

Acc. 13.11.90

Cub - H02908-22 - P024453

AJR

22

American
Journal of
Roentgenology

April 1989

Procedure trays to control costs ...new from E-Z-EM

The objective:

Respond to the demand for a set of disposable trays to help hospitals and private practices control biopsy costs on a per-procedure basis.

The result:

E-Z-EM's new PercuSet line of disposable biopsy trays creating a system of procedure trays—a system of trays which offers the doctor progressive degrees of procedure capability.

The PercuSet Skin Prep Tray includes every implement and agent needed to cleanse, asepsitize, and anesthetize the procedure area—for biopsy, or for any percutaneous procedure.

The PercuSet Basic Biopsy Tray includes all the elements of the Prep Tray, *plus* a needle stop, and a ruler/protractor, *and* the option of an E-Z-EM biopsy needle.

The PercuSet Expanded Biopsy Tray adds a specimen-handling section, for complete biopsy procedure capability, also with the option of an E-Z-EM biopsy needle.

PercuSet Biopsy Trays assure absolute sterility, minimize component handling, eliminate cross-contamination, and are laid out in a logical procedural sequence.

They provide effective cost control, and reduce inventory management of components.

For additional information and a color brochure that details the PercuSet System, contact your local representative, or call E-Z-EM toll-free at 800-645-3052. In New York call 516-333-8230.

E-Z-EM

More than barium—
much more

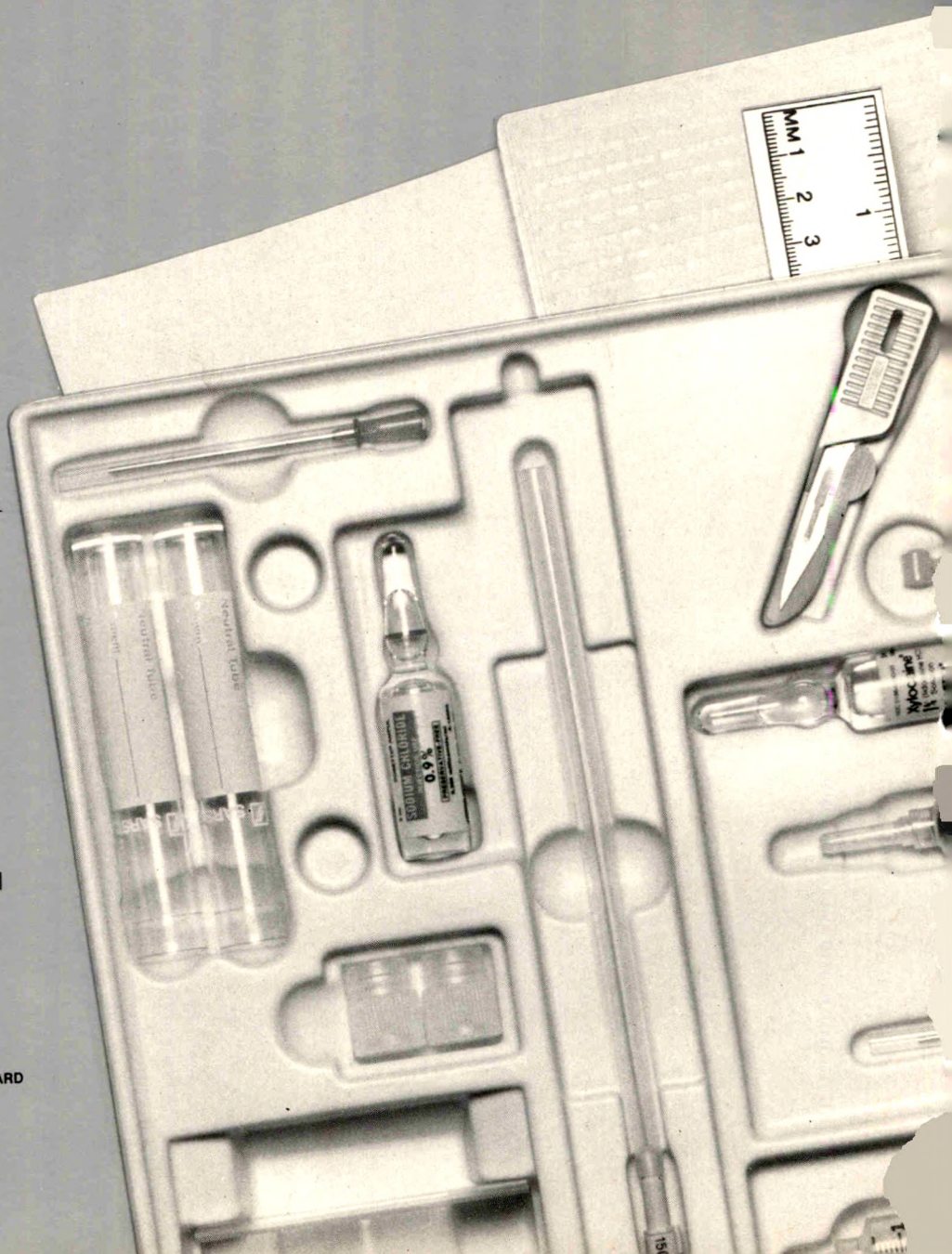


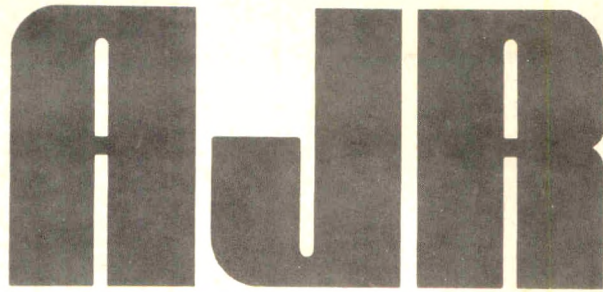
CIRCLE 30 ON READER SERVICE CARD

E-Z-EM, Inc.
7 Portland Avenue
Westbury, N.Y. 11590

© 1986 E-Z-EM, Inc.

PercuSet[™]





American Journal of Roentgenology
Diagnostic Imaging and Related Sciences

Editor-In-Chief Robert N. Berk, *La Jolla, California*
University of California, San Diego
School of Medicine and Medical Center

P24,453

Editor Emeritus Melvin M. Figley, *Seattle, Washington*

Associate Editor Saskia von Waldenburg Hilton, *San Diego, California*

Consulting Editor Juan M. Taveras, *Boston, Massachusetts*

Statistician Charles C. Berry, *San Diego, California*

Editorial Board

John R. Amberg
Itamar Aviad
Lawrence W. Bassett
Gregory P. Borkowski
William G. Bradley, Jr.
Peter L. Cooperberg
N. Reed Dunnick
David K. Edwards
Ronald G. Evens
David S. Feigin
Paul J. Friedman

William R. Hendee
John R. Hesselink
Charles B. Higgins
Melvyn T. Korobkin
Thomas L. Lawson
Bruce L. McClennan
Albert A. Moss
Jeffrey H. Newhouse
Donald L. Resnick
Stewart R. Reuter
Charles A. Rohrmann, Jr.

Peter M. Ronai
Sjef H. J. Ruijs
Carol M. Rumack
Stuart S. Sagel
David J. Sartoris
Stefan C. Schatzki
Edward A. Sickles
Barry A. Siegel
David D. Stark
Edward T. Stewart
Eric vanSonnenberg

Editorial Staff: Margaret Levene, *managing editor*; Katie L. Spiller, Barbara Rose, Barbara L. Halliburton, and Janine Anderson, *manuscript editors*; Nancy Rydbeck, *office manager*; Sheri Smith, *administrative assistant*; Sandra L. Griffin, *administrative secretary*.

AJR, AMERICAN JOURNAL OF ROENTGENOLOGY (ISSN 0361 803X) is the official journal of the American Roentgen Ray Society and is published monthly by Williams & Wilkins, 428 E. Preston St., Baltimore, MD 21202. Annual dues include \$50 for journal subscription. Second-class postage paid at Baltimore, MD, and at additional mailing offices. Postmaster, send address changes (Form 3579) to AJR, 428 E. Preston St., Baltimore, MD 21202. Subscription rates \$100 (\$145 foreign); institutions \$110 (\$155 foreign); in training \$25 (\$70 foreign); single copy \$16 (\$19 foreign). Japanese rates include airfreight. Japanese yen price is available from our sole agent USACO Corporation, 13-12, Shimbashi 1-Chome, Minato-Ku, Tokyo 105, Japan, telephone 03-502-6471. Airmail rates furnished on request. Indexed by *Current Contents* and *Index Medicus*. Copyright © 1989 by American Roentgen Ray Society.

0361-803X/89\$2.00

**COMING
VERY SOON:**



%

**A NEW NONIONIC
THAT PUTS THE
PERCENTAGES IN
YOUR FAVOR**

AJR Guidelines for Authors

Address new and revised manuscripts, correspondence, and classified ads to the Editor:

AJR Editorial Office

2223 Avenida de la Playa, Suite 200

La Jolla, CA 92037-3218

Telephone: (619) 459-2229; FAX: (619) 459-8814

Inquiries regarding subscriptions, display advertising, reprints, or permission to republish *AJR* material should be addressed to the publisher:

The Williams & Wilkins Co.

428 E. Preston St.

Baltimore, MD 21202 Telephone: (301) 528-4133

The *AJR* publishes original contributions to the advancement of medical diagnosis and treatment. Submitted manuscripts should not contain previously published material and should not be under consideration for publication elsewhere. Papers dealing with neuroradiology should be addressed to: American Journal of Neuroradiology, Dept. of Radiology, Massachusetts General Hospital, Boston, MA 02114. At the discretion of the *AJR* Editor, *AJNR* articles that are of interest to the general reader may be republished in the *AJR*. Neuro-radiologic papers sent to the *AJR* will be forwarded to the Editorial Office of the *AJNR*.

Manuscript decisions are based on peer review. Reviewers receive manuscripts without title pages to ensure an unbiased review. Statements made in the article, including changes made by the Editor or manuscript editor, are the responsibility of the author and not of the *AJR* or its publisher. Authors will be sent the edited manuscript, galley proof, and proofs of illustrations. If the corresponding author will be unavailable to review galleys, arrangements should be made for a coauthor or colleague to read and return the proof.

The following guidelines are based on instructions set forth in the **Uniform Requirements for Manuscripts Submitted to Biomedical Journals** (*Ann Intern Med* 1988;108:258-265). Articles will be edited, however, to conform to the individual style of *AJR*.

General Guidelines for Major Papers

Abstract. Clearly state (in 200 words or less) the purpose, methods, results, and conclusions of the study. Include actual data.

Introduction. Briefly describe the purpose of the investigation, including relevant background information.

Methods. Describe the research plan, the materials (or subjects), and the methods used, in that order. Explain in detail how disease was confirmed and how subjectivity in observations was controlled.

Results. Present results in a clear, logical sequence. If tables are used, do not duplicate tabular data in text, but do describe important trends and points.

Discussion. Describe the limitations of the research plan, materials (or subjects), and methods, considering both the

purpose and the outcome of the study. When results differ from those of previous investigators, explain the discrepancy.

AUTHOR'S CHECKLIST

For priority handling, complete the following checklist, sign the copyright form on the reverse side of this page, and include both with the manuscript.

_____ Two copies of the manuscript (the original and a photocopy) and two complete sets of figures are submitted. One copy has been retained by the author.

_____ If appropriate, *AJR* Guidelines for case reports, technical notes, pictorial essays, or letters to the Editor have been followed. (See page A5.)

_____ The manuscript, including references, figure legends, and tables, is typed double-spaced on 8½ × 11 in. (21.6 × 27.9 cm) nonerasable paper. Right-hand margins are not justified.

_____ All manuscript pages are numbered consecutively beginning with the abstract. Authors' names do not appear on the manuscript pages.

_____ The manuscript is organized as follows: title page, blind title page (title only), abstract, introduction, methods, results, discussion, acknowledgments, references, tables, figure legends, and figures.

_____ Informed consent has been obtained from patients who participated in clinical investigations. If experiments were performed on animals, authors complied with NIH guidelines for use of laboratory animals.

_____ Use of unfamiliar acronyms and abbreviations is kept to a minimum. When abbreviations are used they are defined at first mention, followed by the abbreviation in parentheses.

_____ Metric measurements are used throughout, or the metric equivalent is given in parentheses.

_____ Names and locations (city and state only) of manufacturers are given for equipment and nongeneric drugs.

Title Page

_____ The following information is given: title of article; names and complete addresses (including zip code) of all authors; current addresses of authors who have moved since study; acknowledgment of grant or other assistance. The corresponding author is clearly identified, and a current address, phone number, and Fax number are given.

_____ Two copies of a blind title page are included giving only the title (without the authors' names) for use in the review process.

Abstract

_____ An abstract of approximately 200 words concisely states the purpose, methods, and results of the study in one paragraph. Actual data are included. Conclusions are stated in a second, summary paragraph.

_____ No abbreviations or reference citations are used.

References

References (not to exceed 35) are typed double-spaced starting on a separate page and are **numbered consecutively in the order in which they appear in the text**.

All references are cited in the text and are enclosed in brackets and typed on line with the text (not superscript).

Unpublished data are not cited in the reference list, but are cited parenthetically in the text, for example, (Smith DJ, personal communication), (Smith DJ, unpublished data). This includes papers submitted, but not yet accepted, for publication.

Inclusive page numbers (e.g., 333–335) are given for all references.

Journal names are abbreviated according to *Index Medicus*.

Style and punctuation of references follow the format illustrated in the following examples (all authors are listed when six or less; when seven or more authors, the first three are listed, followed by “et al.”):

Journal article

1. Long RS, Roe EW, Wu EU, et al. Membrane oxygenation: radiographic appearance. *AJR* 1986;146:1257–1260

Book

2. Smith LW, Cohen AR. *Pathology of tumors*, 6th ed. Baltimore: Williams & Wilkins, 1977:100–109

Chapter in a book

3. Breon AJ. Serum monitors of bone metastasis. In: Clark SA, ed. *Bone metastases*. Baltimore: Williams & Wilkins, 1983:165–180

Paper presented at a meeting

4. Lau FS, Kirk AN. MR imaging of the spine. Presented at the annual meeting of the American Roentgen Ray Society, Washington, DC, April 1986

Tables

Each table is typed double-spaced on a separate page without vertical or horizontal rules; each has a short, descriptive title. Tables do not exceed two pages in length and contain at least four lines of data.

Tables are numbered in the order in which they are cited in the text.

Abbreviations are defined in an explanatory note below each table.

Tables are self-explanatory and do not duplicate data given in the text or figures.

All arithmetic (percentages, totals, differences) has been double checked for accuracy, and tabular data agree with data given in the text.

Figures and Legends

Two complete sets of original figures are submitted unmounted in labeled envelopes.

Figures are clean, unscratched, 5 × 7 in. (13 × 18 cm) glossy prints with **white borders**. A separate print is submitted for each figure part.

All figure parts relating to one patient have the same figure number.

Each figure is labeled on the back with the figure number and an arrow indicating “top.” For black-and-white figures, labeling is done on a gummed label, which is then affixed to the back of the print. *Never* use labels on color figures, but write figure number on the back lightly in pencil. *Never* use ink on front or back of any figures.

Author’s names are *not* written on the backs of figures.

Only removable (rub-on) arrows and letters are used on the figures. Symbols are uniform in size and style and are not broken or cracked.

Images are uniform in size and magnification.

Line drawings are done in black ink on a white background. They are professional in quality, and all use the same size type. (Only glossy prints are acceptable.)

Written permission has been obtained for use of all previously published illustrations (and copies of permission letters are included), and an appropriate credit line is given in the legends.

Legends are typed double-spaced, and figure numbers correspond with the order in which the figures are cited in the text.

Transfer of Copyright Agreement, Conflict of Interest Acknowledgment, Certification of Coauthors, and Exclusive Publication Statement

Complete copyright to the article entitled: _____

is hereby transferred to the American Roentgen Ray Society (for United States government employees to the extent transferable), effective if and when the article is accepted for publication in the *American Journal of Roentgenology*. In the case of the authors who are officers or employees of the United States government, the American Roentgen Ray Society recognizes that works prepared by officers or employees of the United States government as part of their official government duties are in the public domain.

Authors reserve all proprietary rights other than copyright, such as patent rights and the right to use all or part of this article in future works of their own. The authors retain the right of replication, subject only to crediting the original source of publication and receiving written permission from the publisher.

Authors guarantee that this manuscript contains no matter that is libelous or otherwise unlawful, invades individual privacy, or infringes any proprietary rights.

Authors understand that they will receive no royalty or other compensation from the American Roentgen Ray Society or the publisher.

Authors guarantee that the editor has been or will be informed of any proprietary or commercial interest or conflicts of interest the authors may have that relate directly or indirectly to the subject of this article.

All authors certify that they have made substantive and specific intellectual contributions to the article and assume public responsibility for its content.

Finally, the authors certify that none of the material in this manuscript has been published previously or is currently under consideration for publication elsewhere.

First author/date

Second author

Third author

Fourth author

Fifth author

Sixth author

This agreement must be signed by all authors in order for the manuscript to be published.

Case Reports

A case report is a brief description of a special case that provides a message that transcends the individual patient.

Format. There is no abstract. The introduction should be a short paragraph giving the general background and the specific interest of the case. No more than one case should be described in detail (similar ones can be mentioned briefly in the discussion). Emphasis should be on the radiologic aspects; clinical information must be limited to that necessary to provide a background for the radiology. The discussion should be succinct and should focus on the specific message and relevance of radiologic methods. A review of the literature is not appropriate.

Length. Maximum of five double-spaced, typewritten pages, including the references but not the title page or figure legends.

References. Maximum of eight.

Figures. Maximum of three or four, unless the text is shortened accordingly. Legends must not repeat the text.

Tables and Acknowledgments. Not appropriate in case reports.

Technical Notes

A technical note is a brief description of a specific technique or procedure, modification of a technique, or equipment of interest to radiologists.

Format. No abstract, headings, or subheadings are required. If headings are used, they should be a combination of "Case Report," "Materials and Methods," "Results," and "Discussion." A brief one-paragraph introduction should be included to give the general background. Discussion should be limited to the specific message, including the uses of the technique or equipment. Literature reviews and lengthy case reports are not appropriate.

Length. Maximum of five double-spaced, typewritten pages, including the references but not the title page or figure legends.

References. Maximum of eight.

Figures. Maximum of two, unless the text is shortened accordingly.

Tables and Acknowledgments. Not appropriate in technical notes.

Pictorial Essays

A pictorial essay is an article that conveys its message through illustrations and their legends. Unlike other *AJR* articles, which are based on original research, pictorial essays serve primarily as teaching tools, like exhibits at a scientific meeting. They are not encyclopedic book chapters. No abstract is necessary.

Length. Maximum of four double-spaced, typewritten pages, including the references but not the title page or figure legends.

References. Maximum of four.

Figures. Maximum of 30 figure parts. Number should be as few as necessary to convey the message of the paper.

Tables and Acknowledgments. Not appropriate in pictorial essays.

Letters to the Editor and Replies

Letters to the Editor and Replies should offer objective and constructive criticism of published articles. Letters may also discuss matters of general interest to radiologists. Do not end a letter with a hand-written signature.

Format. All letters should be typed double-spaced on nonletterhead paper, with no greeting or salutation. Name and affiliation should appear at the end of the letter. Titles for letters should be short and pertinent. The title for a reply is simply "Reply."

Length. Maximum of two double-spaced, typewritten pages, including references.

References. Maximum of four.

Figures. Maximum of two.

Tables and Acknowledgments. Not appropriate in Letters to the Editor and Replies.

Opinions, Commentaries, and Perspectives

Opinions, commentaries, and perspectives are special articles dealing with controversial topics or issues of special concern to radiologists.

Format. Include a title page but no abstract. Headings may be used to break up the text.

Length. Maximum of five double-spaced, typewritten pages.

References. Maximum of five.

Tables and Figures. Maximum of four.

Computer Page Articles

Articles published on the computer page deal with practical computer applications to radiology.

Format. Include a title page but no abstract.

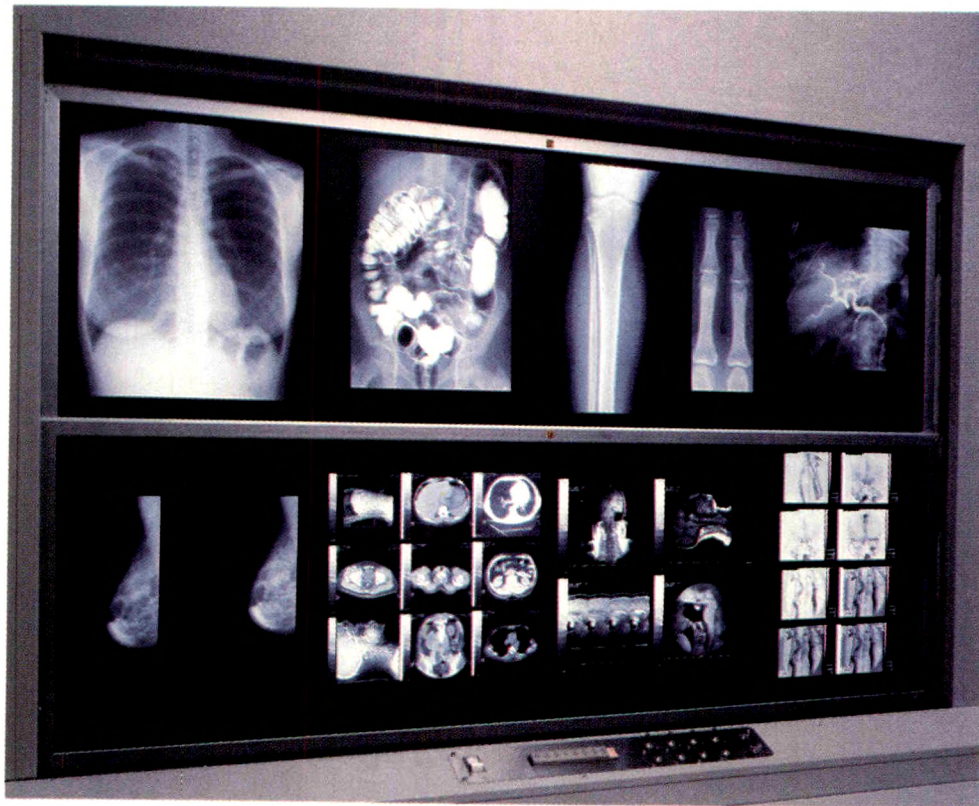
Length. Maximum of eight double-spaced, typewritten pages.

References. Maximum of five.

Figures and Tables. Maximum of five. Computer printouts are not acceptable. Figures must be submitted as 5 × 7 in. glossy prints.

All submissions to the *AJR* must be accompanied by a completed copy of the Author's Checklist and the signed Copyright Agreement.

**THE
RIGHT FILM.
FOR EVERY
SUBJECT
FROM
KODAK**



Whatever the procedure, there's always a Kodak film for the job. Always with the quality you've come to expect from Kodak.

There's a Kodak film for every diagnostic imaging modality and procedure—including extremities, mammography, photofluorography, cinefluorography, duplicating and radiation therapy. In fact, there's usually an array of films for each purpose, so there's not only one that's right for the job, but right for the particular subject as well.



They're all there when you need them, each with the consistent quality you expect from any Kodak product. All with the service and support that help make them as cost-effective as they are good. Your Kodak representative has the details.

The new vision of Kodak



How to stay on top of MR



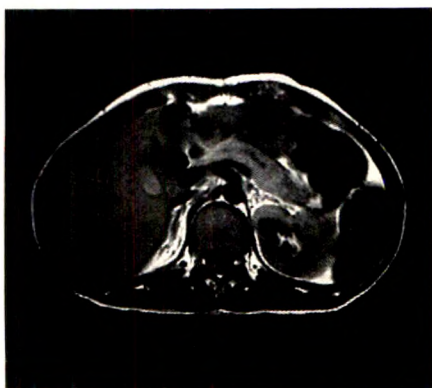
Signa.

Signa... The standard of excellence

It takes a lot to stay on top of MR. You need a high-performance system that offers comprehensive applications and superior images. A system with the flexibility to give you the competitive edge today and tomorrow. That's why more hospitals and imaging centers are using Signa® than any other MR system.

Signa is designed to give you high throughput and reliability. Signa users image an average of more than 13 patients/day. That's well above the typical break-even figure of 8 patients/day.

That's performance.



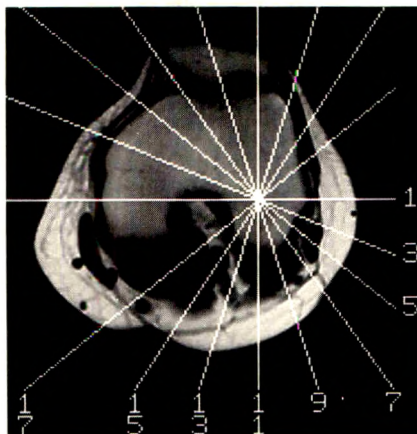
Signa's motion compensation capabilities provide excellent body images.

Superior image quality

Signa image quality gives you a clear advantage throughout the entire body. And that's a distinct edge for generating referrals.

■ Signa's high signal-to-noise ratio allows thin slice, small FOV, single-excitation imaging with superior contrast and resolution.

■ Multi-slice, multi-angle, single acquisition techniques help give you greater diagnostic sensitivity and efficiency.



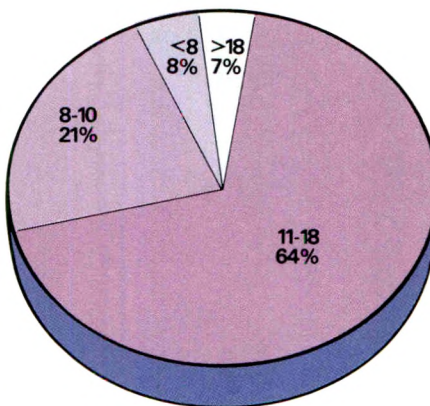
Signa can perform multi-plane/multi-angle techniques in a single acquisition.

■ Three types of motion compensation techniques help minimize motion artifacts.

■ Cine review of fast scan acquisitions helps increase applications by providing a dynamic review of anatomy, such as knees and temporomandibular joints.

■ Off-center FOV imaging with surface coils yields submillimeter resolution of fine anatomy.

■ Shielded gradient coils are designed to help ensure the future performance of your system.



SIGNA SITE STUDIES PER DAY

High study volumes are routine at the majority of Signa sites, based on a 1987 survey.

Options to expand performance

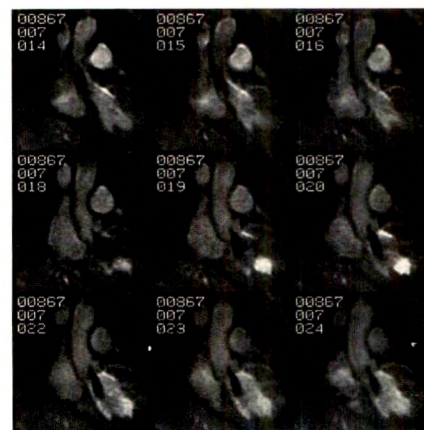
Signa gives you access to a full range of system options.

■ Cine Plus for dynamic heart and cerebrovascular system studies.

■ Peripheral gating for rapid patient preparation and easy acquisition of gated images.

■ Full range of surface coils to increase resolution in small, specific areas.

■ Automatic record-keeping systems to help effectively manage site performance.



Cine Plus gives Signa the ability to acquire and display anatomy dynamically.

Leading-edge capability

Signa is designed to grow with you. From studies that helped establish MR's diagnostic power, to new applications like cine, angiography,* and spectroscopy,* GE's commitment to Signa will help keep you on top of MR.

For more information, please contact your GE Representative or call us toll free at:

(800) 624-5692.

*Some Signa system features are currently classified as investigational and are limited by federal law to investigational use.



CIRCLE 3 ON READER SERVICE CARD

GE Medical Systems

There's never been a better time to choose GE

AJR Business and Subscriber Information

The American Roentgen Ray Society

AJR, *American Journal of Roentgenology*, is published monthly to disseminate research on current developments in the radiologic sciences and commentary on topics related to radiology. It is published by the American Roentgen Ray Society, 1891 Preston White Dr., Reston, VA 22091; (703) 648-8992. Inquiries regarding society business, the annual ARRS meeting, and membership should be addressed to the Society at the above address.

Correspondence Concerning the AJR

Correspondence regarding display (not classified) advertising, subscriptions, address changes, reprints, and permission requests should be addressed to Williams & Wilkins, 428 E. Preston St., Baltimore, MD 21202; (301) 528-4000.

Correspondence regarding editorial matters and classified advertising should be addressed to Editorial Office, *AJR*, 2223 Avenida de la Playa, Ste. 200, La Jolla, CA 92037-3218; telephone (619) 459-2229; FAX (619) 459-8814. For information on manuscript submission, see Guidelines for Authors, pages A3-A5.

Subscriber Information

Subscription requests and inquiries should be sent to Williams & Wilkins, 428 E. Preston St., Baltimore, MD 21202. ARRS annual dues include \$50 for journal subscription. Subscription rates are as follows: nonmembers, \$100/year (\$135 foreign); institutions, \$110 (\$145 foreign); nonmember in-training, \$25 (\$50 foreign). Single copies of the Journal may

be purchased for \$16 (\$19 foreign). Airmail rates will be furnished on request.

Japanese rates include airfreight. Japanese yen price is available from our sole agent, USACO Corporation, 13-12, Shimbashi 1-Chome, Minato-Ku, Tokyo 105, Japan; telephone 03-502-6471.

If a subscriber receives a damaged copy of the *AJR* or fails to receive an issue, the subscriber should notify Williams & Wilkins (428 E. Preston St., Baltimore, MD 21202) within 60 days of publication (90 days for foreign subscribers) and that issue will be replaced.

Change of address information should be sent to Williams & Wilkins, 428 E. Preston St., Baltimore, MD 21202. Allow 90 days for address changes.

Copyrights, Permissions, and Reprints

The American Roentgen Ray Society holds the copyright for all material published in the *AJR*. No part of this publication may be reproduced without permission from the ARRS. Requests for such permission should be addressed to Williams & Wilkins, 428 E. Preston St., Baltimore, MD 21202.

For reprints of a particular article, please contact the author designated in the footnotes for that article.

Indexes

The *AJR* provides volume and yearly indexes (subject and author) in the June and December issues each year. *AJR* articles are also indexed in *Current Contents*, *Index Medicus*, and the cumulative index published by *Radiology*.



For CT scanning...

**A neurotoxicity
profile superior to
any other contrast
medium.*^{1,2}**

Low neurotoxicity is of particular importance in cranial CT scanning, where the blood-brain barrier may be compromised.^{†3,4}

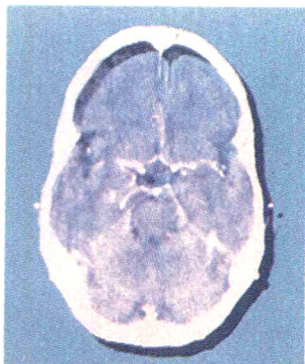
Nonionic OMNIPAQUE is also the only nonionic contrast medium indicated for infusion administration during CT scanning.


And after 15 million radiographic procedures,[‡] you can feel confident about using nonionic OMNIPAQUE in CT scanning. No other nonionic contrast medium has been studied more!⁵

*According to a study of myelographic² comparing nonionic iohexol to iopamidol and metrizamide (based on visual evoked response latency and headache).

†The use of any radiographic contrast medium must be assessed on an individual risk-to-benefit basis.

‡Approximation of over 15 million radiographic procedures worldwide is based on quantities of nonionic iohexol sold, used at recommended dosages.



NONIONIC
OMNIPAQUE®
(IOHEXOL) 
**The image of safety
in CT scanning.**

See next page for important product information concerning contraindications, warnings, adverse reactions, patient selection, and prescribing and precautionary recommendations.

OMNIPAQUE® 240 300 350

INJECTION (IOHEXOL)

INTRAVASCULAR/BODY CAVITIES

PLEASE CONSULT FULL PRODUCT INFORMATION BEFORE USING.
A SUMMARY FOLLOWS:

DESCRIPTION: OMNIPAQUE is a sterile, pyrogen- and preservative-free, nonionic, water-soluble radiographic contrast medium for intravascular administration in concentrations of 240, 300, and 350 mgI/mL. OMNIPAQUE 240 contains 518 mg of iohexol equivalent to 240 mg of organic iodine per mL; OMNIPAQUE 300 contains 647 mg of iohexol equivalent to 300 mg of organic iodine per mL; and OMNIPAQUE 350 contains 755 mg of iohexol equivalent to 350 mg of organic iodine per mL. Each milliliter of iohexol solution contains 1.21 mg tromethamine and 0.1 mg edetate calcium disodium with the pH adjusted between 6.8 and 7.7 with hydrochloric acid or sodium hydroxide. Unused portions must be discarded. Iohecol solution is sensitive to light and should be protected from exposure.

CONTRAINDICATIONS: OMNIPAQUE should not be administered to patients with a known hypersensitivity to iohecol.

WARNINGS: OMNIPAQUE should be used with extreme care in patients with severely impaired renal and/or hepatic function; severe thyrotoxicosis, hyperthyroidism, or an autonomously functioning thyroid nodule; diabetes with a serum creatinine level above 3 mg/dL. It is not recommended for use in patients with anuria.

Patients with known or suspected pheochromocytoma should receive a minimum of contrast medium if the benefit of the examination is judged to outweigh its risk; blood pressure should be monitored throughout the procedure, and measures for the treatment of hypertensive crisis should be readily available.

Contrast agents are potentially hazardous in patients with multiple myeloma or other paraproteinemia, particularly those with therapeutically resistant anuria. The combination of contrast agent and dehydration may precipitate myeloma protein in the renal tubules. No form of therapy, including dialysis, has been successful in reversing the effect. Myeloma, which occurs most commonly in persons over age 40, should be considered before instituting intravascular administration of contrast agents.

Ionic contrast media, when injected intravenously or intra-arterially, may promote sickling in individuals who are homozygous for sickle cell disease.

PRECAUTIONS: Diagnostic procedures that involve the use of radiopaque diagnostic agents should be carried out under the direction of personnel with the prerequisite training and with a thorough knowledge of the particular procedure to be performed. Appropriate facilities should be available for coping with any complication of the procedure, as well as for emergency treatment of severe reactions to the contrast agent itself. Competent personnel and emergency facilities should be available for at least 30 to 60 minutes, since severe delayed reactions have occurred (see ADVERSE REACTIONS). The possibility of serious, life-threatening, fatal, anaphylactoid, or cardiovascular reactions should always be considered (see ADVERSE REACTIONS). It is of utmost importance that a course of action be carefully planned in advance for immediate treatment of serious reactions. Preparatory dehydration is dangerous and may contribute to acute renal failure in patients with advanced vascular disease, in diabetic patients, and in susceptible nondiabetic patients (often elderly with preexisting renal disease), infants, and small children. Patients should be well hydrated prior to and following iohecol administration. Careful consideration of the potential risk of acute renal failure should be given before performing excretory urography in diabetic patients with diabetic nephropathy and in susceptible nondiabetic patients (often elderly with preexisting renal disease). Immediately following surgery, excretory urography should be used with caution in renal transplant recipients. The possibility of an idiosyncratic reaction in susceptible patients should always be considered (see ADVERSE REACTIONS). The susceptible population includes, but is not limited to, patients with a history of a previous reaction to contrast media, patients with a known sensitivity to iodine per se, and patients with a known clinical hypersensitivity: bronchial asthma, hay fever, and food allergies. A thorough medical history with emphasis on allergy and hypersensitivity, prior to the injection of any contrast media, may be more accurate than pretesting in predicting potential adverse reactions.

A positive history of allergies or hypersensitivity does not arbitrarily contraindicate the use of a contrast agent where a diagnostic procedure is thought essential, but caution should be exercised (see ADVERSE REACTIONS). Premedication with antihistamines or corticosteroids to avoid or minimize possible allergic reactions in such patients should be considered and administered using separate syringes. Recent reports indicate that such pretreatment does not prevent serious, life-threatening reactions but may reduce both their incidence and severity.

Even though the osmolality of OMNIPAQUE is low compared to diatrizoate- or iohalalate-based ionic agents of comparable iodine concentration, the potential transitory increase in circulatory osmotic load in patients with congestive heart failure requires caution during injection. These patients should be observed for several hours following the procedure to detect delayed hemodynamic disturbances.

General anesthesia may be indicated in the performance of some procedures in selected adult patients; however, a higher incidence of adverse reactions has been reported in these patients and may be attributable to the inability of the patient to identify untoward symptoms or to the hypotensive effect of the anesthesia, which can reduce cardiac output and increase the duration of exposure to the contrast agent.

Angiography should be avoided whenever possible in patients with homocystinuria, because of the risk of inducing thrombosis and embolism.

In angiographic procedures, the possibility of dislodging plaques or damaging or perforating the vessel wall should be borne in mind during the catheter manipulations and contrast medium injection. Test injections to ensure proper catheter placement are recommended.

Selective coronary arteriography should be performed only in those patients in whom the expected benefits outweigh the potential risk. The inherent risks of angiocardiology in patients with chronic pulmonary emphysema must be weighed against the necessity for performing this procedure.

When OMNIPAQUE is to be injected using plastic disposable syringes, the contrast medium should be drawn into the syringe and used immediately.

The inhibitory effects of nonionic contrast media on mechanisms of hemostasis have been shown, in vitro, to be less than those of ionic contrast media at comparable concentrations. For this reason, standard angiographic procedures should always be followed: angiographic catheters should be flushed frequently, and prolonged contact of blood with contrast media in syringes and catheters should be avoided.

If nondisposable equipment is used, scrupulous care should be taken to prevent residual contamination with traces of cleansing agents.

Parenteral products should be inspected and discarded if particulate matter or discoloration is present.

Drug/Laboratory Test Interaction: If iodine-containing isotopes are to be administered for the diagnosis of thyroid disease, the iodine-binding capacity of thyroid tissue may be reduced for up to 2 weeks after contrast medium administration. Thyroid function tests which do not depend on iodine estimation, eg, T₃ resin uptake or direct thyroxine assays, are not affected. Many radiopaque contrast agents are incompatible in vitro with some antihistamines and many other drugs; therefore, no other pharmaceuticals should be admixed with contrast agents.

Carcinogenesis, Mutagenesis, Impairment of Fertility: No long-term animal studies have been performed to evaluate carcinogenic potential, mutagenesis, or whether OMNIPAQUE can affect fertility in men or women.

Pregnancy Category B: Reproduction studies have been performed in rats and rabbits with up to 100 times the recommended human dose. No evidence of impaired fertility or harm to the fetus has been demonstrated due to OMNIPAQUE. There are, however, no studies in pregnant women. Because animal reproduction studies are not always predictive of human response, this drug should be used during pregnancy only if clearly needed.

Nursing Mothers: It is not known to what extent iohecol is excreted in human milk. However, many injectable contrast agents are excreted unchanged in human milk. Although it has not been established that serious adverse reactions occur in nursing infants, caution should be exercised when intravascular contrast media are administered to nursing women. Bottle feedings may be substituted for breast feedings for 24 hours following administration of OMNIPAQUE.

Pediatric Use (Indicated for Angiocardiology and Urography): Pediatric patients at higher risk of experiencing adverse events during contrast medium administration may include those having asthma, a sensitivity to medication and/or allergens, congestive heart failure, a serum creatinine > 1.5 mg/dL, or those less than 12 months of age.

ADVERSE REACTIONS: Usually mild to moderate in severity. However, serious, life-threatening, and fatal reactions, mostly of cardiovascular origin, have been associated with the administration of iodine-containing contrast media, including OMNIPAQUE. The injection of contrast media is frequently associated with the sensation of warmth and pain, especially in peripheral angiography; pain and warmth are less frequent and less severe with OMNIPAQUE than with many contrast media.

OMNIPAQUE® injection (iohecol)

Cardiovascular System: Arrhythmias including PVCs and PACs (2%), angina/chest pain (1%), and hypotension (0.7%). Others including cardiac failure, asystole, bradycardia, tachycardia, and vasovagal reaction were reported with an individual incidence of less than 0.4%. In controlled clinical trials involving 1,270 patients, one fatality occurred. A cause-and-effect relationship between this death and iohecol has not been established.

Nervous System: Vertigo (including dizziness and lightheadedness) (0.6%), pain (3%), photomas (2%), headache (2%), and taste perversion (1%). Others including anxiety, blurred vision, fever, motor and speech dysfunction, convulsion, paresthesia, somnolence, stiff neck, hemiparesis, syncope, and nystagmus were reported, with an individual incidence of less than 0.3%.

Respiratory System: Dyspnea and laryngitis, with an individual incidence of 0.1%.

Gastrointestinal System: Nausea (2%) and vomiting (0.6%). Others including diarrhea, dyspepsia, and dry mouth were reported, with an individual incidence of less than 0.2%.

Skin and Appendages: Urticaria (0.3%), purpura (0.1%), and pruritus (0.1%).

Pediatric angiocardiology and urography: In controlled clinical trials involving 324 patients, adverse reactions following the use of OMNIPAQUE 300 and OMNIPAQUE 350 were generally less frequent than with adults. **Cardiovascular System:** Ventricular tachycardia (0.6%), 2:1 heart block (0.6%), hypertension (0.3%), and anemia (0.3%).

Nervous System: Pain (0.6%), fever (0.6%), and convulsion (0.3%).

Respiratory System: Congestion (0.3%) and apnea (0.3%).

Gastrointestinal System: Nausea (1%), hypoglycemia (0.3%), and vomiting (2%).

Skin and Appendages: Rash (0.3%).

Body Cavities:

Cardiovascular System: Hypertension (0.4%).

Nervous System: Pain (29%), headache (0.4%), somnolence (0.8%), fever (0.4%), dizziness (0.4%), muscle weakness, burning and unwell feeling, each with an individual incidence of 0.4%.

Respiratory System: None.

Gastrointestinal System: Nausea (0.4%), vomiting (0.4%), diarrhea (0.8%), flatulence (1%), and pressure (0.4%).

Skin and Appendages: Hematoma, injection site (0.4%), swelling (26%), heat (8%).

General Adverse Reactions to Contrast Media: The following reactions have been reported after administration of other intravascular iodinated contrast media, and rarely with iohecol. **Reactions due to technique:** hematomas and ecchymoses. **Hemodynamic reactions:** vein cramp and thrombophlebitis following intravenous injection.

Cardiovascular reactions: rare cases of cardiac arrhythmias, reflex tachycardia, chest pain, cyanosis, hypertension, hypotension, peripheral vasodilatation, shock, and cardiac arrest. **Renal reactions:** occasionally transient proteinuria; rarely, oliguria or anuria. **Allergic reactions:** asthmatic attacks, nasal and conjunctival symptoms, dermal reactions such as urticaria with or without pruritus, as well as pleomorphic rashes, sneezing, and lacrimation; rarely, anaphylactoid reactions. Rare fatalities have occurred due to these or unknown causes. **Signs and symptoms related to the respiratory system:** pulmonary or laryngeal edema, bronchospasm, dyspnea, or to the nervous system: restlessness, tremors, convulsions. **Other reactions:** flushing, pain, warmth, metallic taste, nausea, vomiting, anxiety, headache, confusion, pallor, weakness, sweating, localized areas of edema (especially facial cramps), neutropenia, and dizziness. Rarely, immediate or delayed rigors can occur, sometimes accompanied by hyperpyrexia. Infrequently, "iodism" (salivary gland swelling) from organic iodinated compounds appears 2 days after exposure and subsides by the sixth day.

In general, the reactions that are known to occur upon parenteral administration of iodinated contrast agents are possible with any nonionic agent. Approximately 95% of adverse reactions accompanying the use of water-soluble intravascularly administered contrast agents are mild to moderate in degree. However, severe, life-threatening anaphylactoid reactions, mostly of cardiovascular origin, have occurred. Reported incidences of death range from 6.6 per 1 million (0.00066%) to 1 in 10,000 (0.01%). Most deaths occur during injection or 5 to 10 minutes later; the main feature being cardiac arrest, with cardiovascular disease as the main aggravating factor. Isolated reports of hypotensive collapse and shock are found in the literature. The incidence of shock is estimated to be 1 out of 20,000 (0.005%) patients.

Adverse reactions to injectable contrast media fall into two categories: chemotoxic reactions and idiosyncratic reactions.

Chemotoxic reactions result from the physicochemical properties of the contrast media, the dose, and the speed of injection. All hemodynamic disturbances and injuries to organs or vessels perfused by the contrast medium are included in this category.

Idiosyncratic reactions include all other reactions. They occur more frequently in patients 20 to 40 years old. Idiosyncratic reactions may or may not be dependent on the amount of dose injected, the speed of injection, and the radiographic procedure. Idiosyncratic reactions are subdivided into minor, intermediate, and severe. The minor reactions are self-limited and of short duration; the severe reactions are life-threatening and treatment is urgent and mandatory.

The reported incidence of adverse reactions to contrast media in patients with a history of allergy is twice that in the general population. Patients with a history of previous reactions to a contrast medium are three times more susceptible than other patients. However, sensitivity to contrast media does not appear to increase with repeated examinations.

Most adverse reactions to injectable contrast media appear within 1 to 3 minutes after the start of injection, but delayed reactions may occur.

Regardless of the contrast agent employed, the overall estimated incidence of serious adverse reactions is higher with angiocardiology than with other procedures. Cardiac decompensation, serious arrhythmias, angina pectoris, or myocardial ischemia or infarction may occur during angiocardiology and left ventriculography. Electrocardiographic and hemodynamic abnormalities occur less frequently with OMNIPAQUE than with diatrizoate meglumine and diatrizoate sodium injection.

OVERDOSAGE: Overdosage may occur. The adverse effects of overdosage are life-threatening and affect mainly the pulmonary and cardiovascular systems. The symptoms include cyanosis, bradycardia, acidosis, pulmonary hemorrhage, convulsions, coma, and cardiac arrest. Treatment of an overdosage is directed toward the support of all vital functions and prompt institution of symptomatic therapy.

The intravenous LD₅₀ values of OMNIPAQUE (in grams of iodine per kilogram body weight) are 24.2 in mice and 15.0 in rats.

References: 1. Gonsette RE, Liesenborgs L: Iohecol: A new nonionic contrast medium for myelography and cisternography with markedly reduced neurotoxicity. *Invest Radiol* 1985;20(January-February suppl):32-36. 2. Broadbridge AT, Bayliss SG, Brayshaw CI: The effect of intrathecal iohecol on visual evoked response latency: A comparison including incidence of headache with iopamidol and metrizamide in myelographic studies. *Clin Radiol* 1987;38:71-74. 3. Skajpe IO: Enhancement with water-soluble contrast media in computed tomography of the brain and abdomen: Survey and present state. *Acta Radiol* 1983; suppl 366, pp 72-75. 4. Pfeiffer FE, Homburger HA, Houser OW, et al: Elevation of serum creatine kinase B-subunit levels by radiographic contrast agents in patients with neurologic disorders. *Mayo Clin Proc* 1987;62:351-357. 5. Data on file, Winthrop Pharmaceuticals.

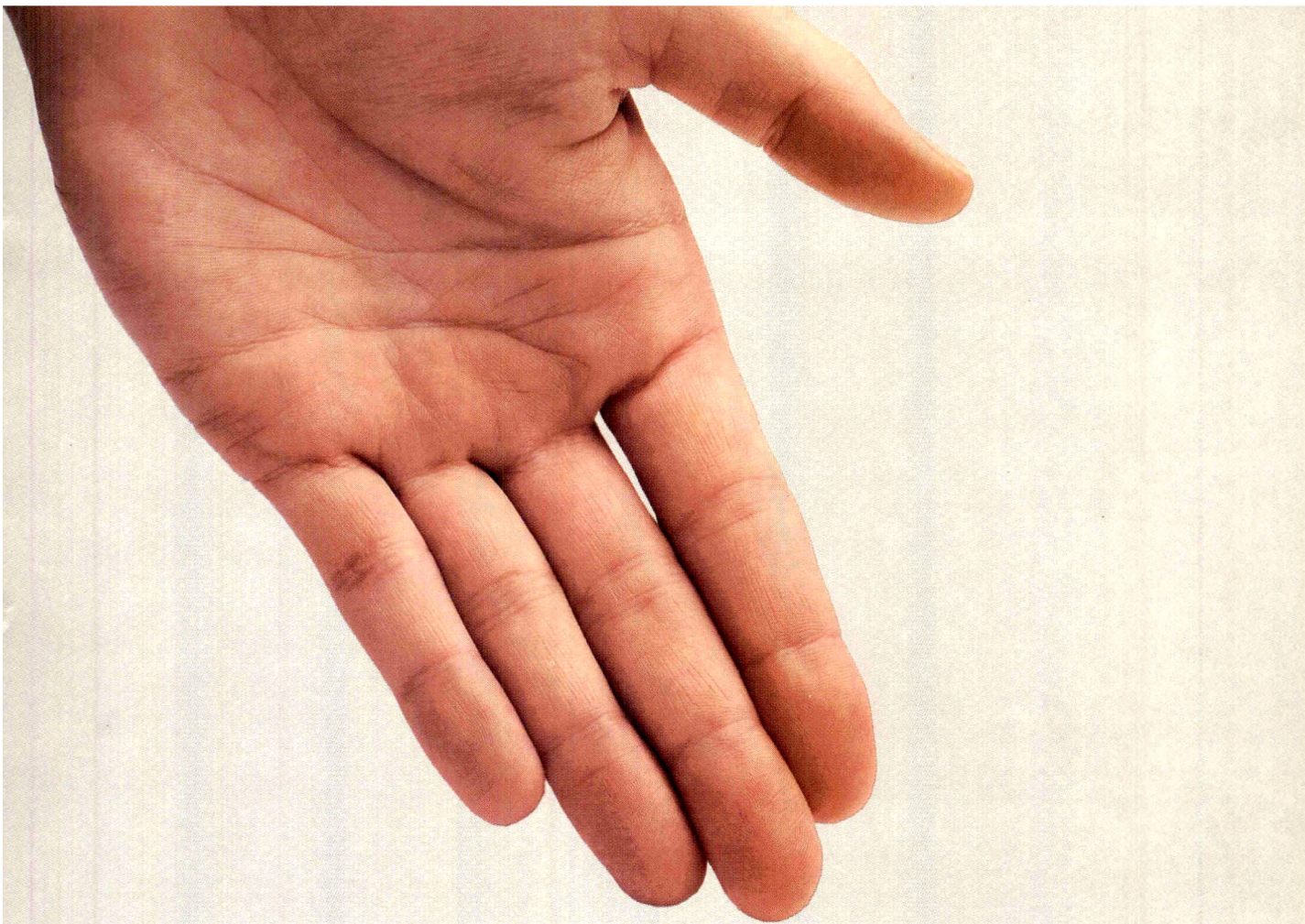
CIRCLE 24 ON READER SERVICE CARD



DIAGNOSTIC IMAGING DIVISION
Winthrop Pharmaceuticals
Division of Sterling Drug Inc.
New York, NY 10016

© 1989 WINTHROP PHARMACEUTICALS

9001/3511

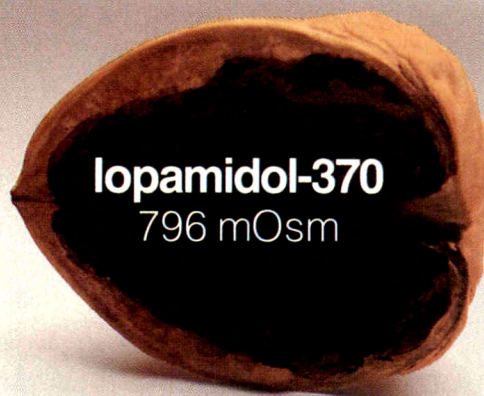


**For greater patient comfort
and the lowest osmolality,
the choice is yours...**

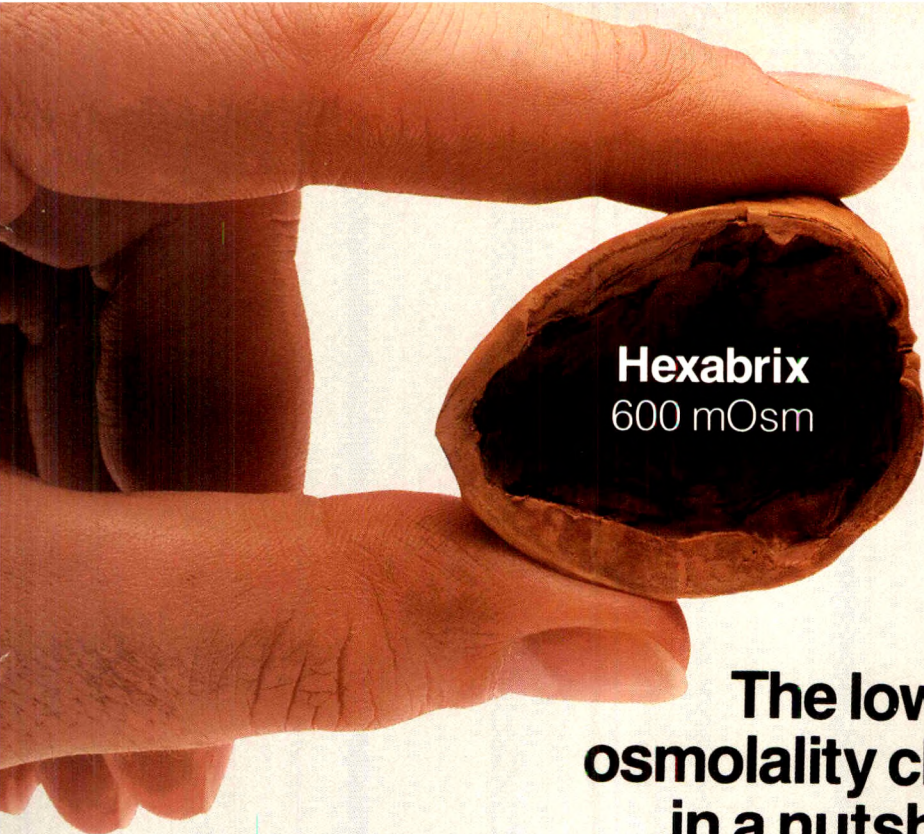




Iohexol-350
844 mOsm



Iopamidol-370
796 mOsm



Hexabrix
600 mOsm

The low osmolality choice, in a nutshell

Compare Hexabrix with the nonionics, and you'll find that Hexabrix not only has the lowest osmolality, but also the least amount of patient discomfort in interventional procedures.

Least heat and pain

Recent comparative studies demonstrate that Hexabrix produces significantly less heat¹ and pain¹⁻³ than iopamidol and/or iohexol during arteriography procedures.¹⁻³

Less risk of clotting *in vitro*

Hexabrix has been shown to be a stronger inhibitor of clotting^{4,5} and platelet aggregation^{5,6} *in vitro* than iopamidol or iohexol.

Good angiographic technique should be followed in all procedures involving contrast media. Even when meticulous technique is used, some mixing of blood with contrast media in syringes and catheters is possible. Prolonged contact of blood and contrast media in syringes and catheters can lead to clot formation.

Lowest viscosity

Hexabrix has the lowest viscosity at 37°C (7.5 cps), compared to iohexol-350 (10.4 cps) or iopamidol-370 (9.4 cps).

HEXABRIX[†]

(ioxaglate meglumine 39.3%/
ioxaglate sodium 19.6% injection)

Please see following page for references and brief summary of prescribing information.

N C K B O D T

HEXABRIX[†] (ioxaglate meglumine 39.3%/ioxaglate sodium 19.6% injection)

HEXABRIX[®]
Each milliliter of HEXABRIX contains 393 mg of ioxaglate meglumine, 196 mg of ioxaglate sodium and 0.10 mg edetate calcium disodium as a stabilizer. The solution contains 3.48 mEq (0.15 mEq) sodium in each milliliter and provides 32% (320 mg/mL) organically bound iodine.

CONTRAINDICATIONS

HEXABRIX is contraindicated for use in myelography. Refer to PRECAUTIONS concerning hypersensitivity. Hysterosalpingography should not be performed during the menstrual period, in pregnant patients, in patients with known infection in any portion of the genital tract, or in patients in whom cervical conization or curettage has been performed within 30 days. Arthrography should not be performed if infection is present in or near the joint.

WARNINGS

Serious or fatal reactions have been associated with the administration of iodine containing radiopaque media. It is of utmost importance to be completely prepared to treat any contrast medium reaction.

As with any contrast medium, serious neurologic sequelae, including permanent paralysis, can occur following cerebral arteriography, selective spinal arteriography and arteriography of vessels supplying the spinal cord. The injection of a contrast medium should never be made following the administration of vasopressors, since they strongly potentiate neurologic effects.

In patients with subarachnoid hemorrhage, a rare association between contrast administration and clinical deterioration, including convulsions and death, has been reported. Therefore, administration of intravascular iodinated contrast media in these patients should be undertaken with caution.

A definite risk exists in the use of intravascular contrast agents in patients who are known to have multiple myeloma. In such instances anuria has developed, resulting in progressive uremia, renal failure and eventually death. Although neither the contrast agent nor dehydration has separately proved to be the cause of anuria in myeloma, it has been speculated that the combination of both may be a causative factor. The risk in myelomatous patients is not a contraindication to the procedure; however, partial dehydration in the preparation of these patients for the examination is not recommended since this may predispose to precipitation of myeloma protein in the renal tubules. No form of therapy, including dialysis, has been successful in reversing the effect. Myeloma, which occurs most commonly in persons over 40, should be considered before instituting intravascular administration of contrast agents.

Administration of radiopaque materials to patients known or suspected to have pheochromocytoma should be performed with extreme caution. It is the opinion of the physician, the possible benefits of such procedures outweigh the considered risks, the procedures may be performed, however, the amount of radiopaque medium injected should be kept to an absolute minimum. The blood pressure should be assessed throughout the procedure, and measures for treatment of a hypertensive crisis should be available.

Since intravascular administration of contrast media may promote sickling in individuals who are homozygous for sickle cell disease, fluid restriction is not advised.

In patients with advanced renal disease, iodinated contrast media should be used with caution and only when the need for the examination dictates, since excretion of the medium may be impaired. Patients with combined renal and hepatic disease, those with severe hypertension or congestive heart failure and recent renal transplant recipients present an additional risk.

Renal failure has been reported in patients with liver dysfunction who were given an oral cholecystographic agent followed by an intravascular iodinated radiopaque agent and also in patients with occult renal disease, notably diabetes and hypertension. In these classes of patients there should be no fluid restriction and every attempt made to maintain normal hydration prior to contrast medium injection. Since dehydration is the single most important factor influencing further renal impairment.

Caution should be exercised in performing contrast medium studies in patients with endotoxemia and/or those with elevated body temperatures.

Reports of thyroid storm occurring following the intravascular use of iodinated radiopaque agents in patients with hyperthyroidism or with an autonomously functioning thyroid nodule, suggest that this additional risk be evaluated before use of this drug. Iodine-containing contrast agents may alter the results of thyroid function tests which depend on iodine estimation, e.g., PBI, and may also affect results of radioactive iodine uptake studies. Such tests, if indicated, should be performed prior to the administration of this preparation.

PRECAUTIONS

Diagnostic procedures which involve the use of iodinated intravascular contrast agents should be carried out under the direction of personnel skilled and experienced in the particular procedure to be performed. All procedures utilizing contrast media carry a definite risk of producing adverse reactions. While most reactions are minor, life-threatening and fatal reactions may occur without warning, and this risk must be weighed against the benefit of the procedure. A fully equipped emergency cart, or equivalent supplies and equipment, and personnel competent in recognizing and treating adverse reactions of all types should always be available. If a serious reaction should occur, immediately discontinue administration. Since severe delayed reactions have been known to occur, emergency facilities and competent personnel should be available for at least 30 to 60 minutes after administration. (See ADVERSE REACTIONS.)

Preparatory dehydration is dangerous and may contribute to acute renal failure in infants, young children, the elderly, patients with pre-existing renal insufficiency, patients with multiple myeloma, patients with advanced vascular disease and diabetic patients.

Acute renal failure has been reported in diabetic patients with diabetic nephropathy and in susceptible non-diabetic patients (often elderly with pre-existing renal disease) following the administration of iodinated contrast agents. Therefore, careful consideration of the potential risks should be given before performing this radiographic procedure in these patients.

Severe reactions to contrast media often resemble allergic responses. This has prompted the use of several provocative pretesting methods, none of which can be relied on to predict severe reactions. No conclusive relationship between severe reactions and antigen-antibody reactions or other manifestations of allergy has been established. The possibility of an

idiosyncratic reaction in patients who have previously received a contrast medium without ill effect should always be considered. Prior to the injection of any contrast medium, the patient should be questioned to obtain a medical history with emphasis on allergy and hypersensitivity. A positive history of bronchial asthma or allergy (including food), a family history of allergy, or a previous reaction or hypersensitivity to a contrast agent may imply a greater than usual risk. Such a history may be more accurate than pre-testing in predicting the potential for reaction, although not necessarily the severity or type of reaction in the individual case. A positive history of this type does not arbitrarily contraindicate the use of a contrast agent when a diagnostic procedure is thought essential, but does call for caution. (See ADVERSE REACTIONS.)

Prophylactic therapy including corticosteroids and antihistamines should be considered for patients who present with a strong allergic history, a previous reaction to a contrast medium, or a positive pre-test since in these patients the incidence of reaction is two to three times that of the general population. Adequate doses of corticosteroids should be started early enough prior to contrast medium injection to be effective and should continue through the time of injection and for 24 hours after injection. Antihistamines should be administered within 30 minutes of the contrast medium injection. Recent reports indicate that such pre-treatment does not prevent serious life-threatening reactions, but may reduce both their incidence and severity. A separate syringe should be used for these injections.

General anesthesia may be indicated in the performance of some procedures in selected patients; however, a higher incidence of adverse reactions has been reported in these patients, and may be attributable to the inability of the patient to identify untoward symptoms or to the hypotensive effect of anesthesia which can prolong the circulation time and increase the duration of contact of the contrast agent.

Angiography should be avoided whenever possible in patients with homocystinuria because of the risk of inducing thrombosis and embolism.

PRECAUTIONS FOR SPECIFIC PROCEDURES

Pediatric Arteriography. It is advisable to monitor for ECG and vital signs changes throughout the procedure.

When large individual doses are administered, sufficient time should be allowed for any observed changes to return to or near baseline prior to making the next injection.

Caution should be used when making right heart injections in patients with pulmonary hypertension or incipient heart failure, since this may lead to increased right side pressures with subsequent bradycardia and systemic hypotension. Patients with pulmonary disease present additional risks.

Caution is advised in cyanotic infants since apnea, bradycardia, other arrhythmias and a tendency to acidosis are more likely to occur.

Since infants are more likely to respond with convulsions than are adults, the amount of total dosage is of particular importance. Repeated injections are hazardous in infants weighing less than 7 kg, particularly when these infants have pre-existing compromised right heart function or obliterated pulmonary vascular beds.

Selective Coronary Arteriography with or without left ventriculography. During the administration of large doses of HEXABRIX, continuous monitoring of vital signs is desirable. Caution is advised in the administration of large volumes to patients with incipient heart failure because of the possibility of aggravating the pre-existing condition. Hypotension should be corrected promptly since it may result in serious arrhythmias. Special care regarding dosage should be observed in patients with right ventricular failure, pulmonary hypertension, or stenotic pulmonary vascular beds because of hemodynamic changes which may occur after injection into the right heart outflow tract.

Peripheral Arteriography. Moderate decreases in blood pressure occur frequently with intra-arterial (brachial) injections. This change is usually transient and requires no treatment; however, the blood pressure should be monitored for approximately ten minutes following injection.

Extreme caution during injection of the contrast agent is necessary to avoid extravasation and fluoroscopy is recommended. This is especially important in patients with severe arterial disease.

Cerebral Arteriography. Cerebral angiography should be performed with special caution in patients with advanced arteriosclerosis, severe hypertension, cardiac decompensation, senility, recent cerebral thrombosis or embolism, and migraine.

Intra-Arterial Digital Subtraction Angiography. The risks associated with IA-DSA are those usually attendant with catheter procedures. Following the procedure, gentle pressure hemostasis is required, followed by observation and immobilization of the limb for several hours to prevent hemorrhage from the site of arterial puncture.

Patient motion, including respiration and swallowing, can result in misregistration leading to image degradation and non-diagnostic studies.

Intravenous Digital Subtraction Angiography. The risks associated with IV-DSA are those usually attendant with catheter procedures and include intraluminal thrombosis, vessel dissection and tissue extravasation. The potential risk is reduced when small test injections of contrast medium are made under fluoroscopic observation to insure that the catheter tip is properly positioned and, in the case of peripheral placement, that the vein is of adequate size.

Patient motion, including respiration and swallowing, can result in misregistration leading to image degradation and non-diagnostic studies.

Peripheral Venography. Special care is required when venography is performed in patients with suspected thrombosis, phlebitis, severe ischemic disease, local infection or a totally obstructed venous system.

Extreme caution during injection of contrast media is necessary to avoid extravasation and fluoroscopy is recommended. This is especially important in patients with severe arterial or venous disease.

Excretory Urography. Infants and small children should not have any fluid restrictions prior to excretory urography. (See WARNINGS and PRECAUTIONS concerning preparatory dehydration.)

Contrast Enhancement in Body Computed Tomography. Patient cooperation is essential since patient motion, including respiration, can markedly affect image quality. The use of an intravascular contrast medium can obscure tumors in patients undergoing CT evaluation of the liver, resulting in a false negative diagnosis. Dynamic CT scanning is the procedure of choice for malignant tumor enhancement.

Arthrography. Strict aseptic technique is required to prevent the introduction of infection. Fluoroscopic control should be used to insure proper introduction of the needle into the synovial space and prevent extracapsular injection. Aspiration of excessive synovial fluid will reduce the pain on injection and prevent the dilution of the contrast agent. It is important that undue pressure not be exerted during the injection.

Hysterosalpingography. Caution should be exercised in patients suspected of having cervical or tubal carcinoma to avoid possible spread of the lesion by the procedure. Delayed onset of pain and fever (1-2 days) may be indicative of pelvic infection.

Carcinogenesis, Mutagenesis, Impairment of Fertility. No long-term animal studies have been performed to evaluate carcinogenic potential. However, animal studies suggest that this drug is not mutagenic and does not affect fertility in males or females.

Pregnancy Category B. Reproduction studies have been performed in rats and rabbits at doses up to two times the maximum adult human dose and have revealed no evidence of impaired fertility or harm to the fetus due to HEXABRIX. There are, however, no adequate and well controlled studies in pregnant women. Because animal reproduction studies are not always predictive of human response, this drug should be used during pregnancy only if clearly needed.

Nursing Mothers. Ioxaglate salts are excreted unchanged in human milk. Because of the potential for adverse effects in nursing infants, bottle feedings should be substituted for breast feedings for 24 hours following the administration of this drug.

Pediatric Use. Safety and effectiveness in children has been established in pediatric angiography and intravenous excretory urography. Data have not been submitted to support the safety and effectiveness of HEXABRIX in any other indication.

(Precautions for specific procedures receive comment under that procedure.)

ADVERSE REACTIONS

Adverse reactions to injectable contrast media fall into two categories: chemotoxic reactions and idiosyncratic reactions.

Chemotoxic reactions result from the physicochemical properties of the contrast media, the dose and the speed of injection. All hemodynamic disturbances and effects on organs or vessels perfused by the contrast medium are included in this category.

Idiosyncratic reactions include all other reactions. They occur more frequently in patients 20 to 40 years old. Idiosyncratic reactions may or may not be dependent on the dose injected, the speed of injection, the mode of injection and the radiographic procedure. Idiosyncratic reactions are subdivided into minor, intermediate and severe. The minor reactions are self-limited and of short duration; the severe reactions are life-threatening and treatment is urgent and mandatory.

NOTE. Not all of the following adverse reactions have been reported with HEXABRIX. Because HEXABRIX is an iodinated intravascular contrast agent, all of the side effects and toxicity associated with agents of this class are theoretically possible, and this should be borne in mind when HEXABRIX is administered.

Severe, life-threatening anaphylactoid reactions, mostly of cardiovascular origin, have occurred following the administration of HEXABRIX as well as other iodine-containing contrast agents. Most deaths occur during injection 5 to 10 minutes later, the main feature being cardiac arrest with cardiovascular disease as the main aggravating factor. Isolated reports of hypotensive collapse and shock are found in the literature. Based upon clinical literature, reported deaths from the administration of conventional iodinated contrast agents range from 6.6 per 1 million (0.0066 percent) to 1 in 10,000 patients (0.01 percent).

Regardless of the contrast agent employed, the overall estimated incidence of serious adverse reactions is higher with coronary arteriography than with other procedures. Cardiac decompensation, serious arrhythmias, or myocardial ischemia or infarction may occur during coronary arteriography and left ventriculography.

The most frequent adverse reactions are nausea, vomiting, facial flush and a feeling of body warmth. These are usually of brief duration. In double-blind clinical trials, HEXABRIX produced less discomfort upon injection (pain and heat) when compared to various other contrast agents. Other reactions include the following:

Hypersensitivity reactions. Dermal manifestations of urticaria with or without pruritus, erythema and maculopapular rash. Dry mouth. Sweating. Conjunctival symptoms. Facial, peripheral and angioneurotic edema. Symptoms related to the respiratory system include sneezing, nasal stuffiness, coughing, choking, dyspnea, chest tightness and wheezing, which may be initial manifestations of more severe and infrequent reactions including asthmatic attack, laryngospasm and bronchospasm with or without edema, pulmonary edema, apnea and cyanosis. Rarely, these allergic-type reactions can progress into anaphylaxis with loss of consciousness, coma, severe cardiovascular disturbances, and death.

Cardiovascular reactions. Generalized vasodilation, flushing and venospasm. Occasionally thrombosis or, rarely, thrombophlebitis. Extremely rare cases of disseminated intravascular coagulation resulting in death have been reported. Severe cardiovascular responses include rare cases of hypotensive shock, coronary insufficiency, cardiac arrhythmia, fibrillation and arrest. These severe reactions are usually reversible with prompt and appropriate management; however, fatalities have occurred.

Technique reactions. Extravasation with burning pain, hematomas, ecchymosis and tissue necrosis; vascular constriction due to injection rate; thrombosis and thrombophlebitis.

Neurological reactions. Spasm, convulsions, aphasia, syncope, paresis, paralysis resulting from spinal cord injury and pathology associated with the syndrome of transverse myelitis, visual field losses which are usually transient but may be permanent, coma and death.

Other reactions. Headache, trembling, shaking, chill, without fever, hyperthermia and lightheadedness. Temporal-renal shutdown or other nephropathy.

Pediatric angiography has been complicated by intraluminal injection with marked adverse effects on cardiac function.

During selective coronary arteriography with or without left ventriculography, patients may have clinically insignificant ECG changes. The following adverse effects have occurred in conjunction with the administration of iodinated intravascular contrast agents for this procedure: hypotension, shock, anginal pain, myocardial infarction, cardiac arrhythmias (bradycardia, ventricular tachycardia, ventricular fibrillation) and cardiac arrest. Fatalities have been reported. Complications to the procedure include dissection of coronary arteries, dislodgement of atheromatous plaques, perforation, hemorrhage and thrombosis.

Following peripheral arteriography, hemorrhage and thrombosis have occurred at the puncture site of the percutaneous injection. Brachial plexus injury has been reported following axillary artery injection.

The major causes of cerebral arteriographic adverse reactions appear to be repeated injections of the contrast material, administration of doses higher than those recommended, the presence of occlusive atherosclerotic vascular disease and the method and technique of injection. Adverse reactions are normally mild and transient. A feeling of warmth in the face and neck is frequently experienced. Infrequently, a more severe burning discomfort is observed. Transient visual hallucinations have been reported. Serious neurological reactions that have been associated with cerebral angiography and not listed under Adverse Reactions include stroke, amnesia and respiratory difficulties. Visual field defects with anopia and reversible neurological deficit lasting from 24 hours to 48 hours have been reported. Confusion, disorientation with hallucinations, and absence of vision sometimes lasting for one week have also been reported. Cardiovascular reactions that may occur with some frequency are bradycardia and shock which may decrease in systemic blood pressure. The blood pressure change is transient and usually requires no treatment. Arthrography may induce joint pain or discomfort which is usually mild and transient but occasionally may be severe and persist for 24 to 48 hours following the procedure. Infusion requiring aspiration may occur in patients with rheumatoid arthritis. Fever and pain, cramping and tenderness of the abdomen have been reported following hysterosalpingography.

OVERDOSAGE

Overdosages may occur. The adverse effects of overdosage are life-threatening and affect mainly the pulmonary and cardiovascular systems. The symptoms may include cyanosis, bradycardia, acidosis, pulmonary hemorrhage, convulsions, coma and cardiac arrest. Treatment of an overdose is directed toward the support of all vital functions and prompt institution of symptomatic therapy.

Ioxaglate salts are dialyzable. The intravenous LD₅₀ values of HEXABRIX (in grams of iodine/kg body weight) were 11.2 g/kg in mice, >8 g/kg in rats, >6.4 g/kg in rabbits and >10.2 g/kg in dogs.

DOSAGE AND ADMINISTRATION

Details on dosage are provided in the package insert. **CONSULT FULL PACKAGE INSERT BEFORE USE.**
Rev Jan 1987

References:

1. Stiris MG, Laerum F. Iohexol and ioxaglate in peripheral arteriography. *Acta Radiologica* 1987; 28:767-770.
2. Smith DC, Yahiku PY, Maloney MD, et al. Three new low-osmolality contrast agents: A comparative study of patient discomfort. *Am J Neuroradiol* 1988; 9:137-139.
3. Murphy WA, Campbell DR, Fraser DB. Pain in peripheral arteriography: An assessment of conventional versus ionic and non-ionic low-osmolality contrast agents. *J Can Assoc Radiol* 1988; 39:103-106.
4. Engelhart JA, Smith D, Bull BS, et al. Aspirated blood and low-osmolality contrast agents: An embolic hazard? Presented at the 73rd Meeting of the Radiological Society of North America, Chicago, IL, Dec., 1987.
5. Mosier LD, Joist JH, Chance D, et al. In vitro effects of ionic and nonionic contrast media on coagulation, platelet function, and fibrinolysis. Presented at the 73rd Meeting of the Radiological Society of North America, Chicago, IL, Nov 30, 1987.
6. Stormorken H, Skaltei IO, Testart MC. Effect of various contrast media or coagulation, fibrinolysis, and platelet function: An in vitro and in vivo study. *Invest Radiol* 1986; 21:348-354.

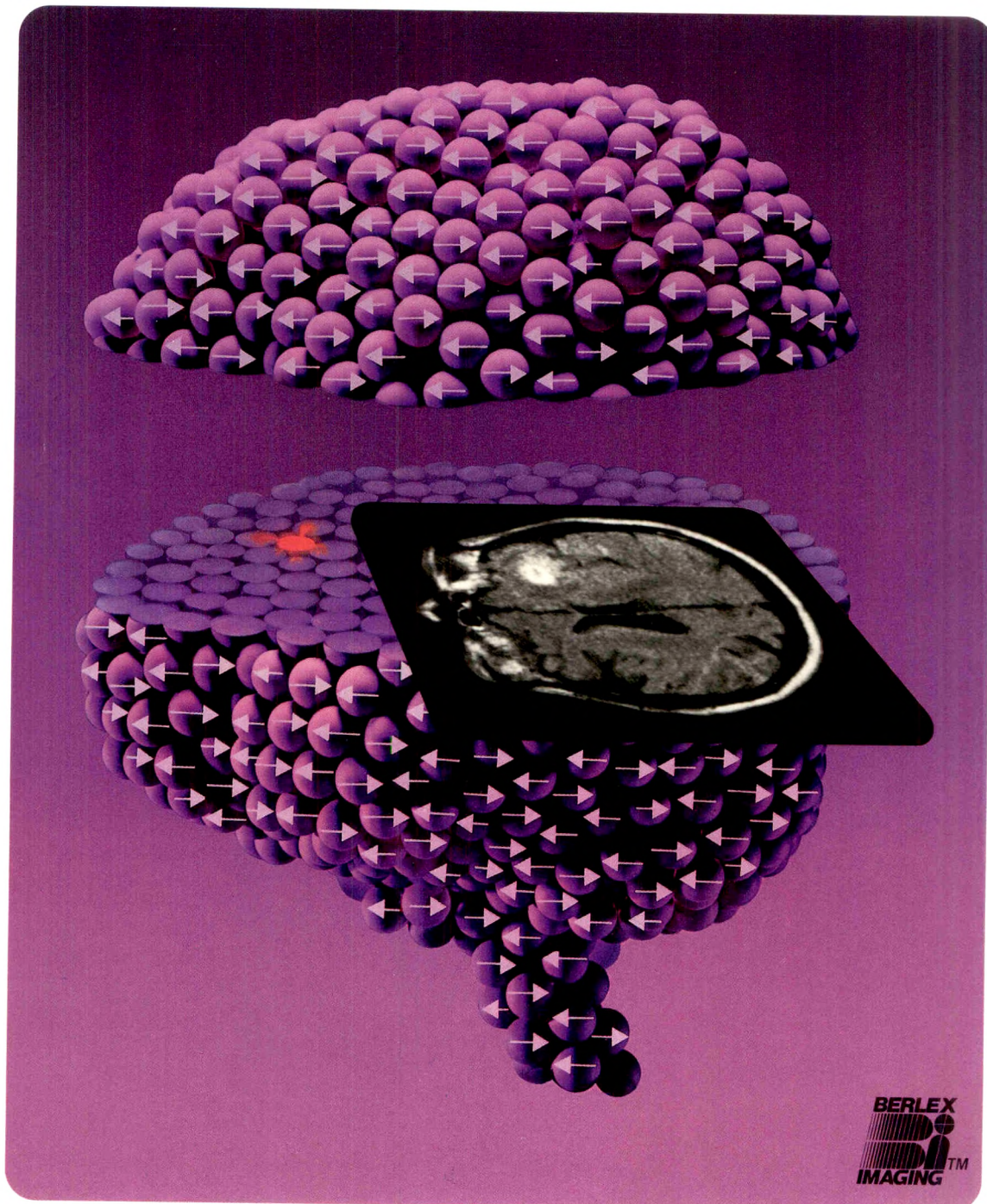


Changing the look of medicine.

**Diagnostic Products Division
Mallinckrodt, Inc.**
Post Office Box 5840
St. Louis, MO 63134
CIRCLE 22 ON READER SERVICE CARD

**For orders,
medical and/or
professional assistance
call
(800) 325-3688 TOLL FREE**

**BETTER MEDICINE
THROUGH
BETTER IMAGES**

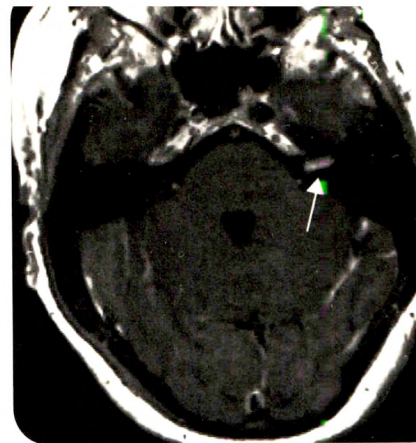
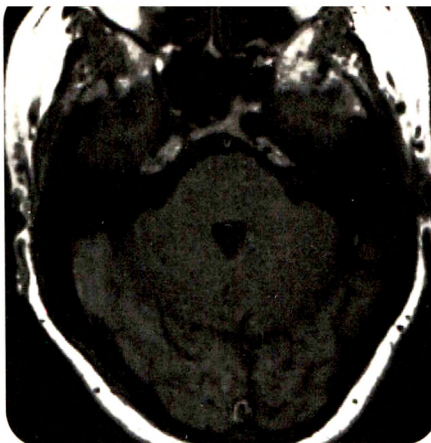


BERLEX
IMAGING™

Magnevist®
(gadopentetate
dimeglumine) INJECTION

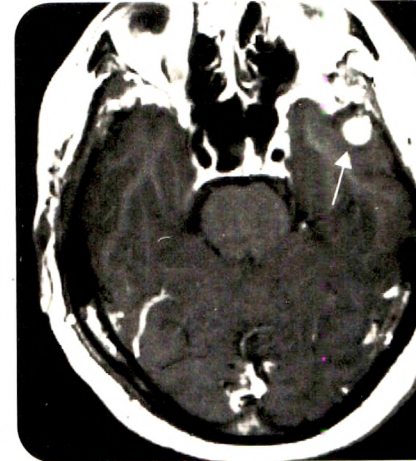
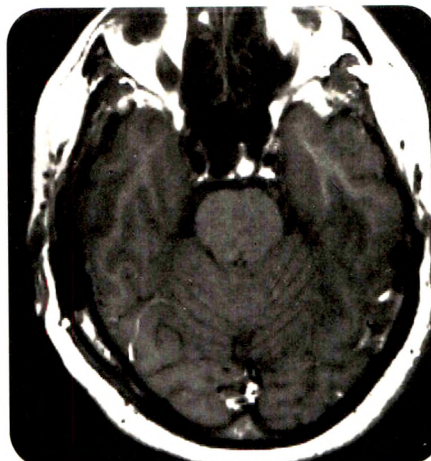
**CONFIRMED
LESION**
**Acoustic
neuroma**

T1-weighted MRI scan
pre-MAGNEVIST® injection.
(TR 400, TE 20)



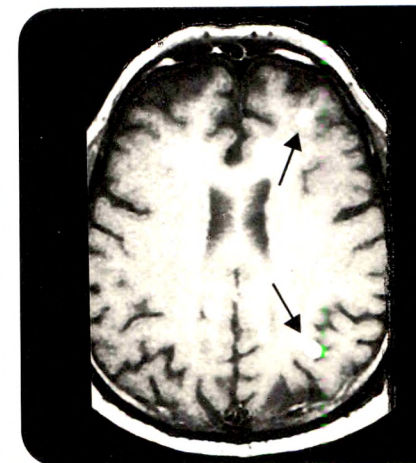
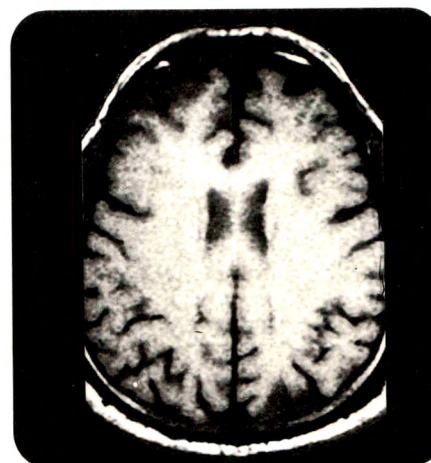
**DEMONSTRATED
SECOND
TUMOR**
Meningioma

T1-weighted MRI scan
pre-MAGNEVIST® injection.
(TR 400, TE 20)



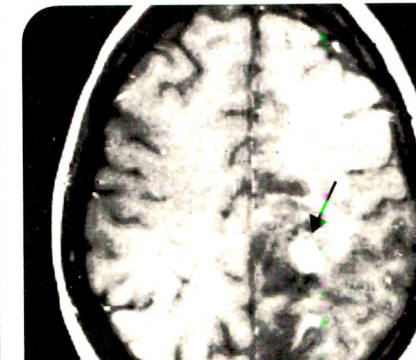
**DETECTED
LESIONS**
Metastases

T1-weighted MRI scan
pre-MAGNEVIST® injection.
(TR 600, TE 20)



**CLEARLY
DELINEATED
LESION**
Glioma

T1-weighted MRI scan
pre-MAGNEVIST® injection.
(TR 650, TE 20)



T1-weighted MRI scan post-MAGNEVIST® injection confirmed intracranial acoustic neuroma. (TR 400, TE 20)

T1-weighted MRI scan post-MAGNEVIST® injection demonstrated second tumor in patient with acoustic neuroma. (TR 400, TE 20)

T1-weighted MRI scan post-MAGNEVIST® injection demonstrated lesions not detected preinjection. (TR 600, TE 20)

T1-weighted MRI scan post-MAGNEVIST® injection showed improved delineation of lesion. (TR 650, TE 20)

Contrast enhancement to facilitate diagnosis.

In the majority of patients, diagnostic ability was facilitated or improved by enhanced contrast with MAGNEVIST® injection.

CONTRAST ENHANCEMENT TO FACILITATE DIAGNOSIS¹

Type of Study	No. of Patients	%
Double-blind	37/57	65
Open-label	70/113	62

Increased number of lesions detected

NUMBER OF LESIONS DETECTED¹

Result of Study	Type of Study	MAGNEVIST® injection	
		No. of Patients	%
Increased no of lesions postinjection	Double-blind	10/43*	23
	Open-label	16/113*	14
Lesions seen postinjection but not preinjection	Open-label	66/232	28
	Total	92/388	24

* The question was answered only for patients with contrast enhancement.

Safety profile. In clinical trials, MAGNEVIST® injection was well tolerated.¹

INCIDENCE OF ADVERSE REACTIONS AMONG 410 PATIENTS

Type of Reaction	% of Patients With Adverse Reactions Related to MAGNEVIST® Injection	Total Reactions
Headache*	4.9%	9.8%
Nausea	3.4%	4.1%
Vomiting	1.5%	1.7%
Other†	<1.0%	<2.0%

* The majority of headaches were transient in nature.

† In clinical trials, two cases of hypotension were reported.

- In clinical trials, 15% to 30% of patients experienced an asymptomatic transient rise in serum iron
- The safety of MAGNEVIST® injection in patients with hemolytic disorders has not been studied

Please see Warnings, Precautions and Adverse Reactions sections in full prescribing information for MAGNEVIST® injection on last page of this advertisement.

¹ Data on file, Berlex Laboratories, Inc.



Magnevist[®]
(gadopentetate dimeglumine) INJECTION

© 1989 Berlex Laboratories, Inc. All rights reserved.

Dosage and administration The recommended dosage of MAGNEVIST® injection is 0.2 mL/kg, administered intravenously, at a rate not to exceed 10 mL per minute. The maximum total dose is 20 mL. The imaging procedure should be completed within one hour of injection.

MAGNEVIST® (brand of gadopentetate dimeglumine) Injection

DESCRIPTION

60621-3

MAGNEVIST® (brand of gadopentetate dimeglumine) Injection is the N-methylglucamine salt of the gadolinium complex of diethylenetriamine pentaacetic acid, and is an injectable contrast medium for magnetic resonance imaging (MRI). Gadopentetate dimeglumine is to be administered by intravenous injection.

Each mL of MAGNEVIST® Injection contains 469.01 mg gadopentetate dimeglumine, 0.39 mg meglumine, 0.15 mg diethylenetriamine pentaacetic acid, and water for injection. MAGNEVIST® Injection contains no antimicrobial preservative.

MAGNEVIST® Injection is provided as a sterile, clear, colorless to slightly yellow aqueous solution.

MAGNEVIST® Injection is a 0.5-mol/L solution of 1-deoxy-1-(methylamino)-D-glucitol dihydrogen [N,N-bis(2-[bis(carboxymethyl)amino]ethyl)glycinate-(5-)]gadolinium (2-)(2-1) with a molecular weight of 938.

MAGNEVIST® Injection has a pH of 6.5 to 8.0. Pertinent physicochemical data are noted below:

PARAMETER

Osmolality (mOsmol/kg water) @ 37° C	1,940
Viscosity (cP) @ 20° C	4.9
@ 37° C	2.9
Density (g/mL)	1.199

MAGNEVIST® Injection has an osmolality 6.8 times that of plasma (285 mOsmol/kg water) and is hypertonic under conditions of use.

CLINICAL PHARMACOLOGY

The pharmacokinetics of intravenously administered gadopentetate dimeglumine in normal subjects conforms to a two compartment open-model with mean distribution and elimination half-lives (reported as mean ± SD) of about 0.2 ± 0.13 hours and 1.6 ± 0.13 hours, respectively.

Upon injection, the meglumine salt is completely dissociated from the gadopentetate dimeglumine complex. Gadopentetate is exclusively eliminated in the urine with 83 ± 14% (mean ± SD) of the dose excreted within 6 hours, and 91 ± 13% (mean ± SD) by 24 hours, post-injection. There was no detectable biotransformation or decomposition of gadopentetate dimeglumine.

The urinary and plasma clearance rates (1.76 ± 0.39 mL/min/kg and 1.94 ± 0.28 mL/min/kg, respectively) of gadopentetate are essentially identical, indicating no alteration in elimination kinetics on passage through the kidneys and that the drug is essentially cleared through the kidney. The volume of distribution (266 ± 43 mL/kg) is equal to that of extracellular water, and clearance is similar to that of substances which are subject to glomerular filtration.

The extent of protein binding and blood cell partitioning of gadopentetate dimeglumine is not known.

Gadopentetate dimeglumine is a paramagnetic agent and, as such, it develops a magnetic moment when placed in a magnetic field. The relatively large magnetic moment produced by the paramagnetic agent results in a relatively large local magnetic field, which can enhance the relaxation rates of water protons in the vicinity of the paramagnetic agent.

In magnetic resonance imaging (MRI), visualization of normal and pathological brain tissue depends in part on variations in the radiofrequency signal intensity that occur with 1) changes in proton density, 2) alteration of the spin-lattice or longitudinal relaxation time (T₁), and 3) variation of the spin-spin or transverse relaxation time (T₂). When placed in a magnetic field, gadopentetate dimeglumine decreases the T₁ and T₂ relaxation time in tissues where it accumulates. At usual doses the effect is primarily on the T₁ relaxation time.

Gadopentetate dimeglumine does not cross the intact blood-brain barrier and, therefore, does not accumulate in normal brain or in lesions that do not have an abnormal blood-brain barrier, e.g., cysts, mature post-operative scars, etc. However, disruption of the blood-brain barrier or abnormal vascularity allows accumulation of gadopentetate dimeglumine in lesions such as neoplasms, abscesses, subacute infarcts.

INDICATIONS AND USAGE

Using magnetic resonance imaging (MRI) in adult patients, gadopentetate dimeglumine provides contrast enhancement in those intracranial lesions with abnormal vascularity or those thought to cause an abnormal blood-brain barrier. Gadopentetate dimeglumine has been shown to facilitate visualization of lesions including but not limited to brain tumors.

CONTRAINDICATIONS None known.

WARNINGS

The accepted safety considerations and procedures that are required for magnetic resonance imaging are applicable when MAGNEVIST® Injection is used for contrast enhancement. In addition, deoxygenated sickle erythrocytes have been shown in *in vitro* studies to align perpendicular to a magnetic field which may result in vaso-occlusive complications *in vivo*. The enhancement of magnetic moment by gadopentetate dimeglumine may possibly potentiate sickle erythrocyte alignment. MAGNEVIST® Injection in patients with sickle cell anemia and other hemoglobinopathies has not been studied.

Patients with other hemolytic anemias have not been adequately evaluated following administration of MAGNEVIST® Injection to exclude the possibility of increased hemolysis.

Hypotension may occur in some patients after injection of MAGNEVIST® Injection. In clinical trials two cases were reported and in addition, there was one case of a vasovagal reaction and two cases of pallor with dizziness, sweating and nausea in one and substernal pain and flushing in the other. These were reported within 25 to 85 minutes after injection except for the vasovagal reaction which was described as mild by the patient and occurred after 6 1/2 hours. In a study in normal volunteers one subject experienced syncope after arising from a sitting position two hours after administration of the drug. Although the relationship of gadopentetate dimeglumine to these events is uncertain, patients should be observed for several hours after drug administration.

PRECAUTIONS - General

Diagnostic procedures that involve the use of contrast agents should be carried out under direction of a physician with the prerequisite training and a thorough knowledge of the procedure to be performed.

Since gadopentetate dimeglumine is cleared from the body by glomerular filtration, caution should be exercised in patients with severely impaired renal function.

Animal studies suggest that gadopentetate dimeglumine may alter red cell membrane morphology resulting in a slight degree of extravascular (splenic) hemolysis. In clinical trials 15-30% of the patients experienced an asymptomatic transient rise in serum iron. Serum bilirubin levels were slightly elevated in approximately 3.4% of patients. Levels generally returned to baseline within 24 to 48 hours. Hematocrit and red blood cell count were unaffected and liver enzymes were not elevated in these patients. While the effects of gadopentetate dimeglumine on serum iron and bilirubin have not been associated with clinical manifestations, the effect of the drug in patients with hepatic disease is not known and caution is therefore advised.

When MAGNEVIST® Injection is to be injected using plastic disposable syringes, the contrast medium should be drawn into the syringe and used immediately.

If nondisposable equipment is used, scrupulous care should be taken to prevent residual contamination with traces of cleansing agents.

Repeat Procedures: If in the clinical judgment of the physician sequential or repeat examinations are required, a suitable interval of time between administrations should be observed to allow for normal clearance of the drug from the body.

Information for Patients:

Patients receiving MAGNEVIST® Injection should be instructed to:

1. Inform your physician if you are pregnant or breast feeding.
2. Inform your physician if you have anemia or any diseases that affect red blood cells.

LABORATORY TEST FINDINGS

Transitory changes in serum iron and bilirubin levels have been reported in patients with normal and abnormal liver function (See PRECAUTIONS - General).

CARCINOGENESIS, MUTAGENESIS, AND IMPAIRMENT OF FERTILITY

No animal studies have been performed to evaluate the carcinogenic potential of gadopentetate dimeglumine.

Gadopentetate dimeglumine did not evoke any evidence of mutagenic potential in the Ames test (histidine-dependent *Salmonella typhimurium*) nor in a reverse mutation assay using tryptophan-dependent *Escherichia coli*. Gadopentetate dimeglumine did not induce a positive response in the (C3H 10T1/2) mouse embryo fibroblast cellular transformation assay, nor did it induce unscheduled DNA repair synthesis in primary cultures of rat hepatocytes at concentrations up to 5000 µg/mL. However, the drug did show some evidence of mutagenic potential *in vivo* in the mouse dominant lethal assay at doses of 6 mmol/kg, but did not show any such potential in the mouse and dog micronucleus tests at intravenous doses of 9 mmol/kg and 2.5 mmol/kg, respectively.

The results of a reproductive study in rats showed that gadopentetate dimeglumine when administered in daily doses of 0.1-2.5 mmol/kg, did not cause a significant change in the pregnancy rate in comparison to a control group. However, suppression of body weight gain and food consumption and a decrease in the mean weights of testis and epididymis occurred in male rats at the 2.5 mmol/kg dose. In female rats a decrease in the number of corpora lutea at the 0.1 mmol/kg dose and the suppression of body weight gain and food consumption at the 2.5 mmol/kg dose were observed.

In a separate experiment, 16 daily intravenous injections were administered to male rats. At a dose of 5 mmol/kg of gadopentetate dimeglumine, spermatogenic cell atrophy was observed. This atrophy was not reversed within a 16-day observation period following the discontinuation of the drug. This effect was not observed at a dose of 2.5 mmol/kg.

PREGNANCY CATEGORY C

Gadopentetate dimeglumine has been shown to retard development slightly in rats when given in doses 2.5 times the human dose, and in rabbits when given in doses of 7.5 and 12.5 times the human dose. The drug did not exhibit this effect in rabbits when given in doses 2.5 times the human dose. No congenital anomalies were noted in either species.

There are no adequate and well-controlled studies in pregnant women. MAGNEVIST® Injection should be used during pregnancy only if the potential benefit justifies the potential risk to the fetus.

NURSING MOTHERS

C¹⁴ labelled gadopentetate dimeglumine was administered intravenously to lactating rats at a dose of 0.5 mmol/kg. Less than 0.2% of the total dose was transferred to the neonate via the milk during the 24-hour evaluation period. It is not known to what extent MAGNEVIST® Injection is excreted in human milk. Because many drugs are excreted in human milk, caution should be exercised when the drug is administered to a nursing mother and consideration should be given to temporarily discontinuing nursing.

PEDIATRIC USE

Safety and effectiveness of MAGNEVIST® Injection in children has not been established.

ADVERSE REACTIONS

The most commonly noted adverse experience was headache with an incidence of 9.8%. The majority of headaches were transient and of mild to moderate severity. In 50% of the cases it was felt that the headaches were not related to MAGNEVIST® Injection. Nausea at 4.1% was the second most common adverse experience.

Localized pain and vomiting occurred in less than 2% of the patients.

The following additional adverse events occurred in less than 1% of the patients:

Body as a Whole: Injection site symptoms, namely, pain, coldness, warmth, burning; localized burning sensation, localized warmth, substernal chest pain, fever, weakness.

Cardiovascular: Hypotension, vasodilation, pallor, non-specific ECG changes.

Digestive: Gastrointestinal distress, stomach pain.

Nervous System: Agitation, paresthesia, dizziness.

Respiratory System: Throat irritation, rhinorrhea.

Skin: Rash, sweating.

Special Senses: Tinnitus, conjunctivitis, visual field defect, taste abnormality, dry mouth.

Laboratory: Transient elevation of serum transaminases.

The following other adverse events were reported. A causal relationship has neither been established nor refuted.

Body as a Whole: Back pain, pain. Allergic-like response including: urticaria, pruritus, wheezing, nasal congestion, sneezing, laryngismus and facial edema.

Cardiovascular: Hypertension, tachycardia, migraine, syncope.

Digestive: Constipation.

Nervous System: Anxiety, anorexia, convulsion, grand mal convulsions, nystagmus, drowsiness, diplopia.

Skin: Urticaria.

Special Senses: Eye pain, ear pain.

Data from foreign studies did not reveal any additional adverse experiences.

OVERDOSAGE

The LD₅₀ of intravenously administered gadopentetate dimeglumine injection in mice is 5-12.5 mmol/kg and in rats it is 10-15 mmol/kg. The LD₅₀ of intravenously administered MAGNEVIST® Injection in dogs is greater than 6 mmol/kg.

Clinical consequences of overdose with MAGNEVIST® Injection have not been reported.

DOSAGE AND ADMINISTRATION

The recommended dosage of MAGNEVIST® Injection is 0.2 mL/kg (0.1 mmol/kg), administered intravenously, at a rate not to exceed 10 mL per minute. More rapid injection rates may be associated with nausea. The maximum total dose is 20 mL. Any unused portion must be discarded.

DOSAGE CHART

Body Weight (kg)	Dose in mL	Approx Duration of Injection in Seconds
40	8.0	50
50	10.0	60
60	12.0	70
70	14.0	80
80	16.0	95
90	18.0	110
100	20.0	120

To ensure complete injection of the contrast medium, the injection should be followed by a 5-mL normal saline flush. The imaging procedure should be completed within 1 hour of injection of MAGNEVIST® Injection.

Parenteral products should be inspected visually for particulate matter and discoloration prior to administration, whenever solution and container permit.

HOW SUPPLIED

MAGNEVIST® Injection is a clear, colorless to slightly yellow solution containing 469.01 mg/mL of gadopentetate dimeglumine. MAGNEVIST® Injection is supplied in 20-mL single dose vials, rubber stoppered, in individual cartons; Boxes of 20, NDC 50419-189-02.

STORAGE

MAGNEVIST® Injection should be stored at controlled room temperature, between 15°-30°C (59°-86°F) and protected from light. DO NOT FREEZE. Should solidification occur in the vial because of exposure to the cold, MAGNEVIST® Injection should be brought to room temperature before use. If allowed to stand at room temperature for a minimum of 90 minutes, MAGNEVIST® Injection will return to a clear, colorless to slightly yellow solution. Before use, examine the product to assure that all solids are redissolved and that the container and closure have not been damaged.

Caution: Federal Law Prohibits Dispensing Without Prescription.

©1988, Berlex Laboratories, Inc. All rights reserved.

Berlex Laboratories, Inc.

Wayne, New Jersey 07470

60621-3

Revised 10/88

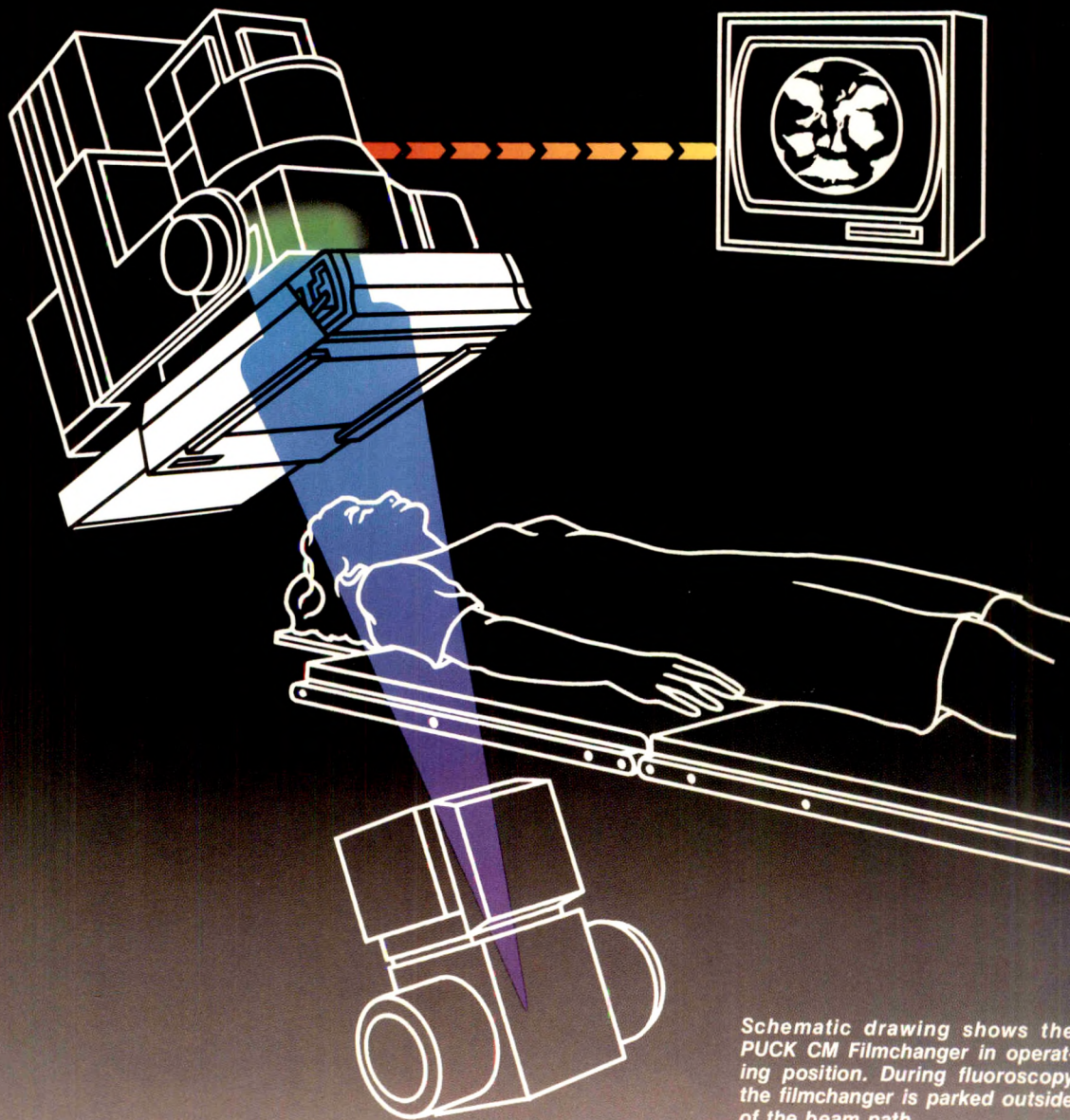


890-49

Printed in USA

April 1989

Now... Real-Time Monitoring with Filmchanger Operation



Schematic drawing shows the PUCK CM Filmchanger in operating position. During fluoroscopy the filmchanger is parked outside of the beam path.

The New PUCK CM Filmchanger... Real-Time Exposure Monitoring

The innovative PUCK CM Filmchanger, when integrated into an appropriate diagnostic X-ray system, permits viewing each individual exposure in a filmchanger series on a TV monitor. Correct catheter position and proper vessel filling can be verified instantaneously, providing the examining physician with an important new control. PUCK CM, of course, performs all position-independent filmchanger functions with or without utilizing the monitoring capability.

This is just one of the many important new features you will benefit from when you choose the new PUCK CM Filmchanger System from Elema-Schonander. Call us for a demonstration.

Elema-Schonander, Inc.

2360 N. Palmer Drive, P.O. Box 94517

Schaumburg, IL 60173-3887

Phone: (312) 397-5900

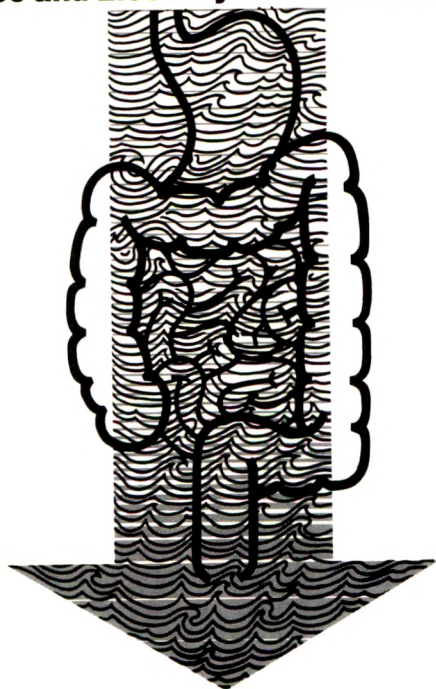
Teletex 26300143

Telefax (312) 397-5943



GoLYTELY[®]

PEG-3350 and Electrolytes for Oral Solution



THE NAME THAT STARTED A REVOLUTION.

The leader
in oral GI lavage.

BRIEF SUMMARY: Before prescribing, see package insert or PDR.

INDICATIONS AND USAGE: GoLYTELY is indicated for bowel cleansing prior to colonoscopy and barium enema x-ray examination.

CONTRAINDICATIONS: GoLYTELY is contraindicated in patients with gastrointestinal obstruction, gastric retention, bowel perforation, toxic colitis, or toxic megacolon.

WARNINGS: No additional ingredients—eg, flavorings—should be added to the solution. GoLYTELY should be used with caution in patients with severe ulcerative colitis.

PRECAUTIONS: General: Patients with impaired gag reflex, unconscious or semi-conscious patients, and patients prone to regurgitation or aspiration should be observed during the administration of GoLYTELY, especially if it is administered via nasogastric tube. If a patient experiences severe bloating, distention, or abdominal pain, administration should be slowed or discontinued temporarily until the symptoms abate. If gastrointestinal obstruction or perforation is suspected, appropriate studies should be performed to rule out these conditions before administration of GoLYTELY.

ADVERSE REACTIONS: Nausea, abdominal fullness, and bloating are the most common adverse reactions (occurring in up to 50% of patients) to administration of GoLYTELY. Abdominal cramps, vomiting, and anal irritation occur less frequently. These adverse reactions are transient and subside rapidly. Isolated cases of urticaria, rhinorrhea, and dermatitis—which may represent allergic reactions—have been reported.

CAUTION: Federal law prohibits dispensing without prescription.

STORAGE: Store in sealed container at 59°-86°F. When reconstituted, keep solution refrigerated. Use within 48 hours. Discard unused portion.

(NDC 52268-0100-01)

Made by Lyne Laboratories, Stoughton, MA 02072,

for BRAINTREE LABORATORIES, INC., P.O. Box 361, Braintree, MA 02184.

© 1989 BRAINTREE LABORATORIES, INC.

CIRCLE 35 ON READER SERVICE CARD

TRE-1037

LABORATORIES, INC.
Braintree

Need shelf space?

Williams & Wilkins is your
source for back issues of
this journal in microform.

Free Up 98%
Of Your Shelf
Space With
Microform
Conversion



MICROFILM editions are available for this journal direct from the publisher. Many Williams & Wilkins journals as well as those journals distributed by the Publishing Services Division of Waverly, Inc., are also available for a single volume year or on a standing order basis.

FOR ORDERING INFORMATION:
Write to the address below or call
TOLL FREE 1-800-638-6423.
In Maryland call 1-800-638-4007.

☐ Please send me microform
back issue ordering information
for _____

Journal Name _____

Name _____

Title _____

Address _____

City/State/Zip _____

Mail to:

Williams & Wilkins

Microform Sales

Attention: Yvonne Hahn

428 East Preston Street

Baltimore, MD 21202

-or-

The Broadway Centre

2-6 Fulham Broadway

London SW6 1AA England

Formats available:

- 16-mm reel
- 35-mm reel
- 16-mm cartridge (3M or Kodak)
- positive or negative film

MICA92 1193

Magnetic Resonance in Medicine

Sample copies and privileged
personal rates are available upon
request. For more information,
please write or call:

ACADEMIC PRESS, INC.
Journal Promotion
Department
1250 Sixth Avenue
San Diego, CA
92101, U.S.A.
(619) 699-6742



CIRCLE 21 ON READER SERVICE CARD

The Most Cited Journal in Radiology and Nuclear Medicine
SCI Citation Reports—1986

Editor-in-Chief
E. Raymond Andrew

University of Florida, Gainesville

Magnetic Resonance in Medicine is an international journal devoted to the publication of original investigations concerned with all aspects of the development and use of nuclear magnetic resonance and electron paramagnetic resonance techniques for medical applications. Basic research and clinical investigations are within the scope of the journal.

Features

- Regular articles
- Communications—preliminary accounts of work of special topicality and importance
- Notes—complete accounts of work of limited scope

Research Areas Include

- Biochemistry
- Biophysics
- Chemistry
- Clinical studies
- Computing
- Engineering
- Mathematics
- Physics
- Physiology

Official Journal of the Society of Magnetic Resonance in Medicine

P24,453

Please enter my subscription for:
Magnetic Resonance in Medicine

- ☐ Volumes 9-12 (1989), 12 issues
ISSN 0740-3194

In the U.S.A. and Canada: \$312.00
All other countries: \$364.00

Please send me:

- ☐ A sample copy.
☐ Privileged personal rate information. Personal subscription rates are available only on orders placed directly with the Publisher and paid for with personal funds. Checks and money orders must be drawn against a U.S. bank.

Method of payment:

- ☐ Our purchase order is enclosed.
☐ My check is enclosed.
☐ Credit information is given.
☐ Enter as a Standing Order (institutions only) hereby authorizing Academic Press to service and bill our account each calendar year until cancelled.

Please note: Payment or credit card information must accompany order. Prices include postage, handling, and air freight where applicable, and are subject to change without notice. Payment must be in U.S. currency, U.S. Bank Draft, International Money Order, or UNESCO coupons. S9119

When paying by credit card, please check one box:

- ☐ Visa/Barclaycard ☐ American Express
☐ MasterCard/Access ☐ Diner's Club

Expiration Date (Mo/Yr): _____

Credit

card
number:

--	--	--	--	--	--	--	--	--	--	--	--	--	--	--	--	--	--	--	--

Signature: _____

Total Amount: \$ _____

Name: _____

Address: _____

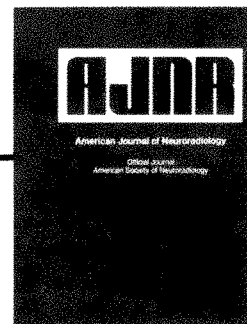
City: _____

State: _____ Zip: _____

Country: _____

Increase your expertise in evaluating CNS lesions

AJNR American Journal of Neuroradiology



Editor: **Juan M. Taveras, MD**, Harvard Medical School; MGH

Outstanding clinical papers on every aspect of CNS imaging, including spinal diagnosis...informed coverage of head and neck radiology...clear, readable CTs, angiographs, MR imaging and ultrasound studies. These are the features you demand of a quality professional journal. You'll find them in every issue of **AJNR: American Journal of Neuroradiology**.

As you are called upon to perform and interpret more and more sophisticated diagnostic tests — from myelography to CT to newborn ultrasound studies — you need a comprehensive, reliable journal that can keep you abreast of all the latest developments. Each bimonthly issue of **AJNR** brings you timely, clinically pertinent information, as well as important clinical research presented with an eye toward immediate practical application.

Here's a brief sampling of the variety of articles you'll find in **AJNR**:

Giant Cavernous Aneurysm Associated with Trigeminal Artery: Treatment by Detachable Balloon. *Higashida RT, Halbach VV, Mehringer CM, Hieshima GB*

Intraoperative Digital Subtraction Neuroangiography: A Diagnostic and Therapeutic Tool. *Hieshima GB, Reicher MA, Higashida RT, et al.*

Characteristic Features of MR Truncation Artifacts.

Czervionke LF, Czervionke JM, Daniels DL, Haughton VM

Neuroimaging of Scuba Diving Injuries to the CNS. *Warren LP Jr, Djang WT, Moon RE, et al.*

Risk of Seizures After Myelography. *Maly P, Bach-Gansmo T, Elmqvist D*


Comparison of MR Imaging and CT in Patients with Intracranial Aneurysm Clips. *Holtas S, Olsson M, Romner B, Larsson E-M, Saveland H, Brandt L*

Comparison of MR Imaging, CT, and Angiography in the Evaluation of the Enlarged Cavernous Sinus. *Hirsch WL Jr, Hryshko FG, Sekhar LN, et al.*

Bimonthly

Personal \$115/yr **Institutions** \$135/yr
In-training \$65/yr (add \$25.00 outside the US)

ORDER FREE BY PHONE. Just call

 **1-800-638-6423** from anywhere in the US.
Maryland residents, call **1-800-638-4007**.

Williams & Wilkins

P.O. Box 23291 Baltimore, Maryland 21203



Subscribe to AJNR for 3 years and SAVE

Avoid future rate increases and ensure uninterrupted service by placing a multi-year subscription at current rates.

☐ New subscription ☐ Renewal
☐ 3 yrs ☐ 2 yrs ☐ 1 yr
☐ **Personal** \$115 ☐ **Institutions** \$135 ☐ **In-training** \$65
(add \$25.00 outside the US)

☐ Also send me the **1989 Bound Volume** at \$65.00 (\$70.00 outside the US). \$2.00 discount for orders placed before October 31, 1989, and for pre-paid orders. I understand that the bound volume is *in addition to* my regular subscription and is available only to subscribers. (To be shipped in early 1990. Sorry, bound volumes for years prior to 1989 are not available.) *All bound volume orders must be received by December 31, 1989.*

☐ Check enclosed ☐ Bill me
☐ VISA ☐ MasterCard ☐ American Express

card # _____ exp. _____

signature/P.O. # _____

printed in USA

Name _____

Address _____

City/State/Zip _____

MD residents, please add 5% sales tax. Subscription orders from outside the US must be prepaid in US dollars only.

Residents, Fellows, Interns, and Students: when applying for the in-training rate, available for 3 years, please specify name of institution and training status. Rates valid through October 31, 1989.

Please allow 8 weeks for order processing and delivery of your first issue. Surface mail delivery to countries outside the US may take up to 16 weeks. Airmail rates available upon request.

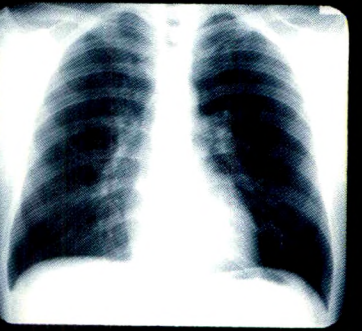
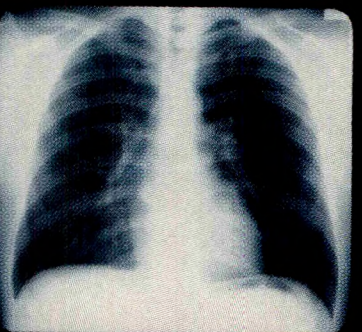
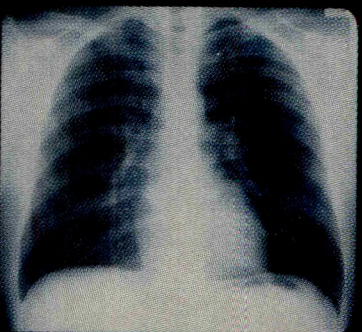
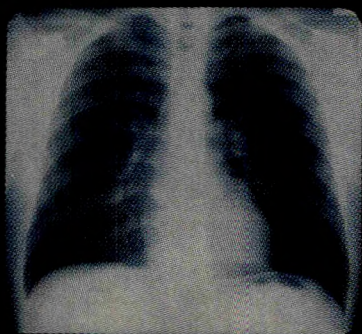
Williams & Wilkins

P.O. Box 23291
Baltimore, Maryland 21203

The Broadway Centre
2-6 Fulham Broadway
London SW6 1AA England



JNRA91 1179



WHICH WOULD YOU RATHER READ?

The difference is *Clear!*
S & S Illuminators provide the brightest, most even light distribution for glare-free "perfect" reading — all day long.

Our commitment to illumination excellence and innovative design has produced an extraordinarily extensive, diversified line of general and "special" purpose illuminators — with configurations to meet *Your* specifications. For example:

- Film formats include 14 x 17, 8 x 10, 14 x 36 and 14 x 51 inches. Plus 18 x 24 and 24 x 30 cm Mammography Series
- Panoramic or divided viewing sections

- High-Low intensity levels as well as high frequency, reduced glare units are available as options
- 1 - 8 banks / Single or double tier configurations
- Straight, console or full range tilt viewing
- Surface or recess mounting or mobile free-standing units
- Economy models thru deluxe models with full range of optional accessories

Tried, tested and trusted for over 40 years, S & S — the world's largest manufacturer of Motorized Viewers — has earned its reputation for setting the **standard** in illumination excellence.

Call us toll-free, or ask your local x-ray representative for our fully illustrated 100+ page catalog of Illuminators, Motorized Viewers and X-Ray Accessories.

CIRCLE 9 ON READER SERVICE CARD



S & S X-RAY PRODUCTS INC.

1101 Linwood Street
Brooklyn, NY 11208

800/347-XRAY • 718/649-8500

FAX 718/257-0219

The difference is Clear!

4X Series with
High-Low Feature
(Model 4X0001 shown)



CLEAR-Pb® LEAD-PLASTIC RADIATION SHIELDING

Up to 6 Sq. Ft. of Overhead X-Ray Barrier Protection

CLEAR-Pb® UNIVERSAL ADAPTER KIT Converts Your Small Overhead Barrier to a BIGGER and BETTER Shield!

- Get more radiation protection at a low cost!
- Generous size and panoramic visibility reduces the need to reposition barrier during procedure.
- Large shielding area can protect two people, if required.

Our Universal Adapter Kit with CLEAR-Pb lead-plastic shield (0.5 mm lead equivalent), enables you to replace your present lead-glass unit with any one of four panoramic shield sizes...from 18" x 24" to 36" x 24". Comes complete with CLEAR-Pb lead-plastic shield, adapter, and all hardware for mounting.

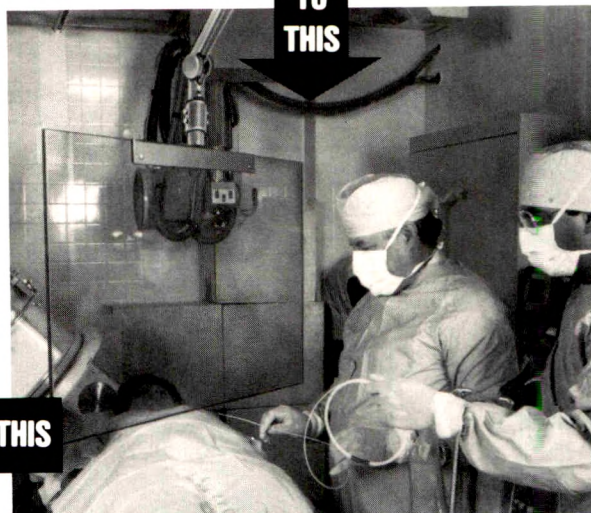


FROM THIS



Present Barrier,
16"W x 12"H
(192 sq. in.)

TO
THIS



WITH THIS

56-626-3624 CLEAR-Pb Barrier
with new adapter 36"W x 24"H (864 sq. in.)

For complete details, request Bulletin 431-44

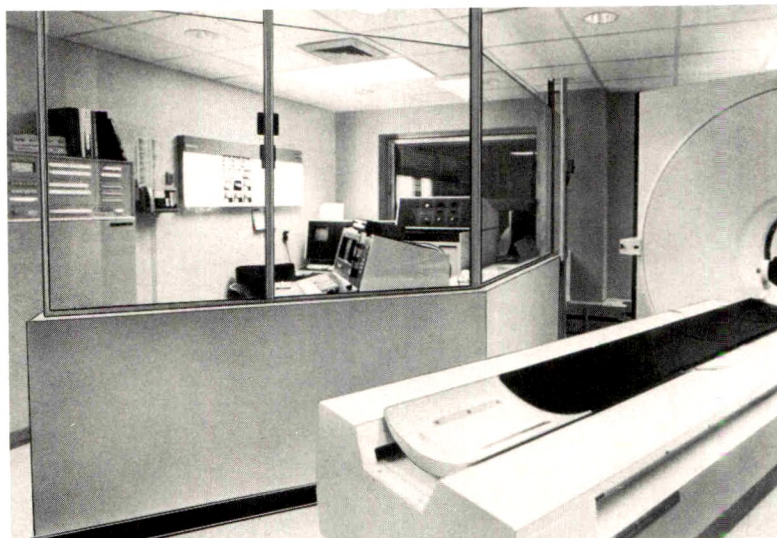
The Unmatched Choice for X-Ray Room Shielding

CLEAR-Pb® Lead-Plastic Modular X-Ray Barriers and Windows

CLEAR-Pb is a lead-impregnated, transparent plastic sheet that combines superb light transmission and complete radiation protection.

It gives you many unique benefits:

- Panoramic viewing areas.
- Simple, quick, on-site modular barrier installation. Modules can be moved or changed without expensive labor or renovations.
- Attractive, space-saving, decorator look. Walls are only about 1 1/2" thick.
- Shatter resistance.
- Choice of lead equivalency - 0.5 to 1.5 mm.



In this CT scanner room, the CLEAR-Pb Modular Barrier provides an unparalleled view of the exam area. Large windows (two 48" x 72" and one 18" x 48") allow the technologist and patient to see each other, giving both a greater feeling of security.
Southern Baptist Hospital, New Orleans, LA.

FREE

- CLEAR-Pb LEAD-PLASTIC SAMPLES.
- CLEAR-Pb "PLANNING GUIDE." Beautifully illustrates dozens of user-designed x-ray room shielding installations to assist you in your planning efforts. Call or write today for your **FREE** materials.

For complete
details, request
Bulletin 3184-44

©Victoreen, Inc.

NUCLEAR ASSOCIATES



A Division of VICTOREEN, INC.
100 VOICE ROAD
CARLE PLACE, NY 11514-1593 U.S.A.
(516) 741-6360
FAX (516) 741-5414

CIRCLE 36 ON READER SERVICE CARD

CLEAR-Pb® MODULAR BARRIERS AND WINDOWS... THE STATE OF THE ART IN X-RAY ROOM SHIELDING

SIEMENS



MG-0000-203 WLM 869

Grasp the future of MR

Introducing the MAGNETOM® SP

An innovation in speed, simplicity and performance.
Available now.

CIRCLE 8 ON READER SERVICE CARD

Siemens Medical Systems, Inc., 186 Wood Avenue South, Iselin, N.J. 08830

Lippincott presents...

Top-notch text/atlasses to help you
face the day-to-day challenges of daily practice.

2,200 superb illustrations!

Gastrointestinal Radiology: A Pattern Approach Second Edition

By
Ronald L. Eisenberg, M.D.

"...This originally conceived and well-executed work does fill a real void... extremely useful in the day-to-day evaluation of GI studies...this superb, moderately priced, and practical textbook is strongly recommended to all who interpret GI tract examinations..."

(JAMA, of the first edition.)

The practical "pattern" approach

Now—the second edition of the first reference to utilize the unique pattern approach—combining in a single source the best features of lists of gamuts with the extensive information of disease-oriented texts.

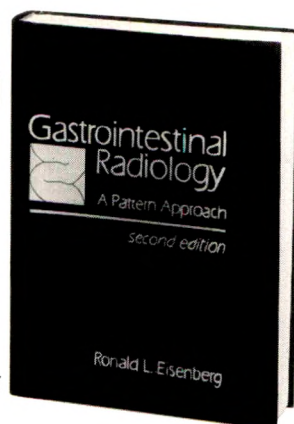
New in the Second Edition:

The new edition has been thoroughly revised and updated to include information on entities described since the first edition. It features approximately 600 additional illustrations, many of which depict newer modalities, such as ultrasound and CT scanning.

Each chapter presents you with:

- a specific radiographic pattern and list of the possible disease entities which this pattern might represent
- an extensive gamut of disease entities for each radiographic finding
- a thorough discussion of differential diagnosis
- approximately 2,200 representative radiographs that illustrate and differentiate between diseases.

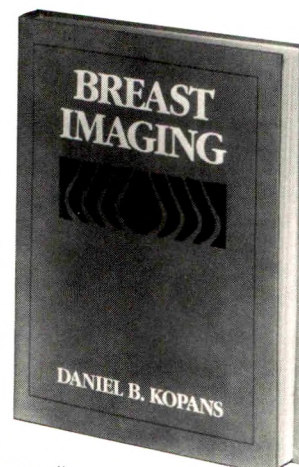
About 992 Pages. 2,200 Illustrations.
June 1989. \$125.00.



**An excellent
text/atlas with
560 illustrations!**

Breast Imaging

By
Daniel B. Kopans, M.D.



A definitive guide to the daily interpretation of breast imaging studies—and a concise overview of the major issues in breast imaging today! In-depth coverage of x-ray mammography—the single most effective means of early breast disease detection—is provided along with detailed discussions on ultrasound and computed breast tomography as diagnostic tools. Also includes:

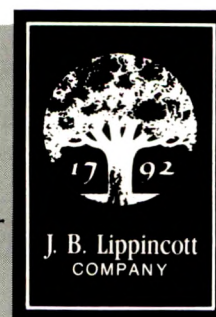
- discussions of techniques such as transillumination, magnetic resonance imaging, digital mammography
- brief reviews of breast anatomy, histology, physiology, pathology
- the clinical importance of staging breast cancer
- aspiration and localization of occult lesions
- the male breast
- the future of breast imaging

About 460 Pages. 560 Illustrations.
1989. \$65.00.



Want it faster?

Call TOLL FREE (USA except AK)
1-800-638-3030. In Maryland, call collect
301-824-7300. Or use the coupon below.
Lippincott books are also available
from your health science bookstore or
Lippincott representative.



J. B. LIPPINCOTT COMPANY • P.O. BOX 1630, HAGERSTOWN, MD 21741

YES! Please send me for 30 days' on-approval examination:

☐ Eisenberg (65-11083) **\$125.00** ☐ Kopans (65-09251) **\$65.00**

Name

Address

City

State Zip

Phone

☐ Payment enclosed* (save postage & handling)

☐ Bill me (plus postage & handling)

☐ Charge it:* (save postage & handling)

☐ MasterCard ☐ VISA ☐ American Express

Card No. Exp. Date

Signature

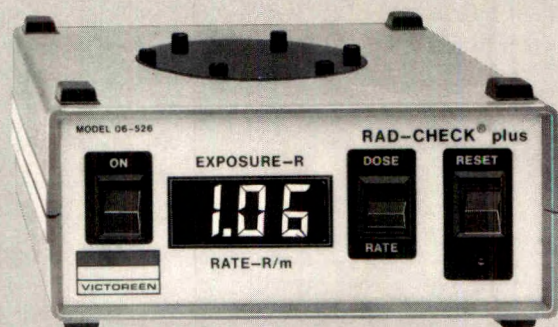
*Add sales tax. Prices in U.S. funds and subject to change. Orders subject to approval of Lippincott. Professional books may be tax deductible. Offer valid in U.S. and Canada only.

120289

Achieve Unmatched Diagnostic Quality

A Simple, Cost-Effective Method for
Determining Entrance Skin Exposures

RAD-CHECK® PLUS X-RAY EXPOSURE METER



To Comply With CDRH and
JCAH Requirements About
Monitoring Doses From
Diagnostic Radiology
Procedures

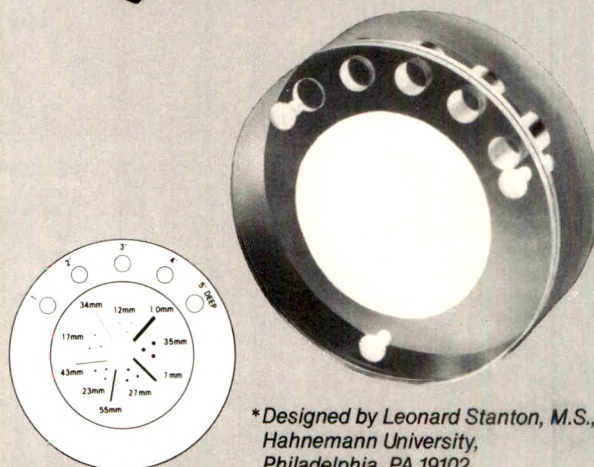
- Measures Entrance Skin Exposure (ESE) to determine the radiation received by a patient.
- Performs fluoroscopy, beam quality, and other QA checks.
- Fast, easy to use; battery operation and built-in detector eliminate set-up time.
- Place Rad-Check Plus on x-ray table, collimate, shoot, and read the result on the large liquid crystal display!
- Dual range: dose to 2R; dose rate to 20R/min.
- Optional remote detectors available in 0-2R and 0-20R ranges; permit measurements in less-accessible areas.

For more details,
request
Bulletin 3561-44

©Victoreen, Inc.

Easy to Use... Easy to Interpret

MAMMOGRAPHIC QA PHANTOM*



**Designed by Leonard Stanton, M.S.,
Hahnemann University,
Philadelphia, PA 19102.*

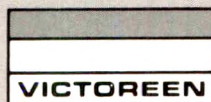
For Evaluating the Overall
Imaging Performance of
a Mammographic System

- Intended as an integral part of a complete mammography QA program: evaluates x-ray generator, screen-film combination and film processor.
- Contains calcium carbonate specks which better simulate actual clinical conditions ("punctate calcifications") in breast cancer.
- Uses nylon fibers to simulate "soft tissue fibrillar extensions in adipose tissue."
- Includes two additional attenuators to check phototiming linearity.
- Includes 5-step air wedge to gauge for image contrast.

For more details,
request
Bulletin 4053-44

CIRCLE 16 ON READER SERVICE CARD

NUCLEAR ASSOCIATES



A Division of VICTOREEN, INC.
100 VOICE ROAD
CARLE PLACE, NY 11514-1593 U.S.A.
(516) 741-6360
FAX (516) 741-5414

WE CARRY A COMPLETE LINE OF MAMMOGRAPHIC QA PRODUCTS

NEW NONIONIC

The logo for Optiray (ioversol) is centered on the page. It consists of a gold-colored rectangle containing the word "OPTIRAY" in a white, serif, all-caps font with a small trademark symbol (TM) to its right. Below "OPTIRAY" is the word "(ioversol)" in a blue, lowercase, serif font. The rectangle is superimposed on a larger, stylized diamond shape. The diamond has a gold outline and is filled with a blue-to-white gradient, with the blue being more prominent at the top and bottom points.

OPTIRAYTM
(ioversol)

COMING VERY SOON.

Review Article

Crystal-Associated Arthropathies

Joel Rubenstein¹ and Kenneth P. H. Pritzker²

The crystal-associated arthropathies are a group of metabolic diseases in which crystals are deposited in and around joints, accompanied by a variable spectrum of clinical, radiographic, and pathologic abnormalities. This article reviews current concepts about the common human arthropathies in which biologically produced crystals are formed. Specifically, these are monosodium urate, calcium pyrophosphate dihydrate, and calcium hydroxyapatite. Other crystals less commonly linked to articular disease (e.g., cholesterol, steroid, oxalate, and cystine) are not discussed [1].

Crystal Characteristics

The clinical identification of crystals plays an essential role in diagnosis. Therefore, a basic knowledge of crystal structure is required to understand the commonly used diagnostic techniques. Crystals are solids of definite form in which the atomic units are arranged in a regular and repetitive manner, creating a three-dimensional lattice [2]. This internal symmetry and the pattern of growth affect the external shape of the crystal, creating facets that vary with the specific crystal, often producing typical microscopic appearances. A given crystal may exist in several forms with different symmetries. Hence, there are six fundamental classes of crystals based on their internal structure and external form: cubic, tetragonal, orthorhombic, monoclinic, triclinic, and hexagonal [3].

This ordered array of atoms allows for the diffraction of X-rays, permitting a precise determination of the internal structure of a given crystal. X-ray diffraction is a commonly used crystallographic technique to study the form, structure, and

aggregation of crystals [4]. Crystals confer similar properties on light, allowing their clinical identification with methods such as polarized light microscopy [5]. Analytical electron microscopy and electron microprobe analysis of calcium to phosphorus molar ratios are other more specialized analytical techniques used in crystal identification [4].

When viewed by polarized light microscopy, urate crystals are needle-shaped, strongly negatively birefringent structures. Although calcium pyrophosphate crystals can be needlelike and similar in size to urate, they are more variable in shape and weakly positively birefringent. With light microscopy, hydroxyapatite crystals are nonbirefringent and appear as spherical aggregates. For the identification of individual hydroxyapatite crystals, which are extremely small ($100 \times 10\text{--}20\text{ nm}$), more sophisticated techniques are required, such as analytical electron microscopy using X-ray spectroscopy and powder X-ray diffraction (Fig. 1). Over the past 25 years, the diagnosis of the various crystal arthropathies has come to rely on these techniques for identification of crystals in synovial fluid [6].

Historical Perspective

The understanding of crystal joint diseases began with interest in gout. The classic description of the inflammatory reaction associated with acute gout was offered by Thomas Sydenham in 1683, more than 175 years before it was first proposed that this disease was caused by crystals [7]:

The victim goes to bed and sleeps in good health.
About two o'clock in the morning he is awakened

Received October 5, 1988; accepted after revision November 28, 1988.

¹ Department of Radiology, Sunnybrook Medical Center, 2075 Bayview Ave., Toronto, Ontario M4N 3M5, Canada. Address reprint requests to J. Rubenstein.

² Department of Pathology, Mount Sinai Hospital, 600 University Ave., Toronto, Ontario M5G 1X5, Canada.

AJR 152:685-695, April 1989 0361-803X/89/1524-0685 © American Roentgen Ray Society

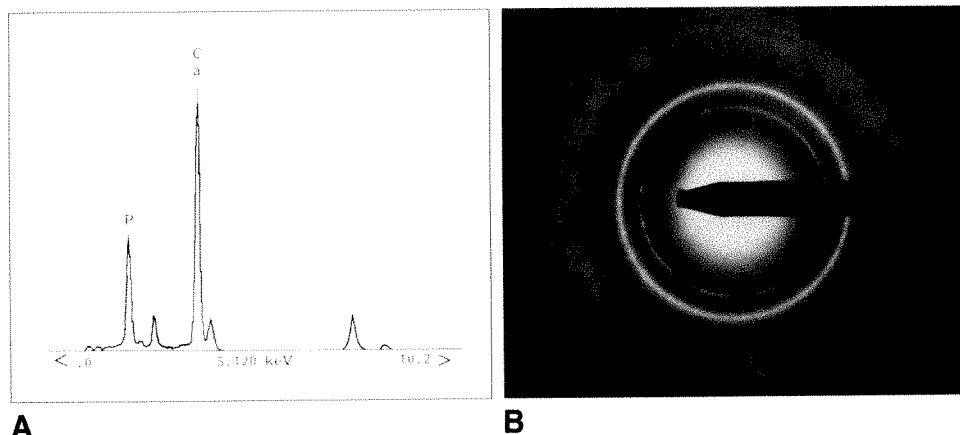


Fig. 1.—Analytical electron microscopic techniques for hydroxyapatite.

A, Energy dispersive X-ray spectrum shows calcium (Ca) and phosphorus (P) ratio equal to 1.67:1, characteristic for hydroxyapatite. Other smaller peaks represent tissue contaminants.

B, X-ray diffraction pattern, recorded on film, is diagnostic for hydroxyapatite. Concentric rings of light result from diffraction of low energy X-rays by sheets of atoms in the crystal. Interplanar spacings are specific for a given crystal.

by a severe pain in the great toe; more rarely in the heel, ankle, or instep. This pain is like that of a dislocation, and yet the parts feel as if cold water were poured over them. Then follow chills and shivers and a little fever. The pain, which was at first moderate, becomes more intense. With its intensity the chills and shivers increase. After a time this comes to its full height, accommodating itself to the bones and ligaments of the tarsus and metatarsus. Now it is a violent stretching and tearing of the ligaments—now it is a gnawing pain and now a pressure and tightening. So exquisite and lively meanwhile is the feeling of the part affected, that it cannot bear the weight of the bedclothes nor the jar of a person walking in the room. The night is passed in torture, sleeplessness, turning of the part affected and perpetual change of posture; the tossing about of the body being as incessant as the pain of the tortured joint, and being worse as the fit comes on. Hence the vain effort by change of posture, both in the body and the limb affected, to obtain an abatement of the pain.

It was not until 1859 that Sir Alfred Baring Garrod [8] suggested that crystals might cause the inflammation occurring with gout. Garrod's hypothesis was proved by Max Freudweiler in 1899. Freudweiler [9] experimentally induced an acute inflammatory reaction in dogs and rabbits, and subsequently in humans, by subcutaneously injecting urate and other crystals. In a related event in 1897, Gustav Riehl [10] had described the phagocytosis of urate crystals by polymorphonuclear white cells, based on his studies of skin topi. These observations subsequently provided a foundation for understanding the inflammatory response to crystals.

It was more than 100 years later (1962) that Faires and McCarty [11] showed that articular inflammation was produced by the intraarticular injection of urate crystals. That same year, McCarty [12] observed that intracellular crystals, contained within neutrophils, were a regular feature of gout. In this same period, by using the polarized light microscope, McCarty and Hollander [13] were the first to identify urate

crystals in the synovial fluid of a patient with gout. In 1962, McCarty et al. [14, 15] also described a different crystal (i.e., calcium pyrophosphate) in the joint fluid of patients who had arthritis simulating acute attacks of gout and referred to this as "pseudogout."

Two common types of joint disease have now been linked to crystal deposition: acute self-limited attacks of joint inflammation and chronic destructive joint disease [16]. Before a crystal can be implicated as the cause of an arthropathy, a modification of Koch's postulates should be satisfied, whereby a well-defined clinical syndrome is consistently associated with identifiable crystals and the injection of the crystals can reproduce the syndrome [17]. Although these criteria have been fulfilled for the acute arthritic syndromes associated with urate, calcium pyrophosphate, and hydroxyapatite crystals, their true relationship to chronic joint disease is yet to be established.

Crystals, Inflammation, and Chronic Joint Disease

The factors responsible for the articular accumulation of crystals and their role in producing joint disease have received much attention [18]. Although the diseases caused by various crystals are different, the biochemical and cellular interactions that cause the acute crystal arthropathies are similar and suggest a common pathogenetic mechanism.

It is generally accepted that a solute excess of a crystal is necessary for its intraarticular deposition, but this may require alteration of the articular connective tissue matrix [4, 19]. Crystals usually are deposited in the connective tissues of joints, often long before causing acute arthritis. They may be found in synovium, cartilage, joint capsule, and periarticular tissues, such as tendon, ligament, and bursa [4]. However, there is evidence that the earliest urate deposits occur in synovial fluid and marginal synovium rather than in cartilage; several reports describe synovial tophi at the time of the first gouty attack [20–22]. This is in contrast to pyrophosphate crystals, in which the initial site of accumulation appears to be in cartilage [22, 23].

The discharge of crystals into the joint cavity results in acute attacks of inflammation. This discharge of crystals may result from de novo precipitation associated with a sudden

elevation of serum uric acid or from the rupture of preformed deposits in synovium and cartilage [24, 25]. The shedding of crystals may result from local trauma, surgery, drug therapy, acute illness, or various factors that increase the solubility of the intraarticular deposits [22]. Rodnan [26] has shown that the acute intraarticular precipitation of urate crystals correlates with rapid lowering of serum urate after its elevation, rather than with the absolute level of serum urate. Thus, a simple relationship does not exist between the serum uric acid level and the presence or number of crystals in the synovial fluid during an acute gouty attack [18]. This correlates with the observation that many hyperuricemic individuals are asymptomatic for long periods of time [1]; acute gouty arthritis developed in only 17% of hyperuricemic patients in one study [27].

The subsequent phagocytosis of free intraarticular crystals by neutrophils plays a central role in the acute inflammatory reaction. Multiple factors appear to influence this phagocytosis, such as protein coating of the crystal [19], crystal size [28], and crystal surface ultrastructure [29, 30].

Urate and pyrophosphate crystals have been shown to be avid binders of various proteins, particularly immunoglobulin G, with a granular surface coating noted around the crystal on scanning electron microscopy (Fig. 2) [31]. This opsonization of crystals has been shown to expedite the phagocytosis of crystals [32]. The crystal is first engulfed by the cell and surrounded by a membrane to produce a phagosome, which then fuses with lysosomes. This leads to the release of multiple enzymes within the cell, resulting in digestion of the surface proteins on the crystal [33]. The crystal itself then appears to be responsible for subsequent membranolytic and cell death, possibly mediated by an electrostatic mechanism, with the enzymes escaping into the extracellular space. This leads to acute synovitis and articular tissue damage [34–36]. The entire process occurs within minutes [37, 38], but its intensity varies with different crystals. For example, pyrophosphate crystals have been shown to have much less membranolytic effect on neutrophils and erythrocytes than do urate crystals [39]. Of added interest is the work of Weissman and Rita [40], who showed a protective effect of 17-estradiol against membranolytic by urate crystals, suggesting a possible explanation for the lower prevalence of gout in women.

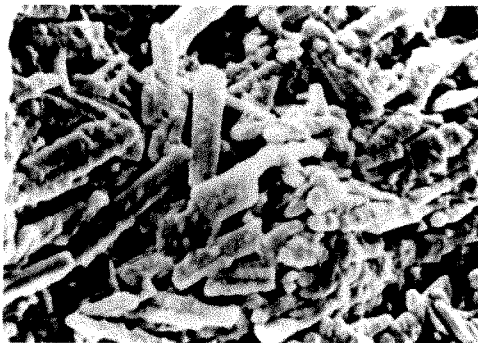


Fig. 2.—Scanning electron photomicrograph shows urate crystals. White coating around crystals is a proteinaceous matrix. ($\times 2500$)

The adsorption to crystals of many other proteins involved in the inflammatory response has also been described, including various immunoglobulins, fibrinogen, elements of the complement system, albumin, acid phosphatase, and β -glucuronidase [18, 32, 41, 42]. Adsorbed proteins with antiphlogistic properties, such as hyaluronate and apolipoprotein B, have also been identified and may play a role in terminating, and even preventing, the inflammatory reaction [43, 44].

Chemotactic factors responsible for mediating inflammation are released from neutrophils after the phagocytosis of crystals. Specifically, a glycoprotein, crystal-induced chemotactic factor, a complement-derived chemotactic factor (C5a), and leukotriene B₄ have been identified [45–47]. The release of these mediators establishes a cycle of additional neutrophil attraction and activation with consequent enhancement of inflammation [48].

The interaction of crystals with cells other than neutrophils may contribute to the clinical signs and symptoms. For example, urate crystals have been shown to stimulate monocytes to release pyrogens, accounting for the fever that occurs with acute gout [49, 50]. Destructive enzymes (e.g., collagenase) and stimulators of inflammation (e.g., prostaglandin E₂) elaborated by type 1 synovial cells also have been incriminated in the pathogenetic process [51, 52]. Additional factors such as crystal structure, pH, temperature, cation concentrations, and mechanical stimuli have been investigated and may be involved in the process [18].

The complete role of crystals in producing joint disease is still not entirely understood, as crystals have been found in joint fluid after inflammation has subsided, as well as in asymptomatic joints, referred to as the "lanthan" state [18].

The relationship between crystals and osteoarthritis is controversial and not fully understood. Some studies conclude that no relationship exists [53, 54] or that osteoarthritis may simply promote the deposition of crystals [55, 56]. Other reports offer evidence that crystals are responsible for the development of osteoarthritis [57, 58] or may produce a distinctive arthropathy simulating osteoarthritis and joint destruction [59–62].

A recent histologic study has shown that the risk of chondrocalcinosis is six times greater in knees resected surgically because of osteoarthritis than in controls matched for age and gender [63]. Crystals are also commonly found in osteoarthritic synovial effusions [55, 64]. Examination of joint fluid from 100 patients with osteoarthritis showed crystals in 60% of patients; 30% contained hydroxyapatite alone, 27% had pyrophosphate alone, and 43% had both. Patients with crystals were older and had osteoarthritis of longer duration and greater severity [55]. There also appears to be a direct correlation between the presence of crystals and the severity of osteoarthritis [65, 66]. However, no studies have determined conclusively that crystals are the cause or result of osteoarthritis.

The clinical and pathologic spectrum of the crystal arthropathies, ranging from an asymptomatic state to acute arthritis and chronic joint destruction, thus results from a complex interaction between multiple factors that are still under investigation.

Urate Crystals (Gout)

Clinical Features

Gout is the best understood crystalline arthropathy, is the easiest to treat, and has the best prognosis. Its full development is characterized by a constellation of abnormalities that include hyperuricemia, recurrent attacks of acute arthritis, tophi, uric acid calculi, and renal disease involving the glomeruli, tubules, and interstitium [67]; however, the term gout should be reserved for hyperuricemic patients with inflammatory arthritis or tophi and not hyperuricemia alone or urolithiasis [68].

Hyperuricemia and gout are divided into primary, secondary, and idiopathic types [69, 70]. The primary type includes patients with renal underexcretion of urate (90% of primary gout), urate overproduction (10%), and specific enzyme defects (<1%). Secondary gout is the consequence of other disease processes, such as myeloproliferative disorders, renal insufficiency, excessive alcohol consumption, and drug therapy. The idiopathic designation refers to cases that cannot be assigned to a precise category.

Gout is mainly a disease of adult men; the peak age at onset is in the fifth decade. Only about 5% of cases occur in women, generally after menopause [71]. Traditionally, gout is divided into four stages; asymptomatic hyperuricemia, acute gouty arthritis, intercritical gout, and chronic tophaceous gout [67].

Asymptomatic hyperuricemia may be present throughout life without any sequelae and is thought to precede the first attack of acute arthritis by many years. Episodes of renal colic may antedate the first attack of gout in 10–40% of patients [69].

The initial attack of acute gouty arthritis is monoarticular in 85–90% of cases; the first metatarsophalangeal joint is the first site of involvement in more than 50% of patients [69]. The onset of the acute attack is abrupt, frequently at night, and often peaks in intensity within the first 12 hr. Untreated attacks are variable in course; mild attacks subside in hours, whereas severe attacks may last for several days to weeks.

Intercritical gout is the asymptomatic period between attacks [69]. A patient with acute gout may never have a second attack, or many years may pass between attacks. However, acute attacks tend to recur in untreated patients, with succeeding episodes gradually becoming more severe, of increased frequency, longer in duration with incomplete recovery, and with an increased likelihood of being polyarticular.

The chronic phase of gout is characterized by the development of tophi, although the prevalence of this type of gout has been dramatically reduced by the advent of effective urate-lowering drugs like allopurinol. A tophus represents a collection of urate crystals oriented radially around an amorphous proteinaceous matrix with a rim of fibroblasts, histiocytes, and multinucleated giant cells [72]. The diameter of tophi varies from a few millimeters to several centimeters. Many years are generally required for tophi to become apparent after the first gouty attack; the average duration is 11.6 years [71]. Common sites for visible tophi are the fingers,

hands, feet, extensor surface of the forearm, olecranon bursa, knees, Achilles tendon, and helix of the ear [73].

Radiographic Features

Radiography generally plays a minor role in the assessment of the initial attacks of acute gouty arthritis. The radiographic findings are nonspecific, consisting of poorly defined soft-tissue swelling, occasionally accompanied by a mild degree of osteoporosis [74, 75]. Fine, striated periosteal new bone may be observed, particularly along the medial aspect of the first metatarsophalangeal joint, and often is best demonstrated on oblique projections [75].

In chronic gout, radiography plays a more important role. In a review by Barthelemy et al. [76], radiographs revealed abnormalities in 24% of asymptomatic patients and in 42% of patients who had no evidence of tophi. Bloch et al. [75] showed that 18% of patients had positive radiographs in the presence of equivocal clinical findings. Treatment is influenced by this radiographic documentation of gouty arthritis; long-term drug therapy is required even in the absence of definite clinical findings [76].

Chronic gout generally results in an asymmetric polyarthropathy with eccentric soft-tissue swelling representing the tophaceous deposits. The peripheral joints are predisposed to involvement, particularly the feet, hands, wrists, elbows, and knees [1, 74]. Normal bony mineralization is maintained in most patients until late in the course of the disease, with osteoporosis then resulting primarily from disuse [77].

Urate crystals initially occupy the superficial layers of cartilage, but the joint space is typically preserved until late in the course of disease, and like the early periosteal changes, gouty erosions may be better delineated on oblique projections (Fig. 3) [1, 75].

Gouty erosions are usually sharply defined with sclerotic margins; an overhanging edge without cortical containment is seen in approximately 40% of patients (Fig. 4) [78]. The overhanging margin is characteristic but not diagnostic, resulting from the gradual enlargement of a tophaceous nidus with periosteal new bone forming at the expanding margin [1]. Pressure erosions of bone commonly develop from deposits in adjacent soft tissues and are one of the described causes of "vanishing bone" [74, 79]. Bony proliferation has been observed at the articular surfaces and along the diaphyses of long bones, as well as at the entheses [1, 77].

Secondary osteoarthritic changes are a common late finding, with areas of bony collapse resulting from pathologic subchondral fractures (Fig. 5) [1, 75]. Subluxation of joints and fibrous ankylosis are described as late complications [74, 75]; bony ankylosis is encountered rarely [77].

Calcification within pure urate tophi is unusual; therefore, calcification suggests the possibility of coexisting calcium-containing crystals such as pyrophosphate or hydroxyapatite (Fig. 6), an underlying abnormality of calcium metabolism, or calcification within cholesterol deposited in the tophus [1, 74, 80]. Intraosseous calcifications have been noted in association with extensive joint destruction or severe renal disease,

Fig. 3.—A and B, Anteroposterior (A) and oblique (B) radiographs show characteristic erosion of dorsomedial aspect of metatarsal head (arrows) in gout, which is seen better on oblique projection. Note preservation of normal joint space.

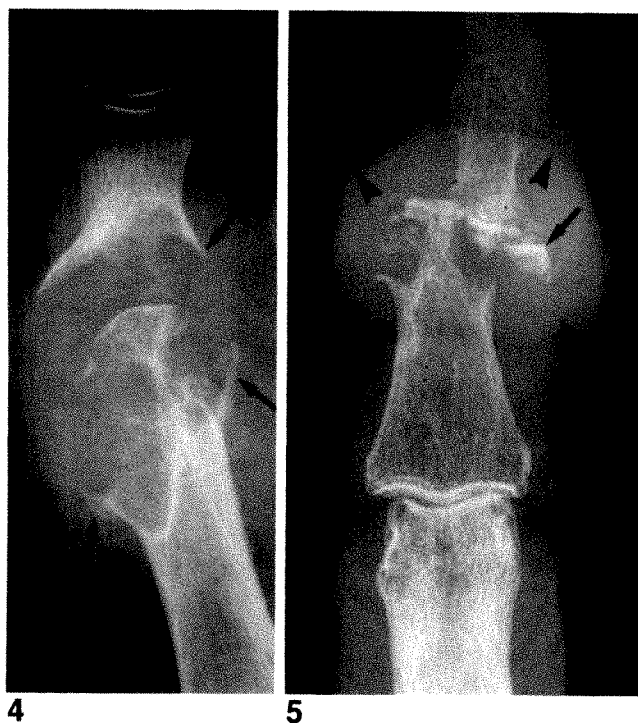
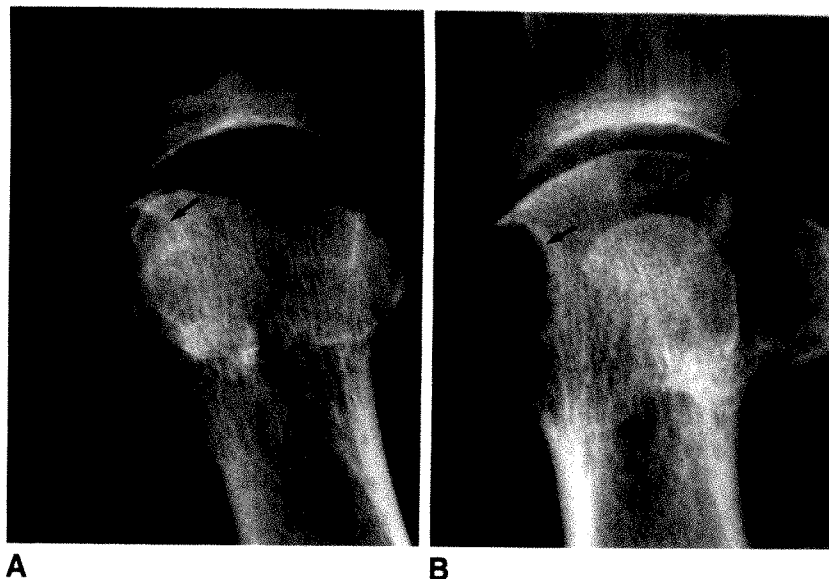


Fig. 4.—Radiograph shows well-defined erosions on both sides of joint and "overhanging margins" (arrows) in patient with gout.

Fig. 5.—Radiograph shows large tophus of distal interphalangeal joint (arrowheads) with marginal erosions and fragmentation (arrow) of subchondral bone in patient with gout who has a pathologic fracture.

simulating enchondromas or bone infarcts [81]. Chondrocalcinosis was noted in 10 of 31 gouty patients reported by Dodds and Steinbach [82], although subsequent reviews [74, 83] have shown no increased association between these two entities. Ossification of tophi is rare, typically occurring in the hand [74, 84].

Calcium Phosphate Crystals

A variety of crystals containing calcium, phosphate, and water can precipitate in human tissues, depending on conditions such as temperature, pH, and mineral concentration [85]. The body is vulnerable to pathologic deposits of these crystals, particularly articular soft tissues. Examples of these types of crystal deposits that have been identified in intraarticular and periarticular structures include calcium pyrophosphate ($\text{Ca}_2\text{P}_2\text{O}_7 \cdot 2\text{H}_2\text{O}$), calcium hydrogen phosphate dihydrate or brushite ($\text{CaHPO}_4 \cdot 2\text{H}_2\text{O}$), octacalcium phosphate ($\text{Ca}_8\text{H}_2(\text{PO}_4)_6 \cdot 5\text{H}_2\text{O}$), and tricalcium phosphate ($\text{Ca}_3(\text{PO}_4)_2 \cdot \text{H}_2\text{O}$).

The most stable form of these crystal species under in vivo conditions seems to be hydroxyapatite ($\text{Ca}_{10}(\text{PO}_4)_6 \cdot (\text{OH})_2$), which is a normal component of tooth enamel and bone [85]. However, hydroxyapatite deposition has also been linked to periarticular and intraarticular pathologic changes.

The following discussion concentrates on pyrophosphate and hydroxyapatite, which have been the most studied and are the best understood examples of these types of crystals linked to joint disease.

Calcium Pyrophosphate Dihydrate Deposition Disease

Clinical features.—Pyrophosphate deposition disease is the most common form of crystalline arthropathy [17], and although it has been linked to familial factors [86] and metabolic diseases [87], it is now apparent that its most common association is with aging [88]. It is estimated that approximately 5% of the adult population have pyrophosphate deposits in the knee joint at the time of death [19]; 25% of patients over the age of 80 have pyrophosphate crystals in articular cartilage or intervertebral disks [54].

Pyrophosphate deposition is responsible for a spectrum of clinical manifestations that can mimic gout, rheumatoid arthritis, a neuropathic joint, or osteoarthritis; however, asymptomatic crystal deposition probably is the most common

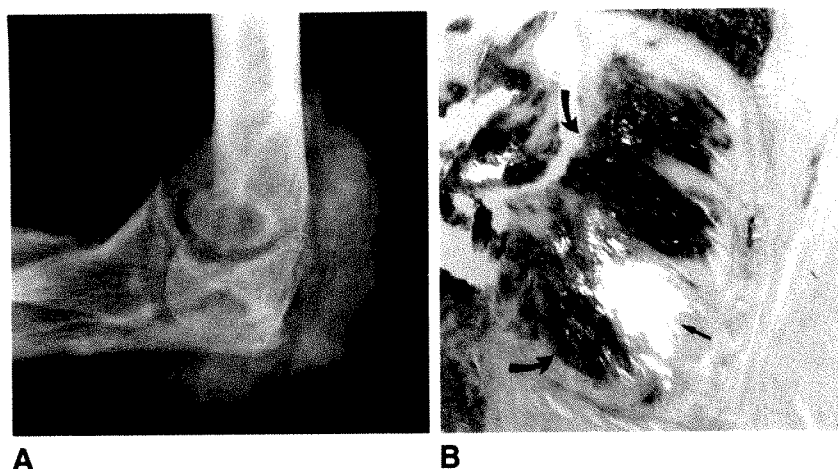


Fig. 6.—Calcification and mixed crystal deposition in gout.

A, Radiograph shows cloudlike calcification within large tophaceous deposit over olecranon of elbow.

B, Polarized light photomicrograph of synovial biopsy specimen shows both urate (straight arrow) and pyrophosphate (curved arrows) crystals. (x400)

clinical pattern, although this has not been documented definitively [19].

The term pseudogout should be reserved for self-limited attacks of acute arthritis simulating acute gout, but precipitated by pyrophosphate rather than urate crystals. Men are affected more often than women, and the presentation usually is monoarticular. The knee is the most common site of involvement; next are the wrist, hip, shoulder, and elbow. Attacks may be provoked by surgery, trauma, or illness [1].

Pseudorheumatoid arthritis accounts for about 5% of cases, with subacute attacks of joint inflammation lasting 4 weeks to several months [19]. A Charcot type of joint destruction in the absence of any neurologic deficit may develop in less than 2% of patients [1].

Joint disease simulating osteoarthritis, with or without acute inflammatory episodes, represents over 50% of cases. Most commonly affected is the knee; next are the wrists, pubic symphysis, metacarpophalangeal joints, and hips [1].

Pathogenesis of pyrophosphate deposition.—Unlike gout, which is a systemic metabolic disorder, pyrophosphate deposition is a local metabolic abnormality; the crystals are found in articular connective tissues only (with rare exceptions). The deposits occur mostly in hyaline and fibrocartilage [54]; the crystals that form in cartilage are localized strictly in the extracellular matrix [89].

The cause of pyrophosphate deposition is not completely understood; however, current data suggest the following factors in the pathogenesis. Early reports documented the accumulation of crystals about the chondrocytes in the midzone of the articular cartilage [89, 90]. A more recent study [91], which was an attempt to look at early deposition, showed crystal deposits at all levels of articular cartilage (i.e., superficial, midzone, and deep), always occurring above the tidemark, with two patterns of accumulation. The most common pattern is agglomerates of pyrophosphate that occupy the entire chondron, associated with necrosis of the chondrocyte; the less frequent pattern is scanty, small deposits at the edge of the chondron. In addition, focal morphologic abnormalities in the midzone of hyaline articular cartilage and a high ratio of keratan sulfate to chondroitin sulfate have been documented at the site of calcium pyrophosphate dihydrate

deposition [92, 93]; a high ratio occurs with aging and may facilitate the deposition of pyrophosphate crystals in cartilage [94]. A recent histochemical study showed specific staining characteristics of chondrocytes around developing pyrophosphate deposits in both hereditary and sporadic forms of the disease, as well as focal areas of chondroid metaplasia in hyaline and fibrocartilage, tendon, ligament, and synovium [95]. These observations suggest an interrelationship in which there is initial focal nucleation of crystals that subsequently agglomerate, with an abnormal matrix facilitating deposition [54].

The mechanism for excess accumulation of pyrophosphate relates to factors that increase its formation and decrease its destruction [54]. Plasma pyrophosphate and urinary excretion of pyrophosphate are normal in patients with pyrophosphate crystal deposition [19]. However, pyrophosphate is a ubiquitous product of intracellular biosynthesis and is produced by ectoenzymes on the plasma membrane of cells, particularly chondrocytes synthesizing glycosaminoglycans [85, 96]. Specifically, the pyrophosphate-generating enzyme, nucleoside triphosphate pyrophosphohydrolase, has been identified on the cell membrane of chondrocytes, with increased levels of activity in the synovial fluid of patients with pyrophosphate deposition and osteoarthritis that correlate with the pyrophosphate concentration [93, 95, 97–99]. In addition, there is some evidence that lower levels of alkaline phosphatase and inorganic pyrophosphatase (which are responsible for enzymatic breakdown of pyrophosphate) are present in cartilage from patients with pyrophosphate crystal deposition compared with normal and osteoarthritic cartilage [100]. These abnormalities thus would favor the accumulation of pyrophosphate in cartilage. It is further speculated that the cartilage matrix may impede movement of macromolecules (i.e., pyrophosphatase) more than small anions (i.e., pyrophosphate), thus protecting pyrophosphate from diffusion of pyrophosphatase elaborated by the chondrocyte and synovium, with pyrophosphate depositing in the abnormal extracellular matrix previously mentioned [54].

Divalent ions have been shown to inhibit pyrophosphatase, contributing to pyrophosphate accumulation [54]. This likely accounts for the association of pyrophosphate crystals with

entities such as hemochromatosis and hyperparathyroidism, in which excess iron and calcium, respectively, inhibit pyrophosphatase. A similar relationship may exist between the copper excess associated with Wilson disease and pyrophosphate deposition, but this association has not been proved [1, 87]. Conversely, pyrophosphate deposition has been documented in association with hypomagnesemia, resulting from a dependence of pyrophosphatase activity on magnesium ions and from a direct relationship between magnesium concentration and calcium pyrophosphate solubility [101, 102].

Radiographic features.—The presence of calcium in pyrophosphate crystals creates an important role for radiography in the identification of pyrophosphate deposits. Although the calcific deposits occur primarily in hyaline and fibrocartilage, they also may be identified in other articular and periarticular structures, including synovium, joint capsule, tendon, ligament, and periarticular soft tissues (Fig. 7) [23]. However, pseudogout also has been observed in the absence of chondrocalcinosis [103].

The most common sites for fibrocartilage deposition are the meniscus of the knee, the triangular cartilage and meniscus of the wrist, the pubic symphysis, the acetabular and glenoid labra, and the anulus fibrosus. A screening examination consisting of frontal views of the knees, symphysis pubis, and both wrists would reportedly detect 100% of patients with chondrocalcinosis [104]. Hyaline cartilage deposits occur most often in the knee, wrist, hip, and elbow [104].

Deposits in synovium and joint capsule usually occur in association with chondrocalcinosis, and are most often seen in the wrist, knee, and metacarpophalangeal and metatarsophalangeal joints [23, 104]. The Achilles, triceps, and quadriceps are the most common sites of deposition in tendons, whereas calcification in the intercarpal space is the most frequent site for deposition in ligaments [23, 104].

Structural changes due to pyrophosphate deposition simulating degenerative joint disease have been described and referred to as pyrophosphate arthropathy (Fig. 8). The changes usually are bilateral but not always associated with

articular calcification [1]. Certain features differentiate this arthropathy from typical degenerative disease [104–106]. The affected articular sites are unusual compared with osteoarthritis, commonly involving the wrist, metacarpophalangeal joints, elbow, and glenohumeral joints. Specific patterns of joint disease have been observed, such as the patellofemoral joint of the knee, radiocarpal joint of the wrist, and talonavicular joint of the foot (Fig. 9). Other suggestive features of this arthropathy are prominent subchondral cysts and progressive articular bone destruction with intraarticular loose bodies resembling neuropathic joint disease. Osteophyte formation may be prominent in some cases but is an inconsistent finding. Involvement of the lumbar spine and sacroiliac joints also has been described [107].

The development of tophaceous deposits of pyrophosphate has been reported, manifest in periarticular locations of the hand and temporomandibular joint [108–110]. The entity is characterized by chondroid metaplasia and calcification related to massive pyrophosphate deposition, and may be associated with episodes of pseudogout.

Hydroxyapatite Crystal Deposition Disease

Clinical features.—Hydroxyapatite serves as the prototype of several basic calcium phosphate crystals (e.g., hydroxyapatite, octacalcium phosphate, and tricalcium phosphate) associated with periarticular deposition. Like the crystals already discussed, chronic and asymptomatic (lanthanic) deposits of hydroxyapatite are common; however, hydroxyapatite has also been described in association with recurrent, painful deposits in periarticular soft tissues [111–113]. Thus, for reasons that are not fully established, hydroxyapatite crystals can stimulate acute inflammation; phagocytosis of hydroxyapatite aggregates has been observed in these instances [17]. Furthermore, over the past 10 years, hydroxyapatite has been linked increasingly to intraarticular deposition, with evidence of acute and chronic manifestations [113–116].

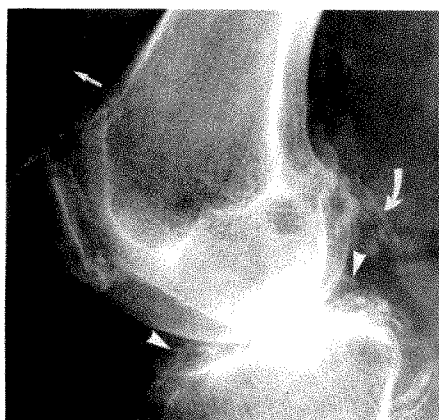


Fig. 7.—Radiograph shows chondrocalcinosis (arrowheads) with deposition of calcium pyrophosphate dihydrate in synovium and joint capsule (curved arrow) and linear calcifications in quadriceps tendon (straight arrow) of knee.



Fig. 8.—Radiograph shows joint-space loss in wrist with subchondral sclerosis and soft-tissue swelling in absence of chondrocalcinosis. Joint aspiration revealed numerous pyrophosphate crystals; culture was negative.

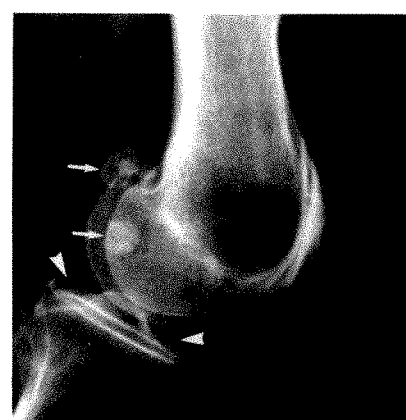


Fig. 9.—Radiograph shows narrowing of patellofemoral joint space with scalloping of anterior femoral cortex, associated with intraarticular osseous bodies (arrows) and chondrocalcinosis (arrowheads).

The study of this group of crystals has been more difficult because of the lack of a readily available method for its identification, primarily because of the nonbirefringence and the very small size of the crystals [117]. Periarticular deposition is encountered most often in the shoulder, especially the tendons of the rotator cuff. Numerous other sites of deposition have also been reported, including the elbow, wrist, hand, foot, ankle, hip, knee, and neck. Acute attacks of inflammation, presumably resulting from release of crystal deposits, generally are monoarticular and self-limited, lasting several days [118]. Occasionally, multiple joints are affected, with simultaneous involvement in one-third of cases and successive involvement in two-thirds [74]. Chronic deposits may be accompanied by mild pain and local tenderness, although they may be asymptomatic [117].

In 1976, with the use of electron microscopy and elemental analysis of phosphorus to calcium ratios, Dieppe et al. [114] first demonstrated hydroxyapatite crystals in the joints of six patients diagnosed with osteoarthritis. Three of these patients had recurrent episodes of acute arthritis associated with joint effusions. Schumacher et al. [115] confirmed this initial observation by identifying hydroxyapatite crystals in the joints of patients with osteoarthritis; like urate and pyrophosphate, hydroxyapatite was noted to undergo phagocytosis, more often by mononuclear cells than by neutrophils, and was found embedded in granular material consisting of immunoglobulins and other proteins. Intraarticular hydroxyapatite crystals have been described in the shoulder, knee, hip, wrist, proximal and distal interphalangeal joint, elbow, and metatarsophalangeal joint [116, 118, 119].

The prevalence and significance of hydroxyapatite crystals with osteoarthritis are not known. Schumacher et al. [65] detected crystals in 44 of 100 osteoarthritic effusions, and Dieppe et al. [120] found hydroxyapatite in nine of 34 unselected osteoarthritic fluids. Hydroxyapatite crystals have also been identified in the cartilage of patients with osteoarthritis [121]. The coexistence of other crystals, particularly pyrophosphate, with hydroxyapatite in osteoarthritic joints (mixed crystal deposition disease) has been reported [122], with some patients developing severe joint damage [123].

The "Milwaukee shoulder," described by McCarty et al. [61, 62], is of particular interest in this regard. They documented a destructive arthropathy in the shoulders of elderly women, characterized by hydroxyapatite crystals in the synovial fluid associated with high levels of activated collagenase and neutral protease enzymes. These findings were accompanied by complete rotator cuff tears in seven of the eight patients. A previous laboratory study by Werb and Reynolds [124] on rabbit synovial fibroblasts showed release of these same enzymes resulting from endocytosis of particulates by the cells; McCarty et al. [125–127] suggested a similar process in the Milwaukee shoulder, and subsequent investigation tends to confirm this hypothesis. A similar type of destructive osteoarthritis has been described by Dieppe et al. [128]; involvement of the knees and other large joints is now recognized [129]. The pathogenesis of the Milwaukee shoulder thus appears to result from a vicious cycle in which the synovial lining cells phagocytose the crystals and particulate collagens, resulting in enzyme release and joint damage,

which in turn contribute to the release of more crystals and collagen [130]. Associated factors that appear to predispose to the development of the Milwaukee shoulder include trauma, overuse, neurologic abnormalities, recurrent dislocations, and renal failure [131].

A recent article [132] reported elevated levels of pyrophosphate in the synovial fluid of patients with basic calcium phosphate deposition, as well as elevated nucleoside triphosphate pyrophosphohydrolase enzyme activity, similar to that described with pyrophosphate deposition. The highest levels of nucleoside triphosphate pyrophosphohydrolase and pyrophosphate were obtained from patients with the Milwaukee shoulder syndrome, suggesting a correlation with the severity of disease. Nearly 75% of the patients with pyrophosphate deposition also had basic calcium phosphate crystals in their synovial fluid, compatible with mixed crystal deposition disease, suggesting solubilization of cartilage as the cause of these abnormalities. However, hydroxyapatite and pyrophosphate formation appear to be mutually exclusive, with metachronous development in adjacent locations, or sequential dissolution of pyrophosphate leading to hydroxyapatite formation [91, 133, 134].

Radiographic features.—The radiologic features of periarticular hydroxyapatite deposition are variable and should be interpreted in the context of the clinical situation. Acute calcific periarthritis can be confused with other entities, such as gout, infection, and fracture; therefore, radiography plays an important role in diagnosis [113]. Sequential radiographs show an initially distinct calcific deposit that changes in appearance to a fluffy, diffuse radiodensity, often followed by disappearance of the calcification related to crystal shedding and phagocytic removal of the crystals (Fig. 10) [112, 113]. Similar periarticular calcification can be seen in the presence of chronic symptoms and in the absence of symptoms [1]. This type of deposit also may be encountered secondary to underlying diseases such as renal failure, collagen vascular disease, and neurologic injury, and after steroid injection [131, 135].

Only a small percentage of patients with intraarticular deposits of hydroxyapatite have calcifications demonstrable on radiographs. When present, the calcifications may be seen in the joint space or periarticularly and generally are not associated with the cartilage and meniscal type of calcification seen with pyrophosphate [116]. Osteoarthritic changes may be present and tend to correlate in severity with the amount of apatite deposition.

Hydroxyapatite deposition should be included in the differential diagnosis of a destructive arthropathy of the shoulder, particularly in women with evidence of an associated rotator cuff tear (Fig. 11) [61]. Likewise, hydroxyapatite deposition is a diagnostic possibility with any severe neuropathic joint [74]. In the knee, typical involvement of the lateral compartment is seen in conjunction with sclerosis, articular collapse, and valgus deformity [129].

Summary

A wide variety of crystals have been described in association with articular disease, and previous investigations have shown a well-defined role for crystals in the pathogenesis of self-limited attacks of acute arthritis.

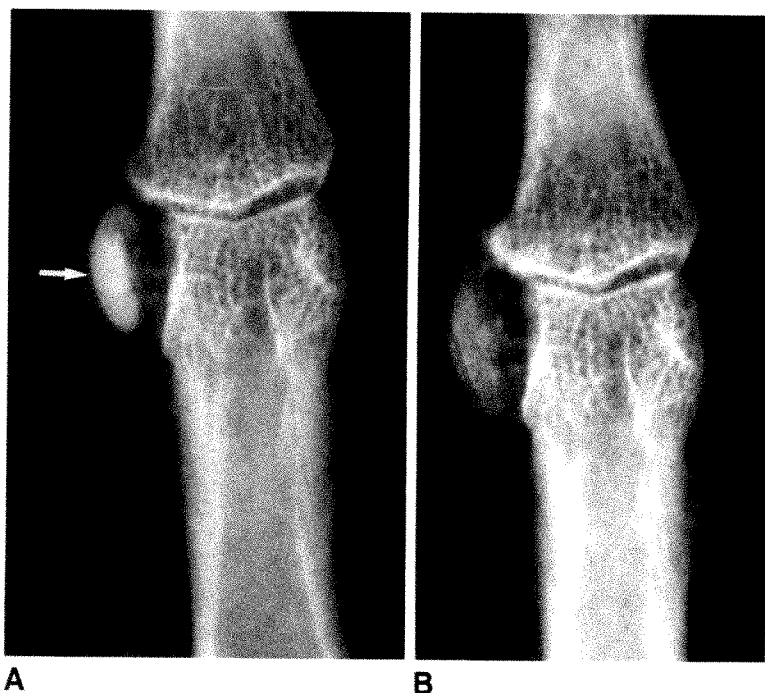


Fig. 10.—A, Radiograph shows dense calcification along radial aspect of proximal interphalangeal joint (arrow) in patient with calcific periarthritis who had acute pain, swelling, and erythema locally.

B, Follow-up 9 days later shows diffusion and decreased density of calcification, correlating with clinical improvement.



Fig. 11.—Radiograph shows destructive changes in proximal humerus with poorly defined areas of calcification and bony fragmentation in patient with Milwaukee shoulder. Numerous hydroxyapatite crystals were identified by electron microscopy of specimen obtained by joint aspiration.

Crystals have also been linked to chronic joint disease, but the relationship between the two is controversial. Diagnostic imaging is important in the assessment of arthropathies, particularly because it provides information about gross pathologic changes that cannot be readily determined by other methods, especially in early disease. Therefore, clinical studies correlating diagnostic imaging with laboratory and histologic findings may ultimately help to elucidate the true relationship between crystals and chronic joint disease.

REFERENCES

1. Resnick D, Niwayama G. *Diagnosis of bone and joint disorders*, 2nd ed. Philadelphia: Saunders, 1988:1619-1764, 1804-1814
2. Crystal structure. In: *McGraw-Hill encyclopedia of science and technology*, 6th ed. New York: McGraw-Hill, 1987:583-589
3. Gait RL. *Exploring minerals and crystals*. Toronto: McGraw-Hill Ryerson, 1972:27-35
4. Dieppe P, Calvert P. *Crystals and joint disease*. London: Chapman & Hall, 1983:24-26
5. Phelps P, Steele AD, McCarty DJ Jr. Compensated polarized light microscopy. *JAMA* 1968;203:508-512
6. McCarty DJ. Synovial fluid. In: McCarty DJ, ed. *Arthritis and allied conditions*, 9th ed. Philadelphia: Lea & Febiger, 1979:60-65
7. Sydenham T. A treatise on gout and dropsy. In: Latham RG, trans. *The works of Thomas Sydenham, M.D.*, Vol. 2. London: Sydenham Society, 1850:124
8. Garrod AB. *The nature and treatment of gout and rheumatic gout*. London: Walton & Maberley, 1859
9. Freudweiler M. Experimentelle Untersuchungen über das Wesen der Gichtknoten. *Eur J Clin Invest* 1901;63:266-355
10. Fiehl G. Zur Anatomie der Gicht. *Wien Klin Wochenschr* 1897;10:761-763
11. Faires JS, McCarty DJ. Acute arthritis in man and dog after intrasynovial injection of sodium urate crystals. *Lancet* 1962;2:682-685
12. McCarty DJ. Phagocytosis of urate crystals in gouty synovial fluid. *Am J Med Sci* 1962;243:288-295
13. McCarty DJ, Hollander JL. Identification of urate crystals in gouty synovial fluid. *Ann Intern Med* 1961;54:452-460
14. McCarty DJ, Kohn NN, Faires JS. The significance of calcium phosphate crystals in the synovial fluid of arthritis patients: the pseudogout syndrome. I. Clinical aspects. *Ann Intern Med* 1962;56:711-737
15. Kohn NN, Hughes RE, McCarty DJ, Faires JS. The significance of calcium phosphate crystals in the synovial fluid of arthritis patients: the pseudogout syndrome. II. Identification of crystals. *Ann Intern Med* 1962;56:738-745
16. Dieppe P, Doherty M, Macfarlane D. Crystal-related arthropathies. *Ann Rheum Dis* 1983;42[suppl]:1-3
17. Pritzker KPH. Crystal-associated arthropathies: what's new in old joints. *J Am Geriatr Soc* 1981;28:439-445
18. Schumacher HR Jr. Pathogenesis of crystal-induced synovitis. *Clin Rheum Dis* 1977;3:105-131
19. McCarty DJ. Calcium pyrophosphate dihydrate deposition disease—1975. *Arthritis Rheum* 1976;19:275-285
20. Brochner-Mortensen K. Gout. *Ann Rheum Dis* 1958;17:1-18
21. Agudelo CA, Schumacher HR. The synovitis of acute gouty arthritis: a light electron microscopic study. *Hum Pathol* 1973;4:265-279
22. McCarty DJ. Pathogenesis and treatment of crystal-induced inflammation. In: McCarty DJ. *Arthritis and allied conditions*. Philadelphia: Lea & Febiger, 1979:1245-1261
23. Resnick D, Niwayama G, Goergen TG, et al. Clinical, radiographic and pathologic abnormalities in calcium pyrophosphate dihydrate deposition disease (CPPD): pseudogout. *Radiology* 1977;122:1-15
24. McCarty DJ. The gouty toe: a multifactorial condition. *Ann Intern Med* 1977;86:234-238
25. Bennett RM, Lehr JR, McCarty DJ. Crystal shedding and acute pseudogout: an hypothesis based on a therapeutic failure. *Arthritis Rheum* 1976;19:93-97

26. Rodnan GP. The pathogenesis of aldermanic gout: procataratic role of fluctuations in serum urate concentration in gouty arthritis provoked by feast and alcohol. *Arthritis Rheum* 1980;23:737
27. Healey LA. Epidemiology of hyperuricemia. *Arthritis Rheum* 1975;18:709-712
28. Schumacher HR, Fishbein P, Phelps P, Tse R, Krauser R. Comparison of sodium urate and calcium pyrophosphate crystal phagocytosis by polymorphonuclear leucocytes: effects of crystal size and other factors. *Arthritis Rheum* 1975;18:783-792
29. Mandel NS. The structural basis of crystal-induced membranous lysis. *Arthritis Rheum* 1976;19[suppl]:439-445
30. Pritzker KPH, Zahn CE, Nyburg SC, Luk SC, Houghton JB. The ultrastructure of urate crystals in gout. *J Rheumatol* 1978;5:7-18
31. Kozin F, McCarty DJ. Protein adsorption to monosodium urate, calcium pyrophosphate dihydrate and silica crystals. *Arthritis Rheum* 1976;19[suppl]:433-438
32. Ginsberg MH, Kozin F, Chow D, May J, Skosey JL. Adsorption of polymorphonuclear leukocyte lysosomal enzymes to monosodium urate crystals. *Arthritis Rheum* 1977;20:1538-1542
33. Cheung HS, Bohan S, Kozin F. Kinetics of collagenase and neutral protease release by neutrophils to microcrystalline sodium urate. *Connect Tissue Res* 1983;11:78-85
34. Burt HM, Jackson JK. Monosodium urate monohydrate crystal induced changes in membrane fluidity: a fluorescence polarization study. *J Rheumatol* 1988;15:1144-1151
35. Terkeltaub R, Ginsburg MH. Molecular mechanisms of gouty arthritis: new insights into an old disease. *Pathol Immunopathol Res* 1984;3:386-396
36. Burt HM, Jackson JK. Characterization and membranolytic effects of triclinic calcium pyrophosphate dihydrate crystals. *J Rheumatol* 1987;14:968-973
37. Rajan KT. Observations on phagocytosis of urate crystals by polymorphonuclear leucocytes. *Ann Rheum Dis* 1975;34:54-61
38. Schumacher HR, Phelps P. Sequential changes in human polymorphonuclear leukocytes after urate crystal phagocytosis: an electron microscopy study. *Arthritis Rheum* 1968;11:145-150
39. Wallingford WR, McCarty DJ. Differential membranolytic effects of microcrystalline sodium urate and calcium pyrophosphate dihydrate. *J Exp Med* 1971;133:100-112
40. Weissman G, Rita GA. Molecular basis of gouty inflammation: interaction of monosodium urate crystals with lysosomes and liposomes. *Nature* 1972;240:167-172
41. Hasselbacher P. Crystal-protein interactions in crystal-induced arthritis. In: Weissmann G, ed. *Advances in inflammation research*, Vol. IV. New York: Raven, 1982:25-44
42. Terkeltaub R, Tenner AJ, Kozin F, Ginsberg MH. Plasma protein binding by monosodium urate crystals: analysis by two-dimensional gel electrophoresis. *Arthritis Rheum* 1983;26:775-783
43. Brandt KD. The effects of synovial hyaluronate on the ingestion of monosodium urate crystals by leukocytes. *Clin Chim Acta* 1974;55:307-315
44. Terkeltaub R, Curtiss LK, Tenner AJ, Ginsberg MH. Lipoproteins containing apoprotein B are a major regulator of neutrophil responses to monosodium urate crystals. *J Clin Invest* 1984;73:1719-1730
45. Phelps P, Andrews R, Rosenbloom J. Demonstration of chemotactic factor in human gout: further characterization of occurrence and structure. *J Rheumatol* 1981;8:889-894
46. Ward PA, Zvaifler NJ. Complement derived leukotactic factors in inflammatory synovial fluids of humans. *J Clin Invest* 1971;50:606-616
47. Rae SE, Davidson EM, Smith MJH. Leukotriene B₄, an inflammatory mediator in gout. *Lancet* 1982;2:122-138
48. Terkeltaub RA, Ginsberg MH. The inflammatory reaction to crystals. *Rheum Dis Clin North Am* 1988;14:353-364
49. Atkins E, Duff GW, Malawista SE. The fever of gout: urate crystals as endogenous stimulators of endogenous pyrogen. *Clin Res* 1983;31:551A
50. Malawista SE, Duff GW, Atkins E, Cheung HS, McCarty DJ. Crystal-induced endogenous pyrogen production. *Arthritis Rheum* 1985;28:1039-1046
51. Schumacher HR. Pathology of the synovial membrane in gout. *Arthritis Rheum* 1975;18:771-782
52. Schumacher HR. The synovitis of pseudogout: electron microscopic observations. *Arthritis Rheum* 1968;11:426-435
53. Pritzker KPH, Renlund RC, Cheng P-T. Which comes first: crystals or osteoarthritis? A study of surgically removed femoral heads. *J Rheumatol* 1983;10:38-39
54. Pritzker KPH. Calcium pyrophosphate crystal arthropathy: a biomineralization disorder. *Hum Pathol* 1986;17:543-545
55. Schumacher HR, Gibilisco P, Reginato A, Cherian V, Gordon G. Implications of crystal deposition in osteoarthritis. *J Rheumatol [Spec Issue]* 1983;9:40-41
56. Wilkins E, Dieppe P, Maddison P, Evison G. Osteoarthritis and articular chondrocalcinosis in the elderly. *Ann Rheum Dis* 1983;42:280-284
57. Gordon GV, Villanueva T, Schumacher HR, Gohel V. Autopsy study correlating degree of osteoarthritis, synovitis and evidence of articular calcification. *J Rheumatol* 1984;11:681-686
58. Zitnan D, Sitaj S. Natural course of articular chondrocalcinosis. *Arthritis Rheum* 1976;19:363-390
59. Markel SF, Hart WR. Arthropathy in calcium pyrophosphate dihydrate crystal deposition disease: pathologic study of 12 cases. *Arch Pathol Lab Med* 1982;106:529-533
60. Menkes CK, Simon F, Delrieu F. Destructive arthropathy in chondrocalcinosis articularis. *Arthritis Rheum* 1976;19:329-348
61. McCarty DJ, Halverson PB, Carrera GF, Brewer BJ, Kozin F. "Milwaukee shoulder": association of microspheroids containing hydroxyapatite crystals, active collagenase, and neutral protease with rotator cuff defects. I. Clinical aspects. *Arthritis Rheum* 1981;24:464-473
62. Halverson PB, Cheung HS, McCarty DJ, Garancis J, Mandel N. "Milwaukee shoulder": association of microspheroids containing hydroxyapatite crystals, active collagenase, and neutral protease with rotator cuff defects. II. Synovial fluid studies. *Arthritis Rheum* 1981;24:474-483
63. Sokoloff L, Varma AA. Chondrocalcinosis in surgically resected joints. *Arthritis Rheum* 1988;31:750-755
64. Gibilisco PA, Schumacher HR Jr, Hollander JL, Soper KA. Synovial fluid crystals in osteoarthritis. *Arthritis Rheum* 1985;28:511-515
65. Schumacher HR, Gordon G, Paul H, et al. Osteoarthritis, crystal deposition and inflammation. *Semin Arthritis Rheum* 1981;11:116-119
66. Halverson PB, McCarty DJ. Identification of hydroxyapatite crystals in synovial fluid. *Arthritis Rheum* 1979;22:389-395
67. Wyngaarden JB, Kelley WN. *Gout and hyperuricemia*. New York: Grune & Stratton, 1976:213-226
68. Wyngaarden JB. Gout. In: Wyngaarden JB, Smith LH Jr, eds. *Cecil textbook of medicine*. Philadelphia: Saunders, 1988:1161-1170
69. Kelley WN, Fox IH. Gout and related disorders of purine metabolism. In: Kelley WN, Harris ED Jr, Ruddy S, Sledge CB, eds. *Textbook of rheumatology*. Philadelphia: Saunders, 1985:1359-1398
70. Boss GR, Seegmiller JE. Hyperuricemia and gout: classification, complications and management. *N Engl J Med* 1979;300:1459-1468
71. Grahame R, Scott JT. Clinical survey of 354 patients with gout. *Ann Rheum Dis* 1970;29:461-468
72. Silberberg R. Diseases of joints. In: Kissane JM, ed. *Anderson's pathology*, 8th ed. St. Louis: Mosby, 1985:1838-1840
73. Holmes EW. Clinical gout and pathogenesis of hyperuricemia. In: McCarty DJ. *Arthritis and allied conditions*. Philadelphia: Lea & Febiger, 1985:1445-1480
74. Watt I. Radiology of the crystal-associated arthritides. *Ann Rheum Dis* 1983;42[suppl]:73-80
75. Bloch C, Hermann G, Yu T-F. A radiologic reevaluation of gout: a study of 2,000 patients. *AJR* 1980;134:781-787
76. Barthelemy CR, Nakayama DA, Carrera GF, Lightfoot RW Jr, Wortmann RL. Gouty arthritis: a prospective radiographic evaluation of sixty patients. *Skeletal Radiol* 1984;11:1-8
77. Watt I, Middlemiss H. The radiology of gout. *Clin Radiol* 1975;26:27-36
78. Martel W. The overhanging margin of bone: a roentgenologic manifestation of gout. *Radiology* 1968;91:755-756
79. Wright JT. Unusual manifestations of gout. *Australas Radiol* 1966;10:365-374
80. Schumacher HR Jr. Pathology of crystal deposition diseases. *Rheum Dis Clin North Am* 1988;14:269-288
81. Resnick D, Broderick TW. Intraosseous calcifications in tophaceous gout. *AJR* 1981;137:1157-1161
82. Dodds WJ, Steinbach HL. Gout associated with calcification of cartilage. *N Engl J Med* 1966;275:745-749

83. Good AE, Rapp R. Chondrocalcinosis of the knee with gout and rheumatoid arthritis. *N Engl J Med* 1967;277:286-290
84. Lichtenstein L, Scott HW, Levin MH. Pathologic changes in gout: survey of 11 necropsied cases. *Am J Pathol* 1956;32:871-895
85. Dieppe P, Calvert P. *Crystals and joint disease*. London: Chapman & Hall, 1983:189-222
86. Zitnan D, Sitaj S. Mnohopocetna familiaria Kalcifaciz artikularchy chrupek. *Bratisl Lek Listy* 1958;28:217-224
87. Hamilton EBD. Diseases associated with CPPD deposition disease. *Arthritis Rheum* 1976;19[suppl]:353-357
88. Doherty M. Pyrophosphate arthropathy: recent clinical advances. *Ann Rheum Dis* 1983;42[suppl]:38-44
89. Bjelle AO. Morphological study of articular cartilage in pyrophosphate arthropathy (chondrocalcinosis articularis or calcium pyrophosphate dihydrate crystal deposition disease). *Ann Rheum Dis* 1972;31:449-456
90. Reginato AJ, Schumacher HR, Martinez VA. The articular cartilage in familial chondrocalcinosis: light and electron microscopic study. *Arthritis Rheum* 1974;17:977-992
91. Pritzker KPH, Cheng P-T, Renlund RC. Calcium pyrophosphate crystal deposition in hyaline cartilage: ultrastructural analysis and implications for pathogenesis. *J Rheumatol* 1988;15:828-835
92. Bjelle AO. The glycosaminoglycans of articular cartilage in calcium pyrophosphate dihydrate (CPPD) crystal deposition disease. *Calcif Tissue Int* 1973;12:37-46
93. Bjelle A. Cartilage matrix in hereditary pyrophosphate arthropathy. *J Rheumatol* 1981;8:959-964
94. Hunter GK, Grynpas MD, Cheng P-T, Pritzker KPH. Effect of glycosaminoglycans on calcium pyrophosphate crystal formation in collagen gels. *Calcif Tissue Int* 1987;41:164-170
95. Ishikawa K. Chondrocytes that accumulate proteoglycans and inorganic pyrophosphate in the pathogenesis of chondrocalcinosis. *Arthritis Rheum* 1985;28:118-119
96. Ryan LM, Wortmann RL, Karas B, McCarty DJ Jr. Cartilage nucleoside triphosphate (NTP) pyrophosphohydrolase. I. Identification as an ectoenzyme. *Arthritis Rheum* 1984;27:404-409
97. Muniz O, Pelletier J-P, Martel-Pelletier J, Morales S, Howell DS. NTP pyrophosphohydrolase in human chondrocalcinotic and osteoarthritic cartilage: I. Some biochemical characteristics. *Arthritis Rheum* 1984;27:186-192
98. Howell DS, Martel-Pelletier J, Pelletier J-P, Morales S, Muniz O. NTP pyrophosphohydrolase in human chondrocalcinotic and osteoarthritic cartilage. II. Further studies on histologic subcellular distribution. *Arthritis Rheum* 1984;27:193-199
99. Rachow JW, Ryan LM, Adenosine triphosphate pyrophosphohydrolase and pyrophosphatase activities in human synovial fluids. *Clin Res* 1983;31:806A
100. Tenenbaum J, Muniz O, Schumacher HR, Good AE, Howell DS. Comparison of phosphohydrolase activities from articular cartilage in calcium pyrophosphate deposition disease and primary osteoarthritis. *Arthritis Rheum* 1981;24:492-500
101. Cheng P-T, Pritzker KPH. The effect of calcium and magnesium on calcium pyrophosphate crystal formation in aqueous solutions. *J Rheumatol* 1981;8:772-782
102. Bennett RM, Lehr JR, McCarty DJ. Factors affecting the solubility of calcium pyrophosphate dihydrate crystals. *J Clin Invest* 1975;56:1571-1579
103. Resnick D, Utsinger PD. The wrist arthropathy of "pseudogout" occurring with and without chondrocalcinosis. *Radiology* 1974;113:633-641
104. Resnik CS, Resnick D. Calcium pyrophosphate dihydrate crystal deposition disease. *Curr Probl Diagn Radiol* 1982;11:7-40
105. Martel W, Champion CK, Thompson GR, Carter TL. A roentgenologically distinctive arthropathy in some patients with the pseudogout syndrome. *AJR* 1970;109:587-605
106. Genant HK. Roentgenographic aspects of calcium pyrophosphate dihydrate crystal deposition disease (pseudogout). *Arthritis Rheum* 1976;19:307-328
107. Martel W, McCarty DK, Solsky MA, et al. Further observations on the arthropathy of calcium pyrophosphate crystal deposition disease. *Radiology* 1981;141:1-15
108. Ling D, Murphy WA, Kyriakos M. Tophaceous pseudogout. *AJR* 1982;138:162-165
109. Leisen J. Calcium pyrophosphate dihydrate deposition disease: tumorous form. *AJR* 1982;138:962
110. Pritzker KPH, Phillips H, Luk SC, Kovern IH, Kiss A, Houpt JB. Pseudotumor of temporomandibular joint: destructive calcium pyrophosphate dihydrate arthropathy. *J Rheumatol* 1976;3:70-81
111. Pinals RS, Short CL. Calcific periarthritis involving multiple sites. *Arthritis Rheum* 1966;9:566-574
112. McCarty DJ Jr, Gatter RA. Recurrent acute inflammation associated with focal apatite crystal deposition. *Arthritis Rheum* 1966;9:804-819
113. Fam AG, Pritzker KPH, Stein JL, Houpt JB, Little AH. Apatite associated arthropathy: a clinical study of 14 cases and 2 patients with calcific bursitis. *J Rheumatol* 1979;6:461-471
114. Dieppe PA, Crocker P, Huskisson EC, Willoughby DA. Apatite deposition disease: a new arthropathy. *Lancet* 1976;1:266-269
115. Schumacher HR, Somlyo AP, Tse RL, Maurer K. Arthritis associated with apatite crystals. *Ann Intern Med* 1977;87:411-416
116. Schumacher HR, Cherian PV, Reginato AJ, Bardin T, Rothfuss S. Intra-articular apatite crystal deposition. *Ann Rheum Dis* 1983;42[suppl]:54-59
117. Paul H, Reginato AJ, Schumacher HR. Alizarin red S-staining as a screening test to detect calcium compounds in synovial fluid. *Arthritis Rheum* 1983;26:191-200
118. Faure G, Daculsi G. Calcified tendinitis: a review. *Ann Rheum Dis* 1983;42[suppl]:49-53
119. Schumacher HR, Miller JL, Ludvico C, Jessar RA. Erosive arthritis associated with apatite crystal deposition. *Arthritis Rheum* 1981;24:31-37
120. Dieppe PA, Crocker PR, Corke CF, Doyle DV, Huskisson EC, Willoughby DA. Synovial fluid crystals. *Q J Med* 1979;48:533-553
121. Ali SY. Apatite-type crystal deposition in arthritic cartilage. *Scan Electron Microsc* 1985;4:1555-1566
122. Doyle DV, Dieppe PA, Crocker PR, Ibe K, Willoughby DA. Mixed crystal deposition in an osteoarthritic joint. *J Pathol* 1977;123:1-4
123. Dieppe PA, Doyle DV, Huskisson EC, Willoughby DA, Crocker PR. Mixed crystal deposition disease and osteoarthritis. *Br Med J* 1978;1:150
124. Werb Z, Reynolds JJ. Stimulation by endocytosis of the secretion of collagenase and neutral protease from rabbit synovial fibroblasts. *J Exp Med* 1974;140:1482-1497
125. McCarty DJ, Lehr JR, Halverson PB. Crystal populations in human synovial fluid: identification of apatite, octacalcium phosphate and tricalcium phosphate. *Arthritis Rheum* 1983;26:1220-1224
126. Halverson PB, Garancis JC, McCarty DJ. Histopathological and ultrastructural studies of synovium in Milwaukee shoulder syndrome: a basic calcium phosphate crystal arthropathy. *Ann Rheum Dis* 1984;43:734-741
127. Cheung HS, Halverson PB, McCarthy DJ. Release of collagenase, neutral protease and prostaglandins from culture mammalian synovial cells by hydroxyapatite and calcium pyrophosphate dihydrate crystals. *Arthritis Rheum* 1981;24:338-344
128. Dieppe PA, Doherty M, Macfarlane DG, Hutton CW, Bradfield JW, Watt I. Apatite associated destructive arthritis. *Br J Rheumatol* 1984;23:84-91
129. Halverson PB, McCarty DJ, Cheung HS, Ryan LM. Milwaukee shoulder syndrome: eleven additional cases with involvement of the knee in seven (basic calcium phosphate crystal deposition disease). *Semin Arthritis Rheum* 1984;14:36-44
130. Cheung HS, McCarty DJ. Mechanisms of connective tissue damage by crystals containing calcium. *Rheum Dis Clin North Am* 1988;14:365-376
131. Halverson PB, McCarty DJ. Clinical aspects of basic calcium phosphate crystal deposition. *Rheum Dis Clin North Am* 1988;14:427-439
132. Rachow JW, Ryan LM, McCarty DJ, Halverson PB. Synovial fluid inorganic pyrophosphate concentration and nucleotide pyrophosphohydrolase activity in basic calcium phosphate deposition arthropathy and Milwaukee shoulder syndrome. *Arthritis Rheum* 1988;31:408-413
133. Cheng P-T, Pritzker KPH. Pyrophosphate/phosphate ion interaction. *J Rheumatol* 1983;10:769-777
134. Hearn PR, Guiland-Cumming PF, Russell RGG. Effect of orthophosphate and other factors on the crystal growth of calcium pyrophosphate in vitro. *Ann Rheum Dis* 1983;42[suppl]:101
135. Bonavita JA, Dalinka MK, Schumacher HR Jr. Hydroxyapatite deposition disease. *Radiology* 1980;134:621-625

Book Review

Fundamentals of Skeletal Radiology. By Clyde A. Helms. Philadelphia: Saunders, 1989. \$35, soft cover

This short, soft-cover text is a unique and refreshing approach to the teaching of skeletal radiology that has been written primarily for medical students, interns, and residents. Its masterful, creative, and unconventional author uses his unorthodox approach to instruction in what undoubtedly will be an exceptionally popular book among its targeted readership. As stated in the preface, the book is not intended to be a reference but rather a compendium of practical lessons, pearls, and differential diagnoses that may be thought of appropriately as the Cliff's Notes or the Classic Comic Book of skeletal radiology, thus filling a void in the existing literature.

The book begins untraditionally with a brief chapter on unnecessary examinations. This is followed sequentially by individual sections considering benign cystic lesions, malignant bone tumors, trauma, arthritis, and metabolic bone disease. A unique chapter entitled "'Don't Touch' Lesions" is provided also. The book concludes with an appendix consisting of extremely useful lists of differential diagnoses, which are repeated inside the front and back covers for easy reference. A comprehensive index affords ready access to information on specific topics throughout the text. Throughout the book, illustrations are numerous and of exquisite quality and include newer imaging techniques such as CT and MR imaging when appropriate. A number of useful tables and line drawings are provided also.

Positive aspects of the book include the unique teaching style of its author, its superb visual components, its bold and attractive typography, and its handy physical size, which is amenable to both cover-to-cover reading and on-the-spot reference during a working day. Short, pertinent reference lists are provided at the end of each chapter for readers desiring additional information on specific topics. The book has no identifiable negative aspects in attempting to meet its stated purpose. It is fair to say that those who read the work in its entirety will not know everything that there is to know about

skeletal radiology, but they will know the most important practical concepts.

With regard to other comparable texts on skeletal radiology, the book most closely resembles the second edition of *Basic Bone Radiology* by Griffiths in purpose, scope, and format. From the standpoint of comprehensiveness, the book does not compete with the soon-to-be-published condensed version of Resnick and Niwama's second edition of *Diagnosis of Bone and Joint Disorders*, but it is certainly more enjoyable to read.

The book is well worth its affordable price and would be an extremely valuable personal acquisition for any physician-in-training who aspires to acquire basic skills in skeletal radiologic interpretation. Although targeted to this audience, the book also would be a useful and quick review for radiologists, orthopedic surgeons, rheumatologists, and other physicians already in practice. The book would be a good library acquisition for any academic department or institution in which the training of physicians is a high priority. As pointed out in the preface, mastery of the book will allow more comprehensive tests to be handled more easily, and it is an excellent review for radiology board examinations. Indeed, I predict that the book's bold red cover will become a familiar site at the Louisville, KY, airport during many Mays to come.

In summary, the author is to be complimented highly for constructing a truly effective and infinitely practical instructive tool that should find widespread use for many years to come. Having heard the author lecture and having read this and many of his previous outstanding publications, I can wholeheartedly echo the words of Hideyo Minagi, who wrote the book's foreword: "Clyde Helms can teach!"

David J. Sartoris
University of California, San Diego, Medical Center
San Diego, CA 92103

Review Article

Current Status of Temporomandibular Joint Imaging for the Diagnosis of Internal Derangements

Phoebe A. Kaplan¹ and Clyde A. Helms²

Temporomandibular joint (TMJ) pain and dysfunction are common and important clinical problems. With the recent advances in imaging technology, radiologists have made major contributions to the understanding of TMJ diseases. The purpose of this article is to review the anatomy of the TMJ and to put into perspective the relative merits of each imaging technique (conventional radiography and tomography, scintigraphy, CT, MR imaging, and arthrography) as it pertains to diagnosing internal derangement, the most common disorder of the joint.

Normal Anatomy and Function

The anatomy of the TMJ can be understood best by considering the osseous, soft-tissue, and functional anatomy separately as described by Murphy [1] (Fig. 1).

The TMJ is a synovial articulation formed by the condyle of the mandible and the glenoid (mandibular) fossa and articular eminence of the temporal bone at the base of the skull. The glenoid fossa and eminence form a smooth sigmoid curve. The condyle is approximately twice as long in the mediolateral dimension as it is in the anteroposterior dimension and is oriented perpendicular to the ramus of the mandible. The joint surfaces are smooth, and the condyle is located symmetrically in the fossa with a uniform joint space. The articular surfaces of the joint are covered by fibrocartilage rather than hyaline cartilage.

The condyle is held in place relative to the temporal bone by muscles, ligaments, and the joint capsule. The most sig-

nificant soft-tissue structure is the dense fibrous disk (or meniscus). The disk is interposed between the condyle and temporal bone, completely separating the joint into two joint spaces (superior and inferior) that do not communicate. The superior joint space is about three times as large as the inferior space. The inferior space is arbitrarily divided into anterior and posterior recesses. The ovoid disk is thin centrally with a thickened peripheral ridge. The anterior and posterior ridges of the disk are called the anterior and posterior bands; the posterior band is larger than the anterior. The anterior band of the disk is in continuity with the anterior margin of the condyle and the articular eminence, as well as with the joint capsule. The disk is attached to the neck of the condyle medially and laterally and to the superior head of the lateral pterygoid muscle anteromedially. The posterior band of the disk is continuous with the highly vascular and well-innervated elastic connective tissue called the bilaminar zone (or posterior attachment). The superior portion of the bilaminar zone attaches to the posterior wall of the mandibular fossa; the inferior portion attaches to the posterior condyle.

Both TMJs function synchronously. Motion of the disk is closely coordinated with condylar motion. The synovial recesses formed in the superior and inferior joint spaces are redundant, allowing normal motion of the condyle and disk. The normal position of the disk with the mouth closed is with the apex of the condyle immediately subjacent to the posterior band of the disk. The initial phase of mouth opening is a hinge action (rotation about a horizontal axis that passes through the condyles). The hinge action is a function of the inferior

Received October 6, 1988; accepted after revision December 16, 1988.

¹ Department of Radiology, University of Nebraska Medical Center, 42nd and Dewey Ave., Omaha, NE 68105. Address reprint requests to P. A. Kaplan.

² Department of Radiology, University of California, San Francisco, San Francisco, CA 94143.

AJR 152:697-705, April 1989 0361-803X/89/1524-0697 © American Roentgen Ray Society

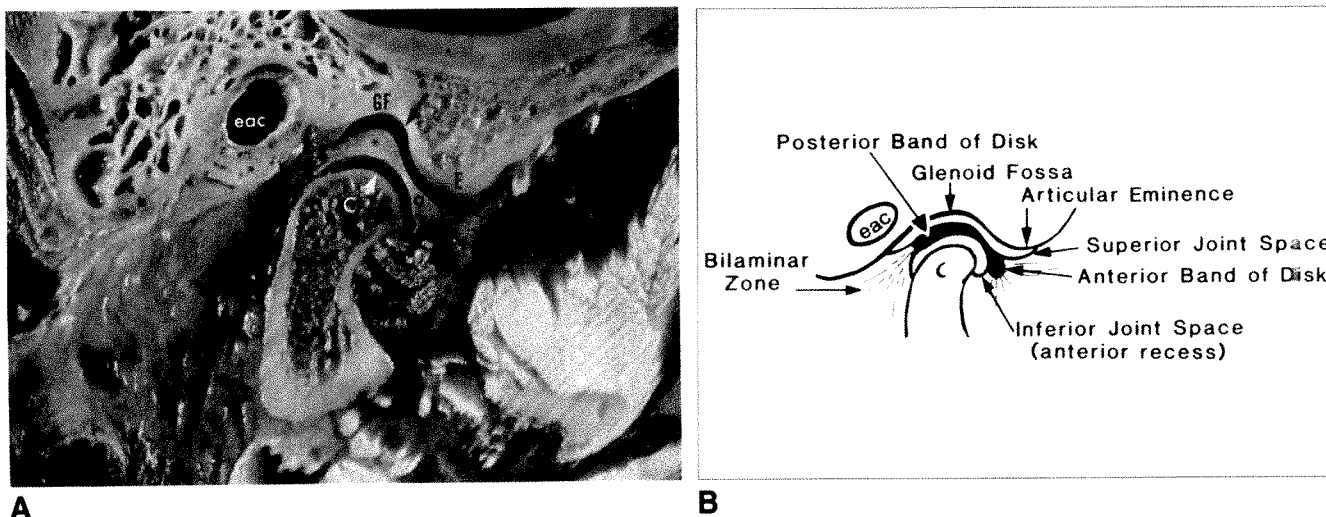


Fig. 1.—A and B, Cadaveric section (A) and diagram (B) of normal osseous and soft-tissue structures of temporomandibular joint. Inferior joint space (white arrow); superior joint space (black arrow); posterior band of disk (*). eac = external auditory canal; GF = glenoid fossa; E = articular eminence; C = condyle; o = anterior band.

joint space as the condyle rotates forward so that it articulates with the thin central zone of the disk. The second action of mouth opening occurs from deformation of the superior joint space and consists of anterior translation of the condyle under the eminence. With incremental mouth opening, there is a coordinated relationship among disk, condyle, and eminence with the posterior band of the disk coming to rest posterior to the condyle. These relationships reverse as the mouth closes. All interactions are smooth and continuous.

Internal Derangement

Various disorders of the TMJ occur; however, the most common is internal derangement [1–4]. Internal derangement is defined as an abnormal relationship (subluxation or dislocation) of the disk relative to the condyle, fossa, and articular eminence. The disk usually is displaced anteriorly, but it may also sublux medially, laterally, or (rarely) posterior to the condyle [5].

Internal derangement occurs in up to 28% of the adult population [3]. Despite the prevalence of this disorder, it has been poorly understood and investigated until only recently. Historically, derangements of the TMJ were initially described in the 1830s and in 1887 by Cooper (cited in [1]) and Annandale [6], respectively. Other scattered reports mainly concerned surgery of the TMJ, but not until 1951 did another investigator publish work concerning possible causes of internal derangement [7], and this study passed relatively unnoticed. In the late 1960s, Laskin [8] popularized the myofascial pain-dysfunction syndrome (facial pain originating in soft-tissue structures without a detectable origin or defect). It was believed that secondary anatomic abnormalities of the TMJ could occur as a result of the syndrome. An organic basis for TMJ pain and dysfunction was supported by the work of Farrar [9] and Farrar and McCarty [10] in the 1970s and has since been confirmed by numerous investigators.

Internal derangement of the TMJ is three to five times more common in women than in men. Symptoms usually occur in early adulthood, typically in the fourth decade of life [11]. No predisposing factors are found in most patients; however, a history of trauma just before the onset of symptoms can be elicited in approximately 25% of patients [12]. A traumatic origin is more common in men and children than in women. About one-third of the trauma-induced derangements are iatrogenic, usually from procedures that hyperextend the jaw such as endoscopy, third molar tooth extraction, and tonsillectomy [12]. A loss of elasticity of the bilaminar zone and other ligaments that control disk position and function is probably the underlying defect regardless of the cause of the ligamentous laxity.

Internal derangement is classically divided into three categories progressing from least to most severe (Fig. 2) [1, 2, 11]. These categories are (1) anterior displacement with reduction of the disk to normal position with mouth opening, (2) anterior displacement without reduction of the disk to normal position with mouth opening, and (3) anterior displacement with perforation of the disk. Frequently patients have a history typical of sequential progression from one category to the next.

Anterior displacement of the disk with reduction usually causes joint noise (popping, clicking) with or without associated pain. The disk is displaced (usually anteriorly but may also be subluxed medially or laterally) with the mouth closed and returns to normal position as the mouth opens and the click is heard. The click occurs during both opening and closing (reciprocal clicking) but is much louder during opening. The click is a result of friction between the posterior band of the disk and the condyle as they move in opposite directions and the disk returns to normal position relative to the condyle. In general, the later the click during mouth opening, the more severe the derangement (greater loss of elasticity of the bilaminar zone). The extent of mouth opening is normal in this category.

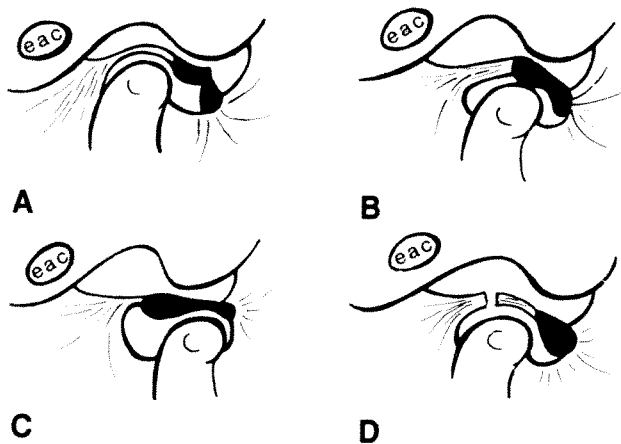


Fig. 2.—Disk position in internal derangement. eac = external auditory canal.

A, Anteriorly displaced disk with both anterior and posterior bands in front of condyle.

B, Disk reduces to normal position as mouth opens. Friction between condyle and posterior band passing in opposite directions is one cause of audible click.

C, Disk after reduction to normal position when mouth is completely open.

D, Displaced disk with perforated bilaminar zone.

Disk displacement without reduction occurs when the loss of elasticity is so great the disk is unable to return to normal position with the condyle and remains displaced anterior to it. The displaced disk forms a physical barrier to the condyle and there is limited anterior translation. The condyle continuously impacts on the innervated bilaminar zone and causes pain. Generally, these patients have limited mouth opening ("closed lock"), with the midline of the mandible deviated to the abnormal side. Usually no joint noise is heard because the posterior band of the disk does not reduce over the condyle into normal position.

Chronic disk displacement without reduction may lead to a perforated disk. The perforation usually is in the bilaminar zone or occasionally is in the disk. These patients have pain and limitation of mouth opening. Paradoxically, mouth opening may be normal because of chronic stretching of the bilaminar zone. Chronic disk displacement can lead to a thickened disk that may not function properly even if it is in the correct position. Degenerative joint disease generally occurs in those with a perforated disk as bone articulates with bone. Joint noise may be present owing to secondary degenerative joint disease.

Pain in patients with internal derangement may occur directly over the TMJ or in the neck, ear, face, or head. Clicking of a TMJ may occur in patients without a displaced disk reducing to normal position [13]. Similarly, restricted mouth opening may have numerous causes other than a displaced disk. Diagnostic imaging is important to confirm a clinically suspected diagnosis, particularly because many disorders may cause similar symptoms.

TMJ Imaging

Conventional radiography is well suited to evaluation of the osseous structures of the TMJ [11, 14–16]. However, more

detailed osseous anatomy may be seen via other methods such as CT or conventional tomography. Several different views are required to show all aspects of the joint. The location of the TMJ in the base of the skull with numerous superimposed structures makes imaging difficult and often not reproducible without meticulous attention to positioning and technique. The transcranial lateral view (opened and closed mouth) is the most valuable (Figs. 3A and 3B). It shows the joint in profile as well as showing the range of motion of the joint. It is obtained by angling the tube or the patient's head so the TMJ is projected above the structures in the base of the skull. A small variation in positioning can significantly alter the appearance of the condyle. Special positioning units have been developed to standardize radiographs and alleviate such problems [17–19].

Supplementary views used to depict the osseous anatomy include the Towne and submentovertex projections, which show the medial and lateral poles of the condyle as well as different portions of the cortical surface. Panoramic radiographs, which are used routinely for evaluation of the mandible and dentition, can also be used to show the TMJs simultaneously and in a near-lateral projection. Most physicians believe that the transcranial lateral radiographs are most useful and may use the other views mentioned in unusual circumstances to clarify the anatomy. The Towne projection is probably the most valuable view to supplement the transcranial lateral view.

Conventional tomography shows osseous anatomy with even greater detail than plain films. For many years before sectional imaging and TMJ arthrography, tomography was used as the main technique for radiographic evaluation of the joint [1, 11, 20, 21].

The abnormalities that can be seen on conventional radiographs and tomograms in patients who have internal derangement are infrequent and nonspecific [11]. Limitation of anterior translation of the condyle can be shown, but the cause is not evident. Degenerative joint disease with osteophytosis, flattening, and sclerosis of the condyle is virtually diagnostic of a displaced and perforated disk; unfortunately, this is present in only a few patients and is a late manifestation of the disease process (Fig. 3D). A radiographic feature of degenerative joint disease that may occur first is an erosion of the apex of the condyle (Fig. 3C). The cause of the erosion is not clear from the plain films, and similar radiographic changes occur with infection or inflammatory arthritides, or as a consequence of a condylar shaving surgical procedure.

TMJ arthrography was pioneered by Norgaard [22] in the mid 1940s, but it did not become popular until the late 1970s. There are several related methods of performing TMJ arthrography [23–30]. In general, the patient is prepared in a sterile fashion and injected with a local anesthetic as for any arthrogram. A small-gauge needle is inserted into the posterior recess of the lower joint space via a preauricular approach, and about 0.5 ml of contrast media are injected under fluoroscopic guidance. Some radiologists also inject the superior joint space followed by arthrotomography. If tomography is not used, routine static images are obtained. Videofluoroscopy to document the dynamic function of the joint is essential in all patients [29, 31]. The only true contraindication to

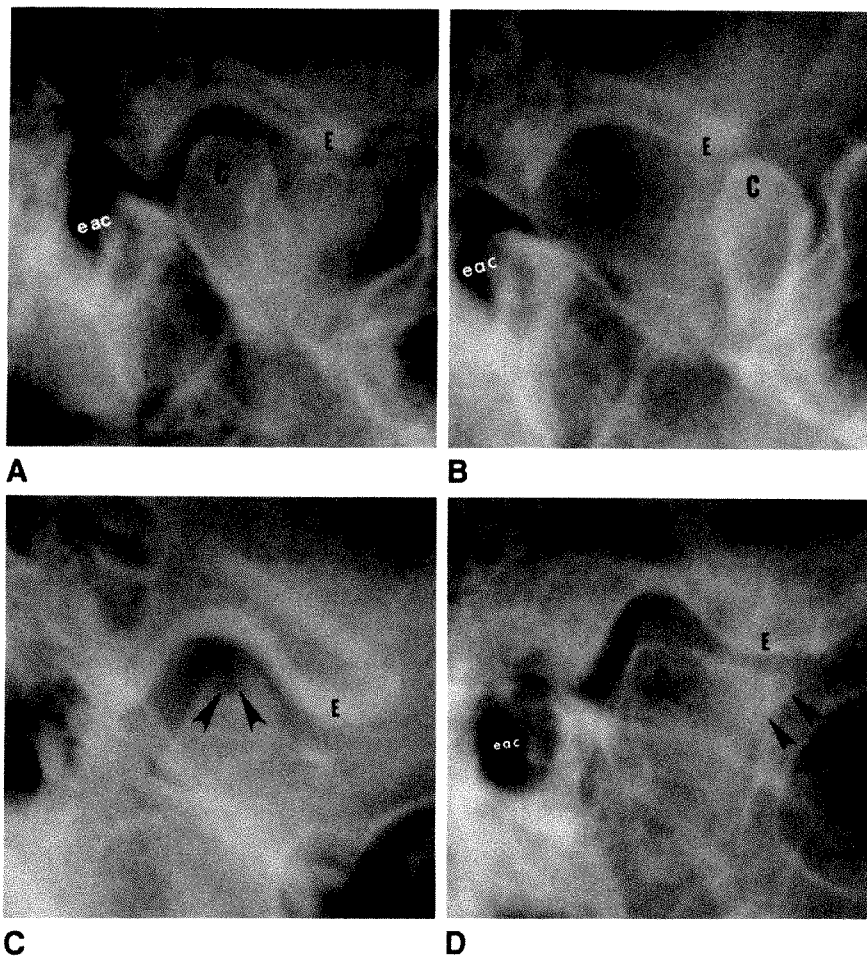


Fig. 3.—A and B, Plain films show normal temporomandibular joint in closed-mouth (A) and open-mouth (B) positions. Note central location of condyle (C) within glenoid fossa with mouth closed (A). Apex of condyle passes to, or slightly beyond, eminence (E) with mouth fully opened (B). eac = external auditory canal.

C and D, Plain films show degenerative changes that occur as a result of internal derangement. C shows an erosion of condyle (arrowheads) that not only may occur with derangements but also may be seen with other entities, such as infection and arthritis. D shows a patient with a displaced and perforated disk who developed a degenerative osteophyte (arrowheads) on anterior condyle.

arthrography is a local skin infection that might contaminate the joint.

The elements that can be evaluated by arthrography are the osseous anatomy; disk position, size, or shape; presence of a perforated disk; reduction of the disk to normal position; dynamic anatomy; and range of motion (Fig. 4).

In the closed position, the posterior recess has a thin curvilinear configuration that conforms to the outline of the condyle. The anterior recess is larger and forms a teardrop configuration directed obliquely downward. The contrast material outlines the undersurface of the disk. The superior aspect of the anterior recess may be straight and smooth or else concave owing to the impression made by the anterior band of the disk, which varies in size in different people [32]. As the mouth opens, the condyle and disk move together in a smooth and coordinated manner. The anterior recess decreases in size until it is a small, crescent-shaped collection of contrast material collapsed against the anterior condyle. Simultaneously, the posterior recess enlarges and the superior aspect becomes concave because of the impression made by the posterior band of the disk. The condyle articulates with the posterior band while the mouth is closed and with the thin central zone during all stages of mouth opening. All relationships reverse as the mouth closes.

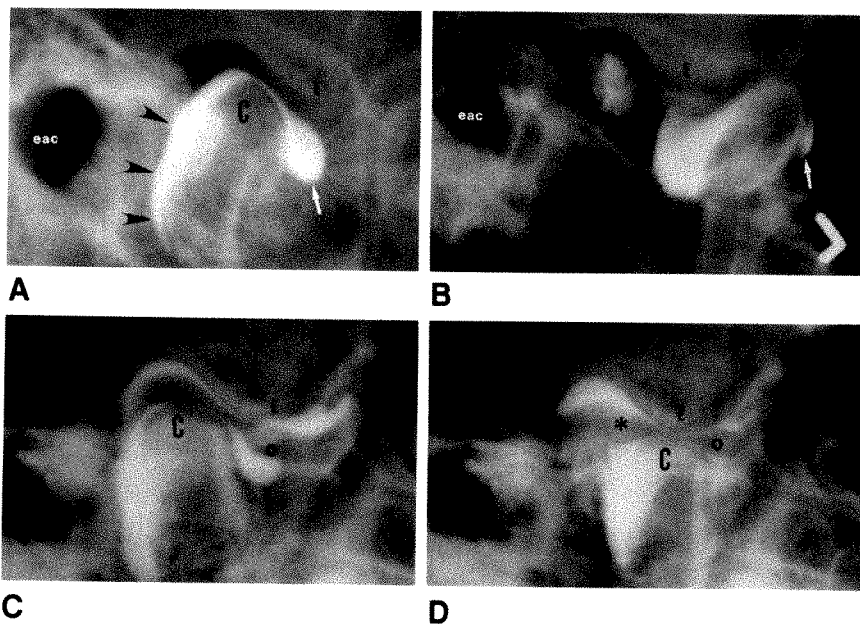
When there is internal derangement, the disk is displaced anterior to the condyle. The posterior band creates a large concave impression on the anterior recess that is diagnostic of disk displacement [1, 11, 23–28]. There is commonly a biconcave appearance of the anterior recess formed by both the anterior and posterior bands while the disk is folded on itself in the thin central zone. The anterior recess is larger in patients with disk displacement than in normal patients (Fig. 5).

As the mouth opens, the concavity formed by the posterior band on the anterior recess is accentuated until the posterior band and condyle pass over one another in opposite directions, creating a friction rub manifest as an audible click. Irregular movements with sudden changes in configuration of contrast material are seen at fluoroscopy as this occurs. As soon as the disk has reduced to normal position, the arthrographic appearance is identical to that of a normal joint. If, however, the disk does not reduce with mouth opening, there is a persistent concave defect on the anterior recess, and this frequently is associated with limited translation of the condyle. The most severe category of derangements occurs when the disk is displaced without reduction and has a perforation. A perforation is diagnosed by the simultaneous appearance of contrast material in both the superior and inferior joint spaces

Fig. 4.—Normal temporomandibular joint arthrography.

A and B, Closed-mouth (A) and open-mouth (B) arthrograms, with contrast material in inferior joint space only, show teardrop-shaped anterior recess that becomes very thin when mouth opens (arrows). Conversely, posterior recess is very thin with mouth closed and increases in anteroposterior dimension with opening (arrowheads). Top of posterior recess is concave from posterior band of disk impinging on it. E = eminence; eac = external auditory canal; C = condyle.

C and D, Arthrograms show normal position of disk relative to condyle with mouth closed (C) and open (D) with contrast material in superior and inferior joint spaces. Condyle is directly subjacent to posterior band (*) with mouth closed and articulates with thin central zone of disk during all phases of mouth opening. Anterior recess (arrow). o = anterior band.



when contrast material was injected into the inferior space only.

Arthrography has also been reported as being useful in determining the cause of postoperative symptoms and intra-articular adhesions, and in developing splints for treatment of mild derangements [33–36].

Despite the high yield of diagnostic information from TMJ arthrography, the technique has been criticized because it is more technically demanding to learn to perform than other kinds of arthrography, and it is an invasive procedure. Despite these contentions, the morbidity from TMJ arthrography has been reported to be minimal if performed by someone experienced with the procedure [37, 38]. Investigations have showed also that postprocedural discomfort could be diminished further by using nonionic contrast agents [37, 39].

Scintigraphy with single-photon emission CT (SPECT) reportedly detects alterations of the TMJ [40]. Unfortunately, the findings are nonspecific, indicating only that a biomechanical or inflammatory process exists but not specifying the nature or precise location of the alteration. Because of these inherent limitations, scintigraphy plays no practical role in the diagnosis or management of TMJ disorders. It may be valuable in detecting other causes of facial pain unrelated to the TMJ.

CT has been shown to be an accurate method of diagnosing displaced menisci [41–47]. It requires some technical expertise, depending on whether the axial or direct sagittal technique is used, but both methods are highly accurate and easily learned. CT scanners are widely available throughout the world; therefore, availability is not an issue. No morbidity is associated with CT scanning of the TMJ, and radiation dose is thought to be relatively low.

The direct axial technique requires that 15–20 thin-section slices be obtained of the TMJs with subsequent sagittal reformations. The identity or “blink” mode is then used to help differentiate the tissue densities anterior to the condyle. A

density anterior to the condyle that is greater than that of normal muscle is consistent with an anteriorly displaced disk (Fig. 6). Multiple sagittal slices through each condyle are examined for this increased density, and the medial aspect of each condyle usually has the majority of positive findings because the lateral pterygoid muscle tends to pull the disk anteromedially.

The direct sagittal technique requires the patient's head to be turned sideways in the gantry so that the slices run sagittally through the condyles; thus, reformations are unnecessary. Approximately 10% of patients cannot tolerate this position and are unable to be studied with this technique. The images obtained from the direct sagittal technique are superior to those obtained with the axial method with reformations; however, no increase in diagnostic accuracy has been reported. By imaging with the direct sagittal technique, the lens of the eye is often seen, which allows an inordinate amount of radiation exposure (4–6 rad [40–60 mGy]) to a radiosensitive organ.

Regardless of which technique is used, the evaluation of the bony structures is superb with CT. Early degenerative disease is seen easily and can be localized as to medial or lateral in position on the condylar head. The cost of a CT examination is roughly twice that of unilateral arthrography. The accuracy of diagnosing a displaced disk is about the same as with arthrography, and there is no morbidity. A perforation of the disk cannot be diagnosed with CT; however, many clinicians do not alter their treatment on the basis of the presence or absence of a perforation. Likewise, joint dynamics cannot be obtained with CT but are not believed to be essential for many clinicians. Many centers have replaced arthrography with CT scanning of the TMJ and have subsequently supplanted CT with MR.

MR imaging is highly accurate in diagnosing TMJ meniscus displacement [48–56]. Because of its ability to image hydrogen protons, information about the state of disk hydration

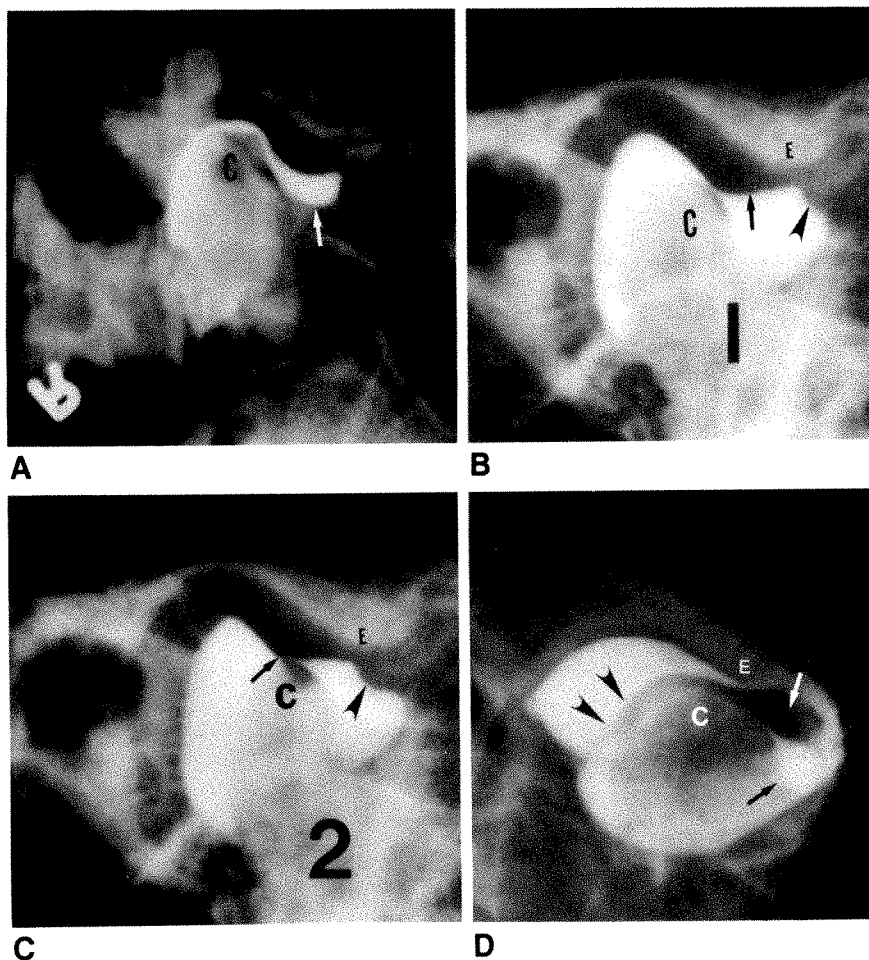


Fig. 5.—Abnormal temporomandibular joint arthrography. E = eminence; C = condyle.

A, Displaced disk has caused large concave defect on superior aspect of anterior recess. Recess (arrow) is also abnormally elongated.

B, Biconcave defect of anterior recess is formed by displaced anterior (arrowhead) and posterior (arrow) bands that are folded at thin central zone.

C, As mouth opens, there is a clicking noise as condyle and posterior band (arrow) pass over one another going in opposite directions. Anterior band (arrowhead).

D, Limited anterior translation of condyle with mouth opening occurs because of displaced disk that does not reduce (white arrow). Contrast medium simultaneously fills superior and inferior joint spaces, indicative of perforated disk. Anterior recess (black arrow); bilaminar zone (arrowheads).

can perhaps be ascertained and used to classify the degree of disk abnormality. This is done routinely in imaging the lumbar spine and may be useful in imaging the TMJ. The histopathology of the disk is similar to that of the lumbar spine disk; hence, one might expect similar MR appearances [57]. Both structures are made up of proteoglycans, which break down under stress. The normal lumbar spine disk has high signal on T2 weighting, as does the normal TMJ disk (Fig. 7).

As a result of technical innovations available in the past few years, MR of small anatomic areas such as the TMJ has improved dramatically, allowing higher spatial resolution and a greater signal-to-noise ratio. Not only can the position of the disk be accurately ascertained, but the size and shape of the disk as well as its signal characteristics can be seen (Figs. 8 and 9). Bony changes can be evaluated also, although not with the clarity afforded by conventional tomography and CT. Use of certain fast-scan techniques in conjunction with an automatic mouth-opening device makes a dynamic MR study possible [58]. It remains to be seen if this information is truly useful to the clinicians treating these patients.

MR scanning techniques vary among different examiners and with different types of magnets; however, most agree that surface coils are necessary for an acceptable study. Most investigators state that only T1-weighted images are necessary, and most recommend only sagittal images. If only T1-

weighted sagittal images are acquired, the study can be performed rapidly, thus reducing the time and cost of the examination. T2-weighted images can be obtained rapidly with gradient-echo refocusing techniques. These afford evaluation of joint fluid and the state of hydration of the disk (Fig. 10). Although this information does not currently alter treatment, it may eventually be valuable. In most centers, a bilateral study with closed- and open-mouth positions can be performed in 30 min. The cost for this examination is about equal to that of a CT examination, or roughly twice that of unilateral arthrography.

There is some debate as to whether full open-mouth images are necessary. It is generally accepted that disk reduction can be determined clinically in most cases. Also, whether a disk reduces and at which degree of opening it does reduce seems to be quite variable from week to week in many patients; therefore, the information obtained during the MR study may be different 1 week later when the clinician examines the patient. Furthermore, these patients experience pain and difficulty in wide mouth opening; therefore, when placed in a wide-open-mouth position for 10–15 min, they often have muscle spasm and pain, resulting in motion and degradation of the image. For these reasons, many radiologists study patients in closed-mouth and partial-open-mouth (before a click) positions. The partial-open-mouth position

Fig. 6.—A, Sagittally reformatted CT scan through right temporomandibular joint with identity or blink mode reveals increased soft-tissue density anterior to condyle (arrow), which is consistent with anteriorly displaced disk.

B, Similar image in another patient has no increased soft-tissue density anterior to condyle. This is consistent with normally positioned disk.

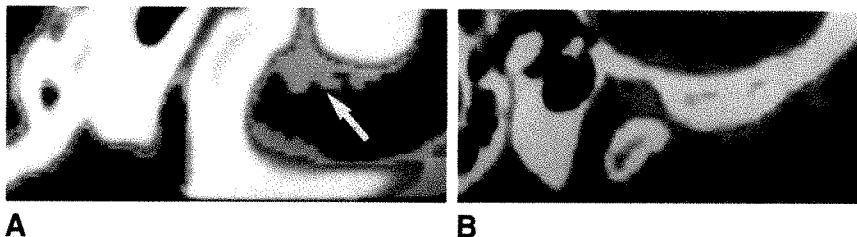


Fig. 7.—A, T1-weighted image in normal temporomandibular joint shows disk in normal position with some intermediate signal in posterior band (arrow).

B, Same joint imaged with gradient refocusing shows posterior band to have high signal, consistent with normal hydration. A small amount of increased signal can also be appreciated in remainder of disk.

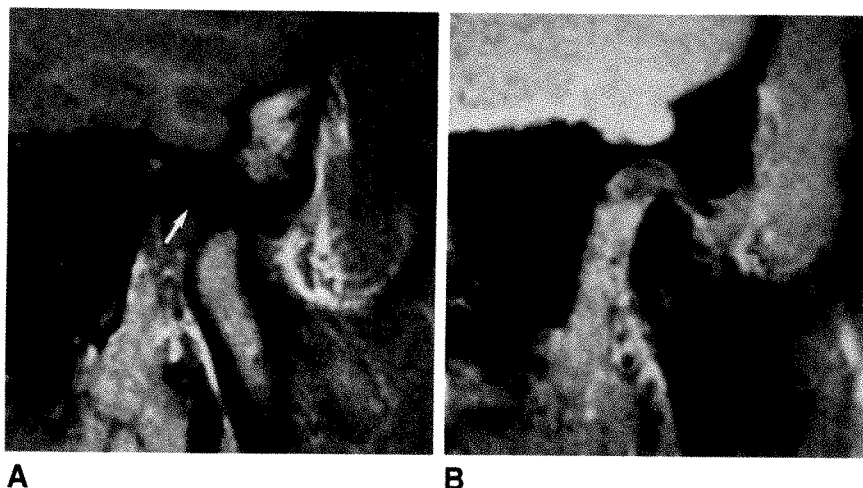
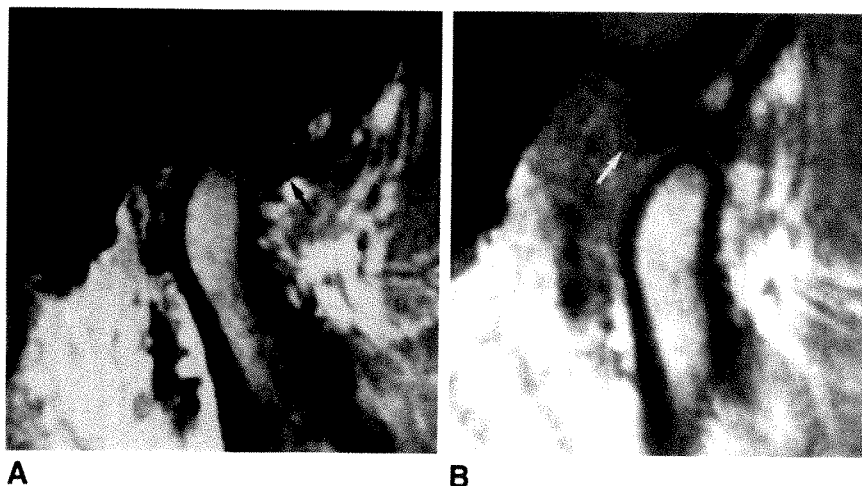


Fig. 8.—A, T1-weighted sagittal MR image in normal individual with mouth closed. Posterior band is seen as low-signal-intensity structure above apex of condyle; anterior band (arrow) is just anterior to condyle. Thin intermediate zone is not clearly seen but is between two most closely opposed cortical surfaces of temporal bone and condyle. Anterior is to the right.

B, Same as in A with mouth open. Condyle is translated anteriorly. Posterior band of disk (arrow) is just posterior to condyle and has intermediate signal. Thin intermediate zone remains between two closely opposed cortical surfaces of temporal bone and condyle.



removes the condyle from the glenoid fossa slightly and allows the disk to be seen with greater clarity than does the closed-mouth position.

As MR of the TMJ continues to be investigated, additional imaging parameters undoubtedly will be recommended and evaluated. Too many variables exist—both clinically and with MR—to ever obtain a general consensus on how to best image these patients. MR does offer the hope that more than just disk position can be assessed. In many centers, MR has completely replaced arthrography and CT as the imaging study of choice because of its ability to visualize directly the disk and its lack of associated morbidity and radiation.

Conclusions

The ideal imaging technique for diagnosing internal derangements should provide (at a reasonable cost) information about the status of the osseous structures, disk, and dynamic function. The severity of the disease process should be delineated to determine the type of therapy to be used and the prognosis. Controversy exists as to which technique is best suited to this task. The relative advantages and disadvantages of each are summarized below.

Conventional radiography is of limited value because only the osseous anatomy can be evaluated, and most of those

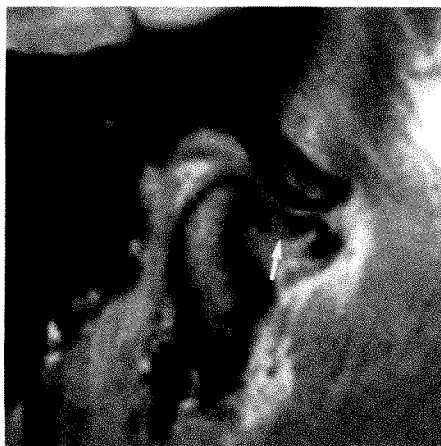


Fig. 9.—T1-weighted sagittal MR image in patient with acute onset of pain and locking of temporomandibular joint. Posterior band is clearly seen to be displaced anteriorly (arrow) and has some intermediate signal. Disk is folded downward at intermediate zone.



A



B

Fig. 10.—A, T1-weighted image in patient with anteriorly displaced disk shows some intermediate signal in posterior band (arrow).

B, Same joint imaged with gradient refocusing shows disk anteriorly displaced and high signal in posterior band (arrow). This image was obtained in half the time of A.

with derangements will show either no abnormalities or non-specific findings. Plain films have a limited role as an inexpensive screening method either to show degenerative changes or to exclude old traumatic abnormalities or congenital deformities that may mimic symptoms of internal derangement.

CT and MR imaging have certain advantages: they are noninvasive and do not require direct supervision by a radiologist while the procedure is being performed. They both image the disk directly. An additional advantage of MR is that it does not expose the patient to ionizing radiation. The disadvantages are that both techniques are relatively expensive and that they do not show functional anatomy or perforations of the disk. In addition, MR is not yet available at many institutions.

A perforated disk can be diagnosed reliably only by arthrography. Arthrography also is the best examination to show the dynamic anatomy of the joint and joint capsule adhesions. Arthrography is relatively inexpensive. Disadvantages are that (1) it requires a physician's time to perform the study, (2) it is technically more difficult to learn to perform than other kinds of arthrography, and (3) it is an invasive examination in that it requires a needle puncture and therefore may be painful.

The radiologist and referring physician must decide on an individual basis which examination best fulfills their needs. Some oral surgeons want to know if a perforated disk exists because they will treat this without delay and with an open surgical procedure, whereas arthroscopic surgery will be used for less severe alterations of the joint. Arthrography must be done for these physicians because it is the only examination that can yield this information with a high degree of certainty. In many situations, surgeons find it necessary to confirm only the location of the disk and do not determine treatment by ancillary radiographic findings. In these circumstances, MR, CT, and arthrography are all excellent choices for diagnosis. The examination performed will depend on the surgeon's

requirements, availability of equipment, and skill and predilection of the radiologist.

REFERENCES

- Murphy WA. The temporomandibular joint. In: Resnick D, Niwayama G, eds. *Diagnosis of bone and joint disorders*, 2nd ed. Philadelphia: Saunders, 1988:1816-1863
- Manzione JV, Katzberg RW, Manzione TJ. Internal derangements of the temporomandibular joint. 1. Normal anatomy, physiology, and pathophysiology. *Int J Periodontol Rest Dent* 1984;4:9-27
- Solberg WK, Woo MW, Houston JB. Prevalence of mandibular dysfunction in young adults. *J Am Dent Assoc* 1979;98:25-34
- Morgan DH. The great impostor: diseases of the temporomandibular joint (commentary). *JAMA* 1976;235:2395
- Khoury MB, Dolan E. Sideways dislocation of the temporomandibular joint meniscus: the edge sign. *AJNR* 1986;7:869-872
- Annandale T. Displacement of the interarticular cartilage of the lower jaw, and its treatment by operation. *Lancet* 1887;1:411-414
- Ireland VE. The problem of the clicking jaw. *J R Soc Med* 1951;44:363-372
- Laskin DM. Etiology of the pain-dysfunction syndrome. *J Am Dent Assoc* 1969;79:147-153
- Farrar WB. Differentiation of the temporomandibular joint dysfunction to simplify treatment. *J Prosthet Dent* 1972;28:629-636
- Farrar WB, McCarty WL. Inferior joint space arthrography and characteristics of condylar paths in internal derangements of the TMJ. *J Prosthet Dent* 1979;41:548-555
- Helms CA, Katzberg RW, Dolwick MF, et al. *Internal derangements of the temporomandibular joint*. San Francisco: Radiology, Research, and Education Foundation; 1983
- Katzberg RW, Dolwick MF, Helms CA, Hopens T, Bales DJ, Coggs GC. Arthrotomography of the temporomandibular joint. *AJR* 1980;134:995-1003
- Miller TL, Katzberg RW, Tallents RH, Bessette RW, Hayakawa K. Temporomandibular joint clicking with nonreducing anterior displacement of the meniscus. *Radiology* 1985;154:121-124
- Yune HY, Hall JR, Hutton CE, Klatte EC. Roentgenologic diagnosis in chronic temporomandibular joint dysfunction syndrome. *AJR* 1973;118:401-414
- Murphy WA, Adams RJ, Gilula LA, Barbier JY. Magnification radiography

- of the temporomandibular joint: technical considerations. *Radiology* 1979;133:524-527
16. VanSickels JE, Blanco HJ, Pifer RG. Transcranial radiographs in the evaluation of the craniomandibular (TMJ) disorders. *J Prosthet Dent* 1983;49:244-249
 17. Updegrave WJ. An evaluation of temporomandibular joint roentgenography. *J Am Dent Assoc* 1953;46:408-419
 18. Buhner WA. A headholder for oriented temporomandibular joint radiographs. *J Prosthet Dent* 1973;29:113-117
 19. Preti G, Arduino A, Pera P. Consistency of performance of a new craniostat for oblique lateral transcranial radiographs of the temporomandibular joint. *J Prosthet Dent* 1984;52:270-274
 20. Stanson AW, Baker HL. Routine tomography of the temporomandibular joint. *Radiol Clin North Am* 1976;14:105-127
 21. Rozenciveig D, Martin G. Selective tomography of the TMJ and the myofascial pain-dysfunction syndrome. *J Prosthet Dent* 1978;40:67-74
 22. Norgaard F. Arthrography of the mandibular joint. *Acta Radiol [Diagn] (Stockh)* 1944;25:679-685
 23. Lynch TP, Chase DC. Arthrography in the evaluation of the temporomandibular joint. *Radiology* 1978;123:667-672
 24. Katzberg RW, Dolwick MF, Bales DJ, Helms CA. Arthrotomography of the TMJ: new technique and preliminary observations. *AJR* 1979;132:949-955
 25. Murphy WA. Arthrography of the temporomandibular joint. *Radiol Clin North Am* 1981;19:365-378
 26. Dolwick MR, Katzberg RW, Helms CA, Bales DJ. Arthrotomographic evaluation of the temporomandibular joint. *J Oral Maxillofac Surg* 1979;37:793-799
 27. Westesson P-L, Rohlin M. Diagnostic accuracy of double-contrast arthrotomography of the temporomandibular joint: correlation with postmortem morphology. *AJNR* 1984;5:463-468
 28. Campbell RL, Alexander JM. Temporomandibular joint arthrography: negative pressure, nontomographic techniques. *Oral Surg Oral Med Oral Pathol* 1983;55:121-126
 29. Bell KA, Walters PJ. Videofluoroscopy during arthrography of the temporomandibular joint. *Radiology* 1983;147:879
 30. Jacobs JM, Manaster BJ. Digital subtraction arthrography of the temporomandibular joint. *AJR* 1987;148:344-346
 31. Kaplan PA, Tu HK, Sleder PR, Lydiatt DD, Laney TJ. Inferior joint space arthrography of normal temporomandibular joints: reassessment of diagnostic criteria. *Radiology* 1986;159:585-589
 32. Kaplan PA, Tu HK, Williams SM, Lydiatt DD. The normal temporomandibular joint: MR and arthrographic correlation. *Radiology* 1987;165:177-178
 33. Manzione JV, Tallents R, Katzberg RW, Oster C, Miller TL. Arthrographically guided splint therapy for recapturing the temporomandibular joint meniscus. *Oral Surg Oral Med Oral Pathol* 1984;57:235-240
 34. Bronstein SL. Postsurgical TMJ arthrography. *J Craniomandib Pract* 1984;2:165-175
 35. Kaplan PA, Reiskin AB, Tu HK. Temporomandibular joint arthrography following surgical treatment of internal derangements. *Radiology* 1987;163:217-220
 36. Schellhas KP, Wilkes CH, Omlie MR, et al. The diagnosis of temporomandibular joint disease: two-compartment arthrography and MR. *AJR* 1988;151:341-350
 37. Kaplan PA, Tu HK, Lydiatt DD, Sleder PR, Williams SM. Temporomandibular joint arthrography of normal subjects: prevalence of pain with ionic versus nonionic contrast agents. *Radiology* 1985;156:825-826
 38. Lydiatt D, Kaplan P, Tu H, Sleder P. Morbidity associated with temporomandibular joint arthrography in clinically normal joints. *J Oral Maxillofac Surg* 1986;44:8-10
 39. Katzberg RW, Miller TL, Hayakawa K, Manzione JV, Tallents RH. Temporomandibular joint arthrography: comparison of morbidity with ionic and low osmolality contrast media. *Radiology* 1985;155:245-246
 40. Collier BD, Carrera GF, Messer EJ, et al. Internal derangement of the temporomandibular joint: detection by single-photon emission computed tomography. *Radiology* 1983;149:557-561
 41. Helms CA, Vogler JB III, Morrish RB Jr, Goldman SM, Capra RE, Proctor E. Temporomandibular joint internal derangements: CT diagnosis. *Radiology* 1984;152:459-462
 42. Manzione JV, Katzberg RW, Brodsky GL, Seltzer SE, Mellins HZ. Internal derangements of the temporomandibular joint: diagnosis by direct sagittal computed tomography. *Radiology* 1984;150:111-115
 43. Wilkinson T, Marynuik G. The correlation between sagittal anatomic sections and computerized tomography of the TMJ. *J Craniomandib Pract* 1983;1:38-45
 44. Thompson JR, Christiansen EL, Sauser DD, Hasso AN, Hinshaw DB. Contrast arthrography versus computed tomography for the diagnosis of dislocation of the temporomandibular meniscus. *AJNR* 1984;5:747-750
 45. Manco LG, Messing SG, Busino LJ, Fasulo CP, Sordill WC. Internal derangements of the temporomandibular joint evaluated with direct sagittal CT: a prospective study. *Radiology* 1985;157:407-412
 46. Westesson P, Katzberg RW, Tallents RH, Sanchez-Woodworth RE, Svensson SA. CT and MR of the temporomandibular joint: comparison with autopsy specimens. *AJR* 1987;148:1165-1171
 47. Cohen HR, Carroll MS, Schatz SL, Mohamed MM. Correlation of sagittal computed tomography of the temporomandibular joint with surgical findings. *J Craniomandib Pract* 1985;3:352-357
 48. Westesson P, Katzberg R, Tallents R, et al. TMJ: comparison of MR images with cryosectional anatomy. *Radiology* 1987;164:59-64
 49. Roberts D, Schenck J, Joseph P, et al. Temporomandibular joint: magnetic resonance imaging. *Radiology* 1985;154:829-830
 50. Katzberg RW, Schenck J, Roberts D, et al. Magnetic resonance imaging of the temporomandibular joint meniscus. *Oral Surg Oral Med Oral Pathol* 1985;59:332-335
 51. Helms CA, Richardson ML, Moon KL, Ware WH. Nuclear magnetic resonance imaging of the temporomandibular joint: preliminary observations. *J Craniomandib Pract* 1984;2:219-224
 52. Harms SE, Wilk RM, Wolford LM, Chiles DG, Milam SB. The temporomandibular joint: magnetic resonance imaging using surface coils. *Radiology* 1985;157:133-136
 53. Cirbus MT, Smilack MS, Beltran J, Simon DC. Magnetic resonance imaging in confirming internal derangement of the temporomandibular joint. *J Prosthet Dent* 1987;57:488-494
 54. Donlon WC, Moon KL. Comparison of magnetic resonance imaging, arthrotomography and clinical and surgical findings in temporomandibular joint internal derangements. *Oral Surg Oral Med Oral Pathol* 1987;64:2-5
 55. Helms CA, Gillespy T III, Sims RE, Richardson ML. Magnetic resonance imaging of internal derangement of the temporomandibular joint. *Radiol Clin North Am* 1986;24:189-192
 56. Schellhas KP, Wilkes CH, Fritts HM, Omlie MR, Heithoff KB, Jahn JA. Temporomandibular joint: MR imaging of internal derangements and postoperative changes. *AJR* 1988;150:381-389
 57. Scapino RP. Histopathology associated with malposition of the human temporomandibular joint disc. *Oral Surg Oral Med Oral Pathol* 1983;55:382
 58. Burnett KR, Davis CL, Read J. Dynamic display of the temporomandibular joint meniscus by using "fast-scan" MR imaging. *AJR* 1987;149:959-962

Book Review

Color Blood Flow Imaging of the Heart. By Dierk A. Redel. New York: Springer-Verlag, 122 pp., 1988. \$169.50

Although not directly stated in the introduction, the author's purpose in this book is to discuss and illustrate the use of color blood-flow imaging in the heart. The book has four short introductory chapters. The first is on the principles of the technique, the second covers artifacts, the third discusses the color-display formats, and the fourth introduces the normal flow-velocity patterns in the heart and great vessels.

The fifth chapter is the largest in the book. It can best be described as an atlas of the flow and velocity patterns in various cardiac diseases. This chapter is organized logically. Shunts around the heart and great vessels are presented in order of blood flow, that is, from the atrial septal defects through the ventricular septal defects and then to patent ductus arteriosus. In each area, the variants and combinations are noted also. Then, the abnormalities associated with diseases of the mitral, aortic, and tricuspid valves are illustrated. Again, variations and conceptually allied conditions, such as aortic coarctation, mitral valve prolapse, and pulmonary artery banding, are included.

Even though the illustrations are well labeled and are reproduced in vivid color, additional line diagrams with vector arrows would have

augmented the actual images immeasurably. Additionally, the composite images that include both color M-mode and color two-dimensional information are confusing. The author has used the acronyms VCI and VCS for the inferior vena cava and the superior vena cava, respectively. The acronyms IVC and SVC would have been more familiar to American readers. The explanations in the initial chapters are too terse to allow a beginner to follow along. Finally, a frustrating feature of this book is that the textual description of the color Doppler findings of an abnormality occasionally is located in a different section of the book than the illustration of the image.

This book is small and rather expensive for its size. It can serve as an atlas of cardiac abnormalities. It cannot serve as an introduction to the subject. I do not know the size of the audience the author or publisher had envisioned for this book, but from the content and illustrations, I can only estimate it will be useful for a small, select group of specialists.

David S. Martin
Chesterfield, MO 63017

Review Article

Clinical Doppler Imaging

Edward G. Grant,¹ Franklin N. Tessler, and Rita R. Perrella

Doppler sonography has played a pivotal role in noninvasive vascular diagnosis for many years. Simple, hand-held Doppler units are familiar to every nurse or house officer who has attempted to confirm the presence of a faintly pulsatile artery. Rapid technological advances, however, have created a complex world of Doppler technology that, in many ways, seems to be challenging even the accepted gold standard of arteriography.

The general radiology community has taken notice of Doppler only recently. Certainly, the appeal of "listening" as a method of making a diagnosis is lacking for most visually oriented radiologists. Likewise, spectral displays rarely, if ever, generate the excitement of an interesting angiogram or MR image. As early as 1974, however, Barber et al. [1] successfully combined crude real-time sonography and Doppler in an effort to direct the *Doppler* beam better. Considering the resolution of ultrasound in 1974, the possibility of simultaneously investigating the vessel walls was probably not even entertained. In a brief period of time, duplex technology reached a level of sophistication that would have been considered fantasy by its originators. Pulse-gating and fast-Fourier transformation now allow us to display the flow characteristics of one or more known points within a vessel graphically; high-resolution real-time ultrasound simultaneously produces elegant images of the walls.

Even as modern duplex Doppler examinations are beginning to become well established in many radiology facilities, a newer and far more advanced technology is emerging—color-flow Doppler. The leap from duplex to color flow represents a technological breakthrough, and many contended until quite recently that such imaging was impossible. Color-

flow Doppler is only in its infancy, but its potential, given its advantages, is tremendous. This article attempts to strike a practical balance between the technical frustrations so common with duplex Doppler and the largely untested promise of color Doppler imaging.

Color Doppler Imaging of the Carotid Arteries

Atherosclerosis at the carotid bifurcation underlies most strokes, the third most common cause of mortality and morbidity in the United States [2, 3]. The carotid bifurcation is ideally situated for examination with ultrasound. The superficial location of the vessels allows the use of high-resolution real-time technique and assures accessibility in almost all patients. Carotid examinations are best performed by using the highest frequency real-time transducer possible. The choice depends on the patient's body habitus and the technical characteristics of the machine being used.

In the older population, nonhemodynamically significant plaques (plaques that narrow the lumen <50%) are common. Most elderly patients, in fact, have at least a few smooth, fibrofatty atheromata (with or without calcifications) in their carotids. In general, these fibrofatty plaques are not thought to have serious prognostic implications [4, 5]. Although high-resolution scans identify numerous plaques, sonography has not been particularly successful in predicting the presence or absence of ulceration [6, 7]. Some consider this insensitivity a serious shortcoming of the technique. On the other hand, arteriography is also known to be relatively insensitive in identifying plaque ulcerations [8, 9].

Received October 4, 1988; accepted after revision December 2, 1988.

¹ All authors: Department of Radiological Sciences, University of California, Los Angeles, Medical Center, Los Angeles, CA 90024. Address reprint requests to E. G. Grant.

Although the ability of ultrasound to identify ulcerated plaque may be in question, studies by Bluth et al. [10] and Lusby et al. [11] have described other sonographic features of atheromata that may be of greater importance. Both groups found that inhomogeneous or anechoic areas often correspond to regions of intraplaque hemorrhage. The role of intraplaque hemorrhage in cerebral infarction remains incompletely understood. In a large study, however, Imparato et al. [12] found that intraplaque hemorrhage was the most common lesion in patients who had strokes. Some theorize that an acute intraplaque hemorrhage may enlarge an existing atheroma or rupture through the intima and serve as a source of emboli. Prospective, longitudinal studies are needed, but high-resolution real-time sonography may eventually prove to be capable of identifying those patients who are at highest risk for cerebral damage from bifurcation disease.

Real-time scanning yields exquisitely detailed images of the carotid walls. Doppler, however, remains the basis for practical clinical diagnosis. The identification of hemodynamically significant lesions is still the major reason for patient referral. Well-performed Doppler examinations should yield impressive results. When compared with angiography, most duplex studies have reported an 85–95% accuracy in the detection of rate-limiting lesions [13–17]. Although the accuracy of duplex Doppler in the detection of luminal narrowing greater than 50% is quite high, this technique is not highly effective in the identification of lesser degrees of narrowing [14, 18]. In these situations, however, unless significant ulceration is present, intervention is not considered. In our experience, nonhemodynamically significant lesions are better characterized with real time than with Doppler.

The criteria for Doppler diagnosis of luminal narrowing at the carotid bifurcation are relatively well defined, considering the technical difficulty of performing an adequate scan. Interpretation is usually based on two types of diagnostic information. The simpler of the two is the most widely used and equates increasing flow velocity and associated turbulence with increasing severity of stenosis. The older diagnostic criteria of Jacobs et al. [14] or Blackshear et al. [15] remain accurate, though both groups used raw kilohertz data. A recent reevaluation of the optimum diagnostic criteria for internal carotid stenoses by Robinson et al. [16] using angle-

adjusted velocity measurements and newer equipment, in fact, is remarkably similar to the original. As an update, Table 1 provides both kilohertz and angle-adjusted velocity measurements. Relatively good correlation exists between peak velocity and the degree of stenosis. However, tightly stenotic lesions (>90–95%) eventually lead to a decrease in maximum systolic velocity. Such lesions, therefore, may be impossible to diagnose on the basis of peak velocity but can be recognized by the marked distortion of their Doppler spectra and a fairly characteristic hissing sound. Though nonspecific, the appearance of high-resistance flow in the common carotid artery (externalization of the common carotid) should further support the diagnosis of a subtotal stenosis in the ipsilateral internal carotid artery.

Diagnostic accuracy and confidence can be further increased by using the patient as his or her own standard and comparing flow velocity in one portion of the carotid system with another. Although numerous velocity ratios have been evaluated, the most commonly used is the comparison of the internal carotid artery to the ipsilateral common carotid artery [19]. Although many would rely heavily on either peak systolic velocity or one or more ratios, we recommend using both. Within reason, the more diagnostic criteria used, the greater the diagnostic accuracy [20]. The use of color Doppler imaging is rapidly expanding in the diagnosis of carotid disease. Color Doppler clearly increases confidence and decreases scan time. Many of the technical pitfalls associated with carotid duplex Doppler may, in fact, be eliminated altogether by using color-flow imaging (Fig. 1) [21]. Thus far, however, the diagnosis of carotid stenosis is still made with meticulously performed spectral analysis.

Color Doppler Imaging of the Heart

A detailed discussion of cardiac Doppler imaging is beyond the scope of this article, and the interested reader is referred to existing texts on the subject [22, 23]. Suffice it to say, Doppler plays a major role in cardiac diagnosis, and since large areas of often high-velocity flow are present, color-flow technology has been applicable to the heart for some time.

TABLE 1: Criteria for Carotid Stenosis

Percent Stenosis	kHz Shift (cm/sec)	Waveform
0–50	<4.0 (<125)	Minimal or no spectral broadening
51–75	4–6 (125–175)	Sonic window progressively fills
76–90	6–8 (175–250)	Waveform remains recognizable, window filled in
>90	>8 (>250)	Window filled in; waveform becoming distorted
95–99	Variable ^a	Waveform markedly distorted
100	0	No Doppler signal; series of dots seen along baseline

^a Can be <4 kHz.

Fig. 1.—Advantages of color Doppler imaging of the carotid arteries. (Reprinted from [21], with permission.)

A, Section through normal carotid bifurcation shows both internal and external vessels. Branches (straight arrows) clearly identify lower vessel as external carotid artery (ECA). Note prominent area of flow reversal (curved arrow) in proximal internal carotid artery (ICA). This boundary-separation zone may produce unusual but normal Doppler spectra.

B, Large anechoic plaque (A) is outlined by color. Anechoic lesions cannot be seen by real-time examination, rendering them difficult to localize with pulse-gated Doppler. Diagnosis is still made with spectral analysis, but placement of cursor can be facilitated by color imaging.

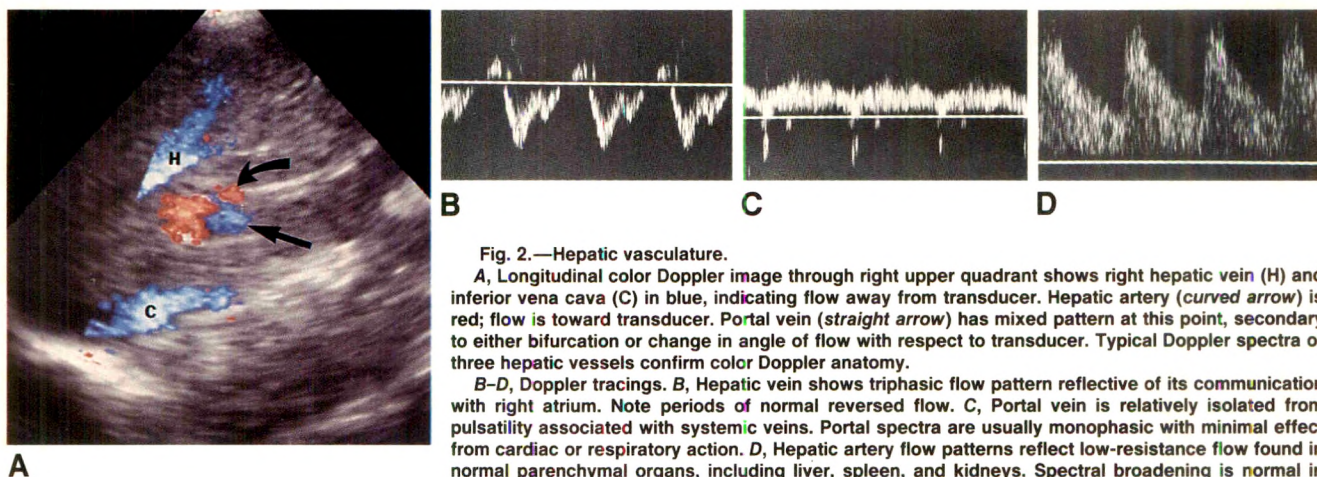
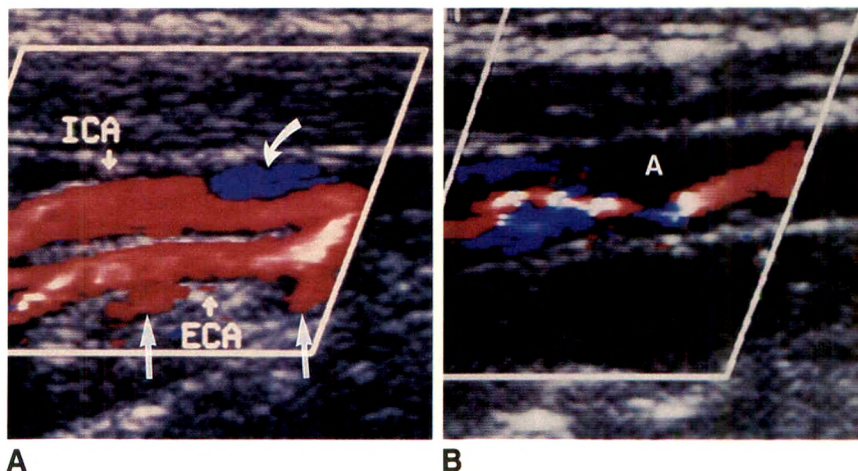


Fig. 2.—Hepatic vasculature.

A, Longitudinal color Doppler image through right upper quadrant shows right hepatic vein (H) and inferior vena cava (C) in blue, indicating flow away from transducer. Hepatic artery (curved arrow) is red; flow is toward transducer. Portal vein (straight arrow) has mixed pattern at this point, secondary to either bifurcation or change in angle of flow with respect to transducer. Typical Doppler spectra of three hepatic vessels confirm color Doppler anatomy.

B–D, Doppler tracings. B, Hepatic vein shows triphasic flow pattern reflective of its communication with right atrium. Note periods of normal reversed flow. C, Portal vein is relatively isolated from pulsatility associated with systemic veins. Portal spectra are usually monophasic with minimal effect from cardiac or respiratory action. D, Hepatic artery flow patterns reflect low-resistance flow found in normal parenchymal organs, including liver, spleen, and kidneys. Spectral broadening is normal in vessels of this size.

Color Doppler Imaging of the Abdomen

Below the diaphragm, there are a host of areas where Doppler evaluations are applicable. The list will undoubtedly expand rapidly as abdominal color-flow technology becomes more widely available. The liver provides a logical starting point, as much of the upper abdominal vasculature is in one way or another associated with this large organ. The liver has unusual circulatory dynamics, but the major hepatic vessels each possess a unique Doppler signature [24]. By means of Doppler signals alone, therefore, one is usually able to distinguish between the hepatic veins, the hepatic artery, and the vessels of the portal system (Fig. 2).

Thrombosis, cavernous transformation, aneurysms, fistulae, and other anatomic abnormalities of the portal venous system should be readily characterized with Doppler imaging (Fig. 3) [25–28]. The ability of Doppler to yield directional information is also a great advantage in the diagnosis of portal hypertension. Thus far, the relatively few large studies that have actually evaluated the accuracy of duplex Doppler im-

aging in portal hypertension have found it sufficiently accurate to recommend its use as the primary noninvasive technique [29, 30]. Unfortunately, small, cirrhotic livers may be difficult to scan, and such patients represent a significant portion of those referred for the examination. Again, meticulous technique will usually produce good results.

The hepatic artery is more difficult to locate than the portal vein because of its small size and its almost perpendicular relationship to the Doppler beam when scanning is performed through the ribs in the area of the portal vein bifurcation. If the patency of the hepatic artery is difficult to establish, an anterior subcostal approach often places a branch of the vessel parallel to the Doppler beam, thereby optimizing the Doppler angle. The status of the hepatic artery is actually of little consequence in patients with chronic liver disease. In patients with cirrhosis, in fact, the arterial signal is often far more prominent than that of the portal vein, as the artery assumes a greater role in supplying blood to the liver. Doppler spectra from the hepatic artery have not been found to be of any diagnostic value thus far. The increased arterial flow in

the liver of patients who have cirrhosis, however, may cause dilatation of the vessel. Likewise, normal elderly patients may have relatively ectatic hepatic arteries. This dilatation is often manifested by the identification of intrahepatic arterial branches on real-time studies. Within the liver, the normal hepatic artery is near [31] or below the resolution of ultrasound. Tubular structures adjacent to portal vein branches, therefore, may be confused with dilated intrahepatic biliary radicals [32]. Doppler can make this distinction very easy and can be of practical value in differentiating between ectatic hepatic arteries and dilated biliary radicals (Fig. 4) [33].

The evaluation of the hepatic artery is unnecessary in most patients. Patients who have undergone liver transplantation, however, must have a patent hepatic artery, and duplex Doppler is the primary screening technique [34, 35]. Finding the hepatic artery may be time-consuming, and patency is diagnosed solely by identifying the characteristic Doppler signal. Doppler is quite sensitive but, at this point, is not specific enough to avoid angiography. Again, our initial experience with color-flow Doppler in liver transplant patients has been encouraging. We should emphasize that thrombosis of the hepatic artery may be identified by Doppler before major degeneration of liver function occurs. Because delayed intervention will worsen prognosis, any patient in whom arterial Doppler signals are not clearly identified should have arteriography.

In addition to excluding the possibility of hepatic artery thrombosis, the hepatic parenchyma can be evaluated for focal lesions and the patency of the portal and hepatic veins established. The inferior vena cava should also be investigated if possible. Our experience has been similar to that of Dalen et al. [36], who have found compromise of the inferior

vena cava fairly common after transplantation (Fig. 5). Close inspection of the inferior vena cava, in fact, almost always shows at least some narrowing at the surgical anastomosis. Although even total occlusion of the inferior vena cava seems of relatively little clinical consequence in transplant patients, the position of the thrombus should be noted to assure that it does not extend into the renal veins.

Considering the success of duplex Doppler in evaluating the portal vein, one would logically conclude it to be an excellent method of diagnosing hepatic vein occlusion as well. A review of the literature produces many inferences to this effect, but no real series have appeared. To begin with, hepatic venoocclusive disease or Budd-Chiari syndrome is relatively rare; few centers see a large number of cases. Beyond this, evaluation of the hepatic veins in the diseased liver is not as straightforward as it seems. In patients with hepatomegaly, the veins are frequently compressed and not visible. Likewise, the hepatic veins of patients with small cirrhotic livers are often impossible to define by using real time, again precluding adequate placement of a duplex Doppler cursor. In our series [37], color-flow Doppler imaging effectively overcame the inherent problems of conventional duplex Doppler in evaluating the hepatic veins. Our study suggests that color Doppler is an effective method for screening patients suspected of having Budd-Chiari syndrome (Fig. 6).

Doppler imaging has also found considerable use in the evaluation of portosystemic shunts [38]. These surgically created communications are most often constructed to relieve portal hypertension. Portocaval shunts are easily visualized because the liver acts as a sonographic window. Portosystemic communications elsewhere (splenorenal, mesocaval, or

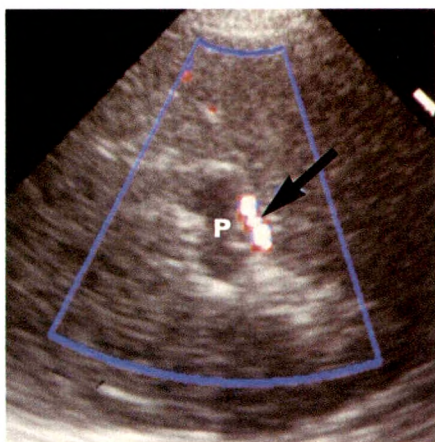
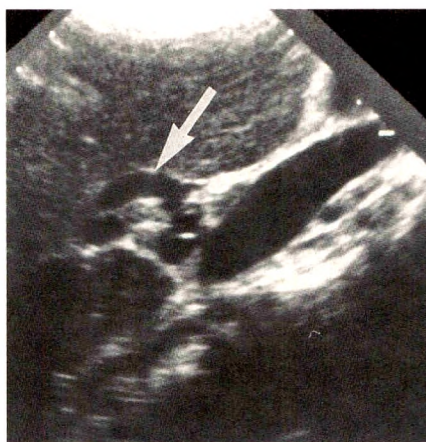
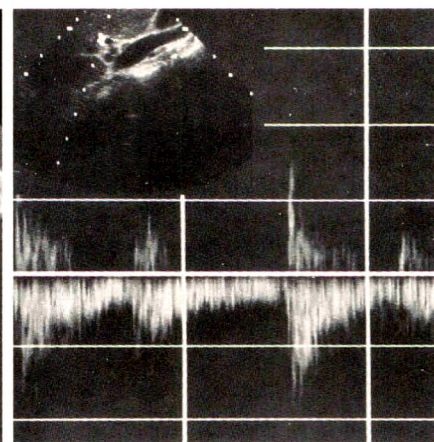


Fig. 3.—Portal vein thrombosis in patient with chronic active hepatitis and acute clinical degeneration. Color Doppler evaluation fails to identify flow in portal vein (P); hepatic artery signals (arrow) are accentuated. Absent flow was confirmed by spectral analysis and later MR. When performing color-flow analysis, the operator must be certain that flow is actually absent and not merely perpendicular to Doppler beam or below threshold of Doppler filters.



A



B

Fig. 4.—Ectatic hepatic artery.

A, Real-time section from patient with jaundice depicts 7-mm tubular structure anterior to portal vein (arrow). Mildly dilated common bile duct was suspected. No evidence of intrahepatic biliary dilatation is noted.

B, Doppler evaluation shows vascular nature of structure; flow pattern confirms vessel is hepatic artery.

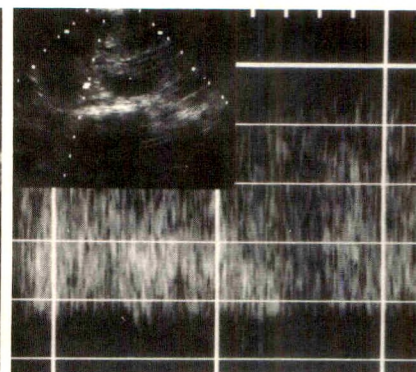
Fig. 5.—Partial occlusion of inferior vena cava.

A, Longitudinal real-time image shows abrupt decrease in caliber of intrahepatic inferior vena cava (arrows). Patency of vessel is uncertain; lumen cannot be followed into right atrium.

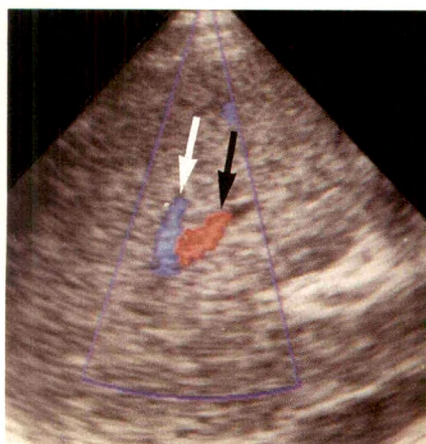
B, Doppler signals can be followed from inferior border of thrombus to right atrium. Velocities are markedly elevated, typical of stenosis. Doppler patterns inferior to thrombotic area show sluggish flow in appropriate direction; normal triphasic pattern is absent. Respiratory velocity change is accentuated.



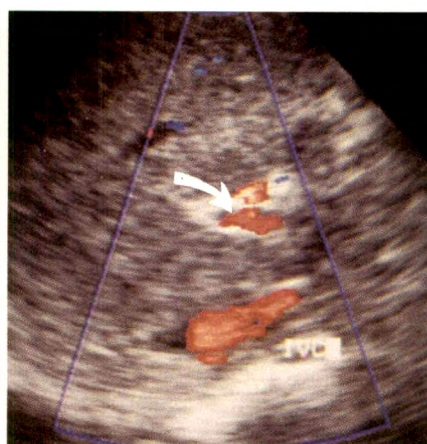
A



B



A



B

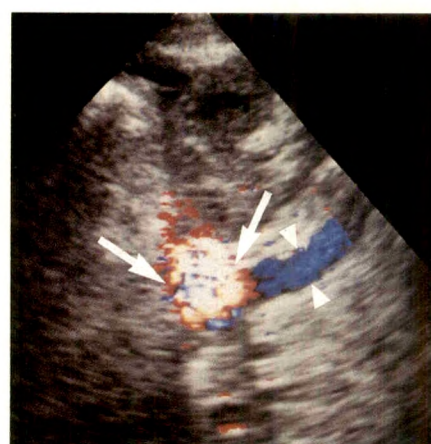


Fig. 6.—Color Doppler images from patient with Budd-Chiari syndrome and thrombosed mesoatrial shunt.

A, Longitudinal section through periphery of right lobe shows pattern typical of Budd-Chiari syndrome. More cephalad hepatic vein branch is directed normally (white arrow). Flow in adjacent branch is reversed (black arrow) and shunts blood toward collaterals on surface of liver. Other intrahepatic abnormalities identified include large intrahepatic collateral and reversed flow in superficial portions of left hepatic veins.

B, Flow in inferior vena cava is reversed, whereas portal vein flow (arrow) is directed toward liver. Patients with patent mesoatrial shunts normally have reversed flow in portal vein. Sonographic findings were confirmed by inferior venacavogram and superior mesenteric arteriogram.

Fig. 7.—Color Doppler image of mesocaval shunt. Flow in superior mesenteric vein is reversed. Brightly echogenic walls of synthetic graft are seen, but with considerable difficulty. Angling cephalad from area above iliac crest, junction between shunt (arrows) and distal inferior vena cava (arrowheads) is visualized.

Warren shunts), however, may be difficult to visualize because the postsurgical anatomy is inconstant and bowel gas may obscure sonographic detail (Fig. 7). Locating the shunt can be facilitated by consulting earlier radiographic studies or the surgeon before beginning the examination. An unusual group of patients with shunts in whom Doppler examinations are of particular value are those who have undergone mesoatrial shunts. Mesoatrial shunts are constructed to relieve hepatic congestion in patients with Budd-Chiari syndrome [39]. In effect, the portal vein is converted into an outflow tract. Blood is shunted directly into the right atrium, bypassing a compromised inferior vena cava. Mesoatrial shunts are located beneath the anterior abdominal wall, and Doppler (either duplex or color flow) should be used as the primary screening technique [37]. The ability to assess shunt patency with duplex Doppler varies with the site of the surgical anastomosis. Again, color flow adds considerable confidence and may actually improve accuracy in the evaluation of the more anatomically problematic shunts.

Doppler also has been used in the investigation of hepatic masses. Typically, hemangiomas produce no Doppler signals at all, whereas hepatomas reportedly have high flow velocities as a result of direct arteriovenous communications [40]. Metastases typically produce Doppler patterns that fall somewhere between those of hemangiomas and hepatomas, but a significant percentage of metastatic lesions produce no detectable Doppler signals. Metastases, therefore, cannot be reliably differentiated from hemangiomas by using Doppler. In addition, we have only very rarely identified the characteristic high-velocity pattern in hepatomas. In general, we have not found duplex Doppler to be particularly helpful in narrowing the differential diagnosis of hepatic masses.

Vascular lesions in the upper abdomen that are not in some way associated with the liver are relatively unusual. Pseudoaneurysms do, however, occur with sufficient frequency to warrant discussion. These lesions are typically associated with pancreatic disease or trauma [41], and their benign appearance may be misleading to the radiologist [42]. The

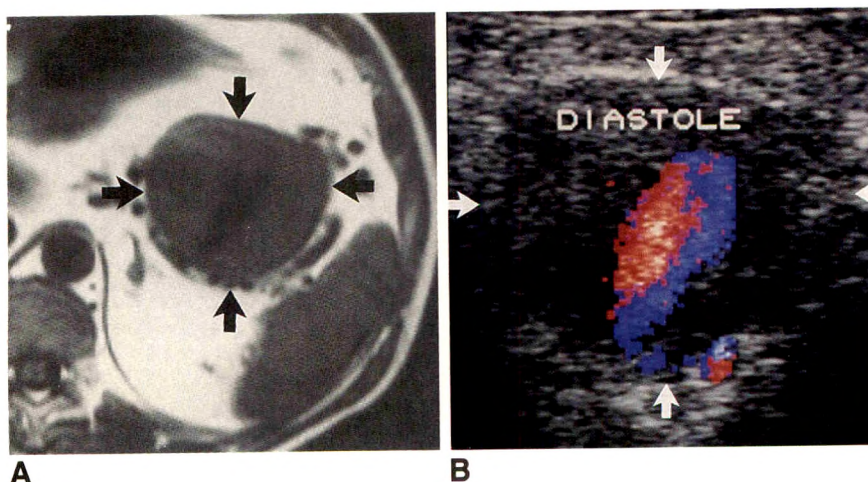


Fig. 8.—Splenic artery pseudoaneurysm in patient with history of abdominal trauma. (Case contributed by Donald Mitchell, Thomas Jefferson Hospital, Philadelphia, PA, with permission.)

A, Axial T1-weighted MR image shows left upper quadrant mass (arrows) with central region of signal void.

B, Color Doppler image identifies mass as pseudoaneurysm of splenic artery. Note thick, hypoechoic area of peripheral thrombus (arrows) and classic "to and fro" (alternating blue and red) pattern of swirling blood centrally.

vascular nature of pseudoaneurysms may not be apparent on routine imaging procedures, and their often cystic sonographic features invite percutaneous puncture/drainage (Fig. 8). It goes without saying that the simple act of diagnosing a pseudoaneurysm with Doppler can be a diagnostic coup. This easily made diagnosis can also save considerably in legal fees if it is made before the insertion of a large catheter.

Color Doppler Imaging of the Kidneys

Doppler has found numerous uses in both the native and transplanted liver. In the kidney, however, Doppler has been used far more often in the transplanted organ. The native renal arteries are usually difficult to localize, and scanning transversely across the upper abdomen places their origins almost perpendicular to the Doppler beam. Useful Doppler information, therefore, is best obtained by scanning through the flanks in the coronal plane. Taylor et al. [43] have found this technique successful for locating the renal artery origins in most of their patients being evaluated for renovascular hypertension. The search for the renal artery origins, however, can be time-consuming and has not been widely practiced in most centers. Color-flow Doppler may simplify the identification of the renal artery origins and popularize sonography as a screening evaluation in suspected renovascular hypertension.

Duplex Doppler may also be of value in patients with renal vein thrombosis. A noninvasive method of diagnosing this clinically elusive entity would be of great benefit. Duplex Doppler can suggest renal vein thrombosis in cases of complete occlusion. Partial or segmental thrombosis, however, will most likely go undetected, as the residual venous flow will produce a Doppler signal. Similar to hepatic vein thrombosis, Doppler diagnosis of renal vein thrombosis should be more definitive with color-flow technology.

As opposed to the native kidneys, renal transplants are well situated for ultrasound examination and Doppler has become a routine part of their evaluation. Doppler is valuable in the diagnosis of both acute rejection and renal transplant artery stenosis. In the former, Doppler takes advantage of the increase in vascular resistance that often accompanies rejection. In general, beyond the first week after transplanta-

tion, the normal low-resistance flow of the kidney changes to high resistance, resulting in a progressive decrease in diastolic flow [44–46]. Although early studies tended to promote the use of signals from the arcuate vessels, the more peripheral arteries may not yield as much diagnostic information as those closer to the hilar area (Fig. 9).

The Doppler diagnosis of acute rejection is relatively specific when diastolic flow is completely absent. As a practical method of quantifying less obvious circulatory abnormalities, however, we often use the resistive index (peak systolic velocity – end-diastolic velocity/peak systolic velocity) [47]. To simplify, as the resistive index rises beyond 0.90, suspicion of acute rejection becomes increasingly significant. Unfortunately, a worrisome proportion of patients with acute rejection have normal or nearly normal flow patterns, and the recent work of Jenkins et al. [48] has questioned the specificity of increased vascular resistance in rejection as well. The ability to accurately diagnose acute rejection with Doppler may depend on the percentage of patients with vascular vs cellular/interstitial rejection. Although the existence of these two forms of rejection is not entirely accepted by all authorities, patients with mild to moderate cellular rejection should have normal flow patterns. Though spectral analysis plays an important role in the diagnosis of renal transplant rejection, further investigation is needed to more fully understand the mechanisms that do (or do not) cause flow alterations.

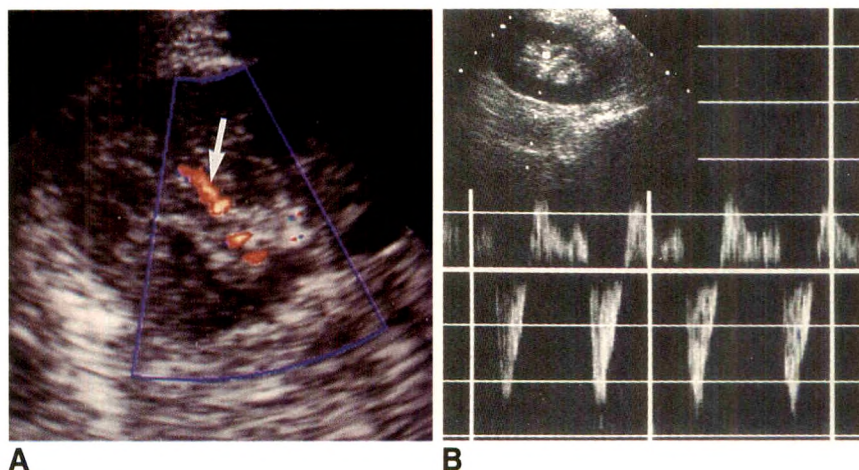
Numerous investigators have evaluated Doppler in the diagnosis of renal transplant rejection, but little attention has been given to its use in renal artery stenosis [49]. As elsewhere in the body, an area of luminal narrowing should produce a segmental region of abnormal flow. This is true in the renal transplant artery, but this diagnosis is not straightforward. Complicating the identification of stenosed renal arteries are the small size of the artery, the difficulty of visualizing the entire vessel, and, most problematic, areas of marked tortuosity. In our experience, even if the Doppler angle is meticulously accounted for, tight curves and areas in which the artery is parallel to the Doppler beam may artifactually produce very high flow velocities. We have found that the most useful diagnostic criterion is actually the identification of a segmental area of extreme spectral broadening and/or frank distortion of the Doppler waveform.

Fig. 9.—Renal transplant rejection 2 weeks after renal transplantation in patient with rapidly increasing creatinine. Nuclear medicine scan was unable to establish blood flow within kidney.

A, Color Doppler image clearly defines internal arterial flow in both main renal and arcuate arteries (arrow).

B, Spectral analysis is typical of acute rejection and shows unusually high vascular resistance. Note prominent negative flow in diastole.

Patient did not respond to immunotherapy; kidney was removed 1 week after initial scan. Pathologic evaluation of nephrectomy specimen revealed severe acute rejection.



Color Doppler Imaging of the Pelvis

Aside from pregnancy, the use of Doppler in the pelvis has been limited. Basic anatomy renders the examination of the major pelvic vessels difficult. Doppler may be of value in determining the vascular nature of iliac aneurysms. Iliac aneurysms, however, are relatively unusual. Because of their inaccessibility, Doppler has not proved overly useful in the diagnosis of luminal compromise in the iliac arteries themselves. Likewise, the iliac veins are often difficult to evaluate directly. Fortunately, thrombosis of the common and external iliac veins can be implied with Doppler in many patients when respiratory variation is absent or lack of response to the Valsalva maneuver is observed in the easily accessible common femoral vein [50].

Although the iliac vessels hide deep within the pelvis, the arteries of the uterus and ovaries are easily found by real-time examination and can be localized with duplex Doppler. One study of interest found that the vascular dynamics of the ovary changed from high to low resistance at the time of ovulation [51]. Such information could prove important to those involved with the treatment of infertility. Another potential use for Doppler in the pelvis may be the identification of ectopic pregnancies. Although endovaginal technique has improved our ability to identify a gestational sac implanted outside the endometrial cavity [52], a significant percentage of ectopic pregnancies remain undetected. Doppler reportedly is capable of identifying the hypervascular zone surrounding an ectopic pregnancy as an intense area of Doppler signal (Merritt C, personal communication). Obviously, only the global view of the pelvic vasculature provided by color flow can be of practical value in this situation. The hypervascular nature of gestational tissue has also been taken advantage of in identifying recurrent trophoblastic disease. An intense low-resistance signal from the endometrial area in a patient with elevated chorionic gonadotrophin is strong evidence that the malignancy has recurred [53].

Color Doppler Imaging in Pregnancy

The pregnant uterus has been the subject of innumerable Doppler investigations. Unfortunately the existing body of

literature does not inspire a great deal of confidence in the examination, as many contradictory conclusions have been drawn. Recent concerns about bioeffects have also limited its use in the radiology community. Pulsed Doppler is not yet approved by the Food and Drug Administration (FDA) for routine obstetric evaluations, and the indications for its use remain unclear. At present, we perform duplex sonographic examinations on patients when there is a specific clinical question about the dynamics of the maternal-fetal circulation. Intrauterine growth retardation (IUGR) [54, 55], fetal congestive heart failure [56], twin/twin transfusion syndrome [57], and other disease processes of vascular origin fall into this category. Before any fetal evaluations are performed, however, we recommend checking the Doppler output of individual machines and their transducers with the manufacturer to ascertain the maximum power output that falls within the FDA guidelines. As a working rule, the lowest power settings possible should be used when examining the fetus. Power settings can be reduced considerably (often to less than 20% of maximum on our machines) and have little effect on the ability to obtain an adequate signal. When there is concern about power output, system gain (amplification) or even sample volume size can be increased to compensate for decreasing power.

A typical maternal-fetal Doppler examination should proceed to three specific areas: the umbilical arteries, the fetal aorta, and the subserosal region of the uterus. Signals from the umbilical artery should reflect the status of its end organ, the placenta. Doppler tracings can be obtained easily by decreasing the size of the sample volume as much as possible (to avoid signals from the adjacent umbilical vein) and insonating the umbilical cord at an appropriate angle. Doppler signals that lack diastolic flow should be rechecked carefully to assure that the angle is not near perpendicular before they are considered abnormal. The fetal aorta is also easily evaluated by Doppler imaging. Most investigators have (for a variety of reasons) taken aortic samples from the area of the diaphragm. Unlike in the adult aorta, diastolic flow is always present in the fetal aorta. This low-resistance pattern reflects the fact that 60–80% of the aortic flow volume is diverted into the umbilical circulation at the level of the iliac arteries [58]. As might be expected, aortic samples tend to be some-

what more reflective of the status of the fetus than those taken from the umbilical arteries. A final area that should be evaluated is the uterus. The study of Trudinger and Cook [59] found Doppler patterns in the uterine/arcuate arteries to be abnormal in 60% of their patients with IUGR. Problems on the maternal side of the fetal circulatory unit, including hypertension, diabetes, and collagen vascular disease, would logically affect the uterine arteries preferentially over those in the fetus. The normal uterine vessels are not visible on real-time sonography but lie in a fairly dense network beneath the serosa. Signals are usually easily obtained by opening the Doppler sample volume and placing the cursor in the appropriate position (Fig. 10).

The Doppler diagnosis of IUGR has been widely investigated [54, 55, 60]. Again, however, results have not been entirely consistent, and severely growth-retarded infants may have normal prenatal Doppler examinations. Unfortunately, IUGR has numerous underlying causes, not all of which are vascular. The study of Wladimiroff et al. [60], in fact, is of interest in that their growth-retarded population with normal Doppler patterns had a significant percentage of congenital abnormalities. On the basis of this information, Doppler could be used to determine which fetuses are asymmetrically growth-retarded noninvasively (and potentially require intervention) and which are not.

In general, decreasing diastolic flow in the fetal aorta or umbilical arteries has been associated with worsening prognosis. This situation, however, is relatively complex because vascular resistance of the maternal-fetal unit decreases as the pregnancy matures. Reuwer et al. [61] found no diastolic flow in fetuses before 20 weeks gestation. Our own experience, however, with carefully angled duplex examinations has shown that diastolic flow should be identified in normal fetuses as immature as 16 weeks.

Laurin et al. [62] recently evaluated resistive index and visual waveform analysis in the diagnosis of IUGR. Their results showed that significant differences in outcome were manifest only when diastolic flow was actually absent; resistive index, therefore, was not of practical value. Patients suspected of IUGR on clinical grounds without diastolic flow

should be considered at high risk and monitored closely. Patients who have developed a negative component to their Doppler waveform are at an even higher risk. Multiple studies, in fact, have equated the appearance of a negative arterial component with a high likelihood of fetal death [63–65].

Other fetal complications of pregnancy in which diagnostic information may be obtained with Doppler include fetal congestive heart failure (typically associated with alpha-thalassemia or erythroblastosis fetalis) [55] and twin/twin transfusion syndrome [57]. In the former, abnormal Doppler signals were obtained from the fetal aorta and inferior vena cava during periods of congestive failure but returned to normal after successful treatment. In the latter, Pretorius et al. [58] reported abnormal signals in a significant percentage of patients with twin/twin transfusion syndrome. Unfortunately, the abnormalities did not consistently identify which twin was the recipient and which twin was the donor.

Color Doppler Imaging of the Extremities

In the limbs, Doppler evaluation of the veins and arteries proceeds along highly divergent courses and each will be discussed separately. Doppler technology has seen limited success in the peripheral arterial system outside of the carotids. The femoral and popliteal arteries are readily accessible to Doppler, and lesions confined to these areas are accurately diagnosed [66]. Unfortunately, the iliac arteries are impossible to examine in an unacceptable number of patients, and the region of the adductor canal is often equally problematic. As these two regions are common sites for atherosclerotic disease, duplex Doppler has not gained popularity as a screening procedure.

Although the arteries of the legs are not well situated for duplex Doppler evaluation, bypass grafts tend to be superficially located and, therefore, easily accessible. Femoropopliteal grafts run beneath the skin of the medial thigh and can be found readily by scanning over the surgical scar. Femorofemoral and axillary-femoral grafts are also accessible to high-frequency transducers, as are hemodialysis access grafts.

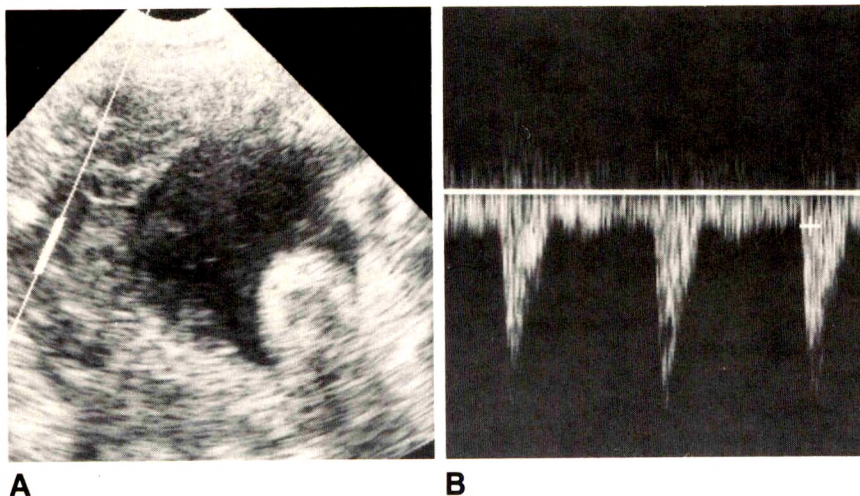


Fig. 10.—Intrauterine growth retardation in patient with history of systemic lupus erythematosus and severe hypertension. Clinical examination did not show adequate interval growth.

A, Real-time sonogram shows oligohydramnios. Doppler sample volume was opened; cursor placed in subserosal region of uterine wall.

B, Doppler spectra indicate decreased diastolic flow. Systolic/diastolic (A/B) ratio is greater than 7.0. A/B ratio should be less than 2.0 by third trimester of pregnancy.

Although the basic question of patency is easily answered, other graft complications can be diagnosed with ultrasound as well. In particular, the duplex or color-flow Doppler features of pseudoaneurysms should allow definitive differentiation from hematomas or abscesses and eliminate the need for contrast studies [67, 68].

The value of ultrasound has not been sufficiently appreciated in regard to its ability to detect venous disease. Numerous studies have attested to its accuracy and noninvasive nature [50, 69–72]. For various reasons, however, contrast venography continues to be performed on a routine basis in many institutions, despite the well-known possibility of its causing the very problem it was used to diagnose. In 1989, deep venous thrombosis of the legs should be investigated first with sonography. The technique is relatively simple and the examination of both legs can be completed in 15–30 min at most. Although Doppler has a definite role in this examination, real time provides the diagnosis in most cases. Color-flow Doppler imaging should further simplify the sonographic evaluation of deep venous thrombosis and eliminate the use of contrast venography in all but the most unusual cases.

An ultrasound examination for femoral venous thrombosis should begin as high in the affected groin as possible. In this region the femoral vein and artery should be in a superficial location in most patients and, therefore, be easily accessible. We recommend the transverse orientation initially and use both compression and Doppler. In or slightly below the groin, the saphenous vein joins the common femoral. The saphenous vein lies directly beneath the skin and is easily missed if more than the slightest amount of pressure is applied. The evaluation proceeds rapidly down the thigh with frequent stops for compression and Doppler samples. In the mid/distal thigh the vein is often lost and may be picked up again by scanning in the popliteal fossa. Although the inability to image the entire length of the vein is of some concern, a few simple Doppler maneuvers should assure the operator that the veins

in question are patent. An augmentation procedure (firmly squeezing the calf) forces blood out of the calf and is reflected by a sharp change in the Doppler signal proximally. A normal augmentation implies the femoral and popliteal veins are patent. Likewise, respiratory motions (a Valsalva maneuver or, better yet, deep breathing) should be reflected at the groin and if absent, raise the possibility of iliac thrombosis. Although cases of deep venous thrombosis occasionally may present a diagnostic challenge, most are readily evident and expand the affected vein with hypoechoic clot (Fig. 11). Although ultrasound may not be accurate in the diagnosis of isolated calf vein thrombosis, clot located below the popliteal vein does not embolize and is of no danger.

Other Uses of Color Doppler Imaging

Numerous areas of the body aside from those mentioned above have been scrutinized with Doppler. The neonatal brain [73, 74], thyroid [75], breast masses [76], . . . the list grows monthly. All viable tissues contain blood vessels, so it seems probable that eventually most body parts will be evaluated with one form of Doppler or another. In some cases the examination may be an immediate success; in others, as we have seen, results may prove the examination impractical. Doppler technology has undergone tremendous change in recent years and its diagnostic abilities have expanded greatly. Although duplex Doppler is a relatively new technology, we now find ourselves referring to it as "conventional duplex." The new technology is already being challenged by the next generation of color-flow Doppler machines. Duplex Doppler has, indeed, opened new horizons in ultrasound diagnosis. The potential of color flow is staggering, and the technology is now only in its infancy. The growth of Doppler technology has been fascinating to watch, and, in our opinion, the most exciting phase is only beginning.

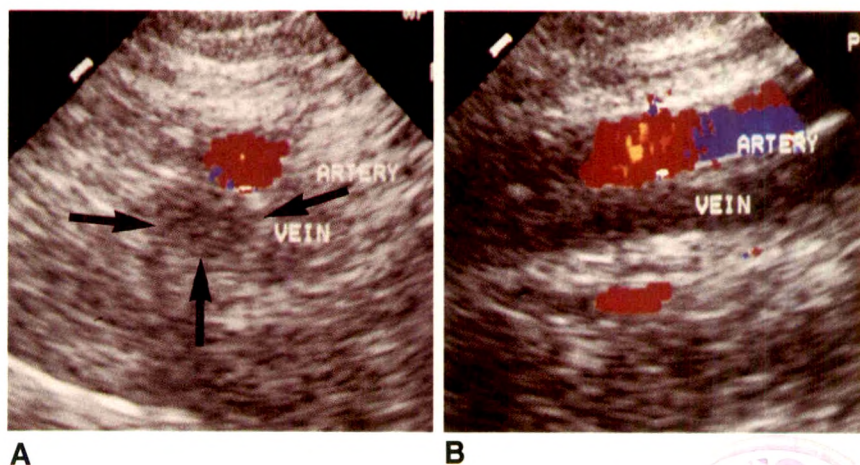


Fig. 11.—A and B, Deep venous thrombosis in patient with painful, swollen right leg after neurosurgery. Transverse (A) and longitudinal (B) color Doppler images of right groin reveal that common femoral vein (VEIN, arrows) is enlarged and filled with hypoechoic material. Adjacent common femoral artery (ARTERY) is patent. Thrombosis was confirmed by inability to compress vein and absence of spectral Doppler signal. Thrombus extended into mid/inferior vena cava.

REFERENCES

- Barber FE, Baker DW, Nation AW, Strandness DE Jr, Reid JM. Ultrasonic duplex echo-Doppler scanner. *IEEE Trans Biomed Eng* 1974;21:109-113
- Callow AD, David M. Hume memorial lecture. An overview of the stroke problem in the carotid territory. *Am J Surg* 1980;140:181-191
- Strother CM, Crummy AB. Cervical arteriosclerosis: diagnostic in need of a clinical answer. *Stroke* 1982;13:551-556
- O'Donnell TF Jr, Erdoes L, Mackey WC, et al. Correlation of B-mode ultrasound imaging and angiography with pathology findings at carotid endarterectomy. *Arch Surg* 1985;120:443-449
- Imparato AM, Riles TS, Gorstein F. The carotid bifurcation plaque: pathologic findings associated with cerebral ischaemia. *Stroke* 1979;10:238-245
- Bluth EL, McVay LV 3rd, Merritt CR, Sullivan MA. The identification of ulcerative plaque with high resolution duplex carotid scanning. *J Ultrasound Med* 1988;7:73-76
- Wolverson MK, Heiberg E, Sundaram M, Tantanavongse S, Shields JB. Carotid atherosclerosis: high-resolution real-time sonography correlated with angiography. *AJR* 1983;140:355-361
- Edwards JH, Kricheff II, Riles T, Imparato A. Angiographically undetected ulceration of the carotid bifurcation as a cause of embolic stroke. *Radiology* 1979;132:369-373
- Eikelboom BC, Riles TR, Mintzer R, Baumann FG, DeFillip G, Lin J. Inaccuracy of angiography in the diagnosis of carotid ulceration. *Stroke* 1983;14:882-885
- Bluth E, Kay D, Merritt C, et al. Sonographic characterization of carotid plaque: detection of hemorrhage. *AJNR* 1986;7:311-315
- Lusby RJ, Ferrell LD, Ehrenfeld WK, Stoney RJ, Wylie EJ. Carotid plaque hemorrhage: its role in production of cerebral ischemia. *Arch Surg* 1982;117:1479-1488
- Imparato AM, Riles TS, Mintzer R, Baumann FG. The importance of hemorrhage in the relationship between gross morphologic characteristics and cerebral symptoms in 376 carotid artery plaques. *Ann Surg* 1983;197:195-203
- Driesbach JM, Seibert CE, Smazal SF, Stavros AT, Daigle RJ. Duplex disease. *AJNR* 1983;4:678-680
- Jacobs NM, Grant EG, Schellinger D, Byrd MC, Richardson JD, Cohan SL. Duplex carotid sonography: criteria for stenosis, accuracy, and pitfalls. *Radiology* 1985;154:385-391
- Blackshear WM, Phillips DJ, Chikos PM, Harley JD, Thiele BL, Strandness DE Jr. Carotid artery velocity patterns in normal and stenotic vessels. *Stroke* 1980;11:67-71
- Robinson ML, Sacks D, Perlmutter GS, Marinelli DL. Diagnostic criteria for carotid duplex sonography. *AJR* 1988;151:1045-1049
- Blasberg DJ. Duplex sonography for carotid artery disease: an accurate technique. *AJNR* 1982;3:609-614
- Zweibel WJ, Crummy AB. Sources of error in Doppler diagnosis of carotid occlusive disease. *AJNR* 1981;2:231-242
- Garth KE, Carroll BA, Sommer FG, Oppenheimer DA. Duplex ultrasound scanning of the carotid arteries with velocity spectrum analysis. *Radiology* 1983;147:823-827
- Vaisman V, Wojciechowski M. Carotid artery disease: new criteria for evaluation by sonographic duplex scanning. *Radiology* 1986;158:253-255
- Grant EG, Wong W, Tessler F, Perrella R. Cerebrovascular ultrasound imaging. *Radiol Clin North Am* 1988;26:1111-1130
- Doherty FJ, McInerney KP. Cardiac Doppler. In: Grant EG, White EM, eds. *Duplex sonography*. New York: Springer-Verlag, 1988:69-128
- Omoto R. *Color atlas of real-time two dimensional Doppler echocardiography*. Tokyo: Sinden-To-Chiryosha, 1987
- Taylor KJ, Burns PN, Woodcock JP, Wells PN. Blood flow in deep abdominal and pelvic vessels: ultrasonic pulsed-Doppler analysis. *Radiology* 1985;154:487-493
- Miller VE, Berland LL. Pulsed Doppler duplex sonography and CT of portal vein thrombosis. *AJR* 1985;145:73-76
- Weltin G, Taylor KJ, Carter AR, Taylor CR. Duplex Doppler: identification of cavernous transformation of the portal vein. *AJR* 1985;144:999-1001
- Huey H, Cooperberg PL, Bogoch A. Diagnosis of giant varix of the coronary vein by pulsed-Doppler sonography. *AJR* 1984;143:77-78
- Bezzi M, Mitchell DG, Needleman L, Goldberg BB. Iatrogenic aneurysmal portal-hepatic venous fistula. *J Ultrasound Med* 1988;7:457-461
- Patriquin HB, Lafortune M, Burns PN, Dauzat M. Duplex Doppler examination in portal hypertension: technique and anatomy. *AJR* 1987;149:71-76
- Nelson RC, Lovett KE, Chezmar JL, et al. Comparison of pulsed Doppler sonography and angiography in patients with portal hypertension. *AJR* 1987;149:77-81
- Bressler EL, Rubin JM, McCracken S. Sonographic parallel channel sign: a reappraisal. *Radiology* 1987;164:343-346
- Wing VW, Laing FC, Jeffrey RB, Guyon J. Sonographic differentiation of enlarged hepatic arteries from dilated intrahepatic bile ducts. *AJR* 1985;145:57-61
- Berland LL, Lawson TL, Foley WD. Porta hepatis: sonographic discrimination of bile ducts from arteries with pulsed Doppler with new anatomic criteria. *AJR* 1982;138:833-840
- Flint EW, Sumkin JH, Zajko AB, Bowen A. Duplex sonography of hepatic artery thrombosis after liver transplantation. *AJR* 1988;151:481-483
- Taylor KJ, Morse SS, Weltin GG, Riely CA, Flye MW. Liver transplant recipients: portal duplex US with correlative angiography. *Radiology* 1986;159:357-363
- Dalen K, Day DL, Ascher NL, Hunter DW, et al. Imaging of vascular complications after hepatic transplantation. *AJR* 1988;150:1285-1290
- Grant EG, Perrella RR, Tessler FN, Lois J, Busuttill R. Budd-Chiari syndrome: results of duplex and color Doppler imaging. *AJR* 1989;152:377-381
- Lafortune M, Patriquin H, Pomier G, et al. Hemodynamic changes in portal circulation after portosystemic shunts: use of duplex sonography in 43 patients. *AJR* 1987;149:701-706
- Cameron JL, Kadir S, Pierce WS. Mesosplenic shunt: a prosthesis modification. *Surgery* 1984;96:114-116
- Taylor KJ, Ramos I, Morse SS, Fortune KL, Hammers L, Taylor CR. Focal liver masses: differential diagnosis with pulsed Doppler US. *Radiology* 1987;164:643-647
- Guida PM, Moore SW. Aneurysm of the hepatic artery. Report of five cases with a brief review of the previously reported cases. *Surgery* 1966;60:299-310
- Falkoff GE, Taylor KJW, Morse S. Hepatic artery pseudoaneurysm: diagnosis with real-time and pulsed Doppler US. *Radiology* 1986;158:55-56
- Taylor DC, Kettler MD, Moneta GL, et al. Duplex ultrasound scanning in the diagnosis of renal artery stenosis: a prospective evaluation. *J Vasc Surg* 1988;7:363-369
- Rigsby CM, Burns PN, Weltin GG, Chen B, Bia M, Taylor KJW. Doppler signal quantitation in renal allografts: comparison in normal and rejecting transplants, with pathologic correlation. *Radiology* 1987;162:39-42
- Steinberg HV, Nelson RC, Murphy FB, et al. Renal allograft rejection: evaluation by Doppler US and MR imaging. *Radiology* 1987;162:337-342
- Buckley AR, Cooperberg PL, Reeve CE, Magil AB. The distinction between acute renal transplant rejection and cyclosporine nephrotoxicity: value of duplex sonography. *AJR* 1987;149:521-525
- Rifkin MD, Needleman L, Pasto ME, et al. Evaluation of renal transplant rejection by duplex Doppler examination: value of the resistive index. *AJR* 1987;148:759-762
- Genkins SM, Sanfilippo FP, Carroll BA. Duplex Doppler sonography of renal transplants: lack of sensitivity and specificity in establishing pathologic diagnosis. *AJR* 1989;152:535-539
- Taylor KJ, Morse SS, Rigsby CM, Bia M, Schiff M. Vascular complications in renal allografts: detection with duplex Doppler US. *Radiology* 1987;162:31-38
- Appelman PT, DeJong TE, Lampmann LE. Deep venous thrombosis of the leg: US findings. *Radiology* 1987;163:743-746
- Taylor KJ, Burns PN, Wells PNT, Conway DI, Hull MG. Ultrasound Doppler flow studies of the ovarian and uterine arteries. *Br J Obstet Gynaecol* 1985;92:240-246
- Nyberg DA, Mack LA, Jeffrey RB Jr, Laing FC. Endovaginal sonographic evaluation of ectopic pregnancy: a prospective study. *AJR* 1987;149:1181-1186
- Taylor KJ, Schwartz PE, Kohorn EI. Gestational trophoblastic neoplasia: diagnosis with Doppler US. *Radiology* 1987;165:445-448
- Wladimiroff JW, Tonge HM, Stewart PA. Doppler ultrasound assessment of cerebral blood flow in the human fetus. *Br J Obstet Gynaecol* 1986;93:471-475
- Jouppila P, Kirkinen P. Increased vascular resistance in the descending

- aorta of the human fetus in hypoxia. *Br J Obstet Gynaecol* **1984**;91:853-856
56. Woo JS, Liang ST, Lo RL, Chan FY. Doppler blood flow velocity waveforms in alpha-thalassemia hydrops fetalis. *J Ultrasound Med* **1987**;6:679-684
 57. Lingman G, Dahlstrom JA, Eik-Nes SH, et al. Haemodynamic evaluation of fetal heart arrhythmias. *Br J Obstet Gynaecol* **1983**;91:647-652
 58. Pretorius DH, Manchester D, Barkin S, et al. Doppler ultrasound of twin transfusion syndrome. *J Ultrasound Med* **1988**;7:117-124
 59. Trudinger BJ, Cook CM. Umbilical and uterine artery flow velocity waveforms in pregnancy associated with major fetal abnormality. *Br J Obstet Gynaecol* **1985**;92:666-670
 60. Wladimiroff JW, Tonge HM, Stewart PA, Reuss A. Severe intrauterine growth retardation; assessment of its origin from fetal arterial flow velocity waveforms. *Eur J Obstet Gynecol Reprod Biol* **1986**;22:23-28
 61. Reuwer PJ, Nuyen WC, Beijer HJ, et al. Characteristics of flow velocities in the umbilical arteries, assessed by Doppler ultrasound. *Eur J Obstet Gynecol Reprod Biol* **1984**;17:397-408
 62. Laurin J, Lingman G, Marsal K, et al. Fetal blood flow in pregnancies complicated by intrauterine growth retardation. *Obstet Gynecol* **1987**;69:895-902
 63. Trudinger BJ, Giles WB, Cook CM. Flow velocity waveforms in the maternal uteroplacental and fetal umbilical placental circulations. *Am J Obstet Gynecol* **1985**;152:155-163
 64. Erskine RL, Ritchie JWK. Umbilical artery blood flow characteristics in normal growth retarded fetuses. *Br J Obstet Gynaecol* **1985**;92:605-610
 65. Trudinger BJ, Giles WB, Cook CM, Bombardier J, Collins L. Fetal umbilical artery flow velocity waveforms and placental resistance: clinical significance. *Br J Obstet Gynaecol* **1985**;92:23-30
 66. Jager KA, Phillips DJ, Martin RL, et al. Noninvasive mapping of lower limb arterial lesions. *Ultrasound Med Biol* **1985**;11:515-521
 67. Helvie MA, Rubin JM, Silver TM, Kresowik TF. The distinction between femoral artery pseudoaneurysms and other causes of groin masses: value of duplex Doppler sonography. *AJR* **1988**;150:1177-1180
 68. Mitchell DG, Needleman L, Bezzi M. Femoral artery pseudoaneurysm: diagnosis with conventional duplex and color Doppler US. *Radiology* **1987**;165:687-690
 69. Raghavendra BN, Rosen RJ, Lam S, Riles T, Horii SC. Deep venous thrombosis: detection by high-resolution real-time ultrasonography. *Radiology* **1984**;152:789-793
 70. Cronan JJ, Dorfman GS, Scola FH, Schepps B, Alexander J. Deep venous thrombosis: US assessment using vein compression. *Radiology* **1987**;162:191-194
 71. Vogel P, Laing FC, Jeffrey RB Jr, Wing VW. Deep venous thrombosis of the lower extremity: US evaluation. *Radiology* **1987**;163:747-751
 72. Langsfeld M, Hershey FB, Thorpe L, et al. Duplex B-mode imaging for the diagnosis of deep venous thrombosis. *Arch Surg* **1987**;122:587-591
 73. Grant EG, White EM, Schellinger D, Choyke PL, Sarcone AL. Cranial duplex sonography of the infant. *Radiology* **1987**;163:177-185
 74. Mitchell DG, Merton D, Needleman L, et al. Neonatal brain: color Doppler imaging. Part I. Technique and vascular anatomy. *Radiology* **1988**;167:303-306
 75. Ralls PW, Mayekawa DS, Lee KP, et al. Color-flow Doppler sonography in Graves disease: "thyroid inferno." *AJR* **1988**;150:781-784
 76. Schoenberger SG, Sutherland CM, Robinson AE. Breast neoplasms: duplex sonographic imaging as an adjunct in diagnosis. *Radiology* **1988**;168:665-668

Book Review

Atlas of Sectional Human Anatomy. Frontal, Sagittal, and Horizontal Planes, 2nd ed. By Jean Georges Koritké and Henri Sick. Baltimore: Urban & Schwarzenberg, 329 pp., 1988. \$165

This attractive book is the second edition of an anatomy atlas first published in 1982. This second edition, a single volume with the drawings relabeled in English and with a minimum of abbreviations, should appeal to a wider audience. The book is technically superb and should be useful to students of three-dimensional anatomy. However, it is unlikely to be as useful to radiologists.

The atlas contains photographs of cadaveric sections in axial, coronal, and sagittal planes through the head and torso; these are illustrated as viewed from above and below, from the front and the back, and from the left and the right. A clearly labeled drawing of each section is displayed on the page opposite each black-and-white photograph. A clear and concise statement of the orientation of the photograph and an indication of the vertebral levels and degree of magnification accompany each photograph. Approximately 25% of the book is devoted to the head and neck, about 30% to the thorax, and the remaining 150 pages to the abdomen and pelvis. The pelvis and perineum of both males and females are shown. The shoulder joint and the hip joint are included as separate sections of the upper thorax and pelvis.

The photographs of the torso are excellent. Sagittal and coronal planes printed in a large page size provide an excellent overview of the viscera and should be helpful in teaching anatomic relationships to students. However, detailed anatomy of closely contiguous planes is lacking, especially in the head and spine. Because of its use of sagittal, coronal, and axial views, this atlas may have some use for radiologists who are struggling with the complex anatomy encountered in CT or MR examinations. However, the detail provided in the legends and labels probably will not be adequate for most radiologists. Other atlases such as Eycleshymer and Schoemaker's *A Cross Section Anatomy*, or Wagner and Lawson's *Segmental Anatomy*, or Schnitzlein and Murtagh's *Imaging Anatomy of the Head and Spine* may be more appropriate for radiologists. However, this volume is an excellent supplement to other anatomy textbooks. Although the book is expensive, the quality of the images probably justifies the price.

Robert A. Clark
H. Lee Moffitt Cancer Center & Research Institute
Tampa, FL 33682-0179

Editorial

Irresponsible Coauthorship

Robert N. Berk¹

At the Conference on Ethics and Policy in Scientific Publications sponsored by the Council of Biology Editors in Washington, DC, October 1988, leaders in the field of scientific publications discussed the problem of irresponsible coauthorship (unearned listing as an author). After 3 days of analysis, the basic question went unanswered; that is, "Why is an investigator who is otherwise impeccably trustworthy, someone who would never even remotely consider falsifying research data, willing to participate in deceit by allowing his name to be used as a coauthor, when he made no genuine contribution to the paper?"

A coauthor is any author of a publication other than the one listed first. As every reader of medical journals knows, the number of coauthors listed per paper has burgeoned. Chew [1] calculated that the *AJR* and *Radiology* have experienced an exponential increase in the number of authorships with only a linear increase in the number of papers published since 1950. Some of the increase in the number of authors per article is warranted in view of the greater complexity of the average report now compared with 1950 and because of the greater opportunity today to collect material from a number of sources. However, assignment of coauthorship has obviously been abused; coauthorship no longer guarantees that the listed person truly has made a substantive contribution to the manuscript.

Harmful Effects of Irresponsible Coauthorship

At the Washington Conference on Ethics, Edward Huth, editor of the *Annals of Internal Medicine*, emphasized that authorship is the currency of academic medicine. As such, it

is the bargaining chip used for promotion, salary increases, grant funding, research time, laboratory space, and other rewards of academia. Gratuitous coauthorship debases the value of this currency. Moreover, it dilutes the satisfaction that comes from being responsible for a contribution to the literature. Arnold Relman, editor of the *New England Journal of Medicine*, said, "Irresponsible coauthorship vitiates the dignity of authorship and raises concern for intellectual honesty." Such authorship is fraud, which, like a stain, can extend to other transgressions such as falsification of data.

Coauthorship implies personal responsibility for the content of the paper. Hence, gratuitous coauthorship makes coauthors vulnerable to charges of fraud, if the content of the paper is subsequently shown to have been falsified. It is no defense for the coauthor to claim, "I am not guilty of fraud. I really had nothing to do with the paper." The coauthor is, indeed, guilty — unwittingly perhaps — but guilty nevertheless.

In other circumstances, by assigning coauthorship irresponsibly, the first author gives the coauthor the legal right to steal his work. Coauthors are free to use the work in any way they see fit and to claim it as their own without recognition of the first author. The first author may have no defense when he sees that his work has been republished by a gratuitous coauthor without credit to the person who truly did the work.

Definition of Responsible Coauthorship

Responsible coauthorship requires the coauthor to have made a substantial and specific intellectual contribution to the work. It indicates active participation with contribution of

This work is an excerpt of information and ideas presented at the Conference on Ethics and Policy in Scientific Publication, sponsored by the Council of Biology Editors, Washington, DC, October 16–19, 1988.

¹ Editor-in-Chief, *American Journal of Roentgenology*, 2223 Avenida de la Playa, Ste. 200, La Jolla, CA 92037-3218. Address reprint requests to R. N. Berk.

thought and effort, and it guarantees that the coauthor has the ability to defend the results and that he assumes responsibility for them. It is different from names that appear in an acknowledgment, which serves to recognize lesser contributions.

At the Conference on Ethics, Vernon Houk, assistant surgeon general, reviewed the qualifications for coauthorship. To be listed as a coauthor, the person must have done one or more of the following: provided the idea (not just suggested that the first author work on a certain problem), designed the protocol, played a leadership role in the acquisition of the data, executed the study, analyzed the data, reviewed the literature, and/or written and revised the manuscript.

It is inappropriate to assign coauthorship as a courtesy (honorary coauthorship), as a gift (gratuitous coauthorship), or solely because the person is a member of a "team" (cronyism). Likewise, coauthorship is not indicated if the individual's only contribution was technical, financial, or editorial or if his sole involvement was having his name on the grant that supported the work. Coauthorship is not warranted if the person served only as a department or laboratory manager, chief of the service, or chairman of the department. Someone whose sole contribution was to refer the cases included in the investigation or to carry out and interpret routine studies on these patients does not deserve to be listed as a coauthor. Recognition and appreciation for these various services should be given in an acknowledgment.

Role of Editors in Preventing Irresponsible Coauthorship

Huth believes that editors may decide either to do nothing and let others assume responsibility for the problem or to act as lawgivers and gatekeepers. The first choice is for those who believe it is more important for editors to be an author's colleague than his policeman, assuming he cannot be both at the same time. In this case (the present situation with most journals), the editor simply trusts authors to act ethically, just as the editor trusts that data presented by the authors have been collected and analyzed honestly.

Editors can attack the problem by serving as lawgivers; that is, they can provide guidelines to define ethical coauthorship and require coauthors to certify that they truly qualify. The *AJR* requires that all authors sign a form guaranteeing that they "have made substantive and specific intellectual contributions to the article and assume public responsibility for its content." (*AJR* Guidelines for Authors, published monthly in the Journal.) Even so, the editor still must act on trust, having no way of knowing if the coauthors' signatures are forged or if they reflect the true situation.

Editors can act as gatekeepers and limit the number of coauthors allowed per paper. This would prevent such ab-

surdities as having 10 coauthors of a single case report. The problem could be solved also by listing the specific contribution of each coauthor next to his name on the title page. Relman recommends categories such as "with the assistance of" or "in collaboration with." Constance Conrad of Emory University suggests that credits be given as they are in motion pictures and television programs. The idea is to list specific contributions; for example, coauthors could be identified as fund raiser, study design adviser, or manuscript editor. Another solution would be to use print size in proportion to the contribution. The first author's name would appear in the largest type.

Role of the Universities in Preventing Unethical Coauthorship

The best solution to the problem would be to devalue the currency; that is, to decrease the value of coauthorship. This will occur when department chairmen and promotions committees ignore the *number* of papers published by an individual when considering promotion and the allocation of resources [2]. Only the candidate's best papers should be considered.

Department chairmen and senior faculty should establish and circulate guidelines that define ethical coauthorship for department members. Most importantly, they should eschew honorary and gift coauthorship for themselves and frown on it for others.

Conclusion

The question, "Why do certain people who are otherwise completely honest and ethical allow themselves to be involved with the cheating that is inherent in irresponsible coauthorship?", has no simple answer. The notions that most people do it and it is considered acceptable by many are part of the answer. These are the same excuses used by people who would not steal money, but who cheat on their income tax.

The purpose of the Washington Ethics Conference and the intent of this editorial are to help solve the problem of irresponsible coauthorship by focusing attention on it. If specific guidelines to distinguish responsible from irresponsible coauthorship are available and if irresponsible coauthorship is called by its true name — fraud — authors, nearly all of whom pride themselves on being honest, are much less likely to be a party to it.

REFERENCES

1. Chew FS. Coauthorship in radiology journals. *AJR* 1988;150:23-26
2. Berk RN. Threats to the quality of peer-reviewed radiology journals. *AJR* 1988;150:19-21

Bayesian Analysis Revisited: A Radiologist's Survival Guide

Paul J. Chang¹

Today's clinicians are confronted by a bewildering number of new, occasionally intimidating, diagnostic imaging tests. Increasingly, colleagues are calling on the radiologist not only to interpret imaging studies but also to provide guidance in the rational selection of appropriate tests and to offer opinions as to the clinical usefulness of newer techniques. Addressing the latter concerns will be significantly more important for the radiologist in light of present and future economic (and other external) constraints. Although thoroughly trained to perform and interpret diagnostic imaging studies, radiologists in general are not adequately trained to address these important concerns regarding analytic decisions.

Much of the radiologist's advice to the clinician (as well as our enthusiasm for newer imaging techniques) is derived from our review of the radiologic literature. Recently, there has been increasing criticism of this literature with respect to the evaluation of the clinical efficacy of our newer techniques (e.g., MR imaging, transrectal sonography); much of this criticism comes from the same clinicians who depend on radiologists to give them accurate advice [1-5]. A number of workers have raised serious concerns about the design and interpretation of radiologic experimental studies; they point out that many papers contain significant design errors/biases that make our recommendations (and enthusiasm) regarding certain newer imaging tests suspect [1, 5].

A review of the radiologic literature supports this concern; many studies reflect a basic misunderstanding of the fundamental principles of Bayesian analysis. This problem is compounded by the fact that most practicing radiologists feel uncomfortable with Bayesian analysis and, as a result, cannot

critically evaluate the "validity" of the literature. This ability is crucial for the radiologist, who must make an informed contribution to the clinical management of patients.

Thus, it is time to revisit Bayes' theorem. One reason that radiologists have trouble understanding and correctly using this analytical tool is that we were originally exposed to Bayesian analysis in a rather dry, theoretical manner, with a confusing array of contingency tables and equations that soon were forgotten. Although this approach is rigorous, it does not yield an *intuitive* understanding of the concepts. The purpose of this paper, therefore, is not to give an exhaustive, formal exposition of Bayesian analysis but to give radiologists an intuitive feel for the basic principles involved.

What the Clinician Knows and Wants to Know

Prior Probability

Before the selection or evaluation of a specific diagnostic imaging test is considered, it is important to understand clearly what confronts the referring clinician: a patient with a constellation of historical, physical, and laboratory findings, all of which suggest a tentative clinical or differential diagnosis. This leads to the important Bayesian concept of the *prior* or "*pretest*" probability, the clinician's initial assessment (i.e., *before* the imaging test is performed) of how likely it is that the patient truly has a specific disease.

Many workers use the term *prevalence* interchangeably with "prior probability." This is misleading because the clinician usually has significantly more information than the disease

Received June 10, 1988; accepted after revision December 14, 1988.

¹ Department of Diagnostic Radiology and Nuclear Medicine, Stanford University School of Medicine, Stanford, CA 94305. Address reprint requests to P. J. Chang.

AJR 152:721-727, April 1989 0361-803X/89/1524-0721 © American Roentgen Ray Society

prevalence before referral to the radiologist. However, disease prevalence is important in deriving a reasonable prior probability and, occasionally, may be the only information available before referral.

Action Threshold

Clinicians institute therapy or other intervention only if they are convinced that the probability that the patient has the disease in question is beyond an "action threshold" probability. In addition, most physicians will not exclude a diagnosis unless the probability is below an "exclusion threshold." In most cases, the prior or pretest probability will lie somewhere between these threshold values (Fig. 1). Therefore, the purpose of the diagnostic test is to obtain additional information to move the *posterior* or "*posttest*" probability either above the action threshold or below the exclusion threshold.

It is important for the radiologist to determine whether the clinician truly has an action and/or exclusion threshold before a test is recommended; if no threshold exists, the rationality of performing *any* test must be questioned (e.g., the frequently encountered scenario in which the results of a requested imaging test will *not* alter a clinician's decision to institute therapy). Similarly, if the clinician's prior probability is already beyond either the action or exclusion threshold, the usefulness of performing any additional confirmatory tests must be questioned.

This principle applies primarily to tests used for *diagnosis*. There are, of course, other valid reasons for performing imaging tests that are not strictly for diagnostic purposes, such as providing anatomic information for surgical planning, tumor staging, and evaluating treatment response. In these cases, patients would have prior probabilities beyond the action threshold.

How Good Is the Imaging Test?

After the clinician determines the prior probability and the action and exclusion threshold values, the radiologist is ready

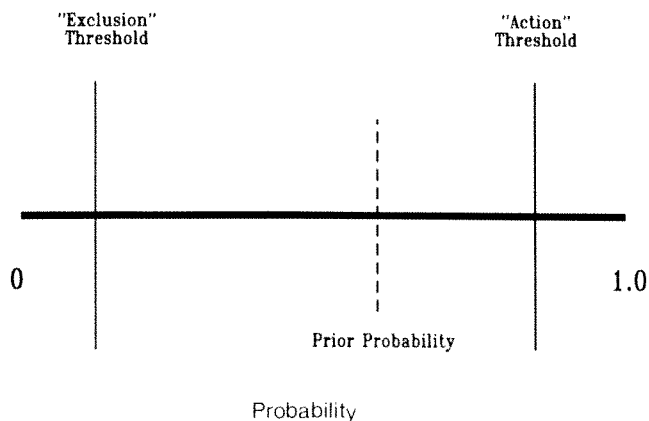


Fig. 1.—Goal of diagnostic test is to update prior or "pretest" probability above or below "action" or "exclusion" threshold, respectively. This updated "posttest" probability represents posterior probability.

to suggest an appropriate diagnostic imaging test. An important consideration in the selection of a test is the test's ability to discriminate between those who have the disease in question and those who do not. The characterization of the test's discriminating performance involves principles derived from Bayesian analysis; these principles should be explicitly addressed by any experimental study evaluating the efficacy of an imaging technique.

The Gold Standard

Determining who has the disease and who does not *must* be done on some basis other than the examination being evaluated. This gold standard may represent pathologic and/or surgical correlation; occasionally, it may correspond to the results of another diagnostic test (i.e., pulmonary angiography for pulmonary embolism or contrast venography for deep venous thrombosis). Despite its label, the gold standard is frequently "imperfect," and it is subject to both false-positive and false-negative results. In addition, one gold standard may be replaced by another as a result of such factors as improved technology or surgical or laboratory advances. The important point is that any experimental study that evaluates the efficacy of diagnostic imaging tests *must* have an explicitly defined, independently derived gold standard. For the purposes of Bayesian analysis, the gold standard is considered to be "perfect," with no false-positive or false-negative results assumed.

Discriminant Criteria

Discriminant criteria are defined specifically for each diagnostic test. For example, possible discriminant criteria for the diagnosis of a malignant liver mass by CT could include the size/configuration of the lesion, attenuation, or contrast enhancement characteristics. (For the purposes of this discussion, let us assume that there is a single discriminant criterion used in our test.) The test is then performed on a population (ideally in a prospective manner), and this discriminant criterion is used with the classification of those with and without the disease defined independently by the gold standard (Fig. 2).

Positivity Criterion

Unfortunately, an overlap almost always exists between those with the disease and those without when the defined discriminant criterion is used. Accordingly, a threshold or "positivity" criterion must be selected according to which an individual is to be called "positive" or "negative" by the test (Fig. 2). The definition of this positivity criterion should be stated explicitly when the efficacy of diagnostic tests is evaluated.

Sensitivity and Specificity

The discriminating power of the imaging test is characterized by the degree of overlap between the diseased and

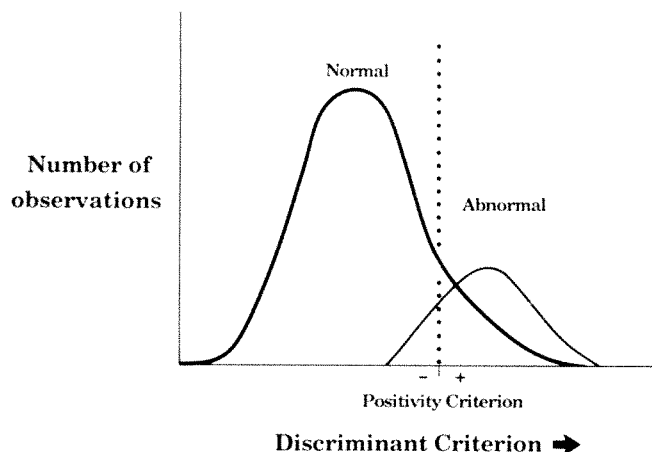


Fig. 2.—Degree of separation between abnormal and normal populations when a specific discriminant criterion is used determines discriminating ability of test. Selected positivity criterion defines a positive or negative test.

disease-free populations present when the defined discriminant and positivity criteria are used. This discriminating power can be described by the *sensitivity* and *specificity* of the test. Sensitivity is defined as the true-positive rate, the proportion of those with the disease (as defined by the gold standard) who test positive when the defined discriminant criteria and positivity criteria are used (Fig. 3A). Specificity is one minus the false-positive rate, where the false-positive rate is defined as the proportion of those without the disease who test positive (Fig. 3B).

Bayes' Theorem

Bayes' theorem models the performance of a diagnostic test as it relates to a specific clinical application by incorporating not only the discriminating power of the diagnostic test

(as measured by sensitivity and specificity) but also the prior or pretest probability to derive the posterior or posttest probability. The formula for Bayes' theorem is a familiar one (Fig. 4); unfortunately, it is also easily forgotten or blindly applied without true understanding of its underlying meaning. It is not important to memorize this formula; it can be looked up as needed. The absolutely crucial point to remember from Bayes' theorem is that *the prior probability (or pretest clinical assessment) is as important as the sensitivity and specificity of the diagnostic test in the determination of the posterior probability (the probability that the patient with a positive test truly has the disease)*.

The foregoing statement can be demonstrated by the use of dreary contingency tables and mathematical formulas; however, a more intuitive understanding of this principle can be achieved by a simple illustration:

Suppose a 25-year-old woman comes to the gynecology clinic worried that she might have syphilis. Assume the sensitivity of the VDRL is 0.90 and the specificity is 0.85. A VDRL is performed and is POSITIVE. What is the probability that this patient truly has syphilis?

An informal survey of physicians at our institution revealed that most clinicians and radiologists believed the probability that this hypothetical patient had syphilis would be relatively high, say about .75–.80. I encourage readers to estimate their own probabilities for this scenario. Now consider the following scenario:

Scenario One: The woman has a past history of multiple episodes of pelvic inflammatory disease and is an IV drug abuser.

Given this information, most physicians updated their probability upward to around .90–.99. The next scenario demonstrates the essential Bayesian principle:

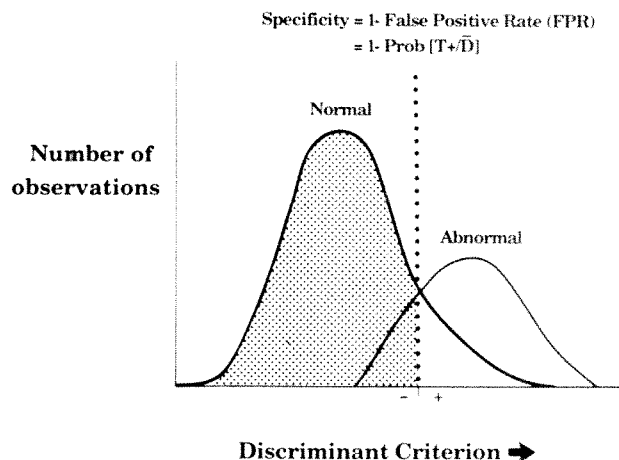
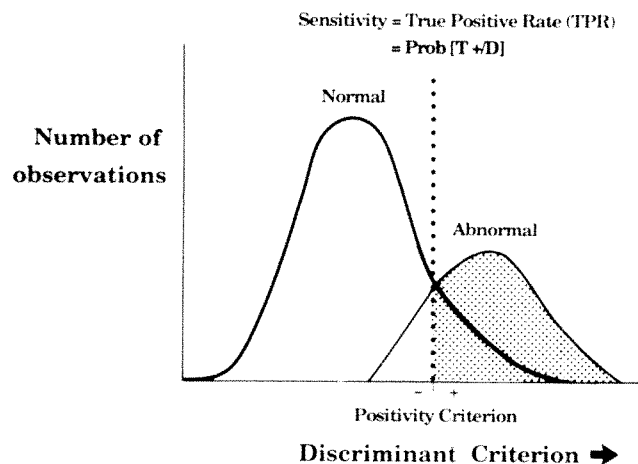


Fig. 3.—Discriminating ability of a test using defined discriminant and positivity criteria is characterized by sensitivity (A) and the specificity (B). Prob [T + D] represents the probability of a positive test in those with the disease. Prob [T + \bar{D}] represents the probability of a positive test in those who do not have the disease.

Bayes' Theorem:

$$P [D|T+] = \frac{(TPR \times \text{Prior Prob})}{(TPR \times \text{Prior Prob}) + [FPR \times (1 - \text{Prior Prob})]}$$

Fig. 4.—Bayes' theorem shows how posterior probability ($P[D|T+]$ represents probability of having disease if test is positive) is a function not only of test efficacy (as defined by sensitivity and specificity) but also of prior probability. TPR = true positive rate or sensitivity; FPR = false positive rate or $[1 - \text{specificity}]$.

Scenario Two: The woman is a virgin studying to be a nun and is afraid that she might have caught syphilis by thinking "impure, immoral thoughts."

With this alternative scenario, all physicians surveyed dramatically lowered their estimate to be less than .10. The important observation is that in both scenarios, *the performance characteristics of the test (as described by the sensitivity and specificity) did not change; it was only the prior probability that changed.* Clearly, the posterior probability (the probability the patient with a positive test truly has the disease) depends not only on test efficacy but, to a high degree, on the prior probability. This simple illustration provides an intuitive understanding of the essential principle behind Bayes' theorem that is not as easily forgotten as the mathematical formula.

The Fluidity of the Positivity Criterion: The ROC Curve

Examination of Figures 2 and 3 suggests that the observed test sensitivity and specificity can be changed by moving the positivity criterion (Figs. 5A and 5B). By moving this threshold criterion, the sensitivity of our test is increased but at the expense of the specificity and vice versa. This change in test sensitivity and specificity as a function of the positivity criterion does *not* alter the intrinsic discriminating power of the examination (the degree of overlap between diseased and undiseased populations).

The selection of the positivity criterion can be quite fluid and specific to the application, especially when the test interpretation is subjective and observer-dependent. This can be demonstrated in any radiology department: a vague, somewhat "nodular" shadow on a chest film can be interpreted either as "worrisome for metastasis, suggest aggressive workup" (in the case of a patient with known malignancy) or as "the probable confluence of normal vascular and osseous structures" (in the case of the "routine" preemployment chest film). This familiar example represents the shifting of the positivity criterion toward improved sensitivity (in the first patient) or specificity (in the second patient).

Accordingly, a wide variation can be observed in test sensitivity and specificity corresponding to identical discriminant criteria and test efficacy. This makes the interpretation of published test performance expressed in terms of sensitivity and specificity alone sometimes difficult and misleading. Clearly, the scalar values of sensitivity and specificity do not describe adequately the intrinsic discriminating power of a test subject to variation in the positivity criterion.

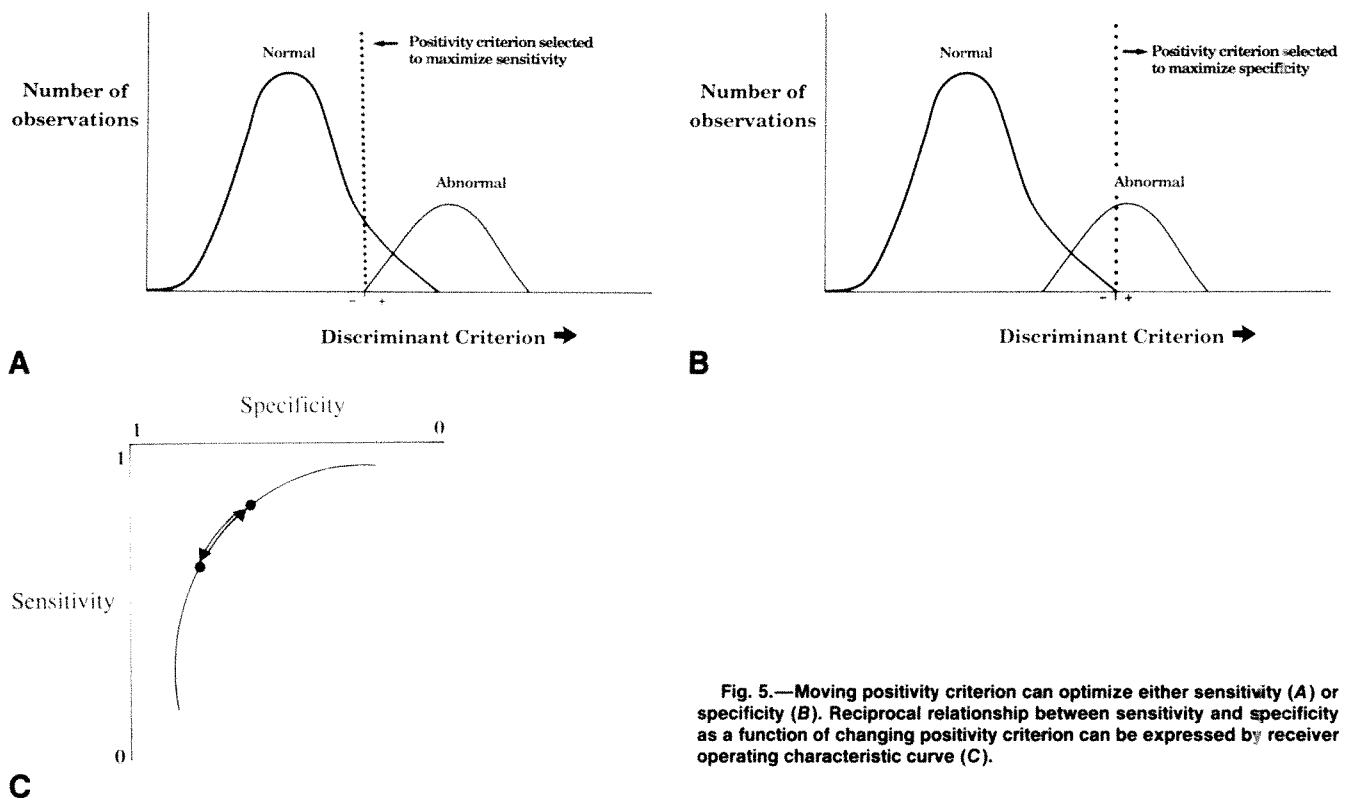


Fig. 5.—Moving positivity criterion can optimize either sensitivity (A) or specificity (B). Reciprocal relationship between sensitivity and specificity as a function of changing positivity criterion can be expressed by receiver operating characteristic curve (C).

The reciprocal relationship between sensitivity and specificity as a function of varying the positivity criterion can be represented more effectively by the use of the receiver operating characteristic (ROC) curve (Fig. 5C). This curve is a more meaningful representation of the intrinsic discriminating power of a given test and enables the direct comparison of the relative performance of different tests, especially when these tests are subject to variation in the positivity criteria. A discussion of the power and elegance of ROC analysis is beyond the scope of this paper; the interested reader is directed to the excellent review by Metz [6].

The foregoing discussion emphasizes the importance of obtaining accurate and thorough clinical information from the referring physician before imaging tests are selected and performed. Without adequate "clinical history," the radiologist is unable to select an appropriate positivity threshold, which results in unacceptably high false-negative or false-positive interpretations. Thorough clinical information also enables the radiologist to help the clinician select an appropriate imaging test: knowledge of the prior probability and the action/exclusion thresholds can be used with Bayes' theorem to select a test with appropriate sensitivity/specificity characteristics [7].

Pitfalls

With this introduction to Bayesian analysis, one can now discuss the various misinterpretations of the theory found in our literature and in our everyday practice; the investigator as well as the practicing radiologist must be able to recognize these potential pitfalls.

No Gold Standard

One cannot meaningfully discuss "sensitivity" or "specificity" without an explicitly defined, independently derived gold standard. Unfortunately, some recent articles, especially those regarding MR imaging, have lacked an *independent* gold standard or used the imaging techniques being evaluated themselves as the gold standard. This leads to misleadingly high "sensitivities" and "specificities."

Ignoring the Importance of the Prior Probability

Bayes' theorem shows that the probability of having the disease given a positive test (the posterior probability) is not the same as the probability of a positive test given the disease (the sensitivity). The relationship between these two values is defined by Bayes' formula and is highly dependent on the prior probability. Radiologists must remind clinicians of this fact before and *after* an examination is performed. We should not be "seduced" by performance characteristics of an imaging test with "high" sensitivity and/or specificity; the interpretation and clinical usefulness of the test are highly dependent on the prior probability—a "positive" test does not necessarily confirm a diagnosis.

Failure to Take Operator-Dependence into Account

The previously discussed variation in observed test sensitivity and specificity as a function of the positivity criterion

suggests that these scalar values do not describe adequately the intrinsic discriminating power of the test when intraobserver variability exists. We must be wary of reported sensitivities and specificities with any imaging technique in which there is considerable observer dependence; your personal experience probably will be different. An ROC curve analysis should be used in the evaluation of tests subject to intraobserver variability.

Avoid "Positive Predictive Value"

In the radiologic literature, authors tend to publish the positive predictive value (PPV) in addition to sensitivity and specificity. The PPV is identical to the posterior or posttest probability discussed previously. I would encourage investigators to avoid stating this value; readers should ignore this number. I believe that the PPV has great potential to mislead. As has been shown, the PPV is highly dependent not only on the performance characteristics of the test being evaluated, but also on the prior probability. Because most studies evaluating imaging are performed at tertiary referral medical centers, the prior probability (which incorporates the prevalence seen at that center) will almost always be much higher than what the "average" practicing radiologist will see. (This is known as *referral bias* [8]. In addition, the prior probability at such centers can be overestimated by a form of *work-up bias*, in which prior test results contribute to the inclusion or exclusion of a patient [8]. As a result, patients with "negative" prior tests may not be evaluated with the imaging technique being studied, thus falsely overestimating the prior probability in retrospective studies.) The high prior probability seen by the investigator usually results in a very high PPV for almost any imaging test being evaluated. Because some will remember that the formal definition of the PPV is "the probability of a patient truly having the disease given a positive test," the practicing radiologist can be given a false sense of security and have ill-founded high expectations for test performance; the actual posttest probability of a positive test will almost always be lower for the practicing radiologist.

Ignoring the Dynamic Nature of Diseases

Occasionally, one sees in the literature a relatively wide variation in observed sensitivities and specificities when the same imaging technique is evaluated. Two "classic" Bayesian hypotheses frequently are used to explain this apparent discrepancy: (1) The various investigators were using different positivity criteria. This would result in a reciprocal relationship between sensitivity and specificity on the *same* ROC curve as seen in Figure 5C; studies claiming high sensitivities would also show lower specificities and vice versa. (2) There is great operator/machine dependence; some investigators are either "better" observers or technically "superior"; alternatively, some workers have "better" or more advanced equipment ("my machine is better than yours"). This would correspond to *different* ROC curves, with one showing superior performance in both sensitivity and specificity relative to another (Fig. 6). Another explanation is intuitively clear but frequently ignored by investigators and practicing radiologists reviewing the literature: "*sensitivity*" and "*specificity*" are actually func-

tions of time and both will change as the disease progresses with time, independent of the intrinsic "goodness" of the test. This is shown in Figures 7A and 7B. Early in almost any disease, significant overlap between diseased and disease-free populations is expected, regardless of the diagnostic test or discriminant criteria (Fig. 7A). However, as the disease continues, overlap between the two populations will be progressively less *regardless of the specific imaging test used* (e.g., a liver metastasis will increase in size, change attenuation values, and increasingly disrupt surrounding parenchyma as it grows, thus making it easier to detect by CT). As a result, we will observe improvement in both the sensitivity and specificity of any test over time as the disease progresses (Fig. 7B). Clearly, the observed sensitivity and specificity of any test will be highly dependent on the temporal stage of the disease.

Radiologists must be aware of this temporal dependency of sensitivity and specificity on the dynamic progression of the disease process. The extrapolation of sensitivity/specificity data derived from relatively advanced disease or from consolidating data spanning all stages of a disease (especially neoplasm) to draw inferences about the performance of an imaging test in the direction of *early* lesions is highly mislead-

ing. Investigators must explicitly control for the temporal stage of the disease being tested.

Comparing Techniques

An important extension of this principle involves studies that attempt to compare the relative performance of various imaging techniques (e.g., comparing CT, MR, and sonography in the detection of liver metastasis). Again, the radiologist must recognize the temporal dependency of sensitivity/specificity on the dynamic progression of the disease. If this dependency is ignored, comparative studies of imaging techniques can be misleading.

The following hypothetical example comparing CT and transrectal sonography in the detection of prostatic carcinoma illustrates the problem. We have already shown that sensitivity (and specificity) are actually functions of time, so it is reasonable to regard Figure 8A as a conceivable sensitivity function curve for CT in the detection and/or staging of prostate cancer. The S shape of the curve reflects the relatively low sensitivity of CT for detecting intraparenchymal lesions that have yet to invade the periprostatic fat or the seminal vesicles. Once the disease progresses through the capsule and in-

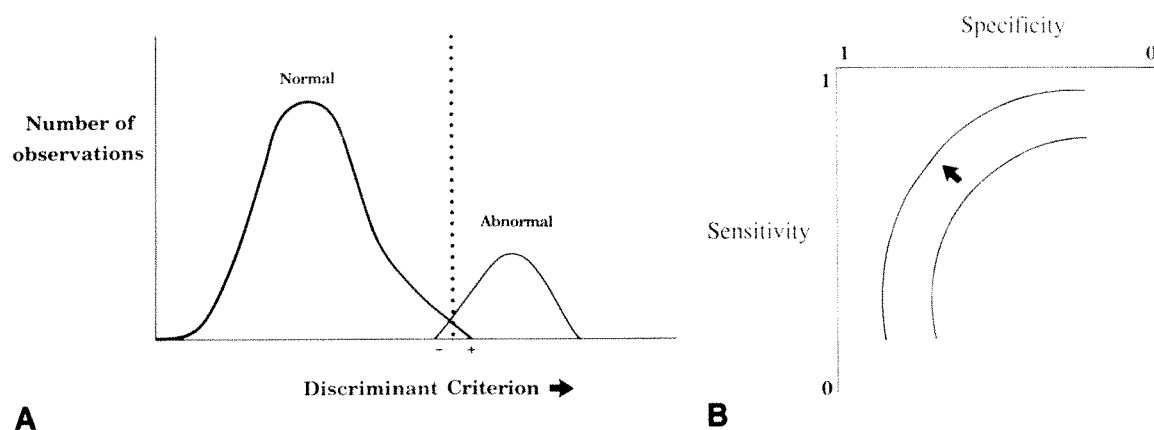


Fig. 6.—We can improve our discriminating ability by using a different test (or by using a different discriminant criterion); this improvement in test performance is due to less overlap between abnormal and normal populations (A). Improvement in both sensitivity and specificity corresponds to moving to a different receiver operating characteristic curve (B).

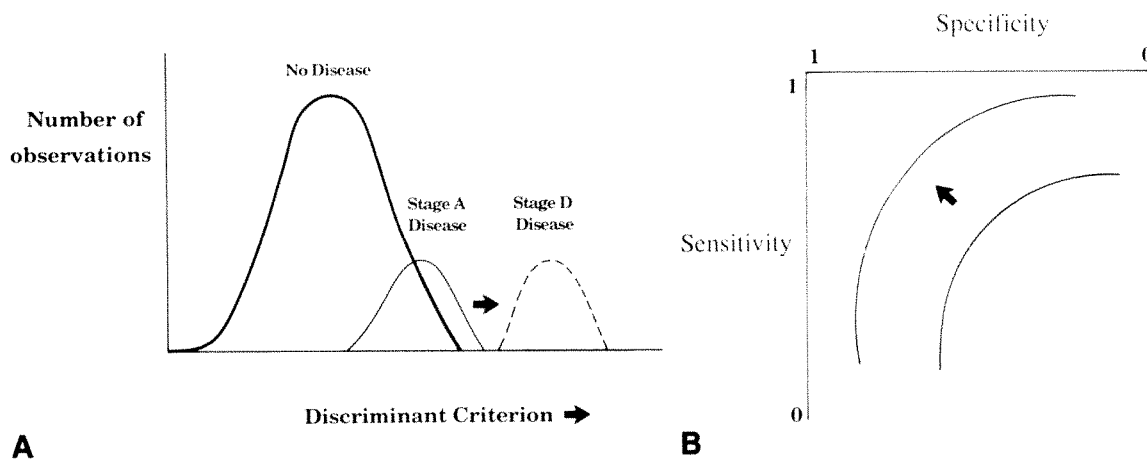
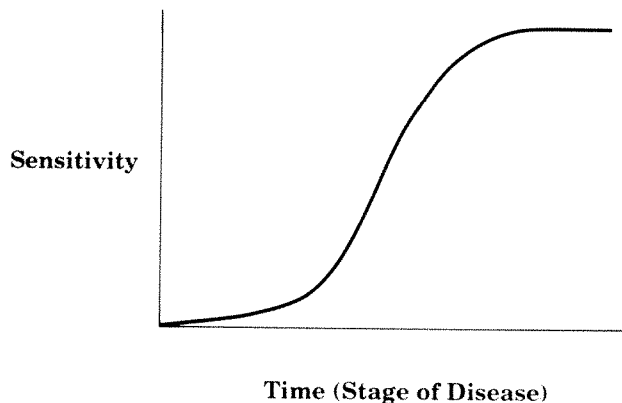
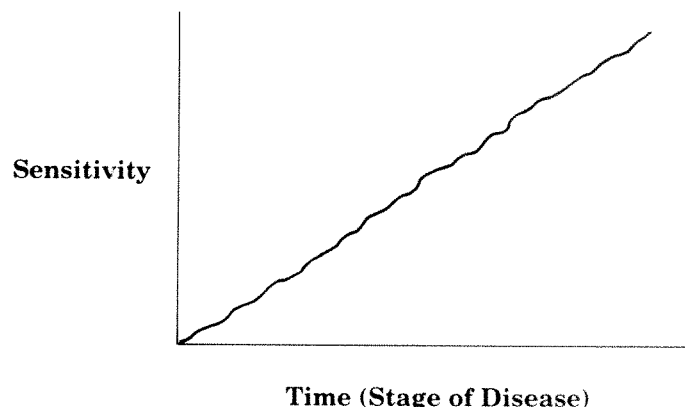


Fig. 7.—By waiting, one will observe both improved sensitivity and specificity. This results from dynamic nature of disease process, which results in progressively less overlap between populations (A) and thus better discriminating ability (B). This improvement in test performance is independent of "intrinsic goodness" of test.

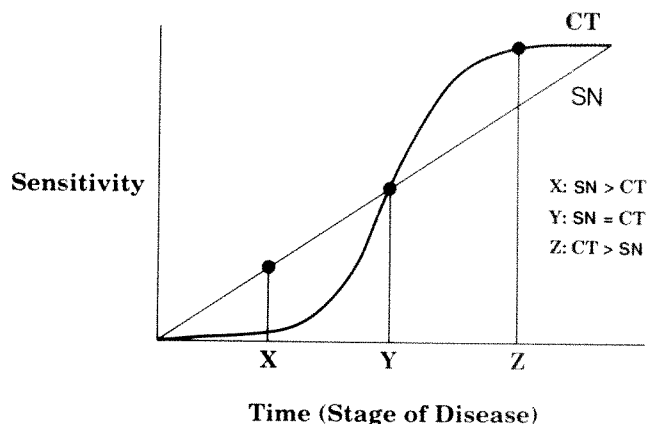


A



B

Fig. 8.—Hypothetical sensitivity of CT (A) and transrectal sonography (B) in detection of prostatic carcinoma as a function of stage of disease. Note how relative “superiority” of one technique compared with the other is highly dependent on temporal stage (X,Y,Z) of disease (C).



C

vades the seminal vesicles, however, sensitivity (as well as specificity) increases rapidly. The corresponding sensitivity curve for transrectal sonography should be somewhat different (Fig. 8B). We expect this curve to increase monotonically in a more “linear” fashion as the disease progresses. This reflects the observation that sonography is better able to differentiate intraparenchymal lesions because of subtle changes in echogenicity well before capsular invasion or other morphologic distortion has occurred.

Overlapping these two curves illustrates the potential misunderstanding (Fig. 8C): *depending on the stage of the disease, we can come to three totally different conclusions regarding the performance of sonography relative to that of CT.* Failure to control carefully for disease stage will almost always guarantee misleading conclusions. Therefore, we must be wary of retrospective multiinstitution comparative studies in which one author compares results of one imaging technique obtained in one clinical setting with results evaluating another imaging test obtained at another institution. Even if disease stage is carefully controlled, such multiinstitutional studies can be misleading because controlling *precisely* for disease stage is extremely difficult. With regard to clinical stage, a wide spectrum occurs within each defined stage. This definition is frequently physician-dependent and open to subjective assessment. One clinician’s “stage B1” lesion may be “stage B2” according to another, even if both are using the same “objective” criteria. The argument can be made that the only rigorous method to compare different imaging techniques critically is to perform all tests on all patients at the same place and time.

Design Bias

Other, somewhat more subtle, experimental design biases can result in overly optimistic sensitivity and specificity claims. These include biases in selection, workup, and test interpretation (including diagnosis and test review bias). Discussion of these pitfalls is beyond the scope of this article; readers are encouraged to read the concise review by Begg and McNeil [8].

ACKNOWLEDGMENT

I am grateful for the helpful advice, assistance, and enthusiastic encouragement received from Gerald Friedland.

REFERENCES

1. Kent DL, Larson EB. Magnetic resonance of the brain and spine: is clinical efficacy established after the first decade? *Ann Intern Med* **1988**;108:402–418
2. Kent DL, Larson EB. Magnetic resonance imaging of the brain and spine: health and public policy committee. *Ann Intern Med* **1988**;108:474–476
3. Kent DL, Larson EB. Editorial. Diagnostic technology assessments: problems and prospects. *Ann Intern Med* **1988**;108:759–761
4. Miller-Catchpole R. Diagnostic and therapeutic technology assessment. *JAMA* **1988**;259:2757–2759
5. Cooper LS, Chalmers TC, McCally M, Berrier J, Sacks HS. The poor quality of early evaluations of magnetic resonance imaging. *JAMA* **1988**;259:3277–3280
6. Metz CE. Basic principles of ROC analysis. *Semin Nucl Med* **1978**;8:283–298
7. Doubilet P. A mathematical approach to interpretation and selection of diagnostic tests. *Med Decis Making* **1983**;3:177–195
8. Begg CB, McNeil BJ. Assessment of radiologic tests: control of bias and other design considerations. *Radiology* **1988**;167:565–569

Book Review

Pulmonary Pathology. Edited by David H. Dail and Samuel P. Hammar. New York: Springer-Verlag, 1200 pp., 1988. \$200

A modern encyclopedic text on lung pathology has been needed for some years now. This impressive reference work fills that need. The book is both thorough and oriented to practical clinical questions. Thirty-four contributing authors represent a "who's who" of the field. The text is generally well written, and illustrations are plentiful. Photographs of gross specimens (i.e., pictures of prime interest to radiologists) are well represented in most chapters. Radiographs also appear in many of the chapters.

Organization is along traditional lines, including anatomy (although gross anatomy is minimally presented), congenital and acquired pediatric diseases, infections (extensively and handsomely presented), emphysema (by Philip Pratt, beautifully illustrated), neoplasms (including current staging concepts for bronchogenic carcinoma), pneumoconioses, and the host of idiopathic entities. Cytology, asbestos, and tobacco each are given separate chapters. A separate radiologic chapter by Paul Friedman is written for an audience of pathologists; although elegantly illustrated, it will be of only modest interest to radiologists.

The presentations of the interstitial pneumonias, unfortunately, are a classic example of fragmentation in a text written by several authors. The contributions of seven authors (six pathologists and a radiologist) are scattered throughout seven chapters. No unifying organization can be found. For instance, Carlos Bedrossian has a nicely crafted section on desquamative interstitial pneumonia, but it is buried between pulmonary hypertension and lipid pneumonia in a

chapter on iatrogenic and toxic injury. Moreover, neither Friedman's nor Bedrossian's discussion of desquamative interstitial pneumonia is indicated in what otherwise appears to be a comprehensive index.

Physically, the book is a visual delight. The 1614 illustrations are reproduced with extraordinary clarity on high-quality paper. The book does test the biceps: it weighs in at 4.5 kg (nearly 10 lb.) and is 6 cm (2 3/8 in.) thick. The chapters are each well referenced, some exceedingly so.

The premier book on pulmonary pathology for the radiologist still remains E. R. Heitzman's *The Lung: Radiologic-Pathologic Correlations* (2nd ed, St. Louis: Mosby, 1984, 546 pp., \$64.95). Providing many direct correlations of radiographs with gross and microscopic specimens, Heitzman's book is packed with radiologic-pathologic perspectives at reasonable cost. However, as a text focused on the everyday entities, it is not a full reference work for the entire range of pulmonary pathology, common or rare. Dail and Hammar's book, on the other hand, clearly is such a work. Unfortunately, the cost of Dail and Hammar's tome necessarily will limit its market (although at \$20/lb it can be argued that it is a good buy). This book deserves a place in departmental libraries and in the personal library of any radiologist who has a major interest in the lung.

John H. M. Austin
Columbia-Presbyterian Medical Center
New York, NY 10032

Comparison of Cine MR Imaging with Doppler Echocardiography for the Evaluation of Aortic Regurgitation

Peter W. Pflugfelder¹
 Joel S. Landzberg²
 Mark M. Cassidy²
 Melvin D. Cheitlin²
 Nelson B. Schiller^{1,2}
 Wolfgang Auffermann¹
 Charles B. Higgins¹

Regurgitant blood flow is associated with localized signal loss of the blood pool within the recipient chamber on cine MR images, which may be useful for assessing regurgitant valvular disease. To evaluate the potential of this technique for determining the severity of aortic regurgitation, multilevel cine MR imaging was performed in 10 normal volunteers and in 25 patients with aortic regurgitation documented and graded for severity by Doppler echocardiography. Cine MR images were analyzed to obtain cardiac chamber volumes and to measure the extent of the signal loss associated with regurgitation. All regurgitant lesions were visualized on cine MR images as areas of diastolic signal loss extending from the aortic valve into the left ventricle. The extent of signal loss and the regurgitant volume determined from analysis of MR images correlated with the echocardiographic severity of the lesion. The total area of diastolic left ventricular signal loss was 0 cm² in 10 normal volunteers, 24 ± 13 (\pm SD) cm² in eight patients with mild aortic regurgitation, 49 ± 11 cm² in nine patients with moderate aortic regurgitation, and 62 ± 20 cm² in eight patients with severe aortic regurgitation ($p < .05$ for moderate and severe vs mild). Left ventricular volumes calculated from MR images correlated well with echocardiographic volumes ($r = .92$, SEE = 30 ml, $p < .0001$). Regurgitant fraction calculated from analysis of cine MR images was $4 \pm 7\%$ in normal volunteers and $31 \pm 8\%$ in mild, $45 \pm 11\%$ in moderate, and $56 \pm 9\%$ in severe aortic regurgitation ($p < .05$ for moderate and severe vs mild and normal).

Thus, cine MR imaging can provide useful qualitative and quantitative data regarding cardiac dimensions and regurgitant valvular flow in patients with aortic regurgitation.

Cine MR imaging uses shallow flip angles, short repetition and echo times, and gradient-recalled echoes to acquire multiple images encompassing the cardiac cycle [1, 2]. Signal intensity of the blood pool is normally high on images obtained with this sequence. However, its intensity is significantly decreased by disturbances in blood flow [3]. High velocity or perhaps turbulent blood flow across abnormal valves results in discrete areas of signal loss, particularly in patients with mitral and aortic regurgitation [2]. We previously demonstrated that it is possible to measure right and left ventricular end-diastolic and end-systolic volumes by using MR imaging [4, 5], and that the stroke volumes of the two ventricles obtained in this way are equivalent in normal subjects [5]. In this study, both echocardiographic and cine MR studies were performed in 25 patients with chronic aortic regurgitation to correlate left ventricular volumes obtained by the two cardiac imaging techniques. Other information obtained from the analysis of cine MR images, including the total area of diastolic signal loss and the volume of regurgitant blood flow, was related to the Doppler echocardiographic severity of aortic regurgitation.

Subjects and Methods

Subjects

Twenty-five patients 23–87 years old (mean \pm SD, 50 ± 18) with known chronic aortic insufficiency were evaluated by Doppler echocardiography and cine MR. Both studies were

Received August 26, 1988; accepted after revision November 28, 1988.

Presented at the annual meeting of the American Heart Association, Anaheim, CA, November 1987.

P. W. Pflugfelder is supported by a grant from the Canadian Heart Foundation.

¹ Department of Radiology, C309, Box 0628, University of California School of Medicine, San Francisco, CA 94143. Address reprint requests to C. B. Higgins.

² Department of Medicine, Division of Cardiology, University of California School of Medicine, San Francisco, CA 94143.

AJR 152:729–735, April 1989

0361–803X/89/1524–0729

© American Roentgen Ray Society

performed on the same day if possible. Fifteen of 25 subjects had the two studies within 7 days of each other, four subjects had studies between 1 and 4 weeks of each other, and six subjects had studies more than 4 weeks apart (mean, 18 weeks). Ten normal subjects served as controls for comparison of intracavitary signal phenomena and volume measurements; details about these subjects have already been reported [5]. All patients and five of the normal volunteers had complete Doppler echocardiographic examinations for the assessment of regurgitant blood flow and determination of left ventricular end-diastolic and end-systolic volumes. In addition, 22 of 25 patients had color Doppler echocardiography to visualize the aortic regurgitant jet.

Echocardiography

Two-dimensional echocardiographic and Doppler studies were performed by using the Irex Meridian (Johnson and Johnson, New Brunswick, NJ). Patients were imaged from the parasternal and apical windows in the 90° left lateral decubitus position. Angular and translational adjustments of the transducer were made to maximize chamber size as well as Doppler flow velocity and signal intensity. Pulsed Doppler mapping of the aortic regurgitant jet was performed in the parasternal short and long axis; apical two- and four-chamber views were obtained as well. Continuous-wave Doppler sonography was used to obtain the optimal aortic regurgitant envelope for measurement of the pressure half-time [6, 7]. Color Doppler flow mapping was performed by using the Aloka 880 (Corometrics Medical Systems, Wallingford, CT) with 2.5- and 3.5-MHz transducers [8]. Gain adjustments were made to maximize the size of the color flow signal of the aortic regurgitant jet recorded in the parasternal and apical views.

Measurement of left ventricular volumes from the two-dimensional echocardiographic images was made by using a commercially available Diasonics (Milpitas, CA) light-pen digitizing system [9, 10]. End-diastolic volumes were traced at the peak of the R wave of the ECG or just after mitral valve closure. The end-systolic volumes were traced at the frame preceding mitral valve opening. The pressure half-time of the aortic regurgitant flow was measured off-line on the Irex Meridian.

A qualitative estimate of the severity of aortic regurgitation (mild, moderate, or severe) was made independently by two observers. The following aspects were considered: (1) the depth, width, and intensity of the aortic regurgitant jet in the parasternal and apical views [11]; (2) the pressure half-time of the aortic regurgitant jet [6, 7]; (3) the depth and size of the aortic regurgitant jet on the color Doppler study [8]; and (4) the left ventricular volumes [12]. In cases of discrepancy, the study was reviewed by the two observers and a consensus was obtained. Discrepancies between the two reviewers occurred in only five cases. All studies were analyzed without knowledge of the findings of the cine MR study. On the basis of this analysis, aortic regurgitation was graded as mild in eight patients, moderate in nine, and severe in the remaining eight.

Cine MR Imaging

Cine MR images were acquired by using methods previously described [2, 5]. Briefly, the technique used shallow flip angles of 30°, an echo delay time of 12 msec, and an interpulse repetition time of 21 msec. The read gradient was inverted before data acquisition, leading to a so-called gradient-refocused echo. The ECG signal was recorded simultaneously and stored in a microcomputer that controlled advancement of the phase-encoding gradient with the R wave. To limit total imaging time, multiple levels were imaged simultane-

ously. The RF pulses alternated between two levels (four subjects) and three levels (21 subjects), resulting in a temporal resolution of 42 or 63 msec/frame, respectively. For the multislice acquisition, a 1-cm gap was used between each slice in the acquisition. The next multislice acquisition acquired alternating 1-cm slices so that the gap was filled on the subsequent acquisition. The number of time frames acquired per cardiac cycle was inversely proportional to the subject's heart rate and the number of levels scanned simultaneously. The acquisition matrix was 128×256 and was interpolated to 256×256 for display, resulting in a normal pixel size of 1.25×1.25 mm. Two data acquisitions were averaged to improve the signal-to-noise ratio, and thus images were acquired over 256 R-R intervals. Physiologic variations in heart rate were compensated by linear interpolation between neighboring time frames to provide a constant number of images within each R-R interval. Computer reconstruction time was approximately 5 min for each cine imaging series.

An initial multislice ECG-gated spin-echo sequence in the coronal plane was used to localize the inferior and superior borders of the heart. This sequence required approximately 2 min to complete. The transverse cine series began at the inferior border and continued until the bifurcation of the main pulmonary artery and roof of the left atrium were visualized. The heart was usually encompassed in 12 contiguous imaging planes of 10-mm slice thickness. The nominal total imaging time, which was determined by the subject's heart rate and the number of imaging levels acquired, ranged from 15 to 30 min:

$$\text{Imaging time} = (\text{phase-encoding steps} \times 2 \text{ excitations} \times \text{No. of series}) / \text{heart rate}$$

However, the study was done on a prototype system, which necessitated a substantially longer time in actual practice; the total time per study, including setup and computer reconstruction time, was 70–90 min.

Analysis of Cine Images

For analysis, images were first displayed on the computer monitor in a movie display to evaluate cardiac function and changes in blood-pool signal intensity during the cardiac cycle. The shape, extension, and timing of areas of altered signal intensity were noted. The end-systolic and end-diastolic images were identified by the movement of the tricuspid and mitral valves. End-systole was defined as the last image showing closed atrioventricular valves and end-diastole as the last image with these valves open. The appearance of regurgitant blood flow further aided in the timing of cardiac events. In the patients with aortic regurgitation, the onset of diastole was marked by the appearance of signal loss within the left ventricular blood pool in continuity with the aortic valve. The end-diastolic time frame was the last one showing an area of left ventricular signal loss.

All images were analyzed by one observer. The signal void could not be measured in one patient in the moderate category because it was inadvertently deleted. Images of 10 randomly selected patients were analyzed independently by a second observer. The first observer also reanalyzed 10 randomly selected studies after a period of at least 4 weeks from the first analysis. The qualitative echocardiographic grading of aortic regurgitation was not known by either observer at the time of analysis. Because the window and level settings are critical for visual edge detection, the level setting on the computer display was standardized to the mean of the signal intensities of myocardium and blood determined from two regions of interest in the respective areas on the first image after the R wave at the midventricular level. The width of the window was arbitrarily set to 50–75% of the level and was maintained constant at these settings for analysis in each individual patient. At each anatomic level, the

endocardium was outlined by using a track-ball cursor system on the end-diastolic and end-systolic images. Smaller trabeculations, commonly noted along the anterolateral wall of the left ventricle and in the right ventricle, were included in the ventricular volumes. However, the papillary muscles of the left ventricle and the moderator band

were excluded from the ventricular volumes. The insertion points of the atrioventricular valves were clearly visible, facilitating the distinction of ventricles from atria. The aortic valve cusps usually could be visualized, and therefore it was possible to distinguish the ventricular outflow tract from the aortic root. The transition from right ventricular

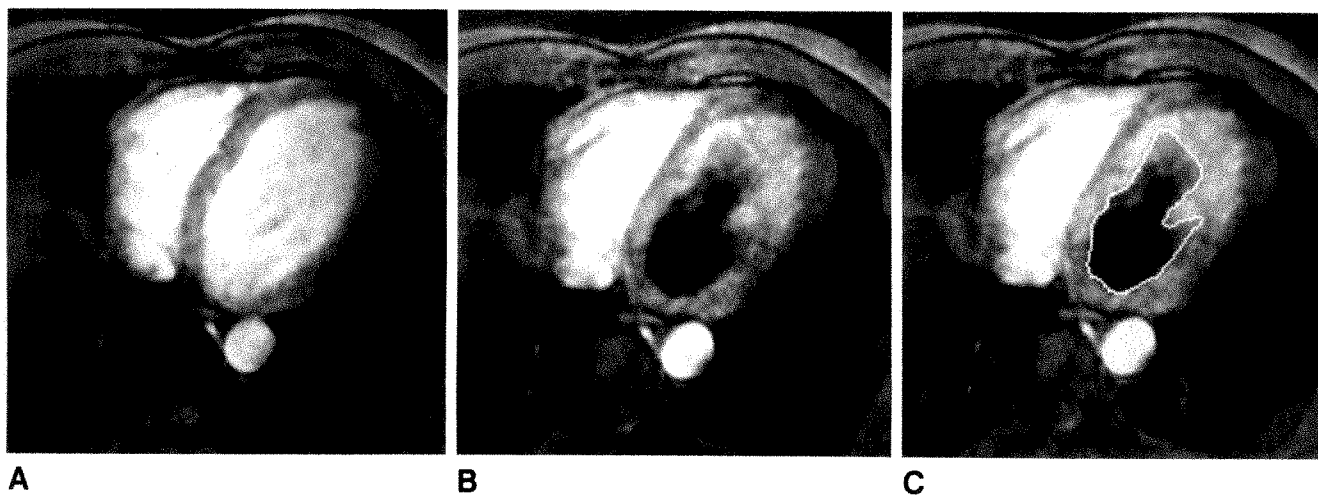


Fig. 1.—Cine MR images show alterations in blood-pool signal in severe aortic regurgitation. A, Midventricular image. First frame of systole shows blood pool has high signal intensity. B, Mid-diastolic frame shows signal loss caused by aortic regurgitation. C, Typical region of interest to quantify area of signal loss. Tracing outlines flow void caused by aortic regurgitation.

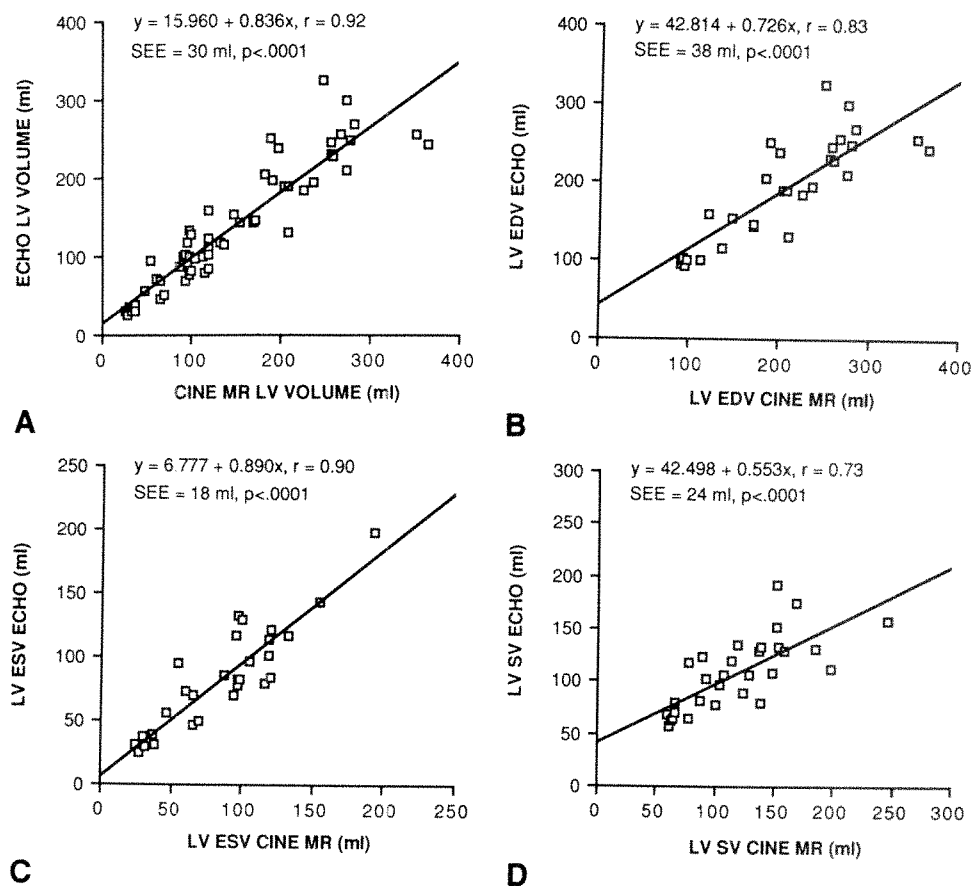


Fig. 2.—A, Correlation for both end-diastolic and end-systolic volumes determined by echocardiography and cine MR.

B, Correlation for end-diastolic volumes.

C, Correlation for end-systolic volumes.

D, Correlation for stroke volumes.

Echo = echocardiography; LV = left ventricular; EDV = end-diastolic volume; ESV = end-systolic volume; SV = stroke volume.

outflow tract to main pulmonary artery was marked by the absence of myocardium at the root of the pulmonary artery and in most patients by visualization of the cusps of the pulmonic valve.

The cross-sectional area of the ventricular cavities on each image was calculated by the display program. Ventricular volumes were obtained by summing the product of the areas of blood pool and slice thickness in the end-systolic and end-diastolic images at each level [5]. Volume determinations required between 20 and 30 min for a trained observer. Stroke volumes were calculated as the difference between end-diastolic and end-systolic volumes for each ventricle. The regurgitant volume was calculated as left ventricular stroke volume minus right ventricular stroke volume. The regurgitant fraction was calculated as (left ventricular stroke volume - right ventricular stroke volume)/left ventricular stroke volume.

In addition to volume determinations, the area of diastolic signal loss was also measured at each level in which it was visible. The area of signal loss was outlined by using the track-ball cursor system as before, yielding the cross-sectional area of the signal void at each level. This procedure was then repeated at each anatomic level to obtain the total area (sum of areas at each level with signal void) of signal loss for each patient. The dimension of the base of the jet (signal void) in contact with the aortic valve was measured, as was the absolute (in millimeters) and relative penetration of signal loss into the left ventricle (extent of jet into the left ventricle [mm]/distance [mm] from aortic valve to apex). A total of 59 areas of signal loss (59 images containing signal void) in 11 randomly selected patients were reanalyzed after a period of more than 4 weeks had elapsed to assess intraobserver reproducibility. Fifty-four areas of signal loss in 10 further randomly selected patients were analyzed by a second observer to evaluate the interobserver reproducibility of the measurement of signal loss.

Statistical Analysis

Mean values \pm one standard deviation are given. Differences between normal volunteers and patients with different severities of aortic regurgitation were tested for statistical significance by using single-factor analysis of variance. Comparisons of severity were also made among the three groups. Scheffe's test for multiple contrasts [13] was applied to significant differences defined by the analysis of variance. The correlation between cardiac volumes by cine MR and echocardiography was also assessed with linear regression analysis. Inter- and intraobserver variabilities were assessed by using linear regression analysis. A p value $< .05$ was considered significant.

Results

In all 25 patients with aortic regurgitation, the valvular lesion was visible as an area of diastolic low signal intensity or signal void during diastole (Fig. 1), extending from the aortic valve for a variable distance into the body of the left ventricle. The area of signal void was present throughout diastole in all patients.

Correlation with Echocardiographic Volumes

The correlation for combined left ventricular end-diastolic and end-systolic volumes obtained by cine MR with echocardiographic volumes was good ($r = 0.92$, standard error of estimate (SEE) = 30 ml, and $p < .0001$) (Fig. 2). The correlation for left ventricular end-diastolic volume alone was $r =$

.83, SEE = 38 ml, and $p < .0001$. For the end-systolic volume, the correlation between volumes obtained by the two techniques was somewhat better: $r = .90$, SEE = 18 ml, and $p < .0001$. For left ventricular stroke volume the correlation was $r = .73$, SEE = 24 ml, and $p < .0001$. Correlation for the ejection fraction obtained by the two techniques was $r = .76$, SEE = 6 ejection fraction units, and $p < .0001$.

Cine MR Parameters and Echocardiographic Severity

Among the normal subjects, the ratio of left to right ventricular stroke volume approached unity (Figs. 3 and 4), reflected in the regurgitant volume of 3 ± 5 ml. In patients with mild aortic regurgitation, the stroke volume ratio was 1.5 ± 0.2 and the regurgitant volume (Fig. 4) was 30 ± 12 ml. Because of the small number of patients in this group with mild regurgitation, these values did not reach statistical significance compared with the normal subjects. In moderate aortic regurgitation, the stroke volume ratio was 1.9 ± 0.4 and the regurgitant volume was 60 ± 20 ml ($p < .05$ vs normal). In severe aortic regurgitation stroke, the volume ratio was 2.3

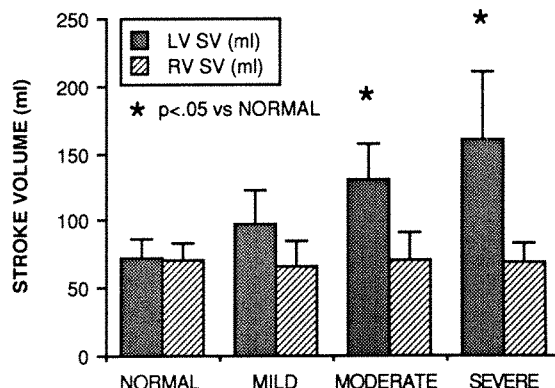


Fig. 3.—Right and left ventricular stroke volumes from cine MR images related to severity of aortic regurgitation. Right ventricular stroke volume (RV SV) remains constant as left ventricular stroke volume (LV SV) increases in relation to severity.

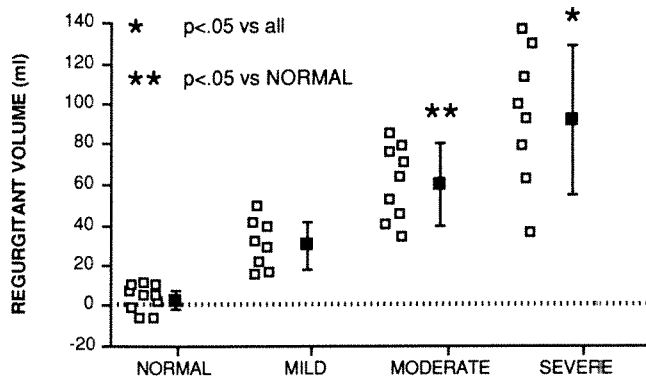


Fig. 4.—Individual values of regurgitant volumes derived from cine MR. In one patient with severe regurgitation, volumes could not be measured due to technical problems.

± 0.5 and the regurgitant volume was 92 ± 37 ml ($p < .05$ vs mild and $p = .01$ vs normal). Among normal subjects, the calculated regurgitant fraction was $4 \pm 7\%$; in mild aortic regurgitation, $31 \pm 8\%$ ($p < .01$ vs normal); in moderate, $45 \pm 10\%$ ($p < .05$ vs mild and $p < .01$ vs normal); and in severe, $56 \pm 9\%$ ($p < .01$ vs mild and normal).

The area of diastolic signal loss also reflected the echocardiographic severity of aortic regurgitation (Figs. 5 and 6). Diastolic signal loss emanating from the aortic valve was not visualized in any normal subjects. The total area of diastolic signal loss (Fig. 7) was 24 ± 13 cm² in patients with mild aortic regurgitation, 49 ± 11 cm² in moderate, and 62 ± 20

cm² in severe ($p < .01$ for moderate and severe vs mild). Neither the dimension of the base of the aortic regurgitant jet measured from cine MR images nor the relative penetration of the jet into the left ventricular cavity correlated with echocardiographic severity.

Inter- and Intraobserver Variability

The inter- and intraobserver variability among the normal volunteers has been reported previously [5]. In the present study, intra- and interobserver correlation for both volume measurements and measurement of areas of signal loss in patients with aortic regurgitation was good (Table 1).

Fig. 5.—A, First frame of systole in patient with mild aortic regurgitation.

B, Mid-diastolic frame shows small area of signal loss (arrows) abutting anterior papillary muscle.

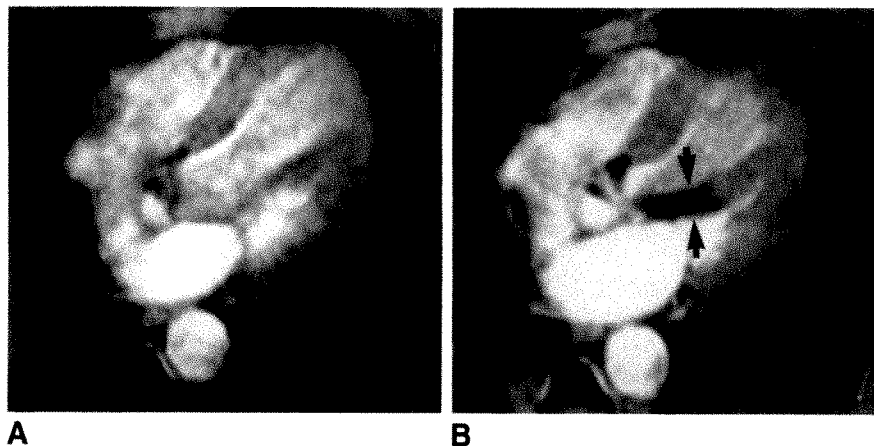
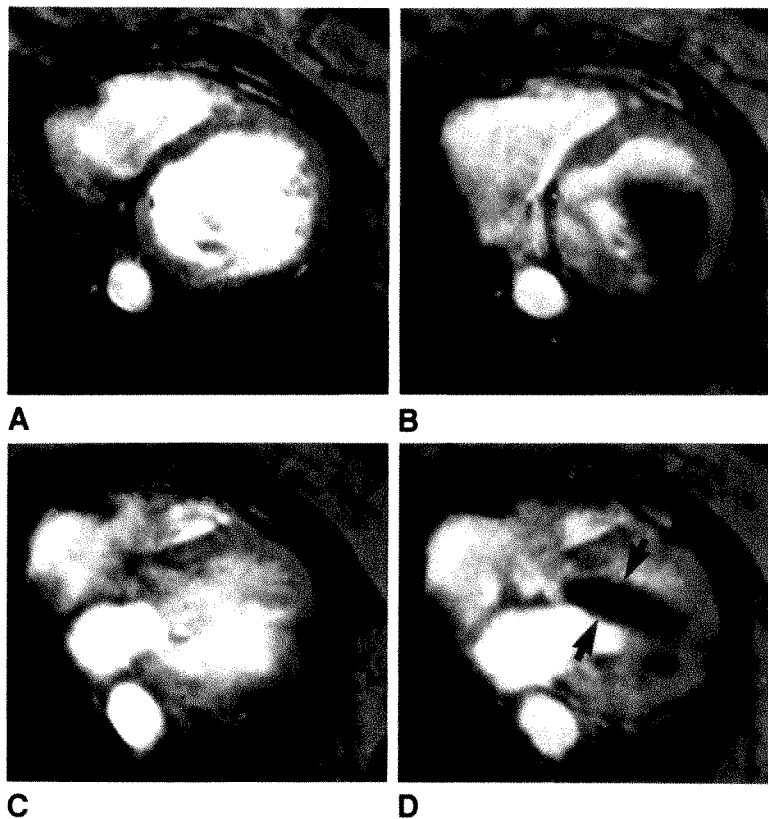


Fig. 6.—A, Cine MR image at midventricular level at end-diastole in patient with severe aortic regurgitation.

B, Cine MR image at mid-diastole in patient with severe aortic regurgitation.

C, Cine MR image at level of aortic outflow tract at end-diastole.

D, Cine MR image at level of aortic outflow tract at mid-diastole. Extensive signal loss (arrows) in left ventricular chamber in mid-diastole indicates aortic regurgitation.



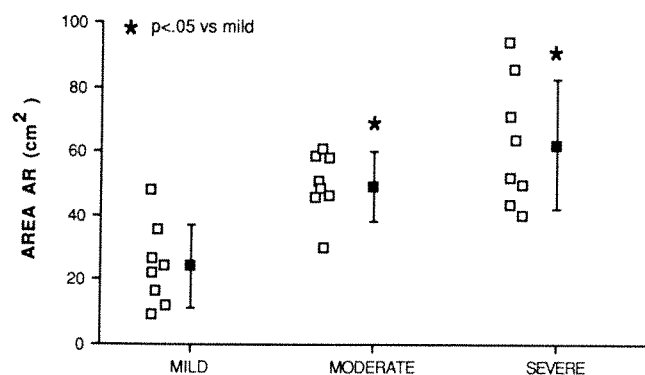


Fig. 7.—Individual summed areas of diastolic signal loss. AR = aortic regurgitation.

TABLE 1: Intra- and Interobserver Variability for Measurement of Volumes

Variable	Intraobserver		Interobserver ^a	
	r	SEE	r	SEE
End-diastolic volume	.99	7.4 ml	.99	12.1 ml
End-systolic volume	.98	6.4 ml	.98	8.6 ml
Stroke volume	.99	7.1 ml	.98	9.4 ml
Ejection fraction	.96	2.6%	.94	3.6%
Regurgitant volume	.96	10.6 ml	.95	14.2 ml
Regurgitant jet (signal void)	.96	1.8 cm ²	.93	2.2 cm ²

^a Two observers were used for determination of interobserver variability.

Discussion

In the current study, the severity of aortic regurgitation defined by cine MR had an overall correlation with the severity defined by Doppler echocardiography. However, individual variances were observed also. This new technique provides another method for detecting aortic regurgitation and can estimate severity by quantitative parameters derived from the images.

Regurgitant Blood Flow on Cine MR Images

On images obtained by cine MR, blood flowing at normal velocities has a higher signal intensity than myocardium. This results from the use of the short repetition and echo times and the constant flow of unsaturated spins from outside into the imaging plane. Valvular regurgitation (or stenosis) results in high velocity and disturbed blood flow across the abnormal valve [14, 15]. This area of abnormal blood flow is reflected as an area of low signal intensity on cine MR images, possibly due to severe dephasing of spins caused by very high velocities [3, 16]. As a result of multiple contiguous sectioning through the entire heart, cine MR images are able to give a three-dimensional impression of the extent and direction of the regurgitant jet and can convey a qualitative estimate of the severity of the valvular lesion on this basis alone.

The orientation of the image voxel in relationship to the direction of the regurgitant flow can be expected to influence the size of the flow void and the contrast between the low intensity of regurgitant flow and the remainder of the intracavitary blood pool. The area of the flow void can be expected to vary somewhat for the sagittal plane, long axis plane, and short axis plane compared with the transverse plane due to the relationship of intravoxel dephasing effects to voxel orientation and voxel dimensions. The size of the void is also variable in relation to the echo time and flip angle used for imaging. Thus, direct comparison of results among various groups pursuing cine MR for quantitating regurgitation may be possible only if techniques are identical.

Cardiac Volumes

Cardiac volumetric determinations, particularly of the right ventricle, can be problematic and there is no ideal method for determination of absolute volumes. The accuracy of noninvasive techniques has been compared with volumes determined by cardiac angiograms. The limitations of comparing an essentially three-dimensional imaging process consisting of multiple tomographic components with a planar technique dependent on geometric assumption are considerable. Moreover, the hemodynamic status of patients can be expected to be different in the noninvasive laboratory and during cardiac catheterization. In this study, the cardiac volumes obtained by MR were compared with an established tomographic imaging technique, and, in general, compared favorably with those volumes obtained by analysis of two-dimensional echocardiographic images. There appeared to be a systematic overestimation of the end-diastolic volume by MR. This may have been related to the exclusion of trabeculation in the two-dimensional echocardiographic images or foreshortening of the ventricle in the apical views (i.e., not imaging to the apex). In addition, the cardiac volumes from echocardiographic images were derived geometrically, whereas the volumes obtained from cine MR resulted from summation of the anatomic cross section of the ventricular blood pool at each level at which it was visible. Despite the overestimation, however, there was good correlation in terms of the magnitude of the volume and with the stroke volume of the left ventricle.

Evaluation of aortic regurgitation now tends to be carried out with noninvasive imaging techniques. Sequential studies are used to determine the time for aortic valve replacement. As such, these techniques are of considerable clinical importance. Although ventricular function can be assessed easily, noninvasive quantification of regurgitant blood volume has been difficult. The gold standard for this measurement has been cardiac catheterization and comparison of the cardiac output derived by the Fick method with the angiographic cardiac output [17]. Noninvasive quantification of regurgitant blood flow in aortic regurgitation by means of radionuclide angiography has been described [18, 19]. By this technique, stroke counts can be obtained from both the right and left ventricle, and the ratio of left to right ventricular stroke counts provides an index of the severity of regurgitation [18, 19]. Anatomic resolution by radionuclide methods is suboptimal.

In comparison with radionuclide methods, cine MR has the potential advantage of also being able to confirm and define the site and extent of the regurgitant valvular lesion and can, in addition, give an estimation of the regurgitant blood volume by direct comparison of right ventricular stroke volume to left ventricular stroke volume. Doppler echocardiography has been shown to be reliable not only for the detection but for the quantification of some regurgitant lesions [20, 21].

Potential Problems

Defining the severity of aortic regurgitation is not without difficulty. In previous studies, the severity of both mitral and aortic regurgitation by Doppler echocardiography or contrast angiography has not always shown a close relationship to the regurgitant fraction [22], although the angiographic grade [23] and Doppler grade of aortic regurgitation generally correlate well [11, 24]. In this study, the severity of aortic regurgitation determined by echocardiography, although qualitative, took into account not only the extent of the regurgitant jet, but also other factors that are related to the volume of regurgitant flow. In the current study, echocardiographic severity correlated both with the regurgitant volume and total area of maximum diastolic signal loss within the left ventricle as determined by cine MR.

In summary, cine MR imaging shows promise for the detection and estimation of the severity of aortic regurgitation. Inasmuch as it also can evaluate ventricular structure and function, it can be a comprehensive imaging technique for the heart.

REFERENCES

1. Frahm J, Haase A, Matthai D. Rapid NMR imaging of dynamic processes using the FLASH technique. *Magn Reson Med* **1986**;3:321-327
2. Sechtem U, Pflugfelder PW, White RD, et al. Cine MR imaging: potential for the evaluation of cardiovascular function. *AJR* **1987**;148:239-246
3. Evans AJ, Herfkens RJ, Spritzer CE, et al. The effect of turbulent flow on MRI signal intensity using gradient refocused echoes. Presented at the annual meeting of the Society of Magnetic Resonance in Medicine, New York City, August **1987**
4. Markiewicz W, Sechtem U, Kirby R, et al. Measurement of ventricular volumes using nuclear MR. *J Am Coll Cardiol* **1987**;10:170-177
5. Sechtem U, Pflugfelder PW, Gould RG, Higgins CB. Measurement of right and left ventricular volumes in healthy individuals using cine MR imaging. *Radiology* **1987**;163:697-702
6. Teague SM, Heinsimer JA, Anderson JL, et al. Quantification of aortic regurgitation utilizing continuous wave Doppler ultrasound. *J Am Coll Cardiol* **1986**;8:592-599
7. Masuyama T, Kodama K, Kitabatake A, et al. Noninvasive evaluation of aortic regurgitation by continuous-wave Doppler echocardiography. *Circulation* **1986**;73:460-466
8. Perry GJ, Helmke F, Nanda NC, et al. Evaluation of aortic insufficiency by Doppler color flow mapping. *J Am Coll Cardiol* **1987**;9:952-959
9. Daigle R, Reineter W, Anderson N, Schiller NB. A light pen measurement system for cross-sectional echocardiography. *J Ultrasound Med* **1977**;4:44-47
10. Schiller NB, Acquetena H, Ports TA, et al. Left ventricular volume from paired biplane 2D echocardiography. *Circulation* **1979**;60:547-555
11. Ciobanu M, Abbasi AS, Allen M, et al. Pulsed Doppler echocardiography in the diagnosis and estimation of severity of aortic insufficiency. *Am J Cardiol* **1982**;49:339-343
12. Henry WL, Bonow RO, Rosing DR, Epstein SR. Observations on the optimum time for operative intervention for aortic regurgitation. II. Serial echocardiographic evaluation of asymptomatic patients. *Circulation* **1980**;61:484-492
13. Scheffe H. A method for judging all contrasts in the analysis of variance. *Biometrika* **1953**;40:87-104
14. Feigenbaum H. *Echocardiography*. Philadelphia: Lea & Febiger, **1986**: 35-38
15. Burton AC. Kinetic energy in the circulation; streamline flow and turbulence; measurement of arterial pressure. In: Burton AC. *Physiology and biophysics of the circulation*. Chicago: Year Book, **1972**:104-114
16. van Dijk P, Guilfoyle DN, Snaar JEM, Bohning DE. Characterization of flow dynamics by fast multiphase imaging. Presented at the annual meeting of the Society of Magnetic Resonance in Medicine, Montreal, Canada, August **1986**
17. Sandler H, Dodge HT, Hay RE, Rackley CE. Quantitation of valvular insufficiency in man by angiocardiology. *Am Heart J* **1963**;65:501-509
18. Rigo P, Alderson PO, Roberson RM, et al. Measurement of aortic and mitral regurgitation by gated cardiac blood pool scans. *Circulation* **1979**;60:306-312
19. Manyari DE, Nolewajka AJ, Kostuk WJ. Quantitative assessment of aortic valvular insufficiency by radionuclide angiography. *Chest* **1982**;81:169-176
20. Blumlein S, Bouchard A, Schiller NB, et al. Quantitation of mitral regurgitation by Doppler echocardiography. *Circulation* **1986**;74:306-314
21. Rokey R, Sterling LL, Zobghbi WA, et al. Determination of the regurgitant fraction in isolated mitral or aortic regurgitation by pulsed Doppler two-dimensional echocardiography. *J Am Coll Cardiol* **1987**;7:1273-1278
22. Croft CH, Lipscomb K, Mathis K, et al. Limitations of qualitative angiographic grading in aortic or mitral regurgitation. *Am J Cardiol* **1984**;53:1593-1598
23. Austen WG, Edwards JE, Frye RL, et al. A reporting system on patients evaluated for coronary artery disease. *Circulation* **1975**;51[suppl 1]:5-40
24. Quinones MA, Young JB, Waggoner AD, et al. Assessment of pulsed Doppler echocardiography in detection and quantification of aortic and mitral regurgitation. *Br Heart J* **1980**;44:612-620

Book Review

Handbook of Cardiovascular and Interventional Radiologic Procedures. By Krishna Kandarpa. Boston: Little, Brown, 254 pp., 1988. \$25, soft cover

This little handbook differs from most radiologic publications in a number of respects, not the least of which are that it is indeed little and that it has the limited scope of a work designed to be used on the run. It is organized in outline form and written in short, clear statements without superfluous clauses or confusing modifiers. Its 254 pages are packed with practical, complete, and easy-to-find information.

The first series of chapters covers vascular and nonvascular diagnostic and interventional procedures, with each chapter devoted to a single procedure or clinical problem. Each chapter sets out the indications for the procedure, instructions for preparation of the patient, a step-by-step summary of exactly how to perform the procedure, recommendations for management of the patient after the procedure, a review of the results as culled from recent literature, a list of potential complications, and a list of references. These chapters are brief, six to eight pages, but surprisingly inclusive. For example, when the author recommends that a laboratory test be checked, he gives the accepted range of normal values for that test and also the limits that can be considered safe for performing the procedure. In addition to a check list of steps to follow, the procedural protocols provide explanations and line drawings that make technical maneuvers clear. All of the chapters devoted to procedures are excellent, but the three chapters on angioplasty (coronary, renal, and extremity) are particularly strong. They present complex problems succinctly and clearly.

The remaining chapters and appendixes are devoted to material that can be considered background information. These are less consistent in quality than the chapters on procedures. Chapters on noninvasive vascular and radionuclide studies describe only a few of the many complimentary procedures that should be covered if these subjects are considered worthy of space in this manual. Chapters on radiation safety and on catheters and guidewires seem to be aimed at readers who have less experience than is presupposed by the remainder of the book.

The chapter on contrast media, however, is superb and in itself may be sufficient reason to buy this book. In a few short pages,

reams of research and published controversy are analyzed and summarized into simple, commonsense recommendations about how and when to use the various media, how to manage patients who have had previous minor or major reactions to a contrast medium, and how to treat each of the various reactions if a reaction should occur. Chapters that discuss commonly used drugs, nursing care, and outpatient care of tubes are also excellent. These subjects, which are crucial to clinical vascular and interventional radiology, are often carelessly or incompletely covered in major reference works. They are appropriate to the purpose of this handbook and are done well.

This is a detail book. Although a person who is thoroughly familiar with all the details surrounding these procedures may not find much use for this handbook, it will be invaluable for the radiology resident or fellow or the radiologist who performs angiographic or interventional procedures only occasionally.

The internist or surgeon who counsels patients about diseases in which these procedures play a role will find this handbook a quick, complete summary of how each interventional procedure is performed, what results can be anticipated, whether the procedure can be done on an outpatient basis, what laboratory test should be ordered beforehand, and what complications should be discussed with the patient. Technologists in the angiography/interventional suite will find the book useful to ensure accurate answers to their patients' questions and to review injection rates and film sequences appropriate to each procedure. Departmental nurses will refer to it to review the drug doses and precautions relevant to the procedure.

This book is a thin, lightweight paperback that will fit easily into the pocket of a lab coat. It seems destined to become a smudged, thoroughly fingered, dog-eared, and written-on silent partner in many briefcases, offices, pockets, and lockers. It ought to be on a bookshelf in every angiography/interventional suite.

Morton G. Glickman
Yale University School of Medicine
New Haven, CT 06510

Coronary Angiography in Atrial Myxoma: Findings in Nine Cases

George A. Fueredi¹
 Thomas E. Knechtges
 David J. Czarnecki

We report the findings on selective coronary angiography in nine patients with atrial myxomas. The angiograms were obtained because the patients were suspected of having coronary artery disease. In each case, the diagnosis of myxoma had been made earlier by echocardiography. Coronary angiography in five (55%) of the nine patients showed neovascularity in the tumor without calcification. In one patient, the angiogram showed a varix of the myocardium at the base of the tumor. The angiograms in three (33%) of the nine patients did not show neovascularity but showed tumoral calcification. Six (67%) of the nine patients had significant coronary artery disease that required coronary artery bypass grafting along with resection of the myxoma.

These data suggest that the incidence of neovascularity in atrial myxomas is higher than previously reported. Furthermore, a significant number of this older population presented with operable artery disease as well as atrial myxoma.

Cardiac myxomas are rare neoplasms that are potentially curable with surgical resection. The patients typically present with a triad of obstructive, embolic, and constitutional symptoms that mimic common systemic illnesses. Although echocardiography is now the imaging technique of choice, MR imaging, scintigraphy, and cine CT also have proved useful in diagnosis [1].

We describe the coronary angiographic findings in nine patients with cardiac myxoma. In each case, the diagnosis of atrial myxoma was made by echocardiography, and the patients had selective coronary angiography because of suspected coronary artery disease.

Materials and Methods

Between 1968 and 1987, atrial myxoma was diagnosed in 16 patients (15 left atria and one right atrium) at St. Luke's Medical Center. There were eight men and eight women from 21 to 79 years old (average, 59 years). One patient died during surgery for an abdominal catastrophe, which at autopsy proved to be due to total occlusion of the proximal abdominal aorta resulting from embolism by a left atrial myxoma. Another patient, in whom mitral stenosis was diagnosed by cardiac catheterization and aortic root cineangiography, proved to have a left atrial myxoma at surgery. The remaining 14 patients all had atrial myxomas diagnosed by echocardiography. Eleven of these patients, seven men and four women from 49 to 79 years old (mean, 64 years) also were suspected of having coronary insufficiency. These patients presented with congestive heart failure, angina, or both, and all had selective coronary angiograms. Nine of 11 of these selective coronary angiograms were available for retrospective review. This group of patients consisted of six men and three women. All of the selective coronary angiograms were initially interpreted by an experienced radiologist without previous knowledge of the clinical history or the results of the echocardiograms. All angiograms were then blindly reviewed retrospectively by a second radiologist, with 100% correlation.

Results

The largest average diameter of the 16 atrial myxomas was 5.9 cm, with a range of 4–8 cm. Twelve (75%) of the 16 myxomas were pedunculated with a broad-based attachment to the atrium. Four (25%) showed prolapse into the left ventricle on either echocardiography or angiocardiography. The amount of prolapse appeared to be related to the proximity of the tumor to the mitral valve. Thirteen (87%)

Received October 11, 1988; accepted after revision December 9, 1988.

¹All authors: Department of Radiology, St. Luke's Medical Center, 2900 W. Oklahoma Ave., Milwaukee, WI 53215. Address reprint requests to G. A. Fueredi.

AJR 152:737–738, April 1989
 0361–803X/89/1524–0737
 © American Roentgen Ray Society

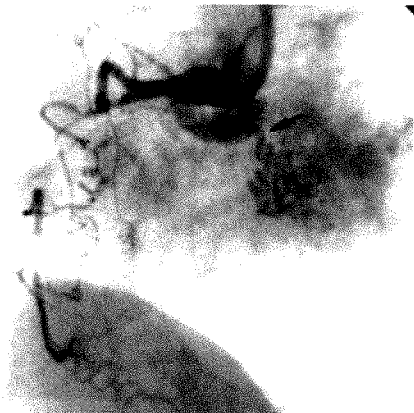


Fig. 1.—Right coronary angiogram (left anterior oblique projection) in 75-year-old woman shows extensive neovascularity in a left atrial myxoma supplied by a large right atrial branch of proximal right coronary artery (arrow). Right coronary artery is occluded in its midsegment with reconstitution distally.

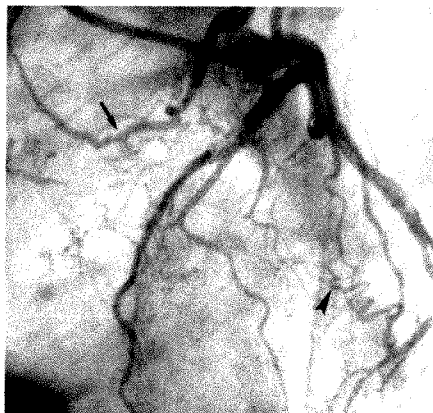


Fig. 2.—Left coronary angiogram (left anterior oblique projection) shows neovascularity in a right atrial myxoma. Blood supply to tumor is from a large right atrial branch of proximal (arrow) and distal (arrowhead) portions of left circumflex artery. No significant coronary artery disease is evident.

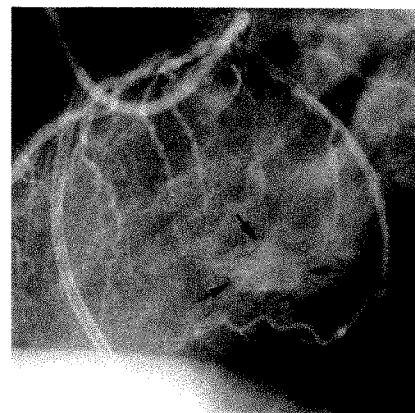


Fig. 3.—Left coronary artery angiogram (anterior oblique projection) in 60-year-old man with extensive calcification of a left atrial myxoma (arrows) without evidence of neovascularity. Moderate stenosis of midcircumflex and mild irregularity of proximal left anterior descending arteries are evident.

of the 15 left atrial myxomas were attached to the interatrial septum at or near the fossa ovalis. One myxoma was attached to the dome of the left atrium near the aortic root origin; another was attached along the posterolateral free wall of the left atrium. The single right atrial myxoma was attached to the inferior portion of the interatrial septum.

In five (55%) of the nine patients whose coronary angiograms were reviewed, abnormally dilated atrial branches supplying the tumor were seen. The neovascularity consisted of clusters of tortuous vessels with blood pooling and tumor blush (Figs. 1 and 2). No evidence of arteriovenous shunting was seen. The abnormal vessels moved with the tumor mass. The extent of neovascularity did not correlate with the size of the myxoma.

The vascular supply to three left atrial myxomas was from atrial branches of the right coronary artery (Fig. 1). One right atrial myxoma derived its vascular supply from right atrial branches of the proximal circumflex artery as well as branches of the third marginal circumflex artery (Fig. 2). One left atrial myxoma derived its supply from an atrial branch of both the right and proximal left coronary arteries. At its base, this myxoma had an underlying varix of the myocardium. This patient was described previously by Rasmussen et al. [2].

Three of the four nonvascular tumors showed varying degrees of calcification, consisting of amorphous flecks that moved with the tumor (Fig. 3). The extent of calcification was not helpful in estimating tumor size. The single right atrial myxoma showed no discernible calcification angiographically, but tumoral calcification was seen on both gross and microscopic examination.

Six (67%) of nine patients had operable coronary artery disease. Of these, five were men, from 49 to 78 years old, with an average age of 59 years. The woman was 75 years old. Five patients had severe disease of two or three coronary arteries (Figs. 1 and 3). A sixth patient had a single 60% stenosis of the left anterior descending artery.

Discussion

Cardiac myxomas are rare tumors, occurring most commonly in patients who are 30–60 years of age. Most authori-

ties believe that cardiac myxomas are true benign cardiac neoplasms [3]. The left atrium is the most common site; 75% of left atrial myxomas are pedunculated and attached to the atrial septum near the fossa ovalis. Twenty percent occur in the right atrium, and 5% are found in the ventricles [1].

Calcification is rare and is reported to occur more commonly in tumors of the right atrium [1]. However, we found calcification in one-third of the patients. All of these patients had myxomas of the left atrium, and none showed any evidence of neovascularity.

Cardiac myxomas are considered highly vascular tumors [4]; however, to the best of our knowledge, only seven cases with neovascularity have been reported [1, 2, 5–8]. The sensitivity of coronary angiography for depicting neovascularity in the tumors is not known. Neovascularity associated with coronary artery disease has only been reported in one case [8]. All cases with neovascularity in our series showed tortuosity of the vessels within the tumor as well as contrast pooling and tumor blush. Although cardiac myxomas are the most common cause of neovascularity, other diagnostic considerations include organized atrial thrombi, cavernous hemangioma, and venous malformations.

REFERENCES

1. Markel ML, Waller BF, Armstrong WF. Cardiac myxoma: a review. *Medicine (Baltimore)* **1987**; 66(2):114–125
2. Rasmussen KJ, Peebles TC, Nellen JR. Unusual variant on tumor vascularity associated with left atrial myxoma. *AJR* **1983**; 141:927–928
3. Wold LE, Lie JT. Atrial myxomas: a clinicopathologic profile. *Am J Pathol* **1980**; 101(1):219–240
4. Borgen HG. Angiocardiography. In: Taveras JM, Ferrucci JT, eds. *Radiology: diagnostics, imaging, intervention*, vol. 2. Philadelphia, PA: Lippincott. **1988**; Chapter 60:3
5. Marshall WH, Steiner RM, Wexler L. "Tumor vascularity" in left atrial myxoma demonstrated by selective coronary arteriography. *Radiology* **1969**; 93:815–816
6. Chan AU. Myxomas of the heart. *McLaren Med Bull* **1974**; 1:1
7. Berman ND, McLaughlin PR, Bigelow WG, March JE. Angiographic demonstration of blood supply of right atrial myxoma. *Br Heart J* **1976**; 38:764–766
8. Levin H, Cha SD, Sumathisen, Gonzales-Lavin L, Gooch AS, Maranhao V. Detection of right atrial myxoma by coronary cinearteriography. *Cathet Cardiovasc Diagn* **1986**; 12:414–416

Case Report

CT Diagnosis of Acute Pericardial Tamponade After Blunt Chest Trauma

Laurence Goldstein,¹ Stuart E. Mirvis,¹ Irene S. Kostrubiak,¹ and Stephen Z. Turney²

CT has been used to diagnose injury after both blunt and penetrating thoracic trauma [1–4]. Applications include the diagnosis of mediastinal hemorrhage, subtle pneumothorax, pulmonary laceration, parenchymal hematomas, and pleural and pericardial effusions [1–4]. Although CT is valuable for detection and evaluation of pericardial effusions and may show signs that suggest pericardial constriction, such as a dilated inferior vena cava, a deformed ventricular contour, or an angulated interventricular septum [5], the diagnosis of acute pericardial tamponade following trauma is usually established by clinical signs. These signs include tachycardia, diminished cardiac output, increased central venous pressure, elevated systemic vascular resistance, distended neck veins, and muffled cardiac sounds. Emergency bedside cardiac sonography can document the presence of pericardial effusion before surgical intervention [2].

We present a case of acute pericardial tamponade shown by emergency CT scanning of the thorax after closed blunt chest trauma. A triad of CT findings diagnostic for acute pericardial tamponade is illustrated.

Case Report

A 19-year-old man was admitted to our trauma center after a motor vehicle accident. Four hours had elapsed from the time of injury. On admission, the patient complained of pain in his chest and right hip. Physical examination revealed an alert individual with a systolic blood pressure of 104 mm Hg and a pulse rate of 140 beats per minute. The upper thorax looked dusky, and the neck veins were distended.

The right hip was fixed in internal rotation. The abdomen was firm, and the bowel sounds were hypoactive. On admission, the hematocrit was 52.5%. An anteroposterior chest radiograph obtained on admission was interpreted as normal.

The patient received rapid IV fluid resuscitation, with an increase in systemic blood pressure to 120/80 mm Hg. Arteriography indicated that the thoracic aorta was not injured. Abdominal CT with IV contrast enhancement was then done to exclude intraabdominal or retroperitoneal injuries. Initial CT sections through the lower chest revealed a pericardial effusion with a CT density of 35–45 H, consistent with hemorrhage (Fig. 1). Because of the pericardial effusion, we obtained more cephalad sections through the thorax to include the entire pericardial space. The superior and inferior vena cavae and the renal veins were distended (Fig. 1). Areas of linear low attenuation paralleling the portal veins were thought to represent periportal lymphedema or tracking of periportal blood (Fig. 1). The rest of the CT study was unremarkable.

Because the clinical and CT findings were compatible with pericardial tamponade, the patient underwent a median sternotomy. The pericardium was tense, and after incision, unclotted blood flowed freely from the pericardial space. A 1.5-cm laceration of the right auricular appendage near the entrance of the superior vena cava was identified and oversewn. After pericardial blood was evacuated, the systemic blood pressure increased to 200/120 mm Hg and the pulse rate decreased from 130 to 90 beats per minute. Orthopedic injuries to the right hip and acetabulum were repaired later.

The patient's postoperative course was complicated by pneumonia. On a follow-up abdominal CT, obtained 2 weeks after admission, the inferior vena cava was considerably less prominent and appeared flattened in the anteroposterior dimension. The periportal lymphedema pattern in the liver had resolved (Fig. 1). After gradual improvement, the patient went home 36 days after surgery.

Received November 10, 1988; accepted after revision December 27, 1988

¹ Department of Diagnostic Radiology, University of Maryland Medical System, 22 S. Greene St., Baltimore, MD 21201. Address reprint requests to S. E. Mirvis.

² Maryland Institute for Emergency Medical Services Systems, University of Maryland Medical System, 22 S. Greene St., Baltimore, MD 21201.

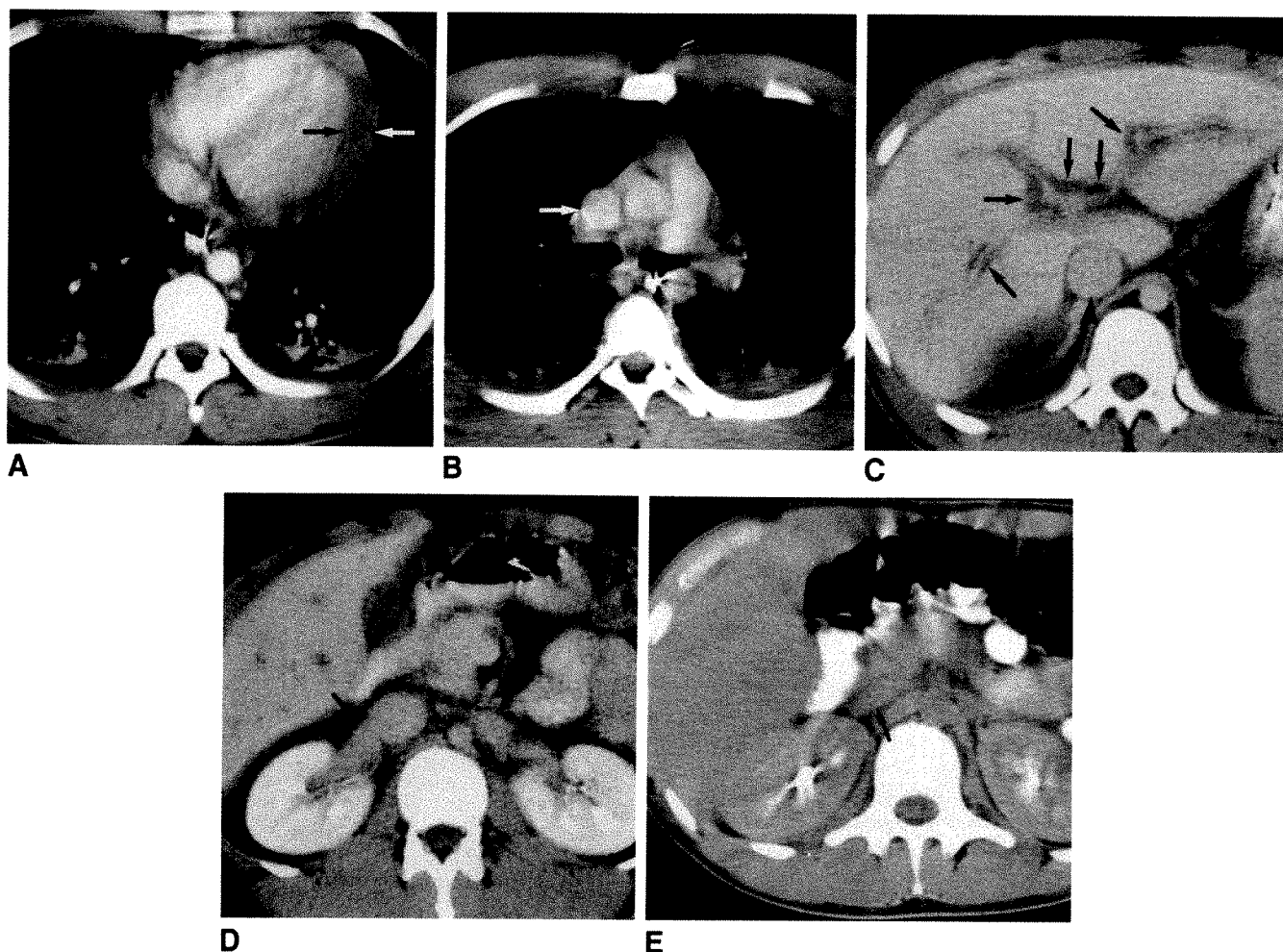


Fig. 1.—CT of pericardial tamponade.

A, Enhanced CT scan through midcardiac level shows small pericardial effusion (arrows). Density was between 35 and 45 H compatible with hemorrhagic fluid. Also note small, bilateral, pleural effusions and increased density around descending aorta consistent with mediastinal hemorrhage. Thoracic aortogram revealed no injury.

B, Axial scan at level of proximal great vessels shows distended superior vena cava (arrow) approximating size of aortic root.

C, Scan at midhepatic level shows diffuse low density paralleling portal venous structures (arrows), most suggestive of periportal lymphedema due to high venous hydrostatic pressure. Note markedly distended inferior vena cava (arrowhead).

D, Scan at more caudal level shows distended right renal vein (arrow). Left renal vein, partially shown, was also markedly dilated.

E, Scan through upper abdomen obtained 2 weeks after admission shows anatomic changes after correction of cardiac tamponade. Inferior vena cava is considerably less prominent and narrowed in anteroposterior dimension (arrow). Periportal lymphedema has resolved.

Discussion

Acute cardiac rupture after blunt chest trauma is a rare and often fatal injury. Most often the left ventricle is involved, resulting in rapidly fatal pericardial tamponade [6]. Rupture of the atria after blunt chest trauma is rare [6]. Bleeding into the pericardium from the lower-pressure atria can produce a slower accumulation of pericardial blood, which permits survival long enough to reach a medical facility. Typically, diagnosis of cardiac tamponade depends on recognition of a physiologic pattern of tachycardia, elevated central venous pressure, elevated systemic vascular resistance, muffled cardiac sounds, distended neck veins, and diminished cardiac output. Recognition of these findings may lead to prompt pericardiectomy or pericardiocentesis, perhaps after emer-

gency bedside cardiac sonography to confirm the presence of pericardial fluid.

In this patient, despite suggestive physical signs, pericardial tamponade was not considered likely, and the patient remained hemodynamically stable with IV administration of fluid. Emergency aortography and abdominal CT were performed to exclude other injuries. In our institution, abdominal CT scanning is started at the lower thorax to exclude pneumothorax, pleural effusions, parenchymal lung injury, and pericardial effusion. CT showed pericardial effusion with a density compatible with blood. Continued scanning through the abdomen revealed distension of the inferior vena cava and renal veins and periportal low density compatible with lymphedema. Increased pericardial pressure most likely resulted in increased central venous pressure with distension of the inferior

vena cava and renal veins and development of periportal lymphedema. We think that the long time from initial injury to CT scanning permitted development of periportal lymphedema. Although the superior vena cava also appeared enlarged in this patient, it was less distended than the inferior vena cava. Doppman et al. [5] have observed that superior vena caval distension is not as striking a finding as inferior vena caval distension on CT studies of patients with constrictive pericarditis.

Although a similar CT appearance for periportal tracking of blood after liver trauma has been described [7], we think that the uniform and diffuse pattern of periportal low density and the lack of CT evidence of liver parenchymal injury favor lymphedema as the most likely cause of this pattern. Other causes of periportal lymphedema include liver transplantation and masses at the liver hilum obstructing venous drainage [8].

CT diagnosis of pericardial tamponade has been reported in a patient with metastatic disease of the pericardium [9]. The authors described a moderate-sized pericardial effusion with high CT numbers but did not comment on any other signs of elevated central venous pressure. The rate of accumulation of pericardial effusion is more significant in establishing pericardial tamponade than the ultimate size or composition of the pericardial fluid. Thus, recognition of simultaneous signs of elevated central venous pressure is most significant in diagnosing this condition by CT.

Although diagnosis of pericardial tamponade after acute thoracic trauma should rarely be made by CT, occasionally

the pathophysiologic pattern of tamponade may not be fully developed or may be masked by rapid IV administration of fluid, use of vasopressors to maintain systemic blood pressure, or more apparent injuries. The triad of CT findings of hemorrhagic pericardial fluid, distended central veins (e.g., the vena cavae or renal veins), and periportal lymphedema should suggest the diagnosis and lead to therapeutic intervention.

REFERENCES

1. Toombs BD, Sandler CM, Lester RG. Computed tomography of chest trauma. *Radiology* 1981;140:733-738
2. Grumbach K, Mechlin MB, Mintz MC. Computed tomography and ultrasound of the traumatized and acutely ill patient. *Emerg Med Clin North Am* 1985;3(3):607-624
3. Mirvis SE, Kostrubiak I, Whitley NO, Goldstein LD, Rodriguez A. Role of CT in excluding major arterial injury after blunt thoracic trauma. *AJR* 1987;149:601-605
4. Wall SD, Federle MP, Jeffrey RB, Brett CM. CT diagnosis of unsuspected pneumothorax after blunt abdominal trauma. *AJR* 1983;141:919-921
5. Doppman JL, Rienmuller R, Lissner J, et al. Computed tomography in constrictive pericardial disease. *J Comput Assist Tomogr* 1981;5(1):1-11
6. Tobin HM, Hiratzka LF, Vargish T. Ruptured right atrium from nonpenetrating trauma of the chest. *South Med J* 1986;79:499-501
7. Foley DW, Cates JD, Kellman GH, et al. Treatment of blunt liver injuries: role of CT. *AJR* 1987;634:635-638.
8. Kcsin DB, Stanley RJ, Berland LL, Shin MS, Dalton SC. Hepatic perivascular lymphedema: CT appearance. *AJR* 1988;150:111-113
9. Johnson FE, Wolverson MK, Sundaran M, Heiberg E. Unsuspected malignant pericardial effusion causing cardiac tamponade: rapid diagnosis by computed tomography. *Chest* 1982;82:501-503

Book Review

Atlas of Mammography. Histologic and Mammographic Correlations, 2nd ed. By John E. Martin. (A volume in Golden's Diagnostic Radiology series, edited by John H. Harris.) Baltimore: Williams & Wilkins, 524 pp., 1988. \$91.50

This extensively revised, second edition on mammographic diagnosis is a classic and is of value to those who use film-screen techniques as well as xeroradiography. Emphasized from the beginning is the direct involvement of the radiologist in the entire diagnostic experience. Throughout the text, the author cites his enormous personal experience and knowledge of the field to emphasize and highlight important aspects.

I especially appreciated succinct chapters on the "radiation controversy," and on breast cancer screening. An innovative chapter, "How to Approach A Mammogram," is illustrated with xerograms that illustrate the problems in localization common in clinical practice. The chapter entitled "Histologic and Mammographic Correlations of Malignant Disease of the Breast" is a brief but lucid introduction to the subsequent chapters on malignant disease. Both direct and indirect indications of malignancy are reviewed in a thorough manner, with many explicit xerographic illustrations. Common and unusual benign breast lesions, skin lesions, and breast prostheses are covered in separate chapters. The last chapter deals with the male breast.

The author has achieved his goal of providing as thorough, thoughtful, and authoritative a text as is available in this burgeoning field of mammographic diagnosis. The illustrations are clear and instructive, even for someone inexperienced with the xerographic technique; it is easy to transfer the appearance mentally to a film-screen image. Obviously, this is not the sort of text to consult for information on film-screen techniques or on alternative diagnostic techniques such as sonography or transillumination. Books by Drs. Wende Logan, Richard Gold, and Valerie Jackson, among others, are available on these subjects, so I do not consider this a shortcoming; although perhaps more than an allusion to these methods might have enhanced the book's usefulness.

Richard M. Klein
Kettering Medical Center
Kettering, OH 45429

Acquired Tracheomegaly in Adults as a Complication of Diffuse Pulmonary Fibrosis

John H. Woodring¹
 Penni A. Barrett¹
 Stanley R. Rehm²
 Pamela Nurenberg^{1,3}

We studied the chest radiographs of 34 consecutive patients with diffuse pulmonary fibrosis to determine the presence of tracheomegaly and to follow its progression with time. Patients had been identified by a computer search of medical records. We measured the internal transverse diameter of the trachea 2 cm above the top of the aortic arch on erect posteroanterior chest radiographs. Transverse diameters greater than 25 mm in men and 21 mm in women were considered indicative of tracheomegaly. Pulmonary-function tests, available in 30 of the 34 patients, showed restrictive lung disease. The transverse tracheal measurements were compared with the cause of fibrosis, severity of restriction, duration of illness, and other clinical variables. Tracheomegaly was present in 10 (29%) of the patients, including four with fibrosing alveolitis, four with sarcoidosis, and two with chronic progressive histoplasmosis. In seven of these patients, serial radiographs showed that the tracheal dilatation had progressed with time. Nine of 24 patients without tracheomegaly also had progressive increase in transverse tracheal diameter over time. Of the 10 patients with tracheomegaly, pulmonary-function tests were available in eight and showed moderate restrictive lung disease in six and severe restrictive lung disease in two. The duration of illness was 3–6 months in two patients, 10–22 years in five patients, and not recorded in three patients. Chronic cough and repeated respiratory infections were slightly more common in those patients with tracheomegaly than in those without.

These data suggest that tracheomegaly develops as a complication of diffuse pulmonary fibrosis in patients who have at least moderate restrictive lung disease and prolonged illness, and it may have some association with chronic cough and repeated respiratory infection.

Breatnach et al. [1] established the normal range of the internal coronal and sagittal diameters of the trachea in 808 adult patients with no clinical or radiographic evidence of respiratory disease. Using a normative range of three standard deviations from the mean, or 99.7% of the normal population, they found the upper limits were 25 and 27 mm (coronal and sagittal, respectively) in men and 21 and 23 mm in women. The lower limit for both dimensions was 13 mm in men and 10 mm in women. Tracheal dimensions greater than or less than these values indicate pathologic tracheal widening or narrowing [1].

Abnormal tracheal enlargement or tracheomegaly has been reported in congenital tracheobronchomegaly (Mounier-Kuhn syndrome) [1–11], Ehlers-Danlos syndrome [10, 11], and diffuse acquired tracheomalacia from a number of inflammatory conditions, including chronic cigarette smoking, chronic bronchitis, emphysema, cystic fibrosis, and relapsing polychondritis [11–13]. Although acquired tracheal dilatation is known to occur in pulmonary fibrosis [13–15], this relationship has received only scant mention in the radiology literature [15]. Over the last several years we have observed progressive tracheal dilatation in several patients with diffuse pulmonary fibrosis. We have evaluated a series of patients with diffuse pulmonary fibrosis and report the features of those patients who developed tracheomegaly as a complication of their disease.

Received October 3, 1988; accepted after revision November 28, 1988.

¹ Department of Diagnostic Radiology, Albert B. Chandler Medical Center, University of Kentucky, 800 Rose St., Lexington, KY 40536-0084. Address reprint requests to J. H. Woodring.

² Department of Internal Medicine, Division of Pulmonary Medicine, Albert B. Chandler Medical Center, University of Kentucky, 800 Rose St., Lexington, KY 40536-0084, and Chief, Pulmonary Section, Veterans Administration Medical Center, Lexington, KY 40511.

³ Present address: Department of Diagnostic Radiology-114, Veterans Administration Medical Center, 4500 S. Lancaster, Dallas, TX 75216.

AJR 152:743–747, April 1989

0361–803X/89/1524–0743

© American Roentgen Ray Society

Materials and Methods

The study group consisted of a consecutive series of 24 men and 10 women (age range, 20–79 years; average, 56 years) with well-documented diffuse pulmonary fibrosis. Patients were identified by a computer search of the medical records of the University of Kentucky Medical Center and the Veterans Administration Medical Center. The causes of the fibrosis were fibrosing alveolitis in 16 patients (documented by open-lung biopsy in 11 and transbronchial biopsy in five), sarcoidosis in 12 (documented by open-lung biopsy in three, transbronchial biopsy in six, and peripheral lymph node biopsy in three), histiocytosis X in three (documented by open-lung biopsy), chronic progressive histoplasmosis in two (documented by transbronchial biopsy and culture), and radiation fibrosis in one (documented by history and transbronchial biopsy). The duration of illness was known in 19 patients and ranged from 2 months to 22 years (average, 7.7 years).

Pulmonary-function tests were available in 30 of the 34 patients. These showed reduction in vital capacity consistent with restrictive lung disease in all 30 patients. The severity of restrictive lung disease was classified as mild in seven patients (vital capacity 60–75% of predicted), moderate in 12 (vital capacity 50–60% of predicted), and severe in 11 (vital capacity less than 50% of predicted) [14].

Other clinical variables evaluated included the following. Of the 34 patients, 23 were cigarette smokers with a smoking history ranging from seven to 250 pack-years (average, 58.8 pack-years), and 11 were nonsmokers. Four had occupational exposure to coal or asbestos dust; however, lung biopsy in these patients did not show pneumoconiosis to be the cause of the pulmonary fibrosis. The tuberculin skin test was positive in eight and was negative in 26; however, none had clinical evidence of active tuberculosis at any time during the course of their disease. One patient had been on chronic medication with nitrofurantoin at the time he developed pulmonary fibrosis, and the drug was thought to have caused the fibrosis in this case. No other patients were on medications known to cause pulmonary fibrosis. Seven patients had endotracheal intubation late in their disease; however, none had a history of intubation before developing pulmonary fibrosis. Sixteen patients had a history of a chronic cough associated with their pulmonary disorder. In these patients, the chronic cough lasted from 6 months to 20 years. Fourteen patients had a history of respiratory infection, including acute bronchitis or pneumonia concurrent with their pulmonary fibrosis. In 12 of these patients, the respiratory infections were recurrent, occurring at intervals from several months to several years.

At the University, chest radiographs were obtained in maximum inspiration in the posteroanterior projection by using a focal film distance of 6 ft (1.83 m) and a 10:1 focused grid for scatter reduction. Exposures were phototimed and made at 135 kVp. At the Veterans Administration Medical Center, radiographs were obtained in maximum inspiration in the posteroanterior projection using a focal film distance of 10 ft (3.05 m) and a 6-in. (15.2 cm) air gap for scatter reduction. Exposures were phototimed and made at 125 kVp. This technique is consistent with that used by Breatnach et al. [1] and results in a midplane magnification factor of 1.08, slightly less than the magnification factor of 1.10 obtained with the more conventional 6-ft focal film distance and grid technique used at the University.

Tracheal diameter was measured from posteroanterior radiographs because lateral radiographs were not available in all cases. The internal transverse (coronal) diameter was measured at a level 2 cm above the top of the aortic arch [1] in all 34 patients. For 24 of these patients, serial radiographs obtained over a period of months or years (range, 4 months to 21 years; average, 6.9 years) were available. In these 24 patients, transverse tracheal diameters were measured

serially. For measurements obtained from radiographs taken at a 6-ft focal film distance, the diameters were multiplied by a factor of 0.9818 to correct for the difference in magnification compared to values obtained from the 10-ft focal film distance radiographs and to standardize our method with that of Breatnach et al. [1].

The transverse (coronal) internal diameter measurements of the trachea were compared with the cause of pulmonary fibrosis, severity of restriction, and duration of the illness. The development of tracheomegaly was also compared with the other clinical variables evaluated in these patients.

Results

Tracheomegaly was present in 10 (29%) of the 34 patients with diffuse pulmonary fibrosis, including four with fibrosing alveolitis, four with sarcoidosis, and two with chronic progressive histoplasmosis (Figs. 1 and 2). This included six men with transverse tracheal dimensions ranging from 27 to 48 mm (upper limit of normal, 25 mm) and four women with transverse tracheal dimensions ranging from 23 to 27 mm (upper limit of normal, 21 mm). The degree of restrictive lung disease was classified as moderate in six patients and severe in two patients; pulmonary-function tests were unavailable in two cases. The duration of illness was 3–6 months in two patients, 10–22 years in five patients, and not recorded in three patients. In seven of these 10 patients, serial radiographs were available, spanning a period of 4 months to 13 years, and in all seven the initial transverse tracheal dimensions were normal, progressing to abnormal values as the pulmonary fibrosis progressed. Nine of the 24 patients without tracheomegaly had serial radiographs showing progressive increase in the transverse diameter of the trachea.

A comparison of the clinical variables examined in the group with tracheomegaly, compared with the group without tracheomegaly, produced the following results. Six (60%) of the 10 patients with tracheomegaly were smokers, compared with 13 (54%) of 24 patients without tracheomegaly. One (10%) of 10 patients with tracheomegaly had occupational exposure to noxious dusts, compared with three (13%) of the 24 patients without tracheomegaly. Two (20%) of the 10 patients with tracheomegaly had a positive tuberculin skin test, compared with six (25%) of the 24 patients without tracheomegaly. No patient with tracheomegaly had been exposed to any medication known to cause pulmonary fibrosis, compared with one (4%) of the 24 patients without tracheomegaly. Two (20%) of the 10 patients with tracheomegaly had a history of endotracheal intubation, compared with five (21%) of 24 patients without tracheomegaly. Therefore, these variables appeared to have no relationship to the development of tracheomegaly. Six (60%) of 10 patients with tracheomegaly had a chronic cough, compared with 10 (42%) of 24 patients without tracheomegaly. Five (50%) of the 10 patients with tracheomegaly had one or more episodes of respiratory infection, compared with nine (38%) of the 24 patients without tracheomegaly, suggesting that chronic cough and superimposed infection may be slightly more common in those patients with diffuse pulmonary fibrosis who develop tracheomegaly.

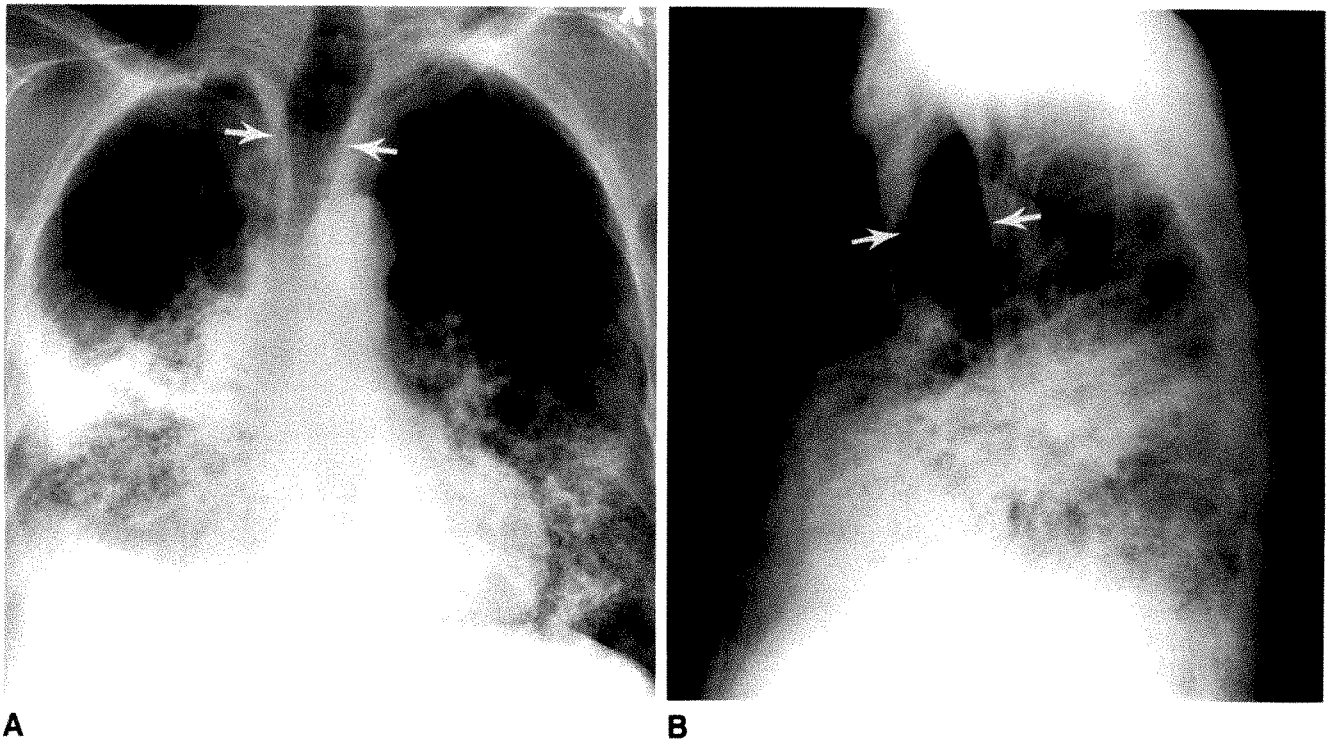


Fig. 1.—Acquired tracheomegaly from fibrosing alveolitis of 6 months duration causing severe restrictive lung disease in a 64-year-old man.
A, On posteroanterior radiograph, transverse internal diameter of trachea 2 cm above aortic arch is 28 mm (arrows), confirming tracheomegaly.
B, On lateral view, sagittal diameter is 32 mm (arrows) and anterior wall shows numerous outpouchings that contribute to mucus stagnation and superimposed infection.

Discussion

The pathogenesis of tracheomegaly is multifactorial and complicated. In some conditions, such as Mounier-Kuhn and Ehlers-Danlos syndromes, the primary cause of tracheal dilatation is thought to be a congenital deficiency in the tracheal and bronchial cartilaginous and membranous tissues resulting in a thinned, atrophic, abnormally flaccid tracheobronchial tree that typically is diffusely enlarged [2–11]. In prolonged endotracheal intubation, acquired tracheomalacia may result from pressure necrosis, impairment of blood supply, infection, and cyclic friction on dry tracheal mucosa [13]. This usually results in focal stenosis of the trachea, but may occasionally cause focal or even diffuse tracheomegaly [13]. A number of inflammatory and infectious conditions have been associated with acquired tracheomalacia and diffuse tracheomegaly. These conditions, including chronic cigarette smoking, chronic bronchitis, emphysema, cystic fibrosis, and relapsing polychondritis, may cause abnormal flaccidity and dilatation of the trachea as a result of chronic infection or inflammation of the tracheal wall [11–13]. Microscopic examination of the trachea in older patients with long-standing cystic fibrosis and tracheomegaly has shown severe inflammation, focal epithelial metaplasia, hypertrophy and hyperplasia of the mucous glands, degenerative changes in the muscle of the pars membranacea, and death of cartilage cells [12]. In cystic fibrosis and the other inflammatory causes of tracheomegaly, it is thought that the

combination of prolonged inflammation and frequent, vigorous coughing damage the tracheal wall [11–13]. It is of interest to note that the most common complication of congenital deficiency of the tracheal wall is bronchiectasis and repeated respiratory infections [2–11]. This suggests that tracheal-wall deficiency and tracheal inflammation may combine to cause progressive tracheal abnormality.

In diffuse pulmonary fibrosis, the primary cause of tracheomegaly is thought to be increased traction on the tracheal wall [13, 14]. Although the trachea is mediastinal and is separated from the lung by two layers of pleura, pulmonary fibrosis can cause traction on the trachea in two ways. The first is through increased elastic recoil pressure in the lungs. Tracheal caliber is a function of the composition of the tracheal wall and the magnitude of the pressure differential across the wall [14]. In diffuse pulmonary fibrosis, lung volume is decreased, but the elastic recoil pressure at the reduced lung volume may be greatly increased because of the abnormal amount of fibrotic tissue in the lung parenchyma [14]. As a result, in those forms of pulmonary fibrosis in which the airways themselves are not involved by the disease, the increased elastic recoil pressure in both lungs exerts opposing traction on the trachea, which may result in tracheomegaly [14]. The results of our study support this view. None of the patients in our series with mild restrictive lung disease, as determined by pulmonary-function tests, developed tracheomegaly. Tracheomegaly only developed in those patients with

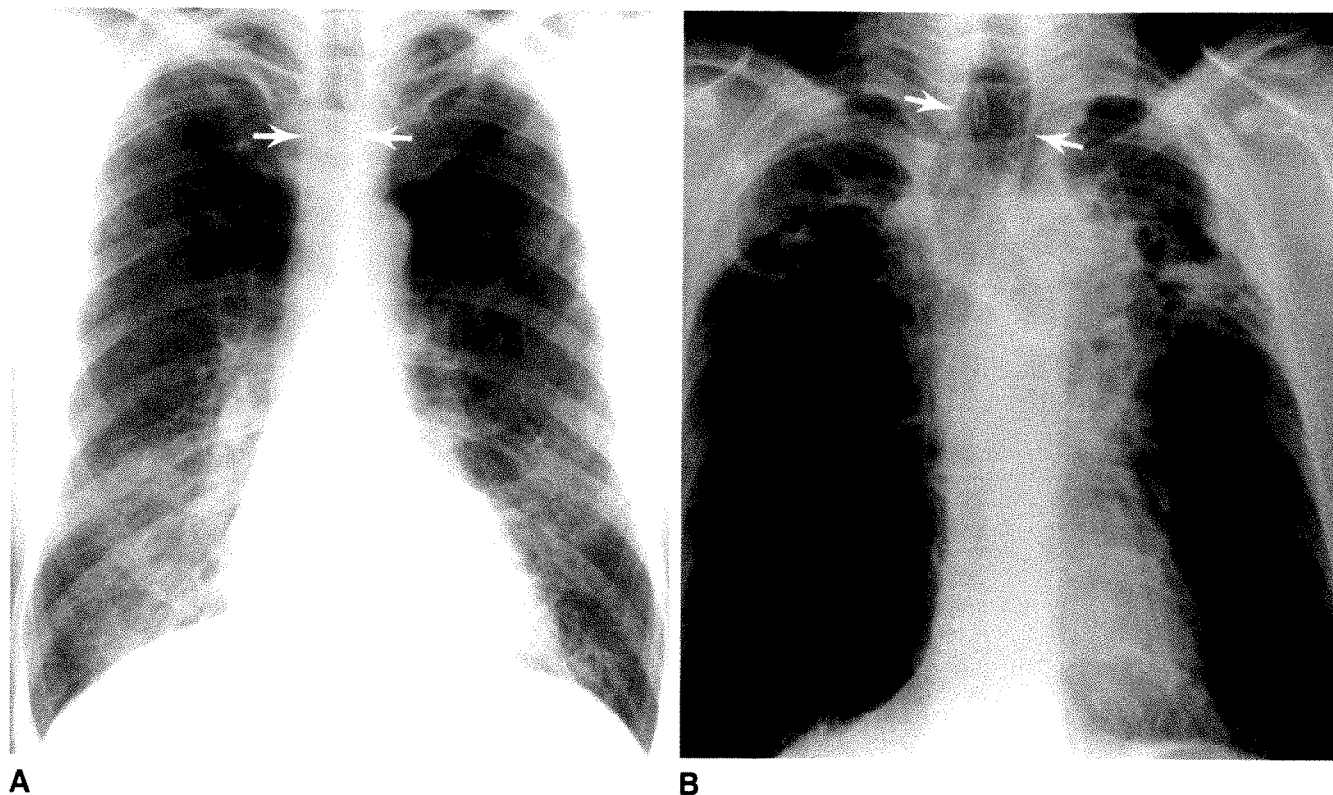


Fig. 2.—Acquired tracheomegaly from chronic progressive histoplasmosis causing moderate restrictive lung disease in a 65 year-old-man.
A, Initial radiograph shows minimal nodular opacities in both upper lobes from histoplasmosis. Transverse internal diameter of trachea 2 cm above aortic arch is normal at 23 mm (arrows).
B, Radiograph 5 years later shows extensive bilateral upper lobe fibrosis and cavitation from chronic progressive disease. Trachea now is 31 mm in transverse diameter (arrows), confirming that tracheomegaly has developed as a result of long-standing pulmonary fibrosis.

long-standing fibrosis with at least moderate or severe restrictive lung disease. In addition, nine of the 24 patients whose tracheal diameters remained within the upper limit of normal showed progressive tracheal dilatation on serial radiographs, suggesting that with longer duration of their illness tracheomegaly may have occurred. A second mechanism by which pulmonary fibrosis may exert abnormal traction on the trachea is the direct formation of adhesions to the tracheal wall [13]. The formation of tracheal adhesions, coupled with increased elastic recoil pressure, may accentuate the tendency to develop tracheomegaly in diffuse pulmonary fibrosis.

An exception to this is sarcoidosis, in which granulomatous involvement of the tracheal wall may result in a narrowed trachea [14]. We have found that acquired tracheomegaly may be observed in a variety of conditions that result in diffuse pulmonary fibrosis. In our series sarcoidosis was a common cause; none of our patients with sarcoidosis showed tracheal narrowing from granulomatous involvement of the trachea. Fibrosing alveolitis (idiopathic pulmonary fibrosis or usual interstitial pneumonitis) and chronic progressive histoplasmosis were observed also to cause acquired tracheomegaly.

In acquired tracheomegaly from pulmonary fibrosis, tracheal dynamics may be severely altered. There may be excessive widening of the tracheal lumen with marked irregular-

ity of its outline [13, 15]. In some instances, true herniations or diverticula develop, and mucus stagnation in these may contribute to chronic infection [15]. Fluoroscopy shows that the trachea may distend disproportionately and unevenly during inspiration and collapse irregularly during expiration; on coughing, marked narrowing or obstruction may occur [13]. The abnormal degree of tracheal collapse during cough further hinders clearance of secretions and contributes to infection [13]. In our series, we did not evaluate tracheal dynamics fluoroscopically.

Although abnormal traction on the trachea is the major cause of tracheomegaly in patients with pulmonary fibrosis, chronic cough and superimposed infection may play a secondary role. Westcott and Cole [16] have shown that acquired "traction" bronchiectasis develops in the lungs in most patients with end-stage pulmonary fibrosis and frequently contributes to the radiographic picture of honeycombing in these patients. Bronchiectasis and chronic infection are known not to be the primary disease in these patients, but rather they develop as a late complication of the fibrotic process in the areas of greatest involvement [16]. In patients with traction bronchiectasis, cough effectiveness is impaired and secretions are retained [16]. As in the congenital forms of tracheobronchial deficiency, it is likely that superimposed infection, coupled with chronic cough, may cause further damage to

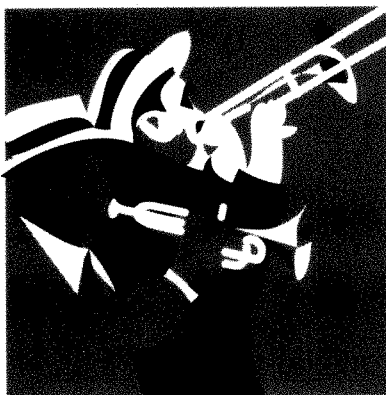
the tracheobronchial tree in patients with pulmonary fibrosis, resulting in progressive airway dilatation.

The altered tracheobronchial dynamics in patients with traction bronchiectasis and/or tracheomegaly may contribute to the high prevalence of pneumonia in patients with extensive pulmonary fibrosis [15, 16]. In our series of 34 patients with diffuse pulmonary fibrosis, superimposed respiratory infections were common, as was chronic cough, occurring in 14 (41%) and 16 (47%) patients, respectively. The prevalence of these complications was slightly higher in those with tracheomegaly, supporting this opinion.

The differential diagnosis of acquired tracheomegaly would include the conditions of congenital tracheobronchomegaly, Ehlers-Danlos syndrome, and diffuse inflammatory tracheomalacia. However, the progressive enlargement of the trachea during the development of diffuse pulmonary fibrosis should be sufficient to distinguish it from these other entities.

REFERENCES

1. Breatnach E, Abbott GC, Fraser RG. Dimensions of the normal human trachea. *AJR* 1984;142:903-906
2. Beachley MC, Ghahremani GG. Tracheobronchiomegaly (Mounier-Kuhn syndrome). *South Med J* 1976;69:1228-1229
3. Hunter TB, Kuhns LR, Roloff MA, Holt JF. Tracheobronchiomegaly in an 18 month old child. *AJR* 1975;123:687-690
4. Johnston RF, Green RA. Tracheobronchiomegaly: report of five cases and demonstration of familial occurrence. *Am Rev Respir Dis* 1965;91:35-50
5. Bateson EM, Woo-Ming M. Tracheobronchomegaly. *Clin Radiol* 1973;24:354-358
6. Ratliff JL, Campbell GD, Reid MV. Tracheobronchiomegaly: report of two cases with widely differing symptomatology. *Ann Otol Rhinol Laryngol* 1977;86:172-175
7. Al-Mallah Z, Quantock OP. Tracheobronchomegaly. *Thorax* 1968;23:320-324
8. Katz I, LeVine M, Herman P. Tracheobronchiomegaly: the Mounier-Kuhn syndrome. *AJR* 1962;88:1084-1094
9. Fiser F, Tomanek A, Rimanova V, Sedivy V. Tracheobronchomegaly. *Scand J Respir Dis* 1969;50:147-155
10. Shin MS, Jackson RM, Ho K-J. Tracheobronchomegaly (Mounier-Kuhn syndrome): CT diagnosis. *AJR* 1988;150:777-779
11. Fraser RG, Paré JAP. *Diagnosis of diseases of the chest*, 2nd ed., Vol. 3. Philadelphia: Saunders, 1979:1322-1325
12. Griscom NT, Vawter GF, Stigol LC. Radiologic and pathologic abnormalities of the trachea in older patients with cystic fibrosis. *AJR* 1987;148:691-693
13. Feist JH, Johnson TH, Wilson RJ. Acquired tracheomalacia: etiology and differential diagnosis. *Chest* 1975;68:340-344
14. Tisi GM. *Pulmonary physiology in clinical medicine*. Baltimore: Williams & Wilkins, 1980:53-73, 175-188
15. Shanks SC, Kerley P. *A textbook of x-ray diagnosis by British authors in six volumes*, 4th ed., Vol. 3. Philadelphia: Saunders, 1973:89
16. Westcott JL, Cole SR. Traction bronchiectasis in end-stage pulmonary fibrosis. *Radiology* 1986;161:665-669



Come to the
American Roentgen Ray Society

89th

ANNUAL MEETING



New Orleans Hilton
May 7-12, 1989



Scientific Program (200 papers)

Instructional Courses (60 hours)

Categorical Course on Genitourinary Radiology

The Caldwell Lecture

Award Papers

Scientific Exhibits

Social, Golf, and Tennis Programs

Guest Programs



Pulmonary Edema as a Complication of Interleukin-2 Therapy

Emily F. Conant¹
Kevin R. Fox²
Wallace T. Miller¹

Eight patients underwent IV bolus therapy with recombinant interleukin-2 (Cetus Corporation, Emeryville, CA) for treatment of metastatic melanoma or renal cell carcinoma. The patients were randomized to receive interleukin-2 alone or interleukin-2 in combination with lymphokine-activated killer cells. Radiographs showed pulmonary edema in five of the eight patients. The changes ranged from mild interstitial edema (two patients) to frank pulmonary edema (three patients). The edema generally resolved within 4 days after the termination of therapy (four patients), however, one patient developed edema and arrhythmias approximately 7 days after interleukin-2 therapy ended. Seven of the eight patients had either cardiac arrhythmias or angina. The mechanisms that contribute to the pathogenesis of these cardiac complications with interleukin-2 therapy remain unclear. The development of pulmonary edema is thought to be caused by capillary leakage and cardiac pulmonary edema due to cardiac toxicity of the drug. The radiologic appearances of these types of pulmonary edema were indistinguishable from one another and from other causes of pulmonary edema.

Our study shows that interleukin-2 can cause pulmonary edema, cardiac arrhythmias, and unstable angina. The severity of these conditions is unrelated to dose.

Interleukin-2 (IL-2) has been shown to cause regression of tumor bulk when given by IV bolus to patients with disseminated cancer. When using the high doses necessary for tumor response, however, researchers have found a high rate of multisystem organ toxicity. In all series, patients have developed a "capillary leak syndrome" resulting in anasarca and multiorgan system dysfunction [1]. Interleukin-2 administration is also associated with hemodynamic alterations similar to those seen in septic shock [2]. Although completely reversible on termination of IL-2 therapy, the increase in vascular permeability leads to varying degrees of interstitial pulmonary edema during treatment, which has produced major cardiovascular and respiratory compromise in some cases [1, 2]. Because the radiographic features of the cardiopulmonary toxicity have not been described, we analyzed these features in eight patients who received therapy and correlated these findings with the dose of the drug and the patients' clinical course.

Subjects and Methods

Eight patients (34 to 58 years old) were randomized to receive IL-2 alone (five patients) or in combination with lymphokine-activated killer (LAK) cells (three patients) for treatment of either metastatic renal cell carcinoma (seven patients) or malignant melanoma (one patient). Patients were excluded from the study if cardiac-stress thallium studies and pulmonary-function tests showed significant cardiac or pulmonary dysfunctions. The patients received an IL-2 infusion based on body weight (100,000 units/kg) every 8 hr for 5 days. After a 5-day recovery period, we gave a second course using the same dose. Individual doses were withheld if toxicity such as hypotension, oliguria, or somnolence occurred. If patients had been randomized to receive LAK cells also, they underwent leukapheresis in the recovery phase, and LAK cells were reinfused at specified intervals during the second course of IL-2.

Received September 23, 1988; accepted after revision November 23, 1988.

¹ Department of Radiology, The Hospital of the University of Pennsylvania, 3400 Spruce St., Philadelphia, PA 19104. Address reprint requests to W. T. Miller.

² Department of Hematology-Oncology, The Hospital of the University of Pennsylvania, Philadelphia, PA 19104.

AJR 152:749-752, April 1989

0361-803X/89/1524-0749

© American Roentgen Ray Society

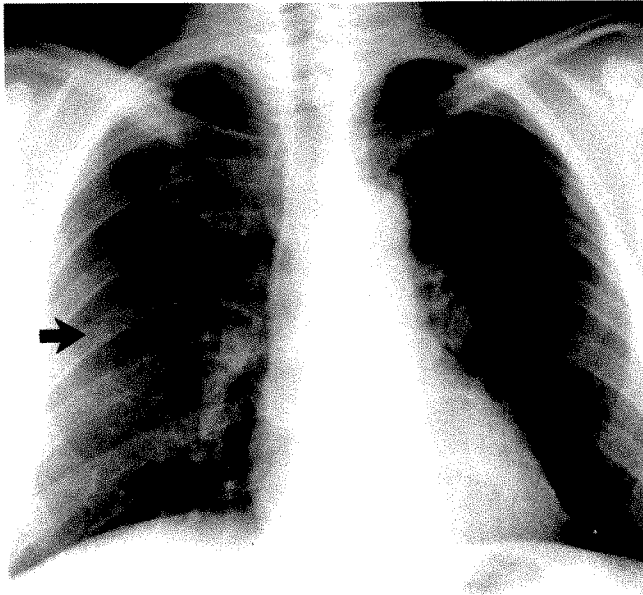
In all patients, serial blood cultures were used to exclude sepsis as a cause for the pulmonary and hemodynamic disorders.

All patients were weighed daily and had their central venous pressures monitored by an in-dwelling catheter. Radiographs were obtained before therapy, daily during IL-2 administration, and as clinically indicated thereafter. The radiographs were reviewed by two experienced chest radiologists.

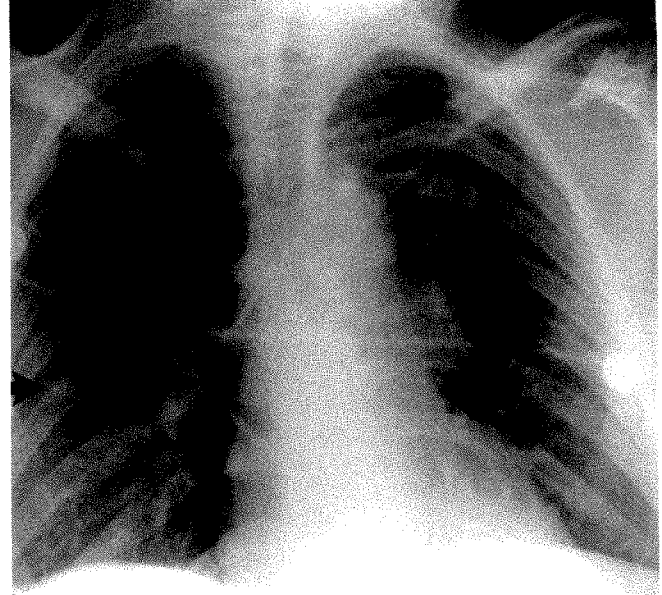
Results

Five of the eight patients developed some degree of pulmonary edema ranging from mild interstitial edema (two pa-

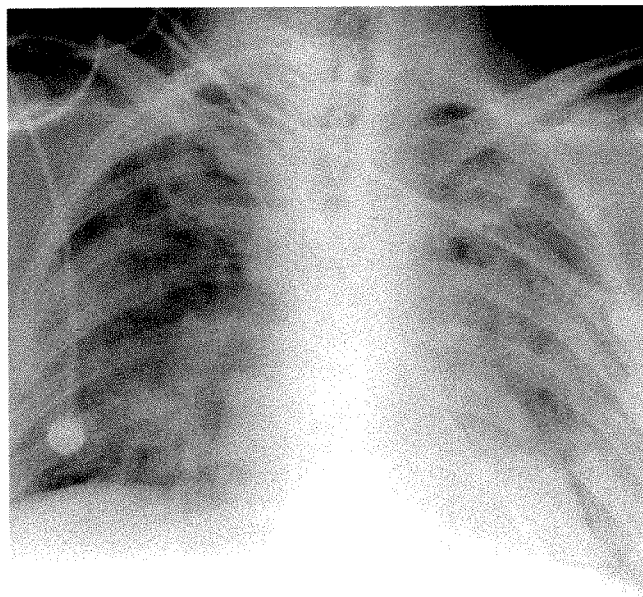
tients) to frank pulmonary edema (three patients). In four of the five patients, pulmonary edema developed within 2 to 8 days of initiation of IL-2 therapy. The fifth patient developed pulmonary edema 7 days after termination of a complete double course of therapy. Percentage weight gain during therapy (relative to initial weight pretherapy) and presence of anasarca with therapy did not always correlate with the degree of pulmonary edema. Percentage weight gain with therapy varied from 6% to 25% (mean = 14%). The patient with a 25% weight gain developed anasarca with bilateral effusions but only mild asymptomatic interstitial edema. A



A



B



C

Fig. 1.—49-year-old man with metastatic melanoma.

A, Radiographs show a 1-cm nodule (arrow) in right middle lobe; CT scan of chest showed multiple pulmonary nodules and bone metastases.

B, 1 day after starting interleukin-2 (IL-2) bolus infusions. Chest radiograph shows mild interstitial edema. It is uncertain whether this edema was due to cardiac toxicity or capillary leak. A left subclavian central venous pressure line is seen. Nodule (arrow) in right middle lobe is seen again.

C, On fifth day of therapy, patient had refractile hypotension, anuria, ECG changes consistent with an inferior wall myocardial infarction, and a chest radiograph showing pulmonary edema. IL-2 therapy was terminated.

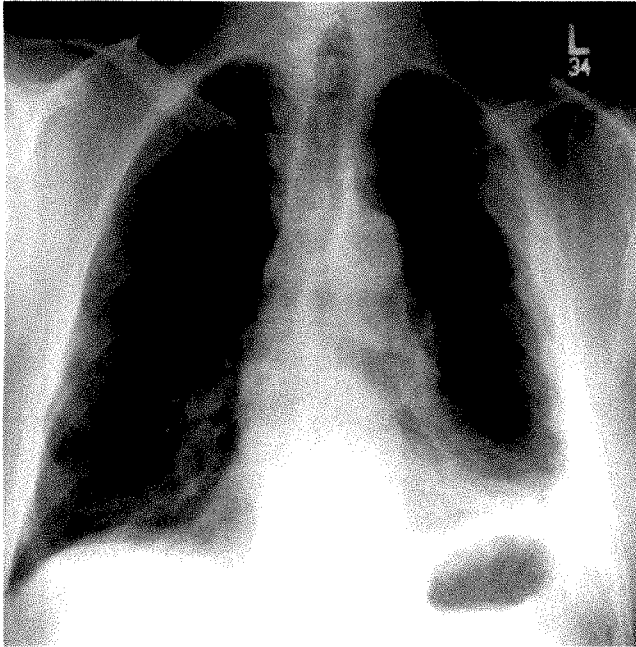
patient with an 11% weight gain developed mild interstitial edema after 3 days, but 2 days later developed severe pulmonary edema (Fig. 1). Two of the three patients randomized to receive LAK with IL-2 developed pulmonary edema, one with mild interstitial edema and the other with more diffuse pulmonary edema. There was no correlation between dose and severity of pulmonary edema.

Seven of the eight patients developed cardiac complications ranging from supraventricular tachycardias (three patients), severe bradycardia (one patient; Fig. 2), and frequent ventric-

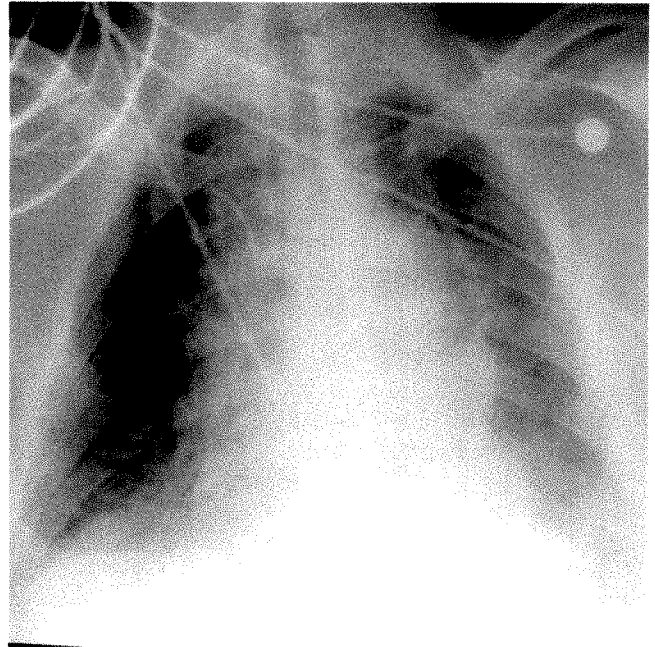
ular premature beats (three patients) to unstable angina with significant electrocardiographic changes that required termination of therapy (three patients). The cardiovascular effects did not appear to be related to dose or correlated with percentage weight gain.

Discussion

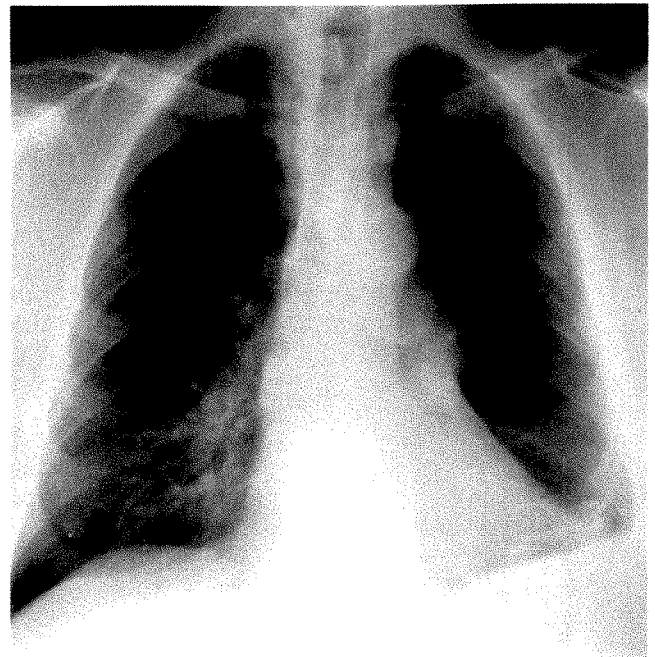
In 1976, Morgan et al. [3] described a factor produced by phytohemagglutinin-activated human T cells that was capable



A



B



C

Fig. 2.—58-year-old man with renal cell carcinoma metastatic to retroperitoneum and chest.

A, Chest radiograph shows metastases to left hilum and pleura (arrow).
B, 5 days after initiation of interleukin-2 (IL-2) therapy, patient had episodes of bradycardia and ventricular arrhythmias and required neosynephrine and dopamine to maintain adequate systolic blood pressures. Chest radiograph shows mild pulmonary edema.

C, 21 days after initiation of IL-2 therapy. Note marked regression of the pleura-based metastases. Mediastinal and left hilar adenopathy are still evident (arrow).

of mediating the expansion of a human T-cell line in vivo. This glycoprotein factor, named T-cell growth factor or interleukin-2 (IL-2), is as potent a mediator of the immune response in vitro as in vivo and has been shown to mediate a spectrum of immunologic effects, including cytotoxic reactivity against autologous tumor cells [4, 5]. The presumed mechanism of IL-2-mediated cytotoxicity is the production of circulating LAK cells. LAK cells are of presumed T-cell or natural-killer-cell origin and are capable of lysing fresh autologous tumor cells in vitro while sparing normal tissues. Treatment of tumor-bearing patients with IL-2 has produced partial remission of metastases in a variety of malignancies, particularly renal cell carcinoma and melanoma. Enthusiasm over human tumor response has been tempered by the severity of toxic reactions associated with systemic administration [6].

A unique capillary leak syndrome has produced major morbidity in patients receiving IL-2 [1]. This increase in vascular permeability has manifested itself by multiorgan system dysfunction and generalized fluid accumulation, with over 10% weight gain in 16 of 25 patients in one series [7]. A more troublesome effect of the syndrome has been the extravasation of fluid in the lung, which produces pulmonary edema in the absence of clinical congestive heart failure, necessitating both ventilatory support and/or termination of IL-2 therapy in extreme cases.

IL-2 administration affects the endothelium and causes emigration of the lymphoid cells from the peripheral blood. Rosenstein et al. [1], using radiolabeled ^{125}I -albumin to measure intravascular plasma volume, assayed varying tissues for vascular fluid extravasation during IL-2 therapy. The IL-2-induced vascular leak showed a characteristic pattern of development requiring at least 3 days of infusion. Continuation of high-dose IL-2 for up to 6 days led to a progressive increase in the level of fluid and colloid pooling in affected tissues. Rosenstein et al. [1] showed a direct dose-response relationship between IL-2 and the level of fluid leakage.

Lotze [8], also studying the capillary leak syndrome using radiolabeled albumin, showed a 20% increase in measured plasma volume associated with a vasodilatory effect of IL-2. Also noted were other cardiovascular and respiratory sequelae including hypotension, tachycardia, decreases in systemic vascular resistance, and increases in cardiac index.

Multiple mechanisms have been proposed for the capillary leak syndrome, but no clear causes have been elucidated. Possible mechanisms postulated include: (1) a direct effect on the integrity of blood vessels by IL-2 factors possessing direct vasoactive properties, (2) an excipient substance in the IL-2 that may be responsible for development of the leak syndrome, and (3) a yet undefined IL-2-mediated host mechanism that initiates the cascade of lymphokines and lymphocytic factors [1]. LAK cells obtained by leukapheresis and later reinfused into patients appear to make no contribution to this vascular toxicity.

At present it is unclear whether IL-2-mediated vascular permeability is necessary for the therapeutic efficacy of the drug. Several therapies have been given in an attempt to abrogate this toxicity, including pretreatment radiation, cyclophosphamide, and concurrent therapy with steroids [1]. None has yet been efficacious, and in fact, some may diminish the antitumor efficacy of IL-2.

Our patients have shown the spectrum of pulmonary leaky capillary syndrome from asymptomatic bilateral effusions, to mild interstitial edema, to frank pulmonary edema (Figs. 1, 2). However, seven of the eight also showed degrees of cardiac toxicity ranging from supraventricular tachycardias, frequent ventricular premature beats, sinus pauses, or runs of ventricular tachycardia to unstable angina with significant electrocardiographic changes. These cardiopulmonary effects are not necessarily related to variations in central venous pressure or percentage weight gain, nor were the pulmonary or cardiovascular effects related to dose or correlated with the addition of LAK cells.

In a series of five patients with similar doses and infusion schedules, Ognibene et al. [2] showed that by day four of therapy, all patients developed tachycardia, decreased mean arterial blood pressure, decreased systemic vascular resistance, and a significant reduction in the left ventricular ejection fraction. These hemodynamic and cardiovascular alterations are very similar to those seen in septic shock. As in sepsis, the mechanisms of these changes are not entirely known. In the use of IL-2, it has been speculated that the changes are due to the drug's ability to activate other mediators such as complement, kinins, or prostaglandins or they may result from a primary toxicity of IL-2 to the myocardium and conducting system [2]. If the latter is contributory, a portion of the pulmonary edema seen radiographically may result from a direct cardiac toxicity rather than purely from the leaky capillary syndrome and noncardiac pulmonary edema. The question of direct myocardial toxicity is being investigated.

It is important for radiologists to be aware of the frequent complication of pulmonary edema in patients receiving IL-2 therapy.

ACKNOWLEDGMENTS

We would like to thank both Mary Dee McEvoy and Lorelei Cannon for gathering data and for managing patients. We also thank Karen Weiss for her typing expertise.

REFERENCES

1. Rosenstein M, Ettinghausen SE, Rosenberg SA. Extravasation of intravascular fluid mediated by the systemic administration of recombinant interleukin 2. *J Immunol* **1986**;137:1735-1742
2. Ognibene FB, Rosenberg SA, Lotze M, et al. Interleukin-2 administration causes reversible hemodynamic changes and left ventricular dysfunction similar to those seen in septic shock. *Chest* **1988**;94(4):750-754
3. Morgan DA, Rusceth FW, Gallo RC. Selective in vitro growth of T lymphocytes from normal human bone marrows. *Science* **1976**;193:1007-1008
4. Grimm EA, Mazumder A, Zhang HZ, Rosenberg SA. Lymphokine-activated killer cell phenomenon: lysis of natural killer-resistant fresh solid tumor cells by interleukin 2-activated autologous human peripheral blood lymphocytes. *J Exp Med* **1982**;155:1823-1841
5. Oldham RK, ed. In vivo effects of interleukin-2. Proceedings of the National Cancer Institute — biological response modifiers program workshop. Bethesda, MD, April 1984. *J Biol Response Mod* **1984**;3:455-532
6. West WH, Tauer KW, Yanelli JR, et al. Constant-infusion recombinant interleukin-2 in adoptive immunotherapy of advanced cancer. *N Engl J Med* **1987**;316:898-905
7. Rosenberg SA, Lotze MT, Muul LM, et al. Observations in the systemic administrations of autologous lymphokine-activated killer cells and recombinant interleukin-2. *N Engl J Med* **1985**;313:1485
8. Lotze MT. Biology and clinical applications of interleukin-2. In: Rosenberg SA, moderator. New approaches to the immunotherapy of cancer. *Ann Intern Med* **1988**;108:853-864

Case Report

Cavitating and Noncavitating Granulomas in AIDS Patients with *Pneumocystis* Pneumonitis

Jeffrey S. Klein,¹ Martha Warnock,² W. Richard Webb,¹ and Gordon Gamsu¹

Pneumocystis carinii pneumonitis is the most common opportunistic lung infection in patients who have AIDS. Although it most commonly presents as parahilar or diffuse granular opacities, several authors have identified atypical radiographic features [1, 2]. We describe a case in which nodular pulmonary densities represented focal granulomatous *P. carinii* infection on pathologic examination. The patient was receiving azidothymidine.

Case Report

A 44-year-old homosexual man first presented in 1986 with shortness of breath of several weeks duration. Chest radiographs revealed a pattern of bilateral interstitial opacities. Examination of induced sputum showed *P. carinii* organisms. The patient was hospitalized after an allergic reaction to oral Septra (trimethoprim-sulfamethoxazole), and IV pentamidine was administered with good clinical and radiographic response.

In early 1987, the patient was started on prophylactic inhaled pentamidine and 3'-azido-3'-deoxythymidine (AZT). In late 1987, his shortness of breath recurred, and chest radiographs showed bilateral coarse linear opacities in the middle to upper lung. Examination of bronchoalveolar lavage fluid showed *P. carinii*. IV pentamidine again brought prompt symptomatic improvement, with resolution of most of the radiographic abnormalities; focal parenchymal scarring was noted on subsequent radiographs.

The patient was admitted to the hospital in March 1988, with progressive clinical deterioration. A frontal chest radiograph at this time revealed a new 1.5 × 2.5 cm nodule with central cavitation in

the left upper lung (Fig. 1A). Despite empiric antibiotic therapy, he died on the 11th hospital day.

Postmortem slices of inflation-fixed lungs revealed three thin-walled cavities up to 2.5 cm in diameter, containing friable yellow exudate. Fibrosis radiated from the cavity walls to surround adjacent bronchovascular bundles (Fig. 1B). Histologically, the cavities were surrounded by foamy macrophages, scattered giant cells, and an outer fibrous wall. The cavity lumen contained foamy pink exudate and proteinaceous debris that was focally calcified. The fibrotic walls of these cavities all contained scattered small granulomas with granular pink centers and surrounding foamy epithelioid cells and fibrosis (Fig. 1C). A Gomori methenamine-silver stain showed numerous *P. carinii* organisms in both the cavities and granulomas. Other smaller granulomas had calcified centers. The scar tissue surrounding the cavities contained muscular arteries with intimal thickening and luminal narrowing (endarteritis obliterans). Viral, mycobacterial, and routine bacterial cultures of lung tissue were negative.

Discussion

Pulmonary infection with *P. carinii* has been associated with lymphoreticular malignancies, immunosuppressive therapy, and AIDS [3]. The classic chest radiographic finding is parahilar "ground glass" or reticulonodular opacities that may progress to more diffuse lung involvement [1]. Atypical radiographic appearances include a normal chest film, lobar or segmental abnormality, sparing of previously irradiated lung, a miliary pattern of abnormality, thin-walled cysts, cavitation,

Received November 7, 1988; accepted after revision December 12, 1988.

¹ Department of Radiology, University of California, San Francisco, Medical Center, San Francisco, CA 94143-0628. Address reprint requests to W. R. Webb, U. C. Medical Center, 505 Parnassus Ave., M396, San Francisco, CA 94143-0628.

² Department of Pathology, University of California, San Francisco, Medical Center, San Francisco, CA 94143-0506.

AJR 152:753-754, April 1989 0361-803X/89/1524-0753 © American Roentgen Ray Society

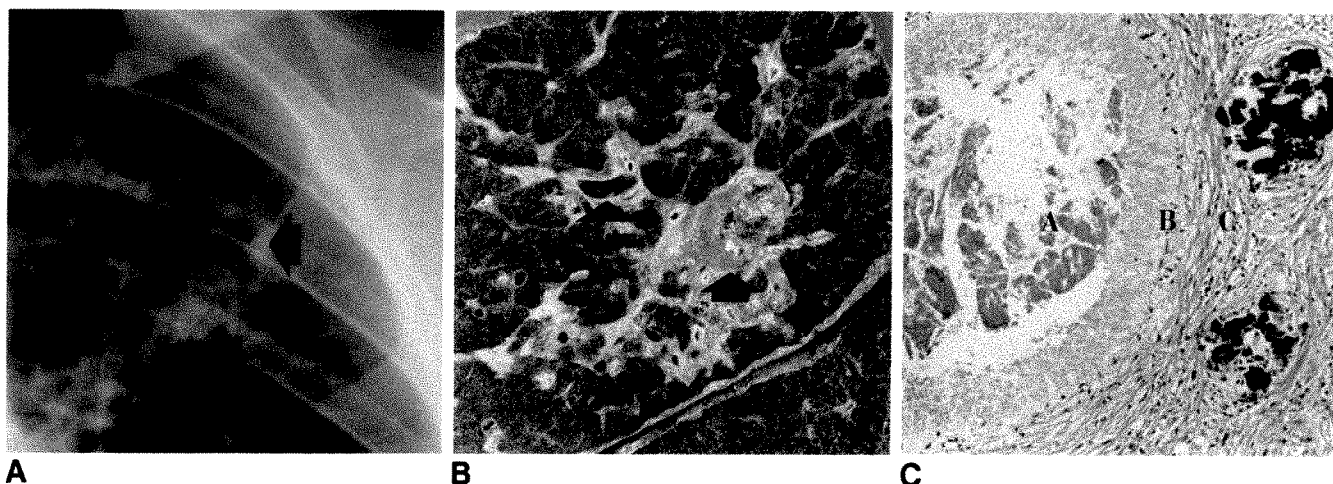


Fig. 1.—*Pneumocystis carinii* pneumonia.

A, Coned-down view of a posteroanterior chest radiograph shows a thin-walled cavity in left upper lobe (arrows).

B, Parasagittal slice of left lung shows two cavities in upper lobe. Larger (arrow), 2.0 × 1.5 cm, has a shaggy wall and granular contents. Smaller (arrowhead) is 1.2 cm long and has a smooth wall. Irregular fibrosis surrounds cavities. (×1.4)

C, Photomicrograph shows granuloma with central cavity (A) that showed multiple *Pneumocystis* organisms on silver stain. Foamy histiocytes (B) and fibroblasts (C) make up wall of granuloma. Two rounded dark bodies adjacent to large granuloma are calcified small granulomas. (H and E, ×200)

pneumothorax, pleural effusion, hilar and mediastinal lymphadenopathy, bilateral apical consolidation, and solitary or multiple pulmonary nodules.

Several studies have described *Pneumocystis* pneumonia with nodular opacities on chest radiographs [4, 5]. In the few cases with pathologic confirmation obtained by using transbronchial or open-lung biopsy or postmortem examination, a granulomatous response to the organism was seen. On microscopic examination, our patient with nodular abnormalities on chest radiograph was shown to have localized granulomatous inflammation associated with *P. carinii*. The cavitation seen was probably caused in part by ischemic necrosis due to vascular narrowing (endarteritis obliterans) in the wall of the nodule. The parenchymal scarring seen on the radiographs and during the pathologic examination is most likely due to the patient's three episodes of *P. carinii* pneumonia. We later saw a second patient with nodular radiographic opacities, in whom granulomatous *Pneumocystis* pneumonitis was diagnosed on the basis of transbronchial lung biopsy. The patient had received AZT. In this patient, although the nodules were not directly biopsied, the coexistence of more typical radiographic findings and the absence of other pathogens on culture suggest that the nodules may represent a focal form of pneumocystosis. Large nodules need not be seen in granulomatous *Pneumocystis* infection; as in our second patient and other reported cases, granulomas also were detected in lung areas that lacked nodules.

Granuloma formation reflects an immune response not usually present in patients with AIDS and *P. carinii* pneumonia. Hartz et al. [5] proposed that the solitary granulomatous nodule in their patient with lymphoma was related to intermittent, rather than continuous, chemotherapy, which had better preserved host immunity. In our patients, AZT (an antiviral agent in clinical use since 1985 for patients with AIDS or AIDS-related complex) may have modified the radiologic and pathologic manifestations of *P. carinii* pneumonia by

boosting immune response. AZT has been shown to increase helper T lymphocytes and to restore delayed hypersensitivity skin reactivity in previously anergic patients [6]. Improved host defenses also may be the result of better therapy against the organism or of the absence of cofactors such as sexually transmitted diseases. Two previously reported AIDS patients with granulomatous *P. carinii* pneumonia had not received AZT [7].

Our two cases suggest that focal lung disease in AIDS patients, manifested radiographically as well-defined nodules or nodular infiltrates, may be related to localized granulomatous inflammation associated with *P. carinii* pneumonia. Thus, *P. carinii* pneumonia, along with fungal and mycobacterial infections, intrathoracic Kaposi sarcoma, and lymphoma, should be considered in the differential diagnosis of nodular pulmonary disease in AIDS patients.

REFERENCES

1. Suster B, Akerman M, Orenstein M, Wax M. Pulmonary manifestations of AIDS: review of 106 episodes. *Radiology* 1986;161:87-93
2. Doppman J, Geelhoed G, DeVita V. Atypical radiographic features in *Pneumocystis carinii* pneumonia. *Radiology* 1975;114:39-44
3. Walzer P, Powell R, Yoneda K, Rutledge M, Milder J. Growth characteristics and pathogenesis of experimental *Pneumocystis carinii* pneumonia. *Infect Immun* 1980;27:928-937
4. Barrio J, Suarez M, Rodriguez J, Saldana M, Pitchenik A. *Pneumocystis carinii* pneumonia presenting as cavitating and noncavitating solitary pulmonary nodules in patients with the acquired immunodeficiency syndrome. *Am Rev Respir Dis* 1986;134:1094-1096
5. Hartz J, Geisinger K, Schary M, Muss H. Granulomatous pneumocystosis presenting as a solitary pulmonary nodule. *Arch Pathol Lab Med* 1985; 109:466-469
6. Yarchoan R, Klecker R, Weinhold K, et al. Administration of 3'-azido-2',3'-deoxythymidine, an inhibitor of HTLV III/LAV replication, to patients with AIDS or AIDS-related complex. *Lancet* 1987;1(8481):575-580
7. Blumenfeld W, Basgoz N, Owen W, Schmidt D. Granulomatous pulmonary lesions in patients with the acquired immunodeficiency syndrome (AIDS) and *Pneumocystis carinii* infection. *Ann Intern Med* 1988;109(6):565-507

Percutaneous Transhepatic Embolization of Gastroesophageal Varices: Results in 400 Patients

C. L'Herminé¹
 P. Chastanet¹
 O. Delemazure¹
 P. L. Bonnière²
 J. P. Durieu¹
 J. C. Paris²

During a 7-year period, bleeding esophageal varices were treated by means of percutaneous transhepatic embolization in 400 cirrhotic patients, including 258 patients with Child's class C cirrhosis (65%) and 142 patients with Child's class B cirrhosis (35%). Embolization was performed either with bucrylate or with absolute ethanol and stainless-steel coils. Variceal hemorrhage was controlled in 245 (83%) of the 297 patients in whom percutaneous transhepatic embolization was performed as an emergency treatment. The 10-day survival rate in the series was 76%, with 97 deaths occurring shortly after the procedure as a result of recurrent bleeding or liver failure. The actuarial rate of recurrent bleeding was 55% at 6 months (38% Child's class B, 70% Child's class C) and 81% at 2 years (71% Child's class B, 90% Child's class C). One-half the cases of recurrent bleeding were easily controlled by medical treatment; 56% of these patients were still alive at 6 months (79% Child's class B, 42% Child's class C), 48% were alive at 1 year, and 26% were alive at 5 years. Results indicated that the survival rate was significantly higher ($p < .01$) in Child's class B patients than in Child's class C patients during the 5-year follow-up period. The overall technical failure and complication rates were 9% and 7%, respectively, but these rates declined progressively as we gained more experience with the procedure.

In this large series, transhepatic embolization was a safe, easy-to-perform, and effective treatment for the control of variceal bleeding and was somewhat more efficacious than previously reported.

When first described by Lunderquist and Vang [1] in 1974, percutaneous transhepatic embolization (PTE) of gastroesophageal varices appeared to be a highly promising procedure for the management of variceal hemorrhage in cirrhotic patients. Indeed, subsequent reports indicated that this method was successful in controlling bleeding in 70–90% of such patients [2–10]. However, because the underlying portal hypertension and hepatic insufficiency are not affected by PTE, further experience showed that the value of the procedure was limited. Recurrent bleeding occurred in 37–65% of patients within a few months after embolization. Long-term survival rates after the procedure have been difficult to evaluate because the prognosis in these patients depends mainly on the degree of hepatic insufficiency. PTE was considered difficult to perform and time-consuming and was associated with a significant rate of technical failure and complications. For these reasons, the method was thought by many to be less effective than endoscopic sclerotherapy for the treatment of esophageal varices; its subsequent use declined substantially [11, 12].

In our hospital, PTE has long been considered a useful therapeutic procedure and, despite the advent of endoscopic sclerotherapy, it has been used frequently. Having amassed a large series of patients, the aim of our study was to assess retrospectively the usefulness of PTE in the management of bleeding varices.

Materials and Methods

Between 1980 and 1987, PTE was attempted 593 times in patients with variceal bleeding and a patent portal vein. The procedure failed in 55 cases (9%); 538 embolizations were

Received January 21, 1988; accepted after revision October 3, 1988.

Presented at the annual meeting of the American Roentgen Ray Society, Miami Beach, FL, April 1987.

¹ Department of Radiology, Centre Hospitalier Universitaire, Place de Verdun, F-59037 Lille, France. Address reprint requests to C. L'Herminé.

² Department of Gastroenterology, Centre Hospitalier Universitaire, Place de Verdun, F-59037 Lille, France.

AJR 152:755–760, April 1989

0361–803X/89/1522–0755

© American Roentgen Ray Society

successful in 482 patients. Of those, 82 were not included in the retrospective analysis either because the follow-up period was less than 3 months or because the patients previously had undergone another hemostatic procedure (endoscopic sclerosis, surgical decompression). Therefore, the clinical outcome of PTE was assessed in 400 patients who were treated exclusively with this procedure and who were followed for at least 3 months. Three hundred sixty-one patients underwent PTE only once; the procedure was repeated twice in 33 patients and three times in six patients in order to treat recurrent bleeding.

Recurrent bleeding and survival rates were calculated according to the actuarial method by using the chi-square test. With the exception of the 39 patients in whom recurrent bleeding was again treated by PTE, either surgery, endoscopic sclerotherapy, balloon tamponade, and/or vasopressin was used for the treatment of recurrent hemorrhage. However, as soon as patients underwent an endoscopic or surgical procedure, they were excluded from the actuarial curve for recurrent bleeding and survival.

Of the 400 patients, 271 were men (68%) and 129 were women (32%). Forty patients (10%) were less than 40 years old, 275 (69%) were between 40 and 60 years old, and 85 (21%) were more than 60 years old. Cirrhosis was of alcoholic origin in 90% of patients and was nonalcoholic in 10% of patients. When grouped according to the Child and Pugh classification (Table 1), 142 patients were classified as Child's class B (35%) and 258 were classified as Child's class C (65%). Because Child's class C is a relatively heterogeneous grouping, it was subdivided into groups C1 and C2 according to whether the Child's score was evaluated as 10–12 or as 13–15, respectively. One hundred seventy-four patients (44%) belonged to the C1 group

and 84 patients (21%) belonged to the C2 group. PTE was performed as an emergency procedure in 297 patients (74%), whereas the remaining 103 patients (26%) were not actively bleeding at the time of embolization.

Percutaneous transhepatic portography was performed according to the method described by Lunderquist et al. [8]. After premedication with 50 mg clorazepate (Tranxene, Clin-Midy, Paris) plus 0.25 mg atropine and local anesthetic, the liver was punctured through the axillary line with the tip of a 19-gauge, 27- to 40-cm-long Teflon-sheathed needle directed toward the 11th dorsal vertebra. The puncture site was situated as high as possible relative to the position of the costodiaphragmatic pleural fossa and in a frontal plane 2 cm above the medial frontal plane in order to facilitate entry into the portal vein. Generally, selective catheterization of the gastric veins was readily achieved through the use of the Lunderquist guidewire by bending its smooth distal and stiff proximal portions to accommodate the shape of the venous tract.

Embolization was performed by using either 0.5–2 ml isobutyl 2-cyanoacrylate mixed with lipiodol or absolute ethanol and stainless-steel coils. During the first years of the study, cyanoacrylate was used after injection of 20–80 ml of 66% hypertonic glucose to decrease variceal hepatofugal flow. This method was abandoned in 1984, and variceal obliteration was achieved by injection of 5–25 ml absolute ethanol; occlusion of the vein itself was completed by using stainless-steel coils [13]. After embolization, portography was performed and the tip of the catheter was inserted into the splenic vein to ascertain left gastric vein obliteration and to detect the presence of other venous collaterals for eventual occlusion (Fig. 1). Subsequent embolization of the needle tract proved to be unnecessary and was rapidly abandoned without engendering further complications.

TABLE 1: The Child and Pugh Classification System

Parameter	Score		
	1	2	3
Bilirubin (mg/l)	20	20–30	30
Albumin (g/l)	35	30–35	30
Prothrombin time (%)	60	60–40	40
Ascites	Absent	Mild	Obvious
Encephalopathy	Absent	Mild	Obvious

Note.—The Child's class is determined by the sum of the scores of the different parameters. Child's class A = 4–6; Child's class B = 7–9; Child's class C = 10–15.

Results

Complications

Of the 538 successful embolizations, significant complications occurred in 40 procedures (7%), resulting in 13 deaths (2%). Hemoperitoneum was observed in seven patients, hemothorax and pneumothorax in eight patients, and pulmonary embolism in five patients; three patients died as a result of pulmonary embolism. One patient died immediately after embolization with bucrylate as a result of a cerebral embolism.

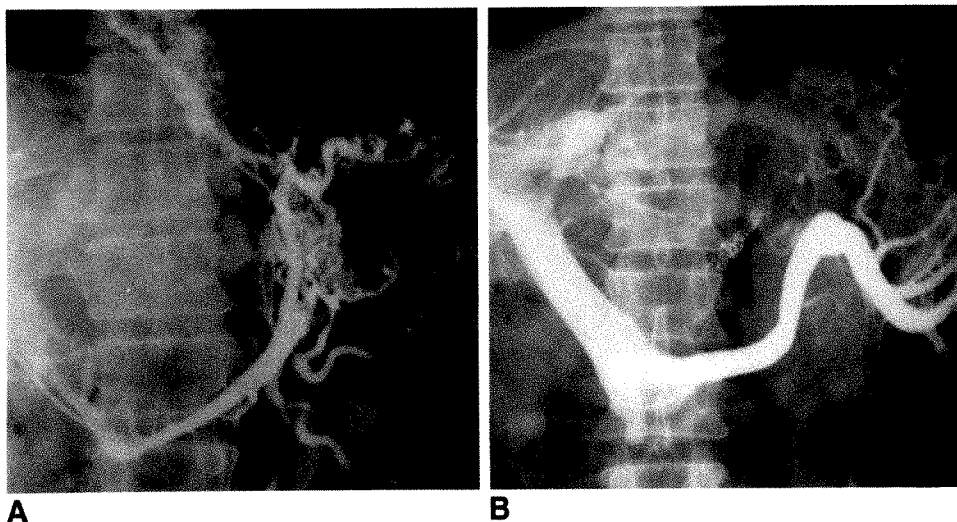


Fig. 1.—Percutaneous transhepatic embolization in an actively bleeding patient with Child's class C alcoholic cirrhosis.

A, Selective catheterization of left gastric vein shows esophageal varices. Portal pressure was 25 cm H₂O.

B, After embolization with 10 ml absolute alcohol and stainless-steel coils, left gastric vein is occluded; portography shows no other veins feeding varices.

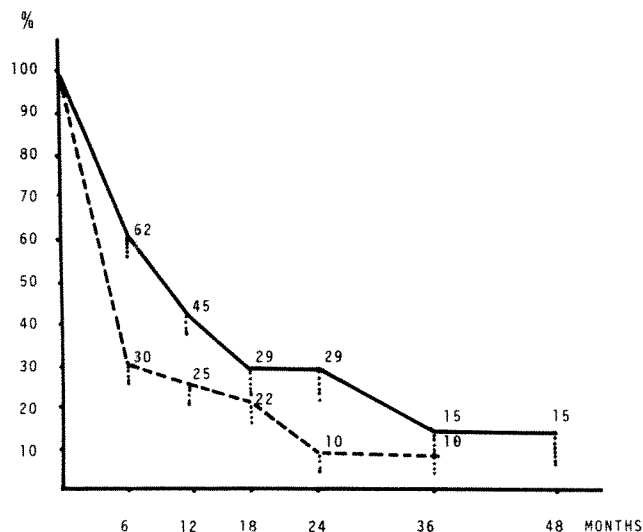


Fig. 2.—Recurrent bleeding rate after percutaneous transhepatic embolization according to Child's classification in 348 patients, including 245 actively bleeding patients in whom hemorrhaging was controlled and 103 patients who were not bleeding at the time of embolization. Actuarial percentage of patients who did not have recurrent bleeding is indicated. Child's class B group, SD = 7% (solid line); Child's class C group, SD = 4–5% (dashed line).

The use of absolute ethanol was responsible for transient convulsions and coma in one patient and respiratory difficulties in two patients. Rupture of the distal tip of the Lunderquist guidewire or migration of a stainless-steel coil within the portal vein was encountered three times.

Ten of the 482 patients in our series had portal vein thrombosis after PTE. Of the 50 patients who subsequently underwent percutaneous transhepatic portography for recurrent bleeding after PTE, eight patients (16%) had portal vein thrombosis.

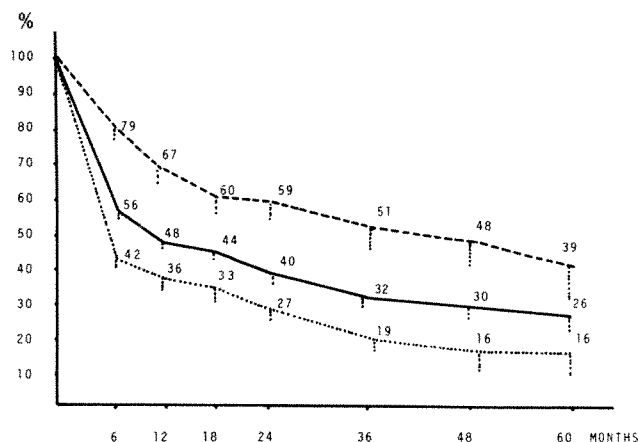


Fig. 3.—Life-table analysis curve after percutaneous transhepatic embolization in 348 patients, including 245 actively bleeding patients in whom hemorrhaging was controlled and 103 who were not actively bleeding at the time of embolization. Actuarial percentage of surviving patients is indicated. Intergroup difference in survival rate was statistically significant ($p < .01$) during the entire 5-year period. Total 348-patient group, SD = 2–4% (solid line); Child's class B group, SD = 4–6% (dashed line); Child's class C group, SD = 2–5% (dotted line).

The number of complications decreased as we gained more experience with the procedure: The complication rate was 12% in 1980, 7% in 1981 (9% in the 125 first procedures), and 5% after 1982.

Short-Term Outcome

Cessation of bleeding was observed in 245 (83%) of the 297 actively bleeding patients, with a higher success rate in Child's class B patients (94%) than in Child's class C patients (78%). Hemorrhaging was not arrested in 52 of these patients, 90% of whom belonged to Child's class C.

Despite successful control of hemorrhaging initially, a marked number of patients died within 10 days of the procedure because of recurrent bleeding or liver failure. The 10-day survival rate was 76%. Of the 97 patients who died, 11 belonged to Child's class B and 86 to Child's class C (49 C1, 37 C2). The early mortality rate was then 8% in Child's class B, 28% in the C1 group, and 44% in the C2 group.

Long-Term Outcome

The long-term evaluation of recurrent bleeding and patient-survival rates was based on a cohort of 348 patients, including (1) the 245 actively bleeding patients in whom the bleeding was initially controlled after embolization and (2) the 103 patients in whom PTE was electively performed after the bleeding had been controlled with conservative treatment. The results were calculated actuarially at 6-month intervals from the day of embolization until 4 or 5 years later.

The recurrent bleeding rate for the entire 348-patient series was 55% at 6 months, 66% at 12 months, 74% at 18 months, 81% at 2 years, 88% at 3 years, and 92% at 4 years. As seen in Figure 2, recurrent bleeding after PTE occurred less

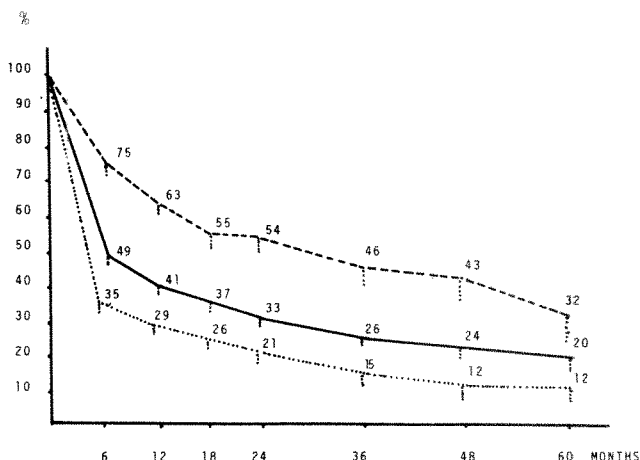


Fig. 4.—Life-table analysis curve for entire series of 400 patients, including the 52 actively bleeding patients whose hemorrhage was not initially controlled after percutaneous transhepatic embolization. Actuarial percentage of surviving patients is indicated. Total 400-patient group, SD = 2–4% (solid line); Child's class B group, SD = 4–6% (dashed line); Child's class C group, SD = 4–5% (dotted line).

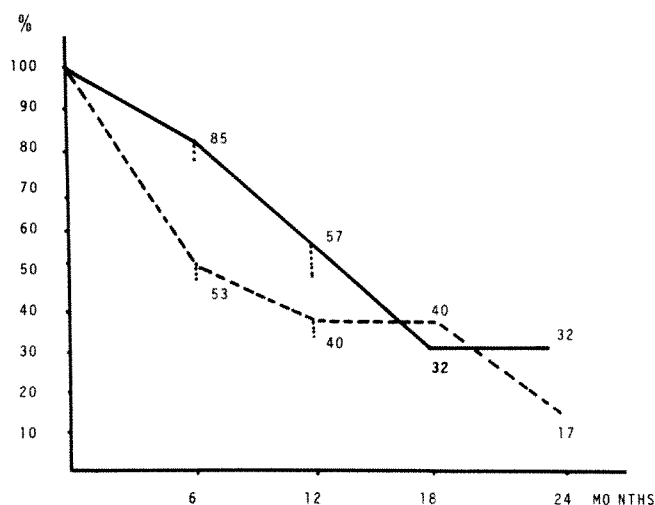


Fig. 5.—Life-table analysis curve compares survival rates among Child's class C patients in C1 group treated once or twice by means of percutaneous transhepatic embolization. Actuarial percentage of surviving patients is indicated. 20 patients were reembolized for recurrent bleeding, SD = 7–11% (solid line); 73 patients underwent only one embolization, SD = 4–5% (dashed line).

frequently in the Child's class B group than in the Child's class C group, at least within the first 3 years after the procedure.

Analysis of the 5-year survival curves (Fig. 3) indicated that the survival rate was significantly higher ($p < .01$) in Child's class B patients than in Child's class C patients during the entire 60-month follow-up period. After the first 6 months, during which mortality proved to be particularly high (58%) in the class C patients, the survival curves declined in parallel at slower rates but with a 30% greater chance of survival for Child's class B patients.

Within the first 2 years after PTE, survival rates differed significantly between Child's class C patients in the C1 group and those in the C2 group (data not shown). The 6-month mortality rate was high in the C2 group (74%), as compared with the C1 group (51%). However, every Child's C2 patient who had survived 6 months was still alive at 18 months; the actuarial survival rate in this group was still 21% at 2 years and 18% at 3 years.

The total survival rate among the 400 patients in whom PTE was successfully achieved—regardless of whether bleeding was controlled initially—was 49% at 6 months, 41% at 1 year, and 33% at 2 years (Fig. 4).

Of the 33 patients in whom rebleeding was treated by reembolization, 20 belonged to Child's class C1. In order to evaluate the usefulness of reembolization, the survival rate in these 20 patients was compared with that in 73 Child's class C1 patients who were not reembolized, although 75% of them had had recurrent bleeding within 1 year after PTE. As seen in Figure 5, the 6-month actuarial survival rates in patients who were reembolized and in those who were not reembolized were 85% ($\pm 7\%$) and 53% ($\pm 4\%$), respectively. The survival rates in these same groups 1 year after PTE were 57% ($\pm 9\%$) and 40% ($\pm 4\%$), respectively.

Discussion

Although technical difficulties have been considered an important drawback of PTE resulting in a consistent failure rate of about 20%, regardless of whether the transhepatic [10] or transjugular [5] route was used, our results indicate that these obstacles can be overcome with increasing experience. Our technical failure rate (9% for the entire series) decreased from 15% during the 125 first attempts to about 5% after 1982. Complications of PTE seem to be more frequent or more severe in patients who have end-stage liver disease—that is, in patients in whom PTE is often the only lifesaving therapeutic measure available in an emergency situation.

PTE was tolerated relatively well by our patients, especially in view of the generally poor condition of the actively bleeding alcoholic cirrhotics in whom it was performed. In our series, hemoperitoneum was a rare complication, despite the severe coagulation defects in some patients and our decision not to embolize the transhepatic needle tract.

The frequency of portal vein thrombosis, another commonly encountered complication of PTE, is difficult to evaluate. The 16% rate of portal vein thrombosis in our group of 50 patients who underwent angiography for recurrent bleeding was similar to that previously reported [8]. However, in three of our eight patients who had recurrent bleeding shortly after PTE, portal vein thrombosis was due to technical failure because a reflux of bucrylate was noted within the vein during embolization. In two other patients, portal vein thrombosis was not discovered until 14 and 18 months after embolization, respectively, when the patients were treated for recurrent bleeding. We do not know whether the thrombosis was initially due to PTE or occurred spontaneously after the procedure. Therefore, as previously stated, PTE is not associated with a high risk of portal vein thrombosis—and the occurrence of thrombosis will be even lower if the use of bucrylate declines. When embolizing varices connecting the portal and caval systems through relatively short and high flow-rate pathways, the use of bucrylate should be avoided because of the potential risk of pulmonary embolism.

PTE has been reported to control acute variceal hemorrhage in 70–95% of cases and to increase the 1-month survival rate from 37% to 73%, as compared with medical treatment [14]. Our results are in agreement with those in the literature because bleeding was controlled in 83% of our patients. Moreover, this arrest of acute hemorrhage compares favorably with the outcome of endoscopic sclerotherapy, which is said to control bleeding in about 75% of cases [15, 16]. Therefore, the immediate efficacy of PTE for acute bleeding is undeniable. In our series, although the early mortality rate was closely related to the degree of liver failure according to the Child's classification, the 10-day survival rate (data not included) was three times higher when PTE was successful in controlling bleeding than when it was not successful. Therefore, it can be shown that the control of bleeding plays a major role in early survival after embolization, regardless of the degree of liver failure.

The results of PTE for recurrent bleeding may appear to be discouraging because most of the patients in both Child's

classes had recurrent bleeding after 3 years (55% at 6 months, 81% at 2 years) (Fig. 2). However, although it is clear that PTE does not prevent long-term recurrent bleeding from new variceal channels or recanalized occluded varices, the new varices are often smaller, resulting in more benign hemorrhage in about half the cases [8]. Nonetheless, it remains to be shown whether PTE has an impact on subsequent mortality caused by recurrent bleeding.

Our series confirms that the mortality rate after successful embolization is highest within the first 6 months and is considerably higher as liver failure becomes more severe; prognosis in Child's C2 patients is particularly poor. Of the 143 patients in whom cause of death was accurately determined, 66 died from bleeding and 77 died from liver insufficiency or other causes unrelated to recurrent bleeding. Thus, in 54% of the patients who died after successful embolization, death cannot be attributed to recurrent bleeding.

Although it is difficult to compare PTE with other hemostatic procedures, the rate of survival after this procedure appears to be higher than that usually reported after conservative treatment. According to Novis et al. [17], the survival rate after medical treatment and use of the Sengstaken tube is 21% at 1 year and 12% at 2 years. The use of endoscopic sclerotherapy was reported to result in a 1-year survival rate ranging from 32% to 82% [15, 16, 18, 19]. However, the higher survival rates occurred in patients with portal hypertension that was unrelated to alcoholic cirrhosis, whereas the lower rates occurred in patients with Child's class C alcoholic cirrhosis [18]. The 32% 1-year survival rate is similar to the 36% and 29% rates observed in the same class of patients in our series (Figs. 3 and 4).

In the case of recurrent bleeding, reembolization improved the survival rate in 20 Child's C1 patients as compared with that in 73 similarly classified patients who underwent only one embolization. Insofar as the Child's classification is a reliable indicator for intergroup comparison, reembolization seems to result in a decreased mortality rate within the first year after bleeding, with a statistically significant difference at 6 months ($p < .01$) (Fig. 5).

Although the long-term efficacy of PTE remains unknown, the results obtained in this extended follow-up of the largest series of patients treated with PTE suggest that this procedure is more valuable in the management of variceal bleeding than has been reported previously [20, 21]. The impact of PTE as well as that of other oblitative variceal procedures is difficult to evaluate in the cirrhotic patient in whom recurrent bleeding and survival depend mainly on the course of hepatic insufficiency. Moreover, most of the studies assessing PTE have been based on relatively small and heterogeneous groups of patients. Higher technical failure and complication rates have occurred in the smaller series of patients; however, many of these studies included a larger number of patients with end-stage liver disease. In our experience, the use of PTE in the treatment of actively bleeding patients leads to a marked reduction in both the amount of blood required and the length of hospitalization.

The efficacy of PTE for control of bleeding may be similar to that of endoscopic sclerotherapy and, although their mode of action differs, both procedures are useful. PTE may be

considered for use in every case of variceal bleeding, provided that the portal vein is patent, regardless of the patient's condition and the site of the varices (esophageal, gastric, or intestinal) [22]. Endoscopic sclerotherapy may be easier to perform because it does not depend on the configuration of the portal vein, but its use is restricted to esophageal varices. Thus, although endoscopic sclerotherapy currently is preferred as the initial hemostatic procedure in most cases involving variceal hemorrhage, PTE also is a useful therapeutic method, particularly when endoscopic sclerotherapy is either contraindicated or fails or when alternative measures are required in patients who have recurrent bleeding after endoscopic sclerotherapy.

ACKNOWLEDGMENTS

We thank R. Beuscart and the Centre d'Etudes et de Recherches en Informatique Médicale (CERIM) for statistical analysis of the data. We are also grateful to Mr. and Mrs. F. Shapiro (Syntaxis-Brugge, Belgium) for editorial assistance.

REFERENCES

1. Lunderquist A, Vang J. Sclerosing injection of esophageal varices through transhepatic selective catheterization of the gastric coronary vein. A preliminary report. *Acta Radiol* 1974;35:546-550
2. Bengmark S, Börjesson B, Hoevels J, Joelsson B, Lunderquist A, Owman T. Obliteration of esophageal varices by percutaneous transhepatic embolization: a follow-up of 43 patients. *Ann Surg* 1979;190:549-554
3. Benner KG, Keefe EB, Keller FS, Rösch J. Clinical outcome after percutaneous transhepatic obliteration of esophageal varices. *Gastroenterology* 1983;85:146-153
4. Franco D, D'Hubert E, Kunslinger F, Bismuth H. Valeur de l'embolisation transhépatique des varices œsophagiennes dans le traitement d'urgence des hémorragies digestives du cirrhotique. *Gastroenterol Clin Biol* 1980;4:921-922
5. Vinei JP, Scotto JM, Levade M, et al. Embolisation des varices œsophagiennes par voie transjugulaire dans les hémorragies digestives graves du cirrhotique. Étude prospective de 83 patients. *Gastroenterol Clin Biol* 1985;9:814-818
6. Hervieu C, Levade M, Pascal JB. Embolisation par voie transcutanée des varices œsophagiennes. *Gastroenterol Clin Biol* 1982;6:692-698
7. Houssin D, Brunet AM, Brochard L, et al. Traitement des hémorragies incontrôlables dues aux varices œsophagiennes chez le cirrhotique. *Presse Med* 1986;15:509-513
8. Lunderquist A, Börjesson B, Owman T, Bengmark S. Isobutyl 2-cyanoacrylate (bucrylate) in obliteration of gastric coronary vein and esophageal varices. *AJR* 1978;130:1-6
9. Passariello R, Thau A, Rossi P, Lombardi M, Simonetti G, Stipa S. Control of gastroesophageal bleeding varices by percutaneous transhepatic portography. *Surg Gynec Obstet* 1980;150:155-160
10. Smith-Laing G, Scott J, Dick R, Sherlock S. Role of percutaneous transhepatic obliteration of varices in the management of hemorrhage from gastroesophageal varices. *Gastroenterology* 1981;80:1031-1036
11. Lunderquist A, Herlinger H, Chuang VP. Direct portography. In: Herlinger H, Lunderquist A, Wallace S, eds. *Clinical radiology of the liver*. Part A. New York: Marcel Dekker 1985;401-427
12. Sos TA. Transhepatic portal venous embolization of varices: pros and cons. *Radiology* 1983;148:569-570
13. Uflacker R. Percutaneous transhepatic obliteration of gastroesophageal varices using absolute alcohol. *Radiology* 1983;146:621-625
14. Widrich WC, Robbins AH, Nabseth DC. Transhepatic embolization of varices. *Cardiovasc Intervent Radiol* 1980;3:298-307
15. Terbianche J, Northover JMA, Bornman P, et al. A prospective controlled trial of sclerotherapy in the long-term management of patients after variceal bleeding. *Surg Gynecol Obstet* 1979;148:323-333

16. Terblanche J, Northover JMA, Bornman P, et al. A prospective evaluation of injection sclerotherapy in the treatment of acute bleeding from esophageal varices. *Surgery* **1979**;85:239-245
17. Novis BH, Duys P, Barbezat GO, Clain J, Bank S, Terblanche J. Fiberoptic endoscopy and the use of the Sengstaken tube in acute gastrointestinal haemorrhage in patients with portal hypertension and varices. *Gut* **1976**;17:258-263
18. Cello JP, Crass R, Turkey DD. Endoscopic sclerotherapy versus esophageal transection in Child's class C patients with variceal hemorrhage. Comparison with results of portocaval shunt: preliminary report. *Surgery* **1982**;91:333-338
19. Clark AW, MacDougall BRD, Westaby D. Prospective controlled trial of injection sclerotherapy in patients with cirrhosis and recent variceal hemorrhage. *Lancet* **1980**;ii:552-554
20. L'Herminé C. *Radiology of liver circulation*. The Hague: Nijhoff, **1985**: 126-127
21. L'Herminé C, Chastanet P. Embolisation des varices oesophagiennes par voie transhépatique percutanée. Résultats chez trois cents malades. *Ann Radiol* **1983**;27:292-293
22. L'Herminé C, Chastanet P, Bonnière P, Gauthier P. Traitement par embolisation des hémorragies par varices intestinales et ombilicales au cours de l'hypertension portale. *Semin Hop Paris* **1987**;63:2650-2654



Scientific Program (200 papers)

Instructional Courses (60 hours)

Categorical Course on
Genitourinary Radiology

The Caldwell Lecture

Award Papers

Scientific Exhibits

Social, Golf, and Tennis Programs

Guest Programs



Come to the American Roentgen Ray Society 89th ANNUAL MEETING



New Orleans Hilton
May 7-12, 1989

Clonorchiasis: Sonographic Findings in 59 Proved Cases

Jae Hoon Lim¹
 Young Tae Ko¹
 Dong Ho Lee¹
 Soon Yong Kim²

Clonorchiasis is a parasitic disease of the bile ducts that occurs in endemic areas after ingestion of the raw flesh of freshwater fish. We analyzed the sonographic findings in 59 patients with clonorchiasis, suspected prospectively from sonographic findings and proved subsequently by demonstration of eggs in their stools. Diffuse dilatation of the small intrahepatic bile ducts with no or minimal dilatation of the large intra- and extrahepatic ducts was observed in all cases. The extrahepatic ducts were patent throughout in all except one case. This characteristic finding reflects diffuse intrahepatic bile duct obstruction and resultant proximal dilatation caused by an adult worm or aggregates of worms, as worms reside diffusely in the medium and small intrahepatic bile ducts. Cholangitis and multifocal periductal fibrosis with proximal dilatation may play an additional role. Increased echogenicity of the intrahepatic bile duct wall was present in 39 cases (66%), reflecting cholangitis and periductal fibrosis. In 17 cases (29%), floating or dependent, discrete, nonshadowing, intraluminal, echogenic foci caused by adult worms in the bile were demonstrated in the gallbladder. These echogenic foci were distinguished from stones because they were fusiform, weak in echogenicity, and floated with a change in position.

Clonorchiasis should be considered when sonography discloses the characteristic pattern of bile duct dilatation with increased wall echogenicity and nonshadowing, discrete, echogenic foci in the gallbladder lumen.

Clonorchiasis is a disease caused by infestation of adult worms of *Clonorchis sinensis*, a liver fluke residing in the medium or small intrahepatic bile ducts and occasionally in the extrahepatic duct and gallbladder. Man is one of the natural definitive hosts and is infested by ingestion of raw flesh of freshwater fish. Most patients are asymptomatic, but heavy long-term infestation produces various gastrointestinal symptoms including jaundice [1, 2]. Although prevalent in the Far East, the disease has been encountered in nonendemic areas as well [3-5] and may be recognized with increasing frequency in the Western world, because the flukes live for decades and the infested persons may immigrate or travel anywhere in the world.

Diagnosis of clonorchiasis usually depends on the demonstration of eggs or adult worms in the feces or bile. Cholangiographic findings have been reported [2-7], but to our knowledge there has been no description of the sonographic features in the English language literature. Several articles in Korean journals have described the sonographic findings [8-10], and the CT findings have been discussed [11, 12]. The purpose of this report is to describe the sonographic features of clonorchiasis in 59 proved cases.

Materials and Methods

In a review of a total of 19,706 abdominal sonograms obtained between April 1985 and July 1988, 59 patients had proved clonorchiasis. Patients with clonorchiasis and concomitant bile duct stones were excluded. There were 52 men and seven women, 25-73 years old

Received September 16, 1988; accepted after revision November 28, 1988

¹Department of Diagnostic Radiology, Kyung Hee University Hospital, 1, Hoeki-dong, Dongdaemun-ku, Seoul 130-702, Korea. Address reprint requests to J. H. Lim.

²Department of Diagnostic Radiology, Han Yang University Hospital, 17, Haengdang-dong, Songdong-ku, Seoul 133-070, Korea.

AJR 152:761-764, April 1989

0361-803X/89/1524-0761

© American Roentgen Ray Society

(mean, 48 years). The patients were studied prospectively and the sonograms were interpreted without knowledge of the clinical history. When sonographic abnormalities of clonorchiasis were found, the diagnosis was proved by stool examination for eggs. All the patients were treated by oral administration of praziquantel. Sonograms were obtained with a 3.5-MHz transducer on commercially available real-time scanners (Toshiba SSA-90A or SAL-55A, Tokyo).

Sonographic abnormalities of the intra- and extrahepatic bile ducts and the gallbladder were analyzed based on the initial interpretation of the sonograms. Dilatation of the intrahepatic bile ducts was considered present if the ducts were equal to or wider than one-half of the accompanying portal venous branches [13] or if ductules were present in the peripheral portion of the liver. The extrahepatic ducts were considered normal if they were less than 6 mm in diameter at the common hepatic duct. The ducts were considered mildly dilated if the diameter was 7–10 mm and moderately dilated if the diameter was 11–15 mm. The echogenicity of the wall of bile ducts was assessed subjectively in each case. Extrahepatic ducts and the gallbladder were examined for the presence of stones or worms, but not every intrahepatic duct was examined meticulously nor was the wall thickness of the ducts measured.

To determine whether worms in the gallbladder produce the same sonographic findings as intraluminal echogenic foci in the gallbladders of patients, we undertook an experimental study with a suspension of worms. Adult worms were collected from the feces of one of our patients and suspended in saline in a surgical glove. Sonograms were obtained with a 3.5-MHz transducer.

Results

Sonograms in all 59 patients showed diffuse dilatation of small intrahepatic ducts (Figs. 1 and 2). In contrast, the extrahepatic ducts were not dilated in 46 cases (78%), minimally dilated (Figs. 1C and 1D) in 12 cases (20%), and moderately dilated in one case (2%). Likewise, though assessed subjectively, the right and left hepatic ducts were normal or minimally dilated. There was no discernible tumor or focal stenotic area throughout the biliary tree. The extrahepatic ducts were patent throughout in 58 cases. In one case only, there was a nonshadowing echogenic cast within the slightly dilated extrahepatic duct (Fig. 3); this was thought to be an aggregate of worms.

The echogenicity of the dilated intrahepatic ductal walls was increased (Figs. 1 and 2) in 39 patients (66%). In 26 cases, (44%) increased echogenicity of the ductal walls produced coarsening of the hepatic parenchymal echo pattern or simulated echogenic nodules if scanned tangentially (Fig. 1B).

Seventeen gallbladders (29%) had fusiform, discrete, echogenic foci measuring 3–6 mm in the lumen (Figs. 1C and 4). In three cases, the echogenic foci floated spontaneously from the dependent portion (Fig. 4), while in nine cases the echogenic foci floated or changed in position with gravity, as the position of the patient was changed. The echogenic foci were

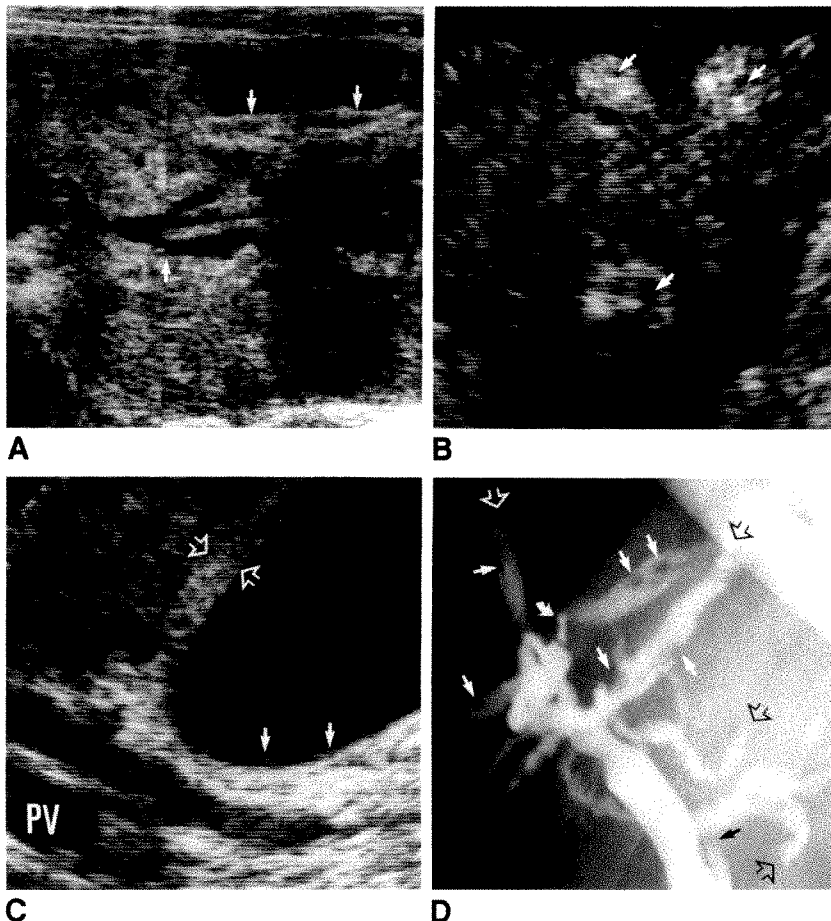


Fig. 1.—38-year-old man with history of raw fish ingestion admitted because of progressive jaundice. Adult worms were expelled in the feces.

A, Transverse scan of left hepatic lobe discloses diffuse severe dilatation of intrahepatic bile ducts with increased echogenicity of duct walls (arrows).

B, Longitudinal scan of left lobe discloses markedly thickened bile ducts mimicking echogenic nodules. Hepatic parenchymal echotexture is coarse. Note dilated small bile ducts (arrows) in center of thick echogenic wall.

C, Parasagittal oblique scan with patient in left decubitus position discloses slightly dilated common hepatic and common bile ducts (8 mm in diameter). Wall of common hepatic duct is thickened. Wall of gallbladder (open arrows) is 7 mm thick. Note faintly echogenic foci (solid arrows) in dependent portion of gallbladder. PV = portal vein.

D, Endoscopic retrograde cholangiogram discloses severe dilatation of intrahepatic bile ducts with irregularity and narrowing (curved arrow). Intraductal filling defects (solid straight white arrows) are caused by adult worms in medium-sized bile ducts. Peripheral small ducts are obstructed (open arrows), as is cystic duct (solid black arrow). Note minimally dilated common hepatic duct.

identified in the dependent portion in the rest of the five gallbladders (Fig. 1C). These fusiform, echogenic foci were distinguished from stones because the echogenicity was weak and nonshadowing and the majority of foci floated with

a change in the position of the patient. During real-time scanning when the position of the patient was unchanged, spontaneous floating movement of these echogenic foci was demonstrated in three cases and was believed to be caused

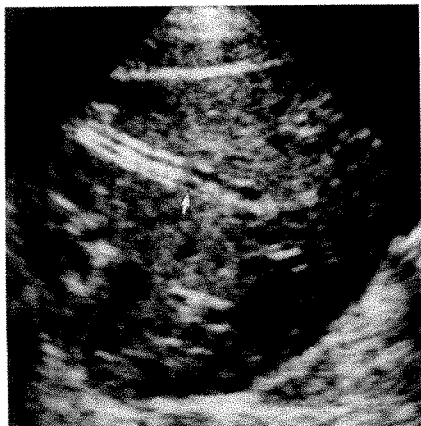


Fig. 2.—43-year-old man examined because of right upper abdominal pain. Longitudinal sonogram of lateral segment of left hepatic lobe discloses echogenic bile duct (arrow) accompanying branch of portal vein to peripheral portion of liver.

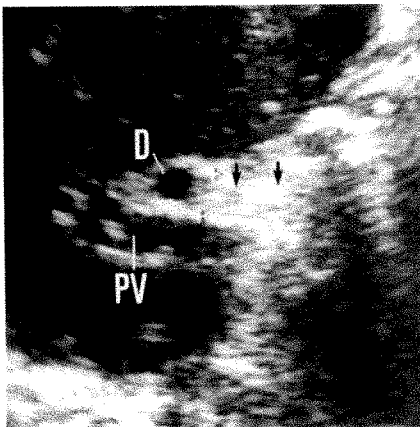


Fig. 3.—73-year-old man with vague abdominal discomfort. Oblique right upper abdominal sonogram shows mild dilatation of common hepatic duct (8 mm in diameter) filled by echogenic cast (arrows). This may represent an aggregate of adult worms. D = common hepatic duct; PV = portal vein.

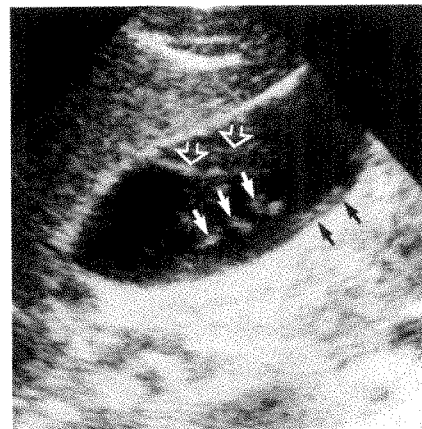


Fig. 4.—31-year-old man with vague abdominal discomfort. Sonogram of gallbladder discloses several discrete, fusiform, floating (solid white arrows), and dependent (black arrows) echogenic foci measuring 5–8 mm. These foci move and float spontaneously, suggesting living worms. Sonographic artifacts (open arrows).

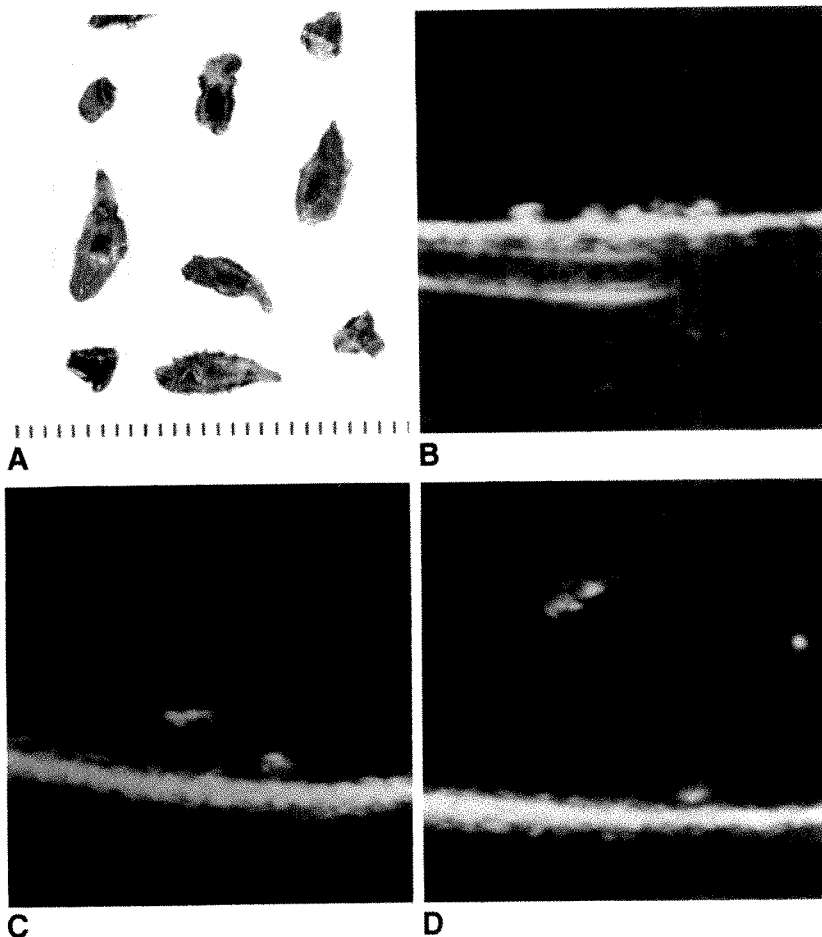


Fig. 5.—Gross appearance and sonograms of adult worms of *C. sinensis* collected from feces of patient in Fig. 1. Sonograms were obtained with worms in saline solution in surgical glove. A 3.5-MHz transducer was used.

A, Gross appearance of adult worms. (Scale increments = 1 mm.)

B, Sonogram of sediment comprising worms.

C and D, Sonograms of floating worms, produced by light blow on surgical glove.

by the movement of living worms, although this was not confirmed.

Eight gallbladders (14%) had stones. The gallbladder wall was thick, over 3 mm (Fig. 1C) in seven cases (12%). A hypoechoic layer was seen within the thick wall in two cases.

In the in vitro study, worms in the glove produced the same echogenic foci as those seen in the gallbladder of patients with clonorchiasis (Fig. 5). The echogenic foci were in the dependent portion but floated after a change in position or a light blow on the glove, due to swirling movement of the saline solution.

Discussion

Our results suggest that clonorchiasis can be suspected on the basis of characteristic sonographic appearances. The specific diagnosis can be made by examination of feces for eggs. Diffuse dilatation of the small intrahepatic bile ducts with no or minimal dilatation of large bile ducts without a focal obstructing lesion (Figs. 1 and 2) is a characteristic finding of clonorchiasis [2, 6–12, 14], not encountered in other bile duct diseases such as tumors of the bile duct, cancer of the pancreas or ampulla of Vater, or choledocholithiasis. In cancer of the bile ducts, including Klatskin tumor, and cancer of the pancreas or ampulla of Vater, the entire biliary tree proximal to the obstructing level dilates diffusely and the obstructing lesion usually can be detected on sonography. In choledocholithiasis, usually stone is demonstrated and the extrahepatic bile duct dilates disproportionately more than in the intrahepatic ducts. In contrast, in clonorchiasis, the extrahepatic ducts are patent throughout and are not dilated. Sclerosing cholangitis may show intrahepatic bile duct dilatation and concentric thickening of the intra- and extrahepatic biliary tree [15], but in sclerosing cholangitis, the thickening of the bile ducts is more severe than in clonorchiasis, and bile duct dilatation is focal and discontinuous, sometimes having a beaded appearance and serpiginous course [16].

The sonographic appearance reflects the basic disease process. Adult worms of the liver flukes reside in the medium and small intrahepatic bile ducts (Fig. 1D) and produce cholangitis [1, 17]. Dilatation of smaller bile ducts is most likely caused by obstruction by the worms per se. The 8 to 15 mm worm or aggregates of worms could easily occlude the small peripheral ducts (Fig. 1D), [1, 12], but larger ducts such as right and left hepatic ducts and extrahepatic ducts are wide enough to be patent, even if worms are lodged within them. However, the mechanism of obstruction cannot be explained by worm size alone, as the worms are flat, willow leaf-like, and 1.5–5 mm thick (Fig. 5A). Mucosal hyperplasia [1], mucus in the ducts caused by cholangitis [6], periductal inflammation [1, 17], fibrosis, and stricture (Fig. 1D) may play additional roles in the occlusion of ducts and resultant proximal small intrahepatic duct dilatation.

In general, a worm or worms that occlude the small intrahepatic bile ducts are not seen on sonography. Demonstration of a worm or worms depends on the size of the worm or its aggregation and the degree of bile duct dilatation. One report described intraductal echoes suggesting worms [8]. In our opinion, the worms or their aggregate in the dilated intrahepatic and extrahepatic ducts can be demonstrated by meticulous examination with high-resolution sonographic equipment (Fig. 3).

Floating or dependent, discrete, nonshadowing echogenic foci in the gallbladder lumen are produced by adult worms of *C. sinensis* (Figs. 1C and 4). The intrahepatic bile ducts are the usual habitat of worms, but occasionally the extrahepatic duct and the gallbladder also may be involved [18]. Worms can be shown within the lumen of the gallbladder on cholangiography [14]. Usually worms sink in the dependent portion (Fig. 1C), but float with a change in position or a light blow on the gallbladder with the transducer, as the position change or light blow causes swirling movement of bile within the gallbladder and the worms float. When worms occasionally float spontaneously (Fig. 4), we believe it is because of movement by living worms. These discrete, echogenic foci are not considered stones as they are fusiform, weakly echogenic, and nonshadowing. In our experimental study done with a suspension of adult worms in saline, the same floating and dependent echogenic foci were demonstrated by sonography (Fig. 5). The discrepancy between the size of the worms on sonograms (Fig. 4) and the real worms (Fig. 5A) may be explained by the fact that worms are usually scanned axially or obliquely (Figs. 5B and 5C) rather than longitudinally (Fig. 5D).

ACKNOWLEDGMENTS

We thank Jong Kwon Won and Byung Do Kim for sonographic assistance and Nan Ok Yeo for secretarial assistance in manuscript preparation.

REFERENCES

1. Yamaguchi T. *Clinical parasitology*. London: Wolfe Medical, 1981:50–57
2. Hatfield PM, Wise RE. Parasitic diseases. In: *Radiology of the gallbladder & bile ducts*. Baltimore: Williams & Wilkins, 1976:252–253
3. Cremin BJ. Biliary parasites. *Br J Radiol* 1969;42:506–508
4. Hartley JPR, Douglas AP. A case of clonorchiasis in England. *Br Med J* 1975;6:575
5. Baker MS, Baker BH, Woo R. Biliary clonorchiasis. *Arch Surg* 1979;114:748
6. Okuda K, Emura T, Morokuma K, Kojima S, Yokagawa M. Clonorchiasis studied by percutaneous cholangiography, and a therapeutic trial of tol-uene-2, 4-diiso-thiocyanate. *Gastroenterology* 1973;65:457–461
7. Choi TK, Wong KP, Wong J. Cholangiographic appearance in clonorchiasis. *Br J Radiol* 1984;57:681–684
8. Kim JW, Kim JG, Sol CH, Kim BS. An observation of ultrasonographic findings in clonorchiasis. *J Korean Radiol Soc* 1983;19:538–545
9. Lim JH, Ko YT, Kim SY, Ryu HS. Ultrasonographic diagnosis of clonorchiasis. *J Korean Radiol Soc* 1984;20:644–647
10. Lim JH, Ko YT, Lee DH, Min YI. Ultrasound findings of clonorchiasis. *J Korean Soc Med Ultrasound* 1987;6:193–194
11. Kim SY, Ko YT, Suh SJ. Computed tomography in evaluation of jaundiced patients due to *Clonorchis sinensis*. *J Korean Radiol Soc* 1978;14:460–464
12. Choi BI, Park JH, Kim YI, et al. Peripheral cholangiocarcinoma and clonorchiasis: CT findings. *Radiology* 1988;169:149–153
13. Bressler EL, Runin JM, McCracken S. Sonographic parallel channel sign: a reappraisal. *Radiology* 1987;164:343–346
14. Lee JI, Yoo JH, Lim GS, Lee CH, Min YI, Lim JH. ERCP findings in clonorchiasis. *J Korean Soc Gastrointest Endosc* 1981;1:29–32
15. Carrol BA, Oppenheimer DA. Sclerosing cholangitis: sonographic demonstration of bile duct wall thickening. *AJR* 1982;139:1016–1018
16. Ferrucci JT, Adson MA, Mueller PR, Stanley RJ, Stewart ET. Advances in the radiology of jaundice: a symposium and review. *AJR* 1983;141:1–20
17. Hou PC. The pathology of *Clonorchis sinensis* infestation of the liver. *J Pathol* 1955;70:53–64
18. Rim HJ. The current pathobiology and chemotherapy of clonorchiasis. *Korean J Parasitol* 1986;24[suppl]:7–20

Duplex Sonography of the Portal Venous System: Pitfalls and Limitations

H. Richard Parvey¹
 Ronald L. Eisenberg¹
 Vishan Giyanani^{1,2}
 Carol A. Krebs¹

Duplex pulsed-Doppler sonographic examinations of the portal venous systems of 14 patients were reviewed, and the results were compared with the findings of other examinations including endoscopy and angiography. The sonograms of virtually every patient in the sample showed at least one of four pitfalls. The "mirror-image" artifact, in which the Doppler signal contained simultaneous and symmetric elements on both sides of the zero baseline, was identified in 11 patients (79%). The "flip" artifact, in which the Doppler signal would either flip from one side of the zero baseline to the other or would indicate a direction of blood flow opposite to that normally expected, was seen in six patients (43%). In four patients (29%), a Doppler flow signal could not be obtained from small vessels that were identified on standard real-time images. In 10 patients (71%), important vascular channels including bleeding gastroesophageal varices were obscured by bowel gas, ascites, or the patient's body habitus.

Duplex sonography may still provide useful information about portal venous hemodynamics. However, it remains a prodigious technical undertaking whose accuracy can be severely hampered by artifacts and inherent technical difficulties.

Duplex pulsed-Doppler sonography has recently been used to show blood flow within both the main tributaries and abnormal collaterals of the portal venous system [1, 2]. In the patient with portal hypertension, in particular, this relatively new technique has been used to document the presence and direction of blood flow at multiple sites including the main portal vein, left coronary vein, and gastroesophageal varices [3-6].

We have encountered some fairly consistent pitfalls and technical difficulties that compromise the ability of duplex studies to accurately depict portal venous hemodynamics. These potential difficulties have not been discussed adequately in the literature. In this report, therefore, we describe the nature, cause, significance, and implications of the particular artifacts we observed in 14 patients in whom duplex sonography was used to investigate the portal venous system. To our knowledge, this communication is the first to include a detailed discussion of two of these pitfalls—the "mirror-image" and "flip" artifacts.

Subjects and Methods

Patients

Fourteen patients (10 males and four females) with a variety of hepatic diseases underwent real-time and duplex pulsed-Doppler sonographic examination of the liver and portal venous system over a 9-month period. One 11-year-old girl had congenital extrahepatic biliary atresia, and two boys (7 and 15 years old) had cavernous transformation of the portal vein. Of the remaining 11 patients (37-78 years old), seven had alcoholic liver disease and/or cirrhosis, two had chronic hepatitis, and one had chronic passive hepatic congestion caused by chronic congestive heart failure. One 56-year-old man had clinical features suggesting both alcoholic liver disease and chronic passive hepatic congestion.

All 14 had at least one diagnostic procedure in addition to sonography that, in most cases, showed evidence of hepatocellular disease or portal hypertension. Five of six patients

Received September 19, 1988; accepted after revision December 13, 1988.

¹ Department of Radiology, Louisiana State University Medical Center, P.O. Box 33932, Shreveport, LA 71130. Address reprint requests to H. R. Parvey.

² Present address: South Arkansas Radiation Therapy Institute, 503 N. Thompson, El Dorado, AR 71730.

AJR 152:765-770, April 1989

0361-803X/89/1524-0765

© American Roentgen Ray Society

undergoing upper gastrointestinal endoscopy had lower esophageal varices. Upper abdominal CT in six patients showed abnormally prominent portal-systemic venous collaterals in all (splenic–left renal vein collaterals in two and lower esophageal, left gastric, and/or retroperitoneal collaterals in four). Four patients (two with alcoholic cirrhosis and two with cavernous transformation of the portal vein) had angiographic studies including wedged hepatic vein injections and pressure readings, superior mesenteric and/or celiac arteriography with delayed venous films, and percutaneous splenoportography. These examinations revealed gastroesophageal varices in three of the four patients and splenomegaly with an enlarged and tortuous splenic vein in the other. Two patients underwent upper gastrointestinal barium studies; both studies showed possible varices in the lower esophagus. Two patients had nuclear sulfur-colloid liver-spleen scans; both studies showed diminished isotope accumulation within the liver and increased uptake within the adjacent spleen and bone marrow. The echocardiograms of two patients with chronic passive hepatic congestion showed cardiomegaly and decreased left ventricular function.

Sonographic Examinations

Real-time and duplex Doppler sonograms were performed on a Picker ARTIS (advanced real-time imaging system) unit with either a 5.0-MHz (imaging)/3.5-MHz (Doppler) transducer or a 3.5-MHz (imaging)/2.25-MHz (Doppler) transducer by using methods similar to those described elsewhere [3–6]. Patients were supine during most of the examination; they were, if necessary, moved into an oblique or decubitus position to better visualize more laterally placed vessels. In most cases, the stomach was not filled with water.

Our particular sonographic machine permits the examiner to orient the Doppler signal tracing either above or below the zero baseline for a given blood flow direction away from or toward the transducer. Attempts were made to visualize (1) the main, left, and right portal veins, the superior mesenteric vein, and the splenic vein and artery; (2) the splenic hilar collateral veins (including short gastric veins); (3) the left coronary collaterals or gastroesophageal varices in the region of the lesser omentum; and (4) a dilated or recanalized umbilical vein.

Each patient's examination was then analyzed for potential errors or pitfalls. In particular, the frequency and circumstances of each of the following were assessed: (1) suboptimal or absent visualization of portal venous channels on real-time examination; (2) absent, equivocal, or technically inadequate Doppler signals; and (3) flow directions

indicated by Doppler that were opposite to that normally expected (e.g., splenic arterial flow going away from the spleen).

Results

Review of the duplex sonographic examinations revealed at least one of the following artifacts or pitfalls in each of the 14 patients.

Mirror-Image Doppler Signal Artifact

This pitfall occurred when the Doppler signal contained simultaneous and symmetric elements on both sides of the zero baseline; the apparent orientation of blood flow therefore was "bidirectional" or ambiguous. This error was identified in at least one vessel in 11 (79%) of the 14 patients. It occurred most often in the main portal vein (six cases), but the error also appeared in the superior mesenteric and splenic veins (three cases each), in the umbilical vein and periportal collaterals (two cases each), and within the hepatic and splenic arteries and within a left coronary venous collateral (one case each).

Both patients with cavernous transformation of the portal vein and one patients with alcoholic cirrhosis showed a mirror-image Doppler signal from periportal collaterals and from the hepatic artery, respectively. These patients' angiographic studies, meanwhile, revealed normal unidirectional hepatopetal flow in these vessels. In another cirrhotic patient, a mirror-image signal was obtained from the main portal vein, but the venous phase of his superior mesenteric arteriogram showed maintained hepatopetal flow.

The mirror-image was more noticeable when the interrogating Doppler beam was nearly perpendicular to the vessel being examined. In four instances (one each in the umbilical vein, the main portal vein, the left portal vein, and a left coronary collateral), readjustment of either transducer alignment or of machine gain yielded a Doppler signal that more clearly indicated flow in only one direction (Fig. 1). In another

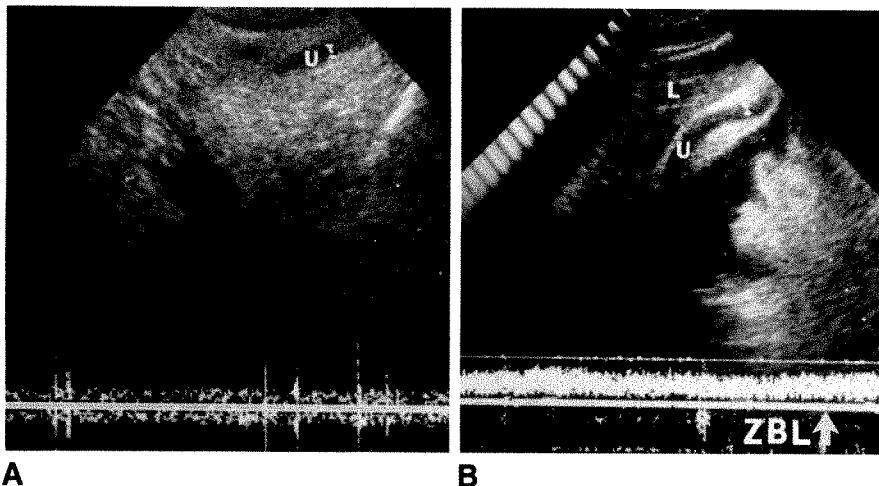


Fig. 1.—Mirror-image artifact in umbilical vein. A, Initial longitudinal duplex image of umbilical vein (U) shows mirror-image Doppler signal on both sides of zero baseline. B, Slight adjustment of transducer position and gain results in more distinctly unidirectional signal on only one side of zero baseline (ZBL). In this case, Doppler signal above baseline indicates flow away from transducer. L = liver.

case, switching the pulsed-Doppler range gate from the main portal vein to the differently aligned left portal vein had a similar effect (Fig. 2).

Ambiguity of Ostensible Flow Direction: Flip Artifact

Unlike the cases with the mirror-image artifact, the Doppler signal in this second condition was indeed unidirectional. The signal, however, would flip suddenly from one side of the zero baseline to the other, or would indicate a direction of blood flow opposite to that normally expected. This artifact was seen in six (43%) of the 14 patients. In four cases it originated from the splenic artery or vein; in each of two other cases, it was encountered in a periportal or splenorenal venous collateral.

In two cases, splenic vein flow appeared to flip spontaneously from a normal hepatopetal direction into a hepatofugal one. Only a slight alteration of transducer placement in one patient with cavernous portal vein transformation caused a comparable change of the Doppler signal from a periportal collateral. This latter patient's splenoportogram and the venous phase of his superior mesenteric arteriogram, however, revealed unidirectional hepatopetal flow. Advancing the pulsed-Doppler range gate around a tortuous "bend" of a splenorenal collateral in one patient and within the distal splenic vein of another (Figs. 3A-3D) caused a similar flip. In the latter individual, the venous phase of a celiac arteriogram and a transverse duplex sonographic image near the pancreas both showed normal hepatopetal splenic vein flow.

In two patients with splenomegaly, left coronal images visualized only short segments of the splenic artery and seemed to indicate arterial flow going away from the spleen. In one of these two patients, the left coronal duplex image also inferred splenic vein flow going *into* the spleen, whereas a transverse duplex image revealed normally directed hepatopetal flow. Two chronic alcoholics with large perisplenic collaterals also had duplex images suggesting splenic vein flow going *into* the spleen. One of these had been admitted several times for hepatic encephalopathy and showed prominent splenorenal collaterals on CT.

Inability to Obtain Doppler Flow Signal from Small Vessels Seen on Standard Real-Time Sonography

This difficulty was encountered in four patients (29%). In three patients, short gastric veins were visualized near the splenic hilum on left coronal sonograms; a splenoportogram had revealed some flow within these small vessels in one of these individuals. In another patient, two small venous channels were seen in the vicinity of the lesser omentum, extending from the main portal vein toward the gastroesophageal junction (Fig. 4). In all four cases, the patient's movement and breathing during the study prevented the exact placement of the pulsed-Doppler range gate within these tiny vessels. Consequently, an adequate Doppler flow signal could not be obtained.

Obscuration of Important Vascular Channels due to Ascites or Bowel Gas

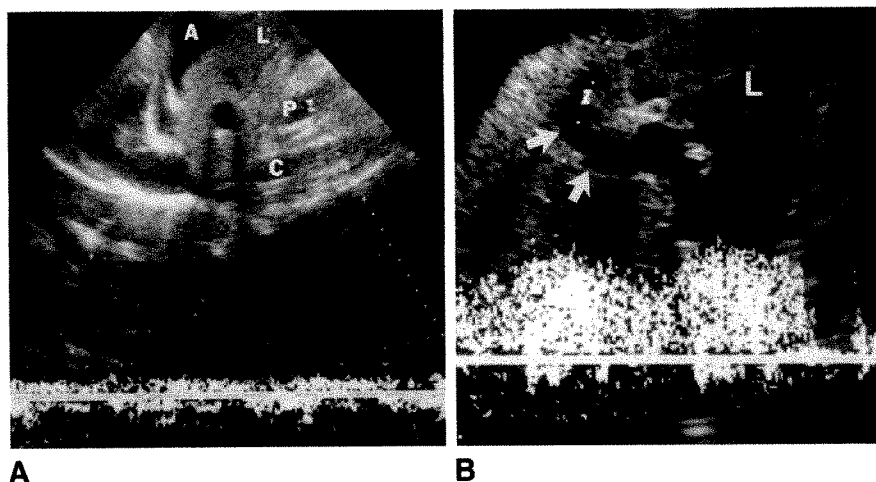
This problem was seen in 10 patients (71%). Bowel gas precluded visualization of nearly all portal venous channels in one patient with ascites and in two without ascites. In these patients, only "gassy" real-time images and weak mirror-image Doppler signals were elicited from the splenic vein on a left coronal view, from the main portal vein below the porta, and from a recanalized umbilical vein beneath the anterior abdominal wall.

Two patients had large bleeding esophageal varices seen both on endoscopy and on real-time sonograms in which Doppler interrogation confirmed hepatofugal flow. In three other patients, however, small to moderate varices were visualized on endoscopy but obscured entirely on sonography by copious intestinal gas. Two of these three patients also had significant ascites. One of the two, a chronic alcoholic with cirrhosis, had had multiple hemorrhages; his varices were shown not only at endoscopy but also during the venous phase of a superior mesenteric arteriogram (Fig. 5). In an additional patient who had not undergone endoscopy, lower esophageal varices identified on an upper gastrointestinal barium study were completely hidden also on both real-time and Doppler images.

Fig. 2.—Mirror-image artifact.

A, Duplex image of main portal vein (P) with mirror-image Doppler signal. Doppler beam is nearly perpendicular to portal vein. L = liver; A = ascites; C = inferior vena cava.

B, Pulsed-Doppler sample volume is moved to left portal vein (arrows), which is more parallel to Doppler beam. Resultant signal is now more clearly unidirectional. Flow in this case is going toward transducer. L = left lobe of liver.



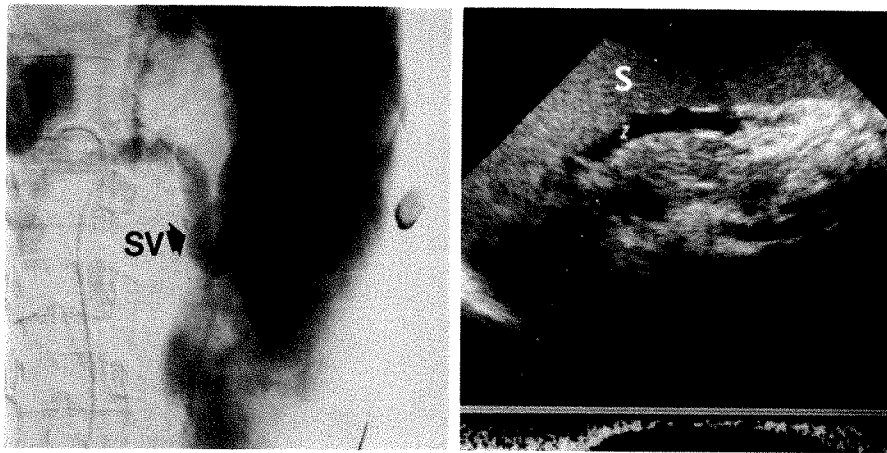


Fig. 3.—Flip artifact.

A, Venous phase of splenic arteriogram. Tortuous curve in splenic vein (SV) near splenic hilum.

B–D, Doppler study of splenic vein. With Doppler range gate near splenic hilum (B), flow is apparently toward transducer. With gate in curve itself (C), direction is predominantly away from transducer but partially toward it. As gate is moved into splenic vein medial to bend (D), flow appears to be completely away from transducer. S = spleen.

E, Proposed mechanism for flip artifact. Slight movement of patient or transducer moves relative position of transducer from position A to position B, bringing an inverted loop of tortuous vessel or collateral vein into sample volume. Consequently, flow relative to transducer face is apparently reversed.

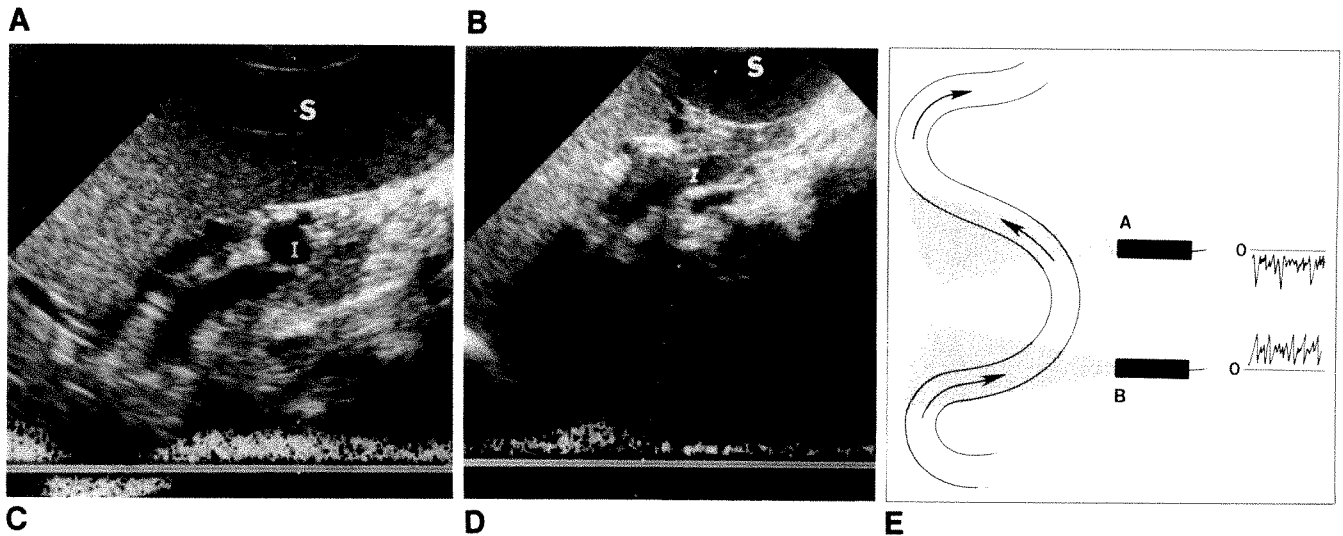


Fig. 4.—Lack of Doppler signal from small vessels seen on real-time sonogram. Small left coronary venous collaterals (arrows) on longitudinal sonogram. Doppler signal was not obtainable from these small vessels even though they could be followed to main portal vein. SA = splenic artery; SV = splenic vein; C = celiac axis; SM = superior mesenteric artery.

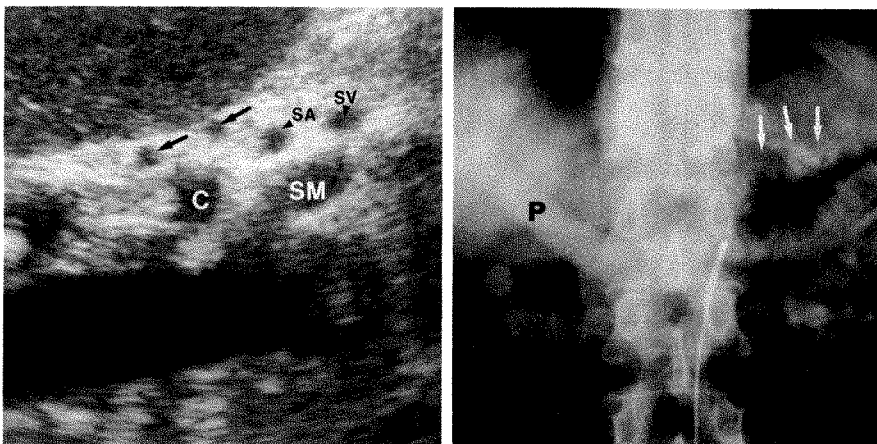


Fig. 5.—Venous phase of superior mesenteric arterial injection. Faintly opacified varices near proximal lesser curvature aspect of stomach (arrows) were also seen on endoscopy but were invisible on both real-time and Doppler sonography. P = portal vein.

Prominent splenorenal collaterals were identified in three patients. In two of these, Doppler showed flow going away from the spleen and toward the region of the adjacent left renal vein, but interposed bowel gas precluded visualization of the left renal vein itself or its junction with the collateral. In the third patient, prominent splenorenal collaterals were seen

on CT; however, all but a small portion of the splenic vein near the splenic hilum was obscured by gas on sonography.

In three patients, retroperitoneal collaterals were seen near the origins of the superior mesenteric artery or celiac axis on CT but not on duplex sonograms. In two other patients, retroperitoneal venous collaterals were observed on duplex

sonography near the pancreatic head, but their exact origin or destination was also indeterminate because of gas.

Bowel gas and ascites also made it difficult to obtain adequate transverse duplex images of the splenic vessels behind the pancreas; splenic vein flow was documented on 11 coronal images but on only six transverse images, whereas splenic artery flow was seen on five coronal and two transverse images. In one patient, the splenic artery and vein were seen in both transverse and coronal planes, although detail on the former was quite indistinct.

Discussion

Several reports describe the use of duplex pulsed-Doppler sonography to show the abnormal portal venous hemodynamics associated with hepatic disease in general and with portal hypertension in particular [1-6]. This procedure, however, is compromised by several persistent difficulties that we noticed in almost every patient in our study.

First, duplex sonography entails the same major technical problem that is encountered in non-Doppler studies: obscuration of detail by ascites, bowel gas, and body habitus. In several of our patients, these exigencies prevented visualization of collaterals shown by other techniques. In three cases, bowel gas almost completely precluded any satisfactory real-time images or Doppler signals. In other patients, gas or ascites hindered the resolution of the origin or connections of retroperitoneal or splenorenal collaterals in which duplex examination had identified flow. Bowel gas also often precluded acceptable transverse images of the splenic vein behind the pancreas, a bothersome dilemma because transverse images (compared with the customary left coronal ones) can determine more accurately the direction of splenic vein flow by visualizing a longer and clearer portion of this vessel that is more appropriately aligned (i.e., not perpendicular) to the interrogating Doppler beam [3]. Obtaining an adequate Doppler flow signal still can be impossible even if bowel gas is *not* a problem, as occurred in four of our patients with dilated short gastric veins or left coronary collaterals (Fig. 4). Accurately placing a 2- to 3-mm range gate in a small, deep vessel for enough time to obtain a diagnostic flow tracing can be painstakingly difficult, especially if the patient cannot hold his or her breath or is uncooperative (as is often the case in patients with cirrhosis or portal hypertension).

Gastroesophageal varices are particularly important because of their frequency [7] and because of their propensity to catastrophic hemorrhage. Therefore, it is quite disconcerting that gas and ascites prevented us from adequately showing either the left gastric vein or gastroesophageal varices in one patient who had suffered multiple severe acute upper gastrointestinal bleeds, had required emergency endoscopic sclerotherapy, and had varices shown on angiography (Fig. 5). It is true that the visibility of gastroesophageal varices [7, 8], as well as their chance of bleeding [9], are directly related to their size. In our series, in fact, the endoscopically visible varices in which we were able to document flow on Doppler were larger than those in which we were unable to do so. Nevertheless, bowel gas, ascites, or the patient's habitus can

obscure even clinically significant varices, especially if these vessels are deep or are adjacent to gas-containing bowel structures.

The mirror-image artifact probably arises during the electronic analysis of the Doppler signal. During this process, sensitive electronic circuits ascertain the direction of blood flow relative to the transducer by "looking" for miniscule phase or frequency differences between returning echo and initially transmitted ultrasonic pulse [10, 11] (Burns PN, personal communication). Several conditions may "confuse" these delicate electronics and thereby obscure the often subtle directional signal data; consequently, the sonographic machine may erroneously "think" that blood is flowing in *both* directions simultaneously, producing an apparent mirror-image. With the interrogating Doppler beam nearly perpendicular to the vessel being examined, for example, the vector component of blood flow velocity along the beam axis is reduced. Therefore, tiny directional signal differences between the blood cells traveling in one direction and those traveling in the opposite direction can be blurred. Similarly, excessive Doppler gain or examining an artery with high-velocity flow can "overwhelm" the electronics in much the same way that excessive amplification can distort the sound of a high-fidelity stereo. Moreover, amplification of a weak Doppler signal (which could easily originate from the often deep or obscured venous channels in a patient with portal hypertension) can increase *both* signal and noise and therefore can actually *lower* the ratio between the two. Therefore, it is not surprising that a perpendicular Doppler beam, a high Doppler gain, or signals near the extremes of dynamic amplitude range commonly produce a mirror-image artifact. In addition, a particular sonographic machine's electronic "quirks" might be at least partially contributory. Adjustment of Doppler gain or beam-vessel angle (Fig. 1) [11] or interrogation of a more appropriately aligned vessel (Fig. 2) can reduce or eliminate the mirror-image. However, these manipulations may be impossible if they require use of an acoustic window that is too small for optimal imaging.

We also observed curious "flips" in the orientation of the Doppler signal, as well as instances in which flow direction (particularly within the splenic vessels) was opposite to that normally expected. These pitfalls were particularly evident while we were imaging only short portions of seemingly tortuous collateral vessels. For example, we observed them on left coronal views of the splenic vein near the splenic hilum (Fig. 3), in a tortuous venous collateral near the inferior tip of the spleen, and during the examination of tortuous periportal collaterals in cavernous transformation of the portal vein. Similar flow-direction ambiguities from within portal vessels have also been described by others [3, 4, 6].

These flips may be authentic and could result from respiratory fluctuations in portal vein flow. However, such fluctuations often are diminished or absent in patients with portal hypertension [12], and outright flow reversal would not be expected. Inflow of blood from nonvisualized perforating or anastomotic vessels also could produce apparent flow inversion [13]. Advanced cirrhosis may lead to an intermediate stage of "to-and-fro" portal vein flow before actual flow rever-

sal [14]. Blood also may travel in a retrograde manner from the superior mesenteric vein into the systemic circulation via the splenic vein and splenorenal collaterals, resulting (as perhaps in one of our alcoholic patients) in splenic vein flow reversal and hepatic encephalopathy [5].

In many instances, however, these flips probably do *not* indicate flow reversal; in several of our cases, angiography or different sonographic views showed normally directed flow. In these situations, such flips most likely are artifacts related to the difficulty of accurately placing a small pulsed-Doppler range gate within the narrow lumen of a tortuous vessel. Slight patient movement during positioning of the gate could move easily an inverted vascular loop or collateral into the sampling volume, resulting in the false impression of reversed flow (Fig. 3E). This particular difficulty is exacerbated if the vessel is deep or narrow or if the patient is agitated or uncooperative. Furthermore, as noted earlier, gas, ascites, or adipose tissue can prevent the visualization of a longer, more easily identified, or less tortuous segment of vessel.

In summary, the technically optimal duplex examination of the portal venous system requires placement of a small pulsed-Doppler range gate in the correct position over a sufficiently long segment of an often tiny, deep, or tortuous vessel for enough time to obtain an acceptable Doppler signal tracing, and use of a satisfactory acoustic window that avoids excessive gas. At the same time, the beam-vessel angle must be kept between 45° and 60° in order to maximize the resultant Doppler signal. Multiple different vessels must each be sequentially and painstakingly inspected [1], with some vessels still not generating an adequate Doppler signal. Even if a signal is obtained, bothersome technical artifacts can hamper the accurate determination of both the presence and the direction of blood flow. Moreover, the entire procedure must be performed in a patient who is often acutely ill and is most likely agitated and uncooperative. An adequate diagnostic examination therefore can be a prodigious technical undertaking.

The duplex examination may still provide useful hemodynamic information in the patient with hepatic disease or portal hypertension. Furthermore, potential future improvements in-

cluding the use of transesophageal transducer [15] or two-dimensional color-coded Doppler [1, 2] may be helpful. At present, however, the use of duplex Doppler sonography in the patient with liver disease must be tempered by an awareness of this technique's inherent technical pitfalls.

REFERENCES

1. Becker CD, Cooperberg PL. Sonography of the hepatic vascular system. *AJR* **1988**;150:999-1005
2. Koslin DB, Berland LL. Duplex Doppler examination of the liver and portal venous system. *JCU* **1987**;15:675-686
3. Alpern MB, Rubin JM, Williams DM, Capek P. Porta hepatis: duplex Doppler US with angiographic correlation. *Radiology* **1987**;162:53-56
4. Nelson RC, Lovett KE, Chezmar JL, et al. Comparison of pulsed Doppler sonography and angiography in patients with portal hypertension. *AJR* **1987**;149:77-81
5. Ohnishi K, Saito M, Sato S, Sugita S, Tanaka H, Ojuda K. Clinical utility of pulsed Doppler flowmetry in patients with portal hypertension. *Am J Gastroenterol* **1986**;81:1-8
6. Patriquin H, Lafortune M, Burns PN, Dauzat M. Duplex Doppler examination in portal hypertension: technique and anatomy. *AJR* **1987**;149:71-76
7. Subramanyam BR, Balthazar EJ, Madamba MR, Raghavendra BN, Horii SC, Lefleur RS. Sonography of portosystemic venous collaterals in portal hypertension. *Radiology* **1983**;146:161-166
8. Bolondi L, Caletti GC, Ferrentino M, et al. Ultrasonographic findings in portal hypertension: correlation with the presence and the size of oesophageal varices. *Ultrasound Med Biol* **1982**;8[suppl 1]:58
9. Lebrech D, De Fleury P, Rueff B, Nahum H, Benhamou JP. Portal hypertension, size of esophageal varices, and risk of gastrointestinal bleeding in alcoholic cirrhosis. *Gastroenterology* **1980**;79:1139-1144
10. Powis RL, Powis WJ. Stealing techniques from the bats: Doppler and pulsed-Doppler techniques. In: *A thinker's guide to ultrasonic imaging*. Baltimore: Urban & Schwarzenberg, **1984**:171-200
11. Burns PN. The physical principles of Doppler and spectral analysis. *JCU* **1987**;15:567-590
12. Bolondi L, Gandolfi L, Arienti V, et al. Ultrasonography in the diagnosis of portal hypertension: diminished response of portal vessels to respiration. *Radiology* **1982**;142:167-172
13. McCormack TT, Smith PM, Rose JD, Johnson AG. Perforating veins and blood flow in oesophageal varices. *Lancet* **1983**;2:1442-1444
14. Reuter SR, Redman HC, Cho KJ. *Gastrointestinal angiography*, 3rd ed. Philadelphia: Saunders, **1986**:382-445
15. Sukigara M, Komazaki T, Yamazaki T, Anzai H, Koyama I, Omoto R. Colour flow mapping of oesophagogastric varices and vessels in and around the liver with trans-oesophageal real-time two-dimensional Doppler US. *Clin Radiol* **1987**;38:487-494

Detection of Liver Metastases with Superparamagnetic Iron Oxide in 15 Patients: Results of MR Imaging at 1.5 T

G. Marchal¹
 P. Van Hecke¹
 P. Demaerel¹
 E. Decrop¹
 C. Kennis²
 A. L. Baert¹
 E. van der Schueren²

The first clinical results of using superparamagnetic ferrite particles as a tissue-specific contrast agent for MR of the liver are reported at high fields (1.5 T). Fifteen patients with proved secondary liver malignancies were studied with plain and contrast-enhanced MR. Superparamagnetic iron oxide was administered IV in a dose of 20 $\mu\text{mol/kg}$. Intermediate TR, 820/30, 60 (TR/TE), and long TR, 2200/22, 70, spin-echo sequences were used before and 1 hr after injection of contrast material. Before injection, the largest number of lesions (437) was detected with the T2-weighted sequence. Lesion-to-liver contrast, expressed as the difference between the tumor and liver signal-to-noise, improved after ferrite administration in both sequences from -1 to 20 and from 7 to 15 for the 820/30, 60 sequence and from 9 to 34 and 15 to 21 for the 2200/22, 70 sequence. Despite this significant improvement in terms of the number of lesions detected, contrast-enhanced images did not show significantly more metastases than the unenhanced T2-weighted images did (383, 421, 407, and 407 vs as many as 437, respectively).

In this limited study at 1.5 T, the benefit of ferrite enhancement was only marginal when postcontrast images were compared with heavily T2-weighted precontrast scans.

The potential of small crystalline ferrite particles as a tissue-specific contrast agent for liver and spleen MR has been studied in laboratory animals [1-3]. When injected IV, these small particles (100 nm) are cleared from the blood by the reticuloendothelial system of the liver and spleen.

Ferrite is a crystalline iron oxide with a large magnetic moment and superparamagnetic properties. It causes local field inhomogeneities that produce rapid dephasing of neighboring proton spins, resulting in a shortening of T2. In the liver and spleen this results in a blackening of the normal parenchyma that lasts for up to 6 hr [4-6]. Liver tumors, which do not possess reticuloendothelial cells, are for this reason not systematically affected by the contrast medium, and stand out more clearly on postcontrast images.

The first clinical study using ferrite particles in 15 patients with liver metastasis was reported recently by Stark et al. [7]. These authors used "intermediate"-field 0.3- and 0.6-T systems and found significant diagnostic improvement after administration of contrast material. We report our results in 15 patients with liver metastasis, studied with ferrite in a high-field 1.5-T system.

Subjects and Methods

The protocol of this study was submitted to and approved by the ethics committee of our institution. Informed consent was obtained for all patients. Five men and 10 women (age range, 45-76 years) with a known primary cancer were selected for study.

All had liver metastasis detected by other techniques (sonography, CT, or biopsy) and proved by liver biopsy or biopsy of the primary cancer. The metastases were from the following primary tumors: breast adenocarcinoma (seven), lung carcinoma (three), adnexal carcinoma (one), duodenal leiomyosarcoma (one), bladder carcinoma (one), uterine carcinoma (one), and rectal adenocarcinoma (one).

Received October 11, 1988; accepted after revision November 29, 1988.

P. Van Hecke is a Research Associate of the Belgian Foundation for Medical Scientific Research.

¹ Department of Radiology, University Hospitals K.U. Leuven, Herestraat 49, B-3000 Leuven, Belgium. Address reprint requests to G. Marchal.

² Department of Oncology, University Hospitals K.U. Leuven, B-3000 Leuven, Belgium.

AJR 152:771-775, April 1989

0361-803X/89/1524-0771

© American Roentgen Ray Society

Patients with any of the following were excluded from the study: allergic predisposition, age younger than 18 years, pregnancy or lactation, hemochromatosis, autoimmune disease, multiple myeloma, blood clotting disorders, or abnormal renal function. Also excluded were patients with bilirubin, glutamic-oxaloacetic transaminase, glutamic-pyruvic transaminase, or alkaline phosphatase exceeding five times the normal value.

Superparamagnetic iron oxide (AMI 25, Guerbet, France) was administered at a dose of 20 $\mu\text{mol/kg}$ (0.1 ml/kg body weight). The nondiluted ferrite suspension was given by a slow IV injection at a rate of 1 ml/min. Possible side effects were evaluated by carefully monitoring the patient and recording both subjective complaints and objective clinical findings. The analysis included the type of side effect and the delay of onset; its duration, intensity, and evolution; and the type of therapy when administered.

MR imaging was performed on a 1.5-T superconductive imaging system (Magnetom 1.5 T, Siemens, Erlangen, W. Germany). Two different spin-echo sequences were used to image the liver before and 1 hr after injection of ferrite: an intermediate TR spin-echo sequence, 820/30, 60 (TR/TE), and a long TR spin-echo sequence, 2200/22, 70 (except for one patient, 2500/22, 70), with flow compensation of the second echo (gradient nulling) (Fig. 1).

For both sequences a rectangular matrix of 128×256 was used, with four acquisitions leading to a scan time of 7 min for TR = 820

msec and 19 min for TR = 2200 msec; the slice thickness was 8 mm and the slice gap 4 mm. Image quality and lesion-to-liver contrast were analyzed for both the pre- and postcontrast series. For each patient and for each sequence, the signal-to-noise (S/N) ratio was calculated for well-defined lesions and for normal liver tissue. The contrast-to-noise (C/N) ratio was calculated by subtracting the signal intensities of lesion and liver, divided by the noise signal. Mean values and standard deviations of the S/N and C/N ratios of the 15 patients were then calculated for each sequence. Furthermore, the overall diagnostic improvement was assessed for each patient by comparing the number of lesions detected on the various pre- and postcontrast images obtained with the two types of sequences. This approach provides only a crude approximation, since it is highly subjective and is compounded by methodologic difficulties (e.g., partial-volume effects, interslice gap, slightly different position between pre- and postcontrast scans, and observer bias).

Results

MR scans in two of the 15 patients showed reduced signal intensity in the liver and spleen before ferrite administration, due to previous blood transfusion. Both were excluded from the study. The drastic changes in S/N and C/N ratios caused

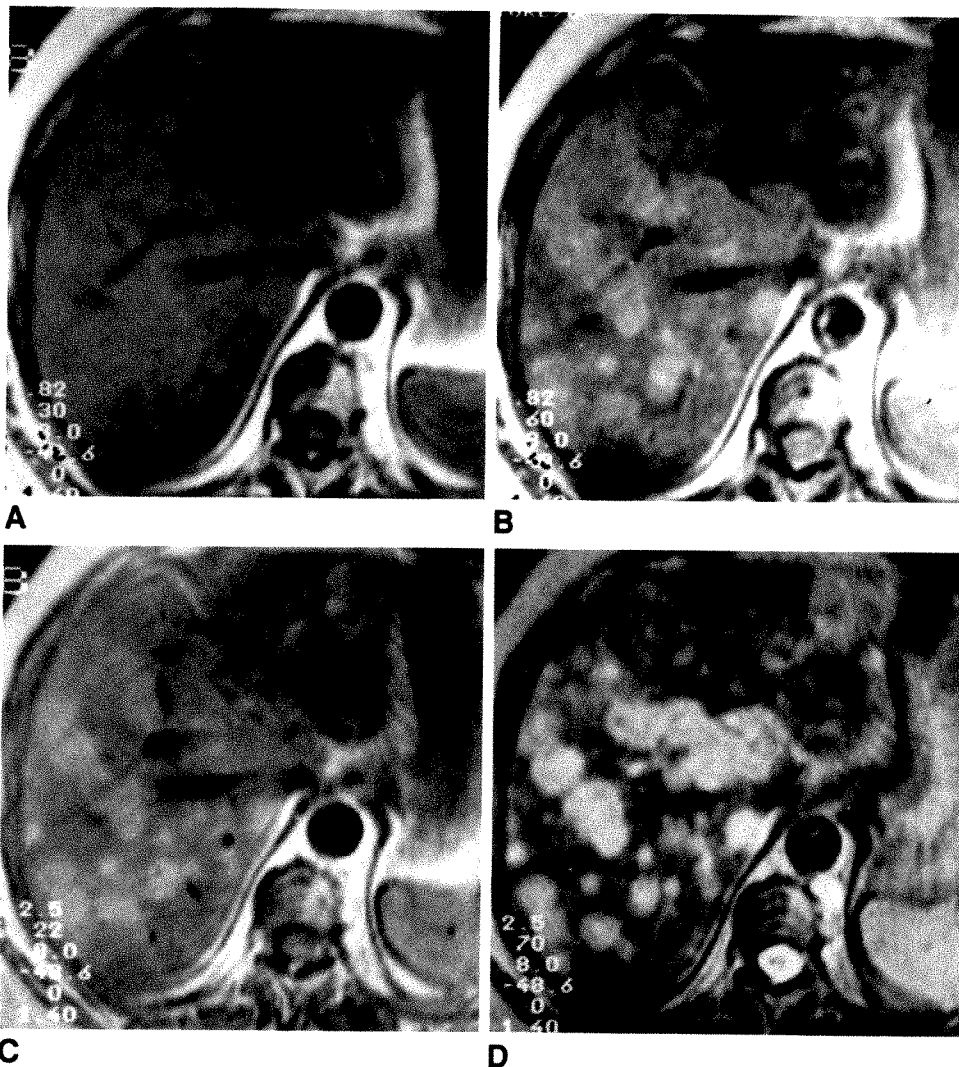


Fig. 1.—MR images of metastases from breast carcinoma before (A–D, this page) and 1 hr after (E–H, facing page) administration of ferrite show effect of ferrite on lesion-liver contrast for different pulse sequences. Lesion-liver contrast is increased on long TE images (B, D, F, and H). Though ferrite images yield somewhat higher contrast, lesion detection is not significantly improved compared with unenhanced T2-weighted images (D). Pre- and postcontrast series are not exactly comparable because patient was moved out of magnet for ferrite injection.

A, B, E, and F, 820/30, 60.
C, D, G, and H, 2500/22, 70.

by the injection of ferrite are shown in Table 1 and Figure 1. As expected, the signal of the lesions was not significantly affected by ferrite administration, in contrast to the intensity of the normal liver parenchyma. The largest effect on liver intensity, expressed as the liver S/N ratio before and after injection, occurred in those sequences providing the highest initial liver intensity (i.e., 820/30 and 2200/22).

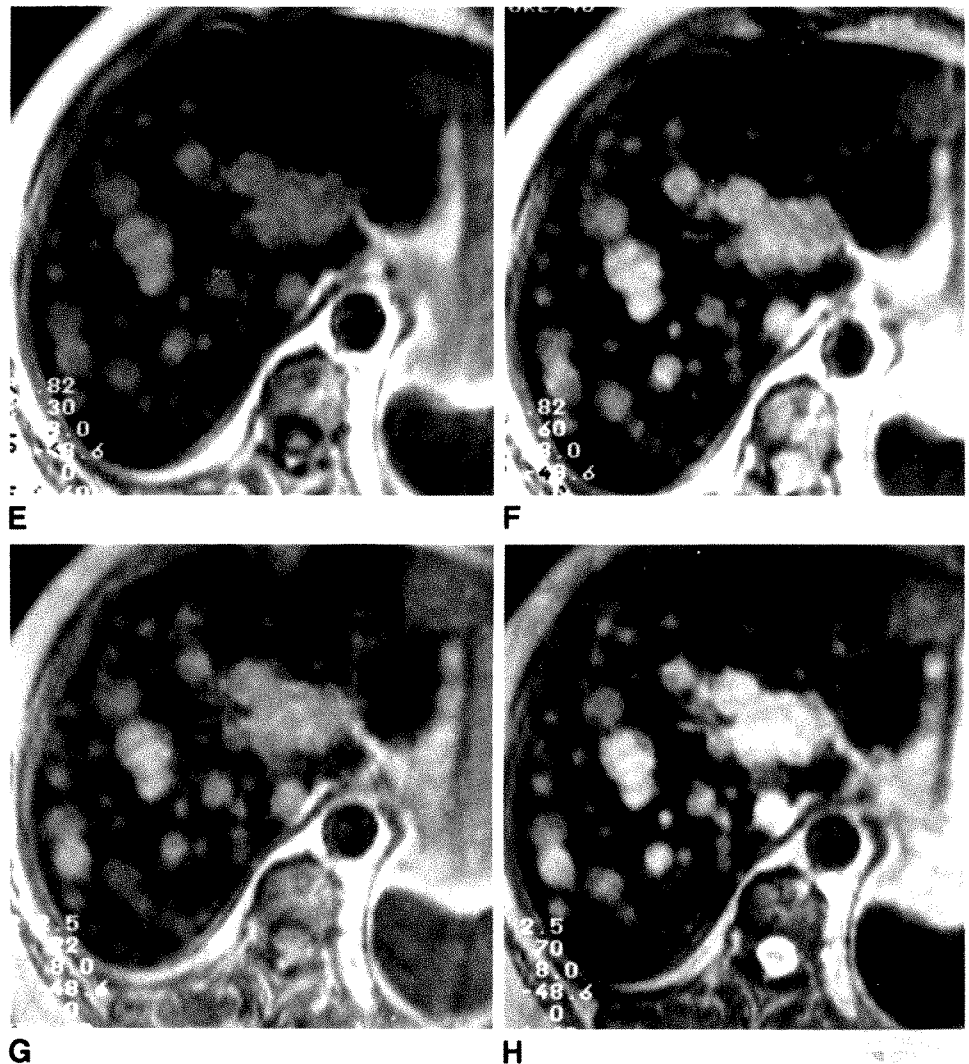
The maximal tumor-liver C/N ratio was obtained with the 2200/22 sequence. This value was significantly higher than the values for the tumor-liver C/N ratio obtained with the three other sequences; the latter three values did not differ significantly from each other. Significances ($p = .05$) were calculated with Student's *t* test. The results of the assessment of the diagnostic improvement of the different sequences are shown in Table 2. On unenhanced images, there was a progressive increase in lesion detection as a function of T2-weighting, with a maximum for the 2200/70 sequence (Fig. 1). This improvement was much less obvious on ferrite images, with only minimal benefit for the 2200/70 series (Fig. 2). Further, the number of lesions detected after contrast administration was not higher than the number detected before contrast administration with the 2200/70 sequence. In

only one of 13 patients were more lesions detected with the T2-weighted sequence (2200/70) after ferrite administration. In one patient (Fig. 2), metastases were characterized by a peripheral hypointense rim on the nonenhanced images, which greatly facilitated identification. This feature, however, disappeared after ferrite administration, making detection more difficult. In another patient, with a rather low intensity metastasis on the T2-weighted sequence, ferrite administration greatly increased C/N (Fig. 3). There were neither subjective nor objective side effects during or after infusion of ferrite.

Discussion

The efficiency of liver MR in detecting liver tumors largely depends on the sequence used. In general, both T1 and T2 are increased in tumor tissue. Therefore, liver tumors are generally shown as hypointense areas on T1-weighted images and as hyperintense areas on T2-weighted images. Although theoretically, T2-weighted images yield the highest diagnostic sensitivity, such sequences suffer from drawbacks, including long acquisition times, low S/N ratios, and high

Fig. 1.—*continued*



susceptibility to motion artifacts. Some of these problems can be avoided by signal averaging and gradient nulling sequences for motion artifact reduction.

In this study we analyzed how ferrite either improved the diagnostic content of the MR scan or reduced the examination time. By using a contrast-enhanced intermediate TR/long TE sequence (820/30, 60), similar lesion-to-liver contrast ratios were achieved in a much shorter acquisition time than with

an unenhanced (heavily T2-weighted) long TR/long TE sequence (2200/70) (Table 1 and Fig. 1).

As already stated, counting the number of lesions detected provides only a very crude estimation of diagnostic efficacy and is compounded by a number of methodologic difficulties. Nevertheless, the trends in these figures allow us to draw some conclusions. The number of lesions detected by the intermediate TR sequences (820/30, 60) after contrast administration was almost as high as the number detected before contrast administration with the 2200/70 sequence (383 and 421 vs 437). The use of contrast material in the sequence with a longer TR (2200/22, 70) did not further improve the number of tumors detected (407 and 407 vs 437) (Table 2). The latter finding is in agreement with the observation that for only one of 13 patients were more lesions detected with the T2-weighted sequence (2200/70) after ferrite administration.

It should also be noted that the 2200/22 sequence, which showed the highest tumor-liver contrast after ferrite injection, did not provide better tumor detection than the other contrast-enhanced sequences (Table 2). In one patient, the use of ferrite obscured one of the signs of the metastases, making the diagnosis somewhat more difficult (Fig. 2).

Our observations on the effects of ferrite for liver tumor detection at high fields clearly differ from those of Stark et al. [7] for low and intermediate fields (0.3 and 0.6 T). The dramatic improvement (four- to 16-fold) in tumor detection numbers obtained by Stark et al. with ferrite for both T1 (500/28) and T2 (1500/40, 80) sequences was not observed in our high-field system. Compared with our standard T2 sequence (2200/70) for clinical evaluation of liver lesions, none of the sequences used with the ferrite contrast agent substantially improved detection. On the other hand, the same sensitivity was obtained with the contrast-enhanced intermediate TR sequence (820/30, 60). However, this sequence did not provide the same tissue characterization as was obtained from a T2-weighted sequence (Fig. 4). The high performance of our standard T2 sequence (2200/70) is due to the improved S/N ratio at high fields and the use of gradient nulling motion

TABLE 1: Effect of Ferrite Enhancement on Signal-to-Noise (S/N) and Contrast-to-Noise (C/N) Ratios in 13 Patients

Spin-Echo Pulse Sequence (TR/TE)	Mean Ratio \pm SD		
	Tumor S/N	Liver S/N	Tumor-Liver C/N
820/30			
Precontrast	28 \pm 7	28 \pm 8	-1 \pm 5
Postcontrast	29 \pm 12	8 \pm 4	20 \pm 10
820/60			
Precontrast	20 \pm 6	13 \pm 6	7 \pm 6
Postcontrast	19 \pm 2	3 \pm 2	15 \pm 6
2200/22			
Precontrast	49 \pm 20	40 \pm 12	9 \pm 9
Postcontrast	46 \pm 21	12 \pm 6	34 \pm 17
2200/70			
Precontrast	30 \pm 11	14 \pm 6	15 \pm 7
Postcontrast	27 \pm 12	6 \pm 9	22 \pm 11

Note.—Postcontrast images were obtained 1 hr after administration of ferrite.

TABLE 2: Effect of Ferrite Enhancement on the Detection of Lesions in 13 Patients

Spin-Echo Pulse Sequence (TR/TE)	No. of Lesions	
	Unenhanced Image	Enhanced Image
820/30	114	383
820/60	280	421
2200/22	221	407
2200/70	437	407

Note.—Enhanced images were obtained 1 hr after administration of ferrite. Scan times: 820/30, 60, 7 min; 2200/22, 70, 19 min.

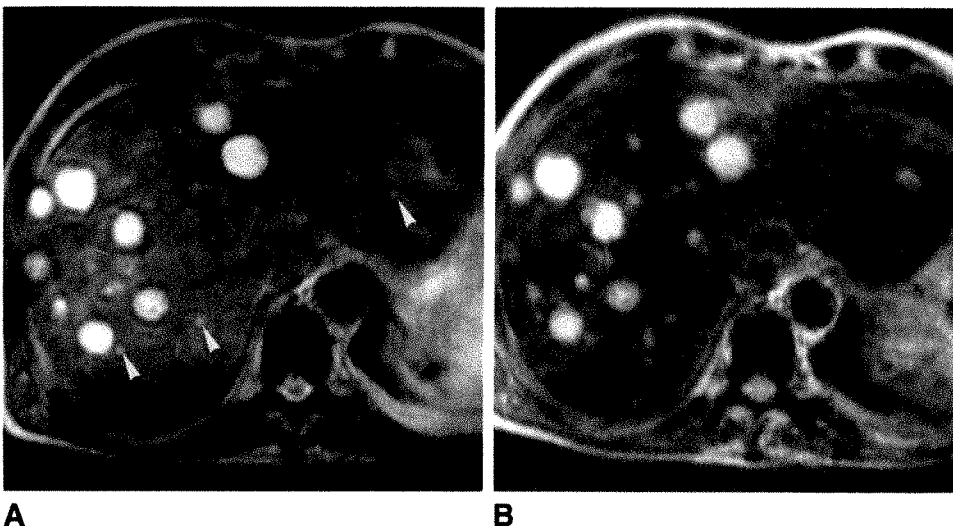


Fig. 2.—T2-weighted MR images (2200/70) of metastases from bladder carcinoma.

A. Unenhanced image. High intensity of metastases surrounded by hypointense rim permits detection of millimeter-sized lesions (arrowheads).

B. Ferrite-enhanced image. Despite increased lesion-to-liver contrast, lesion detection is not improved. This is partially due to disappearance of rim feature in background noise of ferrite images.

Fig. 3.—T2-weighted MR images of metastases of rectal carcinoma.

A, Unenhanced image, 2200/70. Large low-intensity lesion (arrowheads) is seen at lateral aspect of right liver lobe and small high-intensity lesion in dorsolateral subcapsular area (arrow).

B, Ferrite-enhanced image, 820/60. Visualization of large low-intensity tumor is improved. Lower intensity of small lesion is probably due to volume averaging and reduced T2-weighting.

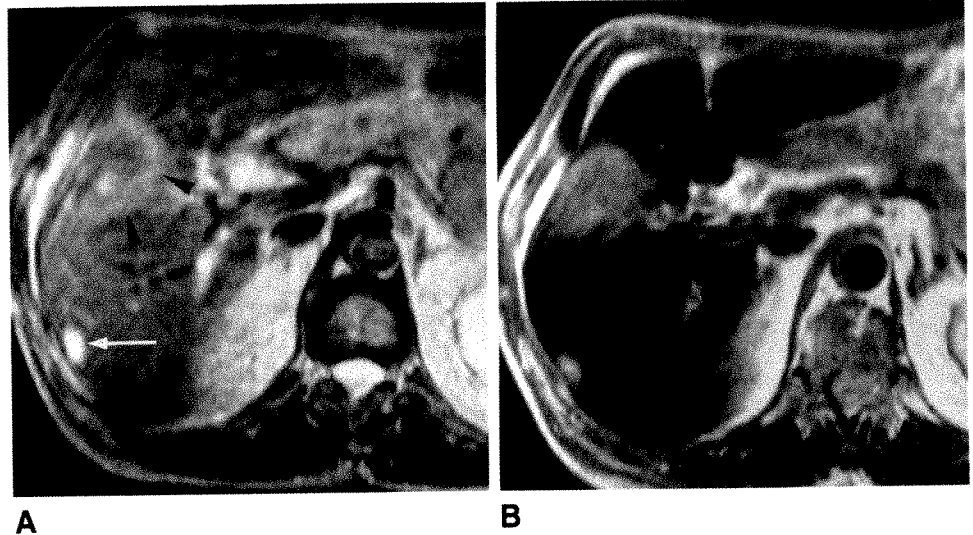
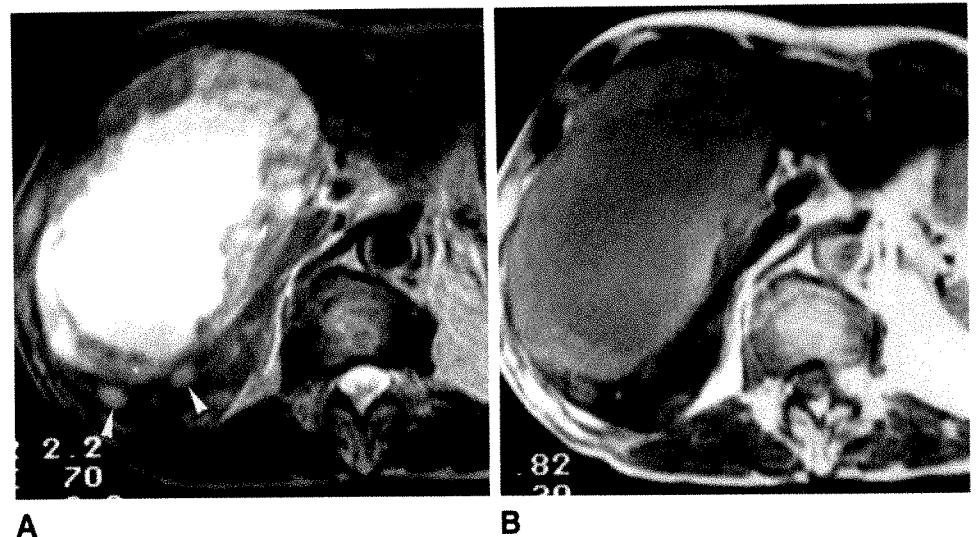


Fig. 4.—T2-weighted MR images of metastases from bronchus carcinoma.

A, Unenhanced image, 2200/70. Large metastasis with clear central necrosis and multiple satellite nodules (arrowheads) are seen in right lobe of liver.

B, Ferrite-enhanced image, 820/30. Though lesion detection is similar, tumor is characterized less well.



compensation. This is reflected in the much larger tumor-liver C/N ratio at high fields (15 ± 7) compared with the value (3.4 ± 3.8) obtained at lower fields by Stark et al. As a result, we obtained the highest tumor detection before contrast administration with T2-weighted sequences, while Stark et al. reported a progressive decrease in detection with progressive T2 weighting.

Tolerance for ferrite was excellent in this study, as no side effects were detected. However, it has to be emphasized that the drug was given by a slow IV injection and that patients with allergic predispositions were excluded from the study.

REFERENCES

1. Saini S, Stark DD, Hahn PF, Wittenberg J, Brady TJ, Ferrucci JT Jr. Ferrite particles: superparamagnetic MR contrast agent for the reticuloendothelial system. *Radiology* 1987;162:211-216
2. Mendoca-Dias MH, Lauterbur PD. Ferromagnetic particles as contrast agents for magnetic resonance imaging of the liver and spleen. *Magn Reson Med* 1986;3:328-330
3. Van Hecke P, Marchal G, Decrop E, Baert AL. Experimental study of the pharmacokinetics and dose response of ferrite particles used as a contrast agent in MR of the normal liver of the rabbit. *Invest Radiol* (in press)
4. Saini S, Stark DD, Hahn PF, et al. Ferrite particles: a superparamagnetic MR contrast agent for enhanced detection of liver carcinoma. *Radiology* 1987;162:217-222
5. Tsang YM, Stark DD, Chen MC, Weissleder R, Wittenberg J, Ferrucci JT. Hepatic micrometastases in the rat: ferrite enhanced MR imaging. *Radiology* 1988;167:21-24
6. Weissleder R, Stark DD, Compton CC, Wittenberg J, Ferrucci JT. Ferrite-enhanced MR imaging of hepatic lymphoma: an experimental study in rats. *AJR* 1987;149:1161-1165
7. Stark DD, Weissleder R, Elizondo G, et al. Superparamagnetic iron oxide: clinical application as a contrast agent for MR imaging of the liver. *Radiology* 1988;168:297-301

Book Review

Hysterosalpingography and Pelvic Ultrasound. Imaging in Infertility and Gynecology. By Isabel C. Yoder. Boston: Little, Brown, 204 pp., 1988. \$75

This book, according to the author, is intended to be a standard text on hysterosalpingography. She has accomplished that purpose to a high degree and certainly has written an excellent book on the subject. The part on preparation of the patient is quite good, and the book has excellent examples of normal and abnormal studies. The bibliography is extensive and current. New methods of diagnosis and treatment are well covered.

The book is divided into five chapters. The first covers techniques, normal anatomy, and complications. The others discuss diseases of the fallopian tubes, fallopian tube surgery, diseases of the uterus, and congenital uterine anomalies. The latter is particularly well written. The inclusion of sonographic studies in this book is sparse, and the illustrations are fair to excellent. Line drawings accompanying the sonograms are used for clarification. Although the addition of sonographic information may be considered as an extra benefit, it does not particularly add to the discussions.

Selected areas do require some comment. The author is too dogmatic about the advantages of the Foley catheter technique for hysterosalpingography over other methods. This is unfortunate be-

cause that system, as well as others, has drawbacks. We find the Cook catheter easier to use and far more versatile. The description of salpingostomy is good, though glossed over; the technique is not nearly as simple as described. Rosch's results do show improvement in fertility status in contradistinction to the statement on page 48. The chapter on congenital anomalies is excellent. However, although the figures mention angulation, the book has no discussion of measurements of the cornual angle or the depth of fundus concavity, which some believe important. The use or mention of the Mullerian anomaly classification (I-VI of Buttram and Gibbons) also is omitted.

These comments, however, should not obscure the fact that this book is an excellent addition to any department that does hysterosalpingography. The author can be congratulated for this up-to-date publication.

Edward I. Miller
Stephen D. Sholkoff
Hoag Memorial Hospital Presbyterian
Newport Beach, CA 92658-8912

Peritubal Adhesions in Infertile Women: Diagnosis with Hysterosalpingography

Stephen Karasick¹
Alvin F. Goldfarb²

We studied the efficacy of hysterosalpingography in the detection of peritubal adhesions without tubal occlusion by using laparoscopy as the gold standard for the diagnosis. Peritubal adhesions were diagnosed on hysterosalpingography by using the following radiographic criteria alone or in combination: (1) convoluted fallopian tube, (2) loculation of spillage of contrast medium into the peritoneal cavity, (3) ampullary dilatation, (4) peritubal halo effect (double-contour appearance of the tubal wall), and (5) vertical fallopian tube. The first 100 patients with the diagnosis of adhesions on hysterosalpingography who also had laparoscopy were included in the study. Seventy-five patients had the diagnosis confirmed on laparoscopy, resulting in a 25% false-positive diagnosis of adhesions with hysterosalpingography. Thirty-nine (52%) of these 75 patients had one radiographic finding alone, and 20 of these patients had loculation of spillage of contrast medium. Although the patients with adhesions tended to have two or more of the radiographic findings, the difference was not statistically significant. The most frequent radiographic findings found in combination were convoluted fallopian tube and loculation of spillage of contrast medium.

These findings suggest that hysterosalpingography can be the diagnostic procedure of choice in the initial investigation of infertility due to peritubal adhesions.

Obstruction of the fallopian tube by peritubal adhesions resulting from surgery or infectious salpingitis is a frequent cause of infertility. Anatomic blockage can occur when adhesions occlude the abdominal orifice of the fallopian tube. Functional blockage can result when adhesions cause retraction of the ovary and/or tube with subsequent enlargement of the space between the ovary and orifice of the tube interfering with oocyte pickup by the fimbriae.

Numerous reports in the literature document the shortcoming of hysterosalpingography (HSG) in establishing the diagnosis [1-15]. With the use of specific radiographic criteria alone or in combination, we investigated the efficacy of HSG in the detection of peritubal adhesions without tubal occlusion in 100 infertile women.

Materials and Methods

Between 1982 and 1987 more than 1000 HSG studies were performed at Thomas Jefferson University Hospital on outpatients who were infertile. HSG was performed by the reproductive endocrinologist during the early proliferative phase of the menstrual cycle. All procedures were monitored fluoroscopically and interpreted by a radiologist before laparoscopy. All of the HSG studies were considered technically satisfactory. Peritubal adhesions were diagnosed on HSG if one or more of the following findings were identified: (1) convoluted or corkscrew configuration of the fallopian tube; (2) loculation of spillage of contrast medium into the peritoneal cavity as represented by irregular, sharply marginated collections in the absence of freely dispersed contrast medium; (3) dilatation of the ampullary segment of the fallopian tube; (4) peritubal halo effect (double-contour appearance of the tubal wall); and (5) vertical position of the fallopian tube.

Received August 16, 1988; accepted after revision December 1, 1988.

¹ Department of Radiology, Thomas Jefferson University Hospital, 111 S. 11th St., Philadelphia, PA 19107. Address reprint requests to S. Karasick.

² Department of Obstetrics and Gynecology, Thomas Jefferson University Hospital, Philadelphia, PA 19107.

AJR 152:777-779, April 1989

0361-803X/89/1524-0777

© American Roentgen Ray Society

In this retrospective analysis, the first 100 patients with the diagnosis of adhesions on HSG who also had laparoscopy were studied for adhesions. In 74, the HSG studies were performed with oil-base contrast material (Ethiodol, Savage Laboratories, Melville, NY), and in 26, the studies were performed with water-soluble contrast media (Conray, Mallinckrodt, St. Louis, MO). Spot-film radiographs were obtained in the supine, anteroposterior, and oblique positions. Delayed prone radiographs after drainage of contrast medium from the uterine cavity were obtained as needed after 15 min in patients examined with water-soluble medium and after 30 min in those in whom oil-soluble medium was used.

Laparoscopy under general anesthesia with pneumoperitoneum was performed by the reproductive endocrinologist. The laparoscope was introduced just below the umbilicus, and tubal anatomy and patency were established by visual inspection of the tube and after transcervical injection of dye (chromopertubation).

Results

Peritubal adhesions were diagnosed by HSG in 100 patients. In 75 of those patients, laparoscopic findings confirmed the presence of peritubal adhesions (Table 1). Thirty-nine of the 75 patients had one radiographic finding only. Of these, 20 patients had loculation of spillage of contrast medium. A vertically oriented fallopian tube, found in nine (12%) of the 75 patients, was found only in conjunction with other radiographic findings. Sixteen of the 25 patients without adhesions on laparoscopy had one radiographic finding; loculation of spillage of contrast medium was seen in 50% of these cases. Delayed prone radiographs were of value in equivocal cases of peritubal adhesions, especially when the spillage of contrast medium retained the same configuration or if ampullary dilatation persisted.

When comparing patients with and without adhesions, there was a tendency for those with adhesions to have two or more of the radiographic findings; this correlation, however, was not statistically significant ($\chi^2 = .87$; $p = .38$). The most frequent combined radiographic findings were convoluted fallopian tube and loculation of spillage of contrast medium ($\chi^2 = 5.19$; $p < .05$; significant).

Discussion

Peritubal adhesions are usually formed as a result of inflammation from pelvic inflammatory disease or surgery. In chronic infection with frequent episodes of acute exacerbation, inflammatory changes involve all of the layers of the fallopian tube. Serosal involvement produces a perisalpingitis, which can lead to formation of adhesions. These adhesions disturb the delicate anatomic relationship between the tube and ovary, interfering with normal ovulation or preventing normal capture and transport of the ovum.

Because laparoscopy allows direct visualization of peritubal adhesions and their nature, extent, and distribution, it is recognized as an accurate and informative procedure to assess tubal patency and peritubal adhesions [6]. However, HSG is a safe, simple procedure with lower cost and less inconvenience to patients.

TABLE 1: Frequency of Findings on Hysterosalpingography (HSG) in 75 Patients with Peritubal Adhesions Diagnosed by Laparoscopy

HSG Finding	No. (%)	
	Only One Finding ^a	Combination of Findings ^b
Convoluted tube	8 (21)	24 (67)
Loculated spill	20 (51)	20 (56)
Ampullary dilatation	7 (18)	14 (39)
Peritubal halo	4 (10)	10 (28)
Vertical tube	0 (0)	9 (25)

^a $n = 39$.

^b $n = 36$. Because of multiple findings, some patients are included in more than one category; therefore, the total number of patients listed in this column exceeds the total number of patients in the group.



Fig. 1.—Hysterosalpingogram in patient with bilateral peritubal adhesions shows peritubal halo effects (curved arrows) with loculation of spillage of contrast medium (straight arrows).

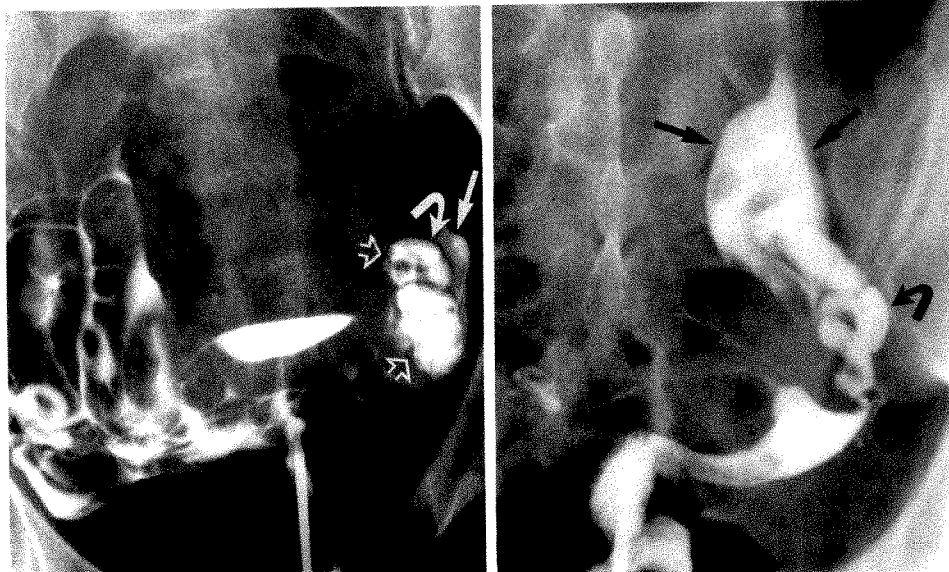
Few reports clearly define the objective criteria needed for accurate diagnosis of peritubal adhesions on HSG. This may explain the discrepancies frequently reported between HSG and laparoscopy. Seventy-five of the 100 (sensitivity = 75%) cases of peritubal adhesions were correctly predicted in our study in contrast to sensitivity findings on previous studies, which ranged from 34% to 46% [1–4, 10]. Our improved sensitivity of HSG in the detection of peritubal adhesions was achieved when these specific radiographic criteria were used: (1) convoluted fallopian tube, (2) loculation of spillage of contrast medium into the peritoneal cavity, (3) ampullary dilatation, (4) peritubal halo effect (double-contour appearance of the tubal wall), and (5) vertical fallopian tube. Similar radiographic findings of peritubal adhesions have been described by Siegler [16, 17].

Peritubal adhesions cannot be reliably distinguished from tubal occlusion on HSG. In patent tubes, close observation must be paid to the configuration of the contrast medium passing from the distal end of the fallopian tube into the peritoneal cavity. Fluoroscopic evaluation and documentation of spillage with spot films are usually sufficient in most instances. However, a delayed prone radiograph after contrast

Fig. 2.—Hysterosalpingogram in patient with left-sided peritubal adhesions shows convoluted tube with ampullary dilatation (open arrows). Peritubal halo effect (curved arrow) and loculation of spillage of contrast medium (straight solid arrow) are also present.



Fig. 3.—Hysterosalpingogram in patient with left-sided peritubal adhesions shows vertically oriented and convoluted fallopian tube (curved arrow) with loculation of spillage of contrast medium (straight arrows).



2

3

medium has been drained from the uterine cavity is helpful in equivocal cases of peritubal adhesions [7]. Localized pooling or loculation of the contrast medium around the distal end of the tube with limited intraperitoneal spillage strongly suggests peritubal adhesions (Fig. 1). This was the most frequent finding in our group of patients with adhesions. Dilatation of the ampullary segments of the tubes, especially if it has persisted on delayed radiographs, also suggests peritubal adhesions.

The peritubal halo effect is due to contrast medium in the peritoneal cavity extending back along the external surface of the tube. This produces a double-contour image, which allows assessment of the thickness of the tubal wall (Fig. 2). Such thickening usually is related to chronic interstitial salpingitis. The fallopian tube may have a convoluted or corkscrew configuration due to peritubal adhesions (Fig. 3). The combination of a convoluted fallopian tube and loculation of spillage of contrast medium into the peritoneal cavity strongly indicates peritubal adhesive disease. The convoluted appearance may be associated with retrograde menstruation and endometriosis, which could, in turn, be a cause of peritubal adhesions [18]. With peritubal adhesive disease (especially if due to endometriosis), retroflexion, lateral deviation, and rotation of the uterus may occur; the fallopian tubes subsequently may appear stretched and vertically oriented without mobility when viewed in various degrees of obliquity [19].

Although laparoscopy is considered the gold standard for the diagnosis of peritubal adhesions, HSG can detect peritubal adhesions in up to 75% of cases when certain objective radiographic criteria are used. The presence of a convoluted fallopian tube and loculation of spillage of contrast medium into the peritoneal cavity should alert the radiologist to the presence of peritubal adhesive disease.

ACKNOWLEDGMENTS

We thank Sandra Ehrlich for contributions and Ann Prather for manuscript preparation.

REFERENCES

- Gomel V. Laparoscopy prior to reconstructive tubal surgery for infertility. *J Reprod Med* 1977;18:251-253
- Hutchins CJ. Laparoscopy and hysterosalpingography in the assessment of tubal patency. *Obstet Gynecol* 1977;49:325-327
- Maathuis JB, Horbach JGM, van Hall EV. A comparison of the results of hysterosalpingography and laparoscopy in the diagnosis of fallopian tube dysfunction. *Fertil Steril* 1972;23:428-431
- Philipsen T, Hansen BB. Comparative study of hysterosalpingography and laparoscopy in infertility patients. *Acta Obstet Gynecol Scand* 1981;60:149-151
- Horwitz RC, Morton PCG, Shaff MI, Hugo P. A radiological approach to infertility—hysterosalpingography. *Br J Radiol* 1979;52:255-262
- Corson SL. Use of the laparoscope in the infertile patient. *Fertil Steril* 1979;32:359-369
- Duff DE, Fried AM, Wilson EA, Haack DG. Hysterosalpingography and laparoscopy: a comparative study. *AJR* 1983;141:761-763
- Kasby CB. Hysterosalpingography: an appraisal of current indications. *Br J Radiol* 1980;53:279-282
- Swolin K, Rosencrantz M. Laparoscopy vs hysterosalpingography in sterility investigations: a comparative study. *Fertil Steril* 1972;23:270-273
- Bateman BG, Nunley WC, Kitchin JD, Kaiser DL. Utility of the 24-hour delay hysterosalpingogram film. *Fertil Steril* 1987;47:613-617
- Hulka JF, Omran K, Berger GS. Classification of adnexal adhesions: a proposal and evaluation of its prognostic value. *Fertil Steril* 1978;30:661-665
- Diamond MP, Daniell JF, Martin DC, Feste J, Vaughn WK, McLaughlin DS. Tubal patency and pelvic adhesions at early second-look laparoscopy following intraabdominal use of the carbon dioxide laser: initial report of the intraabdominal laser study group. *Fertil Steril* 1984;42:717-723
- Snowden EU, Jarrett JC, Yusoff Dawood M. Comparison of diagnostic accuracy of laparoscopy, hysteroscopy, and hysterosalpingography in evaluation of female infertility. *Fertil Steril* 1984;41:709-713
- El-Minawi MF, Abdel-Hadi M, Ibrahim AA, Wahby O. Comparative evaluation of laparoscopy and hysterosalpingography in infertile patients. *Obstet Gynecol* 1978;51:29-32
- Nielsen DT, Rasmussen F, Justesen P. A comparative study of hysterosalpingography and endoscopy/laparotomy in infertile patients. *Eur J Radiol* 1987;7:260-262
- Siegler AM. *Hysterosalpingography*, 2nd ed. New York: Medcom, 1974:125-157
- Siegler AM. Hysterosalpingography. *Fertil Steril* 1983;40:139-157
- Cohen BM, Katz M. The significance of the convoluted oviduct in the infertile woman. *J Reprod Med* 1978;21:31-35
- Karasick S, Karasick D. *Atlas of hysterosalpingography*. Springfield, IL: Charles C Thomas, 1987:115-121

Book Review

Ultrasound of the Prostate. By Matthew D. Rifkin. New York: Raven, 293 pp., 1988. \$79

This book by Matthew D. Rifkin reviews in 16 relatively short chapters the present state-of-the-art in ultrasound examination of the prostate. Encumbered by the author's attempt to cover a relatively new field in which the technology is changing rapidly, and in which many of the statistics are still being accumulated, this volume, by one of the leaders in the field, nevertheless could serve to bring the reader up to date in a rather limited discipline.

After the introduction, chapter 2, on embryology and normal anatomy, is an excellent starting point and review of the details of the development of the prostate and surrounding tissues and of the newer concepts of zonal anatomy, which are lacking in most standard anatomy references. Except for the last few pages on scanners, chapter 3 is the obligatory review of the physical principles of ultrasound imaging. Anyone who does ultrasound should know this or have much more complete texts and references immediately available.

Chapter 4, on scanning techniques, equipment, and preparation of the patient, is destined for a rapid obsolescence, what with new machines and probes entering the market every day. It has too many simplistic diagrams and pictures of equipment and procedures. Six pictures, for instance, covering two pages, are devoted to the "single sheath" technique (or how to place a condom over a probe) and two more pictures to the "double cover" technique (or . . .).

Chapter 5, "Normal Sonographic Anatomy," is almost completely concerned with the endorectal approach to the prostate gland, and rightfully so. One criticism of this chapter, as well as of much of the book, is the filling of a whole page with two figures—an inefficient use of space. This chapter is excellent. Chapter 6 is short (seven pages) and discusses several methods of measuring the prostate and seminal vesicles. Chapter 7 is concerned with the sonographic approach to the diagnosis of prostatic disease. After flow charts are presented to help in the evaluation of the prostate and lesions thereof, quite short paragraphs then provide a discussion of lesions of various echogenicities. Illustrations (two and sometimes one to a page) are of average quality.

Chapter 8, on biopsy techniques, discusses a full range of core and aspiration techniques and the various approaches (ie, transperineal and transrectal) and equipment pertaining thereto. Chapter 9 is a brief review of prostatic cancer. It includes pathogenesis, development, classification, grading and staging, and metastatic potential. Once again, using a whole page for a simple line graph that shows

the increase in new cases and deaths over the last 20 years seems quite inefficient. Otherwise, this chapter is a good discussion. Chapter 10, on sonographic characteristics of cancer, discusses the relationship of size to echogenicity of prostate cancer and methods of staging. That much is known, but that there is even more to determine in the future is the conclusion of this chapter. Chapter 11, a five-page chapter with 2.5 pages of figures, discusses percutaneous use of radiation treatment.

Chapter 12 discusses benign prostatic hypertrophy, a ubiquitous disease, and its sonographic manifestations, pathogenesis, clinical manifestations, and some associated benign diseases. A one-line paragraph and a four-line paragraph on transperineal and endorectal ultrasound, respectively, hardly seem worth mentioning; likewise, the extremely short section on conventional ultrasound. The sections on endorectal ultrasound and other benign diseases are worthwhile.

Chapters 13 and 14 cover inflammatory diseases, infertility, and seminal vesicle diseases and are quite informative. Chapter 15, on the prostatic urethra, is about 60% illustrations and will be of primary interest to urologists. The final chapter attempts to tie together the clinical usefulness of endorectal prostatic ultrasound. Statistical reinforcement is evidently limited, but the examination is likely to be useful, and great hope is expressed for the future of the technique. Five hundred fifty-nine references are cited, and the index is reasonably inclusive.

Overall, the quality of the prose is fair. The organization suffers from an annoying habit of fragmenting short chapters further into extremely short paragraphs or sections with major headings, some of which contain only a few lines. The book has too many figures and illustrations and too many simple diagrams and pictures of transducers, many of which are redundant or too large in relationship to the book and the text. Although the basic physical, clinical, pathologic, anatomic, and statistical information is useful, some is too simplistic for the radiologist and some is too simplistic for the urologist. Nevertheless, especially for those just entering this field, this might be a handy reference text to have on hand. It can reasonably be expected that the book will become obsolete in the next few years, at least in terms of image quality and statistical information.

Hano A. Siegel
Mercy Hospital
San Diego, CA 92103

Pregnancies in Septate Uteri: Outcome in Relation to Site of Uterine Implantation as Determined by Sonography

Luigi Fedele¹
Milena Dorta
Diana Brioschi
Maria Natalina Giudici
Giovanni Battista Candiani

Sonography was used to study the site of uterine implantation of 12 pregnancies in eight patients with complete septation of the uterus. The purpose was to determine the incidence of septal implantation in these patients and its relation to the outcome of the pregnancies. The live-birth rate in the 12 pregnancies was 33%. Three pregnancies (25%) went to term and ended in live neonates. One (8%) resulted in a premature delivery and the neonate survived. Eight (67%) ended in abortion. Sonograms showed that in all four pregnancies that were not aborted, implantation was in the lateral wall of the uterus. In comparison, in the eight pregnancies that terminated in abortion, implantation was septal in six, mixed in one, and undetermined in one.

Our experience with this small group of patients suggests that pregnancies in septate uteri have a poor prognosis and that abortion is related to septal implantation.

Septate uteri [1] are usually considered to be müllerian anomalies with a poor reproductive prognosis. Patients with septate uteri usually do not have difficulty conceiving, but the pregnancies frequently end in abortion or premature birth. The live-birth rate is under 30% [2, 3]. The mechanism by which the malformation interferes with the normal course of pregnancy is uncertain. Of the various hypotheses proposed, an insufficient vascular supply at septal implantation sites is the most attractive [4].

We used sonography to study the implantation and course of pregnancies in septate uteri to determine whether septal implantation is common in this malformation and if it has a poor gestational prognosis.

Subjects and Methods

Twelve consecutive pregnancies in eight patients with complete septate uteri (subclass Va of Buttram and Gibbons [1]) were monitored by sonography beginning at the sixth week. The mean age of the patients at the start of the pregnancy was 27 years (range, 22–35). In two patients, the diagnosis of septate uterus was made by sonography and pelvic exploration. The diagnoses in the other six were made by hysterosalpingography, performed because of primary infertility in two and a previous single abortion in four. In three patients, a longitudinal vaginal septum was removed. Ten of the pregnancies started spontaneously and two were induced with clomiphene citrate.

Sonography was performed with a real-time sector scanner and 3.5-MHz transducer. In the first weeks of pregnancy the scans were obtained with half-full bladders in order to visualize the fundal perimetrium, septum, and endometrial hemicavities simultaneously, as described previously [5, 6]. The scans were obtained weekly until week 14 and monthly thereafter. In each pregnancy the following were noted: (1) presence of the fetal heart beat and the degree of development of the products of conception in relation to the onset of amenorrhea; (2) site of implantation (septal, lateral, or mixed), based initially on study of the site of greatest decidual thickening of the gravid hemiuterus and subsequently on localization of the umbilical cord attachment and the placental topography; (3) characteristics of the decidual reaction in the nongravid hemiuterus (insufficient, normal, or florid) by study of the mucosal thickness and corrugations and the presence of a central fluid mass; (4) diameter

Received September 19, 1988; accepted after revision November 28, 1988.

¹All authors: Clinica Ostetrico-Ginecologica I, Università di Milano, via della Commenda, 12-20122, Milano, Italy. Address reprint requests to L. Fedele.

AJR 152:781-784, April 1989
0361-803X/89/1524-0781
© American Roentgen Ray Society

and configuration of the cervical canal of the gravid hemiuterus (normal, hypotonic, or incontinent) compared with the cervical canal of the nongravid hemiuterus; and (5) any associated pelvic disease (e.g., fibroids or ovarian cysts).

Results

The sonographic data were related to the pregnancy outcome. In 11 pregnancies sonographic visualization of the gestation sac was adequate from the first weeks, whereas in one it was difficult to see until week 11 because of slight retroversion of the uterus. In 10 pregnancies the fetal heart beat was visualized from week 6 and in one at week 8 (delayed conception); in another the embryo was never visible (blighted ovum). In the pregnancies that progressed beyond the third month, the development of the product of conception always corresponded to the duration of amenorrhea, except in one case in which slight fetal growth retardation was observed at 18 weeks followed weeks later by abortion.

The site of implantation was lateral in three cases (25%), mixed in two (17%), septal in six (50%), and could not be

evaluated in one (8%). The decidual reaction in the nongravid hemiuterus was normal with respect to the duration of amenorrhea in five cases (42%), initially normal and subsequently insufficient in three (25%), always insufficient in three (25%), and not evaluable in one (8%). The tone of the cervical canal of the gravid hemiuterus was normal in the pregnancies with a favorable course and became hypotonic after disappearance of the fetal heart beat in the pregnancies that ended in abortion. Associated diseases were observed in three women. Two subserous fibromas 2 cm in diameter were detected in one and an intramural fibroma 1.5 cm in diameter was detected in another; in a third, a lutein cyst remained visible until week 14.

Eight (67%) of the 12 pregnancies studied ended in abortion, one (8%) in premature birth at 35 weeks, and three (25%) in a term birth, so that the live-birth rate was 33%. One of the eight abortions occurred at 8 weeks, five within 13 weeks, one at 16 weeks, and one at 20 weeks. Cytogenetic examination of the abortus was possible in five of the eight cases, and did not show any abnormalities.

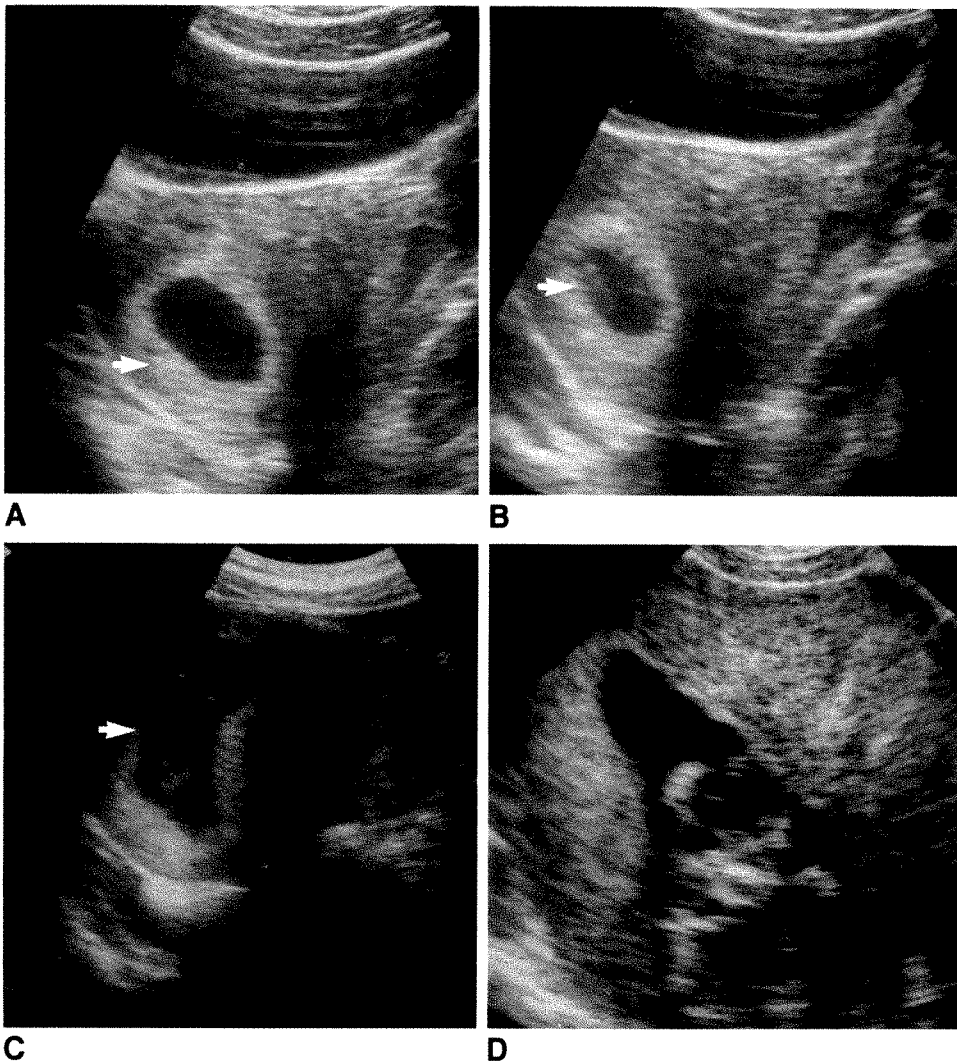


Fig. 1.—Sonograms show course of pregnancy with lateral implantation in septate uterus.

A, 7 weeks. Gestation sac is visible in left hemiuterus with trophoblastic thickening (arrow) localized on lateral myometrium; decidual reaction of non-gravid hemiuterus is florid.

B, 7 weeks. Embryonic pole appears at site of trophoblastic thickening (arrow).

C, 10 weeks. Subsequent umbilical cord attachment (arrow) is seen.

D, 14 weeks. Placenta is fully formed and embryo visible.

When the sonographic data were compared with pregnancy outcome, it was found that in all four pregnancies that reached or nearly reached term, implantation was lateral and the decidual reaction in the nongravid hemiuterus was normal or florid (Fig. 1). In the eight pregnancies that ended in abortion, implantation was septal in six (75%) (Fig. 2), mixed in one (13%), and not evaluable in one (13%). The decidual reaction was normal in the pregnancy that aborted at 16 weeks, initially normal and subsequently insufficient in the pregnancy that ended at 20 weeks, and always insufficient or poorly evaluable in the other pregnancies that aborted in the first trimester. The fibromas were observed in the pregnancies with a favorable course and the lutein cyst in the pregnancy that terminated at 20 weeks.

Discussion

Only pregnancies in complete septate uteri (subclass Va of Buttram and Gibbon [1]) were considered in this study. Because this type of uterus is relatively rare [2], our series is small. The main reason for limiting this study to patients with

complete septate uteri was that many partial septate uteri may not be diagnosed if they do not cause reproductive problems. It is possible, therefore, that all the partial septate uteri recognized have been selected for additional infertility factors and not only for the malformation. On the contrary, complete septate uteri should not escape diagnosis regardless of the reproductive performance of the patients because the double cervix is easily detected at physical examination, as is a vaginal septum. The reproductive implications of uterine septa, therefore, can be analyzed more completely in a study of pregnancies in complete septate uteri. Furthermore, the partially septate uterus subclass includes a range of malformation varieties with septa of different lengths, and uterine vascularization may differ according to the septal length.

Our results confirmed that pregnancies in these patients have a poor reproductive prognosis. In fact, the live-birth rate was 33% (25% when the four abortions in the patients' histories are included). In 1983, Buttram [2] analyzed the outcome of 208 pregnancies in septate uteri in his own patients and in those reported in the literature and found an

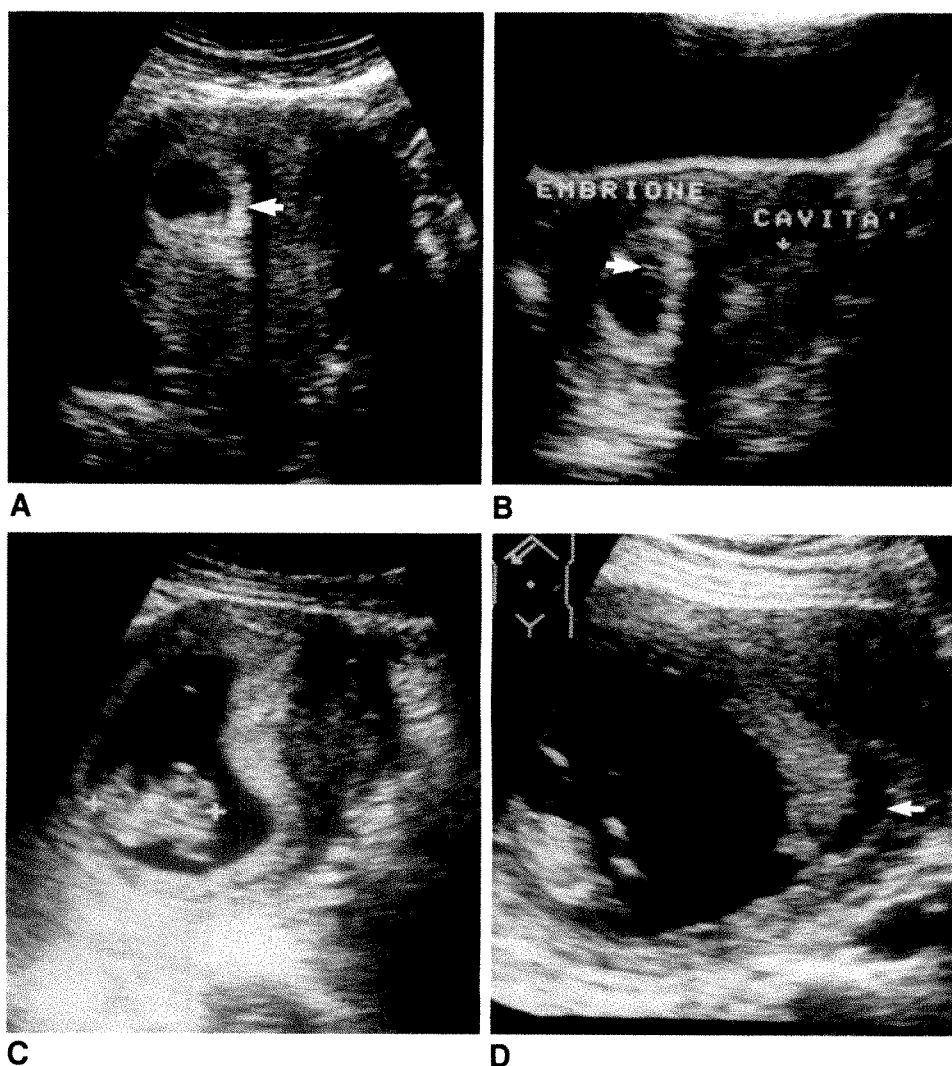


Fig. 2.—Sonograms show course of pregnancy with septal implantation in septate uterus.

A, 7 weeks. Gestation sac can be seen in left hemiuterus, with trophoblastic thickening on septum (arrow).

B, 7 weeks. Embryonic pole is evident at site of trophoblastic thickening (arrow), and there is normal decidual reaction in nongravid uterus.

C, 10 weeks. Embryo is visualized with placenta attached only to septum.

D, 12 weeks. Placenta is partially detached (arrow); abortion occurred a few hours later.

abortion rate of 67% and a live-birth rate of 28%. The fact that our data, which refer only to pregnancies in complete septate uteri, are comparable to the overall data of Buttram suggests that the partial septate uterus also has the same reproductive prognosis.

Our findings also show that the septum is a frequent site of implantation. In fact, of the 12 pregnancies, septal implantation was observed in six (50%) and partial septal implantation in two (17%). This may relate to the fact that the septal mucosa is analogous to the antimesometrial area in which nidation occurs in mammals with bicornuate uteri [7], and would explain why pregnancy is possible in a septate uterus in 25% of cases but ends in abortion in 75%. Furthermore, elective implantation in the septum could support the hypothesis of Buttram [2] that the larger the extension of the uterine septum the greater the impairment of gestational capacity.

In our study it was clearly demonstrated that when implantation is septal the pregnancy outcome is extremely poor, whereas with lateral implantation it is good. The cause of the very poor prognosis of septal implantation could be related to the scanty vascularization of the septum. The uterine vasculature is of fundamental importance for normal placentation and thus for pregnancy outcome. In an angiographic study, Burchell et al. [8] showed that the intervillous space develops in a linear manner along the course of the arcuate arteries. The blood reaches the intervillous space through the spiral arteries, the terminal branches of the radial arteries. Candiani et al. [9] showed that an orderly distribution of the vessels is lacking in the intermediate myometrial layer of the uterine septum and that differentiation of the endometrial basal layer is scanty. These findings could be indicative of an abnormal configuration of the myometrial-endometrial vascular relations at this site. In fact, whereas in the normal uterus all the various endometrial sites are reached directly by spiral arterioles supplied by valid radial arteries, in the uterine septum, relatively poor in vessels, the mucosa is vascularized indirectly and collaterally. It was shown by Candiani et al. [9]

that these vascularization alterations do not interfere with the cyclic modifications of the endometrium and its receptivity, but they could instead have a negative influence on the development phases after implantation and particularly on the establishment of the maternofetal relations preceding placentation.

In our study, sonography was found to be a useful method of monitoring pregnancy in a septate uterus. As soon as the site of implantation is identified, a reliable gestational prognosis can be made and the pregnancies with septal implantation can be followed with particular attention, whereas those with lateral implantation need only normal care. In our study, the decidual reaction in the nongravid hemiuterus had scanty prognostic value. Monitoring the cervical conditions demonstrated that cervical incompetence of the gravid hemiuterus is infrequent, confirming that cerclage is not necessary.

REFERENCES

1. Buttram VC Jr, Gibbons WE. Müllerian anomalies: a proposed classification (an analysis of 144 cases). *Fertil Steril* 1979;32:40-48
2. Buttram VC Jr. Müllerian anomalies and their management. *Fertil Steril* 1983;40:159-165
3. Candiani GB, Fedele L. Clinical management of uterine anomalies. *Acta Eur Fertil* 1981;12:83-101
4. Fedele L, Zamberletti D, D'Alborton A, Vercellini P, Candiani GB. Gestational aspects of uterus didelphys. *J Reprod Med* 1988;33:353-356
5. Fedele L, Ferrazzi E, Dorta M, Vercellini P, Candiani GB. Ultrasonography in the differential diagnosis of "double" uteri. *Fertil Steril* 1988;50:361-364
6. Fedele L, Dorta M, Vercellini P, Brioschi D, Candiani GB. Ultrasound in the diagnosis of subclasses of unicornuate uterus. *Obstet Gynecol* 1988;71:274-277
7. Mossman HW. Comparative morphology of the fetal membranes and accessory uterine structures. *Contrib Embryol Carnegie Inst* 1937;26:129-138
8. Burchell RC, Creed F, Rasoulpour M, Whitcomb M. Vascular anatomy of human uterus and pregnancy wastage. *Br J Obstet Gynaecol* 1978;85:698-702
9. Candiani GB, Fedele L, Zamberletti D, De Virgiliis G, Carinelli S. Endometrial patterns in malformed uteri. *Acta Eur Fertil* 1983;14:311-318

Pictorial Essay

Imaging of Abdominal Aortic Aneurysms

Lorraine L. LaRoy,¹ Peter J. Cormier, Terence A. S. Matalon, Suresh K. Patel, David A. Turner, and Bruce Silver

Abdominal aortic aneurysm is a common disease with potentially catastrophic complications. Untreated, these aneurysms enlarge and eventually rupture with a high mortality of 50–90%. Conversely, elective surgical resection has an excellent prognosis and low mortality (2–4%) and currently is the treatment of choice [1]. Because most patients are asymptomatic, the diagnosis of abdominal aortic aneurysm frequently is unsuspected. Evaluation of these patients is heavily dependent on imaging, and the radiologist is in a unique position to direct the workup.

A true aneurysm of the abdominal aorta is a localized dilatation of the wall greater than 3 cm in diameter. All three layers of the vessel (intima, media, and adventitia) are involved. A false aneurysm (pseudoaneurysm) is essentially a perforation of the aorta with subsequent hematoma formation limited by adventitia or surrounding vascular tissues (Fig. 1).

Most abdominal aortic aneurysms are secondary to atherosclerosis. Other causes include trauma, infection, syphilis, cystic medial necrosis, inflammation, and Marfan syndrome. Atherosclerotic plaques cause fibrosis and atrophy of the underlying media of the aortic wall. Loss of medial elastic fibers seen with advancing age compounds this insult. The weakened media can no longer adequately support the vessel wall, resulting in aortic dilatation. Increasing dilatation and decreasing wall thickness result in a rapid increase in wall tension (Laplace's law). This leads to progressive dilatation and eventual rupture (Fig. 2).

Inflammatory aortic aneurysm is a distinct clinical entity distinguished from uncomplicated atherosclerotic aneurysms by dense perianeurysmal fibrosis and thickened aortic wall. Surgical repair of these aneurysms is difficult, with increased morbidity and mortality compared with simple aneurysms.

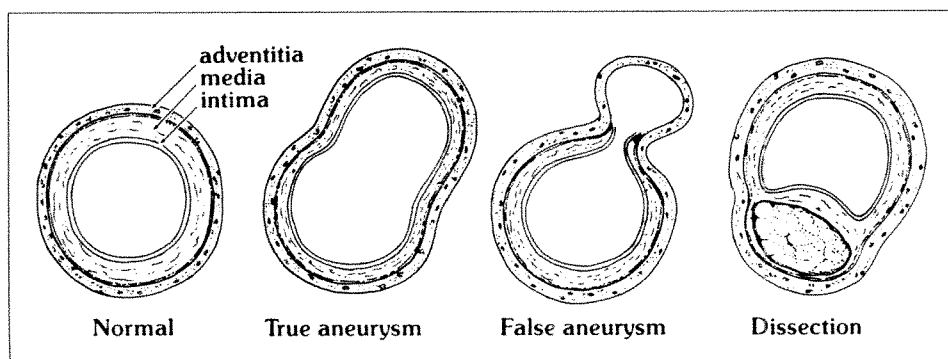


Fig. 1.—Types of aortic aneurysms.

Received August 18, 1988; accepted after revision November 28, 1988.

Presented at the annual meeting of the American Roentgen Ray Society, San Francisco, May 1988.

¹ All authors: Department of Diagnostic Radiology and Nuclear Medicine, Rush-Presbyterian-St. Luke's Medical Center, 1653 W. Congress Pkwy., Chicago, IL 60612. Address reprint requests to T. A. S. Matalon.

AJR 152:785–792, April 1989 0361–803X/89/1524–0785 © American Roentgen Ray Society

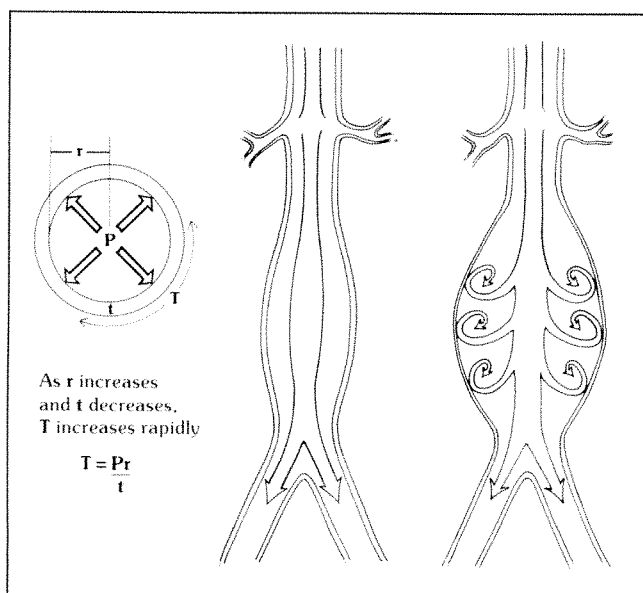


Fig. 2.—Enlargement of abdominal aortic aneurysm is explained by Laplace's law. Wall tension (T) is proportional to the product of the intraluminal pressure (P) and the radius (r), and inversely proportional to the wall thickness (t).

Abdominal aortic aneurysms 3–6 cm in diameter grow approximately 4 mm/year. The risk of rupture relates primarily to the size of the aneurysm, with a clear increase in risk over 5 cm (Fig. 3) [2]. Even small aneurysms are more likely to rupture if significant enlargement is demonstrated on sequen-

SIZE	RUPTURE RISK
< 5 cm	≤ 5%
> 6 cm	16%
> 7 cm	76%

Fig. 3.—Data showing risk of rupture in relation to size of aneurysm. (Data from [2].)

tial studies. Consequently, it has been proposed that even small, asymptomatic aneurysms be reexamined 3–6 months after diagnosis and then at 12-month intervals. Regardless of size, symptomatic aneurysms imply rapid growth or rupture. The most common surgical treatment is endoaneurysmorrhaphy, which consists of the placement of a prosthetic graft within the aneurysm. The aneurysm wall is then wrapped around the graft, providing important protection against aortoenteric fistulas (Figs. 4 and 5). Complete resection of the aneurysm with graft placement can be performed also.

Imaging

Several techniques are available for imaging the aorta. All have strengths and limitations, and there is some controversy regarding their role [3]. Ideally, the aorta should be imaged in two planes. Measurements based on axial images only can be potentially misleading. Tortuosity of the aorta can lead to false estimation of aneurysm size or extent, or to confusion regarding branch vessel involvement.

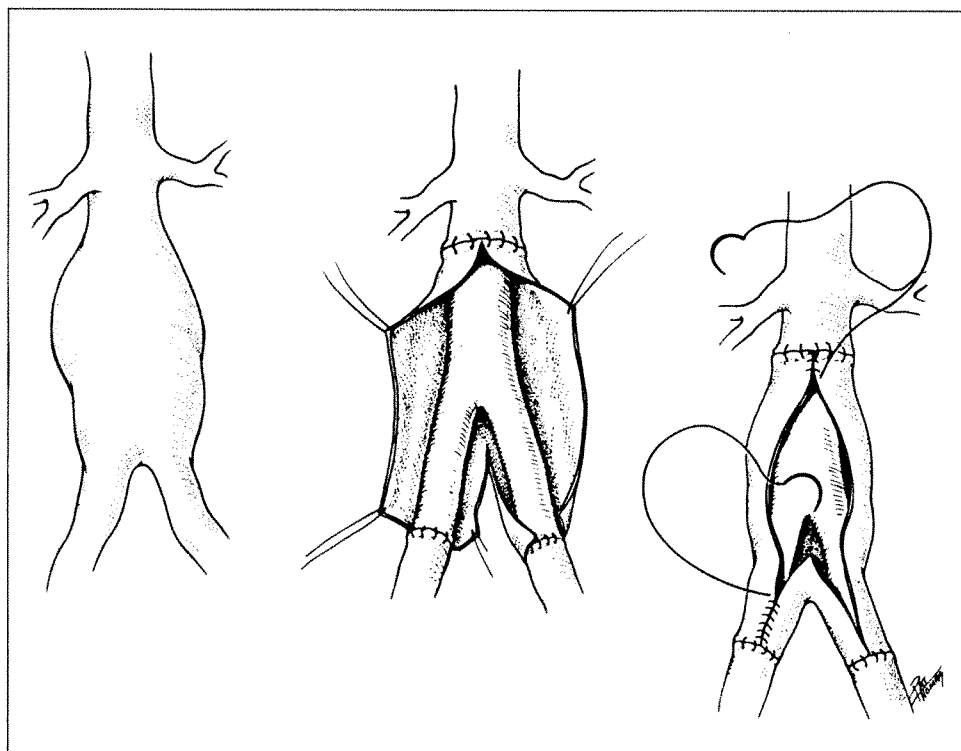
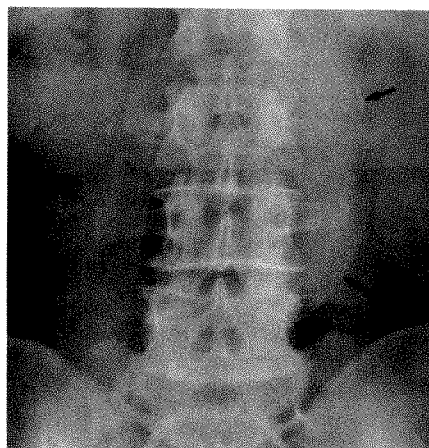


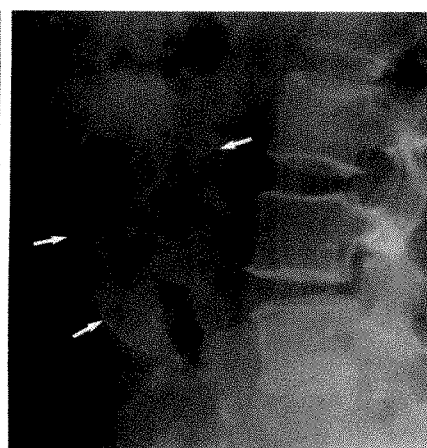
Fig. 4.—Procedure of endoaneurysmorrhaphy.



Fig. 5.—Autopsy specimen after endoaneurysmorrhaphy. Prosthetic graft (arrowheads) is surrounded by native aneurysm (arrows) wall and thrombus. Graft has been opened, revealing an intraluminal thrombus.

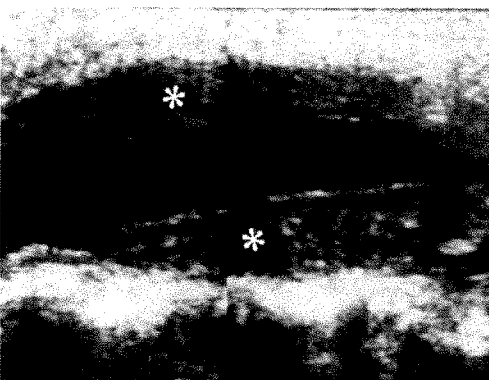


A

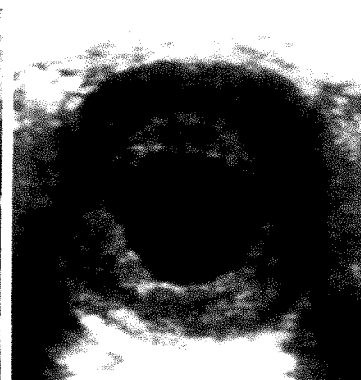


B

Fig. 6.—A and B, Anteroposterior (A) and lateral (B) plain abdominal radiographs show intimal calcifications (arrows) in wall of aortic aneurysm.



A



B

Fig. 7.—Sonograms show 6.0-cm aneurysm lined with thrombus (asterisks).

A, Longitudinal sonogram.

B, Transverse sonogram better depicts circumferential nature of thrombus.

Plain Radiography

Curvilinear calcifications may provide the first clue to the presence of an aneurysm. Approximately 55–85% contain enough calcium to be detected on plain films. Once an aneurysm is suspected, other studies are required for further characterization and staging (Fig. 6).

Sonography

Sonography is the standard method for screening and follow-up of aortic aneurysms. It approaches 100% accuracy in detection, and measurements correlate within 3 mm of surgical specimens. Sonograms may show thrombus, periaortic abnormalities, dissections, cephalic and caudal extent, as well as complications such as hydronephrosis (Fig. 7).

Sonography is limited in obese patients or those with abundant overlying bowel gas. In addition, the renal arteries are rarely visualized directly, and suprarenal extension frequently can only be inferred by the relationship of the aneurysm to the superior mesenteric artery. Availability, cost, and

noninvasiveness, combined with accuracy in detection and measurement, make sonography ideal for screening and follow-up of uncomplicated aneurysms.

CT

CT is a more thorough method of evaluating aortic aneurysms. It accurately demonstrates the size and usually is able to detect intraluminal thrombus (Figs. 8 and 9). CT defines the craniocaudal extent of the aneurysm better than sonography does. Additional advantages include visualization of the retroperitoneum, allowing the detection of aneurysmal leak, ureteral obstruction, perianeurysmal fibrosis, or other unsuspected causes of abdominal or back pain. When performing CT, oral contrast material should be used whenever possible to opacify bowel loops that can mimic periaortic fluid collections or hematoma. In urgent cases, administration of oral contrast material may not be possible because of the time needed to adequately opacify the bowel. In addition, pre- and postinfusion scans should be obtained. Postinfusion scans

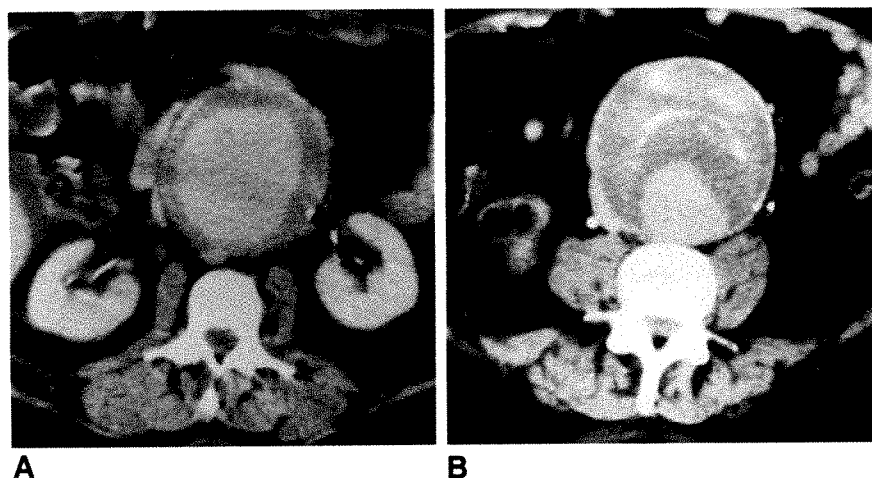


Fig. 8.—A and B, Postinfusion CT scans. Opacified abdominal aortic aneurysm lined with low-attenuation thrombus. Note that thrombus is partially calcified.

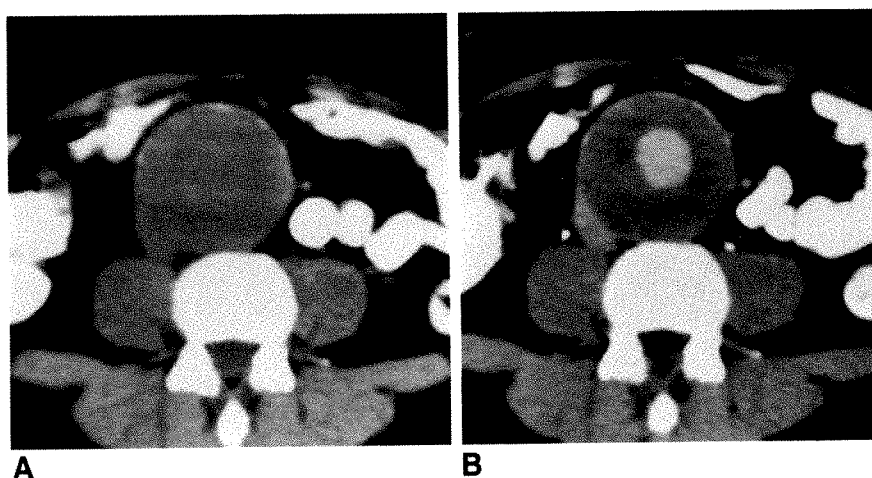


Fig. 9.—A and B, Preinfusion (A) and post-infusion (B) CT scans show importance of IV contrast material to differentiate lumen from thrombus.

opacify the patent lumen of the aneurysm, differentiating it from surrounding intraluminal thrombus. Acute periaortic hematomas tend to be more apparent on preinfusion scans because of the relatively high density of extravasated blood compared with adjacent soft tissues. IV contrast material can also differentiate between periaortic hematoma and periaortic fibrosis. CT of inflammatory aortic aneurysm shows a thickened, often calcified aortic wall surrounded by a low-attenuation soft-tissue mass. Periaortic fibrosis typically enhances after infusion, in contrast to periaortic hematoma, which does not.

Some controversy exists regarding the efficacy of CT in determining involvement of renal arteries, particularly when multiple renal arteries are present. CT cannot always differentiate between thrombus-lined aneurysm and clot within the false lumen of a dissection. Aortography may be required in these cases.

CT is the technique of choice for evaluation of the aorta after surgical repair. Complications after aneurysm repair include perigraft abscess, retroperitoneal hemorrhage, pseudoaneurysm, ureteral obstruction, groin infection, aortoenteric fistulas, and lymphoceles. Many of these complications manifest as perigraft fluid or gas collections ideally demonstrated on CT. In the perioperative period, fluid and gas collections

about the surgical site are normal in most patients. The majority of these collections resolve within 1 month. The presence of gas or fluid around the graft after the fourth postoperative week or increasing amounts at any time are ominous signs. CT is an excellent procedure for both pre- and postoperative evaluation of abdominal aortic aneurysms (Figs. 10–12) [4].

Angiography

Angiography is the gold standard for demonstrating visceral-branch involvement and variations in vascular anatomy (Fig. 13). Repair of suprarenal aneurysms is technically difficult and is associated with increased morbidity and mortality (Fig. 14). Evaluation of mesenteric blood supply is critical to prevent postoperative bowel ischemia. A prominent marginal artery of Drummond and a patent inferior mesenteric artery suggest stenosis of the superior mesenteric artery. If the inferior mesenteric artery is sacrificed during surgery, bowel ischemia may ensue. Biplane angiography is often necessary to completely evaluate mesenteric-branch involvement and is recommended in patients with symptoms of intestinal angina.

Angiography can underestimate both the size and extent of thrombus-filled aneurysms because only the patent lumen

Fig. 10.—Pseudoaneurysm occurring after prosthetic graft repair of aortic aneurysm.

A, CT shows well-circumscribed low-attenuation collection (arrows) to right of infrarenal aorta.
B, CT scan just above bifurcation shows this collection (arrow) communicates with aorta.

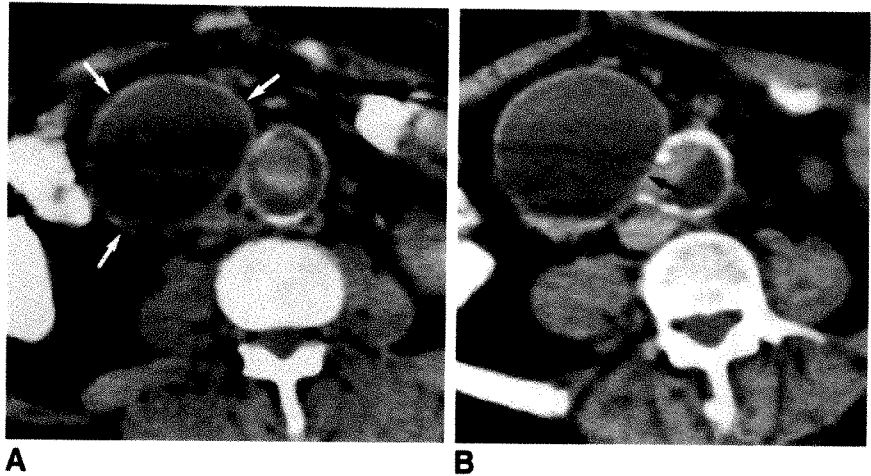
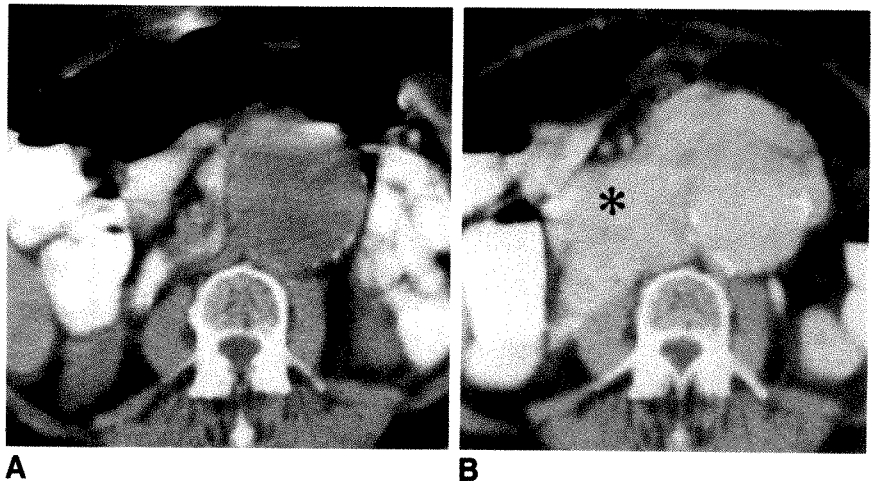


Fig. 11.—Rupture of aortic aneurysm occurring between pre- and postinfusion scans.

A, Preinfusion CT scan shows aneurysm with calcified wall.
B, Postinfusion CT scan at same level shows large periaortic collection (asterisk), not present on preinfusion scan due to periaortic hemorrhage.



is opacified (Fig. 15). Additional information about the abdomen and retroperitoneum can be better obtained by other less invasive procedures.

The routine use of angiography for preoperative evaluation is controversial. Some have advocated only its selective use in those patients suspected of having occlusive disease or branch involvement, such as patients with hypertension or intestinal angina. In the final analysis, the preference of the individual surgeon may determine whether a preoperative angiogram is obtained.

MR Imaging

MR imaging is well suited for imaging the aorta. It is noninvasive, has multiplanar display capability, and shows inherent contrast between flowing blood and adjacent structures. MR imaging is also accurate in the detection and measurement of aortic aneurysms. Extent and visceral-branch involvement often can be determined, and MR imaging can be sufficient for preoperative evaluation of aneurysms in selected cases (Figs. 16 and 17).

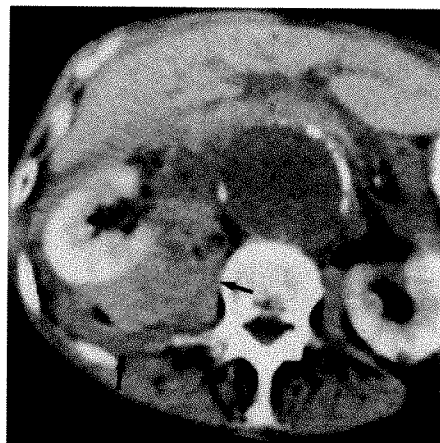


Fig. 12.—Postinfusion CT scan shows perinephric hematoma (arrows) caused by leaking aortic aneurysm.

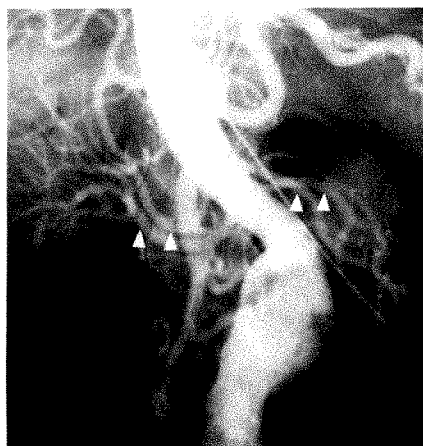


Fig. 13.—Angiogram shows infrarenal aneurysm without compromise to renal blood flow. Note presence of multiple renal arteries (*arrowheads*).

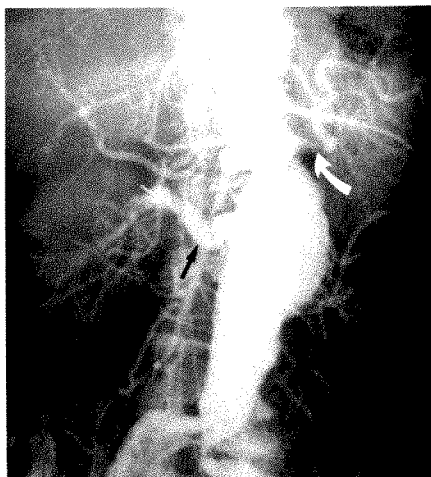


Fig. 14.—Angiogram shows aortic aneurysm involving renal arteries. There is high-grade stenosis of left renal artery (*curved arrow*), while right renal artery (*straight arrow*) arises directly from aneurysm.

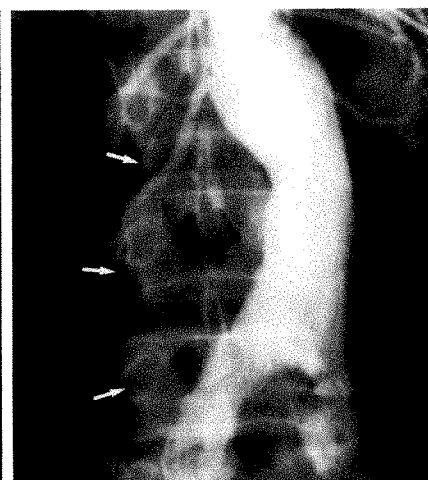
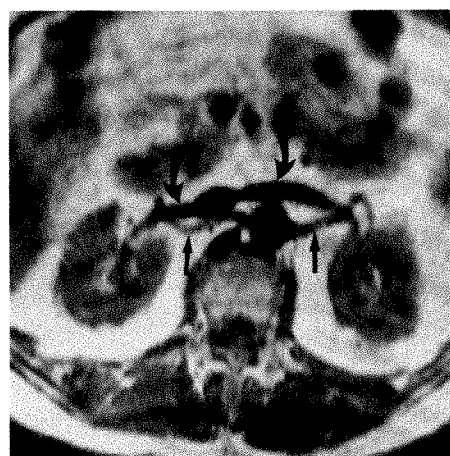
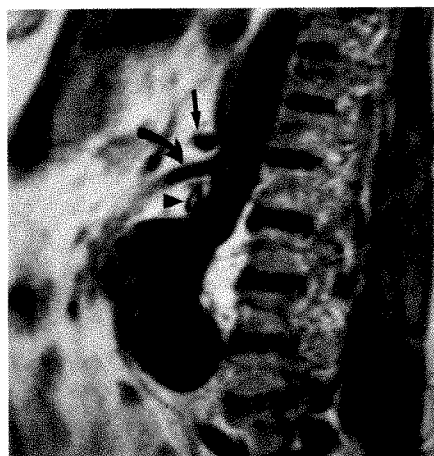


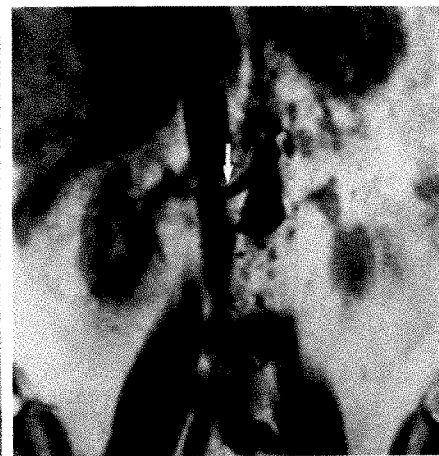
Fig. 15.—Angiogram shows lumen of aortic aneurysm. True diameter of aneurysm is defined by intimal calcifications (*arrows*).



A



B



C

Fig. 16.—MR scans show aortic aneurysm and adjacent vascular anatomy.

A, Axial T1-weighted image, 600/32 (TR/TE), at level of renal hilus shows renal arteries (*straight arrows*) and renal veins (*curved arrows*). Aorta is normal in size.

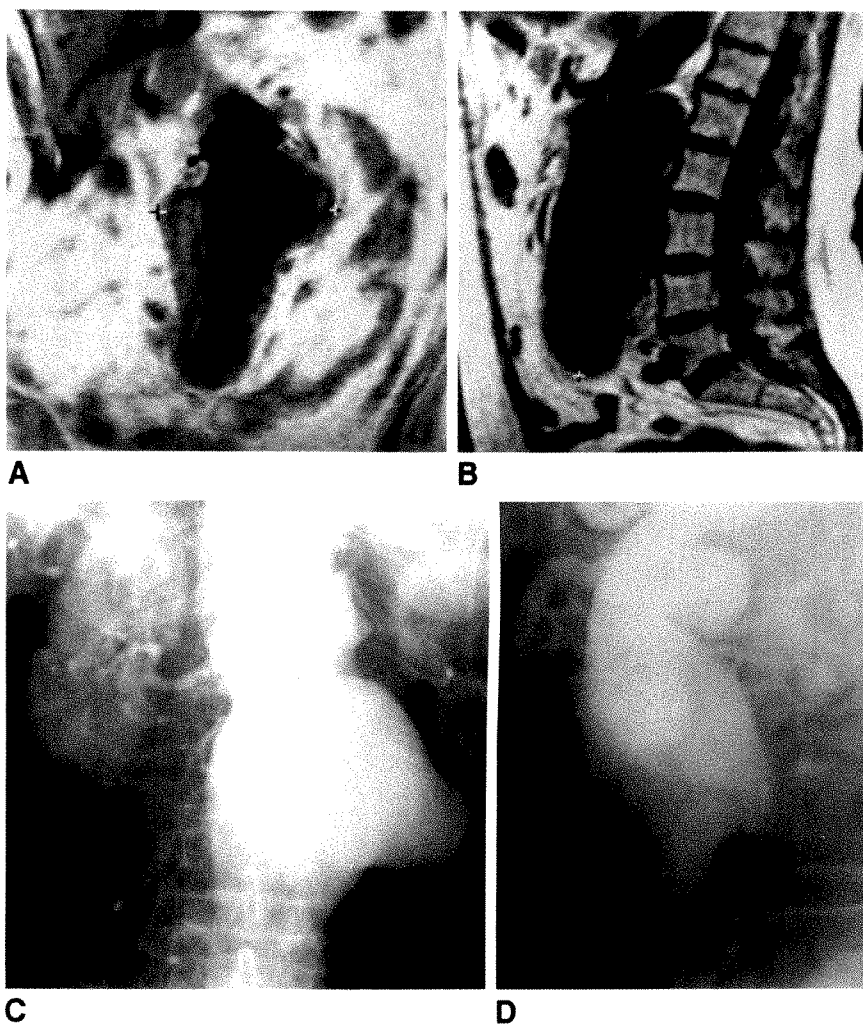
B, Sagittal image, 600/32, shows aortic aneurysm. Superior mesenteric artery (*curved arrow*), celiac axis (*straight arrow*), and left renal vein (*arrowhead*) are also seen.

C, Coronal image shows right renal artery (*arrow*).

Fig. 17.—A-D: A and B, Coronal (A) and sagittal (B) MR images, 730/30 (TR/TE), show thrombus-lined aortic aneurysm.

C and D, Frontal (C) and lateral (D) angiograms show lumen.

Fig. 17 is continued on following page.



When imaging the abdominal aorta with a conventional spin-echo imaging technique, it is best to use a relatively short TE and TR. Although cardiac gating is very useful in imaging the thoracic aorta, it is not helpful when examining the abdominal aorta. Images in the sagittal projection usually show the entire extent of an abdominal aortic aneurysm best and are optimal for measuring its diameter. However, it is important to obtain transaxial and coronal images as well, since this facilitates visualization of the renal arteries and detection of associated abnormalities of the iliac arteries.

One limitation of MR imaging is difficulty in distinguishing slowly flowing blood within the false lumen of a dissection from thrombus within an aneurysm. However, newer fast imaging techniques may improve assessment of flow pat-

terns. Limited availability and high cost inhibit the widespread use of MR imaging. The magnet often precludes the evaluation of seriously ill patients who require respirators or monitoring equipment [5].

Summary

There is no single correct approach to evaluate aortic aneurysm. Variations in individual cases, equipment availability, technical expertise, and surgeons' preference frequently dictate the workup. Sonography is optimal for screening and follow-up in uncomplicated cases. CT is excellent in preoperative and postoperative evaluation of aneurysms and their

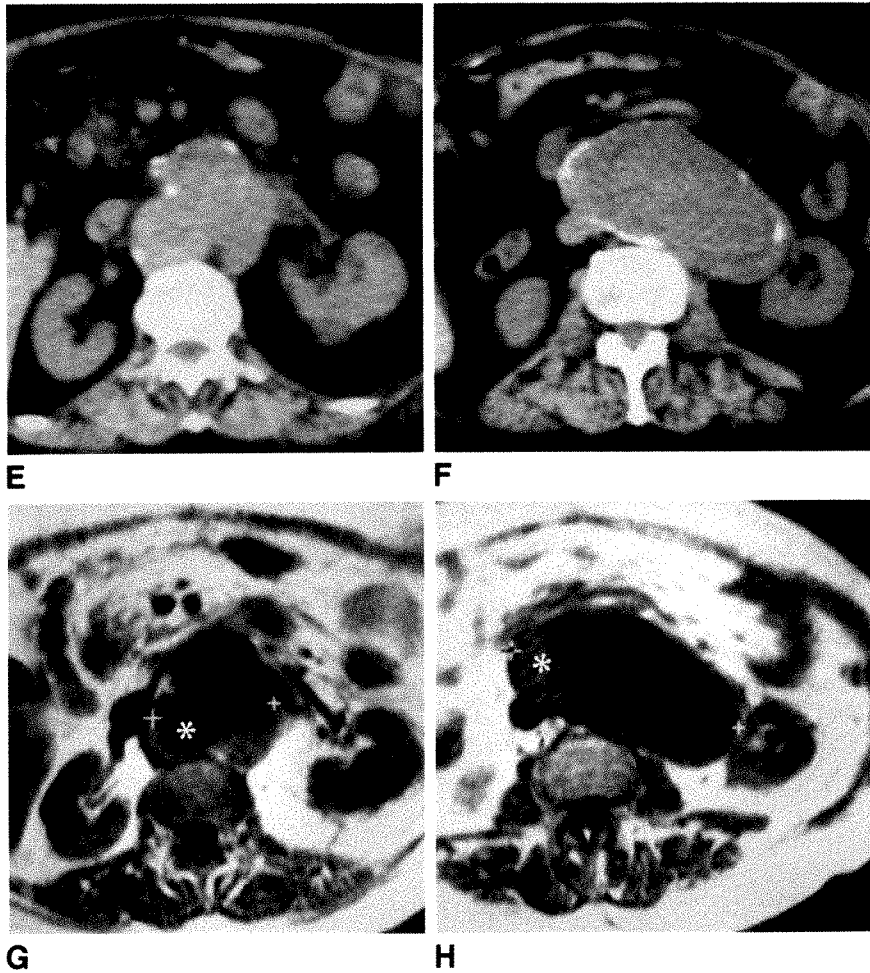


Fig. 17.—E-H, Axial CT scans (E and F) and MR images, 630/30 (G and H), at approximately the same levels. MR better differentiates patent lumen from thrombus (asterisks) in patient to whom IV contrast material could not be given.

potential complications. Angiography is used to determine visceral-branch involvement and define variations in vascular anatomy, although its routine preoperative use is controversial. MR imaging has emerged as a powerful tool to visualize and stage aneurysms.

REFERENCES

1. Pasch AR, Ricotta JJ, May AG, Green RM, DeWeese JE. Abdominal aortic aneurysm: the case for elective resection. *Circulation* 1984;70 [suppl 1]: I-1-I-4
2. Thompson JE, Garrett WV, Patman RD, Talkington CM, Williams SJ III. Surgery for abdominal aortic aneurysms. In: Bergan J, Yao J, eds. *Aneurysms diagnosis and treatment*. New York: Grune & Stratton, 1982: 287-299
3. Ramchandani P, Ball D. Abdominal aortic aneurysms: diagnosis, measurement and treatment. *Postgrad Radiol* 1986;6:259-278
4. Hilton S, Megibow AJ, Naidich DP, Bosniak MA. Computed tomography of the postoperative abdominal aorta. *Radiology* 1982;145:403-407
5. Lee JKT, Ling D, Heiken JP, et al. Magnetic resonance imaging of abdominal aortic aneurysms. *AJR* 1984;1197-1202

Case Report

Transcaval Ureter with Hydronephrosis: Radiologic Demonstration

Max P. Rosen,¹ T. Gregory Walker,¹ James F. Brennan,² Richard K. Babayan,² and Alan J. Greenfield¹

Transcaval ureter is a rare congenital anomaly in which a segment of the inferior vena cava encircles the right ureter in a vascular ring. Seven single cases of this entity have been reported [1-7]. We report a case of transcaval ureter shown by a combination of IV urography, CT, and venacavography and confirmed at surgery.

Case Report

A 42-year-old woman presented with a 3-month history of right flank pain and increased urinary frequency. Her past medical history was unremarkable. An IV urogram (Fig. 1A) showed obstruction of the proximal right ureter. CT scan (Fig. 1B) suggested either a transcaval or retrocaval right ureter. Preoperative venacavography was done to clarify the CT findings. The venacavogram showed a short, segmental duplication of the inferior vena cava at the level of the ureteral obstruction, consistent with a right periureteric venous ring (Fig. 1C). A right retrograde pyelogram showed a normal distal ureter, but no contrast material passed into the renal pelvis. On surgical exploration, we confirmed a transcaval right ureter as the cause of obstruction (Fig. 1D). The patient underwent a segmental ureteral resection and ureteroureterostomy, and an indwelling ureteral stent was placed. Pathologic examination of the resected 1-cm portion of ureter showed mild chronic inflammation with focal fibrosis. The patient's postoperative course was uneventful.

Discussion

The retroperitoneal venous system develops from three paired fetal veins (posterior cardinal, subcardinal, and supra-

cardinal veins), which arise and regress in a well-described chronologic order [8]. Various congenital anomalies of the inferior vena cava, renal veins, and ureters occur when certain embryologic segments fail to regress. Persistence of both the right posterior cardinal and right supracardinal veins forms a vascular ring through which the right ureter passes [8]. On excretory urography, the appearance of the ureter may mimic that of a retrocaval ureter. The latter anomaly is characterized by hydronephrosis and extreme medial deviation ("fish hook deformity") of the middle ureteral segment where it passes behind the inferior vena cava, usually at the L3 vertebral level [8, 9]. In transcaval ureters, the deviated portion of the ureter splits the inferior vena cava and therefore courses less medially than in retrocaval ureters. In addition, the level of obstruction may be slightly more cephalad or caudad [1]. The preoperative diagnosis of this entity is made by CT or venacavography, rather than by urography [4, 5]. Although a rare anomaly, transcaval ureter should be considered when excretory urography suggests retrocaval ureter.

REFERENCES

1. LePage JR, Baldwin GN. Obstructive periureteric venous ring. *Radiology* 1972;104:313-315
2. Radcliffe A, Goode AW, Snell ME. A case of ureteric obstruction due to a double right vena cava forming a periureteric venous ring. *Br J Urol* 1981; 53:478
3. Dharman K. Transcaval ureter. *J Urol* 1980;123:575-576
4. Hattori N, Fujikawa K, Saga T, Nagata Y, Kohno S, Tanabe M. CT diagnosis

Received September 29, 1988; accepted after revision October 27, 1988.

¹ Department of Radiology, Boston University Medical Center, Boston University School of Medicine, 88 E. Newton St., Boston, MA 02118. Address reprint requests to T. G. Walker.

² Department of Urology, Boston University Medical Center, Boston University School of Medicine, 88 E. Newton St., Boston, MA 02118.

AJR 152:793-794, April 1989 0361-803X/89/1524-0793 © American Roentgen Ray Society

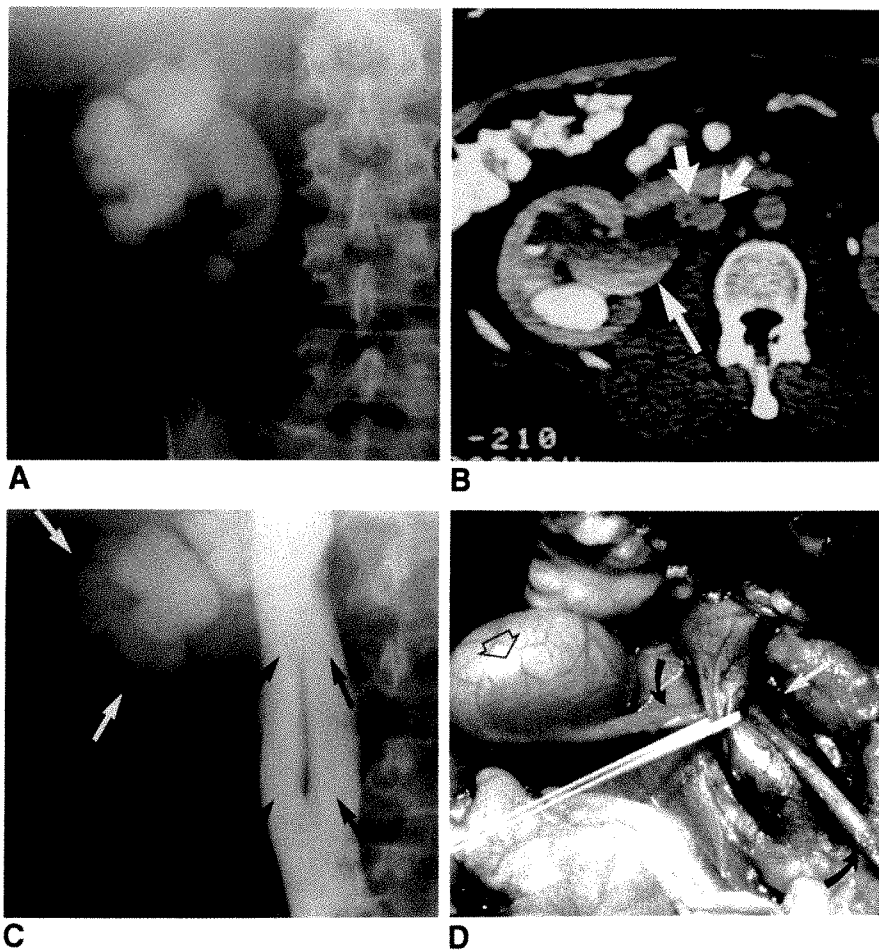


Fig. 1.—A, IV urogram shows proximal right ureteral obstruction and moderate hydronephrosis.

B, Contrast-enhanced CT scan shows dilated right renal pelvis and proximal ureter (long arrow) posterolateral to two segments of duplicated inferior vena cava (short arrows).

C, Inferior venacavogram shows segmental duplication of inferior vena cava (black arrows). Contrast material is present in dilated renal collecting system (white arrows).

D, Surgical photograph shows right ureter (curved arrows) passing through duplicated portion of inferior vena cava (IVC). Lateral segment of duplicated IVC is retracted by a surgical loop. The medial segment (white arrow) is less well seen. Large cystic structure is dilated renal pelvis (open arrow).

of periureteric venous ring. *J Comput Assist Tomogr* 1986;10:1078-1079

5. Sasai K, Snao A, Imanaka K, et al. Right periureteric venous ring detected by computed tomography. *J Comput Assist Tomogr* 1986;10:349-351
6. Irikura H, Minami T, Machida T, Sasaki T, Watanabe H, Ueda M. A rare case of retrocaval ureter. *Nippon Hinyokika Gakkai Zasshi* 1973;64:319-323
7. Fujioka H, Kitamura K, Kawanishi H, Kashiwai K, Takahashi K. Retrocaval ureter with right periureteric venous ring. *Nippon Hinyokika Gakkai Zasshi*

1977;86:788-794

8. Philipps E. Embryology, normal anatomy and anomalies. In: Ferris FJ, Hipona FA, Kahn PC, Philipps E, Shapiro JH, eds. *Venography of the inferior vena cava and its branches*. Baltimore, MD: Williams & Wilkins, 1969:1-32
9. Carion H, Gatewood J, Politano V, Morillo G, Lynne C. Retrocaval ureter: report of 8 cases and the surgical management. *J Urol* 1979;121:514-517

Osteomyelitis of the Foot in Diabetic Patients: Evaluation with Plain Film, ^{99m}Tc -MDP Bone Scintigraphy, and MR Imaging

William T. C. Yuh¹
 John D. Corson²
 Henry M. Baraniewski²
 Karim Rezai¹
 Asad R. Shamma²
 Mary H. Kathol¹
 Yutaka Sato¹
 Georges Y. El-Khoury¹
 Donald R. Hawes¹
 Charles E. Platz³
 Reginald R. Cooper⁴
 Robert J. Corry²

Diagnosis of osteomyelitis of the foot in diabetic patients may be difficult because of the coexistence of chronic cellulitis, vascular insufficiency, and peripheral neuropathy. This study compared the diagnostic accuracies of plain films, bone scans, and MR imaging studies in diabetic patients with suspicion of osteomyelitis of the foot. Twenty-nine plain radiographs, 20 bone scans, and 30 MR studies were obtained in 24 patients. Twenty-nine bones from 14 patients were pathologically proved either positive (25 bones) or negative (four bones) for osteomyelitis. Another 15 bones (10 patients) studied with MR had no pathologic proof, but the bones healed with only local wound care and/or a short course of oral antibiotics. These patients had trauma, cellulitis, or unhealed ulcers. The sensitivity and specificity of plain films were both 75%. Bone scans had a very low specificity (100% false-positive rate). A negative bone scan should strongly exclude the probability of osteomyelitis. Unlike the findings in previous reports, MR had much higher sensitivity and specificity than bone scans in detecting osteomyelitis in diabetic patients. When the 10 patients without pathologic proof (those who presumably had neuroarthropathy, vascular insufficiency, and/or cellulitis) were included, the sensitivity and specificity of all three techniques decreased.

Our experience with this small group of patients suggests that MR is a useful imaging technique for diagnosing osteomyelitis of the foot in diabetic patients.

The diagnosis of osteomyelitis of the foot in patients with diabetes is often difficult to establish. The radiographic changes frequently are subtle or obscured by superimposed destructive processes such as peripheral neuroarthropathy.

To determine the value of MR for detecting osteomyelitis of the foot in diabetic patients, we correlated the MR findings in 24 patients with the pathologic findings and the results of other imaging tests.

Materials and Methods

Twenty-nine plain radiographs, 20 technetium-99m methylene diphosphonate (^{99m}Tc -MDP) bone scans, and 30 MR studies of the foot were obtained in 24 consecutive diabetic patients (age range, 32–74 years; mean, 58.2 years). These patients had clinical suspicion of osteomyelitis and/or nonhealing foot ulcers. All bone scans and plain films were obtained within 48 hr of the MR examinations.

Most MR examinations (28) were performed with a 0.5-T unit (Picker International, Highland Heights, OH) and the rest (two) were performed with a 1.5-T unit (Signa, General Electric Medical Systems, Milwaukee, WI). The imaging techniques included 5- to 7.5-mm T1- and T2-weighted pulse sequences parallel to the long axis of the foot (sagittal). T1-weighted 7.5- to 10-mm images were also obtained perpendicular to the long axis of the foot (axial). Sagittal short-tau inversion recovery (STIR) (2250–2450/125–150) scans with 5-mm-thick slices were obtained in 18 patients. We also evaluated lesion detectability among various techniques including T1-weighted, T2-weighted, and STIR pulse sequences. All studies were performed by using a head coil with the foot in neutral position (15°–30° external rotation). When studies were obtained with a 1.5-T unit, a 2.5-mm gap was used between each slice. Evidence of osteomyelitis seen on MR examination included low signal intensity on T1-weighted images

Received August 15, 1988; accepted after revision December 20, 1988.

Presented at the annual meeting of the American Roentgen Ray Society, San Francisco, CA, May 1988.

¹ Department of Radiology, The University of Iowa Hospitals and Clinics, Iowa City, IA 52242. Address reprint requests to W. T. C. Yuh.

² Department of Surgery, The University of Iowa Hospitals and Clinics, Iowa City, IA 52242.

³ Department of Pathology, The University of Iowa Hospitals and Clinics, Iowa City, IA 52242.

⁴ Department of Orthopaedic Surgery, The University of Iowa Hospitals and Clinics, Iowa City, IA 52242.

AJR 152:795–800, April 1989
 0361–803X/89/1524–0795
 © American Roentgen Ray Society

and high signal intensity on both STIR and T2-weighted images within the bone marrow of the suspected bone.

Triple-phase ^{99m}Tc -MDP bone scans were performed after IV injection of 20–25 mCi (740–925 MBq) of ^{99m}Tc -MDP. Criteria for positive scintigrams included increased blood flow and blood-pool activity (5 min) and abnormally increased intensity localized to the bone. The scintiscan was considered negative for osteomyelitis if the affected foot had only increased flow and blood-pool activity but minimal increased activity in the region of the bone on the delayed images. Routine plain films of the suspected bones with orthogonal views were obtained in 39 bones (24 positive osteomyelitis, four negative osteomyelitis, and 11 nonosteomyelitis). Criteria for positive plain films included permeated radiolucencies, destructive changes, and/or periosteal new-bone formation.

Four radiologists who did not know the results of other studies independently interpreted the MR studies, bone scans, and plain films retrospectively. Limited clinical information, including the site of symp-

toms and previous surgery, was provided. Different studies of each technique were interpreted at different sessions by each of the four radiologists. The results of the four radiologists' interpretations of each study were collated and disagreements were resolved in conference by all four radiologists without knowledge of pathologic reports or results from other techniques. Minor discrepancies occurred with one plain film, three bone scintiscans, and one MR study. All cases of positive or negative osteomyelitis had pathologic and/or bacteriologic proof.

Results

Twenty-nine bone specimens from 14 patients were obtained by either biopsy (six patients) or amputation (eight patients). All specimens were obtained within 48 hr of the last radiographic examination. Twenty-five of these were patho-

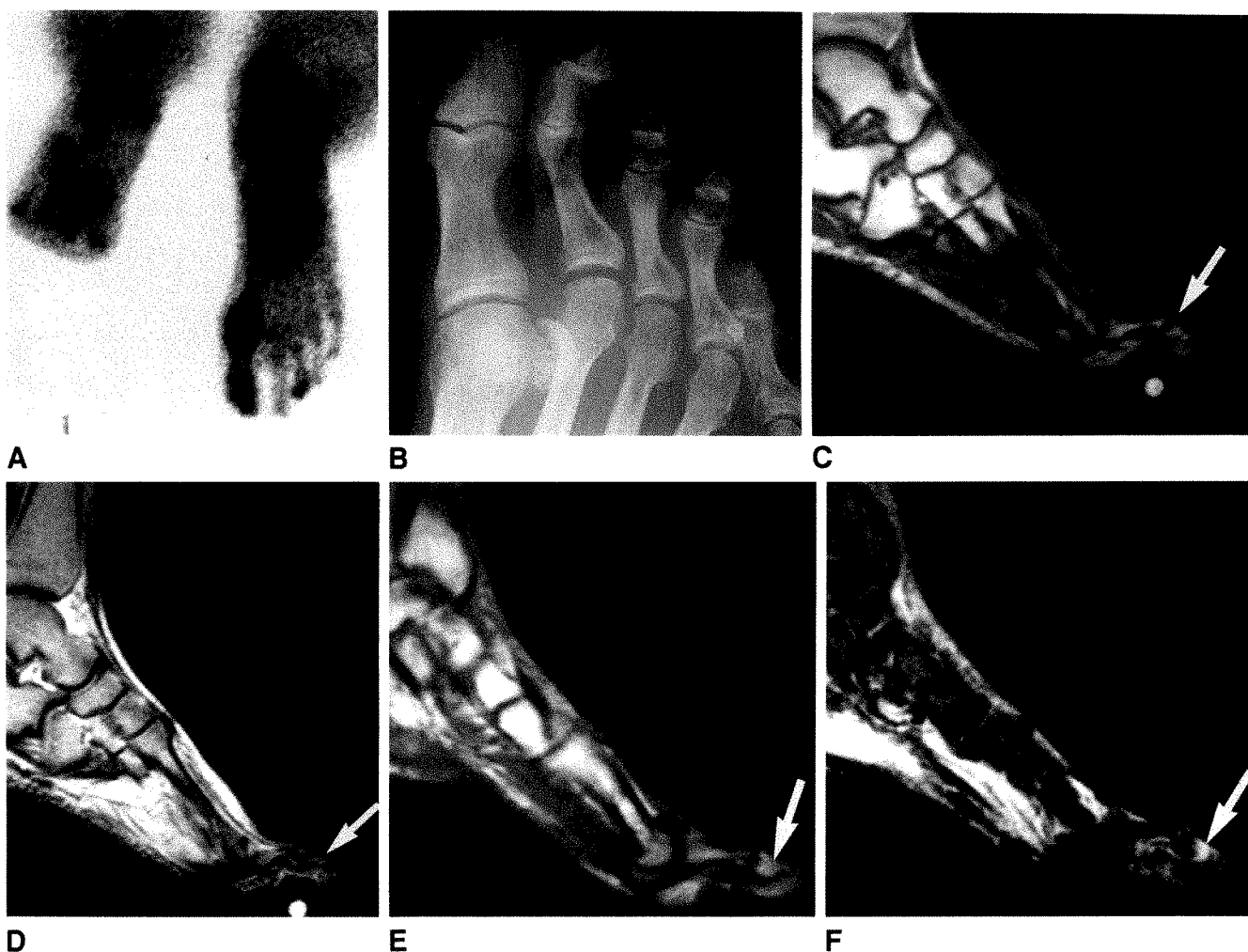


Fig. 1.—Cellulitis of third toe and neurotrophic changes of big toe in 55-year-old man. ^{99m}Tc -methylene diphosphonate (MDP) bone scintigram (A) shows increased uptake in region of first and third toes. Plain radiograph (B) shows essentially normal third toe and destructive changes of asymptomatic big toe. Findings in big toe are consistent with neurotrophic changes. MR of third toe (C and D, arrow) shows essentially normal bone-marrow signal on both T1-weighted (683/20) (C) and T2-weighted (2016/100) (D) images. High-signal bath-oil bead at ventral aspect of third toe is a marker for ulcer. MR of big toe also shows normal bone marrow on T1-weighted image (683/20) (E, arrow) and closely corresponding short-tau inversion recovery (STIR) image (2116/150) (F). Soft-tissue edema (F, arrow) around big toe near destructive area can be seen on STIR image. Abnormal signal in soft tissue on dorsal and plantar aspects of foot, best shown on T2-weighted (D) and STIR (F) images, occurs frequently in diabetic patients with or without evidence of infection.

logically positive for osteomyelitis (positive osteomyelitis) and four were negative (negative osteomyelitis). Fifteen bones (10 patients) had resolution of foot ulcers or cellulitis with only local wound care and/or a short course of oral antibiotics. These cases were considered clinically not to have osteomyelitis (nonosteomyelitis) because there was no pathologic proof of bone infection.

The MR examinations were correct (Figs. 1–4) in all 29 pathologically proved bones (25 positive osteomyelitis and four negative osteomyelitis). A negative MR study had characteristic normal bone-marrow signal on both T1- and T2-weighted images. MR signal intensity of osteomyelitis was similar to that of the surrounding soft-tissue edema on both STIR and T2-weighted images, and it was similar to that of muscle but higher than that of the tendon sheath on T1-weighted images. Osteomyelitis was better shown on both T1-weighted and STIR images than on T2-weighted images. MR had the best performance, followed by plain films, and

then bone scintiscans. The results of each diagnostic technique with respect to pathologically proved positive, negative, and nonosteomyelitis bones are summarized in Table 1. Both MR and bone scans had a very low false-negative rate in the diagnosis of osteomyelitis. The false-positive rate was highest for bone scans, followed by plain films. When cases of nonosteomyelitis were included (Table 1), there were increased false-positives in all three techniques, presumably caused by acute or recent trauma, soft-tissue infection, and/or vascular insufficiency. MR was not able to differentiate the abnormal bone-marrow signal caused by trauma (Fig. 5) from an infectious process in two of three patients with recent bony trauma (fracture or surgery). However, nine other subacute fractures presumably due to peripheral neuroarthropathy had normal MR signal in the bone marrow, despite abnormal bone scans and/or plain radiographs (Figs. 1 and 4).

Six follow-up examinations were performed on three patients with evidence of osteomyelitis and responsiveness to

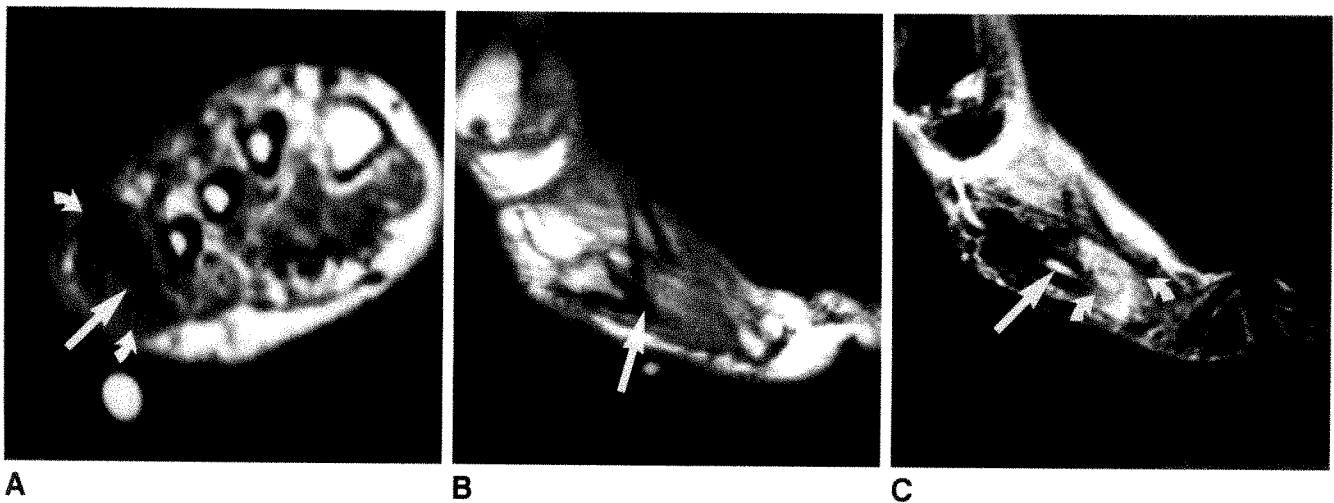


Fig. 2.—Osteomyelitis of fifth metatarsal in 62-year-old man. Abnormal bone-marrow signal (straight arrow) of distal fifth metatarsal is shown on the axial T1-weighted (483/20) (A), sagittal T1-weighted (683/20) (B), and sagittal short-tau inversion recovery (STIR) (2233/125) (C) images. Soft-tissue abscess (curved arrows) adjacent to osteomyelitis can also be seen on T1-weighted (A) and STIR (C) images, but is better shown on STIR image. Note suppressed fat signal within normal bone marrow on STIR image (C).

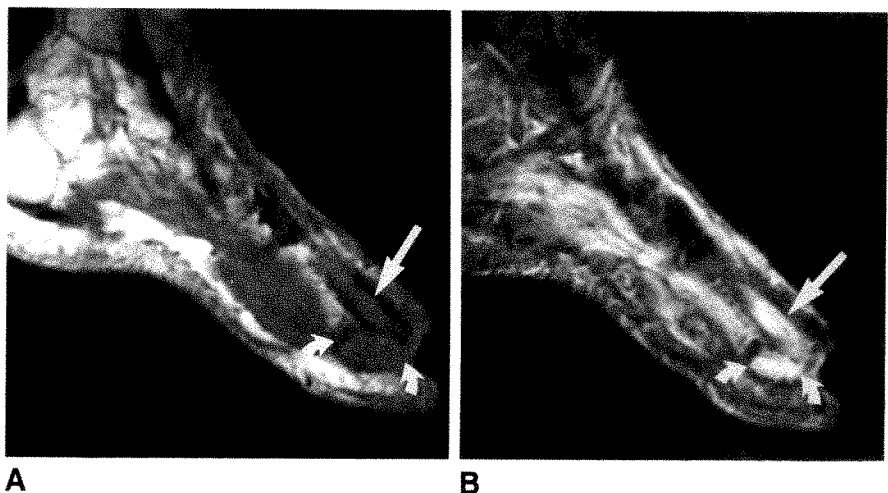


Fig. 3.—Recurrent osteomyelitis and abscesses in 46-year-old man. Osteomyelitis (straight arrow) and abscess (curved arrows) of metatarsal are readily shown on T1-weighted (683/20) (A) and T2-weighted (2016/100) (B) images. Abscess is better shown on T2-weighted image (B).

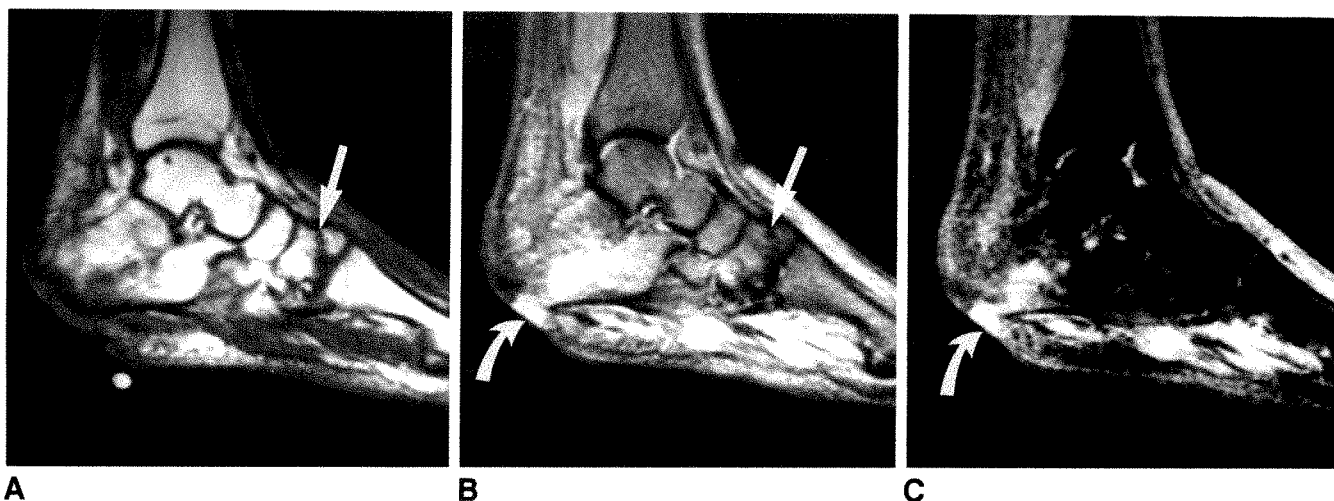


Fig. 4.—Old fracture and osteomyelitis of calcaneus with sinus tract in 38-year-old man. Abnormal calcaneus signal is shown on T1-weighted (583/20) (A), T2-weighted (2000/100) (B), and short-tau inversion recovery (2000/125) (C) images. Note sinus tract (curved arrow) extending from open wound into calcaneus. An old fracture (straight arrow), presumably due to peripheral neuropathy, shows normal bone-marrow signal in bony fragments on all pulse sequences.

TABLE 1: Results of Examinations Obtained with Each Technique in Positive, Negative, or Nonosteomyelitis Cases

Category (No. of Bones)	MR		Bone Scan		Plain Film	
	Positive	Negative	Positive	Negative	Positive	Negative
Positive osteomyelitis (25)	25/25	0/25	17/18	1/18	18/24	6/24
Negative osteomyelitis (4)	0/4	4/4	3/3	0/3	1/4	3/4
Nonosteomyelitis (15)	2/15	13/15	6/8	2/8	5/11	6/11

Note.—Results are expressed as number of positive or negative examinations/total number of bones examined.

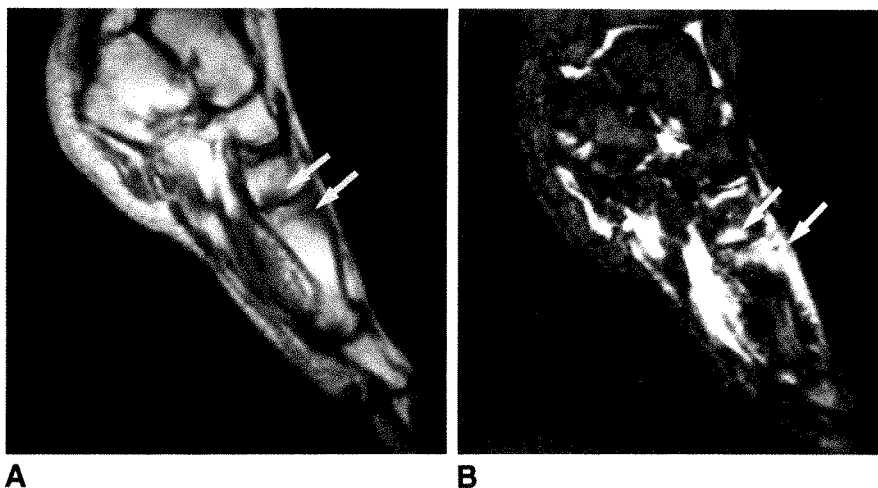


Fig. 5.—Presumed acute trauma (nonosteomyelitis) in 33-year-old woman. Patient recovered without treatment, and her symptoms were most likely caused by an acute fracture. Abnormal signal is shown at metatarsal head and cuboid (arrows) on both T1-weighted (683/20) (A) and short-tau inversion recovery (STIR) (2416/150) (B) images. MR findings of this patient cannot be differentiated from those of osteomyelitis. Small joint effusion can also be seen on STIR image (B).

IV antibiotic treatment. In spite of persistent abnormal signal intensity that lasted for several months, there was a significant decrease in the intensity of the abnormal signal in the bone marrow and the surrounding soft tissue on both T1- and T2-weighted images compared with that of the previous examination obtained during the acute infection.

Soft-tissue high signal intensity was noted frequently on STIR and T2-weighted images in the dorsal subcutaneous tissue and/or in the plantar fascia with or without evidence of

infection in many of these feet of diabetic patients (Figs. 1–5). The pattern of the abnormal signal within the soft tissue was frequently scattered in the dorsal subcutaneous tissue and diffuse and/or ill-defined in the plantar soft tissue. Small joint effusions also were seen frequently in patients with or without evidence of infection (Figs. 1, 4, and 5). Cellulitis could not be differentiated by MR from the soft-tissue edema that was frequently coexistent in this group of patients. Twelve soft-tissue abscesses were detected by MR and could be

differentiated from the soft-tissue edema or cellulitis by a smooth margin and higher signal intensity than that of the surrounding edema on STIR or T2-weighted images (Figs. 2 and 3). MR missed two relatively small abscesses (1.5 cm) on the plantar aspect because of their size and the reduced contrast between the abscess and the high-signal-intensity background. T1-weighted images, despite better sensitivity in detecting osteomyelitis than T2-weighted images, provided limited information about abscesses because of a lack of appreciable contrast between the abscess and the surrounding tissue and/or edema. Similarly, STIR images did not provide the superior contrast of the T2-weighted images in differentiating the abscess. The ^{99m}Tc -MDP radionuclide scans detected one large abscess, which showed a central photopenic area with peripheral increased uptake.

Discussion

Plain radiography with or without tomography is usually a sensitive technique for detecting osteomyelitis. However, the bony changes associated with osteomyelitis may not be seen on plain films for 7–15 days after the onset of the acute infectious process. Early subtle changes from acute osteomyelitis seen on plain film are not easily differentiated from other superimposed changes in feet of diabetic patients. CT has contributed significantly in the evaluation of musculoskeletal pathologic processes. However, CT of the feet may have some disadvantages because of limited soft-tissue contrast, lack of multiplanar ability compared with MR, and poor visualization of soft tissue adjacent to the bone due to beam-hardening artifacts. Radionuclide studies, including ^{99m}Tc -MDP bone scintigraphy, ^{111}In -labeled leukocyte scintigraphy, and ^{67}Ga -citrate scans, are also accurate and sensitive techniques for the detection of bone infection [1–7]. Because there is a lack of spatial resolution and direct visualization of bone marrow, the scintigraphic findings may be equivocal and it may be difficult to estimate the extent of involvement and to distinguish between soft-tissue infections and osteomyelitis [8–11]. Frequently, coexisting osseous pathologic processes, such as osteoarthropathy or diabetic neuroarthropathy, can also make radionuclide scintigraphy unreliable. Significant false-positive rates in diabetic patients have been reported by Maurer et al. [8] and Unger et al. [12].

Although the number of patients was small and pathologic correlation was limited, preliminary studies [12–20] reported that MR imaging had a high sensitivity and specificity in detecting osteomyelitis and provided more detailed information regarding the extent of involvement than did radionuclide studies. Our results were in part similar to those of Berquist et al. [17], who compared MR with CT and ^{111}In -labeled leukocyte scans and concluded that MR imaging was more accurate for the detection of infections involving bone or soft tissue than plain film or CT. They also concluded that MR was less helpful when compared with ^{111}In -labeled leukocyte images in the evaluation of patients who had recently undergone surgery [17].

Recent reports by Beltran et al. [16, 19] also showed no significant differences between MR imaging and bone/gallium radionuclide studies in detecting uncomplicated osteomyelitis in both human and animal studies. We had similar results,

except that we observed a significantly higher false-positive rate with bone scans in our series. One explanation for this is that diabetic osteomyelitis is not usually the result of hematogenous spread, but is a secondary infection from soft-tissue spread. The relatively chronic changes of the soft tissue and/or bone caused by either infection, vascular insufficiency, or peripheral neuropathy in feet of diabetic patients can add significantly to the false-positive rate of bone scans. Similar difficulty in detecting osteomyelitis in feet of diabetic patients may also be encountered, but to a lesser degree, in plain film and CT.

MR had the lowest false-positive rate compared with those of bone scans and radiographs in our series. MR can visualize bone marrow directly, which significantly reduces the false-positive rate and therefore improves the sensitivity and specificity. Our false-positive rate with MR was even lower than that reported by Beltran et al. [19], who evaluated their experimental infection in an animal model. One possible explanation was the trauma caused by injection of the bone with either sterile or contaminated fluid in their animal model. Similar to plain film and CT, MR cannot differentiate the abnormal signal caused by acute trauma from that of osteomyelitis. Presumably, a significant change in the water content of bone marrow is produced by both processes. However, chronic fractures in our series showed no significant increase in MR signal intensity within the bone marrow. This is presumably because of resolution of the local edema produced during acute trauma. A similar mechanism also may account for the decrease of abnormal signal within the bone marrow in the follow-up examination in patients with clinical evidence of improvement after IV antibiotic treatment.

In our limited experience, a significant number of patients with or without infections had abnormal soft-tissue signals and small joint effusions best shown on STIR and T2-weighted images. The exact cause of this fluid is unknown. The mechanism of ulcer formation in the plantar aspect of the foot in diabetic patients is usually related to the uneven distribution of body weight caused by peripheral neuropathy similar to that of decubitus ulcer formation. The diffusely abnormal accumulation of fluid in the soft tissue in the plantar aspect of the foot in diabetic patients may be related in part to the same mechanism of ulcer formation, with resultant stasis and fluid accumulation. The scattered pattern of the abnormal signal on the dorsal aspect of the foot may be explained by random traumatic episodes due to the peripheral neuropathy as opposed to the uneven weight distribution in the plantar aspect. Peripheral neuropathy may also be the cause of the frequently seen small joint effusion. Other possible causes of abnormal signal in the soft tissue include soft-tissue infection and vascular insufficiency.

Our results are similar to those of Beltran et al. [16, 19] and Unger et al. [12], who reported that MR could be used to distinguish soft-tissue disease from bone-marrow disease and abscess from cellulitis. However, we encountered more difficulty in some of our diabetic patients because of reduced contrast between the abscess and the frequently coexistent abnormal signal in the soft tissue. This is especially true for a small abscess in the plantar aspect of the foot in diabetic patients. Nevertheless, we found that MR is more sensitive

than plain films and bone scans in detecting abscesses. The three diagnostic techniques may not always be able to differentiate cellulitis from noninfectious edema, as shown in previous reports [12,16,19].

In our experience with MR, osteomyelitis is best shown by T1 and STIR imaging. The contrast between osteomyelitis and the surrounding abnormal soft-tissue signal may not be as distinct in the relatively T2-weighted image as it is in the STIR and T1-weighted images. Abscesses, however, are better shown on T2-weighted images than on STIR and T1-weighted images. On STIR pulse sequences, the surrounding abnormal signal in the soft tissue has extremely high signal intensity, which may obscure the abscess. Similarly, very poor contrast between abscess and soft tissue was noted on T1-weighted images. In the feet of diabetic patients, the small field of view in MR does not appear to be a significant limiting factor because the entire foot can be examined easily with the use of a head coil, which also significantly improves the resolution and signal-to-noise ratio.

Our study comprised a retrospective evaluation of the MR, bone scan, and plain film examinations that were performed within a 3-day period before surgery in 24 patients, not all of whom underwent all three examinations. The majority of our osteomyelitis patients had serious and complicated foot infection involving the bone and soft tissues, and coexistent bony changes caused by trauma or diabetic neuroarthropathy. This patient profile may have been responsible in part for the high sensitivity and specificity of MR and the relatively high false-positive rate of ^{99m}Tc -MDP bone imaging reported in this series. We did not include ^{67}Ga or ^{111}In -leukocyte imaging studies, which appear to be essential for decreasing a false-positive outcome by scintigraphy. Bone scintigraphy undoubtedly is the technique of choice for whole-body imaging when hematogenously spread osteomyelitis is suspected. Our findings indicate that MR is an extremely useful technique for assessing osteomyelitis in localized regions of the skeleton such as the foot of a diabetic patient. The ultimate role of MR in the diagnosis of osteomyelitis has to be defined by further studies, with a larger number of patients and more imaging techniques such as CT scan, gallium scan, and/or ^{111}In -WBC scan with single-photon emission CT.

ACKNOWLEDGMENTS

The authors gratefully acknowledge Phyllis Bergman and Linda Mohr for their assistance in manuscript preparation.

REFERENCES

1. Park HM, Wheat LJ, Siddiqui AR, et al. Scintigraphic evaluation of diabetic osteomyelitis: concise communication. *J Nucl Med* 1982; 23:569-573
2. Seldin DW, Heiken JP, Feldman F, Alderson PO. Effect of soft-tissue pathology on detection of pedal osteomyelitis in diabetes. *J Nucl Med* 1985; 26:988-993
3. Lisbona R, Rosenthal L. Observations on the sequential use of ^{99m}Tc -phosphate complex and ^{67}Ga imaging in osteomyelitis, cellulitis, and septic arthritis. *Radiology* 1977; 123:123-129
4. Gilday DL, Eng B, Paul DJ, Paterson J. Diagnosis of osteomyelitis in children by combined blood pool and bone imaging. *Radiology* 1975; 117:331-335
5. Duszynski DO, Kuhn JP, Afshani E, Riddlesberger MM Jr. Early radionuclide diagnosis of acute osteomyelitis. *Radiology* 1975; 117:337-340
6. Reba RC, Chandeysson PL. Imaging infection with indium 111-labeled leukocytes. In: Takor ML, ed. *Radiolabeled cellular blood elements: pathophysiology, techniques, and scintigraphic applications*. New York: Plenum, 1985:305-318
7. Sfakianakis GN, Al-Sheikh W, Heal A, Rodman G, Zeppa R, Serafini A. Comparison of scintigraphy with In-111 leukocytes and Ga-67 in the diagnosis of occult sepsis. *J Nucl Med* 1982; 23:618-626
8. Maurer AH, Millmond SH, Knight LC, et al. Infection in diabetic osteoarthropathy: use of indium-labeled leukocytes for diagnosis. *Radiology* 1986; 161:221-225
9. Gilday DL. Problems in the scintigraphic detection of osteomyelitis. *Radiology* 1980; 135:791
10. Garnett ES, Cockshott WP, Jacobs J. Classical acute osteomyelitis with a negative bone scan. *Br J Radiol* 1977; 50:757-760
11. Handmaker H. Acute hematogenous osteomyelitis: has the bone scan betrayed us? *Radiology* 1980; 135:787-789
12. Unger E, Moldofsky P, Gatenby R, Hartz W, Broder G. Diagnosis of osteomyelitis by MR imaging. *AJR* 1988; 150:605-610
13. Smith FW, Runge V, Permezel M, Smith CC. Nuclear magnetic resonance (NMR) imaging in the diagnosis of spinal osteomyelitis. *Magn Reson Imaging* 1984; 2:53-56
14. Fletcher BD, Scoles PV, Nelson AD. Osteomyelitis in children: detection by magnetic resonance. *Radiology* 1984; 150:57-60
15. Modic MT, Feiglin DH, Piraino DW, et al. Vertebral osteomyelitis: assessment using MR. *Radiology* 1985; 157:157-166
16. Beltran J, Noto AM, McGhee RB, Freedy RM, McCalla MS. Infections of the musculoskeletal system: high-field-strength MR imaging. *Radiology* 1987; 164:449-454
17. Berquist TH, Brown ML, Fitzgerald RH Jr, May GR. Magnetic resonance imaging: application in musculoskeletal infection. *Magn Reson Imaging* 1985; 3:219-230
18. Tang JSH, Gold RH, Bassett LW, Seeger LL. Musculoskeletal infection of the extremities: evaluation with MR imaging. *Radiology* 1988; 166:205-209
19. Beltran J, McGhee RB, Shaffer PB, et al. Experimental infections of the musculoskeletal system: evaluation with MR imaging and Tc-99m MDP and Ga-67 scintigraphy. *Radiology* 1988; 167:167-172
20. Quinn SF, Murray W, Clark RA, Cochran C. MR imaging of chronic osteomyelitis. *J Comput Assist Tomogr* 1988; 12:113-117

Voiding Cystourethrography as a Predictor of Reflux Nephropathy in Children with Urinary-Tract Infection

Mikael Hellström^{1,2}
Bo Jacobsson³
Staffan Mårild⁴
Ulf Jodal⁴

Most children who develop renal damage (scarring) after urinary-tract infection have vesicoureteral reflux. Voiding cystourethrography is therefore usually recommended as the initial radiologic study in children with urinary-tract infection. However, renal damage may occur also in the absence of reflux. The aim of this investigation was to determine the sensitivity and predictive value of reflux during voiding cystourethrography in identifying children at risk for renal damage. Eighty-four consecutive children, 2 months to 6 years old, with nonobstructive, first-known, febrile urinary-tract infection underwent voiding cystourethrography and urography. Twenty-seven (32%) had reflux and 10 (12%) had or developed renal damage. Two of the children and four of the kidneys with renal damage had no reflux at initial examination. The sensitivity of reflux as a marker for renal damage was 80%, specificity was 74%, positive predictive value was 30%, and negative predictive value was 96%.

Thus, most children who develop renal damage after urinary-tract infection have reflux during voiding cystourethrography. However, there is a risk, albeit small, for renal damage to occur in the absence of reflux.

Symptomatic urinary-tract infection during childhood occurs in 3–5% of girls and 1–2% of boys [1]. Renal damage (scarring), also termed reflux nephropathy, develops in 5–15% of these children. The main objective is to identify those at risk for development of renal damage early enough to institute effective preventive measures. Much interest has been focused on defining the optimal radiologic workup [2–5], including new imaging methods like renal sonography and scintigraphy (isotope cystography and renal scintigraphy). The central role of vesicoureteral reflux and intrarenal reflux in the development of renal damage in children with urinary-tract infection is well recognized, as stressed by Smellie et al. [6] and Smellie and Normand [7], who have stated that renal damage is almost always associated with vesicoureteral reflux. It has therefore been suggested that voiding cystourethrography (VCUG) be the initial radiologic study in children with urinary-tract infection and that those with reflux should be selected for more thorough workup [3]. However, it seems appropriate to consider the risk of developing similar renal damage after urinary-tract infection in the absence of reflux. Otherwise, the sensitivity and predictive value of such a diagnostic approach cannot be estimated. The aim of this study was to provide such data on the basis of a prospective, consecutive, epidemiologic study of children with febrile urinary-tract infection.

Subjects and Methods

All children from 2 months to 6 years old who had their first known episode of febrile urinary-tract infection diagnosed at the Children's Hospital in Gothenburg from September 1979 to May 1981 were enrolled in this study. The inclusion criteria were fever (body temperature $\geq 38.5^{\circ}\text{C}$) and bacteriuria. Bacteriuria was diagnosed as ≥ 1000 bacteria/ml urine in samples obtained by suprapubic aspiration ($n = 52$), or as $\geq 100,000$ bacteria/ml of identical

Received June 14, 1988; accepted after revision December 12, 1988.

This work was supported by grants from the Gothenburg Medical Society.

¹ Department of Radiology, Sahlgren's Hospital, 41345 Gothenburg, Sweden. Address reprint requests to M. Hellström.

² Present address: Department of Radiology, King Faisal Specialist Hospital and Research Centre, P.O. Box 3354, Riyadh 11211, Saudi Arabia.

³ Department of Radiology, King Faisal Specialist Hospital and Research Centre, P.O. Box 3354, Riyadh 11211, Saudi Arabia.

⁴ Department of Pediatrics, East Hospital, 41685 Gothenburg, Sweden.

AJR 152:801–804, April 1989

0361–803X/89/1524–0801

© American Roentgen Ray Society

strains in two midstream or urine-bag samples ($n = 30$), or as $\geq 100,000$ bacteria/ml in urine obtained by one midstream or urine-bag sample along with a positive nitrite test ($n = 6$). Of 50 children under 1 year of age, 41 were diagnosed by suprapubic aspiration. Leukocyturia of at least 50 cells/ml unspun urine occurred in 87 children (median, 750 cells/ml). No cases with neurogenic urinary-tract abnormalities were included.

A total of 88 children (65 girls and 23 boys) fulfilled the criteria. The median age at inclusion was 10 months (range, 2–70 months). Informed consent was obtained from the parents of all but one child who consequently did not participate in the investigation. One child had no VCUG performed; one had urethral valve stenosis and one had distal ureteral stenosis and both were, therefore, excluded. Thus, 84 children remained for analysis. The combination of bacteriuria (*Escherichia coli* in all cases), fever, elevated C-reactive protein, and reduced concentrating capacity made it likely that these patients had acute pyelonephritis at the time of inclusion in the study [8]. In children under 1 year of age, blood was obtained for culture; only one of 45 had growth of bacteria (*E. coli*). According to the local tradition, most patients with febrile urinary-tract infection are handled at the Children's Hospital, and an estimated 90% of all children in Gothenburg with this type of infection during the inclusion period participated in the study. Management of patients was standardized by a detailed study protocol on diagnostic workup, antibiotic treatment, follow-up schedule, and other aspects of management. All children were immediately given appropriate antibiotic treatment for 10 days.

VCUG was performed according to a standardized procedure, adhering to the recommendations of the International Reflux Study in Children [9], using drip infusion of contrast medium by gravity from a standardized height. Intermittent fluoroscopy with an image inten-

sifier and 70-mm film for documentation was used during bladder filling and voiding. Reflux was graded according to the International Reflux Study in Children [9].

Urography was performed according to a standardized procedure [10]. Renal damage (scarring) was defined as reduction of parenchymal thickness with or without caliceal deformity [11]. Radiographs were evaluated jointly by two radiologists without knowledge of presence of reflux.

The radiologic workup (VCUG and urography) was as follows: (1) in association with the febrile urinary-tract infection, after normalization of body temperature: VCUG ($n = 84$) and urography ($n = 84$); (2) after approximately 6 months: VCUG ($n = 61$) and urography ($n = 80$); (3) after 2.2 years or more: VCUG ($n = 22$) and urography ($n = 77$).

Results

The initial VCUG showed reflux in 27 (32%) of 84 children. Renal damage, in the absence of urinary-tract obstruction, occurred in 10 (12%) of the 84. In three children, the renal damage was documented at initial urography, and in seven children it was documented at follow-up after 2.3–4.1 years (median, 3 years) (Figs. 1 and 2). Eight of the children with renal damage had reflux, whereas two showed no reflux at VCUG.

In total, 13 renal units showed signs of damage. Of these, one had grade-one reflux, three had grade two, five had grade three, and four had no reflux. The four renal units without reflux did not show renal damage at initial urography, and all

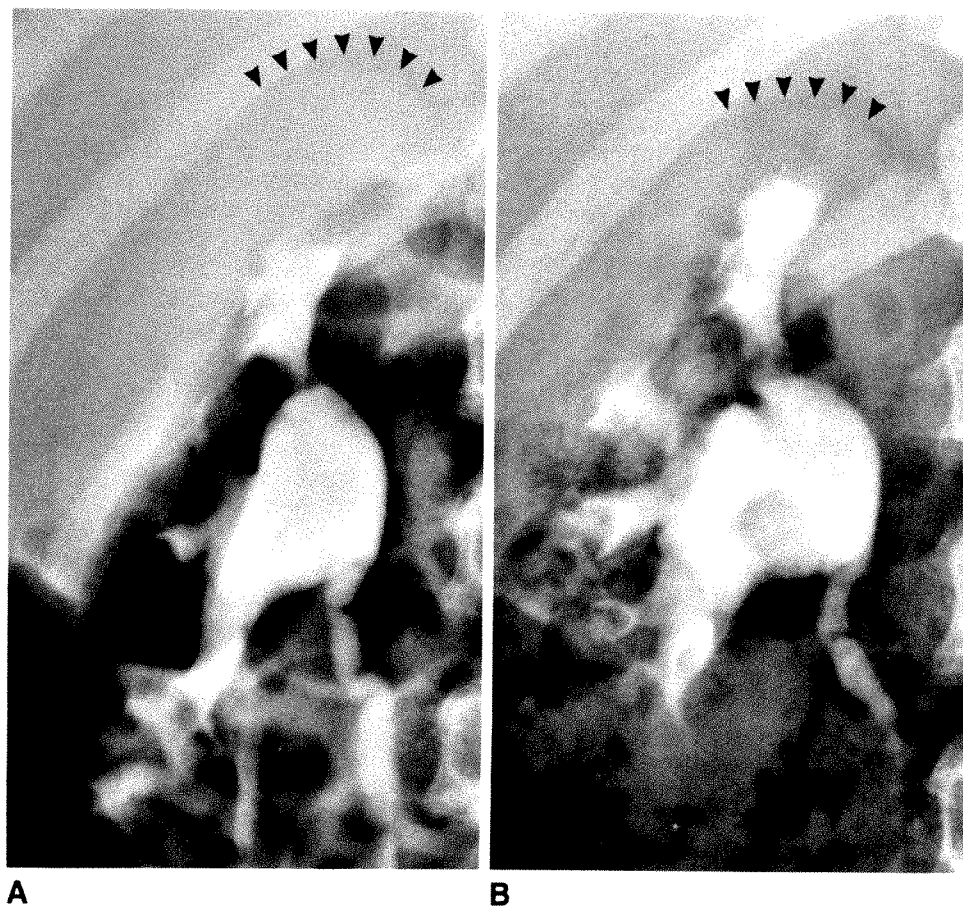
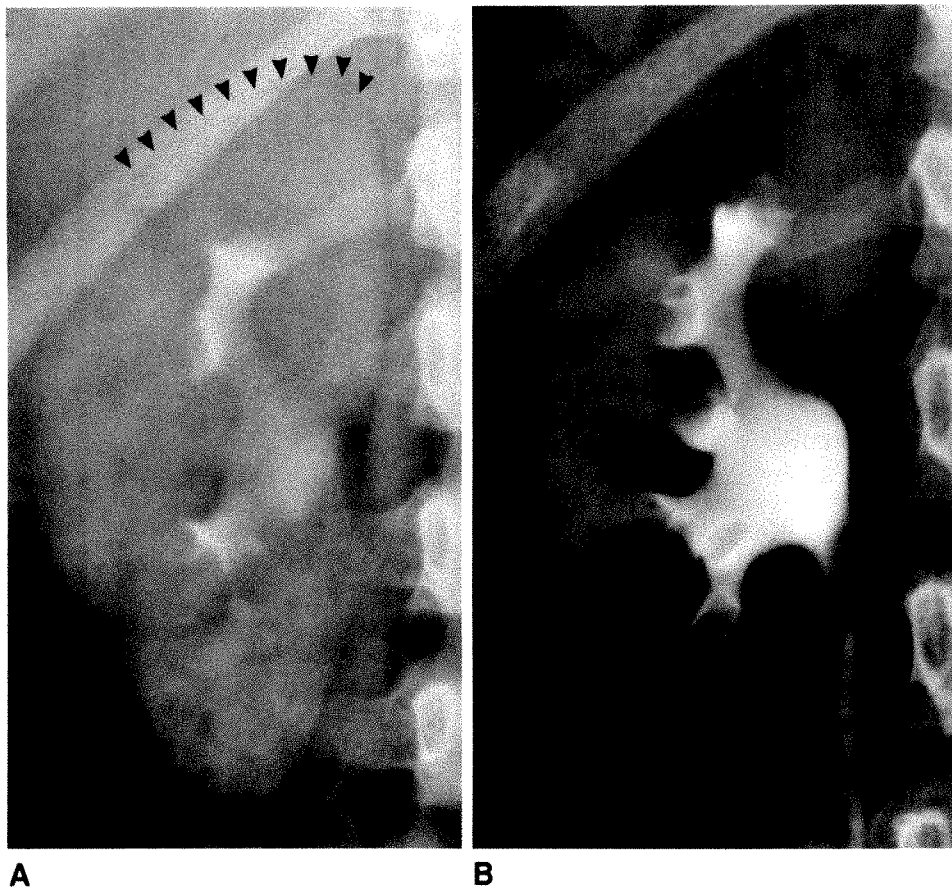


Fig. 1.—Girl with first known urinary-tract infection at 5 years of age. Urography in association with the infection and 7 months later (A) showed normal right upper pole (arrowheads). At follow-up 3 years after infection (B), marked parenchymal reduction (arrowheads) and calyceal clubbing have developed. No reflux was shown on initial voiding cystourethrogram (VCUG). Follow-up VCUG 7 months after infection showed grade-one reflux.

Fig. 2.—Girl with first known urinary-tract infection at 4 years of age. Urography in association with the infection and 6 months later (A) showed normal right upper pole (arrowheads). At follow-up 2.5 years and 4 years (B) after infection, parenchymal reduction in upper pole has developed (arrowheads). No reflux was shown on initial voiding cystourethrogram (VCUG), nor on follow-up VCUGs 7 months and 2.5 years after infection.



were subjected to one or two subsequent VCUGs, which showed no reflux in three renal units and grade-one reflux in one.

If the occurrence of reflux at the initial VCUG was used as a marker for renal damage, the sensitivity was 80%, the specificity 74%, the positive predictive value 30%, and the negative predictive value 96%.

Discussion

The frequency of reflux in the present study of children with nonobstructive, febrile urinary-tract infection was 32%, which is in agreement with previous studies [12, 13]. The proportion of children with renal damage was 10 of 84 (12%). Previous studies have shown renal damage of similar frequency: Winberg et al. [13] found 6.4%; Segura et al. [14] and Smellie et al. [12] found 15%.

Eight of the 10 children (80%) in the present study in whom renal damage developed despite therapy had reflux. However, the majority (70%) of treated children with reflux did not develop renal damage.

Renal damage was infrequent in children without reflux, two (4%) of 57 children. Still, two of 10 children and four of 13 kidneys that developed such damage did not have reflux at initial examination. Segura et al. [14] also found that 20% of the children with urinary-tract infection who developed

scarring had no reflux, and in fact, the corresponding frequency was 15% in the study by Smellie et al. [12]. In an epidemiologic study of boys 1–12 months old who had urinary-tract infection, Bergström et al. [15] found that in five boys who developed renal scarring, three (60%) had no reflux.

Cavanagh and Sherwood [2] stated that mild and moderate reflux did not appear important in the context of renal damage. However, in the present study eight of 13 damaged kidneys had either no reflux or only nondilating reflux (less than grade three). This is in good agreement with Winberg et al. [16], who, in an epidemiologic long-term follow-up study of about 600 children, found that two-thirds of those with scarring had either no reflux or nondilating reflux.

These findings may be explained by the presence of *E. coli* bacteria that can bind to specific receptors on uroepithelial cells, so called P-fimbriated bacteria. In studies on monkeys, Roberts et al. [17, 18] showed that such bacteria caused ureteral malfunction, whereas nonadhering bacteria did not. It was proposed that in humans, renal infection may be caused by P-fimbriated bacteria that ascend into the ureter either by the turbulent flow at the orifice or by mild reflux. By attaching to receptors in the mucosa, preventing washout with the urinary flow, the bacteria could persist and induce ureteritis leading to functional disturbance of the ureter, thus facilitating the introduction of bacteria into the kidney. This hypothesis is supported by the finding of a significant correlation between ureteral dilatation and bacterial adherence in nonrefluxing

children with febrile urinary-tract infection, as well as in infants with asymptomatic bacteriuria [19].

In the present study, four normal-appearing renal units without reflux at the first examination developed renal damage (Figs. 1 and 2). In three of them, repeated VCUGs failed to reveal any reflux, whereas the fourth one had a grade-one reflux at follow-up. The possibility that reflux was an important causal factor in the development of renal damage therefore seems remote in these cases.

Another possible route for bacteria to reach the kidney is by the bloodstream. In the present study, hematogenous spread seemed unlikely also, as only one of 45 infants had a positive blood culture, and none of the older children showed clinical signs of sepsis.

As the time required for a detectable renal scar to develop usually is several months, and may be up to 2 years for complete development [20], urography or renal sonography frequently is interpreted as normal in the initial radiologic workup after childhood urinary-tract infection. Thus, normal VCUG, in combination with normal urography or sonography does not conclusively prove the patient is free from risk of renal damage. The final outcome in these cases can only be determined by delayed examination of the kidney.

The term reflux nephropathy was introduced in the 1970s to focus on the significance of reflux in the development of renal damage [21,22]. There is, however, an inherent risk in using this term; children who do not have reflux but who develop renal damage after urinary-tract infection may be overlooked.

REFERENCES

1. Jodal U, Winberg J. Management of children with unobstructed urinary tract infection. *Pediatr Nephrol* **1987**;1:647-656
2. Cavanagh PM, Sherwood T. Too many cystograms in the investigation of urinary tract infection in children? *Br J Urol* **1983**;55:217-219
3. Blickman JG, Taylor GA, Lebowitz RL. Voiding cystourethrography: the initial radiologic study in children with urinary tract infection. *Radiology* **1985**;156:659-662
4. Haycock G. Investigation of urinary tract infection. *Arch Dis Child* **1986**;61:1155-1158
5. Lebowitz RL, Mandell J. Urinary tract infection in children: putting radiology in its place. *Radiology* **1987**;165:1-9
6. Smellie JM, Edwards D, Hunter N, Normand ICS, Prescod N. Vesico-ureteric reflux and renal scarring. *Kidney Int* **1975**;8:65-72
7. Smellie JM, Normand ICS. Urinary infections in children 1985. *Postgrad Med J* **1985**;61:895-905
8. Jodal U, Lindberg U, Lincoln K. Level diagnosis of symptomatic urinary tract infection in childhood. *Acta Paediatr Scand* **1975**;64:201-208
9. International Reflux Study in Children. International system of radiographic grading of vesicoureteric reflux. *Pediatr Radiol* **1985**;15:105-109
10. Hellström M, Hjälmås K, Jacobsson B, Jodal U, Oden A. Normal ureteral diameter in infancy and childhood. *Acta Radiol [Diagn] (Stockh)* **1985**;26:433-439
11. Hodson CJ. The radiological contribution toward the diagnosis of chronic pyelonephritis. *Radiology* **1967**;88:857-871
12. Smellie JM, Hodson CJ, Edwards D, Normand ICS. Clinical and radiological features of urinary infection in childhood. *Br Med J* **1964**;2:1222-1226
13. Winberg J, Andersen HJ, Bergström T, Jacobsson B, Larson H, Lincoln K. Epidemiology of symptomatic urinary tract infection in childhood. *Acta Paediatr Scand [Suppl]* **1974**;252:1-20
14. Segura JW, Kelalis P, Stickler G, Burke E. Urinary tract infection in children: a retrospective study. *J Urol* **1971**;105:591-593
15. Bergström T, Jacobsson B, Larson H, Lincoln K, Winberg J. Symptomatic urinary tract infection in boys in the first year of life with special reference to scar formation. *Infection* **1973**;1:192-199
16. Winberg J, Bollgren I, Källén G, Möllby R, Svenson SB. Clinical pyelonephritis and focal renal scarring. A selected review of pathogenesis, prevention and prognosis. *Pediatr Clin North Am* **1982**;29:801-814
17. Roberts JA, Kaach B, Källén G, Möllby R, Winberg J, Svenson S. Receptors for pyelonephritogenic *Escherichia coli* in primates. *J Urol* **1984**;131:163-168
18. Roberts JA, Suarez G, Kaach B, Källén G, Svenson S. Experimental pyelonephritis in the monkey. VII. Ascending pyelonephritis in the absence of vesicoureteral reflux. *J Urol* **1985**;133:1068-1075
19. Mård S, Wettergren B, Hellström M, et al. Bacterial virulence and inflammatory response in infants with febrile urinary tract infection or screening bacteriuria. *J Pediatr* **1988**;112:348-354
20. Filly R, Friedland GW, Govan DE, Fair WR. Development and progression of clubbing and scarring in children with recurrent urinary tract infections. *Radiology* **1974**;113:145-153
21. Bailey R. The relationship of vesico-ureteric reflux to urinary tract infection and chronic pyelonephritis-reflux nephropathy. *Clin Nephrol* **1973**;1:132-141
22. Heale WF, Weldon AP, Hewstone AS. Reflux nephropathy: presentation of urinary tract infection in childhood. *Med J Aust* **1973**;1:1138-1140

Case Report

MR Imaging of Coronary Artery Aneurysms in a Child with Kawasaki Disease

George S. Bisset III,¹ Janet L. Strife,¹ and John McCloskey²

In Kawasaki disease, early attention was focused on prompt recognition, acute management, and efforts to determine the origin. As knowledge of the disease has evolved, it has become evident that the major mortality arises from complications of coronary artery aneurysm formation.

The utility of cardiac MR imaging, when coupled with an ECG gating system, has been well documented [1-4]. In a recent report describing the use of MR imaging for evaluating the anatomy of the normal aortic root and major proximal portions of the coronary arteries in adults [2], questions were raised concerning its limitations. However, there is evidence for application of this noninvasive imaging technique in selected clinical situations. We describe the use of MR imaging for evaluating coronary artery aneurysms in a child with Kawasaki disease.

Case Report

The patient was a 7-month-old boy with typical clinical features of Kawasaki disease. Two-dimensional echocardiogram, performed 1 week after the onset of the symptoms, revealed multiple right and left coronary artery aneurysms. Selective right and left coronary angiography and left ventriculography were performed the next day. Figures 1A and 1B are representative views from the left and right coronary angiograms, respectively. Multiple giant aneurysms were identified in both coronary arteries. Flow in both vessels was stagnant, without evidence of thrombosis.

On the subsequent day, cardiac MR imaging was done. MR scanning was performed with a General Electric 1.5-T Signa system with the use of a spin-echo technique. The patient was sedated before the examination with chloral hydrate (80 mg/kg) by mouth. Images were obtained during ECG gating with a 256×128 pixel matrix size. The TE was 20 msec, and the TR was based on the R-R interval of the ECG tracing (480 msec). All scans were 3-5 mm thick with 1-mm interslice gaps. Initial sagittal localizing scans were obtained through the midline, after which nonangled axial scans were obtained from the apex of the heart to the proximal ascending aorta (Figs. 1C and 1D). Coronal scans were then obtained through the aortic root. The patient was treated with aspirin and discharged.

Three weeks later, the patient returned to the emergency room with marked irritability. Repeat two-dimensional echocardiogram revealed thrombi in the proximal right and left coronary arteries. Repeat MR (Figs. 1E and 1F) with identical techniques showed thrombi in the aneurysms in proximal left and right coronary arteries. A coronal scan (Fig. 1G) showed thrombosed aneurysms in the axillary arteries as well.

We have had success in imaging coronary aneurysms with MR imaging in three additional cases, one of which is illustrated (Fig. 2).

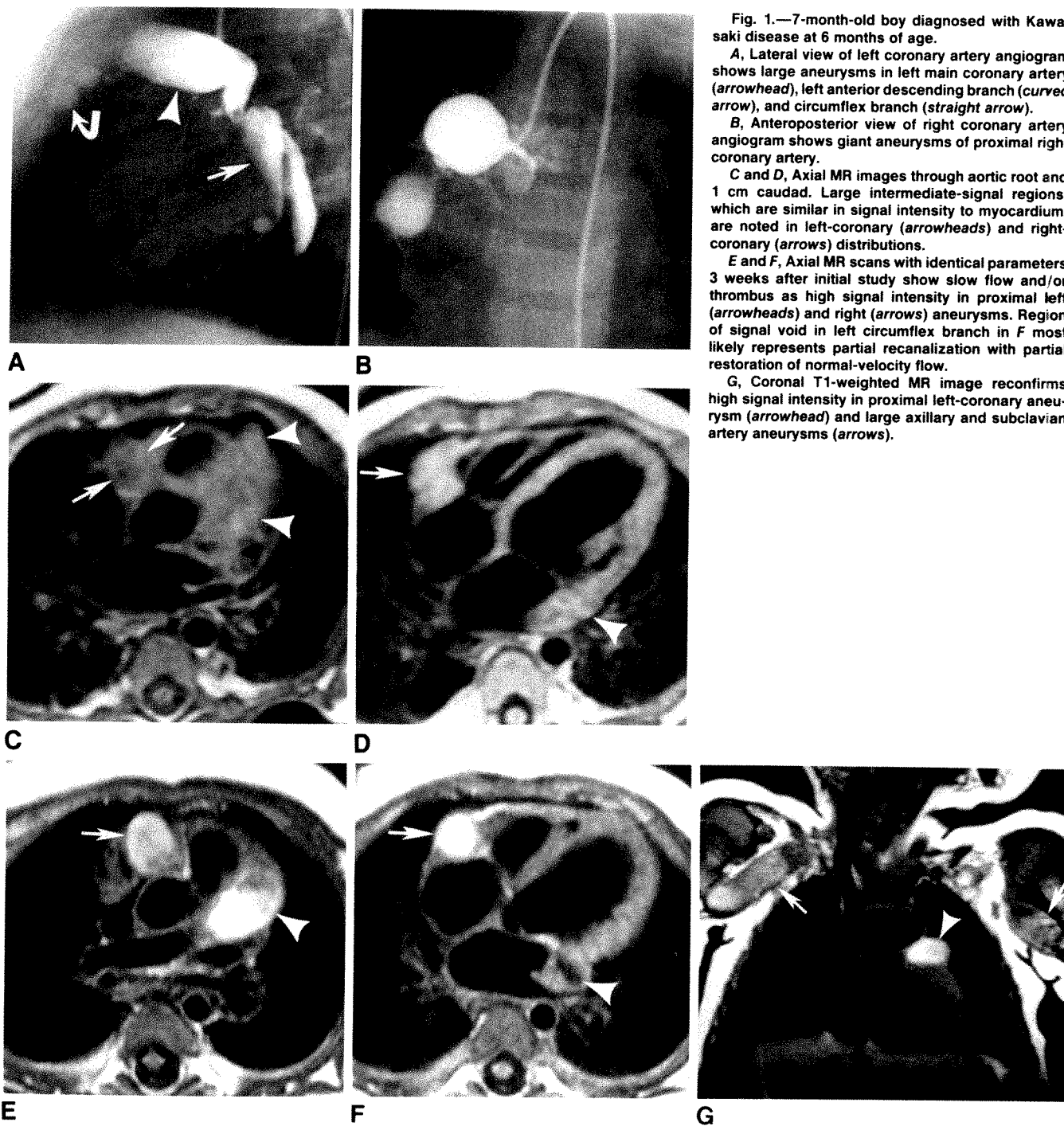
Discussion

Kawasaki disease was initially described in 1967 [4]. Since then, there has been a marked increase in the incidence of this disease, perhaps related to better recognition [5]. The major complication leading to morbidity and mortality is the

Received August 12, 1988; accepted after revision November 8, 1988.

¹ Departments of Radiology and Pediatrics, Children's Hospital Medical Center, and the Department of Radiology, University of Cincinnati College of Medicine, Cincinnati, OH 45229-2899. Address reprint requests to G. S. Bisset III, Department of Radiology, Children's Hospital Medical Center, Elland and Bethesda Aves., Cincinnati, OH 45229-2899.

² Division of Cardiology, Children's Hospital Medical Center, Cincinnati, OH 45229-2899.



development of coronary artery aneurysms, occurring in approximately 10–20% of the patients with this disease [5, 6].

Cardiac imaging in these patients has centered around the use of two-dimensional echocardiography [7]. This technique has been proved accurate and reliable in the investigation of the coronary arteries. Coronary angiography also plays a role in the evaluation of these patients [8]. Although associated with some morbidity, selective coronary arteriography pro-

vides accurate delineation of the entire coronary system. Silent occlusions, coronary thrombosis, and stenotic lesions may be identified more readily with this technique [7].

Previous reports have indicated that ECG-gated MR imaging is capable of visualizing coronary arteries [1, 2]. With the gating capability, each image is obtained at one point in the cardiac cycle; hence, a "freeze-frame" image of the coronary arteries may be achieved at one particular phase of systole

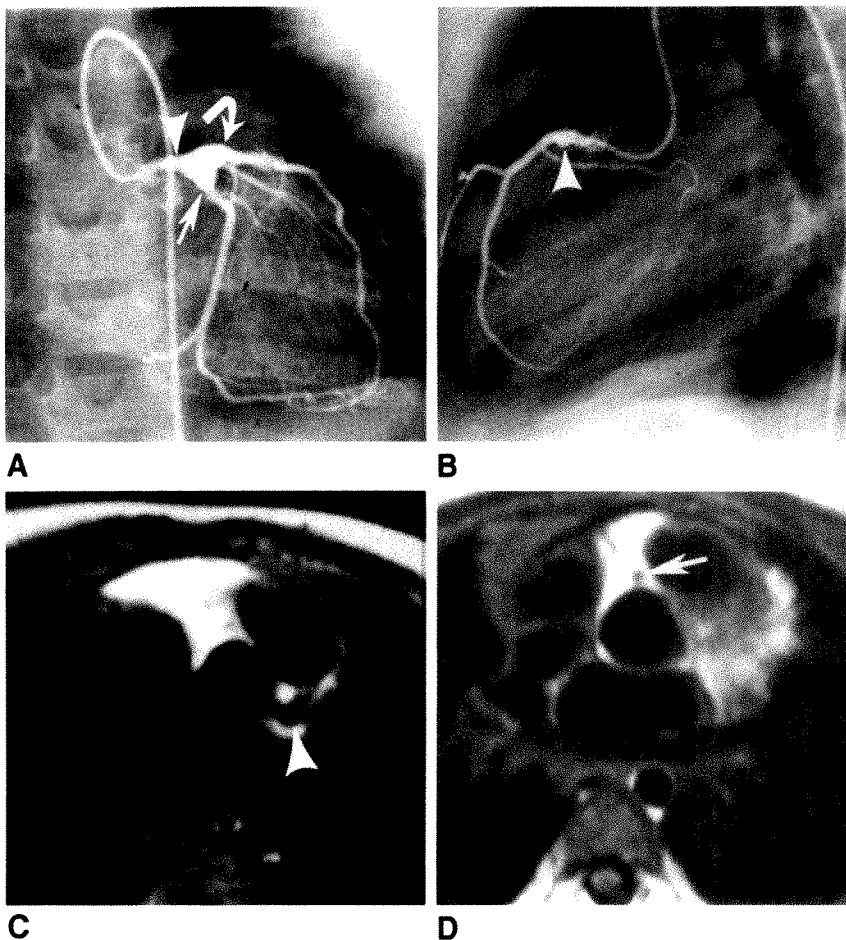
Fig. 2.—17-month-old girl diagnosed with Kawasaki disease 1 month before investigation.

A, Anteroposterior view of left coronary artery angiogram. Aneurysm is seen extending from just distal to origin of left main coronary artery (arrowhead) to origins of left anterior descending branch (curved arrow) and circumflex branch (straight arrow).

B, Lateral view of right coronary artery angiogram. Small proximal aneurysm is seen just distal to origin (arrowhead).

C, Axial oblique view through aortic root shows aneurysm of proximal left coronary artery and proximal left anterior descending branch (arrowhead).

D, Axial view through right coronary artery shows small aneurysm of proximal right coronary artery (arrow).



or diastole. Inconsistencies may result, however, because of respiratory changes in the cardiac orientation and because of the multidirectional orientations of the coronary arteries.

MR imaging also may demonstrate additional anatomic and functional information in patients with Kawasaki disease. In our patient, multiple axillary and subclavian artery aneurysms were detected. From an angiographic standpoint, evaluation of these lesions would require an additional aortic arch angiogram or selective bilateral subclavian angiography.

Flow characteristics within the aneurysmally dilated vessels may also be discerned with this technique. In our patient, MR imaging initially confirmed the presence of angiographically identified slow coronary blood flow. On the later MR evaluation, coronary thrombi were identified. Although it may be difficult to distinguish slow blood flow from thrombus, flow may be characterized definitively as normal (low signal intensity) or abnormal (high signal intensity) in the aneurysms.

Currently the real-time imaging capabilities, low cost, and portability of two-dimensional echocardiography make it the primary noninvasive imaging technique for screening coronary artery anatomy in patients with Kawasaki disease. MR imaging, however, may play an increasing role in the noninvasive identification or follow-up of aneurysms in some patients. Additional prospective comparative studies will be needed to

evaluate the utility of MR imaging as a primary imaging technique in these patients. New improvements in cine MR imaging and spatial resolution may permit even better imaging of these structures in the future.

REFERENCES

1. Higgins CB. New horizons in cardiac imaging. *Radiology* 1985;156:577-588
2. Paulin S, von Schulthess GK, Fossel E, Krayenbuehl HP. MR imaging of the aortic root and proximal coronary arteries. *AJR* 1987;148:655-670
3. Didier D, Higgins CB, Fisher MR, Osaki L, Silverman NH, Cheitlin MD. Congenital heart disease: gated MR imaging in 72 patients. *Radiology* 1986;158:227-235
4. Kawasaki T. Mucocutaneous lymph node syndrome—clinical observation of 50 cases. *Jpn J Allergy* 1967;16:178-182
5. Bell DM, Morens DM, Holman RC, Hurwitz MD, Hunter MK. Kawasaki syndrome in the United States. *Am J Dis Child* 1983;137:211-214
6. Kawasaki T, Kosaki F, Okawa S, Shigematsu I, Yanagawa H. A new infantile acute febrile mucocutaneous lymph node syndrome (MLNS) prevailing in Japan. *Pediatrics* 1974;54:271-276
7. Capannari TE, Daniels SR, Meyer RA, Schwartz DC, Kaplan S. Sensitivity, specificity and predictive value of two-dimensional echocardiography in detecting coronary artery aneurysms in patients with Kawasaki disease. *J Am Coll Cardiol* 1986;7:355-360
8. Onouchi Z, Shimazu S, Kiyosawa N, Takamatsu T, Hamaoka R. Aneurysms of the coronary arteries in Kawasaki disease. An angiographic study of 30 cases. *Circulation* 1982;66:6-13

FORTHCOMING ARTICLES

PROGRESS IN RADIOLOGY

Diagnostic and therapeutic interventional gallbladder procedures. *Teplick SK*

Imaging hepatic metastases from colorectal carcinoma: identification of candidates for partial hepatectomy. *Seltzer SE, Holman BL*

REVIEW ARTICLES

Radiology of penile prostheses. *Cohan RH, Dunnick NR, Carson CC*

Percutaneous insertion of the Greenfield filter. *Pais SO, Tobin KD*

CONTRAST MEDIA

A prospective trial of ionic vs nonionic contrast agents in routine clinical practice: comparison of adverse effects. *Wolf GL, Arenson RL, Cross AP*

Commentary. Nonionic vs ionic contrast media: what do the data tell us? *Lasser EC, Berry CC*

Case report. Acute thrombocytopenia after IV administration of a radiographic contrast medium. *Chang JC, Lee D, Gross HM*

CARDIOPULMONARY RADIOLOGY

Pictorial essay. Surgical defects of the pericardium: radiographic findings. *Takasugi JE, Godwin JD*

Leptospirosis of the lung: radiographic findings in 58 patients. *Im J-G, Yeon KM, Han MC, et al.*

Pulmonary lymphangioliomyomatosis: high-resolution CT findings in four cases. *Rappaport DC, Weisbrod GL, Herman SJ, Chamberlain DW*

Case report. Rounded atelectasis of the lung: MR appearance. *Verschakelen JA, Demaerel P, Coolen J, Demedts M, Marchal G, Baert AL*

BREAST RADIOLOGY

Sedimented calcium in benign breast cysts: the full spectrum of mammographic presentations. *Linden SS, Sickles EA*

GASTROINTESTINAL RADIOLOGY

CT of primary lymphoma of the liver. *Sanders LM, Botet JF, Straus DJ, Ryan J, Filippa DA, Newhouse JH*

Distinction between hemangioma of the liver and hepatocellular carcinoma: value of labeled RBC imaging. *Kudo M, Ikekubo K, Yamamoto K, et al.*

Case report. Hepatic perfusion in cavernous transformation of the portal vein: evaluation by using CT angiography. *Nakao N, Miura K, Takahashi H, et al.*

Is routine chest radiography required with biliary lithotripsy? *Malone DE, Becker CD, Müller NL, Burhenne HJ*

Pneumatosis intestinalis in bone-marrow transplantation patients: diagnosis on routine chest radiographs. *Bates FT, Gurney JW, Goodman LR, Santamaria JJ, Hansen RM, Ash RC*

Pictorial essay. Primary tumors of the small intestine: CT evaluation. *Dudiak KM, Johnson CD, Stephens DH*

Diagnosis of fistulae and sinus tracts in patients with Crohn disease: value of MR imaging. *Koelbel G, Schmiedl U, Majer MC, et al.*

ONCOLOGIC RADIOLOGY

CT of adrenal tumors: frequency and clinical significance of low-attenuation lesions. *Miyake H, Maeda H, Tashiro M, et al.*

Subcutaneous metastases from malignant melanoma: prevalence and findings on CT. *Patten RM, Shuman WP, Teefey S*

MUSCULOSKELETAL RADIOLOGY

Pictorial essay. MR imaging of the finger: correlation with normal anatomic sections. *Erickson SJ, Kneeland JB, Middleton WD, et al.*

Detection of osteomyelitis at fracture nonunion sites: comparison of two scintigraphic methods. *Seabold JE, Nepola JV, Conrad GR, et al.*

PEDIATRIC RADIOLOGY

MR imaging determination of the location of the normal conus medullaris throughout childhood. *Wilson DA, Prince JR*

Review. Imaging of infants and children with AIDS. *Haney PJ, Yale-Loehr J, Nussbaum AR, Gellad FE*

Blunt renal and ureteral trauma in childhood: CT patterns of fluid collections. *Siegel MJ, Balfe DM*

Closed spinal dysraphism: analysis of clinical, radiological, and surgical findings in 104 consecutive patients. *Scatliff JH, Kendall BE, Kingsley DPE, Britton J, Grant DN, Hayward RD*

Absolute intracranial blood flow velocities evaluated by duplex Doppler sonography in asymptomatic preterm and term neonates. *Horgan JG, Rumack CM, Hay T, Manco-Johnson ML, Merenstein GB, Esola C*

Color Doppler imaging of intracranial vessels in the neonate. *Wong WS, Tsuruda JS, Liberman RL, Chirino A, Vogt JF, Gangitano E*

NEURORADIOLOGY

MR imaging of brain abscesses. *Haimes AB, Zimmerman RD, Morgello S, et al.*

Gd-DTPA-enhanced MR imaging of spinal tumors. *Parizei PM, Balériaux D, Rodesch G, et al.*

VASCULAR RADIOLOGY

Pulsed-spray pharmacomechanical thrombolysis: preliminary clinical results. *Bookstein JJ, Fellmeth B, Roberts A, Valji K, Davis G, Machado T*

Color-flow Doppler and conventional duplex scanning of the carotid bifurcation: a prospective, double-blind, correlative study. *Hallam MJ, Reid JM, Cooperberg PL*

Case report. Pelvic arteriovenous malformation diagnosed by color-flow Doppler imaging. *Musa AA, Hata T, Hata K, Kitao M*

Case report. Aorto-left renal vein fistula diagnosis by duplex sonography. *Mansour MA, Russ PD, Subber SW, Pearce WH*

DIGITAL RADIOLOGY

A report-coding system for integration into a digital radiology department. *Bramble JM, Chang CHJ, Martin NL*

Comparison of 2048-line digital display formats and conventional radiographs: an ROC study. *Hayrapetian A, Aberle DR, Huang HK, et al.*

DEPARTMENT MANAGEMENT

Perspective. Strategies for resolving interpersonal conflicts in radiology. *Virapongse C*

TECHNICAL NOTE

Percutaneous procedures guided by color-flow Doppler sonography. *McNamara MP Jr*

Case Report

MR Imaging of the Criss-Cross Heart

Kerry M. Link,¹ Kenneth M. Weesner,² and Augustin G. Formanek¹

The ability of MR imaging to view simultaneously all components of the heart in the transaxial, coronal, and sagittal body planes makes this technique particularly useful for evaluating complex congenital heart defects. One such defect is criss-cross heart (CCH) [1, 2], an unusual rotational malposition in which it was originally assumed that the appropriate physiologic ventricle lies on the contralateral side with respect to the connected atrium [3, 4] (Fig. 1). However, the pertinent connections and relationships of the heart compartments in this anomaly have been difficult to show with angiography. Hoping to show these features clearly, we used MR to image the heart of a 13-month-old boy with CCH previously studied

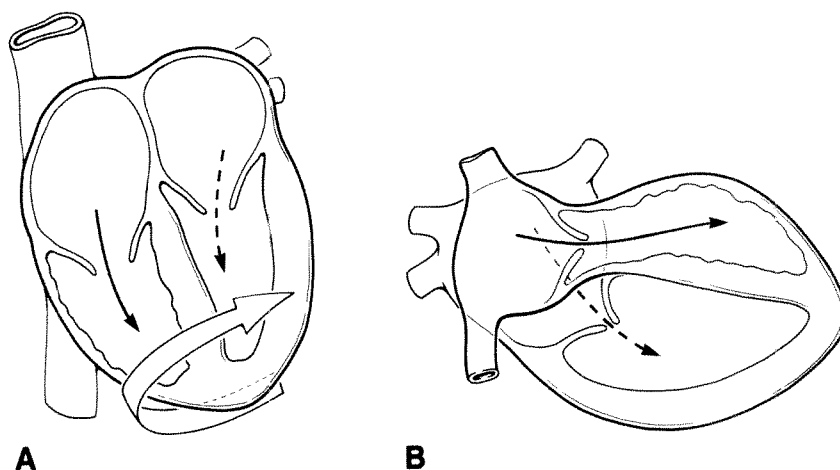
by angiography. The MR scans depicted the anatomy well, highlighting the difficulties of angiographic evaluation of the anomaly.

Case Report

In this patient, catheterization data were compatible with a ventricular septal defect and obstruction to pulmonary flow. Cineangiography confirmed the ventricular septal defect with shunting from the systemic ventricle into the pulmonary ventricle (Fig. 2). However, the intracardiac anatomy was unusual. The ventricular septum was oriented horizontally, and a typical right ventricular infundibulum (a "right-

Fig. 1.—Diagram of abnormal clockwise cardiac rotation resulting in criss-cross heart.

A, Normally rotated heart.
B, Criss-cross heart. Note secondary rotation of a normally looped heart (broad arrow, A). This rotation causes a superior-inferior relationship of the two ventricles. Position of atrioventricular valves is not affected significantly, consequently two venous inflows must cross (right inflow—solid arrow; left inflow—broken arrow).



Received September 6, 1988; accepted after revision November 1, 1988.

This work was supported by a grant from the George Link, Jr. Foundation, New York.

¹ Department of Radiology, The Bowman Gray School of Medicine, Wake Forest University, 300 S. Hawthorne Rd., Winston-Salem, NC 27103. Address reprint requests to K. M. Link.

² Department of Pediatrics, The Bowman Gray School of Medicine, Wake Forest University, 300 S. Hawthorne Rd., Winston-Salem, NC 27103.

AJR 152:809-812, April 1989 0361-803X/89/1524-0809 © American Roentgen Ray Society

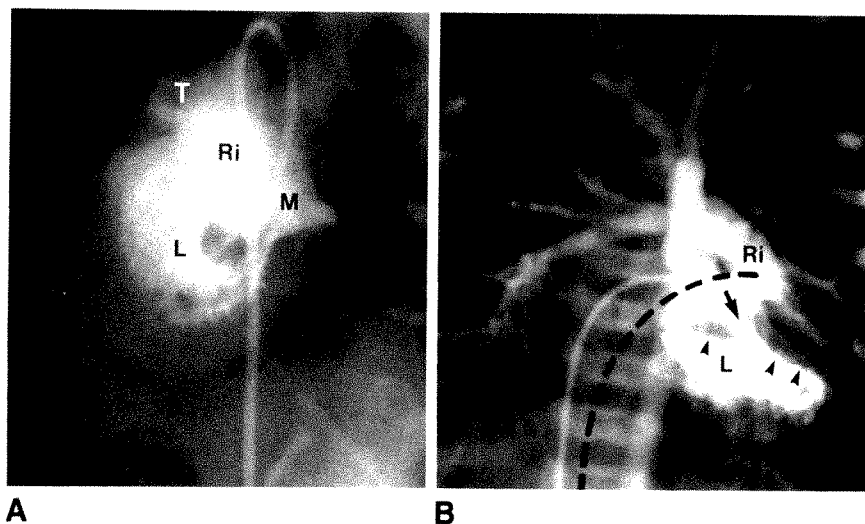


Fig. 2.—Cine left ventriculograms in angulated left anterior oblique (A) and slight right oblique (B) projections. Right ventricular infundibulum is visualized via a ventricular septal defect (arrow) and is above and to left of morphological left ventricle. A horizontal interventricular septum is shown (arrowheads). Unusual craniad position of small right atrioventricular valve is shown well. Round radiolucent structure belongs to catheter balloon. Dashed line marks course of catheter, which entered earlier during catheterization into right ventricle via right atrioventricular valve.

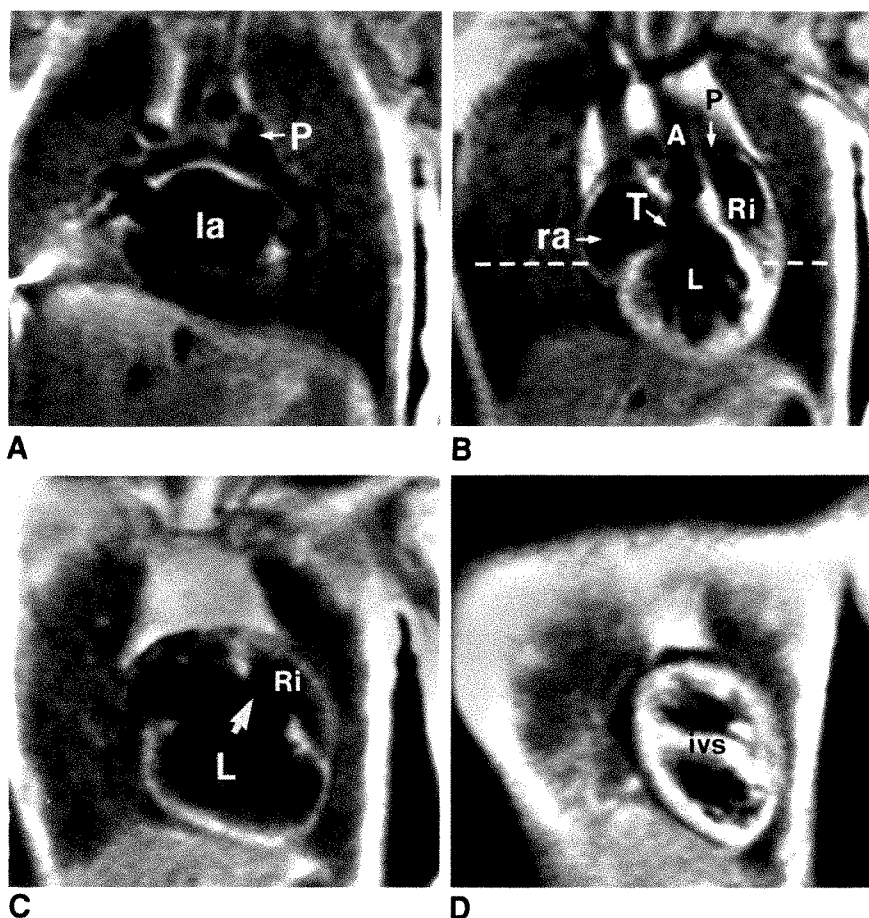


Fig. 3.—Coronal MR scans in posteroanterior sequence.

A and B, Small right atrium is positioned more craniad than left atrium, and its atrioventricular valve is a right-sided structure.

C and D, Large arrow indicates septal defect. Sinus (inflow) portion of right ventricle is above horizontally oriented septum, apex of left ventricle is below it.

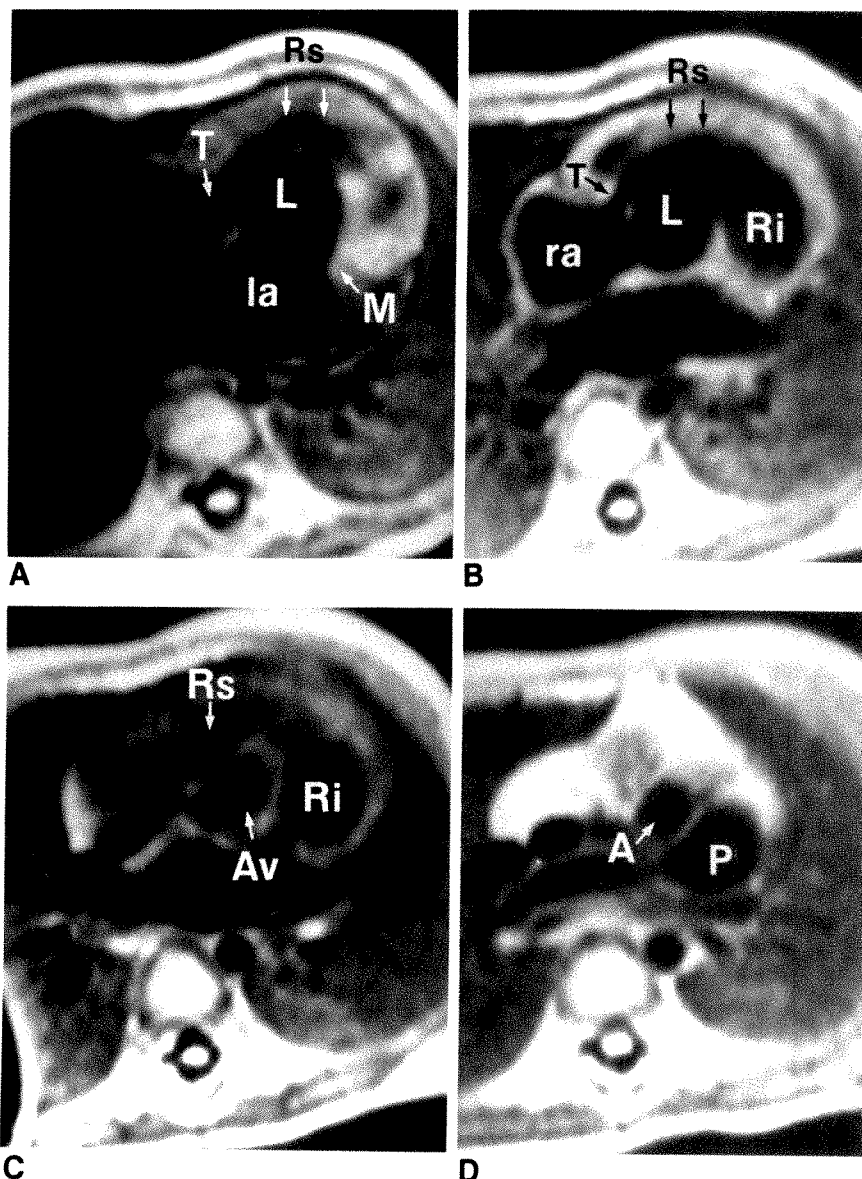
sided" structure) was positioned to the left and above the morphologic left ventricle. Despite the left-to-right shunt, the right ventricle appeared smaller than the left. The connections of the great arteries were normal (concordant): the pulmonary artery arose from the anatomic right ventricle to the left of the aorta, which originated from the anatomic left ventricle. That the atrioventricular connections were

also correct (concordant) was proved by the course of the catheter, which entered the right ventricle from the right atrium and later entered the left ventricle via the foramen ovale and the left atrium. The unusual features, then, were the "contralateral" positions of the right atrium connected to the small morphologic right ventricle, the horizontal septum, and the seemingly inverted (i.e., reversed in the

Fig. 4.—A–D, Transaxial MR scans in caudo-cranial sequence starting at level shown on Fig. 3B (line). Small right atrioventricular valve is located to right and anterior to large left atrioventricular valve. Sinus (inflow) portion of right ventricle is elongated, narrow, and courses from right to left anterior to left ventricle.

Key to Abbreviations Used in Figures

R	right ventricle (morphological)
Ri	right ventricular infundibulum
Rs	right ventricular sinus (inflow)
L	left ventricle (morphological)
ra	right atrium
T	right atrioventricular valve
la	left atrium
M	left atrioventricular valve
A	aorta
Av	aortic valve
P	pulmonary artery
ivs	interventricular septum



left–right direction) relationship of the two ventricles. These findings indicate a variant of CCH in which the ventriculoarterial connections are concordant.

ECG-gated MR imaging was performed on a 0.15-T Picker (Highland Heights, OH) Imager by using a T1 spin-echo pulse sequence. The right atrioventricular (tricuspid) valve, which appears smaller than the left atrioventricular (mitral) valve, occupies the normal position to the *right* of the midline (Figs. 3B and 4A). Because of the entirely left-sided location of the infundibulum, the inflow portion of the right ventricle is elongated and courses horizontally from right to left in front of the left ventricle (Figs. 4A–C and 5A–C). The mitral valve is located to the left of the tricuspid valve and opens into the left ventricle, which is directly anterior to the left atrium (Figs. 4A and 5A). The position of the morphologic left ventricle is below, to the right of the infundibulum, but still posterior to the body of the right ventricle (Figs. 3B and C, 4A, and 5A). The horizontal orientation of the interventricular septum, with a large septal defect, is shown clearly (Figs. 3C and 3D). MR also confirmed the concordant origin of the great arteries (Figs. 3B, 4C, and 4D).

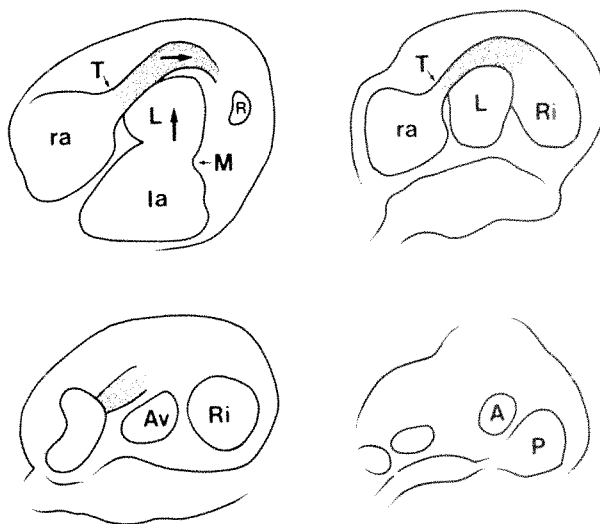


Fig. 5.—Drawing of scans in Fig. 4. Right ventricular sinus (inflow) portion is shaded. Arrows indicate direction of inflowing blood from atria into appropriate ventricles.

Discussion

In discussing positional and rotational anomalies of the heart such as CCH, it is important to distinguish between "connections" and "relations" [5]. *Connection* refers to the sequential order of the adjacent cardiac segments, while *relation* refers to the spatial arrangement of the cardiac segments.

The long-prevailing concept of contralateral atrioventricular connections resulted from the interpretation of angiographic findings in CCH that showed the seemingly contralateral location of the atria and their respective ventricles [2-4]. Van Praagh et al. [6] suggested first, however, that crossed atrioventricular connections (i.e., atrium connected to the contralateral ventricle) are merely angiographic artifacts and, therefore, an illusion. The abnormal clockwise axial rotation during the developmental stage (Fig. 1) causes the outflow portions of the ventricles to shift to the side opposite their inflow portions. This is shown well in our patient, in whom the infundibulum of the right ventricle forms the upper left portion of the cardiac mass. A normal-sized infundibulum is easily recognized angiographically; however, the sinus or inflow portion of the right ventricle, usually underdeveloped in CCH [7], is difficult to identify by conventional contrast studies. Hence the impression on angiography is that the right-sided atrium is connected to an entirely left-sided, small morphologic right ventricle. Axial MR images show conclusively that only the infundibular component is left sided, whereas the atrioventricular connection remains correctly right sided, and that the narrow elongated right ventricular inflow tract extends from right to left between the right atrium and the infundibulum and anterior to the left ventricle. Thus, the blood flows in a right-to-left direction. At the same time, the blood flows from the left atrium into the left ventricle in a posteroanterior direction, with the mitral valve remaining correctly to the left of the tricuspid valve. Whereas in the normal heart the courses of the two ventricular inflows are nearly parallel, in CCH they are perpendicular in the horizontal plane — in reality, crosswise (Fig. 5); hence, the origin of the term

"criss-cross" heart [1]. The other features of CCH are also well illustrated on the MR images — the horizontally oriented interventricular septum, the small tricuspid orifice, and the concordant ventriculoarterial connections. This last feature is of particular interest because normally related and connected great arteries with CCH have been considered an exception [7]. The coronal MR scans show that this anatomic situation occurs, even if rarely, in CCH with concordant atrioventricular connections [4].

This case presentation illustrates well the advantage of MR over angiocardiology when all components of the heart must be shown simultaneously to elucidate the existing connections. This ability is invaluable in the diagnosis of various rotational anomalies of the heart.

REFERENCES

1. Anderson RH, Shinebourne EA, Gerlis LM. Criss-cross atrioventricular relationships producing paradoxical atrioventricular concordance or discordance. Their significance to nomenclature of congenital heart disease. *Circulation* 1974;50:176-180
2. Freedom RM. Supero-inferior ventricle and criss-cross atrioventricular connections: an analysis of the myth and mystery. *Mod Probl Pediatr* 1983;22:48-62
3. Sato K, Kano I, Fukuda M, Yoshida Y, Sasaki T, Hoshino H. Angiographic findings and morphogenesis of criss-cross heart with situs solitus, concordant atrioventricular relationships and L-transposition. *Tohoku J Exp Med* 1976;119:377-384
4. Freedom RM, Culham G, Rowe RD. The criss-cross and superoinferior ventricular heart: an angiographic study. *Am J Cardiol* 1978;42:620-628
5. Anderson RH. Criss-cross hearts revisited. *Pediatr Cardiol* 1982;3:305-313
6. Van Praagh R, Weinberg PM, Van Praagh S. Malposition of the heart. In: Moss AJ, Adams FH, Emmanouilides GC, eds. *Heart disease in infants, children and adolescents*. Baltimore, MD: Williams & Wilkins, 1977
7. Van Praagh S, LaCorte M, Fellows KE, et al. Supero-inferior ventricles: anatomic and angiographic findings in ten postmortem cases. In: Van Praagh R, Takao A, eds. *Etiology and morphogenesis of congenital heart disease*. New York: Futura, 1980:317-378

Multicenter Double-Blind Placebo-Controlled Study of Gadopentetate Dimeglumine as an MR Contrast Agent: Evaluation in Patients with Cerebral Lesions

Eric J. Russell¹
 Thomas F. Schaible²
 William Dillon³
 Burton Drayer⁴
 Joseph LiPuma⁵
 Anthony Mancuso⁶
 Kenneth Maravilla⁷
 Harold A. Goldstein²

This article appears in the January/February 1989 issue of *AJNR* and the April 1989 issue of *AJR*.

Received December 28, 1987; accepted after revision May 9, 1988.

Presented at the annual meeting of the American Society of Neuroradiology, New York City, May 1987.

This work was supported by a grant from Berlex Laboratories, Inc., Cedar Knolls, NJ.

¹ Department of Diagnostic Radiology, Northwestern Memorial Hospital and Northwestern University Medical School, Olson Pavilion, 710 N. Fairbanks Ct., Chicago, IL 60611. Address reprint requests to E. J. Russell.

² Berlex Laboratories, Inc., Cedar Knolls, NJ 07927.

³ Department of Radiology, University of California School of Medicine, San Francisco, CA 94143-0638.

⁴ Barrow Neurological Institute, Phoenix, AZ 85013.

⁵ Department of Radiology, University Hospitals, Cleveland, OH 44106.

⁶ Department of Radiology, University of Florida College of Medicine, Gainesville, FL 32610.

⁷ Department of Radiology, University of Washington School of Medicine, Seattle, WA 98195.

AJR 152:813-823, April 1989

0361-803X/89/1524-0813

© American Roentgen Ray Society

A multicenter double-blind randomized study was designed to evaluate and compare the safety and diagnostic efficacy of gadopentetate dimeglumine (Gd-DTPA) (0.1 mmol/kg) against a saline placebo for use as an IV contrast agent for MR. The randomization code provided for a 2:1 ratio of Gd-DTPA and saline patients. Six investigators studied 88 patients with signs and symptoms of a cerebral lesion. Although safety data were complete in all 88 cases, only 83 had valid efficacy data (57 received Gd-DTPA, 26 placebo). Three patients were excluded from efficacy evaluation because of incomplete scans or scans with severe motion artifacts. Two patients were excluded for protocol variations (did not have a mass lesion). The protocol required that spin-echo MR images be acquired both before and after infusion at mode 1, 500/30/2 (TR/TE/excitations), and at a single-echo mode 2 sequence within a selected range, 1500-2000/56-90/2. Additional TEs could also be used at the discretion of each investigator. Efficacy was determined by comparing post- with preinjection images for relative degree of enhancement and improvement of diagnostic ability after injection, and by comparing these results with placebo results. Enhancement was reported in 43 (75%) of 57 Gd-DTPA patients and in none of the 26 placebo patients. Improvement of diagnostic ability was noted in 37 of 57 Gd-DTPA patients and in no placebo patients. Of 17 patients receiving Gd-DTPA for whom no diagnosis could be made before infusion, nine of 17 were diagnosed after infusion. By comparison, none of five patients not diagnosed before infusion of placebo could be diagnosed after infusion. Of 43 patients in whom lesion enhancement was observed after Gd-DTPA infusion, the diagnosis changed after infusion in 16 (37%) and the number of lesions detected after infusion increased in 10 (23%). Safety studies showed no clinically significant abnormal trends. Minor changes in blood pressure, pulse, and serum iron levels were noted in a higher percentage of Gd-DTPA patients.

This study confirms that Gd-DTPA is an efficacious contrast agent for use with MR and that it exhibits excellent patient tolerance. Enhancement allows for a decisive diagnosis to be made in selected cases in which such capability had previously been lacking with unenhanced MR.

It has been suggested that the lack of a suitable contrast medium limits the specificity and sensitivity of MR imaging. Nonenhanced MR images may fail to detect certain lesions that appear isointense relative to normal brain on one or more pulse sequences, and may fail to reliably define a distinct margin between focal cerebral masses and areas of perifocal edema [1-9]. The search for such an MR contrast medium has led to the development of a new class of agents, paramagnetics, which cause enhancement by locally affecting the magnetic environment of brain water. One such agent, gadopentetate dimeglumine (Gd-DTPA), has been tested extensively in clinical trials both in the United States and Europe [10-16]. Gd-DTPA is a hydrophilic chelate that readily crosses the damaged blood-brain barrier in a manner similar to iodinated radiographic contrast media. It influences tissue relaxation times, resulting in T1 and T2 shortening. Although these effects are contradictory in terms of image signal intensity, a desirable increase in intensity in areas of blood-brain barrier breakdown may be achieved by

using T1-weighted pulse sequences, reducing the undesired signal lowering effect of T2 shortening.

Considering early results obtained in clinical trials, a multicenter double-blind placebo controlled study was designed and performed to compare the safety and efficacy of Gd-DTPA with saline placebo, and to compare pre- and postinfusion images for improvement of diagnostic ability and lesion detection. The results of this study are presented here.

Subjects and Methods

This multicenter double-blind randomized clinical trial evaluated gadopentetate dimeglumine (0.1 mmol/kg) against a saline placebo in hospitalized patients with signs and symptoms of a cerebral lesion. The study population consisted of 88 patients at six medical centers in the United States. The randomized code provided for a 2:1 ratio of Gd-DTPA and saline placebo patients. All 88 patients had valid data for safety scoring; 83 of 88 had valid efficacy data, with five patients excluded from efficacy evaluation due to incomplete or artifactually degraded scans or to variations from study protocol (patients without a mass lesion). Of the 83 patients with valid efficacy data, 57 patients received gadopentetate dimeglumine (Gd-DTPA) and 26 received placebo. Strict patient inclusion and exclusion criteria were adhered to (Table 1); these were selected in part to exclude medically unstable individuals. Vital statistics defining the study group are summarized in Table 2, and the specific presumptive diagnoses are listed in Table 3. The study drug, Gd-DTPA, was provided to the investigating sites as a sterile, clear, and colorless aqueous solution in one 20-ml vial, which contained the di-N-methylglucamine salt of the Gd-DTPA complex in a concentration of 0.5 mol/l. Drug osmolality at 37°C was 1.94 osm/kg H₂O, and viscosity was 2.9 cp. All drugs were supplied to the investigators by the sponsor.* One numbered medication

* Berlex Labs., Cedar Knolls, NJ.

TABLE 1: Criteria for Entry of Patients into Controlled Gd-DTPA Study

Criteria
Inclusion:
Between 18 and 75 years old
If female, not of childbearing potential
Prediagnosed by CT to verify or localize lesion to be studied
Willing to sign written informed consent document
Willing or required to remain hospitalized for a continuous period of 48 hr after infusion MR
Exclusion:
Over 100 kg body weight
Medical instability
Contrast-enhanced CT study within 44 hr before study
Concurrent cytostatic or radiation therapy
Severe or uncontrolled hypertension
Cardiac pacemaker
Intracranial clips or external metallic clips within 10 mm of lesion to be studied
Elevation of one or more laboratory parameters:
Serum iron in excess of laboratory normal
Total serum bilirubin in excess of 1½ times normal
SGPT in excess of two times normal
Serum creatinine above 2.0 mg/dl
Receipt of any investigational drug within 30 days of baseline evaluation

TABLE 2: Vital Statistics of Patients in Controlled Gd-DTPA Study

Variable	Gd-DTPA	Placebo
Gender, no. (%):		
Male	42 (70)	16 (57)
Female	18 (30)	12 (43)
Age (years):		
Range	18–75	22–69
Mean (males)	47.4	49.6
Mean (females)	60	56.5
Weight (kg):		
Mean (males)	78.9	77.6
Mean (females)	70.5	68.4

TABLE 3: Presumptive Diagnosis at Time of Patient Entry into Controlled Gd-DTPA Study

Diagnosis	No. of Patients	
	Gd-DTPA	Placebo
Tumor	36	19
Infarct	13	5
Inflammatory	3	1
Vascular	3	1
Degenerative	2	0
Congenital/metabolic	1	0
Demyelinating	1	0
Other	1	2
Total	60	28

package was assigned to each patient entered into the study. Each package contained 20 ml of either Gd-DTPA or saline (0.9%) placebo.

After obtaining informed consent, the patient's participation in the study began after baseline evaluations were initiated and baseline laboratory values were examined and found to qualify the patient. Before injection of contrast material or placebo, a flexible angiocatheter was inserted into a convenient antecubital vein. The undiluted contrast agent or placebo was then injected at a dose of 0.1 mmol/kg body weight, at a flow rate of 10 ml/min. The mean volume of contrast material or placebo administered was 15.2 and 14.8 ml, respectively.

MR images were obtained on several MR systems at various field strengths: 0.15, 0.35, 0.5, 1.0, and 1.5 T. Before imaging, a flexible plastic tube filled with Gd-DTPA (0.4 mmol/l) was placed beside the patient's head to serve as a signal-intensity standard. Spin-echo images in mode 1, 500/30/2 (TR/TE/excitations), and mode 2, 1500–2000/56–90/2, were then obtained before injection and repetitively after injection in the following sequence. Preinjection: (1) mode 1 and (2) mode 2; postinjection: (1) mode 1, (2) mode 2, (3) mode 1, (4) mode 2, and (5) mode 1. Additional T2-weighted echoes were obtained at the discretion of each investigator. Postinjection images were acquired at 3, 25, and 55 min (mode 1) and at 8 and 35 min (mode 2). Films were collected and subsequently interpreted by the principal investigator at each test site, who then filled out an extensive report form designed to evaluate the efficacy of the injected material for improving lesion detection and subsequent interpretive diagnostic accuracy. The series of efficacy evaluation questions asked of each investigator are summarized in Table 4.

TABLE 4: Global Efficacy of Gd-DTPA as Evaluated by Six Investigators

Question	No. of Patients (%)	
	Gd-DTPA (n = 57)	Placebo (n = 26)
(1) Did injection facilitate making a diagnosis?	37 (65)	0
(2) Are postinfusion T1-weighted images sufficient for diagnosis?	39 (68)	11 (42)
(3) Are postinfusion T2-weighted images sufficient for diagnosis?	37 (66) ^a	17 (65)
(4) Did the lesion enhance?	43 (75)	0
If yes to question 4: ^b		
(5) Which sequence was best for lesion conspicuity?		
T1-weighted	41 (95)	—
T2-weighted	2 (5)	—
(6) Which postinfusion scan was most diagnostic (minutes after injection)? ^c		
0–14	24 (56)	—
14–27	6 (14)	—
28–41	10 (23)	—
42–54	0	—
55–69	3 (7)	—
70–100	0	—
(7) Did infusion change the diagnosis?	16 (37)	—
(8) Was there an increase in the number of lesions after infusion?	10 (23)	—

^a Of 56 instead of 57 patients.^b Questions 5–8 refer to the 43 patients for whom the answer to question 4 was Yes.^c The six time intervals represent time elapsed between infusion of contrast material and performance of imaging.

The efficacy of Gd-DTPA was determined by comparing pre- and postinfusion images to demonstrate the relative ability of the agent to improve contrast between the lesion and normal tissue compared with the ability of placebo injection to do the same. Similarly, such comparison was made to determine whether either injection could facilitate the establishment of a definitive diagnosis. Relative pre- and postinfusion intensities were obtained for the detected focal lesion and for surrounding normal brain tissue, and also for any related lesion necrosis and perifocal edema. Film contrast scores were reported on a four-point scale for conspicuity: 0 = no contrast (no enhancement), 1 = equivocal, 2 = good, and 3 = excellent enhancement.

Gd-DTPA and placebo groups were compared for possible adverse reactions and side effects by extensive clinical examination and laboratory testing. Physical and neurologic examinations were performed at baseline (patient entry into the study) and at 2, 24, and 48 hr after injection. ECG and EEG studies were performed at baseline and 2–4 hr after injection. Laboratory examinations performed at baseline and 2, 24, and 48 hr after injection included urinalysis, serum chemistry studies (blood urea nitrogen, creatinine, lactate dehydrogenase, SGOT, SGPT, potassium, sodium, chloride, calcium, inorganic phosphorous, glucose, total protein, alkaline phosphatase, total and direct bilirubin, cholesterol, iron, magnesium, and uric acid) and hematologic studies (hematocrit, hemoglobin, RBC, WBC, differential leukocyte count, mean corpuscular hemoglobin, mean corpuscular volume, partial thromboplastin time, and platelet count).

In addition, all patients were closely monitored for any adverse reactions immediately after injection and for another 48 hr. Reactions, if noted, were graded by individual investigators as mild, moderate, or severe, and were classified according to clinical review by each investigator as definitely, probably, possibly, remotely, or not related to the study drug or study conditions. Date and time of onset and resolution of reactions were recorded. If the study drug was discontinued, this was indicated also.

Results

Efficacy Evaluation

The results of the global efficacy evaluation are summarized in Table 4. Postinfusion images in all 26 patients receiving placebo were judged to be unenhanced and devoid of any added diagnostic information when compared with preinfusion scans. In patients receiving Gd-DTPA, film contrast scores indicated the relative enhancement of mass lesions provided by infusion. Contrast (intensity) scores were graded for normal tissue, mass lesion, perifocal edema, and necrosis, and values obtained were used as a quantitative measure of enhancement. The percentage of Gd-DTPA patients with a higher intensity score after infusion was statistically significantly greater than that found for placebo patients. Higher intensity scores were noted after injection vs before injection for mass lesion in both modes 1 and 2 ($p < .05$) and for mass vs healthy tissue in mode 2 ($p < .01$). A higher contrast ranking was found after injection in 40 (70%) of 57 Gd-DTPA patients in mode 1 and in 14 (25%) of 56 patients in mode 2. No placebo patients had higher contrast rankings after injection in either mode.

The data indicate that a large proportion of patients receiving Gd-DTPA showed lesion enhancement after infusion (43 of 57), and in 37 (65%) of 57, Gd-DTPA was found to facilitate the diagnostic process. In some patients Gd-DTPA administration resulted in enhancement without improvement of diagnostic ability (Fig. 1). Of the 43 patients with enhancement, 41 (95%) had optimal enhancement (and lesion conspicuity) on T1-weighted scans. The most diagnostic image was found within 27 min after contrast infusion in 30 (70%) of 43 patients (Fig. 2; Table 4). In two of 43 patients, T2-weighted scans showed optimal lesion conspicuity after infusion. In these cases, the additive effects of T2 prolongation and residual increased intensity due to T1 shortening provided better definition of the abnormal focus (Fig. 3). Of the 43 patients with enhancement, the initial presumptive diagnosis was changed in 16 (37%) after images were reviewed subsequent to Gd-DTPA infusion (Fig. 4). An increase in the number of lesions detected was noted in 10 (23%) of the 43 enhanced cases, accounting for a significant portion of those cases demonstrating diagnostic change (Fig. 5).

A definitive diagnosis was not possible before injection of contrast material or placebo in 22 patients. Of these, 17 received Gd-DTPA and five received placebo. Of the 17 patients receiving Gd-DTPA for whom no diagnosis was possible before infusion (on either mode 1 or 2 scans), a diagnosis was possible after infusion in nine (53%) (Fig. 4).

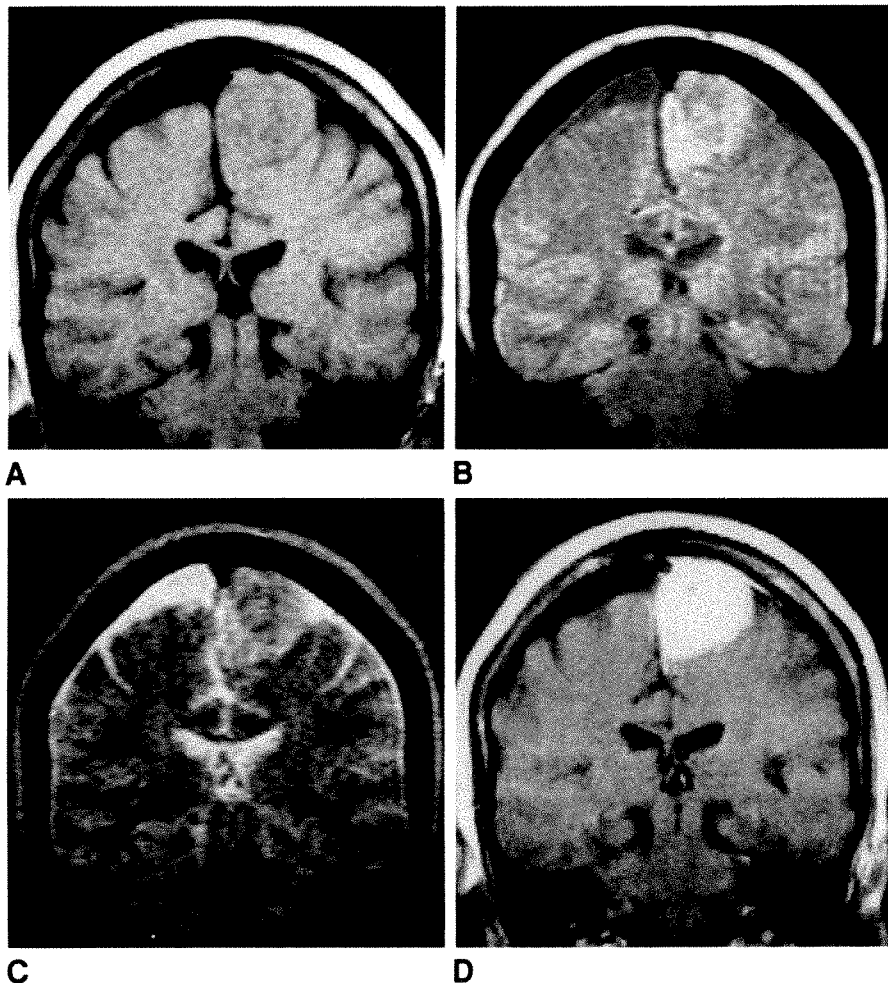


Fig. 1.—Parasagittal meningioma in 64-year-old woman with focal seizures. Contrast enhancement without improvement of diagnostic ability is illustrated.

A–C, Preinfusion coronal spin-echo images 500/30 (A), 2000/60 (B), and 2000/120 (C), acquired at 0.5 T near frontoparietal junction. Mass is isointense relative to brain on short TR/short TE sequence (A), but is still visible by way of regional displacement of gyri and sulcal effacement. Intermediate- and heavily T2-weighted images more clearly define mass and adjacent perifocal edema.

D, Coronal spin-echo image, 500/30, at same level as A after infusion of 0.1 mmol/kg Gd-DTPA. Note marked increase in intensity of tumor improving lesion conspicuity. Improved diagnostic ability was not reported since the mass was clearly detected and delineated before infusion.

No additional diagnostic information was reported in any of the five placebo patients after injection ($p < .01$). Although improvement in diagnostic ability was reported in 65% of all patients receiving Gd-DTPA, a statistically significant difference existed among investigators. Two of the six investigators reported a lower percentage of facilitation; this likely was related to a different case mix, since fewer cases of metastasis and infarction were examined at their institutions. Finally, while 83% of patients were correctly diagnosed after infusion of Gd-DTPA, 67% could be diagnosed on preinfusion mode 1 and 2 images alone.

Safety Evaluation

All patients were evaluated for short-term toxicity to contrast material. Pre- and postinjection clinical evaluations revealed no significantly abnormal trends in physical examination, neurologic status, ECG, EEG, or urinalysis.

Adverse reactions were graded by investigators as mild, moderate, or severe, and as related or unrelated to the injected drug. A similar percentage of patients receiving Gd-DTPA (13 [21.7%] of 60) and placebo (six [21.4%] of 28)

reported at least one adverse reaction ($p > .99$). Three severe reactions were reported in two placebo patients: nausea and hiccups in one patient and headache in the other. None of these was considered to be "drug related." No severe reactions were reported in Gd-DTPA patients. The only adverse reactions reported in more than one patient included headache in three (5%) of the Gd-DTPA patients and five (17.9%) of the placebo patients; hypertension in four (6.7%) of the Gd-DTPA patients and one (3.6%) of the placebo patients; and hypotension in two (3.3%) of the Gd-DTPA patients and none of the placebo patients. Investigators categorized mild or moderate adverse reactions as possibly or definitely drug related in five patients receiving Gd-DTPA. These five patients had 13 reactions, including weakness, conjunctivitis, taste abnormality, local burning at injection site, hypertension, hypotension, nausea and vomiting, and headache.

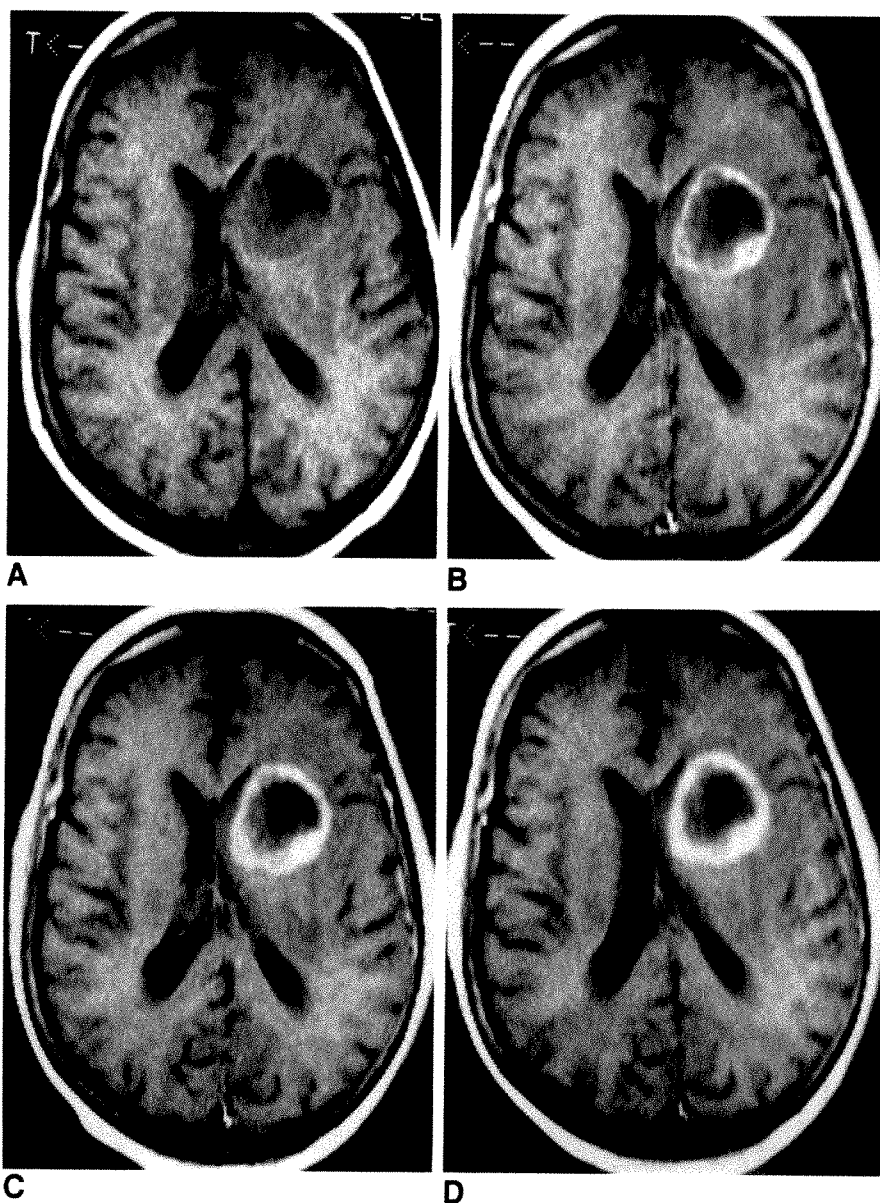
Minor changes were noted in blood pressure and pulse rate in a higher percentage of Gd-DTPA patients. A decrease in systolic blood pressure of more than 25 mm Hg from baseline was noted 25 min after infusion in six Gd-DTPA patients. Further study of this group revealed that five of six were studied at one of the six test sites, and that three of six had baseline systolic pressures in excess of 160 mm Hg. Only

Fig. 2.—76-year-old woman with 4-day history of memory loss and metastases from lung carcinoma. Time dependence of enhancement is illustrated.

A, Axial spin-echo image, 500/30, at 0.5 T before contrast infusion. Central low signal intensity of deep frontal mass is due to necrosis.

B–D, Postinfusion spin-echo images, 500/30, at 5 (B), 25 (C), and 55 (D) min after Gd-DTPA injection. Note relatively thin rim of enhancement observed at 5 min. Delayed scans show thickening of enhanced portion of mass.

As additional information was not available on scans delayed beyond 25 min, optimal enhancement was noted at this point. These findings were typical of cases of necrotic tumors. Immediate postinfusion scans often underestimated extent of eventual tumoral enhancement. Delayed images (most frequently within 25 min) best corresponded to enhancement observed on CT scans.



one of six had an associated decrease in diastolic pressure. Adverse reaction reports noted that two Gd-DTPA patients experienced clinical signs of hypotension. One of the two was a 47-year-old man with symptoms of hypotension 85 min after injection, assessed as unrelated to the drug. The other was a 45-year-old woman who appeared weak and pale and had a blood pressure of 90/60 mm Hg, from a baseline of 120/62, 25 min postinjection; this was considered to be possibly drug related.

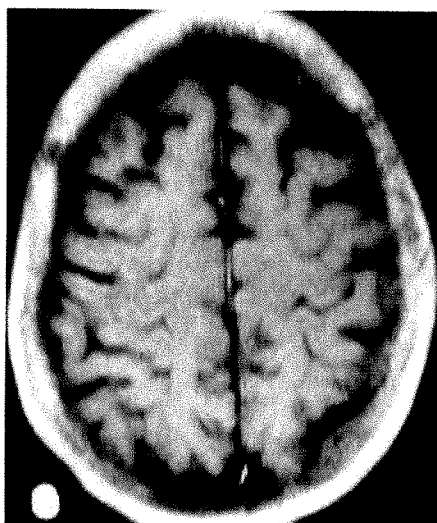
Laboratory studies revealed a generally transient post-Gd-DTPA increase in serum iron concentration. A higher percentage of Gd-DTPA patients had elevated serum iron at 2–4 hr postinjection, and several patients had mildly elevated levels of iron at 48 hr (Table 5).

Discussion

This investigation demonstrated the effectiveness of Gd-DTPA for the detection and definition of cerebral lesions when used in conjunction with MR. It is not surprising that placebo injections were ineffective and that significant increases in signal intensity occurred in a variety of cerebral lesions after Gd-DTPA infusion. Of greater significance was the efficacy demonstrated by Gd-DTPA for providing diagnostic information in nine of 17 cases not elucidated before its administration. Although one might argue that the use of different pulse sequences (such as heavily T1-weighted inversion recovery) might have allowed a greater percentage of diagnoses to be made without infusion of contrast material and that the study



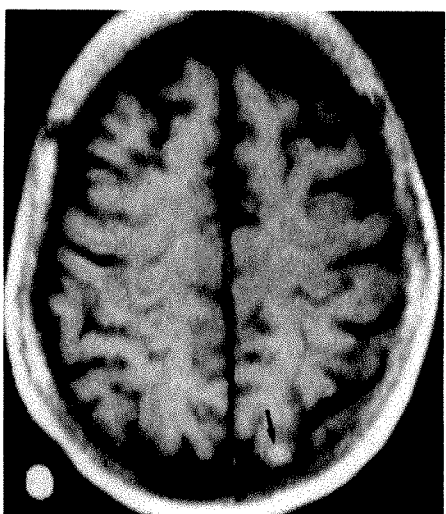
A



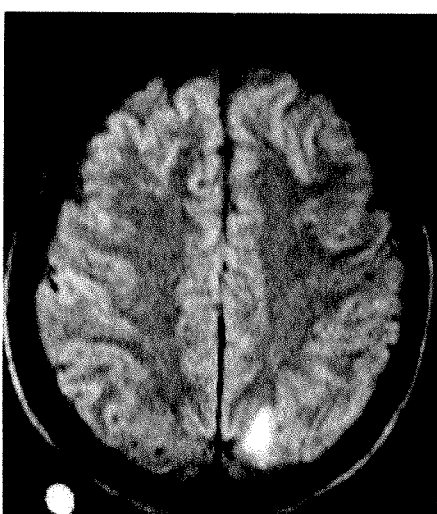
B



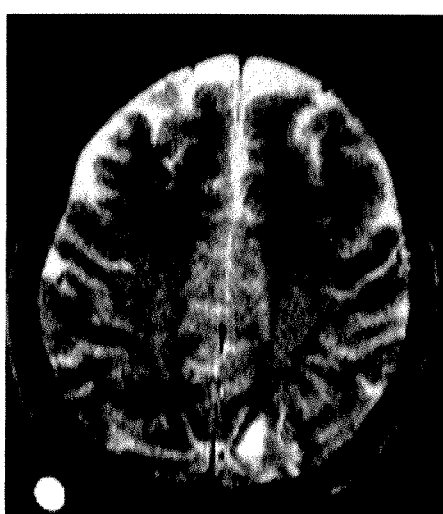
C



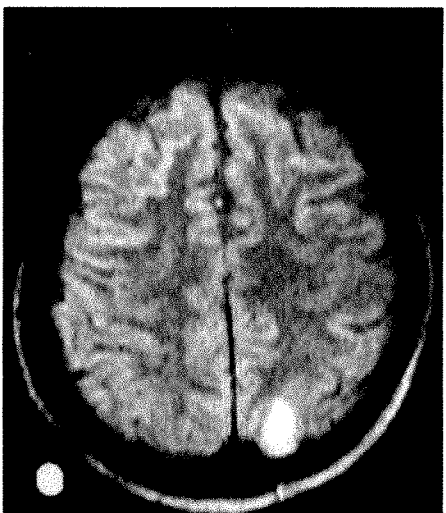
D



E



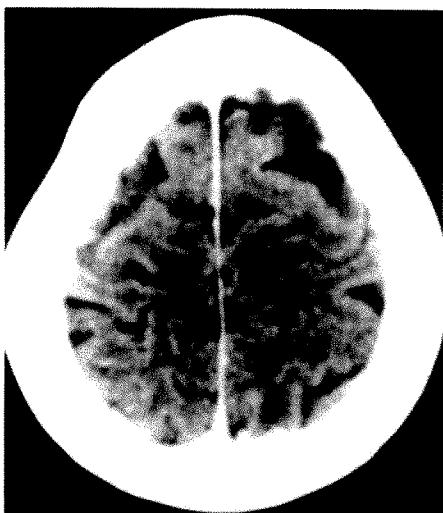
F



G



H



I

◀ Fig. 3.—52-year-old woman with poorly differentiated metastatic lung carcinoma. Lesion is detected readily on all T2-weighted images, but only on 55-min delayed postinfusion T1-weighted study.

A–D, Axial spin-echo images, 500/30, of high convexity before Gd-DTPA infusion (A) and at 5 (B), 25 (C), and 55 (D) min after infusion (acquired at 0.5 T). Note enhancement in small peripheral metastatic nodule detected by independent observers only on last delayed scan (arrow).

E–G, Axial intermediate spin-echo, 2000/60 (E and G), and heavily T2-weighted spin-echo, 2000/120 (F), MR images before (E and F) and after (G) Gd-DTPA infusion. Nodule at periphery is easily detected on preinfusion images because of high-signal edema. Enhancing nodule is also visible posterior to edema (T1 effect) on postinfusion intermediate image (G) (compare with E). Lesion is more conspicuous than on postinfusion T1-weighted studies (B–D).

H and I, CT scans after infusion of iodinated contrast material (adjacent cuts). Nodule is partly hidden by high density of inner table of skull. Contrast this with lack of obscuration by bone on MR studies (D and E).

(Reprinted from [17], with permission.)

was too limited in this respect, the study sequences were representative of current clinical practice. One might also counter that the increase in lesion conspicuity observed in many cases after Gd-DTPA infusion improved diagnostic confidence in a way not indicated by the study data. Improvement in diagnostic ability was reported in 37 of 57 cases qualifying for efficacy determination. The *absence* of enhancement, which led to a more confidently negative diagnosis in some cases, was reflected in this statistic and partly explained the unexpectedly high percentage of such positive responses, although improved lesion conspicuity due to enhancement

did account for the majority of these cases. Because enhancement was observed in 43 of 57 cases, and enhancement facilitated diagnosis in 37 cases, it is evident that enhancement was present in some cases without necessarily improving diagnostic ability (Fig. 1). Although the number of patients in this study is relatively small, there is clear evidence that this carefully controlled investigation supports the utility and even the necessity (in some cases) of using Gd-DTPA (or other contrast agents) in cases not diagnosable or less accurately defined by preinfusion MR alone. Our data also show that improvement in diagnostic ability (reported in 37 of 57

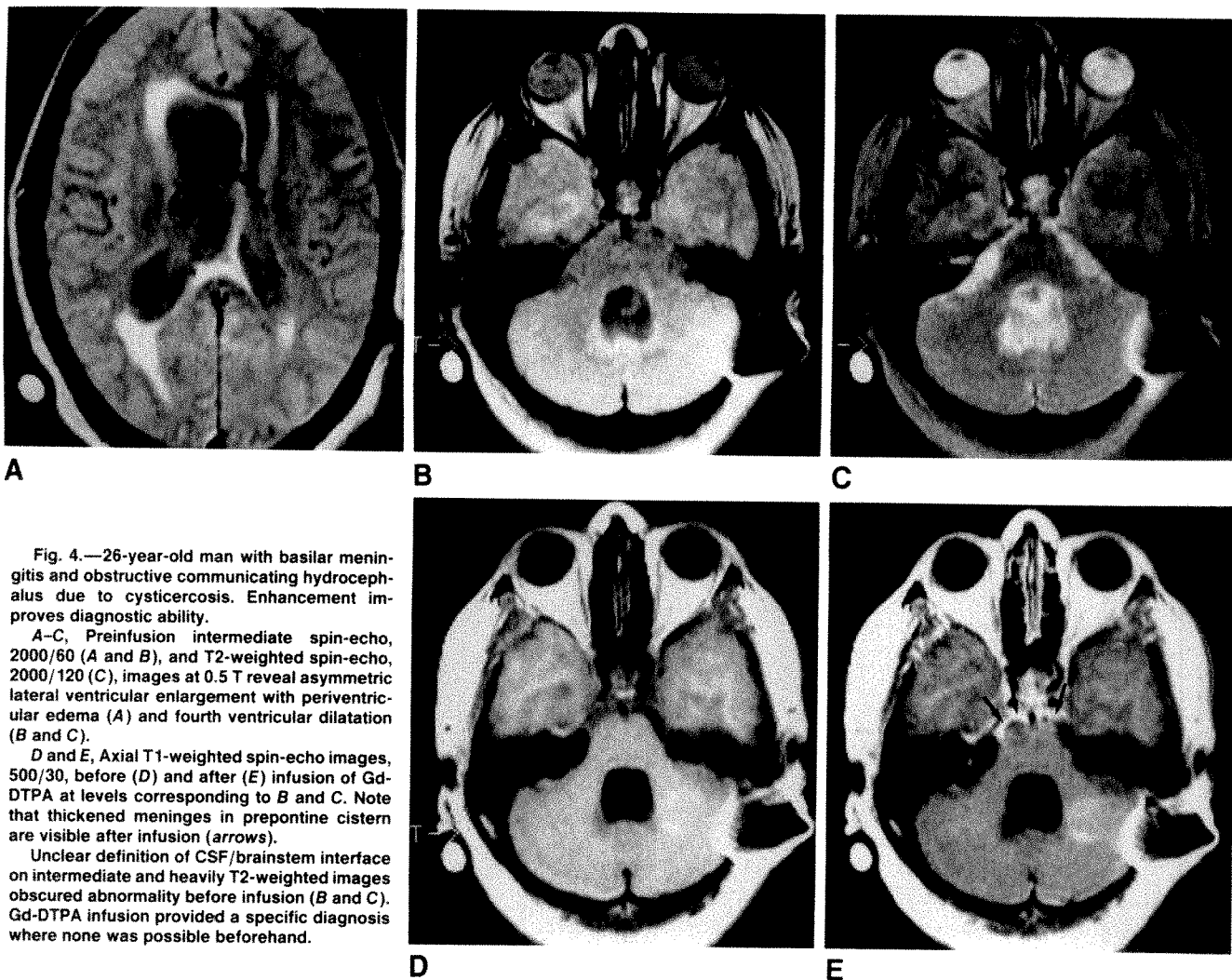


Fig. 4.—26-year-old man with basilar meningitis and obstructive communicating hydrocephalus due to cysticercosis. Enhancement improves diagnostic ability.

A–C, Preinfusion intermediate spin-echo, 2000/60 (A and B), and T2-weighted spin-echo, 2000/120 (C), images at 0.5 T reveal asymmetric lateral ventricular enlargement with periventricular edema (A) and fourth ventricular dilatation (B and C).

D and E, Axial T1-weighted spin-echo images, 500/30, before (D) and after (E) infusion of Gd-DTPA at levels corresponding to B and C. Note that thickened meninges in prepontine cistern are visible after infusion (arrows).

Unclear definition of CSF/brainstem interface on intermediate and heavily T2-weighted images obscured abnormality before infusion (B and C). Gd-DTPA infusion provided a specific diagnosis where none was possible beforehand.

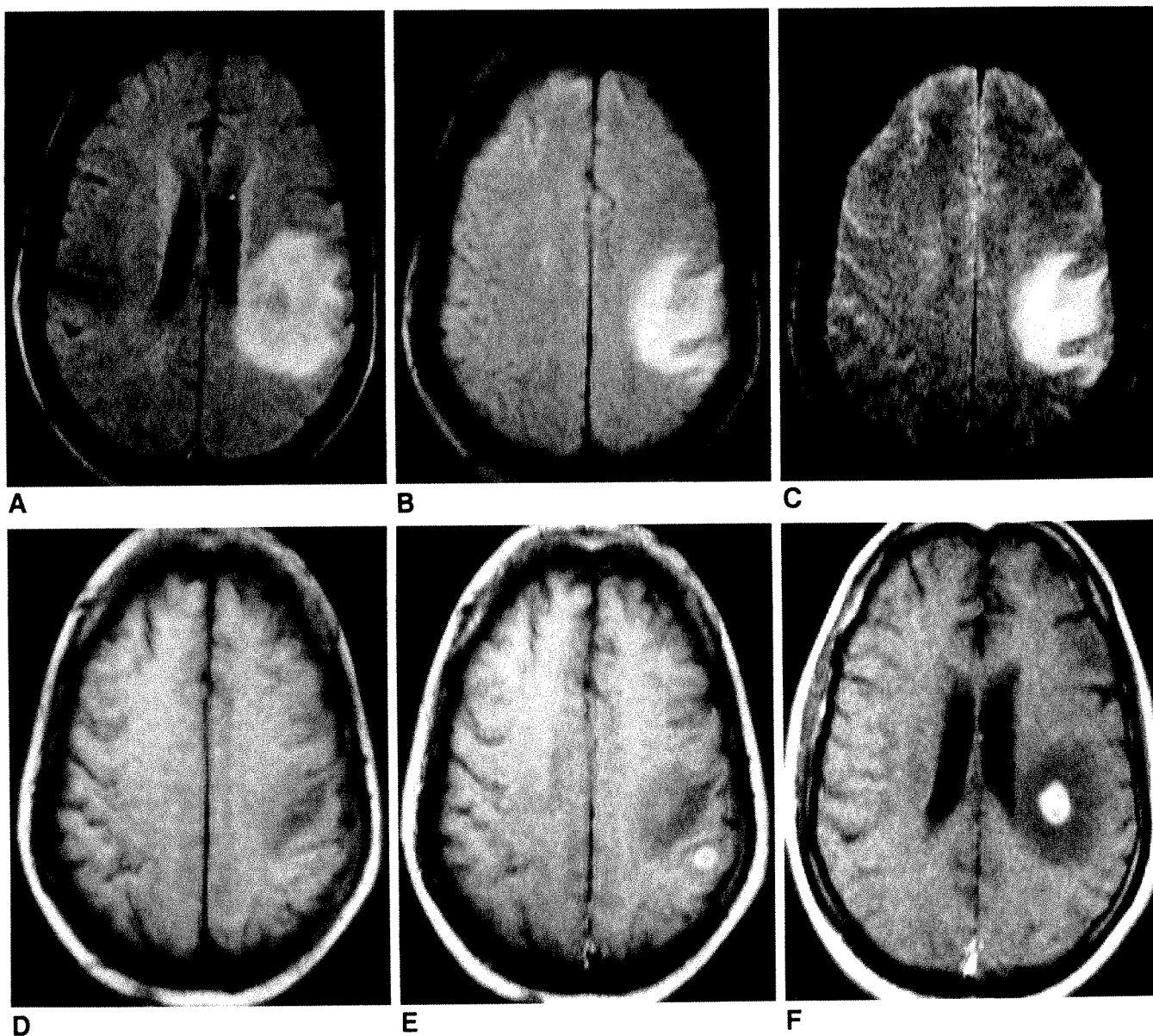


Fig. 5.—47-year-old man with metastases from lung carcinoma. Enhancement facilitates diagnosis with an increase in number of lesions detected. A–C, Preinfusion axial spin-echo images, 2000/60 (A and B) and 2000/120 (C), at 0.5 T. High-signal-intensity edema is easily detected on two adjacent intermediate cuts (A and B), as is a relatively low-signal nodule surrounded by edema (A). Edema also is noted to circumscribe peripheral regions of apparently normal cortex (B and C).

D and E, Axial spin-echo images, 500/30, before (D) and after (E) Gd-DTPA infusion. After contrast administration, a second tumor nodule is clearly defined. This finding is not apparent even in retrospect on any preinfusion image. Infusion studies indicate multiplicity. Improvement in diagnostic ability, therefore, was reported.

F, Postinfusion spin-echo image, 500/30, shows deep lesion detected preinfusion.
(Reprinted from [17], with permission.)

cases) did not always result in a change in diagnosis. Therefore, increased diagnostic confidence is reflected in these numbers; indirectly these data indicate an unexpectedly high underlying lack of confidence in the interpretation of preinfusion MR images, which may be greater than an interpreter might normally express in day-to-day clinical practice where infusion would not be available.

A change in diagnosis after contrast infusion was found most often in patients with multiple lesions. Of 16 patients in whom the diagnosis was changed after pre- and postinfusion images were compared, 10 exhibited an increase in the number of lesions detected. As previously observed in intraparenchymal cerebral metastasis [17], enhancement provides an increase in lesion conspicuity that can overcome the

TABLE 5: Changes in Serum Iron After Infusion of Gd-DTPA or Placebo

Condition: Postinjection Status	No. of Patients (%) ^a					
	Gd-DTPA			Placebo		
	2-4 hr (n = 54)	24 hr (n = 52)	48 hr (n = 43)	2-4 hr (n = 25)	24 hr (n = 24)	48 hr (n = 21)
≥15% rise from baseline	32 (59)	21 (40)	16 (37)	10 (40)	11 (46)	10 (48)
≥15% drop from baseline	8 (15)	18 (35)	16 (37)	7 (28)	7 (29)	7 (33)
Normal baseline:						
Normal	35 (65)	29 (56)	24 (55)	18 (72)	15 (63)	12 (57)
High	7 (13)	6 (12)	5 (12)	1 (4)	3 (13)	2 (10)
Low	1 (2)	7 (13)	6 (14)	1 (4)	3 (13)	4 (19)
High baseline:						
Normal	2 (4)	4 (8)	2 (5)	0	0	0
High	2 (4)	0	0	0	0	0
Low baseline:						
Normal	5 (9)	1 (2)	2 (5)	1 (4)	2 (8)	1 (5)
High	0	1 (2)	0	0	0	0
Low	2 (4)	4 (8)	4 (9)	4 (16)	1 (4)	2 (10)

Note.—No patients in either group with a high baseline had a low postinjection status.

^a The results are derived from those patients with both pre- and postinjection results.

difficulty encountered in detecting small, relatively isointense lesions at the periphery of high-intensity edema, lesions that may be mistaken for regions of normal brain parenchyma (Fig. 5). The failure to detect a second tumor nodule may lead to a failure to make the diagnosis of metastasis, as a solitary mass may represent not only solitary metastasis but other primary lesions of the neuraxis. Difficulty in multilesion detectability is compounded by the failure of noncontrast MR techniques to reliably detect small parenchymal masses not associated with appreciable edema (and focal T2 prolongation) [18-21]. Gd-DTPA-enhanced scans are, in these cases, demonstrably more sensitive to subtle defects in the blood-brain barrier than are noncontrast T2-weighted images.

The data on the optimal pulse sequence for lesion detection not surprisingly confirm the impression that T1-weighted short TR/short TE spin-echo images were superior to long TR images for lesion definition and diagnosis. In several cases, however, the long TR/intermediate TE sequence provided a nice combination of lesion depiction (as an area of short T1) and edema visualization (prolonged T2), and in one composite image all important diagnostic information was provided. Also, the intermediate sequence, in which image intensity is related to both T1 shortening and T2 prolongation, better detected two small lesions not well appreciated as areas of abnormal enhancement on postinfusion T1-weighted images alone (Fig. 3), indicating that T1 and T2 effects may be additive in these images and diagnostic information not available on either T1- or T2-weighted images alone may be produced. This additive effect explains the higher postinfusion contrast ranking and higher intensity scores noted for mass and mass vs normal tissue on T2-weighted scans. A limited number of small extraaxial lesions were studied in this investigation, and data support prior observations [22, 23] that Gd-DTPA infusion dramatically improves visualization in lesions not readily differentiable from adjacent brain substance (before infusion) by differences in inherent intensity alone.

Optimal timing of postinfusion sequences was studied by reviewing responses to question 6. The data summarized in Table 4 indicate that scans obtained within 27 min after infusion were best for detecting enhancement in 70% of cases. Immediate postinfusion imaging is particularly optimal for detecting extraaxial lesions [22, 23]. On the other hand, 13 of 43 cases were best examined after the 27-min time window. Patients best imaged late included those with small parenchymal lesions, which continued to increase in conspicuity on later T1-weighted images due to continued accumulation of contrast material. One lesion was not detected on either of the first two T1-weighted postinfusion sequences, but was noted on the third and last image obtained 55 min after infusion (Fig. 3). This (third) metastatic focus was, however, easily detected as an area of increased signal intensity on T2-weighted images obtained either before or after infusion of contrast material and, therefore, would not have been missed even if delayed postinfusion scans had not been obtained. This type of case certainly supports the need for obtaining preinfusion T2-weighted images routinely in almost all patients studied with Gd-DTPA.

Although some data are available [24], how rapidly one must study patients after Gd-DTPA injection is an issue likely to be determined more by the demands of scanner throughput than by subtle differences in lesion conspicuity, assuming that immediate postinfusion studies detect the vast majority of lesions, a premise supported by the results of our study. The fact that immediate scanning after infusion is likely to be the preferred method is further supported by the tendency of extraaxial lesions to enhance early and then fade [22, 23].

Although no patient's study went from the diagnostic to the nondiagnostic category after Gd-DTPA administration, such an occurrence is certainly possible. Such "enhancement to isointensity" can occur with contrast-enhanced CT when a subtly lucent lesion enhances just enough to blend with adjacent normal brain. One could predict that this phenome-

non would be encountered more often with MR if more heavily T1-weighted (inversion recovery) pulse sequences were used for pre- and postinfusion imaging. Inversion-recovery and very short TE spin-echo sequences show regions of prolonged T1 relaxation times as very distinct areas of low signal intensity, lower than that observed on the "T1-weighted" sequence used in this study. With these heavily T1-weighted sequences, enhancement may fail to overcome this focal low signal, producing isointensity and resulting in lowered diagnostic confidence. Preinfusion MR, therefore, is important not only for the detection of lesions with very short T1 relaxation times, such as hemorrhage (which may be masked by contrast enhancement), but also for the detection of lesions with very long T1 relaxation times to prevent this isointensity phenomenon.

A key question ultimately will be: When is contrast infusion needed? Our data show that a majority of patients are potentially diagnosable without contrast material, although diagnostic confidence and diagnostic accuracy clearly improve after infusion for a significant percentage of patients. This percentage might differ from that obtained at any particular MR facility, since image quality varied from site to site in our study group, and uniformly high-quality images might allow improved lesion detection of noncontrast images. Patients benefiting from infusion also include those who, although clinically suspected of harboring disease, subsequently are found to have a normal postinfusion MR study. We can conclude that infusion is not routinely needed in all patients, but with our current experience, it is not possible to predict with sufficient accuracy which patients do or do not need contrast studies. Unless images obtained before infusion are routinely monitored, and infusion is given only selectively in necessary cases (even this may be difficult to determine), it would appear that contrast material will be more widely used than what might, in retrospect, be required. Broader clinical experience (more widespread use of this agent) should eventually lead to specifically defined uses.

Safety studies performed as part of this placebo-controlled investigation indicate excellent clinical tolerance. No severe reactions were attributed to the drug, and few less severe reactions could even remotely be attributed to Gd-DTPA. Clinical hypotension reported in two patients was "possibly" attributable to Gd-DTPA administration in one, although cardiovascular effects are unlikely at the dose rates used in this study (maximum of 20 ml over 2 min). It is not known whether inadvertently rapid injections were related to the effects observed in this study, since none were reported or indicated in the study data. A lack of exacting technique might be implicated in view of the grouping of five patients with blood pressure abnormalities at one study site. Three of these patients had baseline systolic pressures over 160 mm Hg, suggesting that anxiety prior to the study may have affected later measurements. Such nonuniformities might be expected in a multicenter trial. It would seem likely that factors other than effect of contrast material explain the grouping of abnormal responses in these patients. To be sure, one would need to examine the exact conditions present at all sites before injection of contrast material, such as more stressful

or more relaxed scanning environments, patient education, and patient comfort in each scanner, issues not addressed in this investigation.

Although transient elevations in serum iron have been known to occur after Gd-DTPA administration [15, 16, 25] and were observed in this study (Table 5), there is no evidence that these findings are clinically significant. Animal studies suggest that iron elevation may be related to extrasplenic hemolysis [14-16], although the exact mechanism is unknown. Similar effects may occur with other injected agents. In any case, the low toxicity and low necessary injection volume indicate that Gd-DTPA is well suited for use as a contrast material in patients undergoing MR.

It should also be mentioned that the admission criteria for the study excluded patients with significantly abnormal chemistry and hematology and medical instability, leaving open the possibility that exposure of such patients to the drug may lead to unexpected drug toxicity. Also, because few patients have been reexposed to the agent, the absence of allergic reactions may not indicate that such reactions will not occur when the contrast material becomes more widely used.

In conclusion, Gd-DTPA (0.1 mmol/kg), when administered to patients with presumptive diagnoses of cerebral lesions, demonstrated safety and efficacy as a contrast medium for enhancement of MR images:

1. Gd-DTPA improved diagnostic ability in 65% of the patients and provided enhancement in 75%. For placebo patients, no postinfusion improvement was reported, nor was enhancement seen in any patient.
2. Gd-DTPA permitted diagnosis in nine patients from a group of 17 patients for whom no preinjection image was diagnostic, whereas of five placebo patients for whom no preinjection image was diagnostic, none had postinjection scans that permitted diagnosis.
3. In addition, use of Gd-DTPA resulted in a change in diagnosis in 16 (37%) of the 43 patients who experienced enhancement and permitted visualization of an increased number of lesions in 10 (23%) of the 43 patients.

ACKNOWLEDGMENTS

We thank Dorothy Woodward for manuscript preparation, Jane Washburn-Bleck for administrative assistance, Robert Quencer for editorial advice, and Michael S. Huckman for advice and support.

REFERENCES

1. Brant-Zawadzki M, Norman D, Newton TH, et al. Magnetic resonance of the brain: the optimal screening technique. *Radiology* 1984;152:71-77
2. Bradley WG, Waluch V, Yardley RA, Wyckoff RR. Comparison of CT and MR in 400 patients with suspected disease of the brain and cervical spinal cord. *Radiology* 1984;152:695-702
3. Bydder GM, Steiner RE, Younger IR, et al. Clinical NMR imaging of the brain: 140 cases. *AJNR* 1982;3:459-480, *AJR* 1982;139:215-236
4. Bydder GM, Steiner RE, Thomas DJ, et al. Nuclear magnetic resonance imaging of the posterior fossa: 50 cases. *Clin Radiol* 1983;34:173-188
5. Gadian DG, Payne JA, Bryant DJ, Young IR, Carr DH, Bydder GM. Gadolinium-DTPA as a contrast agent in MRI: theoretical projections and practical observations. *J Comput Assist Tomogr* 1985;9:242-251

6. Carr DH, Brown J, Bydder GM, et al. Clinical use of intravenous gadolinium-DTPA as a contrast agent in NMR imaging of cerebral tumors. *Lancet* **1984**;1:484-486
7. Felix R, Schorner W, Laniado M, et al. Brain tumors: MR imaging with gadolinium-DTPA. *Radiology* **1985**;156:681-688
8. Graif M, Bydder GM, Steiner RE, Neindorf P, Thomas D, Young IR. Contrast enhanced MR imaging of malignant brain tumors. *AJNR* **1985**;6:855-862
9. Claussen C, Laniado M, Kazner E, Schorner W, Felix R. Application of contrast agents in CT and MRI (NMR): their potential in imaging of brain tumors. *Neuroradiology* **1985**;27:164-171
10. Laniado M, Weinmann HJ, Schorner W, Felix R, Speck U. First use of gadolinium/dimeglumine in man. *Physiol Chem Phys Med NMR* **1984**;16:157-165
11. Brasch RC, Weinmann HJ, Wesbey GE. Contrast enhanced NMR imaging: animal studies using gadolinium-DTPA complex. *AJR* **1984**;142:625-630
12. Weinmann HJ, Brasch RC, Press WR, Wesbey GE. Characteristics of gadolinium-DTPA complex: a potential NMR contrast agent. *AJR* **1984**;142:619-624
13. Weinmann HJ, Laniado M, Mutzel W. Pharmacokinetics of Gd-DTPA/dimeglumine after intravenous injection into healthy volunteers. *Physiol Chem Phys Med NMR* **1984**;16:167-172
14. Carr DH, Brown J, Bydder GM, et al. Gadolinium-DTPA as a contrast agent in MRI: initial clinical experience in 20 patients. *AJR* **1984**;142:215-224
15. Bradley WG, Brant-Zawadzki M, Brasch RC, et al. Initial clinical experience with Gd-DTPA in North America: MR contrast enhancement of brain tumors (abstr). *Radiology* **1985**;157:125
16. Runge VM, Price AC. Gd-DTPA: an IV contrast agent for MRI investigation of intracranial neoplastic disease. Presented at the annual meeting of the American Society of Neuroradiology, San Diego, January **1986**
17. Russell EJ, Geremia GK, Johnson CE, et al. Multiple cerebral metastases: detectability with Gd-DTPA-enhanced MR imaging. *Radiology* **1987**;165:609-617
18. Healy ME, Hesselink JR, Press GA, Middleton MS. Increased detection of intracranial metastases with intravenous Gd-DTPA. *Radiology* **1987**;165:619-624
19. Claussen C, Laniado M, Schorner W, et al. Gadolinium-DTPA in MR imaging of glioblastomas and intracranial metastases. *AJNR* **1985**;6:669-674
20. Brant-Zawadzki M, Berry I, Osaki L, Brasch R, Murovic J, Norman D. Gd-DTPA in clinical MR of the brain: 1. Intraaxial lesions. *AJNR* **1986**;7:781-788
21. Woodruff WW Jr, Djang WT, McLendon RE, Heinz ER, Voorhees DR. Intracerebral malignant melanoma: high field-strength imaging. *Radiology* **1987**;165:209-213
22. Berry I, Brant-Zawadzki M, Osaki L, Brasch R, Murovic J, Newton TH. Gd-DTPA in clinical MR of the brain: 2. Extraaxial lesions and normal structures. *AJNR* **1986**;17:789-793
23. Breger RK, Papke RA, Pojuna KW, Haughton VM, Williams AL, Daniels DL. Benign extraaxial tumors: contrast enhancement with Gd-DTPA. *Radiology* **1987**;163:427-429
24. Schorner W, Laniado M, Niendorf HP, Schubert C, Felix R. Time dependent changes in image contrast in brain tumors after gadolinium-DTPA. *AJNR* **1986**;7:1013-1020
25. Neindorf HD, Laniado M, Semmler W, Schorner W, Felix R. Dose administration of gadolinium-DTPA in MR imaging of intracranial tumors. *AJNR* **1987**;8:803-815

Book Review

The Radiologic Clinics of North America. Imaging in Neuroradiology, Part II. Guest editors: S. Howard Lee and Robert A. Zimmerman. Philadelphia: Saunders, September 1988;26(5):893-1155. \$22.95; by subscription, 6 issues annually for \$89

The editors of *Imaging in Neuroradiology, Part II*, S. Howard Lee and Robert A. Zimmerman, state in the preface that this issue is "not a comprehensive review of all the subjects" but rather is meant to "provide basic principles and practical clinical applications . . . of different neurodiagnostic modalities. . . ." (Neurologic MR imaging was presented in part I.)

This volume contains 13 articles. The first seven deal with MR topics, which include common artifacts, contrast agents, and spine lesions (disk disease, tumors, and trauma). Two articles discuss positron emission tomography (PET) and single-photon emission CT (SPECT). Two articles deal with sonography: the first of the infant brain, and the second of vascular disease in the neck. The remaining two articles discuss topics in surgical neuroradiology.

The quality of the illustrations throughout the book is good to excellent. The explanation of each illustration is clear and succinct. The organization of the material in each article is excellent. The progression of thought builds on what has been presented earlier. The discussions are generally clear and free of cryptic or vague presentations. The basic principles, as well as an overview of each

topic, are well presented. A good bibliography is given with each topic, thus providing the reader who desires more information about a topic a source from which to begin. The article on MR contrast agents is erudite but does not provide the level of practical information found in the other articles. The article on PET investigation of CNS disorders is redundant to the article comparing SPECT with PET.

Overall I recommend this book for those who wish to be familiar with the various technologies that are affecting the study of neurophysiology and neuropathology and are or will be important in the diagnosis and treatment of neurologic disease. I know of no other current book that provides this level of overview so concisely and clearly. I recommend this book to radiology and neuroscience residents and to clinicians who care for persons who have neurologic disease.

Richard A. Flom
Barrow Neurological Institute
St. Joseph's Hospital and Medical Center
Phoenix, AZ 85001-2071

Gadolinium-DTPA-Enhanced MR Imaging of the Postoperative Lumbar Spine: Time Course and Mechanism of Enhancement

Jeffrey S. Ross¹
 Richard Delamarter²
 Mark G. Hueftle¹
 Thomas J. Masaryk¹
 Masamichi Aikawa³
 John Carter^{2,3}
 Carolyn VanDyke¹
 Michael T. Modic¹

To define the time course and mechanism of enhancement of epidural fibrosis after gadolinium-DTPA (Gd-DTPA) injection, we undertook a three-part study in humans and dogs with epidural scar after spine surgery. First, the dynamic in vivo contrast-enhancing properties of epidural scar were assessed by using sequential fast (18-sec) spin-echo sequences after contrast injection. Epidural scar in dogs rapidly enhanced; peak enhancement (101%) was 6 min after injection, with a slower decline toward baseline to 45% after 44 min. Epidural fibrosis in patients followed a similar pattern, with a maximum enhancement of 73% after 5 min. Paraspinal muscle had a lower peak enhancement in both patients (36%) and dogs (22%). Second, vascular injection in two dogs with India ink demonstrated multiple small vessels throughout the epidural scar. Third, light and electron microscopy was performed on epidural scar obtained at reoperation in both patients and dogs. Light microscopy showed multiple small capillaries scattered throughout a background of collagen. Electron microscopy demonstrated a wide variation in the junctions between endothelial cells ranging from "tight" to "loose." Regions of endothelial discontinuity were also visualized.

This study suggests that Gd-DTPA diffuses rapidly into the extravascular space in epidural scar, with a slower, net movement toward the intravascular compartment as the agent is renally filtered. The contrast agent transgresses the endothelium through "leaky" intercellular junctions and areas of endothelial discontinuity.

Scar is commonly misconceived as a mass of inert collagen representing the terminus of the healing process. In reality, scar is a dynamic, metabolically active material. This activity and vascularity have been used to some advantage with the administration of iodinated contrast material to enhance scar but not disk [1, 2]. This method is technically demanding, and has not achieved widespread use. We have previously shown that MR imaging is an effective technique in making the distinction between epidural fibrosis (scar) and recurrent disk herniation when gadolinium-DTPA (Gd-DTPA) is used in a way analogous to the use of iodinated contrast material [3]. Immediately after IV injection of Gd-DTPA, epidural scar is seen to enhance, while disk material does not enhance. However, the optimum timing for MR imaging after Gd-DTPA injection in the postoperative patient and the reason for such intense scar enhancement have not been elucidated. In an effort to define the time course and mechanism of the enhancement in epidural fibrosis, we undertook a three-part study in humans and animals with epidural scar after spine surgery: (1) vascular injection with India ink in dogs was performed to define the microvascular anatomy of the epidural scar, (2) light and electron microscopy of human and dog epidural fibrosis was performed to assess the scar vascularity and endothelial ultrastructure, and (3) the dynamic in vivo contrast-enhancing properties of Gd-DTPA and epidural scar were assessed by using sequential fast (18-sec) spin-echo sequences after injection of contrast material.

This article appears in the January/February 1989 issue of *AJNR* and the April 1989 issue of *AJR*.

Received March 25, 1988; accepted after revision July 12, 1988.

¹ Department of Radiology, University Hospitals of Cleveland, Case Western Reserve School of Medicine, 2074 Abington Rd., Cleveland, OH 44106. Address reprint requests to J. S. Ross.

² Department of Orthopaedic Surgery, University Hospitals of Cleveland, Case Western Reserve School of Medicine, Cleveland, OH 44106.

³ Department of Pathology, University Hospitals of Cleveland, Case Western Reserve School of Medicine, Cleveland, OH 44106.

AJR 152:825-834, April 1989
 0361-803X/89/1524-0825

© American Roentgen Ray Society

Materials, Subjects, and Methods

Animal Model

Six adult female beagle dogs (12–14 kg) underwent laminectomy at the L6–L7 level with Silastic banding of the dural tube at the level of the cauda equina 5 months before the Gd-DTPA studies. The banding was performed as part of an unrelated study on cord compression. Four dogs were imaged with MR, and tissue samples were subsequently removed at reoperation for the purpose of light and electron microscopy. Two dogs were used for the India ink vascular preparations. All animals were eventually sacrificed with an overdose of pentobarbital. Epidural scar has previously been shown to consistently form after laminectomy in dogs [4].

Patient Population

Thirty patients were enrolled in an open-label pilot study that used Gd-DTPA in patients with failed back surgery syndrome; the clinical results of that study are described elsewhere [3]. Dynamic MR studies were performed in three patients from this group, the methods of which are described more fully under Imaging Schemes and Pulse Sequences. In 13 patients in this group, signal-intensity measurements of intervertebral disks were obtained before and after contrast enhancement (see the Disk Enhancement section under Data Analysis). Recurrent disk herniation and surrounding scar, which were diagnosed in four patients, were confirmed at surgery.

Imaging Schemes and Pulse Sequences

Imaging experiments were performed on either a 1.0- or 1.5-T superconducting magnet.*

Four dogs were anesthetized with IV sodium pentobarbital, intubated, and placed supine within a 21-cm-diameter resonator coil centered over the lower lumbar spine. Immediately after acquisition of a precontrast axial image through the region of laminectomy, the dimeglumine salt of Gd-DTPA[†] was injected as a bolus (0.1 mmol/kg) into a forefoot vein without changing the position of the dog within the coil. The IV tubing was rapidly flushed with normal saline.

The dynamic MR studies were obtained by using a standard spin-echo sequence, 70/17 (TR/TE). This allowed a single slice (thickness, 10 mm) with two excitations to be performed every 18 sec. With the addition of software recycling time, images could be obtained approximately every 30 sec. Images were obtained every 30 sec for the first 5 min after injection of contrast material, then every 10 min up to 45 min total. There were 128 phase-encoded cycles. During image acquisition, TR, TE, and field of view were held constant.

Similar dynamic studies were performed in three patients with the failed back surgery syndrome in the first 5 min after administration of contrast material (0.1 mmol/kg Gd-DTPA[‡]). Precontrast MR images demonstrated abnormal epidural tissue suggestive of scar in all three cases. A single axial level for the dynamic MR study was chosen on the basis of these images. The administration protocol permitted a maximum contrast injection rate of 10 ml/min. Additional fast spin-echo sequences were then interleaved between the clinical images (approximately one image every 7–10 min). Images obtained for clinical diagnosis of scar or recurrent disk herniation were also used for signal-intensity measurements and consisted of pre- and postcon-

trast T1-weighted sagittal and axial images, 400/15, with a slice thickness of 4 mm and a 256 × 256 matrix.

Data Analysis

Scar.—Signal-intensity values were measured on the precontrast and each postcontrast image in regions of interest (ROIs) over epidural scar and the paraspinal musculature by using a cursor and graphic display device in both dogs and humans. The ROIs covered 0.1 cm² and were held constant in position and size while the pre- and postcontrast signal intensities of each area were measured. Pixel counts ranged from 30 to 50, but were held constant for any one set of images. Percent contrast enhancement was calculated by using the following formula:

$$\text{enhancement} = \frac{\text{postcontrast SI} - \text{precontrast SI}}{\text{precontrast SI}} \times 100.$$

where SI = signal intensity.

Standards were not included on the dog studies because of the difficulty in maintaining correct position and signal intensity with the field dropoff adherent with the use of surface coils. Corn oil standards were placed along the edge of the surface coil in three human patients studied, and these standards showed no signal variation between images.

Disk enhancement.—In 13 patients, similar signal-intensity measurements were obtained on the pre- and postcontrast studies in ROIs over the L3–L4, L4–L5, and L5–S1 intervertebral disks. These measurements were obtained from the central portions of the parent intervertebral disk on sagittal T1-weighted images. Pixel size and methodology were as described above for scar analysis. The post-contrast sagittal images were obtained approximately 5–15 min after injection of contrast material. Percent enhancement was calculated and compared for operated and nonoperated disk levels.

In four patients surgically proved recurrent disk herniations were surrounded by epidural fibrosis. In these cases, signal-intensity measurements and percent enhancement were obtained over the enhancing epidural scar and the central herniated disk material on precontrast axial T1-weighted images as well as on early (1–10 min) and late (33–58 min) postcontrast images.

Signal intensities of scar and paraspinal muscle after administration of contrast material were tested, as appropriate, for significant difference by means of Student's *t* test. A score of *p* < .05 was considered significant.

Vascular Studies

Two dogs were sacrificed and exsanguinated. Subsequently, the abdominal aorta was infused with a 1:1:1 mixture of latex, India ink, and water. The whole lumbar spine was then harvested, fixed in formalin (48 hr), dehydrated in 100% ethanol, and cleared in methyl salicylate. The epidural soft tissues were carefully dissected from the dura at the site of laminectomy for subsequent photography.

Specimen Acquisition

For the human studies, one of us was present during the operation and guided the surgeon to collect specimens as defined by the MR studies. Tissue specimens were obtained at reoperation in both humans and dogs. In general, wide laminectomies were performed, allowing good visualization of the epidural structures and precise tissue localization. A similar approach was used for collection of tissue specimens in dogs.

* Magnetom, Siemens Medical Systems, Iselin, NJ.

[†] Schering AG, Berlin, W. Germany.

[‡] Berlex Laboratories, Cedar Knolls, NJ.

All areas of epidural fibrosis (in patients and laboratory animals) prepared for microscopy demonstrated enhancement on MR after IV injection of Gd-DTPA. In all patients, initial surgery had been performed at least 6 months before. Areas of epidural fibrosis anterior or lateral to the dural tube were removed from seven patients during reoperation. These were immediately placed into the appropriate fixative. Portions of posterior and lateral epidural fibrosis were surgically removed from four dogs and immediately fixed for light and electron microscopy.

Fixations

Light microscopy.—Samples were fixed in 10% formaldehyde and embedded conventionally in paraffin. These samples were stained with hematoxylin and eosin.

Electron microscopy.—Samples were fixed in 2.5% glutaraldehyde buffered to pH 7.4 in 0.1 M sodium cacodylate and 7.5% sucrose for a minimum of 24 hr. Postfixation was performed with 1% osmium tetroxide for 1 hr. Specimens were then dehydrated in graded ethanols and embedded in Epon 812. One-micron-thick sections were examined by light microscopy, which were stained with methylene blue. Portions of interest were then cut with the use of diamond knives and stained with uranyl acetate. Observations were made with a JEM 100 CX electron microscope.

Results

The resolution of the dynamic spin-echo sequences permitted delineation of the vertebral bodies, thecal sac, epidural scar, paraspinal musculature, and other bony structures such as sacroiliac joints. In dogs, before administration of contrast material, the epidural scar was uniformly seen as a homogeneous area of intermediate signal intensity abutting the thecal sac and extending posteriorly a variable distance into the paraspinal musculature. After administration of Gd-DTPA, the epidural scar enhanced rapidly, with a peak enhancement (101%) on images acquired 6 min after injection and a slower decline toward baseline to 45% enhancement after 44 min (Figs. 1 and 2). Paraspinal musculature followed a similar pattern, although the peak enhancement at 4 min was only 22%. The postcontrast scar intensity values were significantly different from their respective postcontrast muscle values ($p < .005$).

In patients, the appearance of scar before contrast administration was of intermediate signal adjacent to the thecal sac (Fig. 3). After injection of Gd-DTPA, the scar enhanced in a pattern similar to that seen in dogs, with a maximum enhancement of 73% after 5 min. The enhancement decreased to



Fig. 1.—Enhancement of dog epidural scar.

Image 8 (top left), Precontrast image shows epidural soft tissue (arrow) to be of low signal, with indistinct thecal sac. Pelvic bones (S) and psoas muscles (P) are well seen.

Images 9–20 were obtained every 0.5 min after administration of Gd-DTPA. Note rapid and marked enhancement of epidural scar (arrows). Thecal sac becomes more well defined.

Images 25–27 (lower right), obtained 25, 26, and 27 min after injection, show decreased intensity within epidural scar.

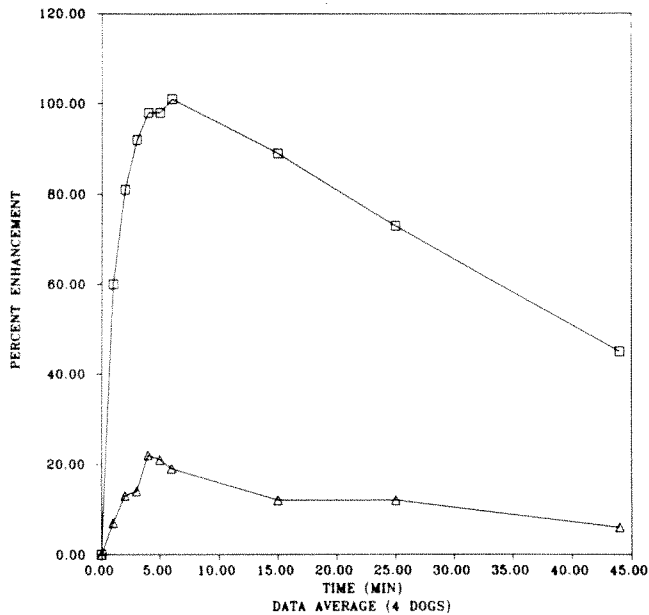


Fig. 2.—Gd-DTPA enhancement in dog epidural scar and muscle. There is rapid enhancement of scar (top curve) over the first 6 min, with a slower decrease over the next 38 min. Muscle enhancement (lower curve) is much less, although peak time is similar.

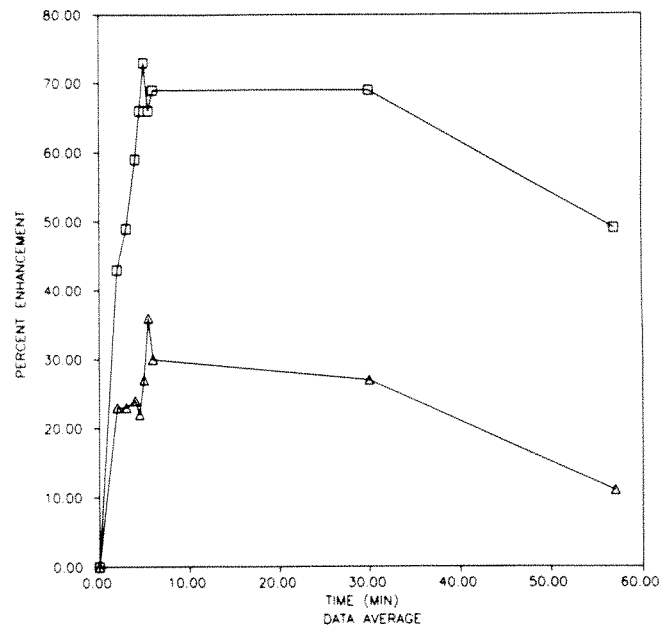


Fig. 4.—Gd-DTPA enhancement in human scar and muscle. Scar enhancement (top curve) follows a course similar to that in dogs, with a peak around 6 min and subsequent slower decline. Muscle follows a similar pattern, but with less overall intensity. Curves are averages from signal-intensity values of three patients with enhancing epidural scar.

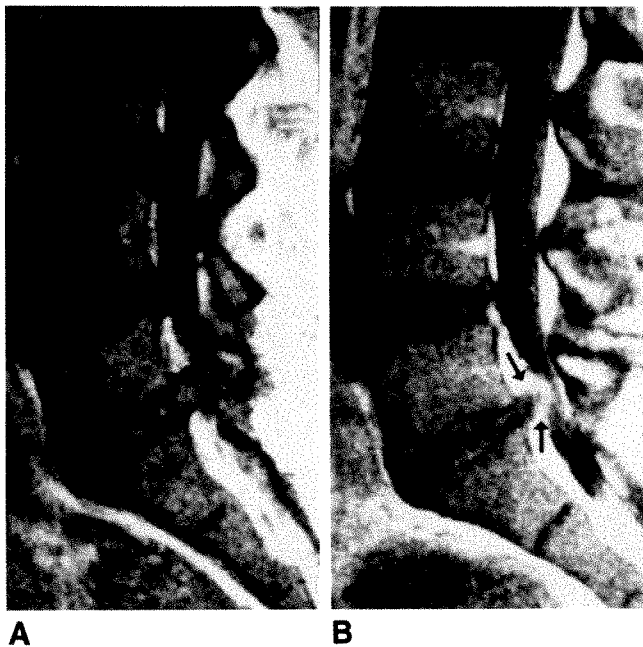


Fig. 3.—Enhancement of epidural scar. Sagittal T1-weighted images. A, Precontrast image shows large soft-tissue signal mass contiguous with L5-S1 disk space. B, Postcontrast image shows enhancement of scar surrounding large disk herniation (arrows). (Surgically proved.)

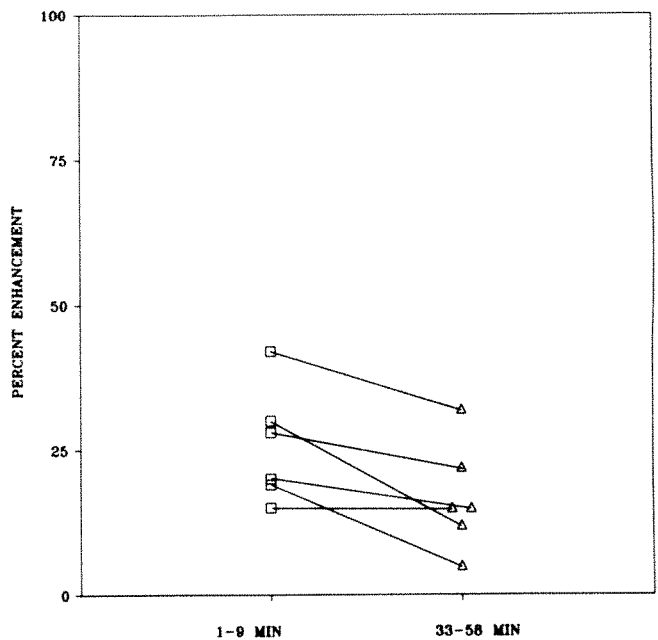


Fig. 5.—Muscle enhancement in six patients derived from signal intensities on spin-echo clinical images. Mild degree of enhancement is seen initially, with slow decrease by 33-58 min, similar to fast spin-echo data.

49% after 57 min. Paraspinal musculature had a lower peak enhancement (36%) after 5.5 min with a decrease to 11% after 57 min (Fig. 4). The postcontrast scar intensity values were significantly different from their respective postcontrast

muscle values ($p < .005$). As a check on the fast spin-echo enhancement of paraspinal muscle, in six patients signal intensities were obtained from ROIs over paraspinal muscle on the pre- and postcontrast clinical axial T1-weighted im-



Fig. 6.—Late enhancement of disk herniation.

A, Preoperative axial T1-weighted MR image shows indistinct thecal sac and posterior laminectomy scar.
 B, Immediate postcontrast image shows enhancement of scar tissue surrounding large nonenhancing disk herniation (solid arrow). Posterior scar also enhances prominently (open arrow).
 C, Late postcontrast image shows smudging of scar/disk herniation interface with enhancement involving disk periphery (arrow). (Surgically proved.)

ages. These enhancement values followed those seen with the fast spin-echo sequences (Fig. 5).

In four patients post-Gd-DTPA images showed enhancement surrounding a recurrent disk herniation. Subsequently, these were all proved histopathologically to be disks "wrapped" in scar after reoperation (Fig. 6). In these patients, the percent enhancement was calculated from ROIs over the enhancing scar, as well as over disk on the postcontrast early and late axial T1-weighted clinical images. The disk material either remained the same intensity or, in three of four cases, increased in signal on the late study. Peridiskal scar signal intensity was more variable, being increased, decreased, or unchanged with time (Fig. 7).

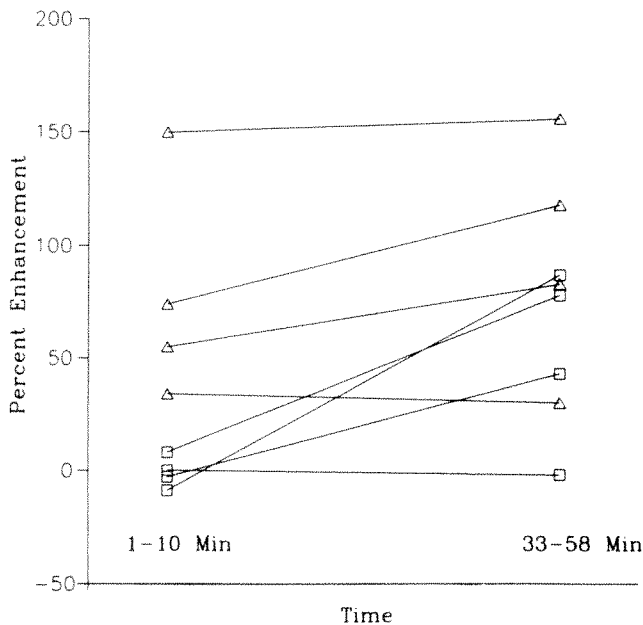


Fig. 7.—Enhancement of disk herniations. Early and late postcontrast enhancement percentages of peridiskal scar (triangles) and disk herniations (squares) in four patients. Enhancement is seen to occur in three disk herniations by the late study.

In certain cases, the central aspect of the intervertebral disk (not disk herniation) enhanced. In 13 patients the percent enhancement was obtained from the pre- and postsagittal clinical images for the L3, L4, and L5 disks. Three intervertebral disks at previously operated levels showed marked enhancement (Fig. 8).

Vascular Injection

The vascular preparations in two dogs showed multiple small vessels extending throughout the epidural scar (Fig. 9).

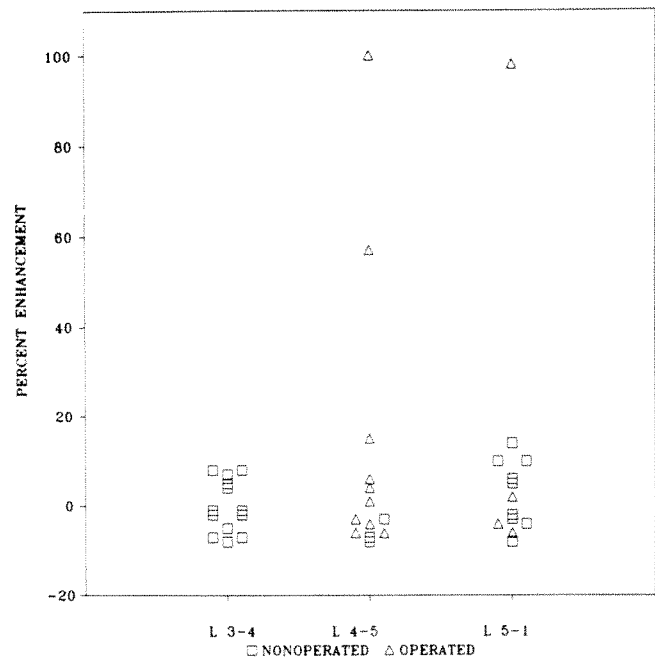


Fig. 8.—Enhancement of central intervertebral disk for operated and nonoperated levels. Levels that enhance markedly had been operated previously ($n = 13$). Signal intensities were obtained 5–15 minutes after injection.

Light Microscopy

Light microscopy of epidural scar from four dogs and seven humans showed scattered fibrocytes, capillaries, and abundant collagen (Fig. 10). In two patients, the scar had two components. One component consisted of plump fibroblasts with multiple small vessels similar to granulation tissue. This tissue surrounded one disk herniation (Fig. 11). The second component showed scanty vessels and fibrocytes, with abundant collagen forming parallel wavy rows representing mature scar.

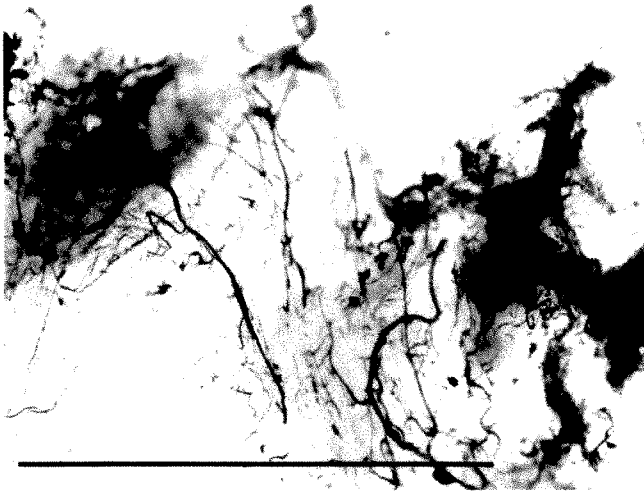


Fig. 9.—Epidural dog scar, India ink vascular injection. Multiple small vessels are distributed throughout scar. Bar represents 1 cm.

Electron Microscopy

Electron microscopy was performed in specimens of scar from two humans and three dogs. These showed three principal findings:

1. True tight junctions (zonulae occludens), where the outer leaflets of the adjoining endothelial cell membranes converged to form a single fused line. These varied in size from a small band of membrane fusion (Fig. 12A) to a focal point of membrane apposition (Fig. 12B). These variations were present in both human and dog scar tissue.

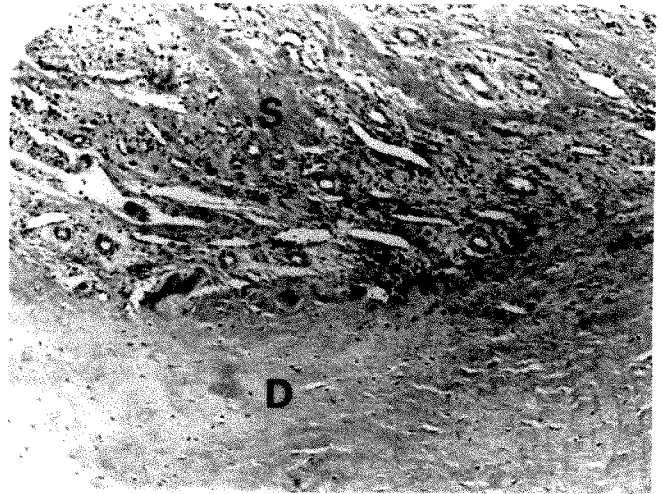
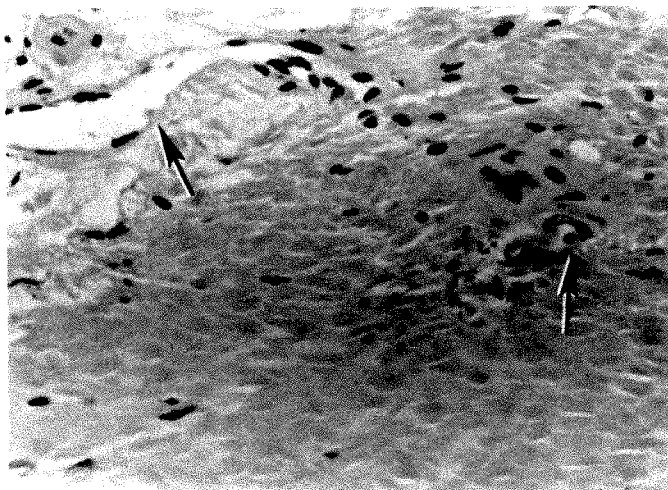
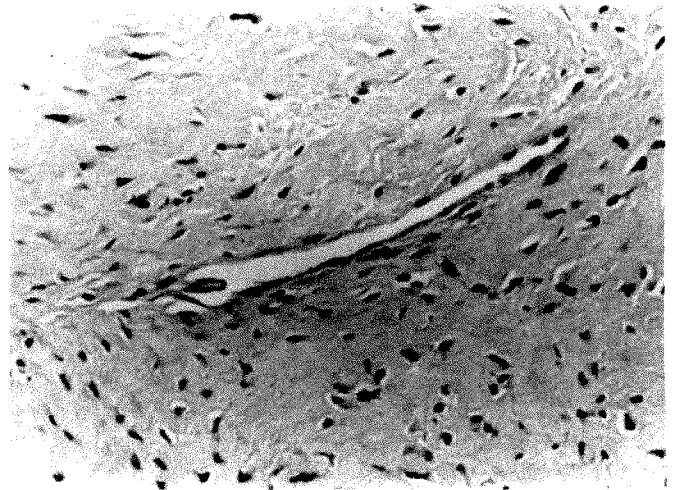


Fig. 11.—Peridiskal scar (same patient as in Fig. 6). Light micrograph shows vascular granulation tissue (S) surrounding avascular disk material (D) (anulus fibrosus). (H and E)



A



B

Fig. 10.—Light micrographs of epidural scar. (H and E)

A, Human scar. Abundant collagen and several capillaries (arrows). (Same patient as in Fig. 3.)

B, Dog scar. Collagen and occasional capillaries, similar in appearance to human scar tissue.

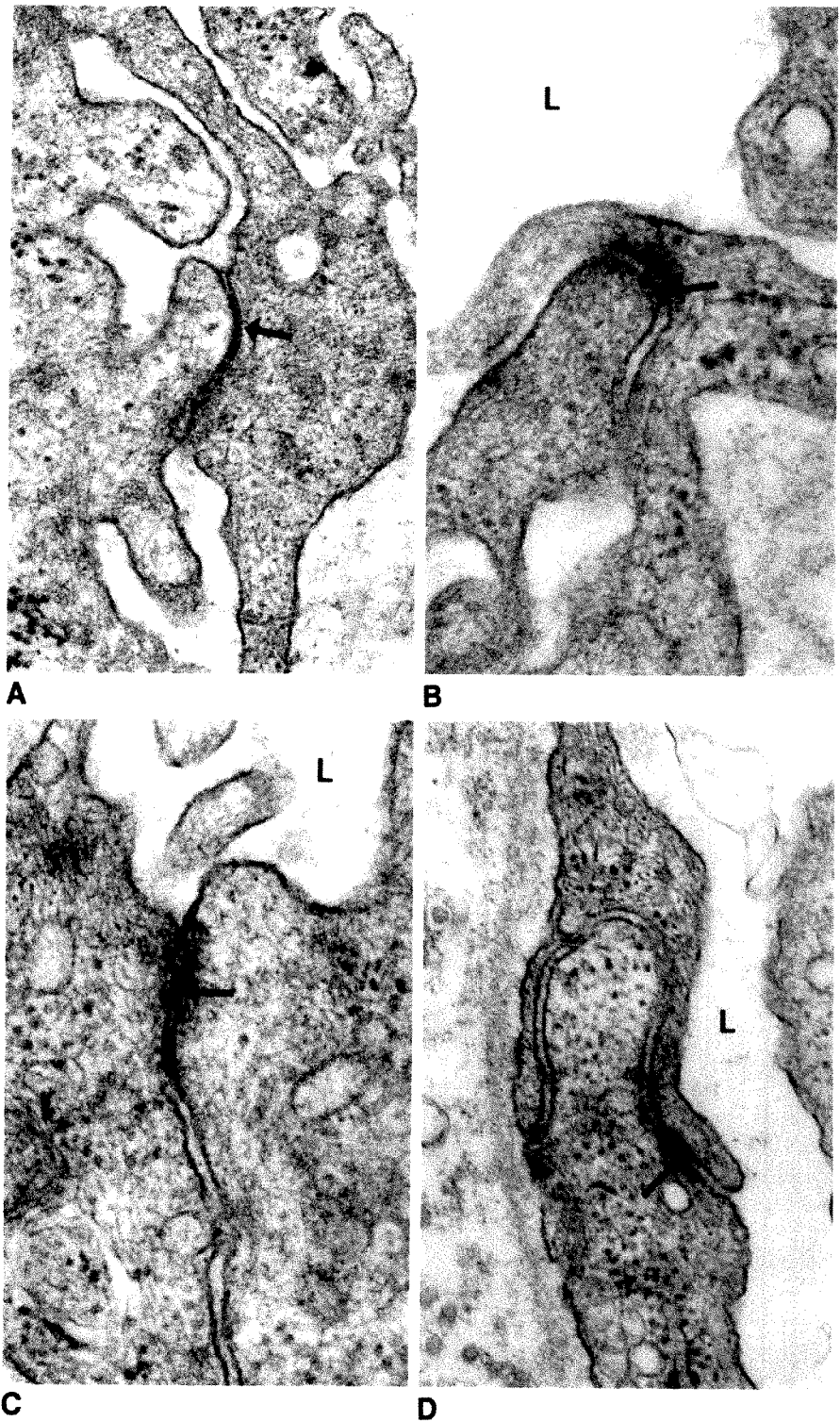
Fig. 12.—Electron micrographs of human (A–C [same patient as in Figs. 3 and 10A]) and dog (D) scar endothelial junctions.

A, Tight junction (arrow) shows linear, electron-dense area representing fusion of inner membranes of adjacent endothelial cells. ($\times 99,000$)

B, "Focal" tight junction (arrow) shows small area of membrane contact. L = lumen. ($\times 99,000$)

C, "Open" junction (arrow) shows slight increased electron density along cell membranes at luminal surface (L), but no areas of membrane contact. ($\times 99,000$)

D, Dog "open" junction (arrow). Appearance of adjacent cell membranes is similar to that in C. ($\times 70,000$)



2. "Loose" tight junctions, where the outer leaflets approached each other but did not fuse (Figs. 12C and 12D). The loose junctions were also visualized in human and dog samples.

3. Intercellular gaps, where there was a wide space between the endothelial cell membranes extending from lumina to basement membrane (Fig. 13). The endothelial cells themselves were otherwise normal in appearance, as were the

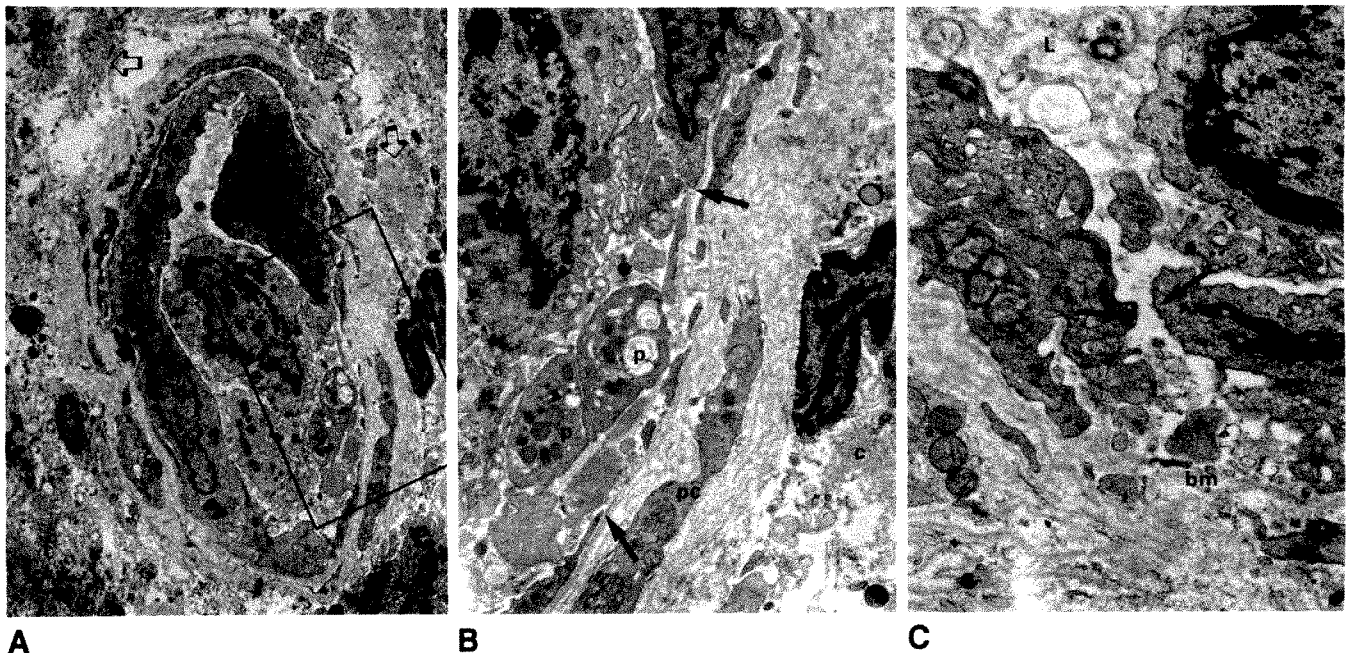


Fig. 13.—Dog epidural scar: discontinuous endothelium.

A, Electron micrograph of scar capillary. Box denotes region of higher magnification in B. Note abundant collagen in extracellular space (arrows). ($\times 6600$)

B, Higher magnification shows ends of adjacent endothelial cells (arrows), with only basement membrane in intervening space. P = platelets; pc = pericytes; c = collagen. ($\times 16,500$)

C, Different area of endothelial discontinuity. Ends of adjacent endothelial cells (arrows) are separated by small space, connecting the lumen (L) directly to basement membrane (bm). ($\times 25,000$)

pericytes and the interstitium. Abundant collagen was present surrounding the vessels.

Discussion

We have previously described the effectiveness of Gd-DTPA in evaluation of the failed back surgery syndrome. Although the biodistribution of Gd-DTPA has been explored for many normal and abnormal tissues, no reports exist concerning the time course of enhancement within epidural fibrosis. In general, three things are necessary for contrast enhancement of any tissue: (1) a vascular supply, (2) a route for the contrast material out of the vasculature, and (3) an interstitial space for sequestering the contrast material. Epidural scar has all of these attributes. Epidural scar has an abundant vascular supply, as shown by the India ink preparations. A potential pathway out of the vasculature was demonstrated by electron microscopy, and the large interstitial or extracellular space was apparent from the light and electron microscopy.

Electron microscopic studies have shown that there are at least four potential passive pathways for molecules through normal endothelium [5]. The smallest is the 0.3- to 0.4-nm hydrophilic pore in the cell membrane. Although this pathway is crucial to ion and water movement between and into the endothelial cells, it is less important in transendothelial transport than are the larger pathways, because of its hydraulic resistance. The next largest pathways are the intercellular

channels, or tight junctions, where under normal conditions the largest molecules that can pass are 2–4 nm. Large molecules such as albumin (4.2 nm and mol wt, 59,000) or horseradish peroxidase (mol wt, 40,000) may be transported through either pinocytotic vesicles or even larger channels. These larger channels would include fenestrated or discontinuous endothelium, as exist in the renal glomeruli or bone marrow, respectively [6].

Our electron microscopic findings suggest that there are two major routes for egress of the small molecule of Gd-DTPA. One is through tight junctions or variants thereof. The zonula occludens closes or seals adjacent cells, which reduces diffusion [7, 8]. These types of junctions allow the creation of gradients between the lumen and the underlying tissues. However, the sealing capacity of tight junctions is quite variable, and relates to cell function. Tissues that need to maintain a steep ionic or osmotic gradient have junctions so tight as to block the movement of small electrolytes and water. "Leakiness" has been related to the freeze-etch morphology of the tissues; "very tight" junctions exhibit a deep zonula occludens with many areas of membrane fusion, while leaky junctions consist of at most one area of fusion [9]. Our electron microscopic observations suggest that the capillaries in scar consist of "leaky" tight junctions with either single areas of fusion or no direct membrane contact. Further, these junctions are relatively short in the apical-basal direction. The second major route for escape of contrast material is the large intercellular gaps. These focal areas of endothelial discontinuity would provide relatively direct access of contrast

material from the lumen into the interstitial space. Discontinuous capillaries normally are found only in organs adapted for free passage of large molecules into and out of the blood; that is, liver, spleen, and bone marrow. In regenerating tissue, endothelial cells within new blood vessels in retina and iris have been shown to be "leaky" to fluorescein and low-molecular-weight tracers secondary to fenestrated capillaries and open intercellular junctions [6]. The leaky junctions and intercellular gaps observed in the endothelium of epidural fibrosis would seem to provide a basic structure-function correlation with Gd-DTPA enhancement.

The biodistribution and kinetics of DTPA-metal ion complexes have been reported for normal tissues [10-14]. The chelates are distributed throughout the extracellular space and are rapidly eliminated by glomerular filtration. Gd-DTPA does not appear to cross intact cell membranes. Gd-DTPA dimeglumine is a small molecule (mol wt, 938) and is similar in size to diatrizoate (mol wt, 600) and iohalamate. This study and others [14-17] suggest that Gd-DTPA diffuses rapidly into the extravascular space. After the equilibration of Gd-DTPA between the intra- and extravascular compartment, the net movement is toward the intravascular compartment, since the agent is renally filtered. Our enhancement curves with Gd-DTPA for scar are very similar to those of the extravascular compartment curves previously described for iohalamate [18]. The increase in the signal intensity of scar tissue would support the theory that tissues with relatively large extravascular spaces and long T1 relaxation times will enhance conspicuously [15, 19, 20]. Certainly, scar tissue, with its abundant collagen, fits this category. Although the overall pattern of enhancement is similar for muscle and epidural scar, there was a qualitative increase in enhancement of scar over muscle with time. This could potentially reflect (1) more vascularity within scar tissue or (2) larger extravascular spaces within scar tissue. Muscle, being an extremely metabolically active tissue, has a large vascular supply and is unlikely to be the cause of the low differential enhancement, as contrasted to epidural scar. However, muscle does have a relatively small extravascular space when compared with scar. The small extravascular space in muscle would not allow the sequestration of contrast material to the same extent as would the large collagen-filled extravascular space in epidural fibrosis.

Our pathologic findings in disk herniations surrounded by scar that enhanced on the late MR studies showed little or no vascularity within the herniations. Although the mechanism of enhancement of disk herniation and intervertebral disk remains speculative, three possibilities should be considered: (1) diffusion of contrast material from the vascular peridiskal scar into the herniation with time, (2) enhancement within intervertebral disks could be secondary to diffusion via vascularized scar from previous curettage of the disk space during surgery, or (3) granulation tissue associated with severe degenerative change. In this group of patients, only the intervertebral disks that were previously curetted showed enhancement. Of course, previous surgical curettage does not mean the parent disk must invariably enhance.

Certain areas of this study deserve further comment. It is highly unlikely that the electron microscopic features of epidural scar could be ascribed to fixation artifact. Great care

was taken to immediately immerse small tissue samples in the fixative. The structure of the other intracellular organelles (such as nuclei, mitochondria, and endoplasmic reticulum) was well defined on the same images and were without obvious fixation artifact. Further, regions of intimate cell-to-cell contact involved in ion exchange (gap junctions) were visualized in our specimens, suggesting adequate fixation of all junctional complexes. The potential for sampling error in the histopathologic studies remains a problem, especially with the electron micrographs. Although the variations in endothelial junctions were seen in both human and dog epidural scar, the discontinuous endothelium was seen by electron microscopy only in dog scar. Whether this variation in endothelial structure actually exists in human scar remains unknown. The enhancement curves of Gd-DTPA might be hampered by the inability to bolus the contrast agent in humans. To what degree, if any, this affected the curves is unknown, but it was also unavoidable due to the drug protocol. We have not directly defined the route of egress of Gd-DTPA into epidural fibrosis. Only autoradiographic electron microscopic techniques would show the course of diffusion of the contrast agent.

One puzzling aspect of this study is the fact that there was rapid egress of contrast material into both scar and paraspinal muscle, while scar has been shown to have "open" junctions and discontinuous endothelium. This fact may be related to the gross assessment of vascular permeability that dynamic MR represents. Small differences in capillary permeability probably are not detected with this technique, as opposed to a more sensitive and invasive technique such as measurement of hydraulic conductivity [21]. However, our hypothesis concerning the permeability of scar endothelium parallels the findings of Giacomelli et al. [22], who found that the permeability of subendocardial capillaries to horseradish peroxidase could be accounted for by larger-sized interendothelial clefts (i.e., open junctions).

In conclusion, we have defined open junctions and areas of discontinuous endothelium within epidural scar. Given the known size of the molecule, its time course of enhancement, and the potential routes for diffusion, we conclude that Gd-DTPA reaches the capacious extravascular space in scar via the "leaky" junctional complexes.

REFERENCES

1. Braun IF, Hoffman JC, Davis PC, Landman JA, Tindall GT. Contrast enhancement in CT differentiation between recurrent disk herniation and postoperative scar. *AJNR* 1985;6:607-612, *AJR* 1985;145:785-790
2. Teplick JG, Haskin ME. Intravenous contrast enhanced CT of the postoperative lumbar spine: improved identification of recurrent disk herniation, scar, arachnoiditis, and diskitis. *AJNR* 1984;5:373-383, *AJR* 1984;143:845-855
3. Hueftle M, Modic MT, Ross JS, et al. Lumbar spine: postoperative MR imaging with Gd-DTPA. *Radiology* 1988;167:817-824
4. LaRocca H. The laminectomy membrane: studies in its evolution, characteristics, effects and prophylaxis in dogs. *J Bone Joint Surg [Br]* 1974;56-B(3):545-550
5. Weinbaum S. Mathematical models for transport across the endothelial cell layers. *Ann NY Acad Sci* 1983;416:92-114
6. Tripathi RC, Tripathi BJ. Functional ultrastructure of endothelium. *Bibl Anat* 1977;16:307-312

MR Imaging Artifacts of the Axial Internal Anatomy of the Cervical Spinal Cord

Andrew J. Curtin¹
 Donald W. Chakeres¹
 Robert Bulas¹
 Carl P. Boesel²
 Mark Finneran¹
 Eric Flint¹

Transverse scans of the spinal cord routinely demonstrate signal variations related to the internal anatomy of the cord that do not accurately conform to histologic cross sections. This study evaluates the MR appearance of the axial anatomy of the spinal cord and provides correlation to histologic sections as a means to understand this discordance so that disease can be recognized more readily. Short TR/TE spin-echo studies, cardiac-gated multiecho spin-echo studies, and gradient-refocused-echo studies of normal excised human spinal cords, a normal volunteer, and gelatin phantoms were obtained by using the same imaging parameters at 1.5 T. Imaging artifacts were further investigated by using both a 128×256 and 256×256 matrix with a varying phase-encoded axis. Histologic sections of the excised cords, which were stained for myelin, iron, and cell bodies (Nissl), were used for correlation to the images. We found that significant Fourier truncation and partial-volume imaging artifacts modulated the MR display of the cord. On short TR/TE images a ring of high signal at the periphery of the cord was due to a truncation artifact. The appearance of the central portions of the gray and white matter was affected variably by partial-volume averaging depending on the matrix size. White-matter tracts of the cord were always lower in signal than was the gray matter on all pulse sequences. This finding was not due to iron deposition or CSF motion artifacts. We suspect that this probably was related to dense, longitudinal organization of spinal tracts and resultant anisotropy of water molecule motion similar to that seen in the pyramidal tracts, tendons, and ligaments.

We recommend the use of a 128×256 matrix with two averages (four excitations) when obtaining axial scans of the spinal cord in living subjects. Although truncation artifacts diminish image quality, the quality is superior to that of images obtained with a 256×256 matrix, in which longer scanning times result in motion artifacts and reduced signal to noise.

Several high-resolution MR imaging studies of the spine have been reported that describe the appearance of the nerve roots, spinal cord, bones, and subarachnoid and epidural spaces [1-8]. This study addresses the normal appearance of the transverse (axial) anatomy of the cervical spinal cord on MR images. With improvement in image quality, owing primarily to surface-coil imaging, recognizable signal variations within the spinal cord are routinely visible. However, the MR appearance does not accurately or simply reflect the normal histologic anatomy. The signal-contrast relationships of the gray and white matter of the cord are different from those of the brain [9]. This study attempts to explain the discordance between the histologic and MR appearances in order to define the normal spinal cord so that disease can be recognized more easily.

Truncation artifacts seen on sagittal images of the cervical cord have already been described [6, 7]. We speculated that some of the findings on axial MR were due to similar technical variations, so a detailed study was undertaken of MR images obtained in cadaver spinal cords, phantoms, and a normal volunteer.

Materials and Methods

Normal fresh human cadaver spinal cords were excised at autopsy. Transverse sections of the formalin-fixed cervical cord were stained for myelin by using Weigert's method, for cell

This article appears in the January/February 1989 issue of *AJNR* and the April 1989 issue of *AJR*.

Received May 11, 1988; accepted after revision September 7, 1988.

¹ Department of Radiology, Division of Neuroradiology, Ohio State University College of Medicine, 410 W. 10th Ave., Columbus, OH 43210. Address reprint requests to A. J. Curtin.

² Department of Pathology, Division of Neuropathology, Ohio State University College of Medicine, Columbus, OH 43210.

AJR 152:835-842, April 1989
 0361-803X/89/1524-0835
 © American Roentgen Ray Society

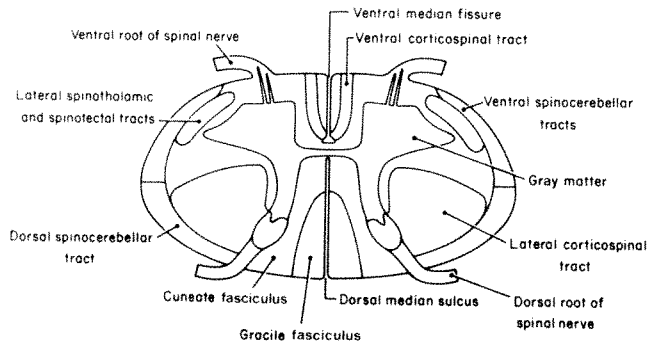


Fig. 1.—Axial anatomy of cord. Schematic drawing shows major spinal white-matter tracts and central gray matter.



Fig. 2.—Myelin stain. Photomicrograph of normal human cervical cord. Transverse section is stained for myelin with Weigert's method. White-matter tracts stain more intensely than does butterfly-shaped central gray matter.



Fig. 3.—Photomicrograph of human cord at level similar to that of Fig. 2. White matter does not stain, but cell bodies in gray matter take up stain, seen as tiny, darker staining areas within gray matter. Very thin, dark rim at periphery is artifact of staining.

bodies by using a Nissl stain, and for ferric iron as per Gans [10] (Figs. 1–3).

All images were generated on a 1.5-T MR unit,* with a 10- by 28-cm license-plate-shaped receive-only surface coil. Slice thickness was

5 mm with a 1-mm gap between slices and one or two averages (two or four excitations). Fields of view were 16 and 20 cm. Both 128×256 and 256×256 matrices were used, varying the direction of the phase-encoded gradient. Imaging parameters included spin-echo images, 800/20/4 (TR/TE/excitations) (imaging times, 13 min 41 sec with a 256×256 matrix and 6 min 50 sec with a 128×256 matrix); gradient-refocused at a steady-state (GRASS) images [11], 1000/12/4, with a low flip angle of 22.5° (imaging times, 17 min 56 sec with a 256×256 matrix and 8 min 58 sec with a 128×256 matrix); as well as cardiac-gated spin-echo images, 2571/40,80/4 (imaging time, 22 min 1 sec with a 256×128 matrix).

Cylindrical, circular gelatin phantoms (1.4 and 2.5 cm in diameter), freshly excised cadaver spinal cords (Figs. 4C, 5C, and 6C), and a single normal volunteer (Figs. 4D, 5D, 6D, and 7C) were imaged with similar scanning parameters. The phantoms and excised cords were imaged both in air and in water baths (Figs. 4B, 5B, 6B, and 7B).

Images of the cadaver cords and the normal volunteer were analyzed and correlated with histologic sections, pixel diagrams, and phantom MR images.

Results

The transverse anatomy of the spinal cord has a central "butterfly" or an H configuration of gray matter (Fig. 1). The ventral collection of anterior horn cells is larger. A thin ventral commissure crosses the midline at the anterior third of the cord. The white-matter tracts are the major components of the cervical cord and surround this gray matter. Weigert's method stains the myelinated white-matter tracts (Fig. 2). The large dorsal columns of white matter form a triangle that appears as an upside-down V posterior to the central gray matter. The lateral and anterior tracts of white matter are composed predominantly of lateral cortical spinal tracts and envelop most of the remainder of the central gray matter. The ventral white-matter columns are much smaller than the posterior columns. The fissure is seen to be broader anteriorly than posteriorly.

Nissl's method stains the cell bodies of the central gray matter, which then appear as small areas of increased staining (Fig. 3). Because there is no peripheral gray matter there is no staining in this region. Iron stains, used to show normal deposits of physiologic iron in the brain, failed to show significant areas of ferric iron deposition (not shown).

Axial scans through the gelatin phantoms demonstrated an apparent ring of high signal at the surface of the gels (Figs. 4B, 5B, and 6B). With the 128×256 matrix, arcs or rings of alternating high and low signal were present within the phantom parallel to the surfaces along the phase and frequency axes only, producing variations in the signal (which one would expect to be homogeneous). These rings occurred in both the frequency- and phase-encoded directions but were thicker in the phase-encoded direction with 128 gradient steps. Switching the axis of the 128 phase-encoded gradient steps changed the direction of the thicker rings (Figs. 4B and 5B). The effect was more pronounced on the images of the smaller 1.4-cm-diameter gel. The artifact was significantly diminished with the 256×256 matrix size (Fig. 6B); however, a thin, bright-signal surface ring persisted. These ring patterns were present on both air and water bath (not shown) images of the phantoms, but were much more apparent on the air studies. In addition to producing apparent signal variations within the homogeneous gels, a geometric distortion also occurred,

* General Electric, Milwaukee.

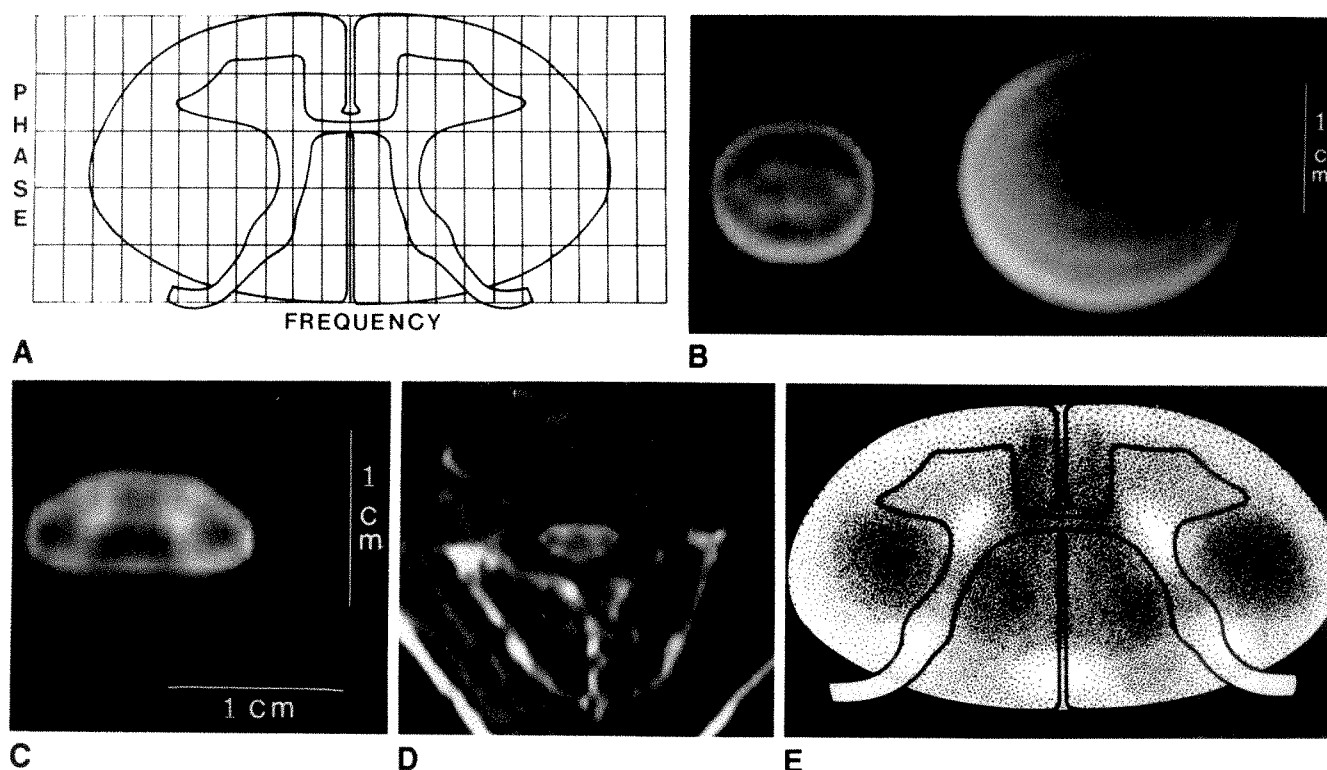


Fig. 4.—Pixel size and orientation.

A, Grid of rectangular boxes overlying transverse section of cord is drawn to scale approximating the number and size of pixels displaying the human cord when a 128×256 matrix and 16-cm field of view is used. Note that when 128 phase-encoded steps run anterior to posterior, only five pixels per row span cord.

B, Gel phantom. Axial scan, 800/20, through cylindrical gelatin phantoms in air with 128×256 matrix and 128 in phase-encoded direction. Artifactual rings of high and low signal traverse internal structure of homogeneous phantom. Note high signal at periphery, which is thicker in phase-encoded direction. Geometric distortion of circular gel to more oval appearance is due to partial-volume effects.

C, Excised cord. Axial scan of excised human cervical cord in air with parameters identical to those of gelatin phantom (B). High-signal rim that is thicker in phase-encoded direction surrounds two lateral circular areas of low signal overlying regions of corticospinal tracts. Butterfly-shaped area of high signal approximates gray matter. Central triangle of low signal approximates anterior and posterior columns.

D, Human volunteer. Axial section of cervical spine, same parameters as B and C. Note that appearance is similar to that seen in excised cord (C).

E, Location of gray-matter tracts with overlay drawing of approximate locations of high and low signal seen on short TR/TE images with 128×256 matrix.

resulting in an oval shape on the transverse section (Figs. 4B and 5B), with the gel appearing more circular on the 256×256 matrix image (Fig. 6B).

The short TR/TE (800/20) MR images (Figs. 4C and 5C) of the excised cadaver cords surrounded by air demonstrated a high-signal ring at the periphery and two low-signal circular regions in the lateral cord substance. A paramidline lower-signal region was seen as a triangle that was broader posteriorly. These low-signal regions outlined two higher-signal regions that approximately, but not exactly, conformed to the central gray matter (Fig. 4E). The exact configuration of these findings varied, depending on the matrix size, voxel size, and direction of the phase-encoded gradient (Figs. 4C, 5C, and 6C). The findings were similar to those in the gelatin phantoms, in which the peripheral ring of high signal was thickest in the phase-encoded direction on the 128×256 matrix images. The appearance of the internal anatomy also changed with the phase-encoded axis, making the gray-matter structures appear to vary in configuration. Slight distortion of the external oval shape of the cord was present depending on the matrix size (Figs. 4C, 5C, and 6C). Visualization of the

internal anatomy of excised human cord was best, and most accurately reflected the true anatomy, when two averages (four excitations) and a 256×256 matrix were used (Fig. 6C). Such high-quality definition of internal anatomy was not obtained in the living subjects with the 256×256 matrix/two averages technique (Fig. 6E).

Excised spinal cord imaged in a water bath with the spin-echo 800/20 technique produced images similar to those found for the cord imaged in air. The image showed the surrounding stationary water bath (not shown) as low signal with a high-signal ring present around the cord that was not as apparent as that seen in air.

The appearance of the excised cord surrounded by air with the GRASS technique appeared nearly identical to that of the short TR/TE sequences in air (Fig. 7A). However, when the cord was placed in a tube filled with water, the high-signal ring disappeared and the periphery was low signal (Fig. 7B). Spin-echo images of the excised cord, 2500/40, 80, were also obtained surrounded by air. The appearance of the internal anatomy on these long TR spin-echo images was similar to that on the other pulse sequences.

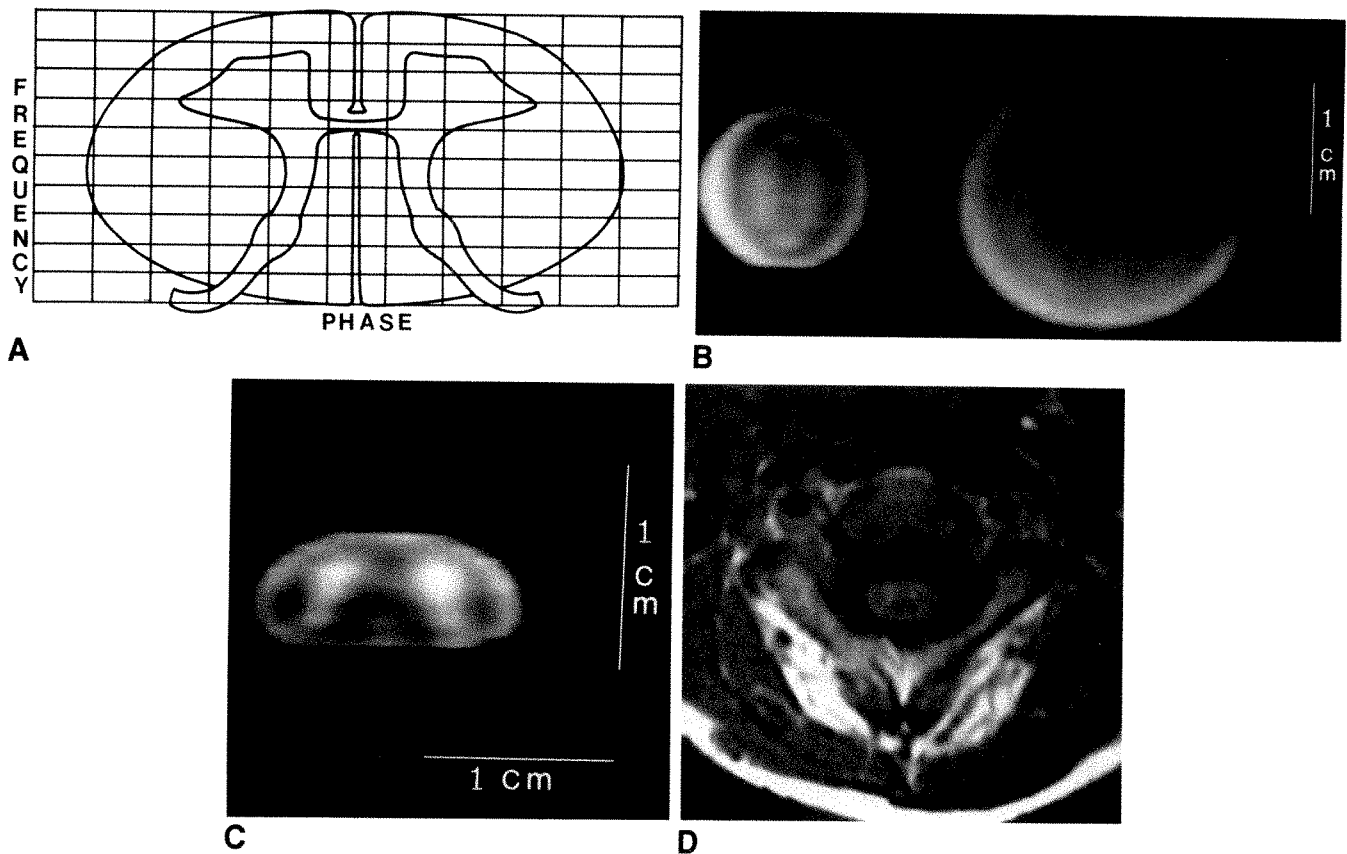


Fig. 5.—Voxel size and orientation, 128×256 matrix.

- A, Pixel grid of 128×256 matrix, similar to Fig. 4A, but phase and frequency directions are reversed.
 B, Gel phantoms identical to those in Fig. 4B with same imaging parameters except phase and frequency directions switched. Note rim of high signal, thicker in phase-encoded direction, now runs from side to side.
 C, Excised cervical cord. Axial scan in air through same human cadaver at same level and with imaging parameters identical to those in Fig. 4C but with phase and frequency directions reversed. Lateral ovals of low signal have changed to more vertical oval orientation due to partial-volume effects, and entire cord has a more oval appearance. The same high-signal rim is apparent but is thicker from side to side in phase-encoded direction.
 D, Human volunteer. Axial scan again shows areas of high and low signal similar to that of excised cord.

The 128×256 matrix volunteer studies with the short TR/TE spin-echo series, cardiac-gated, and non-cardiac-gated techniques produced images of the cord very similar to those of the excised cadaver cord (Figs. 4D and 5D). The use of a 256×256 matrix and only one average resulted in images of poor quality because of reduced signal-to-noise (Fig. 6D). With two averages (four excitations) and cardiac-gating, some of the internal anatomy of the cord was faintly visualized (Fig. 6E), but image quality did not have the resolution seen on the cadaver images. The volunteer studies with the GRASS technique and two averages (four excitations) produced images quite similar to those of the cadaver cord in a water bath (Figs. 7B and 7C), where the surrounding CSF was of high signal and the cord surface of low signal. Cardiac-gated spin-echo images, 2571/40,80 of the volunteer (Fig. 8) demonstrated an internal anatomy similar to that seen on the GRASS images, but the surface of the cord was seen less clearly. Nonetheless, the signal for the central gray and white matter remained constant, with the white matter always of lower signal than the gray matter on all pulse sequences.

As in the images of the gels, decreasing the voxel size by increasing the matrix to 256×256 or using smaller fields of

view (16 cm) did not totally resolve the appearance of the rim of high signal at the periphery of the cord. The small-field-of-view, 256- by 256-matrix image quality of the volunteer studies was degraded by a reduced signal-to-noise ratio, causing poor visualization of the internal anatomy (Figs. 6D and 6E). To optimize visualization of the internal morphology it was necessary to decrease voxel size by using a larger matrix and smaller fields of view, but this required a larger number of averages. The images with the extended scanning times in the volunteer were compromised to some degree by voluntary and involuntary patient motion, so that the cord anatomy was not seen as well on most of the 256×256 images (Figs. 6D and 6E) as on the 128×256 images (Fig. 4D). Although internal cord anatomy was seen best in excised cord with 256×256 matrices and small fields of view, this could not be duplicated in living subjects despite gating and multiple averages.

Discussion

Many MR images of the cord in the axial plane do not correlate with histologic sections. On short TR/TE images, a

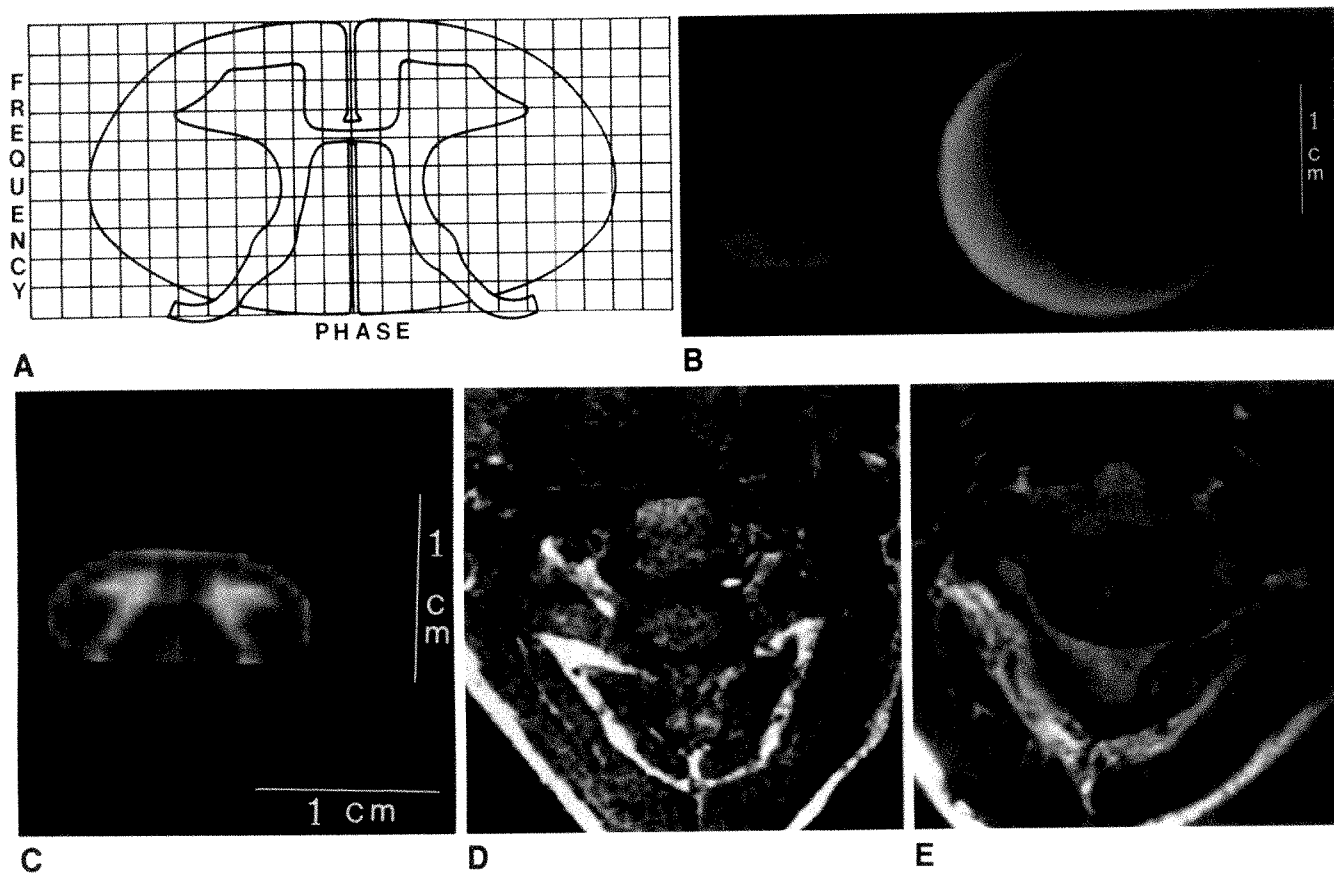


Fig. 6.—Voxel size and orientation, 256×256 matrix.

A, Grid overlays drawing of cord with 256×256 matrix and 16-cm field of view.

B, Gel phantom. With 256×256 matrix, scan of same gelatin phantoms shows marked reduction in ring artifacts. Added data points of increased matrix size lessen effect of data truncation. Thinner peripheral rim of high-signal overshoot persists.

C, Excised cord, same level as in Figs. 4C and 5C, in air. A truer representation of normal transverse anatomy as seen on histologic sections is now shown. Note that a thin rim of high signal persists at periphery.

D, Human volunteer. Axial scan, 800/20, with only two excitations (one average) to maintain imaging time similar to that in Figs. 4 and 5. Image quality is severely diminished because of reduced signal-to-noise ratio of smaller voxel size and poor visualization of internal anatomy.

E, Human volunteer with two averages (four excitations). Increased imaging time required cardiac gating for satisfactory results but still only faintly shows internal cord anatomy.

high-signal ring is seen at the periphery of the cord that has a signal character similar to the central gray matter, but there is no corresponding gray matter at the surface of the cord (Figs. 1–3). Circular low-signal areas overlying regions of the lateral white-matter tracts are seen on MR, but there are no correlating anatomic structures on the histologic sections. The inhomogeneous appearance of the MR images obtained from scanning the gelatin phantoms also suggests that the MR appearance of the gray and white matter is modulated by superimposed artifacts, which may account for the inaccuracies.

Artifacts in MR imaging have been well described in the literature [12–14], including truncation artifacts on sagittal MR images of the cervical cord [6, 7]. Edge artifacts are generally ascribed to chemical shift, motion, and Fourier transformation truncation artifacts (Gibbs phenomenon). Chemical-shift artifacts are spatial errors in image location assignment that occur only in the frequency-encoded direction due to the slightly differing Larmor frequencies of different chemical species of protons. The superimposed artifacts seen in the phan-

tom and spinal cord images occurred in both phase and frequency directions and do not appear to be due to chemical shift. Furthermore, there are no free triglyceride fats in the cord to produce chemical-shift artifacts.

Artifacts due to motion occur predominantly in the phase-encoded direction due to changes in the phase angle of moving protons across the gradients. In addition to simply blurring the images, motion artifacts can occur with sharp edges as “ghost images” or as image harmonics at periodic intervals along the phase-encoded direction that are dependent on TR and TE if there is a periodicity of the motion, as seen with CSF [15, 16]. In the cervical region, pulsatile CSF flow is a source of motion artifact [16, 17], but that does not explain artifacts seen in the cadaver or phantom studies. The cord had a similar appearance on gated and nongated examinations.

A third type of artifact is produced by limitations placed on sampling data for image reconstitution with the two-dimensional Fourier transformation (2DFT) technique [12–14]. The 2DFT techniques transform the frequency- and phase-en-

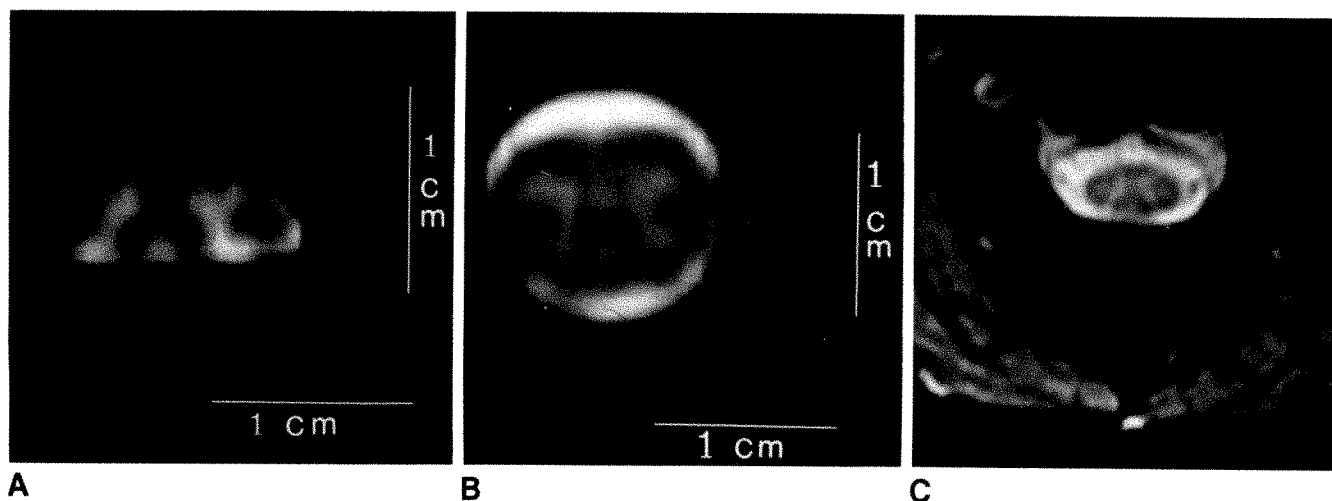


Fig. 7.—GRASS images.

A, Excised cord in air. Axial GRASS scan, 1000/12, of same level through human spinal cord with 22.5° flip angle and 128 × 256 matrix. Phase-encoded direction is anterior to posterior; image is very similar to Fig. 4C with short TR/TE sequence and high-signal overshoot artifact at periphery.

B, Excised cord in water bath. When excised cord is imaged with GRASS technique in a water-filled test tube, higher signal from surrounding water results in boundary artifact that overshoots toward lower signal, giving darker rim to cord. Central gray matter appears as high signal similar to other pulse sequences.

C, Human volunteer. Axial GRASS scan shows darker signal to edge of cord, as seen in cadaver cord within water bath.

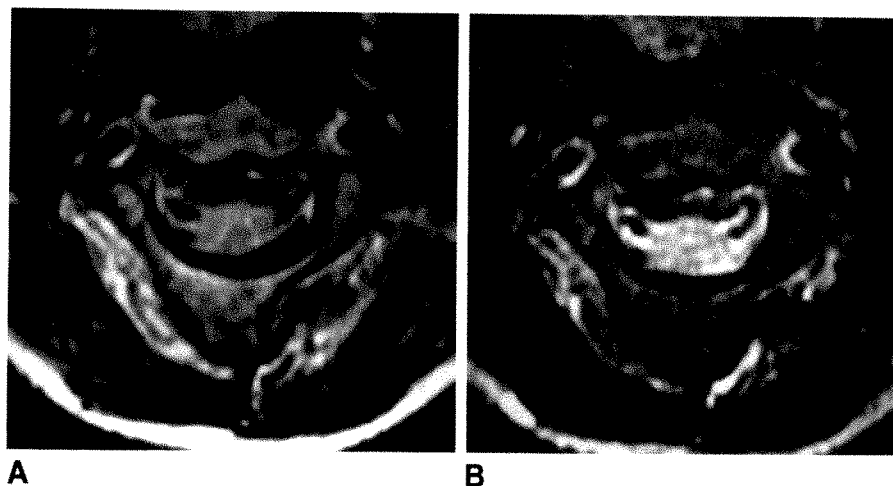


Fig. 8.—Gated spin-echo axial images, normal volunteer.

A, Cardiac gated images have much longer acquisition times, but anatomy is depicted less well. Effective TR is approximately 2500 msec with a TE of 40 msec and 128 × 256 matrix. CSF surrounding cord is isointense relative to gray matter of cord.

B, Second echo of long TR sequence shows good visualization of nerve roots, but internal anatomy is not clear.

coded information into an image. The image is a summation of a multitude of different sinusoidal waveforms. To accurately depict an object, particularly a complex one with abrupt, discrete edges, an infinite number of samples would need to be collected. However, this is not possible due to time constraints, so that data are truncated or approximated. An artifactual over- and undershoot occurs on both sides of the edge discontinuity. This artifact is called the Gibbs' or truncation artifact. In MR imaging, the results of this approximation are artifactual "ring"-like high and low signals parallel to an edge that occur on both sides of the discontinuity. Periodic overshoot and undershoot oscillations are dependent on the matrix size. The oscillations ripple across the image but decay rapidly. The size and periodicity of these striations are dependent on the pixel size in relation to the object and the matrix [6, 7]. 2DFT techniques truncate the data in both the

phase and frequency directions, but the data truncation artifact is most evident in the phase-encoded direction, where data sampling uses only 128 gradient steps to save imaging time.

The edge "ringing" artifacts seen on the stationary gelatin phantom images occurred in both the phase and frequency directions and were the result of truncation artifacts. These artifacts were more severe in the smaller-diameter gel because fewer pixels spanned the section, thus accentuating the artifacts. An artifactual bright ring around the phantom was produced as the 2DFT approximation overshoot the abrupt signal change from the signal void of air to the relatively higher signal of the gelatin. The use of long TR/TE or GRASS techniques to image the cord produced a high-signal CSF surrounding the cord so that the artifactual overshoot going from higher-signal CSF to relatively lower-signal cord resulted

in a lower-signal edge to the cord. The same type of truncation artifacts seem to modulate the images of the excised cadaver spinal cord as well as those of the normal volunteer.

Truncation artifacts can be reduced, although not eliminated, by increasing the matrix size (which increases the amount of data sampled), or by reducing the pixel size (field of view), which in effect reduces the size of the artifact in relation to the object. However, signal-to-noise considerations with smaller fields of view and a larger matrix size require extended imaging times [18], which may not be clinically practical. Even with short TR/TE images the multiple averages needed to obtain adequate signal-to-noise with a 256×256 matrix resulted in an image time of 13 min 41 sec for two averages (four excitations). Cardiac-gated long TR spin-echo images took 22 min 1 sec with two averages (four excitations) and a 128×256 matrix. Although our volunteer had a thin body habitus that maximized the signal and the proximity of the cord to the coil and was extremely cooperative, these protracted imaging times resulted in poorer quality than did shorter scanning times with the 256×128 matrix technique. We routinely use axial images with a 128×256 matrix and two averages (four excitations) for more consistent image quality in a reasonable amount of time (6 min 50 sec). Future development of better cervical spine surface coils may help resolve signal-to-noise considerations to provide greater resolution in a shorter scanning time.

Partial-volume averaging in digital imaging is also an important source of image distortion [19]. Partial-volume averaging occurs when the voxel is larger than the anatomic structure being imaged. Other adjacent structures are averaged, producing distortion of the image. Because the spinal cord is such a small structure, only a few pixels may span the entire cord (Figs. 4A and 5A). As few as five pixels compose the anterior to posterior cord on a 128×256 matrix with a 16-cm field of view (Fig. 4A). The internal appearance of the cord varied with a change in the phase-encoded axis because the pixels are larger than are portions of the cord gray matter, particularly the central commissure and dorsal horns. Geometric distortions to the size and normal oval shape of the cord also are attributable to partial-volume effects.

Previous studies evaluating the syrinxlike artifacts on sagittal images of the cord reported that axial scans obtained with GRASS techniques did not exclude the syrinxlike artifacts [7]. However, we did not find this artifact to be a problem and found that the use of two averages (four excitations) in GRASS-type imaging provides excellent demonstration of the internal anatomy. We suspect this artifact was avoided by using a 16-cm field of view.

The low signal of the white-matter columns in all pulse sequences is different from the appearance found in the brain. The brain white-matter tracts are higher in signal than is the gray matter on short TR/TE images and lower in signal on long TR/TE images. Iron staining of the cord failed to implicate iron deposition as a cause. Relaxation times of white and gray matter in the spinal cord remain an incompletely understood phenomenon. Accurate measurement of spinal cord relaxation times was not possible on our equipment because a region of interest small enough to exclude white matter from the sample area could not be obtained. Carvlin et al.

[20] have reported initial experimental work measuring relaxation times that indicate spinal-cord gray matter has a longer T1, slightly shorter T2, and higher spin density compared with white matter. Yet their highly T1-weighted inversion-recovery images showed contradictory results of high signal to the spinal cord gray matter. They suspected that a higher spin density was the cause of this appearance, but concluded further quantitative studies would be necessary.

We speculate that the low signal of the dorsal and lateral white-matter columns may be due to the extreme longitudinal organization of ascending and descending myelinated axons in these columns, which may be thought of as analogous to the regular array of collagen fibers in a tendon or a ligament. As pointed out by Fullerton et al. [21], the low signal of a tendon is due primarily to the anisotropy of water molecule motion. Indeed, some other areas of white matter seem to show this phenomenon of low signal on all pulse sequences. The pyramidal tracts and medial lemniscus of the brainstem maintain a low signal on all pulse sequences, while the corpus callosum is bright on short TR/TE images. Both are white-matter structures and would be expected to have a similar signal, but the extreme organization of the longitudinal array of tracts in the brainstem most likely exhibits this same anisotropy of water molecule motion.

In summary, the MR appearance of the cervical cord on axial images is a representation of low-signal white-matter tracts and higher-signal gray matter modulated by truncation and partial-volume-averaging artifacts. In excised human spinal cord, the artifacts can be minimized and display of anatomy optimized by using a 256×256 matrix with at least two averages (four excitations). However, when imaging even the most cooperative volunteers in multiple averages, some patient motion and the reduced signal-to-noise aspects of a 256×256 matrix result in poorer image quality, such that the internal anatomy seen in the excised cord cannot be reproduced in the living subject. Although truncation artifacts are more pronounced with a 128×256 matrix, the smaller matrix is the most reliable and practical compromise for displaying the internal anatomy in patients. The use of two averages (four excitations) provides adequate delineation of the anatomy in most clinical situations with acquisition times under 7 min.

ACKNOWLEDGMENTS

We thank Melinda MacCalla, Cheryl Taylor, Linda Chakeres, Margaret O'Brien, and John Crouse for help in manuscript preparation.

REFERENCES

1. Flannigan BD, Lufkin RB, McGlade C, et al. MR imaging of the cervical spine: neurovascular anatomy. *AJNR* 1987;8:27-32
2. Lee BCP, Deck MDF, Kneeland JB, Cahill PT. MR imaging of the craniocervical junction. *AJNR* 1985;6:209-213
3. Norman D, Mills CM, Brant-Zawadzki M, Yeates A, Crooks LE, Kaufman L. Magnetic resonance imaging of the spinal cord and canal. *AJR* 1983;141:1147-1152
4. Modic MT, Weinstein MA, Pavlicek W, Boumpfey F, Starnes D, Duchesneau PM. Magnetic resonance imaging of the cervical spine: technical and clinical observations. *AJR* 1983;141:1129-1136

5. Hyman RA, Edwards JH, Vacirca SJ, Stein HL. 0.6 T MR imaging of the cervical spine: multislice and multiecho techniques. *AJNR* **1985**;6:229-236
6. Levy LM, Di Chiro G, Brooks RA, Dwyer AJ, Wener L, Frank J. Spinal cord artifacts from truncation errors during MR imaging. *Radiology* **1988**;166:479-483
7. Bronskill MJ, McVeigh ER, Kucharczyk W, Henkelman RM. Syrinx-like artifacts on MR images of the spinal cord. *Radiology* **1988**;166:485-488
8. Rubin JB, Enzmann DR. Optimizing conventional MR imaging of the spine. *Radiology* **1987**;163:777-783
9. Wehri FW, MacFall JR, Glover GH, Haughton V, Johanson J. The dependence of nuclear magnetic resonance (NMR) image contrast on intrinsic and pulse sequence timing parameters. *Magn Reson Imaging* **1984**;2:3-16
10. Gans A. Iron in the brain. *Brain* **1923**;46:128-136
11. Enzmann DR, Rubin JB. Cervical spine: MR imaging with partial flip angle, gradient refocused pulse sequences. *Radiology* **1988**;166:467-472
12. Bellon EM, Haacke EM, Coleman PE, et al. MR artifacts: a review. *AJR* **1986**;147:1271-1281
13. Lufkin RB, Pusey E, Stark DD, Brown R, Leikind B, Hanaftee WN. Boundary artifact due to truncation errors in MR imaging. *AJR* **1986**;147:1283-1287
14. Wood ML, Henkelman RM. Truncation artifacts in magnetic resonance imaging. *Magn Reson Med* **1985**;2:517-526
15. Rubin JB, Enzmann DR, Wright A. CSF-gated MR imaging of the spine: theory and clinical implementation. *Radiology* **1987**;163:784-792
16. Rubin JB, Enzmann DR. Harmonic modulation of proton MR precessional phase by pulsatile motion: origin of spinal CSF flow phenomena. *AJNR* **1987**;8:307-318
17. Rubin JB, Enzmann DR. Imaging of spinal CSF pulsation by 2DFT MR: significance during clinical imaging. *AJNR* **1987**;8:297-306
18. Bradley WG, Kortman KE, Cruess JV. Central nervous system high-resolution magnetic resonance imaging: effect of increasing spatial resolution on resolving power. *Radiology* **1985**;156:93-98
19. Chakeres DW. Clinical significance of partial volume averaging of the temporal bone. *AJNR* **1984**;5:297-302
20. Carvlin M, Asato R, Hackney DB, Kasab E, Joseph PM. High resolution MRI of the spinal cord in humans and rats (abstr). *Magn Reson Imaging* **1987**;[Suppl 5]:56
21. Fullerton GD, Cameron IL, Ord VA. Orientation of tendons in the magnetic field and its effect on T2 relaxation times. *Radiology* **1985**;155:433-435

MR Imaging in the Tethered Spinal Cord Syndrome

Narasimhachari Raghavan¹
 A. James Barkovich¹
 Michael Edwards²
 David Norman¹

MR examinations of the spine were reviewed in 25 patients with a clinical diagnosis of tethered spinal cord. In 21 patients (84%), the level of the tip of the conus was below the mid L2 vertebral body. The causes of the tethering were spinal lipomas (72%), tight filum terminale syndrome (12%), diastematomyelia (8%), and myelomeningocele (8%). These entities were readily identified in all instances. Bony dysraphisms were well demonstrated by MR. Interestingly, cavitary lesions/myelomalacia of the conus or the cord adjacent to the tethering lesion were seen with appropriate images in nine of 20 patients. This unexpected finding may have diagnostic and/or prognostic significance.

Spinal MR was found to be extremely useful in the evaluation of the suspected tethered spinal cord. It was able to visualize the conus medullaris, assess the thickness of the filum terminale, identify traction lesions, and evaluate associated bony dysraphisms.

Tethered spinal cord syndrome is often suspected clinically when patients present with motor and sensory dysfunction of lower extremities (unrelated to myotomal or dermatomal pattern), muscle atrophy, decreased or hyperactive reflexes, urinary incontinence, spastic gait, or orthopedic deformities such as scoliosis or foot deformities [1, 2]. Radiographic studies are used to confirm the presence of tethered cord, to ascertain the cause of tethering, and to rule out other diagnostic considerations such as neoplasms, disk herniations, and syringohydromyelia. Traditionally, positive-contrast myelography has been the diagnostic procedure of choice, often supplemented by CT with intrathecal contrast material. With the increasing sophistication of surface-coil technology, MR imaging has been shown to be of considerable value in the diagnosis of intrinsic spinal cord disease [2, 3]. In this article, we report our experience with the MR appearance of suspected tethered spinal cord syndrome.

Materials and Methods

MR examinations of 25 patients with the clinical diagnosis of tethered spinal cord were reviewed retrospectively. The 14 males and 11 females were 0–65 years old (mean, 18 years). All MR scans were obtained before surgical repair. Clinical findings included a fatty lump in the lower lumbosacral region without neurologic deficits, neurogenic bladder with urinary retention, urinary incontinence, decreased perianal sensation, numbness in lower extremities, spastic gait, and lower extremity pain (Table 1). The location of the conus medullaris was identified on axial and sagittal scans. Whenever possible the diameter of the filum terminale at the L5–S1 level was measured. In six cases, tethering was not associated with a well-defined filum. In three cases, images at the L5–S1 level were not available.

The cord was evaluated for the presence or absence of syringohydromyelia/myelomalacia. The cause of tethering was identified. Dysraphic abnormalities of the vertebral bodies and abnormalities of the spinal curvature were characterized. The relative difficulty involved in characterizing the osseous abnormalities was subjectively recorded. The position of the cerebellar tonsils was noted whenever scans at the foramen magnum level were available.

This article appears in the January/February 1989 issue of *AJNR* and the April 1989 issue of *AJR*.

Received March 21, 1988; accepted after revision June 17, 1988.

¹ Department of Radiology, Section of Neuroradiology, L-371, University of California, 505 Parnassus Ave., San Francisco, CA 94143. Address reprint requests to N. Raghavan.

² Department of Neurosurgery, University of California, San Francisco, CA 94143.

AJR 152:843–852, April 1989
 0361–803X/89/1524-0843
 © American Roentgen Ray Society

TABLE 1: Summary of Patients with Tethered Spinal Cord Syndrome

Dysplasia: Case No.	Age	Gender	Conus Level		Filum Thickness (mm)	Syrinx/ Myelomalacia	Skeletal Abnormalities	Clinical Presentation
			Sagittal View	Axial View				
Spinal lipoma ^a :								
1	3	M	Mid L1	Mid L1	No axial view	Poor image	Normal T12–L4	R/O tethered cord
2	37	F	L2–L3	L2–L3	5	No	Normal	Dysesthesias both legs
3	0.6	M	S1	No axial view	No axial view	No axial view	No axial view	Fatty mass over lumbo- sacral spine
4	51	F	Not avail- able	Not avail- able	7	No	Normal L4–S1	Pain in both legs
5	37	M	Mid L3	Mid L3	Cord ends in lesion	No	Normal	Voiding difficulty
6	3	F	Mid–lower L2	Mid L2	3	No	Scoliosis	Urinary incontinence
7	60	M	Mid L3	Mid L3	3	No	Abnormal; poorly evaluable	Decreased perianal sensation
8	17	F	L3	No axial view	No axial view	No	Sacral spina bifida	Neurogenic bladder
9	0.1	M	L3–L4	L3–L4	Cord ends in lesion	Yes	No axial view	Numbness in L leg; atrophy
10	0.3	M	L2–L3	L3–L4	4	Yes	Spina bifida, L5 & S1	Neurogenic bladder; fatty mass over spine
11	65	M	L3–L4	No axial view	5	No axial view	Spina bifida, L5 & S1	Fatty mass over lumbo- sacral spine
12	52	M	Mid L1	Mid L1	5	No	Minimal scoliosis	R/O tethered cord
13	37	F	L5–S1	L5–S1	4	Yes	No axial view	Dysesthesias, both legs
14	1.3	F	L5	L5	3	Poor image	Normal	Numbness in feet; neu- rogenic bladder
15	3	M	L5–S1	L5–S1	Cord ends in lesion	Yes	Spina bifida, L5 & S1	R/O tethered cord
16	12	F	L5–S1	L4–L5	2	No axial view	Mildly asymmetric spina bifida, L4; widely bifid L5 & S1	Neurogenic bladder
17	8	M	L5–S1	L5–S1	6	No	Urinary incontinence; dysesthesias in both legs	Urinary incontinence;
18	11	F	S1	S1	Cord ends in lesion	Yes	Scoliosis; dysraphic at L3–S1	dysesthesias in both legs
None:								
19	16	M	L4–L5	L4–L5	5	Yes	Sacral spina bifida	Toe walking; spasticity
20	7	F	Lower L3	Lower L3	4	Yes	Congenital fusion, L5 & S1; spina bifida occulta, L5; partial sa- cral agenesis	R/O tethered cord
21	5	M	L1–L2	L1–L2	3	Yes	Normal	R/O tethered cord
Myelomeningocele:								
22	4	F	Cord ends in myelo- meningo- cele	Cord ends in myelo- meningo- cele	–	No	Spina bifida, L5–sacrum	Urinary incontinence
23 ^b	0	F	L5–S1	L5–S1	Not seen	No	No axial view	R/O tethered cord
Diastematomyelia:								
24	5	M	L4–L5	Not evalua- ble	3	No	Poorly evaluable	Decreased perianal sensation
25	Age not avail- able	M	Mid L4	L4–L5	5	Yes	Scoliosis; hemi- vertebrae; thick lamina with ever- sion; bony septum at L2	Hyperreflexia; hemi- spastic gait; positive Babinski test
							No bony septum; spina bifida of L5 & S1	R/O tethered cord

Note.—R/O = rule out; L = left.

^a Comprises subtypes lipomyelomeningocele, intramedullary lipoma, and lipoma of filum terminale.^b Skin-covered.

All measurements and observations were made from the hard-copy images by using calipers and the relative MR scale generated on each image.

Most patients were examined on a 1.5-T whole body superconductive magnet* by using surface receiving coils; two patients were studied on a 0.35-T magnet.† Spin-echo sequences were used and data were acquired with either 128 or 256 views in the phase-encoding direction, 256 views in the read-out direction, and two to four excitations by using the two-dimensional Fourier transform method. The field of view was variable but ranged from 20 to 30 cm depending on the plane of imaging. Sagittal T1-weighted images, 600–1000/20–50 (TR/TE), with 3- to 5-mm section thickness were obtained in all patients. Five-millimeter axial spin-echo sections, 1000/20, were also available for 23 of 25 patients. The patients were supine during the examination.

Results

Level of Conus

The level of the conus could be determined in 23 of the 25 patients. In 19 cases, the level of the conus could be identified on both axial and sagittal views. Determination of the level of the conus on axial compared with sagittal views did not vary by more than one-half the vertebral body height in 17 patients and was discrepant by one vertebral body height in two (Table 1; Fig. 1). In five cases, no axial images through the conus tip were available; in one case, the conus was not visualized with certainty on either view owing to the presence of a traction lesion.

In 21 patients, the level of the conus was below the mid L2 vertebral body. In four (16%) of 25 patients, the tip of the conus was at or above the mid L2 level on axial images

(Tables 1 and 2; Fig. 2). Three of these four patients had a spinal lipoma and the other had a thickened filum (normal is 2 mm or less). Cerebellar tonsillar ectopia was present in five of nine patients imaged at this level.

Cause of Tethering

The causes of the tethering are listed in Table 3. Intramedullary lipomas, lipomyelomeningoceles, and lipomas of the filum terminale are collectively referred to as spinal lipomas [4]. The distribution of the lesions in our study differs from the series of 71 patients reported by James and Lassman [5], in which spinal lipomas alone accounted for tethering in only 27% of patients while diastematomyelia was present in 34%.

The tethering lesions were identified readily on the MR studies, as the high signal intensity of fat is easily separable

TABLE 2: Level of Tip of Conus in Patients with Tethered Spinal Cord Syndrome

Level	No. of Patients	
	Sagittal Image	Axial Image
L1	2	2
L1–L2	1	1
L2	1	1
L2–L3	2	1
L3	4	3
L3–L4	2	2
L4	1	0
L4–L5	2	3
L5	1	1
L5–S1	5	4
S1	2	1

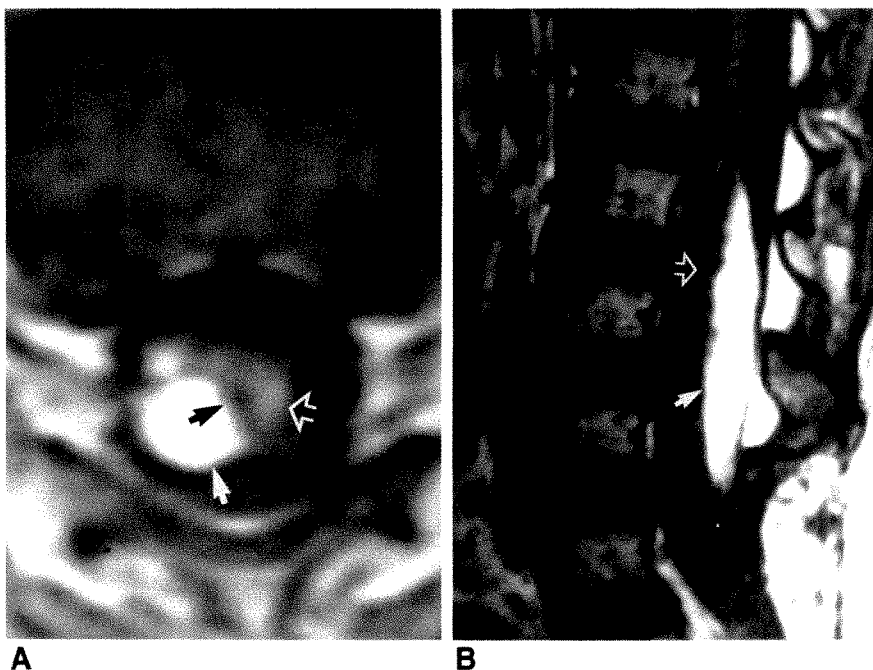
* General Electric, Milwaukee, or Philips Medical Systems, Shelton, CT.

† Diasonics, Milpitas, CA.

Fig. 1.—Case 10: 3-month-old boy with fatty mass over lower lumbosacral spine.

A, Axial spin-echo image, 1000/20, shows cord (open arrow) terminating in lipoma (solid white arrow) opposite L3–L4 disk-space level. Syringohydromyelic cavity/myelomalacia is present in terminal cord (black arrow).

B, Midsagittal spin-echo image, 1000/20. As spinal cord (open arrow) is displaced laterally by lipoma (solid arrow), tip of conus falsely appears to be at L2–L3 level.



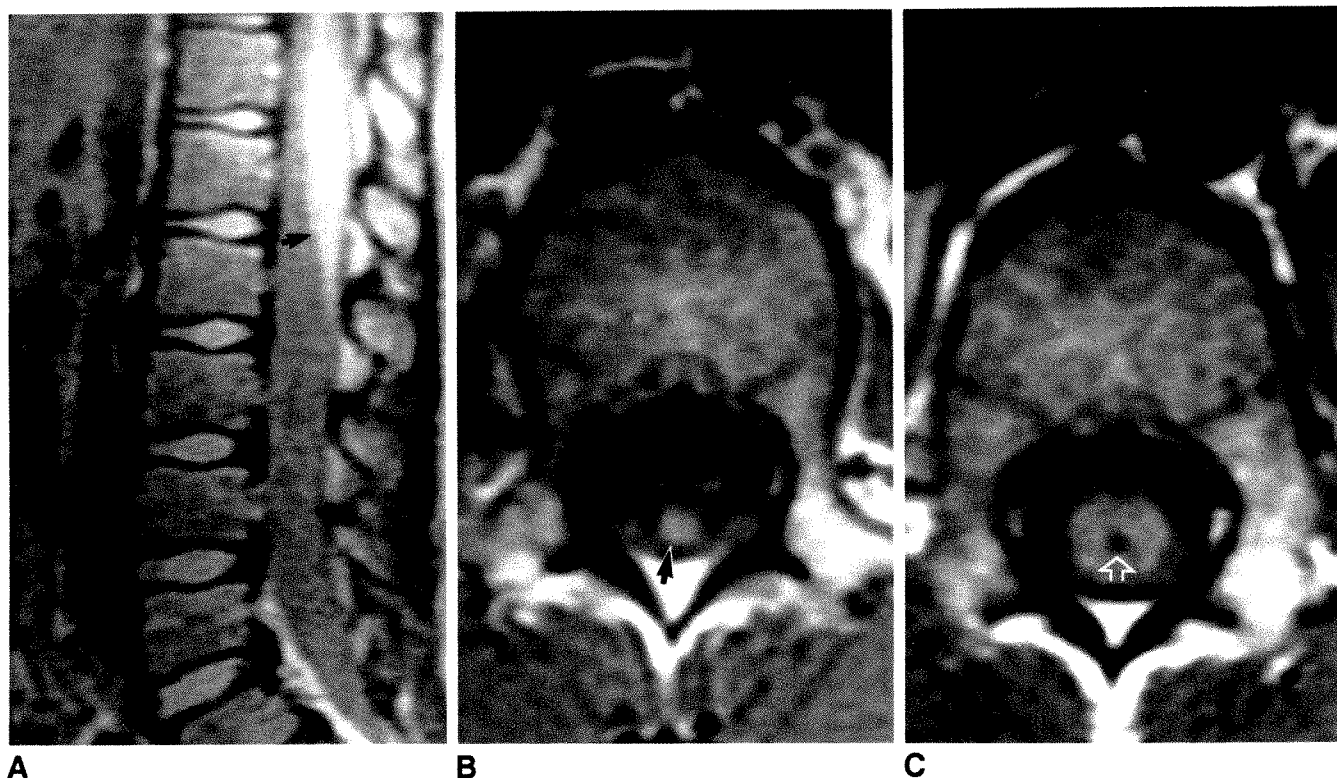


Fig. 2.—Case 21: 5-year-old boy with urinary incontinence. A and B, Spin-echo sagittal, 1000/40 (A) and axial, 1000/20 (B), images confirm position of tip of conus (arrows) to be at L1–L2 interspace. C, Only other radiographic clue is syrigo-hydromyelic cavity/myelomalacia (arrow) (possibly seen on sagittal image as well) from mid T11 to L1–L2 region.

TABLE 3: Causes of Tethering in Tethered Spinal Cord Syndrome

Cause	No. of Patients (%)
Spinal lipoma	18 (72)
Thickened filum (>2 mm) without fat signal	3 (12)
Diastematomyelia	2 (8)
Myelomeningocele	2 (8)
Total	25 (100)

from the signal of the cord and of CSF on short TR/TE images (Fig. 3).

Filum Terminale

Normal filum thickness is stated to be 2 mm or less [6, 7]. Measurements were performed on axial images at the level of the L5–S1 interspace (Fig. 4), and, when clearly separable, the lipomatous elements were excluded from the determination of the filum thickness. In nine of 25 patients, filum thickness could not be measured. In five of these patients, either the cord ended in the traction lesion or the lesion prevented clear visualization of filum terminale. In one case,

the filum could not be differentiated from nerve roots of cauda equina; in the remaining three, the scans did not include the L5–S1 interspace. The filum was greater than 2 mm in diameter in 15 of the 16 patients in whom it could be identified. In the sixteenth patient, the filum measured only 2 mm in width, and in this patient the conus was low-lying, positioned at the L4 vertebral body level.

Cord Architecture

The internal architecture of the spinal cord, judged subjectively on the ability to differentiate gray from white matter, was not well imaged in 20 patients. Nine of 25 subjects had a focal short-length low-intensity lesion representing either a syrigo-hydromyelic cavity or a focus of myelomalacia, measuring 1–4 cm in length and 1–5 mm in diameter in the conus or in the cord adjacent to the tethering lesion if one was present (Fig. 1). These lesions could not be seen with any degree of confidence in the sagittal plane (Fig. 5). Adequate axial images through the cord were not available in five patients; of the 20 subjects with adequate images, nine demonstrated a focal low-intensity cord abnormality. On the short TR/TE axial images, they could be noted with confidence; their signal was similar to that of CSF and lower than that of spinal gray matter. The presence of gliosis or CSF “flow” void could not be evaluated because T2-weighted

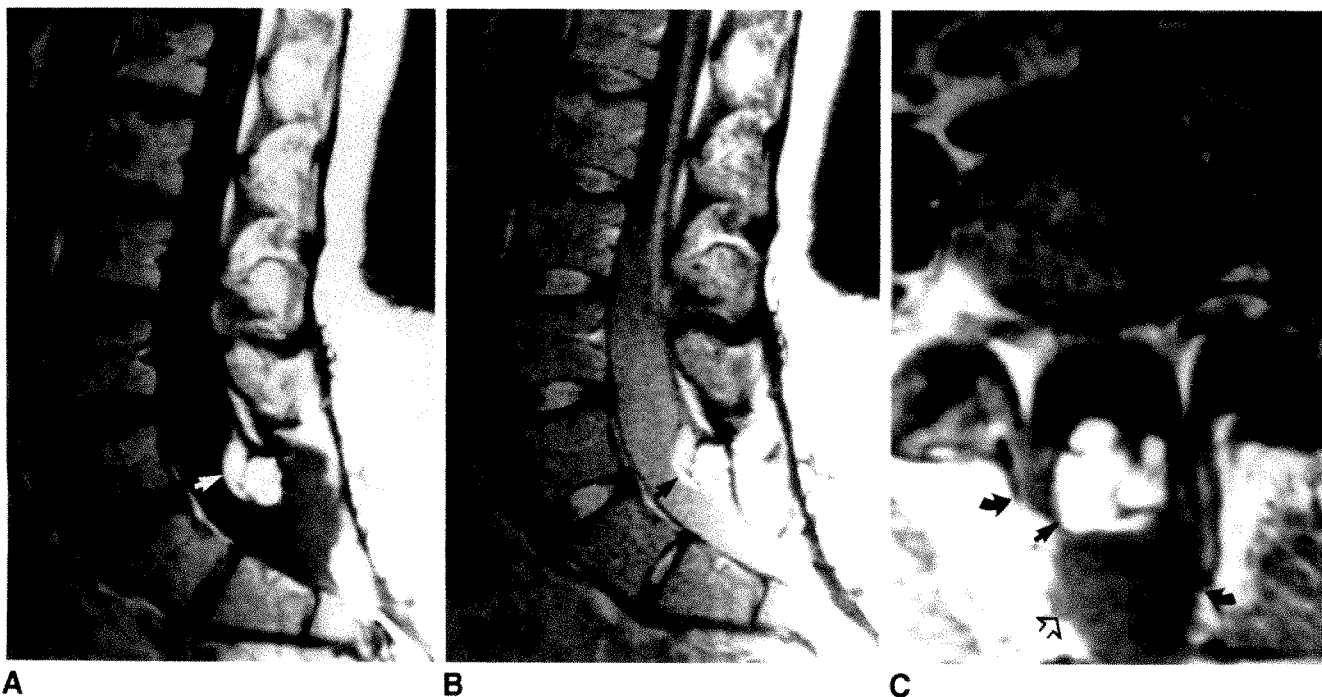


Fig. 3.—Case 2: 37-year-old woman with tethered spinal cord syndrome.

A, Sagittal spin-echo image, 1000/20, depicts low-lying conus tethered by high-intensity lipoma (arrow).

B, Signal of lipoma (arrow) decreases on second echo of sequence, 1000/70.

C, Axial spin-echo image, 1000/20. Bony detail is clearly visualized. Spina bifida (curved arrows), meningocele (open arrow), and lipoma (solid straight arrow) are evident.

studies were not performed. Sagittal MR was performed at the craniocervical junction in four of the nine patients; none had evidence of a Chiari malformation. Scoliosis was not evident in any of these nine patients.

Bony Detail

In 19 of 25 patients, the vertebral architecture was easily characterized. In four patients, axial images were not available for evaluation; in two patients, the presence of a bony abnormality could be appreciated but was not well defined. Six studies demonstrated no bony abnormalities in the region imaged. Both patients with diastematomyelia had thickened, dysplastic, everted laminae. One of the two had a hemivertebra resulting in scoliosis, and a demonstrable bony diastematomyelic septum, shown to be osseous on plain films (Fig. 6). Congenital fusion of L5 and S1, partial sacral agenesis, spina bifida occulta at L5, and frank spina bifida at S1 and S2 were noted in one patient. The remaining 10 patients had spina bifida with varying degrees of laminar eversion. Scoliosis was noted in four subjects; syringohydromyelia/myelomalacia in the terminal cord could not be demonstrated in any of these patients.

Discussion

The spinal cord develops in a relatively orderly manner by the processes of neurulation and disjunction (Fig. 7). Inferior

to the caudal neuropore, the neural tube elongates by canalization and retrogressive differentiation, ultimately forming the distalmost conus medullaris, the ventriculus terminalis, and the filum terminale [7, 8]. Full discussion of the embryology of spinal cord and column formation is beyond the scope of this article, and the interested reader is referred to several excellent discussions on the subject [7, 10–13].

The spinal cord "ascends" relative to the vertebral column because of the differential growth rates of the spinal cord and the vertebral column [6]. The rate of ascent of the conus medullaris is most rapid before the 17th week of gestation, during which period the cord ascends to terminate at the L4 level. Thereafter, the ascent proceeds at a slower pace, reaching the adult level in most patients approximately 2 months after birth [1]. Even though slower ascent can be seen normally, a conus level lower than mid L2 at an age greater than 12 years generally is accepted as abnormal [6]. To achieve the "ascent," the spinal cord must be free from the bony canal and the surrounding subcutaneous tissue [11]. The filum terminale, as previously mentioned, elongates as a result of retrogressive differentiation and is accompanied by an increase in the length of nerve fibers [7, 10]. Failure of either of the delicate processes of neurulation and disjunction can result in anchoring of the spinal cord to the surrounding tissues, thereby preventing the independent growth of the spinal cord. If the spinal cord cannot detach itself from the surrounding meninges, vertebrae, or subcutaneous tissues, the spinal cord cannot ascend relative to the vertebral column.

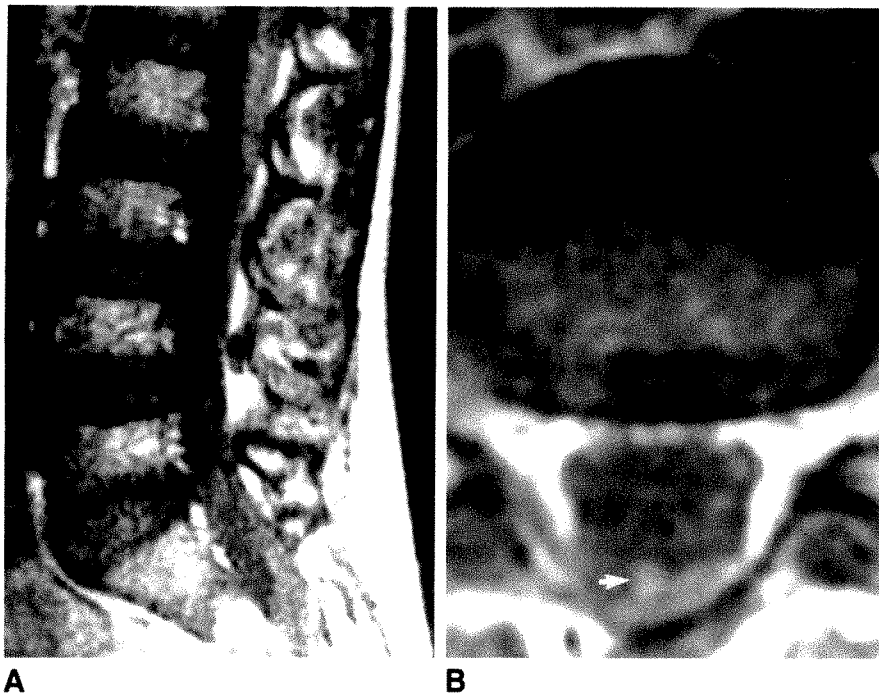


Fig. 4.—Case 20: 7-year-old girl with tethered spinal cord syndrome. Tip of conus is at lower L3 vertebral level.

A, Sagittal spin-echo image, 1000/20, does not show filum terminale clearly.

B, Axial spin-echo image, 1000/20, at L5–S1 interspace. Filum terminale (arrow) is 4 mm thick.

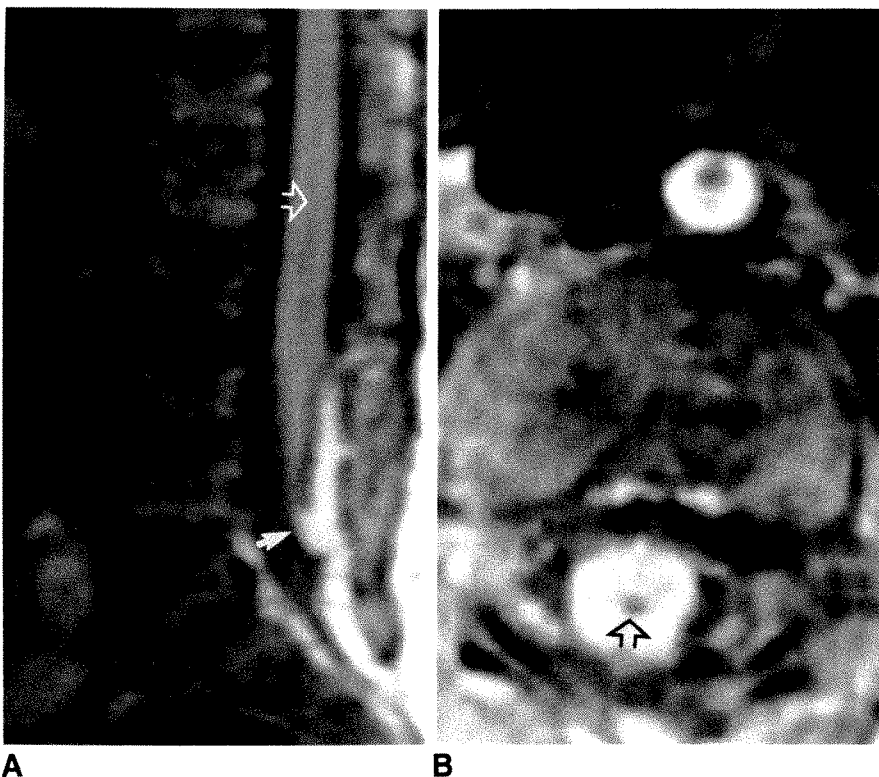


Fig. 5.—Case 9: 3-week-old boy with fatty mass over lumbosacral spine and neurogenic bladder.

A, Sagittal spin-echo image, 1000/20, reveals termination of cord in lipoma (solid arrow) at L3–L4 level. Linear low intensity (open arrow) within cord contour was believed to be artifactual.

B, Axial spin-echo image, 600/20, through L2 vertebral body clearly identifies central syringohydromyelic cavity/myelomalacia (arrow). Lesion was very focal and was not as extensive on axial scans as would have been suggested by linear intensity on sagittal image.

More rapid growth of the spinal column relative to the cord then results in tethering [11, 14].

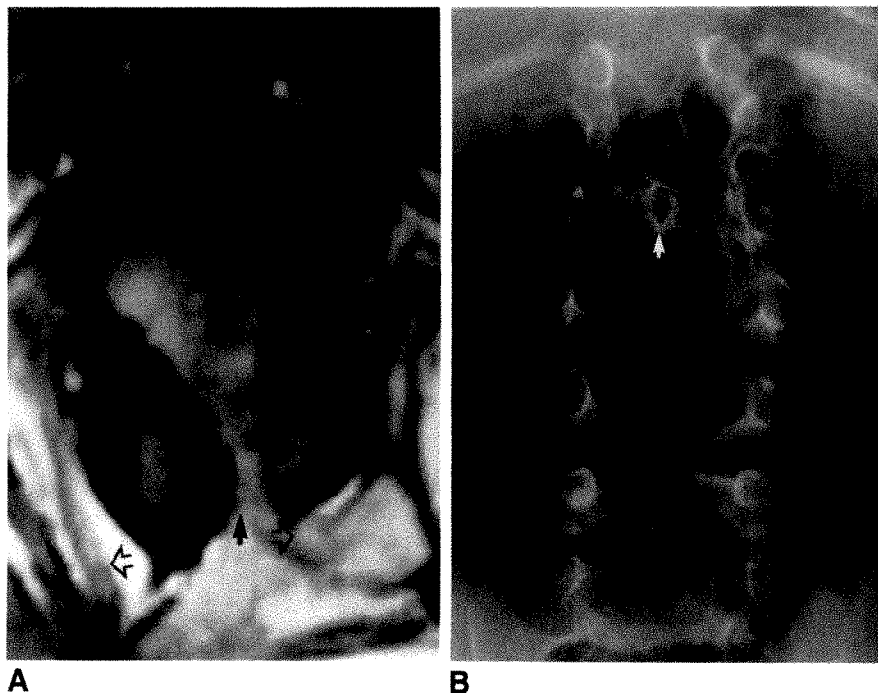
Disturbance in the closure of the neural placode during neurulation with nondisjunction results in myelomeningocele [12]. The edges of the exposed placode blend with a thin

membrane that connects to the surrounding margins [7]. Dorsal dermal sinuses appear to arise from focal incomplete separation of cutaneous ectoderm from neuroectoderm [7]. Focal premature disjunction with exposure of paraxial mesoderm to the dorsal aspect of unfused neural ectoderm induces

Fig. 6.—Case 24: 5-year-old boy with tethered spinal cord syndrome.

A, Axial spin-echo image, 1000/20, through lower thoracic spine clearly reveals diastematomyelia with septum (solid arrow). Thickened everted laminae (open arrows) are evident.

B, Conventional radiograph of lower thoracic upper lumbar spine confirms bony nature of diastematomyelic septum (arrow).



formation of fatty elements, which may prevent fusion of the neural tube and result in the formation of cord lipomas and lipomyelomeningoceles [13]. The fatty mass may attach to the meninges, vertebrae, muscle, or skin. Diastematomyelia is thought to develop from the persistence of an accessory neurenteric canal, which prevents midline fusion of the neural tube [15], or alternatively from formation of two neural tubes as a result of the neural folds turning back ventrally instead of fusing as they approach midline [7]. The presence of a fibrous or bony septum between the hemicords, fibrolipomas at the dorsal aspect of the cleft, adhesions between the hemicords and the meninges, or thickened filum terminale may result in tethering in diastematomyelia [7].

The tight filum terminale syndrome is by definition tethered spinal cord syndrome associated with a short, thickened filum terminale and a low-lying conus. Theoretically the lack of filum elongation from faulty retrogressive differentiation may result in a longer spinal cord, but this in and of itself should not result in cord tethering. Sarwar et al. [16] have postulated that a hemorrhagic or inflammatory insult to the caudal cord may result in reparative elastic or fibrofatty bands that may retract on healing, resulting in tethering of the spinal cord.

The spinal cord is a viscoelastic structure that is fixed and buffered by the dentate ligaments and the filum terminale [17]. The compliance of the filum terminale is far greater than any spinal cord segment and protects the cord from stretching [18]. When the filum is thickened, this protective effect is lost. Elongation of the cord is greatest near the point of tethering [17].

Yamada et al. [19] demonstrated that stretching of the cord results in a highly reduced state of mitochondria, thereby decreasing production of adenosine triphosphonate. Tether-

ing results in stretching, distortion, or kinking of arterioles, venules, and capillaries, but it is unclear if metabolic defects are secondary to ischemia or to some other factor relating to physical stretching of the spinal cord [11]. In any case, metabolic impairment results in functional deterioration of nerve cells. The perikarya (nerve cell bodies) are affected earlier than axons are, and this may account for the earlier appearance of incontinence, muscle atrophy, and hyporeflexia, as opposed to long tract signs such as hyperreflexia and the Babinski sign. Cell damage is reparable up to a point; therefore untethering may result in clinical improvement if the mitochondria are not damaged irreversibly [11].

Repeated acute stretching of the spinal cord may also accentuate the oxidative metabolic changes caused by chronic tethering. The tethered spinal cord syndrome usually presents in childhood, but may present in adults when precipitated by an acute event such as additional tugging when in the lithotomy position, narrowing of the spinal canal by a disk, or direct trauma to the back or buttocks [20]. Twenty-nine percent of our patients were older than 35 years of age.

MR permitted us to confirm the presence of and define the cause of the tethered spinal cord in each case. Myelomeningoceles are obvious clinically and usually are repaired shortly after birth. The majority of patients with skin-covered spinal dysraphisms such as lipomyelomeningoceles are neurologically normal at birth [4, 11]. This may account for the fact that in our series patients undergoing preoperative MR imaging tended to be older and predominantly had skin-covered spinal dysraphisms. Spinal lipomas were the most common traction lesions.

Identification of the level of the conus was concordant in 17 of 19 patients on both sagittal and axial images. In the

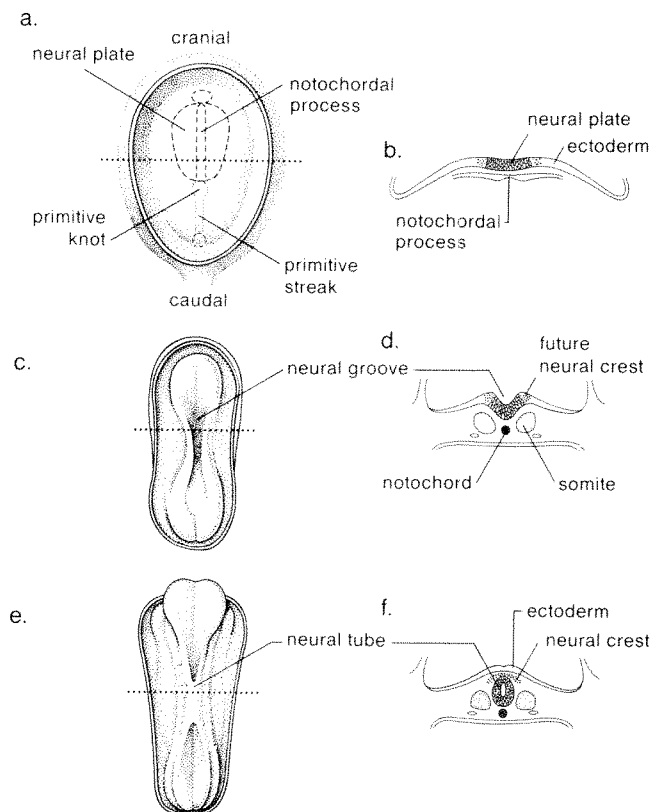


Fig. 7.—Neurulation and disjunction. Dorsal (a, c, and e) and transverse (b, d, and f) sections.

a and b, Thickening of embryonic ectoderm is seen dorsal to notochord to form neural plate.

c and d, Neural plate invaginates along its central axis to form neural groove.

e and f, Neural folds fuse dorsally to form neural tube (neurulation) and simultaneously separate from surface ectoderm (disjunction). First fusion of neural folds is at level of third or fourth somite, and then fusion progresses both cranially and caudally.

(Modified from [8, 9], with permission.)

other two cases, the location on sagittal views was discrepant by at least one vertebral body height from that on axial views. In one case, differentiation of conus from cauda equina was superior on the axial images; the tip of the conus was interpreted as being more cephalad than was suggested on the sagittal study. The inferiorly pointed appearance of the conus usually is readily distinguishable from cauda equina on median sagittal images. However, on sagittal sections slightly off midline, the tip of the conus may be difficult to separate from the roots of cauda equina, which may appear as a uniform structure. Axial images may then be used to confirm the location of the conus termination (Fig. 8) [21]. In the remaining case, the caudal portion of the cord was displaced laterally by a lipoma. Therefore, it was difficult to identify the level of termination of the conus on the sagittal views; the axial images revealed the conus tip to be lower by one vertebral body height (Fig. 1). In all instances, the conus level was assessed more easily and better differentiated from the surrounding cauda equina on axial than on sagittal images.

In 16% of our cases, the tip of the conus was in a normal position. The radiographic diagnosis of tethered spinal cord in these patients had to be determined on the basis of abnormal filum or the presence of a tethering lesion. The thickness of the filum was very useful in the assessment of these patients. We found an abnormally thick filum (greater than 2 mm) at the L5–S1 level in 15 of the 16 patients in whom this measurement could be made. In the patient with a filum thickness of 2 mm, the conus was low-lying. Therefore, the diagnosis of tethered cord was possible even when the filum thickness was normal. Measurements were performed at the L5–S1 interspace level rather than at more cephalad levels, where the filum may appear normal in size due to stretching [11].

A fatty filum terminale was noted as an incidental finding in an additional two patients (33 and 38 years old) whose symptoms could be explained by disk herniations (Fig. 9).

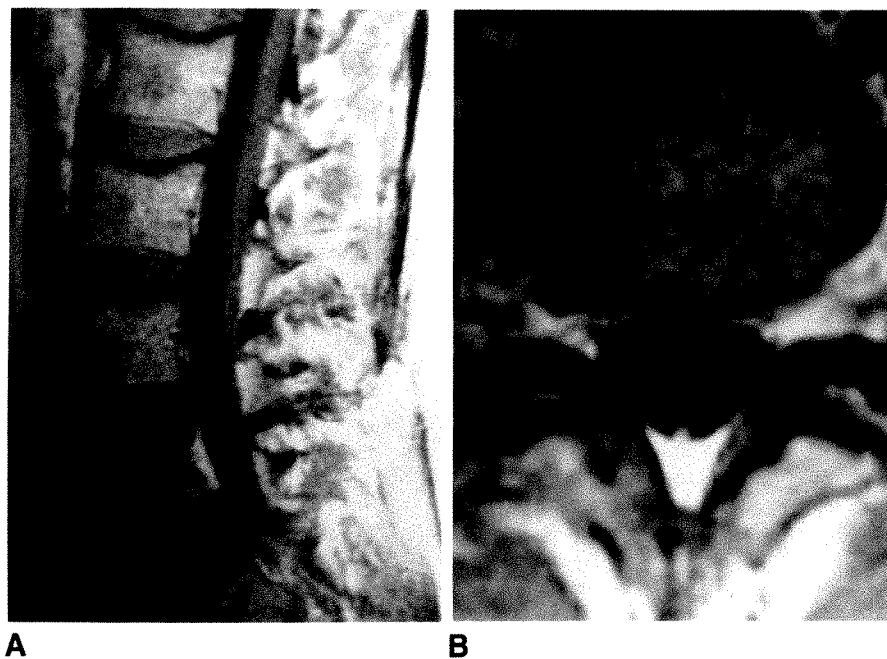


Fig. 8.—Case 12.

A, Slightly off-center sagittal spin-echo image, 1000/20. Cauda equina nerve roots are so uniform as to be confused with conus.

B, Axial spin-echo image 1000/20, confirms presence of cauda equina roots rather than tip of conus at L3–L4 level. Tip of conus was opposite mid L1 vertebral body.

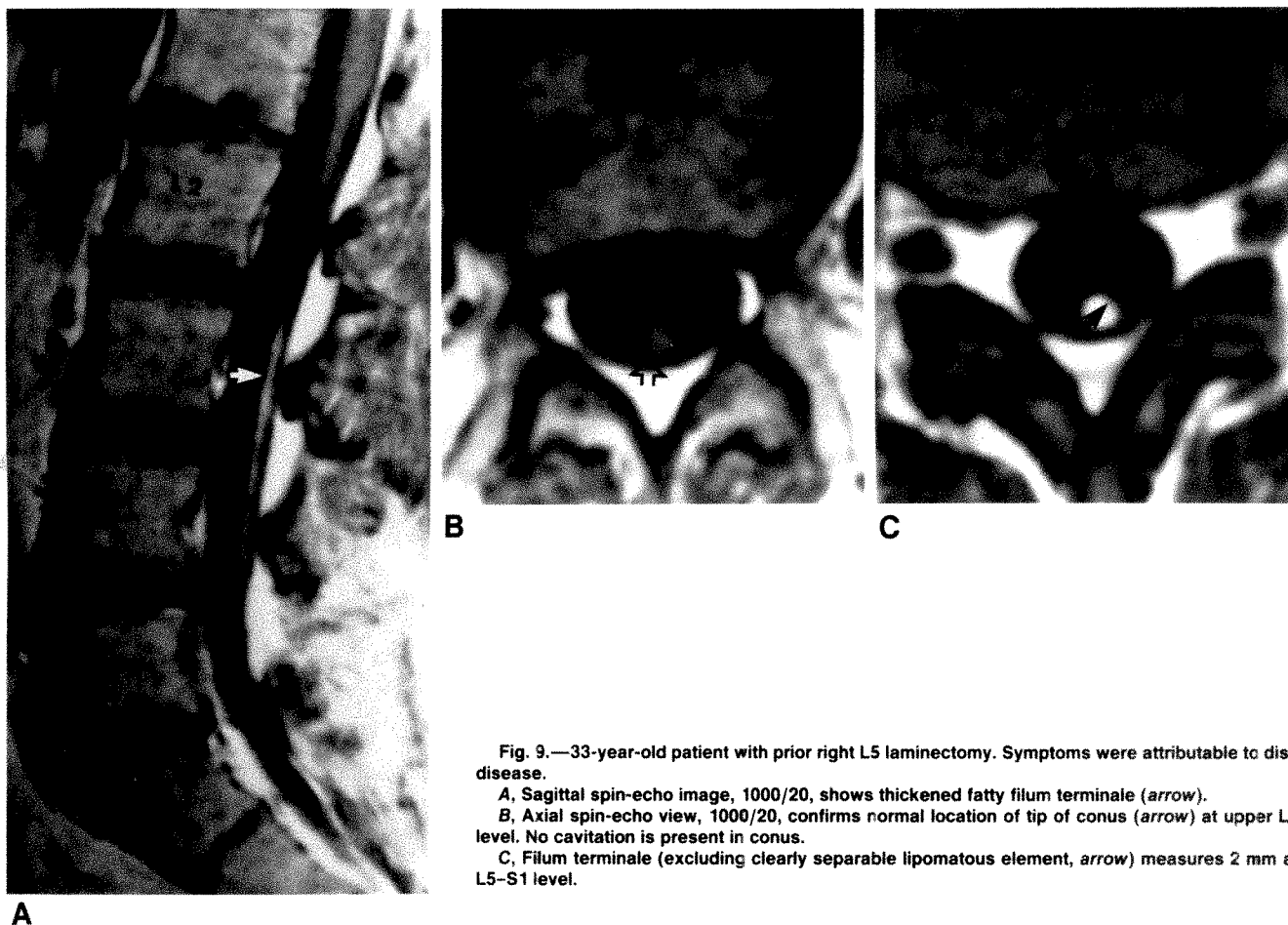


Fig. 9.—33-year-old patient with prior right L5 laminectomy. Symptoms were attributable to disk disease.

A, Sagittal spin-echo image, 1000/20, shows thickened fatty filum terminale (arrow).

B, Axial spin-echo view, 1000/20, confirms normal location of tip of conus (arrow) at upper L2 level. No cavitation is present in conus.

C, Filum terminale (excluding clearly separable lipomatous element, arrow) measures 2 mm at L5-S1 level.

Although tethering may remain subclinical until aggravated by factors that further increase the tension [20], none of the other radiographic criteria of tethered cord were satisfied in either patient. The filum terminale was 2 mm or less in thickness at the L5-S1 level, the conus was above the mid L2 level, and no syringohydromyelic cavity/myelomalacia was identified in the lower spinal cord. Therefore, fatty filum terminale, a possible result of faulty retrogressive differentiation, may not in and of itself be an important radiographic indicator of a tethered spinal cord.

In this study, we did not compare the efficacy of CT with intrathecal contrast material and MR. The inherent advantages of MR are that it is noninvasive and there is no ionizing radiation. Anatomic definition and characterization of the tethering lesions (i.e., lipoma), neural placode, and nerve roots are, in our experience, superior with MR. Flow-compensation gradients and small flip-angle techniques should further improve image quality and nerve root detail by reducing imaging times (less motion artifact) and producing artifact-free myelographic effects. Poor bone definition has always been described as a major limitation of MR compared with CT. In 19 of the 25 patients in our series, the bony dysraphic changes were demonstrated easily. We were able to identify a bony spur and other associated bony changes such as thickened, everted laminae and hemivertebrae in a patient with diaste-

matomyelia (Fig. 6). Vertebral osseous abnormalities are more readily identified and characterized on CT. Identification of neural elements, however, is the primary goal in the evaluation of these patients.

Previous reports have not commented on the association of syringohydromyelia/myelomalacia and tethered spinal cord syndrome except as a postoperative complication or as an additional finding with Chiari malformation [11]. Nine patients in our series had a small, low-intensity cord lesion near to and extending from the conus or the tethering lesions. The syringohydromyelia/myelomalacia could be diagnosed with confidence only on axial images; interpretation on sagittal views was hindered by truncation (Gibbs) and partial-volume artifacts. Given that no axial images were available in five patients, syringohydromyelia/myelomalacia was actually noted in nine of the 20 patients who were adequately evaluated. Six of the nine patients were 11 years old or younger. These small cord lesions probably could not have been detected by any other imaging method. The numbers in this study are small and further experience is necessary, but it is possible that such mild syringohydromyelia/myelomalacia may be a useful ancillary sign in the radiologic diagnosis of tethering.

Stretching of the spinal cord is most prominent in the segment adjacent to the traction lesion [17]. With tethering, oxidative metabolism of the cord is impaired, arterioles and

venules are stretched and distorted, and electron microscopy reveals wrinkling and tearing of the cell membrane [11]. A combination of these factors may be the basis of intramedullary cavity formation. According to the above-proposed mechanism, the cord probably has to go through a stage of myelomalacia (cord softening) before proceeding to actual cavitation [22]. Because we do not have pathologic proof and because a small focus of myelomalacia can be difficult to differentiate with confidence from a small syringohydromyelic cavity on MR, we have referred to the low-intensity cord lesion as syringohydromyelia/myelomalacia.

It is unclear what contribution the focal syringohydromyelic cavity/myelomalacia makes to the symptom complex of tethered spinal cord syndrome and how it may affect the prognosis of treatment. After surgery for tethered cord, motor improvements are seen in 50% of patients, with improvement of urologic function in only 7%. Many deficits stabilize but do not improve [11]. Early prophylactic care is therefore the standard, even in asymptomatic children [4]. The presence of the low-intensity cord lesion may denote some form of irreversibility. Postsurgical follow-up was available in six patients. One of the two patients who remained asymptomatic had a low-intensity focus in the conus. In two patients, symptoms stabilized, and syringohydromyelia/myelomalacia was noted in the one with persistent neurogenic bladder; the other had a hemispastic gait. Syringohydromyelia/myelomalacia was identified in the spinal cords of both of the remaining two patients: one eventually became hemiplegic and the other developed progressive calcaneovalgus deformity.

From a diagnostic point of view, the presence of syringohydromyelia/myelomalacia can be a helpful adjunct when the conus is not low-lying and the diagnosis of tethered spinal cord is clinically suspected. One of our six patients with tethered spinal cord syndrome and a normal conus level had a minimally thickened filum terminale (3 mm) and a low-intensity lesion in the conus.

In summary, MR is very useful in visualizing the conus medullaris, assessing the thickness of the filum terminale, and identifying traction lesions in a patient clinically suspected of having tethered spinal cord syndrome. Associated bony dysraphisms are easily evaluated. We noted a frequent occurrence of focal syringohydromyelia/myelomalacia near the tip of the conus or in the cord near the tethering lesion. This may

be a useful diagnostic sign but the prognostic significance is unclear.

REFERENCES

1. Barson AJ. The vertebral level of termination of the spinal cord during normal and abnormal development. *J Anat* **1970**;106:489-497
2. Smoker WRK, Godersky JC, Knutson RK, Keyes WD, Norman D, Bergman W. The role of MR imaging in evaluating metastatic spinal disease. *AJR* **1987**;149:1241-1248
3. Masaryk TJ, Modic MR, Geisinger MA, et al. Cervical myelopathy: comparison of magnetic resonance and myelography. *J Comput Assist Tomogr* **1986**;10:184-194
4. Edwards MSB. Management of lipomyelomeningoceles in childhood. *Int Pediatr* **1987**;2:120-123
5. James CCM, Lassman LP. *Spinal dysraphism: spina bifida occulta*. New York: Appleton-Century-Croft, **1972**:82-96
6. Fitz CR, Harwood-Nash DC. The tethered conus. *AJR* **1970**;125(3):515-523
7. Newton TH, Potts DG, eds. *Computed tomography of the spine and spinal cord. Spinal dysraphism*, Vol. 1. San Anselmo, CA: Clavadel, **1983**:299-354
8. Moore KL. *The developing human*, 4th ed. Philadelphia: Saunders, **1988**:48-51
9. Cowan M. The development of the brain. *Sci Am* **1979**;241(3):112-133
10. Lemire RJ, Looser JD, Leech RW, Alvord EC. *Normal and abnormal development of the human nervous system*. New York: Harper & Row, **1975**:54-83
11. Holtzman RN, Stein BM, eds. *The tethered spinal cord*. New York: Thieme-Stratton, **1985**:1-147
12. Osaka K, Matsumoto S, Tanimura T. Myeloschisis in early human embryos. *Childs Brain* **1978**;4:347-359
13. McLone DG. The subarachnoid space: a review. *Childs Brain* **1980**;6:113-130
14. Jones PH, Love JG. Tight filum terminale. *Arch Surg* **1956**;73:556-566
15. Bremer JL. Dorsal intestinal fistula; accessory neuroenteric canal; diastematomyelia. *Arch Pathol Lab Med* **1952**;54:132-138
16. Sarwar M, Virapongse C, Bhimani S. Primary tethered cord syndrome: a new hypothesis of its origin. *AJNR* **1984**;5:235-242
17. Sarwar M, Crelin ES, Kier EL, Virapongse C. Experimental cord stretchability and the tethered cord syndrome. *AJNR* **1983**;4:641-643
18. Tani S, Yamada S, Knighton R. Extensibility of the lumbar and sacral cord. *J Neurosurg* **1987**;66:116-123
19. Yamada S, Zinke DE, Sanders D. Pathophysiology of "tethered cord syndrome." *J Neurosurg* **1981**;54:494-503
20. Pang D, Wilberger JE. Tethered cord syndrome in adults. *J Neurosurg* **1982**;57:35-47
21. Monajati A, Wayne WS, Rauschnig W, Ekholm SE. MR of the cauda equina. *AJNR* **1987**;8:893-900
22. Gebarski SS, Maynard FWS, Gabrielson TO, Knake JE, Latack JT, Hoff JT. Post-traumatic progressive myelopathy. *Radiology* **1985**;57:379-385

Comparison of STIR and Spin-Echo MR Imaging at 1.5 T in 90 Lesions of the Chest, Liver, and Pelvis

William P. Shuman¹
 Richard L. Baron
 Michael J. Peters
 Pamela K. Tazioli

Short T1 inversion recovery (STIR) produces both fat suppression and the additive effect of T1 and T2 mechanisms on tissue brightening, in contrast to the subtractive effect of these two mechanisms on spin-echo sequences. In order to compare STIR and spin-echo imaging, we reviewed 90 lesions detected in 76 consecutive MR studies of the chest, liver, or pelvis performed at 1.5 T with both STIR and double-echo spin-echo techniques. Images were compared for the number of individual lesions detected. Lesion conspicuity was scored by using a subjective scale for each sequence. Lesion size was measured with hand-held calipers, and volume was calculated assuming a prolate ellipse. Because of inherent error in such calculations, lesions were judged to be similar in size (within 20%) or dissimilar (more than 20% difference). The presence of a lesion was proved by direct biopsy in 36 (40%), by tissue pathology from some other focus plus follow-up of the lesion in 37 (41%), or by other imaging plus follow-up in 12 (13%). STIR images detected five (6%) more lesions than spin echo and did not miss any of the lesions detected by spin echo. Conspicuity was greater on STIR images than on spin-echo images in 82 (91%) of the lesions. Twenty-six (29%) of the lesions appeared larger on STIR images than on spin-echo images.

For these reasons, STIR may be a useful adjunct to spin echo for body MR in some cases. However, STIR images typically display lower signal-to-noise than spin-echo images do, and all abnormalities (tumor or edema) may appear equally bright on STIR.

At mid field strength (0.6 T), T1-weighted, short-TR and short-TE, spin-echo imaging is sensitive in detecting focal pathology in the liver [1]. At high field strength (1.5 T), T2-weighted, long-TR and long-TE, spin-echo imaging is sensitive in detecting focal pathology in several areas of the body [2-5]. Short T1 inversion-recovery (STIR) sequences at low to mid field strengths and at high field strength also have been reported to be sensitive in detecting focal pathology [6-11]. STIR provides suppression of signal from fat and additive effects of T1 and T2 mechanisms on tissue brightening.

We investigated the utility of STIR imaging in three regions of the body (chest, liver, and pelvis) when it was used as an adjunct to double-echo spin-echo imaging at high (1.5 T) field strength. Specifically, we compared the STIR and spin-echo techniques for (1) the number of individual lesions detected, (2) the subjective conspicuity of individual lesions, and (3) the approximate size of abnormality detected for each lesion.

Materials and Methods

Seventy-six consecutive MR studies of the chest, liver, and pelvis that used both STIR and spin-echo sequences were performed over a 4-month period at our institution. Twenty-two studies were of the chest, 25 were of the liver, and 29 were of the pelvis. Of the 70 patients involved, 29 were men and 41 were women. They were 17-83 years old (average, 48 years).

MR studies were performed on a 1.5-T clinical imager (Signa, General Electric, Milwaukee, WI). All studies used a double-echo spin-echo sequence with mixed- and T2-weighted images

Received August 1, 1988; accepted after revision December 21, 1988.

¹ All authors: Department of Radiology, University of Washington Hospital, Seattle, WA 98195. Address reprint requests to W. P. Shuman.

AJR 152:853-859, April 1989

0361-803X/89/1524-0853

© American Roentgen Ray Society

and included a STIR sequence. The STIR sequence was in the same plane as the spin-echo sequence in all but four studies. Sixteen studies included two separate double-echo spin-echo sequences with different imaging planes. Mixed- and T2-weighted double-echo spin-echo sequences were performed with 2000/20–80 (TR/TE); a matrix of 128 ($n = 19$) or 256 ($n = 73$); two excitations; and a slice thickness of 5 mm ($n = 45$) or 10 mm ($n = 47$) in the coronal ($n = 15$), sagittal ($n = 4$), or axial ($n = 73$) plane. STIR sequences were performed with 2000/110–140/40 (TR/TI/TE); a matrix of 128; two excitations; and a slice thickness of 5 mm ($n = 26$) or 10 mm ($n = 50$) in the coronal ($n = 12$), sagittal ($n = 4$), or axial ($n = 60$) plane. Each STIR sequence required about 8 min to perform. The TI for each STIR sequence was "tuned" to each patient during the manual prescan by minimizing the height of the fat peak on the center-frequency spectral display; this was accomplished in about 2 min by varying the TI in increments of 10 msec between 110 and 140 msec while observing the spectral display. The TI that resulted in the lowest fat peak was selected for use with the STIR imaging sequence (Fig. 1). The TI values used for the 76 STIR imaging sequences were 110 ($n = 2$), 120 ($n = 50$), 130 ($n = 21$), and 140 ($n = 3$).

MR images from the spin-echo and STIR sequences were reviewed retrospectively by three radiologists for the presence of lesions; any differences were resolved by consensus. To compare detection rates, the radiologists evaluated individual lesions detected on any one sequence (mixed-weighted, T2-weighted, and STIR) for detection on the other two types of sequences. To compare conspicuity of lesions, the radiologists scored the conspicuity of each lesion from each

sequence, using the following scale: 0 = not seen, 1 = barely perceptible, 2 = easily seen, and 3 = intensely bright ("light bulb") (Figs. 2 and 3). Although such a conspicuity scale is inherently open to bias, similar subjective scales have produced useful radiologic comparisons, particularly in receiver-operating-characteristic (ROC) methodology [12–14]. The sequence with the highest conspicuity score was noted for each lesion; if conspicuity scores were equal for two sequences, the most conspicuous sequence was selected by direct visual comparison of the images. No attempt was made to measure tissue T1 or T2 values, signal intensities, or contrast-to-noise ratios. Window and level settings selected by experienced MR technologists for routine clinical imaging were accepted for evaluating conspicuity of lesions.

To compare the size of each lesion as detected by the three different sequences, each lesion was measured at its greatest width, length, and height to the nearest 0.5 cm by using hand-held calipers (Fig. 4). The volume of each lesion was calculated (assuming a prolate ellipse) on each sequence. The volume of each lesion on STIR images was compared with the volume from mixed-weighted and T2-weighted images. Considerable inherent error in volume calculations could result from the use of hand-held calipers for measurements and from the assumption that all lesions were prolate ellipse in shape. For these reasons, if the difference in volume of two lesions was less than 20%, they were categorized arbitrarily as being similar in size. Differences in volume of more than 20% resulted in the lesions being categorized as dissimilar in size; in these cases, the greater percent of the larger volume was noted. For volume analysis, lesions seen

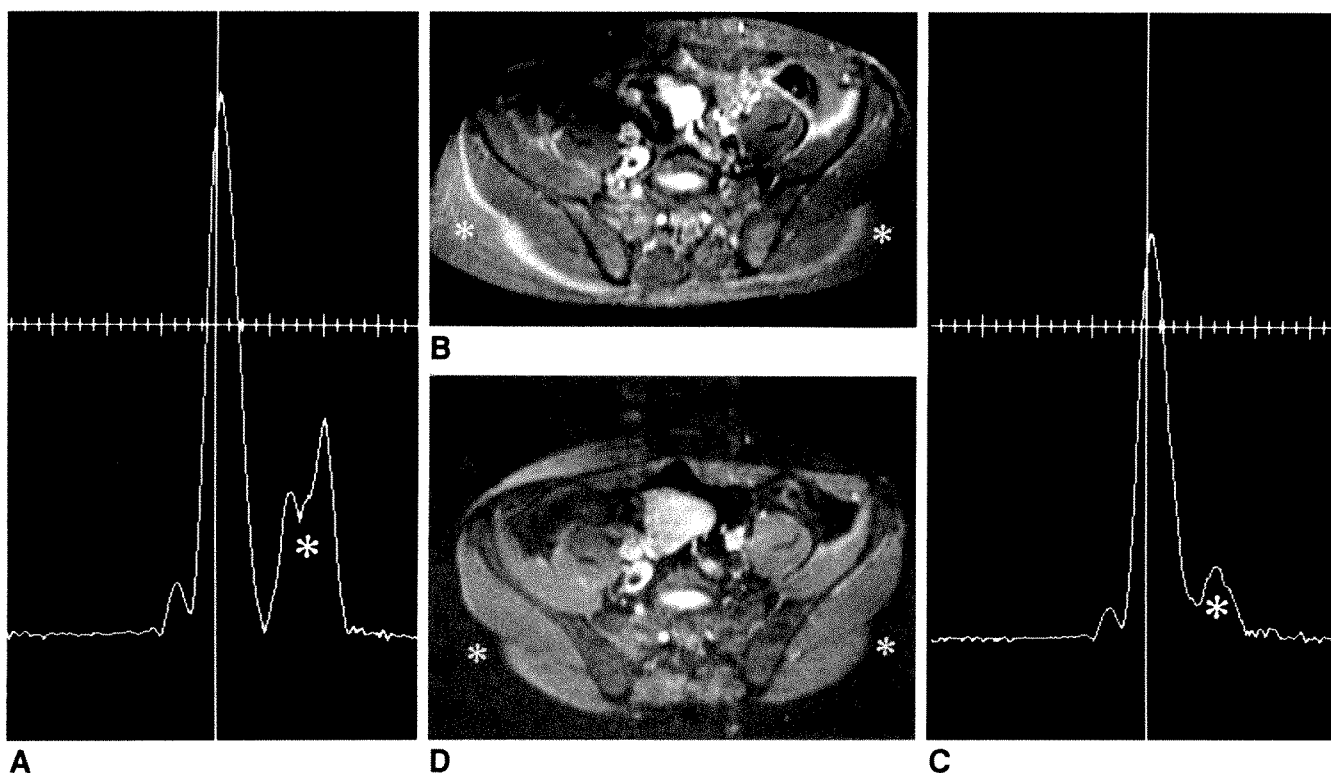


Fig. 1.—Tuning TI to optimize fat suppression. Images and spectral displays at same anatomic location in same volunteer.

A, Center-frequency spectral display, TI = 110. Note height of fat peaks (asterisk). Large central peak is from water signal.

B, Corresponding image (2000/40), TI = 110. Fat signal is suppressed somewhat, but still some signal from subcutaneous fat is seen (asterisks).

C, Center-frequency spectral display, TI = 140. Note decreased height of fat peaks (asterisk) compared with TI of 110.

D, Corresponding image (2000/40), TI = 140. Very little signal comes from subcutaneous fat (asterisks) compared with 110-TI image.

Fig. 2.—Biopsy-proved poorly differentiated metastatic adenocarcinoma in left lobe of liver seen only in STIR images.

A, T2-weighted spin-echo image (2000/80) of liver shows phase-shift artifact but no brightening in left lobe of liver.

B, STIR image (2000/120/40) shows diffuse area of brightening in left lobe of liver (arrows). Sonography identified an identical area of abnormality and was used to obtain a core biopsy, which revealed metastatic adenocarcinoma. Note how area of brightening on STIR is considerably larger than phase-shift artifact area on spin-echo image. STIR conspicuity score was 2.

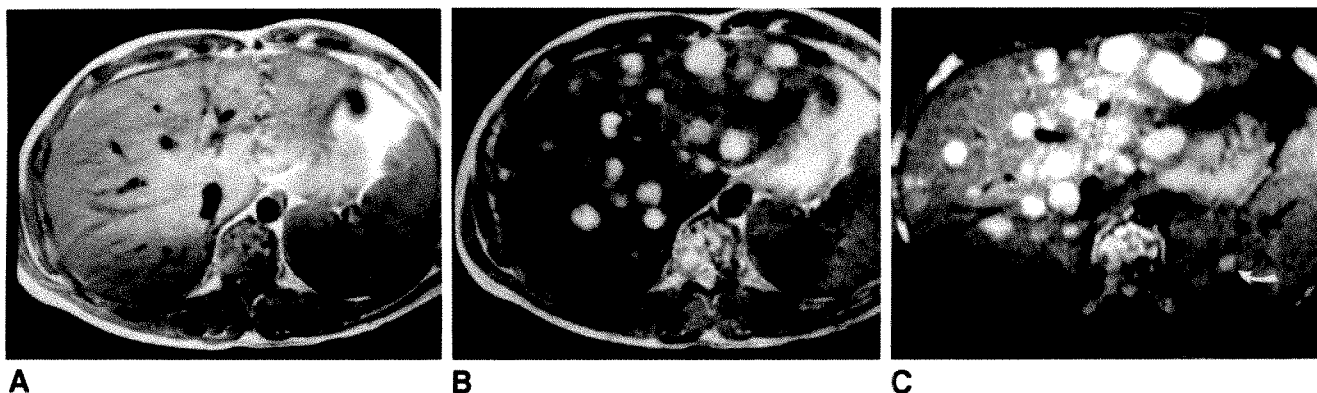
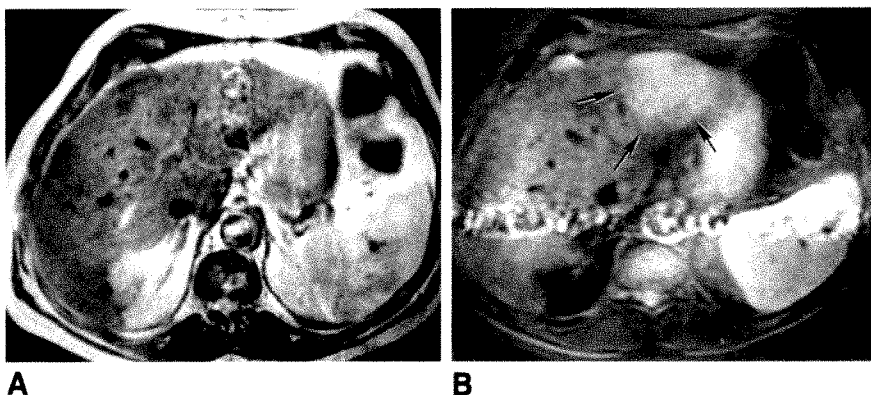


Fig. 3.—Melanoma metastatic to liver (biopsy-proved) not seen on mixed-weighted images but seen equally well on T2 and STIR.

A, Mixed-weighted image (2000/20). No lesions seen in liver or spleen. Arcuate artifacts in liver and spleen are from motion of bright anterior subcutaneous fat.

B, T2-weighted image (2000/80). Multiple bright lesions are seen in liver; conspicuity score was 3. No lesions are seen in spleen. Some arcuate artifact is seen in spleen from motion of bright subcutaneous fat.

C, STIR image (2000/130/40). Same-sized multiple bright lesions are seen in liver; conspicuity score was 3. Note lesion in spleen (arrow). Artifact from subcutaneous fat is absent since fat signal is suppressed.

only on STIR images were arbitrarily assigned a percentage difference of 100%.

Ninety separate lesions were detected in 61 of the 76 MR studies. Proof of the presence and type of pathology was by direct biopsy (either needle or surgical) of the MR lesion in 36 (40%) of the 90; by tissue pathology from some other focus of the patient's disease (other than the MR lesion in question) plus follow-up of the MR lesion for an average of 5.1 months in 37 (41%); or, in 12 (13%) liver hemangiomas, by other imaging studies plus follow-up of the MR lesion for an average of 6.3 months. Five lesions (6%) had no proof but did have follow-up for an average of 5.8 months. The MR study was entirely normal in 15 of the 76 studies. In these 15 normal studies, absence of disease was proved subsequently by negative surgical results in three patients and by clinical follow-up for an average of 6.2 months in 11 patients; one normal MR study had no proof of absence of disease and no follow-up.

Of the 90 lesions detected by MR, 29 lesions were located in the chest; 18 of these were in the chest wall, six in the lung, and five in the mediastinum or adjacent pleural space. Diagnoses for chest pathology included metastases (seven patients); primary breast carcinoma (five); primary lung carcinoma (five); melanoma (four); malignant effusion (two); benign cyst (two); and Ewing sarcoma, malignant fibrous histiocytoma, lymphoma, and lipoma (one each). Thirty-one lesions were located in the liver. Diagnoses for liver pathology included hemangioma (14 patients); metastases (12); and cholangiocarcinoma, adenoma, cyst, sclerosing cholangitis, and fatty infiltration

(one each). Thirty lesions were located in the pelvis. Diagnoses for pelvic pathology included metastases (eight patients); primary carcinoma of the colon (three), penis (two), vagina (two), and prostate, bladder, cervix, and anus (one each); radiation-induced bone fibrosis (four); gestational trophoblastic disease (three); and malignant fibrous histiocytoma, melanoma, Ewing sarcoma, and decubitus ulcer (one each).

Statistical analysis for significant differences in conspicuity scores among the three sequences (mixed-weighted, T2-weighted, and STIR) was performed by using analysis of variance with the Scheffe method of multiple comparisons between groups. Any *p* values less than .05 were accepted as significant.

Results

Of the 90 lesions detected, STIR images identified 89 (99%), T2-weighted images identified 85 (94%), and mixed-weighted images identified 56 (62%). Five lesions (6%) were identified only on STIR images; four malignant lesions were proved by biopsy of the MR lesions, and one case of fatty infiltration of the liver was proved by clinical follow-up and subsequent imaging. One lesion was identified only on T2-weighted images; this lesion was a poorly defined area of brightening in the uterus of a patient who had peritoneal metastases from gestational trophoblastic disease. Subse-

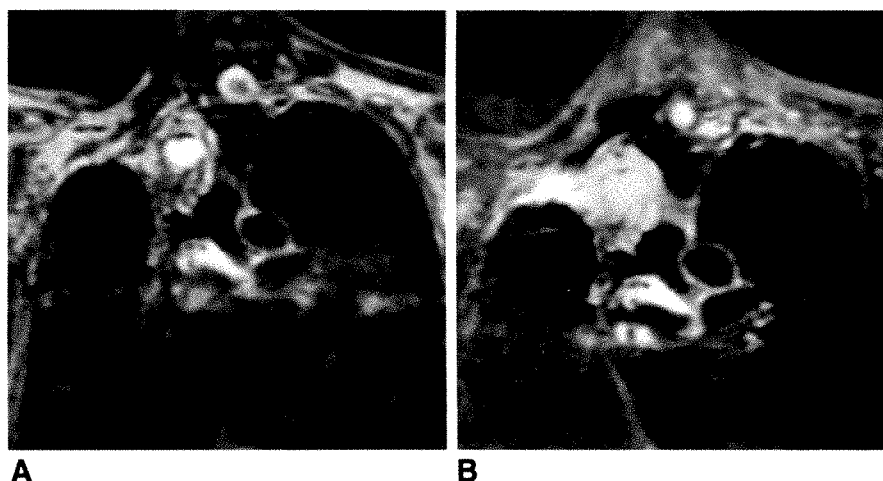


Fig. 4.—Biopsy-proved recurrent bronchogenic carcinoma at right lung apex 5 months after radiation therapy.

A, T2-weighted image (2000/80). Note focal bright tumor with some surrounding darker tissue.

B, STIR image (2000/120/40). Area of bright abnormality is much larger than on T2 image.

quent hysterectomy showed no tumor in the uterus, and the uterine MR lesion was assumed to be a false positive. No lesions were identified on mixed-weighted images only.

Conspicuity scores for the 90 lesions with the three types of images are shown in Table 1. A score of 3 was assigned to the STIR image of a lesion more often than to the T2-weighted image of a lesion (60 vs 23); no mixed-weighted image of a lesion had a score of 3. Good conspicuity (score of 3 or 2) was assigned to the STIR image of a lesion ($n = 87$) more often than to the T2-weighted image of a lesion ($n = 70$) or to the mixed-weighted image of a lesion ($n = 35$). Poor conspicuity (score of 1 or 0) was assigned to the STIR image of a lesion ($n = 3$) less often than to the T2-weighted image of a lesion ($n = 20$) or to the mixed-weighted image of a lesion ($n = 55$). There was a statistically significant difference between the conspicuity scores of STIR vs T2-weighted images ($p < .001$) and STIR vs mixed-weighted images ($p < .001$).

The sequence with the highest conspicuity score was STIR in 50 (56%) of the 90 lesions and was the T2-weighted sequence in one lesion (1%). The STIR score was two higher than the T2 score in seven lesions and was one higher than the T2 score in 43 lesions; the T2 score was one higher than the STIR score in one lesion. In 39 lesions (43%) the conspicuity scores were tied. STIR was the more conspicuous sequence by direct visual comparison when the scores were tied in 32 of these 39 lesions; spin echo was the more conspicuous sequence by direct visual comparison when the scores were tied in seven lesions. Combining categories, STIR was the most conspicuous sequence in 82 lesions (91%) and T2-weighted spin echo was the most conspicuous sequence in eight lesions (9%). The mixed-weighted sequence was the most conspicuous in none of the lesions.

The volume of abnormality was similar ($\leq 20\%$) on STIR and spin-echo sequences in 61 of the 90 lesions. The volume of abnormality was dissimilar (volume on STIR images 20% greater than volume of abnormality on T2-weighted images) in 26 of the 90 lesions (the volume of abnormality on T2-weighted images was \geq the volume on mixed-weighted images in all 26). Ten of the lesions with a greater volume of abnormality on STIR were in the chest; the STIR abnor-

TABLE 1: Distribution of Lesion Conspicuity Scores

Sequence	No. by Score ^a			
	0	1	2	3
STIR	1	2	27	60
T2	5	15	47	23
Mixed	34	21	35	0

^a 0 = not seen; 1 = barely perceptible; 2 = easily seen; 3 = intensely bright.

malty ranged from 26% to 275% greater (average, 126%). Five of the lesions were in the liver; the STIR abnormality ranged from 40% to 209% greater (average, 105%). Eleven of the lesions were in the pelvis; the STIR abnormality ranged from 28% to 150% greater (average, 85%). STIR images for all of these 26 lesions had an average volume of abnormality 105% greater than on T2 images. In three lesions, the margins of the abnormality were too poorly defined to be measured on at least one sequence, so volume comparisons were not obtained.

Discussion

STIR is an inversion-recovery MR imaging sequence that uses a 180° RF pulse followed by a 90° pulse and another 180° pulse (to produce an echo). In "traditional" inversion recovery, the time between the first 180° pulse and the 90° pulse (termed TI) is relatively long (300–500), so that T1-weighting is produced. In STIR, the TI time is made relatively short (100–170) in order to produce fat suppression. To accomplish fat suppression, one must select the TI value such that the 90° pulse occurs exactly when the longitudinal magnetization of fat spins is at zero, while, at the same time, some longitudinal magnetization is still present in water spins. This effectively produces both suppression (blackening) of signal from fat tissue and relative enhancement of signal from water-containing tissues. STIR also enhances differences between the water content of various tissues because it is T1- plus T2-weighted, an additive effect that might potentially highlight disease [10].

In contrast to "traditional" T1-weighted (long T1) inversion recovery, in which long-T1 tissue is dark, in STIR, long-T1 tissue is bright. In addition, the TE in STIR (40 in this study) is longer than in "traditional" T1-weighted inversion recovery in order to make long-T2 tissue bright. Thus, in STIR, long T1 and long T2 have an *additive* effect on tissue brightening: the T1 effect produced by the shorter T1 and the T2 effect produced by the longer TE. Whereas spin-echo sequences are often thought of as T1- or T2-weighted, in fact there are no truly T1- or T2-weighted spin-echo images because T1 and T2 effects are subtractive from each other in their effect on tissue brightening. STIR allows a relatively pure addition of both T1 and T2 mechanisms to result in additive lesion brightening. Thus, STIR might be thought of as being weighted toward tissue, which has both a long T1 plus a long T2. Alternatively, because most pathology has both a long T1 and a long T2 relative to normal tissue, STIR might be thought of as being weighted toward the identification of pathology. This additive effect of T1 and T2 may be what makes pathology more conspicuous with STIR and may account for improved detection of abnormal tissue. However, because all pathology becomes equally bright, STIR is unable to distinguish between different types of abnormal tissue, such as edema or tumor.

STIR has been shown to work well at both low and high field strengths [6–11, 15]. However, at high field strengths, while the T1 increases for all tissue, the difference between the T1 of fat and the T1 of water is greater than at lower field strengths. This makes STIR signal intensity from water-containing tissues relatively greater at higher field strengths and may improve the signal-to-noise ratio [11]. By suppressing fat signal, STIR also controls the chemical-shift artifacts, which are more prominent at high field strengths [11].

Bydder et al. [15] originally described the STIR technique in 1985 and reported that STIR in the liver produced high contrast between normal and diseased liver. They proposed that the high sensitivity of STIR might make it a good screening technique for hepatic pathology. More recently, STIR has been compared with five other spin-echo techniques (including short TR and TE, long TR and TE, and phase contrast) at medium field strengths (1.0 T) for con-

trast-to-noise ratios between normal liver and metastases [10]; STIR yielded the greatest contrast of the six techniques and was believed to be the most sensitive. In other areas of the body, low- to mid-field STIR has been used to evaluate lymphadenopathy, marrow malignancies, and vertebral body metastases and fracture [6, 7, 16, 17]. High-field STIR has been reported in the evaluation of bone marrow and CNS disorders [8, 9, 18]. These reports generally describe a greater number of lesions detected or greater conspicuity for focal pathology with STIR than with spin echo.

Each report on STIR technique to date has used a single T1 time (generally 100 or 150) for all patients in the particular study. Before starting this investigation, we noted that the optimal T1 for fat suppression varied somewhat. Therefore, we adopted a technique of "tuning" the T1 to each individual patient. Tuning was accomplished by altering the T1 between 110 and 140 during prescanning and checking the height of the fat peak (on the center-frequency spectral display) resulting from each T1. The T1 that produced the lowest fat peak was used in the imaging STIR sequence. This technique most commonly resulted in an imaging STIR T1 of 120 (66% of STIR studies), but 130 was used often (28%), and the T1 values 110 or 140 were used occasionally (6%). The reason for variations in the optimal T1 is unknown, but it may be due to variations in the T1 of fat between patients or between different parts of the body. We are currently investigating this question.

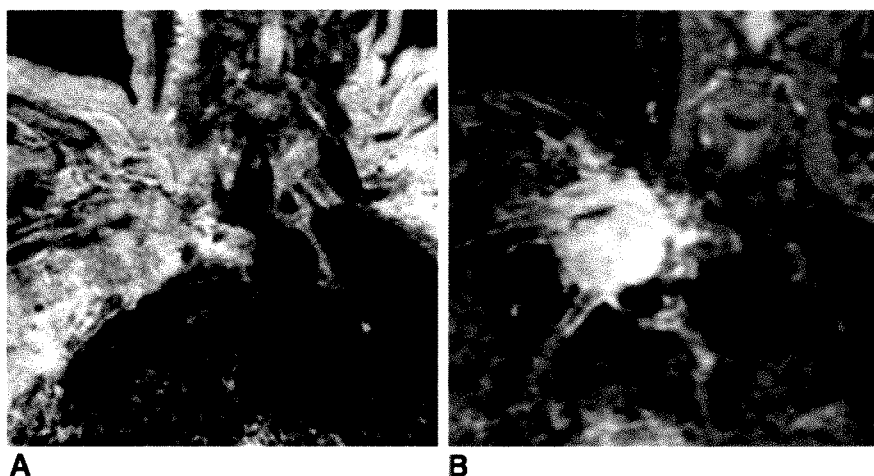
In this sequential series of patients, STIR detected five (6%) more lesions than did double-echo spin-echo sequence and did not miss any lesions detected by spin echo. Additional lesions found by STIR in the liver were an area of infiltrating metastatic disease (Fig. 2) and a region of somewhat diffuse fatty infiltration. Additional lesions found by STIR in the chest wall and pelvis were metastatic breast carcinoma, melanoma, and recurrent vaginal carcinoma, all of which were surrounded by fat.

The most striking feature on the STIR sequence was that conspicuity of most (91%) of the lesions in this series was greater than conspicuity on spin echo. STIR was one or two scores higher in conspicuity in 56% of the lesions. We acknowledge that the conspicuity scale used in this study is

Fig. 5.—Biopsy-proved bronchogenic carcinoma invading right chest wall and brachial plexus region.

A, T2-weighted image (2000/80). Tumor is evident but is isointense relative to surrounding fat and hard to distinguish from it.

B, STIR image (2000/120/40). Abnormality is distinguished from surrounding fat.



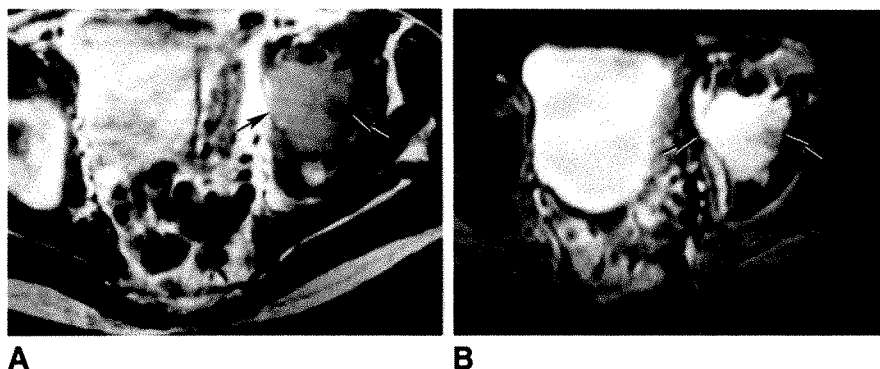


Fig. 6.—Metastatic bronchogenic carcinoma to left acetabulum.

A, Mixed-weighted image (2000/20). Lesion is dark (arrows) and is crossed with arcuate artifacts from bright anterior subcutaneous fat. Conspicuity score was 2.

B, STIR image (2000/130/40). Lesion (arrows) is same size but is bright. No arcuate artifacts are seen because fat signal is suppressed. Conspicuity score was 3.

subjective and inherently open to some preconceived bias. However, visual assessment of lesions detected by MR has been shown to be useful and practical, although it is less accurate than quantitative methods such as contrast to noise ratios [19]. Also, subjective scales frequently are used in radiologic comparison studies that use ROC methodology [12–14].

A substantial proportion (29%) of individual lesions appeared larger on STIR than on spin-echo images. Spatially localized pathologic proof of the cause for additional abnormality (tumor vs peritumoral edema) with STIR was not available in this series. However, we believe that the cause of the larger abnormality detected is the greater sensitivity of STIR to edema surrounding focal tumor and the ability of STIR to better distinguish tumor or peritumoral edema from adjacent fat (Fig. 5). We also observed that in no lesion was STIR able to delineate tumor from adjacent edema, probably because tumor and edema appeared equally bright on STIR. In some clinical instances, this greater ability of STIR to detect peritumoral tissue brightening may be helpful. For example, Beltran et al. [20] showed that up to 27% of extremity sarcomas with peritumoral tissue brightening may have microscopic tumor infiltrating into the adjacent brightened tissue. Such potential microscopic invasion into areas of peritumoral brightening might have important implications for surgical staging or planning radiation therapy.

The STIR sequence does have some significant disadvantages. Because the longitudinal magnetization of water spins may not be great at the time fat spins are passing through zero longitudinal magnetization, signal from the water spins after the 90° pulse may be relatively weak. This means STIR images generally have a poor signal-to-noise ratio and are quite susceptible to artifacts generated by moving tissue or flowing blood. On the other hand, artifact from the respiratory motion of bright subcutaneous fat in the abdominal wall on spin-echo images is absent from STIR images because of suppression of the fat signal (Figs. 3 and 6). An additional disadvantage of STIR imaging is the relatively small number of slices available (8 to 11, depending on the TI). This limitation makes it important to spatially center a STIR sequence on any pathology detected by spin-echo sequences. Alternatively, several contiguous STIR sequences might be used to cover a region of clinically suspected pathology. New artifact- and noise-suppression techniques,

such as narrow bandwidth imaging, saturation pulses, gradient-moment nulling, and gating, have recently become compatible with STIR on our scanner and may help alleviate some of these problems. These techniques also have improved significantly the quality of spin-echo images.

We currently use STIR as an adjunct to spin-echo imaging in many of our body MR studies. We find STIR particularly helpful when there is a clinical need to detect as many individual lesions as possible or to define the full extent of an MR abnormality for therapy planning. The greater conspicuity of lesions on STIR images is also helpful when showing abnormalities to referring clinicians.

ACKNOWLEDGMENTS

We thank Thomas Rudd and Michael Richardson for assistance with data analysis and David Haynor and Rob Newman for manuscript review.

REFERENCES

1. Stark DD, Wittenberg J, Edelman RR, et al. Detection of hepatic metastases: analysis of pulse sequence performance in MR imaging. *Radiology* 1986;159:365–370
2. Foley WD, Kneeland JB, Cates JD, et al. Contrast optimization for the detection of focal hepatic lesions by MR imaging at 1.5 T. *AJR* 1987;149:1155–1160
3. Mitchell DG, Mintz MC, Spritzer CE, et al. Adnexal masses: MR imaging observations at 1.5 T, with US and CT correlation. *Radiology* 1987;162:319–324
4. Togashi K, Nishimura K, Itoh K, et al. Uterine cervical cancer: assessment with high-field MR imaging. *Radiology* 1986;160:431–435
5. Castagno AA, Shuman WP. MR imaging in clinically suspected brachial plexus tumor. *AJR* 1987;149:1219–1222
6. Porter BA, Neumann EB, Olson DO, Nyberg DA, Teefey SA, Shields AF. STIR imaging of lymphadenopathy: advantages over conventional spin-echo techniques. Presented at the annual meeting of the Radiological Society of North America, Chicago, IL, November 1987
7. Wiener SN, Rzeszutarski MS. Thick-section STIR: a screening technique for vertebral metastases. Presented at the annual meeting of the Radiological Society of North America, Chicago, IL, November 1987
8. Unger EC, Moldofsky P, Hartz WH, Clair M, Silver M, McGlone J. MR imaging of bone-marrow disease using STIR. Presented at the annual meeting of the Radiological Society of North America, Chicago, IL, November 1987
9. Larson TC, Newman R, Wehrli FW, Norman D. Early experience with high-field STIR of the central nervous system including fat-suppression techniques. Presented at the annual meeting of the Radiological Society

- of North America, Chicago, IL, November **1987**
10. Paling MR, Abbitt PL, Mugler JP, Brookeman JR. Liver metastases: optimization of MR imaging pulse sequences at 1.0 T. *Radiology* **1988**; 167:695-699
 11. Bydder GM, Young IR. MR imaging: clinical use of the inversion recovery sequence. *J Comput Assist Tomogr* **1985**;9:659-675
 12. Metz CE. ROC methodology in radiologic imaging. *Invest Radiol* **1986**;21:720-733
 13. Poon PY, Bronskill MJ, Henkelman RM, et al. Mediastinal lymph node metastases from bronchogenic carcinoma: detection with MR imaging and CT. *Radiology* **1987**;162:651-656
 14. MacMahon H, Vyborny CJ, Metz CE, Doi K, Sabeti V, Solomon SL. Digital radiography of subtle pulmonary abnormalities: an ROC study of the effect of pixel size on observer performance. *Radiology* **1986**; 158:21-26
 15. Bydder GM, Steiner GM, Blumgart LH, Khenia S, Young IR. MR imaging of the liver using short T1 inversion recovery sequences. *J Comput Assist Tomogr* **1985**;9:1084-1089
 16. Proter BA, Olson DO, Stimac GK, Shields AF, Nelson SJ. Low-field STIR imaging of marrow malignancies. Presented at the annual meeting of the Radiological Society of North America, Chicago, IL, November **1987**
 17. Wiener SN, Neumann DR, Rzeszotarski MS. MRI STIR of acute vertebral fractures. Presented at the annual meeting of the American Roentgen Ray Society, San Francisco, CA, May **1988**
 18. Unger EC, McGlone JS, Silver M. Pulse sequence optimization for STIR inversion recovery sequences. Presented at the annual meeting of the American Roentgen Ray Society, San Francisco, CA, May **1988**
 19. Glazer GM, Woolsey EJ, Borrello J, et al. Adrenal tissue characterization using MR imaging. *Radiology* **1986**;158:73-79
 20. Beltran J, Simon DC, Katz W, Weis LD. Increased MR signal intensity in skeletal muscle adjacent to malignant tumors: pathologic correlation and clinical relevance. *Radiology* **1987**;162:251-255

National Council on Radiation Protection and Measurements

60th Anniversary Meeting

(25th Annual Meeting of the Council)

Washington, DC, April 5-6, 1989

The forerunner organizations of the National Council on Radiation Protection and Measurements (NCRP) were first set up 60 years ago, and the Council itself, in its present form, is 25 years old this year. The annual meeting in this anniversary year will examine the status of radiation protection today—where we have come from, where we are, and where we are going—in a number of important basic and practical areas of radiation protection and measurement. The papers to be presented will concentrate on this theme and will exemplify the role of the NCRP in modern radiation protection as a field of importance to the radiation worker and to the public at large.

The speakers will include Dade W. Moeller, William J. Schull, R. J. Michael Fry, Seymour Abrahamson, Paul Slovic, John W. Baum, William R. Hendee, Marc Edwards, John E. Till, Fred A. Mettler, C. C. Lushbaugh, George M. Wilkening, Richard A. Tell, Paul L. Carson, Gail de Planque, Kenneth R. Kase, Manning Muntzing, and Warren K. Sinclair.

The meeting will be held in the Ballroom of the Vista International Hotel, 14th and M St. N.W., Washington, DC.

All interested are invited to attend. For further information, write to W. Roger Ney, Executive Director, NCRP, 7910 Woodmont Ave., Ste. 800, Bethesda, MD, 20814.

Gastrointestinal Radiology 1989

Focus: New Problems, New Solutions

American Roentgen Ray Society Annual Meeting Friday Symposium

May 12, 1989, New Orleans Hilton, New Orleans, LA

The Immune System and Its Deficiencies

8:00–8:20 a.m.	Immune diseases and the small intestine (<i>Olmsted</i>)
8:20–8:50 a.m.	AIDS and the GI radiologist (<i>Federle</i>)
8:50–9:10 a.m.	Iatrogenic immune suppression (<i>Jones</i>)

The Bile Ducts: Linking Diagnosis and Therapy

9:25–9:45 a.m.	Diagnostic radiology of the bile ducts— 1989 (<i>Balfe</i>)
9:45–10:15 a.m.	Innovative intervention in biliary disease (<i>Teplick</i>)
10:15–10:35 a.m.	Biliary lithotripsy (<i>Ferrucci</i>)

New Horizons in Oncology: Focus on Cancer of the Rectum

10:50–11:10 a.m.	Imaging and immunity: monoclonal antibodies (<i>Wahl</i>)
11:10–11:35 a.m.	Cross-sectional imaging: staging and recurrence (<i>Thompson</i>)
11:35–Noon	Endosonography in the rectosigmoid (<i>Hill</i>)

Computer Page

Semiautomated Slide Identification by Using a Personal Computer and Printer

Irwin M. Feuerstein¹

Many radiologists take great pride in their slide collections of interesting and informative radiographs. Correctly organized and categorized, they are essential for teaching at any level and contribute to research. Slide collections also can contribute to care of patients, because slides are a valuable and readily accessible form of indexed references uniquely tailored to one's individual practice.

The acquisition of a bountiful slide collection requires a substantial time commitment by the radiologist and/or assistants to identify each slide with pertinent data about the patient. Labeling the slides with name, number, and brief historical and diagnostic information gives them more meaning and allows retrieval of original material. Such repetitive and tedious work is ideally suited to the computer. Although there are many commercially available application software packages that have labeling functions, most of them are good for producing larger mailing labels.

We describe here a simple program that accomplishes the identification of large numbers of radiologic slides quickly and with a finished, professional appearance.

Materials and Methods

The computer used in this application was a Compaq Portable Personal Computer Model III, an IBM-compatible, 12-MHz, 80286-based machine (Compaq Computer Corp., Houston, TX). The printer was a Brother M-1709 dot-matrix unit, which prints up to 240 characters/sec in draft mode, can simultaneously print compressed/compressed elite (20 characters/in.; 8 characters/cm) and super-

script/subscript (half-height) fonts, and was configured to run in IBM-mode (Brother Industries, Ltd., Japan). The program also has been tested on an IBM PC-XT and Epson FX-286 printer combination (IBM Corp., Danbury, CT; Epson America, Inc., Torrance, CA).

The labels come as a tractor-fed, continuous form of $1\frac{3}{4} \times \frac{3}{8}$ in. (4.5×1 cm) labels, three across, spaced $\frac{1}{2}$ in. (1.3 cm) from top to top vertically, and approximately 2 in. (5 cm) from left side to left side horizontally. They are available from multiple vendors in a variety of configurations.

The program was written using Compaq's Version 3 of Microsoft BASIC A, but it should run on almost all variations of BASIC. The program requires only minimal changes to run on either the IBM- or the Epson-mode printer.

A simple test was run by using a randomly selected list of mock patient names and diagnoses. These labels were handwritten, then printed using the computer. Sample times were recorded and graphed.

Results

Labels are produced in multiples of three because of the three-labels-per-line format (Fig. 1). The finished product with the labels on the slide is shown in Figure 2.

The program asks for patient name, hospital number and/or date, radiographic findings, and a filing code. We employ the American College of Radiology Index for Radiologic Diagnoses (revised 3rd ed., 1986). Loop functions allow alterations of parts of the label without having to reenter the entire data set. The loops can be individualized readily with only a rudimentary knowledge of BASIC. For instance, one can

Received October 17, 1988; accepted after revision November 28, 1988.

¹ Diagnostic Radiology Department, Warren Grant Magnuson Clinical Center, Bldg 10, Rm. 1C-640, National Institutes of Health, Bethesda, MD 20892, and Dept. of Radiology, Georgetown University Medical Center, Washington, DC 20007. Address reprint requests to I. M. Feuerstein at the National Institutes of Health.

AJR 152:861-863, April 1989 0361-803X/89/1524-0861 © American Roentgen Ray Society

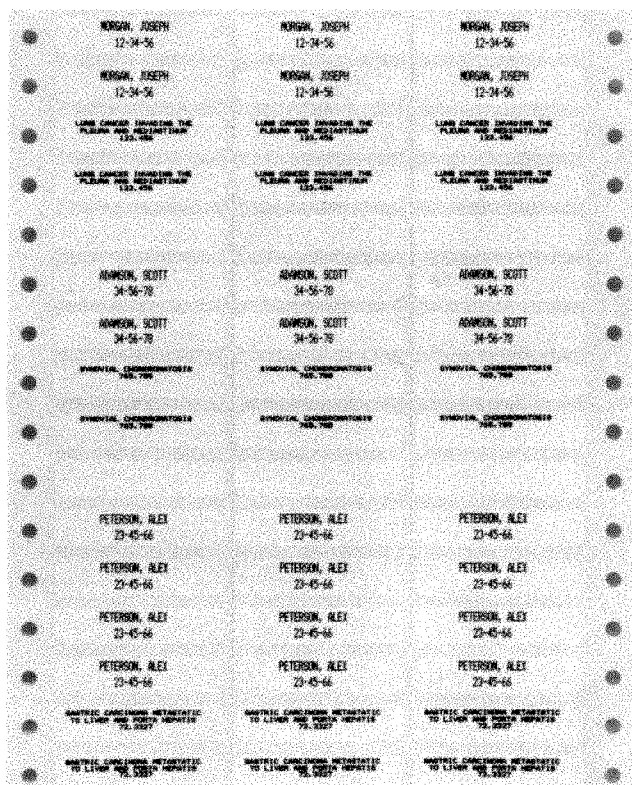


Fig. 1.—Full sheet of labels generated by personal computer and printer, which took 3 min to produce. Same labels required 14 min to make by hand. Actual size is 12 × 6.5 in. (30.5 × 16.5 cm). Names are fictitious. Blank spaces are our preference, but they can be eliminated.

change the descriptive part of the label without having to reenter the patient name and number. If a time interval is the notable item, labels with different dates can be made just by selecting the appropriate option and entering the different dates. If the user finds that a few more labels are needed, additional labels can be produced with just three keystrokes.

Results of the test trial described above are displayed in Figure 3. The individual results for the computer actually overestimate the real time needed to produce labels. Although this factor is difficult to work into the calculations, one will usually be doing something while the labels are printing, such as entering the data for the next label set or mounting the previous labels. This is reflected more accurately in the times necessary to produce a whole sheet of labels. For the sheet produced in Figure 3, computer labeling took just 3 min, while generating the same result by hand took 14 min. In addition, achieving the latter time required writing as fast and as small as possible, with rather sloppy results and strain to the hand and forearm.

Discussion

To many, including the author, the most tedious, repetitive, and time-consuming aspect of building a substantial slide collection is identifying them with important clinical and diagnostic data. This paper describes a short computer program

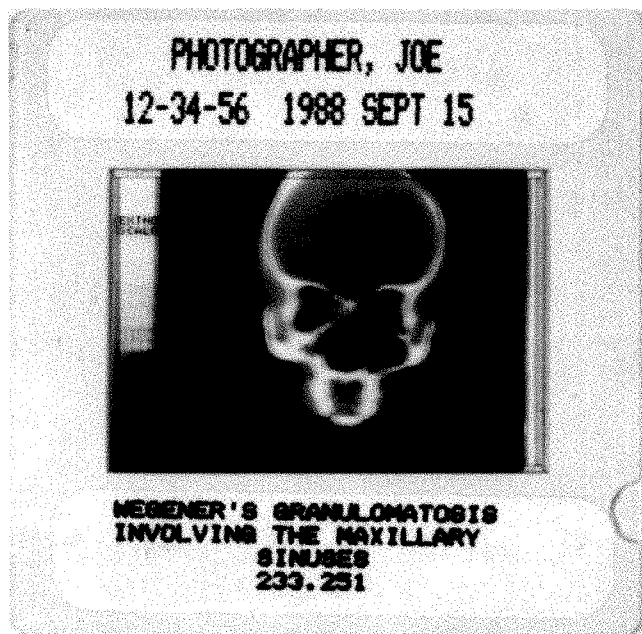


Fig. 2.—Magnified appearance of a 2 × 2 in. (5 × 5 cm) standard radiographic slide with labels applied.

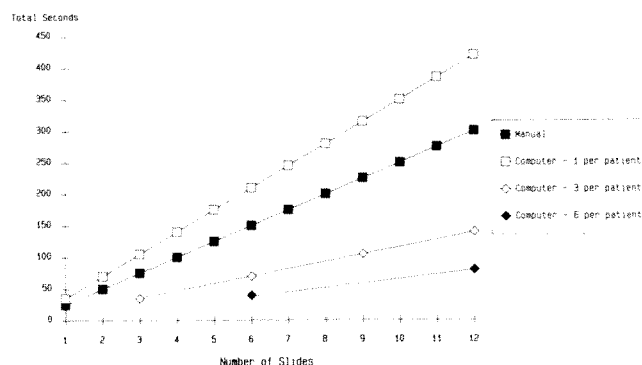


Fig. 3.—Graph showing relative times needed to generate different volumes of slide labels by hand and by computer.

that performs this function quickly and efficiently. Several commercially available software packages can make labels, but these have significant disadvantages. They tend to be expensive and primarily are tailored to make mailing labels. It requires a great deal more expertise to program these software packages than it does simply to use them. Even to those familiar with the programming languages, it is not obvious how to make the software direct the printer to perform the intricate spacing, character sizing, and font changes necessary to print these small labels. On the other hand, BASIC is a much more widely used programming language. The user can easily send instructions to the printer in BASIC and program the loops that make repetitive entry of data unnecessary.

The efficacy of the program depends on a large number of variables. The number of slides and repetitiveness of the data,

amount of information per label, relative speeds of typing and hand printing, and the speeds of the computer (megahertz) and printer (characters/sec) vary widely. Figure 3 allows some conclusions to be drawn at the ends of the slide-volume spectrum. The utility of computer identification is directly proportional to the number of slides labeled. If one makes slides infrequently and makes only one slide per patient, then labeling them by hand is probably faster. However, when multiple examinations are involved and extra slides are made for residents, pathologists, and clinicians, the number of slides can grow rapidly. I often produce more than 20 slides on the same patient that require identical or rather similar labels.

Computer-generated labels would also be quite useful for an assistant whose tasks include making slides for many radiologists. For crowded labels, the small font will generally produce much neater results than handwritten will. The polished appearance of computer-generated labels might even outweigh the minimal time savings for hand-labeling small numbers of slides.

I will supply a listing of the program code, with documentation, described in this report upon written request. The requestor should specify whether the printer runs in IBM or Epson mode. If a floppy disk is enclosed with the request, the program will be furnished on the disk.

American Roentgen Ray Society

89th Annual Meeting

May 7-12, New Orleans, LA

1989 Caldwell Lecturer



The Honorable William Bradley

United States Senator from New Jersey

"Health Care Choices for the 90s"

Categorical Course on Uroradiology

American Roentgen Ray Society 89th Annual Meeting

May 7–11, 1989, New Orleans Hilton, New Orleans, LA

Sunday, May 7

10:00–10:10 a.m.

10:10–10:50 a.m.

10:50–11:30 a.m.

11:30–Noon

Break

1:30–2:15 p.m.

2:15–3:00 p.m.

Break

3:30–4:15 p.m.

4:15–5:00 p.m.

Contrast Media/Infection/Renal Masses (Moderators: Pollack [a.m.] and Mellins [p.m.])

Welcome and Introduction

Contrast media. Comparison of ionic and nonionic agents: pharmacology, physiology, and guidelines for practical usage (*Katzberg*)

Toxicity and reactions to contrast media (*Pfister*)

Evaluation of the azotemic patient (*Talner*)

Acute renal infections (*McClennan*)

Chronic renal infections (*Kenny*)

Cystic diseases of the kidney (*Hartman*)

Neoplasms of the kidney (*Stanley*)

Monday, May 8

1:30–2:15 p.m.

2:15–2:45 p.m.

2:45–3:15 p.m.

Break

3:45–4:15 p.m.

4:15–5:00 p.m.

Prostate/Bladder/Scrotum (Moderator: Davidson)

Imaging of the urinary bladder (*Hattery*)

Epidemiology and natural history of carcinoma of the prostate (*Amis*)

Ultrasonography of the prostate (*Rifkin*)

CT and MRI of the prostate (*Hricak*)

Imaging of the scrotum (*Rosenfield*)

Tuesday, May 9

3:30–4:05 p.m.

4:05–4:40 p.m.

4:40–5:15 p.m.

Stone Disease (Moderator: Newhouse)

Radiological aspects of urolithiasis (*Bush*)

Extracorporeal stone therapy (ESWL) (*LeRoy*)

Interventional procedures in urolithiasis (*Banner*)

Wednesday, May 10

3:30–4:00 p.m.

4:00–4:45 p.m.

4:45–5:15 p.m.

Impotence and Erectile Insufficiency (Moderator: Lang)

Pathology and physiology of impotence (*Goldstein*)

Radiology of impotence (*Bookstein*)

Radiology of penile prostheses (*Cohan*)

Thursday, May 11

3:30–4:05 p.m.

4:05–4:40 p.m.

4:40–5:15 p.m.

Retroperitoneum (Moderator: Hartman)

Adrenal imaging (*Dunnick*)

Perinephric disease (*Levine*)

Retroperitoneal disease (*Lee*)

Technical Note

Composite SPECT-CT Images: Technique and Potential Applications in Chest and Abdominal Imaging

Isaac L. Kaplan¹ and Lawrence C. Swayne

In general, single-photon emission computed tomography (SPECT) and positron emission tomography (PET) provide high-contrast, poor-resolution images of functional significance, whereas radiography, CT, and MR imaging often depict exquisite anatomy, but offer little insight into underlying function. Although separate visual analysis of these studies with subsequent mental integration is adequate in most clinical situations, more precise correlation can be obtained by image fusion. Accordingly, a software program was developed that allowed direct comparison of SPECT and CT in the form of composite SPECT-CT images. A similar approach has been employed for quantitative brain studies using PET with CT or MR images [1-6]; however, the technique has only rarely been applied to chest and abdominal examinations [7, 8].

Materials and Methods

SPECT was done on a rotating gamma camera (7500 Orbiter, Siemens Medical Systems, Des Plaines, IL) interfaced to an independent, compatible computer system (MicroVAX II-driven Max-DELTA, Siemens Medical Systems, Des Plaines, IL). Most studies were made using a 64×64 word matrix, with a 360° orbit rotation containing 64 projections. After uniformity correction using a 120-million-count flood source, reconstruction was performed by filtered back projection with an appropriate Butterworth filter and attenuation correction.

CT examinations were done on a third-generation, whole-body CT scanner (TC/T 9800, General Electric Medical Systems, Milwaukee,

WI) in 10-mm-thick slices. Most examinations were performed immediately after an IV bolus of contrast material (100 ml RENO-M-60, Squibb Diagnostics, Inc., New Brunswick, NJ).

The CT data were transferred to the nuclear computer system via half-inch, nine-track tape. Once in the MaxDelta system, the matrix size for the CT images was converted from a 512×512 to 256×256 pixel matrix. The SPECT matrix was interpolated to a 128×128 pixel matrix.

The SPECT and CT images were initially displayed side by side for subsequent image analysis. Anatomic or externally placed landmarks were selected on both slices and the SPECT image was mapped onto the CT image. The mapping algorithm was a standard two-dimensional scaling, translation, rotation, and stretching transformation. CT pixel values were assigned to the lower (0 to 256) level of the scale and SPECT pixel values were assigned to the upper (256 to 512) level. A color map was constructed to display the lower (CT) values in a high-contrast gray scale and the upper (SPECT) values in a topographic color scale.

Regions of interest (ROI) were then identified on the SPECT image, and background counts were subtracted to enhance ROI contrast. A mask was generated from this slice by setting all values within the ROIs to zero and all other values to negative one. The mask was extracted and mathematically ANDed to the aligned CT image to create a black hole on the future composite SPECT-CT image. The mask was then restored by adding a value of one to the mask and multiplying it by the original values of the SPECT image. The resulting image then contained only the portions of the original slice whose position coincided with that of the mask. The restored SPECT mask was then mathematically ORED to the CT image with the black mask. The final composite SPECT-CT image was thus displayed as color SPECT ROIs superimposed on the appropriate gray-scale CT image.

Received September 29, 1988; accepted after revision November 28, 1988.

Presented at the 35th Annual Meeting of the Society of Nuclear Medicine, San Francisco, CA, June 14-17, 1988.

¹ Both authors: Department of Diagnostic Radiology, Morristown Memorial Hospital, 100 Madison Ave., Morristown, NJ 07960. Address reprint requests to L. C. Swayne.

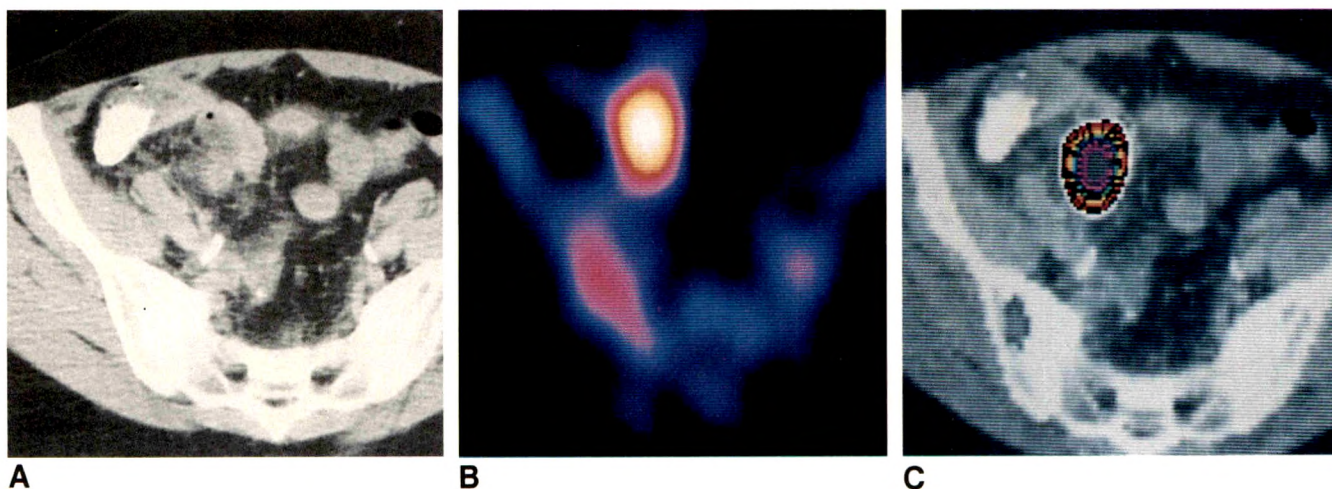


Fig. 1.—A, CT scan. A 55-year-old woman presented with persistent generalized abdominal pain. CT scan shows nonspecific bowel-wall thickening in right lower quadrant.

B, SPECT scan. An indium-111 autologous WBC SPECT study shows a focus of intense increased activity in right lower quadrant.

C, Composite SPECT-CT. Composite image localized activity within pelvis, medial to cecum. At surgery, chronic walled-off perforation of appendix was removed and patient recovered uneventfully.

Results

The method was validated using a standard SPECT phantom (standard model 6250, Data Spectrum, Chapel Hill, NC). Image alignment was accomplished with external markers placed within a carriage specifically designed for the SPECT phantom. The count-weighted centers of selected phantom structures were then automatically calculated for both SPECT and CT images. Registration accuracy was less than 1 mm in all instances.

Twenty composite SPECT-CT studies were performed in selected patients to evaluate suspected pathology in the chest or abdomen. Depending on individual clinical circumstances, several different isotopes were used, including ^{99m}Tc -labeled autologous RBCs, ^{67}Ga -citrate, and ^{111}In -labeled autologous WBCs. Unique advantages of this technique are (1) the establishment of the physiologic status of ambiguous CT objects and (2) identification of minimal anatomic abnormalities of pathologic significance on CT (Fig. 1).

Discussion

The primary advantage of image fusion is precise functional-structural correlation [1–3]. Previous nonneurological applications of image fusion [1–6] have been limited to studies of lung physiology using chest CT and SPECT lung perfusion examinations [7, 8]. The present work, however, suggests several other potential uses. Subtle functional abnormalities identified with SPECT examinations can be accurately localized with SPECT-CT composite images, thus facilitating the planning of subsequent percutaneous biopsies, surgery, or local radiotherapy.

Despite the clinical utility of this technique, there are some apparent limitations. Transfer of the CT data to the nuclear

computer requires that specific transmission and reception software be written to interpret the manufacturer's proprietary format. Operator image alignment may be subjective and inefficient in terms of personnel and machine time. We have found common external landmarks to be most beneficial. Some additional discrepancies between the SPECT and CT images may be due to partial volume averaging, either because of (1) difference in the slice thicknesses (CT = 10 mm and SPECT double thickness = 12 mm) or (2) slight axial differences in the central planes of comparable slices. Finally, compression of the original CT matrix and contrast scale will result in some minimal loss of contrast and resolution on the CT portion of the final composite image [8].

REFERENCES

1. Bajcsy R, Lieberman R, Reivich M. A computerized system for the elastic matching of deformed radiographic images to idealized atlas images. *J Comput Assist Tomogr* 1983;7:618–625
2. Bergstrom M, Boethius J, Eriksson L, Grietz T, Ribbe T, Widen L. Head fixation device for reproducible position alignment in transmission CT and positron emission tomography. *J Comput Tomogr* 1981;5:136–141
3. Bohm C, Grietz T, Kingsley D, Berggren BM, Olsson L. Adjustable computerized stereotaxic brain atlas for transmission and emission tomography. *AJNR* 1983;4:731–733
4. de Leon MJ, George AE, Ferris SH, et al. Regional correlation of PET and CT in senile dementia of the Alzheimer type. *AJNR* 1983;4:553–556
5. Fox PT, Perlmutter JS, Raichle ME. A stereotactic method of anatomical localization for positron emission tomography. *J Comput Tomogr* 1985;9:141–153
6. Miura S, Kanno I, Iida H. Anatomical adjustments in brain positron emission tomography using CT images. *J Comput Tomogr* 1988;12:363–367
7. Moskowitz GW, Vaugois JC, Schiff RG, Levy LM. Improvement of SPECT lung perfusion physiology with CT high resolution structural anatomy. *J Nucl Med* 1986;27:1038
8. Pitcher EM, Stevens PH, Davies ER, Goddard PR, Jackson PC. Transfer and combination of digital image data. *Br J Radiol* 1985;58:701–703

Informed Consent for Contrast Media

William H. Bush¹

The term *informed consent* usually elicits feelings of anxiety and anger on the part of patients and physicians. Patients feel anxious because the need for consent suggests the examination is more dangerous than they imagined. They feel anger that the doctor does not trust them and may be asking them to relinquish their legal rights. The radiologist feels irritation at the legal system for creating a need for such forms and anxiety that he or she may ultimately be defending a lawsuit over a needed diagnostic procedure.

Use of informed consent for contrast media administration is not uniform across the field of radiology; the survey by Spring et al. [1] in 1984 revealed that less than 50% of radiologists used such a device. I was not among them [2]. I subscribed to the philosophy expressed in Lalli's 1974 article [3]; reactions to contrast media can be lessened if the patient's fears are allayed. I felt that informed consent could heighten patients' fears and might increase reactions to contrast media. However, in 1986, a survey by Winfield et al. [4] confirmed Spring's opinions and showed that patients desired more information about their examination; patients in their study did not feel more anxious after reading and signing a consent form, if they understood it.

The advent of nonionic contrast media and use of them for common radiographic procedures (e.g., excretory urography, CT) has changed my opinion about the need for an informed consent form in jurisdictions using a reasonable-patient standard. There is now little doubt that serious anaphylactic-type reactions to contrast media occur less frequently with nonionic agents, such as iopamidol and iohexol [5, 6]. Two schools of thought for the use of nonionic contrast media have emerged: one advocates universal use of nonionic con-

trast media, thereby decreasing the chance of an anaphylactoid reaction in all patients; the other advocates use of nonionic contrast media in patients who can be identified as being at higher risk for having an adverse reaction to contrast media [7, 8]. The dilemma arises because the newer agents are at least 15 times more expensive than conventional ionic agents. Universal use of nonionic contrast media for all patients would be costly [9]. Universal use could divert health-care moneys away from other important problems, such as breast-cancer screening and lower mammography prices, "stop smoking" clinics, or replacement of outdated equipment.

In a recent article, Jacobson and Rosenquist [10] suggest that selective use of nonionic contrast media in high-risk patients may be acceptable on a cost-for-life-lost basis. Additionally, these authors feel, as do others, that this great cost differential will be accepted by juries in defense of selective *nonuse* of nonionic contrast media for low-risk patients [11, 12]. However, most legal opinion also holds that when nonionic contrast medium is used on a selective basis for only high-risk patients in jurisdictions using a reasonable-patient standard, low-risk patients need to be informed that an alternative contrast medium is available [11-13]. A "reasonable patient" would want to know relative risk information to make the best decision [14]. Hence, the requirement in states using the reasonable-patient standard is to inform the patient of this lowering of risk by the use of a nonionic agent.

In dealing with this dilemma, we developed an informational sheet for patients explaining why low-risk patients were being given conventional ionic contrast medium and why others were being given nonionic contrast medium; we have subsequently incorporated this into a consent form that the patients

Received November 9, 1988; accepted after revision December 21, 1988

¹ Department of Radiology, Virginia Mason Clinic, 1100 Ninth Ave., P.O. Box 900, Seattle, WA 98111-0900. Address reprint requests to W. H. Bush.

AJR 152:867-869, April 1989 0361-803X/89/1524-0867 © American Roentgen Ray Society

VIRGINIA MASON MEDICAL CENTER
CONSENT FOR CONTRAST MATERIAL INJECTION

Your doctor has scheduled you for an x-ray examination that requires injection of a contrast agent in your bloodstream. As you know, an x-ray is a picture of what is inside you. The contrast agent (also termed contrast media, or contrast material, or "x-ray dye") shows up white on x-ray film or CT scan images and helps the radiologist interpret the x-rays or CT scans.

The contrast media is given through a small needle placed into a vein, usually on the inside of your elbow or on the back of your hand or through a catheter if angiography is being performed. Normally, contrast media is considered quite safe; however, any injection carries slight risk of harm including injury to a nerve, artery, or vein, infection, or reaction to the material being injected. Occasionally, a patient will have a mild reaction to the contrast agent and develop sneezing or hives. Uncommonly (one case in a thousand) a serious reaction to the contrast occurs. The physicians and staff of the x-ray department are trained to treat these reactions. Very rarely (1:40,000) death has occurred related to contrast administration; the risk of such a severe consequence is similar to that from the administration of penicillin.

Certain patients are at higher risk for experiencing a reaction to the contrast agent, and we are advising those patients to receive a different, more expensive contrast agent, called "low osmolar" or "non-ionic" contrast, which does appear to have a lower incidence of reactions; however, these newer agents are not absolutely free of reactions, even serious ones.

Patients who are at higher risk for adverse effects of contrast are:

- 1) people who have already had a moderate or severe "allergic-like" reaction to contrast material which required treatment;
- 2) people with severe allergies or asthma;
- 3) patients with severe or incapacitating heart disease;
- 4) patients with multiple myeloma, sickle cell disease, polycythemia, or pheochromocytoma;
- 5) patients with severe kidney disease, particularly caused by diabetes.

If you believe you are in one of the above categories, please notify the technologist or radiologist so that we can plan to use a non-ionic or low osmolar contrast agent. Unfortunately, these agents are very expensive (an additional \$90 to \$130 per examination) and your insurance may not cover the additional cost.

If you are not in one of the high risk groups, we recommend use of the standard or conventional ionic contrast agent for your x-ray study. These conventional agents have a long record of safety and effectiveness.

If you have any questions, please ask the x-ray technologist or the attending radiologist.

I have read the above information and have had my questions answered.

(signed) _____

Name _____

Date _____

VMMC FORM 12139 (11-88)

Fig. 1.—Informed consent form.

sign (Fig. 1). It explains that their doctor has ordered the examination; discusses "X-ray dye" and why it is necessary; discusses minor and major adverse effects that may occur, gives basic statistics about reactions (serious reaction, 1:1,000; death, 1:40,000), and gives a comparison to the death rate from penicillin, providing the patient with a reasonable, commonly understood analogy. It indicates that some patients are at higher risk for a contrast reaction and that nonionic contrast media do seem to lower that risk, although not absolutely; provides a listing of what our radiologists consider to be high-risk categories; asks the patients to identify themselves if they are in one of these risk categories; indicates that we want to use nonionic contrast medium for higher risk patients; notes that their insurance may not pay for it and it is more expensive; recommends use of regular conventional ionic agents for low-risk patients; tells them that we would like to answer their questions; and asks them to sign the form. The form is then kept as part of the medical record.

We were concerned that having the patient sign a consent form would deter many of them from having the examination, but such has not been the case. In our survey of 500 outpatients receiving IV contrast for CT, fewer than 5% have had questions after reading the form, fewer than 1% have refused the exam, and fewer than 1% of low-risk patients have requested nonionic contrast. Another smaller survey of patients who received regular ionic contrast medium asked them why, if they were a low-risk patient and still had a choice of having the nonionic agent, they chose the standard ionic agent. Surprisingly, the majority (greater than 80%) said they chose conventional ionic contrast medium because of the information they received in the consent form, rather than because of the cost savings; about 5% indicated cost saving was the major factor, and about 10% indicated that both information and cost were factors.

Our consent form fits the needs of our department and may be adaptable to other radiology practices in reasonable-

patient jurisdictions as they grapple with the need for informed consent in the new era of nonionic contrast use.

REFERENCES

1. Spring DB, Akin JR, Margulis AR. Informed consent for intravenous contrast-enhanced radiography: a national survey of practice and opinion. *Radiology* **1984**;152:609-613
2. Bush WH. Risk factors and clinical considerations in the management of contrast-induced adverse reactions. In: Parvez Z, Moncada R, Sovak M, eds. *Contrast media: biologic effects and clinical application* (3 vols.). Boca Raton, FL: CRC Press, **1987**:137-149
3. Lalli AF. Urographic contrast media reactions and anxiety. *Radiology* **1974**;112:267-271
4. Winfield AC, Ford CV, James AE, Heller RM, Lamballe AK. Response of patients to informed consent for excretory urography. *Urol Radiol* **1986**;8:35-39
5. Palmer FJ. The R.A.C.R. survey of intravenous contrast media reactions: a preliminary report. *Australas Radiol* **1988**;32:8-11
6. Katayama H, Kozuka T, Takashima T, Matsuura K, Yamaguchi K. Adverse reactions to contrast media: high-osmolality versus low-osmolality media. Scientific exhibit at the annual meeting of the Radiological Society of North America, Chicago, IL, November 26-December 2, **1988**
7. Bettman MA. Radiographic contrast agents — a perspective (editorial). *N Engl J Med* **1987**;317:891-893
8. McClellan BL. Low osmolality contrast media: a practical approach. *Diagn Imag* **1987**;9[suppl]:16-18
9. Powe NR, Steinberg EP, Erickson JE, et al. Contrast medium-induced adverse reactions: economic outcome. *Radiology* **1988**;169:163-168
10. Jacobson PD, Rosenquist CJ. The introduction of low-osmolar contrast agents in radiology: medical, economic, legal, and public policy issues. *JAMA* **1988**;260:1586-1592
11. Eisner JM, Casey BJ. Malpractice, informed consent, and the use of low osmolality contrast media. *Conn Med* **1988**;52:87-91
12. Jacobson PD. The availability of low osmolality contrast media: a legal analysis of an emerging technology. *Diagn Imag* **1987**;9[suppl]:22-26
13. Reuter SR. An overview of informed consent for radiologists. *AJR* **1987**;148:219-227
14. Spring DB, Winfield AC, Friedland GW, Shuman WP, Preger L. Written informed consent for IV contrast-enhanced radiography: patients' attitudes and common limitations. *AJR* **1988**;151:1243-1245

Digital Radiography: Uses and Limitations of the Method

Diana L. Novak¹ and Barry F. Bates

As radiology, and indeed all of medicine, strives for more precise quantification of pathology, physicians must ensure they are precisely and consistently recording significant items of measure for any pathologic processes that they encounter. Or, at least that seems like a good idea to us.

To satisfy our compelling urge for quantitative radiographic description, we have been using for some time a technique of digitally determined measurements (DDM) or, when applied to radiology, "Digital Radiography." We have found this to be a handy, accurate, convenient, and very cost-effective method. While innate levels of modesty have prevented our rushing into print about the method, we have noted a number of contributions to the literature claiming experience with, what at first glance would seem to be, applications of our technique, generally under the rubric, "Digital Radiography" [1]. A careful review of the literature has resulted in the somewhat surprising discovery that virtually all the authors claiming expertise in Digital Radiography are in fact reporting about some type of computerized system that has nothing to do with Digital Radiography as we know it. Their use of the term "Digital Radiography" in this context is obviously in error.

As inventors of the true Digital Radiography, we feel compelled to describe, for once and for all, the only tried and true method of Digital Radiography.

Materials and Methods

Use of Digital Radiography requires two elements: (1) a digit (Fig. 1) and (2) a radiograph (Fig. 2). In practice, application of the method

is quite simple. The digit, after calibration, is placed on the radiograph parallel to the dimension in question (Fig. 3). The distance is then read from the digit, the digit reoriented 90° (clockwise or counter-clockwise), and the process is repeated. Continued application of the method as frequently as needed for a given radiograph culminates utilization. From the linear measurements, ratios, areas, and volumes can be calculated by conventional formulas.

There have been attempts to use radiographs of digits in similar applications, with claims that this could be done quite handily. However, difficulties in viewing through the combined density of two radiographs make this approach impractical.

Calibration Technique

In any system of measurement, precise calibration of the device against known standards is crucial. We use a calibration device obtained from the National Unified Technical Standards of Washington, DC (NUTS of Washington) [2]. The digit in question is placed in close proximity to the calibration device, and points of reference are noted (Fig. 4). In the perfect digit, the length between the tip of the digit and the first knuckle (1 knuckle unit or KU) will be 1 in. (2.54321 cm). Assuming no anomalies, each finger will have 3 KUs so that 3 KU = 1 finger knuckle unit or 1 FKU. Once having calibrated a digit, the calibration remains constant, assuming no growth spurts or sudden onset of acromegaly. If the calibrated length is not an easily remembered unit, such as 1 in., the appropriate conversion factor can be tattooed on the digit for ready reference.

Benefits in Operations

The first benefit from the use of our digital system is the elimination of rulers (save for calibration items). As radiologists

Received August 21, 1988; accepted after revision July 29, 1988. Revisions received August 30, September 7, 16, 28, October 9 and 21, final revision November 4, 1988.

This work was supported in part by our own funds. In fact, it was supported entirely by our own funds. There isn't a funding agency anywhere that would give us a penny for this work, and don't think we didn't try! So much for support of scientific research.

¹ Both authors: Samaritan Health Center, 5555 Conner Ave., Detroit, MI 48213. Address reprint requests to D. L. Novak.

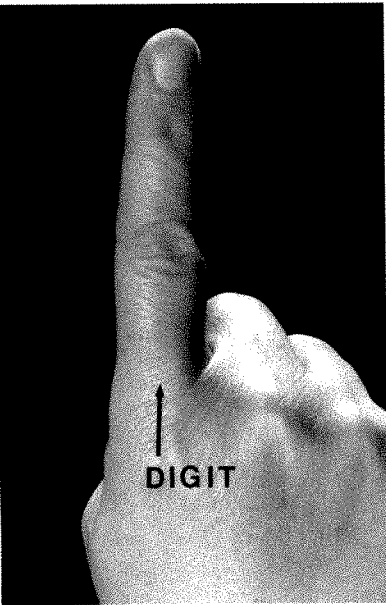


Fig. 1.—Digit suitable for use in Digital Radiography.



Fig. 2.—Radiograph suitable for use in Digital Radiography.



Fig. 3.—Digital Radiography in action! Measurement of dimension of lesion. This developed while patient was traveling in a foreign country, France. This is an example of a French Foreign Lesion.



Fig. 4.—Technique of calibration. Note that fingertip (Tipitus Terminus Digitalis) is even with 1-in. mark, whereas crease of first knuckle joint (Jointus Knucklus Numero Uno) is at reference point.



A



B

Fig. 5.—A, Improper use of digital technique in lay use. This is an incorrect method for requesting "one finger's worth."

B, Correct use of digital technique to request "one finger's worth."

are well aware, rulers have a half-life on the reading bench of 3.5 days. The cause of disappearance of rulers has been speculated on, but no satisfying explanation has come forth. Be that as it may, which it will, replacement of rulers can be a major item in the expense budget of radiology departments. For example, in a department with 10 film-reading stations, if all rulers were replaced immediately on disappearance, the department would need 1,042.85 new rulers a year. With the

digital system, this expense is avoided. Another advantage is the ever-present aspect of the device. Even those rulers that do not spontaneously disappear are frequently mislaid and unavailable for use when needed. However, the digital system is constantly present; one need only go to the elbow, turn right, and there it is.

There are some disadvantages to the system, to be sure. First of all, the technique must be standardized as described

above. One cannot use the width of a digit, as is often done in lay use. For example, liquid libation is often ordered by reference to a form of digital measurement ("Give me one finger's worth!") [3] (Fig. 5A). In true digital measurements, one finger's worth (3 KUs or 1 FKU) would be considerably more (Fig. 5B)!

During physical examination, certain body parts are measured by finger breadth (e.g., liver three fingerbreadths below costal margin). However, this is specifically a *finger-breadth* measurement and is so stated. The term "fingerbreadths" should never be used in Digital Radiography, in order to avoid confusion. Also to be considered is the fingernail length. For obvious reasons, the fingernail length is not included in the DDM method. Measurements are made from the tip of the finger pad (Tipitus Terminus Digitalis) to the first knuckle joint (Jointus Knucklus Numero Uno) (Fig. 4).

Certainly, this article does not investigate fully the multiplicity of advantages of the Digital Radiographic method. Obviously further investigation is indicated, and to this end we urge others to institute aggressive research programs to add knowledge to this most important area of radiologic practice.

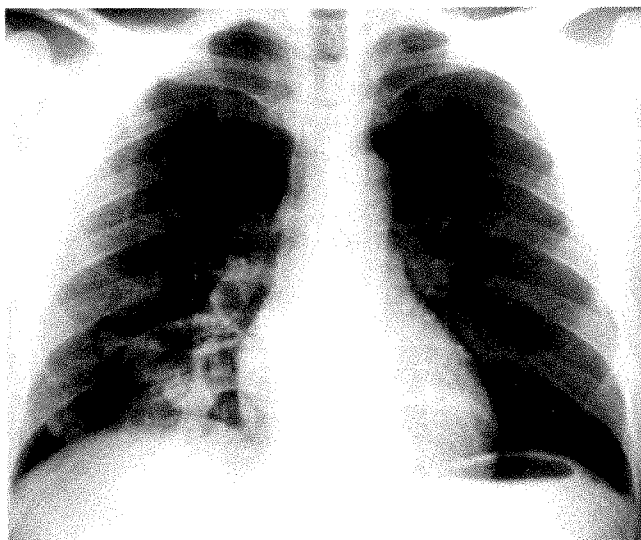
REFERENCES

1. Brody WR. *Digital radiography*. New York: Raven Press, 1984
2. Frustrated IM. Personal communication. (No longer available because of cutbacks to ease the federal budget deficit)
3. Fields WC. *A gentleman's guide to spirits and etiquette*. Los Angeles, CA: Boozer & Co, 1933
4. Other references, such as previous employers, available on request
5. Credit Reference: Credit Bureau of America, 435 W. Madison Ave., New York, NY

Editor's note. Dr. M. M. Figley explained the origin of April Fools' Day quite eloquently in a previous issue (AJR 1984;142:845): "On April Fools' Day, April 1, it is considered appropriate to tell lies and play practical jokes on the unwary. This day, also known as All Fools' Day, is observed almost universally throughout the Western world. The custom is thought to have begun in France, where formal visits were paid to friends on the first day of April, which was 1 week after New Year's Day (March 25 under the Old Style Gregorian calendar). When New Year's Day was moved to January 1 in 1752, mock calls continued to be paid on April 1 as a joke."

General Diagnosis Case of the Day

Harvey S. Glazer,¹ Farrokh Dehdashti,¹ Barry A. Siegel,¹ Bruce L. McClennan,¹ Dennis M. Balfe,¹ and Gerald L. Andriole²



A

Fig. 1.—Case 1: This 37-year-old man presented with a 3-day history of fever, chills, weakness, and pain in right upper quadrant.

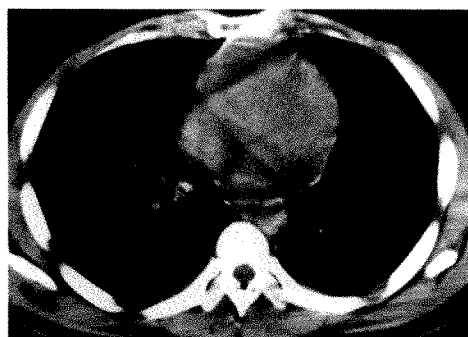
A, Posteroanterior chest radiograph.

B, Precontrast CT scan through level of heart.

C, CT scan with lung window setting.

D, Postcontrast CT scan at a slightly higher level.

E, Postcontrast image through upper abdomen.



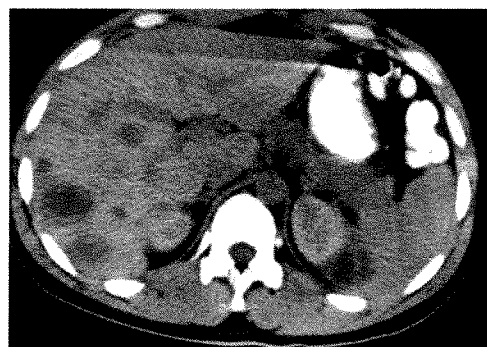
B



C



D



E

¹ Mallinckrodt Institute of Radiology, Washington University School of Medicine, 510 S. Kingshighway Blvd., St. Louis, MO 63110. Address reprint requests to M. J. Siegel at this address.

² Department of Urologic Surgery, Washington University School of Medicine, St. Louis, MO 63110.

Case 1 was prepared by H. S. Glazer. Case 2 was prepared by F. Dehdashti and B. A. Siegel. Case 3 was prepared by B. L. McClennan and G. L. Andriole. Case 4 was prepared by D. M. Balfe. M. J. Siegel is coordinator of the Case of the Day series.

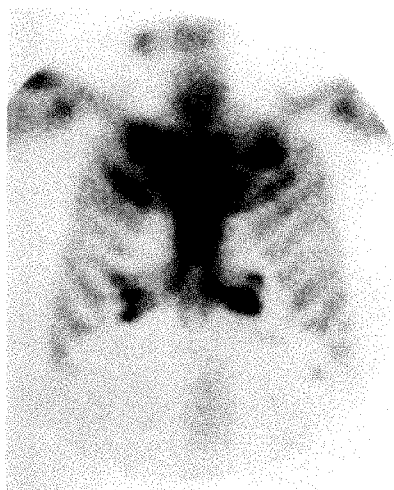
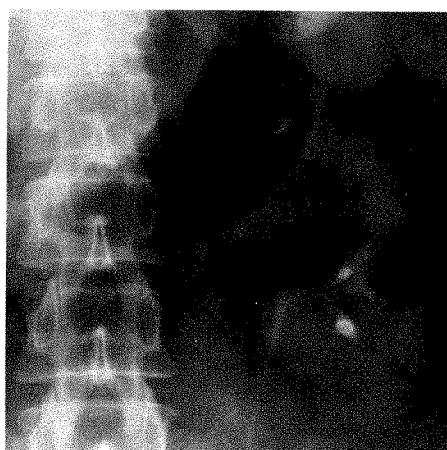
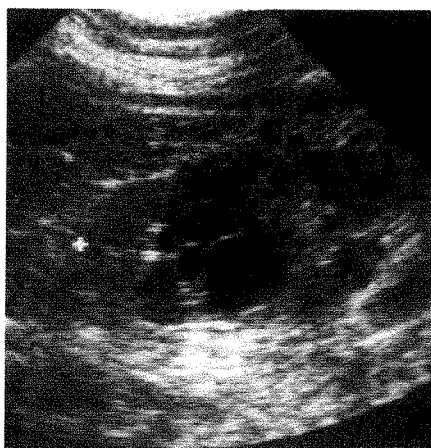


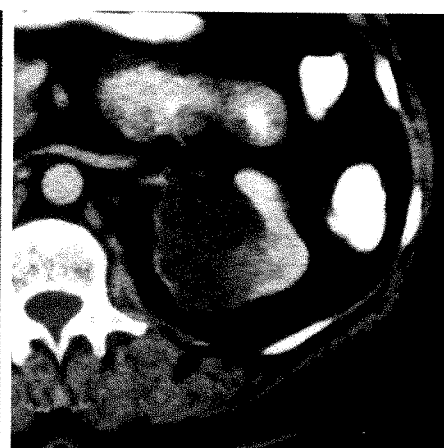
Fig. 2.—Case 2: This 66-year-old previously healthy man was referred for bone scintigraphy because of a recently discovered pulmonary nodule. He was asymptomatic, and all routine laboratory studies (including serum alkaline phosphatase) were normal. An anterior scintigram obtained with ^{99m}Tc -methylene diphosphonate is shown.



A



B



C

Fig. 3.—Case 3: This 67-year-old woman presented with a history of microscopic hematuria.

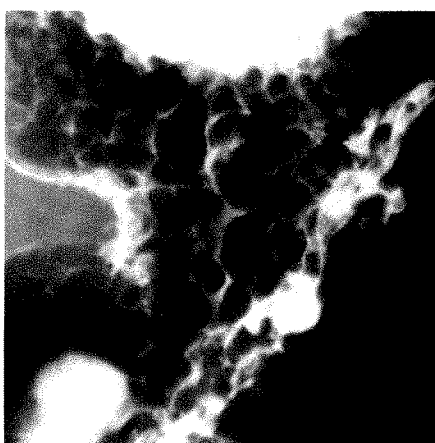
A, Intravenous urogram.

B, Sonogram of left kidney.

C, Postcontrast CT scan of kidney.



A



B



C

Fig. 4.—Case 4: This 38-year-old woman was referred for mild abdominal pain that had not responded to antacid therapy. She had been well before except for a history of seasonal allergies.

A-C, Three views from an upper gastrointestinal series.

Sonography Case of the Day

William D. Middleton,¹ Mary A. Middleton,² and Kimberly Wiele²



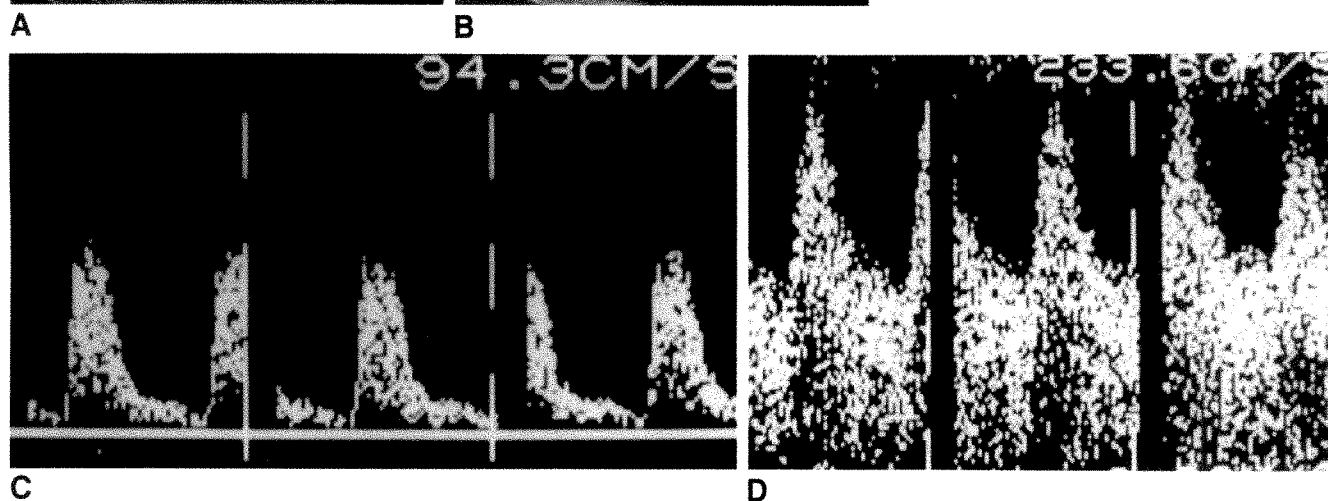
Fig. 1.—Case 1: Patient with hematuria and oliguria following renal transplantation. Previous biopsy had shown mild transplant rejection.

A, Longitudinal sonogram of renal transplant.

B, Transverse sonogram of upper pole of transplant.

C, Pulsed Doppler waveform from lower pole of transplant.

D, Pulsed Doppler waveform from upper pole of transplant.



¹ Mallinckrodt Institute of Radiology, Washington University School of Medicine, 510 S. Kingshighway Blvd., St. Louis, MO 63110. Address reprint requests to M. J. Siegel at this address.

² Deaconess Hospital, St. Louis, 6150 Oakland St., St. Louis, MO 63139.

Cases 1, 3, and 4 were prepared by W. D. Middleton. Case 2 was prepared by M. A. Middleton, W. D. Middleton, and K. Wiele. M. J. Siegel is coordinator of the Case of the Day series.

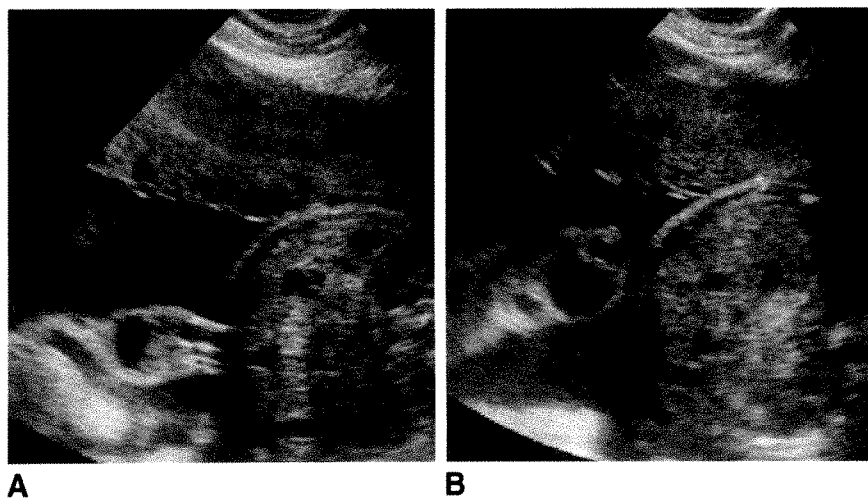


Fig. 2.—Case 2: Asymptomatic patient in second trimester presenting for sonographic dating.
A, Transverse image of fetal abdomen at level of umbilical insertion.
B, Oblique image of umbilical cord.

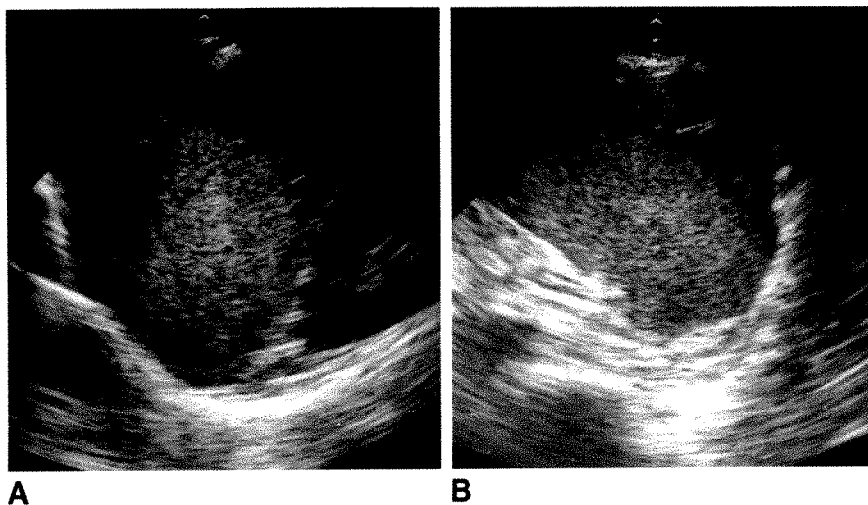


Fig. 3.—Case 3: Young, otherwise healthy man with chronic pain in left upper quadrant.
A, Longitudinal sonogram of left upper quadrant.
B, Transverse sonogram of left upper quadrant.

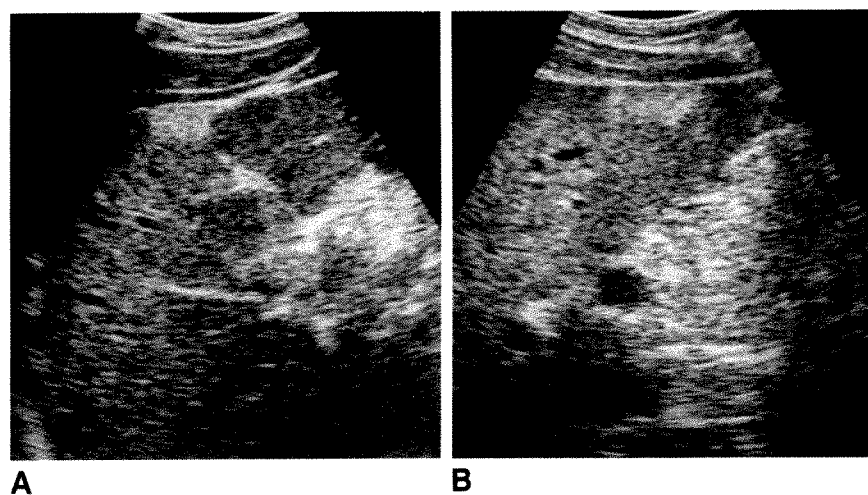


Fig. 4.—Case 4: Otherwise healthy middle-aged woman with mild pain in right upper quadrant, referred for gall-bladder sonography.
A, Transverse sonogram of liver at level of ligamentum teres.
B, Longitudinal image of liver just to right of ligamentum teres.

Pediatric Radiology Case of the Day

William H. McAlister¹ and Marilyn J. Siegel

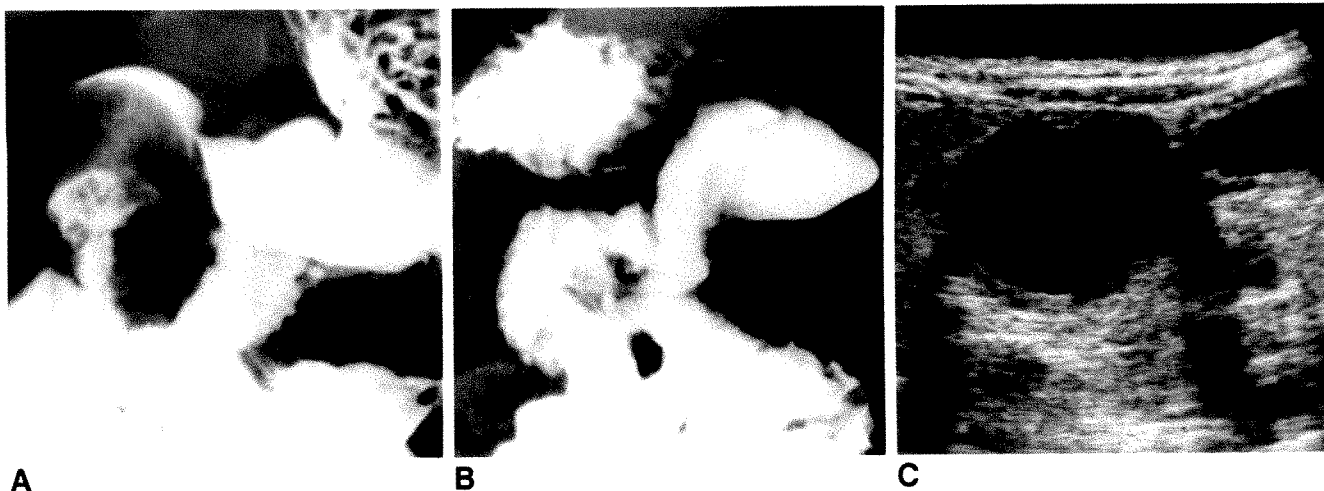


Fig. 1.—Case 1: A 2-month-old boy with a 1-week history of frequent vomiting. Pyloric stenosis was suspected.

A, Anteroposterior radiograph from the upper gastrointestinal study.

B, Lateral radiograph from the upper gastrointestinal study.

C, Sonogram through the upper abdomen.

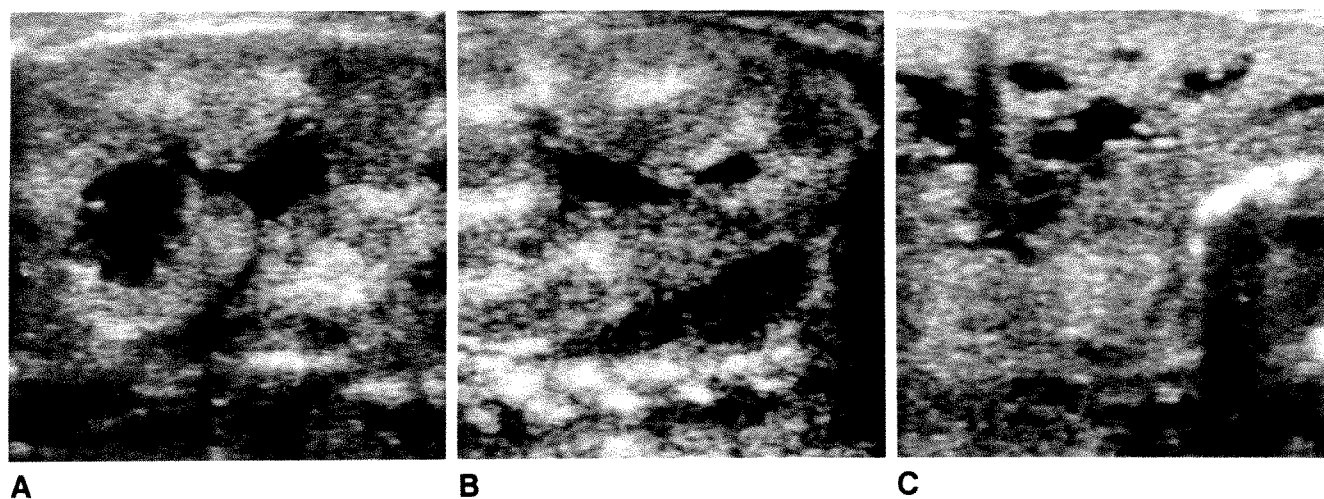


Fig. 2.—Case 2: A premature infant with palpable abdominal masses and a history of maternal oligohydramnios.

A, Longitudinal sonogram of the right kidney.

B, Longitudinal sonogram of the left kidney.

C, Transverse sonogram of the liver.

¹ Both authors: Mallinckrodt Institute of Radiology, Washington University School of Medicine, 510 S. Kingshighway Blvd., St. Louis, MO 63110. Address reprint requests to M. J. Siegel at this address.

M. J. Siegel is coordinator of the Case of the Day series.

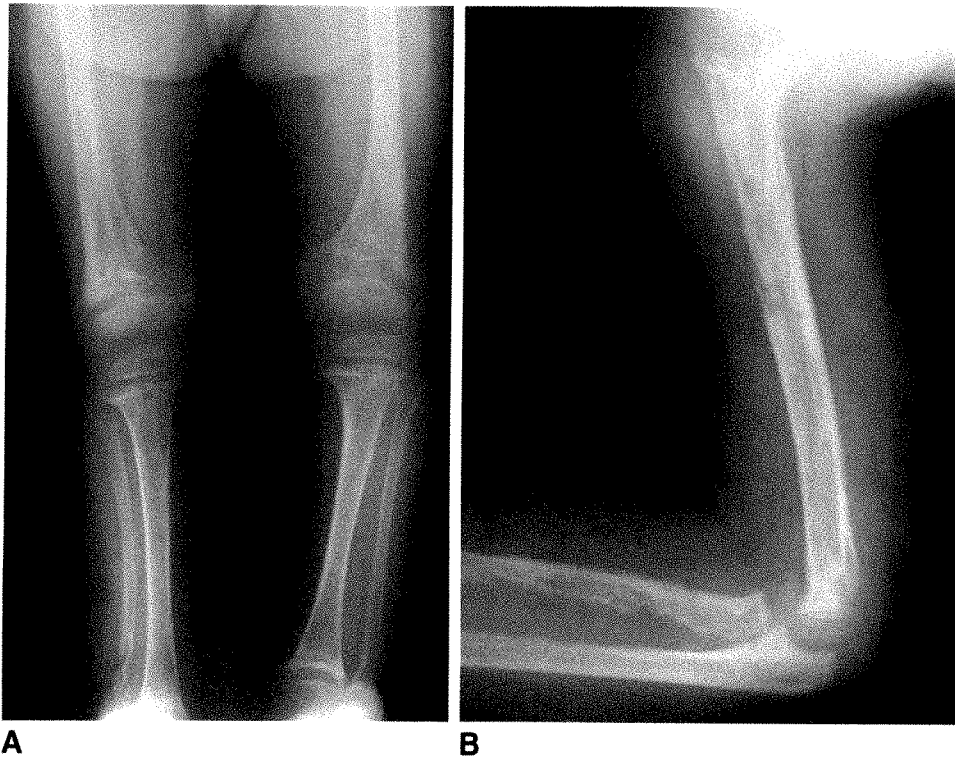


Fig. 3.—Case 3: A 3-year-old girl with bone pain, hyperphosphaturia, hypophosphatemia, and multiple skin lesions believed to represent linear sebaceous nevi.

A, Anteroposterior radiograph of the lower extremities.

B, Lateral radiograph of the right upper extremity.

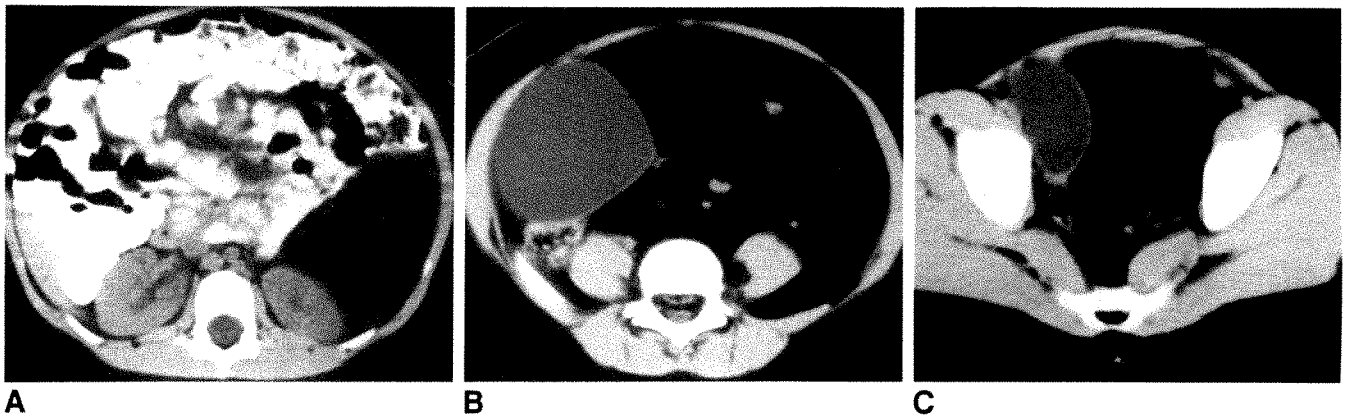


Fig. 4.—Case 4: A 6-year-old girl with a 3-year history of abdominal distention and a newly noted abdominal mass.

A, CT scan through the upper abdomen.

B, CT scan through the lower abdomen.

C, CT scan through the pelvis.

Neuroradiology Case of the Day

Elliot I. Shoemaker,¹ Allan J. Romano, Mokhtar Gado, and Fred J. Hodges III

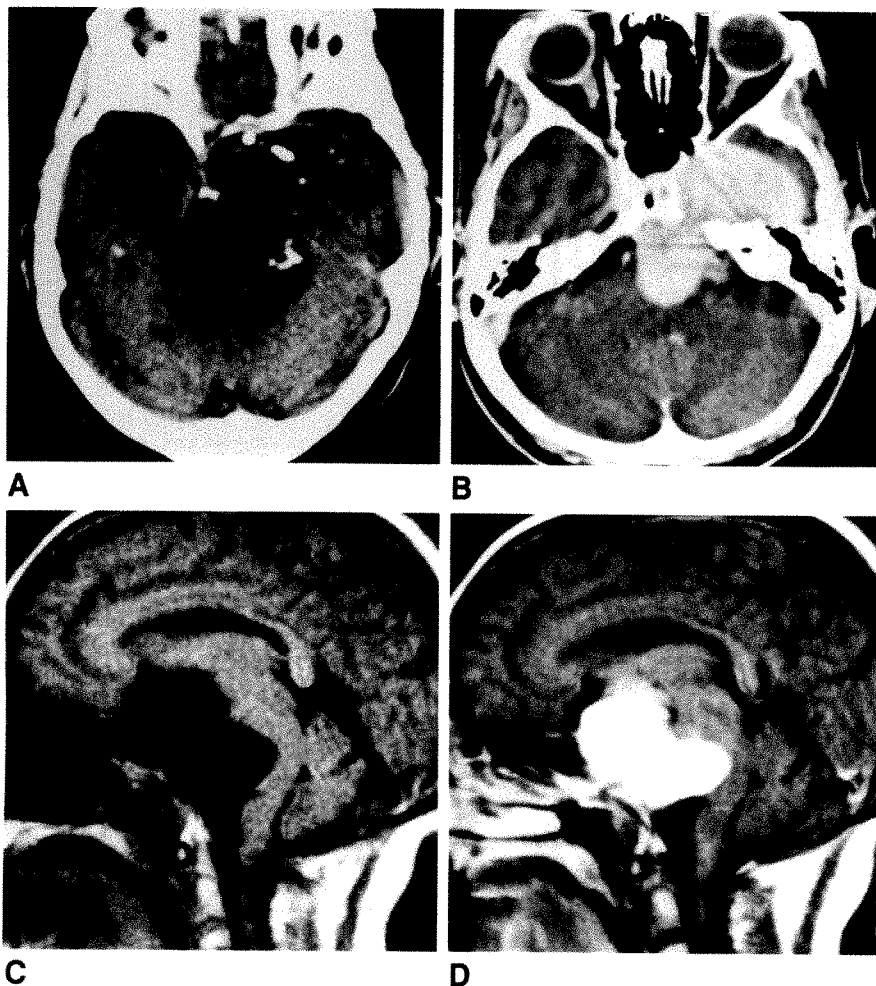


Fig. 1.—Case 1: 55-year-old woman with multiple cranial nerve palsies on left side.

A, Noncontrast CT above level of sella.

B, Contrast CT scan, at level of sella.

C, T1-weighted sagittal MR image, 500/17, near midline.

D, Gadolinium-enhanced, T1-weighted MR image, 700/17.

¹ All authors: Mallinckrodt Institute of Radiology, Washington University School of Medicine, 510 S. Kingshighway Blvd., St. Louis, MO 63110. Address reprint requests to M. J. Siegel at this address.

Cases 1 and 4 were prepared by E. I. Shoemaker, A. J. Romano, and M. Gado. Case 2 was prepared by A. J. Romano, E. I. Shoemaker, and M. Gado. Case 3 was prepared by A. J. Romano, E. I. Shoemaker, M. Gado, and F. J. Hodges III. M. J. Siegel is coordinator of the Case of the Day series.

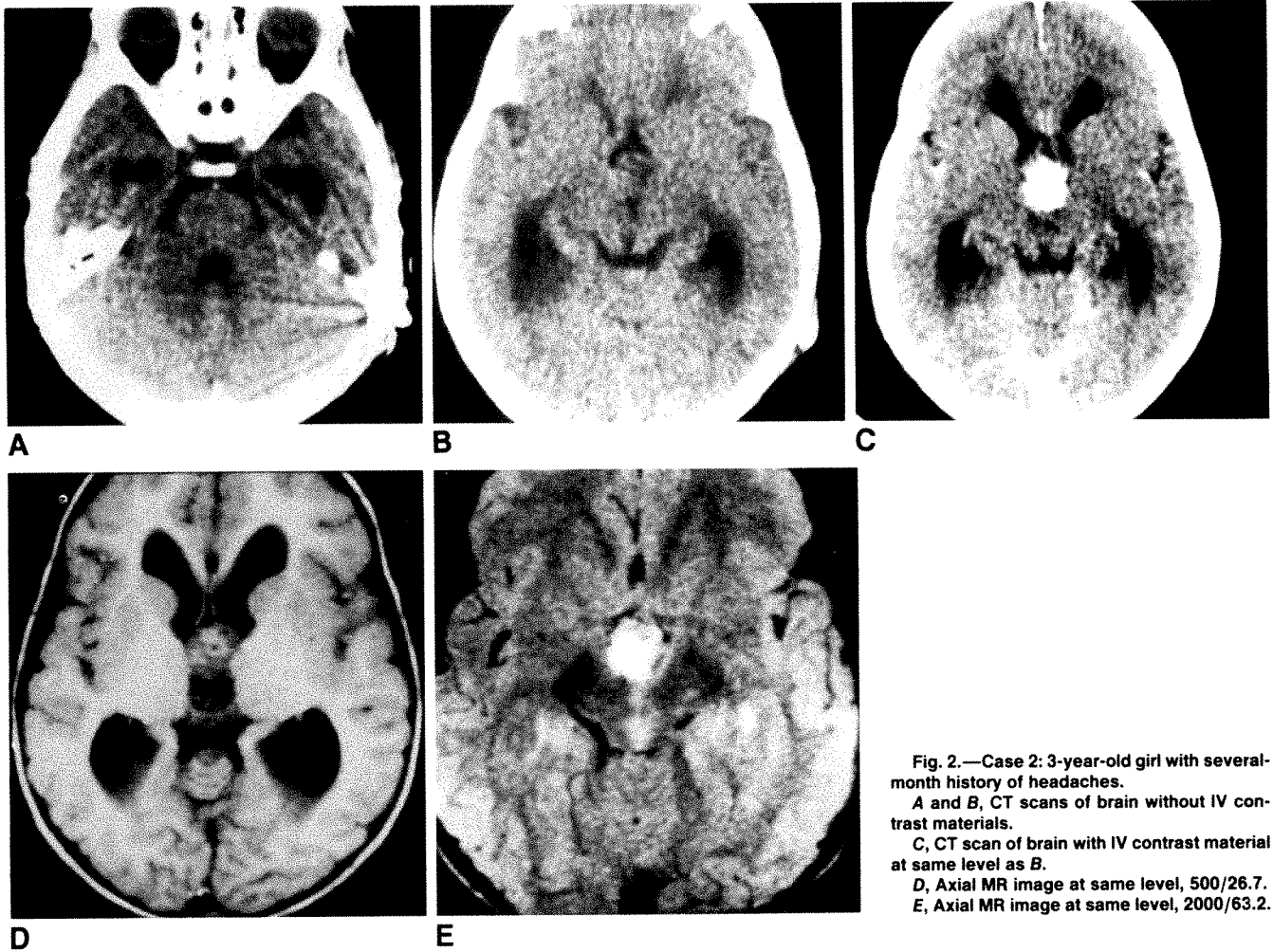


Fig. 2.—Case 2: 3-year-old girl with several-month history of headaches.
A and B, CT scans of brain without IV contrast materials.
C, CT scan of brain with IV contrast material at same level as B.
D, Axial MR image at same level, 500/26.7.
E, Axial MR image at same level, 2000/63.2.

Fig. 3.—Case 3: 70-year-old man with 6-month history of progressive decline in cognitive function and lethargy.

A and B, Noncontrast axial head CT with bone windows.

C and D, Coronal T1 (700/17) and T2 (2000/120) MR images.

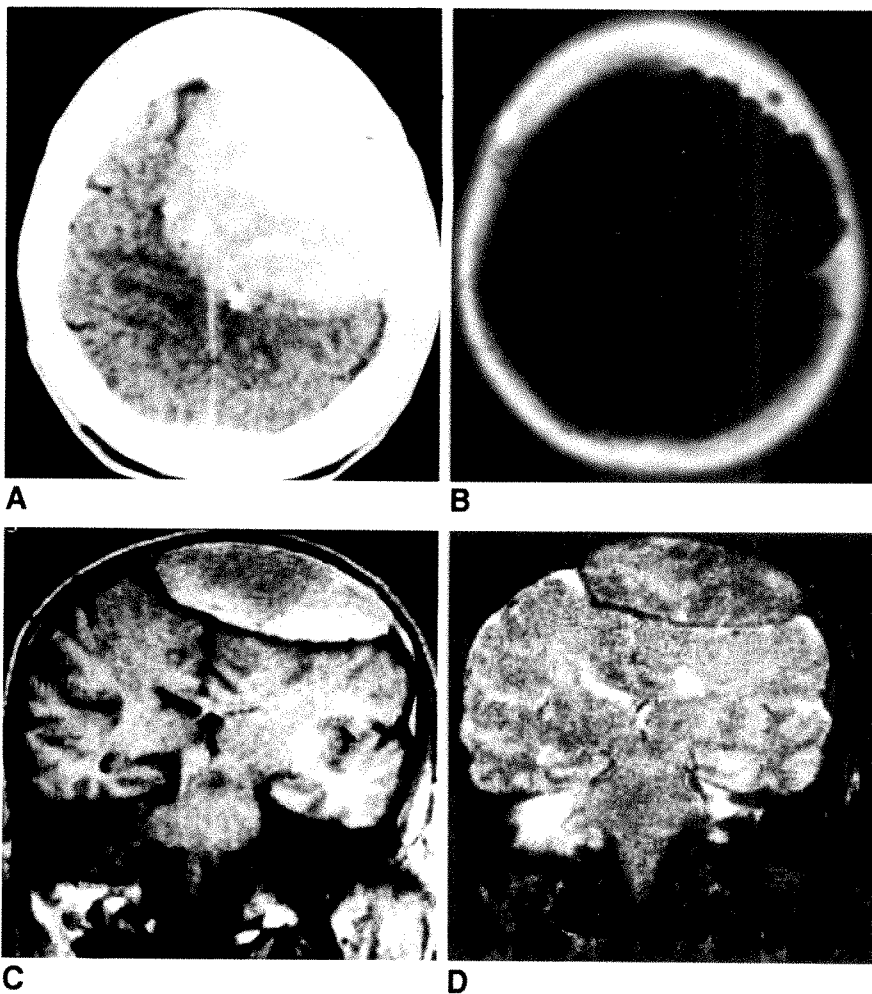
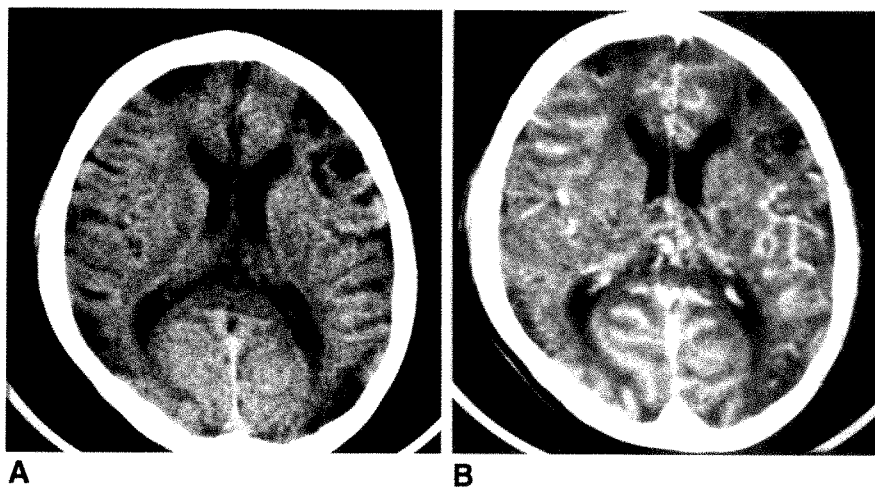


Fig. 4.—Case 4: 10-year-old boy with Down syndrome and progressive intermittent right-sided weakness with exercise.

A, Noncontrast CT.

B, Contrast CT.



Books Received

Receipt of books is acknowledged as a courtesy to the sender. Books considered of sufficient interest are reviewed as space permits. If the book has been reviewed in the *AJR*, the date of its review is given in parentheses.

Fetal Echocardiography. An Atlas. By Kathryn L. Reed, Caroline F. Anderson, and Lewis Shenker. New York: Alan R. Liss, 146 pp., 1988. \$62.50 (1/89)

Small Bowel Radiology. Introduction and Atlas. By Günther Antes and Franz Eggemann. New York: Springer-Verlag, 207 pp., 1988. \$110 (1/89)

Assessing the Skeletal Maturity of the Hand-Wrist. Fels Method. By Alex F. Roche, William Cameron Chumlea, and David Thissen. Springfield, IL: Charles C. Thomas, 339 pp., 1988. \$57.50 (1/89)

The Radiologic Clinics of North America. Imaging in Neuroradiology, Part 1. Guest editors: S. Howard Lee and Robert A. Zimmerman. Philadelphia: Saunders, July 1988;26(4):701-891. \$22.95; by subscription, 6 issues annually for \$89 (1/89)

Fundamentals of Radiology, 4th ed. By Lucy Frank Squire and Robert A. Novelline. Cambridge, MA: Harvard University Press, 355 pp., 1988. \$29.50 (1/89)

Gastrointestinal Nuclear Imaging. Edited by Michael G. Velchik and Abass Alavi. (Vol. 7 of Contemporary Issues in Gastroenterology. Edited by Sidney Cohen and Roger D. Soloway.) New York: Churchill Livingstone, 289 pp., 1988. \$65 (1/89)

Interventional Radiology. Edited by Wilfrido R. Castañeda-Zuñiga and S. Murthy Tadavarthy. (Part of the series Golden's Diagnostic Radiology. Series editor: John H. Harris, Jr.) Baltimore: Williams & Wilkins, 873 pp., 1988. \$149.95 (1/89)

Ultrasonography of the Spleen. By Jean-Noël Bruneton, M. Benozio, M. Bléry, H. A. Gharbi, B. Senecail, and V. Tran-Minh. New York: Springer-Verlag, 84 pp., 1988. \$65.50 (1/89)

Progress in Digital Angiocardiology. Edited by P. H. Heintzen and J. H. Bürsch. Boston: Kluwer Academic, 353 pp., 1988. \$145 (1/89)

Computed Tomography of the Chest. A Teaching File. By M. Elon Gale and Joel B. Karlinsky. Chicago: Year Book Medical, 254 pp., 1988. \$54 (1/89)

Gallenblasensteine. Ihre Morphogenese und Auswahl zur Litholyse. By Carlheinrich Wolpers. Basel: Karger, 202 pp., 1987. DM 190 (1/89)

Imaging of the Foot and Ankle. By D. M. Forrester, Morrie E. Kricun, and Roger Kerr. (From the Clinical Diagnostic Imaging Series. Edited by Morrie E. Kricun.) Rockville, MD: Aspen, 325 pp., 1988. \$93 (1/89)

MRI of the Knee. By Murray A. Solomon. (Videotape 1 of Murray Solomon's Magnetic Resonance Video Review.) Burlingame, CA: Murray Solomon's MRVR, (415) 692-8230, 1988. Single tape, \$125; series of 6 tapes, \$495 (1/89)

Atlas of Fetal Skeletal Radiology. By Asher Ornoy, Zvi Borochowitz, Ralph Lachman, and David L. Rimoin. Chicago: Year Book Medical, 136 pp., 1988. \$75 (2/89)

RSNA Today, Vol. 2, No. 3. Oak Brook, IL: The Radiological Society of North America, 1988. \$75; by subscription, 4 issues annually at \$225 for RSNA members and \$275 for nonmembers (VHS videotape) (2/89)

Imaging Anatomy of the Knee Region. Anatomy-CT-NMR: Frontal Slices, Sagittal Slices, Horizontal Slices. By Henri Sick and Jean-Louis Burguet. Munich: J. F. Bergmann. Verlag, 88 pp., 1988. \$115 (2/89)

Principles of Radiopharmacology. Edited by Harald Deckart and Peter H. Cox. Boston: Nijhoff, 262 pp., 1988. \$67 (2/89)

The Alimentary Tract. The Hollow Organs and Salivary Glands. (Vol. 4 of A Textbook of Radiological Diagnosis, 5th ed.) Edited by K. C. Simpkins. London: H. K. Lewis, 754 pp., 1988. £85 (2/89)

Nuclear Medicine. (Vol. 6 in the series Handbooks in Radiology). By Frederick L. Datz. Chicago: Year Book Medical, 331 pp., 1988. \$19.95 (3/89)

The Chief Resident as Manager. By Neal Whitman, Elaine Weiss, and Lawrence Lutz. Salt Lake City: Department of Family and Preventive Medicine, University of Utah School of Medicine, 143 pp., 1988. \$16 (3/89)

Cerebrovascular Disease. Edited by Masakuni Kameyama, Masanori Tomonaga, and Tadashi Aiba. New York: Igaku-Shoin, 178 pp., 1988. \$60 (3/89)

Nuclear Medicine Annual 1988. Edited by Leonard M. Freeman and Heidi S. Weissmann. New York: Raven, 339 pp., 1988. \$89 (3/89)

How to Write and Publish a Scientific Paper, 3rd ed. By Robert A. Day. Phoenix: Oryx, 211 pp., 1988. \$21.95 (3/89)

The Radiologist's First Reader. By Harry W. Fischer. Rochester, NY: Fischer Associates, 231 pp., 1988. \$18.95 soft cover (3/89)

Exposure of the Population in the United States and Canada from Natural Background Radiation. Recommendations of the National Council on Radiation Protection and Measurements. (NCRP Report No. 94.) Bethesda, MD: National Council on Radiation Protection and Measurements, 209 pp., 1987. \$17 (3/89)

Radiation Exposure of the U.S. Population from Consumer Products and Miscellaneous Sources. Recommendations of the National Council on Radiation Protection and Measurements. (NCRP Report No. 95.) Bethesda, MD: National Council on Radiation Protection and Measurements, 99 pp., 1987. \$14 (3/89)

Public Radiation Exposure from Nuclear Power Generation in the United States. Recommendations of the National Council on Radiation Protection and Measurements. (NCRP Report No. 92.) Bethesda, MD: National Council on Radiation Protection and Measurements, 204 pp., 1987. \$19 (3/89)

Of Critical Importance . . . AIDS Precautions in Radiology. Nashville, TN: Envision Inc., 1988. Purchase, \$295; rental, \$125/5 days (videotape) (3/89)

Smith's Recognizable Pattern of Human Malformation, 4th ed. By Kenneth Lyons Jones. Philadelphia: Saunders, 778 pp., 1988. \$55 (3/89)

The Malformed Fetus and Stillbirth. A Diagnostic Approach. By Robin M. Winter, Simon A. S. Knowles, Frederick R. Bieber, and Michael Baraitser. New York: Wiley & Sons, 376 pp., 1988. \$115.50 (3/89)

Dental Radiographic Diagnosis. By Kavas H. Thunthy. Springfield, IL: Charles C. Thomas, 542 pp., 1988. \$58.75 (3/89)

Magnetic Resonance Imaging. Atlas of the Head, Neck, and Spine. By Catherine M. Mills, Jack de Groot, and Jonathan P. Posin. Philadelphia: Lea & Febiger, 295 pp., 1988. \$98.50 (3/89)

Nuclear Medicine. Self-Study Program I: Part I, Syllabus and Multiple-Choice Questions; Part II, Answers, Critiques, and References for Multiple-Choice Questions. Edited by Barry A. Siegel and Peter T. Kirchner. New York: The Society of Nuclear Medicine, 272 pp., 1988. \$90 for members, \$115 for nonmembers, and \$75 for residents and technologists (3/89)

Fundamentals of Nuclear Medicine, 2nd ed. Edited by Naomi P. Alazraki and Fred S. Mishkin. New York: The Society of Nuclear Medicine, 242 pp., 1988. \$15, soft cover (3/89)

The Scintillation Camera. Edited by Guy H. Simmons. New York: The Society of Nuclear Medicine, 160 pp., 1988. \$30 for members, \$35 for nonmembers, soft cover (3/89)

Radiology: A Practical Guide. Practical Guides for General Practice 3. By R. F. Bury. New York: Oxford University Press, 99 pp., 1988. \$10.95

Practical Gynecologic Oncology. By Jonathan S. Berek and Neville F. Hacker. Baltimore: Williams & Wilkins, 691 pp., 1989. \$59.95

Concepts in Neurosurgery. (Vol. 2 in Stereotactic Neurosurgery.) Edited by M. Peter Heilbrun. Baltimore: Williams & Wilkins, 278 pp., 1988. \$69.50

Sonographie und Szintigraphie der Schilddrüse. Lehrbuch und Atlas. By Von Walter Wiedemann. New York: Thieme-Verlag, 230 pp., 1988.

Radiologia Medica. Edited by Giovanni Juliani. Torino, Italy: Edizioni Minerva Medica, 595 pp., 1988.

Biological, Physical and Clinical Aspects of Hyperthermia. Edited by Bhudatt R. Paliwal, Fred W. Hetzel, and Mark W. Dewhirst. New York: American Institute of Physics, 483 pp., 1988. \$75

Tomodensitometrie du Tronc. Anatomie Normale et Pathologique. By Jacques Hureau and Janine Pradel. Padua, Italy: Piccin, 487 pp., 1988. \$210

Radiology for Dental Hygienists and Dental Assistants. By Olaf E. Langland, Robert P. Langlais, Francis H. Sippy, and Gail F. Williamson. Springfield, IL: Charles C Thomas, 237 pp., 1988. \$29.75

Progress in Cardiology 1/2. Edited by Douglas P. Zipes and Derek J. Rowlands. Philadelphia: Lea & Febiger, 346 pp., 1988. \$29.50

Respiratory Infections in Children. Management in Small Hospitals. a Manual for Doctors. By the World Health Organization. Geneva: Health & Biomedical Programme, 38 pp., 1988. \$3

Environmental Health Criteria 61. Chromium. By The World Health Organization. Geneva: Health & Biomedical Information Programme, 197 pp., 1988. \$17.60

Quality Assurance in Radiotherapy. By the World Health Organization. Geneva: Health & Biomedical Information Programme, 52 pp., 1988. \$6.60

Endourology. New and Approved Techniques. Edited by U. Jonas, N. F. Dabhoiwala, and F. M. J. Debruyne. New York: Springer-Verlag, 162 pp., 1988. \$69.50

Breast Cancer. Collaborative Management. Edited by Jay K. Harness, Harold A. Oberman, Allen S. Lichter, Dorit D. Adler, and Robert L. Cody. Chelsea, MI: Lewis Publishers, 390 pp., 1988. \$69.95

Man-Made Mineral Fibres. Environmental Health Criteria 77. By the World Health Organization. Geneva: World Health Organization, 165 pp., 1988. \$15.20

American Roentgen Ray Society: Officers, Committees, and Membership Information

Officers

President: Lee F. Rogers

President-elect: Ronald G. Evens

1st Vice-president: M. Paul Capp

2nd Vice-president: John A. Kirkpatrick, Jr.

Secretary: Glen W. Hartman

Treasurer: Beverly P. Wood

Executive Council: J. Thrall, J. F. Wiot, L. F. Rogers, R. A. Gagliardi, R. G. Evens, R. N. Berk, B. P. Wood, J. E. Madewell, M. P. Capp, G. W. Hartman, B. G. Brogdon, G. R. Leopold, A. Landry, Jr., A. K. Poznanski, K. H. Vydareny, J. T. Ferrucci, Jr., W. J. Casarella, E. J. Ferris, J. A. Kirkpatrick, Jr., A. E. James, Jr., chairman

Committees

Editorial Policy: S. S. Sagel, R. J. Stanley, C. A. Rohrmann, Jr., N. O. Whitley, S. V. Hilton, J. M. Taveras, R. N. Berk, W. J. Casarella, chairman

Education and Research: C. E. Putman, C. B. Higgins, B. J. Hillman, R. A. McLeod, B. G. Brogdon, chairman

Finance and Budget: A. K. Poznanski, G. R. Leopold, J. R. Thornbury, R. C. Gedgaudas-McClees, J. Thrall, chairman

Nominating: K. L. Krabbenhoft, J. F. Wiot, G. R. Leopold, chairman

Publications: R. J. Stanley, S. S. Sagel, N. O. Whitley, C. A. Rohrmann, Jr., W. J. Casarella, chairman

Membership: E. J. Ferris, G. R. Leopold, K. H. Vydareny, A. K. Poznanski, chairman

Representatives to Other Organizations

American Board of Radiology: E. C. Klatte, L. F. Rogers, J. A. Kirkpatrick, Jr.

American College of Radiology: L. F. Rogers, G. A. Kling, R. A. Gagliardi, J. E. Madewell

American Medical Association House of Delegates: S. F. Ochsner, K. L. Krabbenhoft, alternate

American National Standards Institute: M. Haskin

National Council on Radiation Protection and Measurements: E. L. Saenger, H. L. Friedell

Meeting Arrangements

Annual Meetings: May 7-12, 1989, Hilton, New Orleans; May 13-18, 1990, Sheraton Washington, Washington, DC

Annual Meeting Committee: H. C. Carlson, G. P. Janetos, E. K. Lang, R. R. Lukin, A. Landry, Jr., chairman

Instruction Courses: R. J. Stanley, associate chairman, J. T. Ferrucci, Jr., chairman

Scientific Program: R. J. Alfidi, A. E. Robinson, J. H. Thrall, M. P. Banner, J. J. Gisvold, T. C. McLoud, R. G. Evens, chairman

Scientific Exhibits: A. A. Moss, A. V. Proto, R. J. Churchill, J. E. Madewell, chairman

ARRS Membership

An application form is printed in this April issue of the Journal. For consideration at the 1990 ARRS meeting, send completed forms before February 1, 1990, to American Roentgen Ray Society, 1891 Preston White Dr., Reston, VA 22091. Active members are graduates of an approved medical or osteopathic school or hold an advanced degree in an allied science. They must practice radiology or work in an associated science in the United States or Canada and be certified by the American Board of Radiology, American Osteopathic Board of Radiology, or Royal College of Physicians of Canada or otherwise adequately document training and credentials. Corresponding members are foreign radiologists or scientists who are active in radiology or an allied science. Members-in-training are residents or fellows in radiology or postgraduate students in an allied science. Additional application forms can be obtained from the ARRS offices in Reston, VA.

Business Office

Paul Fullagar, Administrative Director, American Roentgen Ray Society, 1891 Preston White Dr., Reston, VA 22091; (703) 648-8900

Invitation to the 1989 American Roentgen Ray Society Meeting in New Orleans, LA, May 7-12, 1989

I am pleased to extend an invitation to all radiologists to attend the 89th annual meeting of the American Roentgen Ray Society in New Orleans, LA, May 7-12, 1989. In keeping with the ARRS tradition, outstanding scientific and social programs will be provided.

The excitement of a meeting set in New Orleans requires no further description. The opportunity for busy radiologists to attend a major national meeting while enjoying all that New Orleans has to offer is ideal.

The scientific program, instructional courses, and categorical course are certain to be interesting and informative (see Table 1 for schedule).

Scientific Program

Two hundred scientific papers have been selected from more than 400 abstracts. Scientific sessions will be devoted to all major body systems, angiography, interventional techniques, sonography, and mammography, as well as technologies. Special emphasis has been placed on discussion of new developments.

The innovative and extremely well-received Friday morning minisymposium is entitled "Gastrointestinal Radiology Update 1989." An outstanding faculty has been assembled for what I am sure will be a very stimulating program.

Instructional Courses

Joseph T. Ferrucci, Chairman of the Instructional Course Committee, has put together 60 instructional courses. Faculty members have been drawn from across the entire country, with emphasis on luminaries from the South. A superlative educational experience is anticipated, and advance registration is recommended.

Categorical Course

An extraordinary categorical course on genitourinary imaging (uroradiology) has been fashioned. The course covers all aspects of the field, including equipment and principles of diagnosis. This course is certain to be popular, and advance registration is advised.

TABLE 1: Summary of 1989 American Roentgen Ray Society Meeting

Sunday May 7	Monday May 8	Tuesday May 9	Wednesday May 10	Thursday May 11	Friday May 12
	8-9:30 Instructional courses	8-9:30 Instructional courses	8-9:30 Instructional courses	8-9:30 Instructional courses	8-10 Symposium: gastrointestinal imaging update
9-noon Categorical course: genitourinary imaging	10-10:30 Opening cere- monies				
	10:30-12:30 Scientific programs	10-12:30 Scientific programs	10-12:30 Scientific programs	10-12:30 Scientific programs	10:30-12:30 Symposium: gastrointestinal imaging update
1:30-3 Categorical course: genitourinary imaging	1:30-3:30 Categorical course: genitourinary imaging	1:30-3:30 Scientific programs	1:30-3:30 Scientific programs	1:30-3:30 Scientific programs	
3:30-5:30 Categorical course: genitourinary imaging	4-5:30 Instructional courses and cate- gorical course: genitourinary imaging	4-5:30 Instructional courses and cate- gorical course: genitourinary imaging	4-5:30 Instructional courses and cate- gorical course: genitourinary imaging	4-5:30 Instructional courses and cate- gorical course: genitourinary imaging	

Scientific Exhibits

The 220 scientific exhibits coordinated by John Madewell will cover the entire breadth of the field of diagnostic radiology. The technical exhibits will be integrated among the scientific exhibits to enhance the interaction of the attendees with our technical exhibitors.

Caldwell Lecture

The Honorable William Bradley, senator from New Jersey, has agreed to present the Caldwell Lecture at the 1989 meeting. The title of Senator Bradley's presentation will be "Health Care Choices for the Nineties." This promises to be one of the highlights of the meeting.

Social Events

New Orleans offers an unlimited number of diversions, and Abner M. Landry, Jr., Chairman of the Local Arrangements Committee, has engaged Crescent City Consultants to plan a variety of outstanding tours. The annual golf and tennis tournaments for attendees and their companions are scheduled for Monday. The traditional cocktail party given by the society in the exhibit area for all registrants will be Tuesday evening and will provide a convenient meeting place before an evening on the town.

This promises to be a truly outstanding event in exceptional surroundings. I hope you will be able to accept our invitation. Plan now to attend.

Ronald G. Evens
President-Elect, ARRS

1989 ARRS Meeting Summary, May 9-12, 1989 New Orleans, LA

A comprehensive description of the meeting, including the scientific program, Categorical Course in Genitourinary Imaging, and instructional courses, appeared in the February issue of the *AJR*. Meeting and registration forms will be found in the February and March issues. These may be photocopied.

Accreditation

All courses and scientific sessions carry AMA Category I credit on an hour-for-hour basis.

Meeting Format

Scientific Program. Sessions will be grouped in parallel sessions, Monday–Thursday. A total of 189 scientific papers will be presented. In addition, on Wednesday, May 10, the afternoon session will feature award papers and the Caldwell Lecture, which will be delivered by Senator Bill Bradley (D-NJ). On Friday, there will be a special symposium on gastrointestinal imaging.

Categorical Course in Genitourinary Imaging. This 15.5-hr course will be Sunday–Thursday.

Luncheon Sessions. Registrants may enroll in special luncheon sessions, Monday–Thursday. A box lunch will be provided.

Exhibits

Scientific and Technical Exhibits and Case of the Day Presentations will be presented in the Grand Salon of the New Orleans Hilton Riverside and Towers, Monday–Thursday, May 8–11. The Case of the Day will be presented by Marilyn Siegel of Washington University and Mallinckrodt Institute, St. Louis, MO.

Local Activities

General Reception. Tuesday evening, May 9, for all registrants.

Golf Tournament. Monday, May 8, English Turn Country Club. Transportation leaves the hotel at 11 a.m.; shotgun start is at 12:30 p.m.

Men's and Women's Tennis Tournaments. Monday, May 8, at the New Orleans Hilton Riverside and Towers, New Orleans, LA.

Local Tours. Sunday, May 7, 1–4 p.m., Overview of New Orleans; 7:30–10 p.m., Evening on the Mississippi; Monday, May 8, 9 a.m.–4 p.m., Plantations of Old Louisiana; 8–10:30 p.m., Dinner at Gallier Hall; Tuesday, May 9, 9:30 a.m.–3:30 p.m., Elegant Homes of New Orleans; Wednesday, May 10, 9–11:30 a.m., Creole Connection; 12:30–5 p.m., Audubon Zoo/River Cruise; 7–10 p.m., Evening Overlooking the Mississippi; Thursday, May 11, 11 a.m.–2:30 p.m., Cajun Swamp Tour. No refunds after April 20.

Meeting Registration

Preregistration will be accepted until April 7. There will be on-site registration. Official badges and program books will be available at the registration desk, New Orleans Hilton Riverside and Towers. No confirmations will be mailed.

Course Registration

Register early—enrollment is limited. List first, second, and third choices for each period. Also, indicate whether you wish to take the categorical course. Deadline for mail registrations is April 7. All ticket orders will be filled by postmark. Course tickets *will not* be mailed. Tickets will be available on and after Sunday, May 6 (after 1 p.m.), at the ARRS registration desk in the New Orleans Hilton Riverside and Towers. There will be on-site registration for courses not already filled.

Hotel Registration

Reservations are handled by the ARRS Housing Bureau, New Orleans Hilton Riverside and Towers, Attn: Reservations Office, Poydras at the Mississippi River, New Orleans, LA 70140. These must be received by April 7. Make check payable to New Orleans Hilton Riverside and Towers.

Fees

Meeting:

ARRS members and resident members	No fee
Nonmembers	\$250
Nonmember physicians in training (with verification)	25
Categorical course (all who attend)	75
Luncheon sessions/each	12
Golf tournament	75
Tennis tournaments	50
Local tours	20–75

Cancellations and Fee Refunds

Fees will be refunded only if cancellation is received by April 20, 1989. Send to American Roentgen Ray Society, 1891 Preston White Drive, Reston, VA 22091.

Transportation Discounts

United and Delta airlines are offering discounts, up to 40%, on airfares. For United, call (800) 521-4041 and mention ARRS account number 9099D. For Delta, call (800) 241-6760 and reference account number M-0045.

Budget Rent A Car is offering special rates on car rentals. Call (800) 772-3773 and mention that you are attending the American Roentgen Ray Society annual meeting.

Information and Application for Membership in the American Roentgen Ray Society

General Information

The American Roentgen Ray Society, founded in 1900, has been a forum for progress in radiology since shortly after the discovery of x-rays. From its beginning and continuing to today, the ARRS has been guided by dedication to the goal of the advancement of medicine through the science of radiology and its allied sciences.

The goal of the ARRS is maintained through an annual scientific and educational meeting, and through publication of the *American Journal of Roentgenology*.

The annual meeting consists of instructional courses, scientific sessions, a symposium, scientific exhibits, and commercial exhibits. A special categorical course is also offered. Category I CME credits are available on an hour-for-hour basis.

The monthly *American Journal of Roentgenology* is a highly respected peer review journal with a worldwide subscription base. For over 75 years the *AJR* has been accepted as one of the best specialty journals available in the world, and this reputation grows each month.

A recently developed quarterly ARRS newsletter keeps members informed of events and general Society news.

Application Instructions

Candidates for Active Membership

1. An Active member must be a graduate of an approved medical school or hold an advanced degree in one of the physical, chemical or biological sciences and be certified by the American Board of Radiology, the American Osteopathic Board of Radiology, the Royal College of Physicians of Canada, or document training and credentials that are adequate to qualify for membership. Active members shall actively practice radiology or one of its branches in the United States or Canada. Such members are eligible to participate in all activities of the Society, including membership on committees, and have full voting privileges.
2. Application must be on an official form, signed by the applicant and at least two members of the American Roentgen Ray Society, active or emeritus, in good standing, who endorse the applicant.
3. Application fee is \$50 (payable when billed for dues).
4. Annual dues are \$125, payable on January 1 of each year following the initial year. First year dues will be invoiced following candidate election at the annual meeting. Of this amount, \$50 is for a 1-year subscription to the *American Journal of Roentgenology*, beginning with the July issue following election to membership.
5. Application must be received by February 1 for action during the current year's meeting.

Candidates for In-Training Membership

1. In-training members must be serving in a radiology residency program approved by the Radiology Residency Review Committee, the American Osteopathic Board of Radiology, or the Royal College of Physicians of Canada, or in an approved post-residency fellowship, or be a postgraduate student in an allied science. Training status must be verified by the program director. In-training members have special consideration in fees and subscription rates to the Society journal. Such members cannot hold Society offices or vote.
2. Application must be on an official form and signed by the applicant and by the applicant's training or residency program director.
3. In-training status is limited to a maximum of five years starting with the entrance date into the radiology residency. In the last year, each in-training member will receive an application for active membership from the Society. Those who do not apply for transfer to active membership shall be dropped from membership at the end of the fifth year, but can later apply as a new member through the process outlined for active status.
4. There is no application fee. Annual dues are \$25. Membership includes a subscription to the *American Journal of Roentgenology* and admission to the annual meeting without payment of the registration fee.
5. Membership applications will be acted on when received.

Corresponding Membership

A corresponding member must meet the qualifications of active membership, but reside and practice in a foreign country. Corresponding members shall pay dues and fees, but shall not have the privileges of voting nor of holding elective office.

All Applicants

1. Do not remit application fee or dues until requested.
2. Send completed forms to: American Roentgen Ray Society
1891 Preston White Drive
Reston, Virginia 22091

For ARRS
Office Use

Date Rec'd _____

I.D.# _____

AMERICAN ROENTGEN RAY SOCIETY APPLICATION FOR MEMBERSHIP

Date: _____

Category of Membership: ☐ Active
(Check One) ☐ Corresponding
☐ In-Training

Name (Please Print) _____ Degree(s) _____
First Initial Last

Mailing Address _____ Date of Birth _____
Street/Box
City/State/Country Zip Code Telephone () _____

A. Education: (List name of institution, years attended, and degree and type received.)

Undergraduate: _____

Graduate (Medical School, Graduate School, etc.):

Postgraduate (Internship, Residency, Fellowship, etc.):

B. Licensure:

Licensed to practice _____ in _____ since _____
(Type) (State, Province, etc.)

C. Appointments/Memberships: (In-Training applicants: skip to Section F on reverse.)

Present Appointments: Academic _____

Hospitals _____

Memberships in Scientific Societies: _____

Offices or Committee Assignments: _____

Government Service (Military or Civilian) _____
(Position) (Years)

D. Credentials:

I hereby certify that I was issued a certificate of qualification in _____
(Specialty)

in _____ by the _____
(Year) (Name of Qualifying Board)

Other Credentials: _____

Signature: _____

E. References:

We, active or emeritus members in good standing of the American Roentgen Ray Society, and acquainted with the applicant, do recommend him/her for membership in the Society. (Two references are required.)

Name (Please Print) 1. _____ 2. _____

Address _____

Signatures: _____

F. IN-TRAINING APPLICANTS MUST COMPLETE THIS SECTION**Credentials:**

I certify that I am serving as a Resident/Fellow in _____
(Specialty)

at _____ Date program began (begins): _____
(Name of Institution)

date program to end: _____ I understand that in-training membership is limited to a maximum of 5 years.

Applicant Signature: _____

Verification: (Program Director or Department Chairman *only*)

I certify that the applicant is in training at the institution named and qualifies for enrollment as a member-in-training of the American Roentgen Ray Society.

Name (Please Print) _____

Address: _____

Signature _____

Send completed form to: **American Roentgen Ray Society**
1891 Preston White Drive

Letters

I've Got the MR Blues, or T2, Bruté

If MR has you on the ROPES,
And GRASS seemed greener in olden days,
Don't try to COMPENSATE or mope,
The MR Blues are here to stay.

I, too, am feeling STIR crazy,
From GHOSTS and EXORCISTS galore;
My FIELD OF VIEW is shrinking, and
My confidence is out the door.

As if 2 million dollar cost
were not enough to do me in,
Pronouncing GADOLINIUM's
Enough to make my ECHO SPIN.

But still I FLIP from joy INTENSE,
The SEQUENCE of my PULSE does race.
With MULTIPLE EXCITATIONS in store,
I'll die with a smile upon my face.

Joel A. Rubenstein
Reno, NV 89502

Breast Cancer Screening: All's Well That Ends Well, or Much Ado About Nothing?

We mostly agree with the main conclusion reached by Dr. Moskowitz [1] that large-scale routine mammographic screening of asymptomatic women, starting when the women are 40 years old, is a worthwhile endeavor. The only matter of substance where we beg to differ is the assertion that radiologists experienced in mammography can evaluate 20 mammograms/hr. In our experience, this rate can be increased to about 60 mammograms/hr without adversely affecting diagnostic quality. In the DOM project, a large, ongoing breast cancer screening project in Utrecht, the Netherlands, an average of 150 mammograms are evaluated each day [2]. A single mammographic evaluation, once the films have been placed on a belt alternator, takes about 50 sec. Our sensitivity of 96% and specificity of 99% attest to the fact that this rate was not reached by compromising on quality.

Our situation is not unique. Sickels et al. [3] in San Francisco have reported an average evaluation time of 45 sec for each screening mammogram. The Forrest report [4] recommends an evaluation time of 65 sec/mammogram for breast cancer screening centers in the

United Kingdom. The time required for evaluation is not merely an academic issue; it can have major financial implications. In a mass screening setting in which a large number of clients are served rapidly to permit optimal use of professional time, an interpretation fee of \$10 can amount to \$900/hr when the evaluation time is 45 sec. Room for cost cutting is obvious.

D. Beijerinck
J. J. M. Deurenberg
J. J. Rombach
K. Borsje
Preventicon Utrecht
3501 DA Utrecht, the Netherlands

REFERENCES

1. Moskowitz M. Breast cancer screening: all's well that ends well, or much ado about nothing? *AJR* 1988;151:659-665
2. de Waard F, Collette HJA, Rombach JJ, Baanders-van Halewijn EA, Honing C. The DOM project for the early detection of breast cancer, Utrecht, the Netherlands. *J Chronic Dis* 1984;37(1):1-44
3. Sickles EA, Weber WN, Gabirin HB, Ominsky SH, Sollioth RA. Mammographic screening: how to operate successfully at low cost. *Radiology* 1986;160:95-97
4. Forrest P. Breast cancer screening: report to the health ministers of England, Wales, Scotland and Northern Ireland. London: Department of Health and Social Security, 1986

Reply

I thank Dr. Beijerinck et al. for their amplification concerning the number of mammograms read each hour in screening. I wonder sometimes if any statement about screening can be free of controversy. If one radiologist can read more than 20 films/hr (and I believe this is quite obviously the case), then even fewer radiologists would be necessary to handle the projected workload. Apparently, Dr. Beijerinck et al. and I agree that enough radiologists would be available.

I find it extremely interesting that Dr. Beijerinck and his colleagues have achieved a sensitivity of 96% and a specificity of 99%. I certainly am unable to achieve this level in screening. When sensitivity and specificity are evaluated, great care must be taken that the evaluator is not dealing with a self-fulfilling tautology. For example, if the screening mode were only physical examination, with mammography performed either incidentally or on an as-needed basis dictated by suspicious findings, the sensitivity of clinical examination would be in excess of 90%. However, when simultaneous but independent phys-

ical examination and mammography are performed, physical examination has a sensitivity of about 40–60%, and mammography has a sensitivity of about 80–85%. If the cases that occur within 1 year of a negative screening represent failures of the screening process, then the miss rate is quite considerable.

I remember quite clearly when claims of the sensitivity of oral cholecystography for stones were on the order of 97% or higher. Sonography and careful autopsy studies have shown that this is far from the case.

Screening is a humbling experience. Mammography is a tool with limited capabilities. Recognizing its limitation, we can apply it to the general population and, through its judicious application, achieve a significant reduction in mortality. There is no need for hyperbole.

Myron Moskowitz

Breast Imaging Center

University of Cincinnati Medical Center

Cincinnati, OH 45267-0772

Barrett's Esophagus: A Radiologic Diagnosis?

Barrett's esophagus has become the focus of increasing clinical interest. Recent studies have shown that as many as 20% of esophageal cancers arise in ectopic gastric mucosa, as do 20–50% of stomach tumors discovered near the gastroesophageal junction [1–3]. Dr. Levine's interesting review of the topic [4] favorably reports data from Gilchrist et al. [5] suggesting that patients can be classified into high-, moderate-, and low-risk groups for Barrett's esophagus on the basis of double-contrast barium swallows. The low-risk group is spared endoscopy in the face of mounting evidence [6–9] that Barrett's esophagus is caused by chronic gastroesophageal reflux. These investigators are willing to accept a normal esophagram as adequate evidence to exclude reflux.

Although grateful for the attempt to simplify the workup of this clinical challenge, we find two notable problems in applying the proposed algorithm. First, the barium swallow is not a sensitive test for gastroesophageal reflux unless unphysiologic maneuvers are used, which compromise the specificity of the examination and increase the patient's discomfort and exposure to radiation. Second, the moderate-risk group is actually an equivocal category that returns the decision to clinical judgment.

We were surprised, then, that no comment was made about the role of scintigraphic studies in diagnosing a condition that has been imaged successfully since 1973 by using technetium pertechnetate [10–13]. Ectopic gastric mucosa in the esophagus as well as Meckel diverticulum can be identified effectively, and in the latter case, nuclear imaging is currently the examination of choice. Furthermore, scintigraphic techniques are exquisitely sensitive for identifying the gastroesophageal reflux necessary to cause metaplasia of esophageal mucosa.

Scintigraphic methods therefore may be used to clarify the equivocal category and relieve the need for further concern in the low-risk group.

Richard Goldfarb

Fukiat Ongseng

Howard Finestone

Herbert Garcia

Beth Israel Medical Center

New York, NY 10003

REFERENCES

1. Levine MS, Caroline D, Thompson JJ, Kressel HY, Laufer I, Herlinger H. Adenocarcinoma of the esophagus: relationship to Barrett mucosa. *Radiology* 1984;150:305–309

2. Keen SJ, Dodd GD, Smith JL. Adenocarcinoma arising in Barrett's esophagus. *Mt Sinai J Med* 1984;51:442–450
3. Agha FP. Barrett carcinoma of the esophagus: clinical and radiographic analysis of 34 cases. *AJR* 1985;145:41–46
4. Levine MS. Progress in radiology. Barrett's esophagus: a radiologic diagnosis? *AJR* 1988;151:433–438
5. Gilchrist AM, Levine MS, Carr RF, et al. Barrett's esophagus: diagnosis by double-contrast esophagography. *AJR* 1988;150:97–102
6. Mangla JC. Barrett's esophagus: an old entity rediscovered. *J Clin Gastroenterol* 1981;3:347–356
7. Bozyski EM, Herlihy KH, Orlando RC. Barrett's esophagus. *Ann Intern Med* 1982;97:103–107
8. Sjogren RW, Johnson LF. Barrett's esophagus: a review. *Am J Med* 1983;74:313–321
9. Spechler SJ, Goyal RK. Barrett's esophagus. *N Engl J Med* 1986;315:362–371
10. Mangla JC, Brown M. Diagnosis of Barrett's esophagus by pertechnetate radionuclide. *Am J Dig Dis* 1976;21:324–328
11. Berquist TH, Nolan NG, Stephens DH, et al. Radioisotope scintigraphy in diagnosis of Barrett's esophagus. *AJR* 1975;123:401–411
12. Gordon F, Ramirez-Degollado J, Munoz R, et al. Diagnosis of Barrett's esophagus with radioisotopes. *AJR* 1974;121:716–719
13. Berquist TH, Nolan NG, Carlson HC, et al. Diagnosis of Barrett's esophagus by pertechnetate scintigraphy. *Mayo Clin Proc* 1973;276–279

Reply

I thank Dr. Goldfarb et al. for their comments about my recent article on the radiologic diagnosis of Barrett's esophagus [1]. My colleagues suggest that scintigraphic techniques have not been used adequately in diagnosing this condition. However, they cite four articles published more than a decade ago in which Barrett's esophagus was diagnosed scintigraphically in a combined total of only 17 patients (see references 10–13 in their letter). Thus, further investigation is needed to determine the accuracy (i.e., the sensitivity and specificity) of scintigraphy in diagnosing Barrett's esophagus and its ultimate role in evaluating patients with suspected reflux disease.

Regarding the article by Gilchrist et al. [2], my colleagues state that "these investigators are willing to accept a normal esophagram as adequate evidence to exclude reflux." Because scintigraphy is a more sensitive technique for detecting gastroesophageal reflux, Goldfarb et al. conclude that scintigraphic studies might be helpful for documenting gastroesophageal reflux in patients who have a normal esophagram. In the study by Gilchrist et al., however, a normal esophagram did not exclude gastroesophageal reflux or even reflux esophagitis. In that study, the overall sensitivity of double-contrast esophagography in detecting reflux esophagitis was only 52%. However, most cases of reflux esophagitis that were missed radiographically were mild, and only one of 117 patients with a normal esophagram had histologically proved Barrett's esophagus. The data therefore suggest that Barrett's esophagus occurs almost exclusively in patients with reflux esophagitis severe enough to be detected on double-contrast examinations. Thus, patients who have a normal double-contrast esophagram appear to be at low risk for Barrett's esophagus whether or not gastroesophageal reflux is found on scintigraphic studies.

In summary, Goldfarb et al. are concerned that scintigraphic techniques have not been used adequately in evaluating patients with reflux disease and possible Barrett's esophagus. Clearly, further investigation is needed in this area. Nevertheless, the study by Gilchrist et al. suggests that double-contrast esophagography is a useful screening examination for Barrett's esophagus and that unnecessary endoscopy and biopsy can be avoided in the majority of patients who have signs and symptoms of reflux.

Marc S. Levine

Hospital of the University of Pennsylvania
Philadelphia, PA 19104

REFERENCES

1. Levine MS. Progress in radiology. Barrett's esophagus: a radiologic diagnosis? *AJR* 1988;151:433-438
2. Gilchrist AM, Levine MS, Carr RF, et al. Barrett's esophagus: diagnosis by double-contrast esophagography. *AJR* 1988;150:97-102

Esophageal Intramural Pseudodiverticulosis

A 57-year-old obese man had had adult-onset diabetes mellitus for 5 years, which had been well controlled with medication. His chief complaint was the acute onset of dysphagia.

An upper gastrointestinal series revealed rigidity in the upper one-third of the esophagus and multiple, small, flask-shaped outpouchings projecting from the esophageal wall (Fig. 1). The involved length of the esophagus was about 10 cm. The width of the outpouchings was 2-3 mm, and the depth was 3-4 mm.



Fig. 1.—Esophagram shows characteristic multiple, small, flask-shaped outpouches of pseudodiverticulosis in upper esophageal wall.

Endoscopy showed smooth narrowing of the proximal esophagus and numerous small holes 1-2 mm in diameter. Spraying of Lugol's solution revealed normal coloration of the esophageal mucosa. A biopsy specimen showed marked hyperkeratosis and inflammatory cells without evidence of malignancy.

Intramural pseudodiverticulosis of the esophagus was first described by Mendel et al. in 1960 [1]. The usual presenting symptom is acute or chronic progressive dysphagia. The characteristic radiographic findings are multiple, small, flask-shaped outpouchings in the esophageal wall, similar to Rokitsky-Aschoff sinuses in the gallbladder. The width of an outpouching is 1-5 mm, and the depth is usually greater than the width. The outpouchings communicate with esophageal lumen through narrow flask-shaped necks [2].

Endoscopic findings include strictures (72%), inflammation of the mucosa (59%), and the presence of the diverticular orifices (20%) [3]. Pathologic findings are acute or chronic inflammation and fibrosis [4]. Studies of autopsy specimens have shown that the flask-shaped outpouchings are dilated excretory ducts of the deep submucosal or adnexal glands [4].

Akihiko Arakawa
Tadatoshio Tsuchigame
Toshitada Ohkuma
Mutsumasa Takahashi
Kumamoto University Medical School
Kumamoto City 860, Japan

REFERENCES

1. Mendel K, McKay JM, Tanner CH. Intramural diverticulosis of the esophagus and Rokitsky-Aschoff sinuses in the gallbladder. *Br J Radiol* 1960;33:496-501
2. Chc SR, Sanders MM, Turner MA, et al. Esophageal intramural pseudodiverticulosis. *Gastrointest Radiol* 1981;6:9-16
3. Brühlmann WF, Zollikofer CL, Maranta E, et al. Intramural pseudodiverticulosis of the esophagus: report of seven cases and literature review. *Gastrointest Radiol* 1981;6:199-208
4. Umlas J, Sakhuja R. The pathology of esophageal intramural pseudodiverticulosis. *Am J Clin Pathol* 1976;65:314-320

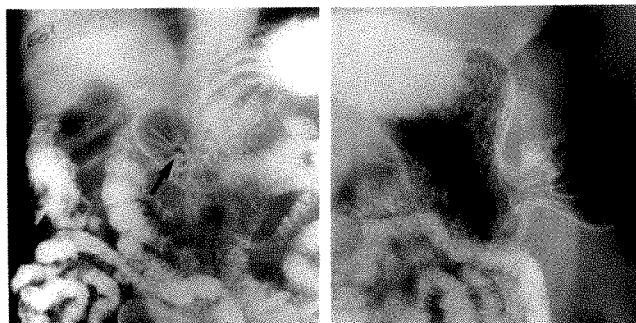
Gastric Involvement in an Epigastric Hernia

An epigastric hernia is a hernia into the abdominal wall above the umbilicus involving the linea alba. It occurs in about 5% of the population and is usually small and asymptomatic. Such a hernia may contain small bowel, omentum, or mesenteric fat, but the presence of other abdominal viscera has been described [1]. Incarceration of a part of the stomach is rare [2, 3].

We saw a 64-year-old obese woman whose chief complaints were severe epigastric pain and vomiting. During the 2 months before admission, abdominal pain, nausea, and vomiting associated with meals had developed. Twenty-two years before, she had had repair of a small umbilical hernia. Physical examination was normal except for a large, painful, nonreducible epigastric mass in the abdominal wall. An upper gastrointestinal series showed that the antrum of the stomach was a hernia in the anterior abdominal wall (Fig. 1). At surgery, an epigastric hernia was found protruding through a 2 x 2 cm opening in the linea alba, containing the midpart of the stomach. The hernia easily was reduced, and the patient's postoperative course was uneventful.

Mobility of the stomach due to ligamentous laxity in the middle-aged or the elderly, particularly multiparous women, may account for the presence of the stomach in the epigastric hernia [3]. The antrum and the distal body are the parts usually herniated because of their greater mobility and proximity to the abdominal wall. Rupture of the stomach may occur if both cardia and pylorus are pulled into the hernial sac, resulting in obstruction.

Francis Serour
Elazar Amsterdam
Shalom Levi
Mayer Krispin
The Edith Wolfson Medical Center
Holon 58100, Israel



A

B

Fig. 1.—Gastric involvement in an epigastric hernia.
A, Anteroposterior radiograph shows neck of gastric hernia (arrow).
B, Lateral radiograph shows antrum.

REFERENCES

1. Ghahremani GG, Meyers MA. Hernias. In: Teplick JG, Haskin ME, eds. *Surgical radiology*, vol. 1. Philadelphia: Saunders, 1981:287-318
2. Johnson CA, Durfresne CR, Bulkley GB. Extraabdominal perforation of gastric ulcer: a complication of incarcerated epigastric hernia. *Am Surg* 1980;46:418-421
3. Bryk D. Gastric involvement in abdominal wall hernias. *Gastrointest Radiol* 1984;9:311-314

Percutaneous Approach to Salvage Failed T-tube Drainage for Malignant Biliary Obstruction

Trans T-tube interventions for malignant biliary obstruction include stenting [1] and trans T-tube catheter drainage [2, 3]. In a case of cholangiocarcinoma, internal biliary drainage was achieved by inserting two catheters through the T-tube tract, one proximally into the left hepatic duct and the other distally into the duodenum. Then both were connected externally to permit internal drainage.

A 74-year-old man first presented in 1986 with obstructive jaundice. Laparotomy at that time showed a stricture of the common hepatic duct. A biopsy of the lesion was done, and a T-tube was inserted. Subsequent histologic studies showed cholangiocarcinoma. Attempted endoscopic stenting failed because of pyloric obstruction, and the patient was left with T-tube drainage.

One year later, drainage via the T-tube progressively decreased, and the patient had three attacks of cholangitis. T-tube cholangiography (Fig. 1A) showed migration of the T-tube with blockage of the distal limb. The stricture had extended proximally, and a sharp kink in the common duct at the point of insertion of the T-tube was present. Another attempt at endoscopic stenting failed because of pyloric obstruction and the distorted anatomy of the common duct. Percutaneous stenting was not attempted because difficulty in negotiating the guidewire through the sharply kinked stricture in the common duct was anticipated.

Internal drainage was achieved as follows: (1) The T-tube tract and the narrowed common duct were negotiated by using a standard 3-mm J guidewire. This was exchanged with a Lunderquist-Ring torque guidewire (Cook, Bloomington, IN). The tract was dilated up to a diameter of 12 French, and a 12-French Silastic tube was inserted. The tip was left in the second part of the duodenum. (2) Another Lunderquist-Ring torque guidewire then was passed through the T-

tube tract and the stricture up into the left hepatic duct. An 8.3-French Ring biliary catheter (Cook) was exchanged with the torque guidewire and positioned in the left hepatic duct. The Ring biliary catheter and the Silastic tube were connected externally. Good biliary drainage was achieved (Fig. 1B). The patient has remained well during a follow-up of 34 weeks. The catheter has been exchanged twice because of blockage by sludge.

C. K. Y. Yip

Joe W. C. Leung

Con Metreweli

Prince of Wales Hospital

Shatin, NT, Hong Kong

REFERENCES

1. Beltran J, Lopez E, Grande J, et al. Placement of biliary endoprosthesis through T-tube tract: case report. *Cardiovasc Intervent Radiol* 1985; 8:106-108
2. McLean GK, Ring EJ, Freiman DB. Therapeutic alternative in treatment of intrahepatic biliary obstruction. *Radiology* 1982;145:289-295
3. Ferrucci JT Jr. Trans T-tube manipulations. In: Ferrucci JT Jr, ed. *Interventional radiology of the abdomen*, 2nd ed. Baltimore: Williams & Wilkins, 1985:345-352

Radiologic Diagnosis of Absent Left Lobe of the Liver

Complete absence of the left lobe of the liver is a rare anomaly. Only a few cases have been reported [1-4], including one case from 19,000 autopsies [1]. The imaging findings in a case that we saw are illustrated.

A 58-year-old woman who was an immigrant from Laos had thyrotoxicosis with mildly elevated levels of serum transaminases. She had no history of abdominal surgery and no stigmata of chronic liver disease. A test for hepatitis B surface antigen was negative; antibodies to core and surface antigens were present. A ^{99m}Tc -sulfur colloid scan did not visualize the left lobe of the liver (Fig. 1). CT showed no hepatic tissue to the left of the gallbladder fossa, confirming the absence of the left lobe.

Before the advent of modern imaging techniques, agenesis of the left lobe of the liver could be diagnosed only at laparotomy or at necropsy. An absent left lobe may be suggested by a U-shaped folding of the stomach, with a high position of the duodenal bulb on an upper gastrointestinal series [2, 4]. Failure to display the falciform

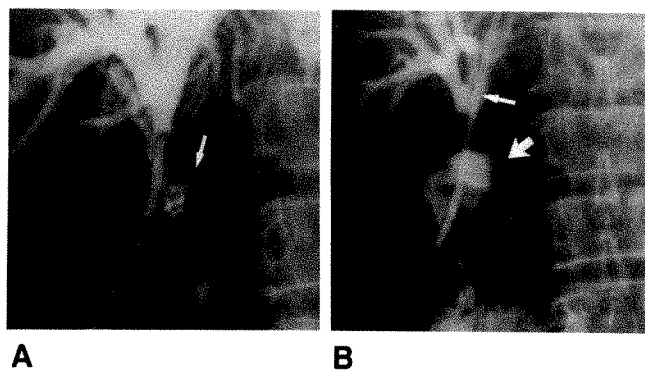


Fig. 1.—A, T-tube tract cholangiogram shows migration of T-tube. Common duct is kinked and narrowed (arrow), and right and left hepatic ducts are dilated.

B, Cholangiogram shows Ring biliary catheter in left hepatic duct (small arrow). Catheter is connected to Silastic tube that has been passed into duodenum (large arrow). Note drainage of contrast material into duodenum.

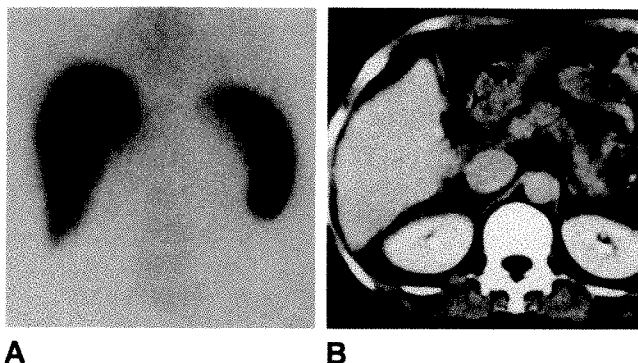


Fig. 1.—Radiologic diagnosis of absent left lobe of the liver.

A, ^{99m}Tc -sulfur colloid scintigram shows a liver with a normal-appearing right lobe but with no uptake over area of left lobe.

B, Contrast-enhanced CT scan shows no liver tissue to left of gallbladder fossa.

ligament or ligamentum teres on sonography supports this diagnosis [2]. The findings on scintigraphy may be misleading [3, 4], but the lack of liver tissue to the left of the gallbladder fossa on CT is considered diagnostic [2]. Reactive hypertrophy of the right and caudate lobes, which has been described in this condition [1, 4], was not present in our patient. Although generally asymptomatic, gastric volvulus has been reported and may not be a simple coincidence [3].

Bhaskar Banerjee

University of Connecticut Health Center
Farmington, CT 06032

David C. Harrison

Hartford Hospital
Hartford, CT 06106

REFERENCES

1. Merrill GG. Complete absence of the left lobe of the liver. *Arch Pathol* 1946;42:232-233
2. Belton RL, VanZandt TF. Congenital absence of the left lobe of the liver: a radiologic diagnosis. *Radiology* 1983;147:184
3. Ahmed AF, Bediako AK, Rai D. Agnesis of the left lobe of the liver with gastric volvulus. *NY State J Med* 1988;88:327-328
4. Yamamoto S, Kojoh K, Saito I, et al. Computer tomography of congenital absence of the left lobe of the liver. *J Comput Assist Tomogr* 1988;12:206-208

The Lateral Ankle Index: Its Usefulness in Detecting Lateral Malleolar Fractures

Injuries to the lateral aspect of the ankle may result in either a lateral ankle sprain or a lateral malleolar fracture. If the major force of the injury is absorbed by the lateral malleolus, a fracture will result. If this force is absorbed by the surrounding soft tissues, more soft-tissue swelling will occur than is seen in the presence of a fracture. By evaluating the presence and amount of posterior soft-tissue swelling on the lateral ankle radiograph and determining the lateral ankle index (LAI), the likelihood of significant osseous injury to the lateral malleolus can be determined.

The plain radiographs of 119 adults with lateral adduction injuries of the ankle were evaluated retrospectively to characterize the amount of soft-tissue swelling found with or without a lateral malleolar fracture. In addition, ankle series of 10 adults with no clinical findings or obvious radiographic signs of trauma were reviewed. The LAI was then formulated. The index is derived by dividing the sagittal length of the distal tibial articulating surface by the distance from the anterior tibial articulating surface to the anterior border of the pre-Achilles fat as shown on the lateral radiograph (Fig. 1). The LAI was determined for each of the 119 patients and for each of the 10 control subjects.

The LAI of patients with a lateral malleolar fracture was 0.71 ± 0.05 (average \pm one standard deviation), which was slightly lower

than the normal control value of 0.72 ± 0.05 . Patients with lateral and posterior soft-tissue swelling without a fracture had a markedly lower LAI of 0.62 ± 0.04 . This is due to the large component of soft-tissue swelling accompanying this injury (Fig. 2). The differences in the LAIs were statistically significant ($p < .0005$) for each of the three groups of patients.

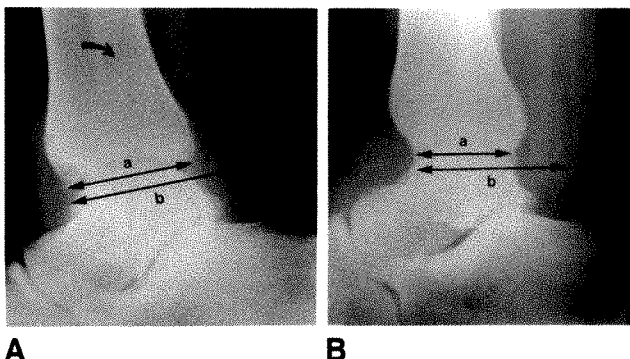


Fig. 2.—A and B, Lateral radiographs show a lateral malleolar fracture (curved arrow, A) and posterior soft-tissue swelling without a fracture (B). LAIs for A and B are 0.72 and 0.62, respectively.

Lateral ankle injuries routinely are diagnosed by plain radiography. The magnitude and direction of the force absorbed during an ankle injury determine the extent of the injury. If the magnitude and direction of the force on the osseous structures are relatively small, the bone will not fracture. The surrounding soft tissues will absorb most of the force, and marked soft-tissue swelling will result. If the force transmitted to the lateral malleolus is great enough, the bone will absorb most of the force and will fracture. The surrounding soft tissues will absorb a small amount of the force, and thus a small amount of soft-tissue swelling will result.

The LAI confirms this hypothesis. Patients with lateral malleolar fractures have a relatively higher LAI (reflecting less soft-tissue swelling) than patients without a fracture, for whom a lower value reflects a larger component of soft-tissue swelling. The soft-tissue swelling seen on the lateral ankle film is located in the peroneal tendon sheath (Fig. 1).

The LAI is a simple measurement that is obtained easily from a lateral ankle radiograph of a patient who has had lateral ankle trauma. A significantly decreased LAI is seen characteristically in patients with marked soft-tissue injury and no fracture, whereas a minimal decrease in the LAI is seen in patients with osseous injury to the lateral malleolus. This index can be used as an aid by the emergency room radiologist in confirming the presence or absence of a lateral malleolar fracture.

Saul Finck

Malcolm D. Jones

University of California, Irvine, Medical Center
Orange, CA 92668

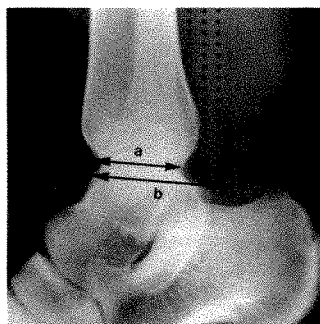


Fig. 1.—Lateral radiograph of a normal ankle. Lateral ankle index (LAI) is defined as a/b . Normal LAI is 0.72 ± 0.05 (average \pm one standard deviation). Asterisks indicate location of peroneal tendon sheath.

Bilateral Distal Tibial Osteonecrosis in Systemic Lupus Erythematosus

Osteonecrosis is the most common disabling orthopedic problem in patients who have systemic lupus erythematosus (SLE). The femoral head or condyle, the humeral head, and the talus are usually the bones involved [1-3]. We describe a woman with SLE in whom disabling osteonecrosis developed in an unusual site: the distal tibiae. The initial radiographic manifestation was metaphyseal periostitis.

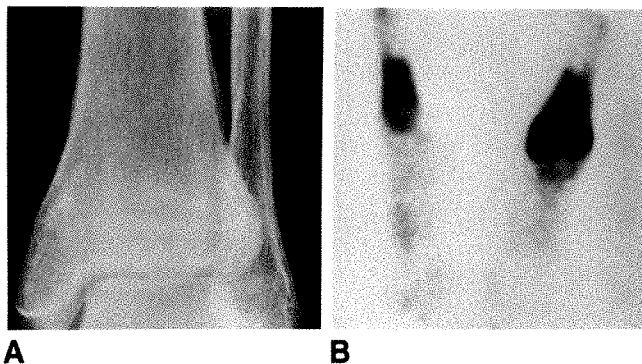


Fig. 1.—Bilateral distal tibial osteonecrosis in a 56-year-old woman with systemic lupus erythematosus.

A, Radiograph of left distal tibia obtained 2 months after onset of symptoms shows periostitis and sclerosis in distal metaphysis.

B, Anterior view of ^{99m}Tc -oxidronate bone scan of ankles shows intense uptake in entire left distal tibia. Increased activity in right distal tibia is less intense and is limited to cortical bone.

A 56-year-old woman who had been taking steroids for 1 year for the treatment of SLE had a gradual onset of progressively worsening bilateral ankle pain. Both ankles were tender, but the tenderness was most marked over the left medial malleolus. Initial radiographs showed bilateral periostitis only. Two months later, radiographs showed sclerosis of the left distal metaphysis (Fig. 1). A bone scan performed 1 month after the onset of symptoms showed intense uptake in the distal tibiae, greater in the left tibia than in the right, reflecting nonspecific increased bone turnover in these areas. Histologic studies after curettage and bone-graft packing of the left distal tibia 6 months later revealed evidence of the reparative phase of osteonecrosis.

This case has unusual features. First, bilateral metaphyseal periostitis only was the first radiographic evidence of osteonecrosis. Tibial periostitis has been reported in several patients with SLE, but it has been thought to be related to vasculitis affecting the periosteum [4]. Second, the distal tibia is an unusual site, although involvement often is not recognized because the findings are nonspecific. Osteonecrosis in SLE has been described in the talus, metatarsals, metacarpals, radial head, and small bones of the hands and feet as well as in the femoral and humeral heads [2, 3]. Resnick et al. [3] and Glickstein et al. [4] have described distal tibial osteonecrosis found in amputation specimens from SLE patients who had severe arterial insufficiency. Our patient had no clinical evidence of vascular insufficiency in her legs; therefore, these infarctions apparently developed as a consequence of steroid therapy and/or the SLE itself.

Eric Outwater

Elizabeth Oates

Robert C. Sarno

Tufts–New England Medical Center
Boston, MA 02111

REFERENCES

- Conklin JJ, Alderson PO, Zizic TM, et al. Comparison of bone scan and radiograph sensitivity in the detection of steroid-induced ischemic necrosis of bone. *Radiology* **1983**;147:221–226
- Klippel JH, Gerber LH, Pollak L, Decker JL. Avascular necrosis in systemic lupus erythematosus: silent symmetric osteonecrosis. *Am J Med* **1979**;67:83–87
- Resnick D, Pineda C, Trudell D. Widespread osteonecrosis of the foot in systemic lupus erythematosus: radiographic and gross pathologic correlation. *Skeletal Radiol* **1985**;13:33–38
- Glickstein M, Neustadter L, Dalinka M, Kricun M. Periosteal reaction in systemic lupus erythematosus. *Skeletal Radiol* **1986**;15:610–612

“Tourniquet Effect” Can Alter Delayed Static Bone Scan

Although release of a tourniquet has been shown to profoundly effect the blood-flow and blood-pool phases of bone scintigraphy in the limb distal to the tourniquet [1–3], abnormally increased regional activity on delayed images has not been attributed to this factor.

To detect asymptomatic skeletal involvement, we performed whole-body skeletal scintigraphy on a 13-month-old infant who had documented visceral histiocytosis. Diffusely increased skeletal activity was seen in the right forearm, wrist, and hand on delayed static bone scintigrams (Fig. 1). Blood-flow and blood-pool images were not obtained. Prolonged application of a tourniquet (15 min) at the right elbow before injection of the radiopharmaceutical was necessary because of a difficult venipuncture. Relatively decreased activity in the first and fifth rays of the right hand may have been related to focal medial and lateral compression of the hand by tape used to secure the hand to an arm board throughout the study period. A radiograph of the right forearm and hand, part of a whole-body skeletal survey, was normal. The infant's extremities remained asymptomatic and follow-up radiographs were normal.

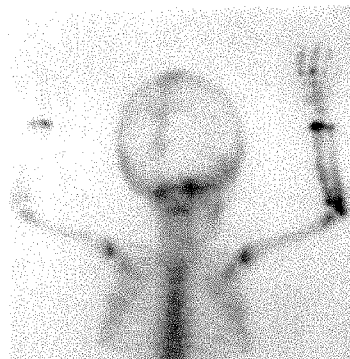


Fig. 1.—Posterior scintigram shows diffusely increased activity in right radius, ulna, and carpal and hand bones.

The tourniquet effect can affect delayed static bone scintigrams, and this explanation should enter into the differential diagnosis of diffusely increased uptake seen in the extremities. Prolonged application of a tourniquet and young age of a patient may be contributing factors.

Joseph A. Orzel

David M. Rosenbaum

Edward Weinberger

University of Washington
Seattle, WA 98195

REFERENCES

- Desai A, Intenzo C. The “tourniquet effect.” *J Nucl Med* **1984**;25:697–699
- Lecklitner ML, Douglas KP. Increased extremity uptake on three-phase bone scans caused by peripherally induced ischemia prior to injection. *J Nucl Med* **1987**;28:108–111
- Kirsh JC, Tepperman PS. Assessment of hand blood flow: a modified technique. *AJR* **1985**;144:781–783

Blood-Fluid Level in Intracerebral Hematoma in an Infant

The CT appearance of multiloculated fluid collections has been described in brain metastasis [1], subdural hematoma [2], and intracerebral hematoma caused by anticoagulation [3]. We report a similar CT finding in an intracerebral hematoma in a neonate who was delivered by forceps.

Fig. 1.—CT scan shows a well-circumscribed, enhancing lesion with a fluid level in left frontoparietal region with no surrounding edema. Another small hematoma is seen in right frontal region.



A 45-day-old, term male infant presented with excessive crying, vomiting, and tense fontanelles of 3 days duration. A lumbar puncture showed blood-stained CSF, and the child deteriorated clinically. The fundi were normal, and no meningeal signs were present. The infant was anemic and had a head circumference of 39 cm and a bulging anterior fontanelle. Hemoglobin was 5 g, WBC was 14,600/ μ l, platelet count was 80,000/ μ l, and clotting times were normal. CT (Fig. 1) showed a left frontoparietal, well-circumscribed, moderately enhancing lesion with a fluid level without surrounding edema and another small hematoma in the right frontal region (caused by previous aspiration through the fontanelle on the right side before the CT scan). Aspiration through the lateral aspect of the anterior fontanelle revealed xanthochromic fluid from the top and blood from the bottom of this cavity. The infant's condition improved after the aspiration but deteriorated later, and he was discharged against medical advice.

Although this finding has no definitive explanation, we hypothesize that the trauma caused by the forceps used during delivery produced the multilayered intracerebral hematoma.

P. Ranganadham

I. Dinakar

Nizam's Institute of Medical Sciences
Panjagutta, Hyderabad 500 482(A.P), India

REFERENCES

1. Kaiser MC, Rodesch G, Capesius P. Blood fluid levels in multiloculated cystic brain metastasis of a hypernephroma. *Neuroradiology* 1983; 25:339-341
2. Finelli PF. Multiloculated fluid blood level with subdural hematoma. *Ann Neurol* 1985;17:103
3. Livoni JP, McGahan JP. Intracranial fluid blood levels in the anticoagulated patient. *Neuroradiology* 1983;25:335-337

Hysterosalpingography: Prone and Supine

Hysterosalpingography is a technique that tends to fall somewhere between the radiology and gynecology departments, and possibly it has not been developed as it might have been because of this. We report an improvement in the technique using a standard radiologic maneuver that not only makes the procedure more comfortable for the patient but also appears to enhance its diagnostic and therapeutic potential.

At our hospital, most hysterosalpingography is carried out by a radiologist. It is an outpatient procedure, and no sedation or analgesia is used. Because the patient is alert and cooperative, she is able to move freely during the procedure. While seeking better visualization of the uterine cavity in its entirety, as well as of the fallopian tubes, we found that having the patient lie in the oblique and lateral positions was helpful. Then we started having the patient turn prone and, to our surprise, found that tubal filling sometimes occurred either spontaneously from the medium already within the uterine cavity or from further injection via the Leech-Wilkinson cannula. This happened in tubes that, despite considerable pressure, we had failed to fill when the patient was lying supine. Furthermore, less pressure was required to produce good tubal filling and free peritoneal spill, so the tendency to leak was less, and the procedure was more comfortable for the patient.

This apparent "unblocking" of tubes caused by having the patient turn to the prone position is the subject of a further communication in which we shall report the high pregnancy rate attributable to hysterosalpingography. Because laparoscopy and instillation of dye can be carried out only with the (anesthetized) patient supine, hysterosalpingography should remain the prime initial investigation in the investigation of the infertile patient (both primary and secondary).

Tubal blockage cannot be presumed from injections carried out when the patient is supine, despite unpleasantly high intrauterine pressures. By having the patient turn to the prone position, bilateral filling can be achieved with readily tolerated intrauterine pressures while at the same time producing a therapeutic as well as diagnostic result. Because of the remarkable and rapid filling achievable by turning the patient, we suggest that the notion of tubal spasm be replaced by the concept of tubal kinking.

Alan E. Hugh

Henry Y. Huang

North Staffordshire Royal Infirmary
Hartshill, Stoke-on-Trent, United Kingdom ST4 7LN

Letters are published at the discretion of the Editor and are subject to editing.

Letters to the Editor must not be more than two double-spaced, typewritten pages. One or two figures may be included. Abbreviations should not be used. See Author Guidelines, page A5.

Material being submitted or published elsewhere should not be duplicated in letters, and authors of letters must disclose financial associations or other possible conflicts of interest.

Letters concerning a paper published in the *AJR* will be sent to the authors of the paper for a reply to be published in the same issue. Opinions expressed in the Letters to the Editor do not necessarily reflect the opinions of the Editor.

Review of Current Literature

Initials and addresses of corresponding authors are provided in parentheses for each article so that the reader can obtain reprints directly. Abstracts are printed verbatim from each journal.

The New England Journal of Medicine

Effects of adjuvant tamoxifen and of cytotoxic therapy on mortality in early breast cancer: an overview of 61 randomized trials among 28,896 women. Early Breast Cancer Trialists' Collaborative Group (EBCTCG Secretariat, ICRF-MRC Clinical Trial Service Unit, Radcliffe Infirmary, Nuffield Dept. of Clinical Medicine, Oxford, OX2 6HE, United Kingdom). *N Engl J Med* 319(26):1681-1692, Dec. 1988

We sought information worldwide on mortality according to assigned treatment in all randomized trials that began before 1985 of adjuvant tamoxifen or cytotoxic therapy for early breast cancer (with or without regional lymph-node involvement). Coverage was reasonably complete for most countries. In 28 trials of tamoxifen nearly 4000 of 16,513 women had died, and in 40 chemotherapy trials slightly more than 4000 of 13,442 women had died. The 8106 deaths were approximately evenly distributed over years 1, 2, 3, 4, and 5+ of follow-up, with little useful information beyond year 5.

Systematic overviews of the results of these trials demonstrated reductions in mortality due to treatment that were significant when tamoxifen was compared with no tamoxifen ($P < 0.0001$), any chemotherapy with no chemotherapy ($P = 0.003$), and polychemotherapy with single-agent chemotherapy ($P = 0.001$). In tamoxifen trials, there was a clear reduction in mortality only among women 50 or older, for whom assignment to tamoxifen reduced the annual odds of death during the first five years by about one fifth. In chemotherapy trials there was a clear reduction only among women under 50, for whom assignment to polychemotherapy reduced the annual odds of death during the first five years by about one quarter. Direct comparisons showed that combination chemotherapy was significantly more effective than single-agent therapy, but suggested that administration of chemotherapy for 8 to 24 months may offer no survival advantage over administration of the same chemotherapy for 4 to 6 months.

Because it involved several thousand women, this overview was able to demonstrate particularly clearly that both tamoxifen and cytotoxic therapy can reduce five-year mortality.

Diminished rates of bone formation in normal black adults. Weinstein RS, Bell NH (RSW, Metabolic Bone Disease Laboratory, Medical College of Georgia, Dept. of Medicine, Rm. BD-248, Augusta, GA 30912). *N Engl J Med* 319(26):1698-1701, Dec. 1988

Blacks have a greater bone mass and a lower incidence of osteoporosis and hip fractures than whites. We performed biopsies of the iliac crest in 12 blacks (6 men and 6 women) and 13 whites (8 men and 5 women) who were matched for age (range, 19 to 46 years) and weight, to determine whether histomorphometric differences between blacks and whites could be identified.

The static measurements of cortical and cancellous bone architecture were not significantly different in the two groups. In contrast, the dynamic measurements, determined with tetracycline markers, showed that the mean rate of bone formation in the blacks was only 35 percent of that in the whites ($P < 0.001$).

We conclude that the rate of bone turnover is lower in blacks than in whites, since bone resorption and bone formation are closely coupled in the steady state. If reconstitution of previously resorbed cavities at remodeling sites is incomplete in osteoporosis, a reduction in the rate of skeletal remodeling could provide a means for maintaining and preserving bone mass in blacks.

Chest

Magnetic resonance for evaluation of the thorax. Fisher MR (MRF, Hospital of the Good Samaritan, University of Southern California, Los Angeles, CA). *Chest* 95:166-173, 1989

Evaluation of diseases in the chest by MR is continually evolving. Early studies showed the potential of the technique for imaging the mediastinal and hilar structures and for demonstrating the normal anatomy of the thorax on sagittal, coronal, and transverse MR images. As more data have been compiled, investigators have compared MR to computed tomography for its ability to assess mediastinal and hilar adenopathy and masses, bronchogenic carcinoma and other pulmonary parenchyma lesions, and for assessment of the pulmonary vascularity. MR has been shown in these situations generally to provide equivalent information to that provided by computed tomography. MR, compared to computed tomography, is still in its infancy in regard to the length of time of its availability and in relation to the MR technology for obtaining images. MR is a technique that has wide variation as to type of image quality obtained depending upon the MR system utilized and the pulse sequence utilized. Because of the diverse nature of potential variables for imaging, many times the images are not equal in quality. As a consequence of this significant variability, the data in the literature are divergent on the precise utility of MR. Although the recommended use of MR may change rapidly, the current feeling is that MR should be used as a procedure complementary to computed tomography in those patients with allergy to iodinated contrast material and to aid in defining equivocal lesions as seen on computed tomography, such as small central hilar bronchogenic carcinomas.

Surgery

Minimally invasive devascularization for variceal bleeding that could not be controlled with sclerotherapy. Berman HL, DelGuercio LRM, Katz SG, Hodgson WJ, Savino JA (HLB, Dept. of Radiology, New York Medical College, Valhalla, NY 10595). *Surgery* 104:500-506, 1988

The appropriate therapy for continued bleeding despite sclerotherapy, remains controversial. This study evaluates a devascularization procedure performed without the risks of major surgery and general anesthesia. Fifty consecutive patients, each with an endoscopically proven variceal hemorrhage that was uncontrollable with sclerotherapy, were treated with minimally invasive devascularization. The procedure was performed in three stages. First, the portal pressure was sharply reduced by angiographic embolization of the midsplenic artery. Then the esophagogastric variceal network was thrombosed by means of a catheter introduced during laparotomy, which created a portoazygos disconnection. Finally, the left gastric and left gastroepiploic arteries were embolized, which completed devascularization of the proximal stomach. According to the Child classification, 16 patients were in class B and 34 were in class C. All Child's class B patients (16/16) and 71% (24/34) of Child's class C patients survived hospitalization. One-year survival was 94% (15/16) for Child's class B and 62% (21/34) for Child's class C patients. Rebleeding occurred in 63% (25/40) of the discharged patients but caused the death of only seven. In conclusion, the 20% initial hospital mortality for these difficult patients was significantly better than that reported for emergency surgery, and the rate of rebleeding was comparable to that seen with other nonshunting therapies.

Gastroenterology

Efficacy and safety of a combination of chenodeoxycholic acid and ursodeoxycholic acid for gallstone dissolution: a comparison with ursodeoxycholic acid alone. Podda M, Zuin M, Battezzati PM, Ghezzi C, De Fazio C, Dioguardi ML (MP, Cattedra di Semeiotica Medica, Universita di Palermo, Palermo, Italy). *Gastroenterology* 96:222-229, 1989

Chenodeoxycholic acid (CDC) and ursodeoxycholic acid (UDC) have distinct physicochemical and metabolic properties which, being complementary, should favor more rapid removal of cholesterol from gallstones when both bile acids are administered together. To see if the combination is more effective and well tolerated, we have compared 5 mg/kg of CDC plus 5 mg/kg of UDC with a 10-mg/kg dose of UDC alone in 120 patients with radiolucent, sonographically confirmed gallstones and characteristics favoring complete dissolution. Ursodeoxycholic acid was chosen as the reference because it dissolves stones faster and is better tolerated than CDC. To minimize the influence of stone size, the major determinant of dissolution, patients were divided, on admission, into two groups according to the maximum stone diameter: 50 had stones ≤ 5 mm, 70 had stones > 5 mm but < 15 mm. The effects of treatment on stone dissolution evaluated by cholecystography and ultrasonography at 6, 12, and 24 mo, were analyzed by the actuarial life-table method. In the group with smaller stones, significantly more patients had obtained complete dissolution after treatment with the combination (52%) than after treatment with UDC alone (24%) at 6 mo. After longer periods, results were still better with the combination, although the differences from UDC alone became smaller. In the patients with larger stones, rates of complete and partial dissolutions were higher after treatment with the combination (51% vs. 24% with UDC) at 6 mo and again the differences had become smaller after longer treatment. Although not statistically significant, stone calcification occurred more often with UDC (7 cases) than with the combination (1 case). We conclude that CDC plus UDC is preferable to UDC alone because it dissolves stones more quickly, with a lower incidence of stone calcification, and may result in reduced cost of treatment.

Reprinted with permission by the American Gastroenterological Association.

Fragmentation of bile duct stones by extracorporeal shock waves: a new approach to biliary calculi after failure of routine endoscopic measures. Sauerbruch T, Stern M, Study Group for Shock-Wave Lithotripsy of Bile Duct Stones (no reprint address available). *Gastroenterology* 96:146-152, 1989

A prospective uncontrolled multicenter trial was performed on 113 patients with bile duct stones in whom routine endoscopic approaches for removal of the calculi had failed. These represented 8.3% of the patients referred to the participating centers for endoscopic extraction of the stones. Extracorporeal shock-wave lithotripsy using the Dornier kidney lithotripter achieved stone disintegration in 103 patients (91%). Complete stone clearance from the bile ducts was obtained in 97 patients (86%) after a median of 4 days following extracorporeal shock-wave lithotripsy. Adverse effects, mostly mild, occurred in 36% of the patients. A 30-day mortality rate of 0.9% (in-hospital mortality rate = 1.8%) of this high-risk group with a mean age of 72 yr and a cholangitis rate of 26% compared favorably with the data given for open surgery. We therefore consider extracorporeal shock-wave lithotripsy a useful method for the treatment of bile duct stones not amenable to routine endoscopic measures.

Reprinted with permission by the American Gastroenterological Association.

Digestive Diseases and Sciences

Effect of body posture on radionuclide measurements of gastric emptying. Moore JG, Datz FL, Christian PE, Greenberg E, Alazraki N (JGM, VA Medical Center/111G, 500 Foothill Blvd., Salt Lake City, UT 84148). *Dig Dis Sci* 33(12):1592-1595, Dec. 1988

The purpose of this investigation was to compare the effect of body posture on gastric emptying measurements of radiolabeled meals. Eight healthy male subjects were studied on four separate days. During each study subjects were fed a standardized meal of beef stew labeled with technetium-99m sulfur colloid, and orange juice. Measurements of solid-phase gastric emptying rates were obtained by a gamma camera. Subjects were studied in the lying, sitting, standing, or combined sitting-standing postures. The results demonstrated that the lying position significantly slowed gastric emptying compared to all other positions. Conversely, a decrease in emptying times of 51% and 35% occurred in the combined sitting-standing position compared to the lying and sitting position. These results support a marked effect of body posture on the radionuclide measurement of gastric emptying.

Upper gastrointestinal tract dysfunction in bulimia. Cuellar RE, Kaye WH, Hsu LKG, Van Thiel DH (DHVT, University of Pittsburgh School of Medicine, Dept. of Medicine, 1000 G Scaife Hall, Pittsburgh, PA 15261). *Dig Dis Sci* 33(12):1549-1553, Dec. 1988

Bulimia nervosa is a health problem of increasing magnitude that is estimated to affect 2-5% of the American adolescent and young adult female population. Because of the magnitude of this clinical problem and because of the importance of the upper gastrointestinal tract in its expression, an intradepartmental program of health care for patients affected with the disease was initiated. Eleven consecutive symptomatic bulimic individuals have been evaluated jointly by the gastroenterology and the psychiatry departments of the University of Pittsburgh. Five of these 11 individuals were found to have clinically important upper gastrointestinal pathology including ulcerative esophagitis, erosive gastritis, duodenal ulcer, and delayed gastric emptying. These gastrointestinal conditions could have been either a result of or have contributed to the symptomatology of these five patients. These data suggest that bulimic subjects have clinically important gastroenterological disease processes that require specific diagnosis and treatment independent of the psychiatric treatment provided for the bulimic condition.

The Journal of Bone and Joint Surgery

The forty-five-degree posteroanterior flexion weight-bearing radiograph of the knee. Rosenberg TD, Paulos LE, Parker RD, Coward DB, Scott SM (RDP, Mount Sinai Medical Center, 1 Mount Sinai Dr., Cleveland, OH 44106). *J Bone Joint Surg [Am]* 70-A(10):1479-1483, Dec. 1988

Posteroanterior weight-bearing radiographs, made with the knee in 45 degrees of flexion, were compared with conventional radiographs for fifty-five patients who had surgical treatment for a lesion causing pain in one knee. Narrowing of the cartilage space of two millimeters or more was defined as indicative of major degeneration (grade III or IV). Comparison of the intraoperatively observed degeneration with the narrowing that was seen on the radiographs revealed that the posteroanterior weight-bearing radiographs that were made with the knee in 45 degrees of flexion were more accurate ($p < 0.01$), more specific (no false-positives) ($p < 0.01$), and more sensitive (fewer false-negatives) than the conventional extension weight-bearing anteroposterior radiographs.

Clinical Orthopaedics and Related Research

Giant-cell tumor of bone with pulmonary metastases: six case reports and a review of the literature. Bertoni F, Present D, Sudanese A, Baldini N, Bacchini P, Campanacci M (MC, Dept. of Orthopaedic Oncology, Istituto Ortopedico Rizzoli, Via Codivilla 9, I-40136 Bologna, Italy). *Clin Orthop* 237:275-285, Dec. 1988

Giant-cell tumor of bone rarely metastasizes to the lung. In three of six cases, lesions in lung tissue were histologically benign. In 39 such cases reported in the literature, the treatments were surgical extirpation, chemotherapy, and radiation therapy. Resection was indicated to definitely diagnose the pulmonary lesions as benign giant-cell tumors. Radiation therapy and/or chemotherapy may be beneficial as adjuvant treatment, especially where the lesions are anatomically inaccessible. Some pulmonary lesions spontaneously regress even in the absence of definitive treatment.

The Journal of Urology

The excretory urogram bowel preparation—is it necessary? Roberge-Wade AP, Hosking DH, MacEwan DW, Ramsey EW (APR-W, Dept. of Surgery, Health Sciences Centre, Winnipeg, Manitoba, Canada). *J Urol* 140:1473-1474, Dec. 1988

A prospective randomized study was undertaken to determine whether prior bowel preparation improves the diagnostic quality of the excretory urogram. From August 1986 to May 1987, 107 outpatients having an excretory urogram on an elective basis were randomized into 3 groups; group 1 received castor oil, group 2 received x-ray preparation and group 3 received clear fluids 24 hours before the study. The quality of the bowel preparation and the excretory urogram was graded separately on a scale of 1 to 5. More than 71 per cent of the bowel preparations were graded as 4 (very good) or 5 (excellent) and more than 91 per cent of the films were graded as 4 or 5 in all 3 groups. The quality of the excretory urogram was graded as 5/5 in a greater number of group 3 cases. Patients reported a high incidence of side effects from both bowel preparations, while no adverse effects were reported from those in group 3. The administration of a bowel preparation compared to that of clear fluids alone made no difference to either the quality of the bowel preparation or the diagnostic quality of the film.

British Journal of Urology

Urethral strictures in childhood. Frank JD, Pocock RD, Stower MJ (JDF, Dept. of Paediatric Surgery, Bristol Royal Hospital for Sick

Children, St. Michael's Hill, Bristol BS2 8BJ, United Kingdom). *Br J Urol* 62:590-592, Dec. 1988

Thirty-six children have been treated for a non-hypospadiac urethral stricture. Of 12 patients with meatal or submeatal stenosis, 10 had undergone circumcision for balanitis xerotica obliterans. The strictures were successfully treated by meatoplasty or meatal dilatation. Twenty-four children had a more proximal urethral stricture: 16 were caused by urethral catheterisation, 4 were post-traumatic, 2 were congenital and 2 were idiopathic. Sixteen children were treated by visual urethrotomy; this was successful in 12 after a maximum of 2 urethrotomies. Two children required 4 or more urethrotomies and 2 required urethroplasty for restricting. Seven children were treated by a formal urethroplasty. There were no complications. Two patients died of unrelated medical conditions. Follow-up was for a mean of 2 years.

Pediatrics

Morbidity for survivors of extracorporeal membrane oxygenation: neurodevelopmental outcome at 1 year of age. Glass P, Miller M, Short B (BLS, ECMO Program, Children's Hospital National Medical Center, 111 Michigan Ave. N.W., Washington, DC 20010). *Pediatrics* 83(1):72-78, Jan. 1989

Extracorporeal membrane oxygenation is an important technology in the treatment of high-risk infants whose long-term outcome is being followed prospectively at our institution. The extracorporeal membrane oxygenation procedure allows temporary cardiopulmonary support for critically ill full-term neonates who are refractory to maximum ventilatory and medical management as a consequence of severe persistent pulmonary hypertension. The technique necessitates both the permanent ligation of the right common carotid artery and jugular vein and systemic heparinization. The survivors constitute a unique group of high-risk infants, from the standpoint of the hypoxic-ischemic insults preceding extracorporeal membrane oxygenation and the risks associated with the procedure. Our results indicate that most of our survivors are developing normally at 1 year. Major morbidity, in terms of either significant developmental delay (Bayley mental and motor indices less than 70) or significant neuromotor abnormality, occurred in only 10% of these infants. Poor outcome was associated with major intracranial hemorrhage and chronic lung disease. Ligation of the right carotid artery and jugular vein was not associated with a consistent lateralizing lesion. Long-term follow-up through school age is essential.

Reprinted by permission PEDIATRICS © 1989.

The Journal of Pediatrics

Acute extrapyramidal syndrome in methylmalonic acidemia: "metabolic stroke" involving the globus pallidus. Heidenreich R, Natowicz M, Hainline BE, et al. (G. T. Berry, Division of Biochemical Development and Molecular Diseases, Children's Hospital of Philadelphia, 1 Children's Center, 34th St. and Civic Center Blvd., Philadelphia, PA 19104). *J Pediatr* 113:1022-1027, Dec. 1988

We report four patients with methylmalonic acidemia who developed acute extrapyramidal disease after metabolic decompensation. The neurologic findings resulted from bilateral destruction of the globus pallidus with variable involvement of the internal capsules. This complication was unrelated to a specific gene defect responsible for methylmalonic acidemia or to cyanocobalamin administration. These lesions constitute a "metabolic stroke," probably because of the accumulation of toxic organic acid metabolites, because they cannot be accounted for by hypoxemia or vascular insufficiency.

Significance of opacification of the maxillary and ethmoid sinuses in infants. Glasier CM, Mallory GB Jr, Steele RW (CMG, Dept. of Radiology, Arkansas Children's Hospital, 800 Marshall St., Little, AR 72202). *J Pediatr* 114:45-50, Jan. 1989

To evaluate the incidence and significance of radiographic sinus opacification in infants, we performed computed tomography (CT) of the maxillary and ethmoid sinuses in conjunction with routine cranial CT in 100 infants from birth to 12 months of age. CT was performed for indications other than sinusitis. Prospective concurrent clinical history was obtained and physical examination of the upper respiratory tract was performed. Of 100 infants, 16 had hypoplasia of the maxillary sinuses; 81% (13/16) of these were less than 2 months of age. The antra showed progressive increase in size during the first year of life. Of the 100 infants, 70 had CT sinus opacification, including 67% of those without historical or physical evidence of upper respiratory tract infection. There was a positive correlation of CT findings between the maxillary and ethmoid sinuses in 80% of the infants older than 2 months of age but in only 49% of the younger infants. Radiographic sinus opacification in infants is of uncertain significance and is not diagnostic of upper respiratory tract infection, much less of sinusitis.

Outcome after posthemorrhagic ventriculomegaly in comparison with mild hemorrhage without ventriculomegaly. Shankaran S, Koepke T, Woldt E, et al. (SS, Children's Hospital of Michigan, 3901 Beaubien Blvd., Detroit, MI 48201). *J Pediatr* 114:109-114, Jan. 1989

The neurodevelopmental sequelae in 33 low birth weight neonates with moderate or severe hemorrhage and ventriculomegaly (VM group) and in 39 neonates with mild hemorrhage only (non-VM group) were evaluated prospectively. Both groups were comparable in birth weight, gestational age, and socioeconomic status. Ventriculoperitoneal shunts were inserted in 23 of the 33 VM group infants at a mean age of 26 days. Eighty-two shunt revisions were performed, for obstruction (71 revisions) or infection (11 revisions), in 18 of the 23 children. At a mean age of 50 months, 19 of 33 children in the VM group had sequelae; 14 children had moderate or severe neurologic deficits, and 5 children had mild sequelae. In the non-VM group, only 3 of 39 children had deficits, all of which were mild ($p < 0.05$). In the VM group, 19 of 33 children had mental developmental delay in comparison with 8 of 39 in the non-VM group ($p < 0.05$), and 17 of 33 children in the VM group had motor developmental delay in comparison with 5 of 39 in the non-VM group ($p < 0.01$). Within the VM group, the number of children with neurodevelopmental sequelae did not differ significantly among the 23 children with shunts, in comparison with the 10 who did not require shunting. Among the children with shunts, a higher incidence of sequelae occurred when lack of ventricular decompression was noted immediately after shunt insertion ($p < 0.005$) and when shunt infections occurred ($p < 0.01$). The most important predictor of mental and motor outcome in the group with shunts was lack of ventricular decompression immediately after shunt insertion. We speculate that, in some infants, loss of brain tissue, cerebral atrophy, or both may occur before insertion of the ventriculoperitoneal shunt, even when the shunt is inserted early.

Pelvic inflammatory disease in adolescents. Golden N, Neuhoof S, Cohen H (NG, Dept. of Pediatrics, Division of Adolescent Medicine, The Brookdale Hospital Medical Center, Linden Blvd. at Brookdale Plaza, Brooklyn, NY 11212). *J Pediatr* 114:138-143, Jan. 1989

Clinical, laboratory, and sonographic data were collected prospectively from 100 female adolescents hospitalized with acute pelvic inflammatory disease (PID). The endocervical isolation rates for *Chlamydia trachomatis* and *Neisseria gonorrhoeae* were 44.7% and 36.4%, respectively. In comparison with adolescents with chlamydia-associated PID, those with gonococcus-associated PID had a shorter duration of pain before admission ($p < 0.05$), higher mean maximum temperatures ($p < 0.01$), and higher leukocyte counts ($p < 0.01$). Pelvic ultrasound studies showed adnexal enlargement or tubo-ovarian abscess (TOA) in 85.2% of the patients. Of the 88 adolescents in whom adequate sonograms were obtained, 17 (19.3%) had TOA. In 12 of the 17 adolescents, the abscesses were identified sonographically before being diagnosed clinically. With clinical criteria alone,

only the leukocyte count and prior history of PID differed significantly between those with TOA and those with uncomplicated PID. These findings support a more liberal use of pelvic ultrasound studies in teenagers with PID. Our high detection rate of *C. trachomatis* and the difficulty in predicting the cause of the infection in an individual patient support treating all adolescents with PID with agents effective against both *C. trachomatis* and *N. gonorrhoeae*.

Journal of Thoracic Imaging

Misconceptions regarding the pathogenicity of silicas and silicates. Feigin DS (DSF, Dept. of Radiology (V-114), University of California, San Diego, La Jolla, CA 92093). *J Thorac Imaging* 4(1):68-80, Jan. 1989

Several inhaled substances, from occupational or other environmental exposure, produce significant pulmonary disease and abnormalities demonstrated by pulmonary imaging. Areas of controversy and misconception relate principally to the extent and nature of both the clinical disease and the imaging abnormalities specific to each substance. The size and shape of the inhaled particles is an important determinant of the nature and severity of the disease produced, with fibrous shapes usually being the most pathogenetic. Fibrogenicity is another important pathogenetic characteristic of talc and kaolin, as well as asbestos. Talc produces four distinct forms of pulmonary disease, depending not only on the other substances with which it is inhaled, but also whether it is inhaled or injected intravenously. When inhaled alone, talc does not appear to produce significant pulmonary fibrosis or malignancy. Kaolin, mica, fuller's earth, zeolite, and fiber-glass all vary in disease production according to their shape and fibrogenicity. Silica, diatomaceous earth, and other forms of silica are all highly fibrogenic and thus produce clinically obvious disease with sufficient inhalation. The largest particles usually produce nodular patterns in the upper pulmonary fields, as is typical of silicosis. The fibrous particles are more likely to manifest themselves as interstitial patterns in the lower pulmonary fields.

Computed tomography in the diagnosis of asbestos-related thoracic disease. Gamsu G, Aberle DR, Lynch D (GG, Dept. of Radiology, Box 0628, University of California, San Francisco, San Francisco, CA 94143-0628). *J Thorac Imaging* 4(1):61-67, Jan. 1989

High-resolution computed tomography (HRCT) has improved the radiologist's ability to detect and potentially quantify the abnormalities of asbestos exposure. It has proved to be more sensitive than chest radiography for detecting pleural plaques and for discriminating between pleural fibrosis and extrapleural fat. HRCT is also more sensitive than chest radiography or conventional CT for detecting parenchymal abnormalities in asbestos-exposed persons. The HRCT findings that correlate with other parameters of asbestosis include (1) septal and centrilobular thickening, (2) parenchymal fibrous bands, (3) honeycomb patterns, (4) subpleural density persisting in the prone position, and (5) subpleural curvilinear lines that persist in the prone position. CT has an important role in evaluating benign and malignant lung and pleural masses in asbestosis.

Gastrointestinal Radiology

Grey Turner's sign and Cullen's sign in acute pancreatitis. Meyers MA, Feldberg MAM, Oliphant M (MAM, Dept. of Radiology, School of Medicine, Health Sciences Center, State University of New York at Stony Brook, Stony Brook, NY 11794). *Gastrointest Radiol* 14:31-37, 1989

Four patients with acute pancreatitis presenting with Grey Turner's sign or Cullen's sign have been studied by computed tomography (CT). These observations help confirm the precise anatomic pathways by which the extravasated pancreatic enzymes and their effects lead to these cutaneous discolorations.

Grey Turner's sign is produced by spread from the anterior pararenal space to between the two leaves of the posterior renal fascia and subsequently to the lateral edge of the quadratus lumborum muscle. Communication may be established to the posterior pararenal space and to the structures of the flank wall. The lumbar triangle, a site of anatomic weakness on the flank wall, may serve as a structural predisposition.

Cullen's sign can be seen to be secondary to the tracking of liberated pancreatic enzymes to the anterior abdominal wall from the inflamed gastrohepatic ligament and across the falciform ligament. Another more direct pathway may be extension from inflammatory changes of the small mesentery or greater omentum to the round ligament, and then to peritoneal fat deep to the umbilicus.

Pneumatosis coli: is there a relationship with sigmoid colon redundancy? Moote DJ, Fried LA, LeBrun GP, Fraser DB (GPL, Dept. of Radiology, Victoria General Hospital, 1278 Tower Rd., Halifax, N.S. B3H 2Y9, Canada). *Gastrointest Radiol* 14:79-82, 1989

Pneumatosis coli (PC) is a process characterized by gas-filled cysts in the wall of the large intestine. The barium enema examinations of 14 patients with idiopathic PC were assessed: 93% involved the sigmoid colon, and 84% of patients with sigmoid pneumatosis had sigmoid colon redundancy in comparison to 14% of the control population ($p < 0.001$). It is proposed that the sigmoid cysts result in redundancy by affecting the mesentery and colon length. This redundancy may account for the increased risk of sigmoid volvulus in this condition.

Radiographic and manometric correlation in achalasia with apparent relaxation of the lower esophageal sphincter. Ott DJ, Richter JE, Chen YM, Wu WC, Gelfand DW, Castell DO (DJO, Dept. of Radiology, Bowman Gray School of Medicine, Winston-Salem, NC 27103). *Gastrointest Radiol* 14:1-5, 1989

We compared the clinical, radiographic, and manometric findings in 10 patients with atypical achalasia showing complete lower esophageal sphincter (LES) relaxation to 39 patients with classic achalasia (i.e., incomplete LES relaxation). Those with atypical achalasia were younger (46.1 vs 60.6 years), had dysphagia of shorter duration (18.7 vs 45.7 mos), had lost less weight (8.2 vs 21.5 lbs), and had less esophageal dilatation (2.8 vs 3.9 cm). However, the mean LES pressures (34.5 vs 37.7 mmHg) and the esophagogastric junction calibers (4.5 vs 4.8 mm) were similar. Radionuclide esophageal emptying studies were done in 15 patients (6 with atypical achalasia; 9 with classic achalasia) and were abnormal in all. Most patients in both groups (90 and 92%) responded well to pneumatic dilatation. We conclude that achalasia with apparent LES relaxation may represent an early form of this motor disorder and that the radiographic findings remain characteristic except for less dilatation of the esophagus.

Pediatric Radiology

Pediatric AIDS: neuroradiologic and neurodevelopmental findings. Price DB, Inglese CM, Haller JO, et al. (DBP, Dept. of Radiology, Box 1208, 450 Clarkson Ave., Brooklyn, NY 11203). *Pediatr Radiol* 18:445-558, 1988

A group of 23 pediatric patients seropositive for HIV antibody were studied by computed tomography and evaluated neurodevelopmentally. Significant neurodevelopmental delays were found in over 95% of the patients studied. CT findings in six patients were normal and thirteen of 23 (57%) had prominence of the CSF spaces. Less frequent findings included calcifications in the basal ganglia and white matter. Cerebral mass lesions included one case of lymphoma and one case of hemorrhage. The CT findings in the pediatric age group

differs from the adult population in that contrast enhancing inflammatory mass lesions are uncommon.

Imaging evaluation of infants with neuroblastoma detected by VMA screening spot test. Fujioka M, Saiki N, Aihara T, Yamamoto K (MF, Dept. of Radiology, Dokkyo University School of Medicine, Mibu, Shimotsuga, Tochigi, Japan). *Pediatr Radiol* 18:479-482, 1988

In the Saitama prefecture in Japan, VMA (vanillyl mandelic acid) screening spot test for detection of neuroblastoma has been performed in 173,046 infants in the years 1981-1986 and 15 infants were found to have neuroblastoma. Two infants had mediastinal tumors and the remainder 13 had intraabdominal tumors. Only 7 infants had palpable masses. Although CT was documented to be the best imaging procedure to provide sufficient information for treatment, conventional radiographic examinations of the chest and abdomen, and abdominal ultrasonography were able, as initial imaging procedures, to detect reasonably small neuroblastomas in infants with a positive VMA screening test.

Journal of Ultrasound in Medicine

Prediction of cesarean section scars with ultrasound imaging during pregnancy. Lonky NM, Worthen N, Ross MG (NML, 1188 N. Euclid St., Anaheim, CA 92801). *J Ultrasound Med* 8:15-19, Jan. 1989

We sought to determine whether a sonographic examination could identify uterine scars in patients with a history of previous cesarean section and further distinguish patients having previous low transverse from vertical uterine incisions. Forty-six antenatal obstetrical patients with a history of prior cesarean section(s) and 30 control patients without prior uterine surgery underwent sonogram examinations to identify the scar. The researcher who later reviewed the sonogram was blinded as to the presence or type of uterine scar. Of the 47 scars examined, uterine scars were visualized in 13 (27.7%). All scars seen were low transverse; no vertical scars were identified by sonography ($p < .05$). No scars were visualized with sonography in the control group and cesarean section scars were seen more easily prior to the third trimester. No information concerning the scar condition (dehiscence) could be obtained with sonography. We conclude it is of benefit to perform sonogram exams in patients with prior cesarean sections of unknown incision to better counsel them as to their risk to rupture. Although vertical cesarean section scars could not be visualized, those patients who had low transverse scars identified could be included in a low-risk vaginal birth population.

Reprinted with permission by the American Institute of Ultrasound in Medicine.

Magnetic Resonance Imaging

Magnetic resonance imaging of the menstrual cycle. Janus CL, Wiczak HP, Laufer N (CLJ, P.O. Box 2247, Charlottesville, VA 22902). *Magn Reson Imaging* 6(6):669-674, Nov./Dec. 1988

This study examines the ability of magnetic resonance imaging (MRI) to monitor follicular and endometrial development during the menstrual cycle. MR scans, sonograms and hormonal levels of estradiol (E_2) and progesterone (P) obtained from five ovulatory volunteers were evaluated on approximately days 4, 8, 12, 16, 20 and 24 of the cycle. MRI reliably demonstrated folliculogenesis in all of the volunteers. Changes depicted in the endometrial and junctional zones of the uterus reflected physiologic events occurring during the normal cycle. Important implications exist for infertile women undergoing stimulated cycles and/or in-vitro fertilization.

MRI of hepatic lymphoma. Weissleder R, Stark DD, Elizondo G, et al. (RW, Dept. of Radiology, Massachusetts General Hospital, Boston, MA 02114). *Magn Reson Imaging* 6(6):675-681, Nov./Dec. 1988

Thirteen patients with biopsy proven hepatic lymphoma (2 Hodgkin, 11 Non-Hodgkin) and a control group of 15 patients with hepatic metastases were analyzed quantitatively and qualitatively by MRI. Focal hepatic lymphoma was most reliably detected (eight of eight patients) and appeared hypointense relative to liver on T_1 weighted (CNR -7.4 ± 2.3) and hyperintense on T_2 weighted (CNR $+8.4 \pm 2.9$) images. The mean T_1 and T_2 relaxation times of focal hepatic lymphoma ($T_1 = 832 \pm 234$ msec, $T_2 = 84 \pm 16$ ms) differed significantly from adjacent non-tumorous liver ($T_1 = 420 \pm 121$ ms, $T_2 = 51 \pm 9$ ms; $p < 0.05$), however CNR values and relaxation times

were similar to those of hepatic metastases. Diffuse hepatic lymphoma (microscopic periportal infiltration) was undetectable by MRI in three patients by either morphologic features or quantitative criteria. A mixed pattern of hepatic lymphoma (focal lesions and diffuse infiltration) showed focal areas of slightly decreased signal intensity on T_1 weighted images (CNR -1.7 ± 0.4) while T_2 weighted images revealed multiple regions of focal hyperintensity (CNR $+13.3 \pm 8.4$) superimposed on a diffusely hyperintense liver. Our experience demonstrates that either T_1 or T_2 weighted techniques are useful in detecting focal and that T_2 weighted techniques are useful in detecting mixed hepatic lymphoma. Conventional image derived relaxation time measurements and quantitative parameters were of no additional diagnostic value.

Visiting Fellowships in Radiology at MGH

Massachusetts General Hospital is offering Visiting Fellowships in Radiology: Diagnosis, Imaging, and Interventional Techniques. The fellowships include 1-week programs in CT, sonography, nuclear medicine, neuroradiology, abdominal imaging, vascular imaging, pediatric radiology, chest radiology, genitourinary radiology, interventional radiology, skeletal radiology, breast imaging, and MR. Program chairman: James H. Thrall. Category 1 credit: 40 hr. Information: Robert H. Cleveland, M.D., Visiting Fellowship Program Director, Dept. of Radiology, Massachusetts General Hospital, Fruit St., Boston, MA 02114; (617) 726-8395.

Biliary Lithotripsy Visiting Fellowships

The Dept. of Radiology, Center for Continuing Education, Hospital of the University of Pennsylvania, is coordinating 5-day visiting fellowships in biliary lithotripsy. The program is designed for physician groups (radiologists, gastroenterologists, or surgeons), technologists, and administrators who are contemplating a joint effort to purchase and operate a biliary lithotripsy unit. It is assumed that participants will have some basic familiarity with diagnostic sonography as applied to the biliary tract. The main activity will be participation in the treatment of patients at the Gallstone Evaluation and Treatment Center, Hospital of the University of Pennsylvania. Lectures will cover subjects such as composition of gallstones; the role of bile salts for litholysis; theory and results of lithotripsy; and the roles of interventional radiology, percutaneous cholecystostomy, and stone dissolution with M-tert-butyl ether. A selection of videotapes covering all aspects of diagnosis and management of biliary tract disorders, including lithotripsy, will be provided. Fee: \$1200. Information: Janice Ford, Dept. of Radiology, Center for Continuing Education, Hospital of the University of Pennsylvania, 3400 Spruce St., Philadelphia, PA 19104; (215) 662-6904.

Clinical MRI: 1989 Update

Massachusetts General Hospital is sponsoring Clinical MRI: 1989 Update, the 7th annual MR imaging postgraduate course, May 17-21, in Boston. Category 1 credit: 31 hr. Fee: physicians, \$525; residents and fellows, \$425. Information: Thomas J. Brady, M.D., Director of MR, Dept. of Continuing Medical Education, Harvard Medical School, Boston, MA 02115; (617) 732-1525.

Advanced Techniques in MRI

The Dept. of Radiology, Duke University Medical School, will present Advanced Techniques in MRI, June 10-15, Kiawah Island,

SC. The course is intended for physicians, physicists, engineers, and technologists who want a fundamental understanding of the technology of MR. The program begins with the basic principles of MR and continues to descriptions of high-speed imaging techniques, cardiac imaging, and spectroscopy. Particular attention will be given to description of the physical basis of the phenomenon of MR and the mechanisms by which it is exploited. Clinical examples will be included when appropriate. Information: G. Allan Johnson, Ph.D., Dept. of Radiology, Box 3302, Duke University Medical Center, Durham, NC 27710; (919) 684-2711, ext. 354.

Emergency Radiology Update 1989

Massachusetts General Hospital is sponsoring the annual Harvard Medical School postgraduate course Emergency Radiology Update 1989: Conventional Imaging Modalities, CT, and MR of Trauma, Three-Dimensional Trauma Imaging, June 19-21, in Boston. Fee: physicians, \$425; residents and fellows, \$325. Information: Dept. of Continuing Medical Education, Harvard Medical School, Boston, MA 02115; (617) 732-1525.

Leeds Gastroenterology Course

The University of Leeds in association with the Royal College of Radiology is sponsoring the 13th Leeds Gastroenterology Course for Radiologists, July 10-14, at St. James University Hospital, Leeds, England. Topics will include diffuse liver disease; liver transplantation; biliary radiology, including lithotripsy; new hepatic contrast material; abdominal trauma; inflammatory bowel disease; and constipation, incontinence, and pelvic floor disorders. Faculty: D. Allison, Clive Bartram, Michael Bernardino, Stan Cope, Oscar Craig, Hans Herlinger, Igor Laufer, and Anders Lunderquist. Fee: \$300 (U.S. dollars). Information: Janice Ford, Dept. of Radiology, Hospital of the University of Pennsylvania, 3400 Spruce St., Philadelphia, PA 19104; (215) 662-6904.

Annual Diagnostic Imaging Seminar

The Dept. of Radiology, Hospital of the University of Pennsylvania, is sponsoring the 11th Annual Diagnostic Imaging Seminar, July 17-21, at the Harbor House Hotel, Nantucket Island, MA. Course director: Peter Arger. Guest faculty: Roy Filly and Eric vonSonnenberg. Category 1 credit: 22 hr (pending). Fee: physicians, \$475; residents, \$375. Information: Janice Ford or Nancy Fedullo, Dept. of Radiology, Hospital of the University of Pennsylvania, 3400 Spruce St., Philadelphia, PA 19104; (215) 662-6904 or 662-6982.

Pathological Effects of Radiation

The Armed Forces Institute of Pathology and the American Registry of Pathology are cosponsoring the short course Pathological Effects of Radiation, Sept. 11–13, in Bethesda, MD. The course will address the morphologic effects of radiation on human tissues and related subjects. It may be of interest to pathologists who examine tissue from patients who have had radiation therapy, radiation therapy residents who wish to review for examinations, and persons who assist in medical management of patients who have acute radiation injury. Course director: David Busch, Ph.D., M.D. Category 1 credit: 21 hr. Fee: nonfederal applicants, \$390. Information: David Busch, Ph.D., M.D., American Registry of Pathology, Armed Forces Institute of Pathology, Washington, DC 20306-6000; (202) 576-2434.

Practical Magnetic Resonance Imaging 1989

The Florida Radiological Society is sponsoring the 3rd annual course, Practical Magnetic Resonance Imaging 1989, Oct. 12–15, at Bally's, Las Vegas, NV. Category 1 credit: 23 hr. Fee: physicians and scientists, \$395; residents, fellows, and military personnel, \$275; nurses and technologists, \$225. Information: Florida Radiological Society, Program Committee, P. O. Box 17241, Tampa, FL 33682; (813) 873-2090 or (800) 338-5901.

The American Board of Radiology Examinations

Written examinations for the American Board of Radiology (ABR) are scheduled for Oct. 12–13, 1989, and Sept. 27–28, 1990. Oral examinations will be held at the Executive West Hotel in Louisville, KY, June 5–9, 1989, and June 4–8, 1990. The ABR will accept applications for admission to the examinations after July 1, but not later than Sept. 30, in the year *preceding* the year in which the examination is to be taken. For application forms and further information: Office of the Secretary, The American Board of Radiology, 300 Park, Ste. 440, Birmingham, MI 48009.

Meeting and Course Review

For the reader's convenience, a summary of upcoming meetings and courses is provided. Detailed listings are given in the *AJR* issue given in parentheses.

Fellowships in Interventional Radiology, times arranged, San Diego (May 1988)

Fellowship Program in Diagnostic Radiology, times arranged, Ann Arbor (June 1988)

Basic and Advanced Training in MRI, times arranged, The Johns Hopkins Hospital, Baltimore (Dec 1988)

St. Moritz 1989: Advances in Diagnostic Imaging, March 25–April 2, St. Moritz, Switzerland (Feb)

University of Wisconsin Ct Conference, March 31–April 1, Madison, WI (Feb)

Joint American-European Course in Davos, April 2–8, Davos, Switzerland (Jan)

Ultrasound in Obstetrics and Gynecology, April 3–5, Ann Arbor (Dec 1988)

Obstetrics and Gynecology, April 3–7, May 22–26, and June 5–9, Philadelphia (Feb)

Visiting Fellowships in MR Imaging at UCLA, April 3–7, May 8–12, and June 5–9, Los Angeles (March)

National Council on Radiation Protection and Measurements Annual Meeting, April 5–6, Washington, DC (Nov 1988)

Spring Seminar, April 5–7, Las Vegas (Jan)

Diagnosis and Treatment of Neoplastic Disorders, April 6–7, Baltimore (March)

Radiation Oncology Clinical Research Seminar, April 6–8, Gainesville, FL (Feb)

American Osteopathic College of Radiology Mid-Year Conference, April 6–9, Washington, DC (Nov 1988)

The Brain, the Self, and Nuclear Medicine, April 7–8, Bonn, W. Germany (Jan)

General Radiology Review at UCLA, April 9–14, Los Angeles (March)

Abdominal Ultrasound, April 10–13 and June 12–15, Philadelphia (Feb)

Mammography for the General Radiologist, April 10–13, May 8–11, Sept. 18–21, and Oct. 23–26, Boston (March)

Society of Computed Body Tomography Annual Course, April 10–14, Washington, DC (Nov 1988)

Courses in Diagnostic Ultrasound at Bowman Gray: Physics, April 12–14; **Obstetrics**, April 17–21 and June 5–9; **Radiology (Abdomen)**, April 24–28 and June 12–16; **Neurovascular**, May 1–5; **Echocardiology**, May 15–19; and **Urology**, May 22–23; Winston-Salem, NC (Jan)

Thomas Jefferson University Hospital Courses in Diagnostic Ultrasound: Prostate Ultrasound, April 14, Philadelphia (Oct 1988)

San Diego Residents' Radiology Review Course, April 16–21, San Diego (Nov 1988)

Radiology Review Course, April 16–21, Orlando, FL (Feb)

Practicums in MR Imaging: Advance Practicum, April 17–21 and Sept. 11–15; **Basic Practicum**, June 19–23 and Oct. 23–27; Baltimore (March)

Tissue Characterization in MR-Imaging, April 18–21, Wiesbaden, Federal Republic of Germany (Feb)

Advances in Radiology, April 19–May 7, Asia (Shanghai, Guilin, Hong Kong, Bangkok, Chiang Mai, Phuket, and Singapore) (Jan)

AFIP Musculoskeletal Radiology Review Course, April 22–23, Bethesda, MD (Jan)

Automated Percutaneous Discectomy Workshop, April 22–23, San Francisco (Jan)

Differential Diagnosis in Radiology, April 22–24, Ann Arbor (Jan)

Ultrasound 1989, April 23–26, Boston (Jan)

Advances in CT and MR Imaging, April 26–28, Ann Arbor (Feb)

Doppler Ultrasound in Vascular Diagnosis, April 26–29 and May 31–June 3, Philadelphia (Feb)

Fleischner Society Symposium on Chest Disease, April 28–30, New York (Dec 1988)

Annual Spring Diagnostic Ultrasound Conference, April 28–30, Los Angeles (Jan)

1989 Neuroradiology Review Course, April 29–30, Oak Brook, IL (March)

International MR Symposium in Italy, April 30–May 5, Venice and Florence (Jan)

Magnetic Resonance Imaging 1989: National Symposium, April 30–May 5, Orlando, FL (Feb)

Surgical Neuroangiography, May 1–5, New York (Dec 1988)

Annual Mid-Pacific Diagnostic Ultrasound Conference, May 2–6, Big Island of Hawaii (Jan)

The Leading Edge in Diagnostic Ultrasound, May 10–12, Philadelphia (Feb and March)

International Congress on Peer Review in Biomedical Publication, May 10–12, Chicago, IL (Sept 1988)

Radiology Review Course, May 14–19, Bal Harbour, FL (March)

Emission Tomography of the Heart, May 20, Seattle (March)

Sonography Symposium, May 26–27, Nashville, TN (Jan)

Radiology in Scandinavia and the Soviet Union, June 17–July 11, Copenhagen, Stockholm, and Leningrad (Jan)

Challenge 89: Decisions in Imaging, June 24–30, London, England (March)

CAR '89, June 25–28, Berlin (Jan)

1989 International Congress of Radiology, July 1–8, Paris (May 1988)

Third World Medicine—Tropical Radiology and the Problem of AIDS, July 19–Aug 5, East Africa (Nairobi, Maasa-Mara, Lake Baringo, Lake Turkana, Mombasa, and Lamu) (Jan)

Symposium on Breast Disease, July 23–26, Mackinac Island, MI (March)

Visiting Fellowship in Mammography, Aug. 28–31 and Oct. 23–27, Los Angeles (March)

Imaging, Intervention, Ireland—1989, Sept. 2–10, Dublin, Cong, and New Market, Ireland (Feb)

Update in Chest Radiology, Sept. 10–23, England and Scotland (Feb)

Society of Uroradiology Postgraduate Course, Sept. 25–28, Hilton Head, SC (Dec 1988)

World Congress for Bronchology, Oct. 18–20, Tokyo, and Oct. 21–22, Kyoto, Japan (Nov 1988)

Royal Australasian College of Radiologists Annual Meeting, Oct.

19–23, Melbourne, Australia (March)

Advances in Chest, Interventional, and Ultrasound, Nov. 25–Dec. 10, South America (Caracas, Isla Margarita, Manaus, Recife, Rio de Janeiro, Buenos Aires, and Bariloche) (March)

AJR carries announcements of courses, symposia, and meetings of interest to its readers if received a minimum of 5 months before the event. There is no charge; receipt of items by the *AJR* Editorial Office is not acknowledged. Submit items for publication typed double-spaced. Provide title, date, location, brief description, sponsor, course directors, fees, category I credit, and address and telephone number for additional information. Faculty from the host institution will not be listed. Guest faculty names will appear **only** if initials are provided. Mail news items to *AJR* Editorial Office, 2223 Avenida de la Playa, Suite 200, La Jolla, CA 92037-3218.

Classified Advertisements

Positions Available

GENERAL AND INTERVENTIONAL RADIOLOGIST—Practice in 200-bed, modern, primary-care hospital with excellent imaging and interventional facility in Troy, MI and rotate in our major, tertiary-care medical center with residency and fellowship training programs. Send applications to Thomas Verhelle, M.D., Chief, Diagnostic Radiology, William Beaumont Hospital, 44201 Dequindre Rd., Troy, MI 48064. 3-5a

THE DEPT. OF RADIOLOGY, VIRGINIA COMMONWEALTH UNIVERSITY/MEDICAL COLLEGE OF VIRGINIA, Richmond, VA seeks faculty for positions in diagnostic radiology for chest, mammography, CT/ultrasound/MR, neuroradiology, pediatrics, ER, angio/interventional, and general radiology. Our 1058-bed facility (205 for pediatric patients) is a Level 1 Trauma Center. ABR certification or eligibility required. Academic rank and salary commensurate with experience. Submit CV to A. V. Proto, M.D., Chairman, Diagnostic Radiology, Medical College of Virginia, MCV Box 47, Richmond, VA 23298-0047. VCU/MCV is an equal opportunity/affirmative action employer. Women and minorities are encouraged to apply. 4-6a

PRACTICE OF RADIOLOGY—A hospital-based practice of 4 radiologists, covering 2 area hospitals serving Wyoming, South Dakota, Colorado, and Nebraska, (recently designated as a rural referral center) seeks an additional radiologist with expertise in all imaging modalities. Excellent compensation and fringe benefits. State-of-the-art facility in a recently constructed wing (1985). Potential to become full partner in 1 yr. Community of approximately 20,000 with medical service population of 110,000. Close to Rocky Mountains (2-5 hr), with excellent hunting and fishing. Alternative opportunity for 1-yr, locum tenens position. If you are board-certified or are soon to be and would like more information about this opportunity, please send CV or call R. G. Heasty, M.D., Regional West Medical Center, 4021 Avenue B., Scottsbluff, NE 69361; (308) 632-0140. 4-6ap

CHIEF, RADIOLOGY SERVICE—BC/BE radiologist with unrestricted license in any state (or District of Columbia), U.S. citizen or permanent resident immigrant, English language proficiency required. 775-bed medical center offers primary and extended care, and outpatient medical and psychiatry services. Salary to \$94,000 (depending on qualifications), federal malpractice protection, 30 days paid vacation, and relocation expenses. Tomah is a city of 7500 in a predominantly rural area that offers affordable real estate and good schools. Conveniently located on I-90/94 midway between Milwaukee and Minneapolis. Call or write R. S. Merrill, M.D., Chief of Staff (11), VA Medical Center, Tomah, WI 54660; (608) 372-1778. EO/AAE. 4-5a

RADIOLOGISTS—Several VAMC salaried positions immediately available to BC, or recently BE, radiologists competent in all areas of radiology. Additional subspecialization in angiography, neuroradiology, and/or interventional procedures sought, but not required for all vacancies. Southwest Ohio. Submit CV to VA Medical Center, Radiology Service (114), 4100 W. Third St., Dayton, OH 45428. An equal opportunity employer. 4a

DIAGNOSTIC RADIOLOGIST—Immediate opening to join large, group practice with multiple hospital and imaging centers. Interventional training desirable. Orange County, NY; 50 mi. from New York City. Competitive salary leading to partnership. Respond to Kenneth S. Schwartz, M.D., Northern Metropolitan Radiology Associates, P. O. Box 199, Jefferson Valley, NY 10535; (914) 245-8935. 4ap

DIAGNOSTIC RADIOLOGIST—The Dept. of Radiology of St. Luke's-Roosevelt Hospital Center in New York City is seeking a general radiologist with a special interest in ultrasound. The hospital is a 1315-bed, voluntary university hospital of Columbia University College of Physicians & Surgeons. Academic rank depends on qualifications and expertise. Excellent facilities and remuneration. Please send inquiries with a CV to Ronald C. Ablow, M.D., Dept. of Radiology, SLRHC, Amsterdam Ave. & 114th St., New York, NY 10025. An equal opportunity employer. 4ap

CHIEF OF ULTRASOUND, PRIVATE PRACTICE HOSPITAL GROUP—Position available at a large, tertiary-care hospital in Phoenix, AZ, for a board-certified radiologist with fellowship training in ultrasound. Prefer postfellowship experience with ability to manage an ultrasound section and promote its services. Experience in obstetrics, general and Doppler ultrasound necessary. This is a unique position, offering academic-style practice with private-practice benefits. Please send letters of inquiry to Aubrey M. Palestrant, M.D. or Theodore Ditchek, M.D., Dept. of Radiology, Good Samaritan Medical Center, 1111 E. McDowell Rd., Phoenix, AZ 85006; (602) 239-4601. 4-7ap

ABDOMINAL RADIOLOGIST—The H. Lee Moffitt Cancer Center and Research Institute at the University of South Florida has a faculty position available for an abdominal radiologist with fellowship training or equivalent subspecialty experience. Interest and expertise in all imaging modalities and procedures related to abdominal radiology are preferred. The position includes clinical service, research, and teaching; academic rank is based on qualifications. Our facility is a new, state-of-the-art complex; the compensation package is excellent. Interested candidates should contact Robert Clark, M.D., Dept. of Radiology, Moffitt Cancer Center, P. O. Box 280179, Tampa, FL 33682-0179. 4-6ap

BOARD-CERTIFIED OR ELIGIBLE RADIOLOGIST to join a hospital and multioffice group practice in North Central Connecticut. Applicant should be competent in all imaging modalities including CT and MRI. Training in interventional radiology is desirable but not essential. Salary first yr leading to full partnership. J. Danigelis, M.D., 151 Berle Rd., South Windsor, CT 06074. 4-6ap

MODERN, 6-MAN RADIOLOGY GROUP seeking 7th man due to expansion. Three private offices and 1 busy hospital, all located in Jamestown, NY, on Chautauqua Lake. Must be board-certified and preferably trained in specials, ultrasound, nuclear medicine, CT, and MRI. Generous salary and benefits. Full partnership in 2 yr. Send CV to Rev. Eugene F. Foley, M.D., 333 E. 5th St., Jamestown, NY 14701, or call Patsy Lydell at (716) 664-9731. 4-6ap

VASCULAR/INTERVENTIONAL RADIOLOGIST—Diagnostic Radiology Dept., National Institutes of Health. Full-time, academic position at assistant- or associate-professor level. Board-certification required, fellowship preferred. Duties include all aspects of vascular/interventional radiology, with particular emphasis on diagnostic angiography. Some cross-sectional imaging and plain film reading required. Numerous research opportunities available in dept. with extensive research facilities and support staff. Salary with excellent fringe benefits. Position includes faculty appointment at Georgetown University. Please send CV with letter to John L. Doppman, M.D., Diagnostic Radiology Dept., Bldg. 10, Room 1C660, National Institutes of Health, Bethesda, MD 20892. 4-6ap

FULL-TIME RADIOLOGIST WANTED—Immediate opening, contact P. O. Box 3932, Poplar Bluff, MO 63901; (314) 785-0125. 4ap

LOCUM COVERAGE—Chattanooga Outpatient Center seeks short- or long-term locum. Excellent equipment. All modalities. No night or weekend work. Generous reimbursement. Contact Desmond Fischer, M.D., 1301 McCallie Ave., Chattanooga, TN 37404; (615) 622-7212. 4-6 ap

VASCULAR/INTERVENTIONAL RADIOLOGIST—The Albany Medical College has an opening at the instructor/assistant professor level for an academic position in the Vascular Radiology Section. The candidate must have completed a 1-yr fellowship in vascular/interventional radiology and be available by July 1989. All angiographic and drainage procedures are performed in the section and a GE Signa MR scanner is available for vascular studies. Clinical responsibilities will also include some involvement in general diagnostic radiology. Academic responsibilities include research and teaching of medical students, residents, and fellows. Interested applicants should forward their CV to James C. Peters, M.D., Acting Chairman, Dept. of Radiology, Albany Medical Center Hospital, 43 New Scotland Ave., Albany NY 12208; (518) 445-3277. 4-5ap

RADIOLOGIST; PERMANENT POSITION—Chattanooga Outpatient Center. Excellent equipment; CT, MRI, ultrasound, nuclear, and mammography. No nights or weekends. Generous reimbursement and vacation package leading to partnership. Contact Desmond Fischer, M.D., 1301 McCallie Ave., Chattanooga, TN 37404; (615) 622-7212. 4-6ap

BC/BE DIAGNOSTIC RADIOLOGIST with expertise in all aspects of diagnostic radiology sought by 7-member, community-based, university-affiliated hospital in Hartford, CT. Latest diagnostic equipment including MRI, GE 9800, and angio. Group expanding to include outpatient office. Send CV to Harold Moskowitz, M.D., Director, Dept. of Radiology, Mount Sinai Hospital, 500 Blue Hills Ave., Hartford, CT 06112. 4ap

RADIOLOGIST—Associate diagnostic radiologist to join a group of 4. Hospital and private practice. All imaging capabilities. Angiography and nuclear medicine. 1 hr from Boston. Reply Box P81, AJR (see address this section). 4-6ap

FACULTY POSITION/ABDOMINAL IMAGER WITH MR EXPERIENCE—The University Hospital is seeking a board-certified radiologist with experience in abdominal imaging and MR. Expertise in clinical service, research, and teaching are required. Salary and rank commensurate with experience. Please contact William Olmsted, M.D., Professor and Director, Division of Diagnostic Radiology, The George Washington University Medical Center, 901 23rd St., N.W., Washington, DC 20037. AA/EOE. 4a

UCSD SCHOOL OF MEDICINE—The Dept. of Radiology is seeking a radiologist to participate in clinical, teaching, and research programs in the Magnetic Resonance Division. Qualifications required are board-eligibility/certification, California medical license, and strong background and experience in MR physics and medical imaging. Title series is assistant or associate professor (in-residence or clinical series—not currently a tenure-track position). Level is based on years experience, salary commensurate with rank, and step of appointment based on the established salary schedule of the UCSD School of Medicine Faculty Compensation Plan. The University of California, San Diego is an equal opportunity/affirmative action employer. All CVs received by May 1, 1989 will be given full consideration. Send to John R. Hesselink, M.D., Associate Professor of Radiology, Dept. of Radiology, UCSD Medical Center, 225 Dickinson St., San Diego, CA 92103. 4a

UCSD SCHOOL OF MEDICINE—The Dept. of Radiology is seeking a neuroradiologist to participate in clinical, teaching, and research programs. Qualifications required are board-eligibility/certification, California medical license, and 2-yr fellowship in neuroradiology including MR imaging (neuro/interventional experience preferred). Title series is assistant professor (in-residence or clinical series—not currently a tenure-track position). Level is based on years experience, salary commensurate with rank, and step of appointment based on the established salary schedule of the UCSD School of Medicine Faculty Compensation Plan. The University of California, San Diego is an equal opportunity/affirmative action employer. All CVs received by May 1, 1989 will be given full consideration. Send to John R. Hesselink, M.D., Associate Professor of Radiology, Dept. of Radiology, UCSD Medical Center, 225 Dickinson St., San Diego, CA 92103. 4a

UCSD SCHOOL OF MEDICINE—The Dept. of Radiology is seeking an interventional radiologist to participate in clinical, teaching, and research programs. Qualifications required are board-eligibility/certification, California medical license, and 1-yr fellowship in interventional radiology. Faculty-level experience is desirable. Title series is assistant professor (in-residence or clinical series—not currently a tenure-track position). Level is based on years experience, salary commensurate with rank, and step of appointment based on the established salary schedule of the UCSD School of Medicine Faculty Compensation Plan. The University of California, San Diego is an equal opportunity/affirmative action employer. All CVs received before May 1, 1989 will be given full consideration. Send to Eric vanSonnenberg, M.D., Associate Professor of Radiology, Dept. of Radiology, UCSD Medical Center, 225 Dickinson St., San Diego, CA 92103. 4a

UCSD SCHOOL OF MEDICINE—The Dept. of Radiology is seeking a cardiovascular radiologist to participate in clinical, teaching, and research programs. Qualifications required are board-eligibility/certification, California medical license, and 1-yr fellowship in angiographic radiology. Faculty-level experience is desirable. Candidate should have a demonstrated interest and ability in clinical and/or laboratory angiographic research, and ability as a scientific writer. Title series is assistant professor (in-residence or clinical series—not currently a tenure-track position). Level is based on years experience, salary commensurate with rank, and step of appointment based on the established salary schedule of the UCSD School of Medicine Faculty Compensation Plan. The University of California, San Diego is an equal opportunity/affirmative action employer. All CVs received before May 1, 1989 will be given full consideration. Send to Joseph J. Bookstein, M.D., Professor of Radiology, Dept. of Radiology, UCSD Medical Center, 225 Dickinson St., San Diego, CA 92103. 4a

ISRAEL, DIAGNOSTIC RADIOLOGY. Opportunities for 3–4 week or longer working vacations in a number of Israeli medical centers, on a volunteer basis. Positions varied, arrangements flexible. For information contact: Jonathan H. Fish, M.D., 1844 San Miguel Dr., #302, Walnut Creek, CA 94596; (415) 947-0560. 2–4xa

HARTFORD, CT—Actively growing practice has position available for board-certified radiologist to join an established group of 7. Practice includes hospital and private offices, performing approximately 70,000 exams per yr. Training and/or experience in CT and MRI necessary. Please send CV with correspondence to M. Lee Wallace, M.D., 40 Hart St., New Britain, CT 06052; (203) 229-2059. 4xa

HARTFORD, CT—Position available for a board-certified radiologist to join an established group of 7. Practice includes hospital and 3 private offices, all fully equipped, including CT, MRI and CT experience is an essential requirement. Competitive starting salary and benefits. Please enclose CV with initial correspondence to Jeffrey Blau, M.D., 40 Hart St., New Britain, CT 06052; (203) 229-2059. 4xa

NEURORADIOLOGIST—Immediate opening for recently trained neuroradiologist in busy, suburban practice in Southwest. Current CT, MRI, and arteriography skills required. Highly competitive salary/benefits. Send CV to Box K49, AJR (see address this section). 4xa

CROSS-SECTIONAL RADIOLOGIST, INTERVENTIONALIST—Board-certified diagnostic radiologist with fellowship training wanted to join 5-member dept. in 214-bed community hospital. Group also active in busy outpatient facilities and free-standing Magnetic Resonance Center. Primary responsibility will be ultrasound, CT, and nonangiography interventional, with back-up for primary angiographer. Competence in Doppler studies desired. Call and/or send CV attention Jon Robins, M.D., or Edward Janon, M.D., 6699 Alvarado Rd., Ste. 2100, San Diego, CA 92120; (619) 583-4214. 4xa

MRI RADIOLOGIST—The Dept. of Radiology at Northwestern University Medical School in Chicago is seeking a radiologist with experience in MRI to serve as Director of the MRI facility at Northwestern Memorial Hospital, a 750-bed university hospital. This is an academic position, requiring a strong interest in clinical teaching and research, as well as patient care. Academic rank depends on qualifications. Send inquiries with a CV to Lee F. Rogers, M.D., Chairman, Dept. of Radiology, Northwestern University Medical School, 710 N. Fairbanks, Chicago, IL 60611. An affirmative action, equal opportunity employer. 3–5ap

DIAGNOSTIC RADIOLOGIST, DALLAS METROPLEX—Position available immediately for BC/BE radiologist to join 3-person group. Our practice includes 2 hospitals and an outpatient clinic. Fellowship training in MRI desired. Reply to Box 072, AJR (see address this section). 3–5ap

BC/BE DIAGNOSTIC RADIOLOGIST to join 4 radiologists at a large, multispecialty, staff model HMO. Practice includes general radiology, mammography, CT, nuclear medicine, and ultrasound. The dept. recently has been outfitted with 2 new GE R&F rooms and a new GE Pace CT scanner. The position offers a competitive salary with a comprehensive benefits program. Medical West Community Health Plan is located in western Massachusetts, approximately 60 min from the Berkshires and 90 min from Boston. Please send CV to Robert P. Newman, M.D., Chief, Dept. of Radiology, MWCHP, Inc., 444 Montgomery St., Chicopee, MA 01020. We are an equal opportunity/affirmative action employer. 3–5a

SOUTHERN INDIANA—Radiologist to join 5-member group in hospital and office practice. Some interest and experience in interventional studies desirable, but all areas of expertise will be considered. All imaging modalities, including MRI, available in 400-bed hospital. 80,000 exams annually. Competitive salary for 2 yr leading to partnership. T. Cook, M.D., P. O. Box 5249, Evansville, IN 47716-5249. 3–5ap

FRAMINGHAM, MA—BC/BE diagnostic radiologist to join 6-member group at 311-bed teaching hospital. Experience in angiography and interventional radiology necessary. Send CV to Herbert D. Weintraub, M.D., c/o Framingham Union Hospital, 115 Lincoln St., Framingham, MA 01701; (508) 626-3525. 3–6ap

UNEXPECTED OPENING JULY 1989 FOR BE/BC DIAGNOSTIC RADIOLOGIST to join 5-man group in Missoula, MT, a university city of 50,000, located in mountainous, western Montana. Looking for a general radiologist with proficiency in MRI, ultrasound, CT, angiography, etc. Administrative skills preferable. Our group of 6 full-time radiologists covers both of Missoula's hospitals (210 and 130 beds). Progressive medical environment with 100+ physicians. One yr to full partner income and 2 yr to partnership. Abundant, nearby recreational opportunities include skiing, fishing, backpacking, hunting, etc. Send CV to Missoula Radiology, Inc., P. O. Box 2039, Missoula, MT 59806; (406) 721-4906. 3–4ap

DIAGNOSTIC RADIOLOGIST—Immediate opening to join 2 other radiologists in a large, multi-specialty group practice serving 4 outpatient offices in Rochester, NY. State-of-the-art Toshiba fluoroscopy, ATL ultrasound, and LoRad mammography equipment. Ultrasound, mammography, and CT experience preferable. 32,000 exams/yr. Please contact Dennis S. Moss, M.D., Rochester Medical Group Associates, P.C., Radiology Dept., 800 Carter St., Rochester, NY 14621; (716) 338-1400 x4096. EOE/MF. 3–5a

IMAGING RADIOLOGIST—If lifestyle is an important consideration in your choice of an employment opportunity, read on. Do you want to hone your skills and become an "expert" in a limited area of radiologic diagnosis instead of being a generalist? Would you like to escape the hassles and bureaucratic entanglements of a hospital environment and also avoid night and weekend call? If you answered "yes" to these questions, you may be interested in joining our 2-man group in an office-based practice that concentrates on diagnostic ultrasound and mammography, with a little general radiology for diversion. This is a full-time position leading to partnership after 3 yr. Salary is competitive and the position is available now. Send resume to AVMAR, 3003 N. Central, #121-249, Phoenix, AZ 85012. 3–4ap

DIAGNOSTIC RADIOLOGIST—The San Francisco VA Medical Center is recruiting a board-certified radiologist with expertise in cross-sectional imaging including ultrasound (primarily), CT, and MRI. Position available July 1, 1989. The SFVA has a fully integrated teaching affiliation with the University of California, San Francisco. Minimum 1 yr of teaching and research experience is essential. Equal opportunity/affirmative action employer. Search continues until position is filled. Submit CV to Susan D. Wall, M.D., Assistant Chief, Radiology (114), VA Medical Center, 4150 Clement St., San Francisco, CA 94121. 3–4a

DIAGNOSTIC RADIOLOGIST—Radiologists seek board-certified radiologist with experience in CT, nuclear medicine, general radiology, and ultrasound including Doppler, for a hospital-based, private practice in 225-bed general hospital in Forest Hills, NY. Immediate opening leading to partnership. Contact M. Tartell, M.D.; (718) 544-5858. 2–4ap

DIAGNOSTIC RADIOLOGISTS, 1 INTERVENTIONAL AND 1 ULTRASOUND—Young, aggressive group in Washington, DC, area has position immediately available for a board-certified diagnostic radiologist in an expanding and diversified hospital and office-based practice with facilities in Maryland and Virginia. Our group covers 2 very progressive hospitals, including a regional trauma center, 3 full-service private offices, and a diagnostic center for women. All imaging modalities represented, including 3 MRI, 6 CT, 5 Acuson 128, and a PIXAR 3-D imaging unit. Dynamic and attractive practice setting. Address inquiries and CV to Radiology Imaging Associates, 8926 Woodyard Rd., Ste. 301, Clinton, MD 20735; (301) 856-3670. 3–5ap

DIAGNOSTIC RADIOLOGIST—Yale New Haven Medical Center is seeking a board-certified or eligible radiologist with additional experience or training in CT and diagnostic ultrasound for a full-time faculty position. Candidates should be able to interpret cross-sectional images and do cross-sectional interventional procedures. This appointment will include work about half time in the Dept. of Diagnostic Radiology at Yale and about half time at the affiliated West Haven VA Medical Center. Academic rank commensurate with experience. Candidates must be U.S. citizens or must qualify as permanent residents in the U.S. Please send CV and bibliography to Arthur T. Rosenfield, M.D., Dept. of Diagnostic Radiology, Yale University School of Medicine, 333 Cedar St., New Haven, CT 06510. Yale University is an equal opportunity/affirmative action employer; applications from women and minority groups are encouraged. Applications should be submitted no later than May 1, 1989. 3-4a

TWO BOARD-CERTIFIED/ELIGIBLE GENERAL DIAGNOSTIC RADIOLOGISTS to join expanding, 9-man group covering 2 hospitals and an MR Imaging Center in a stable midwest community. Ideal private practice using all imaging modalities and interventional techniques. Can start immediately or wait until July 1989. Excellent opportunity with excellent salary and benefits. Send CV to Joseph F. Norfray, M.D., MR Center of Springfield, 319 E. Madison, Springfield, IL 62701. 3-6ap

GENERAL RADIOLOGIST with special interest and expertise in pediatric radiology needed for hospital-based practice in 350-bed community hospital. Candidate also should be familiar with CT, ultrasound, nuclear medicine, and angiography. Reply c/o Petronio T. LeRona, M.D., Maricopa Medical Center, Dept. of Radiology, P.O. Box 5099, Phoenix, AZ 85010; (602) 267-5361. EOE. 3-4a

DIAGNOSTIC RADIOLOGIST—The UCLA Dept. of Radiological Sciences is seeking a board-certified radiologist for its Primary Care/Family Practice Section. Position requires strong interests in teaching, patient care, and knowledge of abdominal CT for evaluation of trauma. Send application, including CV and names and addresses of 3 references, or inquiries to Hooshang Kangaroo, M.D., Chairman, Dept. of Radiological Sciences, UCLA Medical Center, Los Angeles, CA 90024-1721, an EO/AA employer that encourages applications from members of minority groups and women. 2-7a

SKELTAL RADIOLOGIST—The UCLA Dept. of Radiological Sciences has a full- or half-time faculty position available in skeletal radiology. Candidate must be board-certified, have a clinical background in skeletal radiology, and have a strong interest in teaching. Send application, including CV and names and addresses of 3 references, or inquiries to Hooshang Kangaroo, M.D., Chairman, Dept. of Radiological Sciences, UCLA Medical Center, Los Angeles, CA 90024-1721, an EO/AA employer that encourages applications from members of minority groups and women. 2-7a

WILMINGTON, NORTH CAROLINA—Group of 8 radiologists seeking fellowship-trained neuroradiologist and general diagnostic imaging radiologist with staff-level experience. This 400-bed, university-affiliated, regional-referral hospital has all diagnostic imaging capabilities including GE Signa 1.5-T MRI, 2 GE 9800 CT scanners, Toshiba SPECT system, and complete angio/interventional suites. Busy private outpatient office. Progressive growing community in Cape Fear area of coastal North Carolina. Address CV to John Remington, M.D., 2212 Delaney Ave., Wilmington, NC 28403. 2-4ap

SOUTHEAST COAST OF FLORIDA—BC/BE radiologist. No MRI. Experience preferred. Available summer 1989. R. L. Stern, M.D., 3232 Memory Lane, Fort Pierce, FL 34981. 3-5ap

DIAGNOSTIC RADIOLOGIST, PACIFIC NORTHWEST: MRI, CT, AND ULTRASOUND—Progressive group of 4 radiologists seeks board-certified radiologist with subspecialty interest and expertise in MRI, CT, and ultrasound. Busy dynamic practice in regional medical center hospital, privately owned MRI center (presently mobile unit — planning for fixed site, fall 1989), plus private outpatient office. Located in beautiful recreation area in the inland Northwest. World-class lakes for boating and sailing. Excellent skiing, hunting, and fishing. Family-oriented environment 30 min from Spokane. Competitive starting salary with full partnership in 1 yr. Send CV to Richard Hehn, M.D., Radiology Associates of North Idaho, 1104 Ironwood Dr., Coeur d'Alene, ID; (208) 667-0686. 2-4ap

DIAGNOSTIC RADIOLOGIST competent in interventional and MR to join growing 3-man practice in northern Arkansas. Modern hospital-based practice includes CT, ultrasound (including duplex vascular), angiography, DSA, interventional, lo-dose mammography, and computerized nuclear medicine. Mobile MR and on-site Radiation Center being added. Located in beautiful resort area of Ozark Mountains, 110 mi from Springfield, MO, 150 mi from Little Rock, and 190 mi from Memphis, and serves 100,000 area population. Excellent recreational activities in family-oriented rural environment. Competitive starting salary with full-partnership in 1 yr. Contact Marc Trager, M.D., P.O. Box 1137, Mountain Home, AR 72653; (501) 425-1760. 11-4a

THE DEPT. OF RADIOLOGY AT TRIPLER ARMY MEDICAL CENTER, HONOLULU, HI, is recruiting academically oriented radiologists for several divisions of the dept.: ultrasound, imaging (CT and/or MRI), interventional, chest, genitourinary, mammography, pediatric, neuro-radiology, and general diagnostic radiology. We are particularly interested in radiologists with ultrasound training or extensive experience. Our dept. offers a fully-accredited residency program with 18 residents and 15 attending full-time staff. Numerous consultants from across the country lecture on a continuing and regular basis. The hospital is a modern tertiary-care center serving the state and the entire Pacific Basin. A strong residency program, a diverse and interesting patient population, excellent equipment, and a tropical lifestyle are positive aspects of the practice. Academic credentials and/or experience are necessary. Recently graduated fellows are encouraged to apply. Board certification is mandatory. Candidates should be particularly interested in patient care, teaching, and research. Salary and benefits are competitive and generous. Tripler is an EO/EEO employer. Please contact Dr. Mark F. Hansen, Col., MC, Chief, Dept. of Radiology, TAMC, HI 96859-5000; (808) 433-6393. 4-6a

DIAGNOSTIC ONCORADIOLOGIST—The Division of Oncoradiology at the Dana-Farber Cancer Institute, a Harvard University affiliate, has an opening at the instructor/assistant professor level for a general radiologist with an interest in oncology beginning July 1989 or sooner. Patient care responsibilities with a close working relationship with the clinical staff, teaching, and research opportunities abound. There are 52 beds with a large outpatient service. All new equipment is available including a GE-9800 CT scanner. Please send CV to Maxine Jochelson, M.D., Director, Division of Oncoradiology, Dana-Farber Cancer Institute, 44 Binney St., Boston, MA 02115. 11-4a

GENERAL DIAGNOSTIC RADIOLOGIST, THOMAS JEFFERSON UNIVERSITY HOSPITAL—The Dept. of Radiology at Thomas Jefferson University Hospital in Philadelphia has an opening in July 1989 for a faculty-level, general diagnostic radiologist. An interest and/or fellowship training in abdominal radiology (GI/GU) would be helpful, but not mandatory. The individual will have the opportunity to participate in clinical activities, teaching, and research in a progressive and expanding general diagnostic division. Excellent salary and benefits are offered. Contact either Robert M. Steiner, M.D., Co-director of General Diagnostic Radiology or David C. Levin, M.D., Professor and Chairman, Dept. of Radiology, Thomas Jefferson University Hospital, 111 S. 11th St., Philadelphia, PA 19107. Thomas Jefferson University is an equal opportunity/affirmative action employer. 1-6ap

RADIOLOGIST—Full-time, board-certified radiologist with particular interest and experience in nuclear and ultrasound radiology desired for association in 10-man, private practice for a 660-bed, private, tertiary-care, teaching hospital with 2 regional offices. Practice is located in large midwestern city and maintains fully accredited, 4-yr, radiology residency training program. This comprehensive dept. includes 2 state-of-the-art CT scanners, a 1.5-T MRI unit, modern equipment for mammography, sonography, angiography, nuclear medicine, and a wide variety of invasive applications and procedures. Competitive salary and benefits. Full partnership, if mutually agreeable, at 3 yr. Near-future plans include manning of regional outpatient center with CT and general radiologic facilities on site. Send inquiry and CV in reply to Box N63, AJR (see address this section). 1-6ap

PEDIATRIC RADIOLOGIST—Yale New Haven Medical Center, Yale University School of Medicine, is seeking a pediatric radiologist for full-time faculty appointment. Academic rank is at the level of assistant or associate professor, dependent on qualifications. A strong interest in patient care, research, and teaching is required. Please send inquiries along with CV to Marc Keller, M.D., Diagnostic Radiology, Yale University School of Medicine, 333 Cedar St., New Haven, CT 06510. Yale University is an equal opportunity/affirmative action employer; applications from women and minority groups are encouraged. 3-4a

GU RADIOLOGIST, BRIGHAM & WOMEN'S HOSPITAL—The Dept. of Radiology at Brigham & Women's Hospital/Harvard Medical School is seeking a radiologist to direct its GU Section. The position combines clinical activities with teaching and research. Candidates must be board-certified and have experience in all aspects of GU radiology, as well as an interest/commitment to academic work. Please send CV to B. Leonard Holman, M.D., Chairman, Dept. of Radiology, Brigham & Women's Hospital, 75 Francis St., Boston, MA 02115. Harvard Medical School is an affirmative action/equal opportunity educator and employer. 11-4a

ULTRASOUND STAFF RADIOLOGIST, BRIGHAM & WOMEN'S HOSPITAL—The Dept. of Radiology at the Brigham & Women's Hospital/Harvard Medical School is seeking a radiologist for a full-time, academic position in ultrasound. We perform 60-85 scans per day, including OB-GYN, abdominal, Doppler, small parts, neonatal, and interventional. Research and teaching opportunities are available. Candidate must be BC/BE with fellowship training in ultrasound. Please send CV to B. Leonard Holman, M.D., Chairman, Dept. of Radiology, Brigham & Women's Hospital, 75 Francis St., Boston, MA 02115. Harvard Medical School is an affirmative action/equal opportunity educator and employer. 11-4a

FULL-TIME ACADEMIC NEURORADIOLOGIST—

One staff position is currently available in the Division of Neuroimaging at the Children's Memorial Hospital at Chicago. The Division of Neuroimaging is a complete service with 2 CT scanners (1 is a GE-9800), 1 GE 1.5-T Signa MRI scanner (which is inhouse for children), 3 Acuson ultrasound units, myelography and cerebral angiography equipment, as well as an interventional neuroradiology program with Northwestern University. The Division has its own approved fellowship program in neuroradiology. Some training in interventional neuroradiology and/or pediatric neuroradiology is preferred, but not necessary. Send CV to Sharon E. Byrd, M.D., Director of Neuroimaging Division, Children's Memorial Hospital, 2300 Children's Plaza, Chicago, IL 60614; (312) 880-3565. 11-4ap

DIAGNOSTIC RADIOLOGIST—Yale University

School of Medicine is seeking a radiologist with special interest in body MRI including a focus in cardiac MRI for a full-time faculty appointment. Equipment includes 2 GE 1.5-T scanners, a 2-T advanced NMR fast scanner, a 0.4-T superkinetics, a 2-T CSI, and 300- and 20-MHz spectrometers. Academic rank is at the level of assistant professor. A strong interest in patient care, research, and teaching is required. Please send inquiries along with CV to Shirley McCarthy, M.D., Ph.D., Diagnostic Radiology, Yale University School of Medicine, 333 Cedar St., New Haven, CT 06510. Yale University is an equal opportunity/affirmative action employer; applications from women and minority groups are encouraged. 3-4a

DIAGNOSTIC RADIOLOGIST—The University of

S. Florida, Dept. of Radiology, is recruiting for 2 board-certified radiologists. The first position is for a general radiologist with special interest and/or experience in teaching medical students the basics of diagnostic radiology. The second position is for a diagnostic radiologist with a subspecialty or training in thoracic radiology. Both are combined appointments with the Tampa VA Hospital and the Dept. of Radiology, USF, at the assistant or associate professor level, commensurate with prior credentials. Competitive salary and generous fringe benefits are derived from both institutions. Both positions also involve clinical service, the teaching of radiology residents, and research. Please send letter of inquiry with CV to Michael Vermess, M.D., Professor of Radiology, Chief, Radiology Service, James A. Haley Veterans Hospital, 13000 Bruce B. Downs Blvd., Tampa, FL 33612. EOE. 4a

DIAGNOSTIC RADIOLOGIST—GASTROINTESTINAL IMAGING—Yale New Haven Medical

Center, Yale University School of Medicine, is seeking a radiologist with special interest in gastrointestinal imaging including barium radiography, CT, and/or ultrasound. Rank is commensurate with experience. A strong interest in patient care, research, and teaching is required. Please send inquiries along with CV to Morton Burrell, M.D., Professor of Radiology, Director of Gastrointestinal Radiology, Yale University School of Medicine, 333 Cedar St., New Haven, CT 06510. Yale University is an equal opportunity/affirmative action employer; applications from women and minority groups are encouraged. Application deadline is May 31, 1989. 3-5a

DIAGNOSTIC RADIOLOGIST, CLEVELAND, OH—

Position available for BC/BE radiologist to join hospital group at Saint Luke's Hospital. Prefer individual with previous practice experience or fellowship training, with interest in MRI and/or interventional radiology. Submit CV to R. L. Boltuch, M.D., Director, Dept. of Radiology, Saint Luke's Hospital, Cleveland, OH 44104. 2-4ap

RADIOLOGIST—IMMEDIATE OPENING—American

university-educated, board-certified/eligible M.D., with particular interest in imaging including MRI to join large, multihospital group in San Antonio, TX. Please direct inquiries and CV to P. O. Box 120310, San Antonio, TX 78212-9510. 1-4ap

Positions Desired

1976 B/C RADIOLOGIST, with prior academic and private practice experience, seeks opportunity in Denver, CO. Available summer 1989. Excellent health; accustomed to strenuous work schedule. Strong background in business and communications. Extensive general radiologic experience including nuclear medicine and particular expertise in adult and obstetrical ultrasound. Reply Box 074, AJR (see address this section). 3-4bp

Fellowships and Residencies**IMAGING FELLOWSHIP (CT, ULTRASOUND, MRI)—William Beaumont Hospital, a 970-bed,**

modern, tertiary-care teaching and academic institution in southeast MI, offers a 1-yr fellowship in sectional body imaging. The fellowship will provide extensive clinical experience in body CT, ultrasound and MRI, including CT- and ultrasound-guided procedures, conventional and color flow Doppler exams, prostatic and endovaginal sonography. Ample elective time is also provided for other rotations of individual interest. Candidates must be board-certified/eligible in diagnostic radiology and have valid Michigan medical license. Four positions are available for July 1990. Salary and fringe benefits are highly competitive. For further information, write to Ali Shirkhoda, M.D., Chief of Imaging Division, William Beaumont Hospital, 3601 W. 13 Mile Rd., Royal Oak, MI 48072; (313) 541-1001. 3-5c

INTERVENTIONAL RADIOLOGY FELLOWSHIP—

The Rush-Presbyterian-St. Luke's Medical Center is now offering a 1-yr fellowship position beginning July 1, 1990 in interventional radiology. This 750-bed teaching hospital offers extensive experience in all aspects of vascular and nonvascular procedures, with a primary emphasis on patient care and clinical research. Send inquiries to Terence Matalon, M.D., Dept. of Diagnostic Radiology and Nuclear Medicine, Rush-Presbyterian-St. Luke's Medical Center, 1653 W. Congress Parkway, Chicago, IL 60612. 4-7c

CARDIOVASCULAR AND INTERVENTIONAL RADIOLOGY FELLOWSHIP—One-yr fellowship

position available beginning July 1, 1990. 474-bed teaching hospital. Fellow will be trained in all aspects of diagnostic cardiovascular imaging, interventional/angiographic procedures, and nonvascular interventional procedures including biliary intervention, GU intervention biopsy, and abscess drainage. Opportunities for participation in clinical research projects will be available. Candidates should be certified by the American Board of Radiology or eligible for the ABR oral exam. Contact Mark H. Wholey, M.D., Director, Dept. of Radiological Sciences and Diagnostic Imaging, Shadyside Hospital, 5230 Centre Ave., Pittsburgh, PA 15232. 4cp.

CARDIOVASCULAR—INTERVENTIONAL RADIOLOGY FELLOWSHIP—Available July 19, 1989.

One-year fellowship program at a 750-bed teaching hospital. Extensive clinical experience involving all aspects of cardiovascular imaging, interventional vascular and nonvascular procedures, and availability for clinical or animal research. Send CV and inquiries to Oscar H. Gutierrez, M.D., Dept. of Radiology, Box 648, University of Rochester Medical Center, Rochester, NY 14642. An equal opportunity employer (M/F). 3-6c

FELLOWSHIP IN PEDIATRIC IMAGING—The

Dept. of Diagnostic Radiology, Yale University School of Medicine, New Haven, CT, offers a 1- or 2-yr fellowship in pediatric imaging beginning July 1, 1990. Training includes conventional pediatric radiology, body CT, ultrasound (including pulsed and color Doppler), and MRI. All cross-sectional imaging equipment is state-of-the-art. Involvement with new or ongoing research projects will be encouraged. Requirements include satisfactory completion of an accredited diagnostic radiology residency and either board eligibility or certification in diagnostic radiology. A letter of inquiry and CV should be sent to Marc S. Keller, M.D., Chief, Pediatric Imaging Section, Yale University School of Medicine, 333 Cedar St., New Haven, CT 06510; (203) 785-2381. Application deadline is July 1, 1989. 3-4c

NUCLEAR MEDICINE RESIDENCY, JULY 1, 1989—San Francisco General Hospital Medical

Center, University of California, San Francisco, has a Program B, 2-yr, ACGME-approved program satisfying the American Board of Nuclear Medicine training requirements both in basic science and performance/interpretation of imaging and nonimaging in vivo procedures, radioimmunoassay, and radionuclide therapy. Emphasis is on SPECT, nuclear cardiology, and use of computers. Prerequisite is 2-yr, ACGME-approved residency in internal medicine, pathology, pediatrics, or radiology. Send CV to Myron Polycove, M.D., Chief, Nuclear Medicine Dept., San Francisco General Hospital Medical Center, San Francisco, CA 94110. Equal opportunity/affirmative action employer. 3-4c

CARDIOVASCULAR/INTERVENTIONAL RADIOLOGY FELLOWSHIP AT THOMAS JEFFERSON

UNIVERSITY HOSPITAL—A 1-yr fellowship position is available starting 7/1/89. This fellowship includes experience in a wide range of diagnostic angiography and both vascular and nonvascular interventional procedures. These include balloon angioplasty, laser thermal angioplasty, thrombolytic therapy, atherectomy, intravascular stent placement, IVC filter placements, renal and biliary drainage procedures, abscess drainages, and stone retrievals. Optional training also available in coronary angiography. Facilities include state-of-the-art angiographic and digital subtraction equipment. Contact either Geoffrey A. Gardiner, Jr., M.D. or David C. Levin, M.D., Dept. of Radiology, Thomas Jefferson University Hospital, 111 S. 11th St., Philadelphia, PA 19107. Thomas Jefferson University is an equal opportunity/affirmative action employer. 1-6cp

FELLOWSHIP IN PEDIATRIC RADIOLOGY—

Dept. of Radiology, Children's Hospital Medical Center, Cincinnati, OH, offers a 1- or 2-yr fellowship in pediatric radiology beginning July 1, 1989. Children's Hospital Medical Center is a 344-bed institution where approximately 85,000 radiologic exams are done per yr by 10 attending radiologists. Training includes all aspects of pediatric imaging including conventional radiology, neuroradiology, abdominal imaging, ultrasound, nuclear medicine, CT, MRI, and vascular/interventional techniques. Equipment includes digital fluoroscopy, Acuson and ATL ultrasound units with Doppler and color-flow Doppler capabilities, Gamma and SPECT tomographic nuclear cameras, GE 9800 Quick CT Scanner, 1.5-T GE MRI, and angiographic suite with digital vascular imaging. Requirements for the fellowship include completion of a radiology residency with training in the various subspecialties of diagnostic imaging. Contact Donald R. Kirks, M.D., Director, Dept. of Radiology, Children's Hospital Medical Center, Elland & Bethesda Aves., Cincinnati, OH 45229-2899; (513) 559-8058. 12-8cp

DIAGNOSTIC RADIOLOGY RESIDENCY POSITIONS—The University of Miami/Jackson Memorial Medical Center, Dept. of Radiology, is offering 1 third- and 1 fourth-yr diagnostic radiology residency position beginning July 1989. Our program was recently approved for an increase in total number of positions. UM/JMMC is a 1300-bed, tertiary referral center serving Miami, FL, the Southeast, and Latin America. The Dept. of Radiology currently performs approximately 250,000 exams/yr with 33 faculty, 22 residents, and 8 fellows (5 in neuroradiology and 3 in interventional/CT/ultrasound). If interested, please contact by phone or letter with CV, Sandra A. Oldham, M.D., Dept. of Radiology (R-109), University of Miami School of Medicine, P. O. Box 016960, Miami, FL 33101; (305) 549-6894. AA/EOE. 2-6c

FELLOWSHIP IN VASCULAR AND INTERVENTIONAL RADIOLOGY—Due to an unexpected opening, a fellowship position in vascular and interventional radiology is available at the University of Texas Medical Branch, for 1 yr beginning July 1, 1989, and ending June 30, 1990. This position is offered also to those radiologists who desire to return to an academic setting to acquire new skills in the vascular and interventional field. Very active dept. with up-to-date equipment provides an excellent opportunity for training in all interventional modalities. Please contact L. B. Moretin, M.D., Director, Vascular and Interventional Radiology, University of Texas Medical Branch, Galveston, TX 77550; (409) 761-2498. UTMB is an equal opportunity M/F/H/V affirmative action employer. UTMB hires only individuals authorized to work in the United States. 4-6c

GIANTURCO RESEARCH FELLOW—The Dept. of Diagnostic Radiology at The University of Texas M. D. Anderson Cancer Center, Houston, TX is offering a 1-yr training program under the direction of Kenneth C. Wright, Ph.D., Sidney Wallace, M.D., and Cesare Gianturco, M.D. The program is available for laboratory research in the John S. Dunn Research Foundation Center for Radiological Sciences at a salary of \$25,000. The areas of current research include angiographic and interventional technique and devices, microencapsulation of radiopaque contrast materials and chemotherapeutic agents, and a computerized atlas of anatomy and imaging. Appointments may be made during residency, postresidency, or before beginning residency training. For further information, contact Sidney Wallace, M.D., Dept. of Diagnostic Radiology, The University of Texas M. D. Anderson Cancer Center, 1515 Holcombe Blvd., Houston, TX 77030. An equal opportunity/affirmative action employer. 4-6c

DUKE UNIVERSITY, DEPT. OF RADIOLOGY offers 1- or 2-yr fellowship positions in chest radiology, neuroradiology, vascular/interventional radiology, musculoskeletal radiology, CT, ultrasound, MRI, abdominal imaging, pediatric radiology, and nuclear medicine beginning July 1990. The dept. runs an active, clinical service with top-quality equipment including 4 GE 9800-Quick CT scanners, 3 GE 1.5-T MRI units, and 4 fully-equipped vascular/interventional laboratories. In addition to their clinical responsibilities, fellows are provided academic time to pursue investigational interests. Applications should be completed by April 1, 1989 so that interviews can be scheduled for late spring/early summer. For further information and applications, please contact Mrs. Debbie Sykes at the Dept. of Radiology, Box 3808, Duke University Medical Center, Durham, NC 27710; (919) 681-2711. 2-4c

FELLOWSHIP IN MRI NEURO AND BODY—The Christ Hospital and James N. Gamble MR Institute offers a 1-yr fellowship in neuro and body MR and CT. Approximately 4000 MR exams/yr and 7000-8000 CT exams/yr. Two GE 9800 Quick and 1 GE 1.5-T MR unit. Academic endeavors including papers and chapter publication encouraged. The Christ Hospital is an 870-bed multisubspecialty and specialty hospital. Please send CV and 2 letters of reference to Stephen J. Pomeranz, M.D., Division of Radiology and Magnetic Resonance, The Christ Hospital, 2139 Auburn Ave., Cincinnati, OH 45219 or telephone Mrs. Maricarol Glaze at (513) 369-2949. 2-4cp

Tutorials/Courses

CHALLENGE 89—DECISIONS IN IMAGING: LONDON, ENGLAND: JUNE 24-30, 1989—Category I CME, MRI, CT, ultrasound correlative course presented by University of Southern California faculty and a distinguished faculty from the United Kingdom. **Wimbledon Tennis Tournament**. For information contact University Imaging Associates, LAC/USC Medical Center, Box 66, 1200 N. State St., Los Angeles, CA 90033. (213) 226-7245. 4-6dp

FIFTH ANNUAL LONDON-PARIS FALL ULTRASOUND—Sept. 17-23, 1989. Category I accreditation, international faculty. For information, contact Medical Seminars International, 9800 D Topanga Canyon Blvd., Ste. 232, Chatsworth, CA 91311; (818) 700-9821. 3-9d

ALASKA 89—CRUISE THE INLAND PASSAGE—July 8-15, 1989, CME I accreditation, Professor Lawrence Bassett, M.D., Breast Imaging. For information, contact Medical Seminars International, 9800 D Topanga Canyon Blvd., #232, Chatsworth, CA 91311; (818) 700-9821. 1-6d

Other

MOBILE MAMMOGRAPHY VAN—1987, 27-ft Itasca motor home, fully equipped for complete mammography service. Kramex 43S mammography unit, AFP processor. \$85,000. For information respond to, Florida Mobile Imaging, Inc., P. O. Box 2440, Sanford, FL 32772-2440. 4-6ep.

AJR Classified Advertisements Information

Box Responses and Address for Ad Placement

Write Box _____, AJR, 2223 Avenida de la Playa, Suite 200, La Jolla, CA 92037-3218; (619) 459-2229; FAX: (619) 459-8814.

How to Place an Ad

AJR accepts classified advertising for Positions Available, Positions Desired, Fellowships and Residencies, and Tutorials/Courses. Ads are accepted by mail or FAX.

Rates: \$6.00/line with a \$30 minimum charge. Box service is \$10 additional for each month the ad appears. There are discounts for multiple insertions: 10% for 2-3 insertions; 20% for 4 or more. To estimate lines, count all words and divide by 7.

Billing: Ads must be prepaid, or advertisers will be billed after the ad appears providing a purchase order number is submitted with the advertising copy. Terms are net 30 days.

Deadlines: 6 weeks prior to issue date. For specific deadlines, telephone the AJR editorial office.

Estimating Ad Charges

Line charge: divide total words by 7 and multiply by \$6.00	\$
Multiple insertions? If so, multiply by number	x
Subtotal	\$
Discount applies to two or more insertions. Subtract 10% if ad appears 2-3 months, 20% if 4 months or more	-
Subtotal	\$
Box response requested? If so, multiply number of months by \$10.00	+
Approximate advertising charge	\$

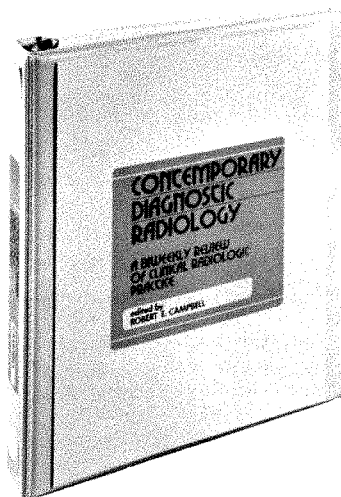
You learn from your experience with **CONTEMPORARY DIAGNOSTIC RADIOLOGY**

Editor: **Robert E. Campbell, M.D.**

A Biweekly Review of Clinical Radiologic Practice—26 issues a year!

One of your toughest jobs is keeping up with the many new developments that affect radiology. That's why you want **Contemporary Diagnostic Radiology**... an effective and convenient way to perfect your skills and maintain your professional status.

Contemporary Diagnostic Radiology is designed as a continuing education program that lets you work at your own pace. Every two weeks you'll receive an issue that covers a single topic or procedure in detail. Read the information and study the clearly reproduced radiographs—and then, if you choose, respond to a comprehensive examination in the strictest confidence. You set the pace. Each biweekly lesson brings you pertinent review of the basics in bone radiology... gastrointestinal radiology... pediatric radiology... genitourinary radiology... MR imaging... and all of the topics you want to know more about.



Contemporary Diagnostic Radiology works two ways. You may choose to subscribe to the non-scoring version, receiving every issue as an important element of your professional reading. The scoring version, however, supplements your reading and computer-coded examinations with confidential result responses, making you eligible for Continuing Medical Education credits co-sponsored by the University of Pennsylvania School of Medicine.

"As an organization for continuing medical education, the University of Pennsylvania School of Medicine designates this continuing medical education activity as meeting the criteria for 1 credit hour per bi-weekly issue in Category I for Educational Materials for the Physician's Recognition Award of the American Medical Association provided it has been completed according to instructions."

You can begin this ongoing program today. **Contemporary Diagnostic Radiology** is a year-round program, so you can join at any time. To begin your lessons, just fill out the enclosed card and return it to us. Or call **FREE** 1-800-638-6423.

In Maryland call 1-800-638-4007. You'll find that **Contemporary Diagnostic Radiology** is the most efficient and inexpensive way to keep up with your dynamic field.

Williams & Wilkins

P.O. Box 23291
Baltimore, Maryland 21203



The Broadway Centre
2-6 Fulham Broadway
London SW6 1AA England

clip & mail

CONTEMPORARY DIAGNOSTIC RADIOLOGY

- ☐ **Yes! I want to keep pace in my field! Begin my 26-issue subscription:**
- ☐ Send me the scoring version (\$230)
 - ☐ Send me the non-scoring version (\$180)
 - ☐ Send me the resident non-scoring version (\$115) (add \$45 for optional air mail delivery outside the U.S.)
 - ☐ new subscription
 - ☐ renewal

name _____

address _____

city/state/zip _____

payment options

- ☐ payment enclosed
☐ American Express

- ☐ bill me
☐ MasterCard

☐ VISA

card # _____

expiration date _____

signature/P.O. # _____

Maryland residents add 5% sales tax. Subscriptions outside the U.S. must be prepaid in U.S. dollars only. Rates subject to change without notice. Please allow 8 weeks for delivery of your first issue, up to 16 weeks for surface delivery outside the U.S. Optional airmail rates add \$45 per subscription.

Residents are eligible for the special in-training rate for up to three years. When requesting this rate, please include training status and institution.



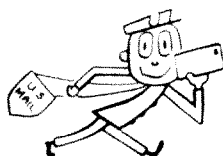
Don't forget: you can order with a **FREE** phone call at 1-800-638-6423. In Maryland, call 1-800-638-4007.

Williams & Wilkins

P.O. Box 23291
Baltimore, Maryland 21203

The Broadway Centre
2-6 Fulham Broadway
London SW6 1AA England

**Help us to
serve you
better.....**



**USE
YOUR
ZIP
CODE**

**Remember, your zip code
provides faster, more direct
delivery of your journals.
Use it on all correspondence,
too.**

WORKSHOP ON FALLOPIAN TUBE CATHETERIZATION

**Oregon Health Sciences University
Portland, Oregon
June 17-18, 1989**

This course offers hands-on and didactic instruction in new transcervical methods for fallopian tube catheterization. Designed for radiologists and gynecologists with a subspecialty interest in infertility, it will allow the participants to: (1) Learn the principles of fallopian tube catheterization for the diagnosis and management of proximal tubal obstruction, for gamete delivery and applications in assisted reproductive technology. (2) Learn to use catheter assemblies and devices for transcervical fallopian tube catheterization by fluoroscopy, ultrasound and hysteroscopy guidance. Lectures address a variety of clinical applications and are supplemented by small group discussions. The course format includes practical experience using the catheter devices in life-size models and the opportunity to view video tapes in a workshop setting. Faculty members are nationally recognized experts in interventional radiology, microsurgery and endoscopy and have pioneered the development of fallopian tube catheterization procedures. A course syllabus including outlines of presentations and pertinent references will be available to all prepaid registrants. Tuition fee is \$400.00.

Course Directors: Amy Thurmond, M.D. and Miles J. Novy, M.D. For more information please contact Continuing Medical Education, Oregon Health Sciences University, Portland, Oregon 97201. Phone (503) 279-8700.

*for prompt
subscription
service...*

attach label here

Please use this coupon and attach a *recent* label in the space provided when writing to us about:

- change of address
- renewal
- questions regarding your subscription

Please use the space below to indicate your *new* address.

Name of Journal _____

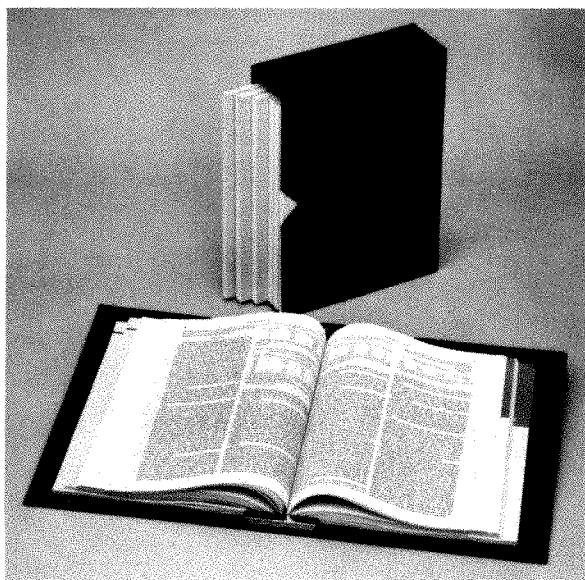
Name _____

Address _____

City/State/Zip _____

THE WILLIAMS & WILKINS COMPANY

428 East Preston Street/Baltimore, Maryland 21202



Protect your copies of

AJR: AMERICAN JOURNAL OF ROENTGENOLOGY

with Jesse Jones Binders or Files

Keep your journals clean, orderly, and readily accessible with Jesse Jones Binders or Files. Two Binders or two box style Files are all you need to accommodate a full year's worth of issues. Both Binders and Files are handsomely made with rich black leatherette covers and gold leaf embossed lettering.

Jesse Jones Binders open flat for easy reading and reference and are economically priced at only \$9.95 each; 3 for \$27.95, or 6 for \$52.95 postpaid. The rugged, compact box Files are only \$7.95 each; 3 for \$21.95, or 6 for \$39.95. Add \$1.00/unit postage and handling. (Outside the U.S. add \$2.50/unit.)

For charge orders call toll free 1-800-972-5858. (\$15.00 minimum).

Free gold transfer slips included for indexing volume and year.

Please allow four to five weeks for delivery.

TO: Jesse Jones Industries
499 E. Erie Avenue, DEPT. AJR
Philadelphia, PA 19134

I enclose my check or money order for \$ _____
(PA residents add 6% sales tax)

Send me ☐ Files ☐ Binders for my journals

Name _____

Address (will not ship to P.O. Box) _____

City/State/Zip _____

Satisfaction guaranteed.

INDEX TO ADVERTISERS

Academic Press, Inc.	A23
Berlex Imaging	A17, A18, A19, A20
Braintree Laboratories	A22
Eastman Kodak	A6, A7
Elema-Schonander, Inc.	A21
E-Z-EM Company	Cover 2
FUJI	Cover 3
General Electric.....	A8, A9
J.B. Lippincott Company	A28
Mallinckrodt, Inc.	A2, A13, A14, A15, A16
Nuclear Associates	A10, A26
Oregon Health Sciences	A31
S & S X-Ray	A25
Siemens Medical Systems, Inc.	A27
Winthrop Laboratories	A11, A12

We try to present an accurate index. Occasionally this may not be possible because of a last-minute change or omission.



Fingertip Processing

With the FTI 200 Thermal Imager, a touch of a button delivers copy of video signals—in room light—in just 22 seconds.

- *Unique*—World's only self-fixing, polyester base thermal film
- *Fast*—Records up to 4 images per minute
- *Versatile*—High line-rate compatibility with optional video interface
- *Sharp & Clear*—Up to 64 shades of gray
- *Convenient*—100% room light loading, no processor needed
- *Useful*—Ultrasound, CT, DSA, MRI with excellent archival qualities

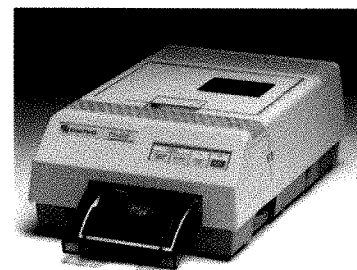
For full details, ask your Fuji sales representative, or call (800) 431-1850. In CT, (203) 353-0300.

CIRCLE 7 ON READER SERVICE CARD



The Reason for Change!

Buckhale Chicago Stamford CT



REVIEW ARTICLES

- 685 **Crystal-associated arthropathies.** Rubenstein J, Pritzker KPH
- 697 **Current status of temporomandibular joint imaging for the diagnosis of internal derangements.** Kaplan PA, Helms CA
- 707 **Clinical Doppler imaging.** Grant EG, Tessler FN, Perrella RR

EDITORIAL

- 719 **Irresponsible coauthorship.** Berk RN

PERSPECTIVE

- 721 **Bayesian analysis revisited: a radiologist's survival guide.** Chang PJ

CARDIOPULMONARY RADIOLOGY

- 729 **Comparison of cine MR imaging with Doppler echocardiography for the evaluation of aortic regurgitation.** Pflugfelder PW, Landzberg JS, Cassidy MM, et al.
- 737 **Coronary angiography in atrial myxoma: findings in nine cases.** Fueredi GA, Knechtges TE, Czarnecki DJ
- 739 **Case report: CT diagnosis of acute pericardial tamponade after blunt chest trauma.** Goldstein L, Mirvis SE, Kostrubiak IS, Turney SZ
- 743 **Acquired tracheomegaly in adults as a complication of diffuse pulmonary fibrosis.** Woodring JH, Barrett PA, Rehm SR, Nurenberg P
- 749 **Pulmonary edema as a complication of interleukin-2 therapy.** Conant EF, Fox KR, Miller WT
- 753 **Case report. Cavitating and noncavitating granulomas in AIDS patients with *Pneumocystis pneumonia*.** Klein JS, Warnock M, Webb WR, Gamsu G

GASTROINTESTINAL RADIOLOGY

- 755 **Percutaneous transhepatic embolization of gastroesophageal varices: results in 400 patients.** L'Herminé C, Chastanet P, Delemazure O, Bonnière PL, Durieu JP, Paris JC
- 761 **Clonorchiasis: sonographic findings in 59 proved cases.** Lim JH, Ko YT, Lee DH, Kim SY
- 765 **Duplex sonography of the portal venous system: pitfalls and limitations.** Parvey HR, Eisenberg RL, Giyanani V, Krebs CA
- 771 **Detection of liver metastases with superparamagnetic iron oxide in 15 patients: results of MR imaging at 1.5 T.** Marchal G, Van Hecke P, Demaerel P, et al.

GENITOURINARY RADIOLOGY

- 777 **Peritubal adhesions in infertile women: diagnosis with hysterosalpingography.** Karasick S, Goldfarb AF
- 781 **Pregnancies in septate uteri: outcome in relation to site of uterine implantation as determined by sonography.** Fedele L, Dorta M, Brioschi D, Giudici MN, Candiani GB
- 785 **Pictorial essay. Imaging of abdominal aortic aneurysms.** LaRoy LL, Cormier PJ, Matalon TAS, Patel SK, Turner DA, Silver B
- 793 **Case report. Transcaval ureter with hydronephrosis: radiologic demonstration.** Rosen MP, Walker TG, Brennan JF, Babayan RK, Greenfield AJ

MUSCULOSKELETAL RADIOLOGY

- 795 **Osteomyelitis of the foot in diabetic patients: evaluation with plain films, ^{99m}Tc-MDP bone scintigraphy, and MR imaging.** Yuh WTC, Corson JD, Baraniewski HM, et al.

PEDIATRIC RADIOLOGY

- 801 **Voiding cystourethrography as a predictor of reflux nephropathy in children with urinary-tract infection.** Hellström M, Jacobsson B, Mårild S, Jodal U

- 805 **Case report. MR imaging of coronary artery aneurysms in a child with Kawasaki disease.** Bisset GS III, Strife JL, McCloskey J
- 809 **Case report. MR imaging of the criss-cross heart.** Link KM, Weesner KM, Formanek AG

NEURORADIOLOGY

- 813 **Multicenter double-blind placebo-controlled study of gadopentetate dimeglumine as an MR contrast agent: evaluation in patients with cerebral lesions.** Russell EJ, Schaible TF, Dillon W, et al.
- 825 **Gadolinium-DTPA-enhanced MR imaging of the post-operative lumbar spine: time course and mechanism of enhancement.** Ross JS, Delamarter R, Hueftle MG, et al.
- 835 **MR imaging artifacts of the axial internal anatomy of the cervical spinal cord.** Curtin AJ, Chakeres DW, Bulas R, Boesel CP, Finneran M, Flint E
- 843 **MR imaging in the tethered spinal cord syndrome.** Raghavan N, Barkovich AJ, Edwards M, Norman D

MAGNETIC RESONANCE IMAGING

- 853 **Comparison of STIR and spin-echo MR imaging at 1.5-T in 90 lesions of the chest, liver, and pelvis.** Shuman WP, Baron RL, Peters MJ, Tazioli PK

COMPUTER PAGE

- 861 **Semiautomated slide identification by using a personal computer and printer.** Feuerstein IM

SPECT-CT

- 865 **Technical note. Composite SPECT-CT images: technique and potential applications in chest and abdominal imaging.** Kaplan IL, Swayne LC

INFORMED CONSENT

- 867 **Opinion. Informed consent for contrast media.** Bush WH

DIGITAL RADIOGRAPHY

- 870 **Technical note. Digital radiography: uses and limitations of the method.** Novak DL, Bates BF

ARRS ANNUAL MEETING CASE OF THE DAY

- 873 **General diagnosis case of the day.** Glazer HS, Dehdashti F, Siegel BA, McClennan BL, Balfe DM, Andriole GL
- 875 **Sonography case of the day.** Middleton WD, Middleton MA, Wiele K
- 877 **Pediatric radiology case of the day.** McAlister WH, Siegel MJ
- 879 **Neuroradiology case of the day.** Shoemaker EI, Romano AJ, Gado M, Hodges FJ III

OTHER CONTENT

- 808 **Forthcoming articles**
- 882 **Books received**
- 884 **American Roentgen Ray Society information**
- 885 **ARRS meeting invitation**
- 887 **ARRS meeting summary**
- 888 **ARRS membership information and application**
- 891 **Letters**
- 898 **Review of current literature**
- 904 **News**
- Book reviews** 696, 706, 718, 728, 736, 742, 776, 780, 824
- 907 **Classified advertisements**
- A3 **Guidelines for authors**
- A10 **AJR business and subscriber information**

WCE 12.11.90

AJR

American
Journal of
Roentgenology

May 1989

Precise localization of non-palpable lesions ...from E-Z-EM

PercuGuideTM

Regardless of your present method of marking non-palpable lesions, PercuGuideTM can improve upon it.

Unlike improvised markers, PercuGuide can't shift with patient movement. It won't disperse over time like a dye. And PercuGuide offers a range of refinements that no other wire guide system can match.

Afterloading of the PercuGuide wire guide eliminates any chance of the barb seating before the needle has been properly positioned. A plastic sheath makes loading easy, and a permanently affixed stiffening cannula protects the wire from being accidentally severed while it acts as a visible guide for the surgeon.

Clearly marked 1 cm gradations on the cannula, and a specially designed gripping hub aid in the precise placement of the needle. A smaller hub is also available for use with compression devices, and each needle is supplied with an E-Z Mark[®] radiopaque marker and a handy ruler.

If you're presently using another system, or if you've never used a wire guide before, PercuGuide can help improve your technique. For more information, contact your local E-Z-EM representative, or call E-Z-EM Interventional Products Marketing at 800-544-4624. In New York call 516-333-8230.

E-Z-EM

More than barium—
much more



E-Z-EM, Inc.,
7 Portland Avenue
Westbury, N.Y. 11590

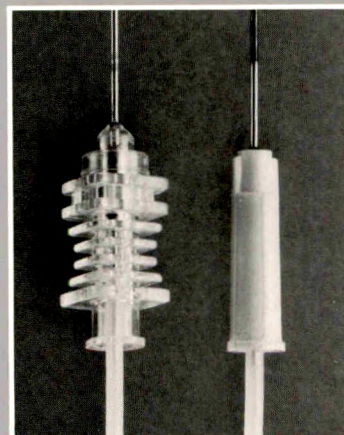
Permanently affixed stiffening cannula
protects wire from being severed
during surgery

Plastic sheath for easy loading and
protection of wire guide

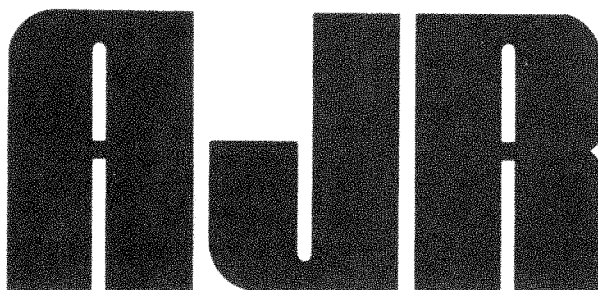
Wire guide is loaded after
positioning needle to eliminate
premature setting of barb in tissue

Your choice of an ergonomically
designed hub for maximum control
or a special, smaller hub for use with
compression devices

1 cm gradations on cannula
for precise depth control



Now available with a
smaller hub for use with
all compression devices.



American Journal of Roentgenology
Diagnostic Imaging and Related Sciences

- Editor-in-Chief** Robert N. Berk, *La Jolla, California*
University of California, San Diego
School of Medicine and Medical Center
- Editor Emeritus** Melvin M. Figley, *Seattle, Washington*
- Associate Editor** Saskia von Waldenburg Hilton, *San Diego, California*
- Consulting Editor** Juan M. Taveras, *Boston, Massachusetts*
- Statistician** Charles C. Berry, *San Diego, California*

Editorial Board


- | | | |
|-------------------------|--------------------------|--------------------|
| John R. Amberg | William R. Hendee | Peter M. Ronai |
| Itamar Aviad | John R. Hesselink | Sjef H. J. Ruijs |
| Lawrence W. Bassett | Charles B. Higgins | Carol M. Rumack |
| Gregory P. Borkowski | Melvyn T. Korobkin | Stuart S. Sagel |
| William G. Bradley, Jr. | Thomas L. Lawson | David J. Sartoris |
| Peter L. Cooperberg | Bruce L. McClennan | Stefan C. Schatzki |
| N. Reed Dunnick | Albert A. Moss | Edward A. Sickles |
| David K. Edwards | Jeffrey H. Newhouse | Barry A. Siegel |
| Ronald G. Evens | Donald L. Resnick | David D. Stark |
| David S. Feigin | Stewart R. Reuter | Edward T. Stewart |
| Paul J. Friedman | Charles A. Rohrmann, Jr. | Eric vanSonnenberg |

Editorial Staff: Margaret Levene, *managing editor*; Katie L. Spiller, Barbara Rose, Barbara L. Halliburton, and Janine Anderson, *manuscript editors*; Nancy Rydbeck, *office manager*; Sheri Smith, *administrative assistant*; Sandra L. Griffin, *administrative secretary*.

AJR, AMERICAN JOURNAL OF ROENTGENOLOGY (ISSN 0361 803X) is the official journal of the American Roentgen Ray Society and is published monthly by Williams & Wilkins, 428 E. Preston St., Baltimore, MD 21202. Annual dues include \$50 for journal subscription. Second-class postage paid at Baltimore, MD, and at additional mailing offices. Postmaster, send address changes (Form 3579) to AJR, 428 E. Preston St., Baltimore, MD 21202. Subscription rates \$100 (\$145 foreign); institutions \$110 (\$155 foreign); in training \$25 (\$70 foreign); single copy \$16 (\$19 foreign). Japanese rates include airfreight. Japanese yen price is available from our sole agent USACO Corporation, 13-12, Shimbashi 1-Chome, Minato-Ku, Tokyo 105, Japan, telephone 03-502-6471. Airmail rates furnished on request. Indexed by *Current Contents* and *Index Medicus*. Copyright © 1989 by American Roentgen Ray Society.

0361-803X/89\$2.00

**COMING
VERY SOON:**



%

**A NEW NONIONIC
THAT PUTS THE
PERCENTAGES IN
YOUR FAVOR**

AJR Guidelines for Authors

Address new and revised manuscripts, correspondence, and classified ads to the Editor:

AJR Editorial Office
2223 Avenida de la Playa, Suite 200
La Jolla, CA 92037-3218
Telephone: (619) 459-2229; FAX: (619) 459-8814

Inquiries regarding subscriptions, display advertising, reprints, or permission to republish *AJR* material should be addressed to the publisher:

The Williams & Wilkins Co.
428 E. Preston St.
Baltimore, MD 21202 Telephone: (301) 528-4133

The *AJR* publishes original contributions to the advancement of medical diagnosis and treatment. Submitted manuscripts should not contain previously published material and should not be under consideration for publication elsewhere. Papers dealing with neuroradiology should be addressed to: American Journal of Neuroradiology, Dept. of Radiology, Massachusetts General Hospital, Boston, MA 02114. At the discretion of the *AJR* Editor, *AJNR* articles that are of interest to the general reader may be republished in the *AJR*. Neuro-radiologic papers sent to the *AJR* will be forwarded to the Editorial Office of the *AJNR*.

Manuscript decisions are based on peer review. Reviewers receive manuscripts without title pages to ensure an unbiased review. Statements made in the article, including changes made by the Editor or manuscript editor, are the responsibility of the author and not of the *AJR* or its publisher. Authors will be sent the edited manuscript, galley proof, and proofs of illustrations. If the corresponding author will be unavailable to review galleys, arrangements should be made for a coauthor or colleague to read and return the proof.

The following guidelines are based on instructions set forth in the **Uniform Requirements for Manuscripts Submitted to Biomedical Journals** (*Ann Intern Med* 1988;108:258-265). Articles will be edited, however, to conform to the individual style of *AJR*.

General Guidelines for Major Papers

Abstract. Clearly state (in 200 words or less) the purpose, methods, results, and conclusions of the study. Include actual data.

Introduction. Briefly describe the purpose of the investigation, including relevant background information.

Methods. Describe the research plan, the materials (or subjects), and the methods used, in that order. Explain in detail how disease was confirmed and how subjectivity in observations was controlled.

Results. Present results in a clear, logical sequence. If tables are used, do not duplicate tabular data in text, but do describe important trends and points.

Discussion. Describe the limitations of the research plan, materials (or subjects), and methods, considering both the

purpose and the outcome of the study. When results differ from those of previous investigators, explain the discrepancy.

AUTHOR'S CHECKLIST

For priority handling, complete the following checklist, sign the copyright form on the reverse side of this page, and include both with the manuscript.

_____ Two copies of the manuscript (the original and a photocopy) and two complete sets of figures are submitted. One copy has been retained by the author.

_____ If appropriate, *AJR* Guidelines for case reports, technical notes, pictorial essays, or letters to the Editor have been followed. (See page A5.)

_____ The manuscript, including references, figure legends, and tables, is typed double-spaced on 8½ × 11 in. (21.6 × 27.9 cm) *nonerasable* paper. Right-hand margins are not justified.

_____ All manuscript pages are numbered consecutively beginning with the abstract. Authors' names do not appear on the manuscript pages.

_____ The manuscript is organized as follows: title page, blind title page (title only), abstract, introduction, methods, results, discussion, acknowledgments, references, tables, figure legends, and figures.

_____ Informed consent has been obtained from patients who participated in clinical investigations. If experiments were performed on animals, authors complied with NIH guidelines for use of laboratory animals.

_____ Use of unfamiliar acronyms and abbreviations is kept to a minimum. When abbreviations are used they are defined at first mention, followed by the abbreviation in parentheses.

_____ Metric measurements are used throughout, or the metric equivalent is given in parentheses.

_____ Names and locations (city and state only) of manufacturers are given for equipment and nongeneric drugs.

Title Page

_____ The following information is given: title of article; names and complete addresses (including zip code) of all authors; current addresses of authors who have moved since study; acknowledgment of grant or other assistance. The corresponding author is clearly identified, and a current address, phone number, and Fax number are given.

_____ Two copies of a blind title page are included giving only the title (without the authors' names) for use in the review process.

Abstract

_____ An abstract of approximately 200 words concisely states the purpose, methods, and results of the study in one paragraph. Actual data are included. Conclusions are stated in a second, summary paragraph.

_____ No abbreviations or reference citations are used.

References

References (not to exceed 35) are typed double-spaced starting on a separate page and are **numbered consecutively in the order in which they appear in the text**.

All references are cited in the text and are enclosed in brackets and typed on line with the text (not superscript).

Unpublished data are not cited in the reference list, but are cited parenthetically in the text, for example, (Smith DJ, personal communication), (Smith DJ, unpublished data). This includes papers submitted, but not yet accepted, for publication.

Inclusive page numbers (e.g., 333–335) are given for all references.

Journal names are abbreviated according to *Index Medicus*.

Style and punctuation of references follow the format illustrated in the following examples (all authors are listed when six or less; when seven or more authors, the first three are listed, followed by "et al."):

Journal article

1. Long RS, Roe EW, Wu EU, et al. Membrane oxygenation: radiographic appearance. *AJR* 1986;146:1257–1260

Book

2. Smith LW, Cohen AR. *Pathology of tumors*, 6th ed. Baltimore: Williams & Wilkins, 1977:100–109

Chapter in a book

3. Breon AJ. Serum monitors of bone metastasis. In: Clark SA, ed. *Bone metastases*. Baltimore: Williams & Wilkins, 1983:165–180

Paper presented at a meeting

4. Lau FS, Kirk AN. MR imaging of the spine. Presented at the annual meeting of the American Roentgen Ray Society, Washington, DC, April 1986

Tables

Each table is typed double-spaced on a separate page without vertical or horizontal rules; each has a short, descriptive title. Tables do not exceed two pages in length and contain at least four lines of data.

Tables are numbered in the order in which they are cited in the text.

Abbreviations are defined in an explanatory note below each table.

Tables are self-explanatory and do not duplicate data given in the text or figures.

All arithmetic (percentages, totals, differences) has been double checked for accuracy, and tabular data agree with data given in the text.

Figures and Legends

Two complete sets of original figures are submitted unmounted in labeled envelopes.

Figures are clean, unscratched, 5 × 7 in. (13 × 18 cm) glossy prints with **white borders**. A separate print is submitted for each figure *part*.

All figure parts relating to one patient have the same figure number.

Each figure is labeled on the back with the figure number and an arrow indicating "top." For black-and-white figures, labeling is done on a gummed label, which is then affixed to the back of the print. *Never* use labels on color figures, but write figure number on the back lightly in pencil. *Never* use ink on front or back of any figures.

Author's names are *not* written on the backs of figures.

Only removable (rub-on) arrows and letters are used on the figures. Symbols are uniform in size and style and are not broken or cracked.

Images are uniform in size and magnification.

Line drawings are done in black ink on a white background. They are professional in quality, and all use the same size type. (Only glossy prints are acceptable.)

Written permission has been obtained for use of all previously published illustrations (and copies of permission letters are included), and an appropriate credit line is given in the legends.

Legends are typed double-spaced, and figure numbers correspond with the order in which the figures are cited in the text.

Transfer of Copyright Agreement, Conflict of Interest Acknowledgment, Certification of Coauthors, and Exclusive Publication Statement

Complete copyright to the article entitled: _____

is hereby transferred to the American Roentgen Ray Society (for United States government employees to the extent transferable), effective if and when the article is accepted for publication in the *American Journal of Roentgenology*. In the case of the authors who are officers or employees of the United States government, the American Roentgen Ray Society recognizes that works prepared by officers or employees of the United States government as part of their official government duties are in the public domain.

Authors reserve all proprietary rights other than copyright, such as patent rights and the right to use all or part of this article in future works of their own. The authors retain the right of replication, subject only to crediting the original source of publication and receiving written permission from the publisher.

Authors guarantee that this manuscript contains no matter that is libelous or otherwise unlawful, invades individual privacy, or infringes any proprietary rights.

Authors understand that they will receive no royalty or other compensation from the American Roentgen Ray Society or the publisher.

Authors guarantee that the editor has been or will be informed of any proprietary or commercial interest or conflicts of interest the authors may have that relate directly or indirectly to the subject of this article.

All authors certify that they have made substantive and specific intellectual contributions to the article and assume public responsibility for its content.

Finally, the authors certify that none of the material in this manuscript has been published previously or is currently under consideration for publication elsewhere.

First author/date

Second author

Third author

Fourth author

Fifth author

Sixth author

This agreement must be signed by all authors in order for the manuscript to be published.

Case Reports

A case report is a brief description of a special case that provides a message that transcends the individual patient.

Format. There is no abstract. The introduction should be a short paragraph giving the general background and the specific interest of the case. No more than one case should be described in detail (similar ones can be mentioned briefly in the discussion). Emphasis should be on the radiologic aspects; clinical information must be limited to that necessary to provide a background for the radiology. The discussion should be succinct and should focus on the specific message and relevance of radiologic methods. A review of the literature is not appropriate.

Length. Maximum of five double-spaced, typewritten pages, including the references but not the title page or figure legends.

References. Maximum of eight.

Figures. Maximum of three or four, unless the text is shortened accordingly. Legends must not repeat the text.

Tables and Acknowledgments. Not appropriate in case reports.

Technical Notes

A technical note is a brief description of a specific technique or procedure, modification of a technique, or equipment of interest to radiologists.

Format. No abstract, headings, or subheadings are required. If headings are used, they should be a combination of "Case Report," "Materials and Methods," "Results," and "Discussion." A brief one-paragraph introduction should be included to give the general background. Discussion should be limited to the specific message, including the uses of the technique or equipment. Literature reviews and lengthy case reports are not appropriate.

Length. Maximum of five double-spaced, typewritten pages, including the references but not the title page or figure legends.

References. Maximum of eight.

Figures. Maximum of two, unless the text is shortened accordingly.

Tables and Acknowledgments. Not appropriate in technical notes.

Pictorial Essays

A pictorial essay is an article that conveys its message through illustrations and their legends. Unlike other *AJR* articles, which are based on original research, pictorial essays serve primarily as teaching tools, like exhibits at a scientific meeting. They are not encyclopedic book chapters. No abstract is necessary.

Length. Maximum of four double-spaced, typewritten pages, including the references but not the title page or figure legends.

References. Maximum of four.

Figures. Maximum of 30 figure parts. Number should be as few as necessary to convey the message of the paper.

Tables and Acknowledgments. Not appropriate in pictorial essays.

Letters to the Editor and Replies

Letters to the Editor and Replies should offer objective and constructive criticism of published articles. Letters may also discuss matters of general interest to radiologists. Do not end a letter with a hand-written signature.

Format. All letters should be typed double-spaced on nonletterhead paper, with no greeting or salutation. Name and affiliation should appear at the end of the letter. Titles for letters should be short and pertinent. The title for a reply is simply "Reply."

Length. Maximum of two double-spaced, typewritten pages, including references.

References. Maximum of four.

Figures. Maximum of two.

Tables and Acknowledgments. Not appropriate in Letters to the Editor and Replies.

Opinions, Commentaries, and Perspectives

Opinions, commentaries, and perspectives are special articles dealing with controversial topics or issues of special concern to radiologists.

Format. Include a title page but no abstract. Headings may be used to break up the text.

Length. Maximum of five double-spaced, typewritten pages.

References. Maximum of five.

Tables and Figures. Maximum of four.

Computer Page Articles

Articles published on the computer page deal with practical computer applications to radiology.

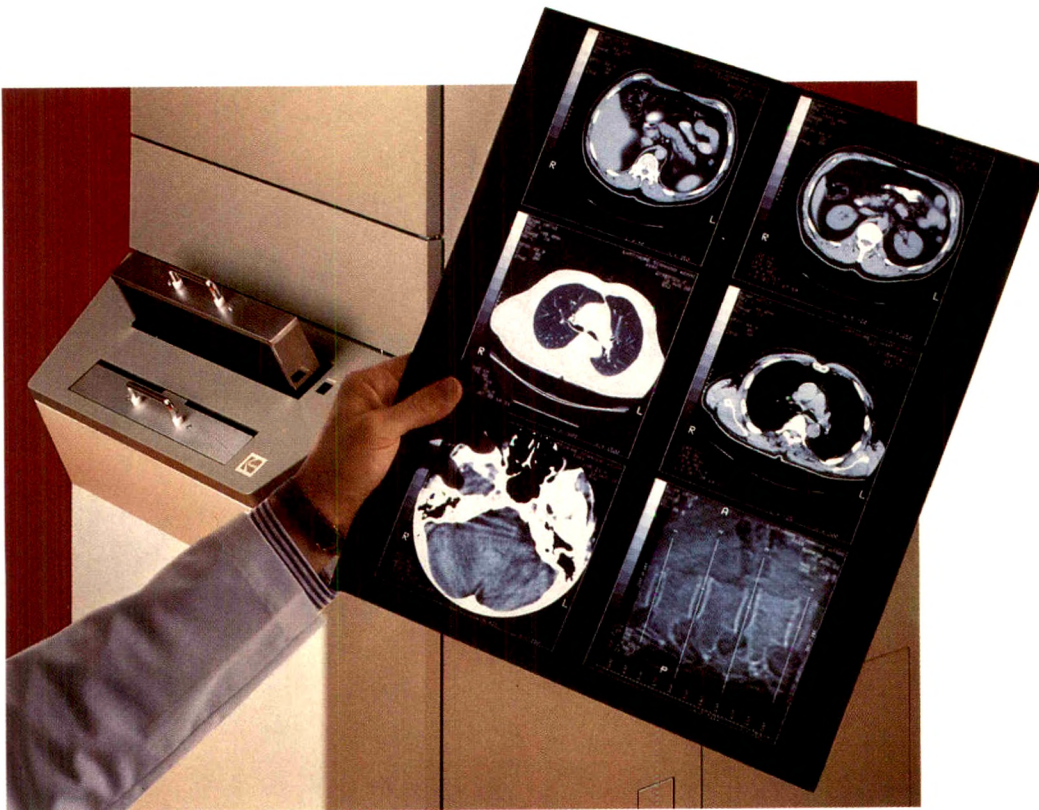
Format. Include a title page but no abstract.

Length. Maximum of eight double-spaced, typewritten pages.

References. Maximum of five.

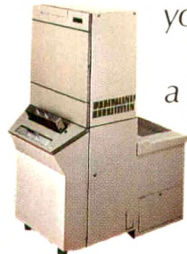
Figures and Tables. Maximum of five. Computer printouts are not acceptable. Figures must be submitted as 5 × 7 in. glossy prints.

**STEP UP
TO LASER
IMAGING
WITH
KODAK**



***Introducing the Kodak Ektascan laser printer, model 100.
The quality of digital imaging for today's and tomorrow's
imaging systems.***

Now you can have consistent, artifact-free, high-resolution digital images from current and future imaging systems. The new Kodak Ektascan laser printer, model 100, is available with custom interfaces for CT, MRI and DSA. Flexible tone scaling gives you the look you like on Kodak Ektascan laser imaging film. And a compact 28 × 30-inch footprint makes it ideal for mobile applications. Part of a complete Kodak imaging system, the Ektascan laser printer, docked to a Kodak processor, gives you maximum productivity.



Ask your Kodak representative for details, or specify a Kodak Ektascan laser printer when you order an imaging system.

The digital imaging advantage.

The new vision of Kodak



The name
that started
a revolution.

*The
Leader*

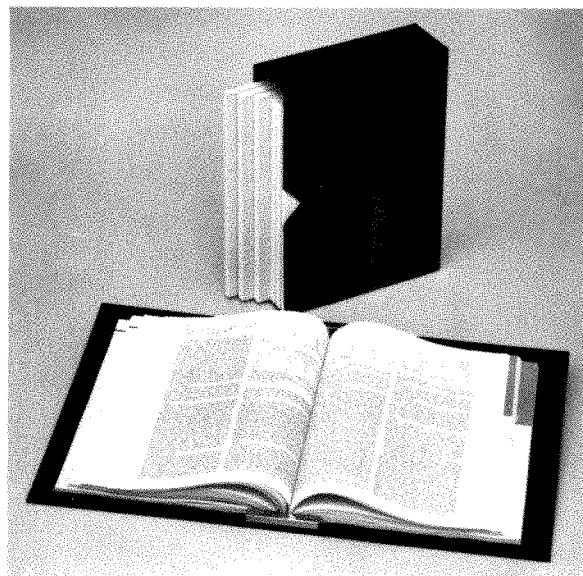
GO LYTE[®]

PEG-3350 and Electrolytes for Oral Solution

CIRCLE 35 ON READER SERVICE CARD

LABORATORIES, INC.
Braintree

© 1989 Braintree Laboratories, Inc.
TRE-1035



Protect your copies of

AJR: AMERICAN JOURNAL OF ROENTGENOLOGY

with Jesse Jones Binders or Files

Keep your journals clean, orderly, and readily accessible with Jesse Jones Binders or Files. Two Binders or two box style Files are all you need to accommodate a full year's worth of issues. Both Binders and Files are handsomely made with rich black leatherette covers and gold leaf embossed lettering.

Jesse Jones Binders open flat for easy reading and reference and are economically priced at only \$9.95 each; 3 for \$27.95, or 6 for \$52.95 postpaid. The rugged, compact box Files are only \$7.95 each; 3 for \$21.95, or 6 for \$39.95. Add \$1.00/unit postage and handling. (Outside the U.S. add \$2.50/unit.)

For charge orders call toll free 1-800-972-5858. (\$15.00 minimum).

Free gold transfer slips included for indexing volume and year.

Please allow four to five weeks for delivery.

TO: Jesse Jones Industries
499 E. Erie Avenue, DEPT. AJR
Philadelphia, PA 19134

I enclose my check or money order for \$.....
(PA residents add 6% sales tax)

Send me ____ ☐ Files ☐ Binders for my journals

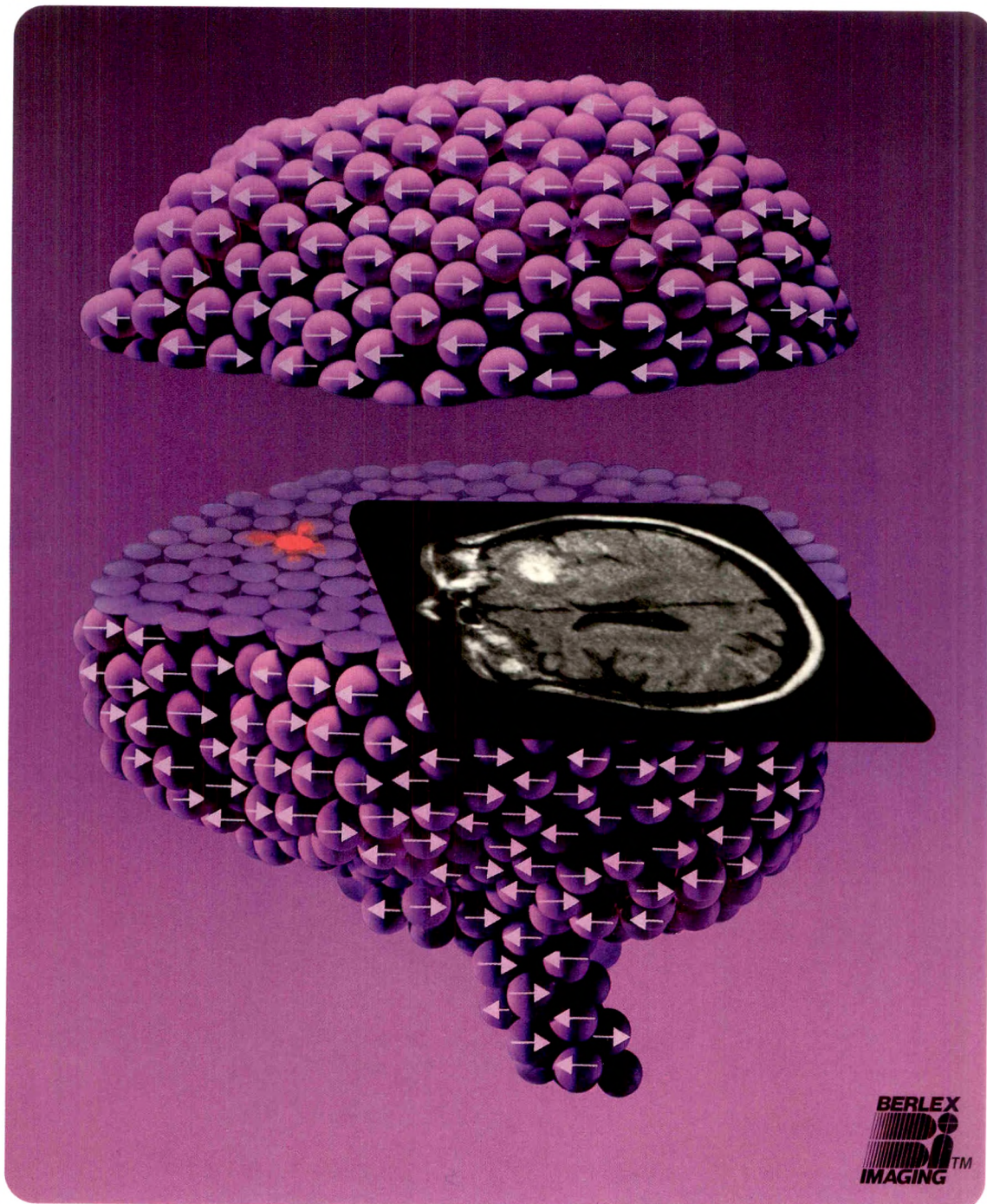
Name

Address (will not ship to P.O. Box)

City/State/Zip

Satisfaction guaranteed.

**BETTER MEDICINE
THROUGH
BETTER IMAGES**

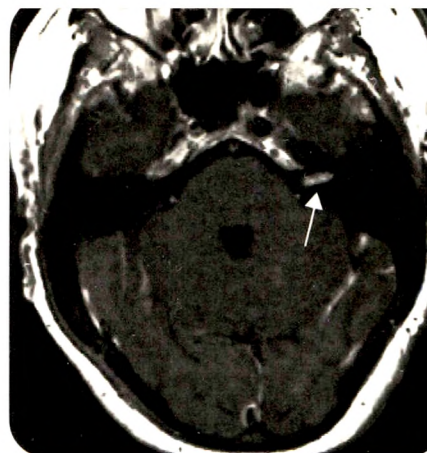
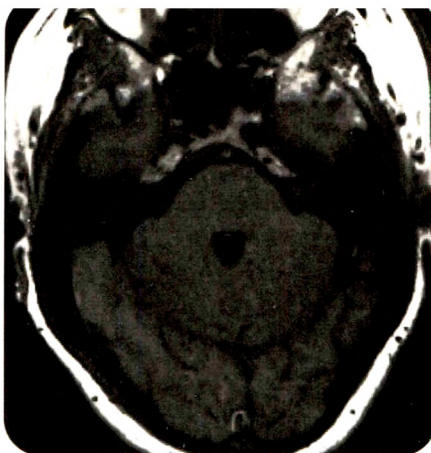


BERLEX
IMAGING™

Magnevist[®]
(gadopentetate
dimeglumine) INJECTION

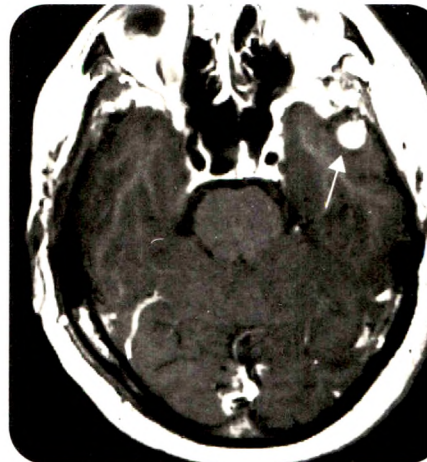
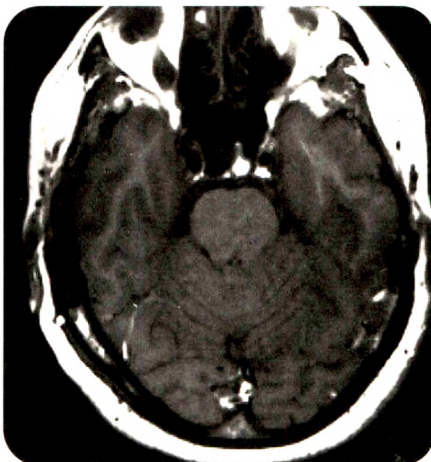
**CONFIRMED
LESION
Acoustic
neuroma**

T1-weighted MRI scan
pre-MAGNEVIST® injection.
(TR 400, TE 20)



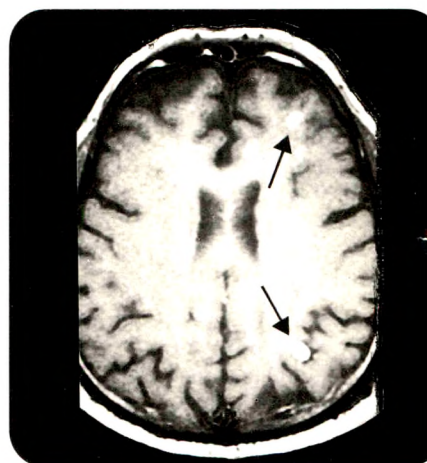
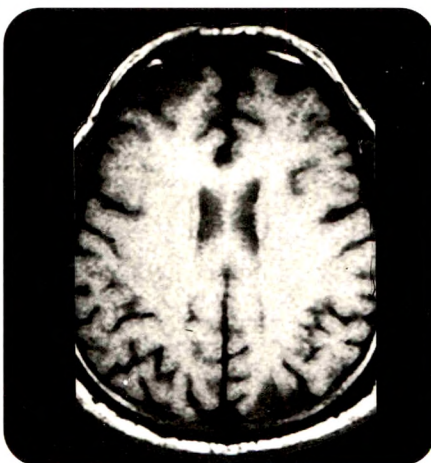
**DEMONSTRATED
SECOND
TUMOR
Meningioma**

T1-weighted MRI scan
pre-MAGNEVIST® injection.
(TR 400, TE 20)



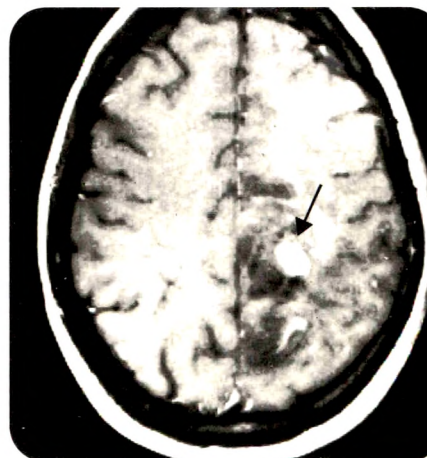
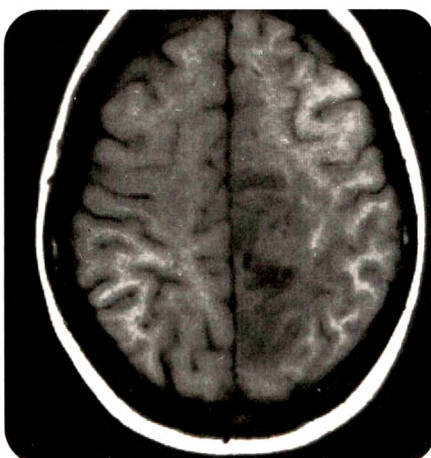
**DETECTED
LESIONS
Metastases**

T1-weighted MRI scan
pre-MAGNEVIST® injection.
(TR 600, TE 20)



**CLEARLY
DELINEATED
LESION
Glioma**

T1-weighted MRI scan
pre-MAGNEVIST® injection.
(TR 650, TE 20)



T1-weighted MRI scan
post-MAGNEVIST® injection
confirmed intracranial
acoustic neuroma.
(TR 400, TE 20)

T1-weighted MRI scan
post-MAGNEVIST® injection
demonstrated
second tumor in patient
with acoustic neuroma.
(TR 400, TE 20)

T1-weighted MRI scan
post-MAGNEVIST® injection
demonstrated lesions
not detected preinjection.
(TR 600, TE 20)

T1-weighted MRI scan
post-MAGNEVIST® injection
showed improved
delineation of lesion.
(TR 650, TE 20)

Contrast enhancement to facilitate diagnosis.

In the majority of patients, diagnostic ability was facilitated or improved by enhanced contrast with MAGNEVIST® injection.

CONTRAST ENHANCEMENT TO FACILITATE DIAGNOSIS¹

Type of Study	No. of Patients	%
Double-blind	37/57	65
Open-label	70/113	62

Increased number of lesions detected

NUMBER OF LESIONS DETECTED¹

Result of Study	Type of Study	MAGNEVIST® injection	
		No. of Patients	%
Increased no of lesions postinjection	Double-blind	10/43*	23
	Open-label	16/113*	14
Lesions seen postinjection but not preinjection	Open-label	66/232	28
	Total	92/388	24

* The question was answered only for patients with contrast enhancement.

Safety profile. In clinical trials, MAGNEVIST® injection was well tolerated.¹

INCIDENCE OF ADVERSE REACTIONS AMONG 410 PATIENTS

Type of Reaction	% of Patients With Adverse Reactions Related to MAGNEVIST® Injection	Total Reactions
Headache*	4.9%	9.8%
Nausea	3.4%	4.1%
Vomiting	1.5%	1.7%
Other†	<1.0%	<2.0%

* The majority of headaches were transient in nature. In children, two cases of hyperventilation were recorded.

- In clinical trials, 15% to 30% of patients experienced an asymptomatic transient rise in serum iron.
- The safety of MAGNEVIST® injection in patients with hemolytic disorders has not been studied.

Please see Warnings, Precautions and Adverse Reactions sections in full prescribing information for MAGNEVIST® injection on last page of this advertisement.

† Data on file, Berlex Laboratories, Inc.



Magnevist
(gadopentetate
dimeglumine) INJECTION

Dosage and administration The recommended dosage of MAGNEVIST® injection is 0.2 mL/kg, administered intravenously, at a rate not to exceed 10 mL per minute. The maximum total dose is 20 mL. The imaging procedure should be completed within one hour of injection.

MAGNEVIST® (brand of gadopentetate dimeglumine) Injection

60621-3

DESCRIPTION

MAGNEVIST® (brand of gadopentetate dimeglumine) Injection is the N-methylglucamine salt of the gadolinium complex of diethylenetriamine pentaacetic acid, and is an injectable contrast medium for magnetic resonance imaging (MRI). Gadopentetate dimeglumine is to be administered by intravenous injection.

Each mL of MAGNEVIST® Injection contains 469.01 mg gadopentetate dimeglumine, 0.39 mg meglumine, 0.15 mg diethylenetriamine pentaacetic acid and water for injection. MAGNEVIST® Injection contains no antimicrobial preservative. MAGNEVIST® Injection is provided as a sterile, clear, colorless to slightly yellow aqueous solution.

MAGNEVIST® Injection is a 0.5-mol/L solution of 1-deoxy-1-(methylamino)-D-glucitol dihydrogen [N,N-bis[2-bis(carboxymethyl)amino]ethyl]glycinate-(5-)-]gadolinium (2-)(2:1) with a molecular weight of 938.

MAGNEVIST® Injection has a pH of 6.5 to 8.0. Pertinent physicochemical data are noted below:

PARAMETER

Osmolality (mOsmol/kg water) @ 37° C	1,940
Viscosity (cP) @ 20° C	4.9
@ 37° C	2.9
Density (g/mL)	1.199

MAGNEVIST® Injection has an osmolality 6.8 times that of plasma (285 mOsmol/kg water) and is hypertonic under conditions of use.

CLINICAL PHARMACOLOGY

The pharmacokinetics of intravenously administered gadopentetate dimeglumine in normal subjects conforms to a two-compartment open-model with mean distribution and elimination half-lives (reported as mean ± SD) of about 0.2 ± 0.13 hours and 1.6 ± 0.13 hours, respectively.

Upon injection, the meglumine salt is completely dissociated from the gadopentetate dimeglumine complex. Gadopentetate is exclusively eliminated in the urine with 83 ± 14% (mean ± SD) of the dose excreted within 6 hours, and 91 ± 13% (mean ± SD) by 24 hours, post-injection. There was no detectable biotransformation or decomposition of gadopentetate dimeglumine.

The urinary and plasma clearance rates (1.76 ± 0.39 mL/min/kg and 1.94 ± 0.28 mL/min/kg, respectively) of gadopentetate are essentially identical, indicating no alteration in elimination kinetics on passage through the kidneys and that the drug is essentially cleared through the kidney. The volume of distribution (266 ± 43 mL/kg) is equal to that of extracellular water, and clearance is similar to that of substances which are subject to glomerular filtration.

The extent of protein binding and blood cell partitioning of gadopentetate dimeglumine is not known.

Gadopentetate dimeglumine is a paramagnetic agent and, as such, it develops a magnetic moment when placed in a magnetic field. The relatively large magnetic moment produced by the paramagnetic agent results in a relatively large local magnetic field, which can enhance the relaxation rates of water protons in the vicinity of the paramagnetic agent.

In magnetic resonance imaging (MRI), visualization of normal and pathological brain tissue depends in part on variations in the radiofrequency signal intensity that occur with 1) changes in proton density; 2) alteration of the spin-lattice or longitudinal relaxation time (T₁); and 3) variation of the spin-spin or transverse relaxation time (T₂). When placed in a magnetic field, gadopentetate dimeglumine decreases the T₁ and T₂ relaxation time in tissues where it accumulates. At usual doses the effect is primarily on the T₁ relaxation time.

Gadopentetate dimeglumine does not cross the intact blood-brain barrier and, therefore, does not accumulate in normal brain or in lesions that do not have an abnormal blood-brain barrier, e.g., cysts, mature post-operative scars, etc. However, disruption of the blood-brain barrier or abnormal vascularity allows accumulation of gadopentetate dimeglumine in lesions such as neoplasms, abscesses, subacute infarcts.

INDICATIONS AND USAGE

Using magnetic resonance imaging (MRI) in adult patients, gadopentetate dimeglumine provides contrast enhancement in those intracranial lesions with abnormal vascularity or those thought to cause an abnormal blood-brain barrier. Gadopentetate dimeglumine has been shown to facilitate visualization of lesions including but not limited to brain tumors.

CONTRAINDICATIONS None known.

WARNINGS

The accepted safety considerations and procedures that are required for magnetic resonance imaging are applicable when MAGNEVIST® Injection is used for contrast enhancement. In addition, deoxygenated sickle erythrocytes have been shown in *in vitro* studies to align perpendicular to a magnetic field which may result in vaso-occlusive complications *in vivo*. The enhancement of magnetic moment by gadopentetate dimeglumine may possibly potentiate sickle erythrocyte alignment. MAGNEVIST® Injection in patients with sickle cell anemia and other hemoglobinopathies has not been studied.

Patients with other hemolytic anemias have not been adequately evaluated following administration of MAGNEVIST® Injection to exclude the possibility of increased hemolysis.

Hypotension may occur in some patients after injection of MAGNEVIST® Injection. In clinical trials two cases were reported and in addition, there was one case of a vasovagal reaction and two cases of pallor with dizziness, sweating and nausea in one and substernal pain and flushing in the other. These were reported within 25 to 85 minutes after injection except for the vasovagal reaction which was described as mild by the patient and occurred after 6-1/2 hours. In a study in normal volunteers one subject experienced syncope after arising from a sitting position two hours after administration of the drug. Although the relationship of gadopentetate dimeglumine to these events is uncertain, patients should be observed for several hours after drug administration.

PRECAUTIONS - General

Diagnostic procedures that involve the use of contrast agents should be carried out under direction of a physician with the prerequisite training and a thorough knowledge of the procedure to be performed.

Since gadopentetate dimeglumine is cleared from the body by glomerular filtration, caution should be exercised in patients with severely impaired renal function.

Animal studies suggest that gadopentetate dimeglumine may alter red cell membrane morphology resulting in a slight degree of extravascular (splenic) hemolysis. In clinical trials 15-30% of the patients experienced an asymptomatic transient rise in serum iron. Serum bilirubin levels were slightly elevated in approximately 3.4% of patients. Levels generally returned to baseline within 24 to 48 hours. Hematocrit and red blood cell count were unaffected and liver enzymes were not elevated in these patients. While the effects of gadopentetate dimeglumine on serum iron and bilirubin have not been associated with clinical manifestations, the effect of the drug in patients with hepatic disease is not known and caution is therefore advised.

When MAGNEVIST® Injection is to be injected using plastic disposable syringes, the contrast medium should be drawn into the syringe and used immediately.

If nondisposable equipment is used, scrupulous care should be taken to prevent residual contamination with traces of cleansing agents.

Repeat Procedures: If in the clinical judgment of the physician sequential or repeat examinations are required, a suitable interval of time between administrations should be observed to allow for normal clearance of the drug from the body.

Information for Patients:

Patients receiving MAGNEVIST® Injection should be instructed to:

1. Inform your physician if you are pregnant or breast feeding.
2. Inform your physician if you have anemia or any diseases that affect red blood cells.

LABORATORY TEST FINDINGS

Transitory changes in serum iron and bilirubin levels have been reported in patients with normal and abnormal liver function (See PRECAUTIONS - General).

CARCINOGENESIS, MUTAGENESIS, AND IMPAIRMENT OF FERTILITY No animal studies have been performed to evaluate the carcinogenic potential of gadopentetate dimeglumine.

Gadopentetate dimeglumine did not evoke any evidence of mutagenic potential in the Ames test (histidine-dependent *Salmonella typhimurium*) nor in a reverse mutation assay using tryptophan-dependent *Escherichia coli*. Gadopentetate dimeglumine did not induce a positive response in the (C3H 10T1/2) mouse embryo fibroblast cellular transformation assay, nor did it induce unscheduled DNA repair synthesis in primary cultures of rat hepatocytes at concentrations up to 5000 µg/mL. However, the drug did show some evidence of mutagenic potential *in vivo* in the mouse dominant lethal assay at doses of 6 mmol/kg, but did not show any such potential in the mouse and dog micronucleus tests at intravenous doses of 9 mmol/kg and 2.5 mmol/kg, respectively.

The results of a reproductive study in rats showed that gadopentetate dimeglumine when administered in daily doses of 0.1-2.5 mmol/kg, did not cause a significant change in the pregnancy rate in comparison to a control group. However, suppression of body weight gain and food consumption and a decrease in the mean weights of testes and epididymis occurred in male rats at the 2.5 mmol/kg dose. In female rats a decrease in the number of corpora lutea at the 0.1 mmol/kg dose and the suppression of body weight gain and food consumption at the 2.5 mmol/kg dose were observed.

In a separate experiment, 16 daily intravenous injections were administered to male rats. At a dose of 5 mmol/kg of gadopentetate dimeglumine, spermatogenic cell atrophy was observed. This atrophy was not reversed within a 16-day observation period following the discontinuation of the drug. This effect was not observed at a dose of 2.5 mmol/kg.

PREGNANCY CATEGORY C

Gadopentetate dimeglumine has been shown to retard development slightly in rats when given in doses 2.5 times the human dose, and in rabbits when given in doses of 7.5 and 12.5 times the human dose. The drug did not exhibit this effect in rabbits when given in doses 2.5 times the human dose. No congenital anomalies were noted in either species.

There are no adequate and well-controlled studies in pregnant women. MAGNEVIST® Injection should be used during pregnancy only if the potential benefit justifies the potential risk to the fetus.

NURSING MOTHERS

C¹⁴ labelled gadopentetate dimeglumine was administered intravenously to lactating rats at a dose of 0.5 mmol/kg. Less than 0.2% of the total dose was transferred to the neonate via the milk during the 24-hour evaluation period. It is not known to what extent MAGNEVIST® Injection is excreted in human milk. Because many drugs are excreted in human milk, caution should be exercised when the drug is administered to a nursing mother and consideration should be given to temporarily discontinuing nursing.

PEDIATRIC USE

Safety and effectiveness of MAGNEVIST® Injection in children has not been established.

ADVERSE REACTIONS

The most commonly noted adverse experience was headache with an incidence of 9.8%. The majority of headaches were transient and of mild to moderate severity. In 50% of the cases it was felt that the headaches were not related to MAGNEVIST® Injection. Nausea at 4.1% was the second most common adverse experience.

Localized pain and vomiting occurred in less than 2% of the patients.

The following additional adverse events occurred in less than 1% of the patients:

Body as a Whole: Injection site symptoms, namely, pain, coldness, warmth, burning; localized burning sensation, localized warmth, substernal chest pain, fever, weakness.

Cardiovascular: Hypotension, vasodilation, pallor, non-specific ECG changes.

Digestive: Gastrointestinal distress, stomach pain.

Nervous System: Agitation, paresthesia, dizziness.

Respiratory System: Throat irritation, rhinorrhea.

Skin: Rash, sweating.

Special Senses: Tinnitus, conjunctivitis, visual field defect, taste abnormality, dry mouth.

Laboratory: Transient elevation of serum transaminases.

The following other adverse events were reported. A causal relationship has neither been established nor refuted.

Body as a Whole: Back pain, pain. Allergic-like response including: urticaria, pruritus, wheezing, nasal congestion, sneezing, laryngismus and facial edema.

Cardiovascular: Hypertension, tachycardia, migraine, syncope.

Digestive: Constipation.

Nervous System: Anxiety, anorexia, convulsion, grand mal convulsions, nystagmus, drowsiness, diplopia.

Skin: Urticaria.

Special Senses: Eye pain, ear pain.

Data from foreign studies did not reveal any additional adverse experiences.

OVERDOSAGE

The LD₅₀ of intravenously administered gadopentetate dimeglumine injection in mice is 5-12.5 mmol/kg and in rats it is 10-15 mmol/kg. The LD₅₀ of intravenously administered MAGNEVIST® Injection in dogs is greater than 6 mmol/kg.

Clinical consequences of overdose with MAGNEVIST® Injection have not been reported.

DOSEAGE AND ADMINISTRATION

The recommended dosage of MAGNEVIST® Injection is 0.2 mL/kg (0.1 mmol/kg), administered intravenously, at a rate not to exceed 10 mL per minute. More rapid injection rates may be associated with nausea. The maximum total dose is 20 mL. Any unused portion must be discarded.

DOSEAGE CHART

Body Weight (kg)	Dose in mL	Approx Duration of Injection in Seconds
40	8.0	50
50	10.0	60
60	12.0	70
70	14.0	80
80	16.0	95
90	18.0	110
100	20.0	120

To ensure complete injection of the contrast medium, the injection should be followed by a 5-mL normal saline flush. The imaging procedure should be completed within 1 hour of injection of MAGNEVIST® Injection.

Parenteral products should be inspected visually for particulate matter and discoloration prior to administration, whenever solution and container permit.

HOW SUPPLIED

MAGNEVIST® Injection is a clear, colorless to slightly yellow solution containing 469.01 mg/mL of gadopentetate dimeglumine. MAGNEVIST® Injection is supplied in 20-mL single dose vials, rubber stoppered, in individual cartons; Boxes of 20, NDC 50419-189-02.

STORAGE

MAGNEVIST® Injection should be stored at controlled room temperature between 15°-30°C (59°-86°F) and protected from light. DO NOT FREEZE. Should solidification occur in the vial because of exposure to the cold, MAGNEVIST® Injection should be brought to room temperature before use. If allowed to stand at room temperature for a minimum of 90 minutes, MAGNEVIST® Injection will return to a clear, colorless to slightly yellow solution. Before use, examine the product to assure that all solids are redissolved and that the container and closure have not been damaged.

Caution: Federal Law Prohibits Dispensing Without Prescription.

©1988, Berlex Laboratories, Inc. All rights reserved.

Berlex Laboratories, Inc.
Wayne, New Jersey 07470

60621-3

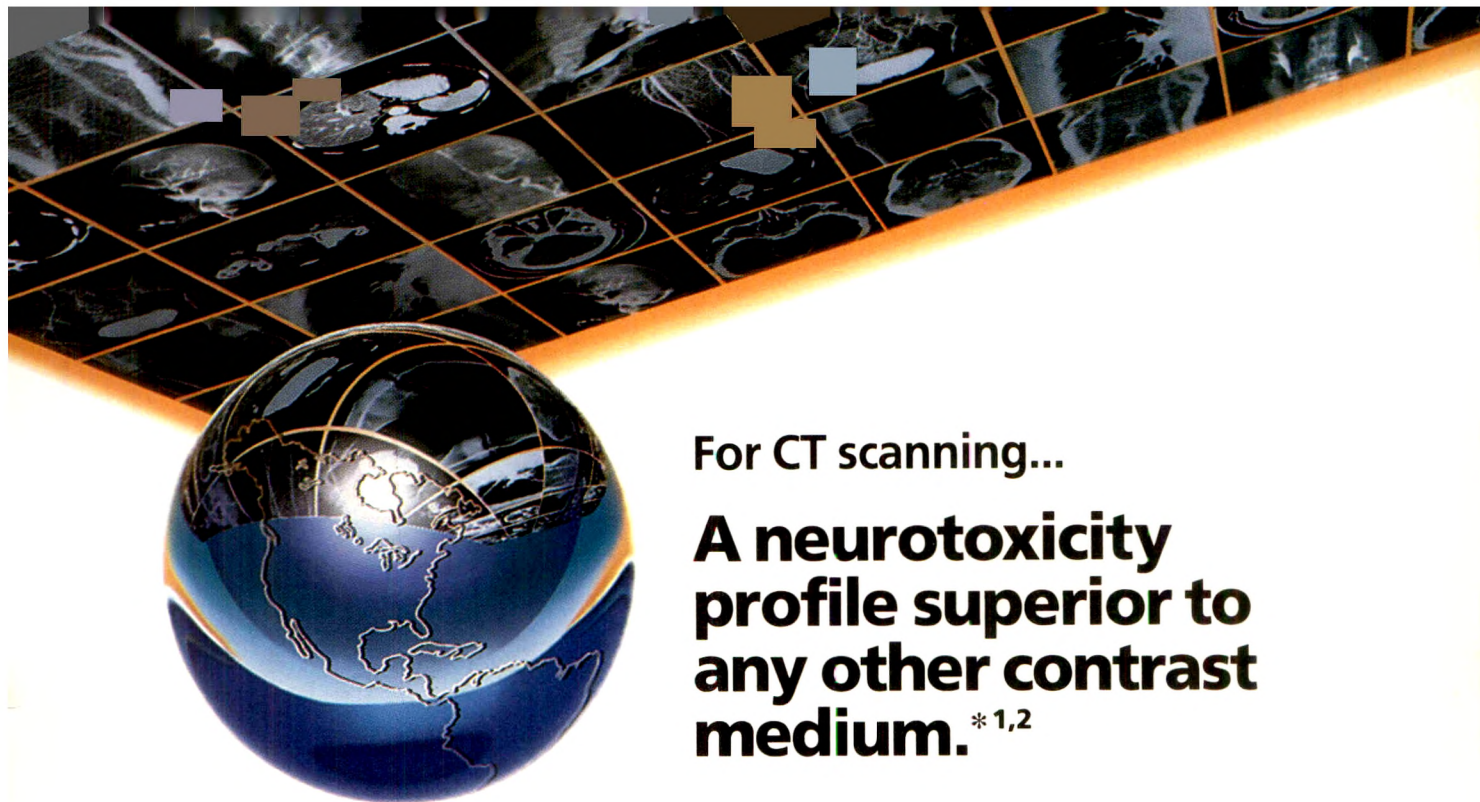
Revised 10/88



890-49

Printed in USA

April 1989



For CT scanning...

**A neurotoxicity
profile superior to
any other contrast
medium.*^{1,2}**

Low neurotoxicity is of particular importance in cranial CT scanning, where the blood-brain barrier may be compromised.^{†3,4}

Nonionic OMNIPAQUE is also the only nonionic contrast medium indicated for infusion administration during CT scanning.

And after 15 million radiographic procedures,[‡] you can feel confident about using nonionic OMNIPAQUE in CT scanning. No other nonionic contrast medium has been studied more!⁵

*According to a study of myelographic² comparing nonionic iohexol to iopamidol and metrizamide (based on visual evoked response latency and headache).

† The use of any radiographic contrast medium must be assessed on an individual risk-to-benefit basis.

‡ Approximation of over 15 million radiographic procedures worldwide is based on quantities of nonionic iohexol sold, used at recommended dosages.



NONIONIC
OMNIPAQUE®
(IOHEXOL)



**The image of safety
in CT scanning.**

See next page for important product information concerning contraindications, warnings, adverse reactions, patient selection, and prescribing and precautionary recommendations.

OMNIPAQUE® 240 300 350

INJECTION (IOHEXOL) INTRAVASCULAR/BODY CAVITIES

**PLEASE CONSULT FULL PRODUCT INFORMATION BEFORE USING.
A SUMMARY FOLLOWS:**

DESCRIPTION: OMNIPAQUE is a sterile, pyrogen- and preservative-free, nonionic, water-soluble radiographic contrast medium for intravascular administration in concentrations of 240, 300, and 350 mgI/mL. OMNIPAQUE 240 contains 518 mg of iothexol equivalent to 240 mg of organic iodine per mL. OMNIPAQUE 300 contains 647 mg of iothexol equivalent to 300 mg of organic iodine per mL. OMNIPAQUE 350 contains 755 mg of iothexol equivalent to 350 mg of organic iodine per mL. Each milliliter of iothexol solution contains 1.21 mg tromethamine and 0.1 mg edetate calcium disodium with the pH adjusted between 6.8 and 7.7 with hydrochloric acid or sodium hydroxide. Unused portions must be discarded. Iothexol solution is sensitive to light and should be protected from exposure.

CONTRAINDICATIONS: OMNIPAQUE should not be administered to patients with a known hypersensitivity to iothexol.

WARNINGS: OMNIPAQUE should be used with extreme care in patients with severely impaired renal and/or hepatic function; severe thyrotoxicosis, hyperthyroidism, or an autonomously functioning thyroid nodule; diabetes with a serum creatinine level above 3 mg/dL. It is not recommended for use in patients with anuria.

Patients with known or suspected pheochromocytoma should receive a minimum of contrast medium if the benefit of the examination is judged to outweigh its risk; blood pressure should be monitored throughout the procedure, and measures for the treatment of hypertensive crisis should be readily available.

Contrast agents are potentially hazardous in patients with multiple myeloma or other paraproteinemia, particularly those with therapeutically resistant anuria. The combination of contrast agent and dehydration may precipitate myeloma protein in the renal tubules. No form of therapy, including dialysis, has been successful in reversing the effect. Myeloma, which occurs most commonly in persons over age 40, should be considered before instituting intravascular administration of contrast agents.

Ionic contrast media, when injected intravenously or intra-arterially, may promote sickling in individuals who are homozygous for sickle cell disease.

PRECAUTIONS: Diagnostic procedures that involve the use of radiopaque diagnostic agents should be carried out under the direction of personnel with the prerequisite training and with a thorough knowledge of the particular procedure to be performed. Appropriate facilities should be available for coping with any complication of the procedure, as well as for emergency treatment of severe reactions to the contrast agent itself. Competent personnel and emergency facilities should be available for at least 30 to 60 minutes, since severe delayed reactions have occurred (see ADVERSE REACTIONS). The possibility of serious, life-threatening, fatal, anaphylactoid, or cardiovascular reactions should always be considered (see ADVERSE REACTIONS). It is of utmost importance that a course of action be carefully planned in advance for immediate treatment of serious reactions. Preparatory dehydration is dangerous and may contribute to acute renal failure in patients with advanced vascular disease, in diabetic patients, and in susceptible nondiabetic patients (often elderly with preexisting renal disease), infants, and small children. Patients should be well hydrated prior to and following iothexol administration. Careful consideration of the potential risk of acute renal failure should be given before performing excretory urography in diabetic patients with diabetic nephropathy and in susceptible nondiabetic patients (often elderly with preexisting renal disease). Immediately following surgery, excretory urography should be used with caution in renal transplant recipients. The possibility of an idiosyncratic reaction in susceptible patients should always be considered (see ADVERSE REACTIONS). The susceptible population includes, but is not limited to, patients with a history of a previous reaction to contrast media, patients with a known sensitivity to iodine per se, and patients with a known clinical hypersensitivity: bronchial asthma, hay fever, and food allergies. A thorough medical history with emphasis on allergy and hypersensitivity, prior to the injection of any contrast media, may be more accurate than pretesting in predicting potential adverse reactions.

A positive history of allergies or hypersensitivity does not arbitrarily contraindicate the use of a contrast agent where a diagnostic procedure is thought essential, but caution should be exercised (see ADVERSE REACTIONS). Premedication with antihistamines or corticosteroids to avoid or minimize possible allergic reactions in such patients should be considered and administered using separate syringes. Recent reports indicate that such pretreatment does not prevent serious, life-threatening reactions but may reduce both their incidence and severity.

Even though the osmolality of OMNIPAQUE is low compared to diatrizoate- or iohalamate-based ionic agents of comparable iodine concentration, the potential transitory increase in circulatory osmotic load in patients with congestive heart failure requires caution during injection. These patients should be observed for several hours following the procedure to detect delayed hemodynamic disturbances.

General anesthesia may be indicated in the performance of some procedures in selected adult patients; however, a higher incidence of adverse reactions has been reported in these patients and may be attributable to the inability of the patient to identify untoward symptoms or to the hypotensive effect of the anesthesia, which can reduce cardiac output and increase the duration of exposure to the contrast agent.

Angiography should be avoided whenever possible in patients with homocystinuria, because of the risk of inducing thrombosis and embolism.

In angiographic procedures, the possibility of dislodging plaques or damaging or perforating the vessel wall should be borne in mind during the catheter manipulations and contrast medium injection. Test injections to ensure proper catheter placement are recommended.

Selective coronary arteriography should be performed only in those patients in whom the expected benefits outweigh the potential risk. The inherent risks of angiocardiology in patients with chronic pulmonary emphysema must be weighed against the necessity for performing this procedure.

When OMNIPAQUE is to be injected using plastic disposable syringes, the contrast medium should be drawn into the syringe and used immediately.

The inhibitory effects of nonionic contrast media on mechanisms of hemostasis have been shown, in vitro, to be less than those of ionic contrast media at comparable concentrations. For this reason, standard angiographic procedures should always be followed: angiographic catheters should be flushed frequently, and prolonged contact of blood with contrast media in syringes and catheters should be avoided.

If nondisposable equipment is used, scrupulous care should be taken to prevent residual contamination with traces of cleansing agents.

Parenteral products should be inspected and discarded if particulate matter or discoloration is present.

Drug/Laboratory Test Interaction: If iodine-containing isotopes are to be administered for the diagnosis of thyroid disease, the iodine-binding capacity of thyroid tissue may be reduced for up to 2 weeks after contrast medium administration. Thyroid function tests which do not depend on iodine estimation, eg, T₃ resin uptake or direct thyroxine assays, are not affected. Many radiopaque contrast agents are incompatible in vitro with some antihistamines and many other drugs; therefore, no other pharmaceuticals should be admixed with contrast agents.

Carcinogenesis, Mutagenesis, Impairment of Fertility: No long-term animal studies have been performed to evaluate carcinogenic potential, mutagenesis, or whether OMNIPAQUE can affect fertility in men or women.

Pregnancy Category B: Reproduction studies have been performed in rats and rabbits with up to 100 times the recommended human dose. No evidence of impaired fertility or harm to the fetus has been demonstrated due to OMNIPAQUE. There are, however, no studies in pregnant women. Because animal reproduction studies are not always predictive of human response, this drug should be used during pregnancy only if clearly needed.

Nursing Mothers: It is not known to what extent iothexol is excreted in human milk. However, many injectable contrast agents are excreted unchanged in human milk. Although it has not been established that serious adverse reactions occur in nursing infants, caution should be exercised when intravascular contrast media are administered to nursing women. Bottle feedings may be substituted for breast feedings for 24 hours following administration of OMNIPAQUE.

Pediatric Use (Indicated for Angiocardiography and Urography): Pediatric patients at higher risk of experiencing adverse events during contrast medium administration may include those having asthma, a sensitivity to medication and/or allergens, congestive heart failure, a serum creatinine > 1.5 mg/dL, or those less than 12 months of age.

ADVERSE REACTIONS: Usually mild to moderate in severity. However, serious, life-threatening, and fatal reactions, mostly of cardiovascular origin, have been associated with the administration of iodine-containing contrast media, including OMNIPAQUE. The injection of contrast media is frequently associated with the sensation of warmth and pain, especially in peripheral angiography; pain and warmth are less frequent and less severe with OMNIPAQUE than with many contrast media.

OMNIPAQUE® injection (iothexol)

Cardiovascular System: Arrhythmias including PVCs and PACs (2%), angina/chest pain (1%), and hypotension (0.7%). Others including cardiac failure, asystole, bradycardia, tachycardia, and vasovagal reaction were reported with an individual incidence of less than 0.4%. In controlled clinical trials involving 1,270 patients, one fatality occurred. A cause-and-effect relationship between this death and iothexol has not been established.

Nervous System: Vertigo [including dizziness and lightheadedness] (0.6%), pain (3%), photomas (2%), headache (2%), and taste perversion (1%). Others including anxiety, blurred vision, fever, motor and speech dysfunction, convulsion, paresthesia, somnolence, stiff neck, hemiparesis, syncope, and nystagmus were reported, with an individual incidence of less than 0.3%.

Respiratory System: Dyspnea and laryngitis, with an individual incidence of 0.1%.

Gastrointestinal System: Nausea (2%) and vomiting (0.6%). Others including diarrhea, dyspepsia, and dry mouth were reported, with an individual incidence of less than 0.2%.

Skin and Appendages: Urticaria (0.3%), purpura (0.1%), and pruritus (0.1%).

Pediatric angiocardiography and urography: In controlled clinical trials involving 324 patients, adverse reactions following the use of OMNIPAQUE 300 and OMNIPAQUE 350 were generally less frequent than with adults.

Cardiovascular System: Ventricular tachycardia (0.6%), 2:1 heart block (0.6%), hypertension (0.3%), and anemia (0.3%).

Nervous System: Pain (0.6%), fever (0.6%), and convulsion (0.3%).

Respiratory System: Congestion (0.3%) and apnea (0.3%).

Gastrointestinal System: Nausea (1%), hypoglycemia (0.3%), and vomiting (2%).

Skin and Appendages: Rash (0.3%).

Body Cavities:

Cardiovascular System: Hypertension (0.4%).

Nervous System: Pain (29%), headache (0.4%), somnolence (0.8%), fever (0.4%), dizziness (0.4%), muscle weakness, burning and unwell feeling, each with an individual incidence of 0.4%.

Respiratory System: None.

Gastrointestinal System: Nausea (0.4%), vomiting (0.4%), diarrhea (0.8%), flatulence (1%), and pressure (0.4%).

Skin and Appendages: Hematoma, injection site (0.4%), swelling (26%), heat (8%).

General Adverse Reactions to Contrast Media: The following reactions have been reported after administration of other intravascular iodinated contrast media, and rarely with iothexol. *Reactions due to technique:* hematomas and ecchymoses. *Hemodynamic reactions:* vein cramp and thrombophlebitis following intravenous injection. *Cardiovascular reactions:* rare cases of cardiac arrhythmias, reflex tachycardia, chest pain, cyanosis, hypertension, hypotension, peripheral vasodilatation, shock, and cardiac arrest. *Renal reactions:* occasionally, transient proteinuria; rarely, oliguria or anuria. *Allergic reactions:* asthmatic attacks, nasal and conjunctival symptoms, dermal reactions such as urticaria with or without pruritus, as well as pleomorphic rashes, sneezing, and lacrimation; rarely, anaphylactic reactions. Rare fatalities have occurred due to these or unknown causes. *Signs and symptoms related to the respiratory system:* pulmonary or laryngeal edema, bronchospasm, dyspnea, or to the nervous system: restlessness, tremors, convulsions. *Other reactions:* flushing, pain, warmth, metallic taste, nausea, vomiting, anxiety, headache, confusion, pallor, weakness, sweating, localized areas of edema (especially facial cramps), neutropenia, and dizziness. Rarely immediate or delayed rigors can occur, sometimes accompanied by hyperpyrexia. Infrequently, "iodism" (salivary gland swelling) from organic iodinated compounds appears 2 days after exposure and subsides by the sixth day.

In general, the reactions that are known to occur upon parenteral administration of iodinated contrast agents are possible with any nonionic agent. Approximately 95% of adverse reactions accompanying the use of water-soluble intravascularly administered contrast agents are mild to moderate in degree. However, severe, life-threatening anaphylactoid reactions, mostly of cardiovascular origin, have occurred. Reported incidences of death range from 6.6 per 1 million (0.00066%) to 1 in 10,000 (0.01%). Most deaths occur during injection or 5 to 10 minutes later, the main feature being cardiac arrest, with cardiovascular disease as the main aggravating factor. Isolated reports of hypotensive collapse and shock are found in the literature. The incidence of shock is estimated to be 1 out of 20,000 (0.005%) patients.

Adverse reactions to injectable contrast media fall into two categories: chemotoxic reactions and idiosyncratic reactions.

Chemotoxic reactions result from the physicochemical properties of the contrast media, the dose, and the speed of injection. All hemodynamic disturbances and injuries to organs or vessels perfused by the contrast medium are included in this category.

Idiosyncratic reactions include all other reactions. They occur more frequently in patients 20 to 40 years old. Idiosyncratic reactions may or may not be dependent on the amount of dose injected, the speed of injection, and the radiographic procedure. Idiosyncratic reactions are subdivided into minor, intermediate, and severe. The minor reactions are self-limited and of short duration; the severe reactions are life-threatening and treatment is urgent and mandatory.

The reported incidence of adverse reactions to contrast media in patients with a history of allergy is twice that in the general population. Patients with a history of previous reactions to a contrast medium are three times more susceptible than other patients. However, sensitivity to contrast media does not appear to increase with repeated examinations.

Most adverse reactions to injectable contrast media appear within 1 to 3 minutes after the start of injection, but delayed reactions may occur.

Regardless of the contrast agent employed, the overall estimated incidence of serious adverse reactions is higher with angiocardiography than with other procedures. Cardiac decompensation, serious arrhythmias, angina pectoris, or myocardial ischemia or infarction may occur during angiocardiography and left ventriculography. Electrocadiographic and hemodynamic abnormalities occur less frequently with OMNIPAQUE than with diatrizoate meglumine and diatrizoate sodium injection.

OVERDOSAGE: Overdosage may occur. The adverse effects of overdosage are life-threatening and affect mainly the pulmonary and cardiovascular systems. The symptoms include cyanosis, bradycardia, acidosis, pulmonary hemorrhage, convulsions, coma, and cardiac arrest. Treatment of an overdosage is directed toward the support of all vital functions and prompt institution of symptomatic therapy.

The intravenous LD₅₀ values of OMNIPAQUE (in grams of iodine per kilogram body weight) are 24.2 in mice and 15.0 in rats.

References: 1. Gonssette RE, Liesenborgs L: Iothexol: A new nonionic contrast medium for myelography and cisternography with markedly reduced neurotoxicity. *Invest Radiol* 1985;20(January-February suppl):32-36. 2. Broadbridge AT, Bayliss SG, Brayshaw CI: The effect of intrathecal iothexol on visual evoked response latency. A comparison including incidence of headache with iopamidol and metrizamide in myelographic studies. *Clin Radiol* 1987;38:71-74. 3. Skajpe IO: Enhancement with water-soluble contrast media in computed tomography of the brain and abdomen. Survey and present state. *Acta Radiol* 1983; suppl 366, pp 72-75. 4. Pfeiffer FE, Homburger HA, Houser OW, et al: Elevation of serum creatine kinase B-subunit levels by radiographic contrast agents in patients with neurologic disorders. *Mayo Clin Proc* 1987;62:351-357. 5. Data on file, Winthrop Pharmaceuticals.

CIRCLE 24 ON READER SERVICE CARD



DIAGNOSTIC IMAGING DIVISION
Winthrop Pharmaceuticals
Division of Sterling Drug Inc.
New York, NY 10016

Easy touch

Put your finger on improved productivity with Advantx R&F systems.

R&F procedures have never been simpler than with an Advantx™ system from GE.

Consider auto-protocol, for example. This software-based option lets you program up to 240 protocols—each accessible at the touch of a “key” on the plasma screen. The result? Ultimate flexibility, instant set-up and consistent results—operator to operator, patient to patient, day to day.

Convenience is also an advantage of the Advantx DR digital photospot option. Unlike conventional systems, Advantx digital recording and post-processing are controlled in the R&F room and films can be annotated right at the Advantx plasma console. The result? Fewer steps, simpler operation and faster exams. More time for you to spend on the patient and completing the exam efficiently.

The Advantx R&F systems. Putting you in touch with greater productivity.

For a free brochure with all the details on Advantx R&F, including the new Advantx DR option, call toll free 1-800-624-5692.



X-ray

GE Medical Systems

AJR Business and Subscriber Information

The American Roentgen Ray Society

AJR, *American Journal of Roentgenology*, is published monthly to disseminate research on current developments in the radiologic sciences and commentary on topics related to radiology. It is published by the American Roentgen Ray Society, 1891 Preston White Dr., Reston, VA 22091; (703) 648-8992. Inquiries regarding society business, the annual ARRS meeting, and membership should be addressed to the Society at the above address.

Correspondence Concerning the AJR

Correspondence regarding display (not classified) advertising, subscriptions, address changes, reprints, and permission requests should be addressed to Williams & Wilkins, 428 E. Preston St., Baltimore, MD 21202; (301) 528-4000.

Correspondence regarding editorial matters and classified advertising should be addressed to Editorial Office, *AJR*, 2223 Avenida de la Playa, Ste. 200, La Jolla, CA 92037-3218; telephone (619) 459-2229; FAX (619) 459-8814. For information on manuscript submission, see Guidelines for Authors, pages A3-A5.

Subscriber Information

Subscription requests and inquiries should be sent to Williams & Wilkins, 428 E. Preston St., Baltimore, MD 21202. ARRS annual dues include \$50 for journal subscription. Subscription rates are as follows: nonmembers, \$100/year (\$135 foreign); institutions, \$110 (\$145 foreign); nonmember in-training, \$25 (\$50 foreign). Single copies of the Journal may

be purchased for \$16 (\$19 foreign). Airmail rates will be furnished on request.

Japanese rates include airfreight. Japanese yen price is available from our sole agent, USACO Corporation, 13-12, Shimbashi 1-Chome, Minato-Ku, Tokyo 105, Japan; telephone 03-502-6471.

If a subscriber receives a damaged copy of the *AJR* or fails to receive an issue, the subscriber should notify Williams & Wilkins (428 E. Preston St., Baltimore, MD 21202) within 60 days of publication (90 days for foreign subscribers) and that issue will be replaced.

Change of address information should be sent to Williams & Wilkins, 428 E. Preston St., Baltimore, MD 21202. Allow 90 days for address changes.

Copyrights, Permissions, and Reprints

The American Roentgen Ray Society holds the copyright for all material published in the *AJR*. No part of this publication may be reproduced without permission from the ARRS. Requests for such permission should be addressed to Williams & Wilkins, 428 E. Preston St., Baltimore, MD 21202.

For reprints of a particular article, please contact the author designated in the footnotes for that article.

Indexes

The *AJR* provides volume and yearly indexes (subject and author) in the June and December issues each year. *AJR* articles are also indexed in *Current Contents*, *Index Medicus*, and the cumulative index published by *Radiology*.

Children's doses

Advantx DR: better R&F images with less dose.

Now there's a digital photospot system that lets you significantly reduce dose levels—without compromising clinical image quality.

The Advantx DR™ system from GE.

It lets you program three different record or fluoro dose levels to your specifications—and switch from one to another during an exam. So you can limit dose, without limiting your procedural flexibility.

This flexibility has big implications, especially for little patients. The mid-level record setting, for example, provides image quality comparable to or better than conventional systems—with 50% less dose than conventional photospot images and 90% less dose than spotfilms.

Other features also make Advantx DR ideal for pediatric cases. For example, the “last image hold” function in digital record or spotfilm mode reduces fluoro dose, and in-room digital post-processing helps minimize required views or retakes.

Advantx DR. “Digital” image quality with significantly less dose.

For a free brochure on Advantx R&F, including the new Advantx DR option, call toll free 1-800-624-5692.



X-ray

GE Medical Systems

THE ONLY JOURNAL PROVIDING A COMPLETE AND SYSTEMATIC

review of the entire field

ALEXANDER R. MARGULIS, Editor

Complete Coverage

Each issue provides a complete systematic review of the past year's developments in one or two sections of radiology. Together the six bimonthly issues cover the entire field of radiology.

Annotated References

With each review, the author selects and annotates the year's most significant papers, highlighting the key findings.

Authoritative Reviews

Each section consists of a series of short, highly illustrated review articles. Using a comprehensive bibliography, leading experts evaluate new findings and developments in their fields.

World Bibliography

In each issue, the complete bibliography of current world literature lists all relevant papers published in the past year. This bibliography is specially compiled by radiologists who scan over 300 journals worldwide.

Current Opinion in RADIOLOGY

Review articles • Recommended reading
Bibliography of the world literature

Vol 1 • 1989 • No 1

No	THIS ISSUE	June
No 1	Chest - JD Godwin Gastrointestinal tract - RF Thoeni	June
No 2	Cardiac imaging, Breast	August
No 3	Genitourinary system, Musculoskeletal radiology	October
No 4	Nuclear medicine, Pediatrics	December
No 5	Neuroradiology, Head and neck	February
No 6	Ultrasound, Angiography and interventional radiology, Technologic advances	April

Volume 1 Number 1 June 1989	
A.R. Margulis	Editorial
Chest	
edited by J.D. Godwin	
N. Muller	High-resolution computed tomography of diffuse lung disease
D. Aberle	Imaging of asbestosis
C. Sanders	Diagnosis of emphysema
H. Libshitz	Imaging of lung cancer
P. Templeton and E. Zerhouni	Computed tomography of the pulmonary nodule and focal pulmonary disease
P. Goodman	AIDS in the chest
L. Goodman and C. Mistrretta	Digital chest radiography
R. Webb	Magnetic resonance imaging of the chest
Gastrointestinal tract	
edited by R. Thoeni	
Gastrointestinal radiology: overview	
S. Glick	Esophagus, stomach, and duodenum
R. Thoeni	Small bowel
D. Gelfand	Colon
Stark and K. Otobi	Liver
H. Goldberg	Biliary system
P. Freeman	Pancreas
J. LaBerge	Interventional radiology in the gastrointestinal tract
S. Wall	AIDS in the gastrointestinal tract
A.R. Margulis	Cross-sectional imaging

Current world literature	
Chest	Gastrointestinal tract
Index to subjects	

Gastrointestinal radiology

- JEFFERY RB JR, FEDERLE MP, TREVINO CS. Periappendiceal inflammatory masses: CT-directed management and clinical outcome in 70 patients. *Radiology* 1988; 167:15-19.
- Twenty patients with periappendiceal inflammatory masses were examined with CT. The CT diagnosis based on the recognition of periappendiceal phlegmons or abscesses was very accurate, but three false positive diagnoses were made in the series.
- WAGNER MM, FRIEDMAN AC, SOWERS E, RICHARDS PL. CT manifestations of peritoneal carcinomatosis. *Am J Roentgenol* 1988; 150:1045-1047.
- Sixty patients with peritoneal tumors were reviewed retrospectively by CT. Ascites was present in 74%, loculation of fluid in 40%, absence of calcified fluid in 17%, and peritoneal thickening of the chest in metastatic disease in 62%. Tumor involvement of bowel was present in 70%.
- LYNCH MA, CHO KC, JEFFERY RB JR, ALTERMAN DD, FEDERLE MP. CT of peritoneal lymphomatosis. *Am J Roentgenol* 1988; 151:713-715.
- Seventy patients with diffuse peritoneal lymphomatosis caused by non-Hodgkin's lymphoma and CT evidence of ascites, omental thickening, and peritoneal implants mimicking carcinomatosis were analyzed. Pathologic findings provided a diagnosis of lymphoma in only one of the seven patients. Although uncommon, lymphoma should be considered in patients who have diffuse peritoneal malignancy, particularly those with ascites.
- ANGELILE G, MACARINI L. CT of the bowel: use of water to enhance depiction. *Radiology* 1988; 169:848-849.
- Dilatation of the stomach with water improved visualization of the gastric wall, was readily accepted by the patient, and allowed detection of irregularity on the inner surface of the stomach with ease, even in the presence of normal wall thickness.
- GUINET D, BEN JN, MAZOR A, MONNER H, GHASSAN M, MALAFOSSE M, GUICHARD M, VADROT D, ECKOFFER J. Preoperative assessment of the extension of rectal carcinoma: correlation of MR, surgical and histopathologic findings. *J Comput Assist Tomogr* 1988; 12:209-214.
- Nineteen patients with rectal carcinoma were evaluated retrospectively. The study shows that MR imaging had sensitivities and specificity of 74% and 100% in the detection of perirectal growth. The comparison with TNM classification demonstrated a correct staging in 79%.
- WOOD ML, RICHARDSON VA, HENDERSON RM. Overcoming motion in abdominal MR imaging. *Am J Roentgenol* 1988; 150:513-522.

Current world literature: Gastrointestinal radiology

THOENI RF, FILLSON RG. Abdominal and pelvic CT: use of oral metoclopramide to enhance bowel opacification. *Radiology* 1988; 169:391-393.

KRENTIN GP, STEINBRICH W, FRIEDMANN G. Recurrent rectal cancer: diagnosis with MR imaging versus CT. *Radiology* 1988; 168:307-311.

LEHR L, RUPP N, SIEWERT JR. Assessment of resectability of esophageal cancer by computed tomography and magnetic resonance imaging. *Surgery* 1988; 103:344-350.

RHEE RS, RAY CG III, KRAVETZ MH, BRALEY L, HARRIS V, GREWE GM, SPIGON DM. Cervical esophageal duplication cyst: MR imaging. *J Comp Assist Tomogr* 1988; 12:693-695.

BAKER ME, LINGERLAIDER R, COOPER C, DENNIS NR, LYNCH MA, CHO KC, JEFFERY RB JR, ALTERMAN DD, FEDERLE MP. CT of peritoneal lymphomatosis. *Am J Roentgenol* 1988; 151:713-715.

LANIADO M, KORNMESSER W, HAMM B, CLAUS W, WEINMANN HJ, FELIX R. MR imaging of the gastrointestinal tract: value of Gd-DTPA. *Am J Roentgenol* 1988; 150:817-821.

ANGELILE G, MACARINI L. CT of the bowel: use of water to enhance depiction. *Radiology* 1988; 169:848-849.

GUINET D, BEN JN, SEZEUR A, MONNER H, GHASSAN M, MALAFOSSE M, GUICHARD M, VADROT D, ECKOFFER J. Preoperative assessment of extension of rectal carcinoma: correlation of MR, surgical and histopathologic findings. *J Comput Assist Tomogr* 1988; 12:209-214.

Call TOLL FREE: (800) 552-5866 or in PA call (215) 790-2279

B SPECIAL PRE-PUBLICATION OFFER!! Save 10% on a 1-year subscription! R6
Current Opinion in RADIOLOGY, Volume 1, 1989 (4 issues)

☐ Yes! Please enter my Personal Subscription. \$65. ONLY \$58.50!
☐ Resident Subscription 30% OFF! Only \$45.50!
☐ Institutional Subscription \$115.

Payment Method: ☐ Check enclosed, payable to Current Science
☐ Bill Me ☐ VISA ☐ Mastercard ☐ American Express

Card Number _____ Exp. _____

Signature _____ Date _____

Name _____

Address _____

City/State/Zip _____

MAIL TO:

CS CURRENT SCIENCE
DEPARTMENT RA
1201 LOCUST STREET
PHILADELPHIA, PA 19107-0924

Future perfect

Tomorrow's R&F capabilities are now on-line with Advantx.

At GE, we've seen the future of R&F. And it's on a floppy disk.

Our Advantx™ R&F systems are designed around a multiplexed, distributed processing digital network called Plexus™. Software, rather than hardware and hardwiring, is the key to adding new capabilities.

For example, the Advantx console is a plasma touch screen—a blank slate, really, with infinite capacity for new protocols. Software allows the console to be instantly updated to accommodate new applications or equipment. No need to add buttons as you add capabilities.

Digital architecture also allows upgrades to be *fully integrated* into the system. Our Advantx DR digital recording system, for example, is operated right from the R&F room. No need for an additional CT-type console or laptop keyboard, as with other digital photospot systems.

Finally, there's speed. Because the entire system is software-driven—including calibration—upgrades are far less time-consuming. In fact, a complete Advantx DR upgrade is on-line typically in about two days.

With Advantx, the future comes easy...and fast.

For a free brochure on the Advantx R&F systems, including the new Advantx DR option, call toll free 1-800-624-5692.

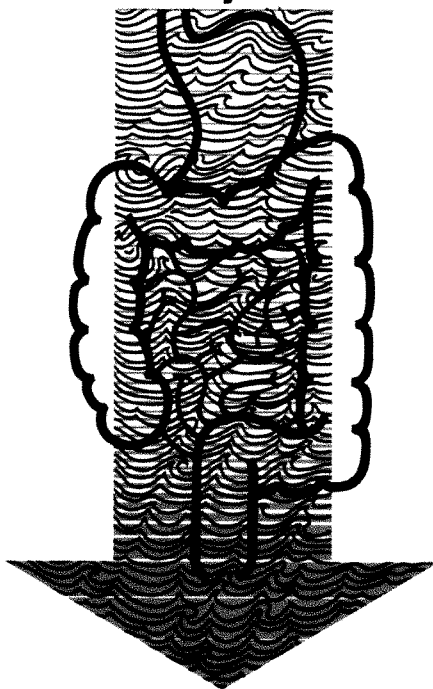


X-ray

GE Medical Systems

GoLYTELY[®]

PEG-3350 and Electrolytes for Oral Solution



THE NAME THAT STARTED A REVOLUTION.

The leader
in oral GI lavage.

BRIEF SUMMARY: Before prescribing, see package insert or PDR.

INDICATIONS AND USAGE: GoLYTELY is indicated for bowel cleansing prior to colonoscopy and barium enema x-ray examination.

CONTRAINDICATIONS: GoLYTELY is contraindicated in patients with gastrointestinal obstruction, gastric retention, bowel perforation, toxic colitis, or toxic megacolon.

WARNINGS: No additional ingredients—eg, flavorings—should be added to the solution. GoLYTELY should be used with caution in patients with severe ulcerative colitis.

PRECAUTIONS: General: Patients with impaired gag reflex, unconscious or semi-conscious patients, and patients prone to regurgitation or aspiration should be observed during the administration of GoLYTELY, especially if it is administered via nasogastric tube. If a patient experiences severe bloating, distention, or abdominal pain, administration should be slowed or discontinued temporarily until the symptoms abate. If gastrointestinal obstruction or perforation is suspected, appropriate studies should be performed to rule out these conditions before administration of GoLYTELY.

ADVERSE REACTIONS: Nausea, abdominal fullness, and bloating are the most common adverse reactions (occurring in up to 50% of patients) to administration of GoLYTELY. Abdominal cramps, vomiting, and anal irritation occur less frequently. These adverse reactions are transient and subside rapidly. Isolated cases of urticaria, rhinorrhea, and dermatitis—which may represent allergic reactions—have been reported.

CAUTION: Federal law prohibits dispensing without prescription.

STORAGE: Store in sealed container at 59°-86°F. When reconstituted, keep solution refrigerated. Use within 48 hours. Discard unused portion.
(NDC 52268-0100-01)

Made by Lyne Laboratories, Stoughton, MA 02072,

for BRAINTREE LABORATORIES, INC., P.O. Box 361, Braintree, MA 02184.

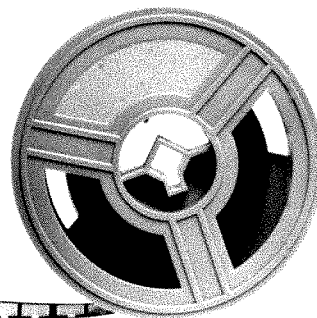
© 1989 BRAINTREE LABORATORIES, INC. CIRCLE 35 ON READER SERVICE CARD TRE-1037

LABORATORIES, INC.
Braintree

Need shelf space?

Williams & Wilkins is your
source for back issues of
this journal in microform.

Free Up 98%
Of Your Shelf
Space With
Microform
Conversion



MICROFILM editions are available for this journal direct from the publisher. Many Williams & Wilkins journals as well as those journals distributed by the Publishing Services Division of Waverly, Inc., are also available for a single volume year or on a standing order basis.

FOR ORDERING INFORMATION:
Write to the address below or call
TOLL FREE 1-800-638-6423.
In Maryland call 1-800-638-4007.

☐ Please send me microform
back issue ordering information
for

Journal Name _____

Name _____

Title _____

Address _____

City/State/Zip _____

Mail to:

Williams & Wilkins

Microform Sales

Attention: Yvonne Hahn

428 East Preston Street

Baltimore, MD 21202

-or-

The Broadway Centre

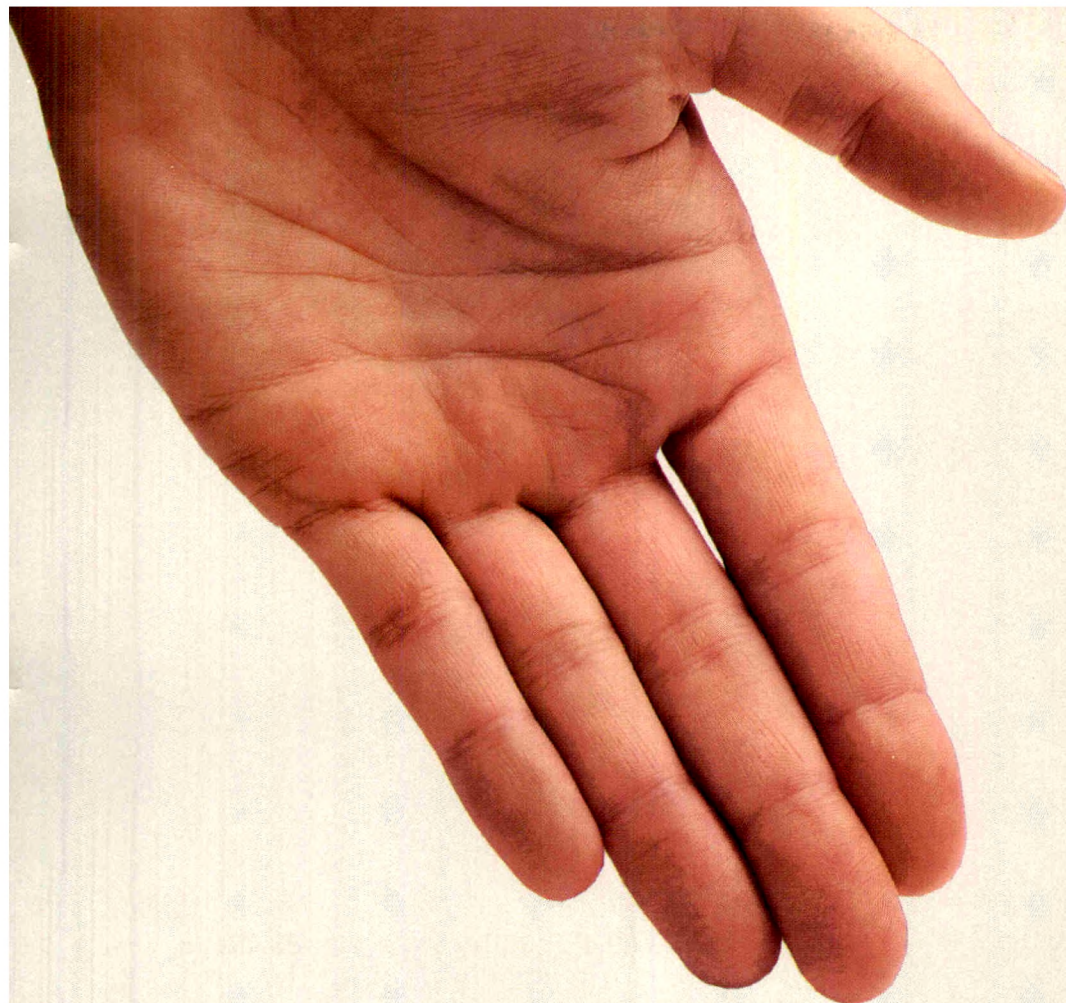
2-6 Fulham Broadway

London SW6 1AA England

Formats available:

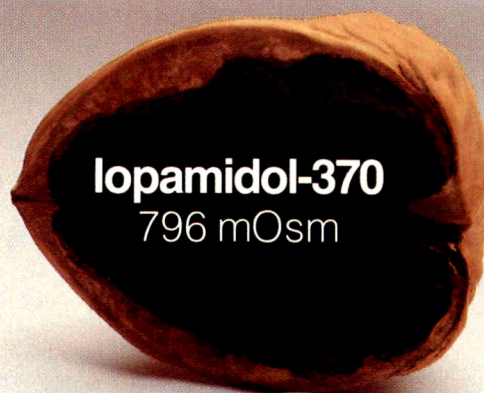
- 16-mm reel
- 35-mm reel
- 16-mm cartridge (3M or Kodak)
- positive or negative film

MICA92 1193




**For greater patient comfort
and the lowest osmolality,
the choice is yours...**





F R O M M A L L



Hexabrix
600 mOsm

The low osmolality choice, in a nutshell

Compare Hexabrix with the nonionics, and you'll find that Hexabrix not only has the lowest osmolality, but also the least amount of patient discomfort in interventional procedures.

Least heat and pain

Recent comparative studies demonstrate that Hexabrix produces significantly less heat¹ and pain¹⁻³ than iopamidol and/or iohexol during arteriography procedures.¹⁻³

Less risk of clotting *in vitro*

Hexabrix has been shown to be a stronger inhibitor of clotting^{4,5} and platelet aggregation^{5,6} *in vitro* than iopamidol or iohexol.

Good angiographic technique should be followed in all procedures involving contrast media. Even when meticulous technique is used, some mixing of blood with contrast media in syringes and catheters is possible. Prolonged contact of blood and contrast media in syringes and catheters can lead to clot formation.

Lowest viscosity

Hexabrix has the lowest viscosity at 37°C (7.5 cps), compared to iohexol-350 (10.4 cps) or iopamidol-370 (9.4 cps).

HEXABRIX[†]

(ioxaglate meglumine 39.3%/
ioxaglate sodium 19.6% injection)

Please see following page for references and brief summary of prescribing information.

I N C K R O D T

HEXABRIX[†] (ioxaglate meglumine 39.3%/ioxaglate sodium 19.6% injection)

HEXABRIX[®]

Each milliliter of HEXABRIX contains 393 mg of ioxaglate meglumine, 196 mg of ioxaglate sodium and 0.10 mg edetate calcium disodium as a stabilizer. The solution contains 3.48 mg (0.15 mEq) sodium in each milliliter and provides 32% (320 mg/mL) organically bound iodine.

CONTRAINDICATIONS

HEXABRIX is contraindicated for use in myelography. Refer to PRECAUTIONS concerning hypersensitivity. Hysterosalpingography should not be performed during the menstrual period in pregnant patients, in patients with known infection in any portion of the genital tract, or in patients in whom cervical ceratization or curettage has been performed within 30 days. Arthrography should not be performed if infection is present in or near the joint.

WARNINGS

Serious or fatal reactions have been associated with the administration of iodine containing radiopaque media. It is of utmost importance to be completely prepared to treat any contrast medium reaction.

As with any contrast medium, serious neurologic sequelae, including permanent paralysis, can occur following cerebral arteriography, selective spinal arteriography and arteriography of vessels supplying the spinal cord. The injection of a contrast medium should never be made following the administration of vasopressors, since they strongly potentiate neurologic effects.

In patients with subarachnoid hemorrhage, a rare association between contrast administration and clinical deterioration, including convulsions and death, has been reported. Therefore, administration of intravascular iodinated contrast media in these patients should be undertaken with caution.

A definite risk exists in the use of intravascular contrast agents in patients who are known to have multiple myeloma. In such instances anuria has developed, resulting in progressive uremia, renal failure and eventually death. Although neither the contrast agent nor dehydration has separately proved to be the cause of anuria in myeloma, it has been speculated that the combination of both may be a causative factor. The risk in myelomatous patients is not a contraindication to the procedure, however, partial dehydration in the preparation of these patients for the examination is not recommended since this may predispose to precipitation of myeloma protein in the renal tubules. No form of therapy, including dialysis, has been successful in reversing the effect. Myeloma, which occurs most commonly in persons over 40, should be considered before instituting intravascular administration of contrast agents.

Administration of radiopaque materials to patients known or suspected to have pheochromocytoma should be performed with extreme caution. It is the opinion of the physician, the possible benefits of such procedures outweigh the considered risks. The procedures may be performed, however, the amount of iodine contrast medium injected should be kept to an absolute minimum. The blood pressure should be assessed throughout the procedure, and measures for treatment of a hypertensive crisis should be available.

Since intravascular administration of contrast media may promote sickling in individuals who are homozygous for sickle cell disease, fluid restriction is not advised.

In patients with advanced renal disease, iodinated contrast media should be used with caution and only when the need for the examination dictates, since excretion of the medium may be impaired. Patients with combined renal and hepatic disease, those with severe hypertension or congestive heart failure and recent renal transplant recipients present an additional risk.

Renal failure has been reported in patients with liver dysfunction who were given an oral cholecystographic agent followed by an intravascular iodinated radiopaque agent and also in patients with occult renal disease, notably diabetes and hypertension. In these cases of patients there should be no fluid restriction and every attempt made to maintain normal hydration prior to contrast medium injection. Since dehydration is the single most important factor influencing further renal impairment.

Caution should be exercised in performing contrast medium studies in patients with endotoxemia and/or those with elevated body temperatures.

Reports of thyroid storm occurring following the intravascular use of iodinated radiopaque agents in patients with hyperthyroidism or with an autonomously functioning thyroid nodule, suggest that this additional risk be evaluated before use of this drug. Iodine-containing contrast agents may alter the results of thyroid function tests which depend on iodine estimation (e.g., PBI) and may also affect results of radioactive iodine uptake studies. Such tests, if indicated, should be performed prior to the administration of this preparation.

PRECAUTIONS

Diagnostic procedures which involve the use of iodinated intravascular contrast agents should be carried out under the direction of personnel skilled and experienced in the particular procedure to be performed. All procedures utilizing contrast media carry a definite risk of producing adverse reactions. While most reactions are minor, life-threatening and fatal reactions may occur without warning, and this risk must be weighed against the benefit of the procedure. A fully equipped emergency cart or equivalent supplies and equipment, and personnel competent in recognizing and treating adverse reactions of all types should always be available. If a serious reaction should occur, immediately discontinue administration. Since severe delayed reactions have been known to occur, emergency facilities and competent personnel should be available for at least 30 to 60 minutes after administration (See ADVERSE REACTIONS).

Preparatory dehydration is dangerous and may contribute to acute renal failure in infants, young children, the elderly, patients with pre-existing renal insufficiency, patients with multiple myeloma, patients with advanced vascular disease and diabetic patients.

Acute renal failure has been reported in diabetic patients with diabetic nephropathy and in susceptible non-diabetic patients (often elderly with pre-existing renal disease) following the administration of iodinated contrast agents. Therefore, careful consideration of the potential risks should be given before performing this radiographic procedure in these patients.

Severe reactions to contrast media often resemble allergic responses. This has prompted the use of several provocative pretesting methods, none of which can be relied on to predict severe reactions. No conclusive relationship between severe reactions and antigen-antibody reactions or other manifestations of allergy has been established. The possibility of an

idiosyncratic reaction in patients who have previously received a contrast medium without ill effect should always be considered. Prior to the injection of any contrast medium, the patient should be questioned to obtain a medical history with emphasis on allergy and hypersensitivity. A positive history of bronchial asthma or allergy (including food), a family history of allergy, or a previous reaction or hypersensitivity to a contrast agent may imply a greater than usual risk. Such a history may be more accurate than pre-testing in predicting the potential for reaction, although not necessarily the severity or type of reaction in the individual case. A positive history of this type does not arbitrarily contraindicate the use of a contrast agent when a diagnostic procedure is thought essential, but does call for caution (See ADVERSE REACTIONS).

Prophylactic therapy including corticosteroids and antihistamines should be considered for patients who present with a strong allergic history, a previous reaction to a contrast medium, or a positive pre-test in these patients. The incidence of reaction is two to three times that of the general population. Adequate doses of corticosteroids should be started early enough prior to contrast medium injection to be effective and should continue through the time of injection and for 24 hours after injection. Antihistamines should be administered within 30 minutes of the contrast medium injection. Recent reports indicate that such pre-treatment does not prevent serious life-threatening reactions, but may reduce both their incidence and severity. A separate syringe should be used for these injections.

General anesthesia may be indicated in the performance of some procedures in selected patients, however, a higher incidence of adverse reactions has been reported in these patients, and may be attributable to the inability of the patient to identify untoward symptoms or to the hypotensive effect of anesthesia which can prolong the circulation time and increase the duration of contact of the contrast agent.

Angiography should be avoided whenever possible in patients with homocystinuria because of the risk of inducing thrombosis and embolism.

PRECAUTIONS FOR SPECIFIC PROCEDURES

Pediatric Angiocardiography. It is advisable to monitor for ECG and vital signs changes throughout the procedure.

When large individual doses are administered, sufficient time should be allowed for any observed changes to return to or near baseline prior to making the next injection.

Caution should be used when making right heart injections in patients with pulmonary hypertension or incipient heart failure, since this may lead to increased right side pressures with subsequent bradycardia and systemic hypotension. Patients with pulmonary disease present additional risks.

Caution is advised in cyanotic infants since apnea, bradycardia, other arrhythmias and a tendency to acidosis are more likely to occur.

Since infants are more likely to respond with convulsions than are adults, the amount of total dosage is of particular importance. Repeated injections are hazardous in infants weighing less than 7 kg, particularly when these infants have pre-existing compromised right heart function or obliterated pulmonary vascular beds.

Selective Coronary Arteriography with or without left ventriculography. During the administration of large doses of HEXABRIX, continuous monitoring of vital signs is desirable. Caution is advised in the administration of large volumes to patients with incipient heart failure because of the possibility of aggravating the pre-existing condition. Hypotension should be corrected promptly since it may result in serious arrhythmias.

Special care regarding dosage should be observed in patients with right ventricular failure, pulmonary hypertension, or stenotic pulmonary vascular beds because of hemodynamic changes which may occur after injection into the right heart outflow tract.

Peripheral Arteriography. Moderate decreases in blood pressure occur frequently with intra-arterial (brachial) injections. This change is usually transient and requires no treatment, however, the blood pressure should be monitored for approximately ten minutes following injection.

Extreme caution during injection of the contrast agent is necessary to avoid extravasation and fluoroscopy is recommended. This is especially important in patients with severe arterial disease.

Cerebral Arteriography. Cerebral arteriography should be performed with special caution in patients with advanced arteriosclerosis, severe hypertension, cardiac decompensation, recently recent cerebral thrombosis or embolism, and migraine.

Intra Arterial Digital Subtraction Angiography. The risks associated with IA-DSA are those usually attendant with catheter procedures. Following the procedure, gentle pressure hemostasis is required. Followed by observation and immobilization of the limb for several hours to prevent hemorrhage from the site of arterial puncture.

Patient motion, including respiration and swallowing, can result in misregistration leading to image degradation and non-diagnostic studies.

Intravenous Digital Subtraction Angiography. The risks associated with IV-DSA include those usually attendant with catheter procedures and include intratumoral injections, vessel dissection and tissue extravasation. The potential risk is reduced when small test injections of contrast medium are made under fluoroscopic observation to insure that the catheter tip is properly positioned and, in the case of peripheral placement, that the vein is of adequate size.

Patient motion, including respiration and swallowing, can result in misregistration leading to image degradation and non-diagnostic studies.

Peripheral Venography. Special care is required when venography is performed in patients with suspected thrombosis, phlebitis, severe ischemic disease, local infection or a totally obstructed venous system.

Extreme caution during injection of contrast media is necessary to avoid extravasation and fluoroscopy is recommended. This is especially important in patients with severe arterial or venous disease.

Excretory Urography. Infants and small children should not have any fluid restrictions prior to excretory urography (See WARNINGS and PRECAUTIONS concerning preparatory dehydration).

Contrast Enhancement in Body Computed Tomography. Patient cooperation is essential since patient motion, including respiration, can markedly affect image quality. The use of an intravascular contrast medium can obscure tumors in patients undergoing CT evaluation of the liver, resulting in a false negative diagnosis. Dynamic CT scanning is the procedure of choice for malignant tumor enhancement.

Arthrography. Strict aseptic technique is required to prevent the introduction of infection. Fluoroscopic control should be used to insure proper introduction of the needle into the synovial space and prevent extracapsular injection. Aspiration of excessive synovial fluid will reduce the pain on injection and prevent the dilution of the contrast agent. It is important that undue pressure not be exerted during the injection.

Hysterosalpingography. Caution should be exercised in patients suspected of having cervical or tubal carcinoma to avoid possible spread of the lesion by the procedure. Delayed onset of pain and fever (1-2 days) may be indicative of pelvic infection.

Carcinogenesis, Mutagenesis, Impairment of Fertility. No long-term animal studies have been performed to evaluate carcinogenic potential. However, animal studies suggest that this drug is not mutagenic and does not affect fertility in males or females.

Pregnancy Category B. Reproduction studies have been performed in rats and rabbits at doses up to two times the maximum adult human dose and have revealed no evidence of impaired fertility or harm to the fetus due to HEXABRIX. There are, however, no adequate and well-controlled studies in pregnant women. Because animal reproduction studies are not always predictive of human response, this drug should be used during pregnancy only if clearly needed.

Nursing Mothers. Ioxaglate salts are excreted unchanged in human milk. Because of the potential for adverse effects in nursing infants, bottle-feeding should be substituted for breast feeding for 24 hours following the administration of this drug.

Pediatric Use. Safety and effectiveness in children has been established in pediatric angiocardiography and intravenous excretory urography. Data have been submitted to support the safety and effectiveness of HEXABRIX in other indications. (Precautions for specific procedures receive comment under that procedure.)

ADVERSE REACTIONS

Adverse reactions to injectable contrast media fall into two categories: chemotoxic reactions and idiosyncratic reactions.

Chemotoxic reactions result from the physicochemical properties of the contrast media, the dose and the speed of injection. All hemodynamic disturbances and reactions to organs or vessels perfused by the contrast medium are included in this category.

Idiosyncratic reactions include all other reactions. They occur more frequently in patients 20 to 40 years old. Idiosyncratic reactions may or may not be dependent on the dose injected, the speed of injection, the mode of injection and the radiographic procedure. Idiosyncratic reactions are subdivided into minor, intermediate and severe. The minor reactions are self limited and of short duration. The severe reactions are life threatening and treatment is urgent and mandatory.

NOTE. Not all of the following adverse reactions have been reported with HEXABRIX. Because HEXABRIX is an iodinated intravascular contrast agent, all of the side effects and toxicity associated with agents of this class are theoretically possible, and this should be borne in mind when HEXABRIX is administered.

Severe life-threatening anaphylactoid reactions, mostly of cardiovascular origin, have occurred following the administration of HEXABRIX as well as other iodine-containing contrast agents. Most deaths occur during injection or 5 to 10 minutes later, the main feature being cardiac arrest with cardiovascular collapse as the main aggravating factor. Isolated reports of hypotensive collapse and shock are found in the literature. Based upon clinical literature, reported deaths from the administration of conventional iodinated contrast agents range from 6.6 per 1 million (0.00066 percent) to 1 in 10,000 patients (0.01 percent).

Regardless of the contrast agent employed, the overall estimated incidence of serious adverse reactions is higher with coronary arteriography than with other procedures. Cardiac decompensation, serious arrhythmias, or myocardial infarction may occur during coronary arteriography and left ventriculography.

The most frequent adverse reactions are nausea, vomiting, facial flush and a feeling of body warmth. These are usually of brief duration. In double-blind clinical trials, HEXABRIX produced less discomfort upon injection (pain and heat) when compared to various other contrast agents. Other reactions include the following:

Hypersensitivity reactions. Dermal manifestations of urticaria with or without pruritus, erythema and maculopapular rash. Dry mouth, Swelling, Conjunctival symptoms. Facial peripheral and angioneurotic edema. Symptoms related to the respiratory system include sneezing, nasal stuffiness, coughing, choking, dyspnea, chest tightness and wheezing which may be initial manifestations of more severe and infrequent reactions including asthmatic attack, laryngospasm and bronchospasm with or without edema, pulmonary edema, apnea and cyanosis. Rarely, these allergic-type reactions can progress into anaphylaxis with loss of consciousness, coma, severe cardiovascular disturbances, and death.

Cardiovascular reactions. Generalized vasodilation, flushing and venospasm. Occasionally thrombosis or rarely thrombophlebitis. Extremely rare cases of disseminated intravascular coagulation resulting in death have been reported. Severe cardiovascular responses include rare cases of hypotensive shock, coronary insufficiency, cardiac arrhythmia, fibrillation and arrest. These severe reactions are usually reversible with prompt and appropriate management, however, fatalities have occurred.

Technique reactions. Extravasation with burning pain, hematomas, ecchymosis and tissue necrosis, vascular constriction due to injection rate, thrombosis and thrombophlebitis.

Neurological reactions. Spasm, convulsions, aphasia, syncope, paresis, paralysis resulting from spinal cord injury and pathology associated with the syndrome of transverse myelitis, visual field losses which are usually transient but may be permanent, coma and death.

Other reactions. Headache, trembling, shaking, chills with or without fever, hyperthermia and lightheadedness. Temporary renal shutdown or other nephropathy.

Pediatric angiocardiography has been complicated by intraluminal injection with marked adverse effects on cardiac function.

During selective coronary arteriography with or without left ventriculography, patients may have clinically insignificant ECG changes. The following adverse effects have occurred in conjunction with the administration of iodinated intravascular contrast agents for this procedure: hypotension, shock, anginal pain, myocardial infarction, cardiac arrhythmias (bradycardia, ventricular tachycardia, ventricular fibrillation) and cardiac arrest. Fatalities have been reported. Complications to the procedure include dissection of coronary arteries, dislodgment of atherosclerotic plaques, perforation, hemorrhage and thrombosis.

Following peripheral arteriography, hemorrhage and thrombosis have occurred at the puncture site of the percutaneous injection. Brachial plexus injury has been reported following axillary artery injection.

The major causes of cerebral arteriographic adverse reactions appear to be repeated injections of the contrast material, administration of doses higher than those recommended, the presence of occlusive atherosclerotic vascular disease and the method and technique of injection. Adverse reactions are normally mild and transient. A feeling of warmth in the face and neck is frequently experienced. Infrequently a more severe burning discomfort is observed. Transient visual hallucinations have been reported. Serious neurological reactions that have been associated with cerebral arteriography and not listed under Adverse Reactions include stroke, amnesia and respiratory difficulties. Visual field defects with anopia and reversible neurological deficit lasting from 24 hours to 48 hours have been reported. Confusion, disorientation with hallucination, and absence of vision sometimes lasting for one week have also been reported. Cardiovascular reactions that may occur with some frequency are bradycardia and either an increase or decrease in systemic blood pressure. The blood pressure change is transient and usually requires no treatment. Arthrography may induce joint pain or discomfort which is usually mild and transient but occasionally may be severe and persist for 24 to 48 hours following the procedure. Eufusion requiring aspiration may occur in patients with rheumatoid arthritis. Fever and pain, cramping and tenderness of the abdomen have been reported following hysterosalpingography.

OVERDOSAGE

Overdosages may occur. The adverse effects of overdosage are life-threatening and affect mainly the pulmonary and cardiovascular systems. The symptoms may include cyanosis, bradycardia, acidosis, pulmonary hemorrhage, convulsions, coma and cardiac arrest. Treatment of an overdose is directed toward the support of all vital functions and prompt institution of symptomatic therapy.

Ioxaglate salts are dialyzable. The intravenous LD₅₀ values of HEXABRIX (in grams of iodine/kg body weight) were 11.2 g/kg in mice, ~8 g/kg in rats, ~6.4 g/kg in rabbits and ~3.0 g/kg in dogs.

DOSAGE AND ADMINISTRATION

Details on dosage are provided in the package insert. **CON-SULT FULL PACKAGE INSERT BEFORE USE.**
Rev Jan 1987

References:

1. Stris MG, Laerum F. Iohexol and ioxaglate in peripheral angiography. *Acta Radiologica* 1987; 28:767-770.
2. Smith DC, Yahiku PY, Maloney MD, et al. Three new low-osmolality contrast agents. A comparative study of patient discomfort. *Am J Neuroradiol* 1988; 9:137-139.
3. Murphy WA, Campbell DR, Fraser DB. Pain in peripheral arteriography. An assessment of conventional versus ionic and non-ionic low-osmolality contrast agents. *J Can Assoc Radiol* 1988; 39:103-106.
4. Engelhart JA, Smith D, Bull BS, et al. Aspirated blood and low-osmolality contrast agents: An embolic hazard? Presented at the 73rd Meeting of the Radiological Society of North America, Chicago, IL, Dec 1, 1987.
5. Mosier LD, Joist JH, Chance D, et al. In vitro effects of ionic and nonionic contrast media on coagulation, platelet function, and fibrinolysis. Presented at the 73rd Meeting of the Radiological Society of North America, Chicago, IL, Nov 30, 1987.
6. Stormorken H, Skaltei IO, Testart MC. Effect of various contrast media on coagulation, fibrinolysis, and platelet function. An in vitro and in vivo study. *Invest Radiol* 1986; 21:348-354.



Changing the look of medicine.

**Diagnostic Products Division
Mallinckrodt, Inc.**
Post Office Box 5840
St. Louis, MO 63134
CIRCLE 22 ON READER SERVICE CARD

**For orders,
medical and/or
professional assistance
call
(800) 325-3688 TOLL FREE**

ARMY COMMUNITY HOSPITALS PROVIDE QUALITY MEDICINE AROUND THE WORLD.



Army physicians have opportunities to practice in a variety of clinical settings. Comprehensive primary and secondary care are provided by Army Community Hospitals, such as Florence A. Blanchfield at Fort Campbell, Kentucky, and 32 others located at Army installations in the U.S., eight in Europe and one in Korea. All Army medical facilities are staffed by well trained health care professionals.

Part of the Community Hospital mission is training. Community Hospital staff physicians receive ample opportunities to teach and train medical personnel. Some of the hospitals offer highly competitive Family Practice and Emergency Medicine Residency Programs. Approximately 21 Community Hospitals in the United States and West Germany are involved in instructing, annually, 450 American medical students enrolled in the Army Health Professions Scholarship Program.

All of the primary medical and surgical specialties, such as internal medicine, general surgery, pediatrics, psychiatry and pathology, are represented at these hospitals. Subspecialties are also staffed by American-trained, board-eligible or certified physicians.

Multiple professionally rewarding opportunities to practice high-quality medicine are available in all Army Community Hospitals. Medicine is practiced without concern for patient ability to pay. Excellent clinical support staffs assist physicians treating patients with a wide variety



of diseases and disorders. Most significant, these hospitals provide excellent medical care for some of America's most important citizens, American soldiers and their families.

If you would like the opportunity to visit an Army hospital near you and observe Army medicine first-hand, write to Army Medical Opportunities, P.O. Box 7711, Clifton, New Jersey 07015.

CIRCLE 38 ON READER SERVICE CARD

ARMY MEDICINE. BE ALL YOU CAN BE.

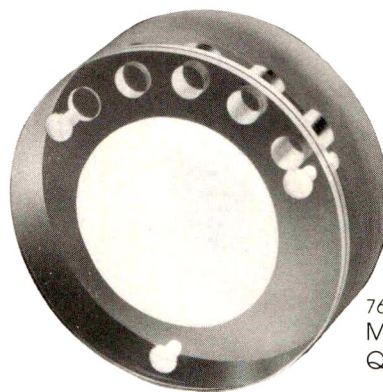
MAMMOGRAPHIC QA

INSTRUMENTS AND ACCESSORIES

For Evaluating the Overall Imaging Performance
of Your Mammographic System



07-492
Mammographic Digital kVp Meter



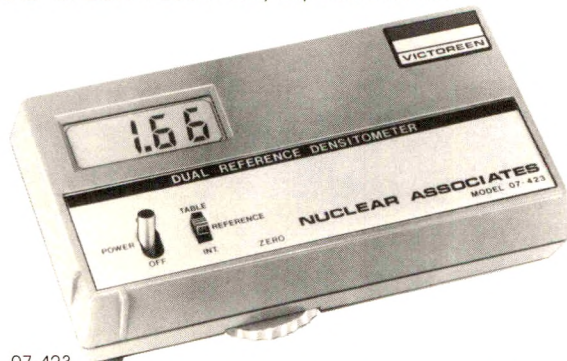
76-001
Mammographic
QA Phantom



06-526
RAD-CHECK® PLUS X-Ray Exposure Meter



07-417
Hand-Held Dual-Color
Sensitometer



07-423
Hand-Held Dual-Reference Digital Densitometer



07-402
Digital Thermometer

WE CARRY A COMPLETE LINE OF MAMMOGRAPHIC QA PRODUCTS

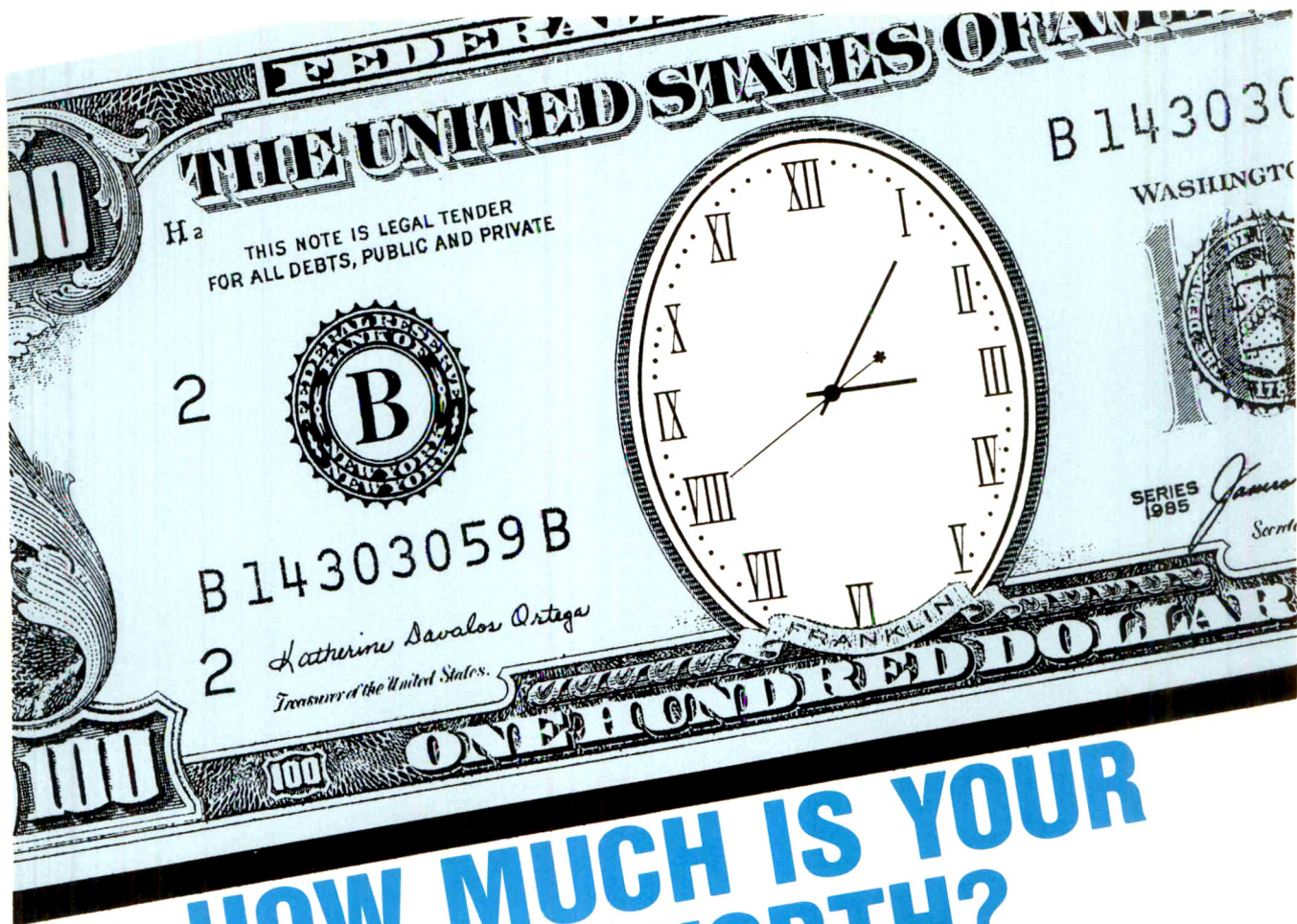
For more information,
request Bulletin 405-44

NUCLEAR ASSOCIATES



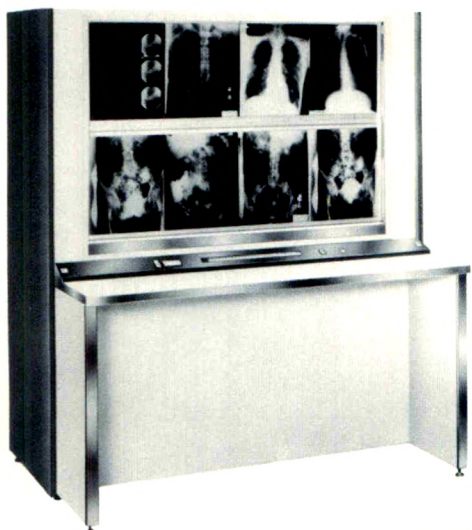
A Division of VICTOREEN, INC.
100 VOICE ROAD
CARLE PLACE, NY 11514-1593
(516) 741-6360

® Victoreen, Inc.



HOW MUCH IS YOUR TIME WORTH?

If, like most Radiologists, you spend 30% or more of your day **handling** films, let us show you how S & S Motorized Viewers eliminate those **COSTLY WASTED HOURS!**



Model MV216

- From 48 up to 324 14" x 17" films can be pre-loaded and stored in proper sequence to be recalled when needed for viewing in as little as 7 seconds—by simply pressing a button!
- All 12 models feature illumination brighter than most other viewers, plus individual panel light controls which promote viewer concentration and increase reading efficiency.
- Some models feature an optional "floating bright spot" which illuminates dense area—at the touch of a button.

- Optional remote controls eliminate need to stand directly in front of viewer to operate it.
- Smaller capacity units on casters provide room-to-room mobility as needed.
- Specially dedicated models are also available for MAMMOGRAPHY, ULTRASOUND, CT and NUCLEAR FILM VIEWING.

Ideal for Teaching, Lecturing or Consultation, S & S Motorized Viewers turn waste into efficiency. **How much is YOUR time worth?** Call S & S or your local x-ray dealer **today.**

CIRCLE 9 ON READER SERVICE CARD

S & S X-RAY PRODUCTS INC.

1101 Linwood Street
Brooklyn, NY 11208
800/347-XRAY
718/649-8500
FAX 718/257-0219



F R O M M A L L I N C K R O D T

NEW NONIONIC

The logo for Optiray (ioversol) is centered on the page. It consists of a gold-colored diamond shape with a blue triangle at the top and a blue triangle at the bottom. Inside the diamond, the word "OPTIRAY" is written in a white, serif, all-caps font. Below it, the word "(ioversol)" is written in a blue, lowercase, serif font. The entire logo is set against a gold-colored rectangular background.

OPTIRAYTM
(ioversol)

COMING VERY SOON.

Progress in Radiology

Diagnostic and Therapeutic Interventional Gallbladder Procedures

Steven K. Teplick¹

The percutaneous insertion of needles and catheters into the gallbladder for a variety of diagnostic and therapeutic purposes is one of the newest areas of interventional radiology. As use of the procedures is becoming more common, their efficacy and safety must be evaluated. In this article, the various diagnostic and therapeutic interventional gallbladder procedures are reviewed. Diagnostic procedures include needle aspiration of bile, needle-aspiration biopsy of the gallbladder, and transcholecystic cholangiography. The most common therapeutic procedure is percutaneous cholecystostomy.

General Considerations

Both CT and sonography can visualize the gallbladder in nearly every instance, so either technique can be used to guide needles or catheters into the gallbladder. Sonographic guidance is, in our experience, usually quicker than CT and sonographic equipment is more readily available.

All patients should be treated with antibiotics 12–24 hr before the study. These prevent infections caused by the organisms commonly found in bile and should include an aminoglycoside and a cephalosporin derivative.

Pain control is important, especially for catheter insertions. This generally requires use of a local anesthetic along with narcotic sedation. We obtain excellent control of pain by having an anesthesiologist administer a high thoracic epidural block. This procedure also reduces the need for narcotics, the use of which is often risky in critically ill patients, particularly those who have preexisting low blood pressure. It has

the added advantage of allowing continuous monitoring of the patient by the anesthetist during the procedure and afterward in the recovery room, and it is better accepted by patients than is sedation with narcotics.

In order to minimize bile leakage, small-gauge needles or Teflon sheaths (20–22 gauge) can be used for the diagnostic procedures. For percutaneous cholecystostomy, larger catheters (5–12 French) are required. The size of the catheter depends on the purpose of the procedure. For example, larger catheters are better suited to drain an empyema of the gallbladder, whereas smaller catheters are sufficient for stone dissolution with methyl *tert*-butyl ether. A variety of catheters are commercially available. Accordion or pigtail catheters that retain their curves (e.g., Hawkins accordion or Cope loop, Cook Inc., Bloomington, IN) are less likely to be dislodged inadvertently than are straight catheters.

Aspiration of Bile and Needle-Aspiration Biopsy

Indications

The major reason for percutaneous needle aspiration of bile is to determine if the gallbladder is a source of infection. This procedure is usually indicated in patients with suspected acalculous cholecystitis, but also can be used to help confirm the presence of calculous cholecystitis. Acalculous cholecystitis occurs most often in patients with complicated and multiple medical or surgical problems. Percutaneous needle aspiration of bile is generally used when other techniques for diagnosing acute acalculous cholecystitis, such as sonogra-

Received September 26, 1988; accepted after revision December 27, 1988.

¹ Department of Diagnostic Radiology, Hahnemann University Hospital, Broad and Vine Sts., Philadelphia, PA 19102. Address reprint requests to S. K. Teplick.

phy and scintigraphy, are inconclusive. For example, the presence of a dilated gallbladder containing sludge on sonography raises the possibility of acalculous cholecystitis, but the diagnosis is inconclusive unless additional findings, such as a thickened gallbladder wall or pericholecystic fluid collection, are identified. Hepatobiliary scintigraphy can be misleading. False-positive studies (nonfilling of the gallbladder, suggesting cystic duct obstruction) are not rare in seriously ill patients.

Sonographic or CT demonstration of an intraluminal or intramural mass in the gallbladder that is not due to stones is unusual. However, one can perform a biopsy on these lesions when present, much as biopsies are performed on mass lesions in other areas of the body. Even small lesions, 1 to 2 cm in size, can be sampled by biopsy. The indication for needle-aspiration biopsy of a gallbladder mass is basically the same as for needle-aspiration biopsies elsewhere, specifically, to diagnose malignancy either in lieu of or before surgery.

Materials and Methods

Gallbladder interventional procedures can be performed in the radiology department under sonographic or CT guidance or, if necessary, at the bedside with the use of mobile sonographic equipment.

A small needle (20–22 gauge) is inserted into the gallbladder via the most direct anterior or anterolateral route, as determined by the imaging technique. Care should be taken not to puncture the back wall of the gallbladder, which would increase the risk of bile spillage.

Gram stains and cultures are made of the aspirated bile. If the bile is obviously infected, insertion of a cholecystostomy catheter should be considered. It is helpful to have a cytologist present during biopsies to ensure that adequate material is obtained. At the end of the procedure, the gallbladder should be decompressed by aspirating as much bile as possible before the needle is removed.

Results

The success rate of inserting small needles into the gallbladder has not been established. In our experience with 60 needle insertions, we had only one failure. This occurred in an uncooperative patient who, after several unsuccessful needle passes were made, refused to continue. Other investigators [1, 2] have not reported any technical failures.

Recently, the usefulness of obtaining bile samples for culture to determine if the gallbladder is the source of infection has been questioned [1]. Usually, a positive bile culture is consistent with the diagnosis of acute cholecystitis. However, negative gram stains and cultures do not exclude cholecystitis, because many patients have already begun antibiotic therapy.

Needle aspiration biopsy of an intraluminal or intramural gallbladder mass is useful preoperatively to establish the presence or absence of malignancy. For example, we performed a biopsy on intraluminal mass lesions of the gallbladder in two patients, both of whom were thought to have cholecystitis and cancer of the gallbladder. At the time of the biopsy, the patients were considered poor candidates for cholecystectomy. In both patients, the cytologic diagnosis was acute and chronic inflammation and no malignancy. The patients responded to medical treatment for cholecystitis.

One subsequently underwent elective cholecystectomy (no cancer was found), and the other has remained asymptomatic for 8 months.

Complications

McGahan and Lindfors [1] reported a series of 36 bile aspirations without complications. One of our cases had transient bacteremia (fever and chills) after a needle-aspiration biopsy. In addition, a small but real risk of bile peritonitis and hemorrhage exists.

Transcholecystic Cholangiography

Indications

In our experience, transcholecystic cholangiography is a safe, rapid, and useful method to visualize nondilated ducts in patients with suspected biliary disease [3]. In addition, it can be used to visualize dilated bile ducts if the site of obstruction is distal to the insertion of the cystic duct.

In our series of 33 patients, the most common reason for transcholecystic cholangiography was to visualize the biliary tree when transhepatic cholangiography and/or endoscopic retrograde cholangiopancreatography were unsuccessful in patients with or without dilated bile ducts. More recently, we have replaced transhepatic cholangiography with transcholecystic cholangiography in patients who do not show dilated intrahepatic ducts on CT or sonography. Other indications for transcholecystic cholangiography are (1) to evaluate patency of the cystic duct in patients with possible acute acalculous cholecystitis when the results of sonography and scintigraphy are equivocal, (2) to confirm suspected injury to the bile duct after endoscopic retrograde cholangiopancreatography, and (3) to evaluate the bile ducts in patients with suspected ampullary stenosis and failed endoscopic retrograde cholangiopancreatography.

Materials and Methods

Under sonographic guidance, a small-bore needle or Teflon sheath (20–22 gauge) is inserted into the gallbladder. We generally aspirate 10–30 ml of bile, depending on the size of the gallbladder, and then, under fluoroscopy, inject as much contrast material as is necessary to visualize the bile ducts. This varies from 30 to 150 ml. At the end of the study, and if there is no obstruction, the gallbladder should be decompressed before the needle is removed. The patient ingests either clear liquids or nothing for 4–6 hr to decrease gallbladder contractions. If obstruction of the common bile duct or cystic duct is found, insertion of a drainage catheter should be considered.

Results

Although vanSonnenberg et al. [2] did not visualize the intrahepatic ducts in four of 10 patients undergoing transcholecystic cholangiography, this has not been our experience. The intrahepatic and extrahepatic ducts had excellent visualization in all our patients. When necessary, complete ductal opacification can be obtained by changing the patient's posi-

tion. Small stones in the gallbladder are best seen by diluting the contrast material with saline solution and, occasionally, by making radiographs with the patient upright.

Complications

Illescas et al. [4] and vanSonnenberg et al. [2] reported no complications with transcholecystic cholangiography in their series of five and 10 patients, respectively. In our series of 33 patients, four (12%) had minor complications consisting of transient mild abdominal or right shoulder pain. In all cases, the pain did not require treatment and subsided shortly after the procedure. Two patients (6%) had more serious complications (probable local peritonitis) consisting of abdominal pain, tenderness, and fever lasting 1–2 days. These patients were maintained on antibiotics and pain medication and recovered completely. None of the patients had hemorrhage or vasovagal reactions.

Percutaneous Cholecystostomy

Indications

Percutaneous cholecystostomy is primarily indicated in patients with acute cholecystitis (often acalculous cholecystitis) who do not respond to medical therapy and who are not candidates for cholecystectomy. Other indications are (1) decompression of obstructed bile ducts when transhepatic decompression is either unsuccessful or unsafe because of underlying liver disease and (2) elective stone dissolution with methyl *tert*-butyl ether or Mocketanin (monooctanoin) [Ethitek Pharmaceuticals, Skokie, IL] and/or (3) basket stone extraction.

Materials and Methods

Usually the gallbladder is localized and punctured under sonographic guidance, and catheter placement is performed under fluoroscopic guidance. However, the entire procedure can be done with sonography or CT alone.

Either the Seldinger exchange technique or the trocar approach is used to insert the catheter. The latter, as advocated by some authors [5–7], is a one-step procedure in which the final catheter is preloaded onto a smaller guidance system. This eliminates the need for dilator exchanges during which bile may leak. However, no proof that either method is safer is available.

Results

Approximately 231 percutaneous cholecystostomies have been reported in the English-language literature [2, 5, 6–25]. Pearse et al. [7] mention the only case in which an attempted percutaneous cholecystostomy failed. Undoubtedly, as percutaneous cholecystostomy is performed more often, this high success rate will decrease, but in general the gallbladder is readily accessible and catheter insertion is relatively easy.

Nearly all the reported cases of acute cholecystitis, acute hydrops, or empyema of the gallbladder that were treated by percutaneous cholecystostomy were cured or sufficiently im-

proved clinically to allow elective cholecystostomy. Vogelzang and Nemcek [25] reported three failures in 16 patients with suspected cholecystitis. We have had a considerably lower success rate. In our experience with six patients who had definite acute cholecystitis (two had empyema), only three were cured by catheter drainage. One improved transiently, then became septic again. At cholecystostomy, this patient was found to have necrosis of the gallbladder wall. Vogelzang and Nemcek [25] also reported a case in which percutaneous cholecystostomy failed in a patient with a necrotic gallbladder. Two of our six patients never recovered from sepsis and died; one had empyema as well as metastatic breast carcinoma, and the other had acute cholecystitis plus extensive liver necrosis following arterial embolization of the liver for bleeding. In five of our patients with suspected biliary sepsis, it was not possible to determine if the gallbladder was the source of infection. Four of the five showed no improvement after percutaneous cholecystostomy even though the sonographic or scintigraphic findings suggested cholecystitis. One patient died from underlying cardiac disease 12 hr after percutaneous cholecystostomy. Three of these patients had several potential sources of chronic sepsis and never recovered. One of five patients improved after percutaneous cholecystostomy, but was improving from chronic sepsis before percutaneous cholecystostomy. Our low success rate with percutaneous cholecystostomy for treating patients with sepsis and suspected cholecystitis in part reflects the difficulty in diagnosing acute cholecystitis in patients with multiple medical and surgical problems. Many of our patients had sepsis for several weeks before the gallbladder was considered the primary or secondary cause of sepsis, and many had several sources of infection.

Percutaneous cholecystostomy can be used to decompress the bile ducts in patients with distal common-bile-duct obstructions [2, 5, 7–9]. The single exception was a case reported by Vogelzang and Nemcek [25]. The patient had carcinoma of the pancreas and did not have adequate reduction of serum bilirubin preoperatively. This patient subsequently underwent percutaneous transhepatic biliary drainage.

Complications

Of the 231 percutaneous cholecystostomies reported in the English-language literature [2, 5, 6–25], only three cases (1%) of bile peritonitis and one death have been reported [7]. In our series of 21 patients, one had peritonitis, which subsided after antibiotic treatment for 4 days.

Other reported complications are four cases of severe vasovagal reactions [2]; one case of acute cholecystitis when a stone became lodged in the cystic duct [2]; five patients with hemobilia, none of whom required treatment [8, 17]; and one transient decrease in blood pressure [17]. The overall reported complication rate is 18/231 (8%).

Unresolved Issues

Several unanswered questions remain concerning percutaneous cholecystostomy. No controlled study has been per-

formed to compare the safety of inserting the catheter into the gallbladder through the liver or the safety of insertion through the peritoneal cavity. The transhepatic approach is advocated by most authorities [5, 9, 21, 26]. In our series and in others [2], both the transhepatic and transperitoneal approaches were used, without an apparent difference in the prevalence of bile peritonitis between the two. New anchoring devices that fix the gallbladder to the abdominal wall, similar to a surgical cholecystostomy, may make the transperitoneal approach preferable [27]. Fixation to the abdominal wall may be especially useful to create a short tract for basket extraction of stones from the gallbladder.

Five of our patients with percutaneous cholecystostomy catheters in place had a cholecystectomy within 5–7 days. In three of the five patients whose catheters did not traverse the liver, omentum covered the site where the catheter entered the gallbladder. No omentum was present at the time of surgery when the catheter traversed the liver. Possibly this omental cover helps reduce bile peritonitis when the liver is not traversed.

There is also uncertainty about when it is safe to remove the catheter from the gallbladder, and if the transhepatic route increases the safety of early removal. Pearse et al. [7] reported one death from peritonitis due to inadvertent early removal of the catheter. Four patients whose catheters accidentally were removed shortly after insertion had no complications. No mention was made of whether or not the catheters were inserted transhepatically. Others also have reported patients whose catheters dislodged without complications [9, 17, 24]. In a series of six patients, Eggermont et al. [15] safely removed the catheters from the gallbladder in 10–21 days. In our series of 21 patients, we were able to remove the catheter in only five patients (5–14 days). The rest either underwent surgery or died with the catheter still in the gallbladder.

Conclusions

In the past, the only treatment for gallbladder disease was surgery. Now, with the use of interventional procedures, it is possible to manage cholecystitis and cholelithiasis nonsurgically. The trend toward greater use of nonsurgical techniques appears to be increasing and is likely to accelerate as more experience is accumulated.

ACKNOWLEDGMENT

The author thanks Ms. Constance Brennan for her technical assistance in the preparation of this manuscript.

REFERENCES

- McGahan JP, Lindfors KK. Acute cholecystitis: diagnostic accuracy of percutaneous aspiration of the gallbladder. *Radiology* **1988**;167:669–671
- vanSonnenberg E, Wittich GR, Casola G, et al. Diagnostic and therapeutic percutaneous gallbladder procedures. *Radiology* **1986**;160:23–26
- Teplick SK, Haskin PH, Sammon JK, et al. Common bile duct obstruction: assessment by transcholecystic cholangiography. *Radiology* **1986**;161:135–138
- Illescas FF, Braun SD, Cohan RH, Bowie JD, Dunnick NR. Ultrasonically guided percutaneous transhepatic transcholecystocholangiography in the nondilated biliary tree. *Gastrointest Radiol* **1986**;11:77–80
- Klimberg S, Hawkins I, Vogel SB. Percutaneous cholecystostomy for acute cholecystitis in high-risk patients. *Am J Surg* **1987**;153:125–129
- McGahan JP, Walter JP. Diagnostic percutaneous aspiration of the gallbladder. *Radiology* **1985**;155:619–622
- Pearse DM, Hawkins IF, Shaver R, Vogel S. Percutaneous cholecystostomy in acute cholecystitis and common duct obstruction. *Radiology* **1984**;152:365–367
- Makucchi M, Yamazaki S, Hasegawa H. Ultrasonically guided cholangiography and bile drainage. *Ultrasound Med Biol* **1984**;10(5):617–623
- Larssen TB, Gothlin JH, Jensen D, Arnesjo B, Soriede O. Ultrasonically and fluoroscopically guided therapeutic percutaneous catheter drainage of the gallbladder. *Gastrointest Radiol* **1988**;13:37–40
- Laffey KJ, Martin EC. Percutaneous removal of large gallstones. *Gastrointest Radiol* **1986**;11:165–168
- Teplick SK, Wolferth CC Jr, Hayes MF Jr, and Amrom G. Percutaneous cholecystostomy in obstructive jaundice. *Gastrointest Radiol* **1982**;7:259–261
- Teplick SK, Brandon JC, Haskin PH, Pavlides CA, Huppert A. Percutaneous cholecystostomy in patients at high risk: treatment of acalculous cholecystitis. *Postgrad Med* **1987**;81(1):209–214
- vanSonnenberg E, Hofmann AF, Neoptolemus J, Wittich GR, Princenthal RA, Willson SW. Gallstone dissolution with methyl-tert-butyl ether via percutaneous cholecystostomy: success and caveats. *AJR* **1986**;146:865–867
- Kerlan RK Jr, LaBerge JM, Ring EJ. Percutaneous cholecystolithotomy: preliminary experience. *Radiology* **1985**;157:653–656
- Eggermont AM, Lameris JS, Jeekel J. Ultrasound-guided percutaneous transhepatic cholecystostomy for acute acalculous cholecystitis. *Arch Surg* **1985**;120:1354–1356
- Shaver RM, Hawkins IF Jr, Soong J. Percutaneous cholecystostomy. *AJR* **1982**;138:1133–1136
- Lohela P, Soiva M, Suramo I, Taavitsainen M, Holopainen O. Ultrasonic guidance for percutaneous puncture and drainage in acute cholecystitis. *Acta Radiol [Diagn]* (Stockh) **1986**;27(5):543–546
- Dunham F, Marliere P, Mortier C, Guibis A. Ultrasound-guided percutaneous and transhepatic cholecystostomy: a complementary procedure to therapeutic endoscopy. *Endoscopy* **1985**;17:153–156
- Allen MJ, Borody TJ, Bugliosi TF, May GR, LaRusso NF, Thistle JL. Rapid dissolution of gallstones by methyl tert-butyl ether. *N Engl J Med* **1985**;312(4):217–220
- Longmaid HE III, Bassett JG, Gottlieb H. Management of gallbladder perforation by percutaneous cholecystostomy. *Crit Care Med* **1985**;13(8):686–687
- Lameris JS, Jeekel J, Havelaar IJ, vonSeyen AJ. Percutaneous cholecystostomy. *ROFO* **1985**;142(1):80–82
- Quinn SF, Fazio F, Jones E. Torsion of the gallbladder: findings on CT and sonography and the role of percutaneous cholecystostomy. *AJR* **1987**;148:881–882
- Radder RW. Ultrasonically guided percutaneous catheter drainage of gallbladder empyema. *Diagn Imag* **1980**;49:330–333
- McGahan JP. A new catheter design for percutaneous cholecystostomy. *Radiology* **1988**;166:49–52
- Vogelzang RL, Nemcek HA Jr. Percutaneous cholecystostomy: diagnostic and therapeutic efficacy. *Radiology* **1988**;168:29–34
- vanSonnenberg E, Wing VW, Pollard JW, Casola G. Life-threatening vagal reactions associated with percutaneous cholecystostomy. *Radiology* **1984**;51:377–380
- Cope C. Percutaneous subhepatic cholecystostomy with removable anchor. *AJR* **1988**;151:1129–1132

Progress in Radiology

Imaging Hepatic Metastases from Colorectal Carcinoma: Identification of Candidates for Partial Hepatectomy

Steven E. Seltzer¹ and B. Leonard Holman

In 1989, there will be 145,000 new cases of colorectal cancer in the United States [1]. The overall 5-year survival rate for patients with this condition remains poor, approximating 30%. However, despite the gloomy population-wide statistics, the last two decades have witnessed enormous progress in the battle against this disease. The 1970s saw the introduction of aggressive surgical techniques to control limited metastatic disease in the liver. The 1980s brought both the development and refinement of imaging techniques to depict hepatic lesions in great detail.

In 1982, Dr. Martin Adson, in his Cannon Lecture to the Society of Gastrointestinal Radiologists [2], summarized progress in hepatic surgery and emphasized the importance of cooperation between radiologists and surgeons: "I know that the radiologist and surgeon both can serve the patient better if they understand each other and look at things together. This can be easy because both are anatomists trained to understand the relation between structure and disease, and both literally hope to see what is happening. . . . A surgeon's success or failure may depend, in part, on the radiologist." He went on to remind his audience that at the close of the 1970s, hepatic imaging techniques were not sufficiently refined to meet the needs of the surgeon: "At least one half of resected patients had large parts of their livers removed for naught. That is, in a way, where you as radiologists come in—for these patients died not from what you saw and we took out, but from what you couldn't see and we left in. Your view of hidden things has so improved in recent years that more precise staging of cancer is likely just

around the corner. When those invisible lesions can be seen, at least one-half of such patients can be spared a useless operation."

Patients with colon cancer can be divided into two groups—one (with a resectable primary tumor and with three or fewer hepatic metastases) can be helped by hepatic surgery; the other (with either no liver metastases or widely disseminated intra- or extrahepatic disease) cannot. The focus of this paper is on strategies available to detect the presence, number, and location of liver metastases and to differentiate malignant from benign lesions. Additionally, the requirements for the identification of patients with colorectal carcinoma who are candidates for partial hepatectomy (i.e., those with limited disease, amenable to a technically feasible operation) are addressed.

It is critical for the radiologist to make these determinations accurately. Only in this way will patients with potentially "curable" disease be given the best chance of survival, and those with "incurable" disease be spared the morbidity, mortality, and costs of unnecessary surgery.

General Concepts

Survival rates in colorectal cancer depend critically on the stage of the disease at diagnosis and initial treatment. The pattern of its metastatic spread is consistent with an orderly "cascade" hypothesis [3]. If the primary tumor can be resected before it has spread to regional lymph nodes, 5-year survival rates should be near 90%. Once lymph nodes are involved,

Received August 26, 1988; accepted after revision January 17, 1989.

¹ Both authors: Department of Radiology, Harvard Medical School, Brigham & Women's Hospital, 75 Francis St., Boston, MA 02115. Address reprint requests to S. E. Seltzer.

5-year survival decreases to about 60%. If the tumor has reached the liver and is not treated, 5-year survival is nil [4, 5].

Adson [6], Adson et al. [7], and others [8–19] observed that when the number of liver metastases is small (three or fewer), resection of these deposits improves survival. As an aggregate, these surgical teams reported an average of 25% 5-year survival in patients undergoing surgery to remove three or fewer liver lesions (compared with 0% in control groups).

It is generally accepted that the timing of the surgical removal of metastatic foci is not a critical determinant of survival. The prognosis is similar for patients after removal of synchronous or metachronous metastases [11, 20]. This fact, coupled with the substantial morbidity and mortality associated with surgery on both the colon and the liver at one time, has led to the general acceptance of a two-step strategy—initial removal/bypass of the primary tumor and removal of metastases a few weeks later.

Although hepatic metastases can be removed, and the patient possibly cured in the process, it is critical that the surgeon have a clear, detailed map of the liver's involvement with tumors. Patients with three or fewer metastases that involve three or fewer hepatic segments are clearly candidates for hepatic metastasectomy—their prognosis is at least fairly good, and they would be left with a sufficient remnant of liver tissue. When more lesions are present, the surgery is useless.

Diagnostic Tests

Nonimaging tests, such as biochemical tests of liver function, carcinoembryonic antigen measurements, and visual inspection of the liver surface through a laparoscope or at surgery are generally agreed to be insufficiently sensitive or specific to be useful for either the detection of metastases or the identification of operable candidates [21–25].

Scintigraphy

Although scintigraphy was the mainstay of liver tumor detection for decades, the test lacks sufficient spatial resolution and tissue characterization to be of value as a primary diagnostic tool. Technical advances, including development of single-photon emission CT (SPECT), have improved resolving power. The "full-width, half-maximum" values that describe the spatial resolution of SPECT are in the range of 15–20 mm, still much coarser than CT or MR [26].

Technetium sulfur colloid is the agent of choice for tumor detection. However, this test cannot determine the nature of the liver lesion. A second test using labeled red cells, gallium citrate, or labeled white cells is required for lesion characterization.

Because of these drawbacks, scintigraphy does not play an important role in the detection of metastases or in the identification of operable candidates.

Sonography

Transabdominal sonography also lacks sufficient spatial resolution and tissue specificity, although recent technical

advances have improved this test. The most optimistic sonographic study used linear array transducers and reported detection of lesions as small as 11 mm [27].

Intraoperative sonography, in which the transducer is placed directly on the liver surface, is proving effective in finding additional metastatic deposits (not detected with transabdominal sonography or CT) at surgery [28–30]. The procedure is not in widespread use, but it is gaining recognition. Kane et al. [28] found the intraoperative procedure to be superior to transabdominal sonography or CT, particularly because of its high sensitivity for detecting small liver lesions. They reported that intraoperative sonography detected approximately 25% more lesions than any other test. Specificities were not calculated. Others report that in up to 25% of patients, additional lesions were seen or new information gathered from the intraoperative study, often resulting in a change in the surgical approach and management [29, 30].

Intraoperative sonography is performed immediately before partial hepatectomy to determine precisely the number and location of metastases, as well as to confirm that the surgery is warranted. It is usually considered impractical to do the sonogram at the time of resection of the primary tumor—in this case exposing the liver involves extending the incision and prolonging the procedure.

CT

Alderson et al. [31] compared the results of scintigraphy, sonography, and CT for the detection of liver metastases in patients with colon (and breast) cancer. CT proved to have the best sensitivity and specificity for tumor detection. ROC curves showed that CT had a higher true-positive ratio at every false-positive rate. The authors found that at the inflection point on its ROC curve (a point that maximizes true positives and minimizes false positives) [32], CT could operate at a 91% true-positive rate and a 13% false-positive rate for the identification of patients with hepatic metastases. The most common cause of false-positive errors is mislabeling of benign lesions (e.g., hemangiomas), normal structures (e.g., vessels), or artifacts. This and other studies confirmed that, as of the mid-1980s, CT was superior to scintigraphy and sonography [33–45].

Other investigators attempted to improve the accuracy of CT still further by administering contrast materials directly into the superior mesenteric artery or into the portal vein [33–36]. Although these procedures improve identification of hepatic segmental anatomy and may show small tumors, they are too invasive and specialized for use as a screening test. Additionally, portography has been cited as having a high false-positive rate [37]. Similarly, although enhanced CT with ethiodized oil emulsion (EOE-13) improves the CT detection of liver metastases [37, 38], this contrast material is not available commercially.

Two practical techniques that use standard IV contrast agents both improve diagnostic accuracy of CT and are practical for routine use. One of these is "dynamic" sequential hepatic CT performed by scanning the liver rapidly after bolus injection of large amounts of contrast material (30–50 g iodine)

[39]. This technique exploits the fact that normal liver tissue and hepatic metastases have different blood supplies. The normal liver is fed 75% from the portal vein and 25% from the hepatic artery, while metastases receive nearly 100% of their blood supply from the hepatic artery. Although the pharmacokinetics of delivery/diffusion of contrast material to normal and pathologic tissues are complex, a generally successful strategy is to start imaging about 20 sec after injection and continue for 2 min. During this short span, iodine is entering the normal liver via the portal vein and is flooding its extracellular space, brightly enhancing normal liver tissue. Most metastatic deposits contain little contrast agent during this predominantly portal venous phase, and show up as filling defects. The technique requires a fast scanner with the ability to move the table automatically and rapidly so that the entire liver can be scanned within 2 min, the "prime time" for tumor visualization. Delayed hepatic CT is performed 4 to 6 hr after the injection of 50 g iodine [40]. Here, imaging is performed during the time in which normal hepatocytes contain the small fraction of the contrast dose that is secreted into the bile. The normal liver is, therefore, slightly enhanced. Liver metastases lack the ability to take up and hold contrast in this delayed phase and are visible as filling defects.

Compared with unenhanced CT, use of dynamic sequential hepatic CT does not markedly increase the number of patients correctly diagnosed as having liver metastases. On the other hand, the number of lesions detected can be increased by as much as 40% [41–43]. In a study by Bernardino et al. [40], delayed CT appeared superior to dynamic CT when the two techniques were used in the same patients. Although both identified the same number of abnormal patients, the delayed study provided better definition of the metastases in 58% of patients and visualized more lesions in 27%. A smaller number of lesions (11%) were better seen on the dynamic than on the delayed images. No false-positive examinations were reported with either technique. An added advantage of using iodinated contrast material is that accurate identification of vessels, depiction of segmental anatomy, and differentiation of benign from malignant tumors are all facilitated, reducing the risk of false-positive interpretations and imprecise localizations [44, 45].

MR Imaging

MR is also an effective procedure for the detection of hepatic metastases. Although results vary with the technique and instrumentation used [46–61], several studies indicate that optimally performed MR is at least as sensitive as contrast-enhanced CT.

Controversy exists about the optimum field strength and optimum pulse sequence to use for liver metastasis detection. Initial reports recommended use of moderate field strength magnets (0.15 to 1.0 T) along with T1-weighted pulse sequences (either short-TR/short-TE spin echo or inversion recovery). However, a recent multiinstitutional trial suggested that there is a "trend" for liver images at high field strength (1.5 T) to be superior to lower fields [60]. At high field strength, there is less difference in T1 values separating normal liver

and tumor tissue, leading to less contrast between these two tissue types on T1-weighted images. T2 is less dependent (if at all) on field strength. Therefore, it has been generally considered that T2-weighted spin-echo pulse sequences (long TR/long TE) are best for tumor depiction at 1.5 T [57, 58]. However, a recent report challenges this concept and suggests that T1-weighted inversion recovery sequences are superior to T2-weighted spin-echo sequences at high field strength [61]. Certainly, additional data are needed to sort out these conflicting results.

Stark et al. [46] found MR superior to CT in a group of 135 patients (57 with liver metastases, 27 with focal benign hepatic conditions, 51 normal). They reported sensitivities of 82% and 80% for MR and CT, respectively, when results were analyzed on a per-patient basis; sensitivities were 64% and 51% when analyzed on a per-lesion basis. Specificities were 99% for MR and 94% for CT. MR has the added potential strength of being able to differentiate benign lesions (e.g., the extremely prevalent hemangioma) from malignant deposits [62].

MR performance may be improved further with the use of contrast media. A novel, particulate agent, superparamagnetic iron oxide, has proved effective in patients [63]. This agent is taken up selectively by normal liver tissue, sharply shortening T2 values and leading to dramatic intensity decreases on T2-weighted images. Tumor deposits cannot ingest the agent, so they stand out brightly as areas of high signal. This technique is under development and must be fully evaluated before it is considered as a viable alternative to unenhanced MR or contrast CT.

The drawbacks of MR are limited availability, prolonged examination time, and limited depiction of extrahepatic structures.

At present, it is not clear which test will prove best. Chezmar et al. [64] point out that availability, experience, extrahepatic visualization, and throughput favor CT, particularly if dynamic CT (an accurate marker of patients with hepatic metastases) is used as the initial examination and delayed imaging (an accurate marker of the number of lesions) is added for those patients who appear to have resectable disease on the dynamic study. With experience, increased availability, and improved techniques, MR might become the imaging procedure of choice.

Selection of an Appropriate Imaging Strategy

Certain assumptions will be made in considering a strategy for liver metastasis detection in patients with colorectal cancer. These assumptions necessarily introduce some biases, but they are necessary to make the analysis feasible. The assumptions include: (1) The primary colonic tumor will be resected or bypassed in all cases. (2) Resection of the primary tumor and hepatic metastases should not be done at one time because of the risk of excessive blood loss and prolonged anesthesia time. (3) There is little risk to the patient of waiting about 6 weeks after resection of the primary tumor before imaging and perhaps operating on the liver. (4) Some patients require CT imaging of the primary tumor site to

determine its resectability (e.g., extensive rectal cancers that could be technically unremovable). These patients would be studied preoperatively by CT.

We will use the term "truth data" to describe the actual condition of the liver in a cohort of 100 hypothetical patients with newly diagnosed colon cancer. Such truth data are presented in Figure 1. If the findings of Finlay and McArdle [25] were applied to this group of 100 such cases, 29 would be considered "incurable" on the basis of the findings at resection of the primary tumor—17 would have overt, disseminated liver metastases and 12 would have unresectable primary tumors. The remaining 71 patients would be considered curable. On the basis of their data, 51 of these 71 would, indeed, have no liver metastases (or any residual disease), whereas 20 would have occult liver metastases—invisible and not palpable. Of these 20 with secondary tumors in the liver, the data of Cady and McDermott [11] and Adson [6] suggest that about one fifth, or four patients, would have four or more deposits and be considered unresectable, whereas about four fifths, or 16 patients, would have three or fewer deposits and could be helped by hepatic resection. These truth data, although based on small numbers of cases, will be used in the analysis of the imaging strategy.

Several additional assumptions are required for the analysis: MR and CT have similar sensitivities for liver metastasis detection (both on a per-patient and per-lesion basis). MR is slightly more specific because it can differentiate heman-

giomas from metastases better than CT. For this analysis, the simplifying assumption will be made that either test can differentiate benign from malignant lesions with perfect accuracy.

Although the sensitivity and specificity rates for MR and CT are becoming better delineated on both a per-patient and per-lesion basis, few or no data are available on the precision with which either test permits an accurate count of the exact number, segmental distribution, and potential resectability of liver metastases in an individual patient. Specifically, we have little insight into the number of times patients characterized as having three or fewer lesions (resectable) actually have four or more (unresectable), or vice versa. In fact, developing such data will be an important research endeavor. For the present analysis, we will make the following tenuous, yet plausible, assumption: when a patient is correctly determined to have metastatic deposits, the precise number and distribution of the lesions are also correctly determined (resectability is correctly determined). Such an assumption is tenuous, because it asserts that per-lesion accuracy rates will be the same in patients with advanced or with limited disease. It is plausible, because it is likely that the appearances of all lesions in an individual patient are highly correlated; that is, if any lesion is detectable, then all that are present are likely to be similarly detectable. Nevertheless, the 25% 5-year survival for patients with apparently resectable disease who undergo partial hepatectomy suggests that the number of undetected

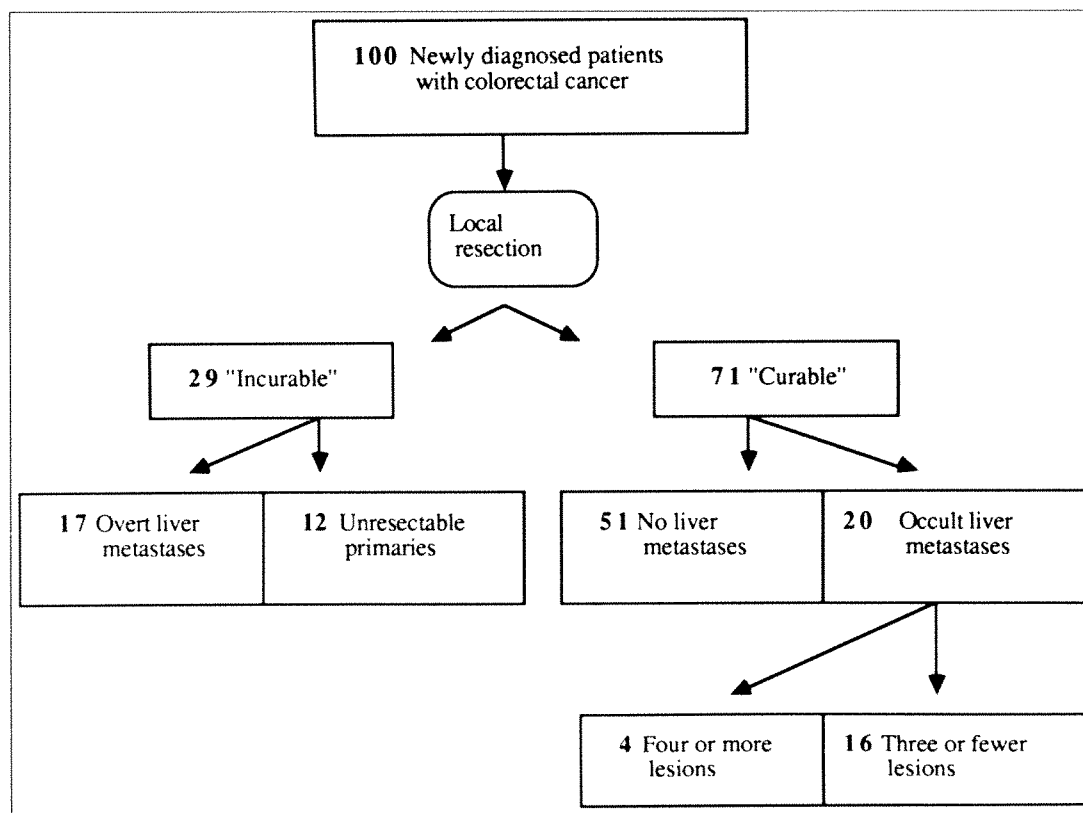


Fig. 1.—Truth data: analysis of 100 hypothetical patients.

liver metastases may be quite high. Despite the stated limitations, in the flowchart accompanying the strategy that follows, it will be assumed that the assessment of "resectability" is made with 100% accuracy.

Postoperative Hepatic Imaging by Using MR or CT

Because all patients require at least palliative colon surgery during which the surgeon can look at the liver, imaging before surgery is unwarranted. Therefore, the strategy presented is postoperative imaging with MR or CT.

The flowchart in Figure 2 tracks the fate of the cohort of 71 patients out of the original 100 with newly diagnosed colon cancer who would still be considered curable after their primary surgery. Assuming that MR and CT are each about 92% sensitive and 95% specific for the detection and characterization of hepatic tumors, 49 of 51 patients without hepatic metastases would be correctly called normal by using this technique. (Two false-positives would be generated.) Of the 20 with occult liver metastases, about 19 would be correctly identified, about one would be missed. Of the 16 patients with potentially resectable hepatic metastases, 15 would be detected (one would be missed). Most of the four patients with unresectable hepatic metastases would be identified (a small fraction would be misclassified as normal).

All told, for about 53 patients a decision against hepatic surgery would be made appropriately; for one patient, this decision would be made inappropriately, and this individual would miss out on a chance for "cure." Fifteen patients would have hepatic surgery appropriately; in just over two patients, this surgery would be performed unnecessarily.

Assuming a 25% 5-year survival rate for the 15 patients identified with resectable liver tumors, about four additional lives would be saved by pursuing this strategy.

Of the 17 patients having surgery, 15 (88%) would have surgery appropriately, and about four (24%) would be cured. The other two (12%) would have surgery unnecessarily. All 17 patients would experience the added morbidity and mortality of this surgery. No generalizable data are available to pinpoint what these extra risks might be—this type of hepatic

surgery is quite specialized, and surgical results would be expected to vary widely from one institution to another.

MR and CT have nearly offsetting special strengths and weaknesses. MR has slightly superior specificity; CT depicts extrahepatic sites of disease with great clarity. MR is costly both in time and dollars; CT requires use of contrast media.

For the foreseeable future, both MR and CT imaging will be accepted procedures for liver evaluation and should yield similar results.

Costs of Imaging Relative to Costs of Treatment

An important point in the foregoing analysis is that the costs of treatment dwarf the costs of imaging tests and impact the costs of the overall strategy. Looking at the strategy proposed, 71 of the initial 100 patients would undergo an MR or CT examination that costs about \$600 [65]. The \$42,600 cost of imaging is quite small compared with the cost of 17 hepatic surgeries (approximately \$37,000 apiece), which amounts to \$629,000 (J. Courtemanche, personal communication). The ratio of surgical costs to imaging costs is 15:1. The cost of imaging to diagnose and "save" the four patients with limited hepatic metastases would be \$10,500 per case (\$42,600 divided by four).

It should be noted that this economic analysis is necessarily quite limited. It does not take into account the treatment costs beyond the hepatic surgery. Certainly, the costs of treatment for the complications of surgery or the terminal care of patients with advanced tumors would have to be considered as part of a thorough economic analysis.

The high cost of treatment reemphasizes the critical need for accurate imaging tests. Better tests would identify more precisely the patients who can actually benefit from partial hepatectomy. Survival rates in this operated group should improve; unnecessary surgery on patients with subtle, but advanced, disease would diminish, ameliorating the human and economic costs. There is reason to be optimistic. Adson's 5-year survival statistics for hepatectomy patients were tabulated before the advent of the promising imaging tests (MR, CT with optimal contrast agent use, intraabdominal sonog-

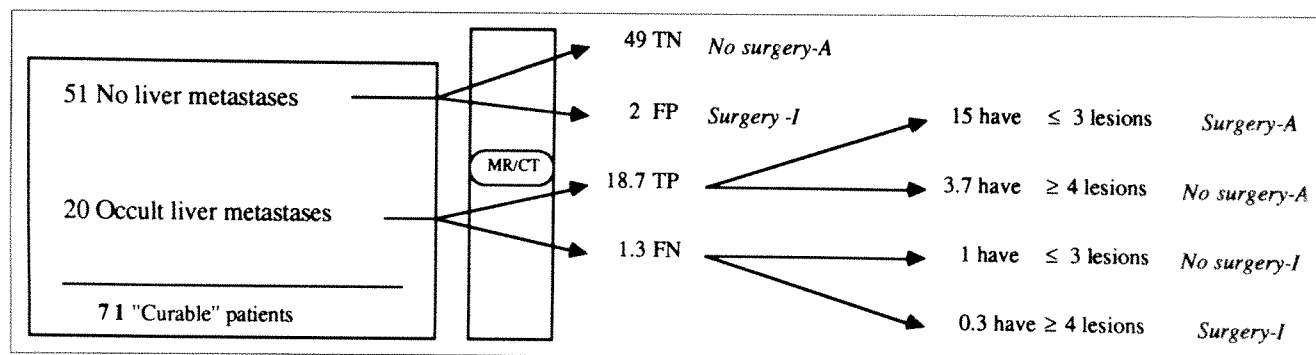


Fig. 2.—Imaging strategy: analysis of outcome of diagnostic tests. TN = true negative; FP = false positive; TP = true positive; FN = false negative; No Surgery-A = no hepatic surgery, appropriately; No Surgery-I = no hepatic surgery, inappropriately; Surgery-A = hepatic surgery, appropriately; Surgery-I = hepatic surgery, inappropriately.

raphy) that are available now and will be with us into the next century.

ACKNOWLEDGMENTS

The authors thank Peter Doubilet for his comments and thoughtful review and Susan McLaughlin for manuscript preparation.

REFERENCES

- Silverberg E, Lubera JA. Cancer statistics 1988. *CA* **1988**;38:5-22
- Adson MA. Cannon lecture: hepatic metastases in perspective. *AJR* **1983**;140:695-700
- Weiss L, Grundmann E, Torhord J, et al. Haematogenous metastatic patterns in colonic carcinoma: an analysis of 1541 necropsies. *J Pathol* **1986**;150:195-203
- Chapuis PH, Fisher R, Dent OL, Newland RC, Pheils MT. The relationship between different staging methods and survival in colorectal carcinoma. *Dis Colon Rectum* **1985**;28:158-161
- Gastrointestinal tumor study group. Adjuvant therapy of colon cancer: results of a prospectively randomized trial. *N Engl J Med* **1984**;310:737-743
- Adson MA. Mass lesions of the liver. *Mayo Clin Proc* **1986**;61:362-368
- Adson MA, Van Heerden JA, Adson MH, Wagner JS, Ilstrup DM. Resection of hepatic metastases from colorectal cancer. *Arch Surg* **1984**;119:647-651
- Logan SE, Meier SJ, Ramming KP, Morton DL, Longmire WP Jr. Hepatic resection of metastatic colorectal carcinoma: a ten-year experience. *Arch Surg* **1982**;117:25-28
- Rajapal S, Dashahapatra KS, Ledesma EJ, Mittelman A. Extensive resections of isolated metastasis from carcinoma of the colon and rectum. *Surg Gynecol Obstet* **1982**;155:813-816
- Malt RA. Current concepts: surgery for hepatic neoplasms. *N Engl J Med* **1985**;313:1591-1595
- Cady B, McDermott WV. Major hepatic resection for metachronous metastases from colon cancer. *Ann Surg* **1985**;201:204-209
- Iwatsuki S, Esquivel CO, Gordon RD, Starzl TE. Liver resection of metastatic colorectal cancer. *Surgery* **1986**;100:804-810
- Coppa GF, Eng K, Randon JHC, Gouge TH, Localio SA. Hepatic resection for metastatic colon and rectal cancer. *Ann Surg* **1985**;205:203-208
- Gennari L, Doci R, Vozzetti F, Bignami P. Surgical treatment of hepatic metastases from colorectal cancer. *Ann Surg* **1986**;203:49-54
- Petrelli NJ, Nambisan RM, Herrera L, Mittelman A. Hepatic resections for isolated metastasis from colorectal carcinoma. *Am J Surg* **1985**;149:205-209
- August DA, Sugarbaker PH, Otow RT, Gianola FJ, Schneider PD. Hepatic resection of colorectal metastases: influence of clinical factors and adjuvant intraperitoneal 5-fluorouracil via Tenckhoff catheter on survival. *Ann Surg* **1985**;201:210-218
- Hughes KS, Simon R, Songhorabodi S, et al. Resection of the liver for colorectal carcinoma metastases: a multi-institutional study of patterns of recurrence. *Surgery* **1986**;100:278-284
- Butler J, Attiye FF, Daly JM. Hepatic resection for metastases of the colon and rectum. *Surg Gynecol Obstet* **1986**;162:109-113
- Ekberg H, Tranberg K-G, Andersson R, et al. Determinants of survival in liver resection for colorectal secondaries. *Br J Surg* **1986**;73:727-731
- August DA, Sugarbaker PH, Schneider PD. Lymphatic dissemination of hepatic metastases: implication for the follow-up and treatment of patients with colorectal cancer. *Cancer* **1985**;55:1490-1494
- Kemeny MN, Sugarbaker PH, Smith TJ, et al. A prospective analysis of laboratory tests and imaging studies to detect hepatic lesions. *Ann Surg* **1982**;195:163-167
- Lowenstein MS, Zancheck N. Carcinoembryonic antigen in the liver. *Gastroenterology* **1977**;72:161-166
- Schulz W, Hagen CH, Hort W. The distribution of liver metastases from colonic cancer: a quantitative postmortem study. *Virchows Arch [A]* **1985**;406:279-284
- Hogg L, Pack G. Diagnostic accuracy of hepatic metastases at laparotomy. *Arch Surg* **1956**;72:251-252
- Finlay IG, McArdle CS. Occult hepatic metastases in colorectal carcinoma. *Br J Surg* **1986**;73:732-735
- VanHeertum RL, Brunetti JC, Yudd AP. Abdominal SPECT imaging. *Semin Nucl Med* **1987**;17:230-246
- Sheu J-C, Chen D-S, Sung J-L, et al. Hepatocellular carcinoma: US evolution in the early stage. *Radiology* **1985**;155:463-467
- Kane RA, Clarke M, Hamilton ES, et al. Prospective comparison of pre-operative imaging and intraoperative US in the detection of liver tumors. *Radiology* **1987**;165(P)[suppl]:286-287
- Rifkin ND, Rosato FE, Branch M, et al. Intra-operative ultrasound of the liver: an important adjunctive tool for decision making in the operating room. *Ann Surg* **1987**;205:466-471
- Machi J, Isomoto H, Kurohiji P, et al. Detection of unrecognized liver metastases from colorectal cancers by routine use of operative ultrasonography. *Dis Colon Rectum* **1986**;29:405-409
- Alderson PO, Adams DF, McNeil BJ, et al. Computed tomography, ultrasound and scintigraphy of the liver in patients with colon or breast carcinoma: a prospective comparison. *Radiology* **1983**;149:225-230
- Swets JA, Pickett RN. *Evaluation of diagnostic systems: methods from signal detection theory*. New York: Academic Press, **1982**
- Moss AA, Dean PB, Axel L, Goldberg HI, Glazer GM, Friedman MA. Dynamic CT of hepatic masses with intravenous and intraarterial contrast material. *AJR* **1982**;138:847-852
- Botet JF, Sanders L, Watson RC, Kemeny N, Cohen A. Comparison of dynamic CT portography and conventional CT in the preoperative evaluation of colorectal metastasis to the liver. *Radiology* **1987**;165(P)[suppl]:232
- Chamsangavej C, Carrasco CH, Richli WR, Lorrigan JG, Wallace S. Portal venous contrast-enhanced CT in the detection of hepatic metastases. *Radiology* **1987**;165(P)[suppl]:232
- Pessar ML, Zerhouni EA, Sitzmann J, Fishman EK, Kaufman SL, Soulen RL. Evaluation of resectability of hepatic malignancy with computed tomographic angiography and MR imaging: comparative study with surgical and histologic correlation. *Radiology* **1987**;165(P)[suppl]:231
- Miller DL, Simmons JT, Chang R, et al. CT detection of hepatic metastases: comparison of arterial portography, delayed scanning and EOE-13 for contrast enhancement. *Radiology* **1987**;165(P)[suppl]:232
- Miller DL, Verness M, Doppman JL, et al. CT of the liver and spleen with EOE-13: review of 225 examinations. *AJR* **1984**;19:570-573
- Foley WD, Berland LL, Lawson TL, Smith DF, Thorsen NK. Contrast enhancement technique for dynamic hepatic computed tomographic scanning. *Radiology* **1983**;147:797-803
- Bernardino ME, Erwin DC, Steinberg HV, Baumgartner BR, Torres WE, Gedgaudas-McClees RK. Delayed hepatic CT scanning: increased confidence and improved detection of hepatic metastases. *Radiology* **1986**;159:71-74
- Berland LL, Lawson TL, Foley WD, Melrose BL, Chintapali KN, Taylor AJ. Comparison of pre- and postcontrast CT in hepatic masses. *AJR* **1982**;138:853-858
- Burgener FA, Hamlin DJ. Contrast enhancement of hepatic tumors in CT: comparison between bolus and infusion techniques. *AJR* **1983**;140:291-295
- Alpern MD, Lawson TL, Foley WD, et al. Focal hepatic masses and fatty infiltration detected by enhanced dynamic CT. *Radiology* **1986**;158:45-49
- Freeny PC, Marks WM. Patterns of contrast enhancement of benign and malignant hepatic neoplasms during bolus dynamic and delayed CT. *Radiology* **1986**;160:613-618
- Itai Y, Araki T, Furui S, Tasaka A. Differential diagnosis of hepatic masses on computed tomography, with particular reference to hepatocellular carcinoma. *J Comput Assist Tomogr* **1981**;5:834-842
- Stark DD, Wittenberg J, Butch RJ, Ferrucci JT. Hepatic metastases: randomized, controlled comparison of detection with MR imaging and CT. *Radiology* **1987**;165:399-406
- Reinig JW, Dwyer AJ, Miller DL, et al. Liver metastasis detection: comparative sensitivities of MR imaging and CT scanning. *Radiology* **1987**;162:43-47
- Bernardino ME. Focal hepatic mass screening: MR imaging or CT scanning? *Radiology* **1987**;162:282-283
- Glazer GM, Aisen AM, Francis IR, Gross BH, Gyves JW, Ensminger WD. Evaluation of focal hepatic masses: a comparative study of MRI and CT. *Gastrointest Radiol* **1986**;11:263-268

50. Stark DD, Wittenberg J, Edelman RR, et al. Detection of hepatic metastases: analysis of pulse sequence performance in MR imaging. *Radiology* **1986**;159:365-370
51. Stark DD, Wittenberg J, Middleton MS, Ferrucci JT. Liver metastases: detection by phase-contrast MR imaging. *Radiology* **1986**;158:327-332
52. Heiken JP, Lee JKT, Glazer HS, Ling D. Hepatic metastases studied with MR and CT. *Radiology* **1985**;156:423-427
53. Paling MR, Abbitt PL, Mugler JP, Brookman JR. Liver metastases: optimization of MR imaging pulse sequences at 1.0 T. *Radiology* **1988**;167:695-699
54. Wittenberg J, Stark DD, Forman BH, et al. Differentiation of hepatic metastases from hepatic hemangioma and cysts by using MR imaging. *AJR* **1988**;151:79-84
55. Frank JA, Dwyer AJ, Choyke PL, et al. Detection of hepatic metastases in colorectal carcinoma: correlating EOE-13 enhanced CT, MR imaging, and surgery. *Radiology* **1987**;165(P)[suppl.]:341
56. Nelson RC, Chezmar JL, Steinberg HB, et al. Focal hepatic lesions: detection by dynamic and delayed computed tomography versus short TE/TR spin-echo and fast field echo magnetic resonance imaging. *Gastrointest Radiol* **1988**;13:115-122
57. Foley WD, Kneeland JB, Cates JD, et al. Contrast optimization for detection of focal hepatic lesions by MR imaging at 1.5 T. *AJR* **1987**;149:1155-1160
58. Henkelman RM, Hardy P, Poon PY, Bronskill MJ. Optimal pulse sequence for imaging hepatic metastases. *Radiology* **1986**;161:727-734
59. Glazer GM. MR imaging of the liver, kidneys, and adrenal glands. *Radiology* **1988**;166:303-312
60. Wittenberg J, Tosteson AA, Karstaedt N, et al. MR imaging versus CT: a multiinstitutional comparison of hepatic metastatic tumor detection accuracy. *Radiology* **1988**;169(P)[suppl]:63
61. Reinig JW, Dwyer AJ, Miller DL, Frank JA, Adams GW, Chang AE. Liver metastases: detection with MR imaging at 0.5 and 1.5 T. *Radiology* **1989**;170:149-154
62. Stark DD, Felder RC, Wittenberg J, et al. Magnetic resonance imaging of cavernous hemangioma of the liver: tissue specific characterization. *AJR* **1985**;145:213-222
63. Stark DD, Weissleder R, Elizondo G, et al. Superparamagnetic iron oxide: clinical application as a contrast agent for MR imaging of the liver. *Radiology* **1988**;168:297-301
64. Chezmar JL, Rumancik WM, Megibow AJ, Hulnick DH, Nelson RC, Bernardino ME. Liver and abdominal screening in patients with cancer: CT vs MR imaging. *Radiology* **1988**;168:43-47
65. Evens RG, Evens RG Jr. Economic and utilization analysis of MR imaging units in the United States in 1987. *Radiology* **1988**;166:27-30

What kind of kid do you suppose Thomas Edison was?



Bet he looked at problems and saw solutions. Like Maurice Scales who invented Baby No-Mash to prevent doors from closing on little fingers.

Bet he saw how things were done, and imagined better ways to do them. Like Lillian Lukas who invented the Puddle Detecting Cane for the blind.

Maurice and Lillian were two of the thousands of winners in the Invent America! education program.

And you know that small genius can grow up to become big genius—with the capacity to make America number one again.

To participate, just write Invent America!, 510 King Street, Suite 420, Alexandria, VA 22314, or call 703/684-1836.

If you're wondering if it's all worthwhile, just imagine what Edison would have said.

Invent America!

For now—as never before—our country needs an inventive spark.

**INVENT
AMERICA!**

Bringing bright ideas out of young minds

Ad Council
A Public Service of This Publication

Invent America! is a nonprofit program in partnership with business, industry and education. Call or write today to join this vital national effort.

Book Review

Imaging of the Pelvis. By Madeleine R. Fisher and Morrie E. Kricun. (A volume in the Clinical Diagnostic Imaging series. Series editor: Morrie E. Kricun.) Rockville, MD: Aspen, 401 pp., 1989. \$115

At first blush, a book about radiology of the pelvis is not so unusual. There are books about radiology of the chest, or the head, or the abdomen, so why not a book about the pelvis? The problem, as I see it, is that the pelvis is not a self-contained region of the body. Many things go through or end in the pelvis, but few are wholly contained there. The colon, the appendix, the ureters, the small bowel, and the spine are all contained in the pelvis, but they are not properly considered pelvic structures and are not discussed in this book. What is discussed are the bony structures; conventional radiology of the bladder and urethra; and sonography, MR, CT, and nuclear medicine of the pelvis. There is also a brief chapter on interventional procedures. All good stuff, to be sure, but presented in somewhat limited depth.

The first chapter, on pelvic anatomy, consists of less than a page of text followed by numerous multiplanar MR images. This is fair enough, but it is somewhat mind numbing when up to six pictures are packed onto a page, and the pertinent anatomy is defined by somewhat cryptic overlying abbreviations: GMn, OI, LA, and ADD, to list but a few. As an aid to identification, the chapter is prefaced with a "Key to Abbreviations" listing 153 of the devils.

The second chapter, on conventional radiography, presents the usual topics (e.g., calcifications, bone tumors, trauma) that are found in basic radiologic texts such as that by Paul and Juhl. For example, osteoporosis as seen in the pelvis is about the same as osteoporosis seen in long bones. This is well outlined in numerous other texts and needs no repeating here.

The third chapter, on conventional contrast procedures (meaning mostly the bladder), is a little gem. The authors nicely discuss abnormalities in shape, position, and size of the bladder and summarize the findings in tables of differential diagnoses. Infections, fistulae, trauma to both the bladder and the urethra, and a brief section on hysterosalpingography round out the chapter.

Three chapters on sonography of the pelvis follow. The chapter on adult pelvic sonography is too wordy, with too few pictures. Obstetric sonography is well handled and well written, but it is too brief, I fear, to be of use to any practicing radiologist. Read Peter Callen's book instead. Pediatric pelvic sonography is a fair chapter and probably worth reading. CT, MR, and nuclear medicine each get a chapter, but these consist of basically the same material as is covered in books devoted to individual imaging techniques, and they are repetitious here.

I firmly believe that the basic premise of this book is wrong. It serves no need. Imaging in the pelvis has been well covered in other books that present essentially the same material in a more comprehensive, detailed form. For CT of the pelvis, read Lee, Sagel, and Stanley; for MR, read Moss; for bone diseases, read Greenfield.

Peter Meyers
Louisiana State University
Shreveport, LA 71115

Review Article

Radiology of Penile Prostheses

Richard H. Cohan¹, N. Reed Dunnick¹, and Culley C. Carson²

Impotence, defined as the persistent inability to achieve or maintain a penile erection adequate for vaginal penetration [1], has been estimated to affect over 10 million middle-aged or elderly men in the United States alone [2]. A survey of 1180 outpatients at the Minneapolis Veterans Administration Medical Center revealed that 34% had some type of erectile dysfunction [3].

It is now recognized that organic impotence is much more common than psychogenic impotence, accounting for as many as 70–80% of cases [3, 4]. Common organic causes include medication effects (e.g., alpramethyldopa, digoxin, cimetidine, propranolol, thiazide diuretics), endocrine disorders (including diabetes mellitus and hyperthyroidism), vascular diseases (aortoiliac aneurysms, occlusions, and atherosclerosis), metabolic derangements (i.e., chronic renal failure and cirrhosis), neurologic processes, and previous surgery (including transurethral resection of the prostate, radical cystoprostatectomy, and abdominal-perineal resection) [3, 5, 6]. Krane [7] has divided the causes of impotence into several broad subsets: "failure to initiate (neurogenic), failure to fill (arteriogenic), failure to store (venogenic), and end-organ disease (Peyronie's, post-priapism)." These subsets can be extremely helpful in planning the diagnostic workup and treatment of affected patients.

Treatment of impotence varies, depending upon the cause. Failure to initiate an erection can be treated with intracorporeal injections of papaverine. Microvascular bypass surgery may prove beneficial in a few selected patients with arteriogenic impotence. Venous ligation may improve the quality of erection in patients with large cavernosal leaks. In each of these cases, however, surgical implantation of a penile prosthesis

has become an accepted alternative therapy. In fact, in many instances the penile prosthesis has become the preferred, rather than the ultimate, treatment option [2, 7, 8].

Types of Penile Prostheses: Normal Appearance

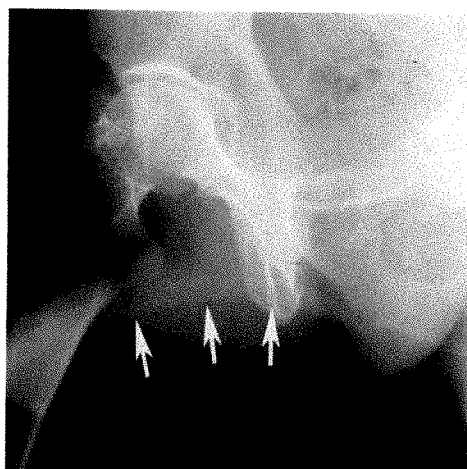
Noninflatable: Semirigid and Malleable

The first successful penile prostheses, developed in the 1960s, consisted of single semirigid acrylic or silicone rods [9–11]. Subsequently, paired semirigid or malleable rods were developed for placement into each corpus cavernosum. The semirigid Small-Carrion prosthesis (Heyer-Schulte Corp., Minneapolis, MN) consists of a medical-grade silicone exterior surrounding a silicone sponge interior [12]. This device is only faintly radiopaque (Fig. 1). The semirigid Finney prosthesis (Surgitek Inc., Racine, WI) is similar in design; however, it has a soft proximal hinge that allows for more flexibility in positioning when the prosthesis is not being used [13]. The AMS600 (American Medical Systems, Minnetonka, MN), Jonas (Dacomed Corp., Minneapolis, MN), and Mentor Malleable (Mentor Corp., Goleta, CA) prostheses are less rigid, but much more malleable, because of a central core of bendable, braided, stainless steel or silver wires (Fig. 2) [14–18]. All but the Finney and Mentor prostheses (which can be tailored for an individual patient) come in many sizes and widths. Penile rigidity, length, and width cannot be altered once a particular device has been inserted, however. These devices are all easily implanted, and complications, which include pain, infection, and perforation or erosion, have been observed in 7–16% of patients [14, 15, 19–22].

Received November 3, 1988; accepted after revision January 5, 1989.

¹ Department of Radiology, Box 3808, Duke University Medical Center, Durham, NC 27710. Address reprint requests to R. H. Cohan.

² Department of Surgery, Division of Urology, Box 3274, Duke University Medical Center, Durham, NC 27710.



1



2

Fig. 1.—Semirigid prosthesis. Oblique radiograph of pelvis in a patient with a Small-Carrion semirigid prosthesis. Silicone prosthesis is only faintly visible (arrows).

Fig. 2.—Malleable penile prosthesis. Anteroposterior radiograph of pelvis in a patient with a Jonas malleable prosthesis. Silver wires (straight arrows) are easily shown. Spherical object in right upper pelvis (arrowhead) is a reservoir for an artificial urethral sphincter (curved arrow).

Most patients (82–90%) [13, 15, 16, 20] are at least fairly satisfied with semirigid or malleable prostheses. Not surprisingly, complaints relate to difficulties in concealment during those times when erection is not desired. A few patients have been dissatisfied also with the limited rigidity afforded by malleable prostheses, despite the fact that satisfactory vaginal penetration can usually be achieved [20].

Inflatable: Multicomponent

In 1973, Scott, Bradley, and Timms [23] devised the first inflatable penile prosthesis (IPP). The IPP represented an improvement over semirigid or malleable prostheses in that both erect and flaccid states could be achieved. Concealment was no longer an embarrassing problem. Furthermore, the quality of the erection was much superior to that attainable by the noninflatable devices.

Unfortunately, the increased number of components in IPPs initially resulted in high mechanical failure rates (approaching 50% in one study [24]). Numerous revisions have significantly reduced the incidence of malfunctions, such that newer versions of the two currently available multicomponent IPPs (AMS700, manufactured by American Medical Systems, and the Mentor IPP, manufactured by the Mentor Corporation) have a 97% chance of functioning properly for 3 to 4 years after insertion [25, 26].

The current AMS700 and Mentor IPPs contain four separate components interconnected by kink-resistant tubing (Fig. 3). Two penile cylinders are made from an expansile silicone rubber polymer so that they can widen and stiffen when inflated [27]. The cylinders are available in four different lengths (12, 14, 18, and 21 cm) [28]. Rear-tip extenders, ranging in length from 1 to 3 cm, can be used to provide an even greater range in sizing, as penile lengths may vary considerably. A hydraulic pump is implanted subcutaneously in the scrotum. A spherical reservoir, now composed of a single durable piece of silicone rubber polymer (to reduce wear and tear and, subsequently, the incidence of fluid leakage), is usually positioned just deep to the rectus abdominis muscles in the pelvis. The entire system is usually filled with

65 ml of isotonic, radiopaque fluid, so that its integrity can be checked easily with plain radiography, should a malfunction occur. Diluted radiographic contrast media (12.5% by weight) is used in all but allergic patients.

Two recent modifications by Surgitek (Uniflate) and Mentor (GFR) have eliminated the reservoir. A larger, more capacious pump serves this function also. The Uniflate and GFR prostheses are easier to implant—because one of the components is no longer necessary—but the degree of rigidity and flaccidity that can be achieved is much more limited because of the greater restrictions on fluid volume in the prosthesis system (the pump/reservoir uses significantly less fluid than does a separate reservoir).

Immediate surgical and medical complications after IPP insertion include infections, erosions, hematomas, seromas, inguinal hernias at the site of reservoir placement, urethrocavernous fistulae, and pain. These have been encountered in 2% to 16% of patients [26, 27, 29]. As experience has increased, the frequency of these problems has diminished considerably. Patient satisfaction is excellent. Scott and co-workers found that 91% of 738 patients were happy with their prostheses [27].

Self-Contained Inflatable and Mechanical Prostheses

Recently, self-contained inflatable penile prostheses (Hydroflex from American Medical Systems, Flexi-Flate I and II from Surgitek, Inc.) and two self-contained mechanical devices (OmniPhase and DuraPhase from Dacomed) have been introduced [7]. The former are changed from flaccid to erect by activation of a distal inflation pump. Fluid is then transferred from a rear reservoir (Hydroflex) or an outer cylinder (Flexi-Flate) into a nondistensible central or inner reservoir [7] (Fig. 4). The OmniPhase prosthesis consists of a number of plastic segments connected by a spring-action cable. When erection is desired, an activating component shortens the cable slightly, allowing all of the plastic segments to tighten against one another, and the prosthesis thereby becomes rigid [7]. The DuraPhase prosthesis is similar to the OmniPhase except

that it exists only in an erect state. The interlocking plastic segments are always closely opposed to one another.

Self-contained inflatable and mechanical prostheses have an advantage over the multicomponent IPPs in that surgical insertion and repair is technically easier. Preliminary reports indicate low surgical and medical complication rates and reasonable patient satisfaction [7], although the penis is less firm and broad in the erect state and less flaccid when deflated in comparison with multicomponent inflatable prostheses.

Radiology of the Malfunctioning Penile Prosthesis

In addition to routine immediate postoperative complications, the urologist is occasionally called upon to evaluate patients with malfunctioning prostheses. Although malfunctions have occurred with all three types of penile prostheses, they have been observed more commonly in patients with IPPs, presumably owing to the greater complexity of the IPP. Evaluation of patients whose prostheses are no longer work-

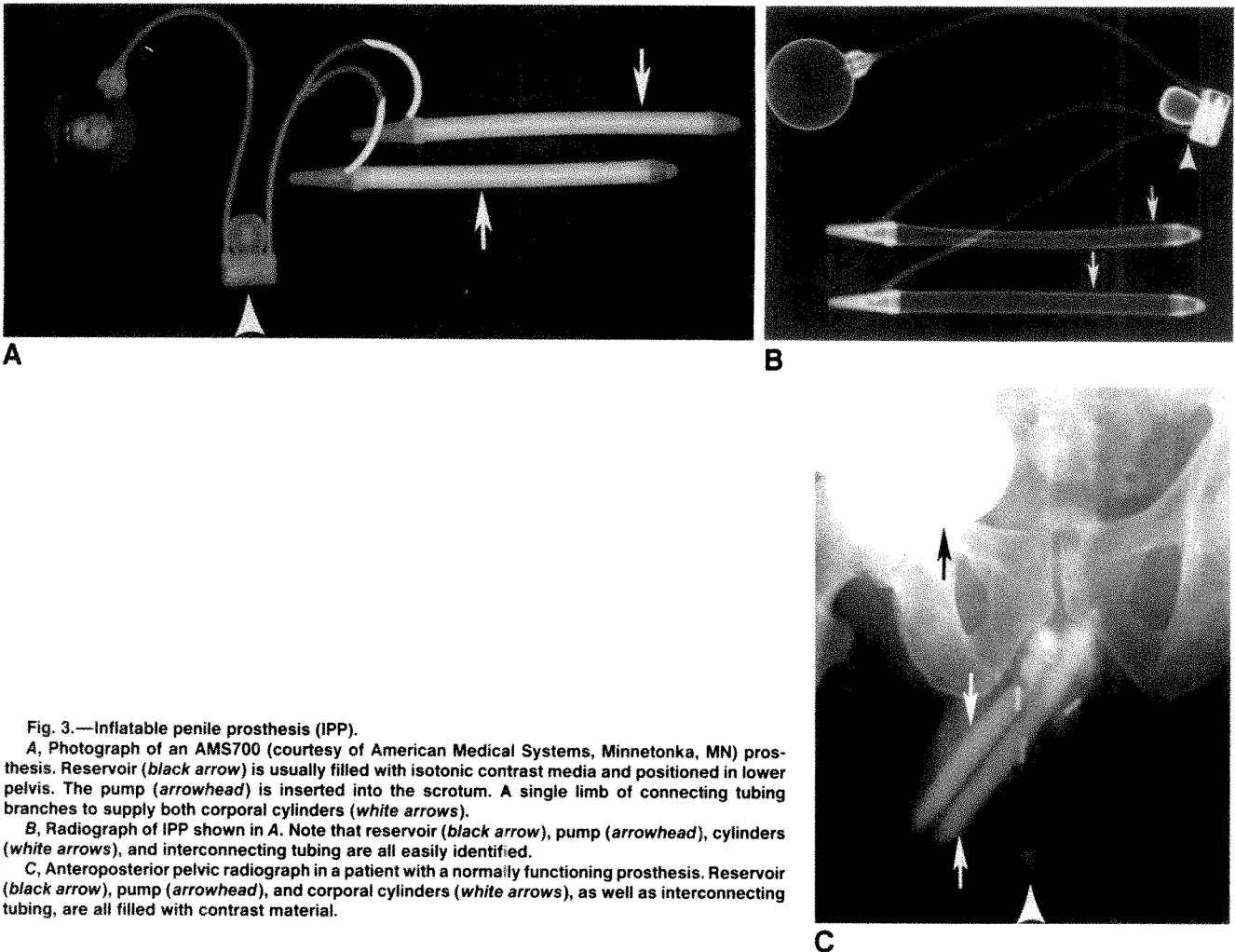


Fig. 3.—Inflation penile prosthesis (IPP).

A, Photograph of an AMS700 (courtesy of American Medical Systems, Minnetonka, MN) prosthesis. Reservoir (black arrow) is usually filled with isotonic contrast media and positioned in lower pelvis. The pump (arrowhead) is inserted into the scrotum. A single limb of connecting tubing branches to supply both corporal cylinders (white arrows).

B, Radiograph of IPP shown in **A**. Note that reservoir (black arrow), pump (arrowhead), cylinders (white arrows), and interconnecting tubing are all easily identified.

C, Anteroposterior pelvic radiograph in a patient with a normally functioning prosthesis. Reservoir (black arrow), pump (arrowhead), and corporal cylinders (white arrows), as well as interconnecting tubing, are all filled with contrast material.

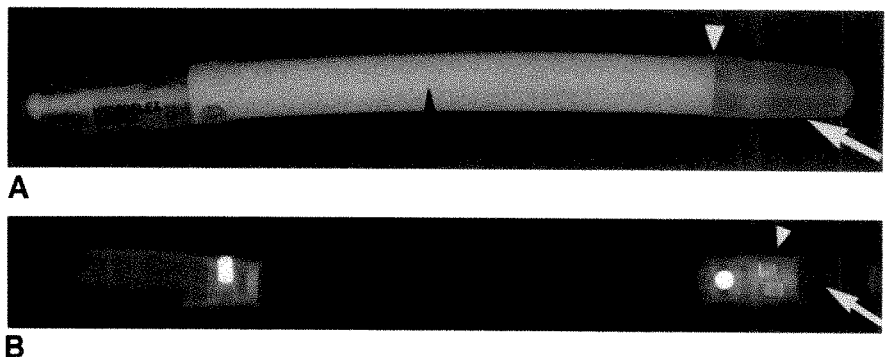


Fig. 4.—Self-contained inflatable prosthesis.

A, Photograph of a single Hydroflex cylinder (courtesy of American Medical Systems, Minnetonka, MN). A distal inflation pump (arrowhead) transfers fluid from rear (white arrow) to central reservoir (black arrow), thereby achieving an erection.

B, Radiograph of the prosthesis shown in **A**. Components (inflation pump, arrowhead; rear reservoir, white arrow; central reservoir, black arrow) are easily seen.

ing appropriately, or who have other chronic complaints, generally consists of gross inspection and one or several pelvic radiographs.

Noninflatable: Semirigid and Malleable

Owing to their simplicity, mechanical complications of these prostheses have been unusual. Radiographic evaluation of malfunctioning noninflatable prostheses is seldom necessary. A single oblique or anteroposterior radiograph of the lower pelvis is usually sufficient, should radiographic visualization be requested.

Fracture.—Rarely, patients may present with complete breaks through semirigid silicone prostheses. Physical examination has been diagnostic in three previously reported cases [30].

Erosion.—Erosion of a semirigid or malleable prosthesis through the skin or into the urethra has been observed in a small minority of patients [12, 14, 20–22]. This is usually obvious on physical examination.

Injury to the metallic core of malleable prostheses.—A number of reports of breaks or fraying of the braided-silver-wire core of the older Jonas prostheses have been published [17, 31]. Diagnosis is often difficult. Some patients complain of loss of rigidity. Audible “crackles” can occasionally be heard on physical examination. Interestingly, despite the excellent radiopacity of the silver core, many fractures have been missed or their severity underestimated on pelvic radiographs using standard radiographic technique [31]. This is probably because of an inability to visualize fraying in the individual wire braids that make up the core. Fortunately, recent revisions in the design of the Jonas prosthesis have greatly reduced the incidence of this complication.

Migration.—Several patients have developed rotational instability (during sexual intercourse) of normally positioned Jonas prostheses [32]. Radiography was not required to make the diagnosis.

Inflatable: Multicomponent

Pelvic radiography plays a vital role in identifying the cause of mechanical malfunctions in inflatable penile prostheses. In contrast with semirigid or malleable devices, physical examination is frequently unrewarding. In most instances, a single oblique pelvic radiograph with the prosthesis inflated is diagnostic [33]. In occasional confusing cases, additional radiographs (an anteroposterior view and/or a radiograph obtained with the prosthesis deflated) may be helpful.

Leaks.—Leakage of fluid from IPPs is usually due to wear and tear on the cylinders from friction with the connecting tubing as it rubs against the cylinder walls, or to kinks in the deflated cylinder's fabric [34, 35]. Although this problem is eventually encountered in 38% to 50% of patients with older models, it has been less common with the newer devices [25, 27, 36]. In our series of 179 patients with a variety of differently modified IPPs, 36 patients (20%) presented with leaks from cylinders (28 patients), connectors (seven patients), or tubing (one patient).

Leaking prostheses cannot be inflated adequately and patients invariably present with inability to achieve a satisfactory erection. Pelvic radiography reveals a marked decrease in the amount of fluid in the reservoir. The penile cylinders are often underinflated (Fig. 5). Once a leak is identified, the defective component can be identified at surgery (by use of an ohmmeter) and then replaced [35].

Aneurysmal dilatation or buckling of the cylinder.—Ballooning or buckling of prosthesis cylinders, resulting from structural weakness in the cylinders themselves, often develops as a late complication (after multiple inflations and deflations) [34, 35]. Preexisting weakness in the tunica albuginea (which can be caused by radiation therapy or by the previous presence of an aneurysmally dilated cylinder) may increase the likelihood of developing cylinder aneurysms or bends [34, 37, 38]. These types of malfunctions have been encountered in 1.6–8.0% of patients [25, 29]. In our series, three of 179 patients (1.7%) developed this problem. As with other me-

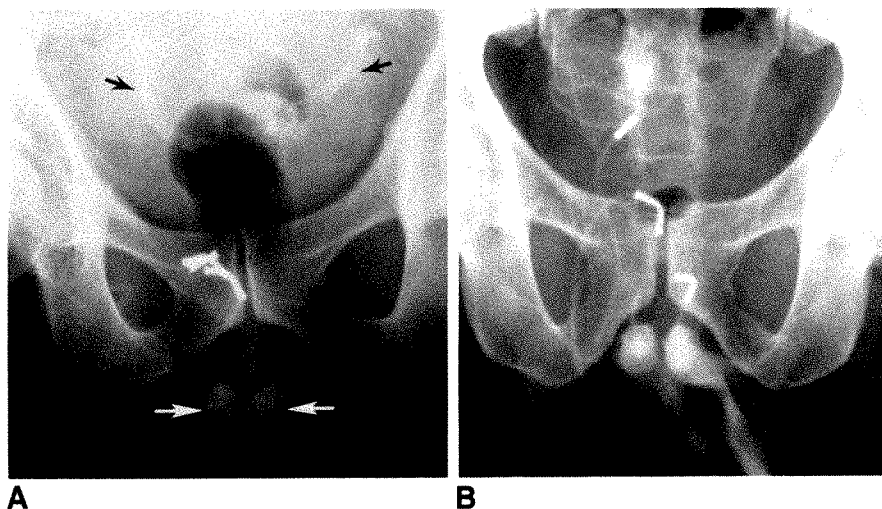


Fig. 5.—Malfunctioning IPP, leak.

A, Only a small amount of fluid is in posterior portion of penile cylinders (white arrows). Reservoir contains virtually no contrast media and cannot be seen. Similarly, no radiopaque fluid is in pump or tubing. Note extensive calcification in vasa deferentia (black arrows) in this diabetic patient.

B, Cylinders are only partially filled in this “inflated” radiograph on another patient. Again, reservoir is empty and cannot be identified.

Fig. 6.—Malfunctioning IPP, aneurysms or buckling of cylinders.

A, Radiograph of inflated prosthesis shows marked ballooning of both cylinders. Reservoir is empty (arrows).

B, Note severe twist in midportions of both cylinders in a second patient (arrows), preventing adequate filling of distal cylinders. Reservoir remains completely filled.

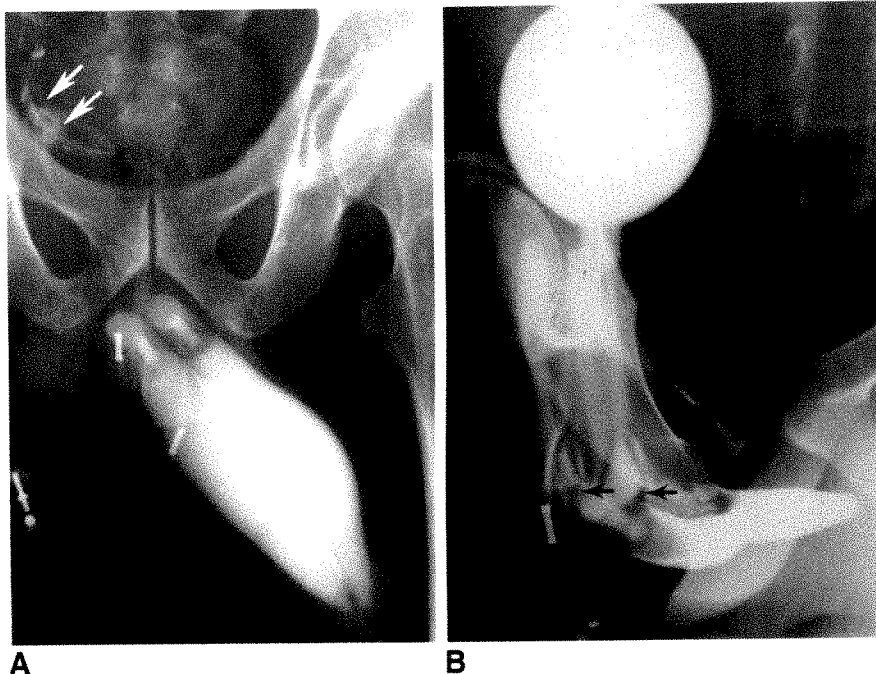
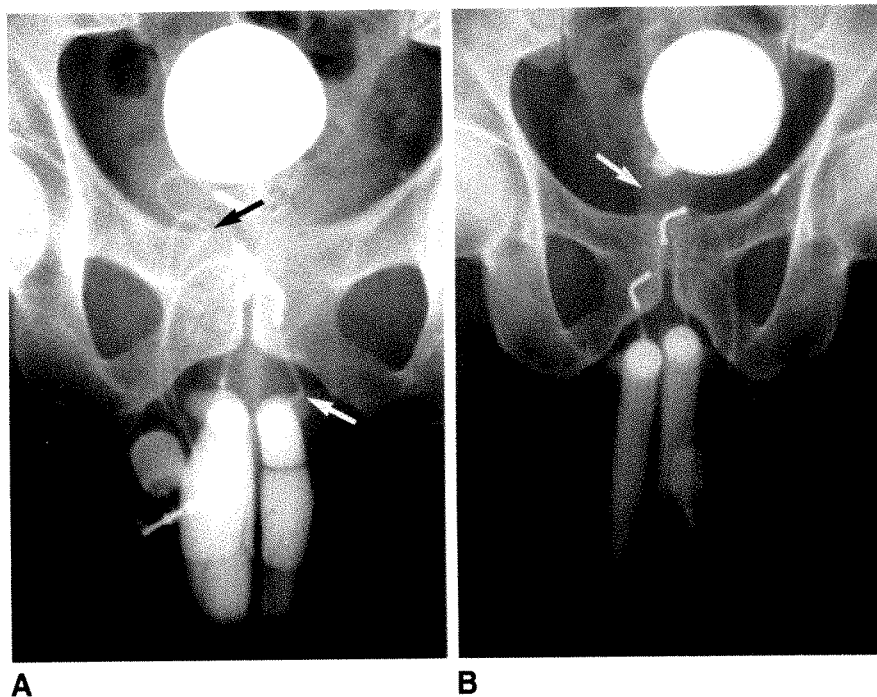


Fig. 7.—Malfunctioning IPP, tubing kinks or separation.

A, At least two kinks are in tubing of this malfunctioning prosthesis (arrows). More cephalad bend is most severe. This complication has been greatly reduced by recent introduction of kinkproof connecting tubing. Note also that moderate aneurysms have developed in both prosthesis cylinders.

B, Connecting tubing has separated completely from reservoir in another patient. Note that reservoir no longer communicates with rest of prosthesis (arrow).



chanical complications, the incidence of cylinder aneurysms is expected to decrease greatly with the newer models.

Patients with aneurysmally dilated cylinders complain of gradual loss of penile rigidity, despite the fact that the patient can inflate his prosthesis until the pump becomes flat (i.e., the reservoir is empty). Alternatively, erections may become angulated or asymmetric [35]. Although physical examination of the penis with the prosthesis in the inflated state is often,

but not always, helpful, the pelvic radiograph is always diagnostic, revealing abnormally shaped cylinders and underfilled reservoirs (Fig. 6).

Treatment involves replacement of the defective cylinders. Because the surrounding tunica albuginea has been expanded, it may have to be reinforced or redundant portions may have to be resected. Persistent weakness in the corpora may predispose these patients to recurrent aneurysms, if

normal cylinders are reinserted. As an alternative, Furlow and Motley [38] and Mulcahy [39] have replaced aneurysmally enlarged cylinders with special controlled expansion cylinders and thus far have met with excellent results.

Kinked or separated tubing.—Kinks in the tubing connecting the reservoir and pump were previously fairly common, occurring in nearly 5% of cases in one series [29] and in 4% of patients in our experience. The introduction of "kink-proof" tubing in recently manufactured models has greatly reduced the incidence of this problem.

Kinks usually develop within the first few months of surgery [34]. Although physical examination is not rewarding, kinks are often easily detected on plain radiography. Connecting tubing may appear excessively long or be acutely angulated (Fig. 7A). Separation of the tubing from the reservoir, pump, or connectors, a much rarer problem, can also be seen easily on plain film (Fig. 7B).

Treatment consists of surgical removal of redundant tubing and/or rerouting [35]. Separated components can be reconnected, or replaced, if defective.

Pump malfunction.—Pump migration or malfunction is unusual, observed in 1.6% of patients in one previous study [25] and in 1.1% of our patients. Pump migration can be detected on gross inspection of the patient. A diagnosis of pump malfunction should be considered in any patient with a nonfunctioning prosthesis whose pelvic radiograph is normal; that is, the reservoir and cylinders are normal in caliber and location, and the tubing is not kinked.

Erosions.—Although erosions often do not result in prosthesis malfunction, the radiologist should be alert to the possibility of erosions of prosthesis components in appropriately symptomatic patients. Encountered in fewer than 1% of patients in one series [40], and in 3% of our patients, erosions probably usually result from local tissue ischemia. Associated infection is common. Most of the erosions observed by Furlow and Goldwasser [40] involved the pump (69%) or the reservoir (25%). Reservoirs usually erode into the bladder [40–43], but erosions into ileal conduits [40, 44], the peritoneal cavity [45], and the sigmoid colon [42] also have been reported. Patients often present with signs and symptoms of local pelvic infection and/or sepsis. Their complaints are frequently nonspecific (pain, hematuria, small bowel obstruction) [41, 45].

Cylinder and pump erosions can be identified on physical examination, and radiography is usually unnecessary. Reservoir erosion, on the other hand, may be difficult to diagnose. Physical examination is often unrewarding. A single pelvic radiograph is recommended but is only helpful if the reservoir is clearly in an abnormal position or has moved since a prior study. Unfortunately, in all of the previously cited reports, the correct diagnosis could not be made until endoscopy or even surgery was performed [41–45].

Although attempts to salvage eroded cylinders have failed, recently it has been shown that conservative surgery directed only toward replacement and repositioning of eroded pumps or reservoirs is often successful [40]. Pump or reservoir erosion associated with widespread prosthesis infection, however, requires removal of the entire device and surgical drainage of the infected site. The prosthesis can only be

replaced when the inflammatory response has completely subsided [46].

Unusual mechanical problems.—A few other causes of IPP malfunction have been observed. Spontaneous inflation (caused by scar capsule formation around the reservoir) can only be diagnosed at surgery, whereas cylinder rupture [29] and dislodgment of a rear-tip extender can be identified on pelvic radiograph.

Inflatable: Self-Contained

Experience with self-contained inflatable prostheses is limited. Mechanical malfunctions will probably be less common than they were in the early days of the multicomponent IPPs. In a recent series [47], leaks were identified in 6% of patients with Hydroflex prostheses. Most had received a prototype model, which has subsequently been improved. A significant minority of patients have had difficulty using the Hydroflex pump [47]. Goulding [48] recently reported a patient who developed a fracture of the posterior reservoir of a Hydroflex prosthesis. Replacement of a malfunctioning self-contained inflatable prosthesis is simple. This procedure is usually done under local anesthesia in an outpatient setting [47].

Conclusions

In many medical centers, insertion of a penile prosthesis is now an accepted treatment for patients presenting with impotence who do not respond to medical management [8, 18]. Because impotence is a common problem, and because these devices are becoming more and more popular, it is likely that an increasing number of radiologists will be asked to evaluate pelvic radiographs of patients presenting with mechanical malfunctions of their prostheses. It is incumbent upon the radiologist to be familiar with the appearance of normal noninflatable and inflatable prostheses, and to be able to recognize the radiographic appearance of the more common causes of malfunction in inflatable penile prostheses.

REFERENCES

1. *Dorland's illustrated medical dictionary*, 26th ed. Philadelphia, PA: Saunders, 1981
2. *Mayo clinical health letter: impotence in America*. Rochester, MN: Mayo Clinic, May 1986:1–8
3. Slag MF, Morley JE, Elson MK, et al. Impotence in medical clinic outpatients. *JAMA* 1983;249(13):1736–1740
4. Padma-Nathan H, Goldstein I, Krane RJ. Evaluation of the impotent patient. *Semin Urol* 1986;4(4):225–232
5. Melman R. Iatrogenic causes of erectile dysfunction. *Urol Clin North Am* 1988;15(1):33–39
6. Wein AJ, Van Arsdalen KV. Drug-induced male sexual dysfunction. *Urol Clin North Am* 1988;15(1):23–31
7. Krane RJ. Penile prostheses. *Urol Clin North Am* 1988;15(1):103–109
8. Kirschenbaum A, Mitty HA. Penile prostheses. *Urol Radiol* 1988;10:160–165
9. Lash H, Zimmerman DC, Loeffler RA. Silicone implantation: inlay method. *Plast Reconstr Surg* 1964;34:75–80
10. Loeffler RA, Sayegh ES. Perforated acrylic implants in management of organic impotence. *J Urol* 1960;84:559–561

11. Pearman RO. Treatment of organic impotence by implantation of a penile prosthesis. *J Urol* **1967**;97:716-719
12. Small MP, Carrion HM, Gordon JA. Small-Carrion penile prosthesis: new implant for management of impotence. *Urology* **1975**;5:479-486
13. Finney RP. New hinged silicone penile implant. *J Urol* **1977**;118:585-587
14. Dorflinger T, Bruskewitz R. AMS malleable penile prosthesis. *Urology* **1986**;28(6):480-485
15. Moul JW, McLeod DG. Experience with the AMS 600 malleable penile prosthesis. *J Urol* **1986**;135:929-931
16. Benson RC Jr, Patterson DE, Barrett DM. Long-term results with the Jonas malleable penile prosthesis. *J Urol* **1985**;134:899-901
17. Tawil EA, Hawatmech I, Apte S, Gregory JG. Multiple fractures of the silver wirestrands as a complication of the silicone-silver wire prosthesis. *J Urol* **1984**;132:762-763
18. Questions and Answers; diagnostic and therapeutic technology assessment (DATTA): penile implants for erectile impotence. *JAMA* **1988**;260(7):997-1000
19. Krane RJ, Freedberg PS, Siroky MD. Jonas silicon-silver penile prosthesis: initial experience in America. *J Urol* **1981**;126:475-476
20. Benson RC, Barrett DM, Patterson DE. The Jonas prosthesis: technical considerations and results. *J Urol* **1983**;130:920-922
21. Montague DK. Experience with Jonas malleable penile prosthesis. *Urology* **1984**;23[suppl]:83-85
22. Small MP. Surgical treatment of impotence with Small-Carrion prosthesis. *Urology* **1984**;23[suppl]:93-97
23. Scott FB, Bradley WE, Timms GW. Management of erectile impotence: use of implantable inflatable prosthesis. *Urology* **1973**;11(1):80-82
24. Joseph DB, Bruskewitz RC, Benson RC Jr. Long-term evaluation of the inflatable penile prosthesis. *J Urol* **1984**;131:670-673
25. Furlow WL, Goldwasser B, Gundian JC. Implantation of model AMS 700 penile prosthesis: long-term results. *J Urol* **1988**;139:741-742
26. Merrill DC. Clinical experience with the Mentor inflatable penile prosthesis in 301 patients. *J Urol* **1988**;140:1424-1427
27. Scott FB, Fishman IJ, Light JK. A decade of experience with the inflatable penile prosthesis. *World J Urol* **1983**;1:244-250
28. AMS 700CX inflatable penile prosthesis (operating room manual), 3rd ed. Minnetonka, MN: American Medical Systems, **1987**:1-28
29. Furlow WL. Inflatable penile prosthesis: Mayo Clinic experience with 175 patients. *Urology* **1979**;13(2):166-171
30. Agatstein EH, Farrer JH, Raz S. Fracture of semirigid penile prosthesis: a rare complication. *J Urol* **1986**;135:376-377
31. Tawil EA, Gregory JG. Failure of the Jonas prosthesis. *J Urol* **1986**;135:702-703
32. Pedersen B, Mieza M, Melman A. Instability and rotation of silver silicone penile prosthesis. *Urology* **1988**;31(2):116-118
33. Kossoff J, Krane RJ, Naimark A. Inflatable penile implant for impotence: radiologic evaluation. *AJR* **1981**;136:1109-1112
34. Furlow WL, Barrett DM. Inflatable penile prosthesis: new device design and patient-partner satisfaction. *Urology* **1984**;24(6):559-563
35. Fishman IJ. Complicated implantations of inflatable penile prostheses. *Urol Clin North Am* **1987**;14(1):217-239
36. Kabin JN, Kessler R. Five-year followup of the Scott inflatable penile prosthesis and comparison with semirigid penile prosthesis. *J Urol* **1988**;140:1428-1430
37. Fein RL. Cylinder problems with AMS 700 inflatable penile prosthesis. *Urology* **1988**;31(4):305-308
38. Furlow WL, Motley RC. The inflatable penile prosthesis: clinical experience with a new controlled expansion cylinder. *J Urol* **1988**;139:945-1031
39. Mulcahy JJ. Use of CX cylinders in association with AMS700 inflatable penile prosthesis. *J Urol* **1988**;140:1420-1421
40. Furlow WL, Goldwasser B. Salvage of the eroded inflatable penile prosthesis: a new concept. *J Urol* **1987**;138:312-314
41. Dupont MC, Hochman HI. Erosion of an inflatable penile prosthesis reservoir into the bladder, presenting as bladder calculi. *J Urol* **1988**;139:367-368
42. Leach GE, Shapiro CE, Hadley R, Raz S. Erosion of inflatable penile prosthesis reservoir into bladder and bowel. *J Urol* **1984**;131:1177-1178
43. Fitch WP III, Roddy T. Erosion of inflatable penile prosthesis reservoir into bladder. *J Urol* **1986**;136:1080
44. Godiwalla SY, Beres J, Jacobs SC. Erosion of an inflatable penile prosthesis reservoir into an ileal conduit. *J Urol* **1987**;137:297-298
45. Nelson RP, Jr. Small bowel obstruction secondary to migration of an inflatable penile prosthesis reservoir: recognition and prevention. *J Urol* **1988**;139:1053-1054
46. Carson CC. Infections in genitourinary prostheses. *Urol Clin North Am* **1989**;16:139-148
47. Mulcahy JJ. The Hydroflex self-contained inflatable prosthesis: experience with 100 patients. *J Urol* **1988**;140:1422-1423
48. Goulding FJ. Fracture of Hydroflex penile implant. *Urology* **1987**;30(5):490-491

Book Review

Radiologic Clinics of North America. Arthritis and Other Arthropathies. Guest editors: Aaron S. Weinstein and Kenneth R. Kattan. Philadelphia: Saunders, November 1988;26(6):1157-1398. \$22.95; by subscription, 6 issues annually for \$89

In this volume of this popular review journal, selected topics in rheumatologic imaging are considered by the editors and by a variety of authors representing radiology, rheumatology, and pathology. The individual contributions do not provide a coherent whole: some are organized as to radiologic findings; others deal with etiology; and others deal with pathologic findings, arthritis of specific age groups, anatomic location of disease, or evaluation of clinical problems. Indeed, the chapter on mixed connective tissue disease, even though it is elegantly written by Dr. Feldman, deals with something that may not even exist as a distinct clinical entity.

In spite of the organizational shortcomings, much of merit can be found in this volume. The first chapter, "Advances in Rheumatology," by Mongey and Hess, is an excellent review of such topics of current interest as the immunogenetics of the spondyloarthropathies and recent advances in the understanding of crystal deposition diseases. Any radiologist who deals with rheumatologists should be facile with this material. "The Differential Diagnosis of Geodes," by Bullough and Bansal, is useful in understanding the pathogenesis of those subchondral holes. The authors succinctly review the controversy as to whether the intrusion of synovial fluid into subchondral bone or the ingrowth of granulation tissue causes the geodes of osteoarthritis, and they differentiate these geodes from the marginal erosions of rheumatoid arthritis. The chapter ends with short sections on pathologic explanations for the radiologic findings in several other arthritides. The short chapter by Kern et al. is interesting for descriptions of occupational hazards of lumberjacks, stone masons, and corn pickers, although Figure 4 is printed upside down.

One of the most important chapters is that by Gold et al., which deals with radiologic changes in seronegative arthritis. The brief clinical reviews that begin each section are useful, and the radiologic findings are well described and illustrated. In the section on ankylosing spondylitis, it might have been worthwhile for the authors to discuss relative roles of imaging techniques in the diagnosis of early sacroiliitis, such as angled vs oblique plain radiographs, CT, and nuclear medicine studies. Also, it is curious that the arthritis of inflammatory bowel disease is not mentioned along with the other seronegative

spondyloarthropathies. Perhaps it was considered identical to ankylosing spondylitis.

Wilkinson and Weissman have written an excellent review of arthritis in childhood. It is particularly valuable in the discussion of lesions not commonly thought of as causing arthritis, such as enchondromatosis, leukemia, and eosinophilic granuloma. Unfortunately, it has no illustrations of early findings, such as osteoporosis, subtle cartilage loss, or widening of the obturator fat stripe in septic arthritis of the hip. Figure 17 in the chapter on septic arthritis shows such a case, but it is cumbersome to page back and forth to see an example. The authors do make the important point that aspiration should be performed in all cases in which this diagnosis is suspected.

The format of the chapter by Rogers and Hendrix is helpful in that it deals with a clinical problem, shoulder pain, rather than describing findings in a series of related diseases. The authors emphasize that the 30° posterior oblique view should be a part of the routine shoulder series, and they show the usefulness of computed arthrotomography in evaluation of glenohumeral instability. It should be stressed that routine arthrography usually is satisfactory for evaluation of the rotator cuff, but that CT should be added to the examination if such instability is suspected. Today, MR may have a role not only in evaluation of masses and osteonecrosis, as the authors say, but also in the diagnosis of tears of the rotator cuff and in the impingement syndrome.

This volume is not useful for residents who are seeking a beginning text in rheumatologic radiology or for those who are preparing for board examinations. Too many areas are not covered, and information must be obtained from several chapters to provide a cohesive view of any one disease or clinical problem. The work is an adequate review of selected topics and a guide to "what's new" in rheumatologic radiology, with laboratory and pathologic correlation, for practicing radiologists who see such diseases.

Ethan M. Braunstein
Indiana University Hospital
Indianapolis, IN 46223

Review Article

Percutaneous Insertion of the Greenfield Filter

S. Osher Pais¹ and Katherine D. Tobin

The Greenfield filter has been used for inferior vena caval (IVC) interruption since 1973 [1]. The technique of percutaneous insertion was first described in 1984 [2]. Since 1984, there have been several reports describing percutaneous Greenfield filter insertion [3–8]. On the basis of this work, it is now possible to evaluate the advantages and complications of percutaneous as compared with surgical insertion. The broader issues of the safety and efficacy of the Greenfield filter in preventing pulmonary embolism, except as these relate to the method of insertion, have been reviewed elsewhere [9–12].

History

The first attempt to prevent pulmonary embolism by venous interruption was reported by Homans in 1934 [13]. The procedure he described was ligation of the femoral vein, which proved to be ineffective. In the mid 1940s, Oschner and DeBakey [14], and O'Neil [15] proposed IVC ligation to prevent recurrent emboli. Although the procedure was effective in reducing the incidence of recurrent emboli to 6% [10], the average mortality was 12%, and there was significant morbidity due to venous stasis. IVC stapling, clipping, and plication were attempted later [12, 16]. With these techniques, IVC patency was about 80% [17], and although the rate of recurrent embolization was reduced to 4%, surgical mortality remained high at about 10% [12].

The next phase of development was the introduction of transvenous devices, which could be placed within the IVC lumen from either the femoral or jugular veins. The first such

device to gain widespread popularity was the Mobbin-Uddin umbrella, which was introduced in 1967 [18]. This device consisted of six stainless-steel spokes radiating from a central hub, and was covered on both sides by heparin-coated fenestrated silastic sheets (Fig. 1). The original umbrella was 23 mm in diameter and was associated with a significant rate of proximal migration [19, 20]. The umbrella was later enlarged to 28 mm diameter; this decreased the incidence of migration, but did not eliminate the problem.

The Mobbin-Uddin umbrella was effective in preventing recurrent embolism, and morbidity and mortality associated with its insertion were low. However, the IVC occlusion rate was 60% [20, 21]. This device was withdrawn from the market in 1986.

The Greenfield filter has been in use since 1973 [1] and is now the most widely used means of IVC interruption in the United States [22, 23]. The filter consists of six stainless steel legs extending from a central hub to form a cone. A hole in the apex allows the filter to be passed over a 0.035-in.-diameter wire. The base of each leg ends in a finely curved hook which engages the caval wall to prevent migration. The filter is 4.6 cm long and has a diameter at the base of 30 mm (Figs. 2A and 2B). It is designed to trap thrombi 3 mm or larger in the apex of the cone. The flow geometry of this device is such that when 70% of the filter's vertical height is filled with thrombus, 49% of the cross-sectional area is still free for flow (Fig. 3). Maximal blood filtration occurs when the filter is within the middle of the caval lumen at an angle of less than 15°; greater angulation can allow larger thrombi to pass between the filter legs [22].

Received October 3, 1988; accepted after revision January 10, 1989.

¹ Both authors: Department of Diagnostic Radiology, University of Maryland Medical System/Hospital, 22 S. Greene St., Baltimore, MD 21201. Address reprint requests to S. O. Pais.

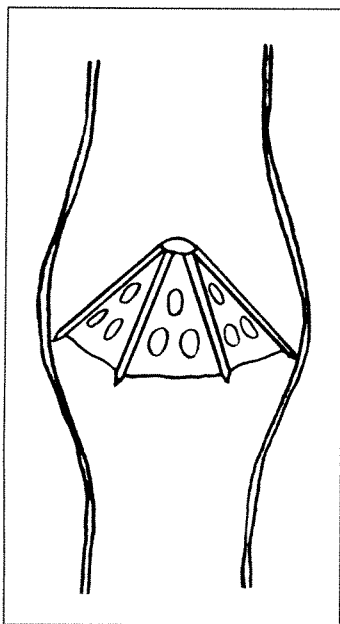
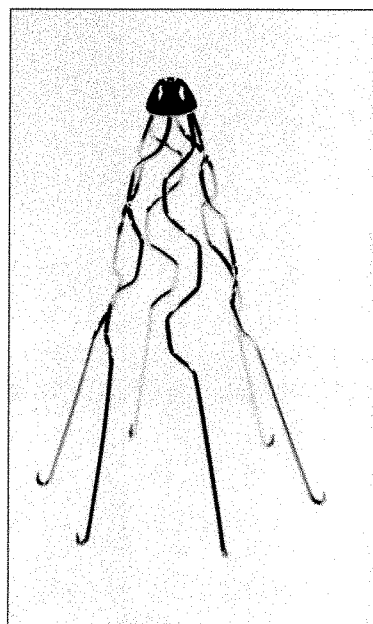
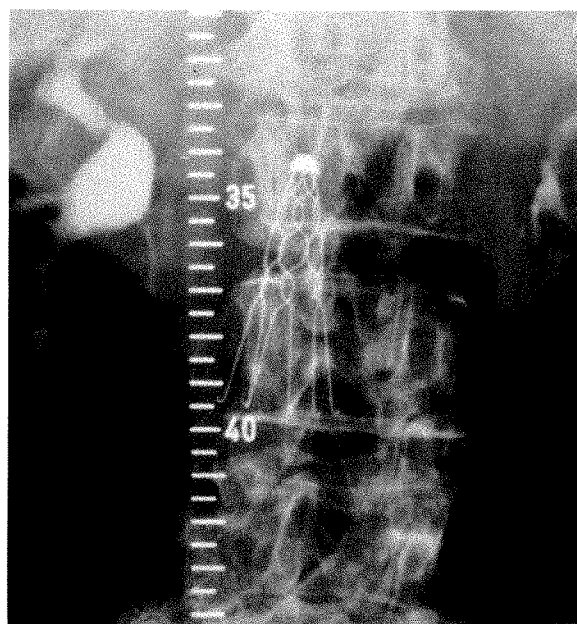


Fig. 1.—Mobbin-Uddin filter.



A



B

Fig. 2.—A, Greenfield filter.

B, Abdominal radiograph showing Greenfield filter in place.

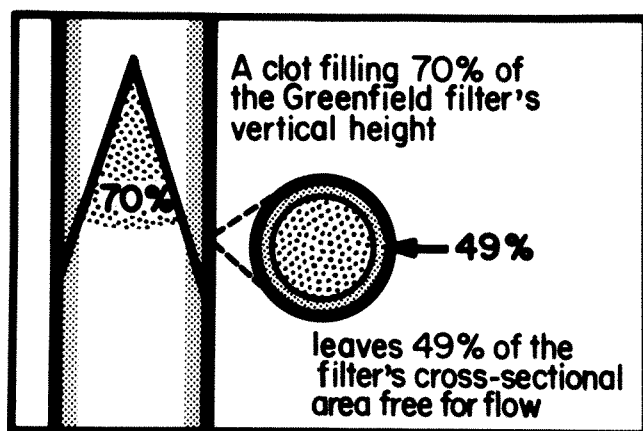


Fig. 3.—Diagram of flow geometry of Greenfield filter.

The problems associated with the Mobbin-Uddin umbrella have been largely resolved by the Greenfield filter. The incidence of recurrent embolization is 5% [9]; the incidence of IVC thrombosis is only 3–5% [9, 20]. If properly used, migration does not occur [8]. Before 1984, the usual means of filter insertion was through a cutdown of either the right internal jugular vein [12] or a femoral vein [24]. Percutaneous insertion of the Greenfield filter was first described in 1984 by Tadarthy et al. [2]. A number of subsequent reports have described additional experience with the procedure.

Technique of Filter Insertion

Percutaneous insertion of the Greenfield filter has been described in several reports [2–8]. The filter may be inserted

through either common femoral vein or the right internal jugular vein. Several authors have noted or theorized more difficulty when insertion is through the left femoral vein, due to the often large angle of the left iliac vein with the IVC [3, 5, 6]. In our experience, however, insertion from the left side has been no more difficult than from the right [8].

Using the Seldinger technique, a pigtail catheter is inserted into the appropriate femoral vein, and an inferior venacavogram is done. Pais et al. [4, 8] emphasized the importance of performing an inferior vena cavogram before filter insertion, to determine IVC diameter, position of the renal veins, presence of iliac vein or IVC thrombus, and presence of congenital variations in IVC anatomy. Twenty-six percent of 97 patients had one or more findings on the inferior vena cavogram, knowledge of which was essential for inserting the filter [8]. It was also noted that in five (5%) of 97 patients the IVC diameter was greater than 30 mm. Because the diameter of the filter base is only 30 mm, placing a filter in a patient with a caval diameter greater than 30 mm can result in filter migration. In four of these five patients, a filter was placed in each iliac vein.

An incision large enough to accommodate a 24-French sheath is made at the puncture site. The site is dilated using either dilators [2, 5] or an angioplasty balloon catheter of 8-mm diameter [4, 25]. A 24-French Coons/Amplatz sheath (Medi-tech, Inc, Watertown, MA) is then inserted. This has a flexible sleeve attached to it that may be pinched shut to control bleeding. The filter is loaded into the carrier in accordance with the manufacturer's instructions. The carrier is inserted over the guidewire, through the sheath, and released in the appropriate location in the IVC. Ideally, the filter should be positioned with the apex just below the renal veins, although considerations of IVC anatomy or pathology may

require a somewhat different location. It is occasionally difficult to traverse the iliac vein with the carrier. Flexing the hip on the side of insertion will often facilitate passage of the carrier through the vein. If passage through the iliac vein is impossible, the right internal jugular vein is used. This occurred in one of 50 patients (2%) and in two of 97 patients (2%) in two different series [3, 8]. A stiff wire with a straight, tapered tip, such as the Coons interventional wire (Cook, Inc., Bloomington, IN) or the Amplatz super stiff wire (Mediatech, Inc., Watertown, MA), is preferable to the wire that comes with the filter assembly, which has a tendency to catch on the filter as the wire is withdrawn [4]. Care must be taken that the wire is not inadvertently advanced into the right ventricle, which can result in potentially dangerous arrhythmias.

Insertion through the right internal jugular vein is necessary if the following circumstances occur: (1) The filter carrier will not negotiate the pelvis. (2) A large thrombus is at the IVC bifurcation. (3) Thrombus is in both iliac veins. In our series of 97 patients, jugular insertion was performed in 12 patients (12%) [8]. The technique of right internal jugular vein insertion is essentially the same as that for femoral vein insertion [4]. Puncture of this vein is facilitated by placing the tip of a catheter that has been inserted via a femoral vein into the right jugular vein. This can usually be done even when filter insertion through the femoral vein cannot. The vein can then be punctured under fluoroscopy by using this catheter as a target.

Except for the original paper by Tadavarthi et al. [2], all subsequent authors have preferred the femoral approach to the jugular approach [3–8]. A summary of the reasons for this preference is as follows: (1) Passage of the catheter through the iliac vein into the IVC is usually easily accomplished. (2) The risks of air embolism, pneumothorax, and inadvertent carotid puncture are avoided. (3) Radiologists are more familiar and more comfortable with puncturing the femoral vein.

Complications

In order to assess the morbidity associated with percutaneous Greenfield filter placement, the complications of this technique can be compared with those associated with surgical insertion. The complications related to filter placement include migration, misplacement or tilting, caval thrombosis, and local complications at the site of insertion.

The incidence of caval thrombosis (2–3%) after percutaneous filter placement [5, 8] is comparable to that reported in multiple surgical series [9–11, 20, 26–28]. This is to be expected because this complication is inherent in the design of the filter and is independent of the method of insertion.

Several series have reported long-term follow-up of correctly positioned Greenfield filters [19, 22, 29]. These studies indicate that 30–60% of filters may migrate up to several centimeters caudally, and as many as 20% can migrate cephalad 2–12 mm. It has been theorized that the change in filter position is a result of a combination of fibrosis, endothelialization, and caval wall penetration [22]. If migration does

not involve movement of the filter into a renal, hepatic, or iliac vein, this degree of migration does not affect filter function. Whereas there have been no reports of significant migration of percutaneously placed filters, there are three case reports of filter migration to the heart or pulmonary artery after surgical insertion [30–32]. A cavogram was not done to assess caval diameter before filter placement in any of the cases in which migration was reported.

The incidence of percutaneously inserted filters that have been misplaced or tilted more than 15° is 1–4% [4–8]. This compares favorably with the incidence of surgical misplacement or tilting of 1.5–14% [7, 10, 11, 20, 26–28, 33]. Filter misplacement into a renal, hepatic, or iliac vein does not protect the patient adequately from pulmonary emboli. This problem can be corrected by positioning a second filter in the cava [8, 34]. No reports have been made of renal or hepatic insufficiency associated with misplaced filters.

There have been 18 cases of intracardiac misplacement reported in the literature; one filter was percutaneously placed [5] and the others were surgically inserted [27, 34–41]. Intracardiac misplacement or migration is the most feared complication of filter insertion. Possible consequences include arrhythmias, thrombosis, myocardial perforation, and valvular damage. However, many patients are asymptomatic, with a few reports of arrhythmias [36, 37], chest pain [41], or hypoxia [30]. Most filters were immediately removed operatively [35–38]. Greenfield [34] has reported retrieval of an intracardiac filter with a transvenous retrieval device. Several filters have been percutaneously retrieved from the heart [39–41] or renal vein [42]. The indications for retrieval have not been defined. Three intracardiac filters have been left in place with no sequelae [6, 31, 32]. This complication should not occur if the cava is delineated and measured with cavography and if the filter is properly inserted.

One mortality associated with percutaneous filter insertion has been reported [8]. Although, to our knowledge, no other mortality associated with filter placement has been reported, the widespread use of this device increases the possibility of random individual fatalities.

Complications may occur at the insertion site with either percutaneous or surgical placement. These include the risk of a pneumothorax or air embolism from the jugular approach and local hematoma, infection, vascular injury, or venous thrombosis from either jugular or femoral insertion. The incidence of pneumothorax following jugular insertion is low and occurred only in two patients after both percutaneous [8] and surgical [43] insertion. Symptomatic air embolism has occurred in two patients during surgical placement [9, 10]. Air embolism has not been reported with percutaneous insertion. This may reflect the larger number of surgically placed filters via the jugular route.

Three cases of a femoral arteriovenous fistula occurring with percutaneous insertion have been reported [5, 44]. They were repaired surgically with no sequelae. This complication has been attributed to an abnormally low venous puncture site with simultaneous puncturing of the femoral vein and superficial femoral artery [44].

Despite the use of a 24-French sheath, the incidence of hematoma formation with percutaneous placement is only 0–

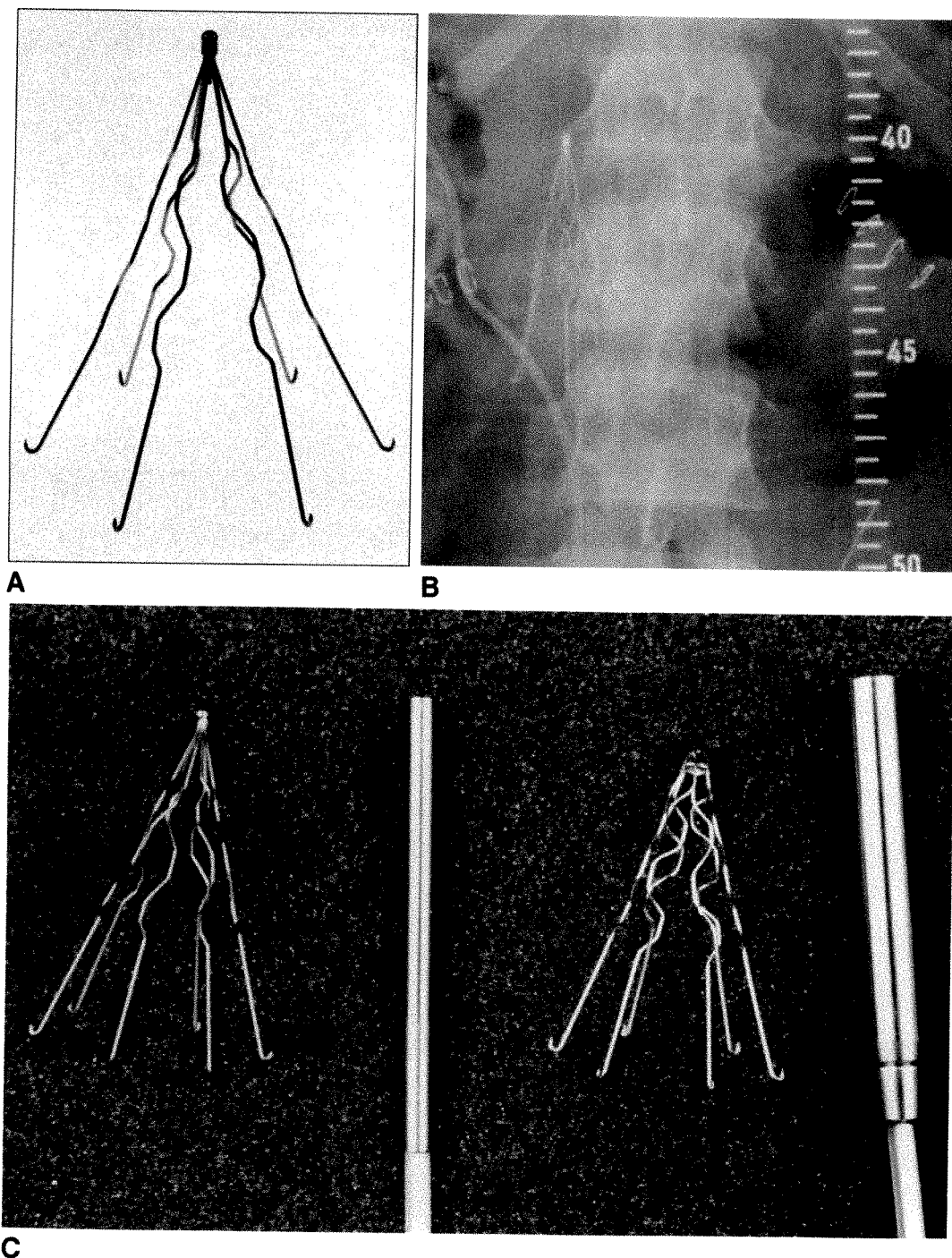


Fig. 4.—A, Modified Greenfield filter.

B, Abdominal radiograph showing modified Greenfield filter in place.

C, Comparison of standard and modified Greenfield filters. Modified Greenfield filter and carrier on left. Standard Greenfield filter and carrier on right.

2% [4–7], and no infections at the site of insertion have been reported. This compares favorably with several surgical series, which have described a 5–14% incidence of local hematoma [10, 27, 28], and two cases of wound infection [27, 45].

The primary complication of percutaneous filter placement is the development of femoral vein thrombosis after insertion via the femoral route. A significant probability of this complication was theorized by Tadavarthy et al. [2], because of the need to use a large sheath to introduce the filter carrier. This is one of several reasons they prefer the jugular approach, because jugular thrombosis is believed to be of little clinical importance. However, a symptomatic jugular vein thrombosis

following surgical filter insertion has been reported [43]; therefore, this complication may not be totally innocuous. The reported incidence of femoral vein thrombosis varies from 0% to 41% [4–6, 8, 25, 46, 47]. This wide range reflects the method of evaluation of the patient.

Thrombosis has a low incidence (2–12%) in patients in whom the presence of thrombosis was determined by clinical examination [4–7, 46]. However, the clinical diagnosis of deep venous thrombosis is known to be markedly inaccurate [48–50]. The true incidence of procedure-related thrombosis should be based on objective studies. Evaluation of patients by sonography [8] or venography [47] after filter placement by the femoral route, has shown a 33% and 41% incidence,

respectively, of femoral vein thrombosis. In the series that used venography, the thrombus was limited to the puncture site and was, therefore, due to manipulation of the vein for filter insertion. In addition, only 13% of patients in the sonography series and 24% in the venography series were symptomatic for venous thrombosis. This is in accord with the low reported incidence of thrombosis in those series relying on clinical assessment for the diagnosis of this complication. Although these two studies suggest a rather high incidence of femoral vein thrombosis, only two cases of chronic venous sequelae related to filter insertion have been reported [5]. One other patient underwent thrombectomy for procedure-related thrombosis and had no further complications [6].

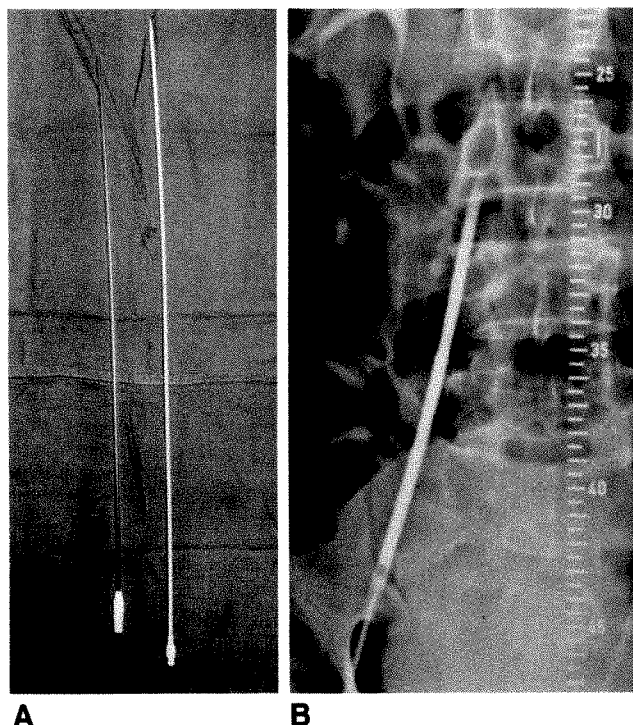
The incidence of femoral vein thrombosis after percutaneous filter insertion needs further study. It should be noted that the incidence of femoral vein thrombosis after surgical filter insertion has not been studied. The incidence of this complication after percutaneous, as opposed to surgical, insertion is therefore not known. This is a relevant consideration, because in several surgical series 19% to 48% of patients had filters inserted via the femoral vein [9, 11, 26, 33].

A recent study by Dorfman et al. [51] used an animal model to evaluate pathologic changes that occur during percutaneous tract dilatation with dilators and angioplasty balloon catheters. Although both techniques resulted in venous injury, the dilators produced significantly more vascular damage, which extended as far distally as they were advanced. To minimize venous injury and thrombosis, Dorfman et al. recommend that balloon dilatation catheters be used and that the 24-French sheath be advanced into the vein as short a distance as possible. In spite of the above-cited study, no clinical data show that balloon dilatation is less thrombogenic than sequential dilators. However, in view of the increased ease of dilatation using balloon catheters, as well as their apparently less traumatic effect on the vein, it would seem prudent to use them rather than dilators.

The Future

The attributes of an "ideal" IVC filter are as follows: (1) It can be inserted safely and easily by physicians of reasonable skill. (2) It prevents recurrent emboli. (3) No mortality or morbidity is associated with its insertion. (4) Chronic sequelae, including IVC thrombosis, do not occur. The Greenfield filter approximates these ideal properties. The only possible drawback of the Greenfield filter is the apparent high incidence of femoral vein thrombosis, which may be related to the large sheath necessary for its insertion. However, the true incidence and significance of this complication are unknown, because the information available is based on a small number of patients [8, 47].

A number of other IVC filters have been developed in recent years, including the Gianturco bird's nest filter [52], the Amplatz filter [53], the Gunther basket filter [54], and the nitinol filter [55]. As these use smaller delivery systems (from 8 to 14 French), it is tempting to assume that the incidence of femoral vein thrombosis will be lower. However, no data have been collected that either support or refute this assumption.



A 14-French sheath/dilator set.
B Abdominal radiograph showing contrast-filled sheath in place before insertion of carrier and filter.

A modified Greenfield filter also has been developed (Fig. 4). This is made from a titanium alloy, which has elastic properties that allow it to be compressed into a 12-French carrier. It is slightly longer than the standard stainless steel filter (4.7 cm), and broader at the base (38 mm). It has been shown experimentally to be comparable to the standard Greenfield filter in its ability to trap emboli and maintain IVC patency [56]. A report of preliminary clinical experience in 40 patients [57] indicates that insertion is easier than for the standard filter. A long 14-French dilator/sheath assembly is passed over a guidewire into the IVC. When the sheath and dilator are in the IVC at the level of filter placement, the wire and dilator are removed (Fig. 5). The 12-French carrier/filter assembly is passed through the sheath, and the filter is released under fluoroscopic control at the appropriate site. The carrier and sheath are then removed. No sutures are necessary at the puncture site, and bleeding is minimal.

It is not the purpose of this review to evaluate the merits of other filters. However, it is germane to note that any other filter, whether currently in use or yet to be developed, must be measured against the Greenfield filter, which represents the current "gold standard." Furthermore, the introduction of a modified Greenfield filter with a smaller delivery system eliminates the major apparent advantage of the other filters currently being evaluated. The accumulated experience with the Greenfield filter represents many thousands of patients over many years. In order to determine whether any of the other filters now being evaluated is superior, or even comparable, many patients will have to be observed over a period of several years.

REFERENCES

- Greenfield LJ, McCurdy JR, Brown PP, Elkins RC. A new intracaval filter permitting continued flow and resolution of emboli. *Surgery* **1973**;73:599-606
- Tadavarthy SM, Castaneda-Zuniga W, Salomonowitz E, et al. Kimray-Greenfield vena cava filter: percutaneous introduction. *Radiology* **1984**;151:525-526
- Denny DF, Cronan JJ, Dorfman GS, Esplin C. Percutaneous Kimray-Greenfield filter placement by femoral vein puncture. *AJR* **1985**;145:827-829
- Pais SO, Mirvis SE, DeOrchis DF. Percutaneous insertion of the Kimray-Greenfield filter: technical considerations and problems. *Radiology* **1987**;165:377-381
- Rose BS, Simon DC, Hess ML, Van Aman ME. Percutaneous transfemoral placement of the Kimray-Greenfield vena cava filter. *Radiology* **1987**;165:373-376
- Welch TJ, Stanson WS, Sheedy PF, Johnson MJ, Miller WE, Johnson CD. Percutaneous placement of the Greenfield vena cava filter. *Mayo Clin Proc* **1988**;63:343-347
- Denny DF, Dorfman GS, Cronan JJ, Greenwood LH, Morse SS, Yoselevitz M. Greenfield filter: percutaneous placement in 50 patients. *AJR* **1988**;150:427-429
- Pais SO, Tobin KD, Austin CB, Queral L. Percutaneous insertion of the Greenfield inferior vena cava filter: experience with 96 patients. *J Vasc Surg* **1988**;8:460-464
- Greenfield LJ. Current indications for and results of Greenfield filter placement. *J Vasc Surg* **1984**;1:502-504
- Gomez GA, Cutler BS, Wheeler HB. Transvenous interruption of the inferior vena cava. *Surgery* **1983**;93:612-619
- Greenfield LJ, Peyton R, Crute S, Barnes R. Greenfield vena caval filter experience: late results in 156 patients. *Arch Surg* **1981**;116:1451-1456
- Mansour M, Chang AE, Sindelar WF. Interruption of the inferior vena cava for the prevention of recurrent pulmonary embolism. *Am Surg* **1985**;51:375-380
- Homans J. Thrombosis of the deep veins of the lower leg causing pulmonary embolism. *N Engl J Med* **1934**;211:993-997
- Oschner A, DeBakey M. Intravenous clotting and its sequelae. *Surgery* **1943**;14:679-690
- O'Neil EE. Ligation of the inferior vena cava in the prevention and treatment of pulmonary embolism. *N Engl J Med* **1945**;232:641-646
- Ravitch MM, Snodgrass E, McEnany T. Compartmentalization of the vena cava with the mechanical stapler. *Surg Gynecol Obstet* **1966**;122:561-566
- Miles RM, Richardson RR, Wayne L, Elsea PW, Stewart SB, Duncan D. Long term results with the serrated Teflon vena caval clip in the prevention of pulmonary embolism. *Ann Surg* **1969**;169:881-891
- Mobbin-Uddin K, Smith PE, Martinez LO, Lombardo CR, Jude JR. A vena caval filter for the prevention of pulmonary embolus. *Surg Forum* **1967**;18:209-211
- Mobbin-Uddin K, Trinkle JK, Bryant LR. Present status of the inferior vena caval umbrella filter. *Surgery* **1971**;70:914-919
- Cimochowski GE, Evans RH, Zarins CK, Lu CT, DeMeester TR. Greenfield filter versus Mobin-Uddin umbrella: the continuing quest for the ideal method of vena caval interruption. *J Thorac Cardiovasc Surg* **1980**;79:358-365
- Mobbin-Uddin K, Utley JR, Bryant LR. The inferior vena cava umbrella filter. *Prog Cardiovasc Dis* **1975**;17:391-399
- Messmer JM, Greenfield LJ. Greenfield caval filters: long-term radiographic follow-up study. *Radiology* **1985**;156:613-618
- Jones TK, Barnes RW, Greenfield LJ. Greenfield vena caval filter: rationale and current indications. *Ann Thorac Surg* **1986**;42[suppl]:S48-S55
- Greenfield LJ. Technical considerations for insertion of vena caval filters. *Surg Gynecol Obstet* **1979**;148:422-426
- Shetty PC, Bok LR, Burke MW, Rajinder PS. Balloon dilatation of the femoral vein expediting percutaneous Greenfield vena caval filter placement. *Radiology* **1986**;161:275
- Carabasi RA, Moritz MJ, Jarrell BE. Complications encountered with the use of the Greenfield filter. *Am J Surg* **1987**;154:163-168
- Scurr JH, Jarrett PE, Wastell C. The treatment of recurrent pulmonary embolism: experience with the Kimray Greenfield vena cava filter. *Ann R Coll Surg Engl* **1983**;65:233-234
- Jarrell BE, Posuniak E, Roberts J, Osterholm J, Cotler J, Ditunno J. A new method of management using the Kimray Greenfield filter for deep venous thrombosis and pulmonary embolism in spinal cord injury. *Surg Gynecol Obstet* **1983**;157:316-320
- Berland LL, Maddison FE, Bernhard VM. Radiologic follow-up of vena cava filter devices. *AJR* **1980**;134:1047-1052
- Moore R, Dagher FJ, Tavares S, Attar S. Migration of Kim-Ray Greenfield umbrella to the heart. *South Med J* **1983**;76:946-947
- Castaneda F, Herrera M, Cragg AW, et al. Migration of a Kimray-Greenfield filter to the right ventricle. *Radiology* **1983**;149:690
- Friedell ML, Goldenkranz RJ, Parsonnet V, et al. Migration of a Greenfield filter to the pulmonary artery: a case report. *J Vasc Surg* **1986**;3:929-931
- Otchy DP, Elliott BM. The malpositioned Greenfield filter: lessons learned. *Am Surg* **1987**;53:580-583
- Greenfield LJ, Crute SL. Retrieval of the Greenfield vena caval filter. *Surgery* **1980**;88:719-722
- Greenfield LJ, Zocco J, Wilk J, Schroeder TM, Elkins RC. Clinical experience with the Kim-Ray Greenfield vena caval filter. *Ann Surg* **1977**;185:692-698
- Villard J, Dentry L, Clermont A, Pinet F. Huit filtres de Greenfield dans les cavités cardiaques droites: traitement chirurgical. *Ann Radiol (Paris)* **1987**;30(2):102-104
- Hirsch SB, Harrington EB, Miller CM, Estioko MR, Haimov M. Accidental placement of the Greenfield filter in the heart: report of two cases. *J Vasc Surg* **1987**;6:609-610
- Akins CW, Thurer RL, Waltman AC, Margolies MN, Schneider RC. A misplaced caval filter. *Arch Surg* **1980**;115:1133
- Yakes WF. Percutaneous retrieval of Kimray-Greenfield filter from right atrium and placement in inferior vena cava. *Radiology* **1988**;169:849-851
- Tsai FY, Myers TV, Ashraf A, Shah DC. Aberrant placement of a Kimray-Greenfield filter in the right atrium: percutaneous retrieval. *Radiology* **1988**;167:423-424
- Deutsch LS. Percutaneous removal of intracardiac Greenfield vena caval filter. *AJR* **1988**;151:677-679
- Schneider PA, Bednarkiewicz M. Percutaneous retrieval of Kimray-Greenfield vena caval filter. *Radiology* **1985**;156:547
- Golueke PJ, Garrett WV, Thompson JE, Smith BL, Talkington CM. Interruption of the vena cava by means of the Greenfield filter: expanding the indications. *Surgery* **1988**;103:111-117
- Grassi CJ, Bettmann MA, Rogoff P, Reagan K, Harrington DP. Femoral arteriovenous fistula after placement of a Kimray-Greenfield filter. *AJR* **1988**;151:681-682
- Swann KW, Black PM, Baker MF. Management of symptomatic deep venous thrombosis and pulmonary embolism on a neurosurgical service. *J Neurosurg* **1986**;64:563-567
- Weinstein JK, Ramchandani P, Soulen RL, Desai SA. Complications of the percutaneous femoral approach for Kimray Greenfield filter placement. Presented at the annual meeting of the Radiological Society of North America, Chicago, November **1987**
- Kantor A, Glanz S, Gordon DH, Sciafani SJA. Percutaneous insertion of the Kimray-Greenfield filter: incidence of femoral vein thrombosis. *AJR* **1987**;149:1065-1066
- Sigel B, Popky GL, Wagner DK, Boland JP, Mapp EM, Feigel P. Comparison of clinical and Doppler ultrasound evaluation of confirmed lower extremity venous disease. *Surgery* **1988**;64:332-338
- Cranley JJ, Canos AJ, Sull WJ. The diagnosis of deep venous thrombosis: fallibility of clinical symptoms and signs. *Arch Surg* **1976**;111:34-36
- Sandler DA, Martin JF, Duncan JS, et al. Diagnosis of deep vein thrombosis: comparison of clinical evaluation, ultrasound, plethysmography, and venoscan with x-ray venogram. *Lancet* **1984**;2(8405):716-719
- Dorfman GS, Esparza AR, Cronan JJ. Percutaneous large bore venotomy and tract creation: comparison of sequential dilator and angioplasty balloon methods in a porcine model. *Invest Radiol* **1988**;23:441-446
- Roehm JOF Jr, Gianturco C, Barth MH. Bird's nest inferior vena caval filter. *Semin Intervent Radiol* **1986**;3:205-213
- Darcy MD, Hunter DW, Lund GB, Cardella JF. Amplatz retrievable vena caval filter. *Semin Intervent Radiol* **1986**;3:214-219
- Gunther RW, Schild H. Basket filter for prevention of pulmonary embolism. *Semin Intervent Radiol* **1986**;3:220-226
- Cragg A, Castaneda-Zuniga WR. Nitinol spiral vena caval filter. *Semin Intervent Radiol* **1986**;3:227-230
- Burke PE, Michna BA, Harvey CF, Crute SL, Sobel M, Greenfield LJ. Experimental comparison of percutaneous vena caval devices: titanium Greenfield filter versus bird's nest filter. *J Vasc Surg* **1987**;6:66-70
- Greenfield LJ, Cho KJ, Pais SO, Van Aman M. Preliminary clinical experience with the titanium Greenfield vena cava filter. *Arch Surg* **1989** (in press)

A Prospective Trial of Ionic vs Nonionic Contrast Agents in Routine Clinical Practice: Comparison of Adverse Effects

Gerald L. Wolf¹
 Ronald L. Arenson²
 Anne P. Cross³

A multicenter study of adverse effects of ionic and nonionic contrast agents was conducted in three similar time periods. In 1985, before approval of the nonionic contrast agents by the Food and Drug Administration, 6006 consecutive patients received iv ionic agents for urography or CT. After approval of the nonionic agents, 7170 consecutive patients referred for the same examinations were studied. The two groups of patients were significantly different, but the differences were small and did not uniformly favor either group. The incidence of adverse effects in the patients given ionic contrast material was significantly higher than that of the nonionic group (4.17% vs 0.69%, $p < .001$). The reactions were also more severe in the ionic group than in the nonionic group ($p < .005$). A patient questionnaire disclosed that many patients did not feel well for hours to days after the procedure and also did not immediately resume normal activities of daily living. The nonionic agent was significantly less distressful than the ionic agent.

We conclude that nonionic agents cause fewer and less severe adverse effects. Reducing adverse effects can save the patient or the examining site either time or money. However, this study does not show that nonionic agents are more cost-effective than ionic agents.

In December 1985, the Food and Drug Administration (FDA) approved two new nonionic, water-soluble radiographic contrast agents for IV use. Extensive animal experiments had shown that these new agents were much safer than the members of the ionic class of agents. A few good clinical studies were available from Scandinavia [1] and Europe [2], and there were reports of very large series of patients with much lower mortality rates from new nonionic agents or a low osmolal nonionic-ionic dimer [3]. However, the incidence and severity of morbidity as well as mortality of such contrast agents varies according to the prevalence of associated risk factors in the population studied [4-11]. Methods used to determine adverse effects of contrast agents range from surveys [4-7], to consecutive series [8, 9], to randomized clinical trials [10, 11]. Each of these methods has its strengths and weaknesses. In addition to the lower risk and equivalent effectiveness of the new nonionic agents, they are much more expensive, which concerns both medical scientists and the lay press [12-18].

As it became evident that such agents would be approved as safe and effective for use in the United States, we became concerned that little information would be available on adverse reactions that affect relative cost-effectiveness of the ionic or nonionic agents when used for routine clinical studies. The following study was performed to provide some information before ethical concerns made random assignment of agents with differing safety impossible.

Materials and Methods

This study was designed to compare the incidence and severity of adverse effects caused by IV water-soluble contrast agents in routine clinical care. Because some investigators consider that adverse events with these agents are influenced by the consent procedure

Received March 7, 1988; accepted after revision January 13, 1989.

G. L. Wolf is supported, in part, by the Veterans Administration Research Service. The iohexol and some financial support for data collection and analysis were provided by Sterling-Winthrop.

¹ Department of Radiology, University of Pittsburgh, and Pittsburgh NMR Institute, 3260 Fifth Ave., Pittsburgh, PA 15213. Address reprint requests to G. L. Wolf at the Pittsburgh NMR Institute.

² Department of Radiology, University of Pennsylvania, 3400 Spruce St., Philadelphia, PA 19104.

³ Cooperative Studies Program Coordinating Center, Veterans Administration Medical Center, W. Spring St., West Haven, CT 06516.

AJR 152:939-944, May 1989
 0361-803X/89/1525-0939
 © American Roentgen Ray Society

itself [19], we wanted to study patients under usual clinical conditions. Thus, the research had to fit paragraph 46.111 of FDA regulations, "research involving no more than minimal risks," in order that a separate informed consent document would not be required. In particular, we followed two specific items from these regulations: item 8, program activities that entail no deviation for subjects from normal requirements of their involvement in the program being identified, and item 9, survey activities in which responses are recorded in such manner that individuals cannot be identified.

These items necessitated a design using best available care and historic controls. Eleven hospitals agreed to gather information on all patients referred for diagnostic examinations requiring IV contrast agents. The technologist completed one form requesting demographic and risk-factor information on each such patient. The demographic questionnaire included information about race, previous reactions to contrast media, use of any premedication, or potential risk factors: congestive heart failure, coronary artery disease, hypertension, vascular disease, renal disease, renal failure or insufficiency, stroke, diabetes mellitus, gout, pheochromocytoma, sickle cell disease, multiple sclerosis, multiple myeloma, hypoalbuminemia, asthma, allergic rhinitis, drug allergy, or food allergy.

If the patient experienced a reaction that the technologist observed or elicited by questioning, a second form describing the adverse reaction was completed. If an adverse reaction occurred, the technologist classified it as minor, moderate, severe, or death according to the criteria of Ansell [4]. Minor reactions were nausea, retching, mild vomiting, and limited urticaria; moderate reactions included faintness, severe vomiting, extensive urticaria, facial or glottic edema, dyspnea or bronchospasm, chest or abdominal pain, and severe headache; severe reactions included loss of consciousness, cardiac arrest, shock, or symptomatic cardiac arrhythmia. Finally, each patient was given a questionnaire and a mailer to complete voluntarily and return a few days later. Figure 1 is a copy of this questionnaire. Under these conditions, the University of Pittsburgh Institutional Review Board concluded that the protocol involved no more than minimal risk.

The first phase of this study was performed with the standard ionic contrast agent formulation, dose, and injection rate used in each site for the patient's indication. There were no exclusions for the purpose of the study. Each center was asked to complete the study forms for every patient who received an IV contrast agent for urography or CT. No center reported withholding any patients from the study. The ionic-agent phase began in May 1985 and was terminated in December 1985, when the FDA approved iopamidol and iohexol, two nonionic agents with clinical indications covering the patients in our study. There were 6006 consecutive patients in this experimental set.

The second phase of the study was conducted in the same hospitals, during a similar time period of May–December 1986. We obtained funding for the nonionic agent (iohexol) used in all these patients but had to restrict this phase of the study to patients referred for IV urography because iohexol was not approved for CT at that time. The dose of iohexol (300 mg I/ml formulation) and its rate of administration were not modified from that used for ionic agents. In this experimental period, 2247 consecutive patients were studied.

Because of concern that the adverse reaction rate might be different for patients undergoing urography and CT, a third phase was performed with consecutive patients in five hospitals between May and November 1988. In this experimental period, 4923 patients were studied; 3422 were with CT and 1501 with urography.

The questionnaire information from technologists and patients was collated and analyzed by computer. As is common under these conditions, some information requested was not completed, in whole or in part. For those items, the results were recorded and analyzed only for those responses known. Where data categories were less

Dear Patient,

On _____, you had a diagnostic Radiology examination where an x-ray dye was injected. Would you please complete this questionnaire so that we can find out more about how this procedure affected you afterwards?

1. Did you notice any change in how you felt after the procedure?

☐ No ☐ Yes

2. How much change did you notice?

Place an X on the line below to show how you felt

Felt much worse	No change	Felt much better
1 1 1	1 1	1 1 1

3. How long were you affected?

☐ Couple hours ☐ Whole day ☐ Two or more days

4. When did you resume your usual activities such as work or enjoyable hobbies (as much as before the examination)?

☐ Couple hours ☐ Next day ☐ Two or more days

5. If you want to share any particular symptoms or observations you think may have been caused by the examination, please do so here.

COMMENTS:

Fig. 1.—Reproduction of questionnaire given to each patient. Questionnaire was coded to match technologist's report and was returned in a preaddressed, stamped envelope.

than 95% complete, the number of responses available was given. Statistical comparisons were made by using the t-test with unequal variance or chi-square analysis.

Results

The first two phases of the study were done in the same sites, by the same personnel, using the same doses and rates of administration, in a similar time and season but 1 year apart. The third phase was done in only five sites, 2 years later. The strength of the consecutive series design is that all patients were studied. The demographic comparisons of the two study populations are shown in Table 1. Because of the large sample size in each group, there are some statistically significant differences, but the differences were not large in clinical terms. The iohexol group had more prior reactors, less premedication, and somewhat fewer risk factors. Corticosteroid was infrequently used as a premedication for either the ionic or nonionic agent (Table 2). In phase 1, where the clinical indication was not requested, the technologists listed 1912 patients for CT, 538 patients for urography, and did not record the examination performed in 3556 patients.

The incidence and severity of the reactions were significantly less with the nonionic than with the ionic agent (Table 3). A large and highly significant difference was found in the incidence of reactions. If the severity of reactions is considered, the ionic-agent reactors had more moderate and severe reactions by proportion while the nonionic reactors had no severe reactions, fewer moderate reactions, and predomi-

nantly mild reactions. The same proportion of the adverse reactions in the iohexol group were given drugs to alleviate the symptoms or signs of the reaction as in the ionic group, but there were many fewer patients receiving nonionic agents who required treatment.

Technologists were asked to complete the demographic questionnaire as well as the adverse drug response (ADR) form. Although there is less likelihood of underreporting when all patients are in a study, it might be questioned whether the incidence of reported ADRs diminished as the study progressed. There is also a possibility of seasonal factors from summer to fall. Figure 2 presents the reported incidence of ADRs by time in each phase of the study. In phase 1, there were 82 ADRs in 1378 patients during May–June, 74 ADRs in 2274 patients in July–August, 91 ADRs in 2342 patients in September–October, and 12 forms with incomplete examination date. In phase 2, there were 11 ADRs in 591 patients in May–June, nine ADRs in 840 patients in July–August, four

ADRs in 796 patients in September–December, and 20 forms with incomplete examination dates. In phase 3, there were six ADRs in 1303 patients in May–June (1988), seven ADRs in 1586 patients in July–August, 13 ADRs in 2027 patients in September–November, and seven forms with incomplete examination dates. Both the ionic-agent phase and the last iohexol phase are consistent over time. The first use of iohexol in phase 2 seems to show a learning curve where reported ADRs are higher in the first 2 months and then decline. In the last 2 months of phase 2, the ADR rate was similar to that of all of phase 3.

The results from the questionnaires given to patients also were interesting. There was a reasonably high rate of return of the questionnaire, and each study group returned the questionnaire in about the same proportion (Table 4). As the patients responded to question 2 by marking on a nine-point analog scale, no change would be rated as a score of 4.5. A significantly higher proportion of patients receiving the ionic

TABLE 1: Demographics of Patients Receiving Ionic Contrast Agents or Iohexol

Demographic Factor ^a	Ionic Agents ^b (n = 6006)	Iohexol ^c (n = 7170)
Born		
1890–1919	29.6	25.0
1920–1939	37.4	38.9
1940–1959	24.3	27.0
1960–1979	7.5	8.9
Race		
White	76	78
Black	22	19
Other	2	3
Prior contrast study	61	58
Prior adverse reaction	3.7	6.7
Any risk factor	46	42
Any premedication	7.0	2.0

^a $p < .001$ for all factors.

^b Numbers in this column are percentages of the total 6006 patients receiving ionic contrast agents.

^c Numbers in this column are percentages of the total 7170 patients receiving iohexol.

TABLE 3: Comparison of the Incidence and Severity of Reactions in Patients Receiving Ionic Agents or Iohexol

Reactions ^a	Ionic Agents (% of 6006 patients)	Iohexol (% of 7170 patients)
Incidence	247 (4.1)	50 (0.69)
Severity		
Mild	152 (2.5)	42 (0.58)
Moderate	71 (1.2)	8 (0.11)
Severe	24 (0.4)	0 (0)
Treatment required		
Yes	79 (1.3)	17 (0.2)
No	168 (2.7)	33 (0.5)

^a Chi-square test for two-way tables yielded $p < .001$ for incidence and for treatment required, and $p < .005$ for severity.

TABLE 2: Pretreatment Regimens and Adverse Reactions for CT and Urography^a

	Phase 1 Ionic Agents			Phase 2 Iohexol EU (n = 2247)	Phase 3 Iohexol	
	CT (n = 1912)	EU ^b (n = 538)	NR ^c (n = 3556)		CT (n = 3422)	EU (n = 1501)
Pretreatment						
Steroids alone	1.4	0.9	2.2	1.1	0.1	0.3
Benadryl alone	0.4	1.7	1.6	2.3	1.2	2.1
Steroids and other drugs	1.0	1.2	2.1	1.2	0.1	0.3
Other	0.3	3.1	1.2	4.3	0.0	0.0
None	96.9	93.2	92.9	91.1	98.6	97.3
Adverse reactions						
Mild	2.6	2.4	2.7	0.9	0.32	0.26
Moderate	1.3	1.2	1.2	0.2	0.11	0.26
Severe	0.4	0.4	0.3	0.0	0.0	0.0

^a Numbers in table are percentages of total number of patients (n) listed at the top of their respective columns.

^b EU = excretory urography.

^c Examination not recorded in Phase 1.

class of agents reported that they felt worse (score < 4.5). These patients also reported a significant difference in the time they were affected (question 3 of Fig. 1, Table 5) and in the time elapsed before they returned to usual activities (question 4 of Fig. 1, Table 5). Again this difference favored nonionic agents, but there are some possible inconsistencies in the responses because fewer patients reported feeling

worse when using the analog scale than when reporting their response on questions 3 and 4. A higher proportion of the patients in the ionic study wrote comments on their responses than those in the nonionic study (32% vs 19%). Many patients were pleased that the investigators were interested in their responses. Not all of the comments were unfavorable, and some ranged from humorous to bizarre.

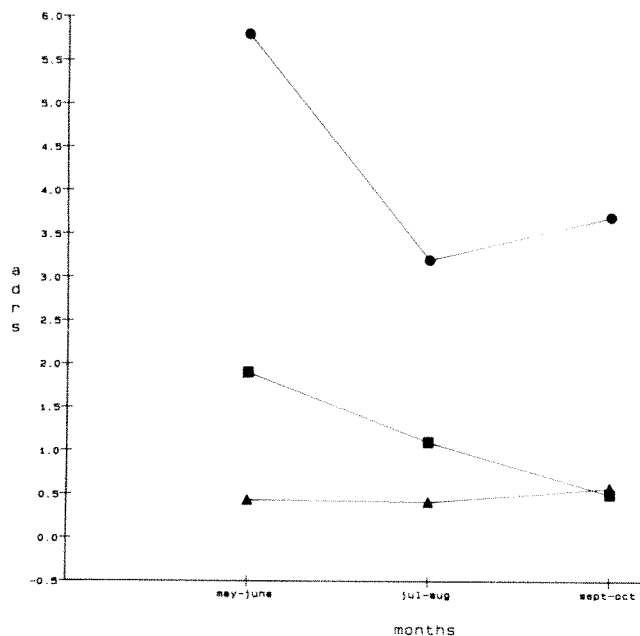


Fig. 2.—Incidence (%) of adverse drug reactions by 2-month period in all three phases of this consecutive series from multiple centers. Phase 1 (circles) was performed with ionic agents in 1985, phase 2 (squares) with iohexol for urography in 1986, and phase 3 (triangles) with iohexol in 1988.

TABLE 4: Patients Reporting Feeling Worse

Condition of Patient ^a	Ionic Agents (% of 6006 patients)	Iohexol (% of 7170 patients)
Felt worse	866 (14.4)	624 (8.7)
Did not feel worse	2295 (38.2)	2959 (41.3)
No response	2845 (47.4)	3587 (50.0)

^a Chi-square = 97.2, df = 2, $p < .0001$.

Discussion

Many different experimental designs have been used to study adverse responses to contrast media, and each has strengths and weaknesses. Randomized clinical trials (RCTs) reduce bias but are very expensive and usually study a highly selected subset of patients. When patients are the subjects, clinical exigencies usually rule out the use of a placebo to control for the nonspecific adverse reactions due to an IV injection or the stress of the circumstances. When properly done, they offer the best answer to an often narrowly posed question. RCTs comparing ionic agents with ioxoglate, iohexol, or iopamidol recently have been collated and roundly criticized [10]. The RCT of Lasser et al. [11] was very well done, but studied premedication in hospitalized patients undergoing CT or urography. It is obviously difficult to do a large RCT of ionic agents vs a newer agent without exclusions in a setting that mimics routine clinical practice [20].

As very large sample sizes are required to find significant differences between uncommon events, some investigators have resorted to surveys where centers are requested to report their own adverse reaction rates [4–7]. This is less expensive per case than an RCT but worrisome for accurate reporting of both ADRs and total patients at risk. Another common method is a consecutive series. Hartman et al. [8] and Witten et al. [9] reported consecutive patients from the Mayo Clinic using ionic agents. Consecutive series are less subject to reporting bias and can be from a single center or several centers. The latter choice also has tradeoffs including uniformity of methods versus diversity of case mix.

Few RCTs have enough data to detect a difference between severe reactions and death. On the other hand, the fatality rate in the Shehadi survey [6] was 1:14,000, and in the Mayo Clinic consecutive series it was 1:75,000 [8].

TABLE 5: Patients Reporting Length of Time Affected

Response	Ionic Agents (% of 6006 patients)	Iohexol (% of 7170 patients)
How long were you affected? ^a		
Couple of hours	795 (13.2)	776 (10.8)
Whole day	326 (5.4)	243 (3.4)
2 or more days	211 (3.5)	114 (1.6)
No response	4674 (77.8)	6037 (84.2)
When did you resume your usual activities? ^b		
Couple of hours	1307 (21.8)	1613 (22.5)
Next day	604 (10.0)	526 (7.3)
2 or more days	191 (3.2)	151 (2.1)
No response	3904 (65.0)	4880 (68.1)

^a Chi-square = 25.4, df = 2, $p < .0001$.

^b Chi-square = 34.1, df = 2, $p < .0001$.

If there is good reason to believe there is a difference in risk between the two agents, there are ethical concerns in assigning patients an ionic agent or a nonionic agent, whether by randomization or another protocol. This study was planned as a multicenter, consecutive series to be performed in routine clinical practice using the best available FDA-approved agent. Consent to participate in an experimental study, lab tests, and exclusions were all avoided.

Phase 1 was performed with ionic agents in patients studied by CT and urography, whereas Phase 2 was performed with iothexol and urography only because CT was not an FDA-approved indication for iothexol in 1986. The literature had not described a difference in ADRs for CT and urography, and we did not routinely collect this information in phase 1. Unexpectedly, Lasser et al. [11] found a difference in ADRs for CT and urography with ionic agents in hospitalized patients. Thus, it became necessary to do phase 3 in both CT and urography to resolve concerns that the difference in clinical indication accounted for some or all of the differences in ADRs between ionic agents and iothexol. Although the study is much improved, there remains a concern about the use of patients receiving ionic agents in 1985 to compare with iothexol in 1986 and 1988. We do not feel that the pattern of care has changed much in this time frame. The iothexol group did have fewer risk factors, but more prior ADRs and less premedication. It is unlikely that the large differences between ionic agents and iothexol are due to differences in the patients studied.

As the results show, there were significant differences in the incidence and severity of adverse effects from ionic agents vs iothexol in standard clinical care. The patients in the ionic-agent phase were receiving IV contrast agents for both urography and CT. Our results are qualitatively and quantitatively similar to the self-reported survey of Australian radiologists [7]. In phase 3 of our study, the incidence of ADRs in patients having CT and in those undergoing urography was not different. This result differs from that of Lasser et al. [11], possibly because no patients were excluded, outpatients and inpatients were used, premedication was infrequent, and the contrast agent was nonionic.

Many of the adverse effects experienced by patients are subjective and recorded by another party. In our study, technologists' reports show a highly significant difference between the standard ionic agent and iothexol. There is no reason to suspect bias in reporting, although the study was not blinded. The decision to treat an observed reaction is made by the radiologist. This is a subjective decision as well. Radiologists treated the same proportion of ADRs in the ionic and nonionic groups but many fewer ADRs occurred with iothexol and significantly fewer iothexol patients required treatment.

In addition to our concerns about relative safety in routine clinical practice, it was also considered likely that there would be large differences in cost of the new agents. New drug applications do not require cost-effectiveness assessments. We felt that good data on the incidence and severity of reactions between similar patients receiving ionic agents and nonionic agents could be used to approximate relative total medical costs. However, we also found there was no information on how the patients felt after leaving the radiographic

suite. If there were differences in return to usual daily activities, this could also impact estimated costs for the two agents. The results of surveys strongly depend upon the exact wording of the questions [21], and we have chosen to reproduce the questionnaire (Figure 1) for the reader rather than attempt to interpret the results at this time.

The patient responses were surprising. Those receiving ionic agents felt significantly worse and took longer to return to their usual activities than those receiving iothexol. If there were acceptable data available on the cost of a minor, moderate, or severe reaction and on the cost of not feeling well for a few hours or days, then our data could be used to estimate relative costs of using ionic agents or iothexol. As the more expensive agent produces fewer adverse effects, it is apparent that the cost-effectiveness of using the safer agent is different from the ratio of the cost of the two classes of diagnostic agents.

The availability of two classes of FDA-approved diagnostic agents with equivalent efficacy but different safety and cost poses a serious dilemma for decision makers [12-18]. The apparently large difference in safety may make further direct comparisons with randomized trials in routine care difficult. Thus, data from this and similar studies, uncontrolled clinical reports, and tightly controlled randomized trials with exclusions may be all the information available.

ACKNOWLEDGMENTS

The following participated in phases 1 and 2 of this study and we are grateful for their contribution: Frank Yarussi, Cannonsburg General Hospital, Cannonsburg, PA; Ronald Clearfield, Citizens General Hospital, New Kensington, PA; David Wilder, Connemaugh Valley Memorial Hospital, Johnstown, PA; Gary Becker, Indianapolis University Hospital, Indianapolis, IN; Julius Mazer, Magee-Womens Hospital, Pittsburgh, PA; Manfred Boehnke, Montefiore Hospital, Pittsburgh, PA; Chester Kay, North Hills Passavant Hospital, Pittsburgh, PA; Howard Pollock, Hospital of the University of Pennsylvania, Philadelphia, PA; Chester Jarmolowski, Shadyside Hospital, Pittsburgh, PA; Peter Joseph, West Penn Hospital, Pittsburgh, PA; and O. F. Gabrielle, West Virginia University Hospital, Morgantown, WV. Phase 3 included the Hospital of the University of Pennsylvania and Montefiore Hospital, as well as Mark Mishkin, Thomas Jefferson Hospital, Philadelphia, PA; Sue Roux, Long Beach Memorial Hospital, Long Beach, CA; and Richard Pfister, Massachusetts General Hospital, Boston, MA. We also thank Darin Wolf, Joe Gillen, and Janis Gottlieb for computer analysis.

REFERENCES

1. Schrott KM, Behrends B, Clauss W, Kaufmann J, Lehnert J. Iothexol in excretory urography: results of the drug monitoring program. *Fortschr Med* 1986;104:153-156
2. Danilstrom K, Shaw DD, Claus W, Andrew E, Sveenk. Summary of U.S. and European intravascular experience with iothexol based on the clinical trial program. *Invest Radiol* 1985;20:5117-5120
3. McClellan BL. Low-osmolality contrast media: premises and promises. *Radiology* 1987;182:1-8
4. Ansell G. Adverse reactions to contrast agents: scope of the problems. *Invest Radiol* 1970;5:374-384
5. Ansell G, Tweedie MCK, West CR, Evans P, Couch L. The current status of reactions to intravenous contrast media. *Invest Radiol* 1980;15:532-539

6. Shehadi WH. Contrast media adverse reactions: occurrence, reoccurrence, and distribution patterns. *Radiology* **1982**;143:11-17
7. Palmer FJ. The R.A.C.R. survey of intravenous contrast media reactions: a preliminary report. *Australas Radiol* **1988**;32:8-11
8. Hartman GW, Hattery RR, Witten DM, Williamson B Jr. Mortality during excretory urography: Mayo Clinic experience. *AJR* **1982**;139:919-922
9. Witten DM, Hirsch FD, Hartman GW. Acute reactions to urographic contrast medium. Incidence, clinical characteristics and relationship to history of hypersensitivity states. *AJR* **1973**;119:832-840
10. Powe NR, Kinnison ML, Steinberg EP. Quality assessment of randomized controlled trials of contrast media. *Radiology* **1989**;170:377-380
11. Lasser EC, Berry CC, Talner LB, et al. Pretreatment with corticosteroids to alleviate reactions to intravenous contrast material: a randomized multi-institutional study. *New Engl J Med* **1987**;317:845-849
12. Wolf GL. Safer, more expensive iodinated contrast agents: how do we decide? *Radiology* **1986**;159:557-558
13. White RI Jr, Halden WJ Jr. Liquid gold: low-osmolality contrast media. *Radiology* **1986**;159:559-560
14. Grainger RG. The clinical and financial implications of the low-osmolar radiological contrast media. *Clin Radiol* **1984**;35:251-252
15. Evans RG. Economic impact of the low-osmolality contrast agents on radiology procedure and departments. *Radiology* **1987**;162:267-268
16. Fischer HW, Spartaro RF, Rosenberg PM. Medical and economic considerations in using a new contrast medium. *Arch Intern Med* **1986**;146:1717-1721
17. Linton A. New drugs or lives: a moral minefield. *The Globe and Mail* (Montreal), Aug. 19, 1986, p A7.
18. Holtas S, Cronquist S, Renaa T. Contrast enhanced CT: comparison between iohexol and metrizoate. *Invest Radiol* **1985**;20:562-564
19. Lalli AF. Urographic contrast media reactions and anxiety. *Radiology* **1974**;112:267-271
20. Wolf GL. Poor quality of clinical research in radiology: another indictment. *Radiology* **1989**;170:311-312
21. Schuman H, Scott J. Problems in the use of survey questions to measure public opinion. *Science* **1987**;236:957-959

The reader's attention is directed to the commentary on this article, which appears on the following pages.

Nonionic vs Ionic Contrast Media: What Do the Data Tell Us?

Elliott C. Lasser¹ and Charles C. Berry²

Currently, most United States radiologists use low-osmolality contrast media only in certain high-risk situations or when comfort of the patient is a special factor, even though these newer media are perceived to be safer than the high-osmolality agents. Undoubtedly, this reflects the 10- to 15-fold higher price of the nonionic media. In the long run, however, it will be the patients without an identifiable risk factor who will constitute the majority of future reactors, and if cost were to be removed from the equation, maximal benefit of the new agents would result from universal use.

Given their increased cost, does the increased safety of nonionic media warrant universal use? The answer depends on the margin of safety to be expected from using these media, the margin of safety that can be provided by pretreatment of patients receiving ionic media, the added cost of nonionic media, and the health benefits that might be purchased by directing the funds used to purchase nonionic media elsewhere.

Many randomized clinical trials (RCTs) have compared low- and high-osmolality contrast media. Kinnison et al. [1] reviewed 45 such RCTs judged to be of higher quality and noted that the low-osmolality media have a lower incidence of heat sensation and pain and produce fewer cardiovascular changes, but have not shown a reduction in nephrotoxicity, neurotoxicity, life-threatening reactions, or death. Failure to show a difference in the case of life-threatening reactions or death may reflect the small sample sizes ($n < 500$) of these studies; no large-scale RCT has compared the incidence of life-threatening reactions and death when using low- and high-osmolality contrast media. Recently, two randomized controlled studies of moderate size have failed to show a difference in the incidence of nephrotoxicity in patients receiving ionic vs nonionic contrast media [2, 3].

Three earlier large-scale prospective (nonrandomized, nonblinded) studies have dealt with the safety of nonionic agents [4–6]. The largest is the study of Katayama and associates [4], who evaluated 169,284 patients receiving ionic contrast

media and 168,363 patients receiving nonionic media. For patients receiving the ionic media, they found an incidence of all types of reactions of 13%; severe reactions, 0.22%; and very severe reactions (intervention of an anesthesiologist or hospitalization was required), 0.04%. For the patients receiving the nonionic media, the incidence of all types of reactions was 3%; severe reactions, 0.04%, and very severe reactions, 0.004%. there was one death in each group.

It is worth noting that Katayama's data imply that one "severe" reaction (on average) can be prevented by using nonionic contrast media for 555 patients. For patients with a history of previous reaction, use of nonionic agents in 182 patients would prevent one severe reaction, while they would need to be used in 621 patients with no such history to prevent one severe reaction. Thus, if the incremental price were \$70 per patient, the use of nonionic contrast media in patients who do not have a previous history of reaction would require \$43,470 per severe reaction prevented.

In our clinical trial of 6763 patients receiving ionic contrast media [7], those randomized to receive two doses of corticosteroid before the contrast injection experienced a lower incidence of reaction. For all types of reactions, the incidence was 6% for those receiving two doses of corticosteroid vs 9% for those who did not. For the most serious category (grade III), the incidence was 0.20% for those receiving two doses of corticosteroid vs 0.52% otherwise. These are smaller reductions by using nonionic media than Katayama reported. However, our grade III reaction category was more broadly defined than the severe category of Katayama, and the incremental cost of corticosteroid pretreatment is almost negligible.

The precision needed to weigh safety vs cost in the wider use of nonionic contrast media requires large-scale studies. Because the only large-scale studies of nonionic vs ionic contrast media are nonrandomized and nonblinded, researchers must understand how biases may arise in such studies and appreciate the magnitude of these biases. For example,

This article is a commentary on the preceding article by Wolf et al.

¹ Department of Radiology, University of California, San Diego, School of Medicine, La Jolla, CA 92093. Address reprint requests to E. C. Lasser.

² Department of Community/Family Medicine, University of California, San Diego, School of Medicine, La Jolla, CA 92093.

the method of collecting reports of reactions to contrast media affects the reported incidence of reactions. In a 12-month period, Ansell et al. [8] collected a detailed form for every patient seen in each of 272 participating hospitals during two randomly selected weeks. During the remaining weeks, these forms were to be filled out only on patients considered to have had intermediate (i.e., those necessitating treatment) or severe reactions or those who died. The reported rate of intermediate reactions was 10 times greater during the two selected weeks, while the reported rate of severe reactions was six times greater during the two selected weeks. Such underreporting cannot be expected to provide data that can be used reliably in a comparative study.

In the preceding article, Wolf et al. report a prospective study of the safety of nonionic contrast media. The patients in one phase of the study received ionic contrast media, whereas patients during two other phases received nonionic media. The authors focus on the differing rates of reaction to the different contrast media, but it is also interesting to examine differences in the rates of reaction between groups of patients who received the same media. Especially intriguing is the difference in incidence of reaction between phase 2 and phase 3. During those phases, all patients received nonionic media, but there was a twofold difference in rates between phases ($p = .011$ by Pearson's chi-square). This may reflect a bias due to the comparison of patients in different institutions or variations in the reporting of reactions by personnel in the different institutions involved in each phase. In any case, it is interesting to consider how these results might have been interpreted if the contrast medium used in phase 2 had been labeled "Brand Y" and that used in phase 3 labeled "Brand X". No doubt, some would claim the superiority of Brand X.

During the first phase (ionic agents only), there were significant differences ($p < .001$ by Pearson's chi-square) in incidence among the patients, depending on the month in which the examination was performed. The incidence during July–August was about half that for May–June. During phase 2 the incidence during September–December was less than one-third that of May–June, and the differences among months were almost significant ($p = .053$ by Pearson's chi-square). Perhaps these differences reflect seasonal trends in adverse reactions like those reported by De Albertis et al. [9] and Belli and Crespi Porro [10]. It is again interesting to consider how the results might have been interpreted if patients in May–June of phase 1 had received contrast labeled Brand Y and those in July–August received Brand X.

These observations emphasize that comparisons of contrast agents outside of large randomized studies can produce spurious differences in the apparent safety of the agents. Blinding in randomized studies functions not only to prevent

bias in the reporting of data, but also to prevent bias in the assignment to treatment or control groups [11]. To minimize such bias in nonrandomized studies, where the potential for assignment bias is great, the patients studied should be a consecutive series. Exclusions from these series need to be based on objective criteria and the excluded cases must be accounted for in the analysis of data. Given the number and character of the institutions involved, Wolf's data appear to include half or fewer of the patients seen in the participating institutions during the study months, although he clearly intended to include all patients.*

These observations point out preventable sources of bias in nonrandomized studies. We agree with Wolf that it is difficult to do a large RCT of ionic agents vs a newer agent without exclusions in a setting that mimics routine clinical practice. Therefore, special consideration should be given to designing prospective nonrandomized studies of adverse reactions. Such studies should cover a long enough period of time and include a large enough group of institutions to minimize extraneous effects; preferably, patients receiving different media should be enrolled concurrently and patients receiving each type of media should be enrolled from each institution. Finally, the patients studied should constitute a consecutive series to avoid possible assignment bias.

It seems unlikely that a definitively large, randomized clinical trial of adverse reactions in nonionic vs ionic contrast media will ever be conducted. Nonionic contrast media apparently confer protection, but a precise, unbiased quantification of degree of protection is lacking. Better, more detailed prospective studies are needed. Perhaps the American College of Radiology's projected comparison of nonionic with ionic contrast media will satisfy that need [12].

REFERENCES

1. Kinnison ML, Powe NR, Steinberg EP. Results of randomized controlled trials of low- versus high-osmolality contrast media. *Radiology* **1989**;170:381–389
2. Schwab SJ, Hlatky MA, Pieper KS, et al. Contrast nephrotoxicity: a randomized controlled trial of a nonionic and an ionic radiographic contrast agent. *N Engl J Med* **1988**;320:149–153
3. Parfrey PS, Griffiths SM, Barrett BJ, et al. Contrast material–induced renal failure in patients with diabetes mellitus, renal insufficiency, or both. A prospective controlled study. *N Engl J Med* **1988**;320:143–149
4. Katayama H, Kozuka T, Takashima T, Matsuura K, Yamaguchi K. Adverse reactions to contrast media: high-osmolality versus low-osmolality media. A scientific exhibit presented at the annual meeting of the Radiological Society of North America, November **1988**
5. Schrott KM, Behrends B, Clauss W, Kaufman J, Lehnert J. Iohexol in der Ausscheidungsurographie: Ergebnisse des drug-monitoring. *Fortschr Med* **1986**;104:153–156
6. Palmer FJ. The R.A.C.R. survey of intravenous contrast media reactions. A preliminary report. *Australas Radiol* **1988**;32:8–11
7. Lasser EC, Berry CC, Talner LB, et al. Pretreatment with corticosteroids to alleviate reactions to intravenous contrast material. *N Engl J Med* **1987**;317:845–849
8. Ansell G, Tweedie MCK, West CR, Evans P, Couch L. The current status of reactions to intravenous contrast media. *Invest Radiol* **1980**;15[suppl]:S32–S39
9. De Albertis P, Piccoli N, Ricci G, Balestra V. Medico-statistical findings about minor reactions in kidney and gallbladder contrast radiography. *Radiol Med* **1968**;59:650–656
10. Belli I, Crespi Porro R. Is there a connection between variations of geot-mospheric environment in acute accidents due to water-soluble organic iodized contrast medium? *Radiol Med* **1968**;59:657–670
11. Chalmers TC, Celano P, Sacks HS, et al. Bias in treatment assignment in controlled clinical trials. *N Engl J Med* **1983**;309:1358–1361
12. Mishkin MM, Edeiken J. The current efficacious use of water soluble contrast agents for intravascular injections. *ACR Bull* **1988**;44:10

* After submission of this commentary, and at Dr. Wolf's suggestion, we canvassed a number of the participating hospitals by telephone. We were able to contact 12 of the 16 institutions included in the study. All reported that, to the best of their knowledge, consecutive patients were studied. However, based on their individual estimates of the number of patients having contrast CT scans and IVPs, and the reported duration of the study, we calculated that less than 50% of the expected numbers of patients in phases 1 and 3 actually appeared in the study. The reasons for this disparity are unclear. Some institutions may not have participated for the full duration of each reported phase or CT patients seen after normal working hours may not have been included. This points up the fact that, despite the best intentions of all concerned, there must be a built-in mechanism to validate fully that a series is consecutive.

Case Report

Acute Thrombocytopenia After IV Administration of a Radiographic Contrast Medium

Jae C. Chang,¹ Daniel Lee, and Howard M. Gross

Although adverse effects of radiographic contrast medium, ranging from minor rashes to anaphylactic reactions, are not rare during various radiologic procedures, thrombocytopenia has been extremely rare, and only a few cases of acute severe thrombocytopenia have been described [1-8]. In five reported patients, thrombocytopenia developed after oral administration of radiographic contrast material [1-4, 6], and in four patients it followed IV injection [5, 7, 8]. In this report, another case of acute severe thrombocytopenia due to an IV contrast medium is described.

Case Report

A 66-year-old woman was admitted to the hospital for evaluation and treatment of recurrent angina. The medication at the time of the admission was diltiazem hydrochloride, chlorzoxazone with acetaminophen, and lorazepam. The patient denied any history of allergy and had no history of exposure to a contrast medium. The hemogram revealed a hemoglobin of 13.3 g/dl, hematocrit 38.3%, white cell count 9000/ μ l, and platelet count 230,000/ μ l. After initial cardiac evaluation, the patient underwent a right and left cardiac catheterization, left ventriculography, and selective coronary angiography. Moderate stenosis of the anterior descending branch of the left coronary artery was shown. During the procedure, 90 ml of Renografin-76 (diatrizoate: sodium 10% and meglumine 66%; Squibb Diagnostics, Inc., New Brunswick, NJ), with 1000 units of heparin flush, were used. Four hours after cardiac catheterization, the platelet count decreased markedly to 10,000/ μ l (Fig. 1). Both prothrombin

time and activated partial thromboplastin time were normal. Fibrinogen level was 280 mg/dl, Factor VIII level was 100%, and fibrin split product was absent. On the basis of these findings, disseminated intravascular coagulation was excluded. No cause of thrombocytopenia was evident; the patient was not taking any drug known to cause acute thrombocytopenia, and heparin-induced thrombocytopenia was ruled out on clinical grounds and the lack of the heparin-dependent, platelet-aggregating factor [9]. Six units of platelet concentrates were transfused, and the patient had no unusual bleeding. The platelet count gradually returned to normal in several days (Fig. 1). Because of the thrombocytopenic episode, no immediate coronary artery surgery was advised, and the patient was discharged on medical treatment of the angina.

Three weeks later the patient was readmitted for percutaneous coronary angioplasty because of unstable angina despite treatment with nitroglycerin, dipyridamole, and verapamil hydrochloride. The platelet count was 320,000/ μ l on admission. During the angioplasty, the patient again received 90 ml of Renografin-76. The patient tolerated the procedure well, and angioplasty was successfully completed. Heparin was not used. However, 3 hr later, marked thrombocytopenia of 9000/ μ l developed. The diagnosis of acute thrombocytopenia induced by Renografin-76 was well established. The patient was not given a platelet transfusion, but the platelet count was closely monitored. Over the next several days, the platelet count increased spontaneously to more than 300,000/ μ l (Fig. 1). Bone-marrow aspiration showed normal erythroid and granulocytic precursors with abundant megakaryocytes during the thrombocytopenic stage, which was consistent with thrombocytopenia due to increased peripheral destruction.

Received December 5, 1988; accepted after revision January 23, 1989.

This work was supported in part by the Oncology Fund of the Samaritan Foundation.

¹ All authors: Department of Medicine, Wright State University School of Medicine, and Hematology and Oncology Section, Good Samaritan Hospital and Health Center, Dayton, OH 45406. Address reprint requests to J. C. Chang at Good Samaritan Hospital.

AJR 152:947-949, May 1989 0361-803X/89/1525-0947 © American Roentgen Ray Society

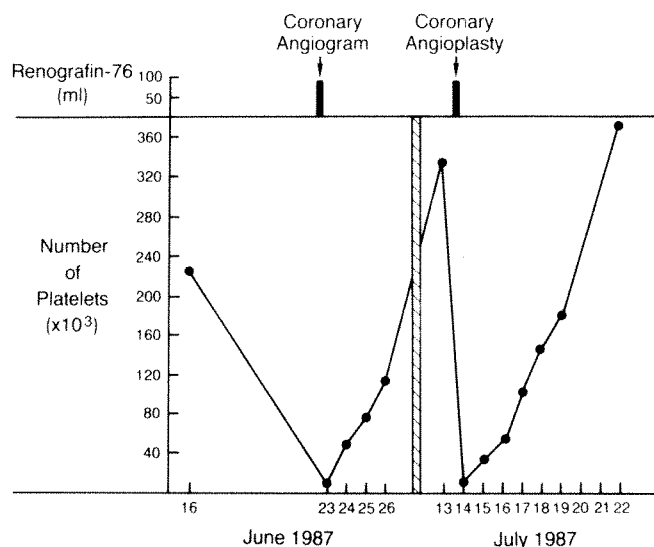


Fig. 1.—Graph showing changes in platelet count after IV administration of Renografin-76 during coronary angiogram and coronary angioplasty. Note sudden onset of severe thrombocytopenia and gradual return to normal platelet counts in about 4 days.

Laboratory Investigation

Immunologic Study

When the patient recovered from acute thrombocytopenia after the percutaneous coronary angioplasty, her serum and platelets were collected for immunologic studies. Platelet-associated immunoglobulin was not detected, and the platelet antigen was positive for PL^{A1}. The complement-dependent cytotoxicity test using the patient's platelets and Renografin-76 was negative. These results suggest thrombocytopenia was not immunologically mediated and tend to exclude drug-induced immune thrombocytopenia and thrombocytopenia due to alloantibody anti-PL^{A1}. Also, these findings suggest Renografin-76 caused thrombocytopenia through a mechanism other than immune pathogenesis.

Platelet Aggregation Test

To rule out the possibility of in-vivo consumption of platelets by aggregation, the Renografin-induced platelet aggregation test was performed by using the patient's plasma and Renografin-76 in a similar manner to show the heparin-dependent, platelet-aggregating factor [9]. No Renografin-76-dependent platelet-aggregating factor was shown. This finding suggests Renografin-induced thrombocytopenia was not caused by in-vivo aggregation of platelets.

In-Vitro Effect of Renografin-76 on Platelets

To examine the possibility of a direct chemical effect of Renografin-76 on the patient's platelets, the patient's platelet-

rich plasma was incubated in various concentrations of Renografin-76, and the platelet count was done at 30-min intervals from 0 to 2 hr. No significant changes in platelet count were observed between samples with and without the radiographic contrast medium. This result tends to exclude a direct chemical destruction of the patient's platelets by Renografin-76.

Comments

It is now well established that various radiographic contrast media can cause acute severe thrombocytopenia. A review of the literature reveals that thrombocytopenia has occurred after administration of four agents: iopanoic acid, ipodate, and iocetamic acid administered orally for cholecystogram [1–4, 6], and diatrizoate administered IV for cardiac catheterization or percutaneous nephrostography (Table 1) [5, 7, 8]. Our patient is added to the cases with diatrizoate. In all five reported cases with diatrizoate, thrombocytopenia followed IV administration of the contrast material, and all cases involved the use of mixed meglumine and sodium salts. Four of the five cases involved cardiac angiography. Radiologic contrast media also are known to cause in-vivo and in-vitro abnormalities of platelet function [10]. Because of possible induction of functional abnormalities of platelets by contrast media, acute severe thrombocytopenia may cause serious bleeding in certain patients.

The mechanism for acute thrombocytopenia due to contrast media is essentially unknown. In our patient, the laboratory investigation suggests that Renografin-76-induced thrombocytopenia is not caused by the immune mechanism,

TABLE 1: Reported Cases of Acute Thrombocytopenia Due to Contrast Medium

Case	Contrast Medium ^a	Radiologic Procedure	Lowest Platelet Count (per μ l)	Reference Citation
1	Iopanoic acid (PO)	Cholecystogram	N.D. ^b	1
2	Ipodate (PO)	Cholecystogram	N.D.	2
3	Iopanoic acid (PO)	Cholecystogram	1,000	3
4	Iopanoic acid (PO)	Cholecystogram	21,000	4
5	Diatrizoate (IV)	Cardiac catheterization	4,000	5
6	Iocetamic acid (PO)	Cholecystogram	N.D.	6
7	Diatrizoate (IV)	Cardiac catheterization	20,000	7
8	Diatrizoate (IV)	Percutaneous nephrostogram	6,000	7
9	Diatrizoate (IV)	Cardiac catheterization	2,000	8
10	Diatrizoate (IV)	Cardiac catheterization	9,000	Present case

^a PO = oral administration, IV = intravenous administration.

^b N.D. = platelet not detected on peripheral blood smear.

in-vivo aggregation resulting in platelet consumption, or direct chemical destruction. Also, clinically, the lack of history of previous exposure to contrast medium tends to argue against antibody-mediated immune destruction. On the other hand, proliferation of megakaryocytes in the marrow, sudden-onset thrombocytopenia and rapid rise in platelet count after Renografin administration are consistent with thrombocytopenia due to rapid destruction of platelets. A more complicated immune mediation, however, cannot be excluded.

As seen in Table 1, thrombocytopenia has occurred after both oral and IV administration of contrast media. Fortunately, all the reported cases have recovered without serious complications, which was possible because of timely recognition of the problem and the shortness of the thrombocytopenic episodes. Often, contrast media are considered not to be drugs, and clinicians generally overlook these agents in the list of drugs when evaluating acute thrombocytopenia. In such instances, thrombocytopenia may be diagnosed as idiopathic, and another radiographic examination with the contrast medium may cause bleeding.

REFERENCES

1. Bishopric GA. Athrombocytosis following oral cholecystography. *JAMA* **1964**;189:771-772
2. Stacher, VA. Schwerste thrombopenie durch ein perorales trijodiertes Gallenkontrastmittel. *Wien Klin Wochenschr* **1966**;7:286-288
3. Hysell JK, Hysell JW, Gray JM. Thrombocytopenic purpura following iopanoic acid ingestion. *JAMA* **1977**;237:361-362
4. Curradi F, Abbritti G, Agnelli G. Acute thrombocytopenia following oral cholecystography with iopanoic acid. *Clin Toxicol* **1981**;18:221-224
5. Wein P, Handler M, Chadda KD. Severe thrombocytopenia as a result of contrast left ventricular angiography. *Cathet Cardiovasc Diagn* **1982**;8:495-499
6. Insausti CLG, Lechin F, Van der Dijs B. Severe thrombocytopenia following oral cholecystography with iocetamic acid. *Am J Hematol* **1983**;14:285-288
7. Shojania AM. Immune-mediated thrombocytopenia due to an iodinated contrast medium (diatrizoate). *Can Med Assoc J* **1985**;133:123
8. Lacy J, Bober-Sorcinelli KE, Farber LR, Glickman MG. Acute thrombocytopenia induced by parenteral radiographic contrast medium. *AJR* **1986**;146:1298-1299
9. Chang JC. White clot syndrome associated with heparin-induced thrombocytopenia: a review of 23 cases. *Heart Lung* **1987**;16:403-407
10. Stein HI, Hilgartner MW. Alteration of coagulation mechanism of blood by contrast media. *AJR* **1968**;104:458-463

Book Review

Proceedings of the Chest Imaging Conference 1987. Edited by W. W. Peppler and A. A. Alter. Madison, WI: Department of Medical Physics, University of Wisconsin, and Medical Physics Publishing, 423 pp., 1988. \$25

This book on the chest imaging conference held at the University of Wisconsin August 31–September 2, 1987, is a formidable undertaking. The conference was an update of a previous symposium devoted to optimization of chest radiography, which also was held at the University of Wisconsin in the spring of 1979. Since that first meeting, considerable changes have occurred in chest radiology. New electronic imaging techniques have appeared that deserve careful scrutiny. These technologies include digital imaging, optical processing, dual-energy systems, new and varied methods of scattered rejection, and improved methods of evaluating pattern recognition.

The conference sponsors were an outstanding group of organizations, which included the Society of Thoracic Radiology, the Fleishner Society, and the American Society of Physicists in Medicine. Cochairmen were Charles Mistretta and Lawrence Goodman. The contributors and planning committee represent the who's who of chest imaging. The text makes a herculean attempt to cover what is new in electronic chest diagnostic techniques.

The proceedings are divided into six sections, which include conventional film radiography, image processing and perception, electronic detection and recording, storage transmission, and quality control and assurance testing. One additional section is devoted to financial implications of the new techniques. Little information is given about the impact of CT and MR on diagnosis of chest disorders except for the usual old bromide of extolling potential and promise based on anticipated improvements in software and hardware. The book has a soft cover, and the paper is of low grade. However, the illustrations of the radiographs and charts are quite acceptable.

One would hope that definitive answers would emanate from such a meeting of minds. However, as in all searches for truth, confusion exists as to the benefit of the new technologies. The demands of chest imaging are compounded by the extreme dynamic range of chest densities, the wide spectrum of diseases and their nonspecific presentation, and the dynamic effects of flowing blood through the thoracic cavity. These questions are addressed in succinct outline, summary form. The reader will be struck by the variations of opinion

and the diversity of solutions. The undercurrent theme throughout the book is that chest radiography is a complex perception task. Altering resolution and contrast in different anatomic compartments affects the detection of lung disease differently (i.e., nodules, low-density and low-contrast infiltrates, and mediastinal diseases). For example, there are varied opinions on the following: What minimal pixel size is necessary in electronic imaging to achieve adequate diagnostic accuracy? What is the best scatter rejection method? Will electronic imaging ever make financial sense and challenge the place of chest radiography?

The need for this dissertation is evident; chest radiology remains the most frequent of all radiologic diagnostic tests. Chest radiography has withstood the test of time and has endured. The proceedings challenge us to develop methods of chest diagnosis that will find new diseases, measure extent, classify and determine the effect of treatment, and document progress—all on a single image. Evidence to the contrary is given that the new technologies will ever resolve this challenge. Despite postprocessing, the newer methods do not yet justify their greater financial expense and expenditure of time, nor have they proved more accurate.

The book addresses these concerns and gives further insight into the state-of-art in conventional chest radiography, the array of new electronic systems, methods of quality evaluations, and future expectations. The reader will find the proceedings difficult to digest because they represent synopses of conference talks. Each article is quite compact and contains considerable data and facts.

The text makes a valiant attempt to assess where chest radiology is today (omitting CT and MR). It is for the thoughtful student and serious practitioner. The time and energy invested will be rewarded, particularly if the reader is interested in purchasing any of the new devices.

Edward Buonocore
University of Tennessee Medical Center
Knoxville, TN 37920

Pictorial Essay

Surgical Defects of the Pericardium: Radiographic Findings

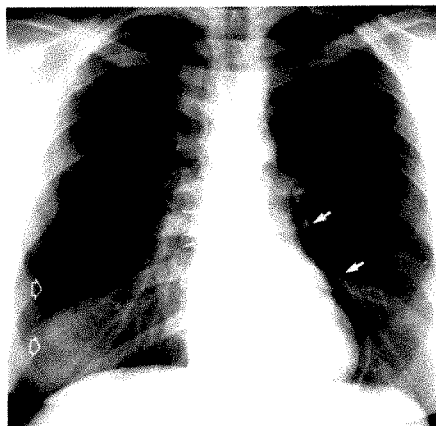
Julie E. Takasugi¹ and J. David Godwin²

Although more common than congenital defects, acquired pericardial defects are less familiar to radiologists. Such acquired defects usually result from surgery and much less frequently from penetrating or blunt trauma (deceleration injury) or from erosion caused by peptic ulcer disease [1]. A variety of surgical procedures can cause the defect. Sometimes a part or all of the pericardium is removed in order to treat pericardial disease. More often the pericardium is opened incidentally during an operation on the heart, mediastinum, or lung, and a defect may persist if the surgeon decides not to close the pericardium. Least commonly a piece of pericardium is removed in order to reconstruct the diaphragm

or to create an intracardiac baffle. It is not known how often such a defect occurs after surgery or how often it is clinically significant or radiographically visible, but it is clear that any of the procedures mentioned above can result in a pericardial defect with striking radiographic manifestations.

A defect of the pericardium is manifested radiographically by the abnormal passage of gas or fluid between the pleural and pericardial cavities or by an abnormal mediastinal contour caused by herniation of part or all of the heart. In this essay we illustrate the radiographic appearances of acquired pericardial defects (Figs. 1–6) and compare the findings with those of congenital defects (Figs. 7 and 8).

Fig. 1.—Asymptomatic right-sided surgical pericardial defect noted 3 months after open repair of atrial septal defect. Chest radiograph shows pneumothorax (*open arrows*) and air in pericardium (*solid arrows*). Both findings occurred after right intercostal nerve block for treatment of postthoracotomy pain.



1

Fig. 2.—Right-sided surgical pericardial defect after extrapleural pneumonectomy (and partial pericardiectomy) for treatment of mesothelioma. Chest radiograph shows air and fluid in pericardium (*solid arrow*) accompanying right hydropneumothorax (*open arrows*). These findings developed after spontaneous drainage of fluid through cutaneous fistula 2 weeks after surgery. Communication between pericardial and pleural sacs is expected after such extensive pericardial resection.



2

Received November 7, 1988; accepted after revision December 23, 1988.

¹ Department of Radiology, 114, Veterans Administration Medical Center, 1660 S. Columbian Way, Seattle, WA 98108. Address reprint requests to J. E. Takasugi.

² Department of Radiology, SB-05, University of Washington, Seattle, WA 98195.

AJR 152:951-954, May 1989 0361-803X/89/1525-0951 © American Roentgen Ray Society

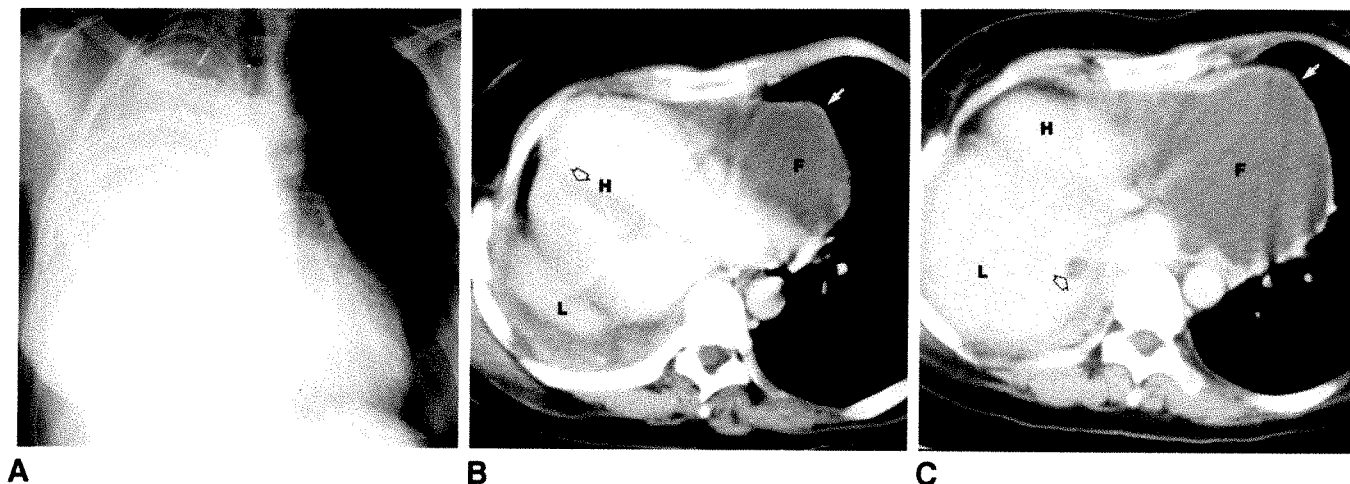


Fig. 3.—Right-sided surgical pericardial defect after extrapleural pneumonectomy (and partial pericardiectomy) for treatment of mesothelioma.

A, 7 months after surgery. Right hemithorax is opacified and heart appears to be in normal location.

B, CT scan shows that heart (H) is actually rotated into right hemithorax through pericardial defect. Pericardium is visible in left chest, but can be followed to right only as far as sternum. Fluid in pericardial sac (F) creates false impression of left heart border (solid arrow). Interventricular septum of heart (open arrow).

C, CT scan 2 cm lower shows distended pericardial sac forming apparent cardiac apex (solid arrow). Patchy pericardial thickening most likely represents metastatic tumor. Low-attenuation lesion in liver (L) is thought to be cyst (open arrow).

Discussion

A surgical defect may be large or small. When a pericardial window is created to drain a malignant pericardial effusion to the pleural space, a small opening usually suffices. On the other hand, when the pericardium is resected to treat constrictive pericarditis, decortication of the right and left ventricles and the diaphragmatic surface of the heart may be required. It may even be necessary to remove the pericardium from the atria, venae cavae, or pulmonary veins.

Parts of the pericardium may be resected during removal of the whole lung or pleura for treatment of locally invasive lung cancer or mesothelioma (Figs. 2–4). A synthetic graft (such as Dexon mesh) may be used to patch the pericardium. The graft may be recognizable on radiographs if its rough texture creates a serrated pattern at the mediastinal margin (Fig. 4). A pericardial defect can also result from intrapericardial pneumonectomy for treatment of lung cancer. This intrapericardial approach sometimes provides technically easier control of the pulmonary arteries and veins. Closure of the pericardium after this type of pneumonectomy is optional, but may help to prevent cardiac herniation.

The most common operation that involves the pericardium is coronary artery bypass grafting, but it rarely creates a radiographically visible pericardial defect, even though the surgeon does not always close the pericardium. A defect is unusual because only a linear incision is made in the pericardium; no tissue is removed, and rapid healing can occur. Also, the pericardial incision is made immediately under the sternum. When the sternotomy is closed, the overlying sternum and ribs prevent anterior herniation of the heart. Further, the right ventricle, the part of the heart that underlies the pericardial incision, does not pulsate as vigorously as other parts of the heart.

The tendency of the heart to herniate through a pericardial defect does not correlate with the size of the defect [2], since herniation can occur through a small defect as well as a large one. The likelihood of herniation reflects several factors. One is the adjacent pleural pressure. After lobectomy or pneumonectomy, pleural pressure is reduced, and the decreased pressure may draw the heart out through a pericardial defect. Pleural drainage by tube thoracostomy with negative pressure may similarly promote cardiac herniation. As was mentioned



Fig. 4.—Left-sided surgical pericardial defect resulting from lung cancer surgery. Because tumor extended to pericardium, local pericardial resection was required in addition to pneumonectomy. Pericardial defect is covered with Dexon patch. Chest radiograph shows serrated texture of patch (arrows) silhouetted against postpneumonectomy space.

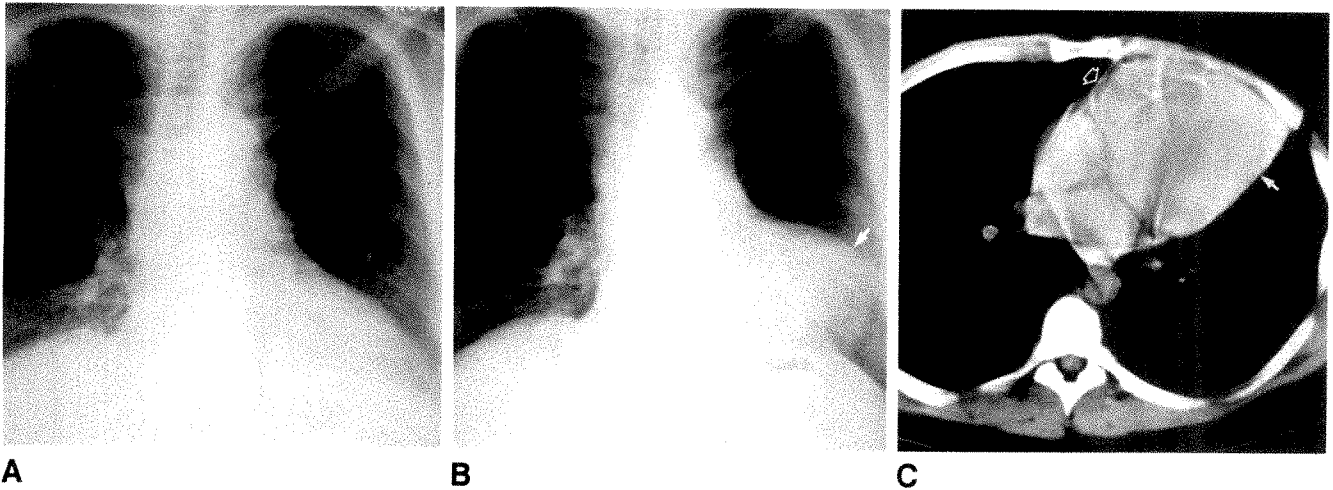


Fig. 5.—Left-sided surgical pericardial defect after pericardial biopsy.

A, Before surgery. Heart contour is normal.

B, After surgery. Left ventricle (arrow) bulges through pericardial defect.

C, CT scan near apex shows left ventricle (solid arrow) herniating through defect. Note normal right pericardium (open arrow). No pericardium is visible at site of defect.

Fig. 6.—Left-sided surgical pericardial defect after creation of pericardial window for treatment of uremic pericarditis.

A, Chest radiograph shows herniation of left ventricle through defect. Cardiac apex is elevated, and lung is insinuated between it and hemidiaphragm.

B, CT scan at level of left coronary artery (arrows) shows abnormally high position of right (1) and left (2) ventricles.

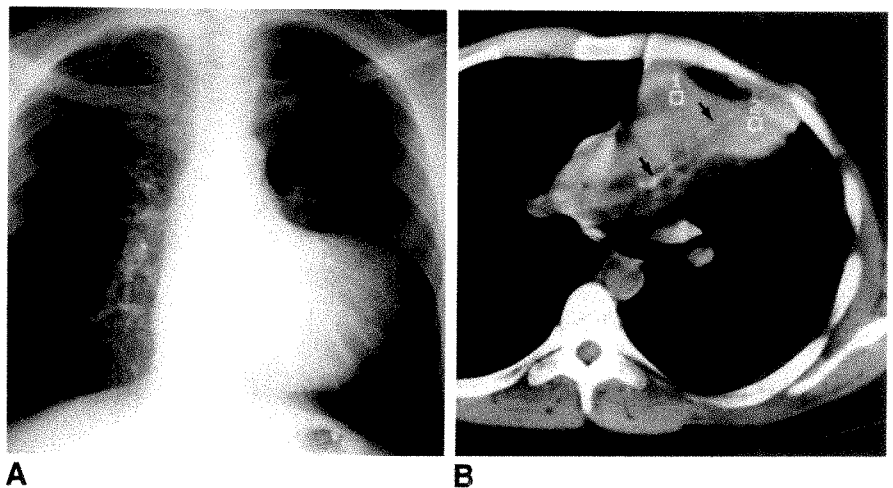
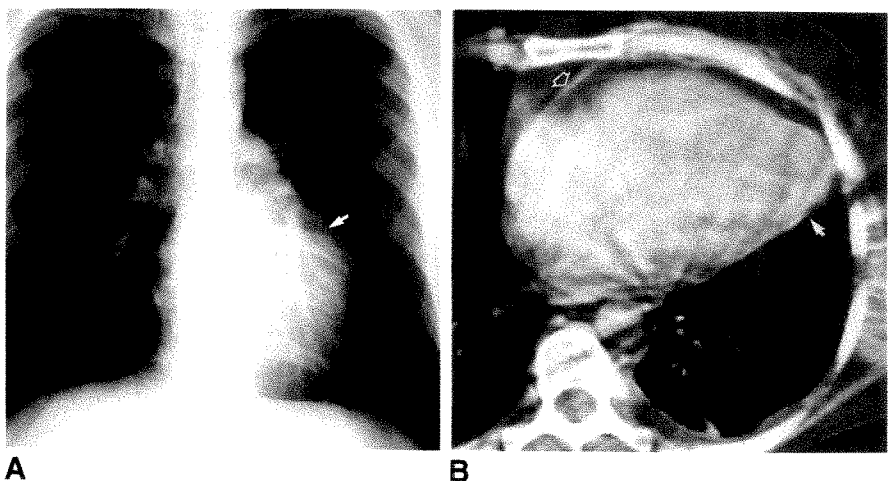


Fig. 7.—Left-sided congenital pericardial defect.

A, Chest radiograph shows herniation of left atrial appendage (arrow) and adjacent parts of left ventricle.

B, CT scan at level of left ventricle shows normal right pericardium (open arrow), but absence of left pericardium and slight bulging of left ventricle (solid arrow).



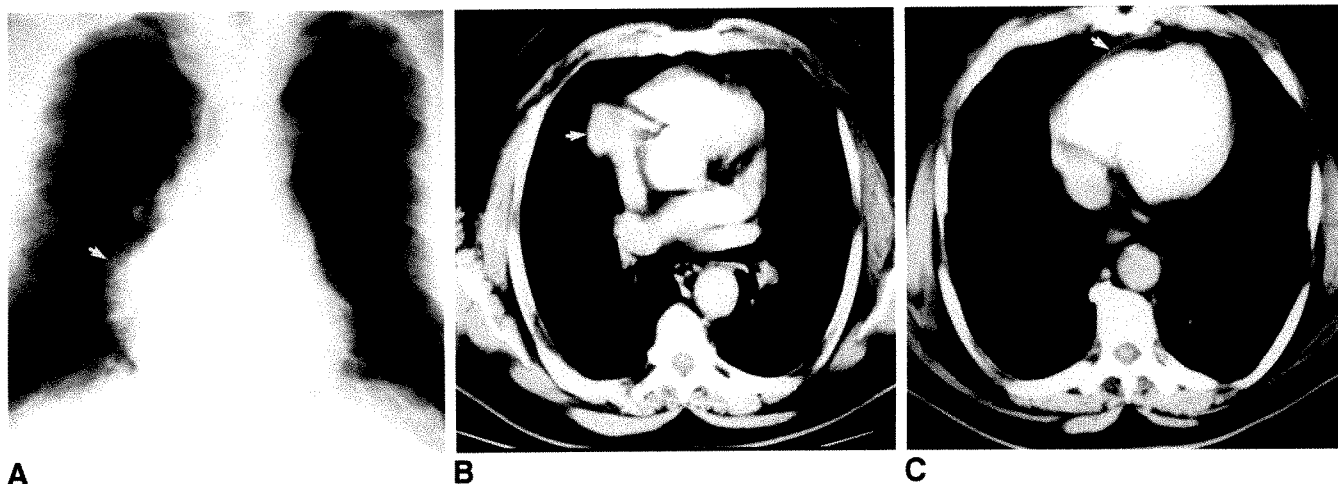


Fig. 8.—Right-sided congenital pericardial defect.

A, Chest radiograph shows herniation of right atrium (arrow).

B, CT scan shows herniation of right atrial appendage (arrow). No pericardium is visible over herniated chamber.

C, CT scan at level of inferior vena cava shows presence of right pericardium (arrow) anterior to defect.

above, the part of the heart underlying the defect probably also plays a role; for instance the vigorous motion of the left ventricle may predispose it to herniation.

The presentation of cardiac herniation varies from asymptomatic to catastrophic. In severe cases there may be strangulation of the ventricles with myocardial ischemia or there may be torsion of the great vessels with hypotension from decreased venous return to the heart [3]. Acute cardiac herniation usually occurs in the immediate postoperative period, almost always within 24 hr of surgery. It may be triggered by a change in the patient's position, endotracheal suction, or coughing. Acute cardiac herniation into the right chest may cause the superior vena cava syndrome, but a more gradual shift need not cause caval obstruction (Fig. 3).

The radiographic manifestations of pericardial defects vary. A pericardial defect can be inferred when pneumopericardium (or hydropneumopericardium) develops in the presence of pneumothorax (or hydropneumothorax) (Figs. 1 and 2). Indeed, in the past, a definite radiographic diagnosis of pericardial defect depended on demonstrating gas in the pericardium after injection of air into the pleural space. With CT or MR imaging, the pericardium and the defect can be identified directly (Figs. 7 and 8) [4]. Similarly, a surgical defect appears as a discontinuity in the parietal pericardium at the site of resection (Figs. 5 and 6).

Congenital absence of the pericardium usually represents partial absence of the parietal pericardium; it occurs more often on the left side than the right. In congenital partial absence of the left pericardium, plain radiographic findings consist of a focal bulge along the mid-left heart border, near the left hilum (Fig. 7). On CT scans, the herniated pulmonary trunk or left atrium can be seen to be the cause of the apparent mediastinal mass. CT also may reveal the gap in the overlying parietal pericardium (Fig. 7). In congenital right pericardial defect, it is the right atrium or ventricle that herniates and produces a focal bulge or rounded right heart border. Again, CT may show the herniated structure and the absence of the adjacent pericardium (Fig. 8).

Most acquired pericardial defects have appearances distinctly different from congenital defects. However, congenital absence of the whole left pericardium can resemble surgical removal of a large portion of the left pericardium (Fig. 6). In both cases, the heart rotates into the left pleural cavity. The left lung may insinuate itself between the aorta and main pulmonary artery, or between the heart and left hemidiaphragm. The absence of the sternopericardial ligaments allows the heart to fall away from the sternum when the patient is supine. On CT scans, the absence of the left pericardium may be apparent.

When acute cardiac herniation occurs in the immediate postoperative period, the diagnosis usually can be made from a chest radiograph, and surgery should not be delayed in order to perform additional radiographic procedures. If the herniation is not acute, then CT may be appropriate to confirm the diagnosis (Fig. 3).

In conclusion, acquired pericardial defects have become more common because of the increasing number of surgical procedures that affect the pericardium. The radiographic patterns of acquired defects are varied and sometimes confusing. An abnormal mediastinal contour or an unusual gas or fluid collection near the heart in a patient who has had thoracic surgery should bring to mind the possibility of a pericardial defect. CT may then be considered for further evaluation.

REFERENCES

1. Ellis K, Malm JR, Bowman FO, King DL. Roentgenographic findings after pericardial surgery. *Radiol Clin North Am* 1971;9(2):327-341
2. Gates GF, Sette RS, Cope JA. Acute cardiac herniation with incarceration following pneumonectomy. *Radiology* 1970;94:561-562
3. Castillo M, Oldham S. Cardiac volvulus: plain film recognition of an often fatal condition. *AJR* 1985;145:271-272
4. Moncada R, Baker M, Salinas M, et al. Diagnostic role of computed tomography in pericardial heart disease: congenital defects, thickening, neoplasms and effusions. *Am Heart J* 1982;103(2):263-282

Leptospirosis of the Lung: Radiographic Findings in 58 Patients

Jung-Gi Im¹
Kyung Mo Yeon¹
Man Chung Han¹
Chu-Wan Kim¹
W. Richard Webb²
Jung Sang Lee³
Yong Chol Han³
Woo Hyun Chang⁴
Je Geun Chi⁵

Leptospirosis is the disease produced by any of the group of spirochetes of the genus *Leptospira*. The main organs involved are the liver, central nervous system, kidneys, skeletal muscle, and lungs. Thirty-seven (64%) of 58 patients with leptospirosis, proved by positive serology, had pulmonary radiographic findings. Three radiographic patterns were evident: (1) 21 (57%) of the 37 patients had small nodular densities, (2) six (16%) had large confluent areas of consolidation, and (3) 10 (27%) had diffuse, ill-defined, ground-glass density. Serial radiographs showed a tendency for the nodular pattern to be followed by confluent consolidation and/or ground-glass density. Abnormalities were bilateral, nonlobar in all cases, and had a marked tendency toward peripheral predominance. Pulmonary abnormalities resolved within 15 days, except in eight patients who died because of respiratory failure (six patients) or other causes (two patients). In order to correlate pathology with the radiographic findings, *Leptospira*, isolated from a patient, was injected intraperitoneally into 20 guinea pigs. All lungs from the guinea pigs showed petechial hemorrhage, which progressed to large confluent areas of hemorrhage.

The typical pulmonary radiographic findings of leptospirosis are compatible with the multifocal pulmonary hemorrhage seen in the guinea pigs.

Leptospirosis is an acute, febrile, systemic disease caused by spirochetes of the genus *Leptospira*. The typical clinical features of the leptospiremic phase include fever, headache, conjunctivitis, myalgia, and jaundice, which last 4–9 days [1–4]. In patients who have died with hepatic involvement (Weil syndrome), renal involvement, or both, the significant gross changes include hemorrhage and bile staining of tissues. The hemorrhage is widespread but is most prominent in skeletal muscle, kidneys, adrenal glands, liver, stomach, spleen, and lungs [4]. In about 30% of leptospirosis patients, however, jaundice is absent, and patients may present predominantly with pulmonary, influenzal, or meningitic symptoms [5].

Pulmonary involvement in this disease consists primarily of hemorrhagic pneumonitis and is usually considered incidental [6]. However, reports from some Far East countries indicate that many patients with leptospirosis present with hemorrhagic pneumonitis or frank pulmonary hemorrhage manifesting bizarre clinical and radiographic features [5, 7–11].

We reviewed the chest radiographic findings in 58 patients with serologically proved leptospirosis, 26 of whom had the pulmonary form of this disease, and correlated those findings with the pathologic abnormalities occurring in guinea pigs with experimentally induced leptospirosis.

Materials and Methods

Study of Patients

We retrospectively reviewed medical records and chest radiographs of 58 patients (including high-resolution CT scans of two patients) in whom leptospirosis was diagnosed and treated between September 1984 and October 1987, primarily at the Seoul National University

Received November 2, 1988; accepted after revision January 3, 1989.

This work was supported in part by a grant from Seoul National University Hospital Fund.

¹ Department of Radiology, College of Medicine, Seoul National University, 28 Yeongun-Dong, Chongro-Ku, Seoul 110-744, Korea. Address reprint requests to J.-G. Im.

² Department of Radiology, University of California, San Francisco, School of Medicine, San Francisco, CA 94143-0628.

³ Department of Internal Medicine, College of Medicine, Seoul National University, Seoul 110-744, Korea.

⁴ Department of Microbiology, College of Medicine, Seoul National University, Seoul 110-744, Korea.

⁵ Department of Pathology, College of Medicine, Seoul National University, Seoul 110-744, Korea.

AJR 152:955–959, May 1989

0361-803X/89/1525-0955

© American Roentgen Ray Society

Hospital (39 cases). Initial radiographs were made within 4 days of the onset of clinical symptoms in most cases. Follow-up intervals were usually 1–3 days during the first week and 3–5 days thereafter. Forty-three patients were men and 15 were women. Their ages ranged from 16 to 85 years, with a mean of 44 years. In 49 (85%) of the 58 patients, the disease occurred in October or November, which is the harvest season in Korea. All patients had a history of working in damp rice fields, typically after a heavy rain.

Of the 51 patients who had complete medical records, 45 (88%) presented with the acute onset of a febrile disease, followed by symptoms of multiple organ involvement. Thirty-four (67%) of the 51 patients had respiratory symptoms such as cough (63%), dyspnea (55%), and hemoptysis (50%). In 26 (51%) of the 51 patients, pulmonary symptoms were the major clinical problem. Nineteen patients (37%) had clinical jaundice. Of the eight patients who died, major causes of death were massive hemoptysis with asphyxia in three patients, respiratory failure with or without renal failure in three patients, and hepatorenal failure in two patients. One autopsy was done, and the lung specimens were compared with the radiographs.

The diagnosis was based on a single high-agglutination titer for leptospirosis (1:100) and/or a fourfold rise in titer in successive studies [3]. In eight cases, leptospiral spirochetes were identified in the blood.

From the chest radiographs of these patients, the frequency, pattern, distribution, and sequential changes of the radiographic abnormalities were analyzed. For the analysis of distribution, the lungs were divided in half by a line drawn along the midpoint between the lateral thoracic wall and the hilum.

Experimental Study

Microorganisms of *Leptospira interrogans*, serovar lai, were isolated from one patient's serum and cultured by using Ellinghausen McCullough Johnson Harris (EMJH) [12] media for 5 days at 86°F. One-milliliter cultures containing approximately 2×10^7 leptospirae were injected into the peritoneal cavity of each of 20 guinea pigs, whose body weights ranged from 160 to 200 g [13, 14]. Two or three guinea pigs were sacrificed at 24, 48, 72, 96, 120, 144, 288, and 356 hr of infection. The lungs were isolated and examined grossly and microscopically.

Results

Study of Patients

Of the total 58 patients, 37 patients (64%) had a radiograph showing pulmonary abnormality. In 21 (57%) of these 37 patients, the radiographic abnormalities appeared between the third and seventh day after the onset of clinical symptoms.

The radiographic patterns of lung disease changed during the course of the disease. However, on the basis of initial radiographs, three radiographic patterns were evident. Of the 37 patients who had abnormal chest radiographs, 21 (57%) had multiple, predominantly nodular densities, ranging from 1 to 7 mm in diameter, with or without larger, focal areas of consolidation. Small nodules often had sharp margins (Fig. 1). High-resolution CT in a patient with the nodular pattern on a chest radiograph showed findings typical of an air-space nodule (Fig. 2). Six (16%) of the 37 patients had large confluent areas of air-space consolidation (Fig. 3). Chest radiographs of 10 (27%) of the 37 patients showed a diffuse, ill-defined, ground-glass appearance in the lungs (Fig. 4). One patient's chest radiograph, obtained just before the patient died, showed mixed nodular lesions and confluent air-space

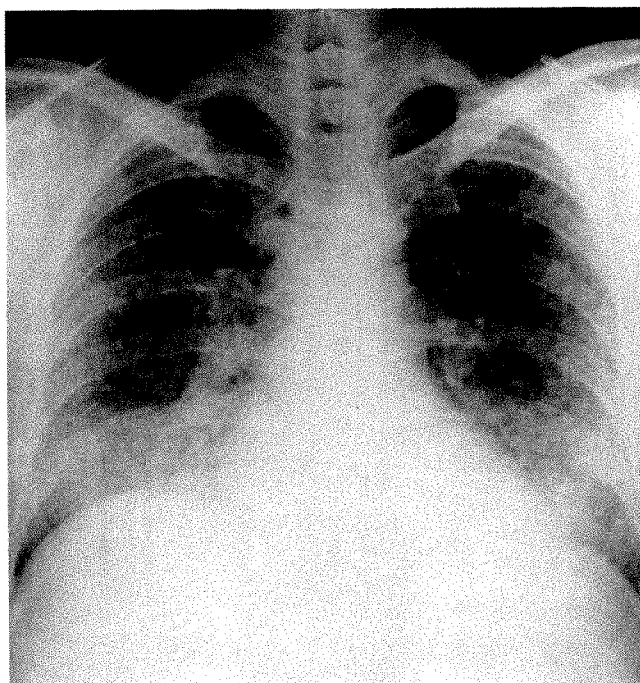


Fig. 1.—Chest radiograph 2 days after onset of symptoms shows well-circumscribed, small nodular densities in both lungs, predominantly at periphery.

consolidation; a gross lung specimen in that patient showed petechial hemorrhage and consolidation with frothy material. Microscopically, foci of intraalveolar and interstitial hemorrhage with pronounced pulmonary edema were seen.

Analysis of the sequence of radiographic abnormalities, from their appearance to resolution, was possible in 21 patients. Thirteen of the 21 patients in whom the sequence of radiographic abnormalities was analyzed, initially had predominantly nodular densities. Radiographs of nine (69%) of those 13 patients showed a change to diffuse, ill-defined, ground-glass densities before complete resolution. Radiographs of two (15%) of the 13 patients with predominantly nodular densities showed a sequential change to large, confluent air-space consolidation and then to diffuse, ground-glass densities before resolution. Two cases presenting with large confluent air-space consolidation changed to diffuse, ground-glass densities before resolution. Eight cases did not show a change in pattern.

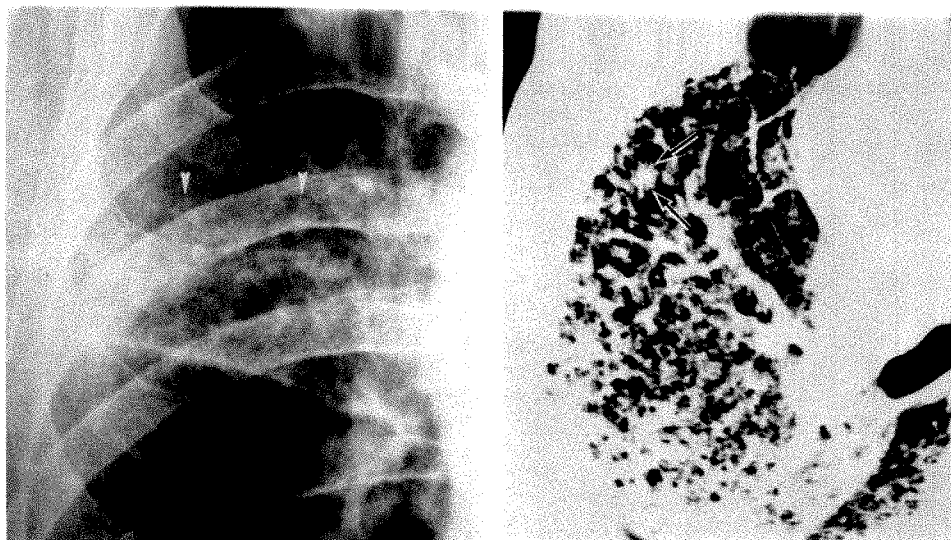
All 37 patients whose radiographs showed pulmonary abnormality had a bilateral pulmonary lesion without a lobar or segmental distribution. Seventeen (46%) of the 37 patients had pulmonary lesions that were predominantly peripheral (Figs. 1 and 3), whereas the remaining 20 patients (54%) had uniformly distributed lesions. In 20 patients (54%), the pulmonary lesions were predominantly on the right side (Fig. 3), whereas the other 17 patients (46%) had bilaterally distributed lesions.

A small pleural effusion was seen in seven (19%) of the 37 patients. In six patients, the effusion was on the right side only, and one patient had bilateral effusion. Four patients had interlobular septal thickening (Kerley B lines). Ten (27%) of the 37 patients had cardiomegaly.

Fig. 2.—A, Portion of a chest radio-

graph with predominantly nodular opacities shows poorly margined nodular lesions in right upper lobe (arrowheads).

B, 1.5-mm collimation, high-resolution CT shows fluffy, ill-defined air-space nodules within secondary pulmonary lobules (arrows).



A

B

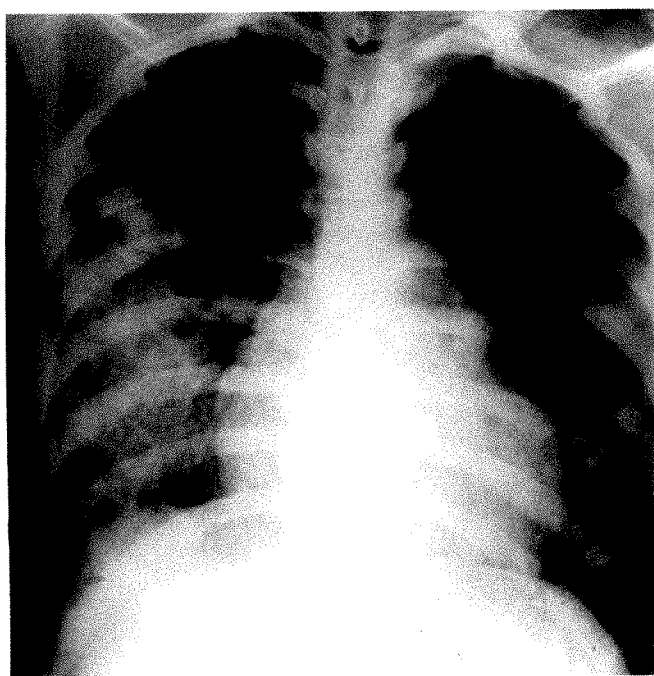


Fig. 3.—Chest radiograph 4 days after onset of symptoms shows large confluent areas of consolidation in both lungs. Note right lung and peripheral predominance of abnormalities.

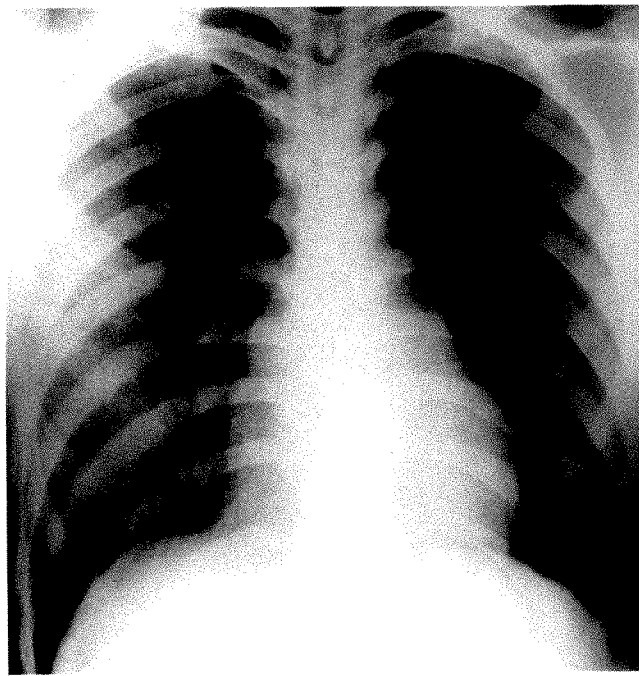


Fig. 4.—Chest radiograph 6 days after presentation shows a diffuse, ill-defined, ground-glass appearance in both lungs, especially at periphery.

In all 19 patients who had pulmonary lesions and serial chest radiographs from the onset to resolution, the lesions resolved completely. The pulmonary lesions resolved in 5 to 10 days in 13 patients (68%) (Fig. 5) and in 11 to 15 days in six patients (32%). Eight patients who had pulmonary lesions and who died did not have resolution. The radiographic abnormalities of these patients were large air-space consolidation (six patients) and small nodular lesions with focal patch densities (two patients). Pulmonary lesions in the patients who died were similar to, but more severe than, lesions in patients who recovered.

Experimental Study

Guinea-pig lungs resected 24 hr after infection showed sparse, subpleural, petechial hemorrhages, approximately 1

mm in diameter. Microscopically, these lesions represented round areas of intraalveolar hemorrhage. At 72 hr, the hemorrhagic foci increased in number and size, but remained less than 2 mm in diameter.

By the fifth and sixth days after infection, the severity of pulmonary hemorrhage reached its peak, showing 3- to 15-mm areas of confluent hemorrhage, with various degrees of associated edema. By the 12th and 15th days of infection, there were no areas of fresh hemorrhage, but hemosiderin from resolving hemorrhage was evident.

Discussion

Leptospirosis occurs when humans come into contact with the urine or tissues of infected animals, or infection can occur

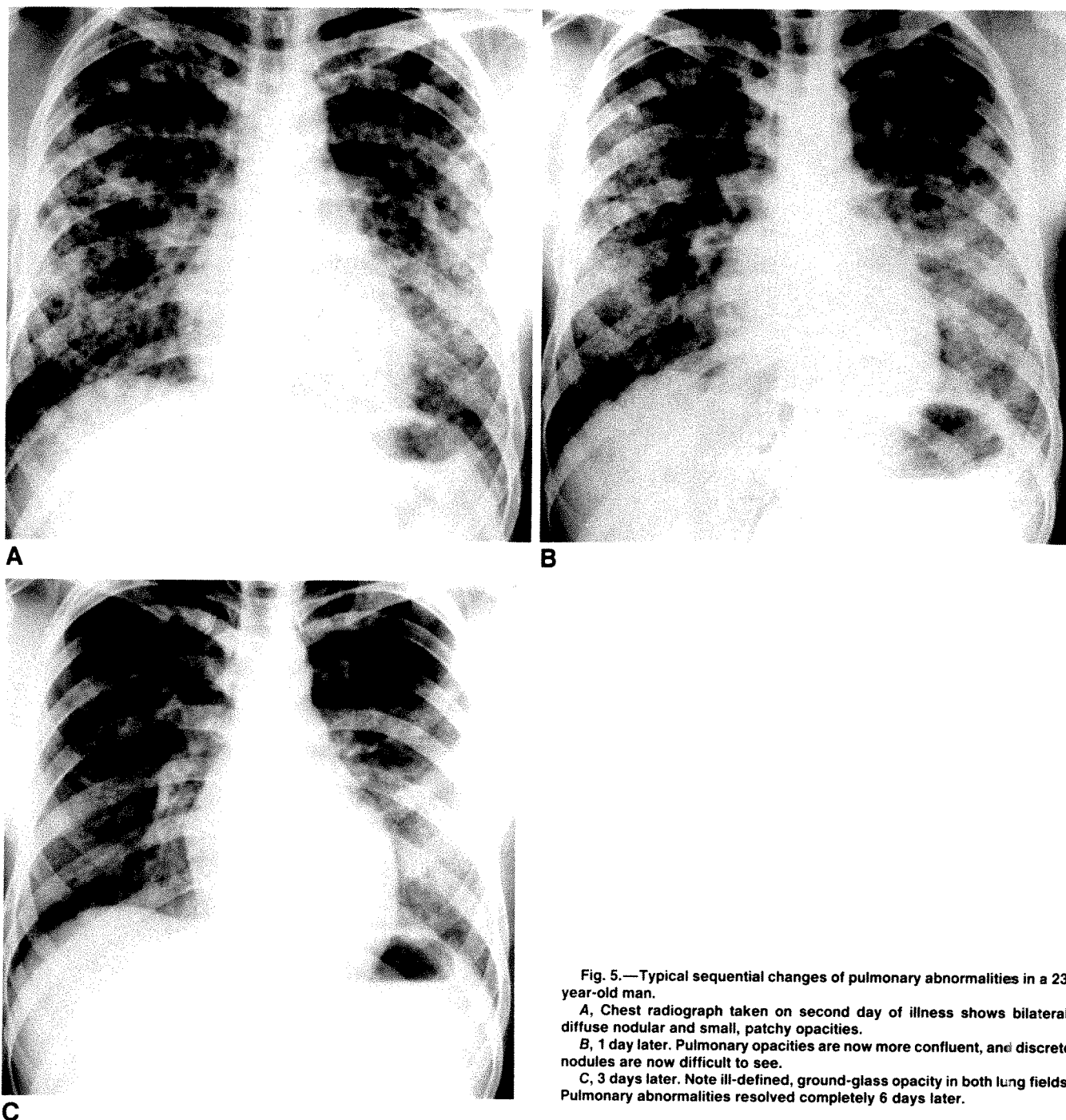


Fig. 5.—Typical sequential changes of pulmonary abnormalities in a 23-year-old man.

A, Chest radiograph taken on second day of illness shows bilateral, diffuse nodular and small, patchy opacities.

B, 1 day later. Pulmonary opacities are now more confluent, and discrete nodules are now difficult to see.

C, 3 days later. Note ill-defined, ground-glass opacity in both lung fields. Pulmonary abnormalities resolved completely 6 days later.

indirectly through contaminated water, soil, or vegetation. The usual points of entry are abraded skin, particularly around the feet, and mucous membranes [1–4].

Although leptospirosis is not common in the United States, it occurs in all regions of the country. Between 1964 and 1978, from 50 to 150 cases were reported annually [1, 3]. In the United States, a wide variety of domestic and wild animals including rats, raccoons, and opossums, harbor *Leptospira*, and infectivity rates of 10–50% in these species are not unusual. Currently, less than 20% of patients in the United States who develop this disease have direct contact with animals [1, 3]. Most have incidental exposure [2, 3], and swimming or partial immersion in contaminated water has

been implicated in approximately 20% [4]. Leptospirosis is more common in tropical and subtropical climates, particularly in the Far East. In the current study, as in a series reported from China [8], most patients had a history of working barefoot in flooded rice fields. We believe that the main causes of the disease in our cases are heavy rain, which leads to wide propagation of *Leptospira*, and the working environment during the harvest, which promotes skin abrasion.

Leptospirosis is typically a biphasic illness. The leptospiremic or first phase lasts 4–9 days with an abrupt onset (75–100%) of chills, fever, headache, and myalgia. The second or immune phase usually lasts 1–3 days after a relatively asymptomatic period of 1–3 days [4]. The reported mortality rate

varies from 2% to 14% [1, 4, 8, 15]. In the current study, the mortality rate is 14%. Complete recovery after acute illness is usual. However, iridocyclitis, lobar pneumonia, acute cholecystitis, abscesses, or pretibial fever are the reported complications in a few cases [8, 15].

Pulmonary involvement in leptospirosis consists primarily of hemorrhagic pneumonitis. Pathologically, petechiae are scattered throughout the lungs and tracheobronchial tree. In advanced cases, extensive pulmonary hemorrhage and edema have been found. Little associated inflammation is present [6, 9, 10]. These findings, which are identical to what was found in an autopsy and in the guinea pigs we studied, presumably result from a direct toxic effect of the organisms or a circulating *Leptospira* endotoxin, both of which result in widespread capillary damage [10, 13, 14].

The reported frequency of abnormalities shown on chest radiographs in patients with leptospirosis varies from 11% to 67% [1, 10, 16]. This wide range probably reflects natural differences in the virulence of the disease in different parts of the world, differences in individual reactivity, and differences in selection of patients. In the present study of both icteric and nonicteric patients, the frequency of abnormalities seen on radiographs was 64%.

The patterns of abnormalities shown on chest radiographs have been variously described as "small patchy localized infiltrations," "confluent massive areas of consolidation," "widely disseminated small infiltrations," "localized patchy cloudings of different sizes," and "snowflake-like small patchy lesions" [6, 7, 10]. Miliary opacities also have been reported [6, 16]. In our study, we categorized patients with abnormal radiographs as having 3 types of pulmonary abnormalities, and in those patients who had follow-up radiographs showing the evolution of these abnormalities, a characteristic sequence of findings was observed. We believe that the different radiographic appearances observed by previous authors are different stages in the disease. Our studies in guinea pigs also support this conclusion.

Most of the patients we studied presented with small nodular lesions, ranging from 1 to 7 mm in diameter, that were sometimes associated with larger areas of consolidation. In the guinea pigs infected with *Leptospira*, small nodular foci of hemorrhage were present within the first few days of infection, probably correlating with this radiographic finding. Larger confluent areas of consolidation, seen in 16% of patients at presentation, appear to correlate with the progressive hemorrhage seen in the guinea pigs by the fifth and sixth days of infection. The diffuse, ground-glass appearance seen in 27% of patients at presentation probably correlates with the resolving hemorrhage seen in the guinea pigs by 12 to 15 days. Also in support of these conclusions is the fact that small nodular lesions typically progressed to large confluent air-space consolidation or diffuse ground-glass lesions before resolving. In patients with large air-space consolidation, progression to diffuse, ground-glass lesions was characteristic.

In our study and in the study reported by Wang et al. [10], pulmonary opacities were often peripherally distributed.

Manifestations of leptospirosis on chest radiographs may mimic viral pneumonia, bronchopneumonia, miliary or endobronchial spread of tuberculosis, other causes of pulmonary hemorrhage such as Goodpasture syndrome, or adult respiratory distress syndrome. However, we believe that rapidly evolving, predominantly peripheral, diffuse nodular or confluent pulmonary lesions are typical of leptospirosis and, along with fever and an appropriate history, could reasonably suggest the diagnosis. Serologic tests for *Leptospira* generally do not become positive until the sixth to 12th day of the disease [3]. However, because the radiograph typically shows abnormality in the first 24 to 72 hr, it can often allow an early diagnosis.

ACKNOWLEDGMENTS

We acknowledge Tae Hwan Lim and Kyung Soo Lee for providing the cases.

REFERENCES

1. Heath CW, Alexander AD, Galton MM. Leptospirosis in the United States (concluded). Analysis of 483 cases in man, 1949-1961. *N Engl J Med* 1965;273(17):915-922
2. Turner LH. Leptospirosis. *Br Med J [Clin Res]* 1973;1:537-540
3. Feigin RD, Aderson DC. Human leptospirosis. *CRC Crit Rev Clin Lab Sci* 1975;5:413-467
4. Beeson PB, McDermott W. *Textbook of medicine*, 16th ed. Philadelphia, PA: Saunders, 1987:1595-1597
5. Poh SC, Soh CS. Lung manifestations in leptospirosis. *Thorax* 1970;25:751-755
6. Silverstein CM. Pulmonary manifestations of leptospirosis. *Radiology* 1953;61:327-334
7. Chiu YC, Liu HH. Report on observation of roentgenologic pulmonary changes in 48 cases of leptospirosis. *Chin J Radiol* 1959;7:374-375
8. Wang CN, John L, Chang TF, Cheng WJ, Luo MY, Hung AT. Studies on anicteric leptospirosis. I. Clinical manifestations and antibiotic therapy. *Chin Med J [Engl]* 1965;84:283-291
9. Research Laboratory of the Sino-Soviet Friendship Hospital and Peking People's Hospital. Pathophysiological studies on leptospirosis. IV. Roentgenological manifestations of chest films. *Chin J Int Med* 1959;7:971-978
10. Wang CP, Chi CW, Lu FL. Studies on anicteric leptospirosis. III. Roentgen observation of pulmonary changes. *Chin Med J [Engl]* 1965;84:298-305
11. Lee JS. Clinical observation of leptospirosis. *Korean J Int Med* 1985;37th Annual Convention Abstract:121-124
12. Ellinghausen HC Jr, McCullough WG. Nutrition of *Leptospira pomona* and growth of 13 other serotypes: fractionation of oleic albumin complex and a medium of bovine albumin and polysorbate 80. *Am J Vet Res* 1965;26:45-51
13. Areean VM, Sarasin G, Green JH. The pathogenesis of leptospirosis: toxin production by *Leptospira icterohemorrhagiae*. *Am J Vet Res* 1964;25:836-843
14. Brito TD, Bohm GM, Yasuda PH. Vascular damage in acute experimental leptospirosis of the guinea-pig. *J Pathol* 1979;128:177-182
15. Chung H-L, Ch'iu F-H, Wu H-T, Hou T-C, K'uang C-H. Leptospirosis: a clinical and statistical study of 182 cases. *Chin Med J [Engl]* 1958;77(3):207-234
16. Lee REJ, Terry SI, Walker TM, Urquhart AE. The chest radiograph in leptospirosis in Jamaica. *Br J Radiol* 1981;54:939-943

Book Review

Mammography. 83 Radiological Exercises for Students and Practitioners. By P. Haehnel and Ch. Kleitz. Translated from the French by Marie-Thérèse Wackenheim. New York: Springer-Verlag, 137 pp., 1988. \$49

This relatively short book contains 142 illustrations that make up 83 radiologic exercises in mammography. All mammographic images shown use film technique. Several pneumocystograms and ductograms as well as a few breast ultrasound images are also illustrated. The subjects covered are divided into six major sections: the normal breast, diffuse opacity, architectural rupture or star-shaped opacities, oval opacities, microcalcifications, and intraductal and intracystic pathology.

The text is translated from the French. Some of the phrases are not used in the American literature, making it difficult to understand the authors' real meaning. Examples of this are "harmonious breast," "architectural rupture," "rugged appearance," and "ramous prolongation."

Some of the images are accompanied by line drawings to make the findings under discussion easier to perceive. However, too often the abnormal findings are difficult to appreciate in the other cases.

There are major omissions in the topics covered. Entities such as dermal calcium, milk of calcium, the postsurgical breast, and the irradiated breast are not mentioned. There is no discussion of the authors' philosophy on management of mammographic abnormalities that have a high probability of representing benign disease. The back cover of the text states that the authors explain the step-by-step procedure in diagnosis. Unfortunately, much is not explained, and I do not believe that the material will be helpful in developing an approach to mammographic interpretation.

Marc J. Homer
Tufts University School of Medicine
New England Medical Center Hospital
Boston, MA 02111

Pulmonary Lymphangiomyomatosis: High- Resolution CT Findings in Four Cases

Daniel C. Rappaport¹
Gordon L. Weisbrod¹
Stephen J. Herman¹
Dean W. Chamberlain²

Lymphangiomyomatosis is a rare disease of unknown cause that affects women of reproductive age. It is characterized by progressive proliferation of smooth muscle in the lung. The patients present with progressive shortness of breath, pneumothorax, chylous effusion, and hemoptysis. Four patients with biopsy-proved lymphangiomyomatosis of the lung were evaluated using high-resolution CT. In all patients, the scan showed well-defined cystic air spaces, surrounded by uniformly thin walls, distributed diffusely throughout both lungs. The cystic air spaces ranged in size from a few millimeters to 5 cm. Pathologically, these cysts were predominantly bounded by normal-looking parenchymal components, with occasional patchy involvement by a smooth-muscle proliferative process. The CT appearance of lymphangiomyomatosis differs quite distinctly from that of other diseases that can cause cystic air spaces, such as fibrosing alveolitis, neurofibromatosis, and bronchiectasis, and less distinctly from pulmonary emphysema and eosinophilic granuloma.

Our experience in these few cases suggests that the high-resolution CT findings in lymphangiomyomatosis are characteristic of the disease.

Lymphangiomyomatosis (LAM) is a rare disease of unknown cause that affects the lungs of women. The patients are usually in the reproductive years. They present with progressive shortness of breath, often associated with chylous pleural effusions, hemoptysis, and/or pneumothoraces. The diagnosis is usually made by open-lung biopsy.

We report the CT findings in four patients with biopsy-proved LAM.

Patients and Methods

Four patients with an age range of 36 to 51 years underwent high-resolution CT of the lungs. All four patients had shortness of breath, two had recurrent pneumothoraces, one had recurrent episodes of hemoptysis, and one had recurrent chylous pleural effusions. Two patients initially became symptomatic during pregnancy.

All patients had pulmonary function tests that showed a marked reduction in diffusion capacity and moderate to severe gas trapping compatible with obstructive lung disease.

Three of the four patients were being assessed for suitability for lung transplantation. These three patients had been symptomatic for 4–16 years, and all had a biopsy-proved diagnosis of LAM. One patient did not have a diagnosis at the time of her CT examination, but was subsequently proved by open-lung biopsy to have LAM. Posteroanterior chest radiographs and high-resolution CT examinations were analyzed in all four patients.

CT exams were performed by using a GE 9800 (General Electric Medical Systems, Milwaukee, WI) CT scanner. Technique included 1.5-mm collimation (120–140 kV, 140–170 MA) and reconstruction by using GE bone algorithm in three patients and a standard algorithm in one patient. Retrospective target reconstructions were performed on one patient. All CT examinations were reviewed retrospectively by three independent radiologists. Any interobserver variations were resolved by mutual consensus.

Received November 7, 1988; accepted after revision January 9, 1989.

¹ Department of Radiology, Toronto General Hospital, 200 Elizabeth St., Toronto, Ontario M5G 2C4, Canada. Address reprint requests to G. L. Weisbrod.

² Department of Pathology, Toronto General Hospital, 200 Elizabeth St., Toronto, Ontario M5G 2C4, Canada.

AJR 152:961–964, May 1989

0361–803X/89/1525–0961

© American Roentgen Ray Society

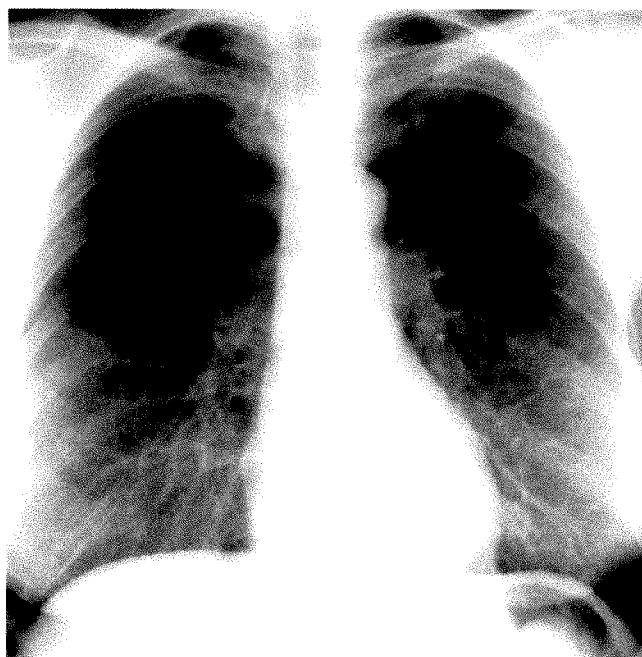
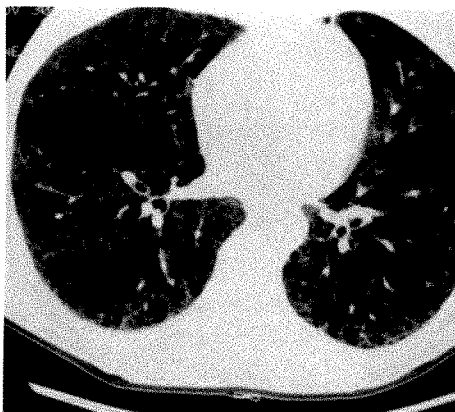
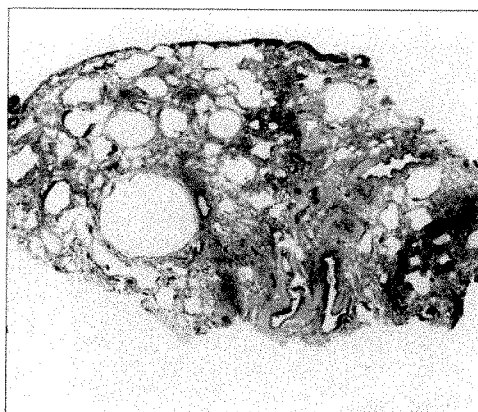
**A**

Fig. 1.—**A**, Posteroanterior radiograph of a 51-year-old woman with lymphangioleiomyomatosis and a 2-year history of progressive dyspnea. There is a subtle increase in interstitial markings at both bases. No definite cystic air spaces can be seen.

B, High-resolution CT reveals well-defined cystic air spaces diffusely distributed through both lungs.

C, Whole section from open-lung biopsy shows small spherical cysts (H and E, $\times 6$).

**B****C**

Results

All CT studies showed a remarkable similarity. CT scans of all four patients revealed well-defined cystic air spaces that affected both central and peripheral portions of the lungs diffusely. The patient with the least advanced disease had relative apical sparing (Figs. 1A and 1B). The cystic air spaces ranged from a few millimeters in size in all patients (Fig. 2) to 5 cm in one patient (Fig. 3). Most of the cysts measured approximately 1 cm in diameter. No nodularity or irregularly thickened interlobular septal lines were present in any of the patients. One patient showed a very slight increase in linear interstitial markings between the cysts. No relationship between the cystic air spaces and pulmonary vessels was apparent, and no vascular destruction could be seen. In addition, all patients showed normal to increased lung volumes.

The open-lung biopsies were similar in appearance in all cases, except for the finding in one patient of mild multifocal

hemosiderosis. All showed a striking increase in smooth muscle, which was irregularly distributed in relation to lymphatics, blood vessels, and small airways. Also, muscle tissue could be found in varying degrees randomly distributed throughout the interstitium, including that of alveolar walls. Despite the marked cellularity and haphazard arrangement of the muscle in many areas, very little cytomorphologic abnormality was evident, and mitotic figures were difficult to find. Cyst formation was prominent (Fig. 1C). The cysts had an appearance similar to that of centriacinar emphysema, except that their distribution within secondary lobules seemed more random. The cysts were bound by relatively normal-looking parenchymal components (mainly compressed alveolar walls) exhibiting an occasional patchy involvement by the smooth-muscle proliferative process (Fig. 4). This probably corresponded to the uniform thin walls seen on CT scans in all four patients. Larger cysts seen both pathologically and radiologically appeared to be formed by coalescence of smaller cysts.

Discussion

Lymphangioleiomyomatosis is characterized by progressive proliferation of smooth muscle, which, in the lung, is patchy in distribution and which principally involves lymphatics, airways, and blood vessels. This accounts for the common sequelae of chylous pleural effusion, postobstructive ectasia of air-containing structures within secondary lobules, and hemorrhage, respectively [1]. The air-space ectasia becomes a prominent anatomic feature with time. It is first seen as small, randomly distributed parenchymal defects within the lobules. With enlargement and coalescence, cystic cavities arise, ranging from millimeters to several centimeters in size and characteristically involving the lung diffusely.

CT is more sensitive than the chest radiograph in the detection of interstitial lung disease [2]. By scanning relatively thin slices in the transverse plane, the problem of superim-

position of densities is diminished. Also, differences in density between normal lung and parenchymal lesions are more readily appreciated with CT's superior contrast resolution, allowing a more accurate indication of the extent and distribution of disease in the lung parenchyma [2]. The distribution and morphology of interstitial diseases have specificity and therefore aid in diagnosis [3]. CT also can aid in showing the presence or absence of adenopathy and pleural effusions.

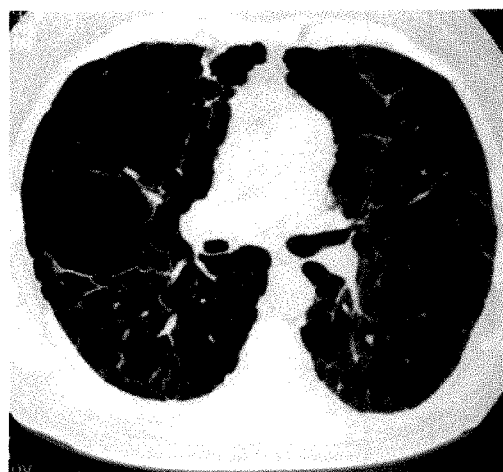
Recently, high-resolution CT (HRCT) has been proposed as a valuable tool for the early detection and characterization of parenchymal lung disease because it minimizes volume averaging of parenchymal structures, resulting in excellent radiologic-pathologic correlation [3-8]. The optimal technique for HRCT of lungs includes 1.5-mm collimation and targeted reconstruction by means of a high-spatial-frequency algorithm (GE bone algorithm) [9].

Fig. 2.—High-resolution CT of a 36-year-old woman with lymphangioleiomyomatosis (who presented during pregnancy 4 years earlier with a chylous effusion) shows cystic air spaces up to 2 cm in diameter. Pulmonary function tests revealed a total lung capacity of 120% and residual volume of 200%. Diffusion capacity was reduced to 29% of predictive value.



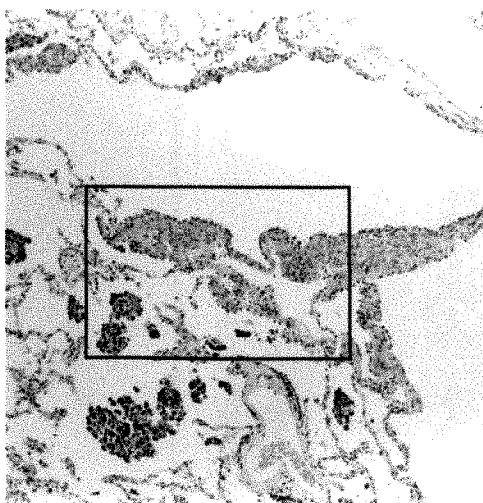
2

Fig. 3.—High-resolution CT of a 42-year-old woman with lymphangioleiomyomatosis and a 10-year history of dyspnea dating back to her first pregnancy shows a 5-cm bulla with cystic air spaces. The patient had a history of bilateral recurrent spontaneous pneumothoraces. She required continuous oxygen therapy because of hypoxemia at rest.



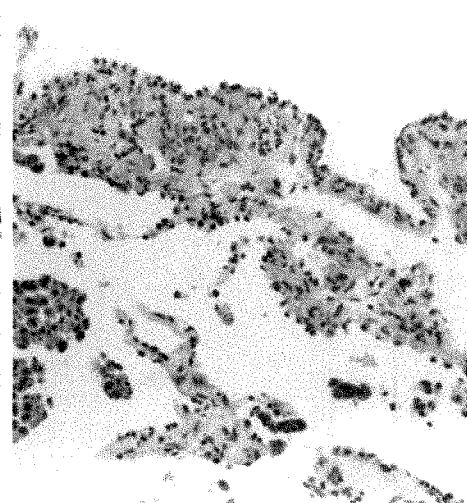
3

Fig. 4.—A, Open-lung biopsy specimen from 28-year-old woman with lymphangioleiomyomatosis, dyspnea, and hemoptysis shows early cyst formation and hemosiderosis involving adjacent alveoli. This patient's pulmonary function tests 8 years after biopsy showed a forced expiratory volume in first second (FEV1.0) of 0.3 l, 10% of predicted value. Sonography showed multiple bilateral echogenic renal masses, consistent with angiomyolipomas.



A

B, High-power view of the area marked in Figure 4A shows cyst wall focally bordered by abnormal smooth muscle (H and E, $\times 63$ and 160).



B

Routine CT has been reported to show lung cysts in LAM [10, 11]. In our patients, HRCT showed the morphology of the cysts more clearly. Recently, HRCT findings of well-defined lung cysts in a single patient with LAM have been described [12]. Similarly, we found that the cystic air spaces were distributed diffusely throughout both lungs, varying in size from a few millimeters up to 5 cm, and were surrounded by uniformly thin walls. The intervening interstitium was difficult to evaluate because of diffuse involvement of the lung parenchyma. The lung volumes were normal or increased. No nodularity, thickened interlobular septal lines, distortion of lung architecture, or vascular destruction was evident. We feel that this HRCT appearance is sufficiently characteristic to allow the diagnosis of LAM to be at least strongly suspected. Lack of experience with the HRCT appearance of other diseases that can cause cystic air spaces precludes saying that the HRCT appearance of LAM is pathognomonic. Cystic air spaces have been reported in fibrosing alveolitis [2-5, 7], neurofibromatosis [2], bronchiectasis [13], eosinophilic granuloma [14, 15], and emphysema [4, 6, 8].

In fibrosing alveolitis and end-stage interstitial pulmonary fibrosis (honeycomb lung), cystic spaces can range from 1 mm to 2.5 cm in diameter, but they are much more patchy in their distribution, generally have thicker walls, and are associated with irregular interlobular septal thickening. In addition, interlobular bands of fibrous tissue with resulting loss of lung volume, bronchiectasis, and gross distortion of lung architecture are evident [4]. A peripheral subpleural accentuation of the disease is also characteristic [2, 3, 5].

Neurofibromatosis also may have cystic or bullous air spaces on CT examination. The spaces differ from LAM in that they occur in an apical location and are associated with a basilar increase in linear markings [2].

Bronchiectasis also may show cystic air spaces on HRCT, but the bronchial distribution and thickened walls, often with air-fluid levels, are sufficiently characteristic to differentiate it from LAM [13].

The most difficult disease to differentiate from LAM on HRCT is pulmonary emphysema. Murata et al. [6] have shown small, round, low-density areas in contact with the terminal pulmonary artery and separated from the corresponding interlobular septum by 3-5 mm in centrilobular emphysema. In our patients, we found it difficult to identify these structures in the secondary pulmonary lobule, and therefore the relationship of the cystic space to the structures in the secondary pulmonary lobule, on thin-section HRCT. Webb et al. [4] studied three lungs with pathologic centrilobular emphysema on HRCT and found focal areas of decreased density (compared with normal lung) that lacked a recognizable wall or septal thickening. Although it was sometimes difficult to determine the centrilobular nature of the disease, involvement of lobules did not appear to be uniform [4]. The cystic air spaces in LAM, compared with those in emphysema, tend to be more uniform, better defined, and less variable in size. Also, the cystic air spaces in LAM generally are not associated with the very large bullae seen in emphysema [8]. These differences may or may not be present, and HRCT appearances of emphysema [16] may mimic LAM. Correlation of the

HRCT appearance with the patient's age, sex, and clinical presentation will aid in the differential diagnosis.

HRCT findings in eosinophilic granuloma can be strikingly similar to those in LAM. The presence of cystic air spaces with thin or indiscernible walls, ranging from 2 mm to 4 cm in size, has been described recently [14, 15]. In addition, reticular nodular densities, cavitating nodules, and apical predominance were also described. In distinction, no nodularity, irregularly thickened interlobular septal lines, or apical predominance was seen in our four patients.

Although the exact role for HRCT in the diagnosis of interstitial disease remains to be defined, the HRCT findings in LAM appear to be very suggestive, if not specific, for this disease. HRCT can show diffuse parenchymal abnormalities in these patients, even in those with a normal or near-normal chest radiograph, and correlate more closely with the severe clinical and pathophysiologic disturbances that are characteristic of LAM.

ACKNOWLEDGMENT

We thank Ms. E. Coretti for preparing the manuscript.

REFERENCES

- Corrin B, Liebow AA, Friedman PJ. Pulmonary lymphangiomyomatosis: a review. *Am J Pathol* 1975;79:348-382
- Bergin CJ, Muller NL. CT in the diagnosis of interstitial lung disease. *AJR* 1985;145:505-510
- Bergin CJ, Muller NL. CT of interstitial lung disease: a diagnostic approach. *AJR* 1987;148:8-15
- Webb WR, Stein MG, Finkbeiner WE, Im JG, Lynch D, Gamso G. Normal and diseased isolated lungs: high-resolution CT. *Radiology* 1988;166:81-87
- Nakata H, Kimoto T, Nakayama T, Kido M, Miyazaki N, Harada S. Diffuse peripheral lung disease: evaluation by high-resolution computed tomography. *Radiology* 1985;157:181-185
- Murata K, Itoh H, Todo G, et al. Centrilobular lesions of the lung: demonstration by high-resolution CT and pathologic correlation. *Radiology* 1986;161:641-645
- Zerhouni EA, Naidich DP, Stitik FP, Khouri NF, Siegelman SS. Computed tomography of the pulmonary parenchyma. Part II: Interstitial disease. *J Thorac Imag* 1985;1:54-64
- Meziane MA, Hruban RH, Zerhouni EA, et al. High resolution CT of the lung parenchyma with pathologic correlation. *RadioGraphics* 1988;8:27-54
- Mayo JR, Webb WR, Gould R, et al. High-resolution CT of the lungs: an optimal approach. *Radiology* 1987;163:507-510
- Berger JL, Shaff MI. Pulmonary lymphangiomyomatosis. *J Comput Assist Tomogr* 1981;5:565-567
- Merchant RN, Pearson MG, Rankin RN, Morgan WKC. Computerized tomography in the diagnosis of lymphangiomyomatosis. *Am Rev Respir Dis* 1985;131:295-297
- Bergin C, Roggli V, Coblentz C, Chiles C. The secondary pulmonary lobule: normal and abnormal CT appearances. *AJR* 1988;151:21-25
- Grenier P, Maurice F, Musset D, Nahum H. Bronchiectasis: assessment by thin section CT. *Radiology* 1986;161:95-99
- Godwin JD, Buschman DL, Moore ADA, et al. High-resolution CT in eosinophilic granuloma (Histiocytosis-X) of the lung. Presented at the annual meeting of the Radiological Society of North America, Chicago, IL, December 1988
- Brauner M, Grenier P, Mouelhi MM, Mompont D, Lenoir S. Pulmonary Histiocytosis-X: high resolution CT evaluation. Presented at the annual meeting of the Radiological Society of North America, Chicago, IL, December 1988
- Hruban RH, Meziane MA, Zerhouni EA, et al. High-resolution computed tomography of inflation-fixed lungs radiologic-pathologic correlation of centrilobular emphysema. *Am Rev Respir Dis* 1987;136:935-940

Case Report

Rounded Atelectasis of the Lung: MR Appearance

J. A. Verschakelen,¹ P. Demaerel,¹ J. Coolen,¹ M. Demedts,² G. Marchal,¹ and A. L. Baert¹

Rounded atelectasis of the lung is a pseudotumor located in the dorsobasal part of the chest and caused by enfolding of atelectatic lung tissue. It is a radiologic entity that usually can be diagnosed on follow-up chest radiographs and conventional tomograms. CT can be helpful in some cases.

To the best of our knowledge, no reports have been published on the MR appearance of this entity. We describe this appearance in one patient.

Case Report

A 76-year-old man was admitted to the hospital because of progressive shortness of breath and a superimposed acute respiratory infection. Physical examination was normal except for slight percussion dullness and diminished breathing sounds at the posterior right lung base. Clubbing of the fingers and pitting edema also were evident.

Plain chest radiographs (Fig. 1A) showed a right pleural effusion and a rather sharply outlined mass in the posterobasal segment of the right lower lobe. Lateral tomograms showed the mass was more or less round, lying against thickened posterior pleura. CT (Fig. 1B) confirmed the presence of a mass in the medial posterobasal region of the right lower lobe. This mass was pleura based, and in lung-window setting, vessels and bronchi were seen curving toward the mass, suggesting rounded atelectasis. However, because a neoplastic process could not be excluded, bronchoscopy and transthoracic lung biopsy under CT guidance were performed. These disclosed unspecific inflammation of the parenchyma.

MR scans showed an oval mass with density similar to liver tissue in the posterobasal segment of the right lower lobe on the sagittal T1-weighted images (Figs. 1C and 1D). The mass was lying against a low-intensity area. In the lesion, curling hypointense lines were seen at the base, continuous with the bronchovascular structures of the lower lobe (Fig. 1D). The pleural effusion was seen as a hyperintense area on the T2-weighted images.

The patient was discharged with a diagnosis of rounded atelectasis.

Discussion

Rounded atelectasis is a less-well-known form of lung collapse. The first reports on this entity appeared in older German and French literature describing a special type of atelectasis that occurred in conjunction with collapse therapy for tuberculosis [1-3]. Hanke [4] was the first to present a hypothesis for the pathogenesis of this disorder and introduced the descriptive term "rounded atelectasis." He postulated that the first step in the pathogenesis is a pleural effusion, which causes an area of atelectasis within a part of the compressed lobe. This atelectatic lung tissue floats within the effusion and is tilted upward or downward when the fluid diminishes. This tilted lung tissue remains atelectatic and becomes engulfed by the surrounding visceral pleura of the remainder of the reexpanded lobe, producing a "mass" that consists of atelectatic pulmonary tissue folded around thickened pleural indentations. This lung folding causes the blood vessels and bronchi to curve. For mechanical reasons, rounded atelectasis occurs mostly in the posterior and basal part of the lower lobes. Occasionally, it is located in the middle lobe or lingula.

Although a few cases have been presented without history of pleural disease [5, 6], most authors agree that there has to be some pleural pathologic change (i.e., pleural effusion or, as in the early cases, a pneumothorax). The higher frequency of rounded atelectasis in patients with asbestosis [7-10] is also probably related to the pleural reaction caused by this disease.

Received October 11, 1988; accepted after revision November 29, 1988.

¹ Department of Radiology, University Hospitals K. U. Leuven, Herestraat 49, B-3000 Leuven, Belgium. Address reprint requests to J. A. Verschakelen.

² Department of Pneumology, University Hospitals K. U. Leuven, B-3000 Leuven, Belgium.

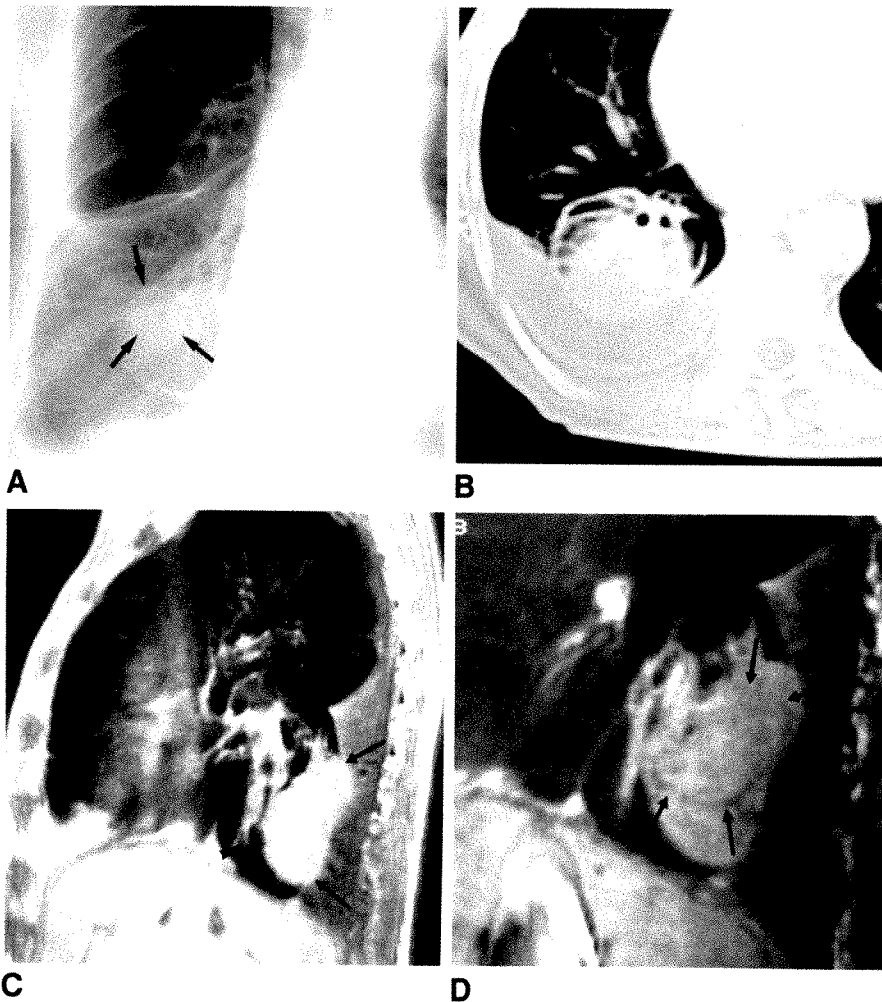


Fig. 1.—Rounded atelectasis in a 76-year-old man.

A, Plain chest film shows a right pleural effusion and a rather sharply outlined mass (arrows) in right lower lobe.

B, CT scan shows a pleura-based mass with vessels and bronchi curving toward mass.

C, Sagittal T1-weighted MR image shows an oval mass with density similar to liver tissue (arrows) in posterobasal segment of right lower lobe. Mass lies against a low-intensity area representing pleural fluid. Blood vessels are curving toward its lower pole (arrowheads).

D, Sagittal MR image shows hypointense lines (arrows) within lesion. These are probably caused by thickened pleural indentations.

Rounded atelectasis is a radiologic diagnosis that can be made on follow-up conventional chest films and sagittal tomograms showing the appearance of a masslike lesion with bronchial and vascular structures extending toward the mass ("comet tail"). Also, CT can be diagnostic, and characteristic features have been described [11, 12]. However, some authors warn that these features do not always allow a definite diagnosis [13]. Moreover, since the major part of the bronchi and blood vessels is in the longitudinal axis (according to the pathogenesis as formulated by Hanke), one would expect imaging techniques that can make longitudinal slices to be more accurate for making the diagnosis [14]. For this reason, we expected that sagittal slices on MR could be used to diagnose rounded atelectasis.

In our case, MR images showed the position of the vascular structures in relation to the inferior pole of the mass (Fig. 1C). On T1-weighted sequences, the mass showed a signal intensity similar to liver tissue. This density is definitely higher than the density of the adjacent pleural fluid; this may be caused by the high protein content of the exudate in atelectatic lung tissue. Differentiation between mass and pleural fluid is possible with CT also, but can be difficult on conventional tomograms. Moreover, MR showed curved low-signal lines in the atelectatic lung tissue (Fig. 1C), which probably are caused by thickened indentations of the visceral pleura. This feature, which is well known from histology, can be seen on MR only and is, in our opinion, together with the comet tail in lung parenchyma, diagnostic of rounded atelectasis.

REFERENCES

1. Amschler H. Die "segmentären" Atelektasen in der Pneumothorax-Behandlung. *Tuberk Bibl* Nr. 94. Leipzig: Barth, 1958
2. Roche G, Parent J, Daumet P. Atelectasies parcellaires du lobe inférieur et du lobe moyen au cours du pneumothorax thérapeutique. *Rév Tuberc* 1956;20:87-94
3. Roche G, Rousselin L. Opacités pulmonaires multiples dues au pneumothorax thérapeutique. *Rév Tuberc* 1957;21:506-512
4. Hanke R. Rundatelektasen (Kugel- und Walzenatelektasen). *Fortschr Geb Röntgenstr Nuklearmed Ergänzungsband* 1971;114:164-183
5. Choffel CL, Verdoux P, Milleron B. Les atelectasies rondes pseudotumorales sans antécédents pleuraux avérés. *Poumon* 1977;33:295-302
6. Schneider HJ, Felson B, Gonzales LL. Rounded atelectasis. *AJR* 1980;134:225-232
7. Blesovsky A. The folded lung. *Br J Dis Chest* 1966;60:19-22
8. Hillerdal G, Hemmingsson A. Pulmonary pseudotumors and asbestosis. *Acta Radiol [Diag]* (Stockh) 1980;21:615-620
9. Mintzer RA, Gore RM, Vogelzang RL, Holz S. Rounded atelectasis and its association with asbestos induced pleural disease. *Radiology* 1981;139:567-570
10. Tylen U, Nilsson U. Computed tomography in pulmonary pseudotumors and their relation to asbestos exposure. *J Comput Assist Tomogr* 1982;6:229-237
11. Doyle TC, Lawler GA. CT features of rounded atelectasis of the lung. *AJR* 1984;134:225-228
12. Grabowski W. Computed tomographic diagnosis of rounded atelectasis: a case report. *Comput Radiol* 1983;7:301-304
13. Greyson-Fleg RT. Lung biopsy in rounded atelectasis. *AJR* 1985;144:1316-1317
14. Verschakelen JA, Baert AL, Demedts M, Van Dyck H. Rounded atelectasis of the lung: diagnosis on conventional radiology and CT. *Eur J Radiol* 1986;6:305-308

Sedimented Calcium in Benign Breast Cysts: The Full Spectrum of Mammographic Presentations

Sarah S. Linden^{1,2}
Edward A. Sickles¹

We retrospectively reviewed the mammograms of 318 patients that showed sedimented calcifications within benign breast cysts to describe the natural history and full spectrum of the mammographic appearances. Sedimented calcifications are seen in approximately 4% of symptomatic women undergoing mammography. Their recognition is important to avoid unnecessary workup, follow-up, or biopsy. Key to recognition is the difference in their radiographic features on lateral and craniocaudal views. The classic appearance is that of milk of calcium, seen as linear, curvilinear, or teacup-shaped particles on horizontal-beam lateral views and as ill-defined smudges on vertical-beam craniocaudal views. The most common presentation is multiple, bilateral, scattered and occasionally clustered calcifications within microcysts. Other presentations include milk of calcium within microcysts in a unilateral, clustered distribution; milk of calcium within macrocysts; sandlike calcifications (discrete particles rather than smudges on craniocaudal view) within cysts of various sizes; and rarely, milk of calcium within the lipid cysts of either fat necrosis or galactoceles. None of our cases has proved to be malignant. However, adjacent malignancies are a potential pitfall. We encountered eight patients with carcinoma presenting as clustered microcalcifications in a breast also containing typical sedimented calcifications. In each of these cases, the malignant calcifications could be distinguished by their mammographic appearance.

The recognition of sedimented calcifications present in about 4% of symptomatic women undergoing mammography is important because these characteristic calcifications are an indication of benignity. Malignant-appearing microcalcifications found in the vicinity of sedimented calcifications can be distinguished and require biopsy.

Sedimented calcium in the breast is a benign entity that occurs in 4–6% of symptomatic women presenting for mammography [1, 2]. When it is recognized, unnecessary workup, follow-up, or biopsy can be avoided. It may have several different appearances on mammography. Our aim in this study was to document the various appearances of sedimented calcium, determine their relative frequency, and describe their natural history.

Materials and Methods

We retrospectively reviewed the reports of 26,360 consecutive mammography examinations performed at the University of California, San Francisco, between January 1, 1980, and June 30, 1988. From these, more than 1000 examinations showing sedimented calcium were identified, representing 335 different patients. Films for 318 of these patients were available for review.

Microfocal spot mammograms were done by using either screen-film technique or xeromammography. Craniocaudal projections were obtained with a vertical X-ray beam. With a few exceptions, lateral views were true lateromedial views, taken with a horizontal X-ray beam. A mediolateral oblique view was obtained instead in the remaining cases. Magnification views were obtained when indicated. Each case was classified according to the mammographic appearance of sedimented calcium, the number of calcific particles, the distribution of particles in the breast(s), changes over time, and the results of any biopsies.

Received October 24, 1988; accepted after revision December 27, 1988.

¹ Department of Radiology, Box 0628, University of California, San Francisco, San Francisco, CA 94143. Address reprint requests to E. A. Sickles.

² Present address: Department of Radiology, Box 3808, Duke University Medical Center, Durham, NC 27710.

AJR 152:967–971, May 1989

0361–803X/89/1525–0967

© American Roentgen Ray Society

Results

Our population of patients was heavily weighted toward symptomatic women. The age range of the study group was 28–82 years (mean, 46.3 years; median, 45 years). Both breasts were examined in 287 women. Only one breast was examined in 31 women, either because the patient had had a mastectomy (10 women) or because she was referred for evaluation of a specific problem in one breast (21 women).

Follow-up mammographic examinations were available for 183 of the 318 patients in this study. Follow-up intervals ranged from 1 to 97 months (mean, 30.9 months; median, 25 months).

The mammographic appearances of sedimented calcium and their prevalence in our study population are listed in Table

TABLE 1: Mammographic Appearance of Sedimented Calcium in 318 Women

Appearance	Both Breasts Examined	One Breast Examined
Milk of calcium within microcysts	268	29
Bilateral, scattered and clustered	168	0
Bilateral, clustered	4	0
Unilateral, scattered and clustered	28	13
Unilateral, clustered	56	12
Solitary	12	4
Milk of calcium within macrocysts	11	1
Milk of calcium within a lipid cyst	1	0
Sandlike particles within cysts	7	1
Total	287	31

1. Almost all our patients had other types of benign or nonspecific calcifications as well.

Milk of calcium within microcysts (cysts <2 mm in diameter) was by far the most common presentation of sedimented calcium in the breast, accounting for 297 (93%) of our 318 patients. In particular, milk of calcium within microcysts that were both scattered and occasionally clustered in distribution accounted for 209 (66%) (Fig. 1). In half of these 209 patients, the total was more than 30 calcifications. In the other half, approximately equal numbers of women had 1 to 10, 11 to 20, and 21 to 30 calcifications.

Considering the 287 women in whom both breasts were examined, the bilateral scattered and occasionally clustered distribution was by far the most common, occurring 58% of the time. Microcysts were distributed symmetrically between the two breasts in two thirds of these women and asymmetrically in the remaining one third. However, it was not uncommon for microcysts to be limited to one breast, occurring 33% of the time. In this subgroup, a single cluster of microcysts was seen in 58% (Fig. 2), scattered and clustered microcysts in 29%, and a solitary microcyst in 13%. The single clusters of microcysts usually contained fewer than 10 calcifications.

Considering the 31 women in whom only one breast was examined, the scattered and occasionally clustered distribution was again the most common, occurring 42% of the time. A single cluster of microcysts was seen 39% of the time and a solitary microcyst 13% of the time.

The prevalence of milk and calcium within macrocysts was significantly less common than within microcysts, occurring in 4% of our total population (Fig. 3). Sandlike calcific particles

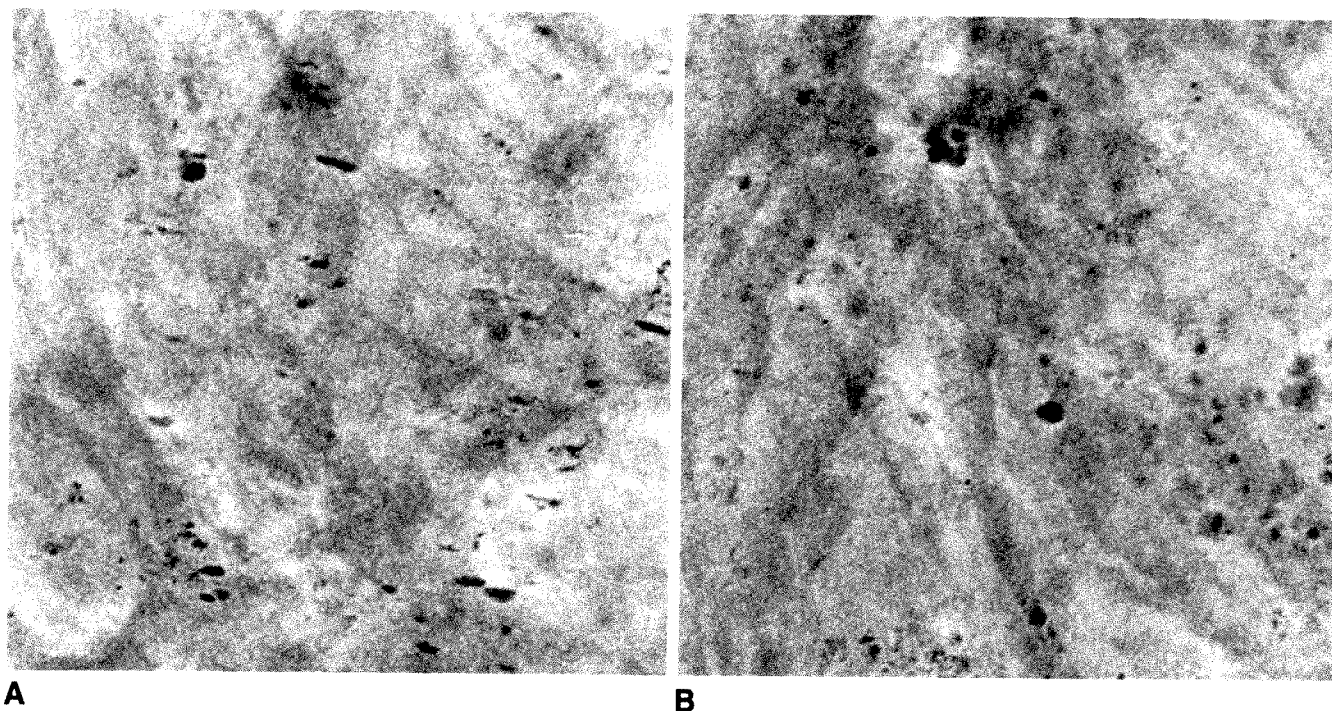


Fig. 1.—Xeromammograms show numerous microcalcifications, both scattered and clustered, with typical configuration of milk of calcium within microcysts. This is single most common presentation of sedimented calcium in breast. Note that actual walls of microcysts are not visible. Opposite breast had a similar appearance.

A. On lateral view, calcifications are seen as linear, curvilinear, or teacup shapes with a horizontal orientation.

B. On craniocaudal view, they are seen as slightly indistinct smudges.

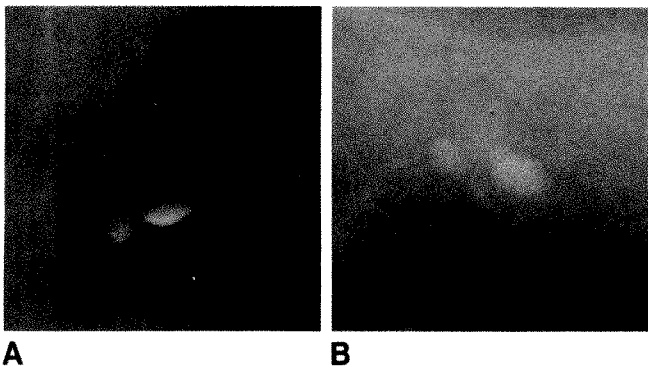


Fig. 2.—A and B, Screen-film mammograms show unilateral, clustered microcysts. Milk of calcium within microcysts may be limited to a single area of one breast. This is second most common presentation of sedimented calcium in breast. Typical appearance on both lateral (A) and craniocaudal (B) views allows them confidently to be called benign. No calcifications were seen in opposite breast.

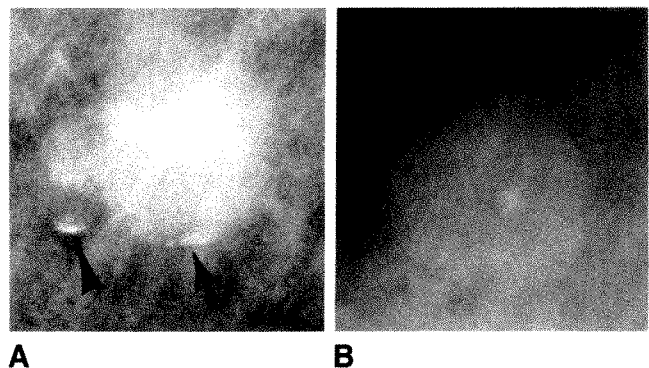


Fig. 3.—Screen-film mammograms show milk of calcium within a macrocyst. When present, milk of calcium allows diagnosis of cyst on basis of mammography alone, without need for sonography.

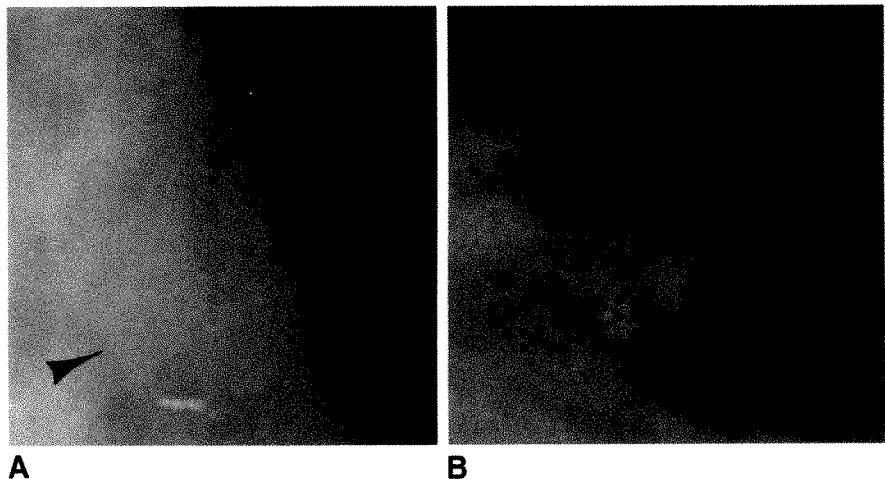
A, Lateral view shows milk of calcium layering dependently within a 1-cm cyst (arrow). Fluid within cyst is seen as water density. Margins of cyst are faintly visible. Milk of calcium is also seen layering dependently in an adjacent, much smaller cyst (arrowhead).

B, Craniocaudal view shows milk of calcium as a smudge centered within water-density cyst. Again, margins of cyst are visible.

Fig. 4.—Screen-film mammograms show sandlike calcifications. Occasionally, sedimented calcium takes form of discrete particles, like grains of sand, which layer dependently within a cyst.

A, Lateral view shows calcium as a linear density with a horizontal orientation. Individual particles are difficult to appreciate. Margins of this 1-cm cyst are faintly visible (arrowheads).

B, Craniocaudal view shows discrete nature of particles better. Margins of cyst are not visible on this view.



within cysts of various sizes were still less common, occurring in 2% of our total population (Figs. 4 and 5). One woman had milk of calcium within a lipid cyst of fat necrosis (Fig. 6).

Of the 183 patients for whom follow-up was available, the sedimented calcifications were unchanged over time in 143 (78%). They increased in number in 19% and decreased in 3% of the 183 patients.

Eight women had biopsy-proved carcinoma, and two had hyperplasia with cellular atypia in breasts that also contained sedimented calcium (Fig. 7). In each case, the carcinoma or atypia was associated with calcifications different in appearance from sedimented calcium, but near or right next to it. These suspicious calcifications prompted biopsy. No biopsies were done when only typical sedimented calcium was seen, but in no case did malignancy develop in one of these benign-appearing areas, as determined by clinical and mammographic follow-up for a period of up to 97 months.

Discussion

Sedimented calcium in the breast can be recognized readily once its various appearances are familiar. The major clue is

the difference in appearance on the two standard views obtained. On the true lateral view, obtained with a horizontal X-ray beam, well-defined, horizontally oriented linear, curvilinear, or teacup shapes are seen, depending on the amount of milk of calcium present [1]. The upper margin of each calcification represents the interface between water-density cystic fluid above and heavier milk of calcium below; the curving lower margin reflects the rounded inferior margin of the cyst. If an oblique view rather than a true lateral is obtained initially, milk of calcium may have an intermediate appearance, but often it is seen as linear or curvilinear shapes with an oblique orientation. On the craniocaudal view, obtained with a vertical X-ray beam, milk of calcium is seen as somewhat ill-defined smudges. These smudges represent heavier, nonparticulate calcific material puddled in the central, most dependent part of cysts. In the case of a microcyst, the margins of the cyst and the water-density fluid it contains will not be visible, although the margins of a macrocyst may be visible.

On the lateral view, sandlike calcific particles sediment within a cyst such that they also are seen as linear, curvilinear, or teacup shapes with a horizontal orientation. Occasionally,

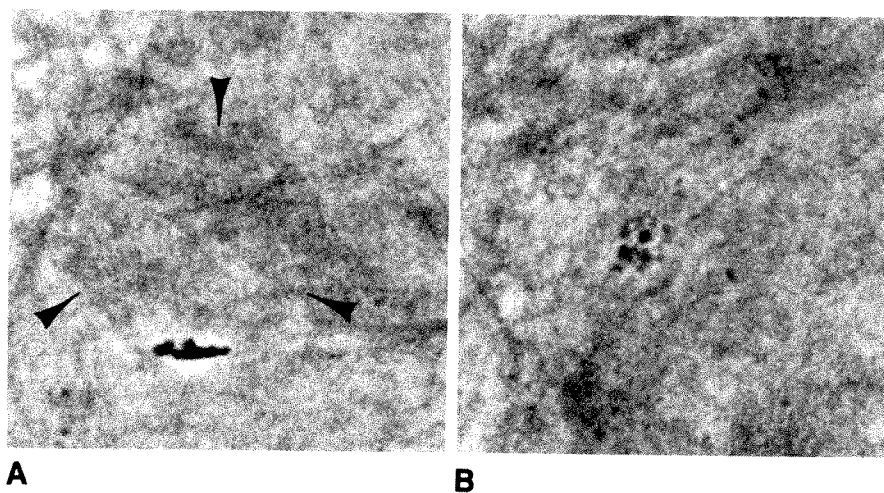


Fig. 5.—Xeromammograms show sandlike calcifications.

A, Lateral view shows calcium as a linear density with a horizontal orientation. Note suggestion of discrete particles piled on each other. Margins of cyst are faintly visible (arrowheads).

B, Craniocaudal view shows discrete particles distinctly.

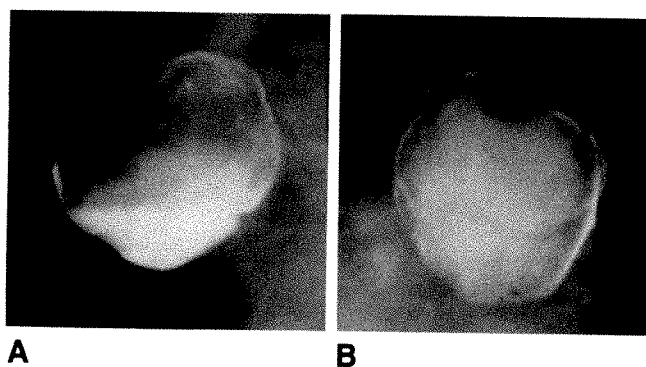


Fig. 6.—Screen-film mammograms show milk of calcium within a lipid cyst of fat necrosis.

A, Lateral view shows fat-calcium layer within a cyst. Rim of cyst is calcified.

B, Craniocaudal view shows milk of calcium as a smudge within calcified rim of cyst.

discrete particles are visible within or immediately above the fluid/calcium interface. On the craniocaudal view, individual calcific particles are usually seen instead of smudges, lying grouped together in the central, most dependent part of the cyst.

Fine-detail magnification views, obtained in the true lateral and craniocaudal projections, are usually helpful in making the confident diagnosis of sedimented calcium.

The most common presentation of sedimented calcium is as milk of calcium within microcysts that are distributed symmetrically between the two breasts, in a scattered and occasionally clustered fashion. The second most common presentation is a single, unilateral cluster of microcysts containing milk of calcium. This distribution, described in several previous reports [1–3], is particularly important to recognize, because other types of unifocal clustered calcifications may suggest malignancy.

Microcysts that are scattered and clustered, but asymmetrically distributed between the two breasts or limited to only one breast, are the third and fourth most common presentations, respectively.

Much less common than any of these is milk of calcium within macrocysts. However, this appearance is important to

recognize as it allows the unequivocal diagnosis of cyst on mammograms, eliminating the need for aspiration or sonography. Another relatively uncommon presentation is discrete, sandlike particles either within microcysts or macrocysts. This form has been described recently [4]. An uncommon presentation is milk of calcium within a lipid cyst of fat necrosis, of which we have seen only one example. This can be distinguished from a simple cyst by the fat density seen within it. Milk of calcium within a galactocele, another fat-density mass, also has been reported [5].

Regarding the natural history of sedimented calcium, the majority (78%) of our cases remained unchanged in appearance during follow-up. However, in 19%, microcysts containing milk of calcium either appeared de novo during follow-up or increased in number. This increase should not raise a suspicion of malignancy, so long as the calcifications have the typical appearance of sedimented calcium. In the single case of milk of calcium within a lipid cyst, the amount of calcium within the cyst increased moderately over 19 months, initially occupying an estimated one third of the cyst volume and later an estimated two thirds. In six of our cases, cysts containing sedimented calcium decreased in number during follow-up. This was apparently a result of spontaneous involution in five cases and aspiration of a macrocyst in the sixth case.

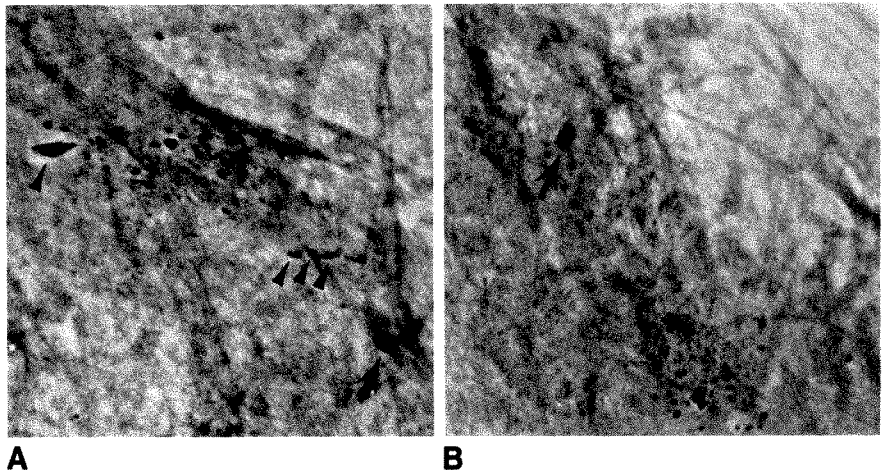
Microcysts in the breast occur so commonly as to be considered normal [6]. Microcysts containing milk of calcium appear to be a subset of this benign condition. Fortunately, carcinoma may arise adjacent to microcysts, and therefore it is important to analyze carefully the characteristics of all the calcifications seen in a given case. We saw eight cases of carcinoma and two of atypical hyperplasia in our primarily symptomatic population; these invariably were associated with microcalcifications different in appearance from sedimented calcium.

In conclusion, the key to recognizing sedimented calcium on mammography is the difference in its appearance between the craniocaudal and lateral or oblique views. When suspected on a combination of oblique and craniocaudal views, a true lateral view should be obtained to confirm the typical appearance. Fine-detail views are often helpful for confident diagnosis. It is important to recognize typical sedimented

Fig. 7.—Xeromammograms show milk of calcium within microcysts, with adjacent carcinoma. This large cluster of microcalcifications includes some typical milk of calcium within microcysts. However, note also numerous irregular tiny calcifications, which prompted biopsy, revealing infiltrating ductal carcinoma.

A, Lateral view shows milk of calcium as tea-cup shapes (densest marked with arrow, others marked with arrowheads). Other calcifications are pleomorphic.

B, Craniocaudal view shows densest collection of milk of calcium as a smudge (arrow). Smaller collections cannot be readily seen. Malignant calcifications are visible as discrete particles, as they appeared on lateral view.



calcium because it is invariably benign. However, it may coexist with other types of calcifications, including malignant calcifications. Thus, consideration should be given to biopsy unless all calcific particles are characteristic of sedimented calcium.

REFERENCES

1. Sickles EA, Abele JS. Milk of calcium within tiny benign breast cysts. *Radiology* **1981**;141:655-658
2. Lanyi M. *Diagnosis and differential diagnosis of breast calcifications*. Berlin: Springer-Verlag, **1986**;11, 51-66
3. Homer MJ, Cooper AG, Pile-Spellman ER. Milk of calcium in breast microcysts: manifestation as a solitary focal disease. *AJR* **1983**;150:789-790
4. Pennes DR, Rebner M. Layering granular calcifications in macroscopic breast cysts. *Breast Dis* **1988**;1:109-112
5. Sickles EA, Vogelaar PW. Fluid level in a galactocoele seen on lateral projection mammogram with horizontal beam. *Breast* **1981**;7(2):32-33
6. Haagensen CD. *Diseases of the breast*, 3rd ed. Philadelphia: Saunders, **1986**:81

Book Review

Antibody-Mediated Delivery Systems. Edited by John D. Rodwell. (Vol. 1 in the series Targeted Diagnosis and Therapy.) New York: Marcel Dekker, 388 pp., 1988. \$99.75

This volume, the first in the series Targeted Diagnosis and Therapy directed toward development and application of antibody conjugates useful for tumor diagnosis and therapy, is a collection of 12 chapters contributed by eminent scientists in the field. Although the text is not divided into sections, the chapters are well organized into three major groups. The first six chapters are devoted to the synthesis and preclinical evaluation of monoclonal antibodies conjugated to a variety of chemotherapeutic agents: daunomycin, Adriamycin (and analog), vinblastine, methotrexate, melphalan (and chlorambucil), and the photoreactive chemical hematoporphyrin. The next two chapters deal with in vitro studies of antibodies coupled to biological-response modifiers: cobra venom factor and ricin toxin A-chain. The last four chapters describe the preparations and applications of monoclonal antibodies conjugated with radioisotopes iodine-131, indium-111, copper-67, and yttrium-90. With the exception of the last chapter, which describes the application of ^{90}Y -conjugated antibodies in animals and in patients for radioimmunotherapy, this excellent reference book is directed mainly toward preclinical evaluations of conjugated antibodies. Several books with collections of chapters from experts who are pursuing research on monoclonal antibodies with appropriate specificities are currently available, but the uniqueness of this volume is that the contributors have presented a detailed review of a particular type of conjugate and the rationale and the chemistry used in its preparation. Most chapters have both an appendix that contains a detailed description of the materials and methods used and an

extensive reference section. Investigators interested in pursuing this field will find the thoroughly described experimental protocols most useful. The style and figures in this volume are of highest quality. Fewer than a dozen typographic errors can be found throughout the text.

Overall, we recommend this reference book enthusiastically to all investigators interested in the state-of-the-art for conjugated antibodies. However, individual investigators may not want to purchase this volume because as with all books describing current methodologies, its usefulness may be limited to a few years. However, this book is a must for all medical libraries, as immunologists, biochemists, radio-pharmacists, radiochemists, biotechnologists, nuclear medicine specialists, and medical oncologists will find it useful.

In the introduction, the editor states that this volume is the first in the series Targeted Diagnosis and Therapy and that near-term books to follow will include subjects such as interferon, interleukin, tissue plasminogen activator, and gene therapy. If the quality of this book is in any way a preview of the quality of books to follow, we eagerly await the publication of the next volumes.

Leela P. Kasi
E. Edmund Kim
The University of Texas
M. D. Anderson Cancer Center
Houston, TX 77030

CT of Primary Lymphoma of the Liver

Linda M. Sanders¹
 Jose F. Botet²
 David J. Straus³
 John Ryan⁴
 Daniel A. Filippa⁵
 Jeffrey H. Newhouse¹

Primary lymphoma of the liver is a rare disease. In each of six cases, a large, often poorly defined mass of low attenuation was present within the liver. Four lesions originated in the right lobe and two originated in the left lobe. Satellite nodules were seen at presentation in one case and developed after presentation in two others. Other features, such as enhancement after contrast administration, necrosis, and calcification, were variable. Three of six lesions had areas of very low density, suggestive of necrosis. One mass had calcifications. After IV contrast administration, no enhancement occurred in three tumors, patchy enhancement occurred in two, and an enhancing ring was seen in the remaining tumor. The radiologic presentation of primary lymphoma of the liver differs from that of secondary involvement of the liver in systemic lymphoma. Whereas secondary lymphoma is often diffusely infiltrative and difficult to detect on CT, the lesions of primary lymphoma of the liver are easily identified on CT scans even before the administration of IV contrast material.

Although rare, primary lymphoma of the liver should be included in the differential diagnosis of a large, hypodense liver mass on CT.

Primary lymphoma of the liver (PLL) is a rare entity, first documented in 1965 [1]. Since then a total of 40 cases have been reported in the clinical and pathologic literature [2-19]. Although descriptions of the appearance of the lesions were included in those reports, no CT images have been published except in one unproved case. In this article, we describe the CT features in six of those patients and discuss the appearance of PLL compared with secondary involvement of the liver in systemic lymphoma.

Subjects and Methods

PLL was diagnosed in nine patients at Memorial Sloan-Kettering Cancer Center between 1972 and 1986. Six of these patients had CT scans that were available for review. We have included the clinical aspects of all nine patients in this section in order to describe the clinical features of this rare entity. The data were obtained from a review of the patients' charts. All nine patients were white men, aged 27 to 76 years (mean, 55.8 years). Presenting symptoms included abdominal pain, fever, night sweats, and weight loss. Physical examination showed hepatomegaly without splenomegaly or adenopathy in all patients. Laboratory data were notable for elevated alkaline phosphatase levels in six patients and elevated serum glutamic oxalacetic transaminase level in four patients. The carcinoembryonic antigen level was within normal range in all seven patients in whom it was measured; the alpha-fetoprotein levels were also within normal limits in all eight patients in whom it was measured.

All nine patients underwent either percutaneous or open liver biopsies and were found pathologically to have malignant, non-Hodgkin lymphoma of the liver. Histologies were predominantly large cell (diffuse histiocytic lymphoma), with or without immunoblastic variation, although one patient had small cell, follicular lymphoma (nodular, poorly differentiated lymphoma). All patients subsequently underwent further staging; this included bone-marrow biopsies in seven patients, CT scans of the chest, abdomen, and pelvis in seven patients, and an exploratory laparotomy in eight patients. In no case did we see involvement of any other site that would have suggested systemic disease; that is, the diagnosis of liver lymphoma was considered primary by all clinical, radiologic, and surgical criteria.

Received October 31, 1988; accepted after revision December 27, 1988.

¹ Department of Radiology, Columbia Presbyterian Medical Center, 622 W. 168th St., New York, NY 10032. Address reprint requests to L. M. Sanders.

² Department of Medical Imaging, Memorial Sloan-Kettering Cancer Center, 1275 York Ave., New York, NY 10021.

³ Department of Medicine, Hematology/Lymphoma Service, Memorial Sloan-Kettering Cancer Center, 1275 York Ave., New York, NY 10021.

⁴ Department of Surgery, Memorial Sloan-Kettering Cancer Center, 1275 York Ave., New York, NY 10021.

⁵ Department of Pathology, Memorial Sloan-Kettering Cancer Center, 1275 York Ave., New York, NY 10021.

AJR 152:973-976, May 1989

0361-803X/89/1525-0973

© American Roentgen Ray Society

Initial CT scans of the liver and abdomen were available for review in six of the nine patients. Nineteen follow-up scans were available in four cases. Of these 25 scans, 17 were performed at Memorial Sloan-Kettering on either a General Electric 9800 scanner or a Technicare 2020 scanner using 10-mm slice thickness. Of the six initial examinations, pre- and postcontrast scans were performed in five; one patient had only a contrast-enhanced study. Between 50 and 100 ml of high osmolality contrast material were administered as a bolus through an antecubital vein; scanning was performed immediately. Scans were analyzed to determine the size and location of the liver masses as well as the presence of necrosis, calcification, and enhancement characteristics of the tumors.

Four of the nine patients underwent partial liver resection. Eight patients received chemotherapy with or without steroids. Four patients received radiation to the liver and abdomen. Of the nine patients, to date six are alive; five are in complete remission and one has shown extraabdominal tumor spread.

Results

Initial CT Findings

Lesions were easily identified as hepatic in origin. Four originated in the right lobe of the liver and two originated in the left lobe. In five cases, the lesions were solitary, multilobulated, and large, ranging in size from 11 × 5 cm to 12 × 17 cm (Fig. 1). In one case, satellite lesions were identified (Fig. 2). Without IV contrast administration, the masses were all hypodense compared with normal liver parenchyma, but higher density than water. Three masses contained central or peripheral areas of very low density, suggestive of necrosis. One mass contained an area of calcification that measured 1.5 × 1.5 cm (Fig. 3). Contrast-enhanced scans were done in six patients—no enhancement at all occurred in three lesions. Patchy, central enhancement was definitely present in one; in one patient with only a postcontrast scan, areas of increased attenuation strongly suggested that enhancement had occurred (Fig. 4). An enhancing ring was present within one lesion.

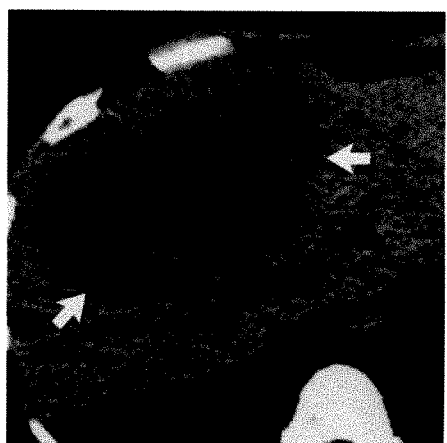
No splenomegaly (defined as one splenic dimension greater than 15 cm) was noted. No mediastinal or retroperitoneal adenopathy (defined as lymph-node diameter greater than 1.0 cm) was present in any patient. No ascites was noted. The portal vein was patent in all cases.

One patient with a mass in the left lobe also had a 4 × 4 cm mass in the porta hepatis, which was felt at surgery to be consistent with regional lymphatic spread of tumor from the primary lesion in the liver. Although this patient's disease could have originated in the portal nodes and metastasized to the liver, the large size of the hepatic tumor in comparison with the small portal mass suggests that the liver lesion was primary. The periportal mass resulted in slight biliary-tree dilatation within the right lobe of the liver. One study showed tumor invasion of the duodenum, which was confirmed at surgery (Fig. 1B).

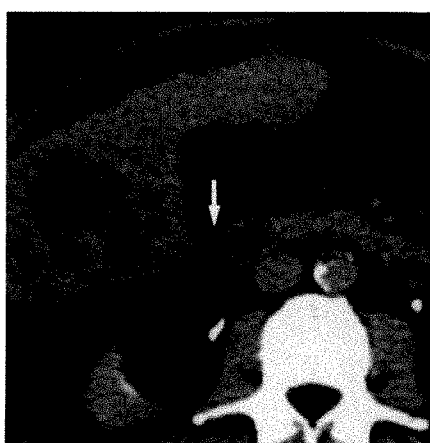
Follow-up CT Scans

Follow-up CT scans were available in four cases. In one patient, who had undergone extended right hepatectomy and combination chemotherapy, follow-up studies revealed compensatory hypertrophy of the left lobe. Lobulated low-density masses appeared in the inferior aspect of the left lobe. Massive ascites was also present. This patient's last study showed resolution of the ascites and only minimal residual low-density areas in the left lobe; however, this patient died.

In a second patient, treated with combination chemotherapy and radiation to the abdomen, follow-up studies at first showed continuing resolution of the mass (Fig. 3B). Subsequently, numerous low-density hepatic masses developed, accompanied by mild splenomegaly and enlarged peripancreatic lymph nodes (Fig. 3C). He underwent a second cycle of combination chemotherapy; his most recent study was normal, and he is currently without evidence of disease, more than 42 months after presentation.



A



B



Fig. 1.—A, Precontrast scan shows large, solitary, low-density mass in right lobe of liver involving medial segment of left lobe (arrows).

B, CT slice at a more caudal level shows tumor invasion of duodenum (arrow), confirmed at surgery.

Fig. 2.—Precontrast scan shows large mass in right lobe with small satellite lesions (arrow).

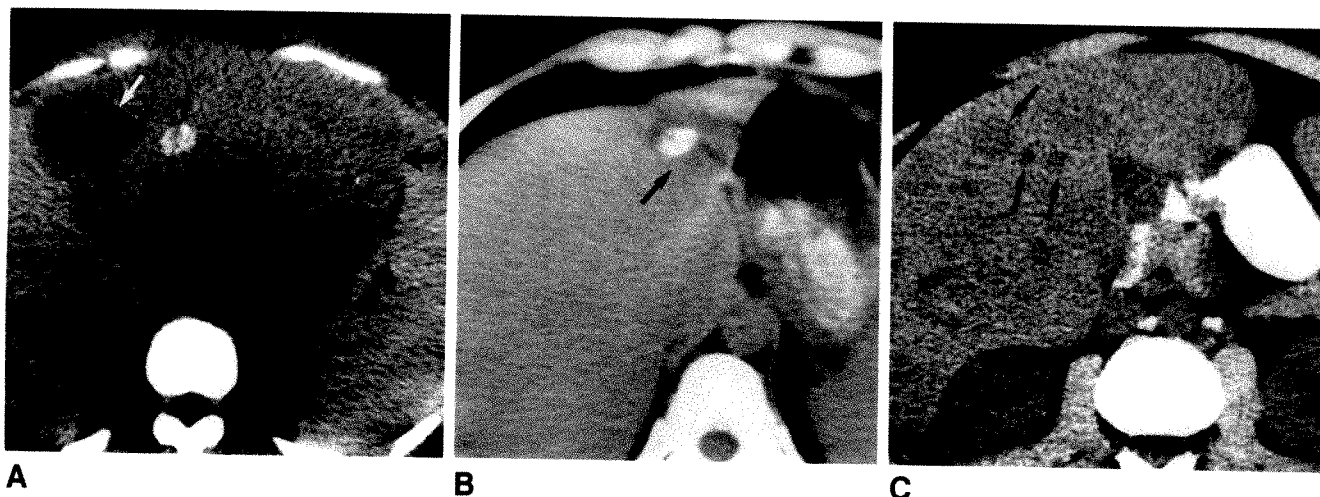


Fig. 3.—A, Postcontrast scan shows large mass in left lobe (large black arrows) with areas of calcification (small black arrow) and necrosis (white arrow).

B, Precontrast scan 13 months later, after chemotherapy and hepatic radiotherapy (800 rad, 8 Gy), shows regression of lesion with residual low density area and calcification (arrow).

C, 15 months after scan in B, follow-up examination shows diffuse liver involvement (arrows), which subsequently regressed with additional chemotherapy. Interaortocaval and left paraaortic structures with dense regions represent enlarged lymph nodes opacified by earlier lymphangiogram.

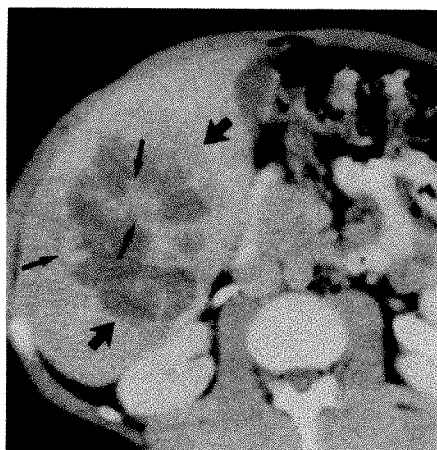


Fig. 4.—Right hepatic lobe mass (large arrows) with patchy enhancement (small arrows) after IV contrast. Left paraaortic low-density structure behind left renal vasculature may represent a small (<1 cm) necrotic lymph node.

In a third patient, treated only with combination chemotherapy, subsequent CT examinations showed regression of the initial lesion followed by progression and development of several satellite lesions. In response to eight additional cycles of combination chemotherapy, both initial and subsequent masses resolved with minimal residual abnormality. The patient shows no evidence of disease 18 months after diagnosis.

The most recent CT on the fourth patient, who was also treated with combination chemotherapy, showed resolution of the liver and the portal masses and no evidence of intraabdominal disease. A cranial CT scan performed 1 year post-presentation showed a large mass in the right temporoparietooccipital lobes that proved to be lymphoma at biopsy.

Discussion

Primary lymphoma of the liver is a rare tumor of the gastrointestinal tract. The stomach and small bowel are the two gastrointestinal organs most frequently involved with primary lymphoma, the CT appearance of which has been well-described [20]. Review of the literature reveals 40 cases of PLL. The disease has a male predominance (31 males, 9 females). Mean age of these patients was 53.4 years (range, 7–84 years).

The liver is often a secondary site of lymphomatous involvement, however; this has been found in approximately half of patients with non-Hodgkin lymphoma and in approximately 60% of patients with Hodgkin disease at autopsy [21–23]. The incidence of hepatic involvement at presentation is much lower. Pathologically, the lesions are often diffusely infiltrative. Discrete nodular lesions are exceedingly uncommon in Hodgkin disease, but occur in half of patients with non-Hodgkin lymphoma [24]. However, nodule size is usually small, under 1 cm [25]. Therefore, the most typical patterns of liver involvement are beyond the resolution for CT detection, even with IV contrast administration. Zornoza and Ginaldi [24] reported that the sensitivity of CT alone in detection of liver lymphoma was 64% and the specificity was 88%. Almost all positive CT scans revealed discrete masses, suggesting that the radiologic detection of liver involvement depends on the presence of extensive disease.

The ability of CT to distinguish PLL from hepatic involvement in systemic lymphoma may be explained by the different sizes of each lesion. Whereas secondary involvement is diffusely infiltrative or sometimes micronodular, PLL seems to present as a large, multilobulated mass. However, the pathologic specificity of this appearance is low. Many other primary tumors of the liver may have this pattern on CT, including benign tumors such as giant cavernous hemangioma [26], focal nodular hyperplasia and adenoma [27], as well as malig-

nant neoplasms such as hepatocellular carcinoma [28], cholangiocarcinoma [29], and certain sarcomas [30]. Metastatic masses may become confluent and also have this appearance [31]. Except in one case with prominent central ring enhancement, enhancement was generally not a significant feature and might help to differentiate PLL from hemangioma, focal nodular hyperplasia, adenoma, or hepatoma. Calcification was definitely present in one case and perhaps two others. Necrosis was seen frequently, in half of the initial CT examinations. Follow-up studies in four patients often showed dramatic resolution of both initial and recurrent lesions, although some minimal residual abnormality was usually evident. This occurred in two patients who are currently doing well and in two other patients, one of whom died and the other of whom developed CNS involvement. Thus, lesion resolution did not always correlate with clinical response.

Earlier descriptions of CT studies of patients with PLL support our findings [15, 16, 19]. Of the 10 cases reported by Osborne et al. [15], nine had focal masses (solitary in three and multiple in six) and one had diffusely infiltrative disease. Three patients in their series, however, also had positive bone-marrow biopsies at the time of diagnosis, which may account for the slight difference in appearance from our six patients, all of whom had negative bone-marrow biopsies at presentation.

REFERENCES

- Ata AA, Kamal IA. Primary reticulum cell sarcoma of the liver: a case report. *J Egypt Med Assoc* 1965;48:514-521
- Rudders RA, Ross ML, DeLellis RA. Primary extranodal lymphoma response to treatment and factors influencing prognosis. *Cancer* 1978;40:406-416
- Hirsch EF. Primary lymphosarcoma of the liver with metastases to the marrow and secondary anemia. *Arch Pathol* 1937;23:674-678
- Torres A. Primary lymphocytic follicular lymphoma of the liver. *Cancer* 1969;23:1185-1189
- Torres A, Bollozos GD. Primary reticulum cell sarcoma of the liver. *Cancer* 1971;27:1489-1492
- Chambers TJ, O'Donoghue DP, Stansfield AG. A case of primary lymphoma of the liver. *J Clin Pathol* 1976;29:967-970
- Talamo TS, Dekker A, Gurecki J, Singh G. Primary hepatic malignant lymphoma: its occurrence in a patient with chronic active hepatitis, cirrhosis and hepatocellular carcinoma associated with hepatitis B viral infection. *Cancer* 1980;46:336-339
- Rauber G, Mehaut M, Schmitt J, Duprez A. Sarcome hépatique de type reticulomyloïde: guérison apparente après 3 ans. *Arch Anat Cytol Pathol* 1966;14:191-194
- Alami SY, Boman RO, Reese MH, Race GJ. Extranodal lymphosarcoma of the left lobe with paraproteinemia. *Arch Intern Med* 1969;123:64-68
- Miller ST, Wollner N, Meyers PA, Exelby P, Jereb B, Miller DR. Primary hepatic or hepatosplenic non-Hodgkin's lymphoma in children. *Cancer* 1983;52:2285-2288
- Fekete F, Molas G, Tossen JC, Degott C, Languille O, Potet F. Lymphome histiocyttaire primitif du foie: étude de deux cas et revue de la littérature. *Gastroenterol Clin Biol* 1983;7:785-791
- Francillon J, Vignal J, Lesbros F, Guyon JM, Jissot E. Lymphosarcome à localisation hépatique pure. *Chirurgie* 1974;100:566-570
- Carter JB. Macroglobulin-producing histiocytic lymphoma of hepatic origin. *Minn Med* 1974;57:22-24
- Leahy MF, Ibrahim EM, Worth AJ. Primary hepatic lymphoma—two case reports and a review of the literature. *Med Pediatr Oncol* 1982;10:575-581
- Osborne BM, Butler JJ, Guarda LA. Primary lymphoma of the liver—ten cases and a review of the literature. *Cancer* 1985;56:2902-2910
- Daniel SJ, Attiye FF, Dire JJ, Pyun HJ, Carroll DS, Attia A. Primary lymphoma of the liver treated with extended left hepatic lobectomy. *Cancer* 1985;55:206-209
- Strayer DS, Reppum TS, Levin M, Deschryver-Keckemetti K. Primary lymphoma of the liver. *Gastroenterology* 1980;78:1571-1576
- Ryan J, Straus DJ, Lange C, et al. Primary lymphoma of the liver. *Cancer* 1988;61:370-375
- Bechtold RE, Karstaedt N, Wolfman NT, Glass TA. Prolonged hepatic enhancement on computed tomography in a case of hepatic lymphoma. *J Comput Assist Tomogr* 1985;9:186-189
- Megibow A, Blathazar E, Naidich D, Bosniak M. Computed tomography of gastrointestinal lymphoma. *AJR* 1983;141:541-547
- Levitan R, Diamond H, Graves L. The liver in Hodgkin's disease. *Gut* 1971;2:60-71
- Kim H, Dorfman R, Rosenberg S. Pathology of malignant lymphoma in the liver: applications in staging. In: Popper H, Schaffner F, eds. *Progress in liver disease*, Vol. 5. New York: Grune & Stratton, 1976:683-698
- Rosenberg S, Diamond H, Jaslowitz B, et al. Lymphosarcoma, a review of 1269 cases. *Medicine* 1961;40:31-84
- Zornoza J, Ginaldi S. CT in hepatic lymphoma. *Radiology* 1981;138:405-410
- Thomas JL, Bernardino ME, Vermess M, et al. EOE-13 in detection of hepatic lymphoma. *Radiology* 1982;145:629-634
- Scatarige JC, Kenny JM, Fishman EK, Herlong FH, Siegelman SS. CT of giant cavernous hemangioma. *AJR* 1987;149:83-85
- Welch TJ, Sheedy PF, Johnson CM, et al. Focal nodular hyperplasia and hepatic adenoma—comparison of CT, ultrasound and scintigraphy. *Radiology* 1985;156:593-595
- Kunstlinger F, Federle MP, Moss MA, Marks W. Computed tomography of hepatocellular carcinoma. *AJR* 1980;134:431-437
- Thorsen MK, Quiroz F, Lawson TL, Smith DF, Foley WD, Stewart ET. Primary biliary carcinoma: CT evaluation. *Radiology* 1984;152:479-483
- Ros PR, Olmsted WW, Dachman AH, Goodman ZD, Ishak KG, Hartman DS. Undifferentiated embryonal sarcoma: radiologic-pathologic correlation. *Radiology* 1986;160:141-145
- Heiken JP, Lee JK, Glazer HS, Ling D. Hepatic metastases studied with MR and CT. *Radiology* 1985;156:423-427

Distinction Between Hemangioma of the Liver and Hepatocellular Carcinoma: Value of Labeled RBC-SPECT Scanning

Masatoshi Kudo^{1,2}
 Katsuji Ikekubo³
 Kazutaka Yamamoto⁴
 Yasuyoshi Ibuki¹
 Megumu Hino³
 Shusuke Tomita¹
 Hideshi Komori¹
 Akio Orino¹
 Akio Todo¹

The role of adding single-photon emission CT (SPECT) to ^{99m}Tc-labeled RBC imaging of the liver was evaluated by specifically focusing on the differentiation between hepatic hemangioma and hepatocellular carcinoma. Planar RBC imaging followed by blood-pool SPECT scanning was performed in 77 patients with a total of 108 hemangiomas and in 29 patients with a total of 46 hepatocellular carcinomas. All lesions were smaller than 5 cm in diameter. Thirty-six (33%) of 108 hemangiomas were detected by planar delayed RBC imaging, whereas 63 (58%) were detected by the delayed RBC-SPECT scan. The smallest hemangioma shown by delayed RBC-SPECT scanning was 1.4 cm in diameter, compared with 1.7 cm by planar RBC scanning. When confined to nodules larger than 1.4 cm in diameter, 42% of hemangiomas (36/85) were detected by planar delayed RBC imaging, whereas 74% (63/85) were detected by delayed RBC-SPECT. Increase in sensitivity was noted in nodules 2.1–4.0 cm in diameter. No hepatocellular carcinomas were shown by delayed RBC planar or SPECT scans.

We concluded that with the addition of SPECT, the sensitivity of delayed RBC scans in the detection of small hemangiomas is considerably improved. Delayed RBC-SPECT scanning can be used to distinguish hemangioma from hepatocellular carcinoma.

Cavernous hemangioma is the most common benign tumor of the liver. With the recent development of high-resolution real-time sonographic equipment, small hemangiomas often have been found incidentally. It has become important to distinguish hemangioma from other malignant tumors, especially hepatocellular carcinoma (HCC), which is a common malignant tumor in the Far East and Africa. The confirmation of hemangioma with sonography or CT is not possible in all cases [1, 2]. Conventional ^{99m}Tc-RBC imaging is a highly specific test for hemangioma [3, 4]; however, its low sensitivity for hemangiomas less than 3 cm in diameter or deeply seated hemangiomas has prevented its widespread use as a confirmation test for hemangioma. Another major controversy is whether or not ^{99m}Tc-RBC imaging can differentiate hemangioma from HCC nodules correctly since both are highly vascular tumors [5, 6].

In this report, we evaluated the role of single-photon emission CT (SPECT) in ^{99m}Tc-RBC imaging of the liver with special concern for the differentiation between hemangiomas and HCCs. In order to clarify its sensitivity in small lesions, small hemangiomas and HCCs less than 5 cm in diameter were selected for study.

Materials and Methods

From July 1981 to April 1988, ^{99m}Tc-labeled RBC planar imaging and SPECT scanning were performed in patients with suspected hemangiomas that were detected by sonography or CT. Of these studies, 77 patients (36 men, 41 women) 24–67 years old (mean, 51) with a total of 108 confirmed hemangiomas smaller than 5 cm in diameter were reviewed. Forty-six proved HCCs smaller than 5 cm in diameter in 29 patients (24 men, 5 women) 38–75 years old (mean, 62) were also studied by ^{99m}Tc-RBC planar and SPECT scanning and were reviewed. The total number of patients included in this study was 105; one patient had HCC

Received November 2, 1988; accepted after revision December 23, 1988.

¹ Department of Medicine, Division of Gastroenterology, Kobe City General Hospital, 4-6, Minatojima-Nakamachi Chuo-ku, Kobe 650, Japan.

² Present address: Divisions of Gastroenterology and Nuclear Medicine, University of California, Davis Medical Center, 4301 X St., Prof. Bldg., Room 2110, Sacramento, CA 95817. Address reprint request to M. Kudo.

³ Department of Nuclear Medicine, Kobe City General Hospital, Kobe 650, Japan.

⁴ Departments of Radiology and Nuclear Medicine, Kyoto University School of Medicine, Shogoin-Kawaramachi, Sakyo-ku, Kyoto 606, Japan.

AJR 152:977–983, May 1989

0361–803X/89/1525–0977

© American Roentgen Ray Society

and hemangioma concurrently. Eighteen of 77 hemangioma patients had multiple hemangiomas.

The diagnosis of hemangioma was confirmed in all patients by angiography ($n = 53$), biopsy ($n = 2$), or clinical follow-up of more than 2 years ($n = 22$). The diagnosis of HCC was confirmed in all patients by surgery ($n = 11$) or clinically ($n = 18$). Clinical confirmation of HCC was based on the fulfillment of the following criteria: underlying chronic liver cirrhosis, no evidence of other malignancy, rising trend of increased α -fetoprotein (>400 ng/ml), characteristic angiographic features, and distinct tumor growth demonstrated by a second angiogram. All 18 patients had angiography more than two times for the purpose of hepatic arterial embolization therapy or infusion chemotherapy. Hemangioma size was measured by angiography ($n = 79$) or sonography ($n = 29$). The size of the HCC nodule was measured by angiography ($n = 35$) or resected specimen ($n = 11$). Thirty-seven of 77 patients with hemangiomas also had chronic hepatitis or liver cirrhosis, and were categorized in the high-risk group for HCC [7]. Eleven of 77 patients with hemangioma had a history of malignancy (one uterine cancer, four colorectal cancer, two gastric cancer, one thyroid cancer, and three breast cancer). Twenty-nine of 77 patients with hemangioma had normal liver function tests and no history of malignancy. All 29 patients with HCC had underlying liver cirrhosis or chronic hepatitis. Patients with suspected hemangiomas were placed in two categories on the basis of this clinical information. Category 1 comprised patients with normal liver function tests and no history of malignancy. Patients who had either an abnormal liver function test or a history of malignancy were assigned to category 2.

RBC labeling was performed in vitro with 20 mCi (740 MBq) of ^{99m}Tc -pertechnetate by using a ^{99m}Tc -RBC labeling kit (CIS kit, Compagnie Oris Industrie S.A., France) [8]. The patients were positioned under a large-field-of-view gamma camera (Ohio Nuclear, Solon, OH; Omega 500, Technicare, Cleveland, OH; or Sigma 410, Sigma, St. Louis, MO) with a low-energy all-purpose parallel-hole collimator. The optimal position was based on lesion location by sonography, CT, or colloid liver scanning. Blood-flow images of the liver were obtained every 4 sec for the first 60 sec after a bolus injection in 66 of 77 hemangioma patients (94 of 108 nodules) and 21 of 29 HCC patients (31 of 46 nodules). For a total of 19 patients, flow studies were not performed since the major goal of the current study was to evaluate the delayed-phase RBC scan. Static images, including anterior, right anterior oblique, right lateral, and posterior views, were obtained at 20 min for 1 million counts in all patients. Delayed blood-pool images at 2 hr were acquired in these four projections. After the conventional RBC blood-pool 2-hr images were obtained, delayed RBC-SPECT scans (360° rotation, 64 view angles, 10 sec/view) were obtained with a General Electric (Milwaukee, WI) model 400T rotating gamma camera and minicomputer. Three tomographic images—transverse, coronal, and sagittal views—were reconstructed by using the filtered

back-projection method with a 0.12 attenuation correction. The images were displayed in 64×64 pixel matrix elements; section thickness was 12.8 mm.

All 105 patients had sonographic examinations with a high-resolution real-time scanner (models 250, 256, 258, and/or 280, Aloka, Tokyo) or sector scanner (model EUB40, Hitachi, Tokyo) with a 3.5-MHz transducer. All 105 patients had precontrast and contrast-enhanced CT studies (General Electric 8800) with ($n = 42$) or without ($n = 63$) a dynamic study. Selective celiac angiography, including infusion hepatic angiography [9], was performed in all 29 HCC patients and in 59 of 77 hemangioma patients.

Two independent investigators with knowledge of the lesion location analyzed the planar RBC and delayed RBC-SPECT images to determine if there was definite increased blood-pool activity compared with normal liver activity at the site of nodules previously shown by sonography or CT. Information about the final diagnosis or the sonographic/CT findings were not given to the investigators at the time of interpretation.

Results

RBC Blood-Flow Imaging

Increased perfusion was shown in 12 of 94 hemangiomas and in 13 of 31 HCCs with ^{99m}Tc -RBC blood-flow imaging. Decreased perfusion was shown in nine hemangiomas and in none of the 31 HCCs. In most of the hemangiomas and HCCs, radioactivity in the tumor was equal to that of the surrounding liver.

RBC Blood-Pool Imaging

The results of ^{99m}Tc -RBC delayed blood-pool imaging for hemangioma and HCC are summarized by categorizing them into five groups according to size (Table 1). No hemangiomas smaller than 1.0 cm in diameter, which were detected incidentally through angiography for coexisting larger hemangiomas, were shown on either planar or SPECT images. Among the hemangiomas 2.1–3.0 and 3.1–4.0 cm in diameter, sensitivity was notably improved with the addition of SPECT, from 43% to 83% and from 62% to 92%, respectively. None of the 46 HCCs that were smaller than 5 cm in diameter were shown with either planar delayed RBC imaging or delayed RBC-SPECT scanning. The relationship between

TABLE 1: Sizes of Hemangioma and Hepatocellular Carcinoma Nodules and Their Detection on ^{99m}Tc Delayed Blood-Pool Imaging

Type of Nodule: Study	No. of Nodules (% of Total) by Size (in cm)					Total
	≤ 1	1.1–2.0	2.1–3.0	3.1–4.0	4.1–5.0	
Hemangioma:						
Planar	0	3 (10)	15 (43)	8 (62)	10 (91)	36 (33)
SPECT	0	11 (38)	29 (83)	12 (92)	11 (100)	63 (58)
Total	20	29	35	13	11	108
Hepatocellular carcinoma:						
Total ^a	1	5	14	12	14	46

^a None of the 46 hepatocellular carcinoma nodules smaller than 5 cm were detected with either planar delayed RBC imaging or RBC-SPECT scanning.

lesion size and results with delayed RBC planar and SPECT scanning are shown in Figure 1. The smallest hemangioma shown with delayed RBC-SPECT scanning was 1.4 cm in diameter, whereas 1.7 cm was the smallest detected with planar delayed RBC scanning. When confined to nodules larger than 1.4 cm, the sensitivity improved from 42% with planar delayed RBC scanning to 74% with the addition of SPECT (Table 2).

Of 45 false-negative nodules detected with delayed RBC-SPECT scans, 28 were smaller than 1.4 cm, two were located adjacent to the heart, two were located adjacent to the right kidney, and four were located adjacent to the large portal vein branch.

Differentiation of Hemangioma from HCC

The specificities for hemangioma by both planar RBC imaging and RBC-SPECT were 100%, resulting in a positive predictive value for hemangioma of 100%. With the addition of SPECT, 27 additional nodules that were not detected with planar RBC scanning were depicted. As a result, hemangiomas were correctly diagnosed and HCCs were correctly excluded by a positive test result from the delayed RBC-SPECT scan in 63 of 85 hemangiomas (Table 2). In an HCC high-risk patient with two hepatic nodules that were both hyperechoic on sonography, only one nodule showed a positive result on the delayed RBC-SPECT scan. Subsequent surgery revealed one nodule to be a hemangioma and the other an HCC. Differentiation between hemangioma and HCC with delayed RBC-SPECT scanning in HCC high-risk patients and an oncology patient are shown in Figures 2–5.

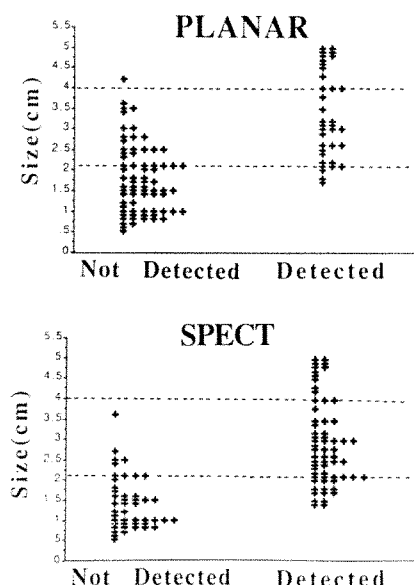


Fig. 1.—Graphs show relationship between size of hemangiomas and results of detection with delayed RBC planar and SPECT scans. SPECT scans significantly depicted nodules in 2.1- to 4.0-cm range (between broken lines), which were not detected on planar scans.

TABLE 2: Differentiation of Hemangioma from Hepatocellular Carcinoma Nodules 1.4–5.0 cm in Diameter on Delayed RBC Scanning

Technique	Hemangioma (n = 85)	Hepatocellular Carcinoma (n = 45)
Planar imaging ^a		
Positive	36	0
Negative	49	45
SPECT ^b		
Positive	63	0
Negative	22	45

^a Sensitivity = 42%; specificity = 100%; accuracy = 62%; positive predictive value = 100%; negative predictive value = 48%.

^b Sensitivity = 74%; specificity = 100%; accuracy = 83%; positive predictive value = 100%; negative predictive value = 67%.

Discussion

RBC Blood-Flow Imaging

Most hemangiomas and HCCs showed perfusion equal to that in surrounding liver on the blood-flow study. This finding does not suggest that most hemangiomas and HCCs have the same vascularity as the surrounding liver, but it does suggest that the planar blood-flow study is not sensitive enough to show the vascular characteristics in the small lesions. As our study shows, the blood-flow study does not appear to contribute to the diagnosis of small hemangiomas less than 5 cm in diameter. However, since this result was obtained from the study dealing with only small hemangiomas, this evidence should not be extrapolated to larger nodules. In some cases of relatively large nodules, a blood-flow study is reported to be essential in the diagnosis of hemangioma [6].

RBC Delayed Blood-Pool Imaging: Contribution of SPECT

The sensitivity of the delayed RBC blood-pool scan was improved with the addition of SPECT. This evidence supports previous studies with smaller numbers of patients [6, 10]. A 74% sensitivity for hemangiomas 1.4–5.0 cm in diameter is considered to be quite satisfactory since this technique is a confirmation test for hemangiomas rather than a screening test. The increase in sensitivity in the detection of nodules 2.1–4.0 cm in diameter (from 48% to 85%) seen in our data is especially encouraging. This is one of the major contributions of SPECT since hemangiomas in this size range are almost commonplace and difficult to detect with planar RBC scanning.

The sensitivities of both planar and SPECT scanning in our study were relatively low compared with previously reported sensitivities of 83–89% for planar RBC scanning [3, 5] and 100% for RBC-SPECT scanning [10]. The reason for this is because the nodules included in our study are considerably smaller than those in previous reports. Our data agree with those of similar series dealing with hemangiomas smaller than 5 cm in diameter [6].

Delayed RBC-SPECT scanning did not detect lesions smaller than 1.4 cm in diameter. This is attributed to the limit

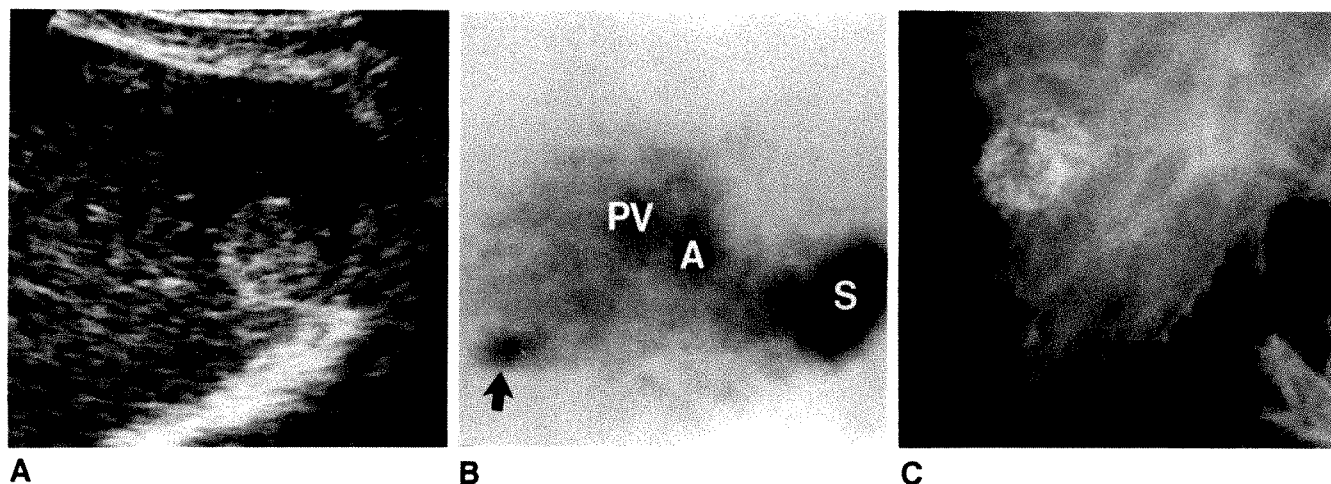


Fig. 2.—Typical sonographic appearance of hemangioma in patient at high risk for hepatocellular carcinoma.

A, Right subcostal sonogram shows solitary, homogeneous, hyperechoic nodule, typical for hemangioma.

B, Transverse image of delayed RBC-SPECT scan shows increased blood-pool activity in lesion (arrow). A = aorta; PV = portal vein; S = spleen.

C, Right hepatic arteriogram, late venous phase, shows findings typical of cavernous hemangioma, which measured 1.7 cm.

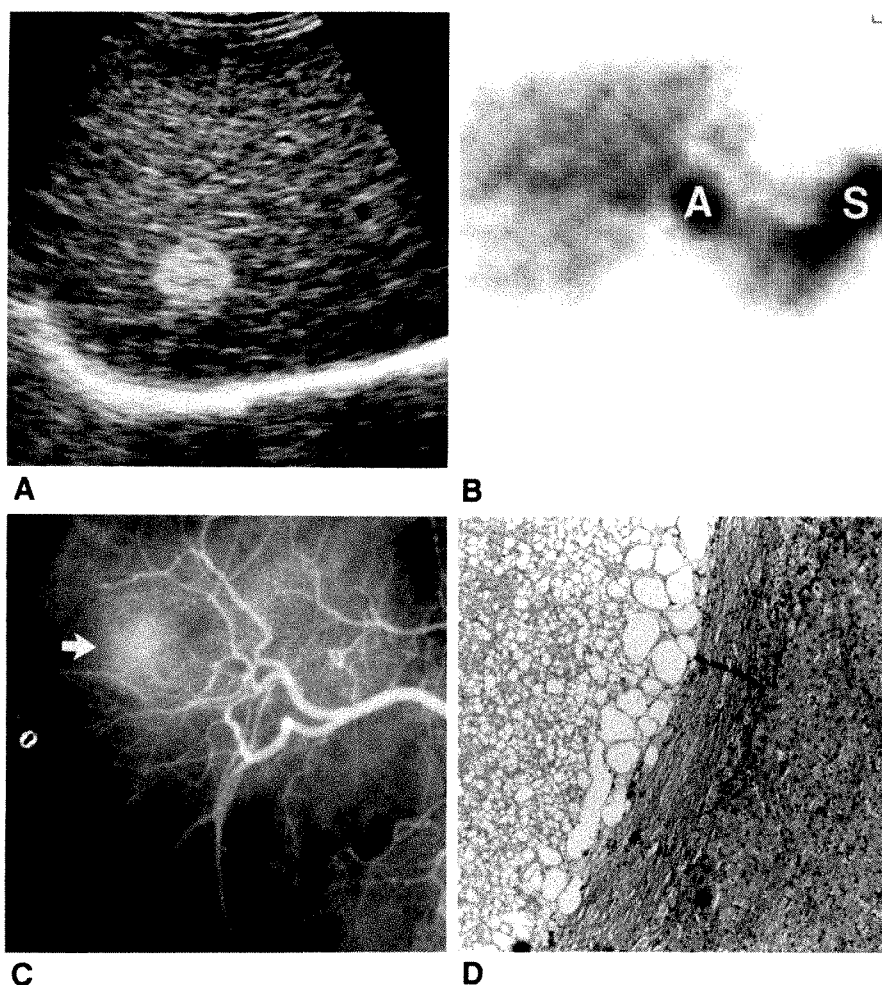


Fig. 3.—Hepatocellular carcinoma simulating hemangioma on sonography.

A, Right subcostal sonogram shows solitary, homogeneous, hyperechoic nodule in right posterior superior segment, which is similar to hemangioma.

B, Delayed RBC-SPECT scan shows no blood-pool activity in corresponding area, suggesting possibility of hepatocellular carcinoma (HCC). A = aorta; S = spleen.

C, Right hepatic arteriogram shows round tumor staining, a finding supportive of small hepatocellular carcinoma (arrow).

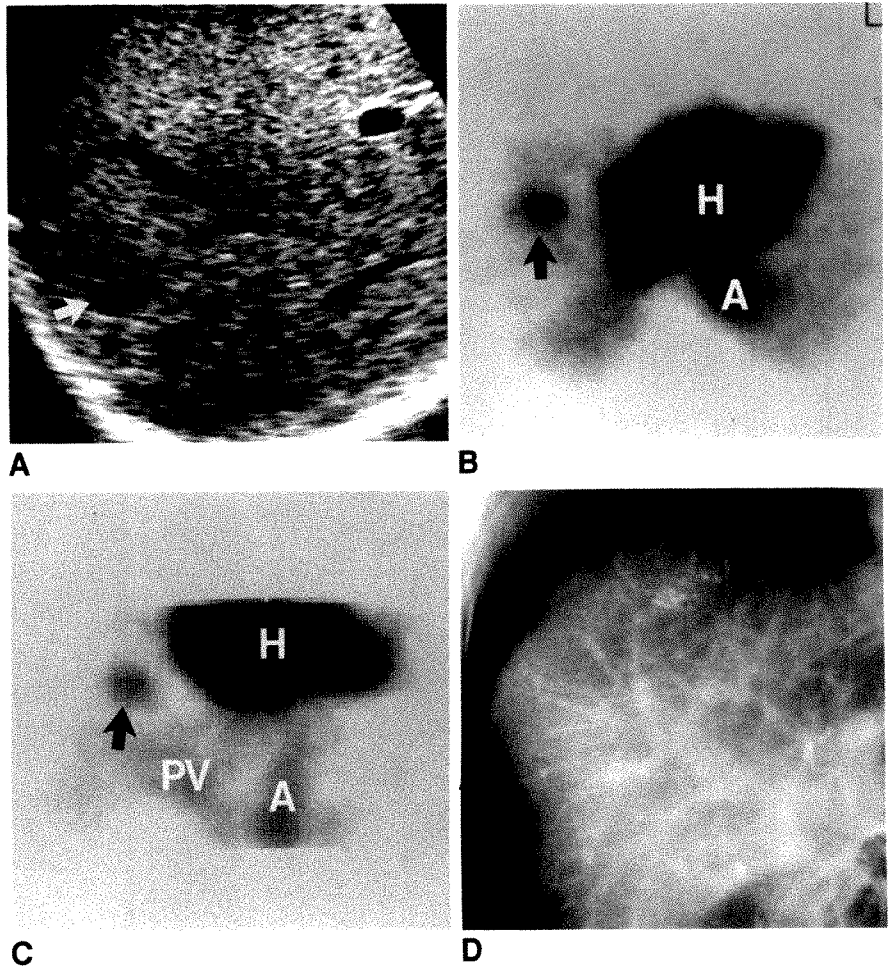
D, Microphotograph of resected specimen shows highly fatty, degenerated (fatty metamorphosis) Edmondson type I-II hepatocellular carcinoma, which is presumed to have caused hyperechoic pattern on sonography, mimicking hemangioma.

Fig. 4.—Atypical sonographic appearance of hemangioma in patient at high risk for hepatocellular carcinoma.

A, Right subcostal sonogram shows solitary, homogeneous, hypoechoic nodule (arrow) in posterior segment of right lobe.

B, and C, Transverse (B) and coronal (C) images of delayed RBC-SPECT scan show increased blood-pool activity, diagnostic for hemangioma (arrows). A = aorta; H = heart; PV = portal vein.

D, Right hepatic arteriogram shows cotton-wool pooling, consistent with hemangioma.



of the resolution of this technique. In addition to these tiny lesions, delayed RBC-SPECT scanning failed to depict lesions adjacent to vascular-rich organs such as heart, kidney, or portal vein. Fibrosis of the lesion is also reported to cause false negatives [4, 5]. Consideration of the disadvantages of this technique is essential in the interpretation of the RBC image and in the management of a suspected hemangioma with a negative RBC study.

Differentiation of Hemangioma from HCC and Other Tumors

No tumors other than hemangiomas have been shown to yield positive findings on delayed blood-pool RBC scanning, except for three HCC cases reported by Rabinowitz et al. [5] and by Drum [11] and one case of hemangiosarcoma reported by Ginsberg et al. [12]. There is an argument as to whether HCC could show increased uptake on delayed RBC scanning. Some authors have stated that HCC could not be excluded on delayed RBC scans because of the three HCC patients with positive delayed RBC studies [5, 6]. A possible explanation for the positive delayed RBC scans in the three HCC patients reported by Rabinowitz et al. and by Drum is that the HCCs were relatively large and advanced so that the delayed RBC scans might have depicted the blood pooling in

the necrotic space (vascular lake), not pooling in the tumor itself. Another possible explanation would be that the three HCCs might have been associated with tumor thrombi in the portal trunk, which are common in advanced HCCs [13], resulting in an increased tumor to nontumor blood-flow ratio due to the lack of portal blood flow. Generally, the relative activity in the hepatic tumor on the delayed RBC scan is a function of the vascularity of the tumor and the blood-flow ratio of hepatic artery to portal vein. Therefore, it is possible that an extremely hypervascular HCC nodule superimposed on severe liver cirrhosis could show increased uptake compared with surrounding liver parenchyma on delayed RBC scans. However, although our series also included such cases as extremely hypervascular HCCs with severe cirrhosis, the results with SPECT, which permits precise analysis of the vascularity in the tumor by improved image contrast, clearly revealed that HCC had no blood pooling during the delayed phase of the RBC scan in nodules less than 5 cm in diameter. Therefore, from our present experience and other reports [3, 4], we believe HCC lesions less than 5 cm in diameter can be correctly ruled out by delayed RBC-SPECT scanning if a positive result is obtained. Further experience, however, is necessary to determine whether or how advanced-stage HCC could appear positive on delayed RBC scanning.

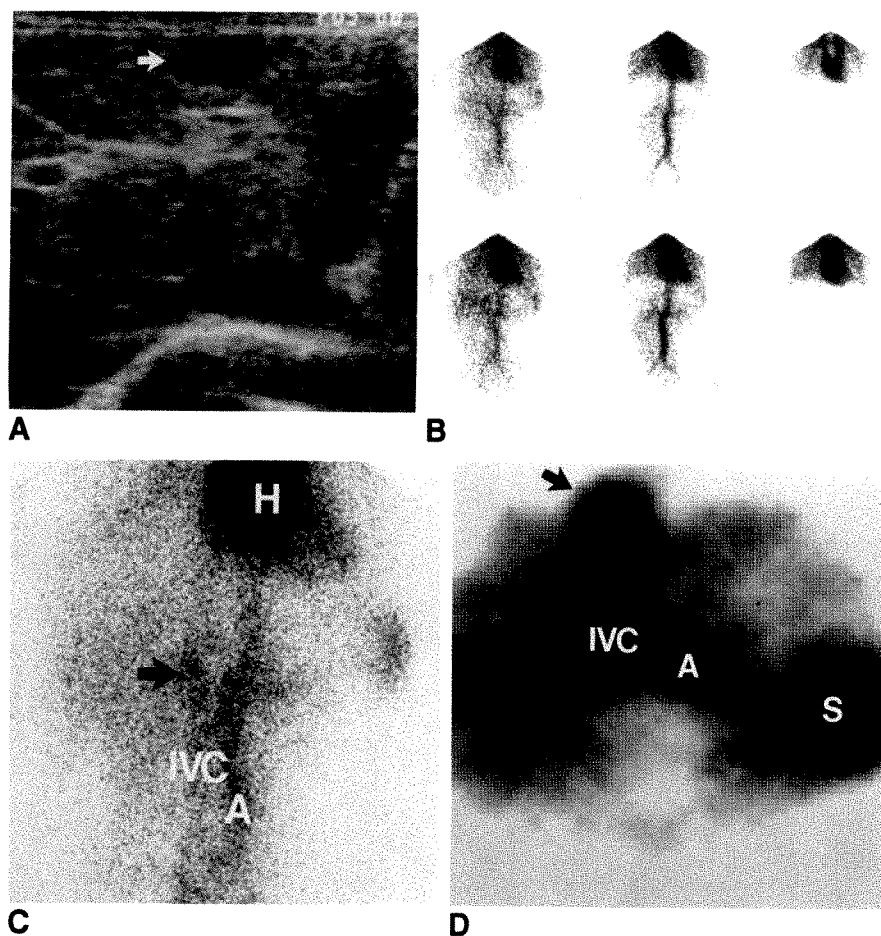


Fig. 5.—Atypical sonographic appearance of hemangioma in patient with history of colon cancer and chronic hepatitis.

A, Right subcostal sonogram shows hypoechoic oval nodule measuring 1 × 2 cm in medial segment of left lobe (arrow).

B, RBC blood-flow study shows perfusion equal to that in surrounding liver.

C, Delayed RBC blood-pool planar scan shows increased uptake at region corresponding to sonogram (arrow). However, this finding is not definite because uptake is overlapping with inferior vena cava (IVC). H = heart; A = aorta.

D, Delayed RBC-SPECT scan clearly shows increased uptake at region corresponding to sonogram, confirming hemangioma (arrow). Size and pattern of nodule remained constant during 4 years of CT and sonographic follow-up. A = aorta; IVC = inferior vena cava; S = spleen.

Ginsberg et al. [12] reported a case of hepatic hemangiosarcoma that showed a positive delayed blood-pool scan. Considering a histology similar to hemangioma, it is possible that hemangiosarcoma shows findings similar to those of hemangiomas on delayed RBC blood-pool scans. However, because selective arteriography is not the gold standard for the diagnosis of hemangiosarcoma [14, 15] and because hemangiosarcoma is a very rare tumor [16], the possibility of hemangiosarcoma is almost negligible except in the patients with a history of chronic exposure to thorotrast, vinyl chloride, arsenicals, or radium, or with a history of hemochromatosis. Other tumors such as liver metastasis [3, 5, 6, 10, 17], abscess [5, 6, 10], cyst [3, 5, 10], adenoma [6], and cirrhotic nodule [3] have been proven to show no increased accumulation on the delayed-phase RBC scan.

Management Scheme for Suspected Hemangioma

With the development of sonography and CT, hemangiomas can be diagnosed without angiography or biopsy. A confirmation test is not necessary for the patient in category 1 with typical CT and/or sonographic findings. However, a confirmation test is still essential for category 1 patients with atypical CT/sonographic findings and for category 2 patients regardless of the CT/sonographic findings.

The CT findings of hemangioma are not specific, although its utility in the diagnosis is well established [2, 18–20]. When strict criteria are applied to improve the specificity by using the delayed dynamic bolus CT technique, the sensitivity decreases to 55% [2]. The complete isodense fill-in on the delayed CT scan is a fairly specific finding for hemangioma; however, since it is very difficult to determine the exact time it should occur, the role of dynamic CT in the confirmation of hemangioma is still limited.

Similarly the sonographic findings of hemangioma are not specific, even if the typical findings of solitary, homogeneous, hyperechoic lesions are demonstrated. A solitary, homogeneous, hyperechoic mass can also be seen in liver cell adenoma, focal nodular hyperplasia, solitary metastasis, and HCC [1, 21–24]. Small HCCs with fatty metamorphosis are often shown on sonography as hyperechoic nodules very similar to hemangiomas, which is a big pitfall in the diagnosis of HCC [25]. Liver metastasis can also present a hyperechoic pattern, especially in adenocarcinoma, with relatively well-developed fibrous tissue [23]. Therefore, even if sonography shows typical findings of hemangioma, patients in category 2 need to have further confirmation testing to rule out HCC or metastasis.

Delayed RBC scanning has been used as a noninvasive confirmation tool for hemangioma, yet it was not sensitive

enough to depict small or deeply seated lesions. However, with the sufficient improvement in sensitivity with the addition of SPECT, as well as the 100% positive predictive value demonstrated in this study, we wish to emphasize that delayed RBC-SPECT scanning should be included routinely as a noninvasive confirmatory tool in the management scheme of suspected hemangiomas. Itai et al. [20] recommend angiography for nodules smaller than 3 cm in oncology patients or in patients at high risk for HCC, even when sonography and CT have yielded findings supportive of hemangioma. We generally agree with the described management scheme for suspected hemangiomas; however, we do suggest that these patients be tested with the delayed RBC-SPECT scan before angiography so that angiography can be avoided in some cases. In our series, one patient had both HCC and hemangioma. Therefore, even if one of the multiple nodules detected on CT or sonography shows a positive result with delayed RBC-SPECT scanning, angiography is strictly recommended for the negative nodules, especially in category 2 patients.

Conclusions

With the addition of SPECT, the sensitivity of delayed RBC scanning for showing hemangiomas 1.4–5.0 cm in diameter was improved from 42% to 74%. The increase in sensitivity was notable, especially in the hemangiomas 2.1–4.0 cm in diameter (from 48% to 85%). In addition, delayed RBC-SPECT scanning has a 100% positive predictive value with a positive test result for the diagnosis of hemangioma so that further invasive diagnostic tests can be avoided. With this improvement in diagnostic capability, we recommend that delayed RBC-SPECT scanning be performed to confirm the diagnosis of hemangiomas detected by sonography or CT, especially in patients in the high-risk group for HCC or with a history of malignancy.

ACKNOWLEDGMENTS

We thank Robert C. Stadalnik, Division of Nuclear Medicine; John P. McGahn, Division of Diagnostic Radiology; and Dr. Anthony Haulk, Division of Gastroenterology, University of California, Davis Medical Center, for critical review of the manuscript. We also thank Dusan P. Hutak, Katherine E. Kanagaki, and Cheryl H. Kirito for help in manuscript preparation.

REFERENCES

- Bree RL, Schwab RE, Neiman HL. Solitary echogenic spot in the liver: is it diagnostic of a hemangioma? *AJR* 1983;140:41–45
- Freeny PC, Marks WM. Hepatic hemangioma: dynamic bolus CT. *AJR* 1986;147:711–719
- Engel MA, Marks DS, Sandler MA, Shetty P. Differentiation of focal intrahepatic lesions with ^{99m}Tc -red blood cell imaging. *Radiology* 1983;146:777–782
- Moinuddin M, Allison JR, Montgomery JH, Rockett JF, McMurray JM. Scintigraphic diagnosis of hepatic hemangioma: its role in the management of hepatic mass lesions. *AJR* 1985;145:223–228
- Rabinowitz SA, McKusick KA, Strauss HW. ^{99m}Tc red blood cell scintigraphy in evaluating focal liver lesions. *AJR* 1984;143:63–68
- Brodsky RI, Friedman AC, Maurer AH, Radecki PD, Caroline DF. Hepatic cavernous hemangioma: diagnosis with ^{99m}Tc -labeled red cells and single-photon emission CT. *AJR* 1987;148:125–129
- Kudo M, Hirasa M, Takakuwa H, et al. Small hepatocellular carcinomas in chronic liver disease: detection with SPECT. *Radiology* 1986;159:697–703
- Bardy A, Fouye H, Gobin R, et al. Technetium-99m labeling by means of stannous pyrophosphate: application to bleomycin and red blood cells. *J Nucl Med* 1975;16:435–437
- Wirtanen GW. A new angiographic technique in the diagnosis of liver tumor. *Radiology* 1973;108:51–54
- Tumeh SS, Benson C, Nagel JS, English RJ, Holman BL. Cavernous hemangioma of the liver: detection with single photon emission computed tomography. *Radiology* 1987;164:353–356
- Drum DE. The radiocolloid liver scan in space-occupying disease. *Appl Radiol* 1982;11:115–122
- Ginsberg F, Slavin JD Jr, Spencer RP. Hepatic angiosarcoma: mimicking of angioma on three-phase technetium-99m red blood cell scintigraphy. *J Nucl Med* 1986;27:1861–1863
- Okuda K, Nakashima T. Primary carcinomas of the liver. In: Berk JE, ed. *Bockus gastroenterology*, vol. 5, 4th ed. Philadelphia: Saunders, 1985:3315–3376
- Whelan JG, Creech JL, Tamburro CA. Angiographic and radionuclide characteristics of hepatic angiosarcoma found in vinyl chloride workers. *Radiology* 1976;118:549–557
- Kudo M, Hirasa M, Takakuwa H, et al. A case of hepatic hemangiosarcoma associated with Kasabach-Merritt syndrome and intraperitoneal bleeding. *Acta Hepatol Jpn (Kanzou)* 1984;25:1605–1611
- Locker GY, Doroshov JH, Zwelling LA, et al. The clinical features of hepatic angiosarcoma: a report of four cases and a review of the English literature. *Medicine (Baltimore)* 1979;58:48–64
- Front D, Israel O, Groshar D, Weininger J. Technetium-99m-labeled red blood cell imaging. *Semin Nucl Med* 1984;14:226–250
- Freeny PC, Vimont TR, Barnett DC. Cavernous hemangioma of the liver: ultrasonography, arteriography, and computed tomography. *Radiology* 1979;132:143–148
- Barnett PH, Zerhouni EA, White RI Jr, Siegelman SS. Computed tomography in the diagnosis of cavernous hemangioma of the liver. *AJR* 1980;134:439–447
- Itai Y, Ohtomo K, Araki T, Furui S, Iio M, Atomi Y. Computed tomography and sonography of cavernous hemangioma of the liver. *AJR* 1983;141:315–320
- Green B, Bree RL, Goldstein HM, Stanley C. Gray scale ultrasound evaluation of hepatic neoplasms: patterns and correlations. *Radiology* 1977;124:203–208
- Kamin PD, Bernardino ME, Green B. Ultrasound manifestations of hepatocellular carcinoma. *Radiology* 1979;131:459–461
- Scheible W, Gosink BB, Leopold GR. Gray scale echographic patterns of hepatic metastatic disease. *AJR* 1977;129:983–987
- Taboury J, Porcel A, Tubiana JM, Monnier JP. Cavernous hemangiomas of the liver studied by ultrasound. *Radiology* 1983;149:781–785
- Yoshikawa J, Matsui O, Takashima T, et al. Fatty metamorphosis in hepatocellular carcinoma: radiologic features in 10 cases. *AJR* 1988;151:717–720

Book Review

X-Ray Differential Diagnosis in Small Bowel Disease. A Practical Approach. By J. L. Sellink. Boston: Kluwer, 182 pp., 1988. \$99.50

This text on diagnosis of diseases of the small bowel by means of enteroclysis is the latest of several similar volumes written by Sellink since 1971. Sellink pioneered the use of single-contrast enteroclysis, and this volume is a distillation of his vast experience with this examination.

The first 40 pages of the book are devoted to the practical aspects of performing single-contrast enteroclysis and how to avoid the common errors and pitfalls. The remainder is an atlas of diseases of the small bowel as demonstrated by this method. The pathologic material is presented in a "pattern" approach and is divided into sections dealing with normal appearances, changes in intestinal length and diameter, thickening of mucosal folds, destruction of the mucosa, and so forth. In each section, an extensive differential diagnosis is presented. The quality of the illustrations is excellent.

This text is unique in at least two aspects. First, it brings to the reader the enormous experience of Dr. Sellink in performing enteroclysis for the past two decades. Dr. Sellink is one of the world's great gastrointestinal radiologists, and this book is replete with hundreds of unique observations on both the technical and interpretive aspects of radiology of the small bowel. Second, the book is an exposition on the technique and findings of the single-contrast method of enteroclysis, which is widely used in Europe for detailed examination of

the small bowel. Having learned to perform single-contrast enteroclysis from Dr. Sellink, I can testify as to its effectiveness as a method for examination of the small bowel.

This textbook does have some negative aspects that should be noted. First, Dr. Sellink occasionally uses spelling and medical terminology that is not standard English usage. These variances appear to be improper translations of medical terms of European origin. Second, the book has neither references nor an index. The lack of an index is compensated for by the detailed table of contents. However, the excellent reference lists included in the author's previous books should have been included in this text also.

Despite its deficiencies, this is one of the most valuable books in print on radiology of the small bowel. It is challenged only by Sellink's earlier 1982 volume written with Roscoe E. Miller. For the reader looking for an unequalled presentation of the radiology and differential diagnosis of diseases of the small bowel, this latest work by Sellink is highly recommended.

David W. Gelfand
Bowman Gray School of Medicine
Winston-Salem, NC 27103

Case Report

Hepatic Perfusion in Cavernous Transformation of the Portal Vein: Evaluation by Using CT Angiography

Norio Nakao,¹ Kohi Miura,¹ Hideo Takahashi,¹ Takashi Miura,¹ Hiroshi Ashida,² Yoshio Ishikawa,² and Joji Utsunomiya²

Dilatation of the small periportal veins sometimes occurs when the main trunk of the extrahepatic portal vein is obstructed, creating hepatopetal collateral pathways that carry blood from the portal vein to the liver. This results in a condition termed cavernous transformation of the portal vein. To our knowledge, few detailed studies have been done to examine the intrahepatic distribution of blood supplied through such collateral pathways via the liver hilum.

The authors performed CT angiography during the arterial and portal phases in a case of cavernous transformation to evaluate in detail the hepatic distribution of arterial and portal blood. The blood distribution could be mapped clearly and divided into three main areas supplied, respectively, by the hepatic artery, the portal vein, and both vessels.

Case Report

An 18-year-old woman was admitted with the diagnosis of esophageal varices. Past medical history was not remarkable. The RBC count was $333 \times 10^4/\text{ml}$, hemoglobin 8.4 g/dl, hematocrit 25.0%, WBC 3900/ml, platelet count $1.5 \times 10^4/\text{ml}$, total plasma proteins 73 g/l, serum glutamic-oxaloacetic transaminase 317.3 nmol sec⁻¹/l, serum glutamic-pyruvic transaminase 350.7 nmol sec⁻¹/l, total bilirubin 7 $\mu\text{mol/l}$, albumin 34.8 g/l, lactic dehydrogenase 5126.9 nmol sec⁻¹/l, alkaline phosphatase 83.5 nmol sec⁻¹/l, and alpha-fetoprotein 5 ng/dl.

Barium examination revealed esophageal and gastric varices. CT scans showed splenomegaly and a normal liver.

Angiography revealed that the left hepatic artery arose from the celiac artery, and the right hepatic artery arose from the superior mesenteric artery. A selective right hepatic arteriogram (Fig. 1) revealed mild dilatation of the hepatic artery and a slightly hypervascular

area in the liver hilum. Branches of the left hepatic artery and left portal vein were also visualized in the hilum.

A superior mesenteric portogram (Fig. 2) revealed obstruction of the main trunk of the portal vein. Blood was carried to the liver through hepatopetal collaterals around the obstructed portal vein. These collaterals appeared to end in the medium-sized intrahepatic portal veins.

CT arteriography and portography (Fig. 3) showed that the liver could be divided with respect to perfusion into three areas of almost equal size: an area perfused by the artery, another perfused by the portal vein, and a third area perfused by both.

The varices were treated by endoscopic sclerotherapy, followed 2 months later by splenectomy and esophageal transection. During surgery, we found marked stenosis of the main trunk of the portal vein (about 5 mm in diameter). Portal blood pressure was 19.9 mm Hg. Liver biopsy disclosed dilatation of the central vein, as well as moderate parenchymal fibrosis.

Two years after the operation, the esophageal varices recurred. In the 6 years since the surgery, the patient has occasionally had slight hematemesis but is presently enjoying satisfactory health.

Discussion

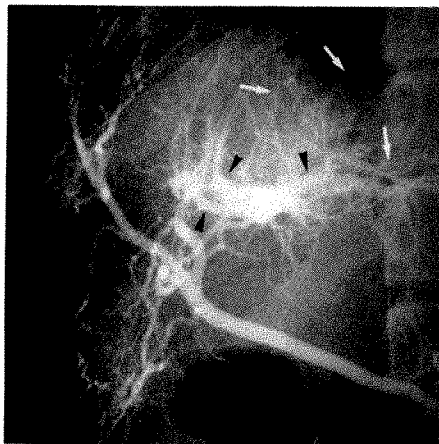
Cavernous transformation of the portal vein was first reported by Balfour and Stewart in 1869 [1]. Since then, many investigators have studied the condition [2-4]. Most agree that it is induced by obstruction of the extrahepatic portal vein. It may be a compensatory phenomenon for maintaining portal blood flow to the liver.

The CT findings of cavernous transformation have been described [5, 6]. However, no detailed study of the intrahepatic distribution of portal blood in such patients has been reported. CT angiography in our patient showed three distinct

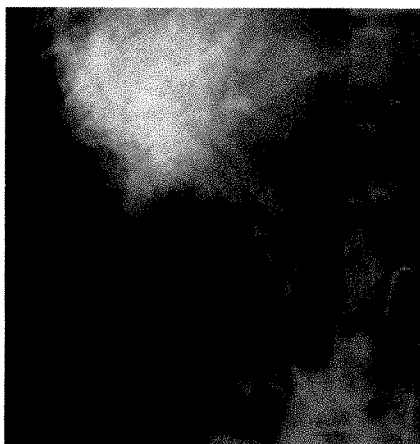
Received September 7, 1988; accepted after revision October 25, 1988.

¹ Department of Radiology, Hyogo College of Medicine, 1-1 Mukogawa-cho, Nishinomiya 663, Japan. Address reprint requests to N. Nakao.

² Department of Surgery, Hyogo College of Medicine, 1-1 Mukogawa-cho, Nishinomiya 663, Japan.



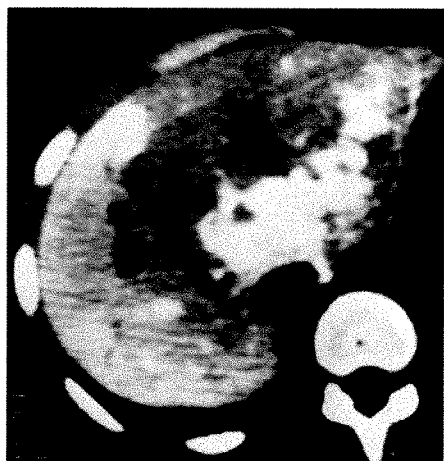
1



2

Fig. 1.—Right hepatic arteriogram shows a hypervascular area near liver hilum. Branches of left hepatic artery (arrows) and portal vein (arrowheads) are also visible in hilum.

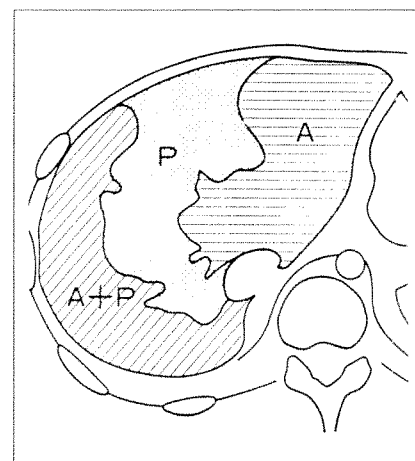
Fig. 2.—Superior mesenteric portogram shows obstruction of extrahepatic portal vein. Cavernous transformation terminates in medium-sized intrahepatic portal veins.



A



B



C

Fig. 3.—A, Dynamic CT arteriogram 20 sec after infusion of 8 ml of contrast material through hepatic artery reveals uneven intrahepatic distribution of arterial blood.

B, CT portogram 20 sec after infusion of 20 ml of contrast material through superior mesenteric artery reveals an uneven distribution of portal blood.

C, Diagram shows a maplike area perfused by hepatic artery (A) and/or portal vein (P).

areas of blood perfusion. The large irregular area of low density with diminished hepatic arterial blood flow in the center of the liver shown on the CT arteriogram (Fig. 3A) is probably due to partial obstruction of the intrahepatic arterial branches as a consequence of perinatal infection. One indication is the area in the center of the right lobe with diminished blood flow in the intrahepatic arterial branches.

Perinatal infection is also strongly indicated by the hypervascular lesion with an arteriportal shunt visible in the liver hilum on the hepatic arteriogram. The liver hilum and left lobe appear as areas of high density on the CT arteriogram because of the hypervascular lesion in the liver hilum and the arterial blood flowing slowly through the thick, tortuous portal vein via the arteriportal shunt.

In the CT portogram (Fig. 3B), the left lobe of the liver is an area of low density. Although this may partially be caused by incomplete recanalization of the intrahepatic portal branches, the principal reason is that high-pressure arterial blood is flowing into the branches of the portal vein through the arteriportal shunt, preventing low-pressure portal blood from flowing into these branches.

The localized area of high density visible in the low-density area in the left lobe of the liver (Fig. 3B) corresponds to the portoportal collaterals and their feeding area near the liver

hilum, as shown in the superior mesenteric portogram (Fig. 2).

Although the cause of portal obstruction in this case was not identified, the obstruction was found to be a presinusoidal portal vein obstruction, because liver biopsy revealed no liver cirrhosis and there were no stenotic changes in the central vein. Only moderate fibrosis was found in the liver parenchyma. Moreover, hepatic venography indicated numerous venous-venous anastomoses, which are typical in presinusoidal portal vein obstruction.

REFERENCES

1. Balfour GW, Stewart G. Case of enlarged spleen complicated with ascites, both depending upon varicose dilatation and thrombosis of the portal vein. *Edinburgh Med J* 1869;14:589-599
2. Klemperer P. Cavernomatous transformation of the portal vein. *Arch Pathol* 1928;6:353-377
3. Parker RA, Seal RME. Cavernous transformation of the portal vein. *J Pathol Bacteriol* 1955;70:97-103
4. Rosch J, Dotter CT. Extrahepatic portal obstruction in childhood and its angiographic diagnosis. *AJR* 1971;112:143-149
5. McCain AH, Bernardino ME, Sones PJ Jr, Berkman WA, Casarella WJ. Varices from portal hypertension: correlation of CT and angiography. *Radiology* 1985;154:63-69
6. Mathieu D, Vasile N, Dibia C, Grenier P. Portal cavernoma: dynamic CT features and transient differences in hepatic attenuation. *Radiology* 1985;154:743-748

Is Routine Chest Radiography Required with Biliary Lithotripsy?

Dermot E. Malone¹
 Christoph D. Becker^{1,2}
 Nestor L. Müller¹
 H. Joachim Burhenne¹

Routine pre- and postlithotripsy chest radiographs are usually obtained on patients undergoing biliary extracorporeal shock-wave lithotripsy. To evaluate the need for this procedure, we reviewed posteroanterior and lateral chest radiographs obtained before and after 107 lithotripsy sessions in 75 patients. In each case, posteroanterior and lateral chest radiographs were obtained as a routine baseline (not to detect incidental abnormalities) before the patient was scheduled for lithotripsy. Posteroanterior and lateral chest radiographs were obtained routinely after each lithotripsy session. Seventy-five patients had 107 lithotripsy sessions on a second-generation lithotripter. Sixty had gallbladder stones, five had cystic duct stones, and 10 had common duct stones. All chest radiographs were reviewed by a chest radiologist. No pulmonary or pleural changes occurred after lithotripsy.

We conclude that routine pre- and postlithotripsy chest radiographs are not warranted in patients undergoing biliary lithotripsy.

Biliary extracorporeal shock-wave lithotripsy is a rapidly developing field. The method involves focusing shock waves on the gallstones. Any soft-tissue damage is undesirable. Some instances of pulmonary abnormalities following experimental lithotripsy in animals have been reported [1, 2]. In our hospital, all patients undergoing biliary lithotripsy have had preliminary chest radiographs, and each lithotripsy session has been followed by chest radiographs. A similar approach has been adopted by the leading European lithotripsy group [3]. No reports of pulmonary damage due to the procedure in humans have appeared in the literature. We performed this retrospective study to evaluate the role of routine chest radiographs with biliary lithotripsy.

Subjects and Methods

Between November 1987 and July 1988, 85 patients with cholelithiasis had 130 biliary extracorporeal shock-wave lithotripsy sessions in this institution. All patients had posteroanterior (PA) and lateral chest radiographs performed in the radiology department within 24 hours of the lithotripsy. Only lithotripsy sessions for which both preliminary and postlithotripsy PA and lateral radiographs were available were included in this study. If there were no preliminary radiographs for the first lithotripsy session, but those obtained after the session were normal, they were accepted as preliminary radiographs for any subsequent lithotripsy sessions.

Posteroanterior and lateral chest radiographs were available for 107 lithotripsy sessions (75 patients). Sixty-five sets of films were from first-session treatments, 28 were from second-session treatments, and 14 were from third-session treatments. The mean time between treatments was 18 days (range: 2–188 days). Sixty of these patients had gallbladder stones, 10 had common duct stones, and five had cystic duct stones.

The patients were treated on an unmodified second-generation extracorporeal lithotripter (Lithostar, Siemens, Erlangen, West Germany). The shock waves were generated electromagnetically. The undertable shockhead was advanced, with the patient prone, and the shockhead membrane was coupled with the patient's skin using coupling gel. Fluoroscopy

Received November 14, 1988; accepted after revision December 30, 1988.

¹ Department of Radiology, University of British Columbia and Vancouver General Hospital, 855 W. 12th Ave., Vancouver, B.C., Canada V5Z 1M9. Address reprint requests to H. J. Burhenne at Vancouver General Hospital.

² Present address: Department of Diagnostic Radiology, University of Bern, Inselspital, 3010 Bern, Switzerland.

AJR 152:987–989, May 1989

0361–803X/89/1525–0987

© American Roentgen Ray Society

was used for targeting. Oral cholecystographic contrast medium (Telepaque [iopanoic acid] 6 g and Orografin [ipodate sodium] 3 g) was given to patients who had gallbladder stones. Patients with stones in the common bile duct or cystic duct received a direct injection of contrast (Conray [iothalamate meglumine] 60%) via a nasobiliary or percutaneous transhepatic catheter.

The capacitor voltage of the shock-wave generator ranged from 10 to 19 kV. At an intermediate capacitor voltage (15.1 kV), focal positive peak pressure in vitro was approximately 25 MPa. The focal region, in which the pressure was more than 50% of the maximum, measured about 90 mm in the long axis and 10 mm in the transverse axis [4]. In all cases, we directed the long axis of the shock-wave field away from the lungs.

All chest radiographs were reviewed by an experienced chest radiologist. Posteroanterior and lateral radiographs obtained before and after lithotripsy were compared directly and evidence of pulmonary or pleural changes was sought. At no time did the chest radiologist know whether he was looking at preliminary or postlithotripsy radiographs for any one session.

Results

Direct comparison of preliminary and postlithotripsy radiographs from 107 lithotripsy sessions revealed no evidence of any postlithotripsy changes. Apart from six patients, who had the same degree of emphysema/chronic obstructive airways disease on their preliminary and postlithotripsy radiographs, all chest radiographs were normal. Specifically, no patient developed atelectasis, airspace consolidation, pleural effusion, or any other abnormality after lithotripsy.

Discussion

Hospitals offering biliary lithotripsy as a treatment option for gallstones report different routine pre- and postlithotripsy protocols [3, 5]. In our hospital, patients have routinely had preliminary and postlithotripsy chest radiographs and selected preliminary and postlithotripsy biochemical studies including measurement of serum bilirubin, alkaline phosphatase, amylase, and aspartate aminotransferase levels. As experience with lithotripsy increases, guidelines are required to establish which routine investigations are necessary when patients are referred for this treatment. This article reports our evaluation of the role of routine preliminary and postlithotripsy chest radiography in patients undergoing the procedure.

Evidence of pulmonary alveolar hemorrhage after lithotripsy has been reported in animals [1, 2]. Histologic changes of alveolar hemorrhage were found in eight of 24 dogs who had undergone lithotripsy with electrohydraulically generated shock waves in a first-generation lithotriptor [1]. Delius et al. [2] used an in vivo pressure probe in dogs and a similar first-generation lithotriptor to estimate the distance between the focal point of the pressure field and the lung at which 1000 shock waves caused no histological evidence of lung hemorrhage. They found that on the long axis of the shock-wave field this distance was 15 cm and that, perpendicular to the long axis, it was 4 cm.

Another animal study performed recently at our institution with the same second-generation lithotriptor on which our patients' gallstones were treated showed that implanted human cholesterol calculi could be fragmented without produc-

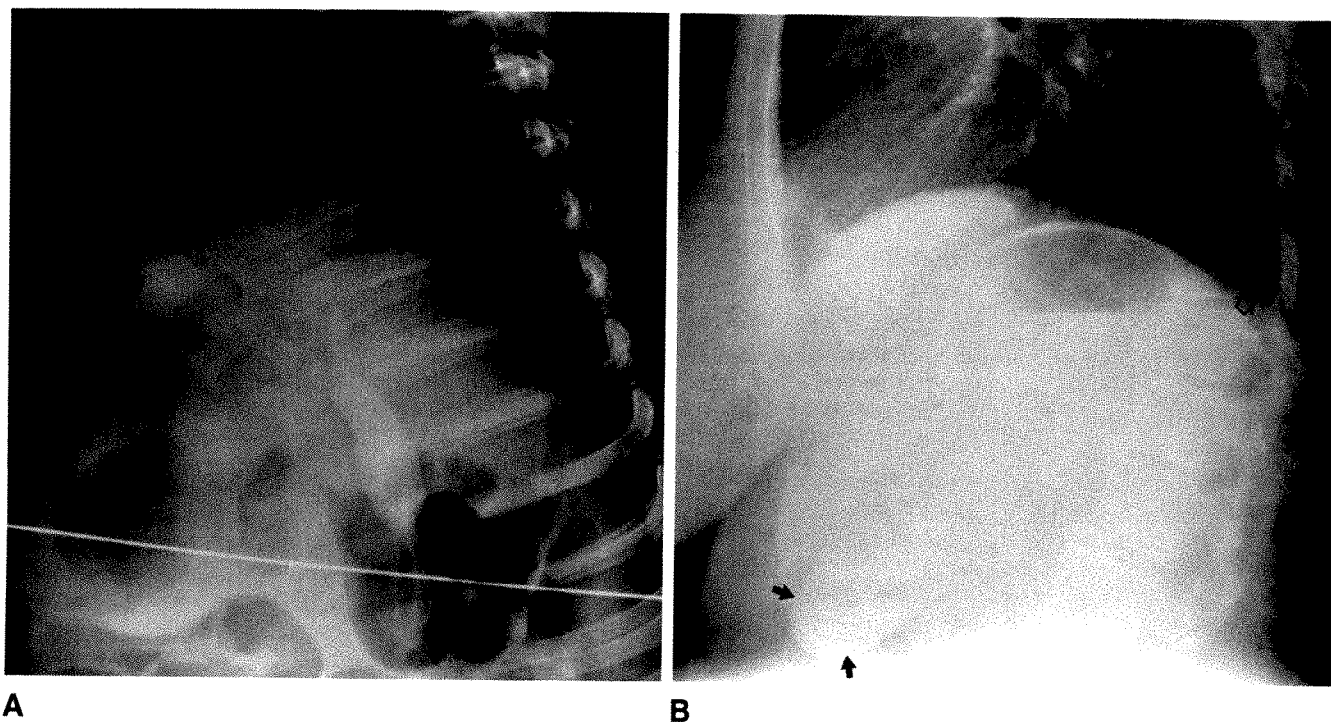


Fig. 1.—Lateral chest radiographs in a pig (A) and a human (B). Cholecystocholangiography shows gallbladder stones. Note species difference in relationship between gallbladder (black arrows) and posterior costophrenic angle (open arrow), which makes pigs more likely to suffer pulmonary hemorrhage from biliary lithotripsy.

ing any macroscopic change in lung tissue. In that study, 24 pigs underwent biliary lithotripsy. The long axis of the shock-wave field was directed away from the lungs. At autopsy, there was no macroscopic evidence of pulmonary hemorrhage. Subsequent histologic examination showed microscopic evidence of alveolar hemorrhage in three of the 24 animals [4].

The literature suggests that, if effective gallstone lithotripsy is to be achieved without pulmonary complications, care must be taken to direct the long axis of the shock-wave field away from the lungs [2, 6]. Humans might, in any event, be expected to be at a lower risk for pulmonary complications than many animals. This is because the posterior costophrenic sulcus is much deeper in many animals than it is in humans [1] (Fig. 1). Our retrospective review of 107 sets of preliminary and postlithotripsy radiographs confirms this impression. Direct comparison of preliminary and postlithotripsy radiographs (with dates masked to eliminate observer bias) revealed no evidence of pulmonary or pleural changes in any of the postlithotripsy radiographs.

At present, few experimental studies have compared different lithotripsy machines [7]. However, the literature does contain reports of series of patients who have undergone lithotripsy with different machines [3, 5]. We have used electromagnetically generated shock waves, and others have used electrohydraulically or piezoceramically generated shock waves [3, 5]. Worldwide, approximately 1000 patients have, by now, undergone lithotripsy. No pulmonary complications in humans have been reported.

We define a routine radiograph as one that is requested for every patient undergoing a particular procedure, whether or not there is any clinical indication for the radiograph. The literature suggests that routine admission and preoperative

chest radiographs do not improve patient care [8]. Our results show that routine preliminary and postlithotripsy chest radiographs are not required with lithotripsy. Adopting this policy in lithotripsy units will reduce the patient's exposure to ionizing radiation and reduce the overall cost of the procedure. If sonography, rather than oral cholecystography, is used to localize the focal point for the shock waves on gallbladder stones, exposure to ionizing radiation during lithotripsy of gallbladder stones can be eliminated.

ACKNOWLEDGMENTS

We thank Sandra Ashby of the Vancouver General Hospital Biliary ESWL Unit for technical assistance and Betty Fowler for manuscript preparation.

REFERENCES

1. Brendel W, Enders G. Shockwaves for gallstones: animal studies. *Lancet* 1983;1:1054
2. Delius M, Enders G, Heine G, Starr J, Remberger K, Brendel W. Biological effects of shock waves: lung hemorrhage by shock waves in dogs—pressure dependence. *Ultrasound Med Biol* 1987;13:61–67
3. Sackmann M, Delius M, Sauerbruch T, et al. Shock-wave lithotripsy of gallbladder stones—the first 175 patients. *N Engl J Med* 1988;318:393–397
4. Becker CD, Blake-Gilks C, Burhenne HJ. Biological effects of biliary shockwave lithotripsy in swine. *Invest Radiol* (in press)
5. Hood KA, Keightley A, Dowling RH, Dick JA, Mallinson CN. Piezo-ceramic lithotripsy of gallbladder stones: initial experience in 38 patients. *Lancet* 1988;1:1322–1324
6. Brendel W. Shock waves: a new physical principle in medicine. *Eur Surg Res* 1986;18:177–180
7. Coleman AJ, Saunders JE. A comparison of commercial extracorporeal shockwave lithotripters based on measurements of the acoustic field. *J Acoust Soc Am* 1988;83[suppl]:71
8. Tape TG, Mushlin AI. The utility of routine chest radiographs. *Ann Intern Med* 1986;104:663–670

Book Review

Endosonography in Gastroenterology. By Thian Lok Tio. New York: Springer-Verlag, 120 pp., 1988.

Intercavitary sonography of the gastrointestinal tract is an experimental technique useful for evaluating the mucosa and wall of the gut. Its use in Europe is growing, perhaps related to the fact that many gastroenterologists there perform standard transabdominal sonography as well. This book summarizes recent progress and trends in echoendoscopy.

This work is divided into 12 chapters that discuss instrumentation and technique; the detection and staging of esophageal, gastric, duodenal, rectal, pancreatic, and biliary neoplasms; the normal sonographic appearance of the gut in vivo and in vitro; benign tumors and lymphoma of the stomach; and a comparison of endosonography with other imaging techniques. Although this book has only one author, the chapters read like separate articles, much like a collection of abstracts from a symposium rather than a cohesive text. Indeed, much of this material was published in a special supplement to the *Scandinavian Journal of Gastroenterology* in 1986.

This book is well illustrated; however, the images are poorly labeled and are misleading. This book is clearly not for the novice sonographer. The author concedes that gastroenterologists who perform echoendoscopy must have extensive experience with conventional transabdominal sonography because the field of view of many of the scopes is quite small. If and when this technique becomes popular in the United States, radiologists who do abdominal imaging may expect many calls from the endoscopy suite.

Another serious problem with this text lies in the chapters comparing endosonography with other imaging techniques. Unfortunately, many misleading and erroneous statements are made. For example, the author claims that this technique is superior to CT for staging pancreatic and peripancreatic malignancy, apparently discounting the need to completely visualize the liver. In a similar vein, conventional sonography is dismissed because "it cannot adequately visualize lesions of the distal common bile duct." In discussing gastric lymphoma, the author states that echoendoscopy is superior to CT, failing to note the importance of finding paraaortic and deep mesenteric adenopathy, which this new technique cannot do. This misleading assessment of other imaging techniques reflects the fact that the radiologic references date primarily from 1984 and earlier.

This book may be of some interest to gastroenterologists, providing they have a thorough knowledge of conventional sonography. If this book is any indication of the current state of endosonography, abdominal radiologists can heave a collective sigh of relief about this latest challenge to their imaging turf.

Richard M. Gore
Northwestern University Medical School
Chicago, IL 60611

Pneumatosis Intestinalis in Bone-Marrow Transplantation Patients: Diagnosis on Routine Chest Radiographs

Forrest T. Bates¹
 Jud W. Gurney^{1,2}
 Lawrence R. Goodman¹
 Julio J. Santamaria³
 Richard M. Hansen³
 Robert C. Ash³

We report seven cases of pneumatosis intestinalis that was initially detected on routine chest radiographs made in adult bone-marrow transplantation patients. The cases were collected over a 13-month period. The chest radiographs generally underestimated the extent of the pneumatosis, as subsequently seen on plain abdominal films. However, the portions of bowel most extensively involved were those seen on the chest radiographs (transverse colon, hepatic and splenic flexures, stomach). One patient had pneumoperitoneum also. Pneumatosis developed within 6–293 days after transplantation. The cause of pneumatosis intestinalis was multifactorial. Three patients were asymptomatic. Clinical management of all seven patients was altered because of the detection of pneumatosis. The dose of steroids was increased in three patients to treat graft-vs-host disease, antibiotic drugs were given to three patients for enteric pathogens, and bowel rest was prescribed for one patient with mucosal injury from intense chemotherapy and radiation therapy.

These cases show that the chest radiograph makes early diagnosis of pneumatosis intestinalis possible in posttransplantation patients.

Bone-marrow transplantation has, in the last decade, developed into an important treatment technique for many diseases, including the leukemias and aplastic anemia. Bone-marrow transplantation is associated with numerous complications affecting multiple organ systems. Pulmonary complications are frequent and include the development of opportunistic infections, nonspecific pneumonitis associated with graft-vs-host disease (GVHD), drug toxicity, and recurrence of the original disease [1]. Because of the serious nature of these pulmonary complications, the routine chest radiograph is a mainstay in evaluation of the patient after transplantation.

The intestinal mucosa also is highly susceptible to injury in bone-marrow transplantation patients. Chemotherapy, radiation therapy, and GVHD are insults that may injure the rapidly dividing cells in the intestinal mucosa [2, 3]. Pneumatosis intestinalis is a specific sign indicating loss of mucosal integrity, and in this group of patients it may herald significant pathology [4–8]. Because abdominal symptoms may not be present early in the course of disease, we report our experience in seven patients with pneumatosis intestinalis detected on routine chest radiographs during a 13-month period.

Subjects and Methods

From July 1987 through July 1988, 48 adult patients underwent bone-marrow transplantation at the Medical College of Wisconsin. Previously, 77 adult patients had undergone transplantation, and of these, 29 were alive and monitored in the transplant clinic. Thus, a total of 77 patients (48 + 29) were observed from July 1987 through July 1988. The frequency and number of chest radiographs performed depended on the patient's clinical status. In an uncomplicated course, radiographs were obtained weekly during hospitalization. After the patients were discharged, chest radiographs were obtained biweekly for 3–6 months, and

Received October 31, 1988; accepted after revision January 17, 1989.

¹ Department of Radiology, Medical College of Wisconsin, 8700 W. Wisconsin Ave., Milwaukee, WI 53226.

² Present address: Department of Radiology, University of Nebraska Medical Center, 42nd and Dewey Ave., Omaha, NE 68105-1065. Address reprint requests to J. W. Gurney.

³ Department of Internal Medicine, Medical College of Wisconsin, 8700 W. Wisconsin Ave., Milwaukee, WI 53226.

AJR 152:991–994, May 1989

0361–803X/89/1525–0991

© American Roentgen Ray Society

less frequently thereafter. Supplemental radiographs were obtained more frequently in patients with complications, a not rare occurrence. All cases of pneumatosis intestinalis were collected prospectively during daily review of the radiographs. All patients with bone-marrow transplants were clearly identified on requisition slips, and their radiographs were searched carefully for pneumatosis intestinalis. Once pneumatosis intestinalis was detected on chest radiographs, all had abdominal films for confirmation and to evaluate the extent of disease. The site of pneumatosis on chest radiographs and abdominal films was compared.

From the records of these patients, we then tabulated symptomatology, drug and immunosuppressive therapy, degree of GVHD, and infections at the time of development of pneumatosis, and the ultimate outcome.

Results

Seven patients with pneumatosis intestinalis were detected prospectively during the routine interpretation of chest radiographs. Abdominal films were not obtained initially in any of these seven patients. Thirty-two other bone-marrow transplantation patients had abdominal films made over the same time period, and none had pneumatosis intestinalis. These seven patients ranged in age from 20 to 47 years (mean, 36 years) and included five men and two women. Bone-marrow transplantation was performed for aplastic anemia (two patients), acute myelogenous leukemia (one patient), acute lymphoblastic leukemia (one patient), chronic myelogenous leukemia (two patients), and essential thrombocytosis (one pa-

tient). The interval from bone-marrow transplantation to the development of pneumatosis intestinalis ranged from 6 to 293 days (mean, 134 days). The duration of pneumatosis ranged from 4 to 43 days (mean, 21 days). Three patients were asymptomatic, and abdominal disease was entirely unsuspected at the time pneumatosis was detected on chest radiographs (Fig. 1). The four symptomatic patients complained of diarrhea, nausea and vomiting, and abdominal pain. There was no correlation between the onset or duration of pneumatosis intestinalis and the presence or absence of symptoms.

On chest radiographs, pneumatosis intestinalis was identified on the posteroanterior and lateral views in three patients, the posteroanterior view only in two patients, and the lateral view only in two patients. Transverse colon, hepatic flexure, or splenic flexure was involved in five patients, and the fundus of the stomach in two patients. The chest radiograph did not show the full extent of pneumatosis intestinalis but did show pneumoperitoneum or retroperitoneal air (Fig. 2). The findings of pneumatosis intestinalis on chest radiographs were frequently subtle, and in two of our patients, findings were present but unrecognized on films taken 1 week earlier.

Subsequent abdominal films showed pneumatosis intestinalis of the colon in five patients, one of whom also had small-bowel involvement. The right colon and hepatic flexure were involved in all patients with pneumatosis intestinalis of the colon. Two patients showed pneumatosis intestinalis of the stomach alone (Fig. 3). Two patients had retroperitoneal air, and one had pneumoperitoneum. No false-positive diagnoses

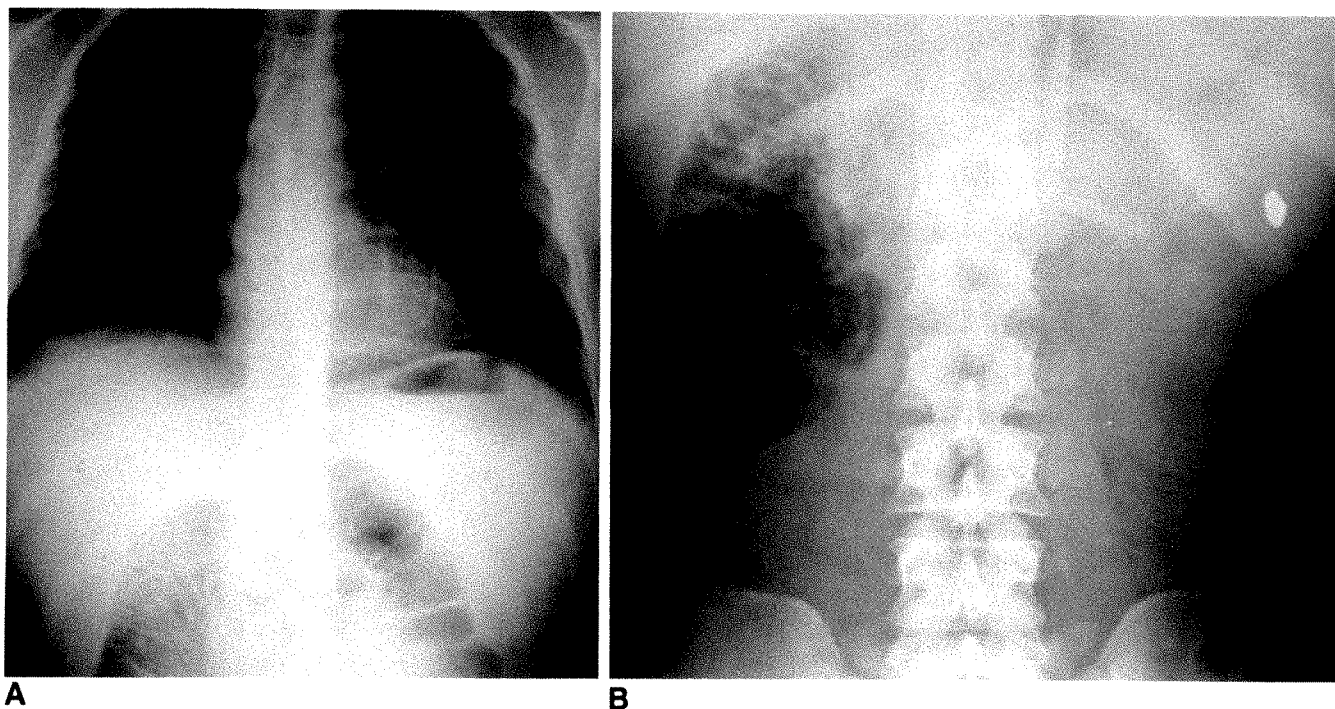


Fig. 1.—A, Routine chest radiograph made in an asymptomatic posttransplantation patient shows pneumatosis in hepatic flexure of colon. Spleen is mildly enlarged.

B, Follow-up abdominal radiograph better delineates pneumatosis in ascending and transverse colon. Pneumatosis resolved after treatment with antibiotics.

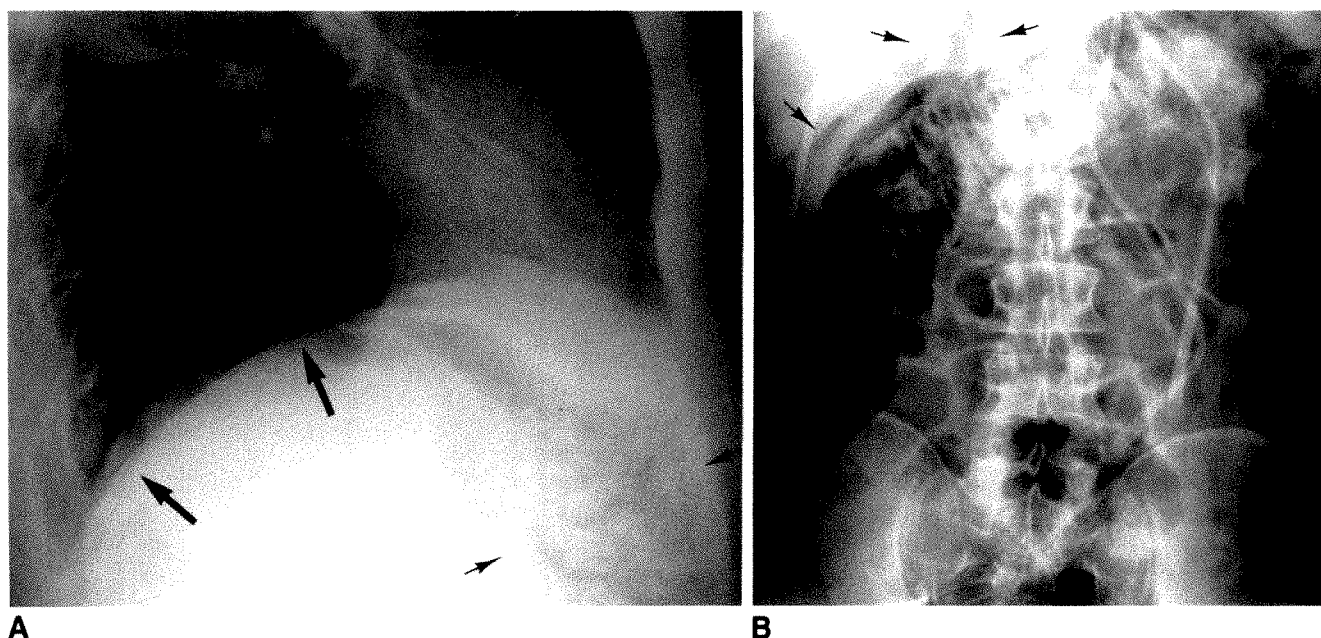


Fig. 2.—A, Routine lateral chest radiograph made 39 days after transplantation shows gas in bowel in abdomen (small arrows). Pneumoperitoneum also is present (large arrows).

B, Plain abdominal radiograph made 1 day later shows pneumatosis intestinalis in the ascending and transverse colon. Retroperitoneal air is present (arrows). Stool sample was positive for *Clostridium difficile* toxin. Patient was treated with antibiotics with resolution of pneumatosis. During this time, patient was asymptomatic.

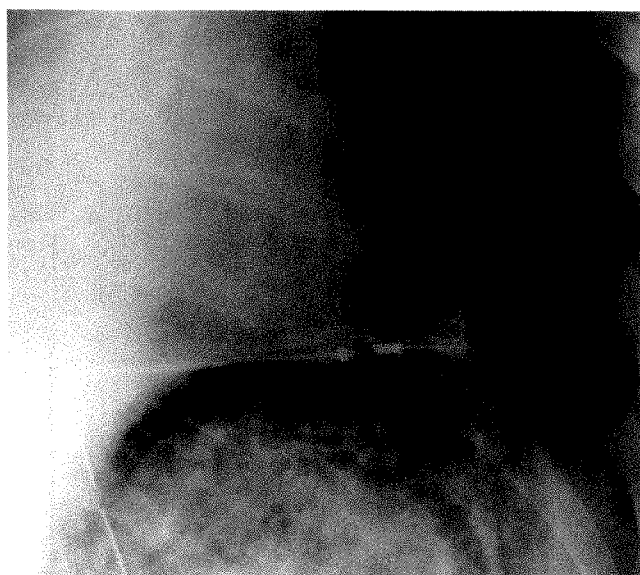


Fig. 3.—Chest radiograph (coned view of diaphragm) shows extensive gastric emphysema. Remainder of bowel was normal. The patient had nausea and vomiting and diarrhea. Rectal biopsy was negative for cytomegalovirus but positive for graft vs host disease. Pneumatosis resolved after treatment of graft vs host disease.

of pneumatosis intestinalis were made on the basis of chest radiographs.

A cause for pneumatosis intestinalis was sought in each patient. Six had skin biopsies documenting GVHD, and five were receiving treatment for GVHD with corticosteroids when

pneumatosis intestinalis developed. Three of these six patients underwent rectal biopsies during their episode of pneumatosis, documenting GVHD of the gastrointestinal tract. Four patients were under treatment for cytomegalovirus (CMV) infection, but rectal biopsies in two of these four patients were negative for CMV. One of the two patients with gastric emphysema had a gastric biopsy that was negative for CMV. The other had a rectal biopsy that was negative for CMV but positive for GVHD. One patient grew *Candida albicans* from stool cultures, and another was positive for *Clostridium difficile* (toxin-producing strain). The final outcome varied. One patient died of sepsis in the presence of pneumatosis. Three patients eventually died, remote from their episodes of pneumatosis; one of them had acute typhlitis of the right colon 3 months after resolution of an asymptomatic episode of pneumatosis of the right colon. The others responded to specific treatment and the pneumatosis resolved.

Clinical management was altered in all seven patients. Three patients were given larger doses of steroids for GVHD, and three patients were given antibiotics for enteric pathogens. One was treated conservatively with bowel rest for pneumatosis of the stomach occurring 6 days after transplantation.

Discussion

Pneumatosis intestinalis was identified in all our patients on chest radiographs alone. Over the 13-month period, no patients were identified with pneumatosis intestinalis on abdominal films who had not had the diagnosis identified or suspected on earlier chest radiographs.

As only a small amount of bowel is normally visible beneath the hemidiaphragms on chest radiographs, the detection of pneumatosis suggests two possibilities: (1) pneumatosis intestinalis associated with bone-marrow transplantation may be more common than initially thought, or (2) pneumatosis intestinalis predilectively involves bowel segments, such as transverse colon or stomach, that are encompassed fortuitously on chest radiographs.

In general, two conditions must be met for the development of pneumatosis intestinalis: there must be a source of gas and the mucosal integrity must be disrupted [9]. In the upright position, gas collects in the transverse colon, colonic flexures, and stomach — common locations for pneumatosis intestinalis in our series and areas of bowel that are included on routine chest radiographs. This distribution is seen by others also; in a recent series of 18 patients with pneumatosis intestinalis, the right hemicolon was involved in 17 patients, with only one having pneumatosis of the small bowel alone [4]. In addition, Navari et al. [8] discovered pneumatosis intestinalis on routine chest radiographs in two of three patients. The lack of identification of pneumatosis on abdominal films in our transplantation population suggests also that the chest radiographs encompass those regions of the bowel more likely to be involved with pneumatosis.

Because the standard chest radiography technique may not be optimal for visualizing infradiaphragmatic structures, we found the radiographic findings of pneumatosis intestinalis frequently subtle and easily overlooked if not actively sought. In fact, in two of our patients, the diagnosis of pneumatosis intestinalis could have been made 1 week earlier if subtle findings had been made on previous examinations.

Two of our seven patients had pneumatosis intestinalis involving the stomach and, to our knowledge, these are the only cases reported in patients after bone-marrow transplantation. Abnormalities of the stomach are known to develop following transplantation. On gastrointestinal examination, Jones et al. [10] identified seven patients with gastric abnormalities: dilatation and atony with delayed emptying, the presence of retained secretions, antral deformity, and an unusual coating pattern felt to be caused by either an infectious disorder or GVHD. In all their patients with gastric dilatation and atony, CMV gastritis was present, a pattern noted also in four patients reported by Strayer et al. [11]. CMV, however, was not detected in either of our patients with pneumatosis intestinalis involving the stomach.

Pneumatosis intestinalis was not an incidental finding. All patients were intensively investigated once pneumatosis was identified, and clinical management was altered in all seven cases. Specific treatment included adjustment of immunosuppressive therapy in patients with increased GVHD and administration of a specific antibiotic treatment when an infectious agent was identified.

As the chest radiograph is integral in overall evaluation and follow-up of patients undergoing bone-marrow transplantation, the detection of pneumatosis intestinalis is important in making an early diagnosis of varied abdominal disease occurring in the transplantation population.

ACKNOWLEDGMENT

The authors thank Sylvia L. Bartz for editorial assistance and manuscript preparation.

REFERENCES

1. Krowka MJ, Rosenow EC III, Hoagland HC. Pulmonary complications of bone-marrow transplantation. *Chest* 1985;87:237-246
2. McDonald GB, Shulman HM, Sullivan KM, Spencer GD. Intestinal and hepatic complications of human bone marrow transplantation. Part I. *Gastroenterology* 1986;90:460-477
3. McDonald GB, Shulman HM, Sullivan KM, Spencer GD. Intestinal and hepatic complications of human bone marrow transplantation. Part II. *Gastroenterology* 1986;90:770-784
4. Day DL, Ramsay NKC, Letourneau JG. Pneumatosis intestinalis after bone-marrow transplantation. *AJR* 1988;151:85-87
5. Hall RR, Anagnostou A, Kanojia M, Zander A. Pneumatosis intestinalis associated with graft-versus-host disease of the intestinal tract. *Transplant Proc* 1984;16:1666-1668
6. Maile CW, Frick MP, Crass JR, Snover DC, Weisdorf SA, Kersey JH. The plain abdominal radiograph in acute gastrointestinal graft-vs.-host disease. *AJR* 1985;145:289-292
7. Yeager AM, Kanof ME, Kramer SS, et al. Pneumatosis intestinalis in children after allogeneic bone-marrow transplantation. *Pediatr Radiol* 1987;17:18-22
8. Navari RM, Sharma P, Deeg HJ, McDonald GB, Thomas ED. Pneumatosis cystoides intestinalis following allogeneic marrow transplantation. *Transplant Proc* 1983;15:1720-1724
9. Meyers MA, Ghahremani GG, Clements JL Jr, Goodman K. Pneumatosis intestinalis. *Gastrointest Radiol* 1977;2:91-105
10. Jones B, Kramer SS, Saral R, et al. Gastrointestinal inflammation after bone-marrow transplantation: graft-versus-host disease or opportunistic infection? *AJR* 1988;150:277-281
11. Strayer DS, Phillips GB, Barker KH, Winokur T, DeSchryver-Kecskemeti K. Gastric cytomegalovirus infection in bone-marrow transplant patients. *Cancer* 1981;48:1478-1483

Pictorial Essay

Primary Tumors of the Small Intestine: CT Evaluation

Kika M. Dudiak,¹ C. Daniel Johnson, and David H. Stephens

The diagnosis of tumors of the small intestine can be a challenge for both clinician and radiologist. Typically nonspecific in their clinical presentation, these uncommon neoplasms are seldom high on the list of diagnostic considerations. Consequently, CT, a common method to evaluate patients with vague abdominal symptoms, is likely to afford the initial opportunity to detect and characterize a tumor of the small intestine. This essay, based on the retrospective analysis of a large series of patients with primary neoplasms of the small bowel, focuses on the association of specific CT features with individual tumor types.

Materials and Methods

CT examinations of 63 patients with primary tumors of the small bowel diagnosed between January 1982 and September 1987 were reviewed retrospectively. Pathologic proof was obtained in 62 patients; the remaining case (multiple small-bowel lipomas) was confirmed radiographically. Periampullary adenocarcinomas of the duodenum and disseminated or purely mesenteric lymphomas were not included. The CT examinations had been performed before percutaneous biopsy or surgical confirmation in all but four patients who had undergone open biopsy without tumor resection. All patients had ingested water-soluble contrast material before scanning and had been given IV contrast material unless the clinical history contraindicated it. Ten-millimeter collimation at 10- to 15-mm incrementation had been used. Twenty-six patients had had barium examinations of the small bowel in addition to CT; in 22 the CT scan had preceded the barium study.

The 63 patients included 19 with lymphoma; 15 with adenocarcinoma; 15 with carcinoid tumor; six with leiomyosarcoma; five with leiomyoma; and one each with Kaposi sarcoma, villous adenoma, and lipoma.

Results

Tumor Detection by CT

The primary tumor, in the form of a mass or other abnormality of the small bowel, was identified on CT in 46 (73%) of the 63 study patients. All of the leiomyosarcomas and all but one lymphoma and one adenocarcinoma were identifiable on CT.

Seventeen (27%) of 63 primary tumors were not detected by CT. Four of the five leiomyomas were undetected; all were found incidentally at surgery. Nine (60%) of the 15 patients with carcinoid tumors had primary sites also not detected by CT, but four of these nine patients had characteristic mesenteric metastases and three others had liver metastases as the only CT abnormality. Of the 17 undetected tumors, all were 3 cm or less in diameter, and 11 were 2 cm or smaller. No size was specified pathologically for the remaining four unidentified tumors.

Characteristic CT Features of Specific Tumor Types

Despite overlapping CT features among the various primary small intestinal tumors, distinctive morphologic patterns on CT were often highly suggestive of specific tumor types.

Lymphoma.—The 19 non-Hodgkin lymphomas were variable in appearance but tended to be large and annular. Two patients with lymphoma had diffusely infiltrative tumors on CT, manifested predominantly by nodular-type fold thickening (Fig. 1). The remaining 16 identified lymphomas appeared as single or multiple regional small-bowel masses. The average

Received November 21, 1988; accepted after revision December 27, 1988.

¹ All authors: Department of Diagnostic Radiology, Mayo Clinic and Mayo Foundation, 200 First St. S.W., Rochester, MN 55905. Address reprint requests to C. D. Johnson.

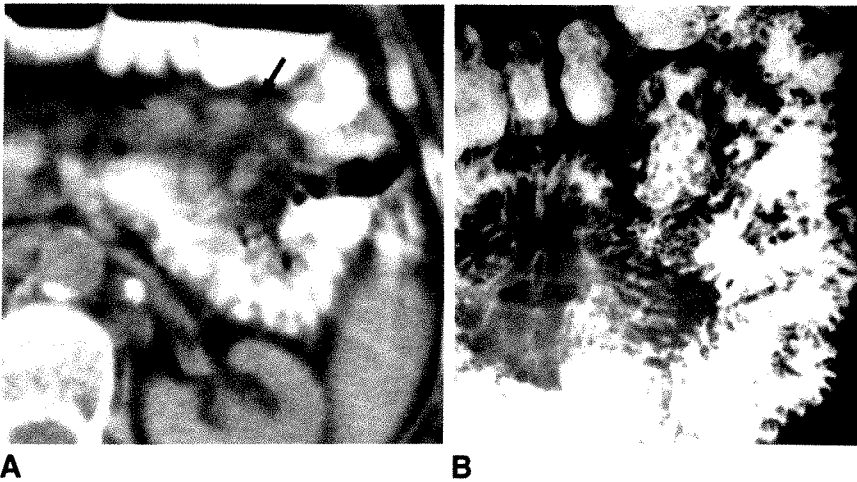


Fig. 1.—Lymphoma diffusely infiltrating small bowel with extensive nodular fold thickening. Changes are apparent on both CT (A) and barium (B) evaluations. Mesenteric (arrows) and paraaortic lymphadenopathy is seen on CT.

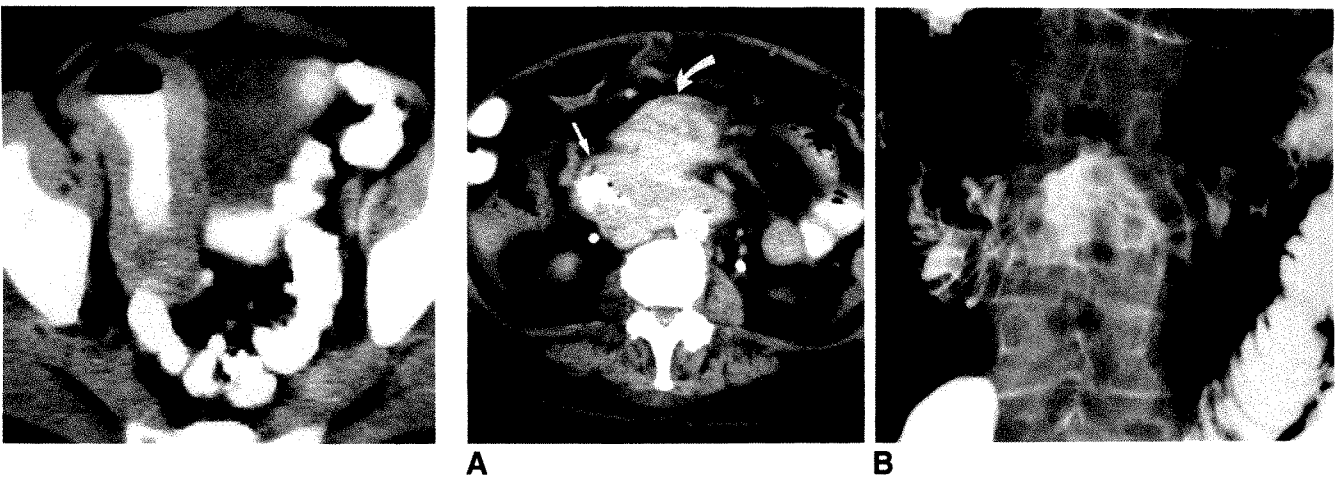


Fig. 2.—Lymphoma of ileum with circumferentially thickened wall and aneurysmal ulceration (arrow).

Fig. 3.—A, CT scan shows duodenal lymphoma (straight arrow) and bulky mesenteric lymphadenopathy (curved arrow). B, Corresponding barium examination shows only primary tumor.

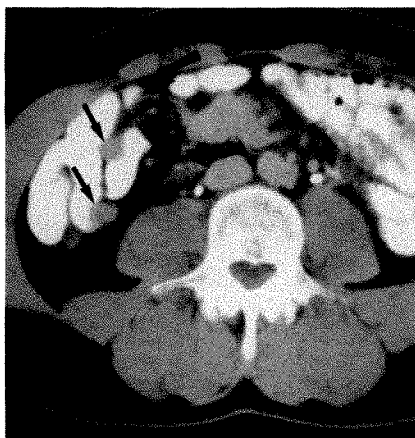


Fig. 4.—Carcinoid tumor of ileum. CT shows multiple mesenteric implants (straight arrows) and increased stranding of mesenteric soft tissues (curved arrows) due to extension.

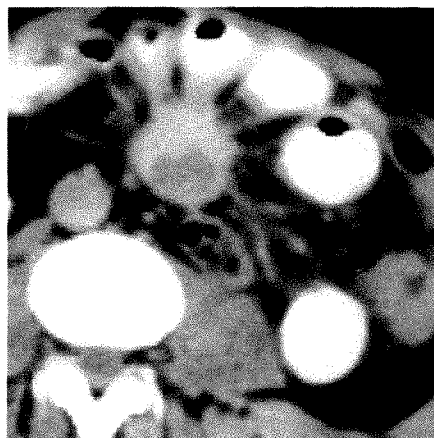


Fig. 5.—Carcinoid tumor of ileum. Metastatic centrally necrotic mass, seen instead of primary tumor, is associated with prominent stranding of mesenteric soft tissues.



Fig. 6.—Ileal carcinoid tumor with retractile mesenteric extension. Mesenteric mass (curved arrow), retraction of small bowel into mesentery (straight arrow), and soft-tissue stranding.

tumor size (greatest cross-sectional diameter or greatest length of affected bowel, excluding the two patients with diffuse infiltrative tumors) was 9.5 cm. Twelve (63%) of the 19 primary tumors were ulcerated. In half these patients, aneurysmal ulceration (larger luminal diameter than the adjacent unaffected bowel) was present (Fig. 2). Mesenteric or retroperitoneal lymphadenopathy (Fig. 3) was seen on the scans of 10 (53%) of the 19 patients.

Carcinoid.—Carcinoid tumors were best recognized on CT on the basis of the features of the secondary tumor. Thirteen (87%) of 15 patients with carcinoid tumors had mesenteric tumor spread (seven patients) or hepatic metastases (seven patients) or both (one patient) (Fig. 4). In seven patients (47%), these findings were seen in lieu of the primary tumor. Mesenteric extension characteristically appeared as a mesenteric mass with an associated stellate pattern of soft-tissue stranding that often was retractile (Figs. 5 and 6). Lymphadenopathy was present on the scans of five patients (33%).

Adenocarcinoma.—Adenocarcinomas frequently appeared as solitary proximal small-bowel masses (Figs. 7 and 8) and were rarely greater than 8 cm in diameter. The average tumor size on CT was 6.5 cm, and all but one of the 15 tumors were located either in the duodenum or in the jejunum. Ulceration

was apparent in six (40%) of the 15 tumors. Seven patients (47%) had lymphadenopathy. These enlarged lymph nodes, however, were not as bulky as those characteristically seen in patients with lymphoma.

Leiomyosarcoma.—Leiomyosarcomas were bulky tumors on CT, averaging 11 cm in diameter, and were frequently situated eccentrically relative to the bowel lumen (Fig. 9). Central necrosis (Fig. 10), seen in three of the six primary tumors, typically involved the larger tumors and was found in only one patient with a tumor (carcinoid metastasis) other than leiomyosarcoma. One leiomyosarcoma was calcified centrally. Two of the six tumors had invaded neighboring organs. Lymphadenopathy was distinctly absent.

Lipoma.—In our one patient (previously reported [1]) with multiple small-bowel lipomas, the tumors had a homogeneous low attenuation of fat (Fig. 11), a finding considered diagnostic of lipoma.

On the basis of the previously described CT features of each tumor type, it was possible to suggest retrospectively a specific tumor diagnosis in the single patient with multiple lipomas of the small bowel, 60% of the patients with adenocarcinoma, 58% of the patients with lymphoma, and one-third of the patients with carcinoid tumor and leiomyosarcoma.

Fig. 7.—Adenocarcinoma of duodenum.
A, CT shows annular mass (arrows) with luminal narrowing.
B, Corresponding barium examination shows similar findings.
Hepatic metastases (not shown) were seen on CT at time of diagnosis.

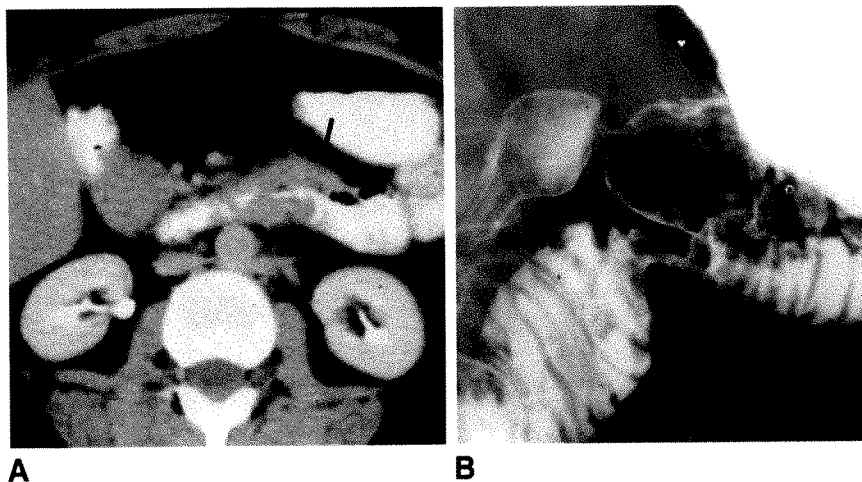


Fig. 8.—Jejunal adenocarcinoma.
A, CT shows polypoid intraluminal filling defects (arrows). Apparent defects in bowel proximal to affected segment did not persist on contiguous scans and represent peristaltic wave.
B, Corresponding barium study was prompted by CT findings.

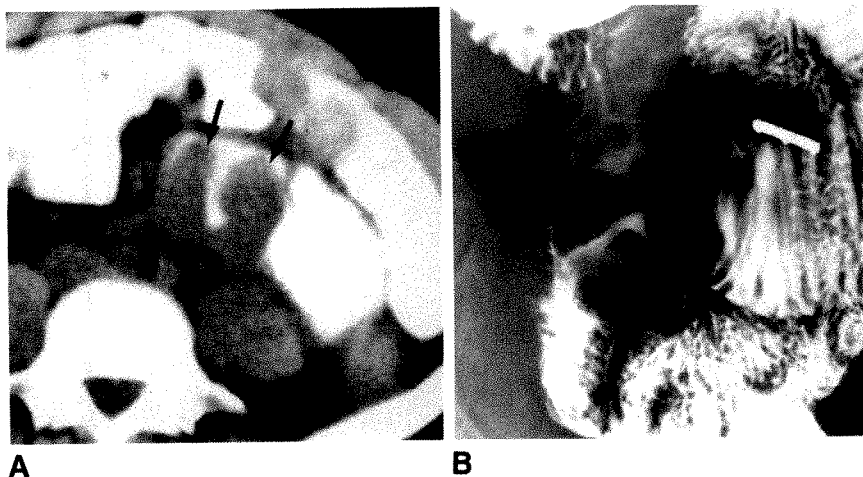




Fig. 9.—Leiomyosarcoma of ileum. Large mass (arrows) with central necrosis and ulceration is situated eccentrically relative to bowel lumen and immediately adjacent to fluid-filled uterus.

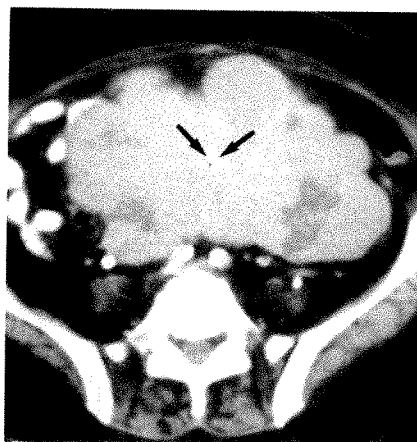


Fig. 10.—Bulky leiomyosarcoma of ileum. Ileal lumen (arrows) can be seen centrally traversing large, lobulated mass. Several areas of tumor necrosis are evident.



Fig. 11.—Multiple small-bowel lipomas (arrows). Well-circumscribed mass with homogeneous low attenuation of fat is diagnostic.

None of the features in the remaining tumors allowed a specific retrospective diagnosis.

Correlation with Conventional Small-Bowel Barium Examination

Of the twenty-six patients who also had a conventional small-bowel barium study, the tumor was identified in 20 (77%) by both techniques. In four patients, all of whom had carcinoid tumors, both studies failed to reveal any abnormality. In two patients, one with lymphoma and another with carcinoid tumor, only the CT scan was positive. None of the tumors seen on the barium studies were missed by CT.

Discussion

Recognizing tumors of the small intestine on CT scans is important, because CT is commonly used as a screening examination in patients with vague abdominal symptoms. CT not only allows recognition of the primary tumor mass but also provides simultaneous imaging of neighboring structures and distant sites that are often characteristically affected by

tumor spread. Certain patterns of CT findings may enable the radiologist to diagnose or at least strongly suggest individual tumor types [1–4]. Characteristic CT features include: (1) lymphoma—large, annular, often “aneurysmally” ulcerated mass, together with bulky lymphadenopathy; (2) adenocarcinoma—annular proximal mass, commonly ulcerated; (3) carcinoid—mesenteric mass associated with desmoplastic changes, with or without hepatic metastases or lymphadenopathy; (4) leiomyosarcoma—large, locally spreading, bulky, inhomogeneous, and occasionally calcified mass; and (5) lipoma—well-circumscribed, homogeneous, fat-density mass.

REFERENCES

1. Ormson MJ, Stephens DH, Carlson HC. CT recognition of intestinal lipomas. *AJR* 1985;144:313–314
2. Picus D, Glazer HS, Levitt RG, Husband JE. Computed tomography of abdominal carcinoid tumors. *AJR* 1984;143:581–584
3. Clark RA, Alexander ES. Computed tomography of gastrointestinal leiomyosarcoma. *Gastrointest Radiol* 1982;7:127–129
4. Hulnick DH, Megibow AJ. CT of small intestine neoplasms. In: Fishman EK, Jones B, eds. *Contemporary issues in computed tomography: computed tomography of the gastrointestinal tract*. New York: Churchill Livingstone, 1988:205–227

Diagnosis of Fistulae and Sinus Tracts in Patients with Crohn Disease: Value of MR Imaging

Gerhard Koelbel¹
 Udo Schmiedl²
 Martin C. Majer¹
 Paul Weber³
 Harro Jenss³
 Klaus Kueper¹
 Clemens F. Hess²

To investigate the potential of MR imaging in the evaluation of sinus tracts or fistulae associated with Crohn disease, 17 patients with pelvic or abdominal fistulae or sinus tracts underwent MR imaging with multislice spin-echo techniques, 500/15 and 1600/22,80 (TR/TE). The presence of fistulae and/or sinus tracts was confirmed by contrast-enhanced CT ($n = 17$) and/or sonography ($n = 8$), sinography ($n = 6$), or barium studies ($n = 4$). In all but three cases the fistulae and extramucosal inflammatory abnormalities were shown by MR. T1-weighted images provided excellent delineation of the extension of the fistulae relative to sphincters and adjacent hollow viscera and showed inflammatory changes in fat planes. T2-weighted images showed fluid collections within the fistulae, localized fluid collections in extraintestinal tissues, and inflammatory changes within muscles. The supralelevator and infralevator compartments were well defined on coronal images. Thus, the perirectal spread of fistulae and sinus tracts with respect to the levator ani could be demonstrated in all cases.

Our results suggest that MR imaging is useful for the demonstration and evaluation of pelvic and abdominal sinus tracts or fistulae associated with Crohn disease.

Crohn disease is a chronic recurrent inflammatory bowel disease primarily involving the small intestine and colon with a high rate of extraintestinal complications [1-3]. Transmural inflammation is characteristic and is responsible for the formation of internal fistulae in 16% and perianal disease in 36% of patients [3]. Accurate assessment of fistulae, extraluminal fluid collections, and abscesses is crucial for the clinical management of these patients.

The role of CT for the detection of complications has been emphasized [4-11]. It has been shown that abscess and fistula formation can be well assessed by CT with the combined use of IV and oral or rectal contrast media. We investigated the value of MR imaging in the evaluation of fistulae and sinus tracts in patients with Crohn disease.

Subjects and Methods

Seventeen patients with histologically proved Crohn disease and with known fistulae or sinus tracts were studied prospectively by MR imaging at 1.5 T (Magnetom, Siemens, Erlangen, W. Germany). Informed consent was obtained from each individual before the study. T1- and T2-weighted multislice (13 to 15 slices) spin-echo (SE) images, 500/15 and 1600-2000/22,80 (TR/double-echo TE), with a slice thickness 5-8 mm and a gap of 2-4 mm were acquired. The image matrix was 256×256 pixels. Transverse and coronal slices were obtained in all cases and sagittal views were acquired also in seven cases. The total scan time ranged between 11 and 32 min. In five cases involving perineal disease, a round, fixed spine coil was used in addition to the whole-body coil to further improve anatomic resolution.

Nine patients with fistulae or sinus tracts involving the rectum or pararectal space and eight patients with fistula formation in the lower or mid abdomen were included in the study. In four patients fistulae were associated with inflammatory masses involving bowel loops or the urinary bladder. In seven patients fistulae to a surgical incision developed between 3 months and 6 years after bowel resection.

Received September 26, 1988; accepted after revision December 23, 1988.

¹ Radiologische Klinik (Abt. Diagnostik), Eberhard-Karls-Universität, Tübingen, West Germany. Address reprint requests to G. Koelbel, Radiologische Klinik, Abt. Kernspintomographie, Otfried Mueller Str. 22, D-7400 Tübingen, West Germany.

² Radiologische Klinik (Abt. Radiotherapie), Eberhard-Karls-Universität, Tübingen, West Germany.

³ Medizinische Klinik (Abt. Gastroenterologie), Eberhard-Karls-Universität, Tübingen, West Germany.

AJR 152:999-1003, May 1989
 0361-803X/89/1525-0999
 © American Roentgen Ray Society

Involvement of adjacent muscles, nerves, vessels, and the urogenital system was analyzed on the MR scans. The results of blinded interpretation of MR scans were compared with blinded interpretation of contrast-enhanced CT ($n = 17$), sonography ($n = 8$), sinography ($n = 6$), barium studies ($n = 4$), and endoscopy ($n = 10$).

The CT scans were obtained with a third-generation scanner (DR3, Siemens, Erlangen, W. Germany) by using a combination of orally and IV administered contrast material in 17 patients. CT scans were obtained with a slice thickness of 8 mm at 1-cm intervals. Multiplanar abdominal sonography was performed by using 3.5- and 5.0-MHz transducers (Picker, Highland Heights, OH) in all patients.

In two patients with pelvic fistulae, the results of MR imaging could be compared with the findings at surgery. In the remaining 15 patients the presence or absence of fistulae or sinus tracts was established

by the combined information provided by CT, sonography, sinography, and barium studies. The entire diagnostic workup of each patient was completed within 4 weeks.

Special attention was given to distinguishing between fistulae and abscesses in the supralevator and infralevator spaces by assessing the levator ani on axial and coronal MR images (Fig. 1).

Results

Fistulae and sinus tracts were seen on T1-weighted images as linear/tubular structures of low signal intensity extending from one bowel segment to another or from bowel to another structure. Cutaneous openings of fistulae were clearly visualized as defects in the subcutaneous fat (Figs. 2–4). On T2-weighted and proton-density-weighted images fistulae had a relatively high signal intensity (Figs. 5 and 6). Inflammation of muscle associated with sinus tracts was relatively hypointense on T1-weighted images and appeared brighter on T2-weighted and proton-density-weighted images (Fig. 7).

Fistulae or sinus tracts were shown by MR imaging in 14 of 17 patients. In two patients in whom fistulae were shown by barium or sinographic studies, MR, CT, and sonography failed to show the fistulae, which were encased by extensive inflammatory masses. In one patient the proved fistula could not be identified by MR because of motion artifacts. The origins of fistulae or sinus tracts in the bowel wall were shown in eight of nine patients with involvement of the rectum and in five of eight patients with involvement of the small bowel or colon. The intestinal termination of enterocutaneous fistulae present in six patients was identified by MR in five cases.

The levator ani and the superficial perineal muscles were identified on coronal and transverse scans in all MR studies of the pelvis. Coronal scans were particularly helpful in defining the supralevator and infralevator spaces (Figs. 8 and 9). The perirectal fascia dividing the supralevator space into the perirectal and pararectal compartment [8] could not be identified reliably. Fistulae or sinus tracts of the rectum in nine

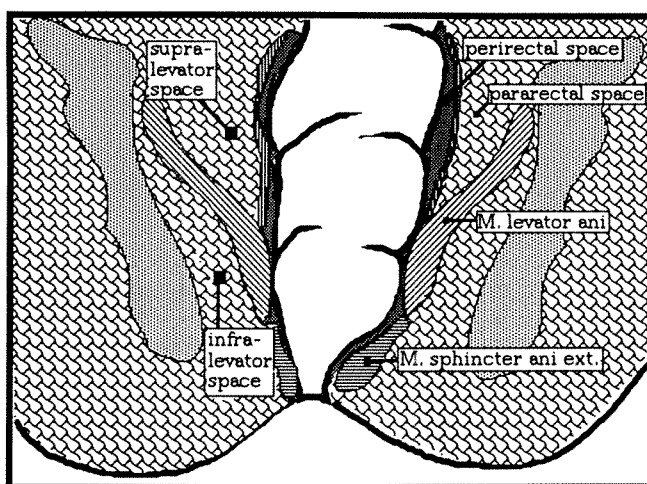


Fig. 1.—Coronal diagram shows anatomy of pararectal spaces and possible locations of perirectal abscesses and fistulae in relation to levator ani muscle (M. levator ani). Inflammation of rectal wall may spread into supralevator and/or infralevator space, giving rise to simple or highly complex pattern of fistulae. M. sphincter ani ext. = external sphincter muscle of anus.

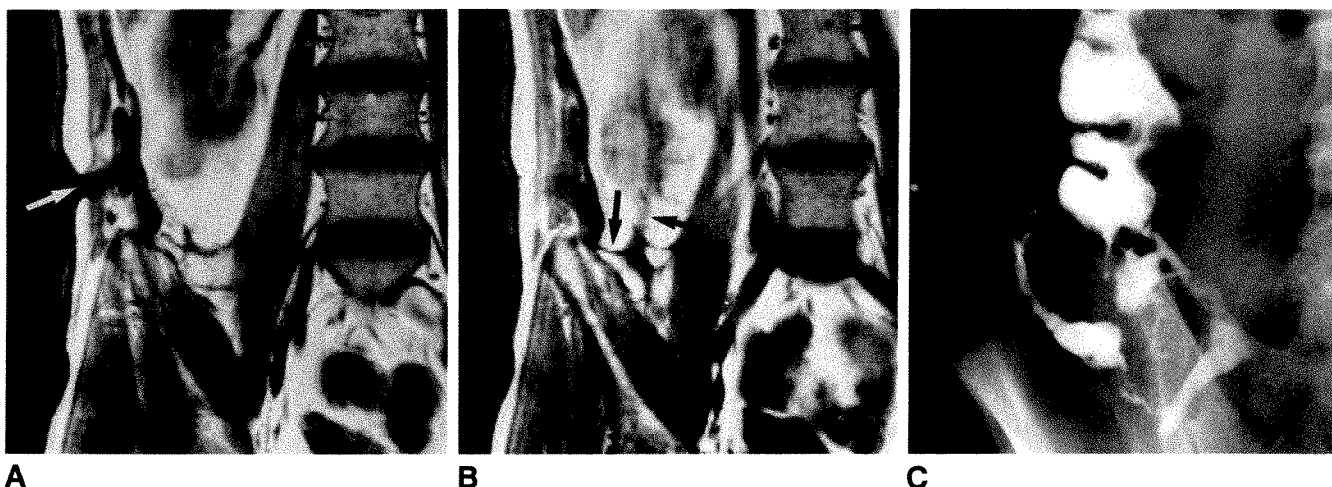
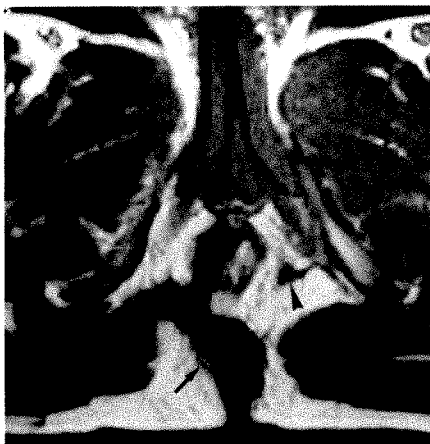


Fig. 2.—A, Coronal MR image (SE 500/15) in patient with recurrent Crohn disease shows cutaneous opening of fistula in flank (arrow). B, Termination of fistula is seen in region of anastomosis between new distal ileum and ascending colon (arrows). C, Sinogram shows full extent of fistulae. Cutaneous opening is marked by lead ball.



Fig. 3.—MR image (SE 500/15) shows fistula from ileum to anterior abdominal wall in patient with ileosigmoidostomy (arrows). Mass surrounds small bowel loops.



A



B

Fig. 4.—A, MR image (SE 500/15) shows sinus tract extending from rectum into subcutaneous fat (arrow). Second fistula (arrowhead).

B, CT scan after administration of IV contrast material shows enhancement of fistula wall, fluid collection (short arrow), and air (long arrow).

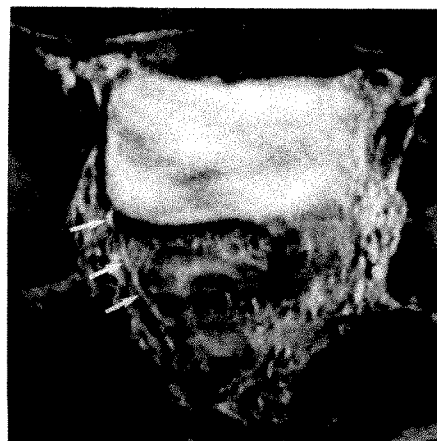


Fig. 5.—Relatively T2-weighted transverse MR image (SE 1600/80) shows fistula (arrows) from sigmoid colon anteriorly to bladder wall.



Fig. 6.—MR image (SE 2000/22) shows fistula orifice in rectal wall (arrowheads). Numerous fistulae and inflammation of gluteal muscles are seen (arrows).



Fig. 7.—MR image (SE 2000/22) shows normal right levator muscle as area of low signal intensity (arrowhead). Left levator ani appears brighter, indicating inflammation of muscle (arrow) caused by spread of inflammation of rectum.

patients were seen to involve the supralelevator space only in one patient, the infralevator space in four patients (Fig. 10), and both compartments in four patients. A fistula connecting the bowel with a fluid collection involving the supralelevator space was identified in one patient.

The MR findings corresponded closely to the abnormalities identified on the CT scans (Fig. 11). In two patients, the presence and extension of fistulae as shown on MR were confirmed by surgery.

Discussion

Barium studies and endoscopy of the lower and upper gastrointestinal tract are commonly used to diagnose Crohn

disease [12–15] and to evaluate relapses in patients in whom the diagnosis is established [16]. Although these procedures reveal mucosal abnormalities, perianal disease, fistula, and abscesses are often not shown. Several investigators have emphasized the value of CT [3–11] and sonography [17–19] for this purpose. CT has been shown to be superior to sonography in the assessment of abscesses and fistulae, particularly if lesions involve multiple loops of small bowel, the mesentery, or the perirectal area [4]. On CT, fistulae may be mistaken for inflammation of muscles, however, and their enteric orifices may not be shown [11]. Inflammation of fat associated with sinus tracts may be simulated by partial-volume averaging of the ischiocavernosus muscle and the anal sphincter or confused with fat or vascular structures of



Fig. 8.—Coronal MR image (SE 500/15) shows fistula from rectum to supralelevator space (arrow) with connection to right levator ani muscle.



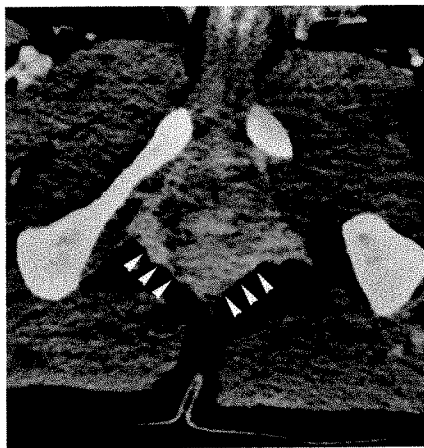
Fig. 9.—Coronal MR image (SE 500/15) shows numerous fistulae in region of anal sphincters. Levator ani muscles are asymmetric (arrows). Fistulae are confined to infralevator space. Streaking of fat in left ischioirectal fossa is present (arrowhead).



Fig. 10.—MR image (SE 500/15) shows well-delineated sinus tract originating from rectum in left ischioirectal fossa (arrows).



A



B

Fig. 11.—A, MR image (SE 1600/22) shows thickening of perirectal tissue with fluid accumulation posterior to rectum (arrowheads).

B, CT scan shows inflammation of perirectal fat, caused by dorsal circumferential spread of fistulae (arrowheads).

the pelvic floor. Furthermore, the levator ani, an important landmark for the distinction between supralelevator and infralevator abscesses, often cannot be seen on CT.

Patients with Crohn disease often experience repeated episodes of acute exacerbation during their chronic illness. The diagnostic workup in these mostly young patients may be difficult, requiring repeated imaging studies, many of which lead to a significant gonadal radiation exposure.

Therapeutic concepts in patients with fistulae and abscesses include drug therapy and surgical intervention. Clinically important decisions include the exclusion of abscesses before initiating cortisone therapy, monitoring drug therapy, and the exact preoperative assessment of the extension of fistulae. In patients treated with a temporary intestinal stoma, the presence of other fistulae must be excluded before continuity can be reestablished.

Our results indicate that MR imaging may overcome some of the limitations of CT in the evaluation of sinus tracts and fistulae in patients with Crohn disease. MR images showed the orifice of the fistulae or sinus tracts in the bowel wall in 13 of 17 patients and showed their connections to muscles, hollow viscera, and skin. In particular, the perirectal spread of fistulae and abscesses with respect to the levator ani was well demonstrated on coronal MR images, and both supralelevator and infralevator compartments were well defined. Neural and vascular structures in the perineum such as the pudendal and inferior gluteal arteries, however, may be mistaken for fistulae on MR scans.

The appearance of fistulae on MR images is fairly characteristic. We believe that the linear structures with low signal intensity on T1-weighted images and high signal intensity on T2-weighted images are due to fluid within fistulae.

Our results suggest that the three-dimensional imaging capabilities, the high soft-tissue contrast resolution, and the lack of ionizing radiation are advantageous features of MR over CT in showing the exact extension of fistulae and sinus tracts in patients with Crohn disease.

ACKNOWLEDGMENT

We thank Sue Romanick-Schmiedl, M.D., for editorial contributions.

REFERENCES

1. Farmer RG, Hawk WA, Turnbull RB Jr. Clinical patterns in Crohn disease: a statistical study of 615 cases. *Gastroenterology* **1975**;68:627-636
2. Greenstein AJ, Janowitz HD, Sachar DV. The extraintestinal complications of Crohn's disease and ulcerative colitis: a study of 700 patients. *Medicine (Baltimore)* **1976**;55:401-412
3. Rankin GB, Watts HD, Melnyk CS, Kelley ML Jr. National comparative Crohn's disease study: extraintestinal manifestations and perianal complications. *Gastroenterology* **1979**;77:914-920
4. Gore RM. Cross sectional imaging of inflammatory bowel disease. *Radiol Clin North Am* **1987**;25:115-131
5. Fishman EK, Wolf EJ, Jons B, Bayless TM, Siegelman SS. CT evaluation of Crohn's disease: effect on patient management. *AJR* **1987**;148:537-540
6. Goldberg HI, Gore RM, Margulis AR, Moss AA, Baker EL. Computed tomography in the evaluation of Crohn's disease. *AJR* **1983**;140:277-282
7. Gore R, Main C, Kirby D, et al. CT findings in ulcerative granulomatous and indeterminate colitis. *AJR* **1984**;143:279-284
8. Guillaumin E, Jeffrey RB Jr, Shea WJ, Asling CW, Goldberg HI. Perirectal inflammatory disease. CT findings. *Radiology* **1986**;161:153-157
9. Kerber GW, Greenberg M, Rubin JM. Computed tomography evaluation of local and extraintestinal complications of Crohn's disease. *Gastrointest Radiol* **1984**;9:143-148
10. Kleinhaus U, Weich Y. Computed tomography of Crohn's disease—a reevaluation. *ROFO* **1987**;147:607-611
11. Yousem DM, Fishman EK, Jones B. Crohn disease: perirectal and perianal findings at CT. *Radiology* **1988**;167:331-334
12. Goldberg HI, Caruthers SB, Nelson JA, Singleton JW. Radiographic findings of the national cooperative Crohn's disease study. *Gastroenterology* **1979**;77:925-937
13. Bartram CL. Radiology in the current assessment of ulcerative colitis. *Gastrointest Radiol* **1977**;1:383-392
14. Carlson HC. Perspective: the small bowel examination in the diagnosis of Crohn's disease. *AJR* **1986**;147:63-65
15. Thoeni RF, Margulis AR. Radiology in inflammatory disease of the colon: an area of increased interest for the modern clinician. *Invest Radiol* **1980**;4:281-292
16. Hildell J, Lindstrom C, Wenckert A. Radiographic appearances in Crohn's disease. IV. The new distal ileum after surgery. *Acta Radiol [Diagn] (Stockh)* **1980**;21:221-227
17. DiCandio G, Mosca F, Campatelli A, Bianchini M, D'Elia F, Dellagiovani PC. Sonographic detection of postsurgical recurrence of Crohn's disease. *AJR* **1986**;146:523-526
18. Jenss H, Klott KJ, Malchow H. Sonographie: Darstellung von Fistein und Abszessen beim Morbus Crohn. *Leber Magen Darm* **1980**;6:317-320
19. Kaftori JK, Percy M, Kleinhaus U. Ultrasonography in Crohn's disease. *Gastrointest Radiol* **1984**;9:137-142

Book Review

MIRD Primer for Absorbed Dose Calculations. By Robert Loevinger, Thomas F. Budinger, and Evelyn E. Watson. New York: The Society of Nuclear Medicine, 128 pp., 1988. \$35 for members, \$50 for nonmembers

MIRD is an acronym for medical internal radiation dose and is a technique for determining the absorbed dose to organs from internally deposited radionuclides. The system was initiated by the Society of Nuclear Medicine more than 20 years ago for the estimation of dose to nuclear medicine patients. The result is an elegant methodology for determining internal dose.

The dose (D) to a target organ from radioactivity deposited in a source organ can be expressed in terms of only two parameters, \bar{A} and S , where $D = \bar{A}S$. \bar{A} is the effective total activity that has contributed to the dose over time (cumulated activity), and S is a factor that relates the dose deposited in a target organ to unit cumulated activity in a source organ. The user is required only to supply the value of \bar{A} from a knowledge of the activity administered and appropriate biological data. The S factor has been tabulated for most medically important radionuclides by using a computer model for standard organ sizes and separations. Other necessary parameters, such as the fraction of energy absorbed in an organ for each of the emissions from a particular radionuclide, also have been incorporated into the S factor.

The MIRD system has been refined over the years and until now has been available as a series of 13 pamphlets published by the Society of Nuclear Medicine between 1968 and 1981. Report No. 33 from the National Council on Radiation Protection and Measurement and report No. 32 from the International Commission on Radiation Units and Measurements also contain worthwhile summaries of the technique.

The MIRD primer is divided into four parts. Part 1 is an introduction to the rationale for the technique and explains the meaning and derivation of each factor contained in \bar{A} and S . A discussion of biokinetics and the still evolving question of the appropriate units to be used is given also. Part 2 is a set of examples of an escalating level of difficulty and complexity. For readers already familiar with the MIRD protocol, this is the most instructive part of the book and gives fresh insight into the value and power of the technique. Part 3 is a collection of 12 absorbed-dose-estimate reports that includes radio-pharmaceuticals containing the common iodine isotopes and also covers the dosimetry of several ^{99m}Tc -labeled imaging agents. Part 4 contains three appendixes, the first of which lists the previously published MIRD pamphlets. The other two are reprints of pamphlets 1 and 12—the scientific underpinnings of the method. Pamphlet 11 is not included. This contains the S factors to be used for routine calibrations and must be purchased separately.

The MIRD primer should be a part of any nuclear medicine department's library, not only for the wealth of information summarized in the volume but also for the rich bibliography that follows each section.

Douglas R. Shearer
Rhode Island Hospital
Providence, RI 02902

CT of Adrenal Tumors: Frequency and Clinical Significance of Low-Attenuation Lesions

Hidetoshi Miyake¹
Hirofumi Maeda¹
Makoto Tashiro¹
Koji Suzuki¹
Hidehiro Nagatomo¹
Hisayuki Aikawa²
Akira Ashizawa¹
Seiji Ichika³
Akira Moriuchi⁴

The CT values of adrenal tumors were evaluated in 36 patients to determine the frequency and significance of negative CT values. Twenty-seven patients had adrenocortical adenomas (13 had primary aldosteronism, 12 had Cushing syndrome, and two had nonhyperfunctioning adenoma), one had adrenocortical carcinoma, and eight had pheochromocytomas. The CT values in primary aldosteronism (mean, 1.8 ± 9.9 H) were lower than those in Cushing syndrome (27.6 ± 12.0 H) and pheochromocytoma (35.9 ± 9.8 H). Six adrenocortical adenomas had homogeneous, low CT attenuation, with CT values ranging from -20 to -0.4 H. Four of these had primary aldosteronism, one had Cushing syndrome, and one had nonhyperfunctioning adenoma.

Our results suggest that adrenal tumors with homogeneous, slightly negative CT attenuation are likely to be adrenocortical adenomas, mainly primary aldosteronism and nonhyperfunctioning adenomas. This finding may be especially useful in diagnosing nonhyperfunctioning adenoma.

CT is an established procedure for detecting and evaluating adrenal lesions [1]. Several authors have reported examples of adrenal tumors with low attenuation on CT [2, 3]. We studied the CT scans of 36 pathologically proved adrenal tumors to determine the frequency and significance of negative CT values.

Patients and Methods

Thirty-six patients with pathologically proved adrenal tumors (10 men and 26 women, age 18–74 years) had CT scans done at the Medical College of Oita and the Nagasaki University School of Medicine. Thirteen had primary aldosteronism caused by an adrenal adenoma (ranging from 1.0 to 4.0 cm). Twelve had Cushing syndrome caused by an adrenal adenoma (2.5–4.0 cm in size), two had nonhyperfunctioning adenoma (3.4 and 4.0 cm), and one had adrenocortical carcinoma (14 cm). Eight had pheochromocytoma (5.0–9.0 cm). Cases of adrenal myelolipoma were excluded from the study.

CT scans were performed at 5- or 10-mm intervals using cuts of 5- or 10-mm thickness. A GE CT/T 9800 (General Electric, Milwaukee, WI) was used at Medical College of Oita (16 cases) and a GE CT/T 8800 was used at Nagasaki University School of Medicine (20 cases). In 30 patients, the CT scans were performed before and after IV infusion of contrast material (65% Angiografin, 100 ml, Nihon Schering, Osaka, Japan). In the remaining six patients, only noncontrast CT scans were done.

Results

The CT values of the 27 adrenocortical adenomas and the eight pheochromocytomas on pre- and/or postcontrast CT scans are shown in Figure 1. The adrenocortical carcinoma showed attenuation values of 42 H on precontrast CT scans and 55 H on postcontrast scans. The CT values in the primary aldosteronism on noncontrast CT scans ranged from -18 to 13 H (mean, 1.8 ± 9.9 H). In cases with Cushing syndrome, the range was -0.4 to 46 H (mean, 27.6 ± 12.0 H). In

Received October 3, 1988; accepted after revision January 19, 1989.

¹ Department of Radiology, Medical College of Oita, 1-1506, Idaigaoka, Hazama-machi, Oita-gun, Oita 879-56, Japan. Address reprint requests to H. Miyake.

² Department of Radiology, Nagasaki University School of Medicine, 7-1 Sakamoto-machi, Nagasaki, 852, Japan.

³ Department of Urology, Medical College of Oita, 1-1506, Idaigaoka, Hazama-machi, Oita-gun, Oita 879-56, Japan.

⁴ Department of Pathology, Medical College of Oita, 1-1506, Idaigaoka, Hazama-machi, Oita-gun, Oita 879-56, Japan.

AJR 152:1005–1007, May 1989
0361–803X/89/1525–1005
© American Roentgen Ray Society

cases of pheochromocytoma, the range was 21 to 50 H (mean, 35.9 ± 9.8 H).

Six of 36 patients had adrenal tumors with negative CT values (-20 to -0.4 H) on noncontrast CT scans. All of the tumors showed a homogeneous interior before and/or after IV administration of contrast material (Fig. 2A). On these six patients, four had primary aldosteronism (-18 to -5 H), one had Cushing syndrome (-0.4 H), and one had a nonhyperfunctioning adenoma (-20 H).

Histologically, the adenomas of four patients with primary aldosteronism and one patient with nonhyperfunctioning adenoma were composed of vacuolated, large clear cells (Fig. 2B). Large amounts of cytoplasmic lipid were confirmed with oil red O stain in one patient (Fig. 2C). Unlike the other patients with Cushing syndrome, the adenoma in one patient with Cushing syndrome comprised more clear cells than compact cells.

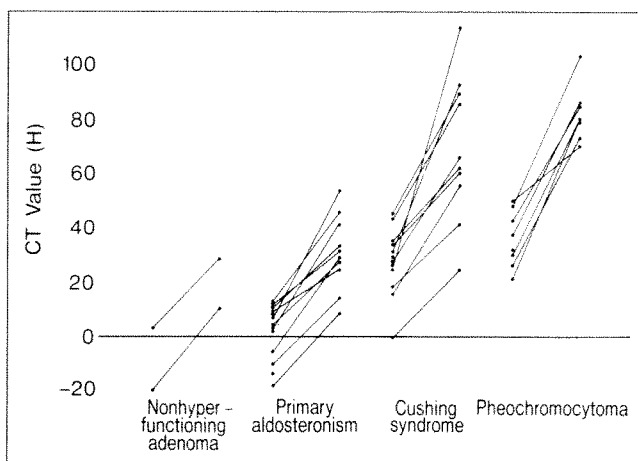


Fig. 1.—CT values of adrenocortical adenomas and pheochromocytoma on noncontrast-enhanced and/or contrast-enhanced CT.

Discussion

Adrenocortical tumors are classified as those associated with Cushing syndrome, primary aldosteronism, adrenogenital syndrome, and nonhyperfunctioning tumor on the basis of clinical and biochemical evidence of hormonal hypersecretion. However, the adenomas in Cushing syndrome generally are composed of enlarged, lipid-laden clear cells scattered among more common compact cells. The cells in primary aldosteronism are mostly large, lipid-laden clear cells similar to those seen in the zona fasciculata [4]. Therefore, cytoplasmic lipid is apt to occur more commonly in primary aldosteronism than in Cushing syndrome.

The CT values of tumors in our cases of primary aldosteronism were lower than those in the patients with Cushing syndrome and pheochromocytoma. Thirty-one percent (4/13) of tumors associated with primary aldosteronism had slightly negative CT values on noncontrast CT scans. In Cushing syndrome, adenomas with more clear cells than compact cells may show slightly negative CT values. The vacuolated, large clear cells of the adenomas are presumed to cause the negative CT values in these cases [5].

It may be that nonhyperfunctioning adenoma cells are unable to use the lipid, resulting in the accumulation of droplets within the cells [6]. There was one nonhyperfunctioning adenoma with negative CT values on precontrast CT scans in our series. Liessi and Spigariol [3] have reported five nonhyperfunctioning adenomas with negative CT values (-20 to -10 H), but there have also been a few reports in which the mean attenuation values varied from -2 to 38 H [7, 8].

In our series, we found homogeneous, slightly negative attenuation on CT scans of adrenocortical adenomas, mainly in cases of primary aldosteronism and nonhyperfunctioning adenoma, not in adrenocortical carcinoma and pheochromocytoma. This finding is not rare in primary aldosteronism, but, to our knowledge, it has not been described. Homogeneous, slightly negative CT attenuation may be especially useful in

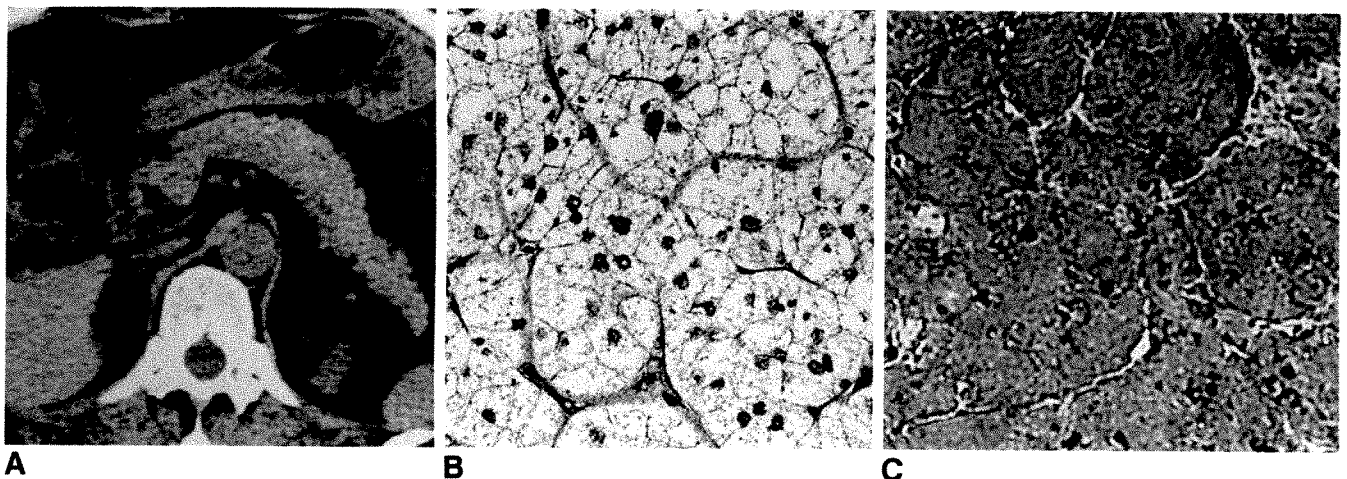


Fig. 2.—58-year-old woman with nonhyperfunctioning adenoma.

A, Precontrast CT scan shows left adrenal tumor with homogeneous low attenuation (-20 H). (window level: 0, window width: 300) B and C, Photomicrographs of pathologic specimen. B, Adenoma is composed of vacuolated, enlarged clear cells (hematoxylin/eosin stain, $\times 200$). C, Enlarged clear cells are filled with large amounts of lipid (oil red O stain, $\times 200$).

distinguishing nonhyperfunctioning adenoma from primary aldosteronism diagnosed by clinical and biochemical evidence of hormonal hypersecretion. Metastatic adrenal tumors containing fat and adrenal myelolipomas may be included in the differential diagnosis of adrenal masses with negative CT values. Metastatic adrenal tumors containing fat are extremely rare [9]. The CT numbers in myelolipomas depend on the relative contents of fat, bone-marrow elements, and other tissue. Myelolipomas usually have an inhomogeneous interior with fat on CT and have no clinical and biochemical evidence of hormonal hypersecretion [10, 11].

In conclusion, homogeneous, slightly negative CT attenuation on noncontrast CT scans is not rare in adrenocortical adenoma, especially in cases of primary aldosteronism and nonhyperfunctioning adenoma. This finding may be especially useful in differentiating nonhyperfunctioning adenoma from other adrenal tumors that do not show clinical and biochemical evidence of hormonal hypersecretion.

REFERENCES

1. Eghrari M, McLoughlin MJ, Rosen IE, et al. The role of computed tomography in assessment of tumoral pathology of the adrenal glands. *J Comput Assist Tomogr* **1980**;4:71-77
2. Haertel M, Probst P, Bollmann J, Zingg E, Fuchs WA. Computertomographische Nebennierendiagnostik. *Fortschr Geb Roentgenstr Nuklearmed Ergänzungsband* **1980**;132:31-36
3. Liessi G, Spigariol F. Ruolo della TC e degli US nella diagnosi delle neoplasie surrenali a matrice adiposa. *Radiol Med (Torino)* **1988**;75:195-199
4. Sommers SC. Adrenal gland. In: Anderson WAD, Kissane JM, eds. *Pathology*, 7th ed. Saint Louis, MO: Mosby, **1977**:1658-1679
5. Schaner EG, Dunnick NR, Doppman JL, Strott CA, Gill JR, Javadpour N. Adrenal cortical tumors with low attenuation coefficients: a pitfall in computed tomography diagnosis. *J Comput Assist Tomogr* **1978**;2:11-15
6. Matsuo K, Kawai K, Tsuchiyama H. Non-functioning adrenocortical adenoma in culture, quantitative and morphological observations. *Acta Pathol Jpn* **1985**;35:871-884
7. Glazer HS, Weyman PJ, Sagel SS, Levitt RG, McClennan BL. Nonfunctioning adrenal masses: incidental discovery on computed tomography. *AJR* **1982**;139:81-85
8. Mitnick JS, Bosniak MA, Megibow AJ, Naidich DP. Non-functioning adrenal adenomas discovered incidentally on computed tomography. *Radiology* **1983**;148:495-499
9. Greene KM, Brantly PN, Thompson WR. Adenocarcinoma metastatic to the adrenal gland simulating myelolipoma: CT evaluation. *J Comput Assist Tomogr* **1985**;9:820-821
10. Behan M, Martin EC, Muecke EC, Kazam E. Myelolipoma of the adrenal: two cases with ultrasound and CT findings. *AJR* **1977**;129:993-996
11. Vick CW, Zeman RK, Mannes E, Cronan JJ, Walsh JW. Adrenal myelolipoma: CT and ultrasound findings. *Urol Radiol* **1984**;6:7-13

Book Review

Diagnostic Nuclear Medicine, vols. 1 and 2, 2nd ed. Edited by Alexander Gottschalk, Paul B. Hoffer, and E. James Potchen. Baltimore: Williams & Wilkins, 1153 pp., 1988. \$215

The exciting developments in CT, sonography, and, particularly, MR imaging in the last decade have tended to overshadow, and perhaps blur, the advances in nuclear medicine. The sleeping bear is alive and well. For those who have any doubt, this masterly new edition in Golden's Diagnostic Radiology series will convince them otherwise.

The editors have completely revised the old text and expanded it into two volumes. Their aim remains the same, namely to provide a reference work for radiologists with substantial interest in nuclear medicine. Their basic introductory and how-to approach in each area will help the novice get a solid foundation. Their contributor's discussions on the traditional areas of nuclear medicine, as well as some new metabolic and physiologic approaches to imaging, are often encyclopedic. Thus, they both provide a good review for the already initiated and go beyond to the frontiers of technology, for example, with a discussion of antibody imaging. Virtually every chapter is thorough, covering normal variants, special techniques, and a wide range of pathologic states. The book has discussions of many new concepts and radiopharmaceuticals that are still investigational. It should be up-to-date for some time.

This edition has much more emphasis than the first on functional applications. The principles of basic physics, computers, and instru-

mentation are included in early chapters. The section on cardiovascular nuclear medicine has been expanded to 16 chapters and provides a sound basis of the general principles, including the pathologic basis of coronary artery disease, as well as correlative clinical discussions on the applications and value of various techniques. In recognition that nuclear medicine is not an island unto itself, chapters have been written on how it correlates with other imaging techniques in the liver, in the hepatobiliary system, and in diseases of the thyroid and kidney. The section on thyroid tests includes a good review of thyroid physiology and a primer on radioimmunoassays, subjects sometimes ignored in imaging texts.

The quality of the photographic images is excellent. References are relatively current. The type could be a little larger in future editions. In summary, this is an excellent text, and we suggest its purchase to those involved in nuclear medicine, whether at a basic or advanced level.

Chester Kay
Andrew J. DeRogatis
St. Luke's/Roosevelt Hospital Center
New York, NY 10019

Subcutaneous Metastases from Malignant Melanoma: Prevalence and Findings on CT

Randall M. Patten¹
William P. Shuman²
Sharlene Teefey³

We reviewed 197 body CT studies on 53 sequential patients who had a histologic diagnosis of malignant melanoma in order to determine the CT appearance, pattern of spread, and prevalence of subcutaneous melanoma metastases. Seventeen (38%) of 45 patients with CT evidence of metastatic melanoma had subcutaneous nodules shown on CT. Five patients (11%) had subcutaneous nodules as the only indication of metastatic disease on their CT scans. All patients who developed subcutaneous metastases had primary lesions classified as Clark level IV or V. (The Clark classification is based on the depth of tumor invasion and is rated I to V.) Metastases appeared as small, discrete rounded densities in the subcutaneous fat; lesions were occasionally subtle because of their small size and peripheral location. The location of subcutaneous nodules could not be predicted consistently on the basis of the site of the primary malignancy.

We conclude that subcutaneous metastases are common with melanoma in patients with Clark level IV or V lesions. These subcutaneous nodules are readily detected on CT scans if the subcutaneous tissues are carefully examined. The detection of these lesions may affect management or prognosis of patients, especially in those cases where subcutaneous nodules are the only CT evidence of metastatic disease.

Malignant melanoma is an unpredictable disease [1]. The tumor may be localized or widely metastatic at initial clinical presentation. Metastatic lesions can spread hematogenously, through lymphatic channels, or by direct local invasion and thus may occur in any organ of the body. The most common sites of metastatic involvement are the lung, liver, bone, and brain [2, 3].

Although the role of imaging in screening for melanoma metastases is controversial [2, 4], CT has been advocated as an important imaging adjunct for accurate staging of the tumor and for treatment planning [5, 6]. Although the prognosis in malignant melanoma is most dependent on the depth and location of the primary tumor [7, 8], information regarding the presence and extent of metastatic lesions also may be of important prognostic value [9, 10] and can help determine the subsequent extent or type of therapy.

Previous reports have suggested some propensity for melanoma to metastasize to subcutaneous tissues, where small nodules may not be detected by the patient and clinician [11, 12]. CT can detect these small soft-tissue lesions within the lower density subcutaneous fat [11]. The purpose of this study was to evaluate the CT appearance, pattern of spread, and prevalence of subcutaneous nodules in a group of patients at risk for metastases from primary melanoma.

Methods

We reviewed body CT studies and medical records of 53 sequential patients at risk for metastatic melanoma. These patients all had biopsy-proved primary malignant melanoma and were referred for body CT imaging over a 4-year period. A total of 197 CT studies were performed on these 53 patients (average, 3.72 studies/patient).

The study group included 29 men and 24 women with an average age of 51 years (range, 23–76 years). Within this group, the primary melanoma was located on the trunk in 33%, in

Received October 31, 1988; accepted after revision December 23, 1988.

Presented at the annual meeting of the American Roentgen Ray Society, New Orleans, LA, May 1989.

¹ Department of Radiology (ZA-65), University of Washington, and Harborview Medical Center, 325 Ninth Ave., Seattle, WA 98104. Address reprint requests to R. M. Patten at Harborview Medical Center.

² Department of Radiology (SB-05), University of Washington, and University Hospital, 1959 N.E. Pacific St., Seattle, WA 98195.

³ Department of Radiology (ZB-20), University of Washington, and Veterans Administration Medical Center, Seattle, WA 98108.

AJR 152:1009–1012, May 1989

0361–803X/89/1525–1009

© American Roentgen Ray Society

the face and neck region in 27%, on the lower extremity in 25%, on the upper extremity in 10%, and in the vulvar region in 5%. In one patient, the site of the primary melanoma was unknown. Primary melanomas in these patients were classified according to the depth of tumor invasion (Clark classification I–V) at initial diagnosis. Most patients in the study group had relatively deep primary lesions at either Clark level IV (18 patients) or V (six patients). Nine patients had primary tumors classified as Clark III and seven patients had shallow primary lesions at either Clark I (two cases) or Clark II (five cases). Depth of tumor invasion was not known for 13 patients.

CT scans on these patients were examined for the presence or absence of subcutaneous nodules in the neck, chest, abdomen, and pelvis. The body regions studied varied from patient to patient; regions were studied on the basis of clinical suspicion for metastatic disease in 16%, as a metastatic screening protocol in 28%, or as a follow-up of known metastases in 56%. Included in this series were 10 CT studies of the neck, 56 studies of the chest, 78 studies of the abdomen, and 53 studies of the pelvis. The time from initial diagnosis of melanoma to the first CT study averaged 2.5 years (range, 1 month–9 years, 3 months).

A study was considered positive for subcutaneous metastases if nonanatomic nodules larger than 3 mm were present within the subcutaneous fat. Confirmation of the malignant character of the subcutaneous nodules was provided by histologic material obtained from biopsy (24%) and autopsy (29%), or was implied by subsequent growth in size and/or number of lesions on follow-up CT studies (47%).

The location of these subcutaneous nodules was recorded in conjunction with the anatomic location of the primary malignancy. If subcutaneous lesions developed in a body section contiguous to the site of a known primary lesion, along its lymphatic drainage pathway, or contiguous to a body section that already harbored subcutaneous metastases, these lesions were categorized as arising in an expected location. If subcutaneous nodules developed in a site remote from the primary malignancy without involvement of intervening body regions or remote from areas of expected lymphatic drainage, these lesions were categorized as arising in an unexpected location.

All CT studies were performed on a General Electric (Milwaukee, WI) 8800 or 9800 scanner with either 2-, 4.6-, or 9.6-sec scan times.

Oral, IV, and rectal contrast agents were administered routinely in the abdomen and pelvis; IV contrast agent was administered routinely in the neck and chest. Axial scans with 1-cm collimation were performed through the chest and abdomen at 1-cm intervals, and through the pelvis with either 1-, 1.5-, or 2-cm intervals. In the neck, 5-mm collimation and scanning intervals of 5 mm were used.

Results

Forty-five (85%) of 53 patients in the study group had CT evidence of metastatic disease, with 99 of the 197 CT studies positive for metastases (50%). Seventeen (38%) of the 45 patients with metastatic disease had subcutaneous nodules shown on CT scans. Five patients (11%) had subcutaneous nodules as the only indication of metastatic disease on their CT scans. All patients who developed subcutaneous metastases had primary lesions classified as Clark level IV or V.

Subcutaneous nodules were identified on 34 of the 197 studies reviewed. Nodules ranged from 0.5 to 2.5 cm in size. CT appearance of subcutaneous nodules included well-defined borders in 94% of cases and ill-defined borders in conjunction with hazing of subcutaneous fat in 6% of cases (Figs. 1–3). Nodules were homogeneous in 25 (74%) of the 34 studies and showed areas of inhomogeneity or necrosis in nine (26%) of the studies (Fig. 4). All nodules were of soft-tissue density with Hounsfield attenuation values between 10 and 40.

The location of subcutaneous metastatic nodules could not be predicted consistently from the anatomic site of the primary tumor. Subcutaneous nodules developed in expected locations (adjacent to the site of the primary lesion or along lymphatic drainage pathways) in 56% of patients and in unexpected locations in 44%. We found seven examples of subcutaneous nodules developing remotely from the site of primary malignancy with no evidence for metastases in the

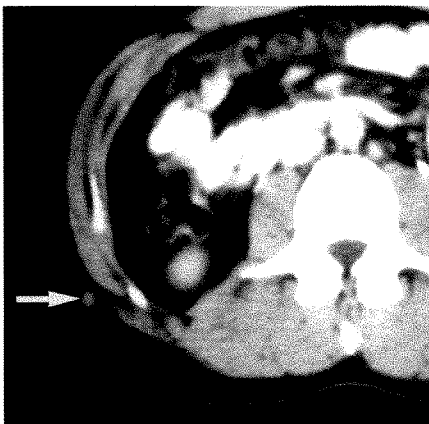


Fig. 1.—Clinically unsuspected, biopsy-proved melanoma metastasis to subcutaneous tissues of right flank (arrow). CT scan shows a well-circumscribed, homogeneous soft-tissue nodule within surrounding subcutaneous fat. Additional scattered subcutaneous nodules were identified on contiguous axial images.

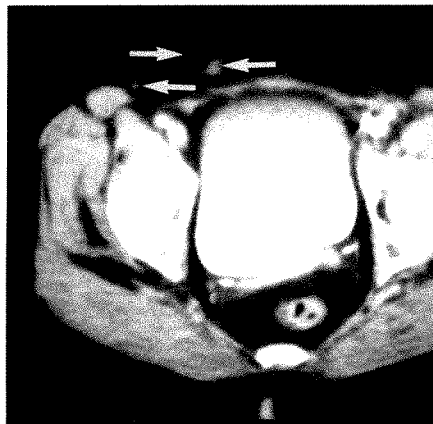


Fig. 2.—CT scan shows several tiny subcutaneous metastases (arrows) in subcutaneous tissues of pelvis. Patient had undergone left inguinal lymph-node dissection for lymphatic metastases.

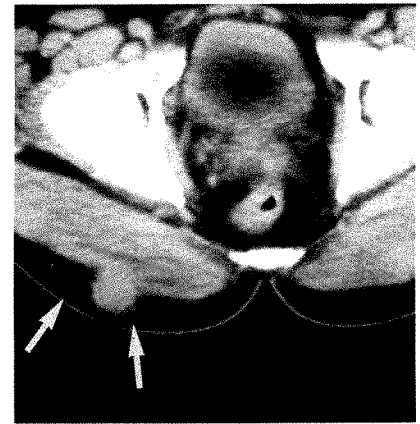
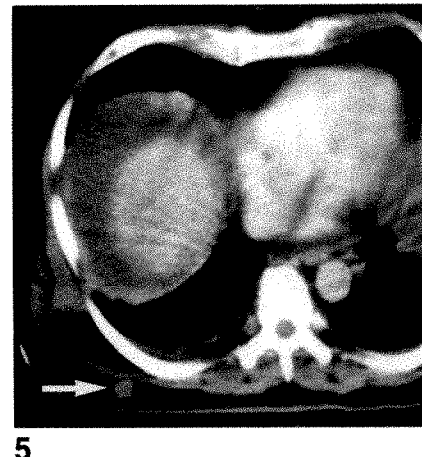


Fig. 3.—Biopsy-proved melanoma metastasis. CT shows 2-cm subcutaneous metastasis in right buttock with poor definition of surrounding fat (arrows).

Fig. 4.—Palpable subcutaneous metastasis in abdominal wall (arrow). CT scan shows central low density of metastasis.



Fig. 5.—CT scan shows a small metastasis in subcutaneous fat (arrow) that is easily overlooked. Note ascites and peritoneal tumor implants.



intervening subcutaneous tissues. Examples include a patient with a primary melanoma of the distal ankle who presented 2 years later with subcutaneous metastases to the chest as the only evidence of metastatic disease and a patient with ocular melanoma whose screening abdominal CT showed multiple subcutaneous metastases despite negative studies of the neck and chest.

Discussion

Melanoma is the most malignant skin cancer and is increasing in epidemic proportions [4]. It represents approximately 1–3% of total cancers in the United States, with an estimated 14,000 new cases diagnosed yearly [13, 14]. Newer and more effective therapeutic regimens, including specific immunotherapy, major obliterative surgery, and chemotherapeutic regimens, have been used with some modest improvement in survival [3, 15, 16].

Determination of the most effective treatment depends in part on accurate staging of the tumor [17]. Such staging depends on the anatomic site and depth of invasion of the primary tumor, but also depends on demonstration of the presence, sites, and extent of metastases [7–10]. Even in patients with advanced melanoma, the documentation of additional sites of metastases may have therapeutic implications [3]. Metastatic lesion detection may be helpful in planning radiation portals, assessing the effectiveness of chemotherapy, and monitoring recurrence following surgery [11]. CT has been advocated as an accurate and reliable imaging technique for detecting metastatic melanoma [18].

Malignant melanoma is commonly recognized as a tumor that may metastasize widely, sometimes spreading to unexpected sites. Although involvement of the subcutaneous tissues by metastatic melanoma has been reported, the prevalence of detection of these lesions by CT has not been addressed. Subcutaneous melanoma metastases are detectable by CT because of the marked contrast between the soft-tissue density of the nodules and the surrounding lower attenuation subcutaneous fat. However, these subcutaneous metastatic foci may be missed because of their small size and

peripheral location, necessitating a careful search of the subcutaneous tissues (Fig. 5). Additionally, technical factors that tend to exclude large portions of the subcutaneous tissues from the photographed image—such as the routine use of magnification to maximize the size of thoracic or abdominopelvic viscera or the use of inappropriately small scan diameters to acquire CT data—may result in the failure to detect subcutaneous melanoma metastases.

Benign subcutaneous nodules (sebaceous cysts, injection granulomata, lipomas) and subcutaneous blood vessels are frequently identified on CT scans and must be differentiated from malignant subcutaneous nodules. Hounsfield attenuation coefficients compatible with fat or calcium may suggest a benign lesion, and in patients at risk for metastatic disease, multiplicity of lesions or change in size and number over time may suggest malignancy. Subcutaneous vessels may simulate a nodule on a single axial image, but they can be identified on contiguous cuts and are smaller and even more sharply defined than the metastatic lesions. Finally, the location of the nodule within the subcutaneous tissue may be helpful: sebaceous cysts are usually just below the skin whereas metastases may be distant from the skin.

Our data suggest that subcutaneous metastases from primary melanoma are common in those patients with CT evidence of metastatic disease. This was especially true for those patients with relatively deep primary lesions, staged at Clark level IV or V at initial diagnosis. However, despite the relatively high rate of subcutaneous metastases found in this population of patients, we suspect that the true prevalence of subcutaneous nodules in metastatic melanoma may be higher than detected in our study for three reasons. First, not all subcutaneous tissues on all patients were examined by CT, and thus some patients may have had clinically occult subcutaneous melanoma metastases that were not detected by CT. Second, some body sections were examined by noncontiguous slices, and thus small nodules could have been missed in the skipped intervals between slices. Third, because multiplicity of nodules was a criterion for positive study, we may have missed solitary metastatic subcutaneous foci and therefore underestimated the true prevalence of subcutaneous metastatic lesions.

In this series, subcutaneous metastases did not always occur in predictable locations when such predictions were based on expected patterns of lymphatic drainage or on proximity to the site of the primary lesion. That subcutaneous metastases can be remote from the site of a known primary malignancy and its lymphatic drainage suggests that CT studies limited to regions of expected metastases may miss clinically occult disseminated disease and thereby potentially understage metastatic malignant melanoma. Similarly, the unpredictable occurrence and pattern of metastatic dissemination makes it difficult to tailor studies to those areas of greatest yield. Because scanning the entire body is impractical and may not be cost effective, monoclonal antibodies directed against human-melanoma-associated antigens might eventually be a more efficient technique for both imaging and treating the metastases of melanoma [19, 20].

We conclude that subcutaneous metastases from primary melanoma are common in patients with Clark level IV or V lesions and are detectable by CT. Such metastases may be subtle and easily overlooked, arising in unexpected locations remote from the site of the primary malignancy. In evaluation of patients with known melanoma, a small but significant number may be understaged, both clinically and by imaging, unless the fortuitous inclusion of subcutaneous metastases is recognized. Occasionally, subcutaneous metastases may be the only CT manifestation of metastatic disease.

REFERENCES

1. Breslow A. Thickness, cross-sectional areas and depth of invasion in the prognosis of cutaneous melanoma. *Ann Surg* 1970;172:902-908
2. Lee YN. Non-invasive screening tests for metastatic melanoma: rationale and results. *Am J Clin Oncol* 1983;6:225-233
3. Lee YTN. Malignant melanoma, pattern of metastasis. *CA* 1980;30:137-142
4. Zartman GM, Thomas MR, Robinson WA. Metastatic disease in patients with newly diagnosed malignant melanoma. *J Surg Oncol* 1987;35:163-164
5. Bydder GM, Kreel L. Body computed tomography in the diagnosis of malignant melanoma metastases. *CT* 1981;5:21-24
6. Strauss AV, Dritschilo A, Carter BL, Nathanson L, Piro AJ. Diagnostic testing for radiation treatment planning of malignant melanoma with special emphasis on CT scanning. *CT* 1981;5:37-42
7. McGovern VJ. The nature of melanoma. A critical review. *J Cutan Pathol* 1982;9:61-81
8. Drzewiecki KT, Andersen PK. Survival with malignant melanoma: a regression analysis of prognostic factors. *Cancer* 1982;49:2414-2419
9. Amier MH, Al-Sarraf M, Kaitkervicuis VK. Clinical presentation, natural history and prognostic factors in advanced malignant melanoma. *Surg Gynecol Obstet* 1979;149:687-692
10. Einhorn LH, Burgess MA, Vallejos C, et al. Prognostic correlations and response to treatment in advanced malignant melanoma. *Cancer Res* 1974;34:1995-2004
11. Dunnick NR, Schaner EG, Doppman JL. Detection of subcutaneous metastases by computed tomography. *J Comput Assist Tomogr* 1978;2:275-279
12. Berdeaux DH, Moon TE, Meyskens FL. Clinical-biologic patterns of metastatic melanoma and their effect on treatment. *Cancer Treat Rep* 1985;69:397-401
13. *Cancer facts and figures*. New York: American Cancer Society, Inc., 1979
14. Adam YG, Efron G. Cutaneous malignant melanoma: current views on pathogenesis, diagnosis, and surgical management. *Surgery* 1983;93:481-494
15. Siegler HF, Fetter BF. Current management of melanoma. *Ann Surg* 1977;186:1-12
16. Karakousis CP, Moore R, Holyoke ED. Surgery in recurrent malignant melanoma. *Cancer* 1983;52:1342-1345
17. Chen JTT, Dahmash NS, Ravin CE, et al. Metastatic melanoma to the thorax: report of 130 patients. *AJR* 1981;137:293-298
18. Doiron MJ, Bernardino ME. A comparison of noninvasive imaging modalities in the melanoma patient. *Cancer* 1981;47:2581-2584
19. Larson SM, Carrasquillo JA, McGuffin RW, et al. Use of I-131 labeled, murine Fab against a high molecular weight antigen of human melanoma: preliminary experience. *Radiology* 1985;155:487-492
20. Natali PG, Aguzzi A, Veglia F, et al. The impact of monoclonal antibodies on the study of human malignant melanoma. *J Cutan Pathol* 1983;10:514-528

Pictorial Essay

MR Imaging of the Finger: Correlation with Normal Anatomic Sections

Scott J. Erickson,¹ J. Bruce Kneeland,¹ William D. Middleton,² A. Jesmanowicz,¹ J. Hyde,¹ Thomas L. Lawson,¹ and W. Dennis Foley¹

The imaging evaluation of the hand to date has primarily consisted of plain-film radiography. Although the plain film yields accurate information about the bones, it gives poor or indirect information about the cartilage and soft tissues.

MR imaging yields a wealth of information about the soft tissues of the musculoskeletal system. Only a small amount of work on the MR appearance of the finger has been published [1-3], mainly because of the considerable demands on the imaging system by the small dimensions involved. To perform this investigation of normal finger anatomy, we wrote software for our MR system that permits the acquisition of images with a 4-cm field of view and we built a highly optimized local coil to obtain a sufficient signal-to-noise ratio to support this small field of view.

Materials and Methods

All imaging was performed on a 1.5-T Signa MR system (General Electric Medical Systems, Milwaukee, WI). The pulse programming language provided by General Electric for the Signa system was used, and a multisection spin-echo sequence was implemented that could be used to obtain fields of view as small as 4 cm and section thicknesses as small as 1 mm. This was obtained by essentially lengthening the duration of the gradients with a concomitant reduction in the sampling rate. This results in an increase in the minimum TE attainable. In order to reduce this minimum TE, the shape of the phase-encoding gradient was changed from its usual half-sine configuration to a trapezoid, increasing its area per unit of time [4]. A

dedicated transmit/receive saddle coil was built [5] by using 0.635-mm copper tubing for the inductance, Cuflon (Polyflon, New Rochelle, NY) for the fixed capacitance, and an 8- to 30-pF variable capacitor (Oxley Development, Ulverston, United Kingdom) for tuning. The coil was 8 cm long and 3.5 cm in diameter (Fig. 1).

Imaging was performed on six asymptomatic volunteers (four women and two men 21-30 years old). All images were obtained with a 4-cm field of view, a 256×256 acquisition matrix, and a

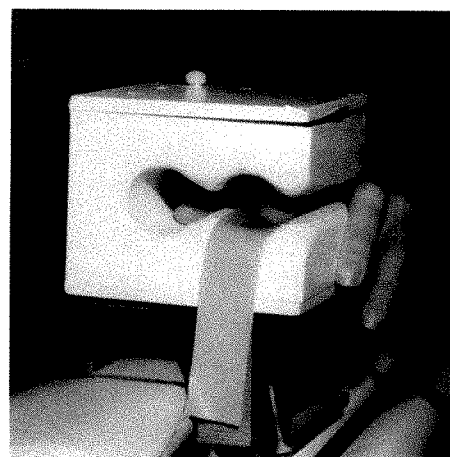


Fig. 1.—Specialized surface coil used for imaging the finger.

Received September 6, 1988; accepted after revision December 6, 1988.

¹ Department of Radiology, Medical College of Wisconsin, 8700 W. Wisconsin Ave., Milwaukee, WI 53226. Address reprint requests to S. J. Erickson.

² Department of Radiology, Mallinckrodt Institute of Radiology, Washington University School of Medicine, 510 S. Kingshighway Blvd., St. Louis, MO 63110.

Key to Abbreviations Used in Figures 2–12

cl	collateral ligament
clc	collateral ligament (cordlike portion)
clf	collateral ligament (fanlike portion)
ddv	dorsal digital vein
dp	distal phalanx
dtml	deep transverse metacarpal ligament
edt	extensor digitorum tendon
ee	extensor expansion
eit	extensor indicis tendon
fa	flow artifact
fdpt	flexor digitorum profundus tendon
fds	fibrous digital sheath
fdst	flexor digitorum superficialis tendon
hc	hyaline cartilage
iom	interosseous muscle
iot	interosseous tendon
lm	lumbrical muscle
mh	metacarpal head
mp	middle phalanx
n	nail
nb	nail bed
PALMAR	palmar aspect
pda	palmar digital artery
pdn	palmar digital nerve
pp	proximal phalanx
RADIAL	radial aspect
sus	subungual space
vp	volar plate

3-mm section thickness. Although thinner slices were possible, the resultant decrease in signal-to-noise was prohibitive. A spin-echo pulse sequence was used with a TR/TE of 500/28 and either two or four excitations.

Anatomic sections of three sets of fingers (one each in axial, sagittal, and coronal planes) were obtained with a cryomicrotome (PMV 2250, LKB, Stockholm, Sweden). Blocks of tissue were frozen in carboxymethyl cellulose and placed on the stage of a cryomicrotome. As each millimeter of tissue was removed, a color photograph of the surface was taken.

Anatomic identifications were established by correlating the cryomicrotome sections and MR images (Figs. 2–12). Standard anatomic texts were used as needed [6, 7].

Results

Bones and Joints

The finger contains the proximal, middle, and distal phalanges. The three articulations are the metacarpophalangeal joint, the proximal interphalangeal joint, and the distal interphalangeal joint. Hyaline cartilage is seen as a layer of medium signal intensity superficial to the low-signal-intensity cortex (Figs. 3–6 and 10). The metacarpophalangeal joint allows limited abduction and adduction as well as flexion and extension. The interphalangeal joints permit flexion and extension only.

Ligaments

The metacarpophalangeal joint is supported by a number of ligaments. The palmar ligament, or volar plate, is a fibrocartilaginous plate extending from the base of the proximal

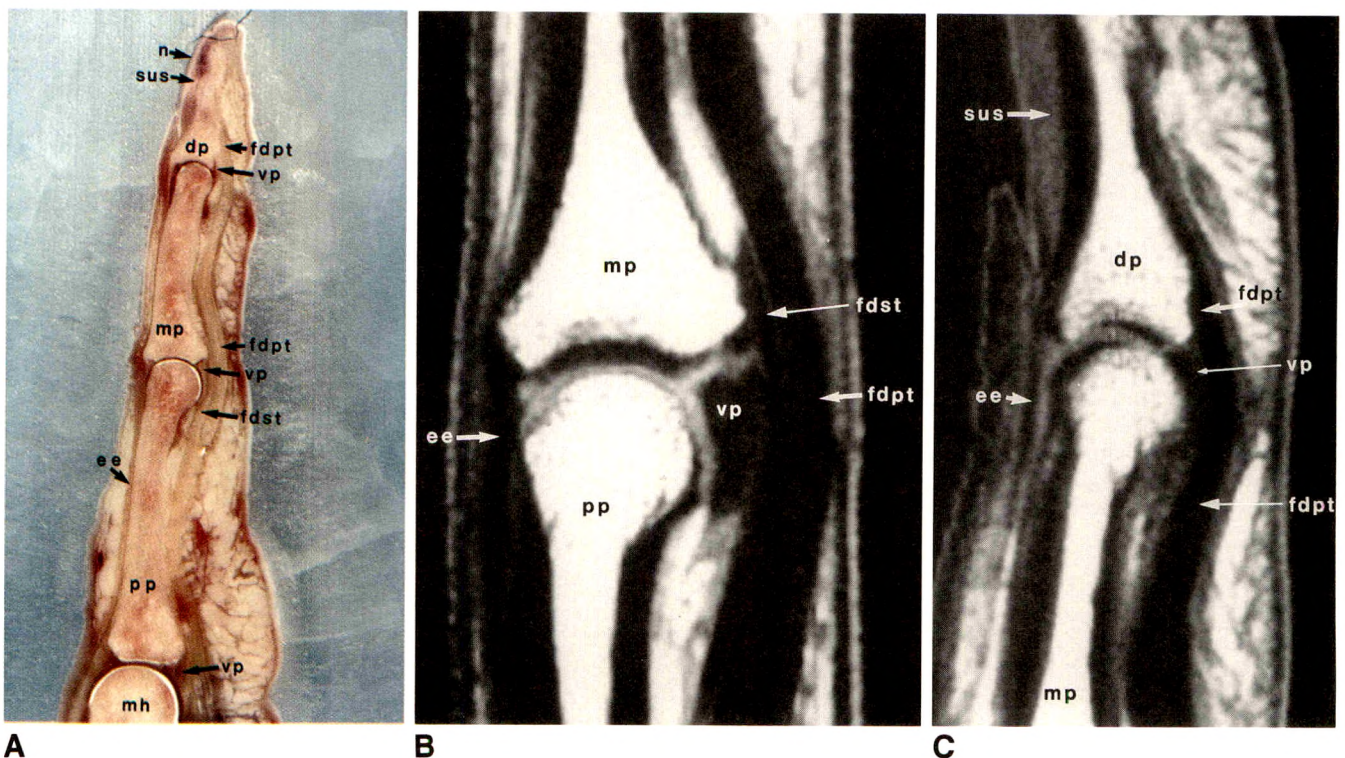


Fig. 2.—Midsagittal sections through finger. See abbreviation key on this page.

A, Cryomicrotome section.

B, MR image through proximal interphalangeal joint.

C, MR image through distal interphalangeal joint.

Fig. 3.—Midsagittal sections through metacarpophalangeal joint. See abbreviation key on page 1014.

A, Cryomicrotome section.
B, MR image.

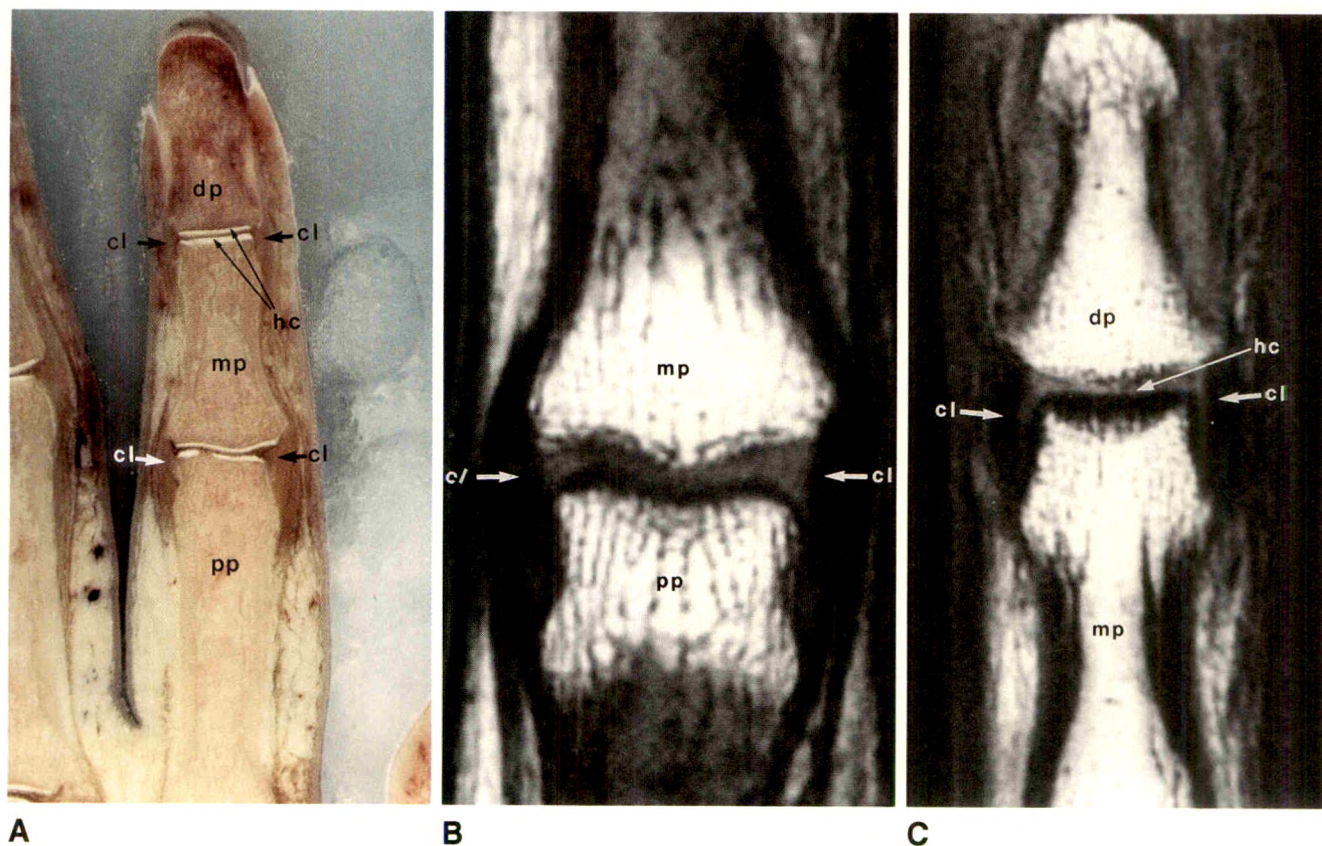
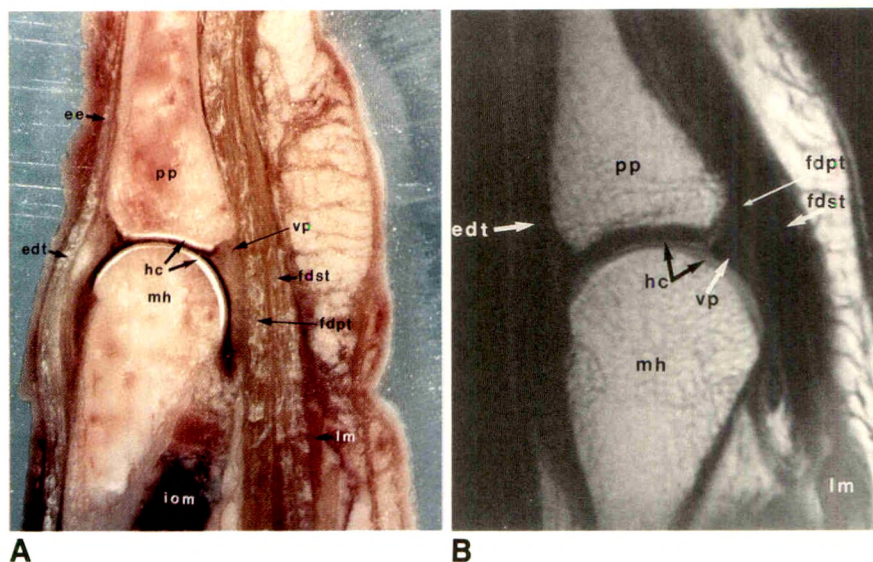


Fig. 4.—Coronal sections through finger. See abbreviation key, page 1014.

A, Cryomicrotome section.
B, MR image through proximal interphalangeal joint.
C, MR image through distal interphalangeal joint.

phalanx to the metacarpal head (Figs. 3, 6, and 7). The deep transverse metacarpal ligaments are three flat bands that connect the palmar ligaments of the second through the fifth metacarpophalangeal joints. The lumbrical muscles are located superficial to, and the interosseous muscles deep to,

these ligaments (Fig. 7). The collateral ligaments lie along the sides of the metacarpophalangeal joints and are composed of two parts. The weaker, more proximal, fanlike portion acts to fix the volar plate to the metacarpal head. The stronger, cordlike part is the more distal component (Figs. 5 and 6).

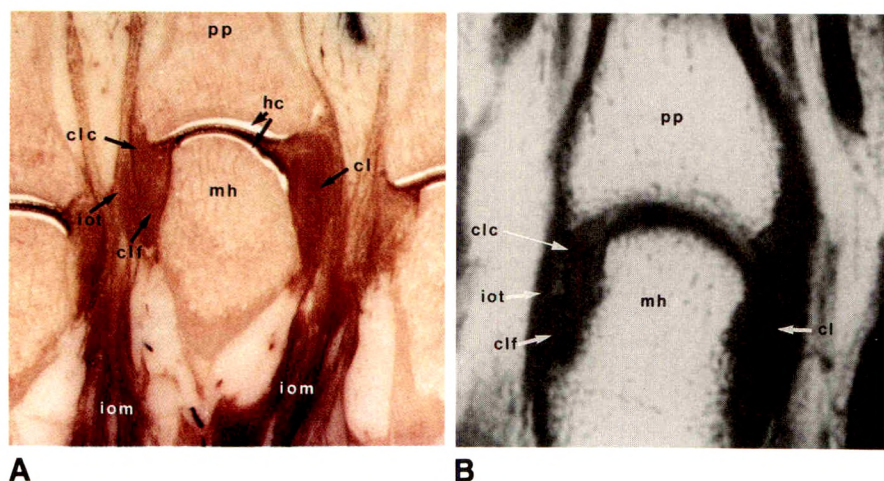


Fig. 5.—Coronal sections through metacarpophalangeal joint. See abbreviation key, page 1014.

A, Cryomicrotome section.
B, MR image.

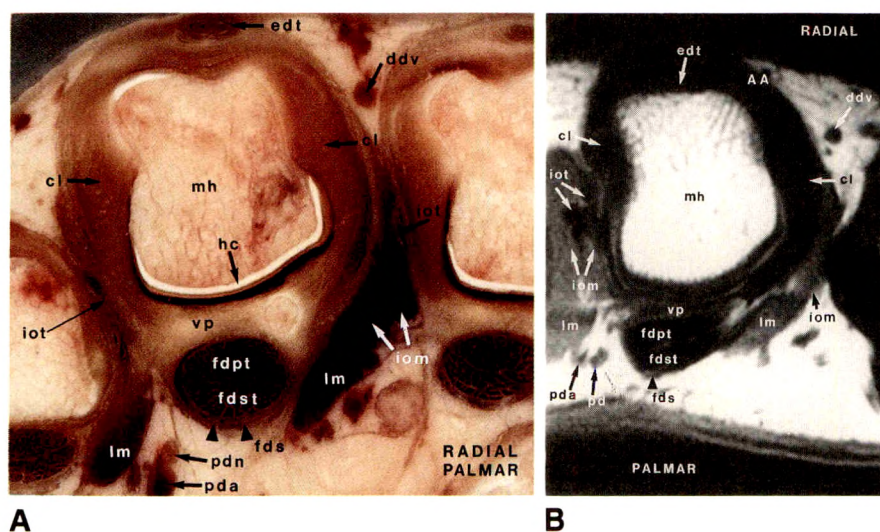


Fig. 6.—Axial sections just proximal to metacarpophalangeal joint. See abbreviation key, page 1014.

A, Cryomicrotome section.
B, MR image.

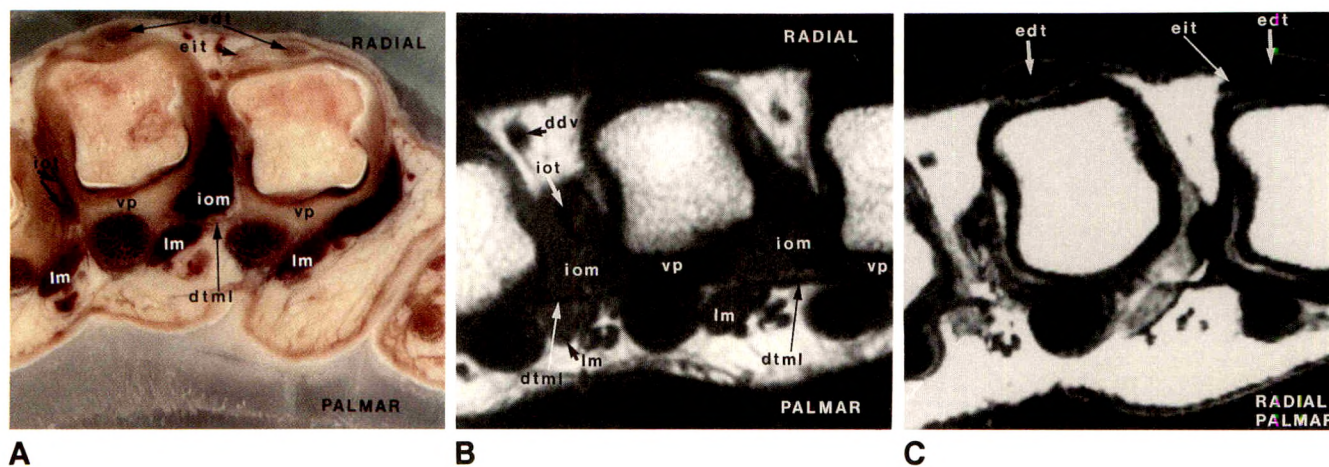


Fig. 7.—Axial sections at about the same level as Fig. 6 with attention to the deep transverse metacarpal ligament. See abbreviation key, page 1014.

A, Cryomicrotome section.

B, MR image.

C, MR image displayed at narrow window shows extensor tendons to better advantage.

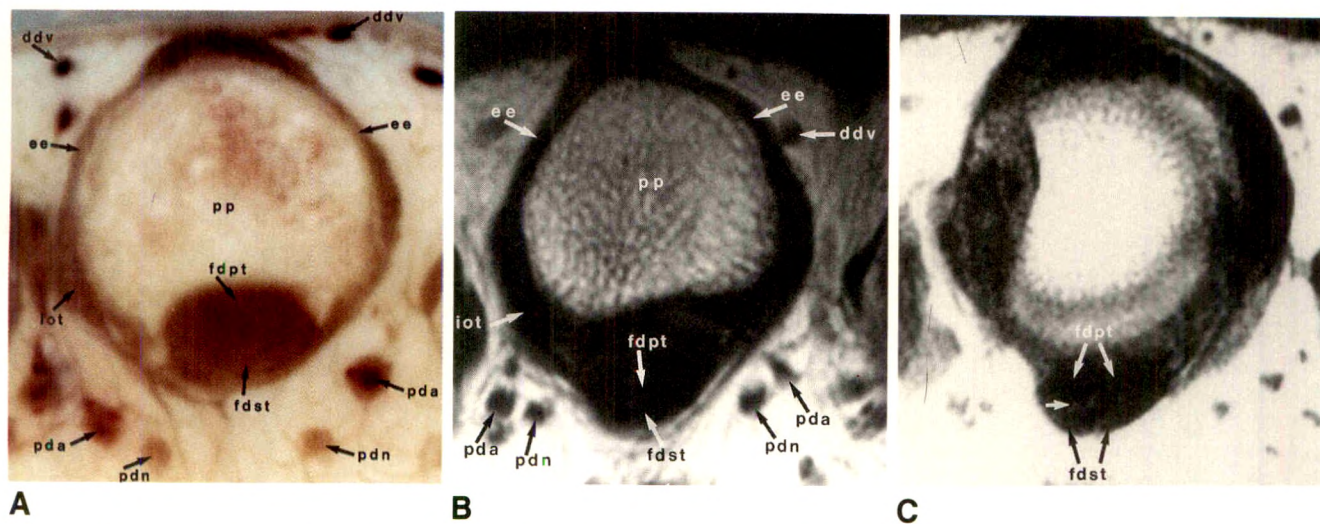


Fig. 8.—Axial sections just distal to metacarpophalangeal joint. See abbreviation key, page 1014.

A, Cryomicrotome section.

B, MR image.

C, MR image at slightly different level and displayed at narrow window shows separation between flexor digitorum tendons (short arrow).

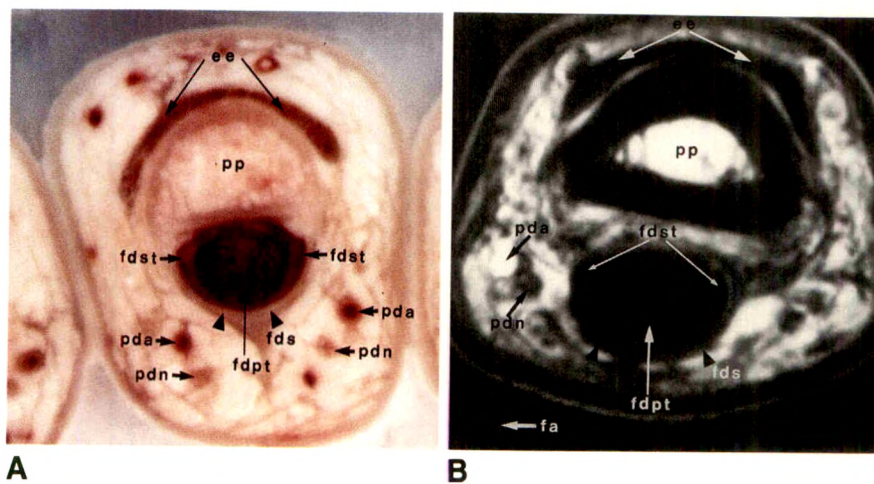


Fig. 9.—Axial sections through midproximal phalanx. See abbreviation key, page 1014.

A, Cryomicrotome section.

B, MR image.

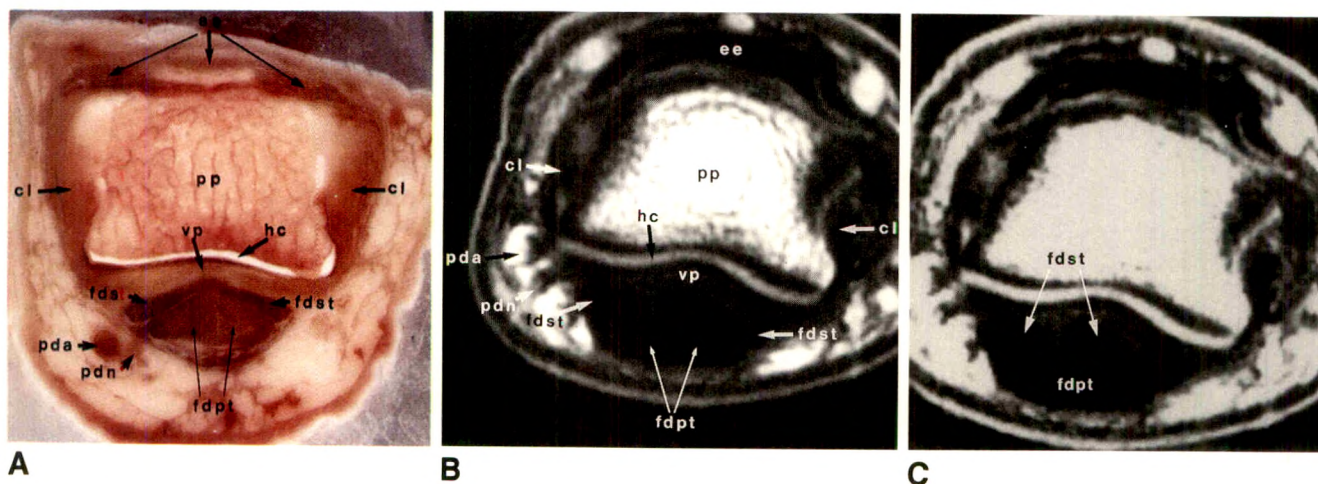


Fig. 10.—Axial sections through proximal interphalangeal joint. See abbreviation key, page 1014.

A, Cryomicrotome section.

B, MR image.

C, MR image displayed at narrow window distinguishes flexor digitorum tendons.

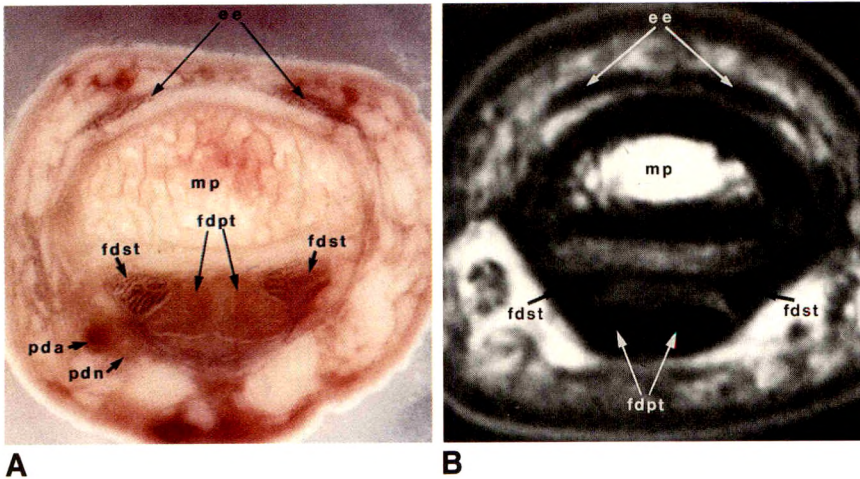


Fig. 11.—Axial sections through middle phalanx. See abbreviation key, page 1014.
A, Cryomicrotome section.
B, MR image.

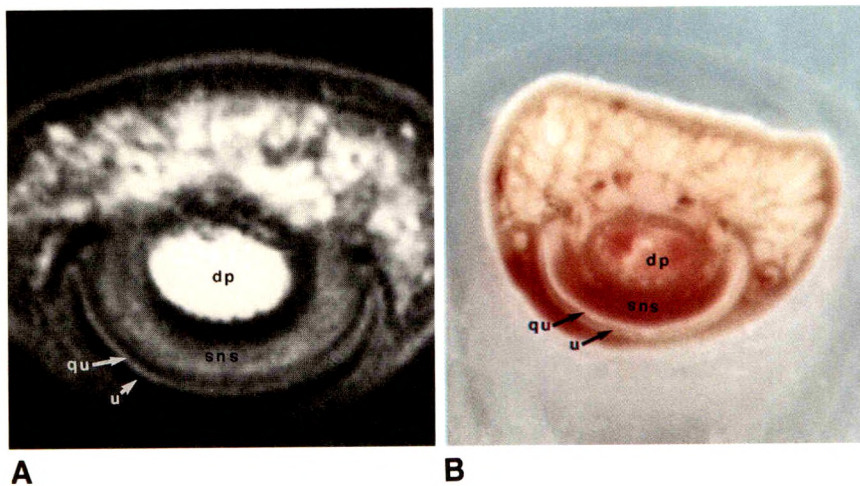


Fig. 12.—Axial sections through distal phalanx. See abbreviation key, page 1014.
A, MR image.
B, Cryomicrotome section.

The interphalangeal joints possess palmar and collateral ligaments that have the same morphology as those of the metacarpophalangeal joint (Figs. 2, 4, and 10). Ligaments are generally seen as structures with a low signal intensity, although the volar plate displayed a slightly greater signal intensity than the other ligaments.

Muscles and Tendons

The flexor digitorum tendons are seen as structures of low signal intensity that pass from the palm of the hand onto the palmar surface of the digits. The flexor digitorum superficialis tendon is superficial to the flexor digitorum profundus tendon at, and just distal to, the level of the metacarpophalangeal joint (Figs. 3, 6, and 8). The superficialis tendon subsequently splits to lie first on each side of the profundus tendon at the level of the midproximal phalanx (Fig. 9) and then deep to the profundus tendon at the level of the proximal interphalangeal joint where the two slips reunite (Fig. 10); finally, it divides again to insert on the sides of the shaft of the midportion of the middle phalanx (Fig. 11). The flexor digitorum profundus tendon inserts onto the base of the distal phalanx (Fig. 2).

The superficialis and profundus tendons each have their own synovial sheaths and also are housed by a common synovial sheath. This common sheath is then housed in a fibrous digital sheath, which consists of both transverse (annular) and crossed (cruciate) fibers that arch to cross the anterior surface of the tendons and attach to the margins of the phalanges. This fibrous sheath occasionally may be visualized with MR as a thin, low-intensity structure (Figs. 6 and 9).

The extensor digitorum tendons pass from the dorsum of the hand onto the dorsal surface of each finger (Figs. 3, 6, and 7). The extensor indicis tendon accompanies the extensor digitorum tendon to the index finger and lies on its ulnar (Fig. 7) aspect. The extensor digiti minimi tendon accompanies the extensor digitorum tendon to the little finger. The extensor expansion consists of the expanded lower ends of the extensor digitorum tendons (Figs. 2, 3, and 8–11). The central fibers of the expansion insert onto the base of the middle phalanx on its dorsal surface. The medial and lateral fibers of the expansion insert onto the base of the distal phalanx.

The four lumbrical muscles (Figs. 3, 6, and 7) arise from the flexor digitorum profundus tendons and insert onto the radial aspect of the extensor expansion. The interosseous

muscles (Figs. 3 and 5-7) arise from the metacarpal bones and insert onto the expansion and also onto the bases of the proximal phalanges (Figs. 5-8). There are three palmar interossei and four dorsal interossei, which act as finger adductors and abductors, respectively.

Neurovascular and Miscellaneous

The neurovascular supply to the finger consists of both palmar and dorsal digital branches of nerves, veins, and arteries. The palmar digital arteries and nerves (Figs. 6 and 8-11) are larger than the dorsal arteries and veins. The dorsal digital veins, however, are more conspicuous than the palmar digital veins (Figs. 6 and 8). The nail, nail bed, and subungual space are seen well with MR (Figs. 2 and 12).

REFERENCES

1. Weiss KL, Beltran J, Shaman OM, Stilla RF, Levey M. High-field MR surface coil imaging of the hand and wrist. Part I. Normal anatomy. *Radiology* **1986**;160:143-146
2. Weiss KL, Beltran J, Lubbers LM. High-field MR surface coil imaging of the hand and wrist. Part II. Pathologic correlations and clinical relevance. *Radiology* **1986**;160:147-152
3. Beltran J, Noto AM, Herman LJ, Lubbers LM. Tendons: high-field-strength surface coil imaging. *Radiology* **1987**;162:735-740
4. Jesmanowicz A, Hyde JS, Kneeland JB. Pulse sequences for small fields of view. Presented at the annual meeting of the Society of Magnetic Resonance in Medicine, San Francisco, CA, August **1988**
5. Ginsberg DM, Melchner MJ. Optimum geometry of saddle shaped coils for generating a uniform magnetic field. *Rev Sci Instrum* **1970**;41:122-123
6. Anderson JE. *Grant's atlas of anatomy*. Baltimore: Williams & Wilkins, **1978**
7. Carter BL, Morehead J, Wolpert SM, Hammerschlag SB, Griffiths HJ, Kahn PC. *Cross-sectional anatomy*. East Norwalk, CT: Appleton-Century-Crofts, **1977**.

Book Review

Handbook of Radiologic Orthopaedic Terminology. By R. F. Kilcoyne and Edward Farrar. Chicago: Year Book Medical, 152 pp., 1986. \$21, soft cover

This soft-cover volume is intended to be a quick reference of orthopedic terminology. The first two chapters are an overview. Chapter 1 provides a glossary of fractures, with eponyms or descriptive terminology, and chapter 2 gives an excellent review of orthopedic terminology for fractures and of treatment of fractures. The remainder of the chapters covers anatomic regions, including the shoulder and humerus, the elbow and forearm, the wrist and hand, the pelvis and hip, the knee, the ankle, the foot, and the spine. Within the specific regions, anatomy, types of fractures, treatment, and complications are reviewed briefly.

The book does have several weaknesses, which may limit its appeal. It would be helpful, for example, if more pertinent references were added to the end of each chapter to augment the short text. In addition, the only areas of orthopedics that are covered are fractures and dislocations, so the title is therefore misleading. The quality of the print is distracting, with large gaps between words, most preva-

lent in the beginning chapters. No reproductions of radiographs are included, and the reader must infer the radiographic appearances from the provided line diagrams. Although in many cases these illustrations are entirely adequate, in some it is difficult to make the necessary transition from diagram to radiograph (e.g., pelvic fractures).

The strengths of the book are its glossary, terse coverage of fractures, and clear presentation of treatment and complications. Its small size and low price make it a practical volume to keep at the reading station. Overall, the authors have fulfilled their goal, and this book is a handy reference source for fracture terminology.

Barbara N. Weissman
Brigham and Women's Hospital
Boston, MA 02115

Detection of Osteomyelitis at Fracture Nonunion Sites: Comparison of Two Scintigraphic Methods

James E. Seabold¹
 James V. Nepola²
 Gary R. Conrad³
 J. Lawrence Marsh²
 William J. Montgomery⁴
 John A. Bricker¹
 Peter T. Kirchner¹

Forty-nine patients with 50 fracture nonunions 4–48 months after injury underwent technetium-99m methylene diphosphonate (^{99m}Tc-MDP) scintigraphy on day 1, combined ^{99m}Tc-MDP and indium-111 leukocyte (¹¹¹In-WBC) scintigraphy on day 2, and gallium-67 (⁶⁷Ga) scintigraphy on day 3. The results were compared to evaluate the relative abilities of these scintigraphic techniques to detect osteomyelitis. Nine patients had clinical evidence of infection at the time of imaging, and 40 patients (41 fractures) did not. Open-biopsy cultures were performed at all fracture sites and were positive at 21 (42%) of the 50 sites. Combined ^{99m}Tc-MDP/¹¹¹In-WBC images were interpreted with the use of two criteria. A positive study by the first criterion required ¹¹¹In-WBC localization in the region of the nonunion fracture. A positive study by the second criterion required ¹¹¹In-WBC localization in bone at the fracture site. The first criterion yielded a sensitivity of 84%, specificity of 72%, and accuracy of 74%; the specificity improved to 97% with an accuracy of 88% when the second criterion was used. Ten (25%) of the 40 patients thought not to have osteomyelitis by clinical criteria at the time of imaging had true-positive ^{99m}Tc-MDP/¹¹¹In-WBC studies by biopsy culture results. Gallium-67 studies were interpreted as nondiagnostic if localization of radioisotope at fracture sites was equal to that with ^{99m}Tc-MDP, positive if ⁶⁷Ga localization was greater than that of ^{99m}Tc-MDP, and negative if it was less than that of ^{99m}Tc-MDP. Twenty-one ⁶⁷Ga studies were interpreted as nondiagnostic; 11 (52%) of the 21 had culture-positive fracture sites. The accuracy of ⁶⁷Ga/^{99m}Tc-MDP imaging was 39%.

Combined ^{99m}Tc-MDP/¹¹¹In-WBC imaging is useful in the detection of osteomyelitis at fracture nonunion sites and improves the specificity of ¹¹¹In-WBC imaging by differentiating inflammation/infection in adjacent soft tissue from osteomyelitis at the fracture site. Gallium-67 with ^{99m}Tc-MDP imaging is not sufficiently reliable in this clinical setting to be useful as an indicator for osteomyelitis.

Infection is a known cause for fracture nonunion [1, 2] and is of particular concern in patients with a history of open fracture or multiple surgical procedures. Nevertheless, subclinical osteomyelitis can be difficult to detect by standard radiographic examinations [3]. An imaging technique that can reliably detect infection would be a useful adjunct for therapeutic management of patients with delayed union of fracture (improper healing within 6 months) or fracture nonunion (failure of union after 6 months).

¹¹¹In-labeled leukocyte (¹¹¹In-WBC) imaging can be useful for detection of acute or chronic osteomyelitis and several forms of complicated musculoskeletal infection, including prosthetic joint infection [4–16]. Two clinical studies have reported ¹¹¹In-WBC imaging to be superior to combined gallium-67 (⁶⁷Ga)/technetium-99m methylene diphosphonate (^{99m}Tc-MDP) imaging for detection of low-grade osteomyelitis in the presence of other conditions that produce increased bone remodeling [6, 7]. Preliminary reports also suggest that ¹¹¹In-WBC imaging alone is useful to detect infection associated with nonunited fracture, whereas combined ^{99m}Tc-MDP/⁶⁷Ga cannot differentiate infected from noninfected sites of delayed union [17, 18].

This prospective study compares the results of sequential preoperative ^{99m}Tc-MDP/¹¹¹In-WBC and ^{99m}Tc-MDP/⁶⁷Ga imaging for detection of infection associated

Received August 26, 1988; accepted after revision November 25, 1988.

Presented in part at the annual meeting of the American Academy of Orthopaedic Surgeons, Atlanta, GA, February 1988.

¹ Department of Radiology, The University of Iowa Hospitals and Clinics, Iowa City, IA 52242. Address reprint requests to J. E. Seabold.

² Department of Orthopaedic Surgery, The University of Iowa Hospitals and Clinics, Iowa City, IA 52242.

³ Department of Radiation Medicine, University of Kentucky Medical Center, Lexington, KY 40536.

⁴ Gainesville Radiology Group, 1026 S.W. Second Ave., Gainesville, FL 32601.

AJR 152:1021–1027, May 1989
 0361–803X/89/1525–1021
 © American Roentgen Ray Society

with delayed-union or nonunion fractures (≥ 4 months) in 54 consecutive patients, without regard to history or clinical presentation.

Subjects and Methods

Between November 1984 and November 1987, 54 consecutive patients with 55 delayed-union or nonunion fracture sites were admitted to the study. All patients underwent open biopsy and culture of the fracture site(s) within 3 weeks of imaging. Some patients had biopsy and culture of former external-fixator pin sites at the time of fracture biopsy. Five patients received antibiotics for concurrent infections between the time of imaging and that of open-bone biopsy cultures and were excluded from the final tabulation in an effort to avoid possible false-negative culture results. None of the remaining 49 patients (50 fractures) had received antibiotics during the 6 weeks before imaging. Each patient was studied with sequential three-phase ^{99m}Tc -MDP scintigraphy (day 1) and combined ^{99m}Tc -MDP/ ^{111}In -WBC scintigraphy (day 2). Forty-five of the 49 patients were studied with ^{67}Ga scintigraphy (day 3).

Each of the patients had sustained a fracture (47 patients) or had undergone attempted arthrodesis (two patients) 4 months to 4 years (mean, 17.5 months) previously. The 37 men and 12 women ranged in age from 19 to 75 years (mean, 34 years). Five patients had insulin-dependent diabetes mellitus. Each of the fracture sites showed sufficient radiographic arrest of healing to warrant consideration for surgical intervention. Nine patients (group 1) had overt clinical evidence of active infection, such as draining open wounds or sinus tracts near the fracture site (Table 1). Seventeen patients with 18 fractures (group 2) had a history of treatment for infection in or adjacent to the fracture site, but these 17 had no evidence of infection at the time of imaging. Eleven of these 18 were open fractures at the time of injury. Twenty-three patients (group 3) had neither history of infection nor clinical evidence of infection at the time of imaging. Nine of these 23 patients also had open fractures. There were 35 fractures

of the tibia/fibula, 10 of the femur, four of the humerus, and one of the radius-ulna.

Twenty-eight patients had sustained open fractures and 22 closed fractures. Thirteen of the 22 patients with closed fractures had undergone at least one open operation. Serial radiographs were considered diagnostic for osteomyelitis in only one of the 49 patients. This patient had radiographic evidence of sequestrum. Positive cultures were obtained from 21 (42%) of the 50 fracture sites. Fourteen (67%) of these 21 cases had no clinical evidence of infection at the time of imaging.

Scintigraphy

WBC labeling with ^{111}In -oxine was accomplished by using a modification [19] of the technique reported by Thakur et al. [20]. On day 1, after informed consent was obtained, each patient underwent three-phase bone scintigraphy with 20 mCi (740 MBq) of IV ^{99m}Tc -MDP. Ten-minute bone images were obtained 3 hr after injection by using a large-field-of-view gamma camera, a high-resolution collimator, and a 15% window centered at 140 keV. Immediately after bone scintigraphy, 400–500 μCi (14.8–18.5 MBq) of ^{111}In -WBCs were injected intravenously. On the next day (16–24 hr after injection), sequential 5-min ^{99m}Tc -MDP bone and 15-min ^{111}In -WBC scintigraphy was performed without moving the patient between each pair of images. Duplicate copies of the images were made so that the ^{111}In -WBC images could be superimposed over the ^{99m}Tc -MDP images. A medium-energy collimator was used. A 10% window centered at 140 keV was used for the ^{99m}Tc -MDP images, whereas a 5% window centered at the 173-keV photopeak and a 20% window for the 247-keV photopeak were used for the ^{111}In -WBC images. Images of the fracture site were obtained in three or four projections with at least two projections perpendicular to each other. After combined ^{99m}Tc -MDP/ ^{111}In -WBC imaging, each patient received 5 mCi (185 MBq) of IV ^{67}Ga . Three-view 10-min images were obtained on day 3 (18–24 hr after ^{111}In -WBC imaging). The ^{67}Ga images were obtained in the same projection as the ^{99m}Tc -MDP images with a medium-energy collimator. Summation of data from the 91-, 189-, and 296-keV photopeaks (15% windows) was used for these images. The ^{67}Ga images were compared with the 3-hr bone images obtained on day 1.

The ^{99m}Tc -MDP/ ^{111}In -WBC and ^{99m}Tc -MDP/ ^{67}Ga images were interpreted by nuclear physicians without knowledge of the patients' histories or clinical findings. A radiologist evaluated the preoperative bone radiographs for signs of osteomyelitis. Serial radiographs also were reviewed when available in an attempt to establish a diagnosis of osteomyelitis. The scintigrams also were interpreted in a second setting in conjunction with the radiographs, to determine the location of old pin sites, hardware, and (when possible) bone grafts. Combined ^{99m}Tc -MDP/ ^{111}In -WBC images were interpreted with the use of two criteria. The first criterion for a positive study required abnormal ^{111}In -WBC localization in the region of the fracture site. This uptake had to be greater than that in normal marrow of adjacent bone or contralateral extremity. The second criterion required that ^{111}In -WBC localization correspond to a region of increased ^{99m}Tc -MDP activity at the fracture site and be greater than that in nonadjacent or contralateral bone marrow. Studies were interpreted as equivocal if the localization was not sufficient to determine the location of uptake with respect to the fracture site and negative if no focus of abnormal uptake was identified. ^{99m}Tc -MDP and ^{67}Ga images were evaluated for the distribution as well as the degree of uptake relative to adjacent normal bone. Combined ^{99m}Tc -MDP/ ^{67}Ga images were interpreted as follows: positive if ^{67}Ga uptake was greater in intensity or spatial distribution than ^{99m}Tc -MDP uptake; negative if the degree or extent of ^{67}Ga uptake was less than ^{99m}Tc -MDP uptake; or equivocal if ^{67}Ga and ^{99m}Tc -MDP uptake were equal in intensity and spatially con-

TABLE 1: Scintigraphic Results: Comparison of ^{99m}Tc -MDP/ ^{111}In -WBC and ^{99m}Tc -MDP/ ^{67}Ga at Fracture Sites with the Use of ^{111}In -WBC Uptake in Bone at Fracture Site

Result and Type of Study	No. of Fractures by Group			Total (n = 50)
	1, Clinically Infected (n = 9)	2, History of Infection (n = 18)	3, No Prior Infection (n = 23)	
True positive				
^{99m}Tc -MDP/ ^{111}In -WBC	6 ^a	6 ^a	4	16
^{99m}Tc -MDP/ ^{67}Ga	2	0	0	2
True negative				
^{99m}Tc -MDP/ ^{111}In -WBC	2 ^a	10	16	28
^{99m}Tc -MDP/ ^{67}Ga	1	5	10	16
False positive				
^{99m}Tc -MDP/ ^{111}In -WBC	0	0	1	1
^{99m}Tc -MDP/ ^{67}Ga	0	0	0	0
False negative				
^{99m}Tc -MDP/ ^{111}In -WBC	0	2	1	3
^{99m}Tc -MDP/ ^{67}Ga	0	5	2	7
Equivocal				
^{99m}Tc -MDP/ ^{111}In -WBC	1 ^{a,b}	0	1	2
^{99m}Tc -MDP/ ^{67}Ga	5	7	9	21
Not done				
^{99m}Tc -MDP/ ^{111}In -WBC	0	0	0	0
^{99m}Tc -MDP/ ^{67}Ga	1	1	2	4

^a One patient had additional ^{111}In -WBC uptake at culture-positive former external-fixator pin sites. (Not tabulated with fracture sites.)

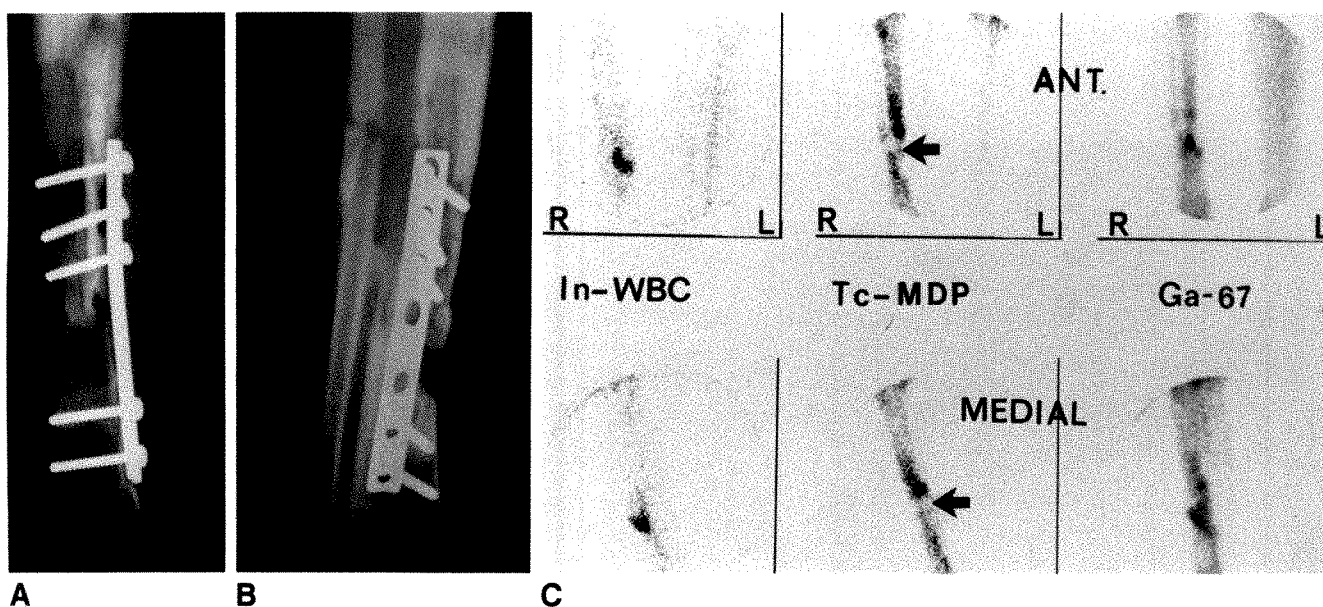


Fig. 1.—32-year-old man with persistent drainage from a mid-tibia/fibula nonunion fracture previously treated for osteomyelitis. A and B, Radiographs show marked osteolysis at tibial fracture site and under side plate, plus bony fragments near upper screws. C, True-positive combined ^{111}In -WBC/ $^{99\text{m}}\text{Tc}$ -MDP and ^{67}Ga / $^{99\text{m}}\text{Tc}$ -MDP images. Scintigrams show abnormal ^{111}In -WBC localization at fracture site. ^{67}Ga images show spatially discordant uptake compared with $^{99\text{m}}\text{Tc}$ -MDP images. Comparison of $^{99\text{m}}\text{Tc}$ -MDP images with other studies shows nonviable infected bone at distal end of proximal fragment (arrows).

gruent. Intraobserver disagreements were resolved by joint review of the images by both observers and consensus with a third observer.

Results

By using the second criterion for a positive study, 17 studies showed localization of ^{111}In -WBCs in bone at fracture nonunions whose locations were identified by means of the paired $^{99\text{m}}\text{Tc}$ -MDP images (Fig. 1). Sixteen of these 17 studies gave true-positive results for osteomyelitis at culture-positive fracture sites (Table 1). One of the 17 showed false-positive ^{111}In -WBC localization at a nonunion site and the adjacent wrist joint. This patient was an insulin-dependent diabetic with an atrophic nonunion fracture (pseudoarthrosis) adjacent to a neuropathic wrist joint. Cultures of both sites were negative, but the synovium surrounding the pseudoarthrosis revealed inflammatory infiltrates. Two of the 16 true-positive studies also showed ^{111}In -WBC localization at infected sites of former external-fixator pins.

Twenty-eight ^{111}In -WBC/ $^{99\text{m}}\text{Tc}$ -MDP studies yielded true-negative results, whereas three studies gave false-negative results (Table 1). All three false-negative cases also had false-negative $^{99\text{m}}\text{Tc}$ -MDP/ ^{67}Ga images. Two leukocyte studies were interpreted as equivocal because of poorly defined uptake that could not be localized with certainty to bone. One patient was in a hip-spica cast at the time of imaging, and optimal views were not obtained. A second study showed abnormal ^{111}In -WBC localization corresponding to infected former external-fixator pin sites, but was interpreted as equivocal at the culture-positive fracture site.

The overall accuracy of combined $^{99\text{m}}\text{Tc}$ -MDP/ ^{111}In -WBC scintigraphy by the second criterion was 88%, with a sensitivity of 84% and a specificity of 97% (Table 2). If the first criterion was used as a positive study for osteomyelitis, seven

TABLE 2: Fracture-Site Results

Finding	$^{99\text{m}}\text{Tc}$ -MDP/ ^{111}In -WBC		$^{99\text{m}}\text{Tc}$ -MDP/ ^{67}Ga
	First Criterion	Second Criterion	
True positive (No.)	16	16 ^a	2
True negative (No.)	21	28 ^b	16
False positive (No.)	8	1	0
False negative (No.)	3	3	7
Equivocal (No.)	2 ^b	2 ^b	21
Sensitivity (%)	84	84	22
Specificity (%)	72	97	100
Accuracy (%)	74	88	39

Note.—Sensitivity = true positive/(true positive + false negative); specificity = true negative/(true negative + false positive); accuracy = (true positive + true negative)/total studies.

^a Two patients had true-positive localization at former external-fixator pin sites.

^b One patient had ^{111}In -WBC uptake at culture-positive former external-fixator pin sites.

additional false-positive results occurred because of soft-tissue localization adjacent to the fracture. Superimposition of the ^{111}In -WBC images over the corresponding $^{99\text{m}}\text{Tc}$ -MDP images allowed for optimal assessment of the anatomic site of ^{111}In -WBC localization in many of these cases. Such soft-tissue localization was caused by trauma, inflammation with or without infection, or heterotopic bone formation. Therefore, without correlative bone scintigraphy, the sensitivity would have been 84%, but the specificity would have fallen to 72%, with an accuracy of 74% (Table 1).

For the combined $^{99\text{m}}\text{Tc}$ -MDP/ ^{67}Ga studies, two results were true positive; 16, true negative; none, false positive; and seven, false negative (Table 1). Figures 1 and 2 are examples

of true-positive and false-negative ^{67}Ga studies, respectively. Four patients did not have ^{67}Ga imaging, and 21 studies were interpreted as nondiagnostic or equivocal. The equivocal cases showed the same extent and degree of ^{67}Ga localization at the fracture site as did the corresponding $^{99\text{m}}\text{Tc}$ -MDP bone images (Fig. 3). Eleven (52%) of these equivocal cases

had culture-positive fracture sites at open biopsy. Thus, only 18 of the 47 combined $^{99\text{m}}\text{Tc}$ -MDP/ ^{67}Ga studies yielded correct and clinically useful information. The overall accuracy of $^{99\text{m}}\text{Tc}$ -MDP/ ^{67}Ga imaging was 39%, with a sensitivity of 22% and a specificity of 100% (Table 2). If the equivocal ^{67}Ga studies were tabulated as positive for osteomyelitis, the sen-

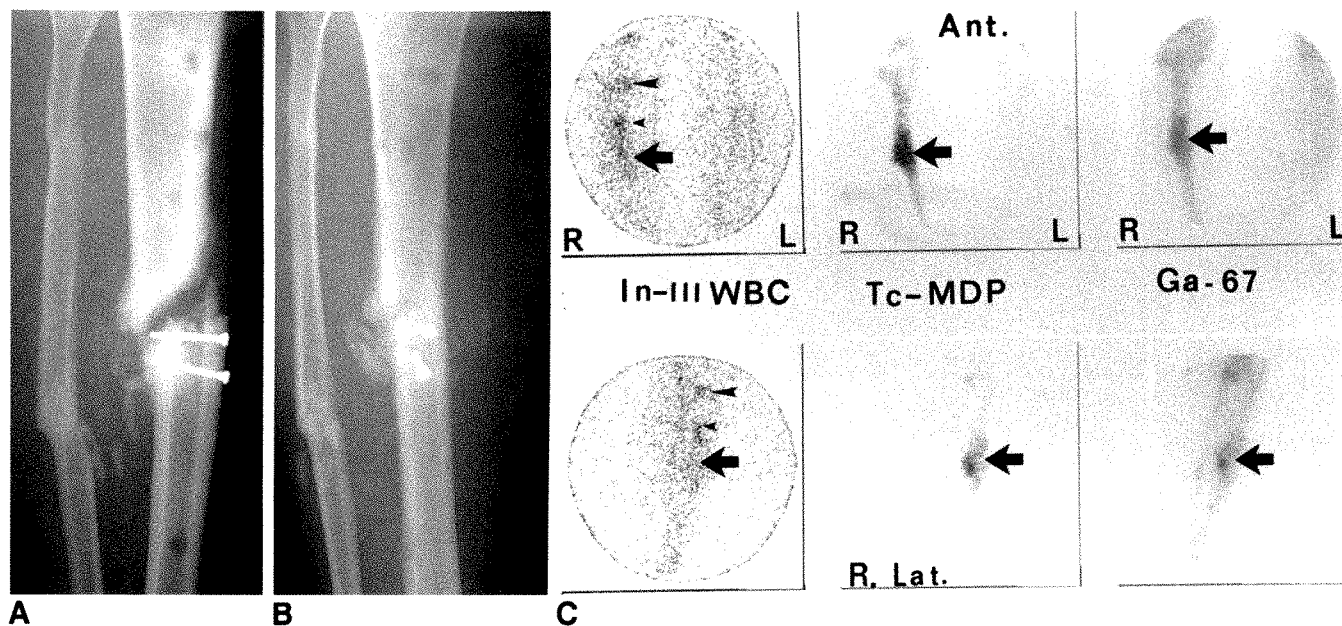


Fig. 2.—26-year-old man developed superficial pin-tract infection 4 months after external fixation of open tibia/fibula fracture.

A and B, Radiographs show distraction of tibial fragments and sclerosis of proximal fragment.

C, False-negative combined $^{67}\text{Ga}/^{99\text{m}}\text{Tc}$ -MDP study. Scintigrams show abnormal ^{111}In -WBC localization at former proximal pin sites (arrowheads) extending into fracture site (arrows). $^{99\text{m}}\text{Tc}$ -MDP images show uptake of tracer at former pin sites and marked uptake at fracture site (arrows). There is less ^{67}Ga uptake than $^{99\text{m}}\text{Tc}$ -MDP uptake at fracture site (arrows).

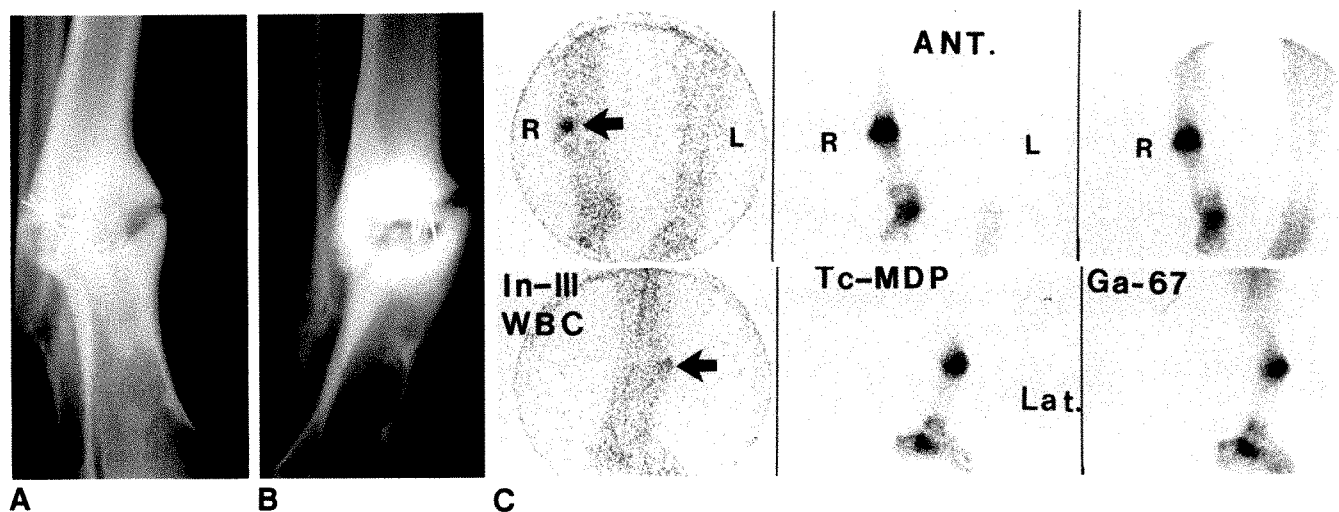


Fig. 3.—21-year-old man with culture-positive fracture site developed osteomyelitis after bone grafting of nonunited mid-tibia/fibula fracture. Infection responded to antibiotic treatment and there was no clinical evidence of recurrent infection despite nonunion.

A and B, Radiographs show hypertrophic and sclerotic changes at fracture site and resorption along electrodes.

C, Equivocal combined $^{67}\text{Ga}/^{99\text{m}}\text{Tc}$ -MDP study. Scintigrams show abnormal ^{111}In -WBC localization in anterolateral portion of fracture site (arrows). ^{67}Ga localization is concordant with $^{99\text{m}}\text{Tc}$ -MDP localization, which is increased relative to adjacent normal shaft.

sitivity improved to 65%, but the specificity decreased to only 61%. If the equivocal ^{67}Ga studies were tabulated as negative, the sensitivity decreased to 9% and the specificity remained 100%.

Discussion

Detection of active osteomyelitis can be difficult in bone that has been altered by processes that affect bone structure and metabolism, such as prior infection and trauma. In the presence of bone injury and repair, plain radiographs are difficult to interpret and bone scintigraphic findings often are nonspecific. In a series of 104 patients, sequestration was the only reliable plain-film finding of acute osteomyelitis when there was prior surgery, fracture, or bone infection [3]. Newly discovered osteolysis or linear periosteal reaction might suggest active osteomyelitis but these findings often are due to other disease processes [3]. In our series, only one (5%) of 21 culture-positive cases had plain-film changes considered diagnostic of osteomyelitis.

Three-phase bone scintigraphy cannot differentiate osteomyelitis from other causes of active bone remodeling, such as recent fracture, neoplasm, loose prosthesis, septic arthritis, and diabetic osteoarthropathy [9, 15, 17, 21]. The value of three-phase bone scintigraphy for the detection of osteomyelitis at nonunion fracture sites was examined in the first 21 patients of this series. We found a sensitivity of 88% and a specificity of only 15% [22]. Others also have reported poor diagnostic specificity for three-phase bone scintigraphy in patients with existing osseous abnormalities [9, 15, 17]. Therefore, we did not attempt to assess the results of three-phase bone scintigraphy in all 50 cases evaluated.

Gallium-67 imaging is sensitive for the detection of osteomyelitis [6, 8, 23]. Gallium-67 localizes in experimentally induced osteomyelitis, but it also shows preferential uptake in a number of diseases that increase bone remodeling [24]. To improve the specificity of ^{67}Ga imaging at sites of preexisting skeletal disease, investigators have compared the pattern of ^{67}Ga uptake with that of $^{99\text{m}}\text{Tc}$ -labeled bone tracers [6–8, 17, 24–28]. Most of these studies show that when the intensity of distribution of ^{67}Ga uptake exceeds that of the bone tracer, osteomyelitis typically is present, and when it is less than that of the bone tracer, osteomyelitis is unlikely. Tumeh et al. [27] also concluded that when ^{67}Ga uptake is approximately equal to that seen on the bone images, the probability of osteomyelitis increases slightly, but not sufficiently to make this combination of scintigraphic findings a reliable standard for osteomyelitis. In the study by Schauwecker et al. [6], 72% of patients with preexisting osseous abnormalities (i.e., prosthesis, neuropathic osteoarthropathy, acute fracture, or nonunion) had equivalent or nondiagnostic $^{67}\text{Ga}/^{99\text{m}}\text{Tc}$ -MDP studies.

The results of our study also indicate that combined $^{99\text{m}}\text{Tc}$ -MDP/ ^{67}Ga imaging is not reliable for predicting osteomyelitis complicating fracture nonunion. Twenty-one (46%) of the 46 cases showed ^{67}Ga localization equivalent to the extent of $^{99\text{m}}\text{Tc}$ -MDP uptake at nonunion fracture sites (nondiagnostic studies). Eleven (52%) of these 21 cases had culture-positive fracture sites. Furthermore, of the 23 sites in which ^{67}Ga

uptake was less than that of $^{99\text{m}}\text{Tc}$ -MDP, seven were culture-positive or false-negative studies. Thus, the accuracy of $^{99\text{m}}\text{Tc}$ -MDP/ ^{67}Ga imaging was only 39%, compared with an accuracy of 88% for combined $^{99\text{m}}\text{Tc}$ -MDP/ ^{111}In -WBC imaging.

Possibly, our ^{67}Ga results might have been better if we had extended the time of ^{67}Ga imaging to 48–72 hr. Although 48- to 72-hr ^{67}Ga imaging improves detection of neoplasms, we are unaware of reports of improved detection of osteomyelitis with delayed imaging. In addition, ^{67}Ga background levels present in the extremities at 24 hr did not interfere with interpretation of images.

^{111}In -WBC imaging has been used to detect subclinical osteomyelitis in patients with a loose or painful prosthesis [7, 8, 10–16]. The reported results have varied somewhat, depending on the imaging technique and the criteria used for interpretation. Johnson et al. [16] have reported improved specificity when ^{111}In -WBC imaging is compared with $^{99\text{m}}\text{Tc}$ hydroxydiphosphonate images obtained 48 hr earlier. Although we studied a different type of disease process, our results indicate that same-day $^{99\text{m}}\text{Tc}$ -MDP/ ^{111}In -WBC imaging improves specificity compared with ^{111}In -WBC imaging alone. This was accomplished by differentiating localization in adjacent soft tissue from bony localization at the fracture site (Fig. 4). Seven more ^{111}In -WBC studies were false positive if the first criterion was used, which decreased the specificity from 97% to 72% (Table 2). The use of sequential $^{99\text{m}}\text{Tc}$ -MDP/ ^{111}In -WBC images in at least two orthogonal projections helped to differentiate soft-tissue inflammation or infection from osteomyelitis.

Early fracture callus, acute bone infarct, heterotopic bone formation, inflammatory arthritis, and rarely, neoplasia have been reported to cause ^{111}In -WBC localization [28–30]. In our series, none of the patients had bone infarcts, but two cases had ^{111}In -WBC in soft tissues at the site of heterotopic bone formation. Serial radiographic correlation helped to clarify the cause of the ^{111}In -WBC soft-tissue localization in both cases. We did not attempt to use ^{111}In -WBC scintigraphy to detect osteomyelitis in fractures less than 4 months old, because we were uncertain about the reliability of this technique in the early stages of bone healing. Others have observed ^{111}In -WBC localization in acute noninfected fractures for up to 3 months [29]. We observed ^{111}In -WBC localization at culture-negative fracture sites in only one case. In this false-positive case, ^{111}In -WBC localization was present in a grossly mobile pseudoarthrosis as well as in the adjacent neuropathic wrist joint. Although bone cultures were negative at the fracture site, synovial biopsies showed histologic findings of acute inflammation.

Esterhai et al. [18] reported a series of nonunion fractures evaluated with radiography and ^{111}In -WBC imaging. They concluded that ^{111}In -WBC imaging could be used to assess the presence, but not the extent, of infection. Our series suggests that combined $^{99\text{m}}\text{Tc}$ -MDP/ ^{111}In -WBC imaging can help identify the extent, as well as the location, of infection. For example, $^{99\text{m}}\text{Tc}$ -MDP/ ^{111}In -WBC imaging identified osteomyelitis at former external-fixator pin sites in two patients with culture-positive fracture sites (Fig. 2). In addition, $^{99\text{m}}\text{Tc}$ -MDP/ ^{111}In -WBC detected infected pin sites in one patient

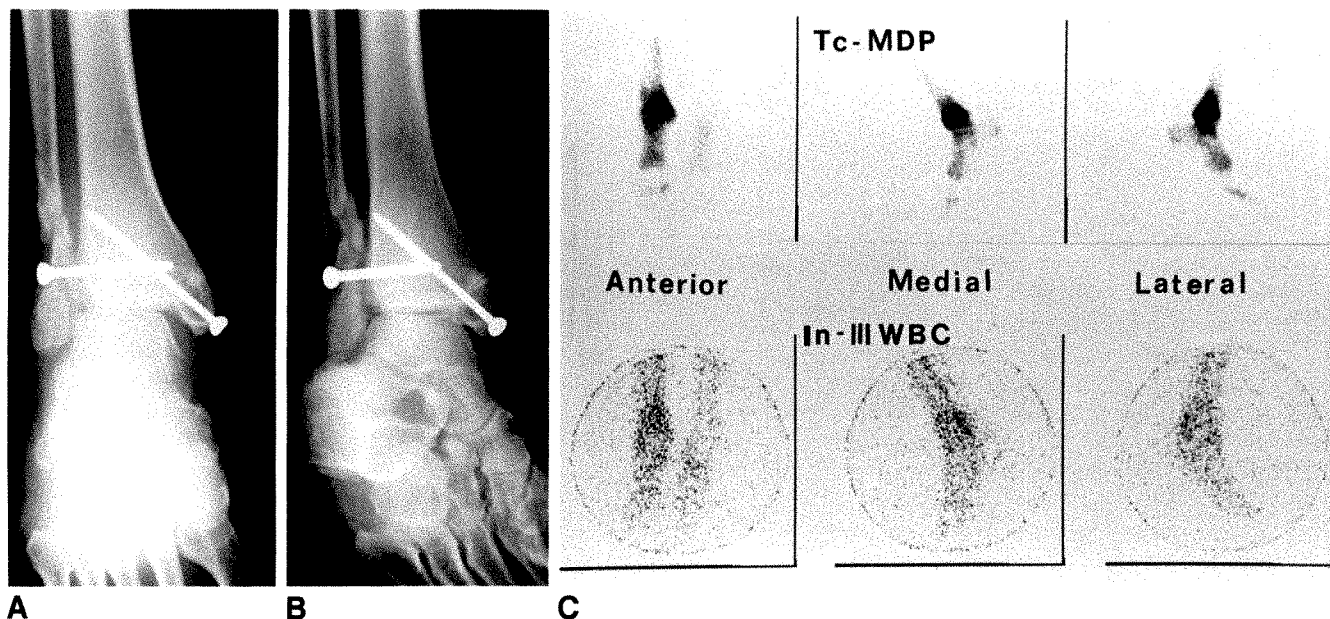


Fig. 4.—64-year-old man with swollen right ankle 5 months after internal fixation of distal right tibia/fibula fracture. A and B, Radiographs show osteolysis along medial screw and nonunion of medial malleolus, plus multiple bony fragments along distal fibula. C, Combined ^{99m}Tc -MDP (upper)/ ^{111}In -WBC (lower) images show markedly increased bone remodeling at distal tibia/fibula with diffuse soft-tissue ^{111}In -WBC localization.

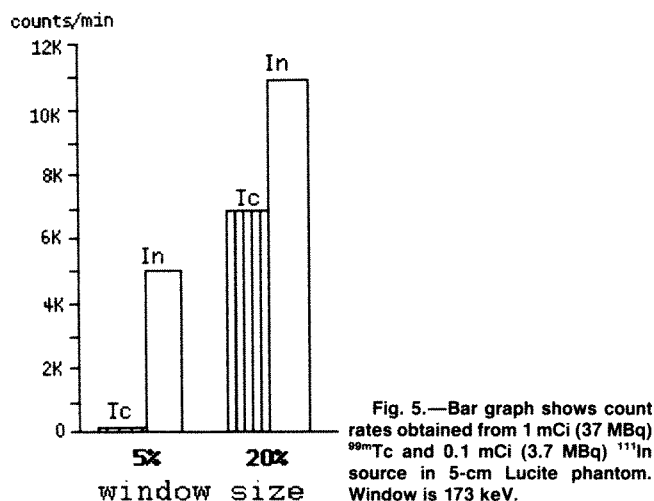


Fig. 5.—Bar graph shows count rates obtained from 1 mCi (37 MBq) ^{99m}Tc and 0.1 mCi (3.7 MBq) ^{111}In source in 5-cm Lucite phantom. Window is 173 keV.

whose fracture site was considered "nondiagnostic" and in one patient with a true-negative fracture site (Table 2). In at least one case, the spread of infection along hardware was shown. Furthermore, 10 (25%) of 40 patients (41 fractures) without clinical evidence of infection at the time of imaging (groups 2 and 3) had true-positive ^{111}In -WBC images for osteomyelitis at the fracture site (Table 1, groups 2 and 3).

Although combined ^{99m}Tc -MDP/ ^{111}In -WBC imaging improves the diagnostic specificity for osteomyelitis, false-positive results may occur because of artifacts from spectral overlap. When a 20% window centered at 173 keV is used to image the lower energy of ^{111}In in the presence of bone tracer that has been injected within 24 hr, residual ^{99m}Tc activity can result in false-positive ^{111}In -WBC images [31]. To

avoid this problem, some investigators image only the 247-keV photopeak of ^{111}In [7]. We have found that the use of a 5% window centered on the 173-keV photopeak excludes ^{99m}Tc counts while improving ^{111}In count rates that are obtained by using the 247-keV peak alone (Fig. 5).

In summary, combined ^{99m}Tc -MDP/ ^{111}In -WBC imaging is useful for the detection of osteomyelitis in patients with fracture nonunion. Combined imaging improves the specificity of ^{111}In -WBC imaging alone by differentiating soft-tissue localization from localization in bone at the fracture site. Combined imaging also can identify the presence of infection at former external-fixator pin sites and may help determine the extent of infection. The high specificity achieved in this series indicates that ^{111}In -leukocyte localization is not likely to occur in uninfected fracture callus that is at least 4 months old.

ACKNOWLEDGMENTS

We thank LuAnn Osdoba and Jan Widmer for secretarial assistance, Phyllis Bergman for editorial assistance, and John Johnson and Steve Moon for photographic assistance in the preparation of this manuscript.

REFERENCES

- Nicoll EA. Fractures of the tibial shaft. A survey of 705 cases. *J Bone Joint Surg [Br]* 1964;46-B:373-387
- Heiple KG, Herndon CH. The pathologic physiology of nonunion. *Clin Orthop* 1965;43:11-21
- Tumeh SS, Aliabadi P, Weissman BN, McNeil BJ. Disease activity in osteomyelitis: role of radiography. *Radiology* 1987;165:781-784
- Propst-Proctor SL, Dillingham MF, McDougall IR, Goodwin D. The white blood cell scan in orthopedics. *Clin Orthop* 1982;168:157-165
- Raptopoulos V, Doherty PW, Goss TP, King MA, Johnson K, Gantz NM. Acute osteomyelitis: advantage of white cell scans in early detection. *AJR* 1982;139:1077-1082

6. Schauwecker DS, Park HM, Mock BH, et al. Evaluation of complicating osteomyelitis with Tc-99m MDP, In-111 granulocytes, and Ga-67 citrate. *J Nucl Med* **1984**;25:849-853
7. Merkel KD, Brown ML, Dewanjee MK, Fitzgerald RH Jr. Comparison of indium-labeled-leukocyte imaging with sequential technetium-gallium scanning in the diagnosis of low-grade musculoskeletal sepsis. A prospective study. *J Bone Joint Surg [Am]* **1985**;67-A:465-476
8. Al-Sheikh W, Sfakianakis GN, Mnaymneh W, et al. Subacute and chronic bone infections: diagnosis using In-111, Ga-67 and Tc-99m MDP bone scintigraphy and radiography. *Radiology* **1985**;155:501-506
9. Mauer AH, Millmond SH, Knight LC, et al. Infection in diabetic osteoarthropathy: use of indium-labeled leukocytes for diagnosis. *Radiology* **1986**;161:221-225
10. Ouzounian TJ, Thompson L, Grogan TJ, Webber MM, Amstutz HC. Evaluation of musculoskeletal sepsis with indium-111 white blood cell imaging. *Clin Orthop* **1987**;221:304-311
11. Mulamba L, Ferrant A, Leners N, de Nayer P, Rombouts JJ, Vincent A. Indium-111 leukocyte scanning in the evaluation of painful hip arthroplasty. *Acta Orthop Scand* **1983**;54:695-697
12. Pring DJ, Henderson RG, Rivett AG, Krausz T, Coombs RRH, Lavender JP. Autologous granulocyte scanning of painful prosthetic joints. *J Bone Joint Surg [Br]* **1986**;68-B:647-652
13. Prchal CL, Kahen HL, Blend MJ, Barmada R. Detection of musculoskeletal infection with the indium-111 leukocyte scan. *Orthopedics* **1987**;10:1253-1257
14. Wukick DK, Abreu SH, Callaghan JJ, et al. Diagnosis of infection by preoperative scintigraphy with indium-labeled white blood cells. *J Bone Joint Surg [Am]* **1987**;69-A:1353-1360
15. Magnuson JE, Brown ML, Hauser MF, Berquist TH, Fitzgerald RH Jr, Klee GG. In-111-labeled leukocyte scintigraphy in suspected orthopedic prosthesis infection: comparison with other imaging modalities. *Radiology* **1988**;168:235-239
16. Johnson JA, Christie MJ, Sandler MP, Parks PF Jr, Homra L, Kaye JJ. Detection of occult infection following total joint arthroplasty using sequential technetium-99m HDP bone scintigraphy and indium-111 WBC imaging. *J Nucl Med* **1988**;29:1347-1353
17. Esterhai J, Alavi A, Mandell GA, Brown J. Sequential technetium-99m/gallium-67 scintigraphic evaluation of subclinical osteomyelitis complicating fracture nonunion. *J Orthop Res* **1985**;3:219-225
18. Esterhai JL Jr, Goll SR, McCarthy KE, et al. Indium-111 leukocyte scintigraphic detection of subclinical osteomyelitis complicating delayed and nonunion long bone fractures: a prospective study. *J Orthop Res* **1987**;5:1-6
19. Ponto JA, Seabold JE. Time course of indium-111 oxine labelling of human leukocytes. *Nucl Med Commun* **1984**;5:769-773
20. Thakur ML, Coleman RE, Mayhill CG, et al. Preparation and evaluation of In-111 labeled leukocytes as an abscess imaging agent in doses. *Radiology* **1976**;119:731-732
21. Graham GD, Lundy MM, Moreno AJ, Fredrick RJ. The role of Tc-99m MDP and Ga-67 citrate in predicting the cure of osteomyelitis. *Clin Nucl Med* **1983**;8:344-346
22. Seabold JE, Conrad GR, Claverie JG, Bricker JA, Nepola JV. Three phase bone scintigraphy (TPBS), indium-111-leukocyte imaging (In-WBC) and gallium-67 imaging for the detection of osteomyelitis associated with nonunion fractures. *J Nucl Med* **1986**;27:915
23. McKillop JH, McKay I, Cuthbert GF, Fogelman I, Gray HW, Sturrock RD. Scintigraphic evaluation of the painful prosthetic joint: a comparison of gallium-67 citrate and indium-111 labelled leucocyte imaging. *Clin Radiol* **1984**;35:239-241
24. Hadjipavlou A, Lisbona R, Rosenthal L. Difficulty of diagnosing infected hypertrophic pseudoarthrosis by radionuclide imaging. *Clin Nucl Med* **1983**;8:45-49
25. Lewin JS, Rosenfield NS, Hoffer PB, Downing D. Acute osteomyelitis in children: combined Tc-99m and Ga-67 imaging. *Radiology* **1986**;158:795-804
26. Lisbona R, Rosenthal L. Observations in the sequential use of Tc-99m phosphate complex and Ga-67 imaging in osteomyelitis, cellulitis and septic arthritis. *Radiology* **1977**;123:123-129
27. Tumeh SS, Aliabadi P, Weissman BN, McNeil BJ. Chronic osteomyelitis: bone and gallium scan patterns associated with active disease. *Radiology* **1986**;158:685-688
28. Kim EE, Pjura GA, Lowry PA, Gobuty AH, Traina JF. Osteomyelitis complicating fracture: pitfalls of ¹¹¹In leukocyte scintigraphy. *AJR* **1987**;148:927-930
29. Van Nostrand D, Abreu SH, Callaghan JJ, Atkins FB, Stoops HC, Savory CG. In-111-labeled white blood cell uptake in noninfected closed fracture in humans: prospective study. *Radiology* **1988**;167:495-498
30. Fortner A, Datz FL, Taylor A Jr, Alazraki N. Uptake of ¹¹¹In-labeled leukocytes by tumor. *AJR* **1986**;146:621-625
31. Fernandez-Ulloa M, Hughes JA, Krugh KB, Chin D. Bone imaging in infections: artefacts from spectral overlap between a Tc-99m tracer and In-111 leukocytes. *J Nucl Med* **1983**;24:589-592

Book Review

Biomedical Magnetic Resonance Imaging. Principles, Methodology, and Applications. Edited by Felix W. Wehrli, Derek Shaw, and J. Bruce Kneeland, New York: VCH, 601 pp., 1988. \$95

This book is organized into 13 chapters written by acknowledged experts in the field. A wide variety of subjects are covered: principles of MR, instrumentation, imaging techniques, contrast mechanisms, blood flow, sodium imaging, contrast media, clinical applications (brain, cardiovascular system, abdomen, pelvis, musculoskeletal system), and safety aspects. Although the main thrust of the book is imaging, it has discussions on spectroscopy in three chapters.

The first three chapters cover fundamental principles in MR imaging and spectroscopy. These chapters explain the principles by using excellent diagrams and examples of MR images. Although an extensive physics background is not necessary to understand the text, some mathematics and elementary physics would be useful for a more complete understanding of the principles. The author of the first chapter does an exquisite job of explaining imaging pulse sequences and localized spectroscopic techniques. The book has many discussions on the relationship between signal intensity and the biological mechanisms involved. For example, in order to explain the biological meaning of the signal intensity in T1-weighted images, chapter 3 discusses a biochemical model in which hydration of water to macromolecules is an important determinant of T1 relaxation rate. Another good example is in the chapter on sodium imaging in which depletion of adenosine triphosphate is used to explain the increase in intracellular sodium as the sodium-potassium pump begins to fail. The

chapter on contrast agents gives an excellent introduction and then some examples of the effect of the agents in different pathologic conditions. The clinical chapters are filled with images demonstrating the MR characteristics of the various diseases. In these chapters, I would like to see a little more quantitative image analysis and statistics. The chapter on flow has a remarkably complete discussion on the biophysics of flow and a mathematical description of flow-induced signal modulation. Chapter 12 contains a good discussion on cellular energetics and metabolism, but because the field of in vivo spectroscopy is changing so fast, this chapter is lacking some of the latest results on spectroscopy in humans. The last chapter covers the bioeffects of RF power deposition and magnetic fields (static and time varying).

In summary, I recommend the purchase of this book to the radiologist, the MR imaging scientist, the biomedical engineer, and the MR technician interested in MR imaging and flow. However, I do not recommend this book to those who are looking for a detailed discussion on in vivo spectroscopy.

Todd Richards
University of Washington
Seattle, WA 98195

John Caffey Award

MR Imaging Determination of the Location of the Normal Conus Medullaris Throughout Childhood

Don A. Wilson¹
John R. Prince

This retrospective study was designed to determine the location of the conus medullaris in normal children by reviewing a series of MR images of the lumbar spine. The study group consisted of 184 children ranging in age from newborn to 20 years who had a normal conus level as reported by the radiologist of record. The range of conus levels for the entire group of normal children was T12 to L3. The range for the 0-2-year-old group was T12 to L2-L3 with an average of L1-L2. The range of conus levels for the 19-20-year-old group was L1 to L2 with an average of L1-L2.

We conclude that the conus medullaris does not ascend throughout childhood as stated by previous authors but attains the adult level sometime during the first few months of life. A conus level at L2-L3 or above should be considered normal at any age. A conus level at L3 is indeterminate, since it is possible for a normal or a tethered conus to be located at this level.

In order to diagnose a low-lying or tethered cord in children, it is necessary to know the level at which the normal conus medullaris terminates. This is a topic that has not received a great deal of attention in the literature. Commonly used reference texts for pediatric neuroradiology and pediatric imaging [1, 2] state that the lower level of the conus is normally at the third lumbar vertebral body (L3) at birth and that it reaches L2-L3 by age 5, L2 by age 12, and eventually arrives at about L1 by adulthood. This series of age-related levels clearly suggests that the conus ascends throughout childhood and that different criteria of normality should be used for different ages. The purpose of this study was to develop a better statistical basis for determining the location of the normal conus medullaris throughout childhood by reviewing a large series of MR images. Comparisons were also made with a group of children who had surgically proved tethered cord syndrome.

Materials and Methods

MR images of the lumbar spine were retrospectively reviewed in 184 children ranging in age from newborn to 20 years. The subjects were divided into two groups. Group I consisted of 85 infants and children (42 girls and 43 boys) who were studied for reasons other than spinal dysraphism. These patients were referred for MR imaging because of low back pain or back injury (37, or 43%), possible infection or tumor of the spine or cord (21, or 25%), brain tumor to exclude dropped metastasis (11, or 13%), leukemia (11, or 13%), and abdominal mass (5, or 6%). The average age of this group was 10.8 years.

Group II contained 99 subjects (50 females and 49 males) referred with possible symptoms of tethered cord syndrome but reported to be normal by the radiologist of record. The clinical indications for these studies were as follows: poor bowel and/or bladder control (39, or 39%), scoliosis (27, or 27%), abnormal muscle tone or gait (25, or 25%), spina bifida (13, or 13%), foot deformities (13, or 13%), and sacral dimple or hairy patch (8, or 8%). The clinical indications exceed the total number of patients in the group because many of the patients had multiple symptoms. The age range for this group was 5 days to 20 years, with an average age of 7.9 years.

Over the same time span in which the normal subjects were being studied (approximately

This article appears in the March/April 1989 issue of *AJNR* and the May 1989 issue of *AJR*.

Recipient of the John Caffey gold award at the annual meeting of the Society for Pediatric Radiology, San Diego, 1988.

¹ Both authors: Magnetic Resonance Center, Oklahoma Medical Center, 940 NE 13th St., P.O. Box 26307, Oklahoma City, OK 73126. Address reprint requests to D. A. Wilson.

AJR 152:1029-1032, May 1989
0361-803X/89/1525-1029
© American Roentgen Ray Society

3 years), 40 infants and children (25 girls and 15 boys) from our institution were diagnosed and surgically confirmed to have the tethered cord syndrome. These children ranged in age from birth to 19 years, with an average age of 6.7 years. These cases were reviewed to determine the range of pathologic conus levels in our population.

MR scans of the lumbar spine were also reviewed in 100 young adults who were referred for lumbar disk disease but who did not have symptoms or signs of myelodysplasia. This group was used to establish the MR criteria for the normal adult conus level. There were 37 women and 63 men ranging in age from 21 to 40 years. The average age of this group was 32 years.

All the imaging studies for both groups were obtained on superconducting magnets operating at 0.5 T* or 1.5 T.[†] To be included in this retrospective investigation, an MR study had to consist of a good-quality sagittal T1-weighted image of the lumbar spine that included visualization of the distal spinal cord and conus medullaris. The pulse sequences used were 350–600/20–30/2–4 (TR range/TE range/number of excitations). The slice thickness was 3 mm for 62/85 (73%) of the subjects in group I and 68/99 (69%) of the subjects in group II. The remainder of the examinations were done at 5-mm slice thickness. The matrix was 128 × 256 or 256 × 256, with a 20–40-cm field of view. The level of the conus medullaris was determined in each instance by first locating the lumbosacral junction on the sagittal MR image and assuming that there were five lumbar vertebral bodies. The intervertebral disk space or midpoint of the vertebral body closest to the tip of the conus was recorded as the conus level. Coronal T1-weighted images were also obtained by using the same pulse sequences cited above for the sagittal images in 52/85 (61%) of group-I subjects and in 92/99 (93%) of group-II subjects. The coronal images were correlated with the sagittal images to confirm the level of conus termination (Fig. 1). Some of the subjects also had balanced and T2-weighted sagittal images with parameters of 2000–2100/20–30, 80–100/2. These images were used for additional confirmation of the findings on the T1-weighted images. In the total study

group of 184 subjects, only 11 (6%) who were imaged at a 5-mm slice thickness did not have coronal images. All of the lumbar spine MR images were obtained by using rectangular surface coils with dimensions of 10 cm × 20 cm or 10 cm × 40 cm (Philips) or 13 cm × 28 cm (GE).

Radiographs of the lumbar spine were available for review in 46/85 (54%) of the group-I subjects and in 50/99 (51%) of the group-II subjects. The true number of lumbar vertebrae and the occurrence of transitional vertebrae were noted in each case and adjustments were made to the designated level of conus termination as necessary.

For statistical analysis, the anatomic level determined for each conus was converted to ordinal data using the following schema. The S4 through S1 vertebral bodies were assigned a score of 1 through 4, respectively. The L5/S1 disk space was assigned a score of 5, L5 a score of 6, the L4–L5 disk space a score of 7, and so on through T11, which was assigned a score of 18. The means and standard deviations were determined by age intervals for both groups. These ranking scores were further analyzed for statistical differences between groups as a whole and by age intervals using the Mann-Whitney test.

Results

The range of conus levels, in brackets, and the mean score ± 1 standard deviation, in parentheses, by age intervals rounded to the nearest year for group-I subjects (normal controls) were: 0–2 years [T12.5[‡]–L1.5](13.8[§] \pm 0.57), 3–4 years [T12.5–L3](13.6 \pm 1.58), 5–6 years [L1–L2](13.4 \pm 0.89), 7–8 years [T12.5–L1](14.1 \pm 0.38), 9–10 years [L1–L2](13.3 \pm 1.15), 11–12 years [L1.5](13), 13–14 years [L1–L1.5](13.2 \pm 0.44), 15–16 years [L1–L1.5](13.6 \pm 0.53), 17–18 years [T12.5–L1.5](13.8 \pm 0.75), 19–20 years [L1–L2](13.1 \pm 0.78).

* S5 Gyroscan (Philips, Shelton, CT).

[†] S15 Gyroscan (Philips, Shelton, CT) or Signa G. E., Milwaukee, WI).

[‡] T12.5 indicates the T12–L1 disk space, etc.

[§] 13 indicates the L1–L2 disk space, 14 indicates the L1 vertebral body.

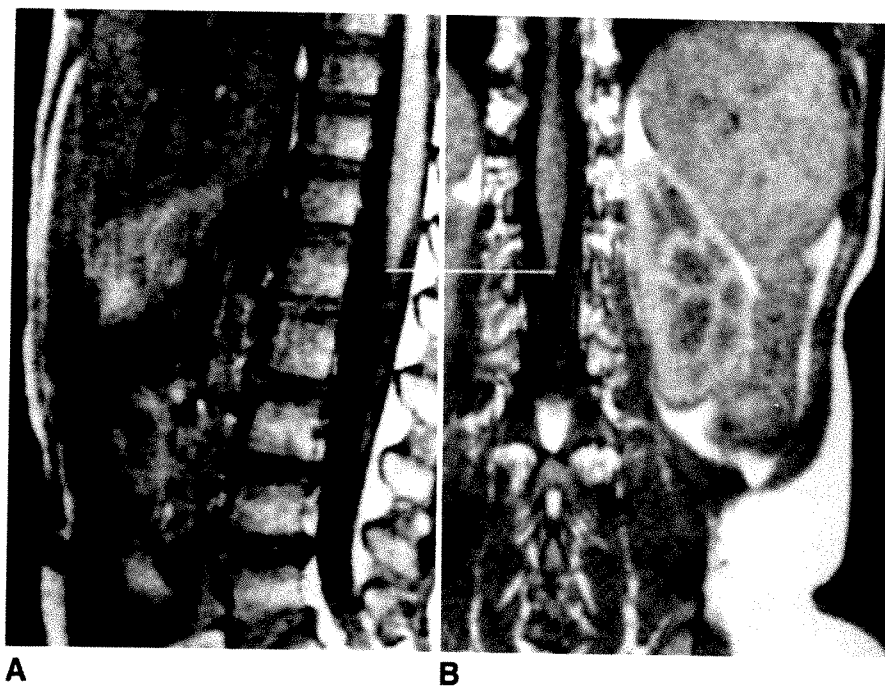


Fig. 1.—Sagittal (A) and coronal (B) MR images (600/20) show good correlation of conus location at L1 in this normal 2-year-old girl.

The range of conus levels, in brackets, and the mean \pm 1 standard deviation, in parentheses, by age intervals rounded off to the nearest year for group-II subjects (patients with symptoms but whose MR findings were normal) were: 0–2 years [T12–L2.5](13 \pm 1.45), 3–4 years [T12.5–L2.5](13.5 \pm 1.30), 5–6 years [T12.5–L2](13.2 \pm 0.97), 7–8 years [T12–L2](14.1 \pm 1.46), 9–10 years [T12–L2.5](13.2 \pm 1.48), 11–12 years [L1–L2](12.9 \pm 0.78), 13–14 years [T12–L2.5](12.8 \pm 1.48), 15–16 years [L1–L2.5](12.0 \pm 1.73), 17–18 years [T12.5–L2](13.0 \pm 1.22), 19–20 years [L1–L1.5](13.7 \pm 0.58).

The mean conus level for groups I and II was compared and found to be the same at each age interval at a confidence level of 95%. Consequently, groups I and II were compared as a whole. The means and standard deviations were 13.5 \pm 0.85 and 13.2 \pm 1.32 for groups I and II, respectively. There was no statistical difference between these groups at a confidence level of 95%. These two groups were therefore combined, giving a grand mean and standard deviation for both groups of 13.3 \pm 1.13. This corresponds to an approximate anatomic level of the L1–L2 intervertebral disk space and two standard deviations would be T12 to L2–L3. The ranges and averages for the combined groups are given in Figure 2.

The conus level in the 100 normal adults ranged from T11–T12 to L2–L3 with the average level at L1.

The patients with surgically proved tethered cords had conus levels ranging from L3 to S4, with the average level of termination at L4–L5. No age-related pattern was observed in these patients.

There were radiographs of the lumbosacral spine available for review on 96/184 (52%) of the group I and group II subjects. We found eight children with transitional vertebrae, two children with four lumbar vertebral bodies, and two children with six lumbar vertebral bodies. The appropriate corrections were made in each instance to reflect the true level of conus termination. The conus level of termination was corroborated by myelography in six cases from group I and in five cases from group II.

Discussion

The volume of data used to develop the present-day criteria for the normal conus level in children is in fact rather small.

There are three anatomic studies of children in the recent literature that evaluated conus level by the dissection of cadavers. The most widely quoted study, by Barson [3] in 1969, is actually a study of cord levels in the fetus (only 12 specimens over the age of 1 year were examined). He demonstrated conclusively that the conus level does ascend throughout fetal life, but, on the basis of data from a very small number of infants and children, suggested that the adult level of L1–L2 was attained by the age of 8 weeks. In another anatomic study, Jit and Charnalia [4] reported the average location of the tip of the conus in 10 newborn infants as the middle of L2, with a range from L1–L2 to L2–L3. No older children were studied. These researchers accepted the adult level as L1–L2 and noted that there was a change of only half a vertebral body from birth to adulthood. The other anatomic study with information pertinent to this problem was published in 1972 by James and Lassman [5], who examined the conus level in autopsies of 25 children ranging in age from newborn to 8 years. They reported that the conus reached the L2 level no later than the age of 5 months, but they examined only three specimens over the age of 1 year.

The combined anatomic data from these three studies contain only 15 measurements in children over the age of 1 year. This is insufficient evidence to justify the accepted level of termination of the normal conus throughout childhood. No imaging studies of significant size have been performed to better define the level of the normal conus in children, even though it is well accepted that myelography [1, 6] and MR imaging [7] can accurately make this determination.

Our study contradicts the conventional wisdom that the conus medullaris ascends throughout childhood. We found that there is no significant difference in the level of conus termination among the various age groups of normal children (see Fig. 2). At any age from birth to 20 years, a conus level of termination at or above L2–L3 was normal. The subjects with a conus level at the L3 level provided some difficulty. We encountered one normal 3-year-old girl with a conus at this level (Fig. 3). There were also two patients with surgically proved tethered cords that terminated at this level. This is not surprising when we note that Reimann and Anson [8] determined from their study and review of 801 adult cadavers that 1.8% of normal adults will have a conus level of termination at L3.

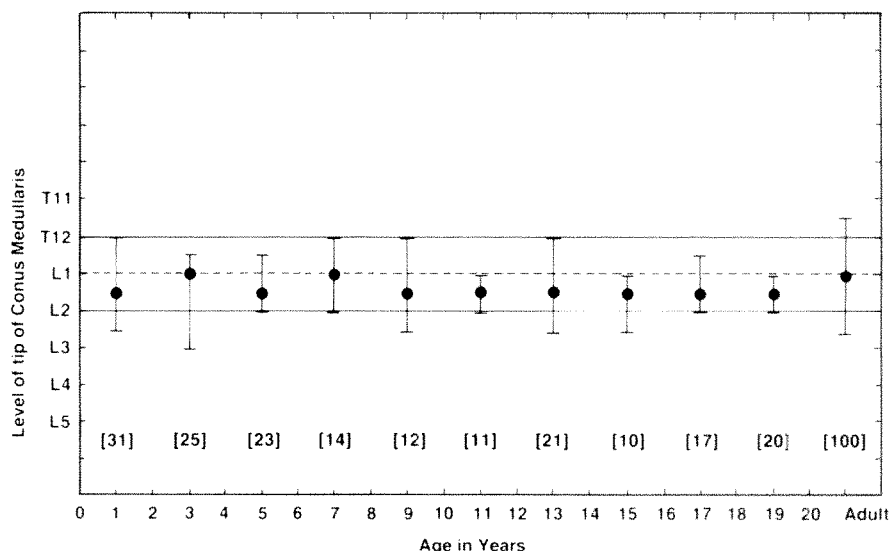


Fig. 2.—Average conus level (dots) and range (vertical bars) are indicated for 184 normal children, ages newborn to 20 years, and for 100 adults.



Fig. 3.—Sagittal MR image (450/30) of lumbar spine in normal 3-year-old girl with a conus tip located at mid-body of L3. 3 = L3 vertebral body.

The possibility that the conus ascends from birth to the adult level by age 8 weeks as reported by Barson [3] could not be confirmed from our data. Only 20 of our subjects were under 1 year old, and of these only six were age 8 weeks or younger. In this small group of subjects, the range of conus levels was T12–L1 to L2–L3, with an average level at L1–L2, results very similar to Jit and Charnalia's [4] group of 10 newborns. Additional study of this early age group by MR imaging seems warranted.

MR imaging appears to be an accurate method of determining the level of conus termination. Myelography agreed with MR in the 11 cases in which both studies were performed. Additional myelographic confirmation was difficult to obtain because of the high level of confidence in our results reported by referring physicians. In the large adult study reported by Reimann and Anson [8], the average level of termination of the adult conus was the lower one-third of L1. The same conclusion was also derived from our series of 100 adult subjects.

The coronal T1-weighted images available in 144/184 (78%) of our subjects did not significantly change the level of conus termination as determined on the sagittal images. The coronal images were definitely useful in increasing our confidence that we were indeed correctly identifying the conus in patients with moderate to severe scoliosis. Correlation of sagittal images with coronal images is essential in patients

with an abnormal conus or thickened filum terminale but would appear to be less important in normal individuals.

The degree of potential error introduced into this study by the possible occurrence of undetected transitional vertebrae or the presence of four or six lumbar vertebrae is considered negligible. Ford and Goodman [9] in a review of 1614 lumbosacral spine films determined the incidence of transitional vertebrae to be about 8%, with four lumbar vertebral bodies occurring in 4.2% of subjects and six lumbar vertebral bodies occurring in 3% of subjects. We corrected for this occurrence in over half (52%) of our patients. For the 88 patients without lumbosacral spine radiographs, the expected incidence of transitional vertebrae would be seven subjects, the incidence of four lumbar vertebral bodies would be four subjects, and the incidence of six lumbar vertebral bodies would be three subjects.

We conclude that the conus medullaris does not ascend throughout childhood as suggested by many authors, but attains the adult level sometime during the first few months of life. Further study of this young age group is warranted. A conus level of termination at L2–L3 or above is normal at any age. A conus level of termination at L3–L4 or below is abnormal (with possible exceptions occurring in premature infants and full-term newborns). The normality of a conus medullaris located at L3 must be determined by other means.

ACKNOWLEDGMENTS

The authors are grateful to Pat Barnes and Dan Galloway (deceased) for the early work they did at Oklahoma Diagnostic Imaging, Inc., in setting up the original spine imaging techniques. Their efforts enhanced our ability to produce the superb quality images that were reviewed for this study. We also thank the radiologists of record on the cases in our study, Pat Barnes, Nguyen Dan, Susan Edwards, Dan Galloway, Edmond Kalmon, Sidney Traub, and Max Walter, for their significant contributions.

We appreciate the support and cooperation we received from the Board of Directors and the staff of Oklahoma Diagnostic Imaging, Inc., for allowing us to use some of their case material in our project, and we are grateful for the assistance of Glenda Sims, Mary Barnard, and Julie Wilson in the preparation of this manuscript.

REFERENCES

1. Harwood-Nash DC, Fitz CR. Myelography. In: *Neuroradiology in infants and children*. St. Louis: Mosby, 1976:1133
2. Kirks DR. Spine and contents. In: *Practical pediatric imaging*. Boston/Toronto: Little, Brown, 1984:134
3. Barson AJ. The vertebral level of termination of the spinal cord during normal and abnormal development. *J Anat* 1969;106:489–497
4. Jit I, Charnalia VM. The vertebral level of the termination of the spinal cord. *J Anat Soc India* 1959;8:93–102
5. James CCM, Lassman LP. Spinal dysraphism. In: *Spina bifida occulta*. London: Butterworth, 1972:20–21
6. Fitz CR, Harwood-Nash DC. The tethered cord. *AJR* 1975;125:515–523
7. Barnes PD, Lester PD, Yamanashi WS, Prince JR. Magnetic resonance imaging in infants and children with spinal dysraphism. *AJNR* 1986;7:465–472, *AJR* 1986;147:339–346
8. Reimann AF, Anson BJ. Vertebral level of termination of the spinal cord with report of a case of sacral cord. *Anat Rec* 1944;88:127–138
9. Ford LT, Goodman FG. X-ray studies of the lumbosacral spine. *South Med J* 1966;59:1123–1128

Review Article

Imaging of Infants and Children with AIDS

Phillip J. Haney,¹ Amy J. Yale-Loehr,¹ Anna R. Nussbaum,² and Fouad E. Gellad¹

The spread of the human immunodeficiency virus (HIV) in the general population is producing an inevitable increase in the number of children afflicted with AIDS. Infected mothers unknowingly are transmitting the virus to their infants in increasing numbers. As of January 1989, 1346 children with AIDS had been reported to the U.S. Centers for Disease Control (personal communication, News Division, Public Health Service); 58% of reported patients have already died [1]. The average lifetime cost of treatment has been estimated to be \$90,347 per child [2]. The U.S. Public Health Service estimates that by 1991 there will be 3000 cases of AIDS in infants and children and up to 20,000 children with HIV infection, who will eventually develop the disease. Novel and characteristic pathologic changes and radiographic findings have recently been described. This report provides a summary and focus to imaging considerations in infants and children who have AIDS.

Although most of the early cases of AIDS in infants and children resulted from transfusions of contaminated blood products, currently about 80% of infants acquire the disease by vertical transmission from an infected mother, which occurs by transplacental exposure during gestation, by exposure to maternal blood during delivery, or by ingestion of the virus during breast feeding [3-7]. There is also concern that sexual abuse of children may produce more infections in the near future [8]. The incubation period is usually 6 months to 2 years, although a significant number of infected children can remain asymptomatic for up to 5 years [9-12].

The diagnosis of AIDS in children is complicated by the presence of passively transferred maternal antibodies. These

may persist in the infected or noninfected infant until the child is 15 months old; thus, early diagnosis requires culture of the virus, demonstration of viral antigens, evidence of immune deficiency, or a characteristic symptom complex [5, 13]. The standard enzyme-linked immunosorbent assay antibody test with confirmation by Western blot assay is sufficient for diagnosis in older patients. Difficulty in establishing the diagnosis also occurs in children with the disease who have no evidence of antibody production [12, 14, 15].

The Centers for Disease Control has devised a classification of AIDS in infants and children that summarizes the possible stages of disease and diagnosis (Table 1). Asymptomatic infants less than 15 months old who have been exposed to an infected mother and therefore have antiviral antibodies have an infection that is classified as indeterminate. Asymptomatic infections are defined as HIV infections without clinical manifestations of the disease. Typical signs and symptoms in a patient with HIV infection indicate symptomatic infection; these include nonspecific findings, neurologic disease, lymphoid interstitial pneumonitis, or secondary infectious diseases and secondary cancers.

AIDS causes varied signs and symptoms in children. Suggestive but nonspecific features include fever, failure to thrive, hepatosplenomegaly, generalized lymphadenopathy, parotitis, and repeated bouts of diarrhea [9]. Other presenting illnesses may be more specific and may have corroborating radiographic changes. These include HIV encephalitis, *Pneumocystis carinii* pneumonia (PCP), and lymphoid interstitial pneumonitis. AIDS in infants and children differs from the typical adult disease in several ways. First, the incubation

Received October 3, 1988; accepted after revision January 23, 1989.

¹Department of Diagnostic Radiology, University of Maryland Medical System/Hospital, 22 S. Greene St., Baltimore, MD 21201. Address reprint requests to P. J. Haney.

²The Russell H. Morgan Department of Radiology and Radiological Sciences, The Johns Hopkins Medical Institution, Baltimore, MD 21205.

TABLE 1: Classification of Human Immunodeficiency Virus (HIV) Infection in Children Under 13 Years Old*

Classification	
Class P-0	Indeterminate infection
Class P-1	Asymptomatic infection
Subclass A	Normal immune function
Subclass B	Abnormal immune function
Subclass C	Immune function not tested
Class P-2	Symptomatic infection
Subclass A	Nonspecific findings
Subclass B	Progressive neurologic disease
Subclass C	Lymphoid interstitial pneumonitis
Subclass D	Secondary infectious diseases
Category D-1	Specified secondary infectious diseases listed in the CDC surveillance definition for AIDS
Category D-2	Recurrent serious bacterial infections
Category D-3	Other specified secondary infectious diseases
Subclass E	Secondary cancers
Category E-1	Specified secondary cancers listed in the CDC surveillance definition for AIDS
Category E-2	Other cancers possibly secondary to HIV infection
Subclass F	Other diseases possibly due to HIV infection

* Reprinted from Centers for Disease Control (CDC) [13], with permission.

period is shorter in infants, probably because of the immaturity of the immune system [9, 16]. This immaturity probably accounts also for the more rapid course of AIDS in children and for the higher mortality [9]. Kaposi sarcoma and hepatitis B viral infections are less common in children than in adults. Bacterial sepsis and lymphocytic interstitial pneumonia, on the other hand, are much more common in children [16].

Chest Disease

Pulmonary disease is the most common clinical feature of AIDS in infants and children and also accounts for most of the morbidity and mortality [16, 17]. HIV-positive children have frequent chest films because of repeated episodes of fever. Plain chest radiography can be helpful in suggesting the diagnosis of AIDS. Lung scans and bronchial washings may also be helpful, but open-lung biopsy has generally been necessary for definitive diagnosis [17, 18].

Lymphocytic interstitial pneumonitis (LIP) is the most frequently encountered pulmonary abnormality and is a characteristic feature of AIDS in infants and children [16, 19]. This entity is a distinct chronic interstitial process associated with progressive alveolocapillary block caused by nodular lymphoid hyperplasia in the bronchiolar epithelium and interalveolar septa [20]. A more diffuse, linear lymphocytic infiltrate similar to that seen in typical LIP in adults may also be present. There is usually a slow, insidious development of respiratory distress with cough and mild to moderate hypoxemia. This is associated with generalized lymphadenopathy, salivary gland enlargement, and digital clubbing. Physical examination of the lungs reveals minimal changes. LIP has a chronic course and a relatively good prognosis; there is often a longer survival time and lower prevalence of other opportunistic infections.

The cause of LIP is unknown. In many patients with LIP, deoxyribonucleic acid specific for Epstein-Barr virus has been isolated from the lungs, and elevated levels of immunoglobulins directed against this virus have been found [19]. LIP may therefore represent a response of the lymphoid system to circulating antigens of the Epstein-Barr virus, *Salmonella*, or other infectious agents [20, 21]. Other investigations suggest that LIP is a response of pediatric pulmonary lymphoid tissue to HIV itself [22].

The chest films of children with LIP usually show small nodules and fine reticular densities that are bilateral and diffuse (Fig. 1). These changes are often mild at first and slowly increase in prominence over a period of weeks to months as clinical symptoms worsen (Fig. 2). Hilar and paratracheal adenopathy may be present, particularly late in the course of the disease, and tend to support the diagnosis of LIP [17, 18]. These patients may also have episodes of fever and acute respiratory distress caused by superimposed bacterial pneumonias, producing focal lobar and segmental infiltrates on the background of interstitial lung disease.

The interstitial changes themselves may be stable for long periods of time. LIP probably includes a spectrum of lymphoid changes in the lung, depending on the exact anatomic structures involved, so that a number of pathologic variants such as desquamative interstitial pneumonitis and bronchus-associated lymphoid tissue may occur [20, 23]. These entities may affect the severity and distribution of radiographic changes, but as yet the changes are not sufficiently specific to allow diagnosis of these variants.

In contrast to LIP, PCP usually presents with high fever, tachypnea with retractions, and markedly abnormal physical findings (wheezing, rhonchi, and diminished breath sounds). The chest film initially shows diffuse interstitial densities that rapidly evolve into coalescent bilateral air-space filling densities with air bronchograms (Fig. 3). The lungs may also show a diffusely granular pattern at this stage. The clinical course generally follows a parallel deterioration, often requiring intubation and mechanical ventilation. Complications such as interstitial emphysema, pneumomediastinum, and pneumothorax may then ensue. Although lung biopsy is necessary for definitive diagnosis, this constellation of clinical and radiographic changes justifies a presumptive diagnosis of PCP and enables early initiation of therapy.

Unfortunately, the chest film occasionally may be entirely normal with PCP, and the clinical findings may not be convincing. Gallium scanning has been shown to be a sensitive tool in detecting early cases of PCP, demonstrating grossly increased uptake bilaterally, in marked contrast to the deceptively benign-appearing chest film [24-26]. The gallium scan is not specific, however. Diffuse increased activity will also be seen with LIP; with other pulmonary infections (which are in the differential diagnosis in this situation); and with various forms of interstitial fibrosis, which also may be present [27].

Cytomegalovirus pneumonia also occurs in children with AIDS and produces reticular, nodular, and occasionally miliary densities on chest films [16-19]. Obviously, these changes are nonspecific. Cytomegalovirus infection may present as an acute respiratory illness (similar clinically and radiographically

Fig. 1.—2½-year-old girl with AIDS.
A and B, Anteroposterior (A) and lateral (B) chest films show small nodular infiltrates throughout both lungs. Open-lung biopsy confirmed lymphocytic interstitial pneumonitis.

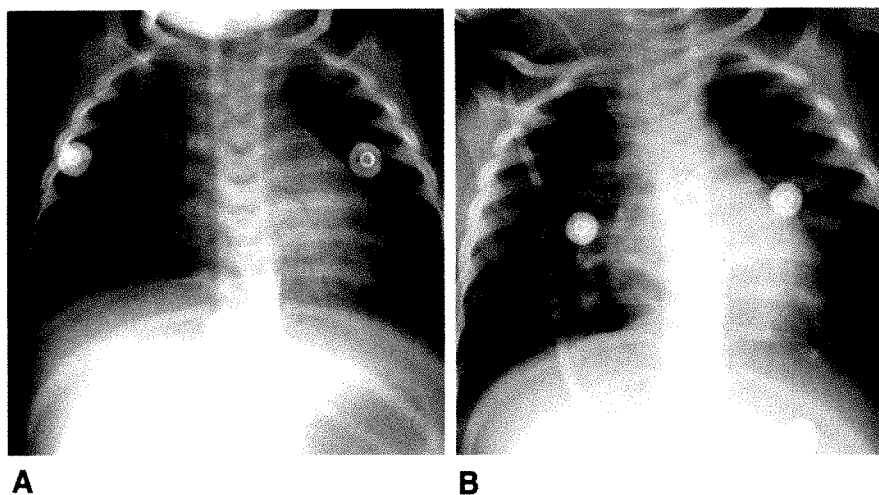
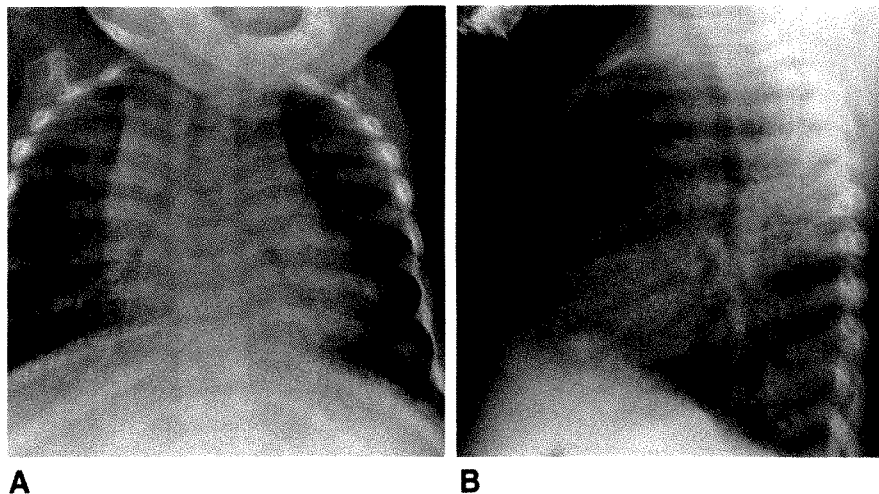


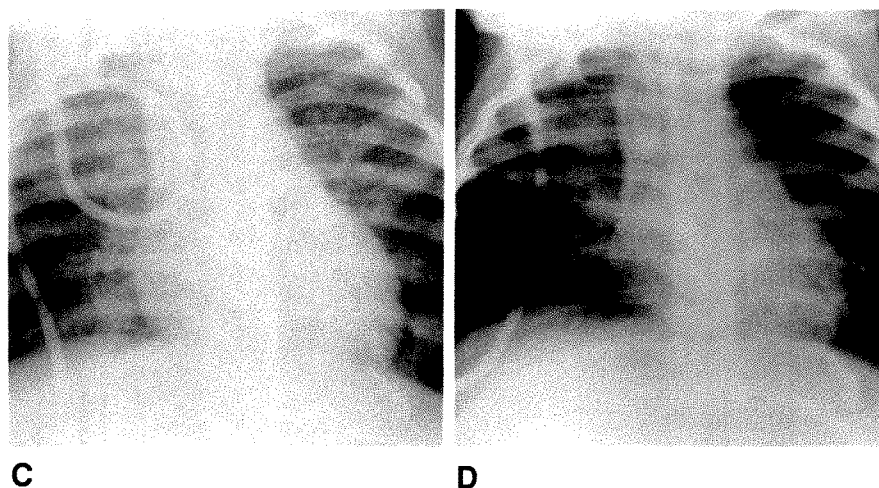
Fig. 2.—Evolution of radiographic changes in lymphocytic interstitial pneumonitis. Serial films at 2-month intervals in 16-month-old girl with AIDS.

A, Initial chest film shows subtle but definite increase in interstitial densities corresponding to onset of cough and tachypnea.

B, Central reticulonodular infiltrates have worsened with possible hilar adenopathy. Biopsy showed lymphocytic interstitial pneumonia.

C, Lung disease continues to progress with more prominent nodules in periphery associated with worsening clinical symptoms.

D, Mild improvement in reticulonodular densities after azidothymidine treatment with new focal right-upper-lobe consolidation. High fever, sepsis, and positive blood culture supported diagnosis of superimposed bacterial pneumonia.



to a typical lower respiratory tract infection); as a chronic, low-grade infection; or as a superinfection complicating LIP or PCP. Diagnosis is made by culture and immunoassay techniques or biopsy. *Mycobacterium avium-intracellulare* is a nontuberculous *Mycobacterium* that usually causes a disseminated systemic infection that may involve the lungs. The

radiographic findings are highly variable and include both alveolar and nodular pulmonary densities. Mediastinal adenopathy is a helpful finding, but can also be seen with LIP. The diagnosis is made from bronchial and sputum washings or by biopsy. Pulmonary infections with parainfluenza viruses and other common childhood viral agents are frequently en-

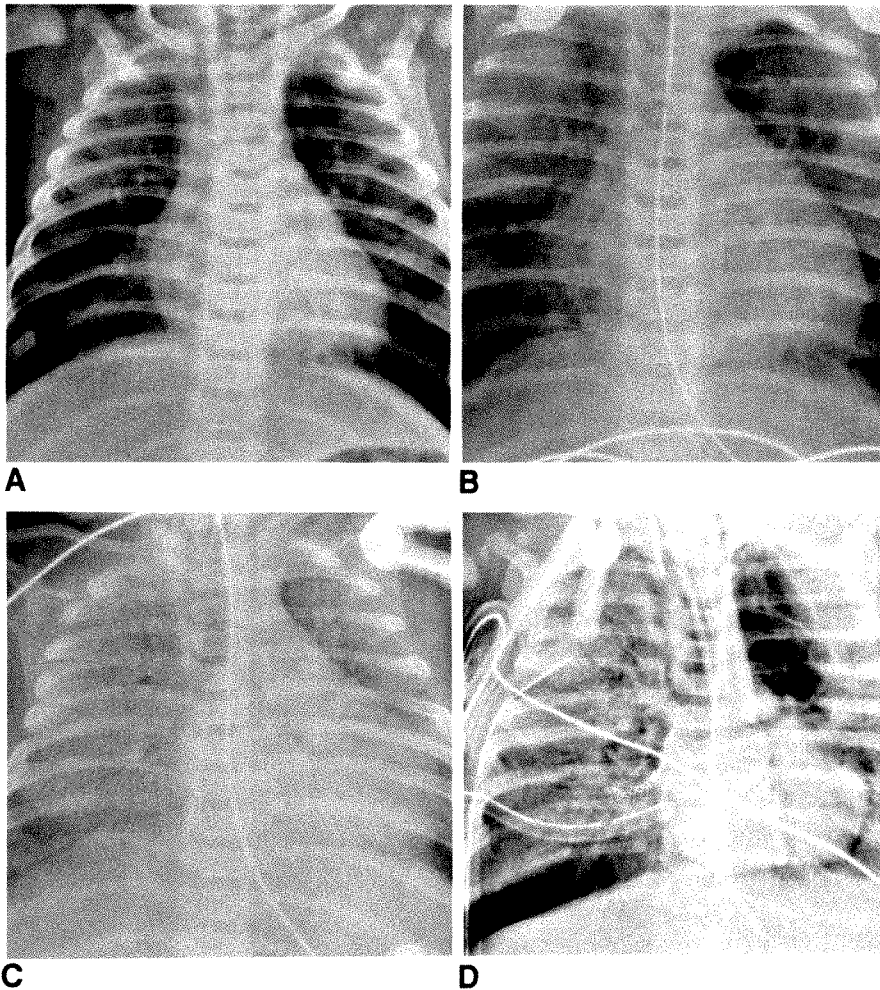


Fig. 3.—*Pneumocystis carinii* pneumonia in 4-month-old girl with AIDS who presented with cough, fever, and dyspnea.

A, Initial chest film shows mild, diffuse interstitial densities.

B, Film 18 hr later shows progression of densities with some confluence and cardiomegaly.

C, Film 2 days later shows diffuse air-space consolidation with air bronchograms. Endotracheal tube is present and staples at right lung base are from biopsy that showed *Pneumocystis*.

D, Film 2 days later shows changes of ventilator therapy, interstitial emphysema, pneumomediastinum, pneumopericardium, and pneumothorax.

countered and show typical radiographic changes of overinflation, perihilar interstitial densities, and atelectasis. These infections tend to be unusually persistent in children with AIDS, and several viral pathogens may be present simultaneously [28].

Bacterial infections can also be seen in these patients, and repeated bouts of pneumonia may be the initial manifestation of AIDS [29]. Superimposed bacterial infections should also be considered in those patients with established lung disease who have sudden worsening of their respiratory status, fever, or sepsis [30]. Typical peripheral infiltrates, segmental or lobar, are usually seen (Fig. 2). Nonspecific alveolar damage can be caused by the various infections themselves as well as by oxygen therapy and mechanical ventilation. This condition has been termed diffuse alveolar damage and is characterized by edema, hemorrhage, hyaline membranes, cuboidal metaplasia of alveolar epithelium, and interstitial fibrosis [23]. Radiographically, diffuse alveolar damage produces nonspecific interstitial densities of variable severity. Baseline films are very helpful in this situation, particularly in the evaluation of a suspected superinfection. Diffuse alveolar damage has also been described as a pathologic feature of nonspecific interstitial pneumonitis, an acute respiratory disease of adults

in which the clinical signs and symptoms are similar to PCP [31]. Nonspecific interstitial pneumonitis may occur de novo or as a sequela of PCP or previous chemotherapeutic regimens, or in association with Kaposi sarcoma. No pathogens are found on lung biopsy or bronchoalveolar lavage. The chest films in 56% of these patients are normal. Whether or not a similar syndrome occurs in children and, if so, what its relationship is to diffuse alveolar damage remains to be seen.

Cardiac disease has been reported in 55–73% of adults with AIDS [32, 33], and several recent reports have described involvement of the heart in children [34, 35]. Pathologically, children have shown a dilated cardiomyopathy with biventricular chamber enlargement and normal pericardium, valves, and coronary arteries. Although a few cases of cytomegalovirus myocarditis have been reported, most AIDS-associated heart disease is a primary myopathic abnormality with no definite evidence of an infectious origin. The pathogenesis remains problematic but may be related to anemia, nutritional deficiencies, immunologic factors, or infection. Most of these patients have cardiomegaly on the chest film, and changes of overt or early pulmonary edema may be seen also (Fig. 4). Confirmation by echocardiography reveals biventricular dilatation, often with some degree of ventricular dysfunction. The

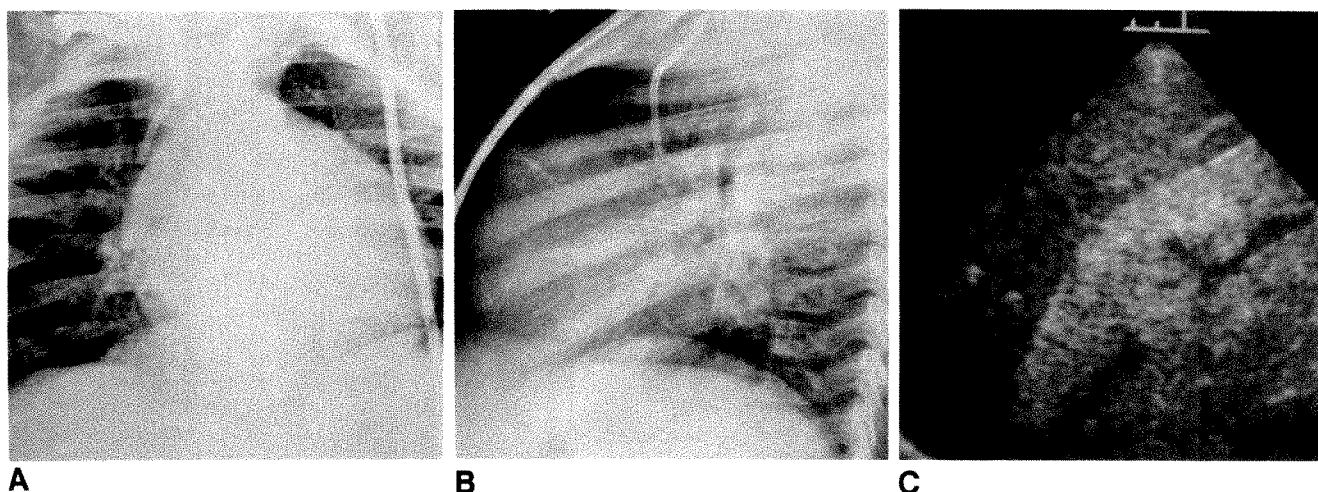


Fig. 4.—7-month-old boy with AIDS and repeated respiratory tract infections presented with cough and tachypnea. A and B, Anteroposterior (A) and lateral (B) chest radiographs obtained to rule out pneumonia show increased heart size and mild prominence of central bronchovascular markings. Echocardiogram confirmed biventricular dilatation and dysfunction, compatible with cardiomyopathy. C, Patient returned 4 months later with proteinuria. Renal sonogram shows increased echogenicity of right kidney compared with liver.

possibility of myocardial involvement should be suggested when serial films show an increase in cardiac size (especially with evidence of failure), because concomitant lung disease and infection may overshadow the clinical features of heart disease. Cardiac involvement probably will increase as survival time is prolonged, and periodic echocardiographic screening may be indicated as the condition responds to treatment with digitalis and diuretics.

Gastrointestinal and Other Abdominal Diseases

A number of characteristic infectious agents involve the gastrointestinal tract in children with AIDS. *Cryptosporidium* can involve the entire length of the gastrointestinal tract from the pharynx and esophagus to the rectum, but most commonly occurs in the small bowel and accounts for many of the cases of chronic diarrhea that are typical of AIDS in children [9, 36]. Contrast studies of the gastrointestinal tract are rarely necessary but if performed generally show a smooth, featureless appearance of the mucosa, with a ribbonlike loss of the normal fold pattern. Enteritis can also be caused by cytomegalovirus and *M. avium-intracellulare*, and diagnosis generally requires culture or biopsy. Esophagitis usually is caused by *Candida* and often is associated with oral thrush [9, 17, 18]. A contrast esophagogram may show ulcers, plaques, and prominent folds; however, these changes can also be seen with esophagitis secondary to cytomegalovirus, herpes simplex, and *Cryptosporidium* (Fig. 5). It should also be kept in mind that most cases of enteritis are secondary to common endemic pathogens such as enteroviruses and *Salmonella*, which also tend to occur more frequently in children with AIDS [9, 16, 21].

On rare occasions opportunistic organisms may produce changes that mimic other diseases. Cytomegalovirus can produce thickening of the pylorus and proximal duodenum, resulting in a high-grade pyloric obstruction with radiographic

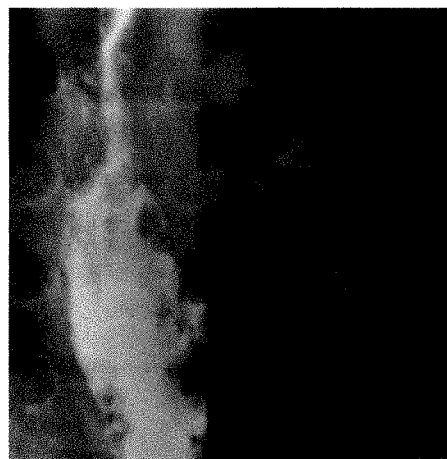


Fig. 5.—Esophagogram in 2-year-old with dysphagia, mucocutaneous thrush, and *Candida* esophagitis shows severely ulcerated esophagus with edematous mucosa.

features similar to those of pyloric stenosis [37]. Appendicitis caused by *M. avium-intracellulare* and cholecystitis caused by cytomegalovirus and *Cryptosporidium* have also been reported [38]. Burkitt lymphoma of the pancreas has been reported to produce enlargement with hypoechoic lesions on sonography [39]. Diagnosis of these unusual entities may require a fair degree of ingenuity in imaging and, in those cases in which they are the presenting abnormality, should suggest the possibility of AIDS.

Adenopathy is probably the most common abdominal manifestation of pediatric AIDS and may be the initial, presenting abnormality [9, 17, 18]. The periaortic, caval, mesenteric, and periportal nodes are usually involved and often demonstrate bulky enlargement (Fig. 6). The degree of echogenicity is variable, perhaps because of the various causes and histologic changes in the nodes. In many cases the enlargement

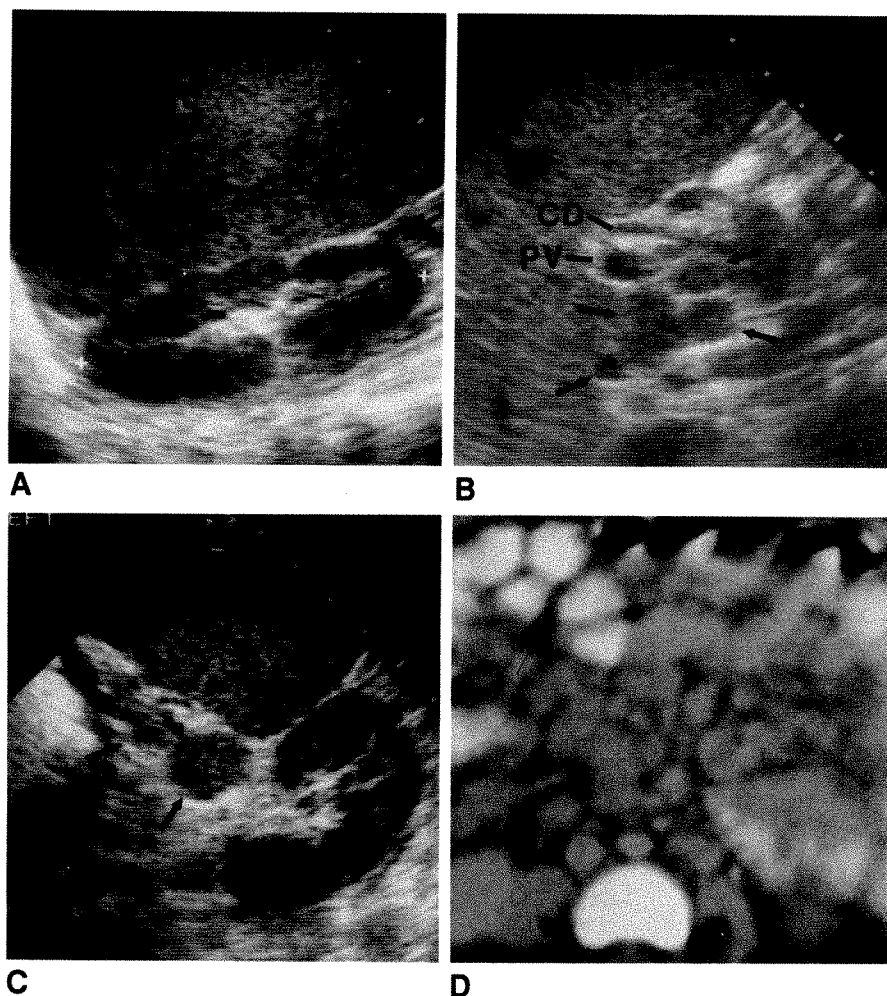


Fig. 6.—4½-year-old girl with transfusion-acquired AIDS who had a history of multiple previous infections and generalized peripheral lymphadenopathy. New elevation of liver function tests and hepatomegaly prompted evaluation.

A, Longitudinal sonogram of right upper quadrant shows hepatomegaly. There were no focal liver lesions or biliary obstruction.

B, Longitudinal sonogram through porta hepatis shows multiple enlarged lymph nodes (arrows). PV = portal vein; CD = common duct.

C, Transverse sonogram of left upper quadrant shows enlarged lymph nodes (arrows) in splenic hilum.

D, Abdominal CT scan shows extensive adenopathy in retroperitoneum and throughout mesentery.

is idiopathic with no evidence of an infectious cause. This has been termed the lymph-node syndrome and often implies generalized adenopathy. Histologically the findings include a spectrum of changes ranging from follicular hyperplasia to follicular atrophy with lymphocytic depletion. *M. avium-intracellulare* is another common cause of mesenteric and retroperitoneal adenopathy, resulting from hematogenous, lymphogenous, or direct spread. Disseminated lymphoid Kaposi sarcoma has also been found at autopsy in infants without clinical manifestations who died of pneumonia and in an older child with AIDS who presented with jaundice, hepatomegaly, and massively enlarged abdominal lymph nodes [40, 41]. Sonography and CT can depict these enlarged nodes, but cannot distinguish among the possible origins.

Hepatosplenomegaly is a common but nonspecific abnormality in children with AIDS (Fig. 6). Liver inflammation is often chronic and may be caused by HIV, cytomegalovirus, *M. avium-intracellulare*, or hepatitis B virus and may progress to liver failure with portal hypertension [17, 18]. Giant cell hepatitis presenting with cholestasis has also recently been described and tentatively attributed to HIV infection [42]. The most common splenic abnormality in adults is infection with *M. avium-intracellulare*, but the spleen is virtually always involved together with other organs by infectious and neoplastic processes [43]. As with adenopathy, changes in size

can be diagnosed readily by CT and sonography, but specific causes cannot be determined. Renal involvement also occurs with AIDS; urinary tract infection and pyelonephritis may not only herald the disease but also account for episodes of sepsis [29]. Patients may also have evidence of renal dysfunction, either as the first manifestation of HIV infection or later in the course of the disease. Edema, proteinuria, and intermittent hematuria are commonly noted, and progressive renal failure usually ensues. Pathologic examination shows focal glomerulosclerosis or mesangial proliferative glomerulonephritis; these lesions may produce increased echogenicity of the kidneys on sonography (Fig. 4). The cause of AIDS-associated renal disease is not known, but it probably results from HIV infection or deposition of immune complexes [44–46]. Acute renal failure is usually associated with dehydration and drug toxicity. Acute tubular necrosis in these cases may result in loss of corticomedullary differentiation on sonography. Renal tubular dilatation producing increased cortical echogenicity has been described in adults with AIDS [47].

CNS Disease

Neurologic changes may be the initial manifestation of AIDS in children or may occur after involvement of other organ systems. There is a fairly typical clinical presentation, including

loss of developmental milestones, apathy, failure of brain growth, and spastic paresis. These signs and symptoms indicate a process that mainly affects the white matter, analogous to the subcortical dementia that occurs in adults [48, 49]. Recent reports suggest that these abnormalities are caused by infection of the brain by HIV and that this infection is by far the most common cause of CNS disease in children and infants who have AIDS [14, 50–52]. The virus itself has been cultured from the CSF and brain tissue in these patients, and both viral antigens and locally produced antiviral antibodies have been demonstrated, even though in some cases there is no systemic antibody production. This HIV encephalopathy generally shows an episodic pattern of progression, with transiently stable plateaus followed by periods of deterioration that correspond to viral replication and release of viral antigens. The prognosis is considerably worse once CNS disease is established.

HIV shows a striking neurotropism, and CNS infection probably occurs early in the course of the disease and is persistent. The immature nervous system also seems to be

particularly vulnerable to infection by retroviruses. A characteristic pathologic change in the brain has been termed calcific vasculopathy and apparently corresponds to the early stage of CNS infection. There is vascular and perivascular inflammatory change in the small and medium-sized vessels of the basal ganglia as well as deposition of calcific plaques in the vessel walls [53, 54]. These changes are reflected in the associated CT and MR abnormalities [55–57]. Contrast CT shows enhancement of the basal ganglia followed by development of calcifications in the same deep cerebral structures as well as in the periventricular white matter in some cases (Fig. 7). Occasionally the findings may be unilateral at first, but most cases eventually show bilateral involvement. Although the calcifications may not be apparent on MR, there are corresponding changes in the basal ganglia and deep white matter; T1-weighted images show areas of diminished signal intensity that increase on the T2-weighted images. There is no evidence of edema or mass effect.

Additional pathologic findings include diminished brain weight, inflammatory cell infiltrates (glial and/or microglial

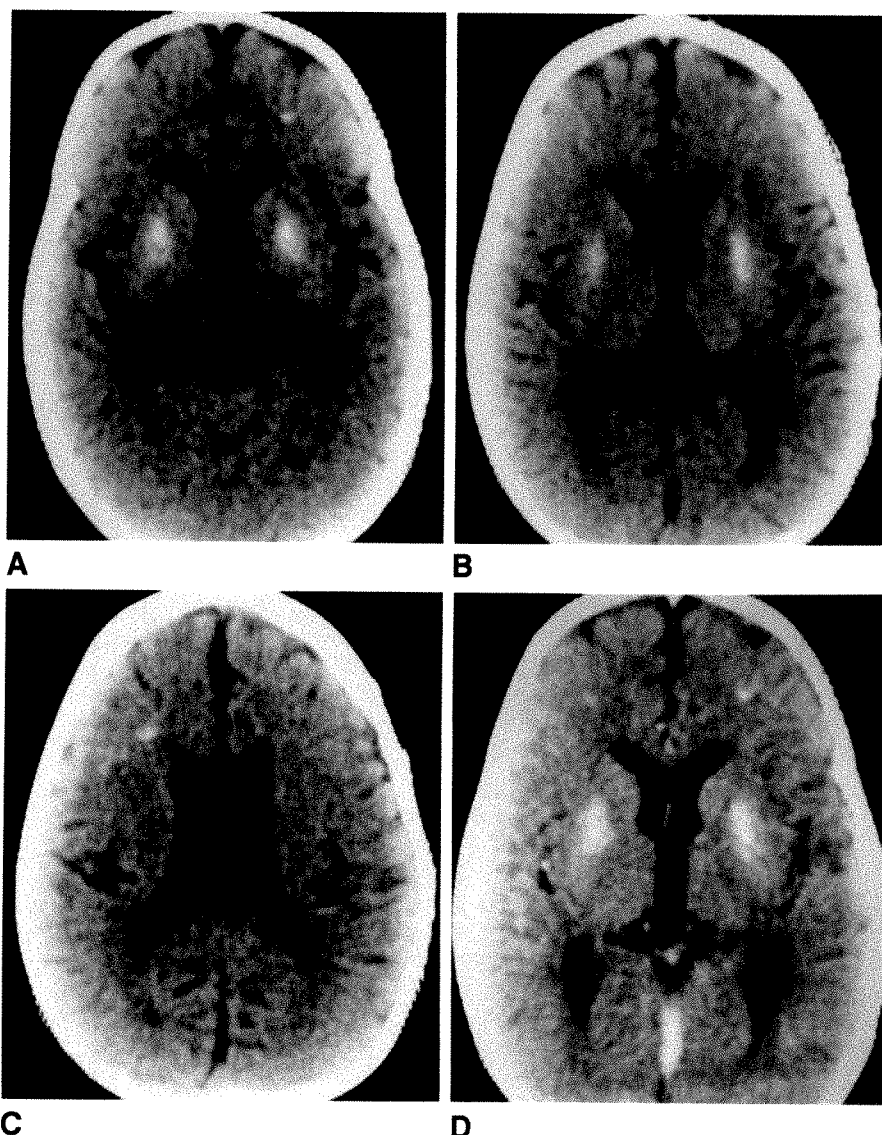


Fig. 7.—Human immunodeficiency virus encephalopathy in 16-month-old boy with AIDS who presented with failure to thrive, loss of developmental milestones, and microcephaly.

A–C, Unenhanced CT scans show enlarged subarachnoid spaces, calcification of basal ganglia, and smaller deposits of calcium in frontal subcortical white matter.

D, Contrast-enhanced CT scan shows enhancement in area of basal ganglia calcifications and punctate regions of enhancement in frontal white matter that do not correspond to previously seen calcifications.

cells, lymphocytes, and monocytes), and multinucleated cells. These changes correspond to the more diffuse findings on CT and MR of cerebral atrophy, a finding that may predate clinical symptoms. There is expansion of the subarachnoid spaces with enlargement of the ventricles, basal cisterns, and interhemispheric fissure as well as prominence of the cerebral sulci. These atrophic changes together with the calcifications and changes in attenuation or signal intensity of the basal ganglia constitute a constellation of findings that is strongly suggestive of CNS infection by HIV in children. Because these patients may present with isolated neurologic disease, the diagnosis of AIDS may first be considered on the basis of neuroimaging studies. The parents may be asymptomatic and appear to have no risk factors on initial evaluation; demonstration of AIDS involving the CNS in one child then indicates the need for further laboratory investigation of the rest of the family [58]. Recent reports [59, 60] document clinical improvement in patients with cerebral HIV infection after treatment with azidothymidine and gamma globulin. This was accompanied by marked improvement of the atrophic changes seen on CT, indicating a role for CT in assessing response to treatment of CNS disease.

Cerebral mass lesions in children with AIDS are usually due to primary lymphoma and usually present with progressive focal neurologic deficits. CT in these cases shows multicentric hyperdense lesions that enhance with contrast medium. MR may show more of the lesions than can be demonstrated on CT [61]. Diagnosis requires biopsy. Opportunistic CNS infections other than those caused by HIV are common in adults but occur rarely in children, probably because they are due to reactivation of latent infections that infants and children have not had time to acquire. However, in some cases this may occur. Infection of the brain in utero by cytomegalovirus may undergo reactivation after birth when immunodeficiency develops. In one recently described case [62], typical periventricular calcifications of cytomegalovirus infection evolved into enhancing mass lesions of active disease in an infant with AIDS. *Toxoplasma* encephalitis has also been described in infants with AIDS. Multiple, small, scattered calcifications were seen on CT, but it was difficult to determine whether this represented intrauterine infection or postnatally acquired disease [63]. The difficulty in diagnosis may be compounded by the inability of these infants to produce specific antibodies.

Other head and neck problems may also require radiographic investigation [29, 64]. Otitis media may be the presenting complaint in children with AIDS and may also be a chronic, persisting problem, although cholesteatoma has not been described in this context. Sinusitis is also frequently suspected clinically, and demonstration of sinus disease in infants may require CT or sonography in addition to routine plain films. Cervical adenopathy occurs in approximately 40% of patients, usually in those with less advanced disease. Parotid enlargement is noted in 30% of cases; pathologically it is associated with lymphocytic infiltration of the gland.

Many of the cited reports deal with small numbers of patients observed over relatively short periods of time. As the number of cases grows and survival lengthens with improved palliation, the clinical and radiographic manifestations of AIDS

in infants and children will no doubt undergo considerable change. Prolonged survival may result in an increase in cardiac and renal involvement and a wider spectrum of pathologic abnormalities and opportunistic infections [34, 35]. The radiographic findings we have described constitute a core of typical abnormalities. Radiology will also play a role in monitoring the response to new therapeutic measures [59]. The chest film and head CT scan may show improvement after drug therapy, and positron emission tomography may confirm improved cerebral function after azidothymidine treatment [60]. We are currently investigating the role of MR and sonography in the evaluation of CNS disease in children with AIDS in the hope that these and other techniques provide a more sensitive and specific depiction of the pathologic anatomy in this new and tragic disease.

REFERENCES

1. Windom RE. From the Assistant Secretary for Health. *JAMA* **1988**;260:18
2. Hegarty JD, Abrams EL, Hutchinson VE, Nicholas SW, Suarez MS, Heagarty MC. The medical care costs of human immunodeficiency virus-infected children in Harlem. *JAMA* **1988**;260:1901-1909
3. Saulsbury FT, Wycoff RF, Boyle RJ. Transfusion-acquired human immunodeficiency virus infection in twelve neonates: epidemiologic, clinical and immunologic features. *Pediatr Infect Dis* **1987**;6:544-549
4. Davids MK. Vertical transmission of HIV. *JAMA* **1988**;260:30-31
5. Pyun KH, Ochs HD, Dufford MTW, Wedgewood RJ. Perinatal infection with human immunodeficiency virus. *N Engl J Med* **1987**;317:611-614
6. Lepage P, Van De Perre P, Carael M, et al. Postnatal transmission of HIV from mother to child. *Lancet* **1987**;2(8555):400-401
7. Secretary Bowen sets department-wide pediatric HIV disease initiative. *Public Health Rep* **1988**;103:325-326
8. Fuller AK, Bartucci RJ. HIV transmission and childhood sexual abuse. *JAMA* **1988**;259:2235
9. Barbour SD. Acquired immunodeficiency syndrome of childhood. *Pediatr Clin North Am* **1987**;34:247-268
10. Centers For Disease Control. Quarterly report to the domestic policy council on the prevalence and rate of spread of HIV and AIDS in the United States. *JAMA* **1988**;259:2657-2661
11. Centers for Disease Control. Update: acquired immunodeficiency syndrome (AIDS)—worldwide. *JAMA* **1988**;259:3104-3107
12. Aiuti F, Luzi G, Messaroma I, Scano G, Papetti C. Delayed appearance of HIV infection in children. *Lancet* **1987**;2(8563):858
13. Centers for Disease Control. Classification system for human immunodeficiency virus (HIV) infection in children under 13 years of age. *MMWR* **1987**;36:225-236
14. Ragni MV, Vabach AH, Taylor S, et al. Isolation of human immunodeficiency virus and detection of HIV DNA sequences in the brain of an ELISA antibody-negative child with acquired immune deficiency syndrome and progressive encephalopathy. *J Pediatr* **1987**;110:892-894
15. Goetz DW, Hall SE, Harbison RW, Reid MJ. Pediatric acquired immunodeficiency syndrome with negative human immunodeficiency virus antibody response by enzyme-linked immunosorbent assay and western blot. *Pediatrics* **1988**;81:356-359
16. Minnefor A, Olesfe J, Connor E, et al. Pediatric AIDS. *Antibiot Chemother* **1987**;38:52-58
17. Amodio JB, Abramson S, Berdon WE, Levy J. Pediatric AIDS. *Semin Roentgenol* **1987**;22:66-76
18. Genieser NB, Hernanz-Schulman M, Krasinski K, Greco MA, Borkowsky W. Pediatric AIDS. In: Federle M, ed. *Radiology of acquired immune deficiency syndrome*. New York: Raven, **1988**:131-141
19. Rubinstein A, Morecki R, Silverman B, et al. Pulmonary disease in children with acquired immune deficiency syndrome and AIDS-related complex. *J Pediatr* **1986**;108:498-503
20. Joshi VV, Oleske JM, Minnefor AB, et al. Pathologic pulmonary findings in children with the acquired immunodeficiency syndrome: a study of ten cases. *Hum Pathol* **1985**;16:244-246

21. Celum CL, Chaisson RE, Rutherford GW, Barnhart JL, Echenberg DF. Incidence of salmonellosis in patients with AIDS. *J Infect Dis* **1987**;156:998-1002
22. Bradford BF, Abdenour GE, Frank JL, Scott GB, Beerman R. Usual and unusual radiologic manifestations of acquired immunodeficiency syndrome (AIDS) and human immunodeficiency virus (HIV) infection in children. *Radiol Clin North Am* **1988**;26:341-353
23. Zimmerman BL, Haller JO, Price AP, Thelmo WL, Fikrig S. Children with AIDS—is pathologic diagnosis possible based on chest radiographs? *Pediatr Radiol* **1987**;17:305-307
24. Levenson SM, Warren RD, Richman SD, et al. Abnormal pulmonary gallium accumulation in *P. carinii* pneumonia. *Radiology* **1976**;119:395-398
25. Turbner EH, Yeh SDJ, Rosen PP, et al. Abnormal gallium scintigraphy in *Pneumocystis carinii* pneumonia with a normal chest radiograph. *Radiology* **1978**;127:437-438
26. Schiff RG, Kabat L, Kamani N. Gallium scanning in lymphoid interstitial pneumonitis of children with AIDS. *J Nucl Med* **1987**;28:1915-1919
27. Zuckier LS, Ongseng F, Goldfarb CR. Lymphocytic interstitial pneumonitis: a cause of pulmonary gallium-67 uptake in a child with acquired immunodeficiency syndrome. *J Nucl Med* **1988**;29:707-711
28. Josephs S, Kim HW, Brandt CD, Parrott RH. Parainfluenza 3 virus and other common respiratory pathogens in children with human immunodeficiency virus infection. *Pediatr Infect Dis* **1988**;7:207-209
29. Bernstein LJ, Krieger BZ, Novice B, Sicklick MJ, Rubinstein A. Bacterial infection in the acquired immunodeficiency syndrome of children. *Pediatr Infect Dis* **1985**;4:472-475
30. Vernon DD, Holzman BH, Lewis P, Scott GB, Birriel JA, Scott MB. Respiratory failure in children with acquired immunodeficiency syndrome and acquired immunodeficiency syndrome-related complex. *Pediatrics* **1988**;82:223-228
31. Suffredini AF, Ognibene FP, Lack EE, et al. Nonspecific interstitial pneumonitis: a common cause of pulmonary disease in the acquired immunodeficiency syndrome. *Ann Intern Med* **1987**;107:7-13
32. Roldan EO. Pathology of the heart in acquired immunodeficiency syndrome. *Arch Pathol Lab Med* **1987**;111:943-946
33. Fink L, Reichel N, St. John Sutton M. Cardiac abnormalities in acquired immune deficiency syndrome. *Am J Cardiol* **1984**;54:1161-1163
34. Steiner L, Brochstein JA, Robins J. Cardiac involvement in congenital acquired immunodeficiency syndrome. *Am J Dis Child* **1986**;140:1241-1244
35. Joshi VV, Gadol C, Connor E, Oleske JM, Mendelson J, Marin-Garcia J. Dilated cardiomyopathy in children with acquired immunodeficiency syndrome: a pathologic study of five cases. *Hum Pathol* **1988**;19:69-73
36. Kazlow PG, Shah K, Benkov KJ, Dische R, LeLeiko NS. Esophageal cryptosporidiosis in a child with acquired immune deficiency syndrome. *Gastroenterology* **1986**;91:1301-1303
37. Victoria MS, Nangia BS, Jindrak K. Cytomegalovirus pyloric obstruction in a child with acquired immunodeficiency syndrome. *Pediatr Infect Dis* **1985**;4:550-552
38. Patrick CC, Hawkins EP, Guerra C, Taber LH. Clinical conference: a patient with leukemia in remission and acute abdominal pain. *J Pediatr* **1987**;111:624-629
39. Graif M, Kessler A, Neumann Y, Martinowitz U, Iizchak Y. Pancreatic Burkitt lymphoma in AIDS: sonographic appearance. *AJR* **1987**;146:1290-1291
40. Buck BE, Scott GB, Valdes-Dapena, Parks WP. Kaposi sarcoma in two infants with acquired immune deficiency syndrome. *J Pediatr* **1983**;103:911-913
41. Kamani N, Kennedy J, Brandsma J. Burkitt lymphoma in a child with human immunodeficiency virus infection. *J Pediatr* **1988**;112:241-244
42. Witzleben CL, Marshall GS, Wenner W, Piccoli DA, Barbour SD. HIV as a cause of giant cell hepatitis. *Hum Pathol* **1988**;19:603-605
43. Klatt EC, Meyer PR. Pathology of the spleen in the acquired immunodeficiency syndrome. *Arch Pathol Lab Med* **1987**;111:1050-1053
44. Rcussean E, Russo P, Lapointe N, O'Regan S. Renal complications of acquired immunodeficiency syndrome in children. *Am J Kidney Dis* **1988**;11:48-50
45. Kaplan MS, Wechsler M, Benson MC. Urologic manifestations of AIDS. *Urology* **1987**;30:441-443
46. Connor E, Gupta S, Joshi V, et al. Acquired immunodeficiency syndrome associated renal disease in children. *J Pediatr* **1988**;113:39-44
47. Hamper UM, Goldblum LE, Hutchins GM, et al. Renal involvement in AIDS: sonographic-pathologic correlation. *AJR* **1988**;150:1321-1325
48. Ultmann MH, Belman AL, Ruff HA, et al. Developmental abnormalities in infants and children with acquired immune deficiency syndrome (AIDS) and AIDS-related complex. *Dev Med Child Neurol* **1985**;27:563-571
49. Belman AL, Ultmann MH, Horoupian D, et al. Neurological complications in infants and children with acquired immune deficiency syndrome. *Ann Neurol* **1985**;18:560-566
50. Gabuzda DH, Hirsch MS. Neurologic manifestations of infection with human immunodeficiency virus: clinical features and pathogenesis. *Ann Intern Med* **1987**;107:383-391
51. Epstein LG, Sharer LR, Oleske JM, et al. Neurologic manifestations of human immunodeficiency virus infection in children. *Pediatrics* **1986**;78:678-687
52. Epstein LG, Goudsmit J, Paul DA, et al. Expression of human immunodeficiency virus in cerebrospinal fluid of children with progressive encephalopathy. *Ann Neurol* **1987**;21:397-401
53. Sharer LR, Epstein LG, Cho E-S, et al. Pathologic features of AIDS encephalopathy in children: evidence for LAV/HTLV III infection of brain. *Hum Pathol* **1986**;17:271-284
54. Rhodes RH. Histopathology of the central nervous system in the acquired immunodeficiency syndrome. *Hum Pathol* **1987**;18:636-642
55. Belman AL, Lantos G, Hordupian D, et al. AIDS: calcifications of the basal ganglia in infants and children. *Neurology* **1986**;36:1192-1199
56. Epstein LG, Berman CZ, Sharer LR, Khademi M, Desposito F. Unilateral calcification and contrast enhancement of the basal ganglia in a child with AIDS encephalopathy. *AJNR* **1987**;8:163-165
57. Post MJD, Tate LG, Quencer RM, et al. CT, MR, and pathology in HIV encephalitis and meningitis. *AJR* **1988**;151:373-380
58. Davis SL, Halsted CC, Levy N, Ellis W. Acquired immunodeficiency syndrome presenting as progressive infantile encephalopathy. *J Pediatr* **1987**;110:884-888
59. Matthew J, Walker LA, Watson JG, Bird AG. AIDS encephalopathy with response to treatment. *Arch Dis Child* **1988**;63:545-547
60. Pizzo PA, Eddy J, Falloon J, et al. Effect of continuous intravenous infusion of zidovudine (AZT) in children with symptomatic (HIV) infections. *N Engl J Med* **1988**;319:889-896
61. Epstein LG, DiCarlo FJ, Joshi VV, et al. Primary lymphoma of the central nervous system in children with acquired immunodeficiency syndrome. *Pediatrics* **1988**;82:355-363
62. Post MJD, Curless RG, Gregorios JB, Scott GB, Sheldon JJ. Reactivation of congenital cytomegalic inclusion disease in an infant with HTLV III associated immunodeficiency: a CT-pathologic correlation. *J Comput Assist Tomogr* **1986**;10:533-536
63. Shanks GD, Redfield RR, Fischer GW. Toxoplasma encephalitis in an infant with acquired immunodeficiency syndrome. *Pediatr Infect Dis* **1987**;6:70-71
64. Williams MA. Head and neck findings in pediatric acquired immune deficiency syndrome. *Laryngoscope* **1987**;97:713-716

Book Review

Radiographic Contrast Agents, 2nd ed. By Jovitas Skucas. Rockville, MD: Aspen, 565 pp., 1989. \$78

This carefully prepared work is a welcome contribution to the field of contrast media in diagnostic radiology. The book consists of nine parts, or sections, with a total of 32 chapters. The longest chapter is 142 pages and the shortest is 13 pages. The sections are gastrointestinal agents, angiographic agents, genitourinary agents, hepatobiliary agents, myelographic agents, ultrasonography, magnetic resonance, miscellaneous agents, and pediatric agents.

The stated purpose of the book is to provide understanding of (1) the basic concepts involved in the application of contrast agents used in different radiologic examinations, (2) the rationale for their use, (3), their advantages, and (4) limitations. In this respect the book has accomplished its purpose quite well. Each chapter is supported by an extensive bibliography. Each chapter presents the historic background in the evolution and development of contrast media in each area of radiologic examination or investigation, stressing technique, chemistry, physics, pharmacology, toxicity, and their application to each organ system.

Ordinarily a book on contrast media in diagnostic radiology would be out of date by the time it goes to press. With the exception of areas of rapid developments, especially nonionic contrast media, this book does not have this shortcoming. Except for cost, the authors

stress the advantages of nonionic contrast media, especially as regards the lower prevalence of adverse reactions. As more data are accumulated, more valuable information will come to light.

This book, edited by Jovitas Skucas, of the Department of Radiology, University of Rochester School of Medicine, has the advantage of having contributions by carefully selected authors of recognized stature from different countries, thus bringing a welcome and valuable international flavor to this work. Twenty authors are from the United States, 12 of whom are from the Department of Radiology, University of Rochester; three are from France; one each is from England, New Zealand, and Sweden; and two each are from Canada, Finland, and Australia.

The work is well organized, sometimes in greater detail than practicing radiologists need or can consume in their daily practices. This book is strongly recommended as a valuable addition to the library of radiology departments, especially those engaged in residents' training programs.

William H. Shehadi
Greenwich, CT 06830

Blunt Renal and Ureteral Trauma in Childhood: CT Patterns of Fluid Collections

Marilyn J. Siegel¹
Dennis M. Balfe

The CT scans of 25 children with blunt renal and ureteral trauma were analyzed to determine the severity of injury, the appearance of retroperitoneal fluid collections, and whether the extent of these collections correlated with the severity of injury. CT showed renal parenchymal injuries in 23 patients and ureteral injuries in two patients. Retroperitoneal fluid was detected in 19 (76%) of 25 patients. Perirenal fluid collections were present in all 19, periureteral fluid in 12, interfascial fluid in eight, anterior pararenal fluid in four, and psoas hemorrhage in three. The presence of perirenal and periureteral fluid was not a good predictor of the extent of renal injury. Fluid collections in the interfascial or anterior pararenal spaces and psoas muscle appeared to correlate with the severity of injury. Patients with these fluid patterns usually had renal fractures, arterial injuries, or ureteral disruptions.

The presence of perirenal and periureteral fluid did not correlate with the extent of renal injury, while the presence of interfascial, anterior pararenal, and psoas muscle fluid correlated somewhat with renal fractures and renal pedicle disruption.

CT is now recognized as the examination of choice for studying severely injured children with real or suspected renal trauma. Although the CT appearances of a wide variety of renal injuries have been described [1-6], the CT patterns of retroperitoneal fluid distribution have not been closely studied in children. Moreover, little attention has been given to the ability of CT to distinguish renal from ureteral injuries. Accordingly, we reevaluated the spectrum of CT findings in children with renal and ureteral injuries and determined whether the presence of retroperitoneal fluid collections correlated with the extent of injury.

Materials and Methods

Between January 1983 and May 1988 abdominal CT scans were obtained in 245 hemodynamically stable children for evaluation of blunt abdominal trauma. In 25 of these patients, CT showed renal or ureteral injuries. Their clinical records were reviewed with attention to type and extent of trauma, operative findings (where applicable), associated injuries, and clinical outcome. Final diagnosis was based on surgical findings in eight patients, subsequent radiologic studies in 10 patients, and clinical follow-up in seven patients.

CT was performed on either the Siemens DR3 or the DRH scanner with a 3- or 4-sec scan time, 1-cm slice thickness, and 1-cm scan interval from the dome of the liver to the lower pole of the kidney and then with 2-cm intervals to the symphysis pubis. All patients received 60% iocinated contrast medium (2-3 ml/kg), given as a bolus injection. Dilute oral contrast material was given by mouth or by nasogastric tube 10-30 min before scanning in 20 patients. In the remaining five patients, the examinations were performed urgently without oral contrast medium. All CT scans were obtained within 24 hr of injury.

The CT scans were reviewed for (1) nature and extent of renal or ureteral injury, (2) visualization of contrast medium in the collecting system or ureter, (3) nature and location of extrarenal fluid collections, and (4) presence of associated injuries. Renal parenchymal lesions were grouped into broad categories based on previously described diagnostic criteria [3, 6]. These included contusions (grade 1), lacerations limited to the cortex (grade 2), complete

Received October 3, 1988; accepted after revision December 27, 1988.

¹ Both authors: The Edward Mallinckrodt Institute of Radiology, Washington University School of Medicine, 510 S. Kingshighway Blvd., St. Louis, MO 63110. Address reprint requests to M. J. Siegel.

AJR 152:1043-1047, May 1989

0361-803X/89/1525-1043

© American Roentgen Ray Society

lacerations extending into the collecting system and fractures (grade 3), shattered kidney (grade 3B), and vascular pedicle injuries (grade 4).

Extrarenal fluid collections were characterized as being in (1) the perirenal space, (2) periureteral space, (3) anterior pararenal space, (4) interfascial space, or (5) psoas space. The interpretations were based on well-established criteria for evaluation of CT anatomy [7].

Results

Twenty-five patients had CT evidence of renal or ureteral trauma. The 17 boys and eight girls were 3–19 years old (mean age, 11 years). The mode of injury included motor-vehicle accidents in 22 cases (pedestrian, $n = 17$; passenger, $n = 5$) and falls in three cases.

The types of injuries, patterns of fluid collections, and need for surgical treatment are shown in Table 1. The left kidney was injured three times more often than the right kidney (left, $n = 17$; right, $n = 6$). In those children with parenchymal injuries, the upper and lower poles were injured with nearly equal frequencies. Both ureteral injuries were on the left side.

Retroperitoneal fluid collections were seen in none of the six patients with contusions but in all of the remaining 17 patients with renal parenchymal or arterial injuries (Figs. 1

and 2). All 17 patients had perirenal fluid collections. In all cases the attenuation values of the perirenal fluid were lower than those of enhanced renal parenchyma. In the patients who required surgical exploration, these collections represented an admixture of blood and urine. Ten of the 17 patients also had unenhanced periureteral fluid collections; six of the 17 had fluid in the interfascial space; two patients had anterior pararenal space fluid collections (Fig. 3) and three patients had fluid collections within the psoas compartment (Fig. 4). With one exception, fluid collections in the interfascial space, anterior pararenal space, and psoas muscle indicated the presence of renal fracture, shattered kidney, or vascular injury.

The remaining two patients with fluid collections had ureteropelvic disruptions, one complete and one incomplete, and their fluid collections contained extravasated contrast medium. Both of these patients had perirenal, periureteral, interfascial, and anterior pararenal fluid collections (Fig. 5). In the patient with complete ureteral disruption, the ipsilateral ureter did not opacify, nor did it appear as a filling defect within the extravasated contrast medium. In the patient with incomplete disruption, contrast medium was visible in the distal ureter.

Extrarenal injuries were present in nine patients. One patient with a contusion had a splenic hematoma. Five patients

TABLE 1: Renal Injury vs Fluid Collection in Renal or Ureteral Trauma

Type of Injuries (No.)	Perirenal Fluid	Periureteral Fluid	Interfascial Fluid	Anterior Pararenal Fluid	Psoas Muscle	Surgical Management
Contusion (6)	0	0	0	0	0	0
Lacerations (10)						
Incomplete	3	0	0	0	0	2
Complete	7	5	1	0	0	0
Fracture (4)	4	3	3	1	0	2
Shattered kidney (1)	1	1	0	0	1	1
Arterial (2)	2	1	2	1	2	1
Ureteral (2)	2	2	2	2	0	2
Total	19	12	8	4	3	8



Fig. 1.—Contusion. CT scan shows persistent segmental obstructive nephrogram (arrows) in midportion of kidney due to contusion. There was no extrarenal fluid collection.



A



B

Fig. 2.—Complete parenchymal laceration. A, CT shows laceration of posterior half of midpole of right kidney with extension to renal sinus. Small fluid collection is present in perirenal space (arrows). B, More inferiorly. Fluid tracking is seen along course of ureter (arrows).

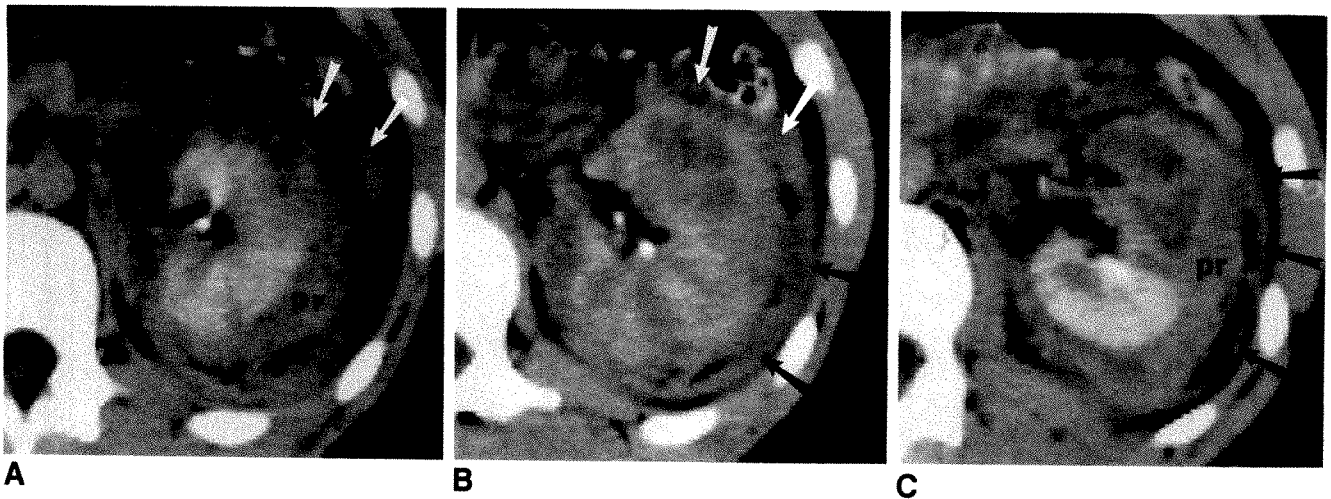


Fig. 3.—Renal fracture.

A, Contrast-enhanced CT scan shows functioning parenchyma in upper pole of left kidney with moderate perirenal hematoma/urinoma.
B, Scan 3 cm lower shows poor enhancement and compression of calices in midpole of kidney, representing hematoma and segmental vascular injury at site of fracture.

C, 2 cm lower, there is parenchymal enhancement of posterior portion of lower pole. Fluid is present in perirenal, interfascial (black arrows), and anterior pararenal spaces.

Anterior pararenal space (white arrows). pr = perirenal space.

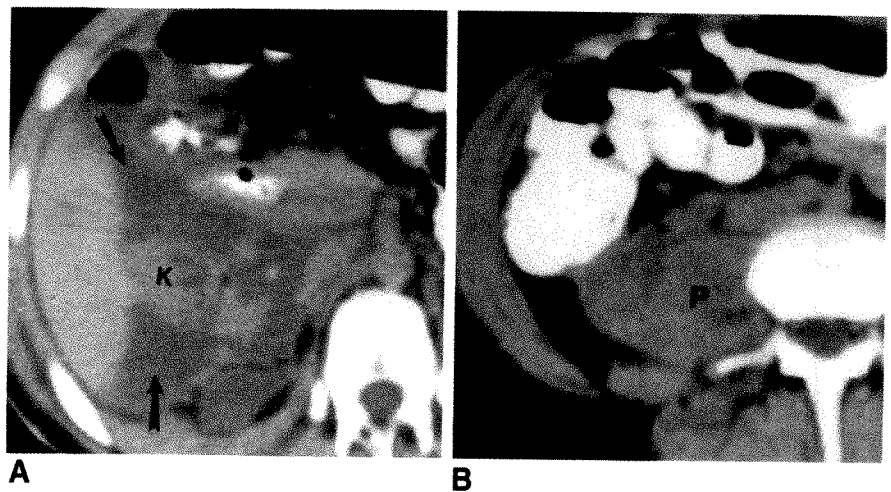


Fig. 4.—Shattered kidney.

A, CT shows unenhanced shattered right kidney (K). Fluid is present in perirenal space (arrows).

B, Lower level. Fluid extends inferiorly into psoas muscle (P), which is enlarged. Diagnosis of shattered kidney was proved at operation; nephrectomy was performed.

with lacerations and/or fractures (grade 2 or 3) had a single concomitant extrarenal injury (two splenic, two hepatic, and one duodenal laceration). Two patients with vascular injuries had splenic lacerations, and one patient with a shattered kidney had a colonic perforation.

Segmental renal infarcts were an associated finding in three of the four patients with renal fractures. On CT, renal infarcts appeared as well-margined, wedge-shaped areas of non-enhancing parenchyma that were surrounded by thin, enhancing cortical rims (Fig. 6). All of these lesions evolved into deep cortical scars on follow-up CT scans obtained 3 months after the initial injury.

Eight of the 25 patients required surgical exploration; no patient with a contusion had surgery. Two patients with incomplete renal lacerations underwent exploration for repair of coexisting congenital ureteropelvic junction obstructions; two other patients with fractures had surgery because of

pancreatic or duodenal lacerations. One patient with an arterial injury and one with a shattered kidney underwent nephrectomy. The other patient with a vascular pedicle injury was treated conservatively because a time delay was thought to nullify the benefits of surgery. Both patients with proximal ureteral injuries had surgical management; one required a ureteropyeloplasty and the other was treated with ureteral stenting. Six patients with complete lacerations or fractures had follow-up CT scans. All had cortical scars at the site of injury. Surgical intervention correlated best with the integrity of renal perfusion and the presence of underlying renal anomalies or associated intraperitoneal injuries.

Discussion

In a previous report, Karp et al. [3] reported small parenchymal injuries (contusions or incomplete lacerations) in ap-

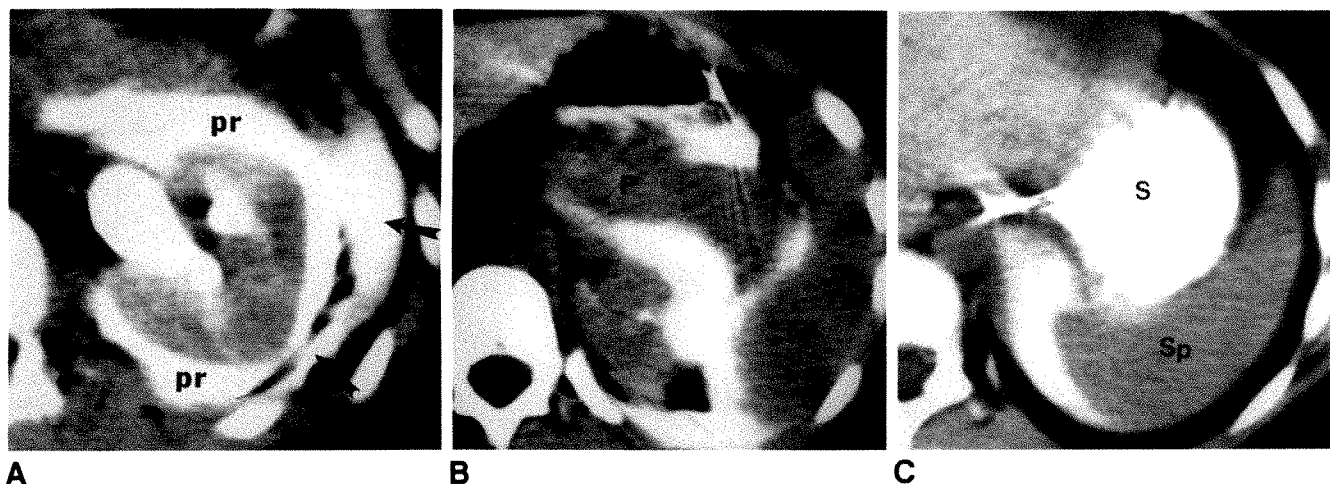


Fig. 5.—Ureteropelvic junction disruption.

A, Left kidney shows intact parenchyma and excretion. Extravasated contrast medium is present in left perirenal (pr) and interfascial (arrows) spaces. **B** and **C**, Higher CT sections through upper pole of left kidney and upper abdomen, respectively, show extravasated contrast medium behind pancreas (P) and in bare area of spleen (Sp), representing fluid in anterior pararenal space. At operation, avulsed ureter was reanastomosed to renal pelvis. S = stomach.

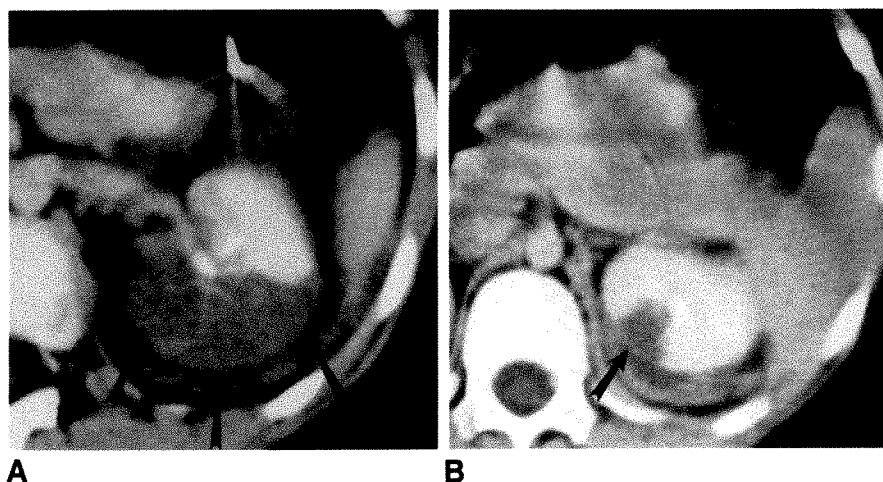


Fig. 6.—Renal infarct.

A, Dynamic CT shows poor enhancement of posterior half of midpole of left kidney, representing absent segmental perfusion to dorsal artery distribution. Also noted is small perirenal fluid collection (arrows).

B, Several centimeters higher. Cephalic extension of nonperfused dorsal vascular territory is seen. Thin, enhancing cortical rim (arrow) reflects perfusion by intact capsular arteries. Appearance is characteristic of segmental infarct. Follow-up CT showed cortical scarring.

proximately 60%, complete lacerations or fractures in 20%, shattered kidney in 14%, and renovascular injuries in 5% of pediatric patients with renal trauma assessed by CT scanning. In our experience, contusions or incomplete lacerations accounted for 39%, complete lacerations and fractures for 47%, shattered kidney for 4%, and arterial injury for 9% of the renal injuries. The reason for difference in the type of injuries is unknown, but possible explanations include differences in patient ages, mechanisms of injuries, or referral patterns. In our series, left renal injuries accounted for three of every four cases of renal trauma. The reason for this predominance is not clear but may be attributed to the fact that the left kidney is less well cushioned by solid perirenal organs (i.e., the liver on the right) and is more easily thrust against the ribs laterally.

An unusual parenchymal injury in our series was the segmental renal infarct present in three patients. Segmental renal infarcts from occlusion of polar arterial branches have been

reported rarely in children. Sandler and Toombs [5] reported a segmental infarct in a 15-year-old patient. Lang et al. [4] reported seven segmental infarcts in 388 patients (296 adults, 92 children) with renal trauma. However, it is unknown if any of these patients were children. Although the diagnosis of a renal infarct does not alter treatment, its presence suggests impaired viability of the affected cortical segment and the possibility of subsequent scar formation.

The most impressive finding in our series was the distribution of the extrarenal fluid collections in patients with ureteral and renal injuries. Kenney et al. [8] reported that the CT findings of ureteropelvic disruption in adults are an intact renal parenchyma, no perirenal hematoma, no opacification of the ipsilateral ureter distal to the disruption, and contrast medium extravasation confined almost exclusively to the medial perirenal space. These authors explained the restricted localization of contrast medium extravasation on the basis of the

separation of the Gerota fascia into a deep and a superficial layer. They suggested that the deep layer of Gerota fascia, which normally surrounds the proximal ureter at the renal hilus, limits the spread of extravasated contrast medium. As both of our cases demonstrate, extravasated contrast medium may not be confined to the medial perirenal space, but may fill the perirenal, periureteral, and anterior pararenal spaces. One possible explanation for the discrepancy is that the trauma in our patients may have been more severe, disrupting the deeper strata of Gerota fascia, and thereby allowing contrast medium to extend further into the perirenal space. Another possibility is that the integrity or thickness of the deeper stratum of Gerota fascia differs in children and adults, or perhaps such medial fascial anatomy is an inconstant finding. Further studies are needed to clarify this issue.

Most previous studies have noted the presence of perirenal fluid in patients with renal injuries, but have not reported accumulations of fluid in other locations. In our experience, collections of blood or urine always involve, but are not limited to, the perirenal space. Extension occurs to four sites: along the ureter, within the interfascial space or interconal fascia, into the anterior pararenal space, and into the psoas compartment. The most common pathway by which fluid escapes from the perirenal space is along the ureter, which normally exits the perirenal fat to accompany the aorta or inferior vena cava. Fluid may use this pathway to enter the pelvis. The extension of fluid into the anterior pararenal space may be explained by the laminar nature of the posterior renal fascia, recently described by Raptopoulos et al. [9]. The posterior renal fascia is divided into two laminae; the anterior lamina continues as the anterior renal fascia, whereas the posterior lamina continues as the lateroconal fascia [7, 9]. Presumably, in trauma, the posterior fascia ruptures and fluid enters the potential space between the laminae. This interfascial space is a posterior continuation of the anterior pararenal space. In turn, such fluid may be seen around the descending colon, posterior to the pancreas, and within the bare area of the

spleen. Finally, perirenal fluid may enter the psoas compartment. In some patients the posterior pararenal fascia caudal to the renal hilus does not extend to the psoas muscle but fuses with the fascia lateral to the psoas muscle, so that a direct communication exists between the medial part of the perirenal space and the psoas compartment [10].

In our patients, extrarenal fluid collections occurred in association with renal lacerations, fractures, shattered kidney, and pedicle injuries, but not with contusions. The presence of larger amounts of retroperitoneal fluid (i.e., fluid in the interfascial or anterior pararenal space or psoas muscle) appeared to be associated with more severe injuries. However, it needs to be stressed that the absence of retroperitoneal fluid does not exclude significant renal trauma. Although uncommon, extrarenal fluid collections may be absent in renal arterial injury [4].

REFERENCES

1. Berger P. CT of blunt abdominal trauma in childhood. *AJR* 1981;136:105-110
2. Federle MP, Kaiser JA, McAninch JW, Jeffrey RB, Mall JC. The role of computed tomography in renal trauma. *Radiology* 1981;141:455-460
3. Karp MP, Jewett TC Jr, Kuhn JP, Allen JE, Dokler ML, Cooney DR. The impact of computed tomography scanning on the child with renal trauma. *J Pediatr Surg* 1986;21:617-623
4. Lang EK, Sullivan J, Frentz G. Renal trauma: radiological studies. *Radiology* 1985;154:1-6
5. Sandler CM, Toombs BD. Computed tomographic evaluation of blunt renal injuries. *Radiology* 1981;141:461-466
6. Yale-Loehr AJ, Kramer SS, Quinlan DM, La France ND, Mitchell SE, Gearhart JP. CT of severe renal trauma in children: evaluation and course of healing with conservative therapy. *AJR* 1989;152:109-113
7. Dodd WJ, Darweesh RMA, Lawson TL, et al. The retroperitoneal spaces revisited. *AJR* 1986;147:1155-1161
8. Kenney PJ, Panicek DM, Witanowski LS. Computed tomography of ureteral disruption. *J Comput Assist Tomogr* 1987;11:480-484
9. Raptopoulos V, Kleinman PK, Marks S Jr, Snyder M, Silverman PM. Renal fascial pathways: posterior extension of pancreatic effusions within the anterior pararenal space. *Radiology* 1986;158:367-374
10. Feldberg MAM, Koehler PR, van Waes PFGM. Psoas compartment disease studied by computed tomography. *Radiology* 1983;148:505-512



The Radiology Outreach Foundation (ROF) is a nonprofit corporation whose goal is to help disadvantaged countries improve their health care by providing radiology equipment, books, consultation, education, and training to their practitioners. This assistance is on an application basis that is independent of political, ethnic, or religious orientation of the grantee. It depends on the need of the people and the ability of the ROF to meet that need. The ROF is approved by the U.S. Internal Revenue Service as a tax-exempt organization. It is endorsed by the following radiologic societies:

American Association of Women Radiologists
American College of Radiology
American Roentgen Ray Society
Association of University Radiologists
Radiological Society of North America
Society of Chairmen of Academic Radiology Departments
Society for Pediatric Radiology
European Society of Pediatric Radiology

All donations to the ROF are tax deductible. Persons who would like to contribute financially to the ROF, would be interested in being a visiting professor, would like to send books or journals to any of the institutions supported by the ROF, or would like further information about the ROF should write to

Charles A. Gooding, M.D.
President
Radiology Outreach Foundation
3415 Sacramento St.
San Francisco, CA 94118 USA

Closed Spinal Dysraphism: Analysis of Clinical, Radiological, and Surgical Findings in 104 Consecutive Patients

James H. Scatliff¹
 Brian E. Kendall²
 Derek P. E. Kingsley²
 Juliet Britton³
 D. Norman Grant⁴
 Richard D. Hayward⁴

We reviewed 104 consecutive cases of closed dysraphism in patients seen at one institution between December 1984 and June 1987. All patients had myelographic studies, and 43 had associated CT examinations. Clinical and surgical findings (64 patients) were correlated with myelographic information. Twenty-three patients (22%) with clinical or plain film findings compatible with dysraphism had normal-appearing cords on conventional myelography, movement between supine and prone positions, and no lesions in the spinal canal. Cerebellar tonsillar ectopia (majority of tonsils between foramen magnum and C1) was found in 17 patients (16%). Six patients (6%) exhibited varying degrees of hydromyelia. In the supine position, CT-myelography of meningoceles, meningomyeloceles, or lipomeningomyeloceles may limit demonstration of the neural placode and nerve roots because of compression of the CSF-containing sac. In the decubitus position, CT scans improved demonstration of neural tissue-CSF space relationships. CT scans were useful in demonstrating anomalous paraspinal bones, diastematomyelia spurs, and spinal and sacral bone deficiency. Axial CT-myelography of intradural lipomas showed apparent neural tissue extension into the lipomas.

We reviewed 104 cases of suspected or proved spinal dysraphism seen at the Hospital for Sick Children, Great Ormond Street, London, from December 1984 through June 1987. Surgical and pathologic data were correlated with clinical and diagnostic imaging findings. Although a considerable number of radiologic reports describing various expressions of spina bifida occulta have appeared in the last 20 years, the assessment of a large number of cases from one hospital is somewhat unique [1-5]. There were 39 postoperative myelograms in 32 patients. (The findings in these studies and their evaluation will be presented in another article.)

This article appears in the March/April 1989 issue of *AJNR* and the May 1989 issue of *AJR*.

Received February 3, 1988; accepted after revision September 12, 1988.

This work was supported in part by the William R. Kenan, Jr., Charitable Trust, Kenan Center, University of North Carolina.

¹ Department of Radiology, University of North Carolina School of Medicine, Chapel Hill, NC 27599. Address reprint requests to J. H. Scatliff.

² Lysholm Radiological Department, The National Hospital, Queen Square, WC1N 3BG, London, UK.

³ Department of Radiology, Atkinson Morley's Hospital, Wimbledon, London, SW20 0NE, UK.

⁴ Department of Neurosurgery, Hospital for Sick Children, Great Ormond St., London WC1N 3JH, UK.

AJR 152:1049-1057, May 1989
 0361-803X/89/1525-1049
 © American Roentgen Ray Society

Materials and Methods

In most cases, imaging studies were performed while the patients were under general anesthesia. Only five patients over the age of 10 were given a local lumbar anesthetic. Plain films were made before or at the beginning of the myelographic procedure. Lumbar punctures with a 22-gauge needle were done off the midline to avoid a low cord or suspected intraspinal component of a lipoma. Iohexol,* 240 mg/l ml, was injected in volumes of 5-15 ml. The great majority of injections were initially subarachnoid, although several mixed (subarachnoid-subdural) injections were made. There was one inadvertent injection into a lumbodorsal hydromyelia. Posteroanterior and lateral films made at right angles during the myelogram showed the needle to be within 2 or 3 mm of the cord or hemicord in most of the studies. In several patients the needle appeared to penetrate or distort the cord. In no study was there evidence of hematomyelia, and there was never any subsequent increase in neurologic findings.

After prone filming and withdrawal of the needle, supine anteroposterior and horizontal-beam lateral films were made in the lumbar region to assess cord movement. In the supine position it was assumed that the cord was not tethered when it floated anteriorly 5 mm or more in the contrast material. Supine filming produced more complete filling of the caudal

* Nyegaard, Oslo, Norway.

sac. Contrast material was advanced to the dorsal region by turning the patient into a decubitus position and then into a supine position. Anteroposterior and lateral films were made of the thoracic and cervical spine areas, the latter to look for tonsillar ectopia.

Conventional tomograms were made in conjunction with some myelograms; however, the majority of CT studies were made with a Toshiba TCT60A CT unit immediately after the myelogram and with maintenance of anesthesia. Delayed scans were done at 5- and 24-hr intervals in patients in whom hydromyelia was suspected. The value of preoperative CT coupled with myelography has been stressed [6-8]. No MR studies were done. Sonography was used in three infants as a screening procedure prior to myelography.

Results

Table 1 shows the types and prevalence of dysraphic pathology observed in the radiographic studies, as well as the frequency of cerebellar tonsillar ectopia and observed hydromyelia. Assignment of the dysraphism to a particular category was made to emphasize the predominant lesion observed in each group. Low cords were found in the majority of abnormal cases, but the associated pathology of tethered cords, lipomas, lipomyelomeningoceles, meningomyeloceles, meningoceles, and dermoids serves as the basis for classification. In two cases focal thinning of the cord was the only abnormality. Although atypical for dysraphic pathology, these patients presented with clinical signs of dysraphism and were therefore placed in the survey. The films of five patients were unavailable for review, and information on these patients was taken from formal reports. Surgical reports were available in 64 patients: 48 had surgery during the review period and 16 before the review period. Clinical notes were not available in four of the surgery cases, and surgery was pending for four other patients.

Normal Myelogram

Five patients had skin dimples or pits in the intergluteal area; one was cervical. Two patients had lumbar nevi or hemangioma; two had displayed abnormal tufts of hair on the

lower back; and two had probable midline lipomas. Plain films showed minimal congenital bone abnormality in five patients and marked bone change in three. One patient had a neuro-pathic bladder with reflux, and one had bowel incontinence. Three patients had disparate leg lengths, and three others had talipes equinovarus in one or both feet. The majority of patients had only one of these findings; however, four patients had two of them.

Twenty-three patients suspected of dysraphism exhibited normal movement of the conus between prone and supine positions. In all except two of the myelograms the conus was between T12 and L3. Barson [9] states that the normal conus medullaris is found between T12 and the L2/L3 interspace at birth. In the two exceptions, the conus was at the L3/L4 interspace; there were cutaneous stigmata of dysraphism, but there was no evidence of cord tethering.

Of interest was moderate widening of the spinal canal and theca in two patients; normal untethered conus were found at T12 and L2, respectively. Both these patients had skin findings seen in dysraphism. It has been suggested [10] that spinal cord pathology is less likely when dysraphic skin lesions are not associated with bone defects. This was true in the present series although, conversely, three cases exhibited prominent bone anomalies without evidence of cord pathology.

One patient had rapid onset of limping after upper respiratory infection; however, the child's gait returned to normal, and in all likelihood there had been a transient viral myelitis. The child's lumbar nevus had prompted myelography. Another child presented with microcephaly, tip-toe walking, and incontinence. Spina bifida at L5 raised the question of more extensive dysraphic pathology, but none was found.

With the exception of one child with bilateral club feet, it was the various stigmata of dysraphism (i.e., skin lesion, feet and legs of unequal size, and congenital bone anomalies) that prompted myelography. The normal or nearly normal position and appearances of the cord, even in the presence of congenital bone anomalies, emphasize that the cord may be normal in myelographic outline and movement in nearly one-fifth of patients examined for suspected dysraphism.

TABLE 1: Diagnostic Studies for Spinal Dysraphism Between December 1984-June 1987 (n = 104)

Finding	Initial Myelograms	Preoperative Myelograms-CT	Postoperative Myelograms	Postoperative Myelograms-CT	Tonsillar Ectopia	Hydromyelia
Normal	23	1				
Tethered cord	14	3	4	3	1	1
Lipoma	10	8	7	2		3
Lipomyelomeningocele	16	10	6	2	6	
Meningomyelocele	7	3	4	1	6	2
Meningocele	3	2	2		1	
Atretic meningocele	2	2			1	
Diastematomyelia:						
Bone spur	18	10	11	1		
Fibrous spur	2	1	1	2	1	
No spur	5	1	3	1		
Dermoid	1					
Dermal sinus	1	1	1		1	
Local atrophy	2	1				
Total	104	43	39	12	17	6

In all probability, specific neuropathologic changes in the cord were not seen. Only one myelographic-CT study was done in this group. It is possible that some cord clefts or other focal changes were not defined by conventional myelography. It is also uncertain that the demonstration of cord movement between supine and prone positions excludes myelodysplasia. Of interest is the finding in two patients included in the series that local atrophy, or hypoplasia, of the cord found on myelography was responsible for lower extremity changes. One patient had disparity of leg lengths from birth, and the other patient had an inverted foot.

Tethered Cord

Fourteen patients had tethered cord. Eight of these had lumbar skin abnormalities characteristic of dysraphia, and six had foot or leg inequality and/or deformity. There were no club feet. Bilateral hydronephrosis was seen in one patient with a conus in the upper sacrum. A neuropathic bladder with bilateral reflux was noted in a patient with sacral dysgenesis.

Twelve of these patients exhibited an abnormally low conal position; nine had varying degrees of filum thickening. The transverse diameter of the filum at L5 ranged from 1.5 to 4.0 mm. In three of these the cord continued without narrowing

down to the point of tethering. Hydromyelia was seen in a postoperative myelogram in one of three patients in whom CT was done. A tethered cord was found in another patient with an occipital encephalocele and lacunar skull. Tonsillar ectopia to C1 was present in a patient whose cord extended to S1 (Fig. 1). Asymmetric hemicords close together were noted only by CT in a patient with typical myelographic findings for a tethered cord (Fig. 2).

All the patients showed decreased movement of the cord as myelographic position changed from prone to supine. This was also true in the two patients whose conus was at a normal level. In one of these patients a thickened filum continued from the conus. In the other the conus was tethered posteriorly by a band evident in the myelogram. The tethering lesions seen at myelography and on CT in all the patients in this category were small lipomas, meningoceles, or fibrous bands.

Lipoma

Ten children had evident or palpable lipomas. Eight of these had urinary or fecal incontinence and six had disparity in leg length as well as foot deformities.

Eight patients had preoperative myelograms, which

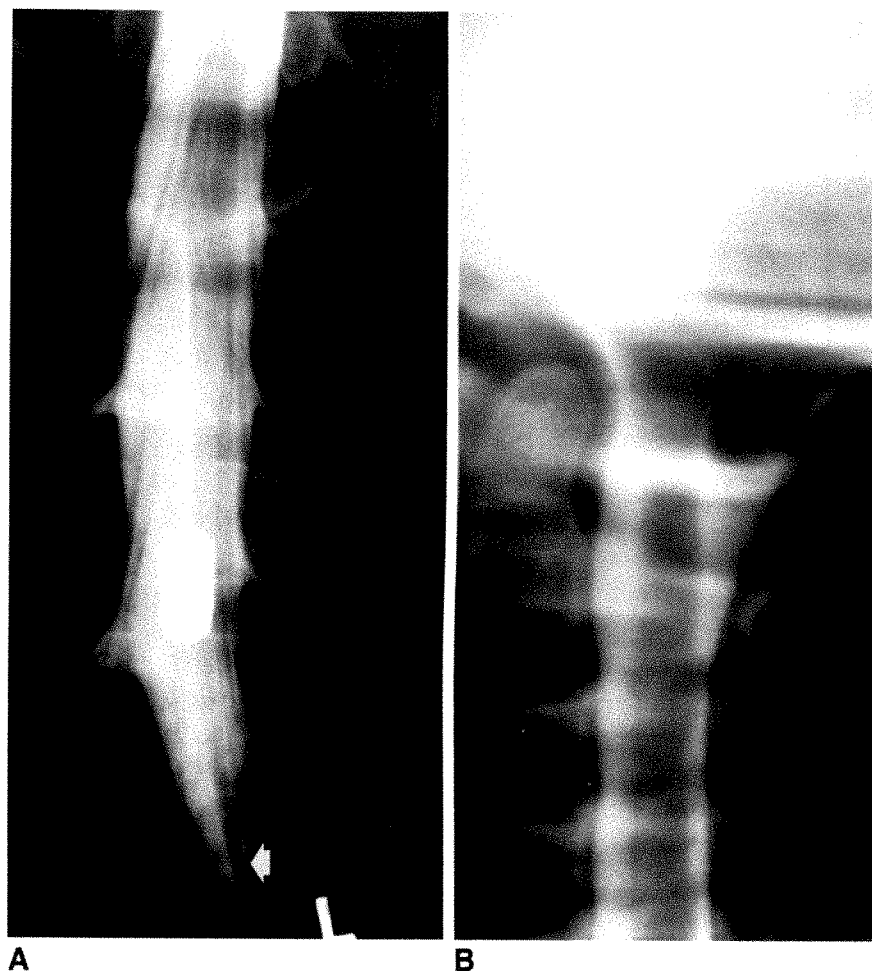


Fig. 1.—9-year-old girl with wasted and weak right leg.

A, Conus extends to L5. Filum is thickened and tethered (arrow).

B, Supine lateral cervical myelogram shows cerebellar tonsillar ectopia to C1.

showed significant intradural lipomas intimately involving the conus and/or nerve roots. The lipomas were in either the lumbar or sacral canal and extended to the subcutaneous tissues of the back. In all these patients the spinal cord was abnormally low, and two of these eight had hydromyelia (Fig. 3). Two of the 10 patients had had surgery in infancy for their lesions, and they were examined for new or continuing symptoms. One of these was found to have a lumbodorsal hydromyelia and the other a neuroenteric cyst adjacent to the upper lumbar cord.

In three patients the spinal cord was displaced anteriorly by the lipoma; in another three the cord was in a central position in the spinal canal as it fused with the lipoma, and in two patients the cord was displaced posteriorly. The initial preoperative studies in two patients were not available. Transverse CT sections in three patients with lipomas are shown in Figure 4. The patient in Figure 4A appeared to have a well-defined interface between the neural placode and lipoma. However, the neurosurgeon found the lipoma contained considerable disorganized tissue, including fibrous elements,

which made the placode difficult to identify. The lipoma was also attached by thick bands of fat and fascia to the walls of the spinal canal, and its dissection was difficult.

The CT sections of patients shown in Figures 4B and 4C had well-defined strands of tissue that could be followed from the cord into the lipoma. At surgery, neural tissue was found in the tumors. Direct correlation of this observation with the CT scans of the lipomas could not be made. In three other patients CT showed relatively homogeneous fat density in the lipomas. The surgical dissection in these patients was difficult, however, because of nerve roots at the margins of the lipomas. These could not be identified in retrospect in the CT studies.

Lipomyelomeningocele

Sixteen patients exhibited varying degrees of lipomatous material closely associated with myelomeningoceles. One patient had previous surgery. All the patients had palpable lumbar or sacral masses, some quite large. Seven patients

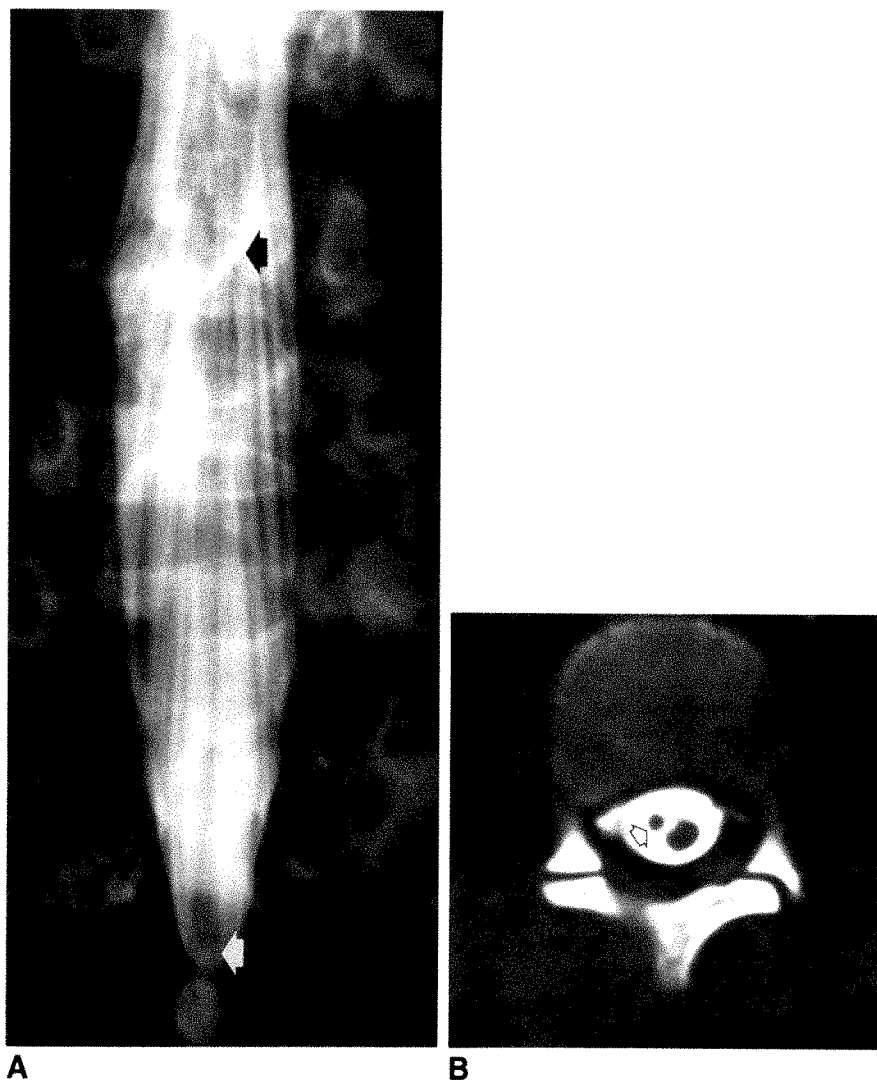


Fig. 2.—8-year-old boy with pain in both lower limbs, urinary frequency, and fecal incontinence. A, Conus is at L3 (black arrow). White arrow shows filum tethered by small meningocele. B, CT at level of conus shows hemicords not seen on conventional myelogram. The small right hemicord (arrow) could be correlated with child's inability to hop or stand on the right foot.

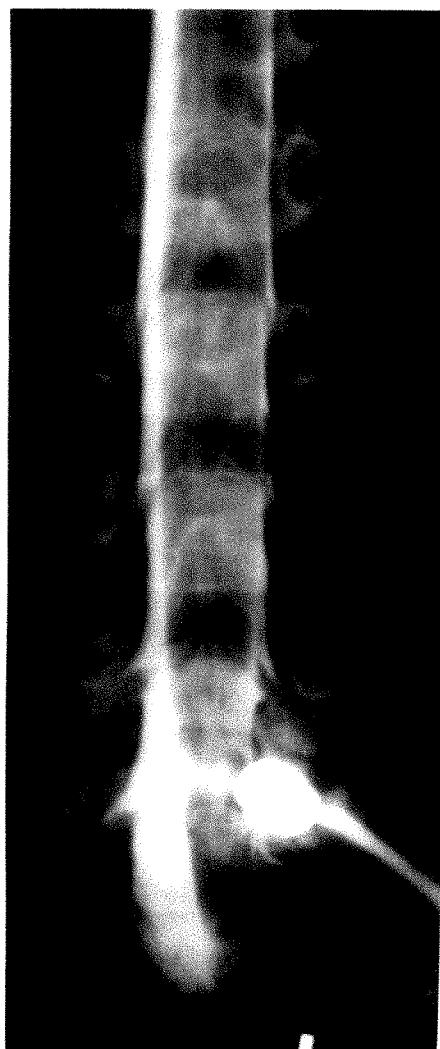


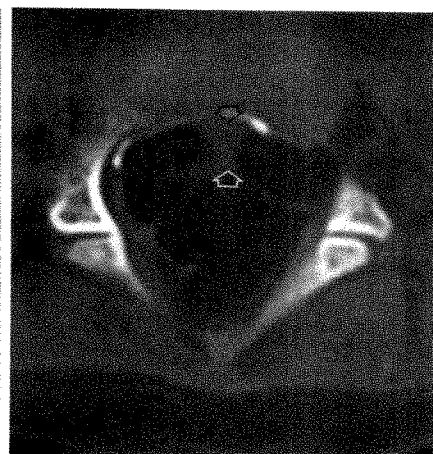
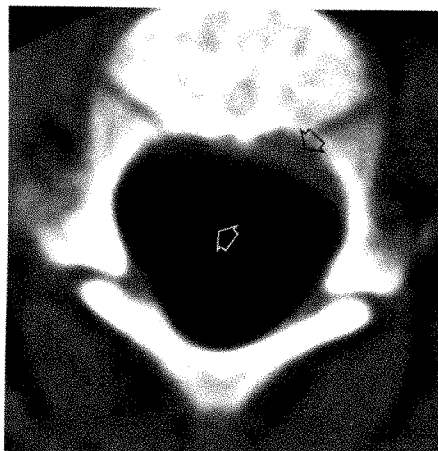
Fig. 3.—4-year-old boy with right leg weakness and double incontinence.
 A, Cord is enlarged and extends to S2.
 B, Hydromyelia (arrow) is noted in a 5-hr delayed scan.
 C, Tethering lipoma expands sacral canal.



A

B

C



A

B

C

Fig. 4.—Intracanalicular lipomas in three patients.
 A, Placode and lipoma interface (arrow) is well defined without change in lipoma to suggest presence of neural tissue. Resection of lipoma was difficult because of fibrous attachments to walls of spinal canal.
 B, Well-margined shadow (white arrow) in lipoma suggests neural tissue associated with placode (black arrow).
 C, Branching bands of probable neural tissue in lipoma (white arrow); placode is at most anterior aspect of spinal canal (black arrow).

had foot or leg abnormalities, including two with unilateral club feet and three with feet and legs of different size and length. Five patients had either urinary incontinence, infection, or reflux. Two patients with urinary tract signs were less than 6 months old. One 8-year-old had fecal incontinence.

The radiologic studies alerted the surgeon that the conus was abnormal in position and involved with the lipoma and the myelomeningocele in all the preoperative patients. In seven of 10 preoperative CT studies the specific relationship between the placode, lipoma, and meningomyelocele could be resolved satisfactorily. The placode–myelomeningocele interface was better defined in one patient as a result of lateral decubitus CT scanning (Fig. 5).

Nerves in the neural sac were seen on four conventional myelograms. CT demonstrated nerve roots in the neural sac in only one patient. Compression of the myelomeningocele in the supine position prevented nerve root visualization in the remaining CT examinations. Nerve roots in the neural canal and their associated placode were seen in CT scans of three patients. The failure to define this relationship with greater frequency was attributed to the complexity of the lesion and incorrect CT windowing.

Preoperative assessment of bone abnormalities associated with the lesion was important. In one patient (Fig. 6) an anomalous bone surrounded by lipoma and not recognized on CT made resection of the lipoma and access to the spinal canal more difficult. In another patient (Fig. 7) hemisacral deficiency was seen on CT with presumed absence of sacral nerve roots. Because of this observation only cosmetic reduction of the large lipoma was planned. Of interest was the prevalence of tonsillar ectopia. Although minimal in three patients, the tonsils were between C1 and C2 in another three.

Meningomyelocele, Meningocele, and Atritic Meningocele

Of the 12 patients in this group, nine presented with palpable masses over the spine. In another patient an anterolateral meningomyelocele was mistaken for a cystic kidney in infancy (1977) and explored without prior myelography or CT.

Two patients were studied postoperatively and a small remaining meningocele was seen in one. Two patients thought clinically to have cervical dermoids with associated sinuses were shown after histologic examination to have atretic meningoceles. Four patients displayed foot abnormalities, and another had urinary incontinence.

The placode and nerve roots were seen well with CT in four patients. In two of these, CT confirmed the presence of nerve roots that were faintly seen on myelograms. CT nicely outlined the complex relationship between a diastematomyelia bone spur and a meningomyelocele with its subcutaneous placode (Fig. 8). In another infant, CT brought out a centrally placed placode subtending two winglike extensions of the meningomyelocele (Fig. 9). Eight of the 13 patients had tonsillar ectopia. The majority of tonsils were between C1 and just below the foramen magnum. However, in one patient with a mid-thoracic meningomyelocele, a Chiari malformation extended to the C5 level.

Diastematomyelia

Twenty-three of the 25 patients in this group had lower extremity signs including disparity of foot size, leg length, and girth. The smaller extremity was associated with the smaller hemicord in these patients. Of the two patients with normal extremities, one was 5 months old and the other was 10 years old. Two infants developed leg abnormalities in early childhood. One child had bilateral clubfeet. Unilateral clubfoot was noted in two patients. One patient had leg wasting and an ipsilateral dislocated hip. One patient had symmetric leg wasting.

Eight of 25 patients had hairy patches at the level of the bony or fibrous spurs. Two patients had meningomyeloceles, which were partially resected at birth, and one extended from T12 to L4. Postoperative adhesions in this case produced prominent arachnoid cysts in the thoracic spinal canal. No urinary or bowel abnormalities were noted in this patient group.

Preoperative CT was performed in 12 patients. Separate dural sheaths around each hemicord could be seen in six



Fig. 5.—8-month-old boy with right buttock mass.

A, Supine CT examination shows outline of a large lipoma extending into sacrum. Myelomeningocele is collapsed (arrow) and associated neural tissue is uncertain.

B, Right lateral decubitus CT scan shows filled out myelomeningocele; neural extension (arrow) into lipoma is better defined.

Fig. 6.—1½-year-old boy with lumbosacral lipoma and right club foot. There was partial previous resection of the lipoma. CT scan shows placode (white arrow) between myelomeningocele and lipoma. Black arrow shows anomalous bone and adjacent lipoma. Resection of lipoma was difficult because of attachment to anomalous bone.

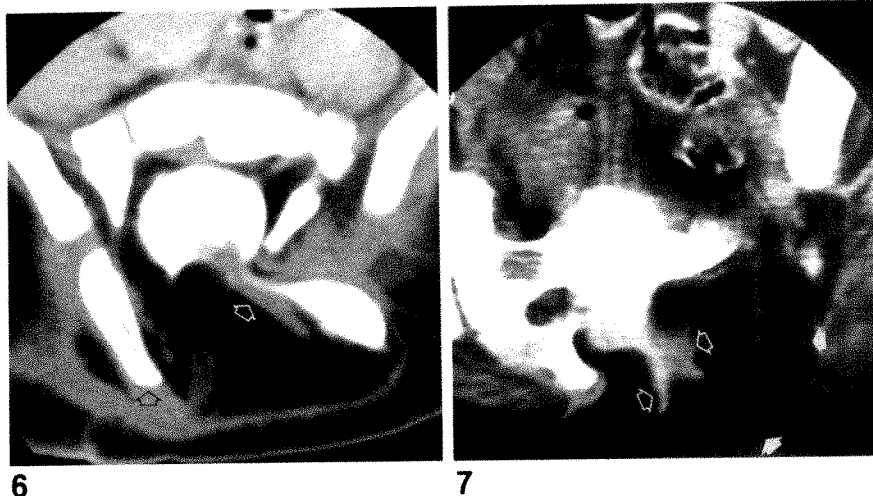


Fig. 7.—8-year-old girl with lumbar lipoma and small deformed feet bilaterally. Lipoma is in left hemisacral region where bone is absent. Lipomatous mass extends to left buttock (solid arrows). Neural tissue in placode (upper open arrow) could be followed into lipoma. Thecal sac is adjacent to placode (lower open arrow).

Fig. 8.—2-year-old boy with lumbosacral hemimyelomeningocele and bone spur. Left leg is shorter and thinner than right leg.

A, Prominent nerve root (upper arrow) spans myelomeningocele and joins placode (lower arrow).

B, Bone spur and adjacent neural tissue (arrow) is seen in next more rostral scan.

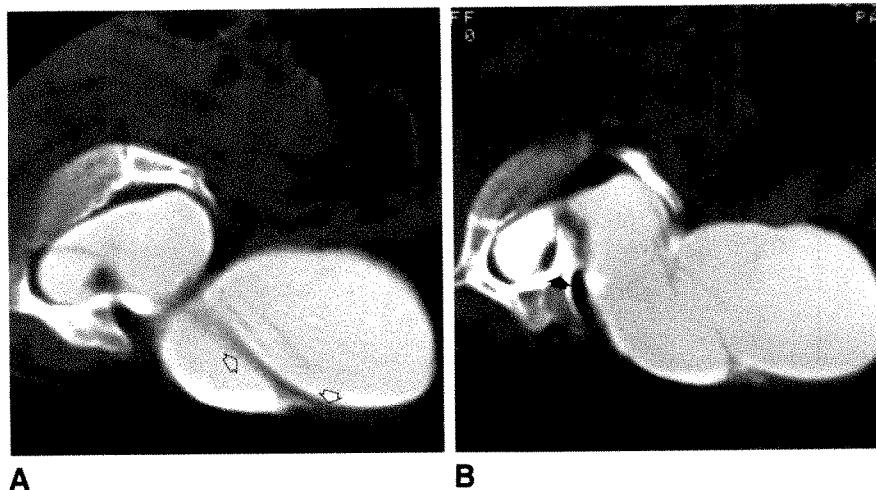
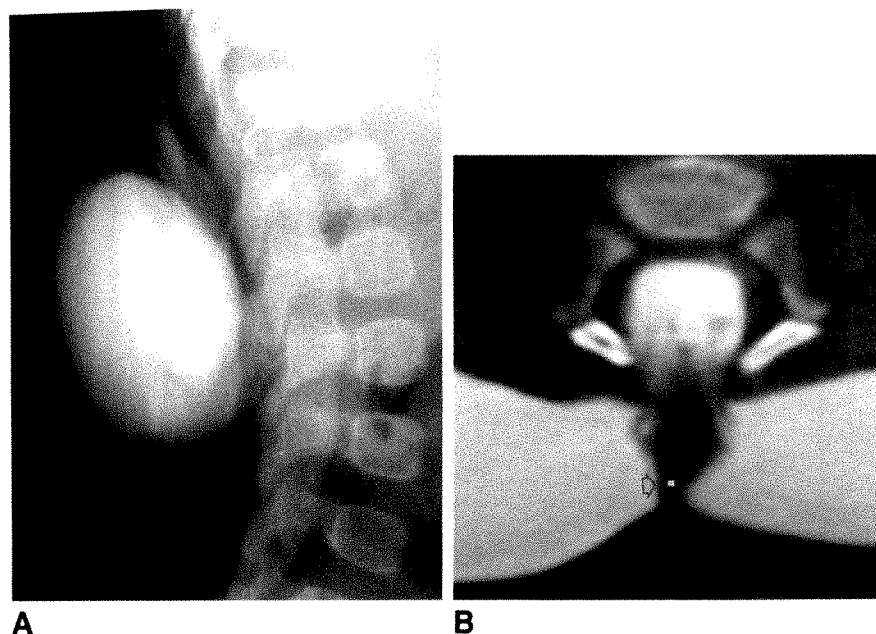


Fig. 9.—6-month-old girl with compressible mass in lumbar region.

A, Myelogram shows apparent myelomeningocele extending into subcutaneous tissue of back.

B, CT clearly brings out relationship between placode (arrow), myelomeningocele, and nerve roots. A cursor was placed at posterior aspect of placode.



patients. Complete or almost complete bone spurs were present in these patients. Four patients had hemicords enclosed in a single dural sheath; two of these had small incomplete spurs, and two had none. One patient had an unusual finding of renal blastema attached to an incomplete bone spur (Fig. 10). CT showed seven bone spurs arising from posterior elements; three came from the posterior vertebral body margin.

Dermoid

One infant had a dermoid with cystic change and hair in the conus. The lesion was brought to clinical attention because of the child's refusal to bear weight on one leg. A preoperative myelogram showed a mass expanding the conus obstructing cephalad flow of contrast material. The second patient presented with a discharging sinus tract connecting with the filum in the sacrum; these findings were confirmed at surgery.

Discussion

The radiology of spina bifida occulta has advanced remarkably over the last 25 years. Lesions in the spinal canal such as dermoids, lipomas, and bone spurs could be seen with Pantopaque (Myodil).[†] Visualization of cord or thecal abnormalities was limited, however [11]. Air-myelography in the 1970s was a step forward, affording better definition of cord outline and movement [12]. However, sufficient detail, especially for conal position, was frequently lacking.

The major breakthrough for more precise resolution of the pathology of closed dysraphism has been the use of nonionic water-soluble contrast material, as well as the advent of CT. Iohexol [13] was used in all the myelograms in this series and there has been no complication from its use other than postexamination headache and nausea, some of which could be attributed to general anesthesia.

CT was used preoperatively in one-half of the positive cases and probably would have added further information in the other half. But CT examination has to be carried out shortly after the conventional myelogram, before dilution of contrast material occurs, and this may not always be possible in a busy radiology department. CT studies also require careful monitoring to ensure cross-sectional imaging at appropriate levels of known pathology. Correct windowing and filter use is important to maximize the details of cord and nerve root relationships in thecal sacs to differentiate meningocele from meningoceles.

This is also true for lipomyelomeningoceles. The usual [14] asymmetric relationship of the lipoma, placode, and meningocele was seen in all the patients in this series. The placode in some lesions was difficult to define, and when seen appeared to be of irregular outline in both the adjacent lipoma and myelomeningocele.

The recognition by CT of neural tissue in lipomas and the lipomatous part of the lipomyelomeningocele in the reported cases was difficult. Although bandlike tissue in two lipomas (Figs. 4B and 4C) could be traced from the placode-lipoma interface, neurosurgical confirmation of this observation was not possible. The neurosurgical reports in several cases in this series indicated that nerve roots or fibrogliotic material were present in lipomatous tissue. This observation has been reported in surgical [15] and pathologic material [16].

Specific correlation of the tissues present in the lipoma could not be made in this series. This was attributed to fractional resection as well as to laser coagulation of the tumor mass. If definite patterns of fibrous and neural tissue can be established by CT or MR, considerable help would then be available for the surgeon in planning the debulking of the lipoma. This information would also be useful in assessing the possibility of untethering the cord and placing it in the spinal canal with only a limited remaining cuff of fatty material.

The surgery for lipomas, lipomyelomeningoceles, and meningocele is often formidable [14]. Myelography and CT can at present show the surgeon major structural points of the lesion and its relationship to the vertebra or sacrum.

[†] Lafayette Pharmacal, Inc., Lafayette, IN.

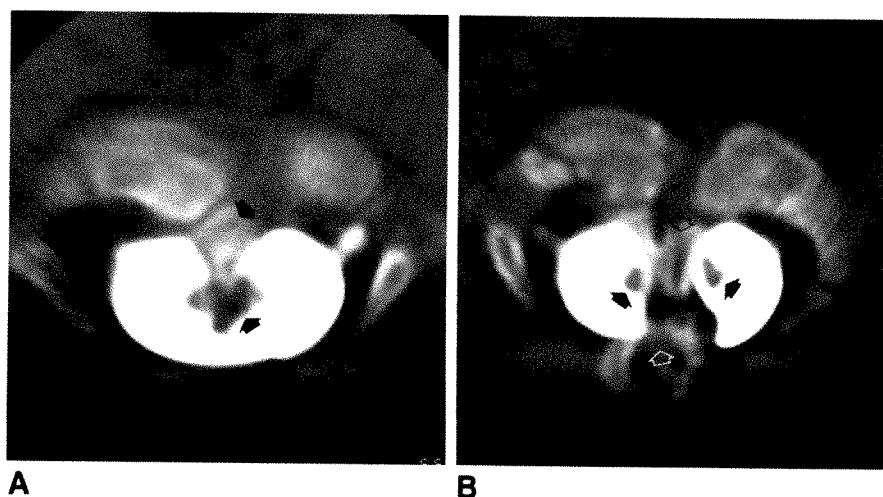


Fig. 10.—5-month-old girl with L5/S1 diastematomyelia. Patient had sacral dimple and no other abnormality.

A, Bone spur is denoted by upper arrow. Lower arrow shows soft tissue at tip of spur. The histologic report for the material was renal blastema and neural tissue.

B, Next rostral scan shows thin hemicords (solid arrows) enveloped by separate dural sheaths. Bone spur (black open arrow) and soft-tissue component of septum (white open arrow) are seen. Note cleft in first sacral segment.

The same is true for various expressions of diastematomyelia. Finer details—such as exact position and number of nerve roots in relation to the placode-lipoma, the presence of fibrous bands or arachnoidal adhesions, or prominent blood vessels—were discovered only at the time of surgery in this series.

An important point in our study is the visualization in plain films and CT of anomalous or deficient bone formation associated with dysraphic lesions. Naidich et al. [14] and others [17, 18] have emphasized recognition of posterior bone masses. Surgery can be facilitated with the foreknowledge that these may need removal for better access to the dysraphic pathology. Noting that a hemisacrum is largely absent and that sacral nerves are probably absent or abnormal may obviate surgery. CT-based 3D reconstruction of bone has now advanced to a level where the skeletal framework of dysraphic lesions can be shown to good advantage. The pathology of diastematomyelia can be shown very well by CT-myelography, as documented by Naidich and Harwood-Nash [5]. Abnormal bones and soft tissues depicted in 3D would be helpful in presurgical assessment. For informative display, however, the increased number of thin CT sections would be time-consuming and could have prohibitive radiation dosage.

The clinical findings in this survey have been enumerated not only to catalogue their prevalence but also to emphasize what dysraphism pathology means to patients, their parents, and their primary physicians. The imaging focus has been strongly directed toward revealing the pathology, with the surgeon operating in the belief that "untethering" the cord will arrest the progress of clinical signs. Unfortunately, this does not always occur. It is evident also from the study that nearly a quarter of patients with suspected dysraphism have a normal-appearing cord without restriction of movement.

ACKNOWLEDGMENT

We thank Patricia A. Dunlop for preparing the manuscript.

REFERENCES

1. James CCM, Lassman LP. *Spinal dysraphism*. London: Butterworth, 1972
2. Burrows FGO. Some aspects of occult spinal dysraphism: a study of 90 cases. *Br J Radiol* 1968;41:496-507
3. Hoffman JH, Taechalam C, Hendrick EB, Humphreys RP. Management of lipomyelomeningoceles. *J Neurosurg* 1985;62:1-9
4. Hilal SK, Marton D, Pollack E. Diastematomyelia in children. Radiographic study of 34 cases. *Radiology* 1974;112:609-621
5. Naidich TP, Harwood-Nash DC. Diastematomyelia hemicord and meningeal sheaths: single and double arachnoid and dural tubes. *AJNR* 1983;4:633-636
6. Rasjo IM, Harwood-Nash DC, Fitz CR, Chuang S. Computed tomographic metrizamide myelography in spinal dysraphism in infants and children. *J Comput Assist Tomogr* 1978;2:549-558
7. Ethier R, King DG, Menancon D, Gelange G, Taylor S, Thompson C. Development of high resolution computed tomography of the spinal cord. *J Comput Assist Tomogr* 1979;3:433-438
8. Scotti G, Musgrave MA, Harwood-Nash DC, Fitz CR, Chuang SH. Diastematomyelia in children: metrizamide and CT metrizamide myelography. *AJNR* 1980;1:403-410
9. Barson AJ. The vertebral level of termination of the spinal cord during normal and abnormal development. *J Anat* 1970;106:489-497
10. Hail DE, Udvarhelyi GB, Altman J. Lumbosacral skin lesions as markers of occult spinal dysraphism. *JAMA* 1981;22:2606-2608
11. Gryspeerdt GL. Myelographic assessment of occult forms of spinal dysraphism. *Acta Radiol* 1963;1:702-717
12. Strand RD. Spinal dysraphism in certain occult forms examined by air myelography without tomography. *Ann Radiol (Paris)* 1969;12:393-399
13. Eldevik OP, Nakstad P, Kendall BE, Hindmarsh T. Iohexol in lumbar myelography: preliminary results from an open noncomparative multicenter clinical study. *AJNR* 1983;4:299-301
14. Naidich TP, McLone DG, Mutluer S. A new understanding of dorsal dysraphism with lipoma (lipomyeloschisis): radiologic evaluation and surgical correction. *AJNR* 1983;4:103-116
15. Dubowitz V, Lorber J, Zachary RB. Lipoma of the cauda equina. *Arch Dis Child* 1965;40:207-213
16. Emery JL, Lendon RG. Lipomas of the cauda equina and other fatty tumors related to neurospinal dysraphism. *Dev Med Child Neurol* 1969;20:62-70
17. McAlister WH, Siegel MJ, Shackelford GD. A congenital iliac anomaly often associated with sacral lipoma and ipsilateral lower extremity weakness. *Skel Radiol* 1978;3:161-166
18. Cohen JY, Lebatard-Sart RER, Lajat Y, Mitard D, David A. Sacral intraspinal lipoma associated with genital iliac anomaly. *Childs Brain* 1981;8:181-188

Book Review

Ultrasonography in Obstetrics and Gynecology, 2nd ed. By Peter W. Callen. Philadelphia: Saunders, 496 pp., 1988. \$60

The second edition of this book has been, by the author's intention, essentially rewritten and expanded to encompass state-of-the-art thinking and developments in all aspects of obstetric and gynecologic sonography. The object is to provide both a reference text with sufficient detail to be used by the experienced sonographer or sonologist and a readable guide that will provide the less experienced practitioner a more basic understanding of a particular topic. The book succeeds admirably in both aims.

The book has 22 chapters, spanning the subject from such basic approaches as chapter 1, "The Obstetric Ultrasound Examination," which provides an excellent overview for the novice, to an extensive and detailed discussion of the fetal heart, which will serve as a reference for all but the most sophisticated sonologist. The text proceeds in a logical and orderly fashion from early to advanced pregnancy and, within each chapter, from the normal to abnormal. Individual chapters treat the first trimester, assessment of fetal age, fetal growth, the neural axis, the genitourinary system, the placenta, an overview of fetal well-being in the biophysical profile, trophoblastic disease, ectopic pregnancy, the ovary, and more. A 20-page appendix provides virtually all of the common measurement tables and methodologies currently in use for evaluating fetal variables, from gestational sac to transverse cerebellar diameter as it relates to the gestational age, and everything in between. The index is complete and allows ready reference to general topics and specific subjects.

Sonograms themselves are of first quality throughout and well reproduced. The temptation to chide the publisher for producing a figure that measures 24 × 37 mm is offset by the fact that even this figure conveys its point adequately. Labeling is clear and pertinent

without being overbearing, and the legends are informative without being overzealous.

The uniformity throughout the book is remarkable despite the 29 contributors; this can only be a testimonial to Dr. Callen's unifying hand along with effective editing on the part of the publisher. A considerable measure of clinical information is incorporated into this work as a result of the inclusion of a number of prominent clinicians as contributors. In this subspecialty perhaps more than any other, the radiologist must be equipped with an adequate understanding of the clinical situation in order to interact appropriately and productively with those directly responsible for care of the patient.

The authors' *modus operandi* is to cover a controversial topic by discussing the most prevalent opinions and pertinent research and, ultimately, stating their opinion and the reasons behind it. This sort of intellectual honesty leaves the reader with an understanding of the various sides of a controversial issue summarized in the well-founded point of view of a recognized authority. Virtually all contributors take this approach. Each chapter is, in addition, provided with a pertinent bibliography of up-to-date references.

In short, this is an outstanding work, second to none in the field. It should be considered essential to every physician in training or practice who deals with obstetric and/or gynecologic sonography.

Andrew M. Fried
University of Kentucky Medical Center
Lexington, KY 40536-0084

Absolute Intracranial Blood-Flow Velocities Evaluated by Duplex Doppler Sonography in Asymptomatic Preterm and Term Neonates

J. Gerard Horgan¹
 Carol M. Rumack¹
 Thomas Hay¹
 Michael L. Manco-Johnson¹
 Gerald B. Merenstein²
 Chris Esola¹

Thirty-eight asymptomatic preterm and term neonates were studied with pulsed Doppler sonography to assess absolute (true) intracranial blood-flow velocities. The middle and posterior cerebral arteries were evaluated by a transcranial approach, and the anterior cerebral artery was evaluated via the anterior fontanelle. Intracranial velocities were seen to increase with increasing gestational age and with increasing age of the neonate. The rate of increase in velocity was greater with higher gestational age. Middle cerebral artery velocities were greater than anterior cerebral velocities. Likewise, antegrade diastolic flow was always seen in these normal neonates.

Intracranial velocities increased with gestational age and with increasing age of the child; the resistive index decreased progressively with age.

Evaluation of the data observed on Doppler examination of the neonatal brain vasculature has prompted much controversy [1, 2]. To date, most studies have used continuous-wave Doppler sonography, which, in the absence of direct imaging of the intracranial structures and blood vessels, assumes the correct anatomic origin of the data obtained. More recently, duplex Doppler sonography has become available, allowing visualization of blood vessels and Doppler evaluation simultaneously. It appears that this technique may provide greater reliability and precision in the evaluation of intracranial vasculature.

Grant et al. [3] reported on the duplex Doppler findings in 75 patients, 19 of whom comprised a mixed group of term and preterm neonates who sustained neither intracranial hemorrhage nor ventriculomegaly. They observed that the intracranial velocities varied by gestational age and, further, that preterm neonates frequently had no diastolic flow. Further, they noted that the anterior cerebral artery (ACA), internal carotid artery (ICA), and basilar arteries had higher velocities than the middle cerebral artery (MCA).

Their study, however, had a number of important limitations. The scan angle was not corrected, a common cause of underestimation of velocity. They used the anterior fontanelle alone as a port of examination, which results in underestimation of velocity in the MCA and posterior cerebral artery (PCA) because of the ensuing high angle of the Doppler examination with this approach. Finally, the clinical condition of their patients was not assessed; hypoxia, hypercapnia, shunts, patent ductus arteriosus, and other clinical variables are known to cause considerable alteration variation in intracranial velocities. Subsequently, Drayton and Skidmore [4] used the temporal approach to the MCA and the anterior fontanelle approach to the ACA in 40 sick and asymptomatic neonates. They found the velocities doubled in preterm neonates in the first 2 days of life. Velocities in term neonates were higher at birth than preterm, and these also increased over the first 2 days.

Clearly, there exists a need for controlled studies in asymptomatic patients to elicit reliable data from which valid conclusions may be drawn.

Received August 17, 1988; accepted after revision January 23, 1989.

Presented at the annual meeting of the Society for Pediatric Radiology, San Diego, CA, April 1988.

¹ Department of Radiology, University of Colorado Health Sciences Center, 4200 E. Ninth Ave., Denver, CO 80262. Address reprint requests to J. G. Horgan.

² Department of Pediatrics, University of Colorado Health Sciences Center, Denver, CO 80262.

AJR 152:1059-1064, May 1989
 0361-803X/89/1525-1059
 © American Roentgen Ray Society

Subjects and Methods

We prospectively evaluated 38 neonates, 19 male and 19 female, who were all judged to be asymptomatic. Table 1 describes the four classes of asymptomatic neonates defined by us. Blood gases, pulse rates, and blood pressure were recorded at the time of sonographic evaluation. No neonate with hypoxia or hypercapnia was entered into the study. Also excluded were all sick neonates, including those who had concurrent patent ductus arteriosus, congenital heart disease, intracranial hemorrhage, shock, severe hyaline membrane disease, bronchopulmonary dysplasia, or pneumothorax. We took particular care to reduce the likelihood of entering patients with significant ductus shunting. In this regard, the possibility of a patent ductus arteriosus was evaluated by careful clinical examination and chest radiograph when necessary. Finally, a high-pulse-velocity differential (systolic minus diastolic velocity) on Doppler examination was helpful in alerting the sonographer to a patent ductus arteriosus. We consider it unlikely that a hemodynamically significant patent ductus arteriosus would have been missed, and we believe the patient population studied conforms to a normal group of physiologically asymptomatic neonates. These considerations are important since the majority of premature neonates can be found to have a patent ductus arteriosus in the first 24 hr of life [5], the presence of which may alter cerebral flow velocities [6].

In a further attempt to assess only asymptomatic neonates, we reevaluated the clinical data at the completion of the study to determine that no sick or otherwise unstable neonates had been entered. It was necessary to exclude only a single study at that time. The gestational ages of the neonates varied between 26 and 42 weeks as determined by clinical examination. Figure 1 shows the distribution of patients by gestational age.

Duplex studies were performed with a UM4 Doppler sonograph (Advanced Technical Laboratories, Bellevue, WA) with the use of a 7.5-MHz probe for imaging and a 5-MHz Doppler probe. Calibration of the Doppler was provided by physics personnel. Verbal consent was obtained from the parent. Both a formal head sonogram and a Doppler evaluation of the cerebral vessels were performed on days 1, 3, 7, and 14 of life. The day-1 study was performed toward the end of the first day of life (so as to reduce the effect of any physiologic ductus). In all, 93 studies were performed in 38 patients (average, 2.5 studies/patient). The Doppler study was performed with a careful Doppler technique: The power setting was low (less than 94 mW/cm² spatial peak temporal average intensity, within Food and Drug Administration recommendations); we limited the duration of the Doppler examination to a maximum of 3 min; a 1.5-mm-wide sample volume was used to interrogate the vessel in view; and all velocities

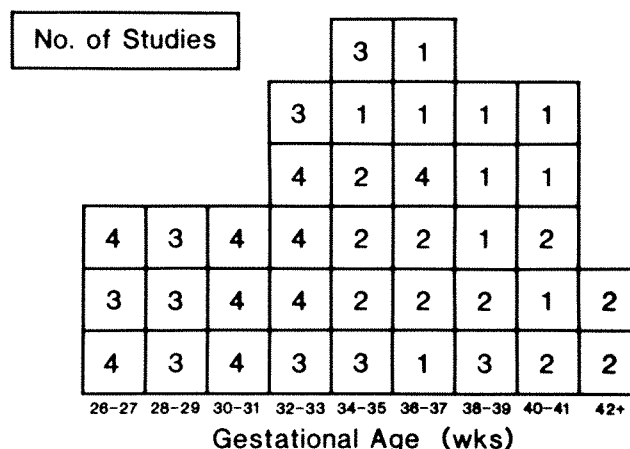


Fig. 1.—Distribution of patients by gestational age. Each box represents one patient; numbers in boxes indicate number of Doppler studies on this patient.

recorded were angle-corrected by appropriate positioning of the crossbar of the Doppler sample volume. Although the ACA frequently is visualized at 0°, the MCA tends to be insonated at 10–30° on average, and the PCA at 45–65°.

To examine the MCA and PCA, we used the transcranial approach proposed by Padayachee et al. [7]. This uses a transtemporal approach, the sonographic image obtained being similar in detail to that seen on an anatomic slice at 10° through the suprasellar cistern (Figs. 2 and 3). This lies at the level of the circle of Willis. The vessels are clearly seen as pulsating structures, the MCA in the sylvian fissure and the PCA lying between the uncus of the temporal lobe and the superior cerebral peduncle. By appropriately placing the sample volume on the vessel under examination and with angle correction (by means of the crossbar), absolute (true) peak systolic and end-diastolic velocities can be determined (Figs. 4 and 5).

For the ACA we used the anterior fontanelle. A suitable location for examination of this vessel is the genu of the corpus callosum, where the vessel can be insonated at close to 0° (Fig. 6). By carefully sweeping medial to lateral, the ACAs can be evaluated independently in most cases.

Absolute peak systolic and diastolic velocities were measured in the MCAs, PCAs, and ACAs. The data were entered into a data base and offloaded to a VAX 11750 computer (Digital Equipment Corp., Boston, MA) for analysis. The data were analyzed with SPSS software (SPSS, Chicago, IL), and linear regressions with 90th percentile prediction intervals were obtained. The latter is essentially the mean \pm 2 SD but is a more appropriate statistic for our data.

TABLE 1: Clinical Classification of Asymptomatic Preterm and Term Neonates

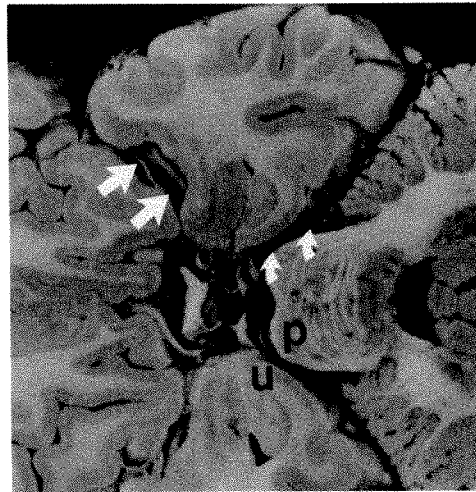
Classification	Description
Normal	Neonate being observed for sepsis but with no signs of disease; previously ill neonate who has recovered
Stable	Neonate requiring minimal additional support (e.g., oxygen, by head box or nasal cannula, or gavage feeding)
Sick, recovering	Neonate requiring decreasing amounts of ventilator support (e.g., less oxygen, lower ventilator rate, or less ventilator pressure)
Sick, stable	Neonate requiring ventilator support but not requiring more oxygen, more ventilator pressure, or higher ventilator rate

Results

Two statistical entities were evaluated: plots of peak velocity vs gestational age and plots comparing velocity and Pourcelot index.

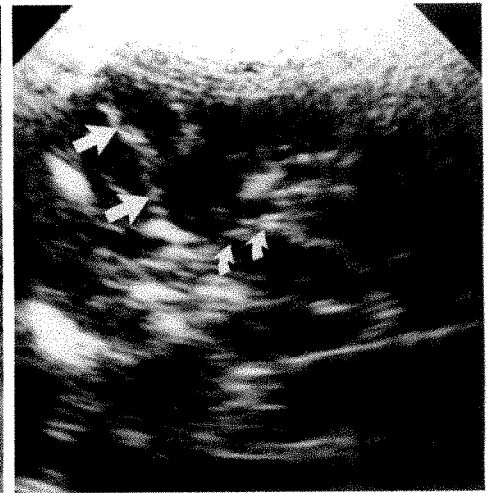
First, systolic and diastolic plots were drawn of the velocity data in centimeters per second against gestational ages 26–42 weeks. The regression plots so obtained demonstrate that velocity in all intracranial vessels increases progressively with gestational age. The plots also show a linearly distributed mean value of peak velocity for gestational age, indicating a direct relationship between velocity and gestational age. By

Fig. 2.—Anatomic slice through suprasellar cistern shows circle of Willis and location of middle cerebral (straight arrows) and posterior cerebral (curved arrows) arteries. u = uncus; p = superior cerebral peduncle. Reprinted from [8], with permission.



2

Fig. 3.—Transcranial sonogram at same level as Fig. 2 shows similar anatomic findings. Middle cerebral (straight arrows) and posterior cerebral (curved arrows) arteries.



3

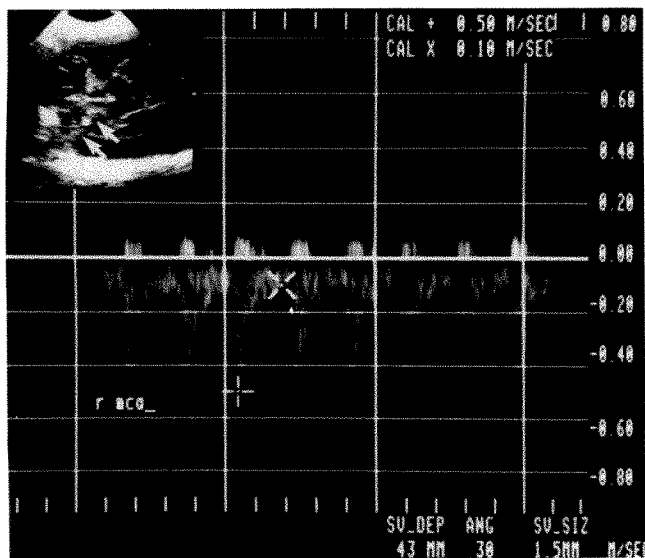


Fig. 4.—Duplex image of contralateral middle cerebral artery. Middle cerebral artery and Doppler cursor (arrows). Velocities are given in upper right-hand corner of image: systolic velocity is 50 cm/sec; diastolic velocity is 10 cm/sec.

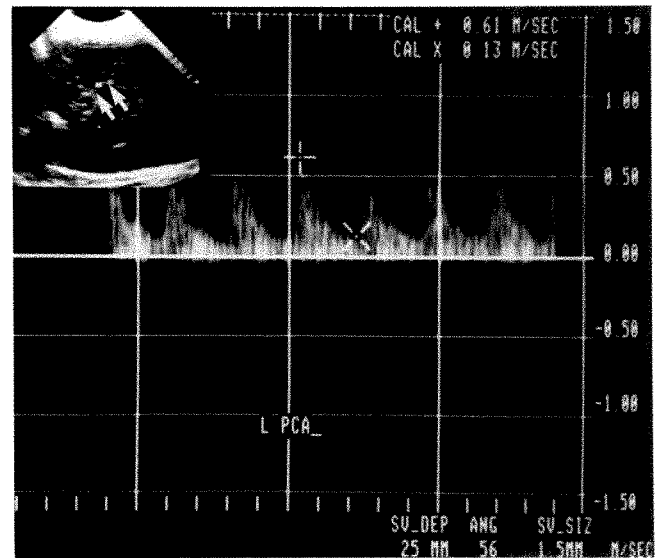


Fig. 5.—Pulsed Doppler study of ipsilateral posterior cerebral artery. Posterior cerebral artery and Doppler cursor (arrows). Doppler angle is 56°; absolute systolic (+) and diastolic (X) velocities are given in upper right-hand corner.

way of example, the left MCA, day-1, systolic velocity regression is shown in Figure 7. While the mean has a linear distribution, we can see that the 90% "confidence" limits are relatively broad.

Comparing the day-1 systolic velocity in the MCA and the ACA on the left, we can see the MCA velocity is greater than the ACA velocity throughout gestational ages 26–42 weeks (Fig. 8).

Evaluating diastolic velocities, it is apparent that these exhibit a slower rate of rise with gestational age than do systolic velocities (Fig. 7). In our experience, antegrade diastolic flow is always seen in normal preterm and term neonates.

For the PCA, we found a wider distribution to the 90% confidence limits, although the mean velocity was again noted

to rise with gestational age and to be distributed linearly (Fig. 9).

Analysis of the data over days 1, 3, 7, and 14 shows there is a progressive rise in velocity (systolic and diastolic) over the first 2 weeks of life, regardless of initial gestational age. However, the higher the initial gestational age, the greater the rate of increase in velocity (Fig. 10).

Plots of resistive index vs gestational age were also compared with the velocity regression plots above. Resistive index (RI) is determined by the velocity equation

$$(\text{Peak systolic} - \text{End-diastolic}) / \text{Peak systolic}$$

With increasing gestational age the resistive index is seen to fall (Fig. 11), whereas the velocity increases (Fig. 12). Similar

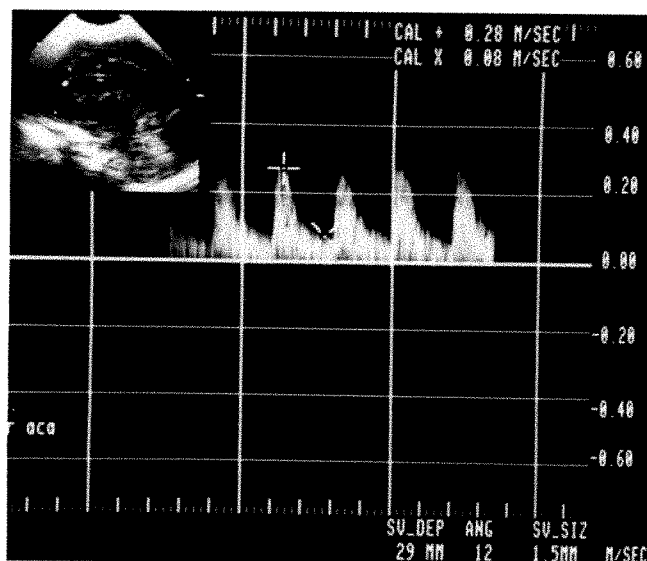


Fig. 6.—Duplex study of anterior cerebral artery. Doppler angle is 12°. Anterior fontanelle is used to insonate this vessel.

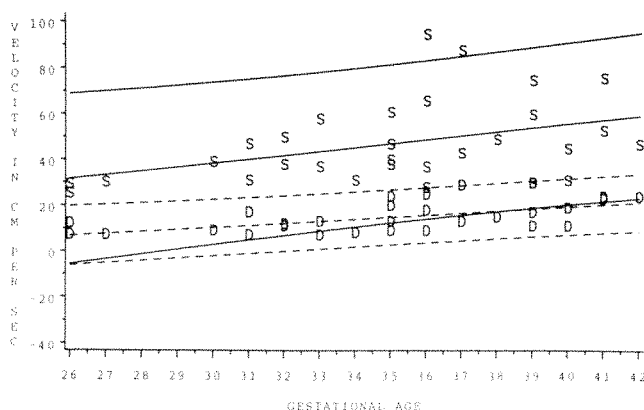


Fig. 7.—Superimposed plots of systolic (S) and diastolic (D) velocities of left middle cerebral artery vs gestational age (in weeks) on day 1. Solid lines show mean systolic velocities and 90% prediction intervals; broken lines show mean diastolic velocities and 90% prediction intervals. Progressive rise in mean systolic velocity of middle cerebral artery (solid center line) is noted with increasing gestational age; rise of systolic velocity is more rapid with increasing gestational age. Antegrade diastolic flow is always seen in normal patients. Middle cerebral systolic correlation coefficient is .42; p value of slope is .02. Diastolic correlation coefficient is .57; p value of slope is .0009.

findings are seen in the ACA and PCA territories. Thus, resistive index and velocity exhibit an opposite trend with time.

Discussion

Duplex Doppler sonography now provides us with a powerful tool to evaluate the neonatal brain in a noninvasive manner. The addition of the transtemporal approach provides a reliable means by which to evaluate velocities in the MCA and, with care, the PCA. The standard anterior fontanelar approach to the ACA is also reliable and reproducible. The

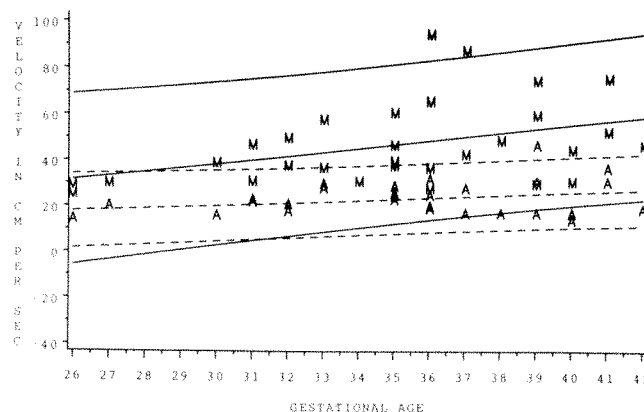


Fig. 8.—Superimposed plots of systolic velocities of left middle cerebral artery (M) and left anterior cerebral artery (A) vs gestational age (in weeks) on day 1. Solid lines show mean left middle cerebral artery velocities and 90% prediction intervals; broken lines show mean left anterior cerebral artery velocities and 90% prediction intervals. Velocities of middle cerebral artery are greater than those of anterior cerebral artery and show a more rapid rise with increasing gestational age. Middle cerebral artery correlation coefficient is .42; p value of slope is .02. Anterior cerebral artery correlation coefficient is .36; p value is .058.

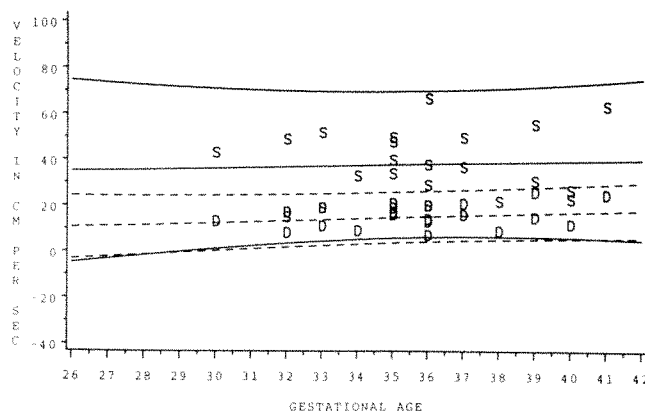


Fig. 9.—Superimposed plots of systolic (S) and diastolic (D) velocities of right posterior cerebral artery vs gestational age (in weeks) on day 1. Solid lines show mean systolic velocities and 90% prediction intervals; broken lines show mean diastolic velocities and 90% prediction intervals. Progressive rise in velocities is noted. Systolic correlation coefficient of right posterior cerebral artery is .07; p value is .76. Diastolic correlation coefficient is .27; p value is .22.

patients in our present study were carefully selected so as to provide normal reference data in asymptomatic neonates. The term *asymptomatic* must be relative, as no neonate of 26- to 36-weeks gestation can be regarded as asymptomatic. Nonetheless, we have striven to exclude many of the variables to which study of the cerebral vasculature is prone. Recent articles in the literature [3, 4] have evaluated mixed heterogeneous groups that included asymptomatic and sick children. Some articles indeed have not addressed the infants' clinical condition when evaluating Doppler data, a major source of error.

We have demonstrated here that absolute systolic and diastolic velocities in asymptomatic neonates show a pro-

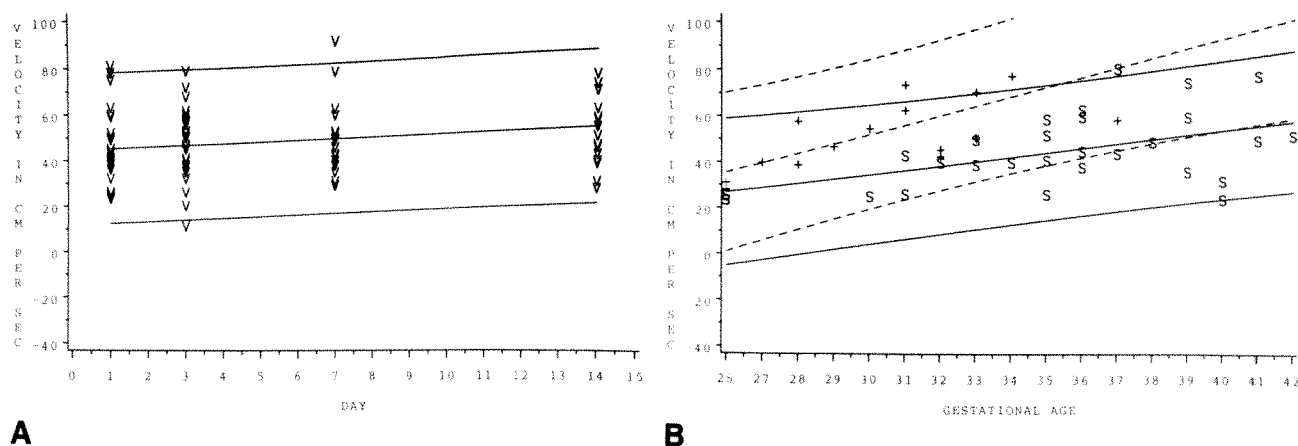


Fig. 10.—A, Composite plot of systolic velocities (V) by days since birth. Solid lines show mean systolic velocity and 90% prediction intervals. Velocities are seen to increase with increasing age of neonate.

B, Superimposed plots of velocities in right middle cerebral artery on day 1 (S) and day 14 (+) vs gestational age (in weeks). Solid lines show mean day-1 velocities and 90% prediction intervals; broken lines show mean day-14 velocities and 90% prediction intervals. Velocities on day 14 are increased over those on day 1, and velocities show a greater increase at higher gestational age. Day 1 correlation coefficient is .51; *p* value is .0048. Day 14 correlation coefficient is .5; *p* value is .0028.

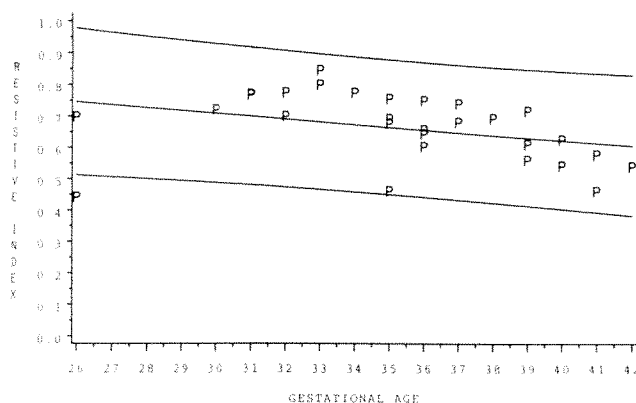


Fig. 11.—Plot of resistive index ($P = 1$ data point) vs gestational age (in weeks) in right middle cerebral artery on day 1. Solid lines show mean resistive index and 90% prediction intervals. Progressive fall in resistive index is seen with increasing gestational age.

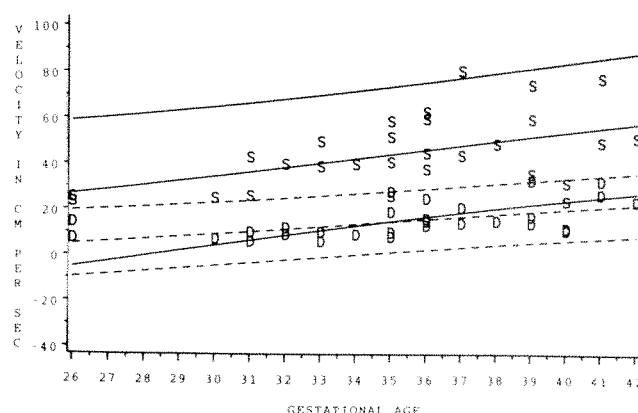


Fig. 12.—Superimposed plots of systolic (S) and diastolic (D) velocities of right middle cerebral artery vs gestational age (in weeks) on day 1. Solid lines show mean systolic velocities and 90% prediction intervals; broken lines show mean diastolic velocities and 90% prediction intervals. Progressive rise in systolic and diastolic velocities is seen with increasing gestational age. Velocity changes contradict resistive index trends (see Fig. 11). Systolic correlation coefficient is .51; *p* value is .0048. Diastolic correlation coefficient is .59; *p* value is .0008.

gressive rise with increasing gestational age. Likewise, velocity is seen to increase with the age of the infant. Contrary to the observations of Grant et al. [3], we found that the MCA velocity is significantly greater than that in the ACA. This presumably is secondary to the greater blood flow to the MCA territory. Further, in no normal patient did we find absent antegrade diastolic flow. These discrepancies can almost certainly be attributed to the use of angle correction and to the absolute (real) nature of our estimations. The previous investigators measured the MCA velocity via the anterior fontanelle, which would provide a large underestimation of true velocity due to the anatomic location of the vessel and the high angle of incidence of the sonographic beam. The lack of angle correction and use of the anterior fontanelle would commonly result in a Doppler angle of incidence in excess of 65° for the MCA, which would have further significantly attenuated their measured velocities.

A practical point in our study was the relatively high angle of interrogation of the PCA, 45–65°. We believe this high angle leads to some degradation of the Doppler data and appears to account for the wider 90° confidence limits observed in this vessel. In calculating velocity with the Doppler equation (velocity is proportional to the inverse of the cosine of the Doppler angle), the cosine of the angle is used. With a Doppler angle of 65° or greater, small errors in estimation of the correct angle cause a progressively larger error with increasing Doppler angles. Thus, a 5° error at 55° causes an error of 12% in the calculation of velocity, and a similar error at 75° causes an error of 35%. We are also of the opinion that absolute velocities are more meaningful than estimation of resistive index in analyzing the data and in looking for changes over time. The popularity of the resistive index (and

similar indexes, e.g., pulsatility index) has arisen for practical reasons.

The resistive index provides a simple device for analysis of the waveform. It is angle-independent. However, it suffers in that absolute velocity data are lost in the calculation. More importantly, our data clearly show the resistive index to fall with increasing gestational age and with age of the neonate, when the velocities, systolic and diastolic, are increasing. Thus, the resistive index exhibits the opposite trend to the true velocity movement. The reason for the falling resistive index is due to the relative increases occurring in systolic and diastolic velocities with time. Although systolic velocity increases more rapidly than diastolic velocity, the proportional increase in diastolic velocity is greater when compared with systolic velocity. Thus, the small diastolic increase in velocity exerts a greater effect on the resistive index equation, (systolic - diastolic)/systolic, than the larger systolic velocity increase (Figs. 11 and 12). This concern is further emphasized when one considers that blood flow in the neonatal brain also increases with gestational age and with the age of the patient [9].

Our data provide a reference for comparison with the velocities noted in various groups of sick children. We are also in a position now to look at various interventions (e.g., extracorporeal membrane oxygenation [10, 11]) and abnormalities (patent ductus arteriosus and hydrocephalus) and to determine the effects of these on the cerebral vasculature.

Finally, we believe that the data may provide some insights into the mechanism of autoregulation and perhaps offer clues in the investigation of intracranial hemorrhage, which may be caused by sudden changes in blood-flow velocity. The known increase in cerebral perfusion with increasing neonatal age, and the progressive rise in our observed velocities with gestational age and with neonatal age of the patients, indicate that the major intracranial vessels are capable of maintaining vascular tone in asymptomatic neonates and thus are vasoactive. Likewise, the relatively low-velocity differential be-

tween systole and diastole in premature neonates indicates a relatively dilated intravascular bed and suggests these neonates may be less able than term neonates to withstand transient vascular disturbances, which may provide a basis for intracranial hemorrhage and ischemia. Additional prospective studies are needed to evaluate the relationship between blood-flow velocities and intracranial hemorrhage.

ACKNOWLEDGMENT

We thank Phil Archer for statistical assistance.

REFERENCES

1. Bejar R, Merrit TA, Coen RW, Mannino F, Gluck L. Pulsatility index, patent ductus arteriosus, and brain damage. *Pediatrics* **1982**;69:818-822
2. Volpe JJ, Perlman JM, Hill A, McMenamin JB. Cerebral blood flow velocity in the human newborn: the value of its determination. *Pediatrics* **1982**;70:147-152
3. Grant EG, White EM, Schellinger D, Choyke PL, Sarcone AL. Cranial duplex sonography of the infant. *Radiology* **1987**;163:177-185
4. Drayton MR, Skidmore R. Vasoactivity of the major intracranial arteries in newborn infants. *Arch Dis Child* **1987**;62:236-240
5. Behaman RE, Vaughan VC. *Nelson textbook of pediatrics*, 12th ed. Philadelphia: Saunders, **1983**:115
6. Wright LL, Baker KR, Hollander DI, Wright JN, Nagey DA. Cerebral blood flow velocity in term newborn infants: changes associated with ductal flow. *J Pediatr* **1988**;112:768-773
7. Padayachee TS, Kirkham FJ, Lewis RR, Gillard J, Hutchinson MCE, Gosling RG. Transcranial measurement of blood velocities in the basal cerebral arteries using pulsed doppler ultrasound: a method of assessing the circle of Willis. *Ultrasound Med Biol* **1986**;12:5-14
8. Matsui T, Hirano A. *An atlas of the human brain for computerized tomography*, 1st ed. Tokyo: Igaku-Shoin, **1978**:63
9. Kirsch JR, Traystman RJ, Rogers MC. Cerebral blood flow measurement techniques in infants and children. *Pediatrics* **1985**;75:887-895
10. Taylor GA, Catena LM, Garin DB, Miller MK, Short BL. Intracranial flow patterns in infants undergoing extracorporeal membrane oxygenation: preliminary observations with Doppler US. *Radiology* **1987**;165:671-674
11. Mitchell DG, Merton D, Desai H, et al. Neonatal brain: color Doppler imaging. Part II. Altered flow patterns from extracorporeal membrane oxygenation. *Radiology* **1988**;167:307-310

Color Doppler Imaging of Intracranial Vessels in the Neonate

Wilson S. Wong¹
 Jay S. Tsuruda^{1,2}
 Ricardo L. Liberman³
 Ana Chirino¹
 John F. Vogt³
 Ernesto Gangitano³

This study was performed to examine the effectiveness of color Doppler imaging (CDI) in demonstrating the neonatal intracranial vessels and altered intracranial flow patterns and to determine the optimal approach in imaging the intracranial vasculature. The study was conducted in two parts. First, 14 neonates were examined with CDI by using a standard approach through the anterior fontanel. Whenever possible, views through the posterior fontanel and the temporal bone were obtained also. The anterior cerebral, M1 segment of the middle cerebral, distal internal carotid, and basilar arteries were demonstrated consistently. Portions of the vertebral, distal middle cerebral, and posterior cerebral arteries were frequently visualized. In the second part of the study, we examined 10 neonates who had undergone extracorporeal membrane oxygenation. In this group of patients, CDI was able to demonstrate occlusion of the right internal carotid artery and the reversal of flow through the ipsilateral A1 segment. Increased flow on the contralateral side and in the basilar artery was observed in several patients.

The anterior fontanel approach was shown to be the most useful in identifying most of the major intracranial arteries and veins with CDI. In addition, the body weights and gestational ages of the neonates were found to significantly influence the success rate in visualizing the intracranial vasculature.

Color Doppler imaging (CDI) is a recent innovation in which color-encoded flow data of a vascular structure are displayed simultaneously on a real-time gray-scale B-mode image [1-3]. In the field of echocardiography, CDI has proved to be effective in the study of normal cardiac anatomy [4], valvular disease [5], cardiomyopathies [6], and congenital heart disease [7]. Extracardiac analysis of blood flow has also been described for evaluation of arterial pseudoaneurysms [8, 9], intratumoral blood flow [10], and abdominal organ perfusion [11]. Its potential application in noninvasive neurovascular imaging has been recognized, and preliminary results with carotid disease [11], intracranial arteriovenous malformations [12], and neonatal intracranial vascular analysis [11] have been reported.

Neonatal cranial sonography has been used mainly in screening premature neonates for intracranial hemorrhage. Additional studies with duplex Doppler imaging have been shown to be helpful in measuring cerebral blood flow and velocity [13-19]. Extracorporeal membrane oxygenation (ECMO) is gaining widespread acceptance as a method of treatment for severe respiratory insufficiency in neonates unresponsive to conventional respiratory therapy [20-23]. This procedure is associated with significant alterations of intracranial hemodynamics [24]. Hence, it would be of great clinical interest to be able to study the intracranial flow patterns of this group of patients noninvasively. Although high-resolution sonography has at times been able to image intracranial vessels in neonates, the ability to demonstrate flow by CDI greatly improves the visualization of these vessels. The objectives of this study were to examine the effectiveness of CDI in demonstrating the neonatal intracranial vessels and altered flow patterns and to determine the optimal approach in imaging the intracranial vasculature.

This article appears in the March/April 1989 issue of *AJNR* and the May 1989 issue of *AJR*.

Received April 22, 1988; accepted after revision July 25, 1988.

Presented at the annual meeting of the American Society of Neuroradiology, Chicago, May 1988.

¹ Department of Radiology, Huntington Memorial Hospital, 100 Congress St., Pasadena, CA 91105. Address reprint requests to W. S. Wong.

² Huntington Medical Research Institutes, Pasadena, CA 91105.

³ Department of Neonatology, Huntington Memorial Hospital, Pasadena, CA 91105.

AJR 152:1065-1070, May 1989
 0361-803X/89/1525-1065
 © American Roentgen Ray Society

Materials and Methods

Patient Population

The patient population consisted of 24 neonates with a mean gestational age of 34 weeks (range, 26–43 weeks). The average weight of the patients was 2176 g (range, 590–4400 g). Neonatal cranial sonography was requested for 11 patients to rule out intracranial hemorrhage and for 10 patients as a routine part of the ECMO procedure. The indications for the remaining three patients were spina bifida, hydrocephalus, and periventricular leukomalacia. In three ECMO patients, serial studies were performed, bringing the total number of studies to 29.

Sonographic Technique

An Acuson 128 color Doppler phase-array scanner* was used for all cases. The examination was performed at the bedside in the neonatal intensive care unit. A conventional B-mode examination was performed with a 5-MHz sector transducer (S519) and was followed by CDI with a 5-MHz linear-array (L538) transducer. The spatial peak temporal average of the equipment estimated *in situ* was maintained at all times below 94 mW/cm². With CDI, the ultrasound signal is detected and analyzed in real time for changes in echo amplitude, frequency, and phase shifts. These changes provide information on the presence and direction of motion relative to the transducer and the relative velocities compared with stationary objects [11]. The results are displayed as a composite image consisting of a background B-mode image with encoded flow information displayed in color. Depending on the direction of flow with respect to the transducer, the data displayed are either red or blue. In this study, for the majority of the images, red was assigned as flow toward and blue as flow away from the transducer. On rare occasions, this was arbitrarily reversed so that venous structures were shown in blue while arterial segments were red. Flow velocity is indicated as the degree of saturation of color, with more saturation indicating higher velocities. In regions of very high velocity and/or turbulent (random) flow, increased color saturation is present and the vessel becomes white. The same machine was equipped with duplex Doppler scanning, which was useful in measuring flow velocity and in distinguishing between arterial and venous flow by spectral analysis after identifying the vessel by CDI. All images were recorded on videotape for later analysis.

Scanning Approaches

Our scanning protocol consisted of three different approaches: the anterior fontanel, the posterior fontanel, and the squamous portion of the temporal bone. The anterior fontanel approach used conventional coronal views obtained from the anteriormost to the posteriormost aspect of the brain (Fig. 1). This was followed by side-to-side parasagittal sections (Fig. 2). All patients were examined with this approach. With the posterior fontanel approach, the transducer was oriented in the axial plane (Fig. 3). Fifteen patients were studied by this approach. For the temporal approach [15], the transducer was also oriented in the axial plane. By placing the transducer 0.5–1 cm anterior to the external auditory canal and superior to the zygomatic process, the ultrasound beam passes through the relatively thin squamous portion of the temporal bone or the anterolateral fontanel, which may be open in neonates (Fig. 4). In the majority of cases, only one side (i.e., left or right temporal view) was obtained, since the depth of penetration of the transducer was adequate to visualize the contralateral vessels. We were able to evaluate 16 patients by the temporal approach. In a minority of patients, either the temporal or the posterior fontanel approach or neither was used when the pa-

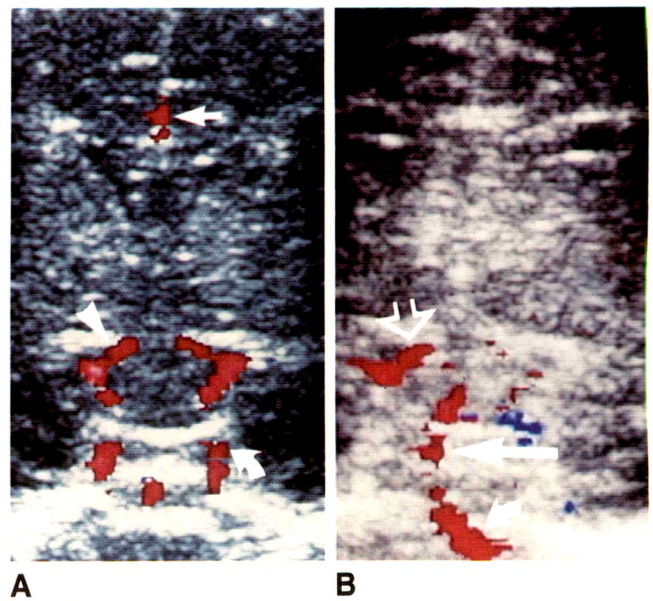


Fig. 1.—Coronal views via anterior fontanel approach.

A, Scan through anterior portion of circle of Willis: right A1 segment (arrowhead), left distal internal carotid artery (curved arrow), and pericallosal artery (straight arrow).

B, Scan slightly posterior to A shows basilar artery (solid straight arrow), left vertebral artery (curved arrow), and portion of right posterior cerebral artery (open arrow). Right vertebral artery (not shown) was also seen, but not in the same imaging plane.

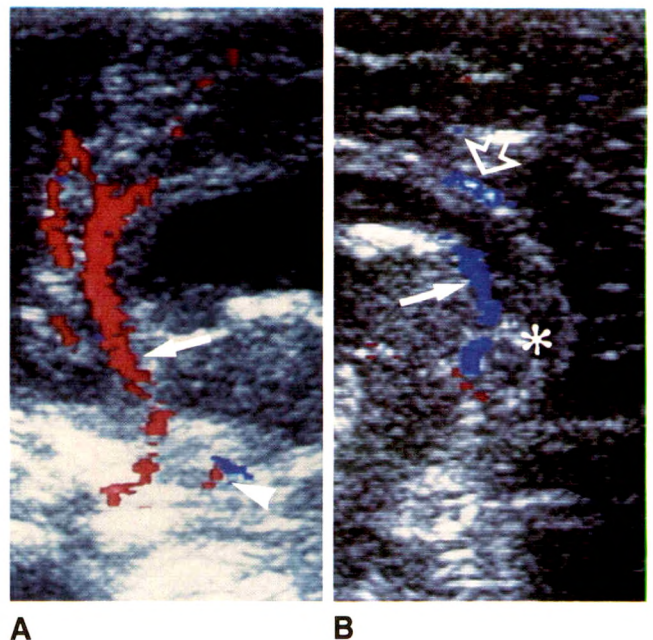


Fig. 2.—Sagittal views through anterior fontanel.

A, Anterior midline sagittal scan shows pericallosal artery (arrow) and its branches and distal portion of basilar artery (arrowhead). Note dilated lateral ventricle.

B, Posterior midline sagittal scan shows internal cerebral vein (solid arrow) and inferior sagittal sinus (open arrow). Asterisk indicates splenium of corpus callosum.

* Acuson, Mountain View, CA.

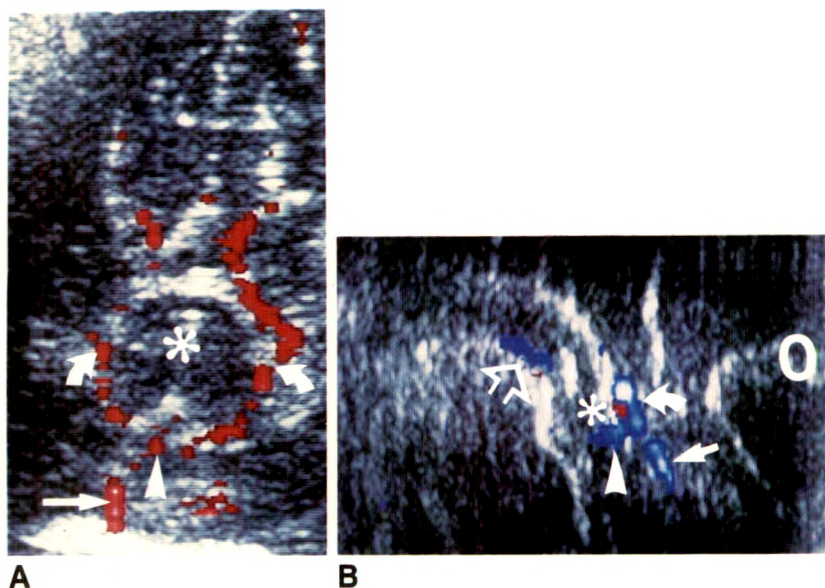


Fig. 3.—Posterior fontanel approach.

A, Axial scan shows posterior cerebral arteries (curved arrows) surrounding brainstem (asterisk), right internal carotid artery (straight arrow), and region of distal end of basilar artery (arrowhead).

B, Midsagittal view shows vein of Galen (arrowhead), straight sinus (straight arrow), inferior sagittal sinus (curved arrow), and internal cerebral vein (open arrow). Splenium of corpus callosum (asterisk) is an important landmark. O indicates occipital region. (Note reversal of color assignment so that venous structures are blue.)

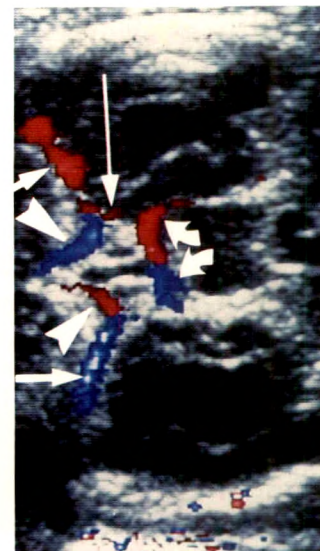


Fig. 4.—Temporal approach.

Transaxial scan through left temporal bone shows circle of Willis: A1 segment of anterior cerebral arteries (left side, blue; right side, red) (arrowheads); M1 segment of middle cerebral arteries (left side, red; right side, blue) (short straight arrows); posterior cerebral arteries (left side, red; right side, blue) (curved arrows); and left posterior communicating artery (long straight arrow).

tient's life-support system prevented adequate access to these areas. In every case, a systematic attempt was made to demonstrate each of the vessels being studied. All examinations were performed by the same technologist and radiologist. The average time to perform a complete study was 15–20 min.

Technical Considerations

Proper adjustment of the velocity scale to match the flow velocity of the vessel was found to be one of the critical factors for the success of the study. A change in the velocity scale directly reflected a change in the pulse repetition frequency or the sampling rate of the scanner. Setting the velocity scale to a high value makes the scanner less sensitive to slow flow within structures such as dural sinuses and internal cerebral veins. Conversely, with the velocity scale set to a low value, high-velocity flow may lead to excessive frequency shift, resulting in aliasing [2, 4], although this was not a serious problem in our patient population.

As with all Doppler examinations, the angle between the direction of flow and the ultrasound beam was an important factor, since a more parallel orientation will enhance color flow visualization of vessels [4, 25]. For example, the coronal view with the anterior fontanel approach demonstrates the M1 segment of the middle cerebral artery poorly. This is due to a nearly perpendicular angle between the direction of flow and the ultrasound beam. By using the temporal approach, the Doppler beam is nearly parallel to flow and the percent visualization is greatly improved.

Because the study is performed in real time, the transducer can be manipulated to optimize the Doppler angle. At the same time, maneuvering the transducer along the course of a tortuous vessel aids in the evaluation of vascular segments. With this method, a more complete appreciation of important structures such as the circle of Willis can be obtained, since only a small portion of this vascular ring

may be seen at any given moment. Its relationship to other important, stationary structures, such as the midbrain and third ventricle, becomes apparent. The color shift from either red or blue based on flow direction aids in identifying a particular vessel and helps to define the contour of small branch vessels such as the distal anterior cerebral branches (Fig. 2A).

Data Analysis

The video recordings were reviewed by two radiologists for the following arteries: anterior cerebral (A1 segments and segments distal to the anterior communicating artery, consisting of the pericallosal artery and its branches), middle cerebral (M1 segments and distal branches including M2 and/or M3 segments), internal carotid, posterior cerebral, basilar, and vertebral. Because the A1 segments, M1 segments, distal middle cerebral branches, internal carotid, posterior cerebral, and vertebrals are paired structures, a numerical score of 0, 1, or 2 was assigned to each paired artery depending on whether none, one, or two of the arteries were seen. This tabulation was performed for each of the three approaches. Distinguishing the two distal anterior cerebral artery segments was not possible because of the closeness of these vessels; therefore, the expected score was 1. The percentage of each artery visualized was computed as follows: percent visualized = total of the numerical score/total number of expected vessels $\times 100$. Although the posterior communicating artery is an important component of the circle of Willis, because of its smaller caliber, it was demonstrated infrequently and was not included as part of the tabulation.

The venous structures, which included the internal cerebral veins, vein of Galen, straight sinus, and superior sagittal/inferior sagittal sinus complex, were studied in a similar fashion. A numerical score of 1 or 0 was assigned to each vessel depending on whether or not it was seen. Like the distal anterior cerebral arterial segments, it was

not possible to distinguish between the right and left internal cerebral veins.

Statistical Analysis

To determine if the patient's gestational age influenced the percent vessel visualization, the entire study group of 24 patients was arbitrarily divided into two subgroups: ≤ 35 weeks (12 patients) and > 35 weeks (12 patients). Comparison was made for each of the three approaches by using a Student *t* test for paired observations. A value of $p < .05$ was considered significant. A similar analysis was performed on the study group as a function of body weight by dividing the patients into two subgroups: ≤ 2000 g (12 patients) or > 2000 g (12 patients).

ECMO Patients

The most common intracranial complication in ECMO patients is intracranial hemorrhage [26, 27]. Serial real-time neonatal cranial sonography was performed mainly to check for development of this problem. In this subgroup of patients, CDI was also used to examine for collateral flow patterns such as flow reversal and change in vascular caliber. In three ECMO patients, CDI was performed serially before and immediately after the ECMO procedure.

Results

Anterior Fontanel Approach

The anterior fontanel approach was the most readily accessible view and yielded the best anatomic detail because of its relatively large size, which provides a good acoustic window. By using a combination of coronal (Fig. 1) and sagittal (Fig. 2) scans, most of the major intracranial vessels could be identified consistently, including the anterior cerebral arteries (A1 and distal segments), internal carotid arteries, and basilar artery. The M1 segments of the middle cerebral artery were demonstrated less well by this approach because the direction of blood flow through this arterial segment is nearly perpendicular to the Doppler beam. With the midsagittal view, the internal cerebral vein was demonstrated relatively well (Fig. 2B) and the vein of Galen was imaged infrequently.

Posterior Fontanel Approach

The posterior fontanel approach was more limited in its field of view because of the comparatively smaller size of this fontanel. An oblique axial approach obtained by angulating the beam toward the midbrain was most effective in defining the arteries of the posterior cerebrum, including the interpeduncular, perimesencephalic, quadrigeminal, and distal segments of the posterior cerebral arteries (Fig. 3A). The distal-most portion of the basilar and internal carotid arteries were visualized inconsistently. If an optimal-flow Doppler beam angle was obtained, flow in the vein of Galen and the straight sinus could be seen (Fig. 3B).

Temporal Approach

The temporal approach through the thin squamous portion of the temporal bone and/or anterolateral fontanel provided detailed images of the midbrain and the vessels forming the circle of Willis, especially the proximal segments of the anterior and middle cerebral arteries (Fig. 4). Compared with the anterior fontanel approach, the middle cerebral arteries were demonstrated better because of the more favorable Doppler angle [15].

Percent Visualization

The percent visualization of both the arteries and veins with respect to the approaches are summarized in Table 1. Data analysis of percent vessel visualization with respect to body weight (≤ 2000 g or > 2000 g) and gestational age (≤ 35 weeks or > 35 weeks) appears in Table 2. For body weight statistical differences in the overall percent vascular visualization was noted in all three approaches, with better demonstration of vessels in the smaller body weight (≤ 2000 g) subgroup. Gestational age had less effect on percent vessel visualization, except for the posterior fontanel approach, which had a higher percent visualization in the ≤ 35 -week subgroup.

ECMO Patients

After right common carotid ligation, reversal of flow direction in the A1 segment of the right anterior cerebral artery was seen consistently in all 10 ECMO patients. This finding was well demonstrated with the anterior and temporal approaches (Fig. 5). Flow within the right middle cerebral artery could be demonstrated also. On occasion, retrograde flow in the distal right internal carotid artery was seen. In a limited number of patients, collateral vessels of the circle of Willis, including the distal portion of the basilar artery, were anecdotally noted to have a greater than expected degree of

TABLE 1: Percent Visualization of Arteries and Veins vs Approach: All Patients

Vessel: Branch	% Visualization via:		
	Anterior Fontanel	Posterior Fontanel	Temporal
Artery:			
Anterior cerebral:			
A1 segments	71	0	9
Distal segments	90	0	0
Middle cerebral:			
M1 segments	44	0	95
Distal segments	23	0	13
Posterior cerebral	66	62	68
Basilar	97	12	30
Vertebral	45	0	0
Internal carotids	82	12	15
Vein:			
Internal cerebral	74	6	0
Vein of Galen	35	47	32
Straight sinus	10	12	0
Superior and/or inferior sagittal sinus	18	6	0

TABLE 2: Percent Arterial and Venous Visualization vs Approach: Effects of Body Weight and Gestational Age

Variable	% Visualization via:		
	Anterior Fontanel	Posterior Fontanel	Temporal
Body weight:			
≤ 2000 g ($n = 12$)	61	22	41
> 2000 g ($n = 12$)	49	5	23
Significance (p)	.036	.011	.043
Gestational age:			
≤ 35 weeks ($n = 12$)	52	19	28
> 35 weeks ($n = 12$)	55	6	25
Significance (p)	NS	.014	NS

Note.—NS = not significant. Significance was determined from paired *t* test.

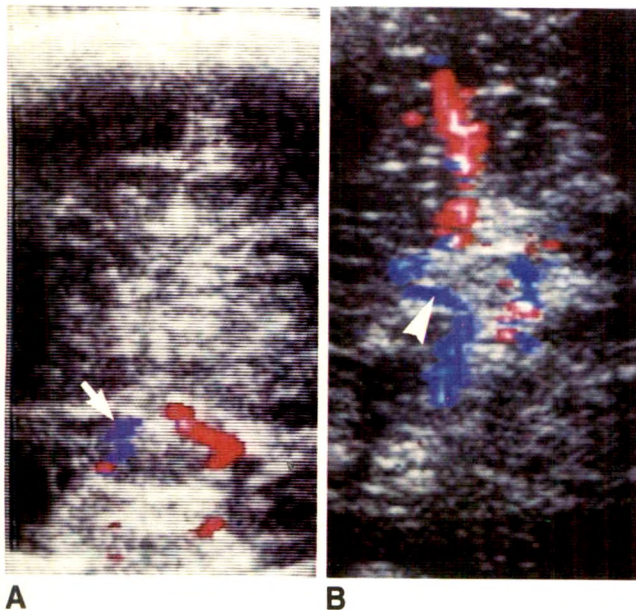


Fig. 5.—Patient who had undergone extracorporeal membrane oxygenation procedure with ligation of right common carotid artery.

A, Coronal view through anterior fontanel shows reversal of flow (blue color indicates flow is away from transducer) in A1 segment (arrow) of right anterior cerebral artery.

B, Transaxial view through left temporal bone shows flow pattern in right A1 segment (arrowhead) similar to that in A. Compare this pattern with that in Fig. 4.

caliber and flow when compared with non-ECMO patients. However, because of the limited access to these critically ill neonates, no attempt was made to further quantify this observation by volumetric flow analysis with pulsed Doppler.

Discussion

In this preliminary study, we have been able to show the effectiveness of CDI in visualizing neonatal intracranial vessels. In most patients, major intracranial arteries and veins could be identified in a high percentage of cases with a high degree of confidence. In addition, the study is noninvasive and rapid and can be performed in the neonatal intensive care unit or nursery on critically ill patients without disturbing life-support systems. Performing this type of examination does require technical skill and the results are highly operator-dependent. We noticed that the ease of obtaining adequate images and the length of time of the examination improved significantly with experience.

From the data presented in Table 1, specific approaches were found to be more useful in demonstrating certain vessels; these are summarized in Table 3. The readily accessible anterior fontanel approach was the most helpful in identifying most of the major intracranial arteries and veins. Of particular importance was its value in visualizing the distal branches of the anterior cerebral artery, as well as the basilar, vertebral, and internal carotid arteries. The midsagittal view from this approach yielded the most information in demonstrating the major intracranial veins and dural sinuses. The temporal approach was the second most useful approach, especially in evaluating the A1 and M1 segments of the anterior and middle cerebral arteries, respectively, due to optimization of the Doppler angle when compared with the anterior fontanel approach (Fig. 4).

TABLE 3: Best Approaches in Imaging the Arteries

Artery	Best Approach
Anterior cerebral:	
A1 segments	Anterior fontanel (coronal) or temporal (axial)
Distal segments	Anterior fontanel (sagittal)
Middle cerebral:	
M1 segments	Temporal (axial)
Distal segments	Anterior fontanel (sagittal)
Posterior cerebral	Posterior fontanel (axial)
Basilar	Anterior fontanel (coronal or sagittal)
Vertebral	Anterior fontanel (coronal)
Internal carotids	Anterior fontanel (coronal)

Finally, on the basis of total percent vessel visualization, the posterior fontanel approach was the least useful. However, in some patients, the posterior fontanel view was excellent in studying the distal branches of the posterior cerebral artery (Fig. 3A), since the direction of flow was directly toward the ultrasound beam. Because the vein of Galen has a similar flow direction, it could be seen in approximately half the patients. Less success was noted in detecting the straight sinus, presumably due to its more inferior flow direction away from the posterior fontanel (Fig. 3B).

The patient population may also affect the overall success of CDI in detecting both arterial and venous structures. From the data summarized in Table 2, a higher, statistically significant percent vessel visualization was obtained with all three approaches in patients weighing 2000 g or less, reflecting the presence of larger fontanel size and smaller brain volume, which allowed better ultrasound beam penetration. In addition, this group included several small-for-gestational-age neonates. In this subgroup, higher intracranial arterial flow velocities have been recorded by standard Doppler analysis [19] and presumably would improve visualization by CDI. Unfortunately, because of the small number of neonates in our study population who were small for gestational age, it was not possible to statistically compare this subgroup with neonates who had appropriate weight for gestational age.

In addition to body weight, gestational age may influence the percent vascular visualization, as outlined in Table 2. After arbitrarily dividing the study population into two subgroups (≤ 35 weeks and > 35 weeks), no significant differences were noted when they were compared for either the anterior fontanel or temporal approach. However, a statistically greater percent visualization was noted in the ≤ 35 -week subgroup when CDI was performed through the posterior fontanel. This difference may be explained by the generally smaller size of this fontanel, which may be closed in term neonates [28].

In ECMO patients, CDI appears to be a sensitive indicator of altered flow patterns. In this procedure, both the right common carotid artery and jugular vein are cannulated with large-caliber catheters. The oxygen-poor blood from the right atrium is drained by gravity into a reservoir via the cannula in the right jugular vein. The blood is then pumped into a thin membrane, which is exposed to a controlled mixture of oxygen, carbon dioxide, and room air. The oxygenated blood is then pumped back to the patient's aortic arch via the catheter in the right carotid artery. These patients provide a unique opportunity to study changes in intracranial flow patterns in vivo, since irreversible ligation of both the common right

carotid artery and jugular vein is performed for the bypass procedure. In addition, other noninvasive studies, including IV digital subtraction angiography and xenon cerebral blood flow determinations, have shown that perfusion of the right cerebral hemisphere by collateral flow is present [23]. This collateral flow pattern, seen as reversal of flow within the right A1 segment of the anterior cerebral artery and antegrade filling of the right M1 segment of the middle cerebral artery, can be demonstrated by CDI. As expected, the posterior communicating arteries would also be important collaterals. Conceptually, the temporal approach would be the optimal view to delineate these vessels. However, because of the nearly perpendicular Doppler beam/flow angle, the posterior communicating arteries were visualized inconsistently (Fig. 4). Reversal of flow within the distal segment of the right internal carotid artery was also seen, which may be an indirect indicator of retrograde supply to other important arteries, such as the right ophthalmic and right external carotid. In patients who had serial studies before and after the ECMO bypass procedure, a qualitative increase in the caliber and pulsation of the intracranial arteries was detected on ECMO, presumably reflecting the known decrease in cerebral vascular resistance and increase in cerebral blood flow as demonstrated by Doppler waveform analysis [24].

CDI may have other potential applications in neurovascular imaging. CDI may assist in the more precise placement of the sample volume for quantitative Doppler spectral analysis and aid in measuring the Doppler angle, thus improving the accuracy of velocity measurements. This technique may also help in diagnosing major intracranial vascular anomalies such as vein of Galen aneurysms, as well as providing intraoperative guidance. We also have begun to apply CDI in evaluating arterioocclusive diseases such as vasculitis and moyamoya. Before performing an ECMO bypass, documenting the lack of collaterals such as an atretic A1 segment may have a role in predicting acute complications such as cerebral infarction and later neurodevelopmental delay. This should be an area of further investigation.

On the other hand, CDI requires considerable operator skill and experience. Care must be taken to detect slow venous flow. In most cases, the major intracranial venous and dural sinuses will not be evaluated adequately, and therefore its use in documenting dural sinus thrombosis may be limited.

In summary, our results show that CDI has a role in the noninvasive evaluation of neonatal intracranial vessels. This technique can be applied readily during the standard B-mode sonographic examination and can provide qualitative information on normal and abnormal flow patterns. With further refinement in the scanner technology, such as the use of sector instead of linear transducers, an improvement in the overall accuracy of this technique is anticipated.

ACKNOWLEDGMENTS

We thank Kathy Cislo and Tom Jedrzejewicz for help in photographing the illustrations and Fred A. Lee and Richard A. Yadley for reviewing the manuscript.

REFERENCES

- Merritt CRB. Doppler blood flow imaging: integrating flow with tissue data. *Diagn Imaging* 1986;8:146-155
- Omoto R, Kasai C. Physics and instrumentation of Doppler color flow mapping. *Echocardiography* 1987;4:467-483
- Taylor KJW. Going to the depths with duplex Doppler ultrasound. *Diagn Imaging* 1987;9:106-116
- Harrison MR, Smith MD, Grayburn PA, Kwan OL, DeMaria AN. Normal blood flow patterns by color Doppler flow imaging. *Echocardiography* 1987;4:485-493
- Perry GJ, Nanda NC. Recent advances in color flow Doppler evaluation of valvular regurgitation. *Echocardiography* 1987;4:503-513
- Mills TJ, Seward JB, Khandheria BK, Klein AL, Oh JK, Tajik AJ. Color flow imaging in cardiomyopathies: observations and implications. *Echocardiography* 1987;4:527-534
- Ritter SB. Application of color flow mapping in the assessment and the evaluation of congenital heart disease. *Echocardiography* 1987;4:543-556
- Mitchell DG, Needleman L, Bezzi M, et al. Femoral artery pseudoaneurysm: diagnosis with conventional duplex and color Doppler US. *Radiology* 1987;165:687-690
- Wong WS. Case report. Detection of a pinhole opening of a false aneurysm by color flow Doppler. *Echocardiography* 1987;4:569-571
- Shinamoto K, Sakuma S, Ishigaki T, Makino N. Intratumoral blood flow: evaluation with color Doppler echography. *Radiology* 1987;165:683-685
- Merritt CRB. Doppler color flow imaging. *JCU* 1987;15:591-597
- Black KL, Rubin JM, Chandler WF, McGillicuddy JE. Intraoperative color-flow Doppler imaging of AVM's and aneurysms. *J Neurosurg* 1988;68:635-640
- Bada HS, Hajjar W, Chua C, Sumner DS. Noninvasive diagnosis of neonatal asphyxia and intraventricular hemorrhage by Doppler ultrasound. *J Pediatr* 1979;95:775-779
- Miles RD, Menke JA, Bashiru M, Colliver JA. Relationships of five Doppler measures with flow in an in vitro model and clinical findings in newborn infants. *J Ultrasound Med* 1987;6:597-599
- Raju TNK, Zikos E. Regional cerebral blood velocity in infants. A real-time transcranial and fontanellar pulsed Doppler study. *J Ultrasound Med* 1987;6:497-507
- van Bel F, van de Bor M, Buis-Liem TN, Stijnen T, Baan J, Ruys JH. The relation between left-to-right shunt due to patent ductus arteriosus and cerebral blood flow velocity in preterm infants. *J Cardiovasc Ultrasonogr* 1987;6:19-25
- van Bel F, van de Bor M, Stijnen T, Baan J, Ruys JH. Aetiological role of cerebral blood-flow alterations in development and extension of perintra-ventricular haemorrhage. *Dev Med Child Neurol* 1987;29:601-614
- van Bel F, van de Bor M, Stijnen T, Baan J, Ruys JH. Cerebral blood flow velocity pattern in healthy and asphyxiated newborns: a controlled study. *Eur J Pediatr* 1987;146:461-467
- van Bel F, van de Bor M, Stijnen T, Ruys JH. Decreased cerebrovascular resistance in small for gestational age infants. *Eur J Obstet Gynecol Reprod Biol* 1986;23:137-144
- Bartlett RH, Gazzaniga AB, Toomasian J, Corwin AG, Roloff D, Rucker R. Extracorporeal membrane oxygenation (ECMO) in neonatal respiratory failure. *Ann Surg* 1986;204:236-245
- Bartlett RH, Roloff DW, Cornell RG, Andrews AF, Dillion PW, Zwischenberger JF. Extracorporeal circulation in neonatal respiratory failure: a prospective randomized study. *Pediatrics* 1985;76:479-487
- Spahr RC. Extracorporeal membrane oxygenation in acute respiratory insufficiency in neonates: a review of the literature. *J Extra-Corporeal Technol* 1985;17:111-116
- Voorhies TM, Tardo CL, Starrett AL, et al. Evaluation of the cerebral circulation in neonates following extracorporeal membrane oxygenation (abstr). *Ann Neurol* 1985;18:380
- Taylor GA, Catena LM, Garin DB, Miller MK, Short BL. Intracranial flow patterns in infants undergoing extracorporeal membrane oxygenation: preliminary observations with Doppler US. *Radiology* 1987;165:671-674
- DeMaria AN, Spain MG, Garrahy P, Grayburn PA, Kwan OL, Smith MD. Considerations in the quantitation of color Doppler flow imaging. *Echocardiography* 1987;4:495-501
- Taylor GA, Fitz CR, Miller MK, Garin DB, Catena LM, Short BL. Intracranial abnormalities in infants treated with extracorporeal membrane oxygenation: Imaging with US and CT. *Radiology* 1987;165:675-678
- Taylor GA, Glass P, Fitz CR, Miller MK. Neurologic status in infants treated with extracorporeal membrane oxygenation: correlation of imaging findings with developmental outcome. *Radiology* 1987;165:679-682
- Harwood-Nash DC, Fitz CR. *Neuroradiology in infants and children*, vol. 1. St. Louis: Mosby, 1976:41-44

Case Report

Hypermagnesemia: A Cause of Abnormal Metaphyses in the Neonate

William A. Cumming¹ and Victor J. Thomas²

A neonate, with radiographic changes in the metaphyses of long bones somewhat reminiscent of those seen in antenatal infection, had been subjected to high levels of magnesium for an unusually long time before birth. No evidence for infection was found, and we believe it likely the abnormal ossification was due to hypermagnesemia.

Case Report

A 28-year-old mother was treated for lupus anticoagulant antibody with 20 mg prednisone daily from the 13th week of pregnancy. Premature labor starting at 15 weeks led to treatment with 250 mg magnesium oxide orally three times a day for about 3 weeks, followed by IV magnesium sulfate in doses ranging from 1 to 4 g per hour until delivery at 28 weeks. Maternal serum Mg levels during this 13-week period ranged from 4.6 to 6.2 mg/dl (normal, 1.8–2.8 mg/dl).

A 1540-g male neonate was delivered at 28 weeks gestation. Apgar score was 1 at 1 min and 8 at 5 min. Respiratory distress syndrome was treated with mechanical ventilation. Ampicillin and gentamicin were given for possible sepsis, but they were discontinued at 72 hr when a negative blood-culture report was received. Indomethacin was given for patent ductus arteriosus. Metaphyseal bone lesions were seen on the initial chest radiograph (Fig. 1A). Antibody titers for toxoplasmosis, rubella, cytomegalovirus, herpes, and syphilis were negative. Screenings for phenylketonuria, hypothyroidism, and galactosemia also were negative. Serum magnesium levels were 4.1 mg/dl on the first day, falling to 2.4 mg/dl by day 20 and remaining normal thereafter. Serum calcium was normal at all times. Alkaline phosphatase, however, was elevated at 677 IU/l initially and fell to 479 IU/l by day 45. Phosphorus was elevated at 9.3 mg/dl on day 10

but normal on day 45. From day 11 to day 30, 400 IU vitamin D was given daily. Aside from necrotizing enterocolitis at 20 days, recovery was uneventful, and the infant was discharged home on day 54.

Initial radiographs showed radiolucent metaphyseal bands in the proximal humeri (Fig. 1A). The bone immediately adjacent to the growth plate, however, was of normal density. A faint longitudinal striation extended to the radiolucent zone. At 11 days, the bone adjacent to the growth plate was sclerotic, and dense longitudinal bands extended into the radiolucent zones (Fig. 1B). The appearance was similar to that seen in patients with congenital rubella infection.

Discussion

The relatively small dose of prednisone given to the mother should not have caused skeletal lesions in this neonate. Although it is not rare for newborn infants to have hypermagnesemia due to treatment of maternal toxemia with magnesium sulfate, rarely is the fetus exposed to 13 weeks of excessive magnesium, as happened in this instance. Neuromuscular depression in such babies is thought to be due to magnesium poisoning, although neurologic signs do not correlate well with serum levels [1]. This patient had a low Apgar score initially, but his condition was considered appropriate for his gestational age of 28 weeks. Even though neonates excrete magnesium poorly [2], normal renal function will usually reduce levels to normal in a few days. The serum level in this patient fell spontaneously to normal in 20 days.

Most neonates with hypermagnesemia do not have radiographic bone lesions, but their exposure to excess magne-

Received November 30, 1988; accepted after revision February 14, 1989.

¹ Departments of Radiology and Pediatrics, Shands Hospital, University of Florida, Gainesville, FL 32605. Address reprint requests to W. A. Cumming.

² Department of Pediatrics, Shands Hospital, University of Florida, Gainesville, FL 32605.

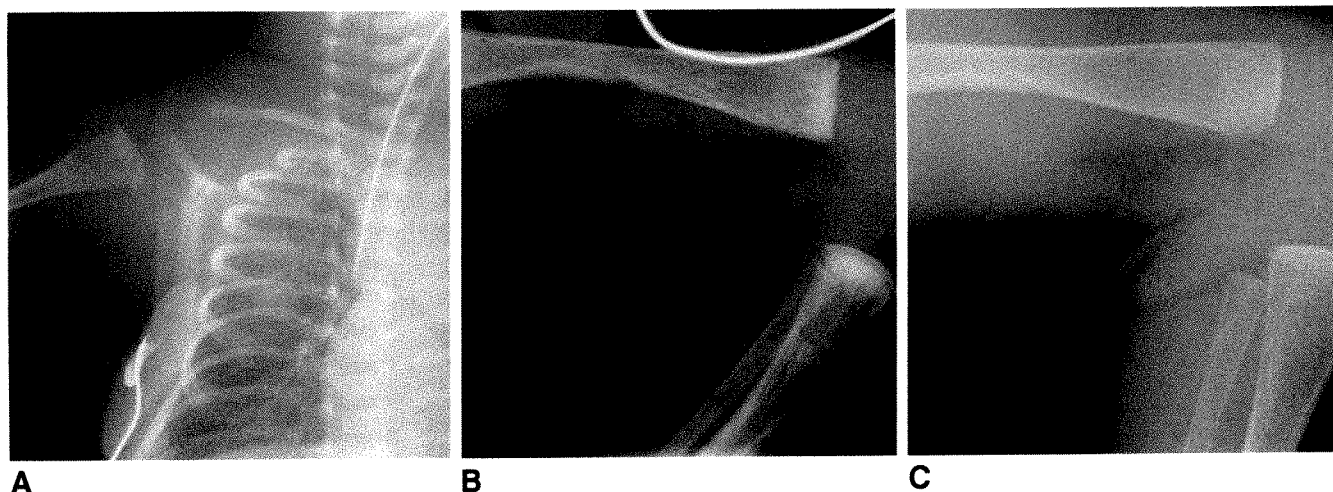


Fig. 1.—A, Chest radiograph on day of birth shows respiratory distress syndrome and radiolucent bands in proximal humeral metaphyses. B, Radiograph of long bones on day 11 shows a band of sclerosis adjacent to growth plates and thin sclerotic columns extending a short distance into radiolucent metaphyses. C, Radiograph on day 45 shows skeletal abnormalities have resolved.

sium has been relatively short. Our patient was subjected to a high level for 13 weeks before delivery. The mechanism of these metaphyseal changes is unclear, although magnesium is known to have an effect on calcium metabolism in both mothers and fetuses [3]. Animal experiments have shown that fetal bone is a site of high concentration of maternally administered magnesium [4], and in-vitro experiments have shown that excess magnesium inhibits calcification of osteoid [5]. Magnesium is known to exchange with calcium in bone, and hypermagnesemic infants have elevated ionized calcium [6]. In the absence of a known cause for the radiologic findings in this patient, we believe it likely the changes are caused by hypermagnesemia.

Lamm et al. [7] recently described two neonates with metaphyseal lesions after maternal magnesium therapy for 13 and 9 weeks, respectively. Both babies had hypocalcemia and were considered by the authors to have congenital rickets. Our patient had normal serum calcium and did not appear to have rickets, but rather a discrete band of osteopenic metaphyseal bone with an intact zone of provisional calcification. By definition, rickets is characterized by defective mineralization of cartilage and osteoid. If hypermagnesemia inhibits mineralization of collagen in vivo as it does in vitro, then the mechanism of the osteopenia is a failure to deposit calcium in osteoid. The sclerosis seen at 11 days is evidence of rapid calcification of previously uncalcified osteoid. Elevated alkaline phosphatase levels in our patient tend to support this

explanation because alkaline phosphatase is known to be part of the process of calcium and phosphorus deposition in collagen. Our case provides evidence of defective fetal bone production during a period of extreme maternal hypermagnesemia. Postnatal radiographs show rapid and complete resolution of these bony abnormalities. Further studies, including pathologic examination of the metaphyseal lesions, are needed to elucidate their anatomic and pathophysiologic basis.

REFERENCES

1. Green KW, Key TC, Coen R, Resnik R. The effects of maternally administered magnesium sulfate on the neonate. *Am J Obstet Gynecol* **1983**;146:29-33
2. Lipsitz PJ. The clinical and biochemical effects of excess magnesium in the newborn. *Pediatrics* **1971**;47:501-509
3. Cruikshank DP, Pitkin RM, Reynolds WA, Williams GA, Hargis GK. Effects of magnesium sulfate treatment on perinatal calcium metabolism. *Am J Obstet Gynecol* **1979**;134:243-249
4. Aikawa JK, Bruns PD. Placental transfer and fetal uptake of Mg 28 in the rabbit. *Proc Soc Exp Biol Med* **1960**;105:95-98
5. Shelling DH, Kramer B, Orent ER. Studies upon calcification in vitro. *J Biol Chem* **1928**;77:157-170
6. Liu CL, Mimouni F, Ho M, Tsang R. In vitro effects of magnesium on ionized calcium concentration in serum. *Am J Dis Child* **1988**;142:837-838
7. Lamm CI, Norton KI, Murphy RJC, Wilkins IA, Rabinowitz JG. Congenital rickets associated with magnesium sulfate infusion for tocolysis. *J Pediatr* **1988**;113:1078-1082

MR Imaging of Brain Abscesses

Alison B. Haimes¹
 Robert D. Zimmerman¹
 Susan Morgello²
 Karen Weingarten¹
 Richard D. Becker^{1,3}
 Richard Jennis¹
 Michael D. F. Deck¹

The MR images and CT scans of 14 patients with surgically verified pyogenic cerebral abscesses were reviewed. The MR findings correlated well with those seen on CT and were believed to be sufficiently characteristic to allow early and accurate diagnosis with MR alone. These features include (1) peripheral edema producing mild hypointensity on short TR/short TE and marked hyperintensity on long TR/intermediate to long TE scans; (2) central necrosis with abscess fluid hypointense relative to white matter and hyperintense relative to CSF on short TR/short TE scans and hyperintense relative to gray matter on long TR/intermediate to long TE scans (the fluid had concentric zones of varying intensity in seven cases, a finding not previously identified in other lesions); (3) extraparenchymal spread (intraventricular or subarachnoid), which was detected more easily on MR than on CT and was manifested by increased intensity relative to normal CSF on both short TR/short TE and long TR/intermediate TE scans; and (4) visualization of the abscess capsule, which was iso- to mildly hyperintense relative to brain on short TR/short TE scans and iso- to hypointense relative to white matter on long TR/intermediate to long TE scans. On the long TR scans, the relative hypointensity of the rim allowed for visualization of the typical morphologic features of the capsule, which in turn aided in differentiation of abscesses from other lesions (as it does on CT). To investigate the cause of the capsular intensity, pathologic studies of the capsules were reviewed when available (10 cases). Fibrosis was identified in all mature abscess capsules, but the combination of the intensities seen on short TR/short TE and long TR/intermediate to long TE scans as well as the temporal changes in intensity were believed to be incompatible with fibrosis as a cause of the capsular changes. Intensity patterns were suggestive of hemorrhage, but neither acute nor chronic hemorrhage was identified on routine H and E stains, while iron stain revealed scant hemorrhage in only two of the eight patients in whom these stains were used. We believe the capsular intensity (in particular the hypointense rims on long TR scans) may reflect paramagnetic T1, and to a greater extent T2, shortening, possibly due to the presence of heterogeneously distributed free radicals that are products of the respiratory burst produced by actively phagocytosing macrophages in the capsule wall.

Distinctive MR features of pyogenic abscesses should afford early and accurate diagnosis.

This article appears in the March/April 1989 issue of *AJNR* and the May 1989 issue of *AJR*.

Received July 13, 1988; accepted after revision October 25, 1988.

Presented at the Symposium Neuroradiologicum, Stockholm, June 1986.

¹ Department of Radiology, New York Hospital-Cornell Medical Center, 525 E. 68th St., New York, NY 10021. Address reprint requests to A. B. Haimes.

² Department of Pathology, New York Hospital-Cornell Medical Center, New York, NY 10021.

³ Department of Radiology, Temple Medical Center, 40-60 Temple St., New Haven, CT 06510.

AJR 152:1073-1085, May 1989

0361-803X/89/1525-1073

© American Roentgen Ray Society

Brain abscesses are potentially fatal lesions that may be treated successfully by medical and/or surgical intervention. Since the advent of CT, there has been a sharp decrease in the mortality of patients with parenchymal brain abscesses from greater than 40% to less than 5% [1-3]. The improved prognosis is attributed to early and accurate diagnosis and localization of these lesions, and to rapid detection of treatment failure and complications [1].

The role of MR imaging in these lesions has not been investigated extensively. The MR findings in 14 patients with pyogenic cerebral abscesses are described. One feature, a dark rim on long TR scans, is particularly notable. Histopathologic correlations are reviewed and a new potential mechanism for hypointensity due to T2 shortening is presented.

Materials and Methods

MR images of 14 patients (23 studies) with surgically verified pyogenic abscesses studied between September 1984 and May 1987 were analyzed retrospectively. In one patient (Case 13), postmortem examination was also performed. The clinical data are summarized in Table 1. In 10 cases, the clinical findings were suggestive of inflammatory disease (e.g., fever or leukocytosis), while the remaining four patients had nonspecific signs of a space-occupying mass. Ten patients were studied preoperatively; two of these were examined both pre- and postoperatively, one at less than 1 week and one at 1 year after surgery. Multiple lesions were identified in another patient (Case 7) in whom MR was performed after surgical drainage of the largest lesion. At least 10 smaller nonsurgical abscesses were identified in this study, the MR features of which were similar and were collectively considered a single preoperative case. Four patients were studied postoperatively only, two with serial scans, one within 1 week and another 1 year after surgical drainage.

MR was performed on a 0.5-T Teslacon unit* in 17 studies (nine preoperative, eight postoperative) and a 1.5-T Signa unit† in six studies (one preoperative, five postoperative). The axial plane was imaged routinely, and coronal and sagittal sections were obtained in selected cases. Slice thickness varied from 5 mm (1.5 T) to 7.5 mm (0.5 T). A variety of pulse sequences were used, particularly on the 0.5-T unit, due to periodic upgrades of these MR scanners. For purposes of comparison, sequences were divided into three groups within which MR images had similar intensities relative to normal CSF, gray matter, and white matter:

1. Short TR/short TE scans, 500–800/25–32/2 (TR/TE/excitations), in 12 patients (18 studies). On these images, which are

considered T1-weighted for brain, CSF was dark, brain parenchyma was bright, and white matter was mildly hyperintense relative to gray matter.

2. Long TR/intermediate TE scans, 1500–2150/40–90/2, in 14 patients (22 studies). On these images, which are considered moderately T2-weighted, CSF was iso- to hypointense relative to white matter and moderately hypointense relative to gray matter.

3. Long TR/long TE scans, 2000–2150/80–120/2, in 14 patients (22 studies). On these images, which are considered heavily T2-weighted, CSF was hyperintense relative to brain.

Typically, multiecho scans were used to obtain long TR/intermediate TE and long TR/long TE scans, but interecho times varied from 30 to 60 msec and the number of echoes from two to four. One single-echo study (1500/90) was performed at 0.5 T (Case 4). Gradient-echo scans, 21/12/4 (TR/TE/excitations), were obtained at 1.5 T in three studies (two patients) with a 10° flip angle. One patient (Case 10) who was scanned at 0.5 T was evaluated before and after the IV injection of Gd-DTPA in a dose of 0.1 mmol.

In all 14 patients, routine CT scans were obtained on third-generation CT scanners. In 12 cases, studies were performed both before and after the administration of IV contrast material. One patient was studied only without contrast enhancement and one patient only after contrast enhancement.

Each lesion was evaluated on MR and compared with corresponding CT scans. Four regions were identified separately on the basis of CT findings and the known pathology of brain abscesses [2, 4–8]:

1. *Peripheral zone of edema*, corresponding to the extracapsular low-attenuation zone on CT. The intensity of this region was compared with that of brain parenchyma and CSF.

2. *Central zone*, corresponding to the central hypodensity within the abscess cavity on CT. The abscess fluid intensity was assessed with respect to CSF, gray matter, and surrounding edema on short TR/short TE and long TR/intermediate to long TE scans.

TABLE 1: Clinical Characteristics of Pyogenic Cerebral Abscesses

Case No.	Age	Gender	Types and Timing of MR Studies	Histologic Findings of Biopsy Specimen
1	2	M	Postop 0.5 T (5 days, 2 weeks) Postop 1.5 T (6, 8, 10, 15 weeks)	Cultured only; no histology
2	10	M	Preop 0.5 T	Organizing abscess with diffuse macrophages
3	24	F	Postop 0.5 T (1 year)	Cultured only; no histology
4	28	F	Preop 0.5 T	Mature abscess capsule; moderate macrophages
5	39	M	Preop 1.5 T	Organizing abscess; focal sheets of macrophages
6	40	M	Preop 0.5 T	Multifocal acute cerebritis with early abscess and scattered macrophages
7	47	M	Preop 0.5 T Postop 0.5 T (1 week)	Granulation tissue with focal necrosis, macrophages
8	52	F	Preop 0.5 T	Cultured only; no histology
9	59	F	Postop 0.5 T (1 week)	Acute cerebritis; early abscess formation with leukocytes and macrophages
10	60	F	Preop 0.5 T Postop 1.5 T (1 year)	Organizing abscess with granulation tissue and diffuse macrophages
11	64	F	Postop 0.5 T (9 days, 5 weeks)	Granulomatous infiltrate with occasional giant cells and focal necrosis
12	65	F	Preop 0.5 T Postop 0.5 T (1 week)	Cultured only; no histology
13	65	F	Preop 0.5 T	Organizing abscess with granulation tissue; sheets of lipid-laden macrophages
14	70	M	Preop 0.5 T	Organizing abscess extending into choroid plexus, with granulation tissue and sheets of lipid-laden macrophages

Note.—Preop = preoperative; postop = postoperative.

3. *Extraparenchymal spread.* Abscess extension was evident by areas of abnormal intensity within adjacent CSF spaces.

4. *Abscess capsule.* The configuration and intensity of the rim of tissue interposed between the peripheral edema and central necrosis were evaluated. Because this fell within the confines of the region of ring enhancement on CT it was believed to represent the abscess capsule.

The intensity of each MR rim was compared with that of frontal gray and white matter on short TR/short TE scans and was graded on long TR/intermediate to long TE scans as follows (Table 2): grade I—iso- to minimally hyperintense relative to frontal white matter and hypointense relative to gray matter; grade II—moderately hypointense relative to frontal white matter, iso- or mildly hyperintense relative to the splenium of the corpus callosum, and hypointense to gray matter; and grade III—moderately to markedly hypointense relative to all white and gray matter. In addition, rim intensities were compared with the intensity of the posterior aspect of the falx cerebri.

All 14 abscesses were surgically drained and cultured. Ten abscess capsule specimens were available for review. The location of seven of the 10 biopsy sites was known from surgical reports and/or postoperative imaging studies. All 10 were routinely evaluated by light microscopy with H and E stains. Each specimen was evaluated for the presence of acute or chronic hemorrhage as manifested by extravascular erythrocytes or hemosiderin-laden macrophages, respectively. Eight specimens were restained with Gomori's modification of Perls' stain for ferric forms of iron. Gram stains for bacteria, Gomori's methenamine silver stain for fungus, Masson stains for collagen, and acid-fast stains for mycobacteria were also used. The abundance of macrophages on H and E stains was graded: grade I—scattered macrophages, grade II—moderate macrophages, and grade III—diffuse macrophages (Table 3).

To further evaluate the causes of hypointensity on MR, three additional patients were reviewed. Their lesions, one tuberculoma and two metastases, demonstrated hypointensity on long TR/intermediate to long TE scans and were pathologically evaluated in the same manner as the abscesses.

Results

The preoperative MR examination of pyogenic cerebral abscesses revealed discrete lesions in all 10 patients. Irregularly marginated subtle hypointensity with respect to brain on short TR/short TE scans (Fig. 1C) and marked hyperin-

TABLE 2: Grades of Rim Intensity of Pyogenic Cerebral Abscesses on Long TR/Intermediate TE and Long TR/Long TE MR Images

Grade	No. of Findings		
	Preoperative MR	Postoperative MR	
		1 Week	1–4 Weeks
I	4 ^a	1	1
II	3	3	1
III	2	0	0
Total	9	4	2

Note.—Grade I = iso- to hyperintense relative to frontal white matter and hypointense relative to gray matter; grade II = hypointense relative to white matter, iso- to hyperintense relative to splenium of corpus callosum, and hypointense relative to gray matter; grade III = hypointense relative to all white and gray matter.

^a In one patient with surgically and pathologically proved acute cerebritis, the entire lesion was of grade I intensity.

TABLE 3: Comparison of Rim Intensities and Histologic Findings in Pyogenic Cerebral Abscesses

Case No.	Grade of Rim Intensity ^a	Grade of Macrophage Infiltration ^b	Presence of Hemorrhage or Iron in Abscess Capsule	
			H and E	Iron Stain
1	II		Histology not performed	
2	II	III	None	None
3	— ^c		Histology not performed	
4	II	II	None	Not performed
5	III	III	None	Not performed
6	I	I	None	None
7	II	II	None	None
8	II		Histology not performed	
9	I	II	None	None
10	I	III	None	Focal/scant
11	II	II	None	None
12	II		Histology not performed	
13	III	III	None	Focal/scant
14	I	III	None	None

^a Grade was determined on long TR images in the initial patient study. Intensity grades are defined in Table 2.

^b Grade I: scattered macrophages; grade II: moderate macrophagic infiltrate; grade III: diffuse macrophages, some in sheets.

^c Scan obtained 1 year postoperatively; no discrete lesion was seen.

tensity on long TR/intermediate to long TE images (Figs. 1–4) correlated well with the hypodense peripheral edema seen on CT. Although the contrast between edema and surrounding tissues was more marked on long TR/intermediate to long TE scans than on CT scans, edema was always well visualized on CT scans.

The signal intensity of the central area corresponding to the abscess cavity on CT was intermediate between that of CSF and brain on all short TR/short TE scans (Fig. 1C). Abscess fluid intensity was consistently greater than that of CSF and was equal to that of gray matter in five of eight cases on long TR/intermediate TE scans (Fig. 3B) and greater than that of gray matter in three cases (Fig. 2C). The signal intensity of the abscess fluid increased as TE was prolonged. Of 10 long TR/long TE scans, one showed fluid intensity equal to that of gray matter, six showed intensity between that of gray matter and edema (Fig. 3C), and the remaining three showed fluid intensity equal to that of edema (Fig. 2D). While central material was homogeneously hypodense (iso- or slightly hyperdense relative to CSF) on CT, this region showed concentric alternating zones of relative hypo- and hyperintensity on seven of 10 MR scans (Figs. 1D and 2E). This appearance was subtle in smaller lesions but became more marked in large abscesses.

Two cases of extraparenchymal abscess extension were noted on preoperative MR, but not on CT. In both cases, intensity was increased relative to CSF, in particular on long TR/intermediate TE scans, while the infected fluid remained isodense relative to CSF on CT. These included one case of surgically confirmed intraventricular extension (Figs. 3A and 3C) and one case of autopsy-confirmed spread into the quadrigeminal plate cistern (Figs. 1B–1D).

In preoperative studies a discrete rim was identified at the margin of the central necrotic zone on both short TR/short TE (seven of nine cases) and long TR/intermediate to long

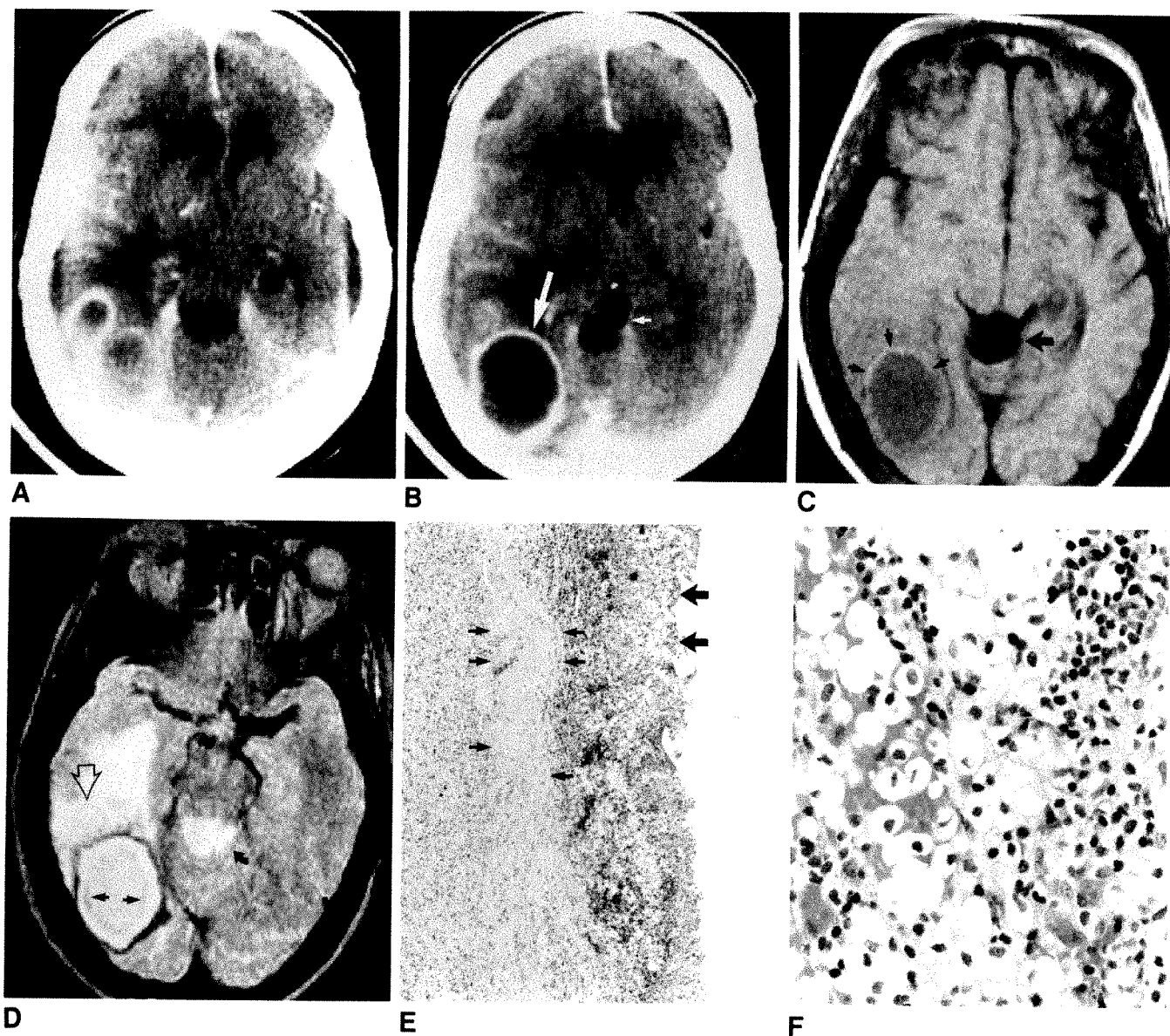


Fig. 1.—Case 13: Preoperative brain abscess.

A and B, CT scans show ring-enhancing lesion in right occipital lobe with adjacent edema. Multiloculation is apparent (A). Note typical mesial wall thinning (large arrow). Quadrigeminal plate cistern (small arrow) is prominent but otherwise normal.

C, MR image, 500/32 (0.5 T), shows central abscess cavity material as hypointense relative to white matter and hyperintense relative to normal CSF in lateral ventricles (not shown). Subtle hyperintense rim is seen at margin (small arrows). Minimal hypointensity in adjacent brain represents edema. Fluid within quadrigeminal plate cistern is subtly hyperintense relative to CSF but less intense than abscess fluid (large arrow).

D, MR image, 2150/64 (0.5 T), shows central area that is hyperintense relative to gray matter and CSF and slightly hypointense relative to edema. More peripherally within abscess cavity, material appears more hyperintense, and zone of relative hypointensity (straight solid arrows) is seen between these regions producing concentric rings of variable signal. Dramatic hypointense rim (grade III) is seen within abscess capsule. Small loculation (open arrow) corresponds to that seen on CT (A). Adjacent edema is hyperintense. Note hyperintensity within quadrigeminal plate cistern (curved arrow).

E, Photomicrograph of abscess wall shows granulation tissue, dense fibrous tissue (small arrows), and numerous lipid-laden macrophages (large arrows). (H and E stain, original magnification $\times 63$)

F, High-power photomicrograph shows lipid-laden macrophages and lymphocytic infiltrate. No evidence of acute or chronic hemorrhage is present (H and E, original magnification $\times 400$)

TE (nine of 10 cases) scans. On short TR/short TE scans the rim was mildly hyperintense relative to white matter in four cases (Fig. 1C) and isointense (delineated by adjacent hypointense peripheral edema and central necrosis) in three cases (Fig. 4A). On long TR/intermediate to long TE scans, the rim was hypointense relative to gray matter in all nine cases. It was hypointense (five cases, e.g., Figs. 1D and 2C–2E) to isointense (four cases, e.g., Figs. 3B, 3C, 4B, and 4C) relative

to white matter and became darker as TE was prolonged (Table 2). One patient with surgically and pathologically confirmed acute cerebritis did not have a discrete rim on short TR/short TE or long TR/intermediate to long TE scans. This lesion was diffusely isointense relative to brain on short TR/short TE scans and isointense relative to white matter (grade I) on long TR/intermediate to long TE scans. The location and configuration of the dark rim on long TR/intermediate to long

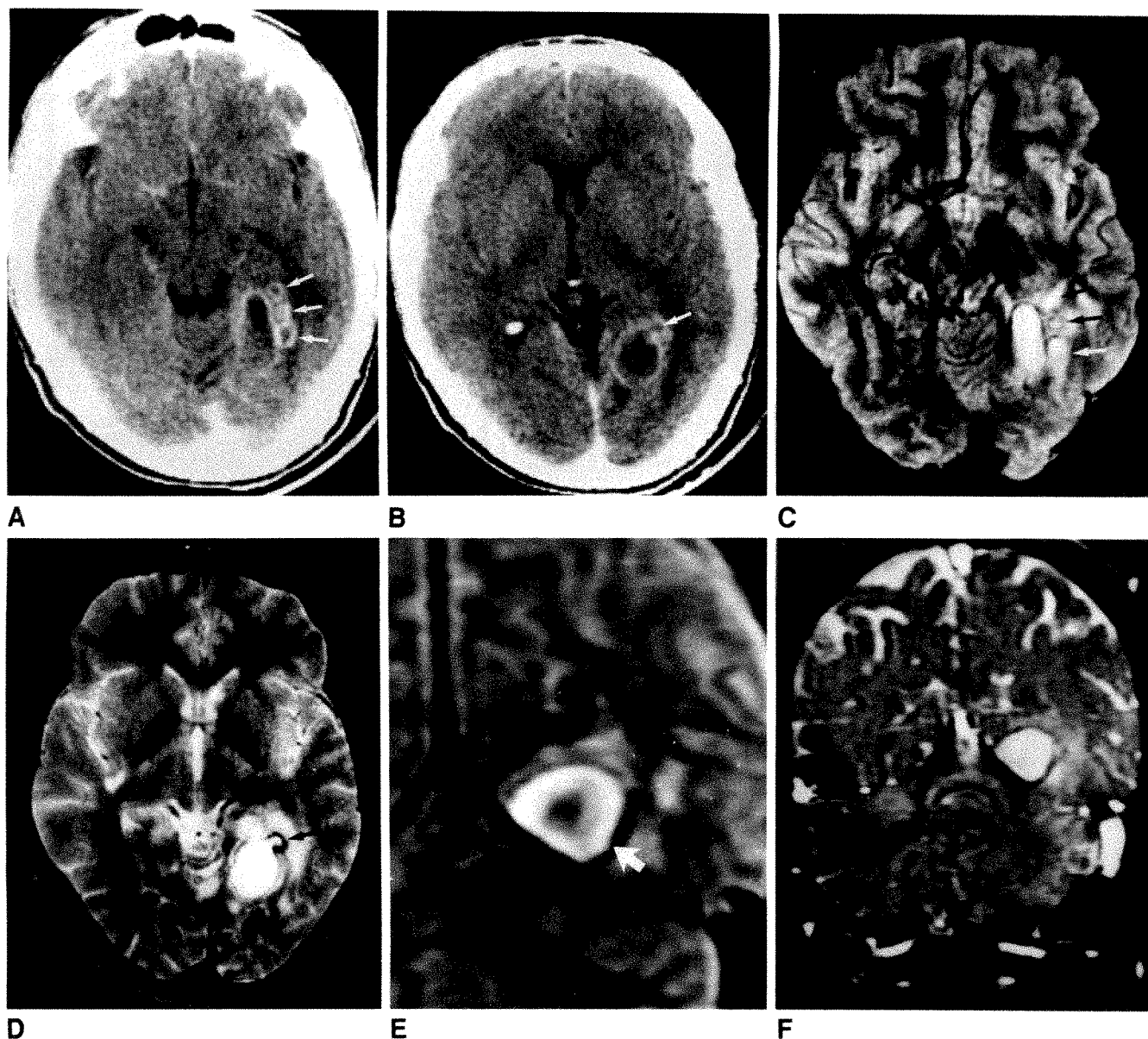


Fig. 2.—Case 5: Preoperative brain abscess.

A and B, Contrast-enhanced CT scans in chronic abscess show large enhancing ring lesion with minimal edema. Note three satellite foci inferiorly (arrows, A) and single, "budlike" projection superiorly (arrow, B).

C and D, MR images, 2000/40 (C) and 2000/80 (D) at 1.5 T, show excellent correspondence. Grade III hypointense rim surrounds abscess, three satellite foci (arrows, C), and bud (arrow, D).

E, Magnified view of coronal image 2000/40 (1.5 T) shows concentric rings in abscess center. Biopsy site is known (arrow) from surgical notes and is hypointense.

F, Rim is hypointense also on gradient-echo image, 21/12 (10° flip angle) at 1.5 T.

TE scans closely matched the enhanced ring visualized on CT; the short TR/short TE rim correlated less well. Subtle loculations and small satellite lesions were seen in all four cases in which these were identified on CT (Figs. 1–3).

The postoperative patients were evaluated on the basis of time from surgical intervention. Evaluation of the four studies performed within 1 week of surgery revealed features similar to the preoperative cases, including peripheral edema, central abscess fluid, and a discrete rim (Figs. 5B, 6A, and 6B). Mild hyperintensity on short TR/short TE scans was noted in the abscess cavity in two cases with evidence of increased central

density on CT, probably indicative of postoperative hemorrhage. The presence of the dark rim allowed visualization of the morphologic characteristics of the abscess, which corresponded well to concurrent CT findings. The intensity of the rim did not change significantly in the one patient studied just before and after surgical drainage (Figs. 5B and 5C), nor was there a significant alteration of intensity when all preoperative and early postoperative cases were compared (Table 2).

More delayed follow-up studies (9 days to 1 year) were available in four patients (nine studies) and showed progressively decreasing edema, mass effect, and abscess cavity

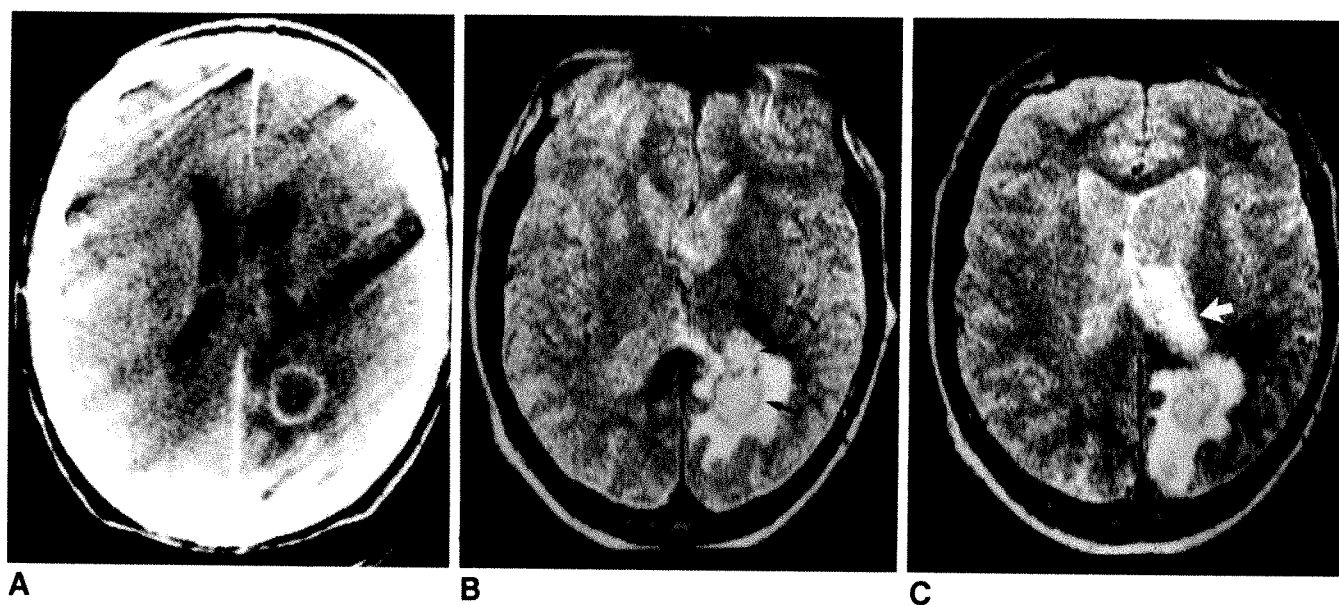


Fig. 3.—Case 14: Preoperative brain abscess.

A, Motion-degraded contrast-enhanced CT scan shows ring-enhancing left occipital abscess with mesial wall thinning. Intraventricular spread cannot be identified.

B and C, MR images, 2150/64 (B) and 2150/96 (C) at 0.5 T, show multilocular lesion with grade I rim intensity (arrows, B) and intraventricular extension of abscess with involvement of choroid plexus (arrow, C). Note hypointensity of falx cerebri.

size. In one patient (Case 11) serial postoperative studies showed progressive diminution of the abscess rim hypointensity. In another patient (Case 1) rim hypointensity decreased between the 5-day and 2-week scans (both obtained at 0.5 T; Figs. 6B and 6C), while a follow-up study at 6 weeks at 1.5 T showed an increase in rim hypointensity without a change in clinical status (Fig. 6D). Further sequential studies up to 15 weeks at 1.5 T revealed complete resolution of the hypointense rim and central necrotic cavity (Fig. 6E). In both serially evaluated patients, contrast-enhanced CT scans obtained close in time to the MR studies continued to demonstrate an enhancing ring. Late follow-up studies at 1 year (Cases 3 and 10, Figs. 4F and 4G) demonstrated only subtle hypointensity on short TR/short TE scans and focal hyperintensity on long TR/long TE scans, without mass effect.

Histopathologic evaluation of the 10 pyogenic abscess biopsy specimens revealed a spectrum of the stages of abscess evolution (Table 1). These include (1) two patients with acute cerebritis or early abscess formation (Cases 6 and 9); (2) seven patients with organizing abscesses (Cases 2, 4, 5, 7, 10, 13, and 14) characterized by granulation tissue containing capillaries, fibroblasts, macrophages, lymphocytes, and polymorphonuclear cells; and (3) one patient (Case 10) with a chronic abscess with a granulomatous infiltrate and foci of necrosis. Macrophages, which were diffusely distributed throughout the capsules of the organizing abscesses, had abundant cytoplasm that ranged from eosinophilic to vacuolated in appearance (Figs. 1E and 1F). Large discrete collections of lipid-laden macrophages were seen in two patients (Cases 13 and 14). Macrophagic infiltration ranged from grade II to III in mature and chronic abscesses and was grade I only in a patient with cerebritis (Table 3). Neither extravas-

cular erythrocytes nor iron pigment was detected by H and E stains in any of the 10 biopsy specimens. Iron stains were performed in eight of 10 specimens. No iron was detected in six specimens, while scant, focal iron deposition was present in only two abscess capsules, one with grade I (Case 10) and one with grade III (Case 13) rim intensity on long TR/intermediate to long TE scans. (Iron was present in the inflamed choroid plexus of one patient [Case 14] and in the leptomeninges of another [Case 9].) Collagen was present in all organizing and chronic abscesses, but was not seen in the cases of cerebritis.

MR and pathologic evaluations of the three patients without pyogenic abscess were performed. One tuberculous granuloma was diffusely hypointense (grade III) on long TR/intermediate to long TE scans. The two metastatic foci had rim appearances similar to those of the majority of the abscesses, including grade II hypointensity of the rim on long TR/intermediate to long TE images (Figs. 7B and 7C). Pathologic evaluation of the tuberculoma revealed granulation tissue with fibroblasts, capillaries, and grade II macrophagic infiltration. In both cases of metastatic carcinoma, the neoplasms were surrounded by sheets of lipid-laden macrophages (grade III), scattered lymphocytes, and proliferating vessels (Fig. 7D). Collagen was not a feature of the metastatic lesions. No hemorrhage or iron was detected in the tuberculoma or the metastatic carcinomas.

On microbacteriologic evaluation, a variety of organisms was cultured. In four cases, two organisms were identified. The most prevalent bacteria were *Streptococcus milleri* and *Peptostreptococcus*, each seen in three cases. No organisms were cultured in two patients in whom antibiotic therapy had been initiated long before surgery.

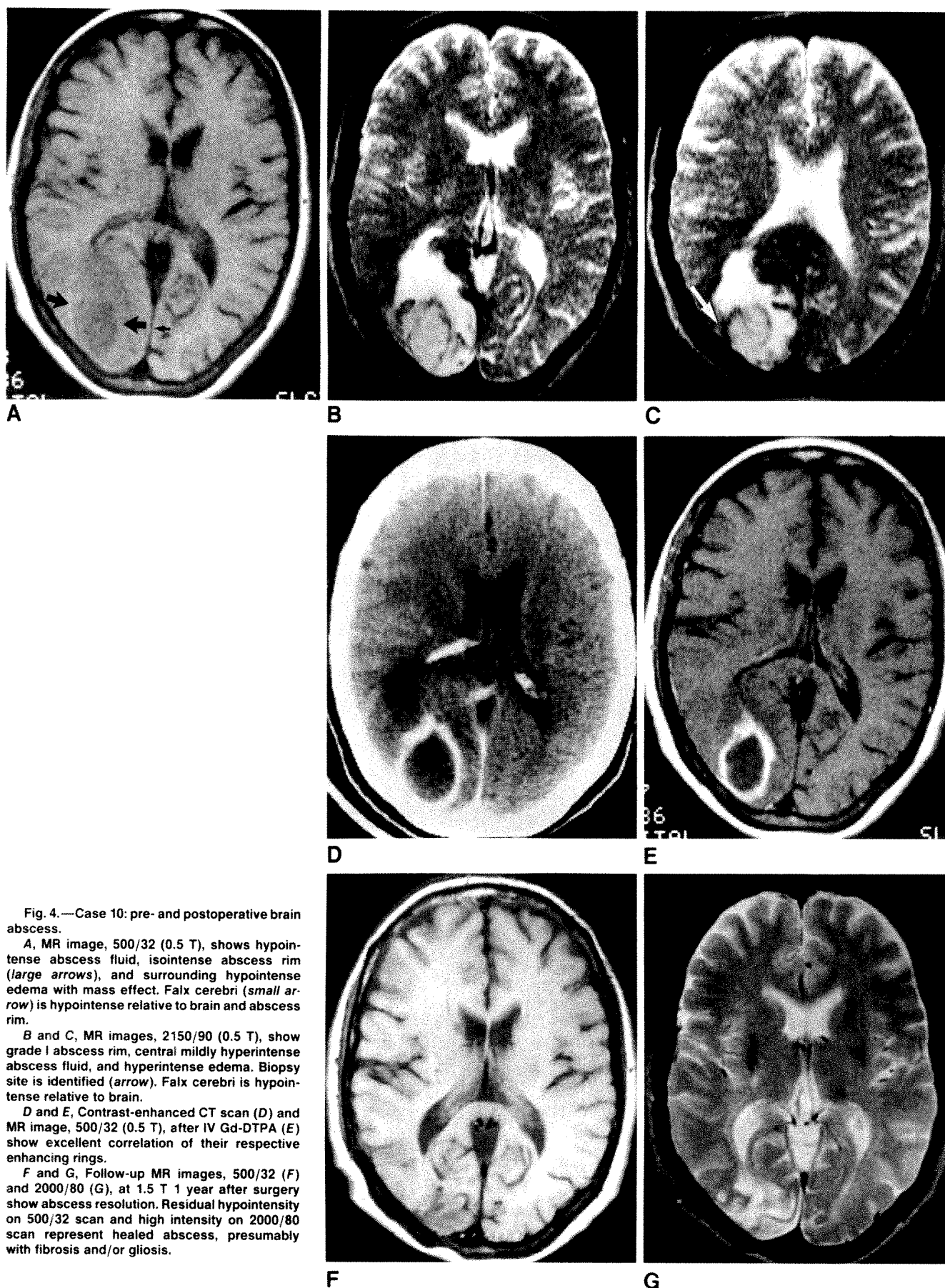


Fig. 4.—Case 10: pre- and postoperative brain abscess.

A, MR image, 500/32 (0.5 T), shows hypointense abscess fluid, isointense abscess rim (large arrows), and surrounding hypointense edema with mass effect. Falx cerebri (small arrow) is hypointense relative to brain and abscess rim.

B and C, MR images, 2150/90 (0.5 T), show grade I abscess rim, central mildly hyperintense abscess fluid, and hyperintense edema. Biopsy site is identified (arrow). Falx cerebri is hypointense relative to brain.

D and E, Contrast-enhanced CT scan (D) and MR image, 500/32 (0.5 T), after IV Gd-DTPA (E) show excellent correlation of their respective enhancing rings.

F and G, Follow-up MR images, 500/32 (F) and 2000/80 (G), at 1.5 T 1 year after surgery show abscess resolution. Residual hypointensity on 500/32 scan and high intensity on 2000/80 scan represent healed abscess, presumably with fibrosis and/or gliosis.

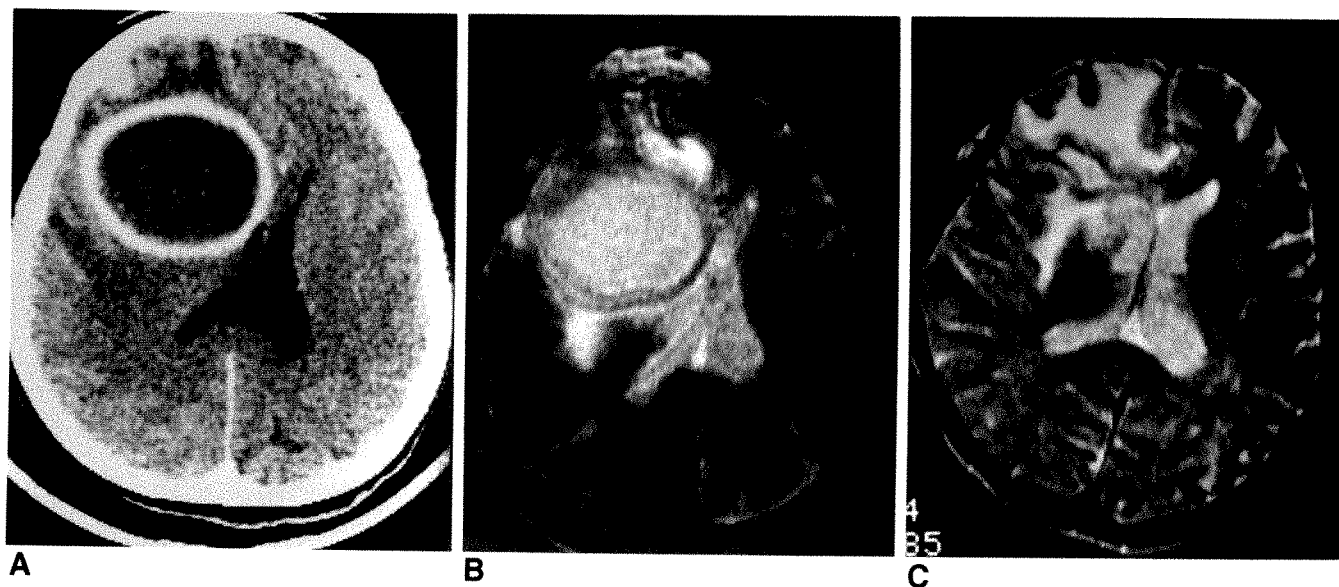


Fig. 5.—Case 12: Pre- and postoperative chronic brain abscess.
 A, Contrast-enhanced CT scan reveals thick-walled chronic abscess.
 B, Motion-degraded MR image, 2150/60 (0.5 T), shows grade II rim intensity.
 C, Follow-up image, 2150/60 (0.5 T), within 1 week of drainage shows collapse of abscess capsule comparable to that seen on CT (not shown). There is no significant change in grade of rim hypointensity when compared with preoperative scan.

Discussion

During the past decade, CT has proved to be an excellent technique for the evaluation of intracranial abscesses, and has been a major factor in the improved survival and reduced mortality now associated with these lesions [1–3]. A constellation of CT features that differentiate abscesses from primary and metastatic neoplasms, infarction, and noninfectious inflammatory lesions is based on pathologic findings and includes (1) peripheral hypodensity due to edema, (2) central hypodensity due to necrosis, (3) intraventricular hyperdensity and/or periventricular enhancement due to extraparenchymal spread, and (4) a highly characteristic pattern of ring enhancement reflecting the unique pathogenesis of the abscess capsule [2, 4–8]. Review of the cases in this series indicates that MR is valuable for detecting and characterizing brain abscesses by demonstrating features corresponding to the CT findings as well as additional features not seen on CT.

Mild hypointensity on short TR/short TE images and marked hyperintensity on long TR/intermediate to long TE images were noted surrounding all preoperative and early postoperative abscesses, reflecting prolongation of T1 and T2 relaxation times due to vasogenic edema [9]. Though edema was identified on CT in every case, contrast between edema and adjacent brain was higher on MR than on CT due to the greater sensitivity of MR to changes in tissue water content (Figs. 1–4) [9]. This might offer a potential advantage in the detection of subtle edema in the early stages of abscess evolution. Serial MR scans showed resolution of hypointensity on short TR/short TE scans and a decrease in the extent of hyperintensity on long TR/intermediate to long TE scans 1–2 months after surgical drainage, indicative of decreasing edema (Fig. 6).

The abscess center demonstrated hyperintensity relative to CSF and hypointensity relative to white matter on short TR/short TE images, hyperintensity relative to CSF and iso- to hyperintensity relative to gray matter on long TR/intermediate images, and iso- to mild hyperintensity relative to CSF and gray matter on long TR/long TE images. This intensity pattern, also encountered in cystic and/or necrotic neoplasms, reflects the proteinaceous character of the abscess fluid with resultant T2 prolongation relative to brain and T1 shortening relative to CSF [9–11]. The development of mild hyperintensity on short TR/short TE images in the abscess cavity without interval change in intensity on long TR/intermediate to long TE images was seen in two early postoperative cases, and was possibly the result of intraoperative hemorrhage. Postoperative reduction in the size of the abscess cavity on MR (two of two cases studied serially; Figs. 5 and 6) correlated with similar changes on CT and with clinical improvement and, thus, was indicative of abscess healing [2].

One additional feature of the abscess cavity detected on long TR/intermediate to long TE scans in seven of 10 preoperative cases was the presence of concentric bands of varying intensity and thickness (Figs. 1D and 2E), a feature not encountered on MR in other cystic or necrotic lesions or on CT studies in this series, where the abscess cavity was uniformly hypodense (Fig. 1B) [12]. The cause of this MR finding is unknown. Pathologic studies have demonstrated necrotic debris without viable bacteria or host inflammatory cells; the consistency of the debris varies from a homogeneous liquid to nonuniform, disorganized, gelatinous material [13]. The findings on MR suggest a greater level of organization within the necrotic center than has been previously appreciated on CT (likely due to the greater sensitivity of MR).

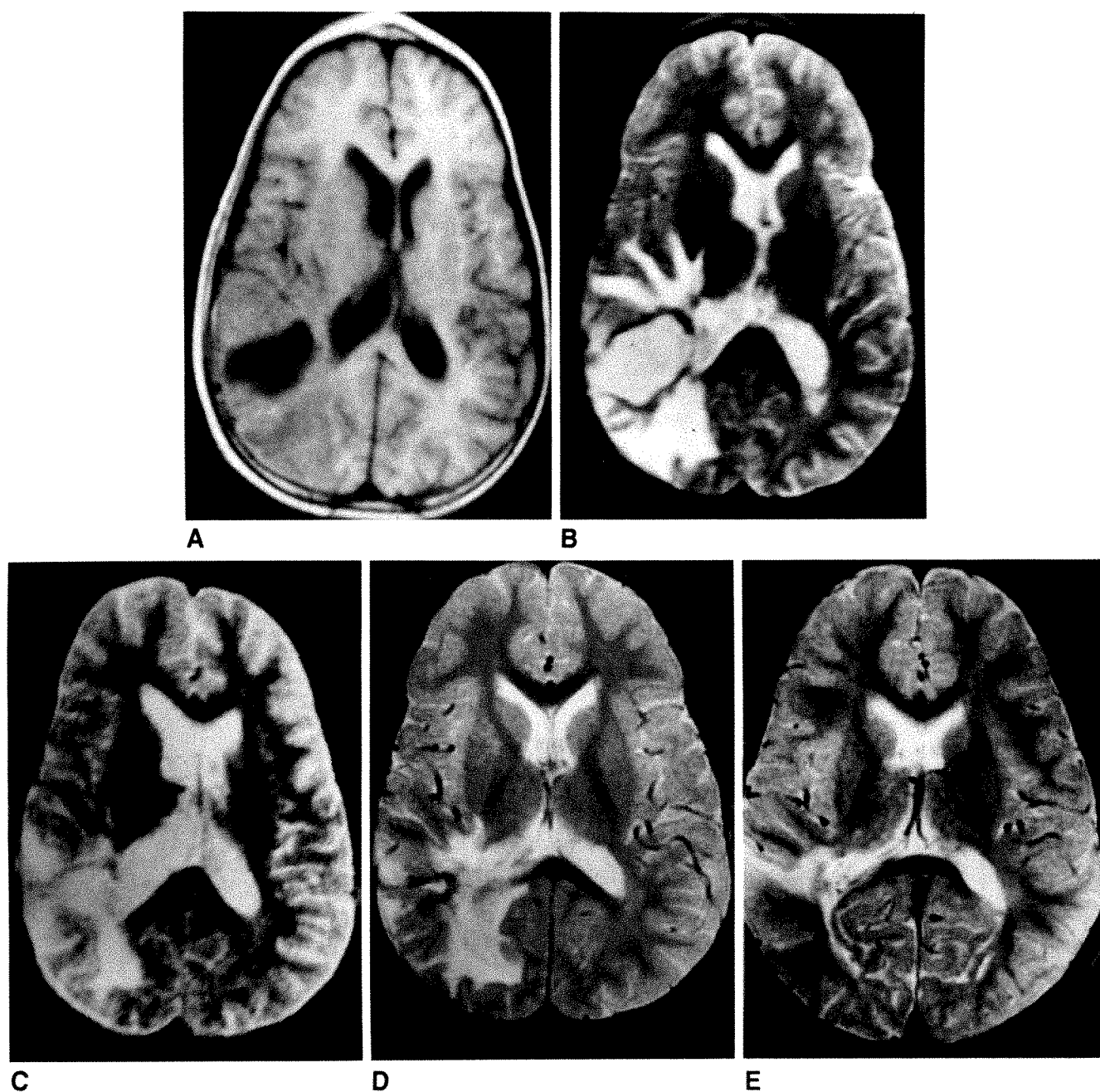


Fig. 6.—Case 1: Serial studies of postoperative brain abscess.

A and B, MR images, 500/32 (A) and 2150/120 (B), at 0.5 T 5 days after drainage of abscess show characteristic central fluid, edema, and rim intensities (grade II on 2150/120 scan).

C, MR image, 2150/120, at 0.5 T 2 weeks after surgery shows decreased mass effect and rim hypointensity.

D, MR image, 2000/80, at 1.5 T 6 weeks after surgery shows increase in rim hypointensity possibly related to increased sensitivity to magnetic susceptibility effects at higher field strength. Note collapse of abscess capsule.

E, MR image, 2000/80, at 1.5 T 15 weeks after surgery shows resolution of mass effect and hypointense rim, with residual high intensity (probable gliosis and/or fibrosis).

or at surgical or postmortem evaluation (possibly due to destruction of this organization by these invasive procedures).

Spread of inflammation into the ventricles and subarachnoid spaces is more conspicuous on MR than on CT. Extension into the quadrigeminal plate cistern (Fig. 1) and lateral ventricle

(Fig. 3) resulted in hyperintensity in these spaces relative to CSF, especially on long TR/intermediate TE images, with no change in density on CT, reflecting the enhanced ability of MR to characterize proteinaceous fluids [9–11]. Extraparenchymal spread is an important differential diagnostic feature

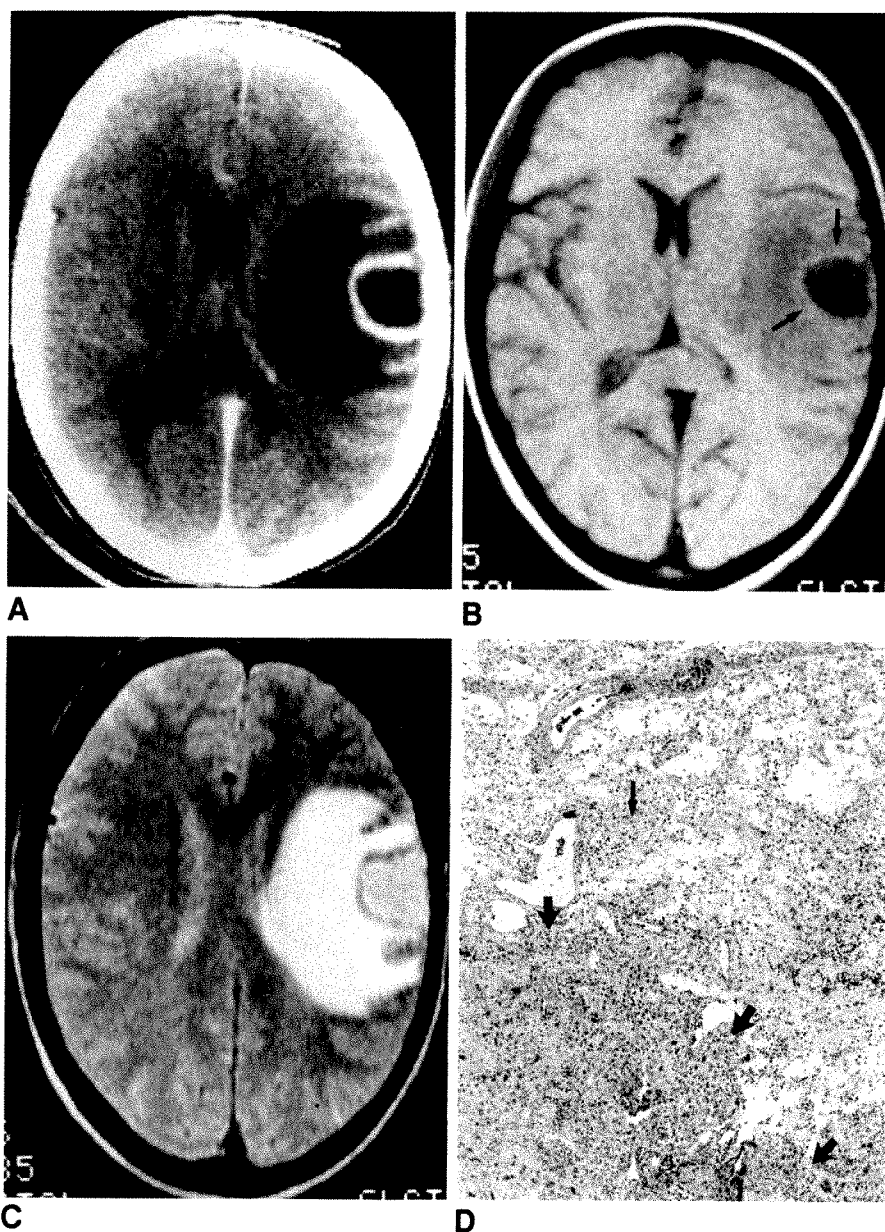


Fig. 7.—Metastatic papillary adenocarcinoma to left parietal lobe.

A, Contrast-enhanced CT scan shows ring enhancement, surrounding low-density edema, mass effect, and cortical location.

B, MR image, 500/32 (0.5 T), shows isointense rim (arrows) with adjacent hypointense peripheral edema and central necrosis.

C, MR image, 2150/96 (0.5 T), shows hyperintense central material, grade II intensity rim, and high-intensity surrounding edema.

D, Photomicrograph shows metastatic tumor (large arrows) surrounded by lipid-laden macrophages (small arrow), chronic inflammatory infiltrate, and numerous vessels. No evidence of acute or chronic hemorrhage or fibrosis is present. (H and E, original magnification $\times 63$)

separating abscesses from other space-occupying lesions [2], and its detection has important therapeutic and prognostic implications.

A striking, unexpected, and clinically useful MR feature, noted in nine of 10 preoperative and four of four early postoperative cases, was the presence of a discrete rim interposed between the necrotic center and peripheral edema. The rim was iso- to mildly hyperintense relative to white matter on short TR/short TE images (Figs. 1C and 6A) and, more importantly, iso- to hypointense relative to white matter and hypointense relative to gray matter on long TR/intermediate to long TE images (Figs. 1D, 2C–2E, 5B, 5C, and 6B); Tables 2 and 3). This rim, present in all mature and chronic abscesses and absent only in the surgically and pathologically proved case of acute cerebritis, corresponded in location and config-

uration to the enhanced ring seen on CT. The rims were thin, smooth, and ovoid in contour, reflecting, as do CT rings, the unique pathology of abscess capsules and aiding differentiation from other lesions. Other characteristic CT findings duplicated by the dark rim on MR included gracile internal loculations and small satellite lesions (Figs. 1D, 2C, 2D, and 3B).

The rim on MR differed from the ring on CT in two respects, one morphologic and one temporal. Mesial wall thinning was more conspicuous on contrast-enhanced CT than on MR, though IV Gd-DTPA was able to duplicate this feature (Figs. 4B–4E). In the early postoperative period, decrease in the size of the rim on MR occurred simultaneously with decrease in size on CT (Fig. 5C). In the late postoperative period, however, rim resolution on MR preceded ring resolution on

CT. Because CT contrast enhancement may persist for at least 8 months after abscess healing [2, 14], rim resolution on MR may prove to be a more accurate assessment of healing.

Though a rim that is iso- to hypointense relative to white matter on long TR images occasionally may be seen in other lesions including subacute and chronic hematomas [15, 16], metastases [17], granulomatous lesions [18], and, rarely, gliomas [17], its presence in all abscesses studied and its uniform, circumferential appearance in each capsule are both unusual and noteworthy. Even extremely thin rim components such as satellite lesions were detected despite partial-volume effects from adjacent hyperintense edema and central necrosis (Figs. 1D and 3C). Normal white matter is hypointense relative to gray matter on long TR/intermediate to long TE images [9] (regions such as the splenium of the corpus callosum are nearly devoid of signal on long TR/long TE scans) because of decreased tissue water. In contrast, most intracerebral lesions are hyperintense relative to gray matter on long TR/intermediate to long TE images because of increased tissue water [19–24]. Thus, abscess rims that are either iso- or hypointense relative to white matter can be described as "hypointense" lesions, a term applied to some hematoma rims also [25] (Figs. 4E and 5B).

Various mechanisms were sought to explain the intensity pattern of the abscess rim that would be compatible with the observed pathologic and MR findings. Fibrosis and hemorrhage were initially considered likely causes. As expected, fibrous collagen was present in the mature abscess capsules [7, 13, 26] submitted for pathologic examination (Fig. 1E); however, the intensities of the rims did not match those seen in normal or pathologic intracranial fibrous tissue. Normal fibrous structures such as the falx and tentorium are hypointense on both short TR/short TE and long TR/intermediate to long TE images due to their low water and proportionately high protein content (Figs. 3B, 3C, and 4A–4C) [9, 10, 27], while the abscess rims are iso- to mildly hyperintense on short TR/short TE images. Pathologic fibrosis is rarely encountered intracranially, but several histologically proved examples of meningeal fibrosis demonstrated hyperintensity on long TR/intermediate to long TE images [28]. Furthermore, the temporal changes in rim intensity correlate poorly with the sequential changes of abscess healing. Specifically, deposition of collagen progresses with abscess maturation and persists after abscess resolution as a focal scar [13, 26]; thus, the dark rim should become progressively more prominent and persist with abscess healing. In fact, the rim showed only moderate (grade II) hypointensity in the most chronic preoperative abscesses (Cases 11 and 12, Fig. 5), and diminished and/or resolved on serial examinations in two patients studied 1 year after surgical drainage. Residual hyperintensity rather than hypointensity was seen in these two patients 1 year after successful treatment.

Though spontaneous hemorrhage into abscesses is rarely encountered clinically or documented pathologically [29], hemorrhage was considered a possible cause of the capsular intensities because of similarities to intensities seen in some stages of hematoma evolution. Thus, mild hyperintensity in

the rim on short TR/short TE images may reflect paramagnetic proton-electron dipole-dipole interaction (T1 shortening) [9, 15], and hypointensity on long TR/intermediate to long TE images may reflect preferential T2 proton relaxation enhancement due to a heterogeneously distributed paramagnetic substance [15, 16, 30–32]. This capsular intensity pattern can be seen during the late acute stage of hemorrhage due to the presence of intracellular methemoglobin and/or a combination of extracellular methemoglobin and intracellular deoxyhemoglobin. In chronic hemorrhage, a hypointense rim, similar in appearance to the abscess rim, is seen because of the presence of hemosiderin-laden macrophages in the hematoma capsule [15, 30]. Support for the hypothesis that the intensities are due to paramagnetic T2 shortening comes from the findings of more pronounced hypointensity at 1.5 T than at 0.5 T (Cases 1 and 5) and the presence of hypointensity on gradient-echo pulse sequences [30].

However, careful review of our surgical reports and pathologic specimens showed no evidence of hemorrhage. Routine H and E stains (on which the presence of microscopic hemorrhage is commonly identified) showed no hemorrhage in the 10 cases in which specimens were available for review. Eight of these cases were restudied with Perls' stain for the presence of iron; no iron was found in six. The possibility that hemorrhage into the abscess capsule was missed due to the sampling error (e.g., only a small portion of the capsule was available for pathologic evaluation) seems unlikely since all but one of the biopsied rims were diffusely and relatively homogeneously hypointense. In the one inhomogeneous rim (Fig. 2E), surgical notes confirmed that pathologic material was indeed obtained from a portion of the capsule with grade III intensity.

The presence of scant amounts of iron in two abscess capsules is unlikely to have been the primary cause of hypointensity on long TR images in these cases, because the degree of hypointensity did not correspond to the extent of iron deposition; that is, marked hypointensity (grade III) was seen in one case (Case 13, Fig. 1) while mild hypointensity (grade I) was seen in the other (Case 10, Fig. 4). In addition, scant amounts of iron are probably insufficient to cause hypointensity on long TR/intermediate to long images at 0.5 T, the field strength at which both patients were studied. Because preferential T2 shortening is, in part, dependent on field strength and the concentration of the intracellular paramagnetic substance [15, 33], small chronic hematomas often fail to produce discernible hypointensity on long TR spin-echo images at 0.5 T [34, 35]. In addition, careful histologic studies have revealed that lesions with scant hemorrhage may fail to demonstrate hypointensity on long TR/long TE images [19]. For instance, in Case 14 (Fig. 3), a scant amount of iron was microscopically identified in the choroid plexus, which was hyperintense on long TR/intermediate to long TE images, while the adjacent hypointense abscess rim did not contain iron.

Finally, the rapid temporal changes known to occur in hematoma intensity are difficult to reconcile with the constant intensity pattern in the abscess rim. In acute hemorrhage, hyperintensity on short TR/short TE images begins to develop

on approximately the third postictal day and persists for weeks to months, and hypointensity on long TR/intermediate to long images is transiently present from approximately the second to the 10th day [16, 32]. Thus, the combination of hyperintensity on short TR/short TE images and hypointensity on long TR/intermediate to long TE images, the pattern seen in abscess rims, is transiently present for approximately 1 week during hematoma evolution. However, the cases in this series were evaluated at various times after the onset of symptoms and at various pathologic stages of abscess evolution (Table 1), yet demonstrated a constant pattern of rim intensities. Furthermore, comparison of pre- and postoperative MR scans demonstrated no change in capsular intensities, with or without intraoperative hemorrhage (Case 12, Fig. 5). On the other hand, in the chronic stage, hemorrhage would be expected to demonstrate persistent hypointensity, particularly at high fields [15], in contrast to resolution of hypointensity seen with abscess healing at high fields (Case 10, Fig. 4; Case 1, Fig. 6).

Though hemorrhage is not the primary cause of the capsular intensities, the MR findings remain highly characteristic of paramagnetic T1 and T2 shortening. One possible source of a paramagnetic substance that heretofore has not been considered comes from the macrophages that are present in abundance in all abscess capsules (Table 3) [26]. In association with phagocytosis, macrophages (and neutrophils) undergo a respiratory burst, generating free radicals that destroy, or help destroy, the ingested microorganisms [36–38]. The initial step in this process is the conversion of molecular oxygen to the free radical superoxide, which then undergoes a variety of complex reactions to produce a large number of free radicals. For instance, the Haber-Weiss reaction converts superoxide to hydrogen peroxide, hydroxyl radical, and atomic oxygen. These free radicals, called reactive oxygen intermediates [38], are short-lived [39] and are generally detected by indirect biochemical methods, though they have been demonstrated by direct in vitro sampling of activated macrophages by electron spin resonance techniques [40–42].

These reactive oxygen intermediates differ in one major respect from paramagnetic substances more familiar to radiologists such as deoxyhemoglobin, methemoglobin, or melanin [19, 21] in that they are unstable and extremely short-lived. Therefore, capsular hypointensity cannot result from a single, easily measurable substance produced by a static group of cells, but rather (if this hypothesis is correct) from the continuous production of a string of short-lived free radicals generated during active phagocytosis by macrophages constantly entering the capsule from the vascular bed.

Another possible source of paramagnetic effects are the enzymes that catalyze these reactions [39]. For example, the Haber-Weiss reaction is catalyzed by copper and iron molecules, possibly in the form of nonheme paramagnetic proteins such as lactoferrin and transferrin [43], which are more stable than the reactive oxygen intermediates.

Certainly, this hypothesis will require extensive in vivo and in vitro evaluation, in particular to determine if activated macrophages and their associated respiratory burst are ca-

pable of producing detectable T1 and T2 shortening. Pending these evaluations, however, there is indirect evidence to support this hypothesis. First, pathologic evaluation of two metastatic foci with rim intensities mimicking those seen in abscesses revealed extensive macrophagic infiltrate in their rims (Fig. 7D). Except for these macrophages, no other histologic feature was common to both the metastases and the abscesses. Specifically, no fibrosis or hemorrhage was demonstrated in the metastases. Second, pathologic evaluation of the diffusely hypointense (on long TR scans) parenchymal tuberculoma demonstrated no fibrosis or hemorrhage, though macrophages were present in abundance. (Similar intensities have been reported in other tuberculomas [18, 44].)

Evaluation of the temporal changes in rim intensity also supports the hypothesis that hypointensity is a reflection of macrophage activity (host response). In the acute cerebritis stage, when the capsule is poorly formed, discrete hypointensity is not seen, and poorly defined hypointensity at this stage may reflect early macrophage reaction. In the early mature abscess stage, host response is maximal, as is the degree of hypointensity. In chronic untreated abscesses (Fig. 5), hypointensity is less marked, suggesting that the infection is partially contained and macrophage activity is waning. With treatment and healing, macrophage activity continues to decrease until hypointensity is no longer visualized (Figs. 4 and 6).

In conclusion, findings in 14 patients with pyogenic abscesses indicate a characteristic set of features that should allow for early and accurate diagnosis on MR. In addition, two important general conclusions seem warranted. First, intensities indicative of paramagnetic T1 and T2 shortening may be seen in the absence of hemorrhage. Second, the hypointense rim in pyogenic abscesses and possibly in other inflammatory lesions may prove to be an indicator of macrophage activity and, therefore, of host response. This may, in turn, have interesting implications for the experimental and clinical evaluation of these lesions and their therapy.

ACKNOWLEDGMENTS

We thank Anna Maria Giambruno and Luis Cintrone for preparation of special histopathologic slides.

REFERENCES

1. Rosenblum ML, Hoff JT, Norman D, Weinstein PR, Pitts L. Decreased mortality from brain abscesses since the advent of computerized tomography. *J Neurosurg* 1978;49:658–668
2. Whelan MA, Hilal SK. Computed tomography as a guide in the diagnosis and follow-up of brain abscesses. *Radiology* 1980;135:663–671
3. Claveria LE, du Boulay GH, Mosley IF. Intracranial infections: investigation by computerized tomography. *Neuroradiology* 1976;12:54–71
4. Nielson H, Gyldensted C. Computed tomography in the diagnosis of cerebral abscess. *Neuroradiology* 1977;12:207–217
5. Braun IF, Chambers E, Leeds NE, Zimmerman RD. The value of unenhanced scans in differentiating lesions producing ring enhancement. *AJNR* 1982;3:643–647
6. Enzmann DR, Britt RH, Placone R. Staging of human brain abscess by computed tomography. *Radiology* 1983;146:703–708
7. Enzmann DR. Focal parenchymal infection. In: Enzmann DR, ed. *Imaging*

- of infections and inflammations of the central nervous system: computed tomography, ultrasound, and nuclear magnetic resonance. New York: Raven, 1984:27-102
8. Holtas S, Tornquist C, Cronqvist S. Diagnostic difficulties in computed tomography of brain abscesses. *J Comput Assist Tomogr* 1982;6(4):683-688
 9. Bradley WG Jr. Pathophysiologic correlates of signal alterations. In: Brant-Zawadzki M, Norman D, eds. *Magnetic resonance imaging of the central nervous system*. New York: Raven, 1987:23-42
 10. Mitchell DG, Burk DL Jr, Vinitski S, Rifkin MD. The biophysical basis of tissue contrast in extracranial MR imaging. *AJR* 1987;149:831-837
 11. Kjos BO, Brant-Zawadzki M, Kucharczyk W, et al. Cystic intracranial lesions: magnetic resonance imaging. *Radiology* 1985;155:363-369
 12. Danziger A, Price H, Schechter MM. An analysis of 113 intracranial infections. *Neuroradiology* 1980;19:31-34
 13. Alvord EC, Shaw C-M. Infectious, allergic, and demyelinating diseases of the nervous system. In: Newton TH, Potts DG, eds. *Radiology of the skull and brain*, Vol. 3. *Anatomy and pathology*, 1st ed. St. Louis: Mosby, 1977:3088-3172
 14. Dobkin JF, Heaton EB, Dickinson PCT, Brust JCM. Nonspecificity of ring-enhancement in "medically cured" brain abscesses. *Neurology* 1984;34:139-144
 15. Gomori JM, Grossman RI, Goldberg HI, Zimmerman RA, Bilaniuk LT. Intracranial hematomas: imaging by high field MR. *Radiology* 1985;157:87-93
 16. Zimmerman RD, Heier LA, Snow RB, Liu DP, Kelly AB, Deck MDF. MR imaging features of acute intracranial hemorrhage studied at 0.5T with emphasis on sequential intensity changes on multiple pulse sequences. *AJNR* 1988;9:47-57, *AJR* 1988;150:651-661
 17. Fleming CA, Zimmerman RD, Haines A, Morgello S, Deck MDF. The diagnostic significance of rim intensity and edema patterns in the differentiation of intracranial mass lesions on MRI (abstr). *AJNR* 1987;8:454
 18. Gupta RK, Jena A, Sharma A, Guha DK, Khush S, Gupta AK. MR imaging of intracranial tuberculomas. *J Comput Assist Tomogr* 1988;12(2):280-285
 19. Woodruff WW Jr, Diang WT, McLendon RE, Heinz ER, Voorhees DR. Intracerebral malignant melanoma: high-field-strength MR imaging. *Radiology* 1987;165:209-213
 20. Komiya M, Yagura H, Baba M, et al. MR imaging: possibility of tissue characterization of brain tumors using T1 and T2 values. *AJNR* 1987;8:65-70
 21. Brant-Zawadzki M. MR imaging of the brain. *Radiology* 1988;166:1-10
 22. Zimmerman RA, Bilaniuk LT, Johnson MH. MRI of central nervous system: early clinical results. *AJNR* 1986;7:587-594
 23. Lee BCP, Kneeland JB, Cahill PT, Deck MDF. MR recognition of supratentorial tumors. *AJNR* 1985;6:871-878
 24. Brant-Zawadzki M, Norman DC, Newton TH, et al. Magnetic resonance of the brain: the optimal screening technique. *Radiology* 1984;152:71-77
 25. Atlas SW, Grossman RI, Gomori JM, et al. Hemorrhagic intracranial malignant neoplasms: spin-echo MR imaging. *Radiology* 1987;164:71-77
 26. Robbins SL, Cotran RS, Kumar V. Inflammation and repair. In: Robbins SL, Cotran RS, Kumar V, eds. *Pathologic basis of disease*, 3rd ed. Philadelphia: Saunders, 1984:40-84
 27. Daniels DL, Pojunaas KW, Kilgore DP. MR of diaphragma sellae. *AJNR* 1986;7:765-769
 28. Destian S, Heier LA, Zimmerman RD, Deck MDF. Meningeal fibrosis in patients with chronic ventriculoperitoneal shunts. Presented at the annual meeting of the American Society of Neuroradiology, Chicago, May 1988
 29. Bach D, Goldenberg MH. Hemorrhage into a brain abscess. *J Comput Assist Tomogr* 1983;7(6):1067-1069
 30. Edelman RR, Johnson K, Buxton R, et al. MR of hemorrhage: a new approach. *AJNR* 1986;7:751-756
 31. Zimmerman RD, Deck MDF. Intracranial hematomas: imaging by high field MR (letter). *Radiology* 1986;159:565-566
 32. Gomori JM, Grossman RI, Hackney DB, et al. Variable appearance of subacute intracranial hematomas on high-field spin-echo MR. *AJNR* 1987;8:1019-1026
 33. Thulborn KR, Waterton JC, Matthews PM, Radda CK. Oxygenation dependence of the transverse relaxation time of water protons in whole blood at high field. *Biochim Biophys Acta* 1982;714:265-270
 34. Zimmerman RD. Magnetic resonance imaging of intracranial hemorrhage. In: Sarwar M, Batnitzky S, eds. *Non-traumatic ischemia and hemorrhagic disorders of the CNS*. Boston: Martinus Nijhoff (in press)
 35. Bradley WG Jr. MRI of hemorrhage and iron in the brain. In: Stark DD, Bradley WG Jr, eds. *Magnetic resonance imaging*. St. Louis: Mosby, 1988:359-375
 36. Eisen HN. Cell-mediated hypersensitivity and immunity. In: Davis BD, Dulbecco R, Eisen HN, Ginsberg HS, eds. *Microbiology, including immunology and molecular genetics*, 3rd ed. Hagerstown: Harper & Row, 1980:494-521
 37. Johnston RB Jr. Oxygen metabolism and the microbicidal activity of macrophages. *Fed Proc* 1978;37:2759-2764
 38. Adams DO, Hamilton TA. The cell biology of macrophage activation. *Annu Rev Immunol* 1984;2:283-318
 39. Southorn PA, Powis G. Free radicals in medicine: I. chemical nature and biologic reactions. *Mayo Clin Proc* 1988;63:381-389
 40. Hume DA, Gordon S, Thornalley PJ, Bannister JV. The production of oxygen-centered radicals by Bacillus-Calmette-Guérin-activated macrophages: an electron paramagnetic resonance study of the response to phorbol myristate acetate. *Biochim Biophys Acta* 1983;763:245-250
 41. Bannister JV, Bellavite P, Serra MC, Thornalley PJ, Rossi F. An EPR study of the production of superoxide radicals by neutrophil NADPH oxidase. *FEBS Lett* 1982;145(2):323-326
 42. Harbour JR, Bolton JR. Superoxide formation in spinach chloroplasts: electron spin resonance detection by spin trapping. *Biochim Biophys Res Commun* 1975;64(3):803-807
 43. Koenig SH, Schillinger WE. Nuclear magnetic relaxation dispersion in protein solution. II. Transferrin. *J Biol Chem* 1969;244(23):6520-6526
 44. Venger BH, Dion FM, Rouah E, Handel SF. MR imaging of pontine tuberculoma (letter). *AJNR* 1987;8:1149-1150

Memorial

Robert S. Sherman, Jr., 1917–1988



Dr. Robert Stanton Sherman, Jr., a highly respected radiation oncologist of the San Francisco Bay area for 39 years, died at his home on May 23, 1988. Born in 1917, the son of a San Francisco physician, Dr. Sherman graduated from the University of California, Berkeley, and received his M.D. from the University of California School of Medicine, San Francisco, in 1942. After an internship at San Francisco General Hospital, he served as a physician in the United States Naval

Reserve from 1943 to 1946. He completed his residency in radiology at the University of California Medical Center, San Francisco, in 1949. He was on the full-time faculty in radiation therapy at that institution until 1953, becoming a diplomate of the American Board of Radiology in 1950. He was an American Cancer Society fellow in clinical therapeutic radiology at the Royal Marsden Hospital, London; Christie Hospital and Holt Radium Institute, Manchester; Foundation Curie, Paris; and Radiumhemmet and Karolinska Institute, Stockholm, from 1953 through 1954. He was a member of the attending staff in radiation therapy at Memorial Hospital, New York, and a member of the faculty of Cornell University Medical School in 1955 and 1956.

Dr. Sherman served on the clinical faculty of the University of California, San Francisco (UCSF), from 1953 until his death, as associate clinical professor of radiology since 1973. He was director of therapeutic radiology at Children's Hospital and Adult Medical Center from 1956 to 1977, at the Veterans Administration Hospital, from 1964 to 1969, and at St. Mary's Hospital from 1960 to 1977, all in San Francisco. He was engaged in the private practice of radiation therapy in Los Gatos, CA, from 1977 to 1983. He re-

mained a consultant in radiation oncology at UCSF until 1987. Dr. Sherman was the president of the UCSF Medical School Alumni-Faculty Association from 1969 through 1971 and of the UCSF Medical School Clinical Faculty Association from 1985 through 1986.

He was a member of the American Society of Therapeutic Radiologists, American Radium Society, Radiological Society of North America, American Roentgen Ray Society, British Institute of Radiology Society, Society of Nuclear Medicine, Pan-American Medical Association, the San Francisco and California Radiological Societies, San Francisco Medical Society, California Medical Association, American Medical Association, World Medical Association, California Academy of Medicine, and the Northern California Radiation Therapy Association. He became a fellow of the American College of Radiology in 1950.

Bob was an enthusiastic, experienced yachtsman and active in community affairs. He was a devoted husband and father. He is survived by his wife, Alice, and four children, Elizabeth, Alice, James, and Robert. He is remembered by his family, colleagues, and friends for his thoughtfulness and ready smile and his deep concern for his patients.

John C. Bennett
San Rafael, CA 94901

Gd-DTPA-Enhanced MR Imaging of Spinal Tumors

Paul M. Parizel^{1, 2}
 Danielle Balériaux¹
 Georges Rodesch¹
 Christoph Segebarth³
 Benjamin Lalmand¹
 Catherine Christophe³
 Marc Lemort³
 Philippe Haesendonck³
 H. Peter Niendorf⁴
 J. Flament-Durand⁵
 Jacques Brotchi⁶

This article appears in the March/April 1989 issue of *AJNR* and the May 1989 issue of *AJR*.

Received March 21, 1988; accepted after revision July 20, 1988.

Presented in part at the annual meeting of the American Society of Neuroradiology, New York City, May 1987.

¹ Department of Radiology, Clinic of Neuroradiology, Hôpital Erasme, Université Libre de Bruxelles, Route de Lennik 808, B-1070 Brussels, Belgium. Address reprint requests to D. Balériaux.

² Present address: Department of Radiology, Antwerp University Hospital, B-2520 Edegem, Belgium.

³ Magnetic Resonance Unit, Hôpital Erasme, Université Libre de Bruxelles, B-1070 Brussels, Belgium.

⁴ Department of Radiology, FB Medizin, Schering AG, P.O. Box 65 03 11, D-1000 Berlin 65, W. Germany.

⁵ Department of Pathology, Hôpital Erasme, Université Libre de Bruxelles, B-1070 Brussels, Belgium.

⁶ Department of Neurosurgery, Hôpital Erasme, Université Libre de Bruxelles, B-1070 Brussels, Belgium.

AJR 152:1087-1096, May 1989
 0361-803X/89/1525-1087
 © American Roentgen Ray Society

Forty-eight Gd-DTPA-enhanced MR examinations of the spine were performed in 40 patients referred for MR because of clinically suspected spinal tumor or for further evaluation of an expanded cord. The study group consisted of 32 patients with spinal tumors (seven ependymomas; seven astrocytomas; four hemangioblastomas; two arteriovenous malformations; two unidentified intramedullary neoplasms; four meningiomas; and single cases of metastatic breast carcinoma, cavernous hemangioma with associated hematomyelia, neurinoma, angiolioma, drop metastasis from medulloblastoma, and epidermoid with diastematomyelia). In the remaining eight patients, other diagnoses were established: thoracic disk herniation (two patients), lumbosacral meningocele (one), syringomyelia secondary to arachnoiditis (four), and expanded cord secondary to gliotic tissue (one). All but two diagnoses were proved histologically by biopsy, surgery, or autopsy; in the two patients with arteriovenous malformations, the definitive diagnosis was made by spinal angiography. Contrast enhancement occurred in 30 of the 32 spinal tumors, and Gd-DTPA-enhanced T1-weighted images proved helpful in defining and outlining intra- and extramedullary spinal neoplasms. All ependymomas and astrocytomas (including low-grade astrocytomas) enhanced. In meningiomas, an immediate and uniform contrast uptake was demonstrated. Additional advantages of Gd-DTPA MR include the differentiation of solid tumor components vs syrinx or cyst or pseudotumoral areas of cord expansion, and the differentiation of residual or recurrent tumor from scar tissue in postoperative patients.

Our results suggest that IV-injected Gd-DTPA improves MR sensitivity and specificity in the evaluation of spinal lesions.

Increasingly, MR imaging has become the method of choice in viewing the normal and diseased spinal cord. Although the effectiveness of MR imaging in the neuro-radiologic evaluation of spinal tumors has been well documented, several problems remain unsolved: the low specificity of noncontrast MR, tumor vs edema differentiation, accurate delineation of the lesion, recognition of solid tumor nodule vs associated syrinx, and study of the postoperative spine. Several recent reports have indicated the usefulness of the paramagnetic MR contrast agent gadolinium-DTPA-dimeglumine (Gd-DTPA) in outlining spinal neoplasms [1-10]. The purpose of the present study of 40 patients was to determine to what extent the use of Gd-DTPA increases both the MR sensitivity in defining and localizing spinal tumors and the MR specificity in the diagnosis of spinal lesions.

Subjects and Methods

Forty-eight Gd-DTPA-enhanced MR examinations of the spine were performed in 40 patients with suspected spinal neoplasm (six patients had Gd-DTPA-enhanced studies both before and after surgery; one patient had three examinations). All patients were referred for MR, either because of clinically suspected spinal tumor or for further investigation of an expanded cord as detected by myelography, CT, or CT-myelography; spinal arteriography was performed in two patients. The patient population included 19 males and 21 females, 14-72 years old (mean age, 44.8).

TABLE 1: Histologic Diagnoses and Results of Gd-DTPA-Enhanced MR Imaging

Case No.	Age	Gender	Level	Diagnosis (Histology)	Enhancement
Intramedullary tumors:					
1	27	M	T10-T11	Ependymoma (grade 3)	+
2	58	F	C6-C7	Ependymoma	+
3	58	M	C5-T1	Ependymoma (grade 2)	+
4	39	F	C7-T1	Ependymoma	+
5	40	M	C2-C5	Ependymoma	+
6	35	F	C2-C5	Ependymoma (poorly differentiated)	+
7	47	F	C1-T1	Ependymoma	+
8	21	M	C1-C5	Astrocytoma (low grade)	+
9	15	F	C1-C3	Astrocytoma (low grade)	+
10	33	M	T9-T12	Astrocytoma (grade 2)	+
11	68	M	Conus medullaris	Astrocytoma (grade 1)	+
12	22	F	C1-C4	Astrocytoma (low grade)	+
13	28	F	Conus medullaris	Astrocytoma (low grade)	+
14	60	M	T9-L1	Astrocytoma (low grade)	±
15	64	F	C2-C3	Unidentified intramedullary tumor + syrinx	+ ^a
16	14	F	C4-C6	Unidentified intramedullary tumor (patient with neurofibromatosis)	+ ^a
17	48	F	C4-C6	Metastasis from breast carcinoma	+
18	23	M	C5-C6	Hemangioblastoma + large syrinx	+
19	38	M	C4-C7	Hemangioblastoma + large syrinx	+
20	45	M	C7-T1 and T9-T10	Multiple hemangioblastomas + large syrinx (von Hippel-Lindau syndrome)	+
21	72	M	T6	Hemangioblastoma + associated syrinx	+
22	64	F	T5-T6	Cavernous hemangioma + hematomyelia	-
23	29	M	C4-C6	Arteriovenous malformation	+ ^b
24	66	M	T7-T8	Arteriovenous malformation	+ ^b
Extramedullary tumors:					
25	34	F	C1-C3	Meningioma	+
26	66	M	C1-C2	Meningioma	+
27	56	F	T3-T4	Meningioma	+
28	57	F	T3	Meningioma (psammomatous type)	+
29	50	F	L3-L4	Neurinoma	+
30	55	F	Sacrum	Drop metastasis from medulloblastoma	+
31	29	F	T12-L5	Epidermoid + diastematomyelia	-
32	37	F	T4-T8	Angiolipoma (posterior extradural space)	+
Other extramedullary lesions:					
33	20	F	L5-sacrum	Lumbosacral meningocele	-
34	55	F	T8-T9	Disk herniation	- ^c
35	51	M	T6-T7	Disk herniation	- ^c
Tumorlike conditions:					
36	57	M	T3-T10	Syringomyelia secondary to arachnoiditis	-
37	59	M	T3-T7	Syringomyelia secondary to arachnoiditis	-
38	62	M	T5-L1	Syringomyelia secondary to arachnoiditis	-
39	28	F	T4-T8	Syringomyelia secondary to arachnoiditis	-
40	62	M	C1-C6	Gliosis (unspecified)	±

^a No definitive histology available.

^b In the two patients with arteriovenous malformations, the definitive diagnosis was made by spinal angiography. In the 38 other patients the diagnosis was established histologically by biopsy, surgery, or autopsy.

^c The thoracic disk as such did not enhance, but enhancement of the posterior longitudinal ligament was observed, as well as triangular areas of contrast uptake above and below the herniated disk. At surgery, these areas were found to correspond to engorged epidural veins with stagnant blood flow and vascular granulation tissue along the inflamed posterior ligament.

After obtaining written informed consent, a standard Gd-DTPA-dimeglumine solution* was injected IV in a dosage of 0.1 mmol/kg body weight. There is evidence that this is a well-tolerated and effective dose for MR imaging [11-15]. All examinations were performed on a superconductive unit,[†] initially operating at a 0.5 T field strength (10 patients) and subsequently at 1.5 T (30 patients).

Both T1- and T2-weighted images were obtained before contrast administration with the use of spin-echo sequences, 250-600/30 and 2000/30, 100 (TR/TE), respectively. After IV Gd-DTPA injection, sequential T1-weighted scans were obtained with short TR spin-echo

sequences and in some instances a fast-field-echo technique. All patients were examined within 5-40 minutes after administration of Gd-DTPA. The acquisition matrix was 256 × 256 with two to four averages. The slice thickness was 5 mm in all instances. Patient tolerance to the Gd-DTPA injection was excellent. There were no side effects during the MR examination or in the subsequent 24-48 hr. Patients with impaired renal and/or hepatic function were excluded from the study.

Results

Our results are summarized in Table 1. Spinal tumors were identified in 32 of 40 patients, including seven ependymomas

* Schering AG, Berlin, W. Germany.

[†] Gyroscan S15, Philips Medical Systems, Eindhoven, Netherlands.

(cases 1–7); seven astrocytomas (cases 8–14); two unidentified intramedullary neoplasms (cases 15 and 16; case 16 was a patient with neurofibromatosis who presented with a large posterior fossa meningioma and an unidentified cervical intramedullary tumor); metastatic breast carcinoma (case 17); five hemangioblastomas with a large syrinx cavity (cases 18–21); cavernous hemangioma with associated hematomyelia (case 22); two arteriovenous malformations (cases 23 and 24); four meningiomas (cases 25–28); and single cases of neurinoma (case 29), drop metastasis from posterior fossa medulloblastoma (case 30), epidermoid with associated diastematomyelia (case 31), and angiolipoma (case 32). All except two diagnoses were established histologically (biopsy, definitive surgery, or autopsy). All tumors showed contrast enhancement with Gd-DTPA, except for the epidermoid and the cavernous hemangioma.

Thoracic disk herniations were found in two patients (cases 34 and 35) and a large lumbosacral meningocele was found in one patient (case 33).

The remaining five patients had tumorlike conditions (widening of the cord on nonenhanced MR scans), but no evidence of an underlying neoplastic lesion was found. This group included four patients (cases 36–39) with a syrinx cavity and irregular thickening of the cord secondary to arachnoiditis, initially believed to represent an intramedullary neoplasm. The lesions did not enhance. The diagnosis was surgically confirmed in all four patients. One patient (case 40) was diagnosed as having an infiltrating intramedullary tumor on non-enhanced MR; there was heterogeneous contrast enhancement throughout the cervical spine. A surgical biopsy revealed diffuse gliosis, without evidence of a true neoplasm.

Discussion

Intramedullary Tumors

The diagnostic usefulness of paramagnetic contrast agents such as Gd-DTPA in the evaluation of intraaxial (i.e., intramedullary) gliomas is based on the fact that they do not cross the intact blood-brain barrier (BBB). Thus, in order for a tumor to enhance, there must be an active breach of the BBB. Because the hydrophilic contrast agent, which has a high molecular weight, leaks out of the vascular compartment into the interstitial spaces, progressive contrast enhancement is to be expected. This gradual increase in signal intensity produced by Gd-DTPA on T1-weighted images reaches a plateau and then signal intensity drops slowly. This pattern has been well established in brain tumors [16]. Variations in time-dependent contrast enhancement have also been described in spinal tumors [17].

In summary, Gd-DTPA is a marker for alterations of the BBB, like a conventional CT contrast agent.

Ependymomas ($n = 7$) are seen on plain MR studies as areas of widening of the cord. On T1-weighted images, ependymomas are isointense with respect to the spinal cord; therefore, their boundaries are difficult to define, unless they are outlined, as is sometimes the case, by syrinx cavities capping the upper and lower poles of the tumor. On T2-

weighted sequences, ependymomas may have a multinodular appearance, but the differentiation of tumor vs surrounding edema is virtually impossible, since both have prolonged T2 relaxation times, presumably reflecting increased water content.

The use of Gd-DTPA allows better definition of the upper and lower limits of these intramedullary tumors. In our experience, ependymomas as a rule showed intense, homogeneous, and sharply margined focal enhancement (Fig. 1). They tend to occupy the whole width of the spinal cord in the affected segment, which is consistent with a centrifugal expansion originating in the ependymal cells lining the central canal or in cellular components scattered in the white matter of the spinal cord.

In some instances, ependymomas have intratumoral cavities. In these cases, Gd-DTPA not only brings out superb tumor-border definition but is also highly accurate in the delineation of central low-signal-intensity components, corresponding to intratumoral cysts [1]. These areas of cystic degeneration were identified after Gd-DTPA injection in three of seven ependymomas in our series and subsequently confirmed at surgery.

Conversely, astrocytomas ($n = 7$) tend to enhance in a more patchy, irregular way, consistent with a more diffusely infiltrating tumor. All astrocytomas, even low-grade astrocytomas, did enhance. The areas of contrast enhancement are often eccentrically located (usually in the posterior aspect of the spinal cord) and are less well defined with slightly fuzzy margins; they may be separated by regions of low signal intensity consistent with areas of necrosis or cystic change (Fig. 2). In addition, in some astrocytomas an exophytic tumor component may be identified as an area of contrast enhancement, which could be verified readily at surgery.

These slightly different patterns of contrast uptake had initially suggested that Gd-DTPA might prove to be a useful tool in predicting the histology of intraspinal neoplasms. However, there is considerable overlap. Of particular interest are some of the errors we made when using our own criteria as described above. Figure 3 illustrates the case of a 28-year-old woman with a tumor at the level of the conus medullaris that showed marked, homogeneous, and sharply margined contrast enhancement both on sagittal and coronal sequences. The tumor appeared very well defined. We expected this tumor to be an ependymoma, especially since ependymomas (particularly of the myxopapillary type) are common in this location. Surgery revealed an infiltrating intramedullary lesion; there was no clear cleavage plane and the tumor could not be completely resected. Pathologic examination showed a well-differentiated (low-grade) astrocytoma. A follow-up Gd-DTPA-enhanced MR scan was clearly superior to plain MR in the delineation of residual tumor tissue (Figs. 3E and 3F).

Conversely, in one patient with an ependymoma, the slightly inhomogeneous pattern of contrast enhancement as well as the asymmetric appearance of the tumor led us initially to consider a low-grade astrocytoma as the first differential diagnosis.

In summary, although we did find different patterns of contrast enhancement in some ependymomas and astrocy-

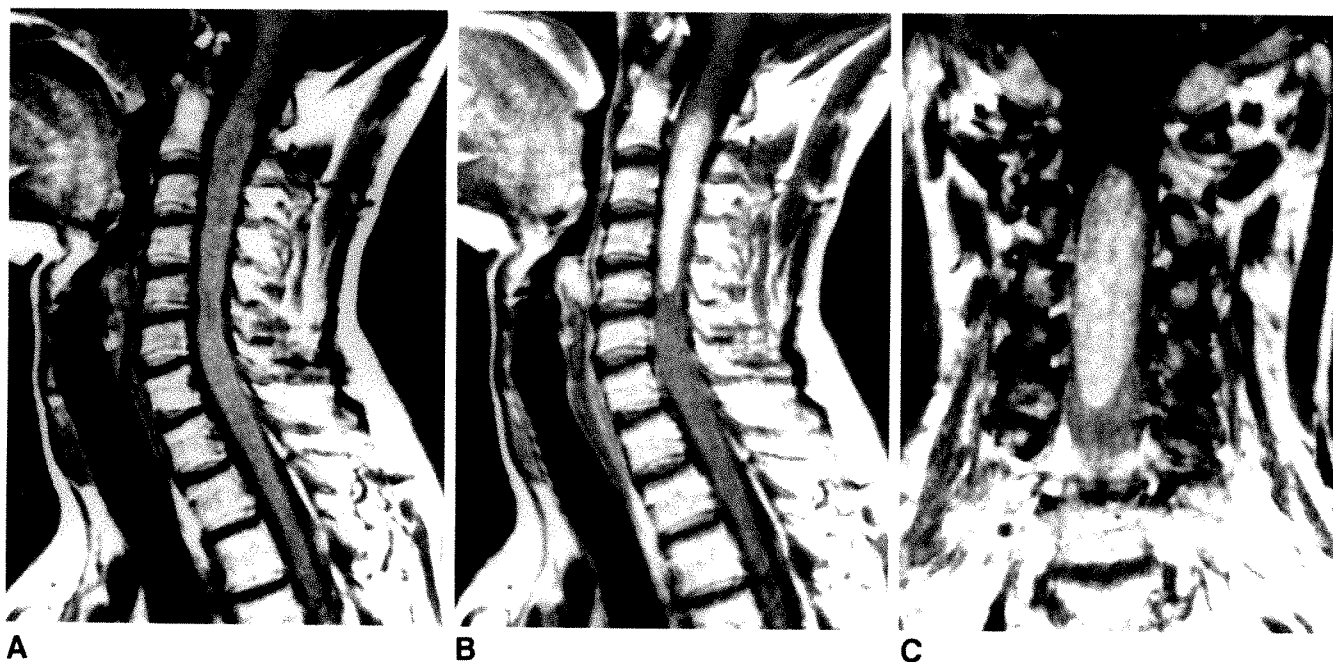


Fig. 1.—Case 6: Ependymoma.

A, Nonenhanced sagittal T1-weighted spin-echo image, 400/30, reveals widening of cervical cord from C1 to T2, suggesting intramedullary tumor.

B, Sagittal T1-weighted spin-echo image, 400/30, immediately after Gd-DTPA injection shows well-defined, oval area of contrast uptake extending from C2 to C5.

C, Enhancing lesion is confirmed on coronal T1-weighted spin-echo image, 400/30, 13 min after contrast injection.

At surgery, an ependymoma was found, sharply defined and limited to region of contrast uptake. Swelling of cord above and below tumor was found to represent edema.

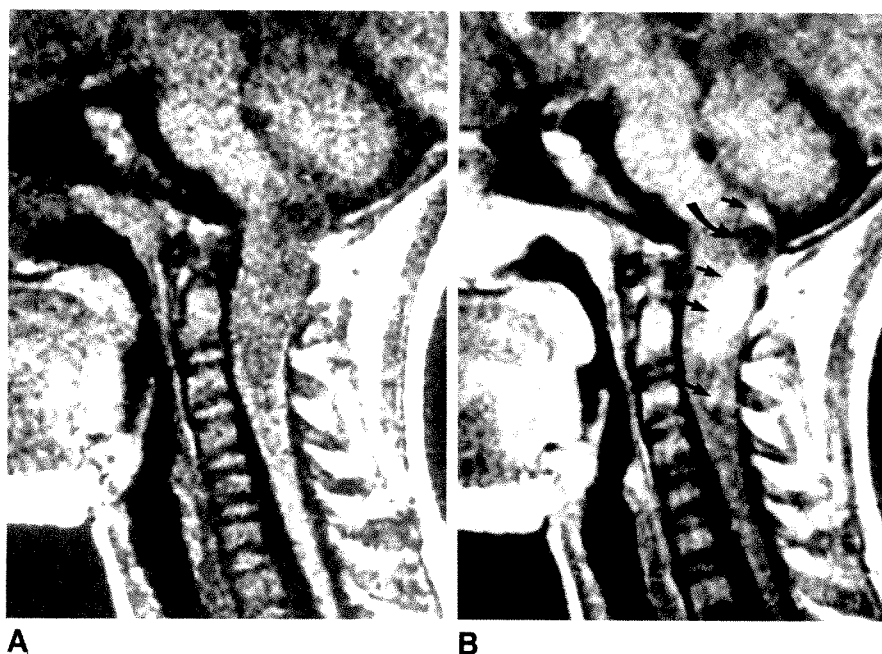


Fig. 2.—Case 9: Partially cystic low-grade astrocytoma.

A, Precontrast sagittal T1-weighted spin-echo image, 250/30, shows widening of upper cervical spinal cord with relatively low-signal-intensity area extending into medulla oblongata.

B, Postcontrast T1-weighted spin-echo image, 250/30, shows irregular areas of contrast uptake (straight arrows), with predilection for posterior aspect of cord. Hypointense, presumably cystic component is seen posteriorly (curved arrow) at junction of upper cervical cord and medulla oblongata. The use of Gd-DTPA allows sharp demarcation between nonenhancing cystic-necrotic component and enhancing tumor infiltration.

At surgery, partially cystic well-differentiated low-grade astrocytoma was discovered.

tomas, as described earlier, an accurate prediction of tumor histology is impossible. At the present time, we must conclude that these two neoplasms cannot be differentiated by MR. Both histologic types can be either solid or cystic with nodules [18].

In a patient with an intramedullary metastasis (metastatic breast carcinoma), the precontrast MR examination (T1- and T2-weighted images) revealed widening of the cord contour and changes in signal intensity. After Gd-DTPA administration, a small localized enhancing nodule was discovered. This

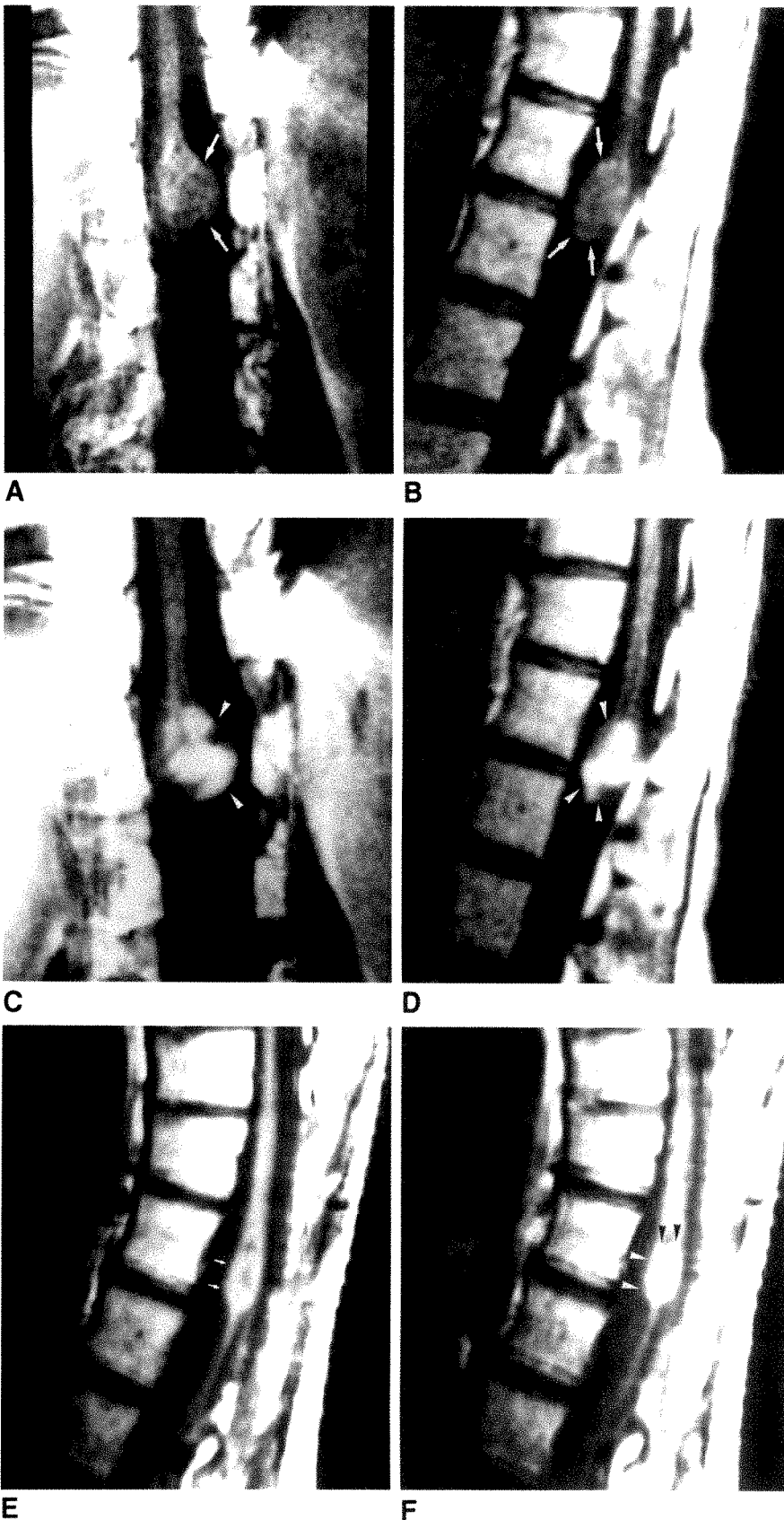
Fig. 3.—Case 13: Low-grade astrocytoma.

A and B, Nonenhanced coronal (A) and sagittal (B) T1-weighted spin-echo images, 400/30, of thoracolumbar spine. Mass lesion is clearly identified (arrows). Tumor is appended to conus medullaris and is lateralized to left, displacing upper part of cauda equina to right.

C and D, After Gd-DTPA administration, coronal (C) and sagittal (D) T1-weighted spin-echo images, 400/30, show sharply defined, homogeneous contrast uptake throughout tumor (arrowheads). At surgery, a low-grade astrocytoma was partially resected; there was no cleavage plane.

E, Nonenhanced sagittal T1-weighted image 3 months after surgery shows increased diameter of conus medullaris (arrows), with heterogeneous signal intensity.

F, After Gd-DTPA injection, residual tumor appears as sharply margined area of contrast uptake (arrowheads), clearly outlined from conus medullaris.



finding indicates that much of the cord enlargement is due to perifocal edema.

In the patients with hemangioblastoma ($n = 5$, in four patients), noncontrast MR displayed irregular and diffuse widening of an apparently infiltrated spinal cord in its cervical and thoracic segments. The intrinsic cord signal was heterogeneous, with low-intensity areas supposedly representing a vast syrinx cavity, alternating with isointense areas of thickening of the cord. In one patient, the syrinx extended from the upper cervical to the lower thoracic cord.

The use of IV-administered Gd-DTPA allows accurate recognition of the highly vascular tumor nidus within a large area of cystic change, thus providing the neurosurgeon with very useful information and directing surgery to the level of the solid tumor component. Some authors have described how the signal characteristics of a tumor nodule may be separated from those of the cyst by using long TR and long TE sequences, since the T2 of the cyst is usually longer [8, 18]. However, in our experience, T2-weighted pulse sequences also are more apt to show artifacts and often are of poorer quality; the Gd-DTPA-enhanced T1-weighted image was superior in highlighting a vascular tumor nodule within an associated cyst. In our limited experience, the association of a strongly enhancing solid tumor nodule within a vast syrinx is very suggestive of hemangioblastoma.

In the patient with a cavernous hemangioma, plain MR revealed an ovoid intramedullary lesion with heterogeneous signal characteristics. A large area of hematomyelia extended below the lesion. The mixed high- and low-signal-intensity components of cavernous hemangiomas presumably indicate the presence of mixed subacute and chronic hemorrhage [19]. After IV Gd-DTPA administration, no definite contrast uptake could be seen. It is likely that in this patient the characteristic crescent-shaped high-signal-intensity hemorrhagic focus (as a result of the formation of methemoglobin) and the surrounding low-signal rim (important concentration of hemosiderin) may mask an area of contrast uptake [8].

The arteriovenous malformations ($n = 2$) had a markedly heterogeneous appearance, both on the pre- and postcontrast MR examinations, due to the presence of old hemorrhagic components and calcifications. The lesions contained serpiginous areas of signal void, reflecting vascular structures with rapidly flowing blood. There was some contrast uptake after Gd-DTPA injection. The final diagnosis was made by spinal angiography.

Extradural Intradural Tumors

The mechanism of contrast enhancement in extraaxial tumors is different, since these lesions have no BBB. Therefore, the degree of T1 shortening after IV injection of Gd-DTPA is a function of tumor vascularization, in much the same way that highly vascular extraaxial tumors such as meningiomas and neurinomas will enhance on CT. Theoretically, one might predict a more immediate contrast enhancement, as opposed to the progressive contrast enhancement in intraaxial gliomas, which is based on the gradual leaking of Gd-DTPA molecules through a ruptured BBB.

Meningiomas ($n = 4$) most often appear isointense with respect to the spinal cord on nonenhanced T1-weighted images and may have a slightly higher signal intensity on T2-weighted images [20, 21]. The isointense mass may be seen in a typical extramedullary intradural location displacing and compressing the cord.

After IV injection of Gd-DTPA, and with the use of a fast-field-echo technique to obtain rapid sequential scans, we could demonstrate immediate and uniform contrast enhancement, as evidenced by marked T1 shortening (Fig. 4). Indeed, because meningiomas are highly vascular extraaxial lesions and have no BBB, they are ideal candidates for enhancement with a paramagnetic contrast agent [22, 23]. This type of contrast uptake is similar to what is reported in the CT literature.

Our series included one patient with a neurinoma, at the left L3-L4 level. After injection of Gd-DTPA, the lesion enhanced homogeneously.

Gd-DTPA has also been reported to be helpful in the evaluation of metastatic disease of the spine, including leptomeningeal tumor spread, where contrast-enhanced MR scans were far superior to examinations performed without contrast agents [24-26]. Our series included one patient with a drop metastasis from a vermian medulloblastoma (Fig. 5). The lesion is identified on T1-weighted images as a mass lesion within the sacral canal, encasing and narrowing the distal caudal sac. There is marked destruction of the sacrum. The T2-weighted images reveal heterogeneous signal intensity within the tumor. After Gd-DTPA injection, areas of T1 shortening are identified; at surgery they are found to be richly vascularized parts of an otherwise highly vascular drop metastasis of a medulloblastoma. The areas of enhancement correlate well with the regions of prolonged T2 on T2-weighted images.

No contrast enhancement was seen in a single patient with an intradural epidermoid (with associated diastematomyelia) in the lumbar spine. These congenital tumors with associated bony malformations are essentially avascular in nature and therefore do not enhance.

Extradural Lesions

Marked contrast uptake was present in a patient with a large tumor in the posterior extradural space, extending from T4 to T8. At surgery this lesion was found to be an angiolioma.

In two patients with suspected spinal tumor, thoracic disk herniations were found. The herniated disk material as such did not enhance. However, in both patients we observed triangular areas of contrast uptake above and below the herniated disk, as well as enhancement of the posterior longitudinal ligament. At surgery they were found to correspond to engorged epidural veins with stagnant blood flow and vascular granulation tissue along the inflamed posterior longitudinal ligament.

Tumorlike Conditions

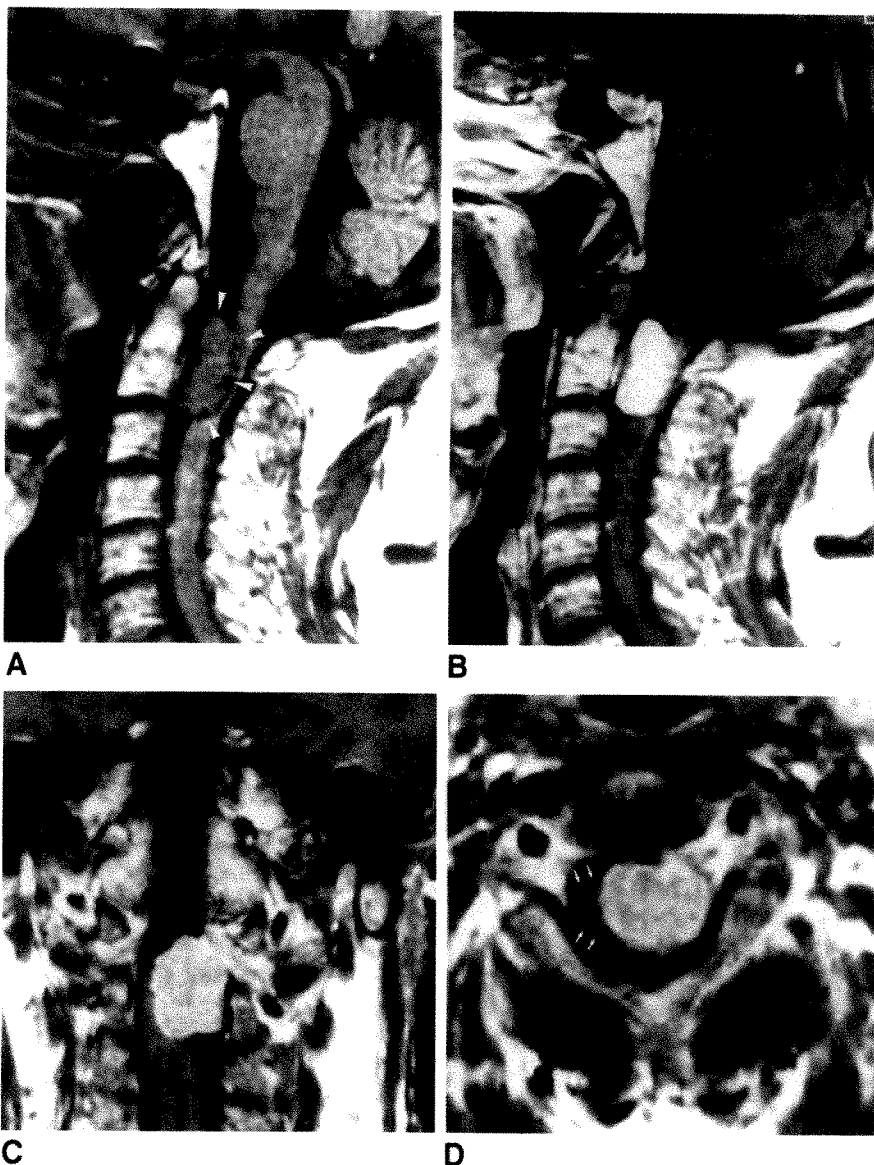
Of particular interest were four cases of syringomyelia secondary to arachnoiditis. In these patients, nonenhanced

Fig. 4.—Case 26: Meningioma.

A, Nonenhanced sagittal T1-weighted image, 600/30, cervical spine shows soft-tissue mass (arrowheads), which is slightly hypointense with respect to spinal cord.

B–D, After IV injection of Gd-DTPA, sagittal (B), coronal (C), and axial (D) T1-weighted images, 600/30, reveal rapid, intense, and homogeneous contrast uptake, providing superior discrimination between tumor and cord. Note enhancement of thickened dura behind C2 vertebral body (B). Tumor has typical intradural extramedullary topography. Spinal cord is flattened and displaced posteriorly and to the right (arrows).

The lesion was a meningioma at C1–C2.



MR was highly suggestive of intramedullary tumor: focal swelling of the spinal cord and central low-signal area compatible with an area of necrotic/cystic change (Fig. 6). However, whereas in our experience the majority of intramedullary tumors did enhance, no T1 shortening was seen in these cases after Gd-DTPA injection. In two patients (cases 36 and 37), the arachnoiditis was presumed to be secondary to an episode of tuberculous meningitis many years before; one patient (case 38) had a history of spinal trauma. The patient illustrated in Figure 6 (case 39) was clinically asymptomatic and underwent the MR examination as a "normal" volunteer. Surgical exploration revealed an area of adhesive arachnoiditis covering the cord, with a subjacent syrinx, but no tumor could be identified. No specific cause for the arachnoiditis was identified. This early experience suggests that Gd-DTPA can help to distinguish neoplastic from benign disease.

In one patient MR was suggestive of an intramedullary tumor. There was minimal heterogeneous contrast enhancement throughout the cervical spine. A surgical biopsy revealed

what was broadly defined as "gliotic tissue," but no true neoplasm could be found (case 40).

No contrast enhancement was present in a lumbosacral meningocele that initially was misdiagnosed as a spinal tumor, because the cyst fluid had signal characteristics different from those of CSF.

In conclusion, paramagnetic contrast agents such as Gd-DTPA offer a means of positive contrast enhancement of spinal tumors, as opposed to the displacement of contrast material in myelography and CT-myelography. There is little doubt that Gd-DTPA-enhanced MR imaging is superior to plain MR (T1- and T2-weighted images) in the diagnosis and anatomic definition of spinal lesions and in assessing tumor vascularity [4, 5, 7, 9, 10]. The increased sensitivity of Gd-DTPA-enhanced MR examinations of the spine is the result of several factors: greater inherent tissue contrast with improved tumor border definition, possibility of lesion vs edema differentiation, identification of foci of necrosis, and intratumoral cystic components.

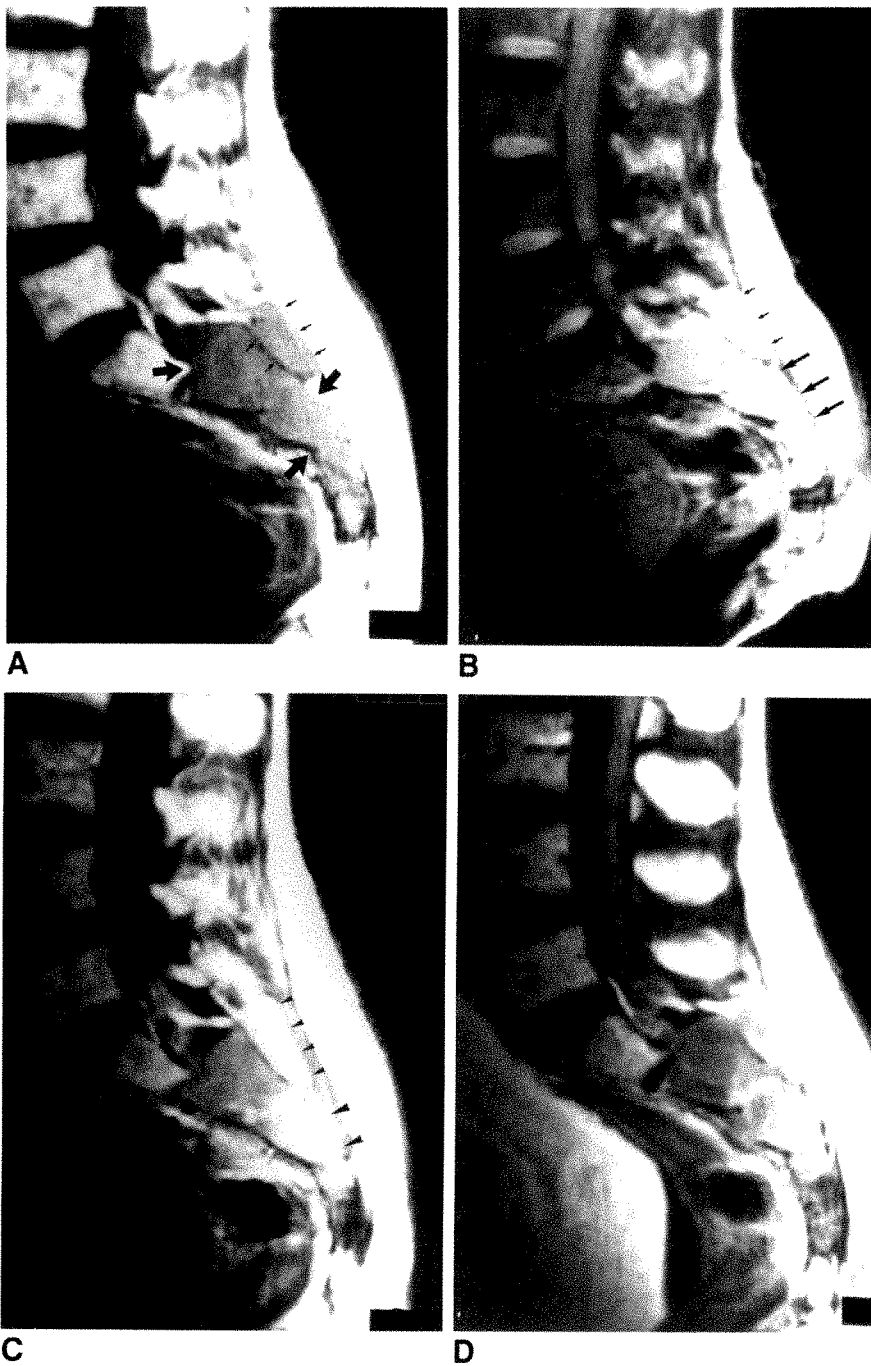


Fig. 5.—Case 30: Drop metastasis from posterior fossa medulloblastoma.

A, Nonenhanced sagittal T1-weighted image, 400/30, displays mass lesion with large anterior component infiltrating in sacral canal and destroying bone (*large arrows*) and smaller posterior component (*small arrows*).

B, Moderately T2-weighted image, 2000/50, reveals heterogeneous signal intensities within tumor. Posterior component (*small arrows*) and inferior portion of intrasacral lesion (*large arrows*) are markedly hyperintense.

C, Sagittal T1-weighted spin-echo image, 400/30, 3 min after IV injection of Gd-DTPA. Contrast uptake is seen to correspond to those regions that had a prolonged T2 (*arrowheads*).

D, 13 min after injection, degree of enhancement has diminished, but differences in contrast uptake between different parts of tumor remain.

Surgery revealed strongly vascularized drop metastasis from posterior fossa medulloblastoma.

It has been suggested that precontrast T2-weighted images might be more sensitive than postcontrast T1-weighted images, since the former identify all lesions with an increased water content, both with and without an active BBB breakdown, whereas the contrast enhancement in the latter depends on an active disruption of the BBB and a viable blood supply. This may be true in the brain, but in the spine our experience shows that the Gd-DTPA-enhanced MR studies were superior to scans obtained without contrast material. Indeed, even when the disease is obvious on a standard MR

scan and the lesion is clearly identified on the T2-weighted image, a Gd-DTPA-enhanced study may still be useful in helping to characterize the lesion or in tumor vs edema differentiation. In addition, the enhanced spin-echo T1-weighted images have shorter acquisition times and fewer artifacts than do the longer T2-weighted spin-echo images, thereby allowing more accurate visualization of spinal lesions.

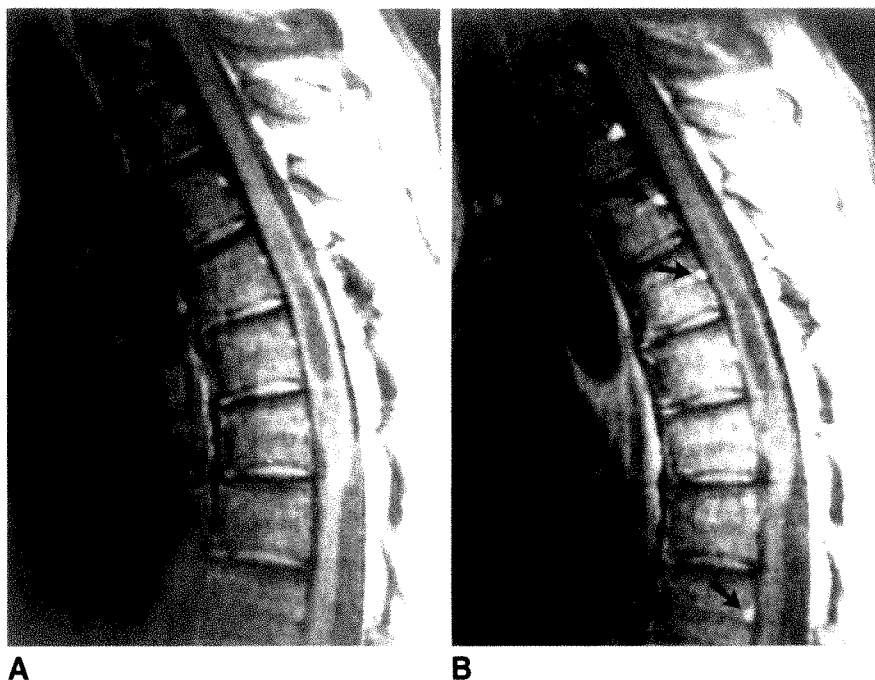
The improved visualization and delineation of spinal tumors on the Gd-DTPA-enhanced MR examination often guides the neurosurgical approach [10]. We found this to be particularly

Fig. 6.—Case 39: Adhesive arachnoiditis with syrinx.

A, Nonenhanced sagittal T1-weighted image, 400/30, shows increased diameter of midthoracic spinal cord with central area of cavitation. Posterior subarachnoid spaces are partially obliterated. Intramedullary tumor was suspected.

B, After IV injection of Gd-DTPA, no contrast uptake is seen within intramedullary lesion (identical pulse sequence). Note enhancement of basivertebral veins (arrows).

Surgical exploration revealed adhesive arachnoiditis, with syrinx cavity, believed to be secondary to arachnoiditis. There was no intramedullary tumor.



true for lesions with a solid enhancing tumor nodule within an associated intramedullary cavity (e.g., hemangioblastoma).

Another very promising result appears to be the possibility of differentiating residual or recurrent tumor from scar tissue in the postoperative spine [4, 7, 9].

We conclude that Gd-DTPA-enhanced MR imaging improves the reliability of spinal tumor diagnosis and increases MR sensitivity and specificity. It is still too early to conclude whether the pattern of enhancement may contain characteristic or even pathognomonic information regarding the differential diagnosis of intramedullary tumors (ependymoma vs astrocytoma). On the other hand, our findings show that contrast enhancement does occur in the vast majority of tumors, enabling differentiation of cystic tumor from nontumoral cyst or syrinx [6, 27, 28], including pseudotumoral syringomyelia secondary to arachnoiditis. In this way, Gd-DTPA can help differentiate neoplastic tissue from benign disease.

ACKNOWLEDGMENT

We thank J. Haustein for reviewing the manuscript and offering bibliographic advice.

REFERENCES

- Bydder GM, Brown J, Niendorf HP, Young IR. Enhancement of cervical intraspinal tumors in MR imaging with intravenous gadolinium-DTPA. *J Comput Assist Tomogr* 1985;9(5):847-851
- Yoshikawa K, Aoki S, Momose T, et al. Gd-DTPA as contrast agent in MR imaging of spinal intramedullary tumors. Presented at the annual meeting of the Society of Magnetic Resonance in Medicine, Montreal, Canada, August 1986
- Fenzl G, Lissner J, Heywang SH, et al. MR of spinal lesions with Gd-DTPA as contrast medium. Presented at the annual meeting of the Society of Magnetic Resonance in Medicine, Montreal, Canada, August 1986
- Treich J, Claussen C, Massih M, Kornmesser W, Felix R. Intraspinal tumors in plain and Gd-DTPA-enhanced magnetic resonance imaging. Presented at the annual meeting of the Society of Magnetic Resonance in Medicine, Montreal, Canada, August 1986
- Stimac GK, Porter BA, Olson DO, Gerlach R, Genton M, Nelson S. Gadolinium DTPA/dimeglumine-enhanced MR of spinal neoplasms: preliminary experience. Presented at the annual meeting of the Society of Magnetic Resonance in Medicine, New York City, August 1987
- Jenkins JPR, Stack JP, Watson Y, Isherwood I. Magnetic resonance imaging of spinal lesions: the role of gadolinium-DTPA. Presented at the annual meeting of the Society of Magnetic Resonance in Medicine, New York City, August 1987
- Balériaux D, Parizel PM, Niendorf HP, Rodesch GL, Segebarth C. Value of intravenous Gd-DTPA contrast injection in the MRI evaluation of spinal tumors. Presented at the annual meeting of the American Society of Neuroradiology, New York City, May 1987
- Sigal R, Halimi Ph, Doyon D, Hurth M, Pigeau I, Thibault M. High-field MR imaging of spinal cord tumors using contrast media. Presented at the annual meeting of the Radiological Society of North America, Chicago, November 1987
- Dillon WP, Bolla K, Mark AS, Tsudura JS, Norman D, Newton TH. Gd-DTPA MR imaging enhancement of spinal cord tumors. Presented at the annual meeting of the Radiological Society of North America, Chicago, November 1987
- Valk J. Gd-DTPA in MR of spinal lesions. *AJNR* 1988;9:345-350, *AJR* 1988;150:1163-1168
- Laniado M, Weinmann HJ, Schorner W, Felix R, Speck U. First use of Gd-DTPA/dimeglumine in man. *Physiol Chem Phys Med NMR* 1984;16:157-165
- Weinmann HJ, Laniado M, Mutzel W. Pharmacokinetics of Gd-DTPA/dimeglumine after intravenous injection into healthy volunteers. *Physiol Chem Phys Med NMR* 1984;16:167-172
- Weinmann HJ, Brasch RC, Press WR, Wesbey GE. Characteristics of gadolinium-DTPA complex: a potential NMR contrast agent. *AJR* 1984;142:619-624
- Carr DH, Brown J, Bydder GM, et al. Gadolinium-DTPA as a contrast agent in MRI: initial clinical experience in 20 patients. *AJR* 1984;143:215-224

15. Carr DH, Brown J, Bydder GM, et al. Intravenous chelated gadolinium as a contrast agent in NMR imaging of cerebral tumors. *Lancet* **1984**;1:484-486
16. Schorner W, Laniado M, Niendorf HP, Schubert C, Felix R. Time-dependent changes in image contrast in brain tumors after gadolinium-DTPA. *AJNR* **1986**;7:1013-1020
17. Laniado M, Kornmesser W, Treisch J, Felix R, Deimling M. Gd-DTPA-enhanced fast magnetic resonance imaging of brain and spinal tumors: early clinical experience. In: Runge VM, et al., ed. *Contrast agents in magnetic resonance imaging. Proceedings of an international workshop, January 1986, San Diego, California*. Amsterdam: Excerpta Medica, **1986**:136-140
18. Scotti G, Scialfa G, Colombo N, Landoni L. Magnetic resonance diagnosis of intramedullary tumors of the spinal cord. *Neuroradiology* **1987**;29:130-135
19. Fontaine S, Melanson D, Cosgrove R, Bertrand G. Cavernous hemangiomas of the spinal cord: MR imaging. *Radiology* **1988**;166:839-841
20. Scotti G, Scialfa G, Colombo N, Landoni L. MR imaging of intradural extramedullary tumors of the cervical spine. *J Comput Assist Tomogr* **1985**;9:1037-1041
21. Boisserie-Lacroix M, Kien P, Caille JM. L'imagerie des tumeurs intradurales et extra-médullaires: les neurinomes et les méningiomes. *J Neuroradiol* **1987**;14:66-81
22. Berry I, Brant-Zawadzki, Osaki L, Brasch RC, Murovic J, Newton TH. Gd-DTPA in clinical MR imaging of the brain: 2. Extraaxial lesions and normal structures. *AJNR* **1986**;7:789-793
23. Bydder G, Kingsley P, Brown J, Niendorf H, Young I. MR imaging of meningiomas including studies with and without gadolinium-DTPA. *J Comput Assist Tomogr* **1985**;9:690-697
24. Sze G, Abramson A, Krol G, Zimmerman R, Deck MDF. Metastatic disease of the spine: MR evaluation with Gd-DTPA. Presented at the annual meeting of the Radiological Society of North America, Chicago, November **1987**
25. Sze G, Abramson A, Krol G, et al. Gadolinium-DTPA in the evaluation of leptomeningeal tumor spread in the spine. Presented at the annual meeting of the Society of Magnetic Resonance in Medicine, New York City, August **1987**
26. Sze G, Abramson A, Krol G, et al. Gadolinium-DTPA in the evaluation of intradural extramedullary spinal disease. *AJNR* **1988**;9:153-163, *AJR* **1988**;150:911-921
27. Slasky BS, Bydder GM, Niendorf HP, Young IR. MR imaging with gadolinium-DTPA in the differentiation of tumor, syrinx, and cyst of the spinal cord. *J Comput Assist Tomogr* **1987**;11:845-850
28. Slasky BS, Niendorf HP, Steiner RE, Bydder GM, Young IR. Does Gd-DTPA help in separating tumor from syrinx or cyst in the spinal cord? Presented at the annual meeting of the Radiological Society of North America, Chicago, November **1987**

Pulsed-Spray Pharmacomechanical Thrombolysis: Preliminary Clinical Results

Joseph J. Bookstein¹
Brian Fellmeth
Anne Roberts
Karim Valji
Gary Davis
Thomas Machado

Pulsed-spray pharmacomechanical thrombolysis was used to treat 41 patients with 47 complete thrombotic occlusions of hemodialysis grafts ($n = 29$), arterial bypass grafts ($n = 10$), or peripheral native arteries ($n = 8$). The procedure involves the use of small pulses of highly concentrated urokinase, which are forcefully sprayed throughout the thrombus during systemic heparinization. Virtually complete lysis was achieved in 46 of 47 occlusions. In the 46 thrombi that lysed, mean time for completion of lysis was 63 ± 35 min and initial partial return of flow required 26 ± 18 min. Complications included small peripheral emboli in one treated bypass graft (which cleared promptly after further pulse-spray therapy) and bleeding in three cases (one case of hematoma in the infused field at the site of recent surgery, one case of bilateral hematomas at the femoral puncture sites, and one minor delayed self-limited gastrointestinal hemorrhage).

Results to date suggest that the pulsed-spray pharmacomechanical method augments the speed, consistency, safety, and cost efficacy of clinical thrombolysis. Further study is warranted.

Persistent problems of selective thrombolysis include a significant failure rate, prolonged infusion times, hemorrhagic complications, early rethrombosis [1-4], and cost. In these regards, early work with animals [5, 6] showed a quantifiable advantage for three adjuncts: (1) intrathrombic rather than parathrombic infusions, (2) high concentrations of urokinase (UK) or tissue plasminogen activator but not streptokinase (SK), and (3) most importantly, augmenting the area of interface between clot and fibrinolytic agent by simultaneous thrombolysis and mechanical clot disruption. The value of the first and second adjuncts has also been shown in several clinical series [2-4]. The value of the third adjunct has been confirmed recently in a report from an independent experimental laboratory [7] and also by our previous clinical series [8].

This article describes a further modification of technique, largely based on exploitation of the third adjunct. The method is termed pulsed-spray pharmacomechanical thrombolysis, and it involves high-pressure spray of small pulses of concentrated UK homogeneously and simultaneously throughout the thrombus. The resultant mechanical and enzymatic degradation of the clot is analogous to the complementary roles of saliva and chewing in the digestion of food.

Methodology is undergoing continuing refinement in dogs and will be reported in detail as optimal methods are developed. Laboratory observations indicate that pulsed intrathrombic injections of saline may produce rapid recanalization of sub-acute thrombi, but with an unacceptable risk of extensive downstream embolization. By using concentrated UK, a slow pulse frequency ($\sim 2/\text{min}$), and systemic heparinization, lysis is complete in under 1 hr, without significant downstream emboli. On the basis of these promising observations in dogs, concurrent animal and clinical evaluation of the pulsed-spray method was considered warranted.

Received September 26, 1988; accepted after revision January 4, 1989.

This work was supported in part by a grant from the Veterans Administration.

¹ All authors: Departments of Radiology, University of California, San Diego and the Veterans Hospital, La Jolla, CA 92093. Address reprint requests to J. J. Bookstein, Dept. of Radiology, Hospital of the University of California, San Diego, 225 W. Dickinson St., San Diego, CA 92103.

AJR 152:1097-1100, May 1989
0361-803X/89/1525-1097

© American Roentgen Ray Society

Methods and Materials

Between January 1988 and January 1989, 47 thrombi in 41 patients were treated by thrombolytic therapy. Patients were selected for pharmacomechanical thrombolysis when angiography showed complete thrombotic occlusion of a dialysis graft, arterial bypass graft, or peripheral native artery, and a guidewire could be passed at least partially through the obstruction (indicating absence of complete organization). Twenty-nine thrombi, 15 to 50 cm long, involved polytetrafluoroethylene hemodialysis grafts (Gortex, W. L. Gore Assoc. Inc., Flagstaff, AZ or Impira, Impira Co., Tempe, AZ), with estimated duration of occlusion of 2 ± 0.7 days (range, 1–4 days). Ten thrombi, 20 to 75 cm long, involved arterial bypass grafts of the lower extremity, with occlusions lasting 12 ± 11 days (range, 1–30 days). Eight thrombi, 5 to 30 cm long, involved native arteries, with occlusions lasting 84 ± 102 days (range, 1–300 days).

Proper administration of the thrombolytic agent required modified catheter assemblies, highly concentrated UK, systemic heparinization, and special methods of injection.

Catheter assemblies, which combined the advantages of end-hole and side-hole systems, were formed as follows. End-hole polyethylene catheters of 5-French diameter were tapered at the tip so that they would be completely occluded by a 0.032-in. (0.81-mm) beaded wire (Cook Inc., Bloomfield, IN). Holes were created in a spiral pattern by puncturing the catheter every 8–10 mm with the tip of a #27- or #30-gauge needle. The length of the segment of the catheter with side holes varied with the length of occlusion, but did not exceed 15 cm. Injections were made via the side arm of a Y-gasket device, with the gasket tightly gripping the protruding end of the occluding bead wire. For thrombosed dialysis grafts, two catheters were inserted in criss-cross fashion from sites central and distal to the midportion of the graft [8], so as to allow injection of the entire graft. A single catheter was used in the treatment of most thrombosed native vessels or bypass grafts.

We dissolved 250,000 units of UK (Abbott Inc., North Chicago, IL) in 10 ml of nonbacteriostatic sterile water, yielding a concentration of 25,000 units/ml. About 150,000 units were then injected over a period of 10–20 min, in ~0.2-ml increments, at a repetition rate of 2–4 pulses per minute, often via a special pulse injector. The catheter was turned about 90° and advanced or withdrawn intermittently to promote continuous homogeneous distribution throughout the clot. After the initial relatively rapid period of deposition, the concentration of UK was usually reduced to 5,000–10,000 units/ml, and administration was continued at a pulse frequency of 1–2 per minute or by continuous slow infusion at 2000 units/min/catheter.

A heparin bolus, 3000–5000 units, was administered with the onset of lysis. Further increments of 1000–2000 units per hour were given if the procedure took longer than 1 hr, and 3000–5000 additional units were injected before any required transluminal angioplasty. Heparinization was not generally reversed before withdrawal of catheters, although the catheter or sheath was sometimes left in place for 1–2 hr while the patient was observed until heparin levels waned. After hemostasis had been achieved, heparin was commonly administered IV for 24 hr.

A prototype pulse injector was used in 14 cases. Its basic features include (1) an air-driven piston syringe, (2) adjustable volumes, rates, frequencies, and pressures of pulse injection, (3) a nearly square-wave pressure pulse, and (4) capability of rapidly developing pressures over 2000 psi (13.8×10^6 Pa). This first model proved somewhat inconvenient and unreliable, and in the remaining 33 cases, injection was done by hand via tuberculin syringe; 0.2 ml was injected as suddenly and forcefully as possible, according to the schedule indicated above. Improved models of the pulse injector are being developed.

In treating thrombosed dialysis grafts, lysis was initially directed at the venous end, to minimize bleeding from prior punctures after arterial patency was reestablished. In treating native or graft arterial obstruction, lysis was begun proximally, and the last centimeter or so of thrombus was left relatively undisturbed until last, to act as a plug to minimize downstream embolization and to maintain high UK concentration in the region of thrombus.

In 32 patients, percutaneous transluminal angioplasty (PTA) was performed on stenoses that persisted after thrombolysis; dilatation was successful in 30 patients. In dialysis grafts, PTA often was applied while small to moderate amounts of thrombus persisted. In bypass grafts or native arteries, however, PTA was withheld until almost all clot had disappeared.

Results

The clot disappeared almost completely in all cases but one. In the 46 thrombi that lysed, partial return of pulse or flow was observed after 26 ± 18 min. Lysis was considered complete after 63 ± 35 min (range, 15–180 min). In one patient with extremely poor peripheral runoff and dry gangrene of a thigh stump, the iliac artery rethrombosed 30 min after completion of lysis, and repeat thrombolysis was considered unwarranted. In the remaining cases, good patency was achieved, which persisted for at least 1 week, or until operation, if such was performed.

Total required doses of UK varied from 100,000 to 600,000 units, with a mean of $368,000 \pm 132,000$ units. Because UK is supplied in 250,000-unit ampoules, most patients received either 250,000 or 500,000 units. Of the 46 successful treatments, one ampoule was sufficient in 23, two ampoules in 21, and three ampoules in two.

Rates of lysis differed only slightly when comparing dialysis grafts with bypass grafts or native arteries (Table 1). Complete lysis was only marginally slower in thrombi 4–300 days of age than in those less than 3 days of age (Table 1). Although these rate differences were statistically significant ($p < .05$), they were not important clinically.

In 44 of 47 treatments, there was no clinical or angiographic evidence of embolism after UK. Downstream emboli occurred in one case with occlusion of a bypass artery. After advancing the catheter to the emboli, additional pulsed spray produced prompt embololysis. Of the 25 patients with treated dialysis grafts, two developed an instantaneous "stitch" in the chest that might have represented an embolus. The pain disap-

TABLE 1: Time Required for Thrombolysis in 46 Successful Cases

Location and Duration of Thrombi	N	First Return Pulse or Flow (min)	Total Lysis (min)
Dialysis graft	29	19±15	49±22
Bypass graft	10	35±18	91±32
Peripheral native artery	7	42±16	75±29
Thrombi 1–3 days	32	21±16	52±25
Thrombi 4–300 days	14	40±16	85±33
All cases	46	26±18	63±35

peared promptly without shortness of breath or other symptoms, and further diagnostic evaluation was not done.

No severe hemorrhagic complications occurred. In one patient in whom a femoral graft thrombus was treated 1 day after an ipsilateral hip operation, mild bleeding occurred in the field directly perfused. This complication had been anticipated and was considered an acceptable cost of reperfusion. In another patient, bilateral hematomas requiring surgical evacuation developed 6 hr after the procedure, at the sites of femoral punctures, while the patient was on heparin. A third patient developed mild self-limited gastrointestinal hemorrhage 6 hr after the procedure, while fully heparinized. The remaining patients had no hemorrhagic sequelae, and hemostasis was achieved with only mild delay after withdrawal of catheters and sheaths. Because of large recently administered doses of heparin, perhaps three patients were observed for 1–2 hr to allow heparin levels to wane before withdrawal of catheter/sheaths. After treatment of dialysis grafts, heparin was reversed with 10–30 mg of protamine sulfate in another three or four patients.

No patient showed evidence of intimal injury or subintimal injection associated with the pulsed-spray injections.

Discussion

Pulsed-spray pharmacomechanical thrombolysis has increased the speed and consistency of thrombolysis. The mean lysis time of 63 min in this series is 36 times faster than the 38-hr mean time reported in our initial clinical series using SK [1]. In dialysis grafts, the present series shows a 43% acceleration, from 86 to 49 min mean, when comparing the pulsed-spray technique with our earlier pharmacomechanical method [8].

The pulsed-spray method is also somewhat faster than other methods recently reported. McNamara and Fischer [2] used intrathrombic UK in concentration of 2500 units/ml, administered at a rate of 240,000 units/hr until pulse return, then 60,000–120,000 units/hr; total calculated dose was approximately 2,000,000 units. They obtained complete lysis in 83% of completed infusions within mean lysis time of 18 ± 20 hr [2]. Partial recanalization was achieved after 3.3 hr (mean), and hemorrhagic complications occurred in 8%. Hess et al. [3], by advancing the catheter under fluoroscopic control as lysis occurred, obtained satisfactory lysis with SK in 1–5 hr, but in only 69% of cases. It is also of some interest to compare our results with those achieved with systemic administration of urokinase. The urokinase/pulmonary/embolism trial [9], for example, indicated that 24 hr of systemic UK lysed an average of 44% of pulmonary embolic volume, whereas complete lysis probably did not occur within 24 hr, and moderate or severe hemorrhage developed in 35%.

In comparing those of our cases treated with or without the pressure device, no significant difference in lysis times is apparent. This homemade prototype injector had a number of deficiencies, however, and conclusions regarding the value of such a device must await completion of an improved commercial model.

The acceleration afforded by the pulsed-spray technique has important clinical implications. Rapid lysis increases the acceptability of the procedure to both patients and physicians. Because a degree of patency and arterial flow are usually established after about 30 min, accelerated thrombolysis usually enables much faster partial reoxygenation of ischemic tissues than does surgery. This is particularly true if catheter access has already been achieved for diagnostic angiography.

Older thrombi have been thought to lyse much more slowly than fresh ones. Our experience does not support such a conclusion. So long as a thrombus was easily traversed by a guidewire, reflecting absence of organization, thrombolysis almost always proceeded rapidly. Although statistical differences were observed, the difference in lysis times between thrombi aged 3 days or less (lysis time = 52 min) and thrombi aged 4 to 300 days (lysis time = 85 min) was not important clinically (Table 1). In one patient, for example, in whom a 75-cm segment of saphenous vein bypass had been occluded for 3 weeks, partial patency of the entire length was regained after 30 min, without visible downstream emboli. The oldest thrombus in this series, an iliac occlusion of 300 days duration, required 45 min until first-observed return of flow and 120 min for completion of lysis.

Rapid lysis also favorably impacts health costs. At our institution, patients undergoing long-term fibrinolytic infusion must be admitted to intensive-care units. With the pulsed-spray technique, however, the entire thrombolytic procedure, as well as any necessary PTA, can be accomplished within the angiography suite in a few hours. Admission to an intensive-care unit then becomes superfluous, effecting a cost saving of \$1000 per day.

The pulsed-spray method has increased the consistency of lysis, as well as its rate. In this series, lysis proved effective in 97.9% of cases. This compares with success rates of 74% [1], 83% [2], and 69% [3] in the series cited earlier. By selecting patients on the basis of at least partial passage of the guidewire and early lytic response, we have avoided the prolonged futile thrombolytic attempts that sometimes occurred in the past. McNamara and Fischer [2] also noted the predictive value of these maneuvers. In two cases that have come to operation because of persistent intraluminal defect after otherwise effective lysis, the residua have been neointimal hyperplasia or atherosclerotic plaque, but not thrombus.

We cannot satisfactorily explain the single case in which lysis failed completely. This 65-year-old diabetic man had claudication for 3 years, which had become worse over the past 3 weeks. Arteriography showed occlusion from the origin of the right common iliac artery to the common femoral bifurcation, plus occlusion of most of the superficial femoral artery. After percutaneous puncture of the occluded right common femoral artery, the guidewire passed into the aorta with only minor difficulty. There was no evidence of lysis after 500,000 units of UK had been injected in 2 hr, and the procedure was abandoned. We postulate that the thrombus may have been organized and that the guidewire had passed via a small residual channel or intramurally.

The absence of major hemorrhage or apparent systemic thrombolytic state in our patients may be attributed to a

number of factors. Our total dose of 250,000–500,000 units is relatively small compared with standard recommended systemic doses of several million units over 12–24 hr, or compared with up to 2,000,000 units per hour that have been used for myocardial infarction [10]. The short biological half-life of UK (~10 min) also minimizes fibrinogen degradation [11]. In addition, intrathrombic insertion of small volumes (large volumes cannot be accommodated within thrombus) probably sequesters thrombolytic agent until lysis has occurred. Such sequestration might further minimize systemic effects, while protecting the UK from systemic inhibitors in plasma [12–15]. Thus, intrathrombic injection promotes efficient use of thrombolytic agent, minimizing both costs and side effects.

Although we have evaluated fibrinogen levels in the past, we did not feel obligated to do so in the present series because (1) the presence of high circulating levels of heparin requires special methods for determination of fibrinogen levels that are not always available at our laboratories, and (2) clinically important coagulation disturbances were absent in our experiences with these and similar methods [8].

Numerous methodologic details require further evaluation. For example, pulse frequency and pressures and optimal methods for avoiding downstream embolization require additional theoretical and empirical investigation. Catheter materials and design, the size and separation of holes, leak-proof couplings capable of withstanding brief pressures of thousands of pounds per square inch, and the pressure injector—all must be optimized.

REFERENCES

1. Mori KW, Bookstein JJ, Heeney DJ. Selective streptokinase infusion: clinical and laboratory correlates. *Radiology* **1983**;148:677–682
2. McNamara TO, Fischer JR. Thrombolysis of peripheral arterial and graft occlusions: improved results using high-dose urokinase. *AJR* **1985**;144:769–775
3. Hess H, Ingrisch H, Mietaschk A, Rath H. Local low-dose thrombolytic therapy of peripheral arterial occlusions. *N Engl J Med* **1982**;307:1627–1630
4. van Breda A, Katzen BT, Scales FE. Streptokinase vs urokinase in local thrombolytic therapy. *Radiology* **1987**;165:109–111
5. Bookstein JJ, Saldinger E. Accelerated thrombolysis: in vitro evaluation of agents and methods of administration. *Invest Radiol* **1985**;20:731–735
6. Valji K, Bookstein JJ. Fibrinolysis with intrathrombic injection of urokinase and tissue-type plasminogen activator: results in a new model of subacute venous thrombosis. *Invest Radiol* **1987**;22:23–27
7. Kandarpa K, Dinker PA, Singer SJ, Caramore D. Forceful pulsatile local infusion of enzyme accelerates thrombolysis: in vivo evaluation of a new delivery system. *Radiology* **1988**;168:739–744
8. Davis GB, Dowd CF, Bookstein JJ, Maroney TP, Lang EV, Halasz N. Thrombosed dialysis grafts: efficacy of intrathrombic deposition of concentrated urokinase, clot maceration, and angioplasty. *AJR* **1987**;149:177–181
9. Sasahara AA, Hyers TM, eds. The urokinase/pulmonary embolism trial. *Circulation* **1973**; 47 [suppl II]
10. Mathey DG, Schofer J, Sheehan FH, Becher H, Tilsner V, Dodge H. Intravenous urokinase in acute myocardial infarction. *Am J Cardiol* **1985**;55:878–882
11. Collen D. On the regulation and control of fibrinolysis. *Thromb Haemost* **1980**;43:77–89
12. Kruithof EK, Tran-Thang C, Bachmann F. The fast-acting inhibitor of tissue-type plasminogen activator in plasma is also the primary plasma inhibitor of urokinase. *Thromb Haemost* **1986**;55:65–69
13. Binnema DJ, van Iersel JJ, Dooijewaard G. Quantitation of urokinase antigen in plasma and culture media by use of an ELISA. *Thromb Res* **1986**;43:569–577
14. Stump DC, Thienpont M, Collen D. Purification and characterization of a novel inhibitor of urokinase from human urine. Quantitation and preliminary characterization in plasma. *J Biol Chem* **1986**;261:12759–12766
15. Lijnen HR, DeWeede K, Demarsin E, Collen D. Biological and thrombolytic properties of proenzyme and active forms of human urokinase—IV. Variability in fibrinolytic response of plasma of several mammalian species. *Thromb Haemost* **1984**;52:31–33

Color-Flow Doppler and Conventional Duplex Scanning of the Carotid Bifurcation: Prospective, Double-Blind, Correlative Study

Michelle J. Hallam¹
Janice M. Reid¹
Peter L. Cooperberg^{1,2}

Color-flow Doppler is a useful adjunct in duplex sonography of peripheral vessels. This study was undertaken to see if color-flow Doppler could give semiquantitative information about the degree of stenosis at the origin of the internal carotid artery. The factors evaluated on color flow are the width of the lumen as estimated from the color-flow image relative to the width of the vessel, the degree of turbulence (evidenced by the mosaic pattern), and the pulse-repetition frequency necessary to prevent aliasing. A double-blind comparison with conventional duplex scanning in 146 carotid bifurcations in 74 patients was carried out. In 91%, the color-flow assessment was in complete agreement with the duplex assessment. In the remaining 9%, the color flow differed from the duplex by only one stenosis group, and the distributions of over- and under-estimation were equal.

These results showed comparable assessment of the degree of stenosis with conventional duplex and color Doppler technology.

In numerous reports in which carotid arteriography is used as the gold standard, duplex sonography (a combination of real-time B-scanning with pulsed Doppler spectral analysis) has proved to be a useful, effective, accurate, and noninvasive method to evaluate arteriosclerotic disease at the carotid bifurcation [1-3]. However, duplex sonography of the carotids is a technically demanding and time-consuming procedure. Real-time B-scanning can show a relatively large segment of the vessel wall and lumen, but flow information (to search for flow disturbances and increased flow velocity) can be obtained only from one small area at a time. Color-flow Doppler [4, 5] allows virtually simultaneous detection of Doppler information throughout the whole section and displays the flowing blood cells in color superimposed on the real-time image.

This study was undertaken to determine if the information from color-flow Doppler imaging could match that from conventional duplex scanning.

Subjects and Methods

During a 1-year period ending in September 1987, 74 patients were randomly selected from those referred for carotid duplex sonographic examinations. The selection was determined more by the availability of the extra room and technician than by any factor related to the patients. A total of 146 separate carotid bifurcations were evaluated. The mean age of the 37 men and 37 women studied was 64 years (range, 32-82 years). The conventional duplex scans were obtained by one of three experienced sonographers in one room. The color-flow examination was then performed in another room by one sonographer. In 22 patients, the color-flow examination was performed first; in the remaining 52 patients, the duplex examination was first. This was for the purpose of convenience only. The results of the conventional duplex study were not known to the subsequent sonographer until after the results for that patient had been documented.

The conventional duplex sonogram was obtained with a Dasonics DRF 400 unit (Dasonics, Inc., Milpitas, CA). A small-parts scanner incorporating a water path with a mechanically

Received April 18, 1988; accepted after revision January 4, 1989.

¹ Department of Radiology, University of British Columbia and Vancouver General Hospital, 855 W. 12th Ave., Vancouver, B.C. V5Z 1M9, Canada.

² Present address: Department of Radiology, St. Paul's Hospital, 1081 Burrard St., Vancouver, B.C. V6Z 1Y6, Canada. Address reprint requests to P. L. Cooperberg.

AJR 152:1101-1105, May 1989
0361-803X/89/1525-1101
© American Roentgen Ray Society

moving 10-MHz imaging transducer and a 4.5-MHz movable Doppler crystal were used. Spectral analysis was performed on the Doppler signal by using a real-time fast-Fourier-transform processor incorporated into the unit. The peak velocity, degree of spectral broadening, and internal carotid/common carotid peak velocity ratios were used to determine the percentage stenosis groupings (Table 1) [6, 7]. To differentiate the most severe degree of stenosis, we used an end-diastolic peak velocity of 100 cm/sec (Figs. 1–3) [7, 8].

The color-flow examination was performed with a prototype Aloka 350 unit (Aloka Imaging Systems, Tokyo, Japan) with a 5-MHz, electronic, curved, linear phased-array transducer. Real-time, gray-scale echo, and color-depicted blood flow information are obtained simultaneously. In this particular unit, flow away from the transducer is always represented by blue and flow toward the transducer by orange red. The brighter the color, the higher the relative velocity of flow. When there is turbulence, which would be displayed as spectral broadening on the spectral analysis of duplex scanning, green is admixed to red or blue, resulting in either yellow or turquoise, respectively. High-grade turbulence with fast tumbling blood flow is

TABLE 1: Criteria to Determine Percentage of Stenosis by Using Conventional Duplex Doppler Sonography

% Stenosis	Peak Systolic Velocity (cm/sec)	ICA/CCA Ratio
0–40	< 80	<1
40–60	80–120	1–1.8
60–80	120–175	>1.8
80–99	>175 (diastolic >100)	>1.8
Occlusion	No flow	No flow

Note.—ICA/CCA = internal carotid artery/common carotid artery.

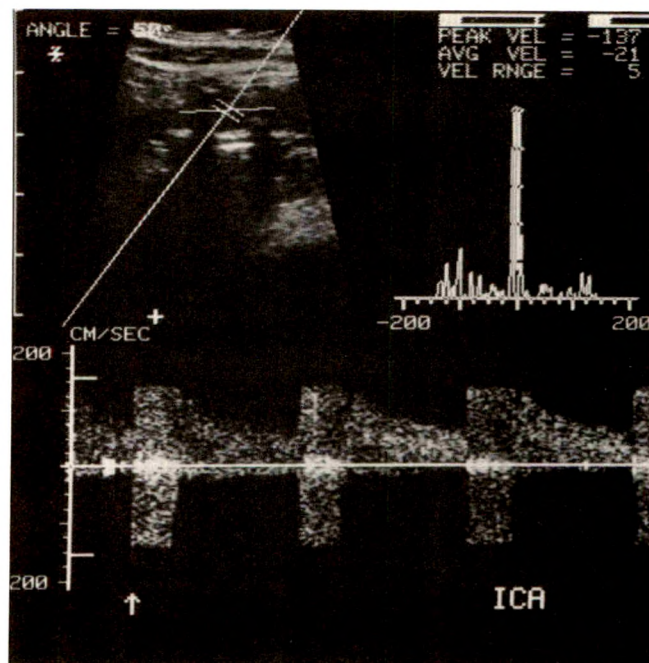


Fig. 2.—Duplex sonogram of internal carotid artery (ICA) just distal to moderate (60–80%) stenosis shows considerable aliasing, with peak velocity (including aliased portion) summated to 270 cm/sec. There is considerable spectral broadening, but end-diastolic velocity is less than 100 cm/sec.

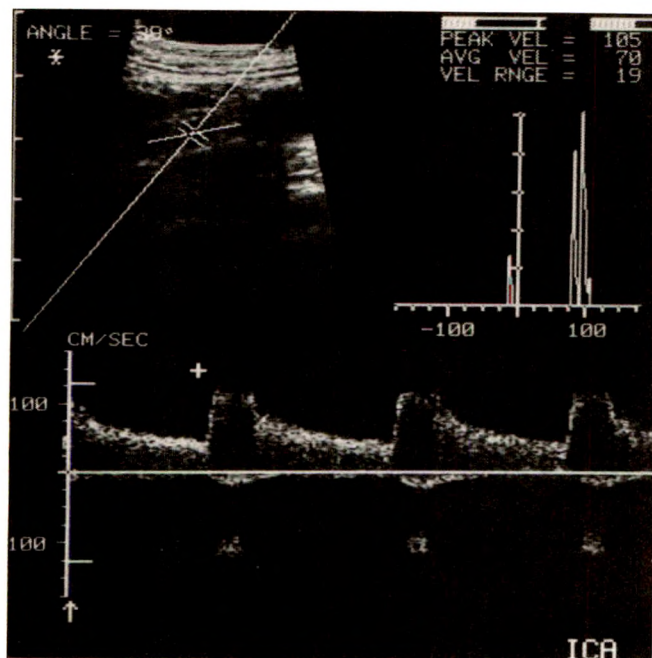


Fig. 1.—Duplex scan of proximal internal carotid artery (ICA) just distal to mild (40–60%) stenosis shows slight degree of aliasing, with peak velocity summated to 151 cm/sec (including aliased portion). Minimal degree of spectral broadening indicates milder degree of stenosis than peak velocity would suggest.

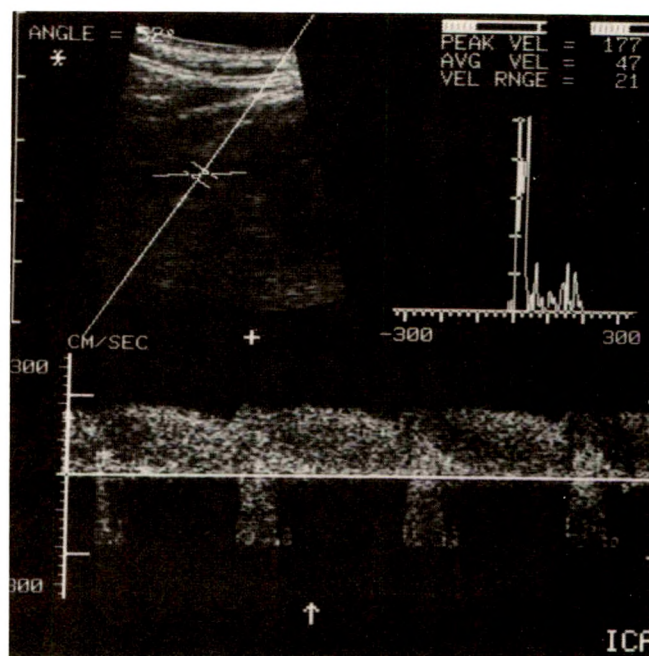


Fig. 3.—Duplex sonogram of internal carotid artery (ICA) just distal to severe (80–99%) stenosis shows considerable aliasing with summated peak velocity (including aliased portion) of 395 cm/sec. Note maximal velocity at end diastole is approximately 180 cm/sec, and spectral broadening indicates considerable turbulence.

displayed as a mosaic pattern with a mixture of red, blue, yellow, turquoise, and green just distal to the stenosis. Aliasing is shown as a reversal of color (an "island" of red within a blue stream) [9, 10]. Aliasing occurs as with conventional duplex scanning when the Doppler shift frequencies exceed the Nyquist limit (one-half the pulse-repetition frequency).

The color-flow equipment is capable of performing conventional pulsed Doppler spectral analysis and providing an audible presentation of the Doppler signal. For this study, this capability was not used. The examinations were interpreted only by observing the color of the flow and any focal area of narrowing of the vessel. The degree of luminal narrowing as evidenced by the width of the color-flow pattern at its narrowest portion, relative to the size of the vessel, was estimated subjectively. Similarly, the degree of the mosaic pattern distal to the stenosis was also estimated subjectively. On this unit, the pulse-repetition frequency could be set to 4, 6, 8, 10, or 12 kHz. By raising the pulse-repetition frequency and observing at what point aliasing disappeared, an approximate kilohertz-shift value could be obtained.

The direction of the ultrasound beam should be maintained at approximately 45°–60° relative to the artery being examined because the appearance of aliasing for the direction of the blood flow cannot be corrected during scanning [11]. The criteria developed to differentiate different degrees of stenosis (as correlated with the duplex scan) are listed in Table 2 (Figs. 4–8).

Cohen's kappa statistic was applied to measure the interrater reliability [12].

Results

The results of this study are displayed in Table 3. Seventy-four patients were examined; 146 bifurcations were included in the study. The examinations in the remaining two bifurcations were not evaluated due to inadequate time on those two occasions. There was disagreement in only 13 of the 146 bifurcations, and in no case was there disagreement by greater than 1 degree of severity. Thus, in 91%, there was complete agreement with the duplex assessment.

On statistical analysis, the kappa value according to Cohen was 0.81. This indicates a significantly better than chance agreement.

Discussion

Real-time two-dimensional color-flow Doppler imaging has been a major technologic advance in diagnostic sonography [13]. The ability to display color where there is flowing blood

TABLE 2: Criteria to Determine Percentage of Stenosis by Using Color-Flow Doppler Sonography

% Stenosis	Criteria
0–40	Blue flow in systole and diastole at 6 kHz; blue flow in diastole at 4 kHz; blue flow, or blue flow with island of red (aliasing), in systole at 4 kHz
40–60	Blue flow with island of red (aliasing) in systole at 6 kHz; blue flow in diastole at 6 kHz; focal narrowing of vessel
60–80	Mosaic colors in systole at 6 kHz; focal narrowing of vessel
80–99	Mosaic colors in systole at 10 or 12 kHz OR blue flow with red island (aliasing) at 12 kHz; focal narrowing of vessel
Occlusion	Absence of color

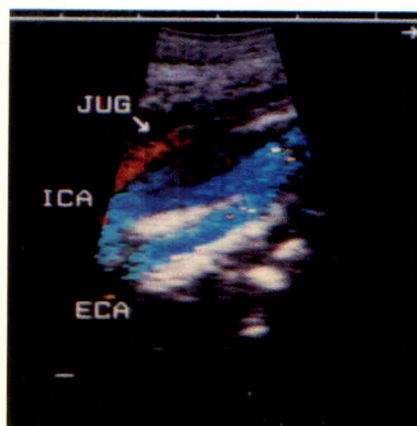


Fig. 4.—Normal carotid bifurcation. Note red (toward transducer) flow in jugular vein (JUG) and blue flow in internal (ICA) and external (ECA) carotid arteries. In superficial portion of carotid bulb normal flow reversal is indicated by red (toward transducer) flow.

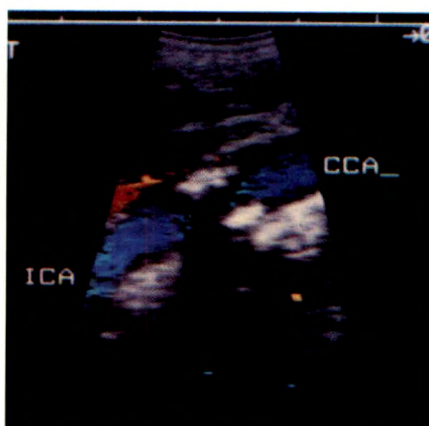


Fig. 5.—Color-flow image of considerable plaque formation at origin of internal carotid artery (ICA) causing shadowing. However, the lack of significant disturbance to flow (even at 4-kHz pulse repetition frequency) indicates no significant (0–40%) stenosis. CCA = common carotid artery.

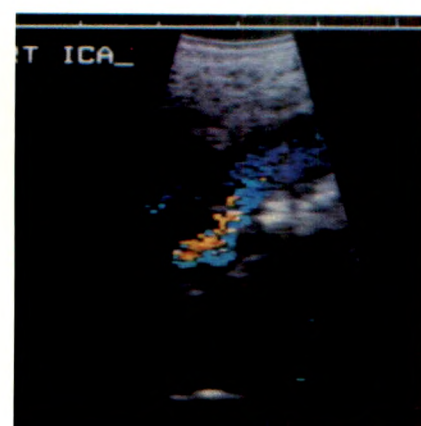


Fig. 6.—Color-flow Doppler image shows moderate (60–80%) stenosis. Mosaic colors are seen in systole at 6 kHz distal to moderate focal narrowing. ICA = internal carotid artery.

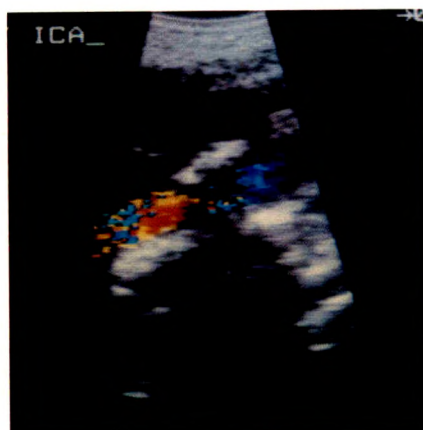


Fig. 7.—Color-flow Doppler image shows severe (80–99%) stenosis demonstrating aliasing and mosaic pattern extending distal to severe stenosis. ICA = internal carotid artery.



Fig. 8.—Color-flow Doppler image shows complete occlusion of internal carotid artery distal to calcified plaque. Note red flow in internal jugular vein, blue flow in common carotid artery proximal to occlusion, and thrombus with no evidence of flow distal to calcified plaque in internal carotid artery.

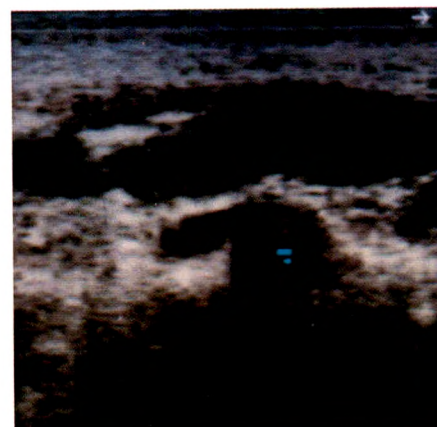


Fig. 9.—Transverse color-flow image shows short axis of common carotid artery with considerable circumferential soft plaque and tiny blue dot representing trickle of flow in severely stenotic lumen.

TABLE 3: Comparison of Diagnostic Results: Conventional Duplex Doppler vs Color-Flow Doppler Sonography

Conventional Findings (% Stenosis)	Color-Flow Doppler Findings (% Stenosis)				
	0–40	40–60	60–80	80–99	Occlusion
0–40	101	3	0	0	0
40–60	3	10	1	0	0
60–80	0	2	5	3	0
80–99	0	0	1	10	0
Occlusion	0	0	0	0	7

Note.—Values are number of bifurcations ($n = 146$).

has a dramatic effect on all those who see it on the television monitor as the patient is being examined. In most cases, there is greatly increased confidence in the diagnostic capabilities of this noninvasive technique. Furthermore, whereas conventional duplex scanning can be complicated and technically demanding, the addition of color-flow information can be a simple adjunctive procedure during real-time scanning. Furthermore, color flow can help direct attention to areas of stenosis within a vessel for a more detailed duplex examination.

This study shows that by using the color-flow information alone we have been able to predict, with a reasonable degree of accuracy, the findings on duplex scanning. In 91%, there was complete agreement with the duplex assessment. In 9%, there was a disagreement by only one adjacent stenotic group. In no case was there a disagreement by more than one stenotic group. Also, the disagreements were evenly divided between over- and underestimation by color flow.

The color-flow studies took approximately 20 min to perform. The time to perform the color-flow examination decreased considerably during the course of the study. The average time for a duplex scan is approximately 35 min, and this average has become stable after several years of experience.

Cohen's kappa statistical analysis measures interrater reliability [12]. This analyzes the agreement that could be expected to happen simply by chance. The lowest value of -1 indicates a poorer than chance agreement. Zero is purely chance. A value of $+1$ means perfect agreement. A value of 0.81 indicates a very good agreement beyond chance.

In practice, with the use of color-flow Doppler, the operator does not have to be limited to the use of the visual analysis of the color flow only. Pulsed Doppler and spectral analysis are available on all color-flow Doppler equipment. Also, the audible signal can greatly aid in the differentiation of the vessels and the detection of poststenotic turbulence and jets. In this study, we restricted the analysis to the color-flow component only.

In practice, color-flow scanning has two major advantages. One of these is to allow the sonographer to scan the neck quickly in transverse section and to identify the region of the bifurcation and the direction taken by the internal and external carotids. This is especially helpful if there is tortuosity of the vessels. Then, in longitudinal examination, a quick survey can show the region of the bifurcation and areas of narrowing, and, because the areas of high flow and turbulence are brighter, the areas of stenosis are easy to identify. Then, one can switch to the duplex mode and place the sample volume

in the appropriate region to confirm the color-flow analysis and provide more precise quantification and hard-copy recording.

Secondly, the sonologist can confirm much more easily the sonographer's results with color flow. With conventional duplex scanning, checking the examination requires almost a complete repetition of what the sonographer has already performed. Confident verification of the sonographer's results is much quicker and easier with the two-dimensional color-flow imaging.

Also, color-flow Doppler has proved useful in specific areas in the diagnosis of carotid disease [4]. If the stenosis is very high grade, only a very narrow trickle of blood may be seen through the stenotic segment. This can be missed more easily with duplex scanning if the sample volume is not placed in the precise position. This can result in the misdiagnosis of a complete occlusion when a surgically correctable high-grade stenosis is actually present. Scanning with color flow in a transverse plane of section can show even a tiny lumen with relatively slow flow (Fig. 9).

Color-flow facilitates the demonstration of the carotid vessels when they are tortuous because the flow is easier to detect on color than the lumen of the vessel on real-time scanning, especially if the patient has a large neck or considerable calcification within the vessel. The ability to detect flow also allows the branches of the external carotid to be identified more easily. This facilitates the differentiation of the external from the internal carotid artery, especially if the internal carotid is completely occluded.

The equipment used for this study was a prototype. Numerous improvements are being incorporated and color flow is becoming available on virtually all sonographic equipment. This should allow color flow to become an even more useful adjunct in the future. This study shows, even with a relatively early prototype, that the results of color imaging can be a

reliable confirmation and predictor of duplex sonographic analysis of the carotid bifurcation.

ACKNOWLEDGMENTS

We thank Jeri Patterson of Overseas Monitor Corp. (Aloka) Ltd. for technical support and Betty Fowler for manuscript preparation.

REFERENCES

1. Clark WH, Hatten HP. Noninvasive screening of extracranial carotid disease: duplex sonography with angiographic correlation. *AJNR* 1981;2:443-447
2. Bendick PJ, Jackson WP, Becker GJ. Comparison of ultrasound scanning/Doppler with digital subtraction angiography in evaluating carotid arterial disease. *Med Instrum* 1983;3:220-222
3. Cardullo PA, Cutler BS, Wheeler HB, et al. Accuracy of duplex scanning in the detection of carotid artery disease. *Bruit* 1984;8:181-186
4. Middleton WD, Foley WD, Lawson TL. Color-flow Doppler imaging of carotid artery abnormalities. *AJR* 1988;150:419-425
5. Becker CD, Cooperberg PL. Progress in radiology. Sonography of the hepatic vascular system. *AJR* 1988;150:999-1005
6. Blackshear WM, Phillips DJ, Chikos PM, Harley JD, Thiele BL, Strandness DE Jr. Carotid artery velocity patterns in normal and stenotic vessels. *Stroke* 1980;11:67-71
7. Bluth EI, Stavros AT, Marich KW, Wetzner SM, Aufrichtig D, Baker JD. Carotid duplex sonography: a multicenter recommendation for standardized imaging and Doppler criteria. *RadioGraphics* 1988;8:487-506
8. Garth KE, Carroll BA, Summer FG, Oppenheimer DA. Duplex ultrasound scanning of the carotid arteries with velocity spectrum analysis. *Radiology* 1983;147:823-827
9. Bommer WJ. Basic principles of flow imaging. *Echocardiography* 1985;2:501-509
10. Omoto R, Kaisai C. Basic principles of Doppler color flow imaging. *Echocardiography* 1986;3:463-473
11. Zweibel WJ. *Introduction to vascular ultrasonography*, 2nd ed. Orlando: Grune & Stratton, 1986
12. Fleiss J. *Statistical methods for rates and proportions*, 2nd ed. New York: Wiley, 1981
13. Omoto R. *Color atlas of real-time two-dimensional Doppler echocardiography*, 2nd ed. Tokyo: Shindan-to-Chiryō, 1987

Book Review

Operative Ultrasonography, 2nd ed. By Bernard Sigel. New York: Raven Press, 219 pp., 1988. \$69

This book is intended primarily to make surgeons and their radiologic colleagues more aware of the usefulness of this new form of operative imaging, which is witnessing rapid advances. It is divided into 10 chapters. The first three are dedicated to basic physics of ultrasound, instrumentation and general techniques of sterilization, deployment of instrumentation in the operating room, placement of transducers, and scanning maneuvers. These chapters can be of significant help to surgeons in general and to part-time sonographers in their first exposure to the operating room. Chapter 4, which addresses operative ultrasonography in liver surgery, is the most elaborate and the most complete. This may be because intraoperative ultrasonography has gained wider acceptance in surgery of the liver than in that of other abdominal organs. This is followed by chapters on biliary tract, pancreatic, renal, and vascular surgery. Although brief, these four chapters are designed with the same easy format (technique, findings, results, conclusions, and recommended applications), which conveys a clear message to the readers. They also contain a tabulation of the author's experience. Chapter 9 on operative sonography during brain and spinal cord procedures is well crafted and offers a good number of excellent illustrations. Considering my belief that ultrasonography is a necessity rather than a luxury to neurosurgeons, I think that a longer chapter on this topic would have been welcome. The last chapter mentions briefly areas

in which operative ultrasonography may play a role in the future, such as in breast, cardiac, and endocrine surgery.

The book is well written and easy to read and covers a wide spectrum of applications. Its main shortcoming is the lack of emphasis on operator-dependency, time consumption, and the need for advanced technical skills that require highly motivated surgeons to undertake formal training or sonographers to dedicate substantial amounts of their time to the operating room. This deficiency is shared with other textbooks on operative ultrasonography, and it has been commented on by colleagues in other reviews as well as in original articles on the same subject. However, the book can be extremely helpful to surgeons who are interested in this new form of operative imaging and to radiologists who practice ultrasonography on a part-time basis and who are contemplating involvement in the operating room. Experienced sonographers who may be familiar with most of the book's contents could use some tips from the author's recommended applications. In sum, I think that the book should be added to all libraries as an authoritative reference on a field with constantly increasing demand.

Joseph Fakhry
New York Medical College
Valhalla, NY 10595

Case Report

Aorto-Left Renal Vein Fistula: Diagnosis by Duplex Sonography

M. Ashraf Mansour,¹ Paul D. Russ,² Stephen W. Subber,² and William H. Pearce¹

Arteriovenous fistulae complicating abdominal aortic aneurysms are uncommon. Most of these fistulae are aortocaval. Rarely, the fistula is to a retroaortic left renal vein [1]. Before surgery, the anatomic location of a fistula must be defined clearly to avoid intraoperative misadventures. Sonography, CT, MR, and angiography are well-established diagnostic imaging techniques currently used to evaluate abdominal aortic aneurysms [2-4]. In the present case, duplex sonography confirmed and precisely localized an aorto-left renal vein fistula, which was suspected on a preoperative arteriogram.

Case Report

A 63-year-old man was referred to our institution for evaluation of a pulsatile abdominal mass. On physical examination, a nontender pulsatile mass was felt just above the umbilicus. A faint, continuous bruit was heard over the left side of the abdomen. Routine laboratory tests were normal except for a serum creatinine level of 1.9 mg/dl and a urinalysis showing microhematuria and proteinuria.

An abdominal sonogram showed a 7.5 × 8.3 cm abdominal aortic aneurysm. Routine preoperative CT showed a retroaortic left renal vein posterior to the aneurysm. The left kidney was mildly enlarged and nonfunctioning. There was no evidence of aortic rupture. In order to delineate the renovascular anatomy, aortography was performed, which showed the aortic aneurysm and early opacification of the inferior vena cava and left renal vein, indicating either an aortocaval fistula or an aorto-left renal vein fistula (Fig. 1).

Duplex sonography was then performed (Fig. 2). Retrograde arterialized flow in the retroaortic left renal vein and arterialized flow

in the inferior vena cava were noted. At real-time examination, posterior-wall disruption of the abdominal aortic aneurysm at the level of the retroaortic left renal vein was shown (Fig. 2A). Doppler interrogation of this small defect showed high-velocity turbulent flow between the abdominal aortic aneurysm and the left renal vein near its confluence with the inferior vena cava (Fig. 2B).

Discussion

Spontaneous formation of a fistula between an abdominal aortic aneurysm and an adjacent venous structure occurs in 1% of all aneurysms and 2.3% of ruptured aneurysms [1, 5]. The most common type of aortovenous fistula is a communication between the aorta and the inferior vena cava [1, 5, 6]. In a recent report, two patients with an aorto-left renal vein fistula were described [1]. In their review, the authors found only 10 previously reported cases of aorto-left renal vein fistula, and a retroaortic left renal vein was encountered in 92% of these 12 cases.

The clinical presentation of patients with aorto-left renal vein fistula is variable. Most patients have abdominal or left-flank pain. On physical examination, a pulsatile mass is felt and auscultation of the abdomen reveals a bruit [1, 5, 6]. Hematuria, gross or microscopic, is seen in 92% of reported cases [1]. A nonvisualized left kidney on urogram and impaired renal function are common findings. In most cases, renal function returns to normal postoperatively [1, 6].

Although several authors have recently described the detection of aortocaval fistulae by CT and MR, most aorto-

Received November 10, 1988; accepted after revision December 12, 1988.

¹ Department of Surgery, Vascular Surgery Section, University of Colorado Health Sciences Center, 4200 E. 9th Ave., Denver, CO 80262. Address reprint requests to M. A. Mansour, Box C306, at the University of Colorado Health Sciences Center.

² Imaging Service, Veterans Administration Medical Center, 1055 Clermont St., Denver, CO 80220.

AJR 152:1107-1108, May 1989 0361-803X/89/1525-1107 © American Roentgen Ray Society

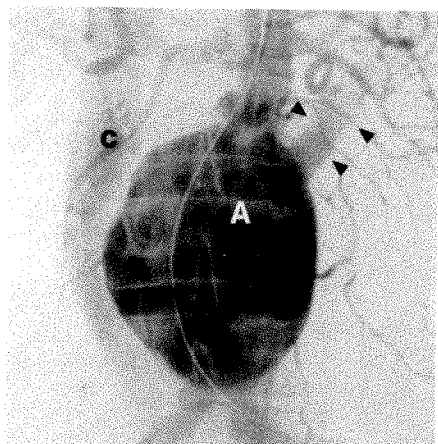


Fig. 1.—Left transfemoral aortogram showing an aneurysm (A) and early opacification of both inferior vena cava (C) and left renal vein (arrowheads).

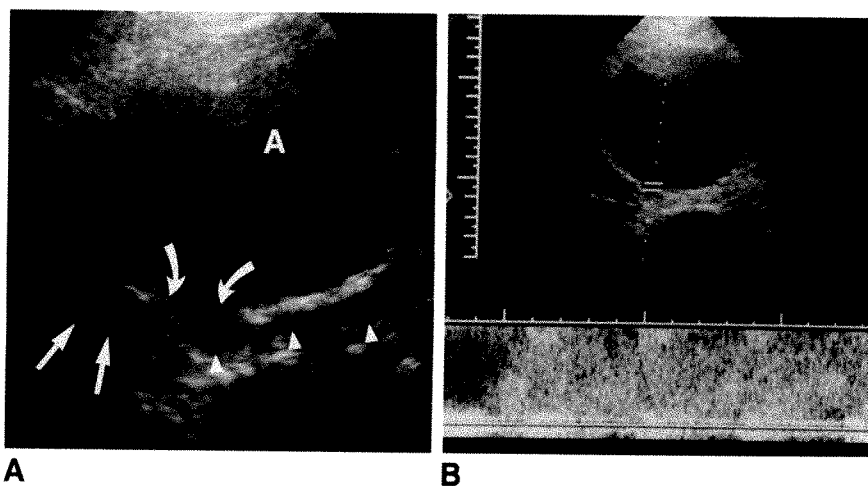


Fig. 2.—Duplex sonography showing abdominal aortic aneurysm and adjacent venous structures. A, Posterior wall disruption (curved arrows) of aneurysm (A) is visible at level of retroaortic left renal vein (arrowheads) near its confluence with inferior vena cava (straight arrows). B, Doppler interrogation of small defect reveals high-velocity turbulent flow confirming an aorto-left renal vein fistula.

left renal vein fistulae have been diagnosed by angiography [7, 8]. Early venous filling is seen on aortography; however, it is often difficult to distinguish between an aortocaval and an aorto-left renal vein fistula by angiography alone, because the fistula may not be visible when the standard biplane filming technique is used. If the anatomy cannot be defined by arteriography, duplex sonography allows for real-time imaging and Doppler interrogation of venous structures next to the abdominal aortic aneurysm. The fistula is localized by detecting vascular-wall disruption with associated high-velocity turbulent flow (Fig. 2).

The operative management of aorto-left renal vein fistula consists of securing proximal and distal control of the aorta and then opening the aneurysm and oversewing the fistula under direct vision. Digital compression of the left renal vein will reduce the amount of bleeding from the fistula. Therefore, the preoperative diagnosis and precise localization of aorto-left renal vein fistula is a helpful guide to the surgeon for safe closure of the fistula without excessive blood loss.

In this case, the abdominal aortic aneurysm was initially diagnosed by sonography. The routine preoperative CT study was done to detect associated iliac aneurysms, venous anomalies, and other intraabdominal disease. The retroaortic left renal vein and enlarged nonfunctioning left kidney were incidental findings. Abdominal bruit on physical

exam is reported in most patients with aortovenous fistula; however, this finding does not exclude other diseases. Although the arteriogram documented an aortovenous fistula, the exact location of the fistula could not be ascertained by angiography alone. Duplex sonography confirmed the presence of the aortovenous fistula and established its exact location.

REFERENCES

1. Celoria GM, Friedmann P, Rhee SW, Berman J. Fistulas between the aorta and the left renal vein. *J Vasc Surg* 1987;6:191-193
2. Leopold GR, Goldberger LE, Bernstein EF. Ultrasonic detection and evaluation of abdominal aortic aneurysms. *Surgery* 1972;72:939-945
3. Axelbaum SP, Schellinger D, Gomes MN, Ferris RA, Hakka HG. Computed tomographic evaluation of aortic aneurysms. *AJR* 1976;127:75-78
4. Lee JKT, Ling D, Heiken JP, et al. Magnetic resonance imaging of abdominal aortic aneurysms. *AJR* 1984;143:1197-1202
5. Merrill WH, Ernst CB. Aorta-left renal vein fistula: hemodynamic monitoring and timing of operation. *Surgery* 1981;89:678-682
6. Suzuki M, Collins GM, Bassinger GT, Dilley RB. Aorto-left renal vein fistula. *Ann Surg* 1976;184:31-34
7. Middleton WM, Smith DF, Foley WD. CT detection of aortocaval fistula. *J Comput Assist Tomogr* 1987;11:344-347
8. Lupetin AR, Dash N, Contractor FM. MRI diagnosis of aortocaval fistula secondary to ruptured infrarenal abdominal aneurysm. *Cardiovasc Intervent Radiol* 1987;10:24-27

A Report-Coding System for Integration into a Digital Radiology Department

John M. Bramble¹
C. H. Joseph Chang
Norman L. Martin

Report-coding systems allow the radiologist to generate a typewritten radiographic report with a computer. Typically, the report is generated by selecting bar codes, speaking key words, or selecting items on a screen. MAMM REPORT is a report-coding system for mammography, developed by radiologists, that runs on a microcomputer (Amiga, Commodore Co., West Chester, PA). MAMM REPORT speaks questions to the radiologist, who responds by pressing one of two buttons on a computer mouse, thus generating the report. MAMM REPORT allows labeling of digital images and reduction of data required to store the report in computer memory (data compression). Data compression is useful for improving computer operating speed. Digital image labeling and data compression facilitate use of MAMM REPORT on a future digital radiology workstation for an all-digital radiology department. Sixty mammographic reports, reviewed by a radiologist who is not a specialist in mammography, were entered into MAMM REPORT. The mammography specialists who dictated the original reports then judged whether the reports generated by MAMM REPORT would be acceptable replacements on the basis of descriptions of findings, diagnoses, and recommendations for further study. Data compression was measured by calculating the ratio of the number of bytes for storage of the reports in original form to a standard storage form (Huffman encoding) and to the MAMM REPORT coded form. All 60 coded reports were acceptable replacements for the original reports. For computer storage, MAMM REPORT produced a compression ratio of 135 to 1 and Huffman encoding, 1.1 to 1. Huffman encoding did not compress most reports because of their brevity.

The results indicate that report coding can produce data compression of radiographic reports. The standard method of text storage, Huffman encoding, is not suitable for application to mammographic reports, which tend to be brief.

Radiographic report-coding systems allow the generation of consultation reports without actually typing the report. Reports can be generated by selecting bar codes, speaking key words, or selecting items from a screen. Several coding systems have been available over the years but have not received widespread acceptance [1-3]. With the advent of the "all-digital" radiology department [4], report-coding systems deserve further investigation. In the all-digital environment, coding systems can improve the efficiency of data analysis for quality assurance, diagnosis coding for third-party payers, and research. Report coding also can be used to improve the efficiency of information networks for storage and communication of diagnostic images and reports in the all-digital radiology department.

MAMM REPORT is a mammographic report-coding system designed for integration into an all-digital radiology department. Two additions to coding systems that are useful for integration are the ability to label the digital images with important findings and the ability to store reports in coded form. Storing reports in coded form decreases the amount of data to be stored for each report (data compression). The coded data are thus made readily available for data analysis.

The system's ability to reduce and store the text of mammogram reports was measured and compared with standard storage methods [5].

Received October 11, 1988; accepted after revision January 11, 1989.

¹ All authors: Department of Diagnostic Radiology, University of Kansas Medical Center, 39th St. and Rainbow Blvd., Kansas City, KS 66103. Address reprint requests to J. M. Bramble.

AJR 152:1109-1112, May 1989

0361-803X/89/1525-1109

© American Roentgen Ray Society

Methods

MAMM REPORT was written in the "C" programming language by John Bramble. The program allows the radiologist to produce a mammogram report by responding to questions from the computer. The questions are spoken by the computer through earphones worn by the radiologist while viewing the exam. The radiologist responds to the questions by pressing either the right or left button on a computer mouse. The report may then be printed on consultation forms and stored on computer disks. A second program was added, which allowed the labeling of digital images of the mammograms. The digital images of the mammograms were obtained by use of a video digitizing system (Digi-View, New Tek, Topeka, KS). The digital images currently are not of diagnostic quality and are included solely to show labeling. The original mammograms were interpreted by two radiologists with 45 years combined experience interpreting mammograms.

Sixty transcribed mammogram reports, randomly selected from work logs, were collected for evaluation. A standard method for storing text, Huffman encoding, was applied to the original reports. Huffman encoding was done using the program PACK [6], which is part of UNIX System 5 (AT&T Bell Laboratories, Holmdale, NJ). The original reports were read by a third radiologist, who entered the findings, diagnoses, and recommendations into the MAMM REPORT program. The third radiologist did not reinterpret the mammograms. The number of computer bytes required for storing the reports was recorded. The report generated by MAMM REPORT was printed for comparison with the original reports.

The original radiologists reviewed the original and computer-generated reports. The computer-generated reports were judged acceptable if the original radiologists determined that all essential findings and recommendations in the original report were contained in the final report. To compare the number of computer bytes, a compression ratio was calculated as the ratio of the number of bytes for the original report to the number of bytes in the coded reports [7]. The higher the compression ratio, the smaller the size of the compressed stored report.

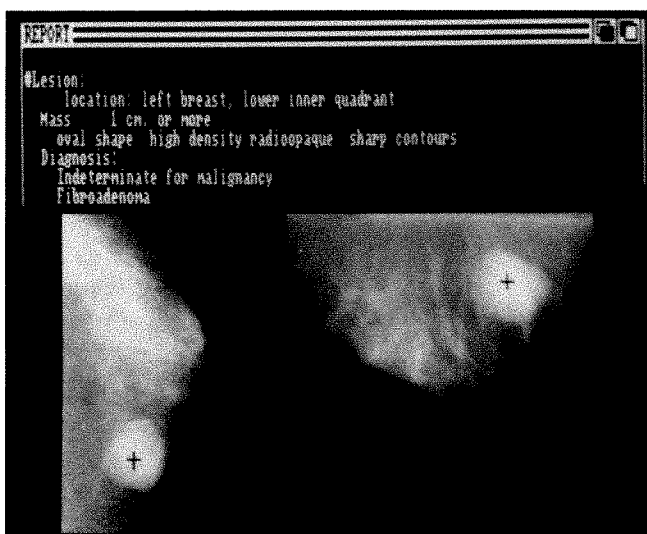


Fig. 1.—Computer-generated report and labeled digital image as it might appear to referring physician. Digital images of breast may be rearranged on screen by clicking a computer mouse button, so that entire report is visible.

TABLE 1: Original Report

BILATERAL MAMMOGRAMS: Both breasts show partial involutional changes. No abnormal calcifications are identified. Skin and vascularity are unremarkable. There is a 3×3.5 cm, well-demarcated soft-tissue mass, seen in the lower-inner quadrant of the left breast. Diagnostic considerations would include a benign cyst and fibroadenoma. Medullary carcinoma, however, remains in the differential diagnosis. Sonography is suggested to determine whether the mass is cystic or solid. There is no dominant mass in the right breast. The axilla are free of adenopathy.

CONCLUSION: The right breast shows partial involutional changes, with no radiographic evidence of malignancy. The left breast reveals a soft-tissue mass, as described above, with recommendations.

Note.—This is the original report dictated by the mammographer of the case shown in Figure 1.

TABLE 2: Computer-Generated Report

CHARACTERISTICS: partial involutional

FINDINGS:

#Lesion:

location: left breast, lower inner quadrant

Mass 1 cm or more

oval shape high density radiopaque sharp contours

Diagnosis:

Indeterminate for malignancy

Fibroadenoma

Benign cyst

RECOMMENDATIONS: Biopsy

Sonography

Note.—This is the computer-generated report of the case shown in Figure 1.

Times required to generate the 60 reports were not measured because the third radiologist did not originally interpret or dictate the mammograms. An informal study was done, during which the times were recorded for comparison of dictation to report coding. The two mammography specialists were timed during the direct dictation of 12 additional cases in the clinical workload. Subsequently, the mammography specialists were timed during the entry of codes for the same cases on the MAMM REPORT system.

Results

PACK did not compress 76% of the reports. The data show that brief reports of less than 500 bytes (or 500 characters) are not compressed. Of the compressed reports, the average compression ratio is 1.5 to 1. For all reports, the average compression ratio is 1.1 to 1. MAMM REPORT produced a compression ratio of 135:1, based on the average for all reports. All reports were compressed, regardless of length.

Figure 1 is a sample computer-generated report with a digitized mammographic image. Part of the report is obscured by the digitized image. Tables 1 and 2 list the entire dictated and computer-generated report for the case depicted in Figure 1. Table 3 lists the computer queries that the radiologist would hear and the user (radiologist) responses (indicated by clicking the left or right button on the computer mouse) during the review of the case in Figure 1. The compression ratio of 93:1 is less than average because of the presence of an abnormality. Reports of "normal," "no change from prior

TABLE 3: Computer Queries and User Responses During Generation of the Mammographic Report

C: Prior exam?	C: Halo sign: yes or no?
U: No	U: No
C: Dense breasts?	C: Calcifications?
U: No	U: No
C: Involutional?	C: Stellate lesion?
U: No	U: No
C: Partial involutional?	C: Possibly malignant?
U: Yes	U: Yes
C: Fibrocystic disease?	C: Indeterminate for malignancy?
U: No	U: Yes
C: Normal?	C: Fibrocystic disease?
U: No	U: No
C: Any lesion?	C: Fibroadenoma?
U: Yes	U: Yes
C: Both breasts?	C: Intramammary lymph node?
U: No	U: No
C: Left or right?	C: Benign cyst?
U: Left	U: Yes
C: Scattered or focal?	C: Focal fibrocystic disease?
U: Focal	U: No
C: Subareolar or central?	C: More diagnoses?
U: No	U: No
C: Upper on CC view?	C: End diagnosis?
U: No	U: Yes
C: Lower on CC view?	C: More lesions?
U: Yes	U: No
C: Outer half on ML view?	C: More findings?
U: No	U: No
C: Inner half on ML view?	C: Recommendations: standard or special?
U: Yes	U: Special
C: Mass lesion?	C: Biopsy?
U: Yes	U: Yes
C: Size: greater or less than 1 cm?	C: Follow up in 3 months?
U: Greater than 1 cm	U: No
C: Shape: oval or lobulated?	C: Follow up in 6 months?
U: Oval	U: No
C: Density: lucent or dense?	C: Follow up in 1 year?
U: Dense	U: No
C: Radiodense: mixed or uniform?	C: Mammographic CT?
U: Uniform	U: No
C: Uniform density: high or low?	C: Sonography?
U: High	U: Yes
C: Contours: sharp or unsharp?	
U: Sharp	

Note.—The case illustrated is the same as Figure 1. C = computer query, U = user response. Forty-three responses are required for the generation of the report. This yields a compression ratio (the number of computer bytes in the original dictated report to the number of computer bytes in the MAMM REPORT coded form) of 93:1.

exam," and "fibrocystic disease" produce the highest compression ratios. The original radiologists judged all of the computer-generated reports acceptable in information content. Twelve additional cases required 772 sec for dictation directly to a transcriptionist. The same 12 cases required 732 sec when coded by MAMM REPORT.

Discussion

Data compression is used to decrease the amount of data in text or images without significantly changing the information content. A reduction of the amount of data can improve the efficiency of computer systems designed to process the information. Efficiency is improved because less time is spent moving the data around in computer memory and on and off

computer storage devices. The results indicate that report coding systems such as MAMM REPORT can be much more efficient than standard methods for storing reports.

The data compression that is possible with report-coding systems is not essential for digital radiology departments. The amount of data required for reports is miniscule compared with the amount of data in images. Inexpensive computer storage media can store many reports [8]. Rather, data compression is a useful side effect that can be taken advantage of, particularly in radiology information networks, which use multiple copies of reports at multiple stations.

The primary advantages of report coding are cost savings and ready availability of data for analysis. Cost savings are realized by the reduction of salary for transcription. Data analysis is useful for generation of diagnosis codes for billing,

quality assurance reports, and compilation of statistics of disease and incidence of radiographic findings. The statistics gathered would be useful for setting guidelines for screening. Information correlating risk factors, radiographic findings, and disease incidence also can be presented to the radiologist to aid diagnostic decisions.

The major disadvantage of report coding has been the inconvenience for the radiologist compared with dictation. Two inconveniences of report coding are that most coding systems are slower than dictation and that most require the radiologist to look away from the film. The results of an informal study of time for report generation suggests that report coding will not be significantly slower. However, a more extensive study would be necessary for more reliable results. The use of computer-generated voices eliminates the need for the radiologist to look away from the films. Radiologists' responses also are confirmed orally and they review the final report on the screen before printing.

The MAMM REPORT system is currently being modified (changing printers and customizing questions to the radiologist's preference). After the system is finalized, more rigorous testing of speed and acceptance by radiologists can be completed.

In summary, report-coding systems can be easily integrated into the all-digital radiology department. There are certain

advantages to be gained by using report coding as opposed to dictation/transcription. Information contained in the reports is accessible for data analysis and is recorded much more efficiently.

ACKNOWLEDGMENTS

The authors thank Sam Dwyer, Ken Hensley, and Theresa Stika for assistance in performing the study and preparing the manuscript.

REFERENCES

1. Adams HG, Campbell AF. Automated radiographic report generation using barcode technology. *AJR* **1985**;145:177-180
2. Choplin RH, Boehme JM, Cowan RJ, et al. A computer-assisted radiologic reporting system. *Radiology* **1984**;150:345-348
3. Jeanty P. A simple reporting system for obstetrical ultrasonography. *J Ultrasound Med* **1985**;4:591-593
4. Templeton AWT, Cox GG, Dwyer SJ III. Digital image management networks: current status. *Radiology* **1988**;169:193-199
5. Reghbati HK. An overview of data compression techniques. *IEEE Computer* **1981**;14:71-76
6. *Uniplex + System V user's manual*. Berkeley, CA: UniSoft Systems, **1984**
7. Huang HK. *Elements of digital radiology: a professional handbook and guide*. Englewood Cliffs, NJ: Prentice-Hall, **1987**
8. Jost RG. Radiology reporting. *Radiol Clin North Am* **1986**;24(1):19-26

Comparison of 2048-Line Digital Display Formats and Conventional Radiographs: An ROC Study

Alek Hayrapetian¹
 Denise R. Aberle¹
 H. K. Huang¹
 Robert Fiske^{1,2}
 Craig Morioka¹
 Dan Valentino¹
 M. Ines Boechat¹

Observer performance tests were conducted to compare the effects on diagnostic accuracy of digital hard copy and video display formats versus conventional radiographic film. Digital images were obtained by digitizing conventional chest radiographs to a 2048 × 2048 matrix with a laser film scanner. Three digital display formats were used: laser-printed digital film, a 2048-line video monitor without user interaction, and a 2048-line video monitor with user interaction. Thirty-one posteroanterior chest radiographs, determined by consensus of four thoracic radiologists to contain septal lines ($n = 11$), parenchymal nodules ($n = 7$), nodules and septal lines ($n = 7$), or neither abnormality ($n = 6$), were used for the study. Images were interpreted by four radiologists in four separate viewing sessions. Diagnostic accuracy was determined by receiver-operating-characteristic analysis for each observer with each viewing technique. No statistical differences in diagnostic accuracy, determined by the area under the receiver-operating-characteristic curve, were found between the analog film, the digital film, and the two video digital display formats.

This preliminary study suggests that 2048-line digital displays may be an acceptable alternative to the traditional lightbox viewing method for the perception of these two abnormalities commonly seen on chest radiographs.

Present digital technology provides a variety of display formats for digitally acquired images. Previous studies have addressed variations in the size of matrix display, hard-copy (film) versus soft-copy (video monitor) format, and numerous enhancements that can affect the diagnostic quality of the digital image [1-4]. Video display systems offer image manipulation and potentially improved diagnostic accuracy by virtue of interactive windowing, tonal reversal, magnification, and unsharp masking.

In some instances, these image-enhancement techniques have been shown to compensate for the effect of limited spatial resolution inherent in current digital display systems, suggesting the importance of controlled studies of digital imaging that incorporate user interaction [5]. We have recently installed a 2048-line digital display station for clinical use. Using this video system, we designed an experiment to examine the detection of two abnormalities commonly seen on chest radiographs, pulmonary nodules and septal lines. We compared their detection in analog films with that in three digital displays of 2048 matrix: digital hard copy, static video display, and video display with user interaction.

Materials and Methods

Thirty-one conventional chest radiographs were chosen from among hospitalized and ambulatory clinic patients in a university setting that incorporated both medical and surgical practice. These radiographs showed septal lines ($n = 11$), parenchymal lung nodules ($n = 7$), nodules and septal lines ($n = 7$), or neither abnormality ($n = 6$). The presence or absence of abnormality as well as the visibility of abnormality (from subtle to obvious) were determined by unanimous agreement among four thoracic radiologists who did not participate in the

Received September 22, 1988; accepted after revision January 9, 1989.

This work was supported in part by Public Health Service grant no. 2 R01 CA 39063 awarded by the National Cancer Institute.

¹Department of Radiological Sciences, UCLA Medical Center, BL-428 CHS, University of California, Los Angeles, Los Angeles, CA 90024-1721. Address reprint requests to H. K. Huang.

²Present address: Rockwell International Corp., P. O. Box 92098, Los Angeles, CA 90009.

AJR 152:1113-1118, May 1989

0361-803X/89/1525-1113

© American Roentgen Ray Society

TABLE 1: Characteristics of the 31 Radiographs Used for the ROC Study

Case Number	Abnormality 1	Abnormality 2
1	Septal (O)	(—)
2	Septal (O)	Nodule (not used)
3	(—)	Nodule (O)
4	Septal (I)	(—)
5	Septal (O)	(—)
6	Septal (S)	Nodule (low contrast, I)
7	Septal (I)	(—)
8	Septal (S)	Nodule (low contrast, O)
9	(—)	Nodule (low contrast, O)
10	(—)	(—)
11	Septal (O)	(—)
12	Septal (O)	(—)
13	Septal (O)	(—)
14	Septal (I)	Nodule (O)
15	Septal (I)	(—)
16	(—)	Nodule (low contrast, S)
17	(—)	Nodule (O)
18	(—)	(—)
19	Septal (I)	(—)
20	Septal (I)	Nodule (O)
21	(—)	(—)
22	Septal (I)	Nodule (low contrast, I)
23	(—)	(—)
24	(—)	Nodule (S)
25	(—)	(—)
26	(—)	Nodule (O)
27	(—)	(—)
28	Septal (S)	Nodule (low contrast, I)
29	(—)	Nodule (low contrast, I)
30	Septal (O)	(—)
31	Septal (S)	Nodule (O)
Total	13 (—), 18 Septal	16 (—), 14 Nodule

Note.—(O) = obvious, (I) = intermediate, (S) = subtle, (—) not present.

receiver-operating-characteristic (ROC) study, by using the conventional radiographs together with additional clinical and radiographic data. Nodules were chosen as a test of diagnostic accuracy because their presence is a frequent concern in the clinic patients with malignancies followed at our institution. Septal lines have been used in other ROC studies as a measure of the spatial-resolution requirements of imaging systems.

There were a total of 14 nodules shown on the 31 radiographs. The average diameter of the nodules was 12.4 mm (range, 8–40 mm). The locations of the nodules varied, with seven projecting over skeletal structures, over the heart, or into areas of diffuse lung disease. These were thought to represent threshold lesions by virtue of structured noise or low contrast with their surroundings. Among these nodules, ease of visibility of the abnormality was considered subtle in two, intermediate in four, and obvious in eight. Eighteen of the images contained septal lines visible in the costophrenic angles, lung periphery, or perihilar regions. Of these, ease of visibility of the abnormality was considered subtle in four, intermediate in seven, and obvious in seven. Table 1 shows the characteristics of these 31 radiographs.

All radiographs were of high quality, the majority had been exposed at 130 kV with a 10:1 grid using a Fuji KYOKKO screen and Fuji HRL film (Tokyo, Japan). The analog films of 35×35 cm² (14×14 in²) were digitized to $2048 \times 2048 \times 8$ bit digital images using a laser film scanner (Konica Photo Industrial Co., Tokyo, Japan) with a spatial resolution of 0.175 mm/pixel. Hard-copy images of 33×33 cm (13×13 in²), in which the pixel size was 0.08 mm (hence, the image size was 6% smaller), were printed using a 4096×4096 matrix laser film printer (3M P831 Laser Imager, St. Paul, MN). The laser printer used the pixel-replication technique in which one pixel value in the digital image was duplicated to 2×2 pixels in the printed image.

Soft-copy images of 29×29 cm² (11×11 in²) were displayed on a 2048×2048 interlaced monitor with a long persistent phosphor-tainted screen having a spatial resolution of 0.142 mm/pixel (Mitsubishi Electric Company, Kyoto, Japan). The video display was 2:1 interlaced with a 30-Hz vertical frequency, with a 120-MHz bandwidth and an 18.5-in. diagonal screen. The video monitor is capable of displaying 256 gray scales. The whole image was 19% smaller than the original analog image.

For the video display conditions with and without user interaction, the contrast and brightness of the monitor were established at the beginning of each reading session and were not altered thereafter. The observers were shown a palette of 256 gray levels and were told to fix the contrast at the maximum and to adjust the brightness level such that they could not see the first two gray levels (numbers zero and one), that is, gray level two was established as the lower bound. For the interactive video display condition, the observers were trained about the possible interactive window and level adjustments. Observers initially were shown training images of an anthropomorphic model containing lung nodules in different locations. They were told of the locations of the nodules and were allowed to alter the contrast window and level in order to familiarize themselves with interactive conditions. During the ROC viewing sessions, the training case was repeated after every 10 test images to refamiliarize readers with the interactive video features.

Four radiologists (two chest, one pediatric, and one senior resident) with limited experience with video display monitors and interactive windowing were used as observers to evaluate the images. The radiologists were provided no clinical information and did not know the proportion of cases containing abnormality. Each observer reviewed four image sets consisting of 31 different images each. For each ROC study, the reader was informed that the images might contain nodules or septal lines. They were asked to evaluate each image for these independent observations. They were not asked to evaluate for all possible chest abnormalities. Viewing sessions for each observer were separated by at least 2 days; many were separated by weeks or months. Each viewing session consisted of pure image sets for the conventional film, laser-printed digital film, video monitor without user interaction, or video monitor with user interaction. No time constraints were imposed on the observers. To counteract possible learning effects, observers encountered the four display conditions in different orders, and the order of presentation of images was randomized for each test. Correct diagnoses for the images were not revealed to observers until they had reviewed all four image sets. All these precautions were to minimize the effects of recall. Figure 1 shows the four display conditions, and Figure 2 depicts an example of one case in each of the four display conditions.

For each image, the observer rated the presence of septal lines and nodules as two separate judgments using a six-point confidence-rating scale, with "1" as the most certain that abnormality is not present and "6" as the most certain that abnormality is present.

The performance measure was A_z , the area under the ROC curve constructed separately for each disease, for each display condition, and for each observer. After the ROC curve was generated, the area under the curve was computed by using the trapezoidal rule. Each

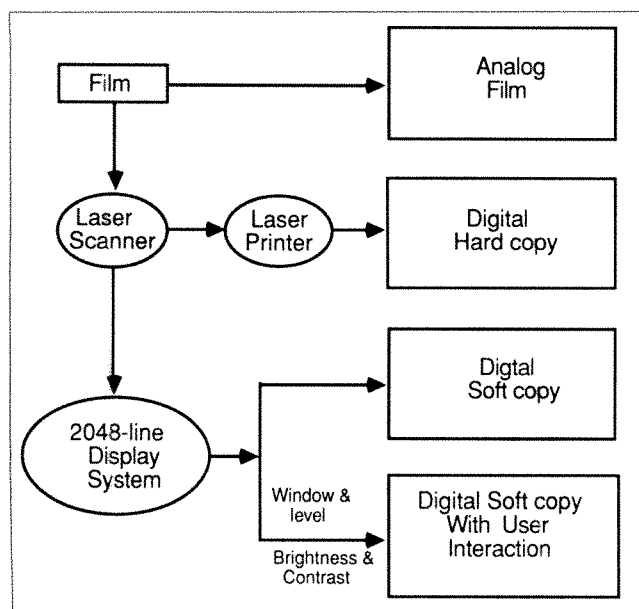


Fig. 1.—Block diagram showing method of obtaining four display formats.

ROC test on a complete image set was treated as a separate measurement; no pooling of observations was performed. We used the analysis of variance technique (ANOVA) with the standard F ratio to accept or reject a hypothesis. In each case, the F ratio was calculated and then compared with the tabulated value of F (r,s), where r and s are the degrees of freedom of the given experiment.

Results

Figure 3 shows the area under the ROC curve for each of the two abnormalities and for each of the four viewing formats. For each condition, the area under the ROC curve was obtained by averaging the results from the four observers. The standard deviations (SD) shown in Figure 3 were computed by the formula

$$SD = \sqrt{\frac{\sum_{i=1}^N (A_i - A)^2}{N - 1}}$$

where A is the average area of a viewing format, and A_i is the area of an observer. The 95% confidence level was used, that is, the null hypothesis was rejected if the p value was less than .05. The statistical analysis is given in the Appendix.

For detecting septal lines, analysis of composite ROC data indicated that diagnostic accuracy with conventional film was statistically equivalent to that with digital film (hard copy). Video display without user interaction yielded similar results. Diagnostic accuracy did not improve significantly with the interactive video display.

For detecting pulmonary nodules, diagnostic accuracy was equivalent between conventional film and digital hard copy. Similarly, the two video display conditions were equivalent, and there was no significant difference between the soft-copy

or hard-copy display conditions. For each display condition, the diagnostic accuracy of nodules was inferior to that of septal lines, and this difference was uniform among the four display conditions.

There were no interaction effects, that is, the differences in the ROC scores between septal line detection and nodule detection were statistically equal for all four display formats. This means that the display formats did not exhibit significant advantage over each other in the detection of the two diseases. Overall diagnostic accuracy with each display technique was calculated by averaging the ROC data for each of the lung abnormalities. Diagnostic accuracy was statistically equal for all of the display conditions.

Discussion

Relatively few papers have addressed the effects on diagnostic accuracy of video display formats relative to hard copy for detecting abnormalities commonly seen on chest radiographs. In this study, the two video display conditions used a 2048-line video monitor that is capable of displaying a pixel size of 0.14 mm. All images were digitized using a laser film scanner with a spatial resolution of 0.175 mm/pixel; thus, the overall spatial resolution was limited to 0.175 mm/pixel by the digitization process.

We chose to use septal lines as a measure of the spatial-resolution requirement because they are one of the smallest finite densities visible on the chest radiograph. We attempted to sample a spectrum of conspicuity of abnormality, as determined by radiologists not participating in the ROC tests. In our study, septal lines were seen as well on hard-copy and soft-copy digital display systems as on conventional radiographs. This is consistent with the observations of Lams and Cocklin [1] who compared the detectability of nodules and septal lines on conventional film with that under varying video display conditions ranging in pixel size from 0.2 to 1.6 mm. They concluded that, among readers experienced with digital and video display systems, observer performance with digital images of 0.4-mm pixel size was comparable to that achieved with conventional film. They found a small, but not significant, decrease in observer performance with the highest resolution digital images (0.2-mm pixel size), which was not explained.

MacMahon et al. [2] compared digital images of spatial resolution from 0.1 to 1.0 mm/pixel with conventional film for the detectability of interstitial infiltrates without septal lines and subtle pneumothoraces. They concluded that diagnostic accuracy increased significantly as the pixel size was reduced to 0.1 mm and that accuracy was greatest for both abnormalities with the conventional radiographs. Many of their examples of interstitial infiltrate did not contain discrete septal lines, but rather, hazy or ill-defined patterns with obscuration of normally sharp vessel margins. Although this pattern of interstitial abnormality complicates the determination of diagnostic "truth," it may provide a more rigorous test of minimum spatial-resolution requirements in imaging systems.

In our study, diagnostic performance also was evaluated with respect to nodule detection. Nodules were chosen as a test because of the frequency with which they are questioned

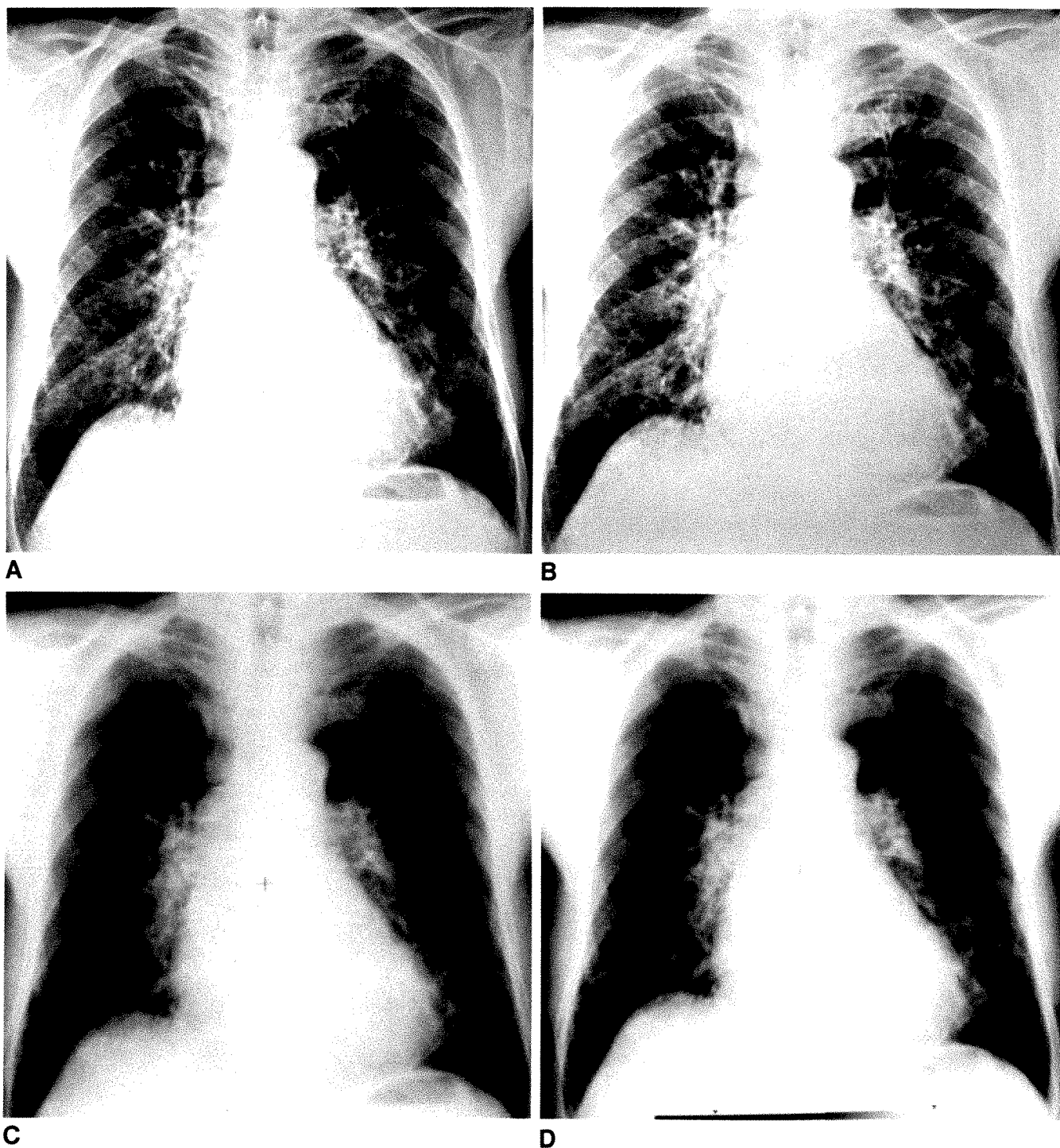


Fig. 2.—Appearance of a test image with septal lines (case 1) in each of four display formats. Film was digitized at 0.175 mm/pixel. A, analog film; B, digital hard copy; C, soft copy (2048-line monitor); D, soft copy with user interaction. Cross on C and D is cursor; in D, window and level scale are shown in lower portion of image.

in clinical practice. The detection of nodules is less dependent on spatial resolution than is interstitial disease; their conspicuity is highly dependent on the differences in their contrast relative to background [1, 3]. Some image-processing meth-

ods, such as unsharp masking, have been studied to determine whether altering contrast and improved edge enhancement may compensate for a lesser degree of spatial resolution [5].

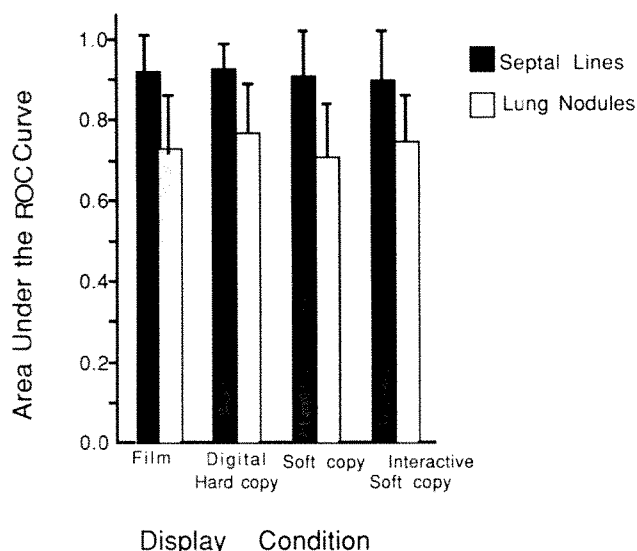


Fig. 3.—Average detectability of septal lines and nodules under each display condition tested. Error bars show one standard deviation above mean.

Similarly, video-display conditions that allow for interactive windowing have been used to achieve higher display contrast and greater diagnostic yield. Chakraborty et al. [3] compared diagnostic performance in detecting nodules on images of an anthropomorphic phantom on a 512-line video display with interaction and on conventional film. They found that more nodules were detected with the conventional system when projected over the lungs; however, many more nodules were identified by video when the nodules projected over the mediastinum. In another study using simulated nodules, analog film was compared to laser-digitized images displayed on a 1024-line video monitor. The study concluded that there was no statistical difference in detectability [6]. Recently, MacMahon et al. [7] compared diagnostic accuracy for nodule detection of hard copy, conventional video, and reversed-gray-scale video display formats. Composite ROC curves showed that the conventional video was slightly superior to hard-copy display, although the difference was not significant. In this study, observers were not allowed to manipulate the video controls.

We were interested in determining the additional benefit, if any, to be gained from interactive windowing. Cases were chosen to include nodules in areas of relatively poor contrast, such as the retrocardiac areas, or in regions of crossing skeletal structures. Furthermore, observers were required to evaluate nodules in the presence of coexistent interstitial disease. The nodule detection among the four readers was in the range of diagnostic accuracy, with A_z ranging from 0.7076 to 0.7512. We found that performance on the two video display conditions was equivalent to that achieved with hard copy. No additional benefit was derived from interactive windowing.

The implications of this finding are not clear. It may be that within the confines of an ROC test, readers are alerted to the

high probability of a particular abnormality being present and are not likely to overlook an abnormality unless it is extremely subtle. The nodules chosen were taken from routine clinical cases in which the interpretation of the chest radiograph indicated possible disease; these cases may have been insufficiently subtle to provide differentiation between display conditions, especially when comparing digital display formats of relatively high spatial resolution. In addition, although formal teaching sessions were incorporated into the ROC test, the readers were relatively inexperienced in the use of interactive windowing for projectional images. Conceivably, with readers more experienced in digital radiography and interactive windowing, the results with the interactive video display could have been improved.

Nonetheless, our preliminary experience with a 2048-line matrix video display system has been promising for the perception of septal lines and nodules, two abnormalities seen relatively commonly on chest radiographs. In our study, although we used only 31 cases, the experimental outcome was as effective as two studies, each of which was composed of 31 cases. This is because the experimental design requested the readers to evaluate the two abnormalities as two separate, independent observations. Additional studies using more subtle cases are needed to generalize our results and further investigate differences in the performance obtained on different digital-display conditions.

Appendix: Test of Hypotheses

For the two abnormalities and the four display formats shown in Figure 3, we tested the following five hypotheses. (1) The ROC scores for all four display formats for detection of septal lines are statistically equal. (2) The ROC scores for all four display formats for the detection of nodules are statistically equal. (3) The average ROC scores (averaged over the two abnormalities) for the four display formats for detection of septal lines and nodules are statistically equal. (4) The ROC score of a display format for detection of septal lines is statistically equal to the corresponding score for detection of nodules. (5) The differences in the ROC scores between the detection of septal lines and nodules are statistically equal for all four display conditions. The level of significance used for testing all four hypotheses is $\alpha = 0.05$.

In testing the first hypothesis on the septal-line detection, the computed F ratio is

$$F_c(u - 1, [u - 1][n - 1]) = F_c(3, 9) = 0.4440$$

where $u = 4$ is the number of display formats, $n = 4$ is the number of observers. Because the tabulated value $F_{T,0.95}(3,9) = 3.86$ and $F_c(3,9) < F_{T,0.95}(3,9)$, we do not reject the hypothesis that all four display formats are statistically equal for detection of septal lines. For the second hypothesis on nodule detection, $F_c(3,9) = 3.0448$ and $F_{T,0.95}(3,9) = 3.86$. Because $F_c(3,9) < F_{T,0.95}(3,9)$, we do not reject the hypothesis that all four display formats are statistically equal for detection of nodules. For the third hypothesis on combining both septal line and nodule detection, we first averaged the ROC scores over the two diseases and computed the F_c . The result is $F_c(3,9) = 2.532$ and $F_{T,0.95}(3,9) = 3.86$. Because $F_c(3,9) < F_{T,0.95}(3,9)$, we do not reject the hypothesis that all four display formats are statistically equal for detection of septal lines and nodules.

The fourth hypothesis is to test the superiority of septal line to nodule detection using the four display formats. Two different tests

were used. First, the $F_{\alpha}(v-1, [V-1][n-1])$ ratios were computed for $n = 4$ observers, $v = 2$ diseases, and each of the four display formats. The results are $F_{\alpha}(1,3) = 56.82, 7.25, 76.20$, and 420.26 for analog film, digital hard copy, soft copy, and interactive soft copy, respectively. Because $F_{T,0.95}(1,3) = 10.1$, we reject the hypothesis that detection of septal lines is statistically equal to detection of nodules. We also computed the average ROC score (averaged over the four display formats) for detection of septal lines and for nodules. In this case, $F_{\alpha}(v-1, [n-1]) = F_{\alpha}(1,3) = 52.783$ where $v = 2$ is the number of diseases. Because $F_{T,0.95}(1,3) = 9.280$ and $F_{T,0.95}(1,3) < F_{\alpha}(1,3)$, we reject the hypothesis that the detection of septal lines is statistically equal to detection in all of the display conditions of nodules. Since the A_z for septal-line detection is larger than that for nodule detection in all four display formats, we conclude that septal-line detection is superior to nodule detection using any one of the four display formats.

The last hypothesis is to test for interaction effects between septal-line and nodule detection and the four display formats. In this case, $F_{\alpha}(3,9) = 0.988$ and $F_{T,0.95}(3,9) = 3.86$. Because $F_{\alpha}(3,9) < F_{T,0.95}(3,9)$, we do not reject the hypothesis, which means that there are no interaction effects.

REFERENCES

1. Lams PM, Cocklin ML. Spatial resolution requirements for digital chest radiographs: an ROC study of observer performance in selected cases. *Radiology* **1986**;158:11-19
2. MacMahon H, Vyborny CJ, Metz CE, Doi K, Sabeti V, Solomon SL. Digital radiography of subtle pulmonary abnormalities: an ROC study of the effect of pixel size on observer performance. *Radiology* **1986**;158:21-26
3. Chakraborty DP, Breatnach ES, Yester MV, Soto B, Barnes GT, Fraser RG. Digital and conventional chest imaging: a modified ROC study of observer performance using simulated nodules. *Radiology* **1986**;158:35-39
4. Goodman LR, Foley WD, Wilson CR, Rimm AA, Lawson TL. Digital and conventional chest images: observer performance with film digital radiography system. *Radiology* **1986**;158:27-33
5. Kundel HL. Digital projection radiography of the chest. *Radiology* **1986**;158:274-276
6. Carterette ED, Fiske RA, Huang HK. Receiver operating characteristic (ROC) evaluation of a digital viewing station for radiologists. *PACS IV, SPIE* **1986**;626:441-446
7. MacMahon H, Metz CR, Doi K, Kim T, Giger ML, Chan H-P. Digital chest radiography: effect on diagnostic accuracy of hard copy, conventional video, and reversed gray scale video display formats. *Radiology* **1988**;168:669-673

Perspective

Strategies for Resolving Interpersonal Conflicts in Radiology

Chat Virapongse¹

In the last decade, the imaging revolution and changes in societal expectations of medicine have placed major stresses on radiology departments and their personnel. Increasing technological and organizational complexity have been coupled with pressure to perform state-of-the-art imaging in a cost-containment environment surrounded by medicolegal vulnerability. Under these circumstances, intradepartmental conflicts for time, support, space, and equipment are apt to arise. Hitherto, conflict-handling techniques have not been discussed in radiologic journals, even though they are abundantly covered in other literature. In this communication, I offer an overview of the dynamics of interpersonal conflicts and techniques that can be used to solve issues of concern to radiologists.

Definition and Classification of Conflict

Conflict can be defined as incompatible preference ordering between individuals [1], or a situation where one party perceives that the other has frustrated or is about to frustrate his concern. Conflict is constructive when the differences are resolved in outcomes favorable to group cohesiveness, organizational innovation, increased performance, and productivity. It is destructive when the outcomes are divisiveness, poor productivity, and loss of personnel and morale, possibly with debilitating physical and psychological hardship [2]. In fact, some conflicts may be necessary to attain optimum organizational effectiveness [3]. Organizations with too little conflict may ultimately stagnate. But how can we harvest the

positive attributes of conflict and convert them into an organizational gain?

Conflict Dynamics

According to Woodtli [2], a conflict consists of a series of events called "the conflict episode," which has a set of predictable dynamics. Two issues are important to the participants of the conflict: the outcome of the conflict and the relationship of the participants after the conflict. When the conflict becomes uncontrolled and grows disproportionately, it is considered a crisis. According to Caplan's [4] model, the conflict has four levels of intensity. In the first, there is initial rise in tension. During this phase, the participants attempt to cope with the conflict. Failure to solve the conflict results in greater uneasiness. Subsequently, tension rises further until it finally reaches uncontrolled (crisis) proportion.

In a crisis, participants are apt to seek outside support to gain better bargaining power. A victory or defeat may depend on the ability of the participants to canvass support. For example, a junior staff member in conflict with his section chief may seek support among similar-level colleagues, residents, and clinicians, personnel with whom he has a meaningful relationship, while the section chief may seek support from other section chiefs, the chairman, etc. Once an interpersonal conflict has grown into a group conflict and a crisis looms, resolution becomes difficult; the outcome may be disastrous for the losing party.

Received August 26, 1988; accepted after revision December 28, 1988.

¹ Department of Radiology, Veterans Administration Medical Center, University of Florida, Gainesville, FL 32602. Address reprint requests to C. Virapongse.

AJR 152:1119-1122, May 1989 0361-803X/89/1525-1119 © American Roentgen Ray Society

Solutions

Positive attributes of conflict are now recognized, especially for organizations that are confronted with changing technology and working environment, such as radiology. As a result, the focus has now shifted from conflict avoidance and reduction to more constructive approaches to conflict resolution [5]. There are essentially two parts to the solution of a conflict: diagnosis and intervention.

Diagnosis

The first step is the recognition of a conflict and identification of its source and participants [2]. Difficulty arises when participants hesitate to speak openly about the conflict because of its emotional impact. Indeed, emotions tend to cloud issues and need to be stripped away so that participants can fully grasp their differences in a more objective light. A confrontation session where the nature and source of the conflict can be separated from emotional overlay is recommended. Its timing and place should be considered carefully [6]. Only the issues should be probed, not the individual's reaction to them [5]. A neutral third party should listen carefully, avoiding criticism or defense of either participant. He should maintain a strong focus on the need to clarify and solve the problem without getting sidetracked into irrelevant issues.

In a report about conflicts between medical staffs and hospital management, factors cited as important in resolving the conflicts were (a) definition of the responsibilities of the medical staff and the management, (b) adequacy of communication, (c) sensitivity and responsiveness of management, and (d) involvement of the medical staff in decisions affecting the hospital [7]. The perceptions of each participant in the conflict should be voiced freely, because lack of communication often contributes to the origin of the conflict.

Intervention

The milestone work by Sherif et al. [8] on intergroup conflict revealed that conflict occurs when mutually incompatible goals exist between two competing parties, as opposed to common (superordinate) goals, which tend to promote group cooperation. If the conflict relates to the mission of the department, long- and short-term goals need to be specified and the participants encouraged to comment freely on their roles in achieving these objectives. Role-playing sessions may be helpful, where members of conflicting groups are asked to assume the roles of their adversaries, thus putting role identities and overlaps into fresh perspective. This may reveal difficulties with communication and with formalization of rules and procedures. Review and clarification may be necessary to restore a sense of order where ambiguities lead to misunderstanding.

Strategy

One of five choices can be made from a matrix of strategy modes on the basis of the desire for a good outcome or for a good relationship (Fig. 1) [9]:

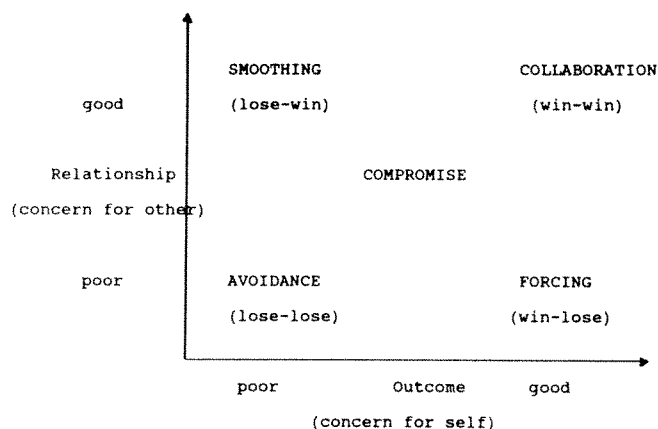


Fig. 1.—Strategy matrix for resolving conflicts.

Collaboration, a win-win resolution.—Participants agree collaboratively to a mutually acceptable goal with mutually anticipated rewards. They face issues in such a way that they can develop a resolution fully satisfactory to both. The needs, desires, and feelings of participants are taken into account and the concerns of both parties are expressed. Each party joins the search for the best resolution to the conflict in a constructive manner. This is the ideal objective of conflict resolution, where both sides are winners and emerge mutually satisfied.

Example: Intergroup conflict is brewing between skeletal radiology, abdominal imaging, and neuroradiology sections over time sharing of the only high-field MR machine in the department. Members of skeletal radiology and abdominal imaging are accusing the chief of neuroradiology (and associate chairman) of being unfair, by using his nominal power as the associate chairman to designate more service and research time to neuroradiology. Clinicians have already been drawn into the conflict and have made several phone calls to the associate chairman, each supporting his subspecialty. The situation is clearly reaching a crisis level. The chairman calls a meeting between the parties and asks each to explain his perception of the problem. Each is requested to look into the volume of patients in his subspecialty requiring high-field MR and to develop time requirements of research protocols so that time sharing can be dealt with objectively. At the next meeting, time sharing was formulated on the basis of projected needs of each party. All felt satisfied with the solution and the conflict dissipated.

Forcing, a win-lose resolution.—Here, concern for the outcome is high. This mode requires the use of authority by the forcing individual. The user of this strategy is firm, not willing to give ground, intent on pursuing his goals. The forcing strategy is frequently used between peers or between parties from different organizations. When both parties use this strategy, considerable hostility is likely, because each is trying to gain the upper hand. In the short run during an interpersonal conflict, the strategy can be used quite effectively, but it often builds up resentment and hostility. Only one participant or group will be happy with the outcome, usually with loss of friendship.

Example: A senior staff member in vascular radiology wants to take a 2-week vacation in July and hands the section chief a vacation slip 2 weeks in advance (within regulation time limit). The section chief is reluctant to let him go, because he would be faced with a work overload and untrained fellows to assist him during the early part of the academic year. He decides that he cannot let his staff member go and tells him so in an authoritative fashion. The staff member is very unhappy about the outcome, because he has already made arrangements for the vacation. The section chief talks to the staff member and explains the reasons for his decision and asks that the staff member postpone his vacation until October. The staff member accepts but is still dissatisfied with the outcome.

Smoothing, a lose-win resolution—Here, concern for the relationship is high, and the user is willing to give the favorable outcome to his adversary in order to maintain a good relationship. In smoothing, the user gives in to the demands of his adversary. This outcome produces a loser and a winner. The problem with this strategy is that it provides only a temporary solution to the immediate encounter. The issues still exist and the feelings are likely to intensify. The underlying assumption in this strategy is that agreement is impossible and that the use of power will ultimately resolve the problem.

Example: A junior staff member in skeletal radiology is requested by his chief to reduce his academic time from the customary 20% to 10%, so that his chief can have additional nonclinical time. At this point, each of them is getting 20% (1 day/week). The chief is an older tenured professor who has been unproductive in research for several years, partly because of his lack of interest in the new imaging techniques, CT and MR. His argument for more academic time is that he is spending more time on administration because of the added responsibility of the new imaging techniques (turf battles with other sections). The problem has been taken to the chairman, who is afraid to challenge the chief's decision for fear of reprisal and because he needs the chief's support in another matter. Feeling exploited and frustrated, the junior staff member begins to think that the only way he can solve this dilemma is to leave the department.

Withdrawal/avoidance, a lose-lose resolution—Here, there is a lack of concern for either the relationship or outcome. Each side evades the issues and fails to confront the reality of the conflict by rationalizing or by delegating the problem to another party. The outcome is the least desirable and produces no winner while isolating both parties. The assumption in this strategy is that conflict is unnecessary and irrelevant to either party and/or that there is no interdependency to make resolution worthwhile.

Example: Neuroradiology and vascular staff radiologists are interested in using Doppler sonography for studying carotid bifurcation disease in patients with transient ischemic disease, but are afraid to confront the chief of sonography with the plan for a joint research venture because of his reputation as being very "territorial." They have tried approaching him informally, but he was not interested. They decide that the situation is hopeless and that he would never listen to their suggestions. The chief of sonography feels that both staff radiologists are poor investigators and their pro-

posal would never amount to much, so he does his best to avoid them. The project never gets underway. Each feels a strong resentment toward the other, and their relationship is strained.

Compromise—Here, there is concern for outcome as well as relationship. Both parties try to reach an agreement that would give both some of what they want and have no effect on their relationship [6]. This could be considered a lose-lose strategy, because neither is likely to feel fully satisfied with the result, and the relationship is likely to be strained. In some arenas, the compromise mode has become a primary means of resolving conflict. It is frequently used in labor and political negotiations, but in an interpersonal conflict it is not considered constructive. The strategy seeks to modify the positions of both parties by trying to find a middle ground. It inhibits creativity that may have found a better solution while improving relations [6].

Example: Gastrointestinal (GI) and sonography sections are short of staff personnel. None of the fellows wanted to stay on the staff because of the reputation of both chiefs as being "difficult to work for," nor could the chairman recruit personnel for either section externally. A junior staff member on the GI team decides that sonography offers a greater opportunity for research publication and therefore would like to do sonography full time, much to the delight of the chief of sonography. Sensing a developing conflict, the chief of GI calls a meeting with the chief of sonography and the junior staff member. After much discussion, a compromise is reached whereby the junior staff member will spend 2½ days per week working in each service.

The Choice of Strategy

The choice of strategy may depend on several factors. For example, if one has authoritative power and favorable outcome is essential, one could choose a strategy from the right side of the matrix (Fig. 1), that is, forcing or collaboration. But, if one is concerned about maintaining a good relationship, then the upper echelon strategy modes (i.e., collaboration or smoothing) are more appropriate. If time is not available, only smoothing or forcing strategies may be possible. Preferably, conflict resolution should always be aimed at collaboration, because both sides gain mutual advantage.

Interestingly, a survey performed on 158 deans of accredited nursing colleges showed that deans use the five conflict-handling modes in the following order of frequency: compromising, collaborating, avoiding, smoothing, and forcing, regardless of conflict source or perceived conflict effect [10]. Collaboration was not the most popular mode, as might be expected of an ideal strategy, and forcing was the least frequently used.

The Role of the Chairman

The chairman has three key roles: his interpersonal role is to act as the authority, counselor, and arbitrator; his informational role is to act as monitor and disseminator; his managerial role is to act as entrepreneur, resource allocator,

disturbance handler, and decision maker (11). Conflict handling is an inevitable part of his job. How frequently he plays the role of the neutral third party depends on his administrative skill [10], his sense of fairness, and his ability to respond to the disparate needs of his associates. Seldom will he have the resources to satisfy all the demands of the faculty. According to Sherif et al. [8], resolution "was obtained through the introduction of a series of superordinate goals, which had compelling appeal value for both groups, but which could not be achieved by the efforts and resources of one group alone. When a state of interdependence between groups was thus produced, the groups realistically faced common problems. They took them up as common problems, jointly moving toward their solution, proceeding to plan and to execute the plans they had jointly envisaged."

Thus, a greater emphasis should be placed on the goals and objectives of the department and the needs of each imaging section placed within the overall framework of these departmental objectives. The staff should be made aware of the constraints in space, support personnel, and time sharing of equipment; individual needs may have to be reduced according to resource availability. A better relationship between imaging sections can be fostered by increasing group interactions to reduce intersectional conflicts. Interpersonal conflicts can be avoided before they reach crisis proportion by group meetings where the collaborative approach and teamwork effort toward research and clinical service are

heavily stressed. The dwindling financial resource caused by cost-containment measures during this period of rapid expansion of imaging cries out for strong leadership; this leadership requires knowledge of good conflict-handling techniques in order to convert potentially destructive conflict situations into constructive ones.

REFERENCES

1. Guy ME. Interdisciplinary conflict and organizational complexity. *Hosp Health Serv Admin* **1986**;111-121
2. Woodtli AB. Conflict: insights before intervention. *J Nurs Educ* **1987**;12(2):22-26
3. Rahim MA. A strategy for managing conflict in complex organizations. *Hum Relat* **1985**;38(1):81-89
4. Caplan G. *Principles of preventive psychiatry*. New York: Basic Books, **1964**
5. Wolfe DE, Bushardt SC. Interpersonal conflict: strategies and guidelines for resolution. *J Am Med Rec Assoc* **1985**;56(2):18-22
6. Tappen RM. Strategies for dealing with conflict: using confrontation. *J Nurs Educ* **1978**;17(5):47-52
7. Burda D. Role-playing reduces doctor-hospital tension. *Modern Healthcare*, July **1988**:78-84
8. Sherif M, Harvey OJ, White BJ, Hood WR, Sherif CW. *The Robbers cave experiment*. Middletown, CT: Wesleyan University Press, **1988**
9. Blake RR, Mouton JS. *The managerial grid*. Houston, TX: Gulf Publishing, **1964**
10. Woodtli AB. Deans of nursing: perceived sources of conflict and conflict handling modes. *J Nurs Educ* **1987**;26(7):272-277
11. Numerof RE. The manager as conflict negotiator. *Healthcare Supervisor* **1985**;3(3):1-15

Technical Note

Percutaneous Procedures Guided by Color-Flow Doppler Sonography

Michael P. McNamara, Jr.¹

Interventional procedures have long been done under sonographic guidance. A-mode [1, 2], static gray scale [3], and real-time gray scale methods [4, 5] have been described. Recently, McGahan and Anderson [6] described the use of duplex Doppler sonography for guidance. In this article, I relate my preliminary experience with using linear-array and sector color-flow imaging for planning and real-time guidance of percutaneous procedures.

Materials and Methods

The Acuson 128 (Acuson Computed Tomography, Mountain View, CA) was used for all procedures. The L538 linear-array probe was used for the following real-time monitored "freehand" procedures: one liver biopsy (14-gauge Tru-Cut, Travenol Laboratories, Inc., Deerfield, IL), one neck-mass biopsy (18-gauge needle), and one paracentesis (18-gauge sheathed needle). It was used also to plan an entry point and route for a difficult thoracentesis.

The S328 sector probe, with an offset needle guide, was used for three liver biopsies (one with 18-gauge needle and two with 14-gauge Tru-Cut), one renal-mass biopsy, and one nephrostomy. The color-flow software for the sector probe was a prerelease version from Acuson.

Preliminary work to establish feasibility of the procedure was done on a dog, by using an 18-gauge needle (Fig. 1). In the dog, as well as in the clinical cases, the standard prebiopsy planning was done: the target was identified and the shortest route to it that avoided traversal of vasculature or unnecessary penetration of other organs was chosen. Just before the needle was inserted, the color-flow Doppler option was engaged to produce a dynamic, real-time, color-flow overlay on the gray-scale image, and the chosen route to the

target was reassessed. The needle path was modified to avoid vessels that became visible with color-flow imaging. The procedures were then carried out without difficulty. No complications occurred.

Results

In four of the nine cases, adjustments were made to the path that had been considered "final" when standard gray-scale imaging alone was used. In two of the liver biopsies (done with 14-gauge cutting needles), small vessels obliquely crossing the anticipated needle path were seen only when the color Doppler option was on. During the renal-mass biopsy, several large tumor vessels were entirely invisible without color Doppler imaging (Fig. 2). The thoracentesis patient was obese and had pleural thickening and a bloody effusion. The pleural fluid could not be seen until the color Doppler imaging was engaged; at that time, the to-and-fro movement of the pleural fluid (in response to cardiac motion and augmented by coughing) appeared as a snowstorm of color, and the aspiration route was planned easily.

Color Doppler imaging did not add information for the other two liver biopsies (perhaps because the initial biopsy path decided on with gray-scale imaging alone fortuitously did not contain any small, obliquely oriented vessels). It was not helpful for the nephrostomy either. The patient was obese, and the native renal vessels could not be seen clearly with the version of color software used. Color-flow imaging was useful in planning paracentesis; the patient was cirrhotic and had abdominal wall varices that were avoided. However,

Received October 4, 1988; accepted after revision December 7, 1988.

¹ Department of Medical Imaging, Adams County Hospital, West Union, OH 45693. Address reprint requests to M. P. McNamara, Jr.

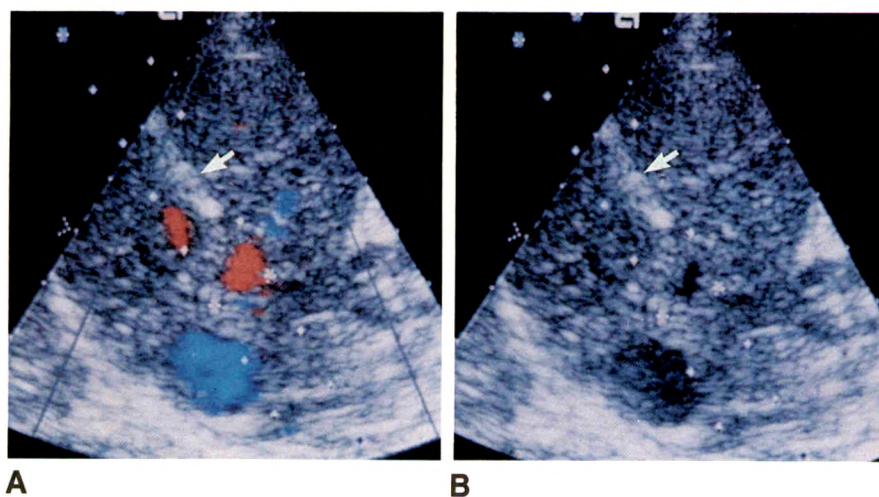


Fig. 1.—A and B, Doppler sonograms of dog liver biopsy with (A) and without (B) color-flow overlay. Color-flow data allow for easier visualization and avoidance of vessels during biopsy (arrows = needle).

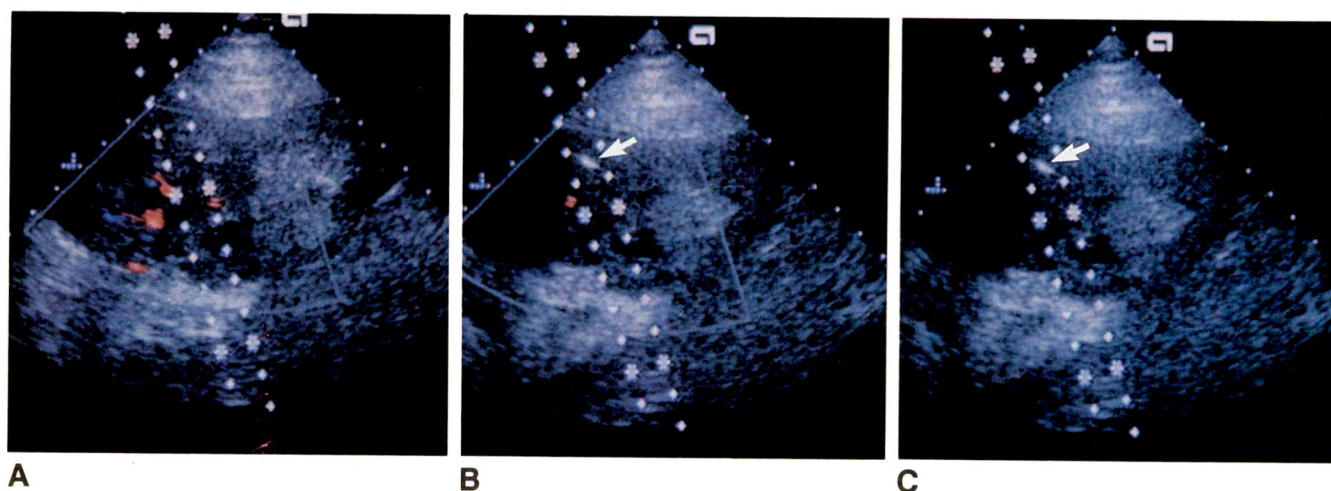


Fig. 2.—Doppler images of renal-mass biopsy.
A, Numerous tumor vessels were noted near anticipated biopsy path when color-flow Doppler was turned on. Biopsy path was then adjusted to minimize proximity to tumor vessels.
B and C, Final biopsy path with (B) and without (C) color-flow overlay (arrow = needle-tip echo).

placement of the needle with real-time sonographic guidance resulted in obscurement of the needle in a snowstorm artifact caused by movement of the fluid by the needle as it was inserted.

Discussion

With standard gray-scale imaging, the best spatial resolution is achieved when the ultrasound beam is at 90° (perpendicular) to the structure being imaged. However, the best Doppler signal results when the structure being imaged is at 0° (parallel) to the Doppler beam. Thus, the two techniques can complement one another. With pulsed Doppler imaging, only a small region of interest can be evaluated at any given time; with color-flow Doppler imaging, all flow within this image plane can be seen, provided that its velocity exceeds the minimum sensitivity of the instrument and the vessel is not at 90° to the Doppler line of sight.

Color-flow Doppler information, superimposed on the real-time, gray-scale image, heightens awareness of native and tumor vasculature. It provides easy recognition of vessels whose appearance on the gray-scale image alone is subtle and lets one see vessels that are otherwise not apparent because they are either small or obliquely oriented (either within the plane of the image or crossing it). Vessels with flow away from the transducer were color-coded blue, and those with flow toward the transducer were color-coded red.

The color-flow option can be turned off, once the path has been checked, or it can be left on and the needle placement done under real-time color Doppler imaging. If the latter is elected, it is important to adjust properly the color Doppler sensitivity of the system. Otherwise, any movement of the patient or the transducer during the procedure causes a color snowstorm that temporarily replaces all or part of the gray-scale image and blinds the operator. Movement in pleural or ascitic fluid can have a similar effect. However, this effect can

be useful in a difficult thoracentesis. The snowstorm can be avoided by using the largest color-velocity scale that still allows vessels to be identified, placing the overall color Doppler gain at the lowest possible setting, and using wall filters. Newer Acuson software releases minimize the problem. The importance of cooperation by the patient and excellent local anesthesia, to minimize movement, cannot be emphasized enough.

The number of cases that constitute this report is small. However, my preliminary experience with this new method of guidance indicates that it can increase the margin of safety when large-bore (14-gauge) cutting needles are used for liver biopsy because it allows visualization of native vessels that are small or obliquely oriented to the imaging plane. Color-flow guidance also should be useful in biopsies of neoplasms; tumor vessels are not arranged in a predictable pattern and are harder to see than native vessels with gray scale alone. Color-flow guidance can also be useful for planning a difficult thoracentesis, because the snowstorm appearance caused by movement of pleural fluid allows easy differentiation of the fluid from pleural thickening, even in an obese patient. In this patient, the needle was not placed under real-time visualization, because movement of the fluid with respiration or as a result of insertion of the needle resulted in currents in the fluid and a snowstorm artifact that obscured the needle. Color-flow guidance for nephrostomy could not be evaluated as the patient was obese, and the renal vascularity could not be

seen adequately with the software used. Color-flow guidance should also help avoid noncalcified, unsuspected aneurysms and pseudoaneurysms, and it may provide increased safety for renal transplant biopsy and a way of monitoring conventional and laser angioplasty in real time.

ACKNOWLEDGMENTS

The author gratefully acknowledges the assistance of Debbie Ryan, Linda Copas, Rick Bailey DVM, and George T. Riffle, as well as the support of the Acuson Corporation and the following Acuson personnel: Robert V. McCormick, Eileen Ellsworth, Robert J. Royea, Wayne Milam, Robert Peterson, Pete Ross, and Rob Steins.

REFERENCES

1. Holm HH, Kristensen JK, Rasmussen SN, Northeved A, Barlebo H. Ultrasound as a guide in percutaneous puncture technique. *Ultrasonics* **1972**; 10(2):83-86
2. Goldberg BB, Pollack HM. Ultrasonic aspiration-biopsy transducer. *Radiology* **1973**;108:667-671
3. Skolnick ML, Dekker A, Weinstein BJ. Ultrasound guided fine-needle aspiration biopsy of abdominal masses. *Gastrointest Radiol* **1978**;3: 295-302
4. Pederson JF. Percutaneous puncture guided by ultrasonic multitransducer scanning. *JCU* **1977**;5(3):175-177
5. Saitoh M, Watanabe H, Ohe H, et al. Ultrasonic realtime guidance for percutaneous puncture. *JCU* **1979**;7:269-272
6. McGahan J, Anderson M. Pulsed Doppler sonography as an aid in ultrasound-guided aspiration biopsy. *Gastrointest Radiol* **1987**;12:279-284

FORTHCOMING ARTICLES

PROGRESS IN RADIOLOGY

- Diagnostic imaging of bone and joint abnormalities associated with sickle cell hemoglobinopathies.** *Sebes JI*
- Three-dimensional techniques and artificial intelligence in thallium-201 cardiac imaging.** *DePuey EG, Garcia EV, Ezquerra NF*
- Computer applications in radiology education: a challenge for the 1990s.** *Tessler FN*

CARDIOPULMONARY RADIOLOGY

- Pictorial essay. Low-attenuation mediastinal masses on CT.** *Glazer HS, Siegel MJ, Sagel SS*
- The CT findings of pulmonary sarcoidosis: analysis of 25 patients.** *Müller NL, Kullnig P, Miller RR*
- Chronic lung diseases: specific diagnosis using CT.** *Bergin CJ, Coblentz CL, Chiles C, Bell DY, Castellino RA*
- Treatment of pleural effusions and pneumothorax with catheters placed percutaneously under imaging guidance.** *Reinhold C, Illescas FF, Atri M, Bret PM*
- Case report. Apical *Pneumocystis carinii* pneumonia after inhaled pentamidine prophylaxis.** *Conces DJ Jr, Kraft JL, Vix VA, Tarver RD*
- Case report. Goblet cell metaplasia causing alveolar disease of the lung: radiographic and pathologic findings.** *Nazarian GK, Gross BH, Del Buono EA*

GASTROINTESTINAL RADIOLOGY

- Characterization of splenic structure in Hodgkin disease by using narrow-band filtration of backscattered ultrasound.** *Friedman PA, Sommer FG, Chen H-S, Rachlin DJ, Hoppe R*
- SPECT of the peritoneal cavity: a method for delineating intraperitoneal fluid distribution.** *Wahl RL, Gyves J, Gross BH, et al.*
- Diagnosis of acute cholecystitis by cholescintigraphy: significance of pericholecystic hepatic uptake.** *Swayne LC, Ginsberg HN*
- MR appearance of the liver after partial hepatectomy.** *Arrivé L, Hricak H, Goldberg HI, Thoeni RF, Margulis AR*
- Giant cavernous hemangioma of the liver: CT and MR imaging in ten cases.** *Choi BI, Han MC, Park JH, Kim SH, Han MH, Kim C-W*
- Case report. Pancreatic plasmacytoma: CT findings.** *Wilson TE, Korobkin M, Francis IR*
- Case report. Cecal diverticulitis differentiated from appendicitis by using graded-compression sonography.** *Townsend RR, Jeffrey RB, Laing FC*

GENITOURINARY RADIOLOGY

- Stab wounds of the renal artery branches: angiographic diagnosis and treatment by embolization.** *Fisher RG, Ben-Menachem Y, Whigham C*
- Testicular ischemia: color Doppler sonographic findings in five patients.** *Middleton WD, Melson GL*

SKELETAL RADIOLOGY

- MR imaging of the temporomandibular joint: comparison of images of autopsy specimens made at 0.3 T and 1.5 T with anatomic cryosections.** *Hansson L-G, Westesson P-L, Katzberg RW, et al.*

PEDIATRIC RADIOLOGY

- MR imaging of the abdomen in children.** *Boechat MI, Kangaroo H*
- Case report. Hypercalciuric Bartter syndrome: resolution of nephrocalcinosis with indomethacin.** *Matsumoto J, Han BK, de Rovetto CR, Welch TR*

ENDOCRINE RADIOLOGY

- Case report. Recurrent occult medullary thyroid carcinoma detected by MR imaging.** *Crow JP, Azar-Kia B, Prinz RA*

NEURORADIOLOGY

- Alzheimer's disease: longitudinal CT studies of ventricular change.** *de Leon MJ, George AE, Reisberg B, et al.*
- Juvenile pilocytic astrocytomas: CT and MR characteristics.** *Lee Y-Y, Van Tassel P, Bruner JM, Moser RP, Share JC*
- MR imaging of intracranial carotid occlusion.** *Katz BH, Quencer RM, Kaplan JO, Hinks RS, Post MJD*
- The anatomic basis of vertebrogenic pain and the autonomic syndrome associated with lumbar disk extrusion.** *Jenkins JR, Whittemore AR, Bradley WG*
- MR imaging of experimental demyelination.** *Teresi LM, Hovda D, Seeley AB, Nitta K, Lufkin RB*

VASCULAR RADIOLOGY

- Stenosis of the internal carotid artery: assessment using color Doppler imaging compared with angiography.** *Erickson SJ, Mewissen MW, Foley WD, et al.*
- Blood flow in the carotid arteries: quantification using phase-sensitive MR imaging.** *Bendel P, Buonocore E, Bockisch A, Besozzi MC*

COMMENTARY

- The perception of visual data: a summary of the ACR meeting on visualization science in engineering, computing, and medicine.** *Hendee WR*

CASE OF THE DAY

- General diagnosis case of the day.** *Glazer HS, Dehdashti F, Siegel BA, McClennan BL, Balfe DM, Andriole GL*
- Sonography case of the day.** *Middleton MA, Middleton WD, Wiele K*
- Pediatric radiology case of the day.** *McAlister WH, Siegel MJ*
- Neuroradiology case of the day.** *Shoemaker EI, Romano AJ, Gado M, Hodges FJ III*

Letters

The Staggering Cost of Endoscopy

In an article in the *Wall Street Journal* discussing the refusal of insurers to pay for needless medical tests [1], Ruffenach listed the approximate number and cost of selected medical tests performed in hospitals and doctors' offices in 1987. The source of the information was the National Center for Health Statistics, Robert Wood Johnson Foundation, Blue Cross and Blue Shield Association, Health Care Financing Administration, and McGraw-Hill Inc.

I was astounded to see that the total annual cost of endoscopy performed in 1987 (\$10 billion) was estimated to be more than double the cost of all of the chest radiographs (\$2.75 billion) and sonograms (\$1.25 billion) done that year. Moreover, the cost of endoscopy was about equal to the total cost of five of the most common diagnostic tests: urinalysis (\$3 billion), blood cholesterol (\$3 billion), peripheral blood counts (\$2 billion), electrocardiograms (\$1.5 billion) and pap smears (\$0.8 million).

In view of the efficacy of the upper gastrointestinal series and barium enema examination for the diagnosis of gastrointestinal diseases, the ease with which they can be performed, and their relatively low cost, spending \$10 billion annually for endoscopy is a national disgrace. Those responsible for deciding which procedures to perform should not be allowed to continue to ignore barium studies.

Adam B. Sacks
La Jolla, CA 92037

REFERENCE

1. Ruffenach G. Medical tests go under the microscope. *Wall Street Journal*, 1989 Feb. 7:120:B-1

Willard Gibbs and the Gibbs Phenomenon

Czervionke et al. [1] have provided an excellent analysis of the artifacts that result from the truncation of the data set used in MR imaging. However, they consistently misspell the name of the effect, which should be designated the Gibbs phenomenon rather than the Gibb phenomenon. It is worthwhile correcting this spelling because J. Willard Gibbs (1839–1903), who became professor of mathematical physics at Yale in 1871, was a great scientist, known for his modesty, whose immense accomplishments include the development of some of the most fundamental concepts in modern science [2]. These have had great consequences for technology in general and, as indicated in the article by Czervionke et al., for MR imaging in particular. Gibbs often is considered the foremost American scientist, and he has been referred to—along with Lincoln, Melville, and Whitman—as one of

the four greatest Americans of his time [3]. Along with Heaviside, he developed modern vector analysis [4, 5], and essentially by himself he developed the science of statistical mechanics [6]. He had many additional accomplishments, but these two are used throughout physical science. If examples from MR imaging are considered, vector analysis provides the mathematical framework for the description of magnetic fields, and statistical mechanics is basic to the description of the evolution and relaxation of nuclear spin systems.

In comparison with these accomplishments, the description of the Gibbs phenomenon was practically a throwaway. In 1898, Gibbs wrote a brief letter [7] to *Nature* commenting on some problems of the convergence of the Fourier series that represents a sawtooth waveform. Later, he realized he had missed a subtlety in the argument and corrected himself in a second brief letter (*Nature* 1899;59:606), which began, "I should like to correct a careless error which I made in describing the limiting form of the family of curves represented by the equation $y = 2(\sin x - \frac{1}{2} \sin 2x + \dots \pm \frac{1}{n} \sin nx)$ as a zigzag line consisting of alternate inclined and vertical portions." The correction of this "careless error" is the basis of the artifactual phenomenon now routinely seen in MR images. Carslaw [8] provides additional references and some historical background on the Gibbs phenomenon.

It is characteristic of the work of this great scientist that it remains fundamental today and is relevant to a modern imaging technique that could not, in his lifetime, have been imaged.

John F. Schenck
General Electric Corporate Research and Development Center
Schenectady, NY 12309

REFERENCES

1. Czervionke LF, Czervionke JM, Daniels DL, Haughton VM. Characteristic features of MR truncation artifacts. *AJR* 1988;151:1219–1228
2. Wheeler LP. *Josiah Willard Gibbs: the history of a great mind*. New Haven, CT: Yale University Press, 1962
3. Rukeyser M. *Willard Gibbs*. New York: Dutton, 1964
4. Crowe MJ. *A history of vector analysis*. South Bend, IN: Notre Dame Press, 1967. Reprinted, New York: Dover, 1985
5. Wilson EB. *Vector analysis, a text-book for the use of students of mathematics and physics founded upon the lectures of J. Willard Gibbs*, 2nd ed. New York: Scribner's, 1909. Reprinted, New York: Dover, 1960
6. Gibbs JW. *Elementary principles in statistical mechanics*. New York: Scribner's, 1902. Reprinted, Woodbridge, CT: Ox Bow Press, 1981
7. Gibbs JW. *The scientific papers of J. Willard Gibbs*. London: Longmans, Green, 1906. Reprinted, New York: Dover, 1961
8. Carslaw HS. *An introduction to the theory of Fourier's series and integrals*, 3rd ed. New York: Macmillan, 1930. Reprinted, New York: Dover, 1950

Reply

This letter is in reply to the comments made by Dr. John Schenck in a letter pertaining to Willard Gibbs and the Gibbs phenomenon mentioned in the article "Characteristic Features of MR Truncation Artifacts" [1], which appeared in the December 1988 issue of *AJR*.

At some point between production of the original manuscript and the final draft of the manuscript, the letter s at the end of Gibbs was inadvertently omitted, and regrettably I did not detect this omission. The purpose of mentioning the Gibbs phenomenon several times in the article was to recognize the contributions of this great mathematician and certainly not to misspell his name. I wish to extend my appreciation to Dr. Schenck for pointing out this unfortunate error and also for providing the interesting historical information on Willard Gibbs.

Leo F. Czervionke
Medical College of Wisconsin
Milwaukee, WI 53226

REFERENCE

1. Czervionke LF, Czervionke JM, Daniels DL, Haughton VM. Characteristic features of MR truncation artifacts. *AJR* 1988;151:1219-1228

Stopper Fragments: A Potential Hazard in Contrast Media

Adverse reactions to contrast media have been attributed to a variety of causes, both intrinsic and extrinsic [1]. Contaminants from rubber in plastic syringes have been implicated in some cases [2]. More commonly, when a contaminant is suspected, no abnormality is detected at the time of extensive laboratory analysis.

Recently, we have recognized a contaminant but have not proved its association with reactions to contrast media. When a needle punctures the rubber stopper that seals a bottle of contrast medium, a core may be produced. This small plug and its fragments may be found inside the bottle and, occasionally, inside the syringe after aspiration (Fig. 1). This came to our attention because we recently switched from using bottles sealed with white stoppers to ones sealed with black stoppers. The black particles are obvious, especially after initial recognition. As a result, they have been detected in numerous instances.

I am convinced that such particles easily may be overlooked and thereby inadvertently injected into a patient. Whether any potential and/or significant sequelae result from this is yet to be determined. Persons who use contrast media should be alert to this contaminant.

Arthur J. Segal
Rochester General Hospital
Rochester, NY 14534

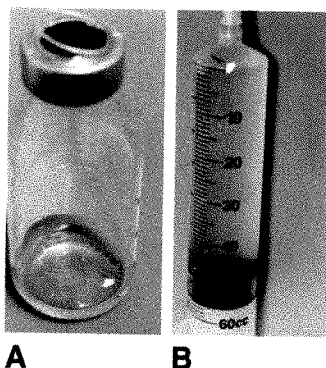


Fig. 1.—A and B, Almost empty bottle (A) of contrast medium and filled syringe (B) contain black particles (white arrows) thought to be fragments of rubber stopper used to seal bottle.

REFERENCES

1. Cohan RH, Dunnick NR. Progress in radiology. Intravascular contrast media: adverse reactions. *AJR* 1987;149:665-670
2. Hamilton G. Re: Contamination of contrast agents by rubber components of 50-ml disposable syringes (letter). *Radiology* 1984;152:539-540

Duodenal Angioma: Transcatheter Embolotherapy

Most upper gastrointestinal bleeding is caused by well-known diseases [1], such as duodenal and gastric ulcers and esophageal varices. However, other rare causes may occur. One of these is duodenal angioma, of which only a few cases have been reported [2].

A 61-year-old man with a history of chronic pulmonary disease had weakness, weight loss, and anemia. His hemoglobin level was 3.5 g/dl. At gastroscopy, a protruding submucosal lesion thought to be an angioma was observed in the duodenum. An angiogram showed a vascular lesion typical of an angioma. The inferoposterior pancreaticoduodenal trunk was catheterized selectively (Fig. 1). Because the patient was not considered a candidate for surgery, the lesion was embolized by introducing a few small particles (2 × 2 mm) of absorbable gelatin sponge (Gelfoam). The hemoglobin level returned to normal after a few days, and signs of bleeding did not occur during 6 months of follow-up.

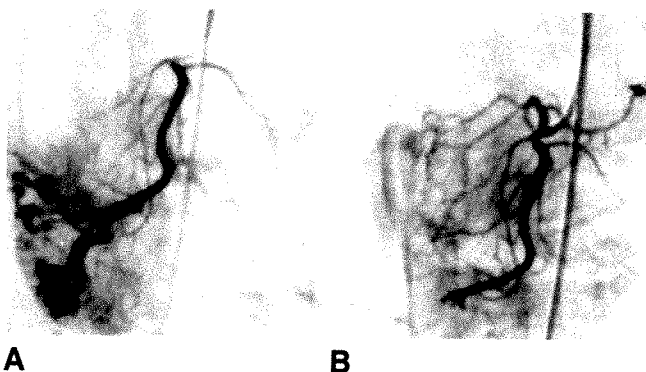


Fig. 1.—Transcatheter embolotherapy of a duodenal angioma. A, Angiogram performed by catheterization of inferoposterior pancreaticoduodenal trunk shows angioma in second part of duodenum. B, Angiogram made after introduction of a few particles of an absorbable gelatin sponge shows no vascular filling of angioma.

Endoscopically, duodenal angiomas appear as submucosal, expansive, broad-based growths protruding into the lumen with intact overlying mucosa [2]. Differential diagnosis includes duodenal varices and angiodysplasia. A definitive diagnosis can be made by using angiography. The treatment is controversial; usually surgery is required [2].

J. I. Bilbao
J. Longo
D. Aquerreta
P. San Julián
M. Muñoz
Clínica Universitaria de Navarra
Pamplona, Spain

REFERENCES

1. Rosch J, Kozak BE, Keller FS. Unusual sources of gastrointestinal bleeding. *Semin Intervent Radiol* 1988;5:64-72
2. Plausic B, Jevseb-Provic B. Radiologic and endoscopic diagnosis of duodenal angioma. *Acta Radiol [Diagn]* (Stockh) 1987;28:735-758

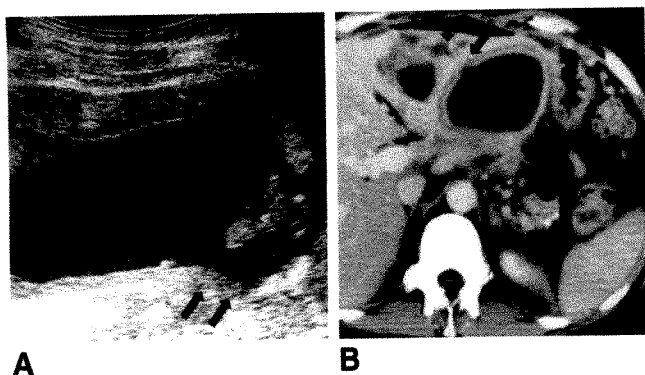


Fig. 1.—Intrahepatic rupture of a pancreatic pseudocyst.
A. Longitudinal sonogram shows extension of a pancreatic pseudocyst into liver. Arrows mark point of penetration through liver capsule.
B. CT scan shows intrahepatic pseudocyst. Point of rupture into liver (long arrow) and fluid collection (short arrow) are visible. Pancreatic part of pseudocyst is not visible in this scan. Note also smaller pseudocyst to tail and pancreatic calcifications.

Intrahepatic Rupture of a Pancreatic Pseudocyst: Sonographic and CT Demonstration

A 42-year-old woman who had a long history of excessive alcohol ingestion presented with acute exacerbation of epigastric pain. She was known to have a large intrahepatic pancreatic pseudocyst (estimated volume, 500 ml). Sonography on this admission showed a 9-cm intrahepatic cyst, but the estimated volume was only 150 ml (Fig. 1). Adjacent areas of low attenuation were noted in the liver. CT confirmed the diagnosis of rupture of the intrahepatic pseudocyst into the liver. Aspiration of the pseudocyst 1 week later revealed brown-red fluid with a high content of amylase (24,800 U/l). Sonograms made 2 weeks later showed that the liver parenchyma around the pseudocyst had returned to normal. At surgery 3 weeks later, a large pseudocyst with intrahepatic extension and a small fibrotic pancreas with several smaller cysts was found. A cystojejunostomy with a Roux-en-Y loop was performed. The patient recovered, and serum amylase levels returned to normal.

To our knowledge, no previous case of spontaneous rupture of an intrahepatic pancreatic pseudocyst into the liver has been reported.

Jan A. Lantink
 Ben G. F. Heggelman
 Rolf A. Geerdink
 St. Elisabeth Hospital
 Amersfoort, the Netherlands

Radiologic Evaluation of Cholangiocarcinoma

I read with great interest the article by Nesbit et al. [1] in which they conclude that CT and sonography are complementary to direct cholangiography in the diagnosis and assessment of resectability of cholangiocarcinoma. This article is important because it restates the need for adequate imaging in the evaluation of obstruction of bile ducts and highlights the contribution noninvasive sectional imaging can make when attention is paid to careful technique and to analysis of images. In this sense, the conclusions are in broad agreement with the reports of others [2, 3].

Nesbit et al. found that CT was superior to sonography in detection and assessment of resectability of cholangiocarcinoma. This may be partially explained, as the authors suggest, by the retrospective nature of the study, which severely hinders the interpretation of the details of sonographic findings. In a previous prospective study [2] that included a substantial proportion of patients with cholangiocar-

cinoma, sonography was superior to CT in detection and assessment of resectability of hilar tumors.

Direct cholangiography, preferably percutaneous transhepatic, is necessary for accurate determination of the proximal extent of hilar tumors, including cholangiocarcinomas, but CT and sonography can show important factors that affect resectability, such as intra- and extrahepatic spread of tumor and involvement of the portal vein [2, 3]. In individual practices, physicians should, of course, use the combination of procedures in which they have the greatest expertise, but even with optimal techniques each of these procedures can be complementary.

Criteria for resectability vary between practices. Nesbit et al. contend that lobar atrophy does not in itself have predictive value for resectability. Although this may appear to be true when taken as an isolated factor in the case of hilar tumors, in particular, cholangiocarcinomas, the presence of lobar atrophy on one side does become important if resection of the tumor requires resection of the contralateral lobe. Lobar atrophy therefore was regarded as an important factor in assessment of resectability in our previous study [2] and remains so in our current practice. Careful evaluation of these various aspects of hilar tumors, including cholangiocarcinomas, is important not only for preoperative assessment but also for planning the most appropriate approach to palliative drainage by insertion of a catheter or endoprosthesis [4].

Robert N. Gibson
 The University of Melbourne
 The Royal Melbourne Hospital
 Victoria 3050, Australia

REFERENCES

1. Nesbit GM, Johnson CD, James EM, MacCarty RL, Nagorney DM, Bender CE. Cholangiocarcinoma: diagnosis and evaluation of resectability by CT and sonography as procedures complementary to cholangiography. *AJR* 1988;151:933-938
2. Gibson RN, Yeung E, Thompson JN, et al. Bile duct obstruction: radiologic evaluation of level, cause, and tumor resectability. *Radiology* 1986;160:43-47
3. Reiman TH, Balfe DM, Weyman PJ. Suprapancreatic biliary obstruction: CT evaluation. *Radiology* 1987;163:49-56
4. Gibson RN, Yeung E, Hadjis N, et al. Percutaneous transhepatic endoprotheses for hilar cholangiocarcinoma: value in patients unsuitable for surgical resection or bypass. *Am J Surg* 1988;156:363-367

Reply

We appreciate the interest and thoughtful comments of Dr. Gibson that highlighted the significant points of our article [1]. It is difficult to compare our study directly with the prospective study of Gibson et al. [2] as they reviewed all causes of biliary obstruction (of which 22 were cholangiocarcinomas) to arrive at an assessment of level, cause, and resectability. In our study, we reviewed cases of known cholangiocarcinoma, evaluating detection, appearance, and resectability. The major cause of unresectability in our group was metastatic adenopathy, which was not mentioned specifically in the article of Gibson et al.

We agree that cross-sectional imaging techniques are complementary to direct cholangiography because of their ability to directly visualize the extrabiliary disease extent. Also, in many instances, CT and sonography can be complementary to each other.

Surgical resectability can vary between practices and even among patients because of the patients' age, functional status, and hepatic reserve. We included those criteria that are accepted at our institution by our surgeons. The criteria we used are derived from articles by Voyles et al. [3] and Blumgart et al. [4]. In the specific instance of lobar atrophy involving one lobe and resectability requiring resection of the contralateral lobe, the finding of lobar atrophy would be

regarded as an important factor in determining resectability. Our contention is that the finding of lobar atrophy does not in itself have predictive value in resectability as the atrophic lobe usually is involved by tumor and therefore is the lobe requiring resection; in fact, in our study all of the nine patients who had lobar atrophy had predominant involvement of the ducts draining the atrophic lobe. We would again like to thank Dr. Gibson for his thoughtful comments and hope that these discussions will further delineate the role of cross-sectional imaging techniques in evaluating cholangiocarcinoma.

Gary M. Nesbit
Mayo Clinic and Mayo Foundation
Rochester, MN 55905

REFERENCES

1. Nesbit GM, Johnson CD, James EM, MacCarty RL, Nagorney DM, Bender CE. Cholangiocarcinoma: diagnosis and evaluation of resectability by CT and sonography as procedures complementary to cholangiography. *AJR* 1988;151:933-938
2. Gibson RN, Yeung E, Thompson JN, et al. Bile duct obstruction: radiologic evaluation of level, cause, and tumor resectability. *Radiology* 1986;160:43-47
3. Voyles CR, Bowley NJ, Allison DJ, Benjamin IS, Blumgart LH. Carcinoma of the proximal extrahepatic biliary tree: radiologic assessment and therapeutic alternatives. *Ann Surg* 1983;197:188-194
4. Blumgart LH, Hadjis NS, Benjamin IS, Beazley R. Surgical approaches to cholangiocarcinoma at confluence of hepatic ducts. *Lancet* 1984;1:66-70

Sonographic Findings in Torsion of a Meckel Diverticulum

An 11-year-old girl complained of 24 hr of generalized abdominal pain, anorexia, and 10 hr of vomiting. Physical examination showed moderate tenderness with guarding in the right lower quadrant. No mass was palpable. The patient was afebrile, and her WBC count was normal. Sonography showed a sonolucent, noncompressible mass $2.5 \times 2.5 \times 4$ cm in the right lower quadrant (Fig. 1) that was suggestive of an inflamed, dilated appendix. The walls were characteristic of bowel with an echogenic inner layer consistent with mucosa and submucosa surrounded by a hypoechoic muscular layer. The thickness of the wall was 3-5 mm.

At surgery, a Meckel diverticulum was discovered that had twisted 360° at its point of attachment to the ileum. The diverticulum was twisted around a vitelline duct remnant that attached it to the umbilicus. The wall of the diverticulum was hemorrhagic and necrotic with no evidence of perforation.

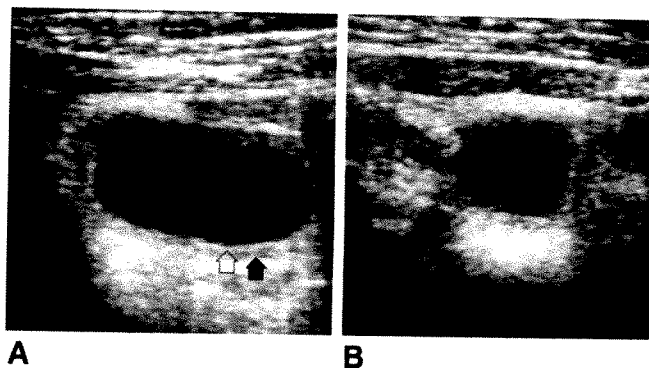


Fig. 1.—Twisted Meckel diverticulum.

A, Longitudinal sonogram through Meckel diverticulum shows a fluid-filled center surrounded by hyperechoic mucosa and submucosa (open arrow) that subsequently is surrounded by a hypoechoic muscularis (solid arrow).

B, Transverse sonogram through twisted Meckel diverticulum.

A Meckel diverticulum is a persistence of the proximal part of the vitelline or omphomesenteric duct. The reported mortality rate of patients who have complicated Meckel diverticulum is between 5% and 10% [1]. As sonography is used more often for evaluation of pain in the right lower quadrant, a complicated Meckel diverticulum should be considered part of the differential diagnosis. To our knowledge, the sonographic appearance of a torsion of a Meckel diverticulum has not been described before in the literature. The sonographic findings in our case are similar to those seen in acute appendicitis. However, both conditions require surgery.

James Larson
Doug Ellinger
Michigan State University
East Lansing, MI 48824

REFERENCE

1. Griffin WO. Meckel's diverticulum. In: Sabiston DC, ed. *Textbook of surgery*, 13th ed. Philadelphia: Saunders, 1986:946-948

Clinical Indications for Arteriography of Penetrating Wounds of the Extremities

I read the article by Reid et al., "Wounds of the Extremities in Proximity to Major Arteries: Value of Angiography in the Detection of Arterial Injury" [1], with great interest, and I congratulate the authors for the high sensitivity and accuracy of their angiographic diagnosis. They cite their low 3.6% true-positive yield and recommend that "angiography of wounds in proximity to major extremity arteries should be reserved for situations in which exclusion of injury is critical to overall management of the patient." I fully agree with the authors' conclusions and support their plea for more stringent clinical criteria. I would like to emphasize further that the presence or absence of a significant hematoma is an excellent criterion for selection of patients for arteriography.

In studies in animals and with 75 patients with penetrating injuries of the extremities [2], my colleagues and I showed that significant hematomas consistently were associated with arterial injuries and were present even when pulse or neurologic deficits or signs of ischemia were absent. A significant hematoma may be associated with a fracture or massive muscle injury, as in shotgun wounds, even without major arterial injury. However, a significant hematoma was not encountered when arterial injuries were absent. Therefore, formation of a hematoma is an important factor in determining whether arteriography is indicated.

Another noteworthy finding in our studies of experimentally induced transverse and longitudinal arterial lacerations in animals was that whereas transverse lacerations were identified consistently, several instances of longitudinal laceration were not shown by arteriography. We concluded that this was a potential pitfall of arteriography. The reported sensitivity of 100% of Reid et al. could, therefore, mean that longitudinal lacerations were infrequent or not represented in their patients or, perhaps, could be attributed to the authors' meticulous attention to technique, as evidenced by inclusion of at least two views of each artery.

Rubem Pochaczewsky
Long Island Jewish Medical Center
New Hyde Park, NY 11042

REFERENCES

1. Reid JDS, Redman HC, Weigelt JA, Thal ER, Francis H III. Wounds of the extremities in proximity to major arteries: value of angiography in the detection of arterial injury. *AJR* 1988;151:1035-1039
2. Pochaczewsky R, Mufti MA, LaGuerra JN, et al. Arteriography of penetrating wounds of the extremities: help or hindrance? *J Can Assoc Radiol* 1973;24:354-361

I appreciate Dr. Pochaczewsky's comments on our article [1]. We agree that a significant hematoma is a good criterion for selection of patients for arteriography. However, our study addressed asymptomatic patients who had no signs or symptoms of arterial injury but did have a wound in proximity to the artery [2]. Attempts to identify occult injuries in this population are difficult and currently are done by arteriography. The decision of when and where not to perform arteriography in these patients is the crux of our article.

We feel strongly that any stable patient with signs or symptoms of arterial injury should undergo arteriography. These signs and symptoms would include a large hematoma, pulsatile or not; a pulse deficit distal to the injury; a bruit or thrill in the area of the injury; and a history of arterial bleeding or shock [2, 3]. These patients should undergo arteriography if clinical conditions allow. We certainly would expect the true-positive yield in this population to be higher than the 3.6% reported for our population of asymptomatic patients.

I appreciate the information on transverse and longitudinal arterial lacerations; however, we have no information about these findings in our patients. We do insist that two views of each artery always be obtained unless a gross abnormality is seen.

John A. Weigelt

University of Texas, Southwestern Medical Center
Dallas, TX 75235

REFERENCES

1. Reid JDS, Redman HC, Weigelt JA, Thal ER, Francis H III. Wounds of the extremities in proximity to major arteries: value of angiography in the detection of arterial injury. *AJR* 1988;151:1035-1039
2. Snyder WH III, Thal ER, Bridges RA, et al. The validity of normal arteriography in penetrating trauma. *Arch Surg* 1978;113:424-428
3. McCorkell SJ, Harley JD, Morishima MS, et al. Indications for angiography in extremity trauma. *AJR* 1985;145:1245-1247

Osseous Invasion by Soft-Tissue Sarcoma Seen Better on MR Than on CT

A 25-year-old female IV drug abuser had noted an enlarging, mildly tender mass in her foot over a period of 11 months. Plain films and CT scans (Fig. 1A) showed a noncalcified soft-tissue mass and were interpreted as showing osteopenia adjacent to the mass without invasion of bone. T2-weighted MR images (Fig. 1B) showed signal heterogeneity of the mass. The major part, which was intermediate in intensity, blended almost imperceptibly with the normal marrow fat. Proton-density MR images (Figs. 1C and 1D) clearly showed invasion of the intermediate-intensity mass into the high-signal-intensity marrow fat of the navicular and cuneiform bones.

Percutaneous biopsy was followed by below-the-knee amputation. The histologic diagnosis was synovial sarcoma with areas of spindle cells, glandlike components, necrosis, and bone invasion.

Invasion of bone is rare in soft-tissue sarcomas; it was 5% of cases in one study [1]. This is true even if the tumors are in intimate contact with the bone [1]. Although CT is well recognized as the most sensitive method for detecting destruction of cortical bone, T1-weighted or proton-density MR images are more sensitive and specific for involvement of the marrow [2]. This is well illustrated in our case in which invasion of bone was not apparent on the CT scan. Indeed, the cortex appeared intact with adjacent marrow rarefaction similar to that caused by osteoporosis. The cortex may appear relatively intact on CT if local extension is by a tumor that is so aggressive that it simply grows through the cortex without significantly destroying it or if the plane of the CT scan is not ideal for showing cortical violation. Detection of marrow disease in cases of very aggressive soft-tissue tumors then becomes a more sensitive indicator of bone invasion. T1-weighted and proton-density MR images are preferred because they provide the highest difference in contrast between tumor (dark) and marrow (bright). In our case, a malignant tumor was suspected because of the bone invasion seen

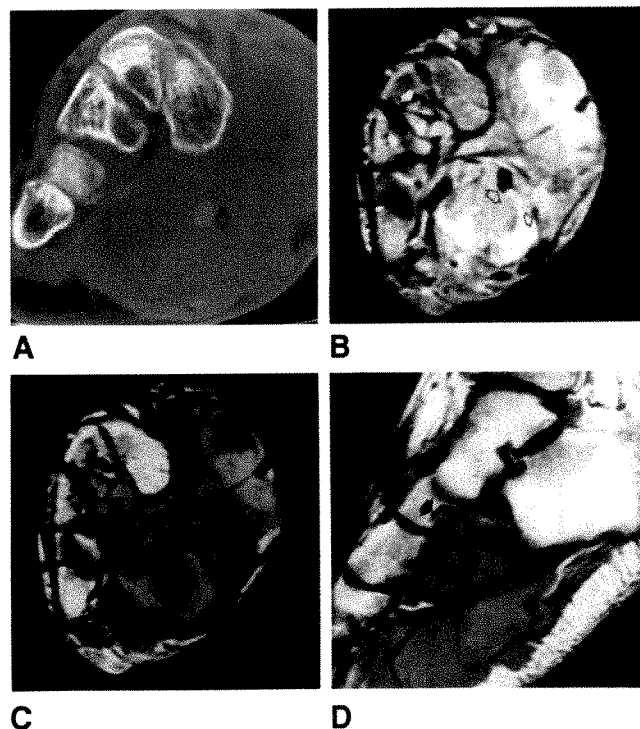


Fig. 1.—Osseous invasion by soft-tissue sarcoma.

A, Coronal CT scan shows a large soft-tissue mass enveloping tendons (open arrow). Solid arrows indicate intact cortex. Note areas of diminished mineralization of bone consistent with osteoporosis.

B and C, Coronal T2-weighted (B) and proton-density (C) MR images at same level as CT scan show invasion of mass into second and third cuneiform bones (solid arrows). Dark structures (open arrows) are tendons enveloped by tumor.

D, Sagittal proton-density MR image shows navicular invasion (arrow).

on MR. In general, however, MR is poor for distinguishing benign from malignant soft-tissue lesions as judged by signal characteristics or margination [3].

Dean Berthoty
Parviz Haghighi
David J. Sartoris
Donald Resnick

University of California, San Diego Medical Center
San Diego, CA 92103

REFERENCES

1. Weinberger G, Levinsohn EM. Computed tomography in the evaluation of sarcomatous tumors in the thigh. *AJR* 1978;130:115-118
2. Sartoris DJ, Resnick D. MR imaging of the musculoskeletal system: current and future status. *AJR* 1987;149:457-467
3. Totty WG, Murphy WA, Lee JK. Soft-tissue tumors: MR imaging. *Radiology* 1986;160:135-141

Pneumomediastinum Due to a Sucking Wound of the Knee

We report a case in which extensive subcutaneous emphysema, pneumoretroperitoneum, pneumoscrotum, pneumomediastinum, and air in the neck developed from a small sucking wound of the knee. Such findings associated with a sucking wound have not been described before.

A 38-year-old male heroin addict presented with malaise, shivering, and swelling of the neck. Nine years before he had had a surgical repair of his right patellar tendon; he had refused to cooperate in his treatment, and the tendon had ruptured again. After several operations in different hospitals, he was left with a stiff knee and an ulcer below the patella. The ulcer had become inflamed before presentation

at our institution. On examination, his body temperature was 38.5°C. He had extensive subcutaneous emphysema of the right lower limb, left thigh, scrotum, abdomen, chest, and neck. The ulcer below the right patella was 2 cm in diameter and appeared to be infected. Thigh, abdominal, and chest radiographs (Fig. 1) showed air in soft-tissue planes from thigh to neck, including pneumoscrotum, pneumoretroperitoneum, and pneumomediastinum. Close examination of the ulcer showed a tiny sinus in its base. This opened on flexion of the knee and closed on extension. An audible hiss occurred on the flexion as air entered the soft tissues through the sinus, and bubbles were expelled on extension. The ulcer was treated with occlusive dressings, the knee was splinted, and broad-spectrum antibiotics were given orally. The subcutaneous emphysema resolved rapidly, but the patient discharged himself early and did not return for review.

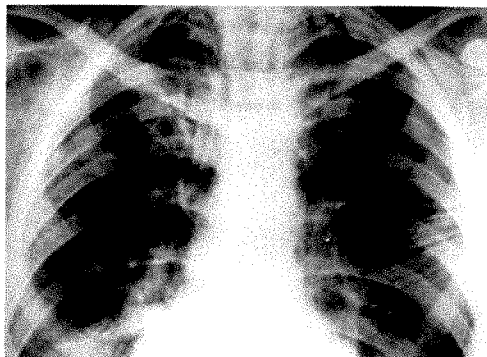


Fig. 1.—Coned view of chest radiograph shows pneumomediastinum and subcutaneous emphysema.

Saleh and Bollen [1] described a sucking wound that prompted fears of gas gangrene, but in that instance the air was localized to the area of trauma. Pneumomediastinum and such extensive subcutaneous emphysema as a result of a sucking wound have not been described before. In our patient, the diagnosis was clear on close clinical examination. It is important to be aware that a sucking wound, although tiny, can give rise to symptoms and signs far removed from the wound site and that, if found, it may alleviate fears of gas gangrene.

Samuel Hamilton
Mark J. Towers
J. Michael Pegum
Meath Hospital
Dublin 8, Ireland

REFERENCE

1. Saleh M, Bollen SR. Sucking wound of the knee: not gas gangrene. *Br Med J* 1984;289:1348

Transabdominal and Transvaginal Sonography in Early Pregnancy

I wonder, is there a misprint in the recent article by Jain, Hamper, and Sanders [1] that compares transabdominal and transvaginal

sonography in early pregnancy? I find it difficult to believe that an institution with the sonographic experience of Johns Hopkins could detect only 20% of intrauterine pregnancies by the transabdominal route as stated in the article. Do the authors mean that without the transvaginal study they would have diagnosed 80% of normal pregnancies incorrectly as ectopic pregnancies? Surely not. If this were so, transabdominal sonography could not have acquired its status as the foremost diagnostic procedure for suspected ectopic pregnancy.

I do not mean to impugn the value of the transvaginal approach; there is little doubt that it gives a better look at most of the pelvis than does the transabdominal scan. However, in their enthusiasm for the new transducer, the authors unfairly have denigrated the value of the older method. Unfortunately, readers who do not have direct experience with pelvic sonography could conclude from this article that the transabdominal examination is inadequate. Nearly two decades of clinical experience have shown that this is not the case.

Royal J. Bartrum, Jr.
Central Vermont Hospital
Barre, VT 05641

REFERENCE

1. Jain KA, Hamper UM, Sanders RC. Comparison of transvaginal and transabdominal sonography in the detection of early pregnancy and its complications. *AJR* 1988;151:1139-1143

Reply

At 4.5 to 5.5 weeks, only 20% of intrauterine pregnancies could be diagnosed by transabdominal scanning, whereas almost all could be diagnosed at this stage by transvaginal scanning. The better anatomic detail of endovaginal scans yielded additional information that was helpful in making earlier diagnosis of a normal intrauterine pregnancy. I trust this point is clarified in the rest of the article.

Kiran A. Jain
Ulrike M. Hamper
Roger C. Sanders
The Johns Hopkins Medical Institutions
Baltimore, MD 21205

Dogout Attacks

When and where to split a word at the end of a line is always an editorial problem. I am aware that it may be acceptable to split a word at the end of a syllable, but it may have unexpected effects if not done according to the word's derivation. For example, "pseudogout" should be split "pseudo" and "gout." In Dr. Resnick's paper [1] in the December 1988 *AJR*, the word "pseudogout" is split into "pseu" and "dogout." We thus read of "dogout attacks" on page 1087, with, no doubt, a howl of protest!

Frank I. Jackson
Cross Cancer Institute
Edmonton, Alberta, Canada T6G 1Z2

REFERENCE

1. Resnick D, Eugene W. Caldwell Lecture. Common disorders of synovium-lined joints: pathogenesis, imaging abnormalities, and complications. *AJR* 1988;151:1079-1093

Letters are published at the discretion of the Editor and are subject to editing.

Letters to the Editor must not be more than two double-spaced, typewritten pages. One or two figures may be included. Abbreviations should not be used. See Author Guidelines, page A5.

Material being submitted or published elsewhere should not be duplicated in letters, and authors of letters must disclose financial associations or other possible conflicts of interest.

Letters concerning a paper published in the *AJR* will be sent to the authors of the paper for a reply to be published in the same issue. Opinions expressed in the Letters to the Editor do not necessarily reflect the opinions of the Editor.

Review of Current Literature

Initials and addresses of corresponding authors are provided in parentheses for each article so that the reader can obtain reprints directly. Abstracts are printed verbatim from each journal.

The New England Journal of Medicine

Effects of ursodeoxycholic acid and aspirin on the formation of lithogenic bile and gallstones during loss of weight. Broomfield PH, Chopra R, Sheinbaum RC, et al. (JW Marks, Division of Gastroenterology, Cedars-Sinai Medical Center, 8700 Beverly Blvd., No. 7511, Los Angeles, CA 90048). *N Engl J Med* 319(24):1567-1572, Dec. 1988

We attempted to determine whether the administration of aspirin or ursodeoxycholic acid during loss of weight could prevent the development of lithogenic changes in bile and the formation of gallstones. Sixty-eight obese subjects without gallstones who were entered in a program (520 kcal per day) to lose weight were randomly assigned to receive ursodeoxycholic acid (1200 mg per day), aspirin (1300 mg per day), or placebo in double-blind fashion for up to 16 weeks. At entry, at four weeks of treatment, and at three weeks after the completion of treatment, the subjects underwent ultrasonography to detect gallstones and duodenal drainage of bile to detect cholesterol crystals and to determine the bile saturation index and glycoprotein concentration.

No gallstones or cholesterol crystals formed in the patients treated with ursodeoxycholic acid. Among the patients given placebo, gallstones formed in five ($P < 0.05$ vs. ursodeoxycholic acid) and cholesterol crystals in six ($P < 0.001$ vs. ursodeoxycholic acid); among those given aspirin, gallstones formed in two and cholesterol crystals in one (no significant difference from ursodeoxycholic acid treatment). By the fourth week, the bile saturation index increased in the placebo group (from 1.07 ± 0.26 to 1.29 ± 0.27 ; $P < 0.001$), decreased in the ursodeoxycholic acid group (from 1.11 ± 0.34 to 0.91 ± 0.24 ; $P < 0.001$), and did not change significantly in the aspirin group. The concentration of glycoprotein in bile increased in the placebo group (27.9 ± 14.5 percent; $P < 0.001$) but did not change significantly in the groups treated with ursodeoxycholic acid or aspirin.

We conclude that ursodeoxycholic acid prevents lithogenic changes in bile and the formation of gallstones in obese subjects during loss of weight.

Effect of ultraviolet radiation on cataract formation. Taylor HR, West SK, Rosenthal FS, et al. (HRT, Wilmer Institute, 600 N. Wolfe St., Baltimore, MD 21205). *N Engl J Med* 319(22):1429-1433, Dec. 1988

To investigate the relation of ultraviolet radiation and cataract formation, we undertook an epidemiologic survey of 838 watermen (mean age, 53 years) who worked on Chesapeake Bay. The annual

ocular exposure was calculated from the age of 16 for each waterman by combining a detailed occupational history with laboratory and field measurements of sun exposure. Cataracts were graded by ophthalmologic examination for both type and severity.

Some degree of cortical cataract was found in 111 of the watermen (13 percent), and some degree of nuclear cataract in 229 (27 percent). Logistic regression analysis showed that high cumulative levels of ultraviolet B exposure significantly increased the risk of cortical cataract (regression coefficient, 0.70; $P = 0.04$). A doubling of cumulative exposure increased the risk of cortical cataract by a factor of 1.60 (95 percent confidence interval, 1.01 to 2.64). Those whose annual average exposure was in the upper quartile had a risk increased by 3.30 (confidence interval, 0.90 to 9.97) as compared with those in the lowest quartile. Analysis using a serially additive expected-dose model showed that watermen with cortical lens opacities had a 21 percent higher average annual exposure to ultraviolet B (t-test, 2.23; $P = 0.03$). No association was found between nuclear cataracts and ultraviolet B exposure or between cataracts and ultraviolet A exposure.

We conclude that there is an association between exposure to ultraviolet B radiation and cataract formation, which supports the need for ocular protection from ultraviolet B.

Contrast nephrotoxicity: a randomized controlled trial of a nonionic and an ionic radiographic contrast agent. Schwab SJ, Hlatky MA, Pieper KS, et al. (SJS, Division of Nephrology, Box 3014, Duke University Medical Center, Durham, NC 27710). *N Engl J Med* 320(3):149-153, Jan. 1989

Experimental studies have suggested that nonionic contrast agents are less nephrotoxic than ionic contrast agents. To examine the relative nephrotoxicity of the two types of agents, we randomly assigned 443 patients to receive either iopamidol (nonionic) or diatrizoate (ionic) for cardiac catheterization. The patients were stratified into low-risk ($n = 283$) or high-risk ($n = 160$) groups, on the basis of the presence of diabetes mellitus, heart failure, or preexisting renal insufficiency (base-line serum creatinine level, $>133 \mu\text{mol}$ per liter). Serum and urine analyses were performed at base line and 24 and 48 hours after the infusion of contrast material. Nephrotoxicity was defined as an increase in the serum creatinine level within 48 hours of at least $44 \mu\text{mol}$ per liter.

The median maximal rise in the serum creatinine level was $18 \mu\text{mol}$ per liter in both the diatrizoate group ($n = 235$) and the iopamidol group ($n = 208$) (P not significant; power to detect a difference $>9 \mu\text{mol}$ per liter, >90 percent). Creatinine levels increased by at least $44 \mu\text{mol}$ per liter (0.5 mg per deciliter) in 10.2 percent of the patients receiving diatrizoate and 8.2 percent of the patients receiving iopamidol (P not significant). Among the high-risk patients, creatinine levels increased by at least $44 \mu\text{mol}$ per liter in 17 percent of the patients in the diatrizoate group, as compared with 15 percent of the patients in the iopamidol group (P not significant).

We were unable to demonstrate a difference in the incidence of nephrotoxicity between patients receiving a nonionic contrast agent and those receiving an ionic contrast agent.

Contrast material-induced renal failure in patients with diabetes mellitus, renal insufficiency, or both: a prospective controlled study. Parfrey PS, Griffiths SM, Barrett BJ, et al. (PSP, Division of Nephrology, Health Sciences Centre, St. John's, Newfoundland A1B 3V6, Canada). *N Engl J Med* 320(3):143-149, Jan. 1989

To determine the risk of nephrotoxicity induced by the infusion of radiographic contrast material, we undertook a prospective study of consecutive patients undergoing radiographic procedures with intravascular contrast material. There were three study groups: patients with diabetes mellitus and normal renal function ($n = 85$), patients with preexisting renal insufficiency (serum creatinine level, $\geq 150 \mu\text{mol}$ per liter) without diabetes ($n = 101$), and patients with both diabetes and renal insufficiency ($n = 34$). The control group consisted of patients undergoing CT scanning or abdominal imaging procedures without the infusion of contrast material who had diabetes mellitus ($n = 59$), preexisting renal insufficiency ($n = 145$), or both ($n = 64$).

Clinically important acute renal failure (defined as an increase of >50 percent in the serum creatinine level) attributable to the contrast material did not occur in nondiabetic patients with preexisting renal insufficiency or in diabetics with normal renal function. The incidence of clinically important contrast-induced renal failure among the diabetic patients with preexisting renal insufficiency was 8.8 percent (95 percent confidence interval, 1.9 to 23.7 percent), as compared with 1.6 percent for the controls.

The incidence of acute renal insufficiency, more broadly defined as an increase of >25 percent in the serum creatinine level after the infusion of contrast material, was 11.8 percent among all patients with preexisting renal insufficiency. After the exclusion of patients whose acute renal insufficiency could be attributed to other causes, the incidence was 7.0 percent (95 percent confidence interval, 3.2 to 12.8 percent), as compared with 1.5 percent in the control group. The risk of acute renal insufficiency attributable to the contrast material was therefore 5.5 percent, and the relative risk associated with the infusion of contrast material was 4.7. These rates were similar whether the osmolality of the contrast material was high or low.

We conclude that there is little risk of clinically important nephrotoxicity attributable to contrast material for patients with diabetes and normal renal function or for nondiabetic patients with preexisting renal insufficiency. The risk for those with both diabetes and preexisting renal insufficiency is about 9 percent, which is lower than previously reported.

The efficacy of endoscopic sphincterotomy after cholecystectomy in patients with sphincter-of-Oddi dysfunction. Geenen JE, Hogan WJ, Dodds WJ, Toouli J, Venu RP (WJH, Gastroenterology Division, Froedtert Memorial Lutheran Hospital, 9200 W. Wisconsin Ave., Milwaukee, WI 53226). *N Engl J Med* 320:82-87, Jan. 1989

Forty-seven patients thought to have dysfunction of the sphincter of Oddi were randomly assigned to undergo endoscopic sphincterotomy or sham sphincterotomy in a prospective double-blind study. All the patients had pain resembling biliary pain, had previously undergone a cholecystectomy, and had clinical characteristics suggesting biliary obstruction. The patients were randomly assigned to the treatment ($n = 23$) or nontreatment ($n = 24$) group before manometric examination of the sphincter of Oddi was performed.

Sphincterotomy resulted in improvement in pain scores at one-year follow-up in 10 of 11 patients with elevated sphincter pressure. In contrast, there was improvement in only 3 of 12 patients with elevated basal sphincter pressures who underwent the sham procedure. In patients with normal sphincter pressure, pain scores were similar regardless of treatment. After one year, sphincterotomy was performed in 12 symptomatic patients who had undergone the sham procedure—7 with elevated sphincter pressures and 5 with normal sphincter pressures. Forty patients were followed for four years. Of the 23 patients with increased sphincter pressure, 10 of the original 11 who underwent sphincterotomy remained virtually free of pain; 7

others who subsequently underwent sphincterotomy also benefited from it. Thus, 17 of 18 patients with sphincter-of-Oddi dysfunction verified by manometry benefited from sphincterotomy. In patients with normal sphincter pressure, sphincterotomy was no more beneficial than sham therapy.

Our observations suggest that endoscopic sphincterotomy offers long-term relief of pain in a group of patients with verified sphincter-of-Oddi dysfunction.

Cancer

Small bowel carcinoma in Crohn's disease: distinguishing features and risk factors. Senay E, Sachar DB, Keohane M, Greenstein AJ (AJG, Dept. of Surgery, Box 1259, Mount Sinai Medical Center, New York, NY 10029). *Cancer* 63:360-363, 1989

An 86-year-old woman who developed small bowel adenocarcinoma 40 years following in-continuity bypass of a 60-cm segment of regional ileitis represents the 22nd reported patient with this complication of bypassed Crohn's disease. Her case demonstrates several of the typical clinical features of such cancers: late recrudescence of disease following a 40-year period of relative quiescence; delayed diagnosis due to misinterpretation of the clinical picture (intestinal obstruction, abdominal mass, intraabdominal abscess, and fistula formation) as due to inflammatory bowel disease; and an exceedingly poor prognosis with rapid widespread local dissemination and death. Histologically, severe dysplasia was demonstrated both in close proximity to and at a distance from the lesion. The increasing number of case reports of adenocarcinoma arising at the site of long-standing Crohn's disease, many with dysplasia within areas of diseased bowel, is further evidence that Crohn's disease is a precancerous condition. Physicians must continue to search for methods of earlier diagnosis to improve the prognosis of small bowel carcinoma in Crohn's disease.

Reprinted by permission from the American Cancer Society.

Is there an increased incidence of adenomatous polyps in breast cancer patients? Jouin H, Baumann R, Derlon A, et al. (HJ, Service d'Hépatogastroentérologie et, d'Assistance Nutritive, Chu Haute-pierre, 67098 Strasbourg Cedex, France). *Cancer* 63:599-608, 1989

Using flexible proctosigmoidoscopy, the incidence of adenomatous polyps was studied in 161 patients previously operated on for breast cancer and also in 147 hospitalized controls not presenting with colorectal symptoms. The acceptance and tolerance of the examination were good in both populations. The mean age and length of the colons explored were not statistically different for the two groups. The incidence of adenomas was high in the breast cancer group (14.2%) in comparison to the control group (4.7%) ($P < 0.01$). This strong incidence especially concerned very small polyps with a diameter smaller than 3 mm. There were also two polyps with superficial carcinomas in the breast cancer group. Breast cancer does indeed seem to represent a condition with a high risk of colorectal adenomas. Our results prompt us to propose the adoption of systematic screening measures and a surveillance schedule as soon as the breast cancer is found.

Reprinted by permission from the American Cancer Society.

Osteomyelitis in pediatric patients with leukemia. Murphy RG, Greenberg ML (MLG, Division of Hematology/Oncology, The Hospital for Sick Children, 555 University Ave., Toronto, Ontario, Canada). *62:2628-2630, 1988*

An 11-year retrospective study showed that there were nine patients with osteomyelitis in our population of pediatric patients with leukemia. Six patients had acute lymphoblastic leukemia (ALL) and three had acute nonlymphoblastic leukemia (ANLL). Seven of nine patients were in remission at the time of diagnosis of osteomyelitis. The delay in diagnosis, which exceeded 2 weeks in seven patients, was typical. Surgical intervention was required for diagnostic or therapeutic purposes in five patients. *Staphylococcus aureus* was isolated from only three patients. Informative diagnostic studies in-

cluded nuclear scans that yielded abnormal results in all patients and erythrocyte sedimentation rates (ESR) that were elevated to greater than 70 mm/h in seven patients. The recognition of features that differ from osteomyelitis in the normal population may facilitate earlier diagnosis.

Reprinted by permission from the American Cancer Society.

Preoperative cutaneous lymphoscintigraphy in malignant melanoma. Lock-Andersen J, Rossing N, Drzewiecki KT (JL-A, Syvbjergvej 95, DK-2625 Vallensbaek Denmark). *Cancer* 63:77-82, 1989

To identify the regional lymph node basins cutaneous lymphoscintigraphy with technetium 99m rhenium sulfide colloid ($^{99m}\text{Tc-ReS}$) was performed in 45 patients and with technetium 99m antimony sulfide colloid ($^{99m}\text{Tc-Sb}_2\text{S}_3$) in seven patients after excisional biopsy of the primary tumor. All patients had skin tumors located in the face or neck or on the trunk with 47 cases of cutaneous malignant melanoma and 5 cases of benign or premalignant lesions. In 48 patients the scintiscans 1 hour after perilesional injection of the tracer colloid clearly showed the lymphatic drainage patterns from the tumor sites, of them 25 patients demonstrated unidirectional drainage, whereas the remaining 23 patients had multidirectional drainage to two or three lymph node groups. There were technical difficulties in performing the examinations in four patients. The authors recommend cutaneous lymphoscintigraphy as a safe, simple and reliable technique for mapping the lymphatic drainage preoperatively in patients with Stage I cutaneous malignant melanoma of axial localization.

Reprinted by permission from the American Cancer Society.

Analysis of the possibility that transurethral resection promotes metastasis in prostate cancer. Sandler HM, Hanks GE (GEH, Dept. of Radiation Therapy, The Fox Chase Cancer Center, Philadelphia, PA 19111). *Cancer* 62:2622-2627, 1988

The issue of transurethral resection (TURP) in patients with known prostatic adenocarcinoma is a current clinical controversy. Data have accumulated to associate this procedure with an adverse risk of distant spread and death for a defined subset of patients with moderate and poorly differentiated, T3 and T4 (Stage C) tumors. Review of available literature demonstrates that examination of this subset is incomplete in studies that do not find an adverse prognosis. The reason for the association of TURP and metastasis may be related directly to the resection via mechanical dissemination of tumor or indirectly through association with unknown adverse factors. Retrospective review may be unable to separate these two hypotheses, but hazard function analysis is presented and is consistent with surgical enhancement of metastases. Strategies for avoiding the adverse effect represent areas for possible further clinical research.

Reprinted by permission from the American Cancer Society.

Gastroenterology

Histologic correlates of gastrointestinal ultrasound images. Kimmey MB, Martin RW, Haggitt RC, Wang KY, Franklin DW, Silverstein FE (MBK, Dept. of Medicine, University of Washington, Seattle, WA). *Gastroenterology* 96:433-441, 1989

Endoscopic ultrasound imaging has potential for improving the diagnosis of gastrointestinal disease. However, the anatomic correlates of gastrointestinal ultrasound images have not been precisely defined. We have compared ultrasound images with the corresponding histologic sections of 81 specimens of resected and postmortem, normal and diseased gastrointestinal tissue. The five layers seen on ultrasound images of the normal gastrointestinal tract correspond to (1) superficial mucosa, (2) deep mucosa, (3) submucosa plus the acoustical interface between the submucosa and muscularis propria, (4) muscularis propria minus the acoustical interface between the submucosa and muscularis propria, and (5) serosa and subserosal fat. This interpretation takes into consideration the echoes produced by the tissue layers and the echoes produced by the interfaces between layers. Abnormal findings on ultrasound images of neoplastic

and inflammatory diseases correspond to histologic tissue structure. When properly interpreted, ultrasound images of the gastrointestinal wall can provide potentially useful diagnostic information.

Reprinted with permission by the American Gastroenterological Association.

Colonoscopic screening of persons with suspected risk factors for colon cancer: II. Past history of colorectal neoplasms. Grossman S, Milos ML, Tekawa IS, Jewell NP (SG, Division of Gastroenterology, Dept. of Medicine, Kaiser Permanente Medical Center, Oakland, CA). *Gastroenterology* 96:299-306, 1989

Colonoscopic screening has been recommended for all persons who have had a colorectal adenoma or carcinoma. Such persons have been assumed to be at increased risk of having additional, asymptomatic colorectal neoplasms, the removal of which would reduce morbidity and mortality from colorectal cancer. In this prospective study, initial colonoscopy was performed on 544 asymptomatic subjects with past histories of colorectal index lesions ranging from small tubular adenomas to invasive cancers. In 402 subjects whose worst index lesion was an adenoma, the prevalence of neoplasms detected at colonoscopy, above the reach of the rigid sigmoidoscope, increased with age, male sex, black race, and the number and size of their index adenomas. In 142 subjects whose worst index lesion was invasive cancer, colonoscopy findings were marginally related to age and white race. A subgroup of 133 subjects whose worst index lesion was a single, small (<10 mm) tubular adenoma and who had no first-degree relatives with colorectal cancer had only a 3% prevalence of advanced colonic neoplasms (tubular adenomas ≥ 10 mm in diameter; tubulovillous, villous, or severely dysplastic adenomas; or invasive cancers) found on colonoscopy—no greater than would be expected in the general population. Subgroups of the remaining 411 subjects, who had advanced or multiple index lesions, had prevalences of advanced neoplasms ranging from 8% to 18%. These findings indicate that for persons whose only risk factor is a single small tubular adenoma, current screening guidelines could be modified to recommend techniques less costly and less invasive than colonoscopy.

Reprinted with permission by the American Gastroenterological Association.

Ileocolonoscopy in seronegative spondylarthropathy. De Vos M, Cuvelier C, Mielants H, Veys E, Barbier F, Elewaut A (MDV, Dept. of Gastroenterology, State University of Ghent, Ghent, Belgium). *Gastroenterology* 96:339-344, 1989

A prospective endoscopic and histologic study of terminal ileum and colon in 211 patients with seronegative spondylarthropathy revealed macroscopic inflammatory lesions varying from erythema to superficial erosions in 30% of the patients and microscopic inflammation in 61%. Two types of inflammation were observed: an acute inflammation resembling an infectious enterocolitis and a chronic inflammation. In idiopathic reactive arthritis both types of inflammation were equally present, whereas chronic inflammation predominated in patients with ankylosing spondylitis. In 32% of patients with chronic inflammation, the lesions particularly resembled early Crohn's disease. Repeat ileocolonoscopy on 19 patients demonstrated a parallel evolution of joint symptoms and histologic lesions. All patients with acute inflammation went into clinical and histologic remission, whereas lesions persisted in patients with Crohn-like inflammation. In patients with chronic inflammation, remission and persistence were observed equally. This study identified a group of patients with seronegative spondylarthropathy which, even in the absence of gastrointestinal symptoms, showed evidence of gut inflammation, probably inducing an increased gut permeability with transgression of the oral tolerance and absorption of provocative antigens into the circulation. It is also possible that both diseases reflect a common underlying process.

Reprinted with permission by the American Gastroenterological Association.

Digestive Diseases and Sciences

Reliability of 24-hour home esophageal pH monitoring in diagnosis of gastroesophageal reflux. Mattioli S, Pilotti V, Spangaro M, et

al. (SM, Clinica Chirurgica II, Via Massarenti, 9, 40138 Bologna, Italy). *Dig Dis Sci* 34(1):71-78, Jan. 1989

Twenty-four-hour home esophageal pH monitoring is proposed in order to study gastroesophageal reflux (GER) so that prolonged use of costly hospital equipment and staff can be curtailed and the diagnostic accuracy of the examination improved. Eighty-six patients affected by GER symptoms and 20 healthy volunteers underwent 24-hr home esophageal pH monitoring, x-rays, and endoscopy of the upper gastrointestinal tract to investigate reliability of outpatient recording. Fifteen more patients consecutively underwent out- and inpatient recording to detect possible differences between these methods in the two daily periods. Outpatient monitoring was well tolerated in 94.7% of the patients; 14.3% of them markedly reduced their routine activities. The range of normality of outpatient recording does not differ from that of inpatients. In the 15 patients who consecutively underwent out- and inpatient monitoring, no significant differences were reported. The sensitivity of 24-hr home esophageal pH recording is 0.85, the specificity 1, the accuracy for negative prediction 0.68, and the accuracy for positive prediction 1. The reliability of 24-hr home esophageal pH monitoring is comparable to inpatient recording. It allows hospital cost reduction and is also better tolerated by patients but has not greatly improved the diagnostic accuracy of the gastroesophageal reflux pH monitoring.

Idiopathic recurrent pancreatitis: an approach to diagnosis and treatment. Venu RP, Geenen JE, Hogan W, Stone J, Johnson GK, Soergel K (JEG, 1333 College Ave., Racine, WI). *Dig Dis Sci* 34(1):56-60, Jan. 1989

The cause of recurrent acute pancreatitis can be identified in the majority of patients. A small group of patients in whom an etiological association is not obvious is characterized as idiopathic recurrent pancreatitis (IRP). During the last seven years, we used endoscopic retrograde cholangiopancreatography (ERCP) and sphincter of Oddi (SO) manometric pressure studies to investigate 116 patients initially diagnosed as IRP. Forty-four of the 116 patients were found to have a demonstrable cause of their pancreatitis. Appropriate therapeutic intervention was carried out in 43 of these patients with a favorable outcome in the majority of patients noted during long-term follow-up.

Gastrointestinal Endoscopy

Endoscopic retrograde cholangiography in the diagnosis of biliary malformations in infants. Heyman MB, Shapiro HA, Thaler MM (MBH, Dept. of Pediatrics, M-680, Division of Gastroenterology/Nutrition, University of California, San Francisco, CA 94143). *Gastrointest Endosc* 34(6):449-453, 1988

The differentiation of infantile biliary malformations from primary parenchymal diseases is difficult. The recent development of a pediatric side-viewing endoscope (PJF Endoscope; Olympus Corporation of America) provided an opportunity to investigate the usefulness of endoscopic retrograde cholangiography (ERC) for precise visualization of the extrahepatic biliary passages in infants with persistent cryptogenic cholestasis. ERC was performed in 12 patients, with visualization of the existing extrahepatic bile ducts in 4. The entire biliary system was visualized in one, excluding extrahepatic biliary atresia and choledochal cyst. The reduced caliber of the intrahepatic bile ducts and histological observations in a percutaneous liver biopsy supported the diagnosis of intrahepatic biliary hypoplasia in this case. An intact hepatic portochole cystostomy was documented in one, although the intrahepatic biliary system was not delineated. Atresia of the hepatic bile ducts proximal to the gallbladder was documented in two. Of the eight patients in whom extrahepatic bile ducts were not visualized by ERC, six had extrahepatic biliary atresia confirmed at exploratory laparotomy. The papilla of Vater could not be located in four of these six infants. The remaining two had neonatal hepatitis. ERC may offer a useful alternative to operative cholangiography in selected infants with persistent cholestasis and acholic stools.

The Journal of Bone and Joint Surgery

Correlation of the findings of magnetic resonance imaging with those of bone biopsy in patients who have stage-I or II ischemic

necrosis of the femoral head. Seiler JG III, Christie MJ, Homra L (JGS III, Dept. of Orthopaedics and Rehabilitation, Vanderbilt University Medical Center, Nashville, TN 37232). *J Bone Joint Surg [Am]* 71-A:28-32, Jan. 1989

A prospective study was undertaken to determine the diagnostic accuracy of magnetic resonance imaging in the evaluation of a symptomatic hip for which a diagnosis of early ischemic necrosis of the femoral head was suspected. Fifteen patients (sixteen symptomatic hips), for whom the findings of magnetic resonance imaging were consistent with a diagnosis of osteonecrosis of the femoral head, had a core decompression and a biopsy of the contents of the core. Preoperative magnetic-resonance imaging was useful for planning which segment of the femoral head should be biopsied. Plain radiographs and tomograms of the hips were also made. On the basis of the plain radiographs, ten hips were determined to have Stage-I findings and six hips, Stage-II ischemic necrosis, according to the system of Ficat and of Arlet and Ficat.

Histological study revealed evidence of necrosis in all of the biopsy specimens of bone. We concluded that findings of magnetic resonance imaging that are characteristic of osteonecrosis correlate well with the results of biopsies of bone in patients who have an early stage of ischemic necrosis. Magnetic resonance imaging is a highly sensitive and specific method for both the diagnosis and the location of Stage-I and Stage-II osteonecrosis.

Clinical Orthopaedics and Related Research

Adamantinoma of the tibia masked by fibrous dysplasia. Schajowicz F, Santini-Araujo E (FS, St. Louis University Medical Center, 1325 S. Grand Blvd., St. Louis, MO 63104). *Clin Orthop* 238:294-301, Jan. 1989

Three cases of adamantinoma of the tibia associated with and mimicking fibrous dysplasia or osteofibrous dysplasia are reported in children aged three, nine, and 16 years. The roentgenographic features were typical of intracortical fibrous dysplasia (osteofibrous dysplasia). These entities are not two distinct diseases, but rather are different histologic expressions of essentially the same process, which varies depending on location (predominantly intracortical or medullary) and age. Adamantinoma in children under ten years of age is not as rare as reported in the literature and was found in two of 14 cases in our files (14.3%). In some cases the fibrous dysplasia-like component predominates over the scarce epithelioid islands of tumor cells and consequently is not recognized as adamantinoma. That may explain the frequent recurrences after incomplete excisions of supposed intracortical fibrous dysplasia lesions in young children. An extensive histopathologic study of the biopsy and/or surgical specimen by a specialized pathologist is therefore advisable.

The Journal of Urology

Outpatient angiographic evaluation of living renal donors. Spencer W, Streem SB, Geisinger MA, et al. (SBS, Dept. of Urology, The Cleveland Clinic Foundation, 9500 Euclid Ave., Cleveland, OH 44106). *J Urol* 140:1364-1366, Dec. 1988

A total of 71 potential living kidney donors was evaluated on an outpatient basis with either a modification of standard catheter angiography (30 patients) or intra-arterial digital subtraction angiography (41 patients). Both procedures provided accurate assessment of the main renal vasculature as proved at the time of donor nephrectomy. Neither technique was associated with any significant morbidity. We conclude that complete angiographic evaluation of potential kidney donors can be performed accurately and safely on an outpatient basis.

British Journal of Urology

Serial residual volumes in men with prostatic hypertrophy. Birch NC, Hurst G, Doyle PT (NCB, General Surgery, Hinchingsbrooke

Hospital, Huntingdon, Cambridgeshire, United Kingdom). *Br J Urol* 62:571-575, Dec. 1988

Thirty men with prostatic hypertrophy were scanned on 3 occasions on the day before TURP. Five commonly used formulae to estimate residual urine were used. All of these methods are subject to large degrees of error; 66% of these patients had residual volumes that varied significantly on the same day.

We suggest that it is of no clinical value to perform a single residual urine measurement in patients with prostatic hypertrophy.

Pediatrics

Unusual clustering of allergic bronchopulmonary aspergillosis in children with cystic fibrosis. Maguire S, Moriarty P, Tempary E, FitzGerald M (SM, Grenagh, 30 Fosters Ave., Blackrock, Dublin, Ireland). *Pediatrics* 82(6):835-839, Dec. 1988

Allergic bronchopulmonary aspergillosis has been recognized in association with cystic fibrosis in children since 1965. Since then, however, there have been a paucity of reports of pediatric cystic fibrosis complicated by allergic bronchopulmonary aspergillosis, and, in most cases, these have been diagnosed retrospectively. A cluster of five acute cases seen during a 4-month period in a single cystic fibrosis center with a systemic illness and deterioration in respiratory status are described. In all five patients, reversible bronchoconstriction and infiltrative changes on x-ray films suggested the diagnosis. This was confirmed by the presence of (1) peripheral blood eosinophilia, (2) elevated total IgE and *Aspergillus fumigatus*-specific IgE, and (3) circulating serum precipitins against *A. fumigatus* in all cases. All children tested had positive type 1 immediate hypersensitivity to skin tests for *A. fumigatus*, in sputum eosinophilia, and *Aspergillus* cultured from sputum. Only three of five children were previously noted to be atopic and none had severe advanced suppurative lung disease. All children had previously received bronchodilator therapy and appropriate antibiotics. Following treatment with corticosteroids, acute symptoms and radiologic changes resolved for 1 to 5 months. To date, no children have had recurrence of their allergic bronchopulmonary aspergillosis while receiving alternate-day steroid treatment for 6 months.

Reprinted by permission of PEDIATRICS © 1988.

The Journal of Nuclear Medicine

Successful imaging of malignant melanoma with technetium-99m-labeled monoclonal antibodies. Eary JF, Schroff RW, Abrams PG, et al. (JFE, Division of Nuclear Medicine, University Hospital RC-70, Seattle, WA 98195). *J Nucl Med* 30(1):25-32, Jan. 1989

$F(ab')_2$ and Fab fragments of murine monoclonal antibody 9.2.27, that recognizes the 250 kD melanoma-associated antigen, were labeled with ^{99m}Tc using the bifunctional chelate method of Fritzberg et al. Twenty-seven (27) patients received, intravenously, 10 mg of either $F(ab')_2$ (8), or the Fab (27), labeled with up to 30 mCi of ^{99m}Tc . These doses were preceded by an infusion of cold irrelevant antibody. The average serum $T_{1/2}$ of the $F(ab')_2$ and the Fab were 11 hr and 2 hr, respectively. Twenty-two percent (22%) of the total injected $F(ab')_2$ dose was excreted in the urine in 20 hr, compared to 55% for the Fab group. Imaging was optimal 6-9 hr postinjection for the Fab patients. No nonspecific uptake in liver, spleen, bone marrow, or lung was observed for either antibody form. Overall, (43/53) 81% of known metastases were seen with visualization of tumors as small as 250 mg and tumor localization as high as 0.03% injected dose/g. Immunoperoxidase staining of freshly-frozen tumor nodules removed 24 hr postinjection confirmed antibody deposition in the tumor. Thirty-six previously unknown ("occult") metastatic sites were detected. To date, 12/36 of these sites have been confirmed. We conclude that ^{99m}Tc -labeled antibody to melanoma produces high resolution images with a high sensitivity of detecting metastatic melanoma. The detection of previously unknown sites of disease has proven helpful in

directing additional diagnostic studies (i.e., CT) as well as planning of therapeutic options.

Journal of Ultrasound in Medicine

Fetal choroid plexus lesions: relationship of antenatal sonographic appearance to clinical outcome. Hertzberg BS, Kay HH, Bowie JD (BSH, Dept. of Radiology, Box 3808, Duke University Medical Center, Durham, NC 27710). *J Ultrasound Med* 8:77-82, Feb. 1989

The sonograms and clinical outcomes of 31 fetuses with antenatally detected choroid plexus lesions were retrospectively reviewed. Lesions were classified as simple cysts in 22 cases (71%) and complex lesions in 9 (29%). Simple cysts tended to be smaller in size than the complex lesions and no adverse sequelae were attributed to the sonographic detection of simple cysts. Although complex choroid plexus lesions appeared to be an incidental finding in seven of nine cases (78%), one of the remaining fetuses developed ventriculomegaly with focal cerebral cortical thinning and in utero viral infection is suspected in the other. Amniocentesis was performed in nine patients (five with simple cysts and four with complex lesions) and no chromosomal abnormalities were detected during the study period, although after these data were collected we encountered a fetus in which bilateral large complex choroid plexus lesions were associated with trisomy 18.

These findings suggest that antenatally detected choroid plexus lesions are more variable in appearance than previously recognized. We consider fetuses with small simple cysts and otherwise normal sonograms to be at relatively low risk for developing adverse sequelae and recommend repeat sonography in 1 to 2 months to confirm the benign nature of the process. The presence of large and/or complicated lesions is of more concern, although the majority of these lesions (78%) also represented an incidental finding. We suggest consideration of amniocentesis, TORCH titers, and close sonographic follow-up of pregnancies with large or complex choroid plexus lesions.

Reprinted with permission by the American Institute of Ultrasound in Medicine.

Magnetic Resonance Imaging

Femoral head avascular necrosis in sickle cell anemia: MR characteristics. Rao VM, Mitchell DG, Steiner RM, et al. (VMR, Dept. of Radiology, Thomas Jefferson University Hospital, 1033 Main Bldg., 10th and Sansom Sts., Philadelphia, PA 19107). *Magn Reson Imaging* 6:661-667, 1988

Since considerable expansion of hematopoietic marrow occurs in patients with sickle cell anemia (SCA), magnetic resonance images of 20 hips in 10 patients with known homozygous SCA were reviewed to determine a) if low signal hematopoietic marrow extended into the femoral capital epiphysis and b) if the MR characteristics of avascular necrosis (AVN) differed depending on the type of epiphyseal marrow. Our results revealed variable epiphyseal marrow type; mixed (fatty and hematopoietic) marrow (42%), fatty marrow (32%), hematopoietic marrow (16%) and hemosiderotic marrow (10%). AVN occurred irrespective of the underlying marrow. Segmental areas of low signal intensity in variable shapes (ring, band, crescent or large homogeneous area) was the most consistent MR manifestation of AVN in SCA. A low signal intensity peripheral rim surrounding a central zone, isointense with epiphyseal marrow on T_1 and T_2 weighted images, was most frequently observed similar to that described in patients without hemoglobinopathy. The notable difference, however, was of segmental areas within the same femoral head that demonstrated variable central zone signal on T_2 weighted images. Further, while an increase in hip joint fluid is commonly seen with both early and advanced AVN in patients without hemoglobinopathy; it was increased in only one hip in patients with SCA. The observed differences in MR characteristics may be due to different pathophysiology of AVN in patients with SCA.

Clinical Seminar in Diagnostic Ultrasound

The Western Pennsylvania Hospital is sponsoring the 3rd Annual Clinical Seminar in Diagnostic Ultrasound, May 19–21, at the Westin William Penn Hotel, Pittsburgh, PA. This weekend course for physicians and technologists will focus on diagnostic applications and will explore the role of ultrasound among imaging techniques. Lectures will be given on Doppler color flow imaging and its application to carotid and vertebral duplex sonography, deep abdominal and peripheral arterial and venous Doppler studies, abdominal sonography, transvaginal and transrectal ultrasound, pediatric ultrasound, neurosonography, obstetric and gynecologic sonography, fetal imaging, and breast and scrotal sonography. Workshops for physicians and sonographers will be offered in transvaginal and transrectal sonographic techniques, carotid Doppler techniques, and noninvasive imaging. Program directors: Marcela Bohm-Velez and Ellen B. Mendelson. Category 1 credit: 20 hr; ECE credit: 20 credits. Fee: physicians: before March 17, \$395; after March 17, \$425; residents, technicians, and other health professionals: before March 17, \$195; after March 17, \$225. Information: Dept. of Continuing Medical Education, The Western Pennsylvania Hospital, 4800 Friendship Ave., Pittsburgh, PA 15224; (412) 578-6926.

Doppler in Diagnostic Imaging (Color and Duplex)

The Dept. of Ultrasound, Yale University, will present Doppler in Diagnostic Imaging (Color and Duplex), June 5–6, in New Haven, CT. The course will provide an introduction to Doppler physics; vascular and abdominal Doppler imaging, including duplex and color flow imaging of the carotid arteries in correlation with angiography; Doppler examination of the deep abdominal and pelvic vessels; applications in obstetrics; other perinatal applications; and Doppler signals from tumors. Course director: Kenneth J. W. Taylor. Category 1 credit: 14 hr. Fee: physicians, \$300; residents and sonographers, \$250. Information: Office of Graduate and Continuing Education, 333 Cedar St., P. O. Box 3333, New Haven, CT 06510; (203) 785-4578.

Obstetrical and Gynecological Ultrasound

The 6th Annual Seminar in Obstetrical and Gynecological Ultrasound will be presented June 9–10 at NYU Medical Center, New York City. The course will provide a comprehensive introduction to vaginal ultrasound scanning. Previous knowledge of ultrasound is not required. Didactic sessions, panels, workshops, and meetings with the faculty will be included. Category 1 credit: 10.5 hr. Fee: \$395.

Information: NYU Medical Center, Post-Graduate Medical School, 550 1st Ave., New York, NY 10016; (212) 340-5295 (24-hr service).

Napa Valley Imaging Update—MRI 1989

The Dept. of Radiology and the Office of Continuing Medical Education, University of California, Davis, School of Medicine, are sponsoring Napa Valley Imaging Update—MRI 1989, July 30–Aug. 3, at the Silverado Country Club, Napa Valley, CA. This annual symposium has been developed to bring together national and international experts in diagnostic imaging. This year's program will emphasize the newer applications of MR imaging. Specific areas to be covered are MR imaging of the head and neck; new concepts, including MR of the bony spine and extremities; state-of-the-art imaging of the thorax, including CT and MR; and newer percutaneous techniques and lithotripsy of the gallbladder, biliary tract, and kidney. Category 1 credit: 17 hr. Fee: physicians, \$435; others, \$335. Information: Nina Musselman, Office of Continuing Medical Education, University of California, Davis, School of Medicine, 2701 Stockton Blvd., Sacramento, CA 95817; (916) 453-5390.

Radiation, Physics, and Biology

Radiation, Physics, and Biology will be presented Aug. 28–Sept. 1 at the NYU Medical Center, New York City. This intensive review course is designed especially for residents in diagnostic radiology and nuclear medicine. The presentation is concentrated, so students are advised to prepare for the course by reading one or more of the basic texts in diagnostic radiologic physics and radiation biology. Category 1 credit: 32 hr. Fee: physicians, \$575; residents, \$431. Information: NYU Medical Center, Post-Graduate Medical School, 550 1st Ave., New York, NY 10016; (212) 340-5295 (24-hr service).

Registry Preparation Courses for Sonographers

Registry preparation courses for sonographers will be presented by Frederick W. Kremkau (Physics and Doppler Physics) and Kenneth J. W. Taylor (Abdomen and Obstetrics and Gynecology). Physics: Sept. 8–10, Holiday Inn DFW South, Dallas, TX; Sept. 22–24, Hyatt Regency Crystal City, Washington, DC; Sept. 29–Oct. 1, Sheraton Plaza La Reina, Los Angeles, CA; Oct. 6–8, Hyatt Regency O'Hare, Chicago, IL. Fee: \$300. Doppler Physics: Sept. 21, Hyatt Regency Crystal City, Washington, DC; Oct. 2, Sheraton Plaza La Reina, Los Angeles, CA. Fee: \$100. Abdomen: Sept. 26–27, Hyatt Regency Crystal City, Washington, DC. Fee: \$200. Obstetrics and Gynecology,

Sept. 25, Hyatt Regency Crystal City, Washington, DC. Fee: \$100. Information: Louise Nixon, Center for Medical Ultrasound, Bowman Gray School of Medicine, Winston-Salem, NC 27103; (919) 748-4505.

1989 Interventional Neuroradiology

The Dept. of Radiology and Radiological Science, The Johns Hopkins University School of Medicine, is sponsoring 1989 Interventional Neuroradiology, Sept. 11-13, at The Johns Hopkins Medical Institutions, Baltimore, MD. The course will be an in-depth discussion of treatment of cerebral aneurysms, fistulas, and brain arteriovenous malformations by means of state-of-the-art interventional neurologic procedures. Hands-on workshops will be included. Course director: Gerard Debrun. Category 1 credit: 26.5 hr. Fee: physicians, \$550; residents and fellows, \$350 (letter required); technicians, \$350. Information: Francette Boling, Program Coordinator, The Johns Hopkins Medical Institutions, Office of Continuing Education, Turner Bldg., 720 Rutland Ave., Baltimore, MD 21205; (301) 955-2959.

Transrectal Ultrasound and Prostate Cancer

Huron Valley Radiology and the Catherine McAuley Health Center, Ann Arbor, MI, will present the 4th Annual International Symposium on Transrectal Ultrasound in the Diagnosis and Management of Prostate Cancer, Sept. 14-16, in Chicago. Topics will include imaging, biopsy, staging, screening, prostate specific antigen, DNA ploidy, radical surgery, and radiation and endocrine therapy. Attendees can take part in the discussion in the "2 minute-2 slides" presentations. A poster exhibition will be held also. Cochairmen: Fred Lee and Richard D. McLeary. Category 1 credit: 21 hr. Information: Deborah S. Highfield, Symposium Coordinator, Diversified Conference Management, Inc., 1471 Morehead, Ann Arbor, MI 48103; (313) 665-2535.

Radiology on Ischia

The Universities of Connecticut and Naples are sponsoring the 11th annual International Radiology Congress, Radiology on Ischia, Sept. 23-Oct. 1, in Lacco Ameno, Island of Ischia, Bay of Naples, Italy. Topics will include MR imaging; CT; sonography, including Doppler sonography; mammography; and interventional radiology. Guest faculty: Barbara Carroll, I. I. Kircheff, T. L. Lawson, M. T. Modic, A. Y. Proto, S. S. Sagel, and E. A. Sickles. Category 1 credit: 35 hr. Fee: physicians, \$650; residents, \$325. Information: D. Beatty Crawford, M.D., Dept. of Radiology, University of Connecticut Health Center, Farmington, CT 06032; telephone: (203) 679-3322; fax (203) 679-3145.

Seminar in Diagnostic Ultrasound

Seminar in Diagnostic Ultrasound

The Dept. of Radiology, University of Michigan Medical School, is sponsoring the 12th Annual Seminar in Diagnostic Ultrasound, Oct. 5-7, at the Towsley Center, Ann Arbor, MI. The objectives of the course are to review currently used techniques and applications of diagnostic sonography, emphasizing new information and advances in this field, especially in Doppler imaging and obstetrics, that have occurred within the last year. Course director: Terry M. Silver. Guest faculty: P. H. Arger, P. W. Callen, J. W. Charboneau, C. A. Mittelstaedt, and Laurence Needleman. Category 1 credit: 13 hr. Information: Debra DeSmyther, Program Assistant, Office of Continuing

Medical Education, G-1100 Towsley Center, Box 0201, University of Michigan Medical School, Ann Arbor, MI 48109-0201; (313) 763-1400.

Practical Radiology

The University of Virginia will offer its 12th annual postgraduate course, Practical Radiology, Oct. 9-12, at the Boar's Head Inn, Charlottesville, VA. Guest faculty: P. R. Mueller, R. M. Quencer, D. D. Stark, and W. R. Webb. Category 1 credit: 20 hr. Fee: \$385. Information: Theodore E. Keats, M.D., Professor and Chairman, Dept. of Radiology, University of Virginia School of Medicine, Charlottesville, VA 22908.

International Seminar of Medical Imaging

The Chinese University of Hong Kong and the Medical College of Wisconsin are sponsoring the 2nd Annual International Seminar of Medical Imaging, Oct. 30-Nov. 4, in Shatin, Hong Kong, in the New Territories. The 6-day course will consist of a series of seminars and lectures covering imaging of the abdomen and chest. The conference will focus on integrated imaging and the advantages of various radiologic techniques in problem solving. Faculty will include Joe Ariyama, Iain Birchall, Jay Heiken, Yuji Itai, Louis Kreel, T. L. Lawson, Joe Leung, Con Metreweli, Stuart Sagel, and Anna Throton. Category 1 credit: 35 hr. Fee: \$475. Information: Thomas L. Lawson, M.D., Dept. of Radiology, Milwaukee County Medical Complex, 8700 W. Wisconsin Ave., Milwaukee, WI 53226; (414) 257-6024.

International Conference on Gallstones and Their Management

The International Conference on Gallstones and Their Management will be held in Jerusalem, Israel, Feb. 25-28, 1990. The conference will cover diverse aspects of gallstone disease: epidemiology, natural history, pathogenesis, biliary imaging, motility, and others. Particular attention will be directed to the new therapeutic techniques: shock-wave lithotripsy, direct dissolution, medical dissolution, and endoscopic management, as well as the role of surgery and the long-term problems of recurrence and prevention. Information: Gallstone Conference, Vered Congress, 15 Weizman St., Nes Ziona 70400, Israel; telephone: 08-400777, 8,9; 400562; telex: 381361 VERED IL; fax: 972-8-404142.

Congress of the European Federation of Societies for Ultrasound in Medicine and Biology

The 7th Congress of the European Federation of Societies for Ultrasound in Medicine and Biology will take place in Jerusalem, Israel, May 6-11, 1990. Cochairpersons: Haim Zakut and Yacov Itzhak. Information: 7th Congress of the European Federation of Societies for Ultrasound in Medicine and Biology, c/o P. O. Box 50006, Tel Aviv 61500, Israel.

The American Board of Radiology Examinations

Written examinations for the American Board of Radiology (ABR) are scheduled for Oct. 12-13, 1989, and Sept. 27-28, 1990. Oral examinations will be held at the Executive West Hotel in Louisville, KY, June 5-9, 1989, and June 4-8, 1990. The ABR will accept applications for admission to the examinations after July 1, but not

later than Sept. 30, in the year *preceding* the year in which the examination is to be taken. For application forms and further information: Office of the Secretary, The American Board of Radiology, 300 Park, Ste. 440, Birmingham, MI 48009.

Meeting and Course Review

For the reader's convenience, a summary of upcoming meetings and courses is provided. Detailed listings are given in the *AJR* issue given in parentheses.

Fellowship Program in Diagnostic Radiology, times arranged, Ann Arbor (June 1988)

Basic and Advanced Training in MRI, times arranged, Baltimore (Dec 1988)

Visiting Fellowships in Radiology at MGH, times arranged, Boston (April)

Biliary Lithotripsy Visiting Fellowships, times arranged, Philadelphia (April)

Advances in Radiology, April 19–May 7, Asia (Shanghai, Guilin, Hong Kong, Bangkok, Chiang Mai, Phuket, and Singapore) (Jan)

International MR Symposium in Italy, April 30–May 5, Venice and Florence, (Jan)

Magnetic Resonance Imaging 1989: National Symposium, April 30–May 5, Orlando, FL (Feb)

Surgical Neuroangiography, May 1–5, New York (Dec 1988)

Courses in Diagnostic Ultrasound at Bowman Gray: Neurovascular, May 1–5; **Echocardiology**, May 15–19; **Urology**, May 22–23; **Obstetrics**, June 5–9; and **Radiology (Abdomen)**, June 12–16; Winston-Salem, NC (Jan)

Annual Mid-Pacific Diagnostic Ultrasound Conference, May 2–6, Big Island of Hawaii (Jan)

Mammography for the General Radiologist, May 8–11, Sept. 18–21, and Oct. 23–26, Boston (March)

Visiting Fellowships in MR Imaging at UCLA, May 8–12 and June 5–9, Los Angeles (March)

International Congress on Peer Review in Biomedical Publication, May 10–12, Chicago, IL (Sept 1988)

The Leading Edge in Diagnostic Ultrasound, May 10–12, Philadelphia (Feb and March)

Radiology Review Course, May 14–19, Bal Harbour, FL (March)

Clinical MRI: 1989 Update, May 17–21, Boston (April)

Emission Tomography of the Heart, May 20, Seattle (March)

Obstetrics and Gynecology, May 22–26 and June 5–9, Philadelphia (Feb)

Sonography Symposium, May 26–27, Nashville, TN (Jan)

Doppler Ultrasound in Vascular Diagnosis, May 31–June 3, Philadelphia (Feb)

Advanced Techniques in MRI, June 10–15, Kiawah Island, SC (April)

Abdominal Ultrasound, June 12–15, Philadelphia (Feb)

Radiology in Scandinavia and the Soviet Union, June 17–July 11, Copenhagen, Stockholm, and Leningrad (Jan)

Emergency Radiology Update 1989, June 19–21, Boston (April)

Practicums in MR Imaging: Basic Practicum, June 19–23 and Oct. 23–27; **Advanced Practicum**, Sept. 11–15; Baltimore (March)

Challenge 89: Decisions in Imaging, June 24–30, London, England (March)

CAR '89, June 25–28, Berlin (Jan)

1989 International Congress of Radiology, July 1–8, Paris (May 1988)

Leeds Gastroenterology Course, July 10–14, Leeds, England (April)

Annual Diagnostic Imaging Seminar, July 17–21, Nantucket Island, MA (April)

Third World Medicine—Tropical Radiology and the Problem of AIDS, July 19–Aug. 5, East Africa (Nairobi, Maasa-Mara, Lake Baringo, Lake Turkana, Mombasa, and Lamu) (Jan)

Symposium on Breast Disease, July 23–26, Mackinac Island, MI (March)

Visiting Fellowship in Mammography, Aug 28–31 and Oct. 23–27, Los Angeles (March)

Imaging, Intervention, Ireland—1989, Sept. 2–10, Dublin, Cong, and New Market, Ireland (Feb)

Update in Chest Radiology, Sept. 10–23, England and Scotland (Feb)

Pathological Effects of Radiation, Sept. 11–13, Bethesda, MD (April)

Society of Uroradiology Postgraduate Course, Sept. 25–28, Hilton Head, SC (Dec 1988)

Practical Magnetic Resonance Imaging 1989, Oct. 12–15, Las Vegas, NV (April)

World Congress for Bronchology, Oct. 18–20, Tokyo, and Oct. 21–22, Kyoto, Japan (Nov 1988)

Royal Australasian College of Radiologists Annual Meeting, Oct. 19–23, Melbourne, Australia (March)

Advances in Chest, Interventional, and Ultrasound, Nov. 25–Dec. 10, South America (Caracas, Isla Margarita, Manaus, Recife, Rio de Janeiro, Buenos Aires, and Bariloche) (March)

AJR carries announcements of courses, symposia, and meetings of interest to its readers if received a minimum of 5 months before the event. There is no charge; receipt of items by the *AJR* Editorial Office is not acknowledged. Submit items for publication typed double-spaced. Provide title, date, location, brief description, sponsor, course directors, fees, category I credit, and address and telephone number for additional information. Faculty from the host institution will not be listed. Guest faculty names will appear **only** if initials are provided. Mail news items to *AJR* Editorial Office, 2223 Avenida de la Playa, Suite 200, La Jolla, CA 92037-3218.

American Roentgen Ray Society: Officers, Committees, and Membership Information

Officers

President: Lee F. Rogers

President-elect: Ronald G. Evens

1st Vice-president: M. Paul Capp

2nd Vice-president: John A. Kirkpatrick, Jr.

Secretary: Glen W. Hartman

Treasurer: Beverly P. Wood

Executive Council: J. Thrall, J. F. Wiot, L. F. Rogers, R. A. Gagliardi, R. G. Evens, R. N. Berk, B. P. Wood, J. E. Madewell, M. P. Capp, G. W. Hartman, B. G. Brogdon, G. R. Leopold, A. Landry, Jr., A. K. Poznanski, K. H. Vydareny, J. T. Ferrucci, Jr., W. J. Casarella, E. J. Ferris, J. A. Kirkpatrick, Jr., A. E. James, Jr., chairman

Committees

Editorial Policy: S. S. Sagel, R. J. Stanley, C. A. Rohrmann, Jr., N. O. Whitley, S. V. Hilton, J. M. Taveras, R. N. Berk, W. J. Casarella, chairman

Education and Research: C. E. Putman, C. B. Higgins, B. J. Hillman, R. A. McLeod, B. G. Brogdon, chairman

Finance and Budget: A. K. Poznanski, G. R. Leopold, J. R. Thornbury, R. C. Gedgaudas-McClees, J. Thrall, chairman

Nominating: K. L. Krabbenhoft, J. F. Wiot, G. R. Leopold, chairman

Publications: R. J. Stanley, S. S. Sagel, N. O. Whitley, C. A. Rohrmann, Jr., W. J. Casarella, chairman

Membership: E. J. Ferris, G. R. Leopold, K. H. Vydareny, A. K. Poznanski, chairman

Representatives to Other Organizations

American Board of Radiology: E. C. Klatte, L. F. Rogers, J. A. Kirkpatrick, Jr.

American College of Radiology: L. F. Rogers, G. A. Kling, R. A. Gagliardi, J. E. Madewell

American Medical Association House of Delegates: S. F. Ochsner, K. L. Krabbenhoft, alternate

American National Standards Institute: M. Haskin

National Council on Radiation Protection and Measurements: E. L. Saenger, H. L. Friedell

Meeting Arrangements

Annual Meetings: May 7-12, 1989, Hilton, New Orleans; May 13-18, 1990, Sheraton Washington, Washington, DC

Annual Meeting Committee: H. C. Carlson, G. P. Janetos, E. K. Lang, R. R. Lukin, A. Landry, Jr., chairman

Instruction Courses: R. J. Stanley, associate chairman, J. T. Ferrucci, Jr., chairman

Scientific Program: R. J. Alfidi, A. E. Robinson, J. H. Thrall, M. P. Banner, J. J. Gisvold, T. C. McLoud, R. G. Evens, chairman

Scientific Exhibits: A. A. Moss, A. V. Proto, R. J. Churchill, J. E. Madewell, chairman

ARRS Membership

An application form is printed in the April issue of the Journal. For consideration at the 1990 ARRS meeting, send completed forms before February 1, 1990, to American Roentgen Ray Society, 1891 Preston White Dr., Reston, VA 22091. Active members are graduates of an approved medical or osteopathic school or hold an advanced degree in an allied science. They must practice radiology or work in an associated science in the United States or Canada and be certified by the American Board of Radiology, American Osteopathic Board of Radiology, or Royal College of Physicians of Canada or otherwise adequately document training and credentials. Corresponding members are foreign radiologists or scientists who are active in radiology or an allied science. Members-in-training are residents or fellows in radiology or postgraduate students in an allied science. Additional application forms can be obtained from the ARRS offices in Reston, VA.

Business Office

Paul Fullagar, Administrative Director, American Roentgen Ray Society, 1891 Preston White Dr., Reston, VA 22091; (703) 648-8900

Classified Advertisements

Positions Available

CHIEF, RADIOLOGY SERVICE—450-bed, Northwestern University Medical School-affiliated VA Lakeside Medical Center in Chicago seeks a board-certified radiologist to serve as Chief, Dept. of Radiology. Dept. includes general diagnostic radiology, CT scanner, and DSA unit. MRI is available nearby. Interest in teaching and research preferred. Administrative experience is desirable. Address inquiry and CV to Lee F. Rogers, M.D., Chairman, Dept. of Radiology, Northwestern University Medical School, 710 N. Fairbanks, Chicago, IL 60611; (312) 908-5103. An equal opportunity employer. 5ap

PEDIATRIC RADIOLOGIST—The University of Tennessee, Memphis/University Physicians Foundation has an opening for a pediatric radiologist effective July 1, 1989. Faculty rank of assistant or associate professor based on experience. Applicant must be board-certified/eligible in diagnostic radiology. At least 1 yr of postgraduate training in a recognized program in pediatric radiology is required. Primary work sites will be LeBonheur Children's Medical Center and St. Jude Children's Research Hospital. Blacks, women, handicapped, and other minorities are encouraged to apply. The University of Tennessee, Memphis/University Physicians Foundation is an affirmative action/equal opportunity employer. Address inquiries to Barry Fletcher, M.D., Chairman, Diagnostic Imaging Dept., St. Jude Children's Research Hospital, 332 N. Lauderdale, Memphis, TN 38101; or Robert A. Kaufman, M.D., Director, Dept. of Radiology, The University of Tennessee, Memphis/LeBonheur Children's Medical Center, 800 Madison Ave., Memphis, TN 38163. 5-7a

TAMPA BAY AREA RADIOLOGY GROUP seeking board-certified generalist primarily for office position, some hospital work. Candidate must be able to perform routine radiologic CT, ultrasound, mammography, and venography, in addition to general radiologic duties. Send CV to Radiology Group, P. O. Box 17319, Tampa, FL 33682. 5-6a

UNIVERSITY OF SOUTH CAROLINA, SCHOOL OF MEDICINE—The Radiology Dept. plans to add a physicist to participate in the general educational and research program of the medical school. The physicist would participate with others in the administration of the university radiation safety program and a similar radiation safety program of the affiliated VA hospital. The position requires a Ph.D. from a radiation-related program. Applicants should have an interest in teaching and applied research. Send resume and salary requirements to James J. Farrell, M.D., University of South Carolina, School of Medicine, Dept. of Radiology, Columbia, SC 29208; (803) 733-3295. AA/EOE. 5ap

ULTRASOUND/GENERAL RADIOLOGIST—Position available for a board-certified radiologist with experience in ultrasound (preferably obtained by fellowship) and also capable of performing general diagnostic studies, to join 15-member group in Pittsburgh, PA. Two hospitals, 675 beds, private office, and MRI center. Active radiology residency program. Excellent salary and benefits. Send CV to Robert E. Gates, M.D., c/o Mercy Hospital, Dept. of Radiology, 1400 Locust St., Pittsburgh, PA 15219. 5ap

SAN FRANCISCO BAY AREA, DIAGNOSTIC RADIOLOGY—Full-time position available as of July 1989 for BC/BE radiologist to join established group based in growing SF Bay area communities. Competence in all modalities including MRI and angiography required; fellowship training desirable. Contact J. Fish, M.D., c/o Walnut Creek Radiology, 1844 San Miguel Dr., #302, Walnut Creek, CA 94596; (415) 947-0560. 5a

GENERAL RADIOLOGIST—BC/BE radiologist needed in Morehead, KY. All modalities employed, including duplex ultrasound, mammography, nuclear medicine, angiography, interventional procedures, and CT. MRI within 2 yr. This 130-bed hospital covers a referral population base of 50,000-70,000. There is an affiliation with University of Kentucky and its training programs. Starting salary is competitive, with full partnership available. Ideal recreational area with easy access to Lexington, Louisville, Huntington, and Cincinnati. Interested parties forward CV and calls to E. G. Barker, M.D., St. Claire Medical Center, Morehead, KY 40351; (606) 784-6661, ext. 313. 5ap

DIAGNOSTIC RADIOLOGIST, FLORIDA GULF COAST—Position available July 1, 1989 for board-certified/eligible radiologist to join busy women's diagnostic imaging practice including women's hospital and 2 outpatient imaging centers. Send CV to Lisa A. Nemecek, M.D., Chairman, Dept. of Radiology, 1260B S. Greenwood Ave., Clearwater, FL 34616. 5ap

CHIEF, DEPT. OF RADIOLOGY—The University of California, San Francisco (UCSF), is seeking a Chief of Radiology for San Francisco General Hospital (SFGH), 1 of 3 core teaching hospitals. Candidate will be appointed at the level of associate professor or professor of radiology (depending on qualifications) and also serve as Vice-Chairman of the Dept. of Radiology at UCSF. The SFGH Chief of Radiology must be an excellent teacher, and an experienced administrator, who will supervise all clinical, teaching, and research programs in radiology at SFGH. Physician staffing consists of 8 full-time radiologists, 4 fellows in radiology, and 11 radiology residents. Demonstrated record of ability in clinical and experimental academic research in several modalities such as MRI/MRS, ultrasound, CT, conventional radiology, and familiarity with angiography/interventional procedures is desirable. The University of California is an equal opportunity/affirmative action employer. Minority groups, women, and handicapped are encouraged to apply. Send CV to Charles A. Gooding, M.D., Chair, Search Committee, UCSF, Dept. of Radiology, Box 0628, San Francisco, CA 94143-0628. 5a

MRI RADIOLOGIST—The Dept. of Radiology of St. Luke's-Roosevelt Hospital Center in New York City is seeking a radiologist with experience beyond fellowship in body MRI. A strong interest in clinical teaching and research, as well as in patient care, is required. Academic rank at assistant or associate professor level depends on qualifications. The hospital is a 1315-bed, voluntary, university hospital of Columbia University College of Physicians & Surgeons. Send inquiries with CV to Ronald C. Ablow, M.D., Dept. of Radiology, SLRHC, Amsterdam Ave. & 114th St., New York, NY 10025. Columbia University takes affirmative action to ensure equal opportunity. 5ap

CHIEF, RADIOLOGY SERVICE—VA Medical Center, Augusta, GA, is seeking a qualified radiologist for Chief, Radiology Service. Board certification required. Subspecialty interest in chest, skeletal, GI, or interventional radiology is desirable, but not essential. Faculty appointment commensurate with qualifications and experience. This 1,142-bed, tertiary-care, medical center is affiliated with the Medical College of Georgia. Augusta enjoys a moderate climate, reasonable cost of living, numerous recreational facilities, and institutions of higher learning. Augusta is known as the Garden City of the South and home of the Masters Golf Tournament. An equal opportunity employer. For additional information, contact Henry M. Altharis, Sr., M.D., Chief of Staff; (404) 823-2224. 5a

THE OREGON HEALTH SCIENCES UNIVERSITY, Dept. of Diagnostic Radiology, Portland, OR, invites applications for faculty positions in MRI, neuroradiology, pulmonary radiology, mammography, skeletal radiology, vascular and interventional radiology, GU radiology, computed body tomography, and ultrasound. A Ph.D. NMR scientist also is being sought. The Oregon Health Sciences University is an affirmative action, equal opportunity employer. Send CV to Richard W. Katzberg, M.D., Chairman of Diagnostic Radiology, L340, The Oregon Health Sciences University, 3181 S.W. Sam Jackson Park Rd., Portland, OR 97201-3098. 5-4ap

PORTLAND, OR—Group of 8 radiologists seeking general diagnostic radiologist. Limited amount of ultrasound and nuclear medicine. Practice includes CT, MRI, and angiography. Group covers large trauma hospital and 4 outpatient offices. Send CV or call Randy Greene, M.D. or Blaine Kozak, M.D., Dept. of Radiology, 2801 N. Gantenbein, Portland, OR 97227; (503) 280-4032. 5-7ap

RADIOLOGIST—Requirements: interpretation of diagnostic x-rays, ultrasound, mammography, computed tomography, nuclear medicine, magnetic resonance imaging, digital subtraction angiography, general radiology. Worker is to be a medical doctor who has completed three years specialty training in diagnostic radiology and obtained certification from the American Board of Radiology (Diplomate of the American Board of Radiology). At least one year experience in neuro-radiology is needed. Salary \$10,000 per month. 40-hour work week. Send all resumes to Tennessee Department of Employment Security, Job Service, Attention: Mr. Charles Turner, 400 Georgia Ave., Chattanooga, TN 37402-4599. 5ap

ACADEMIC RADIOLOGY POSITION—Creighton University is seeking a board-certified diagnostic radiologist to head the Section of Chest Radiology. The Dept. of Radiology at Creighton University has excellent facilities and equipment including MRI and PET. There is generous time allotment for academic endeavors and competitive pay. All faculty members participate in clinical service and teaching. Academic rank depends on qualifications and experience. Interested applicants should contact Mathis P. Frick, M.D., Professor and Chairman, Dept. of Radiology, Creighton University Medical Center, 601 N. 30th St., Omaha, NE 68131. An equal opportunity employer. 5a

UCSD SCHOOL OF MEDICINE—The Dept. of Radiology is seeking a physician to participate in clinical, teaching, and research programs in nuclear medicine. Board eligibility/certification in nuclear medicine and California medical license required. Title series: assistant professor (in-residence or clinical series—not currently a tenure-track position), level based on years experience and salary commensurate with rank and step of appointment, based on the established salary schedule of the UCSD School of Medicine Faculty Compensation Plan. The University of California, San Diego is an equal opportunity/affirmative action employer. All CVs received by July 1, 1989 will be given full consideration. Send to William L. Ashburn, M.D., Professor of Radiology, Dept. of Radiology, UCSD Medical Center, 225 Dickinson St., San Diego, CA 92103. 5a

NEW HAMPSHIRE—Excellent opportunity for young, BC/BE, general radiologist with MRI experience to join well-established, busy, small group. Live and work in beautiful Connecticut Valley Region close to lakes and skiing. Competitive compensation package leading to partnership. Please send CV to New England Health Search, 63 Forest Ave., Orono, ME 04473; (207) 866-5680 or (207) 866-5685. 5-7ap

PEDIATRIC RADIOLOGIST—Vacancies are available in various parts of the Pediatric Radiology Dept. at The Hospital for Sick Children, Toronto. The hospital is a 560-bed, tertiary-care, pediatric center situated in downtown Toronto and affiliated with the University of Toronto. 100,000 exams are performed each yr, and the staff includes 17 full-time pediatric radiologists and 7 fellows. Positions are available in general pediatric radiology areas as well as in more specialized areas such as neuroradiology. The dept. is equipped with state-of-the-art equipment. Applicants must have pediatric radiology experience, including 1- and preferably 2-yr fellowship, and staff radiologists with greater experience are certainly most welcome. For further information, please contact A. Daneman, M.D., Radiologist-in-Chief, Dept. of Radiology, The Hospital for Sick Children, 555 University Ave., Toronto, Ontario, M5G 1X8, Canada; (416) 598-6026. 5-8a

ATLANTA, GA—One radiology position. The Southeast Permanente Medical Group, Inc., Georgia Region, is seeking an additional radiologist for a growing radiology dept. serving several medical centers throughout the Atlanta area. Interested and qualified candidates must be board-certified in radiology with expertise in general radiology to include CT, ultrasound, and mammography. Address inquiries and CVs to Alex Daley, M.D., Chief of Radiology, c/o The Southeast Permanente Medical Group, Inc., 3355 Lenox Rd., Ste. 1000, Atlanta, GA 30326; (404) 233-0666, ext. 192. 5-10ap

RADIOLOGIST—The Elko Regional Medical Center seeks a BC/BE general diagnostic radiologist to work at the medical center as well as the local community hospital. CT, mammography, ultrasound, nuclear medicine, and some interventional training or experience required. Guaranteed salary for 6 mo leading to full partnership. Excellent benefits package including malpractice insurance. Elko is a thriving community surrounded by mountains and wilderness areas. Recreation yr round. Please send CV to Cherie Atwood, Administrator, Elko Regional Medical Center, 762 14th St., Elko, NV 89801; (702) 738-3111. 5-7ap

RADIOLOGIST—Expanding radiology practice has an opening for a radiologist with fellowship or postgraduate experience in interventional radiology. Exceptional general radiology talents also needed. Special competency in nuclear medicine and MRI a plus, but not mandatory. Practice is located in Albuquerque, NM and consists of 13 physicians serving 3 major hospital facilities and a separate MRI center. Climate and living conditions are outstanding. Qualified applicants may send CV and references to Radiology Associates of Albuquerque, P.A., 4001 Indian School Rd., N.E., Ste. 300, Albuquerque, NM 87110, Attn: J. R. Ellison, Business Manager. 5ap

PRACTICE OF RADIOLOGY—A hospital-based practice of 4 radiologists, covering 2 area hospitals serving Wyoming, South Dakota, Colorado, and Nebraska, (recently designated as a rural referral center) seeks an additional radiologist with expertise in all imaging modalities. Excellent compensation and fringe benefits. State-of-the-art facility in a recently constructed wing (1985). Potential to become full partner in 1 yr. Community of approximately 20,000 with medical service population of 110,000. Close to Rocky Mountains (2-5 hr), with excellent hunting and fishing. Alternative opportunity for 1-yr, locum tenens position. If you are board-certified or are soon to be and would like more information about this opportunity, please send CV or call R. G. Heasty, M.D., Regional West Medical Center, 4021 Avenue B., Scottsbluff, NE 69361; (308) 632-0140. 4-6ap

GENERAL AND INTERVENTIONAL RADIOLOGIST—Practice in 200-bed, modern, primary-care hospital with excellent imaging and interventional facility in Troy, MI and rotate in our major, tertiary-care medical center with residency and fellowship training programs. Send applications to Thomas Verhelle, M.D., Chief, Diagnostic Radiology, William Beaumont Hospital, 44201 Dequindre Rd., Troy, MI 48084. 3-5a

THE DEPT. OF RADIOLOGY, VIRGINIA COMMONWEALTH UNIVERSITY/MEDICAL COLLEGE OF VIRGINIA, Richmond, VA seeks faculty for positions in diagnostic radiology for chest, mammography, CT/ultrasound/MR, neuroradiology, pediatrics, ER, angio/interventional, and general radiology. Our 1058-bed facility (205 for pediatric patients) is a Level 1 Trauma Center. ABR certification or eligibility required. Academic rank and salary commensurate with experience. Submit CV to A. V. Proto, M.D., Chairman, Diagnostic Radiology, Medical College of Virginia, MCV Box 47, Richmond, VA 23298-0047. VCU/MCV is an equal opportunity/affirmative action employer. Women and minorities are encouraged to apply. 4-6a

CHIEF, RADIOLOGY SERVICE—BC/BE radiologist with unrestricted license in any state (or District of Columbia), U.S. citizen or permanent resident immigrant, English language proficiency required. 775-bed medical center offers primary and extended care, and outpatient medical and psychiatry services. Salary to \$94,000 (depending on qualifications), federal malpractice protection, 30 days paid vacation, and relocation expenses. Tomah is a city of 7500 in a predominantly rural area that offers affordable real estate and good schools. Conveniently located on I-90/94 midway between Milwaukee and Minneapolis. Call or write R. S. Merrill, M.D., Chief of Staff (11), VA Medical Center, Tomah, WI 54660; (608) 372-1778. EO/AEE. 5a

CHIEF OF ULTRASOUND, PRIVATE PRACTICE HOSPITAL GROUP—Position available at a large, tertiary-care hospital in Phoenix, AZ, for a board-certified radiologist with fellowship training in ultrasound. Prefer postfellowship experience with ability to manage an ultrasound section and promote its services. Experience in obstetrics, general and Doppler ultrasound necessary. This is a unique position, offering academic-style practice with private-practice benefits. Please send letters of inquiry to Aubrey M. Palestrant, M.D. or Theodore Ditchek, M.D., Dept. of Radiology, Good Samaritan Medical Center, 1111 E. McDowell Rd., Phoenix, AZ 85006; (602) 239-4601. 4-7ap

ABDOMINAL RADIOLOGIST—The H. Lee Moffitt Cancer Center and Research Institute at the University of South Florida has a faculty position available for an abdominal radiologist with fellowship training or equivalent subspecialty experience. Interest and expertise in all imaging modalities and procedures related to abdominal radiology are preferred. The position includes clinical service, research, and teaching; academic rank is based on qualifications. Our facility is a new, state-of-the-art complex; the compensation package is excellent. Interested candidates should contact Robert Clark, M.D., Dept. of Radiology, Moffitt Cancer Center, P. O. Box 280179, Tampa, FL 33682-0179. 4-6ap

BOARD-CERTIFIED OR ELIGIBLE RADIOLOGIST to join a hospital and multi-office group practice in North Central Connecticut. Applicant should be competent in all imaging modalities including CT and MRI. Training in interventional radiology is desirable but not essential. Salary first yr leading to full partnership. J. Danigelis, M.D., 151 Berie Rd., South Windsor, CT 06074. 4-6ap

LOCUM COVERAGE—Chattanooga Outpatient Center seeks short- or long-term locum. Excellent equipment. All modalities. No night or weekend work. Generous reimbursement. Contact Desmond Fischer, M.D., 1301 McCallie Ave., Chattanooga, TN 37404. 4-6 ap

VASCULAR/INTERVENTIONAL RADIOLOGIST—The Albany Medical College has an opening at the instructor/assistant professor level for an academic position in the Vascular Radiology Section. The candidate must have completed a 1-yr fellowship in vascular/interventional radiology and be available by July 1989. All angiographic and drainage procedures are performed in the section and a GE Signa MR scanner is available for vascular studies. Clinical responsibilities will also include some involvement in general diagnostic radiology. Academic responsibilities include research and teaching of medical students, residents, and fellows. Interested applicants should forward their CV to James C. Peters, M.D., Acting Chairman, Dept. of Radiology, Albany Medical Center Hospital, 43 New Scotland Ave., Albany NY 12208; (518) 445-3277. 4-5ap

MODERN, 6-MAN RADIOLOGY GROUP seeking 7th man due to expansion. Three private offices and 1 busy hospital, all located in Jamestown, NY, on Chautauqua Lake. Must be board-certified and preferably trained in specials, ultrasound, nuclear medicine, CT, and MRI. Generous salary and benefits. Full partnership in 2 yr. Send CV to Rev. Eugene F. Foley, M.D., 333 E. 5th St., Jamestown, NY 14701, or call Patsy Lydell at (716) 664-9731. 4-6ap

VASCULAR/INTERVENTIONAL RADIOLOGIST—Diagnostic Radiology Dept., National Institutes of Health. Full-time, academic position at assistant- or associate-professor level. Board-certification required, fellowship preferred. Duties include all aspects of vascular/interventional radiology, with particular emphasis on diagnostic angiography. Some cross-sectional imaging and plain film reading required. Numerous research opportunities available in dept. with extensive research facilities and support staff. Salary with excellent fringe benefits. Position includes faculty appointment at Georgetown University. Please send CV with letter to John L. Doppman, M.D., Diagnostic Radiology Dept., Bldg. 10, Room 1C660, National Institutes of Health, Bethesda, MD 20892. 4-6ap

RADIOLOGIST; PERMANENT POSITION—Chattanooga Outpatient Center. Excellent equipment; CT, MRI, ultrasound, nuclear, and mammography. No nights or weekends. Generous reimbursement and vacation package leading to partnership. Contact Desmond Fischer, M.D., 1301 McCallie Ave., Chattanooga, TN 37404. 4-6ap

RADIOLOGIST—Associate diagnostic radiologist to join a group of 4. Hospital and private practice. All imaging capabilities. Angiography and nuclear medicine. 1 hr from Boston. Reply Box P81, AJR (see address this section). 4-6ap

ISRAEL, DIAGNOSTIC RADIOLOGY. Opportunities for 3-4 week or longer working vacations in a number of Israeli medical centers, on a volunteer basis. Positions varied, arrangements flexible. For information contact: Jonathan H. Fish, M.D., 1844 San Miguel Dr., #302, Walnut Creek, CA 94596; (415) 947-0560. 5-7xa

TWO BOARD-CERTIFIED/ELIGIBLE GENERAL DIAGNOSTIC RADIOLOGISTS to join expanding, 9-man group covering 2 hospitals and an MR Imaging Center in a stable midwest community. Ideal private practice using all imaging modalities and interventional techniques. Can start immediately or wait until July 1989. Excellent opportunity with excellent salary and benefits. Send CV to Joseph F. Norrmy, M.D., MR Center of Springfield, 319 E. Madison, Springfield, IL 62701. 3-6ap

NEURORADIOLOGIST—Immediate opening for recently trained neuroradiologist in busy, suburban practice in Southwest. Current CT, MRI, and arteriography skills required. Highly competitive salary/benefits. Send CV to Box K49, *AJR* (see address this section). 5xa

MRI RADIOLOGIST—The Dept. of Radiology at Northwestern University Medical School in Chicago is seeking a radiologist with experience in MRI to serve as Director of the MRI facility at Northwestern Memorial Hospital, a 750-bed university hospital. This is an academic position, requiring a strong interest in clinical teaching and research, as well as patient care. Academic rank depends on qualifications. Send inquiries with a CV to Lee F. Rogers, M.D., Chairman, Dept. of Radiology, Northwestern University Medical School, 710 N. Fairbanks, Chicago, IL 60611. An affirmative action, equal opportunity employer. 3-5ap

DIAGNOSTIC RADIOLOGIST, DALLAS METROPLEX—Position available immediately for BC/BE radiologist to join 3-person group. Our practice includes 2 hospitals and an outpatient clinic. Fellowship training in MRI desired. Reply to Box O72, *AJR* (see address this section). 3-5ap

DIAGNOSTIC RADIOLOGISTS, 1 INTERVENTIONAL AND 1 ULTRASOUND—Young, aggressive group in Washington, DC, area has position immediately available for a board-certified diagnostic radiologist in an expanding and diversified hospital and office-based practice with facilities in Maryland and Virginia. Our group covers 2 very progressive hospitals, including a regional trauma center, 3 full-service private offices, and a diagnostic center for women. All imaging modalities represented, including 3 MRI, 6 CT, 5 Acuson 128, and a PIXAR 3-D imaging unit. Dynamic and attractive practice setting. Address inquiries and CV to Radiology Imaging Associates, 8926 Woodyard Rd., Ste. 301, Clinton, MD 20735; (301) 856-3670. 3-5ap

GENERAL DIAGNOSTIC RADIOLOGIST, THOMAS JEFFERSON UNIVERSITY HOSPITAL—The Dept. of Radiology at Thomas Jefferson University Hospital in Philadelphia has an opening in July 1989 for a faculty-level, general diagnostic radiologist. An interest and/or fellowship training in abdominal radiology (GI/GU) would be helpful, but not mandatory. The individual will have the opportunity to participate in clinical activities, teaching, and research in a progressive and expanding general diagnostic division. Excellent salary and benefits are offered. Contact either Robert M. Steiner, M.D., Co-director of General Diagnostic Radiology or David C. Levin, M.D., Professor and Chairman, Dept. of Radiology, Thomas Jefferson University Hospital, 111 S. 11th St., Philadelphia, PA 19107. Thomas Jefferson University is an equal opportunity/affirmative action employer. 1-6ap

RADIOLOGIST—Full-time, board-certified radiologist with particular interest and experience in nuclear and ultrasound radiology desired for association in 10-man, private practice for a 660-bed, private, tertiary-care, teaching hospital with 2 regional offices. Practice is located in large midwestern city and maintains fully accredited, 4-yr, radiology residency training program. This comprehensive dept. includes 2 state-of-the-art CT scanners, a 1.5-T MRI unit, modern equipment for mammography, sonography, angiography, nuclear medicine, and a wide variety of invasive applications and procedures. Competitive salary and benefits. Full partnership, if mutually agreeable, at 3 yr. Near-future plans include manning of regional outpatient center with CT and general radiologic facilities on site. Send inquiry and CV in reply to Box N63, *AJR* (see address this section). 1-6ap

BC/BE DIAGNOSTIC RADIOLOGIST to join 4 radiologists at a large, multispecialty, staff model HMO. Practice includes general radiology, mammography, CT, nuclear medicine, and ultrasound. The dept. recently has been outfitted with 2 new GE R&F rooms and a new GE Pace CT scanner. The position offers a competitive salary with a comprehensive benefits program. Medical West Community Health Plan is located in western Massachusetts, approximately 60 min from the Berkshires and 90 min from Boston. Please send CV to Robert P. Newman, M.D., Chief, Dept. of Radiology, MWCHP, Inc., 444 Montgomery St., Chicopee, MA 01020. We are an equal opportunity/affirmative action employer. 3-5a

DIAGNOSTIC RADIOLOGIST—The UCLA Dept. of Radiological Sciences is seeking a board-certified radiologist for its Primary Care/Family Practice Section. Position requires strong interests in teaching, patient care, and knowledge of abdominal CT for evaluation of trauma. Send application, including CV and names and addresses of 3 references, or inquiries to Hooshang Kangarloo, M.D., Chairman, Dept. of Radiological Sciences, UCLA Medical Center, Los Angeles, CA 90024-1721, an EO/AA employer that encourages applications from members of minority groups and women. 2-7a

SKELETAL RADIOLOGIST—The UCLA Dept. of Radiological Sciences has a full- or half-time faculty position available in skeletal radiology. Candidate must be board-certified, have a clinical background in skeletal radiology, and have a strong interest in teaching. Send application, including CV and names and addresses of 3 references, or inquiries to Hooshang Kangarloo, M.D., Chairman, Dept. of Radiological Sciences, UCLA Medical Center, Los Angeles, CA 90024-1721, an EO/AA employer that encourages applications from members of minority groups and women. 2-7a

SOUTHERN INDIANA—Radiologist to join 5-member group in hospital and office practice. Some interest and experience in interventional studies desirable, but all areas of expertise will be considered. All imaging modalities, including MRI, available in 400-bed hospital. 80,000 exams annually. Competitive salary for 2 yr leading to partnership. T. Cook, M.D., P. O. Box 5249, Evansville, IN 47716-5249. 3-5ap

THE DEPT. OF RADIOLOGY AT TRIPLER ARMY MEDICAL CENTER, HONOLULU, HI, is recruiting academically oriented radiologists for several divisions of the dept.: ultrasound, imaging (CT and/or MRI), interventional, chest, genitourinary, mammography, pediatric, neuro-radiology, and general diagnostic radiology. We are particularly interested in radiologists with ultrasound training or extensive experience. Our dept. offers a fully-accredited residency program with 18 residents and 15 attending full-time staff. Numerous consultants from across the country lecture on a continuing and regular basis. The hospital is a modern tertiary-care center serving the state and the entire Pacific Basin. A strong residency program, a diverse and interesting patient population, excellent equipment, and a tropical lifestyle are positive aspects of the practice. Academic credentials and/or experience are necessary. Recently graduated fellows are encouraged to apply. Board certification is mandatory. Candidates should be particularly interested in patient care, teaching, and research. Salary and benefits are competitive and generous. Tripler is an EO/EEO employer. Please contact Dr. Mark F. Hansen, Col., MC, Chief, Dept. of Radiology, TAMC, HI 96859-5000; (808) 433-6393. 5a

DIAGNOSTIC RADIOLOGIST—Immediate opening to join 2 other radiologists in a large, multi-specialty group practice serving 4 outpatient offices in Rochester, NY. State-of-the-art Toshiba fluoroscopy, ATL ultrasound, and LoRad mammography equipment. Ultrasound, mammography, and CT experience preferable. 32,000 exams/yr. Please contact Dennis S. Moss, M.D., Rochester Medical Group Associates, P.C., Radiology Dept., 800 Carter St., Rochester, NY 14621; (716) 338-1400 x4096. EOE/MF. 3-6a

FRAMINGHAM, MA—BC/BE diagnostic radiologist to join 6-member group at 311-bed teaching hospital. Experience in angiography and interventional radiology necessary. Send CV to Herbert D. Weintraub, M.D., c/o Framingham Union Hospital, 115 Lincoln St., Framingham, MA 01701; (508) 626-3525. 3-6ap

SOUTHEAST COAST OF FLORIDA—BC/BE radiologist. No MRI. Experience preferred. Available summer 1989. R. L. Stern, M.D., 3232 Memory Lane, Fort Pierce, FL 34981. 3-5ap

DIAGNOSTIC RADIOLOGIST—GASTROINTESTINAL IMAGING—Yale New Haven Medical Center, Yale University School of Medicine, is seeking a radiologist with special interest in gastrointestinal imaging including barium radiography, CT, and/or ultrasound. Rank is commensurate with experience. A strong interest in patient care, research, and teaching is required. Please send inquiries along with CV to Morton Burrell, M.D., Professor of Radiology, Director of Gastrointestinal Radiology, Yale University School of Medicine, 333 Cedar St., New Haven, CT 06510. Yale University is an equal opportunity/affirmative action employer; applications from women and minority groups are encouraged. Application deadline is May 31, 1989. 3-5a

Fellowships and Residencies

FELLOWSHIP IN PEDIATRIC RADIOLOGY—LeBonheur Children's Medical Center/St. Jude Children's Research Hospital/The University of Tennessee, Memphis/University Physicians Foundation, Inc. combined program in pediatric radiology offers a 1- or 2-yr fellowship in pediatric radiology. There are approximately 70,000 pediatric exams performed annually by 10 full-time radiologists. Experience to include general pediatric, neuro, nuclear, oncologic, neonatal, and cardiovascular radiology. Facilities include Doppler ultrasound, CT, and MRI. Opportunity to participate in MRI and other imaging research. Blacks, women, handicapped, and other minorities are encouraged to apply. The University of Tennessee, Memphis/University Physicians Foundation, Inc. is an affirmative action/equal opportunity employer. Address inquiries to Barry D. Fletcher, M.D., Chairman, Diagnostic Imaging Dept., St. Jude Children's Research Hospital, 332 N. Lauderdale, Memphis, TN 38101; or Robert A. Kaufman, M.D., Director, Dept. of Radiology, LeBonheur Children's Medical Center/University of Tennessee, Memphis, 800 Madison Ave., Rm. 114C Chandler, Memphis, TN 38163. 5-7c

ANGIOGRAPHY AND INTERVENTIONAL RADIOLOGY FELLOWSHIP TO BEGIN JULY 1990—568-bed teaching hospital. Fellows will participate in all vascular and nonvascular/interventional procedures, including angioplasties, biliary, GU, biopsies, abscess drainages, and angiography. Fellows also will be actively involved in diagnostic CT, MRI, and ultrasound. Send inquiries to Harvey L. Neiman, M.D., Chairman, Dept. of Radiology, West Penn Hospital, 4800 Friendship Ave., Pittsburgh, PA 15224. 5-8c

ULTRASOUND, MR, AND CT IMAGING FELLOWSHIP TO BEGIN JULY 1990—568-bed teaching hospital. Over 130,000 exams are performed yearly in the radiology dept. All imaging modalities are integrated into the fellowship program, which will emphasize diagnostic ultrasound (including obstetrical and Doppler with color flow), MRI, and body CT. Send inquiries to Harvey L. Neiman, M.D., Chairman, Dept. of Radiology, West Penn Hospital, 4800 Friendship Ave., Pittsburgh, PA 15224. 5-8c

ANGIOGRAPHY/INTERVENTIONAL RADIOLOGY FELLOWSHIP—New York Medical College announces the availability of a 1-yr fellowship to begin July 1, 1990. The program includes training in all phases of diagnostic angiography and interventional radiologic techniques. Approximately 900 procedures were performed in 1988. The program is based at Westchester County Medical Center, a 650-bed, tertiary-care center located on the campus of the medical college in prestigious suburban setting only about 1/2 hr from New York City. Active participation in clinical management of patients is emphasized. Current research interests include transmesenteric sclerosis of portal varices and hepatic arterial chemoembolization. A new interventional/imaging suite will open in 1989. For additional information and application, contact Stuart Katz, M.D., Dept. of Radiology, New York Medical College, Valhalla, NY 10595; (914) 285-8388. 5-6c

INTERVENTIONAL RADIOLOGY FELLOWSHIP—The Rush-Presbyterian-St. Luke's Medical Center is now offering a 1-yr fellowship position beginning July 1, 1990 in interventional radiology. This 750-bed teaching hospital offers extensive experience in all aspects of vascular and nonvascular procedures, with a primary emphasis on patient care and clinical research. Send inquiries to Terence Matalon, M.D., Dept. of Diagnostic Radiology and Nuclear Medicine, Rush-Presbyterian-St. Luke's Medical Center, 1653 W. Congress Parkway, Chicago, IL 60612. 4-7c

CARDIOVASCULAR—INTERVENTIONAL RADIOLOGY FELLOWSHIP—Available July 19, 1989. One-year fellowship program at a 750-bed teaching hospital. Extensive clinical experience involving all aspects of cardiovascular imaging, interventional vascular and nonvascular procedures, and availability for clinical or animal research. Send CV and inquiries to Oscar H. Gutierrez, M.D., Dept. of Radiology, Box 648, University of Rochester Medical Center, Rochester, NY 14642. An equal opportunity employer (M/F). 3-6c

VASCULAR-INTERVENTIONAL RADIOLOGY FELLOW (JULY 1989)—Unexpected opening for vascular-interventional radiology fellow in university-affiliated program. Send letter of inquiry with CV to Souheil Saddekni, M.D., Director, Vascular-Interventional Division, Dept. of Radiology, St. Luke's-Roosevelt Hospital Center, 114th St. at Amsterdam Ave., New York, NY 10025. 5cp

VASCULAR/INTERVENTIONAL RADIOLOGY FELLOWSHIP at the University of Maryland Medical Center. A 1-yr fellowship position available beginning July 1, 1989. The University is a 750-bed, acute-care hospital and tertiary referral center, including a new 135-bed trauma hospital. Training is offered in all aspects of angiography and interventional radiology including laser angioplasty, percutaneous insertion of inferior vena caval filters, embolization, biliary and GU interventional procedures. There are approximately 2000 procedures done annually. Please contact Joseph Whitley, M.D., Dept. of Radiology, University of Maryland Medical Center, 22 S. Greene St., Baltimore, MD 21201; (301) 328-3477. 5c

FELLOWSHIP IN DIAGNOSTIC IMAGING (MRI, ULTRASOUND, AND CT)—Fellowship available July 1990 at Rhode Island Hospital, a major affiliate of Brown University Medical School. The radiology staff serves this 715-bed general hospital and a 200-bed, lying-in hospital. Over 190,000 exams are performed yearly. The fellowship will emphasize MRI, ultrasonography, and CT, along with associated interventional procedures. A busy mammography area is included. Send inquiries to Daniel J. Hanson, M.D., Radiologist-in-Chief, Dept. of Diagnostic Radiology, Rhode Island Hospital, 593 Eddy St., Providence, RI 02902. 5c

GIANTURCO RESEARCH FELLOW—The Dept. of Diagnostic Radiology at The University of Texas M. D. Anderson Cancer Center, Houston, TX is offering a 1-yr training program under the direction of Kenneth C. Wright, Ph.D., Sidney Wallace, M.D., and Cesare Gianturco, M.D. The program is available for laboratory research in the John S. Dunn Research Foundation Center for Radiological Sciences at a salary of \$25,000. The areas of current research include angiographic and interventional technique and devices, microencapsulation of radiopaque contrast materials and chemotherapeutic agents, and a computerized atlas of anatomy and imaging. Appointments may be made during residency, postresidency, or before beginning residency training. For further information, contact Sidney Wallace, M.D., Dept. of Diagnostic Radiology, The University of Texas M. D. Anderson Cancer Center, 1515 Holcombe Blvd., Houston, TX 77030. An equal opportunity/affirmative action employer. 4-6c

FELLOWSHIP IN VASCULAR AND INTERVENTIONAL RADIOLOGY—Due to an unexpected opening, a fellowship position in vascular and interventional radiology is available at the University of Texas Medical Branch, for 1 yr beginning July 1, 1989, and ending June 30, 1990. This position is offered also to those radiologists who desire to return to an academic setting to acquire new skills in the vascular and interventional field. Very active dept. with up-to-date equipment provides an excellent opportunity for training in all interventional modalities. Please contact L. B. Moretini, M.D., Director, Vascular and Interventional Radiology, University of Texas Medical Branch, Galveston, TX 77550; (409) 761-2498. UTMB is an equal opportunity M/F/H/V affirmative action employer. UTMB hires only individuals authorized to work in the United States. 4-6c

ABDOMINAL IMAGING FELLOWSHIP, JULY 1, 1989—One-yr fellowship in abdominal imaging available in all aspects of diagnostic ultrasound, CT, GI and GU radiology, and body MR. Applicants must have completed an approved residency program in diagnostic radiology and be board-eligible/certified. Send letter of inquiry with CV to William W. Olmsted, M.D., The George Washington University Hospital, Dept. of Radiology, 901 23rd St., N.W., Washington, DC 20037. The George Washington University Hospital is an EEO/affirmative action employer. 5c

FELLOWSHIP POSITIONS AVAILABLE IN ABDOMINAL IMAGING (CT/ULTRASOUND/MRI), CHEST RADIOLOGY, AND VASCULAR/INTERVENTIONAL RADIOLOGY at State University of New York, Health Science Center Syracuse, Dept. of Radiology beginning July 1989 and July 1990. For information and applications, contact Beverly A. Spirt, M.D. (abdominal imaging—CT/ultrasound/MRI), Stuart A. Groskin, M.D. (chest radiology), or John B. Weigle, M.D. (vascular/interventional radiology) at the Dept. of Radiology, SUNY Health Science Center Syracuse, 750 E. Adams St., Syracuse, NY 13210. 5cp

IMAGING FELLOWSHIP (CT, ULTRASOUND, MRI)—William Beaumont Hospital, a 970-bed, modern, tertiary-care teaching and academic institution in southeast MI, offers a 1-yr fellowship in sectional body imaging. The fellowship will provide extensive clinical experience in body CT, ultrasound and MRI, including CT- and ultrasound-guided procedures, conventional and color flow Doppler exams, prostatic and endovaginal sonography. Ample elective time is also provided for other rotations of individual interest. Candidates must be board-certified/eligible in diagnostic radiology and have valid Michigan medical license. Four positions are available for July 1990. Salary and fringe benefits are highly competitive. For further information, write to Ali Shirkhoda, M.D., Chief of Imaging Division, William Beaumont Hospital, 3601 W. 13 Mile Rd., Royal Oak, MI 48072; (313) 541-1001. 3-5c

DIAGNOSTIC RADIOLOGY RESIDENCY POSITIONS—The University of Miami/Jackson Memorial Medical Center, Dept. of Radiology, is offering 1 third- and 1 fourth-yr diagnostic radiology residency position beginning July 1989. Our program was recently approved for an increase in total number of positions. UM/JMMC is a 1300-bed, tertiary referral center serving Miami, FL, the Southeast, and Latin America. The Dept. of Radiology currently performs approximately 250,000 exams/yr with 33 faculty, 22 residents, and 8 fellows (5 in neuroradiology and 3 in interventional/CT/ultrasound). If interested, please contact by phone or letter with CV, Sandra A. Oldham, M.D., Dept. of Radiology (R-109), University of Miami School of Medicine, P. O. Box 016960, Miami, FL 33101; (305) 549-6894. AA/EOE. 2-6c

CARDIOVASCULAR/INTERVENTIONAL RADIOLOGY FELLOWSHIP AT THOMAS JEFFERSON UNIVERSITY HOSPITAL—A 1-yr fellowship position is available starting 7/1/89. This fellowship includes experience in a wide range of diagnostic angiography and both vascular and nonvascular interventional procedures. These include balloon angioplasty, laser thermal angioplasty, thrombolytic therapy, atherectomy, intravascular stent placement, IVC filter placements, renal and biliary drainage procedures, abscess drainages, and stone retrievals. Optional training also available in coronary angiography. Facilities include state-of-the-art angiographic and digital subtraction equipment. Contact either Geoffrey A. Gardiner, Jr., M.D. or David C. Levin, M.D., Dept. of Radiology, Thomas Jefferson University Hospital, 111 S. 11th St., Philadelphia, PA 19107. Thomas Jefferson University is an equal opportunity/affirmative action employer. 1-6cp

FELLOWSHIP IN PEDIATRIC RADIOLOGY—Dept. of Radiology, Children's Hospital Medical Center, Cincinnati, OH, offers a 1- or 2-yr fellowship in pediatric radiology beginning July 1, 1989. Children's Hospital Medical Center is a 344-bed institution where approximately 85,000 radiologic exams are done per yr by 10 attending radiologists. Training includes all aspects of pediatric imaging including conventional radiology, neuro-radiology, abdominal imaging, ultrasound, nuclear medicine, CT, MRI, and vascular/interventional techniques. Equipment includes digital fluoroscopy, Acuson and ATL ultrasound units with Doppler and color-flow Doppler capabilities, Gamma and SPECT tomographic nuclear cameras, GE 9800 Quick CT Scanner, 1.5-T GE MRI, and angiographic suite with digital vascular imaging. Requirements for the fellowship include completion of a radiology residency with training in the various subspecialties of diagnostic imaging. Contact Donald R. Kirks, M.D., Director, Dept. of Radiology, Children's Hospital Medical Center, Elland & Bethesda Aves., Cincinnati, OH 45229-2899; (513) 559-8058. 12-8cp

Tutorials/Courses

CHALLENGE 89—DECISIONS IN IMAGING: LONDON, ENGLAND; JUNE 24–30, 1989—Category I CME, MRI, CT, ultrasound correlative course presented by University of Southern California faculty and a distinguished faculty from the United Kingdom. **Wimbledon Tennis Tournament.** For information contact University Imaging Associates, LAC/USC Medical Center, Box 66, 1200 N. State St., Los Angeles, CA 90033; (213) 226-7245. 4–6dp

FIFTH ANNUAL LONDON-PARIS FALL ULTRASOUND—Sept. 17–23, 1989. Category I accreditation, international faculty. For information, contact Medical Seminars International, 9800 D Topanga Canyon Blvd., Ste. 232, Chatsworth, CA 91311; (818) 700-9821. 3–9d

ALASKA 89—CRUISE THE INLAND PASSAGE—

July 8–15, 1989, CME I accreditation, Professor Lawrence Bassett, M.D., Breast Imaging. For information, contact Medical Seminars International, 9800 D Topanga Canyon Blvd., #232, Chatsworth, CA 91311; (818) 700-9821. 1–6d

Other

MOBILE MAMMOGRAPHY VAN—1987, 27-ft Itasca motor home, fully equipped for complete mammography service. Kramex 43S mammography unit, AFP processor. \$85,000. For information respond to, Florida Mobile Imaging, Inc., P. O. Box 2440, Sanford, FL 32772-2440. 4–6ep.

AJR Classified Advertisements Information

Box Responses and Address for Ad Placement

Write Box _____, AJR, 2223 Avenida de la Playa, Suite 200, La Jolla, CA 92037-3218; (619) 459-2229; FAX: (619) 459-8814.

How to Place an Ad

AJR accepts classified advertising for Positions Available, Positions Desired, Fellowships and Residencies, and Tutorials/Courses. Ads are accepted by mail or FAX.

Rates: \$6.00/line with a \$30 minimum charge. Box service is \$10 additional for each month the ad appears. There are discounts for multiple insertions: 10% for 2–3 insertions; 20% for 4 or more. To estimate lines, count all words and divide by 7.

Billing: Ads *must* be prepaid, or advertisers will be billed after the ad appears *providing* a purchase order number is submitted with the advertising copy. Terms are net 30 days.

Deadlines: 6 weeks prior to issue date. For specific deadlines, telephone the AJR editorial office.

Estimating Ad Charges

Line charge: divide total words by 7 and multiply by \$6.00	\$
Multiple insertions? If so, multiply by number	x
Subtotal	\$
Discount applies to two or more insertions. Subtract 10% if ad appears 2–3 months, 20% if 4 months or more	–
Subtotal	\$
Box response requested? If so, multiply number of months by \$10.00	+
Approximate advertising charge	\$



THE JOHNS HOPKINS MEDICAL INSTITUTIONS MRI PRACTICUMS

The MRI Division of The Johns Hopkins Medical Institutions offers uniquely structured BASIC and ADVANCED week long practicums for radiologists who wish to rapidly achieve clinical proficiency in MRI.

The practicums consist of a series of formal lectures on basic principles and practice of clinical MRI (brain, spine and body), followed by intensive small group interactive sessions and review of our large file of instructive cases. Scanning techniques, protocols and procedures will be emphasized. Ample opportunity to participate in our daily case load of over 35 patients is provided.

Course Directors:

Elias A. Zerhouni, M.D.
R. Nick Bryan, M.D.
Clare Tempany, M.D.

Credit: 40 AMA Category I

Fee: \$1250

ATTENDANCE IS LIMITED

Course Dates:

Basic Practicum

June 19-23, 1989
October 23-27, 1989
January 22-26, 1990
May 21-25, 1990

Advanced Practicum

September 11-15, 1989
December 11-15, 1989
March 19-23, 1990

The Johns Hopkins Medical Institutions
MRI Meeting: November 10-12, 1989
Sheraton Inner Harbor, Baltimore, Maryland

For further information contact: Program Coordinator, Office of Continuing Education, The Johns Hopkins Medical Institutions, Turner Building, 720 Rutland Ave., Baltimore, Maryland 21205-2195, (301) 955-2959.

CHIEF, RADIOLOGY SERVICE

University of Michigan Affiliated Ann Arbor VA Hospital

The University of Michigan is seeking to recruit a Board certified radiologist to serve as Chief of the Radiology service at the 300 bed affiliated Ann Arbor Veterans Administration Medical Center. The position also includes a faculty appointment at the University.

The VA Radiology Department is well staffed and has modern equipment, including magnetic resonance, computed tomography, and ultrasound. Forty-two thousand examinations are performed annually. University of Michigan radiology residents and medical students rotate through the department monthly.

Three or more years of experience beyond residency is essential. Previous administrative experience, as well as cross-sectional imaging experience, are desirable. Rank and salary commensurate with credentials.

Contact:

William Martel, M.D.
Chairman, Department of Radiology
University Hospitals
1500 E. Medical Center Drive
Ann Arbor, MI 48109-0030

A nondiscriminatory, affirmative action employer.

DIAGNOSTIC RADIOLOGY RESIDENCY

A position as a fourth year resident in Diagnostic Radiology is available at Lenox Hill Hospital beginning July 1, 1989. Lenox Hill Hospital is a 650 bed voluntary hospital in Manhattan which is academically affiliated with Cornell University Medical College. Please send your c.v. to **Lewis M. Rothman, M.D., Director of Radiology.**

LENOX HILL HOSPITAL



100 E. 77th Street
New York, NY 10021
an equal opportunity employer



SUBSCRIPTION QUESTIONS OR PROBLEMS?

Call us on our **free** line, 1-800-638-6423 to get your problem solved. In Maryland call 1-800-638-4007.

We can help you most efficiently if the mailing label from your latest issue is in front of you when you call. If the problem concerns your payment, please have your canceled check in front of you so that we can solve the problem over the phone. For speedier service, refer to the six digit number at the end of the top line of your address label.

Subscription Fulfillment Department
Williams & Wilkins
428 East Preston Street
Baltimore, Maryland 21202



MOVING?

Let us serve you better.

Attach your current address label in the space below. To be sure you don't miss any issues of the journal, please notify us at least eight weeks before you move.

CURRENT LABEL:

Name _____
Address _____
City _____ State _____ Zip _____
Journal Title _____

NEW ADDRESS:

Name _____
Address _____
City _____ State _____ Zip _____

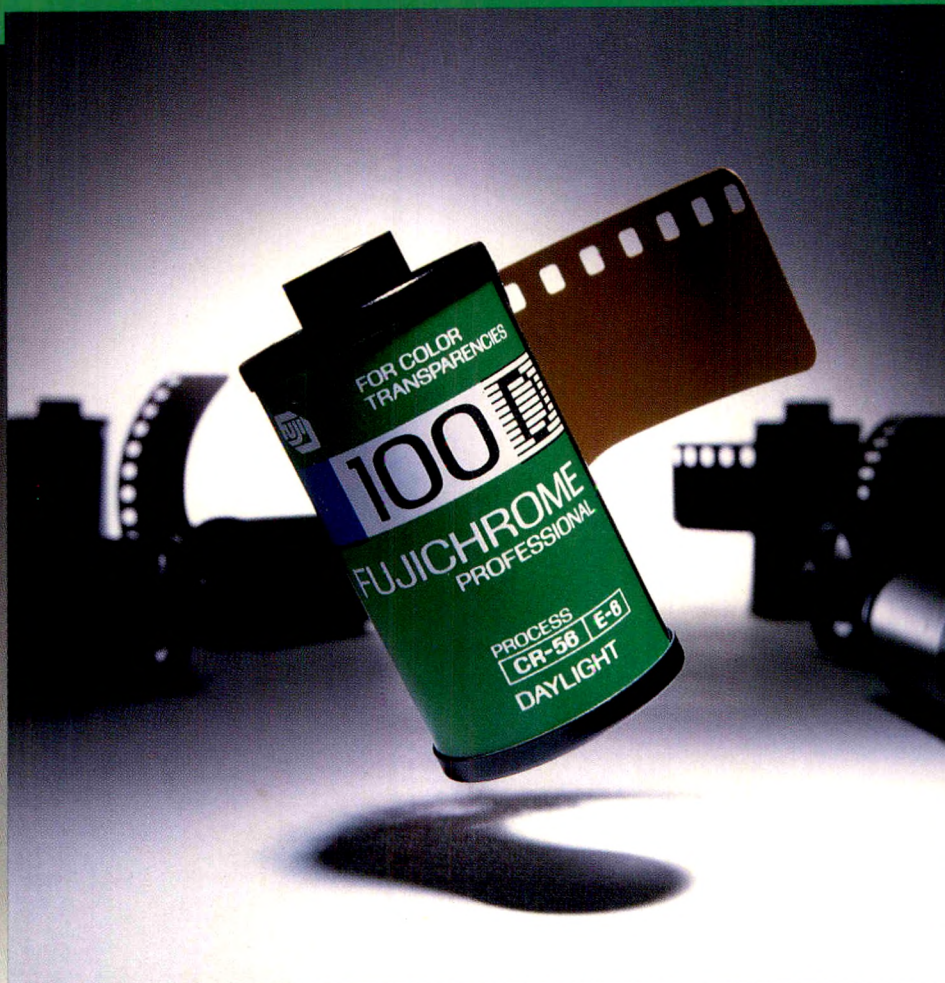
Subscription Fulfillment Department
Williams & Wilkins
428 East Preston Street
Baltimore, Maryland 21202



INDEX TO ADVERTISERS

Berlex Imaging	A9, A10, A11, A12
Braintree Laboratories	A8, A20
Current Science	A18
Eastman Kodak	A6, A7
E-Z-EM Company	Cover 2
FUJI	Cover 3
Johns Hopkins Medical Institutions	A29
General Electric	A15, A17, A19
Lenox Hill Hospital	A29
Mallinckrodt, Inc.	A2, A21, A22, A23, A24
University of Michigan	A29
Nuclear Associates	A26
S & S X-Ray	A27
Siemens Medical Systems, Inc.	A27
U.S. Army	A25
Winthrop Laboratories	A13, A14

We try to present an accurate index. Occasionally this may not be possible because of a last-minute change or omission.



The reason for change . . . It's better

No one likes change . . . particularly professional and serious amateur photographers. So when they began switching to Fuji color film world wide, there could only be one reason . . . the right reason. It's better!

Have you evaluated Fuji Medical radiographic films lately?

Call your Fuji representative or 800-431-1850.

CIRCLE 7 ON READER SERVICE CARD



The Reason for Change!



PROGRESS IN RADIOLOGY

- 913 Diagnostic and therapeutic interventional gallbladder procedures. *Teplick SK*
- 917 Imaging hepatic metastases from colorectal carcinoma: identification of candidates for partial hepatectomy. *Seltzer SE, Holman BL*

REVIEW ARTICLES

- 925 Radiology of penile prostheses. *Cohan RH, Dunnick NR, Carson CC*
- 933 Percutaneous insertion of the Greenfield filter. *Pais SO, Tobin KD*

CONTRAST MEDIA

- 939 A prospective trial of ionic vs nonionic contrast agents in routine clinical practice: comparison of adverse effects. *Wolf GL, Arenson RL, Cross AP*
- 945 Commentary. Nonionic vs ionic contrast media: what do the data tell us? *Lasser EC, Berry CC*
- 947 Case report. Acute thrombocytopenia after IV administration of a radiographic contrast medium. *Chang JC, Lee D, Gross HM*

CARDIOPULMONARY RADIOLOGY

- 951 Pictorial essay. Surgical defects of the pericardium: radiographic findings. *Takasugi JE, Godwin JD*
- 955 Leptospirosis of the lung: radiographic findings in 58 patients. *Im J-G, Yeon KM, Han MC, et al.*
- 961 Pulmonary lymphangiomyomatosis: high-resolution CT findings in four cases. *Rappaport DC, Weisbrod GL, Herman SJ, Chamberlain DW*
- 965 Case report. Rounded atelectasis of the lung: MR appearance. *Verschakelen JA, Demaerel P, Coolen J, Demedts M, Marchal G, Baert AL*

BREAST RADIOLOGY

- 967 Sedimented calcium in benign breast cysts: the full spectrum of mammographic presentations. *Linden SS, Sickles EA*

GASTROINTESTINAL RADIOLOGY

- 973 CT of primary lymphoma of the liver. *Sanders LM, Botet JF, Straus DJ, Ryan J, Filippa DA, Newhouse JH*
- 977 Distinction between hemangioma of the liver and hepatocellular carcinoma: value of labeled RBC-SPECT scanning. *Kudo M, Ikekubo K, Yamamoto K, et al.*
- 985 Case report. Hepatic perfusion in cavernous transformation of the portal vein: evaluation by using CT angiography. *Nakao N, Miura K, Takahashi H, et al.*
- 987 Is routine chest radiography required with biliary lithotripsy? *Malone DE, Becker CD, Müller NL, Burhenne HJ*
- 991 Pneumatosis intestinalis in bone-marrow transplantation patients: diagnosis on routine chest radiographs. *Bates FT, Gurney JW, Goodman LR, Santamaria JJ, Hansen RM, Ash RC*
- 995 Pictorial essay. Primary tumors of the small intestine: CT evaluation. *Dudiak KM, Johnson CD, Stephens DH*
- 999 Diagnosis of fistulae and sinus tracts in patients with Crohn disease: value of MR imaging. *Koelbel G, Schmiedl U, Majer MC, et al.*

ONCOLOGIC RADIOLOGY

- 1005 CT of adrenal tumors: frequency and clinical significance of low-attenuation lesions. *Miyake H, Maeda H, Tashiro M, et al.*
- 1009 Subcutaneous metastases from malignant melanoma: prevalence and findings on CT. *Patten RM, Shuman WP, Teefey S*

MUSCULOSKELETAL RADIOLOGY

- 1013 Pictorial essay. MR imaging of the finger: correlation with normal anatomic sections. *Erickson SJ, Kneeland JB, Middleton WD, et al.*

- 1021 Detection of osteomyelitis at fracture nonunion sites: comparison of two scintigraphic methods. *Seabold JE, Nepola JV, Conrad GR, et al.*

PEDIATRIC RADIOLOGY

- 1029 MR imaging determination of the location of the normal conus medullaris throughout childhood. *Wilson DA, Prince JR*
- 1033 Review. Imaging of infants and children with AIDS. *Haney PJ, Yale-Loehr AJ, Nussbaum AR, Gellad FE*
- 1043 Blunt renal and ureteral trauma in childhood: CT patterns of fluid collections. *Siegel MJ, Balfe DM*
- 1049 Closed spinal dysraphism: analysis of clinical, radiological, and surgical findings in 104 consecutive patients. *Scatliff JH, Kendall BE, Kingsley DPE, Britton J, Grant DN, Hayward RD*
- 1059 Absolute intracranial blood-flow velocities evaluated by duplex Doppler sonography in asymptomatic preterm and term neonates. *Horgan JG, Rumack CM, Hay T, Manco-Johnson ML, Merenstein GB, Esola C*
- 1065 Color Doppler imaging of intracranial vessels in the neonate. *Wong WS, Tsuruda JS, Liberman RL, Chirino A, Vogt JF, Gangitano E*
- 1071 Case report. Hypermagnesemia: a cause of abnormal metaphyses in the neonate. *Cumming WA, Thomas VJ*

NEURORADIOLOGY

- 1073 MR imaging of brain abscesses. *Haimes AB, Zimmerman RD, Morgello S, et al.*
- 1087 Gd-DTPA-enhanced MR imaging of spinal tumors. *Parizel PM, Balériaux D, Rodesch G, et al.*

VASCULAR RADIOLOGY

- 1097 Pulsed-spray pharmacomechanical thrombolysis: preliminary clinical results. *Bookstein JJ, Fellmeth B, Roberts A, Valji K, Davis G, Machado T*
- 1101 Color-flow Doppler and conventional duplex scanning of the carotid bifurcation: prospective, double-blind, correlative study. *Hallam MJ, Reid JM, Cooperberg PL*
- 1107 Case report. Aorto-left renal vein fistula: diagnosis by duplex sonography. *Mansour MA, Russ PD, Subber SW, Pearce WH*

DIGITAL RADIOLOGY

- 1109 A report-coding system for integration into a digital radiology department. *Bramble JM, Chang CHJ, Martin NL*
- 1113 Comparison of 2048-line digital display formats and conventional radiographs: an ROC study. *Hayrapetian A, Aberle DR, Huang HK, et al.*

DEPARTMENT MANAGEMENT

- 1119 Perspective. Strategies for resolving interpersonal conflicts in radiology. *Virapongse C*

TECHNICAL NOTE

- 1123 Percutaneous procedures guided by color-flow Doppler sonography. *McNamara MP Jr*

OTHER CONTENT

- Book reviews 924, 932, 950, 960, 972, 984, 990, 1004, 1008, 1020, 1028, 1042, 1058, 1106
- 1086 Memorial, Robert S. Sherman, Jr
- 1126 Forthcoming articles
- 1127 Letters
- 1133 Review of current literature
- 1138 News
- 1141 American Roentgen Ray Society information
- 1142 Classified advertisements
- A3 Guidelines for authors
- A8 AJR business and subscriber information

Acc 13.11.90

AJR

American
Journal of
Roentgenology

June 1989

PercuCut™ Cut-Biopsy Needles from E-Z-EM provide reliable results in virtually all soft-tissue biopsies. Patented, specially designed "keyhole" cutting-edges on the cannula tip precisely core tissue samples. Ultra-thin-wall tubing maximizes sample size while minimizing needle gauge and patient trauma.

Three PercuCut needle designs allow the physician complete flexibility in obtaining a biopsy sample.

Cut-Biopsy Needle—a keyhole cutting-edge cannula with stylet. Includes a unique syringe which creates and maintains negative pressure during the biopsy procedure.

Coaxial Sheath Cut-Biopsy Needle—a three-part sheath/cannula/stylet design for multiple samples through a single puncture. Our unique aspirating syringe system is also included.

Self-Aspirating Cut-Biopsy Needle—a biopsy needle that combines our keyhole-cutting technology with a specially designed self-aspirating diaphragm hub which permits one-hand operation without a syringe.

PercuCut Needles have proven their ability to provide excellent, reliable histological and cytological samples in virtually all soft-tissue biopsies. All use a straight-tracking trocar pointed stylet for precise placement, and are available in gauges and lengths to suit any application.

For additional information on all of the PercuCut products, contact your local representative, or call E-Z-EM toll-free at 1-800-544-4624. In New York call 516-333-8230.

E-Z-EM
More than barium—much more



E-Z-EM, Inc.
7 Portland Avenue
Westbury, N.Y. 11590

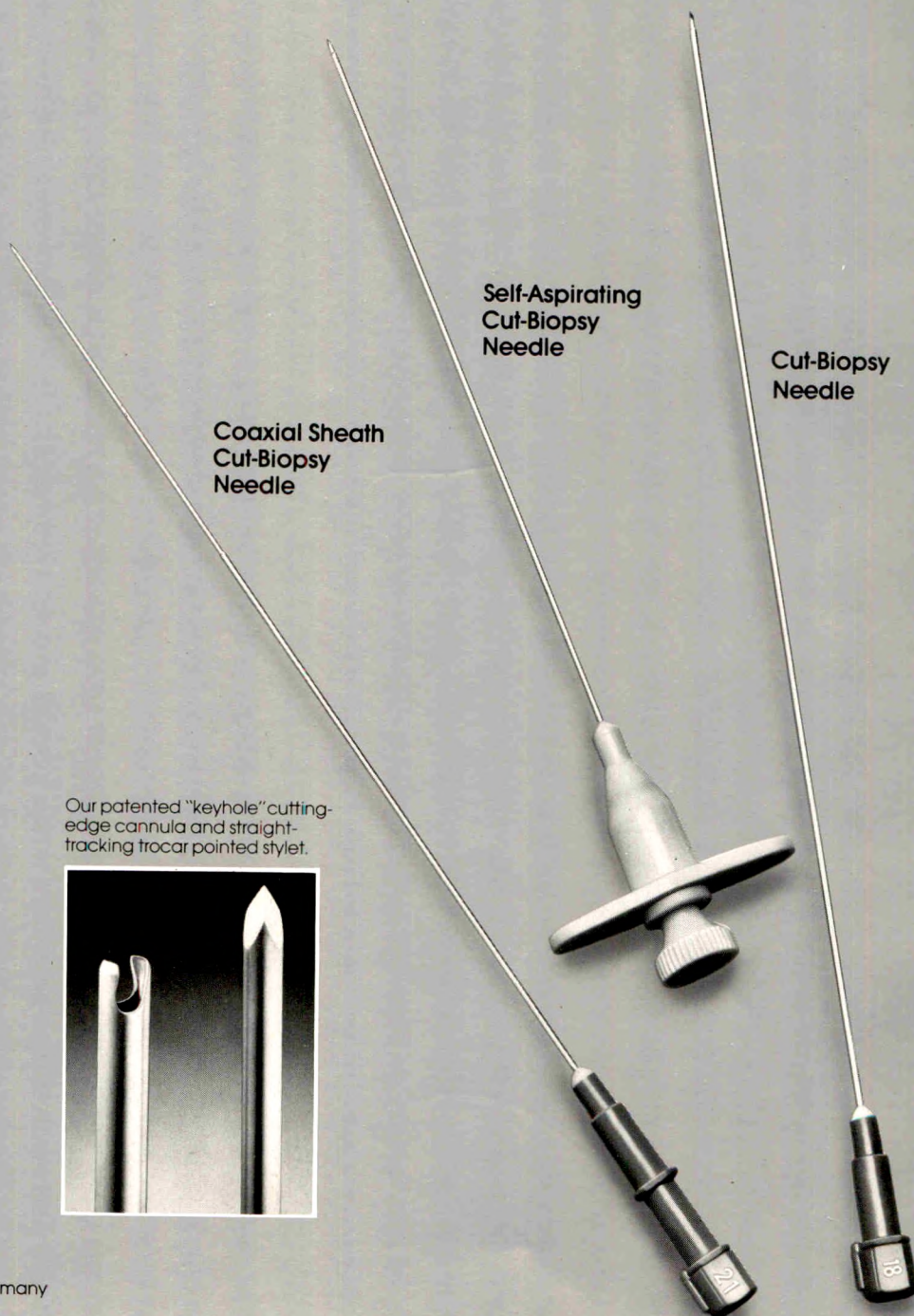
CIRCLE 5 ON READER SERVICE CARD

© 1987 E-Z-EM, Inc.

Manufactured for E-Z-EM by Angiomed®, West Germany

Reliable histological
and cytological
fine needle
aspiration biopsies
...from E-Z-EM

PercuCut™

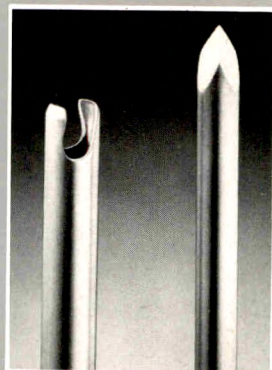


Coaxial Sheath
Cut-Biopsy
Needle

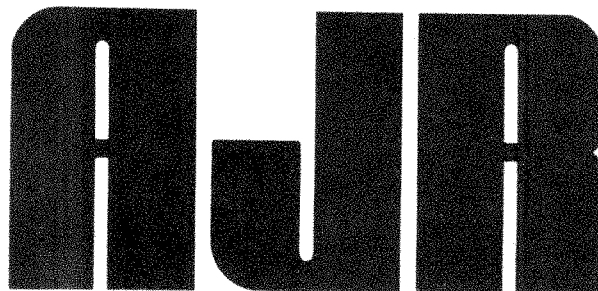
Self-Aspirating
Cut-Biopsy
Needle

Cut-Biopsy
Needle

Our patented "keyhole" cutting-edge cannula and straight-tracking trocar pointed stylet.



Official Journal of the American Roentgen Ray Society



American Journal of Roentgenology
Diagnostic Imaging and Related Sciences

- Editor-In-Chief** Robert N. Berk, *La Jolla, California*
University of California, San Diego
School of Medicine and Medical Center
- Editor Emeritus** Melvin M. Figley, *Seattle, Washington*
- Associate Editor** Saskia von Waldenburg Hilton, *San Diego, California*
- Consulting Editor** Juan M. Taveras, *Boston, Massachusetts*
- Statistician** Charles C. Berry, *San Diego, California*

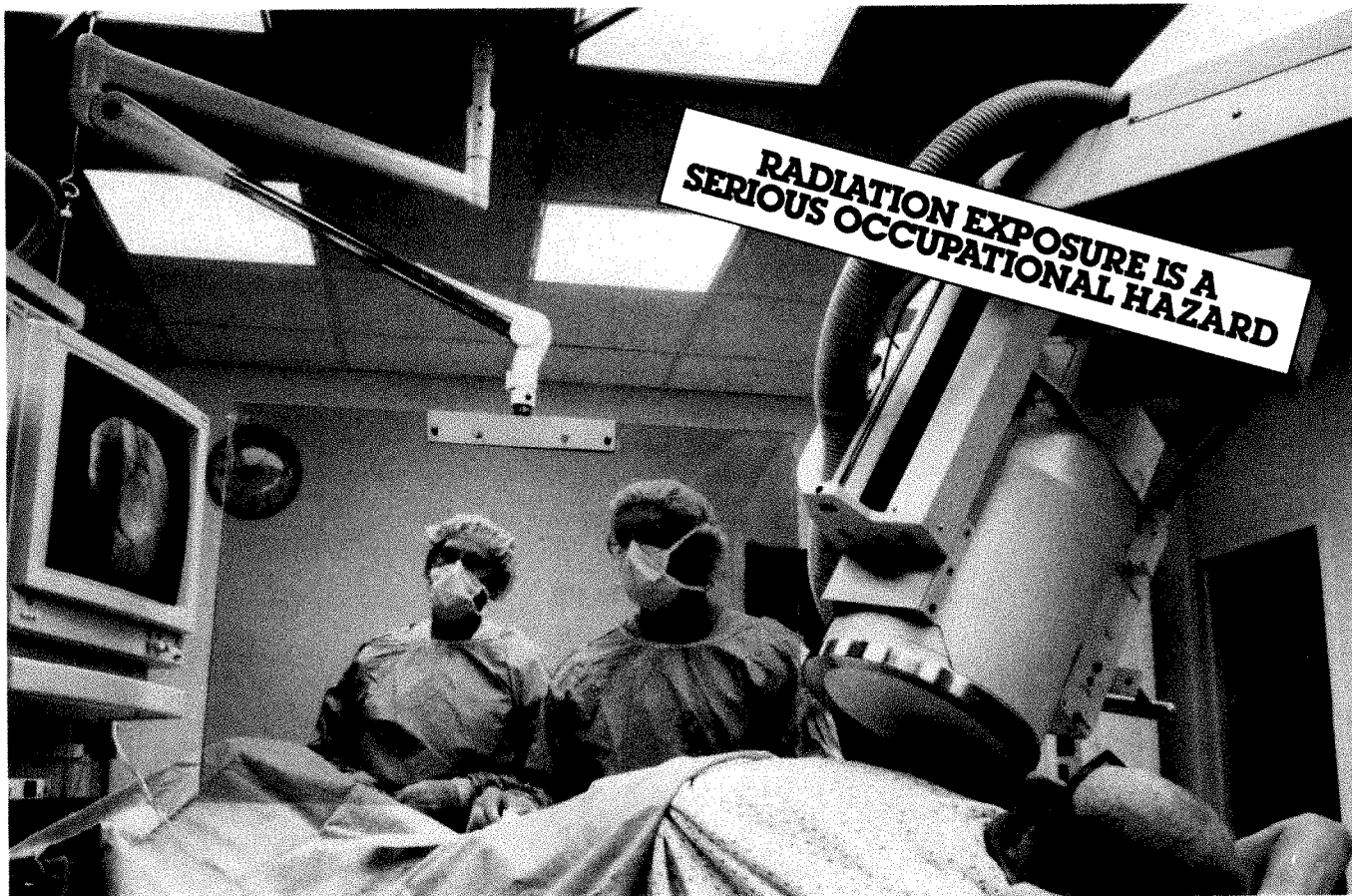
Editorial Board

- | | | |
|-------------------------|--------------------------|--------------------|
| John R. Amberg | William R. Hendee | Peter M. Ronai |
| Itamar Aviad | John R. Hesselink | Sjef H. J. Ruijs |
| Lawrence W. Bassett | Charles B. Higgins | Carol M. Rumack |
| Gregory P. Borkowski | Melvyn T. Korobkin | Stuart S. Sagel |
| William G. Bradley, Jr. | Thomas L. Lawson | David J. Sartoris |
| Peter L. Cooperberg | Bruce L. McClennan | Stefan C. Schatzki |
| N. Reed Dunnick | Albert A. Moss | Edward A. Sickles |
| David K. Edwards | Jeffrey H. Newhouse | Barry A. Siegel |
| Ronald G. Evens | Donald L. Resnick | David D. Stark |
| David S. Feigin | Stewart R. Reuter | Edward T. Stewart |
| Paul J. Friedman | Charles A. Rohrmann, Jr. | Eric vanSonnenberg |

Editorial Staff: Margaret Levene, *managing editor*; Katie L. Spiller, Barbara Rose, Barbara L. Halliburton, and Janine Anderson, *manuscript editors*; Nancy Rydbeck, *office manager*; Sheri Smith, *administrative assistant*; Sandra L. Griffin, *administrative secretary*.

AJR, AMERICAN JOURNAL OF ROENTGENOLOGY (ISSN 0361 803X) is the official journal of the American Roentgen Ray Society and is published monthly by Williams & Wilkins, 428 E. Preston St., Baltimore, MD 21202. Annual dues include \$50 for journal subscription. Second-class postage paid at Baltimore, MD, and at additional mailing offices. Postmaster, send address changes (Form 3579) to AJR, 428 E. Preston St., Baltimore, MD 21202. Subscription rates \$100 (\$145 foreign); institutions \$110 (\$155 foreign); in training \$25 (\$70 foreign); single copy \$16 (\$19 foreign). Japanese rates include airfreight. Japanese yen price is available from our sole agent USACO Corporation, 13-12, Shimbashi 1-Chome, Minato-Ku, Tokyo 105, Japan, telephone 03-502-6471. Airmail rates furnished on request. Indexed by *Current Contents* and *Index Medicus*. Copyright © 1989 by American Roentgen Ray Society.

0361-803X/89\$2.00



Cardiac Cath and Special Procedures Personnel...

NOW YOU CAN GET GREATER RADIATION PROTECTION WITH CLEAR-Pb® Fixed-Mount Overhead X-Ray Barriers

*In 4 panoramic shield sizes...18" x 24" to 36" x 24"..
at budget-pleasing prices.*

- **Unsurpassed radiation protection;** shatter-resistant, transparent lead-plastic (0.5mm lead equivalency).
- **Bigger shielding area and panoramic visibility;** no need to reposition the barrier during procedure; protects two people, if required.
- **Easy-to-use, adjustable, spring-loaded fixed ceiling mounted suspension system;** pull down to use, push up and out of the way at the end of the procedure.

Existing lead-glass overhead barriers (usually 16" x 12" or 20" x 16") are so small that when you move, you must also move the barrier to avoid exposure. Now, depending on your needs and budget, you can select from 4 CLEAR-Pb Overhead Barriers with panoramic shield sizes from 18" x 24" to 36" x 24", and get greater protection from scatter radiation.

For complete details, request Bulletin 423-44

CIRCLE 16 ON READER SERVICE CARD

NUCLEAR ASSOCIATES



A Division of VICTOREEN, INC.
100 VOICE ROAD
CARLE PLACE, NY 11514-1593 U.S.A.
(516) 741-6360
FAX (516) 741-5414

® Victoreen, Inc.

AJR Guidelines for Authors

Address new and revised manuscripts, correspondence, and classified ads to the Editor:

AJR Editorial Office

2223 Avenida de la Playa, Suite 200

La Jolla, CA 92037-3218

Telephone: (619) 459-2229; FAX: (619) 459-8814

Inquiries regarding subscriptions, display advertising, reprints, or permission to republish AJR material should be addressed to the publisher:

The Williams & Wilkins Co.

428 E. Preston St.

Baltimore, MD 21202 Telephone: (301) 528-4133

The AJR publishes original contributions to the advancement of medical diagnosis and treatment. Submitted manuscripts should not contain previously published material and should not be under consideration for publication elsewhere. Papers dealing with neuroradiology should be addressed to: American Journal of Neuroradiology, Dept. of Radiology, Massachusetts General Hospital, Boston, MA 02114. At the discretion of the AJR Editor, AJNR articles that are of interest to the general reader may be republished in the AJR. Neuro-radiologic papers sent to the AJR will be forwarded to the Editorial Office of the AJNR.

Manuscript decisions are based on peer review. Reviewers receive manuscripts without title pages to ensure an unbiased review. Statements made in the article, including changes made by the Editor or manuscript editor, are the responsibility of the author and not of the AJR or its publisher. Authors will be sent the edited manuscript, galley proof, and proofs of illustrations. If the corresponding author will be unavailable to review galleys, arrangements should be made for a coauthor or colleague to read and return the proof.

The following guidelines are based on instructions set forth in the **Uniform Requirements for Manuscripts Submitted to Biomedical Journals** (*Ann Intern Med* 1988;108:258-265). Articles will be edited, however, to conform to the individual style of AJR.

General Guidelines for Major Papers

Abstract. Clearly state (in 200 words or less) the purpose, methods, results, and conclusions of the study. Include actual data.

Introduction. Briefly describe the purpose of the investigation, including relevant background information.

Methods. Describe the research plan, the materials (or subjects), and the methods used, in that order. Explain in detail how disease was confirmed and how subjectivity in observations was controlled.

Results. Present results in a clear, logical sequence. If tables are used, do not duplicate tabular data in text, but do describe important trends and points.

Discussion. Describe the limitations of the research plan, materials (or subjects), and methods, considering both the

purpose and the outcome of the study. When results differ from those of previous investigators, explain the discrepancy.

AUTHOR'S CHECKLIST

For priority handling, complete the following checklist, sign the copyright form on the reverse side of this page, and include both with the manuscript.

_____ Two copies of the manuscript (the original and a photocopy) and two complete sets of figures are submitted. One copy has been retained by the author.

_____ If appropriate, AJR Guidelines for case reports, technical notes, pictorial essays, or letters to the Editor have been followed. (See page A5.)

_____ The manuscript, including references, figure legends, and tables, is typed double-spaced on 8½ × 11 in. (21.6 × 27.9 cm) *nonerasable* paper. Right-hand margins are not justified.

_____ All manuscript pages are numbered consecutively beginning with the abstract. Authors' names do not appear on the manuscript pages.

_____ The manuscript is organized as follows: title page, blind title page (title only), abstract, introduction, methods, results, discussion, acknowledgments, references, tables, figure legends, and figures.

_____ Informed consent has been obtained from patients who participated in clinical investigations. If experiments were performed on animals, authors complied with NIH guidelines for use of laboratory animals.

_____ Use of unfamiliar acronyms and abbreviations is kept to a minimum. When abbreviations are used they are defined at first mention, followed by the abbreviation in parentheses.

_____ Metric measurements are used throughout, or the metric equivalent is given in parentheses.

_____ Names and locations (city and state only) of manufacturers are given for equipment and nongeneric drugs.

Title Page

_____ The following information is given: title of article; names and complete addresses (including zip code) of all authors; current addresses of authors who have moved since study; acknowledgment of grant or other assistance. The corresponding author is clearly identified, and a current address, phone number, and Fax number are given.

_____ Two copies of a blind title page are included giving only the title (without the authors' names) for use in the review process.

Abstract

_____ An abstract of approximately 200 words concisely states the purpose, methods, and results of the study in one paragraph. Actual data are included. Conclusions are stated in a second, summary paragraph.

_____ No abbreviations or reference citations are used.

References

References (not to exceed 35) are typed double-spaced starting on a separate page and are **numbered consecutively in the order in which they appear in the text**.

All references are cited in the text and are enclosed in brackets and typed on line with the text (not superscript).

Unpublished data are not cited in the reference list, but are cited parenthetically in the text, for example, (Smith DJ, personal communication), (Smith DJ, unpublished data). This includes papers submitted, but not yet accepted, for publication.

Inclusive page numbers (e.g., 333–335) are given for all references.

Journal names are abbreviated according to *Index Medicus*.

Style and punctuation of references follow the format illustrated in the following examples (all authors are listed when six or less; when seven or more authors, the first three are listed, followed by "et al."):

Journal article

1. Long RS, Roe EW, Wu EU, et al. Membrane oxygenation: radiographic appearance. *AJR* 1986;146:1257–1260

Book

2. Smith LW, Cohen AR. *Pathology of tumors*, 6th ed. Baltimore: Williams & Wilkins, 1977:100–109

Chapter in a book

3. Breon AJ. Serum monitors of bone metastasis. In: Clark SA, ed. *Bone metastases*. Baltimore: Williams & Wilkins, 1983:165–180

Paper presented at a meeting

4. Lau FS, Kirk AN. MR imaging of the spine. Presented at the annual meeting of the American Roentgen Ray Society, Washington, DC, April 1986

Tables

Each table is typed double-spaced on a separate page without vertical or horizontal rules; each has a short, descriptive title. Tables do not exceed two pages in length and contain at least four lines of data.

Tables are numbered in the order in which they are cited in the text.

Abbreviations are defined in an explanatory note below each table.

Tables are self-explanatory and do not duplicate data given in the text or figures.

All arithmetic (percentages, totals, differences) has been double checked for accuracy, and tabular data agree with data given in the text.

Figures and Legends

Two complete sets of original figures are submitted unmounted in labeled envelopes.

Figures are clean, unscratched, 5 × 7 in. (13 × 18 cm) glossy prints with **white borders**. A separate print is submitted for each figure *part*.

All figure parts relating to one patient have the same figure number.

Each figure is labeled on the back with the figure number and an arrow indicating "top." For black-and-white figures, labeling is done on a gummed label, which is then affixed to the back of the print. *Never* use labels on color figures, but write figure number on the back lightly in pencil. *Never* use ink on front or back of any figures.

Author's names are *not* written on the backs of figures.

Only removable (rub-on) arrows and letters are used on the figures. Symbols are uniform in size and style and are not broken or cracked.

Images are uniform in size and magnification.

Line drawings are done in black ink on a white background. They are professional in quality, and all use the same size type. (Only glossy prints are acceptable.)

Written permission has been obtained for use of all previously published illustrations (and copies of permission letters are included), and an appropriate credit line is given in the legends.

Legends are typed double-spaced, and figure numbers correspond with the order in which the figures are cited in the text.

Transfer of Copyright Agreement, Conflict of Interest Acknowledgment, Certification of Coauthors, and Exclusive Publication Statement

Complete copyright to the article entitled: _____

is hereby transferred to the American Roentgen Ray Society (for United States government employees to the extent transferable), effective if and when the article is accepted for publication in the *American Journal of Roentgenology*. In the case of the authors who are officers or employees of the United States government, the American Roentgen Ray Society recognizes that works prepared by officers or employees of the United States government as part of their official government duties are in the public domain.

Authors reserve all proprietary rights other than copyright, such as patent rights and the right to use all or part of this article in future works of their own. The authors retain the right of replication, subject only to crediting the original source of publication and receiving written permission from the publisher.

Authors guarantee that this manuscript contains no matter that is libelous or otherwise unlawful, invades individual privacy, or infringes any proprietary rights.

Authors understand that they will receive no royalty or other compensation from the American Roentgen Ray Society or the publisher.

Authors guarantee that the editor has been or will be informed of any proprietary or commercial interest or conflicts of interest the authors may have that relate directly or indirectly to the subject of this article.

All authors certify that they have made substantive and specific intellectual contributions to the article and assume public responsibility for its content.

Finally, the authors certify that none of the material in this manuscript has been published previously or is currently under consideration for publication elsewhere.

First author/date

Second author

Third author

Fourth author

Fifth author

Sixth author

This agreement must be signed by all authors in order for the manuscript to be published.

Case Reports

A case report is a brief description of a special case that provides a message that transcends the individual patient.

Format. There is no abstract. The introduction should be a short paragraph giving the general background and the specific interest of the case. No more than one case should be described in detail (similar ones can be mentioned briefly in the discussion). Emphasis should be on the radiologic aspects; clinical information must be limited to that necessary to provide a background for the radiology. The discussion should be succinct and should focus on the specific message and relevance of radiologic methods. A review of the literature is not appropriate.

Length. Maximum of five double-spaced, typewritten pages, including the references but not the title page or figure legends.

References. Maximum of eight.

Figures. Maximum of three or four, unless the text is shortened accordingly. Legends must not repeat the text.

Tables and Acknowledgments. Not appropriate in case reports.

Technical Notes

A technical note is a brief description of a specific technique or procedure, modification of a technique, or equipment of interest to radiologists.

Format. No abstract, headings, or subheadings are required. If headings are used, they should be a combination of "Case Report," "Materials and Methods," "Results," and "Discussion." A brief one-paragraph introduction should be included to give the general background. Discussion should be limited to the specific message, including the uses of the technique or equipment. Literature reviews and lengthy case reports are not appropriate.

Length. Maximum of five double-spaced, typewritten pages, including the references but not the title page or figure legends.

References. Maximum of eight.

Figures. Maximum of two, unless the text is shortened accordingly.

Tables and Acknowledgments. Not appropriate in technical notes.

Pictorial Essays

A pictorial essay is an article that conveys its message through illustrations and their legends. Unlike other *AJR* articles, which are based on original research, pictorial essays serve primarily as teaching tools, like exhibits at a scientific meeting. They are not encyclopedic book chapters. No abstract is necessary.

Length. Maximum of four double-spaced, typewritten pages, including the references but not the title page or figure legends.

References. Maximum of four.

Figures. Maximum of 30 figure parts. Number should be as few as necessary to convey the message of the paper.

Tables and Acknowledgments. Not appropriate in pictorial essays.

Letters to the Editor and Replies

Letters to the Editor and Replies should offer objective and constructive criticism of published articles. Letters may also discuss matters of general interest to radiologists. Do not end a letter with a hand-written signature.

Format. All letters should be typed double-spaced on nonletterhead paper, with no greeting or salutation. Name and affiliation should appear at the end of the letter. Titles for letters should be short and pertinent. The title for a reply is simply "Reply."

Length. Maximum of two double-spaced, typewritten pages, including references.

References. Maximum of four.

Figures. Maximum of two.

Tables and Acknowledgments. Not appropriate in Letters to the Editor and Replies.

Opinions, Commentaries, and Perspectives

Opinions, commentaries, and perspectives are special articles dealing with controversial topics or issues of special concern to radiologists.

Format. Include a title page but no abstract. Headings may be used to break up the text.

Length. Maximum of five double-spaced, typewritten pages.

References. Maximum of five.

Tables and Figures. Maximum of four.

Computer Page Articles

Articles published on the computer page deal with practical computer applications to radiology.


Format. Include a title page but no abstract.

Length. Maximum of eight double-spaced, typewritten pages.

References. Maximum of five.

Figures and Tables. Maximum of five. Computer printouts are not acceptable. Figures must be submitted as 5 × 7 in. glossy prints.

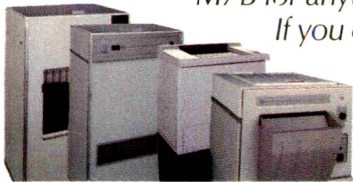
**WHERE
TO FIND
RELIABLE
PROCESSORS
BY
KODAK**

A decorative horizontal bar consisting of a thick grey line with a thin yellow line running parallel just below it, positioned behind the word KODAK.



Kodak processors set the standards for reliability and dependability—and support—in departments of every size in medical facilities everywhere.

Kodak developed the roller transport film processor, and the rest of the world has been playing catch-up ever since. Kodak X-Omat processors are known for reliability, dependability, and consistency. And for support: Kodak representatives and service people stand behind every one. The line now includes the M35A for the smallest operations. Plus the M8 and M6B for the largest, and the M7B for anything in between.



If you don't yet have the speed and consistency of automation, or if you don't have the reliability and backup of Kodak, talk to your Kodak representative.

The new vision of Kodak



AJR Business and Subscriber Information

The American Roentgen Ray Society

AJR, *American Journal of Roentgenology*, is published monthly to disseminate research on current developments in the radiologic sciences and commentary on topics related to radiology. It is published by the American Roentgen Ray Society, 1891 Preston White Dr., Reston, VA 22091; (703) 648-8992. Inquiries regarding society business, the annual ARRS meeting, and membership should be addressed to the Society at the above address.

Correspondence Concerning the *AJR*

Correspondence regarding display (not classified) advertising, subscriptions, address changes, reprints, and permission requests should be addressed to Williams & Wilkins, 428 E. Preston St., Baltimore, MD 21202; (301) 528-4000.

Correspondence regarding editorial matters and classified advertising should be addressed to Editorial Office, *AJR*, 2223 Avenida de la Playa, Ste. 200, La Jolla, CA 92037-3218; telephone (619) 459-2229; FAX (619) 459-8814. For information on manuscript submission, see Guidelines for Authors, pages A3-A5.

Subscriber Information

Subscription requests and inquiries should be sent to Williams & Wilkins, 428 E. Preston St., Baltimore, MD 21202. ARRS annual dues include \$50 for journal subscription. Subscription rates are as follows: nonmembers, \$100/year (\$135 foreign); institutions, \$110 (\$145 foreign); nonmember in-training, \$25 (\$50 foreign). Single copies of the Journal may

be purchased for \$16 (\$19 foreign). Airmail rates will be furnished on request.

Japanese rates include airfreight. Japanese yen price is available from our sole agent, USACO Corporation, 13-12, Shimbashi 1-Chome, Minato-Ku, Tokyo 105, Japan; telephone 03-502-6471.

If a subscriber receives a damaged copy of the *AJR* or fails to receive an issue, the subscriber should notify Williams & Wilkins (428 E. Preston St., Baltimore, MD 21202) within 60 days of publication (90 days for foreign subscribers) and that issue will be replaced.

Change of address information should be sent to Williams & Wilkins, 428 E. Preston St., Baltimore, MD 21202. Allow 90 days for address changes.

Copyrights, Permissions, and Reprints

The American Roentgen Ray Society holds the copyright for all material published in the *AJR*. No part of this publication may be reproduced without permission from the ARRS. Requests for such permission should be addressed to Williams & Wilkins, 428 E. Preston St., Baltimore, MD 21202.

For reprints of a particular article, please contact the author designated in the footnotes for that article.

Indexes

The *AJR* provides volume and yearly indexes (subject and author) in the June and December issues each year. *AJR* articles are also indexed in *Current Contents*, *Index Medicus*, and the cumulative index published by *Radiology*.

F R O M M A L L I N C K R O D T

Introducing
new nonionic
OPTIRAY[®]
(ioversol)

F R O M M A L

NEW NONIONIC OPTIRAY® (ioversol)

Providing confidence in imaging procedures

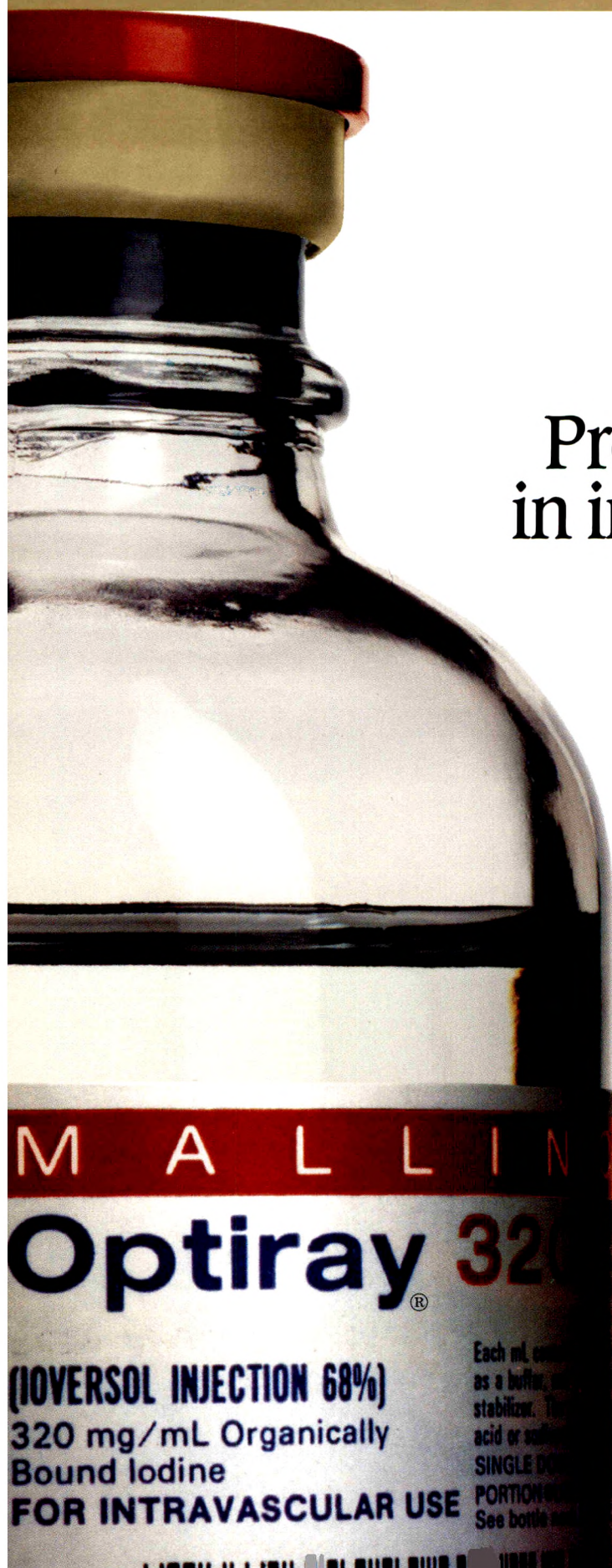
Confidence from patient comfort and safety profile

In clinical trials, individual drug-related adverse reactions were less than 1% for OPTIRAY.

Incidence of drug-related adverse reactions (n = 1,186)*

ALLERGIC:	Urticaria	0.2%
	Sneezing	0.3%
	Periorbital edema	0.1%
	Pruritus	0.1%
CARDIOVASCULAR:	Angina	0.2%
	Bradycardia	0.1%
CNS:	Headache	0.5%
	Blurred vision	0.2%
	Disorientation	0.2%
	Lightheadedness	0.3%
	Vertigo	0.1%
	Vasovagal reaction	0.1%
GASTROINTESTINAL:	Nausea	0.8%
	Vomiting	0.3%
RESPIRATORY:	Coughing	0.1%
	Nasal congestion	0.3%
	Hypoxia	0.1%
MISCELLANEOUS:	Shaking, chills	0.3%
	Bad taste	0.1%

*Data on file, Mallinckrodt Medical, Inc.



Versatile iodine concentrations

Osmolality and Viscosity of Nonionic Contrast Agents			
	Concentration (mg Iodine/mL)	Osmolality (mOsm/kg H ₂ O)	Viscosity at 37°C (CPS)
Iopamidol*	370	796	9.4
Iohexol†	350	844	10.4
OPTIRAY 320§ (ioversol)	320	702	5.8
Iohexol	300	672	6.3
Iopamidol	300	616	4.7
Iohexol	240	520	3.4
OPTIRAY 240 (ioversol)	240	502	3.0
Iopamidol	200	413	2.0
Iohexol	180	408	2.0
OPTIRAY 160 (ioversol)	160	355	1.9
Iopamidol	128	290	1.4

*Marketed by Squibb Diagnostics under license from Bracco Industria Chimica, S.p.A., Italy.

†Marketed by Winthrop Pharmaceuticals under license from Nycomed AS, Norway.

§Marketed by Mallinckrodt Medical, Inc. Developed and manufactured by Mallinckrodt Medical, Inc. in the U.S.A.

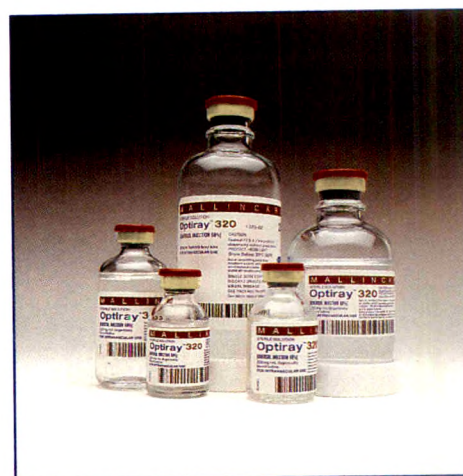
Indications for OPTIRAY

Optiray is indicated for the following imaging procedures:

- Venography
- Intravenous urography
- Head CT
- Body CT
- Cerebral arteriography
- Aortography, visceral and renal arteriography
- Intra-arterial digital subtraction angiography
- Peripheral arteriography
- Selective coronary arteriography, with or without left ventriculography

Wide variety of sizes

Concentration	Vial/Bottle Sizes
OPTIRAY 320	20 mL, 30 mL, 50 mL vials 100 mL, 150 mL, 200 mL bottles
OPTIRAY 240	50 mL vial 100 mL, 200 mL bottles
OPTIRAY 160	50 mL vial 100 mL bottle



Changing the look of medicine.

Mallinckrodt Medical, Inc.
An operating unit of Mallinckrodt, Inc.
Post Office Box 5840
St. Louis, MO 63134

For orders,
medical and/or
professional assistance
call
(800) 325-3688 TOLL FREE

Please see the following page for brief summary of prescribing information.

OPTIRAY® 160 240 320 (Ioversol Injection)

DESCRIPTION: Each milliliter of OPTIRAY 160 (ioversol injection 34%) provides 339 mg of ioversol with 3.6 mg of tromethamine as a buffer and 0.2 mg of edetate calcium disodium as a stabilizer. OPTIRAY 160 provides 16% (160 mg/mL) organically bound iodine.

Each milliliter of OPTIRAY 240 (ioversol injection 51%) provides 509 mg of ioversol with 3.6 mg of tromethamine as a buffer and 0.2 mg of edetate calcium disodium as a stabilizer. OPTIRAY 240 provides 24% (240 mg/mL) organically bound iodine.

Each milliliter of OPTIRAY 320 (ioversol injection 68%) provides 678 mg of ioversol with 3.6 mg of tromethamine as a buffer and 0.2 mg of edetate calcium disodium as a stabilizer. OPTIRAY 320 provides 32% (320 mg/mL) organically bound iodine.

CONTRAINDICATIONS: None.

WARNINGS: Nonionic iodinated contrast media inhibit blood coagulation, in vitro, less than ionic contrast media. Clotting has been reported when blood remains in contact with syringes containing nonionic contrast media.

Serious, rarely fatal, thromboembolic events causing myocardial infarction and stroke have been reported during angiographic procedures with both ionic and nonionic contrast media. Therefore, meticulous intravascular administration technique is necessary, particularly during angiographic procedures, to minimize thromboembolic events. Numerous factors, including length of procedure, catheter and syringe material, underlying disease state and concomitant medications may contribute to the development of thromboembolic events. For these reasons, meticulous angiographic techniques are recommended including close attention to guidewire and catheter manipulation, use of manifold systems and/or three-way stopcocks, frequent catheter flushing with heparinized saline solutions and minimizing the length of the procedure. The use of plastic syringes in place of glass syringes has been reported to decrease but not eliminate the likelihood of in vitro clotting.

Serious or fatal reactions have been associated with the administration of iodine-containing radiopaque media. It is of utmost importance to be completely prepared to treat any contrast medium reaction.

As with any contrast medium, serious neurologic sequelae, including permanent paralysis, can occur following cerebral arteriography, selective spinal arteriography and arteriography of vessels supplying the spinal cord. A cause-effect relationship to the contrast medium has not been established since the patients' pre-existing condition and procedural technique are causative factors in themselves. The arterial injection of a contrast medium should never be made following the administration of vasopressors since they strongly potentiate neurologic effects.

Caution must be exercised in patients with severely impaired renal function, combined renal and hepatic disease, severe thyrotoxicosis, myelomatosis, or anuria, particularly when large doses are administered.

Intravascularly administered iodine-containing radiopaque media are potentially hazardous in patients with multiple myeloma or other paraproteinemia, particularly in those with therapeutically resistant anuria. Myeloma occurs most commonly in persons over age 40. Although neither the contrast agent nor dehydration has been proved separately to be the cause of anuria in myelomatous patients, it has been speculated that the combination of both may be causative. The risk in myelomatous patients is not a contraindication to the procedure; however, special precautions, including maintenance of normal hydration and close monitoring, are required. Partial dehydration in the preparation of these patients prior to injection is not recommended since this may predispose the patient to precipitation of the myeloma protein.

Administration of radiopaque materials to patients known or suspected of having pheochromocytoma should be performed with extreme caution. If, in the opinion of the physician, the possible benefits of such procedures outweigh the considered risks, the procedures may be performed; however, the amount of radiopaque medium injected should be kept to an absolute minimum. The blood pressure should be assessed throughout the procedure, and measures for treatment of a hypertensive crisis should be available.

Contrast media may promote sickling in individuals who are homozygous for sickle cell disease when administered intravascularly.

Risks of thyroid storm following the intravascular use of iodinated radiopaque agents in patients with hyperthyroidism or with an autonomously functioning thyroid nodule, suggest that this additional risk be evaluated in such patients before use of any contrast medium.

PRECAUTIONS: General: Diagnostic procedures which involve the use of iodinated intravascular contrast agents should be carried out under the direction of personnel skilled and experienced in the particular procedure to be performed. A fully equipped emergency cart, or equivalent supplies and equipment, and personnel competent in recognizing and treating adverse reactions of all types should always be available. Since severe delayed reactions have been known to occur, emergency facilities and competent personnel should be available for at least 30 to 60 minutes after administration.

Preparatory dehydration is dangerous and may contribute to acute renal failure in patients with advanced vascular disease, diabetic patients, and in susceptible non-diabetic patients (often elderly with pre-existing renal disease). Patients should be well hydrated prior to and following the administration of OPTIRAY.

The possibility of a reaction, including serious, life-threatening, fatal, anaphylactoid or cardiovascular reactions, should always be considered (See ADVERSE REACTIONS). Increased risk is associated with a history of previous reaction to a contrast medium, a known sensitivity to iodine and known allergies (i.e., bronchial asthma, hay fever and food allergies) or hypersensitivities.

The occurrence of severe idiosyncratic reactions has prompted the use of several pretesting methods. However, pretesting cannot be relied upon to predict severe reactions and may itself be hazardous to the patient. It is suggested that a thorough medical history with emphasis on allergy and hypersensitivity, prior to the injection of any contrast medium, may be more accurate than pretesting in predicting potential adverse reactions. A positive history of allergies or hypersensitivity does not arbitrarily contraindicate the use of a contrast agent when a diagnostic procedure is thought essential, but caution should be exercised. Premedication with antihistamines or corticosteroids to avoid or minimize possible allergic reactions in such patients should be considered. Reports indicate that such pretreatment does not prevent serious life-threatening reactions, but may reduce both their incidence and severity.

General anesthesia may be indicated in the performance of some procedures in selected patients, however, a higher incidence of adverse reactions has been reported in these patients, and may be attributable to the inability of the patient to identify untoward symptoms or to the hypotensive effect of anesthesia which can prolong the circulation time and increase the duration of exposure to the contrast agent.

In angiographic procedures, the possibility of dislodging plaques or damaging or perforating the vessel wall should be considered during catheter manipulations and contrast medium injection. Test injections to insure proper catheter placement are suggested.

Angiography should be avoided whenever possible in patients with hemocystinuria because of the risk of inducing thrombosis and embolism. Patients with congestive heart failure should be observed for several hours following the procedure to detect delayed hemodynamic

disturbances which may be associated with a transitory increase in the circulating osmotic load.

Selective coronary arteriography should be performed only in selected patients and those in whom the expected benefits outweigh the procedural risk. The inherent risks of angiocardiology in patients with chronic pulmonary emphysema must be weighed against the necessity for performing this procedure.

Extreme caution during injection of a contrast medium is necessary to avoid extravasation. This is especially important in patients with severe arterial or venous disease.

Drug Interactions: Renal toxicity has been reported in a few patients with liver dysfunction who were given oral cholecystographic agents followed by intravascular contrast agents. Administration of any intravascular contrast agent should therefore be postponed in patients who have recently received a cholecystographic contrast agent.

Other drugs should not be mixed with ioversol injection.

Drug Laboratory Test Interactions: The results of PBI and radioactive iodine uptake studies, which depend on iodine estimation, will not accurately reflect thyroid function for up to 16 days following administration of iodinated contrast media. However, thyroid function tests not depending on iodine estimations, e.g., T3 resin uptake and total or free thyroxine (T4) assays are not affected.

Carcinogenesis, Mutagenesis, Impairment of Fertility: No long term animal studies have been performed to evaluate carcinogenic potential. However, animal studies suggest that this drug is not mutagenic and does not affect fertility.

Pregnancy Category B: No teratogenic effects attributable to ioversol have been observed in teratology studies performed in animals. There are, however, no adequate and well controlled studies in pregnant women. It is not known whether ioversol crosses the placental barrier or reaches fetal tissues. However, many injectable contrast agents cross the placental barrier in humans and appear to enter fetal tissue passively. Because animal teratology studies are not always predictive of human response, this drug should be used during pregnancy only if clearly needed. X-ray procedures involve a certain risk related to the exposure of the fetus.

Nursing Mothers: It is not known whether ioversol is excreted in human milk. However, many injectable contrast agents are excreted unchanged in human milk. Although it has not been established that serious adverse reactions occur in nursing infants, caution should be exercised when intravascular contrast media are administered to nursing women because of potential adverse reactions, and consideration should be given to temporarily discontinuing nursing.

Pediatric Use: Safety and effectiveness in children have not been established.

ADVERSE REACTIONS: Adverse reactions following the use of OPTIRAY formulations are usually mild to moderate, of short duration and resolve spontaneously (without treatment). However, serious, life-threatening and fatal reactions, mostly of cardiovascular origin, have been associated with the administration of iodine-containing contrast media.

Injections of contrast media are often associated with sensations of warmth and pain. In controlled double-blind clinical studies, significantly less warmth and pain were associated with the injection of OPTIRAY than with iohalate meglumine, diatrizoate meglumine, and diatrizoate sodium.

When OPTIRAY 320 is used for coronary arteriography and ventriculography in double-blind clinical trials, electrocardiographic and hemodynamic changes occur with less frequency and severity with ioversol injection than with diatrizoate meglumine and diatrizoate sodium.

Following coronary artery and left ventricular injection, electrocardiographic parameters were affected less with OPTIRAY (ioversol injection) than with diatrizoate meglumine and diatrizoate sodium injection. These parameters included the following: bradycardia, tachycardia, T-wave amplitude, ST depression and ST elevation.

OPTIRAY has also been shown to cause fewer changes in cardiac function and systemic blood pressure than conventional ionic media. These include cardiac output, left ventricular systolic and end-diastolic pressure, right ventricular systolic and pulmonary artery systolic pressures and decreases in systolic and diastolic blood pressures.

The following table of incidence of reactions is based upon clinical trials with OPTIRAY formulations in over 1100 patients. This listing includes all adverse reactions which were contributory to the administration of ioversol regardless of their direct attributability to the drug or the procedure. Adverse reactions are listed by organ system and in decreasing order of occurrence. Significantly more severe reactions are listed before others in a system regardless of frequency.

System	Adverse Reactions	
	> 1%	≤ 1%
Cardiovascular	none	angina pectoris hypotension vascular spasm bradycardia conduction defect false aneurysm hypertension transient arrhythmia vascular trauma
Digestive	none	nausea vomiting
Nervous	none	cerebral infarct headache blurred vision vertigo lightheadedness vasovagal reaction disorientation dysphasia paresthesia visual hallucination laryngeal edema nasal congestion sneezing coughing hypoxia
Respiratory	none	periorbital edema urticaria facial edema flush pruritus
Skin	none	extravasation shaking chills bad taste general pain
Miscellaneous	none	

Regardless of the contrast medium employed, the overall incidence of serious adverse reaction is higher with coronary arteriography than with other procedures. Cardiac decompensation, serious arrhythmias, myocardial ischemia or myocardial infarction may occur during coronary arteriography and left ventriculography.

General Adverse Reactions to Contrast Media
The following adverse reactions are possible with any parenterally administered iodinated contrast medium. Severe life-threatening reactions and fatalities, mostly of cardiovascular origin, have occurred. Most deaths

occur during injection or 5 to 10 minutes later, the main feature being cardiac arrest with cardiovascular disease as the main aggravating factor. Isolated reports of hypotensive collapse and shock are found in the literature. Based upon clinical literature, reported deaths from the administration of conventional iodinated contrast agents range from 6.6 per 1 million (0.00066 percent) to 1 in 10,000 patients (0.01 percent).

The reported incidence of adverse reactions to contrast media in patients with a history of allergy is twice that of the general population. Patients with a history of previous reactions to a contrast medium are three times more susceptible than other patients. However, sensitivity to contrast media does not appear to increase with repeated examinations.

Adverse reactions to injectable contrast media fall into two categories: chemotoxic reactions and idiosyncratic reactions.

Chemotoxic reactions result from the physicochemical properties of the contrast medium, the dose and the speed of injection. All hemodynamic disturbances and injuries to organs or vessels perfused by the contrast medium are included in this category.

Idiosyncratic reactions include all other reactions. They occur more frequently in patients 20 to 40 years old. Idiosyncratic reactions may or may not be dependent on the dose injected, the speed of injection, the mode of injection and the radiographic procedure. Idiosyncratic reactions are subdivided into minor, intermediate and severe. The minor reactions are self-limited and of short duration; the severe reactions are life-threatening and treatment is urgent and mandatory.

In addition to the adverse reactions reported for ioversol, the following additional adverse reactions have been reported with the use of other contrast agents and are possible with any water soluble, iodinated contrast agent:

Nervous: muscular spasm, convulsions, aphasia, syncope, paralysis, visual field losses which are usually transient but may be permanent, coma and death.

Cardiovascular: angioneurotic edema, peripheral edema, vasodilation, thrombosis and rarely thrombophlebitis, disseminated intravascular coagulation and shock.

Skin: maculopapular rash, erythema, conjunctival symptoms, ecchymosis and tissue necrosis.

Respiratory: choking, dyspnea, wheezing which may be an initial manifestation of more severe and infrequent reactions including asthmatic attack, laryngospasm and bronchospasm, pulmonary edema, apnea and cyanosis. Rarely these allergic-type reactions can progress into anaphylaxis with loss of consciousness, coma, severe cardiovascular disturbances and death.

Miscellaneous: hyperthermia, temporary anuria or other nephropathy.

Other reactions may also occur with the use of any contrast agent as a consequence of the procedural hazard, these include hemorrhage or pseudoaneurysms at the puncture site, brachial plexus palsy following axillary artery injections, chest pain, myocardial infarction, and transient changes in hepatorenal chemistry tests. Arterial thrombosis, displacement of arterial plaques, venous thrombosis, dissection of the coronary vessels and transient sinus arrest are rare complications.

In cerebral arteriography, cardiovascular reactions that may occur with some frequency are bradycardia and either an increase or decrease in systemic blood pressure. Neurological reactions that may occur are: seizures, drowsiness, transient paresis, and mild disturbances in vision.

Central nervous system reactions with OPTIRAY in controlled clinical studies in cerebral arteriography that occurred with frequencies greater than 1% were: vertigo (4%) and blurred vision (3%).

In aortography, depending on the technique employed, the risks of this procedure also include the following: injury to the aorta and neighboring organs, pleural puncture, renal damage including infarction and acute tubular necrosis with oliguria and anuria, retroperitoneal hemorrhage from the transumbilical approach and spinal cord injury and pathology associated with the syndrome of transverse myelitis. Under conditions of slowed aortic circulation there is an increased likelihood for aortography to cause muscle spasm. Occasional serious neurologic complications, including paraplegia, have also been reported in patients with aortic atherosclerosis, femoral artery obstruction, abdominal compression, hypotension, hypertension, spinal anesthesia, and injection of vasopressors to increase contrast. In these patients the concentration, volume, and number of repeat injections of the medium should be maintained at a minimum with appropriate intervals between injections. The position of the patient and catheter tip should be carefully monitored.

Entry of a large aortic dose into the renal artery may cause, even in the absence of symptoms, albuminuria, hematuria, and an elevated creatinine and urea nitrogen. Rapid and complete return of function usually follows.

Cardiovascular system reactions with OPTIRAY in controlled clinical studies in coronary arteriography with left ventriculography that occurred with frequencies greater than 1% were: angina (1.2%) and nausea (1.2%).

PRECAUTIONS FOR SPECIFIC PROCEDURES:

Cerebral Arteriography

Extreme caution is advised in patients with advanced arteriosclerosis, severe hypertension, cardiac decompensation, senility, recent cerebral thrombosis or embolism, and migraine.

Peripheral Arteriography

Pulsation should be present in the artery to be injected. In thromboangiitis obliterans, or ascending infection associated with severe ischemia, angiography should be performed with extreme caution, if at all.

Coronary Arteriography and Left Ventriculography

Mandatory prerequisites to the procedure are specialized personnel, ECG monitoring apparatus and adequate facilities for immediate resuscitation and cardioversion. Electrocardiograms and vital signs should be routinely monitored throughout the procedure.

Venography

Special care is required when venography is performed in patients with suspected thrombosis, phlebitis, severe ischemic disease, local infection or a totally obstructed venous system. In order to minimize extravasation during injection, fluoroscopy is recommended.

OVERDOSAGE: The adverse effects of overdosage are life-threatening and affect mainly the pulmonary and cardiovascular system. Treatment of an overdosage is directed toward the support of all vital functions, and prompt institution of symptomatic therapy.

Ioversol does not bind to plasma or serum protein and is therefore, dialyzable.

The intravenous LD₅₀ values (g/kg) for ioversol in animals were 17 (mice), and 15 (rats).

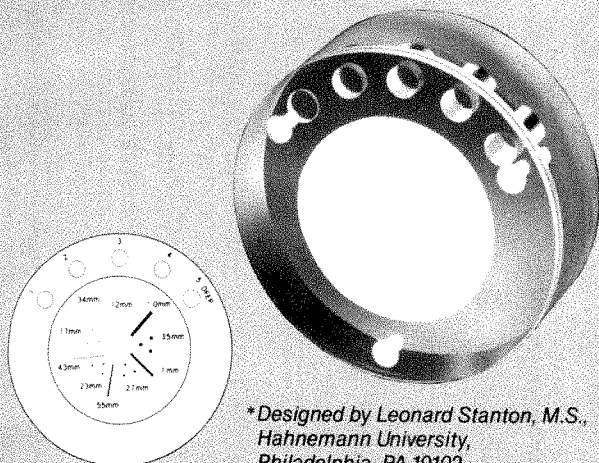
DOSAGE AND ADMINISTRATION: Details on dosage are provided in the package insert. CONSULT FULL PACKAGE INSERT BEFORE USE.



Ensure Mammographic Diagnostic Quality

Easy to Use... Easy to Interpret

MAMMOGRAPHIC QA PHANTOM*



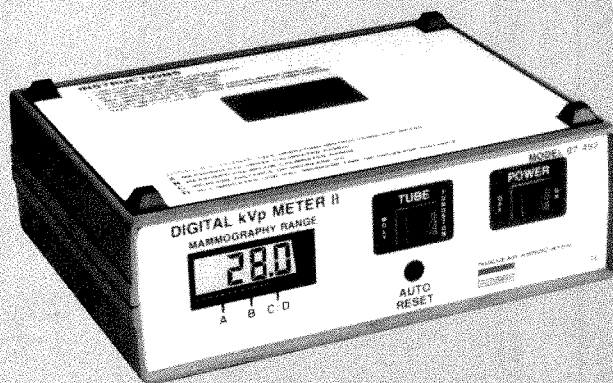
*Designed by Leonard Stanton, M.S.,
Hahnemann University,
Philadelphia, PA 19102.

For Evaluating the Overall Imaging Performance of a Mammographic System

- Intended as an integral part of a complete mammography QA program: evaluates x-ray generator, screen-film combination and film processor.
- Contains calcium carbonate specks which better simulate actual clinical conditions ("punctate calcifications") in breast cancer.
- Uses nylon fibers to simulate "soft tissue fibrillar extensions in adipose tissue."
- Includes two additional attenuators to check phototiming linearity.
- Includes 5-step air wedge to gauge for image contrast.

Affordable, Non-Invasive

MAMMOGRAPHIC DIGITAL kVp METER



For Quick and Accurate Measurements of X-Ray Generator Tube Potential

- Accuracy ± 1.5 kVp.
- Range 22-50 kVp (0.1 kVp resolution).
- Automatic display reset.
No remote control cables.
- Mo/W selector switch.
- Scope output for waveform analysis.
- Compact, lightweight, battery-operated.

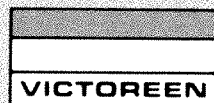
SO EASY TO USE

1. Place instrument on x-ray table.
2. Set the Mo/W selector switch for your type of tube.
3. Make an exposure.
4. Read the kVp.

For more details,
request
Bulletin 4053-44

CIRCLE 36 ON READER SERVICE CARD

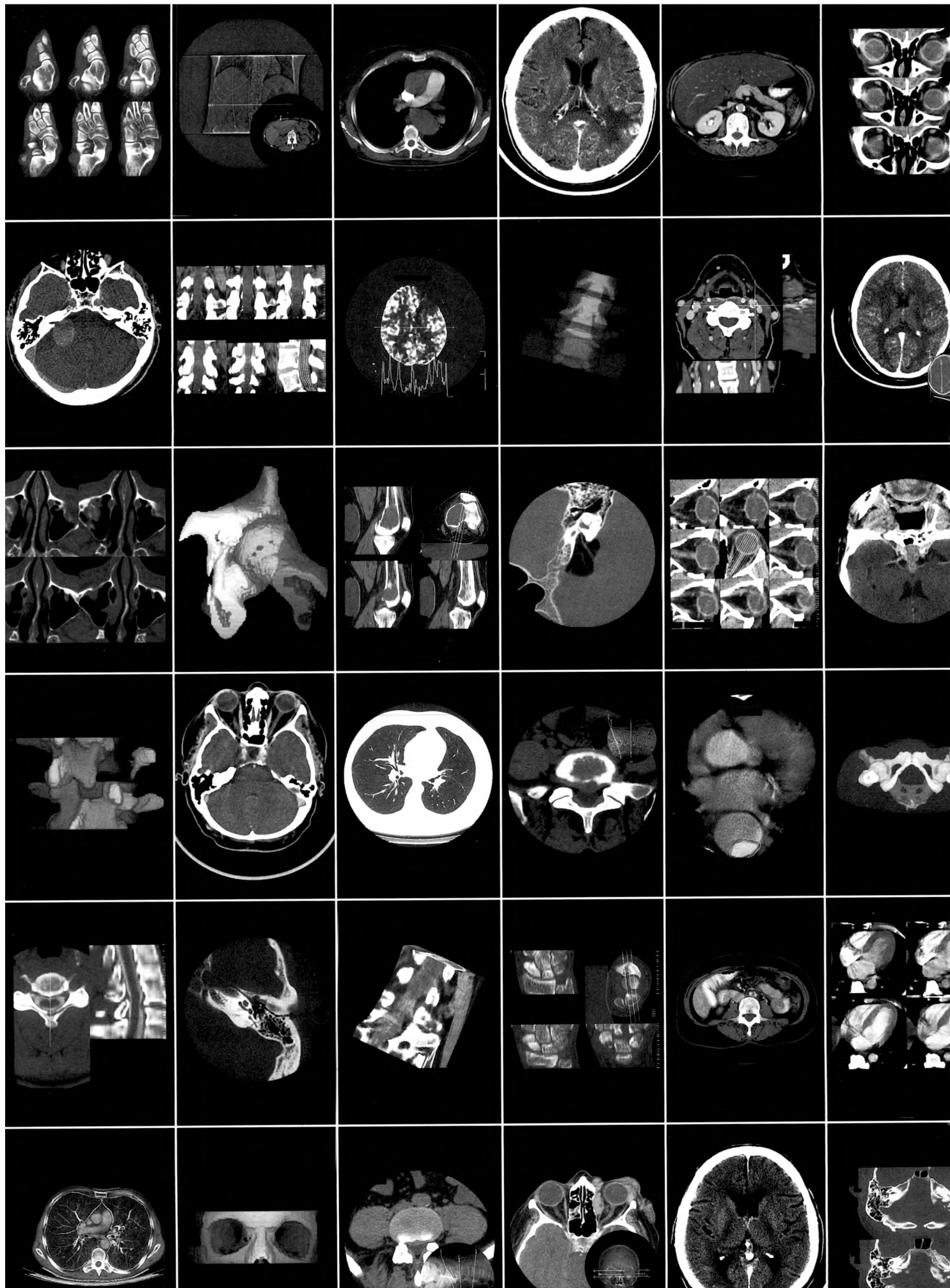
NUCLEAR ASSOCIATES



A Division of VICTOREEN, INC.
100 VOICE ROAD
CARLE PLACE, NY 11514-1593 U.S.A.
(516) 741-6360
FAX (516) 741-5414

For more details,
request
Bulletin 421-44

WE CARRY A COMPLETE LINE OF MAMMOGRAPHIC QA PRODUCTS



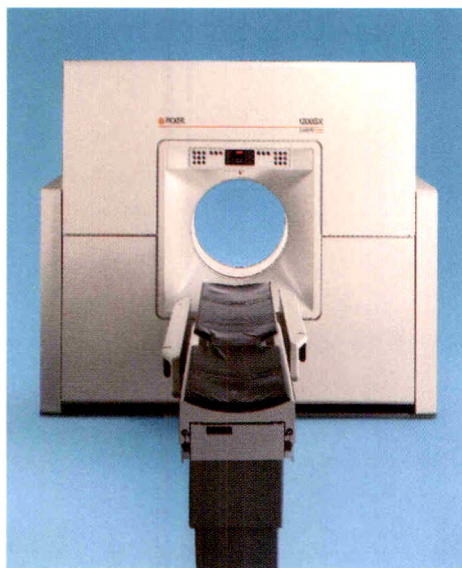
It's all in a day's work.

Consistent performance throughout your busy day.

Expert™ CT performance. The ability to achieve unsurpassed throughput without sacrificing image quality or versatility. And, attaining that performance consistently, day after day, image after image, study after study. Proven dependable through an installed base of over 1000 systems.

Let's talk about throughput. Many of our users achieve throughput levels of 30 or more patients per day. With uptime greater than 98%. Providing a return on investment that makes the Expert a smart business decision.

And our unquestionably superb throughput is not achieved by sacrificing application versatility. It's being achieved with



a mix of routine studies and specialty cases like trauma, pediatric, neuro and orthopedic, as well as advanced applications like 3-D, Xenon blood flow, bone mineral analysis, therapy planning and more.

And, of course, there is Picker's undisputed leadership in image quality to consider. The Expert delivers world class image quality in all types of studies, with resolution as high as 15 lp/cm. Image quality that gets you the right results the first time, every time.

So if you want your day's work to look like our day's work, give us a call. Maybe it's time you stepped up to a CT that can work as hard as you do. For complete information and documented success call: 1-800-543-4331, in Ohio, 216-473-3364.



PICKER

THE IMAGE OF EXCELLENCE.

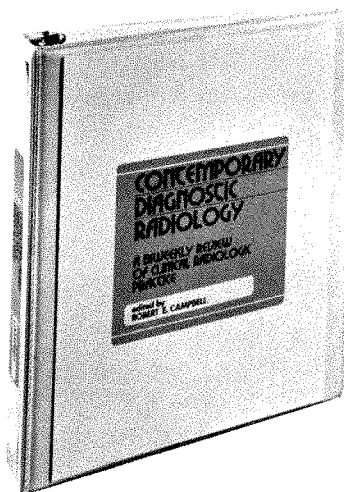
You learn from your experience with **CONTEMPORARY DIAGNOSTIC RADIOLOGY**

Editor: **Robert E. Campbell, M.D.**

A Biweekly Review of Clinical Radiologic Practice—26 issues a year!

One of your toughest jobs is keeping up with the many new developments that affect radiology. That's why you want **Contemporary Diagnostic Radiology**... an effective and convenient way to perfect your skills and maintain your professional status.

Contemporary Diagnostic Radiology is designed as a continuing education program that lets you work at your own pace. Every two weeks you'll receive an issue that covers a single topic or procedure in detail. Read the information and study the clearly reproduced radiographs—and then, if you choose, respond to a comprehensive examination in the strictest confidence. You set the pace. Each biweekly lesson brings you pertinent review of the basics in bone radiology... gastrointestinal radiology... pediatric radiology... genitourinary radiology... MR imaging... and all of the topics you want to know more about.



Contemporary Diagnostic Radiology works two ways. You may choose to subscribe to the non-scoring version, receiving every issue as an important element of your professional reading. The scoring version, however, supplements your reading and computer-coded examinations with confidential result responses, making you eligible for Continuing Medical Education credits co-sponsored by the University of Pennsylvania School of Medicine.

"As an organization for continuing medical education, the University of Pennsylvania School of Medicine designates this continuing medical education activity as meeting the criteria for 1 credit hour per bi-weekly issue in Category I for Educational Materials for the Physician's Recognition Award of the American Medical Association provided it has been completed according to instructions."

You can begin this ongoing program today. **Contemporary Diagnostic Radiology** is a year-round program, so you can join at any time. To begin your lessons, just fill out the enclosed card and return it to us. Or call **FREE** 1-800-638-6423. In Maryland call 1-800-638-4007. You'll find that **Contemporary Diagnostic Radiology** is the most efficient and inexpensive way to keep up with your dynamic field.

Williams & Wilkins

P.O. Box 23291
Baltimore, Maryland 21203



The Broadway Centre
2-6 Fulham Broadway
London SW6 1AA England

clip & mail

CONTEMPORARY DIAGNOSTIC RADIOLOGY

☐ **Yes!** I want to keep pace in my field! Begin my 26-issue subscription:

- ☐ Send me the scoring version (\$230)
- ☐ Send me the non-scoring version (\$180)
- ☐ Send me the resident non-scoring version (\$115) (add \$45 for optional air mail delivery outside the U.S.)
- ☐ new subscription
- ☐ renewal

name _____

address _____

city/state/zip _____

payment options

- ☐ payment enclosed
- ☐ American Express

- ☐ bill me
- ☐ MasterCard

☐ VISA

card # _____

expiration date _____

signature/P.O. # _____

Maryland residents add 5% sales tax. Subscriptions outside the U.S. must be prepaid in U.S. dollars only. Rates subject to change without notice. Please allow 8 weeks for delivery of your first issue, up to 16 weeks for surface delivery outside the U.S. Optional airmail rates add \$45 per subscription.

Residents are eligible for the special in-training rate for up to three years. When requesting this rate, please include training status and institution.



Don't forget: you can order with a **FREE** phone call at 1-800-638-6423. In Maryland, call 1-800-638-4007.

Williams & Wilkins

P.O. Box 23291
Baltimore, Maryland 21203

The Broadway Centre
2-6 Fulham Broadway
London SW6 1AA England

WHICH WOULD YOU RATHER READ?

The difference is *Clear!*
S & S Illuminators provide the brightest, most even light distribution for glare-free "perfect" reading — all day long.

Our commitment to illumination excellence and innovative design has produced an extraordinarily extensive, diversified line of general and "special" purpose illuminators — with configurations to meet *Your* specifications. For example:

- Film formats include 14 x 17, 8 x 10, 14 x 36 and 14 x 51 inches. Plus 18 x 24 and 24 x 30 cm Mammography Series
- Panoramic or divided viewing sections

- High-Low intensity levels as well as high frequency, reduced glare units are available as options
- 1 - 8 banks / Single or double tier configurations
- Straight, console or full range tilt viewing
- Surface or recess mounting or mobile free-standing units
- Economy models thru deluxe models with full range of optional accessories

Tried, tested and trusted for over 40 years, S & S — the world's largest manufacturer of Motorized Viewers — has earned its reputation for setting the **standard** in illumination excellence.

Call us toll-free, or ask your local x-ray representative for our fully illustrated 100+ page catalog of Illuminators, Motorized Viewers and X-Ray Accessories.

CIRCLE 9 ON READER SERVICE CARD



S & S X-RAY PRODUCTS INC.

1101 Linwood Street
Brooklyn, NY 11208
800/347-XRAY • 718/649-8500
FAX 718/257-0219

The difference is Clear!

4X Series with
High-Low Feature
(Model 4X0001 shown)



A top-down view of a white GE front-loading washing machine. The machine is enclosed in a clear, rectangular protective enclosure. A vertical metal bar is positioned in front of the circular door. The GE logo is prominently displayed on the top panel. The control panel is located just above the door, featuring a digital display and several buttons. The machine is situated on a light-colored tiled floor.

MR

Look under the hood



The high homogeneity of the magnet in the MR Max Plus system enables high quality, off-center FOV imaging (shoulder, 15 cm FOV).



The MR Max Plus system consistently yields excellent image quality and resolution (sagittal head, 5 mm, gradient echo, 256 x 256 matrix).

The magnet makes the difference in MR Max Plus

Some people think that all MR magnets are alike. Not so. We've got the numbers—and the images—to prove it.

The MR Max Plus™ system features a self-shielded magnet designed, manufactured and serviced by GE. A magnet that has the *highest level of homogeneity currently available* in mid-field systems—up to four times higher than other systems.

The result is better image quality and consistency. Particularly in thin slice (3 mm), small FOV images—such as those required for C-spine studies, a mainstay of MR imaging volume.

Of course, superb image quality is only one reason to choose MR Max Plus. There's also:

- ▶ Minimal capital and operating costs.
- ▶ Low break-even.
- ▶ Full range of sophisticated features.
- ▶ Uncomplicated installation and simple operation.
- ▶ And the security of having GE equipment.

No matter how you look at it—feature by feature, image for image, magnet to magnet—there is no better mid-field system than MR Max Plus.

For a free 24" x 36" poster of MR Max Plus images, call toll free 1-800-624-5692.



CIRCLE 15 ON READER SERVICE CARD

GE Medical Systems

We bring good things to life.

The only journal providing a complete and systematic review of the entire field

ALEXANDER R. MARGULIS, Editor

Complete Coverage

Each issue provides a complete systematic review of the past year's developments in one or two sections of radiology. Together the six bimonthly issues cover the entire field of radiology.

Annotated References

With each review, the author selects and annotates the year's most significant papers, highlighting the key findings.

Authoritative Reviews

Each section consists of a series of short, highly illustrated review articles. Using a comprehensive bibliography, leading experts evaluate new findings and developments in their fields.

World Bibliography

In each issue, the complete bibliography of current world literature lists

relevant papers published in the past year. This bibliography is specially compiled by radiologists who scan over 300 journals worldwide.

Current Opinion in RADIOLOGY

Review articles · Recommended reading
Bibliography of the world literature

Vol 1 · 1989 · No 1

No 1	THIS ISSUE	June
	Chest · JD Godwin Gastrointestinal tract · RF Thoeni	
No 2		August
	Cardiac imaging, Breast	
No 3		October
	Genitourinary system, Musculoskeletal radiology	
No 4		December
	Nuclear medicine, Pediatrics	
No 5		February
	Neuroradiology, Head and neck	
No 6		April
	Ultrasound, Angiography and interventional radiology, Technologic advances	



Volume 1 Number 1 June 1989

A.R. Margulis Editorial

Chest

edited by J.D. Godwin

- Thoracic radiology: overview
N. Müller High-resolution computed tomography of diffuse lung disease
D. Aberle Imaging of asbestosis
C. Sanders Diagnosis of emphysema
H. Libshitz Imaging of lung cancer
P. Templeton et al. Computed tomography of the pulmonary nodule and focal pulmonary disease
P. Goodman AIDS in the chest
L. Goodman and C. Mistretta Clinically chest radiography
R. Webb Magnetic resonance imaging of the chest

Gastrointestinal tract

edited by R. Thoeni

- Gastrointestinal radiology: overview
S. Glick Esophagus, stomach, and duodenum
R. Thoeni Small bowel
D. Gelfand Colon
S. K. Otho Liver
H. Goldberg Biliary system
P. Freeny Pancreas
J. LaBerge Interventional radiology in the gastrointestinal tract
S. Wall AIDS in the gastrointestinal tract
A.R. Margulis Cross-sectional imaging

Current world literature

- Chest
Gastrointestinal tract
Index to subjects

Gastrointestinal radiology

8. JEFFERY RB JR, FEDERLE MP, TOLENTINO CS. **Periappendiceal inflammatory masses: CT-directed management and clinical outcome in 70 patients.** *Radiology* 1988; 167:13-16.

Twenty patients with periappendiceal inflammatory masses were examined with CT. The CT diagnosis, based on the recognition of periappendiceal phlegmons or abscesses, was very accurate, but three false-positive diagnoses were made in the series.

9. WALKER MM, FREEDMAN AC, SOHOTA P, RADICKE PD. **CT manifestations of peritoneal carcinomatosis.** *AJR* 1988; 150:1035-1041.

Sixty patients with peritoneal tumors were reviewed retrospectively by CT. Ascites was present in 74%, loculation of fluid in 46%, absence of col-decuss fluid in 17%, and peritoneal thickening of the chest in metastatic disease in 62%. Tumor involvement of bowel was present in 50%.

10. LYNCH MA, CHO KC, JEFFERY RB JR, ALTERMAN DD, FEDERLE MP. **CT of peritoneal lymphomatosis.** *AJR* 1988; 151:713-715.

Seven patients with diffuse peritoneal malignancy caused by non-Hodgkin's lymphoma and CT evidence of ascites, omental infiltration and peritoneal implants mimicking carcinomatosis were analyzed. Paracentesis provided a diagnosis of lymphoma in only one of the seven patients. Although uncommon, lymphoma should be considered in patients who have diffuse peritoneal malignancy, particularly those who are at risk for AIDS.

Twenty volunteers were studied with T₂ T₂- and proton-density-weighted MR imaging scans of the abdomen following administration of gadolinium-DTPA either alone or with mannitol. The results suggest that oral administration of gadolinium-DTPA (1 mL) given with mannitol (15 g/L) is effective as an MR contrast agent for the gastrointestinal tract.

12. ANGELELLI G, MACARINI L. **CT of the bowel: use of water to enhance depiction.** *Radiology* 1988; 169:848-849.

Distention of the stomach with water improved visualization of the gastric wall, was readily accepted by the patient, and allowed detection of irregularity on the inner surface of the stomach with ease, even in the presence of normal wall thickness.

13. GUINET D, BLY JN, SEZEUR A, MOSNIER H, GHASSAN M, MALAFOSSE M, GUTVARCH M, VADROT D, ECOIFFER J. **Preoperative assessment of the extension of rectal carcinoma: correlation of MR, surgical and histopathologic findings.** *J Comput Assist Tomogr* 1988; 12:209-214.

Nineteen patients with rectal carcinoma were evaluated retrospectively. The study shows that MR imaging had sensitivities and specificities of 75% and 100% in the detection of perirectal growth. The comparison with TNM classification demonstrated a correct staging in 79%.

14. WOOD ML, RUNGE VM, HENDRICKS RM. **Overcoming motion in abdominal MR imaging.** *AJR* 1988; 150:513-522.

Current world literature: Gastrointestinal radiology

- THOENI RF, FILON RG. **Abdominal and pelvic CT: use of oral metoclopramide to enhance bowel opacification.** *Radiology* 1988; 169:391-393.
- KRESTIN GP, STEINBRICH W, FRIEDMANN G. **Rectal cancer: diagnosis with MR imaging versus CT.** *Radiology* 1988; 168:307-311.
- LEHR L, RUPP N, SIEWERT JR. **Assessment of resectability of esophageal cancer by computed tomography and magnetic resonance imaging.** *Surgery* 1988; 103:344-350.
- RHEE RS, RAY CG III, KRAVETZ MH, BRADLEY L, HARRIS V, GREWE GM, SPIGOS DM. **Cervical esophageal duplication cyst: MR imaging.** *J Comp Assist Tomogr* 1988; 12:693-695.
- BAKER ME, LINGERHAIDER R, COOPER C, DUNNICK NR.

- LYNCH MA, CHO KC, JEFFERY RB JR, ALTERMAN DD, FEDERLE MP. **CT of peritoneal lymphomatosis.** *AJR* 1988; 151:713-715.
- LANIADO M, KORNMESSER W, HAMM B, CLAUS W, WEINMANN HJ, FELIX R. **MR imaging of the gastrointestinal tract: value of Gd-DTPA.** *AJR* 1988; 150:817-821.
- ANGELELLI G, MACARINI L. **CT of the bowel: use of water to enhance depiction.** *Radiology* 1988; 169:848-849.
- GUINET D, BLY JN, SEZEUR A, MOSNIER H, GHASSAN M, MALAFOSSE M, GUTVARCH M, VADROT D, ECOIFFER J. **Preoperative assessment of extension of rectal carcinoma: correlation of MR, surgical and histopathologic findings.** *J Comput Assist Tomogr* 1988; 12:209-214.

Call TOLL FREE: (800) 552-5866 or in PA call (215) 790-2279

RB SPECIAL PRE-PUBLICATION OFFER!! Save 10% on a 1-year subscription! R

Current Opinion in RADIOLOGY, Volume 1, 1989 (4 issues)

- ☐ Yes! Please enter my **Personal Subscription**. \$65. ONLY \$58.50!
☐ **Resident Subscription** 30% OFF! Only \$45.50!
☐ **Institutional Subscription** \$115.

Payment Method: ☐ Check enclosed, payable to Current Science
☐ Bill Me ☐ VISA ☐ Mastercard ☐ American Express

Card Number _____ Exp. _____

Signature _____ Date _____

Name _____

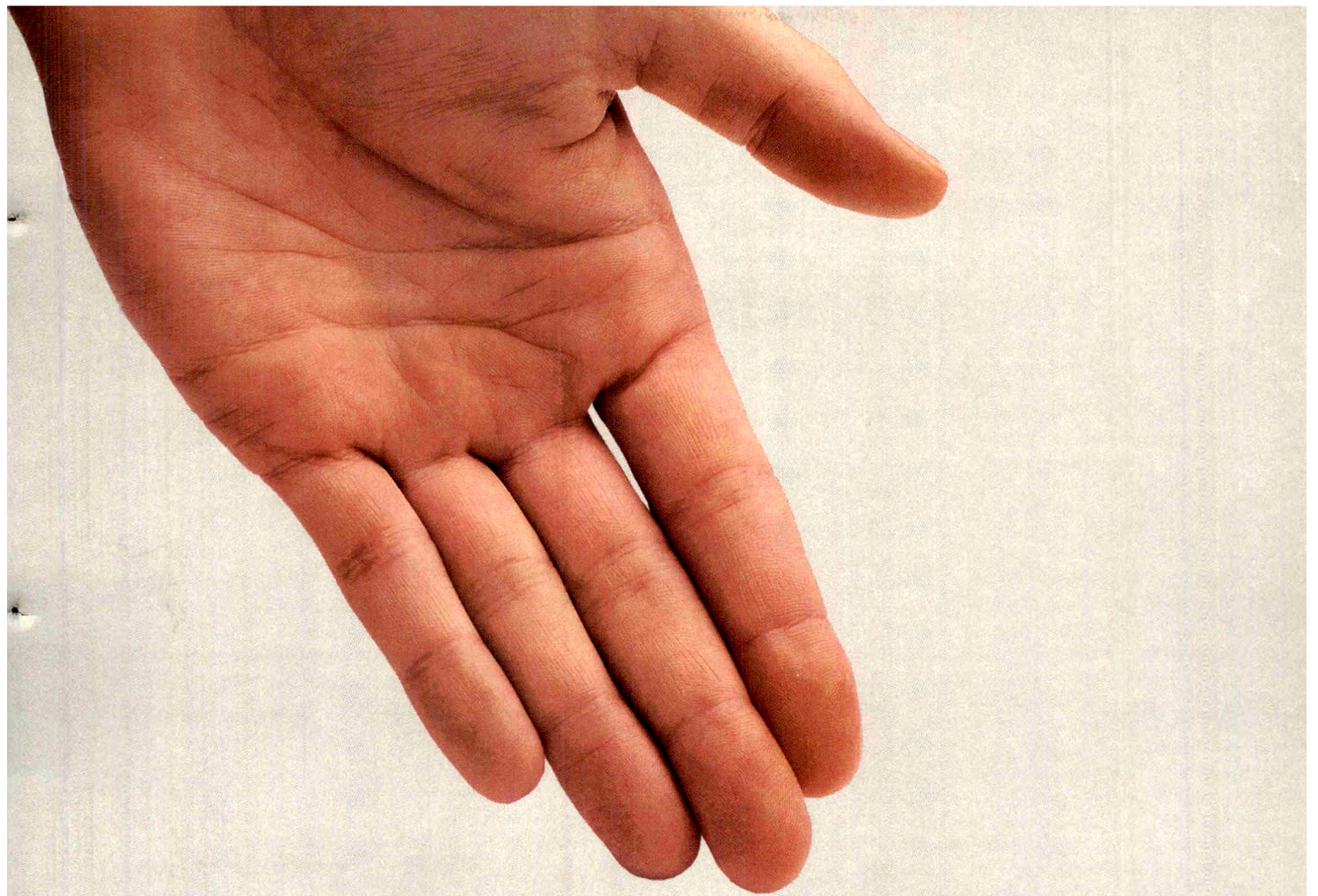
Address _____

City/State/Zip _____

MAIL TO:



CURRENT SCIENCE
DEPARTMENT RA
1201 LOCUST STREET

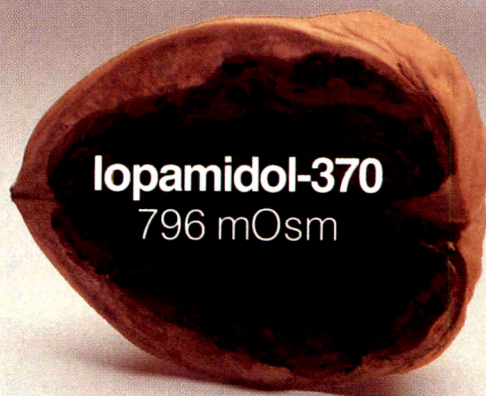


**For greater patient comfort
and the lowest osmolality,
the choice is yours...**

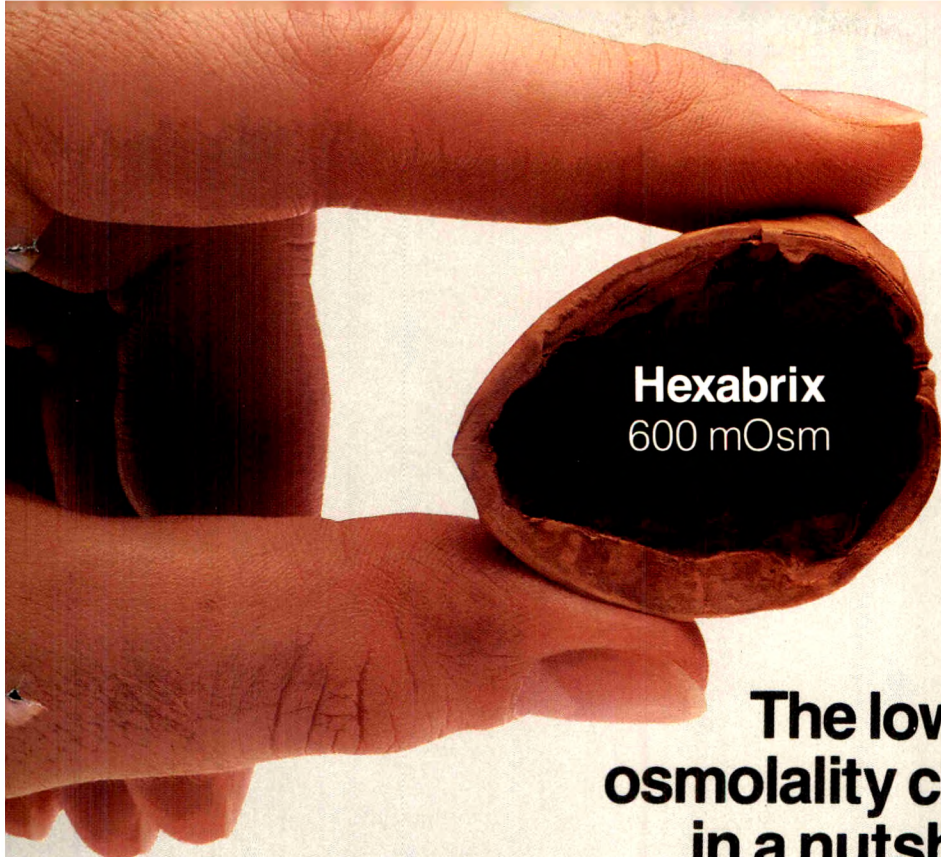




Iohexol-350
844 mOsm



Iopamidol-370
796 mOsm



Hexabrix
600 mOsm

The low osmolality choice, in a nutshell

Compare Hexabrix with the nonionics, and you'll find that Hexabrix not *only* has the lowest osmolality, but also the least amount of patient discomfort in interventional procedures.

Least heat and pain

Recent comparative studies demonstrate that Hexabrix produces significantly less heat¹ and pain¹⁻³ than iopamidol and/or iohexol during arteriography procedures.¹⁻³

Less risk of clotting *in vitro*

Hexabrix has been shown to be a stronger inhibitor of clotting^{4,5} and platelet aggregation^{5,6} *in vitro* than iopamidol or iohexol.

Good angiographic technique should be followed in all procedures involving contrast media. Even when meticulous technique is used, some mixing of blood with contrast media in syringes and catheters is possible. Prolonged contact of blood and contrast media in syringes and catheters can lead to clot formation.

Lowest viscosity

Hexabrix has the lowest viscosity at 37°C (7.5 cps), compared to iohexol-350 (10.4 cps) or iopamidol-370 (9.4 cps).

HEXABRIX[†]

(ioxaglate meglumine 39.3%/
ioxaglate sodium 19.6% injection)

Please see following page for references and brief summary of prescribing information.

I N C K B O D T

HEXABRIX[†] (ioxaglate meglumine 39.3%/ioxaglate sodium 19.6% injection)

HEXABRIX[®]

Each milliliter of HEXABRIX contains 393 mg of ioxaglate meglumine, 196 mg of ioxaglate sodium and 0.10 mg of edetate calcium disodium as a stabilizer. The solution contains 3.48 mEq (0.15 mEq) sodium in each milliliter and provides 32% (320 mg/mL) organically bound iodine.

CONTRAINDICATIONS

HEXABRIX is contraindicated for use in myelography. Refer to PRECAUTIONS concerning hypersensitivity. Hysterosalpingography should not be performed during the menstrual period, in pregnant patients, in patients with known infection in any portion of the genital tract or in patients in whom cervical ceratization or curettage has been performed within 30 days. Arthrography should not be performed if infection is present in or near the joint.

WARNINGS

Serious or fatal reactions have been associated with the administration of iodine containing radiopaque media. It is of utmost importance to be completely prepared to treat any contrast medium reaction.

As with any contrast medium, serious neurologic sequelae, including permanent paralysis, can occur following cerebral arteriography, selective spinal arteriography and arteriography of vessels supplying the spinal cord. The injection of a contrast medium should never be made following the administration of vasopressors, since they strongly potentiate neurologic effects.

In patients with subarachnoid hemorrhage, a rare association between contrast administration and clinical deterioration, including convulsions and death, has been reported. Therefore, administration of intravascular iodinated contrast media in these patients should be undertaken with caution.

A definite risk exists in the use of intravascular contrast agents in patients who are known to have multiple myeloma. In such instances, anuria has developed, resulting in progressive uremia, renal failure and eventually death. Although neither the contrast agent nor dehydration has been separately proved to be the cause of anuria in myeloma, it has been speculated that the combination of both may be a causative factor. The risk in myelomatous patients is not a contraindication to the procedure, however, partial dehydration in the preparation of these patients for the examination is not recommended since this may predispose to precipitation of myeloma protein in the renal tubules. No form of therapy, including dialysis, has been successful in reversing the effect. Myeloma, which occurs most commonly in persons over 40, should be considered before instituting intravascular administration of contrast agents.

Administration of radiopaque materials to patients known or suspected to have pheochromocytoma should be performed with extreme caution. If, in the opinion of the physician, the possible benefits of such procedures outweigh the considered risks, the procedures may be performed, however, the amount of radiopaque medium injected should be kept to an absolute minimum. The blood pressure should be assessed throughout the procedure, and measures for treatment of a hypertensive crisis should be available.

Since intravascular administration of contrast media may promote sickling in individuals who are homozygous for sickle cell disease, fluid restriction is not advised.

In patients with advanced renal disease, iodinated contrast media should be used with caution and only when the need for the examination dictates, since excretion of the medium may be impaired. Patients with combined renal and hepatic disease, those with severe hypertension or congestive heart failure and recent renal transplant recipients present an additional risk.

Renal failure has been reported in patients with liver dysfunction who were given an oral cholecystographic agent followed by an intravascular iodinated radiopaque agent and also in patients with occult renal disease, notably diabetes and hypertensives. In these classes of patients there should be no fluid restriction and every attempt made to maintain normal hydration prior to contrast medium injection. Since dehydration is the single most important factor influencing further renal impairment.

Caution should be exercised in performing contrast medium studies in patients with endotoxemia and/or those with elevated body temperatures.

Reports of thyroid storm occurring following the intravascular use of iodinated radiopaque agents in patients with hyperthyroidism or with an autonomously functioning thyroid nodule, suggest that this additional risk be evaluated before use of this drug. Iodine-containing contrast agents may alter the results of thyroid function tests which depend on iodine estimation, e.g., PBI, and may also affect results of radioactive iodine uptake studies. Such tests, if indicated, should be performed prior to the administration of this preparation.

PRECAUTIONS

Diagnostic procedures which involve the use of iodinated intravascular contrast agents should be carried out under the direction of personnel skilled and experienced in the particular procedure to be performed. All procedures utilizing contrast media carry a definite risk of producing adverse reactions. While most reactions are minor, life-threatening and fatal reactions may occur without warning, and this risk must be weighed against the benefit of the procedure. A fully equipped emergency cart, or equivalent supplies and equipment, and personnel competent in recognizing and treating adverse reactions of all types should always be available. If a serious reaction should occur, immediately discontinue administration. Since severe delayed reactions have been known to occur, emergency facilities and competent personnel should be available for at least 30 to 60 minutes after administration. (See ADVERSE REACTIONS.)

Preparatory dehydration is dangerous and may contribute to acute renal failure in infants, young children, the elderly patients with pre-existing renal insufficiency, patients with multiple myeloma, patients with advanced vascular disease and diabetic patients.

Acute renal failure has been reported in diabetic patients with diabetic nephropathy and in susceptible non-diabetic patients (often elderly with pre-existing renal disease) following the administration of iodinated contrast agents. Therefore, careful consideration of the potential risks should be given before performing this radiographic procedure in these patients.

Severe reactions to contrast media often resemble allergic responses. This has prompted the use of several provocative pretesting methods, none of which can be relied on to predict severe reactions. No conclusive relationship between severe reactions and antigen-antibody reactions or other manifestations of allergy has been established. The possibility of an

idiosyncratic reaction in patients who have previously received a contrast medium without ill effect should always be considered. Prior to the injection of any contrast medium, the patient should be questioned to obtain a medical history with emphasis on allergy and hypersensitivity. A positive history of bronchial asthma or allergy (including food), a family history of allergy, or a previous reaction or hypersensitivity to a contrast agent may imply a greater than usual risk. Such a history may be more accurate than pre-testing in predicting the potential for reaction, although not necessarily the severity or type of reaction in the individual case. A positive history of this type does not arbitrarily contraindicate the use of a contrast agent when a diagnostic procedure is thought essential, but does call for caution. (See ADVERSE REACTIONS.)

Prophylactic therapy including corticosteroids and antihistamines should be considered for patients who present with a strong allergic history, a previous reaction to a contrast medium, or a positive pre-test, since in these patients the incidence of reaction is two to three times that of the general population. Adequate doses of corticosteroids should be started early enough prior to contrast medium injection to be effective and should continue through the time of injection and for 24 hours after injection. Antihistamines should be administered within 30 minutes of the contrast medium injection. Recent reports indicate that such pre-treatment does not prevent serious life-threatening reactions, but may reduce both their incidence and severity. A separate syringe should be used for these injections.

General anesthesia may be indicated in the performance of some procedures in selected patients, however, a higher incidence of adverse reactions has been reported in these patients, and may be attributable to the inability of the patient to identify untoward symptoms or to the hypotensive effect of anesthesia which can prolong the circulation time and increase the duration of contact of the contrast agent.

Angiography should be avoided whenever possible in patients with homocystinuria because of the risk of inducing thrombosis and embolism.

PRECAUTIONS FOR SPECIFIC PROCEDURES

Pediatric Angiography. It is advisable to monitor for ECGs and vital signs changes throughout the procedure.

When large individual doses are administered, sufficient time should be allowed for any observed changes to return to or near baseline prior to making the next injection.

Caution should be used when making right heart injections in patients with pulmonary hypertension or incipient heart failure, since this may lead to increased right side pressures with subsequent bradycardia and systemic hypotension. Patients with pulmonary disease present additional risks.

Caution is advised in cyanotic infants since apnea, bradycardia, other arrhythmias and a tendency to acidosis are more likely to occur.

Since infants are more likely to respond with convulsions than are adults, the amount of total dosage is of particular importance. Repeated injections are hazardous in infants weighing less than 7 kg, particularly when these infants have pre-existing compromised right heart function or obliterated pulmonary vascular beds.

Selective Coronary Arteriography with or without left ventriculography. During the administration of large doses of HEXABRIX, continuous monitoring of vital signs is desirable. Caution is advised in the administration of large volumes to patients with incipient heart failure because of the possibility of aggravating the pre-existing condition. Hypotension should be corrected promptly since it may result in serious arrhythmias.

Special care regarding dosage must be observed in patients with right ventricular failure, pulmonary hypertension, or stenotic pulmonary vascular beds because of hemodynamic changes which may occur after injection into the right heart outflow tract.

Peripheral Arteriography. Moderate decreases in blood pressure occur frequently with intra-arterial (brachial) injections. This change is usually transient and requires no treatment, however, the blood pressure should be monitored for approximately ten minutes following injection.

Extreme caution during injection of the contrast agent is necessary to avoid extravasation and fluoroscopy is recommended. This is especially important in patients with severe arterial disease.

Cerebral Angiography. Cerebral angiography should be performed with special caution in patients with advanced atherosclerosis, severe hypertension, cardiac decompensation, recently recent cerebral thrombosis or embolism and migraine.

Intra-Arterial Digital Subtraction Angiography. The risks associated with IA-DSA are those usually attendant with catheter procedures. Following the procedure, gentle pressure hemostasis is required, followed by observation and immobilization of the limb for several hours to prevent hemorrhage from the site of arterial puncture.

Patient motion, including respiration and swallowing, can result in misregistration leading to image degradation and non-diagnostic studies.

Intravenous Digital Subtraction Angiography. The risks associated with IV-DSA include those usually attendant with catheter procedures and include intraluminal injections, vessel dissection and tissue extravasation. The potential risk is reduced when small test injections of contrast medium are made under fluoroscopic observation to insure that the catheter tip is properly positioned and, in the case of peripheral placement, that the vein is of adequate size.

Patient motion, including respiration and swallowing, can result in misregistration leading to image degradation and non-diagnostic studies.

Peripheral Venography. Special care is required when venography is performed in patients with suspected thrombosis, phlebitis, severe ischemic disease, local infection or a totally obstructed venous system.

Extreme caution during injection of contrast media is necessary to avoid extravasation and fluoroscopy is recommended. This is especially important in patients with severe arterial or venous disease.

Excretory Urography. Infants and small children should not have any fluid restrictions prior to excretory urography. (See WARNINGS and PRECAUTIONS concerning preparatory dehydration.)

Contrast Enhancement in Body Computed Tomography. Patient cooperation is essential since patient motion, including respiration, can markedly affect image quality. The use of an intravascular contrast medium can obscure tumors in patients undergoing CT evaluation of the liver, resulting in a false negative diagnosis. Dynamic CT scanning is the procedure

of choice for malignant tumor enhancement.

Arthrography. Strict aseptic technique is required to prevent the introduction of infection. Fluoroscopic control should be used to insure proper introduction of the needle into the synovial space and prevent extracapsular injection. Aspiration of excess synovial fluid will reduce the pain on injection and prevent the dilution of the contrast agent. It is important that undue pressure not be exerted during the injection.

Hysterosalpingography. Caution should be exercised in patients suspected of having cervical or tubal carcinoma to avoid possible spread of the lesion by the procedure. Delayed onset of pain and fever (1-2 days) may be indicative of pelvic infection.

Carcinogenesis, Mutagenesis, Impairment of Fertility. No long-term animal studies have been performed to evaluate carcinogenic potential. However, animal studies suggest that this drug is not mutagenic and does not affect fertility in males or females.

Pregnancy Category B. Reproduction studies have been performed in rats and rabbits at doses up to two times the maximum adult human dose and have revealed no evidence of impaired fertility or harm to the fetus due to HEXABRIX. There are, however, no adequate and well controlled studies in pregnant women. Because animal reproduction studies are not always predictive of human response, this drug should be used during pregnancy only if clearly needed.

Nursing Mothers. Ioxaglate salts are excreted unchanged in human milk. Because of the potential for adverse effects in nursing infants, bottle feedings should be substituted for breast feedings for 24 hours following the administration of this drug.

Pediatric Use. Safety and effectiveness in children has been established in pediatric angiography and intravenous excretory urography. Data have not been submitted to support the safety and effectiveness of HEXABRIX in any other indication. Precautions for specific procedures receive comment under that procedure.

ADVERSE REACTIONS

Adverse reactions to injectable contrast media fall into two categories: chemotoxic reactions and idiosyncratic reactions.

Chemotoxic reactions result from the physicochemical properties of the contrast media, the dose and the speed of injection. All hemodynamic disturbances and injuries to organs or vessels perfused by the contrast medium are included in this category.

Idiosyncratic reactions include all other reactions. They occur more frequently in patients 20 to 40 years old. Idiosyncratic reactions may or may not be dependent on the dose injected, the speed of injection, the mode of injection and the radiographic procedure. Idiosyncratic reactions are subdivided into minor, intermediate and severe. The minor reactions are self-limited and of short duration, the severe reactions are life-threatening and treatment is urgent and mandatory.

NOTE. Not all of the following adverse reactions have been reported with HEXABRIX. Because HEXABRIX is an iodinated intravascular contrast agent, all of the side effects and toxicity associated with agents of this class are theoretically possible, and this should be borne in mind when HEXABRIX is administered.

Severe, life-threatening anaphylactoid reactions, mostly of cardiovascular origin, have occurred following the administration of HEXABRIX as well as other iodine-containing contrast agents. Most deaths occur during injection or 5 to 10 minutes later, the main feature being cardiac arrest with cardiovascular disease as the main aggravating factor. Isolated reports of hypotensive collapse and shock are found in the literature. Based upon clinical literature, reported deaths from the administration of conventional iodinated contrast agents range from 6.6 per 1 million (0.00066 percent) to 1 in 10,000 patients (0.01 percent).

Regardless of the contrast agent employed, the overall estimated incidence of serious adverse reactions is higher with coronary arteriography than with other procedures. Cardiac decompensation, serious arrhythmias or myocardial ischemia or infarction may occur during coronary arteriography and left ventriculography.

The most frequent adverse reactions are nausea, vomiting, facial flush and a feeling of body warmth. These are usually of brief duration. In double-blind clinical trials, HEXABRIX produced less discomfort upon injection (pain and heat) when compared to various other contrast agents. Other reactions include the following:

Hypersensitivity reactions. Dermal manifestations of urticaria with or without pruritus, erythema and maculopapular rash. Dry mouth. Sweating. Conjunctival symptoms. Facial peripheral and angioneurotic edema. Symptoms related to the respiratory system include sneezing, nasal stuffiness, coughing, choking, dyspnea, chest tightness and wheezing, which may be initial manifestations of more severe and infrequent reactions including asthmatic attack, laryngospasm and bronchospasm with or without edema, pulmonary edema, apnea and cyanosis. Rarely, these allergic-type reactions can progress into anaphylaxis with loss of consciousness, coma, severe cardiovascular disturbances and death.

Cardiovascular reactions. Generalized vasodilation, flushing and venospasm. Occasionally thrombosis or rarely, thrombophlebitis. Extremely rare cases of disseminated intravascular coagulation resulting in death have been reported. Severe cardiovascular responses include rare cases of hypotensive shock, coronary insufficiency, cardiac arrhythmia, fibrillation and arrest. These severe reactions are usually reversible with prompt and appropriate management, however, fatalities have occurred.

Technique reactions. Extravasation with burning pain, hematomas, ecchymosis and tissue necrosis, vascular constriction due to injection rate, thrombosis and thrombophlebitis.

Neurological reactions. Spasm, convulsions, aphasia, syncope, paresis, paralysis resulting from spinal cord injury and pathology associated with the syndrome of transverse myelitis. Visual field losses which are usually transient but may be permanent, coma and death.

Other reactions. Headache, trembling, shaking, chills without fever, hyperthermia and lightheadedness. Temporary renal shutdown or other nephropathy.

Pediatric angiography has been complicated by intraluminal injection with marked adverse effects on cardiac function.

During selective coronary arteriography with or without left ventriculography, patients may have clinically insignificant ECG changes. The following adverse effects have occurred in conjunction with the administration of iodinated intravascular contrast agents for this procedure: hypotension, shock, anginal pain, myocardial infarction, cardiac arrhythmias (bradycardia, ventricular tachycardia, ventricular fibrillation) and cardiac arrest. Fatalities have been reported. Complications to the procedure include dissection of coronary arteries, dislodgement of atheromatous plaques, perforation, hemorrhage and thrombosis.

Following peripheral arteriography, hemorrhage and thrombosis have occurred at the puncture site of the percutaneous injection. Brachial plexus injury has been reported following axillary artery injection.

The major causes of cerebral arteriographic adverse reactions appear to be repeated injections of the contrast media, administration of doses higher than those recommended, the presence of occlusive atherosclerotic vascular disease and the method and technique of injection. Adverse reactions are normally mild and transient. A feeling of warmth in the face and neck is frequently experienced. Infrequently, a more severe burning discomfort is observed. Transient visual hallucinations have been reported. Serious neurological reactions that have been associated with cerebral arteriography and not listed under Adverse Reactions include stroke, amnesia and respiratory difficulties. Visual field defects with anopia and reversible neurological deficit lasting from 24 hours to 48 hours have been reported. Confusion, disorientation with hallucinations and absence of vision sometimes lasting for one week have also been reported. Cardiovascular reactions that may occur with some frequency are bradycardia and either an increase or decrease in systemic blood pressure. The blood pressure change is transient and usually requires no treatment. Arthrography may induce joint pain or discomfort which is usually mild and transient but occasionally may be severe and persist for 24 to 48 hours following the procedure. Eufusion requiring aspiration may occur in patients with rheumatoid arthritis. Fever and pain, cramping and tenderness of the abdomen have been reported following hysterosalpingography.

OVERDOSAGE

Overdosages may occur. The adverse effects of overdoses are life-threatening and affect mainly the pulmonary and cardiovascular systems. The symptoms may include cyanosis, bradycardia, acidosis, pulmonary hemorrhage, convulsions, coma and cardiac arrest. Treatment of an overdose is directed toward the support of all vital functions and prompt institution of symptomatic therapy.

Ioxaglate salts are dialyzable. The intravenous LD₅₀ values of HEXABRIX (in grams of ioxaglate/kg body weight) were 11.2 g/kg in mice, >8 g/kg in rats, >6 g/kg in rabbits and >10.2 g/kg in dogs.

DOSEAGE AND ADMINISTRATION

Details on dosage are provided in the package insert. **CON-SULT FULL PACKAGE INSERT BEFORE USE.**

Rev. Jan 1987

References:

1. Striss MG, Laerum F. Iohexol and ioxaglate in peripheral arteriography. *Acta Radiologica* 1987; 28:767-770.
2. Smith DC, Yahiku PY, Maloney MD, et al: Three new low-osmolality contrast agents: A comparative study of patient discomfort. *Am J Neuroradiol* 1988; 9:137-139.
3. Murphy WA, Campbell DR, Fraser DB: Pain in peripheral arteriography: An assessment of conventional versus ionic and non-ionic low-osmolality contrast agents. *J Can Assoc Radiol* 1988; 39:103-106.
4. Engelhart JA, Smith D, Bull BS, et al: Aspirated blood and low-osmolality contrast agents: An embolic hazard? Presented at the 73rd Meeting of the Radiological Society of North America, Chicago, IL, Dec 1, 1987.
5. Mosier LD, Jost JH, Chance D, et al: In vitro effects of ionic and nonionic contrast media on coagulation, platelet function, and fibrinolysis. Presented at the 73rd Meeting of the Radiological Society of North America, Chicago, IL, Nov 30, 1987.
6. Stormorken H, Skaltei IO, Testart MC: Effect of various contrast media on coagulation, fibrinolysis, and platelet function: An in vitro and in vivo study. *Invest Radiol* 1986; 21:348-354.



Changing the look of medicine.

Diagnostic Products Division

Mallinckrodt, Inc.

Post Office Box 5840

St. Louis, MO 63134

CIRCLE 22 ON READER SERVICE CARD

For orders,

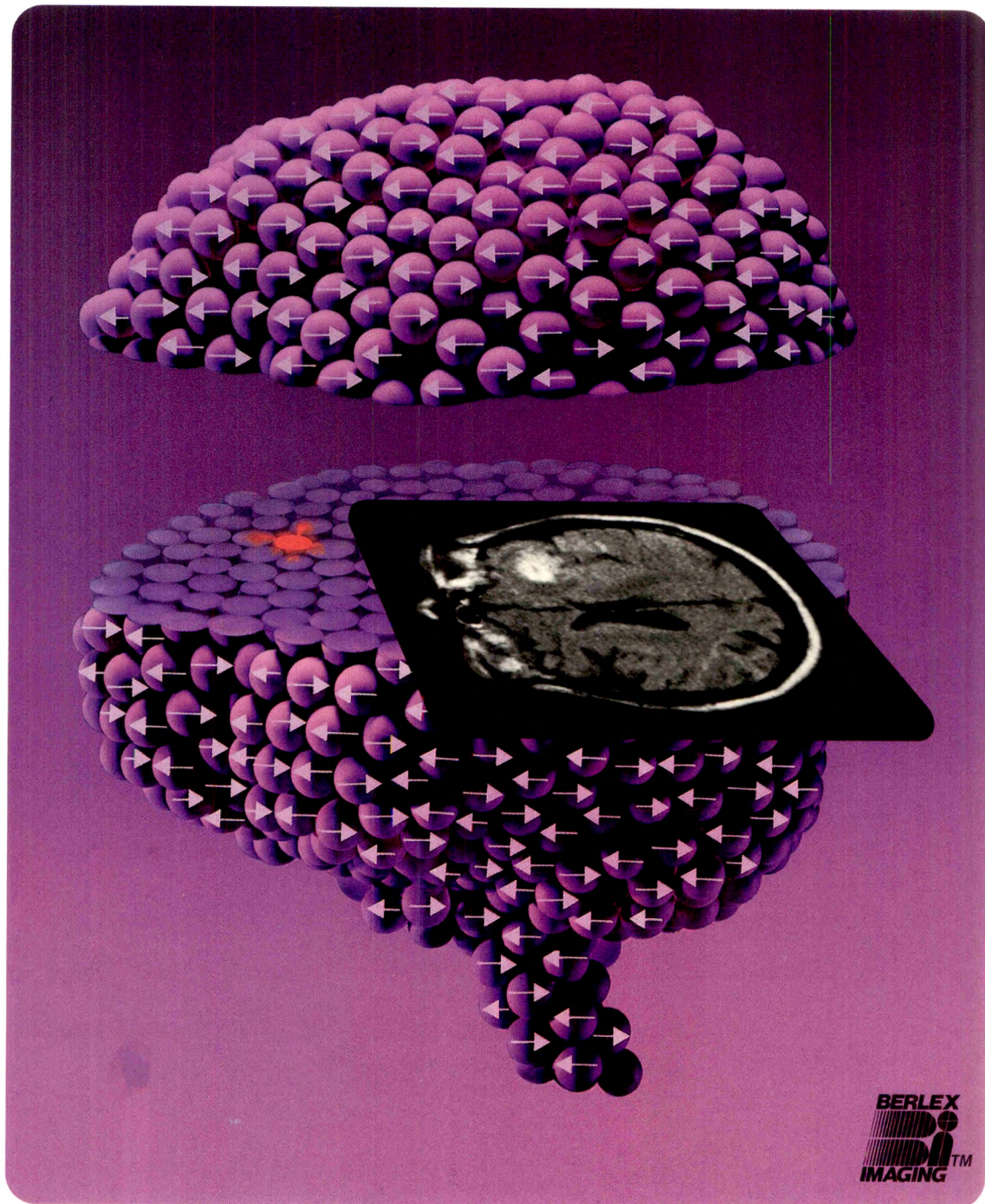
medical and/or

professional assistance

call

(800) 325-3688 TOLL FREE

**BETTER MEDICINE
THROUGH
BETTER IMAGES**

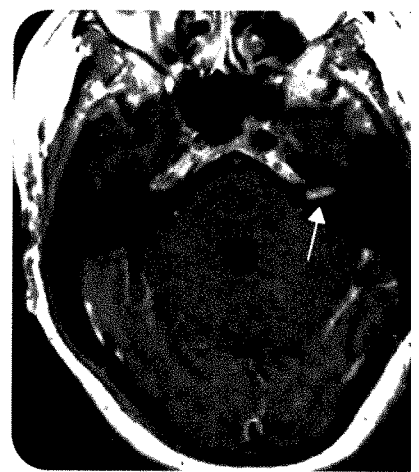


BERLEX
IMAGING™

Magnevist®
(gadopentetate
dimeglumine) INJECTION

**CONFIRMED
LESION
Acoustic
neuroma**

T1-weighted MRI scan
pre-MAGNEVIST® injection.
(TR 400, TE 20)



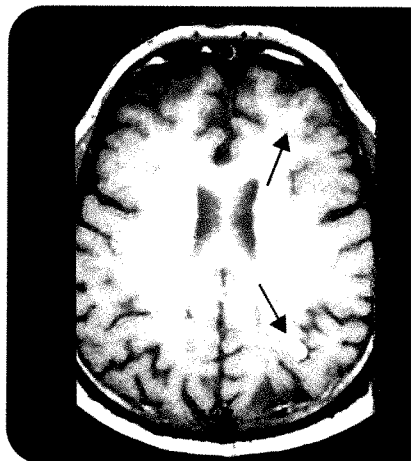
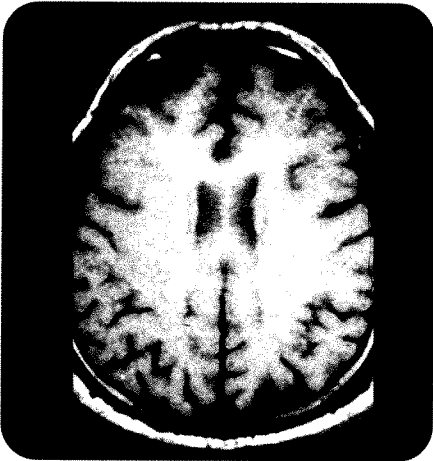
**DEMONSTRATED
SECOND
TUMOR
Meningioma**

T1-weighted MRI scan
pre-MAGNEVIST® injection.
(TR 400, TE 20)



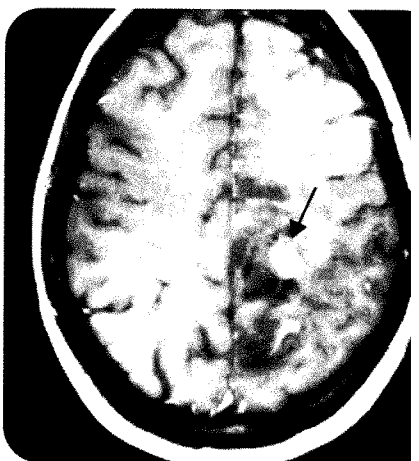
**DETECTED
LESIONS
Metastases**

T1-weighted MRI scan
pre-MAGNEVIST® injection.
(TR 600, TE 20)



**CLEARLY
DELINEATED
LESION
Glioma**

T1-weighted MRI scan
pre-MAGNEVIST® injection.
(TR 650, TE 20)



T1-weighted MRI scan post-MAGNEVIST® injection confirmed intracanalicular acoustic neuroma. (TR 400, TE 20)

T1-weighted MRI scan post-MAGNEVIST® injection demonstrated second tumor in patient with acoustic neuroma. (TR 400, TE 20)

T1-weighted MRI scan post-MAGNEVIST® injection demonstrated lesions not detected preinjection. (TR 600, TE 20)

T1-weighted MRI scan post-MAGNEVIST® injection showed improved delineation of lesion. (TR 650, TE 20)

Contrast enhancement to facilitate diagnosis

In the majority of patients, diagnostic ability was facilitated or improved by enhanced contrast with MAGNEVIST® injection.

CONTRAST ENHANCEMENT TO FACILITATE DIAGNOSIS¹

Type of Study	No. of Patients	%
Double-blind	37/57	65
Open-label	70/113	62

Increased number of lesions detected

NUMBER OF LESIONS DETECTED¹

Result of Study	Type of Study	MAGNEVIST® injection	
		No. of Patients	%
Increased no of lesions postinjection	Double-blind	10/43*	23
	Open-label	16/113*	14
Lesions seen postinjection but not preinjection	Open-label	66/232	28
	Total	92/388	24

*The question was answered only for patients with contrast enhancement.

Safety profile. In clinical trials, MAGNEVIST® injection was well tolerated.¹

INCIDENCE OF ADVERSE REACTIONS AMONG 410 PATIENTS

Type of Reaction	% of Patients With Adverse Reactions Related to MAGNEVIST® Injection	Total Reactions
Headache*	4.9%	9.8%
Nausea	3.4%	4.1%
Vomiting	1.5%	1.7%
Other†	<1.0%	<2.0%

*The majority of headaches were transient in nature.
†In clinical trials, two cases of hypotension were reported.

- In clinical trials, 15% to 30% of patients experienced an asymptomatic transient rise in serum iron.
- The safety of MAGNEVIST® injection in patients with hemolytic disorders has not been studied.

Please see Warnings, Precautions and Adverse Reactions sections in full prescribing information for MAGNEVIST® injection on last page of this advertisement.

¹ Data on file, Berlex Laboratories, Inc.



Magnevist®
(gadopentetate dimeglumine) INJECTION

Dosage and administration The recommended dosage of MAGNEVIST® injection is 0.2 mL/kg, administered intravenously, at a rate not to exceed 10 mL per minute. The maximum total dose is 20 mL. The imaging procedure should be completed within one hour of injection.

MAGNEVIST®

(brand of gadopentetate dimeglumine)
Injection

DESCRIPTION

MAGNEVIST® (brand of gadopentetate dimeglumine) Injection is the N-methylglucamine salt of the gadolinium complex of diethylenetriamine pentaacetic acid, and is an injectable contrast medium for magnetic resonance imaging (MRI). Gadopentetate dimeglumine is to be administered by intravenous injection.

Each mL of MAGNEVIST® Injection contains 469.01 mg gadopentetate dimeglumine, 0.39 mg meglumine, 0.15 mg diethylenetriamine pentaacetic acid and water for injection. MAGNEVIST® Injection contains no antimicrobial preservative. MAGNEVIST® Injection is provided as a sterile, clear, colorless to slightly yellow aqueous solution.

MAGNEVIST® Injection is a 0.5-mol/L solution of 1-deoxy-1-(methylamino)-D-glucitol dihydrogen [N,N-bis(2-{bis(carboxymethyl)amino}ethyl)glycinate-(5-)]gadolinolide (2-)(2:1) with a molecular weight of 938.

MAGNEVIST® Injection has a pH of 6.5 to 8.0. Pertinent physicochemical data are noted below:

PARAMETER	
Osmolality (mOsmol/kg water) @ 37° C	1940
Viscosity (cP) @ 20° C	49
@ 37° C	29
Density (g/mL)	1.199

MAGNEVIST® Injection has an osmolality 6.8 times that of plasma (285 mOsmol/kg water) and is hypertonic under conditions of use.

CLINICAL PHARMACOLOGY

The pharmacokinetics of intravenously administered gadopentetate dimeglumine in normal subjects conforms to a two-compartment open-model with mean distribution and elimination half-lives (reported as mean \pm SD) of about 0.2 ± 0.13 hours and 1.6 ± 0.13 hours, respectively.

Upon injection, the meglumine salt is completely dissociated from the gadopentetate dimeglumine complex. Gadopentetate is exclusively eliminated in the urine with $83 \pm 14\%$ (mean \pm SD) of the dose excreted within 6 hours, and $91 \pm 13\%$ (mean \pm SD) by 24 hours, post-injection. There was no detectable biotransformation or decomposition of gadopentetate dimeglumine.

The urinary and plasma clearance rates (1.76 ± 0.39 mL/min/kg and 1.94 ± 0.28 mL/min/kg, respectively) of gadopentetate are essentially identical, indicating no alteration in elimination kinetics on passage through the kidneys and that the drug is essentially cleared through the kidney. The volume of distribution (266 ± 43 mL/kg) is equal to that of extracellular water, and clearance is similar to that of substances which are subject to glomerular filtration.

The extent of protein binding and blood cell partitioning of gadopentetate dimeglumine is not known.

Gadopentetate dimeglumine is a paramagnetic agent and, as such, it develops a magnetic moment when placed in a magnetic field. The relatively large magnetic moment produced by the paramagnetic agent results in a relatively large local magnetic field, which can enhance the relaxation rates of water protons in the vicinity of the paramagnetic agent.

In magnetic resonance imaging (MRI), visualization of normal and pathological brain tissue depends in part on variations in the radiofrequency signal intensity that occur with 1) changes in proton density, 2) alteration of the spin-lattice or longitudinal relaxation time (T₁), and 3) variation of the spin-spin or transverse relaxation time (T₂). When placed in a magnetic field, gadopentetate dimeglumine decreases the T₁ and T₂ relaxation time in tissues where it accumulates. At usual doses the effect is primarily on the T₁ relaxation time.

Gadopentetate dimeglumine does not cross the intact blood-brain barrier and, therefore, does not accumulate in normal brain or in lesions that do not have an abnormal blood-brain barrier, e.g., cysts, mature post-operative scars, etc. However, disruption of the blood-brain barrier or abnormal vascularity allows accumulation of gadopentetate dimeglumine in lesions such as neoplasms, abscesses, subacute infarcts.

INDICATIONS AND USAGE

Using magnetic resonance imaging (MRI) in adult patients, gadopentetate dimeglumine provides contrast enhancement in those intracranial lesions with abnormal vascularity or those thought to cause an abnormal blood-brain barrier. Gadopentetate dimeglumine has been shown to facilitate visualization of lesions including but not limited to brain tumors.

CONTRAINDICATIONS None known.

WARNINGS

The accepted safety considerations and procedures that are required for magnetic resonance imaging are applicable when MAGNEVIST® Injection is used for contrast enhancement. In addition, deoxygenated sickle erythrocytes have been shown in *in vitro* studies to align perpendicular to a magnetic field which may result in vaso-occlusive complications *in vivo*. The enhancement of magnetic moment by gadopentetate dimeglumine may possibly potentiate sickle erythrocyte alignment. MAGNEVIST® Injection in patients with sickle cell anemia and other hemoglobinopathies has not been studied.

Patients with other hemolytic anemias have not been adequately evaluated following administration of MAGNEVIST® Injection to exclude the possibility of increased hemolysis.

Hypotension may occur in some patients after injection of MAGNEVIST® Injection. In clinical trials two cases were reported and in addition, there was one case of a vasovagal reaction and two cases of pallor with dizziness, sweating and nausea in one and subdermal pain and flushing in the other. These were reported within 25 to 85 minutes after injection except for the vasovagal reaction which was described as mild by the patient and occurred after 6-1/2 hours. In a study in normal volunteers one subject experienced syncope after arising from a sitting position two hours after administration of the drug. Although the relationship of gadopentetate dimeglumine to these events is uncertain, patients should be observed for several hours after drug administration.

PRECAUTIONS - General

Diagnostic procedures that involve the use of contrast agents should be carried out under direction of a physician with the prerequisite training and a thorough knowledge of the procedure to be performed.

Since gadopentetate dimeglumine is cleared from the body by glomerular filtration, caution should be exercised in patients with severely impaired renal function.

Animal studies suggest that gadopentetate dimeglumine may alter red cell membrane morphology resulting in a slight degree of extravascular (splenic) hemolysis. In clinical trials 15-30% of the patients experienced an asymptomatic transient rise in serum iron. Serum bilirubin levels were slightly elevated in approximately 3.4% of patients. Levels generally returned to baseline within 24 to 48 hours. Hematocrit and red blood cell count were unaffected and liver enzymes were not elevated in these patients. While the effects of gadopentetate dimeglumine on serum iron and bilirubin have not been associated with clinical manifestations, the effect of the drug in patients with hepatic disease is not known and caution is therefore advised.

When MAGNEVIST® Injection is to be injected using plastic disposable syringes, the contrast medium should be drawn into the syringe and used immediately.

If nondisposable equipment is used, scrupulous care should be taken to prevent residual contamination with traces of cleansing agents.

Repeat Procedures: If in the clinical judgment of the physician sequential or repeat examinations are required, a suitable interval of time between administrations should be observed to allow for normal clearance of the drug from the body.

Information for Patients

Patients receiving MAGNEVIST® Injection should be instructed to:

1. Inform your physician if you are pregnant or breast feeding.
2. Inform your physician if you have anemia or any diseases that affect red blood cells.

LABORATORY TEST FINDINGS

Transitory changes in serum iron and bilirubin levels have been reported in patients with normal and abnormal liver function (See PRECAUTIONS - General).

CARCINOGENESIS, MUTAGENESIS, AND IMPAIRMENT OF FERTILITY
No animal studies have been performed to evaluate the carcinogenic potential of gadopentetate dimeglumine.

Gadopentetate dimeglumine did not evoke any evidence of mutagenic potential in the Ames test (histidine-dependent *Salmonella typhimurium*) nor in a reverse mutation assay using tryptophan-dependent *Escherichia coli*. Gadopentetate dimeglumine did not induce a positive response in the (C3H 10T1/2) mouse embryo fibroblast cellular transformation assay, nor did it induce unscheduled DNA repair synthesis in primary cultures of rat hepatocytes at concentrations up to 5000 µg/mL. However, the drug did show some evidence of mutagenic potential *in vivo* in the mouse dominant lethal assay at doses of 6 mmol/kg, but did not show any such potential in the mouse and dog micronucleus tests at intravenous doses of 9 mmol/kg and 2.5 mmol/kg, respectively.

The results of a reproductive study in rats showed that gadopentetate dimeglumine when administered in daily doses of 0.1-2.5 mmol/kg, did not cause a significant change in the pregnancy rate in comparison to a control group. However, suppression of body weight gain and food consumption and a decrease in the mean weights of testes and epididymis occurred in male rats at the 2.5 mmol/kg dose. In female rats a decrease in the number of corpora lutea at the 0.1 mmol/kg dose and the suppression of body weight gain and food consumption at the 2.5 mmol/kg dose were observed.

In a separate experiment, 16 daily intravenous injections were administered to male rats. At a dose of 5 mmol/kg of gadopentetate dimeglumine, spermatogenic cell atrophy was observed. This atrophy was not reversed within a 16-day observation period following the discontinuation of the drug. This effect was not observed at a dose of 2.5 mmol/kg.

PREGNANCY CATEGORY C

Gadopentetate dimeglumine has been shown to retard development slightly in rats when given in doses 2.5 times the human dose, and in rabbits when given in doses of 7.5 and 12.5 times the human dose. The drug did not exhibit this effect in rabbits when given in doses 2.5 times the human dose. No congenital anomalies were noted in either species.

There are no adequate and well-controlled studies in pregnant women. MAGNEVIST® Injection should be used during pregnancy only if the potential benefit justifies the potential risk to the fetus.

NURSING MOTHERS

C14 labelled gadopentetate dimeglumine was administered intravenously to lactating rats at a dose of 0.5 mmol/kg. Less than 0.2% of the total dose was transferred to the neonate via the milk during the 24-hour evaluation period. It is not known to what extent MAGNEVIST® Injection is excreted in human milk. Because many drugs are excreted in human milk, caution should be exercised when the drug is administered to a nursing mother and consideration should be given to temporarily discontinuing nursing.

PEDIATRIC USE

Safety and effectiveness of MAGNEVIST® Injection in children has not been established.

ADVERSE REACTIONS

The most commonly noted adverse experience was headache with an incidence of 9.8%. The majority of headaches were transient and of mild to moderate severity in 50% of the cases it was felt that the headaches were not related to MAGNEVIST® Injection. Nausea at 4.1% was the second most common adverse experience.

Localized pain and vomiting occurred in less than 2% of the patients.

The following additional adverse events occurred in less than 1% of the patients:

Body as a Whole: Injection site symptoms, namely, pain, coldness, warmth, burning, localized burning sensation, localized warmth, subdermal chest pain, fever, weakness.

Cardiovascular: Hypotension, vasodilation, pallor, non-specific ECG changes.

Digestive: Gastrointestinal distress, stomach pain.

Nervous System: Agitation, paresthesia, dizziness.

Respiratory System: Throat irritation, rhinorrhea.

Skin: Rash, sweating.

Special Senses: Tinnitus, conjunctivitis, visual field defect, taste abnormality, dry mouth.

Laboratory: Transient elevation of serum transaminases.

The following other adverse events were reported. A causal relationship has neither been established nor refuted.

Body as a Whole: Back pain, pain. Allergic-like response including: urticaria, pruritus, wheezing, nasal congestion, sneezing, laryngismus and facial edema.

Cardiovascular: Hypertension, tachycardia, migraine, syncope.

Digestive: Constipation.

Nervous System: Anxiety, anorexia, convulsion, grand mal convulsions, nystagmus, drowsiness, diplopia.

Skin: Urticaria.

Special Senses: Eye pain, ear pain.

Data from foreign studies did not reveal any additional adverse experiences.

OVERDOSAGE

The LD₅₀ of intravenously administered gadopentetate dimeglumine injection in mice is 5-12.5 mmol/kg and in rats it is 10-15 mmol/kg. The LD₅₀ of intravenously administered MAGNEVIST® Injection in dogs is greater than 6 mmol/kg.

Clinical consequences of overdose with MAGNEVIST® Injection have not been reported.

DOSAGE AND ADMINISTRATION

The recommended dosage of MAGNEVIST® Injection is 0.2 mL/kg (0.1 mmol/kg), administered intravenously, at a rate not to exceed 10 mL per minute. More rapid injection rates may be associated with nausea. The maximum total dose is 20 mL. Any unused portion must be discarded.

DOSAGE CHART

Body Weight (kg)	Dose in mL	Approx Duration of Injection in Seconds
40	8.0	50
50	10.0	60
60	12.0	70
70	14.0	80
80	16.0	95
90	18.0	110
100	20.0	120

To ensure complete injection of the contrast medium, the injection should be followed by a 5-mL normal saline flush. The imaging procedure should be completed within 1 hour of injection of MAGNEVIST® Injection.

Parenteral products should be inspected visually for particulate matter and discoloration prior to administration, whenever solution and container permit.

HOW SUPPLIED

MAGNEVIST® Injection is a clear, colorless to slightly yellow solution containing 469.01 mg/mL of gadopentetate dimeglumine. MAGNEVIST® Injection is supplied in 20-mL single dose vials, rubber stoppered, in individual cartons. Boxes of 20, NDC 50419-189-02.

STORAGE

MAGNEVIST® Injection should be stored at controlled room temperature, between 15°-30°C (59°-86°F) and protected from light. DO NOT FREEZE. Should solidification occur in the vial because of exposure to the cold, MAGNEVIST® Injection should be brought to room temperature before use. If allowed to stand at room temperature for a minimum of 90 minutes, MAGNEVIST® Injection will return to a clear, colorless to slightly yellow solution. Before use, examine the product to assure that all solids are redissolved and that the container and closure have not been damaged.

Caution: Federal Law Prohibits Dispensing Without Prescription.

©1988, Berlex Laboratories, Inc. All rights reserved.
Berlex Laboratories, Inc.
Wayne, New Jersey 07470

60621-3

Revised 10/88

890-49

Printed in USA

April 1989





FIFTH ANNUAL LONDON-PARIS FALL ULTRASOUND CONGRESS



September 16-23, 1989

—London Sessions—

Kensington Hilton Hotel, September 17-19

—Paris Sessions—

Grand Hotel, September 20-23

Attend one **or** both sessions
offering CME I accreditation

Faculty: Peter L. Cooperberg, M.D. joined in London by an invited faculty including Drs. David Cosgrove, Andrew Hine, William Lees and Philip Shorvon, and in Paris by Drs. Marc Giwerc, Jean-Francois Moreau, Marie Christine Plainfosse and Valerie Vilgrain.

Ronald J. Friedman, M.D. — Meeting Coordinator
University of Southern California

Registration/Information: Medical Seminars International, 9800 D. Topanga Canyon Blvd., Suite 232, Chatsworth, CA 91311, (818) 700-9821.

For Travel Information: Rebel Tours, Inc., 4455 Van Nuys Blvd., Sherman Oaks, CA 91403, (818) 990-2400 or (800) 22-REBEL, FAX (818) 990-0479, TELEX 662417.

MAMMOGRAPHY FELLOWSHIP JULY 1989

The Department of Radiology at the University of Michigan has an unexpected opening for a 6 or 12 month fellowship in mammography. This may be combined with a 6 month fellowship in another subspecialty within the Department, including magnetic resonance imaging. Approximately 8,000 mammograms are performed annually.

The fellowship offers extensive training in all aspects of breast imaging including film/screen mammography, breast ultrasound, fine needle aspiration biopsy, and preoperative localizations. Ample research opportunities including MRI and color-flow Doppler are available.

Direct inquiries to:

Dorit Adler, M.D.
Director, Division of Mammography
University of Michigan Hospitals
TC 2910P
Ann Arbor, MI 48109-0326
Phone: 313-936-4351

The name
that started
a revolution.

*the
leader*

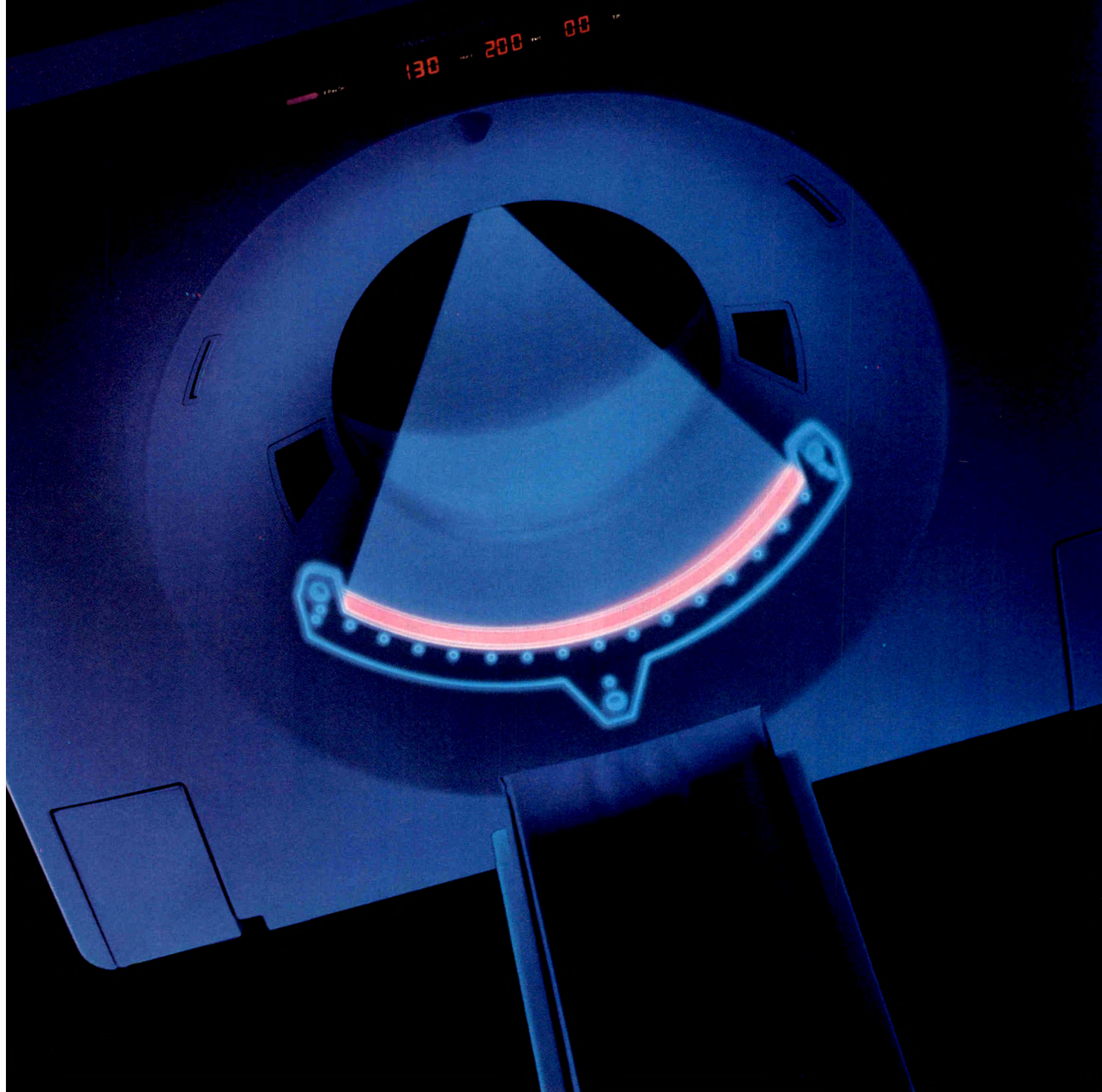
GO LYTE
PEG-3350 and Electrolytes for Oral Solution

CIRCLE 35 ON READER SERVICE CARD

LABORATORIES, INC.
Braintree

© 1989 Braintree Laboratories, Inc.
TRE-1035

HiLight



New light in computed tomography

GE is bringing new light to computed tomography. The CT 9800 HiLight™ Detector.

It's a revolutionary new detector from the scientists at GE that provides you with fast scan times, low dose levels, high throughput and extraordinary images.

With efficiency and sensitivity far beyond other detectors, HiLight brings even greater spatial resolution and low-contrast detectability to the CT 9800 Quick™ system.

In a standard 2-second scan, for example, spatial resolution measures 0.65 mm. In the high resolution mode—0.35 mm. Low contrast detectability is equally impressive—2.5 mm at 0.25% contrast (≤ 4 rads).

Extraordinary images

As a result, clinical images are remarkable—even by GE standards. Improved definition between grey and white matter in head studies. Superior detection of liver lesions, periaortic structures and mesenteric vasculature. Clear presentation of the smallest details of anatomy and pathology in studies of the spine, chest, inner ear and orbits.



No compromises

Perhaps the most significant aspect of imaging with the CT 9800 Quick/HiLight system is that there are no compromises. In any study you can combine fast scan times with low dose levels and still get superior images.

Which means better pediatric studies. More comprehensive dynamic scanning. More efficient throughput with fewer tube cooling delays.

Dose for dose, scan time for scan time, there is no better image quality available to you in CT today.

Still the standard

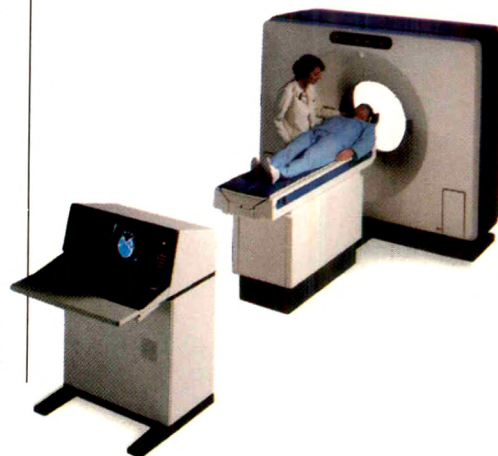
CT 9800 Quick continues to be the system by which all others are measured in computed tomography. Its standard features have always been exceptional. Routine 2-second scanning. Ability to scan, reconstruct, display and film slices in less than 16 seconds. Real-time ScoutView™ dynamic scanning. Arrange™ reformatting and a host of other features that enhance both the clinical effectiveness and efficiency of your CT department.

And now, with the HiLight Detector, we've raised our image quality standards even higher—so you can continue to provide the ultimate in CT imaging to your patients.

The CT 9800 Quick system with the HiLight Detector. An extraordinary combination from GE.

For more information, call GE Medical Systems toll free:

(800) 624-5692.



CIRCLE 3 ON READER SERVICE CARD

GE Medical Systems

*There's never been
a better time to choose GE*



14th Annual International BODY IMAGING CONFERENCE

Hyatt Regency Waikoloa — Waikoloa, Kona, Hawaii

October 14-22, 1989

This correlative conference presents topics in Magnetic Resonance Imaging, Computed Tomography, Ultrasonography, and Interventional Radiology, and offers Category I CME accreditation.

Invited Faculty

William G. Bradley, Jr. M.D., Ph.D.

Huntington Research Center

Arthur C. Fleischer, M.D.

Vanderbilt University

Gary Glazer, M.D.

Stanford University

R. Edward Hendricks, M.D.

University of Colorado

J. Bruce Kneeland, M.D.

Medical College of Wisconsin

James Lear, M.D.

University of Colorado

Angelo Lurus, M.D.

Holy Family Hospital

Michael Manco-Johnson, M.D.

University of Colorado

Richard Sano

Philips Medical Systems

Hervey Segall, M.D.

University of Southern California

Patrick Sheedy, M.D.

Mayo Clinic

Terry Silver, M.D.

University of Michigan

Arina van Breda, M.D.

Alexandria Hospital

Paul van Waes, M.D., Ph.D.

Academische Ziekenhuis Utrecht

Meeting Coordinator: **Ronald J. Friedman, M.D.**, University of Southern California

Registration Fee: US \$460 to June 30, 1989, US \$495 thereafter — (Residents, Interns, Nurses, Technicians less US \$100)

Upcoming Meetings:

Challenge 89 - Decisions in Imaging, London and Cambridge, England, June 24-30, 1989

Alaska 89 - Cruise the Inland Passage, July 7-14, 1989

Fifth Annual London-Paris Fall Ultrasound Congress, September 16-23, 1989

Eighth European Winter Ski Congress, March 1990, Site to be Announced

Registration/Information: Annual Body Imaging Conference, 9800 D. Topanga Canyon Blvd., Suite 232, Chatsworth, CA 91311.

For Travel Information: Rebel Tours, Inc., 4455 Van Nuys Blvd., Sherman Oaks 91403, (818) 990-2400 or (800) 22-REBEL, FAX (818) 990-9479, TELEX 662417.

SAY IT WITH STYLE!

AMA MANUAL OF STYLE

The one to consult

Whether it's a multi-volume work or a short article, you'll find the write stuff in the **AMA Manual of Style**.

This 8th Edition, a major revision, is the standard among medical publishers. All major aspects of manuscript preparation are covered in five sections which outline:

- Preparing an article for publication
- Style • Terminology • Measurement and Quantitation • Technical Information and Bibliography.

You'll find everything you need to make your article a success including: • Legal and Ethical Matters • Grammar • Punctuation • Word Use • Foreign Words and Phrases • Diacritics • Abbreviations • Units of Measure • Numbers and Percentages • Mathematics • Statistics • Production and Printing Terms • Editing and Proofreading Marks • Eponyms • Nomenclature • Greek Alphabet • Virus Names • SI Units and Conversion Tables • Expanded Collection of Graphs and Charts • Bibliography • Resources for On-Line Databases.

Next time you have a question about making your medical writing more clear, concise and accurate, be ready with one



simple answer — the **AMA Manual of Style**. Order your copy today!
1988/377 pp/4351-X/\$24.95

Want it faster? Call FREE
1-800-638-0672 from anywhere in the U.S. Maryland residents call 528-4221 COLLECT.

Yes, send me _____ copies of **AMA Manual of Style** (4351-X) at \$24.95 per copy. If not completely satisfied, I may return the book within 30 days at no further obligation (US only).

Payment Options

Save postage and handling charges by enclosing your payment or charging your order.

☐ Check enclosed ☐ Bill me ☐ VISA
☐ MasterCard ☐ American Express

Card # _____ Exp. Date _____

Signature/P.O. # _____

Name _____

Address _____

City/State/Zip _____



Mail Coupon to:

Williams & Wilkins
428 East Preston Street
Baltimore, MD 21202

Meeting News

Society of Cardiovascular & Interventional Radiology: 14th Annual Meeting, March 1989

The fourteenth annual meeting of the Society of Cardiovascular & Interventional Radiology was held March 20–23, 1989, at the San Diego Marriott Hotel and Marina, San Diego, CA. The 1500 attendees listened to presentations in 11 symposia. Sixty workshops were offered, as well as a special practice-management symposium and a laser-certification course. Technical exhibits provided information and demonstrations of the latest relevant products.

Although we regret that all of the program cannot be covered because of space limitations in the Journal, the following summaries reflect the sessions judged to be of greatest general interest to radiologists.

Peripheral Revascularization Symposium

Recent research on peripheral revascularization as an alternative to surgery has provided exciting and encouraging results. New techniques are being developed to enhance the initial results of both percutaneous angioplasty and atherectomy and to reduce the restenosis rates when these procedures are performed for peripheral vascular disease. In an introductory talk, Barry T. Katzen pointed out that, because of the many newer methods being attempted and a growing preference for nonsurgical treatment of peripheral vascular disease, percutaneous transluminal angiography has become the gold standard of percutaneous vascular intervention. Among the techniques discussed at this symposium were different applications of balloon angioplasty, use of lasers in vascular angioplasty, peripheral percutaneous atherectomy, and vascular stenting to unclog arteries.

Balloon Angioplasty

Much current research has focused on the use of balloon catheters to relieve vascular blockage. Charles J. Tegtmeier noted that the balloon itself has been improved: the newer balloons are thinner (0.0004–0.0006 in.) and more flexible, and each balloon can take 8–10 atm of pressure. The new low-profile angioplasty balloons have a high degree of torque and, on the newer guidewires, can be directed around tight corners and preshaped catheters. As reported by Donald E. Schwarten, use of balloon catheters to treat infrapopliteal arteriosclerotic vascular disease has resulted in 2-year limb-salvage rates (86%) that are comparable with those after surgery (89%).

Edward M. Drury discussed a retrograde popliteal approach for femoral percutaneous transluminal angioplasty with balloons that may resolve the problems of performing such procedures both in patients with either a high or occluded origin of the superficial femoral artery and in markedly obese patients. The use of radiofrequency-generated heat to reduce the rate of restenosis, as reported by Gary J. Becker, is another promising balloon method.

Lasers

Although Harold A. Mitty admitted that lasers are not the "be-all and end-all" of revascularization, he also pointed out interesting and encouraging indications that the laser can be a useful tool in certain clinical situations. When the new, larger, 2.5-mm argon laser probe was used for treatment of

peripheral vascular disease in 44 patients (sometimes with and sometimes without subsequent balloon angioplasty), clinical success was achieved in 85%. Moreover, laser therapy alone (no balloon angioplasty) has successfully treated 15 of 17 lesions below the knee, all of which were severe enough to threaten limb salvage. Laser-assisted therapy will result in fewer hospital days and shorter recovery times for patients. Possible complications of laser therapy include laser-probe perforation, arterial rupture, distal embolization, hematoma, and thrombosis. Further data on complications and restenosis rates await results from long-term follow-up.

Percutaneous Atherectomy

Donald E. Schwarten described some of the spectacular results that can be achieved with percutaneous atherectomy, in which atheroma is removed from the clogged vessel. Preliminary studies show a possible restenosis rate as low as 5% at 6-month follow-up; however, researchers do not yet know whether atherectomy actually reduces the restenosis rate or only delays restenosis.

According to Manuel Maynar, the Simpson atherectomy catheter has had an initial success rate of 100% in 13 patients with complete arterial obstruction—at 18-month follow-up, 10 of the 13 patients still had 76% patency. Complications of the procedure included thrombosis, hematoma, and distal intimal separation. Wilfrido R. Castañeda-Zuñiga explained that the ideal diameter for a Simpson atherectomy catheter for any given patient is at least equal to the diameter of the artery being treated; a catheter smaller than the artery may result in an inadequate amount of plaque being removed. Use of a combination of balloon angioplasty and atherectomy will improve the 68% 5-year patency rates now reported for balloon angioplasty of total occlusions in the superficial femoral and popliteal systems.

Vascular Stenting

The balloon-expandable stent now has been used in 200 patients with 100% success, indicating its usefulness in unclogging arteries. Examples presented by Julio C. Palmaz showed remarkable healing of foot ulcers caused by arterial blockages. The stent holds the artery open the width of the balloon inflation, which prevents the problem of relogging that occurs with regular balloon angioplasty. Because the new procedure does leave metal in the artery when the stent is inserted, use of this balloon-expandable stent is not recommended for all patients. However, the exciting results so far indicate that the procedure is a promising alternative when balloon angioplasty has failed.

Complications

Ernest J. Ring explained that, although peripheral transluminal angioplasty does sometimes result in complications, those complications are significantly fewer and less significant than postsurgical complications. In fact, the primary reasons to prefer angioplasty over surgery are less risk, lower cost,

and increased patient comfort. The complications of transluminal angioplasty and their occurrence rates are hematoma, 2–8%; pseudoaneurysm, 0–1%; thrombosis, 1–3%; occlusion, 5–8%; distal emboli, 1–5%; rupture, 0–1%; renal failure, 0.3–6.0%; death, 0–0.5%.

Because of the low risks with angioplasty, it can be done as an outpatient procedure. This reduces the cost and inconvenience for the patient, but the patient must understand the procedure and the risks. William F. Rogers described a study in which 127 outpatient angioplasty procedures were performed on 87 outpatients; in this group, only one serious complication (pseudoaneurysm) occurred. These results indicate that outpatient percutaneous transluminal angioplasty is a safe procedure, if the radiologist communicates well with the patient and if the patient is reliable, able to understand the procedure, and willing to follow the instructions.

Preventing Restenoses

Geoffrey A. Gardiner discussed restenosis, which is the major limitation of percutaneous transluminal angioplasty. Reocclusion rates range from less than 10% in 1 year for short iliac stenoses to 35% in 6 months for coronary blockages. A striking similarity exists between the characteristics of arterial bypass failure and those of restenosis after angioplasty. Prevention of intimal hyperplasia is the key to preventing postangioplasty restenosis, and the goal of research in this area is the development of techniques or agents that will reduce or eliminate vessel-wall injury.

Symposium on Thromboembolic Disease

Thrombolysis is one of the most exciting fields of research today. Techniques are being developed that will obviate surgery in many cases and will help the patient more effectively at lower costs in both time and money. The symposium speakers concentrated on three topics of interest concerning treatment of thromboembolic disease: thrombolysis by means of thrombolytic enzymes, mechanical thrombolysis, and current use of vena caval filters.

Thrombolytic Enzymes

Robert W. Holden listed streptokinase, urokinase, APSAC, scu-PA, and tPA as the major thrombolytic agents that have been studied. Three factors need to be considered in the decision to use such agents: occlusive character of thrombus, age of thrombus, and dose. In respect to occlusive character, an accelerated lysis seems to occur in nonocclusive thrombi (i.e., those clots with greater surface area exposed to the circulating enzymes). The age of a thrombus is inversely proportional to the success of lytic therapy because of the cross-linking of fibrin polymers and retraction of clot. The most effective enzymatic thrombolysis occurs when plasminogen is activated in the thrombus itself. The most effective dose to use with each of these lytic agents is controversial; physicians and pharmacists are working together to try to understand the principles of dosage with these agents. Re-

cently, a coaxial method that administers relatively high doses of urokinase both proximally and distally into the clot has resulted in faster, more effective thrombolysis with fewer bleeding complications. As Thomas O. McNamara explained, this higher dose regimen was helpful particularly in the patients with profoundly ischemic conditions. In a total of 250 thrombolytic procedures, the 10% amputation rate and 5% mortality compared favorably with the surgical results (both amputation and mortality rates ranging between 20% and 30%).

The combination of angioplasty with thrombolytic enzyme therapy (thrombolysisangioplasty) has shown good results also. In a study of 282 such procedures, Amir Motarjeme reported an initial success rate of 80% and a complication rate of only 10.6%. Follow-up studies indicated long-term success, too, especially in iliac arteries (at 2 years, 100% patency; at >2 years, 97.5% patency).

A survey described by Donald L. Miller questioned angiographers about their use of heparin to prevent clots. No consensus was found. For example, when respondents were asked if they used heparin in flush solutions, the answers varied widely, with the concentrations used ranging from 0 IU/l to 12,000 IU/l. The conclusion of the data analysis was that a large-scale, prospective study of the usefulness of systemic heparinization is needed.

Mechanical Thrombolysis

Two speakers discussed the use of mechanical devices to achieve thrombolysis. Joseph J. Bookstein described a pulse-spray technique in which a high-pressure pump is used to "chew a clot out." By this method, the clot is "digested" by fluid pulses that macerate the clot as urokinase is injected to achieve lysis. In 52 of 54 patients, the technique was successful and the mean time for first return of flow was 26 ± 19 min (mean total lysis time = 62 ± 36 min). This thrombolytic device is promising, offering less expensive, less time-consuming, and more successful lysis with no significant sequelae. The second mechanical approach, reported by Glenn P. Moradian, uses a tiny propeller mounted inside a vascular catheter. The propeller macerates clots without use of lytic agents. The most promising application of the propeller technique is in the treatment of clotted arterial bypass grafts.

Vena Caval Filters

In discussing the state of the art in vena caval filters, Ernest J. Ferris stated that the gold standard for vena caval filters is the Kimray-Greenfield 24-French filter; it provides effective prevention of pulmonary embolism with few complications. The "bird's nest" filter has the advantages of easy placement and good tolerance by patients, and it can be studied easily by sonography. In the 40 filters of this type already placed, migrations occurred in two patients; this was a problem with early filters because they were difficult to remove (the newer bird's nest filters are easier to remove). Also effective and safe in 30 placements is the Amplatz 14-French filter. The recently developed "Simon" (Nitinol) filter, however, has a

relatively high complication rate that has so far precluded approval by the FDA.

Dr. Kyung J. Cho discussed the new percutaneous Greenfield 12-French (titanium) filter. Preliminary clinical experience showed a success rate of 100% in 47 patients, but long-term follow-up studies are needed in regard to the clinical effectiveness, as well as complications of angulation, migration, caval-wall perforation, and femoral vein thrombosis. The manufacturer of this titanium filter has recalled the filter and requested that it not be used until modifications are made, particularly in regard to preventing vessel-wall perforation.

Gallbladder Intervention

Extracorporeal shock-wave lithotripsy has created increased public interest in treatment of gallstones and gallbladder disease. This symposium featured presentation of recent studies in percutaneous and thermal treatments of gallbladder disease, as well as a discussion of the latest issues in lithotripsy.

Percutaneous and Thermal Approaches

Radiologists often perform percutaneous cholecystostomy as a drainage procedure. Other potential applications of percutaneous cholecystostomy are biliary decompression, stone removal, and gallbladder ablation. Irvin F. Hawkins described a new technique for this procedure; it involves a needle-guide approach, which seems to result in fewer complications than the accepted Seldinger technique. The needle used prevents the buckling problem and perforation of the posterior wall; it also makes possible as many passes as needed to find the target. Also, the T-form catheter used represents an important advance over the accordion catheter, and its Teflon material allows it to slide in easily. When the needle-guide approach was used in 31 consecutive patients, all of whom were very ill, no procedural complications occurred.

MTBE appears to be an effective agent for percutaneous dissolution of gallstones. Hugh J. Williams described a study in which MTBE was used in 75 patients (none of whom were excluded because of stone size or number). MTBE infusion dissolved gallstones in 69 (95%) of 75; residual debris was seen in 48 of the 69, and in 15 of those 48, the debris cleared in 6–36 months. Anesthesia (three patients), hemolysis (one), and duodenitis (one) were rare complications; nausea and vomiting were common. Future improvements in the use of MTBE to dissolve gallstones include development of an automated pump for infusion and elimination of the risk of intraperitoneal bile leakage.

Carol C. Coleman reported an animal experiment in which gallbladder ablation was attempted by means of hot contrast material. The study addressed the problem of the diseased gallbladder that remains after gallstones are removed non-surgically. In each of 15 dogs, gallstones were placed surgically into the gallbladder. Boiling contrast material was injected by catheter into the gallbladder in 13 dogs. (In the other two control dogs, room-temperature contrast material was injected.) The results indicate that boiling contrast ma-

terial ablates the mucosa as well as the deeper glands of the gallbladder in the dogs. This is an encouraging step in the nonsurgical ablation of the gallbladder.

Lithotripsy

Giving an overview of the use of lithotripsy for gallstones, Eric vanSonnenberg stated the three goals of extracorporeal shock-wave lithotripsy (ESWL): fragmentation of stones, clearing of the gallbladder, and relief of the patient's symptoms. Many patients were excluded from ESWL by number, size, or appearance of stones or because of a nonvisualized gallbladder. Although only 25–30% of patients with gallstones may be treated by ESWL, the treatment has been successful in more than 300 cases. Stones were fragmented by ESWL in 100% of those cases; in 80%, all stones were eliminated. Currently, stone recurrence is the major limitation of ESWL.

A newer type of lithotripsy was described by Franklin J. Miller. In order to test the technique, human gallstones were placed in swine gallbladders. Then investigators used a guide-wire to insert a device with a high-speed rotary tip into each gallbladder. Rotating at 5000–25,000 rpm, the device creates strong fluid currents that turn the gallbladder into a "blender" and its contents into a "homogeneous slurry." The technique was successful in 23 of 26 swine; the only complication was one perforation. The effectiveness of this type of lithotripsy is not limited to certain types, number, or size of gallstones. As with all gallstone treatment, the final goals are the most effective removal of calculi and ablation of the gallbladder with the least cost (in time, money, and complications) to the patient.

William J. Casarella discussed organization of a biliary lithotripsy center. He emphasized that radiologists must be sure that they are a part of the planning process for such a center. Nine manufacturers are trying now to get FDA approval to sell lithotriptors. Stakes are high for these manufacturers, because the market for lithotriptors is small (400–500 in the U.S.) and immediate (the orders will "pour in" with FDA approval). Because radiologists are experienced in sonographic localization and interventional procedures, their skills will be much needed as centers are set up. To maximize involvement of the radiology department in the lithotripsy centers, radiologists should ensure that (1) the center is placed physically so that radiologists have easy access; (2) the director of the center is a radiologist, and the employees at the center report to that director; (3) cooperation is established between radiology and gastroenterology departments to avoid conflicts; and (4) radiologists have a role in establishing billing procedures, training-program criteria, a computerized data base, and a public relations program. Also, as these lithotripsy centers are established, radiologists must take part in establishing criteria for the lithotripsy credential; it was suggested that logically the credential should be weighted on imaging skills, especially experience in sonographic localization.

Symposium on Current Issues

This symposium was the result of member requests for formal discussions of current issues in their subspecialty.

Included in the topics covered were the goals of the SCVIR in the current political environment, turf battles, quality assurance in interventional radiology, and the health and legal dangers faced by radiologists (the risks presented by the AIDS epidemic and informed-consent litigation, respectively).

SCVIR Goals

Barry T. Katzen described the current direction of the Society of Cardiovascular & Interventional Radiology by quoting a recent statement of its mission: "to improve health and quality of life through the practice of cardiovascular and interventional radiology by promoting education and research and by providing leadership in the development of health care policy." The Society's goals include providing information, promoting basic research, assessing the effectiveness and establishing guidelines for use of new techniques, and developing quality-assurance programs and a code of ethics.

Turf Battles

Cardiovascular and interventional radiologists cannot look forward to a successful future unless they more aggressively claim their rightful place in medical care. In one survey described by David C. Levin, respondents from 198 institutions indicated that, of 13 angiographic/interventional procedures, at least five were controlled almost totally by nonradiologist clinicians.

Tony P. Smith reported another survey (715 U.S. radiologist respondents), which showed that vascular and interventional procedures are being "significantly infringed on" by specialists other than radiologists. One way of avoiding such infringement is to set up an interventional radiologic admitting service. Robert I. White described the setting up of such an admitting service in his institution in 1982; by 1987, positive results of the service included decreased length of stay for patients, improved physician-patient relationships and follow-up, and increased professional fees.

Quality Assurance in Radiology

One way to encourage nonradiologist colleagues to refer appropriate procedures to radiologists is to ensure high-quality work. Quality of patient care is, of course, the primary reason for instituting a quality-assurance program. Timothy J. McCowan suggested nine steps to take in establishing such a program: (1) assign responsibility, (2) delineate scope of care, (3) identify important aspects of care, (4) identify indicators of and thresholds for evaluation, (5) collect data, (6) evaluate care, (7) identify problems and implement solutions, (8) assess solutions and document improvement, and (9) communicate results to the organization-wide, quality-assurance program.

Radiologists and AIDS

Although some data indicate that the occurrence rate of AIDS in homosexual men will peak in 1989 and then begin to decline, health-care workers will be dealing with many cases

of AIDS in the future—80,000 new cases per year by 1992. Considering these data, R. Brook Jeffries urged radiologists to take the "universal-precaution" approach: to assume that all blood and blood products may be contaminated and to wear protective gloves during all procedures (and to wear masks, goggles, and gowns during procedures in which blood may be splattered).

Contrast Agents and Lawsuits

Radiologists are concerned also about lawsuits arising from inadequate informed consent for contrast-agent procedures. Stewart R. Reuter encouraged any radiologist involved with contrast media to learn the local legal requirements about informed consent: whether "adequacy" of patient information is based on (1) the information that any reasonable physician would give, (2) the information that any reasonable patient would want, or (3) some other standard. If consent forms are used, they must be complete; in a lawsuit, these forms will reveal exactly what information the patient was not given, as well as what information was given. Other ways that radiologists can protect themselves legally include anticipating any possible challenges to adequacy of information given and providing adequate, legible, and timely documentation on the patient's chart.

Dotter Lecture

"The Decline of Diagnostic Radiology: A Call to Action"

Barry T. Katzen introduced the annual Dotter Lecture by noting that the lecture began 5 years ago and has continued through a substantial endowment. Thomas F. Meaney, this year's lecturer, is a founder and past president of SCVIR, as well as being a leader in many other societies. His many contributions to radiology are widely known.

Dr. Meaney's lecture addressed an important problem in a realistic manner. He emphasized that his statements in this lecture represented his personal observations and conclusions and not those of any organization. Dr. Meaney contends that the market value of the radiologist's expertise has been negatively affected by the development of (1) new technolo-

gies that do not involve ionizing radiation, (2) HMOs and their rigid cost-containment efforts, (3) challenges from nonradiologist specialists who claim ability to interpret imaging studies on the basis of specific organ-system knowledge, and (4) extrapolation challenges in interventional radiology, in which nonradiologists base their qualifications to perform the procedures on their specialized knowledge of specific anatomy and disease processes.

As these factors have resulted in nonradiologists performing radiologic diagnosis and intervention, two other current conditions have complicated resolution of the problem. First, a common perception is that the number of available radiologists is large (certainly this is true in the high-population areas in desirable locations). Therefore, if any radiologists take a firm stand to fight a turf battle, they risk losing their jobs to more cooperative radiologists. Second, profit-oriented companies are marketing their radiology products to nonradiologists—sometimes even with instructions on how to perform the procedure or interpret the image.

The action plan that Dr. Meaney suggests to combat the decline of radiology consists of two components, temporizing measures and fundamental changes. The temporizing measures recommended are (1) encourage state and federal regulation of abuse and fraud arising from overutilization and self-referral; (2) promote quality standards; and (3) testify for patients who have not received optimal care when nonradiologists attempt to perform radiologic duties. These temporizing measures will help in the long run only if at least four fundamental changes are made: (1) increase direct contact between radiologists and patients, (2) implement "primary access radiology" in which patients have direct access to radiologic services, (3) require more clinical training for radiologists, and (4) develop multispecialty groups in which radiologists are the prime movers and diagnostic radiology occupies a central position.

Dr. Meaney concluded with two questions: "Would you choose to enter the specialty of diagnostic radiology 10 years from now? If not, why not?" To stem the decline of diagnostic radiology, radiologists themselves must identify the possible answers to the second question and take action to resolve the problems.

Book Review

Anatomy and MRI of the Joints. A Multiplanar Atlas. Edited by William D. Middleton and Thomas L. Lawson. New York: Raven, 312 pp., 1988. \$125

This atlas of MR imaging as applied to the anatomy of individual articulations is a much needed reference that undoubtedly will become an important contribution to the literature on diagnostic imaging. The MR images included permit ready identification of articular and periarticular structures. They were obtained from live volunteers by using a 1.5-T system, commercially available surface coils, and standard spin-echo pulse sequences. T1-weighted images are used for all joints except the vertebral column, and two excitations were used uniformly. The slice thickness was 3 mm for smaller joints and 5 mm for larger articulations, including the hip and those of the spine; the imaging field of view varied according to region. The MR images are compared with anatomic sections obtained from frozen cadavers. The joint specimens were cut into tissue blocks and sequentially sliced on the stage of a cryomicrotome unit. Color photographs of the exposed surfaces were taken at less than 1-mm intervals. Representative serial sections in the axial, sagittal, and coronal planes are depicted in the atlas.

The book was written by authors who are recognized experts in musculoskeletal MR. Individual chapters on the temporomandibular joint, shoulder, elbow, wrist, finger, vertebral column, hip, knee, and ankle are provided. Each section begins with a brief description of the anatomy of the specific joint under consideration and includes exquisitely drawn and detailed line sketches. Reference drawings also are provided with each MR image and anatomic section for purposes of orientation. Clear and detailed labeling of structures on both images and sections makes it easy to identify important anatomic components. A comprehensive and up-to-date compilation of recommended readings, organized by site, is provided at the end of

the atlas, along with a complete subject index to individual anatomic structures. The book really has no negative aspects, although an anatomist might argue that the labeling of structures could have been more detailed. As pointed out in the preface, the MR images undoubtedly will become less than state-of-the-art as technologic improvements in MR become available. However, the atlas never will become obsolete as cryomicrotome methodology has already reached its zenith.

In summary, the authors are to be commended for an outstanding and timely contribution to the MR literature; the atlas should be a valuable reference for years to come. The book will be valuable to a wide audience, including radiologists involved in interpretation of musculoskeletal CT and MR studies, clinicians who refer patients for such studies, residents and fellows in training, gross anatomists, and medical students engaged in learning human anatomy. The atlas is well worth its moderate cost and unquestionably would be a worthwhile addition to any departmental library, in an academic or private practice. The quality and comprehensiveness of articular anatomy provided by this book are far superior to those of other currently available MR atlases not limited to musculoskeletal sites, such as *Sectional Human Anatomy* by Han and Kim, and its scope is broader than that of works limited to a single joint, such as *Imaging Anatomy of the Knee Region* by Sick and Burquet.

David J. Sartoris
University of California, San Diego, Medical Center
San Diego, CA 92103

Progress in Radiology

Diagnostic Imaging of Bone and Joint Abnormalities Associated with Sickle Cell Hemoglobinopathies

Jeno I. Sebes¹

Since James Herrick's [1] first description of sickle cell anemia in 1910, much has been learned about the anatomic and pathologic aspects of the various manifestations of sickle cell hemoglobinopathies. The explosive development of imaging techniques in recent years has contributed to the basic understanding of bone and joint manifestations in the sickling disorders and has had significant impact on diagnosis and treatment of this disease. In the last decade, significant advances have been made in plain film diagnosis, radionuclide imaging, CT, and MR imaging of bone and joint abnormalities. The controversial issues and the important advances made with each imaging technique are reviewed, and their potential impact on the management of sickle cell disease is discussed.

History

Although it is generally believed that Herrick was first to describe sickle cell anemia, there is evidence that the disease had been recognized before Herrick's observation. Lebby [2] may have been first to report sickle cell anemia, found during an 1834 autopsy of a young black male. Later reports trace the existence of this disease further into the past. In 1971, Bohrer and Connah's [3] paleoradiologic investigation of 700-year-old Nigerian skeletons revealed bone changes consistent with sickle cell disease. Although the exact origin of the sickle cell disease remains controversial, sickle cell genes most likely originated in the Arabian peninsula and then spread worldwide [4].

In the United States, the prevalence of homozygous individuals for the sickle cell gene is estimated to be 0.15% to 0.2% in the black population, affecting more than 50,000 individuals. The heterozygous individuals are much more common, representing 8% of the black population [5].

In 1934, Diggs and Ching [6] were first to study the pathology, radiology, and clinical manifestations of sickle cell hemoglobinopathies. Understanding of sickle cell hemoglobin structure was advanced by Pauling et al. [7], who showed a significant difference in the electrophoretic mobility of the sickle cell and normal hemoglobins. Pauling's work in the 1940s paved the way for modern studies of this disease at a molecular level. In 1956, Ingram [8] discovered that the change in hemoglobin S, the most common hemoglobin variant, was due to substitution of valine for glutamic acid at the sixth position of the beta chain. In hemoglobin C, the second most common hemoglobin variant, lysine is substituted for glutamic acid in the sixth position of the beta chain [9]. The nomenclature and genotypes of the major sickling disorders are presented in Table 1.

The sickle hemoglobinopathies are a group of diseases in which the common denominator is the presence of the sickle hemoglobin, hemoglobin S. Hemoglobin S becomes less soluble when the erythrocyte undergoes deoxygenation. Decreased solubility results from polymerization of hemoglobin S, an effect of hypoxemia. Having the highest concentration of hemoglobin S, the erythrocytes are the most viscous and sickle most abruptly. With worsening hypoxemia, the abnormal stiffness of the sickle cell increases blood viscosity,

Received September 30, 1988; accepted after revision January 24, 1989.

¹Department of Radiology, University of Tennessee, Memphis, 800 Madison Ave., Room 114C Chandler, Memphis, TN 38163. Address reprint requests to J. I. Sebes.

AJR 152:1153-1159, June 1989 0361-803X/89/1526-1153 © American Roentgen Ray Society

TABLE 1: Major Genotypes of Sickle Cell Disease

Type of Anemia	Genotype	Anemia
Sickle cell anemia, homozygous sickle cell disease	SS disease	Severe
Sickle cell anemia with α thalassemia	SS- α thalassemia	Severe
Sickle cell- β^0 thalassemia	S β^0 thalassemia	Severe
Sickle cell- β^+ thalassemia	S β^+ thalassemia	Mild
Sickle cell-hemoglobin C disease	SC disease	Mild

compromising microvascular flow. Hemolytic anemia is thus created, with infarction and eventual multiorgan failure [10]. In the femoral and humeral heads, marginally adequate vascular supply [11] and increased intraosseous pressure contribute to infarction of the epiphyses [12].

Bone and Joint Abnormalities

Numerous reports based on plain film radiographs describe bone and joint abnormalities in sickle cell disease and sickle cell anemia, and the subject is thoroughly covered by Reynolds [13], Bohrer [14], and Serjeant [15]. Numerous studies analyzing avascular necrosis in the hips and shoulders [9, 13, 14, 16–23] report a wide variation in the incidence of avascular necrosis as a complication of sickle cell anemia.

As a result of the National Sickle Cell Anemia Control Act of 1972, the National Institutes of Health initiated a multicenter cooperative study of sickle cell disease in 1978. One purpose of this study was to evaluate avascular necrosis arising in the hips and shoulders of patients with sickle cell hemoglobinopathies. During this study in 22 clinical centers, a total of 9736 plain film radiographs of the shoulders and hips were evaluated in 1184 patients suffering from one of the hemoglobinopathies.

The classification of Ficat and Arlet [24], the most widely used staging system of the several radiologic classifications and staging systems of avascular necrosis, was adopted for the study [25–27] (Table 2). Patients were recorded as having avascular necrosis of the femoral head when stage II, III, or IV changes were noted on radiographs. In the humeral head, sclerosis, flattening, and/or subchondral lytic lesions were interpreted as evidence of avascular necrosis. The cooperative study [28] found avascular necrosis of the femoral and humeral head with equal frequency. Pain or limitation of motion was observed in half of the patients with avascular

necrosis of the femoral head and in 25% of the patients with avascular necrosis of the humeral head (A. P. Kraus, unpublished data). Table 3 summarizes the findings.

Treatment

Early diagnosis impacts treatment because avascular necrosis in stages I and II may be treated successfully with limited surgical procedures whereas more advanced lesions usually require total arthroplasties. Despite the advent of modern prosthetic devices, total hip replacements have not produced anticipated results because revisions are often necessary due to pain, loosening, infection, or an unacceptable range of motion. Patients with arthroplasties are at high risk for infection both soon after and long after surgery. Additional complications include a high incidence of fractures of the femoral shaft at the tip of the stem [20, 29, 30], protrusio acetabuli, fracture of the prosthetic stem [20, 31], and sepsis [19, 29, 30–33]. Long-term follow-up of hip arthroplasties reveals a failure rate of up to 50% after the fifth postoperative year [31]. For these reasons, the recent trend has been toward more conservative methods of treatment. These procedures include electrical stimulation to produce new bone formation, core decompression to decrease intraosseous pressure, rotational osteotomy to shift the weight-bearing area from the necrotic portion of the femoral head, drilling of holes in the femoral head to stimulate reestablishment of vascular channels, and insertion of bone grafts to stimulate bone growth. In order to intervene early for the purpose of preserving the joint rather than replacing it, early diagnosis of avascular necrosis of the hip has become increasingly important.

Radionuclide Scintigraphy

In sickle cell anemia, the bones are affected by bone-marrow expansion created by the demand for increased erythropoiesis and by vascular occlusion with bone infarction. The plain radiograph is not helpful in showing early changes produced by either process. In the last 20 years, many studies have proved the effectiveness of radionuclide scintigraphy in patients with sickle cell disease [34–38]. Radionuclide imaging is particularly helpful in detection of avascular necrosis because the transport of the radionuclide to the site of uptake depends on blood flow. Vascular occlusion, which produces a photopenic defect in the femoral or humeral head, is regarded as the earliest evidence of avascular necrosis [38].

TABLE 2: Radiologic Classification of Ischemic Necrosis of the Femoral Head*

Stage	Joint Space	Femoral Head Contour	Trabeculae	Diagnosis by Plain Film Radiography
I	Normal	Normal	Normal or slight osteoporosis	Uncertain
II	Normal	Normal	Osteoporosis/osteosclerosis	Probable
III	Normal	Flattened, subchondral infraction, collapse	Sclerosis, sequestrum	Certain
IV	Narrowed	Collapsed	Destroyed	Differential diagnosis: necrosis, arthrosis, inflammatory arthritis

* Modified from [24].

Technetium-99m phosphate compounds (polyphosphate, methylene diphosphonate, and pyrophosphate) are cortical bone-seeking radiopharmaceuticals that localize in areas of increased osteoblastic activity. Although these agents are sensitive in the detection of avascular necrosis, they are not specific. Increased perfusion in medullary osteonecrosis, when imaged with cortical agents, may reveal either increased or decreased activity, depending on the combination of vessels occluded and the stage of infarction [39-41]. Osteomyelitis and foci of metastatic carcinoma also stimulate increased uptake with these agents. Therefore, bone scans performed with cortical bone-seeking agents alone must be interpreted in the proper clinical setting. The most effectively used agent

for bone-marrow scanning is ^{99m}Tc -sulfur colloid. This agent accumulates in the reticuloendothelial system (RES); RES activity in normal bone marrow is sufficient to produce an image [35]. In sickle cell anemia, the chronic hemolysis causes substantial expansion of the erythropoietic marrow extending well into long bones. The marrow expansion produces increased activity; conversely, areas of infarction lead to decreased activity and consequent photopenia resulting from the lack of ^{99m}Tc -sulfur colloid uptake in nonviable marrow.

Introduction of infection-seeking agents allows differentiation between bone infarction and osteomyelitis. Gallium-67 citrate and indium-111 leukocytes accumulate in foci of osteomyelitis [40]. Combined radionuclide imaging with ^{99m}Tc -sulfur colloid and ^{67}Ga -citrate allows differentiation of infarction from osteomyelitis [42, 43]. Acute bone infarcts less than 1 week old are usually photopenic on both ^{99m}Tc -sulfur colloid and ^{67}Ga -citrate images. Older infarcts produce photopenic areas on marrow scans and exhibit normal gallium uptake. Osteomyelitis results in increased gallium uptake in the area corresponding to the photopenic defect on the ^{99m}Tc -sulfur colloid marrow scan [44] (Fig. 1).

Recently, single-photon emission CT (SPECT) has been used successfully to investigate early avascular necrosis. SPECT can improve diagnostic accuracy by identifying on sequential tomographic images photopenic defects in the femoral head, which are obscured by acetabular activity on planar scans [45]. The disadvantages of radionuclide imaging

TABLE 3: Avascular Necrosis (AVN) of the Femoral Head

Type of Anemia	Mean Age at Diagnosis (yr)	No. of Patients	No. Patients with AVN of Hip (%)
Sickle cell anemia with α thalassemia	27.9	282	39 (13.8)
Sickle cell anemia without α thalassemia	24.5	708	62 (8.8)
Sickle cell-hemoglobin C disease	33.9	459	23 (5.0)
Sickle cell- β^0 thalassemia	22.3	91	12 (13.2)
Sickle cell- β^+ thalassemia	36.2	121	6 (5.0)

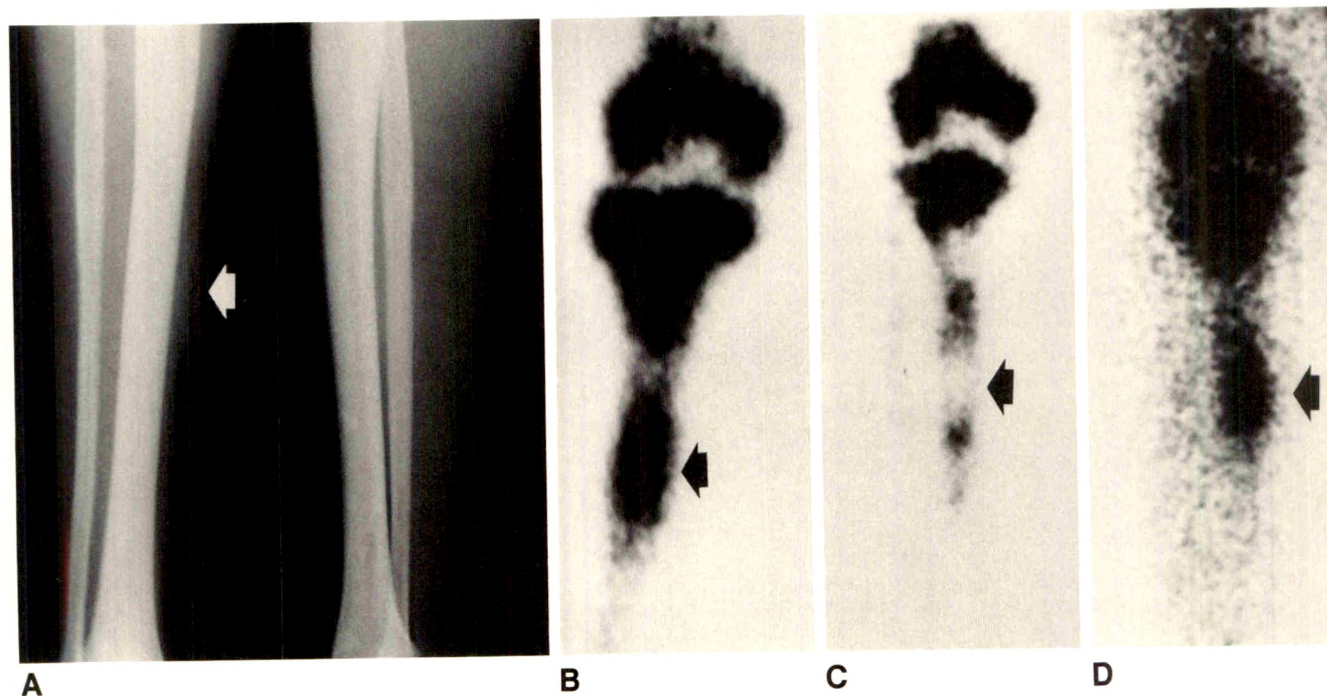


Fig. 1.—Osteomyelitis in a proximal tibial medullary bone infarct.

A, Anteroposterior and lateral radiographs of right leg in a 31-year-old woman with sickle cell anemia who presented with focal bone pain in proximal tibia and swelling of right leg (arrow).

B, ^{99m}Tc -methylene diphosphonate (^{99m}Tc -MDP) scan of right leg. Increased activity is seen in proximal tibia (arrow).

C, ^{99m}Tc -sulfur colloid scan reveals photopenic areas in tibia. Entire distal tibia is infarcted and there are two areas of focal infarction in proximal tibia. Large oval photopenic area (arrow) corresponds to focus of increased uptake on the ^{99m}Tc -MDP scan.

D, ^{67}Ga -citrate scintigram with increased accumulation of radionuclide in area corresponding to photopenic focus (arrow) on marrow scan indicating an infected medullary infarction.

of avascular necrosis, compared with CT and MR imaging, reside in its inability to localize the extent of the disease accurately and to assess the associated bone deformity resulting from it.

Computed Tomography

CT has proved useful in the diagnosis of avascular necrosis. In 1982, Dihlmann [46] described the "asterisk sign" of ischemic necrosis of the femoral head. The normal star or asterisk pattern on CT of the femoral head is the increased area of sclerosis produced by the compressive trabeculae. The alteration of the asterisk by loss of its rays or by increased peripheral densities as well as complete loss of the asterisk results from extensive necrosis of the femoral head. Although these CT findings may reveal avascular necrosis at a stage when plain films are still normal, complete destruction of the asterisk and sclerosis are advanced changes seen when plain film diagnosis is no longer doubtful. Early diagnosis of avascular necrosis on CT is difficult because some of the many normal variations of the asterisk appear similar to those seen in avascular necrosis. Osteoporosis and cysts of arthritic, metabolic, and neoplastic processes also can mimic avascular necrosis (Fig. 2). Therefore, it is unlikely that CT in its current state of technology can provide diagnosis at an earlier stage

than MR imaging. CT with multiplanar reconstruction can reveal subtle changes in trabecular pattern and minimal contour deformities in the femoral head, improving accuracy of staging and possibly affecting treatment of avascular necrosis. Diagnostic capability can be improved by using multiplanar reconstruction, which provides views of the hip from different perspectives and reveals the precise location of early and subtle deformities of the femoral head [47].

MR Imaging

During the last 4 years, MR imaging has become a widely used technique for detecting avascular necrosis [48–52] and bone-marrow necrosis [53–57]. Avascular necrosis in the sickling disorders has the same appearance as avascular necrosis from any other cause. MR imaging has been studied by Glickstein et al. [58], who report specificity of 98% with sensitivity of 85% for MR in differentiating avascular necrosis from nonnecrotic conditions and 97% sensitivity of MR in differentiation of avascular necrosis from normality. Conversely, when high-risk patients are studied with MR imaging and biopsy of the hip, the sensitivity of MR in detection of early avascular necrosis may be less than 50% [59]. The question of how early the diagnosis of avascular necrosis can be made is being studied [59]. Despite the controversy about

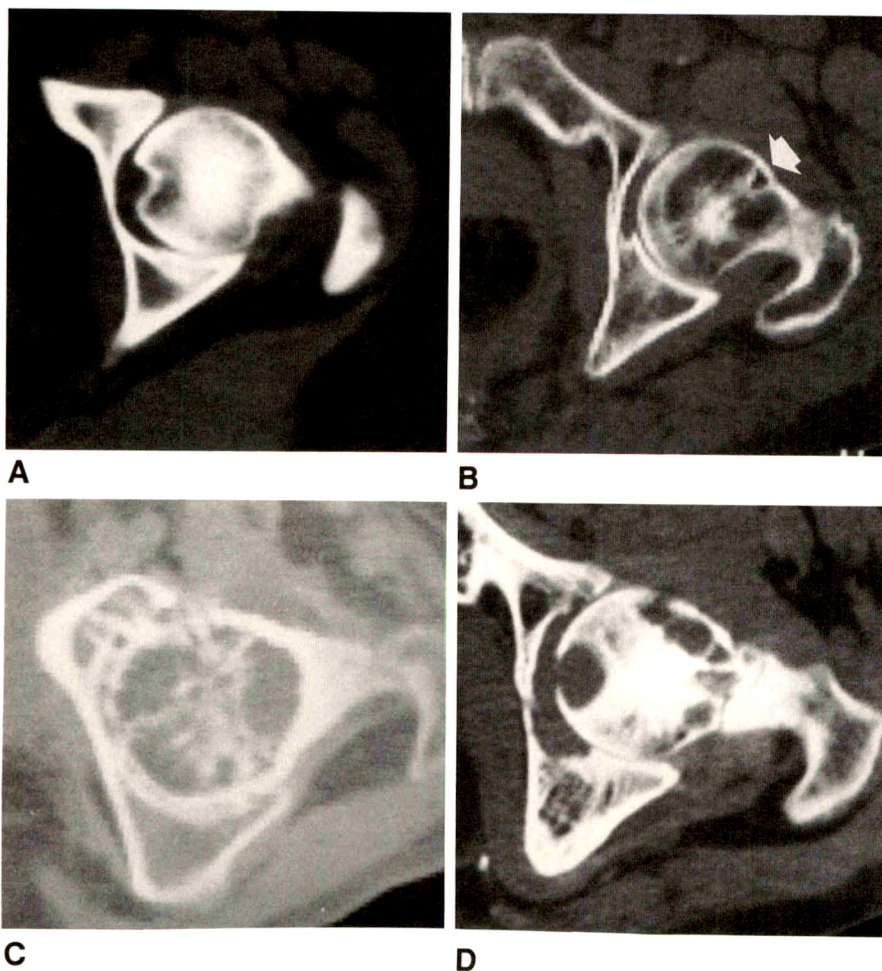


Fig. 2.—Various manifestations of "asterisk" sign. Transverse CT scans with 6-mm sections through femoral head.

A, Normal asterisk. Central density with a star-shaped arrangement of normal compressive trabeculae radiating from center.

B, Avascular necrosis of femoral head in a 24-year-old patient with sickle cell anemia. Note loss of some rays of asterisk and an intraosseous cyst anteriolaterally (arrow).

C, Almost complete loss of rays of asterisk due to severe osteoporosis in a 23-year-old woman with advanced rheumatoid arthritis. Note marked joint-space narrowing.

D, Large cystic lesions in a 47-year-old man with renal osteodystrophy. Peripheral rays of asterisk are destroyed by cysts. Note fracture of femoral neck.

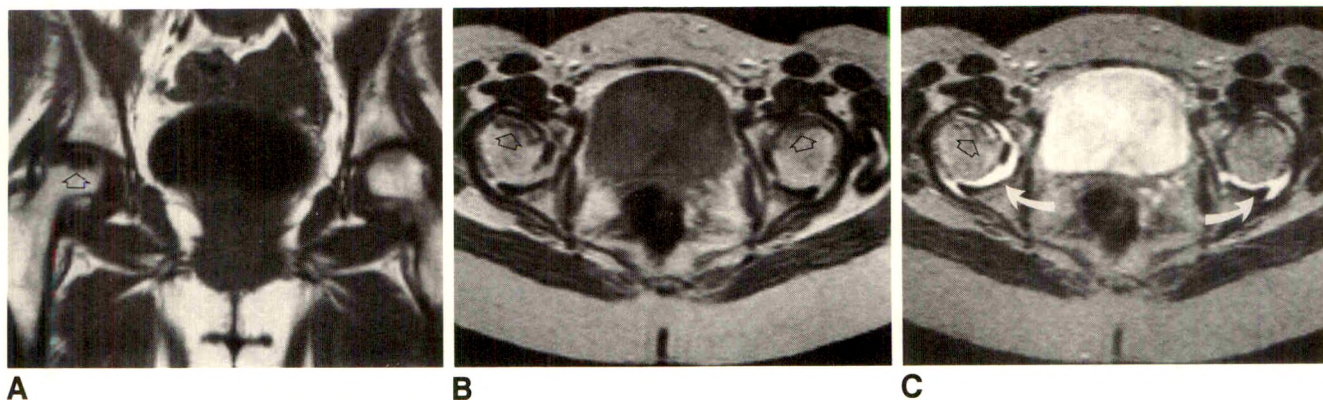


Fig. 3.—MR imaging of avascular necrosis of femoral heads in a 33-year-old man with hemoglobin SC disease.
 A, Coronal T1-weighted MR image (550/17) shows focus of low-signal area in right femoral head (arrow) with well-preserved fatty marrow in ilium and femur.
 B, Axial proton-density image (2500/35) reveals bilateral avascular necrosis with subchondral fractures (arrows).
 C, Axial T2-weighted image (2500/90). High-intensity lesion of acute avascular necrosis with a low-intensity rim (black arrow). Similar smaller lesion in left femoral head anteriorly. Note bright signal from bilateral joint effusion (white arrows).

the sensitivity of MR in detecting avascular necrosis in its earliest phase, it is currently the imaging choice.

Avascular necrosis produces a number of different patterns of MR imaging. These include a low signal intensity that may be homogeneous, heterogeneous, or a ring pattern of decreased signal surrounding the high signal intensity of fatty marrow on T1-weighted images. When the inner margin of the ring converts to a high signal of T2-weighted images, a ring or a double line is seen. Rao et al. [60] studied patients with sickle cell hemoglobinopathies by using MR imaging during sickle cell crises. The conversion from low signal intensity on short TR/TE pulse sequences to high signal intensity on long TR/TE images correlated well with pain, representing edema in the acute infarction phase. Low signal intensity on both short and long TR/TE images was seen in patients with old infarction and fibrosis. This conversion or lack of conversion of signal intensity differentiates between acute and chronic avascular necrosis (Fig. 3). Cystic lesions in the femoral head do not show the conversion to high signal intensity on long TR/TE images because there is no reactive interface with hyperemia and granulation tissue in cysts of arthritic or neoplastic origin. Therefore, the "ring sign" or the "double-line sign" is very useful in the differential diagnosis of avascular necrosis from other lesions and virtually diagnostic of avascular necrosis [61]. Because the length of time required for signal alteration in acute infarction may be several days while marrow cells, osteocytes, and fat cells die, it may be necessary to combine MR imaging with bone scintigraphy in patients who are at high risk for avascular necrosis. Additionally, T1-weighted images alone are insufficient for staging acute and chronic infarction; therefore, intermediate [62] or long TR/TE sequences should be used.

Prevention and Treatment

Despite the new additions to knowledge of the pathogenesis at the molecular, cellular, and clinical level as well as the use of newer imaging techniques, allowing earlier diagnosis,

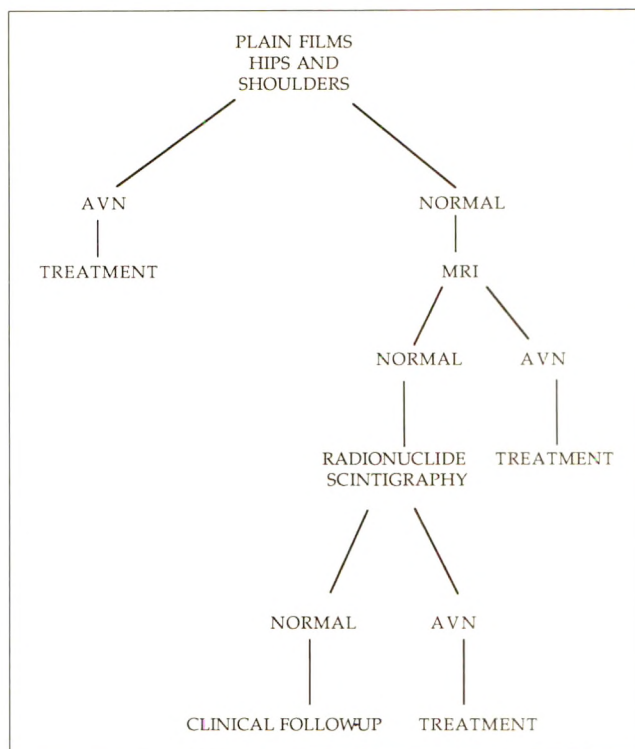


Fig. 4.—Algorithm for diagnosis of avascular necrosis (AVN) in high-risk patients with sickle cell anemia.

there is still no cure for sickle cell anemia, and treatment remains entirely symptomatic. Avascular necrosis of the hips and shoulders and bone infarction seriously disable patients with sickle hemoglobinopathies [63]. Chronic pain, severely limited motion of hips and shoulders, and development of osteoarthritis, as well as life-threatening complications including sepsis, hemolytic or splenic crises, and cerebral infarction require highly skilled specialists committed to long-term care. Ultimately, a cure may be found when it becomes possible to

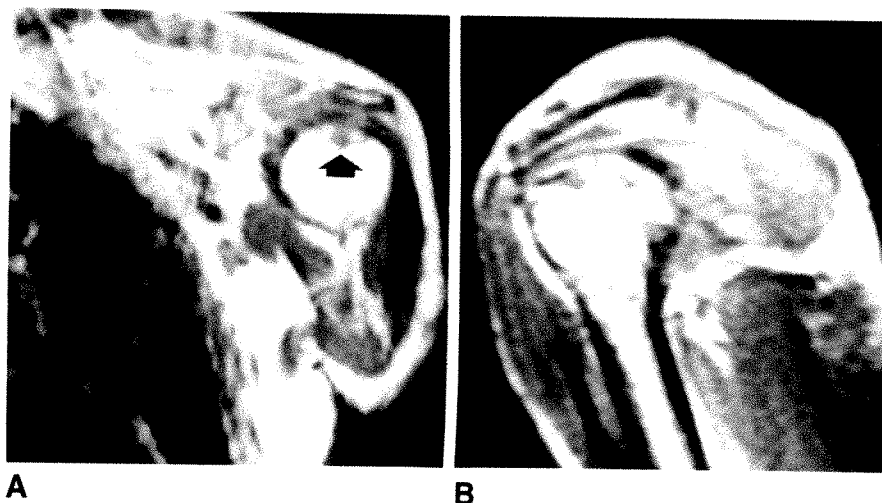


Fig. 5.—Avascular necrosis of left humeral head in a 57-year-old man with sickle cell anemia.

A, Coronal MR image through left shoulder (600/20) shows necrosis of humeral head (arrow).

B, Oblique view (2500/20) of infarcted left humeral head with high-signal-intensity lesion surrounded by low-signal-intensity ring. (Courtesy of Robert M. Steiner, M.D., and Vijay M. Rao, M.D., Thomas Jefferson University Hospital, Philadelphia, PA.)

inhibit hemoglobin S production genetically. Currently, attempts at improving therapy are being explored. A number of drugs with antisickling properties are under investigation [64, 65]. Bone-marrow transplantation also is being explored as a potential therapy [66, 67]. Until the sickling process can be controlled, noninvasive techniques will play a primary role in diagnosis of bone and joint disorders.

The Cooperative Study of Sickle Cell Disease revealed important data for potential screening by identifying the subgroups that are at highest risk for avascular necrosis. Various algorithms for detecting avascular necrosis have been proposed [59, 68, 69] (Fig. 4). For screening, however, these approaches are costly. The data from the cooperative study indicate that screening should start early in the second decade. Because half the patients developed avascular necrosis at the second site within 2 years after diagnosis of avascular necrosis at the first site, it may be necessary to screen the high-risk groups at 6-month intervals. Because avascular necrosis was found to occur as frequently in the humeral head as in the hip, it is apparent that in addition to the hips, the shoulders should be imaged. MR imaging for the detection of avascular necrosis in the shoulder has received little attention in the literature, and the shoulder (Fig. 5) is a difficult area to study [70, 71]. However, it is clear that both sites should be screened for avascular necrosis in patients with high-risk hemoglobinopathies. For screening purposes it may be sufficient to use MR imaging only with T1-weighted coronal images of the hips and shoulders.

It is hoped that the newer diagnostic imaging methods will have a beneficial impact on treatment of bone infarction. Some patients with sickle cell hemoglobinopathies can now be prevented from progressing to extensive bone and joint damage. Because the newer methods allow diagnosis of small segmental areas of necrosis, it may be possible to begin treatment before development of extensive necrosis and subsequent articular damage.

ACKNOWLEDGMENTS

The author thanks Geneva Reid and Dorothy M. Easter for their expert assistance in the preparation of this manuscript.

REFERENCES

- Herrick JB. Peculiar elongated and sickle shaped red blood corpuscles in a case of severe anemia. *Arch Intern Med* 1910;6:517-521
- Lebby R. Case of absence of the spleen. *South J Med Pharmacol* 1846;1:481-483
- Bohrer PS, Connah GE. Pathology in 700-year-old Nigerian bones. *Radiology* 1971;98:581-584
- Lehman H. Origin of the sickle cell. *S Afr J Sci* 1954;4:478-483
- Mills ML. Life-threatening complications of sickle cell disease in children. *JAMA* 1985;254:1487-1491
- Diggs LW, Ching RE. Pathology of sickle cell anemia. *South Med J* 1934;27:839-845
- Pauling L, Hano HA, Singer SJ, et al. Sickle cell anemia, a molecular disease. *Science* 1949;110:543-548
- Ingram VM. A specific chemical difference between the globins of normal human and sickle cell anemia hemoglobin. *Nature* 1956;178:792-794
- Chung SMK, Ralston EL. Necrosis of the femoral head associated with sickle-cell anemia and its genetic variants. *J Bone Joint Surg [Am]* 1969; 51-A:33-57
- Horne MK. Sickle cell anemia as a rheological disease. *Am J Med* 1981;70:288-298
- Trueta J, Harrison MHM. The normal vascular anatomy of the femoral head in adult man. *J Bone Joint Surg [Am]* 1953;35-A:442-461
- Barton CJ, Cockshott PW. Bone changes in hemoglobin SC disease. *AJR* 1962;88:223-232
- Reynolds J. *The roentgenological features of sickle cell disease and related hemoglobinopathies*. Springfield, IL: Thomas, 1965
- Bohrer SP. *Bone ischemia and infarction in sickle cell disease*. St. Louis: Warren H. Green, 1981
- Serjeant GR. *Sickle cell disease*. Oxford: Oxford University Press, 1985
- Tanaka KR, Clifford GO, Axelrod AR. Sickle cell anemia (homozygous) with aseptic necrosis of femoral head. *Blood* 1956;11:998-1008
- Hill MC, Oh KS, Bowerman JW, Siegelman SS, James AE Jr. Abnormal epiphyses in the sickling disorders. *AJR* 1975;124:34-43
- Golding JSR, MacIver JE, Went LN. The bone changes in sickle cell anemia and its genetic variants. *J Bone Joint Surg [Br]* 1959;41-B:711-718
- Lee REJ, Golding JSR, Serjeant GR. The radiological features of vascular necrosis of the femoral head in homozygous sickle cell disease. *Clin Radiol* 1981;32:205-214
- Sebes JI, Kraus AP. Avascular necrosis of the hip in the sickle cell hemoglobinopathies. *J Can Assoc Radiol* 1983;34:136-139
- Macht SH, Roman PW. The radiological changes in sickle-cell anemia. *AJR* 1948;51:697-707
- Hewett WV, Nice M Jr. Radiography manifestations of sickle cell anemia. *Radiol Clin North Am* 1964;2:249-259
- Moseley JE. Skeletal changes in the anemias. *Semin Roentgenol* 1974;9:169-184
- Ficat RP, Arlet J. Ischemia and necrosis of bone. In: Hungerford DS, ed. *Ischemia and necrosis of bone*. Baltimore: Williams & Wilkins, 1980:68

25. Catterall A. The natural history of Perthe's disease. *J Bone Joint Surg [Br]* **1971**;53-B:37-53
26. Cruess RL. Osteonecrosis of bone. Current concepts as to etiology and pathogenesis. *Clin Orthop* **1986**;208:30-39
27. Marcus ND, Enneking WF, Massam RA. The silent hip in idiopathic aseptic necrosis. *J Bone Joint Surg [Am]* **1973**;55-A:1351-1366
28. Gaston MH. Sickle cell disease: an overview. *Semin Roentgenol* **1987**;22:150-159
29. Chung SMK, Ralston EL. Necrosis of the femoral head associated with sickle-cell anemia and its genetic variants. A review of the literature and study of thirteen cases. *J Bone Joint Surg [Am]* **1969**;51-A:33-58
30. Gunderson C, D'Ambrosia RD, Shoji H. Total hip replacement in patients with sickle-cell disease. *J Bone Joint Surg [Am]* **1977**;59-A:760-762
31. Hanker JI, Amstutz HC. Osteonecrosis of the hip in sickle-cell diseases. Treatment and complications. *J Bone Joint Surg [Am]* **1988**;70-A:499-506
32. Bishop AR, Robertson JR, Eckman JR, Flemming LL. Total hip arthroplasty in patients who have sickle-cell hemoglobinopathy. *J Bone Joint Surg [Am]* **1988**;70-A:853-855
33. Epps CH Jr, Castro O. Complication of total hip replacements in sickle cell disease. *Orthop Trans* **1978**;2:236-237
34. Alavi A, Schumacher HR, Dowart D, Kuhl DE. Bone marrow scan evaluation of arthropathy in sickle cell disorders. *Arch Intern Med* **1976**;136:436-440
35. Alavi A, Bond JP, Kuhl DE, Greech RH. Scan detection of bone marrow infarcts in sickle cell disorders. *J Nucl Med* **1974**;15:1003-1007
36. Lutzker LG, Alavi A. Bone and marrow imaging in sickle cell disease: diagnosis of infarction. *Semin Nucl Med* **1976**;6:83-93
37. Pierce RO Jr. Aseptic necrosis of the hip in sickle cell disease. *J Natl Med Assoc* **1979**;71:45-48
38. Lee CK, Hansen HT, Weiss AB. The "silent hip" of idiopathic ischemic necrosis of the femoral head in adults. *J Bone Joint Surg [Am]* **1980**;62-A:795-800
39. Rocha AFG, Harbert JC. *Textbook of nuclear medicine: clinical applications*. Philadelphia: Lea & Febiger, **1979**:124-126
40. Meyers MH, Telfer ND, Moore TM. Determination of the vascularity of the femoral head in the technetium ^{99m}sulfur colloid. *J Bone Joint Surg [Am]* **1977**;59-A:658-664
41. Webber MM, Wagner J, Cragin MD. Radionuclide patterns of femoral head disease. *Int J Nucl Med Biol* **1977**;4:167-177
42. Amundsen TR, Siegel MJ, Siegel BA. Osteomyelitis and infarction in sickle-cell hemoglobinopathies. Differentiation by combined technetium and gallium scintigraphy. *Radiology* **1984**;153:807-812
43. Graham GD, Lundy MM, Frederick MR, Berger DE, O'Brian AW, Brown TJ. Scintigraphy detection of osteomyelitis with ^{99m}Tc-MDP and ⁶⁷Ga-citrate. *J Nucl Med* **1983**;24:1019-1022
44. Armas RR, Goldsmith SJ. Gallium scintigraphy in bone infarction: correlation with bone imaging. *Clin Nucl Med* **1984**;9:1-3
45. Collier DB, Carrera GF, Johnson RP, et al. Detection of femoral head avascular necrosis in adults by SPECT. *J Nucl Med* **1985**;26:979-987
46. Dihlmann W. CT analysis of the upper end of the femur: the asterisk sign and ischaemic bone necrosis of the femoral head. *Skeletal Radiol* **1982**;8:251-258
47. Magid D, Fishman EK, Scott WW, et al. Femoral head avascular necrosis. CT assessment with multiplanar reconstruction. *Radiology* **1985**;157:751-756
48. Steinberg ME, Brighton CT, Steinberg DR, Tooz SE, Hayken GD. Treatment of avascular necrosis of the femoral head by combination of bone grafting decompression and electrical stimulation. *Clin Orthop* **1984**;186:137-153
49. Totty WG, Murphy WA, Ganz WI, et al. Magnetic resonance imaging of the normal and ischemic femoral head. *AJR* **1984**;143:1273-1280
50. Mitchell DG, Kressel HY, Arger PH, Dalinka MK, Spritzer CE, Steinberg ME. Avascular necrosis of the femoral head: morphologic assessment by MR imaging with CT correlation. *Radiology* **1986**;161:739-742
51. Mitchell MD, Kundel JL, Steinberg ME, Kressel HY, Alavi A, Axel L. Avascular necrosis of the hip: comparison of MR, CT, and scintigraphy. *AJR* **1986**;147:67-71
52. Bassett LW, Gold RH, Reichter MA, et al. Magnetic resonance imaging in the early diagnosis of ischemic necrosis of the femoral head: preliminary results. *Clin Orthop* **1987**;214:237-248
53. Coleman BG, Kressel HY, Dalinka MK, Scheibler ML, Burk DL, Cohen EK. Radiographically negative avascular necrosis: detection with MR imaging. *Radiology* **1988**;168:525-528
54. Vogler JB III, Murphy WA. Bone marrow imaging. *Radiology* **1988**;168:679-693
55. Kangaroo H, Dietrich RB, Taira RT, et al. MR imaging of bone marrow in children. *J Comput Assist Tomogr* **1986**;10:205-209
56. Porter BA, Shields AF, Olson DO. Magnetic resonance imaging of bone marrow disorders. *Radiol Clin North Am* **1988**;24:269-289
57. Powers JA. Magnetic resonance imaging in marrow diseases. *Clin Orthop* **1986**;206:79-85
58. Glickstein MF, Burk LD Jr, Schiebler ML, et al. Avascular necrosis versus other diseases of the hip: sensitivity of MR imaging. *Radiology* **1988**;169:213-215
59. Genez BM, Wilson MR, Houk RW, et al. Early osteonecrosis of the femoral head: detection in high-risk patients with MR imaging. *Radiology* **1988**;168:521-524
60. Rao VM, Fishman M, Mitchell DG, et al. Painful sickle cell crisis: bone marrow patterns observed with MR imaging. *Radiology* **1986**;161:211-215
61. Mitchell DG, Joseph PM, Fallon M, et al. Chemical-shift MR imaging of the femoral head: an in vitro study of normal hips and hips with avascular necrosis. *AJR* **1987**;148:1159-1164
62. Lang P, Jergesen HE, Moseley ME, Block JE, Chafetz NI, Genant HK. Avascular necrosis of the femoral head: high-field-strength MR imaging with histologic correlation. *Radiology* **1988**;169:517-524
63. Hawker H, Neilson H, Hayes RJ, Serjeant GR. Haematological factors associated with avascular necrosis of the femoral head in homozygous sickle cell disease. *Br J Haematol* **1982**;50:29-34
64. Dean J, Schechter N. Sickle-cell anemia: molecular and cellular bases of therapeutic approaches. *N Engl J Med* **1978**;299:752-763
65. Chang H, Ewert SM, Bookchin RM, Nagel RL. Comparative evaluation of 15 antisickling agents. *Blood* **1983**;61:693-704
66. Johnson FL, Look AT, Gockerman T, Ruggiero MR, Dalla-Pozzo L, Billings FT III. Bone marrow transplantation in a patient with sickle-cell anemia. *N Engl J Med* **1984**;311:780-783
67. Thomas ED. Marrow transplantation for nonmalignant disorders. *N Engl J Med* **1985**;312:46-48
68. Ehman RL, Berquist TH, McLeod RA. MR imaging of the musculoskeletal system: a 5-year appraisal. *Radiology* **1988**;166:313-320
69. Beltran J, Herman LJ, Burk JM, et al. Femoral head avascular necrosis: MR imaging with clinical-pathologic and radionuclide correlation. *Radiology* **1988**;166:215-220
70. Kieft GJ, Bloem JL, Obermann WR, Verbout AJ, Rozing PM, Doornbos J. Normal shoulder: MR imaging. *Radiology* **1986**;159:741-745
71. Seeger LL, Ruszkowski JT, Bassett LW, Kay SP, Kahmann RD, Ellman H. MR imaging of the normal shoulder: anatomic correlation. *AJR* **1987**;148:83-99

Book Review

Ultrasound. Its Chemical, Physical, and Biological Effects. Edited by Kenneth S. Suslick. New York: VCH, 336 pp., 1988. \$65

This clearly written text is aimed primarily at engineers, physicists, and chemists. However, four of its eight chapters might be of interest to radiologists and radiologic physicists specializing in ultrasound. In addition to a complete bibliography and description of the major research on the biological, physical, and chemical effects of ultrasound, the authors describe each phenomenon in concise but readable text and supply the relevant equations needed for theoretical prediction. They are careful to identify those effects for which theoretical descriptions do not match experimental results, and they describe the experimental difficulties in measuring the effects of ultrasound.

Chapter 1, by A. A. Atchley and L. A. Crum, on acoustic cavitation and bubble dynamics covers the same material as G. R. ter Haar in chapter 12 of C. R. Hill's *Physical Principles of Medical Ultrasonics* (New York: Wiley & Sons, 1986), but in much more detail. In addition, the separate effects of the fluid's physical factors on cavitation thresholds are explored thoroughly. This chapter is the best one in the book, and the material it contains is not available elsewhere in such an easily readable form.

Chapter 2, by J. A. Rooney, on other nonlinear acoustic phenomena, is of marginal interest to the radiologic physicist. However, it clearly describes acoustic streaming, emulsification and bubble oscillation. A section on measurement of radiation force for acoustic dosimetry is the only part of the book that describes the measurement of ultrasound pressure or power. Chapters titled "Industrial Applications of Ultrasound," "Homogeneous Sonochemistry," "Heterogeneous Sonochemistry," and "Sonoluminescence" are not applicable to the effects of medical ultrasound.

The book ends with two chapters on the biological effects of ultrasound, one by L. A. Frizzell and one by G. R. ter Haar. Some of the material in these chapters overlaps, but this repetition allows each chapter to be read independently. Dr. Frizzell's chapter covers the biological effects of cavitation and discusses experiments with cells, plants, and insects. Although this is a short chapter, the references are quite complete. The last chapter, by G. R. ter Haar, covers the same material that was covered in chapter 12 of Hill's book, but in less detail. One excellent feature of this chapter, however, is the summary list that relates cavitation threshold values to acoustic pressure, frequency, gas content, sample temperature, and sample viscosity. Dr. ter Haar also catalogs the mechanical effects of ultrasound by the physical structure of the insonated tissue, which helps clarify the effects previously described.

The only disappointment in this text is the poor index, which apparently was matched to an earlier version of the book containing fewer pages. By chapter 4, indexed references are incorrect by five pages.

Although this book may be too technical for many radiologists, it does provide information about the effects of ultrasound and the reasons why physicists cannot completely rule out all possibility of biological damage from some intensity levels of medical ultrasound.

Carolyn Kimme-Smith
University of California, Los Angeles
Los Angeles, CA 90024-1721

Progress in Radiology

Three-Dimensional Techniques and Artificial Intelligence in Thallium-201 Cardiac Imaging

E. Gordon DePuey,¹ Ernest V. Garcia,¹ and Norberto F. Ezquerro²

Tomographic myocardial perfusion imaging is gaining widespread acceptance as the noninvasive imaging technique of choice for the diagnosis of coronary artery disease and myocardial ischemia. However, interpretation of complex multiprojection tomographic data is difficult, particularly for the novice observer. For this reason a number of tools have been developed that aid in identifying perfusion defects, determining whether they represent actual coronary disease or artifact, assigning them to coronary vascular territories, and deciding whether they represent scar or ischemia. These tools include polar-coordinate maps and three-dimensional (3-D) surface displays, which compress data from multiprojection tomographic slices into single images. Moreover, artificial intelligence (AI) techniques, which replicate the thought processes of well-trained experts in image interpretation, allow inexperienced observers to rapidly become competent in the use of this new imaging technique.

Polar-Coordinate Maps

There is increasing evidence that single-photon emission CT (SPECT) offers a significant advantage over planar imaging for thallium-201 myocardial perfusion imaging. The ability to separate the left ventricular myocardium from overlying background activity results in considerable improvement in image contrast resolution. Furthermore, the ability to resolve the entire myocardium in multiple oblique, orthogonal tomo-

graphic slices avoids the problem of superimposition of myocardial walls inherent to planar techniques. Therefore, with ²⁰¹Tl-SPECT, the individual vascular territories of the major coronary arteries can be resolved, thereby improving our ability not only to detect but also to localize coronary disease. Investigators have demonstrated SPECT to be superior to planar imaging in the detection of remote myocardial infarction in humans [1, 2]. Reports have shown that SPECT is also superior in the identification and localization of myocardial ischemia in images obtained immediately after injection of thallium-201 at peak exercise [3-6]. In particular, disease of the left circumflex coronary artery, detected by planar imaging with sensitivities considerably less than 50% in most reported series, is detected with sensitivities comparable to those in other coronary lesions.

Despite these advantages of SPECT imaging, review and interpretation of multislice tomographic data are often difficult and time-consuming, particularly for the physician accustomed to the conventional planar images used in the majority of general nuclear medicine imaging procedures. Typically a myocardial SPECT study comprises about 10 short-axis slices, eight vertical long-axis slices, and eight horizontal long-axis slices for both immediate postexercise and also 3- to 4-hr delayed studies. Thus, there are a total of about 52 images to review for each study. To make interpretation even more tedious, differentiation of scar from ischemia requires that corresponding stress and delayed slices be compared.

Received November 2, 1988; accepted after revision January 6, 1989.

This work was supported in part by grant R29-LM 04692 from the National Library of Medicine and by a seed grant from the Emory/Georgia Tech Biomedical Technology Research Center.

¹Department of Radiology, Emory University School of Medicine, 1364 Clifton Rd. N.E., Atlanta, GA 30322. Address reprint requests to E. G. DePuey.

²Office of Interdisciplinary Programs, Georgia Institute of Technology, Atlanta, GA 30332.

Display of such multislice data on conventional X-ray or nuclear medicine film is awkward, and it is difficult to match image intensity and contrast for both the immediate and delayed images. Review of multislice data in dynamic format directly on the computer cathode ray tube is preferable, but nevertheless requires considerable interpretive expertise. For these reasons, to allow for easier assimilation of 3-D tomographic data, a number of display formats have been devised.

In a method developed at Emory University School of Medicine, 3-D tomographic myocardial data are displayed two-dimensionally (2-D) by using a polar-coordinate or bull's-eye map [7]. This map is constructed from tomographic slices obtained in orthogonal planes parallel to and perpendicular to the long axis of the left ventricle (Fig. 1). From the vertical long-axis slice with the largest cavity length, the operator selects the short-axis cuts, which extend from the base of the left ventricle to the apical cap. To ensure proper slice selection, guidelines for slice selection must be followed carefully. For instance, the apical-most slice must include as much apical myocardium as possible without extending into the left ventricular cavity. From the short-axis cut, falling halfway between the apex and the base, the operator then defines the center of the left ventricular cavity and the radius of search.

The maximal count circumferential profiles for each short-axis cut are then generated automatically from the most apical to the most basal cut. The actual raw counts are extracted and used without normalization. This procedure is performed for each stress and each delayed tomographic study. Percent washout of circumferential profiles is also calculated by using the profiles of the corresponding anatomic cut for stress and delayed tomography, respectively.

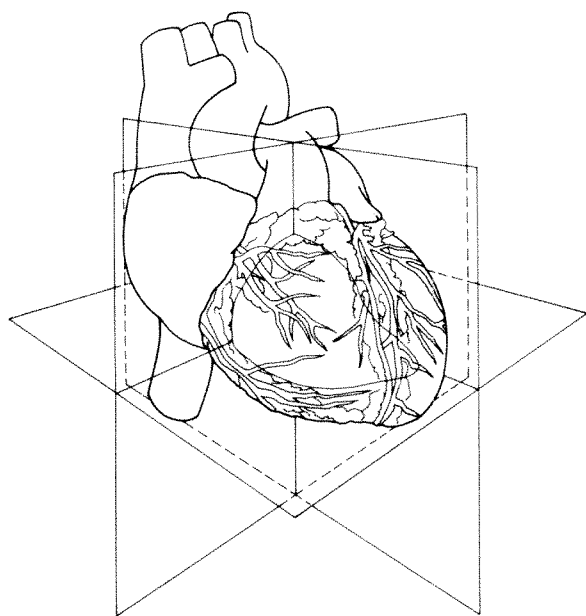


Fig. 1.—Orthogonal planes oriented parallel and perpendicularly to long axis of left ventricle, from which tomographic myocardial slices are reconstructed.

In Figure 2A, alternating short-axis slices of the left ventricle are displayed from base to apex. Approximately 12 slices are obtained from a normal-sized heart. In this example there is a defect in the septum, which is highlighted in the middle slice. In Figure 2B this slice has been divided into 40 sectors, each 9° . The septum is represented by the sectors from 90° to 180° . The maximal counts per pixel within each sector is determined. In Figure 3 these 40 values have been plotted as a circumferential profile of the maximal counts/pixel vs angular location. A similar profile is constructed for each slice except the first two containing the apex, which are represented by a single value representing the maximal counts/pixel within the entire slice. In most cases the apical slice extends somewhat beyond the actual apex of the heart, encompassing both myocardium and background activity distal to the apex. Therefore, the count density of the apical portion of the bull's-eye is dependent not only on the count density within the apical myocardium, but also on the distance beyond the apex that the apical slice extends. This is the *partial-volume effect*. To account for variations in the number of slices per study, these circumferential count-density profile curves are interpolated to produce a total of 15 profiles. Each of the rectangular coordinate profiles is translated into a polar-coordinate profile (Fig. 3B), which displays the curve as a circle composed of 40 pixels. In Figure 3C these data are displayed as a polar map called a bull's-eye plot, which consists of a series of 15 concentric rings with the apex at the center and the base at the periphery. Individual bull's-eyes are constructed for the stress and delayed images (Fig. 4). In this display format the stress and delayed bull's-eyes are adjusted by multiplying

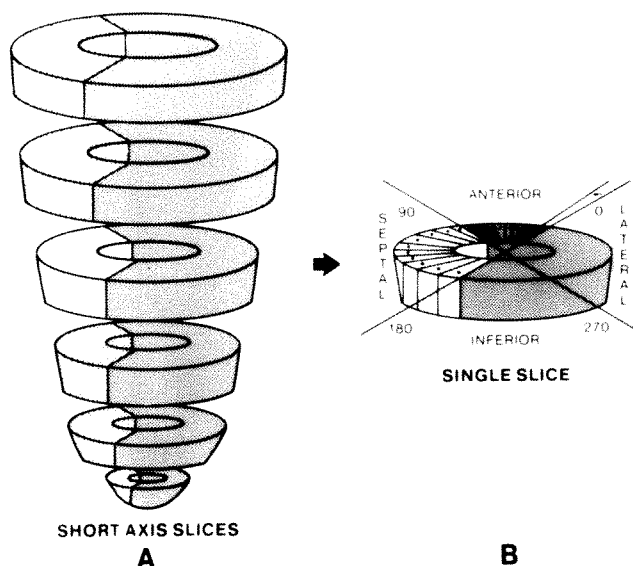


Fig. 2.—Division of short-axis tomographic myocardial slices into 9° wedges for circumferential profile analysis. (Reprinted with permission from DePasquale et al. [7].)

Fig. 3.—Circumferential profile analysis with translation into polar-coordinate bull's-eye plot. ANT. = anterior; SEP. = septal; INF. = inferior; LAT. = lateral. (Reprinted with permission from DePasquale et al. [7].)

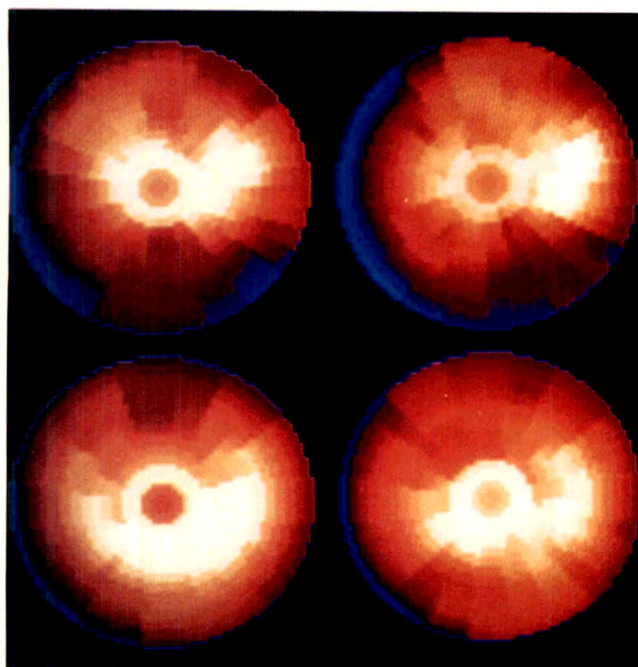
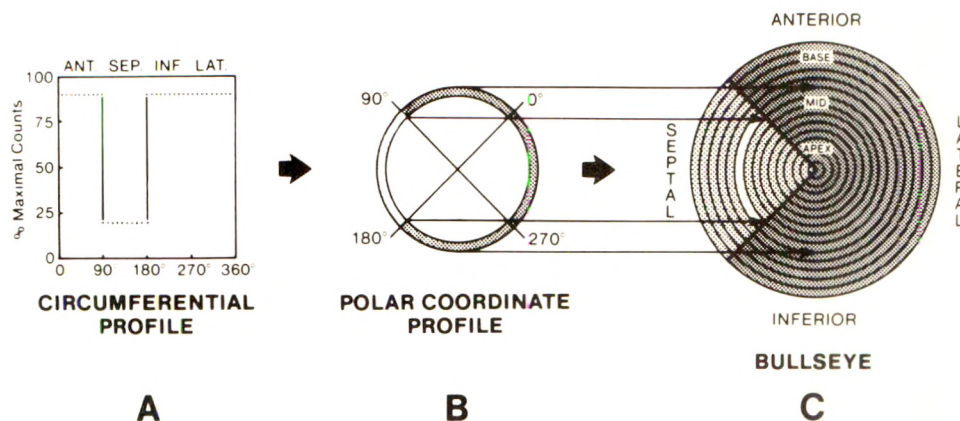


Fig. 4.—Bull's-eye circumferential profile plots obtained immediately after exercise (left) and at 3-hr delayed interval (right) are shown for normal male (top) and normal female (bottom).

each pixel in the delayed bull's-eye by the ratio of the maximal counts/pixel in the stress bull's-eye to the maximal counts/pixel in the delayed bull's-eye.

In addition, functional plots of thallium-201 washout (stress minus delayed counts per pixel divided by stress counts per pixel) can be displayed. A reversibility plot, highlighting areas of tracer redistribution into areas of ischemia present immediately after exercise, has also been developed [8].

A similar method of circumferential profile analysis with polar-coordinate plots has been developed at Cedars Sinai Medical Center in Los Angeles [9]. In the Cedars approach the apical (central) portion of the plot is derived from vertical long-axis slices passing through the apex. Apical count density is therefore much less dependent on operator selection of the apical-most short-axis slice, and the partial-volume effect influencing the count density of the apex is somewhat less marked. The arcs between 60° and 120° of each vertical

long-axis cut are mapped into the central region of the display to depict apical thallium-201 distribution. Immediately surrounding the apical region, the entire (0–360°) most apical short-axis stress profile is mapped with all of the following short-axis count profiles being mapped in increasingly larger circles until the most basal count profile is reached. In the 2-D Cedars polar map, the size of the display always remains the same, so the size of the left ventricle is reflected by the number of count profiles that are mapped. Thus, in larger left ventricles, the band representing each slice is thinner compared with smaller left ventricles. In the Emory bull's-eye method, the circumferential profiles are scaled for display to a percentage of maximum counts in the entire left ventricle [10], whereas in the method developed at Cedars, each profile is normalized to the maximum pixel value for that profile.

Anatomic features of the left ventricle, count-density distribution, attenuation effects, and artifacts seen in oblique tomographic slices are also present in polar-coordinate maps, which again are only a 3-D representation of the 2-D tomographic slices. However, the polar-coordinate maps allow relationships of count density in various myocardial regions to be compared more readily. Salient features of normal count-density distribution within the left ventricular myocardium can be noted for males and females in the normal bull's-eye images in Figure 3. In both men and women, lateral-wall count density is greater than that in the septum (lateral:septal ratio equals approximately 1.2:1). This is because the lateral wall is thicker than the septum in normal individuals [11] and also because the septum is attenuated to a greater degree in the 180° imaging arc. In nearly all patients, count density is markedly decreased at the base of the septum, partly because the proximal one-fourth to one-third of the septum consists of a membrane rather than muscle and also because of partial-volume effects. In men, the inferior wall of the left ventricle has a lower count density because of attenuation of the inferior wall by the left hemidiaphragm and also the overlying right ventricle. In women, this effect is counterbalanced by attenuation of the anterior wall by the breast. Attenuation of the anterior wall in women will depend on the size, density, and position of the overlying breast. The appearance of the apex is variable, in part because of the methods used to reconstruct the apex in the polar-coordinate map, but also

because the degree of physiologic apical thinning varies among patients.

Quantitative Analysis of Circumferential Profile Maps

In order to facilitate interpretation of bull's-eye plots and to provide a quantitative estimate of the extent of abnormalities and their severity, patient data are compared with a composite file of gender-matched normal control subjects, each with a less than 5% likelihood of coronary artery disease as determined by Bayesian analysis of risk factors.

Comparison of patient data with normal limits results in the conversion of the bull's-eye into a *standard deviation map* displaying pixels color-coded to the number of standard deviations (SD) below normal [7]. Pixels 1–2 SD below mean normal are coded in tan, pixels 2–3 SD below normal in brown, pixels 3–5 SD below normal in blue, pixels 5–7 SD below normal in green, and pixels more than 7 SD below normal in black. This analysis results in establishing additional profile curves representing 2.5 SD below the mean normal response as the threshold for defect detection. Points falling below this established normal limit are plotted in a *blackout bull's-eye*, in which the black region within the bull's-eye plot defines the extent of the perfusion abnormality (Fig. 5). The location, size, and shape of these blacked-out regions are used in conjunction with heuristic rules developed from the

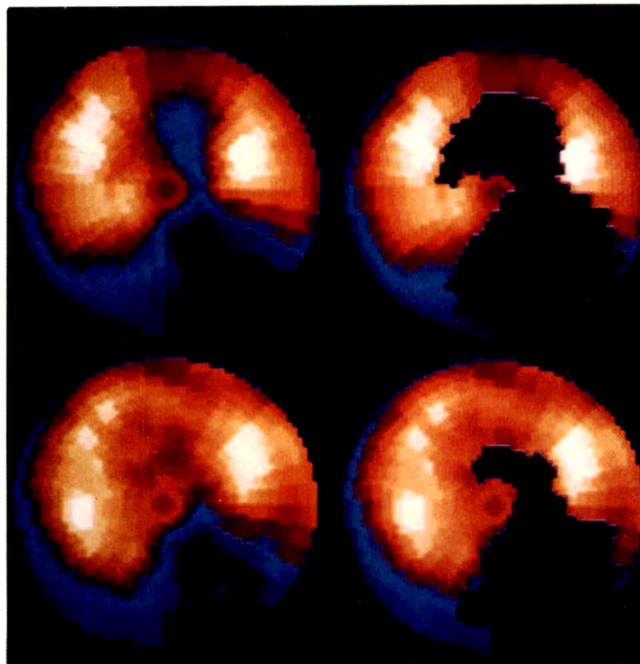


Fig. 5.— ^{201}Tl -SPECT study in 56-year-old man with prior myocardial infarct who presented with recurrent angina pectoris.

Top, Immediate postexercise images show moderate perfusion defect involving anterolateral wall and large defect in inferior/inferolateral wall. Blackout standard deviation map (top right), in which pixels >2.5 SD below mean normal limits are blackened, highlights abnormalities.

Bottom, Delayed images show considerable anterolateral redistribution, indicating ischemia. Inferior/inferolateral defect is fixed, consistent with prior infarction and myocardial scarring.

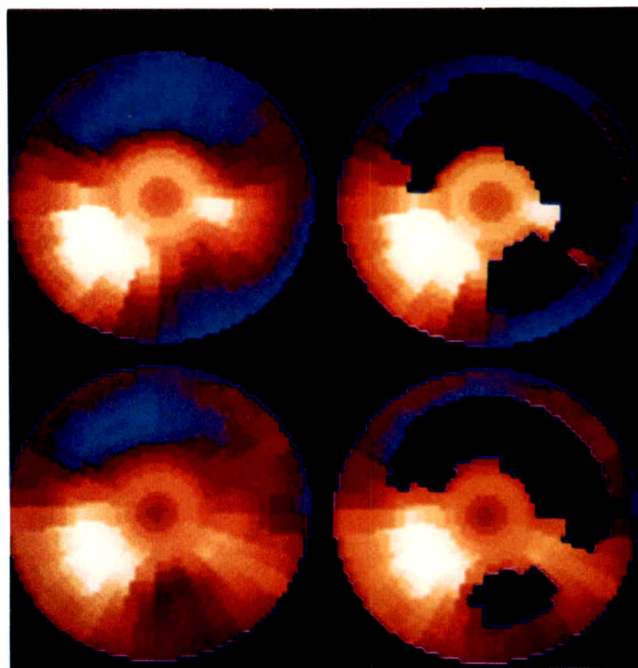


Fig. 6.—Woman with large anteriorly and laterally positioned breasts. Soft-tissue attenuation creates apparent anterior and lateral defect in both immediate postexercise (top) and delayed (bottom) images, mimicking myocardial infarction.

pilot group to identify the stenosed coronary artery associated with specific patterns of perfusion abnormality.

It must be emphasized, however, that this method does not eliminate the problem of scan artifacts. In fact, since areas of the left ventricle that deviate from the normal count-density distribution are highlighted, artifacts are accentuated. For example, in a woman with large breasts, the decrease in anterior count density is greater than that predicted by the normal female file, consisting of women with average-sized breasts. If such a patient's quantitative bull's-eye plots were compared with the normal female file, there would be an apparent fixed anterior defect, mimicking anterior myocardial infarction (Fig. 6).

Clinical Applications

Application of the Emory bull's-eye quantitative technique to a prospective group of 210 patients (179 with and 31 without coronary artery disease) resulted in an overall sensitivity of 95%, specificity of 74%, and accuracy of 92% for detecting the presence or absence of $\geq 50\%$ coronary luminal diameter narrowing [7]. The ability of this analysis to identify individual coronary stenoses is displayed in Figure 7 for each major coronary artery and for the left circumflex and right coronary arteries combined. The results of this prospective evaluation of the method show a high sensitivity and specificity for the detection of coronary artery disease and of individual coronary stenoses. The typical appearance of bull's-eye stress and delayed plots in myocardial ischemia and infarction is displayed in Figure 5.

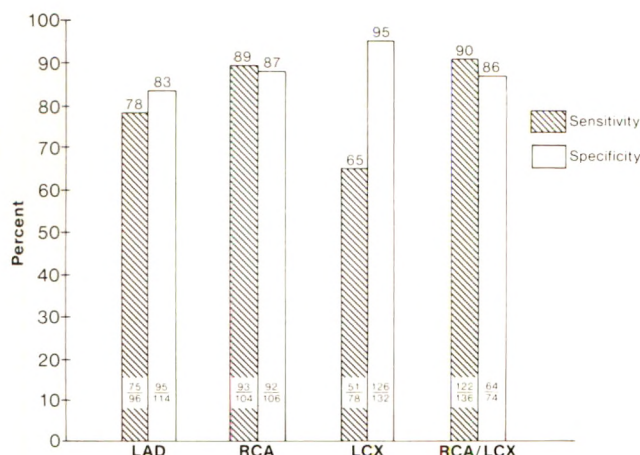


Fig. 7.—Detection of individual coronary artery stenoses with thallium-201 tomography. LAD = left anterior descending; RCA = right coronary artery; LCX = left circumflex. (Reprinted with permission from DePasquale et al. [7].)

3-D Display

Methods are being developed to extend the functional 2-D polar map approaches to 3-D. Three-dimensional representations of myocardial perfusion SPECT studies should aid physicians in the visualization and determination of the extent and severity of perfusion defects. At present, the investigated 3-D rendering methods code the myocardial perfusion information on a 3-D surface. These 3-D surface display approaches either render a surface that approximates the actual myocardial shape [12, 13] or a surface that models the shape of the myocardium, such as an ellipsoid [14, 15].

Surface Rendering

Methods that render the actual myocardial shape have their main processing steps in common with methods developed for 3-D display of bony surfaces from CT imaging [16]. The input is usually a set of contiguous 2-D tomographic slices. Each slice is made up of a matrix of voxels, or volume elements. From these sets of voxels, an algorithm generates a binary representation of the myocardium by determining whether a voxel is part of the myocardium (setting that voxel to 1) or outside the myocardium (setting that voxel to 0). Often a single count threshold is used to determine this classification. Once all the voxels have been classified as 0 or 1, another computer algorithm performs surface tracking of the interface between the zeros and the ones. To represent the myocardium, an outside (epicardium) and an inside (endocardium) surface may be generated, although present methods use a single surface to code the myocardial perfusion information.

Once a 3-D surface is generated in the memory of the computer, it can be used to generate a set of multiple projections that may be animated in cinematic form to give the illusion of a moving 3-D surface. A number of common processing tricks are used to shade the surfaces to give this

illusion a sense of reality. Each projection is coded so that the surfaces "further" from the viewer are shaded dimmer and the ones "closer" are brighter. If a distant surface falls behind a front surface along the viewer's line of sight, it is hidden from the display at that projection. A light source is assumed in generating these projections, so that if a surface is perpendicular to the "rays" from the light source it is shaded brighter, and if it is parallel to the rays it is dimmer. Figure 8 illustrates an application of this methodology as implemented by Nowak [12].

Surface Modeling

A more direct approach to extend the 2-D polar maps (bull's-eye displays) to 3-D is being developed in a joint project between Emory University and the Georgia Institute of Technology [14, 15, 17]. In this approach, the myocardial surface is modeled as a 3-D ellipsoid covered by small tiles of equal dimensions. The same maximal-count circumferential profiles that are mapped onto the 2-D bull's-eye displays are now mapped onto the 3-D ellipsoidal surface with length and width relative to actual myocardial dimensions. Each circumferential profile count value that is used to assign a color to the bull's-eye map is also used to assign the same color to a tile on the ellipsoidal surface representative of the thallium-201 concentration in that region of the myocardium. In addition to this color coding, each tile is further shaded for each generated

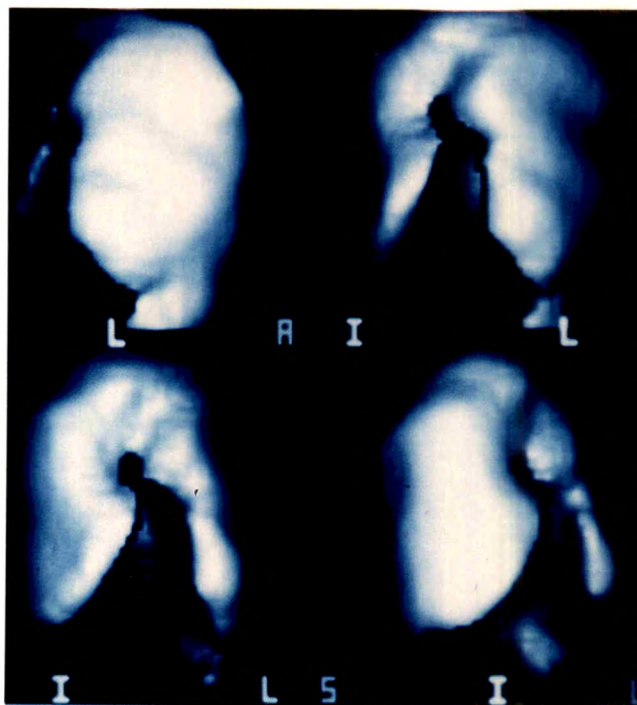


Fig. 8.—Surface rendering of three-dimensional thallium-201 perfusion distribution in patient with left circumflex coronary artery disease. Each panel shows slightly different rotation (apex pointing up) of hypoperfused inferolateral myocardial wall. Perfusion defect is shown by missing region between inferior (I) and lateral (L) walls. (Courtesy of D. Nowak, General Electric, Milwaukee, WI.)

2-D projection to give the illusion of a 3-D display, as described in the surface-rendering section. These projections are then animated to give the illusion of a left ventricular myocardium rotating about the patient's long axis. Figure 9 shows an example of the displays.

Ideally, accurate assessment of the extent and severity of coronary artery disease requires the integration of physiologic information derived from thallium SPECT and anatomic information derived from coronary arteriography. To accomplish this goal, the above-described surface model representing myocardial perfusion is currently being enhanced by superimposing the patient's own coronary arterial tree. The patient-specific coronary arterial tree is obtained from a 3-D geometric reconstruction performed on simultaneously acquired, digital, biplane angiographic images [17]. The coronary arterial tree is approximated by successive conical segments. After the arterial tree is reconstructed in 3-D, it is scaled, transformed (warped), and rotated to fit onto the myocardial ellipsoidal surface. The left and right coronary arteries are fixed onto the myocardial perfusion ellipsoidal model by registering the proximal left anterior descending coronary artery onto the region corresponding to the anterior interventricular groove and the posterior descending artery onto the inferior interventricular groove. The bottom panels of Figure 9 illustrate this unified display.

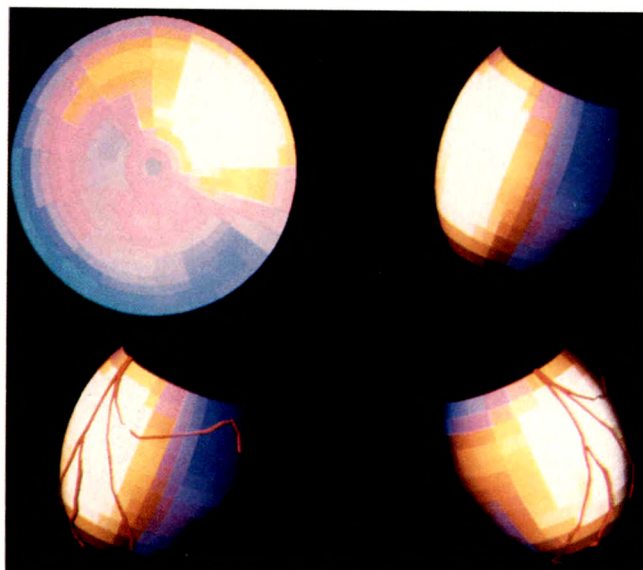


Fig. 9.—Three-dimensional heart models of patient exhibiting hypoperfusion of inferior and inferolateral myocardial walls.

Top left, Bull's-eye polar map is seen with perfusion defect represented by shades of blue.

Top right, Corresponding three-dimensional ellipsoidal model of myocardium.

Bottom, Two different orientations of unified model where patient's left coronary arteries have been registered onto ellipsoidal perfusion model. Bottom left panel shows high-grade lesion at midcourse of left circumflex coronary artery.

(Results generated by C. D. Cooke and J. Peifer.)

Artificial Intelligence

Artificial intelligence (AI) is the ability to emulate or replicate human capabilities, performances, and reasoning with computers [18]. In its purest form, AI is the use of a computer both to store human knowledge and to replicate human reasoning, which can access the knowledge to arrive at new conclusions based on the problem presented. In its most practical form, AI is the ability to arrive at the same or similar conclusions as a knowledgeable human regardless of which method was used.

AI vs Conventional Computer Methods

Traditionally, conventional computer approaches have been developed to perform exact mathematical calculations by using predetermined algorithmic control. These conventional deterministic approaches have the disadvantage that many problems are too complex for a step-by-step algorithmic solution. Moreover, these conventional techniques fail when presented with any input data that are unreliable, ambiguous, conflicting, noisy, or corrupted. AI, on the other hand, deals with symbolic rather than numeric information. AI reaches conclusions through heuristically defined rules derived from such subjective sources as intuitive judgment, knowledge obtained from experience, rules of thumb, and the thought process of experts in the field. Thus, similar to the way humans solve problems, the AI approach is capable of decision making despite incomplete knowledge or incomplete input information by pursuing a line of reasoning rather than a deterministic sequence of steps.

Expert Systems

Four major application areas traditionally have been associated with AI [19]: natural language processing, problem solving and planning, computer vision, and expert systems. Expert systems are becoming commercially popular because they are implemented to circumvent the problem of having few experts in areas where many are needed. Thus, expert systems attempt to capture the knowledge or expertise of the human expert to provide it to a large number of nonexperts.

Most of the working examples of expert systems are in nonimaging areas. However, there are some attempts to develop AI systems in medical imaging. One of the first implementations of knowledge-based approaches in diagnostic imaging has been in image processing operations, where human decision making can be substituted by computer-based decision making. Some AI approaches have already been implemented to automatically delineate the borders of the left ventricle from multiple-gated equilibrium scintigraphic studies [20, 21]. In one approach, proposed by Duncan [20] of Yale University, the program uses the magnitude and direction of those edges that are easy to identify to detect the ventricular edges in noisy regions. Edge points in these noisy regions are only accepted if they conform to the general

shape expected of the left ventricle in the view under analysis. It is not very difficult to envision an improved implementation of the approach that would recognize when the automatic algorithm has failed, warn the operator to manually provide the missing edge strips, and learn from the operator's decisions in filling in the missing information. This type of automation can lead to standardization of acquisition protocols and measured parameters. Such automation should also lead to a reduction in the amount of time that the physician must devote to processing the study and a concomitant reduction in the cost of performing the study.

Example of an Expert System for Interpreting Myocardial Thallium-201 Distribution

An example of the power of AI tools is found in a preliminary version of an expert system that we have developed [22–24] to assist in diagnosing coronary artery disease from thallium-201 3-D myocardial distributions. After reviewing 291 studies from patients with coronary artery disease documented angiographically, we developed heuristic rules that best correlated the presence and location of perfusion defects on ^{201}Tl -SPECT studies with coronary lesions. The perfusion defects were identified from polar bull's-eye maps [7, 9] as pixels below gender-matched normal limits. Approximately 100 rules were structured as part of this preliminary system.

The system implemented is an inference engine where the location, size, and shape of each of the perfusion defects are automatically determined from features extracted from bull's-eye maps, as well as patient-related information. This information is used to fire, or execute, the rules to produce new facts or draw inferences. For each input parameter and for each rule, a certainty factor is assigned that is traced to infer the certainty of the identification and location of the coronary lesion. A diagram depicting how information flows in and out of the expert system is shown in Figure 10.

Figure 11 illustrates how the knowledge base, which contains the heuristic rules, was structured into 10 subsets of rules known as frames. For example, a frame called *DEFECT SHAPE* uses the descriptors of the perfusion defect identified by a feature extraction program to predict the shape of the

perfusion defect in a medically useful representation (such as basal, apical, standard, blob, and wraparound), whereas another frame called *PATIENT* deals with patient-related information independent of the perfusion defects. Ten frames have been defined: (1) *PATIENT*, in which patient-specific information is obtained; (2) *DEFECTS*, which obtains a set of descriptors for the feature extraction program to be used with subsequent frames; (3) *DEFECT SHAPE* and (4) *DEFECT LOCATION*, which use the symbolic description of the descriptors to determine the shape and location of each perfusion defect; (5) *ARTIFACT*, which uses patient information such as gender and age coupled with the defect shape and location to determine if this defect is a possible artifact; (6) *LAD*, (7) *LCX*, and (8) *RCA*, each used to assign incremental evidence that the perfusion defect corresponds to disease in the left anterior descending, left circumflex, and right coronary artery, respectively; (9) *UPDATE CORONARIES*, which combines the incremental evidence of coronary artery disease from all defects; and (10) *PATIENT CONDITION*, which draws conclusions regarding the overall condition of the patient and prints the final report.

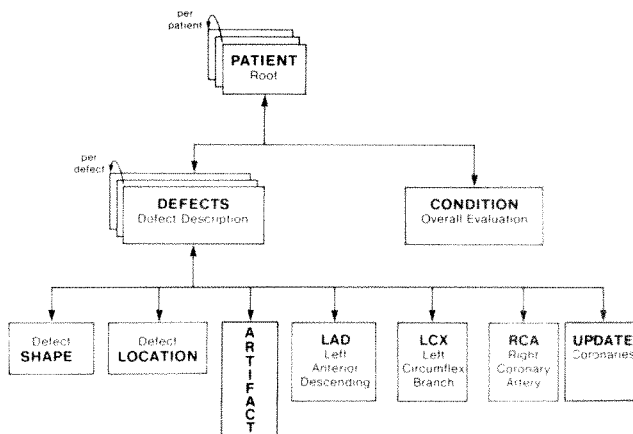


Fig. 11.—Knowledge-base frame configuration.

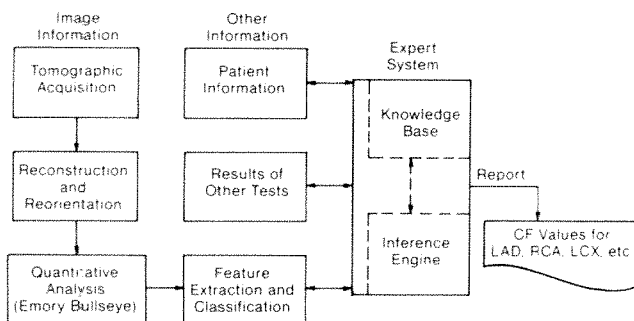


Fig. 10.—Information flow of knowledge-based system for interpreting thallium-201 myocardial distributions. CF = certainty factors; LAD = left anterior descending; RCA = right coronary artery; LCX = left circumflex.

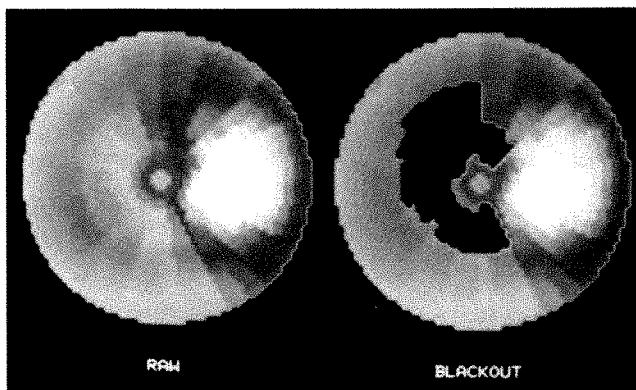


Fig. 12.—Stress bull's-eye polar representation of three-dimensional thallium-201 myocardial distribution before (*raw*) and after (*blackout*) comparison with normal limits in patient with single-vessel left anterior descending coronary artery disease.

A preliminary knowledge base, developed as 30 heuristic rules written in a format similar to the one described above, based on a review of 291 patient studies, was tested with a separate group of 50 patients comparing (1) the conclusions reached by the system, (2) the interpretation made by human experts, and (3) the results obtained from angiography. The results show that there was agreement in the identification of 41 of 42 patients with coronary artery disease, seven of eight normal patients, and 120 of 150 vascular territories when compared with angiographic results. When compared with human experts, there was agreement in the identification of 41 of 42 patients with coronary artery disease, seven of eight normal patients, and 138 of 150 vascular territories. Hence, excellent agreement was obtained with this initial testing set. These preliminary results also helped to identify some of the necessary refinements. Figure 12 shows a sample test patient's stress thallium-201 polar bull's-eye map where the perfusion defect is automatically delineated in black. The results obtained from the expert system for this patient's perfusion defect are as follows. The probability of each conclusion is given in parentheses after each statement: (1) *DEFECT SHAPE* is wraparound left anterior descending (0.4); *POSSIBLE ARTIFACT* is none; *WALL LOCATIONS* are antero-septal (0.83), septoanterior (0.77), septoinferior (0.55), and anterolateral (0.27); *PATIENT CONDITION* is abnormal (0.95); and *DISEASED CORONARIES* are left anterior descending (0.94), right coronary artery (0.27), and left circumflex (0.11).

Summary

Three-dimensional reconstruction techniques including bull's-eye polar-coordinate maps, surface rendering, and surface modeling have been developed that help interpreting physicians assimilate complex 3-D tomographic data. Comparison of patient data with normal files highlights myocardial perfusion abnormalities, thus facilitating their recognition. In addition, AI systems that use heuristically defined rules derived from an expert knowledge base assist inexperienced observers in drawing conclusions regarding scan abnormalities.

REFERENCES

1. Tamaki S, Najajima H, Murakami T, Yui Y, Kambara H, Kadota K. Estimation of infarct size by myocardial emission computed tomography with thallium-201 and its relation to creatine kinase-MB release after myocardial infarction in man. *Circulation* **1982**;66(5):994-1001
2. Ritchie JL, Williams DL, Harp G, Stratton JL, Caldwell JH. Transaxial tomography with thallium-201 for detecting remote myocardial infarction. *Am J Cardiol* **1982**;50:1236-1241
3. Go RT, Cook SA, McIntyre WJ, et al. Comparative accuracy of stress and redistribution thallium-201 cardiac single photon emission transaxial tomography and planar imaging in the diagnosis of myocardial ischemia (abstr). *J Nucl Med* **1982**;23:24
4. Nohara R, Kambara H, Suzuki Y, et al. Stress scintigraphy using single-photon emission computed tomography in the evaluation of coronary artery disease. *Am J Cardiol* **1984**;53:1250-1254
5. Maddahi J, Van Train KF, Wong C, et al. Comparison of thallium-201 SPECT and planar imaging for evaluation of coronary artery disease (abstr). *J Nucl Med* **1986**;27:999
6. Kiat H, Maddahi J, Merz R, et al. Comparison of Tc-99m methoxy isobutyl isonitrile (MIBI) with Tl-201 imaging by planar and SPECT techniques for assessment of coronary disease (abstr). *J Nucl Med* **1988**;29:791
7. DePasquale EE, Nody AC, DePuey EG, et al. Quantitative rotational thallium-201 tomography for identifying and localizing coronary artery disease. *Circulation* **1988**;77:316-327
8. Klein L, Garcia E, DePuey EG, et al. Reversibility bull's-eye: a new polar bull's-eye map to quantify reversibility of stress induced SPECT Tl-201 myocardial perfusion defects (abstr). *J Nucl Med* **1987**;28:642
9. Garcia E, Van Train K, Maddahi J, et al. Quantification of rotational thallium-201 myocardial tomography. *J Nucl Med* **1985**;26:17-26
10. Caldwell J, Williams D, Ritchie J. Single photon emission computed tomography: validation and application for myocardial perfusion imaging. In: Pohost G, Higgins C, Morganroth J, Ritchie J, Schelbert H, eds. *New concepts in cardiac imaging* 1985. Boston: Hall, **1985**:115-136
11. Clausen M, Bice AN, Civelek C, Hutchins GM, Wagner HN. Circumferential wall thickness measurements of the human left ventricle: reference data for thallium-201 single-photon emission computed tomography. *Am J Cardiol* **1986**;58:827-831
12. Nowak DJ. Three dimensional surface display of nuclear medicine images. *J Nucl Med* **1988**;29:967
13. Miller TR, Starren JB, Grothe RA. Three-dimensional display of positron emission tomography of the heart. *J Nucl Med* **1988**;29:530-537
14. Ezquerro NF, Zerbi M, Cooke CD, Garcia E. A method of 3D display of arterial structure superimposed on myocardial perfusion distribution (abstr). *J Nucl Med* **1987**;28:675
15. Peifer JW, Cooke CD, Skelton JP, et al. 3D visualization of coronary arterial tree superimposed on myocardial perfusion distribution (abstr). *J Nucl Med* **1988**;29:810
16. Herman GT. Computerized reconstruction and 3-D imaging in medicine. *Ann Rev Comput Sci* **1986**;1:153-179
17. Cooke C, Jofre L, Klein L, et al. 3-dimensional reconstruction of arterial structure from biplane angiography. In: *Proceedings of IEEE technicon '87 conference*. New York: Institute of Electrical and Electronics Engineers, **1987**; cat. no. 87-82761:31-34
18. Winston PH. *Artificial intelligence*. Menlo Park, CA: Addison-Wesley, **1984**
19. Nilsson N. *Principles of artificial intelligence*. Palo Alto, CA: Toiga, **1980**
20. Duncan J. Intelligent determination of left ventricular wall motion from multiple view, nuclear medicine sequences. In: *Proceedings of 8th annual IEEE SCAMC*. New York: Institute of Electrical and Electronics Engineers, **1984**:265-267
21. Niemann H, Bunke H, Hoffman J, et al. A knowledge based system for analysis of gated blood pool studies. In: *IEEE Trans. Pattern Anal. Machine Intell.* New York: Institute of Electrical and Electronics Engineers, **1985**; PAMI-7, no. 3:246-258
22. Garcia E, Ezquerro N, DePuey EG, et al. An artificial intelligence approach to interpreting thallium-201 3-dimensional myocardial distributions (abstr). *J Nucl Med* **1986**;27:1005
23. Ezquerro NF, Garcia EV, DePuey EG, et al. Development of an expert system for interpreting medical images. In: *Proceedings of IEEE International Conference on Systems, Man and Cybernetics*, vol. 1. New York: Institute of Electrical and Electronics Engineers, **1986**:205-210
24. Ezquerro NF, Shapiro S, Garcia EV, et al. A knowledge based system for interpreting cardiovascular nuclear medicine images. In: *Computers in cardiology*. New York: IEEE Computer Society, **1987**; CH 2476-0:3-8

Progress in Radiology

Computer Applications in Radiology Education: A Challenge for the 1990s

Franklin N. Tessler¹

Of all the medical specialties, diagnostic radiology is the one most dependent on computer technology. Many of the imaging techniques introduced during the last 20 years would not exist were it not for the sophisticated hardware and software that drives them. However, educational applications of computers in the radiologic sciences have been noticeably lacking. Although isolated projects have successfully shown the capability of computers to teach radiology [1-6], progress has lagged behind other specialties [4]. This article begins with a brief review of potential areas of computer application, followed by a discussion of hardware and software development, and concludes with practical suggestions for the radiologist wishing to write instructional software.

Areas of Application

Computer applications in radiology may be classified into three broad categories: computer-aided preparation and filing of teaching materials, computer-assisted testing, and computer-assisted instruction.

Computer-Aided Case Filing and Preparation of Teaching Materials

This area has received the most attention in the literature, and encompasses applications ranging from preparing slides to maintaining and searching for teaching files. Storing instruc-

tive cases is a task for which the desktop computer is well suited [7-9]. Appropriate data-base management software is available for most brands of equipment. In planning a computer-based filing system, the radiologist should carefully consider the uses to which retrieved data will be put. For example, cases kept purely for teaching purposes may not require as much demographic information as those on which research will be based.

Computers also are ideal for preparing educational materials such as lecture handouts, exhibits, and slides [8, 10-12]. Although computers have not revolutionized the process, they have considerably shortened the time from concept to finished product. The quality of 35-mm slides produced with a desktop computer and film recorder rivals the work of expensive service bureaus, at a much lower cost [12]. Film recorders are available for well under \$10,000.

Computer-Assisted Testing

Test generation is another educational task that is amenable to automation [13, 14]. In its simplest form, the computer is used to prepare an examination from a bank of prestored questions. The test is administered manually, however. A more sophisticated approach involves having the examination given and scored by computer. The primary advantage of the latter method is that the student can be given immediate feedback for every response, a feature that has been shown to improve the learning experience [14].

Received November 1, 1988; accepted after revision January 26, 1989.

¹ Department of Radiological Sciences, UCLA School of Medicine, CHS BR-272, 10833 Le Conte Ave., Los Angeles, CA 90024-1721. Address reprint requests to F. N. Tessler.

Computer-Assisted Instruction

Computer-assisted instruction has received the least attention in radiology. In its simplest form, the student works through a lesson in a more-or-less linear fashion. The computer presents text, graphics, and images, and periodically poses questions to grade the student's understanding of the material. This type of computer-assisted instruction has been derisively called "electronic page turning" by some, who feel that it represents a trivial use of the computer [15].

In more sophisticated types of computer-assisted instruction, the computer assumes the role of teacher. Programs of this type must be nonlinear in construction, with many alternative pathways. In writing such a program, the instructor tries to anticipate every possible student response and provide appropriate feedback and remedial exercises. When preparing a lesson, much of the programmer's time is devoted to parts of the program that few students ever see.

The most sophisticated type of teaching application is the simulation of a patient. Typically, the computer presents a case history and reacts to the student's therapeutic decisions. Good simulations are enjoyable and highly effective forms of instruction [15]. Although not a substitute for clinical experience, simulations allow students to experiment and make potentially life-threatening errors without fear of causing harm to patients. Moreover, computer simulations can be used simultaneously by many students.

Computers in Education: Evolving Technology

Hardware

Computer systems of the late 1950s and early 1960s were ill-suited to the needs of the educator. Expensive and difficult to program, they typically processed jobs one at a time and did not allow for interaction with the user. The development of time-sharing systems in the 1960s was a major advance for two reasons. First, time sharing permitted multiple users to access the computer simultaneously, while giving each the impression of having the machine's undivided attention, thereby reducing the cost per user. Even more significant was the ability of time-shared programs to interact with users, enabling programs to alter their execution in response to the user's actions.

The rapid development of mainframe computer systems was paralleled by an evolution in the hardware used to interact with them. The device in most common use through much of the 1960s and 1970s was the teletypewriter terminal. Bulky, slow, and noisy by today's standards, its use in education was limited to presenting brief passages of text and accepting short responses.

The mid 1970s saw the gradual phasing out of hardcopy terminals and the introduction of displays on cathode-ray tubes (CRTs). Although early versions were not much faster than hardcopy devices (usually a limitation of the computer network), they were silent and were more comfortable to use.

Despite these advances in terminal technology, it was clear that general-purpose equipment was lacking in certain features unique to educational applications. For example, standard video terminals were often incapable of displaying even

simple graphics, let alone complex images. Limitations of the keyboard as an input device also were evident, especially when dealing with children or handicapped students. Finally, computer terminals did not contain the hardware necessary to synthesize or reproduce sound.

Several manufacturers responded by offering terminals geared to the needs of the educational market. I used one such terminal to produce a series of computer-assisted learning modules on thoracic radiology. The terminal included a CRT for display of text and graphics, a 35-mm slide projector for presenting radiographs, and a random-access cassette audio device. Both the CRT and the slide screen were touch sensitive, so a student could identify a particular region of interest by pointing to it. The chief drawbacks of the equipment were its high cost and limited distribution.

The most recent milestone in the evolution of hardware was the debut of the desktop computer in the late 1970s. Dollar-for-dollar, the equipment available today is more powerful than the mainframe computers of 20 years ago, both in terms of computing speed and memory capacity. Although many types of computers may be used for teaching, the radiologist's need to display gray-scale and color images limits the choice to high-end machines such as the Apple Macintosh II and the IBM PS 2 series. This is especially important when dealing with high-resolution images such as radiographs. Most future development of instructional material in radiology will probably be done with equipment of this type.

Storage devices have evolved along with computers. Early desktop computers used cassette tapes to store programs and data. Slow and inefficient, they were soon replaced by so-called floppy disks, which remain in widespread use for software distribution. For data storage, floppy disks have largely been replaced by faster hard drives. However, even the 20- to 80-megabyte disks in common use today are insufficient to store the large numbers of images required to teach radiology. (One chest radiograph typically requires 1 megabyte of disk space.) Fortunately, the need for higher capacity devices will soon be filled by optical storage media.

Diagnostic images may be stored in either video (analog) or digital format. Laser videodisks can store 55,000 individual television frames [5, 15], accessible under computer control. However, their resolution is limited, and they do not permit windowing and other image manipulation. In contrast, the CD-ROM (Compact Disk-Read Only Memory) can store any type of data (including CT and MR images) in numeric form. The disks, similar to those used in audio CD players, each can hold approximately 550 megabytes of data. However, CD-ROM is a read-only medium—the disks cannot be recorded on. Furthermore, both videodisks and CD-ROM disks must be manufactured by using an expensive mastering process [16].

Writeable optical disks have become available during the past 2 years. Early disks could be written on but not erased, and so became known as WORM (Write Once Read Many) devices. More recently, optical drives on which data can be recorded and erased repeatedly have appeared. They use removable cartridges with capacities of over 600 megabytes. Currently selling in the \$5000–6000 range, prices can be expected to fall in the future.

Software

One impediment to the development of computer-assisted instruction in radiology has been a lack of software suitable for the task. Traditional computer languages, designed for scientific and systems programming, are poor choices for writing instructional material. Therefore, most of the main-frame-based computer-assisted instruction systems developed over the past 20 years have incorporated languages tailored especially for education [15].

A debate that has raged in the computer-assisted instruction community for many years has centered around the design goals for these languages. Should they be simple enough for educators with little or no computer background to use or should they be rich in features and require traditional programming skills? Fortunately, some of the newer languages developed for the desktop computer market have been successful in combining the best of both philosophies. Excellent software for writing materials for computer-assisted instruction is now available for most major desktop computers (Table 1).

Computer-Assisted Instruction and the Radiologist

Why has radiology lagged behind other specialties in the development of effective computer-assisted instruction? I believe that the answer is twofold. First, the process by which radiology is taught at the viewbox is difficult to duplicate on the computer. Furthermore, those with imaging expertise (radiologists) often lack the requisite knowledge of instructional design and computer programming. Even given the recent advances in software for writing computer-assisted instruction materials noted earlier, the task remains time-consuming and arduous.

The second part of the answer is political. At most academic institutions (the likely source for most computer-assisted instruction research), the incentive to do the work simply does not exist [15]. Unlike journal articles and grants, computer programming is not often considered meritorious when academic promotion is at stake. Junior faculty are more likely to spend their time writing papers and grant proposals than preparing instructional computer programs.

Still, academic radiologists should not be deterred from exploring computer-assisted instruction. The technique has been shown to be effective in many fields, and it is well suited to teaching radiology to medical students and residents. The lack of incentive discussed earlier might be mitigated if commercial publishers were to become involved in developing computer-assisted instruction in the same way that they now promote textbooks.

Radiologists interested in developing educational computer programs should restrain the urge to start by buying expensive hardware and software: such expenditures are apt to meet resistance from cost-conscious administrators. Instead, they should first approach other individuals in their own institution who are experienced in computer-assisted instruction. Schools of education and computer science are excellent places to look for such expertise. The prospective author should prepare a document detailing the nature and scope of the material to be taught.

The choice of equipment and software will be dictated by the nature of the course material and by budgetary and other practical considerations. Again, I suggest that the radiologist start on a small scale, perhaps enlisting the aid of an interested medical student or resident. As instructional programs are developed, their efficacy should be evaluated by means of formal testing. Attention to detail and careful evaluation in the early stages of a project will prove invaluable in attracting favorable attention and grant funding later. Finally, the results of evaluation surveys may be suitable for publication.

Fulfilling the Promise: A Plan for the 1990s

The tools that would permit the computer to play a significant role in postgraduate and continuing radiology education already exist. If the technology is to live up to its promise, however, academic institutions will have to make a firm commitment. Those who make the decisions regarding promotion will need to recognize the merit inherent in developing computer-assisted instruction programs. Universities will have to adopt a team approach to computer-assisted instruction by fostering cooperation between radiologists, educational strategists, and programmers. Only then will the computer assume a larger role in coping with the expanding needs of radiology education in the 1990s and beyond.

TABLE 1: Systems for Writing Computer-Assisted Instruction Materials with Apple and IBM Desktop Computers

Program	Vendor	Computer System	Price (\$)
Course of Action	Authorware, Inc. Minneapolis, MN	Apple Macintosh	695-2500
Course Builder	Telerobotics, Inc. Knoxville, TN	Apple Macintosh	395-995
HyperCard	Apple Computer, Inc. Cupertino, CA	Apple Macintosh	Free with computer
Personal Computer Instructional System	International Business Machines Corp. (IBM)	IBM family	575
InfoWindow PILOT	IBM	IBM family	2050
Video PAssage	IBM	IBM family	7200

Note.—Substantial educational discounts are available for many of these products. Where a range of prices is given, different versions of the product with various capabilities are available.

REFERENCES

1. Starkschall G, Riggs JD, Lowther JR. A computer-aided instructional module for radiological physics. *Int J Radiation Oncol Biol Phys* **1986**; 12:421-426
2. Rowberg AH, Loop JW, Nelp WB. The design of a computer-assisted education system using a CT scanner computer. *J Med Syst* **1984**;8: 111-114
3. Wenzel A, Gotfredsen E. Retention after computer-assisted instruction in intraoral radiography. *J Dent Educ* **1987**;51:244-245
4. Jacoby CG, Smith WL, Albanese MA. An evaluation of computer-assisted instruction in radiology. *AJR* **1984**;143:675-677
5. McEnery KW. Interactive instruction in the radiographic anatomy of the chest. *Comput Methods Programs Biomed* **1986**;22:81-86
6. Andrews CL, Goldsmith DG, Osborn AG, Stensaas SS, Davidson HC, Quigley AC. Neuroradiology computer-assisted instruction using interactive videodisk: pilot project. Presented at the annual meeting of the Radiological Society of North America, Chicago, IL, November **1987**
7. Uri DS, Wall SD. Personalized data management for the radiologist. *AJR* **1988**;150:1415-1417
8. Amis ES Jr. Microcomputer applications for the academic radiologist. *AJR* **1987**;149:187-190
9. Sommer FG. Some applications for a personal computer data-base system in radiology. *AJR* **1986**;147:1075-1077
10. Chew FS, Hefner ML. Computer-aided design and realization of scientific exhibits in radiology. *AJR* **1987**;149:195-198
11. Taylor GA. Microcomputer-based graphics for radiology. *AJR* **1986**;147:1319-1321
12. Chew FS. The use of a microcomputer to make rapid and inexpensive lecture slides. *AJR* **1989**;152:185-188
13. Crass JR. Computer-generated examinations for residents in radiology. *AJR* **1986**;146:413-414
14. Aronberg DJ, Radewald SS, Jost RG. Computer-assisted instruction in radiology. *Radiology* **1985**;154:345-347
15. Piemme TE. Computer-assisted learning and evaluation in medicine. *JAMA* **1988**;260:367-372
16. Weiner E, Gordon J, Anderson R, et al. Interaction videodisc production in a university environment. *Comput Nurs* **1988**;6:108-114

Pictorial Essay

Low-Attenuation Mediastinal Masses on CT

Harvey S. Glazer,¹ Marilyn J. Siegel, and Stuart S. Sagel

A variety of mediastinal masses contain areas with CT attenuation values lower than that of chest wall musculature and higher than that of subcutaneous fat, and, therefore, these areas appear cystic on CT. In some cases, the low attenuation is not absolute but is relative to an enhancing wall of the lesion or to surrounding structures on contrast-enhanced CT images. In these cases, precise determination of the attenuation values discloses a density equivalent to that of soft tissue. In this report the gamut of low-attenuation mediastinal masses seen on CT is illustrated.

Congenital Cysts

Congenital mediastinal cysts include foregut, pericardial, and thymic cysts (Figs. 1–2). Foregut cysts may be classified further as bronchogenic, esophageal duplication, and neurenteric cysts [1].

Bronchogenic cysts are lined by respiratory epithelium and result from abnormal ventral budding of the tracheobronchial tree [1]. Most mediastinal bronchogenic cysts are located in the subcarinal or right paratracheal region. On CT, approximately half of the cysts are homogeneous, near-water-density masses, reflecting their serous nature (Fig. 1). The other half have attenuation values equal to that of soft tissue because of viscid mucoid contents or calcium. Such lesions may be indistinguishable from solid soft-tissue neoplasms, although the complete absence of enhancement after administration of IV contrast material may be a clue to their cause. Those patients who are asymptomatic and have small cysts with typical CT findings can be followed [2]. If a malignant neoplasm is suspected because the CT findings are atypical or the mass has increased in size, surgery or aspiration (percu-

taneous or transbronchial/transesophageal) may be required for diagnosis. Mediastinal cysts rarely resolve spontaneously.

Esophageal duplication cysts are lined by gastrointestinal mucosa and usually are located adjacent to or within the esophageal wall. Their appearance on CT is identical to that of bronchogenic cysts, except for their location in the posterior mediastinum.

Neurenteric cysts are rare posterior mediastinal lesions connected to the meninges through a midline defect in one or more vertebral bodies. Associated vertebral anomalies, present in approximately 50% of cases, suggest the diagnosis.

Pericardial cysts most frequently arise in the right cardiophrenic angle. The majority are sharply margined, somewhat triangular, and of near-water-density.

Congenital thymic cysts are caused by persistence of the thymopharyngeal duct. Except for the location within the thymus, CT features are similar to those of other congenital mediastinal cysts (Fig. 2). Hemorrhage into the cyst can cause a density greater than water.

Neoplasms

Although the CT density of most neoplasms is equal to that of soft tissue, areas of low attenuation may be present secondary to necrosis, old hemorrhage, or intrinsic properties of the neoplasm (Fig. 3) [3–6]. A CT diagnosis of a cystic neoplasm is based on finding an inhomogeneous, relatively low-density mass with thick walls (Figs. 4 and 5), sometimes in conjunction with other CT findings, such as lymphadenopathy elsewhere in the mediastinum or a pulmonary or pleural mass.

Received November 2, 1988; accepted after revision February 2, 1989.

¹ All authors: Mallinckrodt Institute of Radiology, Washington University School of Medicine, St. Louis, MO 63110. Address reprint requests to H. S. Glazer.

Hodgkin disease can be associated with cystic changes in the thymus, probably because of initial involvement of the thymus by Hodgkin disease, rather than as a consequence of therapy (Fig. 5) [3]. These cysts can persist unchanged or even grow after treatment and simulate persistent or recurrent disease.

Enlarged lymph nodes with a cystic appearance on CT caused by their low density may be seen in metastases (e.g., testicular or thyroid carcinoma) and may be present at the time of diagnosis or after chemotherapy/radiation. The decreased density is due to necrosis or cystic degeneration, but also may reflect intrinsic properties of the neoplasm (e.g., teratomatous elements in testicular cancer) (Fig. 6) [4].

Nerve-root tumors, such as schwannomas or neurofibromas, frequently are of lower attenuation on CT than muscle, because of their lipid or mucinous matrix or because of cystic degeneration (Fig. 7) [5]. Various degrees of inhomogeneity and contrast enhancement can be seen in both benign and

malignant neural tumors. Mediastinal nerve-root tumors usually arise from an intercostal nerve and less frequently from the vagus or phrenic nerve. They are usually paravertebral in location and may cause smooth expansion of a vertebral foramen.

Lymphangioma

Lymphangiomas are congenital malformations of lymphoid tissue. Most are seen before the patient is 2 years old and appear as cervical masses posterior to the sternocleidomastoid muscle. Mediastinal lymphangiomas usually are extensions of cervical lesions (Fig. 8). Typically, they are thin-walled, multiloculated, near-water-density masses, but they may have solid components if hemorrhage or infection has occurred. Most are well defined, but they may infiltrate adjacent structures and be difficult to remove surgically.

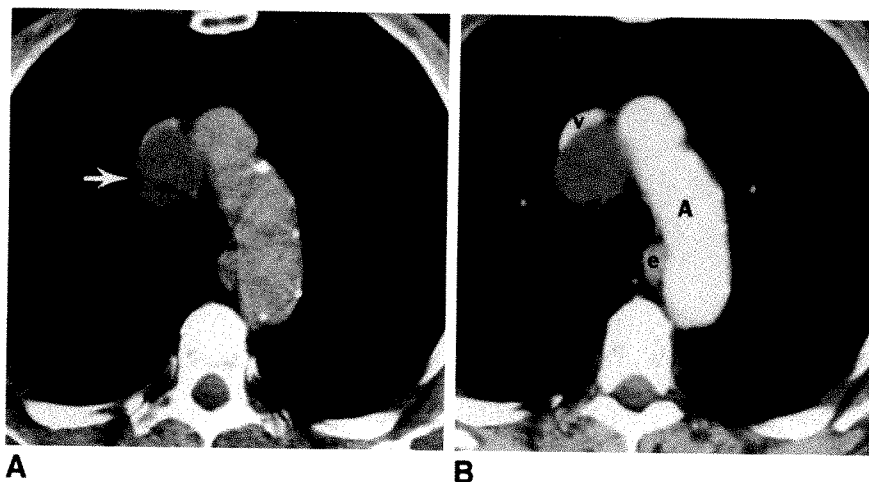


Fig. 1.—Bronchogenic cyst.

A, Noncontrast CT scan shows well-defined, homogeneous, water-density, right paratracheal mass (arrow).

B, Contrast-enhanced CT scan shows no enhancement of mass. Superior vena cava (v) is displaced anteriorly. A = aorta; e = esophagus.

Follow-up chest radiograph 20 months later showed no mass; presumably this was a bronchogenic cyst.

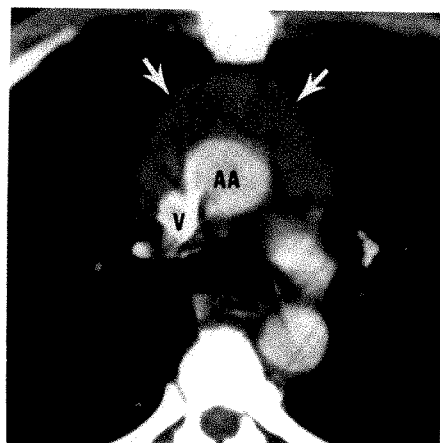


Fig. 2.—Thymic cyst. CT scan shows homogeneous, water-density mass (arrows) that conforms to expected position of right and left lobes of thymus. AA = ascending aorta; V = superior vena cava.

At surgery a thymic cyst was found with occasional Hassall corpuscles in the wall.

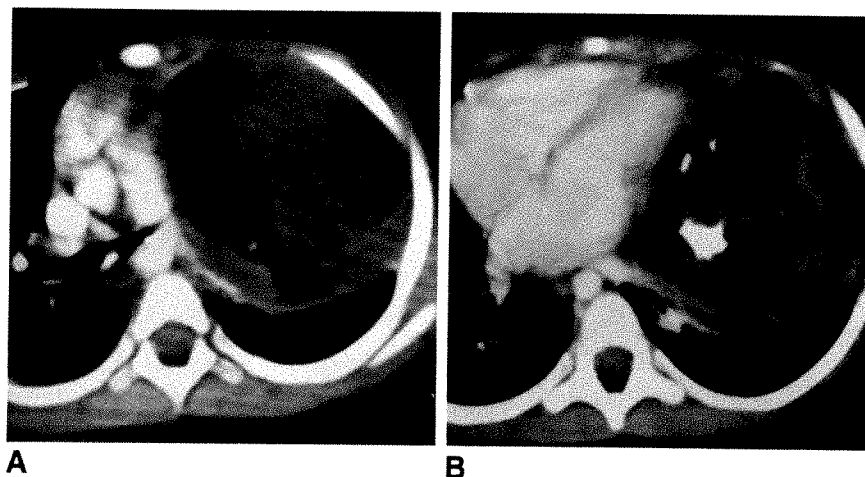


Fig. 3.—Benign mature teratoma.

A and B, CT scans. Large, complex mass containing multiple cysts, fat, and calcification displaces mediastinum to right.

Histology of specimen removed at surgery showed benign mature teratoma, mostly cystic, but also containing fat and embryonic teeth.

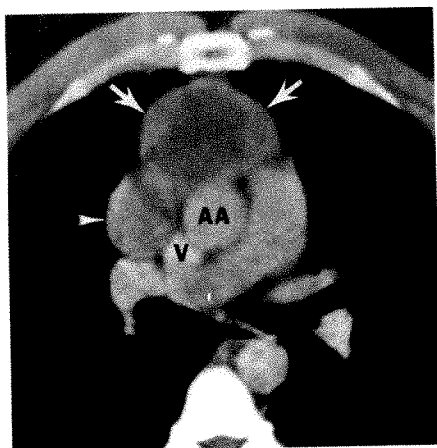
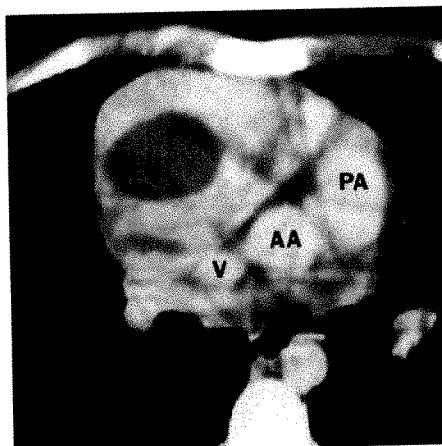


Fig. 4.—Cystic thymoma. CT scan. Large, well-defined mass adjacent to ascending aorta (AA) and superior vena cava (V) contains solid component (arrowhead) and thick-walled cystic component (arrows).

At surgery, a thymoma was found with cystic and solid areas surrounded by a thick fibrous capsule.



A



B

Fig. 5.—Cystic Hodgkin disease.

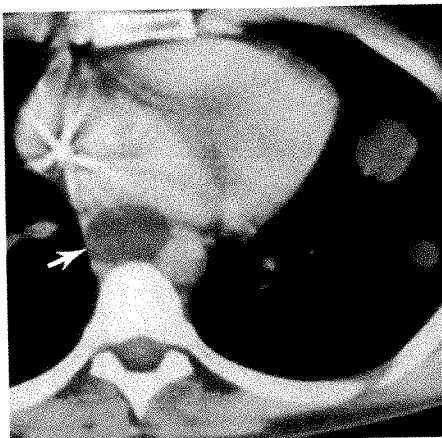
A, CT scan shows soft-tissue mass with well-defined, central low-attenuation component in anterior mediastinum. V = superior vena cava; AA = ascending aorta; PA = pulmonary artery.

B, More cephalad scan at level of aortic arch (A) shows multiple enlarged right paratracheal and anterior mediastinal lymph nodes.

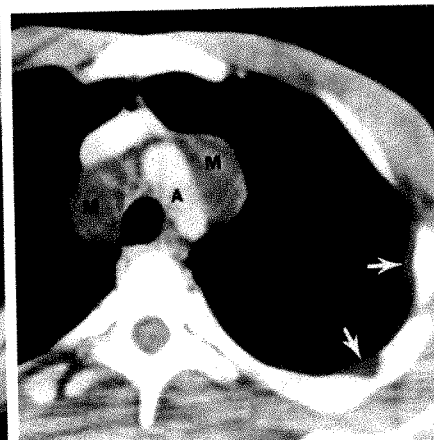
Surgical biopsy of cervical node revealed nodular sclerosing Hodgkin disease.

Fig. 6.—Metastatic testicular cancer. CT scan at level of heart shows low-attenuation paraaortic lymph node (arrow) and two low-attenuation lung nodules. (Reprinted from Yousem et al. [4].)

Previous left orchiectomy disclosed embryonal cell carcinoma. Other scans showed hilar, retrocrural, and retroperitoneal lymphadenopathy.



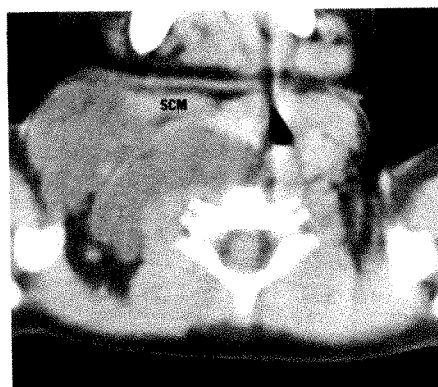
6



7

Fig. 7.—Neurofibromas in patient with neurofibromatosis. CT scan shows bilateral low-attenuation masses (M) adjacent to aortic arch (A). Associated intercostal neurofibromas (arrows).

More cephalad scans showed masses extending from carotid sheaths in expected distribution of vagus nerves. (Courtesy of F. Oakley, Mason City, IA.)



A



B

Fig. 8.—Lymphangioma.

A, CT scan shows large, multiloculated, near-water-density mass in right side of neck posterior and lateral to sternocleidomastoid muscle (SCM).

B, More caudal scan shows extension into superior mediastinum and right axilla. Lymphangioma was found at surgery.

Meningocele

An intrathoracic meningocele is a protrusion of the leptomeninges into the thoracic cavity through an intervertebral foramen. Association with neurofibromatosis is common. On CT, a homogeneous near-water-density paravertebral mass is seen (Fig. 9). Other findings may include enlargement of the intervertebral foramina and associated vertebral and rib anomalies.

Inflammatory Processes

A mediastinal abscess may cause a low-attenuation mass because of its fluid content. Associated CT findings, such as gas bubbles or contiguity or communication with an empyema or subphrenic abscess, and clinical features usually permit differentiation from true cysts or neoplasms. However, percutaneous needle aspiration may be required to distinguish

an abscess from an uninfected postoperative seroma or hematoma.

Central areas of relatively low attenuation have been described in tuberculous lymph nodes, reflecting the presence of caseation and liquefaction [6]. The low-density contents usually are surrounded by an enhancing hypervascular wall.

Goiter

Intrathoracic goiters, which are almost always continuous with the cervical part of the thyroid gland, usually are well defined and may contain calcium deposits (Fig. 10). Parts may have relatively low attenuation values due to cystic degeneration and colloid formation. Thyroid carcinoma with mediastinal extension may be indistinguishable from a benign multinodular goiter, but the presence of poorly defined margins, invasion of adjacent structures, and cervical/mediastinal lymphadenopathy or pulmonary nodules allows differentiation.

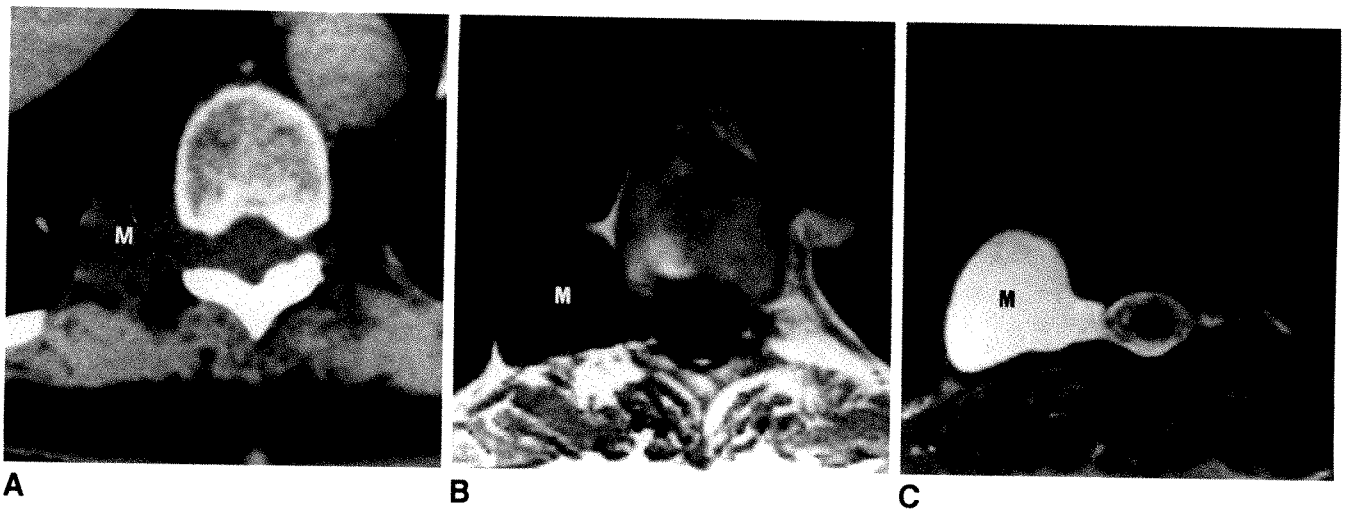


Fig. 9.—Lateral thoracic meningocele.
A, CT scan at level of T10 shows smooth, homogeneous, low-attenuation mass (M) extending into right intervertebral foramen.
B and C, Relatively T1-weighted, 1000/17 (B), and T2-weighted, 3400/90 (C), MR images. Signal characteristics of mass (M) are similar to those of CSF, consistent with meningocele. Lower-signal-intensity nerve roots and spinal cord are seen well on T2-weighted image.

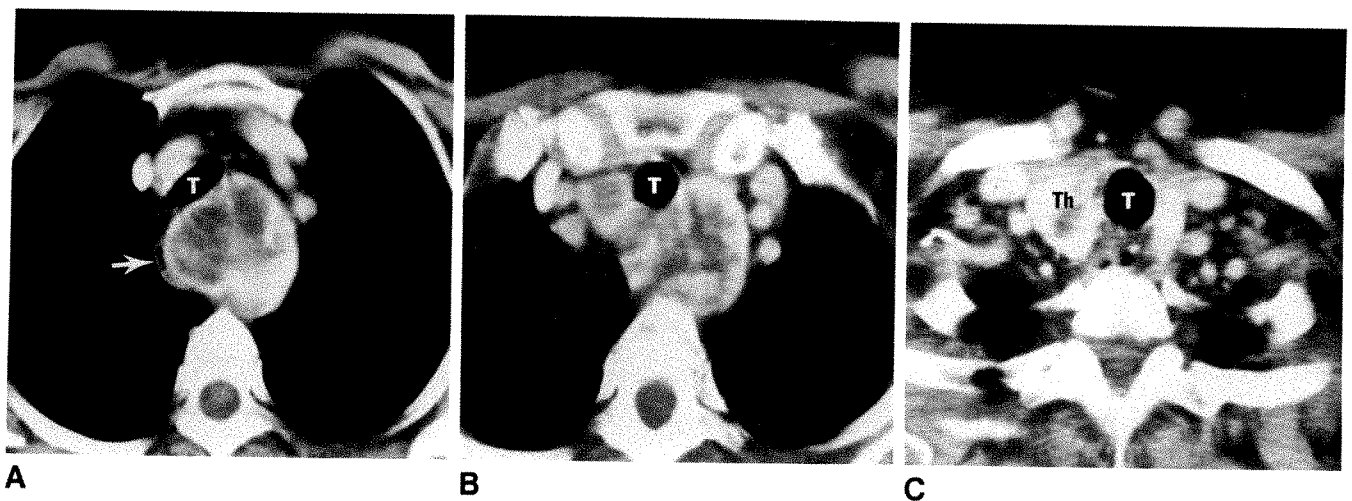


Fig. 10.—Intrathoracic goiter.
A–C, Contrast-enhanced CT scans at progressively cephalad levels show large, well-defined, complex mass posterior to trachea (T) and lateral to esophagus (arrow) that displaces arch vessels laterally and is continuous with right lobe of thyroid (Th).
Clinical and radiographic follow-up over 2.5 years has shown no change in mass.

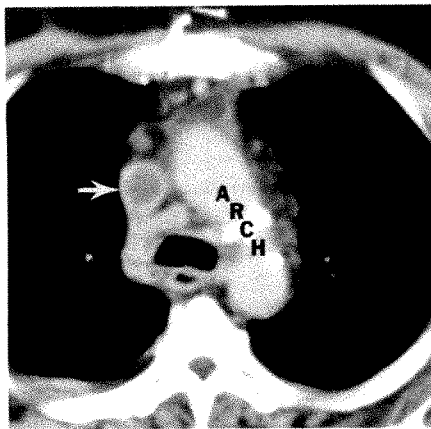


Fig. 11.—Superior vena cava thrombosis. Contrast-enhanced CT scan at level of undersurface of aortic arch (ARCH) shows superior vena cava (arrow) containing relatively low-attenuation thrombus in comparison with enhancing wall. Multiple collateral vessels are seen, especially in chest wall.



Fig. 12.—Colonic interposition. CT scan shows well-defined, near-water-density mass (M) anterior to superior vena cava (V) and aortic arch (A). Changes from previous sternotomy are present. Small amount of air is within mass (arrowhead).

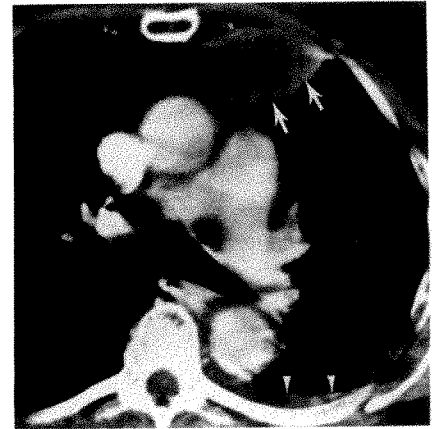
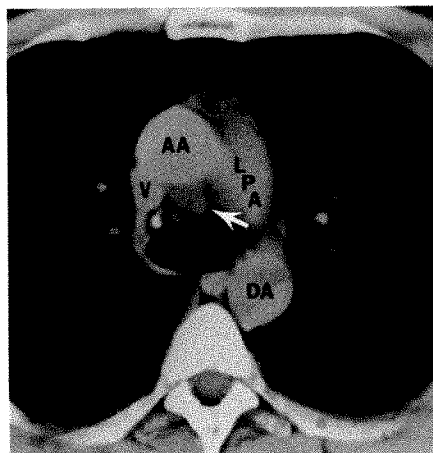


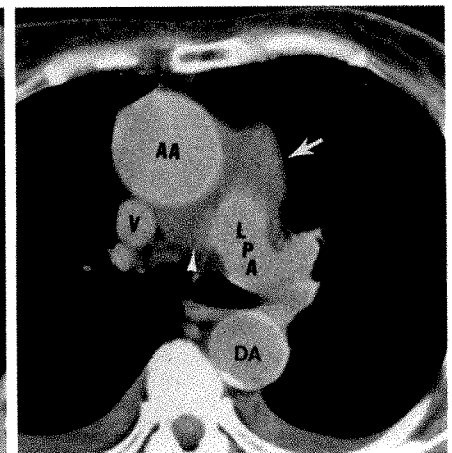
Fig. 13.—Loculated pleural effusion in patient with resolving congestive heart failure. CT scan shows loculated collection of pleural fluid (arrows) adjacent to anterior mediastinum. "Mass" was absent on follow-up chest radiographs. Small left pleural effusion (arrowheads).

Fig. 14.—Pericardial recess. CT scan shows normal superior sinus of pericardium (arrow) as crescentic, near-water-density structure posterior to ascending aorta (AA). DA = descending aorta; V = superior vena cava; LPA = top of left pulmonary artery.



14

Fig. 15.—Pericardial recess in patient with a pericardial effusion. CT scan shows fluid distending superior sinus of pericardium (arrowhead) and aortopulmonary pericardial recess (arrow). Small bilateral pleural effusions are seen. AA = ascending aorta; DA = descending aorta; V = superior vena cava; LPA = left pulmonary artery.



15

Hematoma

Subacute or chronic hematomas of the mediastinum may appear as low-density masses. Occasionally, hematomas have a fluid-fluid level on CT, indicating separation of the low-density serum anteriorly and sedimentation of cellular components.

Miscellaneous

A thrombosed vein may simulate a necrotic lymph node on CT because of peripheral enhancement and a lower-attenuation center (Fig. 11). A correct diagnosis can be achieved by scrutiny of consecutive images and noting secondary signs of venous thrombosis, such as collateral vessels.

A fluid-filled dilated esophagus (e.g., achalasia) or colonic interposition may mimic the appearance of a congenital mediastinal cyst or fluid collection (Fig. 12). Careful review of serial scans and the administration of oral contrast material will reveal the nature of the lesion.

Loculated pleural fluid adjacent to the mediastinum may simulate a low-density mass on CT (Fig. 13). Identification of

pleural fluid elsewhere in the chest usually results in the correct diagnosis.

A fluid-filled pericardial recess may also simulate a low-density mediastinal mass on CT [7]. Knowledge of the characteristic locations of the various pericardial recesses and/or the demonstration of pericardial fluid on other images should allow confident identification (Figs. 14 and 15).

REFERENCES

1. Fitch SJ, Tonkin IL, Tonkin AK. Imaging of foregut duplication cysts. *RadioGraphics* 1986;6:189-201
2. Kuhlman JE, Fishman EK, Wang KP, Zerhouni EA, Siegelman SS. Mediastinal cysts: diagnosis by CT and needle aspiration. *AJR* 1988;150:75-78
3. Lindfors KK, Meyer JE, Dedrick CG, Hassell LA, Harris NL. Thymic cysts in mediastinal Hodgkin disease. *Radiology* 1985;156:37-41
4. Yousem DM, Scatarige JC, Fishman EK, Siegelman SS. Low-attenuation thoracic metastases in testicular malignancy. *AJR* 1986;146:291-293
5. Kumar AJ, Kuhajda FP, Martinez CR, Fishman EK, Jezic DV, Siegelman SS. CT of extracranial nerve sheath tumors. *J Comput Assist Tomogr* 1983;7:857-865
6. Im J-G, Song KS, Kang HS, et al. Mediastinal tuberculous lymphadenitis: CT manifestations. *Radiology* 1987;164:115-119
7. Aronberg DJ, Peterson RR, Glazer HS, Sagel SS. Superior sinus of the pericardium: a pitfall of mediastinal CT. *Radiology* 1984;153:489-492

Book Review

Radiology Report. Editor in chief: Ronald L. Eisenberg. St. Louis: Mosby, November 1988;1(1):1-124. \$25; by subscription, 3 issues annually for \$49.50

"Not another journal?" might well be the reaction of the busy radiologist already inundated with scientific journals, seminars, clinics, reviews, and the commercial newsmagazines and disposable journals. *Radiology Report*, a new journal to be published three times a year, intends to synthesize information on major clinical advances and controversies in the rapidly expanding field of radiology. The sections include new developments, problem solving, case reports, legal issues, literature review, and current controversies.

In this inaugural issue, the section on new developments includes noninvasive bone densitometry, interventional radiology of the pleural space and lung, staging of malignancies of the upper gastrointestinal tract, and interventional radiology of the abdomen. Each subject is covered in detail by a well-recognized expert. Although the reproductions of the radiographs are not of the highest quality, the pertinent findings are shown clearly and are supplemented occasionally by line drawings. Charts, tables, and diagrams are used effectively to enhance the generally well-written, lucid text. Highlighted key statements on a blue background are dispersed throughout the text. Almost all of the material has been published before as journal articles and is presented here more in the integrated form of a book chapter with up-to-date references. The emphasis is transmitting information on state-of-the-art technology and techniques to the practicing radiologist in a well-organized, easily assimilated format.

The section on problem solving follows up the early coverage of noninvasive bone densitometry with a clinician's perspective on the impact of screening on the diagnosis and treatment of menopausal osteoporosis. The subject is examined further in the "Point/Counterpoint" section in which two prominent experts in skeletal radiology debate the value of screening for osteoporosis. For the second contribution to the section on problem solving, the editor in chief integrates information from two textbooks on various techniques for

the diagnosis of deep venous thrombosis. Again, the presentation is concise and authoritative, making it comprehensible even for readers who have no experience in this area.

The four case reports have no connection to the rest of the material in this issue. The radiographic findings are obvious, and the diagnoses should be made readily by any competent general radiologist—as opposed to the so-called zebras shown at film panels that try to stump the experts. The discussions are complete, but no effort is made to integrate these cases into the overall teaching effort of the publication. As a result, they give the impression of being fillers.

Other articles featured in this issue concern the controversy over nonionic contrast material, basic concepts of medical malpractice law, and issues of quality assurance. The literature review has abstracts of recent articles of current interest in radiologic and clinical journals and brief comments by the editors on the impact of the information on radiologic practice.

This inaugural issue seems to have met its goal of furnishing timely and applicable clinical information on the latest developments and controversies in radiology. I hope that future issues will have a more limited focus, providing detailed coverage of fewer subjects and making a greater effort to integrate the material presented in the various sections.

This journal is recommended highly to the general radiologist who is too busy to keep up with all the literature in the field but who wants to keep abreast of the latest developments by reading a publication that uses a more condensed format.

Herbert F. Gramm
New England Deaconess Hospital
Harvard Medical School
Boston, MA 02215

The CT Findings of Pulmonary Sarcoidosis: Analysis of 25 Patients

Nestor L. Müller¹
 Peter Kullnig^{1,2}
 Roberta R. Miller³

We analyzed the CT findings in 25 patients with biopsy-proved pulmonary sarcoidosis. In all 25 patients, 10-mm collimation scans were available. In 16 of the 25 patients, select 1.5-mm scans were obtained. These were retrospectively targeted by using a 20- to 25-cm field of view and a high-spatial-resolution algorithm. The CT and pathologic findings were compared in two patients in whom surgical specimens of the lung were available. CT findings included hilar and mediastinal adenopathy ($n = 22$), subpleural nodules ($n = 19$), and 1- to 10-mm-diameter nodules ($n = 17$) and irregular linear densities ($n = 12$), both mainly along the bronchovascular structures. High-resolution CT was superior to conventional CT in the assessment of subpleural nodules and irregular linear densities, but conventional CT was superior in the assessment of peribronchovascular nodules. The two gross pathologic specimens showed the sarcoid granulomas to be mostly along the lymphatics in the peribronchovascular sheath and, to a lesser extent, in subpleural and interlobar septal lymphatics.

We conclude that the characteristic CT appearance of pulmonary sarcoidosis consists of small nodules and irregular linear densities along the bronchovascular bundles.

Sarcoidosis is a systemic disorder of unknown cause characterized by noncaseating granulomas, which may resolve spontaneously or progress to fibrosis [1]. It may involve almost any organ, but most of the morbidity and mortality is due to pulmonary disease [2]. Pulmonary manifestations are present in 90% of patients, 20–25% of whom have permanent functional impairment [2]. The aim of the present study was to determine the appearance of pulmonary sarcoidosis on conventional and high-resolution CT in 25 patients. In two patients in whom surgical specimens of the lung were available, the CT and pathologic findings were compared.

Materials and Methods

Twenty-five patients with biopsy-proved pulmonary sarcoidosis and CT scans of the chest were included in the study. There were 13 men and 12 women, ranging in age from 28 to 69 years (mean, 45 years; standard deviation, 13). All were white. The diagnosis of sarcoidosis was made on transbronchial biopsy in 12 patients, mediastinal or scalene nodal biopsy in nine, lobectomy in two, bronchial biopsy in one, and bone marrow biopsy in one.

The extent of the pulmonary disease in the 25 patients was estimated by reviewing the chest radiographs with the criteria defined by Scadding and Mitchell [3]. Two patients had normal chest radiographs, five patients showed only hilar and paratracheal lymphadenopathy, nine had lymphadenopathy and parenchymal abnormalities, five had parenchymal abnormalities without lymphadenopathy, and four had fibrosis. Fibrosis was considered to be present when parenchymal abnormalities were associated with distortion of vascular shadows or displacement of mediastinal structures [3].

The CT scans were performed on a GE 8800 (four patients) or 9800 (21 patients) scanner (General Electric, Milwaukee, WI). All scans were obtained at end-inspiration by using 1-cm collimation at 1-cm intervals. They were photographed at windows appropriate for lung parenchyma (level, -600 to -700 H; window width, 1000–2000 H) and mediastinum (level, 30–50 H; width, 350–500 H) by using the standard algorithm. In 16 patients, additional 1.5-

Received December 8, 1988; accepted after revision February 6, 1989.

¹ Department of Radiology, University of British Columbia, and Vancouver General Hospital, 855 W. 12th Ave., Vancouver, B.C., Canada V5Z 1M9. Address reprint requests to N. L. Müller.

² Present address: Universitätsklinik für Radiologie, A-8036, Auenbruggerplatz 9, Graz, Austria.

³ Department of Pathology, University of British Columbia, and Vancouver General Hospital, 855 W. 12th Ave., Vancouver, B.C., Canada, V5Z 1M9.

AJR 152:1179–1182, June 1989

0361-803X/89/1526-1179

© American Roentgen Ray Society

mm collimation scans were obtained at the level of the aortic arch, tracheal carina, and 1 cm above the dome of the diaphragm. These 1.5-mm collimation scans were retrospectively targeted by using a field of view of 20 or 25 cm and a high-spatial-resolution algorithm (bone algorithm). These high-resolution CT images were obtained by using 120 kVp and 360–420 mAs. IV contrast medium was not used, except in five patients suspected of having lymphoma or a bronchogenic carcinoma.

The CT scans were assessed independently by two observers for the presence of hilar and mediastinal adenopathy and for the presence, type, and distribution of parenchymal abnormalities. Hilar and mediastinal nodes were considered enlarged if the short axis was larger than 5 and 10 mm, respectively. Pulmonary opacities were classified as either nodular or linear. The nodules were classified according to size (1–5 mm, 5–10 mm, or mixed) and according to margin (smooth or irregular). The distribution of opacities was classified as peribronchovascular, subpleural, or random. The lung zone most often involved was determined, and the presence and type of thickening of septal lines, pleural thickening, and effusion were noted.

Lobectomy specimens were available in two patients who underwent surgery because of concomitant bronchogenic carcinoma. These were cut in the same transverse plane as the CT scans, and the type and distribution of parenchymal abnormalities were noted. The findings in both specimens were due to true sarcoidosis rather than sarcoid reaction to a tumor, because the mediastinal lymph nodes contained noncaseating granulomas with no malignancy, the pulmonary granulomas were not more numerous around the tumor, and the distribution of the pulmonary granulomas was identical to the known distribution of sarcoidosis.

Results

CT scans showed lymph-node enlargement in 20 patients. Nineteen patients had bilateral hilar adenopathy, and 19 had mediastinal nodal enlargement on CT. These included the four patients with marked fibrosis in whom the hilar region was obscured or distorted on the radiograph.

In only two of seven patients with no parenchymal changes on the radiograph was a parenchymal abnormality detected on CT. Both patients had a few 1- to 5-mm subpleural nodules on CT, and one of them also had a few irregular linear densities. High-resolution CT was performed in only one of the five patients with no parenchymal abnormalities on CT.

CT scans were superior to radiographs for use in assessing the distribution of parenchymal changes. The 20 patients with parenchymal changes had nodular densities on CT. These ranged from 1 to 10 mm in diameter but were 1–5 mm in 15 patients and 5–10 mm in five. In 17 patients, the nodules were located mostly along the bronchovascular bundles (Fig. 1). In 19 patients they also were evident in the subpleural region (Fig. 1). The nodules had sharply circumscribed, smooth margins in three patients and irregular margins in 17 patients. Five patients had conglomerate masses of granulomas or fibrosis measuring up to 4 cm in diameter. Sixteen patients had irregular linear opacities. In 12 of these, a mostly peribronchovascular distribution was evident on CT (Fig. 2).

The distribution of the nodular densities along the bronchovascular structures was easier to appreciate on the 10-mm collimation scans (Fig. 2). However, high-resolution CT allowed better assessment of uneven thickening of bronchi running parallel to the plane of the section (Fig. 3). It was also superior to conventional CT in the assessment of nodular thickening of the pleura, particularly along the major fissures, which was seen in four patients (Fig. 3). High-resolution CT allowed assessment of the secondary pulmonary lobule. Even or uneven thickening of the interlobular septa was seen in 10 patients. A few localized polygonal lines were seen on high-resolution CT in six patients. These lines were thickened, but in five of six patients they had a smooth contour. Distortion of the secondary pulmonary lobules, presumably as a result of fibrosis, was evident on CT in 13 patients. Although high-resolution CT allowed better assessment of parenchymal detail, it did not detect any abnormality when the conventional CT at the same level was normal.

In two patients with definite pulmonary sarcoidosis, which was shown by transbronchial biopsy, no parenchymal abnormality could be seen on CT. In a third patient, a single nodule was seen, which later was proved to be a bronchogenic carcinoma. The concomitant sarcoidosis in this patient was not evident on the radiograph or on CT.

The two lobectomy specimens showed small nodular lesions representing noncaseating granulomas mostly along the bronchovascular sheath and, to a lesser extent, in the subpleural lymphatics and along the interlobular septal lymphatics (Fig. 4).

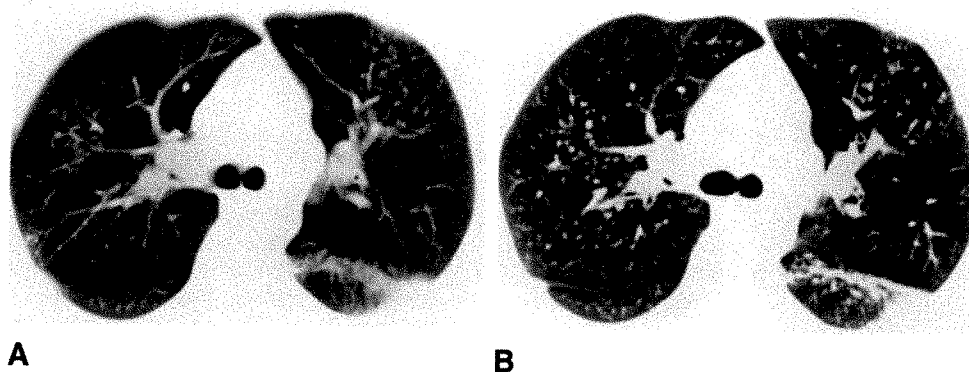


Fig. 1.—28-year-old man with hilar adenopathy and apparently nonfibrotic changes on radiograph.

A, 10-mm collimation scan at level of trachea carina shows mainly peribronchovascular distribution of nodules. A broad area of increased density is present subpleurally in superior segment of left lower lobe.

B, 1.5-mm collimation scan at same level as A shows peribronchovascular distribution of nodules in right upper lobe, but peribronchovascular distribution is more difficult to see in left upper lobe. Area of increased density in superior segment of left lower lobe is presumably due to conglomeration of subpleural granulomas.

Fig. 2.—69-year-old man with fibrotic lung changes. CT scan shows linear fibrotic strands radiating along bronchovascular bundles.

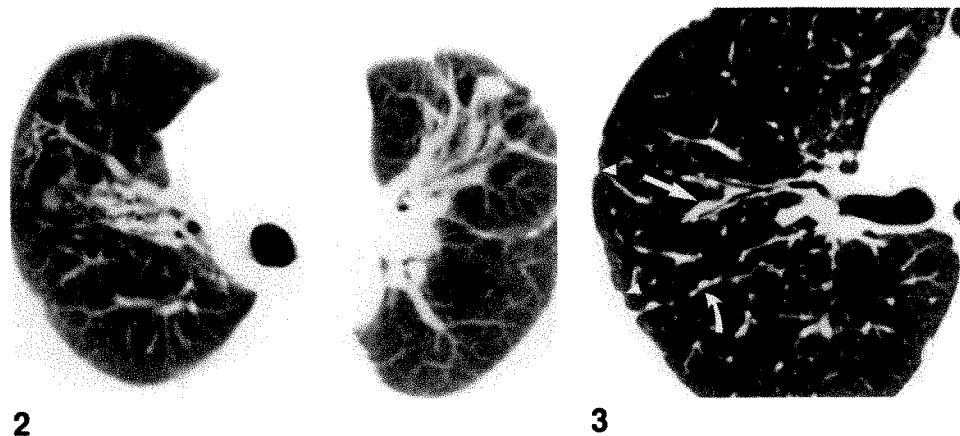


Fig. 3.—High-resolution CT scan in 41-year-old man with hilar adenopathy and apparently nonfibrotic lung changes shows uneven thickening of bronchus (straight arrow) and right major fissure (curved arrow). Also seen are subpleural nodules (arrowheads).



Fig. 4.—55-year-old woman with 5-year history of sarcoidosis developed a neoplastic lesion in right upper lobe and underwent right upper lobectomy. A, 10-mm collimation CT scan shows irregular nodules mostly along bronchovascular bundles (arrows) and in subpleural region. Process is most severe in right lower lobe, where a large pleura-based abnormality presumably is a conglomeration of subpleural granulomas. Only a few peribronchovascular nodules are present in right upper lobe.

B, 1.5-mm collimation scan at same level as A.

C, Specimen from right upper lobe cut in transverse plane shows noncaseating sarcoid granulomas along bronchovascular bundles (long arrows) and in subpleural region (short arrows).

Discussion

Approximately 60–70% of patients with sarcoidosis have a characteristic radiologic appearance consisting of enlarged hilar and paratracheal lymph nodes with or without concomitant parenchymal changes [3–5]. In 25–30% of cases, however, the radiologic findings are nonspecific or atypical, and in 5–10% of patients the radiograph is normal [1–6].

The variable and often nonspecific radiographic findings are surprising given the characteristic pathologic appearance and distribution of sarcoidosis. Sarcoid granulomas, the hallmark of the disease, are distributed along the lymphatics in the bronchovascular sheath and, to a lesser extent, in the interlobar septa and pleura [1, 7, 8]. This distribution is one of the most helpful features in recognizing sarcoidosis pathologically [1]. It can be seen clearly in illustrations of the macroscopic pathologic appearance [1, 9]. This distribution is difficult to appreciate on the radiograph because of the superimposition of the parenchymal shadows, but often it can be seen on CT. A previous report on the CT findings in three patients with sarcoidosis described small nodules along the bronchovas-

cular bundles as well as subpleural nodules in two of the patients [10]. Nakata et al. [11] observed irregular thickening of the bronchial walls in the one patient with pulmonary sarcoidosis they assessed with high-resolution CT. Hamper et al. [6] assessed the typical and atypical CT manifestations in 36 patients. Subpleural nodules were seen in some patients, but no mention was made of peribronchovascular distribution or thickening of the interlobular septa. In the present study, the main parenchymal findings on CT consisted of nodules along the bronchovascular bundles and in the subpleural regions. This reflects the distribution of sarcoid granulomas. Established sarcoid fibrosis, when present, also was more marked along the bronchovascular bundles.

The distribution of sarcoid granulomas along the lymphatics is similar to that seen with pulmonary lymphangitic carcinomatosis. Both conditions cause a beaded appearance of the bronchovascular bundles and of the interlobular septa [12, 13]. However, in the present study, the septal thickening was much less marked than that seen with pulmonary lymphangitic carcinomatosis. Unevenly thickened polygonal lines, which are present in most patients with lymphangitic carcinomato-

sis, were uncommon and when present were usually localized and few. The nodules in sarcoidosis often have irregular margins; those in lymphangitic carcinomatosis are smooth. Irregular linear opacities and evidence of fibrosis are also more suggestive of sarcoidosis. In some patients, however, the pattern of parenchymal involvement of sarcoidosis may be identical to that of lymphatic spread of tumor.

In the present study, CT showed mild parenchymal abnormalities in one of two patients with a normal chest radiograph and a few subpleural nodules in one of five patients with only hilar adenopathy apparent on the radiograph. However, CT showed no evidence of sarcoidosis in three patients with definite pulmonary involvement, which was proved by transbronchial biopsy or lobectomy. Although CT gives a superior pictorial assessment of disease pattern and distribution, it does not correlate better than the radiograph with the clinical and functional impairment in sarcoidosis [14]. In a review of 27 patients with sarcoidosis, 20 of whom were included in the present study, CT and radiographic assessment of disease extent had similar correlations with the severity of dyspnea ($r = .61$ and $.58$, respectively, $p < .001$), total lung capacity ($r = -.54$ and $-.62$, respectively, $p < .01$), and in gas transfer as assessed by the carbon monoxide diffusing capacity ($r = -.62$ and $-.52$, respectively, $p < .01$) [14].

We conclude that the characteristic parenchymal abnormalities of sarcoidosis on CT are nodular densities along the bronchovascular bundles, interlobular septa, major fissures, and subpleural regions. These densities represent granulomas distributed along the lymphatics, a distribution that is the pathologic hallmark of sarcoidosis. When fibrosis occurs, it also involves mainly the peribronchovascular region. Because CT closely reflects the macroscopic appearance, it may show characteristic findings even when the radiographic appearance is nonspecific. However, CT cannot be used to rule out the diagnosis of pulmonary sarcoidosis. Noncaseating granulomas may be present when the radiograph, conven-

tional CT scans, and high-resolution CT scans are completely normal.

REFERENCES

1. Colby TV, Carrington CB. Infiltrative lung disease. In: Thurlbeck WM, ed. *Pathology of the lung*. Stuttgart: Thieme Medical, 1988:425-517
2. Crystal RG, Bitterman PB, Rennard SI, Hance AJ, Keogh BA. Interstitial lung diseases of unknown cause: disorders characterized by chronic inflammation of the lower respiratory tract. *N Engl J Med* 1984;310:235-244
3. Scadding JG, Mitchell DN, eds. *Sarcoidosis*. London: Chapman and Hall Medical, 1985:101-180
4. McLoud TC, Epler GR, Gaensler EA, Burke GW, Carrington CB. A radiographic classification for sarcoidosis: physiologic correlation. *Invest Radiol* 1982;17:129-138
5. Hillerdal G, Nöu E, Osterman K, Schmekel B. Sarcoidosis: epidemiology and prognosis, a 15-year European study. *Am Rev Respir Dis* 1984;130:29-32
6. Hamper UM, Fishman EK, Khouri NF, Johns CJ, Wang KP, Siegelman SS. Typical and atypical CT manifestations of pulmonary sarcoidosis. *J Comput Assist Tomogr* 1986;10:928-936
7. Carrington CB, Gaensler EA, Mikus JP, Schachter AW, Burke GW, Goff AM. Structure and function in sarcoidosis. *Ann NY Acad Sci* 1976;278:265-283
8. Thomas PD, Hunninghake GW. Current concepts of the pathogenesis of sarcoidosis. *Am Rev Respir Dis* 1987;135:747-760
9. Heitzman ER. Sarcoidosis. In: Heitzman ER, ed. *The lung: radiologic-pathologic correlations*. St. Louis: Mosby, 1984:294-310
10. Bergin CJ, Müller NL. CT of interstitial lung disease: a diagnostic approach. *AJR* 1987;148:8-15
11. Nakata H, Kimoto T, Nakayama T, Kido M, Miyazaki N, Harada S. Diffuse peripheral lung disease: evaluation by high-resolution computed tomography. *Radiology* 1985;157:181-185
12. Munk PL, Müller NL, Miller RR, Ostrow DN. Pulmonary lymphangitic carcinomatosis: CT and pathologic findings. *Radiology* 1988;166:705-709
13. Stein MG, Mayo J, Müller N, Aberle DR, Webb WR, Gamsu G. Pulmonary lymphangitic spread of carcinoma: appearance on CT scans. *Radiology* 1987;162:371-375
14. Müller NL, Mawson JB, Mathieson JR, Abboud R, Ostrow DN, Champion P. Sarcoidosis: Correlation of CT with clinical, functional, and radiological findings. *Radiology* 1989;171

Chronic Lung Diseases: Specific Diagnosis by Using CT

Colleen J. Bergin¹
 Craig L. Coblentz²
 Caroline Chiles²
 Dianne Y. Bell³
 Ronald A. Castellino¹

We evaluated patterns of abnormal lung parenchyma on CT scans in six specific chronic lung diseases and then applied those findings in the differential diagnosis of these lung parenchymal patterns in 56 subjects. There were 48 patients with chronic lung diseases (43 with histologic proof) consisting of usual interstitial pneumonia ($n = 20$), sarcoidosis ($n = 16$), lymphangitic carcinomatosis ($n = 7$), lymphangioleiomyomatosis ($n = 2$), drug toxicity ($n = 2$), and eosinophilic granuloma ($n = 1$). Including eight CT scans of normal control subjects, 56 CT scans were assessed independently by two readers (R1 and R2). Chest radiographs, most of which were obtained within 1 week of CT examination, were available in 48 of the 56 subjects. CT scans were evaluated for specific parenchymal features including disease distribution, lung distortion, thickening of bronchovascular bundles and polygon walls, bronchiectasis, cysts, and nodules, to determine the association of each abnormal feature with the different diseases. Diagnosis was then made from the overall CT appearance of the lungs and, on a separate occasion, from the appearance of the chest radiograph. The correct diagnosis was made from the CT appearance in 54 of 56 patients (R1) and in 50 of 56 patients (R2). Correct diagnoses were made from the chest radiographs in 42 of 48 patients (R1) and 43 of 48 patients (R2).

We have identified features that are reproducible and useful when describing CT scans of patients with chronic lung diseases. Interpretation of the appearance of the lung on CT scans was accurate in diagnosing usual interstitial pneumonia, sarcoidosis, and lymphangitic carcinomatosis.

There are recognizable radiologic and pathologic patterns of lung parenchymal abnormality that characterize the various causes of chronic lung disease [1-3]. Although at the cellular level the lung parenchyma has limited ways to respond to disease, the nature of the disease and the host response can result in gross morphologic patterns that can be identified radiologically.

The chest radiograph is a useful, inexpensive examination, which is always part of the initial examination of patients with chronic lung diseases. Recent reports suggest that the decreased superimposition of anatomic structures afforded by CT may make CT better than chest radiographs for this purpose [4-6]; however, the ultimate value of CT has yet to be determined. No studies have been reported that establish whether or not the patterns of parenchymal abnormality detected by CT are characteristic of specific types of chronic lung disease. Furthermore, only limited evaluation of various types of parenchymal abnormalities in different chronic lung diseases has been done [7-11].

This study was designed to identify the parenchymal abnormalities detected on CT in several varieties of chronic lung disease and then to test use of these patterns in the differential diagnosis. We also compared the accuracy of CT with that of chest radiography in diagnosing these specific diseases.

Subjects and Methods

Fifty-six patients were examined in the study, including eight normal control subjects. Forty-three of the 48 patients with chronic lung disease had biopsy-proved diagnoses. In the

Received December 14, 1988; accepted after revision February 1, 1989.

Presented at the annual meeting of the American Roentgen Ray Society, New Orleans, LA, May 1989.

This work was supported in part by grant HL 14212 from the National Heart, Lung, and Blood Institute and by grant RR-30 from the Division of Research Resources, General Clinical Research Centers Program of the National Institutes of Health.

¹ Department of Diagnostic Radiology and Nuclear Medicine, Stanford University School of Medicine, Stanford, CA 94305. Address reprint requests to C. Bergin, Divn. of Diagnostic Radiology/H1307, Stanford University Medical Center, Stanford, CA 94305.

² Department of Radiology, Duke University Medical Center, Durham, NC 27710.

³ Department of Pediatrics, Duke University Medical Center, Durham, NC 27710.

AJR 152:1183-1188, June 1989
 0361-803X/89/1526-1183
 © American Roentgen Ray Society

remaining five cases, the diagnosis of four cases of usual interstitial pneumonia (UIP) and one case of sarcoidosis was based on characteristic clinical findings. There were 20 patients with UIP, 16 with sarcoidosis, seven with lymphangitic carcinomatosis (breast [$n = 2$], prostate gland [$n = 2$], kidney [$n = 1$], lung [$n = 1$], and an unknown primary site [$n = 1$]), two with drug toxicity affecting the lung, two with lymphangioleiomyomatosis, and one with eosinophilic granuloma. The diagnosis of UIP includes patients with idiopathic pulmonary fibrosis ($n = 19$) and mixed connective tissue disease ($n = 1$), because the lung pathology in these conditions is identical. Chest radiographs were available for review in 48 of the 56 patients. Most chest radiographs were obtained within 1 week of the CT examination.

CT scans were performed on a GE 9800 scanner (General Electric Medical Systems, Milwaukee, WI) by using 10-mm collimated contiguous scans in 52 patients. Only limited chest CT scans were available in four patients with UIP. The standard algorithm was used for image reconstruction, and scans were viewed at settings appropriate for lung parenchyma (level, -701 ; width, 1000). Mediastinal windows were not evaluated. In 30 patients, high-resolution CT scans (HRCT) were obtained, consisting of 1.5-mm collimated scans at three levels: the aortic arch, the carina, and 3 cm above the diaphragm. HRCT scans were evaluated in conjunction with the standard CT scans.

Two experienced chest radiologists assessed the CT scans independently on two separate occasions 2 weeks apart to evaluate the reproducibility of their interpretations. There was an initial learning period in which the two readers were shown CT examples of the different diseases along with examples of each CT feature to be evaluated. CT scans were assessed for (1) distribution of disease in the axial plane (i.e., central, peripheral, or diffuse); (2) location (apex, midzone, and base) of polygons; (3) regular or irregular thickening of polygon walls (>1 mm); (4) central dot thickening (>1 mm); (5) distortion of pulmonary vessels, bronchi, and fissures in the lung; (6) bronchovascular-bundle thickening; (7) other linear densities (not obviously bronchovascular bundles or lobular septa); (8) air-space disease; (9) bronchiectasis; (10) unilateral or bilateral disease; (11) the presence, size, extent, and wall thickness of cysts; and (12) the presence, size, and number of nodules. Confidence levels for the first 11 features were scored from 1 to 5 (1 = definitely not present, 2 = probably not present, 3 = undecided, 4 = probably present, and 5 = definitely present). Each defined feature was considered to be present if it was identified with a confidence level of 4 or 5. Nodule size was grouped as <1.0 cm or ≥ 1.0 cm, and the number of nodules was estimated as zero, <20 , and ≥ 20 .

The readers also were required to assign each case to one of six known categories of chronic lung disease (UIP, sarcoidosis, lymphangitic carcinomatosis, drug toxicity, eosinophilic granuloma, lymphangioleiomyomatosis) or to the normal group. A specific diagnosis based on the findings on the 48 available chest radiographs (the type and

distribution of lung parenchymal abnormalities and the presence of mediastinal or hilar adenopathy) also was made in each case by each observer. Sensitivity, specificity, and accuracy of the diagnoses from CT and chest radiograph interpretations were calculated for the 48 patients with both studies.

Results

Some evidence of a learning process in diagnosing diseases from CT parenchymal patterns was seen, with marginally better performances by both readers on their second readings. R1 correctly diagnosed the disease in 52 of 56 and 54 of 56 patients in the first and second readings, respectively, and R2 correctly diagnosed the disease in 48 of 56 and 50 of 56 patients in the first and second readings, respectively.

The most prominent CT parenchymal features of each disease are presented in Table 1. The features that were identified most consistently by the two observers when comparing their first and second readings were disease distribution, thickened central dots within polygons, and the presence of cysts, lung distortion, bronchiectasis, and bronchovascular-bundle thickening. The two readers were internally consistent and consistent with each other in classifying axial disease distribution, except for nine cases of sarcoidosis. The second reader categorized parenchymal disease as being "diffuse" more often than "central" in the cases of sarcoidosis, although noting prominent thickening of bronchovascular bundles. R2 also categorized cases with UIP as being diffuse more often than did R1. The two observers were consistent with each other in their evaluation of lung distortion, the presence of nonseptal linear densities, central dot thickening, and bronchiectasis. The readers were less consistent in their identification of air-space disease and bronchovascular-bundle thickening, particularly in patients with UIP. Interpretation of unilateral or bilateral distribution of disease was consistent both between readings and between readers.

Usual Interstitial Pneumonia

The most consistent findings in 20 patients with UIP were the peripheral distribution of disease and lung distortion of parenchyma (Fig. 1). A peripheral pattern was identified in all 20 patients by R1, and in 16 patients by R2, who categorized four of the 20 patients as having diffuse disease. Bronchiectasis

TABLE 1: Prominent CT Features Identified in Various Chronic Lung Diseases

Disease	Distribution	Bronchovascular-Bundle Thickening	Distortion	Nodules	Polygons	Cysts	Patchy Air-Space Disease
Usual interstitial pneumonia ($n = 20$)	Peripheral	+	++	+	+	++	+
Sarcoidosis ($n = 16$)	Central/diffuse	+++	+++	+++	+	+	+
Lymphangitic carcinomatosis ($n = 7$)	Central/diffuse	+++	0	++	+++	0	+
Lymphangioleiomyomatosis ($n = 2$)	Diffuse	0	+++	0	+	+++	0
Eosinophilic granuloma ($n = 1$)	Diffuse	+	++	+++	+	++	0
Drug toxicity ($n = 2$)	Diffuse	0	+	0	0	0	++

Note.—Key: + = mild or few, ++ = moderate, +++ = severe or numerous, 0 = not seen.

tasis, nonseptal lines, and cysts were other common features of UIP. Most cysts were less than 1 cm in diameter, with walls that were usually thickened. Polygons were visualized in 50% of the patients, but were less well defined than those identified in lymphangitic carcinomatosis. Ill-defined nodules, numbering less than 20 and usually less than 1 cm in size were seen in eight patients.

R1 correctly diagnosed UIP in 19 of 20 patients by using CT, and no misdiagnoses of UIP occurred using CT scans. R2 diagnosed UIP correctly from CT scans in all 20 patients with UIP, but incorrectly interpreted one normal control scan as showing UIP (on the basis of dependent atelectasis).

R1 correctly diagnosed UIP in 10 of 13 patients from the chest radiographs. UIP was misdiagnosed as sarcoidosis in three patients, and sarcoidosis was misdiagnosed as UIP in two patients. R2 correctly diagnosed UIP in 12 of 13 patients from the chest radiographs. Sarcoidosis was misdiagnosed in one patient with UIP. UIP was misdiagnosed in one patient with sarcoidosis and in two patients with lymphangitic carcinomatosis.

Sarcoidosis

Lung distortion was the most frequent abnormality in the 16 patients with sarcoidosis (Fig. 2). Bronchovascular-bundle thickening and nodules were the next most common features.

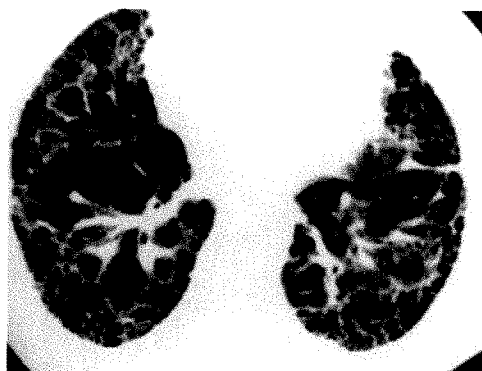


Fig. 1.—Usual interstitial pneumonia. CT section through lung bases shows peripheral rim of small thick-walled cysts and relatively spared central lung parenchyma.

Fig. 2.—Sarcoidosis. Parenchymal distortion is marked and abnormally thickened bronchovascular bundles are prominent in right lung. Small nodules also are visible.

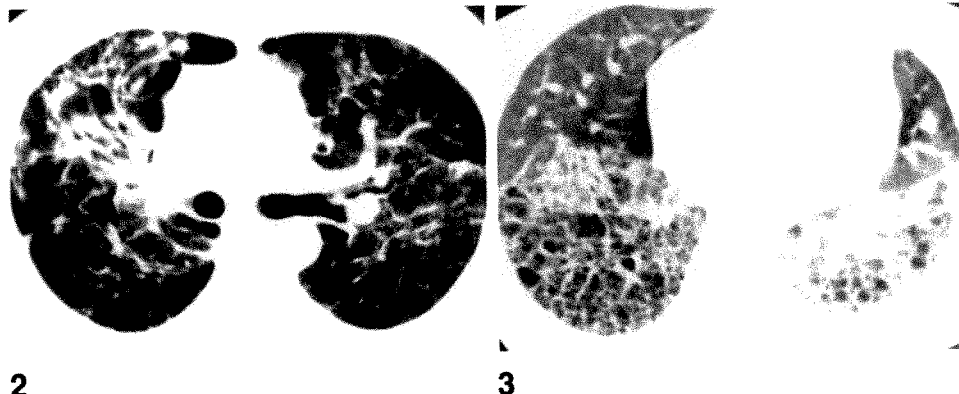


Fig. 3.—Sarcoidosis. This pattern of diffuse cyst formation and distortion is not typical of sarcoidosis and was misdiagnosed as usual interstitial pneumonia.

Nodules were seen in 13 of 16 patients with sarcoidosis and were more numerous than in the other diseases studied (except for the one case of eosinophilic granuloma). Polygons with irregularly and regularly thickened walls were observed by both readers in an average of 33% of patients. Although R1 commonly described distribution of disease as diffuse, prominent involvement of bronchovascular bundles was noted in 75% of the patients. Peripheral disease was described in four patients with sarcoidosis, three of whom had alveolar sarcoidosis. In the fourth patient, peripheral abnormality consisted of minimal patchy air-space disease with no evidence of cysts, lung distortion, or air bronchograms. Bronchiectasis and cystic spaces were seen in sarcoidosis, but less commonly than in UIP. As with UIP, cyst walls were often thickened; however, cystic spaces were frequently larger and more irregular in sarcoidosis than in the other diseases examined.

The correct diagnosis of sarcoidosis was made from CT scans in all 16 patients by R1 and in 15 of 16 patients by R2 (in one patient with sarcoidosis, atypical cysts on CT scans were misinterpreted as UIP [Fig. 3]). UIP was misdiagnosed as sarcoidosis in one patient by R1, and R2 misdiagnosed lymphangitic carcinomatosis in three patients and drug toxicity in one patient as sarcoidosis.

On the basis of chest radiographs, both readers correctly diagnosed sarcoidosis in 14 of 16 patients. Severe UIP was the disease most commonly confused radiographically with sarcoidosis.

Lymphangitic Carcinomatosis

Polygons were seen well in five of the seven patients with lymphangitic carcinomatosis. Their walls were thickened in each case, and their central dots were increased in diameter (R1, five of five; R2, four of five). Nodules were identified in five of seven cases. As opposed to sarcoidosis, lung distortion was uncommon in lymphangitic carcinomatosis, but it was occasionally present in association with a mass. Bronchiectasis was not seen. Disease distribution was categorized as either diffuse or central, and bronchovascular bundles were considered abnormally thick in most patients in this group (R1, seven of seven; R2, six of seven) (Fig. 4). Although most patients in this group had bilateral lung involvement, unilateral disease occurred more commonly in lymphangitic carcinomatosis than in any of the other diseases studied.

The correct diagnosis of lymphangitic carcinomatosis was made from CT images and chest radiographs in all patients by R1. R2 misdiagnosed lymphangitic carcinomatosis as sarcoidosis from the CT appearance in three cases and misdiagnosed the disease in two of the same patients from the chest radiograph. None of the chest radiographs were incorrectly interpreted as showing lymphangitic metastatic disease.

Lymphangioleiomyomatosis, Eosinophilic Granuloma, and Drug Toxicity

CT scans in two patients with lymphangioleiomyomatosis showed numerous cysts with thin walls (<1 mm). These cysts involved the lung parenchyma diffusely and varied in diameter from a few millimeters to 3 cm (Fig. 5). Visibility of polygons was reported with a confidence level of 4 by R1, who considered septal walls to be minimally thickened. Distortion of the lung parenchyma from areas of confluent cysts was prominent in both patients. Nodules were not noted.

CT images in the one patient with eosinophilic granuloma showed diffuse cysts in the upper zones (Fig. 6). These cysts were more widely spaced and had thicker walls than cysts identified in the two patients with lymphangioleiomyomatosis. In addition, numerous nodules were present.

The two patients with pulmonary drug toxicity had patchy bilateral air-space disease (Fig. 7).

Correct CT and chest radiographic diagnoses were made by both readers in the patients with lymphangioleiomyomatosis and eosinophilic granuloma, and in one of two patients with pulmonary drug toxicity.

Normal Control Subjects

R1 considered polygons to be visible on CT scans in four of the eight normal control subjects. The polygons were usually incomplete, with walls less than 1-mm thick. R2 categorized polygons only if they were complete and identified them in one of eight control subjects. One control subject showed sparse dependent, patchy atelectasis on CT images and R2 misdiagnosed early UIP.

Accuracy Data

Diagnostic sensitivity, specificity, and overall accuracy of R1 and R2 for UIP, sarcoidosis, and lymphangitic carcinomatosis are summarized in Table 2. The data base consists of those patients with chronic lung disease ($n = 40$) and the normal control subjects ($n = 8$) who had both CT scans and chest radiographs. R1 was marginally more accurate in diagnosing specific chronic lung disease from CT images than from chest radiographs. Using CT images, R1 correctly diagnosed the disease in four of the six patients whose diseases R1 misdiagnosed with chest radiographs. R2 was equally



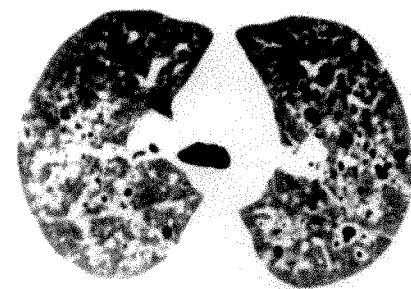
4



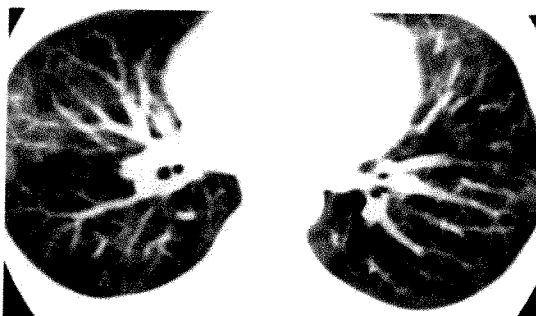
5

Fig. 4.—Lymphangitic carcinomatosis. Secondary lobules (polygons) are clearly delineated in right lung by thickened walls and central dots. Bronchovascular bundles on right also are markedly thickened. No evidence of lung distortion is present.

Fig. 5.—Lymphangioleiomyomatosis. Small thin-walled cysts are distributed throughout lung parenchyma. Note bilateral small chronic pneumothoraces.



6



7

Fig. 6.—Eosinophilic granuloma. Multiple thick- and thin-walled cysts and nodules were more prominent in upper zones and more widely spaced than cysts in lymphangioleiomyomatosis or usual interstitial pneumonia.

Fig. 7.—Drug toxicity. CT section shows bilateral patchy air-space disease.

TABLE 2: Sensitivity, Specificity, and Overall Accuracy of Two Readers (R1 and R2) in Diagnosing Specific Chronic Lung Disease from CT and Chest Radiograph Patterns

Disease ^a	Reader	Sensitivity (%)		Specificity (%)		Accuracy (%)	
		CT	CR ^b	CT	CR	CT	CR
Usual interstitial pneumonia (n = 13)	R1	12/13 (92)	10/13 (77)	35/35 (100)	33/35 (94)	47/48 (98)	43/48 (90)
	R2	13/13 (100)	12/13 (92)	34/35 (97)	32/35 (91)	47/48 (98)	44/48 (92)
Sarcoidosis (n = 16)	R1	16/16 (100)	14/16 (88)	31/32 (97)	29/32 (91)	47/48 (98)	43/48 (90)
	R2	15/16 (94)	14/16 (88)	28/32 (88)	31/32 (97)	43/48 (90)	45/48 (94)
Lymphangitic carcinomatosis (n = 6)	R1	6/6 (100)	6/6 (100)	42/42 (100)	42/42 (100)	48/48 (100)	48/48 (100)
	R2	3/6 (50)	4/6 (67)	42/42 (100)	42/42 (100)	45/48 (94)	46/48 (96)

^a Data calculated for 48 patients (usual interstitial pneumonia = 13, sarcoidosis = 16, lymphangitic carcinomatosis = 6, lymphangioleiomyomatosis = 2, drug toxicity = 2, eosinophilic granuloma = 1, and normal controls = 8) in whom both CT scans and chest radiographs were available.

^b CR = Chest radiograph.

accurate using CT and the chest radiograph. R2 correctly diagnosed the disease by CT but not by chest radiographs in one patient and by chest radiographs but not by CT in two patients; the diseases in four patients were misdiagnosed by R2 with both studies. After using the sign test, we found no significant difference between CT and the chest radiograph.

Thin-section scans (HRCT) improved visualization of specific parenchymal features, particularly polygons, nonseptal linear densities, small cysts, and bronchiectasis. However, an independent assessment comparing HRCT with standard CT scans in identifying specific disease features was not part of this study.

Discussion

CT patterns of abnormal lung parenchyma have been described in various chronic lung diseases [7–11], but the diagnostic accuracy of radiologists using these patterns has not been evaluated previously. In this series, we assessed the frequency of various parenchymal abnormalities in a variety of chronic lung diseases and determined the accuracy of CT pattern recognition in the diagnosis of six specific disease entities.

UIP and sarcoidosis tend to be distributed differently in the lungs, a feature that can be readily appreciated on CT scans [1, 12]. This was the feature that could be used most reliably to distinguish UIP from the other diseases included in this series. In UIP, the peripheral lung is most abnormal, first with a patchy distribution, which then progresses to a uniform rim of fibrosis, cystic spaces, and lung distortion. (In severe disease, these abnormalities can progress beyond their peripheral distribution to involve the lung diffusely) [9]. This pattern of lung fibrosis, characteristic of patients with UIP, is identical, both pathologically and radiologically, to that seen in idiopathic pulmonary fibrosis, rheumatoid arthritis, scleroderma, mixed connective tissue disease and asbestosis; thus, these diseases can be distinguished only by their clinical presentations.

As opposed to UIP, sarcoidosis more commonly affects the central and middle lung compartments [5] and is less prominent peripherally. Septal thickening, parenchymal distortion, bronchiectasis, and cysts were seen in both UIP and sarcoid-

osis; however, cysts were generally smaller, more numerous, and peripheral in distribution of UIP. Linear and irregular nonseptal densities, seen in CT images of both UIP and sarcoidosis, were longer and broader in sarcoidosis, a disease in which sheaths of fibrosis frequently extend from the mediastinum to the pleura [12]. In sarcoidosis, these thick fibrous bands caused distortion of the lung, displacing major vessels and bronchi. Conversely, the position of the major vessels and bronchi in UIP remained normal, with distortion usually affecting only peripheral structures except in severe, advanced disease.

Both readers had difficulty distinguishing UIP from sarcoidosis in patients with severe parenchymal disease, using either the chest radiograph or CT scan. The cause of end-stage lung disease can also be difficult to determine from histologic sections in patients with known severe UIP or sarcoidosis. Even with extensive parenchymal changes, however, a peripheral predominance was noted on CT images in most patients with UIP. When the bases of the lungs were diffusely abnormal in cases of UIP, a peripheral pattern often was still seen above the carina. Other than UIP, no disease studied in this series had a peripheral rim of abnormal parenchyma. When noted in sarcoidosis, peripheral disease was limited to one or two focal segments, and the correct diagnosis was made in each case by the readers, recognizing the spherical or air-space abnormalities of "alveolar" sarcoidosis. Thus, the pattern of a peripheral rim of parenchymal disease in our series proved diagnostic of UIP.

Sarcoidosis was correctly diagnosed by both readers using CT in all but one patient. Bronchovascular-bundle thickening was a more consistent observation in sarcoidosis than in any other disease, except for lymphangitic carcinomatosis. Both sarcoidosis and lymphangitic carcinomatosis prominently involve lymphatic channels, accounting for the observed bronchovascular-bundle thickening [12]. Septal thickening and visibility of polygons representing secondary lobules also were features of both sarcoidosis and lymphangitic carcinomatosis. CT features that best distinguished sarcoidosis from lymphangitic carcinomatosis were lung distortion, cysts, and bronchiectasis, all of which result from the fibrosis prominently associated with sarcoidosis. Thick, nonseptal, linear, and irregular densities causing parenchymal distortion represent

fibrotic bands in sarcoidosis [12]. These bands were not features of lymphangitic carcinomatosis. Although fibrosis has been described with lymphangitic metastases [7, 13], this is a rare histologic finding. Nodules were common in both diseases, but they were more numerous and more clearly defined in patients with sarcoidosis than in patients with lymphatic spread of tumor.

Although patterns in drug toxicity, eosinophilic granuloma, and lymphangioleiomyomatosis were different from those in UIP, sarcoidosis, and lymphangitic carcinomatosis and were accurately diagnosed with both CT and chest radiographs, our limited number of cases precludes meaningful conclusion. Comparing CT patterns of chronic drug toxicity in larger numbers of patients with other types of lung disease is an avenue for further investigation.

Diagnostic accuracy was only marginally better when using pattern recognition from CT images rather than from the chest radiographs, and this difference was not statistically significant. The additional expense of CT is warranted when it might provide evidence sufficiently supportive of a clinical diagnosis to prevent more invasive diagnostic procedures. From our limited series, we consider the peripheral rim of parenchymal fibrosis to be sufficiently specific for the UIP group of diseases that open-lung biopsy may not be necessary for further diagnosis. However, when parenchymal abnormalities are either very mild or very extensive, the imaging diagnosis of UIP is less accurate, and in these cases open-lung biopsy may still be needed. No single parenchymal abnormality was as predictive of sarcoidosis in our series. However, the diagnosis of sarcoidosis was made with a high degree of accuracy by using a combination of parenchymal CT features (i.e., nodules, thickened bronchovascular bundles, and distortion). Thickened bronchovascular bundles identified on CT suggest lymphangitic carcinomatosis or sarcoidosis; both are diseases in which transbronchial biopsy has a higher yield of diagnostic tissue than in other diseases in our series. Thus, recognizing thickened bronchovascular bundles on CT in patients with nondiagnostic chest radiographs should suggest transbron-

chial biopsy as the diagnostic method of choice. Furthermore, the clearer parenchymal detail possible with CT may provide an effective noninvasive tool for following response to therapy in patients with chronic lung disease.

We have identified different combinations of parenchymal abnormalities on CT images of patients with a variety of chronic lung diseases. Two radiologists reliably reproduced their findings from two separate readings and diagnosed specific chronic lung diseases from CT images alone with a high degree of accuracy.

REFERENCES

1. Heitzman ER. *The lung: radiographic-pathologic correlations*, 2nd ed. St. Louis: Mosby, 1984:48-105
2. Fraser RG, Paré JAP. *Synopsis of diseases of the chest*. Philadelphia: Saunders, 1983:640-662
3. McLoud TC, Gaensler EA, Carrington CB. Chronic diffuse infiltrative lung disease: newer approaches. *Clin Chest Med* 1984;5:332-344
4. Bergin CJ, Muller NL. CT of interstitial lung disease: a diagnostic approach. *AJR* 1987;148:8-15
5. Bergin CJ, Roggli V, Coblentz C, Chiles C. The secondary lobule: normal and abnormal CT appearance. *AJR* 1988;151:21-25
6. Webb WR, Stein MG, Finkbeiner WE, Im J-G, Lynch D, Gamsu G. Normal and diseased isolated lungs: high-resolution CT. *Radiology* 1988;165:81-87
7. Munk PL, Müller NL, Miller RR, Ostrow DN. Pulmonary lymphangitic carcinomatosis: CT and pathologic findings. *Radiology* 1988;166:705-709
8. Mezziane MA, Hruban RH, Zerhouni EA, et al. High resolution CT of the lung parenchyma with pathologic correlation. *RadioGraphics* 1988;8:27-54
9. Staples CA, Müller NL, Vedral S, Abboud RT, Ostrow D, Miller RR. Usual interstitial pneumonia: correlation of CT with clinical, functional, and radiologic findings. *Radiology* 1987;162:377-381
10. Aberle DR, Gamsu G, Ray CS, Feuerstein IM. Asbestos-related pleural and parenchymal fibrosis: detection with high-resolution CT. *Radiology* 1988;166:729-734
11. Hamper UM, Fishman EK, Khouri NF, Johns CJ, Wang KP, Siegelman SS. Typical and atypical CT manifestations of pulmonary sarcoidosis. *J Comput Assist Tomogr* 1986;10:928-936
12. Dail DH, Hammer SP. *Pulmonary pathology*. New York: Springer-Verlag, 1988:417-438, 1095-1135
13. Trapnell DH. The radiologic appearance of lymphangitic carcinomatosis of the lung. *Thorax* 1964;19:251-260

Treatment of Pleural Effusions and Pneumothorax with Catheters Placed Percutaneously Under Imaging Guidance

Caroline Reinhold¹
 Fernando F. Illescas
 Mostafa Atri
 Patrice M. Bret

We analyzed our experience with 42 consecutive patients who had pleural effusions (seven benign exudates, 12 malignant exudates, and 15 empyemas) or pneumothoraxes (eight patients) treated over a 3-year period by catheters placed percutaneously under imaging guidance. The catheters ranged in size from 8 French to 14 French. Although the overall success rate was 71% (30/42), the success rate during the first 2 years was 57% (12/21), compared with 86% (18/21) during the third year. The success rates according to collection type were 63% (12/19) for exudates, 80% (12/15) for empyemas, and 75% (6/8) for pneumothoraxes. There were two complications: a vasovagal reaction and a sterile collection converted to an empyema.

After an initial learning period and with accumulated experience, radiologically placed catheters have proved to be an efficacious treatment of pleural effusions and pneumothoraxes that has a low complication rate.

A variety of diseases result in the accumulation of fluid or air in the pleural space. Treatment is usually unnecessary, but drainage by tube thoracostomy is sometimes required [1]. Collections requiring treatment include large pneumothoraxes, malignant effusions, empyema (including complicated parapneumonic effusions), hemothoraxes, and chylothoraxes. In the past, drainage has been achieved by surgically placed large-bore chest tubes. However, the use of catheters placed percutaneously under imaging guidance has gained acceptance [2-4]. We analyzed the results and complications in 42 consecutive patients treated in this fashion over the past 3 years.

Materials and Methods

We undertook a retrospective study of 42 consecutive patients who underwent percutaneous catheter drainage of pleural collections in our department between 1985 and 1987. The 42 cases consisted of 15 empyemas, 19 exudates (12 malignant and seven nonmalignant), and eight pneumothoraxes. Causes of the empyemas included pneumonia (eight cases), iatrogenic contamination of the pleural space (six cases), and postoperative bronchopleural fistula (one case). Malignant effusions resulted from primary tumors of the lung (two cases) and metastases from the urinary tract (four cases), breast (two cases), and the gastrointestinal tract, the tonsils, and an unknown source (one case each). One case was a mesothelioma. Causes of nonmalignant exudates included pneumonia (three cases), effusion after esophageal perforation (one case), sympathetic effusion associated with a subphrenic abscess (one case), and two cases with no clear cause. The pneumothoraxes were complications of transthoracic needle aspiration (seven cases) and, in one case, pneumothorax occurred after a thoracotomy for decortication. There were 26 men and 16 women. The mean age was 63 years, with a range of 31 to 92 years. In 28 patients, only radiologically placed catheters were used, and in 14 patients radiologically placed catheters were inserted after surgically placed chest tubes.

All pleural collections were classified as exudates, empyemas, or pneumothoraxes. Criteria for exudates included at least one of the following features [5]: (1) a pleural fluid to serum protein ratio of greater than 0.5, (2) a pleural fluid lactic dehydrogenase level greater than

Received November 28, 1988; accepted after revision February 6, 1989.

¹All authors: Department of Radiology, McGill University and Montreal General Hospital, 1650 Cedar Ave., Montreal, Quebec, H3G 1A4 Canada. Address reprint requests to F. F. Illescas.

AJR 152:1189-1191, June 1989
 0361-803X/89/1526-1189
 © American Roentgen Ray Society

200 IU, and (3) a pleural fluid to serum lactic dehydrogenase ratio of greater than 0.6. Empyemas were defined as frank pus, fluid shown to be infected by bacteriologic studies, or fluid with a pH less than 7 [6]. Indications for catheter drainage of pleural effusions included empyemas and symptomatic exudative effusions.

Of the 56 catheters used for drainage of exudates and empyemas, 40 catheters were placed under sonographic guidance, 11 catheters under CT guidance, and five catheters under fluoroscopic guidance, mainly to replace existing catheters. For pneumothoraxes, eight catheters were placed under fluoroscopic guidance and one under CT guidance.

Once a collection was localized, its extent and the presence or absence of loculations were noted. Small effusions were drained by using a multistep Seldinger technique, and large effusions were drained by using the trocar technique.

For small collections or where difficult access was anticipated, the initial puncture was made under sonographic or CT guidance. Under local anesthesia, the chest wall was punctured with an 18-gauge sheathed needle (Cook, Bloomington, IN). Several milliliters of fluid were then aspirated and sent for laboratory analysis. Then, under fluoroscopic control, a J-tipped guidewire was inserted through the sheath into the pleural space. After tract dilatation, a single lumen, multi-side-hole catheter was placed, and as much fluid as possible was aspirated. To avoid inducing reexpansion pulmonary edema, the largest amount of fluid removed during one session was 1000 ml [1].

For larger collections, after an initial thoracentesis with a small-gauge localizing needle, the trocar-catheter technique was used under direct radiologic guidance. Once the catheter was in good position, it was connected to underwater-bottle seal with or without low-wall suction.

The catheter size used ranged from 10 French to 14 French, depending on the viscosity of the collection (Sachs catheter, Electro-Catheter Corp., Rahway, NJ; or vanSonnenberg single lumen catheter, Medi-tech, Watertown, MA). After catheter placement, all patients were evaluated periodically with chest radiographs to assess the state of the pleural collection; in addition, complex collections were evaluated with sonography and occasionally with CT.

Indications for drainage of pneumothoraxes with a radiologically placed catheter included a 20% or greater pneumothorax on the initial chest radiograph, significant symptomatology, or progression of the pneumothorax shown on serial radiographs.

In the case of pneumothoraxes, percutaneous drainage was performed by using a pneumothorax set that consisted of a 9-French multi-side-hole catheter (Cook, Bloomington, IN), a stylet within a metal cannula, and a two-way stopcock with plastic tubing, which is used to connect the catheter to the one-way flutter valve (Heimlich valve, Bard-Parker, Rutherford, NJ). The puncture site was selected along the midaxillary line in the fifth or sixth intercostal space. After infiltration with local anesthesia, the catheter-cannula-stylet combination was inserted into the pleural space using the trocar technique under direct fluoroscopic guidance. Once the catheter was placed in the desired anteroapical position, the stylet and metal cannula were withdrawn, and the catheter was connected to the Heimlich valve. Bubbling at the tip of the valve when submersed in water, as well as condensation inside the plastic tubing, confirmed the intrapleural location of the catheter. An upright expiratory chest film was then obtained to document the position of the catheter and resolution of the pneumothorax.

The drainage procedure was considered successful if complete or almost complete evacuation of the pleural collection and significant clinical improvement occurred. In the case of an empyema, treatment was considered successful if surgical intervention was not required.

Results

A total of 65 catheters were used for the 42 patients in the study. Most patients with pneumothoraxes required a single catheter (seven of eight patients had one catheter inserted), whereas for exudates and empyemas, a significant number required several catheters. Eighteen patients each had one catheter inserted, 12 patients had two catheters, two patients had three catheters, and two patients had four catheters. All catheters were placed sequentially, and no patients had more than one catheter placed radiologically at one time.

The overall success rate of percutaneous catheter drainage was 71% (30/42). The success rate for exudates was 63% (12/19), for empyemas 80% (12/15), and for pneumothoraxes 75% (6/8).

In the third year of the study, we were referred the same number of cases as in the first 2 years (21 cases). Our overall success rate improved significantly from 57% (12/21) during the first 2 years to 86% (18/21) in the final year. This improvement occurred for all collections.

Complications were encountered in two of the 42 cases. Of these, only one was clinically significant (conversion of a sterile collection into an empyema). The second patient had a transient vasovagal reaction during the drainage procedure that responded to conservative management.

Discussion

Success rates reported in the literature for drainage with a surgically placed tube vary widely. In the case of empyemas, the range is 35–80% [7]. This compares with 72–88% for catheters placed percutaneously under sonographic or CT guidance [3, 4, 8]. The 86% we achieved in the final year of our study compares favorably with these results.

The success rate for drainage of malignant effusions with surgically placed tubes ranges from 5% to 86%, with a mean of 42% [9]. Our success rate with percutaneously placed catheters was 63% for this subgroup.

Finally, two recent series that used percutaneously placed catheters to drain pneumothoraxes occurring after transthoracic needle aspiration reported success rates of over 90% [2, 10]. We had a slightly lower success rate of 75%, perhaps due to a slightly different patient population. One of our patients was being treated for a persistent pneumothorax after decortication surgery.

In addition to being efficacious, catheters placed percutaneously under CT or sonographic guidance cause fewer complications. Of the two complications encountered in our series, only the conversion of a sterile collection into an empyema was clinically significant. These results are in keeping with reports in the literature to date, in which no major complications have been reported [2–4, 8, 10].

In 12 of the 42 cases, drainage was unsuccessful. Ten of these cases had persistent pleural collections when the catheter was removed. One pneumothorax recurred, and in another case, the patient required a Foley catheter for long-term irrigation of an empyema.

Five of these 10 patients with residual loculated hydropneumothoraxes at the time of catheter removal had malignant effusions. Associated abnormalities that may have prevented lung expansion in these cases include (1) marked pleural thickening caused by metastatic involvement or radiation therapy, (2) radiation-induced parenchymal fibrosis, and (3) lymphangitic tumor spread. In another case, a persistent pneumothorax was present. In this case, extensive fibrothorax from a previous intrapleural hemorrhage probably prevented complete lung expansion. In the remaining four cases, no obvious explanation was found.

As our results show, drainage with radiologically placed catheters is very successful after an initial learning curve. The higher success rates in the final year of the study seem largely to be due to improved catheter management after insertion. Assessments regarding the patient's clinical status and progress of drainage were frequently made. This close follow-up allowed for early investigation with sonography or CT, or for intervention such as catheter repositioning, catheter exchange, or insertion of additional catheters. During the first 2 years of the study, we were less aggressive with catheter manipulations once the catheter was inserted. Also, initially we were not always consulted when catheter drainage was discontinued in favor of surgically placed chest tubes because of presumed failure of the catheter.

In conclusion, this retrospective study shows that drainage of pleural collections with radiologically placed catheters is highly successful and has a low complication rate. When compared with the success rate reported in the literature,

radiologically placed catheters appear to be as efficacious as surgically placed chest tubes. The ease of placement, comparable success rate, and safety of radiologically placed catheters makes them an attractive alternative to surgically placed chest tubes.

REFERENCES

1. Miller KS, Sahn SA. Chest tubes: indications, techniques, management and complications. *Chest* **1987**;91(2):258-264
2. Perlmutt LM, Braun SD, Newman GE, et al. Transthoracic needle aspiration: use of a small chest tube to treat pneumothorax. *AJR* **1987**;148:849-851
3. Westcott JL. Percutaneous catheter drainage of pleural effusions and empyema. *AJR* **1985**;144:1189-1193
4. vanSonnenberg E, Nakamoto SK, Mueller PR, et al. CT and ultrasound-guided catheter drainage of empyemas after chest tube failure. *Radiology* **1984**;151:349-353
5. Light RW, MacGregor ML, Luchsinger PC, Ball WC Jr. Pleural effusions: the diagnostic separation of transudates and exudates. *Ann Intern Med* **1972**;77(4):507-513
6. Light RW. Parapneumonic effusions and empyema. *Clin Chest Med* **1985**;6(1):55-62
7. Lemmer JH, Botham MJ, Orringer MB. Modern management of adult thoracic empyema. *J Thorac Cardiovasc Surg* **1985**;90:849-855
8. Silverman SG, Mueller PR, Saini S, et al. Thoracic empyema: management with image-guided catheter drainage. *Radiology* **1988**;169:5-9
9. Prakash UBS. Malignant pleural effusions. *Postgrad Med* **1986**;80(5):201-209
10. Casola G, vanSonnenberg E, Keightley A, Ho M, Withers C, Lee AS. Pneumothorax: radiologic treatment with small catheters. *Radiology* **1988**;166:89-91

Book Review

Essential Chest Radiology. By J. B. Cookson and D. B. L. Finlay. Stoneham, MA: Butterworths, 151 pp., 1988. \$37.95

The value of any book depends on how well that book satisfies the readers' needs and interests. A problem with many medical books, especially large tomes, is the desire of the author to satisfy everyone. This can result in inclusion of detail so excessive that the average reader is overwhelmed and unable to extract relevant information. One response to this problem is the authorship of concise, terse texts, written to satisfy specific needs and interests.

Essential Chest Radiology was written by a British internist and a British radiologist. The target readers are candidates for certifying examinations in the United Kingdom in those two fields. It is written and illustrated with emphasis on brevity, directness, and relevance. Reflecting the orientation of the senior author, clinical correlation is abundant.

Introductory chapters cover, in summary fashion, radiographic techniques and plain-film anatomy of the chest. Subsequent sections are devoted to specific patterns or anatomic regions and thus include localized and diffuse pulmonary "shadows"; obstructive lung disease; the pleura, diaphragm, and chest wall; the hilum; the mediastinum; and the heart. A short, final section entitled "Special Techniques" briefly discusses chest CT and nuclear medicine.

The bulk of this short volume thus is devoted to the interpretation of plain films of the chest. The discussions are exceedingly terse with regard to radiographic descriptions. The illustrations are ample and have minimal legends. Definitions of pulmonary patterns are arbitrary and not especially conventional. The illustrations are adequate, but close-ups of the lung fields are exceedingly few, and most of the prints lack both the contrast and resolution necessary for optimal exemplification. The illustrations include only one CT scan, a vintage study of a most unusual mesothelioma.

It is possible that this volume perfectly fits the needs of its target readers. If so, I must express concern about the appropriateness of

the examinations for which these readers are studying. Differential diagnoses are based far more on the clinical data than on the information on the images. The differential diagnoses apparently reflect perceived incidence in the United Kingdom, such as the repeated reference that tuberculosis is common only in Asians and that fungal diseases are rare. Reference to immunocompromised individuals is extremely infrequent, and the book has absolutely no mention of human immunodeficiency virus and its consequences. Two references are listed at the end of the text: the 1973 edition of Felson's *Chest Roentgenology* and Simon's 1978 *Principles*.

The targeted readers quite clearly must be experienced in both clinical and imaging arenas as the text has far too little descriptive material to inform the inexperienced reader, such as the medical student or first-year radiology or clinical resident, how to interpret the images.

Essential Chest Radiology may be the ideal review book for its intended audience. Unfortunately, it has little to offer those who are outside the United Kingdom, are not experienced clinicians, or are interested in multimodality imaging of the chest. For those not ready for a complete treatise, namely *Diagnosis of Diseases of the Chest* by Fraser and Pare, several other concise texts are more useful. These include the more recent edition of Felson's book, the Pare and Fraser *Synopsis*, the chapters on chest imaging in the new edition of *Fundamentals of Radiology* by Squire and Novelline, and some of the other texts for medical students.

David S. Feigin
University of California, San Diego
San Diego, CA 92093

Case Report

Apical *Pneumocystis carinii* Pneumonia After Inhaled Pentamidine Prophylaxis

Dewey J. Conces, Jr.,¹ Jean L. Kraft, Vernon A. Vix, and Robert D. Tarver

Pneumocystis carinii pneumonia is the most common pulmonary infection among patients with AIDS [1]. The antiprotozoal agent pentamidine is an effective IV treatment for this infection, but has significant side effects [2]. Inhalation of aerosolized pentamidine recently has been shown to be effective and less toxic, and this route is now being used to administer reduced doses for prophylaxis [3, 4].

We report a case of bilateral apical *P. carinii* pneumonia developing in an AIDS patient receiving aerosolized pentamidine prophylaxis.

Case Report

A 57-year-old man presented with a dry cough. The patient was infected with human immunodeficiency virus and 15 months earlier had suffered his first episode of *P. carinii* pneumonia. Chest radiographs at that time showed diffuse bilateral interstitial infiltrates, which cleared after treatment with IV pentamidine.

For the 9 months before admission, he had received prophylactic aerosolized pentamidine treatments. The initial dosage was 60 mg every 2 weeks, and after 6 months it was increased to 150 mg every 2 weeks. The treatments were administered by the respiratory therapy department, with the patient seated.

The patient had also been receiving zidovudine for 14 months, during which he had experienced persistent anemia, which required many blood transfusions. On the day of admission, the patient had a hemoglobin level of 7.3 g/dl and was given a transfusion. The patient complained of a dry cough and increasing fatigue, but denied fever, shortness of breath, or sputum production. The physical examination was unremarkable. Chest radiography showed bilateral apical infil-

trates (Fig. 1). Arterial blood gas was not measured. The WBC count was 2500, with a normal differential. Bronchoscopy was performed, and bronchoalveolar lavage samples were obtained only from the upper lobes. Numerous *P. carinii* organisms were present, and no other organisms were identified. The patient was treated with trimethoprim and dapsone. The infiltrates cleared gradually, with minimal residual infiltrate remaining in the right apex.

Discussion

The usual radiographic appearance of *P. carinii* pneumonia in patients with AIDS is a diffuse interstitial infiltrate [1]. Some patients have focal infiltrates involving one or more lobes [1]. Milligan et al. [5] reported eight patients who initially were thought to have pulmonary tuberculosis because of the upper-lobe distribution of their infiltrates. One case of apical *P. carinii* infection has been reported in a patient receiving prophylactic inhaled pentamidine [6]. During his first episode of *P. carinii* pneumonia, our patient had typical diffuse interstitial infiltrates. His second episode, which occurred while receiving prophylactic inhaled pentamidine treatments, was confined to the apices.

The standard therapy for *P. carinii* pneumonia is either trimethoprim-sulfa or pentamidine. Both of these agents are effective, but they are frequently associated with toxicity [2]. Recently, inhaled pentamidine has been shown to be effective in the treatment of mild cases of *P. carinii* pneumonia [3]. This method of administration seems ideally suited for the treatment of *P. carinii* pneumonia because the organisms are

Received January 6, 1989; accepted January 26, 1989.

¹ All authors: Department of Radiology, Indiana University School of Medicine and Hospital, X-64, 926 W. Michigan St., Indianapolis, IN 46223. Address reprint requests to D. J. Conces.

AJR 152:1192-1194, June 1989 0361-803X/89/1526-1193 © American Roentgen Ray Society

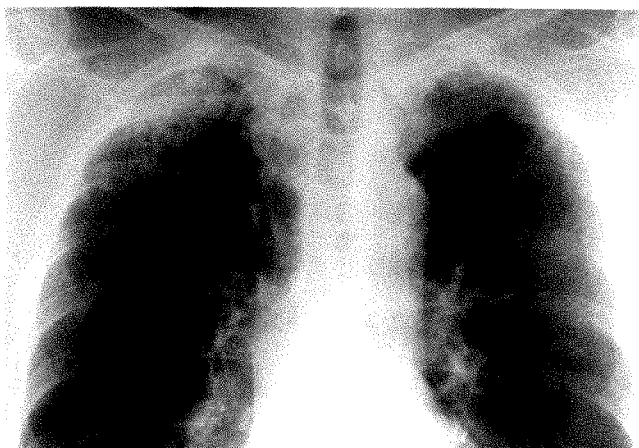


Fig. 1.—Posteroanterior chest radiograph showing bilateral apical infiltrates.

located in the alveoli. Inhaled pentamidine concentrates in the alveoli at levels five to 14 times greater than those reached with IV administration [3]. The prophylactic use of inhaled pentamidine recently has been shown to protect against recurrent *P. carinii* pneumonia [4].

We think that the apical distribution of the recurrent *P. carinii* pneumonia infection in this patient can be explained by factors that affect the regional distribution of inhaled particles in the lung. Ventilation in the normal human has been shown to increase from the apex to the base of the lung [7]. The deposition of particles in the lung is closely related to ventilation, with the greatest deposition occurring where ventilation is greatest [8]. Thus, inhalation of pentamidine leads to greater deposition of the drug in the bases than in the apices. This has been confirmed by measuring regional distribution of a mixture of pentamidine and ^{99}Tc -DTPA administered to

a patient receiving inhaled pentamidine prophylaxis [6]. Because of this, we think that the alveolar concentration of pentamidine in the apices was not high enough to prevent a recurrence of *P. carinii* pneumonia.

Because of the regional differences in the deposition of particulate material, it might be advisable to administer the inhaled pentamidine in the supine position. When the patient is supine, the ventilation gradient is markedly reduced, as compared with the upright position [7, 8]. This decrease in gradient would result in increased deposition of pentamidine in the apices, which may raise the concentration enough to prevent recurrent *P. carinii* infection.

REFERENCES

1. Suster B, Akerman M, Orenstein M, Wax MR. Pulmonary manifestations of AIDS: review of 106 Episodes. *Radiology* **1986**;161:87-93
2. Sattler FR, Cowan R, Nielsen DM, Ruskin J. Trimethoprim-sulfamethoxazole compared to pentamidine for treatment of *Pneumocystis carinii* pneumonia in the acquired immunodeficiency syndrome. *Ann Intern Med* **1988**;109:280-287
3. Conte JE, Hollander H, Golden JA. Inhaled or reduced-dose intravenous pentamidine for *Pneumocystis carinii* pneumonia. *Ann Intern Med* **1987**;107:495-498
4. Van Gundy KP, Akil B, Bill R, Boylen CT. The effect of inhaled pentamidine on the prevention of *Pneumocystis carinii* pneumonia in patients with acquired immunodeficiency syndrome (AIDS). *Am Rev Respir Dis* **1988**;137S:120
5. Milligan SA, Stulbarg MS, Gamsu G, Golden JA. *Pneumocystis carinii* pneumonia radiographically simulating tuberculosis. *Am Rev Respir Dis* **1985**;132:1124-1126
6. Abd AG, Niermans DM, Ilowite JS, Pierson RN, Bell ALL. Bilateral upper lobe *Pneumocystis carinii* pneumonia in a patient receiving inhaled pentamidine prophylaxis. *Chest* **1988**;94:329-331
7. Kaneko K, Milic-Emili J, Dolovich MB, Dawson A, Bates DV. Regional distribution of ventilation and perfusion as a function of body position. *J Appl Physiol* **1966**;21:767-777
8. Chamberlain MJ, Morgan WKC, Vinitski S. Factors influencing the regional deposition of inhaled particles in man. *Clin Sci* **1983**;64:69-78

Case Report

Goblet Cell Metaplasia Causing Alveolar Disease of the Lung: Radiographic and Pathologic Findings

Gwen K. Nazarian,¹ Barry H. Gross,^{1,2} and E. A. Del Buono³

When alveolar disease of the lung occurs in patients in an intensive-care setting, the most common causes are pulmonary edema, pneumonia, or hemorrhage [1]. We report a case of alveolar disease due to mucin production caused by goblet cell metaplasia of uncertain cause. To the best of our knowledge, this is the first such case reported.

Case Report

An 83-year-old man was hospitalized for treatment of pneumonia. He was a nonsmoker who, 3 weeks before admission, had been healthy without any history of chronic bronchitis. He was being treated empirically with antibiotics for presumed pneumonia (the patient refused chest radiographs) when he developed progressive respiratory distress requiring emergent tracheostomy placement. He was transferred to a secondary care center, where he was ventilated at 60–80% inspired oxygen levels. Chest radiographs reportedly showed diffuse bilateral air-space disease. Fiber-optic bronchoscopy showed a large fistula from the left main bronchus to the esophagus. The cause of the fistula was not apparent. An endotracheal tube was placed at bronchoscopy and bronchial washings grew a few yeast cells and rare Gram-negative rods. He was transferred to our hospital for surgery. Surgical repair included ligation of the cervical esophagus and gastroesophageal junction with formation of a blind pouch that communicated through the fistula with the lungs. The cause of the fistula still was not apparent. Chest radiographs 17 days later at our institution revealed diffuse bilateral air-space disease consistent with pulmonary edema or diffuse pneumonia (Fig. 1A). Sputum cultures grew *Pseudomonas aeruginosa* and numerous yeast cells. His post-operative course was complicated by recurrent hypotension and

respiratory failure despite being ventilated at 80–100% inspired oxygen levels, and he died 24 days after his initial presentation.

At autopsy, large cell lymphoma involving the soft tissues surrounding the bronchus and esophagus was found to have caused the fistula. This was confirmed by common leukocyte antigen immunohistochemical stains. The lungs had a gross appearance typical of alveolar cell carcinoma (Fig. 1B). Despite numerous histologic sections, only two microscopic foci of metastatic lymphoma to lung were found, and no evidence was seen of alveolar cell carcinoma. Instead, extensive goblet cell metaplasia involved almost all air spaces, including alveoli, with a copious mucopurulent exudate (Fig. 1C). No significant suppurative consolidation of air spaces, pulmonary edema, or hyaline membranes was present. No large airways were obstructed, although the peripheral airways were plugged by mucin.

Discussion

Communication between the esophagus and the tracheo-bronchial tree allows the introduction of food and refluxed gastric contents into the lungs. Initially this may result in aspiration pneumonia or pulmonary edema [2], the latter sometimes resulting from aspiration of gastric acid (Mendelson syndrome). In some cases, adult respiratory distress syndrome (ARDS) may supervene. Pneumonia, pulmonary edema, and ARDS are all causes of radiographic alveolar disease in the acute-care setting, and these were the major premortem diagnostic considerations in our patient.

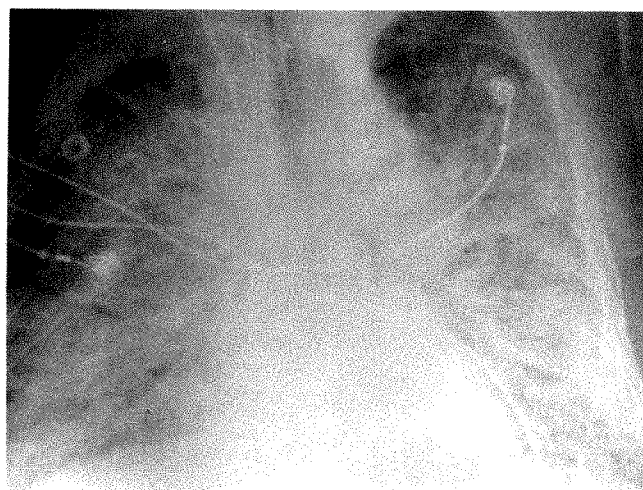
Goblet cell metaplasia typically occurs in the setting of chronic bronchitis, affects primarily bronchi and bronchioles

Received October 31, 1988; accepted after revision January 17, 1989.

¹ Department of Radiology, University of Michigan Hospitals, Ann Arbor, MI 48109.

² Present address: Department of Radiology, Henry Ford Hospital, 2799 W. Grand Blvd., Detroit, MI 48202. Address reprint requests to B. H. Gross.

³ Department of Pathology, University of Michigan Hospitals, Ann Arbor, MI 48109.

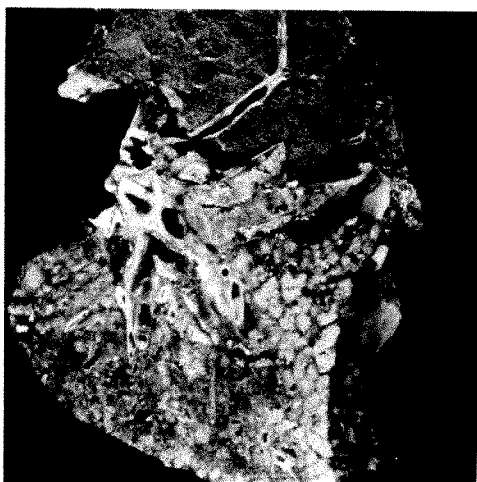


A

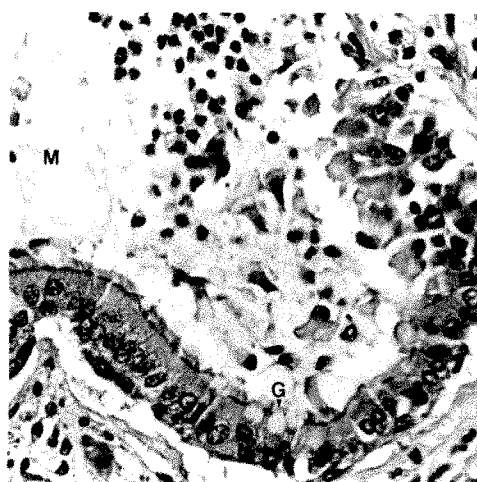
Fig. 1.—A, Anteroposterior chest radiograph reveals diffuse alveolar disease.

B, Photograph showing cut surface of left lung. Diffuse infiltrate has gross appearance of alveolar cell carcinoma.

C, Photomicrograph of left lung shows goblet cell metaplasia. Terminal bronchioles and alveoli are lined by pseudostratified ciliated columnar epithelium with numerous goblet cells (G). Epithelial cells, macrophages, and occasional neutrophils float in a sea of mucin (M). (H and E; original magnification, $\times 400$.)



B



C

to the level of the terminal bronchioles, and results in copious mucin production. To the best of our knowledge, involvement of the alveoli with goblet cell metaplasia has not been reported. The metaplastic response is thought to be caused by chronic irritants [3]. Chronic aspiration in the setting of a bronchoesophageal fistula is the best explanation for the extent and severity of metaplasia occurring in our patient. Copious mucin production was the actual explanation for the radiographic appearance. That mucin can cause radiographic alveolar disease is well known from cases of alveolar cell carcinoma, where mucin and cells fill the alveoli. Because the patient was ventilated at high oxygen levels for several weeks, it is possible that oxygen toxicity contributed to the pathologic

findings, although to the best of our knowledge, no association is known between goblet cell metaplasia and oxygen toxicity [4].

REFERENCES

1. Felson B. The roentgen diagnosis of disseminated pulmonary alveolar diseases. *Semin Roentgenol* 1967;2:3-21
2. Fraser RG, Paré JAP. *Diagnosis of diseases of the chest*, 2nd ed. Philadelphia: Saunders, 1979:1553
3. Thurlbeck WM. The pathology of small airways in chronic airflow limitation. *Eur J Respir Dis* 1982;121:9-18
4. Matsubara O, Takemura T, Nasu M, et al. Pathologic changes of the lungs after prolonged inhalation of high concentrations of oxygen. *Virchows Arch [A]* 1986;408:461-474

Characterization of Splenic Structure in Hodgkin Disease by Using Narrow-Band Filtration of Backscattered Ultrasound

P. A. Friedman¹
F. G. Sommer¹
H.-S. Chen²
D. J. Rachlin²
R. Hoppe³

A preliminary study was performed to evaluate the effectiveness of narrow-band filtration of backscattered ultrasound for the detection of splenic involvement in patients with Hodgkin disease. Regions of interest were identified in the spleens of 14 normal volunteers and eight Hodgkin disease patients before staging laparotomy. An analysis of the narrow-band-filtered waveforms showed that the mean amplitudes of the filtered ultrasonic signals received correlated with the presence of extensive splenic involvement with Hodgkin disease (defined as more than four grossly visible nodules on cut section) ($p = .0004$). Conversely, mean amplitudes of unfiltered ultrasonic backscatter, employed in conventional sonographic imaging, did not correlate with splenic involvement ($p = .5$). Phantom studies were performed to develop a tissue model for the observed phenomena; images of the phantoms and of the involved and uninvolved spleens were made by using techniques involving narrow-band filtration of backscattered ultrasound.

Our results indicate that narrow-band-filtered sonography holds promise for detecting lymphomatous involvement of the spleen, although larger studies, with equipment allowing real-time implementation of narrow-band filtering, are needed.

The importance of detecting extensive splenic involvement (defined as the presence of four or more grossly visible lymphomatous nodules) in patients with pathologic stage IIIA Hodgkin disease is manifest, because this is the single most important factor in determining whether this patient group would benefit from chemotherapy [1, 2]. Contemporary imaging techniques (including conventional sonography) have had poor results in detecting splenic involvement with Hodgkin disease [3-5], and the only new method to show promise has been CT of the spleen using the experimental contrast agent ethiodized oil emulsion (EOE-13) [6]. Preliminary studies with MR imaging indicate that this technique offers no improvement over, or is inferior to, CT and sonography in the detection of lymphomatous involvement of the spleen [7-9]. However, recent work using narrow-band filtration of backscattered ultrasound (a type of sonography that uses a narrow-band filter to process received sound waves) has differentiated between phantoms of different scattering characteristics and between normal and cirrhotic liver tissue, on the basis of differences in the frequency dependence of ultrasonic backscatter [8, 9]. This suggests that the technique may work when applied to the spleen.

In this study, we evaluated the ability of narrow-band-filtered sonography to detect lymphomatous involvement of the spleen. The study of Hodgkin disease patients before staging laparotomy provided an opportunity to correlate in vivo ultrasonic waveform statistics with splenic histology. Additionally, a target phantom composed of two materials of different backscattering characteristics was used as an in vitro model to test the ability of filtered sonographic imaging to detect focal regions of altered scattering properties.

Received November 18, 1988; accepted after revision February 9, 1989.

This work was supported in part by grants CA 37483 and CA 38109 from the National Cancer Institute. F. G. Sommer is partially supported by Research Career Development Award CA 00960 from the National Institutes of Health.

We acknowledge Philips Ultrasound International for providing equipment support for this project.

¹ Department of Diagnostic Radiology, Room H1307, Stanford University Medical Center, Stanford, CA 94305. Address reprint requests to F. G. Sommer.

² Department of Electrical Engineering, Stanford University, Stanford, CA 94305.

³ Department of Therapeutic Radiology, Stanford University Medical Center, Stanford, CA 94305.

AJR 152:1197-1203, June 1989
0361-803X/89/1526-1197
© American Roentgen Ray Society

Methods

A Philips (Santa Ana, CA) SDR 2500 sector scanner was modified to allow the digitization of RF sonographic data from a trapezoidal region of interest (ROI), the size and location of which were chosen in the real-time conventional (unfiltered) image by an operator. Patients were studied with a 19-mm-diameter, 3.0-MHz center-frequency transducer, which has a -3-dB bandwidth of 0.9 MHz and is focused 90 mm from the transducer tip. Each ROI was sampled at 25 MHz with an eight-bit dynamic range, and the RF data were stored on standard 5.25-in. floppy diskettes. After obtaining informed consent, data were recorded from the spleens of eight Hodgkin patients before staging laparotomy and splenectomy and from 14 normal volunteers. Data from six ROIs were obtained from the spleens of all experimental subjects, with an effort to ensure that data were obtained from independent splenic sample volumes in each of the six acquisitions. ROIs were selected at a depth range of approximately 4–10 cm, and typically included approximately 30 A-lines. In selecting an ROI, major specular reflectors were avoided with the help of the real-time image. All data were recorded to a standardized dynamic range by adjusting the depth-gain compensation and by using an amplitude histogram of the received RF echoes.

The algorithms for the narrow-band processing used to generate amplitude statistics and create filtered sonographic images have been described [10, 11]. Briefly, for each ROI, the RF data were passed through a digital 3.4-MHz center-frequency filter with a -6-dB bandwidth of 800 kHz. The waveform envelopes of the filtered and the original unfiltered (control) data were then calculated using the Hilbert transform, and the mean amplitudes of the filtered and unfiltered data were determined. Next, the mean amplitudes were divided by the average power per A-line of the unfiltered waveforms; this normalizing step served to control for operator error in adjusting the depth-gain compensation by using the amplitude histogram when digitizing the A-lines.

After splenectomy in the Hodgkin disease patients, the spleens were evaluated by a pathologist and the following histologic characteristics assessed in each case: histologic type, splenic weight, number of nodules, nodule size range, cellularity of nodules, and collagen deposition. Statistical analysis comparing the pathologist's findings and the ultrasound amplitude statistics was then performed.

Additionally, the RF data acquired from several regions of interest in one normal and one lymphomatous spleen were used to generate images encoding the amplitudes of the backscattered ultrasound. Images were formed from unfiltered (conventional) and narrow-band-filtered ultrasound amplitudes, using a previously described digital technique [11]. The filtered images were created using a 3.4-MHz

center-frequency, 800-kHz bandwidth filter that had been found to be optimal [10]. Bistable (binary gray-scale) images, in which amplitude values above an empirically determined threshold were assigned a white pixel and those below it a darker pixel, and continuous linear gray-scale images, in which increasing amplitudes were assigned lighter shades of gray, were generated.

Also, three different phantoms were constructed to study the ability of narrow-band images to detect focal regions differing in scattering characteristics from their surroundings, as compared with conventional sonography. Two of the phantoms were homogeneous: one was made by suspending 1 g of 50- μ m (average) cellulose uniformly in 500 ml of 1.5% agar gel; a second was built similarly by suspending 1 g of 10- to 120- μ m polystyrene spheres in 500 ml of 1.5% agar gel. The third phantom constructed (the target phantom) contained an oval region of polystyrene microspheres (enclosed by a thin latex membrane) in a background of cellulose scatterers. The sizes and concentrations of the cellulose and polystyrene scatterers in this phantom were the same as for the homogeneous agar-gel phantoms. RF data from six regions containing about 40 A-lines, each at a depth range of 4–10 cm from the transducer tip, were acquired from the phantoms with the same scanner used for clinical studies, but with a nominal 5-MHz, 13-mm-diameter focused transducer. The actual mean recorded backscattered frequency in the phantoms was 4.5 MHz. For the homogeneous phantoms, the average power spectra of all 100 A-lines were computed, normalized, and plotted. For the target phantom, conventional (unfiltered) and narrow-band-filtered images of the phantom were created by using a higher-than-mean center-frequency filter (5 MHz, with a -6-dB bandwidth of 800 kHz) and a lower-than-mean center-frequency filter (4 MHz, with a -6-dB bandwidth of 800 kHz).

Results

A linear multiple regression analysis was performed and the probability of the beta coefficients was used to determine which tissue characteristics correlated with the filtered and unfiltered received waveform amplitudes (the dependent variables). Table 1 lists the pathologic findings for the patients who underwent splenectomy; these findings were tested as independent variables in the multiple regression analysis. The only histologic feature that correlated with the narrow-band-filtered mean amplitudes was the number of lymphomatous nodules. The nodules ranged in size from 0.3 to 4.0 cm, although the vast majority were in the 0.3–0.7 cm range. The

TABLE 1: Pathologic Findings in the Spleens of Patients Who Had Laparotomies

Patient Number	Histologic Type	Cellularity of Nodules	Splenic Weight (g)	Nodule Size Range (cm)	Number of Nodules	Collagen (involved regions)
1	NSHD	1–2+ (2)	230	0.3	5	1+; 3+ (2)
2	NSHD	2+	165		1	2+
3	MCHD	3+ ^a	250	0.5	0	0
4	MCHD	3+	355	0	10	0
				0.5–1.5 (1)		
5	MCHD	0 ^b	240	0	0	0
6	NSHD	3+	116	0.2–0.3 (0.25)	7	0
7	NSHD	3+	210	0.6	6	0
8	MCHD	3+	390	0.5	<4	0

Note.—When there is a range of values, the number in parentheses indicates the value used in the analysis. The number of nodules was divided into three groups for the analysis: zero, less than four, and four or more. MCHD = mixed cellularity Hodgkin disease; NSHD = nodular sclerosing Hodgkin disease.

^a Reactive hyperplasia.

^b Granulomas were present.

average narrow-band-filtered amplitudes of the ROIs of spleens that were extensively involved (defined as more than four visible nodules on cut splenic sections) were significantly different from the similarly filtered amplitudes of the control spleens ($p = .0004$, one tail unpaired Student's t test), although the groups did overlap. The Student's t test was calculated by using each ROI mean amplitude as an independent value belonging to the control or to the involved groups. Only two of the patients who underwent laparotomy had minimal involvement; therefore, the ability of the narrow-band technique to detect minimal involvement (less than four grossly visible nodules, or microscopic disease) could not be significantly determined. Unlike the narrow-band results, neither the number of nodules present ($p = .5$, one tail unpaired Student's t test), nor any other histologic feature of the involved spleens correlated significantly with the mean amplitudes of the unfiltered ultrasound.

Figure 1A shows a plot of the narrow-band-filtered mean amplitude vs the extent of splenic involvement, and Figure 1B shows the corresponding results for the unfiltered data. Each plotted point in Figures 1A and 1B represents the mean of all of the average amplitudes from a given patient, where each average amplitude was calculated from an independent ROI. Note that there is considerably less overlap between the extensively involved and the control groups when using the narrow-band technique than when using conventional sonography and that neither technique separates the control spleens from the minimally involved spleens.

Figure 2 shows the acquisition of data from ROIs in an in vivo normal spleen and an involved spleen, and the results obtained by using conventional processing and the narrow-band technique [10] on the same ROI. Images were formed at each progressive processing step to show the effects of each procedure. It should be stressed that all processing, including filtration and thresholding, was performed in exactly the same manner for all compared images. Figures 2 E-H are images of a spleen that has significant involvement with

Hodgkin disease (Table 1, patient #1). Note in Figures 2A and 2E the unfiltered waveform amplitude histograms (upper left corners) used to convert waveform data to standardized dynamic ranges in each case. The appearance of the normal and the lymphomatous spleens in the conventional sonographic images (Figs. 2B and 2F) is not appreciably different; however, the appearance of the normal and the lymphomatous spleens in the continuous gray-scale, narrow-band-filtered images (Figs. 2C and 2G) is appreciably different. This difference is more striking in the binary thresholded narrow-band images (Figs. 2D and 2H). A number of bright regions corresponding to zones several millimeters in diameter in the ROIs are visible in Figure 2H (the involved spleen), but very little of this bright appearance is apparent in Figure 2D (the uninvolved spleen). Figures 3A and 3B show low-power hematoxylin and eosin images of typical regions of these uninvolved and involved spleens, respectively.

Figure 4A shows the power spectra generated by the study of the homogeneous polystyrene and cellulose phantoms; the spectra show that the polystyrene phantom has a higher frequency dependence of backscatter than the cellulose phantom, because more energy is backscattered at high frequencies for the polystyrene phantom. The spectral difference between the two phantoms is consistent with the difference in the size of their mean scatterers; the presence of two separate peaks in the polystyrene spectrum is probably a result of a resonance effect within the polystyrene phantom. Figure 4B shows the acquisition of data in the target phantom, and Figure 4C shows the image of the target phantom formed by using conventional (unfiltered) sonography; in this case, the target is not visible as a zone of altered echogenicity, although its location can be discerned by the presence of the surrounding latex membrane. Figures 4D and 4E show images of the same target phantom using narrow-band filtration. Note that the polystyrene target is clearly identifiable as a dark region in Figure 4D and as a bright region in Figure 4E, in comparison with the surrounding cellulose material.

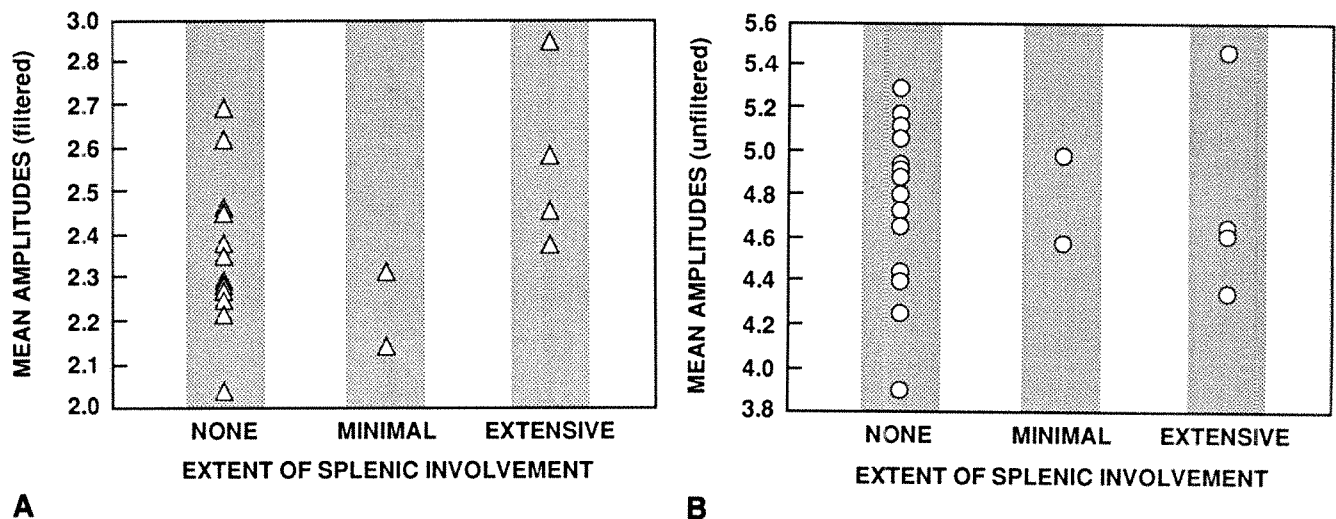


Fig. 1.—Plots of amplitude vs extent of splenic involvement with Hodgkin disease. Uninvolved group includes Hodgkin disease patients and healthy volunteers. Minimal and extensive involvement are defined in text.

A, Narrow-band-filtered amplitude vs extent of splenic involvement.

B, Unfiltered (control) average amplitude vs extent of splenic involvement.

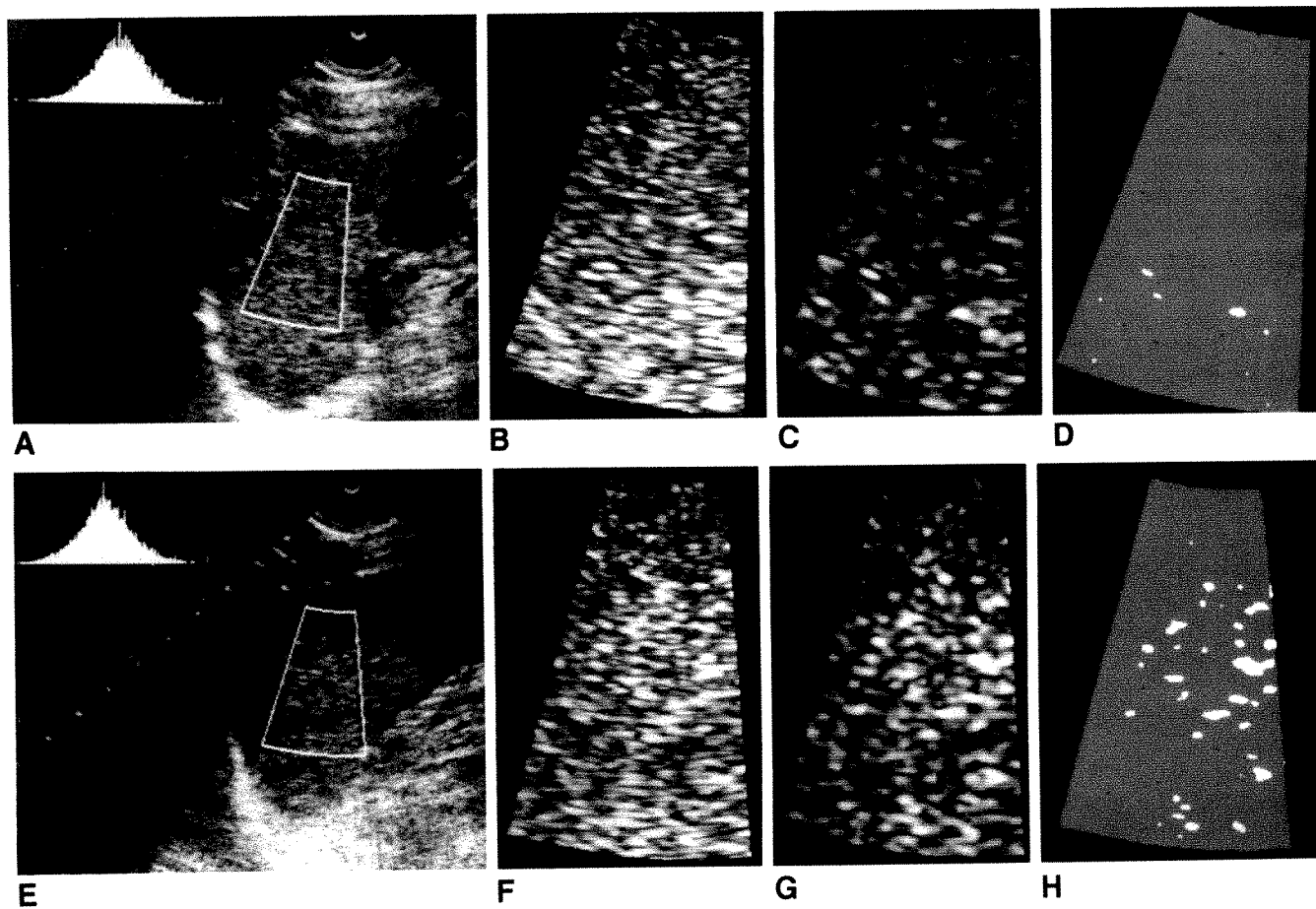


Fig. 2.—A, Image seen by operator during acquisition of ultrasonic waveform data from a region of interest in uninvolved spleen.
 B–D, Images of region of interest in uninvolved spleen acquired in A generated by using unfiltered (conventional) sonography (B), narrow-band-filtered sonography with linear gray-scale postprocessing (C), and narrow-band-filtered sonography with binary gray-scale postprocessing (D).
 E, Image seen by operator during acquisition of ultrasonic waveform data from a region of interest in lymphomatous spleen.
 F–H, Images of region of interest in lymphomatous spleen acquired in E generated by using unfiltered (conventional) sonography (F), narrow-band-filtered sonography with linear gray-scale postprocessing (G), and narrow-band-filtered sonography with binary gray-scale postprocessing (H).

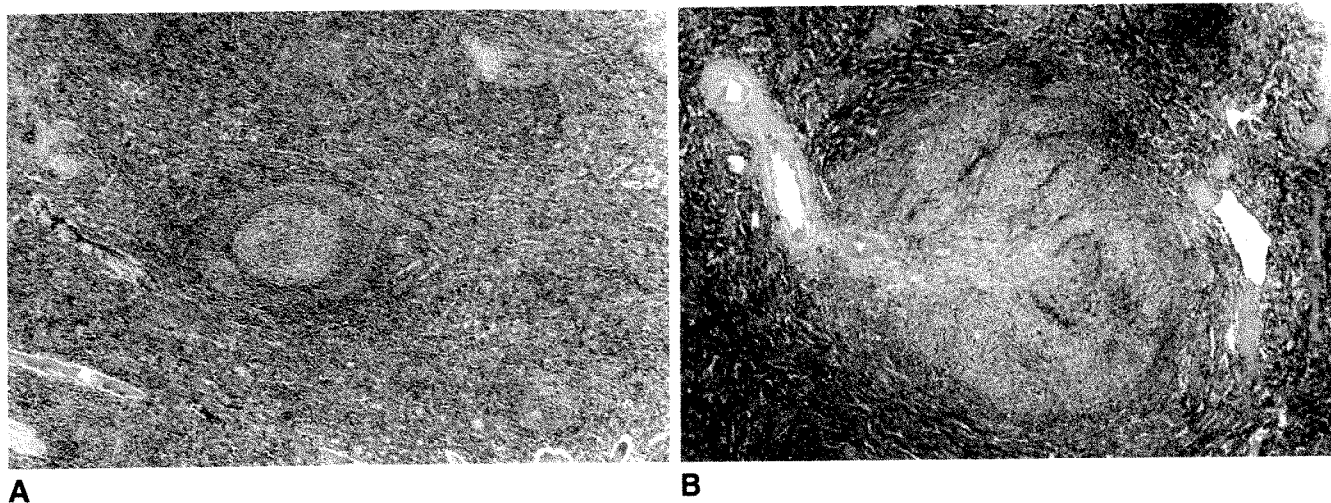


Fig. 3.—Photomicrographs of 10-mm histologic sections of two spleens shown in Figure 2. (H and E, low power).
 A, Uninvolved spleen; only small, 1- to 2-mm lymphoid follicles are shown.
 B, Lymphomatous spleen; note large, typical lymphomatous nodule, measuring about 6 mm in diameter.

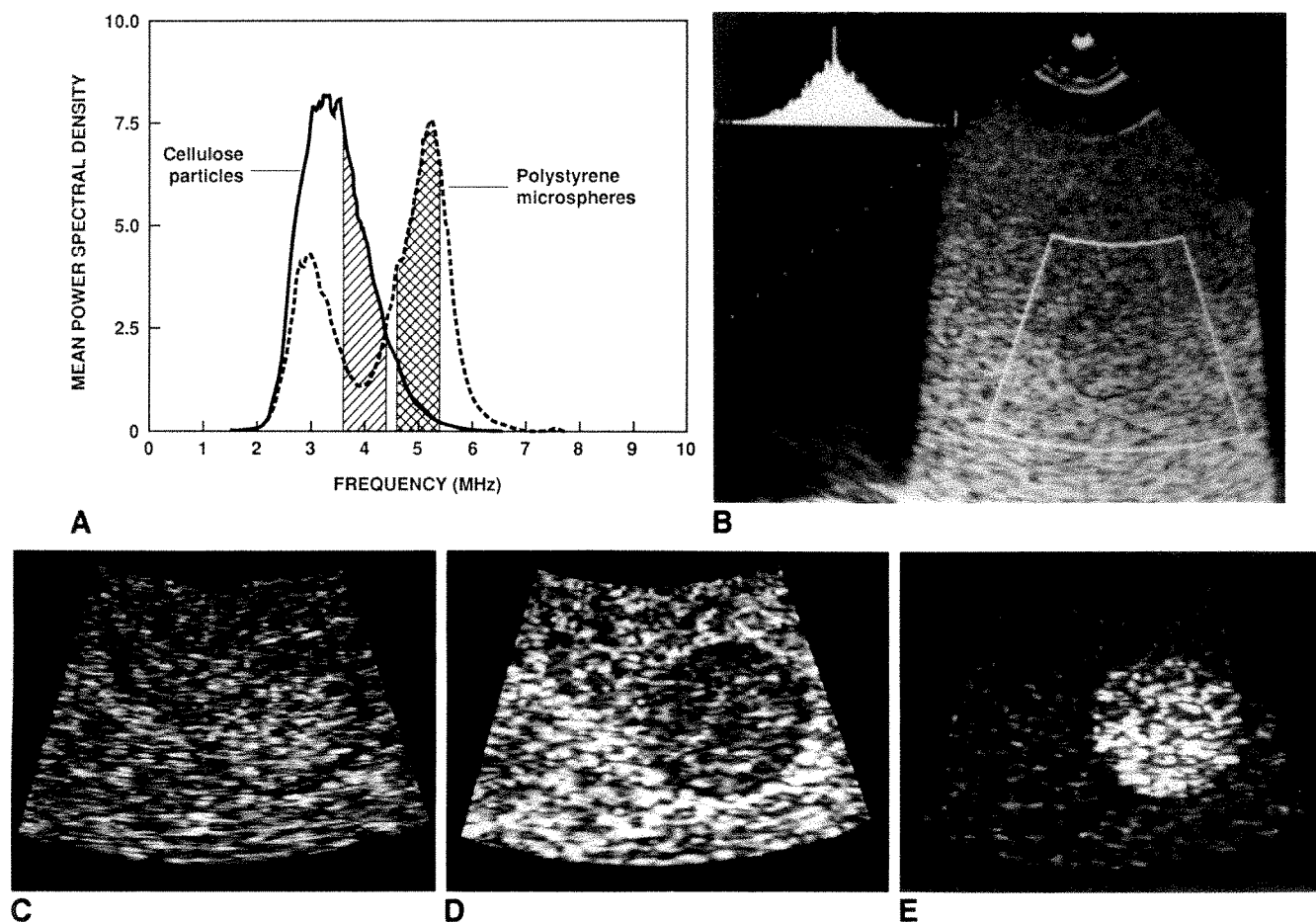


Fig. 4.—A, Power spectra of ultrasound backscattered from polystyrene and cellulose phantoms.
 B, Image seen by operator during acquisition of ultrasonic waveform data from a region of interest in target phantom.
 C–E, Images of region of interest in target phantom acquired in B generated by using unfiltered (conventional) sonography (C), narrow-band-filtered sonography with a low-pass narrow-band filter (D), and narrow-band-filtered sonography with a high-pass narrow-band filter (E).

Discussion

The manner in which narrow-band filtration detects shifts in the frequency dependence of backscatter of different materials can be appreciated by comparing the spectral responses of the polystyrene and cellulose scatterers employed in the phantom study (Fig. 4A). Because the polystyrene phantom preferentially backscatters high-frequency energy, more of the received energy is in the frequency range above the center frequency than below it. The cellulose phantom, on the other hand, reflects more energy in the frequency range below the center frequency because its frequency dependency of backscatter is low. Due to normalization of unfiltered recorded ultrasound, the total energy backscattered is identical in both cases; however, the frequency distribution of the energy is different. Figure 4A illustrates how a filter chosen above the center frequency can be used to detect the differences in frequency dependence of backscatter. Because conventional sonography processes broadband signals, it cannot differentiate tissues on the basis of the frequency content of backscattered ultrasound.

The ability of the narrow-band technique to form images on the basis of differences in the scattering characteristics of various materials is seen in the images of the target phantom (Figs. 4D and 4E). Because the central polystyrene target preferentially backscatters high-frequency signals, a higher proportion of its backscattered energy is in the passband range of the high-frequency narrow-band filter (shown in Figure 4A), so it appears bright (Fig. 4E). The backscatter from the surrounding cellulose, however, is of a lower frequency that is below the filter's passband, so the background of the image is darker. Conversely, the low-pass filter preferentially weights low-frequency energy (Fig. 4A), making the target region appear relatively dark compared with the background (Fig. 4D). Because conventional sonography uses a broadband filter that does not weight some frequencies more heavily than others, the low-frequency energy from the background and the high-frequency energy from the target contribute equally to the image, making the target invisible (Fig. 4C).

Differences in the frequency dependence of backscatter of various tissues may account for the observed difference

between normal and involved spleen narrow-band-filtered amplitude statistics and images. In the normal spleen, the main sources of tissue scatterers may be presumed to be the splenic trabeculae, the blood vessels surrounded by collagen, the collagen in the cords of Bilroth, as well as the supportive reticulin network found throughout the splenic parenchyma. The ultrasonic backscatter from the delicate parenchymal reticulin network most likely approximates Rayleigh scattering, which is fourth-power frequency dependent (f^4), because the scatterers are small compared with the mean incident ultrasonic wavelength. The splenic trabeculae and collagen-surrounded blood vessels, however, act as large cross-section scatterers of dimensions slightly larger than the mean incident ultrasonic wavelength, which produce backscatter that is independent of frequency (f^0). The overall effect of the large scatterers superimposed on the small ones is a backscatter that has a frequency dependency somewhere between zero and fourth power. This has been observed in studies of excised spleens, which have shown a frequency dependence of backscatter of $f^{2.2}$ [12].

The lymphomatous nodules found in the spleens of Hodgkin disease patients represent cellular elements, which would not be expected to produce significant acoustic scattering. However, the increased mass of cellular tissue may act to spread the collagenous trabeculae, so that the tissue path interrogated by a given A-line has a lower probability of containing large specular scatterers than of containing fine reticulin scatterers, giving the lymphomatous spleen scattering characteristics closer to an f^4 frequency dependency. This model is consistent with earlier studies that found that the mean scatterer spacing for splenic tissue was increased by lymphomatous involvement [13–15].

Another way of considering the involved spleen is that lymphomatous nodules act analogously to the polystyrene target: both may be foci with a higher frequency dependency of backscatter than surrounding structures, which may therefore appear as bright spots in narrow-band images, and increase the overall amplitude of the narrow-band-filtered backscatter. This would account for the result shown in Figure 3A: as the number of nodules in the spleens increases, the mean amplitudes of the filtered ultrasonic backscatter also increase.

An alternative explanation for the differentiation between normal and extensively involved spleens achieved via narrow-band filtration could be that the frequency-dependent attenuation overlying and within the ROIs in the normal and involved spleens differed in a systematic way, altering the received frequency spectral-energy content. Because it is impossible for us to acquire data in the near field with the scanner employed (because of near-field reverberation artifacts), and because our prior studies [16] have indicated considerable difficulty in the accurate and reproducible measurement of attenuation frequency dependence in vivo, it was not possible for us to determine experimentally the extent (if any) to which differences in this variable were responsible for our clinical results. Previously reported work [11] with phantoms of identical measured frequency-dependent attenuation, but differing scattering characteristics showed clearly that the

narrow-band filtration image-creation scheme is capable of differentiating materials that differ only in their diffuse scattering properties. Similarly, the target phantom study shows the ability of an analogous image-creation technique to display regions of altered scattering characteristics, which may be invisible in conventional sonographic images. In clinical studies of the narrow-band-filtered imaging technique, either of normal and cirrhotic liver [11], or of normal and abnormal spleens as in the present study, experimental limitations make the physical basis for the observed results less clear-cut than for more controllable phantom studies. In particular, it is not possible to determine whether the bright regions present in the filtered images of the involved spleens (Figs. 2G and 2H) actually represent the locations of lymphomatous nodules. It should be pointed out that the reason for using a higher frequency transducer (5 MHz) with greater bandwidth in the phantom studies was to maximize the differentiation of the phantom components in the filtered images; it was not possible to use the 5-MHz probe in the clinical studies because of inadequate penetration of the in vivo spleens.

Because of the inability of conventional sonography to image lymphomatous involvement of the spleen, the operator could not determine whether or not nodules were present in a particular scan. This was because the real-time images from which the ROIs were selected and the data recorded were generated using conventional sonography. Therefore, some scans of extensively involved spleens might actually have evaluated uninvolved parenchyma. As a consequence, the amplitude statistics shown in Figures 1A and 1B are no doubt adversely affected by the averaging of uninvolved and involved regions in those spleens involved with Hodgkin disease. This probably accounts, at least in part, for the overlap seen between the normal and the involved spleen groups. An obvious step toward improving the detection of involvement would be the real-time implementation of the narrow-band-filtered image creation, which would allow the operator interactively to detect and record images and data from abnormal tissue ROIs. Real-time narrow-band filtration would enable a larger clinical study to be performed, which could determine the role of the narrow-band technique in the staging of Hodgkin disease patients.

ACKNOWLEDGMENT

The authors thank Henry Tazelaar for preparing the histologic sections of Figure 3 and for his very helpful discussions of splenic histopathology.

REFERENCES

1. Hoppe RT, Cox RS, Rosenberg SA, Kaplan HS. Prognostic factors in pathologic stage III Hodgkin's disease. *Cancer Treat Rep* 1982;66:743–749
2. Hoppe RT, Rosenberg SA, Kaplan HS, Cox RS. Prognostic factors in pathological stage IIIA Hodgkin's disease. *Cancer* 1980;46:1240–1246
3. Sekiva T, Meller ST, Cosgrove DO, McCread VR. Ultrasonography of Hodgkin's disease in the liver and spleen. *Clin Radiol* 1982;33(6):635–639

4. Carrol BA. Ultrasound of lymphoma. *Semin Ultrasound* **1982**;3:114-122
5. Kaplan HS. *Hodgkin's disease*, 2nd ed. Cambridge, MA: Harvard University Press, **1980**:209-213
6. Thomas JL, Bernardino ME, Vermess M, et al. EOE-13 in the detection of hepatosplenic lymphoma. *Radiology* **1982**;145:629-634
7. Richards MA, Webb JA, Jewell SE, Stansfeld AG, Lister TA, Wrigley PF. Low field strength magnetic resonance imaging of the spleen: results from volunteers and patients with lymphoma. *Br J Cancer* **1988**;57(4):408-411
8. Nyman R, Rehn S, Glimelius B, et al. Magnetic resonance imaging, chest radiography, computed tomography and ultrasonography in malignant lymphoma. *Acta Radiol* **1987**;28(3):253-262
9. Hahn PF, Weissleder R, Stark DD, Saini S, Elizondo G, Ferrucci JT. MR imaging of focal splenic tumors. *AJR* **1988**;150(4):823-827
10. Sommer FG, Stern RA, Howes PJ, Young H. Envelope amplitude analysis following narrow band filtering: a technique for ultrasonic tissue characterization. *Med Phys* **1987**;14:627-632
11. Sommer FG, Stern RA, Chen HS. Cirrhosis: US images with narrow band filtering. *Radiology* **1987**;165:425-430
12. Nicholas D. In: White DN, ed. *Recent advances in ultrasound in biomedicine*. Forest Grove, OR: Research Studies Press, **1977**:29-54
13. Sommer FG, Hoppe RT, Fellingham L, Carroll BA, Solomon H, Yousem S. Spleen structure in Hodgkin disease: ultrasonic characterization. *Radiology* **1984**;153:219-222
14. Fellingham LL, Sommer FG. Ultrasonic characterization of tissue structure in the *in vivo* human liver and spleen. *IEEE Trans Sonics Ultrasonics* **1984**;SU-31:418-428
15. Sommer FG, Joynt LF, Hayes DL, Macovski A. Stochastic frequency-domain tissue characterization: application to human spleens 'in vivo.' *Ultrasonics* **1982**;March:82-86
16. Sommer FG, Gregory PB, Fellingham LL, et al. Measurement of attenuation and scatterer spacing in human liver tissue: preliminary results. *J Ultrasound Med* **1984**;3:557-561

American Roentgen Ray Society Residents' Award Papers, 1990

The ARRS announces competition for the 1990 President's Award and two Executive Council Awards for the best papers concerning the clinical application of the radiologic sciences.

Awards

The winner of the President's Award will receive a certificate and a \$1000 prize. The winners of the two Executive Council Awards will each be given a certificate and a prize of \$500. The winners will be announced on March 15, 1990. Winning papers will be presented at the ARRS annual meeting at the Sheraton Washington Hotel, Washington, D.C., May 13-18, 1990. Winning papers will be submitted for early publication in the *American Journal of Roentgenology*. All other papers will be returned to the authors.

Regulations

Eligibility is limited to residents or fellows in radiology who have not yet completed 4 years of approved training in a radiologic discipline. A letter from the resident's department chairman attesting to this status must accompany the manuscript. The resident must be the sole or senior author and be responsible for all or most of the project.

Submitted manuscripts must not exceed 5000 words and have no more than 10 illustrations. Four copies of the manuscript and illustrations are required. Submitted manuscripts should not contain previously presented or published material and should not be under consideration for publication elsewhere.

Deadline for submissions is February 16, 1990. Send papers to

B. G. Brogdon, M.D.
Chairman, Committee on Education & Research
American Roentgen Ray Society
Department of Radiology
University of South Alabama Medical Center
2451 Fillingim Street
Mobile, AL 36617

Book Review

Radiolabeled Monoclonal Antibodies for Imaging and Therapy. Edited by Suresh C. Srivastava. (Vol. 152 in NATO Advanced Study Institute series, Series A, Life Sciences.) New York: Plenum, 876 pp., 1988. \$129.50

This volume represents the proceedings of the North Atlantic Treaty Organization Advanced Study Institute on Radiolabeled Monoclonal Antibodies for Imaging and Therapy: Potential, Problems, and Prospects held in Italy, July 20–August 1, 1986. Thus, the book has appeared 2 years after the meeting. The editor states that "no claims are made for a textbook character for this volume." With a wealth of material in 876 pages, however, it begins to assume the role of a near-definitive account of the subject (albeit in many different styles because of the number of authors).

The book is divided into nine parts, followed by a list of participants, an author index, and a subject index. Part 1 (146 pages, 11 chapters) deals with production, selection, and characterization of monoclonal antibodies. Part 2, the shortest, (46 pages, three chapters) is about selection criteria for imaging and therapy, as well as radionuclide production. Part 3 (76 pages, six chapters) is devoted to radiohalogenation and radiometal labeling of monoclonal antibodies. Part 4 (122 pages, eight chapters) considers immunoreactivity and pharmacokinetics. Part 5 (72 pages, five chapters) covers radiobiological and dosimetric considerations for imaging and therapy when radiolabeled monoclonal antibodies are used. Part 6 (118 pages, seven chapters) involves instrumentation, strategies for radioimmunoimaging, and comparison with other imaging techniques. Part 7, the longest section (156 pages, nine chapters), is concerned with preclinical and clinical radioimmunoimaging. Part 8 (56 pages, three chapters) slightly changes pace by examining radioimmunotherapy. Part 9 (54 pages, four chapters) is on monoclonal antibodies for blood-cell labeling and thrombus imaging.

This volume has an extraordinary amount of material, and the reader can be overwhelmed by the variety. A possible approach is to start with a history of the field (page 95), proceed to comments by Beierwaltes (page 143), touch on the immunochemistry of hybridomas (page 3) and criteria for selection (page 168), and then note candidate radionuclides (page 151).

In the midst of all this information, some aspects unnecessarily befuddle the reader. (1) The chapters are not numbered, compounding problems of cross reference. (2) Multiple typefaces appear in this book, which was produced from camera-ready copy. The chapter beginning on page 409 has one typeface on that page, whereas the remaining pages are in another. (3) Most of the pages are well reproduced, but several are faded, probably as a result of the initial typing. (4) Each chapter has a following discussion. This tends to be uneven; for example, the chapter on pages 271–280 is appended with a discussion (pages 281–292) that is longer than the chapter itself. Still, these only slightly detract from the richness of the book. In it can be found information on bifunctional chelates, image subtraction, and a host of topics related to radioimmunoimaging.

The book is indeed weighty (heavy), but it will be a good companion for exploring the present state of radioimmunoimaging. It will find readers from those in the medical community, radiochemistry, dosimetry, physics, instrumentation, and immunology.

Richard P. Spencer
University of Connecticut Health Center
Farmington, CT 06032

SPECT of the Peritoneal Cavity: Method for Delineating Intraperitoneal Fluid Distribution

Richard L. Wahl¹
John Gyves^{1,2}
Barry H. Gross³
Michael Cochran^{1,4}
Jack E. Juni^{1,5}
Nelson B. Arnstein^{1,6}
Diane Lahti¹
Robert J. Ackermann¹

Seventeen single-photon emission CT (SPECT) studies were performed after intraperitoneal administration of ^{99m}Tc-sulfur colloid in patients with a history of colon cancer to assess the extent of intraperitoneal fluid distribution prior to intraperitoneal chemotherapy. Planar gamma images were also obtained in all patients for correlation with the SPECT findings. Four patients had transmission CT scans of the abdomen after intraperitoneal administration of iodinated contrast material. In seven patients, repeat planar and SPECT studies were performed with the original or a different infusion volume to determine if different volumes altered the fluid distribution qualitatively or quantitatively (using a linear profile method). We found that 360° peritoneal SPECT is easily performed after intraperitoneal administration of ^{99m}Tc-sulfur colloid. SPECT provides more detailed anatomic information than planar scans do. Spaces of the upper abdomen, such as the lesser sac, were resolved better with SPECT than with planar imaging. SPECT assessment of intraperitoneal fluid distribution also correlated well with transmission CT scans. Quantitative linear-profile radionuclide plots were reproducible at the same volume and showed no major differences in relative intraperitoneal fluid distribution between the 1.5- and 3.0-l infusion volumes, suggesting that the two delivery volumes were equivalent in relative distribution.

SPECT appears to be a useful procedure to define the extent and location of intraperitoneally administered fluids. Thus, it may be of value in determining the intraperitoneal distribution of drugs and radiopharmaceuticals used in the treatment of intraabdominal tumors.

Received September 6, 1988; accepted after revision February 7, 1989.

This work was supported in part by U.S. Public Health Service/National Cancer Institute grant CA41531, awarded to R. L. Wahl.

¹Department of Internal Medicine, Division of Nuclear Medicine, University of Michigan Medical Center, 1500 E. Medical Center Dr., Ann Arbor, MI 48109-0028. Address reprint requests to R. L. Wahl.

²Present address: E. I. Du Pont de Nemours and Co., Inc. Wilmington, DE 19880-0026.

³Department of Diagnostic Radiology, University of Michigan Medical Center, Ann Arbor, MI 48109-0028.

⁴Present address: Lake Forest Hospital, Lake Forest, IL 60048.

⁵Present address: William Beaumont Hospital, Royal Oak, MI 48072-2793.

⁶Present address: Los Angeles County/University of Southern California Medical Center, Los Angeles, CA 90003-8109.

AJR 152:1205-1210, June 1989
0361-803X/89/1526-1205

© American Roentgen Ray Society

Malignant diseases of the peritoneal cavity are being treated increasingly with intraperitoneal chemotherapy, colloidal phosphorus-32, and most recently radiolabeled monoclonal antibodies [1-10]. For these therapeutic approaches to be successful, there must be free distribution of the therapeutic agent throughout the peritoneal cavity, maximizing contact of the agent with the tumor. At our institution the distribution of infused fluids in the peritoneal cavity has generally been assessed by planar scintigraphy of the abdomen after instillation of several millicuries of ^{99m}Tc-sulfur colloid into the peritoneal cavity. Transmission CT after intraperitoneal administration of iodinated contrast medium has occasionally been used as a supplemental study in difficult cases.

Single-photon emission CT (SPECT) is potentially better suited to evaluate the intricacies of the intraperitoneal distribution of fluid. In this report, we describe our experience with SPECT performed after intraperitoneal injection of ^{99m}Tc-sulfur colloid using a very-large-field-of-view gamma camera capable of examining the entire peritoneal cavity in a single acquisition. We also compare SPECT with standard planar imaging, correlate SPECT studies with contrast-enhanced CT scans of the peritoneal space, describe a technique of quantifying relative regional radiopharmaceutical uptake on these scans, and evaluate the effect of changes in volume on the distribution of radioactivity on the scans.

Materials and Methods

Nine men (41–69 years old) with known colon cancer resected before scanning and referred for abdominal scanning of the intraperitoneal distribution of ^{99m}Tc -sulfur colloid were evaluated by planar and SPECT imaging to determine if they were eligible for a pilot study of adjunct intraperitoneal chemotherapy. None of these patients had known residual tumor at the time of procedure (Table 1).

A total of 1500 or 3000 ml of lactated Ringer's solution were instilled via an implanted Silastic intraperitoneal catheter/port (Infusaid Corp., Norwood, MA) as previously described [7]. Four to 5 mCi (148–185 mBq) of ^{99m}Tc -sulfur colloid were injected followed by a 10-ml saline flush when approximately 1 l had been infused (1.5% Hypaque was given in a similar fashion). After the full volume was infused, the Ringer's solution was infused at 42 ml/hr until completion of imaging. This rate approximates the rate of fluid absorption from the peritoneal cavity [7]. When patients were studied by SPECT and/or CT, the abdomen was filled over 1–2 hr with lactated Ringer's solution (1.5 or 3.0 l), and the volume was maintained by a continuous infusion of Ringer's solution at 42 ml/hr. When patients were studied at 1.5 and 3.0 l on the same day (two patients), the initial 1.5-l volume was maintained with an infusion at 42 ml/hr until the first scan was completed; then, an additional 1.5 l along with additional 4–5 mCi (148–185 mBq) of ^{99m}Tc -sulfur colloid was infused over 1–2 hr with the same maintenance infusion until scan completion. Patients were rolled from side to side and allowed to walk for up to 2 hr before imaging to enhance mixing.

Gamma-camera imaging was then performed in the supine position with a rectangular, very-large-field-of-view 14 by 20-in. (36.8 by 50.8-cm) usable-field-of-view gamma camera (UFOV, Technicare, Omega 500, Solon, OH) fitted with a general-purpose low-energy collimator. Anterior images acquired for 500,000 counts were obtained, the acquisition time was noted, and then both lateral views were obtained for that time. Images were recorded on film as well as stored digitally on floppy disks by using a Technicare 560 computer and a 64- by 64-pixel matrix.

SPECT scanning was performed immediately after planar imaging with the same camera and computer. Acquisitions were in a 360° circular orbit with 90 camera stops and 20 sec of imaging/stop, for a total image acquisition time of slightly over 30 min. Then, 1.2-cm-thick SPECT images in a 64- by 64-pixel matrix were reconstructed in the transverse, sagittal, and coronal planes. A low-pass high-frequency cutoff filter and commercial attenuation correction algorithms for the abdomen were applied (Butterworth order 4, 0.35 cutoff). From the corrected absolute counts, transverse-section his-

tograms of the intraperitoneal distribution were constructed for each patient at each infusion volume. This involved plotting the percentage of total counts in the study associated with each slice corrected for attenuation (10 slices/study is typical) vs slice number (1 = diaphragm, 10 = pelvis, etc.). This allows for a quantitative comparison of relative regional fluid distributions between volumes in the same patient as well as among patients. Abdominal CT scans were performed on the same day as the SPECT scans with a GE 8800 scanner after sterile intraperitoneal instillation of 1.5 (two patients) or 3.0 (two patients) l of 1.5% Hypaque 60 (diatrizoate meglumine 60% w/v) (Table 1). The contrast material was given after approximately 1.0 l of lactated Ringer's solution had been infused.

Planar and SPECT images were reviewed by two observers. Transmission CT images were subsequently also reviewed by two observers, along with the SPECT and planar images. These images were studied in an effort to qualitatively determine if SPECT contributed more or less information than the planar images and if SPECT and CT were in agreement regarding peritoneal fluid distribution.

Results

SPECT scans of satisfactory quality were obtained in all 17 studies in the nine patients. An example of a normal planar study (anterior view) and the corresponding SPECT images is shown in Figure 1. Typical SPECT display options include a rotating display, which is a sequential display of the planar projection images, and the ability to interactively select transverse, coronal, and sagittal views. Although SPECT images were generally of satisfactory quality, occasionally they were degraded by a very localized area of increased activity caused by residual activity in the catheter or injection site. This could be avoided to a large extent by flushing the catheter extensively with saline.

Quantifying the difference between planar and SPECT images was difficult. In general, planar scans showed distribution patterns similar to those on SPECT images (Figs. 1 and 2). In each instance SPECT was able easily to define the extent of the bare area of the liver (Fig. 2C), which was not apparent on planar views (Fig. 2A). Defining the peritoneal spaces about the liver was much easier with SPECT than with planar images, as SPECT addressed the problem of overlap (Figs. 1A, 1C, 1D, 2A, and 2C). The completeness of perfusion to the paracolic gutters and pelvis (Figs. 2D and 2E) was seen to excellent advantage with SPECT. SPECT also was able to show entry of fluid into the lesser sac, which could not be seen on planar images (Fig. 3). Thus, if nonperfusion of these areas occurred, particularly of Morrison pouch, it might not be detected on planar images, but should be detected on SPECT.

Four patients were studied by both intraperitoneal contrast-enhanced CT and intraperitoneal SPECT (two at 1.5 l and two at 3.0 l infused) (Table 1). The overall distributions of intraperitoneal fluid imaged by the nuclear and CT methods were quite similar. It appeared that SPECT might be somewhat more sensitive than CT after intraperitoneal administration of contrast material in detecting very small foci of activity, although contrast-enhanced CT clearly provided superior anatomic detail. Representative images are shown in two different patients (Figs. 2B, 2C, and 3). The similarity of the information provided is apparent. Normal intraperitoneal

TABLE 1: Summary of Planar, Single-Photon Emission CT (SPECT), and Intraperitoneal Contrast-Enhanced CT Studies in Patients with Colon Cancer

Case No.	No. of Studies		
	Planar and SPECT		Contrast-Enhanced CT
	1.5 l	3.0 l	
1	2	1	1
2	2	0	1
3	2	0	0
4	0	1	1
5	1	1	1
6	1	1	0
7	1	1	0
8	1	0	0
9	1	1	0

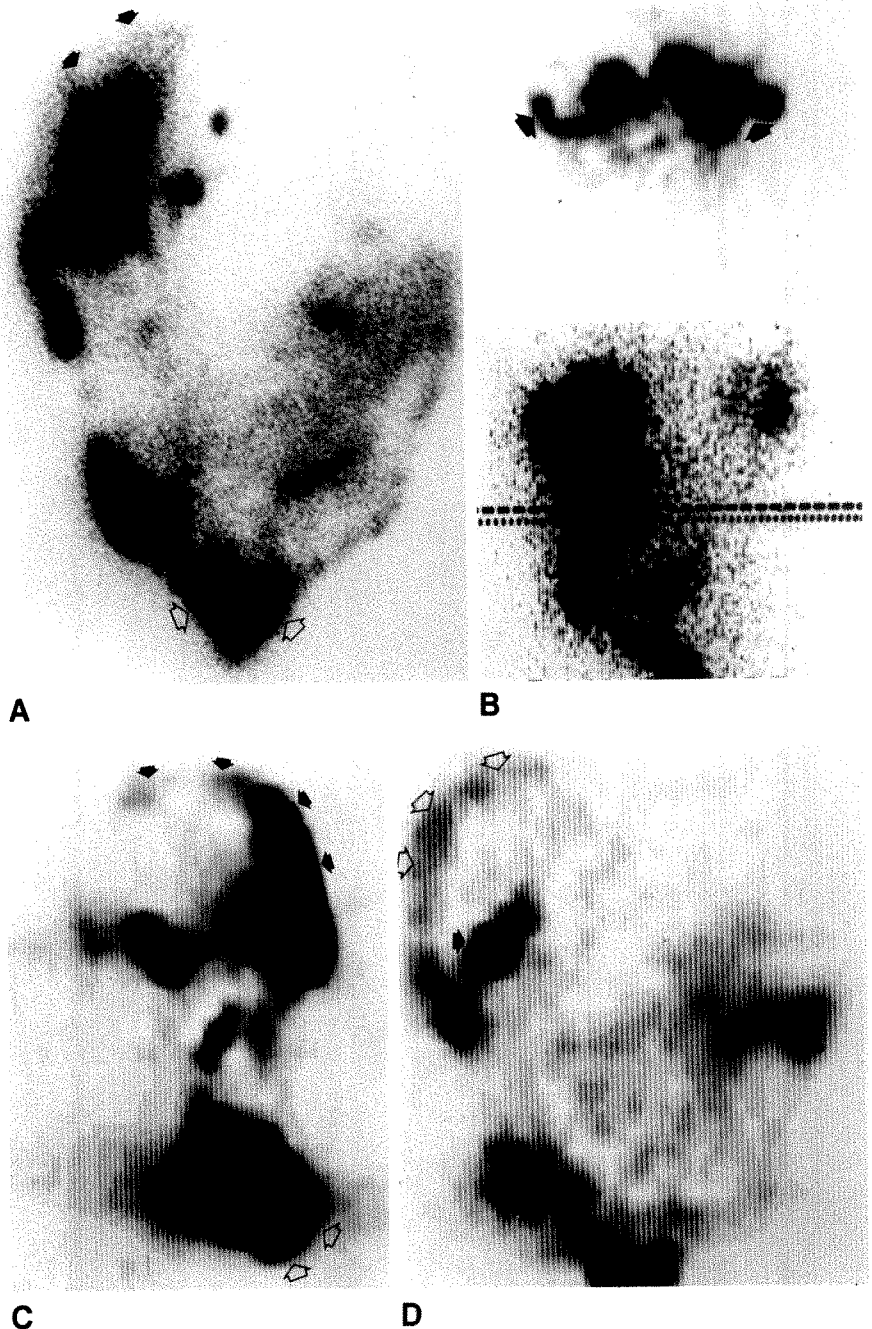
Fig. 1.—Normal SPECT of peritoneal cavity.

A, Anterior planar view of abdomen after administration of ^{99m}Tc -sulfur colloid shows normal fluid distribution over dome of liver (solid arrows) and into anatomic pelvis (open arrows).

B, Transverse SPECT (top) and single-projection anterior planar raw image (bottom) from SPECT study shortly after A. Right and left paracolic gutters (arrows).

C, Sagittal image shows fluid superior and anterior to liver (solid arrows), as well as its extension into anatomic pelvis (open arrows).

D, Coronal image shows excellent visualization of activity over dome of liver (open arrows) and just below right lobe of liver in Morrison pouch (solid arrow).



spaces were seen to excellent advantage on both SPECT and CT images (Figs. 2 and 3).

An example of the quantification approach for a single patient is shown in Figure 4. This histogram is representative in that the bulk of activity is in the mid to lower abdomen, and it also shows the very similar quantitative histograms in a patient imaged twice at the same fluid volume over a 1-month period. Thus, the technique appears to be reproducible. Fluid distributions were comparable in a total of three patients studied on two separate occasions at the same volume (Table 1). This methodology of quantification differs from simply drawing 10 equally spaced, horizontal regions of interest over

the abdomen in that the counts we plotted represent the total acquired, with a correction for attenuation, from all 90 angular projections. Thus, this index equally weights the data from all projections, unlike quantification from just the anterior planar view, which might overly weight anteriorly situated counts.

In five patients, intraperitoneal scans with SPECT were obtained at two different volumes (Table 1). The mean \pm SEM of four of these patients' count histograms is plotted in Figure 5. In the fifth patient, the quantitative data at 1.5 l were lost from the computer; however, planar images at the two volumes showed very similar fluid distributions. These profiles of intraperitoneal radioactivity showed very little change be-

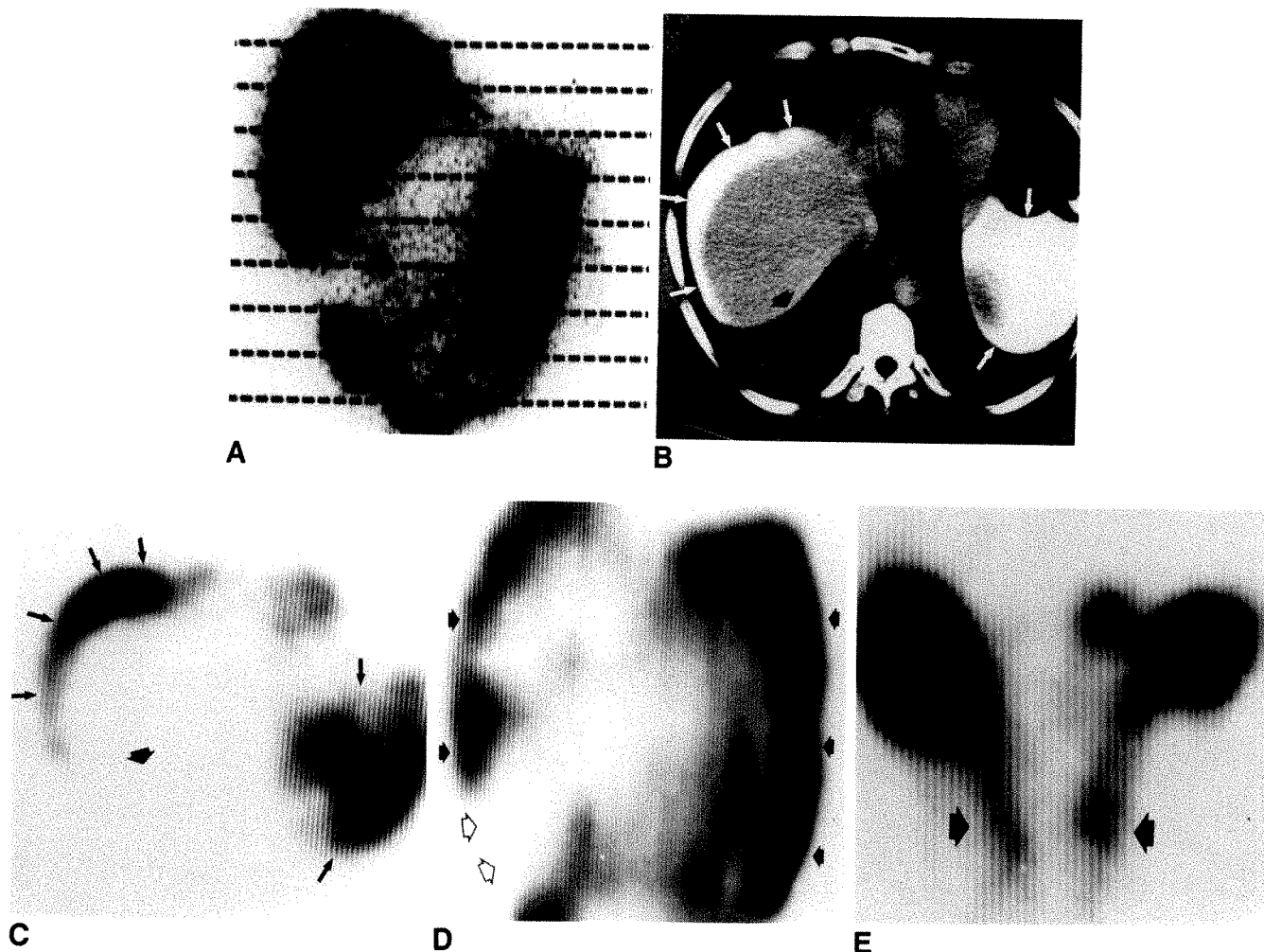


Fig. 2.—Examples of SPECT and CT correlative anatomy.

A, Anterior-projection image from SPECT acquisition shows horizontal levels at which transverse tomographic slices can be selected, and from which quantitative information was drawn.

B, CT scan with intraperitoneal contrast material in upper abdomen anterior and lateral to liver as well as around spleen (white arrows). "Bare area" of liver (black arrow) is not exposed to intraperitoneal contrast material.

C, Corresponding transverse SPECT image. Bare area of liver posteriorly has no radionuclide (short arrow); it corresponds to area of no contrast material in B. Satisfactory fluid accumulation is seen in anterior and left upper abdomen (long arrows).

D, Coronal view shows filling of paracolic gutters (solid arrows), except in right lower quadrant (open arrows). Nonperfusion in this area is not uncommonly related to recurrent tumor mass, though no tumor was identified.

E, Transverse view shows ^{99m}Tc -sulfur colloid activity entering pelvis (arrows).

tween the 1.5- and 3.0-l intraperitoneal infusion volumes, though they suggest that the 3.0-l volume may result in a slight shift of fluid toward the pelvis.

Discussion

SPECT of the peritoneal cavity is performed readily with modern nuclear imaging and computer equipment. The ability to use a very-large-field-of-view gamma camera makes it possible to include the entire abdominal cavity in a single acquisition, which is generally not possible with a smaller camera [11, 12].

Ours is not the first attempt at quantifying intraperitoneal SPECT data. Slosman et al. [13] applied an approach to quantify ^{99m}Tc -human serum albumin distribution. That ap-

proach was applied to individual 1.2-cm-thick slices, and related total counts in six areas of the transverse slice to total area as a percentage or index. The quantitative approach used in our study differed from that of Slosman et al. in that a somewhat more extensive analysis of distribution of abdominal fluid was performed in which the attenuation-corrected percentage of activity present in each of the 10 transverse slices of the abdomen compared with the total activity on all slices was determined and then plotted as a histogram. Thus, our approach should be geometrically less sensitive and assesses all counts plotted from upper abdomen to pelvis.

Our results indicate that the complex recesses of the peritoneal cavity, particularly those of the upper abdomen, are displayed more clearly by SPECT than by planar nuclear images. It seems reasonable to assume that foci of intraperi-

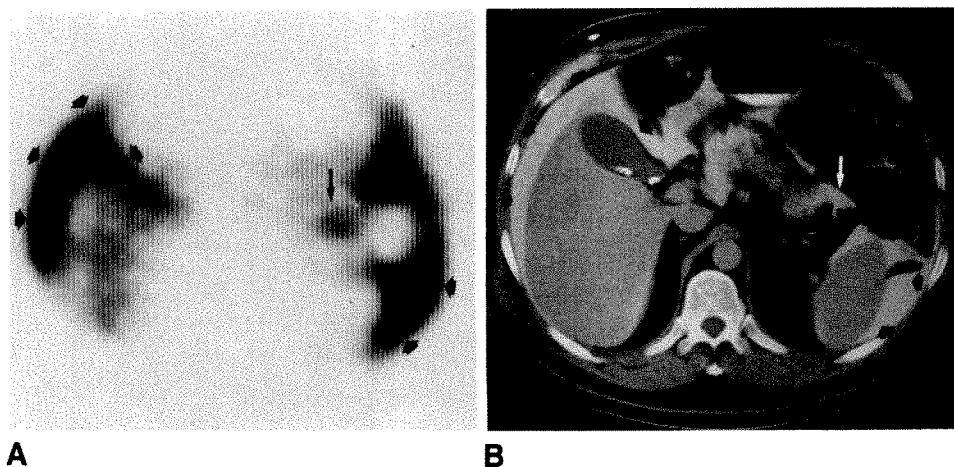


Fig. 3.—Visualization of complex upper abdominal fluid distribution on SPECT and CT.
 A, Transverse SPECT image of intraperitoneal ^{99m}Tc -sulfur colloid distribution in upper abdomen correlates well with CT after intraperitoneal fluid distribution (B). Note fluid in lesser sac (long arrow), as well as about liver and spleen (short arrows).
 B, Transverse CT image corresponding to A after intraperitoneal administration of contrast material. Fluid is seen well in anterior subhepatic space, about spleen (black arrows), and in lesser sac (white arrow).

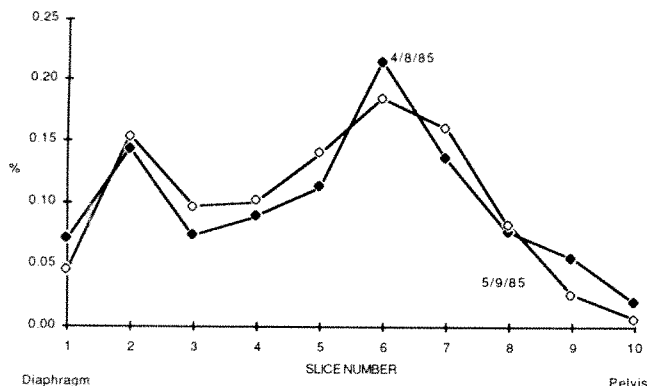


Fig. 4.—Reliability of quantitative SPECT profile graph. Relative count distributions at 1.5-l filling volumes on two occasions are virtually identical.

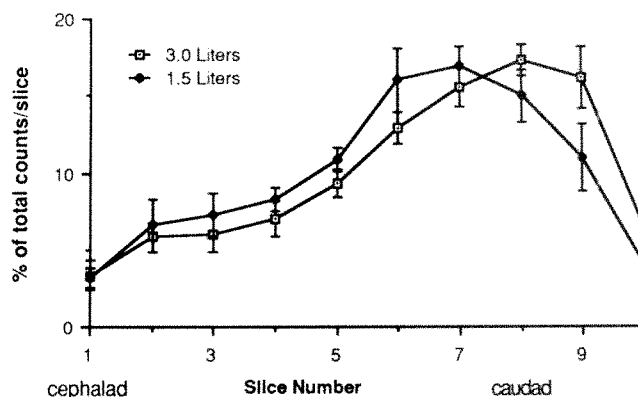


Fig. 5.—Linear relative-count histograms from SPECT images at 1.5- or 3.0-l filling volumes pooled from data of four patients (mean \pm SEM). Note lack of change in relative count distributions with twofold alteration in volume, though there is a suggestion of slightly more activity in anatomic pelvis (slices 8–10) at 3.0-l volume.

toneal nonperfusion would be better identified by SPECT than by planar images (as several areas of normal perfusion are not seen on planar images). If so, disease in these regions would also be relatively inaccessible by the intraperitoneal delivery route and thus potentially more subject to tumor recurrence or progression.

Transverse SPECT images show findings similar to those on transverse transmission CT images after intraperitoneal injection of contrast material and provide an accurate image of the recesses of the peritoneal cavity. The nuclear technique has the advantage of not exposing the patient to iodinated contrast material [11]. For this reason, peritoneal SPECT may be the preferred study for assessing intraperitoneal fluid distribution. It is also possible that the nuclear imaging technique is superior to transmission CT in that smaller foci of fluid potentially may be localized by SPECT. Because only four direct comparisons between SPECT and CT were possible,

this aspect will need considerable further study, especially in patients with recurrent cancers.

The quantitative ability of intraperitoneal SPECT is a potential advantage of this method compared with transmission CT and may be of eventual clinical importance. With the simple quantification method we have described, changes in the distribution of intraperitoneal fluid can be followed objectively. For example, there has been some debate regarding the amount of fluid required to assure adequate intraperitoneal fluid distribution for therapy. Our quantitative data indicate the 1.5-l volume to be virtually equivalent to the 3-l volume in terms of the relative distribution of intraperitoneal fluid [12]. It should be noted that in three patients the 1.5- and 3.0-l volumes were given on separate occasions, whereas in two others the 3.0-l volume was reached by adding 1.5 l and ^{99m}Tc -sulfur colloid to the existing 1.5 l. No major difference was seen between the distribution of the first and second 1.5

I. Obviously, small alterations in the fluid distribution pattern, not resolvable by gamma cameras, would not be detectable by this technique. The distribution data acquired by SPECT should improve treatment planning and response monitoring for intraperitoneal chemotherapy. SPECT may also prove useful in defining the intraperitoneal distribution of radiolabeled monoclonal antibodies.

Previously we have shown visually that apparent changes on intraperitoneal distribution scans can indicate the recurrence of tumor in the abdomen, manifested by diminished fluid reaching the areas of the recurrence of colon cancer [14]. Obviously, visual analysis of the planar and SPECT images is key, but quantitative analysis of the SPECT data may add further information and is relatively easy to achieve as there is signal only where radioactive fluid is present. Quantitative analysis by transmission CT is more difficult in that, at present, such information can only be produced by manually selecting regions of interest delineating the peritoneal fluid, calculating an area, and then developing a percentage of fluid/area that can be plotted in a variety of ways, including a simple linear plot, such as we have used. This approach is extremely labor-intensive. Obviously, if fine anatomic detail is required in addition to assessing the gross pattern of fluid distribution, contrast-enhanced CT of the peritoneal cavity would seem preferable. Further study of the clinical utility of the "relative quantitation" method will be necessary before its routine use can be recommended.

In conclusion, SPECT of the peritoneal cavity is performed simply, adds spatial detail of anatomic areas impossible to resolve on planar images, and allows for the visualization of the complexity of the peritoneal space. SPECT provides less detail than contrast-enhanced CT of the peritoneal cavity does, but it does not expose the patient to the risk of iodinated contrast material, shows fluid distribution clearly, and can be quantified easily. SPECT of the peritoneal cavity is a useful adjunct to planar imaging in the evaluation of the distribution of intraperitoneally administered radioactivity and is a useful alternative to CT after administration of intraperitoneal contrast material. An understanding of the normal and pathologic anatomy seen on such scans will be essential as the intraperitoneal route of drug and radionuclide delivery is used more often.

ACKNOWLEDGMENTS

We thank Michele Curro, Mary Miller, and Wanda Wysor for secretarial assistance.

REFERENCES

1. Jones RB, Myers CE, Guarino AM, Dedrick RL, Hubbard SM, DeVita VT. High volume intraperitoneal chemotherapy ('belly bath') for ovarian cancer. *Cancer Chemother Pharmacol* 1978;1:161-166
2. Dedrick RL, Myers CE, Bungay PM, DeVita VT. Pharmacokinetic rationale for peritoneal drug administration in the treatment of ovarian cancer. *Cancer Treat Rep* 1978;62:1-11
3. Dunnick NR, Jones RB, Doppman JL, Speyer J, Myers CE. Intraperitoneal contrast infusion for assessment of intraperitoneal fluid dynamics. *AJR* 1979;133:221-223
4. Speyer JL, Myers CE. The use of peritoneal dialysis for delivery of chemotherapy to intraperitoneal malignancy. *Recent Results Cancer Res* 1980;74:264-269
5. Ozols RF, Young RC, Speyer JL, et al. Phase I and pharmacological studies of Adriamycin administered intraperitoneally to patients with ovarian cancer. *Cancer Res* 1982;42:4265-4269
6. Epenetos AA, Hooker G, Krausz T, Snook D, Bodner WF, Taylor-Papadimitriou J. Antibody-guided irradiation of malignant ascites in ovarian cancer: a new therapeutic method possessing specificity against cancer cells. *Obstet Gynecol* 1986;68(3):71S-74S
7. Gyves J, Ensimer W, Stetson P, et al. Contrast intraperitoneal infusion of 5-fluorouracil via a totally implanted system. *Clin Pharmacol Ther* 1984;35:83-89
8. Wahl RL, Barrett J, Geatti O, et al. The intraperitoneal delivery of radiolabeled monoclonal antibodies: studies on the regional delivery advantage. *Cancer Immunol Immunother* 1988;26(3):187-201
9. Wahl RL, Liebert M, Fisher S, Boland R. Enhanced radioimmunotherapy of intraperitoneal human colon cancer xenografts by intraperitoneal monoclonal antibody delivery. *Proc Am Assoc Cancer Res* 1987;28:438
10. Colcher D, Esteban J, Carrasquillo JA, et al. Complementation of intracavitary and intravenous administration of a monoclonal antibody (B72.3) in patients with carcinoma. *Cancer Res* 1987;47(15):4218-4224
11. Shehadi W, Toniolo G. Adverse reactions to contrast media: a report from the committee on Safety of Contrast Media of the International Society of Radiology. *Radiology* 1980;137:299-302
12. Rosenshein NB, Blake D, McIntyre PA, et al. The effect of volume on the distribution of substances instilled into the peritoneal cavity. *Gynecol Oncol* 1978;6(1):106-110
13. Slosman D, Forni M, Townsend D, Brioschi PA, Krauer F, Donath A. SPECT study of the fluid distribution in the intra-abdominal space during intraperitoneal treatment of ovarian cancer. *Nucl Med Commun* 1985;6:91-96
14. Arnstein NB, Wahl RL, Cochran M, Gyves J. Adenocarcinoma of the alimentary tract: peritoneal distribution scintigraphy. *Radiology* 1987;162:439-441

Diagnosis of Acute Cholecystitis by Cholescintigraphy: Significance of Pericholecystic Hepatic Uptake

Lawrence C. Swayne¹
Hal N. Ginsberg

Uptake of radionuclide by the liver next to the gallbladder in cholescintigraphy has been described as a useful secondary sign with a high positive predictive value for the diagnosis of acute cholecystitis. We retrospectively examined 780 consecutive cholescintigrams to (1) determine the positive predictive value at 1 hr of this sign for acute cholecystitis and (2) ascertain if the presence or absence of this finding could differentiate acute from gangrenous cholecystitis. Pericholecystic hepatic activity was present at 1 hr in 48 (34%) of 141 scans in which the gallbladder was not visualized, and cholecystectomy was performed within 6 days of scintigraphy. Forty-five of these patients had acute and three had chronic cholecystitis (94% positive predictive value for acute cholecystitis). In addition, 57% of patients with gangrenous cholecystitis exhibited pericholecystic hepatic activity, and the frequency of this finding was significantly higher ($p < .006$) in gangrenous than in acute cholecystitis.

In summary, pericholecystic hepatic uptake is a valuable secondary sign in the cholescintigraphic diagnosis of acute cholecystitis. The significance of the finding is (1) a high positive predictive value for acute disease at 1 hr and (2) a statistically significant increased frequency in patients with gangrenous cholecystitis.

Increased pericholecystic activity by the liver parenchyma in the gallbladder fossa has been described as a useful secondary sign in the cholescintigraphic diagnosis of acute gallbladder disease [1-4]. Brachman et al. [1] originally observed the sign with gallbladder nonvisualization in five patients with acute gangrenous cholecystitis. Smith et al. [2] later reported a high association of the finding with both gangrenous cholecystitis and gallbladder perforation. Eleven of their 13 patients with the sign who underwent cholecystectomy had acute cholecystitis, although the other two had chronic disease. In other series, Meekin et al. [3] (nine patients) and Bushnell et al. [4] (18 patients) found high positive predictive values of the sign for acute cholecystitis at 1 hr. No data were published to determine if the intensity of the pericholecystic activity correlated with the degree of inflammation.

The purpose of this study was to determine the positive predictive value of the sign at 1 hr for acute disease in a larger series of cases and to determine if the presence or absence of increased pericholecystic hepatic uptake of radionuclide could differentiate between acute and gangrenous cholecystitis.

Materials and Methods

We retrospectively analyzed 780 consecutive cholescintigrams obtained in patients with suspected acute cholecystitis at Morristown Memorial Hospital during a 4-year period. The group included 477 females (61%) and 303 males (39%); the age range was 8-96 years. Data analysis was limited to a subset of 226 patients with normal biliary transit who had cholecystectomy within 6 days of their examination.

Cholescintigraphy was performed in all patients after they had fasted for at least 3 hr. If the patients had been fasting for more than 18 hr, they were pretreated with an IV infusion of Sincalide (0.02 $\mu\text{g/kg}$ Kinevac, Squibb, Princeton, NJ). The examination was done after IV

Received December 15, 1987; accepted after revision January 26, 1989.

This work was supported in part by a grant from the R. Franklin Carter Surgical Research Fund, 112 Skyline Dr., Morristown, NJ 07960.

¹ Both authors: Department of Diagnostic Radiology, Morristown Memorial Hospital, 100 Madison Ave., Morristown, NJ 07960. Address reprint requests to L. C. Swayne.

AJR 152:1211-1213, June 1989
0361-803X/89/1526-1211

© American Roentgen Ray Society

administration of 5 mCi (185 MBq) of ^{99m}Tc -labeled diisopropyl-iminodiacetic acid (Disofenin; New England Nuclear, North Billerica, MA) by using a standard large-field-of-view gamma camera and a high-resolution collimator, with a 20% energy window centered at 140 keV. Serial 15-min, 500,000-count images were obtained in the anterior projection for up to 60 min. One hour after injection, additional right lateral and left anterior oblique images were obtained. Delayed images, with shielding of the bowel when appropriate [5], were then obtained until either the gallbladder was satisfactorily visualized or an insufficient amount of activity remained within the hepatic parenchyma to warrant continuation. All studies with gallbladder nonvisualization were continued for at least 2 hr; 4-hr images were not obtained in every case.

If the scintigram failed to show the gallbladder, the examination was considered positive. Two additional patients who had perforation of the gallbladder had gallbladder visualization, but free peritoneal spill of radionuclide was evident. The pathologic criteria used for the diagnosis of acute cholecystitis included edema of the gallbladder wall and neutrophilic infiltration with or without superficial mucosal ulceration. Gangrenous cholecystitis was diagnosed pathologically if hemorrhagic infarction or transmural suppurative necrosis was present. Chronic cholecystitis was diagnosed if fibrous wall thickening and an abundance of Rokitsky-Aschoff sinuses were noted histologically [2].

Two radiologists independently reviewed all of the examinations, without knowledge of the subsequent surgical and pathologic findings. The presence or absence of increased pericholecystic uptake of radionuclide in each case was recorded and graded on the basis of a subjective assessment of the relative observed intensity on scans made at 1 hr, compared with the activity in the hepatic parenchyma and biliary ducts. Grades were assigned as follows: 0 = absent; 1 = trace; 2 = increased activity, less than the adjacent ducts; 3 = activity equal in intensity to the adjacent ducts; and 4 = activity greater than the adjacent common hepatic duct. The pathology and surgery reports were reviewed and correlated with the scintigraphic findings. Statistical evaluations were done by using the chi-square test.

Acute cholecystitis was present in 128 patients with nonvisualized gallbladders. Two additional patients whose gallbladders were visualized before 1 hr also were considered true-positive because of obvious free peritoneal spill. Seventy-eight patients with gallbladder visualization had nonacute disease at surgery. At 2 hr, there were five false-negative examinations and 13 false-positive studies. Thus, cholecystigraphy had a 96% (130/135) sensitivity and an 86% (78/91) specificity for acute disease at 2 hr after injection.

Results

In the data analysis group, 141 patients had gallbladder nonvisualization. Pathologic evidence of acute cholecystitis was found in 135 patients, 46 of whom had additional evidence of gangrenous cholecystitis and/or gallbladder perforation. Increased pericholecystic uptake of radionuclide was present in 48 (34%) of the 141 patients with gallbladder nonvisualization (see Table 1). This sign appeared as a curvilinear band of variable width and intensity in the adjacent gallbladder fossa and was always present by 1 hr (Fig. 1). Of these 48 patients, 45 had pathologic evidence of acute cholecystitis, and three had evidence of chronic cholecystitis (one of the three had a diffusely necrotic gallbladder carcinoma). Increased uptake also was present in 26 (57%) of 46 patients with gangrenous cholecystitis and was observed in four (31%) of the 13 patients with acute gallbladder perforation. In 22

TABLE 1: Relationship of Gallbladder Nonvisualization to Increased Pericholecystic Activity on Cholescintigraphy

Pathologic Changes	Results of Cholescintigraphy	
	Gallbladder Nonvisualization	Increased Pericholecystic Uptake
Acute ($n = 135$)	128 ^a	45
Gangrene ^b ($n = 46$)	44 ^a	26
Perforation ^c ($n = 13$)	11 ^a	4
Chronic ($n = 91$)	13	3
Total ($n = 226$)	141 ^a	48

^a Two other patients had no cholescintigraphic evidence of perforation.

^b Cases of gangrenous cholecystitis are included in the cases of acute cholecystitis.

^c Cases of gallbladder perforation are included in the cases of gangrenous cholecystitis.



Fig. 1.—Grade 4 pericholecystic hepatic uptake in a 64-year-old man with acute right-upper-quadrant pain. Scintigram (anterior view) at 1 hr does not visualize gallbladder but shows diffuse intense increased activity (arrowheads) involving entire inferior border of right lobe of liver and extending medially to porta hepatis. Surgery, performed same day, revealed acute gangrenous cholecystitis and cholelithiasis.

patients with increased pericholecystic activity, no evidence was found of gangrenous cholecystitis or of gallbladder perforation.

The frequency of increased pericholecystic activity in acute disease was thus significantly higher ($p < .000001$) in acute than in chronic cholecystitis. The sign was highly specific, 97% (88/91), and had a high positive predictive value, 94% (45/48), for acute cholecystitis, although the sensitivity was only 33% (45/135) and the negative predictive value was 49% (88/178). Similarly, the sign also has a high specificity, 88% (158/180), for advanced disease (gangrenous cholecystitis and/or acute gallbladder perforation) with a lower sensitivity of 57% (26/46). There was a statistically significant ($p < .006$) increased frequency of the sign in gangrenous vs acute cholecystitis. No significant differences ($p < .05$) were ob-

served, however, between the acute, gangrenous, and perforation groups with regard to the grading distribution of the increased activity. The two radiologists reviewing the examinations agreed on the presence or absence of the finding in 96% (53/55) of the cases. The interobserver reliability of the grading distribution was 86% (47/55). Disagreements were limited to the assignment of cases to the grade 1 or 2 categories and were resolved by mutual agreement.

Discussion

With the advent of ^{99m}Tc -labeled iminodiacetic acid agents, cholescintigraphy has been widely accepted as the diagnostic technique of choice in both acute calculous and acalculous cholecystitis [5, 6]. Recently, increased pericholecystic hepatic activity has been described as a secondary sign of acute disease [1–4, 6–8]. In our series, increased activity was seen in 34% of patients with nonvisualization of the gallbladder who had normal biliary to bowel transit of the radionuclide. This compares favorably with the 21% prevalence reported by others [2]. The frequency of the increased pericholecystic activity in patients with acute gallbladder disease was much higher than in those with nonacute disease, and the difference was highly statistically significant ($p < .000001$).

In addition, the presence of the increased activity at 1 hr was associated with a high positive predictive value (94%) for acute disease. Other authors [3, 4] have reported similar high positive predictive values (94–100%). Because the increased activity, when present, was always evident on the 1-hr scan, the finding may increase the specificity of early cholescintigraphic images and obviate pharmacologic intervention (morphine-augmented cholescintigraphy) [9, 10] or delayed imaging (a delay has caused some authors to express a preference for sonography [11]). Unfortunately, the absence of the finding at 1 hr does not exclude the diagnosis of acute cholecystitis (negative predictive value of only 49%), and delayed imaging in these patients is still required.

Increased pericholecystic activity correlated with the presence of gangrenous cholecystitis or gallbladder perforation. Twenty-six (57%) of the 46 patients with advanced disease had increased pericholecystic hepatic activity. The frequency of the finding in gangrenous cholecystitis was higher than in acute cholecystitis, and the difference was statistically significant ($p < .006$). In our series, visual assessment of the relative intensity of the increased uptake did not correlate with the degree of inflammation. The importance of the finding, therefore, involves only whether it is present or absent.

Previous reports of the sensitivity of the finding in advanced disease have ranged from 22% [7] to 89% [4]; however, the two largest previous series have reported sensitivities of 33% [6] and 44% [8]. The association of the finding with gangrenous cholecystitis or gallbladder perforation is an important observation, because gallbladder perforation has been associated with a mortality rate of 25% even in patients undergoing cholecystectomy [12–14].

In summary, pericholecystic hepatic uptake of radionuclide is a valuable secondary sign in the cholescintigraphic diagnosis of acute cholecystitis. The presence of the sign on 1-hr images may alleviate the need for delayed views in diagnosing acute cholecystitis, because it results in a comparable specificity. In addition, there is a statistically significant increased frequency of the sign in patients with gangrenous vs acute cholecystitis.

REFERENCES

1. Brachman MB, Tanasescu DE, Ramanna L, Waxman AD. Acute gangrenous cholecystitis: radionuclide diagnosis. *Radiology* 1984;151:209–211
2. Smith R, Rosen JM, Gallo LN, Alderson PO. Pericholecystic hepatic activity in cholescintigraphy. *Radiology* 1985;156:797–800
3. Meekin GK, Ziessman HA, Klappenbach RS. Prognostic value and pathophysiologic significance of the rim sign in cholescintigraphy. *J Nucl Med* 1987;28:1679–1682
4. Bushnell DL, Perlman SB, Wilson MA, Polcyn RE. The rim sign: association with acute cholecystitis. *J Nucl Med* 1986;27:353–356
5. Weissmann HS, Frank MS, Bernstein LH, Freeman LM. Rapid and accurate diagnosis of acute cholecystitis with ^{99m}Tc -HIDA cholescintigraphy. *AJR* 1979;132:523–528
6. Swayne LC. Acute acalculous cholecystitis: sensitivity in detection using technetium-99m iminodiacetic acid cholescintigraphy. *Radiology* 1986;160:33–38
7. Shih W-J, Domstad PA, Kenady DE, DeLand FH. Scintigraphic findings in acute gangrenous cholecystitis. *Clin Nucl Med* 1987;12:717–720
8. Smith R, Rosen JM, Alderson PO. Gallbladder perforation: diagnostic utility of cholescintigraphy in suggested subacute and chronic cases. *Radiology* 1986;158:63–66
9. Choy D, Shi EC, McClean RG, Hoschl R, Murray IPC, Ham JM. Cholescintigraphy in acute cholecystitis: use of intravenous morphine. *Radiology* 1984;151:203–207
10. Kim EE, Pjura G, Lowry P, Nguyen M, Pollack M. Morphine-augmented cholescintigraphy in the diagnosis of acute cholecystitis. *AJR* 1986;147:1177–1179
11. Schuman WP, Rudd TG, Rogers JV, Stevenson JK, Larson EB. Radionuclide hepatobiliary imaging and real-time ultrasound in the diagnosis of acute cholecystitis. *Radiology* 1984;152:238
12. Glenn F, Hays D. The age factor in the mortality rate of patients undergoing surgery of the biliary tract. *Surg Gynecol Obstet* 1955;100:11–18
13. Isch JH, Finneran JC, Nahrwold DL. Perforation of the gallbladder. *Am J Gastroenterol* 1971;55:451–458
14. Roslyn J, Busuttill RW. Perforation of the gallbladder: a frequently mismanaged condition. *Am J Surg* 1979;137:307–312

Book Review

Nuclear Medicine Technology and Techniques. Edited by Donald R. Bernier, Paul E. Christian, James K. Langan, and L. David Wells. St. Louis: Mosby, 610 pp., 1989. \$54.95

The mathematics section of this book offers a good background and foundation for understanding and performing quantitative analysis and quality control. An addition to the usual presentation is a nice description of graphing techniques, which should be of value in terms of clinical and administrative applications. This is followed by chapters on physics, instrumentation, and computers. A great deal of material is covered, but day-to-day information on usage, potential problems, and solutions, particularly in terms of computer hardware and software, is not prominent. The next two chapters deal extensively with laboratory science and radiochemistry, but I was surprised to see no mention of preparation and labeling of monoclonal antibodies for immunoscintigraphy. This is mentioned, however, in the chapter on radioimmunoassays. The chapters on radiation safety and quality control are informative and well worth reading. It seems as though the chapter on nuclear magnetic resonance was written more for the clinician than for the technologist; authorship by a technologist would have been useful. A section on the care of patients is useful. Most of the remaining chapters deal with nuclear medicine procedures on an

organ-by-organ basis, and most have two authors, a technologist and a physician. Occasionally, I had the impression that the clinical input in these chapters is overbearing in relation to the basic information needed for a technologist to understand and perform the task being requested. For example, I doubt whether a technologist could perform and process a left-to-right intracardiac shunt study on the basis of the information presented in this book.

In general, I think that the book is well written and contains numerous valuable illustrations. It could be a valuable general reference book for technologists and even could be of interest to physician-trainees in nuclear medicine. However, a reference explaining techniques in more detail should be chosen as a companion. I congratulate the editors on integrating and coordinating the production of a book that contains a significant body of knowledge.

Michael E. Siegel
University of Southern California, School of Medicine
Los Angeles, CA 90033

MR Appearance of the Liver After Partial Hepatectomy

Lionel Arrivé¹
Hedvig Hricak
Henry I. Goldberg
Ruedi F. Thoeni
Alexander R. Margulis

To define the MR appearance of the liver after partial hepatectomy, we reviewed retrospectively 61 MR examinations performed on 25 patients 10 days to 48 months after surgery. Twenty-seven partial hepatectomies performed in the 25 patients included right lobectomy in 11, trisegmentectomy in two, left lobectomy in five, and wedge resection in nine. By using vascular landmarks, demonstration of the falciform ligament, and the presence of surgical clips, we correctly identified the type of partial hepatectomy in 21 of the 25 patients. The signal intensity of the resection margin was similar to that of the remaining parenchyma in 16 of 18 patients and was poorly defined and had a higher signal intensity (T2-weighted image) in the remaining two. Liver regeneration was observed on serial MR scans 2–16 months after surgery. Findings related to chemotherapy, including periportal changes and inhomogeneous appearance of the liver, were shown in six of eight patients. Tumor recurrence was present in nine patients, either intrahepatic (seven patients) or at the resection margin (two patients), and was consistently identified with MR imaging.

The ability of MR imaging to produce images without artifacts from surgical clips is helpful in displaying the MR appearance of the liver after partial hepatectomy. Anatomic landmarks, findings related to chemotherapy, and tumor recurrence were shown well.

The use of partial hepatectomy for the treatment of neoplastic or benign conditions of the liver has increased during recent years [1, 2]. It may be necessary for removal of primary or secondary hepatic neoplasms, for adequate excision of bile-duct tumors, and for management of a variety of benign conditions [2].

In the postoperative follow-up of such patients, radiologic evaluation can be necessary to rule out complications or to detect recurrent neoplasia [3]. So far, CT has been the most important imaging technique after partial hepatectomy [4–7]; however, its usefulness can be limited by artifacts caused by surgical clips [4].

MR imaging has been shown to be an accurate method for the evaluation of benign as well as malignant hepatic conditions. To define the MR findings after partial hepatectomy, including anatomic landmarks, effects of chemotherapy, and detection of tumor recurrence, we retrospectively reviewed 61 MR examinations in 25 patients who had undergone this type of operation.

Materials and Methods

Twenty-five consecutive patients with partial hepatectomy, 11 males and 14 females 2–88 years old (mean, 49 years), composed the study group. The medical records of all patients were reviewed and the following were specifically recorded: type of hepatic disease, type of partial hepatectomy and surgical technique, associated therapy, and postoperative complications. The indications for partial hepatectomy were hepatic metastases ($n = 10$) from colorectal ($n = 8$), renal ($n = 1$), and adrenal carcinoma ($n = 1$); primary hepatic tumors ($n = 9$), including hepatocellular carcinoma ($n = 6$), hepatoblastoma ($n = 1$), angiosarcoma ($n = 1$), and adenoma ($n = 1$); direct extension to the liver ($n = 3$) of biliary duct tumors ($n = 2$) and gallbladder carcinoma ($n = 1$); chronic abscess of the liver ($n = 1$); recurrent cholangitis ($n = 1$); and hydatid cyst of the liver ($n = 1$).

Received December 7, 1988; accepted after revision January 26, 1989.

L. Arrivé is a research fellow in MR Imaging on leave from the Department of Radiology, Hôpital Beaujon, Clichy, France, and is supported by a grant (Bourse Lavoisier) from the French Foreign Office.

¹ All authors: Department of Radiology, Box 0628, University of California School of Medicine, San Francisco, CA 94143. Address reprint requests to H. Hricak.

AJR 152:1215–1220, June 1989

0361–803X/89/1526–1215

© American Roentgen Ray Society

Twenty-seven partial hepatectomies were performed in the 25 patients. Hepatic lobectomy was performed in 18: 11 right lobectomies (associated in two cases with a wedge resection of a portion of the left lobe), two trisegmentectomies, and five left lobectomies. Hepatic wedge resection was performed in nine, including four wedge resections in the right lobe, four in the left lobe, and one in both right and left lobes. After surgery, eight patients underwent chemotherapy.

Sixty-one MR examinations were performed in the 25 patients over a period of 10 days to 48 months after surgery. Ten patients had a single MR examination, seven patients had two examinations, and eight patients had three or more. Those performed 6 months or less after surgery are referred to as early MR examinations ($n = 18$); those obtained after 6 months are referred to as late MR examinations ($n = 43$).

MR imaging was performed with a Diasonics MT/S system (Milpitas, CA) operated at 0.35 T. Multislice spin-echo (SE) images, 500–2000/30,60 (TR range/first-echo TE, second-echo TE), were obtained. Both T1- (SE 500/30) and T2- (SE 2000/30,60) weighted transverse images were obtained in all patients. Slices were contiguous, with a thickness of 10 mm.

MR images were evaluated in conference and discrepancies in interpretation were resolved by consensus. Observers had no knowledge of the hepatic disease, the type of partial hepatectomy and associated therapy, or the results of any procedure (imaging, surgery, or biopsy) consequent to the first surgery. The following were analyzed: (1) the ability to identify the type of partial hepatectomy by showing anatomic landmarks including hepatic veins, portal veins, and falciform ligament [8]; (2) resection margin, regularity, and signal intensity; (3) shape of the liver and size of the segments; (4) signal intensity of the liver in comparison with the pancreas and homogeneity of the liver with special attention to periportal areas as related to different TR and TE settings; and (5) detection of hepatic focal lesions.

MR findings were correlated with histologic results in 11 patients (seven surgery, two biopsy, and two autopsy), with repeat MR and clinical follow-up in seven patients, and with clinical follow-up alone in seven.

Results

MR Appearance after Partial Hepatectomy

The type of partial hepatectomy was correctly identified in 21 of the 25 patients (Figs. 1–3). Identification was based on the recognition of anatomic landmarks, including vascular elements, the falciform ligament, and surgical clips (Table 1). Right lobectomy was correctly identified on MR images in 10

of 11 patients. In one patient, right lobectomy was misinterpreted as a trisegmentectomy because neither the middle hepatic vein nor the falciform ligament was recognized. Trisegmentectomy was correctly identified in the two patients with this type of surgery. Left lobectomy was correctly identified in four of five patients. In one patient, the left lobectomy was misinterpreted as a lateral segmentectomy because a large amount of hepatic tissue between the middle hepatic vein and the resection margin was considered to be the medial segment of the left lobe (Fig. 4). Wedge resection, performed in seven patients, was accurately diagnosed in five. In two patients, wedge resection of the liver was not identified because surgical clips were not seen. After lobectomy, absence of the corresponding branch of the portal vein was noted in all cases. After right lobectomy or trisegmentectomy, the left portal vein was prominent and well visualized in all cases.

The signal intensity of the resection margin was distinct and similar to that of the remaining liver parenchyma in 16 of the 18 patients who underwent lobectomy. In the two remaining patients, the resection margin appeared as a poorly defined area and showed slightly higher signal intensity than the remaining liver did on T2-weighted images. One of these patients had been imaged 2 months after surgery and proved, at subsequent surgery, to have scar tissue and regenerative changes in the liver (Fig. 5). The other patient had been imaged initially 10 days after surgery, and these findings were not duplicated on follow-up MR studies. The patient's clinical history was unremarkable, and therefore it is assumed that the findings represented postsurgical changes.

Surgical clips at the site of resection were demonstrated in 23 of 25 patients. On both T1- and T2-weighted images, they emitted a low signal intensity and a high-signal-intensity halo, but they never obscured the details of hepatic or adipose tissue.

Liver regeneration was observed on serial MR scans 2–16 months after lobectomy and was most marked during the first 6 months. The regenerated liver had the same signal intensity as the normal liver did (i.e., similar to that of the pancreas on both T1- and T2-weighted images). After right lobectomy, liver enlargement assumed either a transverse elongated shape (transverse dimension more than twice the anteroposterior dimension) (Fig. 6) when regeneration affected mostly

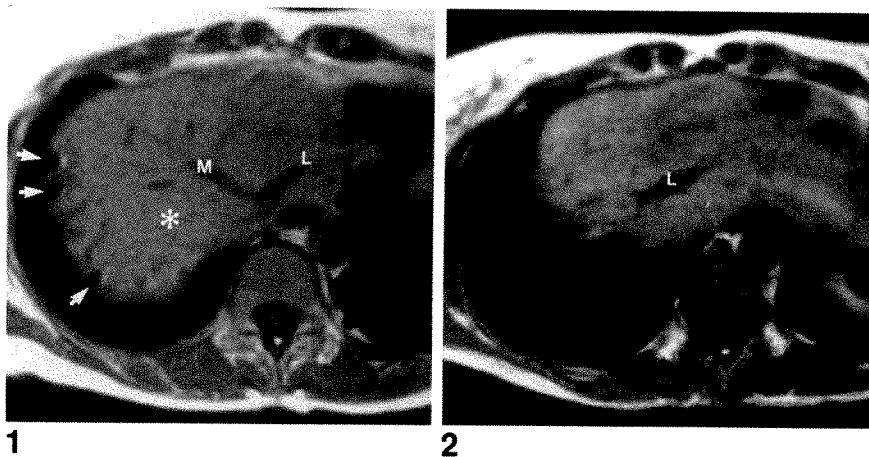


Fig. 1.—Right lobectomy. T1-weighted image (SE 500/30) shows middle (M) and left (L) hepatic veins. A large amount of hepatic tissue (asterisk) is between middle hepatic vein and resection margin, where artifacts caused by surgical clips (arrows) are identified.

Fig. 2.—Trisegmentectomy. T1-weighted image (SE 500/30) shows left hepatic vein (L) only.

Fig. 3.—Left lobectomy. First echo of T2-weighted sequence (SE 2000/30) shows right (R) and middle (M) hepatic veins. Middle hepatic vein is adjacent to resection margin, where artifacts caused by surgical clips (curved arrow) are identified. Small hepatic cyst (straight arrows).

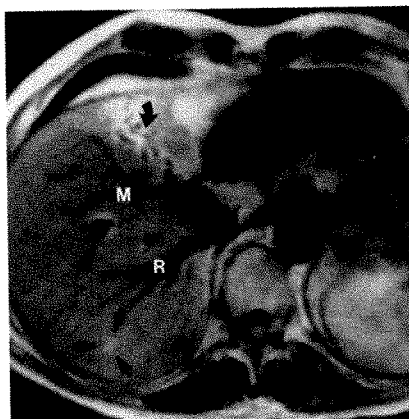


Fig. 4.—Left lobectomy. T1-weighted image (SE 500/30) shows right (R) and middle (M) hepatic veins. Large amount of hepatic tissue (asterisk) between middle hepatic vein and resection margin was misinterpreted as medial segment of left lobe.

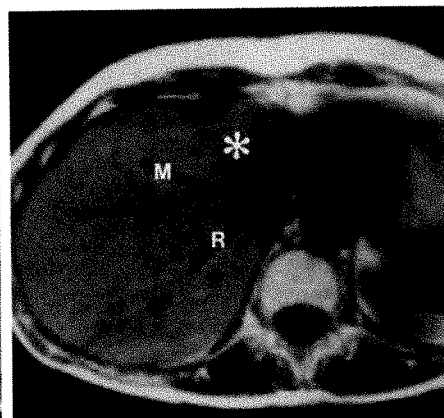


TABLE 1: MR Identification of Anatomic Landmarks and Clips after Partial Hepatectomy

Operation	No. of Patients (n = 25)	MR Identification				
		Right Hepatic Vein	Middle Hepatic Vein	Left Hepatic Vein	Falciform Ligament	Clip
Right lobectomy	11 ^a	0/0	10/11	11/11	10/11	11/11
Trisegmentectomy	2	0/0	0/0	2/2	0/0	2/2
Left lobectomy	5	5/5	5/5	0/0	0/0	5/5
Wedge resection	7 ^a	7/7	7/7	7/7	6/7	5/7

^a Two patients had both right lobectomy and wedge resection of the left lobe. In addition to the findings related to the right lobectomy, MR identified intrahepatic clips.

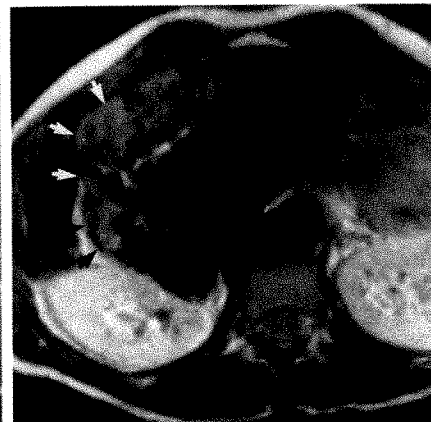
Fig. 5.—Trisegmentectomy. MR examination 2 months after surgery.

A, T1-weighted image (SE 500/30) shows transverse elongated shape of regenerating lateral segment of left lobe. Small, low-intensity area (arrows) is seen.

B, T2-weighted image (SE 2000/60) shows poorly defined areas of slightly higher signal intensity (arrows) than seen in remaining liver. These proved at subsequent surgery to represent scar tissue and regenerative changes in the liver.



A



B

the lateral segment of the left lobe ($n = 6$) or a rounded shape (transverse dimension less than twice the anteroposterior dimension) when regeneration affected both lateral and medial segments of the left lobe ($n = 5$). After trisegmentectomy, enlargement of the lateral segment of the left lobe assumed a transverse elongated shape (Fig. 5). After right lobectomy or trisegmentectomy, the caudate lobe was enlarged in eight of 13 patients, as shown by an increase in the parenchyma between the portal vein and the inferior vena cava. After left lobectomy, regeneration was shown as an enlarged, rounded shape of the residual right lobe; no hypertrophy of the caudate

lobe was observed. After wedge resection of the liver, neither the wedge defect nor the regeneration of bordering parenchyma was shown clearly.

Additional MR Findings

In patients imaged early after surgery, MR showed small right pleural effusions ($n = 3$), small abdominal fluid collections ($n = 3$), areas of perihepatic fat inhomogeneity ($n = 2$), bile lakes ($n = 2$), and a large biloma. This last was percutaneously evacuated. None of the other patients required specific treat-

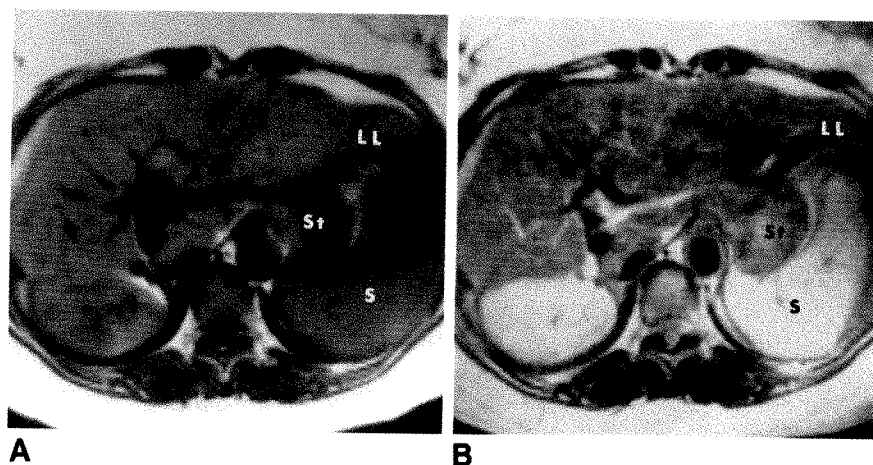


Fig. 6.—Right lobectomy.
A and B, T1-weighted (SE 500/30) (A) and T2-weighted (SE 2000/60) (B) images show transverse elongated shape of regenerating left lobe. Differentiation between lateral segment of left lobe (LL) and spleen (S) is best studied on T2-weighted images. St = stomach.

ment, and serial MR examinations showed spontaneous regression of the above findings.

In two of the eight patients who received chemotherapy, no abnormal finding was demonstrated with MR imaging. Among the remaining six patients, periportal changes showed in three, liver inhomogeneity in two, and both abnormalities in one. Periportal changes appeared as poorly defined areas of abnormal signal intensity localized along both sides of the portal vein and its branches (Figs. 7A and 7B). Their signal intensity was lower than that of remaining liver on T1-weighted images and higher on T2-weighted images. In one patient, subsequent surgery revealed inflammation and arterial intimal proliferation in the porta hepatis. Two of the three other patients had serial MR examinations that showed disappearance of periportal abnormalities after completion of chemotherapy (Figs. 7C and 7D). Liver inhomogeneities were detected only on T2-weighted images, where they appeared as poorly defined regions of signal intensity higher than that of remaining liver (Figs. 7D and 7E). Neither periportal changes nor hepatic inhomogeneity was observed in patients not undergoing chemotherapy.

MR showed tumor recurrence in nine patients. Tumor recurrence was accurately detected regardless of its location (in two patients at the resection margin adjacent to surgical clips and in the remaining patients throughout the liver). The MR findings were confirmed by biopsy ($n = 5$) or MR follow-up ($n = 4$). One false-positive diagnosis of tumor recurrence was made by MR in a patient in whom MR scans showed liver lesions of low signal intensity on T1-weighted and of high signal intensity on T2-weighted images; these lesions proved at surgery to represent duct ectasia with chronic inflammation of the liver.

Discussion

Partial hepatectomy can be performed along an interlobar or intersegmental plane, or a wedge can be resected that does not follow the anatomic division [9]. There are four surgical approaches to controlled excision: right and left lobectomy, trisegmentectomy (removal of the right lobe plus the medial segment of the left lobe), and lateral segmentec-

tomy (removal of the lateral segment of the left lobe) [1, 2]. Chemotherapy can be administered either before surgery, for reduction of tumor volume, or after surgery, in the case of recurrence [10].

In our study, the type of partial hepatectomy was recognized in 21 of the 25 patients. Right lobectomy was characterized by the absence of the right hepatic vein, left lobectomy by the absence of the left hepatic vein and falciform ligament, and trisegmentectomy by the absence of the right and middle hepatic veins and the falciform ligament. After right or left lobectomy, the amount of hepatic tissue between the middle hepatic vein and the resection margin varied depending on the surgical technique, the pattern of hepatic regeneration, and the degree of liver rotation associated with regeneration. A moderate enlargement of the remaining left portal vein was noted after right lobectomy and trisegmentectomy. In canine studies [11], dilatation of intrahepatic portal vein branches, as well as temporary portal hypertension, have been reported after hepatic resection.

A small fluid collection at the resection margin in the first weeks and scar and regeneration tissue in the first months after surgery may be shown as a high-signal-intensity resection margin. This pattern is rare and was observed in only two of the 18 early MR examinations. However, when the resection margin is of high signal intensity on MR images, the differentiation between residual tumor and postsurgical changes is not possible. In the other cases, the resection margin was either of the same signal intensity as the rest of the liver or of low signal intensity in the presence of surgical clips. A small region of low attenuation at the surgical margin has been described by CT [6, 8]. The MR intensity of the artifacts due to surgical clips probably varied in relation to the nature and degree of ferromagnetism of the clip. However, the liver anatomy was never obscured.

Most hepatic regeneration was observed within the first 6 months after surgery. These results agree with those obtained with CT by Nagasue et al. [5]. However, in our study, some hepatic regeneration persisted more than 1 year postoperatively. Although it is known that the ability of the liver to regenerate is seriously compromised and can be slower in cirrhosis of the liver [5], none of our patients had cirrhosis.

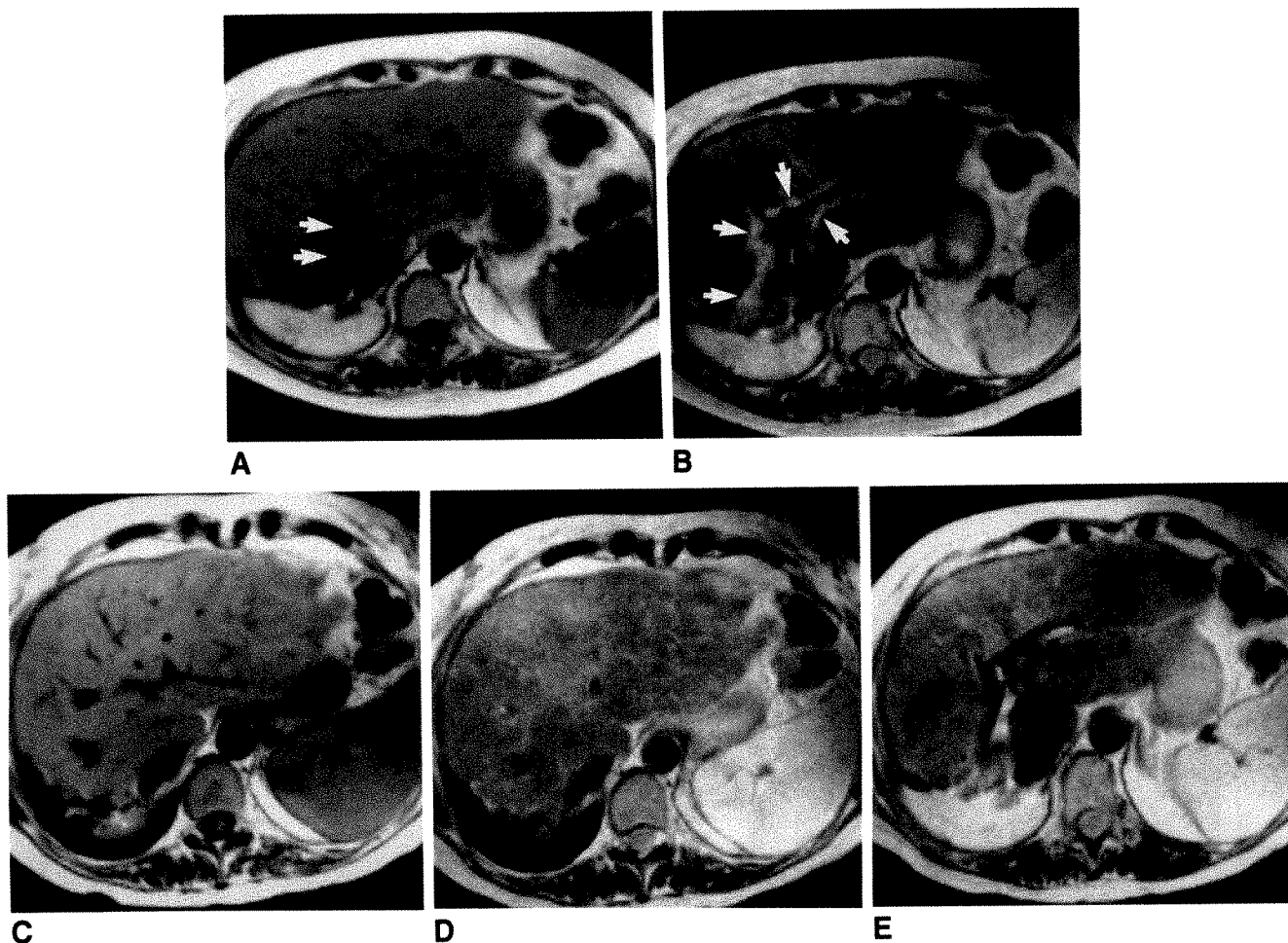


Fig. 7.—Hepatic changes related to chemotherapy. A and B, T1-weighted (SE 500/30) (A) and T2-weighted (SE 2000/60) (B) images during chemotherapy 16 months after right lobectomy show areas of low signal intensity on T1- and high signal intensity on T2-weighted images (arrows) localized along left portal vein. C and D, T1-weighted (SE 500/30) (C) and T2-weighted (SE 2000/60) (D) at upper level. Diffuse hepatic inhomogeneity is observed. E, T2-weighted (SE 2000/60) image at level of portal vein, 6 months after completion of chemotherapy, shows disappearance of periportal abnormalities.

With MR imaging, the signal intensity of the regenerating liver was similar to that of the normal liver. In vitro, Pizzarello et al. [12] found no change in T2 and only a slight increase in T1 relaxation time in rat livers after partial hepatectomy [12].

Periportal abnormalities were observed in four patients, all of whom had received chemotherapy. Symmetric distribution along the portal vessels and disappearance of these abnormalities after completion of chemotherapy allow differentiation from metastases that may involve the periportal area but that are usually more localized, asymmetric, and often well defined [13]. Such periportal abnormalities have been described with CT under various circumstances (liver transplant rejection, viral hepatitis, infectious cholangitis) and have been attributed to lymphocytic portal infiltration or periportal hepatocyte necrosis [14]. Infiltration of the periportal area by proliferating connective tissue, periportal edema secondary to vascular endothelial damage, and periportal hepatocytic necrosis have been described during chemotherapy of the liver without evidence of recurrent disease [15, 16]. Such lesions in the

porta hepatis were found at surgery in one patient with periportal abnormalities and probably explain the abnormalities seen on MR imaging.

Diffuse inhomogeneities of the hepatic parenchyma were seen in three patients who had chemotherapy. Heterogeneous intrahepatic areas have been described with CT after chemotherapy and characterized as perfusion abnormalities resulting from vascular damage due to chemotherapy [17]. Fatty changes also have been described as a consequence of hepatic chemotherapy [18]. With MR imaging, these non-tumoral areas of inhomogeneity appeared as irregularly demarcated regions that contrasted with the remaining normal liver, as opposed to tumor recurrence, which appeared as localized, more sharply demarcated regions of high signal intensity on T2-weighted images. In our series, the MR appearance of tumor recurrence after partial hepatectomy was not different from that of the primary tumor.

MR and CT were not compared in this study. In our institution, follow-up of patients after partial hepatectomy is

performed with either MR or CT, and the only cases in which both were available were those in which CT was nondiagnostic because surgical clips had produced artifacts that obscured the liver. This would have introduced an obvious bias in any comparison.

In conclusion, in patients with partial hepatectomy, the ability of MR to produce images without the artifacts of surgical clips is helpful in displaying the appearance of the liver and determining the type of partial hepatectomy. Chemotherapy-related changes are demonstrated well and tumor recurrence can be detected accurately, particularly at the resection margin, without the artifacts of surgical clips. Therefore, we believe that MR imaging is well suited for the follow-up of patients with partial hepatectomy.

ACKNOWLEDGMENT

This work is dedicated to Jo Wheeler, whose friendship and guidance have helped us learn what research is all about.

REFERENCES

1. Starzl TE, Bell RH, Beart RW, Putnam CW. Hepatic trisegmentectomy and other liver resections. *Surg Gynecol Obstet* 1975;141:429-437
2. Blumgart LH. Hepatic resection. In: Dudley H, ed. *Rob & Smith's operative surgery*. London: Butterworths, 1983:477-499
3. Sugarbaker PH, Gianola FJ, Dwyer A, Neuman NR. A simplified plan for follow-up of patients with colon and rectal cancer supported by prospective studies of laboratory and radiologic test results. *Surgery* 1987;102:79-87
4. Couanet D, Shirkhoda A, Wallace S. Computed tomography after partial hepatectomy. *J Comput Assist Tomogr* 1984;8:453-457
5. Nagasue N, Yukaya H, Ogawa Y, Kohno H, Nakamura T. Human liver regeneration after major hepatic resection. A study of normal liver and livers with chronic hepatitis and cirrhosis. *Ann Surg* 1987;206:30-39
6. Letourneau JG, Steely JW, Crass JR, Goldberg ME, Grage T, Day DL. Upper abdomen: CT findings following partial hepatectomy. *Radiology* 1988;166:139-141
7. Quinn SF, Bodne DJ, Clark RA, Karl RC, Nicosia SV. Upper abdomen: CT findings following partial hepatectomy. *Radiology* 1988;168:879-880
8. Fisher MR, Wall SD, Hricak H, McCarthy S, Kerlan RK. Hepatic vascular anatomy on magnetic resonance imaging. *AJR* 1985;144:739-746
9. Goldsmith NA, Woodburne RT. The surgical anatomy pertaining to liver resection. *Surg Gynecol Obstet* 1957;105:310-318
10. Lotze MT. Surgical management of hepatocellular carcinoma. *Gastroenterol Clin North Am* 1987;16:613-626
11. Enge I. Liver regeneration after surgical resection. In: Herlinger H, Lunderquist A, Wallace S, eds. *Clinical radiology of the liver*, part A. New York: Marcel Dekker, 1983:123-139
12. Pizzarello DJ, Chandra R. Effects of mitotic activity and water content on the proton relaxation times in partially hepatectomized and sham-operated rat livers. *Invest Radiol* 1986;21:320-324
13. Baker ME, Silverman PM, Halvorsen RA Jr, Cohan RH. Computed tomography of masses in periportal/hepatoduodenal ligament. *J Comput Assist Tomogr* 1987;11:258-263
14. Wechsler RJ, Munoz SJ, Needleman L, et al. The periportal collar: a CT sign of liver transplant rejection. *Radiology* 1987;165:57-60
15. Herrmann G, Lorenz M, Kirkowa-Reimann M, Hottenrott C, Hübner K. Morphological changes after intra-arterial chemotherapy of the liver. *Hepatogastroenterology* 1987;34:5-9
16. Vaage J. Local and systemic effects during interleukin-2 therapy of mouse mammary tumors. *Cancer Res* 1987;47:4296-4298
17. Merine D, Fishman EK, Sitzmann JV, et al. Vascular abnormalities following radio- and chemotherapy of hepatic neoplasms: CT angiographic findings. *J Comput Assist Tomogr* 1988;12:584-587
18. Keeling PWN, Thompson RPH. Drug-induced liver disease. *Br Med J* 1979;1:990-993

Giant Cavernous Hemangioma of the Liver: CT and MR Imaging in 10 Cases

Byung Ihn Choi¹
 Man Chung Han
 Jae Hyung Park
 Seung Hyup Kim
 Moon Hee Han
 Chu-Wan Kim

Ten giant cavernous hemangiomas of the liver in eight patients were examined with both MR imaging and dynamic bolus CT. The maximal diameters of the tumors were 6.5–19 cm (mean, 10.8 cm). MR imaging was done with a 2.0-T superconducting magnet and spin-echo imaging. CT was done with single-bolus dynamic scans. On MR images, all 10 hemangiomas had a heterogeneous appearance. The main part of the tumor comprised uniform, well-defined, high-intensity areas on T2-weighted images, with increasing intensity ratios with prolongation of TR and TE. Other parts of the tumor were cleftlike and were of lower intensity than the remainder of the tumor on T1-weighted images and of higher intensity on heavily T2-weighted images. These parts corresponded to the areas of the tumor that were of lower density on dynamic bolus CT scans. Internal septa in the tumor of low intensity were also noted on all MR pulse sequences. These parts corresponded to low-density areas on delayed contrast-enhanced CT.

Familiarity with the characteristics of the internal architecture of giant cavernous hemangiomas on MR imaging or dynamic bolus CT might be useful in making the correct diagnosis of this tumor.

In contrast to small, incidentally discovered hemangiomas, giant cavernous hemangiomas of the liver are less common, more likely to produce symptoms [1, 2], and more often confused with primary or metastatic malignancy [3]. Definitive, noninvasive imaging of giant cavernous hemangioma is important to avoid angiography, biopsy, or exploratory laparotomy.

Dynamic CT has been considered a good imaging technique for evaluation of hemangioma. However, a review of previous reports [4–9] reveals that CT features of hemangiomas include a broad spectrum of morphologic patterns, thus raising questions about the specificity of the CT diagnosis.

Recently, the usefulness of MR imaging in identifying cavernous hemangiomas of the liver has been discussed [10–14]. These reports mainly describe MR findings of small hemangiomas. The MR findings in giant cavernous hemangiomas have not been documented. In this study, we describe the characteristics of giant hemangiomas on MR images and compare these characteristics with those noted on dynamic bolus CT scans.

Materials and Methods

During a 2-year period, 10 giant cavernous hemangiomas in eight patients were studied by MR imaging and dynamic bolus CT. A giant hemangioma was defined as one in which at least one dimension of the tumor exceeded 6 cm. The series included six women and two men (age range, 38–51 years; mean, 45). The diagnosis of giant cavernous hemangioma had been established previously by angiography in six patients and/or unchanging sonographic or CT findings over 1–4 years in two patients. Seven patients had right upper abdominal pain or epigastric discomfort. Three patients had a palpable upper abdominal mass. In one patient, the hemangioma was found incidentally on sonography. Liver function studies were normal

Received December 13, 1988; accepted after revision January 25, 1989.

This work was supported in part by the Special Fund of the Radiological Research Foundation of Korea (1989).

¹ All authors: Department of Radiology, College of Medicine, Seoul National University, 28, Yeongun-Dong, Chongro-Ku, Seoul 110-744, Korea. Address reprint requests to B. I. Choi.

AJR 152:1221–1226, June 1989
 0361–803X/89/1526–1221
 © American Roentgen Ray Society

in all eight patients. The giant hemangiomas were 6.5–19 cm (mean, 10.8 cm) in the largest diameter. Seven tumors were located in the right lobe, two in the left lobe, and one in the caudate lobe.

MR spin-echo (SE) images were obtained by using a superconducting Spectro-20000 (Goldstar, Seoul, Korea) operated at 2.0 T. Images were constructed by using two-dimensional Fourier transform technique. A body coil with a field of view of 35 cm was used. The image matrix of 180×256 elements yielded an in-plane spatial resolution of 1.9×1.4 mm. Two or four data acquisitions were averaged for each image. A multisection/multiecho technique was used to make axial sections with a section thickness of 8 mm and intersection gap of 2 mm. Relatively T1-weighted images, 500/30 (TR/TE), were obtained, as were T2-weighted images, 2000/60, 120, 150, 180 (TR/TE). Neither respiratory nor ECG gating was used.

CT scans were obtained by using a CT 9800 scanner (General Electric, Milwaukee, WI) with a scan speed of 2 sec. In all eight patients, single-level bolus dynamic scans were obtained. Nonenhanced CT scans of the liver were obtained at 10-mm intervals to localize the lesions. Single-level bolus dynamic CT scans were then obtained at the level that contained the largest lesion. Contrast-enhanced CT scans of the liver were obtained after IV bolus injection of 60 ml of 60% iodinated contrast agent (Telebrix 30, Guerbet, Aulnay-Sous-Bois, France). The contrast agent was injected by hand over a period of 15 sec by using a butterfly needle placed in a peripheral vein. Scans at the preselected level were then acquired at 5 sec, 15 sec, 30 sec, 1 min, 2 min, 3 min, 5 min, 10 min, and 15 min after the end of the injection. Delayed scans were obtained until no further increase in lesion attenuation or degree of filling was discernible on serial delayed scans.

MR images and dynamic bolus CT scans were interpreted at the same time for each patient, with emphasis on comparing the MR images and CT scans for evaluation of the internal architecture of the tumor. For analysis of MR imaging, visual estimates of the intensity of the hemangioma were made as follows: low intensity (intensity lower than that of surrounding liver), isointensity (intensity equal to that of surrounding liver), high intensity (intensity higher than that of surrounding liver), and very high intensity (intensity higher than that of fat). In addition, measurements of the ratio of intensity between tumor and surrounding liver were obtained. A region of interest was circumscribed with a cursor on the displayed image. When possible, all intensity measurements were made with the same x coordinate (i.e., same y axis) to minimize artifacts. Intensity was recorded in absolute numbers (mean intensity value). Intensity ratios of hemangiomas to surrounding liver were calculated for all pulse sequences. Dynamic CT scans were reviewed to determine the size, location, and appearance of the hemangiomas on nonenhanced CT scans, as well as changes that occurred after bolus contrast enhancement.

Results

MR Imaging

All 10 hemangiomas had a heterogeneous appearance on T1- and T2-weighted images. All of the tumors comprised a main tumor with cleftlike areas. Five also had internal septa.

On T1-weighted MR images, the main part of the tumor was of high intensity in two cases (Fig. 1A), isointensity in four cases (Fig. 2A), and low intensity in four cases. The intensity ratio of the main part of the tumor was 0.90 ± 0.15 . Cleftlike areas were well defined and were of lower intensity than the main tumor. They were round or ovoid in five cases, linear in three, and irregular in two. Internal septa also were of lower intensity than the main tumor and could not be

differentiated from the cleftlike areas. The contours of the internal septa were linear or curvilinear in all five cases.

On T2-weighted MR images, the main part of the tumor was of high intensity with an increasing intensity ratio with prolongation of TR and TE in all 10 cases (Fig. 2B). On heavily T2-weighted images, 2000/120, seven of 10 tumors were of higher intensity than fat (Fig. 2C), while all 10 tumors were of higher intensity on SE 2000/150, 180 images (Figs. 1B and 2D). Intensity ratios of the main tumor were 3.00 ± 1.02 (SE 2000/60), 7.13 ± 2.55 (SE 2000/120), 11.67 ± 3.91 (SE 2000/150), and 12.71 ± 3.31 (SE 2000/180). Cleftlike areas were of high intensity on T2-weighted images, 2000/60, in all 10 cases and could not be differentiated from the main part of the tumor. However, on heavily T2-weighted images, 2000/150, 180, cleftlike areas showed higher intensity than the main tumor did, and the two could be differentiated from each other in all 10 cases (Figs. 1B and 2D). Internal septa had low intensity on all T2-weighted images (Figs. 2B–2D) and could be differentiated from cleftlike areas, which showed high intensity in all five cases.

Dynamic Bolus CT

On nonenhanced CT scans, all 10 giant hemangiomas showed low-density areas compared with surrounding liver, and all tumors contained cleftlike areas of lower density than the main tumor. The attenuation number of the cleftlike areas varied from +8 to +29 H. The cleftlike areas were round or ovoid in five cases (Fig. 1C), linear in three, and irregular in two (Fig. 2E). Spotty calcification was seen in the tumor in one case.

On dynamic, contrast-enhanced scans, contrast enhancement at the periphery of the tumor was visible in every patient. Delayed imaging at the preselected reference levels showed further centripetal enhancement in each of the tumors (Figs. 1D and 2F). However, complete filling of the tumor with contrast material was never observed. The cleftlike areas of lower density did not enhance completely on delayed scans (Figs. 1D and 2H). The time interval from the end of injection to maximal observed filling was 10–120 min (mean, 32).

Comparison of MR Images and Dynamic Bolus CT Scans

MR imaging was equal to dynamic bolus CT in delineating the extent of the tumor and in diagnosing giant hemangiomas. However, MR imaging was superior to dynamic bolus CT in characterizing the internal architecture. Cleftlike areas of lower density on dynamic bolus CT scans corresponded to the areas of lower intensity on T1-weighted images and of higher intensity on heavily T2-weighted images (Fig. 1) in all 10 cases. Low-density areas of the tumor showing the most recent enhancement on delayed dynamic CT scans corresponded to low-intensity areas on T1- and T2-weighted images that were thick internal septa of giant hemangiomas (Figs. 2A, 2D, 2G, and 2H) in three cases. However, dynamic bolus CT scans could not disclose fine internal septa of giant hemangiomas that were visualized clearly on MR images in five cases.

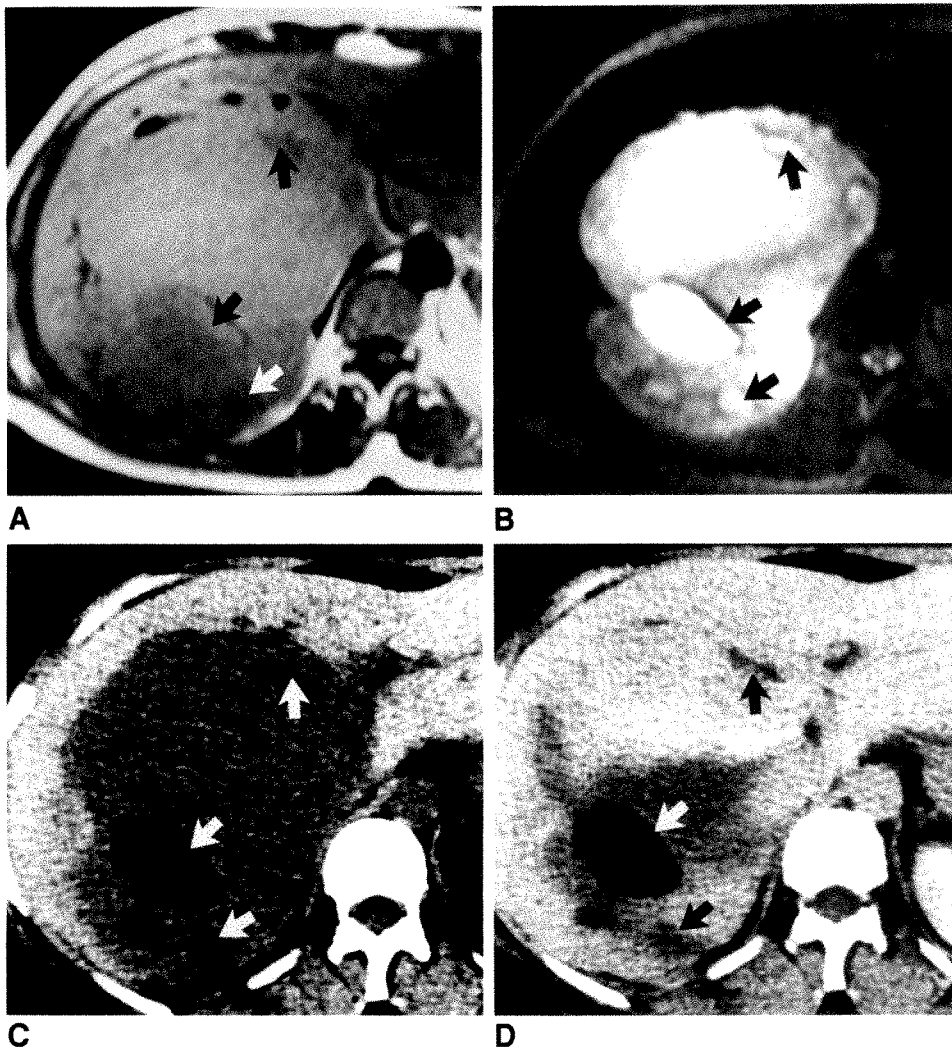
Fig. 1.—Giant cavernous hemangioma of liver in 41-year-old woman with indigestion.

A, Axial SE 500/30 MR image shows main part of tumor with slightly high intensity in entire right hepatic lobe. Lower-intensity areas (arrows) are seen in tumor.

B, Axial SE 2000/180 MR image shows heterogeneous appearance of tumor with smooth, well-defined margin. Main part of tumor shows very high intensity. Round and ovoid cleftlike areas (arrows) show higher intensity than main part does.

C, Nonenhanced CT scan shows ovoid tumor with low attenuation in right hepatic lobe. Cleftlike areas of lower attenuation (arrows) are seen also.

D, Delayed CT scan 15 min after injection of contrast material shows nearly complete filling of tumor. Cleftlike areas (arrows), which are not enhanced, correspond to cleftlike, low-intensity areas in tumor on T1-weighted MR image and higher-intensity areas in tumor on heavily T2-weighted image.



Discussion

Although hemangiomas are the most common benign tumors of the liver, giant hemangiomas with clinical manifestations are rare. Because of the relative infrequency of large symptomatic hepatic hemangiomas, few reports have appeared in the radiologic literature [15, 16]. The definition of giant hemangiomas is still uncertain. Edmondson and Peters [17] described giant hemangiomas as tumors more than 10 or 12 cm in greatest dimension. Adam et al. [18] defined them as tumors measuring more than 4 cm in diameter, because no symptomatic tumor was encountered that was smaller than this. However, all 22 tumors in the series of Adam et al. exceeded 6 cm in at least one dimension. Thus, we defined giant hemangiomas as tumors that exceeded 6 cm in at least one dimension.

In our series, all 10 hemangiomas showed heterogeneous intensity on T1- and T2-weighted MR images. The larger the tumor, the more diverse were the internal components of the tumor. Giant hemangiomas have a spectrum of histopathologic changes, including hemorrhage, thrombosis, extensive

hyalinization, liquefaction, and fibrosis [2, 4, 14, 16, 19]. These features cause a heterogeneous appearance of the tumor on MR imaging. Stark et al. [11] reported that none of the hemangiomas in their series had heterogeneity on T1-weighted images. In our series, however, all hemangiomas had a heterogeneous appearance on T1-weighted images as well as on T2-weighted images. Ros et al. [14] also reported that 80% of hemangiomas in their series were inhomogeneous on T2-weighted images and all hemangiomas were inhomogeneous on cut sections of pathologic specimens.

The characteristic appearance of cavernous hemangiomas on CT scans after bolus contrast enhancement has been reported previously [4–9]. However, controversy still exists concerning which CT criteria must be met for reliable diagnosis of a hemangioma. The 10 giant hemangiomas we report behaved similarly on dynamic CT scans. All tumors showed low-density areas on nonenhanced CT scans, and each contained one or more cleftlike zones of lower density. All tumors displayed early, peripheral enhancement and some degree of centripetal filling. However, none became completely isodense on delayed scans. Because of this, none of our patients

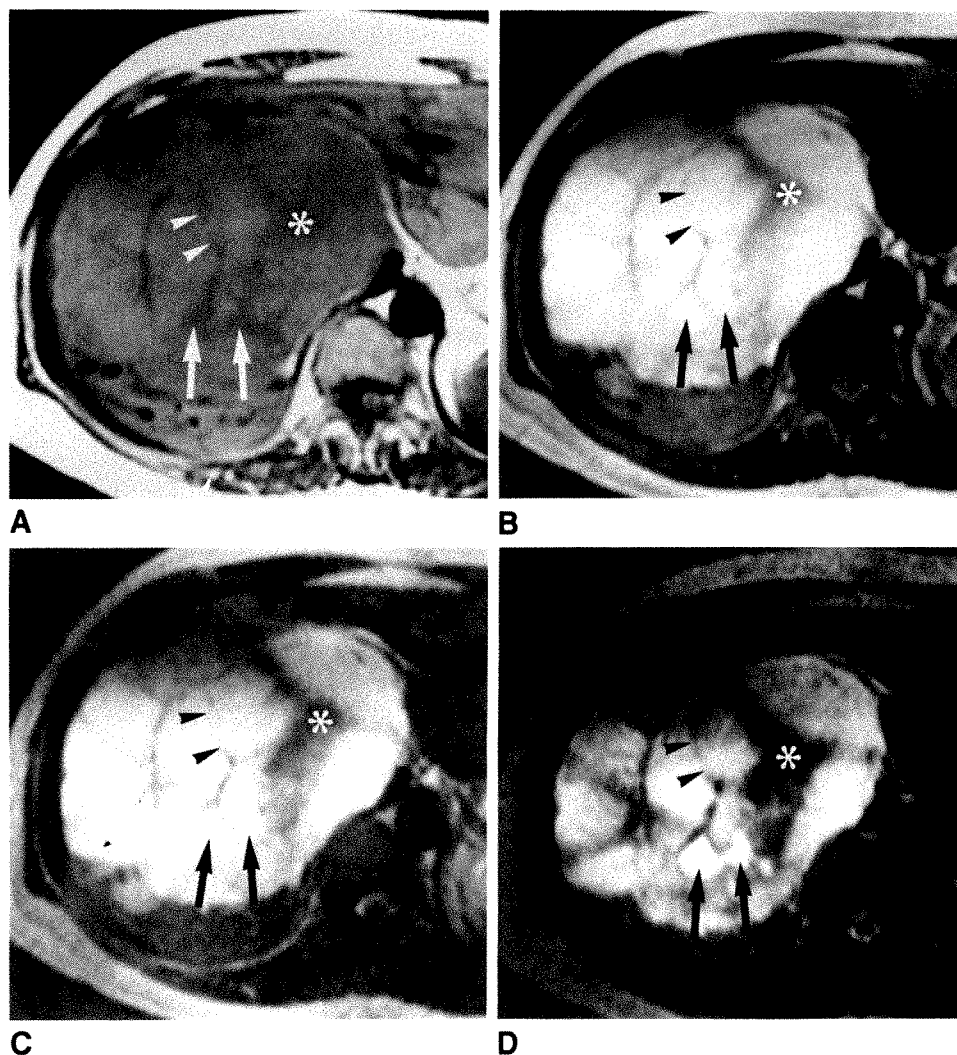


Fig. 2.—Giant cavernous hemangioma of liver in 43-year-old woman with epigastric discomfort. Axial MR images (A–D) are on this page; postcontrast CT findings (E–H) are on facing page.

A, SE 500/30 image shows main part of tumor to be isointense in entire right hepatic lobe. Lower-intensity areas (arrows, arrowheads, asterisk) are seen in tumor.

B, SE 2000/60 image shows heterogeneous appearance of tumor with well-defined, lobulated margins. Irregular cleftlike areas (arrows) are of high intensity. Thin (arrowheads) and thick (asterisk) septa are of low intensity.

C, SE 2000/120 image shows very high intensity of main part of tumor and irregular cleftlike areas (arrows). Internal septa (arrowheads, asterisk) still show low intensity.

D, SE 2000/180 image shows three different parts of hemangioma: main part of tumor, cleftlike part (arrows), and internal septa (arrowheads, asterisk).

had tumors that fulfilled the criteria used by Freeny and Marks [8] for a typical hemangioma. However, all would have been acceptable under the conditions proposed by Ashida et al. [9]. Our results are similar to those reported by Scatarige et al. [15].

The cleftlike areas of hemangiomas noted on MR images or CT scans may be due to areas of cystic degeneration or liquefaction, rather than fibrosis, thrombosis, or hemorrhage, as was postulated by several authors [4, 15]. The reason for this is because the attenuation numbers of the cleftlike areas in all cases were less than +30 H, all of the cleftlike areas did not show contrast enhancement on delayed scans, and the cleftlike areas with lower density on dynamic bolus CT scans corresponded to the areas with lower intensity than the main part of the tumor on T1-weighted images and with higher intensity than the main part on heavily T2-weighted images. Takayasu et al. [19] also reported one case of giant hemangioma of the liver with a central cavity that contained transparent serous fluid. Ros et al. [14] reported that some hemangiomas contained cystic cavities filled with gelatinous material on pathologic examination. The areas of internal

septa of hemangiomas could be explained as poorly cellular fibrous tissue. The areas of internal septa were of low intensity on MR images on all pulse sequences. Fibrosis decreases the water content and shows low intensity. The low-density areas of hemangiomas with the most recent enhancement on delayed scans corresponded exactly to the areas of low intensity on MR images. On the basis of an MR-pathologic correlation in three resected hemangiomas, Ros et al. [14] reported that nodular areas and septations of decreased intensity within a hyperintense tumor on T2-weighted images corresponded to fibrotic nodular areas and fibrotic strands, respectively. Muramatsu et al. [20] described the CT-pathologic correlation of the fibrotic part of a hepatic tumor. On late-enhancing CT scans obtained more than 5 min after administration of contrast material, the fibrotic part showed contrast enhancement because fibrous stromas retained contrast material longer than tumor tissue did. However, on CT scans in the early phase after a bolus administration of contrast material, it was difficult to differentiate tumor tissue from fibrotic connective tissue. Further studies with histologic correlation are needed because none of the hemangiomas in

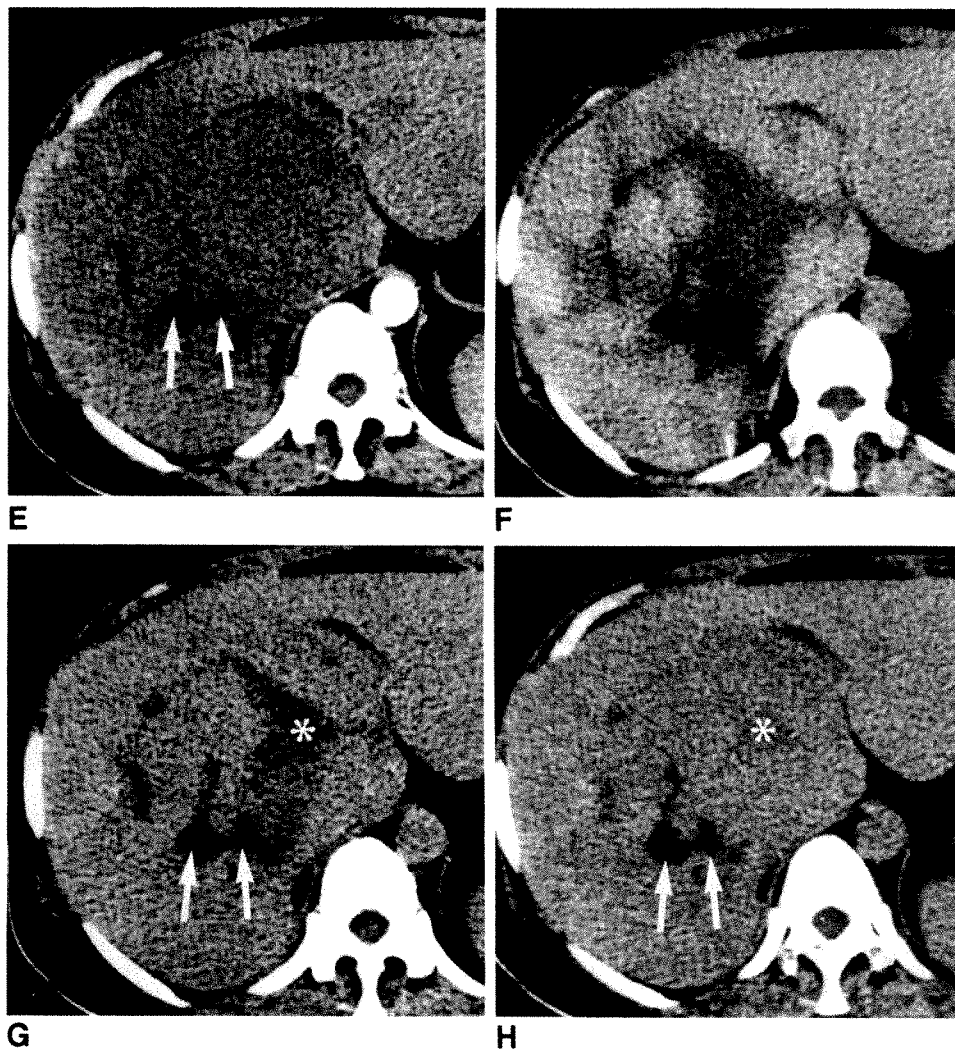
Fig. 2.—E–H, Postcontrast CT scans.

E, 5 sec after bolus injection of contrast material. Large, ovoid tumor with low attenuation is seen in right hepatic lobe. Cleftlike areas of lower attenuation (arrows) are seen also.

F, 15 min after injection. Peripheral contrast enhancement is seen.

G, Delayed scan 30 min after injection shows isodense filling that spares cleftlike areas (arrows) and central part (asterisk), which correspond to central low-intensity zone on MR images. However, delineation of fine internal septa, which are visualized clearly on MR images, is poor.

H, Delayed scan 50 min after injection shows nearly complete filling of mass except for cleftlike areas (arrows), which are not enhanced, and central zone (asterisk), which shows late enhancement.



our series were surgically resected and available for pathologic study.

Giant cavernous hemangiomas have a heterogeneous appearance on MR images. Therefore, there is sometimes confusion between giant hemangiomas and malignant tumors. Necrotic metastatic tumor and hepatoma are included in the differential diagnosis of giant hemangiomas [11]. The characteristic MR findings of giant hemangiomas, such as well-defined, high-intensity areas on T2-weighted images with increasing intensity ratios with prolongation of TR and TE, are useful in differentiating these tumors from necrotic metastases or hepatomas. In addition, focal hemorrhagic necrotic areas with high intensity on T1-weighted images [11, 21] and the presence of a capsule, target, or halo sign [21–24], which are encountered often in hepatomas or metastases, are not seen in hemangiomas.

In summary, we believe that careful evaluation of the internal architecture of giant hemangiomas with MR imaging or dynamic bolus CT makes it possible to facilitate the correct diagnosis in these tumors. The diagnosis of giant cavernous hemangioma should be considered when MR images show

large, well-defined, heterogeneous masses that contain areas with an increasing intensity ratio with prolongation of TR and TE, cleftlike areas of low intensity on T1-weighted images and of higher intensity on heavily T2-weighted images, and low-intensity internal septa on all pulse sequences.

ACKNOWLEDGMENTS

We thank Z. H. Cho and H. W. Park for assistance in manuscript preparation.

REFERENCES

1. Ishak KG, Rabin L. Benign tumors of the liver. *Med Clin North Am* 1975;59:995–1013
2. Ishak KG. Mesenchymal tumors of the liver. In: Okuda K, Peters RL, eds. *Hepatocellular carcinoma*. New York: Wiley, 1976:275–286
3. Cronan JJ, Esparza AR, Dorfman GS, Ridlen MS, Paoletta LP. Cavernous hemangioma of the liver: role of percutaneous biopsy. *Radiology* 1988; 166:135–138
4. Johnson CM, Sheedy PF, Stanson AW, et al. Computed tomography and angiography of cavernous hemangiomas of the liver. *Radiology* 1981; 138:115–121
5. Itai Y, Ohtomo K, Araki T, Furui S, Iio M, Atomi Y. Computed tomography

- and sonography of cavernous hemangioma of the liver. *AJR* **1983**;141:315-320
6. Itai Y, Furui S, Araki T, Yashiro N, Tasaka A. Computed tomography of cavernous hemangioma of the liver. *Radiology* **1980**;137:149-155
 7. Freeny PC, Vimont TR, Barnett DC. Cavernous hemangioma of the liver: ultrasonography, arteriography, and computed tomography. *Radiology* **1979**;132:143-148
 8. Freeny PC, Marks WM. Hepatic hemangioma: dynamic bolus CT. *AJR* **1986**;147:711-719
 9. Ashida C, Fishman EK, Zerhouni EA, Herlong FH, Siegelman SS. Computed tomography of hepatic cavernous hemangioma. *J Comput Assist Tomogr* **1987**;11:455-460
 10. Glazer GM, Aisen AM, Francis IR, Gyves JW, Lande I, Alder DD. Hepatic cavernous hemangioma: magnetic resonance imaging. *Radiology* **1985**;155:417-420
 11. Stark DD, Felder RC, Wittenberg J, et al. Magnetic resonance imaging of cavernous hemangioma of the liver: tissue specific characterization. *AJR* **1985**;145:213-222
 12. Itai Y, Ohtomo K, Furui S, Yamauchi T, Minami M, Yashiro N. Noninvasive diagnosis of small cavernous hemangioma of the liver: advantage of MRI. *AJR* **1985**;145:1195-1199
 13. Ohtomo K, Itai Y, Furui S, Yashiro N, Yoshikawa K, Iio M. Hepatic tumors: differentiation by transverse relaxation time (T2) of magnetic resonance imaging. *Radiology* **1985**;155:421-423
 14. Ros PR, Lubbers PR, Olmsted WW, Morillo G. Hemangioma of the liver: heterogeneous appearance on T2-weighted images. *AJR* **1987**;149:1167-1170
 15. Scatarige JC, Kenny JM, Fishman EK, Herlong FH, Siegelman SS. CT of giant cavernous hemangioma. *AJR* **1987**;149:83-85
 16. Olmsted WW, Stocker JT. Cavernous hemangioma of the liver. *Radiology* **1975**;117:59-62
 17. Edmondson HA, Peters RL. Neoplasms of the liver. In: Schiff L, Schiff ET, eds. *Diseases of the liver*. Philadelphia: Lippincott, **1982**:1144-1145
 18. Adam YG, Huvos AG, Fortner JG. Giant hemangiomas of the liver. *Ann Surg* **1970**;172:230-245
 19. Takayasu K, Moriyama N, Shima Y, et al. Atypical radiographic findings in hepatic cavernous hemangioma: correlation with histologic features. *AJR* **1986**;146:1149-1153
 20. Muramatsu Y, Takayasu K, Moriyama N, et al. Peripheral low-density area of hepatic tumors: CT-pathologic correlation. *Radiology* **1986**;160:49-52
 21. Wittenberg J, Stark DD, Forman BH, et al. Differentiation of hepatic metastases from hepatic hemangiomas and cysts by using MR imaging. *AJR* **1988**;151:79-84
 22. Ebara M, Ohto M, Watanabe Y, et al. Diagnosis of small hepatocellular carcinoma: correlation of MR imaging and tumor histologic studies. *Radiology* **1986**;159:371-377
 23. Itoh K, Nishimura K, Togashi K, et al. Hepatocellular carcinoma: MR imaging. *Radiology* **1987**;164:21-25
 24. Itai Y, Ohtomo K, Furui S, Minami M, Yoshikawa K, Yashiro N. MR imaging of hepatocellular carcinoma. *J Comput Assist Tomogr* **1986**;10:963-968

Case Report

Pancreatic Plasmacytoma: CT Findings

Todd E. Wilson,¹ Melvyn Korobkin,¹ and Isaac R. Francis²

Extramedullary plasmacytoma is a neoplastic proliferation of plasma cells outside the confines of the osseous system. It typically presents as a solitary plasmacytoma of the paranasal and pharyngeal soft tissues or as a preterminal manifestation of multiple myeloma. The spleen, liver, lymph nodes, and kidney are the most commonly involved sites in cases of advanced multiple myeloma [1].

Plasmacytoma of the pancreas is rare. Only five cases with CT of the pancreatic mass have been described [2-6]. All five showed dilated intrahepatic ducts due to a mass in the head of the pancreas. We did CT scans on three patients with this abnormality, one of whom was the basis of an earlier case report [7]. In these three cases, the CT findings were more varied than previously reported.

Case Report

A 52-year-old woman with a 5-year history of multiple myeloma had a generally progressive clinical course with intermittent periods of remission on various chemotherapeutic regimens. During the fifth year of therapy, local radiation therapy was required to treat a pathologic fracture of the left femur due to a focal plasmacytoma. Several months later, the patient had progressive epigastric pain, nausea, and vomiting refractory to her antiemetic regimen. An upper gastrointestinal series revealed compression of the medial aspect of the first and second portions of the duodenum with widening of the duodenal C-sweep. Unenhanced CT examination confirmed the presence of a 4-cm, homogeneous solid mass in the head of the pancreas (Fig. 1). The mass had a density slightly higher than the rest of the pancreas. No evidence was seen of biliary-tract or pancreatic-duct

dilatation. Percutaneous fine-needle biopsy under sonographic guidance showed atypical plasma cells in a background of benign pancreatic acinar epithelium diagnostic of pancreatic plasmacytoma. After radiation therapy, the gastrointestinal symptoms subsided. A new pelvic mass, which proved to be a separate extramedullary plasmacytoma, developed 5 weeks later.

Discussion

Two additional patients had proved pancreatic plasmacytoma, and both underwent contrast-enhanced CT of the abdomen. In one patient, a homogeneous, 4-cm soft-tissue mass was shown in the tail of the pancreas (Fig. 2). In the other patient, CT showed diffuse enlargement of the entire pancreas (Fig. 3), with dilatation of the bile ducts.

CT scans of pancreatic plasmacytoma have been published in six cases [2-7]. In five of these cases, CT showed dilated bile ducts and a focal mass in the head of the pancreas. Our three cases illustrate a greater variety of imaging features. In one patient, we saw diffuse pancreatic enlargement rather than a focal mass; one patient had a mass in the pancreatic tail; the other patient had a mass in the pancreatic head, but without bile-duct dilatation.

Pancreatic plasmacytoma does not present as an isolated primary lesion. In all reported cases, including our three patients, the pancreatic lesion has been associated with advanced multiple myeloma or a previously diagnosed upper respiratory or osseous primary site. Other additional foci of

Received December 19, 1988; accepted after revision January 24, 1989.

¹ Department of Diagnostic Imaging/Radiology, Sinai Hospital of Detroit, and the Wayne State University School of Medicine, Detroit, MI 48235. Address reprint requests to M. Korobkin, Sinai Hospital, 6767 W. Outer Dr., Detroit, MI 48235-2899.

² Department of Radiology, University of Michigan Hospital, Ann Arbor, MI 48109.

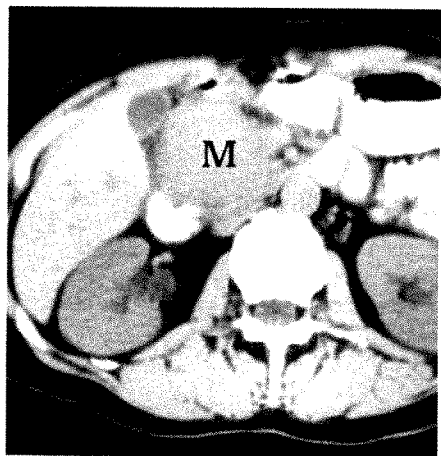


Fig. 1.—Unenhanced CT scan shows a large homogeneous mass (M) in head of pancreas. Other CT sections showed a normal pancreatic body and tail.

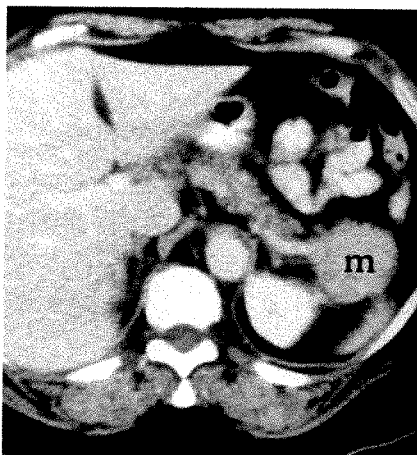


Fig. 2.—Enhanced CT scan shows a homogeneous solid mass (m) in distal portion of tail of pancreas. Remainder of pancreas was normal.

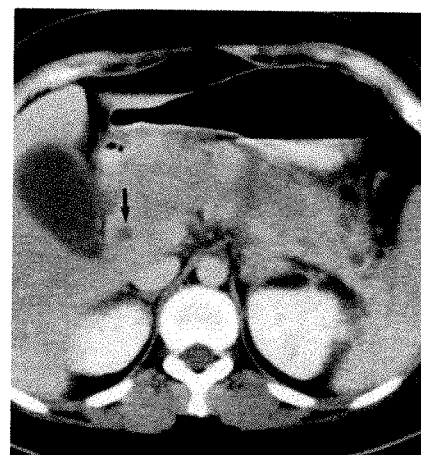


Fig. 3.—Enhanced CT scan shows diffuse enlargement of entire pancreas. Common bile duct (arrow) is near normal size, but higher sections showed mild but definite enlargement of intrahepatic ducts. (Reprinted, with permission, from [7].)

extramedullary plasmacytoma often are documented by clinical or imaging findings or at autopsy.

The CT findings in our cases and those cases previously reported include a focal mass in the pancreatic head (six cases), a focal mass in the pancreatic tail (one case), and diffuse enlargement of the entire pancreas (one case). In all cases, the lesion was homogeneous in density. The absence of irregular hypodensity, often seen with the more common ductal adenocarcinoma, may be an important differentiating characteristic.

In a patient with multiple myeloma or solitary plasmacytoma, a pancreatic mass is most likely due to a pancreatic plasmacytoma. An unrelated pancreatic mass, such as an adenocarcinoma, must be excluded. Percutaneous biopsy is a simple and effective way to establish the correct diagnosis.

REFERENCES

1. Pasmantier MW, Azar HA. Extraskelatal spread in plasma cell myeloma: a review of 57 autopsied cases. *Cancer* 1969;23:167-174
2. Rice NT, Woodring JH. Pancreatic plasmacytoma: sonographic and computerized tomographic findings. *JCU* 1981;9:46-48
3. Twomey BP, Katz D. CT in the diagnosis of extramedullary plasmacytoma. *J Comput Assist Tomogr* 1983;7:407-408
4. Lake G, Shade RR, Van Threl DH. Extrahepatic biliary tract obstruction due to plasmacytoma. *J Clin Gastroenterol* 1983;5:273-276
5. Mitchell DG, Hill MC. Obstructive jaundice due to multiple myeloma of the pancreatic head: CT evaluation. *J Comput Assist Tomogr* 1985;9:1118-1119
6. Speelberg B, Kluin PM, Punt K, et al. Non-secreting extramedullary plasmacytoma with late involvement of the pancreas causing obstructive jaundice. *Neth J Med* 1985;28:291-293
7. Scheiman J, Elta G, Francis I. Biliary obstruction secondary to an extramedullary plasmacytoma of the pancreas: confusion with pancreatitis on computed tomography. *Pancreas* 1987;2:237-239

Case Report

Cecal Diverticulitis Differentiated from Appendicitis Using Graded-Compression Sonography

Ronald R. Townsend,¹ R. Brooke Jeffrey, Jr., and Faye C. Laing

Graded-compression sonography of the right lower quadrant can be useful for diagnosing appendicitis [1, 2]. Sonography also can establish alternative causes of symptoms in patients in whom no evidence of appendicitis is identified [3–5]. Abnormally thickened terminal ileum may be seen on compression sonograms in patients with *Campylobacter* enteritis or Crohn disease and may allow differentiation of these conditions from acute appendicitis [4, 5]. Cecal diverticulitis, a relatively uncommon cause of right-lower-quadrant pain, also can mimic appendicitis clinically. The CT appearance of diverticulitis of the right colon has been reported [6–8], and Puylaert [5] briefly described a case of cecal diverticulitis diagnosed by compression sonography.

We recently examined a patient who was clinically suspected of having appendicitis, in whom compression sonograms revealed cecal wall thickening and calcifications in diverticula. These findings suggested diverticulitis, which was confirmed by CT. Sonographic findings in two other patients with cecal diverticulitis also are discussed.

Case Report

A 60-year-old woman was admitted with clinically suspected appendicitis on the basis of 1 day of anorexia, diarrhea, and right-lower-quadrant/right-flank pain. Her temperature and WBC count were elevated to 38.2°C and 12,700, respectively. Graded-compression sonograms of the right lower quadrant did not show appendicitis. Discrete outpouchings that contained shadowing echogenic material were noted emanating from the wall of an abnormally thickened noncompressible cecum (Fig. 1A). Focal tenderness during compression

maneuvers was observed over the abnormal region. The sonographic diagnosis of diverticulitis was made, and an abdominal CT scan was obtained for confirmation (Fig. 1B). CT revealed several right-side diverticula, calcified enteroliths, and inflammatory changes in the right anterior pararenal space. After treatment with IV-ampicillin, gentamycin, and metronidazole for 7 days, the patient was discharged without symptoms. One recurrence was treated successfully with antibiotics.

Discussion

Cecal diverticulitis is a relatively rare condition that is difficult to diagnose preoperatively either by radiographic or clinical examination. Right-lower-quadrant findings frequently mimic appendicitis, although the pain may not be as well localized. Because the initial treatment for diverticulitis consists of antibiotics, preoperative diagnosis is important. The specific diagnosis can be made by CT if a diverticulum is visualized with adjacent cecal wall thickening [6, 7]. Unfortunately, in many cases CT cannot distinguish diverticulitis from appendicitis [6]. Barium enema examination may provide a firm diagnosis if inflammatory changes are detected in association with diverticula. Not infrequently, however, the findings overlap with those of colonic tumors and appendicitis [6].

Graded-compression sonography of the right lower quadrant is highly sensitive and specific for diagnosing appendicitis and is most useful in patients in whom the clinical diagnosis is uncertain [1, 2]. The patient described earlier is one of three patients with cecal diverticulitis who were referred to our sonography laboratory with a clinical diagnosis of possible

Received November 9, 1988; accepted after revision December 12, 1988.

¹ All authors: Department of Radiology, San Francisco General Hospital, 1001 Potrero Ave., San Francisco, CA 94110. Address reprint requests to R. R. Townsend, Room 1X57.

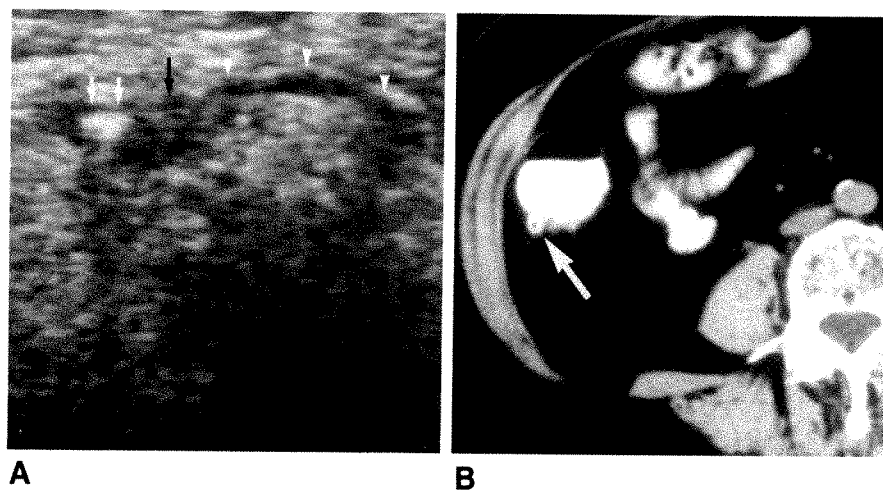


Fig. 1.—A, Compression sonogram of right lower quadrant in patient with cecal diverticulitis. A fecalith with shadowing is present in a diverticulum of lateral wall of cecum (white arrows). Anterior wall of cecum is visible (arrowheads). Thickening of cecal wall next to diverticulum is noted (black arrow).
B, CT scan shows a calcified fecalith in diverticulum (arrow). Inflammatory thickening of cecal wall is evident and was more marked on adjacent images.

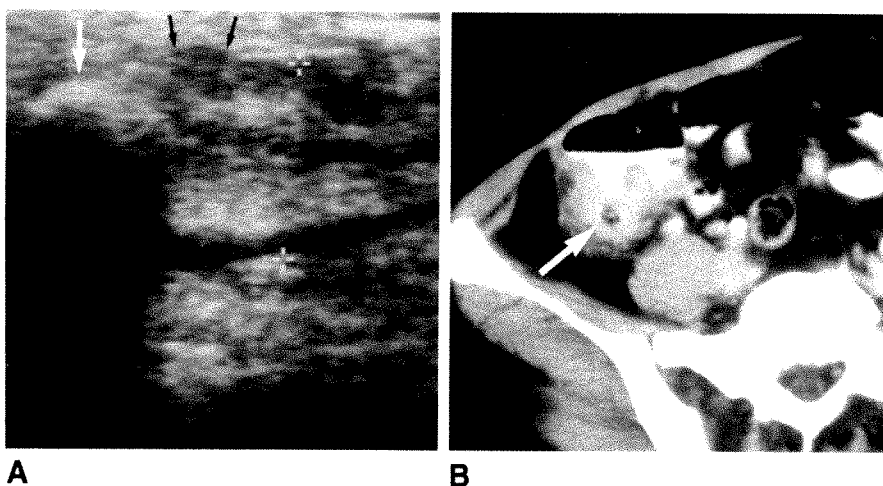


Fig. 2.—A, Compression sonogram in patient with surgically proved cecal diverticulitis. Echo-genic shadowing focus (white arrow) at right margin of cecum is noted with adjacent thickening of cecal wall (black arrows). Cursors mark anterior and posterior margins of cecum. Gas normally present within cecal lumen is displaced by compression maneuver and is not visualized.
B, CT scan shows marked cecal wall thickening around a stool-filled diverticulum (arrow). Probable identification of a normal appendix was made on a more caudal image.

appendicitis. Figure 2 is from a second patient with surgically proved cecal diverticulitis in whom the sonographic diagnosis was made in retrospect. We have since diagnosed diverticulitis in a third patient, whose sonographic appearance was almost identical to that of the second patient. Although surgical proof and/or other confirmatory imaging studies are lacking in this case, the patient's symptoms resolved rapidly with antibiotics.

Although conventional abdominal sonography using a 3.5-MHz sector transducer without compression may identify a pericolic abscess associated with diverticulitis, the examination may be normal in patients with diverticulitis [8] and little experience with sonography of cecal diverticulitis has been reported. Compression sonography with a 5-MHz transducer provides optimal sonographic visualization of the cecum, terminal ileum, and inflamed appendix. Sonographic identification of diverticulum or diverticula with a thickened, noncompressible cecal wall and focal tenderness is highly suggestive of cecal diverticulitis. A fecalith is sometimes present within the diverticulum. A pericolic abscess may be seen. In the absence of a diverticulum, a pericecal inflammatory mass is nonspecific (as with CT) and could be due to diverticulitis, appendicitis, neoplasm (especially if perforated), or Crohn disease.

As graded-compression sonography of the right lower quadrant gains acceptance, a variety of diseases in addition to appendicitis will be encountered in the sonography laboratory. An alternative diagnosis, especially gynecologic or urologic, may be evident in as many as one third of cases

[3]. Puylaert et al. [4, 5] have described findings in Crohn disease, infectious ileitis/mesenteric adenitis, and other rarer conditions. To date, descriptions of cecal diverticulitis by using the graded-compression technique are limited to those of this report and those mentioned briefly by Puylaert [5]. In order to determine the accuracy of this technique for diagnosing cecal diverticulitis, a much larger experience is required. Nonetheless, our experience suggests that identification of cecal diverticulitis may be another benefit of right-lower-quadrant compression sonography.

REFERENCES

1. Puylaert JBCM. Acute appendicitis: US evaluation using graded compression. *Radiology* 1986;158:355-360
2. Jeffrey RB, Laing FC, Townsend RR. Acute appendicitis: sonographic criteria based on 250 cases. *Radiology* 1988;167:327-329
3. Gaensler EHL, Jeffrey RB Jr, Laing FC, Townsend RR. Sonography in patients with suspected acute appendicitis: value in establishing alternative diagnoses. *AJR* 1989;152:49-51
4. Puylaert JBCM, Lalisang RI, van der Werf SDJ, Doornbos L. *Campylobacter* ileocolitis mimicking acute appendicitis: differentiation with graded-compression US. *Radiology* 1988;166:737-740
5. Puylaert JBCM. Graded compression ultrasound in acute disease of the right lower quadrant. *Semin US CT MR* 1987;4:385-402
6. Balthazar EJ, Megibow AUJ, Gordon RB, Hulnek D. Cecal diverticulitis: evaluation with CT. *Radiology* 1987;162:79-81
7. Scatarige JC, Fishman EK, Crist DW, Cameron JL, Siegelman SS. Diverticulitis of the right colon: CT observations. *AJR* 1987;148:737-739
8. Feczko PJ, Nish AD, Craig BM, Simms SM. Acute diverticulitis in patients under 40 years of age: radiologic diagnosis. *AJR* 1988;150:1311-1314

Stab Wounds of the Renal Artery Branches: Angiographic Diagnosis and Treatment by Embolization

Richard G. Fisher¹
Yoram Ben-Menachem²
Cliff Whigham¹

Renal artery branch injury resulting from stab wounds of iatrogenic origin or street violence is an important cause of renal hemorrhage. Over a period of 10 years we accurately diagnosed the injury and successfully managed the associated hemorrhage in 15 patients by using angiography and percutaneous embolization techniques. Nine branch injuries in eight patients were due to street knifings and seven injuries were complications of invasive medical procedures (four from renal biopsy, two from nephrostolithotomy, and one from nephrostomy). All patients had gross hematuria at the time of angiographic evaluation. False aneurysms were present in six patients (one with associated frank extravasation), false aneurysm/arteriovenous fistula in three, false aneurysm/arteriocaliceal fistula in one, and isolated arteriovenous fistula in two. Frank extravasation without associated false aneurysm/arteriovenous fistula was present in two. One patient had two injuries, an upper-pole false aneurysm and a lower-pole false aneurysm/arteriovenous fistula. In the eight patients injured in street knifings, hematuria recurred after surgical exploration and treatment. None of the 16 injuries involved the main renal artery. Gelfoam was used for embolization of nine lesions and steel coils for four. Three others were treated with Gelfoam plus coils. Hemostasis was achieved in all and none required subsequent surgery. Renal tissue loss was small to moderate (less than 30%) in 12 patients and large (30–50%) in three patients. Transient postembolization hypertension occurred in one of the latter.

We consider selective angiography/embolization to be an effective and safe means for diagnosing and treating wounds of the renal artery branches.

Renal angiography has been the preferred means of diagnosing renal artery injury for over two decades [1–3]. In more recent years, transcatheter management of renal artery branch hemorrhage has become increasingly successful [4–6]. Despite this, relatively few instances of therapeutic embolization for renal artery branch laceration due to stab wounds have been reported since the landmark case of Bookstein and Goldstein [7] in 1973. Most of these injuries were the result of iatrogenic trauma, usually renal biopsy [4, 8–24]. Conversely, reports of transcatheter embolization of renal hemorrhage caused by street stabbings have been rare [4, 6, 11, 25, 26].

We report our experience with the angiographic diagnosis and subsequent transcatheter embolization for treatment of hemorrhage in 15 patients with injury of renal artery branches due to stab wounds caused by street fights or medical procedures.

Materials and Methods

Fifteen patients with injury to branches of the renal artery caused by stab wounds were diagnosed angiographically and had treatment with transcatheter embolization between November 1980 and August 1988. None of the injuries involved the main renal artery. There were 13 men and two women 15–60 years old. Nine injuries involved the left kidney, five involved the right kidney, and one involved a renal transplant. Seven were complications of

Received October 13, 1988; accepted after revision February 6, 1989.

¹ Department of Radiology, Baylor College of Medicine, 1 Baylor Plaza, Houston, TX 77030. Address reprint requests to R. G. Fisher.

² Department of Radiology ZA-65, Harborview Medical Center, 325 Ninth Ave., Seattle, WA 98104.

AJR 152:1231–1235, June 1989

0361–803X/89/1526–1231

© American Roentgen Ray Society

medical procedures: four from biopsy, two from percutaneous nephrostolithotomy, and one from nephrostomy. Eight were due to street stabbings; all of these were initially explored surgically.

The common denominator in patient selection for angiographic evaluation and possible embolization in our series as well as in the literature was persistent or recurrent hematuria. The time of onset of bleeding ranged from immediately after the procedure/injury/surgery to weeks or even months later. The hemorrhage was sufficiently severe so as to require multiple transfusions in eight of our 15 patients and in at least 10 of those previously reported [7, 10–13, 17–19]. Preangiographic imaging was used in nine of our patients (two with sonography, one with CT, and six with excretory urography) and in four patients from the literature (three with sonography and one with CT); five of the studies in our patients and three in the literature were abnormal [7, 18, 24, 25].

Angiographic Technique

Angiography was done with the standard percutaneous technique via a femoral artery approach. Abdominal aortography was followed by selective renal arteriography. The latter was accomplished with a 5- or 6-French cobra catheter with a 0.97-mm inner diameter in 14 cases. A 5.5-French Simmons 1 catheter (Cook Corp., Bloomington, IN) was used in the 15th case. Earlier cases were imaged with the conventional single-plane technique. Later cases were supplemented with digital angiography (General Electric DF 3000, DF 5000, or DF 5500, General Electric, Milwaukee, WI), which tended to shorten

procedure time. U-arm fluoroscopy (General Electric L/U-Angio Vascular Imaging System) was also available in later cases.

In each patient the selective catheter was placed as close as possible to the bleeding site before embolization. Materials used for embolization were either surgical gelatin sponge or Gianturco steel coils (Cook) or both. When Gelfoam was used, particle size depended on the perceived size of the artery feeding the lesion. Larger strips (torpedoes) were in the range of $10\text{--}20 \times 4 \times 2$ mm, whereas smaller pledgets were approximately $4 \times 4 \times 2$ mm. When coils were used they were advanced into place with long floppy-tipped wires such as the Newton wire (Cook).

Flow-directed embolization [6] was used in three, two with Gelfoam (one successfully) and one with a 3-mm steel coil (also successfully) (Fig. 1).

Estimates of renal volume loss due to infarction were determined from postembolization arteriograms. Volume loss less than 30% was arbitrarily considered to be small to moderate (12 patients), while loss greater than 30% was considered to be large (three patients).

Results

Angiographic diagnosis was straightforward in most of the patients and the lesion (false aneurysm, arteriovenous fistula, or frank extravasation) was easily seen with the selective angiographic technique. Indeed, in a few cases, abnormalities were recognizable on aortography (Figs. 2A and 3A). In one,

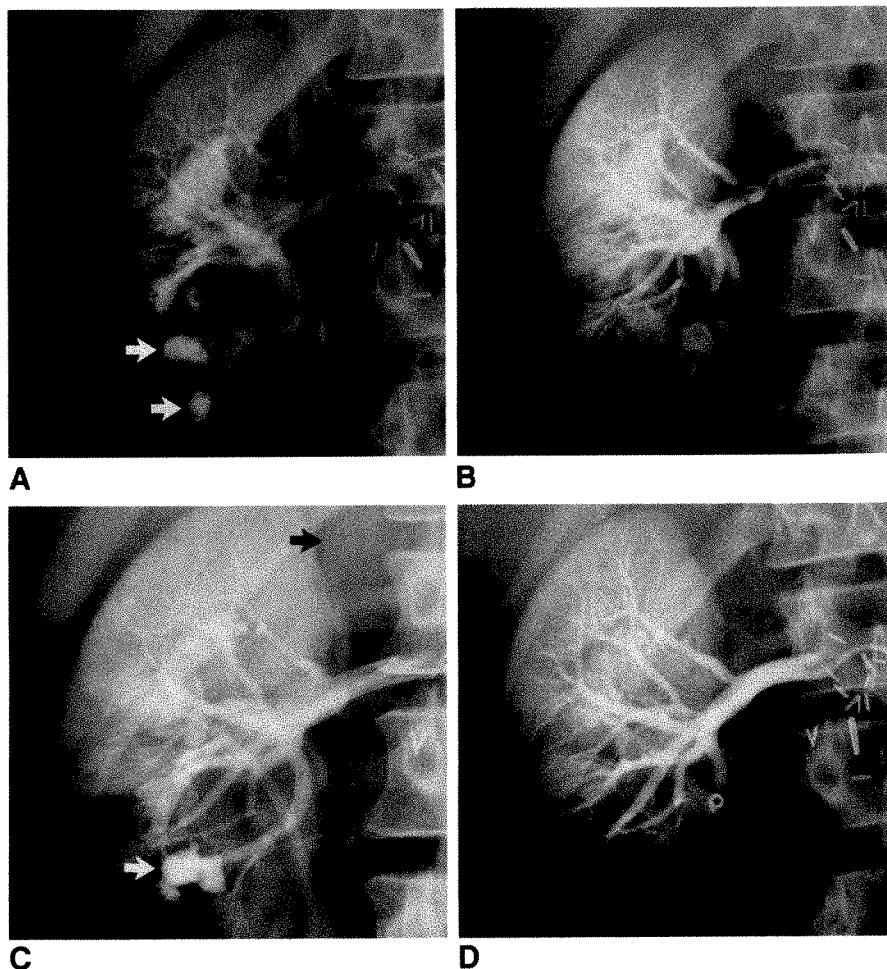


Fig. 1.—Flow-directed coil embolization after failed Gelfoam occlusion.

A, Selective right renal arteriogram shows two false aneurysms (white arrows) and arteriovenous fistula with inferior vena caval opacification (black arrow).

B, Renal arteriogram after subselective embolization with large Gelfoam strip (torpedo) shows occlusion of feeding branch artery and absence of false aneurysms/arteriovenous fistula.

C, Renal arteriogram 7 days later for rebleeding shows one multilobular false aneurysm (white arrow) and arteriovenous fistula with persistent faint inferior vena caval opacification (black arrow).

D, Subselective catheterization was not possible and attempted flow-directed Gelfoam embolization was ineffective. Angiogram shows successful occlusion, which was ultimately achieved after embolization with flow-directed 3-mm coil.

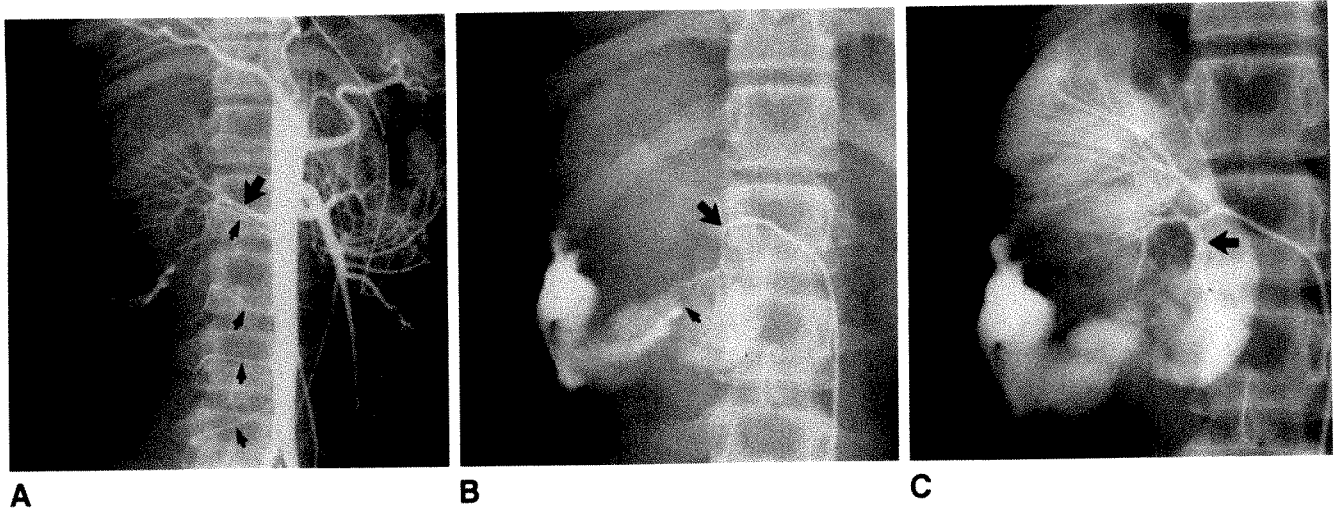


Fig. 2.—Embolization for treatment of postbiopsy renal hemorrhage.

A, Aortogram shows brisk bleeding from lower-pole branch of right renal artery. Giant hematoma displaces aorta, liver, bowel, and right iliac artery and markedly stretches right renal artery (*large arrow*) and lumbar arteries (*small arrows*).

B, Selective opacification of lower-pole branch of right renal artery (*large arrow*) shows massive extravasation (*small arrow*).

C, Arteriogram after embolization with single Gelfoam plug (*arrow*) shows occlusion of lower-pole artery without further extravasation of contrast material. Extravasation lingers from preembolization injections.

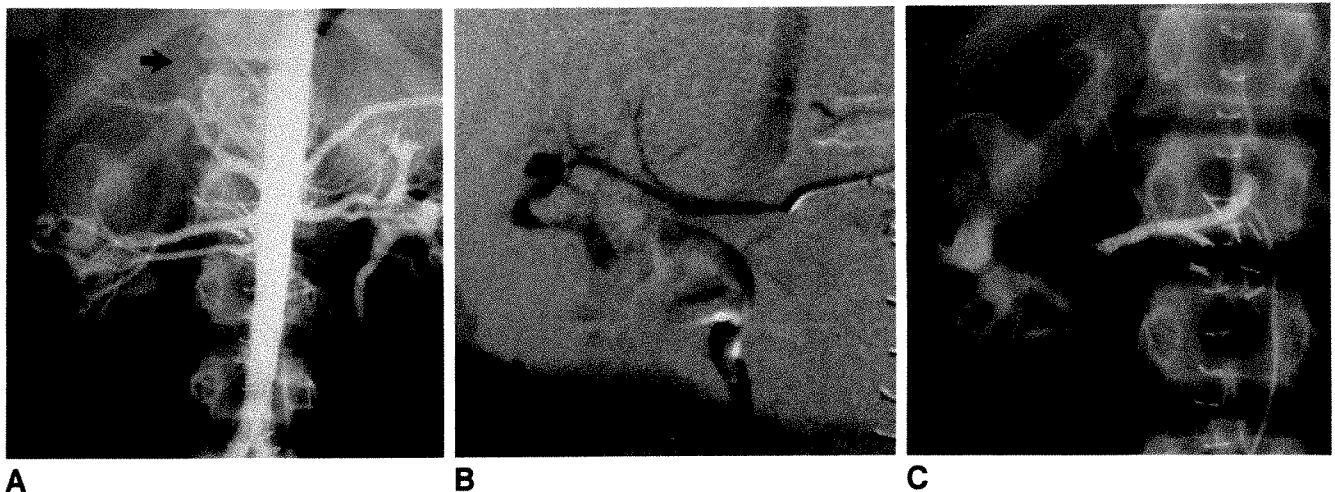


Fig. 3.—Large renal volume loss (30–50%) after embolization of false aneurysm/arteriovenous fistula.

A, Aortogram reveals two right renal arteries and upper-pole false aneurysm with associated extravasation and arteriovenous fistula with inferior vena caval opacification (*arrow*).

B, Digital subselective arteriogram of branch of right superior renal artery confirms that false aneurysm, extravasation, and arteriovenous fistula arise from this vessel.

C, Angiogram shows bleeding branch was catheterized but 3-mm-coil placement displaced catheter, resulting in more proximal positioning of coil with occlusion of trifurcation of most superior duplicate right renal artery.

however, a rapidly flowing arteriovenous fistula was demonstrable only with subselective technique (Figs. 4A and 4B). In another, a false aneurysm was clearly visible but the specific feeding artery was elusive.

Selective renal angiography showed a false aneurysm in five patients, a false aneurysm with an arteriovenous fistula in three, a false aneurysm with an arteriocaliceal fistula in one, a false aneurysm with frank extravasation in one (Fig. 5A), an arteriovenous fistula without a visible false aneurysm in two, and frank extravasation in two others. In the remaining case, a false aneurysm was shown in the upper pole and a false

aneurysm with an arteriovenous fistula in the lower pole, for a total of 16 lesions in 15 patients.

Hemorrhage was completely controlled with embolization in each of the 15 patients with no need for follow-up surgical intervention. Gelfoam was used exclusively and successfully in the treatment of nine lesions: five false aneurysms, two areas of frank extravasation, one false aneurysm with arteriovenous fistula, and one isolated arteriovenous fistula. Gelfoam was used in the false aneurysm/arteriovenous fistula because the arteriovenous communication was tiny and the shunt slow-flowing. The isolated arteriovenous fistula was in

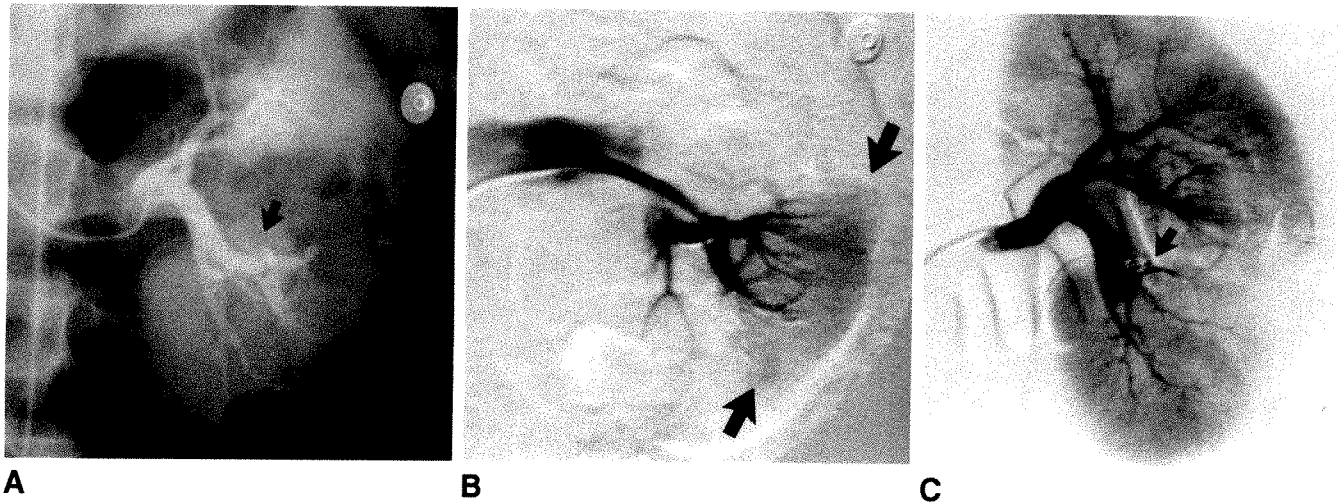


Fig. 4.—Embolization for treatment of arteriovenous fistula caused by knife wound.
A, Selective left renal arteriogram shows only questionable arteriovenous fistula (arrow) in left lower pole.
B, Subselective lower-pole digital arteriogram reveals rapidly flowing arteriovenous fistula. Note area of expected postembolization tissue loss (arrows).
C, Angiogram after embolization with 3-mm coil (arrow) shows occluded feeding artery and arteriovenous fistula. Moderate-sized area of infarction (10–20%) is evident.

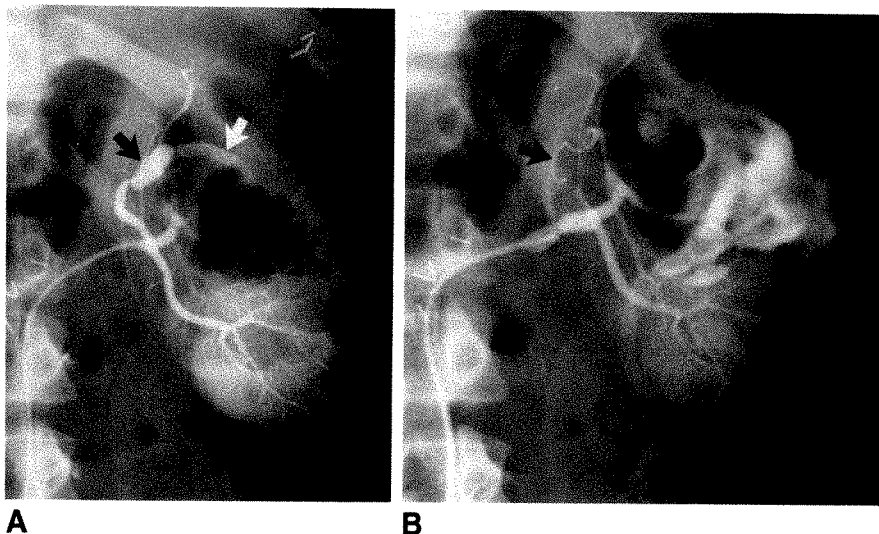


Fig. 5.—Embolization for treatment of false aneurysm with extravasation from knife wound to left kidney.

A, Selective left renal arteriogram shows large false aneurysm (black arrow) with frank extravasation (white arrow) and mass effect of large hematoma.

B, Angiogram shows medium-sized coil (5 mm), initially intended for aneurysm itself, remains partially uncoiled (arrow) in distal feeding artery, which has thrombosed.

a transplanted kidney and Gelfoam embolization was initially attempted in the interest of maximum renal preservation. Fortunately it proved successful and coils were not needed. Two Gelfoam failures were due to embolization of the wrong artery in one and probable recanalization 7 days after embolization in the other (Figs. 1B and 1C). The latter phenomenon was observed by us once before [6].

Coin embolization was used exclusively in four lesions: one false aneurysm with frank extravasation (Fig. 5), two false aneurysms with arteriovenous fistulas, and one isolated arteriovenous fistula. Coils were also used in conjunction with or after Gelfoam failure in three others. Renal volume loss was small to moderate (less than 30%) in 12 and large (30–50%) in three.

No complications were related to the diagnostic angiographic procedures. Complications of embolization occurred in three patients and consisted of large renal volume loss (30–50%). There was no evidence of persistent postembolization

hypertension in any patient, including these three. Two of the patients with large infarctions, however, were lost to follow-up after discharge. The third patient (Fig. 3) developed transient fever, pain, and low-grade hypertension (150/90 mm Hg) immediately after embolization. Two weeks later, the blood pressure was normal (120/80 mm Hg), despite a glomerular filtration rate of 10.3 ml/min in the embolized kidney vs 51.4 ml/min in the normal kidney. The patient is currently being followed as an outpatient and was still normotensive 3 months after embolization.

Discussion

The first reported use of renal arterial embolization for the control of hemorrhage from a stab wound was in 1973 by Bookstein and Goldstein [7]. Their three initial cases were all complications of medical procedures, specifically renal biopsies. Since then at least 42 additional cases have been reported [4, 6, 8–26].

Eighty-four percent (38 of 45) of injuries to renal artery branches diagnosed angiographically and treated by embolization were complications of medical procedures, with biopsies accounting for 24 [7–20]. Four of 38 were embolized for treatment of hemorrhagic complications of surgical procedures [12, 14, 22, 23] and 10 of 38 (all reported since 1981) were treated for bleeding complications caused by other percutaneous procedures: five after nephrostomy [17–19] and five after nephrostolithotomy [20, 21].

The remaining seven patients treated with embolization were injured in street stabbings [4, 11, 25, 26]; three of these were reported by us previously [6]. The five new cases in this series raise the overall published total in this category to 12.

Embolization materials used in our series were surgical Gelfoam and/or steel coils. The type and size of embolic substance used were based on the type of lesion (false aneurysm, arteriovenous fistula, or frank hemorrhage); the character of the lesion (fast- or slow-flowing arteriovenous fistula); and the size of the feeding artery, as shown on selective angiography. When larger vessels were involved, specific measurement of the feeding artery was made directly from a film, uncorrected for magnification.

Gelfoam was considered the preferred substance because of its potential for a more peripheral occlusion and concomitant minimal tissue loss. In addition, there was at least a theoretical potential for ultimate posthealing recanalization. A standard Gelfoam embolus (torpedo) was $10 \times 4 \times 2$ mm, with the volume increased or decreased depending on the estimated size of the lesion and its feeding artery.

Delays in requesting angiography/embolization complicated management in four of our patients. This resulted in shock and the need for multiple transfusions in all four. Furthermore the resultant massive hematoma hampered selective angiography/embolization in two patients (Fig. 2). The precedent exists for delaying aggressive intervention for hematuria (unless it is massive) after renal biopsy, because it usually is self-limiting [7]. However, our experience indicates that any hematuria after surgical treatment of a knife wound to the kidney is worthy of angiographic evaluation. Indeed, angiography and embolization might be well advised in stable patients with renal knife wounds, prior to surgical exploration for suspected injury of adjacent organs.

Hemorrhage was controlled with limited renal volume loss (less than 30%) in 12 of our 15 patients. However, embolization resulted in large-volume tissue loss (30–50%) in the remaining three. This may have been avoided in one of the patients by a more zealous search for the specific bleeding branch before embolization. In another, Gelfoam probably would have produced a better result (Fig. 3), although we were reluctant to use Gelfoam because of the fast-flowing arteriovenous fistula. In the third, multiple embolizations were unavoidable because distorting hematoma prevented subsection and flow direction of the Gelfoam was unsuccessful.

Postembolization hypertension did not develop in 14 patients and was transient in one. Although hypertension is a possibility after renal embolization, Bertini et al. [2] suggest that it may occur only with main renal artery occlusion or occlusion of one of the multiple renal arteries. The latter occurred in our patient who developed hypertension, but fortunately it was self-limiting (Fig. 3).

In conclusion, angiography/embolization is considered to

be an effective means of managing renal artery branches injured by stab wounds, because it offers the potential for maximum renal preservation with relatively low patient risk. Early intervention is encouraged, especially in patients with knife wounds, because delay can seriously complicate the procedure. Meticulous identification of the specific bleeding artery and cautious embolization are essential for optimal results.

REFERENCES

1. Elkin M, Meng CH, DePredes RG. Roentgenologic evaluation of renal trauma with emphasis on renal angiography. *AJR* 1966;98:1–26
2. Bertini JE Jr, Flechner SM, Miller P, Ben-Menachem Y, Fischer RP. The natural history of traumatic branch renal artery injury. *J Urol* 1986;135:228–230
3. Lang EK, Sullivan J, Frentz G. Renal trauma: radiological studies: comparison of urography, computed tomography, angiography and radionuclide studies. *Radiology* 1985;154:1–6
4. Clark RA, Gallant TE, Alexander ES. Angiographic management of traumatic arterial venous fistulas: clinical results. *Radiology* 1983;147:9–13
5. Sclafani SJA, Shaftan GW, Mitchell WG, Nayaranaswamy TS, McAuley J. Interventional radiology in trauma victims: analysis of 51 consecutive patients. *J Trauma* 1982;22:353–360
6. Fisher RG, Ben-Menachem Y. Embolization procedures in trauma: the abdomen-extraperitoneal. *Semin Intervent Radiol* 1985;2:148–157
7. Bookstein JJ, Goldstein HM. Successful management of post-biopsy arteriovenous fistula with selective arterial embolization. *Radiology* 1973;109:535–536
8. Meaney TF, Chicatel PD. Obliteration of renal AVF by transcatheter clot embolization. Case report and experimental observations. *Cleve Clin J Med* 1974;41:33
9. Silber SJ, Clark RE. Treatment of massive hemorrhage after renal biopsy with angiographic injection of clot. *N Engl J Med* 1975;292:1387–1388
10. Goldman ML, Fellner SK, Parrott TS. Transcatheter embolization of renal arteriovenous fistula. *Urology* 1975;6:386–388
11. Chuang VP, Reuter SR, Walter J, Foley WD, Bookstein JJ. Control of renal hemorrhage by selective renal embolization. *AJR* 1975;125:300–306
12. Kaufman SL, Freeman C, Busky SM, White RI Jr. Management of post-operative renal hemorrhage by transcatheter embolization. *J Urol* 1976;115:203–205
13. Maxwell DD, Frankel RS. Wedged catheter management of the bleeding renal pseudoaneurysm. *J Urol* 1976;116:96–97
14. Pontes JE, Parekh N, McGuckin JT, Banks MD, Pierce JM. Percutaneous transfemoral embolization of arteriofundibular-venous fistula. *J Urol* 1976;116:98–100
15. Barbaric ZI, Cutcliff WB. Control of renal arterial bleeding after percutaneous biopsy. *Urology* 1976;8:108–111
16. Kollmeyer KR, Hunt JL, Ellman BA, Fry WJ. Acute and chronic traumatic arteriovenous fistula in civilians. *Arch Surg* 1981;116:697–702
17. Eckhauser ML, Haaga JR, Hampel N, et al. Arterial embolization of renal allograft to control hemorrhage secondary to percutaneous nephrostomy. *J Urol* 1981;126:679–680
18. Cope C, Zeit RM. Pseudoaneurysms after nephrostomy. *AJR* 1982;139:255–261
19. Lalude AO, Conroy RN. Vascular complication of percutaneously placed pigtail uretero stent. *J Urol* 1983;130:553–554
20. Kalash SS, Young JD Jr. Serious complications associated with percutaneous nephrolithotomy. *Urology* 1987;29:290–293
21. Lee WJ, Smith AD, Cubelli V, et al. Complications of percutaneous nephrolithotomy. *AJR* 1987;148:177–180
22. Castaneda-Zuniga WR, Tadavarthy SM, Murphy W, Beranek I, Amplatz K. Nonsurgical closure of large arteriovenous fistula. *JAMA* 1976;236:2649–2650
23. Kerber CW, Freeny PC, Cromwell L, Margolis MT. Cyanoacrylate occlusion of renal arteriovenous fistula. *AJR* 1977;128:663–665
24. McAlistar DS, Johnsrude I, Miller MM, Clap J, Thompson WM. Occlusion of acquired renal arteriovenous fistula with transcatheter electrocoagulation. *AJR* 1979;132:998–1000
25. Chang J, Katzen BT, Sullivan KP. Transcatheter Gelfoam embolization of post-traumatic bleeding pseudoaneurysms. *AJR* 1978;131:645–650
26. White RI Jr, Kaufman SL, Barth KH, DeCaprio V, Strandberg JD. Embolotherapy with detachable silicone balloons. *Radiology* 1979;131:619–627

Videotape Review

RSNA Today, Vol. 2, No. 4. Oak Brook, IL: The Radiological Society of North America, 1988. \$75; by subscription, 4 issues annually at \$225 for RSNA members and \$275 for nonmembers (VHS videotape)

This tape consists of three parts, each on a different subject. The first, "Increased Detectability of Renal Cell Carcinoma," is an interview of Morton Bosniak by Stanley Siegelman. Comparisons are made between work done over two separate time periods, 1974–1977 and 1982–1985, before and after use of CT and sonography was common. Figures are presented that lead to the conclusions that small (less than 3.0 cm) renal neoplasms often are discovered now at a size that yields comparatively superior results after treatment and that partial nephrectomy is becoming a much more viable therapeutic option. It is pointed out that renal cell carcinoma, oncocytoma, and adenoma cannot be differentiated but that some 80% of solid lesions discovered in the kidney are renal cell carcinomas. The conclusion is that early diagnosis of renal cell carcinoma can lead to more frequent use of partial nephrectomy as a curative treatment. The kidneys should be screened carefully on any CT or sonographic examination of the abdomen in hopes of discovering early renal cell carcinoma. This section of the tape is clear and concise. The format and case examples are excellent, and the film quality is good.

The second part, "Imaging the Temporomandibular Joint," examines the roles of cine arthrography and MR imaging in meniscus displacement syndromes. It is presented as a discussion by Richard W. Katzberg (University of Rochester) with videotapes by L. Eriksson and P-L Westesson (University of Lund, Sweden). After an excellent anatomic review, clinical and imaging variables of the normal temporomandibular joint and meniscus displacement with and without reduction are reviewed, as are the indications and materials and methods of the examinations. Excellent correlation between cine arthrography and MR is demonstrated. The conclusion is that arthro-

graphy and MR of the temporomandibular joint are complimentary and useful tools in evaluating meniscus displacement syndromes. The dynamic display of anatomy of the cadaver is superb, and the images are excellent. The presentation is clear and concise, and just enough material is covered.

The third part, "Inflammatory Disease of the Paranasal Sinuses," is a case presentation and discussion by Peter Som (Mt. Sinai Hospital, New York). Imaging signs of inflammatory diseases of the sinuses are discussed, and differential points regarding tumors are included. The importance of water content in MR imaging and contrast enhancement in CT is reviewed. Various diagnostic considerations for benign disease in each of the sinuses and the nasal cavity are offered. The separation of hyperdense material in the sinuses from bone by a layer of mucoid secretions is stressed as a sign of benign disease on CT and on T2-weighted MR images. The conclusion is that CT and MR are useful in the diagnosis of benign diseases of the paranasal sinus and in their differentiation from malignant tumors. The presentation is good but limited. The lack of discussion of coronal CT workup of abnormalities of the ostiomeatal complex treatable by endoscopic therapy is glaring.

Despite certain deficiencies, this tape is of excellent quality overall and is recommended for purchase and viewing by any radiologist who is interested in one or more of the three topics covered.

Hano A. Siegel
Mercy Hospital
San Diego, CA 92103

Testicular Ischemia: Color Doppler Sonographic Findings in Five Patients

William D. Middleton¹
G. Leland Melson

We studied the findings on color Doppler sonography in five men with testicular ischemia (three with acute testicular torsion and two with testicular infarcts after herniorrhaphies). In all five cases, no intratesticular blood flow was identified on the symptomatic side, while normal blood flow was evident on the opposite side. In the three cases of acute torsion, no gray scale sonographic abnormalities were seen, and in the two cases of postoperative infarction, the abnormalities were nonspecific.

These findings suggest that color Doppler sonography can be used to show decreased blood flow in cases of acute testicular ischemia and that it may have a role in evaluating patients with suspected testicular torsion.

Color Doppler sonography allows for simultaneous real-time display of morphology and the temporospatial characteristics of blood flow. We have reported that color Doppler sonography can reliably show normal intratesticular arterial blood flow [1]. This report describes our findings in five patients with testicular ischemia.

Methods

Five patients with suspected testicular ischemia were examined with color Doppler sonography. Three patients (ages 18, 19, and 20 years) presented with acute scrotal pain of less than 6 hr duration. All three had testicular torsion confirmed surgically. The other two patients (ages, 53 and 68 years) developed testicular pain and swelling 2 days after inguinal herniorrhaphies. The diagnosis of testicular ischemia was made in both men on the basis of the color Doppler sonographic examination and clinical follow-up. Both were treated conservatively with scrotal supports, ice packs, and pain medication.

The patients were examined with a commercially available color Doppler sonography unit (QAD-1, Quantum Medical Systems, Issaquah, WA). A 7.5-MHz linear, phased-array transducer was used for all exams. Power output and threshold settings were adjusted to maximize detection of blood flow throughout the field of view without producing visible system noise. Additionally, all exams were performed at low flow settings to allow for optimal detection of slowly flowing blood in the small testicular arteries. Pulsed Doppler sampling was performed on a variety of visible vessels that were identified on the real-time image. All examinations were recorded digitally on videotape and later reviewed on a frame-by-frame basis by using a cine loop function.

The patients were scanned in the supine position. Standard longitudinal transverse planes were used for imaging both testes. When vessels were identified in the testis, oblique images were obtained to show the more vascular planes of the testis.

Results

All three patients with acute testicular torsion had no intratesticular blood flow identified in the symptomatic testis (Fig. 1A), while normal blood flow was documented in multiple intratesticular and testicular capsular arteries on the asymptomatic side (Fig. 1B). Otherwise, the symptomatic testis was completely normal and

Received November 21, 1988; accepted after revision January 9, 1989.

¹ Both authors: Mallinckrodt Institute of Radiology, Washington University School of Medicine, 510 S. Kingshighway Blvd., St. Louis, MO 63110. Address reprint requests to W. D. Middleton.

AJR 152:1237-1239, June 1989
0361-803X/89/1526-1237
© American Roentgen Ray Society

identical in appearance to the contralateral side. Testicular echogenicity was homogeneous and equal to that of the contralateral side. A follow-up examination done 2 days after orchiopexy in one patient showed an increased number of visible intratesticular arteries in the symptomatic testis compared with the asymptomatic testis. This was presumed to be a result of postischemic hyperemia (Fig. 1C).

As with acute torsion, the two postherniorrhaphy patients also had complete lack of identifiable intratesticular blood flow on the symptomatic side and normal blood flow within several intratesticular and testicular capsular arteries on the asymptomatic side (Figs. 2A and 2B). Peritesticular hyperemia also was apparent in both of these patients (Fig. 2C). In addition to the flow abnormalities, both of these patients had morpho-

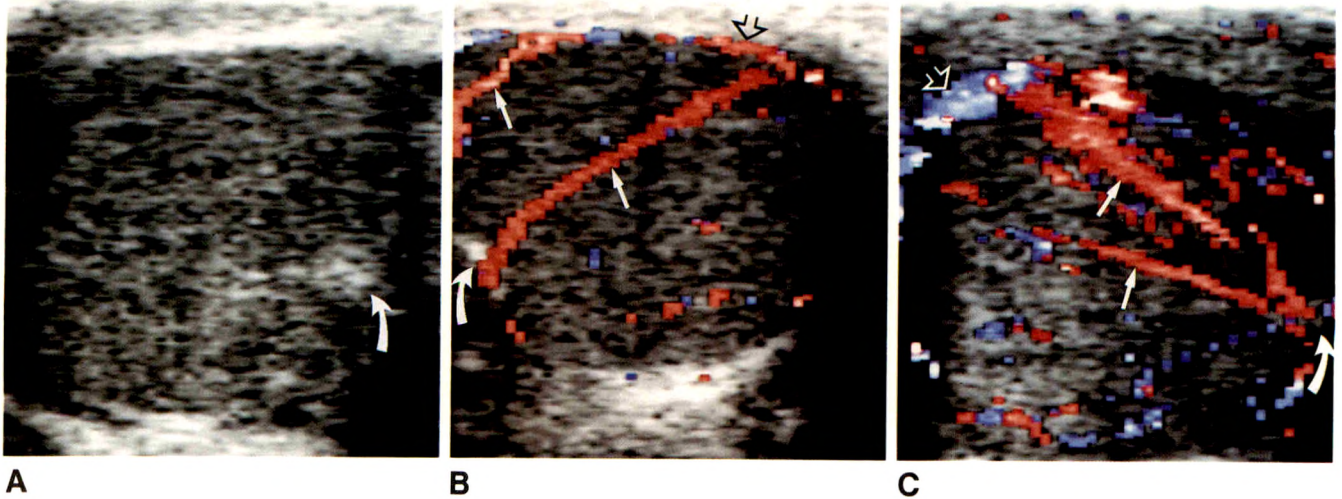


Fig. 1.—19-year-old man with acute testicular torsion.

A, Transverse color Doppler sonographic image of symptomatic testis shows no identifiable testicular blood flow. Mediastinum (curved arrow).
 B, Transverse color Doppler sonographic image of asymptomatic testis shows normal blood flow. Intratesticular arteries (straight arrows), capsular artery (open arrow), mediastinum (curved arrow).
 C, Transverse color Doppler sonographic image of symptomatic testis after orchiopexy shows an increased number of visible intratesticular arteries (straight arrows), consistent with postischemic hyperemia. Capsular artery (open arrow), mediastinum (curved arrow).

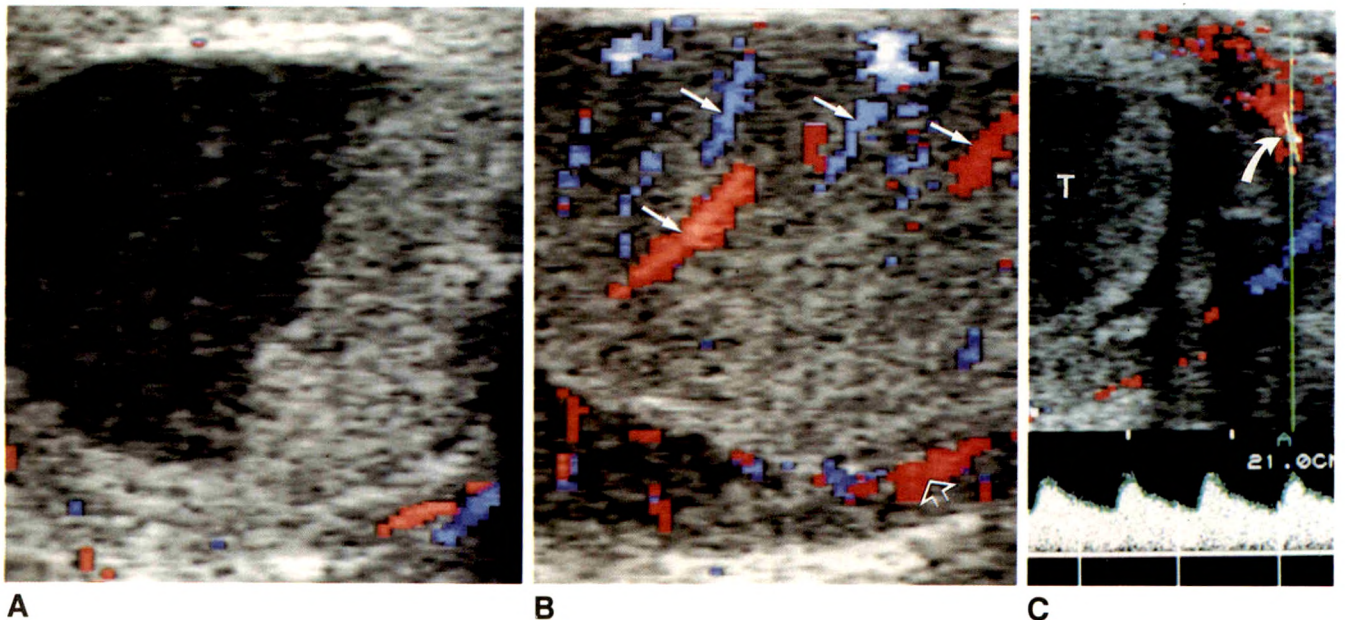


Fig. 2.—53-year-old man with testicular ischemia after herniorrhaphy.

A, Longitudinal color Doppler sonographic image of symptomatic testis shows no visible testicular blood flow and demarcation between hypoechoic upper pole and morphologically normal lower pole.
 B, Longitudinal color Doppler sonographic image of asymptomatic testis shows blood flow in several intratesticular arteries (closed arrows) and capsular artery (open arrow).
 C, Longitudinal color Doppler sonographic image and Doppler waveform of symptomatic testis with range-gated pulsed Doppler cursor placed on peritesticular artery (curved arrow). Increased number of peritesticular vessels and high levels of diastolic flow indicate hyperemia. T = lower pole of testis.

logical abnormalities in the testis that were evident on gray-scale imaging. The first patient had a well-defined region of decreased echogenicity in the upper pole of the testis, which was well demarcated from the more normal-appearing lower pole (Fig. 2A). A follow-up scan in this patient obtained 2 days after the initial study showed extension of this hypoechoic region further caudad, consistent with an evolving infarct. The other patient had testicular enlargement and diffuse decrease in echogenicity on the symptomatic side.

Discussion

Conventional gray-scale sonography without Doppler is a valuable means of identifying morphological abnormalities in the testes. In patients with acute testicular torsion, the reported findings are enlargement of the testis with decrease in the echogenicity of the testicular parenchyma. Often there is associated enlargement of the epididymis [2]. Experimental studies in dogs have shown that the testis generally enlarges and becomes hypoechoic within 15 min after torsion [3]. Unfortunately, identical findings may be present with epididymo-orchitis [4]. In addition, in acute torsion, the testis may be entirely normal on gray-scale imaging [5] as in our three cases. Therefore, gray-scale imaging of the scrotum is often not helpful in definitively establishing the diagnosis of torsion and distinguishing it from scrotal inflammatory processes.

Nonimaging, continuous-wave Doppler techniques have been used to help differentiate testicular torsion from epididymo-orchitis. Initial reports showed that lack of detectable arterial signals over the involved testis was an extremely sensitive sign of testicular torsion [6, 7]. However, subsequent reports have indicated that these methods may not detect torsion in as many as 62–67% of cases [8, 9]. False-negative or indeterminate results presumably occur because arterial flow in peritesticular vessels cannot be distinguished from flow in intratesticular arteries.

The combination of pulsed Doppler and gray-scale imaging that is possible with conventional duplex Doppler equipment allows for determination of the exact origin of arterial signals in the scrotum [3]. This should theoretically increase the accuracy of sonographic evaluation of acute scrotal symptoms. Identification of normal or increased blood flow within the testis would effectively exclude the diagnosis of acute torsion. However, because the testicular vessels are small and not visible on gray-scale imaging and because the flow velocities are low, detection of intratesticular flow can be difficult even in normal testes. Therefore, the diagnosis of acute torsion can be difficult to make with great confidence even with duplex Doppler evaluation. In addition, the meticulous interrogation of the testicular parenchyma that is necessary with conventional duplex Doppler can be quite time-consuming. This is particularly true in the presence of testicular ischemia, where prolongation of the examination is often necessary to distinguish apparent nonperfusion from sampling error. Despite these limitations, in experienced hands, conventional duplex Doppler has been shown to be helpful in diagnosing testicular torsion [10].

Color Doppler sonography offers a number of advantages over conventional sonographic imaging and duplex Doppler

evaluation. In addition to showing the nonspecific gray-scale changes that can occur with testicular ischemia, color Doppler sonography also images blood flow in testicular arteries. Previous work done with normal volunteers has shown that color Doppler sonography can be used confidently and reliably to identify blood flow in the capsular and centripetal arteries of the testis [1]. This normal pattern is easily distinguished from the complete lack of visible intratesticular blood flow in the five patients reported in this series. Because of the striking difference in appearance between perfused and nonperfused testes, we believe that color Doppler sonography will allow for a more rapid and definitive diagnosis of testicular ischemia than conventional sonography or duplex Doppler evaluation.

These results may not be applicable in all clinical situations. All five patients were adults; color Doppler sonography of the testes will undoubtedly be more difficult in neonates and children with acute scrotal symptoms. In addition, the three patients with torsion all presented acutely and it is possible that delayed torsion will be more difficult to diagnose. Finally, the ability to detect absence of testicular perfusion clearly depends on the ability to show blood flow in the normal testis reliably and unequivocally. This ability will vary depending on the sensitivity of the equipment used and on the transmitted frequency.

In summary, our initial experience in using color Doppler sonography to image patients with testicular ischemia has shown that lack of identifiable intratesticular blood flow is a sign of testicular torsion or infarction. In these five patients, the asymmetry in blood flow between the symptomatic and asymptomatic sides was striking and allowed for rapid and definitive diagnosis. Although these results suggest that color Doppler sonography may play a valuable role in evaluating patients with suspected testicular torsion, further comparative studies between color Doppler sonography and testicular scintigraphy in a larger population of patients will be needed before its exact role can be determined.

REFERENCES

1. Middleton WD, Thorne D, Melson GL. Color Doppler ultrasound of the normal testis. *AJR* 1989;152:293–297
2. Bird K, Rosenfield AT, Taylor JKW. Ultrasonography in testicular torsion. *Radiology* 1983;147:527–534
3. Hricak H, Lue T, Filly RA, Alpers CE, Zeineh SJ, Tanagho EA. Experimental study of the sonographic diagnosis of testicular torsion. *J Ultrasound Med* 1983;2:349–356
4. Rifkin MD, Kurtz AB, Goldberg BB. Epididymis examined by ultrasound: correlation with pathology. *Radiology* 1984;151:187–190
5. Chen DCP, Holder LE, Kaplan GN. Correlation of radionuclide imaging and diagnostic ultrasound in scrotal diseases. *J Nucl Med* 1986;27:1774–1781
6. Pedersen JF, Holm HH, Hold T. Torsion of the testis diagnosed by ultrasound. *J Urol* 1975;113:66–68
7. Perri AJ, Slachta GA, Feldman AE, Kendall AR, Karafin L. The Doppler stethoscope and the diagnosis of the acute scrotum. *J Urol* 1976;116:598–599
8. Rodriguez DD, Rodriguez WC, Rivera JJ, Rodriguez S, Otero AA. Doppler ultrasound versus testicular scanning in the evaluation of the acute scrotum. *J Urol* 1981;125:343–347
9. Lee LM, Wright JE, McLoughlin MG. Testicular torsion in the adult. *J Urol* 1983;130:93–94
10. Lewandowski B, Collins J, Gerritzen R. The halo sign revisited: a duplex Doppler, scintigraphy, pathological correlation of testicular torsion. Presented at the annual meeting of the American Institute of Ultrasound in Medicine, Washington, DC, October 1988



The Radiology Outreach Foundation (ROF) is a nonprofit corporation whose goal is to help disadvantaged countries improve their health care by providing radiology equipment, books, consultation, education, and training to their practitioners. This assistance is on an application basis that is independent of political, ethnic, or religious orientation of the grantee. It depends on the need of the people and the ability of the ROF to meet that need. The ROF is approved by the U.S. Internal Revenue Service as a tax-exempt organization. It is endorsed by the following radiologic societies:

American Association of Women Radiologists
American College of Radiology
American Roentgen Ray Society
Association of University Radiologists
Radiological Society of North America
Society of Chairmen of Academic Radiology Departments
Society for Pediatric Radiology
European Society of Pediatric Radiology

All donations to the ROF are tax deductible. Persons who would like to contribute financially to the ROF, would be interested in being a visiting professor, would like to send books or journals to any of the institutions supported by the ROF, or would like further information about the ROF should write to

Charles A. Gooding, M.D.
President
Radiology Outreach Foundation
3415 Sacramento St.
San Francisco, CA 94118 USA

MR Imaging of the Temporomandibular Joint: Comparison of Images of Autopsy Specimens Made at 0.3 T and 1.5 T with Anatomic Cryosections

Lars-Göran Hansson¹
 Per-Lennart Westesson^{2,3}
 Richard W. Katzberg⁴
 Ross H. Tallents⁵
 Kenichi Kurita^{2,6}
 Stig Holtås¹
 S. Alvar Svensson⁷
 Lars Eriksson⁸
 Carl Christian Johansen¹

Received October 26, 1988; accepted after revision February 6, 1989.

This study was performed as a joint project between the Universities of Lund, Sweden, and Rochester, NY. 0.3-T MR imaging and cryosectioning were performed at the University of Lund; 1.5-T MR imaging was performed at the University of Rochester, New York. The study was done while Dr. Kurita was a guest researcher at the University of Lund during 1987 and 1988.

This work was supported by the Swedish Medical Research Council (project nos. 6751, 8164), the Torsten and Ragnar Söderbergs Foundations, NIH (Grant DE-08059), and the Swedish Society of Medical Radiology.

¹ Department of Diagnostic Radiology, University Hospital of Lund, S-221 85 Lund, Sweden.

² Department of Oral Radiology, University of Lund, School of Dentistry, S-214 21 Malmö, Sweden. Address reprints requests to P.-L. Westesson.

³ Present address: Department of Diagnostic Radiology, Box 694, University of Rochester School of Medicine and Dentistry, Rochester, NY 14642.

⁴ Department of Diagnostic Radiology, Box 694, University of Rochester School of Medicine and Dentistry, Rochester, NY 14642.

⁵ Eastman Dental Center, Rochester, NY 14642.

⁶ Present address: The Second Department of Oral and Maxillofacial Surgery, Aichi-Gakuin University, 2-11 Suemon, Chikusa, Nagoya 4-64, Japan.

⁷ Laboratory of Engineering, University of Lund, School of Dentistry, S-214 21 Malmö, Sweden.

⁸ Department of Oral Surgery, University Hospital of Lund, S-221 85 Lund, Sweden.

AJR 152:1241-1244, June 1989

0361-803X/89/1526-1241

© American Roentgen Ray Society

We made MR images of 39 autopsy specimens of the temporomandibular joint at 0.3 and 1.5 T and compared the images with anatomic cryosections. Imaging time and slice thickness were the same on scans made at each field strength. The purpose was to determine which field strength provides the best scans for imaging of the joint. Additionally, we used imaging times two and four times longer on the 0.3-T scanner to assess to what extent image quality and diagnostic accuracy could be improved. The cryosections showed that 27 of the joints were normal. Twelve had disk displacements. Ten of the joints with disk displacement also had disk deformities, and seven had bony abnormalities. Investigators who analyzed the MR images had no knowledge of the findings on the cryosections. The disk position, disk configuration, and bony abnormalities were correctly diagnosed in 85%, 77%, and 100%, respectively, on 1.5-T MR images compared with 46%, 41%, and 85%, respectively, on the 0.3-T images. When the imaging time was increased by a factor of four, the accuracy rate on the 0.3-T system became comparable to that of the 1.5-T MR scanner: 73% for disk position, 67% for disk configuration.

The results suggest that the diagnostic quality of MR images of the temporomandibular joint is better on scans made at 1.5 T than on those done at 0.3 T when comparable imaging times are used.

The magnetic field strength is the most prominent characteristic of MR imaging systems, with field strengths ranging from 0.02 to 2.0 T when the systems are used for clinical diagnosis [1]. Subjective ratings of MR images obtained at different field strengths have suggested that systems with higher field strength provide superior image quality [2]. Theoretical concepts support these observations; the signal-to-noise ratio increases by a factor of four between 0.3 and 1.5 T [3], resulting in superior tissue differentiation and superior spatial resolution. Experimental studies with field-cycling relaxometry suggest, however, that field strengths between 0.2 and 0.6 T are optimal for clinical imaging because the T1 contrast decreases at field strengths higher than 0.6 T [4].

To study the effect of field strength on the quality of MR images of the temporomandibular joint (TMJ), we imaged 39 autopsy specimens of the joint in both an iron-core resistive 0.3-T and a superconducting 1.5-T MR scanner and compared the findings with corresponding cryosectional anatomy. The imaging time and the slice thickness were the same on scans made at each field strength. Other imaging variables were selected individually for each scanner for optimal image quality within the constraints of the preselected imaging time and slice thickness. Additionally, we used imaging times that were two and four times longer on the 0.3-T scanner to assess to what extent image quality and diagnostic accuracy could be improved.

Materials and Methods

Thirty-nine left TMJs were removed as blocks approximately 6 × 6 × 6 cm from fresh cadavers (5–48 hr postmortem) during an autopsy that included the brain. No information

about TMJ symptoms before death was available. The age range of the individuals from whom the specimens were obtained was 47–92 years (mean, 72 years). The specimens were taken from cadavers with either natural teeth or full dentures. Cadavers with no teeth or with unstable dentures were excluded because it was not possible to place the lower jaw into a fixed closed position. No other attempts were made to be selective.

Before the joint specimen was removed, the mouth of the cadaver was closed and the left TMJ region was deep-frozen by repeatedly pouring liquid nitrogen over the joint region. In this manner, the status of the joint components as seen in the subsequent MR images and cryosections was representative of the joint in the closed-jaw position.

Once the joints were removed, fluoroscopy was used as a guide to orient the long axis of the condyle vertically, and the specimens were embedded in square blocks of methyl methacrylate. One side of the block was oriented parallel to the condylar long axis and the other side was perpendicular to it. In this way, the position of the specimen could be standardized during MR imaging and cryosectioning. The acrylic block made it possible to maintain the positional relationships of the joint components when the specimens were thawed for MR imaging.

MR imaging was performed by using two MR systems. One was a superconducting 1.5-T Signa (General Electric, Milwaukee, WI), and the other was an iron-core resistive 0.3-T scanner (Fonar, beta-3000M, Fonar, Melville, NY). Identical imaging variables were not used because the two scanners differ. Only the imaging time (2 min, 34 sec) and the slice thickness (3 mm) were constant. Other imaging variables were selected for each scanner to optimize the image quality. In preparation for this study, we tested many combinations of different imaging settings on both scanners to determine a combination for each scanner that produced an optimal image quality for the scan time and slice thickness selected. These settings were then held constant throughout this protocol.

The body coil was used as transmitter for both scanners. The scanning variables with a 6-cm surface coil on the 1.5-T scanner were 600/25/2 (TR/TE/excitations), 256×128 matrix, 8-cm field of view, and interleaving. Eight 3-mm sagittal planes of imaging were obtained [5]. For the 0.3-T scanner, a 6-cm surface coil (orbit coil) was used as the receiver, and the following scanning variables were used: 600/28/1, 256×256 matrix, and 16-cm field of view. Nine 3-mm sagittal planes of imaging were obtained with an interslice gap of 0.75 mm.

All joints were imaged first on the 0.3-T magnet and then on the 1.5-T magnet. To assess whether repeated thawing and deep freezing affected the image quality of the joint, nine randomly selected joints were imaged a second time on the 0.3-T scanner after they had been thawed and imaged on the 1.5-T scanner. The images were then reassessed without knowledge of previous findings.

Fifteen randomly selected joints were additionally imaged at 5.5- and 11.2-min scanning times on the 0.3-T magnet to determine if image quality could be improved by using greater imaging times. Two and three excitations for 5.5- and 11.2-min scanning times, respectively, were used. The other imaging parameters were held constant.

After all scanning protocols had been completed, the specimens were deep frozen and later cryosectioned on a precision band saw with a fine-toothed metal cutting blade as previously described [5, 6]. The surfaces of the square acrylic block served as the planes of reference for MR imaging and cryosectioning. The newly cut surfaces of the specimens were photographed by using color slide film (Kodak K64, Rochester, NY).

The images from the two scanners were rated side-by-side by two of the authors to determine if the image quality was better at 0.3 T, better at 1.5 T, or equal. The MR images were assessed for diagnosis with respect to the position and the configuration of the disk without knowledge of the cryosectional results. The images from each scan-

ner were assessed independently of each other. All 1.5-T images were assessed in one session, and all 0.3-T images were assessed in another session. Blinded assessment with respect to the scanner was not possible because the origin of the images was obvious. Disk position was classified as normal when the posterior band of the disk was located on top of the condyle or displaced when this band was located anterior to the top of the condyle. Disk configuration was classified as biconcave (normal) or deformed (abnormal). These classifications were made according to previously described criteria [6–8].

The MR images were evaluated for evidence of abnormalities of the bone also. Thus, concavity, erosion, flattening, or osteophytes of the condyle, fossa, or tubercle were classified as abnormalities.

Findings in the MR images later were compared with the anatomy in the cryosections. Thus, position and configuration of the disk and bony changes were assessed in the same way as in the MR images. On cryosections, 27 joints showed normal disk position. Twelve joints showed disk displacement. Disk deformation was seen in nine of the abnormal joints. Bony abnormalities were found in seven of the abnormal joints. The cryosectional findings were used as the morphologic standard, and the diagnostic accuracy was calculated for each MR system as the percentage of joints with the correct diagnosis (true-positive and true-negative diagnoses) out of all joints [9, 10]. In the calculation of diagnostic accuracy, the inconclusive images were included among the false diagnoses. After all analyses were completed, the MR images were compared with the cryosections in an attempt to explain the disparities.

Chi-square tests were used to assess if observed frequencies differed from those expected. The null hypothesis was rejected if $p < .05$.

Results

In 33 (85%) of the 39 joints, the 1.5-T images of the disk were rated as superior to the 0.3-T images (Figs. 1 and 2). In five joints (13%), the image quality was equal for the two scanners, and in one joint (2%), the 0.3-T scanner produced an image that was rated as superior to that of the 1.5-T scanner with respect to delineation of the disk. Subjectively, the images produced by the 0.3-T scanner had higher tissue contrast between the disk and surrounding tissues but were noisier when compared with the 1.5-T images (Figs. 1 and 2). The 1.5-T images gave the subjective impression of having a higher signal-to-noise ratio and provided a superior delineation of fine details (Figs. 1 and 2).

The number of MR images that were not interpretable was higher for the 0.3-T scanner (disk position 41%, disk configuration 46%, bone 3%) than for the 1.5-T scanner (disk position 8%, disk configuration 10%, bone 0%). The diagnostic accuracy was greater with the 1.5-T scanner than with the 0.3-T scanner with regard to disk position ($p < .001$), disk configuration ($p < .001$), and bony abnormalities ($p < .05$) (Table 1).

When the imaging time at 0.3-T field strength was increased to 5.5 min, the images of two of the 15 joints were rated superior to the 2.5-min images, whereas the images of the remaining 13 joints were rated as similar to the 2.5-min images. When the imaging time was increased to 11.2 min, the quality of the images of seven of the 15 joints appeared to be superior when compared with the 2.5-min images (Fig. 3). The diagnostic accuracy for both position and configura-

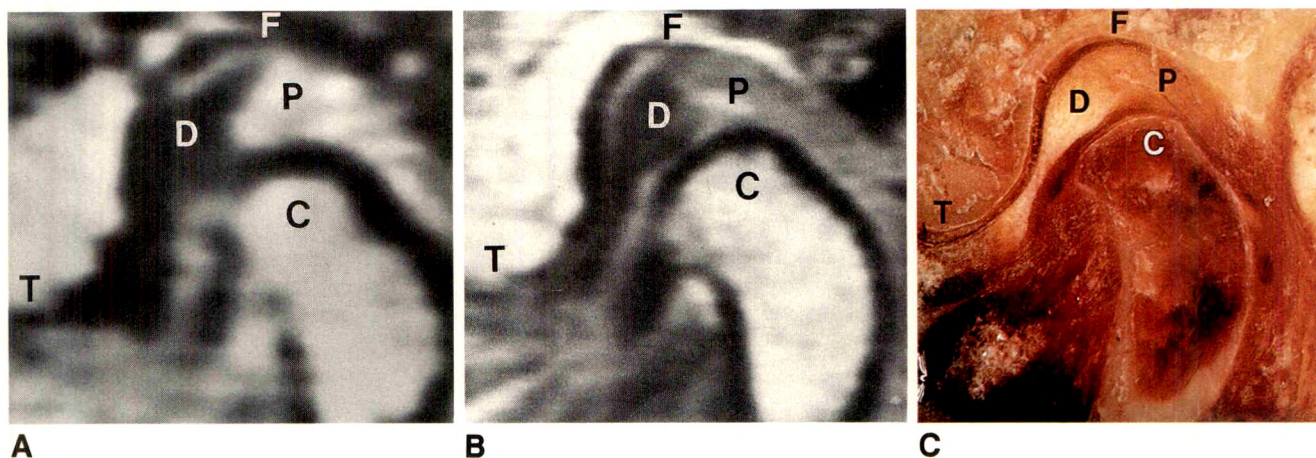


Fig. 1.—A and B, MR images obtained at 0.3 (A) and 1.5 T (B) show normal disk position. Anterior is to left. Quality of 1.5-T image was rated superior to that of 0.3-T image.

C, Cryosection confirms MR diagnosis. F = fossa, D = disk, P = posterior disk attachment, T = tubercle, and C = condyle.

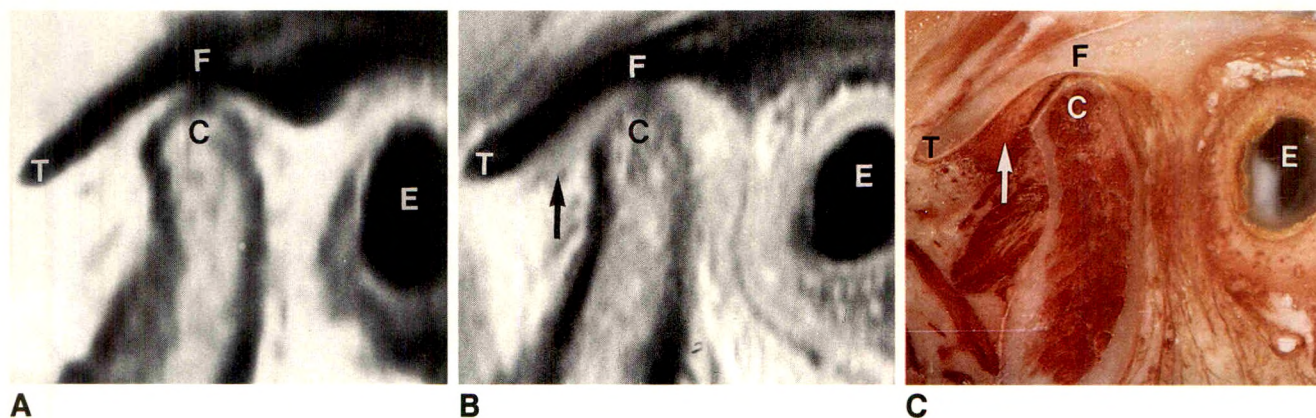


Fig. 2.—A and B, MR images obtained at 0.3 (A) and 1.5 T (B) show anterior displacement of disk. Anterior is to left. Image quality with respect to delineation of disk was rated superior on 1.5-T image (B). Position of disk could not be seen clearly in 0.3-T image (A).

C, Cryosection confirms MR diagnosis. F = fossa, arrow = disk, T = tubercle, E = external auditory meatus, and C = condyle.

tion of the disk was 53% for these 15 joints at both 2.5- and 5.5-min scanning times. At 11.2-min scanning time, the accuracy was 73% for position of the disk and 67% for disk configuration.

Repeated imaging after thawing and freezing was performed in nine joints and resulted in the same image quality in six joints and a slightly deteriorated image in three joints.

Discussion

The results show that the 1.5-T scanner is superior to the 0.3-T scanner with respect to diagnostic accuracy in studies of the TMJ when equivalent imaging times and slice thicknesses are used. The major difference between the two scanners was that the frequency of inconclusive studies was higher at 0.3 T than at 1.5 T. A side-by-side comparison of the images showed that the 0.3-T images were noisier but had a higher tissue contrast than the 1.5-T images. The visualization of fine anatomic detail was poor in the 0.3-T images with this relatively short imaging time. These obser-

TABLE 1: Accuracy (%) of MR Imaging of Temporomandibular Joint at 0.3 and 1.5 T

Structure Assessed	Accuracy (%)	
	0.3 T	1.5 T
Disk position	46	85
Disk configuration	41	77
Bone	85	100

Note.—Accuracy = number of correct diagnoses out of all examined joints (n = 39).

ations are in accordance with earlier studies that compared images of the CNS obtained at different field strengths [2, 11].

In our preliminary studies, we tested multiple parameters on each of the scanners to find an optimal imaging strategy for each one. The parameters used in the study were those determined to provide optimal image quality in fresh TMJ autopsy specimens. Despite these attempts, we cannot be certain that further improvements might not have been pos-

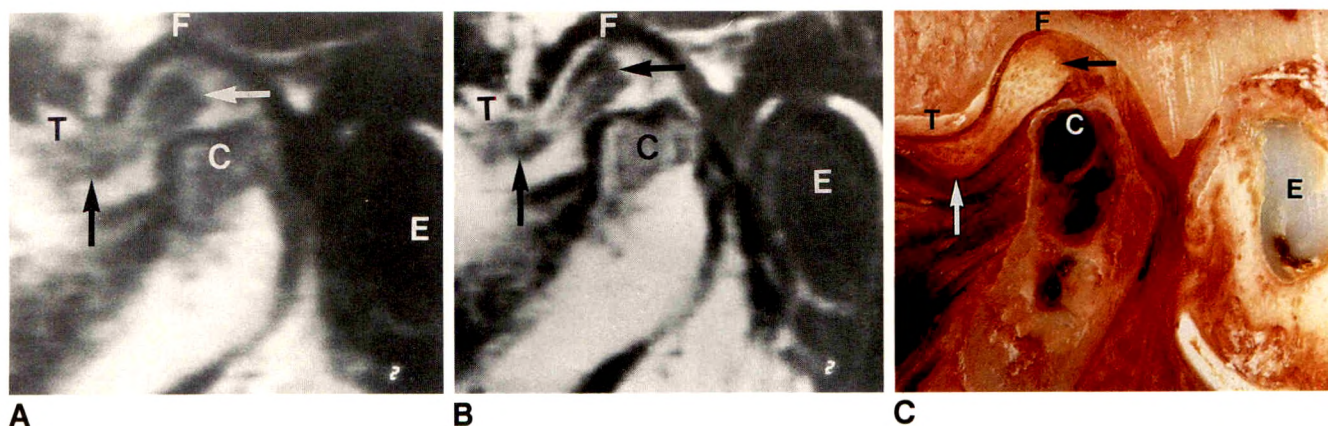


Fig. 3.—A and B, MR images obtained with 0.3-T scanner by using 2.5-min (A) and 11-min (B) scanning times show normal disk position. Anterior is to left. Quality of 11-min images was rated superior to that of 2.5-min images. Erosive change superiorly on condyle is best viewed in 11-min image. C, Cryosection confirms MR diagnosis. F = fossa, arrows = disk, C = condyle, T = tubercle, and E = external auditory meatus.

sible. It should, however, be noted that relatively major changes in imaging parameters resulted in only relatively minor changes in image quality. We found that the only way to improve image quality substantially was to increase acquisition time or to increase slice thickness. It should be emphasized, however, that differences in image quality between the two field strengths used were so dramatic that variations in imaging parameters would not have altered our overall findings.

All specimens were examined at room temperature. The temperature was, however, approximately the same during the examinations in both scanner rooms and the comparison between images therefore should be comparable. Imaging at higher tissue temperature might alter the accuracy rate but probably would not account for the differences in image quality between field strengths.

The results of this study suggest that the image quality and diagnostic accuracy of MR images of the TMJ are better at 1.5 T than at 0.3 T when comparable imaging times are used.

ACKNOWLEDGMENTS

Nils H. Sternby, Department of Pathology, General Hospital, Malmö, Sweden, is acknowledged for support with the cadaver work; William Badger, Aileen MacKay, Ann Nilsson, Titti Owman, Constance White, and Anna Wicks are acknowledged for technical assistance.

REFERENCES

1. Nixon JR. Basic principles and terminology. In: Berquist TH, Ehman RL, Richardson ML, eds. *Magnetic resonance of the musculoskeletal system*. New York: Raven Press, 1987:1-21
2. Keohler RP, Daniels DL, Williams AL, Haughton VM. Technical factors in MR image quality. *Neuroradiology* 1986;28:74-77
3. Luytjens R, Goes E, Osteaux M. MRI tissue differentiation: comparing high and low field strengths. *J Belge Radiol* 1986;69:157-161
4. Rinck PA, Fischer HW, Vander Elst L, Van Haverbeke Y, Muller RN. Field-cycling relaxometry: medical applications. *Radiology* 1988;168:843-849
5. Westesson P-L, Katzberg RW, Tallents RH, Sanchez-Woodworth RE, Svensson SA, Espeland MA. Temporomandibular joint: comparison of MR images with cryosectional anatomy. *Radiology* 1987;164:59-64
6. Westesson P-L, Bronstein SL, Liedberg JL. Internal derangement of the temporomandibular joint: morphologic description with correlation to function. *Oral Surg Oral Med Oral Pathol* 1985;59:323-331
7. Westesson P-L, Rohlin M. Diagnostic accuracy of double-contrast arthro-tomography of the temporomandibular joint: correlation with postmortem morphology. *AJNR* 1984;5:463-468, *AJR* 1984;143:655-660
8. Westesson P-L, Bronstein SL, Liedberg J. Temporomandibular joint: Correlation between single-contrast videarthrography and postmortem morphology. *Radiology* 1986;160:767-771
9. Patton DD. Introduction to clinical decision making. *Semin Nucl Med* 1978;8:273-278
10. Gelfand DW, Ott DJ. Methodologic considerations in comparing imaging methods. *AJR* 1985;144:1117-1121
11. Rinck PA, Muller RN, Fischer H. Feld- und Temperaturabhängigkeit des Kontrastes in der Magnetresonanzbildgebung. *Fortschr Geb Röntgenstr Nuklearmed Ergänzungsband* 1987;147:200-206

Progress in Radiology

MR Imaging of the Abdomen in Children

M. Ines Boechat¹ and Hooshang Kangarloo

Imaging of the pediatric patient has undergone a rapid and profound change during the past decade. Advances in MR imaging have changed the approach to many pediatric diseases because excellent tissue-contrast differentiation, high-resolution multiplanar capability, and lack of ionizing radiation make MR imaging a very useful tool in the evaluation of many pediatric disorders. The role of MR images in evaluating the brain and spine in children is well accepted [1-3]. Recent advances have also clearly defined the advantages of MR imaging in the evaluation of the musculoskeletal system and particularly of bone marrow [4, 5]. The role of MR imaging in the evaluation of the abdomen in children, however, has not been clearly established. This article summarizes selected aspects of abdominal MR imaging with particular emphasis on the evaluation of abdominal masses in children. Because the majority of abdominal masses in children are related to the kidney, the adrenal glands, or the liver, each of these areas is discussed separately.

General Considerations

Sedation and Patient Immobilization

Sedation in young children is required to obtain a good MR study. As a rule, we sedate all patients up to the age of 7 years old. Older children who are apprehensive may also receive sedation. Chloral hydrate, 50-100 mg/kg, is given to children under 3 years old by mouth, whereas intrarectal thiopental, 25 mg/kg, is given to older patients. If an acceptable level of sedation cannot be obtained with these drugs,

the examination is rescheduled and a stronger drug, such as Versed (Roche, Nutley, NJ) or fentanyl, is administered by a pediatric intensive care physician in charge of drug administration and patient monitoring. All sedated patients are connected to an apnea monitor (Biochem, Waukesha, WI), which detects the relative amount of carbon dioxide exhaled by the patient through a nasal cannula. After the examination is completed, the patient, when alert and awake, is discharged. Parental anxiety is decreased by the attending radiologist's explanation about the procedure and by a booklet given to the parents before the study. A parent usually stays in the room with the child during the entire examination.

Patient immobilization is accomplished with a blanket, light sandbags, or sponges. Because scanner beds are designed specifically for adults, adaptations may be necessary for children. To ensure their positioning in the center of the coil with optimal signal emission, placement of extra pads under the patient or of special cradle devices provided by some manufacturers is recommended.

Surface Coil and Imaging Plane

By separating the receiver coil from the transmitter coil, it is possible to optimize each coil for its particular function. The receiver coil should be as small as possible relative to the patient's size (it should fit tightly around the patient's abdomen), and it should have a high quality factor [6-8]. We have used solenoid surface coils, which are made up of several pairs of thin copper coils. The use of flexible copper allows the coil to be applied like a belt around the child's abdomen

Received November 7, 1988; accepted after revision January 25, 1989.

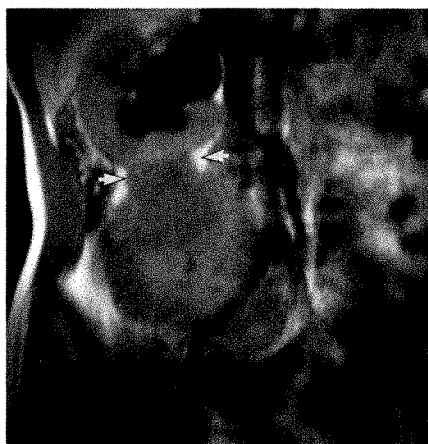
¹ Both authors: Department of Radiological Sciences, University of California, Los Angeles, School of Medicine, Los Angeles, CA 90024-1721. Address reprint requests to H. Kangarloo.

and secured with a Velcro fastener. Various sizes of these coils are available, ranging from 3 to 50 cm in diameter. Strong coupling of the surface coil results in an improved signal-to-noise ratio (SNR), compared with images obtained with the standard body coil. Planar and other noncircumferential surface coils have a marked loss of signal beyond one radius from the center of the coil. This drop in signal intensity limits the effectiveness of the coil when imaging deeper structures in the abdomen. Solenoidal surface coils do not have this limitation and provide images with more uniform intensities [7].

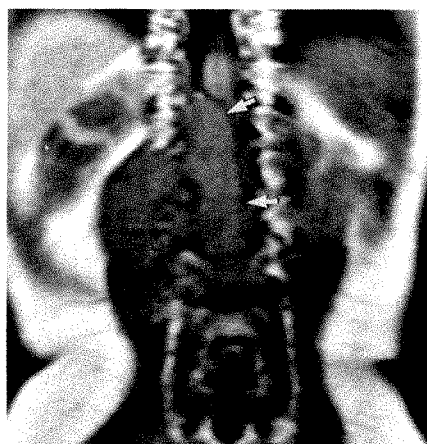
Axial and coronal planes are most often used in evaluating suspected abdominal disease in children. Other imaging planes are occasionally used depending on the findings of initial axial or coronal scans. Coronal images provide a good overview of the abdomen and are useful in defining the organ of origin of an abdominal mass. This imaging plane is particularly useful in differentiating renal and juxtarenal masses (Figs. 1–4). The coronal plane is also useful to visualize the aorta and inferior vena cava in assessing tumor extent (Fig. 4). The axial plane is used for evaluating the liver (Fig. 5) and pancreas, as well as for defining tumor extent by visualizing the celiac axis (Fig. 6).

Field Strength, Slice Section, and Pulse Sequence

Field strength determines the maximum achievable SNR. The signal increases as the square of the field's strength, but noise also increases linearly. Furthermore, as the field strength increases, so does the resonance RF, and as the frequency increases, the RF penetration into the imaged body part decreases. This necessitates an increase in RF power with increasing magnetic field. In light of all of these facts, the SNR is only about linearly proportional to the magnetic field. Hoult et al. [9] reported that the present imaging techniques provide a good argument for the use of a mid field strength. Henkelman et al. [10] suggested that at field strengths less than 15 MHz (0.35 T), a T1-weighted sequence is preferred between 15 and 24 MHz (0.5 and 0.56 T), which is an inversion-recovery sequence, whereas at field strengths greater than 0.56 T, a T2-weighted sequence is optimum for detecting liver metastasis in adults. Among other important aspects that need to be considered is the relative orientation of the magnetic field to the body. A vertical field allows the optimal use of surface coils with concomitant increase in SNR. This is particularly relevant to the small filling factor of pediatric patients.



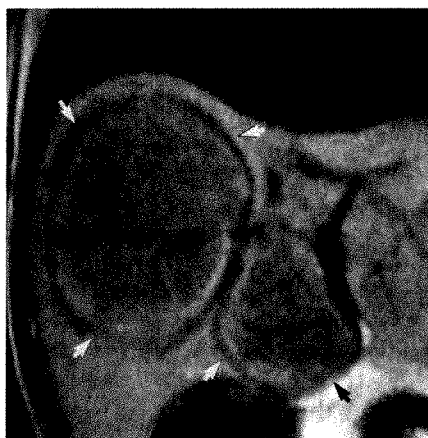
1



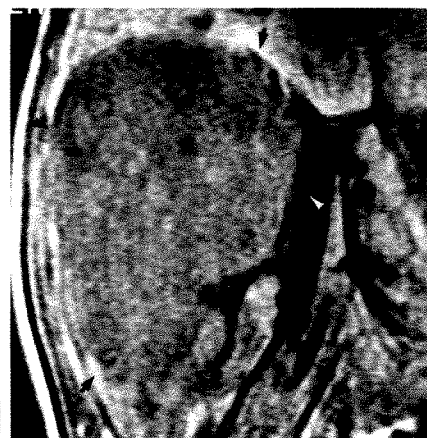
2

Fig. 1.—7-year-old girl with Wilms tumor. Coronal SE T1-weighted image (500/18) depicts exophytic nature of tumor, which arises from lower pole of right kidney (arrows) and causes hydronephrosis due to compression of distal ureter.

Fig. 2.—6-month-old girl with paravertebral neuroblastoma. Coronal SE T1-weighted image (500/28) shows extrarenal origin of lesion, extension into spinal canal (arrows), and cord compression. (Reprinted with permission from Dietrich et al. [24].)



3



4

Fig. 3.—8-year-old girl with hepatoblastoma. Coronal SE T1-weighted image (300/18) shows bilobular tumor (arrows) in liver. (Reprinted with permission from Boechat et al. [30].)

Fig. 4.—4-year-old boy with Wilms tumor (arrows). Coronal SE T1-weighted image (500/28). Void signal provided by flowing blood acts as natural contrast to show medium-signal-intensity mass in lumen of inferior vena cava (arrowhead).

Perhaps one of the most important considerations is the dependence of contrast on the magnetic field strength. T1 is field-dependent, increasing with field strength, but T2 is relatively independent of field strength [11]. A consequence of this can be directly seen, for example, in lesion detectability in the liver. At low and mid field strengths, a short TE/short TR sequence is very efficient in detecting hepatic lesions. A long TR/long TE spin-echo (SE) sequence is more effective at field strengths of greater than 0.7 T. The dependence on field strength occurs because liver lesions generally have prolonged T1 and T2 relaxation times; T1 increases at higher field strengths while T2 does not show appreciable changes. This increase in T1 in tissues at higher field strengths makes the contrast between normal liver and hepatic lesions less evident as the field strength is increased. Thus, T1-weighted sequences are optimal for detecting liver lesions at low and mid field strengths (up to approximately 0.7 T), fully using the differences in the T1 times between normal liver and lesions. This difference decreases at higher field strengths (particularly greater than 1.0 T), reducing the efficacy of the T1-weighted sequences [11]. Long TR/long TE SE sequences thus become better for lesion detection at high field strength [12]. In a recent article, Reinig et al. [13] reviewed the accuracy of detecting liver lesions at 0.5 and 1.5 T in 19 patients with known liver metastasis. They showed that at 0.5 T, an SE 300/22 (TR/TE) sequence prospectively showed 92.4% of liver lesions, whereas SE 300/25 at 1.5 T showed 68.3% of lesions. Furthermore, an SE 2000/80 sequence at 0.5 T showed 52.1% of lesions and, at 1.5 T, 71.6% of lesions. Reinig et al. showed that liver metastasis was not only better detected on a short SE pulse sequence with a lower magnetic field (0.5 T), but also a T1-weighted sequence with a low magnetic field strength was superior to a T2-weighted sequence at a higher field strength (1.5 T).

An important issue to remember is that moving abdominal structures give rise to ghost artifacts propagating along the phase-encoding direction. Fat usually has the highest signal

intensity; this signal is the most frequently registered as the propagator of ghost images. Because the SNR is in general higher in a high field strength, the fat intensity is greater and consequently the ghost images are more evident.

Other important advantages of T1-weighted SE sequences are that they require short scanning times, have good SNRs, and can have slice thicknesses as thin as 3 mm. The drawback is that sequences with a very short excitation time (TE) are not suitable for obtaining contiguous slices. Gaps between sections are undesirable. However, there is a loss of tissue contrast in MR imaging when contiguous sections (using gaussian RF shape pulse) are acquired. This is largely due to the nonideal excitation created by the 180° pulse, which results in partial excitation of neighboring sections [14]. Sinc-shaped RF pulses can be tailored to generate rectangular profiles diminishing section-to-section interference. However, these are of longer duration than gaussian RF pulses. Thus, in order to obtain contiguous sections, a longer TE is required. Another advantage of long SE pulse sequences (T2-weighted images) is that lesions such as hepatic hemangiomas may be specifically diagnosed on T2-weighted images [15–17]. On the basis of the MR appearance alone, however, benign hemangiomas may be difficult to differentiate from metastatic neuroblastomas or other malignant tumors (Figs. 7 and 8). T1-weighted images may also allow for a specific diagnosis (Figs. 9 and 10). At the present time, however, both T1- and T2-weighted images may be necessary in evaluating much of the abdominal pathology in children.

MR Imaging of the Kidneys

The results of early investigations suggest the usefulness of MR imaging in the evaluation of renal disease [18]. A report from our own institution [19] that describes MR imaging in 43 children with renal abnormalities is based on a comparison of MR imaging results with those obtained by more conventional techniques such as sonography, CT, and excretory urogra-

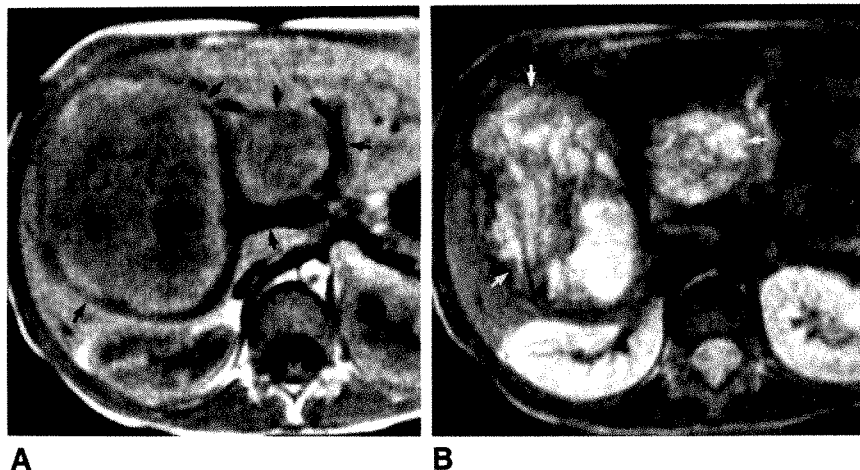
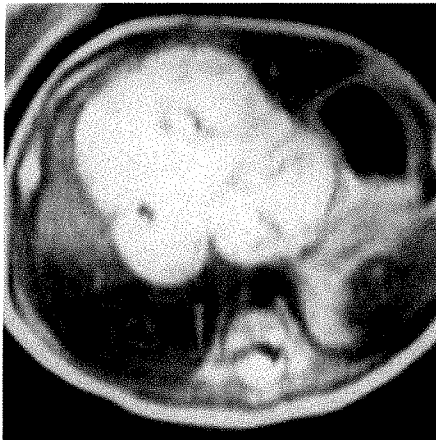


Fig. 5.—Child with hepatoblastoma. A and B, Axial SE T1-weighted (300/18) (A), and T2-weighted (1500/56) (B), images. Well-defined lobulated mass (arrows) is bordered posteriorly by main portal vein, branches of right portal vein, and left portal vein. Vascular anatomy is seen somewhat better on T1-weighted image. (Reprinted with permission from Boechat et al. [30].)



Fig. 6.—8-month-old boy with unresectable neuroblastoma. Axial SE T1-weighted image (500/18) shows encasement of aorta and its branches (arrows) and lateral deviation of right kidney.



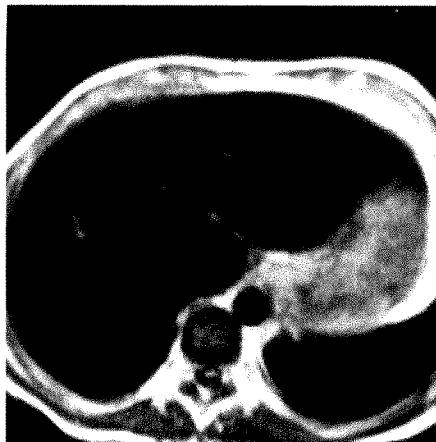
7



8

Fig. 7.—Specificity of T2-weighted image in neonate with cavernous hemangioma. Axial SE T2-weighted image (1500/56) shows marked hyperintensity of lesion (equal or higher than subcutaneous fat) characteristic of hemangioma.

Fig. 8.—Specificity of T2-weighted image in 2-month-old boy with large thrombosed hemangioma in left lobe of liver. Axial SE T2-weighted image (1500/56) shows nonhomogeneous intensity of lesion, with areas of decreased signal intensity, not typical of hemangioma. When lesion is thrombosed, it is not possible to differentiate between benign and malignant lesions. (Reprinted with permission from Boechat et al. [30].)



9



10

Fig. 9.—Specificity of T1-weighted image in child with chronic renal disease with multiple transfusions. Axial SE T1-weighted image (500/28) shows markedly decreased signal intensity of liver as a result of iron overload.

Fig. 10.—Specificity of T1-weighted image in 7-month-old boy with Wolman disease. Coronal SE T1-weighted image (500/18) of the abdomen shows liver and spleen to be of very high signal intensity due to fatty infiltration. In addition, splenomegaly is clearly seen in this coronal plane image.

phy. Our conclusion was that sonography should remain the initial procedure of choice in evaluating a child with a possible renal disorder. Depending on the initial sonographic findings, other imaging procedures should be performed. MR imaging is useful when a solid renal lesion is identified. When compared with CT, MR imaging was the same or more sensitive in detecting various renal abnormalities, with the exception of calcification. Because the renal medulla has a longer relaxation time than the renal cortex, a short SE T1-weighted pulse sequence differentiates these two zones in a normal kidney. Corticomedullary differentiation on noncontrast MR images is superior to that on noncontrast CT [12]. Discrimination between cortex and medulla is useful in evaluating generalized parenchymal disease and is similar to the appearance in adults in evaluating renal transplantation. Long SE T2-weighted sequences do not allow for corticomedullary differentiation, require a longer examination time, and are more likely to produce motion artifacts.

One of the most important roles of imaging in evaluating suspected renal disease in children is to define the origin of an abdominal mass, particularly in differentiating renal and extrarenal origins of a solid lesion (Figs. 1 and 2). It is also important to define tumor extent and resectability by visualizing vascular anatomy. The most common renal tumor in

children is Wilms tumor [20]. MR imaging is an excellent technique to diagnose Wilms tumor and to define tumor size, as well as possible tumor thrombus in the inferior vena cava (Fig. 4). With current techniques, however, MR imaging may not allow detection of small lesions. In one patient with Drash syndrome, with a high incidence of Wilms tumor, diagnosis of a lesion approximately 1 cm in size was not made by MR imaging [21]. Another potential drawback of MR imaging in children with Wilms tumor is the evaluation of the lung parenchyma. At the present time CT remains the imaging technique of choice for evaluating lung metastasis from Wilms tumor [22].

Both coronal and axial imaging planes are useful for evaluating the kidneys. Examination should begin in the coronal plane with a T1-weighted sequence, which allows for a good topographic view of the abdomen, for definition of the tumor origin, and for visualization of vascular anatomy. Other imaging planes and pulse sequences are then tailored depending on the result of the first pulse sequence.

MR Imaging of the Adrenal Glands

Other investigators have shown significant promise for MR imaging in evaluating the adrenal glands [23]. Chang et al.

[23] reported that MR imaging can show the normal adrenal glands in most patients. However, considerable overlap may occur in the signal-intensity ratios of adrenal adenoma and malignant neoplasms [23]. Our own experience in trying to differentiate between benign and malignant adrenal lesions initially was encouraging. Adrenal hemorrhage, which has a high signal intensity on a T1-weighted SE sequence, could be differentiated from a medium-level-signal-intensity neuroblastoma. However, in a recent patient with hemorrhagic neuroblastoma, this lesion could not be differentiated from adrenal hemorrhage.

Probably the most useful role of MR imaging in evaluating adrenal glands in children is in the study of patients with neuroblastoma. The usefulness of MR imaging was compared with that of CT in 15 patients [24]. In this study, all patients were examined in the coronal plane with an SE T1-weighted sequence (500/28), followed by imaging in the axial plane in 13 of these patients, again with a similar T1-weighted sequence. In eight patients, an SE T2-weighted sequence (1500,2000/56,84) was also performed. This retrospective study showed MR imaging to be as useful as CT in the evaluation of neuroblastoma. MR imaging can accurately diagnose adrenal lesions and define the extent of tumors in patients with neuroblastoma. This tumor extension correlated well with surgical findings [24]. The T1-weighted sequence in the coronal plane again appeared to be the most useful initial imaging plane, because it also allows the evaluation of bone marrow, the assessment of extension into the spinal canal and into the mediastinum, and the evaluation of the aorta and the inferior vena cava. However, in order to evaluate the superior mesenteric artery and the celiac axis, and to define tumor resectability, imaging in the axial plane also is essential (Fig. 6). Thus, evaluation of adrenal lesions also requires two different SE pulse sequences. Evaluating the invasion of neuroblastoma into the spinal canal is one of the major contributions of MR imaging (Fig. 2). In this group of patients, MR imaging can replace myelography, which is a more invasive and time-consuming procedure in the pediatric age group.

MR Imaging of the Liver

Evaluation of the liver with MR imaging has been a topic of controversy [25–28]. The major issue in adults has been a comparison between the relative efficacies of MR and CT in the detection of metastasis. In children, concerns are somewhat different and mainly relate to the ability of MR imaging to evaluate hepatic lesions and define tumor resectability. Weinreb et al. [29] compared CT and MR of the liver in 27 children. Fourteen of the children had normal livers and nine had focal liver disease. All patients were examined on a 0.35-T system. This study concluded that MR imaging has the potential to replace CT in evaluating the pediatric liver in many cases. MR was not tissue-specific and focal hepatic lesions were hyperintense on T2-weighted images regardless of their pathology. On the other hand, Glazer et al. [12, 17] reported that hepatic hemangiomas appeared to be specific on SE images at 0.35 T and that the sensitivity of MR imaging for detecting hepatic cavernous hemangiomas exceeded that of

other radiologic tests. Stark et al. [15] reported that MR imaging was 90% sensitive and 92% specific in the diagnosis of hemangioma. This specific appearance, defined as extreme hyperintensity on T2-weighted images, probably reflects slowly flowing blood in these lesions (Fig. 7). It should be remembered, however, that if a hemangioma is thrombosed, this differentiation may not be possible. Thrombosis is a common finding in hemangiomas and hemangioendotheliomas, which originate in the center and progress peripherally. If most of the lesion is thrombosed, then differentiation between these lesions and other tumors may not be possible with MR imaging because a thrombosed hemangioma would lack the characteristic marked hyperintensity on T2-weighted images (Fig. 8).

In a recent report [30], a prospective comparison was made between MR imaging and CT in children with suspected hepatic neoplasms. Twenty-five children were evaluated with both CT and MR imaging, and the diagnoses were compared with surgery and histologic findings in all patients. This study indicates that MR imaging is as accurate as CT in evaluating hepatic lesions and in guiding surgeons for tumor resectability. Resectability of hepatic neoplasms depends largely on the distribution of the liver lesion and its relationship to vascular structures, in particular to those that determine hepatic segmental anatomy [31]. MR imaging seems to be better than CT and angiography in predicting resectability. However, it is not possible to differentiate between hepatoblastomas and hepatocellular carcinomas on the basis of the MR appearance. These tumors both appear heterogeneous with poorly defined margins and are not markedly hyperintense on T2-weighted images compared with uncomplicated hemangiomas.

Generalized parenchymal liver disease has been evaluated only briefly by MR imaging in the pediatric age group. A report from our own institution [32] described MR imaging of iron overload in children with end-stage renal disease. Serum ferritin levels correlated well with the results of MR imaging in documenting the presence and the degree of iron overload in 18 patients who had multiple transfusions with end-stage renal disease.

Other Abdominal Organs

Although the majority of abdominal neoplasms in children are related to the kidneys, adrenal gland, or liver, lesions may arise from other abdominal organs. Pelvic lesions that extend into the abdomen may also present as abdominal masses. MR, with its multiplanar capability, is useful to provide a good overview of the abdomen and to assist in defining the organ of origin when a child has an abdominal mass. Again, specially designed surface coils and good immobilization will allow a satisfactory examination. T1-weighted SE sequences should be the initial imaging technique. Additional pulse sequences are used depending on these initial findings. Results of MR imaging involving abdominal disease in children so far favorably compare with those of high-resolution contrast-enhanced CT. The addition of contrast material may further enhance the ability of MR imaging in evaluating the pediatric abdomen.

REFERENCES

1. Pennock J, Bydder GM, Dubowitz LMS, et al. Magnetic resonance imaging of the brain in children. *Magn Reson Imaging* **1986**;4:1-9
2. Brant-Zawadzki M. MR imaging of the brain. *Radiology* **1988**;166:1-10
3. Davis PC, Hoffman JC Jr, Ball TI, et al. Spinal abnormalities in children: MR imaging findings compared with clinical, myelographic, and surgical findings. *Radiology* **1988**;166:679-685
4. Ehman RL, Berquist TH, McLeod RA. MR imaging of the musculoskeletal system: a 5-year appraisal. *Radiology* **1988**;166:313-320
5. Kangarloo H, Dietrich RB, Taira RT, et al. MR imaging of the bone marrow in children. *J Comput Assist Tomogr* **1986**;10:205-209
6. Axel L. Surface coil magnetic resonance imaging. *J Comput Assist Tomogr* **1984**;3:381-384
7. Lufkin RB, Votruba J, Reicher M, et al. Solenoid surface coils in magnetic resonance imaging. *AJR* **1986**;146:409-412
8. Edelman RR, McFarland E, Stark DD, et al. Surface coil MR imaging of abdominal viscera. *Radiology* **1985**;157:425-430
9. Hoult D, Chen CN, Sank VJ. The field dependence of NMR imaging: arguments concerning an optimal field strength. *Magn Reson Med* **1986**;3:730-746
10. Henkelman RM, Hardy P, Poon PY, Bronskill MJ. Optimal pulse sequence for imaging hepatic metastases. *Radiology* **1986**;161:727-734
11. Bottomley PA, Foster TH, Argersinger RE, Pfeifer LM. A review of normal tissue hydrogen NMR relaxation times and relaxation mechanisms from 1-100 MHz: dependence on tissue type, NMR frequency, temperature, species, excision and age. *Med Phys* **1984**;11:425-448
12. Glazer GM. MR imaging of the liver, kidneys and adrenal glands. *Radiology* **1988**;166:303-312
13. Reinig JW, Dwyer AJ, Miller DL, Frank JA, Adams GW, Chang AE. Liver metastases: detection with MR imaging at 0.5 and 1.5 T. *Radiology* **1989**;170:149-153
14. Runge VM, Wood ML, Kaufman DM, Silver MS. MR imaging section profile optimization: improved contrast and detection of lesions. *Radiology* **1988**;167:831-834
15. Stark DD, Felder RC, Wittenberg J, et al. Magnetic resonance imaging of cavernous hemangioma of the liver: tissue-specific characterization. *AJR* **1985**;145:213-222
16. Brant WE, Floyd JL, Jackson DE, Gilliland JD. The radiological evaluation of hepatic cavernous hemangioma. *JAMA* **1987**;257:2471-2474
17. Glazer GM, Aisen AM, Francis IR, Gyves JW, Lande I, Adler DD. Hepatic cavernous hemangioma: magnetic resonance imaging. *Radiology* **1985**;155:417-420
18. Hricak H, Demas BE, Williams RD, et al. Magnetic resonance imaging in the diagnosis and staging of renal and perirenal neoplasms. *Radiology* **1985**;154:709-715
19. Dietrich RB, Kangarloo H. Kidneys in infants and children: evaluation with MR. *Radiology* **1986**;159:215-221
20. Kangarloo H, Dietrich RB, Ehrlich RM, Boechat MI, Feig SA. Magnetic resonance imaging of Wilms tumor. *Urology* **1986**;28:203-207
21. Boechat MI, Kangarloo H. MR imaging in Drash syndrome. *J Comput Assist Tomogr* **1988**;12(3):405-408
22. Kangarloo H. Chest MRI in children. *Radiol Clin North Am* **1988**;26(2):263-275
23. Chang A, Glazer HS, Lee JKT, Ling D, Heiken JP. Adrenal gland: MR imaging. *Radiology* **1987**;163:123-128
24. Dietrich RB, Kangarloo H, Lenarsky C, Feig SA. Neuroblastoma: the role of MR imaging. *AJR* **1987**;148:937-942
25. Ferrucci JR. MR imaging of the liver. *AJR* **1986**;147:1103-1116
26. Reinig JW, Dwyer AJ, Miller DL, et al. Liver metastasis detection: comparative sensitivities of MR imaging and CT scanning. *Radiology* **1987**;162:43-47
27. Stark DD, Wittenberg J, Edelman RR, et al. Detection of hepatic metastases: analysis of pulse sequence performance in MR imaging. *Radiology* **1986**;159:365-370
28. Stark DD, Wittenberg J, Butch RJ, Ferrucci JT. Hepatic metastases: randomized, controlled comparison of detection with MR imaging and CT. *Radiology* **1987**;165:399-406
29. Weinreb JC, Cohen JM, Armstrong E, Smith T. Imaging the pediatric liver: MRI and CT. *AJR* **1986**;147:785-790
30. Boechat MI, Kangarloo H, Ortega J, et al. Primary liver tumors in children: comparison of CT and MRI. *Radiology* **1988**;169:727-732
31. Mukai JK, Stack CM, Turner DA, et al. Imaging of surgically relevant hepatic vascular and segmental anatomy. Part 2. Extent and resectability of hepatic neoplasms. *AJR* **1987**;149:293-297
32. Querfeld U, Dietrich R, Taira RT, et al. Magnetic resonance imaging of iron overload in children treated with peritoneal dialysis. *Nephron* **1988**;50:220-224

Case Report

Hypercalciuric Bartter Syndrome: Resolution of Nephrocalcinosis with Indomethacin

Jane Matsumoto,¹ Bokyoung Kim Han,¹⁻³ Consuelo Restrepo de Rovetto,⁴ and Thomas R. Welch^{2,4}

Bartter syndrome is defined clinically by hypokalemic alkalosis, hyperreninemia, hyperaldosteronism, and normal blood pressure. This syndrome may be the common clinical expression of a number of tubular defects. In children, a variant is described in which the typical abnormalities of Bartter syndrome are associated with hypercalciuria [1]. Nephrocalcinosis occurs commonly in children with this variant of Bartter syndrome. Treatment with indomethacin effectively reduces urinary calcium excretion. We performed serial sonographic examinations on four children with Bartter syndrome and hypercalciuria before and during indomethacin therapy in order to evaluate changes in nephrocalcinosis. One of these cases is presented in detail.

Case Report

The patient was a 1640-g neonate, small for a 35-week gestation. The pregnancy was remarkable for polyhydramnios (10 l of fluid). The neonate had marked polyuria, hypokalemia, and hypercalciuria. A sonogram obtained at 3 days of age showed normal kidneys (Fig. 1A). A follow-up sonogram at 1 month of age showed diffuse bilateral medullary nephrocalcinosis (Fig. 1B). The patient was evaluated at 10 months of age because of failure to thrive and frequent vomiting. He was below the fifth percentile for height and weight. Extensive metabolic testing showed hypokalemic metabolic alkalosis with elevation of plasma renin activity, serum aldosterone level, and $1\alpha,25$ -dihydroxycholecalciferol ($1,25(\text{OH})_2\text{D}$) level. The value of urinary pros-

taglandin E_2 also was elevated. His serum calcium level was normal, but there was marked hypercalciuria. Serial parathyroid hormone values were normal, and the possibility of rickets was excluded. Renal sonography showed no change in the medullary nephrocalcinosis (Fig. 1C). The diagnosis of hypercalciuric Bartter syndrome was made, and indomethacin therapy was begun.

Within 6 weeks, the patient had gained 1.4 kg and grown 3.75 cm. His urinary calcium excretion and prostaglandin E_2 level decreased to normal. Over the next 12 months, his rate of growth increased, and at 24 months he was at the fifth percentile in length and the 30th percentile in weight. Sonography after 12 months of therapy showed a marked decrease in the echogenicity of the medullary pyramids (Fig. 1D).

Discussion

In 1962, Bartter and colleagues [2] described the syndrome of hypokalemic alkalosis, hyperaldosteronism, hyperreninism, hypertrophy of the juxtaglomerular apparatus, and normotension. Since this time, at least three defects in tubular transport have been shown to cause this syndrome [3].

In one subset, hypercalciuria and nephrocalcinosis complicate the typical clinical picture of Bartter syndrome. Polyuria is typically severe in these children and may cause polyhydramnios in utero, resulting in premature delivery [1]. Hypercalciuria in this variant is uniformly associated with an increase in levels of urinary prostaglandin E_2 [4] and serum $1,25(\text{OH})_2\text{D}$.

Received November 4, 1988; accepted after revision February 6, 1989.

¹ Department of Radiology, Children's Hospital Medical Center and University of Cincinnati College of Medicine, Elland & Bethesda Aves., Cincinnati, OH 45229-2899. Address reprint requests to J. Matsumoto.

² Department of Pediatrics, Children's Hospital Medical Center and University of Cincinnati College of Medicine, Cincinnati, OH 45229-2899.

³ Present address: Department of Radiology, Rush-Presbyterian-St. Luke's Medical Center, 1635 W. Congress Pkwy., Chicago, IL 60612.

⁴ Department of Nephrology, Children's Hospital Medical Center and University of Cincinnati College of Medicine, Cincinnati, OH 45229-2899.

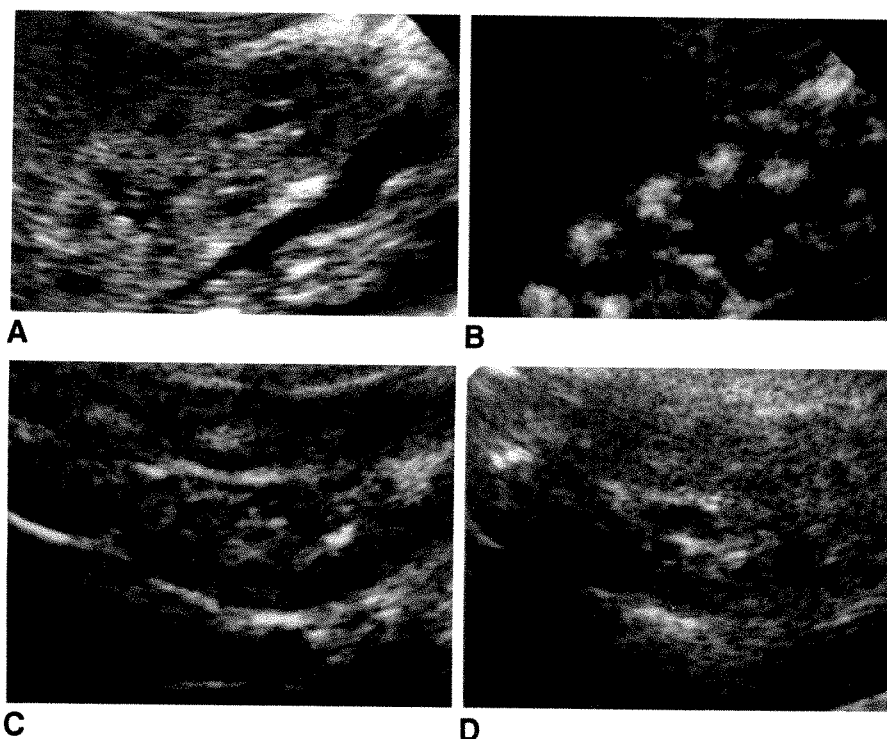


Fig. 1.—A, Renal sonogram of 3-day-old neonate shows normal echogenicity.

B, At 1 month of age, patient had developed marked nephrocalcinosis.

C, At 10 months, patient had persistent nephrocalcinosis, and indomethacin therapy was begun.

D, After 12 months of treatment, patient's urinary calcium excretion returned to normal and sonogram showed a marked decrease in nephrocalcinosis.

the active metabolite of vitamin D. It has been hypothesized that prostaglandin E_2 stimulates the 1α -hydroxylation of 25-OHD, resulting in increased circulating levels of $1,25(OH)_2D$ [5]. This, in turn, increases urinary excretion of calcium and causes nephrocalcinosis [Fig. 2]. Indomethacin acts by inhibiting the cyclooxygenase enzyme, which blocks excess prostaglandin production. Lowering of prostaglandin levels decreases formation of metabolically active vitamin D [6, 7].

We have performed serial sonographic examinations on four patients with Bartter syndrome and hypercalciuria, including the patient reviewed in our case report. In three of our patients, renal sonograms obtained in the neonatal period showed normal kidneys. All three patients developed marked medullary nephrocalcinosis within months. This observation supports the hypothesis that elevated vitamin D levels play an essential role in the hypercalciuria of Bartter syndrome. Nephrocalcinosis occurs after the start of oral feedings, which offer a source of calcium on which vitamin D can act.

After treatment with indomethacin, the urinary calcium excretion decreased to within the normal range (<4 mg/kg/24 hr) in three of the four patients. There was significant improvement but incomplete resolution of nephrocalcinosis in two of the three infants (5–11 months old). The third infant had no change in the nephrocalcinosis. He is still in the early stages of therapy, and urinary calcium excretion studies indicate incomplete correction of his hypercalciuria. In a fourth patient, treated as an adolescent, the urinary calcium excretion decreased without an appreciable change in the nephrocalcinosis on sonography. These findings suggest that the medullary nephrocalcinosis may be reversed in its early stages by correction of the hypercalciuria. It may be more resistant to treatment or even irreversible if present for a long time.

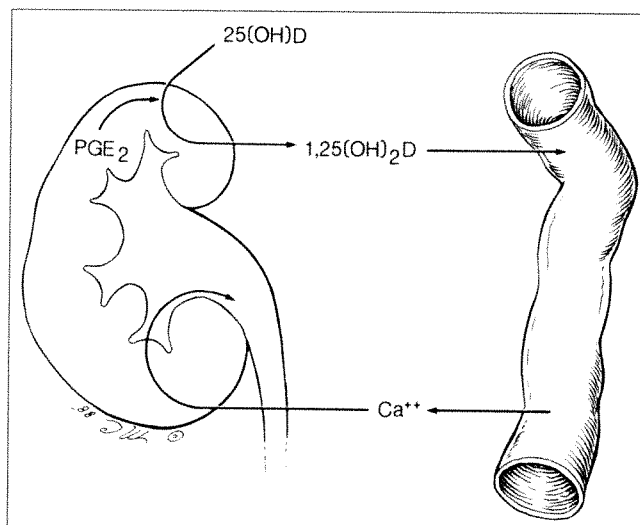


Fig. 2.—Prostaglandin (PG) E_2 is thought to stimulate formation of $1,25(OH)_2D$. This results in increased calcium absorption from bowel and, consequently, hypercalciuria.

Renal sonography is an ideal means of monitoring patients with Bartter syndrome and nephrocalcinosis during treatment with indomethacin. It is a very sensitive imaging technique in the detection of nephrocalcinosis [8, 9]. Normally, the medullary pyramids are less echogenic than the cortex. In nephrocalcinosis, the medullary pyramids display a diffuse increase in echogenicity, becoming more echogenic than the renal cortex. However, this sonographic appearance is not specific for nephrocalcinosis. It can be seen in patients with renal

tubular ectasia and Tamm-Horsefall proteinuria [10]. In the clinical situation that we have described, these findings reflect nephrocalcinosis.

In Bartter syndrome with nephrocalcinosis, the calcifications are often microscopic, and acoustic shadowing is not always present [8, 9]. The plain abdominal radiograph does not show evidence of nephrocalcinosis in most cases. The differential diagnosis of nephrocalcinosis in children includes renal tubular acidosis, chronic therapy with Lasix (Hoechst-Roussel, Somerville, NJ), primary and secondary hyperparathyroidism, vitamin D intoxication, Cushing syndrome, and Fanconi syndrome. Bartter syndrome with hypercalciuria is not widely recognized as a cause of nephrocalcinosis. It should always be considered when nephrocalcinosis is present in a preterm infant with a history of polyhydramnios. Early diagnosis is important, because treatment with indomethacin may result in correction of the hypercalciuria, a decrease in nephrocalcinosis, and preservation of renal function.

REFERENCES

1. Ohlsson A, Sieck U, Cumming W, Akhtar M, Serenius F. A variant of Bartter's syndrome. Bartter's syndrome associated with hydramnios, prematurity, hypercalciuria and nephrocalcinosis. *Acta Paediatr Scand* 1984; 73:868-874
2. Bartter FC, Provone P, Gill JR, MacCradie RC, Diller E. Hyperplasia of the juxtaglomerular complex with hyperaldosteronism and hypokalemic alkalosis. *Am J Med* 1962;33:811-821
3. Stein JH. The pathogenic spectrum of Bartter's syndrome. *Kidney Int* 1985;28:85-93
4. Houser M, Zimmerman B, Davidman M, Smith C, Sinaiko A, Fish A. Idiopathic hypercalciuria associated with hyperreninemia and high urinary prostaglandin E. *Kidney Int* 1984;26:176-182
5. Yamada M, Matsumoto T, Takahashi N, Suda T, Ogata E. Stimulatory effect of prostaglandin E₂ on 1 α , 25-dihydroxyvitamin D₃ synthesis in rats. *Biochem J* 1983;216:237-240
6. Kurose H, Sonn YM, Jafari A, Birge SJ, Avioli LV. Effects of prostaglandin E₂ and indomethacin on 25-hydroxyvitamin D₃-1 α -hydroxylase activity in isolated kidney cells of normal and streptozotocin-induced diabetic rats. *Calcif Tissue Int* 1984;37:625-629
7. de Rovetto CR, Welch TR, Hug G, Clark KE, Bergstrom W. Hypercalciuria with Bartter's syndrome: evidence for an abnormality of vitamin D metabolism. *J Pediatr* (in press)
8. Cumming WA, Ohlsson A. Nephrocalcinosis in Bartter's syndrome: demonstration by ultrasonography. *Pediatr Radiol* 1984;14:125-126
9. Glazer GM, Callen PW, Filly RA. Medullary nephrocalcinosis: sonographic evaluation. *AJR* 1982;138:55-57
10. Avni EF, Spehl-Robberecht M, Lebrun D, Gomes H, Garel L. Transient acute tubular disease in the newborn: characteristic ultrasound pattern. *Ann Radiol (Paris)* 1983;26:175-182

Book Review

Workbook for MRI and CT of the Head and Neck, 2nd ed. By Anthony A. Mancuso, H. Ric Harnsberger, and William P. Dillon. Baltimore: Williams & Wilkins, 251 pp., 1989. \$54.95

This book is unusual because it is a workbook that supplies approaches to using CT in nonneurologic examinations of the head and neck. The first chapter provides an introduction to the technical factors that control quality MR and CT. The authors lay a groundwork for emphasizing the clinical usefulness of each technique to answer specific clinical questions that affect the management of patients. Other chapters cover anatomic regions such as the orbits, temporal bones, salivary glands, nasopharynx, oropharynx, larynx, and general regions of the neck.

Each chapter gives an excellent discussion of the indications for performing an imaging study and the relative values of CT and MR. Techniques are discussed in some detail and are followed by descriptions of anatomy in the various planes of MR and CT. Line drawings are given for each region. After this introduction, examples of disease in each region are shown. These are followed by a series of questions to bring out pertinent facts of anatomy and of management of patients. Extensive tables are provided to give differential diagnoses, clinical triage, and an imaging decision tree that should please any reader interested in computer approaches to radiologic practice.

The major strengths of the workbook are the excellent discussions of indications and CT techniques, anatomic drawings, and the excellent clinical knowledge of the authors. They place radiologic imaging on a sound footing. The quiz cases used throughout the text are excellent. They have enough unusual twists to challenge the experienced radiologist yet not frustrate the beginner by ignoring basic facts of anatomy and pathophysiology.

Weaknesses in the workbook are difficult to find. The worst I can say is that because the book has more than one author, some variation occurs in the quality of MR images. Nevertheless, all pathologic anatomy is illustrated adequately. The authors also have an underlying slight bias to CT, which is probably good in this era of MR euphoria. I am sure that there will be considerable variations in the reception of the recommended treatment techniques because of personal preferences and technical skills in different institutions. The authors do temper their recommendations in a nice way.

This workbook is a must for any trainee in radiology or head and neck surgery who has a serious interest in becoming knowledgeable in head and neck imaging. It serves as an excellent guide to the practicing radiologist who sees only the occasional head and neck case and needs a review of the anatomy or a clinical briefing about a radiologic examination. The average medical student or paramedical person probably will find the information a little too detailed for thorough study but should keep the workbook in mind as an excellent reference when head and neck problems are encountered. The improved diagrams, tables, and updating of images create a new and greatly improved workbook over the first edition.

William Hanalee
University of California, Los Angeles
Los Angeles, CA 90024-1721

Case Report

Recurrent Occult Medullary Thyroid Carcinoma Detected by MR Imaging

John P. Crow,¹ Behrooz Azar-Kia,² and Richard A. Prinz¹

Medullary carcinoma of the thyroid originates in the parafollicular or C cells of the thyroid gland. These C cells produce calcitonin, which is a sensitive marker for the presence of tumor. Measurement of plasma calcitonin level is an important tool for early diagnosis and for monitoring the results of treatment [1, 2]. In patients with medullary carcinoma treated by total thyroidectomy, rising plasma calcitonin levels almost always signify growth of recurrent or residual tumor. In a patient who has a rising level of plasma calcitonin after total thyroidectomy, localization of regional or systemic disease is important for subsequent management. Several methods, including CT scanning [1], sonography [3], ¹³¹I-metaiodobenzylguanidine (¹³¹I-MIBG) scanning [4], and selective venous catheterization with quantitative calcitonin measurement [5], have been reported as useful in detecting the location of medullary thyroid cancer.

We report a patient with rising plasma calcitonin levels whose recurrent tumor was not localized by physical examination, CT scan, or ¹³¹I-MIBG scan. MR imaging clearly showed residual tumor in the neck. This experience suggests that MR may be useful in localizing residual or recurrent disease in patients being monitored for medullary carcinoma of the thyroid.

Case Report

A 63-year-old woman was referred for follow-up of a medullary carcinoma of the thyroid. She had an asymptomatic nodule in the left lobe of the thyroid in 1970, and left thyroid lobectomy was performed for a benign nodular goiter. She did well until 1984, when a new mass

was noted in the right lobe. A completion thyroidectomy was performed, and pathologic examination showed medullary carcinoma. Postoperative calcitonin level was 178 pg/ml (normal, <19 pg/ml). The carcinoembryonic antigen (CEA) was 3.0 ng/ml. She was asymptomatic, with serial calcitonin levels in the range of 200 pg/ml over the next 3 years. In September 1987, she was still asymptomatic, but her plasma calcitonin level was 598 pg/ml. One month later, it had increased to 729 pg/ml. Examination of her neck did not reveal any masses. A CT scan of her neck and upper mediastinum showed no residual or metastatic disease. Plasma calcitonin rose to 22,000 pg/ml in December 1987. Physical examination was normal. A ¹³¹I-MIBG scan showed no abnormal uptake. MR images were obtained in the cranial, sagittal, coronal, and transverse sections with a GE 1.5-T MR imager. These images clearly showed a round area of increased intensity on the T2-weighted pulse sequences in the left thyroid bed (Fig. 1).

At surgery, a 2.5-cm mass was found in the bed of the previously removed left lobe of the thyroid. Resection of this lesion and a central lymph node revealed metastatic medullary carcinoma of the thyroid consistent with the pathologic reports from her resection in 1984. Six months after surgery, the patient remains asymptomatic with a plasma calcitonin level of 231 pg/ml.

Discussion

Measurement of plasma calcitonin level is a sensitive tool for the early detection of medullary carcinoma of the thyroid in families at risk for this disease and for the long-term postoperative follow-up of both the sporadic and familial form of this disease. One vexing problem has been the patient who, after undergoing total thyroidectomy, has no clinically apparent disease but has a rising plasma calcitonin level.

Received November 28, 1988; accepted after revision January 24, 1989.

¹ Department of Surgery, Loyola University Medical Center, 2160 S. First Ave., Maywood, IL 60153. Address reprint requests to R. A. Prinz.

² Department of Radiology, Loyola University Medical Center, 2160 S. First Ave., Maywood, IL 60153.

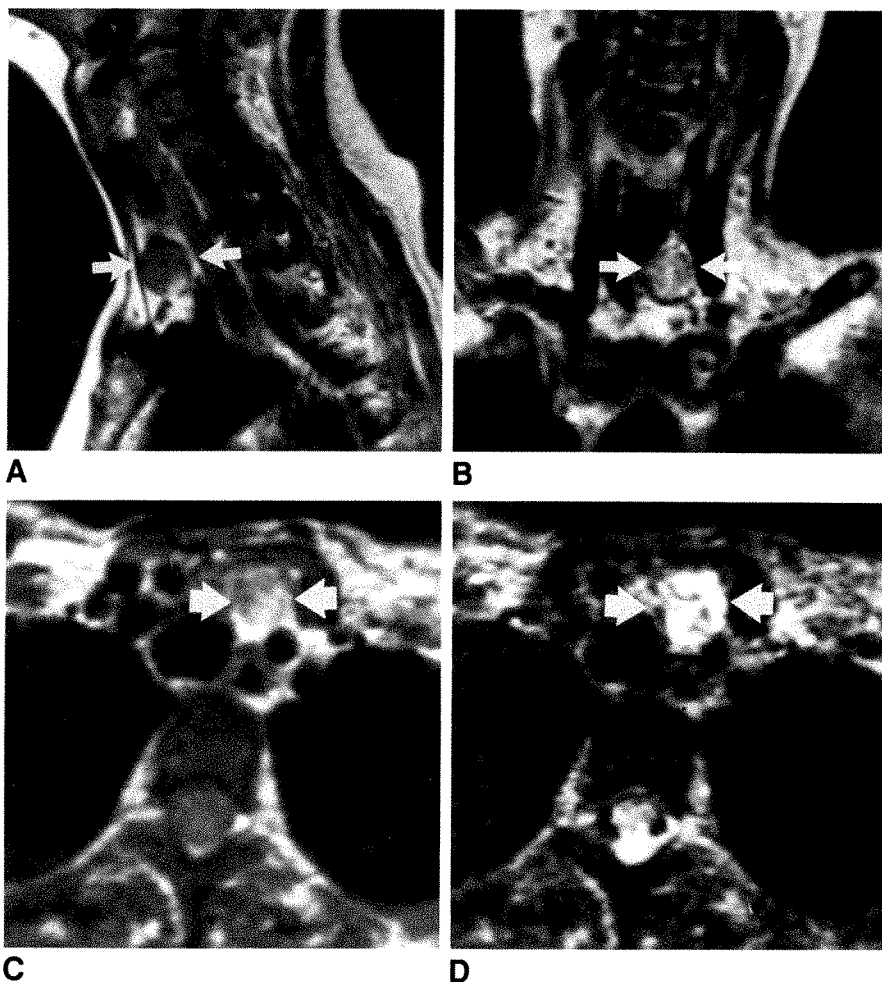


Fig. 1.—Recurrent occult medullary thyroid carcinoma.

A, Sagittal T1-weighted MR image (800/20) shows a well-defined, rounded mass, isointense to soft tissue in anteroinferior aspect of neck (arrows).

B, Coronal proton-density (2500/20) image shows a high-intensity lesion in left thyroid fossa (arrows).

C and D, Axial proton-density (2500/20) MR image (C) and T2-weighted (2500/80) image (D) show high-intensity mass in left thyroid fossa (arrows).

Most investigators believe that such a patient has occult residual or recurrent disease [1, 6]. The problem is to localize the clinically inapparent tumor so that, if possible, it can be removed [5, 7]. Although medullary carcinoma of the thyroid can metastasize widely, in the patient with no clinically apparent disease and a rising level of calcitonin, the tumor is probably confined to the neck. Norton et al. [5] described seven patients who, after thyroidectomy for medullary carcinoma, had elevated levels of plasma calcitonin but no other evidence of disease. Each of these patients had a surgically resectable tumor in the neck. Likewise, Tisell et al. [7] described 11 patients who had continued elevated levels of plasma calcitonin after thyroidectomy but no other clinically apparent disease, all of whom were found to have residual or recurrent tumor within the neck.

Several methods are now available to localize clinically inapparent disease in patients with rising levels of plasma calcitonin after thyroidectomy. CT scanning was originally suggested for this purpose [1], but little evidence indicates it is accurate. Schwerek et al. [3] successfully localized recurrent occult disease in the neck ranging from 1 to 2.5 cm in three patients studied with sonography.

A variety of radionuclides, including ^{131}I -MIBG [4], $^{99\text{m}}\text{Tc}$ -dimercaptosuccinic acid ([V]DMSA), and $^{99\text{m}}\text{Tc}$ -methylene diphosphonate, have been used to identify tumor location in medullary carcinoma [8]. However, none of these scintigraphic methods has been documented to identify occult disease. Selective venous catheterization with sampling and

measurement of calcitonin has been used successfully for finding clinically inapparent disease in the neck. Norton et al. [5] used this technique in seven patients and correctly localized the disease in each patient. However, this is an invasive and expensive procedure that requires special expertise to perform.

REFERENCES

- Stepanas AV, Samaan N, Hill CS Jr, Hickey RC. Medullary thyroid carcinoma: importance of serial serum calcitonin measurement. *Cancer* 1979;43(3):825-837
- Wells SA Jr, Baylin SB, Leight GS, Dale JK, Killely WG, Farndon JR. The importance of early diagnosis in patients with hereditary medullary thyroid carcinoma. *Ann Surg* 1982;195(5):595-599
- Schwerek WB, Grun R, Wahl R. Ultrasound diagnosis of C-cell carcinoma of the thyroid. *Cancer* 1985;55(3):624-630
- Oishi S, Sasaki M, Hirota Y, Takahashi M. Imaging and uptake mechanism of ^{131}I -meta-iodobenzylguanidine in medullary thyroid carcinoma. *Endocrinol Jpn* 1986;33(3):309-315
- Norton JA, Doppman JL, Brennan MF. Localization and resection of clinically inapparent medullary carcinoma of the thyroid. *Surgery* 1980;87:616-622
- Jackson CE, Talpos GB, Kambouris A, Yott JB, Tashjian AH Jr, Block MA. The clinical course after definitive operation for medullary thyroid carcinoma. *Surgery* 1983;94(6):995-1001
- Tisell L, Hansson G, Jansson S, Salander H. Reoperation in the treatment of asymptomatic metastasizing medullary thyroid carcinoma. *Surgery* 1986;99(1):60-66
- Clarke SEM, Lazarus CR, Wraight P, Sampson C, Maisey MN. Pentavalent ($^{99\text{m}}\text{Tc}$)DMSA, (^{131}I)MIBG, and techniques in patients with medullary carcinoma of the thyroid. *J Nucl Med* 1988;29(1):33-38

Alzheimer's Disease: Longitudinal CT Studies of Ventricular Change

Mony J. de Leon¹
 Ajax E. George²
 Barry Reisberg¹
 Steven H. Ferris¹
 Alan Kluger¹
 Leonidas A. Stylopoulos²
 Jeffrey D. Miller²
 Mary Ellen La Regina²
 Clara Chen³
 Jacob Cohen⁴

A 3-year longitudinal study was conducted with 50 Alzheimer's disease patients and 45 elderly control subjects. All study participants received an extensive evaluation that included brain CT at baseline and follow-up. Quantitation of ventricular size, using both linear and volume methods, revealed highly significant cross-sectional and longitudinal differences between the Alzheimer patients and control subjects. Specifically, the annual rate of change in ventricular volume was approximately 9% in the Alzheimer patients and approximately 2% in the controls. The presence of age-related white matter lesions had no effect on the clinical course of the patients or on the changes in ventricular size. Among the Alzheimer patients, the rate of clinical decline was strongly related to the rate of change in ventricular size. Baseline ventricular measurements were of no value in predicting the subsequent rate of clinical deterioration or ventricular enlargement.

The results suggest that changes in ventricular size closely reflect the clinical changes in Alzheimer patients.

Cross-sectional CT studies have repeatedly demonstrated statistically significant differences in ventricular size between Alzheimer's disease patients and elderly normal control subjects. However, it is generally acknowledged that a single observation of ventricular size in aged memory-impaired individuals is of limited clinical utility [1, 2]. Very few longitudinal CT studies of either normal aging or Alzheimer's disease have been reported. Furthermore, there are no reported longitudinal studies that include Alzheimer patients and aged normal individuals with white matter lesions. These lesions are commonly found in elderly groups [3]. After excluding patients with infarcts, it appears that the white matter lesions are caused by microvascular hyalinosis and demyelination [3, 4]. However, the possible role of white matter lesions in the course of Alzheimer's disease or normal aging is unknown.

In one longitudinal study, Naguib and Levy [5] followed up 10 Alzheimer patients after 2 years. Their results indicated that the five patients who demonstrated psychometric decline had significantly greater ventricular areas when compared with the five relatively stable Alzheimer patients. These authors also reported that the baseline CT measurements were of no predictive value in the determination of the subsequent course of Alzheimer's disease. Gado et al. [6] studied 21 Alzheimer patients and 24 control subjects on two occasions separated by an interval of 1 year. Using linear measurements to estimate ventricular size (across two different CT scanners), these researchers obtained results that indicated that the Alzheimer group had a greater rate of longitudinal change. In addition, the Alzheimer group had significantly larger ventricles at each of the two cross-sectional time points. Brinkman and Largent [7] did follow-up CT studies on five "significantly" demented patients after 15–35 months. Their results indicated that their patients had rates of linear ventricular change that exceeded those predicted from published cross-sectional normative data. Luxenberg et al. [8] studied 18 Alzheimer patients and 12 aged control subjects with a follow-up interval that ranged from 6 months to 5

This article appears in the March/April 1989 issue of *AJNR* and the June 1989 issue of *AJR*.

Received April 27, 1988; accepted after revision August 10, 1988.

This work was supported in part by USPHS grants MH36969, AG03051, and MH43965.

¹ Department of Psychiatry, New York University Medical Center, 550 First Ave., New York, NY 10016. Address reprint requests to M. J. de Leon.

² Department of Radiology, New York University Medical Center, New York, NY 10016.

³ Department of Nuclear Medicine, Hospital of the Albert Einstein College of Medicine, Bronx, NY 10461.

⁴ Department of Psychology, New York University, New York, NY 10012.

AJR 152:1257–1262, June 1989

0361–803X/89/1526–1257

© American Roentgen Ray Society

years. Their results indicated significantly increased yearly rates of ventricular enlargement in the Alzheimer group relative to the control group.

The foregoing longitudinal CT studies were carried out with relatively small sample populations. In the study reported here, we followed up a large group of Alzheimer patients and control subjects after a standard 3-year interval. We also report the first longitudinal results on the effect of white matter lesions on ventricular size and clinical outcome. Our CT measurements included both linear and volume studies of ventricular size.

Subjects and Methods

A complete 3-year longitudinal follow-up examination was conducted on 50 Alzheimer patients and 45 control subjects who were comparable in age and follow-up interval (see Table 1). All Alzheimer patients were participants in the New York University Aging and Dementia Research Program, and all met both DSM III [9] and NINCDS-ADRDA diagnostic criteria for Alzheimer's disease [2]. The normal control subjects were volunteers and were mainly derived from the spouses, relatives, and friends of the impaired group. At both baseline and follow-up examinations, all subjects received medical, neurologic, psychiatric, neuropsychological, and CT examinations. Following this standard protocol of assessments, all subjects included in the longitudinal study were diagnosed as normal or as presumed Alzheimer patients at both evaluations. The patients selected for study had no evidence of diseases that could affect brain functioning other than Alzheimer's disease.

In defining these two study groups, subjects with any history of stroke or with neurologic or CT evidence of infarction (sharply marginated low-attenuation lesions of gray or white matter), or modified Hachinski [10] scores >3 were excluded. At baseline, subjects with hypertensive (BP $> 150/90$) and/or clinically significant cardiac disease were excluded. Also excluded were diabetics requiring treatment with insulin or oral medication. Subjects with diabetes under dietary control were not excluded from the study. With these relatively strict subject selection criteria we found no evidence for baseline or follow-up differences between Alzheimer patients and normal subjects on the following medical parameters: hematologic, gastrointestinal, pulmonary, immunologic, cancer, thyroid, or cardiac. Therefore, the two study groups began and remained comparable medically. Over the 3-year interval, less than 4% of all the subjects returning for follow-up showed significant evidence of adverse medical changes. These changes were equally distributed across the two study groups. Within the Alzheimer group, adverse medical changes were not associated with the rate of cognitive decline.

In deriving the study groups we found different attrition rates at the 3-year follow-up for the patient and control groups. Specifically, 87% of the controls contacted returned for follow-up as compared with 48% of the Alzheimer patients. Table 2 summarizes the follow-up attempts for the two study groups. Death was more common in the Alzheimer group, and over 40% of them failed to return due to the severity of the disease and other health-related reasons. However, at least some follow-up information was obtained for approximately 90% of the Alzheimer group. When a visit to the clinic was not possible, information was obtained by phone calls and in some cases by home visits. Lack of clinic follow-up for health-related reasons occurred in less than 8% of the control subjects. Specific study of the separate group of 43 Alzheimer patients who did not return for reexamination, but for whom limited follow-up results were available, revealed that their baseline measurements of age (mean =

TABLE 1: Baseline Ages and Follow-up Intervals for Longitudinal Study Groups

Group	No.	Age (Mean \pm SD)	Years of Follow-up (Mean \pm SD)
Normal	45	68.9 \pm 6.4	3.4 \pm 0.7
Alzheimer	50	71.2 \pm 8.1	2.9 \pm 1.2

TABLE 2: Outcomes for Follow-up Attempts (n = 156)

Outcome	Normal (n = 52)		Alzheimer (n = 104)	
	No.	%	No.	%
Completed follow-up	45	86.5	50	48.0
Limited follow-up				
Deceased	1	1.9	13	12.5
Nursing home	0	0.0	18	17.3
Home contact	3	5.8	12	11.5
No follow-up				
Refused	2	3.8	9	8.6
Lost	1	1.9	2	1.9

72.7 \pm 5.7) and severity of impairment based on the Global Deterioration Scale (GDS) (mean = 3.9 \pm 0.9) [11] did not differ from those of the 50 Alzheimer patients who were successfully followed up (mean age = 71.2 \pm 8.1 years; mean GDS = 3.7 \pm 1.2).

Psychiatric and Neuropsychological Evaluations

As part of the comprehensive clinical examination, all patients and control subjects received the GDS at each observation point. Evaluation of the GDS was done by a clinician and was based on subjective complaints of memory deficit, on observation of deficit during careful clinical interview, and (in the case of Alzheimer patients) on discussions with caretakers concerning the patient's ability to perform tasks of daily living. This scale evaluates the general level of an individual's ability to function. The global status of the subject is rated on a 7-point scale that has specific behavioral anchor points. Higher values on the GDS indicate greater cognitive impairment. For the Alzheimer patients, the GDS at baseline was 3.7 \pm 1.2 and at follow-up 4.5 \pm 1.3. The interrater reliability of the GDS is .90, $p < .01$, as determined by the dual evaluation of 39 patients. This scale is also highly correlated with other dementia scales (e.g., the Mini Mental State [12] $r = -.89$, $n = 170$, $p < .01$).

Formal psychometric evaluations were conducted at both time points. In the interest of reducing the number of psychometric variables, we developed a composite Psychometric Deterioration Score (PDS). The PDS represents an equally weighted combination of scores from the Guild Memory Test [13] and the WAIS [14]. The PDS includes five measures from the Guild Memory Test: the immediate and delayed recall of two paragraphs; the immediate and delayed recall of paired associates; and recall of abstract designs. Four subtests of the WAIS were included: vocabulary; digit symbol substitution, and digits forward and backward. To obtain the PDS, the calculated total average percent correct is divided into a quasi 1–7-point scale, with low numbers representing relatively little impairment and high scores representing poor psychometric test performance. For the Alzheimer patients, the PDS at baseline was 4.8 \pm 1.6 and at follow-up 5.5 \pm 1.9. The test-retest reliability of the PDS is .94, $n = 25$, $p < .001$.

From the GDS and the PDS scores we attempted to define a group of Alzheimer patients who unequivocally demonstrated cognitive decline over the study interval. We defined decliners as those subjects showing changes ≥ 2 units on either the GDS or PDS, with a minimum of 1 unit of change on the other scale. By this calculation we identified 26 decliners among the 50 Alzheimer patients. The remaining 24 Alzheimer patients, who showed relatively less cognitive deterioration, were termed the nondecliners. In this study, ceiling effects in the evaluation of cognitive change longitudinally were not a problem, since mild to moderately severe patients were selected at baseline (i.e., GDS 3–5).

CT Examination

The longitudinal cohort of patients and controls was developed over a period of time (1978–1986) in which three different CT scanners were used. These included the EMI 5005, the Philips Tomoscan 200, and the GE 8800. Scans from all machines were obtained from the base to the vertex of the brain with contiguous 10-mm-thick slices. Each study was done by using a zero scanning angle relative to the canthomeatal plane. All patients had their follow-up study on the GE 8800 CT scanner. The majority of both Alzheimer patients and control subjects who were followed also had baseline CT evaluations on the GE 8800 CT scanner. With respect to the other machines used at baseline, seven controls and six Alzheimer patients were studied on the EMI 5005, and six controls and 10 Alzheimer patients were studied on the Philips machine.

In the interest of utilizing as much of this valuable data as possible, several studies were conducted to determine the potential errors in making comparisons across machines. Water phantom studies revealed that for relatively large volumes, which include the ventricular anatomy, accurate and reproducible volume estimates were possible across machines. However, for water volumes that were relatively small, i.e., in the range of the cortical sulci, the recovery errors combined with partial volume errors were large. Therefore, in the present study only ventricular size was quantitatively determined. We also examined among the normal subjects and the Alzheimer patients the effect of a particular CT machine on the baseline ventricle/brain ratio for both the linear and the volume measures. Our results failed to show significant machine-related effects for these two measures ($F = 1.97$ and 1.84 , $p > .05$, respectively). We also found no evidence for a diagnosis by machine interaction ($p > .05$) for the two ventricle measures. Therefore, data for the three machines were combined in the analyses reported below.

Linear ventricular assessments. For each CT study ventricular size was estimated by using the arithmetic sum of five ratios of linear measurements. Each measurement was corrected for brain size by dividing by a corresponding measurement of the brain width (inner table to inner table) and thereby forming a linear ventricle/brain ratio (VBR-L). These measurements were taken from the one or two CT slices that best depicted the basal ganglia, foramen of Monro, and third ventricle. The measurements included the maximum widths across the frontal horns, the bicaudate diameter, the width of the third ventricle, and the oblique widths of the left and right frontal horns. This procedure is well documented as being a useful index for describing Alzheimer-related changes [15] and is highly reliable across observers. ($r = .91$, $p < .001$, $n = 109$).

Volume ventricular assessment. We estimated ventricular volume by outlining the anatomy of the ventricles and the skull inner table on a transparent plastic overlay. The overlay was digitized by using a video camera connected to a Data General-Grinnell imaging computer station. With this system we are able to precisely determine the number of picture elements in each enclosed component, i.e., the subvolumes of the ventricular anatomy and the whole-slice brain

volume minus the ventricular subvolumes. The volume ventricle/brain ratio (VBR-V) measurement was constructed slice by slice as the ratio of the ventricular area divided by the brain plus ventricular area. Across all machine and subject studies it was determined that the most reliable data would be obtained by using the three contiguous slices that depicted the greatest VBR-V. This procedure avoids measurement of the small ventricular subvolumes in the inferior temporal horns and in the most superior aspects of the bodies of the lateral ventricles. Direct comparison of this procedure with our earlier published ventricular volume method [16] was excellent ($r = .85$, $p < .01$, $n = 61$). The earlier procedure relies on interactive use of the GE 8800 CT computers and the definition of pixel ranges that separately defines CSF and brain (white and gray), and uses seven slices to estimate ventricle volume and three contiguous slices to estimate brain volume.

White matter lesions. All evaluations of white matter lesions were done on the follow-up study by using hard-copy X-ray film from the GE 8800 CT scanner obtained under standard conditions, which included X-ray tube power and window and level settings for the hard-copy imaging. Each CT study was evaluated separately for the presence or absence of white matter lesions. The white matter lesions were defined as areas of reduced CT white matter attenuation, typically in the periventricular white matter. With MR scanning that employed long TR images, these white matter areas show increased signal [17]. At neuropathology these white matter lesions are associated with demyelination and arteriolar hyalinization, and in severe cases there is axonal loss [3]. Using procedures that we have reported elsewhere [3], we categorized each study according to the severity and location of the CT lesions. In the longitudinal analysis, we identified 10 Alzheimer patients and 14 control subjects as having white matter lesions. All subjects with white matter lesions at follow-up had demonstrated white matter lesions at baseline. We did not observe any cases in which white matter lesions either developed or resolved during the 3-year course of the study. In several cases the apparent area of involvement of the white matter lesions increased in size.

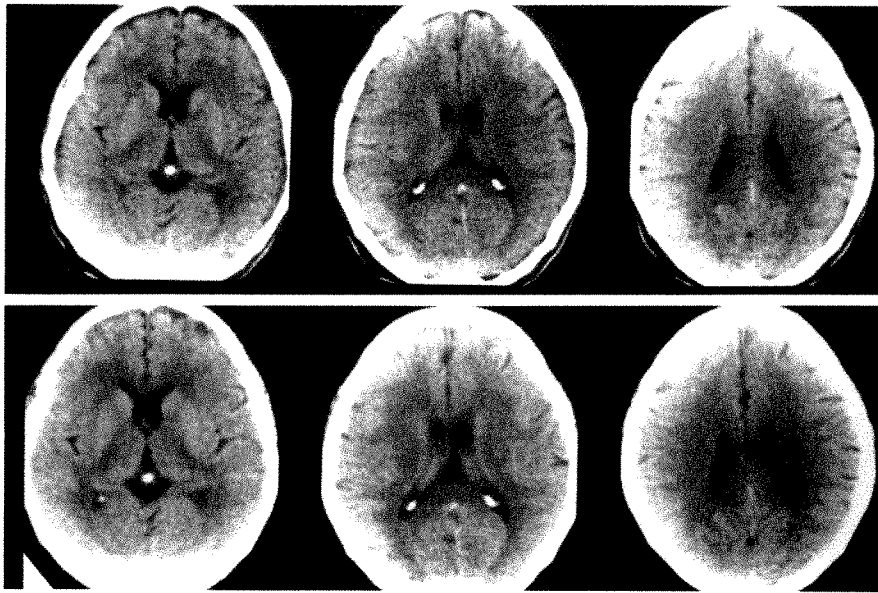
Results

As summarized in Table 3, the results for the linear and volume measurements were remarkably consistent. For both linear and volume VBR measurements two-way Analyses of Variance (ANOVA) (i.e., two diagnostic groups and presence or absence of white matter disease), indicated significant

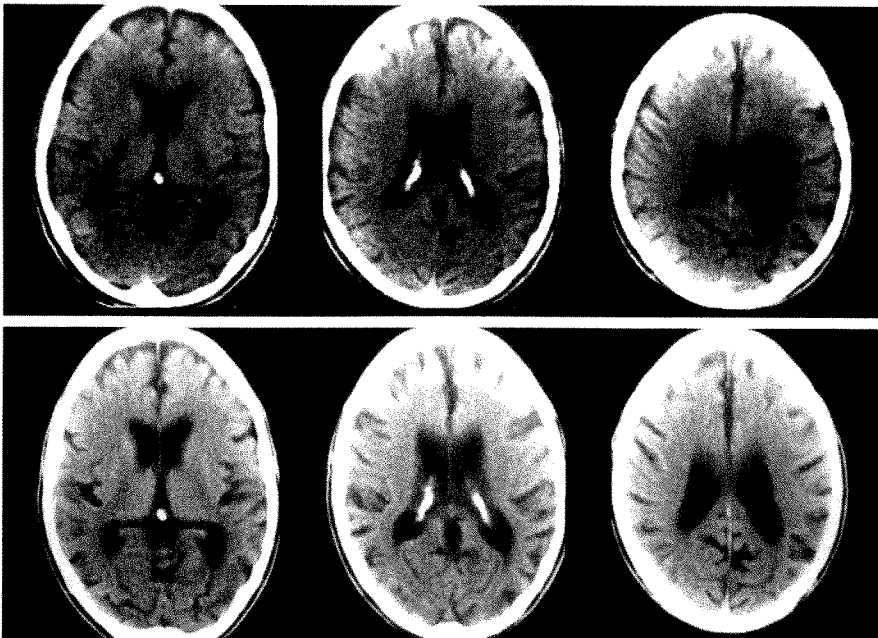
TABLE 3: Comparison of Cross-Sectional and Longitudinal Measures of Ventricular Size in Normal Aging and Alzheimer's Disease

CT Variable	Normal ($n = 45$) Mean \pm SD	Alzheimer ($n = 50$) Mean \pm SD	Percent Change in Alzheimer Group
Linear ventricle/brain ratio $\times 100$			
Time I	63 \pm 12	72 \pm 15*	+14
Time II	65 \pm 11	80 \pm 19*	+23
% change per year	0.7 \pm 1.2	3.4 \pm 4.4*	+385
Volume ventricle/brain ratio $\times 100$			
Time I	90 \pm 29	119 \pm 44*	+32
Time II	98 \pm 30	141 \pm 49*	+44
% change per year	2.3 \pm 3.7	9.3 \pm 12.1*	+304

* Different from normal control $p < .05$.



A



B

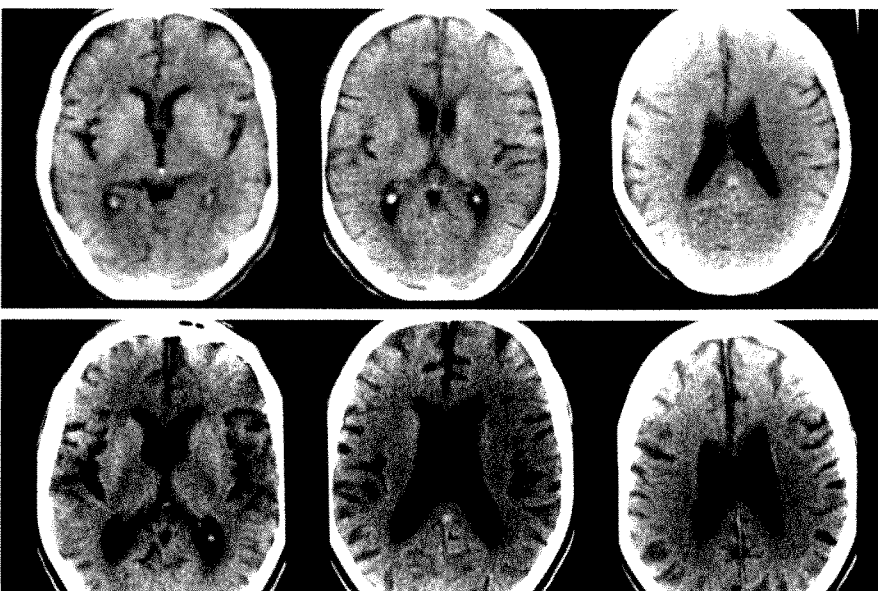


Fig. 1.—Typical 3-year changes in ventricular size in three women 59–65 years old at baseline.
 A, Normal control subject.
 B, Nondeclining Alzheimer patient (level 4 on Global Deterioration Scale).
 C, Declining Alzheimer patient (from level 3 to level 5 on Global Deterioration Scale).

diagnostic group differences at baseline, at follow-up, and for the yearly rate of ventricular enlargement, [F 's (1,90) > 13.5, (p < .01)]. The yearly rate of change was computed by using the following equation:

$$\text{yearly rate} = \frac{[\text{ventricle size follow-up} - \text{ventricle size baseline}]}{\text{Follow-up interval (years)}}$$

The yearly rate of change of ventricle size (either linear or volume) was observed to be three to four times greater in Alzheimer patients than in normal subjects. Figure 1 depicts the average 3-year ventricular changes in Alzheimer patients and in normal subjects.

In the ANOVA, the presence of white matter lesions in both the cross-sectional and longitudinal analyses had no significant effects on ventricular size, and there were no interaction effects on ventricle size between clinical diagnosis and white matter lesions [F 's (1,90) < .8, p > .05]. Figure 2 shows that the average yearly rates of ventricular change differ between the Alzheimer and normal groups, but within each group the rates are unchanged by the presence or absence of white matter lesions.

In further analyses, we examined the hypotheses that (1) patients showing clinical deterioration over the study interval would show larger ventricles at baseline than would the relatively stable patients and thereby demonstrate the predictive value of the ventricle measure, (2) that the deteriorating patients would show correlated changes in the rate of ventricular size, and (3) that the deteriorating patient group would comprise a disproportionate number of patients with white matter disease. Results from one-way analyses of variance showed that on both the linear and volume measures there were no baseline differences between decliners and nondecliners (p > .05). Only at follow-up was there significantly increased ventricular enlargement (p < .05) in the decliner group over the nondecliner Alzheimer group (see Fig. 3). Additionally, the Alzheimer group that did not return for follow-up (n = 43) was no different at baseline than the Alzheimer

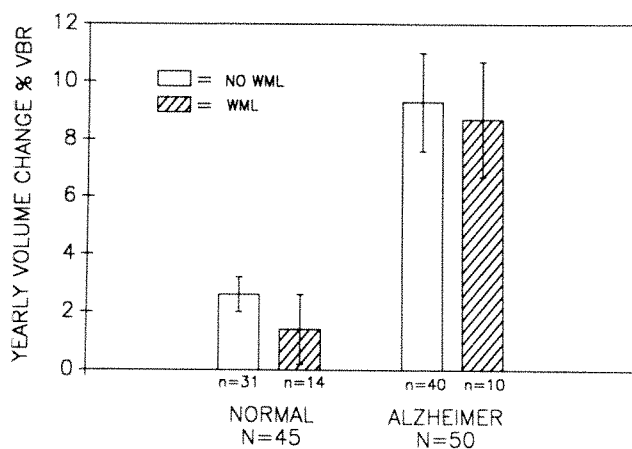


Fig. 2.—Annual rate of change of ventricular volume in Alzheimer patients and control subjects: the effects of white matter lesions (WML).

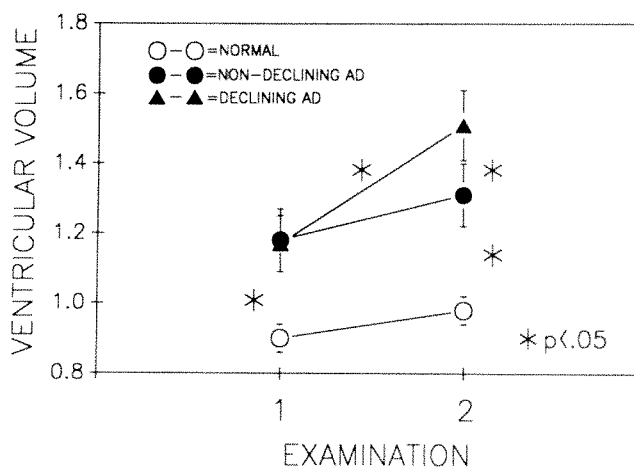


Fig. 3.—Ventricular volume changes in declining (n = 26) and nondeclining (n = 24) Alzheimer disease (AD) patients and control subjects (n = 45).

group that was followed (p > .05). In summary, at baseline there were no age, GDS, or ventricular differences between the Alzheimer groups (p > .05).

With respect to the second hypothesis, one-way analyses of variance with Tukey follow-up procedures showed that the rate of ventricular enlargement was significantly greater (p < .05) in the decliner group than in either the nondeclining Alzheimer group or the control group. The control subjects and the nondeclining Alzheimer patients did not differ significantly with respect to rate of ventricular enlargement. However, these two groups did differ significantly in the amount of ventricular enlargement at each of the two time points. The nondeclining Alzheimer group always showed significantly more ventricular enlargement (see Fig. 3).

The third hypothesis that patients with white matter lesions would be more represented in the declining group was not supported. Specifically, six patients with white matter lesions were in the declining group and four patients with white matter lesions were in the nondeclining group (χ^2 = .41, p > .05).

Discussion

The results of this longitudinal CT study show that Alzheimer patients have more rapid ventricular enlargement than do control subjects. The effects of the accelerated atrophic process in Alzheimer's disease are clearly seen at each of the two cross-sectional time points studied. This result is in agreement with earlier studies [6–8]. Our results also show a strong relationship over the study interval between the magnitude of ventricular enlargement and the presence or absence of significant clinical decline. Also in agreement with the earlier studies, our results show no predictive value for baseline ventricular size in determining the further rate of ventricular enlargement. As such, these data suggest that changes in ventricular size either follow changes in clinical condition or are more closely associated in time to observed clinical deterioration

than our study could have detected after a 3-year time interval.

Surprisingly, the results suggest that coincident white matter lesions have no effect on either (1) the severity of clinical deterioration in Alzheimer patients or (2) the magnitude of ventricular enlargement in the Alzheimer or control groups. These results suggest that in the absence of infarction, the presence of CT white matter disease (microvascular hyalinosis, edematous changes, and demyelination [3, 4, 17]), does not have a measurable impact on the Alzheimer process affecting the patient. Although our previous studies have identified clinical neurologic correlates of white matter lesions (e.g., gait and other motoric dysfunctions) [3, 18], the present longitudinal study was not designed to assess progressive motor changes. However, the results do indicate that white matter lesions had no significant longitudinal effect on cognition, memory, general medical health, or the project's attrition rate. Nevertheless, the relatively small sample size in the present study needs to be substantially expanded before these conclusions can be considered definitive.

Over all analyses, the linear and volumetric ventricular measurements gave the same results. Therefore, our findings suggest that the easily determined linear measures can be substituted for the more laborious area and volume measurements.

ACKNOWLEDGMENTS

We gratefully acknowledge the assistance of our students: Mitchell Brezel, Kevin Courtney, Liz Horowitz, Varghese Mathai, Sandra M. Quintero, Lisa Schwartz, Gwenn Smith, and Robin Weisbrod.

REFERENCES

- George AE, de Leon MJ. Computed tomography (CT and PET) in aging and dementia. In: Latchaw RE, ed. *Computed tomography of the head, neck and spine*. Chicago: Year Book Medical, 1984:415-435
- McKhann G, Drachman D, Folstein M, Katzman R, Price D, Stadlan EM. Clinical diagnosis of Alzheimer's disease: report of the NINCDS-ADRDA work group under the auspices of Department of Health & Human Services Task Force on Alzheimer's disease. *Neurology* 1984;34:939-944
- George AE, de Leon MJ, Gentes CI, et al. Leukoencephalopathy in normal and pathologic aging: 1. CT of brain lucencies. *AJNR* 1986;7:561-566
- Brun A, Englund E. A white matter disorder in dementia of the Alzheimer type: a pathoanatomical study. *Ann Neurol* 1986;19:253-262
- Naguib M, Levy R. CT scanning in senile dementia: a follow-up of survivors. *Br J Psychiatry* 1982;141:618-620
- Gado M, Hughes CP, Danziger W, Chi D. Aging, dementia, and brain atrophy: a longitudinal computed tomographic study. *AJNR* 1983;4:699-702
- Brinkman SD, Lergen J. Changes in brain ventricular size with repeated CAT scans in suspected Alzheimer's disease. *Am J Psychiatry* 1984;141:81-83
- Luxenberg JS, Haxby JV, Creasey H, Sundaram M, Rapoport SI. Rate of ventricular enlargement in dementia of the Alzheimer type correlates with rate of neuropsychological deterioration. *Neurology* 1987;37:1135-1140
- American Psychiatric Association. *Diagnostic and statistical manual of mental disorders*. Washington, DC: American Psychiatric Association, 1980
- Hachinski VC, Lassen NA, Marshall J. Multi-infarct dementia, a cause of mental deterioration in the elderly. *Lancet* 1974;ii:207-210
- Reisberg B, Ferris SH, de Leon MJ, Crook T. The global deterioration scale for assessment of primary degenerative dementia. *Am J Psychiatry* 1982;139:1136-1139
- Folstein MF, Folstein SE, McHugh PR. Mini-mental state: a practical method for grading the cognitive state of patients for the clinician. *J Psychiatr Res* 1975;12:189-198
- Crook T, Gilbert JG, Ferris SH. Operationalizing memory impairment in elderly persons: the Guild memory test. *Psychol Rep* 1980;47:1315-1318
- Wechsler D. *WAIS-R manual*. New York: Psychological Corp., 1981
- de Leon MJ, Ferris SH, George AE, Reisberg B, Kricheff II, Gershon S. Computed tomography evaluations of brain-behavior relationships in senile dementia of the Alzheimer's type. *Neurobiol Aging* 1980;1:60-69
- George AE, de Leon MJ, Rosenbloom S, et al. Ventricular volume and cognitive deficit: a computed tomographic study. *Radiology* 1983;149:493-498
- George AE, de Leon MJ, Kalnin A, Rosner L, Goodgold A, Chase N. Leukoencephalopathy in normal and pathologic aging: 2. MRI and brain lucencies. *AJNR* 1986;7:567-570
- Kluger A, Gianutsos J, de Leon MJ, George AE. The significance of age-related white matter lesions. *Stroke* 1988;8:1054-1055

Juvenile Pilocytic Astrocytomas: CT and MR Characteristics

Ya-Yen Lee¹
Pamela Van Tassel¹
Janet M. Bruner²
Richard P. Moser³
Jane C. Share⁴

Thirty-seven cases of juvenile pilocytic astrocytoma were reviewed retrospectively to determine their CT and MR characteristics. All cases occurred in pediatric patients, except for one in a young adult. There was a propensity for tumors to be located around the third and fourth ventricles. On CT the tumors were all sharply demarcated and smoothly marginated and rarely had associated edema. The lesions tended to be round or oval. The tumor matrix was most often hypo- or isodense with marked enhancement. Cyst formation, either micro- or macrocystic or combined, was frequently observed, and tumor calcification occurred occasionally. On MR the tumors appeared hypo- or isointense on T1-weighted images and hyperintense on T2-weighted images.

The radiologic appearances of juvenile pilocytic astrocytomas are quite characteristic. By using age of presentation, typical location, configuration, and enhancement patterns, the presurgical diagnosis of juvenile pilocytic astrocytoma can be made with a high index of confidence.

Juvenile pilocytic astrocytoma is a distinctive histologic subtype of astrocytoma occurring predominantly in children and young adults and distinguished by a relatively benign clinical course. Histologically it has a characteristic appearance with an alternating pattern of compact bipolar pilocytic (hairlike) astrocytes and loosely aggregated protoplasmic astrocytes, the latter of which often undergo microcystic degeneration.

Although this astrocytoma is well known to neurooncologists and neurosurgeons, its radiologic characteristics have not been well described. In this retrospective study, we evaluated the CT and MR appearances of this distinctive astrocytoma in an attempt to improve presurgical diagnostic accuracy.

Materials and Methods

Thirty-seven cases of histologically proved juvenile pilocytic astrocytomas were collected for this retrospective study. The 17 males and 20 females were 6 months to 28 years old (mean, 7.1 years) at presentation. However, in 29 patients (78%) the disease was diagnosed within the first decade of life; there was only one adult (>20 years). Five patients (14%) had stigmata or a family history of neurofibromatosis.

Thirty-seven pretreatment CT and five MR studies were available for review. CT was performed routinely before and immediately after IV administration of iodinated contrast medium with a slice thickness of 4–10 mm; occasionally, delayed scans were obtained. T1-weighted spin-echo images, 600–800/17–20 (TR/TE); proton-density images, 2000/20–30; and T2-weighted images, 2000/80–90, were obtained in the MR studies. The location, size, configuration, and margins of the tumors were evaluated in addition to the CT density, contrast enhancement, and MR intensity. The presence of tumor calcification, micro- (diameter, ≤ 1 cm) or macro- (diameter, > 1 cm) cyst formation, as well as associated edema or arachnoid cyst was also recorded.

Results

The locations of tumors were: optic chiasm and hypothalamus, 17; cerebellar vermis, seven; cerebellar hemisphere, four; cerebral hemisphere, four (three in the

This article appears in the March/April 1989 issue of *AJNR* and the June 1989 issue of *AJR*.

Received April 27, 1988; accepted after revision August 30, 1988.

¹ Division of Diagnostic Imaging, Department of Diagnostic Radiology, The University of Texas M. D. Anderson Cancer Center, 1515 Holcombe Blvd., Houston, TX 77030. Address reprint requests to Y.-Y. Lee.

² Division of Pathology, Section of Neuropathology, The University of Texas M. D. Anderson Cancer Center, Houston, TX 77030.

³ Division of Surgery, Section of Neurosurgery, The University of Texas M. D. Anderson Cancer Center, Houston, TX 77030.

⁴ Department of Radiology, Boston Children's Hospital, Boston, MA 02215.

AJR 152:1263–1270, June 1989
0361–803X/89/1526–1263

© American Roentgen Ray Society

temporal lobe and one in the frontal lobe); intraventricular, two; septum pellucidum, one; thalamus, one; and optic nerve, one (Table 1). Among 17 cases of chiasmal lesions, nine had downward extension into the pituitary fossa (Fig. 1), three had anterior extension into the optic nerve (Fig. 2), and three

had posterior extension into the postchiasmal optic pathway (Fig. 3). All four cerebellar hemispheric lesions were located medially near the vermis (Fig. 4). The two intraventricular tumors were identified within the anterior lateral ventricles (Fig. 5). The septal and thalamic lesions were located in the

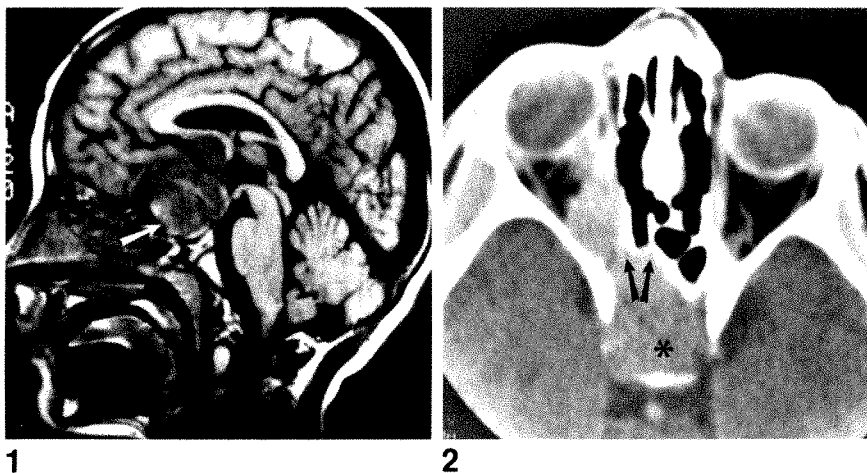


Fig. 1.—T1-weighted sagittal MR image, 600/20. Large chiasmal pilocytic astrocytoma with downward extension into pituitary fossa and sphenoid sinus (arrow).

Fig. 2.—Contrast-enhanced axial CT scan. Anterior extension of chiasmal pilocytic astrocytoma into right orbit. Noted are erosions of right tuberculum sellae and optic canal (arrows), as well as downward extension into pituitary fossa (asterisk).

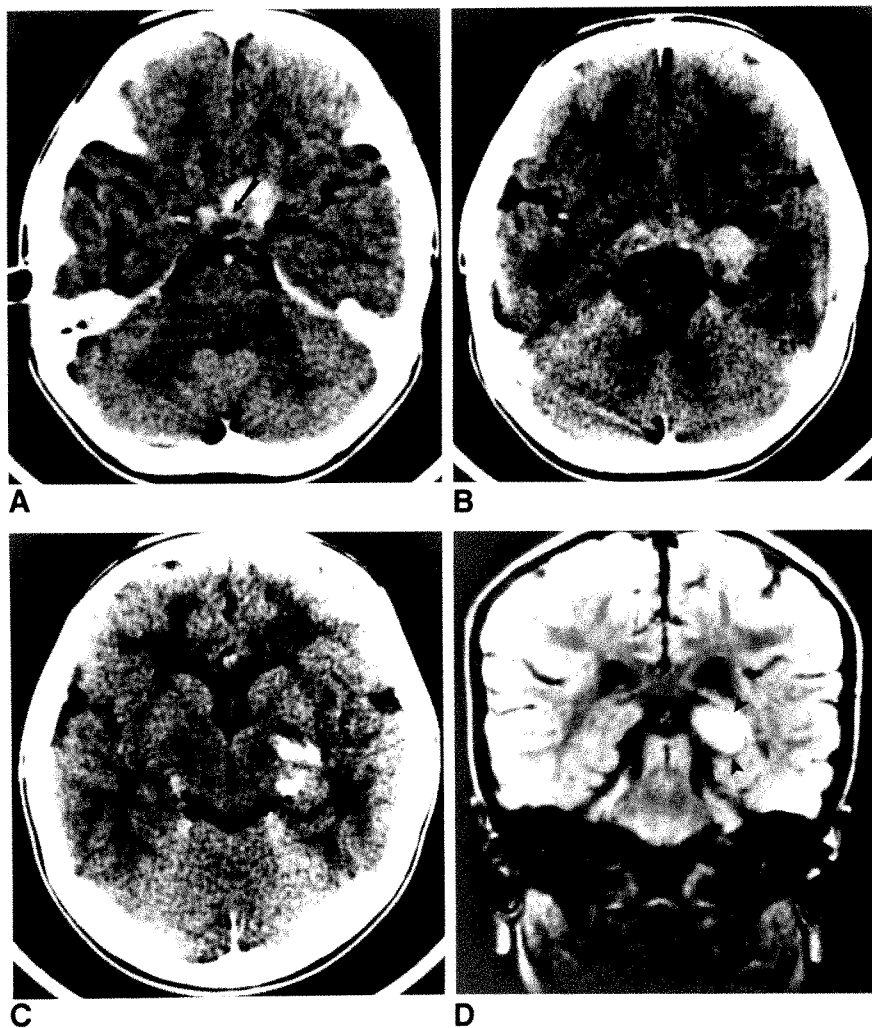


Fig. 3.—A–C, Contrast-enhanced axial CT scans show chiasmal pilocytic astrocytoma with bilateral postchiasmal optic pathway extension. Noted are tumor calcifications in left optic tract and microcyst in chiasmal tumor (arrow). Right optic tract is minimally involved, and there is uncertainty about left lateral geniculate body involvement.

D, Coronal proton-density MR image, 2000/20. Left lateral geniculate body involvement is definite and sharply delineated (arrowheads).

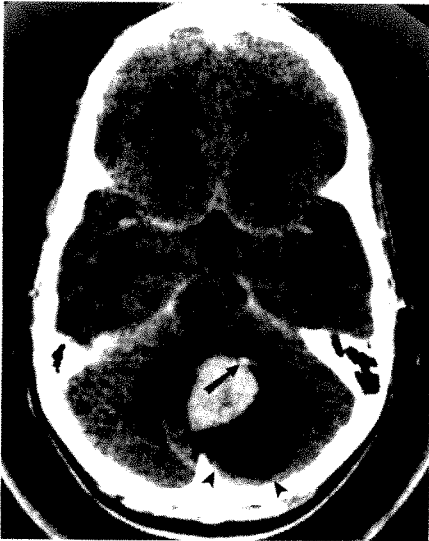
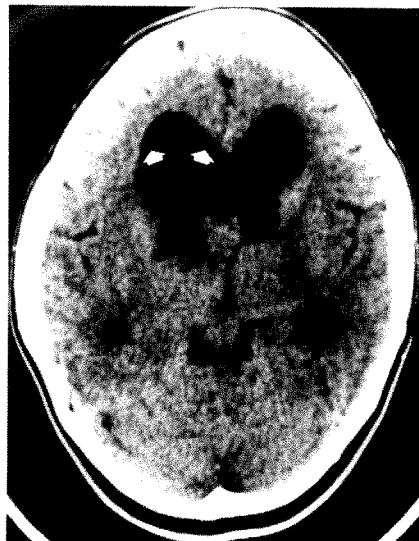
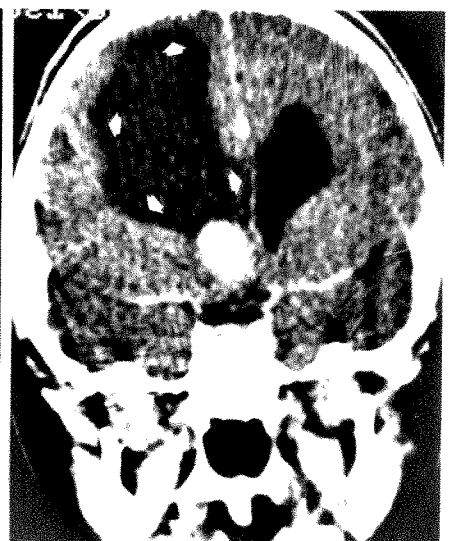


Fig. 4.—Contrast-enhanced axial CT scan shows cystic pilocytic astrocytoma of left medial cerebellar hemisphere. Noted are a small flecklike tumor calcification (*arrow*); a sharply demarcated, solid, enhancing component; and a macrocyst (*arrowheads*). Surrounding edema is minimal. Fourth ventricle is severely deformed with resultant obstructive hydrocephalus.

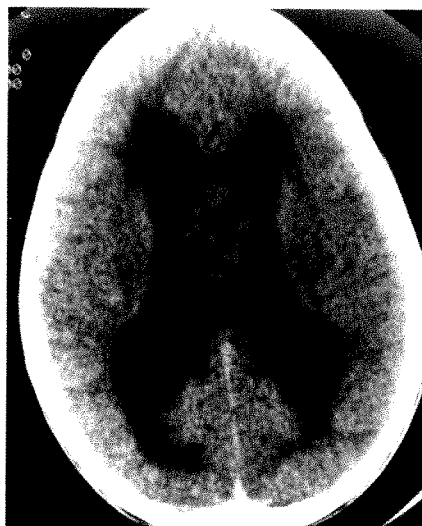


A

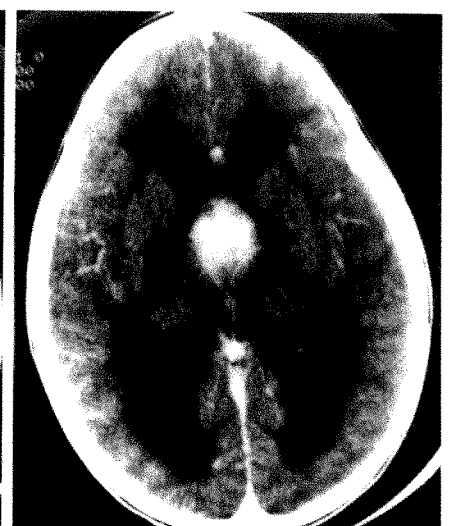


B

Fig. 5.—Nonenhanced axial (A) and enhanced coronal (B) CT scans show intraventricular pilocytic astrocytoma. Large associated intraventricular cyst (*arrows*) has a CT attenuation number slightly higher than that of CSF.

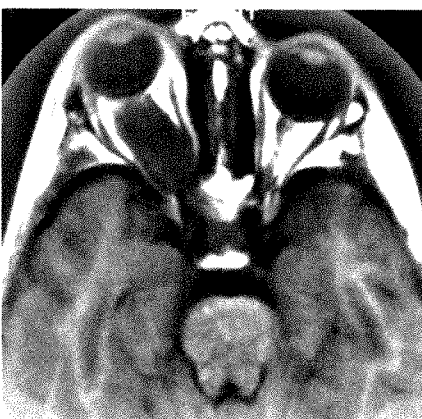


A

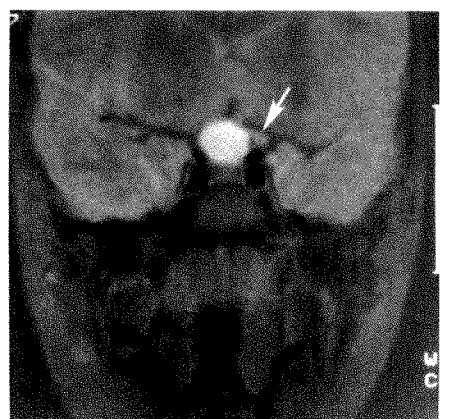


B

Fig. 6.—Nonenhanced (A) and enhanced (B) axial CT scans show isodense enhancing pilocytic astrocytoma arising from septum pellucidum. This sharply demarcated round tumor was proved to be subependymal at surgery.



A



B

Fig. 7.—T1-weighted axial, 600/17 (A), and T2-weighted coronal, 2000/90 (B), MR images show right optic nerve pilocytic astrocytoma with posterior extension into optic chiasm. Tumor is hypointense on T1- and hyperintense on T2-weighted images. Left side of optic chiasm is displaced but uninvolved (*arrow*).

TABLE 1: Summary of Juvenile Pilocytic Astrocytomas

Location	No.	Extension (No.)	Configuration (No.)	No. with Cyst Formation ^a	No. with Calcification	No. with Edema	CT Findings (No.)		MR Findings (No.)		No. with Associated Neuro-fibromatosis
							Tumor Matrix	Contrast Enhancement	T1	T2	
Optic chiasm/hypothalamus	17	Pituitary fossa (9), optic nerve (3), postchiasmal pathway (3)	Multilobulated (10), oval (4), dumbbell (3)	Micro (9), macro (1)	2	0	Hypodense (4), isodense (11), hyperdense (2)	Moderate (6), marked (11)	Hypointense (2), isointense (2)	Hyperintense (4)	3
Cerebellum: Vermis	7	No extension	Round (5), oval (2)	Micro (1), macro (3), combined (3)	0	0	Hypodense (2), isodense (5)	Marked (7)	MR not performed	N	0
Hemisphere	4	No extension	Round (3), oval (1)	Macro (3), combined (1)	1	1	Hypodense (2), isodense (2)	Moderate (1), marked (3)	MR not performed	N	0
Cerebrum: Hemisphere	4	No extension	Round (2), oval (2)	Macro (3)	0	1	Hypodense (3), isodense (1)	Marked (4)	MR not performed	N	0
Intraventricular	2	No extension	Oval (2)	Macro (1)	0	0	Hypodense (2)	Marked (2)	MR not performed	N	1
Subependymal	2	No extension	Oval (2)	No cysts	1	0	Hypodense (2)	Marked (2)	MR not performed	N	0
Optic nerve	1	Optic chiasm (1)	Dumbbell (1)	No cysts	0	0	Hypodense (1)	Marked (1)	Hyperintense (1)	Hyperintense (1)	1

^a Microcysts are ≤ 1 cm in diameter; macrocysts are >1 cm in diameter.

subependymal region around the third ventricle (Fig. 6). One lesion arose in an optic nerve with posterior extension into the optic chiasm (Fig. 7).

The majority of the tumors were either oval or round (23 cases, 62%). Ten lesions were multilobulated; all 10 were chiasmal. One optic nerve and three chiasmal lesions had a dumbbell appearance. The size of the tumors ranged from $2 \times 2 \times 2$ cm³ to $6 \times 5 \times 6$ cm³. All the lesions were sharply demarcated and smoothly margined. The CT density of the tumor matrix was hypodense relative to brain in 16, isodense in 19, and hyperdense in two. All the tumors enhanced on CT after IV contrast administration, at least to a moderate degree and usually markedly. Tumor calcifications were identified in four cases (11%), including two chiasmal lesions, all in the form of flecks (Fig. 8). Twenty-five cases (68%) had cyst formation; microcysts were observed in 10 cases, macrocysts in 11 cases, and a combination of both in four (Fig. 9). Mild vasogenic edema was associated only in two cases, one in the cerebral and the other in the cerebellar hemisphere. An associated arachnoid cyst or subarachnoid-space dilatation was observed in two cases, one associated with a chiasmal lesion (Fig. 10) and the other one in the sylvian fissure with a temporal lesion. The tumors all appeared isointense or slightly hypointense relative to brain on T1-weighted and hyperintense on T2-weighted images in all five patients who had MR.

Discussion

Mature astrocytes are of fibrillary and protoplasmic types, both of which can give rise to astrocytomas. The diffuse astrocytomas of the cerebral hemispheres usually are of the fibrillary type (Fig. 11); this is because protoplasmic astrocytes can acquire fibrillary characteristics under pathologic conditions. Astrocytomas also may be categorized by histologic growth pattern. The pilocytic astrocytomas have an abundance of cells that are elongated and bipolar, thus appearing "hairlike." These tumors are of two distinct types: adult (or diffuse) and juvenile (or biphasic). The juvenile pilocytic astrocytoma has also been referred to as "polar spongioblastoma." Complicating the issue of pilocytic astrocytoma is the tendency of diffuse cerebral and pontine fibrillary astrocytomas of higher grades of anaplasia to infiltrate along existing brain fiber tracts, thus attaining an artificial pilocytic appearance (Fig. 12) [1].

The juvenile pilocytic astrocytoma is a distinct low-grade variant of astrocytoma, both clinically and histopathologically. It is composed of distinct areas of compact pilocytic astrocytes, mostly arranged around vessels, and mixed with areas having a looser, protoplasmic, or partially cystic appearance [2]. This gives a definite biphasic pattern to the tumor when viewed under low-power magnification (Fig. 13). In contrast to the diffuse fibrillary astrocytomas of the cerebral hemispheres, for which a grading system is well established [3], the presence of atypical or multinucleated cells or vascular endothelial hyperplasia does not imply a worse prognosis for the juvenile pilocytic neoplasms. Mitoses and tumor necrosis are found rarely or never [4]. Important histologic and CT features of various gliomas are outlined in Table 2.

Juvenile pilocytic astrocytomas may have a grossly cystic character and contain a mural tumor nodule located in the

Fig. 8.—Nonenhanced (A) and enhanced (B) axial CT scans show calcified chiasmal pilocytic astrocytoma. Noted are microcysts within this strongly enhancing tumor (arrows).

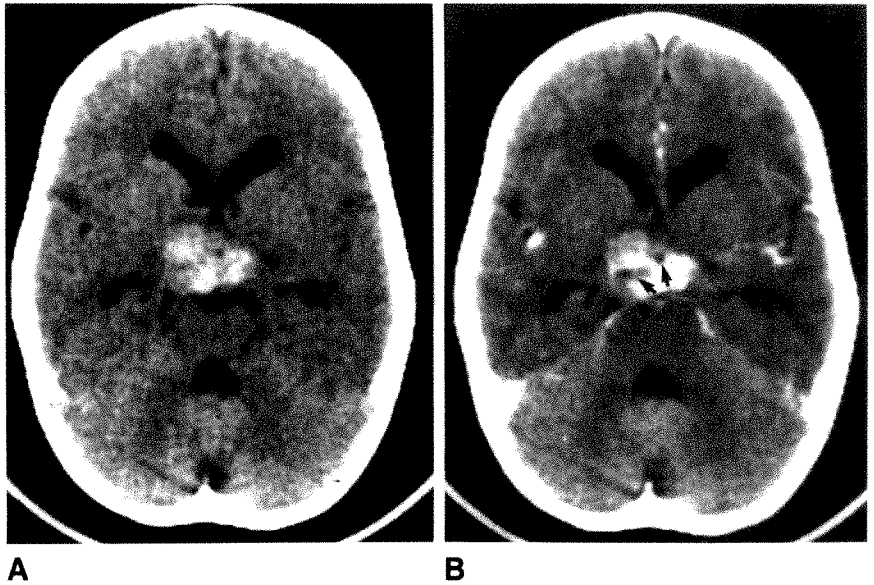


Fig. 9.—Contrast-enhanced axial CT scans. A, Intraventricular pilocytic astrocytoma. Multiple microcysts are identified. B, Right frontal pilocytic astrocytoma. Well-defined macrocyst is associated with strongly enhancing mural nodule.

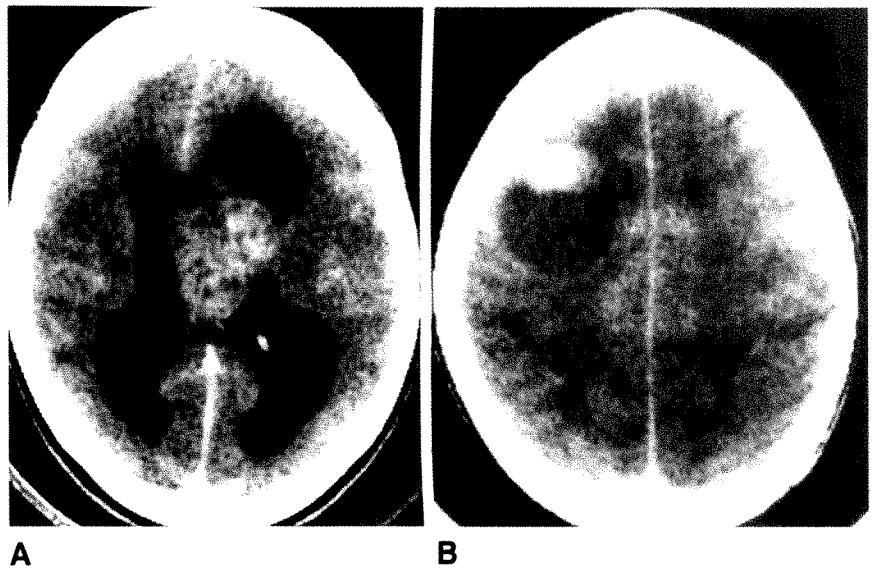
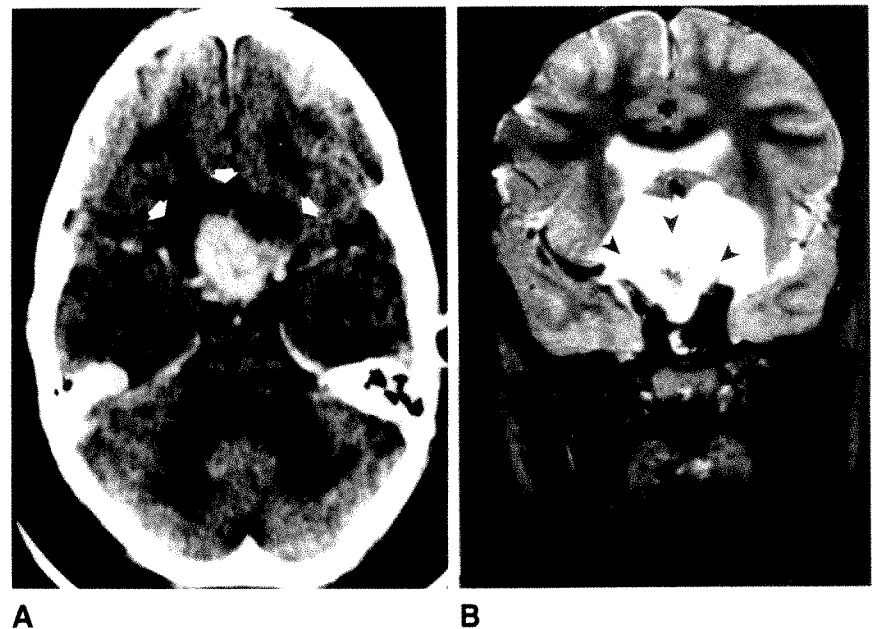


Fig. 10.—A, Contrast-enhanced axial CT scan shows strongly enhanced chiasmal pilocytic astrocytoma surrounded by multilobulated arachnoid cyst (arrows). B, Coronal T2-weighted MR image, 2000/80, shows associated arachnoid cyst draped around tumor (arrowheads). Sagittal T1-weighted MR image, 600/20, in this patient (Fig. 1) did not provide demarcation of tumor from surrounding arachnoid cyst.



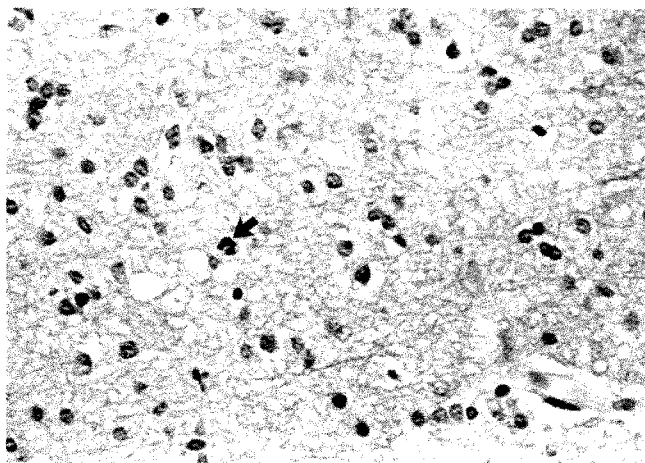


Fig. 11.—Diffuse fibrillary astrocytoma, low grade. Diagnostic features include uneven increase in cellularity, nuclear enlargement, and rounded nuclei with multiple delicate fibrillary processes. One mitotic figure (arrow) is present. (H and E, $\times 600$)



Fig. 12.—Pilocytic growth pattern in pontine glioblastoma multiforme. Neoplastic cells are elongated, with bipolar processes, but growth pattern is diffuse. Other areas of this neoplasm were highly pleomorphic and showed coagulation necrosis. (H and E, $\times 600$)

wall of the cyst. This tumor nodule is soft and red-tan, because of rich vascularity. The tumors commonly occur in children and young adults. The most frequent locations are the cerebellum, the optic nerves or chiasm (optic-nerve glioma), and the region around the third ventricle. Less often, juvenile pilocytic astrocytomas can be found in the cerebral hemispheres and lateral ventricles. These tumors are the most common astrocytic neoplasm in the cerebellum of children. The diffuse (adult type, nonbiphasic) pilocytic astrocytomas are distinctly less common than the juvenile type in children. Biologically, the juvenile tumors are low grade. After complete surgical excision, they almost never recur. Even those examples that are incompletely resected are slow growing, and, unlike diffuse astrocytomas of the cerebrum, do not undergo malignant transformation to a more anaplastic form [4].

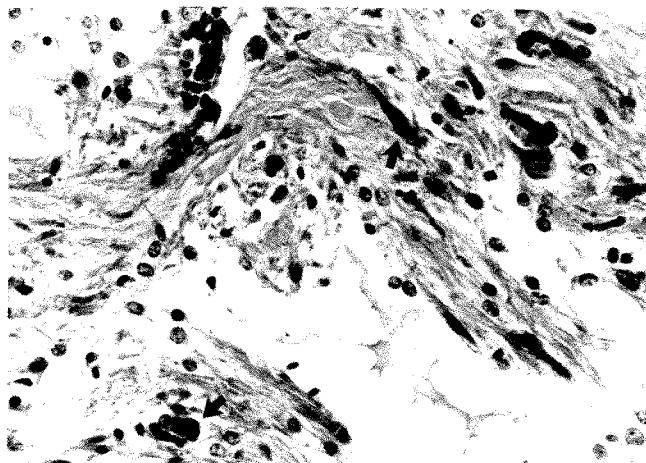


Fig. 13.—Juvenile pilocytic astrocytoma. Characteristic biphasic pattern of dense "hairlike" pilocytic areas alternating with looser microcystic areas. Rosenthal fibers can be identified (arrows). (H and E, $\times 600$)

Juvenile pilocytic astrocytomas are well known for their association with neurofibromatosis, and in this entity they are usually confined to the anterior optic pathways; for example, the optic nerve and chiasm [5–8]. In our series five juvenile pilocytic astrocytomas were associated with neurofibromatosis; three were centered at the optic chiasm, one involved the optic nerve, and one was within the frontal horn of the lateral ventricle.

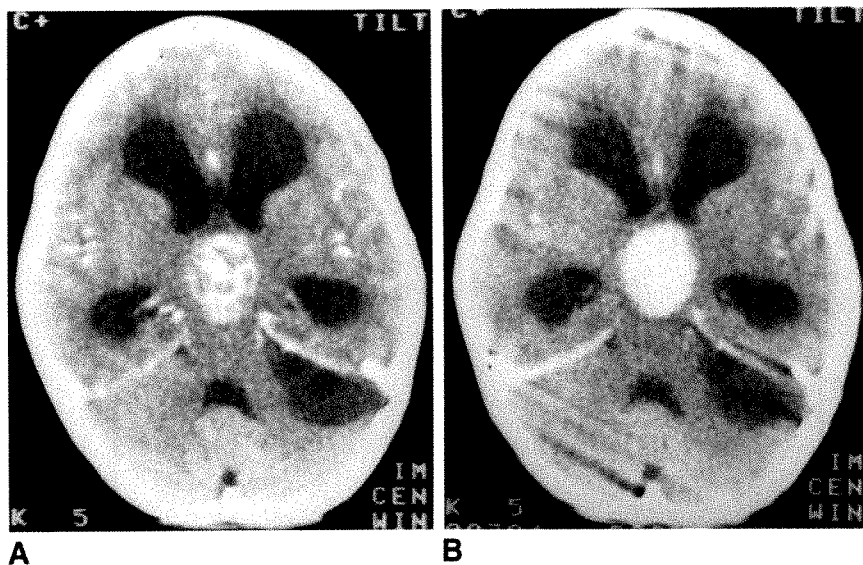
Several characteristic findings were observed in our radiologic review. Except for occasional hemispheric lesions, these tumors tend to be found around the third ventricle supratentorially and the fourth ventricle infratentorially; that is, in the optic chiasm and vermis, respectively. All lesions appear sharply demarcated and smoothly margined and often are round or oval in configuration, except when located in the optic chiasm or optic nerve. At these sites the tumor has a tendency to grow along the optic pathway, giving a multilobulated or dumbbell appearance. Most often the tumor matrix appears hypo- or isodense and enhances strongly on CT. The character of contrast enhancement of juvenile pilocytic astrocytomas is distinctive when compared with the more frequently occurring low-grade fibrillary astrocytomas, which often present as hypodense, nonenhancing masses [9, 10]. This CT observation might be explained by increased tumor vascularity, which is constantly observed in the pilocytic astrocytomas and absent in the low-grade fibrillary astrocytomas. The frequent absence of associated edema is indicative of the low malignancy of this particular astrocytoma. Interestingly, two patients in our series were seen initially with an arachnoid cyst draped around the tumor. Its indolent growth and tendency to infiltrate along the arachnoid with secondary fibrotic changes might explain the secondary development of an arachnoid cyst. To our knowledge, this has not been reported in association with other brain tumors. Tumor calcification, which occurred rarely, tends to be flecklike. Formation of either micro- or macrocysts is observed frequently in pilocytic astrocytomas. Macrocysts tend to occur in cerebral or cerebellar lesions and rarely in the lesions along the optic

TABLE 2: Histologic and CT Features of Various Gliomas

Type of Glioma	Histology	CT
Pilocytic astrocytoma (polar spongioblastoma)	Bipolar and biphasic; increased vascularity; mitosis and necrosis rare or never	Around or in the ventricles; round or oval, multilobulated in chiasmal region; sharply demarcated; contrast enhancement marked; cysts frequent; calcification rare
Fibrillary astrocytoma: (Low-grade) astrocytoma	Multipolar fibrillary or protoplasmic; no increased vascularity	Lobar; round; poorly demarcated; hypodense, nonenhancing; cysts rare; calcification rare; edema?
Anaplastic astrocytoma	Multipolar fibrillary or protoplasmic; mitosis and vascular endothelial proliferation; no necrosis	Lobar; configuration variable; demarcation variable; contrast enhancement variable; cysts rare; calcification rare; edema frequent
Glioblastoma multiforme	Multipolar; markedly cellular and pleomorphic; mitosis and vascular endothelial proliferation marked; necrosis required	Lobar; multilobulated; necrotic center frequent; cysts rare; calcification rare; edema frequent
Oligodendroglioma	Neoplastic oligodendrocytes with round nuclei and clear cytoplasm; prominent fine capillary branching	Peripheral lobar, occasionally around or in ventricle; demarcation variable; contrast enhancement variable; cysts occasional; calcification frequent; edema variable

Fig. 14.—A, Immediate contrast-enhanced CT scan shows multiple microcysts within chiasmal pilocytic astrocytoma. Also noted is arachnoid cyst (asterisk).

B, Delayed contrast-enhanced CT scan. Microcysts fill with contrast medium.



pathway or around the third ventricle. The microcysts are best demonstrated on the immediate postcontrast CT scans because these cysts may fill with contrast medium on delayed scans (Fig. 14). Comparison between MR and concurrent CT scans shows MR to be superior in delineating the tumor extent, particularly in the postchiasmal optic pathway [8, 11, 12].

The differential diagnosis of juvenile pilocytic astrocytoma

includes craniopharyngioma, germinoma, loculated leptomeningeal metastasis, and invasive pituitary adenoma in the chiasmal region; medulloblastoma and ependymoma in the posterior fossa; and intraventricular or subependymal oligodendroglioma and ependymoma in the paraventricular cerebral hemisphere. Craniopharyngiomas tend to be densely calcified and often have macrocysts [13], while chiasmal pilocytic astrocytomas calcify rarely and the cysts are often

small and multiple. Suprasellar germinoma [14] and loculated leptomeningeal metastasis, most often from medulloblastoma in children, can mimic chiasmal pilocytic astrocytoma but without extension into the optic apparatus. These other tumors are often associated with evidence of diffuse leptomeningeal metastases, a finding never observed in pilocytic astrocytoma. Chiasmal pilocytic astrocytomas remain centered in the suprasellar region when they extend into the pituitary fossa, while this midline growth may not be observed when invasive pituitary adenomas extend into the suprasellar cistern. Furthermore, the compressed but noninfiltrated optic chiasm in pituitary adenomas can be appreciated readily on state-of-the-art imaging such as MR. Within the posterior fossa, in contrast to medulloblastoma and ependymoma, which tend to fill and dilate the fourth ventricle, the cerebellar pilocytic astrocytoma often extrinsically obliterates the ventricle. Macrocysts, often observed in cerebellar pilocytic astrocytomas, rarely occur in the former two tumors. Oligodendroglioma within or around the third or lateral ventricles [15, 16] may be very difficult to distinguish from a paraventricular pilocytic astrocytoma, but the age of the patient may provide an important differentiating clue.

In conclusion, the radiologic appearance of pilocytic astrocytomas is quite characteristic although not pathognomonic. They tend to be round or oval, sharply demarcated with smooth margins, usually without vasogenic edema, and located around the third or fourth ventricle. The tumor matrix is often hypo- or isodense on CT with strong contrast enhancement and frequent demonstration of micro- or macrocysts. On the basis of the typical radiologic appearance and age of the patient, a presurgical diagnosis of juvenile pilocytic astrocytoma can be made with confidence.

REFERENCES

1. Russell DS, Rubinstein LJ. *Pathology of tumors of the nervous system*, 4th ed. Baltimore: Williams & Wilkins, 1977:156-163
2. Garcia DM, Fulling KH. Juvenile pilocytic astrocytoma of the cerebrum in adults. *J Neurosurg* 1985;63:382-386
3. Burger PC, Vogel FS, Green SB, Strike TA. Glioblastoma multiforme and anaplastic astrocytoma: pathologic criteria and prognostic implications. *Cancer* 1985;56:1106-1111
4. Clark GB, Henry JM, McKeever PE. Cerebral pilocytic astrocytoma. *Cancer* 1985;56:1128-1133
5. Blah J, Jaffe R, Deutsch M, Adkins JC. Neurofibromatosis and childhood tumors. *Cancer* 1986;57:1225-1229
6. Jacoby CG, Go RT, Beren RA. Cranial CT of neurofibromatosis. *AJNR* 1980;1:311-315
7. Alvord EC, Lofton S. Gliomas of the optic nerve or chiasm. *J Neurosurg* 1988;68:85-98
8. Brown EW, Riccardi VM, Mawad M, Handel S, Goldman A, Bryan RN. MR imaging of optic pathways in patients with neurofibromatosis. *AJNR* 1987;8:1031-1036
9. Steinhoff H, Lanksch W, Kazner E, et al. Computed tomography in the diagnosis and differential diagnosis of glioblastomas. *Neuroradiology* 1977;14:193-200
10. Marks JE, Gado M. Serial computed tomography of primary brain tumors following surgery, irradiation, and chemotherapy. *Radiology* 1977;125:119-125
11. Albert A, Lee BCP, Saint-Louis L, Deck MDF. MRI of optic chiasm and optic pathways. *AJNR* 1986;7:255-258
12. Daniels DL, Herfkens R, Gager WE, et al. Magnetic resonance imaging of the optic nerve and chiasm. *Radiology* 1984;152:79-83
13. Fitz CR, Wortzman G, Harwood-Nash DC, Holgate RC, Barry J, Boldt DW. Computed tomography in craniopharyngiomas. *Radiology* 1987;127:687-691
14. Fields JN, Fulling KH, Thomas PRM, Marks JE. Suprasellar germinoma: radiation therapy. *Radiology* 1987;164:247-249
15. Dolinskas CA, Simeone FA. CT characteristics of intraventricular oligodendrogliomas. *AJNR* 1987;8:1077-1082
16. Lee YY, Van Tassel P. Intracranial oligodendrogliomas: imaging findings in 35 untreated cases. *AJNR* 1989;10:119-127

MR Imaging of Intracranial Carotid Occlusion

Barry H. Katz¹
Robert M. Quencer¹
Jack O. Kaplan^{1,2}
R. Scott Hinks^{1,3}
M. Judith Donovan Post¹

The MR scans of seven patients with intracranial carotid occlusion (five proved, two presumed) were reviewed to evaluate the MR signal characteristics seen in this disorder. Five patients had clinical signs of cerebral infarction. Of the remaining two patients, one was asymptomatic and the other had a long-standing occlusion and headaches. We correlated the MR findings with cerebral angiography in five patients and with CT scans in six patients. All occluded vessels demonstrated MR signal predominantly isointense to brain on proton-density- T1- and T2-weighted images. Since there is an absence of flow, the MR signal is based on the intrinsic properties of the arterial thrombus and possibly on the chronicity of the occlusion. The pathogenesis and histopathology of intravascular thrombus differ significantly from extravascular hematoma, which accounts for the differences in their MR signal characteristics.

The demonstration of occluded intracranial vessels may solidify the diagnosis of stroke in cases in which clinical and/or CT findings are equivocal. In patients presenting with infarction, an occluded carotid artery by MR may obviate the need for angiography; however, the demonstration of a patent carotid in conjunction with infarction suggests the possibility of an embolus, which may require angiography. We believe that MR is a valuable adjunct to CT in evaluating patients with cerebrovascular infarction.

For the past decade, CT has been the radiologic mainstay in the evaluation of cerebral infarction. In most instances, it can reliably define the location, extent, type (bland vs hemorrhagic), and chronicity of the infarction. However, MR imaging has been shown by several authors to be more sensitive in the detection of cerebrovascular accidents (CVAs), especially early in the course of the infarction [1-8]. This sensitivity is the result of the superior ability of MR imaging to detect an increase in water content within ischemic tissue, as manifested by an increase in the tissue T1 and T2 relaxation times. MR can also assess the presence or absence of intravascular flow in a noninvasive manner [9-12]. The characteristic flow void, seen as absence of signal on T1- and T2-weighted images, indicates vascular patency and rapid flow [9-12]. An absence of this finding on routine MR imaging is strongly suggestive of slow flow or thrombosis. The ability to study intracranial structures in multiple planes with MR improves the ability to diagnose vascular occlusion. This can be an important corroborative finding in the evaluation of cerebral infarction, especially when the clinical or radiologic diagnosis is unclear. In this study, intracranial vascular occlusion in seven patients was diagnosed by MR and correlated with the CT findings in six patients and with angiography in five patients. It was our objective to characterize and explain the MR signal changes resulting from carotid occlusion.

Subjects and Methods

Seven patients with cerebrovascular disease were studied with MR. The group included four women and three men 33 to 65 years old (mean, 52.6 years). The two institutions involved in this study used the 1.5-T Signa* (four cases) and the Vista 1.5-T and 0.5-T† (three

This article appears in the March/April 1989 issue of *AJNR* and the June 1989 issue of *AJR*.

Received February 17, 1988; accepted after revision July 6, 1988.

¹ Department of Radiology, University of Miami/Jackson Memorial Medical Center, Miami, FL. Address reprint requests to R. M. Quencer, Department of Radiology (R-308), University of Miami MRI Center, 1115 N.W. 14th St., Miami, FL 33136.

² Department of Medical Imaging, Baptist Hospital of Miami, Miami, FL 33176.

³ Picker International, Inc., NMR Imaging Research at the University of Miami, Miami, FL 33101.

AJR 152:1271-1276

0361-803X/89/1526-1271

© American Roentgen Ray Society

* General Electric, Milwaukee, WI.

† Picker International, Highland Heights, OH.

cases) superconducting magnets. Multisection, spin-echo (SE) pulse sequences were obtained in all patients. Proton-density- T1- and T2-weighted images (using dual echoes) were obtained in all patients scanned on the 1.5-T Signa unit; T1- and single-echo T2-weighted images were obtained in patients scanned on the Picker units. The imaging parameters were 500–1000/25–30/2 (TR range/TE range/excitations) for T1-weighted images and 2000/20–35, 60–120/2 for the proton-density- and T2-weighted images, respectively. The section thickness was 5 mm with an interslice gap varying from 0 to 2 mm. The acquisition matrix varied from 128 × 256 to 256 × 256. Axial, coronal, and/or sagittal images were obtained in most patients. The MR scans were done 4 to 60 days after clinical presentation of stroke (mean, 21.4 days). Of the five patients presenting with stroke, three had cerebral angiography. All three of these arteriograms were performed within 1½ days of the MR scans. Another patient with chronic occlusion had angiography several years before his MR scan. The asymptomatic patient had angiography for the purpose of evaluating significant Doppler abnormalities. Six patients had axial CT scans (on either a GE 9800 or 8800 model) prior to their MR scans (range, 2–6 days). Five of the six CT scans were done only without IV contrast administration; the other scan was performed both pre- and postcontrast. All CT scans were obtained with 10-mm contiguous slices.

The MR and CT examinations were assessed with respect to intraparenchymal abnormalities and the evaluation of intracranial vas-

cular patency. Angiography was performed in order to prove or disprove the MR findings and to determine if the vessel was occluded or highly stenosed.

Results

The findings are presented in Table 1. All seven patients in the study had occluded intracranial carotids demonstrated by MR. In all cases, CT failed to demonstrate that abnormality.

Of the five patients (cases 1–4 and 6) presenting with cerebral infarction, the MR showed the characteristic findings of CVA as well as the occluded blood vessels. Three of these patients underwent cerebral angiography, and the occlusions were corroborated in each case. In each of these patients, CT demonstrated findings of cerebral infarction, but no carotid arterial abnormality was evident. We assume that the occlusions took place in association with the patient's symptoms. Cases 1 and 2 clearly occluded at the time of their symptomatology, as these patients each had several MR scans proving this. Patients 3, 4, and 6 most likely occluded at the time of their symptoms, although one could argue that the occlusions

TABLE 1: Summary of Patients with Intracranial Carotid Occlusion

Case No.	Age	Gender	Clinical Information	CT Findings	Angiographic Findings	MR Findings*
1	52	F	Diabetic with mucormycosis, superior orbital fissure syndrome, and left hemiparesis	Infarct in right frontoparietal area in MCA distribution	Not done	Right MCA infarct with occluded right intracavernous ICA (7 days)
2	33	F	Osteosarcoma of ethmoid sinus; history of radiation therapy; presented with left hemispheric CVA syndrome and meningitis	Gyral and cisternal enhancement	Not done	Left basal ganglia hemorrhage and occluded left MCA (4 days)
3	51	M	Hypertensive with right hemispheric infarct	Right basal ganglionic hemorrhagic infarct	Occluded right common carotid artery	Occluded right intracavernous ICA with subacute hemorrhagic basal ganglionic infarct (30 days); adequate collateral circulation to ipsilateral MCA
4	52	F	2-month history of ataxia, dizziness, and left-sided numbness	Right basal ganglionic infarct	Occluded right intracavernous ICA	Right basal ganglionic infarct with occluded right intracavernous ICA (60 days)
5	61	M	Chronic headaches, with history of "reported" left cerebral infarct 16 years ago; Doppler: complete left ICA occlusion	Normal	Complete left ICA 16 years earlier	Occluded left ICA
6	54	F	Right hemispheric infarct	Acute right MCA in basal ganglia, internal capsule, and temporal lobe	Occluded right MCA	Occluded right intracavernous ICA with infarct in basal ganglia, internal capsule, and temporal lobe (16 days)
7	65	M	Asymptomatic with carotid bruit; Doppler: occluded left ICA and 60–80% stenosis of right ICA	Not done	Occluded left ICA	Occluded left ICA; adequate collaterals to ipsilateral MCA

* Information in parentheses = number of days between onset of clinical signs and symptoms and performance of MR imaging.

Note.—MCA = middle cerebral artery; ICA = internal carotid artery; CVA = cerebrovascular accident.

occurred at an earlier time and that the symptoms appeared in relation to problems with the collateral circulation. We believe that this is unlikely in these cases in that all three had angiography and none of them showed any evidence of collateral vessels. The asymptomatic patient (case 7) and the patient who presented with chronic headaches but without stroke (case 5) had MR and angiographically proved vascular occlusion. Patient 5 had a normal CT scan with no evidence of parenchymal or vascular abnormalities. Both of the patients (cases 1 and 2) who did not have angiographic confirmation of carotid occlusion had serial MR scans. The initial scans demonstrated flow voids in the carotid arteries and no parenchymal abnormality, while the subsequent MR examinations clearly showed parenchymal infarctions in conjunction with an occluded ipsilateral carotid.

Three of the five patients presenting with stroke had occlusion of the intracavernous internal carotid artery (ICA) shown by MR. All three had infarction in a middle cerebral artery (MCA) distribution, yet the ipsilateral MCA was patent by MR and/or angiography. Examples of this are illustrated in Figures 1 (case 3) and 2 (case 4). The former was a hemorrhagic infarct in a hypertensive patient; the latter a bland one. The other two patients presenting with stroke had MR manifestations of MCA infarction with occlusion of the ipsilateral MCA. One of these was a bland infarct, while the other was hemorrhagic. Our asymptomatic patient had complete occlusion at the origin of the ICA (Fig. 3, case 7). The patient with chronic headaches also had an occlusion of the left intracavernous ICA branch.

Although small foci of increased or decreased signal were visualized within some of the occluded vessels by MR, the overall signal intensity was predominantly isointense to brain parenchyma. This was consistently found on all T1-, proton-density, and T2-weighted images.

Discussion

In the evaluation of patients with cerebrovascular disease, an understanding of parenchymal abnormalities and of the patency of the major intracranial vessels is important. To our knowledge, a series of intracranial carotid occlusions documented by MR has not been previously reported. MR can evaluate vascular patency noninvasively, whereas CT evaluation of intracranial vascular patency generally requires the administration of IV contrast material, and even when performed in that manner vascular cutoff may not be visualized. A recent article [13] reported that CT of acute CVAs may show increased attenuation in the occluded vessel (secondary to acute thrombosis) on noncontrast images, especially if 5-mm cuts are obtained. The sensitivity of this finding in the acute setting is yet to be determined prospectively. It is important to note that acute stroke patients are usually imaged with 10-mm-thick cuts, so this potential finding may often go undetected. None of our cases demonstrated any definite vascular occlusion by CT. It is fair to point out, however, that most patients imaged with CT in the acute setting of a stroke are done only without IV contrast administration. Typically, the clinicians want to ascertain primarily whether a bleed has occurred. In our series, only one of six patients who underwent CT scanning were given IV contrast. The ability of MR to image intracranial vessels by showing the presence or absence of a "flow void" is a tremendous advantage in evaluating their patency.

The principles of evaluating blood flow by MR have been well described [9-14]. The signal intensity from blood within the vessel lumen is a function of numerous parameters. These include patient-dependent factors, such as the direction of flow, the spatial distribution of velocities across the lumen, and the changes in velocity due to the flow-dependence on

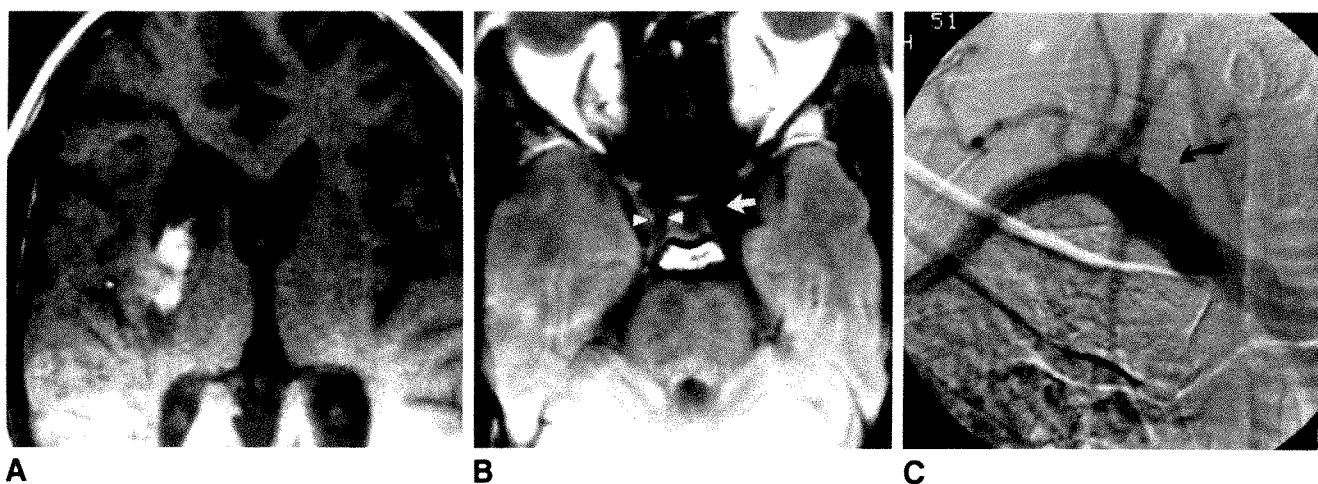


Fig. 1.—Case 3: Hemorrhagic infarct in a right MCA distribution in a patient with occluded common carotid artery.

A, T1-weighted axial image (600/25) shows subacute hemorrhage in basal ganglia.

B, Proton-density-weighted axial image (2000/20) shows absence of flow void within isointense intravascular signal in right intracavernous ICA (arrowheads). Compare with patent left intracavernous carotid (arrow).

C, Digital subtraction angiogram shows stump of occluded right common carotid artery (arrow). Other images (not shown) demonstrated complete occlusion of remainder of right common carotid artery as well as entire internal and external carotids.

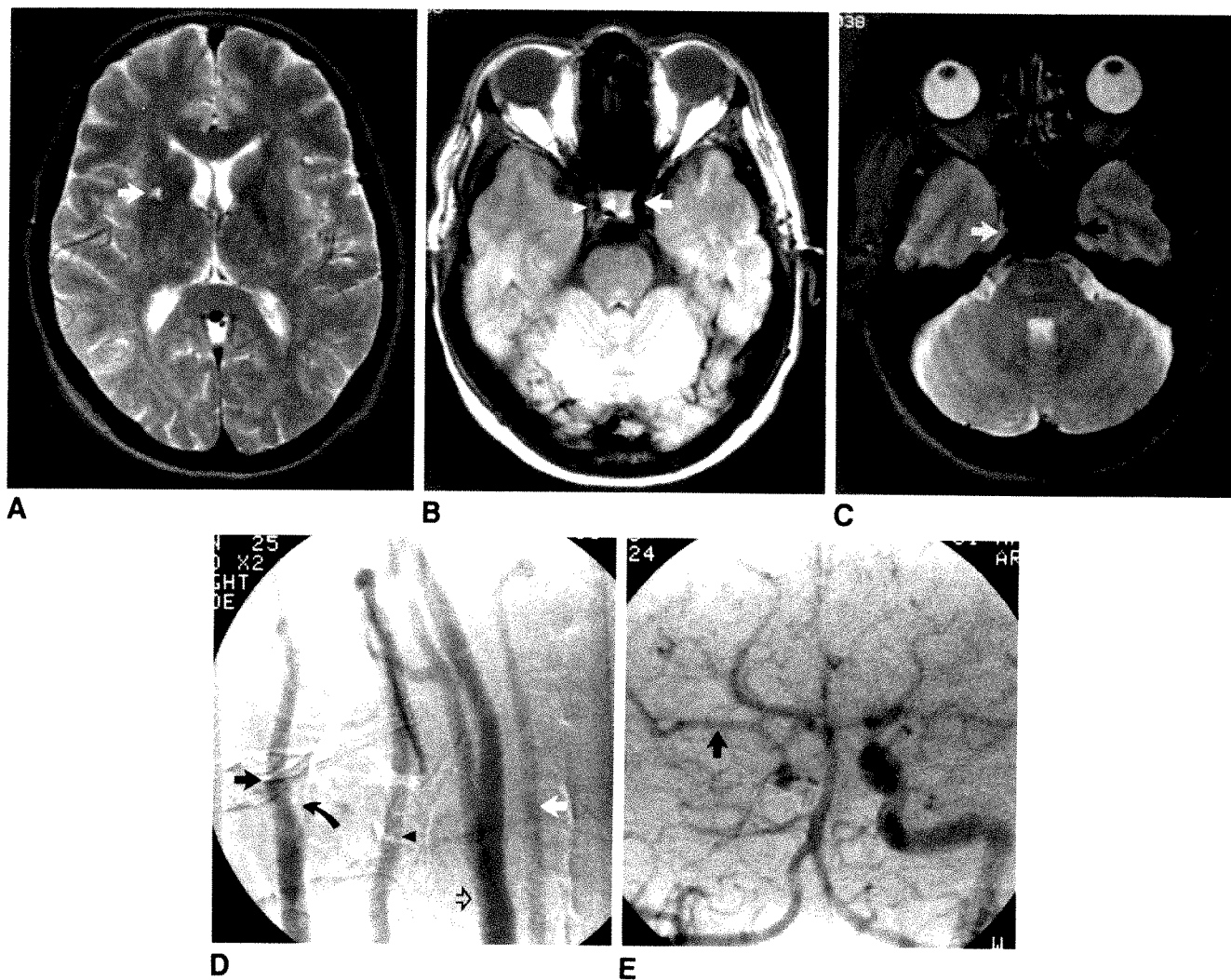


Fig. 2.—Case 4: Basal ganglia infarct in patient with occluded right ICA (60 days after onset of symptoms).

A, Axial T2-weighted image (2000/80) shows basal ganglionic infarct (arrow).

B, Proton-density-weighted axial image (2000/20) shows isointense right intracavernous ICA (arrowheads) compared with flow void seen in normal left ICA (arrow).

C, T2-weighted axial image (2000/80) through precavernous portion of ICA shows absence of right ICA (white arrow) compared with normal left side (black arrow).

D, Digital arch arteriogram shows occluded right ICA (curved black arrow), normal right external carotid artery (straight black arrow), right vertebral artery (arrowhead), left common carotid artery (open arrow), and left vertebral artery (white arrow).

E, Note occluded right ICA but with collateral circulation to fill right MCA (arrow).

the cardiac cycle. MR sequence-dependent factors include the type of pulse sequence, whether the section is an entry or exit slice (flow-related enhancement), the spin-echo type (odd or even), the orientation of the imaging plane and the phase- and frequency-encoding axes within this plane, and whether cardiac gating is employed [11]. In addition, tissue characteristics such as proton density, T1, and T2 relaxation times also play a role in the contrast observed between the vessel lumen and surrounding tissues.

Rapidly flowing blood normally gives a characteristic signal void as a result of a combination of "time-of-flight" effects and turbulence. The "time-of-flight" effect results from the motion of blood through a slice during the time between the 90° and 180° pulses in the sequence. Material that originally receives the 90° excitation pulse moves out of the slice, does not

experience the 180° refocusing pulse, and hence does not form an echo. In addition, material that moves into the slice between the two pulses only experiences the refocusing pulse and likewise does not contribute to the signal. Turbulent flow also contributes to the loss of signal intensity by increasing the amount of dephasing of the signal across the individual pixel. As dephasing increases, the small contributing signals add together less coherently and the received signal decreases.

In all our cases, there was absence of the "flow void" that one usually sees in the lumen of normally flowing arteries. This is secondary to the lack of "time-of-flight" effects and turbulence in the occluded vessels. The intravascular signal seen in all the occluded vessels (in multiple planes) was basically isointense to normal brain on T1-, proton-density,

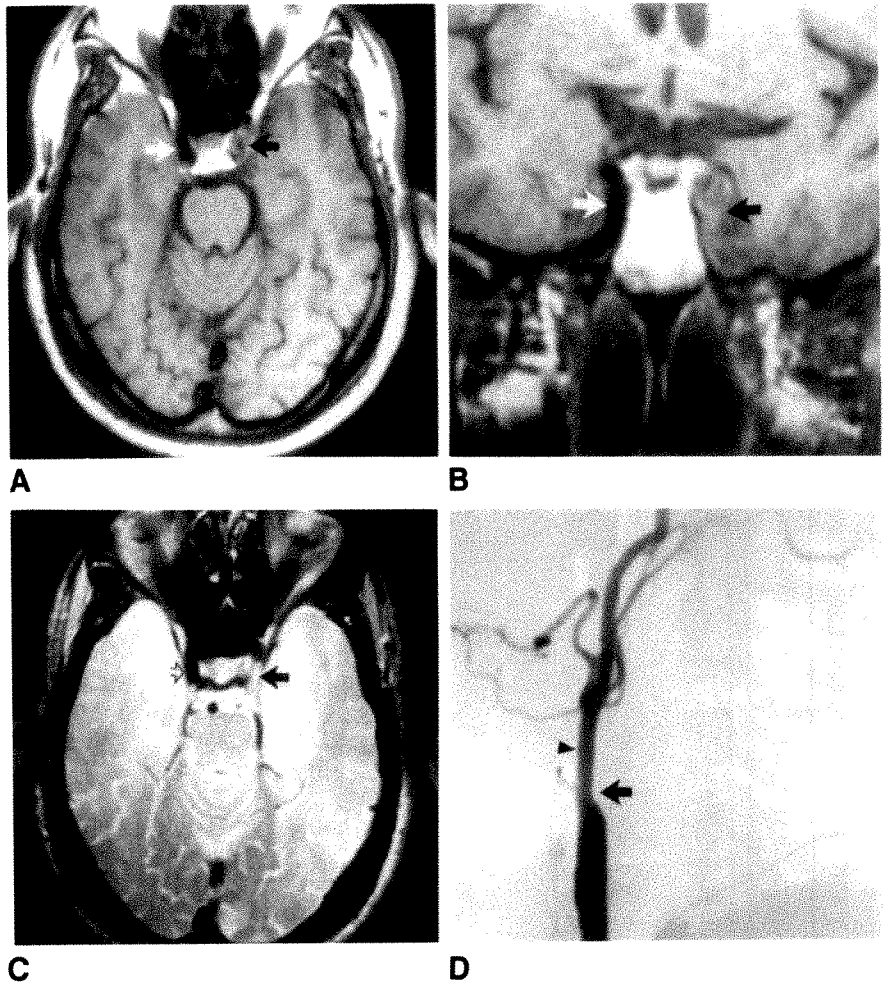
Fig. 3.—Case 7: Occlusion of left ICA in asymptomatic patient.

A. T1-weighted axial image (691/26) shows lack of flow void in left ICA with signal intensity equal to surrounding brain parenchyma (*black arrow*). Normal flow void in right carotids indicated by *white arrows* in A and B.

B. Coronal T1-weighted image (691/26) shows findings similar to those in A (*arrows* are also similar).

C. Axial T2-weighted image (1991/60) again shows predominantly isointense signal in occluded vessel (*closed arrow*) compared with normal right side (*open arrow*).

D. Digital subtraction angiogram of the left common carotid artery injection shows total occlusion at origin of left ICA (*arrow*). Note normal external carotid artery (*arrowhead*).



and T2-weighted images. Likewise, none of the occluded carotids showed hyperintense intraluminal signal. Intravascular hyperintensity can be seen secondary to flow-related enhancement (particularly for entry slices seen with a short TR), diastolic pseudogating, the use of motion-compensating gradients, cardiac gating, and symmetric even-echo rephasing [12]. All these mechanisms may produce increased intraluminal signal in normal veins, where flow is relatively slow compared with arterial flow. In our experience, none of these will produce increased signal in a normally flowing carotid artery. In fact, flow-related enhancement, diastolic pseudogating, and even-echo rephasing require some flow in order to produce a bright signal [9]. No second-echo rephasing was seen in our cases.

In cases 3–6, in which a second echo was utilized, the signal intensity in the occluded carotids was identical (isointense) on both the first and second echoes. We can presume, therefore, that if one sees a high signal in a carotid artery, diminished flow (secondary to a high-grade stenosis or to a low cardiac output state) is present. Since all our MR scans were done at least 4 days after the clinical event, it is presumed that slow flow progressed to complete occlusion in most, if not all, these cases. It is postulated that MR performed within the first 24 hr after a stroke may demonstrate increased signal intensity intravascularly as long as

flow, though diminished, is maintained. Certainly, a gradual thrombotic occlusion would be more likely to produce these findings than would an acute embolic occlusion. Further investigation of these issues may elucidate the flow dynamics of stroke early in its evolution. We therefore contend that when carotid arteries contain neither a flow void nor a high signal, that flow is neither normal nor sluggish. The isointense signal represents stationary protons in an occluded vessel. This is substantiated in our angiographically proved cases in which all demonstrated occlusion rather than stenosis. On the basis of the progression of both intraluminal and parenchymal abnormalities, we do believe that our two patients who had serial MR scans (cases 1 and 2) would have shown a similar angiographic picture. These factors support the conclusion that the observed signal intensities within these occluded vessels is a function of the proton-density and relaxation characteristics of the intravascular thrombus rather than flow, which would dominate the observed signal intensity if these vessels were patent. The proton-density and relaxation characteristics of arterial thrombus are dependent on its histopathologic composition.

Arterial thrombi are composed of alternating layers of fibrin and platelets irregularly united with very small quantities of red blood cells and coagulated blood. These laminated layers are known as the lines of Zahn. Arterial thrombi are known

as white thrombi because of their lack of red cells within the precipitated fibrin network. In the typical thrombotic arterial occlusion, atherosclerotic changes fill the majority of the lumen, with the remainder representing thrombus. It is this combination of arterial wall, atheroma, and thrombus that contributes to the observed signal in the occluded arteries. In no case were we able to definitely separate the arterial wall from its intraluminal contents on MR. On the other hand, venous thrombus as well as intraparenchymal or any extravascular hematoma is composed primarily of red blood cells that simply coagulate, much as blood would clot in a test tube [14]. The MR signal characteristics of intracranial hematomas have been well described on high-field-strength systems [15]. Since intraparenchymal hematomas and venous thrombus are composed mostly of red cells, the MR signal characteristics over time depend on the relaxation times of oxidation breakdown products of hemoglobin (i.e., deoxy-hemoglobin, methemoglobin, and hemosiderin). The occluded carotid vessels, which contain few red cells, do not have any significant contribution from these substances. For example, methemoglobin from lysed red blood cells would give high signal on both T1- and T2-weighted images in the subacute phase of either an intraparenchymal bleed or in a superior sagittal sinus thrombosis. Conversely, the relative lack of methemoglobin in intravascular arterial thrombus will not tend to produce a high signal in the vessel. Heier et al. [16] described the MR signal characteristics of intracranial vascular occlusions in 16 patients in terms of chronicity but did not distinguish between arterial and venous occlusions. We would expect to see signal differences based on the higher percentage of blood elements in a venous thrombus as compared with the predominant intimal atheroma seen in most cases of arterial occlusion. A case report [17] described a high signal intensity in a carotid artery illustrated on the T2-weighted images. An arteriogram was performed, and it was thought from this that thrombus was present in the left internal carotid artery. In addition, there was cross-filling of the left A1 and M1 segments via the anterior communicating artery from the right common carotid artery injection. We believe that the high signal most likely was secondary to retrograde filling of the supraclinoid and cavernous segments of the internal carotid artery with slow flow. Another possibility would be an unusually high content of methemoglobin in an arterial occlusion in relation to the amount of atheroma narrowing the lumen.

We have indicated that arterial occlusion gives, for the most part, an isointense MR signal on all spin-echo sequences. There are, however, small focal areas of either increased or decreased signal intensity scattered within several of the occluded vessels. We believe that focal punctate areas of hyperintensity may represent small amounts of methemoglobin in a subacute thrombus. Conversely, we postulate that small areas of hypointensity may be the result of fibrin and hemosiderin deposits in a chronic, organized thrombus. Both these substances are seen in abundance in chronic thrombi [14] and both may cause diminished MR signal. We do not believe that the small foci of intraluminal hypointensity are secondary to small collateral vessels, since the shape of the low signals are not serpiginous and the angiographic cases did not indicate the presence of any collaterals within or adjacent to the cavernous sinuses.

Several important clinical inferences can be made on the basis of these MR findings. First, in cases in which the clinical signs and/or CT are equivocal, the presence of an occluded carotid artery by MR may serve as an important adjunct in making the diagnosis of cerebral infarction. Second, in patients presenting with CVAs, the presence of an occluded ipsilateral carotid by MR may obviate the need for carotid angiography. Conversely, in patients demonstrating a patent internal carotid artery by MR in conjunction with a cerebral infarction, angiography may be required to look for a possible embolic source.

Until such time as specialized "MR angiography" [18, 19] sequences become available for widespread clinical use, we believe that spin-echo MR can be used to diagnose carotid occlusion. By MR, intravascular signal isointense to brain on proton-density-, T1-, and T2-weighted images strongly suggests this diagnosis. As a result of the superior ability of MR to evaluate both intraparenchymal and intravascular abnormalities, we believe that this imaging technique should serve as an important adjunct to CT in the evaluation of patients with cerebrovascular disease.

REFERENCES

1. Sipponen JT. Visualization of brain infarction with nuclear magnetic resonance imaging. *Neuroradiology* **1984**;387-391
2. Brant-Zawadzki M, Weinstein P, Bartkowski H, Mosley M. MR imaging and spectroscopy in clinical and experimental cerebral ischemia. A review. *AJNR* **1987**;8:39-48
3. Brant-Zawadzki M, Solomon M, Newton TH, Weinstein P, Schmidley J, Norman D. Basic principles of magnetic resonance imaging in cerebral ischemia and initial clinical experience. *Neuroradiology* **1985**;27:517-520
4. Bryan RN, Willcott MR, Schneiders NJ, Ford JJ, Dorman HS. Nuclear magnetic resonance evaluation of stroke. *Radiology* **1983**;149:189-192
5. Sipponen JT, Kaste M, Ketoner L, Sipponen RE, Keteuvuo K, Sivula A. Serial nuclear magnetic resonance (NMR) imaging in patients with cerebral infarction. *J Comput Assist Tomogr* **1983**;7:585-589
6. Pykett IL, Buonanno FS, Brady TJ, Kistler JP. True three-dimensional nuclear magnetic resonance neuro-imaging in ischemic stroke: correlation of NMR, X-ray, CT and pathology. *Stroke* **1983**;14:173-177
7. Bydder GM, Steiner RE, Young IR, et al. Clinical NMR imaging of the brain: 140 cases. *AJNR* **1982**;3:459-480, *AJR* **1982**;139:215-236
8. Bryan RN, Willcott MR, Schneiders NJ, Rose JE. NMR evaluation of stroke in the rat. *AJNR* **1983**;4:242-244
9. Mills CM, Brant-Zawadzki M, Crooks LE, et al. Nuclear magnetic resonance: principles of blood flow imaging. *AJR* **1984**;142:165-170
10. Bradley WG Jr, Waluch V. Blood flow: magnetic resonance imaging. *Radiology* **1985**;154:443-450
11. Von Schulthess GK, Higgins CB. Blood flow imaging with MR: spin-phase phenomena. *Radiology* **1985**;687-695
12. Waluch V, Bradley WG. NMR even echo rephasing in slow laminar flow. *J Comput Assist Tomogr* **1984**;8:594-598
13. Pressman BD, Tourje EJ, Thompson JR. An early CT sign of ischemic infarction: increased density in a cerebral artery. *AJNR* **1987**;8:645-648
14. Robbins SL, Cotran RS. *Pathologic basis of disease*. Philadelphia: Saunders, **1979**:114-129
15. Gomori JM, Grossman RI, Goldberg HI, Zimmerman RA, Bilaniuk LT. Intracranial hematomas: imaging by high-field MR. *Radiology* **1985**;157:87-93
16. Heier LA, Zimmerman RA, Deck MF. Major vascular occlusions: an MR diagnosis. *AJNR* **1987**;8:948 (abstr)
17. Alvarez O, Edwards JH, Hyman RA. MR recognition of internal carotid artery occlusion. *AJNR* **1986**;7:359-360
18. Bryant DJ, Payne JA, Firman DN, Longmore DB. Measurement of flow with NMR imaging using a gradient pulse and phase difference technique. *J Comput Assist Tomogr* **1984**;8:588-593
19. Nishimura DG, Macovski A, Pauly JM. Magnetic resonance angiography. *IEEE Trans Med Imaging* **1986**;5:140-151

The Anatomic Basis of Vertebrogenic Pain and the Autonomic Syndrome Associated with Lumbar Disk Extrusion

John R. Jenkins^{1,2}
 Anthony R. Whittemore¹
 William G. Bradley¹

Extruded lumbar intervertebral disks traditionally have been classified as posterior or central in location. A retrospective review of 250 MR imaging examinations of the lumbar spine that used mid- and high-field imagers revealed 145 positive studies, which included a significant number of extrusions extending anteriorly. With the lateral margin of the neural foramen/pedicle as the boundary, 29.2% of peripheral disk extrusions were anterior and 56.4% were posterior. In addition, a prevalence of 14.4% was found for central disk extrusions, in which there was a rupture of disk material into or through the vertebral body itself. The clinical state of *neurogenic* spinal radiculopathy accompanying posterior disk extrusion has been well defined; however, uncomplicated anterior and central disk extrusions also may be associated with a definite clinical syndrome. The *vertebrogenic* symptom complex includes (1) local and referred pain and (2) autonomic reflex dysfunction within the lumbosacral zones of Head. Generalized alterations in viscerosomatic tone potentially may also be observed. The anatomic basis for the mediation of clinical signs and symptoms generated within the disk and paradiskal structures rests with afferent sensory fibers from two primary sources: (1) posterolateral neural branches emanating from the ventral ramus of the *somatic* spinal root and (2) neural rami projecting directly to the paravertebral *autonomic* neural plexus. Thus, conscious perception and unconscious effects originating in the vertebral column, although complex, have definite pathways represented in this dual peripheral innervation associated with intimately related and/or parallel central ramifications. It is further proposed that the specific clinical manifestations of the autonomic syndrome are mediated predominantly, if not entirely, within the sympathetic nervous system.

The directional differentiation of lumbar disk extrusions by MR, together with a clarification and appreciation of the accompanying clinical somatic and autonomic syndromes, should contribute both to understanding the specific causes as well as to establishing the appropriate treatment of acute and chronic signs and symptoms engendered by many nonspecific disease processes involving the spinal column.

The written history of intervertebral disk herniation originated with Kochner's postmortem description in 1896. Since that time, continued radiologic advancements have successively improved diagnostic efficacy in the evaluation of spinal disk disease. While these methods have been directed chiefly toward the elucidation of posterior disk extrusion (PDE), occasional publications have addressed the diagnosis of anterior disk extrusion (ADE) (i.e., anterior to the confines of the neural foramen) and central disk extrusion (CDE) (i.e., into or through the vertebral body itself) [1-3]. This report details the potential of MR to reveal such extrusions and examines the pathways of pain mediation and autonomic dysfunction engendered by these lesions within the lumbar vertebral column.

Materials and Methods

A random retrospective review was undertaken of 250 MR examinations of the lumbosacral spine on adult subjects completed during the preceding year. These studies were acquired on 0.35-T Diasonics and 1.5-T Philips or General Electric units. Intermediate and T2-weighted

This article appears in the March/April 1989 issue of *AJNR* and the June 1989 issue of *AJR*.

Received January 13, 1988; accepted after revision November 1, 1988.

Presented at the annual meeting of the American Society of Neuroradiology, Chicago, May 1988.

¹ MR Imaging Laboratory, Huntington Medical Research Institutes, 10 Pico St., Pasadena, CA 91105.

² Present address: Neuroradiology Section, University of Texas Health Science Center, 7703 Floyd Curl Dr., San Antonio, TX 78284-7800. Address reprint requests to J. R. Jenkins.

AJR 152:1277-1289, June 1989
 0361-803X/89/1526-1277
 © American Roentgen Ray Society

spin-echo acquisitions were performed in the sagittal and axial planes with 5- and/or 3-mm-thick sections. The system of classification divided the extrusions into three major categories: anterior and posterior peripheral disk extrusions (with the lateral border of the neural foramen used as the boundary) and central extrusions into or through the vertebral body itself. Further subdivisions were used to clarify the vertebral level and the precise radial direction of anterior or posterior extrusion (midline, direct lateral, or antero- or posterolateral). The criteria used in this series for diagnosis of ADE and PDE included two parameters: (1) *focal* extension of high/mixed-intensity disk substance beyond the peripheral margin of the vertebral body, resulting in a balloon configuration with a neck indicating complete annulus rupture and disk extrusion (Fig. 1), and (2) further extension of the mixed-intensity disk fragment superiorly or inferiorly away from the intervertebral disk space, signifying migration (Fig. 2) [4–6]. CDEs were classified as (1) a focal rounded, or square-shaped extrusion of disk substance into the adjacent vertebral body synonymous with the so-called Schmorl node (Fig. 3) and (2) a transosseous extrusion of disk material obliquely through the corner edge of the vertebral body (also termed a limbus vertebra) or an extreme peripheral transvertebral extrusion resulting in a distracted ring epiphysis fragment (designated here as an epiphyseal avulsion) (Fig. 4) [7–9].

The term *herniation* is not used in this classification system, since it is not always possible to differentiate between complete and incomplete herniation on MR. The absolute term of *disk extrusion* is

chosen instead. *Focality* is defined as a localized outward convex contour of the disk margin in the axial plane, extending peripherally beyond the border of the remainder of the intervertebral disk for a total of less than 25% of the entire disk circumference.

None of the patients in this series underwent surgical excision of the demonstrated ADE or CDE. As the majority of the patients in this retrospective review were referred from outside institutions, only fragmentary follow-up was possible on the further care of subjects with PDE.

As an adjunct to this study, and in an effort to place the radiographic findings into a clinical context, the charts of 20 patients with isolated ADEs or CDEs were reviewed. Only ADEs and CDEs were chosen for this small review so that there would be no direct spinal-nerve-root involvement to overlay the element of presumably relatively pure vertebrogenic symptomatology.

Results

Of 250 MR examinations, 145 subjects (58%) demonstrated 236 extrusions, leaving 105 negative studies (42%). Of these 236 extrusions, 69 (29.2%) were ADEs, 34 (14.4%) were CDEs, and 133 (56.4%) were PDEs. The peripheral extrusions revealed 82 midline PDEs, 51 posterolateral PDEs, 32 midline ADEs, 34 anterolateral ADEs, and three direct

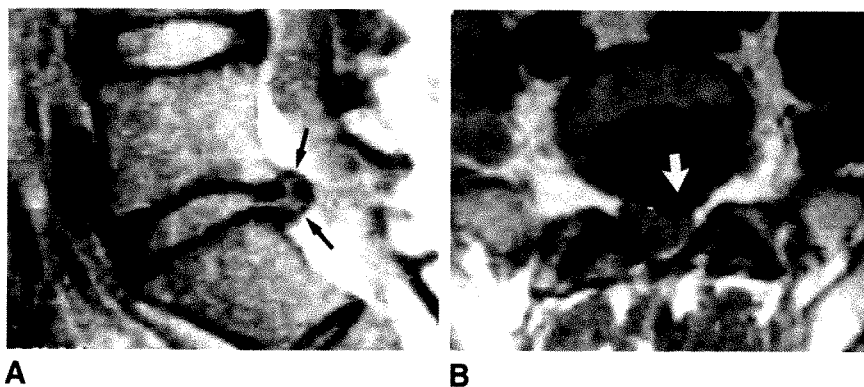


Fig. 1.—Posterior disk extrusion.

A, Sagittal image shows extension of high/mixed-intensity disk substance beyond peripheral margin of vertebral endplate resulting in balloon configuration (arrows).

B, Axial image shows focal nature of extrusion (arrow).

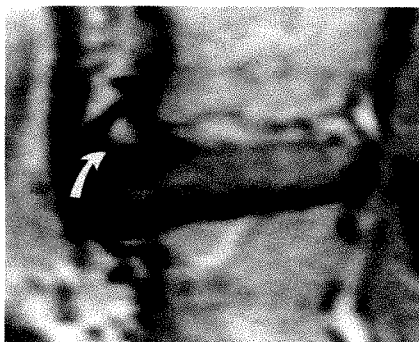


Fig. 2.—Anterior disk extrusion with migration. Sagittal image shows extension of mixed-intensity extruded disk fragment cranial from disk space (arrow).

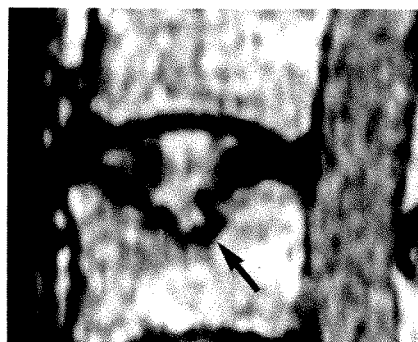


Fig. 3.—Schmorl node. Sagittal section reveals typical focal intraosseous extrusion of high-intensity central disk substance into adjacent vertebral body (arrow).

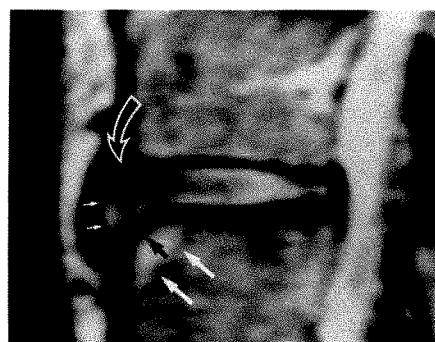


Fig. 4.—Peripheral transosseous epiphyseal avulsion-extrusion. Sagittal image shows avulsed epiphyseal site (black arrow) associated with adjacent high-intensity bony reaction (large solid white arrows), as well as retraction of annular fibers together with low-intensity epiphyseal fragment (open arrow). High-intensity extruded disk fragment is identified beneath anterior longitudinal ligament (small solid white arrows).

lateral ADEs. The total of 34 CDEs represented 26 Schmorl nodes and eight limbus-type extrusions. Of the patients with multilevel lesions, 15 had extrusions at multiple anterior levels, nine at multiple central levels, and 24 at multiple posterior levels. The types of extrusions relative to specific disk levels are summarized in Table 1.

Significant numbers of subjects revealed "isolated" extrusions falling into only one of the three major categories. In this regard, 28 patients (19.3%) of the total 145 with extrusions had isolated ADEs at 39 levels, 13 patients (9%) had isolated CDEs at 17 levels, and 72 individuals (49.7%) had isolated PDEs at 91 levels. This left 22.1%, or 32 subjects with mixed directional extrusions at *different* levels. A separate classification of multivectorial extrusion, or concomitant PDE, CDE, and/or ADE at the *same* intervertebral level, included 18 patients (12.4%) at 21 (9.8%) of a total 215 involved levels. A high frequency (81%) of multivectorial extrusions occurred at the L3-L4/L4-L5 levels. In addition, a

single case each was found of ADE concomitant with antero- and retro-listhesis at the L5-S1 level (Fig. 5). No PDEs or CDEs were identified at levels of spondylolisthesis.

A total of 14 levels with ADE demonstrated disk fragment migration away from the disk space with four migrating cranial and 10 caudad. Of eight levels with PDE manifesting migration, one migrated cranially and seven caudally.

Longitudinally within the lumbar spine, PDE was statistically most common caudally, ADE and limbus-type extrusions were most prevalent in the midlumbar region, and Schmorl nodes were seen with the greatest frequency cranial in the lumbar spine.

Remarkable detail of normal and pathologic intervertebral disk anatomy was seen frequently. MR definition of peripheral annular fibers, presumably Sharpey fibers, is observed in childhood and is better defined anteriorly (Fig. 6). Initial pathologic change within their coarser, denser anatomic configuration was noted in this anterior, peripheral disk location in

TABLE 1: Summary of Lumbar Disk Extrusions in 145 Subjects

Type of Extrusion	No. (%) by Level					Total
	L1-L2	L2-L3	L3-L4	L4-L5	L5-S1	
Posterior disk extrusion:						
Midline	0	5	7	44	26	82
Posterolateral:						
Right	0	0	2	9	11	22
Left	0	1	2	9	17	29
Subtotal	0	6	11	62	54	133 (56.4)
Central disk extrusion:						
Schmorl node	9	10	6	1	0	26
Limbus	0	4	2	1	1	8
Subtotal	9	14	8	2	1	34 (14.4)
Anterior disk extrusion:						
Midline	3	7	11	10	1	32
Anterolateral:						
Right	2	2	7	2	0	13
Left	1	3	6	5	6	21
Direct lateral	0	0	1	1	1	3
Subtotal	6	12	25	18	8	69 (29.2)
Total	15 (6.4)	32 (13.6)	44 (18.6)	82 (34.7)	63 (26.7)	236 (100)
Multivectorial extrusion ^a	0	2	9	8	2	21

^a Multivectorial extrusions were not averaged into totals and percentages. (See text for further explanation.)

Fig. 5.—Spondylolisthetic extrusion. Sagittal image shows grade I anterolisthesis with associated anterior disk extrusion (arrows).



Fig. 6.—Intact peripheral annular fibers (arrow).

5

6

the form of an interruption of normal low intensity by irregular high signal interpreted as shearing or fracturing of the fibers (Figs. 7 and 8).

In frank ADE, the anterior longitudinal ligament was regularly seen to be elevated by the extrusion and suspended over the anterior vertebral border (Fig. 9). On the other hand, direct lateral ADE sometimes demonstrated a poorly defined margin, as no strong ligamentous structures are normally present laterally to confine the disk fragment (Fig. 10).

ADE of presumably long duration engenders osteophyte formation, which has a pincer or clamshell configuration partially enclosing the extruded disk fragment (Fig. 11). This differs from simple degenerative spondylotic osteophytes, which demonstrate predominantly flat, although irregular, inner surfaces.

The chart review of the 20 subjects with anterior or central

extrusions included 15 isolated ADEs and five isolated CDEs (Table 2). Pain in the lower back was noted to be moderate or diffuse in 18 of the 20. The symptoms of pain removed from the lower back were unilateral in five subjects and bilateral in the other 11. Pain was specifically referred, *not* radiating, to the groin in one, the sacroiliac joint in one, the buttock(s) in two, the hip(s) in two, and the posterior/lateral aspect of the lower extremity in 11. In addition to pain, other subjective and objective findings were observed. Two of the subjects had bilateral lower-extremity spasm/cramping. Seven patients experienced nonspecific superficial or deep paresthesias over the buttocks and proximal lower extremities. Finally, a single patient experienced an increased awareness of a periodic bilateral superficial blushing that was accompanied by a sensation of "prickling" heat within the same distribution.



Fig. 7.—Disrupted annular fibers (arrow).



Fig. 8.—Anterior extrusion with ligamentous containment. Extrusion split between fractured fibers is identified as widened area of high intensity interposed between struts of fiber fragments (curved arrow). Disk material is contained within disk space by thick anterior longitudinal ligament (straight arrows).

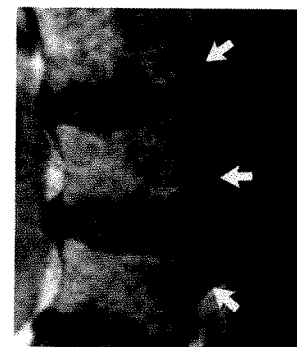


Fig. 9.—Multilevel anterior extrusions. Sagittal image shows multiple anterior disk extrusions with elevation and suspension of thick anterior longitudinal ligament over extruded disk fragments (arrows). Some of the low intensity beneath the ligament is likely due to chronic vertebral reaction to the extrusive ligamentous elevation.

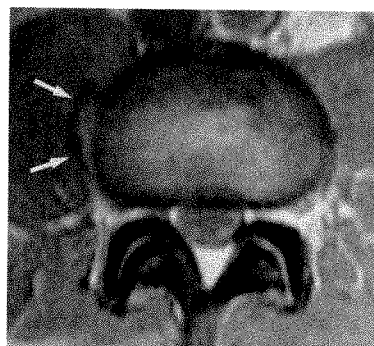


Fig. 10.—Direct lateral extrusion. Axial image shows irregular low-intensity disk extrusion invaginating into psoas muscle on right at L2-L3 (arrows).



A



B

Fig. 11.—Extrusion osteophyte.
A, Sagittal image shows pincer osteophytes (open arrows) partially embracing extruded disk fragment (solid arrow) in clamshell configuration at L4-L5 level.
B, Conventional radiograph at same level shows extrusion osteophytes (arrows).

TABLE 2: Retrospective Clinical Summaries in 20 Random Subjects with Anterior or Central Disk Extrusions

Type of Extrusion and Case No.	Age	Gender	Level(s)	Signs/Symptoms
Anterior disk extrusion:				
1	63	F	L1-L2, L2-L3	Low-back pain, bilateral hip pain
2	53	F	L5-S1	Low-back pain, right lower-extremity pain
3	63	F	L2-L3, L3-L4	Low-back pain, bilateral hip pain
4	58	F	L1-L2	Low-back pain, right sacroiliac pain
5	43	F	L3-L4	Low-back pain, bilateral lower-extremity pain
6	62	M	L1-L2, L2-L3	Low-back pain, right lower-extremity pain and paresthesias
7	47	M	L5-S1	Low-back pain, bilateral lower-extremity pain
8	58	F	L3-L4, L4-L5	Low-back pain, bilateral lower-extremity paresthesias
9	75	M	L3-L4, L4-L5	Low-back pain, bilateral lower-extremity pain and muscle spasm
10	60	F	L3-L4	Bilateral lower-extremity paresthesias
11	51	M	L4-L5	Bilateral buttock pain
12	47	M	L3-L4	Low-back pain, left lower-extremity pain and paresthesias
13	44	F	L4-L5	Low-back pain, left lower-extremity pain
14	28	F	L4-L5	Low-back pain, bilateral buttock pain, bilateral lower-extremity pain, paresthesias, and pallor/blushing
15	55	M	L1-L2	Low-back pain, bilateral lower-extremity pain
Central disk extrusion:				
16	67	F	L2-L3	Low-back pain, bilateral lower-extremity pain
17	31	M	L1-L2, L2-L3	Low-back pain, bilateral groin pain
18	71	M	L1-L2, L2-L3	Low-back pain, bilateral lower-extremity paresthesias
19	32	M	L1-L2, L2-L3, L3-L4, L4-L5	Low-back pain, bilateral lower-extremity paresthesias and muscle spasm
20	50	M	L2-L3, L3-L4	Low-back pain, bilateral lower-extremity pain

Discussion

One of the goals of this study was to evaluate the varying degrees and directions of intervertebral disk extrusion. The highest incidence of ADE in the mid-lumbar spine contrasts with the distribution of PDE that tends to involve the lower lumbar levels. In regard to PDE, most certainly this relates to a difference in stress mechanics caudally with increasing ventral angulation at the lumbosacral junction. More weight is concentrated over the posterior regions of the disk at these lower levels, and therefore the major compacting stresses are aimed posteriorly. In addition, increased potential range of motion caudally may contribute to increased pathologic change at these disk levels. In the mid-lumbar region, however, these forces may be reversed, as forward bending

exaggerates intrinsic disk pressures as well as anteriorly placed stress, possibly leading to an increased incidence of single and multilevel extrusion directed toward the apex of the lumbar lordotic curve [10, 11].

Multivectorial extrusions (i.e., at the same disk level but in different peripheral directions) represent an unexpected phenomenon. Two possible mechanisms may explain the occurrence of these lesions: (1) simultaneous extrusions in different directions at the time of initial incident, or (2) after the initial extrusion, granulation tissue enters the area of injury along with fibrosis resulting in a certain degree of healing, which may effectively "seal" the rupture. With an ensuing traumatic event, then, an extrusion occurs in a different direction [12].

Regardless of the cause of multivectorial extrusion, the total of 21 levels observed indicates a weakness in the

intervertebral disks involved. This tendency toward disk extrusion can be explained on the basis of the dynamic biomechanics of the spinal column [10, 11]. The disks that manifested the greatest multivectorial extrusion, and thus the highest intrinsic extrusive tendency, were the L3–L4 and L4–L5 levels, the two totaling 81% of the lumbar levels with multivectorial extrusions.

The total number of disk extrusions in all directions revealed that the L4–L5 level had the highest in absolute number (34.7%). In decreasing frequency, the L5–S1 level was followed by L3–L4, L2–L3, and finally L1–L2.

A number of CDEs occurred in the younger age group. This is likely due to the fact that the annular fibers themselves are intact and strong in youth with firm anchoring in the adjacent vertebrae [13]. In a given patient, the cartilage endplate overlying the vertebral bodies centrally may be the weaker of the two structures surrounding the nucleus pulposus [10]. Therefore, the disk extrusion preferentially takes place through the cartilage and into the contiguous vertebral body, resulting in a Schmorl node. Although not proved in this patient group, the cases of multiple Schmorl nodes noted superiorly in the lumbar spine may be related to Scheuermann juvenile epiphysitis [9]. In fact, the majority of subjects with multiple upper lumbar Schmorl nodes also had evidence of adjacent nodes extending into the usual location in the thoracic spine. On the other hand, isolated lumbar Schmorl nodes were unassociated with similar thoracic disease. Nevertheless, the rarity of Schmorl nodes caudally within the lumbar spine would seem to indicate a definite vulnerability of the upper lumbar segments to intraosseous disk extrusion, quite possibly because the cartilaginous endplates are simply stronger caudally.

The limbus-type CDE also occurred in relatively higher frequency in the lower age group. However, the larger transosseous fracture/extrusion resulting in a classic limbus vertebra was seen only once in this series. Rather, small parannular avulsions of the ring epiphysis were observed more commonly. The strong Sharpey fibers are very firmly embedded within the epiphysis of the peripheral endplate and form a bond with it that in youth is stronger than the vertebral body itself. This finding was observed only anteriorly and anterolaterally and not posteriorly, apparently because the epiphysis of the vertebral endplate does not exist posteriorly [13]. In a distribution similar to that of ADEs and probably for the same reasons, limbus-type CDEs were found to be most common in the region of the apex of the lumbar lordotic curve.

As a disk extrusion is a traumatic event, it will necessarily incite a reaction at the insertion of Sharpey fibers into the vertebral epiphysis. Anteriorly or laterally, the net chronic result may be the formation of a "pincer"-type osteophyte between adjacent vertebral bodies embracing the extruded disk material, ultimately resulting in the pathologic picture of "spondylosis deformans" [14].

The physical manifestations of PDE have been described extensively in the literature; however, ADE may also be associated with distinct clinical symptomatology. The features of this disease process were originally described in a case report by Cloward [1] in 1952 and include (1) low-back pain of acute onset, (2) possible relation to a specific traumatic

incident, (3) referred pain perceived in the buttock and/or proximal lower extremity(ies), and (4) no evidence of neurologic findings to suggest direct compression of lumbar or sacral nerve roots.

The anatomic basis for diskogenic and therefore vertebrogenic pain generated by all disk extrusions rests partially with somatic fibers originating from the recurrent meningeal nerve (sinuvertebral nerve of Luschka) supplying the posterior longitudinal ligament, the meninges, the blood vessels, the posterior extent of the outermost fibers of the anulus fibrosus, a portion of the periosteum of the vertebral bodies, and the underlying bone. In addition, a small branch from the ventral ramus of the somatic spinal nerve root directly innervates the posterolateral aspect of the vertebral body and related tissues for a variable distance. Any traumatic involvement of these structures may incite well-circumscribed *local somatic pain* due to this somatosensory innervation (Figs. 12 and 13A), and due to the direct nature of the afferent inflow from the segment of origin into the CNS via the somatic spinal nerves (Fig. 13A) [15, 16, 18–22].

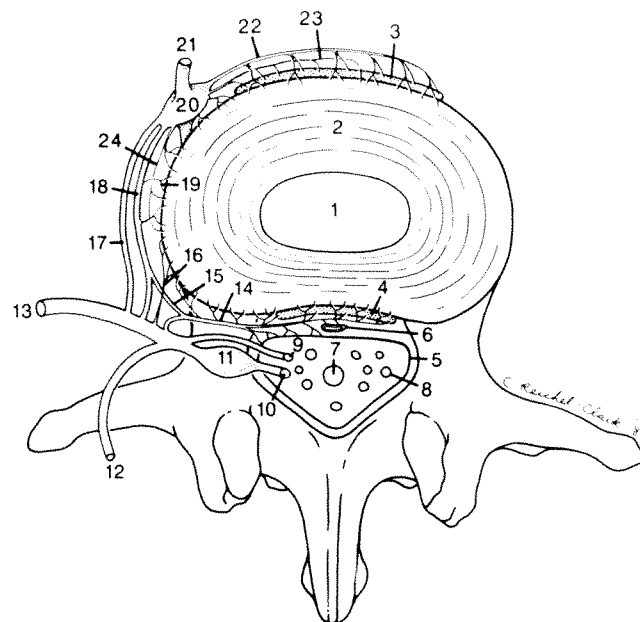


Fig. 12.—Schematic diagram of innervation of anterior spinal canal and structures of anterior aspect of spinal column (modified from [15–17]): 1 = nucleus pulposus; 2 = anulus fibrosus; 3 = anterior longitudinal ligament/periosteum; 4 = posterior longitudinal ligament/periosteum; 5 = leptomeninges; 6 = epidural vasculature; 7 = filum terminale; 8 = intrathecal lumbosacral nerve root; 9 = ventral root; 10 = dorsal root; 11 = dorsal root ganglion; 12 = dorsal ramus of spinal nerve; 13 = ventral ramus of spinal nerve; 14 = recurrent meningeal nerve (sinuvertebral nerve of Luschka); 15 = autonomic (sympathetic) branch to recurrent meningeal nerve; 16 = direct somatic branch from ventral ramus of spinal nerve to lateral disk; 17 = white ramus communicans (not found caudal to L2); 18 = gray ramus communicans (multilevel irregular lumbosacral distribution); 19 = lateral sympathetic efferent branches projecting from gray ramus communicans; 20 = paraspinal sympathetic ganglion (PSG); 21 = paraspinal sympathetic chain; 22 = anterior paraspinal afferent sympathetic ramus(i) projecting to PSG; 23 = anterior sympathetic efferent branches projecting from PSG; 24 = lateral paraspinal afferent sympathetic ramus(i) projecting to PSG. (Note.—Afferent and efferent sympathetic paraspinal branches/rami may be partially combined in vivo.)

However, many of the afferent fibers of the anterior and anterolateral disk and paradiskal structures project immediately to the paraspinal sympathetic ganglia. Polymodal afferent pain fibers to the sympathetic ganglia have been identified in all of the anterior vertebral structures except the nucleus pulposus to include the anterior longitudinal ligament, the most peripheral laminae of the annulus fibrosus, the periosteum of the vertebral body, and the vertebral body itself [15, 17–19]. There is also a major autonomic branch extending posteriorly from the sympathetic ganglion or gray ramus communicans to join the recurrent meningeal nerve [16, 21, 23]. Thus, the *entire* disk periphery, and indeed the whole vertebral column, is supplied with afferent sympathetic fibers. This extensive network was initially fully detailed by Stilwell [17] and is known as the *paravertebral autonomic neural plexus* (Figs. 12 and 14).

Depending on the vertebral level, some of these afferent fibers traverse the sympathetic ganglia and enter the ventral ramus of the somatic spinal nerve via the white ramus communicans. Subsequently, these fibers pass into the dorsal root ganglion where the cell bodies lie. The dorsal root then carries the fibers as they enter the dorsolateral aspect of the spinal cord within the tract of Lissauer, adjacent to the dorsal-horn gray matter.

The embryologic origin and anatomic path of these neural elements within the autonomic nervous system contribute to

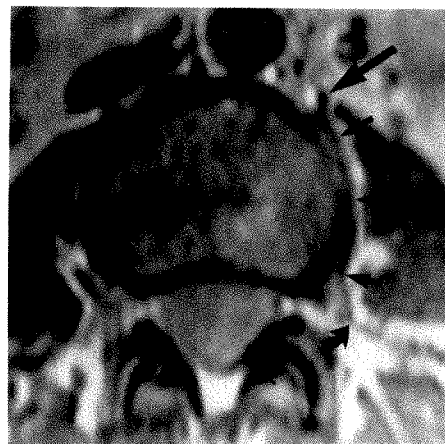


Fig. 14.—Paravertebral autonomic plexus. Axial image at L3 shows sympathetic ganglion on left at anterior sulcus of psoas muscle and vertebral body (partially obscured by chemical shift artifact) (large straight arrow), contiguous rami communicantes (small straight arrows), and junction of latter with ventral ramus of spinal nerve (curved arrow).

the imperfect somatic localization of pain. The conscious somatotopic perception of somatic pain origin is chiefly accomplished by the point of spatial entry of afferent impulses/axons into the CNS. Some entering afferent fibers may result in appropriately localized symptomatology while others are involved with important autonomic reflex functions. However, different afferent fibers will result in the conscious perception of *distant referred pain*. This pain is referred to the region corresponding roughly to the somatic distribution of the afferent fibers of the spinal nerve with which the afferent sympathetic fibers enter the spinal canal.

Referred pain is not the classic, well-discriminated, centrifugally radiating *neurogenic pain* within the cutaneous dermatome as is seen in the radiculopathy of nerve-root compression often associated with PDE [9]. Rather, it is a diffuse, deep, dull, aching, nonspecific pain perceived in the referred pain "zones of Head," which are based loosely on the concept of "somatomes." An example of a classic, well-known Head zone is that of the ischemic myocardium, in which the patient may experience centrifugal pain within the left shoulder, arm, root of the neck, and/or jaw. In the current context, the referred pain zones mediated by primary afferent fibers originating in spinal elements seem to be largely confined to limited regions within the pelvic structures, the lower extremities, and possibly the spine itself and surrounding soft tissues [20, 24–29].

Simply stated, a somatome is defined as a field of somatic and autonomic innervation that is based on the segmental embryologic expression of the somatic tissues [30]. The complete somatome is composed of three elements: the skin (dermatome); the deep musculature (myotome); and the bones, joints, and ligaments (sclerotome). The term *somatic* indicates that these tissues embryonically originate from the precursor somites [31]. Therefore, tissues originating from the same somite will also have a common neural circuitry and thus a common pathway of referral. Pain is distantly referred to these projection fields of innervation within the lumbosacral

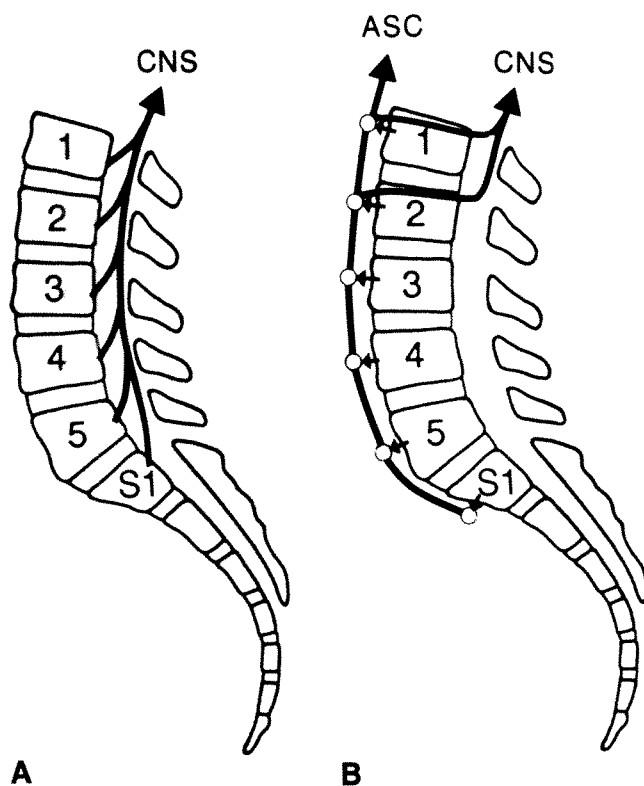


Fig. 13.—Lumbar afferent sensory patterns.

A, Direct somatic afferent inflow into CNS from branches of somatic spinal nerves at all levels.

B, Ascending autonomic (sympathetic) afferent inflow diversion into CNS of sympathetic fibers from S1 to L2 vertebral levels. ASC = ascending sympathetic chain.

somatomes. The conscious perception of that referred pain is within the zones of Head, which are irregular, constricted, asymmetric, and superimposed as well as somewhat inconsistent from subject to subject (Fig. 15) [27]. Importantly, it must be noted that these regions of vertebrogenic pain referral are found in much the same physical distribution as that seen in true radicular neurogenic sciatica. That the *origin* of referred pain is a process intimately involving the peripheral nervous system and that the *perception* of referred pain is a mechanism of the CNS is confirmed by the experimental finding that local anesthesia of the region of impulse origin (spine) abolishes the pain referral; however, anesthesia of the site of referral (zone of Head) does not consistently eliminate this pain [33, 34].

The ill definition of the pain and its referred nature are further complicated by the distribution patterns of the sympathetic afferent fibers of the spine, which overlap craniocaudally as well as across the midline. Stated differently, there is no true anatomic midline or accurate segmental nature of the

lumbosacral paravertebral autonomic (sympathetic) nervous system. In addition, once afferent fibers enter the paraspinal sympathetic ganglia, they do not always exit directly into the nearby somatic ventral ramus of the spinal root. These fibers may instead ascend to a more cranial level before entering the spine. Afferent fibers can, in fact, only join the spinal nerves and subsequently the CNS via the *white* rami communicantes. An important and anatomically confirmed pattern is that there are *no* white rami communicantes below the L2 vertebral level [35]. Therefore, any sympathetic afferent fibers from the lower lumbar and upper sacral region must ascend within the sympathetic chain to, or cranial to, the L2 nerve root before they can enter the spine (Fig. 13B). Because of this ascending sympathetic afferent diversion, sympathetic pain impulses emanating from the lumbosacral regions not having white rami communicantes (below L2) will be referred to the somatome corresponding to the spinal entry level of the afferent fiber at the L2 segment or above. Thus, the conscious perception of sympathetic mediated pain

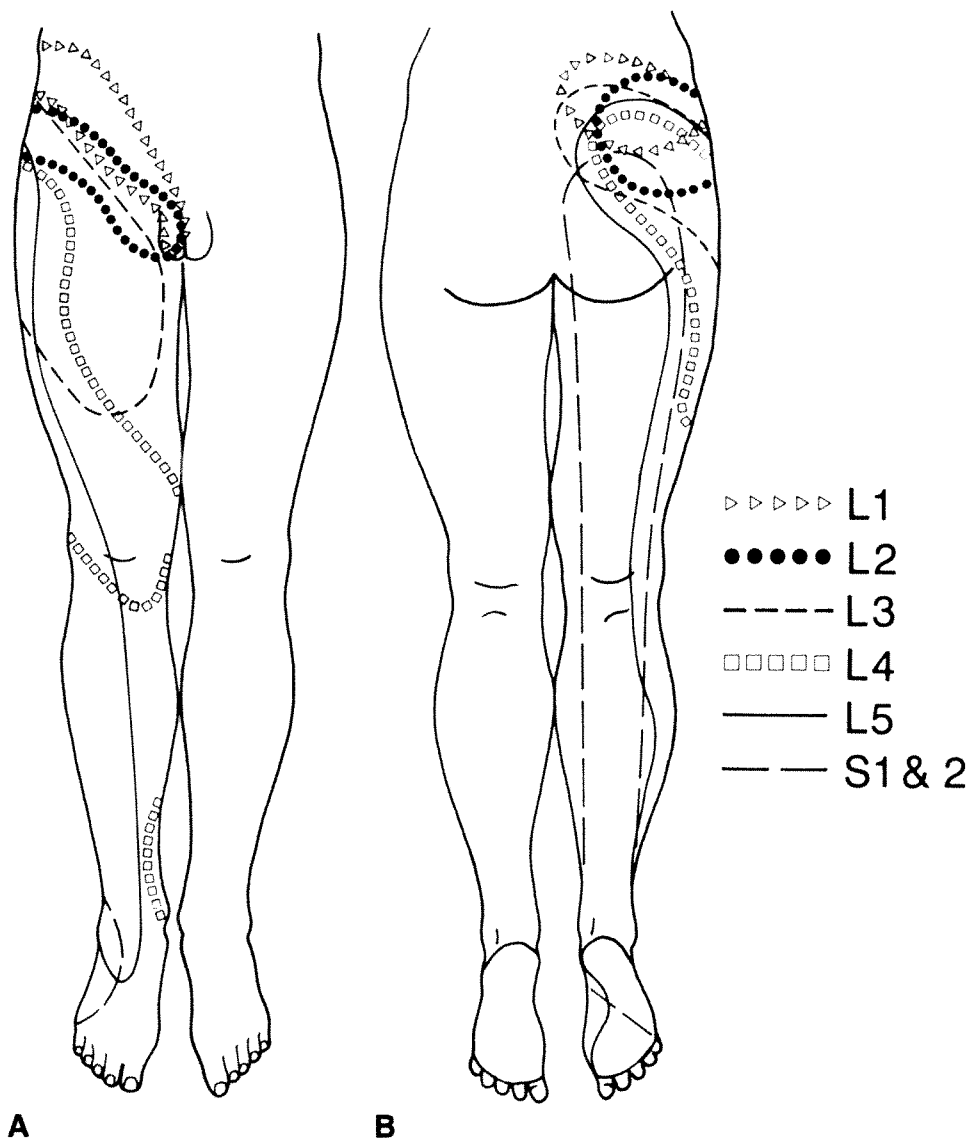


Fig. 15.—Right unilateral composite of lumbosacral Head zones of pain referral and proposed reflex autonomic dysfunction referral from segmental spinal levels. Anterior (A) and posterior (B) aspects. Note constricted, superimposed, and skipped regions. (Modified from [32].)

may be misregistered and referred to a somatome different from what its origin would have indicated, possibly resulting in summing of pain sensation due to superimposition of afferent fiber input [33].

This would explain the partial segmental superimposition of the zones of Head in the lumbosacral region, as depicted in Figure 15. The posteriorly overlapping areas of commonest centrifugal pain referral from *all* lumbar levels in fact fall largely within the superficial somatomes of the upper lumbar spinal nerves. Nevertheless, these effects are not precise, and the referral patterns are rarely completely homosegmental, but instead spread over one or several contiguous segments. However, predominantly extrasegmental pain referral might be termed aberrant, as little or none of the site of impulse origin is within the same embryologically defined somatome as the referred effect, this being a consequence of the ascending autonomic lumbar afferent inflow diversion to the L2 level.

Such unusual lumbosacral innervation patterns may also engender *local referred pain* to the spine itself and its surrounding tissues. Conscious pain originating in the spinal column is referred to the zones of Head, which are linked with vertebral segments and spinal nerves that coincidentally have afferent somatic projection fields within spinal and paraspinal structures. In other words, an integral component of the sclerotomes of spinal nerves includes the spinal elements themselves. In this manner, although the pain is not referred to the precise point of origin in the spine, it is still perceived diffusely in the region of the low back. The local referred, distant referred, and local somatic pain constitute vertebro-genic pain, which, when combined with the sometimes concurrent radiating radicular neurogenic pain, seems to explain the parallel systems operating in the spinal column responsible for the complex syndromes of spinal pain [36].

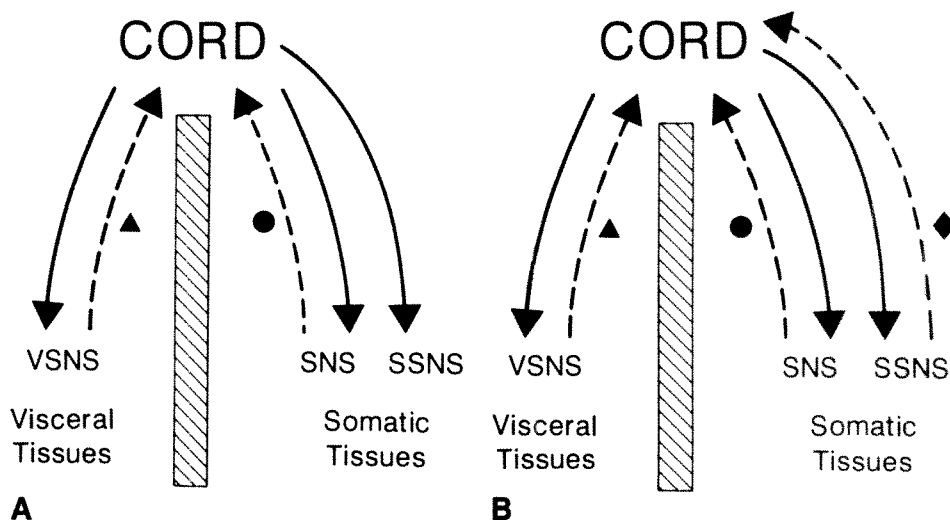
A close inspection of Figure 15 reveals areas of unsuperimposed pain referral extending far distally in the lower extremities. This is explained by the fact that there is direct sympathetic afferent inflow into the S2-S4 pelvic somatic nerve roots, and also because the innervation of spinal struc-

tures may originate from as few as three and as many as five different adjacent spinal levels [20]. Thus, direct sacral inflow and therefore direct pain referral may obtain over wide areas of the lower lumbosacral spine. Stated differently, even though there is a referred component to the pain perception, it will still be largely homosegmental [37, 38]. This might be termed appropriate pain referral, as the site of impulse origin is within the same developmentally determined somatome as the referred effect. The reason for the gaps in somatic coverage in the zones of Head is suggested by the fact that somatic tissues are not as densely populated with autonomic fibers as they are with afferent and efferent somatic fibers. As a result, the autonomic projection fields may therefore be somewhat contracted. The confining, superimposing effects of the ascending lumbar sympathetic afferent diversion may also be a major factor. These anatomic concepts help to clarify some of the peripheral mechanisms responsible for the rather nebulous fields characteristic of the zones of Head.

It may be, as the foregoing seems to indicate, that the entire perception of referred pain is handled within the autonomic (sympathetic) somatotopic organization of the CNS running in parallel with somatic afferent fibers. Embryologically, the peripheral neurologic system follows two patterns. The somatic nervous system has one distribution within the somatome. However, the autonomic nervous system develops along two different pathways. One is within visceral structures and is sometimes referred to as the visceral autonomic nervous system. The other pathway is within the somatic tissues in a distribution similar to that of the peripheral somatic nerves, although possibly not along such discretely demarcated lines. Just as there are functional sympathetic efferent connections within somatic tissues, so too must there be sympathetic afferent links to the CNS in order to complete autonomic reflex arcs. Therefore, functionally at least, the existence of "somatic" afferent sympathetic fibers is proved (Fig. 16). In fact, the presence of these peripheral autonomic afferent fibers within somatic tissues has been demonstrated clinically [39]. Since both visceral and somatic tissues are innervated by the sympathetic nervous system, and assuming

Fig. 16.—Schematic of peripheral nervous system.

A, Current understanding.
B, Proposed configuration.
Efferent pathways (solid arrows), afferent pathways (broken arrows), visceral tissue sympathetic afferent fibers (triangles), somatic tissue somatic afferent fibers (circles), and proposed somatic tissue sympathetic afferent fibers (diamonds). VSNS = visceral sympathetic nervous system; SNS = somatic nervous system; SSNS = somatic sympathetic nervous system.



that both tissues are served by afferent limbs, the CNS may then perceive an impulse origin within either tissue on the basis of a central embryologically predetermined linkage. However, the CNS may not be able to accurately discriminate spatially between the visceral and the somatic ramifications of this network in certain circumstances. In this way, a visceral sympathetic afferent stimulus may erroneously be consciously perceived as arising within the somatic sector of the sympathetic sensory projection field, and by definition is thus referred to this location. The converse of this might also be true.

This concisely explains the finding of referral of visceral sympathetic stimuli to the somatic sympathetic afferent projection field (and vice versa), thus defining the zones of Head predominantly or entirely as a phenomenon of a developmentally dichotomous sympathetic nervous system. In this functional context, referred actions and perceptions are an expected capacity of the autonomic (sympathetic) nervous system, rather than a truly abnormal phenomenon. Hence, the ascending afferent lumbar sympathetic diversion accounts for not only the referred effects and pain but also their *extrasegmental* CNS misregistration and mismatched *superimposition* within the lumbosacral zones of Head [38].

Only so much can be understood within the framework of the peripheral nervous system, and therefore CNS mechanisms of pain referral must also be considered. Experimental anatomic data suggest that somatic and visceral autonomic afferents may have the same or some of the same central connections at the level of the spinal cord, thalamus, and sensory cortex [20, 29, 38, 40, 41]. One simplified theory, referred to above, for the occurrence of referred pain states that since some of the same central pathways are shared by the converging visceral and somatic afferent systems, the CNS cannot precisely distinguish between the two origins of sensory input. Another hypothesis indicates that since the somatotomes are continually relaying noxious stimuli, as op-

posed to the viscera, through a process of pattern recognition, the CNS attributes most of the segmental afferent inflow to somatic origins regardless of the true site of the stimulus [38, 40]. There seems to be no question, however, that some degree of modulation of afferent input from any peripheral source occurs at the level of the spinal cord [20, 42].

The actual problem of the somatotopic misregistration, whether homo- or extrasegmental, thus seems to lie at the level of the spinal cord and above. As noted, complications necessarily arise in stimulus origin localization when multiple afferent systems converge at the same spinal nerve/cord level. There is a definite somatotopic organization of the spinal cord with reference to entering afferent fibers. Not only is the level of cord entry important but so is the point of termination of the fiber spatially within the cord gray matter at any particular level. Somatic afferent fibers largely terminate within laminae II, III, and IV, while visceral afferent fibers end in laminae I and V and within the ventral horn substance (Figs. 17A and 17B). It is a basic observation that the cells on which the visceral afferents terminate are known as viscerosomatic neurons. The reason for this is that many of these neurons are driven by stimuli both from the somatic as well as the visceral tissues [29]. This then would support the concept of discrete sympathetic afferent systems within visceral and somatic tissues. In fact, some "indeterminate" somatic afferents terminate within the visceral field of the cord (on the same viscerosomatic neurons noted above), which may indicate that these neural structures are in actuality the postulated somatic tissue sympathetic afferent fibers (Fig. 17C) [29]. Presumably, many of these somatic sympathetic afferent fibers may never enter the peripheral visceral autonomic pathways but instead travel almost entirely within the somatic nerves of the extremities on their route to the spinal cord. It is only their distinctive, embryonically predetermined points of termination within the gray matter of the cord that distinguish them from nonautonomic somatic afferent fibers.

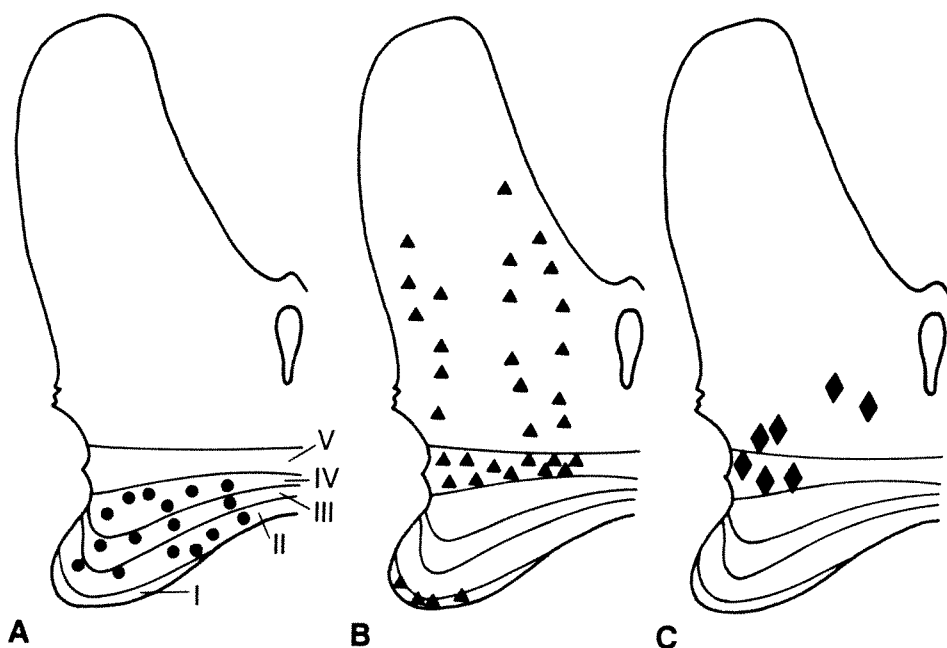


Fig. 17.—Points of termination of visceral and somatic afferent fibers on cord neurons within dorsal and ventral gray matter of right spinal hemicord. I–V = laminae of dorsal horn. (Modified from [29].)

A, Terminations of somatic (somatic tissue somatic) afferent fibers on somatic cord neurons (circles).

B, Terminations of visceral (visceral tissue sympathetic) afferent fibers on viscerosomatic cord neurons (triangles).

C, Terminations of somatic (proposed somatic tissue sympathetic) afferent fibers on viscerosomatic cord neurons (diamonds). Note overlapping regions in B and C.

One other complementary theory for referred pain considers the possibility of bifurcating sympathetic afferent fibers, with one limb entering the visceral tissues while the other ramifies within the somatic tissues (Fig. 18) [29, 43–45]. Regardless of whether one or both these mechanisms are functional, the important concept is that of convergence of multiple afferent axons on the same viscerosomatotopic registration region of the CNS, either primarily or via connecting interneurons, which then causes a false mental image of localization of a sensory event. Therefore, neither radiating nor referred pain has its origin in the mismatched areas of perception. Within this definition of central pain perception, both referred and radiated pain fields are thus "imagined" by the CNS.

However, the autonomic nervous system is involved not only with the conscious perception of painful stimuli: A major role of this network is the mediation of subconscious autonomic function via autonomic reflex arcs occurring at the level of the spinal cord, which in turn are influenced by higher CNS levels [20, 29, 40, 46, 47]. Just as the conscious perception of pain may be spatially misregistered, so too may be various autonomic functions. It is known that somatic as well as autonomic fibers both excite or otherwise share the same

interneurons within the spinal cord [40]. Referred autonomic dysfunction of spinal column origin may be represented in the form of aberrant centrifugal vasomotor, pilomotor, and sudomotor activity [38]. Not only positive sympathetic effects may be seen but also reverse or paradoxical effects, presumably due to pre- and/or postsynaptic efferent inhibition by polysynaptic, polyaxonal afferent spinal cord input [20, 40].

These findings are seemingly minor, however, and are much overshadowed by the manifestations of pain. Often apparently disregarded, such autonomic dysfunction was nevertheless recorded in one of the patients who was studied retrospectively. Quite possibly such phenomena may be more common than realized, and could be elicited with greater frequency if the subjects were carefully screened for such abnormalities at the time of examination.

Another finding, that of somatic muscle spasm, is also associated with autonomic function/dysfunction and was seen in two of the subjects studied [20, 29, 33, 34, 38]. This is commonly seen in clinical medicine in the form of abdominal wall rigidity allied with the visceral insult of peritonitis [38, 40]. Skeletal muscle spasm, which may become a painful process in and of itself, is accomplished by an aberrant reflex arc, as in the other autonomic reflex dysfunction described earlier. This type of referred reflex somatic muscle spasm in the lumbosacral myotome, known as a viscerosomatic reflex, must account for this clinically significant symptomatology [47]. The spasm itself may be produced by an arrest of the usual negative feedback mechanisms that ordinarily affect muscular contraction. This could occur because the stimulus does not originate within the area of the effect, the lumbosacral zone of Head, but instead from a distant referral source, the spine. Alternatively, unopposed positive feedback mechanisms may be responsible for the spasm for the same reasons [40].

In all these conditions of autonomic reflex dysfunction, the afferent limb is carried within the paraspinal sympathetic plexus. As discussed previously, largely because of the ascending sympathetic afferent inflow diversion (entering at or above L2) and because of the peculiarities of the autonomic (sympathetic) nervous system (both in its central and peripheral ramifications), there may be a spatial mismatching of otherwise normal autonomic function, causing the efferent effector limb of the arc to occur in the peripheral somatome (Fig. 19). This autonomic dysfunction might include any one or combination of dermal blushing, pallor, piloerection, diaphoresis, or somatic muscle spasm reflecting genuine peripheral signs and symptoms within the lumbosacral zones of Head [38]. The temporal relationship of these physical findings to the genesis of the vertebral lesion is, however, obscure.

An additional referred phenomenon is that of paresthesias of the somatic tissues within the zones of Head [34, 38]. This was observed in seven of the 20 subjects retrospectively reviewed. Presumably the mechanism for this is at the level of the cord and/or above, which unpredictably facilitates (hyperesthesia) or blocks (hypoesthesia) somatic afferent activity within the somatome in response to elevated paraspinal sympathetic afferent inflow [20].

Final considerations involve the general sympathetic outflow, which is occasionally seen clinically and experimentally

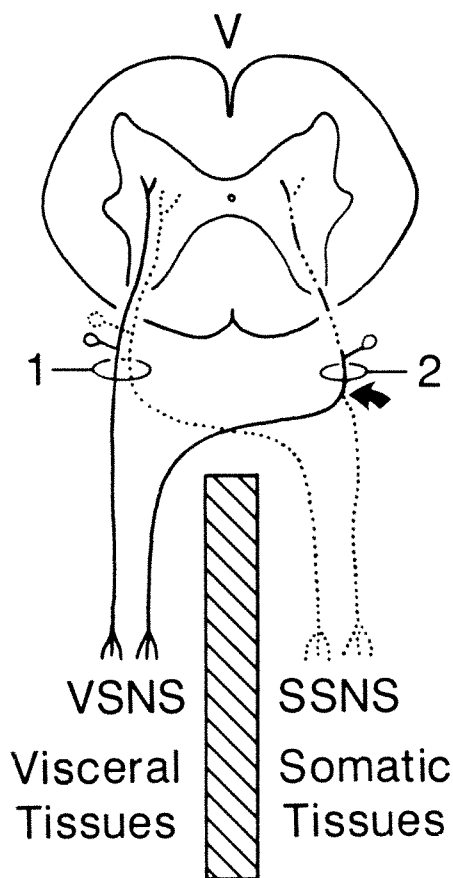


Fig. 18.—General organization of peripheral afferent sympathetic nervous system (hypothetical) [29, 43–45]: 1 = dual afferent axon configuration; 2 = bifurcating (arrow) afferent axon pattern. Visceral sympathetic afferent fibers (solid axons); somatic sympathetic afferent fibers (dotted axons). VSNS = visceral sympathetic nervous system; SSNS = somatic sympathetic nervous system; V = ventral surface of spinal cord.

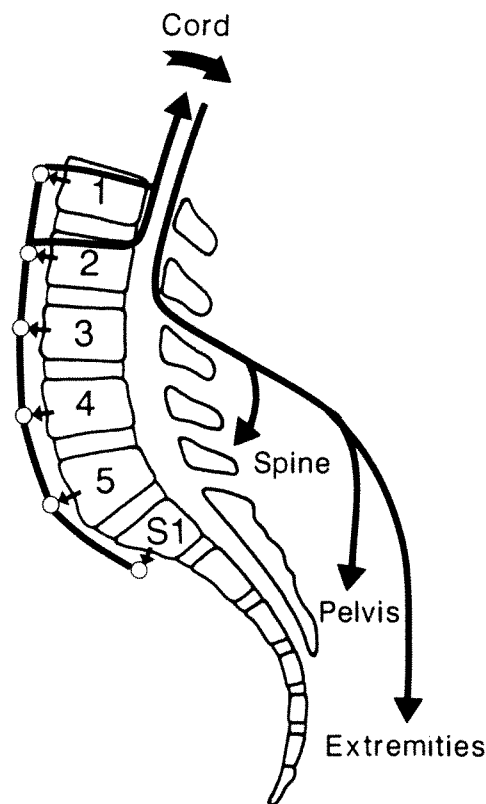


Fig. 19.—Aberrant autonomic reflex arc. Afferent limb is carried within ascending paraspinal sympathetic chain. After synapse in spinal cord, efferent limb is carried within peripheral ramifications of somatic and/or sympathetic components of somatic spinal nerves [47].

in conjunction with acute traumatic stimulation of vertebral elements. This encompasses such viscerosomatic reactions as a change in blood pressure, heart rate, and respiratory rate as well as elevations in alertness accompanied by nausea, all of which are *not* proportional to the severity and extent of the induced pain [16, 29, 34]. These findings were not seen in the small clinical review series, but neither were these parameters carefully evaluated. They may, therefore, occasionally play a role in the overall symptom complex during certain phases of spinal disease.

In closing, a statement should be made concerning primary disease of the posterior spinal elements (e.g., the facet joints and spinous processes) and the regional extraspinal tissues to include the paraspinal structures, the pelvis, and the lower extremities. It must be remembered that abnormalities in these areas may mimic signs and symptoms within the spinal column itself and/or within the somatic distribution of the sciatic nerve. These considerations must be entertained in any evaluation of spinal disease, and may in fact "contaminate" the results of any study concerned primarily with the complex aspects of intervertebral disk disease.

Summary

In common practice, a far-reaching, perplexing, combined somatoautonomic syndrome is known to stem from spinal disease that includes varying degrees of (1) local vertebro-

genic somatic pain, (2) centrifugal vertebrogenic referred pain, (3) centrifugal neurogenic radiating pain, (4) referred sympathetic reflex dysfunction (diaphoresis, piloerection, vasomotor changes, somatic muscle spasm), (5) somatic reflex dysfunction, (6) somatic muscle weakness, (7) peripheral somatic paresthesias, and (8) generalized alterations in viscerosomatic tone (blood pressure, heart rate, respiratory rate, alertness). The *somatic syndrome* (including 1, 3, and 5–7 above) is mediated within the main somatic spinal nerve roots, or direct somatic branches thereof, in conjunction with the CNS. A unified theory is proposed that indicates that the *autonomic syndrome* (2, 4, 7 and 8 above) is predominantly if not entirely mediated within the peripheral and central ramifications of the sympathetic nervous system.

On the one hand, there is a single afferent and efferent arborization of the somatic nervous system that is within the somatic tissues. On the other hand, the sympathetic nervous system has efferent connections within both visceral and somatic tissues. In addition, there are afferent sympathetics within the visceral tissues, and research data support the hypothesis that somatic tissue sympathetic afferents exist as well. Experimental evidence indicates that both somatic and sympathetic nervous system afferents terminate largely within separate regions of the gray matter of the spinal cord. Incoming sympathetic impulses from distantly separated visceral and somatic sources may drive the same viscerosomatic cord neurons by two methods. First, two different sympathetic afferent fibers, one of visceral origin and the other of somatic origin, may terminate on the same cord neuron or associated cord interneurons. Second, bifurcating afferent fibers, with one limb each ramifying within the somatic and the visceral tissues, may terminate a single shared central axon within the spinal cord gray matter. Either or both these anatomic configurations may be operative. A separate mechanism, such as pattern recognition, may determine whether the source of the stimulus is somatotopically or viscerotopically consciously perceived, or both. This would indicate which direction the pain is referred (i.e., to the visceral or to the somatic tissues), if at all, and in turn whether pain may concomitantly be perceived locally at the site of stimulus origin. Inhibition of impulse input as well as facilitation also occurs at the cord level, which further alters cerebral perception. Craniad to the level of afferent fiber entry into the cord, there is evidence of separate or at least partially discrete ascending spinal tracts for central autonomic (sympathetic) and somatic impulse mediation. Most certainly, this input is in turn modified by higher centers, resulting in varying combinations of local somatic, local referred, and distant referred pain.

Analogous to the analysis of pain mediation, referred autonomic reflex dysfunction occurs because of a common spinal cord neuron convergence of peripheral visceral and somatic afferents. This results in a misregistration of viscerosomatic input, which in turn dictates a consonant mismatching of efferent actions. This is true for both visceral as well as somatic functions and may conceivably be manifested in either or both of the two tissues. Thus, regions of referral, or zones of Head, theoretically may be found in both visceral and somatic tissues. The summed expression of these pain sensations and autonomic actions is further altered in the

lumbosacral region by the ascending afferent diversion within the paraspinal sympathetic chain. Finally, owing to the activation of inflow into the autonomic nervous system, generalized sympathetic outflow occurs that may alter the overall viscerosomatic tone.

Any one or combination of neurogenic and/or vertebrogenic signs and symptoms may be observed in an individual subject. This variety of manifestations may mislead the patient and the physician. As discussed above, this is largely due to related patterns of local and centrifugal distribution of peripheral nerve fibers as well as their complex central connections, which consequently result in a concurrent superimposition of focal and diffuse conscious perceptions and unconscious effects. Although it was not possible in the present retrospective study to accurately match the majority of the MR findings with a precise clinical correlation, in the future this input will surely be an important factor in evaluating the relationships and significance of the somatic and autonomic lumbosacral syndromes in patients with any disease process involving the vertebral column.

ACKNOWLEDGMENTS

We thank S. Valdez and J. Murray for manuscript preparation, V. Caullay for manuscript research, the Huntington Medical Research Institutes staff for technical assistance, C. Reichel-Clark for artwork, and S. Valone for photographic reproductions. In addition, we express appreciation to R. Brown for use of selected case material.

REFERENCES

- Cloward RB. Anterior herniation of a ruptured lumbar intervertebral disk. *Arch Surg* 1952;64:457-463
- Johansen JG. Demonstration of anterior intervertebral disc herniation by CT. *Neuroradiology* 1987;29:214
- Kozlowski K. Anterior intervertebral disc herniations in children. *Pediatr Radiol* 1977;6:32-35
- Edelman RR, Shoukimas GM, Stark DD, et al. High-resolution surface-coil imaging of lumbar disk disease. *AJNR* 1985;6:479-485
- Modic MT, Pavlicek W, Weinstein MA, et al. Magnetic resonance imaging of intervertebral disk disease. *Radiology* 1984;152:103-111
- Modic MT, Masaryk T, Boumprey F. Lumbar herniated disk disease and canal stenosis: prospective evaluation by surface coil MR, CT, and myelography. *AJR* 1986;147:757-765
- Fitzer PM. Anterior herniation of the nucleus pulposus: radiologic and clinical features. *South Med J* 1985;78:1296-1300
- Ghelman B, Freiburger RH. The limbus vertebra: an anterior disc herniation demonstrated by discography. *AJR* 1976;127:854-855
- DePalma AF, Rothman RH. Clinical manifestations of lumbar disc syndrome. In: *The intervertebral disc*. Philadelphia: Saunders, 1970:203-248
- White AA, Panjabi MM. *Clinical biomechanics of the spine*. Philadelphia: Lippincott, 1978:1-34, 277-294
- Nachemson A. The load on lumbar disks in different position of the body. *Clin Orthop* 1966;45:107-122
- Hult L. Cervical, dorsal and lumbar spinal syndromes. *Acta Orthop Scand [Suppl]* 1954;17:1-102
- Shapiro R. The herniated intervertebral disk. In: *Myelography*. Chicago: Year Book, 1984:422-496
- Resnick D. Osteophytes, syndesmophytes, and other "sygtes." *Postgrad Radiol* 1981;1:217-232
- Edgar MA, Ghadially JA. Innervation of the lumbar spine. *Clin Orthop* 1976;115:35-41
- Pedersen HE, Blunck CFJ, Gardner E. The anatomy of lumbosacral posterior rami and meningeal branches of spinal nerves (sinu-vertebral nerves). *J Bone Joint Surg [Am]* 1956;38-A:377-391
- Stilwell DL. The nerve supply of the vertebral column and its associated structures in the monkey. *Anat Rec* 1956;125:139-169
- Jackson HC, Winkelman RK, Bickel WH. Nerve endings in the human lumbar spinal column and related structures. *J Bone Joint Surg [Am]* 1966;48-A:1272-1281
- Paris SV. Anatomy as related to function and pain. *Orthop Clin North Am* 1983;14:475-489
- Wyke B. The neurology of low back pain. In: Jayson MIV, ed. *The lumbar spine and back pain*. New York: Churchill-Livingstone, 1987:56-99
- Wiberg G. Back pain in relation to the nerve supply of the intervertebral disc. *Acta Orthop Scand* 1949;19:211-221
- Malinsky J. The ontogenetic development of nerve terminations in the intervertebral discs of man. *Acta Anat (Basel)* 1959;38:96-113
- Kaplan EB. Recurrent meningeal branch of the spinal nerves. *Bull Hosp Jt Dis Orthop Inst* 1947;8:108-109
- Rothman RH, Simeone FA, Bernini PM. Lumbar disc disease. In: Rothman RH, Simeone FA, eds. *The spine*. Philadelphia: Saunders, 1982:508-531
- Brodal A. The autonomic nervous system. In: *Neurological anatomy*. New York: Oxford University, 1981:698-787
- Elliott FA, Schutta HS. The differential diagnosis of sciatica. *Orthop Clin North Am* 1971;2:477-484
- Mooney V, Robertson J. The facet syndrome. *Clin Orthop* 1976;115:149-156
- Hirsch C, Ingelmark BE, Miller M. The anatomical basis for low back pain. *Acta Orthop Scand* 1963;33:1-17
- Cervero F. Visceral nociception: peripheral and central aspects of visceral nociceptive systems. *Philos Trans R Soc Lond* 1985;B308:325-337
- Inman VT, Saunders JB de C. Referred pain from skeletal structures. *J Nerv Ment Dis* 1944;99:660-667
- Parke WW. Development of the spine. In: Rothman RH, Simeone FA, eds. *The spine*. Philadelphia: Saunders, 1982:1-17
- Chusid JG. *Correlative neuroanatomy & functional neurology*. Los Altos, CA: Lange Medical, 1985:238
- Hockaday JM, Whitty CWM. Patterns of referred pain in the normal subject. *Brain* 1967;90:482-496
- Feinstein B, Langton JNK, Jameson RM, Schiller F. Experiments on pain referred from deep somatic tissues. *J Bone Joint Surg [Am]* 1954;36-A:981-997
- Gray H. *Anatomy of the human body*. Philadelphia: Lea & Febiger, 1985:1251-1254, 1264-1265
- DePalma AF, Rothman RH. Salient clinical features of lumbar disc lesions. In: *The intervertebral disc*. Philadelphia: Saunders, 1970:181-202
- Carpenter MB. The autonomic nervous system. In: *Human neuroanatomy*. Baltimore: Williams & Wilkins, 1976:191-212
- Ruch TC. Pathophysiology of pain. In: Ruch TC, Patton HD, eds. *Physiology and biophysics*. Philadelphia: Saunders, 1982:508-531
- Pick J. The principles of the autonomic nervous system. In: *The autonomic nervous system*. Philadelphia: Lippincott, 1970:23-43
- Willis WD, Grossman RG. The spinal cord. In: *Medical neurobiology*. St. Louis: Mosby, 1973:80-115
- Willis WD, Grossman RG. Sensory systems. In: *Medical neurobiology*. St. Louis: Mosby, 1973:227-272
- Hannington-Kiff J. The modulation of pain. In: Helfet AJ, Lee DMG, eds. *Disorders of the lumbar spine*. Philadelphia: Lippincott, 1978:120-136
- Bahr R, Blumberg H, Janig W. Do dichotomizing afferent fibers exist which supply visceral organs as well as somatic structures? A contribution to the problem of referred pain. *Neurosci Lett* 1981;24:25-28
- Dalsgaard CJ, Ygge J. Separate populations of primary sensory neurons project to the splanchnic nerve and thoracic spinal nerve rami of the rat. *Med Biol* 1985;63:88-91
- Pierau F, Fellmer G, Taylor DCM. Somato-visceral convergence in cat dorsal root ganglion neurones demonstrated by double-labelling with fluorescent tracers. *Brain Res* 1984;321:63-70
- Jenkins TW. Physiology of spinal nerves. In: *Functional mammalian neuroanatomy*. Philadelphia: Lea & Febiger, 1978:107-133
- Janig W. The autonomic nervous system. In: Schmidt RF, ed. *Fundamentals of neurophysiology*. New York: Springer-Verlag, 1985:216-269

Book Review

Diagnosis and Management of Orbital Tumors. By Jerry A. Shields. Philadelphia: Saunders, 401 pp., 1989. \$125

This is an excellent, readable text on the diagnosis and management of orbital tumors. The author is a noted leader in the field, and the book has the uniform style and lack of redundancy typical of well-executed texts written by only one author. The book has three sections. The first reviews the anatomy, clinical features, and epidemiology of orbital tumors and briefly discusses evaluation, diagnostic techniques, and management of these lesions. Section two consists of 200 pages describing primary orbital tumors classified as cystic; vasculogenic; peripheral nerve; optic nerve and meningeal; fibrous connective tissue; osseous, fibroosseous, and cartilaginous; lipomatous and myxomatous; myogenic; epithelial lacrimal gland; and primary melanocytic. Section three discusses lymphoid tumors and leukemia, metastases to the orbit, histiocytic tumors and pseudotumors, and secondary orbital involvement by tumors arising elsewhere. Each discussion of an entity includes an introduction, a definition of the lesion, an indication of its incidence, a review of the clinical features, a discussion of the diagnostic approaches used, a review of the pathology and pathogenesis, a description of the goals and practice of management, and a discussion of the prognosis.

This text is not intended primarily for radiologists. Diagnostic radiology of the orbit is covered in six pages, including illustrations. Only two illustrations are devoted to radiologic anatomy, and the book has nearly no discussion of the principles of interpretation of or techniques for performing MR or CT of the orbit. The discussions of imaging techniques and findings are confined to the diagnostic-approaches component of each description. These tend to be brief and lack the detail that would be found in a text primarily concerned with imaging of orbital lesions. There are far more photographs of patients and illustrations of gross and microscopic pathologic speci-

mens than CT or MR images. The CT and MR images included are well chosen and of excellent quality.

The relatively brief discussions of imaging are appropriate for a text intended as a reference source for "ophthalmologists, otolaryngologists, neurosurgeons, pediatricians, internists, and other specialists who have an interest in orbital diseases." Despite these shortcomings, I think that this book should be widely read by radiologists. Discussions of radiologic anatomy and CT and MR techniques are available in the radiologic literature. However, because most radiologic texts give little attention to the clinical, pathologic, or management aspects of orbital disease, this volume is an excellent reference source for any radiologist who is regularly called on to interpret CT or MR studies of the orbit. At 400 pages, this well-written text should be read cover to cover by any radiologist for whom orbital disease is a significant component of practice. The discussions of orbital disease are brief, to the point, and extremely well referenced. Thus, the text serves as a handy first source as well as an introduction to more comprehensive investigations of orbital tumors. I know of no other text that discusses the full range of primary and secondary orbital tumors in this concise, thorough, and readable format. Because the text is extremely well written and well organized, it will serve as a valuable reference for radiology trainees and for radiologists in practice. This book belongs in the library of any radiology department that performs CT or MR studies of the orbit.

David B. Hackney
Hospital of the University of Pennsylvania
Philadelphia, PA 19104

MR Imaging of Experimental Demyelination

Louis M. Teresi¹
David Hovda
Allen B. Seeley
Katherine Nitta
Robert B. Lufkin

Seventeen rabbit sciatic nerves undergoing experimental demyelination and 17 control nerves were imaged in vivo with a 0.3-T MR imaging system using a silicone chamber wrapped around the nerves to isolate them from surrounding tissues. Three pulse sequences were used for each nerve: (1) spin-echo 500/28 (TR/TE), (2) spin-echo 2000/56, and (3) inversion recovery 1000/300/30 (TR/TI/TE). Image intensity data were acquired for each nerve by placing a region of interest over the nerve and measuring pixel brightness within the region of interest by means of a computer algorithm. The mean signal intensity of the experimental nerve was then compared with the mean signal intensity of the contralateral control nerve on the same image. Histologic sections of the nerves were stained with Loyez's stain for myelin and thionin for glial cells. MR findings were then compared with histopathologic data. Experimental nerves showed distinct stages of demyelination. Two fundamental observations were surmised from the data: (1) Perceptible MR signal changes are associated with early nerve degeneration, in which there is demyelination in the absence of glial cell proliferation; these changes are appreciated as increased intensity on heavily T2-weighted sequence. In these nerves no signal changes are seen on T1-weighted sequences. (2) Perceptible MR signal changes are associated with more advanced nerve degeneration, in which there is an increase in the number of glial cells in the absence of further demyelination; these changes are appreciated as decreased intensity on T1-weighted sequences and markedly increased intensity on T2-weighted sequences, respectively.

The results show that MR can distinguish stages of demyelination in degenerating nerves, thereby providing a powerful method for the diagnosis and characterization of demyelinating disease.

The process of demyelination is common to many neurologic diseases in both the central and peripheral nervous systems. MR imaging has shown the potential to differentiate between myelinated and demyelinated nerves and to identify focal lesions in demyelinating disease, such as multiple sclerosis [1-5]. Early studies of demyelination associated with wallerian degeneration have suggested that T1 and T2 values lengthen in this disease process [2, 4]. A limitation of the experimental design used in these studies is that MR data were acquired with a spectrometer, not an imager, without consideration for the cumulative effects of T1, T2, and proton-density data on image signal for a given pulse sequence. Thus, the cumulative effect of changes in proton-density and T1 and T2 values on the resulting signal, as observed on MR routinely generated in the clinical environment, is as yet poorly understood. Determining the MR signal changes associated with the evolving histologic stages of nerve demyelination would contribute significantly to our understanding of the sensitivity and specificity of MR signal changes seen in clinically suspected demyelination in both the central and peripheral nervous systems.

To date, no experimental model of nerve demyelination has allowed direct correlation of histopathologic and MR image data. We developed an animal model, the "silicone chamber model," that allows us to image isolated sciatic nerves in

This article appears in the March/April 1989 issue of *AJNR* and the June 1989 issue of *AJR*.

Received March 9, 1988; accepted after revision November 1, 1988.

Presented at the annual meeting of the American Roentgen Ray Society, San Francisco, CA, May 1988. Recipient of the ARRS Executive Council Award.

¹ All authors: Department of Radiological Sciences, University of California, Los Angeles, School of Medicine, UCLA Medical Center, BL-428, Los Angeles, CA 90024. Address reprint requests to L. M. Teresi.

AJR 152:1291-1298, June 1989
0361-803X/89/1526-1291

© American Roentgen Ray Society

vivo and to readily compare MR findings with histopathologic data. We report the signal changes on MR associated with the progressively more severe histologic stages of demyelination as observed in this unique experimental model.

Materials and Methods

Thirty-four sciatic nerves in 17 large (5–6 kg) adult male New Zealand white rabbits* were studied. After induction of general anesthesia with approximately 1 ml/kg IV thiamylal sodium† titrated to effect, both right and left sciatic nerves were gently dissected from surrounding tissues. In each rabbit, the left sciatic nerve was subjected to experimental demyelination, while the right sciatic nerve served as a control. Experimental demyelination was induced by three methods: (1) crush injury, (2) transection, and (3) exposure to pure alcohol. In seven rabbits, the nerve was crushed with forceps at the level of the sciatic notch, while in five rabbits the nerve was transected with a scalpel at the level of the sciatic notch. In five rabbits the experimental nerve was bathed in a solution of 100% isopropyl alcohol for 3 min. In each rabbit, the contralateral control nerve, although dissected from surrounding tissues, was not manipulated further. The surgical wounds on both the experimental and control sides were then irrigated with isotonic normal saline solution and closed. The animals were then allowed full activity. All rabbits were imaged 14 days after induction of experimental demyelination.

Immediately before imaging, general anesthesia was again induced with IV Surital, and both right (control) and left (experimental) sciatic nerves were gently dissected from surrounding tissues. Each nerve was then inserted into a silicone tube measuring 7 mm in external diameter, 5 mm internal diameter, and 4 cm in length that had been cut along its long axis on a single side (Fig. 1A). The nerve was therefore isolated from surrounding soft tissues within the silicone tube. The surgical wounds on both the experimental and control sides were then irrigated with isotonic normal saline solution and closed. While still under general anesthesia, the rabbit was transferred from the surgical suite to the MR suite for imaging. General anesthesia was continued through the imaging protocol to prevent motion.

Imaging was performed on a 0.3-T hybrid magnet imaging system.‡ The rabbit was positioned on its side in the scanner gantry such that the thighs of the animal were oriented perpendicular to the long axis of the gantry. A solenoid surface receiver coil was then wrapped around the lower extremities. First, a seven-slice axial T1-weighted spin-echo (SE) scout image, SE 500/28/1 (TR/TE/excitations), was obtained. With the rabbit positioned in the gantry in this manner, the axial scout sequence generally would produce an image of the length of the silicone chambers in the rabbit's thighs (Fig. 1B). If the scout image did not provide a satisfactory image of the length of the silicone chambers, the rabbit was repositioned and a second axial scout image was obtained (Fig. 1B).

Using the axial scout image, we then positioned cursor lines across the length of the silicone chambers and obtained three further imaging sequences: (1) SE 500/28/2–4, (2) SE 2000/56/2, and (3) inversion-recovery (IR) 1000/300/30/2 (TR/TI/TE/excitations). In all sequences 5-mm-thick sections with a 2-mm interslice gap were used. All sequences were obtained in precisely the same location with the same scout cursor line positions. This imaging protocol, therefore, produced three directly comparable multislice 5-mm-thick cross-sectional images of both control and experimental nerves isolated from surrounding tissues by their respective silicone chambers (Fig. 2).

Image intensity data were acquired for each nerve by placing a cursor-guided range of interest over the nerve and measuring pixel

brightness within the region of interest with a computer algorithm. Three independent measurements of the signal intensity of the experimental and control nerves were made from each image. The mean signal intensity of the experimental nerve was then compared with the mean signal intensity of the control nerve on the same image.

After imaging, each nerve was transected flush with the proximal and distal ends of the silicone chamber. This segment of nerve contained within the silicone chamber was then removed from the animal in toto with the silicone chamber and its proximal end marked with a single 5–0 suture. Both the nerve and chamber were then transferred directly to a buffered 10% formalin bath. After this procedure, the animal was sacrificed by lethal IV air embolization.

After being fixed in the formalin bath, each nerve was removed from its respective silicone chamber and imbedded in paraffin. With a standard rotary microtome, 25- μ m-thick sections were alternately stained with Loyez's stain for myelin (odd sections) and thionin for Nissl bodies, which are present in glial cells (even sections). Respective sections were then examined under light microscopy.

Results

Control Nerves

Control nerves appeared as rounded or oval structures of intermediate intensity measuring 2–4 mm in diameter surrounded by a circular area of signal void produced by the silicone chamber when imaged in cross section (Figs. 2A–2C). The signal intensity of control nerves approximated that of muscle on SE 2000/56 and SE 500/28 sequences. On IR 1000/300/30 images, control nerves were slightly more intense than muscle. Myelin and thionin histologic preparations on all control nerves showed intact myelin sheaths and a normal number of glial elements, respectively (Figs. 3A and 3B).

Experimental Nerves

Review of the myelin and thionin preparations of nerves subjected to experimental demyelination revealed three distinct categories of histologic changes (Table 1): Category 1 was characterized by beading and fragmentation of myelin around most axon cylinders and some axon cylinders showing complete loss of myelin. These changes in myelin were associated with a doubling of glial elements (Figs. 3C and 3D). Category 2 was characterized by further loss of myelin with only scattered myelin fragments present. In these nerves there was no perceptible increase in the number of glial elements compared with category 1 (Figs. 3E and 3F). Category 3 was characterized by no further loss of myelin compared with category 2, but a more than fourfold increase in the number of glial elements compared with control nerves (Figs. 3F and 3G).

Nerves subjected to crush or transection at the level of the sciatic notch showed variable degrees of demyelination and gliosis, depending on the distance along the nerve distal to the site of injury. In general, more demyelination and proliferation of glial elements was observed in the proximal, compared with the distal, portions of these nerves. Nerves exposed to pure alcohol showed more uniform demyelination and gliosis along the course of the nerve. In all nerves exposed to pure alcohol, demyelination was nearly complete (category

* Irish Farms, Riverside, CA.

† Surital, Parke-Davis, Newark, NJ.

‡ Fonar 3000M, Fonar Corp., Melville, NY.

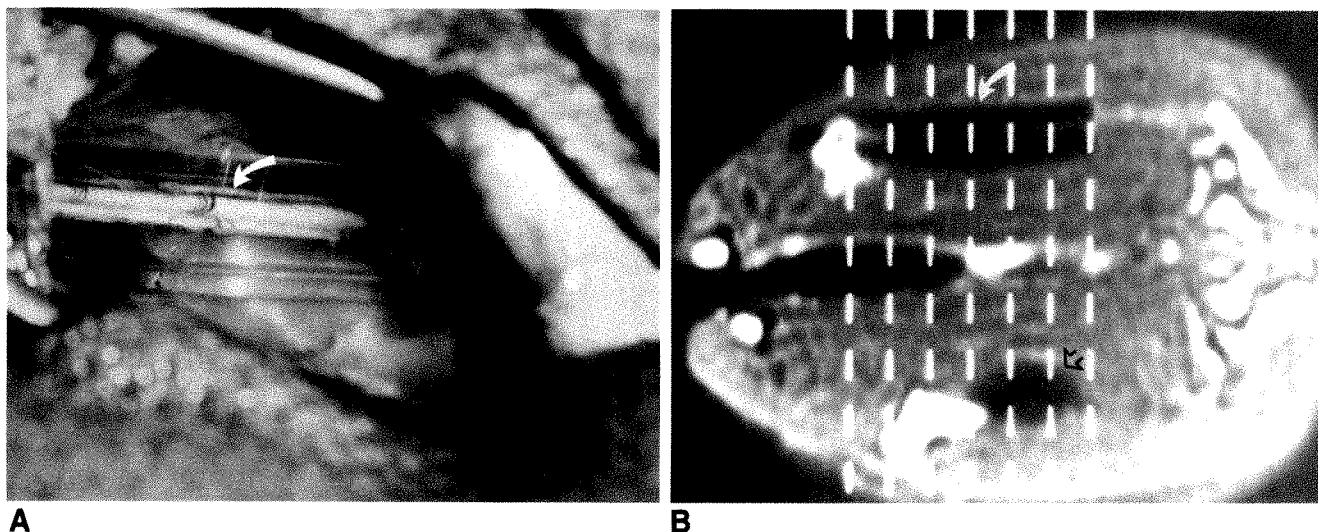


Fig. 1.—A, Intraoperative photograph shows sciatic nerve (arrow) positioned in silicone chamber for imaging. B, SE 500/28. T1-weighted scout image shows length of silicone chamber as low-signal region in leg of rabbit (curved arrow). A small portion of contralateral silicone chamber is seen (open arrow) in other leg on this image, and in its entirety on adjacent slices.

3). Table 2 summarizes the number of nerve segments for each type of injury exhibiting a specific category of histologic changes.

MR images of experimental nerves in each histologic category are shown in Figure 2, and their respective myelin- and thionin-stained histologic sections in Figure 3. Relative signal intensity changes in experimental nerves in each histologic category are summarized in Table 3 and Figure 4. *Relative signal intensity* refers to the mean pixel intensity of the experimental nerve divided by the mean pixel intensity of the control nerve on the same image ($\text{intensity}_{\text{experimental}} / \text{intensity}_{\text{control}}$). Signal intensity values in Table 3 and Figure 4 reflect the mean relative signal intensity of all experimental nerves in a given histologic category plus or minus the absolute range of relative intensity values for all nerves in that category. Of note is that all significant relative signal intensity changes could be appreciated on MR.

Nerves showing category 1 histology evidenced marked increase in signal intensity on the T2-weighted SE 2000/56 sequence, approximately 1.5 times that of respective control nerves. T1-weighted SE 500/28 and IR 1000/300/30 sequences showed no significant signal changes. Nerves showing category 2 histology showed further increase in relative signal intensity on the SE 2000/56 sequence compared with category 1 nerves. Unlike category 1 nerves, category 2 nerves showed a moderate increase in signal intensity on the SE 500/28 sequence. No change in relative signal intensity could be seen on the IR 1000/300/30 sequence for category 2 nerves. Category 3 nerves demonstrated an even further increase in relative signal intensity over category 2 nerves on the SE 2000/56 sequence. Unlike category 2 nerves, category 3 nerves evidenced decreased signal intensity on the IR 1000/300/30 sequence. A slight increase in relative signal intensity was sometimes appreciated on the SE 500/28 sequence for category 3 nerves.

Discussion

To date the cumulative effect of changes in proton density and T1 and T2 values on the resulting signal in degenerating nerves is as yet poorly understood. By using the silicone chamber model, we were able to directly image isolated sciatic nerves in vivo and directly compare MR images with histopathologic data. Thus, we were able to determine the cumulative MR signal intensity changes associated with progressively more severe histologic stages of nerve demyelination with pulsing sequences routinely used in the clinical environment.

In this study we initiated degeneration in rabbit sciatic nerves by transection, crushing, or local application of a toxic substance. Subsequent nerve degeneration and demyelination associated with these techniques have been well described and may be divided into three stages [6–9].

Early in degeneration (stage 1), usually 0–4 days in the peripheral nervous system, the myelin sheath retracts from the axon at the nodes, leaving a greater area of naked axon. This retraction first affects nodes near the lesion, secondarily spreading peripherally. The region of the nerve distal to the lesion becomes incapable of impulse conduction. The retraction of the myelin sheath is followed by the breakdown of the myelin into the so-called “digestion chambers” or ellipsoids in which the remnants of the axis cylinder disintegrate. In this stage there is physical destruction of myelin, without evidence of chemical degradation. Myelin lipids remain unaltered except for a slight diminution of neutral fat.

Between 4 and 7 days after sectioning (stage 2), neuroglial cells proliferate and surround the digestion chambers. The digestion chambers are gradually resorbed, so that by 30 days after nerve section all remnants of the axis cylinder and myelin sheath have disappeared. In this stage there is chemical destruction of myelin. Each of the myelin lipids (free

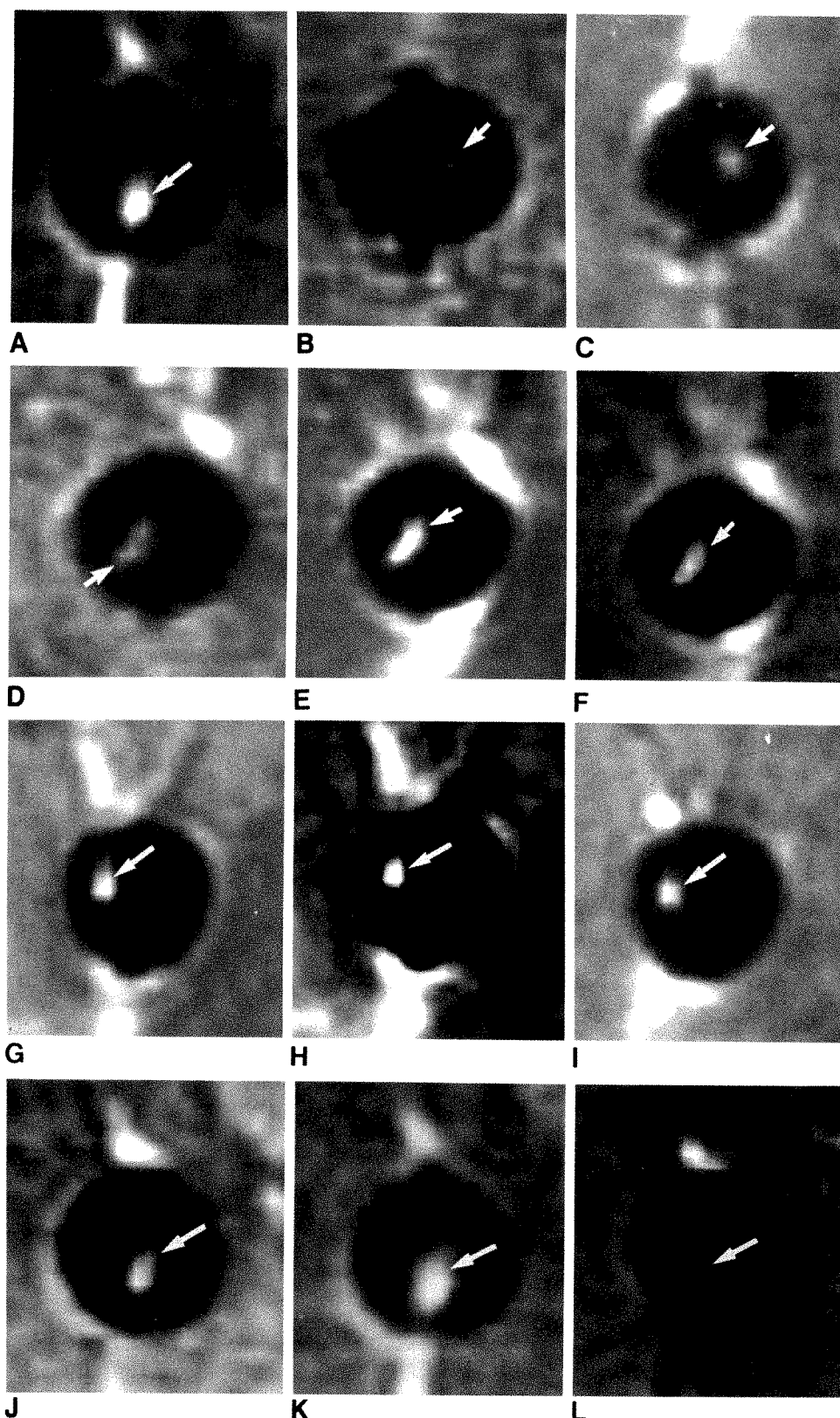


Fig. 2.—MR images of normal and demyelinated nerves.

A–C, Control nerve.

A, SE 500/28. Nerve is seen as small, rounded region of intermediate signal intensity (arrow), similar to muscle, surrounded by circular area of low signal intensity produced by silicone chamber.

B, SE 2000/56, heavily T2-weighted image. Nerve (arrow) appears similar to that seen on relatively T1-weighted sequence (A).

C, IR 1000/300/30, heavily T1-weighted image. Nerve (arrow) appears to be of slightly higher intensity than muscle, and brighter than on relatively T1-weighted (A) and heavily T2-weighted (B) sequences.

D–F, Category 1 nerve.

D, SE 500/28, relatively T1-weighted image. Nerve (arrow) shows no perceptible signal change.

E, SE 2000/56, heavily T2-weighted image. Nerve (arrow) shows marked increase in signal intensity.

F, IR 1000/300/30, heavily T1-weighted image. Nerve (arrow) appears to be of slightly higher intensity than muscle, not unlike control nerve.

G–I, Category 2 nerve.

G, SE 500/28, relatively T1-weighted image. Nerve (arrow) shows slight increase in signal intensity.

H, SE 2000/56, heavily T2-weighted image. Nerve (arrow) shows marked increase in signal intensity.

I, IR 1000/300/30, heavily T1-weighted image. Nerve (arrow) is of slightly higher intensity than muscle, not unlike control nerve.

J–L, Category 3 nerve.

J, SE 500/28, relatively T1-weighted image. Nerve (arrow) shows slight increase in signal intensity.

K, SE 2000/56 heavily T2-weighted image. Nerve (arrow) shows marked increase in signal intensity.

L, IR 1000/300/30, heavily T1-weighted image. Nerve (arrow) shows marked decrease in signal intensity.

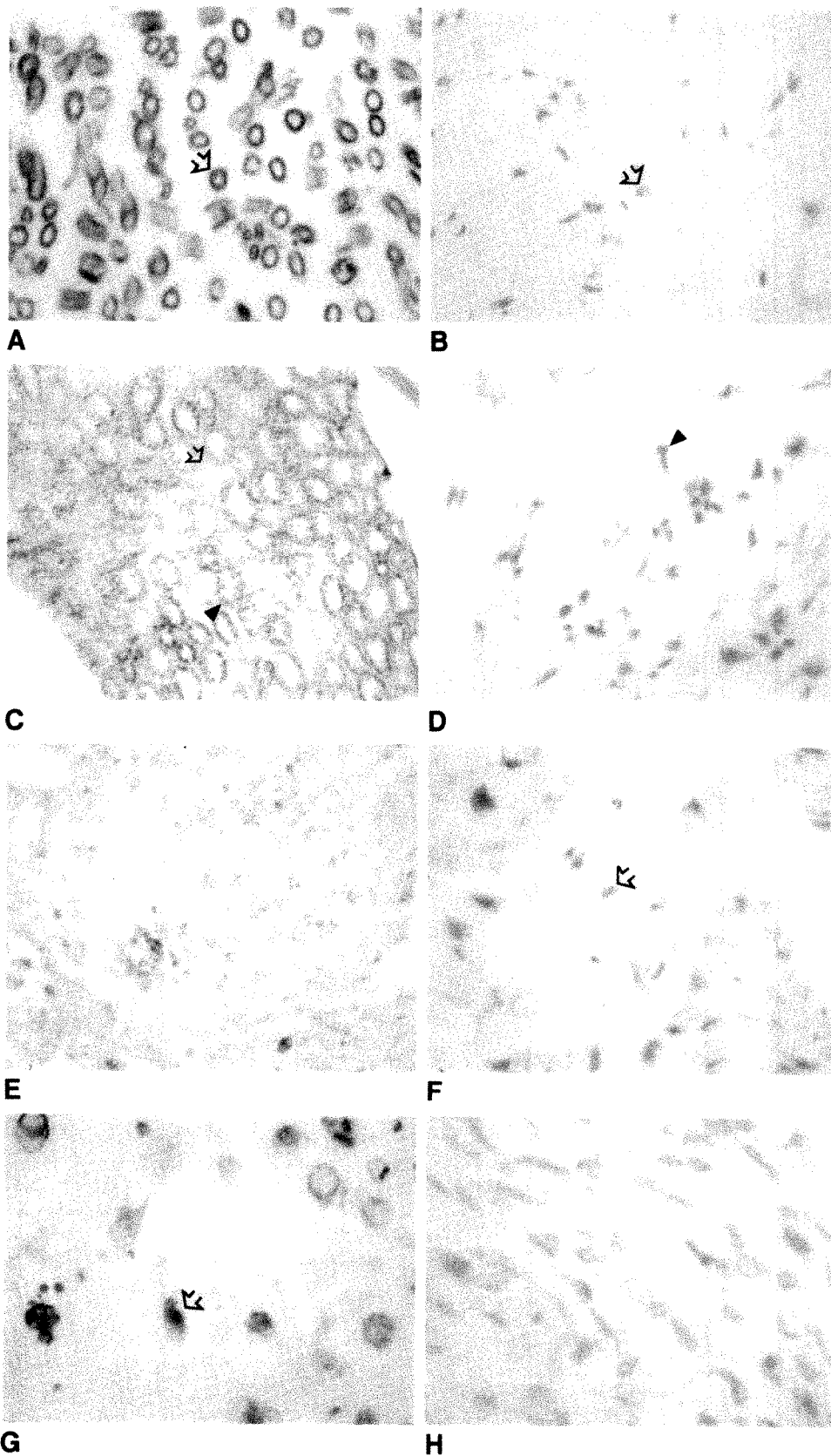
Fig. 3.—Nerve histology.**A, and B, Control nerve.****A, Myelin stain ($\times 10$).** Myelin sheaths appear normal (arrow).**B, Corresponding section stained for thionin ($\times 10$).** Shows a normal number of glial cells (arrow).**C and D, Category 1 nerve.****C, Myelin stain ($\times 10$).** Shows beading of myelin (arrowhead) around most axon cylinders and nearly complete absence of myelin in others (arrow).**D, Corresponding section stained for thionin ($\times 50$).** Nerve shows a twofold increase in number of glial elements (arrowhead).**E and F, Category 2 nerve.****E, Myelin stain ($\times 10$).** Shows scattered dark-staining myelin debris.**F, Corresponding section stained for thionin ($\times 100$).** Shows twofold increase in number of glial elements (arrow).**G and H, Category 3 nerve.****G, Myelin stain ($\times 100$).** Shows scattered, dark-staining myelin debris (arrow).**H, Corresponding section stained for thionin ($\times 100$).** Shows fourfold increase in number of glial elements.

TABLE 1: Categories of Histologic Changes with Myelin and Thionin

Category	Change
1: Myelin	Beading and fragmentation of myelin around most axon cylinders and some axon cylinders showing complete loss of myelin
Glial elements	Doubled relative to control
2: Myelin	Further loss of myelin with only scattered myelin fragments present
Glial elements	No perceptible increase in the number of glial elements compared with category 1
3: Myelin	No further loss of myelin compared with category 2
Glial elements	More than a fourfold increase compared with control nerves

TABLE 2: Categorization of Nerve Segments by Histologic Changes

Injury: Location	Histologic Category		
	1	2	3
Crush (<i>n</i> = 7):			
Proximal	4	3	0
Distal	0	2	5
Transection (<i>n</i> = 5):			
Proximal	2	3	0
Distal	0	1	4
Alcohol (<i>n</i> = 5):			
Proximal	0	0	5
Distal	0	0	5
Total	6	9	19

Note.—Categories of histologic changes are described in Table 1.

TABLE 3: Changes in Relative Signal Intensity by Histologic Categories

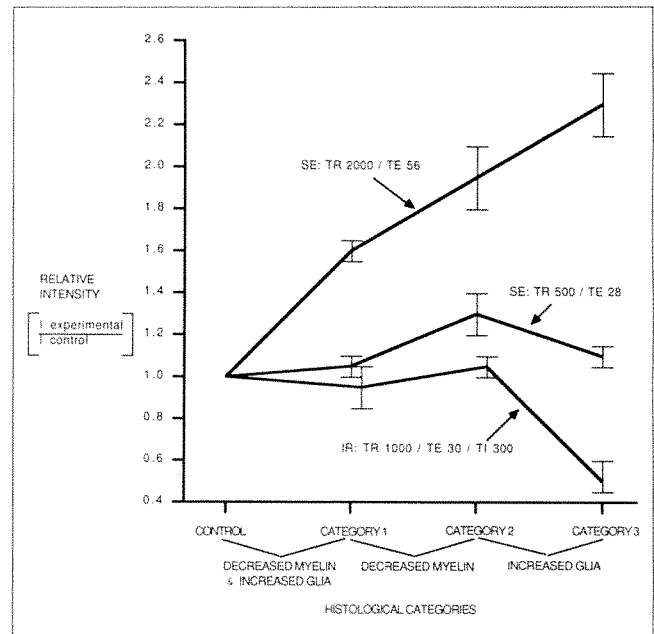
Sequence	Mean Signal Intensity ± Absolute Range		
	Category 1	Category 2	Category 3
SE 500/28	1.08 ± 0.12	1.28 ± 0.14	1.10 ± 0.09
SE 2000/56	1.61 ± 0.11	1.94 ± 0.23	2.26 ± 0.31
IR 1000/300/30	0.94 ± 0.14	1.06 ± 0.12	0.54 ± 0.15

Note.—Categories of histologic changes are described in Table 1.

cholesterol, glycosphingolipid, and sphingomyelin) disappears rapidly and at a similar rate. Cholesterol ester is seen for the first time. When breakdown and resorption of myelin debris is complete, cell multiplication ceases. Total cell population may reach eight times normal.

After 30 days (stage 3), the cytoplasm of the proliferated and hypertrophied neuroglial cells decreases in volume, resulting in the formation of neuroglial cell bands intimately covered by endoneurial sheaths. Nucleic acid concentration returns toward normal and the nerve fibril shows volume loss and fibrosis.

It must be emphasized that studies of the chemistry of degeneration generally involve analyses of the whole nerve.

**Fig. 4.—Plot of changes in relative signal intensity by histologic categories.**

Results, therefore, represent the combined chemical constituents of all structures of the peripheral nerve—axon, myelin, neurilemma, macrophages, collagenous fibers, and other connective tissue elements. Chemical studies on individual components are not yet feasible technically.

The three histologic categories of nerve in our study, therefore, were consistent with evolving phases of stage 2 degeneration. Category 1 nerves exhibited beading and fragmentation of myelin around most axon cylinders with some axon cylinders showing complete loss of myelin, associated with a doubling of glial elements (Figs. 3C and 3D). These nerves showed a marked increase in signal intensity on the T2-weighted SE 2000/56 sequence, approximately 1.5 times that of respective control nerves. Relatively T1-weighted SE 500/28 sequences and heavily T1-weighted IR 1000/300/30 sequences showed no significant signal change. Thus, images of nerves undergoing early demyelination and neuroglial proliferation showed signal changes consistent with significant changes in T2 relaxation time. Signal changes may be attributable to either demyelination or neuroglial proliferation or both.

The fact that signal changes were appreciated only on heavily T2-weighted sequence is of interest. It is unlikely that a significant increase in T2 is unaccompanied by a concomitant increase in T1 in the absence of a paramagnetic effect [10]. Certainly, there is a significant contribution of T2 relaxation to the signal produced with the relatively T1-weighted SE 500/28 sequence. IR sequences, however, are usually purely T1-weighted. In current imaging protocols, however, most IR sequences use a second 180° refocusing pulse to increase readable signal, inducing minimal, but perhaps not insignificant, T2-weighting to the images. Our IR sequence

uses such a refocusing pulse and a TE of 30. Thus, it is likely that marked changes in T2 relaxation mask the contributions of changes in T1 relaxation to the signal, even in this heavily T1-weighted sequence.

Category 2 was characterized by further loss of myelin with only scattered myelin fragments present. In these nerves there was no perceptible increase in the number of glial elements compared with category 1 (Figs. 3E and 3F). These nerves showed further increase in relative signal intensity on the heavily T2-weighted SE 2000/56 sequence compared with category 1 nerves. Unlike category 1 nerves, category 2 nerves showed a moderate increase in signal intensity on the relatively T1-weighted SE 500/28 sequence. Category 2 nerves showed no change in relative signal intensity on the heavily T1-weighted IR 1000/300/30 sequence.

When compared with category 1 nerves, category 2 nerves, therefore, show that there is a change in MR signal intensity with loss of myelin alone, not attributable to a neuroglial proliferation. Again, the further marked increase observed in T2 may account for the moderate increase in signal on the relatively T1-weighted SE sequence and the absence of perceptible signal change on the heavily T1-weighted IR sequence.

Category 3 nerves showed no further loss of myelin; however, there was a more than twofold increase in glial elements compared with category 2 nerves (Figs. 3G and 3H). Category 3 nerves demonstrated an even further increase in relative signal intensity over category 2 nerves on the heavily T2-weighted SE 2000/56 sequence. Unlike category 2 nerves, category 3 nerves evidenced decreased signal intensity on the IR 1000/300/30 sequence. A slight increase in relative signal intensity was sometimes appreciated on the SE 500/28 sequence for category 3 nerves.

MR signal data in category 3 compared with category 2 nerves indicates an increase in both T1 and T2 relaxation times with increase in the number of glial elements alone, independent of the degree of demyelination. In category 3 nerves, despite the increase in signal on the heavily T2-weighted SE sequence, a decrease in signal is seen on the heavily T1-weighted IR sequence. This perceptible decrease in signal on the IR sequence, combined with the relatively insignificant change in signal on the relatively T1-weighted SE sequence, supports the contention that T2 effects dominate the MR signal from category 1 and 2 nerves, masking changes in T1 on conventional T1-weighted sequences.

It is known that the MR signals of myelinated nerves in imaging and relaxation studies are mainly due to water protons. Deuteron exchange experiments have shown that no significant contribution of lipid protons is present in relaxation signals of white matter [9]. Under the experimental conditions used, only water, hydroxyl, and amine protons will exchange with deuterons, which is consistent with the unisexponential decay observed in both T1 and T2 for deuteron-exchanged white matter. This observation is supported by the almost equal proton densities of white matter measured by MR and calculated from water content. The signals arising from lipid protons in white matter are only visible in high-resolution MR spectra after removing a part of the water protons by deuteron

exchange. Thus, the T1 and T2 of white matter mainly reflect the state of the water protons. The changes in signal intensity we observed in evolving demyelination, therefore, are best interpreted by considerations of the changes in nerve water associated with degeneration.

Studies of T2 relaxation times measured by high-resolution MR spectroscopy in the frog sciatic nerve have shown that there are three experimentally distinct compartments of water [10]. A slowly relaxing fraction, amounting to about 21% of the total tissue water, is probably located in the intercellular space, representing the extracellular water. The physical properties of this fraction are the closest to those of a dilute aqueous solution; however, the propinquity to macromolecular surfaces lowers its transverse relaxation time. The fast relaxing component, representing about 29% of the signal, may be ascribed to water closely associated with the proteins and phospholipids of the myelin membrane, having the physical properties strongly affected by this association. The intermediate relaxation time fraction, amounting to about 50% of the whole nerve water, most probably represents the axoplasmic water.

Axonal membranes and myelin surfaces constitute barriers for tissue water protons, creating different macromolecular environments [11, 12]. It has been shown that proton MR relaxation characteristics of body tissue are related to water-surface interactions, and it appears that the tissues with the shorter relaxation times contain an abundance of surfaces, primarily in the form of membranes [11]. Similarly, myelin may not only significantly restrict the motion of water within and upon the membrane itself, but also limit the rate of water exchange between intraaxonal and extraaxonal compartments. Thus, it is conceivable that the process of demyelination and axonal degeneration alters the physical state and compartmentalization of water in the nerve fibers. With demyelination there would be a decrease in membrane-bound water, characterized by a short relaxation time, and a concomitant increase in extracellular water, characterized by a longer relaxation time.

Certainly an increase in absolute nerve water would also produce longer relaxation times. It is known, however, that absolute nerve water associated with demyelination is closely correlated with the number of neuroglial cells [7, 13]. Thus, signal changes observed between our histologic categories 1 and 2, in which there was no change in the number of glial cells, are not well explained by an increase in total water content and are best explained by changes in the physical state and compartmentalization of water. On the other hand, signal changes observed between our histologic categories 2 and 3, in which there was a fourfold increase in the number of glial cells and no change in the appearance of myelin, may be attributable to an increase in the total water content of the nerve.

We cannot yet fully appreciate how specific changes in the quantity, physical state, and compartmentalization of water in the demyelinated nerve influences signal characteristics. This study, however, has yielded two fundamental observations: (1) perceptible signal changes associated with early nerve degeneration, in which there is demyelination in the

absence of glial cell proliferation, are appreciated as increased intensity on heavily T2-weighted sequences and (2) perceptible signal changes associated with more progressive nerve degeneration, in which there is an increase in the number of glial cells in the absence of further demyelination, are appreciated as decreased intensity on T1-weighted sequences and increased intensity on T2-weighted sequences, respectively. The ability of MR to distinguish evolving changes in degenerating nerves provides a powerful method for diagnosing demyelinating disease in both the central and peripheral nervous systems.

REFERENCES

1. Jolesz FA, Polak JF, Adams DF, Ruenzel PW. Myelinated and nonmyelinated nerves: comparison of proton MR properties. *Radiology* **1987**;164:89-91
2. Jolesz F, Polak J, Ruenzel P, et al. Wallerian degeneration demonstrated by magnetic resonance: spectroscopic measurements on peripheral nerve. *Radiology* **1983**;149:345-348
3. Lukes SA, Crooks LE, Aminoff MJ, et al. Nuclear magnetic resonance imaging in multiple sclerosis. *Ann Neurol* **1983**;13:592-601
4. Misra L, Egan W, Vijeswarapu J, et al. Early detection of diabetic neuropathy by NMR relaxation times. Presented at the annual meeting of the Society of Magnetic Resonance Imaging in Medicine, Montreal, Canada, March **1986**
5. Cobb SR, Mehringer CM. Wallerian degeneration in a patient with Schilder disease: MR imaging demonstration. *Radiology* **1987**;162:521-522
6. Rossiter RJ. The chemistry of Wallerian degeneration. In: Folch-Pi, ed. *Chemical pathology of the nervous system*. New York: Pergamon, **1961**:207-227
7. McCaman RE, Robins E. Quantitative biochemical studies of Wallerian degeneration in the peripheral and central nervous systems. I. Chemical constituents. *J Neurochem* **1959**;5:18-31
8. Bottomley PA, Hart HR, Edelstein WA, et al. Anatomy and metabolism of the normal human brain studied by magnetic resonance at 1.5 Tesla. *Radiology* **1984**;150:441-446
9. Kamman RL, Go KG, Muskiet FAJ, Stomp GP, Van Dijk P, Berendson HJK. Proton spin relaxation studies of fatty tissue and cerebral white matter. *Magn Reson Imaging* **1984**;2:211-220
10. Vasilescu V, Katona E, Simplaceau V, Demco D. Water compartments in the myelinated nerve. III. Pulsed NMR results. *Experientia* **1978**;34:1443-1444
11. Cameron IL, Ord VA, Fullerton GD. Characterization of proton NMR relaxation times in normal and pathological tissues by correlation with other tissue parameters. *Magn Reson Imaging* **1984**;2:97-106
12. Jenkinson TJ, Kamat VB, Chapman D. Physical studies of myelin. II. Proton magnetic resonance and infrared spectroscopy. *Biochim Biophys Acta* **1969**;183:427-433
13. Hirose G, Bass NH. A quantitative histochemical study of early cellular events associated with destruction of myelinated axons in rat optic nerve. *Exp Neurol* **1974**;44:82-95

Stenosis of the Internal Carotid Artery: Assessment Using Color Doppler Imaging Compared with Angiography

Scott J. Erickson¹
 Mark W. Mewissen¹
 W. Dennis Foley¹
 Thomas L. Lawson¹
 William D. Middleton²
 Francisco A. Quiroz³
 Stephanus J. Macrander⁴
 Elliot O. Lipchik¹

The percentage of diameter stenosis of the internal carotid artery was estimated directly from color Doppler images obtained in both longitudinal and transverse planes and compared with the results of digital subtraction angiography in 49 patients (95 carotid arteries). Peak systolic velocity measurements were obtained by placing the sample volume in the highest-velocity flow stream with the angle-correction cursor parallel to the color-encoded lumen. Arterial stenoses were categorized on a grade 1–5 scale: 1 = 0–15%, 2 = 16–49%, 3 = 50–75%, 4 = 76–99%, and 5 = occlusion. Percent diameter stenosis could not be determined in 12 color Doppler flow imaging studies (13%) due to calcified plaque. Of the remaining 83 arteries evaluated by both techniques, the respective categories by color Doppler flow imaging/angiography were grade 1 (16/26), grade 2 (25/24), grade 3 (30/19), grade 4 (5/8), and grade 5 (7/6). Percent diameter stenosis determined by color Doppler flow imaging was greater than by angiography in 25% and less than by angiography in 4%. Peak systolic velocity measurements did not separate the hemodynamically insignificant (less than 50% diameter stenosis) grade 1 and grade 2 lesions, but were in agreement in 86% of grades 3–5 stenotic categories, as determined by measurements from the color Doppler flow image.

A direct measurement of percent diameter stenosis from the color Doppler flow image was possible in 87% of cases. Peak systolic velocity provided correlative diagnostic information when assessing hemodynamically significant lesions.

Numerous studies have evaluated the ability of sonography to accurately determine the degree of carotid stenosis [1–3]. Methods include the use of real-time sonography to measure the percentage of diameter reduction and the use of duplex Doppler for measurements of flow velocities and velocity ratios and for assessment of the degree of spectral broadening. The Doppler velocity criteria have been shown to be less accurate when the diameter of the internal carotid artery is reduced less than 50% [1]. Furthermore, assessment of spectral broadening in the evaluation of low-grade lesions is extremely dependent on the use of appropriate receiver gain settings [2].

We present our initial experience with color Doppler flow imaging (CDFI), which previously has been demonstrated to accurately depict flow in the residual lumen over a spectrum of disease [4]. Conventional sonography cannot consistently define the residual lumen; therefore, grading of stenoses often relies on Doppler criteria alone.

We compared the degree of stenosis (the percentage of reduction in diameter) from the real-time color flow image with peak systolic velocity obtained within the stenotic segment. These results were then compared with intraarterial digital subtraction angiography (DSA).

Materials and Methods

Forty-nine patients (98 carotid arteries) who had both CDFI studies and angiography were included in this study. Three carotid arteries were omitted because the bifurcation was not

Received November 14, 1988; accepted after revision January 31, 1989.

¹ Department of Radiology, Medical College of Wisconsin, 8700 West Wisconsin Ave., Milwaukee, WI 53226. Address reprint requests to S. J. Erickson.

² Mallinckrodt Institute of Radiology, 510 S. Kingshighway Blvd., St. Louis, MO 63110.

³ Radiología, Ultrasonido y Medicina Nuclear, S.C., Guanajuato No. 35 Col. Roma, Mexico 7, D.F. C.P. 6700 Mexico.

⁴ Radiology Associates of Appleton, 424 E. Wisconsin Ave., Appleton, WI 54917.

AJR 152:1299–1305, June 1989

0361–803X/89/1526–1299

© American Roentgen Ray Society

visualized at angiography, leaving a total of 95 carotid arteries for evaluation (of these three cases, two had occlusions proximal to the bifurcation that were predicted correctly by CDFI).

CDFI studies were performed with a 7.5-MHz linear-array transducer except in patients in whom the vessel was particularly deep. For these patients, a 5.0-MHz transducer was used (QAD I, Quantum Medical Systems, Issaquah, WA). All studies were performed with a fluid-filled, plastic, wedge-shaped standoff attached directly to the transducer. This created an angle between the sound beam and the longitudinal axis of vessels running parallel to the skin surface. Returning echoes were analyzed for amplitude, phase, and frequency shift. Amplitude data provide a gray scale or tissue image; phase and frequency shifts are produced by moving targets (RBCs). Color assignment (either red or blue) depends on flow direction with respect to the transducer and is operator-selectable. Color saturation or hue reflects the extent of frequency shift, which is dependent on flow velocity and the angle of the sound beam in relation to the longitudinal axis of the flow lumen. High-frequency shifts result in greater color saturation toward the lighter shades of red and blue. The amplitude of the Doppler signal depends on power output, reflectivity of the moving RBCs, and receiver gain. The amplitude of the color flow signal on the video display terminal is controlled by a display threshold setting. Most studies were performed before the availability of "slow-flow" software, which employs slower pulse repetition frequencies resulting in greater sensitivity to lower flow rates. Maximal frame rate is 18 frames/sec, when the 7.5-MHz transducer and minimum depth of 42 mm are used.

CDFI examinations included longitudinal and transverse views of the common carotid artery, carotid bifurcation, and proximal internal carotid artery. The vertebral arteries were examined for flow diameter and flow direction. Examinations were recorded digitally on videotape.

Direct measurements to determine the degree of stenosis (percentage of reduction in diameter) were performed in both the longitudinal and transverse planes. The diameter of the residual lumen of the internal carotid artery (as depicted in color) was divided into the total width of the vessel at the same level (flow lumen diameter/vessel diameter). Peak systolic velocity was recorded by placing the sample volume within the flow stream or flow jet both within and immediately beyond the region of maximal stenosis; angle correction was performed parallel to the residual lumen rather than the vessel wall. We did not use the optional "green tag" function, which encodes velocities above a specified threshold in a green hue. On the basis of measurements of the degree of stenosis obtained from the color-flow image we assigned five grades of disease: grade 1 = less than 15% stenosis, grade 2 = 16–49% stenosis, grade 3 = 50–75% stenosis, grade 4 = 76–99% stenosis, and grade 5 = occlusion. In addition, the grade of stenosis was also inferred from the maximal peak systolic velocity and end-diastolic velocity recorded from the internal carotid artery: grade 1 = peak systolic velocity of less than 100 cm/sec, grade 2 = 100–125 cm/sec, grade 3 = 125–250 cm/sec, grade 4 = greater than 250 cm/sec with end-diastolic velocity greater than 125 cm/sec, and grade 5 = occlusion with absent flow. These velocity determinations are a modification of criteria established by Langlois et al. [3], in which the degree of stenosis was determined from frequency shift measurements assuming a 5.0-MHz frequency transducer and a 60° angle between the interrogating sound beam and the longitudinal axis of the flow stream. We did not include spectral broadening in our modification.

Ninety-three of 95 carotid arteries were evaluated by selective angiography while the remaining two were imaged using arch injections. We used a commercially available digital angiographic unit (General Electric DF 5000, Milwaukee, WI) by using lateral and ipsilateral oblique projections, a 15-cm intensifier input diameter, and a nongrid air-gap magnification technique (0.3-mm focal spot, 1.5× magnification). Each study was performed by using a 5- to 6-ml

injection of 30% iodinated contrast material, a frame rate of three/sec, and an exposure time of 20 msec or less. The subtraction image with the highest contrast concentration and the best registration of soft tissue, skeletal structures, and calcified plaque was selected for analysis. Measurement of the percent reduction in diameter of the internal carotid artery was determined by comparing the diameter at the site of maximal narrowing with presumed normal diameter in the more distal internal carotid artery.

Measurements of stenosis in both the longitudinal and transverse planes on CDFI were compared with those determined by angiography. CDFI and angiographic measurements were considered in agreement if the same grade of stenosis was assigned by using each technique or if numeric values were within 10% of one another.

The grades of stenosis inferred from the velocity measurements from the internal carotid artery were also correlated with measurements of percent diameter stenosis obtained by CDFI in both the longitudinal and transverse planes as well as with measurements obtained by DSA. The grades of stenosis inferred from velocity measurement, CDFI, and DSA were considered to be in agreement if the same grade of stenosis was obtained by each measurement technique.

Results

In 12 CDFI longitudinal-plane examinations (13%), the degree of stenosis could not be measured because of extensive calcified plaque or unfavorable patient body habitus. Of the remaining 83 arteries, the degree of stenosis (percentage of reduction in diameter) determined by CDFI and DSA was in agreement in 59 (71%) of 83 longitudinal CDFI measurements (Fig. 1) and 54 (65%) of 83 transverse CDFI measurements (Fig. 2). The respective categories by longitudinal CDFI/DSA were grade 1 (16/26), grade 2 (25/24), grade 3 (30/19), grade 4 (5/8), and grade 5 (7/6). In three internal carotid arteries (4%) CDFI showed a grade 1 stenosis and DSA showed a grade 2. On subsequent rereview of the selective DSA studies, the CDFI measurements of the percentage of reduction in diameter were considered falsely low. There were 21 cases (25%) in which determination of stenosis from the internal carotid artery by DSA resulted in a lower-grade assignment than measurements on CDFI did. In 12 of these cases, measurements on DSA estimated a grade 1 lesion, whereas those determined on CDFI estimated a grade 2 lesion. In 11 of these 12 cases, the peak systolic velocity in the internal carotid artery was less than 100 cm/sec. In nine (11%) of 83 cases, CDFI determined a grade 3 lesion compared with a grade 2 lesion by DSA. In seven of these nine cases, the peak systolic velocity in the internal carotid artery was greater than 125 cm/sec (i.e., direct measurement and recorded flow velocity were in agreement). In the other two cases, the peak systolic velocity in the internal carotid artery was 100–125 cm/sec, consistent with a grade 2 lesion.

All five patients who had a technically adequate CDFI study showing a high-grade stenosis had a grade 4 lesion on DSA. In addition, there were four CDFI examinations of patients with angiographic grade 4 lesions in which the residual lumen was obscured by calcified plaque. In these four cases, the grade of stenosis inferred by velocity measurement immediately distal to the plaque was in agreement with the angiographic determination in only one instance. In the other eight CDFI studies limited by calcified plaque or unfavorable patient

Fig. 1.—Longitudinal sonography in agreement with angiography.

A, Longitudinal sonogram shows plaques (P1, P2) in bulb and internal carotid artery (ICA). Proximal stenosis measures approximately 45%. Residual lumen (black arrows); overall vessel width (white arrows). CCA = common carotid artery.

B, Angiogram agrees with sonographic findings. P1 = plaque in bulb; P2 = plaque in proximal internal carotid artery.

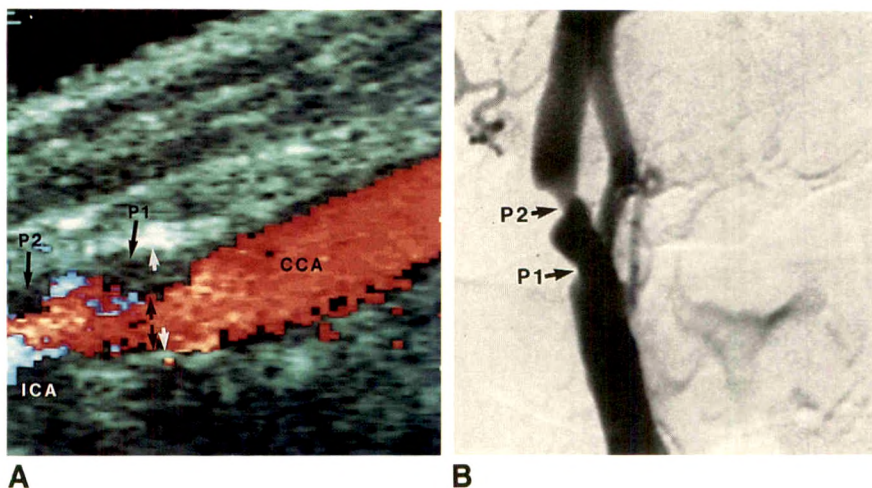
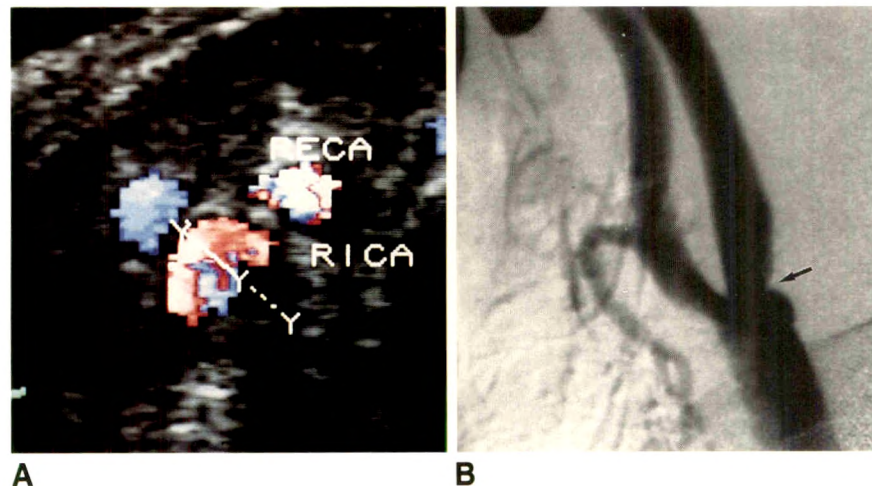


Fig. 2.—Transverse sonography in agreement with angiography.

A, Transverse sonogram shows 40% (grade 2) stenosis involving right internal carotid artery (RICA). RECA = right external carotid artery.

B, Angiogram shows 40% (grade 2) stenosis involving bulb and proximal internal carotid artery (arrow).



body habitus, hemodynamically insignificant stenoses were shown by DSA in seven.

There were seven diagnoses of internal carotid artery occlusion by CDFI, six of which were corroborated by DSA. There was one false-positive CDFI diagnosis of occlusion in which DSA revealed a 99% stenosis and a "string sign."

Comparisons were made between CDFI measurements in the longitudinal plane and peak systolic velocity including cases of occlusion, but excluding examinations limited by plaque calcification or body habitus. CDFI measurements agreed with peak systolic velocity in 66% of cases (55/83). Correlation was 100% (16/16) for grade 1 lesions, 16% (4/25) for grade 2 lesions, 87% (26/30) for grade 3 lesions, 60% (3/5) for grade 4 lesions, and 100% (7/7) for grade 5 lesions. Angiographic measurement agreed with peak systolic velocity in 62% of cases (59/95).

Discussion

Most authors cite angiography as the gold standard for the measurement of atherosclerotic stenosis in the internal carotid artery. Angiographic measurements, however, are imperfect

for a number of reasons. First, prevalence of both intra- and interobserver variability is 10–20% [5]. Second, there is individual variability in the relative diameter of the carotid bulb in comparison with the presumed more distal internal carotid artery. Angiographers have attempted to estimate the percent reduction in diameter directly by comparative measurement of the residual lumen and vessel diameter at the same level in the internal carotid artery. This measurement is performed by determining arterial vessel diameter by using wall calcification as a marker. However, wall calcification is not uniformly shown in diseased vessels. The more reproducible angiographic technique is to compare the diameter of the residual lumen at the site of greatest stenosis of the artery with the diameter of the more distal and presumed normal internal carotid artery. The presence of concentric distal plaque can result in an underestimation of the true distal internal carotid artery diameter and, therefore, result in a falsely low percentage of stenosis. However, this latter measurement artifact is uncommon. Thus, we relied on this measurement technique for angiographic determination of percent stenosis of the internal carotid artery in this study.

When measuring percentage of stenosis with CDFI, we directly compared residual lumen with vessel diameter at the

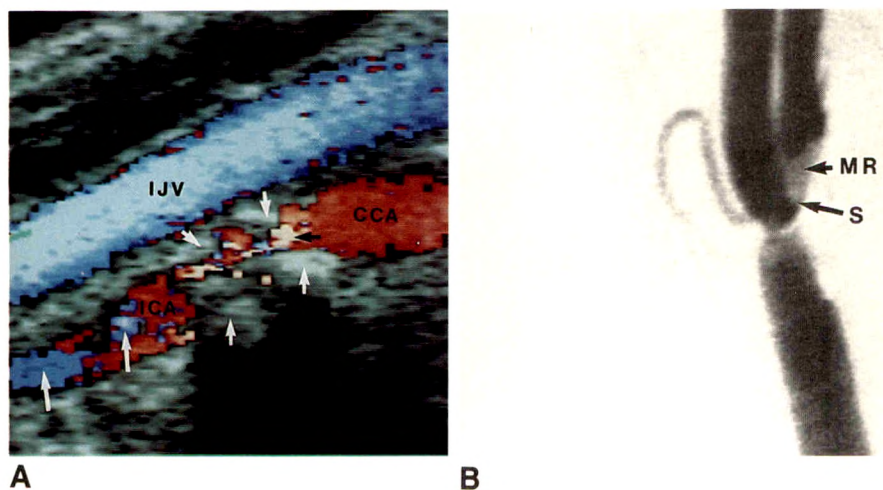


Fig. 3.—High-grade stenosis.

A, Longitudinal sonogram shows high-grade stenosis with resultant flow jet (black arrow) involving bulb and internal carotid artery (ICA). Plaque is heavily calcified (short white arrows), and turbulence manifested by flow reversal is seen distal to lesion (long white arrows). CCA = common carotid artery; IJV = internal jugular vein.

B, Angiogram shows high-grade lesion (S). Extensive calcification results in misregistration artifact (MR).

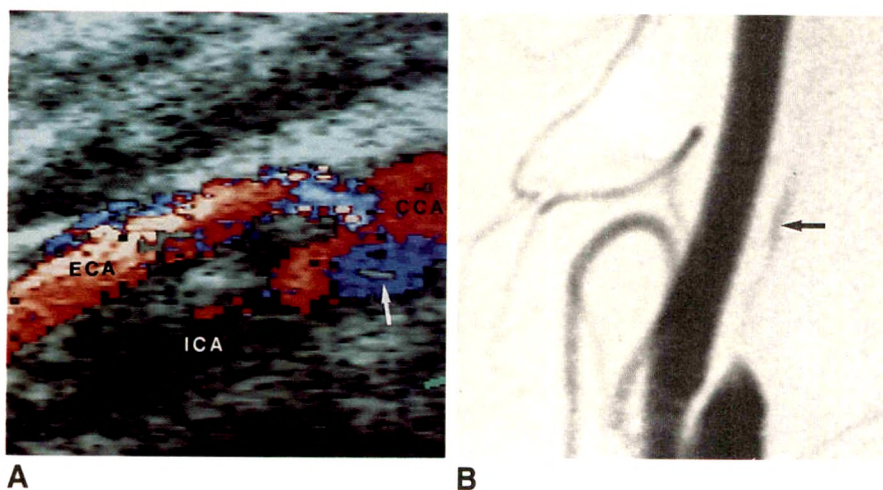


Fig. 4.—False-positive sonographic diagnosis of occlusion.

A, Longitudinal sonogram shows absence of flow in internal carotid artery (ICA), suggesting occlusion. Abnormal early diastolic flow reversal was seen just proximal to lesion (arrow). CCA = common carotid artery; ECA = external carotid artery.

B, Angiogram shows 99% stenosis of internal carotid artery, with "string sign" (arrow).

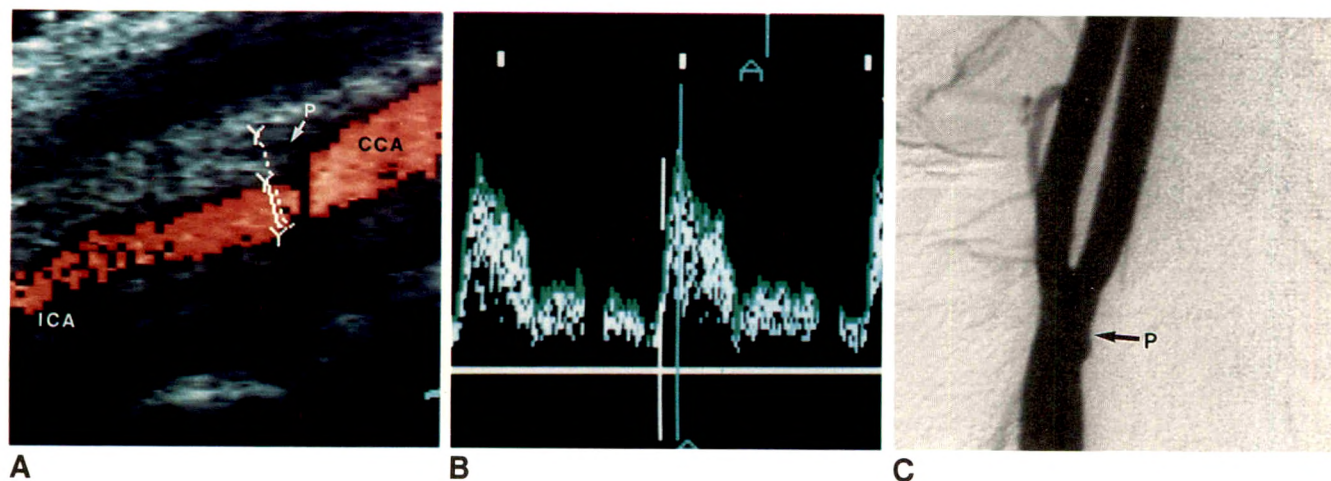


Fig. 5.—Underestimation of degree of stenosis by angiographic and peak systolic velocity criteria.

A, Longitudinal sonogram shows echogenic plaque (P) in carotid bulb; stenosis was measured as 44% (grade 2 lesion). CCA = common carotid artery; ICA = internal carotid artery.

B, Spectral trace shows peak systolic velocity of 97 cm/sec (grade 1 lesion by velocity criteria).

C, Angiogram shows lesion (P) in carotid bulb that was thought to represent 15% (grade 1) stenosis.

same level in the internal carotid artery. This measurement technique corresponds to what authors have attempted to use in angiographic determination of internal carotid artery stenosis and should provide a more correct anatomic estimate of the percentage of stenosis than the measurement technique used in the DSA examinations in this study. We found measurement in the longitudinal plane to be superior to transverse measurement for two reasons. First, the outer vessel wall was better defined in the longitudinal plane. Second, transverse-plane images with simultaneous color Doppler display are obtained with cephalad transducer tilt to provide a Doppler angle resulting in an image that is not a true cross section.

CDFI has two advantages over conventional sonography in the evaluation of carotid atherosclerotic disease. First, atherosclerotic plaques are more conspicuous with CDFI when contrasted with the color flow lumen. With conventional sonography, the degree of stenosis may be underestimated when the atherosclerotic plaque is partly anechoic [6]. Secondly, CDFI readily shows normal or abnormal dynamics at the carotid bulb. Middleton et al. [7] showed transient systolic flow reversal in 99 of 100 normal carotid arteries. Flow reversal reflects boundary-layer separation and disruption of laminar flow, which occur when the arterial flow stream in the common carotid artery reaches the wider-diameter carotid bulb [8]. Lack of normal flow reversal at the carotid bulb suggests atherosclerotic disease in this region. We noted lack of flow reversal in several grade 2 lesions shown by CDFI in which there was no focal constriction of the flow lumen. Flow reversal can be shown with conventional duplex Doppler imaging although it is much more time-consuming.

We found CDFI useful in differentiating high-grade stenoses from occlusions. With high-grade stenoses, a string of color flow (with corresponding increase in peak systolic velocity) is usually evident (Fig. 3). Although the number of occlusions determined by CDFI was small ($n = 7$), we had only one false-

positive case, which was shown to represent a 99% stenosis by selective DSA (Fig. 4). Routine use of slow-flow sensitivity settings when flow is not evident with conventional settings should further enhance the detection of a residual lumen. Other signs suggestive of occlusion are a marked decrease in relative diastolic flow in the common carotid artery in comparison with the opposite carotid, as well as early diastolic flow reversal at the internal carotid artery origin, which is easily discernible with CDFI.

When the percentages of diameter reduction estimated with velocity criteria from the internal carotid artery were compared with direct measurements from the CDFI images, findings were shown similar to those previously described with conventional duplex Doppler, in comparison with selective angiography [1]. Velocity measurement criteria were unable to subquantify lesions in the 50% diameter range or less. When hemodynamically insignificant lesions are located in the carotid bulb, arterial flow velocities are frequently normal, presumably because the carotid bulb can accommodate a relatively large plaque without relative increase in flow velocity. In our study, 21 of 25 stenoses measuring between 16% and 49% (grade 2) by measurement from the CDFI images had peak systolic velocity measurements in the internal carotid artery of less than 100 cm/sec, corresponding to grade 1 lesions (Fig. 5). When atherosclerotic lesions exceeded 50% reduction in diameter, however, there was significantly better correlation between measurement from the CDFI image and stenosis assignment from a peak systolic velocity determination. We noted an 86% concordance between peak systolic velocity measurements and CDFI measurements in grades 3-5 lesions (Fig. 6).

Measurement of peak systolic velocity is of significant benefit when the actual site of atherosclerotic stenosis is obscured by calcified plaque on the CDFI image. Because the actual stenosis cannot be measured, increase in peak systolic velocity may be the only indication of hemodynamically signif-

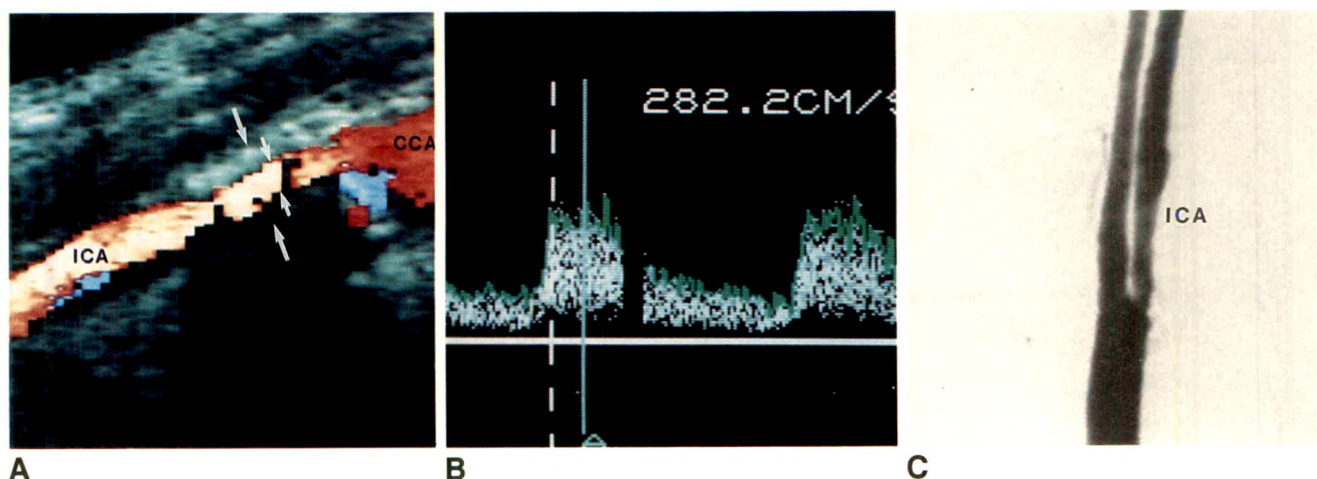


Fig. 6.—Underestimation of degree of stenosis by angiography.

A, Longitudinal sonogram shows 60% (grade 3) stenosis involving carotid bulb and internal carotid artery (ICA). Residual flow lumen (short arrows); overall vessel width (long arrows). CCA = common carotid artery.

B, Spectral trace shows peak systolic velocity of 153 cm/sec (grade 3 by velocity criteria).

C, Angiogram shows lesion involving bulb and internal carotid artery thought to represent 45% (grade 2) stenosis.

icant disease (Fig. 7), as occurred in one of four cases in our series. In some instances, however, a measurement of peak systolic velocity obtained beyond the site of a calcific stenosis will be falsely low, as occurred in three of four cases in our series. When a calcified plaque within a high-grade lesion obscures the residual lumen for more than 1 cm beyond the focal stenosis, the internal carotid artery velocity beyond the plaque may be decreased. Thus, grading of stenosis by velocity criteria would underestimate the degree of stenosis [9]. In the presence of a critical high-grade internal carotid artery stenosis (90–99%), flow velocity immediately distal to

the stenosis will drop precipitously to within a normal range [10]. In this instance, however, the arterial flow waveform often becomes markedly distorted, suggesting an immediately proximal high-grade stenosis (Fig. 8) [2].

In conclusion, the angiographic methods of estimation of percent reduction in diameter suffer from the inability to depict the outer vessel boundary, and conventional sonography is unable to consistently show the residual lumen. Determinations of peak systolic velocity obtained from conventional duplex Doppler instruments are unreliable in assessing low-grade lesions. Other Doppler criteria such as velocity ratios

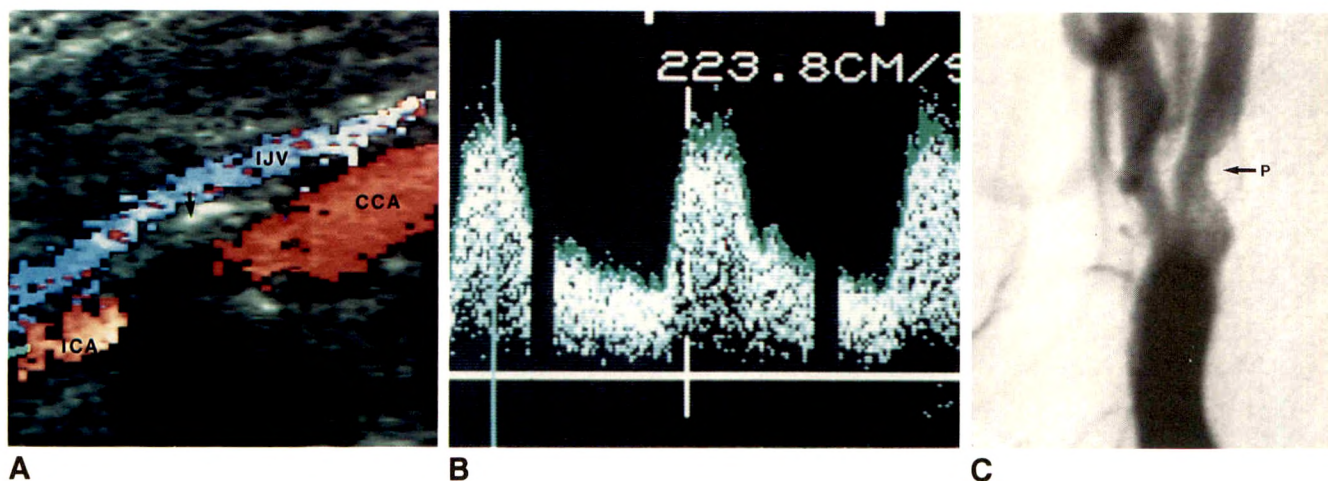


Fig. 7.—Calcified plaque obscuring residual lumen.
 A, Longitudinal sonogram shows calcified plaque (arrow) obscuring bulb region. CCA = common carotid artery; ICA = internal carotid artery; IJV = internal jugular vein.
 B, Spectral trace shows peak systolic velocity of 174 cm/sec (grade 3 by velocity criteria).
 C, Angiogram shows plaque (P) in carotid bulb that was thought to represent 45% (grade 2) stenosis.

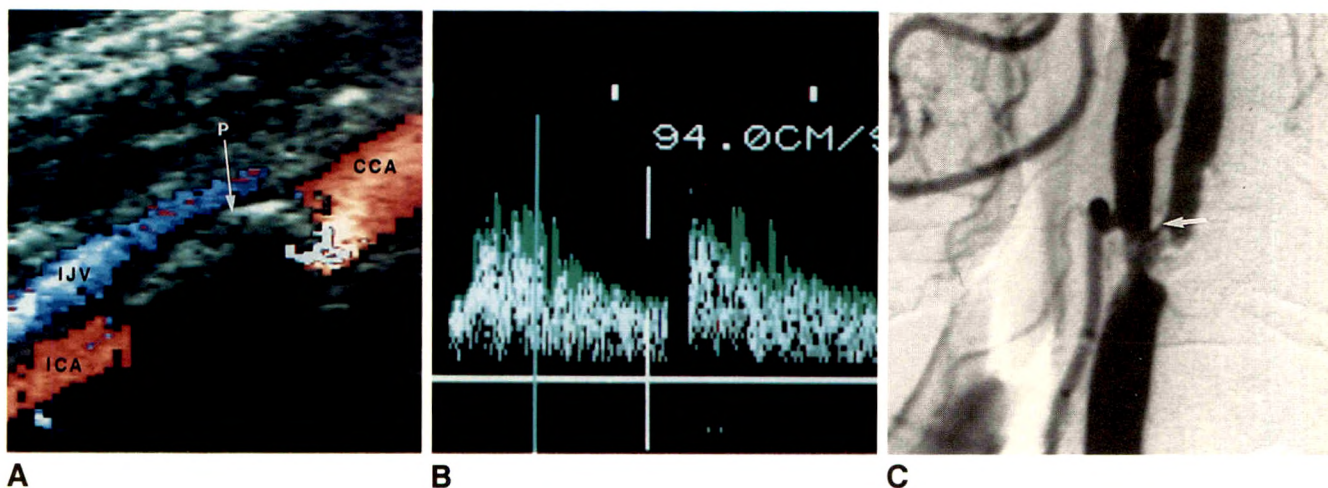


Fig. 8.—Calcified plaque obscuring residual lumen.
 A, Longitudinal sonogram shows heavily calcified plaque (P) obscuring carotid bulb and proximal internal carotid artery (ICA). CCA = common carotid artery; IJV = internal jugular vein.
 B, Spectral trace shows peak systolic velocity of 62 cm/sec. Waveform is distorted, however, suggesting presence of critical (greater than 90%) stenosis.
 C, Angiogram shows high-grade lesion (arrow) thought to represent greater than 90% stenosis. Artifact posterior to stenotic proximal internal carotid lumen represents misregistered calcified plaque.

or spectral broadening may improve sensitivity to such hemodynamically insignificant lesions. CDFI appears to be an accurate method for demonstrating atherosclerotic plaque, for measuring the percentage of stenosis at the site of plaque, and in guiding placement of cursors to obtain the velocity measurements that are useful in categorizing hemodynamically significant stenoses.

REFERENCES

1. Bluth EI, Stavros AT, Marich KW, Wetzner SM, Aufrichtig D, Baker JD. Carotid duplex sonography: a multi-center recommendation for standardized imaging and Doppler criteria. *RadioGraphics* **1988**;8:487-506
2. Jacobs NM, Grant EG, Schellinger D, Byrd MC, Richardson JD, Cohan SL. Duplex carotid sonography: criteria for stenosis, accuracy, and pitfalls. *Radiology* **1985**;154:385-391
3. Langlois Y, Roederer GO, Chan A, et al. Evaluating carotid artery disease: the concordance between pulsed Doppler spectrum analysis and angiography. *Ultrasound Med Biol* **1983**;9(1):51-63
4. Middleton WD, Foley WD, Lawson TL. Color-flow Doppler imaging of carotid abnormalities. *AJR* **1988**;150:419-425
5. Chikos PM, Fisher LD, Hirsch JH, Harley JD, Thiele BL, Strandness DE. Observer variability in evaluating extracranial carotid stenoses. *Stroke* **1983**;14(6):885-892
6. Zweibel WJ. Primer of cerebral vascular ultrasound. Part IV. Normal and abnormal B-mode appearance of the carotid arteries. *Semin Ultrasound CT MR* **1987**;8(1):17-26
7. Middleton WD, Foley WD, Lawson TL. Flow reversal in the normal carotid bifurcation: color Doppler flow imaging analysis. *Radiology* **1988**;167:207-210
8. Phillips DJ, Greene FM, Langlois Y, Roederer GO, Strandness DE. Flow velocity patterns in the carotid bifurcation of young, presumed normal subjects. *Ultrasound Med Biol* **1983**;9:39-49
9. Zweibel WJ. Primer of cerebral vascular ultrasound. Part V. Analysis of carotid Doppler signals. *Semin Ultrasound CT MR* **1987**;8(1):27-50
10. Berguer R, Hang NHC. Critical arterial stenoses: a theoretical and experimental solution. *Ann Surg* **1974**;1980:39-50

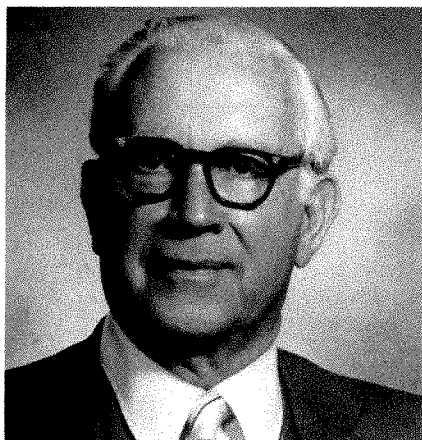
American Society of Emergency Radiology

The American Society of Emergency Radiology (ASER) has been created and incorporated. The purpose of the society is to (1) advance and improve the radiologic aspects of emergent patient care; (2) establish emergency radiology as an area of special interest in the field of diagnostic imaging; (3) improve methods of education in emergency radiology; (4) provide, through formal meetings, a mechanism for presentation of scientific papers on various aspects of emergency radiology; (5) promote research in emergency radiology by residents and investigators; and (6) act as the resource body on emergency radiology for those interested in emergent patient care.

Current officers are John H. Harris, Jr., president; Robert A. Novelline, vice-president and president-elect; and Gordon C. Carson, secretary-treasurer. Active membership is reserved for diplomates of the American Board of Radiology or the American Board of Osteopathic Radiology whose primary professional interest is emergency radiology. Associate membership is reserved for radiologists who are not eligible to be active members but whose credentials and interests indicate significant participation in emergency radiology. The status of member-in-training is limited to physicians in training in the field of radiology (residents or fellows) who have shown an interest in emergency radiology. Membership applications can be obtained from Stuart E. Mirvis, M.D., Dept. of Diagnostic Radiology, University of Maryland Medical System, 22 S. Greene St., Baltimore MD 21201.

Memorial

Joseph L. Morton, 1912–1987



Joseph L. Morton died July 16, 1987, of acute heart failure secondary to multiple myocardial infarctions. Born December 13, 1912, in New Vienna, OH, he was the only child of Lyle G. and Helen Morton. He was

raised in Ohio. He graduated from Ohio State University medical school in 1936. In 1937, he married Mary Frances Boone, a registered nurse. He completed his radiology training at Case Western Reserve in Cleveland in 1939. He served 4 years in the Pacific Theater in World War II. He returned to Columbus, OH, to become a professor of radiology at Ohio State. He and his wife and two sons moved to Indianapolis in 1955, where he became the sole radiologist at St. Vincent Hospital. Under his progressive insight and guidance, the radiology department grew to become one of the most respected private hospital departments in Indiana. The department currently has 18 radiologists. Dr. Morton was board certified in diagnostic radiology, therapeutic radiology, and nuclear medicine. He was a member of several national and international societies in these disciplines. After "retirement" in 1982, he continued to work at locum tenentes in the midwest and adjacent southern states until his death.

He was remarkable for his unquenchable thirst for knowledge. He was able to use new

ideas in his daily practice. He pioneered new techniques in cobalt therapy. He was one of the first to use radioactive seeds in plastic tubing for interstitial radiation therapy. He used strontium for bone scanning in the 1950s. In the 1960s, he experimented with ultrasound for determining midline shift of the brain. He and his first wife financed and maintained a large colony of athymic mice in their basement in the 1970s. He attempted to grow his patients' tumors in these mice and then individualize therapy for his patients.

He was an avid gardener. He took his father's farm and expanded it into a state-of-the-art hog farm. He was a generous man. He also loved music, and he loved singing with the church choir and the Shrine choir.

I often hear from former patients or their families that they were touched by my father. He is survived by Lillian Blanchard Morton, who married him after his first wife's death; my brother, Joe; myself; and three grandchildren.

John A. Morton
Carmel, IN 46032

Blood Flow in the Carotid Arteries: Quantification by Using Phase-Sensitive MR Imaging

Peter Bendel^{1,2}
Edward Buonocore³
Andreas Bockisch⁴
Myrwood C. Besozzi³

The feasibility of MR phase-sensitive imaging for the quantification of blood flow in the carotid arteries was studied in two normal volunteers and six patients with carotid artery and/or cerebrovascular disease. The technique consists of sensitizing the phase of the MR signal to blood flow velocity gated to different times in the cardiac cycle. Flow velocities and volumes were measured by using transverse planes in the common, internal, and external carotid arteries, and flow curves were generated. Measurements made by using flow phantoms correlated well with calculated results. The MR measurements yielded values between 250 and 580 ml/min for the total flow through each of the common carotid arteries in the two normal volunteers. Markedly reduced flow (about 50% below normal) was detected in a patient whose arteriogram showed severe occlusion of the internal carotid artery. In a second patient, who had a large frontal intracranial arteriovenous malformation noted by arteriography, the MR-quantified flow was abnormally high (about 1 liter/min). In the remaining four patients, the findings on phase-sensitive quantification were consistent with those expected from clinical and other laboratory studies (including arteriography and sonography).

These preliminary findings suggest that MR phase mapping may be a feasible tool for the noninvasive quantification of carotid blood flow.

In order to enhance the value of MR imaging of the carotid arteries, a phase-sensitive method of quantitative analysis of flow in the axial projection was applied to the study of two normal volunteers and six patients with carotid and/or cerebrovascular disease. The method uses a gradient-echo sequence with a short TR and low flip angle that is applied in a cardiac-gated synchronized cine mode. Flow information temporally resolved over the cardiac cycle was provided [1]. Previous quantitative MR flow-velocity studies [2-4] in humans have been made with spin-echo sequences without temporal resolution during the cardiac cycle. Other reports [5, 6] include cine mode measurements of flow made by using angiography [6]. The purpose of this report is to validate the accuracy of phase-sensitive imaging for quantitative flow in phantom experiments and its application to the study of carotid arteries.

Materials and Methods

Experiments were performed on a commercial whole-body Gyrex 2TTM MR imager, (Elscent, Inc., Herzlia, Israel) operating at 1.9 T. The pulse technique consisted of the interleaved application of two sequences, which differed in the amount of phase-velocity encoding along the direction of the slice-select gradient (also the principal direction of the flow). In one scan, the gradient waveforms compensated for phase shifts introduced by flow at constant velocity, whereas in the alternate sequence, a phase proportional to velocity was introduced. Both sequences were phase compensated for flow along the view- or frequency-encoding direction.

Excitation pulses with 30° flip angle were applied with TR = 30 msec, and the signal was detected with TE = 18 msec. The increment of the phase-encoding gradient was triggered by the heartbeat. Because the velocity measurements are derived from difference images involving two successive scans, a velocity measurement every 60 msec through the cardiac

Received September 23, 1988; accepted after revision February 3, 1989.

¹ Institute of Biomedical Imaging, University of Tennessee Medical Center, 1924 Alcoa Hwy., Knoxville, TN 37920 and Elscint Magnetic Resonance Imaging Center, Herzlia, Israel.

² Present address: Dept. of Isotope Research, The Weizmann Institute of Science, Rehovot 76100, Israel. Address reprint requests to P. Bendel.

³ Department of Radiology, University of Tennessee Medical Center, 1924 Alcoa Hwy., Knoxville, TN 37920.

⁴ Department of Clinical and Experimental Nuclear Medicine, University of Bonn, Sigmund Freud Strasse 25, 5000 Bonn 1, West Germany. From May to August 1988, A. Bockisch was a visiting scientist in the Dept. of Radiology at the University of Tennessee Medical Center.

AJR 152:1307-1310, June 1989

0361-803X/89/1526-1307

© American Roentgen Ray Society

cycle was obtained. The total measurement time for a 256×256 acquisition was about 5 min, depending on the heart rate of the patient. Slice width was 6 mm, field of view was 22 cm, and velocity encoding was $3^\circ/\text{cm}/\text{sec}$. Signals were detected by the standard spine coil of the system.

Phase intensities were corrected by a simple linear software operation with variables derived from the requirement that the intensity should have an average of zero in areas containing only nonflowing material. Flow directions and velocities were read directly off the images on a pixel-by-pixel basis, and the proportionality constant between velocity and phase was determined by flow-phantom calibrations, described later in the text. The phase images were correlated with the magnitude images, and a phase value of zero was assigned to all pixels whose magnitude intensity was below a certain threshold.

Volume flow rates were derived by drawing a region of interest around the vessel. The area contained in the region was multiplied by the average image intensity. The product of these two values yielded the volume flow rate.

Subjects

Two young, healthy volunteers and six patients with carotid artery stenosis or various degrees of intracerebral vascular diseases were studied (Table 1). Of the six patients, two had carotid artery occlusive disease, one diagnosed by arteriography and the other by carotid sonography and Doppler technique. The remaining four patients had no evidence of carotid-artery narrowing by arteriography. Of these four patients, two had a diagnosis of a remote stroke, and each had normal carotid and cerebral angiograms and was clinically normal. Of the remaining two patients, one had a large arteriovenous malformation and the other was evaluated for neck pain and found to be normal by arteriography and further clinical assessment.

Data Collection

A survey coronal MR image was obtained to choose the position of the transverse planes used for the analysis of blood flow in the

common, internal, or external carotid arteries. In these two planes, phase mapping was performed, as described. Analysis of the data yielded the arterial flow at eight to 11 points of the heart cycle, which made it possible to calculate the total flow by integrating the area under the flow-time graph, or by interpreting the line shape of the graph itself.

Calibration

Measurements were made by using phantoms in which constant-velocity flow was generated in tubes and measured by timing the flow into graduated containers to calibrate our pulse sequence and for subsequent data processing. We tested two sequences that differed in the amount of flow encoding. In one sequence, the flow-induced phase was $2^\circ/\text{cm}/\text{sec}$, and in the other (which was the sequence used in the carotid artery study), the phase encoding by flow was $3^\circ/\text{cm}/\text{sec}$.

Results

The results of the flow-phantom calibration study are shown in Figure 1. A straight-line correlation was produced when phase intensity of the signal was plotted against the measured velocity of flow in the phantom.

Figure 2 illustrates typical magnitude images and difference-phase maps of one of the normal volunteers. Figure 3 shows the flow curves for one of these volunteers. Figures 4 and 5 show flow curves for two other subjects, as indicated in the captions. The patients' relevant data and the total integrated flow volumes are summarized in Table 1.

Discussion

Several MR techniques for studying the morphology and function of the vascular system have been introduced in the

TABLE 1: Carotid Artery Flow Rates (ml/min)^a

Age (years)	Gender	Clinical Status	Common Carotid Artery			Internal Carotid Artery	
			Left	Right	Left/Right Ratio	Left	Right
32	F	Right CVA, normal cerebral angiogram	567	572	1.0	279	208
53	M	Left CVA, severe narrowing of left ICA, mild narrowing of right ICA	171	344	0.50	NM	247
66	F	Stroke 10 months ago, clinically normal	502	416	1.2	329	292
37	M	Large right frontal AVM from both carotids, right > left	959	1182	0.81	ND	ND
59	M	Peripheral vascular disease, Right ICA, 100% occluded; Left ICA, 80% occluded	389	No flow detected	—	—	—
38	F	Throat and neck pain; no cerebral vascular disease	265	275	1.0	NM	165
22	M	Normal volunteer	373	445	0.84	ND	ND
20	F	Normal volunteer	291	311	0.94	231	249

Note.—CVA = cerebral vascular accident, ICA = internal carotid artery, AVM = arteriovenous malformation, NM = not measured, ND = not determined, — = no flow detected.

^a Experimental uncertainties for the flow volumes in this table are estimated at ± 40 ml/min.

last few years [6–8]. MR angiography aims to provide static anatomic images of in-plane blood flow of long segments of vessels, whereas other methods have been designed to provide functional specific quantitative information about flow velocities, volumes, and directions. Quantitative measurement of flow velocities can be achieved by some sort of inflow-outflow tagging technique [2] or by using phase measurements on cross-sectional phase images [4, 9].

The proportionality constant between velocity and phase as determined by our technique could, in principle, be predicted directly from a calculation of the gradient waveform-time integral [9]. Others have pointed out the need for calibrations with flow phantoms [8], so we conducted experiments to determine the accuracy of our calculated phase-sensitive technique (Fig. 1). Using flow phantoms, we found that the measured flow encoding of a given sequence did indeed differ slightly from the calculated phase, if the phase was calculated in a straightforward manner [9]. The measured

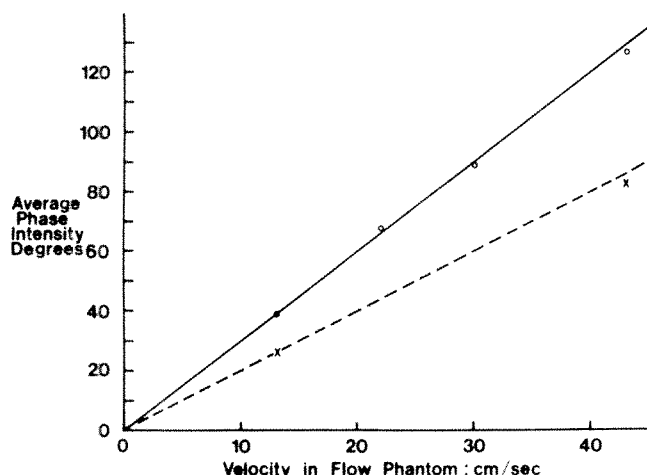


Fig. 1.—Calibration curve of phase-mapping sequences on flow phantom. Vertical scale is average intraluminal phase intensity in tube carrying flowing water, determined by difference phase mapping, as described in text. Horizontal coordinates are velocities measured by timing delivery of measured volumes through the tube. Data are presented for two different pulsing sequences, with calculated velocity phase encoding of $3^\circ/\text{cm}/\text{sec}$ (circles), and $2^\circ/\text{cm}/\text{sec}$ (x), which are also slopes of solid and dashed lines, respectively.

difference in velocity phase encoding between two sequences with slightly different compensating gradients could be predicted accurately by the simple analytical calculation.

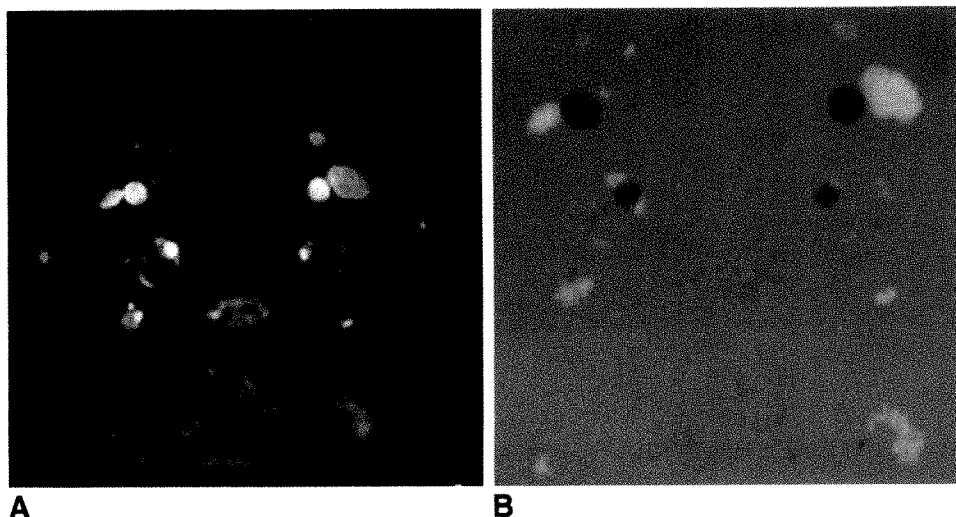
Validation of our phase-sensitive technique of determining blood flow is evidenced by noting that the total integrated flow volumes of normal volunteers (Table 1) are well within the broad range of normal values established in the literature by other methods [10]. The shape of the curves resembles the expected physiologic pressure curves [11], even suggesting the presence of a diastolic notch. Further internal consistency of our measurements is shown by comparing the flow rates in the common carotid artery with the sum of the rates in the internal and external branches farther downstream. The two values should be equal, and as shown in Figure 4, they indeed are within the limits of experimental uncertainty.

Our data reflect volume flow rates, that is, the product of linear velocities and cross-sectional areas. We found these values to be more precise (in terms of evaluation by different observers) than the values of average velocity and cross-sectional area separately, which tend to be more dependent on the tendency of an individual to draw the contour region of interest around the vessel.

A possible limitation of the accuracy of the clinical data may be imposed by acceleration, which was not present in our flow-phantom calibration. Acceleration can cause phase shifts not considered in our analysis. A rough calculation using typical rates of velocity increase or decrease and the gradient timing of our pulse sequence indicates that an inaccuracy of up to 20% in the estimated flow rate could be caused by this omission during peak acceleration. The error would cause overestimation of the rate during acceleration and underestimation during deceleration. The overall effect may simply be a slight temporal shift of the flow-rate curve to the right. This would produce little effect on the integrated total flow volume and is probably of no clinical significance.

In the studies of patients with normal carotid arteriography and stroke due to intracerebral vascular occlusion, we found that the carotid flow was essentially normal. The peak, however, was less pronounced than in the normal volunteers (Fig. 4), possibly because the patients were older than the volunteers. The ratios of the flow rates between left and right carotid arteries in the patients were similar to the ratios calculated for the volunteers. In the patient with intracerebral

Fig. 2.—Magnitude and phase-sensitive MR scans in normal volunteer. Magnitude (A) and zoomed phase-difference image (B) of one cardiac frame (282 msec after R wave) in one volunteer. Phase-difference image was masked by assigning a phase intensity of zero (gray) to all pixels whose magnitude intensity was below a certain threshold. Direction of flow and magnitude are determined. Both common carotid and vertebral arteries (dark) and jugular veins (bright) are well resolved and visualized. Degree of brightness correlates with velocity.



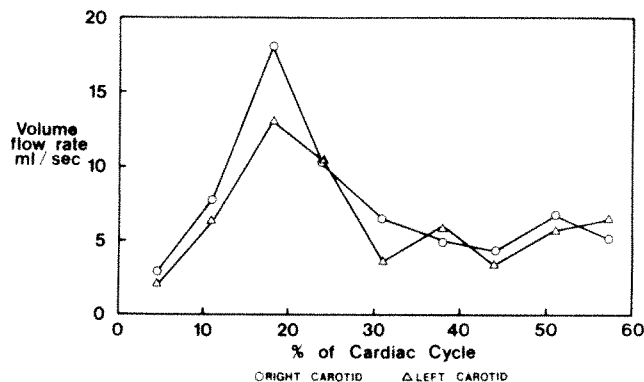


Fig. 3.—Graph showing calculated flow volume rate vs time frame in a cardiac cycle for 22-year-old male volunteer. Solid lines are simple connections between experimental points, for better visualization of time dependence.

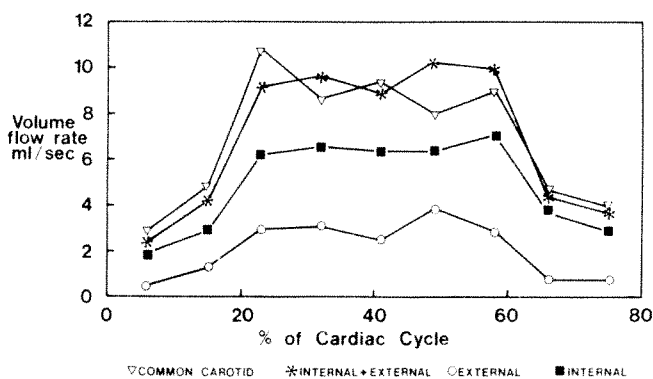


Fig. 4.—Graph showing flow volume rates of right common, internal, and external carotid arteries determined by phase-sensitive MR scanning in a 66-year-old woman with history of a remote stroke and normal arteriography. Note that calculated sum of external and internal curves is equivalent to measured flow curve of right common carotid artery. Note also lower and flattened peak of curves as compared with that of 22-year-old volunteer in Fig. 3.

arteriovenous malformation, carotid artery flow was increased considerably. The flow volume was higher on the right side, as would be expected from the arteriographic findings.

Our investigations of the two patients with severe carotid stenosis were in accord with the arteriographic diagnosis. In one patient, arteriography showed 90% stenosis in the left internal carotid artery and total occlusion on the right side. With MR phase mapping, no flow was detected in either the right or left internal carotid arteries. At the level of the common carotid arteries, normal flow was measured in the left common carotid artery. Flow in the left internal carotid artery could not be detected by MR phase mapping, most likely because of turbulence due to the severe stenosis. Turbulence makes phase analysis of flow impossible. Absence of any enhanced signal from the vessel on the magnitude images corroborated the presence of turbulent flow. On the right side, no flow was detected in the common carotid artery.

In the other patient with carotid artery occlusive disease, correlation of the sonographic findings with phase mapping was as follows. Mild occlusion of the right internal carotid artery and nearly total occlusion of the left internal carotid artery were found by sonography. MR phase mapping indicated normal total flow in the right common carotid artery and

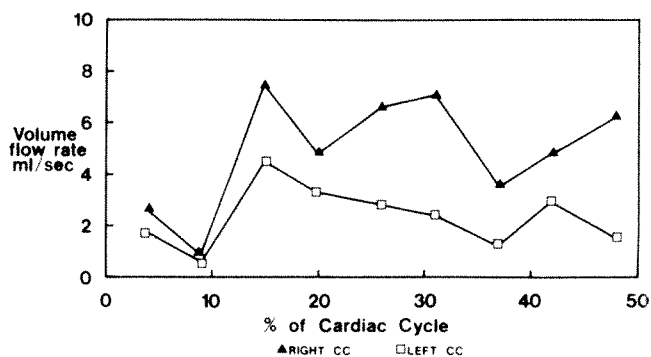


Fig. 5.—Graph showing common carotid artery volume flow rates in a 53-year-old man who had severe narrowing of left and mild narrowing of right internal carotid arteries. Flow-rate ratio of right to left common carotid arteries was 2:1.

reduced flow in the left common carotid artery with an abnormal right/left ratio of 2.0 (Fig. 5).

In summary, although only a limited number of patients have been studied, we found that accurate measurement of blood flow by MR phase mapping is feasible in carotid arteries with normal flow. A principal limitation of the technique is the loss of signal in turbulent flow, whether slow or rapid. This problem may be overcome by measuring flow proximally or distally to the regions of turbulent flow. Because the planes detected by MR easily can be oriented at any angle and detection can reach any depth within the body, MR phase mapping of flow rates may become particularly valuable in deep-lying vessels (e.g., renal or mesenteric arteries), which are not readily accessible by other techniques (e.g., sonography). Although the morphologic information provided by MR imaging may not be as flexible as that provided by digital subtraction angiography, the MR examination described here combines a detailed anatomic image with quantitative functional information, without the use of contrast agents.

REFERENCES

1. Nayler GL, Firmin DN, Longmore DB. Blood flow imaging by cine magnetic resonance. *J Comput Assist Tomogr* **1986**;10:715-722
2. Singer JR, Crooks LE. Nuclear magnetic resonance blood flow measurements in the human brain. *Science* **1983**;221:654-656
3. Feinberg DA, Crooks LE, Hoenninger J, Arakawa M, Watts J. Pulsatile blood velocity in human arteries displayed by magnetic resonance imaging. *Radiology* **1984**;153:177-180
4. Bryant DJ, Payne JA, Firmin DN, Longmore DB. Measurement of flow with NMR imaging using a gradient pulse and phase difference technique. *J Comput Assist Tomogr* **1984**;8:588-593
5. Firmin DN, Nayler GL, Klipstein RH, Underwood SR, Rees RSO, Longmore DB. In vivo validation of MR velocity imaging. *J Comput Assist Tomogr* **1987**;11:751-756
6. Walker MF, Souza SP, Dumoulin CL. Quantitative flow measurement in phase contrast MR angiography. *J Comput Assist Tomogr* **1988**;12:304-313
7. Singer JR. Blood flow rates by nuclear magnetic resonance measurements. *Science* **1959**;130:1652-1653
8. Lenz GW, Haacke EM, Masaryk TJ, Laub G. In-plane vascular imaging: pulse sequence design and strategy. *Radiology* **1988**;166:875-882
9. Moran PR, Moran RA, Karstaedt MB. Verification and evaluation of internal flow and motion. *Radiology* **1985**;154:433-441
10. Ackroyd N, Gill R, Griffiths K, Kossoff G, Appleberg M. Quantitative common carotid artery blood flow: prediction of internal carotid artery stenosis. *J Vasc Surg* **1986**;3:846-853
11. Burton AC. *Physiology and biophysics of the circulation*, 2nd ed. Chicago: Year Book Medical, **1972**

Case Report

Pelvic Arteriovenous Malformation Diagnosed by Color Flow Doppler Imaging

Antoine Abu Musa,¹ Toshiyuki Hata, Kohkichi Hata, and Manabu Kitao

Arteriovenous malformation (AVM) of the female pelvic organs is uncommon. Previous reports have described the roles of angiography [1, 2], CT [3], and MR imaging [4] in the diagnosis. To the best of our knowledge, this is the first report in which the diagnosis of a pelvic AVM is by color flow Doppler sonography.

Case Report

A 71-year-old woman was admitted for management of heart failure due to severe mitral regurgitation and for evaluation of a pelvic mass. Her history was not remarkable except for an uneventful intrauterine curettage 35 years ago.

Real-time sonography showed multiple small, echo-free spaces in the uterus and multicystic masses in both adnexal regions (Fig. 1). Color flow Doppler revealed findings diagnostic of pelvic AVM (Fig. 2). This was confirmed by pelvic angiography (Fig. 3). The patient refused further evaluation and treatment.

Discussion

Pelvic AVMs are uncommon lesions of unknown cause. Congenital AVMs are considered to be undifferentiated vascular structures resulting from arrest of embryonic development at various stages [5]. Acquired AVMs are usually caused by neoplasms or trauma, and procedures such as curettage and uterine surgery have been implicated [2]. These malformations are characterized by their slow growth with a period

of latency before becoming symptomatic. They may produce local or systemic effects, including vaginal bleeding, abdominal pain, urinary symptoms, and high-output congestive heart failure. Pelvic examination may reveal a poorly defined pulsatile adnexal mass or a soft and enlarged uterus that transmits pulsations. In our case, the cause of AVM is unclear; however, the intrauterine curettage done 35 years ago might be related. The patient did not have local symptoms, even at the age of 71. How much the AVM contributed to her cardiac failure is not known, because she refused further evaluation and management.

Many methods have been used to diagnose pelvic AVM. Angiography is the traditional diagnostic tool and is essential to delineate the blood supply to the tumor and to guide treatment [6]. Fakhri et al. [3] recommended the use of CT with bolus contrast enhancement to diagnose pelvic AVM and to assess the degree of local organ involvement. Recently, MR imaging has been suggested as a method for evaluating pelvic AVM [4].

The sonographic findings of pelvic AVM were first described by Torres et al. [1]. These included multiple serpiginous sonolucent structures within the pelvis. With real-time sonography, enlarged bounding vessels can be seen occasionally [2]. Although sonography seemed to be a good screening test, the findings of multiple cystic lesions in the pelvis suggest other entities such as multiloculated ovarian cysts and dilated fluid-filled loops of bowel [1]. This problem in the differential diagnosis can be resolved with color flow Doppler. In our

Received November 28, 1988; accepted after revision December 28, 1988.

¹All authors: Department of Obstetrics and Gynecology, Shimane Medical University, Izumo 693, Japan. Address reprint requests to T. Hata.

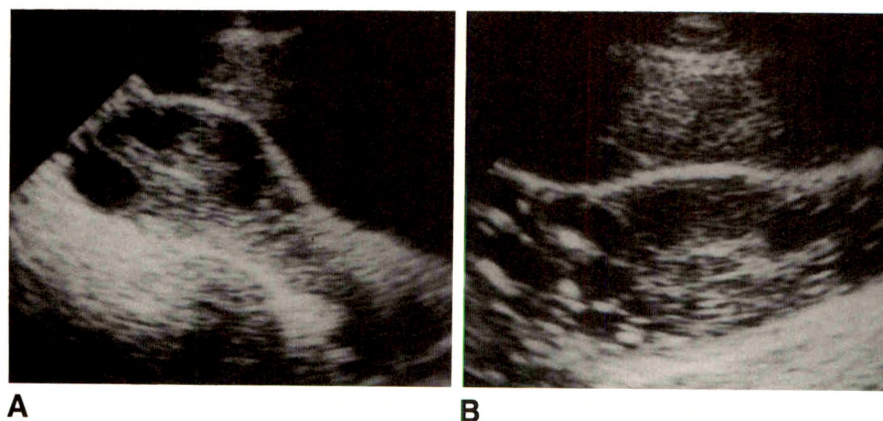


Fig. 1.—Real-time sonogram shows multiple anechoic spaces in the uterus (A) and in both adnexal regions (B).

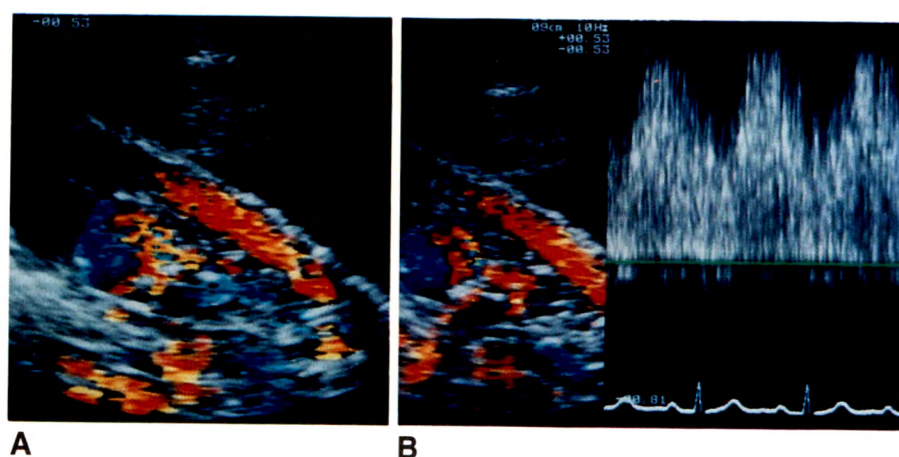


Fig. 2.—Color flow Doppler images show a mosaic pattern with red shades and blue regions in right adnexal mass (A). Pulsed Doppler sonography shows rapid and turbulent systolic blood flow with relatively high-velocity diastolic component (B).

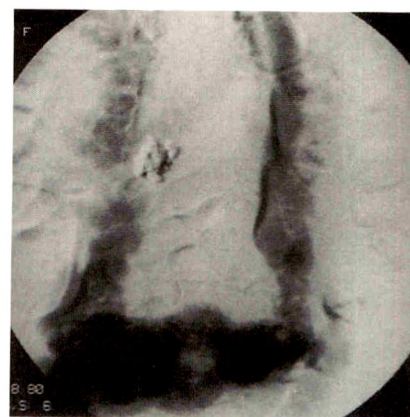


Fig. 3.—Pelvic angiogram shows an extensive hypervascular tumor involving uterus and both adnexa with early venous filling and venous dilatation.

case, real-time sonography revealed multiple cystic lesions in the pelvis. However, color flow Doppler depicted abundant blood flow, with shades of red or blue within the multicystic masses. Moreover, a mosaic pattern with red shades and blue regions was noted within the mass, and pulsed Doppler sonography showed rapid and turbulent systolic flow with a relatively high-velocity diastolic component. The diagnosis of an AVM was confirmed by a pelvic angiogram.

AVM is treated by either surgery, embolization, or both. However, because of the high recurrence rate and the difficulty of treatment in cases of multiple tumors involving adjacent organs, conservative therapy is recommended in most cases, especially in asymptomatic patients [7]. Angiography is essential before treatment, but in cases where AVM is suspected and conservative treatment is anticipated, color flow Doppler alone can establish the diagnosis.

REFERENCES

1. Torres WE, Stones PJ Jr, Thames FM. Ultrasound appearance of pelvic arteriovenous malformation. *JCU* 1979;7:383-385
2. Diwan RV, Brennan JN, Selin MA, et al. Sonographic diagnosis of arteriovenous malformation of the uterus and pelvis. *JCU* 1983;11:295-298
3. Fakhri A, Fishman EK, Mitchell SE, Siegelman SS, White RI. The role of CT in the management of pelvic arteriovenous malformations. *Cardiovasc Intervent Radiol* 1987;10:96-99
4. Amparo EG, Higgins CB, Hricak H. Primary diagnosis of abdominal arteriovenous fistula by MR imaging. *J Comput Assist Tomogr* 1984;8:1140-1142
5. Natakli J, Jue DP, Kieffer E, et al. Arteriovenous fistulae of the internal iliac vessels. *J Cardiovasc Surg* 1984;24:165-172
6. Mitty HA, Baron MG, Jacobson JH. Pelvic arteriovenous malformations. *AJR* 1968;102:424-430
7. Pritchard DA, Maloney JD, Bernatz PE, Symmonds RE, Stanson AW. Surgical treatment of congenital pelvic arteriovenous malformation. *Mayo Clin Proc* 1978;53:607-611

Commentary

The Perception of Visual Data: A Summary of the ACR Meeting on Visualization Science in Engineering, Computing, and Medicine

William R. Hendee¹

Images have always been important to understanding and communicating among people. Long before written communication, images were used to convey information and to express hopes and fears, often within the rubric of myths and legends. Today, images frequently are used to connote patterns of information too complex to describe in other ways. The pilot viewing a radar screen to help guide a runway approach, the surveillance expert using remote cameras to assess the security of an area, and the analyst scanning computer-generated displays of multidimensional data sets are examples of the use of images to characterize information that would otherwise be uninterpretable. Another example is the use of radiologic images in medicine to depict human anatomy and physiology and their alterations by injury and illness.

Radiologic images have improved markedly since their introduction into clinical medicine almost a century ago. Especially notable has been the progress over the past couple of decades as computer-based digital techniques have been applied to radiologic imaging. Today the technology of radiology is truly spectacular, with several recent introductions such as CT and MR imaging complementing digital modifications of existing imaging methods in radiography, sonography, and nuclear medicine. Digital images can be modified to sharpen or reduce their detail, enhance or soften their contrast, and increase or suppress their statistical noise, depending on the wishes of the observer.

Thousands of software routines have been written to alter the appearance of radiologic images to make them more useful to the physician. In general, these routines have not been widely adopted into clinical practice, primarily because the process of information transfer from image to observer is poorly understood. In spite of centuries of curiosity about vision and decades of research on the visual process, we still have little knowledge about how visual information is detected and even less knowledge of how detected information is processed cognitively to arrive at an understanding of images. In medicine today, these limitations impede exploitation of the technology of imaging to improve diagnosis and treatment of patients. This impediment is not very different from those present in other vision-dependent disciplines, including space science, military surveillance, industrial quality assurance, air traffic control, and computer graphics analysis.

Recognizing the common need of several disciplines for improved knowledge about the detection and cognition of visual information, the American College of Radiology convened a 3-day meeting in March 1988, entitled "Visualization Science in Engineering, Computing, and Medicine." The meeting was designed to explore what is understood (and, more importantly, not understood) about the human visual process and the extraction and use of information from visual images. Attending the meeting were over 100 representatives from fields such as aerospace, military intelligence, industry, computer graphics, and medicine. The meeting was presented in

The meeting on visualization science in engineering, computing, and medicine, sponsored by the American College of Radiology, was held March 30–April 1, 1988, in Arlington, VA.

¹ Vice President for Science and Technology, American Medical Association, 535 N. Dearborn St., Chicago, IL 60610. Address reprint requests to W. R. Hendee.

five half-day sessions entitled (1) Detection of Visual Information, (2) Cognitive Processing of Visual Information, (3) Matching of Image and Observer Characteristics, (4) Acquisition and Processing of Visual Information, and (5) Display of Visual Information. Each session was introduced by a keynote speaker, followed by three respondents who commented on the keynote and added their own perspectives. An hour's discussion of the topic with the audience highlighted each session and was perhaps the most enriching feature of the meeting. Comments of the attendees suggested that the meeting was an enlightening experience for most and that multiple pathways for additional research, much of it interdisciplinary, had become apparent during the discussions.

The first keynote speaker was Arthur Ginsburg, President of Vistech Consultants and former vision researcher with the U.S. Air Force. Dr. Ginsburg discussed the three principal models for detecting visual signals: the signal-to-noise, computational, and signal-channel models. The signal-to-noise model characterizes the ability of the observer to detect simple visual signals embedded in a relatively predictable background of noise. The model has been applied successfully to several detection tasks for extracting information from rather simple images. In more complex visual situations, however, the model fails to predict the performance of human observers, suggesting that it is an overly simplistic interpretation of human visual detection. The computational model proposes that an image is detected by first composing a "primal sketch" of fundamental properties (shape, distance, orientation, and motion) of the scene, followed by a more thorough analysis to confirm the initial impression. Development of this model into a useful paradigm has been disappointing, probably because current understanding of the psychophysical aspects of vision is too rudimentary.

The signal-channel model is currently the most promising approach to understanding visual detection. In this model, the visual system is characterized as a series of parallel channels, with each channel sensitive to a different range of spatial frequency information about the image. The image is perceived by mental integration of information across all spatial frequencies, with high and low frequencies typically attenuated to enhance the contribution of intermediate spatial frequencies. This tendency is described by "contrast sensitivity" curves that were proposed by Dr. Ginsburg as useful expressions of an observer's visual performance. The suggestion that these curves be used as a screening test for entry into visually oriented occupations such as air-traffic control, piloting of aircraft, and radiologic diagnosis stimulated considerable controversy. Participants agreed that matching images to the perception characteristics of observers by use of image processing algorithms might be accompanied by efforts to match observer characteristics to images by use of appropriate screening tests. However, many felt that use of contrast sensitivity curves is an overly simplistic response to this challenge.

The keynote speaker for the second session was Richard Gregory, Director of the Brain and Perception Unit at the University of Bristol, who emphasized that detection of visual signals must be distinguished from cognitive interpretation of

those signals as a representation of "reality." He suggested that detection of visual information occurs very quickly, but can be tricked into mistakes and illusions. Cognition invokes "top-down" knowledge to prime perceptions and to provide plausible interpretations of perceptual hypotheses formed during the detection process. Hence, detection and cognition work together in the interpretation of visual images. His comments reminded attendees of Kant's paraphrased adage that "Perception without conception is empty, and conception without perception is blind." They also revealed one of the intrinsic difficulties in improving observer performance; until the role of cognition is better understood, especially the influence of mental templates formed through experience in interacting visually with the external world, progress in matching image and observer may remain elusive.

The third session explored the efficiency of coupling the objective characteristics of images to human interpreters responsible for decisions based on visual information. Robert Wagner of the U.S. Food and Drug Administration's Center for Devices and Radiological Health presented the keynote address, with a contribution from an associate, Kyle Myers. They showed that human observers perform well (within a factor of two of ideal observers) when only first-order statistics (brightness and contrast information) of the images are required for decision making. The performance deteriorates when higher order information (e.g., color, configuration, or texture) is needed for proper interpretation. Humans appear to combine several techniques in interpreting complex images, including template matching, thresholding, and logical-comparison procedures that can be performed by a single-level neural net. Wagner suggested that optimal visual performance might be best approached through a division of labor between humans and artificial intelligence machines, with humans interpreting brightness and contrast information and machines analyzing higher order cues such as texture. Sonographic and CT images may be suited to such an approach at the present time.

In his keynote address, Harrison Barrett of the Optical Sciences Center at the University of Arizona considered the challenge of optimizing observer performance by manipulating variables used in generating images. He demonstrated the use of the "Hoteling observer" as a mathematical model that closely simulates the performance of human observers and suggested that this model could be used to estimate the effects on observer performance of various techniques for acquiring and manipulating images. Barrett proposed that a Hoteling template might be useful as a frequency filter to enhance the recognition of image characteristics that represent abnormal conditions in the object.

The final keynote speaker, Stephen Pizer of the Computer Science Department at the University of North Carolina, discussed the design of image-display workstations to enable the observer to navigate efficiently among many images. He acknowledged that the traditional method of displaying multiple images simultaneously in a contiguous spatial configuration is a relatively efficient approach and that electronic workstations will have to offer significant improvements to be useful. He described several technical limitations impeding

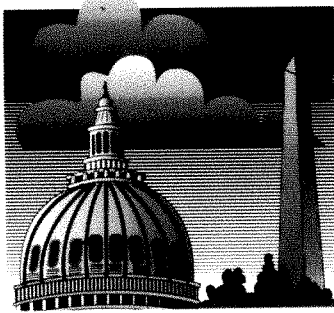
current work on workstations and also outlined various uncertainties in knowledge about the interaction between the observer and multiple image displays. Considerable work is underway in workstation design, and a better understanding of the ergonomics of the workstation environment is sorely needed.

Many recommendations for future research in image perception and cognition evolved from the workshop. The number and depth of these recommendations suggest that image visualization is a potentially fruitful arena for interdisciplinary research and that many activities, including radiology, would benefit from the products of that research. Our present un-

derstanding of how we see, and how we know what we see, is rudimentary; improving that understanding and using the improved understanding to enhance the presentation of visual information to observers could significantly improve the accuracy of radiologic interpretation.

ACKNOWLEDGMENT

This report was edited from a synopsis of the meeting prepared by William R. Hendee, Calvin F. Nodine, Kendall Preston, Jr., Roger H. Schneider, and Peter N. T. Wells.



Scientific Program (200 papers)

Instructional Courses (60 hours)

Categorical Course on
Cardiovascular Imaging

The Caldwell Lecture

Award Papers

Scientific Exhibits

Social, Golf, and Tennis Programs

Guest Programs



Come to the
American Roentgen Ray Society

90th

ANNUAL MEETING

Washington, D. C.

Sheraton Washington Hotel

May 13-18, 1990

FORTHCOMING ARTICLES

PROGRESS IN RADIOLOGY

Imaging advances in the diagnosis of renovascular hypertension. Hillman BJ

Biliary lithotripsy 1989: a progress report. Ferrucci JT

Update on interventional neuroradiology. Viñuela F, Dion J, Lylyk P, Duckwiler G

Radiation detector probes for tumor localization using tumor-seeking radioactive tracers. Woolfenden JM, Barber HB

CARDIOPULMONARY RADIOLOGY

CT features of rounded atelectasis. McHugh K, Blaquiére RM

Septic pulmonary emboli: CT-radiographic correlation. Huang R-M, Naidich DP, Lubat E, Schinella R, Garay SM, McCauley DI

Pictorial essay. MR imaging of secondary cardiac and paracardiac lesions. Barakos JA, Brown JJ, Higgins CB

Case report. CT demonstration of an ossifying bronchial carcinoid simulating broncholithiasis. Shin MS, Berland LL, Myers JL, Clary G, Zorn GL

MAMMOGRAPHY

Commentary. Medicolegal aspects of screening mammography. Brenner RJ

GASTROINTESTINAL RADIOLOGY

Pancreas transplants: evaluation using perfusion scintigraphy. Kuni CC, du Cret RP, Boudreau RJ

Case report. Obliteration of periaarterial retropancreatic fat on CT in pancreatitis: an exception to the rule. Luetmer PH, Stephens DH, Fischer AP

Case report. Use of tetracycline for sclerosis of a biliary-cutaneous fistula. Shaw DWW, Bertino RE, Mulholland MW, Coldwell DM, Goldman ML

Technical note. A technique for embolization of biopsy tracts. Crummy AB, McDermott JC, Wojtowycz M

GENITOURINARY RADIOLOGY

Small renal neoplasms: clinical, pathologic, and imaging features. Levine E, Huntrakoon M, Wetzel LH

Transvaginal sonography in the evaluation of normal early pregnancy: correlation with HCG level. Bree RL, Edwards M, Böhm-Vélez M, Beyler S, Roberts J, Mendelson EB

Fluoroscopically guided retrograde brush biopsy to diagnose transitional cell carcinoma of the upper urinary tract: results in 45 patients. Sheline M, Amendola MA, Pollack HM, Banner MP, de las Morenas A, Wein AJ

Technical note. A new technique for complete temporary occlusion of the ureter. Castañeda F, Moradian GP, Epstein DH, Hunter DW, Castañeda-Zuñiga WR, Amplatz K

Case report. MR imaging findings in renal medullary fibroma. Cormier P, Patel SK, Turner DA, Hoeksema J

Case report. Burkitt lymphoma involving the epididymis and spermatic cord: sonographic and CT findings. Zwanger-Mendelsohn S, Shreck EH, Doshi V

MUSCULOSKELETAL RADIOLOGY

Rotator cuff tears: prospective comparison of MR imaging with arthrography, sonography, and surgery. Burk DL, Karasick D, Kurtz AB, et al.

Temporomandibular joint inflammation: comparison of MR fast scanning with T1- and T2-weighted imaging techniques. Scheelhas KP, Wilkes CH

The radiologic manifestations of alveolar soft part sarcoma. Lorigan JG, O'Keeffe FN, Evans HL, Wallace S

Pictorial essay. MR imaging of aneurysmal bone cysts. Munk PL, Helms CA, Holt RG, Johnston J, Steinbach L, Neumann C

Pictorial essay. Osteolytic lesions of the patella. Ehara S, Khurana JS, Kattapuram SV, Rosenberg AE, El-Khoury GY, Rosenthal DI

Case report. Intramuscular myxoma: a rare but important association with fibrous dysplasia of bone. Sundaram M, McDonald DJ, Merenda G

PEDIATRIC RADIOLOGY

Pictorial essay. Congenital cardiac anomalies: prenatal sonographic diagnosis. Brown DL, Emerson DS, Cartier MS, Felker RE, DiSessa TG, Smith WC

Nuclear cystography and renal sonography: findings in girls with urinary tract infection. Strife JL, Bisset GS III, Kirks DR, et al.

CT of cerebrovascular injury following neonatal extracorporeal membrane oxygenation: implications for neurodevelopmental outcome. Taylor GA, Fitz CR, Glass P, Short BL

Pictorial essay. MR imaging anatomy of the infant hip. Johnson ND, Wood BP, Noh KS, Jackman KV, Westesson P-L, Katzberg RW

NEURORADIOLOGY

Pathophysiology of acute intracerebral and subarachnoid hemorrhage: applications to MR imaging. Hayman LA, Pagani JJ, Kirkpatrick JB, Hinck VC

Angiogenesis and blood-brain barrier breakdown modulate CT contrast enhancement: experimental study in a rabbit brain-tumor model. Zagzag D, Goldenberg M, Brem S

High-signal periventricular lesions in patients with sarcoidosis: neurosarcoidosis or multiple sclerosis? Smith AS, Meisler DM, Weinstein MA, et al.

Hemorrhage within pituitary adenomas: how often associated with pituitary apoplexy syndrome? Ostrov SG, Quencer RM, Hoffman JC, Davis PC, Hasso AN, David NJ

High-resolution sonography of the salivary glands. Gritzmann N

VASCULAR RADIOLOGY

Short-duration, high-dose urokinase infusion for recanalization of occluded saphenous aortocoronary bypass grafts. Marx M, Armstrong WP, Wack JP, et al.

Detection of thrombus using phase-image MR scans: ROC curve analysis. Tavares NJ, Auffermann W, Brown JJ, Gilbert TJ, Sommerhoff C, Higgins CB

COMMENTARY

The economic impact of technology on diagnostic imaging at a university medical center. Evens RG

MEMO TO AUTHORS

AJR achieves new record for speed of publication. Berk RN

General Diagnosis Case of the Day

Harvey S. Glazer,¹ Farrokh Dehdashti,¹ Barry A. Siegel,¹ Bruce L. McClennan,¹ Dennis M. Balfe,¹ and Gerald L. Andriole²

Case 1: Pulmonary Arteriovenous Malformations

A 37-year-old man presented with a 3-day history of fever, chills, weakness and tenderness of the right upper quadrant. A chest radiograph showed multiple nodular masses in the right lower lobe of the lung (Fig. 1). On a CT scan of the chest, these masses, which had a more branched appearance, enhanced to the same degree as other vascular structures and drained into a large, right inferior pulmonary vein. In addition, multiple low-attenuation lesions were seen in the liver and spleen. Subsequent percutaneous aspiration of a large lesion in the spleen yielded 50 ml of purulent fluid, which grew *Streptococcus* and two gram-negative anaerobes. A pulmonary angiogram confirmed the diagnosis of a large arteriovenous malformation (AVM) in the right lower lobe. Two additional smaller malformations (<1 cm diameter) were seen in the right lower lobe as well as in the left lower lobe. The patient underwent right lower lobectomy without complications. Further questioning did not reveal a family history of pulmonary AVMs. Skin or mucous membrane telangiectasis was not seen.

Congenital AVMs represent an abnormal communication between a pulmonary artery and a pulmonary vein, caused by a defect in the capillary bed [1-5]. Thin-walled, dilated vascular spaces result, which are usually supplied by a single artery and drained by a single vein. In some cases, the malformation may be more complex, with many feeding arteries and draining veins. Because blood bypasses the pulmonary capillaries, a right-to-left shunt exists.

In one-third of the cases, there is more than one lesion [2]. In 8-20% of cases, AVMs are seen in both hemithoraces. Forty to 60% of patients with pulmonary AVMs also have lesions elsewhere in the body, such as the skin or mucous membranes (hereditary hemorrhagic telangiectasia or Rendu-Osler-Weber [R-O-W] disease). Approximately 15% of patients with R-O-W disease have pulmonary AVMs.

Although present at birth, most AVMs don't become clinically apparent until adulthood, usually during the third-fourth decade. The most common presenting symptom is dyspnea

[5]. Neurologic symptoms may occur as a result of anoxemia or thrombosis, related in part to polycythemia or cerebral telangiectasis. Fever may result from abscess formation (especially cerebral), which may be caused by microaerophilic streptococci within emboli formed in dilated veins [3]. Moreover, large AVMs may permit infected emboli from systemic veins to pass directly into the systemic arterial system without being filtered in the pulmonary capillary system. Other complications include stroke, hemoptysis, and hemothorax. Physical examination may reveal a bruit, clubbing, cyanosis, or telangiectasis in the skin or mucous membranes. Polycythemia may be caused by shunting and chronic arterial hypoxemia.

On the plain chest radiograph, AVMs are most commonly seen in the lower lobes, where they appear as rounded or lobulated densities ranging in size from less than a centimeter to several centimeters. They may simulate a bronchocele or pulmonary nodule. One may see a feeding artery or draining vein, but this finding is usually better seen on fluoroscopy or CT.

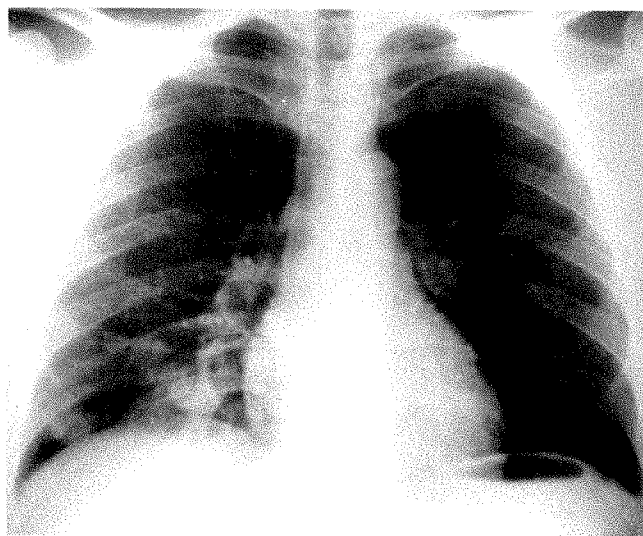
The CT findings of AVMs have been well described [6, 7]. If dynamic scanning is performed, rapid enhancement and washout are usually seen. Enhancement typically occurs after enhancement of the right ventricle and before enhancement of the left atrium and left ventricle. Although the findings are obvious visually, time-density curves may be helpful occasionally in distinguishing an AVM from a vascular neoplasm. A few case reports of highly vascular neoplasms (e.g., metastatic choriocarcinoma) simulating AVMs have been described [8, 9]. As with plain-film radiography, it is important to look for a dilated feeding artery and a dilated draining vein. Associated CT findings (lymphadenopathy, presence of other less-vascular nodules) and clinical history may be helpful in suggesting the diagnosis of neoplasm. Angiography may further clarify confusing cases. Angiography is most important in the pretreatment planning to define the blood supply, extent, number, and location of lesions [1, 4].

The indications for treatment of AVMs are somewhat controversial [5]. It is usually agreed that treatment is indicated

¹ Mallinckrodt Institute of Radiology, Washington University School of Medicine, 510 S. Kingshighway Blvd., St. Louis, MO 63110. Address reprint requests to M. J. Siegel at this address.

² Department of Urologic Surgery, Washington University School of Medicine, St. Louis, MO 63110.

Case 1 was prepared by H. S. Glazer. Case 2 was prepared by F. Dehdashti and B. A. Siegel. Case 3 was prepared by B. L. McClennan and G. L. Andriole. Case 4 was prepared by D. M. Balfe. M. J. Siegel is coordinator of the Case of the Day series.



A

Fig. 1.—Case 1: Pulmonary arteriovenous malformations with hepatic and splenic abscesses.

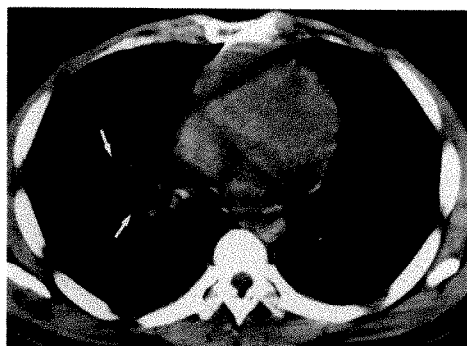
A, Posteroanterior chest radiograph shows multiple nodular masses in right lower lobe of lung.

B, Precontrast CT image through level of heart shows a lobulated mass (arrows) in right lower lobe of lung.

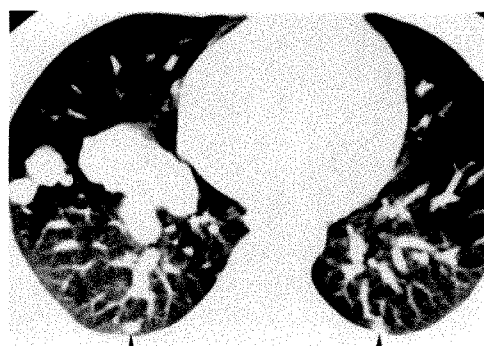
C, Lung window CT image at slightly lower level than B better shows lobulated contour of mass. In addition, two smaller nodules (arrowheads) are seen in right lower lobe and left lower lobe of lung.

D, Postcontrast CT image at a slightly higher level than B shows enhancement of mass. Review of serial images confirmed that nodular masses seen on plain chest radiographs were continuous with each other and drained into a large, right inferior pulmonary vein (V).

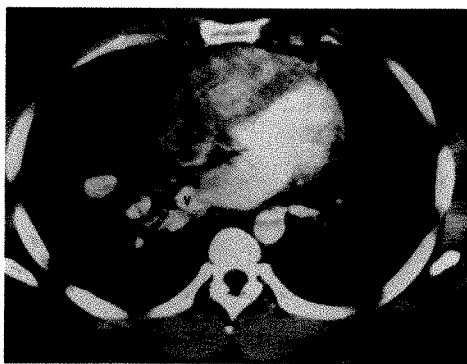
E, Postcontrast image through upper abdomen shows multiple low attenuation lesions in liver and spleen (arrowheads). K = kidney.



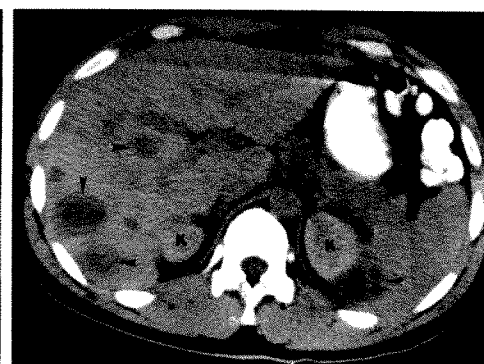
B



C



D



E

in symptomatic patients. Therapeutic options include surgery or embolotherapy (e.g., coil, balloons). The complication rate is generally less with embolotherapy than with surgery, and it is usually the treatment of choice in institutions with significant experience. Asymptomatic patients are still at risk for complications of their AVMs, so it may be reasonable to monitor a small lesion.

Harvey S. Glazer

REFERENCES

1. Cooley RN, Schreiber MH. *Radiology of the heart and great vessels*, 3rd ed. Baltimore, MD: Williams & Wilkins, 1978:416-426
2. Pare JAP, Fraser RG. *Synopsis of diseases of the chest*. Philadelphia, PA: W. B. Saunders, 1983:247-249
3. Spencer H. *Pathology of the lung*, 4th ed. Oxford: Pergamon Press, 1985:990-995
4. Panicek DM, Heitzman ER, Randall PA, et al. The continuum of pulmonary developmental anomalies. *RadioGraphics* 1987;7:747-772

5. Burke CM, Safai C, Nelson DP, Raffin TA. Pulmonary arteriovenous malformations: a critical update. *Am Rev Respir Dis* 1986;134:334-339
6. Rankin S, Faling LJ, Pugatch AD. CT diagnosis of pulmonary arteriovenous malformations. *J Comput Assist Tomogr* 1982;6:746-749
7. Webb WR. CT of solitary pulmonary vascular lesions. *Semin Roentgenol* 1984;19:189-198
8. Haltschlag A, Schulze W, Ungeheuer E, Höer P-W. Pitfall in the CT diagnosis of pulmonary arteriovenous malformation. *J Comput Assist Tomogr* 1983;7:710-712
9. Cirimelli KM, Colletti PM, Beck S. Metastatic choriocarcinoma simulating an arteriovenous malformation on chest radiography and dynamic CT. *J Comput Assist Tomogr* 1988;12:317-319

Case 2: Sternocostoclavicular Hyperostosis

The anterior ^{99m}Tc -methylene diphosphonate (MDP) scintigram of the chest (Fig. 2A) shows moderately increased accumulation of the tracer in the sternal manubrium and in most of the sternal body. Also, ^{99m}Tc -MDP uptake is increased in the anterior aspects of the first and second ribs and the first and second costal cartilages bilaterally, as well as in the lower (fifth, sixth, and seventh) costal cartilages bilaterally. Activity also may be increased in the medial end of the right clavicle, but this is difficult to determine with certainty because of the changes in the first costal cartilage. Posteroanterior and lateral chest radiographs (Figs. 2B and 2C) show sclerosis, cortical thickening, and expansion of the sternum, with apparent fusion at the manubriosternal joint. The first and second costal cartilages bilaterally are ossified and expanded; ossification and widening of lower costal cartilages also can be seen on the lateral radiograph. In addition, the lateral radiograph shows degenerative changes in the lower thoracic spine, with bridging ossification anteriorly, an appearance suggesting diffuse idiopathic skeletal hyperostosis. The scintigrams of the thoracic spine (not shown) showed only minimally increased activity in the lower thoracic spine, indicating that the metabolic activity of the process in the spine is different from that in the sternum and costal cartilages. The changes in the sternum and cartilages were confirmed by CT (Fig. 2D).

The scintigraphic findings (and the confirming radiographic and CT findings) are consistent with sternocostoclavicular hyperostosis. Sternocostoclavicular hyperostosis is a benign disease of unknown cause and pathogenesis. It has been reported most frequently in Japan, affects men more frequently than women, and usually appears in the fourth to sixth decades of life [1-3].

Sternocostoclavicular hyperostosis is characterized by progressive hyperostosis of the clavicles, upper anterior ribs, and sternum, as well as ossification of the costoclavicular ligaments and adjacent soft tissues. Involvement of the lower sternum and costal cartilages, as in this patient, is less typical. In various respects, the disorder simulates the features of psoriatic arthropathy, ankylosing spondylitis, diffuse idiopathic skeletal hyperostosis, and Paget disease. It is frequently associated with pustulosis palmaris et plantaris [1-3], a cutaneous disorder characterized by recurrent bouts of sterile pustules symmetrically involving the palms, soles, or both.

Sternocostoclavicular hyperostosis usually presents with pain, swelling, tenderness, and local heat in the anterior chest; however, it can present with painless swelling or be asymptomatic (as in this patient). Extensive edema has been seen with occlusion of the subclavian vein due to osseous overgrowth [1, 4, 5]. This disease may be associated with elevation of the erythrocyte sedimentation rate, antistreptolysin-O titer, and serum globulins; a positive C-reactive protein; mild leukocytosis; and (occasionally) increased serum alkaline phosphatase [1, 3]. The usually normal level of the latter helps to distinguish sternocostoclavicular hyperostosis from active Paget disease. Serologic tests for HLA-B27 antigen and rheumatoid factor are usually negative [1, 2, 4]. Pathologic examination of the ossified masses reveals marked fibrosis and new bone formation with mild accumulation of granulation tissue and round-cell infiltration [1].

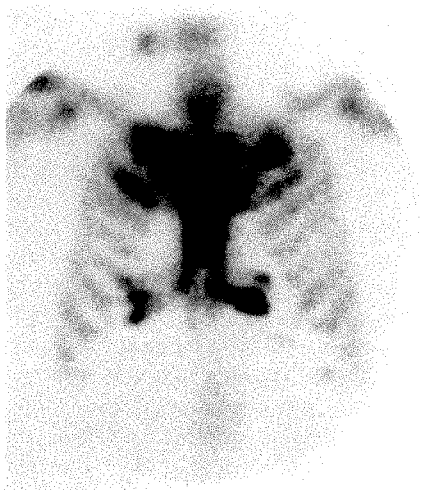
Characteristic radiographic findings include bilateral hyperostosis and bony expansion of the clavicles, anterior upper ribs, and sternum. The sternoclavicular and sternomanubrial junctions may show prominent bone formation and osseous fusion. The costoclavicular ligaments and adjacent soft tissues also are ossified [2]. The radiographic changes of this disease have been graded by Sonozaki et al. [4] according to the degree of bony and soft-tissue abnormalities. In Stage I (localized), ossification is mild and confined to the regions of the costoclavicular ligaments. In Stage II (generalized), ossification spreads beyond the costoclavicular ligaments and surrounding tissues with poor definition of the inferior margin of the clavicles and the superior margin of the first rib. The interspace between the clavicle and first rib is filled with an ossified mass. This is the most common stage of this disorder. Stage III (hyperostotic) is characterized by hyperostosis of the inferior and superior margins of the clavicles and first ribs. The osseous nature of the mass can be confirmed by CT. Bone scintigraphy, as in this patient, shows accumulation of radiopharmaceutical in the areas of bony overgrowth. Scintigraphic changes often can be recognized more easily, especially in the mild form of the disease, where the radiographs may be negative or only subtly abnormal [1-3, 6-8].

Additional radiographic findings may be seen in the vertebral column, and include new bone formation along the anterior aspects of vertebral bodies and intervertebral disks, resembling the changes of diffuse idiopathic skeletal hyperostosis, ankylosing spondylitis, or psoriatic spondylitis [1]. Exuberant anterior bone formation also may be seen in the cervical spine. In the sacroiliac joints, associated changes may consist of either osseous bridging and ligamentous calcification or articular surface erosions, sclerosis, and fusion, simulating ankylosing spondylitis.

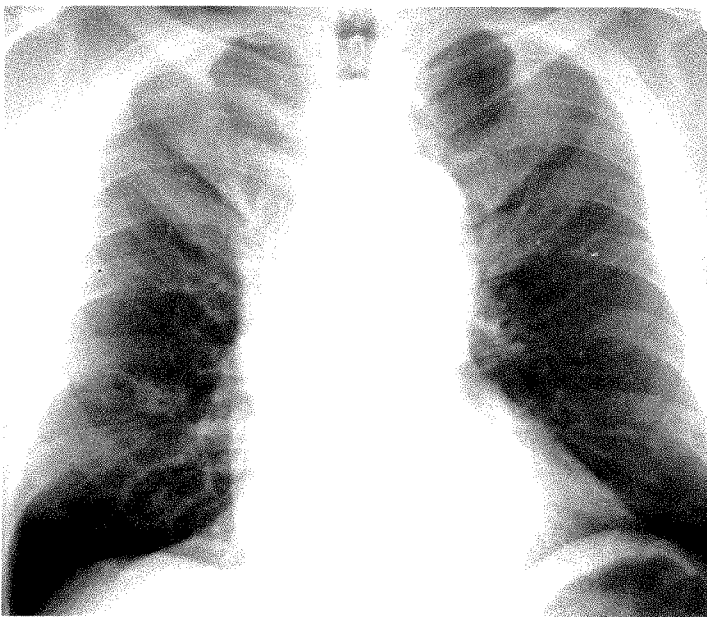
Farrokh Dehdashti
Barry A. Siegel

REFERENCES

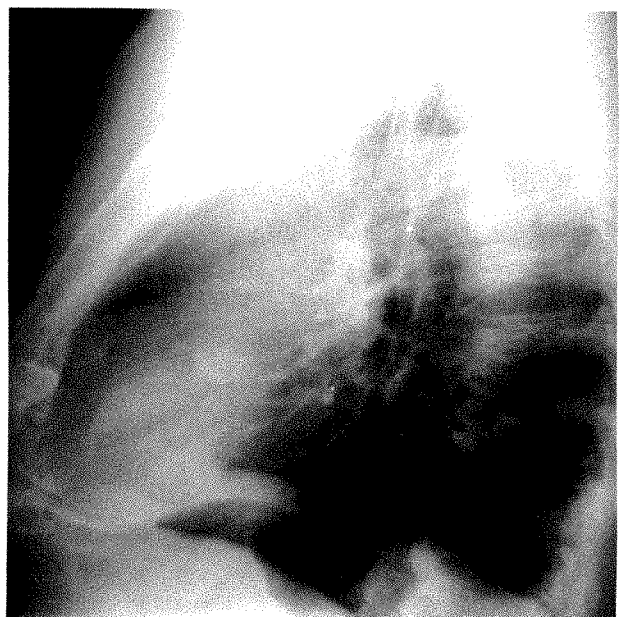
1. Resnick D, Niwayama G. *Diagnosis of bone and joint disorders*, 2nd ed. Philadelphia: Saunders, 1988:4127-4131
2. Resnick D. Sternocostoclavicular hyperostosis. *AJR* 1980;135:1278-1280
3. Sartoris DJ, Schreiman JS, Kerr R, Resnik CS, Resnick D. Sternocosto-



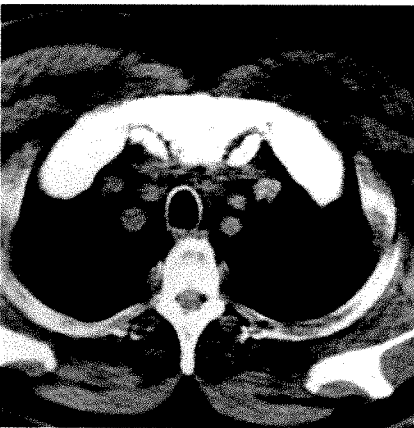
A



B



C



D

Fig. 2.—Case 2: Sternocostoclavicular hyperostosis.

A, Anterior ^{99m}Tc -MDP scintigram shows increased tracer uptake in sternum, several ribs and costal cartilages symmetrically, and possibly medial end of right clavicle.

B and C, Posteroanterior and lateral chest radiographs show a right lung nodule (which prompted the patient's diagnostic evaluation, but was found to be granulomatous inflammation). Note expansion and hyperostosis of sternum, ossification of first and second costal cartilages and lower costal cartilages, and anterior ossification in lower thoracic spine.

D, CT at level of first costal cartilages confirms hyperostosis of sternum and ossification of these costal cartilages.

clavicular hyperostosis: a review and report of 11 cases. *Radiology* **1986**;158:125–128

4. Sonozaki H, Azuma A, Okai K, et al. Clinical features of 22 cases with "intersterno-costo-clavicular ossification." A new rheumatic syndrome. *Arch Orthop Trauma Surg* **1979**;95:13–22

5. Köhler H, Uehlinger E, Kutzner J, West TB. Sternocostoclavicular hyperostosis: painful swelling of the sternum, clavicles, and upper ribs. Report of two new cases. *Ann Intern Med* **1977**;87:192–194

6. Rosenthal L, Burke DL. A radionuclide and radiographic diagnosis of sternocostoclavicular hyperostosis. *Clin Nucl Med* **1986**;11:322–324

7. Ueno K, Rikimaru S, Kawashima Y, Sakai H. Bone imaging of sternocostoclavicular hyperostosis in palmoplantar pustulosis. *Clin Nucl Med* 1986;11:420-425
8. Otsuka N, Fukunaga M, Sone T, et al. Usefulness of bone imaging in diagnosis of sternocostoclavicular hyperostosis. *Clin Nucl Med* 1988;11:651-652

Case 3. Multilocular Cystic Nephroma (MLCN)

A 67-year-old woman presented with a history of microscopic hematuria. She was otherwise in good health. An IV urogram showed an intrarenal mass (arrowheads) separating the collecting system in the left kidney, compressing and displacing the midpole calyces inferiorly, and compressing or indenting the renal pelvis (arrows) (Fig. 3A). A sonographic examination revealed a complex, cystic mass corresponding to the mass effect seen on the urogram. Through-transmission was present but numerous internal echoes or septa were also noted (arrowheads) (Fig. 3B). A CT scan during the drip infusion of IV contrast material was performed. Scan sections at the level of the left renal vein showed a nonenhancing mass within the left kidney. A single septum is noted on this scan slice (small arrow) (Fig. 3C). An enhancing, thickened wall of the mass is present medially (arrowheads). A left nephrectomy was performed and the pathologic diagnosis of multilocular cystic nephroma was made.

Multilocular cystic nephroma (MLCN) is a rare, nonfamilial (noninherited) benign renal neoplasm that is usually well circumscribed or encapsulated, varies in size, but may show interval growth, albeit slow [1-6]. This typically cystic neoplasm consists of well-demarcated, often multiple noncommunicating fluid-filled cysts separated by septa composed of fibrous stroma. These cysts are lined with epithelium and portions of the cystic neoplasm may protrude into the collecting system, specifically the renal pelvis, or cause obstruction

of the pelvis or ureter. The presentation is usually nonspecific, but in an adult, hematuria is often present. In children, an abdominal mass often is noted. The cause is unknown, and usually there are no associated findings or renal anomalies. The hematuria is thought to be due to compression of the collecting system or herniation into the renal pelvis and, on occasion, urinary-tract infection may be present, often along with urinary-tract obstruction. There is a marked female preponderance in adults but a slight male preponderance in children. Multilocular cystic nephroma is seen throughout childhood and adulthood, but rarely seen before the age of 3 months. The treatment is almost always surgical with an emphasis on conservative surgery that spares the kidney whenever possible. Cyst aspiration and/or biopsy usually is not helpful because the cysts do not communicate. The fluid is often clear and cytologically negative. Frequently, the preoperative diagnosis is not definitively made, but an increasing awareness of this benign cystic neoplasm has enabled conservative surgery in selected cases. The IV urographic features include unilateral or bilateral renal masses, usually avascular. Often the septa, thickened walls or rims, can be seen on the tomogram phase of the urogram because of total-body contrast enhancement. Calcifications may be present within the septa or the walls themselves, and herniation into the collecting system can be noted along with obstruction, depending on the size of the mass. Sonographic features include typical renal cystic features, but occasional increased internal echoes are present. The echogenic rims or septa can be noted when imaged, but often the mass has both solid and cystic components.

CT (and MR imaging) mirrors the macroscopic pathologic findings of this lesion [1, 2]. Contrast enhancement occurs only within the septa, or walls, of the lesion. The attenuation of the fluid within the cystic components is often higher than water. Calcifications can be noted and central calcification is

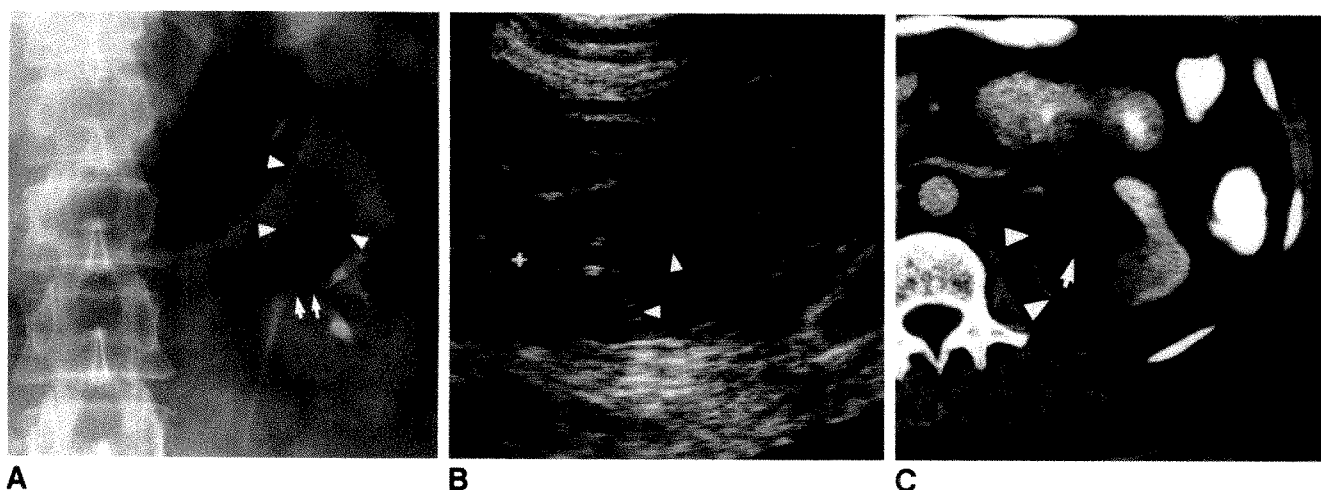


Fig. 3.—Case 3: Multilocular cystic nephroma.

A, IV urogram shows left upper pole mass (arrowheads) displacing upper and midpole calyceal groups. Compression of renal pelvis by mass (herniation?) also is noted (arrows).

B, Sonogram reveals multiloculated, septated (arrowheads) mass corresponding to mass seen on urogram (A). Some through-transmission is noted behind mass, along with fine internal echoes within largely cystic locules.

C, CT scan during contrast drip infusion reveals thick-walled (arrowheads) mass in left kidney. A single septum (arrow) is noted. Central attenuation was slightly higher than water but did not enhance.

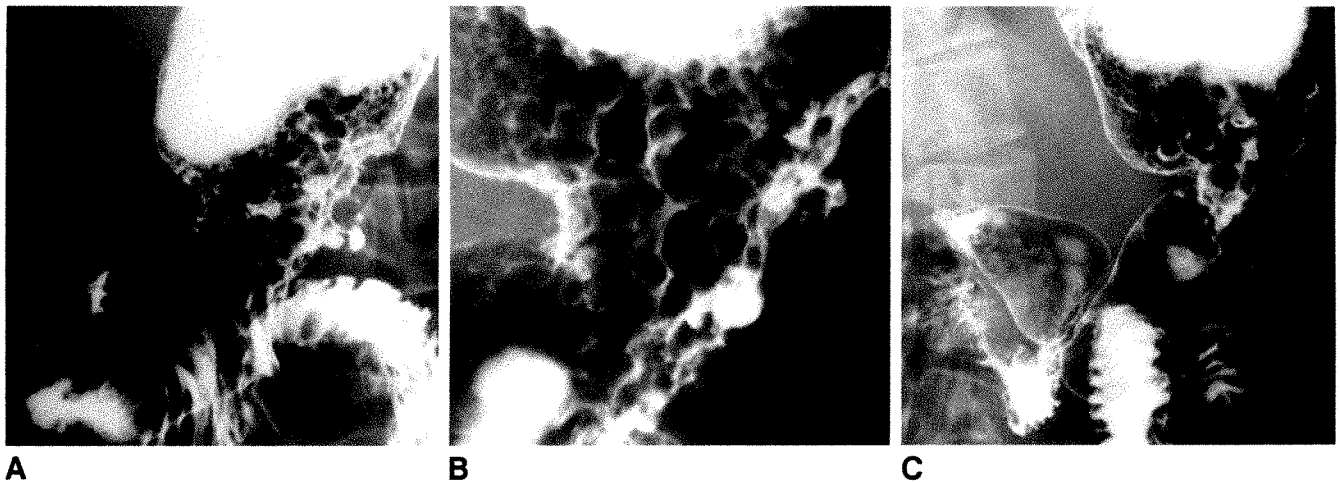


Fig. 4.—Case 4: Eosinophilic gastritis.

A, Right posterior oblique view from upper gastrointestinal examination. Note narrowing of body of stomach; mucosa is markedly nodular in narrowed segment; nodularity extends into gastric fundus.

B, Coned view of abnormal region shows multiple polypoid nodules of various sizes carpeting mucosal surface in narrowed segment.

C, Left posterior oblique view from same examination shows an abrupt transition from abnormal to normal mucosa in central region. Duodenum and proximal small bowel are also normal.

more common; peripheral calcification is less common, but both may occur. The differential diagnosis includes a form of segmental cystic disease, cystic Wilms tumor in children and young adults, and cystic nephroblastoma in children. The most commonly confused entity is a multiloculated or cystic renal cell carcinoma, although renal abscesses, infarctions, or other cystic neoplasms may be considered in the differential diagnosis. Virtually all of the features of multilocular cystic nephroma in adults can be mimicked by cystic renal-cell carcinoma. The combination of findings as noted previously with calcifications within the septa, or walls, of the lesion in an asymptomatic woman should suggest the diagnosis.

Bruce L. McClennan
Gerald L. Andriole

REFERENCES

1. Dikengil A, Benson M, Sanders L, Newhouse JH. MRI of multilocular cystic nephroma. *Urol Radiol* 1988;10:95-99
2. Hartman DS, Davis CJ, Sanders RC, Johns TT, Smirniotopoulos J, Goldman SM. The multiloculated renal mass: considerations and differential features. *RadioGraphics* 1987;7:29-52
3. Alanen A, Nurmi M, Ekfors T. Multilocular renal lesions—a diagnostic challenge. *Clin Radiol* 1987;38:475-477
4. Bosniak MA. The current radiological approach to renal cysts. *Radiology* 1986;158:1-10
5. Madewell JE, Goldman SM, Davis CJ, Hartman DS, Feigin DS, Lichtenstein JE. Multilocular cystic nephroma: a radiographic-pathologic correlation of 58 patients. *Radiology* 1983;146:309-321
6. Banner MP, Pollack HM, Chatten J, Witzleben C. Multilocular renal cysts: radiologic-pathologic correlation. *AJR* 1981;136:239-247

Case 4: Eosinophilic Gastritis

A 38-year-old woman was evaluated for epigastric pain of 3 months duration. At the onset of symptoms, her physician instituted antacid therapy, with transient success. She had

been completely healthy otherwise, except for mild seasonal bronchospasm.

Barium examination of the upper gastrointestinal tract showed circumferential narrowing of the gastric body with coarse irregular nodularity of the mucosal folds in the narrowed region (Figs. 4A and 4B). The nodular folds extended into the gastric fundus, but the antrum and duodenum were normal (Fig. 4C). Endoscopy showed coarse nodularity and friability of the stomach; superficial biopsies revealed edema and infiltration of the lamina propria with eosinophils. A peripheral eosinophilia (7%) was present. The patient responded to a course of steroids and is presently asymptomatic.

Eosinophilic gastroenteritis is a disease of unknown cause and pathogenesis. Criteria for the diagnosis include the presence of peripheral eosinophilia, gastrointestinal dysfunction, and infiltration of some portion of the gastrointestinal tract by eosinophils [1, 2]. The clinical presentation and radiographic appearance [3] are quite variable, depending on the site and extent of alimentary tract involvement; the process may be limited to the mucosa, or (as in this case) involve both the mucosa and the intestinal wall. In most reported cases, the disease affects the gastric antrum and proximal small intestine, but cases of isolated esophageal, ileal, or colonic involvement have been reported.

A specific food allergy is rarely documented, but a short course of oral steroids usually ameliorates the symptoms.

Dennis M. Baife

REFERENCES

1. Cello JP. Eosinophilic gastroenteritis—a complex disease entity. *Ann J Med* 1979;67:1097-1104
2. Johnstone JM, Morson BC. Eosinophilic gastroenteritis. *Histopathology* 1978;2:335-348
3. Goldberg HI, O'Kieffe D, Jenis EH, et al. Diffuse eosinophilic gastroenteritis. *AJR* 1973;119:342

Sonography Case of the Day

Mary A. Middleton,¹ William D. Middleton,² and Kimberly Wiele¹

Case 1: Postbiopsy Renal Transplant Arteriovenous Fistula

This patient experienced decreased renal function 8 days after renal transplantation. A percutaneous renal biopsy showed findings consistent with rejection, and appropriate therapy was initiated. After the biopsy, the patient developed hematuria and decreased urine output. Longitudinal and transverse sonograms of the transplant (Figs. 1A and 1B)

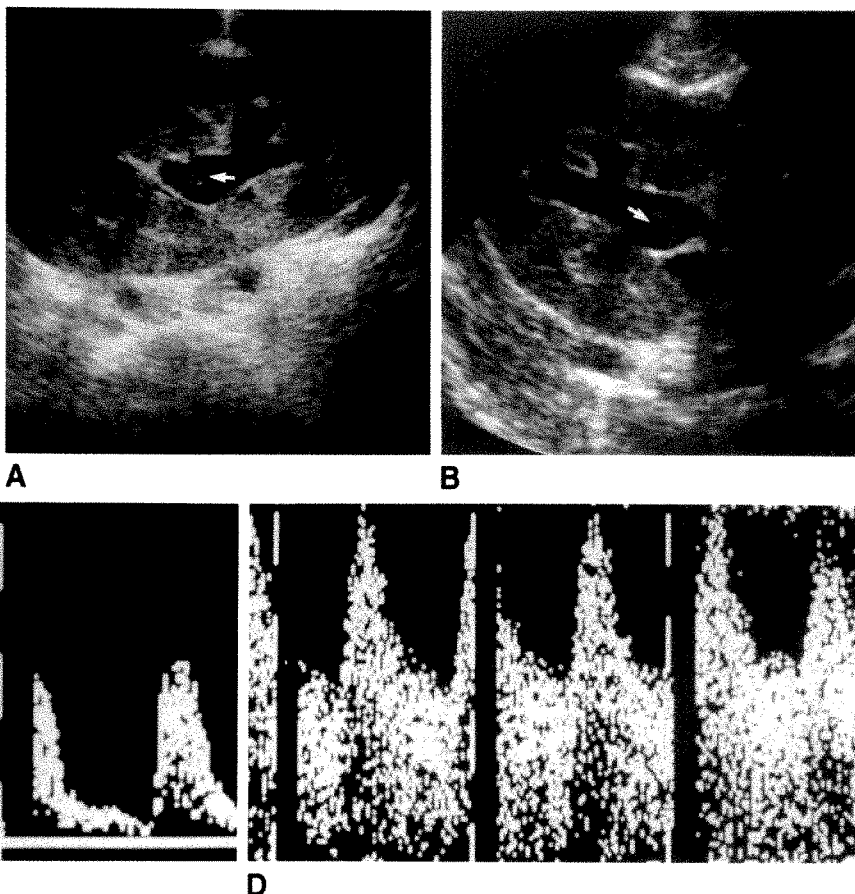
showed hydronephrosis and an echogenic mass in the renal collecting system. In general, pulsed Doppler waveforms from the transplant showed little diastolic flow (Fig. 1C), consistent with the diagnosis of rejection. However, Doppler interrogation in the upper pole showed an area with markedly elevated flow rates and high levels of diastolic flow (Fig. 1D). These findings were all consistent with a postbiopsy renal transplant arteriovenous fistula that had bled and caused hydronephrosis due to obstructing thrombus. Because of the persis-

Fig. 1.—Case 1: Postbiopsy renal transplant arteriovenous fistula.

A and B, Longitudinal and transverse sonograms of transplanted kidney show dilatation of collecting system. Note echogenic area representing clot in collecting system (arrow).

C, Pulsed Doppler waveform from lower pole shows significant reduction in diastolic flow, reflecting rejection.

D, Doppler waveform from upper pole of transplanted kidney reveals very high levels of diastolic flow caused by an arteriovenous fistula.



¹ Deaconess Hospital, St. Louis, 6150 Oakland St., St. Louis, MO 63139.

² Mallinckrodt Institute of Radiology, Washington University School of Medicine, 510 S. Kingshighway Blvd., St. Louis, MO 63110. Address reprint requests to M. J. Siegel at this address.

Cases 1, 3, and 4 were prepared by W. D. Middleton. Case 2 was prepared by M. A. Middleton, W. D. Middleton, and K. Wiele. M. J. Siegel is coordinator of the Case of the Day series.

tent hematuria and intermittent obstruction, angiography was performed to embolize the arteriovenous fistula. This was done successfully, and the patient has been well since then.

Arteriovenous fistulas are an uncommon, but well-described, complication of percutaneous renal biopsies [1, 2]. Angiographic data suggest a frequency of approximately 15% in native kidneys [3, 4]. Animal studies have been performed and have shown a frequency as high as 44% in a rabbit model [5]. In most cases, renal arteriovenous fistulas are clinically occult and resolve spontaneously [3, 4, 6, 7]. However, they can result in hypertension, high-output heart failure, or hematuria, as in our case [1, 2].

Conventional gray-scale sonographic imaging can show morphological abnormalities in chronic arteriovenous fistulas consisting of enlargement and tortuosity of the vessels leading to and from the fistula [8, 9]. However, with acute arteriovenous fistulas, as in this case, duplex Doppler and color Doppler ultrasound are necessary to show the hemodynamic changes that result from the arteriovenous communication. Because resistance to flow in the supplying artery is markedly reduced, flow rates are higher throughout the cardiac cycle and flow velocity increases in diastole compared with systole [10]. These changes were apparent in this patient. The diagnosis can be confirmed by documenting arterialization of the waveform from the draining vein. This is theoretically possible with conventional duplex Doppler sonography. However, color Doppler ultrasound aids tremendously in identifying the draining vein and thus allows for accurate placement of the range-gated Doppler cursor to detect the abnormal venous waveform. Color Doppler sonography aids also in the initial identification of transplant arteriovenous fistulas. The elevated flow velocities in the supplying artery and draining vein make them appear whiter than the normal vessels. In addition, the high flow rates often result in flow turbulence, vessel wall vibration, and ultimately perivascular tissue vibration, which can be seen as random red and blue color assignment to the perivascular soft tissues [11].

The only differential diagnostic consideration in this case is a high-grade intrarenal arterial stenosis. This could account for all of the changes noted in the artery. However, arterial stenosis would not result in arterialization of the venous waveform and, therefore, careful interrogation of the draining vein should allow differentiation of these two entities. In addition, a prior renal transplant biopsy in the region of the sonographic abnormality makes arteriovenous fistula much more likely.

William D. Middleton

REFERENCES

1. Wickre CG, Golper TA. Complications of percutaneous needle biopsy of the kidney. *Am J Nephrol* 1982;2:173-178
2. Altebarmakian VK, Guthinger WP, Yakub YN, Gutierrez OH, Linke CA. Percutaneous kidney biopsies. Complications and their management. *Urology* 1981;18:118-122
3. Bennett AR, Wiener SN. Intrarenal arteriovenous fistula and aneurysm: a complication of percutaneous renal biopsy. *AJR* 1965;95:372-382
4. Ekelund L, Lindholm T. Arteriovenous fistula following percutaneous renal biopsy. *Acta Radiol [Diagn]* 1971;11:38-48
5. Ekelund L. Arteriovenous fistula secondary to renal biopsy. An experimental study in the rabbit. *Acta Radiol [Diagn]* 1970;10:218-224
6. Herschman A, Klein MJ, Blumberg AG. Spontaneous disappearance of iatrogenic renal arteriovenous fistula: report of a case. *J Urol* 1971;105:4-6
7. DeBeukelaer MM, Schreiber MH, Dodge WF, Travis LB. Intrarenal arteriovenous fistulas following needle biopsy of the kidney. *J Pediatr* 1971;78:266-272
8. Subramanyam BR, Lefleur RS, Bosniak MA. Renal arteriovenous fistulas and aneurysms: sonographic findings. *Radiology* 1983;149:261-263
9. Thomas JL, Lymberio MEB, Hunt TH. Ultrasonic features of acquired renal arteriovenous fistula. *AJR* 1977;132:653-655
10. Taylor KJ, Morse SS, Rigsby CM, Bia M, Schiff M. Vascular complications in renal allografts: detection with duplex Doppler US. *Radiology* 1987;162:31-38
11. Middleton WD, Kellman GM, Melson GL, Madrazo B. Color Doppler ultrasound characteristics of renal transplant arteriovenous fistulas. *Radiology* (in press)

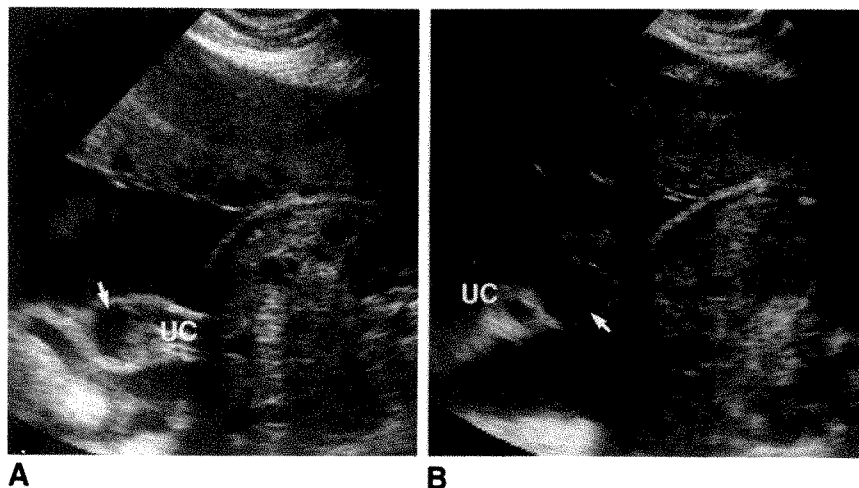
Case 2: Allantoic Cyst of the Umbilical Cord

A 27-year-old asymptomatic patient in her second trimester was referred for sonographic estimation of fetal age. The examination showed a normal 25-week male fetus. A 3 × 2 cm cystic mass in the umbilical cord was identified. The umbilical cord insertion into the fetal abdomen was normal, and the cystic mass was located several centimeters away from the insertion (Fig. 2). Reexamination 5 weeks later showed normal interval fetal growth and no change in the umbilical cord cyst. At delivery, the infant was normal, and the cystic mass was confirmed to be an allantoic cyst.

At term, the normal umbilical cord contains two arteries, one vein, and mesenchymal tissue called Wharton jelly. However, during early embryologic development, the cord also contains the allantois and yolk sac [1]. Remnants of these structures may persist in the cord beyond the first trimester and form allantoic or omphalomesenteric duct cysts. Allantoic cysts may be associated with urinary-tract obstruction, omphalocele, and/or a patent urachus [2-4]. Omphalomesenteric duct cysts may be associated with midgut anomalies such as Meckel diverticulum [4, 5]. Therefore, detection of an umbilical cord cyst should be followed by a particularly careful survey of the fetal gastrointestinal and genitourinary systems. In addition, because any mass of the umbilical cord may cause vascular compression and fetal compromise, fetal growth and biophysical parameters should be monitored.

In addition to allantoic cysts and omphalomesenteric duct cysts, the differential diagnosis in this case includes cystic degeneration of Wharton jelly, knots of the umbilical cord, and true hematomas [4, 6, 7]. Cystic degeneration of Wharton jelly and cystic hematomas may not be distinguishable sonographically. Knots of the umbilical cord can generally be distinguished by careful real-time examination and pulsed Doppler interrogation, if necessary. Tumors of the cord such as teratomas or hemangiomas are rare and should not be confused with umbilical cord cysts because of their hyper-echoic or complex sonographic appearance. Any cord mass located immediately adjacent to the insertion of the fetal

Fig. 2.—Case 2: Allantoic cyst of umbilical cord.
A and B. Transverse (A) and oblique (B) sonograms of fetal abdomen show cystic mass (arrow) in umbilical cord (UC).



abdomen may simulate an omphalocele or gastroschisis. Careful evaluation of the anterior abdominal wall should allow differentiation of these entities.

Mary A. Middleton
William D. Middleton
Kimberly Wiele

REFERENCES

1. The placenta and fetal membranes. In: Moore KL, ed. *The developing human: clinically oriented embryology*. Philadelphia, PA: Saunders, 1988:104–130
2. Sachs L, Fourcroy JL, Wenzel DJ, Austin M, Nash JD. Prenatal detection of umbilical cord allantoic cyst. *Radiology* 1982;145:445–446
3. Fink LJ, Filly RA. Omphalocele associated with umbilical cord allantoic cyst: sonographic evaluation in utero. *Radiology* 1983;149:473–476
4. The umbilical cord. In: Romero R, Pilu G, Jeanty P, Ghidini A, Hobbins JC, eds. *Prenatal diagnosis of congenital anomalies*. Norwalk, CT: Appleton & Lange, 1988:385–402
5. Rosenberg JC, Chevenek FA, Walker BA, Chitkara U, Berkowitz RL. Antenatal sonographic appearance of omphalomesenteric duct cyst. *J Ultrasound Med* 1986;5:719–720
6. Iaccarino M, Balfi F, Perisico O, Palagiano A. Ultrasonographic and pathologic study of mucoid degeneration of umbilical cord. *JCU* 1986;14:127–129
7. Bergman P, Lundin P, Malmström T. Mucoid degeneration of Wharton's jelly. *Acta Obstet Gynecol Scand* 1961;40:372–378

Case 3: Pseudosubcapsular Splenic Hematoma due to Elongation of Left Hepatic Lobe

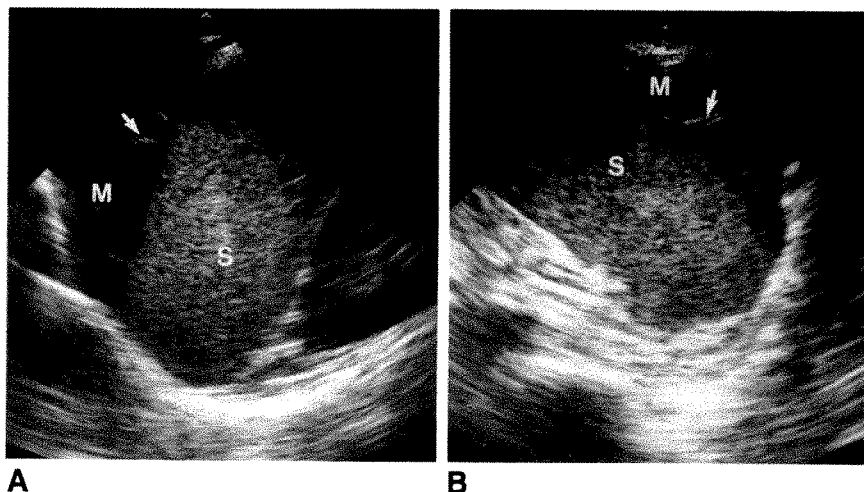
A young man complained of chronic pain in the left upper quadrant. Sonograms of the spleen show a crescent-shaped mass superior to the spleen with low-level internal echoes. The location, shape, and echogenicity of the mass closely simulate a subcapsular or perisplenic hematoma. However, within the mass is a tubular structure seen in cross section on the longitudinal view (Fig. 3A) and along its long axis on the transverse view (Fig. 3B). This finding suggests a vessel coursing within the parenchyma of an organ and is, in fact, characteristic of a portal vein located within an elongated left hepatic lobe.

An elongated left hepatic lobe that extends across the midline and contacts the superior aspect of the spleen is a normal variant that can be a pitfall in left-upper-quadrant sonograms. Although traditional teaching states that the liver

Fig. 3.—Case 3: Pseudosubcapsular splenic hematoma due to elongation of left hepatic lobe.

A. Longitudinal view of left upper quadrant shows crescentic mass (M) with low-level echoes cephalad to spleen (S). Several tubular structures with echogenic walls (arrows) are noted within mass and represent portal veins. Mass, therefore, represents hepatic parenchyma.

B. On a transverse view, relatively hypoechoic mass lies anteriorly and laterally to spleen and represents elongated left lobe of liver.



is equal or greater in echogenicity than the spleen [1, 2], recent reports have shown that the liver is actually significantly lower in echogenicity than the spleen [3]. In fact, three separate studies have shown that when the liver and spleen are seen on the same sonogram, the liver appears so hypoechoic that it may simulate a fluid collection [3–5]. This low echogenicity, combined with the crescentic shape and location superior to the spleen, can closely simulate a subcapsular or perisplenic hematoma. By showing continuity between the elongated left lobe and the remainder of the liver, one can confirm the true reason for this appearance, but this may be difficult to do. Identification of a portal triad, as in this case, can also confirm that the mass is actually hepatic parenchyma and not a fluid collection around the spleen. On real-time examination, the elongated left hepatic lobe can be seen to slide over the spleen with respiratory motion. Finally, the acoustic properties of the left lobe are those of solid tissue, rather than fluid. There is no increase in through-transmission and there are no refractive effects between the left lobe and the spleen, as would be expected for fluid.

General knowledge of this potential sonographic pitfall is adequate to avoid diagnostic error resulting from an elongated left hepatic lobe. If the cause of the sonographic findings remains in doubt, CT can be performed to exclude the possibility of a fluid collection in the left upper quadrant. In actual practice, this should be necessary only in rare instances.

William D. Middleton

REFERENCES

1. Rosenfield AT, Taylor KJW, Jaffe CC. Clinical applications of ultrasound tissue characterization. *Radiol Clin North Am* 1980;18:31
2. Mittelstaedt CA, Partain CL. Ultrasonic-pathologic classification of pelvic abnormalities: grey scale patterns. *Radiology* 1980;134:697–705
3. Li DKB, Cooperberg PL, Graham MF, Callen P. Pseudo perisplenic "fluid collection": a clue to normal liver and spleen echogenic texture. *J Ultrasound Med* 1986;5:397–400
4. Arenson AM, McKee JD. Left upper quadrant pseudolesion secondary to normal variants in liver and spleen. *JCU* 1986;14:558–561
5. Crivello MS, Peterson IM, Austin RM. Left lobe of the liver mimicking perisplenic collections. *JCU* 1986;14:697–701

Case 4: Focal Hepatic Fatty Infiltration Adjacent to Falciform Ligament

This middle-aged woman with pain in the right upper quadrant was referred for gallbladder sonography. Incidentally noted was a focal, homogeneous, hyperechoic region in the peripheral portion of the left lobe of the liver (Fig. 4A). It was situated in the medial segment adjacent to the falciform ligament. It was oval with the long axis oriented vertically (Fig. 4B). Its echo texture, shape, and position were all characteristic of nodular focal fatty infiltration. A follow-up scan done 8 months after the initial study showed resolution of the abnormality.

Fatty infiltration of the liver can be caused by alcohol abuse, diabetes mellitus, chemotherapy, hyperalimentation, obesity, pregnancy, malnutrition, and steroid therapy. Generally, it involves the liver diffusely, but it may be focal [1]. Sonographically, focal fatty infiltration appears as geographically shaped areas of increased hepatic echogenicity. Because it infiltrates otherwise normal liver parenchyma, it does not behave as a space-occupying lesion. Therefore, it does not displace or distort portal triads or hepatic veins [2]. With real-time scanning, it is often possible to show undisturbed hepatic vessels coursing within the focal area of fatty infiltration.

Occasionally, focal fatty infiltration of the liver can appear nodular [3, 4]. In this situation, the differential diagnosis between cavernous hemangioma, metastatic disease, or benign or malignant primary liver tumors can be difficult. In general, other imaging techniques are necessary to establish the diagnosis of focal fatty infiltration when it is nodular. Sulfur colloid radionuclide scans can assist in the diagnosis, if the lesion is large enough, by showing normal distribution of sulfur colloid within the reticuloendothelial system of the liver [3]. MR imaging can also assist in the differential diagnosis, particularly when the lesions are small [5].

Recently, Yoshikawa et al. [6] described a characteristic location of focal fatty infiltration in the medial segment of the left hepatic lobe adjacent to the falciform ligament. They postulate that local tissue hypoxia causes the focal change adjacent to the falciform ligament, although the exact reason for this is unclear. Because it is located superficially in the

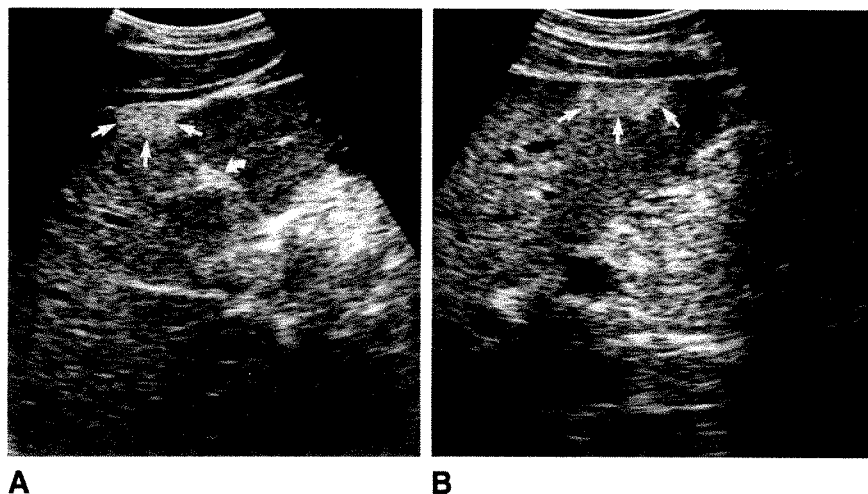


Fig. 4.—Case 4: Focal hepatic fatty infiltration adjacent to falciform ligament.

A, Transverse sonogram at level of ligamentum teres (curved arrow) shows a focal area of increased echogenicity in left lobe of liver, representing fatty infiltration (straight arrows).

B, On longitudinal sonogram of liver, just to right of ligamentum teres, area of fatty infiltration is oval and has sharp margins (arrows), separating it from normal, less echogenic hepatic parenchyma.

liver, it is often overlooked sonographically because of near-field reverberation artifacts. Therefore, focal fatty infiltration adjacent to the falciform ligament is more commonly seen on CT scans of the abdomen.

In patients, such as this one, in whom there is no history of a primary malignancy, the presumptive diagnosis of focal fatty infiltration can be made on the basis of the hyperechoic appearance, oval shape, and typical location of the lesion. Other imaging techniques may be considered in order to confirm the diagnosis if clinically indicated. Invasive procedures such as percutaneous needle biopsy or angiography should not be necessary in most cases.

William D. Middleton

REFERENCES

1. Quinn SF, Gosink BB. Characteristic sonographic signs of hepatic fatty infiltration. *AJR* **1985**;145:753-755
2. Baker MK, Wenker JC, Cockerill EM, Ellis JH. Focal fatty infiltration of the liver: diagnostic imaging. *RadioGraphics* **1985**;5:923-939
3. Yates CK, Streight RA. Focal fatty infiltration of the liver simulating metastatic disease. *Radiology* **1986**;159:83-84
4. Baker ME, Silverman PM. Nodular focal fatty infiltration of the liver: CT appearance. *AJR* **1985**;145:79-80
5. Heiken JP, Lee JKT, Dixon WT. Fatty infiltration of the liver: evaluation by proton spectroscopic imaging. *Radiology* **1985**;157:707-710
6. Yoshikawa J, Matsui O, Takashima T, et al. Focal fatty change of the liver adjacent to the falciform ligament: CT and sonographic findings in five surgically confirmed cases. *AJR* **1987**;149:491-494

Pediatric Radiology Case of the Day

William H. McAlister¹ and Marilyn J. Siegel

Case 1: Duodenal Duplication

The barium study shows extrinsic mass effect on the duodenum and greater curvature of the stomach (Figs. 1A and 1B). On the sonogram (Fig. 1C), the mass looks similar to the adjacent stomach, with a hypoechoic muscle layer, echogenic mucosa, and a fluid-filled interior. The radiographic findings are most consistent with an intestinal duplication. Choledochal cyst was thought to be less likely because of the lack of bile-duct dilatation and posterior displacement of the duodenum. At surgery, the duplication was attached to the immediate postbulbar duodenum. A small communication was present between the duplication and the native duodenum. On gross section, the duplication cyst contained clear fluid and a small ulcer in the base.

Duplications of the gastrointestinal tract can occur anywhere in the abdomen, although they are most common in the ileocecal area [1–3]. The second most common site of

origin is near the duodenum, adjacent to the first and second parts, or proximal jejunum. The cause of intestinal duplications is unknown. Some proposed causes are abnormalities of recanalization, intrauterine vascular accidents, and persistence of embryonic diverticula. Intestinal duplications occur with equal frequency in boys and girls and vary from 2 to 12 cm in size [4]. Patients usually present with symptoms of bowel obstruction, pain, mass, or bleeding, and most cases are diagnosed in the first 2 years of life. The mechanism of bowel obstruction is compression of the normal adjacent bowel, intussusception, or volvulus. Bleeding can occur if there is a communication with the adjacent bowel lumen and if gastric mucosa is present in the duplication [1, 2]. Occasionally, duplications are found on intrauterine sonograms.

Plain radiographs may show a mass that occasionally is calcified or causes bowel obstruction. Duplications that communicate with the bowel can contain air and fluid. Abnormalities of the spine and gastrointestinal and genitourinary mal-

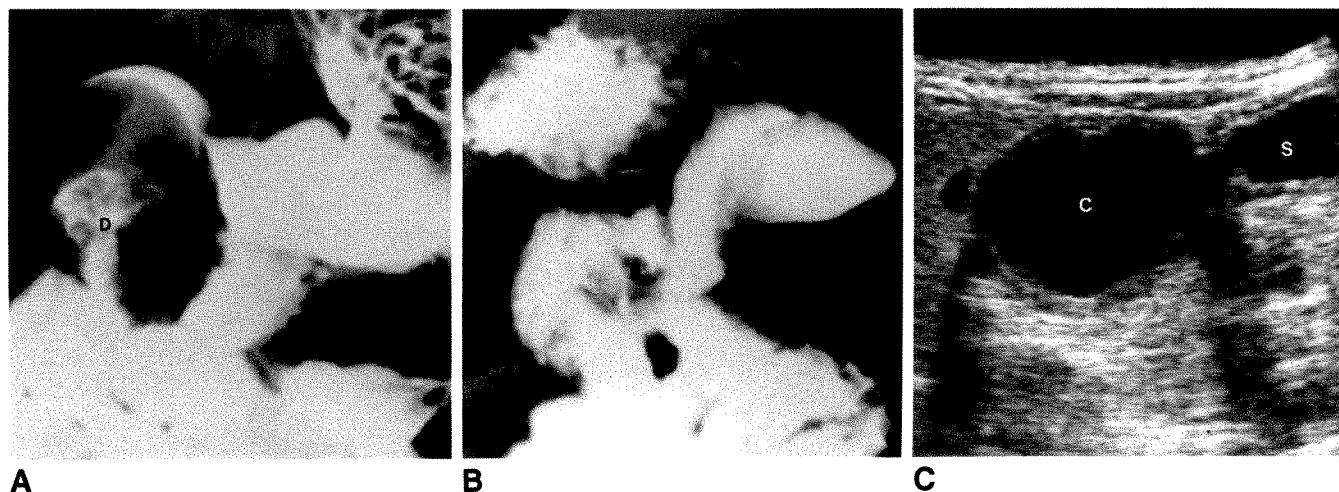


Fig. 1.—Case 1: Duodenal duplication.

A and B, Anteroposterior and lateral radiographs from an upper gastrointestinal series show extrinsic compression of duodenum (D) and greater curvature of stomach.

C, Transverse sonogram through upper abdomen shows a cystic mass, the duplication cyst (C). Cyst is lined by a layer of echogenic mucosa and surrounded by hypoechoic muscle. S = stomach.

¹ Both authors: Mallinckrodt Institute of Radiology, Washington University School of Medicine, 510 S. Kingshighway Blvd., St. Louis, MO 63110. Address reprint requests to M. J. Siegel.

M. J. Siegel is coordinator of the Case of the Day series.

formations are less frequent with abdominal duplications than with thoracic duplications. Rarely, a transdiaphragmatic type of duplication, originating in the duodenum or from the area of the ligament of Treitz, extends into the chest.

On sonograms, the internal contents of the duplication can be sonolucent or echogenic because of increased amounts of mucus and/or blood [5, 6]. Increased through-transmission is common. Occasionally, the mucosal surface or muscle layer of the duplication is seen. This feature is characteristic of a duplication and can help separate duplications from mesenteric, omental, ovarian, or choledochal cysts. However, a fluid-filled Meckel diverticulum may be more difficult to differentiate preoperatively. The findings of intestinal duplications on barium studies are bowel displacement and occasionally opacification of the cyst lumen. Ulcers rarely have been noted in the bowel adjacent to the duplication. A ^{99m}Tc -pertechnetate scan may show increased activity, because between 10% and 35% of duplications contain gastric mucosa [3]. Duplications are treated by surgical resection. The adjacent bowel is often resected because it has a common blood supply with the duplication.

William H. McAlister
Marilyn J. Siegel

REFERENCES

1. Hocking M, Young DG. Duplications of the alimentary tract. *Br J Surg* 1981;68:92-96
2. Bower RJ, Sieber WKN, Kiesewetter WB. Alimentary tract duplications in children. *Ann Surg* 1978;188:669-674
3. Ildstad ST, Tollerud DJ, Weiss RG, Ryan DP, McGowan MA, Martin LW. Duplications of the alimentary tract. *Ann Surg* 1988;208:184-189
4. Walker J, Kapila L. Duodenal duplication—3 new cases. *Z Kinderchir* 1986;41:338-339
5. Kangaroo H, Sample WF, Hansen G, Robinson JS, Sarti D. Ultrasonic evaluation of abdominal gastrointestinal tract duplication in children. *Radiology* 1979;131:191-194
6. Blumhagen JD, Weinberg E. Pediatric gastrointestinal ultrasonography. In: Sanders RC, Hill M (eds.), *Ultrasound annual*. New York: Raven Press, 1986

Case 2: Congenital Hepatic Fibrosis with Saccular Dilatation of the Intrahepatic Bile Ducts and Infantile Polycystic Kidneys

Sonogram of the kidneys of this newborn shows large echogenic kidneys bilaterally with slight sonolucency in the periphery of each kidney (Fig. 2A). A number of small cysts and several larger cysts are seen (Fig. 2B). Several tubular structures consistent with dilated bile ducts are noted in the liver (Fig. 2C). Serial sonograms obtained before the patient's death showed a progressive decrease in the echogenicity of the renal medulla, but no other change. At autopsy, both kidneys were markedly enlarged with normal contours and a smooth surface. Postmortem sonography showed similar findings. On cut surface, the kidney was traversed by radially oriented fusiform or cylindrical tubules. The right and left kidneys weighed 170 and 122 g, respectively. The liver weighed 144 g and, on cut surface, showed numerous dilated bile ducts. Microscopic examination of the liver showed proliferation of bile ducts in the portal areas and hepatic lobules, dilatation of the bile ducts, biliary stasis, and some fibrosis.

This patient had autosomal recessive polycystic kidney disease (RPKD). Although many patients die early in infancy, some survive into early adulthood [1, 2]. The disease is called juvenile polycystic disease in survivors. In RPKD, the typical findings by IV urography include enlarged kidneys, compressed and distorted calyces, and distal tubular opacification (medullary striations). This pattern occasionally can be seen in dominant polycystic kidney disease. The kidneys, by sonography, are large, echogenic, and may contain a number of small cysts. Larger cysts, 1-2 cm in diameter, and a hypoechoic peripheral rim are seen occasionally. The extremely echogenic renal medulla present in our patient is not typical of RPKD. A similar appearance in one reported case was shown to be due to proteinaceous debris, uric acid, and oxylate crystals [3]. The sonographic pattern of the kidneys in RPKD is not pathognomonic and can be seen in a variety

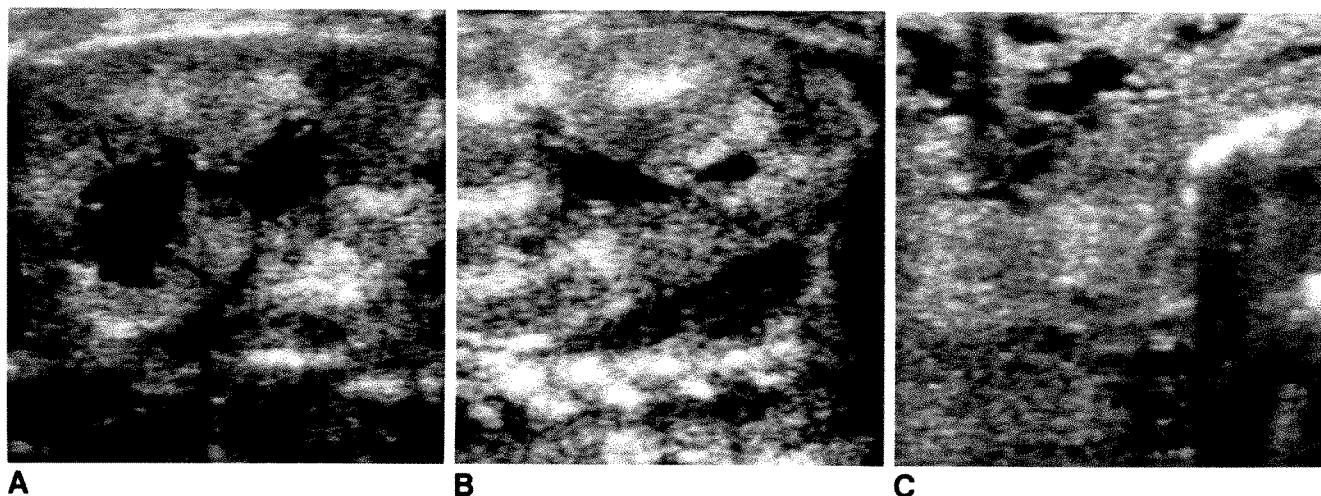


Fig. 2.—Case 2: Congenital hepatic fibrosis with intrahepatic bile-duct dilatation and polycystic kidneys. A and B, Longitudinal sonograms of both flanks show markedly enlarged and echogenic kidneys, although a sonolucent rim can be seen. Several cysts (arrows) of variable size are noted in renal parenchyma. C, Transverse sonogram of liver shows a dilated intrahepatic ductal system.

of conditions, including adult polycystic disease, glomerulocystic kidney disease, congenital nephrosis, glomerulonephritis, acute infantile pyelonephritis, tuberous sclerosis, renal lymphangioma, Beckwith-Wiedemann syndrome, and Laurence-Moon-Biedel syndrome [1, 2, 4]. Renal sonography of the parents and siblings of affected patients may help to exclude other causes of renal enlargement, especially adult polycystic kidney disease [5, 6]. RPKD may be familial.

RPKD is almost always associated with congenital hepatic fibrosis that ranges in severity from mild to severe [1]. Some affected patients have only dilatation of intrahepatic bile ducts and mild fibrosis, as in our patient; others have progressive splenomegaly, esophageal varices, and complications of portal hypertension. Conditions associated with congenital hepatic fibrosis other than RPKD include Caroli disease, choledochal cysts, adult polycystic kidneys, Meckel syndrome, and dysplastic kidneys. Many patients with these disorders also have cystic dilatation of the renal collecting tubules. Rarely, congenital hepatic fibrosis may exist without associated renal lesions.

William H. McAlister
Marilyn J. Siegel

REFERENCES

1. Premkumar A, Berdon WE, Levy J, Amodio J, Abramson SJ, Newhouse JH. The emergence of hepatic fibrosis and portal hypertension in infants and children with autosomal recessive polycystic kidney disease. *Pediatr Radiol* 1988;18:123-129
2. Kaariainen H, Jaaskelainen J, Kivisaari L, Koskimies O, Norio R. Dominant and recessive polycystic kidney disease in children: classification by intravenous pyelography, ultrasound, and computed tomography. *Pediatr Radiol* 1988;18:45-50
3. Davies CH, Stringer DA, Whyte H, Daneman A, Mancier K. Congenital hepatic fibrosis with saccular dilatation of intrahepatic bile ducts and infantile polycystic kidneys. *Pediatr Radiol* 1986;16:302-305
4. Farrell TP, Boal DK, Wood BP, Dagen JE, Rabinowitz R. Unilateral abdominal mass: an unusual presentation of autosomal dominant polycystic kidney disease in children. *Pediatr Radiol* 1984;14:349-352
5. Cole BR, Conley SB, Stapleton FB. Polycystic kidney disease in the first year of life. *J Pediatr* 1987;111:693-699
6. Taitz LS, Brown CB, Blank CE, Steiner GM. Screening for polycystic kidney disease: importance of clinical presentation in the newborn. *Arch Dis Child* 1987;62:45-49

Case 3: Oncogenic Rickets (Feuerstein and Mims Syndrome with Resistant Rickets)

This 3-year-old girl presented with skin lesions characteristic of the linear sebaceous nevus syndrome, muscle weakness, and bone pain. The patient also had clinical findings typical of oncogenic rickets, namely hyperphosphaturia, hypophosphatemia, elevated serum alkaline phosphatase level, normal serum calcium level, low plasma levels of 1,25-dihydrovitamin D (1,25-(OH)₂D), and normal levels of 25-hydrovitamin D (25(OH)D). Radiographs show rachitic changes manifested as widening and irregularity of the epiphyseal plates in addition to several cystlike lesions in the cortex and metaphysis (Fig. 3A and 3B). Some of the bony lesions have a linear appearance. This appearance has been seen in other

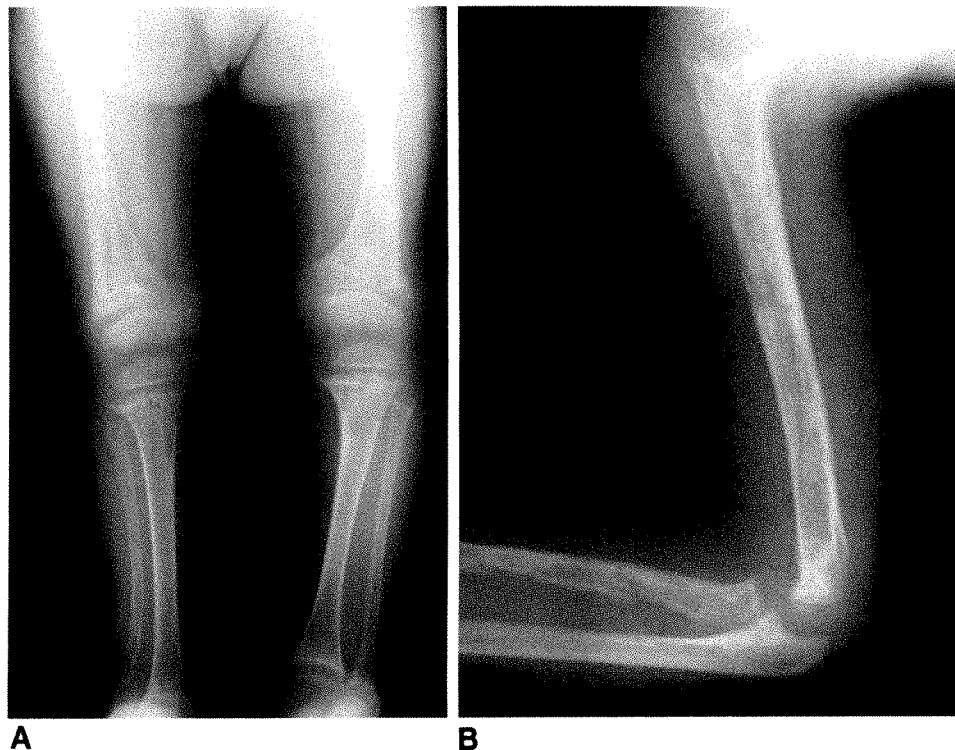


Fig. 3.—Case 3: Oncogenic rickets.
A, Anteroposterior radiograph of lower extremities shows rachitic changes with widening of growth plates, cupping of metaphyseal regions, and demineralization. Also noted are several cystic lesions in bones.
B, Lateral radiograph of right upper extremity shows similar changes.

patients with oncogenic rickets and is uncommon in other forms of rickets. After treatment with 1,25-cholecalciferol and several surgical resections of the linear sebaceous nevi, the patient's bony lesions resolved.

Since the first patient with oncogenic or tumor-associated osteomalacia/rickets was described in 1949 by McCance, roughly 50 patients have been reported [1]. The tumors associated with this form of rickets include ossifying mesenchymal tumors, osteoblastoma, hemangiopericytoma-like tumor, nonossifying fibroma, cavernous hemangioma, giant cell tumor of bone, granuloma, and miscellaneous tumors and conditions such as fibrous dysplasia, fibrohemangioma, hemangioma, nonspecific vascular mesenchymal neoplasms, osteocarcinoma, angiosarcoma, prostate carcinoma, and vascular nevi [1-8]. The associated neoplasms frequently are of mesenchymal origin and contain multinucleated giant cells and extensive vascularity. The lesions arise with equal frequency in bone and soft tissues. Lesions of the skin account for less than 5% of the cases. Oncogenic rickets may be seen in adults or children. In children, the symptoms and signs include growth failure, fractures, and skeletal deformity. In adults, bone pain, weakness, loss of height, fractures, and deformities are seen. The symptoms are often present for a number of years before the condition is diagnosed.

The cause of the decreased renal tubular absorption of phosphate has not been fully explained. A possible explanation is the production of a humoral substance by the tumor. In experimental studies, injection of extracts from some tumors into animals has produced a renal tubular defect that interferes with phosphate reabsorption and a 1,25-dihydroxyvitamin D deficiency. This, in turn, leads to osteomalacia or rickets. Also, some tumors produce humoral factors that inhibit 25-hydroxyvitamin D 1, α -hydroxylase activity [6].

In summary, any patient with atypical rickets, particularly with associated cystic bony lesions, should have a radiographic examination of the entire skeleton and a careful physical examination of the skin and soft tissues to look for associated tumors. MR imaging may be helpful in identifying soft-tissue neoplasms in patients with suspected oncogenic rickets in whom no tumors have been palpated. Removal of the tumor or tumors results in normal serum phosphorus and 1,25-dihydroxyvitamin D levels and in curing the rickets or osteomalacia.

William H. McAlister
Marilyn J. Siegel

REFERENCES

1. Siris ES, Clemens TL, Shane E, Segre GV, Lindsay R, Bilezikian JP. Tumor-induced osteomalacia. *AM J Med* 1987;82:307-312
2. Aschinger LC, Solomon LM, Zeis PM, Justice P, Rosenthal IM. Vitamin D-resistant rickets associated with epidermal nevus syndrome: demonstration of a phosphaturic substance in the dermal lesions. *J Pediatr* 1977;91:56-60
3. Skovby F, Svejgaard E, Møller J. Hypophosphatemic rickets in linear sebaceous nevus sequence. *J Pediatr* 1987;111:855-857
4. Moorjani R, Shaw DG. Feuerstein and Mims syndrome with resistant rickets. *Pediatr Radiol* 1976;5:120-122
5. Sparagana M. Tumor-induced osteomalacia: long-term follow-up of two patients cured by removal of their tumors. *J Surg Oncol* 1987;36:198-205
6. Miyauchi A, Fukase M, Tsutsumi M, Fujita T. Hemangiopericytoma-induced osteomalacia: tumor transplantation in nude mice causes hypophosphatemia and tumor extracts inhibit renal 25-hydroxyvitamin D 1-hydroxylase activity. *J Clin Endocrinol Metab* 1988;67:46-53
7. Carey DE, Drezner MK, Hamdan JA, et al. Hypophosphatemic rickets/osteomalacia in linear sebaceous nevus syndrome: a variant of tumor-induced osteomalacia. *J Pediatr* 1986;109:994-1000
8. Weidner N, Bar RS, Weiss D, Strottmann MP. Neoplastic pathology of oncogenic osteomalacia/rickets. *Cancer* 1985;55:1691-1705

Case 4: Diffuse Infiltrating Lipomatosis

The patient in this case is a 6-year-old girl who presented with a 3-year history of abdominal distention and a newly noted abdominal mass. The CT scan shows a large retroperitoneal mass with a density equal to that of normal fatty tissue. The mass extends from the left kidney inferiorly to the pubic symphysis and causes displacement and elevation of the bowel and urinary bladder (Figs. 4A-4C). Additionally, there is slight lateral displacement of the left psoas muscle. A few linear septa course throughout the mass. The clinical and CT findings are typical of diffuse infiltrating lipomatosis. The patient underwent surgical resection of the mass as well as part of the left iliac vein that was enveloped by the tumor. Microscopically, the tumor was composed of mature fat with a small amount of fibrous tissue interspersed. A final diagnosis of benign, but infiltrating, lipomatosis was made.

Lipomatous tumors are mesenchymal neoplasms that occur predominantly in the retroperitoneal space, but may also arise within the peritoneal cavity. These tumors have a variety of benign and malignant forms. Diffuse infiltrating lipomatosis is a rare condition that affects young people and represents widespread overgrowth of fatty tissue [1]. This tumor is histologically benign and resembles simple lipomas, except for its invasive nature. Complete surgical resection is rarely possible, and therefore, recurrence after attempted resection is frequent. Like the simple lipoma, this lesion has a density on CT scans equal to that of the patient's normal fat. However, it is more extensive, growing along fascial planes and occasionally infiltrating muscle. Thin linear strands of slightly higher density can be seen within the fatty mass, but discrete masses of soft tissue density are absent.

Lipoblastomatosis is also a rare benign tumor occurring almost exclusively in children, with about 90% of cases occurring before the age of 3 years [2, 3]. Most of these tumors are located superficially in the extremities and infrequently in the neck, mediastinum, or retroperitoneum. On CT scans, the tumor has a variable appearance, ranging from a predominantly fatty mass to a heterogeneous mass containing soft-tissue densities [3]. Microscopically, the lesion consists of lobules of fetal or embryonal fat tissue separated by connective tissue septa. The term lipoblastoma is sometimes applied to the circumscribed form and lipoblastomatosis, to the diffuse type. After surgery, the recurrence rate is 14%. The CT findings in the patient in this case could be caused by lipoblastomatosis, but the age of the patient is atypical.

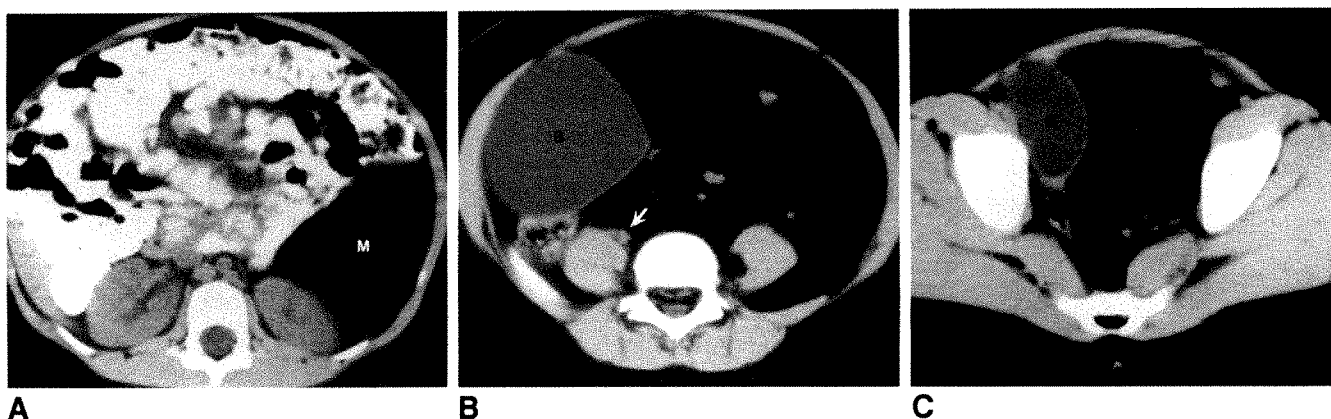


Fig. 4.—Case 4: Diffuse infiltrating lipomatosis.

A, CT scan through upper abdomen shows a fatty mass (M) in left abdomen displacing bowel anteriorly and to right.

B, CT scan through lower abdomen shows lipomatous mass filling almost entire abdomen and displacing urinary bladder (B) to right. Several linear, streaky densities are noted within fatty tissue, corresponding to vessels and fibrous septa. Left iliac vessels are not seen and were found encased by mass at operation. Arrow = right iliac vessels.

C, At a lower level in pelvis, lipomatous tumor elevated bladder (B) to right and cephalad.

Malignant fatty tumors are termed liposarcomas. Liposarcomas usually are inhomogeneous, poorly margined and invasive, and have CT numbers greater than the patient's normal fat. Depending on the amount of fat present, they will have variable densities ranging from soft tissue (poorly differentiated form) to something between water density and fat [4]. Even when large areas of fat density are present, other areas have higher attenuation values similar to that of solid tissue. The absence of discrete masses of higher density than fat make liposarcoma an unlikely diagnosis in this patient.

William H. McAlister
Marilyn J. Siegel

REFERENCES

1. Waligore MP, Stephens DH, Soule EH, McLeod RA. Lipomatous tumors of the abdominal cavity: CT appearance and pathologic correlation. *AJR* **1981**;137:539-545
2. Chung EB, Enzinger FM. Benign lipoblastomatosis. An analysis of 35 cases. *Cancer* **1973**;32:482-492
3. Fisher MF, Fletcher BD, Dahms BB, Haller JO, Friedman AP. Abdominal lipoblastomatosis: radiographic, echographic and computed tomographic findings. *Radiology* **1981**;138:593-596
4. Friedman AC, Hartman DS, Sherman J, Lautin EM, Goldman M. Computed tomography of abdominal fatty masses. *Radiology* **1981**;139:415-429

Neuroradiology Case of the Day

Elliot I. Shoemaker,¹ Allan J. Romano, Mokhtar Gado, and Fred J. Hodges III

Case 1: Chordoma of the Clivus

A 55-year-old woman developed blurred and double vision of the left eye 2 years before these studies. A workup 1 year later showed optic atrophy and a left sixth cranial nerve palsy. Before admission, the patient had two seizures.

Initial noncontrast CT examination showed a low-density mass centered in the left parasellar region, causing bony destruction with a few scattered areas of calcification (Fig. 1A). The contrast examination showed dense homogeneous enhancement of a multilobular mass (Fig. 1B). Definite evidence is present of extension into the left middle cranial fossa and through the incisura of the tentorium into the posterior fossa. On the contrast examination, the floor of the sella appeared intact. An MR examination was obtained with gadolinium. The pre-gadolinium, T1-weighted images showed a low-signal-intensity mass originating from the clivus growing into the suprasellar region with superior and posterior extension (Fig. 1C). The brainstem was deviated posteriorly, and the basal ganglia were displaced superiorly. The postgadolinium, T1-weighted image showed dense homogeneous enhancement (Fig. 1D). The mass showed high signal intensity on the T2-weighted image (Fig. 1E).

Chordoma is a relatively rare neoplasm, accounting for less than 1% of all intracranial tumors [1, 2]. The distribution is approximately 50% sacrococcygeal, 35% cranial, and 15% vertebral [3]. They develop from remnants of the notochord, which is the embryonic precursor of the axial skeleton. This explains their usual midline location. They occur most frequently in the third or fourth decades of life.

These tumors tend to present with the signs and symptoms of a mass compressing the cranial nerves and brainstem, most often the abducens nerve. General symptoms include lethargy, fatigue, and weakness [3].

On CT scans, clival chordomas typically show solitary or multiple areas of low attenuation, probably representing myxoid and gelatinous material found on pathologic examination. Calcification commonly can be seen, representing either tumor calcification or sequestered fragments of bone, and may appear linear, nodular, or mixed. In a review of 30 cases, calcification was present in 47%. The differential diagnosis of a calcified sellar or parasellar lesion would include

craniopharyngioma, aneurysm, or meningioma. After contrast injection, clival chordomas are enhanced. The three major directions of tumor growth are parasellar, prepontine, and nasopharyngeal [4].

On T1-weighted MR images, chordomas tend to be isointense or hypointense. T2-weighted images always show high signal intensity. Seventy percent of chordomas show septa of low signal intensity separated by lobulated areas of high signal intensity. Sagittal MR is useful in disclosing the extent of the tumor in the epidural space. Characterization of the tumor is possible with MR imaging [5]. Chordomas are frequently separated into two pathologic subsets described as typical chordomas and chondroid chordomas. The latter tend to have shorter T1 and T2 relaxation times. Overall, chondroid chordomas tend to have a better prognosis than typical chordomas. MR imaging is less accurate than CT in showing calcification and bone destruction.

Elliot I. Shoemaker
Allan J. Romano
Mokhtar Gado

REFERENCES

1. Firooznia H, Pinto RS, Lin JP, Baruch HH, Zausner J. Chordoma: radiologic evaluation of 20 cases. *AJR* 1976;127:797-805
2. Kendel BE, Lee BC. Cranial chordomas. *Br J Radiol* 1977;50:687-698
3. Tan WS, Spigos D, Khine N. Chordoma of the sellar region. *J Comput Assist Tomogr* 1982;6:154-158
4. Meyer JE, Oot RF, Lindfors KK. CT appearance of clival chordomas. *J Comput Assist Tomogr* 1986;10:34-38
5. Sze G, Uichanco LS, Brant-Zawadzki MN, et al. Chordomas: MR imaging. *Radiology* 1988;166:187-191

Case 2: Choroid Plexus Papilloma, Third Ventricle

A 3-year-old girl presented with a several-month history of headaches. Physical examination was normal except for increased head circumference. Noncontrast CT scans disclosed hydrocephalus. A mass, isodense with brain parenchyma, partially filled the anterior-superior third ventricle and obstructed CSF outflow at the foramina of Monro (Figs. 2A and

¹ All authors: Mallinckrodt Institute of Radiology, Washington University School of Medicine, 510 S. Kingshighway Blvd., St. Louis, MO 63110. Address reprint requests to M. J. Siegel at this address.

Cases 1 and 4 were prepared by E. I. Shoemaker, A. J. Romano, and M. Gado. Case 2 was prepared by A. J. Romano, E. I. Shoemaker, and M. Gado. Case 3 was prepared by A. J. Romano, E. I. Shoemaker, M. Gado, and F. J. Hodges III. M. J. Siegel is coordinator of the Case of the Day series.

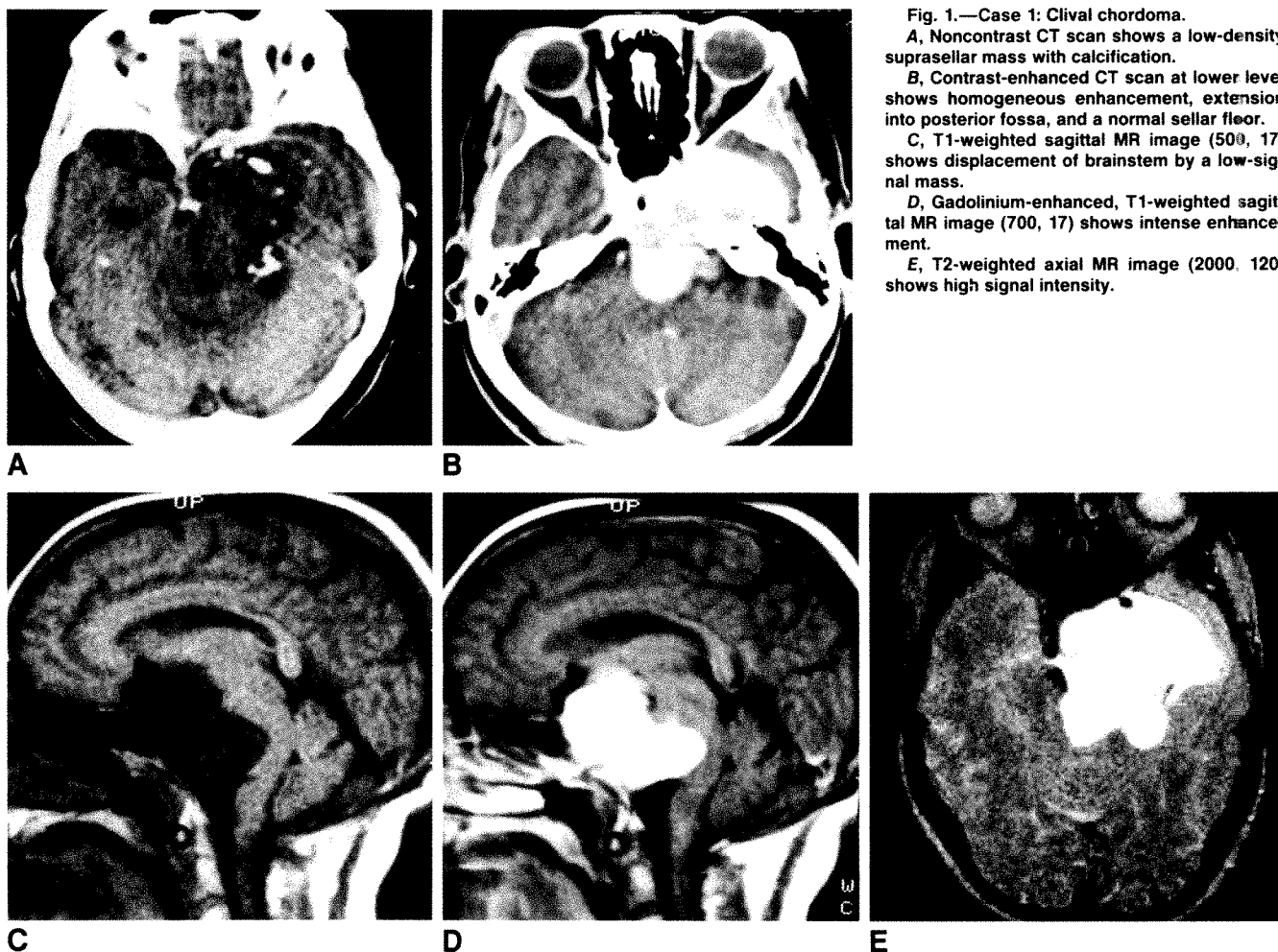


Fig. 1.—Case 1: Clival chordoma.

A, Noncontrast CT scan shows a low-density suprasellar mass with calcification.

B, Contrast-enhanced CT scan at lower level shows homogeneous enhancement, extension into posterior fossa, and a normal sellar floor.

C, T1-weighted sagittal MR image (500, 17) shows displacement of brainstem by a low-signal mass.

D, Gadolinium-enhanced, T1-weighted sagittal MR image (700, 17) shows intense enhancement.

E, T2-weighted axial MR image (2000, 120) shows high signal intensity.

2B). No calcification was shown in the mass. After IV contrast, the mass enhanced intensely and the margins appeared irregular (Fig. 2C). MR images with short and long TR confirmed the location of the mass in the third ventricle and the obstruction at the foramina of Monro (Figs. 2D and 2E). The patient underwent a craniotomy with complete resection of the third ventricle tumor by a transcallosal approach. Histologic examination revealed a benign choroid plexus papilloma.

Choroid plexus papillomas are primary intraventricular neoplasms, accounting for 3% of intracranial neoplasms in children and 0.6% in adults [1, 2]. They arise from the epithelial cells of the choroid plexus and occur wherever choroid plexus is found: lateral ventricles (43%), third ventricle (10%), fourth ventricle (39%), and even the cerebellopontine angles (9%) [2]. In children, papillomas tend to occur in the lateral ventricles, whereas the fourth ventricle is the most common site in adults [1, 3]. In children, 86% of all papillomas occur in the first 5 years of life. Malignant change occurs in up to 20% and is more common in children [3, 4]. Seeding by CSF pathways is reported to occur in both benign and malignant tumors [2, 4]. Choroid plexus papillomas may recur if not completely excised [2, 5].

Patients with choroid plexus papillomas have symptoms of

increased intracranial pressure—headaches, vomiting, and gait abnormality. Physical examination shows increased head circumference in children, abnormal plantar reflexes, and papilledema [3, 4]. Hydrocephalus is a constant feature and may be due to obstruction of CSF pathways, overproduction of CSF by the papilloma, adhesions due to bleeding from the tumor, or a combination of these factors [2, 6]. When the tumor is located in the third ventricle, the cause appears to be obstruction of CSF outflow at the foramina of Monro. This is because of the strategic location of third ventricular papillomas, which are attached at the tela choroidea [2, 7]. Sudden death from acute ventricular obstruction is a well-known complication of third ventricular colloid cysts and also has been reported in choroid plexus papillomas of the third ventricle [1].

On CT scans, three fourths of choroid plexus papillomas are isodense or hyperdense relative to brain parenchyma, and one fourth are hypodense or of mixed density. Tumor margins can be smooth (29%), lobulated (19%), or irregular (52%). Irregular margins are found in both malignant tumors (71%) and benign lesions (43%). Calcification is reported in 24%. All choroid plexus papillomas enhance with IV contrast, and the enhancement is typically intense [3].

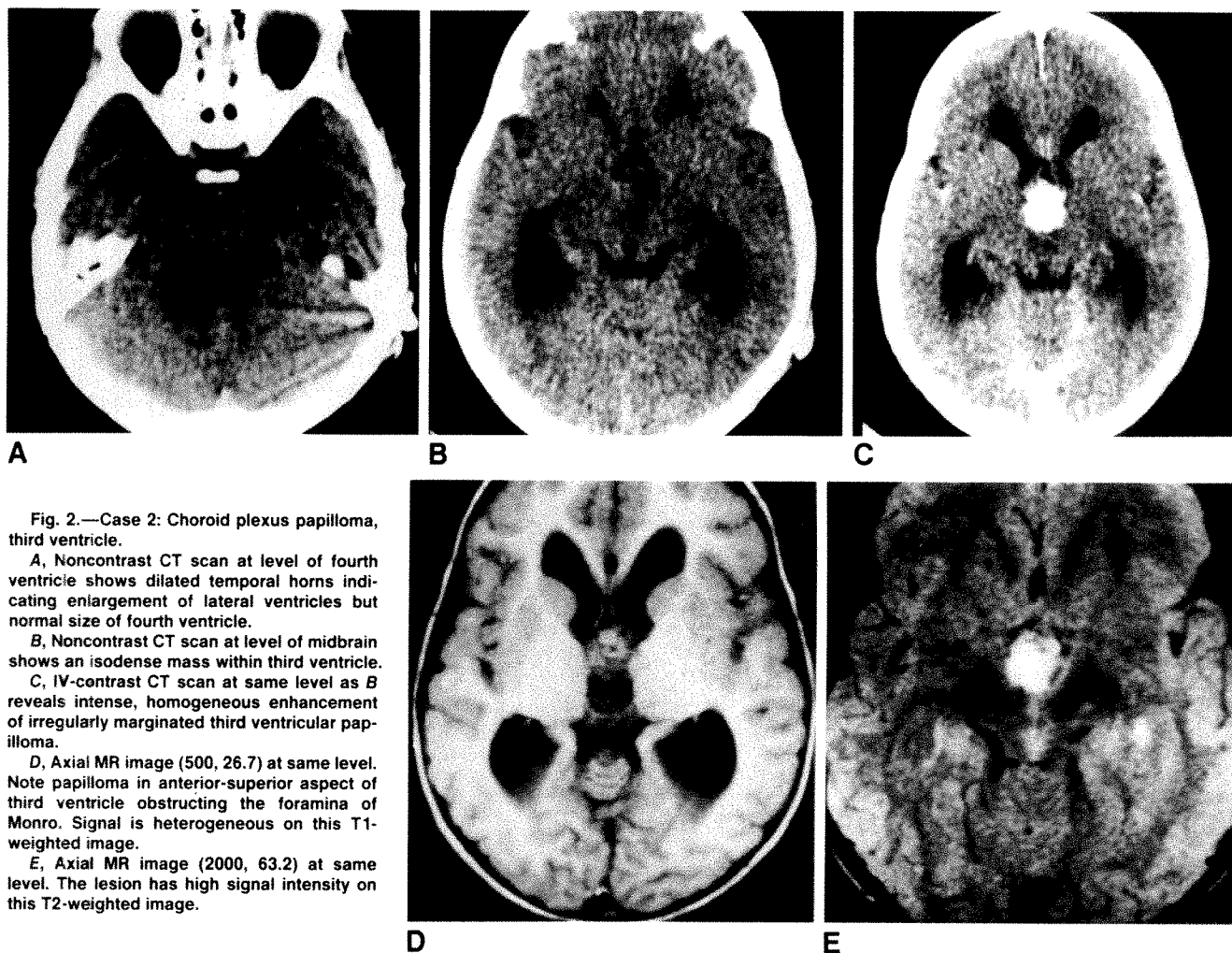


Fig. 2.—Case 2: Choroid plexus papilloma, third ventricle.

A, Noncontrast CT scan at level of fourth ventricle shows dilated temporal horns indicating enlargement of lateral ventricles but normal size of fourth ventricle.

B, Noncontrast CT scan at level of midbrain shows an isodense mass within third ventricle.

C, IV-contrast CT scan at same level as B reveals intense, homogeneous enhancement of irregularly margined third ventricular papilloma.

D, Axial MR image (500, 26.7) at same level. Note papilloma in anterior-superior aspect of third ventricle obstructing the foramina of Monro. Signal is heterogeneous on this T1-weighted image.

E, Axial MR image (2000, 63.2) at same level. The lesion has high signal intensity on this T2-weighted image.

The differential diagnosis of third ventricular tumors includes colloid cyst, meningioma, craniopharyngioma, glioma, ependymoma, dermoid, epidermoid, metastasis, and tumors deposited by CSF seeding. CT and MR features can be used to exclude colloid cyst, meningioma, most craniopharyngiomas, dermoid, and epidermoid tumors [3, 4, 7]. In a young patient, metastasis is unlikely. Supratentorial ependymomas tend to have a smaller intraventricular component compared with a larger portion of the tumor mass invading the adjacent parenchyma. In a child, the most common tumor to spread via CSF pathways is medulloblastoma, but this characteristically involves the cerebellar vermis initially [7]. The features possessed by gliomas and choroid plexus papillomas overlap considerably, making reliable distinction between these tumor types difficult [3].

Allan J. Romano
Elliot I. Shoemaker
Mokhtar Gado

REFERENCES

1. Gradin WC, Taylor C, Fruin AH. Choroid plexus papilloma of the third ventricle: case report and review of the literature. *Neurosurgery* 1983;12:217-220
2. Rovit RL, Schechter MM, Chodraff P. Choroid plexus papillomas—observations on radiographic diagnosis. *AJR* 1970;110:608-617
3. Kendall B, Reider-Grosswasser I, Valentine A. Diagnosis of masses presenting within the ventricles on computed tomography. *Neuroradiology* 1983;25:11-22
4. Thompson JR, Harwood-Nash DC, Fitz CR. The neuroradiology of childhood choroid plexus neoplasms. *AJR* 1973;118:116-132
5. Tomasello F, Albanese V, Bernini FP, Picozzi P. Choroid plexus papilloma of the third ventricle. *Surg Neurol* 1981;16:69-71
6. Joona R, Grand DN. Third ventricle choroid plexus papillomas. *Childs Brain* 1983;10:242-250
7. Hopper KD, Foley C, Nieves NL, Smirniotopoulos JG. The interventricular extension of choroid plexus papillomas. *AJNR* 1987;8:469-472

Case 3: Plasmacytoma of the Skull Vault

A 70-year-old man presented with a 6-month history of progressive decline in cognitive function, lethargy, and mild ataxia. Laboratory evaluation disclosed anemia, hyperproteinemia, increased erythrocyte sedimentation rate, and elevated 24-hour urine protein level. Serum and urine electrophoresis was positive for IgG kappa paraprotein and kappa light chains. Noncontrast CT showed a large hyperdense mass with focal calcifications. The lesion crossed the midline without displacing the adjacent falx cerebri (Fig. 3A). Bone

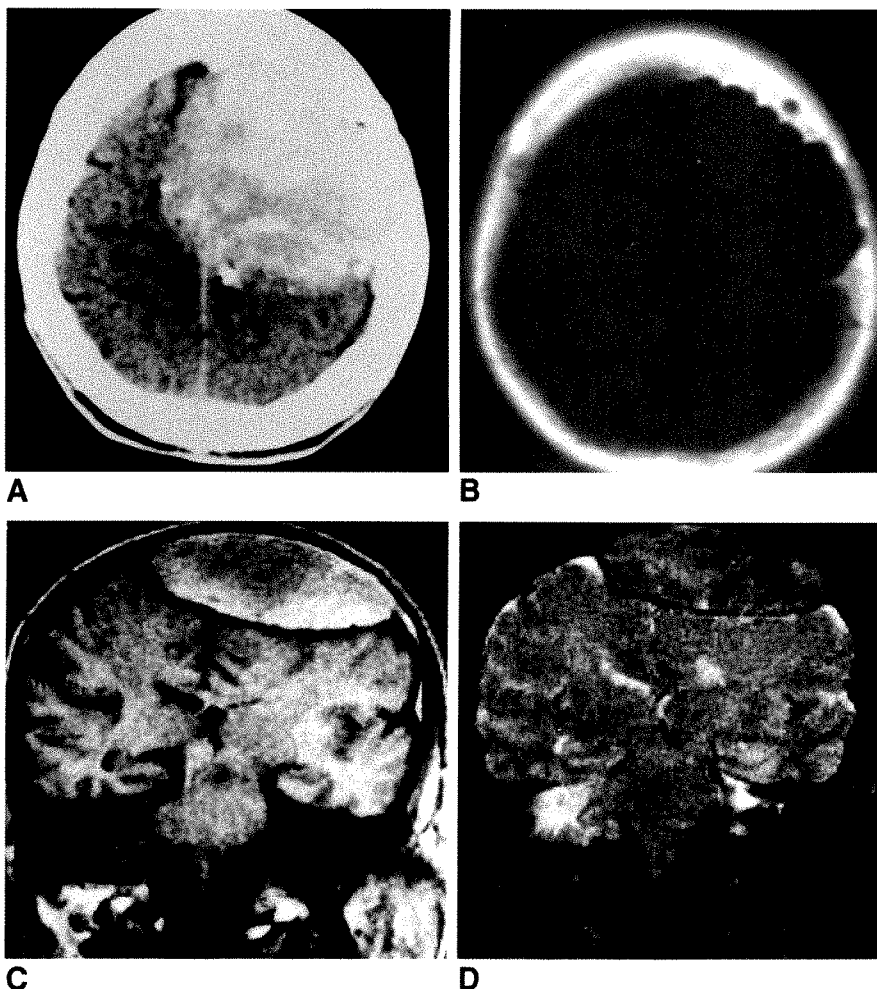


Fig. 3.—Case 3: Plasmacytoma of skull vault.

A, Noncontrast axial head CT scan near vertex shows a hyperdense mass, with focal areas of higher density suggesting calcification. Lesion crosses midline.

B, Bone windows of scan A, showing scalloping of inner table of skull, penetrating diploic space.

C, Coronal MR image (700, 17). Elliptical extradural mass crosses midline and involves inner table and diploic space. It has mixed signal intensity, but generally has a slightly higher signal than brain parenchyma.

D, Coronal MR image (2000, 120). Heterogeneous signal is again noted on this long sequence image. Black line along inner margin of mass represents dura, confirming extradural location.

windows showed erosion of the inner table of the skull extending into the diploic space with preservation of the outer table of bone (Fig. 3B). Coronal short- and long-sequence MR images identified the mass as extradural, with inward displacement of the intact dura and distortion of the adjacent brain and lateral ventricles. Although the cerebral hemispheres were distorted, there was no signal abnormality in the brain (Figs. 3C and 3D). A skeletal survey revealed no definite evidence for other bone lesions. Bone-marrow biopsy showed a mildly cellular marrow with 70–80% plasma cells, consistent with multiple myeloma. A stereotaxic biopsy of the skull lesion confirmed the diagnosis of plasma cell myeloma.

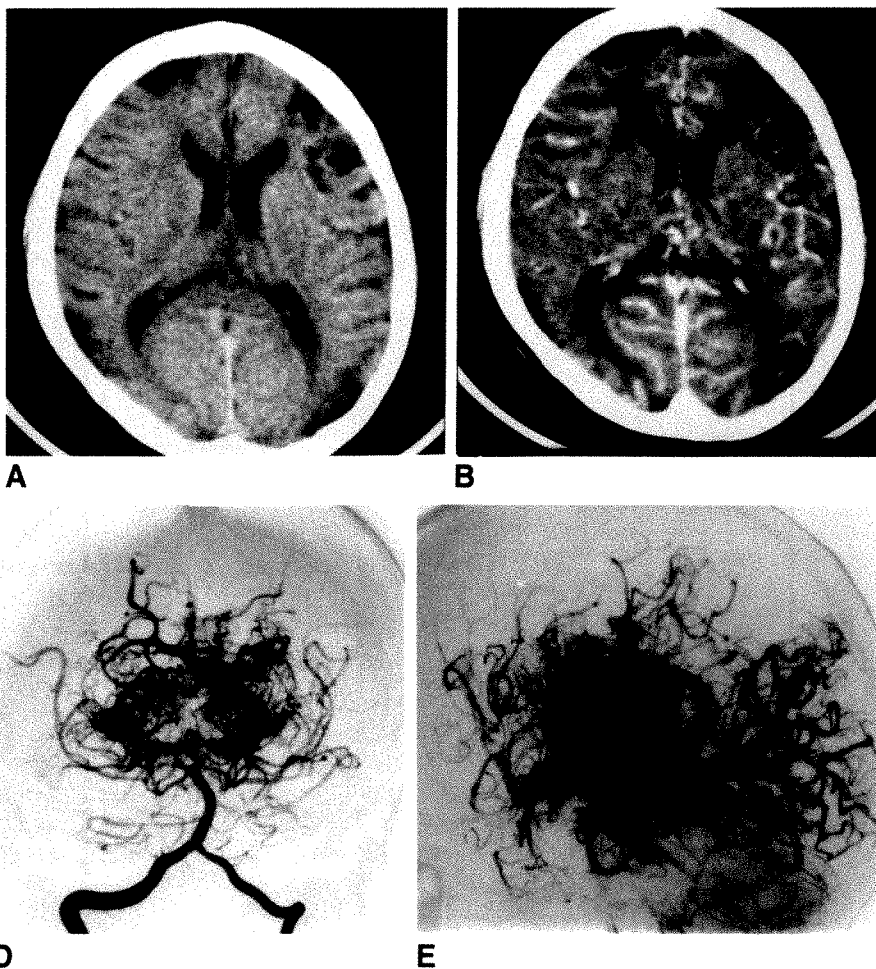
Multiple myeloma accounts for 1% of all malignant disease and slightly greater than 10% of hematologic malignancies [1]. This neoplasm originates from plasma cells, which are derived from the B-lymphocyte [2]. Myeloma is characterized by proliferation of a single clone of abnormal plasma cells, which produce abnormal monoclonal proteins [1]. Three forms of plasma cell proliferation are recognized—solitary plasmacytoma of bone, extramedullary plasmacytoma, and multiple myeloma. These are felt to be different manifestations of the same disease [3, 4]. The criteria for the diagnosis of multiple myeloma are (1) increased numbers of abnormal,

atypical, or immature plasma cells in the bone marrow, and (2) monoclonal protein in the serum or urine, or (3) bone lesions consistent with myeloma [1].

The disease generally occurs in patients between 50 and 70 years old, is more common in men (61%), is typically associated with abnormal protein in both serum (90%) and urine (80%), and presents most often with bone pain (68%). At presentation, 79% of patients have abnormal skeletal radiographs [1]. The flat bones containing red marrow (ribs, vertebrae, sternum, skull, pelvis, and mandible) are involved most often [5].

Although the radiographic presentation is variable, focal abnormalities typically appear as multiple small, rather uniform osteolytic lesions with sharp punched-out margins [1, 2, 5, 6, 7]. This is certainly the classic appearance in the skull, where the earliest lesions may be most conspicuous. Small lesions may coalesce into larger areas of bone destruction. Rarely, a large solitary lesion is observed. The involvement of bone is often associated with an adjacent soft-tissue mass [8]. In the skull, unusually large solitary lesions with an associated soft-tissue mass have rarely been reported to cause deformity of the brain and can be associated with neurologic symptoms due to cerebral compression [9].

Fig. 4.—Case 4: Moyamoya disease.
A, Noncontrast CT scan shows prominent sulci and ventricles.
B, Contrast-enhanced CT scan shows prominence of many cortical vessels.
C, Lateral view of right common carotid angiogram shows occlusion of internal carotid artery with meningeal collaterals.
D and E, Anteroposterior and lateral views of vertebral angiogram. Both posterior cerebral arteries are occluded, with an extensive network of perforating vessels in region of basal ganglia.



The differential diagnosis includes metastasis, osteochondroma, osteochondrosarcoma, meningioma, sarcoma of the dura, and hemangioma of the dura. The sharp borders, little or no bony sclerosis or new bone formation, and the paucity of periosteal reaction are useful in suggesting the correct diagnosis of plasmacytoma. However, in cases of unusual presentation, such as a solitary expansile lesion of considerable size, or advanced disease, reliable distinction may be impossible.

Allan J. Romano
 Elliot I. Shoemaker
 Mokhtar Gado
 Fred J. Hodges, III

REFERENCES

1. Kyle RA. Multiple myeloma, review of 869 cases. *Mayo Clin Proc* 1975;50:29-40
2. Goodman MA. Plasma cell tumors. *Clin Orthop* 1986;204:86-92
3. Tong D, Griffin TW, Laramore GE, et al. Solitary plasmacytoma of bone and soft tissues. *Radiology* 1980;135:195-198
4. Meyer JE, Schulz MD. "Solitary" myeloma of bone. A review of 12 cases. *Cancer* 1974;34:438-440
5. Edeiken J, Hodes PJ. *Roentgen diagnosis of diseases of bone*, 2nd ed. Baltimore: Williams & Wilkins, 1973:1026-1051
6. Meszaros WT. The many facets of multiple myeloma. *Semin Roentgenol* 1974;9:219-228
7. Yentis I. Radiological aspects of myelomatosis. *Clin Radiol* 1961;12:1-7
8. Resnick D, Niwayama G. *Diagnosis of bone and joint disorders*, 2nd ed. Philadelphia: Saunders, 1988:2360-2379
9. Stork RJ, Henson RA. Cerebral compression by myeloma. *J Neurol Neurosurg Psychiatry* 1981;44:833-836

Case 4: Moyamoya Disease

The patient is a 10½-year-old boy with Down syndrome. An episode of lethargy, fever, and right-sided weakness of several weeks duration occurred approximately 2 years before admission. During the few months before this study, the parents noted progressive intermittent right-sided weakness, particularly when the patient exercised.

The noncontrast CT examination showed prominent sulci and ventricles but no parenchymal changes (Fig. 4A). The contrast study showed intense enhancement of many cortical vessels bilaterally (Fig. 4B). An angiogram was obtained. Contrast-material injection in the right common carotid artery showed occlusion of the internal carotid artery just distal to the takeoff of the ophthalmic artery. Enlarged meningeal branches perforated the dura and supplied the anterior portion

of the middle cerebral artery as well as callosomarginal branches anteriorly (Fig. 4C). The contrast-material injection in the left internal carotid artery showed similar findings. Selective injection in the right vertebral artery showed occlusion of the posterior cerebral arteries at their origins. An extensive network of perforating vessels, supplied via the basilar artery, appeared to reconstitute branches of the posterior cerebral artery as well as posterior branches of the middle cerebral artery. These perforating vessels were most prominent in the region of the basal ganglia (Figs. 4D and 4E). The overall appearance was consistent with Moyamoya disease.

In general, Moyamoya disease causes occlusion or stenosis of the supraclinoid portions of the internal carotid arteries, as well as the proximal portions of the anterior and middle cerebral arteries. It tends to be bilateral. The most striking source of collaterals is the dense network of small conglomerate vessels in the region of the basal ganglia and upper brainstem. The anterior or middle cerebral arteries beyond the site of occlusion may be reconstituted by way of this network. Vessels that contribute to this network include the thalamoperforate arteries, the anterior choroidal arteries, and the artery of Heubner, to name a few. Transdural external-to-internal carotid anastomoses can occur via the superficial temporal artery, middle meningeal artery, occipital artery, or the ophthalmic artery. These are called meningeal anastomoses. End-to-end anastomoses on the surface of the cerebral hemispheres can occur, unless the basilar artery is occluded, and are called leptomeningeal anastomoses [1, 2].

Typically, most of these patients are less than 15 years old. Young patients can present with sudden and recurrent paresis of one or two limbs, as well as convulsive seizures. Overall, symptoms due to cerebral ischemia are the main features in childhood. In adults, subarachnoid hemorrhage is the most

common presentation [3]. These patients present with motor weakness, decreased sensation, mental deterioration, and convulsions or headache. In a large series of 96 cases, 10 of the patients had symptoms before the age of 10 years and 73 had symptoms before 24 years of age [1].

In a CT study of 12 patients with Moyamoya disease, moderate dilatation of the ventricular system was found in seven, widening of the sulci in nine, and intracerebral lucent foci representing old infarcts in 11 patients. Most of these features were in the cortex or subcortical white matter [4]. In another study of six patients, focal low-density areas were found in five patients and were felt to represent previous infarcts. The postcontrast CT scans showed curvilinear tortuous densities in the basal ganglia in four patients. Vessels in the cerebral sulci and sylvian fissures were often not seen except in those patients in whom angiography showed extensive parenchymal and leptomeningeal collaterals [3].

Elliot I. Shoemaker

Allan J. Romano

Mokhtar Gado

REFERENCES

1. Taveras JM. Multiple progressive intracranial arterial occlusion: a syndrome of children and young adults. *AJR* 1969;106:235-268
2. Handa J, Handa H. Progressive cerebral arterial occlusive disease: analysis of 27 cases. *Neuroradiology* 1972;3:119-133
3. Takahashi M, Miyauchi T, Kowada M. Computed tomography of Moyamoya disease: demonstration of occluded arteries and collateral vessels as important diagnostic signs. *Radiology* 1980;134:671-676
4. Handa J, Nakano Y, Dkuno T, Komuro H, Hojyo H, Handa H. Computerized tomography in Moyamoya syndrome. *Surg Neurol* 1977;7:315-319

Letters

Agenesis of the Lungs

Developmental defects of the lungs are rare. They usually are associated with congenital malformations that affect primarily the cardiovascular system (most frequently patent ductus arteriosus, spinal abnormalities, and tracheoesophageal fistulas). The agenesis does not cause any signs or symptoms unless it is complicated by bronchopulmonary disease or other anomalies.

A 38-year-old man had fever and a cough. Chest radiographs showed complete opacification of the left hemithorax, shift of the mediastinum to the left, and hyperinflation of the right lung. Bronchoscopy showed absence of the left main bronchus. This was confirmed by bronchography (Fig. 1). CT showed hypoplasia of the left hemithorax, hyperinflation of the right lung, and a shift of the mediastinum to the left. The carina and tracheal bifurcation were not visualized even on slices 2 mm thick.

Agenesis of the right lung is twice as common as agenesis of the left lung [1]. The oldest patient previously reported to have this condition was a 23-year-old man [2]. Our patient, who was 38 years old, had complete absence of the left lung and bronchus and no associated cardiovascular anomalies.

M. C. Pant
P. K. Srivastava
K. N. Sinha
G. N. Agrawal
P. K. Agrawal
A. K. Tripathi
D. K. Agrawal
Kaiserbagh
Lucknow, 226 003 U. P., India

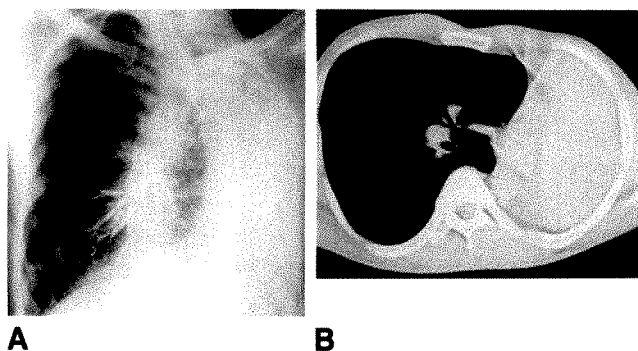


Fig. 1.—Agenesis of lungs.

A, Bronchogram shows absence of left main bronchus.

B, CT scan shows absence of pulmonary parenchyma and pleura on left side.

REFERENCES

1. Pallie W, Alhady SMA, Bin Din O. Agenesis of the right lung as unusual presentation. *Thorax* 1967;22:368
2. Booth JB, Berry CI. Unilateral pulmonary agenesis. *Arch Dis Child* 1967; 42:361

CT Findings of a Posterior False Aneurysm of the Left Ventricle

I describe the CT findings in a case of a false aneurysm, a condition caused by a myocardial rupture into the pericardial space that subsequently is sealed by adhesions [1].

A 64-year-old man with a 7-month history of diabetes, hypertension, and myocardial infarction of the inferior wall had syncope and pain in the lower part of the chest. A grade 2 systolic murmur of new onset was detected at the left second interspace. Chest radiographs showed an enlarged heart with a subcarinal density extending to the diaphragm [2]. Two-dimensional echocardiograms showed hypokinesis of the inferior wall of the left ventricle. A 2-cm defect in the posterior wall communicated with a 5-cm echo-free chamber extending to the region of the left atrium (Fig. 1A). The findings were confirmed by M-mode echocardiography. Doppler examination of the ostium revealed equal biphasic systolic flow toward the false aneurysm and a monophasic diastolic flow toward the left ventricle. Radionuclide ventriculography showed a posterior chamber separate from the left atrium; ejection fraction was 43%. Contrast-enhanced CT showed a persistent collection of contrast material with ill-defined borders adjacent to the left ventricle with absence of adjacent epi-

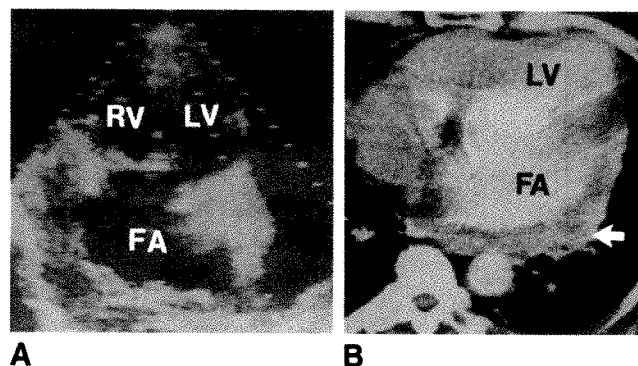


Fig. 1.—Posterior false aneurysm of left ventricle.

A, Two-dimensional echocardiogram shows a false aneurysm (FA) connecting to posterior wall of left ventricle (LV). RV = right ventricle.

B, Nonincremental dynamic CT scan at a plane inferior to left atrium shows contrast material in false aneurysm posterior to left ventricle. Note contrast-enhancing pericardial effusion (arrow).

cardial fat (Fig. 1B). Angiography confirmed the presence of a false aneurysm posterior to the left ventricle with total occlusion of the proximal part of the right coronary artery. Excision of the false aneurysm and bypass grafting of the coronary artery were performed.

A. Escarous

New York Medical College
Lincoln, NY 10451

REFERENCES

1. Roberts WC, Morrow AG. Pseudoaneurysm of the left ventricle: an unusual sequel of myocardial infarction and rupture of the heart. *Am J Med* 1967; 43:639-644
2. Higgins CB, Lipton MJ, Johnson AD, Peterson KL, Vieweg WVR. False aneurysms of the left ventricle. *Radiology* 1978;127:21-27

Superior Mediastinal Widening from Spine Fractures Mimicking Aortic Rupture on Chest Radiographs

In the January 1989 issue of *AJR*, Dennis and Rogers [1] report that if evidence of a fracture of the lower cervical or upper thoracic spine can be found in a trauma patient who has mediastinal widening on chest radiographs, aortic rupture is unlikely in the absence of clinical signs and symptoms that support this diagnosis. The clinical signs and symptoms are not addressed. The implication of this article is that aortography should be deferred unless clinical signs and symptoms of aortic rupture are present. This is a dangerous practice.

Frequently, no signs or symptoms are present until immediately before the patient exsanguinates. In many patients, signs and symptoms of aortic rupture may be masked by concomitant head, skeletal, or visceral trauma. In an article on nonpenetrating traumatic injury of the aorta, Parmley et al. [2] found that 36% of 296 cases had minimal or no external evidence of chest injury and that specific symptoms or signs of cardiovascular injury were rare. Kirsh et al. [3] found that one third of 43 patients with aortic rupture had no external evidence of thoracic injury. They stated further, "Despite the severe nature of the injury the clinical manifestations of aortic rupture are usually deceptively meager." In the series of Parmley et al., 34 of 38 patients who survived for some time after injury had dorsolumbar vertebral fractures. In a review of 17 cases of aortic transections at my institution, I found that two patients had concomitant vertebral fractures. Though this prevalence is considerably lower than that reported by Parmley et al., it is certainly too high to ignore.

Obviously, fracture of a vertebral body can occur without thoracic aortic injury and may be much more frequent than aortic transection. However, a widened mediastinum in a patient with significant trauma requires further evaluation by aortography or possibly contrast-enhanced CT to exclude aortic rupture regardless of the presence or absence of a vertebral body fracture.

E. Heiberg

St. Louis University Medical Center
St. Louis, MO 63104

REFERENCES

1. Dennis LN, Rogers LF. Superior mediastinal widening from spine fractures mimicking aortic rupture on chest radiographs. *AJR* 1989;152:27-30
2. Parmley LF, Mattingly TW, Manion WC, Jahnke EJ Jr. Nonpenetrating traumatic injury of the aorta. *Circulation* 1958;17:1086-1101
3. Kirsh MM, Behrendt DM, Orringer MB, et al. The treatment of acute traumatic rupture of the aorta. *Ann Surg* 1976;184:308-315

Reply

Dr. Heiberg's comments are greatly appreciated. The thesis of our article was that a widened mediastinum on a chest radiograph after trauma is not a specific finding for aortic rupture; it also may be the result of a nonaortic hemorrhage associated with fracture of vertebral bodies. It is our hope that both fractures of the spine and aortic rupture will be considered in the differential diagnosis of a widened mediastinum so as not to overlook either.

In our series, it was unlikely for a patient to have both a spinal fracture and an aortic rupture. However, nowhere in our article do we state or intend to suggest that aortography should be deferred in the evaluation of an aortic rupture in patients who have a widened mediastinum. This would certainly be unwise given the high mortality rate associated with this condition. It was not our intent to discuss the signs and symptoms of aortic rupture or when aortography should be performed, but rather to stress the importance of examining the spine for fracture in patients who sustain chest trauma.

Lee N. Dennis

Lee F. Rogers

Northwestern University Medical School
Chicago, IL 60611

Cost of Breast Localization Devices

We commend Drs. Kopans and Swann for their comprehensive review of preoperative localization procedures performed for nonpalpable breast lesions [1]. It is clear from their descriptions, and from our own experience, that each localization guide involves trade-offs but that all guides can give comparable results in the hands of mammographers and surgeons who are experienced in their use.

Currently popular breast localization devices include those marketed by Cook (Kopans), E-Z-EM (Percu Guide), N.S. Medical (Hawkins), Namik (Homer), and Ranfac (Sadowsky). We recently priced these guides and found that their cost per unit varied from \$12.50 to \$20. Of course, a straight needle is considerably cheaper but, in our hands, less satisfactory. We did not inquire about the possibility of discounted prices for these guides because of volume of purchase or their use by residents in training.

A substantial increase in the market for breast localization guides is predicted, and we are aware of a number of new devices currently being developed. Because of the similarity and equivalent effectiveness of most of these devices, we think that cost should be a substantial factor in their selection.

Ferris M. Hall

Donna M. Tobey

Beth Israel Hospital
Harvard Medical School
Boston, MA 02215

REFERENCE

1. Kopans DB, Swann CA. Preoperative imaging-guided needle placement and localization of clinically occult lesions. *AJR* 1989;152:1-9

Reply

The letter from Dr. Hall and Ms. Tobey strikes to the heart of the question. If in fact all localization techniques give the same result, it would seem that the least costly should be used. In our review [1], we tried to present an objective and unbiased summary of the many approaches used. Unfortunately, the success rates of the various methods are probably not equal. Although few data are published on

the amount of tissue removed and the number of samples required for removal, we know that not all methods give comparable results. Many breast biopsies for nonpalpable lesions involve the removal of a much larger volume of tissue than needed because of variations in the skill and technique of the physician placing the guide, the kind of guide used, and the skill of the surgeon. Low-accuracy techniques require the surgeon to excise a larger amount of tissue than is necessary to ensure excision. It is the accuracy of the overall procedure (guide and placement of the guide) that reduces the trauma to the patient by permitting minimal surgery. We know, for example, that by using our particular approach [2], we can guarantee that the wire system that we use is always within 5 mm of the lesion (in 96%, we pass the guide through or within 2 mm of the lesion), and the three-dimensional stability of the wire we use permits the removal of an extremely small volume of tissue. As stated in our review, we would agree that a "fancy," expensive guide that is unable to produce a three-dimensionally useful marker is unnecessary if it is placed through and beyond the lesion with no effort at depth localization. Such a guide has little to add over merely placing a standard needle through the lesion. However, when used properly, a guide with three-dimensional stability that is positioned accurately can assist the surgeon significantly and reduce the extent of surgery, thus justifying some additional cost. As with all procedures, the operator must evaluate his or her own requirements to ensure the safety of and benefit for the patient and the needs of the surgeon when selecting the techniques and instruments to be used.

Daniel B. Kopans
Massachusetts General Hospital
Boston, MA 02114

REFERENCES

1. Kopans DB, Swann CA. Progress in radiology. Preoperative imaging-guided needle placement and localization of clinically occult breast lesions. *AJR* 1989;152:1-9
2. Kopans DB, Lindfors K, McCarthy KA, Meyer JE. Spring hookwire breast lesion localizer: use with rigid-compression mammographic system. *Radiology* 1985;157:537-538

Fatty-Meal Sonography for Diagnosis of Obstruction of Common Bile Duct

In the July 1988 issue of the *AJR*, Darweesh et al. [1] reported that fatty-meal sonography is a useful noninvasive screening test for patients with suspected obstruction of the common bile duct. Their rationale for the test, as first proposed in 1982 by Simeone et al. [2], was that entry of ingested fat into the duodenum stimulates mucosal release of cholecystokinin in the small intestine, which then exerts its three major effects: contraction of the gallbladder, relaxation of the sphincter of Oddi, and increased flow of bile. A 2-mm or more increase in the diameter of the common bile duct was considered a positive test for obstruction of the common duct. What is disconcerting is the higher number of false-negatives (four of 12) in the patients in group 2 who had no gallbladder when compared with the number of false-negatives (one of seven) in the patients in group 2 whose gallbladders were intact. This raises a question about the validity of the test in those patients who lack a gallbladder either because increased bile flow induced by cholecystokinin is insufficient or because coexisting medical problems have blunted the patients' response to the meal.

Cholecystokinin increases bile flow by increasing bile acid-independent ductular secretion of bile [3]. However, it plays only a minor

role in increasing ductular secretion when compared with secretin [4]. Although experiments in animal models have shown that bile flow increased as much as 5 ml/hr after stimulation with cholecystokinin [3, 4], we do not have enough data in humans on how much cholecystokinin can increase bile secretion. This information is critical to the premise of Darweesh et al. because in patients who lack a gallbladder and have obstruction of the common bile duct, the common duct will dilate as a result of increased ductular secretion of bile after the patient has eaten a fatty meal. If the common bile duct is assumed to be a circular cylinder with a volume described by the formula $V = 3.1416 \times \text{radius}^2 \times \text{height}$, where the height is assumed to be constant at 11 cm, it will require an increment of 2.76 ml of bile flow to dilate an obstructed common duct from 7 mm to 9 mm. A larger volume (3.45 ml) of bile is required to dilate the common duct from 9 mm to 11 mm. It is apparent that a proportionate increase in bile flow is required as the diameter of the duct increases to cause a 2-mm change in size of the duct. Whether cholecystokinin could cause an increment of bile of at least 3 ml over 45 min in humans is not well established. Some of the observations made by Darweesh et al. may have been associated with release of secretin stimulated either by the fatty meal itself and/or by the entry of acidic gastric secretion in the duodenum [5].

Another point is that the article did not include the patients' medical histories and the results of pretest investigations. Of particular interest are celiac disease (defective release of cholecystokinin [6]), diabetes (gastroparesis with consequent decreased duodenal delivery of fat and therefore decreased release of cholecystokinin [3]), levels of serum amylase (obstruction of the duct from pancreatitis), and use of drugs (e.g., barbiturates, theophylline, hydrocortisone, thyroid supplements, insulin, and diuretics [5]) that could alter bile flow. We think that inquiry on these matters should have been made and that if the inquiry was made, the results should have been included in the published article.

Elias Pascual
Brian Weiner
Anthony Foong
Suresh Reddy
Tariq J. Khan
Jersey City Medical Center
Jersey City, NJ 07304

REFERENCES

1. Darweesh RMA, Dodds WJ, Hogan WJ, et al. Fatty-meal sonography for evaluating patients with suspected partial common duct obstruction. *AJR* 1988;151:63-68
2. Simeone JF, Mueller PR, Ferrucci JT Jr, et al. Sonography of the bile ducts after a fatty meal: an aid in detection of obstruction. *Radiology* 1982;143:211-215
3. Shaw RA, Jones RS. The choleretic action of cholecystokinin and cholecystokinin octapeptide in dogs. *Surgery* 1978;84(5):622-625
4. Gardiner BN, Small DM. Simultaneous measurement of the pancreatic and biliary response to CCK and secretin. *Gastroenterology* 1976;70:403-407
5. Erlinger S. Secretion of bile. In: Schiff L, Schiff ER, eds. *Diseases of the liver*, 6th ed. Philadelphia: Lippincott, 1987:77-101
6. Calam J, Ellis A, Dockray G. Identification and measurement of molecular variants of cholecystokinin in duodenal mucosa and plasma. *J Clin Invest* 1982;69:218-225

Reply

In their letter about our article on fatty-meal sonography [1], Dr. Pascual et al. have two concerns. First, from data taken from Figure 3 in the article, they point out that a false-negative result was obtained

in one of seven patients who had a gallbladder and in four of 12 patients who had had a cholecystectomy. However, this trend was not statistically significant; the number of patients who had had their gallbladder removed was twice the number of those who still had a gallbladder. The Chi-square value needed for statistical significance is 3.8, whereas that calculated from the data is only 0.5. Therefore, we do not think that Pascual et al. have raised an important issue based on the data from the article.

The other issue raised by Pascual et al. is how the fatty-meal sonographic test might be positive 45 min after a fatty meal when the gallbladder has been removed. Actually, this issue was dealt with in the Roscoe Miller Award Lecture but inadvertently not included in the discussion published in the *AJR*. As correctly pointed out by Pascual et al., cholecystokinin causes a negligible increase in hepatic bile flow by any direct action on the liver. What cholecystokinin does do, however, is increase hepatic bile flow maximally 30–60 min after onset of its infusion or after a meal because of its effects on small-bowel motility. Cholecystokinin causes a generalized increase in small-bowel motor activity that accelerates the rate of bile transport through the small bowel. Bile acids reaching the terminal ileum are absorbed rapidly, thereby enhancing the enterohepatic circulation of the bile acids. This enhanced circulation produces an increase in bile acid-dependent bile flow. As shown in the opossum and dog [2, 3], this effect approximately doubles hepatic bile flow because of the increased amount of bile acids passing back through the liver. This phenomenon is the reason the optimal time for a positive test result is at 45 min, regardless of whether the gallbladder is present. Thus, a positive test result is not related to the minimal direct effect cholecystokinin has on enhancing hepatic production of bile but rather to the marked increase in the enterohepatic circulation of bile acids.

Wylie J. Dodds
Medical College of Wisconsin
Milwaukee, WI 53226

REFERENCES

1. Darweesh RMA, Dodds WJ, Hogan WJ, et al. Fatty-meal sonography for evaluating patients with suspected partial common duct obstruction. *AJR* 1988;151:63–68
2. Takahashi I, Dodds WJ, Itoh Z, Hogan WJ, Kern MK. Influence of trans-sphincteric fluid flow on spike burst rate of the opossum sphincter of Oddi. *Gastroenterology* 1984;87:1292–1298
3. Scott RB. Factors controlling fasting and postprandial duodenal bile acid delivery (abstr). *Gastroenterology* 1987;92:1629

Portal Hypertension in Behçet Syndrome

Although Behçet syndrome involving the eyes, skin, and mouth was recognized as a clinical entity in 1937 [1], it has become evident that this syndrome is a systemic disorder. We describe a patient with portal hypertension associated with thrombosis of the portal vein (with subsequent recanalization and cavernous transformation) and obstruction of the inferior vena cava.

The patient is a 25-year-old man who was admitted because of abdominal discomfort and joint pain. Physical examination revealed oral and genital aphthous ulcers, bilateral pretibial edema, abdominal collateral veins, ascites, splenomegaly, and a deep pretibial ulcer 3 cm in diameter. An abdominal sonogram showed multiple hypoechoic serpentine vascular channels at the level of the porta hepatis. In addition, the inferior vena cava was obstructed completely, and the portal vein was not identified. Intraarterial digital subtraction angiography showed numerous atypical venous collateral channels replacing the main portal vein (Fig. 1A). CT showed multiple vascular structures in the region of the portal vein, representing venous periportal collat-

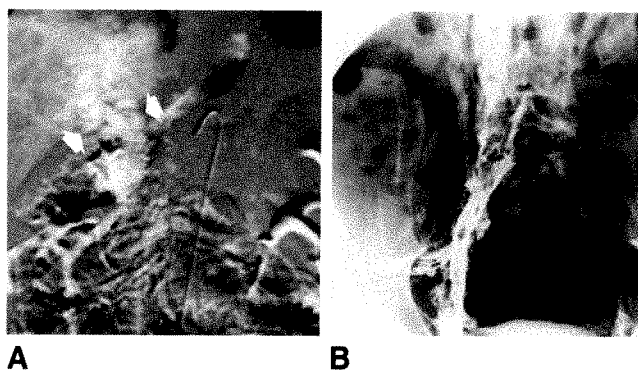


Fig. 1.—Portal hypertension in Behçet syndrome.
A, Digital subtraction angiogram shows multiple vascular structures at level of porta hepatis due to periportal collateral veins (arrows).
B, Cavogram shows obstruction of inferior vena cava with contrast filling of azygos veins.

eral vessels. Cavography showed complete obstruction of the inferior vena cava from the level of the right iliac vein with contrast filling of the azygos veins (Fig. 1B). Follow-up examinations, done on an outpatient basis, have shown that the patient's condition is gradually worsening.

Behçet syndrome, which is not uncommon in Turkey, involves many different organ systems. The main pathologic feature is vasculitis. Superficial venous occlusions and thrombosis of the veins and arteries are common. Kansu et al. [2] and Dündar and Yazici [3] reported thrombosis of the inferior or superior vena cava or both. In the past 20 years, we have seen 30 patients with obstruction of these veins. Castillo et al. [4] reported the first case of Behçet syndrome with portal hypertension associated with thrombosis of the portal vein. To our knowledge, this is the second reported case.

Yusuf Bayraktar
Ferhun Balkanci
Emin Kansu
Semra Dündar
Hasan Telatar
Hacettepe University School of Medicine
Ankara, Turkey

REFERENCES

1. Behçet HH. Über rezidivierende, aphthöse, durch ein Virus verur sachte Geschwüre am Mund, am Auge und an den Genitalien. *Dermatol Wochenschr* 1937;105:1152
2. Kansu E, Ozer FL, Akalin E, et al. Behçet's syndrome with obstruction of the vena cava. *Q J Med* 1972;162:151–168
3. Dündar S, Yazici H. Superior vena cava syndrome in Behçet's disease. *Vasc Surg* 1984;10:28–33
4. Castillo J, Leina M, Alveres-Prechous A, et al. Behçet's disease: report of ten cases and a new clinical manifestation (portal vein thrombosis). *Med Clin (Barc)* 1980;75:279–280

Percutaneous Extraction of Renal Fungal Ball

We have several questions about the article by Doemeny et al. [1] on fluoroscopically guided percutaneous extraction of a renal fungal ball. First, was excretory urography done initially, and, if so, did it show any radiolucent filling defect in the pelvis? If a fungal cause was suspected, was a sample of bladder urine cultured for fungus before the patient had retrograde pyelography? In the absence of evidence of pyelonephritis, fungal infection of the renal pelvis usually is the

result of an ascending infection from the bladder. In such a case, the patient should have signs and symptoms of cystitis, and a diffuse, intense inflammatory reaction should be seen on cystoscopy. Most physicians would treat the infection before doing retrograde pyelography.

Thus, doing retrograde pyelography as the first procedure in this case does not seem necessary or valid. The authors state that the filling defects "did not appear to be as large as they were on a similar study performed 6 months earlier." Why did the size decrease if no antifungal treatment was given?

Renal sonography was normal in this case, but fungal balls are known to show echogenic mass with no acoustic shadowing [2]. What was the CT attenuation value of this fungal ball?

Were samples of the bladder urine cultured for fungus before the authors resorted to percutaneous extraction of the ball? What were the results of histologic or microbiologic examination of the extracted fungal ball? Was fungal serology done for this patient? If so, what were the titers? Was blood sent for fungal culture?

Was micturating cystourethrography done to look for any evidence of vesicoureteric reflux? Did the patient have a history of previous urinary tract infections? Was she passing fungal balls in the urine?

It is well known that ascending infections arise from the bladder and are limited to the bladder, ureter, and renal pelvis; renal parenchymatous infection is rare [3]. Predisposing factors such as antibiotic therapy, indwelling IV tubes, Foley catheters, concomitant bacterial infection, recent surgery, and parenteral hyperalimentation are usually present [4]. Other factors include leukemia, steroid or antimetabolite therapy, radiation, and immunodeficiency. In this case, none of these was present.

Last, *Torulopsis* does not form pseudohyphae, so infections caused by this yeast are not associated with the formation of bezoars [5]. Bezoars usually are associated with *Aspergillus* or *Candida* infections [6], so it is difficult to understand and explain the presence of a fungal ball in a patient who has urinary *Torulopsis* infection.

Neelam Malik
Sudhir Khanna

Postgraduate Institute of Medical Education and Research
Chandigarh 160012, India

REFERENCES

1. Doemeny JM, Banner MP, Shapiro MJ, Amendola MA, Pollack HM. Technical note. Percutaneous extraction of renal fungus ball. *AJR* 1988;150:1331-1332
2. Francesoo A, Glazel GP, Paranello L. Upper urinary tract obstruction in children caused by *Candida* fungal ball. *Eur Urol* 1985;11:188-191
3. Littewood JM. *Candida* infection of the urinary tract. *Br J Urol* 1968;40:293-305
4. Klein JJ, Watanakunakorn C. Hospital acquired fungemia: its natural course and clinical significance. *Am J Med* 1979;67:51-58
5. Schronebeckly J. Fungal infection of the urinary tract. In: *Campbell's urology*, 4th ed., vol. 1. Philadelphia: Saunders, 1986:1033-1034
6. Wise GJ. Treatment of fungal disease of the kidney, ureter, and bladder. In: Kaufmann JJ, ed. *Current urologic therapy*, 2nd ed. Philadelphia: Saunders, 1986:51

Reply

We welcome the interest shown by Drs. Malik and Khanna and their comments about the urologic and radiologic diagnosis of renal fungal infection. In our paper [1], we were unable to address many of the points they raised because our contribution was a technical note.

An excretory urogram was performed at a different hospital 2 weeks before the patient was referred to us for extracorporeal shock-wave lithotripsy (ESWL). It showed multiple radiolucent filling defects

in the right pyelocaliceal system. These were thought to represent a branched, nonopaque, infection-related renal calculus. The renal papillae appeared intact. In preparation for ESWL, a ureteral catheter was inserted easily in retrograde fashion. Cystoscopic examination of the bladder was normal, with no evidence of bladder fungal infection. Routine urine culture showed no growth. The patient was not passing fungal balls in her urine. In fact, fungal infection was not yet clinically suspect.

We think that the normal nephrosonogram in this case is attributable to the absence of hydronephrosis. As previously reported [2], fungal masses may appear as echogenic nonshadowing foci when surrounded by urine. In this case, renal sinus echoes probably blended with and became indistinguishable from echoes from any inflammatory or infectious material in the collecting system.

We do not know the CT attenuation value of the fungal mass. As stated, the mass was slightly more attenuating than urine and less attenuating than either blood or nonopaque calculus. These findings first raised the possibility of a fungal infection.

Micturating cystourethrography was not performed because a bladder source of infection was never suspected. Consequently, neither was vesicoureteral reflux.

Cultures of bladder urine repeatedly were negative for fungus as the infection appeared to be limited to the kidneys. The percutaneously extracted mass (and washings from the retrograde ureteral catheter) showed many budding yeast forms, which grew *Torulopsis glabrata* on culture. Fungal serology and blood cultures were not obtained as there was no systemic evidence of fungemia.

T. glabrata frequently is isolated from the urine of patients who have diabetes mellitus [3], especially those with glycosuria [4]. Although it is usually a saprophyte, this fungus, not unlike *Candida albicans*, can cause pyelonephritis and sepsis, particularly in elderly persons with diabetes mellitus [4]. Our patient was an elderly woman whose diabetes was poorly controlled. She had a 1-year history of intermittent urinary tract infections that had been treated with several antibiotics. We suspect that her renal fungal infection was not the result of hematogenous dissemination or retrograde propagation of a lower urinary tract infection but rather the combination of *T. glabrata* overgrowth, enhanced by the previous administration of antibiotics; fungal colonization; and the formation of renal stone matrix and/or inflammatory debris within the collecting system. We have used the term fungus ball (or bezoar) generically to describe an agglomeration of inflammatory cells, fungus, and necrotic debris and/or stone matrix (i.e., an inflammatory fungal mass). In the context of interventional radiology, there seems to be no purpose in restricting the definition of a fungus ball to a mass composed primarily of hyphae-forming fungi. The technique of removing these masses from the kidney percutaneously depends more on the size and location of the mass than on microbiologic characteristics.

Marc P. Banner
Howard M. Pollack
Marco A. Amendola
John M. Doemeny
Marcelle J. Shapiro

Hospital of the University of Pennsylvania
Philadelphia, PA 19104

REFERENCES

1. Doemeny JM, Banner MP, Shapiro MJ, Amendola MA, Pollack HM. Technical note. Percutaneous extraction of renal fungus ball. *AJR* 1988;150:1331-1332
2. Stuck KJ, Silver TM, Jafee MH, Bowerman RA. Sonographic demonstration of renal fungus balls. *Radiology* 1981;142:473-474

3. Marks MI, Langston C, Eickhoff TC. *Torulopsis glabrata*: an opportunistic pathogen in man. *N Engl J Med* 1970;283:1131-1135
4. Kauffman CA, Tan JS. *Torulopsis glabrata* renal infection. *Am J Med* 1974;57:217-224

Testicular Epidermoid Cyst: Sonographic and MR Findings

Epidermoid cysts of the testicle are uncommon, benign lesions that may not require orchiectomy [1]. Sonographic findings may suggest the diagnosis but cannot be used to differentiate seminoma, teratoma, embryonal carcinoma, and epidermoid cyst [2]. However, the presence of a sharply circumscribed hypoechoic lesion with an echogenic center should raise the possibility of this benign condition.

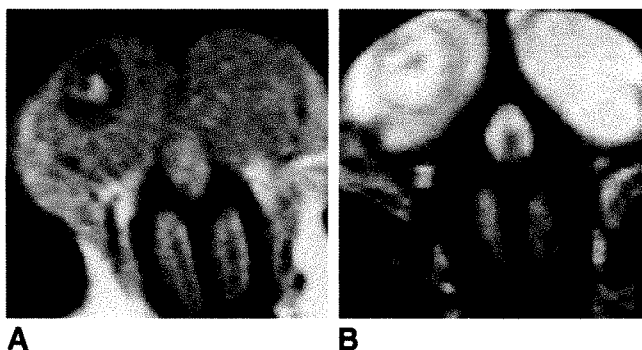


Fig. 1.—A and B, T1-weighted, 330/22, (A) and T2-weighted, 2000/90, (B) MR images show testicular epidermoid cyst.

MR recently has been used to investigate testicular lesions [3]. In our case of an epidermoid cyst, the tumor had a bull's-eye or target appearance on MR examination, which may be a characteristic finding. The outer fibrous capsule, epithelial lining, and adjacent compact keratin produced a peripheral low-signal zone on both T1- and T2-weighted images. The center, composed of dense debris and calcification, also produced low signal. Between these areas on both sequences was a zone of greater signal caused by loose, degenerating, exfoliated squamous cells. The strong signal on T1-weighted images probably is due to a high lipid content (Fig. 1A), whereas the increased signal on T2-weighted images may be due to water (Fig. 1B).

J. S. Brenner
W. A. Cumming
P. R. Ros
University of Florida
Gainesville, FL 32610

REFERENCES

1. Berger Y, Srinivas V, Hajdu SI, Herr HW. Epidermoid cyst of the testes: role of conservative surgery. *J Urol* 1985;134:962-963
2. Schwerk WB, Schwerk WN, Rodeck G. Testicular tumors: prospective analysis of real-time US patterns and abdominal staging. *Radiology* 1987;164:369-374
3. Baker LL, Hajek PC, Burkhard TK, et al. MR imaging of the scrotum: pathologic conditions. *Radiology* 1987;163:93-98

The Laminar Space Sign: Is It Reliable, Specific?

Plain radiographs are still the first imaging study used to evaluate most cervical spine injuries. In this era of high-tech imaging methods,

it was refreshing to read the article by Young et al. [1] describing a new plain-film sign for the diagnosis of unilateral locked facet.

There are already a handful of signs that suggest this injury, but, as the authors point out, none is absolute. The same is true of the authors' new sign, which was positive in 85% (23 of 27) of their cases. The importance of the article is that with yet another sign to help in making this diagnosis, fewer cases should show no obvious signs and thus be missed.

As with any new sign, other investigators must confirm its validity and define its limitations. For instance, the authors refer only to an "abrupt" change in the laminar space size; no measurement is given. Their one measured example shows a 2.5-mm change. Would 1.5 or 1.0 mm be sufficient? After reading the article, I began observing the laminar space critically and noted several patients with no apparent traumatic rotational injury who had an abrupt change in the laminar space. In Figure 1 (p. 1345), laminar spaces are 1 mm at C3, 1-1.5 mm at C4, and 4 mm at C5. Some rotation is apparent, but is this an abrupt change? If so, what is the cause? We know degenerative diseases can allow anterolisthesis and retrolisthesis in the cervical spine; can they also allow rotational changes? What about lax ligaments or inflammatory joint disease?

Daffner, in his new book [2], shows several unilateral pillar fractures with an abrupt change in the laminar distance. The authors' new sign clearly must indicate rotational changes, but only time will tell how specific it may be for unilateral facet lock and what numerical limitations might increase that specificity.

Stanley P. Bohrer
Bowman Gray School of Medicine
Wake Forest University
Winston-Salem, NC 27103

REFERENCES

1. Young JWR, Resnik CS, DeCandido P, Mervis SE. The laminar space in the diagnosis of rotational flexion injuries of the cervical spine. *AJR* 1989;152:103-107
2. Daffner RM. *Imaging of vertebral trauma*. Rockville, MD: Aspen, 1988: 110, 111, Figs. 5-20, 5-21

Reply

We are pleased to reply to Dr. Bohrer's letter about the laminar facet space. It raises several points that we think need clarification.

In cases of unilateral facet dislocation, the abrupt change in the laminar space that we describe occurs at the level of rotation, but it is reflected at all vertebral levels above or below the level of change [1]. In other words, whereas one vertebral body is rotated in relation to its adjacent neighbor, the vertebral bodies above or below will maintain a normal relation to each other. As mentioned in our article, we had two cases in which "normal" spines showed an abrupt change in the laminar space, but only at one level, as in the case provided by Dr. Bohrer (Fig. 1). In one case, our Figure 9, there was a history of a previous articular pillar fracture, which may produce abnormality of the posterior facet line, as has been demonstrated by Daffner [2]. We also have noted a similar appearance in fractures of the articular pillar (Fig. 2). The case provided by Dr. Bohrer has clear evidence of abnormality at the level in question (Fig. 1). There is asymmetry of the C4-C5 disk space, which is mildly widened anteriorly and significantly narrowed posteriorly. In addition, some irregularity of the inferior margin of the posterior facet line is seen, which could be due to an earlier facet/pillar fracture. These changes are quite compatible with a previous hyperextension injury. Furthermore, examination of the laminar spaces from C3 through C6 on this radiograph shows a

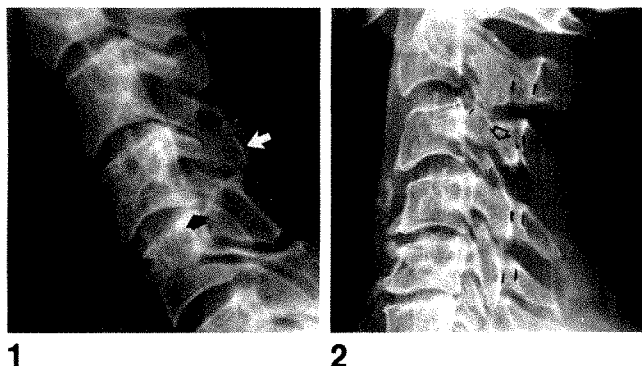


Fig. 1.—Radiograph shows an abrupt change in laminar space from C4 to C5. However, asymmetry of disk space at this level is marked, with widening anteriorly and narrowing posteriorly (black arrows). In addition, there is a "double line" at inferior posterior margin of articular pillar of C4 (white arrow). We (Young et al.) think these changes suggest a previous hyperextension injury, possibly with damage to inferior facet of C4.

Fig. 2.—Radiograph shows a similar but more marked change than in Figure 1. A fracture through articular pillar of C3 (arrow), with posterior displacement of the dorsal fragment, causes localized narrowing in laminar facet space. In this case, there is also some widening of laminar space at C2, probably reflecting rotation due to rotary instability of C3.

gradual progressive widening of all except that at C4. Again, we think that this indicates a local abnormality at C4. We suspect that tomography would confirm abnormality of the articular pillar of C4 but certainly is not indicated in an asymptomatic patient.

The finding of a localized change in the laminar space is not unusual, but it should not be a cause for concern if the patient is asymptomatic. However, if it is present in a symptomatic patient, a pillar fracture should be suspected, and additional studies should be performed.

The sign we describe, however, with an abrupt change reflected at all levels above or below the injury, is an accurate indication of a rotational abnormality, although not specific for unilateral locking. Nine of our cases had pillar/facet fractures, which by definition exclude a locking of the facets. For this reason, we deliberately refer to the injury as unilateral dislocation. This is well shown in Figure 7 of the original article [1].

The size of the change that indicates abnormality is difficult to substantiate fully. Although theoretically a change of only 1 mm could indicate rotation, we found a large number of normal spines with alterations in the laminar/facet space of 1 mm. We agree with Dr. Bohrer that any cause of laxity at a joint, including loss of articular cartilage or ligamentous laxity, could be responsible for this type of anomaly. In all our cases of unilateral facet dislocation, the abrupt change was 2 mm or greater, and in all but three cases, it was greater than 2.5 mm. We think that a change of this size in the laminar space is an extremely accurate indication of abnormality.

Jeremy W. R. Young
Charles S. Resnik
Paula DeCandido
Stuart E. Mirvis

University of Maryland Medical System/Hospital
Baltimore, MD 21201

REFERENCES

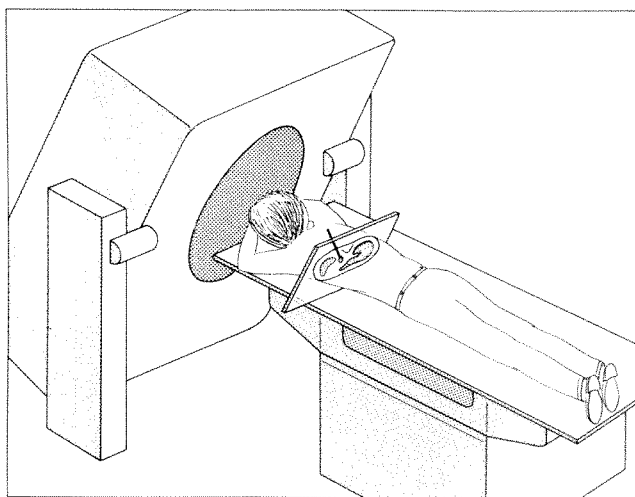
1. Young JWR, Resnik CS, DeCandido P, Mirvis SE. The laminar space in the diagnosis of rotational flexion injuries of the cervical spine. *AJR* 1989;152:103-107

2. Daffner RM. *Imaging of vertebral trauma*. Rockville, MD: Aspen, 1988: 110, 111, Figs. 5-20, 5-21

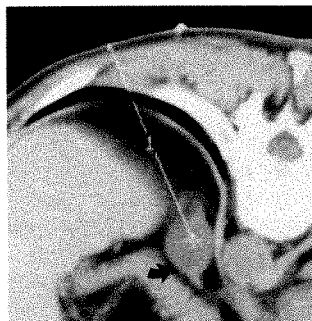
Gantry Angulation for CT-Guided Biopsy or Aspiration

CT-guided biopsies and aspirations usually are performed in the axial plane. This permits the proposed track, and the subsequently introduced needle, to be imaged in their entirety on a single scan. Occasionally, vital structures or bone precludes this approach. This commonly occurs with subdiaphragmatic lesions because of interposed lung and pleura. Triangulation is an indirect method of addressing this problem [1]. We describe an alternative method in which the needle is placed under direct CT guidance by angulating the gantry (Fig. 1).

The possibility that angulating the gantry will permit an alternative, safer approach is usually evident from studying the standard axial images (Fig. 1B). The amount the gantry must be tilted is estimated, and corresponding sections are obtained through the lesion (Fig. 1C). Direct visualization of the lesion in the selected angled plane permits measurement of the length of the proposed needle track. The entry



A



B



C

Fig. 1.—Gantry angulation for CT-guided adrenal biopsy in a patient with primary lung carcinoma.

A, Drawing shows angulation of gantry. Needle is introduced parallel to plane of tilted gantry.

B, Standard axial CT scan performed with patient prone shows barium paste on skin, lesion (arrow), proposed needle track, and interposed lung.

C, Repeat CT scan of mass with patient in similar phase of respiration as in B and gantry angulated 10° shows interposed lung is absent.

site on the skin is chosen, and the needle is introduced in a standard manner while the patient is outside the gantry. The needle is aligned with the angled gantry by means of "eyeballing" in the same manner as vertical alignment is determined in axially oriented localization procedures (Fig. 1A). After the needle is placed, its exact position is determined by corresponding angled CT scans.

On our CT scanner, the gantry can be tilted 20°, but the effective angle can be increased by using bolsters under the patient. However, the method we describe is not applicable when large degrees of angulation are required. Multiplanar approaches are possible; decubitus or oblique positions can be used to rotate the axis of gantry angulation. In the case of a posterior approach to an abscess in the upper abdomen, to decrease the possibility of transgressing pleural space, we have angled the gantry and corresponding needle track even when standard axial sections have shown no intervening lung.

We have used this technique successfully in approximately 10 cases, including lesions in the adrenals, pancreas, liver, spleen, and pelvis. No complications have occurred, and the risks are comparable with those of standard axially oriented procedures. Although this method undoubtedly has been used by others, we could find no description of it in the literature.

Matthew L. Levine
Ferris M. Hall
Beth Israel Hospital
Harvard Medical School
Boston, MA 02215

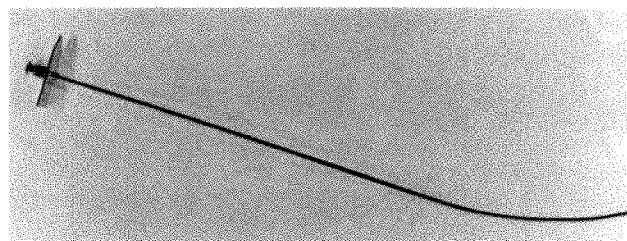
REFERENCE

1. Gerzof SG. Triangulation: indirect CT guidance for abscess drainage. *AJR* 1981;137:1080-1081

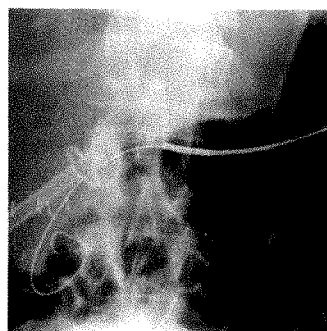
Directable Cannula for Gastrojejunal Catheterization

After percutaneous gastrostomy, a jejunal feeding tube often is inserted either alone or as part of a gastrojejunostomy catheter assembly to prevent aspiration of stomach contents. Placement of the jejunal catheter is often laborious and complex because the catheters and guidewires tend to coil uncontrollably within the gastric lumen when the operator attempts to intubate the duodenum. This is especially common when the stomach is unusually large or J-shaped, when the proximal duodenum is acutely angled, or when the gastrostomy site is poorly placed. Use of a special 8-French, directable, hollow metal cannula can greatly shorten what is often an unnecessarily long procedure.

The 8-French cannula (Cook, Co., Bloomington, IN) that is used is 30 cm long. It is made of soft, malleable stainless steel that can be reshaped by finger pressure into any simple curves needed to reach the pyloric canal from the gastrostomy site. Its lumen accepts a 5.5-French catheter easily, provided the stem is not bent at too sharp an angle. The hub has a directional pointer (Fig. 1). A peel-away sheath introducer properly sized to the feeding tube is inserted percutaneously into the stomach with the aid of an anchoring device [1]. After the stomach is opacified with dilute contrast medium, the reshaped metal cannula with a 5-French cobra or multipurpose catheter threaded through its lumen is advanced through the gastrostomy sheath and with a gentle, circular, probing motion, is directed selectively, under fluoroscopy, to the pyloric canal. The operator holds the cannula in position with one hand, and with the other hand advances the coaxial catheter either alone or together with a J-tip guidewire through the pylorus and duodenum to the jejunum (Fig. 1B). A stiff exchange guidewire is inserted then, the cannula and catheter are removed, and the jejunal tube is threaded to its full length over the wire. Use of this cannula, which allows prompt access to the pyloric canal and prevents intragastric coiling of guidewires,



A



B

Fig. 1.—Directable cannula for gastrojejunal catheterization.

A, 8-French, malleable, steel gastric cannula.

B, Radiograph shows guide-wire advanced into duodenum through gastric cannula without intragastric coiling.

simplifies and shortens the time needed for jejunal intubation to just a few minutes. This technique has been used experimentally in four pigs and clinically in six patients. The tip of the cannula is blunt and is prevented from coming into contact with the stomach wall by the protruding coaxial catheter and guidewire, so the chances of damaging the gastric mucosa or perforating the stomach wall are small. The cannula also has been used within large abdominal abscess cavities to prevent coiling of guidewire and catheters while drains are inserted through complex tracts.

Constantin Cope
Hospital of the University of Pennsylvania
Philadelphia, PA 19104

REFERENCE

1. Cope C. Suture anchor for visceral drainage. *AJR* 1986;146:160-161

Improved Catheter Introducer with Recessed Sheath

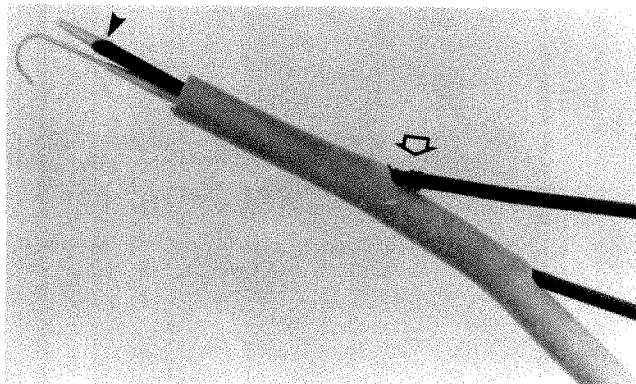
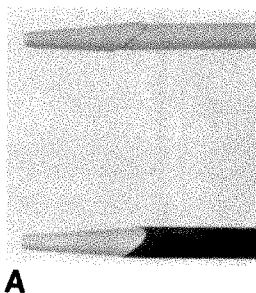
Despite improvements in design and quality control of catheter introducers with regard to the taper and fit of the sheath, it is still not uncommon to have problems with insertion. The rim edge of the sheath is a point of friction that can lead to flaring, retraction, and tearing of the sheath as it is advanced through unexpectedly desmoplastic tissue. This may lead either to inability to advance the sheath, which will fold like an accordion, or to laceration of the arteriotomy with formation of hematomas or intimal dissection. Butto et al. [1] have added a small bulbous protrusion to the dilator just distal to the rim of the fitted sheath to predilate the arteriotomy site so that there is less resistance to the passage of the sheath.

I have used a modification of a previously designed atraumatic sheath needle [2] to devise a catheter introducer that will resist fraying better because the transition between sheath and dilator is smooth and stepless. The recessed-sheath dilator (Cook, Co., Bloomington, IN) (Fig. 1) consists of a Teflon sheath with an angled tip that is mated to a specially designed dilator with a broader distal segment. The protruding part of the dilator is approximately 1 French larger than its main stem; its proximal edge is cut diagonally to the same

Fig. 1.—Improved catheter introducer with recessed sheath.

A, Proximal edge of expanded dilator tip has a diagonal overhanging tip (top) that fits snugly over end of Teflon sheath to produce a smooth, stepless transition zone (bottom).

B, Attempt to insert a standard 8-French catheter introducer over a guidewire through wall of a 28-French rubber tube was unsuccessful because sheath folded up (arrow). 8-French recessed catheter introducer was advanced easily with no damage to tip of sheath (arrow-head).



angle as the tip of the sheath and forms a slightly recessed shelf. When the sheath and dilator are mated perfectly with their hubs interlocked, the abutting edge of the sheath lies nestled within the proximal overhanging rim of the expanded segment of the dilator to form a perfectly smooth area of transition that will pass easily through thick rubber tubing (Fig. 1B). Because the sheath is fitted carefully to the dilator at the factory, it should not be loosened before use. Once inserted into a vessel over a guidewire, the dilator is easily removed from the sheath by turning the dilator's hub and locking the ring counterclockwise and then pulling the dilator out. This maneuver not only separates the interlocking hubs but also causes the diagonal end of the sheath to override the protruding rim of the expanded dilator, thus permitting withdrawal of the dilator. The clinical experience gained with the recessed-sheath dilators includes 18 insertions into the femoral artery (7-French dilator), three percutaneous gastrotomies (7-French peel-away), and four percutaneous cholecystostomies (two 16-French, two 24-French). In all cases, the insertion was perfectly smooth with no sensation of a hang-up as the transition zone of the sheath passed through tissues, some of which were quite desmoplastic. All the edges of the sheath were inspected at the end of each procedure and were found to be intact with no fraying, tearing, or pleating. As interventional procedures become more complex, varied, and demanding, there is an increasing need for the availability of catheter introducers that will pass safely without tearing not only through healthy tissue planes but also through fibrotic postoperative or postinflammatory indurated sites. The present design is a step in that direction.

Constantin Cope
Hospital of the University of Pennsylvania
Philadelphia, PA 19104

REFERENCES

- Butto F, Robinson JD, Vlodaver Z, Hunter DW, Castañeda-Zuñiga WR, Amplatz K. Modified sheath introducer for reduced arterial damage. *Radiology* 1987;163:824-826

- Cope C. Simple method for the introduction of large-gauge plastic catheters. *N Engl J Med* 1958;258:1000-1002

Removal of a Nondeflating Balloon Angioplasty Catheter After Percutaneous Aspiration

Retention of an angioplasty catheter because the balloon fails to deflate is an unusual complication. Removal after percutaneous puncture and aspiration of the balloon has been suggested as a feasible alternative to surgical intervention [1]. Such a procedure has been performed successfully in a 7-week-old mongrel puppy when a balloon failed to deflate during dilatation of an aortic coarctation [2]. We have used the technique successfully in a patient who had a retained catheter.

A 78-year-old man who previously had had angioplasty of a right common iliac stenosis was admitted for investigation of recurrent claudication. Transfemoral arteriography showed that a further stenosis had developed in the right common iliac artery distal to the original lesion. Repeat angioplasty was performed by using a Cordis balloon 3 cm long and 8 mm in diameter on a 7-French catheter (Cordis Corp., Miami, FL). The balloon was inflated and deflated three times with 30% iopamidol, and the postangioplasty arteriogram showed good results. After deflation, the catheter was withdrawn to the groin without applying suction to the balloon. Marked resistance to removal of the catheter was encountered, and fluoroscopy revealed a small amount of contrast medium trapped within the distal end of the balloon. The catheter was readvanced slightly over a guidewire, but nothing more could be aspirated from the balloon. Overinflating the balloon to burst it proved impossible because no more contrast medium could be injected into it.

A 22-gauge spinal needle was inserted vertically down into the balloon under fluoroscopic guidance. The contents were aspirated, and the catheter then was withdrawn easily from the groin. The balloon was severely crumpled, and the puncture hole was visible at its distal end.

We think that groin fibrosis due to the previous angioplasty may have been a factor in preventing deflation. During removal of catheters with polyethylene balloons, suction usually is not applied in case the stiff "wings" tear the arterial wall. Some fluid may remain within the balloon then, and attempts at removal through a fibrotic groin would tend to milk this residue into the distal end. Crumpling of the balloon may be enough then to trap the contrast material and prevent further attempts at deflation.

Perhaps a modification of technique should be considered when a noncompliant fibrous groin is suspected, and gentle suction should be applied during removal of the balloon. If deflation does not occur, percutaneous aspiration should be attempted before resorting to surgical arteriotomy.

Jeremy Price
Linda J. Hands
Edward W. L. Fletcher
John Radcliffe Hospital
Oxford OX3 9DU, United Kingdom

REFERENCES

- Cumberland DC. Percutaneous angioplasty. In: Ansell G, Wilkins RA, eds. *Complications in diagnostic imaging*, 2nd ed. Oxford, England: Blackwell Scientific Publications, 1987:128-147
- Schneider JR, Johnsrude IS, Lund G, Rysavy J, Anderson RW, Amplatz K. Percutaneous catheter balloons: failure to deflate. *Radiology* 1985; 155:832

Sonographic Appearance of Aortic Saddle Embolus

A 78-year-old woman with atrial fibrillation had acute pain in both legs at rest. Physical examination showed mottling of the lower extremities, and no femoral, popliteal, or distal pulses could be detected. The patient had a respiratory arrest, and after resuscitation, a sonogram of the aorta was requested. Real-time sonography showed that the caliber of the abdominal aorta was normal with no evidence of aneurysmal dilatation. Most of the aorta was anechoic with visible pulsations and was externally compressible. However, the terminal part contained intraluminal echogenic material (Fig. 1) that extended distally into the proximal common iliac arteries. No pulsations were present, and these segments were not compressible. At surgery, a large saddle embolus was found at the aortic bifurcation, and embolectomy was performed. The patient survived the operative procedure but died the next day.

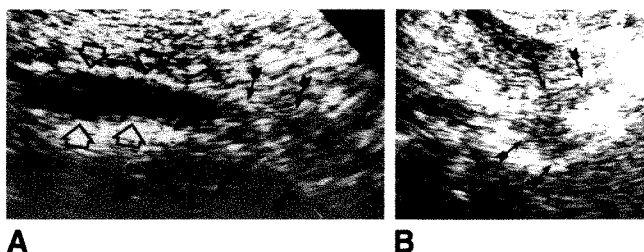


Fig. 1.—Aortic saddle embolus.

A, Sagittal sonogram of distal abdominal aorta shows transition from anechoic, pulsatile vessel (*open arrows*) to nonpulsatile aorta containing echogenic material (*closed arrows*).

B, Sagittal sonogram at aortic bifurcation shows echogenic material extending into common iliac arteries (*arrows*).

Top = anterior; bottom = posterior; left = head; right = foot.

Arterial emboli are a frequent cause of occlusive vascular disease. Most of these form as cardiac mural thrombi resulting from either atrial fibrillation due to atherosclerotic or rheumatic heart disease or from acute myocardial infarction [1]. Most arterial emboli lodge in the lower extremities; however, nearly 14% occur at the aortic bifurcation. Mortality remains high despite prompt surgical intervention [1].

Although the clinical diagnosis of saddle embolus of the distal aorta is rarely in doubt, abdominal aortic aneurysms may thrombose spontaneously, presenting a similar clinical picture [2]. Real-time sonography can be useful in documenting the presence of intraluminal clot and the absence of pulsations while excluding thrombosis of an abdominal aortic aneurysm. This knowledge is helpful in planning emergent surgery; embolectomy is required for the saddle embolus and more complicated aortofemoral bypass for the aneurysm. Sonography has been shown to be effective in detecting aortic thrombosis due to umbilical artery catheterization in neonates [3]; however, to my knowledge, the sonographic features of aortic saddle embolus have not been reported before.

Stanley G. Cooper
Norwalk Hospital
Norwalk, CT 06856

REFERENCES

1. Gordon RD, Fogarty TJ. Peripheral arterial embolism. In: Rutherford RB, ed. *Vascular surgery*, 2nd ed. Philadelphia: Saunders, 1984:449-459.
2. Rutherford RB. Infrarenal aortic aneurysms. In: Rutherford RB, ed. *Vascular surgery*, 2nd ed. Philadelphia: Saunders, 1984:755-771.
3. Rudas G, Bors S. Aortic thrombosis diagnosed by ultrasound. *Pediatr Radiol* 1988;18:77-78.

Gadolinium-DPTA: A Radiographic Contrast Agent

I recently made a serendipitous observation while reviewing an abdominal CT scan of an AIDS patient that I wish to share. Magnevist (gadopentetate dimeglumine; Berlex Laboratories, Inc., Cedar Knolls, NJ) is sufficiently radiopaque to be visible on CT images. I am unaware of any reports of this fact, and I have no previous personal experience nor do I know of any anecdotal experience of others in this regard.

When asked to review an abdominal and pelvic CT scan of a young male AIDS patient who was admitted to our medical center with a diagnosis of an acute abdomen, I noticed that contrast material was present in the renal collecting system. IV contrast material had not been administered for the CT scan, so I was left to explain this finding. A rapid review of the patient's recent radiographic studies failed to reveal a source for the contrast agent. Serendipitously, at that moment, the MR technologist appeared and asked for the patient's film jacket to file the MR brain scan, a study that had been completed 2 hr before the CT scan was performed. Yes, Magnevist had been administered. (It should be known that at my institution MR imaging is done at an outpatient facility across the street from the hospital.) A few hurried telephone calls and a review of a recent comprehensive index of radiologic literature were not helpful.

Thereupon, I scanned vials of Magnevist, Conray 60 (Mallinckrodt, St. Louis, MO), and lidocaine 1% with a Picker SX scanner. The vial of Magnevist was slightly less than half as dense as Conray 60. The patient had been given a dose of Magnevist equivalent to approximately 5 ml of Conray 60. In that Magnevist is excreted fairly rapidly by the kidneys, I had my explanation. An additional volunteer (or should I say "recruit") allowed performance of limited CT of his kidneys after Magnevist-enhanced MR imaging, and the observation was confirmed.

I will leave it to others to work this out more fully. There may be a use for an extremely safe, although expensive (approximately \$4.25/ml) and quite dose-limited, new radiographic contrast material.

Edward A. Janon
Alvarado Hospital Medical Center
San Diego, CA 92120

Simple Method to Identify Sequential Images

We describe a simple method for identifying sequential images produced by multifilm cameras in use for CT, MR, and other imaging techniques.

Although the future promises sophisticated archiving and retrieval of digital images, most radiologists still will be dealing with hard copy for many years. This includes not only images obtained in their own departments but also those accompanying patients referred from other institutions. Frequently, 10 or more sheets of film may be generated from a complex study, and although efforts have been made to segregate them in individual envelopes, they often all end up in the same film jacket.

For the last 4 years we have been using a simple technique that greatly facilitates sorting the several sheets of film containing the sequential images from a study. As soon as the hard copy from the multifilm camera has been processed, the technologist, using a felt-tip, permanent marking pen, marks in the upper left-hand corner of each film the date the examination was carried out and in the upper right-hand corner the position of this sheet of film relative to the total number of films that were used to record the sequence of images (e.g., 3 of 6) (Fig. 1).

This simple, inexpensive technique makes it easy to sort imaging studies both by date performed and by sequence. It is particularly

Fig. 1.—Simple method to identify sequential images.

DATE		#
1-11-89		396

important when patients have more than one examination and when films from these examinations have been commingled. This system is also effective in consultations and conferences, situations in which a radiologist often is presented with a stack of unsorted images and expected to give an instant interpretation. This methodology also will simplify the tasks of file room personnel who prepare images for interpretation and comparison with previous studies or who load films onto a multiviewer.

Raj Dalal
H. Rodney Hartmann
M. I. B. Hospital
Cooperstown, NY 13326

Letters are published at the discretion of the Editor and are subject to editing.

Letters to the Editor must not be more than two *double-spaced*, typewritten pages. One or two figures may be included. Abbreviations should not be used. See Author Guidelines, page A5.

Material being submitted or published elsewhere should not be duplicated in letters, and authors of letters must disclose financial associations or other possible conflicts of interest.

Letters concerning a paper published in the *AJR* will be sent to the authors of the paper for a reply to be published in the same issue. Opinions expressed in the Letters to the Editor do not necessarily reflect the opinions of the Editor.

Review of Current Literature

Initials and addresses of corresponding authors are provided in parentheses for each article so that the reader can obtain reprints directly. Abstracts are printed verbatim from each journal.

The New England Journal of Medicine

Radiologic contributions to the investigation and prosecution of cases of fatal infant abuse. Kleinman PK, Blackburne BD, Marks SC, Karellas A, Belanger PL (PKK, Dept. of Radiology, University of Massachusetts Medical Center, 55 Lake Ave., N., Worcester, MA 01655). *N Engl J Med* 320(8):507-511, 1989

In 1984 we started a two-year program in Worcester (Mass.) and Boston to provide additional radiologic data for the medical investigation of suspected fatal infant abuse. During that period the investigation of 12 cases of unexplained infant death included the review of complete radiographic skeletal surveys by a pediatric radiologist. Autopsies were supplemented with resection, high-detail radiography, and histologic study of all noncranial sites of suspected osseous

Thirty-four bony injuries were noted, including 12 acute and 16 healing fractures of the long-bone metaphyses and posterior-rib arcs in patterns indicative of infant abuse. The investigations determined that there were eight cases of abuse, two accidental deaths, and two natural deaths (sudden infant death syndrome). At this writing, the radiologic and osseous histologic studies appear to have influenced the determination of the manner of death in six of the eight cases of abuse and the criminal prosecution in four of the five convictions.

These findings suggest that a thorough postmortem radiologic evaluation followed by selected histologic studies can have an impact on the investigation and prosecution of cases of fatal infant abuse.

Reduced bone mass in daughters of women with osteoporosis. Seeman E, Hopper JL, Bach LA, et al. (ES, Dept. of Medicine, Austin Hospital, Heidelberg, Melbourne, Victoria 3084, Australia). *N Engl J Med* 320:554-558, March 1989

To determine whether premenopausal daughters of women with postmenopausal osteoporosis have lower bone mass than other women of the same age, we measured the bone mineral content of the lumbar spine and femoral neck and midshaft, using dual-photon absorptiometry, in 25 postmenopausal women with osteoporotic compression fractures and in 32 of their premenopausal daughters; we then compared the results with those in normal controls.

As compared with normal postmenopausal women, women with osteoporosis had lower bone mineral content in the lumbar spine, femoral neck, and femoral midshaft by 33, 24, and 15 percent, respectively ($P < 0.001$ for each comparison by the one-tailed t-test). As compared with normal premenopausal women, the daughters of women with osteoporosis had lower bone mineral content at these

sites by 7, 5, and 3 percent, respectively ($P = 0.03, 0.07$, and 0.15 , respectively, by the one-tailed t-test). In terms of a standardized score, we calculated that the mean (\pm SEM) relative deficits in bone mineral content in the daughters of women with osteoporosis were 58 ± 18 percent (lumbar spine) and 34 ± 16 percent (femoral neck) of the relative deficits in their mothers.

We conclude that daughters of women with osteoporosis have reduced bone mass in the lumbar spine and perhaps in the femoral neck; this reduction in bone mass may put them at increased risk for fractures. We also conclude that postmenopausal osteoporosis may result partly from a relatively low peak bone mass rather than from excessive loss of bone.

Detection of deep-vein thrombosis by real-time B-mode ultrasonography. Lensing AWA, Prandoni P, Brandjes D, et al. (AWAL, Centre for Thrombosis, Haemostasis and Atherosclerosis Research, F4 Rm. 237, Academic Medical Centre, Meibergdreef 9, 1105 AZ, Amsterdam, the Netherlands). *N Engl J Med* 320:342-345, Feb. 1989

In 220 consecutive outpatients with clinically suspected deep-vein thrombosis of the leg, we compared contrast venography with real-time B-mode ultrasonography, using the single criterion of vein compressibility with the ultrasound transducer probe. The common femoral and popliteal veins were evaluated for full compressibility (no thrombosis) and noncompressibility (thrombosis).

Both veins were fully compressible in 142 of the 143 patients with normal venograms (specificity, 99 percent; 95 percent confidence interval, 97 to 100). All 66 patients with proximal-vein thrombosis had noncompressible femoral veins, popliteal veins, or both (sensitivity, 100 percent; 95 percent confidence interval, 95 to 100). For all patients (including 11 with calf-vein thrombi), sensitivity and specificity were 91 (95 percent confidence interval, 82 to 96) and 99 percent, respectively. The sensitivity for isolated calf-vein thrombosis was only 36 percent. The compression ultrasound test was repeated in a subset of 45 consecutive patients by a second examiner, unaware of the results of the first test, whose results agreed in all patients with those of the first examiner ($\kappa = 1$).

We conclude that ultrasonography with the single criterion of vein compressibility is a highly accurate, simple, objective, and reproducible noninvasive method for detecting proximal-vein thrombosis in outpatients with clinically suspected deep-venous thrombosis.

Chest

Chronic thromboembolic occlusion in the adult can mimic pulmonary artery agenesis. Moser KM, Olson LK, Schlusberg M, Daily PO, Dembitsky WP (KMM, UCSD Medical Center (H772), 225 Dickinson St., San Diego, CA 92103). *Chest* 95:503-508, March 1989

In the first 100 patients operated on for C T-E PH, three were referred with the diagnosis of UPAA having been made elsewhere. We found that many features of these two conditions are so similar that differential diagnosis is very difficult. Shared features may include findings on chest x-ray film, pulmonary angiography, CT scan and MRI studies. Since the two conditions vary substantially with respect to the methods of potential surgical correction, recognition of this possible differential diagnostic dilemma is important.

Circulation

Neutrophil function in ischemic heart disease. Mehta J, Dinerman J, Mehta P, et al. (JM, Dept. of Medicine, University of Florida, Box J-277, JHMHC, Gainesville, FL 32610). *Circulation* 79:549-556, 1989

Neutrophils contribute to the healing of and scar formation in myocardium after ischemic injury. Many recent studies indicate that neutrophils may be involved in the genesis and propagation of myocardial ischemia. To characterize neutrophil function in ischemic heart disease, neutrophil chemotaxis, leukotriene B₄ (LTB₄) generation, and elastase release in plasma were measured in 20 patients with stable angina, 17 patients with unstable angina or acute myocardial infarction (AMI), and 20 age-matched control subjects. Neutrophils from patients with stable angina exhibited markedly increased chemotactic activity and LTB₄ generation as compared with the age-matched control subjects ($p < 0.01$). Neutrophils of nine of 17 patients with unstable angina or AMI clumped spontaneously ex vivo and exhibited marked pseudopod formation and granule extrusion on electron microscopy. Subsequent chemotactic activity and LTB₄ generation by neutrophils from these patients was less than in patients with stable angina, suggesting previous in vivo activation. Plasma levels of peptide B β , a product of fibrin degradation by human neutrophil elastase, were approximately 15-fold higher ($p < 0.001$) in patients with unstable angina or AMI (588 ± 171 pmol/l, mean \pm SEM) compared with those in patients with stable angina (37 ± 25 pmol/l) or control subjects (40 ± 22 pmol/l), confirming intense in vivo neutrophil activation. Our study shows enhanced neutrophil function in patients with ischemic heart disease. The increased neutrophil chemotactic activity and LTB₄ generation may be markers of stable angina pectoris. Intense neutrophil activation in unstable angina or AMI, as manifested by morphologic changes in neutrophils and elastase release, may relate to ongoing in vivo cellular activation.

Effect of magnesium on anginal attack induced by hyperventilation in patients with variant angina. Miyagi H, Yasue H, Okumura K, Ogawa H, Goto K, Oshima S (HY, Division of Cardiology, Kumamoto University Medical School, 1-1-1, Honjo, Kumamoto City, Kumamoto 860, Japan). *Circulation* 79:597-602, 1989

To examine whether or not magnesium suppresses coronary spasm, the effect of magnesium infusion on anginal attacks induced by hyperventilation was studied in 20 patients with variant angina. In all patients, anginal attacks associated with ischemic ST segment changes on the electrocardiogram were repeatedly induced by hyperventilation. The study was performed in the early morning successively for 3 days. On days 1 and 3 (control studies), 50 minutes before the hyperventilation test, a 5% glucose solution was infused as a placebo. On day 2 (magnesium study), 50 minutes before the hyperventilation test, magnesium sulfate (0.27 mM/kg body wt) was infused during a 20-minute period. During the control studies, anginal attack was induced by hyperventilation in all 20 patients, whereas during the magnesium study, anginal attack was induced by hyperventilation in only six (30%) of the 20 patients ($p < 0.001$ vs. control studies). The changes in arterial blood pH and Pco₂ caused by hyperventilation were not significant between the control study and the magnesium study. Mean serum magnesium concentration increased from 2.2 ± 0.2 to 6.0 ± 0.5 mg/dl immediately after infusing magnesium and was 4.5 ± 0.6 mg/dl before the hyperventilation test during the magnesium study. We conclude that magnesium sup-

presses anginal attacks induced by hyperventilation in patients with variant angina.

Increasing pericardial effusion in cardiac transplant recipients. Valentine HA, Hunt SA, Gibbons R, Billingham ME, Stinson EB, Popp RL (RLP, Cardiology Division (CVRC), Stanford University School of Medicine, Stanford, CA 94305). *Circulation* 79:603-609, 1989

Although pericardial effusion after cardiac surgery is frequent and usually benign, its etiology and prognosis after cardiac transplantation are unknown. During 1 year (1985-1986), 12 of our current transplant population (total, 189) developed moderate or large pericardial effusions confirmed by two-dimensional echocardiography. These effusions occurred within 1 month of transplantation in 10 patients and at 3 months and 4.5 years in the other two. Pericardiocentesis was performed because of clinical evidence of increasing effusions in eight patients, with demonstrable hemodynamic compromise secondary to tamponade in five. Pericardial fluid was sterile in all but one. Endomyocardial biopsy at the time of increasing effusion revealed moderate acute rejection in five patients, mild rejection in three, and no rejection in four. All three patients with mild rejection had moderate acute rejection on subsequent biopsy performed within 7 days. In two of the four with no rejection, repeat biopsy within 5 days showed moderate acute rejection; in a third, moderate rejection was present on biopsy performed 14 days later. *Legionella dumoffii* was isolated from the pericardial fluid of the fourth patient, whose subsequent biopsies never showed rejection. Three of the 12 patients developed progressive ventricular dysfunction sufficiently severe to require retransplantation. One patient died suddenly 12 months after transplantation, and autopsy examination revealed severe coronary artery disease. Two died of sepsis within 3 months of transplantation. Intense inflammatory infiltrates and thickening of the pericardium and epicardium were characteristically present in explanted and autopsy hearts. The remaining six patients were fully rehabilitated with normal ventricular function at 12-20 months after transplantation. These data suggest a temporal relation between development of moderate or large pericardial effusions and allograft rejection that may involve the pericardium. The clinical course and autopsy findings of these transplant recipients indicate an etiology and prognosis of pericardial effusions different from those associated with other forms of cardiac surgery.

Gastroenterology

Pancreaticobiliary ductal union in biliary diseases: an endoscopic retrograde cholangiopancreatographic study. Misra SP, Gulati P, Thorat VK, Vij JC, Anand BS (SPM, Dept. of Gastroenterology, G. B. Pant Hospital, New Delhi, India). *Gastroenterology* 96:907-912, 1989

To assess whether the anatomy of the pancreaticobiliary ductal drainage into the duodenum has any relationship with biliary diseases we analyzed 259 endoscopic retrograde cholangiopancreatograms. These included 102 normal examinations (control group), 95 patients with gallstone disease, and 21 patients with carcinoma of the gallbladder. In the control group, 64 (63%) subjects had a common channel and 38 (37%) had separate openings for the common bile duct and the main pancreatic duct. By contrast, the prevalence rate of a common channel was significantly lower in gallstone disease [28 (30%); $p < 0.001$]. No such difference, compared with controls, was observed in patients with carcinoma of the gallbladder. The length of the common channel in the control group (mean \pm SD, 4.7 ± 2.5 mm) was similar to that in gallstone disease (4.6 ± 2.6 mm). However, patients with carcinoma of the gallbladder had a significantly longer common channel (8.3 ± 4 mm; $p < 0.001$) compared with the control group. An abnormally long common channel (≥ 8 mm) was seen more frequently in carcinoma of the gallbladder (8 of 21; 38%) compared with normal subjects (3 of 102; 3%) and patients with gallstones (1 of 95, 1%); the difference was highly significant ($p < 0.001$ for each). These observations suggest a close association between the anatomy of the distal ends of the common bile duct and

main pancreatic duct and the development of gallstones and carcinoma of the gallbladder.

Reprinted with permission by the American Gastroenterological Association.

Comparison of three nonsurgical treatments for bleeding esophageal varices. O'Connor KW, Lehman G, Yune H, et al. (KWO, Dept. of Medicine, Division of Gastroenterology, Indiana University School of Medicine, Indianapolis, IN). *Gastroenterology* 96:899-906, 1989

Ninety-seven patients with recent or active variceal bleeding were randomly assigned to oral propranolol, endoscopic sclerotherapy plus oral propranolol, or transhepatic sclerotherapy plus oral propranolol. The effects of treatment on the number of units transfused, rebleeding of any magnitude, major rebleeding, and death were assessed in these patients, 82% of whom were alcoholic and 81% Child's Class C. After a minimum follow-up interval of 2 yr (range, 27-65 mo), major rebleeding rates were 65% for propranolol alone, 45% for endoscopic sclerotherapy plus propranolol, and 60% for transhepatic sclerotherapy plus propranolol. The corresponding death rates were 81% for propranolol alone, 55% for endoscopic sclerotherapy plus propranolol, and 66% for transhepatic sclerotherapy plus propranolol ($p = 0.03$). Thirty-three patients (34%) never received propranolol: 8 due to medical contraindications and 25 because they died or bled enough to meet the definition of treatment failure within 3 or 4 days of randomizations (no significant differences among treatment groups). Patients assigned to propranolol alone bled sooner, bled more units, and had a higher mortality rate than patients treated by endoscopic sclerotherapy plus propranolol. Patients treated with transhepatic sclerotherapy plus propranolol had intermediate results. Propranolol alone is inadequate treatment for esophageal variceal bleeding in patients with advanced liver disease.

Reprinted with permission by the American Gastroenterological Association.

Gallbladder motility before and after extracorporeal shock-wave lithotripsy. Spengler U, Sackmann M, Sauerbruch T, Holl J, Paumgartner G (US, Dept. of Internal Medicine II, Klinikum Grosshadern, University of Munich, Munich, Federal Republic of Germany). *Gastroenterology* 96:860-863, 1989

To determine whether extracorporeal shock-wave lithotripsy of gallbladder stones alters gallbladder motility, gallbladder contraction in response to intravenous cholecystokinin was investigated by ultrasound. Twenty-one patients with symptomatic gallstones were studied before and after shock-wave lithotripsy, 12 with and 9 without concomitant litholytic therapy (combination of ursodeoxycholic acid and chenodeoxycholic acid). Gallbladder emptying was significantly delayed and less complete in both groups of patients before shock-wave treatment (with bile salts: residual volume, $51\% \pm 10\%$ and half-ejection time, 40 ± 5 min; without bile salts: residual volume, $46\% \pm 7\%$; half-ejection time, 30 ± 4 min) compared with healthy controls (residual volume, $15\% \pm 4\%$; half-ejection time, 18 ± 2 min). Gallbladder motility was not altered in either group 1 day and 1 yr after lithotripsy. The findings indicate (a) that extracorporeal shock-wave lithotripsy has no immediate or long-term adverse effects on gallbladder motility and (b) that the defect of gallbladder motility associated with gallstone disease is not abolished by removal of the stone.

Reprinted with permission by the American Gastroenterological Association.

Effect of proctocolectomy for chronic ulcerative colitis on the natural history of primary sclerosing cholangitis. Cangemi JR, Wiesner RH, Beaver SJ, et al. (JRC, Division of Gastroenterology, Mayo Medical School, Clinic, and Foundation, Rochester, MN). *Gastroenterology* 96:790-794, 1989

The effect of proctocolectomy on the primary sclerosing cholangitis that frequently is associated with chronic ulcerative colitis in patients with both conditions is unknown. We have studied prospectively the progression of clinical, biochemical, cholangiographic, and hepatic histologic features in 45 patients with both primary sclerosing cholan-

gitis and chronic ulcerative colitis to compare these variables in the 20 patients who had undergone proctocolectomy with the 25 who had not. The two groups were similar initially with regard to clinical, biochemical, cholangiographic, and hepatic histologic findings. All patients were followed for a minimum of 1 yr and overall duration of follow-up was similar in both groups (4.1 vs. 3.9 yr). Clinically, new onset of hepatomegaly, splenomegaly, esophageal varices, and ascites did not differ in patients with and without proctocolectomy. Biochemically, the serial changes in bilirubin, alkaline phosphatase, aspartate aminotransferase, prothrombin time, and albumin were similar. Histologic progression on liver biopsy did not differ between groups, nor did changes on serial cholangiograms. Proctocolectomy also had no effect on survival. We conclude that proctocolectomy for chronic ulcerative colitis has no beneficial effect on the primary sclerosing cholangitis in patients with both diseases.

Reprinted with permission by the American Gastroenterological Association.

Gastrointestinal Endoscopy

The gastrostomy button: a prospective assessment of safety, success, and spectrum of use. Foutch PG, Talbert GA, Gaines JA, Sanowski RA (PGF, Dept. of Gastroenterology VAMC, 7th St. & Indian School Rd., Phoenix, AZ 85012). *Gastrointest Endosc* 35(1):41-44, 1989

The gastrostomy button is a new, skin level, nonrefluxing, mushroom-tipped feeding device which can be used to replace conventional gastrostomy catheters. We have prospectively evaluated 31 consecutive patients managed with this appliance and our results show that the button can be successfully placed in 90% of cases without serious morbidity or mortality. The procedure is quick to perform, requires minimal intravenous sedation, and is well-suited to a broad range of socially active gastrostomy-dependent patients. Patients found the aesthetics, convenience, and independence of the low profile design attractive and no individual wished to return to the original method of feeding. Small and medium-size buttons were easier to place than larger devices. Gastrocutaneous reflux through the appliance occurred in 11% of cases and was a common cause for replacement. Alert, ambulatory patients with an established gastrostomy and short or medium-sized gastrocutaneous fistulous tracts are ideal candidates for the button.

Endoscopic management of cysts and pseudocysts in chronic pancreatitis: long-term follow-up after 7 years of experience. Cremer M, Deviere J, Engelholm L (MC, Dept. of Gastroenterology, ULB-Hôpital Erasme, route de Lemnik 808, B-1070 Brussels, Belgium). *Gastrointest Endosc* 35(1):1-9, 1989

Endoscopic cystoenterostomy was performed in 33 patients with chronic pancreatitis. Endoscopic cystoduodenostomy (ECD) was done in 22 cases of symptomatic paraduodenal cysts and endoscopic cystagastrostomy (ECG) in 11 cases of retrogastric pseudocysts. The success rates were 96% for ECD and 100% for ECG. The relapse rate was 9% after ECD and 19% after ECG. No significant complications were observed after successful ECD and clinical relief of pain was achieved in 20 patients. ECD was an effective and definitive treatment for 19 of the 22 cases. Two complications of ECG were gastric hemorrhage and iatrogenic pseudocyst infection. In two ECG patients, percutaneous drainage was required. ECG alone was a definitive treatment for 8 of the 11 cases. When restricted to the precise morphological indication (paraintestinal cyst bulging into the duodenal or gastric lumen), ECD is the first choice for treatment of paraduodenal cysts, whereas ECG is an alternative procedure for the drainage of retrogastric pseudocysts, offering at least results as good as percutaneous drainage.

The diagnosis of submucosal tumors of the stomach by endoscopic ultrasonography. Yasuda K, Nakajima M, Yoshida S, Kiyota K, Kawai K (KY, Dept. of Gastroenterology, Kyoto Second Red Cross

Hospital, Kamazadori Marutamachi-agaru Kamigyo-ku, Kyoto 602, Japan). *Gastrointest Endosc* 35(1):10-15, 1989

The clinical value of endoscopic ultrasonography (EUS) in the diagnosis of submucosal tumors (SMTs) of the stomach was examined. We used echo endoscopes with a 7.5 or 10.0 MHz radial-scan transducer made by Olympus Co. Ltd. EUS was carried out on 80 patients with SMTs of the stomach including 54 cases confirmed histologically (24 cases of leiomyoma, 3 of leiomyosarcoma, 12 of cysts, 7 of aberrant pancreas, 4 of lipoma, 2 of carcinoid, and 3 of other diseases). Fifty-nine patients with extraluminal compression were detected by endoscopy and/or x-ray examination. We examined the effectiveness of EUS based on our analysis of the gastrointestinal tract wall seen in the EUS image as a five-layered structure corresponding with that of the histological layers. As a result, SMTs and extragastric compression were easily distinguishable in the EUS images of the lesions. The size, location, and origin of the SMTs could be detected. From the location of the SMT in the five-layered structure seen in the EUS image we could predict its histological nature.

Thus, EUS was a most valuable method not only in the diagnosis of intramural and extramural SMTs but also in the detection of extragastric compressive lesions and organs.

Scandinavian Journal of Gastroenterology

Sclerosing cholangitis in acquired immunodeficiency syndrome: case reports and review of the literature. Dowsett JF, Miller R, Davidson R, et al. (JFD, Dept. of Gastroenterology, The Middlesex Hospital, Mortimer St., London WIN 8AA, United Kingdom). *Scand J Gastroenterol* 23:1267-1274, 1988

Four patients with acquired immunodeficiency syndrome (AIDS) (CDC group IV) were investigated for biliary disease because of the presence of both severe upper abdominal pain and raised levels of serum alkaline phosphatase. None was clinically jaundiced. Upper abdominal ultrasound was abnormal in three. All had endoscopic retrograde cholangiographic evidence of both an intrahepatic sclerosing cholangitis suggestive of primary sclerosing cholangitis and an irregular suprapapillary common bile duct dilation suggestive of papillary stenosis. Three had evidence of gastrointestinal cryptosporidiosis and two of disseminated cytomegalovirus infection. Endoscopic sphincterotomy, performed in two patients, gave good pain relief. We propose the name 'AIDS sclerosing cholangitis' for this form of secondary cholangitis. The cause of this disorder remains unclear. Recent evidence is discussed which suggests that it is not due to HIV itself but to an opportunistic infection. Cryptosporidium appears to be the most likely candidate.

The Journal of Bone and Joint Surgery

Comparison of computerized tomography parameters of the cervical spine in normal control subjects and spinal cord-injured patients. Matsuura P, Waters RL, Adkins RH, Rothman S, Gurbani N, Sie I (PM, Rancho Los Amigos Medical Center, Rm. 121, Harriman Bldg., 7601 E. Imperial Hwy., Downey, CA 90242). *J Bone Joint Surg [Am]* 71-A(2):183-188, Feb. 1989

The cross-sectional area and the sagittal and transverse diameters of the cervical spinal canal were measured, using high-resolution, thin-section computerized-tomography images, in 100 control subjects and forty-two patients who had a traumatic injury to the spinal cord. No significant differences were found between the control and the spinal cord-injured group with regard to the cross-sectional area of the spinal canal; however, the differences between the two groups were significant with regard to mean sagittal and transverse diameters of the spinal canal. The sagittal diameters of the spinal canal of the control group were significantly larger than those of the spinal cord-injured group. Conversely, the transverse diameters of the spinal canal of the spinal cord-injured group were significantly larger than those of the control group.

These findings suggest that certain patients may be predisposed to spinal cord injury, given sufficient trauma. It is not the total volume of space in the spinal canal that is the critical factor; rather, it is the shape. An index of shape is the ratio of the sagittal to the transverse diameter.

The difference between the two groups, based on the ratio of sagittal to transverse diameter, was highly significant. Because this measure is a ratio, there is no need to evaluate an individual on the basis of measurements of absolute values.

Clinical Orthopaedics and Related Research

The quadrangular fragment fracture: roentgenographic features and treatment protocol. Favero KJ, Van Peteghem PK (KJF, Dept. of Orthopaedic Surgery, Shaughnessy Hospital/University of British Columbia, Rm. G423, 4500 Oak St., Vancouver, B.C., Canada V6H 3N1). *Clin Orthop* 239:40-46, Feb. 1989

The quadrangular fragment fracture is a clinically discrete type of cervical lesion that poses a difficult management problem. Physically, it resembles the triangular fragment fracture or teardrop fracture, but it responds very poorly to posterior fusion, the conventional treatment for these fractures. It is characterized by a quadrangular-shaped fragment from the anterior one-third of the vertebral body, a significant degree of posterior subluxation, an angular kyphosis, and an increased interspinous space with facet subluxation due to disruption of the soft tissues. Recognition of the quadrangular fragment may help determine the treatment protocol. A group of 23 patients with quadrangular fragment fracture was treated with the standard protocol and had poor results, including difficulty in maintaining reduction, neck pain, and significant residual kyphosis. A second group of 15 patients received the second treatment protocol, which consisted of one to two weeks of skull traction over an extension bolster, followed by an anterior interbody strut graft to stabilize the fracture and further traction over an extension bolster until four weeks postinjury. Treatment minimized the angular kyphosis apparent at bony healing, and all patients achieved satisfactory union with good alignment and no significant neck pain.

The Journal of Urology

Potential pitfalls in the obstructive renal scan in patients with double-pigtail ureteral catheters. Greenstein A, Chen J, Matzkin H, Baron J, Braf Z (AG, Dept. of Urology, Tel-Aviv Medical Center, Tel-Aviv University, Tel-Aviv, Israel). *J Urol* 141:283-284, Feb. 1989

In 21 patients with a long-standing internal ureteral double-pigtail catheter we demonstrated the adverse effect of a full bladder on upper system drainage. A pseudo-obstructive pattern noted in these patients on routine scans was immediately rectified by mere bladder emptying and a normal pattern was demonstrated. We suggest the bladder be emptied in all patients with indwelling internal ureteral stents before renographic evaluation.

British Journal of Urology

Patients at high risk of cardiovascular complications in oestrogen treatment of prostatic cancer. Hendriksson P, Edhag O, Eriksson A, Johansson S-E (PH, Dept. of Medicine, Huddinge Hospital, S-141 86 Huddinge, Sweden). *Br J Urol* 63:186-190, Feb. 1989

The aim of this study was to predict cardiovascular complications in patients with prostatic cancer treated with oestrogen. A randomised prospective study of oestrogen therapy versus orchiectomy was performed. Patients with pre-existing cardiovascular morbidity were excluded (16%). Prior to the initiation of therapy, patients were subjected to exercise stress tests, physiological evaluation of peripheral circulation, blood volume estimation, chest X-ray, blood test, including hormones, lipoproteins, and antithrombin III, and a physical

examination and history by a cardiologist. The oestrogen treatment and the orchiectomy group did not differ with regard to these pre-treatment variables; 25% of the patient given oestrogen therapy had cardiovascular complications during the initial treatment year compared with none of the orchiectomy group.

Three statistical discriminating techniques were employed and they allowed us to identify 2 strong discriminating variables for cardiovascular complications if oestrogen therapy is instituted in patients with prostatic cancer but without overt clinical cardiovascular disease. These 2 discriminators were luteinising hormone (LH) and ST-segment depression during exercise. This means that a patient with ST-segment depression during an exercise test and/or a high luteinising hormone concentration should not be treated with oestrogen.

Pediatrics

Relationship of benzyl alcohol to kernicterus, intraventricular hemorrhage, and mortality in preterm infants. Jardine DS, Rogers K (DSJ, Dept. of Anesthesiology, University of Washington School of Medicine, RN-10, Seattle, WA 98195). *Pediatrics* 83(2):153-160, Feb. 1989

Intraventricular hemorrhage and death in preterm neonates has been associated with the use of fluid containing benzyl alcohol, a bacteriostatic agent, to flush intravascular catheters. The hospital and autopsy records of infants admitted to a nursery during the last 18 months that benzyl alcohol was in use (218 patients) were reviewed and compared with those of infants admitted in the first 18 months after benzyl alcohol was withdrawn (232 patients). The volume of flush solution administered to each patient was estimated. Exposure to benzyl alcohol was significantly associated with the development of kernicterus ($P < .005$), and intraventricular hemorrhage ($P < .000,000,5$). Kernicterus did not develop in any patient after benzyl alcohol was withdrawn. Many patients with kernicterus or intraventricular hemorrhages received small daily volumes of fluid containing benzyl alcohol. Withdrawal of benzyl alcohol from clinical use had no demonstrable effect on mortality. Medications intended for neonatal use should not contain benzyl alcohol. Our data indicate that patients not exposed to benzyl alcohol have a greatly reduced risk of kernicterus. If this finding is confirmed by other investigators, present indications for exchange transfusions in preterm infants with moderate elevations of serum bilirubin should be reconsidered.

Reprinted by permission of PEDIATRICS © 1989.

The Journal of Pediatrics

Odontoid hypoplasia with vertebral cervical subluxation and ventriculomegaly in metatropic dysplasia. Shohat M, Lachman R, Rimoin DL (DLR, Dept. of Pediatrics, Cedars-Sinai Medical Center, 8700 Beverly Blvd., Los Angeles, CA 90048). *J Pediatr* 114:239-243, Feb. 1989

Our experience with 12 patients with metatropic dysplasia has demonstrated two important and treatable complications: odontoid hypoplasia with subluxation of the first and second cervical vertebrae, and ventriculomegaly. Hypoplasia and lack of ossification of the odontoid process were noted in all cases. Subluxation of these two vertebrae was demonstrated in all six patients who had lateral flexion-extension radiographs; three had subluxation even in a neutral position, and sudden odontoid dislocation developed in another after a simple fall. Four individuals have had surgical fusion of the cervical vertebrae; one child died suddenly, 1 week before scheduled surgery. In the three patients in whom computed tomography scans of the head were obtained, enlarged ventricles were found; one had symptomatic increased intracranial pressure and required a shunt. We recommend that odontoid hypoplasia be evaluated in all patients with metatropic dysplasia. If subluxation is proved, atlantoaxial fusion should be performed before damage to the cervical part of the spinal cord results. Serial head circumference measurements and evaluation for hydrocephalus are also recommended.

Sturge-Weber syndrome: a study of cerebral glucose utilization with positron emission tomography. Chugani HT, Mazziotta JC, Phelps ME (HTC, Division of Pediatric Neurology, Rm. MDCC 22-464, UCLA School of Medicine, Los Angeles, CA 90024). *J Pediatr* 114:244-253, Feb. 1989

We measured local cerebral metabolic rate for glucose (ICMRGlc) using positron emission tomography (PET) in six children with Sturge-Weber syndrome (SWS) and in six neurologically asymptomatic children with facial capillary hemangioma suggestive of SWS. Children with advanced SWS showed markedly depressed ICMRGlc in the anatomically affected cerebral hemisphere in a distribution that extended beyond the abnormalities depicted on computed tomography scan. In two infants with SWS and recent seizure onset, interictal PET revealed a paradoxical pattern of increased ICMRGlc in the cerebral cortex of the anatomically affected hemisphere. In one of these infants, ICMRGlc was also increased in the contralateral cerebellum, suggesting activation of the cortico-ponto-cerebellar circuitry. Subsequent PET (28 months later) in this child revealed the typical ICMRGlc pattern seen in advanced SWS. Further study of this transient ICMRGlc increase may be important in disclosing the pathogenesis of unilateral cerebral degeneration in SWS. In neurologically asymptomatic children with the facial stigmata of SWS and in children with early SWS, PET provides a sensitive measure of the extent and degree of cerebral metabolic impairment. Serial PET studies in children with SWS can be used to assess disease progression and, together with computed tomography or magnetic resonance imaging, may be useful in the selection of suitable candidates for cerebral hemispherectomy or focal cortical resection.

The Journal of Nuclear Medicine

Localization of pheochromocytoma: MIBG, CT, and MRI correlation. Velchik MG, Alavi A, Kressel HY, Engelman K (MGV, Dept. of Radiology, The Hospital of the University of Pennsylvania, Philadelphia, PA 19104). *J Nucl Med* 30:328-336, 1989

Nineteen patients (8 M, 11 F) ranging in age from 15-67 yr old (mean = 39 yr) with clinically diagnosed pheochromocytomas were prospectively evaluated with ^{131}I metaiodobenzylguanidine (MIBG) scintigraphy ($n = 19$), computed tomography (CT) ($n = 19$), and magnetic resonance imaging (MRI) ($n = 17$) in order to determine their relative diagnostic efficacy. Pathologic confirmation was obtained in all 19 patients: 13 intraadrenal and six extraadrenal with metastases in five (Table 1). All three imaging modalities were in agreement in 11 of 14 completed examinations (79%). MIBG and CT agreed in 16 of the 19 patients in whom both were performed (84%). MIBG/MR and CT/MR results were concordant in 12 of 14 (86%) and 13 of 14 (93%) jointly completed examinations, respectively. There was one false-negative (FN) MIBG scan, two FN CT scans, and one FN MR scan. MIBG, CT, and MRI are complementary procedures with MIBG providing more specific functional information and the latter two superior anatomic detail. MIBG scintigraphy is recommended as the initial localizing study of choice (especially for the detection of extraadrenal disease and postoperative recurrence), as a guide for CT and/or MR and specific functional confirmation of their findings. Although MRI is capable of imaging in multiple planes (without exposure to ionizing radiation or the need for i.v. contrast material) with superior contrast compared to CT, it is expensive and has poor patient cooperation. However, it may be capable of differentiating pheochromocytomas from other adrenal masses on the basis of signal characterization.

Gastrointestinal Radiology

Complications of endoscopic retrograde sphincterotomy: computed tomographic evaluation. Kuhlman JE, Fishman EK, Milligan FD, Siegelman SS (EKF, Dept. of Radiology, Johns Hopkins Hospital, 600 N. Wolfe St., Baltimore, MD 21205). *Gastrointest Radiol* 14:127-132, 1989

Although the reported complication rate of endoscopic retrograde cholangiopancreatography (ERCP) with sphincterotomy is low, patients often experience abdominal pain postprocedure. When pain persists, or fever or leukocytosis develop, a procedure-related complication should be suspected. The authors reviewed a series of 36 patients referred to computed tomography (CT) for evaluation of possible complications following ERCP with sphincterotomy. Initial CT scans were obtained within 24 h in 19 patients, and during the second to seventh day in the remainder. Complications detected by CT included acute pancreatitis (23), duodenal perforation (11), retroperitoneal dissection of air (4), pneumoperitoneum (4), and development of retroperitoneal abscess (4). Eight patients had normal CT scans except for air and contrast material in the biliary tree. The severity and extent of injury were readily assessed by CT, and response to therapy effectively monitored by serial CT examinations. Thirty-one cases (31 of 36) were successfully managed conservatively with antibiotics, intravenous hydration, and restriction of oral intake. Four patients required surgical intervention for drainage of a retroperitoneal abscess (3) or a pseudocyst (1). A fifth patient required intensive care resuscitation for septic shock. We conclude that CT is the study of choice for evaluating the patient with suspected complication following ERCP and sphincterotomy.

Journal of Ultrasound in Medicine

Sonography of the simple and complicated ipsilateral fused kidney. Lubat E, Hernanz-Schulman M, Genieser NB, Ambrosino MM, Teele RL (EL, Dept. of Radiology, New York University Medical Center, 550-560 1st Ave., New York, NY 10016). *J Ultrasound Med* 8:109-114, March 1989

Anomalies of renal fusion and their sonographic findings can be straightforward or quite complex. Sonograms of eight cases of simple and complicated anomalies of renal fusion in pediatric patients are reviewed to determine characteristic sonographic findings in such cases. The correct diagnosis can be suspected by evaluation of the following parameters: (1) the echoic texture of the renal "mass"; (2) the differential orientation of the renal pelvises; (3) the content of the contralateral renal fossa; (4) the size of the ipsilateral kidney; (5) extension of the isthmus medially anterior to the spine; and (6) presence of a deep anteroposterior notch. Utilizing these parameters, a rationale for diagnosis and for selecting the appropriate sequence of further studies is suggested.

Reprinted with permission by the American Institute of Ultrasound in Medicine.

Journal of Computer Assisted Tomography

MR imaging of normal nasal cycle: comparison with sinus pathology. Zinreich SJ, Kennedy DW, Kumar AJ, Rosenbaum AE, Arrington JA, Johns ME (SJZ, Meyer 8-140, Johns Hopkins Hospital, 600 N. Wolfe St., Baltimore, MD 21205). *J Comput Assist Tomogr* 12(6):1014-1019, Nov./Dec 1988

Sequential MR examinations of the nasal cavity and paranasal sinuses were performed within a 6-8 h period in five normal volunteers. The nasal mucosal volume and signal intensities (T2 weighted) were shown to alternate from one side to the other during this period. When a topical vasoconstrictor was applied, this cycle was interrupted. These cyclical changes were limited to the mucosa of the

turbinates, nasal cavity, and ethmoid sinus, representative of the nasal cycle. The maxillary, frontal, and sphenoid sinuses were not affected. The hyperintensity of the nasal cycle on T2-weighted images was similar to that shown by inflammatory mucosa. Squamous cell carcinoma within the nasal cavity and paranasal sinuses has characteristically demonstrated a lower signal intensity on T2-weighted images. Awareness of these cyclical nasal and paranasal appearances reduces the likelihood of inflammatory disease being confused with normal physiological changes within the nasal area.

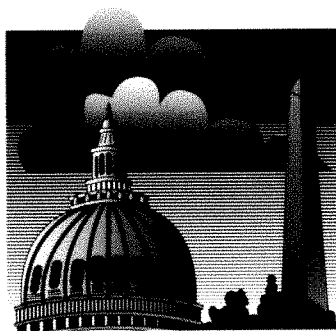
Magnetic Resonance Imaging

Thermoregulatory consequences of cardiovascular impairment during NMR imaging in warm/humid environments. Adair ER, Berglund LG (ERA, John B. Pierce Foundation Laboratory, 290 Congress Ave., New Haven, CT 06519). *Magn Reson Imaging* 7:25-37, 1989

A simple model of physiological thermoregulation, previously adapted to predict the thermoregulatory consequences of exposure to the nuclear magnetic resonance (NMR) imaging environment, has been further adapted to simulate impaired cardiovascular function. Restrictions on the rate of skin blood flow (SkBF), ranging from 0 to 89% of normal, were studied. Predictions of physiological heat loss responses in real time were generated as a function of ambient temperature (T_a), relative humidity (RH) and rate of whole-body radio-frequency (RF) energy deposition (SAR). Under conditions that are desirable in the clinic ($T_a = 20^\circ\text{C}$, 50% RH, still air), moderate restrictions (up to 67%) of SkBF yield tolerable increases in core temperature ($\Delta T_{co} \leq 1^\circ\text{C}$) during NMR exposures ($\text{SAR} \leq 4 \text{ W/kg}$) of 40 min or less. Increased T_a and RH exacerbate the thermal stress imposed by absorbed RF energy; severely impaired SkBF encourages short NMR exposures (e.g., 20 min or less) at SARs $\leq 3 \text{ W/kg}$. In warm/humid environments, sweating is predicted to be profuse and evaporative cooling curtailed, yielding a state of extreme thermal discomfort. Added insulation (e.g., a blanket) is discouraged. Some guidelines, incorporating SkBF restrictions, T_a , RH, and insulation, are offered for the prediction of tolerable NMR exposure conditions.

Marrow infarction in sickle cell anemia: correlation with marrow type and distribution by MRI. Rao VM, Mitchell DG, Rifkin MD, et al. (VMR, Dept. of Radiology, Thomas Jefferson University Hospital, 10th and Sansom Sts., Philadelphia, PA 19107). *Magn Reson Imaging* 7:39-44, 1989

Ischemic necrosis of bone is believed to occur exclusively in areas of predominantly fatty marrow. Sickle cell disease is unusual in that marrow infarction occurs in areas of active hematopoiesis. MR images of long bone obtained in ten patients with sickle cell anemia (SCA) were analyzed to correlate the distribution and appearance of marrow infarction with the type of marrow. While the hematopoietic marrow predominated in metaphyseal and diaphyseal regions of femurs and tibias, the fatty or mixed marrow was the most common pattern in epiphyses. Infarcts occurred in fatty as well as hematopoietic marrow. Marrow infarcts were isointense or minimally hyperintense on T_1 weighted images with the hematopoietic marrow and therefore difficult to detect. On T_2 weighted images, the infarcts showed very high signal. T_2 weighted images are essential for detection of marrow infarction. Soft tissue changes seen as low signal on T_1 and high signal on T_2 , may be secondary to intramuscular injections of analgesics or muscle ischemia occurring during sickle crisis.



Come to the
American Roentgen Ray Society

90th

ANNUAL MEETING

Washington, D. C.

Sheraton Washington Hotel

May 13-18, 1990

Scientific Program (200 papers)

Instructional Courses (60 hours)

Categorical Course on Cardiovascular Imaging

The Caldwell Lecture

Award Papers

Scientific Exhibits

Social, Golf, and Tennis Programs

Guest Programs



News

Ultrasonic Liver Surgery

The Parenteral and Enteral Nutrition Team and the Section of Pediatric Surgery, Dept. of Surgery, University of Michigan Medical School are sponsoring Ultrasonic Liver Surgery, June 2, at the Towsley Center, Ann Arbor, MI. The number of participants in the course will be limited, and a waiting list will be established. Course director: Alfred E. Chang. Category 1 credit: 8 hr. Information: Betty Phillips, Program Assistant, Office of Continuing Medical Education, G-1000 Towsley Center, Box 0201, University of Michigan Medical School, Ann Arbor, MI 48109-0201; (313) 763-1400.

Diagnostic Radiology and Nuclear Medicine

The Dept. of Radiology, Bowman Gray School of Medicine, will hold its 7th Annual Summer Continuing Education Meeting, June 25-30, at the Kingston Plantation, Myrtle Beach, SC. The course will provide the practicing radiologist with an update on contemporary topics pertaining to key subspecialties and techniques. Emphasis will be on newer imaging techniques. Program director: Ronald J. Zagoria. Category 1 credit: 20 hr. Fee: \$450. Information: Pat Rice, Dept. of Radiology, Bowman Gray School of Medicine, Winston-Salem, NC 27103; (919) 748-2470.

Practical Approach to Mammographic Interpretation

The Division of Special Programs, Colby College, is sponsoring Practical Approach to Mammographic Interpretation, July 17-18, in Waterville, ME. This intensive tutorial is designed to teach a pragmatic approach to interpretation of mammograms. It will include all aspects of needle localization. Category 1 credit: 10 hr. Fee: \$275. Information: Dr. Robert Kany, Director, Special Programs, Colby College, Waterville, ME 04901.

Pittsburgh Breast Imaging Seminar

The 9th annual Pittsburgh Breast Imaging Seminar will be held Aug. 4-6 at the Sheraton Hotel at Station Square, Pittsburgh. The seminar is sponsored by four Pittsburgh hospitals: Magee-Womens Hospital, Montefiore Hospital, Shadyside Hospital, and the Western Pennsylvania Hospital. The course will feature state-of-the-art breast imaging. Course codirectors: Kathleen Harris, Ellen Mendelson, Ingrid Naugle, and W. R. Poller. Guest faculty: Ingvar Andersson, S. A. Feig, Gloria Frankl, and V. P. Jackson. Category 1 credit: 19 hr; ECE

credits (ASRT): 19. Fee: physicians, \$375; residents and fellows (with letter of verification), technologists, and other health professionals, \$200. Information: call Terri Smith at (412) 647-1635.

Physics and Biology of Radiology

The Dept. of Radiology, University of California, San Diego, School of Medicine, will present Physics and Biology of Radiology, Aug. 24-27, at the Town & Country Hotel, San Diego. Program director: Michael P. André. Category 1 credit: 25 hr. Fee: \$395. Information: Dawne Ryals, Ryals & Associates, P. O. Box 1925, Roswell, GA 30077-1925; (404) 641-9773.

Imaging on Lake Coeur d'Alene

The Depts. of Radiology, University of Washington, Seattle, and Sacred Heart Medical Center, Spokane, are cosponsoring Imaging on Lake Coeur d'Alene—A Summer Radiology Meeting, Aug. 31-Sept. 2, at the Coeur d'Alene Resort, Coeur d'Alene, ID. This course is designed primarily to meet the educational objectives of practicing general diagnostic radiologists. Topics will include chest and abdominal radiology, diagnostic ultrasound, and digital techniques. Category 1 credit: 20 hr. Fee: \$350 (\$400 after July 15). Information: Kathy Fischer, Course Secretary, Dept. of Radiology, Sacred Heart Medical Center, TAF-C9, Spokane, WA 99220; (509) 455-3352 or 455-3330.

Sonography Update

The Dept. of Radiology, University of California, San Diego, School of Medicine, will present the 5th annual Sonography Update for Physicians and Sonographers, Sept. 7-10, at the San Diego Marriott Hotel and Marina, San Diego. Program director: John R. Forsythe. Category 1 credit: 18 hr. Fee: physicians, \$375; sonographers, technologists, and residents, \$275. Information: Dawne Ryals, Ryals & Associates, P. O. Box 1925, Roswell, GA 30077-1925; (404) 641-9773.

Mammography and the Search for Breast Cancer

Wende Logan-Young and the Rochester Roentgen Ray Society are sponsoring Mammography and the Search for Breast Cancer, Sept. 15-17, in Vancouver, B.C. This intensive course will address all aspects of screen-film mammography and other investigative procedures essential to early accurate diagnosis of breast cancer.

Fee: radiologists, \$400; residents and technologists, \$350. Information: Wende Logan-Young, M.D., 1351 Mt. Hope Ave., Rochester, NY 14620; (716) 442-8432.

Harvard Postgraduate Courses

The Harvard Medical School postgraduate courses, Current Concepts in Neuroradiology, Head and Neck Radiology, and Neuro-MRI, will be given Sept. 18–22 at the Lafayette Hotel, Boston. Category 1 credit: 40 hr. Fee: for combined course, physicians, \$590; residents and fellows, \$450; for Neuroradiology only (Sept. 18–20), \$450; for Head and Neck Radiology only (Sept. 21–22), \$400. Information: Harvard Medical School, Dept. of Continuing Education, Boston, MA 02114; (617) 732-1525.

Nuclear Cardiology Symposium and Workshop

The Cardiovascular Disease Section, University of Wisconsin Medical School, Milwaukee Clinical Campus; Sinai Samaritan Medical Center, Mount Sinai Campus, Milwaukee; and Continuing Medical Education, University of Wisconsin, Madison are cosponsoring the 14th annual Nuclear Cardiology Symposium and Workshop, Sept. 20–22, at the Hyatt Regency Hotel, Milwaukee, WI. The meeting, which will feature workshops and exhibits, is designed to provide a comprehensive review of current techniques. It is intended for cardiologists, radiologists, technicians, and other health professionals interested in nuclear cardiology. Category 1 credits will be awarded. Information: Sarah Aslakson, Continuing Medical Education, 2715 Marshall Ct., Madison, WI 53705; (608) 263-2856.

Applied Duplex Ultrasound

The Dept. of Radiology, University of Alabama, Birmingham, School of Medicine, will present Applied Duplex Ultrasound: A Practical Course for Physicians and Sonographers, Oct. 13–15, at the Wynfrey Hotel Galleria Plaza, Birmingham, AL. The course will provide instruction in the clinical applications of duplex scanning. It is designed for practicing physicians, sonographers, and vascular technologists. Workshops will be offered to demonstrate scanning techniques. Program chairman: Robert J. Stanley; program director: Lincoln L. Berland. Category 1 credit: 18 hr. Fee: practicing physicians, \$375; residents, fellows, nurses, sonographers, and technologists, \$275. Information: Dawne Ryals, Ryals & Associates, P. O. Box 1925, Roswell, GA 30077-1925; (404) 641-9773.

MR Course in Riyadh, Saudi Arabia

The Depts. of Radiology and Medical Studies, Riyadh Armed Forces Hospital, will sponsor their 2nd annual international course on MR imaging, Oct. 2–5, at the Riyadh Armed Forces Hospital, Riyadh, Saudi Arabia. The course will provide a comprehensive overview of MR technology and up-to-date methodology, discussion of present and future uses of MR in the whole body, small workshops, and access to the MR teaching file. The course will be of benefit to those who have started working with or are in the process of selecting MR equipment. Fee: physicians, 1,000 SR; medical staff in training, 500 SR. Information: Dept. of Medical Studies, Armed Forces Hospital, P. O. Box 7897, Riyadh 11159, Saudi Arabia; telephone (01) 477-7714.

Current Trends in Diagnostic Radiology

Massachusetts General Hospital is sponsoring the course Current Trends in Diagnostic Radiology, Emphasizing New Imaging Modalities, Intervention and Administrative Issues—1989, Oct. 2–5, in Boston. Category 1 credit: 31 hr. Fee: \$495. Information: Harvard Medical School, Dept. of Continuing Education, Boston, MA 02115; (617) 732-1525.

Breast Imaging: Problems and Solutions

Massachusetts General Hospital is sponsoring Breast Imaging: Problems and Solutions, Oct. 6, in Boston. Category 1 credit: 7 hr. Fee: \$195. Information: Harvard Medical School, Dept. of Continuing Education, Boston, MA 02115; (617) 732-1525.

Update in Pediatric Imaging

The Dept. of Radiology, Children's Hospital Medical Center, Cincinnati, OH, will present Update in Pediatric Imaging for the Practicing Radiologist, Oct. 2–5, at the Ritz-Carlton, Laguna Niguel, CA. This course is designed to present a wide cross section of basic pediatric imaging for practicing radiologists who devote time to the care of infants and children. Program director: George S. Bisset III; program chairman, Donald R. Kirks. Category 1 credit: 18 hr. Fee: \$395. Information: Dawne Ryals, Ryals & Associates, P. O. Box 1925, Roswell, GA 30077-1925; (404) 641-9773.

Farwest Image Perception Conference

The 3rd Farwest Image Perception Conference will be held Oct. 19–20 at the Westward Look Resort, Tucson, AZ. Information: Office of Medical Education, Arizona Health Sciences Center, Tucson, AZ 85724; (602) 626-7832.

Advanced Neuroradiology Seminar

The Depts. of Radiology, The Tampa General Hospital and the University of South Florida College of Medicine, will sponsor the 7th annual Advanced Neuroradiology Seminar, Oct. 26–28, at the Hyatt Regency Grand Cypress Hotel, Orlando, FL. This is a nonprofit meeting; proceeds will be put into the Radiology Resident Fund at The Tampa General Hospital for medical books, slides, videos, visiting professors, and so forth. The course will emphasize recent advances in MR imaging, CT, and interventional neuroradiology. Topics will include optimizing parameters for MR imaging; MR imaging of brain tumors, infarcts, hemorrhage, and trauma; MR imaging of the lumbar spine, cervical spine, and spinal cord; CT and MR of the orbits and temporal bones; and endovascular therapy of intracranial aneurysms and arteriovenous malformations. Course directors: Charles H. Fisher and Carlos R. Martinez. Guest faculty: R. N. Bryan, R. I. Grossman, R. M. Quencer, Gordon Sze, and Fernando Vinuela. Category 1 credit: 16 hr. Fee: physicians, \$375; residents, fellows, and radiological technologists, \$300. Information: Agnes Bridges, Radiological Services, The Tampa General Hospital, P. O. Box 1289, Tampa, FL 33601; (813) 251-7778.

Advanced Imaging of the Musculoskeletal System

The Dept. of Radiology, University of California, San Diego, School of Medicine, will offer Advanced Imaging of the Musculoskeletal

System, Oct. 28–29, at the Le Meridien San Diego Hotel, Coronado, CA. Program director: Sevil Brahme. Category 1 credit: 12 hr. Fee: physicians, \$200; residents, fellows, and technologists, \$125. Information: Dawne Ryals, Ryals & Associates, P. O. Box 1925, Roswell, GA 30077-1925; (404) 641-9773.

The American Board of Radiology Examinations

Written examinations for the American Board of Radiology (ABR) are scheduled for Oct. 12–13, 1989, and Sept. 27–28, 1990. Oral examinations will be held at the Executive West Hotel in Louisville, KY, June 5–9, 1989, and June 4–8, 1990. The ABR will accept applications for admission to the examinations after July 1, but not later than Sept. 30, in the year *preceding* the year in which the examination is to be taken. For application forms and further information: Office of the Secretary, The American Board of Radiology, 300 Park, Ste. 440, Birmingham, MI 48009.

Meeting and Course Review

For the reader's convenience, a summary of upcoming meetings and courses is provided. Detailed listings are given in the *AJR* issue given in parentheses.

Basic and Advanced Training in MRI, times arranged, Baltimore (Dec 1988)

Visiting Fellowships in Radiology at MGH, times arranged, Boston (April)

Biliary Lithotripsy Visiting Fellowships, times arranged, Philadelphia (April)

Doppler Ultrasound in Vascular Diagnosis, May 31–June 3, Philadelphia (Feb)

Doppler in Diagnostic Imaging (Color and Duplex), June 5–6, New Haven, CT (May)

Courses in Diagnostic Ultrasound at Bowman Gray: Obstetrics, June 5–9; and **Radiology (Abdomen)**, June 12–16; Winston-Salem, NC (Jan)

Obstetrics and Gynecology, June 5–9, Philadelphia (Feb)

Visiting Fellowships in MR Imaging at UCLA, June 5–9, Los Angeles (March)

Obstetrical and Gynecological Ultrasound, June 9–10, New York City (May)

Advanced Techniques in MRI, June 10–15, Kiawah Island, SC (April)

Abdominal Ultrasound, June 12–15, Philadelphia (Feb)

Radiology in Scandinavia and the Soviet Union, June 17–July 11, Copenhagen, Stockholm, and Leningrad (Jan)

Emergency Radiology Update 1989, June 19–21, Boston (April)

Practicums in MR Imaging: Basic Practicum, June 19–23 and Oct. 23–27; **Advanced Practicum**, Sept 11–15; Baltimore (March)

Challenge 89: Decisions in Imaging, June 24–30, London, England (March)

CAR '89, June 25–28, Berlin (Jan)

1989 International Congress of Radiology, July 1–8, Paris (May 1988)

Leeds Gastroenterology Course, July 10–14, Leeds, England (April)

Annual Diagnostic Imaging Seminar, July 17–21, Nantucket Island, MA (April)

Third World Medicine—Tropical Radiology and the Problem of AIDS, July 19–Aug. 5, East Africa (Nairobi, Maasa-Mara, Lake Baringo, Lake Turkana, Mombasa, and Lamu) (Jan)

Symposium on Breast Disease, July 23–26, Mackinac Island, MI (March)

Napa Valley Imaging Update—MRI 1989, July 30–Aug. 3, Napa Valley, CA (May)

Visiting Fellowship in Mammography, Aug. 28–31 and Oct. 23–27, Los Angeles (March)

Radiation, Physics, and Biology, Aug. 28–Sept. 1, New York City (May)

Imaging, Intervention, Ireland—1989, Sept. 2–10, Dublin, Cong, and New Market, Ireland (Feb)

Registry Preparation Courses for Sonographers: Physics: Sept. 8–10, Dallas; Sept. 22–24, Washington, DC; Sept. 29–Oct. 1, Los Angeles; Oct. 6–8, Chicago; **Doppler Physics**: Sept. 21, Washington, DC; Oct. 2, Los Angeles; **Abdomen**: Sept. 26–27, Washington, DC; **Obstetrics and Gynecology**: Sept. 25, Washington, DC (May)

Update in Chest Radiology, Sept. 10–23, England and Scotland (Feb)

Pathological Effects of Radiation, Sept. 11–13, Bethesda, MD (April)

1989 Interventional Neuroradiology, Sept. 11–13, Baltimore (May)

Transrectal Ultrasound and Prostate Cancer, Sept. 14–16, Chicago (May)

Mammography for the General Radiologist, Sept. 18–21 and Oct. 23–26, Boston (March)

Radiology on Ischia, Sept. 23–Oct. 1, Lacco Ameno, Island of Ischia, Bay of Naples, Italy (May)

Society of Uroradiology Postgraduate Course, Sept. 25–28, Hilton Head, SC (Dec 1988)

Seminar in Diagnostic Ultrasound, Oct. 5–7, Ann Arbor, MI (May)

Practical Radiology, Oct. 9–12, Charlottesville, VA (May)

Practical Magnetic Resonance Imaging 1989, Oct. 12–15, Las Vegas, NV (April)

World Congress for Bronchology, Oct. 18–20, Tokyo, and Oct. 21–22, Kyoto, Japan (Nov 1988)

Royal Australasian College of Radiologists Annual Meeting, Oct. 19–23, Melbourne, Australia (March)

International Seminar of Medical Imaging, Oct. 30–Nov. 5, Shatin, Hong Kong, the New Territories (May)

Advances in Chest, Interventional, and Ultrasound, Nov. 25–Dec. 10, South America (Caracas, Isla Margarita, Manaus, Recife, Rio de Janeiro, Buenos Aires, and Bariloche) (March)

International Conference on Gallstones and Their Management, Feb. 25–28, 1990, Jerusalem, Israel (May)

Congress of the European Federation of Societies for Ultrasound in Medicine and Biology, May 6–11, 1990, Jerusalem, Israel (May)

AJR carries announcements of courses, symposia, and meetings of interest to its readers if received a minimum of 5 months before the event. There is no charge; receipt of items by the *AJR* Editorial Office is not acknowledged. Submit items for publication typed double-spaced. Provide title, date, location, brief description, sponsor, course directors, fees, category I credit, and address and telephone number for additional information. Faculty from the host institution will not be listed. Guest faculty names will appear **only** if initials are provided. Mail news items to *AJR* Editorial Office, 2223 Avenida de la Playa, Suite 200, La Jolla, CA 92037-3218.

American Roentgen Ray Society 90th Annual Meeting May 13–18, 1990, Washington, DC Sheraton Washington Hotel

Registration and Hotel Reservations

Forms for advance registration and hotel reservations will be in the February and March 1990 issues of the *AJR*.

Scientific Program

Abstracts of papers to be considered for the program must be submitted by October 2, 1989. Forms on which to submit abstracts are in this issue of the *AJR*. Please photocopy if additional copies are needed. The ARRS Program Committee will select papers and notify authors in early November. The *AJR* has first rights to all papers accepted for presentation at the ARRS meeting. Send abstract, application, and four copies of the abstract to

ARRS President-Elect
c/o Paul R. Fullagar
American Roentgen Ray Society
1891 Preston White Dr.
Reston, VA 22091

Refresher Course Program

A summary of the refresher courses will appear in the *AJR* in February along with advance registration forms. Early registration is an advantage in assuring preferred courses in this popular program. Dr. J. T. Ferrucci, Jr., is program director.

Scientific Exhibits

Proposals for scientific exhibits must reach the Chairman of Exhibits by October 2. Forms, which may be photocopied, are in this issue of the *AJR*. Send completed form to:

John E. Madewell, M.D.
The Pennsylvania State University
The Milton S. Hershey Medical Center
P.O. Box 850
Hershey, PA 17033
Telephone (717) 531-8044

Local Program

A program of sightseeing, shopping, and entertainment will be developed by the Local Arrangements Chairman. Information and advance registration forms will be in the February issue of the *AJR*.

Residents' Award Papers

The society offers several cash awards for the best scientific papers prepared by residents in radiology. The President's Award has a \$1000 prize. There are two Executive Council awards of \$500 each. All are presented at the annual meeting. Papers should be submitted by February 16, 1990, for consideration in this competition. Send entries to:

B. G. Brogdon, M.D.
Dept. of Radiology
University of South Alabama Medical Center
2451 Fillingim Street
Mobile, AL 36617

Deadlines

Abstracts of papers: October 2, 1989
Scientific exhibit proposals: October 2, 1989
Residents' Award papers: February 16, 1990

Call for Papers

**American Roentgen Ray Society
1990 Annual Meeting:
May 13-18, 1990, Washington, DC**

ADDRESS OF PRESENTING AUTHOR

Department _____

Institution _____

Street _____

City, State _____

Zip _____

Phone: _____

Type title, authors, and abstract in the space provided below. (Instructions are on reverse side of this page. Abstract should not exceed 300 words.)

Select one category: _____Angio/Interventional _____Breast _____Chest _____CT _____Gastrointestinal Tract _____Genitourinary Tract _____MR .
Neuroradiology _____Skeletal _____Sonography

Projection Requirements: _____35 mm, single or double (circle one) _____16 mm silent film _____VHS

Has this been presented elsewhere? _____yes _____no. If yes, please describe on reverse side of this page.

(This Form May Be Photocopied)

Instructions for Scientific Abstracts

1. Type the information single-spaced within the lines. Underline the name of the presenting author. Append as a last line of the abstract any research grant support, if applicable (e.g., Supported by USPHS Grant HE-80144). If the abstract is accepted, it will not be proofread; it will appear exactly as typed. Use the following format:

MR IMAGING OF THE SPINE AND NECK
F. S. Lau, M.D., A. N. Kirk, M.D., and R. A. Beck, Ph.D.
University of California, Bakersfield, Bakersfield, CA 92338
2. Abstracts should include four paragraphs devoted sequentially to the following topics: (1) object or purpose of the study, (2) materials, methods, and procedures, (3) results, (4) significance of the results and conclusions. The text should not exceed 300 words. Specific data are essential. The abstract should be a succinct summary of work done rather than a promissory note.
3. The Program Committee will grade each abstract and determine acceptance. Further information will be forwarded to those whose abstracts are accepted for presentation.

Deadline for submission of abstract is October 2, 1989. Mail abstract and two copies to

ARRS President-Elect
c/o Paul R. Fullagar
American Roentgen Ray Society
1891 Preston White Dr.
Reston, VA 22091

Call for Scientific Exhibits

**American Roentgen Ray Society
1990 Annual Meeting:
May 13-18, 1990, Washington, DC**

FOR COMMITTEE USE ONLY

Date Received _____ Application No. _____
Subject _____ Score _____
Rejected _____ Accepted _____
Assigned _____ Space No. _____

Principal Exhibitor's Mailing Address

Name _____ Institution _____
Department _____ Street Address _____ City _____
State _____ Zip Code _____ Telephone: office () home ()

Names of Exhibitors (List principal exhibitor first and telephone number of each person.)

Last	First	Middle	Telephone	Degree (one only)	Member ARRS?
------	-------	--------	-----------	----------------------	--------------

_____	_____	_____	_____	_____	_____
_____	_____	_____	_____	_____	_____
_____	_____	_____	_____	_____	_____
_____	_____	_____	_____	_____	_____
_____	_____	_____	_____	_____	_____

Title of Exhibit _____

Type abstract single-spaced in the space provided below. (See instructions on the reverse side of this page.)

Instructions for Abstract

The abstract should be a brief paragraph that states the purpose, principal information, and conclusions of the exhibit. Promissory statements are not acceptable. Type single-spaced in the space provided on the reverse side. Brevity is desirable but not at the expense of specific information. **The abstract will appear in the program book as submitted.** Please use typewriter and complete the application form on both sides. List space requirements.

What Sort of Exhibit Is Proposed? (Check one and fill in all appropriate blanks.)

_____ **Free-standing.** This is a self-contained display created in total by the exhibitor. It may be a fold-open unit, a unit shipped in cases and assembled on site, or a tabletop unit. Linear feet required _____.

_____ **Poster Board (backboard panels).** Backboard panels are 4×6 or 4×8 ft. (1.2×1.8 or 1.2×2.5 m). Number of panels required _____ 4×6 or _____ 4×8 . If two panels are needed, there will be a $\frac{1}{4}$ -in. frame separating the panels, thus requiring a separation in the presentation.

_____ **Viewbox.** Mounted materials (radiographs and other transparencies) for display on the society's illuminators. Each illuminator is 39.5×59.5 in. (100×151 cm). Number of illuminators required _____. Slides should not be glass mounted.

_____ **Audiovisual.**

Please Indicate Most Appropriate Category.

Diagnostic Radiology

_____ Bone _____ Cardiovascular System _____ Chest _____ Pediatric Radiology _____ Gastrointestinal Tract
_____ Genitourinary Tract _____ Neuroradiology _____ Mammography

Other

_____ Medical Physics _____ Nuclear Medicine _____ Radiation Oncology _____ Radiobiology _____ Sonography

Has the exhibit been shown in whole or in part at any previous meeting? _____ (Previous display does not preclude acceptance.)

If so, where? _____ When? _____

Nature of meeting or name of society _____

Signature of Principal Exhibitor _____

Exhibitors will receive detailed instructions for exhibit preparation.

Applications must be received no later than October 2, 1989. Mail original and five copies to

John E. Madewell, M.D.
The Pennsylvania State University
The Milton S. Hershey Medical Center
P. O. Box 850
Hershey, PA 17033

Telephone: (717) 531-8044

Classified Advertisements

Positions Available

PERMANENT POSITION—Mary Hitchcock Memorial Hospital is seeking a general radiologist to be a member of a 200-physician, academic, multi-specialty group that forms the clinical faculty of Dartmouth Medical School. Board-certification/eligibility required. Position entails responsibility for a full scope of general diagnostic procedures including mammography, ultrasound, and CT. Interest in teaching and research essential. Mary Hitchcock Memorial is a 440-bed hospital with 80 radiology dept. personnel and performs 55,000 inpatient and 45,000 outpatient exams/yr. Dept. consists of 13 staff and 9 resident radiologists with a full range of modern radiologic practice. Write to P. K. Spiegel, M.D., Dartmouth-Hitchcock Medical Center, Dept. of Radiology, 2 Maynard St., Hanover, NH 03756. AAEOE. 6-7ap

OUTPATIENT ANGIOGRAPHER/IMAGER—Rapidly expanding, 6-member group practice, covering 2 full-service imaging centers has an immediate opening. We are looking for an additional board-certified radiologist with an uncommon dedication to excellence in patient care. We currently have a GE Advantax angiography lab with full digital and cine capabilities, as well as a 4-bed outpatient recovery area. Our other capabilities include MR (2 Diasonics), CT (2 GE 9800 Quick Hilight), ultrasound (4 Acuson), mammography (4 CGR), nuclear medicine (GE and Picker SPECT), plus R & F. This is an excellent opportunity for a career position with a well-respected group in a growing community. Send CV to Mark Winkler, M.D., SDMI, 2950 S. Maryland Pkwy., Las Vegas, NV 89109. 6-8ap

POSITION OPEN IMMEDIATELY—Forty-physician multispecialty clinic, serving central and western Kansas, is seeking a board-eligible/certified radiologist. Excellent facilities include diagnostic radiology, CT, diagnostic ultrasound, nuclear medicine, and mobile MR services. An excellent opportunity in a dynamic practice setting. Please send CV to Administrator, Hutchinson Clinic, 2101 N. Waldron, Hutchinson, KS 67502; (316) 663-6121. 6-12ap

STAFF PHYSICIAN/RADIOLOGY, 2 POSITIONS—Vacancy exists for 2 diagnostic radiologists, board-certified or in examining process, with experience in CT, angiography, interventional ultrasound, and nuclear medicine. Hospital located in northeastern Tennessee near ski slopes and Appalachian Trail in Smoky Mountains. Great area for outdoor activities including hiking, golf, tennis, and all water sports. Affiliated with Quillen-Dishner College of Medicine in Johnson City, TN. Direct all inquiries to Harold Ross, M.D., Chief, Radiology Service, VA Medical Center, Mountain Home, TN 37684; (615) 926-1171, ext. 7401. An equal opportunity employer 6-7a

RADIOLOGIST NEEDED IN SOUTHWEST—Radiologist is needed for an outpatient office facility that performs general radiography, sonography, and mammography. Hours: 8-5, Mon-Fri. Attractive compensation package. Must be board-certified. Please submit letter and resume to P.O. Box 80886, Albuquerque, NM 87108-9998. 6ap

RADIOLOGIST WANTED—Progressive hospital located at the foot of the Big Horn Mountains. Quality lifestyle, excellent hunting, fishing, and recreation area. Skills required in diagnostic, ultrasound, mammography, nuclear medicine, and CT. For information, contact Howard Megorden, Administrator, Washakie Memorial Hospital, P.O. Box 700, Worland, WY 82401; (307) 347-3221. 6ap

BC/BE DIAGNOSTIC RADIOLOGIST—Immediate opening to join 7-person group in South Bay area of N. California. Hospital and private office practice. All diagnostic techniques including MRI. Send CV to Box Q92, AJR (see address this section). 6-8ap

THE ST. LOUIS VA MEDICAL CENTER is recruiting a board-certified radiologist with expertise in special procedures imaging, ultrasound, and CT. Position available immediately. The medical center has a fully integrated teaching affiliation with St. Louis University School of Medicine. Faculty appointment commensurate with qualifications and experience. Equal opportunity/affirmative action employer. Search continues until position is filled. Submit CV to C. R. Markivee, M.D., Chief, Radiology (114/JC), VA Medical Center, 915 N. Grand, St. Louis, MO 63106. 6a

LARGE, COMMUNITY-BASED RADIOLOGY GROUP seeks board-certified radiologist interested in part-time position. No night or weekend call. Long-term commitment desired. Responsibilities include general radiography, fluoroscopy, mammography, CT (body), and ultrasound. Ideal practice situation for semiretired radiologist. Desirable Southwest community. Competitive salary and benefits. Send CV to Radiology, Ltd., P.O. Box 12249, Tucson, AZ 85732-2249. 6-9ap

RADIOLOGIST, SARATOGA SPRINGS, NY—Four-member, hospital-based group is seeking board-eligible/certified radiologist. Interventional training or experience is required. This progressive practice includes CT, ultrasound, nuclear medicine, and special procedures. Excellent compensation leading to early partnership plus comprehensive benefit package. Saratoga is a historic, close-knit community, a 1/2-hr drive from Albany, one of the nation's finest capital cities. Saratoga offers lovely neighborhoods in a variety of settings, as well as fine restaurants, specialty shops and entertainment, thoroughbred racing, and the Saratoga Performing Arts Center. Proximity to Lake Placid and the Green Mountains of Vermont gives skiers and outdoor enthusiasts a number of recreational outlets. Forward CV to Saratoga Radiological Associates, c/o Miss Denise Romand, Saratoga Hospital, 211 Church St., Saratoga Springs, NY 12866; (518) 584-6000, ext. 465. 6-8a

NEURORADIOLOGIST—The University of Texas Health Science Center at San Antonio is seeking a qualified academic neuroradiologist to fill an immediate opening. Send cover letter and CV to John R. Jinkins, M.D., Director of Neuroradiology, University of Texas Health Science Center, 7703 Floyd Curl Dr., San Antonio, TX 78284-7800. 6-11ap

CHIEF OF ANGIOGRAPHY/INTERVENTIONAL RADIOLOGY—The Hospital of the University of Pennsylvania is seeking an experienced interventional radiologist to serve as chief of the Angiography/Interventional Radiology Section and professor/associate professor of radiology in the School of Medicine of the University of Pennsylvania. The chief oversees 3 other staff angiographers, 4 fellows, and 1 or 2 rotating residents in an extremely busy clinical practice involving the entire spectrum of angiographic and interventional procedures. Strong academic and research interests are a major requirement for this position. Send inquiries to Stanley Baum, M.D., Professor and Chairman, Dept. of Radiology, Hospital of the University of Pennsylvania, 3400 Spruce St., Philadelphia, PA 19104. The University of Pennsylvania is an equal opportunity employer. 6ap

RADIOLOGY SERVICE—Seeking chief, radiology service, Miami VA Medical Center. The successful candidate must possess the clinical, administrative, and leadership skills necessary to manage a complex radiology service in a tertiary-care teaching hospital and should qualify for academic appointment in the Dept. of Radiology, University of Miami. Applications, including a CV and list of references, should be addressed to Alan L. Bisno, M.D., Radiology Search Committee, Miami VA Medical Center, 1201 N.W. 16th St., Miami, FL 33125. The VA is an equal opportunity employer. 6a

IMMEDIATE OPENING IN SOUTHEAST TEXAS for board-certified radiologist to join another radiologist in well-established, hospital-based, diagnostic radiology practice. Interested physicians should be well-trained in all imaging techniques with proficiency in IVM, ultrasound, CT, MRI, and interventional radiology, in addition to general radiology. Initial salary competitive/commensurate with experience, with partnership arrangement within 18 mo-2 yr. Interested applicants please call (409) 985-0302 collect for further information, or forward CV to Director of Physician Services, P.O. Box 6668, Beaumont, TX 77705-0668. 5-7a

MINNEAPOLIS, MN—Practice opportunity for a board-certified radiologist with subspecialty interest in musculoskeletal imaging. MR expertise and procedural skills mandatory. Large volume of invasive spine and orthopedic procedures. Practice is based at a rapidly growing, privately owned, freestanding, outpatient imaging center equipped with GE 9800 Quick and 8800 CT scanners, 2 GE Signa 1.5-T MR scanners, and related fluoroscopic-radiographic and ultrasound equipment. Practice also includes coverage of a 750-bed, tertiary-care medical center. Three radiologists in practice currently. One distant MR facility operating, another under construction, and plans for more. Investment opportunities for radiologists involved in the practice as well as academic orientation and opportunity for subspecialization. Outstanding benefits. Send CV and responses to Kurt P. Schellhas, M.D., Center for Diagnostic Imaging, 5775 Wayzata Blvd., Ste. 190, Minneapolis, MN 55416. No telephone calls please. All inquiries confidential. 6-9ap

GENERAL RADIOLOGIST to join 3 other radiologists with 55-physician, multispecialty group in La Crosse, WI. Includes provision of all radiology services for Skemp Clinic and St. Francis Medical Center, a 270-bed hospital. Dept. includes CT, ultrasound, nuclear medicine, special procedures, and MRI. Experience in interventional radiology would be a plus. La Crosse is located in western Wisconsin in the Mississippi River Valley, ranked nationally as having one of the highest qualities of life for a city of its size (50,000). Competitive first-year income and comprehensive benefits. Equal shareholder after 2 yr. Contact Dr. Shultz, Skemp Clinic, 815 S. 10th St., La Crosse, WI 54601; (608) 782-9760. 6ap

THE OREGON HEALTH SCIENCES UNIVERSITY, Dept. of Diagnostic Radiology, Portland, OR, invites applications for faculty positions in MRI, neuroradiology, pulmonary radiology, mammography, skeletal radiology, vascular and interventional radiology, GU radiology, computed body tomography, and ultrasound. A Ph.D. NMR scientist also is being sought. The Oregon Health Sciences University is an affirmative action, equal opportunity employer. Send CV to Richard W. Katzberg, M.D., Chairman of Diagnostic Radiology, L340, The Oregon Health Sciences University, 3181 S.W. Sam Jackson Park Rd., Portland, OR 97201-3098. 5-4ap

PORTLAND, OR—Group of 8 radiologists seeking general diagnostic radiologist. Limited amount of ultrasound and nuclear medicine. Practice includes CT, MRI, and angiography. Group covers large trauma hospital and 4 outpatient offices. Send CV or call Randy Greene, M.D. or Blaine Kozak, M.D., Dept. of Radiology, 2801 N. Gantenbein, Portland, OR 97227; (503) 280-4032. 5-7ap

NEW HAMPSHIRE—Excellent opportunity for young, BC/BE, general radiologist with MRI experience to join well-established, busy, small group. Live and work in beautiful Connecticut Valley Region close to lakes and skiing. Competitive compensation package leading to partnership. Please send CV to New England Health Search, 63 Forest Ave., Orono, ME 04473; (207) 866-5680 or (207) 866-5685. 5-7ap

PEDIATRIC RADIOLOGIST—The University of Tennessee, Memphis/University Physicians Foundation has an opening for a pediatric radiologist effective July 1, 1989. Faculty rank of assistant or associate professor based on experience. Applicant must be board-certified/eligible in diagnostic radiology. At least 1 yr of postgraduate training in a recognized program in pediatric radiology is required. Primary work sites will be LeBonheur Children's Medical Center and St. Jude Children's Research Hospital. Blacks, women, handicapped, and other minorities are encouraged to apply. The University of Tennessee, Memphis/University Physicians Foundation is an affirmative action/equal opportunity employer. Address inquiries to Barry Fletcher, M.D., Chairman, Diagnostic Imaging Dept., St. Jude Children's Research Hospital, 332 N. Lauderdale, Memphis, TN 38101; or Robert A. Kaufman, M.D., Director, Dept. of Radiology, The University of Tennessee, Memphis/LeBonheur Children's Medical Center, 800 Madison Ave., Memphis, TN 38163. 5-7a

TAMPA BAY AREA RADIOLOGY GROUP seeking board-certified generalist primarily for office position, some hospital work. Candidate must be able to perform routine radiologic CT, ultrasound, mammography, and venography, in addition to general radiologic duties. Send CV to Radiology Group, P. O. Box 17319, Tampa, FL 33682. 5-6a

DIAGNOSTIC RADIOLOGIST, FLORIDA GULF COAST—Position available July 1, 1989 for board-certified/eligible radiologist to join busy women's diagnostic imaging practice including women's hospital and 2 outpatient imaging centers. Send CV to Lisa A. Nemec, M.D., Chairman, Dept. of Radiology, 1260B S. Greenwood Ave., Clearwater, FL 34616. 6ap

PRACTICE OF RADIOLOGY—A hospital-based practice of 4 radiologists, covering 2 area hospitals serving Wyoming, South Dakota, Colorado, and Nebraska, (recently designated as a rural referral center) seeks an additional radiologist with expertise in all imaging modalities. Excellent compensation and fringe benefits. State-of-the-art facility in a recently constructed wing (1985). Potential to become full partner in 1 yr. Community of approximately 20,000 with medical service population of 110,000. Close to Rocky Mountains (2-5 hr), with excellent hunting and fishing. Alternative opportunity for 1-yr, locum tenens position. If you are board-certified or are soon to be and would like more information about this opportunity, please send CV or call R. G. Heasty, M.D., Regional West Medical Center, 4021 Avenue B., Scottsbluff, NE 69361; (308) 632-0140. 4-6ap

ATLANTA, GA—One radiology position. The Southeast Permanente Medical Group, Inc., Georgia Region, is seeking an additional radiologist for a growing radiology dept. serving several medical centers throughout the Atlanta area. Interested and qualified candidates must be board-certified in radiology with expertise in general radiology to include CT, ultrasound, and mammography. Address inquiries and CVs to Alex Daley, M.D., Chief of Radiology, c/o The Southeast Permanente Medical Group, Inc., 3355 Lenox Rd., Ste. 1000, Atlanta, GA 30326; (404) 233-0555, ext. 192. 5-10ap

RADIOLOGIST—The Elko Regional Medical Center seeks a BC/BE general diagnostic radiologist to work at the medical center as well as the local community hospital. CT, mammography, ultrasound, nuclear medicine, and some interventional training or experience required. Guaranteed salary for 6 mo leading to full partnership. Excellent benefits package including malpractice insurance. Elko is a thriving community surrounded by mountains and wilderness areas. Recreation yr round. Please send CV to Cherie Atwood, Administrator, Elko Regional Medical Center, 762 14th St. Elko, NV 89801; (702) 738-3111. 5-7ap

PEDIATRIC RADIOLOGIST—Vacancies are available in various parts of the Pediatric Radiology Dept. at The Hospital for Sick Children, Toronto. The hospital is a 560-bed, tertiary-care, pediatric center situated in downtown Toronto and affiliated with the University of Toronto. 100,000 exams are performed each yr, and the staff includes 17 full-time pediatric radiologists and 7 fellows. Positions are available in general pediatric radiology areas as well as in more specialized areas such as neuroradiology. The dept. is equipped with state-of-the-art equipment. Applicants must have pediatric radiology experience, including 1- and preferably 2-yr fellowship, and staff radiologists with greater experience are certainly most welcome. For further information, please contact A. Daneman, M.D., Radiologist-in-Chief, Dept. of Radiology, The Hospital for Sick Children, 555 University Ave., Toronto, Ontario, M5G 1X8, Canada; (416) 598-6026. 5-8a

THE DEPT. OF RADIOLOGY, VIRGINIA COMMONWEALTH UNIVERSITY/MEDICAL COLLEGE OF VIRGINIA, Richmond, VA seeks faculty for positions in diagnostic radiology for chest, mammography, CT/ultrasound/MR, neuroradiology, pediatrics, ER, angio/interventional, and general radiology. Our 1058-bed facility (205 for pediatric patients) is a Level 1 Trauma Center. ABR certification or eligibility required. Academic rank and salary commensurate with experience. Submit CV to A. V. Proto, M.D., Chairman, Diagnostic Radiology, Medical College of Virginia, MCV Box 47, Richmond, VA 23298-0047. VCU/MCV is an equal opportunity/affirmative action employer. Women and minorities are encouraged to apply. 4-6a

CHIEF OF ULTRASOUND, PRIVATE PRACTICE HOSPITAL GROUP—Position available at a large, tertiary-care hospital in Phoenix, AZ, for a board-certified radiologist with fellowship training in ultrasound. Prefer postfellowship experience with ability to manage an ultrasound section and promote its services. Experience in obstetrics, general and Doppler ultrasound necessary. This is a unique position, offering academic-style practice with private-practice benefits. Please send letters of inquiry to Aubrey M. Palestrant, M.D. or Theodore Ditchek, M.D., Dept. of Radiology, Good Samaritan Medical Center, 1111 E. McDowell Rd., Phoenix, AZ 85006; (602) 239-4601. 4-7ap

ABDOMINAL RADIOLOGIST—The H. Lee Moffitt Cancer Center and Research Institute at the University of South Florida has a faculty position available for an abdominal radiologist with fellowship training or equivalent subspecialty experience. Interest and expertise in all imaging modalities and procedures related to abdominal radiology are preferred. The position includes clinical service, research, and teaching; academic rank is based on qualifications. Our facility is a new, state-of-the-art complex; the compensation package is excellent. Interested candidates should contact Robert Clark, M.D., Dept. of Radiology, Moffitt Cancer Center, P. O. Box 280179, Tampa, FL 33682-0179. 4-6ap

LOCUM COVERAGE—Chattanooga Outpatient Center seeks short- or long-term locum. Excellent equipment. All modalities. No night or weekend work. Generous reimbursement. Contact Desmond Fischer, M.D., 1301 McCallie Ave., Chattanooga, TN 37404. 4-6 ap

MODERN, 6-MAN RADIOLOGY GROUP seeking 7th man due to expansion. Three private offices and 1 busy hospital, all located in Jamestown, NY, on Chautauqua Lake. Must be board-certified and preferably trained in specials, ultrasound, nuclear medicine, CT, and MRI. Generous salary and benefits. Full partnership in 2 yr. Send CV to Rev. Eugene F. Foley, M.D., 333 E. 5th St., Jamestown, NY 14701, or call Patsy Lydell at (716) 664-9731. 4-6ap

VASCULAR/INTERVENTIONAL RADIOLOGIST—Diagnostic Radiology Dept., National Institutes of Health. Full-time, academic position at assistant- or associate-professor level. Board-certification required, fellowship preferred. Duties include all aspects of vascular/interventional radiology, with particular emphasis on diagnostic angiography. Some cross-sectional imaging and plain film reading required. Numerous research opportunities available in dept. with extensive research facilities and support staff. Salary with excellent fringe benefits. Position includes faculty appointment at Georgetown University. Please send CV with letter to John L. Doppman, M.D., Diagnostic Radiology Dept., Bldg. 10, Room 1C660, National Institutes of Health, Bethesda, MD 20892. 4-6ap

RADIOLOGIST; PERMANENT POSITION—Chattanooga Outpatient Center. Excellent equipment; CT, MRI, ultrasound, nuclear, and mammography. No nights or weekends. Generous reimbursement and vacation package leading to partnership. Contact Desmond Fischer, M.D., 1301 McCallie Ave., Chattanooga, TN 37404. 4-6ap

RADIOLOGIST—Associate diagnostic radiologist to join a group of 4. Hospital and private practice. All imaging capabilities. Angiography and nuclear medicine. 1 hr from Boston. Reply Box P81, *AJR* (see address this section). 4-6ap

ISRAEL, DIAGNOSTIC RADIOLOGY. Opportunities for 3-4 week or longer working vacations in a number of Israeli medical centers, on a volunteer basis. Positions varied, arrangements flexible. For information contact: Jonathan H. Fish, M.D., 1844 San Miguel Dr., #302, Walnut Creek, CA 94596; (415) 947-0560. 5-7xa

FRAMINGHAM, MA—BC/BE diagnostic radiologist to join 6-member group at 311-bed teaching hospital. Experience in angiography and interventional radiology necessary. Send CV to Herbert D. Weintraub, M.D., c/o Framingham Union Hospital, 115 Lincoln St., Framingham, MA 01701; (508) 626-3525. 3-6ap

DIAGNOSTIC RADIOLOGIST—Immediate opening to join 2 other radiologists in a large, multi-specialty group practice serving 4 outpatient offices in Rochester, NY. State-of-the-art Toshiba fluoroscopy, ATL ultrasound, and LoRad mammography equipment. Ultrasound, mammography, and CT experience preferable. 32,000 exams/yr. Please contact Dennis S. Moss, M.D., Rochester Medical Group Associates, P.C., Radiology Dept., 800 Carter St., Rochester, NY 14621; (716) 338-1400 x4096. EOE/MF. 3-6a

THE DEPT. OF RADIOLOGY AT TRIPLER ARMY MEDICAL CENTER, HONOLULU, HI, is recruiting academically oriented radiologists for several divisions of the dept.: ultrasound, imaging (CT and/or MRI), interventional, chest, genitourinary, mammography, pediatric, neuroradiology, and general diagnostic radiology. We are particularly interested in radiologists with ultrasound training or extensive experience. Our dept. offers a fully-accredited residency program with 18 residents and 15 attending full-time staff. Numerous consultants from across the country lecture on a continuing and regular basis. The hospital is a modern tertiary-care center serving the state and the entire Pacific Basin. A strong residency program, a diverse and interesting patient population, excellent equipment, and a tropical lifestyle are positive aspects of the practice. Academic credentials and/or experience are necessary. Recently graduated fellows are encouraged to apply. Board certification is mandatory. Candidates should be particularly interested in patient care, teaching, and research. Salary and benefits are competitive and generous. Tripler is an EO/EEOE employer. Please contact Dr. Mark F. Hansen, Col., MC, Chief, Dept. of Radiology, TAMC, HI 96859-5000; (808) 433-6393. 6a

TWO BOARD-CERTIFIED/ELIGIBLE GENERAL DIAGNOSTIC RADIOLOGISTS to join expanding, 9-man group covering 2 hospitals and an MR Imaging Center in a stable midwest community. Ideal private practice using all imaging modalities and interventional techniques. Can start immediately or wait until July 1989. Excellent opportunity with excellent salary and benefits. Send CV to Joseph F. Norfray, M.D., MR Center of Springfield, 319 E. Madison, Springfield, IL 62701. 3-6ap

DIAGNOSTIC RADIOLOGIST—The UCLA Dept. of Radiological Sciences is seeking a board-certified radiologist for its Primary Care/Family Practice Section. Position requires strong interests in teaching, patient care, and knowledge of abdominal CT for evaluation of trauma. Send application, including CV and names and addresses of 3 references, or inquiries to Hooshang Kangaroo, M.D., Chairman, Dept. of Radiological Sciences, UCLA Medical Center, Los Angeles, CA 90024-1721, an EO/AA employer that encourages applications from members of minority groups and women. 2-7a

SKELETAL RADIOLOGIST—The UCLA Dept. of Radiological Sciences has a full- or half-time faculty position available in skeletal radiology. Candidate must be board-certified, have a clinical background in skeletal radiology, and have a strong interest in teaching. Send application, including CV and names and addresses of 3 references, or inquiries to Hooshang Kangaroo, M.D., Chairman, Dept. of Radiological Sciences, UCLA Medical Center, Los Angeles, CA 90024-1721, an EO/AA employer that encourages applications from members of minority groups and women. 2-7a

GENERAL DIAGNOSTIC RADIOLOGIST, THOMAS JEFFERSON UNIVERSITY HOSPITAL—The Dept. of Radiology at Thomas Jefferson University Hospital in Philadelphia has an opening in July 1989 for a faculty-level, general diagnostic radiologist. An interest and/or fellowship training in abdominal radiology (GI/GU) would be helpful, but not mandatory. The individual will have the opportunity to participate in clinical activities, teaching, and research in a progressive and expanding general diagnostic division. Excellent salary and benefits are offered. Contact either Robert M. Steiner, M.D., Co-director of General Diagnostic Radiology or David C. Levin, M.D., Professor and Chairman, Dept. of Radiology, Thomas Jefferson University Hospital, 111 S. 11th St., Philadelphia, PA 19107. Thomas Jefferson University is an equal opportunity/affirmative action employer. 1-6ap

RADIOLOGIST—Full-time, board-certified radiologist with particular interest and experience in nuclear and ultrasound radiology desired for association in 10-man, private practice for a 660-bed, private, tertiary-care, teaching hospital with 2 regional offices. Practice is located in large midwestern city and maintains fully accredited, 4-yr, radiology residency training program. This comprehensive dept. includes 2 state-of-the-art CT scanners, a 1.5-T MRI unit, modern equipment for mammography, sonography, angiography, nuclear medicine, and a wide variety of invasive applications and procedures. Competitive salary and benefits. Full partnership, if mutually agreeable, at 3 yr. Near-future plans include manning of regional outpatient center with CT and general radiologic facilities on site. Send inquiry and CV in reply to Box N63, *AJR* (see address this section). 1-6ap

BOARD-CERTIFIED OR ELIGIBLE RADIOLOGIST to join a hospital and multi-office group practice in North Central Connecticut. Applicant should be competent in all imaging modalities including CT and MRI. Training in interventional radiology is desirable but not essential. Salary first yr leading to full partnership. J. Dangelis, M.D., 151 Barle Rd., South Windsor, CT 06074. 4-6ap

CHIEF, RADIOLOGY SERVICE—The Colmery-O'Neil VA Medical Center, Topeka, KS, is recruiting a board-certified radiologist to work with 3 staff radiologists in a modern diagnostic imaging dept. Activities include routine radiography, fluoroscopy, limited angiography, CT, ultrasound, percutaneous biopsy, and PTC. This 809-bed medical center is affiliated with the Oral Roberts School of Medicine, which provides staff physicians with teaching opportunities. Excellent school system, several universities within a 60-mi. radius, and a wide variety of cultural and recreational programs are available. Federal benefit package includes liberal holiday and leave programs, malpractice insurance coverage, and tax-deferred retirement options. Please send inquiries to Harold M. Voth, M.D., Chief of Staff (11), VA Medical Center, Topeka, KS 66622. EOE. 6a

BREAST IMAGING RADIOLOGIST, THOMAS JEFFERSON UNIVERSITY HOSPITAL—The Dept. of Radiology at Thomas Jefferson University Hospital in Philadelphia has an immediate opening in a faculty position with emphasis on mammography and breast ultrasound. Some work in the general diagnostic division also is included. Jefferson has a large new Breast Imaging Center currently averaging about 85 studies/day, as well as active research and teaching programs. Excellent salary and benefits are offered. Contact either Stephen A. Feig, M.D., Director of Breast Imaging, or David C. Levin, M.D., Professor and Chairman, Dept. of Radiology, Thomas Jefferson University Hospital, Philadelphia, PA 19107. Thomas Jefferson University is an equal opportunity/affirmative action employer. 6-11ap

CHIEF, RADIOLOGY SERVICE—450-bed, Northwestern University Medical School-affiliated VA Lakeside Medical Center in Chicago seeks a board-certified radiologist to serve as Chief, Dept. of Radiology. Dept. includes general diagnostic radiology, CT scanner, and DSA unit. MRI is available nearby. Interest in teaching and research preferred. Administrative experience is desirable. Address inquiry and CV to Lee F. Rogers, M.D., Chairman, Dept. of Radiology, Northwestern University Medical School, 710 N. Fairbanks, Chicago, IL 60611; (312) 908-5103. An equal opportunity employer. 5-7ap

PACIFIC NORTHWEST—Opportunity for BC/BE general diagnostic radiologist to join group of 5 board-certified radiologists. Experience in all modalities desired. Practice includes 2 hospitals and private office in Southern Oregon. Competitive starting salary with early full partnership. Excellent lifestyle with many outdoor activities from Pacific Coast to Oregon Cascades. Send CV to John McCaffrey, M.D., Roseburg Radiologists, P.C., P. O. Box 1547, Roseburg, OR 97470. 6-8ap

DIAGNOSTIC RADIOLOGIST—Radiologists seek board-certified radiologist with experience in CT, nuclear medicine, general radiology, and ultrasound including Doppler, for a hospital-based, private practice in 225-bed general hospital in Forest Hills, NY. Immediate opening leading to partnership. Contact M. Tartell, M.D.; (718) 544-5858. 6-8ap

DIAGNOSTIC RADIOLOGIST, BODY IMAGING—Young, aggressive group in Washington, DC, area has position immediately available for a board-certified diagnostic radiologist in an expanding and diversified hospital and office-based practice with facilities in Maryland and Virginia. Our group covers 2 very progressive hospitals, including a regional trauma center, 3 full-service private offices, and a diagnostic center for women. All imaging modalities represented, including 3 MRI, 6 CT, 5 Acuson 128, and a PIXAR 3-D imaging unit. Dynamic and attractive practice setting. Address inquiries and CV to Radiology Imaging Associates, 7700 Old Branch Ave., Ste. B-101, Clinton, MD 20735; (301) 858-8718. 6-8ap

Positions Desired

PGY4, MALE (30), UROLOGY RESIDENT MAJOR NYC UNIVERSITY PROGRAM, American medical graduate, also biomedical engineering degree (Johns Hopkins), seeks diagnostic radiology residency training program for July 1989. Call (914) 725-5346. CV and recommendations upon request. 6bp

Fellowships and Residencies

INTERVENTIONAL RADIOLOGY FELLOWSHIP

The Rush-Presbyterian-St. Luke's Medical Center is now offering a 1-yr fellowship position beginning July 1, 1990 in interventional radiology. This 750-bed teaching hospital offers extensive experience in all aspects of vascular and nonvascular procedures, with a primary emphasis on patient care and clinical research. Send inquiries to Terence Matalon, M.D., Dept. of Diagnostic Radiology and Nuclear Medicine, Rush-Presbyterian-St. Luke's Medical Center, 1653 W. Congress Parkway, Chicago, IL 60612. 4-7c

NEURORADIOLOGY FELLOWSHIP

Two yr beginning July 1, 1990. Exposure to all aspects of clinical/academic neuroradiology. Participation in research/teaching. Send cover letter/CV to John R. Jenkins, M.D., Director, Neuroradiology Section, University of Texas Health Science Center, 7703 Floyd Curl Dr., San Antonio, TX 78284-7800. The University of Texas Health Science Center at San Antonio is an affirmative action/equal opportunity employer. 6-8cp

DIAGNOSTIC RADIOLOGY RESIDENCY POSITION

The Methodist Hospital of Brooklyn, NY has a position available for chief resident (4th-yr resident), in diagnostic radiology, effective July 1, 1989. The Dept. of Radiology performs approximately 75,000 exams/yr and has a staff of 9 radiologists and 8 residents. For further information and application, call or write Joseph Giovanniello, M.D., Director of Radiology, The Methodist Hospital, 506 6 St., Brooklyn, NY 11215; (718) 780-3870. 6cp

CARDIOVASCULAR-INTERVENTIONAL RADIOLOGY FELLOWSHIP

Available July 19, 1989. One-year fellowship program at a 750-bed teaching hospital. Extensive clinical experience involving all aspects of cardiovascular imaging, interventional vascular and nonvascular procedures, and availability for clinical or animal research. Send CV and inquiries to Oscar H. Gutierrez, M.D., Dept. of Radiology, Box 648, University of Rochester Medical Center, Rochester, NY 14642. An equal opportunity employer (M/F). 3-6c

FELLOWSHIP IN PEDIATRIC RADIOLOGY

Dept. of Radiology, Children's Hospital Medical Center, Cincinnati, OH, offers a 1- or 2-yr fellowship in pediatric radiology beginning July 1, 1989. Children's Hospital Medical Center is a 344-bed institution where approximately 85,000 radiologic exams are done per yr by 10 attending radiologists. Training includes all aspects of pediatric imaging including conventional radiology, neuroradiology, abdominal imaging, ultrasound, nuclear medicine, CT, MRI, and vascular/interventional techniques. Equipment includes digital fluoroscopy, Acuson and ATL ultrasound units with Doppler and color-flow Doppler capabilities, Gamma and SPECT tomographic nuclear cameras, GE 9800 Quick CT Scanner, 1.5-T GE MRI, and angiographic suite with digital vascular imaging. Requirements for the fellowship include completion of a radiology residency with training in the various subspecialties of diagnostic imaging. Contact Donald R. Kirks, M.D., Director, Dept. of Radiology, Children's Hospital Medical Center, Eland & Bethesda Aves., Cincinnati, OH 45229-2899; (513) 559-8050. 10-2ap

FELLOWSHIP IN PEDIATRIC RADIOLOGY—LeBonheur Children's Medical Center/St. Jude Children's Research Hospital/The University of Tennessee, Memphis/University Physicians Foundation, Inc. combined program in pediatric radiology offers a 1- or 2-yr fellowship in pediatric radiology. There are approximately 70,000 pediatric exams performed annually by 10 full-time radiologists. Experience to include general pediatric, neuro, nuclear, oncologic, neonatal, and cardiovascular radiology. Facilities include Doppler ultrasound, CT, and MRI. Opportunity to participate in MRI and other imaging research. Blacks, women, handicapped, and other minorities are encouraged to apply. The University of Tennessee, Memphis/University Physicians Foundation, Inc. is an affirmative action/equal opportunity employer. Address inquiries to Barry D. Fletcher, M.D., Chairman, Diagnostic Imaging Dept., St. Jude Children's Research Hospital, 332 N. Lauderdale, Memphis, TN 38101; or Robert A. Kaufman, M.D., Director, Dept. of Radiology, LeBonheur Children's Medical Center/University of Tennessee, Memphis, 800 Madison Ave., Rm. 114C Chandler, Memphis, TN 38163. 5-7c

ULTRASOUND, MR, AND CT IMAGING FELLOWSHIP TO BEGIN JULY 1990—568-bed teaching hospital. Over 130,000 exams are performed yearly in the radiology dept. All imaging modalities are integrated into the fellowship program, which will emphasize diagnostic ultrasound (including obstetrical and Doppler with color flow), MRI, and body CT. Send inquiries to Harvey L. Neiman, M.D., Chairman, Dept. of Radiology, West Penn Hospital, 4800 Friendship Ave., Pittsburgh, PA 15224. 5-8c

ABDOMINAL IMAGING FELLOWSHIP—One-yr fellowship in abdominal imaging available at The George Washington University Medical Center. Training provided in all aspects of diagnostic ultrasound, CT, GI and GU radiology, and body MR. Applicants must have completed an approved residency program in diagnostic radiology and be board-eligible/certified. Send letter of inquiry with CV to William W. Olmsted, M.D., The George Washington University Medical Center, Dept. of Radiology, 901 23rd St., N.W., Washington, DC 20037. The George Washington University Medical Center is an EEO/affirmative action employer. 6c

FELLOWSHIP IN ULTRASOUND/CT/ANGIO-INTERVENTIONAL—Available July 1, 1990. A 1-yr fellowship program is available at the Lehigh Valley Hospital Center in Allentown, PA, a 492-bed, acute-care facility with Level I Trauma Center designation. The fellowship program offers training in CT (head and body), ultrasound, angiography (neuro and visceral), and interventional radiography. MRI experience also is available. For further information, contact Robert Kricun, M.D., Dept. of Radiology, Lehigh Valley Hospital Center, P. O. Box 689, Allentown, PA 18105. 6cp

DIAGNOSTIC RADIOLOGY RESIDENCY POSITIONS—The University of Miami/Jackson Memorial Medical Center, Dept. of Radiology, is offering 1 third- and 1 fourth-yr diagnostic radiology residency position beginning July 1989. Our program was recently approved for an increase in total number of positions. UM/JMMC is a 1300-bed, tertiary referral center serving Miami, FL, the Southeast, and Latin America. The Dept. of Radiology currently performs approximately 250,000 exams/yr with 33 faculty, 22 residents, and 8 fellows (5 in neuroradiology and 3 in interventional/CT/ultrasound). If interested, please contact by phone or letter with CV, Sandra A. Oldham, M.D., Dept. of Radiology (R-109), University of Miami School of Medicine, P. O. Box 016960, Miami, FL 33101; (305) 549-6894. AA/EOE. 2-6c

GIANTURCO RESEARCH FELLOW—The Dept. of Diagnostic Radiology at The University of Texas M. D. Anderson Cancer Center, Houston, TX is offering a 1-yr training program under the direction of Kenneth C. Wright, Ph.D., Sidney Wallace, M.D., and Cesare Gianturco, M.D. The program is available for laboratory research in the John S. Dunn Research Foundation Center for Radiological Sciences at a salary of \$25,000. The areas of current research include angiographic and interventional technique and devices, microencapsulation of radiopaque contrast materials and chemotherapeutic agents, and a computerized atlas of anatomy and imaging. Appointments may be made during residency, postresidency, or before beginning residency training. For further information, contact Sidney Wallace, M.D., Dept. of Diagnostic Radiology, The University of Texas M. D. Anderson Cancer Center, 1515 Holcombe Blvd., Houston, TX 77030. An equal opportunity/affirmative action employer. 4-6c

ANGIOGRAPHY/INTERVENTIONAL RADIOLOGY FELLOWSHIP—New York Medical College announces the availability of a 1-yr fellowship to begin July 1, 1990. The program includes training in all phases of diagnostic angiography and interventional radiologic techniques. Approximately 900 procedures were performed in 1988. The program is based at Westchester County Medical Center, a 650-bed, tertiary-care center located on the campus of the medical college in prestigious suburban setting only about 1/2 hr from New York City. Active participation in clinical management of patients is emphasized. Current research interests include transmesenteric sclerosis of portal varices and hepatic arterial chemoembolization. A new interventional/imaging suite will open in 1989. For additional information and application, contact Stuart Katz, M.D., Dept. of Radiology, New York Medical College, Valhalla, NY 10595; (914) 285-8388. 5-6c

CARDIOVASCULAR/INTERVENTIONAL RADIOLOGY FELLOWSHIP AT THOMAS JEFFERSON UNIVERSITY HOSPITAL—A 1-yr fellowship position is available starting 7/1/89. This fellowship includes experience in a wide range of diagnostic angiography and both vascular and nonvascular interventional procedures. These include balloon angioplasty, laser thermal angioplasty, thrombolytic therapy, atherectomy, intravascular stent placement, IVC filter placements, renal and biliary drainage procedures, abscess drainages, and stone retrievals. Optional training also available in coronary angiography. Facilities include state-of-the-art angiographic and digital subtraction equipment. Contact either Geoffrey A. Gardiner, Jr., M.D. or David C. Levin, M.D., Dept. of Radiology, Thomas Jefferson University Hospital, 111 S. 11th St., Philadelphia, PA 19107. Thomas Jefferson University is an equal opportunity/affirmative action employer. 1-6cp

FELLOWSHIP IN VASCULAR AND INTERVENTIONAL RADIOLOGY—A fellowship position in vascular and interventional radiology is available at the University of Texas Medical Branch, for 1 yr beginning July 1, 1990, and ending June 30, 1991. This position is offered also to those radiologists who desire to return to an academic setting to acquire new skills in the vascular and interventional field. Very active dept. with up-to-date equipment provides an excellent opportunity for training in all interventional modalities. Please contact L. B. Moretton, M.D., Director, Vascular and Interventional Radiology, University of Texas Medical Branch, Galveston, TX 77550; (409) 761-2498. UTMB is an equal opportunity M/F/H/V affirmative action employer. UTMB hires only individuals authorized to work in the United States. 4-6c

ANGIOGRAPHY AND INTERVENTIONAL RADIOLOGY FELLOWSHIP TO BEGIN JULY 1990—568-bed teaching hospital. Fellows will participate in all vascular and nonvascular/interventional procedures, including angioplasties, biliary, GU, biopsies, abscess drainages, and angiography. Fellows also will be actively involved in diagnostic CT, MRI, and ultrasound. Send inquiries to Harvey L. Neiman, M.D., Chairman, Dept. of Radiology, West Penn Hospital, 4800 Friendship Ave., Pittsburgh, PA 15224. 5-8c

Tutorials/Courses

CHALLENGE 89—DECISIONS IN IMAGING: LONDON, ENGLAND; JUNE 24-30, 1989—Category I CME, MRI, CT, ultrasound correlative course presented by University of Southern California faculty and a distinguished faculty from the United Kingdom. **Wimbledon Tennis Tournament.** For information contact University Imaging Associates, LAC/USC Medical Center, Box 66, 1200 N. State St., Los Angeles, CA 90033; (213) 226-7245. 4-6dp

FIFTH ANNUAL LONDON-PARIS FALL ULTRASOUND—Sept. 17-23, 1989. Category I accreditation, international faculty. For information, contact Medical Seminars International, 9800 D Topanga Canyon Blvd., Ste. 232, Chatsworth, CA 91311; (818) 700-9821. 3-9d

ALASKA 89—CRUISE THE INLAND PASSAGE—July 8-15, 1989, CME I accreditation, Professor Lawrence Bassett, M.D., Breast Imaging. For information, contact Medical Seminars International, 9800 D Topanga Canyon Blvd., #232, Chatsworth, CA 91311; (818) 700-9821. 1-6d

Other

FOURTEENTH ANNUAL BODY IMAGING CONFERENCE—Hyatt Regency Waikoloa Hotel, October 14-21, 1989. MRI, CT, and ultrasound. Category I accreditation, university faculty. For registration and information, contact Annual Body Imaging Conference, 9800 D. Topanga Canyon Blvd., Ste. 232, Chatsworth, CA 91311; (818) 700-9821. 6-9dp

MOBILE MAMMOGRAPHY VAN—1987, 27-ft Itasca motor home, fully equipped for complete mammography service. Kramex 43S mammography unit, AFP processor. \$85,000. For information respond to, Florida Mobile Imaging, Inc., P. O. Box 2440, Sanford, FL 32772-2440. 4-6ep.

AJR Classified Advertisements Information

Box Responses and Address for Ad Placement

Write Box _____, AJR, 2223 Avenida de la Playa, Suite 200, La Jolla, CA 92037-3218; (619) 459-2229; FAX: (619) 459-8814.

Author Index

Volume 152

Authors of *AJR* articles are also included in the 5-year cumulative index published in *Radiology*.

A

Aberle DR, 152:1113
 Abu Musa A, 152:1311
 Ackermann RJ, 152:1205
 Adam A, 152:527
 Aggarwal S, 152:431
 Agrawal DK, 152:1339
 Agrawal GN, 152:1339
 Agrawal PK, 152:1339
 Aikawa H, 152:1005
 Aikawa M, 152:825
 Aiman J, 152:91
 Akins EW, 152:128
 Alexander JA, 152:128
 Allen KS, 152:77
 Altin RS, 152:629
 Amberg JR, 152:11, 152:10
 Amendola MA, 152:97, 152:1343
 Amodeo C, 152:641
 Amsterdam E, 152:893
 Andriole GL, 152:873, 152:1317
 Aquerreta D, 152:1128
 Arafah BU, 152:597
 Arakawa A, 152:893
 Arata JA Jr, 152:591
 Aronson RL, 152:261, 152:939
 Arger PH, 152:77
 Arnstein NB, 152:1205
 Arrivè L, 152:1215
 Ashida H, 152:985
 Ashizawa A, 152:1005
 Ash RC, 152:991
 Atkins EW, 152:181
 Atri M, 152:1189
 Atuk NO, 152:641
 Auffermann W, 152:729
 Austin JHM, 152:728
 Axel L, 152:653
 Azar-Kia B, 152:1255
 Azzarelli B, 152:131

B

Babayan RK, 152:793
 Bacon BR, 152:167
 Baert AL, 152:771, 152:965
 Baker SP, 152:509
 Balériaux D, 152:1087
 Balfe DM, 152:513, 152:873,
 152:1043, 152:1317
 Balkanci F, 152:1342
 Ballerio C, 152:19
 Balthazar EJ, 152:504
 Banerjee B, 152:894
 Banner MP, 152:97, 152:1343
 Baraniewski HM, 152:795
 Barberena J, 152:202
 Barkovich AJ, 152:353, 152:843

Barloon TJ, 152:501
 Baron RL, 152:853
 Barrett PA, 152:743
 Bartrum RJ Jr, 152:1132
 Barzel E, 152:655
 Bassett LW, 152:35
 Bates BF, 152:870
 Bates FT, 152:991
 Bauman J, 152:275
 Bayraktar Y, 152:1342
 Becker CD, 152:987
 Becker RD, 152:615, 152:1073
 Beijerinck D, 152:891
 Bellah RD, 152:123
 Bell DY, 152:1183
 Bellon EM, 152:597
 Bendel P, 152:1307
 Ben-Menachem Y, 152:1231
 Bennett JC, 152:1086
 Bennett W, 152:63
 Bergin CJ, 152:1183
 Berk RN, 152:719
 Berrey BH Jr, 152:337
 Berry CC, 152:945
 Berry I, 152:153
 Berry M, 152:431
 Berthoty D, 152:1131
 Besozzi MC, 152:1307
 Bezzi M, 152:53
 Bharathi MV, 152:429
 Bilaniuk LT, 152:159
 Bilbao JL, 152:1128
 Bisset GS III, 152:805
 Bittner L, 152:641
 Blumhagen JD, 152:120
 Bockisch A, 152:1307
 Boechat MI, 152:1113, 152:1245
 Boesel CP, 152:835
 Bohrer SP, 152:462, 152:1344
 Bologna S, 152:343
 Bonnière PL, 152:755
 Bookstein JJ, 152:1097
 Borkowski GP, 152:518
 Borsje K, 152:891
 Botet JF, 152:973
 Bowie JD, 152:433
 Bradburg EM, 152:623
 Bradley WG, 152:1277
 Braffman BH, 152:159
 Bramble JM, 152:1109
 Brandon JC, 152:513
 Brauner M, 152:432
 Braunstein EM, 152:932
 Brennan JF, 152:793
 Brenner JS, 152:1344
 Bretagne J-F, 152:434
 Bret PM, 152:1189
 Bricker JA, 152:1021

Brikman I, 152:261
 Brink JA, 152:289
 Brioschi D, 152:781
 Britton J, 152:1049
 Brock JM, 152:623
 Brogdon BG, 152:645
 Brotchi J, 152:1087
 Bruner JM, 152:1263
 Bulas DI, 152:575
 Bulas R, 152:835
 Buonocore E, 152:950, 152:1307
 Burger PC, 152:433
 Burhenne HJ, 152:987
 Bush WH, 152:867
 Busuttill R, 152:377

C

Callaghan JJ, 152:202
 Campbell WL, 152:275, 152:285
 Candiani GB, 152:781
 Capek P, 152:183
 Capobianco A, 152:523
 Carmody RF, 152:475
 Carrasco CH, 152:387
 Carrol CL, 152:19
 Carroll BA, 152:535
 Carson CC, 152:925
 Carson SH, 152:573
 Carter J, 152:825
 Carvalho P, 152:527
 Cassidy MM, 152:729
 Castellino RA, 152:1183
 Chakeres DW, 152:835
 Chaloupka JC, 152:433
 Chamberlain DW, 152:961
 Chang CHJ, 152:1109
 Chang JC, 152:947
 Chang PJ, 152:721
 Chang WH, 152:955
 Chan MKM, 152:529
 Chamsangavej C, 152:387
 Chastanet P, 152:755
 Chehrabi B, 152:623
 Cheitlin MD, 152:729
 Chen C, 152:1257
 Chen HH, 152:319
 Chen H-S, 152:1197
 Chew F, 152:185
 Chi JG, 152:955
 Chiles C, 152:1183
 Chirino A, 152:1065
 Choi BI, 152:281, 152:1221
 Cho K, 152:205
 Choyke PL, 152:267
 Christophe C, 152:1087
 Chu DDM, 152:654
 Clark LR, 152:267
 Clark RA, 152:718

Clark SA, 152:31
 Coblenz CL, 152:1183
 Cochran M, 152:1205
 Cochran ST, 152:299
 Cohan RH, 152:925
 Cohen J, 152:1257
 Compton CC, 152:63, 152:167,
 152:289, 152:493
 Conant EF, 152:749
 Conces DJ Jr, 152:31, 152:1193
 Conrad GR, 152:1021
 Coolen J, 152:965
 Cooper RR, 152:795
 Cooper SG, 152:1348
 Cooperberg PL, 152:1101
 Cope C, 152:183, 152:1346
 Cormier PJ, 152:785
 Corry RJ, 152:795
 Corson JD, 152:795
 Crain MR, 152:430
 Cranney GB, 152:385
 Cross AP, 152:939
 Crow JP, 152:1255
 Culham JAG, 152:431
 Cumming WA, 152:1071, 152:1344
 Curtin AJ, 152:835
 Czarnecki DJ, 152:737
 Czervionke LF, 152:1128

D

Dalal R, 152:1349
 Dalinka MK, 152:229
 D'Amour PG, 152:131
 Darwin R, 152:347
 Davidoff A, 152:41
 Davis G, 152:1097
 DeCandido P, 152:103, 152:1345
 Deck MDF, 152:137, 152:615,
 152:1073
 de Crespigny LC, 152:432
 Decrop E, 152:771
 de Groot J, 152:153
 Dehdashti F, 152:873, 152:1317
 Delamarier R, 152:825
 Del Buono EA, 152:1195
 Delemazure O, 152:755
 de Leon MJ, 152:1257
 Demaerel P, 152:771, 152:965
 Demedts M, 152:965
 Demetris AJ, 152:275, 152:285
 Dennis LN, 152:27, 152:1340
 DePuey EG, 152:1161
 DeRoogatis AJ, 152:1008
 Destian S, 152:137
 Deurenberg JMM, 152:891
 Deutsch AL, 152:333
 Dillon W, 152:813
 Dillon WP, 152:145

Dinakar I, 152:896
 Djang WT, 152:347, 152:433
 Dnauf DG, 152:128
 Dodds WJ, 152:1342
 Doemeny JM, 152:573, 152:1343
 Doenz F, 152:205
 Donaldson JS, 152:115
 Dorta M, 152:781
 Doussset MG, 152:493
 Doyle M, 152:385
 Do YS, 152:281
 Drayer BP, 152:347, 152:813
 Dreesen RG, 152:131
 Druy EM, 152:96
 Dubbins PA, 152:531
 Dudiak KM, 152:995
 Dunder S, 152:1342
 Dunnick NR, 152:451, 152:925
 Durieu JP, 152:755

E

Edwards DK III, 152:573
 Edwards M, 152:843
 Edwards MK, 152:131
 Ehman RL, 152:469
 Eisenberg RL, 152:765
 Eisenman JI, 152:622
 Elizondo G, 152:175
 El-Khoury GY, 152:795
 Ellinger D, 152:1130
 Engelstad BL, 152:167
 Epstein DM, 152:261
 Erba SM, 152:327
 Erickson SJ, 152:371, 152:1013, 152:1299
 Eriksson L, 152:1241
 Escarous A, 152:1340
 Esola C, 152:1059
 Evens RG, 152:200, 152:220, 152:400
 Ezquerro NF, 152:1161

F

Fabrizzi G, 152:73
 Fajardo LL, 152:475
 Fakhry J, 152:1106
 Fan T, 152:623
 Farnum GN, 152:327
 Fearon T, 152:575
 Fedele L, 152:781
 Feigin DS, 152:1192
 Fellmeth B, 152:1097
 Fernbach SK, 152:115
 Ferrell WR, 152:475
 Ferris SH, 152:1257
 Ferrucci JT Jr, 152:11, 152:63, 152:175, 152:289, 152:402, 152:487, 152:493
 Feuerstein IM, 152:861
 Filippa DA, 152:973
 Finck S, 152:895
 Finestone H, 152:892
 Finneran M, 152:835
 Firooznia H, 152:201
 Fishbain D, 152:653
 Fisher RG, 152:1231
 Fishman EK, 152:382
 Fiske R, 152:1113
 Flament-Durand J, 152:1087
 Fletcher EWL, 152:1347
 Flicker S, 152:629
 Flint E, 152:835
 Flodmark O, 152:583
 Flom RA, 152:824
 Foley WD, 152:272, 152:371, 152:1013, 152:1299
 Foong A, 152:1341
 Formanek AG, 152:809
 Forrest JV, 152:18

Fox KR, 152:749
 Fram E, 152:347
 Francis IR, 152:1227
 Franken EA Jr, 152:501
 Franquet T, 152:202
 Freddara U, 152:73
 Frey DG, 152:474
 Fried AM, 152:1058
 Friedman AC, 152:174
 Friedman PA, 152:1197
 Fritts HM, 152:551
 Fueredi GA, 152:737

G

Gado M, 152:879, 152:1333
 Gaensler EHL, 152:49
 Galeazzi R, 152:73
 Gamsu G, 152:753
 Gangitano E, 152:1065
 Garcia EV, 152:1161
 Garcia H, 152:892
 Garin B, 152:432
 Gasparaitis AE, 152:513
 Gastard J, 152:434
 Gearhart JP, 152:109
 Gebarski SS, 152:596
 Geerdink RA, 152:1129
 Gelfand DW, 152:984
 Gellad FE, 152:1033
 Genkins SM, 152:535
 George AE, 152:1257
 Gibson RN, 152:1129
 Gillespie KR, 152:483
 Ginsberg HN, 152:1211
 Giyanani V, 152:765
 Glazer HS, 152:873, 152:1173, 152:1317
 Glick SN, 152:513
 Glickman MG, 152:736
 Glickstein MF, 152:307
 Godwin JD, 152:951
 Goldberg HI, 152:159, 152:1215
 Goldberg M, 152:653
 Goldberg ME, 152:512
 Goldfarb AF, 152:777
 Goldfarb R, 152:892
 Gold RH, 152:35
 Goldstein HA, 152:813
 Goldstein L, 152:739
 Gonzalez G, 152:579
 Gonzalez JF, 152:175
 Goodman LR, 152:991
 Gordillo I, 152:579
 Gordon RL, 152:97
 Gore MD, 152:115
 Gore RM, 152:990
 Gramm HF, 152:52, 152:288, 152:1178
 Grant DN, 152:1049
 Grant EG, 152:377, 152:707
 Graziani L, 152:73
 Greenberg JJ, 152:523
 Greenfield AJ, 152:793
 Griscom NT, 152:123
 Gross BH, 152:1195, 152:1205
 Gross HM, 152:947
 Grossman RI, 152:159
 Guidici MN, 152:781
 Guinto FC Jr, 152:609
 Guion CJ, 152:575
 Guo D-W, 152:345
 Gurney JW, 152:991
 Gyves J, 152:1205

H

Hackney DB, 152:159, 152:1290
 Haesendonck P, 152:1087
 Hagen-Ansert SL, 152:114
 Haghighi P, 152:1131

Hahn PF, 152:63, 152:175, 152:289, 152:487, 152:493
 Haines AB, 152:615, 152:1073
 Hall FM, 152:1340, 152:1345
 Hallam MJ, 152:1101
 Halls J, 152:291
 Hamilton S, 152:1132
 Hammond DI, 152:309
 Hamper UM, 152:1132
 Hanafee W, 152:550, 152:1254
 Han BK, 152:1251
 Han MC, 152:281, 152:955, 152:1221
 Han MH, 152:281, 152:1221
 Han YC, 152:955
 Hands LJ, 152:1347
 Haney PJ, 152:1033
 Hanna PD, 152:521
 Hansen RM, 152:991
 Hansson L-G, 152:1241
 Harms L, 152:91
 Harrill CD, 152:483
 Harrington DP, 152:652
 Harris AB, 152:152
 Harris G, 152:53
 Harrison DC, 152:894
 Hartmann HR, 152:1349
 Hata K, 152:1311
 Hata T, 152:1311
 Hauser GJ, 152:575
 Hawes DR, 152:795
 Hawkins IF Jr, 152:181
 Hayrapetian A, 152:1113
 Hay T, 152:1059
 Hayward RD, 152:1049
 Heekin RD, 152:337
 Heggelman BGF, 152:1129
 Heiberg E, 152:1340
 Heier LA, 152:615
 Heinz ER, 152:347
 Heinz TR, 152:347
 Hellström M, 152:801
 Helms CA, 152:547, 152:697
 Hendee WR, 152:398, 152:1313
 Herfkens RJ, 152:465
 Herlinger H, 152:53
 Herman SJ, 152:961
 Hernanz-Schulman M, 152:318
 Hertzberg BS, 152:433
 Hess CF, 152:999
 Hibbard CA, 152:229
 Higashihara H, 152:204
 Higgins CB, 152:729
 Hill A, 152:583
 Hillman BJ, 152:475
 Hilton SW, 152:578
 Hinks RS, 152:1271
 Hino M, 152:977
 Hodges FJ III, 152:879, 152:1333
 Holman BL, 152:917
 Holt RG, 152:547
 Holtas S, 152:561, 152:1241
 Homer MJ, 152:960
 Hoppe R, 152:1197
 Horgan JG, 152:1059
 Hovda D, 152:1291
 Gross HM, 152:1215
 Hricak H, 152:1215
 Huang HK, 152:1113
 Huang HY, 152:897
 Hueftle MG, 152:825
 Hugh AE, 152:897
 Hurtig HI, 152:159
 Hurwitz J, 152:652
 Hyde J, 152:1013

I

Ibuki Y, 152:977
 Ichika S, 152:1005
 Iio M, 152:505
 Ikekubo K, 152:977

Illescas FF, 152:1189
 Im J-G, 152:955
 Ishikawa Y, 152:985
 Itai Y, 152:505

J

Jackson FI, 152:1132
 Jackson VP, 152:483
 Jacobs JE, 152:307
 Jacobs P, 152:167
 Jacobsson B, 152:801
 Jaffe MH, 152:267
 Jaffe RB, 152:591
 Jain KA, 152:1132
 Janon EA, 152:1348
 Jarvis LJ, 152:531
 Jasper MP, 152:429
 Jeffrey RB Jr, 152:49, 152:1229
 Jelinek JS, 152:337
 Jennis R, 152:1073
 Jenss H, 152:999
 Jesmanowicz A, 152:1013
 Jiang J, 152:165
 Jiménez C, 152:202
 Jinkins JR, 152:1277
 Jodal U, 152:801
 Johansen CC, 152:1241
 Johnson CD, 152:995
 Johnson DW, 152:327
 Johnson JE, 152:475
 Johnson MB, 152:291
 Johnston WW, 152:451
 Jones MD, 152:895
 Julsrud PR, 152:469
 Juni JE, 152:1205

K

Kangaroo H, 152:1245
 Kansu E, 152:1342
 Kaplan IL, 152:865
 Kaplan JO, 152:1271
 Kaplan PA, 152:697
 Kaplan SB, 152:285
 Kaplan WE, 152:115
 Karasick S, 152:777
 Kasi LP, 152:972
 Kathol MH, 152:795
 Katz BH, 152:1271
 Katz BP, 152:483
 Katzberg RW, 152:1241
 Kaufman B, 152:597
 Kaufman BA, 152:597
 Kay C, 152:1008
 Kelly J, 152:41
 Kelly W, 152:153
 Kendall BE, 152:1049
 Kennis C, 152:771
 Khan TJ, 152:1341
 Khanna S, 152:1343
 Kilcoyne RF, 152:82
 Kim C-W, 152:955, 152:1221
 Kim D, 152:523
 Kim EE, 152:972
 Kim HJ, 152:281
 Kim KS, 152:319
 Kim R, 152:523
 Kim SH, 152:1221
 Kim SY, 152:761
 Kimme-Smith C, 152:35, 152:1160
 Kingsley DPE, 152:1049
 Kioumehri F, 152:299
 Kirchner PT, 152:1021
 Kissel P, 152:623
 Kitao M, 152:1311
 Klein JS, 152:753
 Klein RM, 152:742
 Kleinman PK, 152:108
 Kluger A, 152:1257
 Knechtges TE, 152:737

Kneeland JB, 152:1013
 Ko YT, 152:761
 Koelbel G, 152:999
 Koganemaru F, 152:204
 Kokubo T, 152:505
 Komori H, 152:977
 Kopans DB, 152:1, 152:1341
 Korobkin M, 152:26, 152:1227
 Kostrubiak IS, 152:739
 Kraft JL, 152:1193
 Kramer SS, 152:109
 Kransdorf MJ, 152:337
 Krebs CA, 152:765
 Kressel HY, 152:77
 Kricun ME, 152:229
 Krispin M, 152:893
 Krol G, 152:137
 Krueckeberg ST, 152:125
 Kucharczyk J, 152:153
 Kucharczyk W, 152:153
 Kudo M, 152:977
 Kueper K, 152:999
 Kuharik MA, 152:131
 Kullnig P, 152:1179
 Kumar A, 152:431
 Kundel HL, 152:261
 Kurita K, 152:1241

L

Labbe E, 152:653
 Lachman RS, 152:572
 La France ND, 152:109
 Lagrotteria LB, 152:551
 Lahti D, 152:1205
 Laing FC, 152:49, 152:1229
 Laimand B, 152:1087
 Lammert GK, 152:382
 Lampmann LEH, 152:203
 Landzberg JS, 152:729
 Lane RH, 152:83
 Lantink JA, 152:1129
 La Regina ME, 152:1257
 LaRoy LL, 152:785
 Larson J, 152:1130
 Larsson E-M, 152:561
 Lasser EC, 152:945
 Latchaw RE, 152:327
 Laufer I, 152:53
 Lawate PS, 152:429
 Lawson TL, 152:371, 152:1013, 152:1299
 Layfield L, 152:299
 Lebowitz RL, 152:567
 Lecumberri FJ, 152:202
 Lee BCP, 152:623
 Lee D, 152:947
 Lee DH, 152:761
 Lee JS, 152:955
 Lee KP, 152:291
 Lee RR, 152:481
 Lee S-E, 152:654
 Lee SH, 152:281
 Lee Y-Y, 152:361, 152:1263
 Legrand I, 152:432
 Le Jean-Colin I, 152:434
 Lemort M, 152:1087
 Lentle BC, 152:654
 Leung JWC, 152:529, 152:894
 Levi S, 152:893
 Levin DC, 152:199
 Levine ML, 152:1345
 Levine MS, 152:53, 152:513, 152:892
 Lewis J, 152:167
 L'Herminé C, 152:755
 L'Heureux PR, 152:125
 Li C, 152:265
 Li D, 152:583
 Liberman RL, 152:1065
 Liddell RM, 152:120

Lim JH, 152:761
 Linden SS, 152:967
 Link KM, 152:809
 Link MP, 152:343
 Linton OW, 152:191
 LiPuma J, 152:813
 Lo H-H, 152:58
 Lois J, 152:377
 Longo J, 152:1128
 Loréal O, 152:434
 Lorigan JG, 152:387
 Lotan CS, 152:385
 Lufkin RB, 152:1291
 Lund JT, 152:469
 Lupton B, 152:583

M

MacEwan DW, 152:189
 Machado T, 152:1097
 Mack LA, 152:202
 Macrander SJ, 152:371, 152:1299
 Maeda H, 152:1005
 Maglinte DDT, 152:513
 Mail JT, 152:483
 Maile CW, 152:521
 Majer MC, 152:999
 Malik N, 152:1343
 Malone DE, 152:987
 Malt RA, 152:63
 Mamourian A, 152:431
 Manco-Johnson ML, 152:1059
 Mancuso A, 152:813
 Manfrini E, 152:73
 Mansour MA, 152:1107
 Marasco JA Jr, 152:191
 Maravilla K, 152:813
 Marchal G, 152:771, 152:965
 Marfil J, 152:175
 Margulis AR, 152:1215
 Márid S, 152:801
 Marsh JL, 152:1021
 Marshburn PB, 152:433
 Martin DS, 152:706
 Martin NL, 152:1109
 Martin TD, 152:128
 Martinez A, 152:579
 Marx MV, 152:633
 Masaryk TJ, 152:825
 Mastin ST, 152:435
 Matalon TAS, 152:785
 Mathews VP, 152:131
 Matlak ME, 152:591
 Matsumoto J, 152:1251
 Mattrey RF, 152:247
 Mayekawa DS, 152:291
 McAlister WH, 152:877, 152:1328
 McAsey M, 152:91
 McClellan BL, 152:873, 152:1317
 McCloskey J, 152:805
 McLeish WA, 152:309
 McNamara MP Jr, 152:1123
 McNeish LM, 152:202
 Melson GL, 152:293, 152:633, 152:1237
 Merenstein GB, 152:1059
 Merine D, 152:382
 Metreweli C, 152:529, 152:894
 Mewissen MW, 152:1299
 Meyer JE, 152:481
 Meyers P, 152:924
 Mezirch JL, 152:261
 Middleton MA, 152:875, 152:1323
 Middleton WD, 152:91, 152:293, 152:371, 152:633, 152:875, 152:1013, 152:1237, 152:1299, 152:1323
 Millán JM, 152:579
 Miller EI, 152:776
 Miller JD, 152:1257
 Miller L, 152:343

Miller RR, 152:1179
 Miller WT, 152:265, 152:749
 Mindell HJ, 152:47, 152:651
 Mink JF, 152:333
 Miralles M, 152:579
 Mirvis SE, 152:103, 152:739, 152:1345
 Mitchell SE, 152:109
 Miura K, 152:985
 Miura T, 152:985
 Miyake H, 152:1005
 Mladinich C, 152:181
 Modic MT, 152:597, 152:825
 Moler C, 152:35
 Montgomery WJ, 152:1021
 Moonen C, 152:623
 Morgello S, 152:1073
 Morioka C, 152:1113
 Moriuchi A, 152:1005
 Morton JA, 152:1306
 Moser RP, 152:1263
 Moskowitz M, 152:891
 Mueller PR, 152:11, 152:289, 152:487, 152:493
 Mukhopadhyay S, 152:431
 Müller NL, 152:987, 152:1179
 Munk PL, 152:547
 Muñoz M, 152:1128
 Murphey MD, 152:541

N

Nagatomo H, 152:1005
 Naidech HJ, 152:629
 Nakamura T, 152:204
 Nakao N, 152:985
 Nath H, 152:199, 152:430
 Nazarian GK, 152:1195
 Nepola JV, 152:1021
 Nesbit GM, 152:1130
 Newhouse JH, 152:973
 Newman LM, 152:313
 Newton TH, 152:145, 152:153
 Ngo C, 152:299
 Niendorf HP, 152:1087
 Nitta K, 152:1291
 Nocks BN, 152:303
 Norman D, 152:145, 152:153, 152:353, 152:843
 Norman MG, 152:583
 Norton P, 152:41
 Novak DL, 152:870
 Nozaki Y, 152:204
 Nurenberg P, 152:743
 Nussbaum AR, 152:1033

O

Oates E, 152:895
 O'Donnell C, 152:527
 Ohkuma T, 152:893
 Ohtomo K, 152:505
 Okazaki M, 152:204
 O'Keefe F, 152:387
 Olcoz F, 152:579
 Omile MR, 152:551
 Ongseng F, 152:892
 Orino A, 152:977
 Orron DE, 152:523
 Orzel JA, 152:896
 Oster ZH, 152:253
 Ott DJ, 152:462
 Outwater E, 152:895

P

Painter M, 152:523
 Pais SO, 152:933
 Pant MC, 152:1339
 Papanicolaou N, 152:303
 Paris JC, 152:755
 Parizel PM, 152:1087

Park JH, 152:1221
 Parker BR, 152:343
 Parvey HR, 152:765
 Pascual E, 152:1341
 Patel SK, 152:785
 Patten RM, 152:1009
 Paushter DM, 152:267
 Pearce WH, 152:1107
 Peck WW, 152:145
 Pegum JM, 152:1132
 Perlmutter LM, 152:451
 Perrella RR, 152:377, 152:707
 Peters MJ, 152:853
 Pfister RC, 152:303
 Pflugfelder PW, 152:729
 Picus DD, 152:633
 Platz CE, 152:795
 Pochaczewsky R, 152:1130
 Pohost GM, 152:385
 Pollack HM, 152:53, 152:77, 152:97, 152:1343
 Pollack MM, 152:575
 Pond GD, 152:475
 Porter DH, 152:523
 Porterfield JK, 152:382
 Post MJD, 152:1271
 Posteraro RH, 152:465
 Pradines P, 152:432
 Price J, 152:1347
 Prince JR, 152:1029
 Prinz RA, 152:1255
 Pritzker KPH, 152:685
 Pry R, 152:181
 Pulperio JR, 152:579

Q

Quencer RM, 152:1271
 Quinlan DM, 152:109
 Quiroz FA, 152:371, 152:1299

R

Rachlin DJ, 152:1197
 Radowich MS, 152:337
 Radtke R, 152:347
 Rafii M, 152:201
 Raghavan N, 152:843
 Rajani M, 152:429
 Ralls PW, 152:291
 Ranganadham P, 152:896
 Rao VM, 152:313
 Raoul J-L, 152:434
 Rappaport DC, 152:961
 Raptopoulos V, 152:41, 152:509, 152:651
 Rasuli P, 152:309
 Reddy S, 152:1341
 Rehm SR, 152:743
 Reicher MA, 152:573
 Reid JM, 152:1101
 Reiman HM, 152:83
 Reinhold C, 152:1189
 Reisberg B, 152:1257
 Resnick D, 152:241, 152:1131
 Resnik CS, 152:103, 152:1345
 Restrepo de Rovetto C, 152:1251
 Reuter SR, 152:200
 Rezaei K, 152:795
 Richards T, 152:1028
 Richli WR, 152:387
 Robbins S, 152:26
 Roberts A, 152:1097
 Robinson HP, 152:432
 Robkin MA, 152:492, 152:500
 Rodesch G, 152:1087
 Rogers LF, 152:27, 152:319, 152:1340
 Rohmann CA, 152:280
 Roland EH, 152:583
 Rolston DDK, 152:429

Romano AJ, **152:879, 152:1333**
 Rombach JJ, **152:891**
 Ros PR, **152:435, 152:1344**
 Rosen M, **152:793**
 Rosenbaum DM, **152:120, 152:896**
 Rosenfelt FP, **152:333**
 Rosomoff H, **152:653**
 Ross JS, **152:825**
 Rothschild PA, **152:35**
 Rubenstein J, **152:685**
 Rubenstein JA, **152:891**
 Rubesin SE, **152:53**
 Rubin GD, **152:573**
 Rumack CM, **152:1059**
 Rummeny E, **152:63, 152:493**
 Russ PD, **152:1107**
 Russell EJ, **152:319, 152:813**
 Ryan J, **152:973**

S

Sacks AB, **152:1127**
 Sacks BA, **152:523**
 Sagel SS, **152:1173**
 Saini S, **152:63, 152:175, 152:289, 152:487, 152:493**
 Sanders LM, **152:973**
 Sanders RC, **152:1132**
 Sanfilippo FP, **152:535**
 San Julián P, **152:1128**
 Santamaria JJ, **152:991**
 Sarno RC, **152:895**
 Sartoris DJ, **152:76, 152:241, 152:312, 152:696, 152:1131, 152:1152**
 Sato Y, **152:795**
 Scatliff JH, **152:1049**
 Schaible TF, **152:813**
 Scheibler ML, **152:267**
 Schellhas KP, **152:551**
 Schenck JF, **152:1127**
 Schiller NB, **152:729**
 Schmiedl U, **152:999**
 Schuster JJ, **152:509**
 Schwenk GR, **152:31**
 Seabold JE, **152:1021**
 Sebes JJ, **152:1153**
 Seeley AB, **152:1291**
 Sefczek R, **152:431**
 Segal AJ, **152:1128**
 Segebarth C, **152:1087**
 Seibert A, **152:623**
 Selby JB, **152:641**
 Selman WR, **152:597**
 Seltzer SE, **152:917**
 Serour F, **152:893**
 Serrano C, **152:579**
 Shamma AR, **152:795**
 Shapiro MJ, **152:1343**
 Share JC, **152:567, 152:1263**
 Sharma S, **152:429**
 Shearer DR, **152:1004**
 Shehadi WH, **152:1042**
 Sheline ME, **152:261**
 Shkolnik A, **152:115**

Shoemaker EI, **152:879, 152:1333**
 Sholkoff SD, **152:776**
 Shortsleeve MJ, **152:513**
 Shuman WP, **152:853, 152:1009**
 Sibony M, **152:432**
 Sickles EA, **152:967**
 Siegel BA, **152:873, 152:1317**
 Siegel HA, **152:780, 152:1236**
 Siegel ME, **152:464, 152:1214**
 Siegel MJ, **152:877, 152:1043, 152:1173, 152:1328**
 Silver B, **152:785**
 Silverman SG, **152:289**
 Simeone JF, **152:11, 152:289, 152:487, 152:493**
 Sinak LJ, **152:469**
 Singh SP, **152:429**
 Sinha KN, **152:1339**
 Siragusa RJ, **152:181**
 Sivitt CJ, **152:575**
 Smith JL, **152:501**
 Smith SR, **152:299**
 Smithuis RHM, **152:59**
 Som P, **152:253**
 Sommer FG, **152:1197**
 Sostman HD, **152:465**
 Soter CS, **151:508**
 Soto B, **152:199**
 Spencer RP, **152:264, 152:1204**
 Spevak MR, **152:108**
 Spritzer CE, **152:465**
 Squire LF, **152:457**
 Srivastava PK, **152:1339**
 Stadalnik RC, **152:540**
 Stanley RJ, **152:199**
 Stark DD, **152:63, 152:167, 152:175, 152:487, 152:493**
 Steele-Rosomoff R, **152:653**
 Steinbach BG, **152:435**
 Steiner E, **152:487**
 Stephens DH, **152:83, 152:995**
 Stern MB, **152:159**
 Stimac GK, **152:583**
 Stomper PC, **152:481**
 Straus DJ, **152:973**
 Strife JL, **152:805**
 Stylopoulos LA, **152:1257**
 Subber SW, **152:1107**
 Sumkin JH, **152:285**
 Sussman SK, **152:307**
 Suzuki K, **152:1005**
 Svensson SA, **152:1241**
 Swann CA, **152:1**
 Swanson DA, **152:125**
 Swayne LC, **152:865, 152:1211**
 Szasz IJ, **152:654**
 Sze G, **152:137**
 Szucs R, **152:652**

T

Tajik AJ, **152:469**
 Takahashi H, **152:985**
 Takahashi M, **152:893**
 Takasugi JE, **152:951**

Tallents RH, **152:1241**
 Tarver RD, **152:31, 152:1193**
 Tashiro M, **152:1005**
 Taylor GA, **152:575**
 Tazioli PK, **152:853**
 Teehey S, **152:1009**
 Tegtmeyer CJ, **152:641**
 Telatar H, **152:1342**
 Teplick SK, **152:513, 152:913**
 Terashi A, **152:654**
 Teresi LM, **152:1291**
 Tessier FN, **152:377, 152:707, 152:1169**
 Thoeni RF, **152:1215**
 Thomas VJ, **152:1071**
 Thomson JD, **152:337**
 Thorne DA, **152:293**
 Thorsen MK, **152:91**
 Tobey DM, **152:1340**
 Tobin KD, **152:933**
 Todd LE, **152:175**
 Todo A, **152:977**
 Tomita S, **152:977**
 Tomsak RL, **152:597**
 Towers MJ, **152:1132**
 Townsend RR, **152:49, 152:1229**
 Tripathi AK, **152:1339**
 Tristan TA, **152:572**
 Tsuchigame T, **152:893**
 Tsuruda JS, **152:1065**
 Tung G, **152:289**
 Tupler R, **152:181**
 Turner DA, **152:785**
 Turney SZ, **152:739**

U

Usselman JA, **151:474**
 Utsunomiya J, **152:985**
 Utz JA, **152:337**

V

Valentino D, **152:1113**
 Valji K, **152:1097**
 van der Schueren E, **152:771**
 VanDyke C, **152:825**
 Van Hecke P, **152:771**
 van Holsbeeck M, **152:202**
 Van Tassel P, **152:361, 152:1263**
 Verschakelen JA, **152:965**
 Versteylen RJ, **152:203**
 Victorica BE, **152:128**
 Virapongse C, **152:1119**
 Vix VA, **152:1193**
 Vogt JF, **152:1065**
 Vos CG, **152:59**

W

Waggenspack GA, **152:609**
 Wahl RL, **152:1205**
 Waite R, **152:41**
 Walker TG, **152:391, 152:793**
 Wallace S, **152:387**
 Waltman AC, **152:391**

Warnock M, **152:753**
 Waxman AD, **152:333**
 Webb WR, **152:753, 152:955**
 Weber P, **152:999**
 Wechsler RJ, **152:313**
 Weesner KM, **152:809**
 Weigelt JA, **152:1131**
 Weinberger E, **152:896**
 Weiner B, **152:1341**
 Weingarten K, **152:615, 152:1073**
 Weisbrod GL, **152:961**
 Weissleder R, **152:63, 152:167, 152:175, 152:493**
 Weissman BN, **152:1020**
 Welch TH, **152:1251**
 Westesson P-L, **152:1241**
 Whalen E, **152:195, 152:647**
 Whigham C, **152:1231**
 White DL, **152:167**
 White RI Jr, **152:382**
 White SJ, **152:483**
 Whitfield MF, **152:583**
 Whitman GJ, **152:518**
 Whittmore AR, **152:1277**
 Wiele K, **152:875, 152:1323**
 Wilkes CH, **152:551**
 William R, **152:429**
 Wilson CB, **152:145**
 Wilson DA, **152:1029**
 Wilson TA, **152:1227**
 Winzelberg GG, **152:512**
 Wiot JF, **152:456**
 Wittenberg J, **152:63, 152:487, 152:493**
 Wolf GL, **152:939**
 Wong WS, **152:1065**
 Wood LC, **152:644**
 Woodring JH, **152:743**
 Wu A, **152:205**

Y

Yaghmai I, **152:299**
 Yale-Loehr AJ, **152:109, 152:1033**
 Yamamoto K, **152:977**
 Yeon KM, **152:955**
 Yeung EY-C, **152:527**
 Yip CKY, **152:529, 152:894**
 Yoshida H, **152:505**
 Yoshikawa K, **152:505**
 Young G, **152:125**
 Young JWR, **152:103, 152:1345**
 Young SW, **152:19**
 Yuh WTC, **152:795**

Z

Zacher D, **152:653**
 Zajko AB, **152:275, 152:285**
 Zandt-Stastny D, **152:91**
 Zaontz MR, **152:115**
 Zeman RK, **152:267**
 Zimmerman RA, **152:159**
 Zimmerman RD, **152:137, 152:615, 152:1073**
 Zion A, **152:91**
 Zlatkin MB, **152:229**
 Zygmunt S, **152:561**

Subject Index Volume 152

AJR articles are also included in the 5-year cumulative index published in *Radiology*.

Index Key: a = abstract, b = book review, e = editorial, l = letter, m = memorial, p = pictorial essay, v = videotape review

Subjects in this index are cataloged by body part where possible. Disease entities unique to a body part are listed by that part; other more general diseases have separate listings by name. Technical procedures are also listed by part, as appropriate. Because of general interest, subjects dealing with computed tomography, magnetic resonance imaging, sonography, radionuclide imaging, and pediatric radiology are listed under those headings as well as under appropriate body part and/or disease.

A

Abdomen

blunt trauma, non-contrast-enhanced CT, 152:47, 152:41 (commentary)
color Doppler imaging, 152:707
composite SPECT-CT images, 152:865

Abdominal aortic aneurysm

cholelithiasis with, sonography, 152:509
imaging (p), 152:785

Absorptiometry, dual-energy radiographic, bone densitometry, 152:241

Acetabula, teardrop, migration relations (a), 152:658

Acetabular cup, fracture, heterotopic ossification (a), 152:439

Achalasia, radiographic and manometric correlation in, relaxation of lower esophageal sphincter (a), 152:902

Acidemia, methylmalonic, acute extrapyramidal syndrome (a), 152:900

Acquired immune deficiency syndrome

infectious diarrhea in (a), 152:208

pediatric

imaging, 152:1033

neuroradiologic and neurodevelopmental findings (a), 152:902

Pneumocystis pneumonitis with, cavitating and noncavitating granulomas with, 152:753

precaution in radiology (v), 152:504

sclerosing cholangitis in (a), 152:1353

squamous cell carcinoma, esophageal (a), 152:209

Adrenal gland, tumors, CT, 152:1005

Afferent loop, obstruction, direct percutaneous drainage of, 152:521

Alimentary tract, hollow organs and salivary glands (b), 152:280

Alzheimer's disease, ventricular change in, CT, 152:1257

American Roentgen Ray Society

Executive Council award, 152:475
information and application for membership, 152:216

1989 local activities, 152:421

1989 meeting, New Orleans, LA, 152:220, 152:400, 152:664, 152:885

1989 meeting summary, 152:427, 152:675, 152:887

1989 scientific program, 152:415

1990 meeting, Washington, DC, 152:1360

officers, committees, and membership information, 152:219, 152:428, 152:666, 152:884
section on instruction, 152:402

Anatomy, sectional (b), 152:718

Angina, attack induced by hyperventilation, magnesium effects (a), 152:1351

Angiocardiography

cine, aortico-left ventricular tunnel, 152:345

digital, progress (b), 152:26

Angiography

color Doppler sonography comparison

hemodialysis vascular access, 152:633

stenosis of internal carotid artery, 152:1299

coronary, atrial myxoma, 152:737

CT, cavernous transformation of portal vein, 152:985

digital and film-based, coronary artery disease (a), 152:657

digital subtraction, contrast medium and bilateral blurring vision (l), 152:429

esophagojejunal venous shunt, esophagojejunostomy and (l), 152:434

renal artery branch injury, 152:1231

subclavian hemodialysis catheter insertion, 152:641

Angioma, duodenal (l), 152:1128

Angioplasty

balloon, pulmonary hypertension (a), 152:657

coronary, early restenosis after, diet effects (a), 152:206

Ankle

imaging (b), 152:82

malleolar fracture (l), 152:895

Antibody-mediated delivery systems, tumor diagnosis and therapy (b), 152:972

Aortic aneurysms

abdominal

imaging (p), 152:785

cholelithiasis with, sonography, 152:509

Aortic regurgitation, Doppler echocardiography, compared with cine MRI, 152:729

Aortic stenosis, gastrointestinal bleeding, angiodysplasia association (a), 152:657

Appendicitis

cecal diverticulitis differentiated from, graded-compression sonography, 152:1229

suspected, sonography, 152:49

Arteriography

femoral, knee time in (l), 152:203

penetrating wounds of extremities (l), 152:1130

pulmonary, right ventricular enlargement, 152:391

Arteriovenous fistulae, abdominal aortic aneurysms, duplex sonography, 152:1107

Arteriovenous malformation, pelvic, color Doppler imaging, 152:1311

Arthritis, rheumatoid, craniocervical junction, MRI, 152:561

Arthrography, TMJ diagnosis, 152:697

Arthropathies, crystal-associated, 152:685

Asbestos

disorders of the chest, plain-film diagnosis (a), 152:658

thoracic disease related to, CT (a), 152:901

Aspirin, ursodeoxycholic acid and, lithogenic bile and gallstone formation (a), 152:1133

Atelectasis, rounded, lung, MRI, 152:965

Atrial myxoma, coronary angiography in, 152:737

Avascular necrosis

osteochondritis dissecans, mandibular condyle, MRI, 152:551

Autonomic syndrome, vertebrogonic pain and, lumbar disk extrusion, 152:1277

B

Barium studies, prostatic carcinoma, rectal involvement in, 152:53

Bartter syndrome, hypercalciuric, 152:1251

Bayesian analysis, 152:721

Behcet syndrome, portal hypertension in (l), 152:1342

Benzyl alcohol, kernicterus relations, preterm infants (a), 152:1354

Bile duct

malignant obstructions, mushroom-tipped endoprostheses, 152:527

stone removal, percutaneous transhepatic oddisphincter dilatation, 152:73

strictures, scrape biopsy, 152:529

Biliary obstruction

malignant

endoscopy in (a), 152:208

failed T-tube drainage (l), 152:894

Biopsy

CT-guided, gantry angulation (l), 152:1345

needle

blunt, percutaneous access device, 152:181

cold thyroid nodules (a), 152:207

- percutaneous transthoracic, **152:451**
 preoperative image-guided placement, occult breast lesions, **152:1**
 transthoracic aspiration, diagnosis of pulmonary infections, **152:31**
 needle-aspiration, gallbladder, **152:913**
 scrape, malignant biliary stricture, **152:529**
- Blood flow**
 absolute intracranial velocities, preterm and term neonates, **152:1059**
 color imaging, heart (b), **152:706**
 postprandial intestinal, duplex ultrasound (a), **152:437**
- Bone**
 abnormalities, sickle cell hemoglobinopathies and, **152:1153**
 densitometry, dual-energy radiographic absorptiometry, **152:241**
 giant cell tumor, with pulmonary metastases (a), **152:900**
 immature infarcts, MRI, **152:547**
 metastases, bronchial carcinoid (l), **152:202**
- Bone marrow**, transplantation, pneumatosis intestinalis in, routine chest radiographs, **152:991**
- Bone scan**, delayed static, tourniquet effect after (l), **152:896**
- Book reviews**
 anatomy and MRI of the joints, **152:1152**
 antibody-mediated delivery systems, **152:972**
 assessing the skeletal maturity of the hand-wrist, **152:108**
 atlas of fetal skeletal radiology, **152:318**
 atlas of mammography, **152:742**
 atlas of sectional human anatomy, **152:718**
 biomedical magnetic resonance imaging, **152:1028**
 cerebrovascular disease, **152:622**
 color blood flow imaging of the heart (b), **152:706**
 computed tomography of the chest, **152:26**
 dental radiographic diagnosis, **152:550**
 diagnosis and management of orbital tumors, **152:1290**
 diagnostic nuclear medicine, vols 1 and 2, 2nd ed, **152:1008**
 endosonography in gastroenterology, **152:990**
 essential chest radiology, **152:1192**
 exposure of the population in the United States and Canada from natural background radiation, **152:492**
 fetal echocardiography, **152:114**
 fundamentals of nuclear medicine, 2nd ed., **152:540**
 fundamentals of skeletal radiology, **152:696**
 gallenblasensteine, **152:10**
 gastrointestinal nuclear imaging, **152:58**
 handbook of cardiovascular and interventional radiologic procedures, **152:736**
 handbook of radiologic orthopaedic terminology, **152:1020**
 how to write and publish a scientific paper, 3rd ed., **152:644**
 hysterosalpingography and pelvic ultrasound, **152:776**
 imaging anatomy of the knee region, **152:312**
 imaging of the foot and ankle, **152:82**
 imaging of the pelvis, **152:924**
 interventional radiology, **152:96**
 magnetic resonance imaging, **152:596**
 mammography, **152:960**
 MIRD primer for absorbed dose calculations, **152:1004**
 nuclear medicine, **152:474**, **152:508**
 nuclear medicine annual 1988, **152:464**
 nuclear medicine technology and techniques, **152:1214**
 operative ultrasonography, 2nd ed, **152:1106**
 principles of radiopharmacology, **152:264**
 proceedings of the chest imaging conference 1987, **152:950**
- progress in digital angiocardiology, **152:26**
 public radiation exposure from nuclear power generation in the United States, **152:474**
 pulmonary pathology, **152:728**
 radiation exposure of the U. S. population from consumer products and miscellaneous sources, **152:500**
 radiographic contrast agents, 2nd ed, **152:1042**
 radiolabeled monoclonal antibodies for imaging and therapy, **152:1204**
 radiology report, **152:1178**
 RSNA today, vol. 2, no. 4, **152:1236**
 small bowel radiology, **152:52**
 Smith's recognizable patterns of human malformation, 4th ed., **152:578**
 the alimentary tract, **152:280**
 the chief resident as manager, **152:512**
 the malformed fetus and stillbirth, **152:572**
 the radiologic clinics of North America
 arthritis and other arthropathies, **152:932**
 imaging in neuroradiology, part I, **152:152**
 imaging in neuroradiology, part II, **152:824**
 the radiologist's first reader, **152:572**
 the scintillation camera, **152:512**
 ultrasonography in obstetrics and gynecology, 2nd ed, **152:1058**
 Ultrasonography of the spleen, **152:174**
 ultrasound, **152:1160**
 ultrasound of the prostate, **152:780**
 workbook for MRI and CT of the head and neck, **152:1254**
 x-ray differential diagnosis in small bowel disease, **152:984**
- Brain**
 abscesses, MRI, **152:1073**
 congenital malformations, absence of septum pellucidum, **152:353**
 infarct, thrombolytic treatment, spectroscopy, **152:623**
 third ventricle
 anterosuperior, masses, MRI and CT, **152:609**
 herniation into empty sella, **152:597**
- Breast**
 benign cysts, sedimented calcium in, **152:967**
 cancer
 adenomatous polyps in (a), **152:1134**
 adjuvant tamoxifen and cytotoxic therapy (a), **152:898**
 metastatic pattern in recurrence (a), **152:436**
 lesions
 localization devices, cost of (l), **152:1340**
 preoperative imaging-guided needle placement, **152:1**
 mass, pectoralis muscle simulating, **152:481**
Bronchial carcinoid, target metastases from (l), **152:202**
Bronchogenic cyst, mediastinal, prenatal sonography, **152:125**
Bronchopulmonary aspergillosis, allergic, children with cystic fibrosis (a), **152:1137**
Budd-Chiari syndrome, duplex and color Doppler imaging, **152:377**
Bulimia, upper GI tract dysfunction in (a), **152:899**
- C**
- Calcium**, sedimented, benign breast cysts, mammography, **152:967**
Calculi, see specific type
Carcinoma, see specific organ, region
Carotid artery
 bifurcation, color-flow Doppler and conventional duplex sonography, **152:1101**
 blood flow, phase-sensitive MRI, **152:1307**
 color Doppler imaging, **152:707**
 internal, stenosis, color Doppler imaging compared with angiography, **152:1299**
 intracranial occlusion, MRI, **152:1271**
- Case of the day**
 general diagnosis, **152:873**, **152:1317**
 neuroradiology, **152:879**, **152:1333**
- pediatric radiology, **152:877**, **152:1328**
 sonography, **152:875**, **152:1323**
- Cataracts**, formation, ultraviolet radiation and (a), **152:1133**
- Catheter**
 balloon, norepinephrine infusion and, embolization for replaced hepatic artery (l), **152:204**
 balloon angioplasty, removal after percutaneous aspiration (l), **152:1347**
 cope loop, versatility of (l), **152:204**
 internalized double-J, percutaneous transgastric cystogastrostomy, **152:523**
 large-bore suprapubic cystostomy, technique and results, **152:303**
 percutaneous, treatment of pleural effusions and pneumothorax, **152:1189**
 subclavian hemodialysis, fluoroscopy and angiography, **152:641**
 ureteral, double-pigtail, obstructive renal scan in (a), **152:1353**
- Catheterization**, gastrojejunal, directable cannula for (l), **152:1346**
- Celiac disease**, duodenal folds in, endoscopic demonstration (a), **152:206**
- Cerebrovascular disease**, diagnosis (b), **152:622**
- Chemotherapy**, embolization and, primary and metastatic cancer, **152:387**
- Chenodeoxycholic acid**, dissolution of gallstones (a), **152:899**
- Chest**, see Thorax
- Child abuse**, fatal, infants, radiologic contribution to investigation and prosecution (a), **152:1350**
- Cholangiocarcinoma**, radiologic evaluation (l), **152:1129**
- Cholangiography**
 endoscopic retrograde, biliary malformation in infants (a), **152:1136**
 hepatobiliary tuberculosis (a), **152:210**
 intrahepatic abnormalities, liver transplants, **152:275**
 transcholecystic, **152:913**
- Cholangiopancreatography**, endoscopic retrograde, biliary disease (a), **152:1351**
- Cholecystectomy**, endoscopic sphincterotomy after, patients with sphincter-of-Oddi dysfunction (a), **152:1134**
- Cholecystitis**
 acute, diagnosis by cholelescintigraphy, **152:1211**
 acute gangrenous, sonography, **152:289**
- Cholecystostomy**, percutaneous, **152:913**
- Cholelithiasis**
 abdominal aortic aneurysm and, sonography, **152:509**
 dissolution, chenodeoxycholic acid and ursodeoxycholic acid (a), **152:899**
 formation, ursodeoxycholic acid and aspirin effects (a), **152:1133**
 morbid obesity and, sonography (a), **152:209**
 nonsurgical therapy, imaging and, **152:11**
- Cholescintigraphy**, diagnosis of acute cholecystitis, **152:1211**
- Choroid plexus**, lesions, fetal, sonography (a), **152:1137**
- Claustrophobia**, MRI and (l), **152:653**
- Clonorchiasis**
 CT, **152:281**
 sonography, **152:761**
- Colitis**, ulcerative, proctocolectomy effects (a), **152:1352**
- Colon**
 adenomatous polyps, inheritance of susceptibility (a), **152:206**
 cancer, risk factors, colonoscopic screening (a), **152:1135**
 epithelial cell proliferation, aging effects (a), **152:656**
 neoplasms, missed by endoscopy, **152:513**
- Colorectal cancer**

- colonic adenomatous polyps and, inheritance of susceptibility (a), **152:206**
 imaging hepatic metastases from, **152:917**
 model for screening, video endoscopy by nurse practitioner (a), **152:208**
- Computed tomography**
 biopsy guided by, gantry angulation for (l), **152:1345**
 malignant melanoma, subcutaneous metastases from, **152:1009**
 single-photon emission (SPECT)
 composite images, chest and abdomen, **152:865**
 peritoneal cavity, **152:1205**
 three-dimensional techniques, cardiac imaging, **152:1161**
- Computed tomography, abdomen**
 non-contrast enhanced-
 blunt trauma, **152:41 152:47**, (commentary)
 blunt trauma (l), **152:651**
 pseudomyxoma peritonei (l), **152:429**
 small intestine, primary tumors (p), **152:995**
- Computed tomography, adrenal**, low-attenuation lesions, **152:1005**
- Computed tomography, cranium**
 Alzheimer's disease, ventricular change in elderly patients, **152:1257**
 epilepsy, MRI comparison, **152:347**
 intracranial oligodendrogliomas, **152:361**
 masses of anterosuperior third ventricle, **152:609**
 pilocytic astrocytomas, juvenile, **152:1263**
 TMJ diagnosis, **152:697**
- Computed tomography, esophagus**
 giant fibrovascular polyp, **152:518**
 prediction of carcinoma (a), **152:207**
- Computed tomography, head and neck**, work-book (b), **152:1254**
- Computed tomography, heart**, left ventricle, posterior false aneurysm (l), **152:1339**
- Computed tomography, kidney**
 severe trauma, children, **152:109**
 ureter and, blunt trauma, CT patterns of fluid collection, **152:1043**
- Computed tomography, liver**
 clonorchiasis, **152:281**
 contrast enhancement, hepatic metastases, **152:272, 152:267**, (commentary)
 giant cavernous hemangioma, **152:1221**
 lymphoma
 cyclosporine-treated transplant recipients, **152:501**
 primary, **152:973**
 RBC-single-photon emission, liver hemangioma and hepatocellular carcinoma, **152:977**
 transplant rejection, **152:285**
- Computed tomography, lung**
 leptospirosis, **152:955**
 lymphangioleiomyomatosis, **152:961**
- Computed tomography, neck**, subclavian triangle, **152:312**
- Computed tomography, pancreas**
 neoplasms, MRI comparison, **152:487**
 plasmacytoma, **152:1227**
 pseudocyst (l), **152:1129**
- Computed tomography, retroperitoneum**, primary neoplasms (p), **152:83**
- Computed tomography, spine**, comparison of parameters, normal and spinal cord-injured patients (a), **152:1353**
- Computed tomography, thorax**
 asbestos-related disease (a), **152:901**
 blunt trauma, acute pericardial tamponade, **152:739**
 chronic lung diseases, **152:1183**
 introductory text (b), **152:26**
 low-attenuation mediastinal masses (p), **152:1173**
 pulmonary sarcoidosis, **152:1179**
- Computed tomography, ureter**, transcaval ureter with hydronephrosis, **152:793**
- Computed tomography, uterus**, adnexa, before menarche, **152:123**
- Computer page**
 microcomputer, inexpensive lecture slides, **152:185**
 semiautomated slide identification, personal computer and printer, **152:861**
- Contrast medium**
 anticoagulant effects of, **152:309**
 digital subtraction angiography, bilateral blurring vision after (l), **152:429**
 enhancement, suspected hepatic metastases, **152:272, 152:267** (commentary)
 gadopentetate dimeglumine, patients with cerebral lesions, **152:813**
 Gd-DPTA (l), **152:1348**
 induced renal failure and (a), **152:1134**
 informed consent, **152:867**
 ionic and nonionic
 nephrotoxicity and (a), **152:1133**
 prospective trial, **152:945, 152:939**, (commentary)
 IV administration, acute thrombocytopenia after, **152:947**
 perfluorooctylbromide, CT, sonography, and MRI, **152:247**
 radiographic, basic concepts (b), **152:1042**
 stopper fragments in (l), **152:1128**
 superparamagnetic iron oxide, **152:167, 152:175**
- Conus medullaris**, normal, childhood, MRI determination of location, **152:1029**
- Coronary artery**
 aneurysm, Kawasaki disease and, children, MRI, **152:805**
 disease, angiography comparison in (a), **152:657**
 thallium-201 SPECT in (a), **152:209**
- Coronary segments**, intrathoracic spatial location, normal heart (a), **152:437**
- Crohn disease**
 fistulae and sinus tracts, diagnosis, MRI and, **152:999**
 small bowel carcinoma in (a), **152:1134**
- Crystals**, arthropathies associated with, **152:685**
- Cushing disease**, pituitary microadenomas, MRI, **152:145**
- Cystic fibrosis**, allergic bronchopulmonary aspergillosis, children (a), **152:1137**
- Cystogastrostomy**, percutaneous transgastric, internalized double-J catheter, **152:523**
- Cystostomy**, percutaneous suprapubic, technique and results, **152:303**
- Cystourethrography**, voiding, predictor of reflux nephropathy, urinary tract infection, children, **152:801**
- Cytosine arabinoside**, high-dose, cerebellar atrophy caused by, CT and MRI, **152:343**
- D**
- Demyelination**, experimental, MRI, **152:1291**
- Densitometry**, bone, dual-energy radiographic absorptiometry, **152:241**
- Diarrhea**, infections, AIDS patients (a), **152:208**
- Diatrizoate**, anticoagulant effects of, **152:309**
- Discogram**, lumbar, false-negative (a), **152:658**
- Diverticulitis**, cecal, differentiation from appendicitis, sonography, **152:1229**
- Drug testing**, American Board of Radiology oral exams (l), **152:431**
- Dysraphism**, closed, spinal, **152:1049**
- E**
- Echocardiography**
 autosomal dominant polycystic kidney disease (a), **152:436**
 Doppler, cine MRI compared with, aortic regurgitation, **152:729**
 fetal (b), **152:114**
- Echo sequences**, fast spin and gradient field, comparison (a), **152:210**
- Ectopic ureterocele**, urography and sonography, **152:567**
- Editorial**, irresponsible coauthorship, **152:719**
- Embolization**, percutaneous transhepatic, gastroesophageal varices, **152:755**
- Embolotherapy**
 false aneurysm, percutaneous techniques, **152:382**
 transcatheter (l), **152:1128**
- Emphysema**
 clinical, hyperinflation, radiographic measures (a), **152:656**
 density mask, CT (a), **152:437**
- Empyemas**, subdural and epidural, MRI, **152:615**
- Endoprostheses**, biliary, occluded double mushroom-tipped, **152:527**
- Endoscopy**
 cost of (l), **152:1127**
 cysts and pseudocysts, pancreatitis (a), **152:1352**
 large colonic neoplasms missed by, **152:513**
 loss of duodenal folds, diagnosis of celiac disease (a), **152:206**
 malignant biliary obstruction (a), **152:208**
 submucosal tumors, stomach (a), **152:1352**
 video, nurse practitioners (a), **152:208**
- Endosonography**, in gastroenterology (b), **152:990**
- Epididymis**, changes after vasectomy, sonography, **152:531**
- Epigastric artery**, chemotherapy and emboization, primary and metastatic cancer, **152:387**
- Epilepsy**, MR vs CT, **152:347**
- Esophageal sphincter**, relaxation, correlation in achalasia with (a), **152:902**
- Esophageal varices**, bleeding, nonsurgical treatments (a), **152:1352**
- Esophagojejunostomy**, angiography (l), **152:434**
- Esophagus**
 Barrett's (l), **152:892**
 carcinoma, CT prediction (a), **152:207**
 giant fibrovascular polyp, CT and MRI, **152:518**
 intramural pseudodiverticulosis (l), **152:893**
 squamous cell carcinoma, AIDS and (a), **152:209**
- Ethmoid sinus**, opacification, infant (a), **152:900**
- Extracorporeal membrane oxygenation**, morbidity for survivors (a), **152:900**
- Extracorporeal shock-wave lithotripsy**
 biliary, routine chest radiography and, **152:987**
 fragmentation of bile duct stones (a), **152:899**
 gallbladder motility (a), **152:1352**
 gallstones, **152:11**
 long-term follow up (a), **152:209**
- Extraprismatic syndrome**, acute, methylmalonic acidemia (a), **152:900**
- F**
- Felson, Benjamin (m)**, **152:456**
- Femoral artery**, catheterization, pseudoaneurysm and arteriovenous fistula after, **152:629**
- Femoral neck**, fracture, bipolar hemiarthroplasty (a), **152:208**
- Fertility**, experimental testicular torsion effects (a), **152:439**
- Fetus**, malformed, stillbirth and (b), **152:572**
- Film-processor**, mammographic, temperature, development time, and chemistry, **152:35**
- Finger**, normal anatomic sections, MRI (p), **152:1013**
- Foot**
 imaging (b), **152:82**
 neuropathic disease, bone scintigraphy and In-111 leukocytes scans in (a), **152:440**
- Fuzzy cluster**, visual analysis, MRI, **152:19**
- G**
- Gadolinium-DTPA**
 MRI enhanced with
 cardiac transplant rejection (a), **152:437**
 experimental bacterial meningitis, **152:131**

- postoperative lumbar spine, **152:825**
Gadopentate dimeglumine, contrast agent, patients with cerebral lesions, **152:813**
Gallbladder
 bile, gallstone recognition, microscopic examination (a), **152:438**
 diagnostic and therapeutic interventional procedures, **152:913**
 heterotopic gastric mucosa (l), **152:432**
 motility, extracorporeal shock-wave lithotripsy (a), **152:1352**
Gallstones, see Cholelithiasis
Gastrectomy, gastric histology after, bile diversion and (a), **152:438**
Gastric emptying, radionuclide measurement, body posture effects (a), **152:899**
Gastric mucosa, heterotopic, duodenal bulb, peptic ulcer relations, **152:59**
Gastroduodenal motility, abnormal, children and adolescents (a), **152:658**
Gastroesophageal reflux, esophageal pH monitoring in diagnosis (a), **152:1135**
Gastroesophageal varices, percutaneous transhepatic embolization of, **152:755**
Gastrointestinal bleeding
 idiopathic, aortic stenosis and angiodysplasia (a), **152:657**
^{99m}Tc-sulfide colloid and ^{99m}Tc-RBC studies (l), **152:653**
Gastrointestinal motor dysfunction, paraneoplastic visceral neuropathy (a), **152:438**
Gastrointestinal tract, upper, dysfunction in bulimia (a), **152:899**
Gastrostomy
 assessment (a), **152:1352**
 percutaneous nonendoscopic (a), **152:438**
Gibbs phenomenon (l), **152:1127**
Glenoid labrum, normal, variations (l), **152:201**
Glioma, PET in (a), **152:207**
Goblet cell metaplasia, alveolar disease and, lung, **152:1195**
Granulomas, cavitating and noncavitating, AIDS patients with *Pneumocystis* pneumonitis, **152:753**
Greenfield filter, percutaneous insertion, **152:933**
Guidelines for authors, **152:195**

H

- Hallux**, interphalangeal joint, traumatic subluxation (l), **152:652**
Hand, skeletal maturity of (b), **152:108**
Heart
 blood flow, color imaging (b), **152:706**
 color Doppler imaging, **152:707**
 criss-cross, MRI, **152:809**
 double-outlet right ventricle, MRI, **152:128**
 imaging
 continuing training of residents (l), **152:199**
 three-dimensional techniques and artificial intelligence, **152:1161**
 ischemic disease, neutrophil function in (a), **152:1351**
 masses, MRI, **152:469**
 position, left hemidiaphragm and (l), **152:655**
 transplant recipients, pericardial effusions in (a), **152:1351**
Hemangioma
 cavernous, MRI differentiation from hepatoma, **152:505**
 giant cavernous, liver, CT and MRI, **152:1221**
Hematoma, intracerebral, blood-fluid level in, infant (l), **152:896**
Hematopoietic hyperplasia, routine knee MRI and, **152:333**
Hemiarthroplasty, bipolar, fracture of femoral neck (a), **152:208**
Hemodialysis
 subclavian catheters, fluoroscopy and angiography, **152:641**
 vascular access, color Doppler sonography, **152:633**
Hemoglobinopathy, sickle cell, bone and joint abnormalities with, **152:1153**
Hepatectomy
 partial
 hepatic metastases from colorectal carcinoma, **152:917**
 MRI appearance of the liver after, **152:1215**
Hepatic artery, replaced, transcatheter arterial embolization for (l), **152:204**
Hepatocellular carcinoma
 differentiation from cavernous hemangioma, MRI, **152:505**
 liver hemangioma and, RBC-SPECT scanning, **152:977**
Hernia, epigastric, gastric involvement (l), **152:893**
Heterotopic gastric mucosa, gallbladder (l), **152:432**
Hip, painful, children, sonography, **152:579**
Hodgkin disease
 mediastinal osteosarcoma and (a), **152:436**
 splenic structure in, sonography, **152:1197**
Hospital practice, imaging procedures, professional responsibility for (l), **152:199**, **152:652**
Hydronephrosis
 intermittent (a), **152:658**
 transcaval ureter with, IV urography, CT and venacavography, **152:793**
Hyperagnesemia, abnormal metaphyses and, neonate, **152:1071**
Hypertension
 portal, Behcet syndrome (l), **152:1342**
 pulmonary, balloon angioplasty in (a), **152:657**
Hyperventilation, angina attack induced by, magnesium effects (a), **152:1351**
Hysterosalpingography
 diagnosis of peritubal adhesions, infertile women, **152:777**
 pelvic sonography and (b), **152:776**
 prone and supine (l), **152:897**

I

- Ileocolonoscopy**, seronegative spondylarthropathy (a), **152:1135**
Indomethacin
 intrauterine exposure, preterm infants (a), **152:440**
 resolution of nephrocalcinosis, **152:1251**
Infertility, women, peritubal adhesions in, hysterosalpingography diagnosis, **152:777**
Informed consent, update, **152:200**
Interleukin-2, pulmonary edema as a complication of, **152:749**
Intestine, small, primary tumors, CT (p), **152:995**
Intracranial neoplasms, hemorrhagic, MRI, **152:137**
Intracranial vessels, neonate, color Doppler imaging, **152:1065**
Intrauterine growth retardation, Doppler criteria for (a), **152:659**
Iohexol, anticoagulant effects of, **152:309**
Ioxaglate, anticoagulant effects of, **152:309**
Iron oxide
 superparamagnetic
 detection of liver metastases, **152:771**
 pharmacokinetics and toxicity, **152:167**
 splenic lymphoma, MRI diagnosis, **152:175**
Ischemic necrosis, femoral head, MRI and bone biopsy (a), **152:1136**

J

- Joints**
 abnormalities, sickle cell hemoglobinopathies and, **152:1153**
 disease, modern diagnostic imaging, **152:229**

K

- Kawasaki disease**, coronary artery aneurysm with, children, MRI, **152:805**

- Kernicterus**, benzyl alcohol relations, preterm infants (a), **152:1354**

Kidney

- autosomal dominant polycystic disease, echocardiography (a), **152:436**
 color Doppler imaging, **152:707**
 ectopic, delayed radiologic appearance, **152:120**
 fungus ball, percutaneous extraction (l), **152:1343**
 multiloculated mass, renal lymphangiomyoma and, **152:307**
 severe trauma, CT, children, **152:109**
 transplants, duplex Doppler sonography, **152:535**
 ureter and, blunt trauma, CT patterns of fluid collection, **152:1043**
 Wilms tumor, adult patient, **152:299**

Knee

- femoral arteriography (l), **152:203**
 forty-five degree posteroanterior flexion weight-bearing radiograph of (a), **152:900**
 imaging anatomy (b), **152:312**
 wound, pneumomediastinum and (l), **152:1131**

L

- Laminar space**, diagnosis of rotational flexion injuries, cervical spine, **152:103**

- Laminar space sign**, reliability (l), **152:1344**

- Leptospirosis**, lung, CT, **152:955**

- Leukemia**, periaortic infiltration (l), **152:434**

Liver

- absent left lobe, radiologic diagnosis (l), **152:894**
 cirrhosis, upper gastrointestinal lesions (a), **152:438**
 clonorchiasis, CT, **152:281**
 duplex sonography, **152:765**
 hemangioma
 giant cavernous, CT and MRI, **152:1221**
 hepatocellular carcinoma and, RBC-SPECT scanning, **152:977**
 metastases
 CT evaluation, **152:272**, **152:267** (commentary)
 from colorectal carcinoma, **152:917**
 superparamagnetic iron oxide, **152:771**
 neoplasms, MRI (p), **152:493**
 partial hepatectomy, MRI appearance, **152:1215**
 primary lymphoma, CT, **152:973**
 primary tumor, MRI, **152:63**
 radiation-induced injury, sonography (a), **152:440**
 transplant
 intrahepatic cholangiographic abnormalities, **152:275**
 rejection, periportal low-attenuation areas on CT, **152:285**
 transplant recipients, cyclosporine-treated, lymphoma in, sonography and CT, **152:501**
Lumbar disk, autonomic syndrome, vertebroprogenic pain and, **152:1277**

Lung

- agenesis (l), **152:1339**
 alveolar disease, goblet cell metaplasia causing, **152:1195**
 central pulmonary emboli, cine-gradient-refocused MRI, **152:465**
 chronic diseases, CT, **152:1183**
 hemosiderosis, MRI, **152:573**
 hydatid cyst, ruptured (l), **152:431**
 infection, transthoracic aspiration needle biopsy, **152:31**
 leptospirosis, CT, **152:955**
 lobar collapse (a), **152:207**
 lymphangioleiomyomatosis, high-resolution CT, **152:961**
 nodules, comparison of imaging procedures, **152:261**
 pathology (b), **152:728**
 rounded atelectasis, MRI, **152:965**
 sarcoidosis, CT, **152:1179**
Lymphangioleiomyomatosis, pulmonary, high-resolution CT, **152:961**

Lymphangiomyoma, renal, multiloculated renal mass and, **152:307**

Lymphoma

hepatic

cyclosporine-treated transplant recipients, sonography and CT, **152:501**

MRI (a), **152:903**

primary, liver, CT, **152:973**

Lymphoscintigraphy, cutaneous, malignant melanoma (a), **152:1135**

M

Magnetic resonance imaging

biomedical (b), **152:1028**

cardiovascular impairment during, thermoregulatory consequences (a), **152:1355**

cine, Doppler echocardiography compared with, aortic regurgitation, **152:729**

cine-gradient-refocused, central pulmonary emboli, **152:465**

claustrophobia and (l), **152:653**

gastrointestinal nuclear imaging (b), **152:58**

music/audio system (l), **152:653**

pigmented villonodular synovitis (p), **152:337**

spin-echo, STIR comparison, lesions of chest, liver, and pelvis, **152:853**

visual fuzzy cluster analysis, **152:19**

Magnetic resonance imaging, abdomen

fistulae and sinus tracts, patients with Crohn disease, **152:999**

pediatric patients, **152:1245**

Magnetic resonance imaging, bone

femoral head, ischemic necrosis, bone biopsy correlation (a), **152:1136**

immature infarcts, **152:547**

marrow infarction, sickle cell anemia (a), **152:1355**

Magnetic resonance imaging, cranium

brain abscesses, **152:1073**

carotid artery, blood flow, **152:1307**

epilepsy, CT comparison, **152:347**

gadopentetate dimeglumine, patients with cerebral lesions, **152:813**

hemorrhagic intracranial neoplasms, **152:137**

intracranial carotid occlusion, **152:1271**

intracranial oligodendrogliomas, **152:361**

mandibular osteochondritis dissecans, avascular necrosis and, **152:551**

masses of anterosuperior third ventricle, **152:609**

normal nasal cycle, sinus pathology comparison (a), **152:1355**

periventricular leukomalacia, childhood, **152:583**

pilocytic astrocytomas, juvenile, **152:1263**

progressive periventricular hyperintensity (l), **152:654**

spin-echo and gradient-echo sequences, Parkinson disease, **152:159**

subdural and epidural empyemas, **152:615**

temporomandibular joint, autopsy specimens, **152:1241**

TMJ diagnosis, **152:697**

Magnetic resonance imaging, esophagus, giant

fibrovascular polyp, **152:518**

Magnetic resonance imaging, finger, normal anatomic sections (p), 152:1013

Magnetic resonance imaging, foot, osteomyelitis, diabetic patients, 152:795

Magnetic resonance imaging, head and neck

atlas of head, neck, and spine (b), **152:596**

workbook (b), **152:1254**

Magnetic resonance imaging, heart

aortic dissection, fat-shift artifact, **152:385**

cardiac masses, **152:469**

coronary artery aneurysm, child with Kawasaki disease, **152:805**

criss-cross heart, **152:809**

double-outlet right ventricle, **152:128**

gd-DTPA, transplant rejection (a), **152:437**

Magnetic resonance imaging, hip, femoral head,

avascular necrosis, sickle cell anemia and (a), **152:1137**

Magnetic resonance imaging, joints, anatomy (b), 152:1152

Magnetic resonance imaging, knee

hematopoietic hyperplasia detection, **152:333**

videotape (v), **152:76**

Magnetic resonance imaging, liver

after partial hepatectomy, **152:1215**

ferrite, detection of metastases, **152:771**

giant cavernous hemangioma, **152:1221**

hepatic lymphoma (a), **152:903**

hepatocellular carcinoma, differentiation from cavernous hemangioma, **152:505**

neoplasms (p), **152:493**

primary tumor, **152:63**

Magnetic resonance imaging, lung, hemosiderosis, 152:573

Magnetic resonance imaging, pancreas, neoplasms, CT comparison, 152:487

Magnetic resonance imaging, pituitary

microadenomas, Cushing disease, **152:145**

posterior, hyperintense signal, **152:153**

Magnetic resonance imaging, prostate

age-related changes, **152:77**

carcinoma, benign hyperplasia differentiation (a), **152:659**

Magnetic resonance imaging, soft tissue, osseous invasion by sarcoma (l), 152:1131

Magnetic resonance imaging, spine

cervical spinal cord, axial cervical anatomy, **152:835**

conus medullaris location, children, **152:1029**

craniocervical junction, rheumatoid arthritis, **152:561**

experimental bacterial meningitis, CT comparison, **152:131**

experimental demyelination, **152:1291**

Gd-DTPA-enhanced

postoperative lumbar spine, **152:825**

tumors, **152:1087**

pars interarticularis, **152:327**

tethered spinal cord syndrome, **152:843**

Magnetic resonance imaging, spleen, lymphoma, superparamagnetic iron oxide, 152:175

Magnetic resonance imaging, testes, epidermoid cyst (l), 152:1344

Magnetic resonance imaging, thorax, diseases of the chest (a), 152:898

Magnetic resonance imaging, thyroid, recurrent occult medullary carcinoma, 152:1255

Magnetic resonance imaging, uterus, menstrual cycle (a), 152:902

Malformation, human (b), 152:579

Mammography

atlas (b), **152:742**

benign breast cysts, sedimented calcium in, **152:967**

breast cancer screening (l), **152:891**

breast mass, pectoralis muscle simulating, **152:481**

dual-screen, dual emulsion system, evaluation, **152:483**

film-processor, temperature, development time, and chemistry, **152:35**

needle placement and, clinically occult breast lesions, **152:1**

radiological exercise for students and practitioners (b), **152:960**

Mandibular condyle, osteochondritis dissecans, avascular necrosis and, MRI, 152:551

Maxillary sinus, opacification, infant (a), 152:900

Meckel diverticulum, torsion of, sonography (l), 152:1130

Mediastinum, low-attenuation masses, CT (p), 152:1173

Medical internal radiation dose, absorbed dose calculations (b), 152:1004

Melanoma

malignant

lymphoscintigraphy in (a), **152:1135**

subcutaneous metastases from, CT, **152:1009**

^{99m}Tc-labeled monoclonal antibodies (a), **152:1137**

Memorials

Benjamin Felson, 1913–1988, **152:456**

Joseph L. Morton, 1912–1987, **152:1306**

Robert S. Sherman, Jr., 1917–1988, **152:1086**

Meningitis, experimental bacterial, adnexa MRI, CT comparison, 152:131

Menstrual cycle, MRI (a), 152:902

Metatropic dysplasia, vertebral cervical subluxation and ventriculomegaly, odontoid hypoplasia with (a), 152:1354

Methyl-tert-butyl ether, dissolution of gallstones, 152:11

Minerals, bone, measurement, dual-energy radiographic absorptiometry, 152:241

Monoclonal antibodies

radiolabeled

imaging and therapy (b), **152:1204**

thrombus-specific imaging, **152:253**

Morton, Joseph L. (m), 152:1306

Myocardial infarction, recanalization rates and changes, comparison (a), 152:207

N

Nephroblastoma, see Wilms tumor

Nephrocalcinosis, resolution with indomethacin, 152:1251

Nephrotoxicity, contrast (a), 152:1133

Neuroblastoma, infant, VMA screening spot test (a), 152:902

Neutrophils, function, ischemic heart disease (a), 152:1351

Nuclear medicine

annual volume (b), **152:464**

diagnostic (b), **152:1008**

fundamentals (b), **152:540**

handbooks in radiology, vol. 6 (b), **152:474**

self-study program (b), **152:508**

technology and techniques (b), **152:1214**

O

Oddi-sphincter

dysfunction (a), **152:437**

percutaneous transhepatic dilatation, bile duct stone removal, **152:73**

Ogilvie's syndrome, management without colonoscopy (a), 152:658

Oligodendrogliomas, intracranial, 152:361

Oligohydramnios, intrauterine exposure to indomethacin, preterm infants (a), 152:440

Oral bile acid therapy, gallstones, 152:11

Orbital tumors, diagnosis and management (b), 152:1290

Organophosphate insecticide, ingestion, pulmonary edema and, 152:265

Orthopedics, radiologic terminology (b), 152:1020

Orthopedic surgery, vascular complications (a), 152:439

Os perineum, stress fracture (l), 152:430

Osteochondritis dissecans, avascular necrosis and, mandibular condyle, MRI, 152:551

Osteomyelitis

detection at fracture nonunion sites, scintigraphy, **152:1021**

foot, diabetes and, diagnostic methods, **152:795**

leukemia and, pediatric patients (a), **152:1134**

Osteonecrosis, bilateral distal tibial, systemic lupus erythematosus (l), 152:895

Osteoporosis, women, reduced bone mass in daughters of (a), 152:1350

Osteosarcoma, mediastinal, Hodgkin disease and (a), 152:436

Ovulation, imminent, sonography detection of, 152:91

Oxygen, requirement, neonatal period (a), 152:209

P

Pancreas

- neoplasms, MRI and CT comparison, **152:487**
- plasmacytoma, CT findings, **152:1227**
- pseudocysts
 - percutaneous drainage, children, **152:591**
 - sonography and CT (I), **152:1129**

Pancreatitis

- acute, Grey Turner's sign and Cullen's sign (a), **152:901**
- chronic, evolution and regression of calcification (a), **152:207**
- cysts and pseudocysts in, endoscopy (a), **152:1352**
- idiopathic recurrent (a), **152:1136**

Parkinson disease, MRI, spin-echo and gradient-echo sequences, **152:159****Pars interarticularis**, MRI, **152:327****Pectoralis muscle**, simulating breast mass, **152:481****Pediatric radiology**

- absolute intracranial blood-flow velocities, pre-term and term neonates, **152:1059**
 - AIDS
 - infants and children, **152:1033**
 - neuroradiologic and neurodevelopmental findings (a), **152:902**
 - allergic bronchopulmonary aspergillosis, children with cystic fibrosis (a), **152:1137**
 - benzyl alcohol relations to kernicterus, preterm infants (a), **152:1354**
 - cerebellar atrophy, high-dose cytosine arabinoside and, CT and MRI, **152:343**
 - chest radiography, efficacy of, **152:575**
 - choroid plexus lesions, fetal, sonography (a), **152:1137**
 - conus medullaris, normal, MRI, **152:1029**
 - cystic fibrosis, conventional physiotherapy in (a), **152:209**
 - ethmoid and maxillary sinuses, opacification of, infants (a), **152:900**
 - fetal ventriculomegaly (a), **152:439**
 - gastroduodenal motility, abnormal (a), **152:658**
 - hypercalciuric Bartter syndrome, **152:1251**
 - hypermagnesemia, cause of abnormal metaphyses in neonate, **152:1071**
 - intracranial vessels, neonate, color Doppler imaging, **152:1065**
 - intrauterine exposure to indomethacin, preterm infants (a), **152:440**
 - Kawasaki disease, coronary artery aneurysm with, MRI, **152:805**
 - kidney and ureter, blunt trauma, CT patterns of fluid collection, **152:1043**
 - metatropic dysplasia, odontoid hypoplasia (a), **152:1354**
 - MRI of abdomen, **152:1245**
 - neuroblastoma, VMA screening spot test, infant (a), **152:902**
 - normal uterine adnexa, before menarche, CT, **152:123**
 - osteomyelitis, leukemia and (a), **152:1134**
 - painful hip, sonography, **152:579**
 - pancreatic pseudocysts, percutaneous drainage, **152:591**
 - periventricular leukomalacia, MRI, **152:583**
 - premature infants, abnormal pulmonary outcomes (a), **152:209**
 - severe renal trauma, CT, **152:109**
 - Sturge-Weber syndrome, CT (a), **152:1354**
 - urethral strictures (a), **152:900**
 - urinary tract infection, voiding cystourethrography as predictor of reflux nephropathy, **152:801**
- Pelvic inflammatory disease**, adolescents (a), **152:901**
- Pelvis**
- abscess, subarachnoid fistula (I), **152:432**
 - color Doppler imaging, **152:707**
 - imaging (b), **152:924**

Penis, prostheses, radiology of, **152:925****Pentalogy of Cantrell**, prenatal diagnosis, sonography (a), **152:210****Pentamidine**, inhaled prophylaxis, *Pneumocystis carinii* pneumonia after, **152:1193****Peptic ulcer**, see Ulcer**Perfluorooctylbromide**, contrast agent, CT, sonography, and MRI, **152:247****Pericardial effusion**, cardiac transplant recipients (a), **152:1351****Pericardial tamponade**, blunt chest trauma, CT diagnosis, **152:739****Pericardium**, surgical defects (p), **152:951****Peritoneal cavity**, intraperitoneal fluid distribution, SPECT, **152:1205****Periventricular leukomalacia**, childhood, MRI, **152:583****Perurethral transvesical approach**, pyeloureteral interventions by, **152:97****Peutz-Jeghers syndrome**, clinicopathologic survey (a), **152:657****Pheochromocytoma**, localization (a), **152:1354****Physiotherapy**, conventional, cystic fibrosis (a), **152:209****Pigmented villonodular synovitis**, MRI (p), **152:337****Pilocytic astrocytomas**, juvenile, MRI and CT, **152:1263****Pituitary****microadenomas**, MRI, Cushing disease, **152:145****posterior**, hyperintense signal on MRI, **152:153****Pleural effusions**, pneumothorax and, treatment with catheters under imaging guidance, **152:1189****Pneumatosis coli**, sigmoid colon redundancy relations (a), **152:902****Pneumatosis intestinalis**, bone-marrow transplant patients, routine chest radiographs in, **152:991****Pneumocystis carinii****pneumonia**, after inhaled pentamidine prophylaxis, **152:1193****pneumonitis**, AIDS patients, cavitating and non-cavitating granulomas with, **152:753****Pneumomediastinum**, sucking wound of the knee and (I), **152:1131****Pneumonia**, *Pneumocystis carinii*, after inhaled pentamidine prophylaxis, **152:1193****Pneumothorax****detection**, digital and conventional imaging comparison, **152:475****pleural effusions** and, treatment with catheters under imaging guidance, **152:1189****Portal vein****cavernous transformation**, hepatic perfusion in, CT angiography, **152:985****duplex sonography**, **152:765****Pregnancy****color Doppler imaging**, **152:707****early**, transabdominal and transvaginal sonography (I), **152:1132****septate uteri**, sonography, **152:781****sonography during**, prediction of cesarean section scars with (a), **152:902****Proctocolectomy**, chronic ulcerative colitis, effect on primary sclerosing cholangitis (a), **152:1352****Prostate****age-related changes**, MRI, **152:77****cancer****estrogen treatment of**, cardiovascular complications in (a), **152:1353****metastasis**, transurethral resection effects (a), **152:1135****MRI (a)**, **152:659****rectal involvement in**, barium enema findings, **152:53****transrectal ultrasound (a)**, **152:439****Pseudoaneurysms****after femoral artery catheterization**, **152:629****embolotherapy of**, **152:383****Pseudodiverticulosis**, intramural, esophagus (I), **152:893****Pseudomyxoma peritonei**, CT and sonography (I), **152:429****Pulmonary artery**, catheterization, right ventricular enlargement, **152:391****Pulmonary edema****complication of interleukin-2 therapy**, **152:749****organophosphate insecticide ingestion**, **152:265****Pulmonary fibrosis**, acquired tracheomegaly as a complication of, **152:743**

Q

Quadrangular fragment fracture, management (a), **152:1353**

R

Radiation**consumer products and miscellaneous sources**, exposure in U. S. population (b), **152:500****exposure, public (b)**, **152:474****natural background**, United States and Canada (b), **152:492****ultraviolet**, cataract formation and (a), **152:1133****Radiography****conventional****comparison of 2048-line digital display formats**, **152:1113****TMJ diagnosis**, **152:697****dental diagnosis (b)**, **152:550****digital**, **152:870****pneumothorax detection**, **152:475****digital skeletal**, detection of subperiosteal resorption, **152:541****Radiologic journals**, industry support of, **152:189****Radiologic physics**, instruction for diagnostic radiologists, **152:398**, **152:393**, (commentary)**Radiologist**, first reader (b), **152:573****Radiology****chest (b)**, **152:1192****fundamentals (b)**, **152:18****interpersonal conflicts in**, **152:1119****interventional (b)**, **152:96****marketing**, **152:191****radiology report (b)**, **152:1178****skeletal****fetal atlas (b)**, **152:318****fundamentals (b)**, **152:696****Radiology, technique****cardiovascular and interventional procedures (b)**, **152:736****penile prostheses**, **152:925****Radiology, training****computer applications in education**, **152:1169****teaching to medical students**, **152:462**, **152:457**, (commentary)**Radiology department**, digital, report-coding system for, **152:1109****Radiology Outreach Foundation**, **152:1240****Radiopharmacology**, principles (b), **152:264****Rectal ulcer syndrome**, biopsies, diffuse excess mucosal collagen in (a), **152:657****Renal artery**, branches, stab wounds, angiography, **152:1231****Retroperitoneum**, primary neoplasms, CT (p), **152:83**

S

Sarcoma**soft-tissue****MRI and CT (I)**, **152:1131****postradiation (a)**, **152:656****Scientific journals****editing of articles**, **152:647****perspective**, **152:645****Scintigraphy****osteomyelitis**, fracture nonunion sites, **152:1021**

^{99m}Tc-MDP bone, osteomyelitis of the foot, diabetes and, **152:795**
 TMJ diagnosis, **152:697**
Scintillation camera, workings of (b), **152:512**
Sclerotherapy, control of variceal bleeding, minimally invasive devascularization (a), **152:899**
Septum pellucidum, absence of, **152:353**
Sequential images, identification (l), **152:1348**
Sherman, Robert S., Jr. (m), **152:1086**
Shoulder, postoperative, sonography of (l), **152:202**
Sickle cell anemia
 bone and joint abnormalities, **152:1153**
 femoral head avascular necrosis, MRI (a), **152:1137**
 marrow infarction in, MRI (a), **152:1355**
Silicas, pathogenicity (a), **152:901**
Silicates, pathogenicity (a), **152:901**
Small bowel
 carcinoma, Crohn disease and (a), **152:1134**
 radiology (b), **152:52**
 x-ray differential diagnosis (b), **152:984**
Sonography
 chemical, physical, and biological effects (b), **152:1160**
 color Doppler
 Budd-Chiari syndrome, **152:377**
 compared with angiography, stenosis of internal carotid artery, **152:1299**
 conventional duplex and, carotid bifurcation, **152:1101**
 dilated intrahepatic ducts distinguished from vascular structures, **152:291**
 hemodialysis vascular access, **152:633**
 intracranial vessels, neonate, **152:1065**
 lower extremity venous disease, **152:371**
 normal testes, **152:293**
 percutaneous procedures guided by, **152:1123**
 Doppler
 clinical, **152:707**
 intrauterine growth retardation (a), **152:659**
 duplex Doppler
 absolute intracranial blood-flow velocities, preterm and term neonate, **152:1059**
 postprandial intestinal blood flow (a), **152:437**
 obstetrics and gynecology, **152:1058**
 operative (b), **152:1106**
Sonography, abdomen
 acute gangrenous cholecystitis, **152:289**
 aortic aneurysm, cholelithiasis with, **152:509**
 cholelithiasis, morbid obesity and (a), **152:209**
 clonorchiasis, **152:761**
 common bile duct, fatty-meal for diagnosis of obstruction (l), **152:1341**
 duplex, aorto-left renal vein fistula, **152:1107**
 gastrointestinal images, histological correlates of (a), **152:1135**
 graded-compression, cecal diverticulitis differentiated from appendicitis, **152:1229**
 Meckel diverticulum, torsion of (l), **152:1130**
 pregnancy, prediction of cesarean section scars with (a), **152:902**
 pseudomyxoma peritonei (l), **152:429**
 suspected acute appendicitis, **152:49**
Sonography, cranium, landmarks, fetus (l), **152:432**
Sonography, heart, aortic saddle embolus (l), **152:1348**
Sonography, kidney
 duplex Doppler, pathologic diagnosis of transplants, **152:535**
 ipsilateral fused (a), **152:1355**
Sonography, leg, deep-vein thrombosis (a), **152:1350**
Sonography, liver
 duplex, portal venous system, **152:765**
 lymphoma, cyclosporine-treated transplant recipients, **152:501**
 radiation-induced injury (a), **152:440**

Sonography, mediastinum, bronchogenic cyst, prenatal, **152:125**
Sonography, pancreas, pseudocyst (l), **152:1129**
Sonography, pelvis
 color Doppler, pelvic arteriovenous malformation, **152:1311**
 hysterosalpingography and (b), **152:776**
Sonography, prenatal, Pentalogy of Cantrell (a), **152:210**
Sonography, prostate, state-of-the-art (b), **152:780**
Sonography, scrotal, vasectomy, epididymal changes after, **152:531**
Sonography, shoulder, postoperative (l), **152:202**
Sonography, spleen
 Hodgkin disease, splenic structure in, **152:1197**
 monograph (b), **152:174**
Sonography, testes
 color Doppler, testicular ischemia, **152:1237**
 epidermoid cyst (l), **152:1344**
Sonography, transabdominal, early pregnancy (l), **152:1132**
Sonography, transrectal, staging of prostatic carcinoma (a), **152:439**
Sonography, transvaginal
 detection of imminent ovulation, **152:91**
 early pregnancy (l), **152:1132**
Sonography, ureter, ectopic ureterocele, **152:567**
Sonography, uterus, septate uteri, pregnancy in, **152:781**
SPECT, see Computed tomography, single-photon emission
Spectroscopy, cerebral infarct, thrombolytic treatment, **152:623**
Spermatogenesis, experimental testicular torsion effects (a), **152:439**
Sphincterotomy
 endoscopic, after cholecystectomy (a), **152:1134**
 endoscopic retrograde, complications (a), **152:1354**
Spine
 axial internal anatomy, MRI artifacts, **152:835**
 cervical
 flexion teardrop fracture, **152:319**
 rotational flexion injuries, diagnosis, **152:103**
 closed dysraphism, **152:1049**
 fracture
 mediastinal widening from, chest radiographs, **152:27**
 superior mediastinal widening, chest radiographs (l), **152:1340**
 lumbar, pars interarticularis, MRI, **152:327**
 postoperative lumbar, Gd-DTPA-enhanced MRI, **152:825**
 subarachnoid fistula, pelvic abscess and (l), **152:432**
 tethered spinal cord syndrome, MRI, **152:843**
 tumors, Gd-DTPA-enhanced MRI, **152:1087**
Spleen, lymphoma, MRI, superparamagnetic iron oxide, **152:175**
Spondylarthropathy, seronegative, ileocolonoscopy (a), **152:1135**
STIR, spin-echo MRI comparison, lesions of chest, liver, and pelvis, **152:853**
Stomach, submucosal tumors, endoscopic ultrasound (a), **152:1352**
Sturge-Weber syndrome, CT study (a), **152:1354**
Subclavian artery, right, isolation (l), **152:430**
Subclavian triangle, neck, CT, **152:312**
Subperiosteal resorption, detection, digital skeletal radiography, **152:541**
Superior vena cava syndrome
 percutaneous treatment, **152:183**
 thromboembolic events in, anticoagulation role in (a), **152:436**
Suprasellar visual system, herniation into empty sella, **152:597**
Systemic lupus erythematosus, bilateral distal tibial osteonecrosis (l), **152:895**

T

Tamoxifen, adjuvant, cytotoxic therapy and, breast cancer mortality (a), **152:898**
Teflon, subureteric injection, correction of vesicoureteral reflux, **152:115**
Temporomandibular joint
 autopsy specimens, MRI, **152:1241**
 imaging, diagnosis of internal derangements, **152:697**
Testes
 epidermoid cyst, sonography and MRI (l), **152:1344**
 ischemia, color Doppler sonography, **152:1237**
 normal, color Doppler sonography, **152:293**
Thorax
 aortic rupture, superior mediastinal widening from spine fractures mimicking, **152:27**
 asbestos-related disorders, plain-film diagnosis (a), **152:658**
 blunt trauma, acute pericardial tamponade, CT, **152:739**
 composite SPECT-CT images, **152:865**
 essential radiology (b), **152:1192**
 proceedings of the chest imaging conference 1987 (b), **152:950**
 pulmonary nodules, comparison of imaging procedures, **152:261**
 radiography, pediatric, **152:575**
 routine radiography
 biliary lithotripsy and, **152:987**
 pneumatosis intestinalis in bone-marrow transplant patients, **152:991**
Thrombocytopenia, acute, after IV contrast medium, **152:947**
Thrombolysis, pharmacomechanical, pulsed-spray, **152:1097**
Thrombosis, deep-vein, leg, sonography (a), **152:1350**
Thrombus-specific imaging, radiolabeled monoclonal antibodies, **152:253**
Thyroid
 cold nodules, fine-needle aspiration biopsy (a), **152:207**
 occult medullary carcinoma, MRI, **152:1255**
Tibial epiphysitis, distal, triplane fracture (a), **152:208**
Tracheomegaly, acquired, complication of diffuse pulmonary fibrosis, **152:743**
TTNA, see Biopsy, needle, percutaneous transthoracic
Tuberculosis, hepatobiliary, calcifications and cholangiographic findings (a), **152:210**

U

Ulcer, peptic, heterotopic gastric mucosa relations, **152:59**
Ureter, kidney and, blunt trauma, CT patterns of fluid collection, **152:1043**
Urethra, strictures, childhood (a), **152:900**
Urinary tract, infection, reflux nephropathy in children, voiding cystourethrography and, **152:801**
Urography
 ectopic ureterocele, **152:567**
 excretory, bowel preparation (a), **152:900**
 IV, transcaval ureter with hydronephrosis, **152:793**
Ursodeoxycholic acid
 aspirin, lithogenic bile and gallstone formation (a), **152:1133**
 dissolution of gallstones (a), **152:899**
Uterus
 adnexa, before menarche, CT, **152:123**
 implantation of pregnancy, sonography, **152:781**

V

Variceal bleeding, minimally invasive devascularization for, control with sclerotherapy (a), **152:899**

Vasectomy, epididymis changes after, sonography, **152:531**

Vena cava, inferior, interruption, Greenfield filter, **152:933**

Venacavography, transcaval ureter with hydronephrosis, **152:793**

Venous thrombosis, lower-extremity, color Doppler sonography, **152:371**

Ventriculomegaly

fetal (a), **152:439**

posthemorrhagic (a), **152:901**

Vesicoureteral reflux, subureteric injection of teflon, radiographic evaluation of, **152:115**

Videotape reviews

MRI of the knee, **152:76**

of critical importance...AIDS precautions in radiology, **152:504**

RSNA Today, Vol. 2, No. 3, **152:288**

Visualization science, ACR meeting summary, **152:1313**

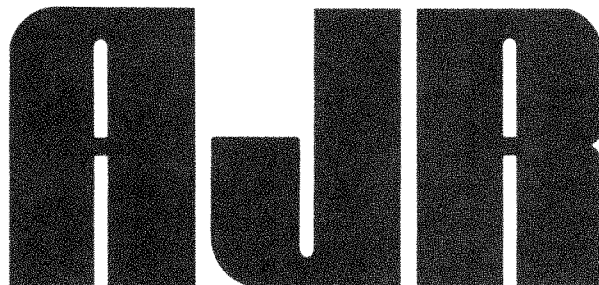
W

Wilms tumor, adult patient, **152:299**

Wrist, skeletal maturity of (b), **152:108**

Volume 152

Official Journal of the American Roentgen Ray Society



American Journal of Roentgenology
Diagnostic Imaging and Related Sciences

Editor-In-Chief Robert N. Berk, *La Jolla, California*
University of California, San Diego
School of Medicine and Medical Center

Editor Emeritus Melvin M. Figley, *Seattle, Washington*

Associate Editor Saskia von Waldenburg Hilton, *San Diego, California*

Consulting Editor Juan M. Taveras, *Boston, Massachusetts*

Statistician Charles C. Berry, *San Diego, California*

Editorial Board

John R. Amberg
Itamar Aviad
Lawrence W. Bassett
Gregory P. Borkowski
William G. Bradley, Jr.
Peter L. Cooperberg
N. Reed Dunnick
David K. Edwards
Ronald G. Evens
David S. Feigin
Paul J. Friedman

William R. Hendee
John R. Hesselink
Charles B. Higgins
Melvyn T. Korobkin
Thomas L. Lawson
Bruce L. McClennan
Albert A. Moss
Jeffrey H. Newhouse
Donald L. Resnick
Stewart R. Reuter
Charles A. Rohrmann, Jr.

Peter M. Ronai
Sjef H. J. Ruijs
Carole M. Rumack
Stuart S. Sagel
David J. Sartoris
Stefan C. Schatzki
Edward A. Sickles
Barry A. Siegel
David D. Stark
Edward T. Stewart
Eric vanSonnenberg

Editorial Staff: Margaret Levene, *managing editor*; Katie L. Spiller, Barbara Rose, Barbara L. Halliburton, and Janine Anderson, *manuscript editors*; Nancy Rydbeck, *office manager*; Sheri Smith, *administrative assistant*; Sandra L. Griffin, *administrative secretary*.

AJR, AMERICAN JOURNAL OF ROENTGENOLOGY (ISSN 0361 803X) is the official journal of the American Roentgen Ray Society, and is published monthly by Williams & Wilkins, 428 E. Preston St., Baltimore, MD 21202. Annual dues include \$50 for journal subscription. Second-class postage paid at Baltimore, MD, and at additional mailing offices. Postmaster, send address changes (Form 3579) to AJR, 428 E. Preston St., Baltimore, MD 21202. Subscription rates \$100 (\$145 foreign); institutions \$110 (\$155 foreign); in training \$25 (\$70 foreign); single copy \$16 (\$19 foreign). Japanese rates include airfreight. Japanese yen price is available from our sole agent USACO Corporation, 13-12, Shimbashi 1-Chome, Minato-Ku, Tokyo 105, Japan, telephone 03-502-6471. Airmail rates furnished on request. Indexed by *Current Contents* and *Index Medicus*. Copyright © 1989 by American Roentgen Ray Society. 0361-803X/89\$2.00

PROGRESS IN RADIOLOGY

- 1 Preoperative imaging-guided needle placement and localization of clinically occult breast lesions. *Kopans DB, Swann CA*
- 11 Nonsurgical therapy of gallstones: implications for imaging. *Simeone JF, Mueller PR, Ferrucci JT*
- 19 Visual fuzzy cluster analysis of MR images. *Young SW, Ballerio C, Carrol CL*

PULMONARY RADIOLOGY

- 27 Superior mediastinal widening from spine fractures mimicking aortic rupture on chest radiographs. *Dennis LN, Rogers LF*
- 31 Transthoracic aspiration needle biopsy: value in the diagnosis of pulmonary infections. *Conces DJ Jr, Clark SA, Tarver RD, Schwenk GR*

BREAST RADIOLOGY

- 35 Mammographic film-processor temperature, development time, and chemistry: effect on dose, contrast, and noise. *Kimme-Smith C, Rothschild PA, Bassett LW, Gold RH, Moler C*

GASTROINTESTINAL RADIOLOGY

- 41 The value of non-contrast-enhanced CT in blunt abdominal trauma. *Kelly J, Raptopoulos V, Davidoff A, Waite R, Norton P*
- 47 Commentary. On the value of non-contrast-enhanced CT in blunt abdominal trauma. *Mindell HJ*
- 49 Sonography in patients with suspected acute appendicitis: value in establishing alternative diagnoses. *Gaensler EHL, Jeffrey RB Jr, Laing FC, Townsend RR*
- 53 Rectal involvement by prostatic carcinoma: barium enema findings. *Rubesin SE, Levine MS, Bezzi M, et al.*
- 59 Heterotopic gastric mucosa in the duodenal bulb: relationship to peptic ulcer. *Smithuis RHM, Vos CG*
- 63 Primary liver tumors: diagnosis by MR imaging. *Rummeny E, Weissleder R, Stark DD, et al.*
- 73 Technical note. Percutaneous transhepatic Oddi-sphincter dilatation for bile duct stone removal. *Graziani L, Fabrizio G, Manfrini E, Galeazzi R, Freddara U*

GENITOURINARY RADIOLOGY

- 77 Age-related changes of the prostate: evaluation by MR imaging. *Allen KS, Kressel HY, Arger PH, Pollack HM*
- 83 Pictorial essay. Primary retroperitoneal neoplasms: CT findings in 90 cases with clinical and pathologic correlation. *Lane RH, Stephens DH, Reiman HM*
- 91 Inability of sonography to detect imminent ovulation. *Zandt-Stastny D, Thorsen MK, Middleton WD, et al.*
- 97 Fluoroscopically guided pyeloureteral interventions by using a perurethral transvesical approach. *Amendola MA, Banner MP, Pollack HM, Gordon RL*

MUSCULOSKELETAL RADIOLOGY

- 103 The laminar space in the diagnosis of rotational flexion injuries of the cervical spine. *Young JWR, Resnik CS, DeCandido P, Mirvis SE*

PEDIATRIC RADIOLOGY

- 109 CT of severe renal trauma in children: evaluation and course of healing with conservative therapy. *Yale-Loehr AJ, Kramer SS, Quinlan DM, La France ND, Mitchell SE, Gearhart JP*
- 115 Radiographic evaluation of subureteric injection of Teflon to correct vesicoureteral reflux. *Gore MD, Fernbach SK, Donaldson JS, Shkolnik A, Zaontz MR, Kaplan WE*
- 120 Case report. Delayed radiologic appearance of bilateral thoracic ectopic kidneys. *Liddell RM, Rosenbaum DM, Blumhagen JD*

- 123 Case report. Torsion of normal uterine adnexa before menarche: CT appearance. *Bellah RD, Griscom NT*
- 125 Case report. Mediastinal bronchogenic cyst: prenatal sonographic diagnosis. *Young G, L'Heureux PR, Krueckeberg ST, Swanson DA*
- 128 Case report. MR imaging of double-outlet right ventricle. *Akins EW, Martin TD, Alexander JA, Knauf DG, Victorica BE*

NEURORADIOLOGY

- 131 Dyke award. Gd-DTPA-enhanced MR imaging of experimental bacterial meningitis: evaluation and comparison with CT. *Mathews VP, Kuharik MA, Edwards MK, D'Amour PG, Azzarelli B, Dreesen RG*
- 137 MR imaging of hemorrhagic intracranial neoplasms. *Destian S, Sze G, Krol G, Zimmerman RD, Deck MDF*
- 145 High-resolution MR imaging of pituitary microadenomas at 1.5 T: experience with Cushing disease. *Peck WW, Dillon WP, Norman D, Newton TH, Wilson CB*
- 153 Histochemical characterization and functional significance of the hyperintense signal on MR images of the posterior pituitary. *Kucharczyk J, Kucharczyk W, Berry I, et al.*
- 159 MR imaging of Parkinson disease with spin-echo and gradient-echo sequences. *Braffman BH, Grossman RI, Goldberg HI, et al.*

MAGNETIC RESONANCE IMAGING

- 167 Superparamagnetic iron oxide: pharmacokinetics and toxicity. *Weissleder R, Stark DD, Engelstad EL, et al.*
- 175 The diagnosis of splenic lymphoma by MR imaging: value of superparamagnetic iron oxide. *Weissleder R, Elizondo G, Stark DD, et al.*

INTERVENTIONAL RADIOLOGY

- 181 Technical note. The blunt needle: a new percutaneous access device. *Akins EW, Hawkins IF Jr, Mladinich C, Tupier R, Siragusa RJ, Pry R*
- 183 Case report. Percutaneous treatment of superior vena cava syndrome. *Capek P, Cope C*

COMPUTER PAGE

- 185 The use of a microcomputer to make rapid and inexpensive lecture slides. *Chew FS*

PERSPECTIVES

- 189 Industry support of radiologic journals and news-magazines. *MacEwan DW*
- 191 Marketing radiology and radiologic services. *Marasco JA Jr, Linton OW*

FROM THE EDITORIAL OFFICE

- 195 An author's guide to the Guidelines for Authors. *Whalen E*

OTHER CONTENT

- 136 ARRS 1989 residents' award papers information
- 158 Books received
- 166 Forthcoming articles
- 199 Letters
- 206 Review of current literature
- 211 News
- 216 ARRS membership information and application
- 219 American Roentgen Ray Society information
- 220 Invitation to the 1989 ARRS meeting
- Book reviews 10, 18, 26, 52, 58, 76, 82, 96, 108, 114, 152, 174
- 222 Classified advertisements
- A3 Guidelines for authors
- A8 AJR business and subscriber information

February 1989

REVIEW ARTICLE

- 229 **Modern diagnostic imaging in joint disease.** *Dalinka MK, Kricun ME, Zlatkin MB, Hibbard CA*

PROGRESS IN RADIOLOGY

- 241 **Dual-energy radiographic absorptiometry for bone densitometry: current status and perspective.** *Sartoris DJ, Resnick D*
 247 **Perfluorooctylbromide: a new contrast agent for CT, sonography, and MR imaging.** *Mattrey RF*
 253 **New perspectives in thrombus-specific imaging: radiolabeled monoclonal antibodies.** *Oster ZH, Som P*

CARDIOPULMONARY RADIOLOGY

- 261 **The diagnosis of pulmonary nodules: comparison between standard and inverse digitized images and conventional chest radiographs.** *Sheline ME, Brikman I, Epstein DM, Mezrich JL, Kundel HL, Arenson RL*
 265 **Case report. Pulmonary edema due to ingestion of organophosphate insecticide.** *Li C, Miller WT, Jiang J*

GASTROINTESTINAL RADIOLOGY

- 267 **CT evaluation of suspected hepatic metastases: comparison of techniques for IV contrast enhancement.** *Paushter DM, Zeman RK, Scheibler ML, Choyke PL, Jaffe MH, Clark LR*
 272 **Commentary. Dynamic hepatic CT scanning.** *Foley WD*
 275 **Intrahepatic cholangiographic abnormalities in liver transplants: correlation with biopsy evidence of rejection and other disorders.** *Bauman J, Campbell WL, Demetris AJ, Zajko AB*
 281 **CT findings of clonorchiasis.** *Choi BI, Kim HJ, Han MC, Do YS, Han MH, Lee SH*
 285 **Periportal low-attenuation areas on CT: value as evidence of liver transplant rejection.** *Kaplan SB, Sumkin JH, Campbell WL, Zajko AB, Demetris AJ*
 289 **The sonographic diagnosis of acute gangrenous cholecystitis: importance of the Murphy sign.** *Simeone JF, Brink JA, Mueller PR, et al.*
 291 **Technical note. The use of color Doppler sonography to distinguish dilated intrahepatic ducts from vascular structures.** *Ralls PW, Mayekawa DS, Lee KP, Johnson MB, Halls J*

GENITOURINARY RADIOLOGY

- 293 **Color Doppler ultrasound of the normal testis.** *Middleton WD, Thorne DA, Melson GL*
 299 **Wilms tumor (nephroblastoma) in the adult patient: clinical and radiologic manifestations.** *Kiomehr F, Cochran ST, Layfield L, Yaghmai I, Ngo C, Smith SR*
 303 **Percutaneous, large-bore, suprapubic cystostomy: technique and results.** *Papanicolaou N, Pfister RC, Nocks BN*
 307 **Case report. Renal lymphangiomyoma—a rare cause of a multiloculated renal mass.** *Jacobs JE, Sussman SK, Glickstein MF*

CONTRAST MATERIAL

- 309 **Anticoagulant effects of contrast materials: in vitro study of iohexol, ioxaglate, and diatrizoate.** *Rasuli P, McLeish WA, Hammond DI*

MUSCULOSKELETAL RADIOLOGY

- 313 **Pictorial essay. The subclavian triangle: CT analysis.** *Wechsler RJ, Rao VM, Newman LM*
 319 **Flexion teardrop fracture of the cervical spine: radiographic characteristics.** *Kim KS, Chen HH, Russell EJ, Rogers LF*
 327 **MR imaging of the pars interarticularis.** *Johnson DW, Farnum GN, Latchaw RE, Erba SM*
 333 **Incidental detection of hematopoietic hyperplasia on routine knee MR imaging.** *Deutsch AL, Mink JH, Rosenfelt FP, Waxman AD*

- 337 **Pictorial essay. Imaging of pigmented villonodular synovitis with emphasis on MR imaging.** *Jelinek JS, Kransdorf MJ, Utz JA, et al.*

PEDIATRIC RADIOLOGY

- 343 **Case report. Cerebellar atrophy caused by high-dose cytosine arabinoside: CT and MR findings.** *Miller L, Link MP, Bologna S, Parker BR*
 345 **Case report. Aortico-left ventricular tunnel: diagnosis by cine angiocardiography.** *Guo D-W*

NEURORADIOLOGY

- 347 **Efficacy of MR vs CT in epilepsy.** *Heinz ER, Heinz TR, Radtke R, et al.*
 353 **Absence of the septum pellucidum: a useful sign in the diagnosis of congenital brain malformations.** *Barkovich AJ, Norman D*
 361 **Intracranial oligodendrogliomas: imaging findings in 35 untreated cases.** *Lee Y-Y, Van Tassel P*

VASCULAR AND INTERVENTIONAL RADIOLOGY

- 371 **Color Doppler ultrasound imaging of lower-extremity venous disease.** *Foley WD, Middleton WD, Lawson TL, Erickson S, Quiroz FA, Macrander S*
 377 **Budd-Chiari syndrome: the results of duplex and color Doppler imaging.** *Grant EG, Perrella R, Tessler FN, Lois J, Busuttill R*
 382 **Case report. Embolotherapy of a high-flow false aneurysm by using an occlusion balloon, thrombin, steel coils, and a detachable balloon.** *Lammert GK, Merline D, White RI Jr, Fishman EK, Porterfield JK*
 385 **Case report. Fat-shift artifact simulating aortic dissection on MR images.** *Lotan CS, Cranney GB, Doyle M, Pohost GM*
 387 **Chemotherapy and embolization via the inferior epigastric artery for the treatment of primary and metastatic cancer.** *O'Keeffe F, Lorigan JG, Charnsangavej C, Carrasco CH, Richli WR, Wallace S*
 391 **Technical note. A technique for pulmonary artery catheterization in patients with right ventricular enlargement.** *Waltman AC, Walker TG*

RADIOLOGIC PHYSICS

- 393 **Perspective. Radiologic physics instruction for diagnostic radiologists: results of an opinion survey.** *Committee on Training of Radiologists, American Association of Physicists in Medicine*
 398 **Commentary. Physics instruction in radiology.** *Hendee WR*

1989 ARRS MEETING SECTION

- 400 **Meeting invitation**
 402 **Section on instruction**
 415 **Scientific program**
 421 **Local activities**
 423 **Registration forms**
 426 **Airline discounts**
 427 **Meeting summary**

OTHER CONTENT

- 370 **Forthcoming articles**
 428 **American Roentgen Ray Society information**
 429 **Letters**
 436 **Review of current literature**
 440 **ARRS 1989 residents' award papers information**
 441 **News**
 Book reviews 264, 280, 288, 312, 318
 445 **Classified advertisements**
 A3 **Guidelines for authors**
 A8 **AJR business and subscriber information**

PROGRESS IN RADIOLOGY

- 451 Percutaneous transthoracic needle aspiration: a review. *Perlmutter LM, Johnston WW, Dunnick NR*

SPECIAL ARTICLES

- 457 Perspective. On teaching radiology to medical students: challenges for the nineties. *Squire LF*
462 Commentary. On teaching radiology to medical students. *Ott DJ, Bohrer SP*

PULMONARY RADIOLOGY

- 465 Cine-gradient-refocused MR imaging of central pulmonary emboli. *Posteraro RH, Sostman HD, Spritzer CE, Herfkens RJ*
469 Cardiac masses: assessment by MR imaging. *Lund JT, Ehman RL, Julsrud PR, Sinak LJ, Tajik AJ*
475 Detection of pneumothorax: comparison of digital and conventional chest imaging. *Fajardo LL, Hillman BJ, Pond GD, Carmody RF, Johnson JE, Ferrell WR*

MAMMOGRAPHY

- 481 Case report. Pectoralis muscle simulating a breast mass. *Meyer JE, Stomper PC, Lee RR*
483 Evaluation of a dual-screen, dual-emulsion mammography system. *Jackson VP, Harrill CD, White SJ, Gillespie KR, Mail JT, Katz BP*

GASTROINTESTINAL RADIOLOGY

- 487 Imaging of pancreatic neoplasms: comparison of MR and CT. *Steiner E, Stark DD, Hahn PF, et al.*
493 Pictorial essay. MR imaging of liver neoplasms. *Rummeny E, Saini S, Wittenberg J, et al.*
501 Hepatic lymphoma in cyclosporine-treated transplant recipients: sonographic and CT findings. *Honda H, Franken EA Jr, Barloon TJ, Smith JL*
505 MR differentiation of hepatocellular carcinoma from cavernous hemangioma: complementary roles of FLASH and T2 values. *Ohtomo K, Itai Y, Yoshida H, Kokubo T, Yoshikawa K, Iio M*
509 Increased prevalence of cholelithiasis in patients with abdominal aortic aneurysm: sonographic evaluation. *Schuster JJ, Raptopoulos V, Baker SP*
513 Large colonic neoplasms missed by endoscopy. *Glick SN, Teplick SK, Balfe DM, et al.*
518 Case report. Giant fibrovascular polyp of the esophagus: CT and MR findings. *Whitman GJ, Borkowski GP*
521 Case report. Direct percutaneous drainage of an obstructed afferent loop. *Maile CW, Hanna PD*
523 Technical note. An internalized double-J catheter for percutaneous transgastric cystogastrostomy. *Sacks BA, Greenberg JJ, Porter DH, et al.*
527 Technical note. A new technique for removing occluded double mushroom-tipped biliary endoprostheses. *Yeung EY-C, O'Donnell C, Carvalho P, Adam A*
529 Technical note. Scrape biopsy of malignant biliary stricture through percutaneous transhepatic biliary drainage tracts. *Yip CKY, Leung JWC, Chan MKM, Metreweli C*

GENITOURINARY RADIOLOGY

- 531 Changes in the epididymis after vasectomy: sonographic findings. *Jarvis LJ, Dubbins PA*
535 Duplex Doppler sonography of renal transplants: lack of sensitivity and specificity in establishing pathologic diagnosis. *Genkins SM, Sanfilippo FP, Carroll BA*

SKELETAL RADIOLOGY

- 541 Digital skeletal radiography: spatial resolution requirements for detection of subperiosteal resorption. *Murphy MD*
547 Immature bone infarcts: findings on plain radiographs and MR scans. *Munk PL, Helms CA, Holt RG*

- 551 MR of osteochondritis dissecans and avascular necrosis of the mandibular condyle. *Schellhas KP, Wilkes CH, Fritts HM, Omlie MR, Lagrotteria LB*
561 Pre- and postoperative MR imaging of the craniocervical junction in rheumatoid arthritis. *Larsson E-M, Holtås S, Zygmunt S*

PEDIATRIC RADIOLOGY

- 567 Ectopic ureterocele without ureteral and calyceal dilatation (ureterocele disproportion): findings on urography and sonography. *Share JC, Lebowitz RL*
573 Case report. Diagnosis of pulmonary hemosiderosis by MR imaging. *Rubin GD, Edwards DK III, Reicher MA, Doemeny JM, Carson SH*
575 Efficacy of chest radiography in pediatric intensive care. *Sivit CJ, Taylor GA, Hauser GJ, et al.*
579 Sonography of the painful hip in children: 500 consecutive cases. *Miralles M, Gonzalez G, Pulpeiro JR, et al.*
583 MR imaging of periventricular leukomalacia in childhood. *Flodmark O, Lupton B, Li D, et al.*
591 Percutaneous drainage of traumatic pancreatic pseudocyst in children. *Jaffe RB, Arata JA Jr, Matlak ME*

NEURORADIOLOGY

- 597 Herniation of the suprasellar visual system and third ventricle into empty sellae: morphologic and clinical considerations. *Kaufman B, Tomsak RL, Kaufman BA, et al.*
609 MR and CT of masses of the anterosuperior third ventricle. *Waggenpack GA, Guinto FC Jr*
615 Subdural and epidural empyemas: MR imaging. *Weingarten K, Zimmerman RD, Becker RD, Heier LA, Haines AB, Deck MDF*
623 ³¹P spectroscopy in thrombolytic treatment of experimental cerebral infarct. *Lee BCP, Brock JM, Fan T, et al.*

VASCULAR RADIOLOGY

- 629 Pseudoaneurysm and arteriovenous fistula after femoral artery catheterization: association with low femoral punctures. *Altin RS, Flicker S, Naidech HJ*
633 Color Doppler sonography of hemodialysis vascular access: comparison with angiography. *Middleton WD, Picus DD, Marx MV, Melson GL*
641 Insertion of subclavian hemodialysis catheters in difficult cases: value of fluoroscopy and angiographic techniques. *Selby JB, Tegtmeyer CJ, Amodeo C, Bittner L, Atuk NO*

PERSPECTIVE

- 645 On journals: the competition for minds and money. *Brogdon BG*

FROM THE EDITORIAL OFFICE

- 647 Why we edit. *Whalen E*

OTHER CONTENT

- 456 Memorial, Benjamin Felson
640 Forthcoming articles
651 Letters
656 Review of current literature
660 News
664 SPR Scientific Program: 32nd annual meeting, April 5-9
666 American Roentgen Ray Society information
667 Invitation to 1989 ARRS meeting
671 ARRS 1989 meeting registration forms
675 ARRS 1989 meeting summary
676 ARRS membership information and application
Book and videotape reviews 464, 474, 492, 500, 504, 508, 512, 540, 550, 572, 578, 596, 622, 644
679 Classified advertisements
A3 Guidelines for authors
A8 AJR business and subscriber information

REVIEW ARTICLES

- 685 **Crystal-associated arthropathies.** *Rubenstein J, Pritzker KPH*
- 697 **Current status of temporomandibular joint imaging for the diagnosis of internal derangements.** *Kaplan PA, Helms CA*
- 707 **Clinical Doppler imaging.** *Grant EG, Tessler FN, Perrella RR*

EDITORIAL

- 719 **Irresponsible coauthorship.** *Berk RN*

PERSPECTIVE

- 721 **Bayesian analysis revisited: a radiologist's survival guide.** *Chang PJ*

CARDIOPULMONARY RADIOLOGY

- 729 **Comparison of cine MR imaging with Doppler echocardiography for the evaluation of aortic regurgitation.** *Pflugfelder PW, Landzberg JS, Cassidy MM, et al.*
- 737 **Coronary angiography in atrial myxoma: findings in nine cases.** *Fueredi GA, Knechtges TE, Czarnecki DJ*
- 739 **Case report: CT diagnosis of acute pericardial tamponade after blunt chest trauma.** *Goldstein L, Mirvis SE, Kostrubiak IS, Turney SZ*
- 743 **Acquired tracheomegaly in adults as a complication of diffuse pulmonary fibrosis.** *Woodring JH, Barrett PA, Rehm SR, Nurenberg P*
- 749 **Pulmonary edema as a complication of interleukin-2 therapy.** *Conant EF, Fox KR, Miller WT*
- 753 **Case report. Cavitating and noncavitating granulomas in AIDS patients with *Pneumocystis pneumonia*.** *Klein JS, Warnock M, Webb WR, Gamsu G*

GASTROINTESTINAL RADIOLOGY

- 755 **Percutaneous transhepatic embolization of gastroesophageal varices: results in 400 patients.** *L'Herminé C, Chastanet P, Delémazure O, Bonnière PL, Durieu JP, Paris JC*
- 761 **Clonorchiasis: sonographic findings in 59 proved cases.** *Lim JH, Ko YT, Lee DH, Kim SY*
- 765 **Duplex sonography of the portal venous system: pitfalls and limitations.** *Parvey HR, Eisenberg RL, Giyanani V, Krebs CA*
- 771 **Detection of liver metastases with superparamagnetic iron oxide in 15 patients: results of MR imaging at 1.5 T.** *Marchal G, Van Hecke P, Demaerel P, et al.*

GENITOURINARY RADIOLOGY

- 777 **Peritubal adhesions in infertile women: diagnosis with hysterosalpingography.** *Karasick S, Goldfarb AF*
- 781 **Pregnancies in septate uteri: outcome in relation to site of uterine implantation as determined by sonography.** *Fedele L, Dorta M, Brioschi D, Giudici MN, Candiani GB*
- 785 **Pictorial essay. Imaging of abdominal aortic aneurysms.** *LaRoy LL, Cormier PJ, Matalon TAS, Patel SK, Turner DA, Silver B*
- 793 **Case report. Transcaval ureter with hydronephrosis: radiologic demonstration.** *Rosen MP, Walker TG, Brennan JF, Babayan RK, Greenfield AJ*

MUSCULOSKELETAL RADIOLOGY

- 795 **Osteomyelitis of the foot in diabetic patients: evaluation with plain films, ^{99m}Tc-MDP bone scintigraphy, and MR imaging.** *Yuh WTC, Corson JD, Baraniewski HM, et al.*

PEDIATRIC RADIOLOGY

- 801 **Voiding cystourethrography as a predictor of reflux nephropathy in children with urinary-tract infection.** *Hellström M, Jacobsson B, Mårild S, Jodal U*

- 805 **Case report. MR imaging of coronary artery aneurysms in a child with Kawasaki disease.** *Bisset GS III, Strife JL, McCloskey J*
- 809 **Case report. MR imaging of the criss-cross heart.** *Link KM, Weesner KM, Formanek AG*

NEURORADIOLOGY

- 813 **Multicenter double-blind placebo-controlled study of gadopentetate dimeglumine as an MR contrast agent: evaluation in patients with cerebral lesions.** *Russell EJ, Schaible TF, Dillon W, et al.*
- 825 **Gadolinium-DTPA-enhanced MR imaging of the postoperative lumbar spine: time course and mechanism of enhancement.** *Ross JS, Delamarter R, Hueftle MG, et al.*
- 835 **MR imaging artifacts of the axial internal anatomy of the cervical spinal cord.** *Curtin AJ, Chakeres DW, Bulas R, Boesel CP, Finneran M, Flint E*
- 843 **MR imaging in the tethered spinal cord syndrome.** *Raghavan N, Barkovich AJ, Edwards M, Norman D*

MAGNETIC RESONANCE IMAGING

- 853 **Comparison of STIR and spin-echo MR imaging at 1.5-T in 90 lesions of the chest, liver, and pelvis.** *Shuman WP, Baron RL, Peters MJ, Tazioli PK*

COMPUTER PAGE

- 861 **Semiautomated slide identification by using a personal computer and printer.** *Feuerstein IM*

SPECT-CT

- 865 **Technical note. Composite SPECT-CT images: technique and potential applications in chest and abdominal imaging.** *Kaplan IL, Swayne LC*

INFORMED CONSENT

- 867 **Opinion. Informed consent for contrast media.** *Bush WH*

DIGITAL RADIOGRAPHY

- 870 **Technical note. Digital radiography: uses and limitations of the method.** *Novak DL, Bates BF*

ARRS ANNUAL MEETING CASE OF THE DAY

- 873 **General diagnosis case of the day.** *Glazer HS, Dehdashti F, Siegel BA, McClennan BL, Balfe DM, Andriole GL*
- 875 **Sonography case of the day.** *Middleton WD, Middleton MA, Wiele K*
- 877 **Pediatric radiology case of the day.** *McAlister WH, Siegel MJ*
- 879 **Neuroradiology case of the day.** *Shoemaker EI, Romano AJ, Gado M, Hodges FJ III*

OTHER CONTENT

- 808 **Forthcoming articles**
- 882 **Books received**
- 884 **American Roentgen Ray Society information**
- 885 **ARRS meeting invitation**
- 887 **ARRS meeting summary**
- 888 **ARRS membership information and application**
- 891 **Letters**
- 898 **Review of current literature**
- 904 **News**
- Book reviews 696, 706, 718, 728, 736, 742, 776, 780, 824
- 907 **Classified advertisements**
- A3 **Guidelines for authors**
- A8 **AJR business and subscriber information**

PROGRESS IN RADIOLOGY

- 913 Diagnostic and therapeutic interventional gallbladder procedures. *Teplick SK*
- 917 Imaging hepatic metastases from colorectal carcinoma: identification of candidates for partial hepatectomy. *Seltzer SE, Holman BL*

REVIEW ARTICLES

- 925 Radiology of penile prostheses. *Cohan RH, Dunnick NR, Carson CC*
- 933 Percutaneous insertion of the Greenfield filter. *Pais SO, Tobin KD*

CONTRAST MEDIA

- 939 A prospective trial of ionic vs nonionic contrast agents in routine clinical practice: comparison of adverse effects. *Wolf GL, Arenson RL, Cross AP*
- 945 Commentary. Nonionic vs ionic contrast media: what do the data tell us? *Lasser EC, Berry CC*
- 947 Case report. Acute thrombocytopenia after IV administration of a radiographic contrast medium. *Chang JC, Lee D, Gross HM*

CARDIOPULMONARY RADIOLOGY

- 951 Pictorial essay. Surgical defects of the pericardium: radiographic findings. *Takasugi JE, Godwin JD*
- 955 Leptospirosis of the lung: radiographic findings in 58 patients. *Im J-G, Yeon KM, Han MC, et al.*
- 961 Pulmonary lymphangioleiomyomatosis: high-resolution CT findings in four cases. *Rappaport DC, Weisbrod GL, Herman SJ, Chamberlain DW*
- 965 Case report. Rounded atelectasis of the lung: MR appearance. *Verschakelen JA, Demaerel P, Coolen J, Demedts M, Marchal G, Baert AL*

BREAST RADIOLOGY

- 967 Sedimented calcium in benign breast cysts: the full spectrum of mammographic presentations. *Linden SS, Sickles EA*

GASTROINTESTINAL RADIOLOGY

- 973 CT of primary lymphoma of the liver. *Sanders LM, Botet JF, Straus DJ, Ryan J, Filippa DA, Newhouse JH*
- 977 Distinction between hemangioma of the liver and hepatocellular carcinoma: value of labeled RBC-SPECT scanning. *Kudo M, Ikekubo K, Yamamoto K, et al.*
- 985 Case report. Hepatic perfusion in cavernous transformation of the portal vein: evaluation by using CT angiography. *Nakao N, Miura K, Takahashi H, et al.*
- 987 Is routine chest radiography required with biliary lithotripsy? *Malone DE, Becker CD, Müller NL, Burhenne HJ*
- 991 Pneumatosis intestinalis in bone-marrow transplantation patients: diagnosis on routine chest radiographs. *Bates FT, Gurney JW, Goodman LR, Santamaria JJ, Hansen RM, Ash RC*
- 995 Pictorial essay. Primary tumors of the small intestine: CT evaluation. *Dudiak KM, Johnson CD, Stephens DH*
- 999 Diagnosis of fistulae and sinus tracts in patients with Crohn disease: value of MR imaging. *Koelbel G, Schmiedl U, Majer MC, et al.*

ONCOLOGIC RADIOLOGY

- 1005 CT of adrenal tumors: frequency and clinical significance of low-attenuation lesions. *Miyake H, Maeda H, Tashiro M, et al.*
- 1009 Subcutaneous metastases from malignant melanoma: prevalence and findings on CT. *Patten RM, Shuman WP, Teefey S*

MUSCULOSKELETAL RADIOLOGY

- 1013 Pictorial essay. MR imaging of the finger: correlation with normal anatomic sections. *Erickson SJ, Kneeland JB, Middleton WD, et al.*

- 1021 Detection of osteomyelitis at fracture nonunion sites: comparison of two scintigraphic methods. *Seabold JE, Nepola JV, Conrad GR, et al.*

PEDIATRIC RADIOLOGY

- 1029 MR imaging determination of the location of the normal conus medullaris throughout childhood. *Wilson DA, Prince JR*
- 1033 Review. Imaging of infants and children with AIDS. *Haney PJ, Yale-Loehr AJ, Nussbaum AR, Gellad FE*
- 1043 Blunt renal and ureteral trauma in childhood: CT patterns of fluid collections. *Siegel MJ, Balfe DM*
- 1049 Closed spinal dysraphism: analysis of clinical, radiological, and surgical findings in 104 consecutive patients. *Scatliff JH, Kendall BE, Kingsley DPE, Britton J, Grant DN, Hayward RD*
- 1059 Absolute intracranial blood-flow velocities evaluated by duplex Doppler sonography in asymptomatic preterm and term neonates. *Horgan JG, Rumack CM, Hay T, Manco-Johnson ML, Merenstein GB, Esola C*
- 1065 Color Doppler imaging of intracranial vessels in the neonate. *Wong WS, Tsuruda JS, Liberman RL, Chirino A, Vogt JF, Gangitano E*
- 1071 Case report. Hypermagnesemia: a cause of abnormal metaphyses in the neonate. *Cumming WA, Thomas VJ*

NEURORADIOLOGY

- 1073 MR imaging of brain abscesses. *Haimes AB, Zimmerman RD, Morgello S, et al.*
- 1087 Gd-DTPA-enhanced MR imaging of spinal tumors. *Parizel PM, Balériaux D, Rodesch G, et al.*

VASCULAR RADIOLOGY

- 1097 Pulsed-spray pharmacomechanical thrombolysis: preliminary clinical results. *Bookstein JJ, Fellmeth B, Roberts A, Valji K, Davis G, Machado T*
- 1101 Color-flow Doppler and conventional duplex scanning of the carotid bifurcation: prospective, double-blind, correlative study. *Hallam MJ, Reid JM, Cooperberg PL*
- 1107 Case report. Aorto-left renal vein fistula: diagnosis by duplex sonography. *Mansour MA, Russ PD, Subber SW, Pearce WH*

DIGITAL RADIOLOGY

- 1109 A report-coding system for integration into a digital radiology department. *Bramble JM, Chang CHJ, Martin NL*
- 1113 Comparison of 2048-line digital display formats and conventional radiographs: an ROC study. *Hayrapetian A, Aberle DR, Huang HK, et al.*

DEPARTMENT MANAGEMENT

- 1119 Perspective. Strategies for resolving interpersonal conflicts in radiology. *Virapongse C*

TECHNICAL NOTE

- 1123 Percutaneous procedures guided by color-flow Doppler sonography. *McNamara MP Jr*

OTHER CONTENT

- Book reviews 924, 932, 950, 960, 972, 984, 990, 1004, 1008, 1020, 1028, 1042, 1058, 1106
- 1086 Memorial, Robert S. Sherman, Jr
- 1126 Forthcoming articles
- 1127 Letters
- 1133 Review of current literature
- 1138 News
- 1141 American Roentgen Ray Society information
- 1142 Classified advertisements
- A3 Guidelines for authors
- A8 AJR business and subscriber information

MEETING NEWS

- 1147 **Society of Cardiovascular & Interventional Radiology:** 14th annual meeting, March 1989.

PROGRESS IN RADIOLOGY

- 1153 **Diagnostic imaging of bone and joint abnormalities associated with sickle cell hemoglobinopathies.** Sebes JI
1161 **Three-dimensional techniques and artificial intelligence in thallium-201 cardiac imaging.** DePuey EG, Garcia EV, Ezquerro NF
1169 **Computer applications in radiology education: a challenge for the 1990s.** Tessler FN

CARDIOPULMONARY RADIOLOGY

- 1173 **Pictorial essay. Low-attenuation mediastinal masses on CT.** Glazer HS, Siegel MJ, Sagel SS
1179 **The CT findings of pulmonary sarcoidosis: analysis of 25 patients.** Müller NL, Kullnig P, Miller RR
1183 **Chronic lung diseases: specific diagnosis by using CT.** Bergin CJ, Coblentz CL, Chiles C, Bell DY, Castellino RA
1189 **Treatment of pleural effusions and pneumothorax with catheters placed percutaneously under imaging guidance.** Reinhold C, Illescas FF, Atri M, Bret PM
1193 **Case report. Apical *Pneumocystis carinii* pneumonia after inhaled pentamidine prophylaxis.** Conces DJ Jr, Kraft JL, Vix VA, Tarver RD
1195 **Case report. Goblet cell metaplasia causing alveolar disease of the lung: radiographic and pathologic findings.** Nazarian GK, Gross BH, Del Buono EA

GASTROINTESTINAL RADIOLOGY

- 1197 **Characterization of splenic structure in Hodgkin disease by using narrow-band filtration of backscattered ultrasound.** Friedman PA, Sommer FG, Chen H-S, Rachlin DJ, Hoppe R
1205 **SPECT of the peritoneal cavity: method for delineating intraperitoneal fluid distribution.** Wahl RL, Gyves J, Gross BH, et al.
1211 **Diagnosis of acute cholecystitis by cholescintigraphy: significance of pericholecystic hepatic uptake.** Swayne LC, Ginsberg HN
1215 **MR appearance of the liver after partial hepatectomy.** Arrivé L, Hricak H, Goldberg HI, Thoeni RF, Margulis AR
1221 **Giant cavernous hemangioma of the liver: CT and MR imaging in ten cases.** Choi BI, Han MC, Park JH, Kim SH, Han MH, Kim C-W
1227 **Case report. Pancreatic plasmacytoma: CT findings.** Wilson TE, Korobkin M, Francis IR
1229 **Case report. Cecal diverticulitis differentiated from appendicitis using graded-compression sonography.** Townsend RR, Jeffrey RB Jr, Laing FC.

GENITOURINARY RADIOLOGY

- 1231 **Stab wounds of the renal artery branches: angiographic diagnosis and treatment by embolization.** Fisher RG, Ben-Menachem Y, Whigham C
1237 **Testicular ischemia: color Doppler sonographic findings in five patients.** Middleton WD, Melson GL

SKELETAL RADIOLOGY

- 1241 **MR imaging of the temporomandibular joint: comparison of images of autopsy specimens made at 0.3 T and 1.5 T with anatomic cryosections.** Hansson L-G, Westesson P-L, Katzberg RW, et al.

PEDIATRIC RADIOLOGY

- 1245 **MR imaging of the abdomen in children.** Boechat MI, Kangaroo H
1251 **Case report. Hypercalciuric Bartter syndrome: resolution of nephrocalcinosis with indomethacin.** Matsumoto J, Han BK, de Rovetto CR, Welch TR

ENDOCRINE RADIOLOGY

- 1255 **Case report. Recurrent occult medullary thyroid carcinoma detected by MR imaging.** Crow JP, Azar-Kia B, Prinz RA

NEURORADIOLOGY

- 1257 **Alzheimer's disease: longitudinal CT studies of ventricular change.** de Leon MJ, George AE, Reisberg B, et al.
1263 **Juvenile pilocytic astrocytomas: CT and MR characteristics.** Lee Y-Y, Van Tassel P, Bruner JM, Moser RP, Share JC
1271 **MR imaging of intracranial carotid occlusion.** Katz BH, Quencer RM, Kaplan JO, Hinks RS, Post MJD
1277 **The anatomic basis of vertebro-genic pain and the autonomic syndrome associated with lumbar disk extrusion.** Jenkins JR, Whittemore AR, Bradley WG
1291 **MR imaging of experimental demyelination.** Teresi LM, Hovda D, Seeley AB, Nitta K, Lufkin RB

VASCULAR RADIOLOGY

- 1299 **Stenosis of the internal carotid artery: assessment using color Doppler imaging compared with angiography.** Erickson SJ, Mewissen MW, Foley WD, et al.
1307 **Blood flow in the carotid arteries: quantification by using phase-sensitive MR imaging.** Bendel P, Buonocore E, Bockisch A, Besozzi MC
1311 **Case report. Pelvic arteriovenous malformation diagnosed by color flow Doppler imaging.** Abu Musa A, Hata T, Hata K, Kitao M

COMMENTARY

- 1313 **The perception of visual data: a summary of the ACR meeting on visualization science in engineering, computing, and medicine.** Hendee WR

ARRS CASE OF THE DAY

- 1317 **General diagnosis case of the day.** Glazer HS, Dehdashti F, Siegel BA, McClennan BL, Balfe DM, Andriole GL
1323 **Sonography case of the day.** Middleton MA, Middleton WD, Wiele K
1328 **Pediatric radiology case of the day.** McAlister WH, Siegel MJ
1333 **Neuroradiology case of the day.** Shoemaker EI, Romano AJ, Gado M, Hodges FJ III

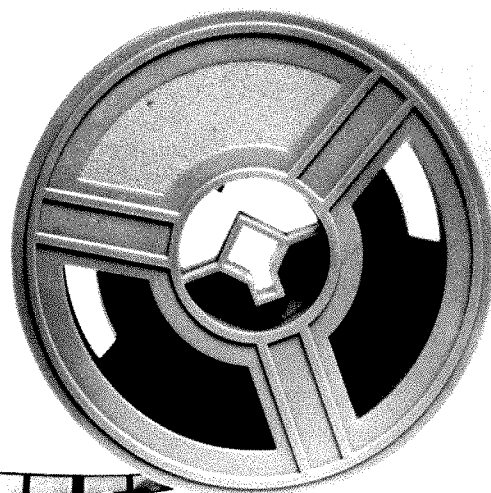
OTHER CONTENT

- Book and videotape reviews,** 1152, 1160, 1178, 1192, 1204, 1214, 1236, 1254, 1290
1306 **Memorial, Joseph L. Morton**
1316 **Forthcoming articles**
1339 **Letters**
1350 **Review of current literature**
1357 **News**
1360 **ARRS 1990 meeting announcement, calls for papers and exhibits**
1365 **Classified advertisements**
1369 **Index, vol. 152**
A3 **Guidelines for authors**
A8 **AJR business and subscriber information**

Need shelf space?

Williams & Wilkins is your source for back issues of this journal in microform.

Free Up 98% Of
Your Shelf Space With
Microform Conversion



MICROFILM editions are available for this journal direct from the publisher. Many Williams & Wilkins journals as well as those journals distributed by the Publishing Services Division of Waverly, Inc., are also available for a single volume year or on a standing order basis.

For ordering information: Write to the address below or call **TOLL FREE 1-800-638-6423**. In Maryland call **1-800-638-4007**.

☐ **Please send me microform back issue ordering information for**

Journal Name _____

Name _____

Title _____

Address _____

City/State/Zip _____

Mail to:

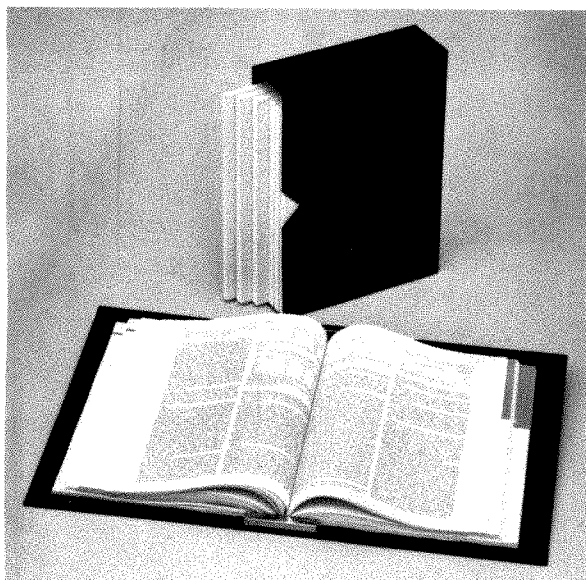
Williams & Wilkins
Microform Sales
Attention: Yvonne Hahn
428 East Preston Street
Baltimore, MD 21202

or

The Broadway Centre
2-6 Fulham Broadway
London SW6 1AA England

Formats available:

- 16-mm reel
- 35-mm reel
- 16-mm cartridge (3M or Kodak)
- positive or negative film



Protect your copies of

AJR: AMERICAN JOURNAL OF ROENTGENOLOGY

with Jesse Jones Binders or Files

Keep your journals clean, orderly, and readily accessible with Jesse Jones Binders or Files. Two Binders or two box style Files are all you need to accommodate a full year's worth of issues. Both Binders and Files are handsomely made with rich black leatherette covers and gold leaf embossed lettering.

Jesse Jones Binders open flat for easy reading and reference and are economically priced at only \$9.95 each; 3 for \$27.95, or 6 for \$52.95 postpaid. The rugged, compact box Files are only \$7.95 each; 3 for \$21.95, or 6 for \$39.95. Add \$1.00/unit postage and handling. (Outside the U.S. add \$2.50/unit.)

For charge orders call toll free 1-800-972-5858. (\$15.00 minimum).

Free gold transfer slips included for indexing volume and year.

Please allow four to five weeks for delivery.

TO: Jesse Jones Industries
499 E. Erie Avenue, DEPT. AJR
Philadelphia, PA 19134

I enclose my check or money order for \$ _____
(PA residents add 6% sales tax)

Send me ☐ Files ☐ Binders for my journals

Name _____

Address (will not ship to P.O. Box) _____

City/State/Zip _____

Satisfaction guaranteed.

INDEX TO ADVERTISERS

Annual Body Imaging Conference.....	A32
Berlex Imaging	A25,A26, A27, A28
Braintree Laboratories	A29
Current Science	A20
Eastman Kodak	A6, A7
E-Z-EM Company	Cover 2
FUJI	Cover 3
General Electric	A18, A19, A30, A31
Mallinckrodt, Inc.	A9, A21, A22, A23, A24
Medical Seminars	A29
University of Michigan	A29
Nuclear Associates	A2, A13
Picker International	A14, A15
S & S X-Ray	A17

We try to present an accurate index. Occasionally this may not be possible because of a last-minute change or omission.



When is the duplicate as good as the original?

In nature the "twin" is almost always as good as the original, but in medical radiography . . . rarely. That's why Fuji developed a superior duplicating film which will consistently give faithful reproductions with contrast and image values right up there with the original.

Frankly, nature still has us beat . . . but that's as it should be. For the next best duplicating process, call your Fuji representative or 800-431-1850.

CIRCLE 7 ON READER SERVICE CARD



The Reason for Change!



MEETING NEWS

- 1147 Society of Cardiovascular & Interventional Radiology: 14th annual meeting, March 1989.

PROGRESS IN RADIOLOGY

- 1153 Diagnostic imaging of bone and joint abnormalities associated with sickle cell hemoglobinopathies. Sebes JI
1161 Three-dimensional techniques and artificial intelligence in thallium-201 cardiac imaging. DePuey EG, Garcia EV, Ezquerro NF
1169 Computer applications in radiology education: a challenge for the 1990s. Tessler FN

CARDIOPULMONARY RADIOLOGY

- 1173 Pictorial essay. Low-attenuation mediastinal masses on CT. Glazer HS, Siegel MJ, Sagel SS
1179 The CT findings of pulmonary sarcoidosis: analysis of 25 patients. Müller NL, Kullnig P, Miller RR
1183 Chronic lung diseases: specific diagnosis by using CT. Bergin CJ, Coblenz CL, Chiles C, Bell DY, Castellino RA
1189 Treatment of pleural effusions and pneumothorax with catheters placed percutaneously under imaging guidance. Reinhold C, Illescas FF, Atri M, Bret PM
1193 Case report. Apical *Pneumocystis carinii* pneumonia after inhaled pentamidine prophylaxis. Conces DJ Jr, Kraft JL, Vix VA, Tarver RD
1195 Case report. Goblet cell metaplasia causing alveolar disease of the lung: radiographic and pathologic findings. Nazarian GK, Gross BH, Del Buono EA

GASTROINTESTINAL RADIOLOGY

- 1197 Characterization of splenic structure in Hodgkin disease by using narrow-band filtration of backscattered ultrasound. Friedman PA, Sommer FG, Chen H-S, Rachlin DJ, Hoppe R
1205 SPECT of the peritoneal cavity: method for delineating intraperitoneal fluid distribution. Wahl RL, Gyves J, Gross BH, et al.
1211 Diagnosis of acute cholecystitis by cholescintigraphy: significance of pericholecystic hepatic uptake. Swayne LC, Ginsberg HN
1215 MR appearance of the liver after partial hepatectomy. Arrivé L, Hricak H, Goldberg HI, Thoeni RF, Margulis AR
1221 Giant cavernous hemangioma of the liver: CT and MR imaging in ten cases. Choi BI, Han MC, Park JH, Kim SH, Han RH, Kim C-W
1227 Case report. Pancreatic plasmacytoma: CT findings. Wilson TE, Korobkin M, Francis IR
1229 Case report. Cecal diverticulitis differentiated from appendicitis using graded-compression sonography. Townsend RR, Jeffrey RB Jr, Laing FC.

GENITOURINARY RADIOLOGY

- 1231 Stab wounds of the renal artery branches: angiographic diagnosis and treatment by embolization. Fisher RG, Ben-Menachem Y, Whigham C
1237 Testicular ischemia: color Doppler sonographic findings in five patients. Middleton WD, Melson GL

SKELETAL RADIOLOGY

- 1241 MR imaging of the temporomandibular joint: comparison of images of autopsy specimens made at 0.3 T and 1.5 T with anatomic cryosections. Hansson L-G, Westesson P-L, Katzberg RW, et al.

PEDIATRIC RADIOLOGY

- 1245 MR imaging of the abdomen in children. Boechat MI, Kangaroo H
1251 Case report. Hypercalciuric Bartter syndrome: resolution of nephrocalcinosis with indomethacin. Matsumoto J, Han BK, de Rovetto CR, Welch TR

ENDOCRINE RADIOLOGY

- 1255 Case report. Recurrent occult medullary thyroid carcinoma detected by MR imaging. Crow JP, Azar-Kia B, Prinz RA

NEURORADIOLOGY

- 1257 Alzheimer's disease: longitudinal CT studies of ventricular change. de Leon MJ, George AE, Reisberg B, et al.
1263 Juvenile pilocytic astrocytomas: CT and MR characteristics. Lee Y-Y, Van Tassel P, Bruner JM, Moser RP, Share JC
1271 MR imaging of intracranial carotid occlusion. Katz BH, Quencer RM, Kaplan JO, Hinks RS, Post MJD
1277 The anatomic basis of vertebro-genic pain and the autonomic syndrome associated with lumbar disk extrusion. Jinkins JR, Whittemore AR, Bradley WG
1291 MR imaging of experimental demyelination. Teresi LM, Hovda D, Seeley AB, Nitta K, Lufkin RB

VASCULAR RADIOLOGY

- 1299 Stenosis of the internal carotid artery: assessment using color Doppler imaging compared with angiography. Erickson SJ, Mewissen MW, Foley WD, et al.
1307 Blood flow in the carotid arteries: quantification by using phase-sensitive MR imaging. Bendel P, Buonocore E, Bockisch A, Besozzi MC
1311 Case report. Pelvic arteriovenous malformation diagnosed by color flow Doppler imaging. Abu Musa A, Hata T, Hata K, Kitao M

COMMENTARY

- 1313 The perception of visual data: a summary of the ACR meeting on visualization science in engineering, computing, and medicine. Hendee WR

ARRS CASE OF THE DAY

- 1317 General diagnosis case of the day. Glazer HS, Dehdashti F, Siegel BA, McClennan BL, Balfe DM, Andriote GL
1323 Sonography case of the day. Middleton MA, Middleton WD, Wiele K
1328 Pediatric radiology case of the day. McAlister WH, Siegel MJ
1333 Neuroradiology case of the day. Shoemaker EI, Romano AJ, Gado M, Hodges FJ III

OTHER CONTENT

- Book and videotape reviews, 1152, 1160, 1178, 1192, 1204, 1214, 1236, 1254, 1290
1306 Memorial, Joseph L. Morton
1316 Forthcoming articles
1339 Letters
1350 Review of current literature
1357 News
1360 ARRS 1990 meeting announcement, calls for papers and exhibits
1365 Classified advertisements
1369 Index, vol. 152
A3 Guidelines for authors
A8 AJR business and subscriber information